FRONTIERS IN CHEMISTRY: RISING STARS

EDITED BY: S. Suib, H. Ju, S. Cosnier, B. Ohtani, J. D. Wade, G. Garnier, N. V. Myung, L. D. Carlos, M. Kassiou, F. Zhang, I. Ojima, P. Musto, T. D. James, T. S. Hofer and S. P. De Visser

PUBLISHED IN: Frontiers in Chemistry

frontiers Research Topics

frontiers

Frontiers eBook Copyright Statement

The copyright in the text of individual articles in this eBook is the property of their respective authors or their respective institutions or funders. The copyright in graphics and images within each article may be subject to copyright of other parties. In both cases this is subject to a license granted to Frontiers.

The compilation of articles constituting this eBook is the property of Frontiers.

Each article within this eBook, and the eBook itself, are published under the most recent version of the Creative Commons CC-BY licence. The version current at the date of publication of this eBook is CC-BY 4.0. If the CC-BY licence is updated, the licence granted by Frontiers is automatically updated to the new version.

When exercising any right under the CC-BY licence, Frontiers must be attributed as the original publisher of the article or eBook, as applicable.

Authors have the responsibility of ensuring that any graphics or other materials which are the property of others may be included in the CC-BY licence, but this should be checked before relying on the CC-BY licence to reproduce those materials. Any copyright notices relating to those materials must be complied with.

Copyright and source acknowledgement notices may not be removed and must be displayed in any copy, derivative work or partial copy which includes the elements in question.

All copyright, and all rights therein, are protected by national and international copyright laws. The above represents a summary only. For further information please read Frontiers' Conditions for Website Use and Copyright Statement, and the applicable CC-BY licence.

ISSN 1664-8714
ISBN 978-2-88963-580-1
DOI 10.3389/978-2-88963-580-1

About Frontiers

Frontiers is more than just an open-access publisher of scholarly articles: it is a pioneering approach to the world of academia, radically improving the way scholarly research is managed. The grand vision of Frontiers is a world where all people have an equal opportunity to seek, share and generate knowledge. Frontiers provides immediate and permanent online open access to all its publications, but this alone is not enough to realize our grand goals.

Frontiers Journal Series

The Frontiers Journal Series is a multi-tier and interdisciplinary set of open-access, online journals, promising a paradigm shift from the current review, selection and dissemination processes in academic publishing. All Frontiers journals are driven by researchers for researchers; therefore, they constitute a service to the scholarly community. At the same time, the Frontiers Journal Series operates on a revolutionary invention, the tiered publishing system, initially addressing specific communities of scholars, and gradually climbing up to broader public understanding, thus serving the interests of the lay society, too.

Dedication to Quality

Each Frontiers article is a landmark of the highest quality, thanks to genuinely collaborative interactions between authors and review editors, who include some of the world's best academicians. Research must be certified by peers before entering a stream of knowledge that may eventually reach the public - and shape society; therefore, Frontiers only applies the most rigorous and unbiased reviews.
Frontiers revolutionizes research publishing by freely delivering the most outstanding research, evaluated with no bias from both the academic and social point of view. By applying the most advanced information technologies, Frontiers is catapulting scholarly publishing into a new generation.

What are Frontiers Research Topics?

Frontiers Research Topics are very popular trademarks of the Frontiers Journals Series: they are collections of at least ten articles, all centered on a particular subject. With their unique mix of varied contributions from Original Research to Review Articles, Frontiers Research Topics unify the most influential researchers, the latest key findings and historical advances in a hot research area! Find out more on how to host your own Frontiers Research Topic or contribute to one as an author by contacting the Frontiers Editorial Office: researchtopics@frontiersin.org

FRONTIERS IN CHEMISTRY: RISING STARS

Topic Editors:
Steve Suib, University of Connecticut, United States
Huangxian Ju, Nanjing University, China
Serge Cosnier, UMR5250 Département de Chimie Moléculaire (DCM), France
Bunsho Ohtani, Hokkaido University, Japan
John D. Wade, University of Melbourne, Australia
Gil Garnier, Bioresource Processing Institute of Australia (BioPRIA), Australia
Nosang Vincent Myung, University of California, Riverside, United States
Luís D. Carlos, University of Aveiro, Portugal
Michael Kassiou, University of Sydney, Australia
Fan Zhang, Fudan University, China
Iwao Ojima, Stony Brook University, United States
Pellegrino Musto, Italian National Research Council, Italy
Tony D. James, University of Bath, United Kingdom
Thomas S. Hofer, University of Innsbruck, Austria
Sam P. De Visser, University of Manchester, United Kingdom

Cover image: 24Novembers/Shutterstock.com

The *Frontiers in Chemistry* Editorial Office team are delighted to present the inaugural "Frontiers in Chemistry: Rising Stars" article collection, showcasing the high-quality work of internationally recognized researchers in the early stages of their independent careers.

All Rising Star researchers featured within this collection were individually nominated by the Journal's Chief Editors in recognition of their potential to influence the future directions in their respective fields. The work presented here highlights the diversity of research performed across the entire breadth of the chemical sciences, and presents advances in theory, experiment and methodology with applications to compelling problems.

This Editorial features the corresponding author(s) of each paper published within this important collection, ordered by section alphabetically, highlighting them as the great researchers of the future.

The *Frontiers in Chemistry* Editorial Office team would like to thank each researcher who contributed their work to this collection. We would also like to personally thank our Chief Editors for their exemplary leadership of this article collection; their strong support and passion for this important, community-driven collection has ensured its success and global impact.

Laurent Mathey, PhD
Journal Development Manager

Citation: Suib, S., Ju, H., Cosnier, S., Ohtani, B., Wade, J. D., Garnier, G., Myung, N. V., Carlos, L. D., Kassiou, M., Zhang, F., Ojima, I., Musto, P., James, T. D., Hofer, T. S., De Visser, S. P., eds. (2020). Frontiers in Chemistry: Rising Stars. Lausanne: Frontiers Media SA. doi: 10.3389/978-2-88963-580-1

Table of Contents

ANALYTICAL CHEMISTRY

14 ***Influence of Fixation and Permeabilization on the Mass Density of Single Cells: A Surface Plasmon Resonance Imaging Study***
Ruoyu Cheng, Feng Zhang, Meng Li, Xiang Wo, Yu-Wen Su and Wei Wang

21 ***ctDNA Detection Based on DNA Clutch Probes and Strand Exchange Mechanism***
Huan Chang, Yiyi Zhang, Fan Yang, Changtao Wang and Haifeng Dong

28 ***Biological Applications of Organic Electrochemical Transistors: Electrochemical Biosensors and Electrophysiology Recording***
Liming Bai, Cristina García Elósegui, Weiqi Li, Ping Yu, Junjie Fei and Lanqun Mao

44 ***An Allosteric-Probe for Detection of Alkaline Phosphatase Activity and its Application in Immunoassay***
Jingjing Guo, Mingxuan Gao, Yanling Song, Li Lin, Kaifeng Zhao, Tian Tian, Dan Liu, Zhi Zhu and Chaoyong James Yang

53 ***Substrate-Assisted Visualization of Surfactant Micelles via Transmission Electron Microscopy***
Zekun Zhang, Kaitao Li, Rui Tian and Chao Lu

61 ***A Threshold-Limited Fluorescence Probe for Viscosity***
Zuhai Lei, Kai Xin, Shaobing Qiu, Liling Hou, Xiangming Meng and Youjun Yang

68 ***Phosphate Assay Kit in One Cell for Electrochemical Detection of Intracellular Phosphate Ions at Single Cells***
Haiyan Xu, Dandan Yang, Dechen Jiang and Hong-Yuan Chen

CATALYSIS AND PHOTOCATALYSIS

77 ***Efficient Light-Driven Hydrogen Evolution Using a Thiosemicarbazone-Nickel (II) Complex***
Stylianos Panagiotakis, Georgios Landrou, Vasilis Nikolaou, Anisa Putri, Renaud Hardré, Julien Massin, Georgios Charalambidis, Athanassios G. Coutsolelos and Maylis Orio

85 ***Highly Active Ni- and Co-Based Bimetallic Catalysts for Hydrogen Production From Ammonia-Borane***
Shinya Furukawa, Genki Nishimura, Tomoaki Takayama and Takayuki Komatsu

92 ***Harnessing Plasmon-Induced Hot Carriers at the Interfaces With Ferroelectrics***
Vineet Kumar, Shaun C. O'Donnell, Daniel L. Sang, Paul A. Maggard and Gufeng Wang

111 ***A Holistic Approach to Model the Kinetics of Photocatalytic Reactions***
Jonathan Z. Bloh

124 ***Flavin Conjugated Polydopamine Nanoparticles Displaying Light-Driven Monooxygenase Activity***
Leander Crocker and Ljiljana Fruk

CHEMICAL AND PROCESS ENGINEERING (FORMERLY CHEMICAL ENGINEERING)

139 ***Porous Boron Nitride Materials: Influence of Structure, Chemistry and Stability on the Adsorption of Organics***
Sofia Marchesini, Xiyu Wang and Camille Petit

148 ***Structural Changes in Polymeric Gel Scaffolds Around the Overlap Concentration***
Han Zhang, Matthew D. Wehrman and Kelly M. Schultz

158 ***Preparation of Renewable Epoxy-Amine Resins With Tunable Thermo-Mechanical Properties, Wettability and Degradation Abilities From Lignocellulose- and Plant Oils-Derived Components***
Louis Hollande, Izia Do Marcolino, Patrick Balaguer, Sandra Domenek, Richard A. Gross and Florent Allais

169 ***Nanocellulose Xerogels With High Porosities and Large Specific Surface Areas***
Shunsuke Yamasaki, Wataru Sakuma, Hiroaki Yasui, Kazuho Daicho, Tsuguyuki Saito, Shuji Fujisawa, Akira Isogai and Kazuyoshi Kanamori

CHEMICAL BIOLOGY

180 ***N,N-Dimethylaminoxy Carbonyl, a Polar Protecting Group for Efficient Peptide Synthesis***
Ryo Okamoto, Emiko Ono, Masayuki Izumi and Yasuhiro Kajihara

186 ***Lighting-Up Tumor for Assisting Resection via Spraying NIR Fluorescent Probe of γ-Glutamyltranspeptidas***
Haidong Li, Qichao Yao, Feng Xu, Ning Xu, Wen Sun, Saran Long, Jianjun Du, Jiangli Fan, Jingyun Wang and Xiaojun Peng

201 ***Imaging of Formaldehyde in Live Cells and* Daphnia magna *via Aza-Cope Reaction Utilizing Fluorescence Probe With Large Stokes Shifts***
Mingwang Yang, Jiangli Fan, Jianjun Du, Saran Long, Jia Wang and Xiaojun Peng

211 ***Near-Infrared Aggregation-Induced Emission-Active Probe Enables* in situ *and Long-Term Tracking of Endogenous ß-Galactosidase Activity***
Wei Fu, Chenxu Yan, Yutao Zhang, Yiyu Ma, Zhiqian Guo and Wei-Hong Zhu

222 ***Chemical Biology Gateways to Mapping Location, Association, and Pathway Responsivity***
Marcus J. C. Long, Xuyu Liu and Yimon Aye

243 ***Elucidating the Lipid Binding Properties of Membrane-Active Peptides Using Cyclised Nanodiscs***
Alan H. Zhang, Ingrid A. Edwards, Biswa P. Mishra, Gagan Sharma, Michael D. Healy, Alysha G. Elliott, Mark A. T. Blaskovich, Matthew A. Cooper, Brett M. Collins, Xinying Jia and Mehdi Mobli

ELECTROCHEMISTRY

261 ***Photochemically Induced Phase Change in Monolayer Molybdenum Disulfide***
Peter Byrley, Ming Liu and Ruoxue Yan

270 ***Low-Loading of Pt Nanoparticles on 3D Carbon Foam Support for Highly Active and Stable Hydrogen Production***
Abdulsattar H. Ghanim, Jonathan G. Koonce, Bjorn Hasa, Alan M. Rassoolkhani, Wei Cheng, David W. Peate, Joun Lee and Syed Mubeen

279 ***Lithium Sulfide–Carbon Composites via Aerosol Spray Pyrolysis as Cathode Materials for Lithium–Sulfur Batteries***
Noam Hart, Jiayan Shi, Jian Zhang, Chengyin Fu and Juchen Guo

286 ***Effect of Surface and Bulk Properties of Mesoporous Carbons on the Electrochemical Behavior of GOx-Nanocomposites***
Tsai Garcia-Perez, Shouzhen Hu, Youngho Wee, Louis Scudiero, Conrad Hoffstater, Jungbae Kim and Su Ha

298 ***The Influence of Interfacial Chemistry on Magnesium Electrodeposition in Non-nucleophilic Electrolytes Using Sulfone-Ether Mixtures***
Laura C. Merrill and Jennifer L. Schaefer

308 ***Localization of Ion Concentration Gradients for Logic Operation***
Nikolay V. Ryzhkov, Pavel Nesterov, Natalia A. Mamchik, Stanislav O. Yurchenko and Ekaterina V. Skorb

317 ***A Review on the Electroless Deposition of Functional Materials in Ionic Liquids for Batteries and Catalysis***
Abhishek Lahiri, Giridhar Pulletikurthi and Frank Endres

GREEN AND SUSTAINABLE CHEMISTRY

333 ***Bioinspired Slippery Lubricant-Infused Surfaces With External Stimuli Responsive Wettability: A Mini Review***
Xian Yang, Yu Huang, Yan Zhao, Xiaoyu Zhang, Jinhua Wang, Ei Ei Sann, Khin Hla Mon, Xiaoding Lou and Fan Xia

340 ***Quantifying the Stability of the Hydronium Ion in Organic Solvents With Molecular Dynamics Simulations***
Alex K. Chew and Reid C. Van Lehn

354 ***A Strategy for Prompt Phase Transfer of Upconverting Nanoparticles Through Surface Oleate-Mediated Supramolecular Assembly of Amino-ß-Cyclodextrin***
Xindong Wang and Guanying Chen

363 ***Membrane-Modified Metal Triazole Complexes for the Electrocatalytic Reduction of Oxygen and Carbon Dioxide***
Skye N. Supakul and Christopher J. Barile

371 ***Photoelectrochemical Gas–Electrolyte–Solid Phase Boundary for Hydrogen Production From Water Vapor***
Fumiaki Amano, Ayami Shintani, Hyosuke Mukohara, Young-Min Hwang and Kenyou Tsurui

381 ***Templated Growth of Crystalline Mesoporous Materials: From Soft/Hard Templates to Colloidal Templates***
Lei Zhang, Lei Jin, Ben Liu and Jie He

INORGANIC CHEMISTRY

399 ***Coordination-Driven Self-Assembly of Silver(I) and Gold(I) Rings: Synthesis, Characterization, and Photophysical Studies***
Cressa Ria P. Fulong, Sewon Kim, Alan E. Friedman and Timothy R. Cook

412 ***Understanding the Role of Yb^{3+} in the Nd/Yb Coupled 808-nm-Responsive Upconversion***
Nan Song, Bo Zhou, Long Yan, Jinshu Huang and Qinyuan Zhang

420 ***Mapping Temperature Distribution Generated by Photothermal Conversion in Graphene Film Using Er,Yb:$NaYF_4$ Nanoparticles Prepared by Microwave-Assisted Solvothermal Method***
Oleksandr A. Savchuk, Joan J. Carvajal, Yolanda Cesteros, Pilar Salagre, Huu Dat Nguyen, Airan Rodenas, Jaume Massons, Magdalena Aguiló and Franscesc Díaz

431 ***Revisiting the Growth of Black Phosphorus in Sn-I Assisted Reactions***
Dongya Wang, Peng Yi, Lin Wang, Lu Zhang, Hai Li, Min Lu, Xiaoji Xie, Ling Huang and Wei Huang

440 ***Upconversion Nanocomposite Materials With Designed Thermal Response for Optoelectronic Devices***
Eduardo D. Martínez, Carlos D. S. Brites, Luís D. Carlos, Ricardo R. Urbano and Carlos Rettori

451 ***Luminescent Schiff-Base Lanthanide Single-Molecule Magnets: The Association Between Optical and Magnetic Properties***
Jérôme Long

458 ***C–X (X = N, O) Cross-Coupling Reactions Catalyzed by Copper-Pincer Bis(N-Heterocyclic Carbene) Complexes***
Jennifer L. Minnick, Doaa Domyati, Rachel Ammons and Laleh Tahsini

467 ***Self-Calibrated Double Luminescent Thermometers Through Upconverting Nanoparticles***
Carlos D. S. Brites, Eduardo D. Martínez, Ricardo R. Urbano, Carlos Rettori and Luís D. Carlos

477 ***Reversible Control of the Mn Oxidation State in $SrTiO_3$ Bulk Powders***
Haneen Mansoor, William L. Harrigan, Keith A. Lehuta and Kevin R. Kittilstved

485 ***Molecular Orbital Insights of Transition Metal-Stabilized Carbocations***
Hannah Goodman, Liangyong Mei and Thomas L. Gianetti

NANOSCIENCE

511 ***Non-covalent Methods of Engineering Optical Sensors Based on Single-Walled Carbon Nanotubes***
Alice J. Gillen and Ardemis A. Boghossian

524 ***Noble Metal Based Alloy Nanoframes: Syntheses and Applications in Fuel Cells***
Farhat Nosheen, Tauseef Anwar, Ayesha Siddique and Naveed Hussain

547 ***Big Potential From Silicon-Based Porous Nanomaterials: In Field of Energy Storage and Sensors***
Rana Zafar Abbas Manj, Xinqi Chen, Waheed Ur Rehman, Guanjia Zhu, Wei Luo and Jianping Yang

561 ***Mesoporous WO_3 Nanofibers With Crystalline Framework for High-Performance Acetone Sensing***
Haiyun Xu, Jie Gao, Minhan Li, Yuye Zhao, Ming Zhang, Tao Zhao, Lianjun Wang, Wan Jiang, Guanjia Zhu, Xiaoyong Qian, Yuchi Fan, Jianping Yang and Wei Luo

572 ***The Impact of Cr^{3+} Doping on Temperature Sensitivity Modulation in Cr^{3+} Doped and Cr^{3+}, Nd^{3+} Co-doped $Y_3Al_5O_{12}$, $Y_3Al_2Ga_3O_{12}$, and $Y_3Ga_5O_{12}$ Nanothermometers***
Karolina Elzbieciak and Lukasz Marciniak

580 ***Phosphorothioate DNA Mediated Sequence-Insensitive Etching and Ripening of Silver Nanoparticles***
Shengqiang Hu, Po-Jung Jimmy Huang, Jianxiu Wang and Juewen Liu

589 ***The Bioavailability, Biodistribution, and Toxic Effects of Silica-Coated Upconversion Nanoparticles* in vivo**
Mingzhu Zhou, Xiaoqian Ge, Da-Ming Ke, Huan Tang, Jun-Zheng Zhang, Matteo Calvaresi, Bin Gao, Lining Sun, Qianqian Su and Haifang Wang

601 ***Air-Stable Na_xTMO_2 Cathodes for Sodium Storage***
Yi Zhang, Renyuan Zhang and Yunhui Huang

616 ***Crucial Breakthrough of Functional Persistent Luminescence Materials for Biomedical and Information Technological Applications***
Huaxin Tan, Taoyu Wang, Yaru Shao, Cuiyun Yu and Lidan Hu

628 ***Reversible Photo-Switching of Dual-Color Fluorescent Mn-Doped CdS-ZnS Quantum Dots Modulated by Diarylethene Molecules***
Yucheng Yuan, Hua Zhu, Yasutaka Nagaoka, Rui Tan, Andrew Hunter Davis, Weiwei Zheng and Ou Chen

637 ***Mesoporous Silica Nanoparticles for Protein Protection and Delivery***
Chun Xu, Chang Lei and Chengzhong Yu

POLYMER CHEMISTRY

653 ***Review on Polymer-Based Composite Electrolytes for Lithium Batteries***
Penghui Yao, Haobin Yu, Zhiyu Ding, Yanchen Liu, Juan Lu, Marino Lavorgna, Junwei Wu and Xingjun Liu

670 ***Sorption of Water Vapor in Poly(L-Lactic Acid): A* Time-Resolved *FTIR Spectroscopy Investigation***
Marianna Pannico and Pietro La Manna

680 ***Pyro-Electrification of Freestanding Polymer Sheets: A New Tool for Cation-Free Manipulation of Cell Adhesion in vitro***
Romina Rega, Oriella Gennari, Laura Mecozzi, Vito Pagliarulo, Martina Mugnano, Emilia Oleandro, Filomena Nazzaro, Pietro Ferraro and Simonetta Grilli

690 ***Ultrasound Reversible Response Nanocarrier Based on Sodium Alginate Modified Mesoporous Silica Nanoparticles***
Xiaochong Li, Zhanhua Wang and Hesheng Xia

701 ***Advances in Organic Solvent Nanofiltration Rely on Physical Chemistry and Polymer Chemistry***
Michele Galizia and Kelly P. Bye

723 ***Stereocomplexation of Poly(Lactic Acid)s on Graphite Nanoplatelets: From Functionalized Nanoparticles to Self-assembled Nanostructures***
Matteo Eleuteri, Mar Bernal, Marco Milanesio, Orietta Monticelli and Alberto Fina

SUPRAMOLECULAR CHEMISTRY

739 ***Molecular Logic as a Means to Assess Therapeutic Antidotes***
Linor Unger-Angel, Leila Motiei and David Margulies

746 ***A Near-Infrared Ratiometric Fluorescent Probe for Highly Selective Recognition and Bioimaging of Cysteine***
Xuan Zhang, Li Zhang, Wei-Wei Ma, Yong Zhou, Zhen-Ni Lu and Suying Xu

754 ***Uncovering the Structural Diversity of Y(III) Naphthalene-2,6-Dicarboxylate MOFs Through Coordination Modulation***
Sarah L. Griffin, Claire Wilson and Ross S. Forgan

763 ***Clustering-Triggered Emission of Carboxymethylated Nanocellulose***
Meng Li, Xiaoning Li, Xuefei An, Zhijun Chen and Huining Xiao

772 ***A Saccharide Chemosensor Array Developed Based on an Indicator Displacement Assay Using a Combination of Commercially Available Reagents***
Yui Sasaki, Zhoujie Zhang and Tsuyoshi Minami

779 ***Self-Assembled Thin-Layer Glycomaterials With a Proper Shell Thickness for Targeted and Activatable Cell Imaging***
Chao Zhang, Guanzhen Wang, Hai-Hao Han, Xi-Le Hu, Robert A. Field, Guo-Rong Chen, Jia Li, Bing Ye, Xiao-Peng He and Yi Zang

786 ***Squaramide—Naphthalimide Conjugates as "Turn-On" Fluorescent Sensors for Bromide Through an Aggregation-Disaggregation Approach***
Lokesh K. Kumawat, Anthony A. Abogunrin, Michelle Kickham, Jyotsna Pardeshi, Orla Fenelon, Martina Schroeder and Robert B. P. Elmes

800 ***Aggregation-Induced Emission: Lighting Up hERG Potassium Channel***
Xiaomeng Zhang, Tingting Liu, Qi Li, Minyong Li and Lupei Du

THEORETICAL AND COMPUTATIONAL CHEMISTRY

809 ***Steric Switching From Photochemical to Thermal N2 Splitting: A Computational Analysis of the Isomerization Reaction*** $\{(Cp^*)(Am)Mo\}_2(\mu\text{-}\eta^1\text{:}\eta^1\text{-}N_2) \rightarrow \{(Cp^*)(Am)Mo\}_2(\mu\text{-}N)_2$
Vera Krewald

823 ***γ-Secretase Studied by Atomistic Molecular Dynamics Simulations: Global Dynamics, Enzyme Activation, Water Distribution and Lipid Binding***
Manuel Hitzenberger and Martin Zacharias

839 ***Bridging the Homogeneous-Heterogeneous Divide: Modeling Spin for Reactivity in Single Atom Catalysis***
Fang Liu, Tzuhsiung Yang, Jing Yang, Eve Xu, Akash Bajaj and Heather J. Kulik

854 ***CherryPicker: An Algorithm for the Automated Parametrization of Large Biomolecules for Molecular Simulation***
Ivan D. Welsh and Jane R. Allison

864 ***Breakthrough Potential in Near-Infrared Spectroscopy: Spectra Simulation. A Review of Recent Developments***
Krzysztof B. Beć and Christian W. Huck

886 ***Advances in Sustainable Catalysis: A Computational Perspective***
Matthew G. Quesne, Fabrizio Silveri, Nora H. de Leeuw and C. Richard A. Catlow

Analytical Chemistry

Wei Wang

Wei Wang received his BSc and MSc degree from the ESE Department of Nanjing University in 1997 and 2000, respectively. He received a PhD degree from the ECE department of the National University of Singapore (NUS) in 2008. He joined the Computer Science and Technology Department of Nanjing University in 2012. Before that, he worked at Microsoft Research Asia (MSRA) as an associate researcher in 2009. His research interests are focused in the areas of wireless networking, including Device-free Sensing, Software Defined Radio, and Mobile Cellular Networks.

Haifeng Dong

Dr Haifeng Dong received his PhD degree from Nanjing University in 2011. He then joined the University of Science & Technology Beijing (USTB) in the same year. He pursued his research as a postdoctoral researcher at the University of Pittsburgh from October 2012 to September 2013. Afterwards, he joined USTB as a Professor. He worked as a visiting Professor at Kyoto University from July 2015 to October 2015. His research interests include the application of functional nanoprobes in DNA biosensors and imaging analysis of intracellular microRNA as well as nanomedicine. His achievements have led to three published books and 70 SCI papers published in Chem. Rev., Angew. Chem. Int. Ed., Adv. Mater., Nano lett., ACS nano, Adv. Funct. Mater., Chem. Sci. and Biomaterials, etc. These papers have been cited over 3,000 times and the most cited paper has been cited 527 times.

Ping Yu

Ping Yu is currently a Professor at the Key Laboratory of Analytical Chemistry for Living Biosystems of the Institute of Chemistry, at the Chinese Academy of Sciences (ICCAS). She received her PhD in Chemistry from ICCAS in 2007 and then joined ICCAS as a faculty member. She was a recipient of the "LU JIAXI Award for Junior Scientists" awarded by the Chinese Academy of Sciences (2014) and the "National Excellent Young Scholars" awarded by National Natural Science Foundation of China (2013). Her ongoing work focuses on ion transport, electrochemistry, chem/(bio)sensors, and *in vivo* analysis.

Zhi Zhu

Prof. Zhi Zhu received her Bachelor's degree in chemistry from Peking University, China in 2006 and her PhD in analytical chemistry from the University of Florida, USA in 2011. She joined Xiamen University, China as an Assistant Professor in 2011 and was promoted to Associate Professor in 2012 and Professor in 2015. She won the Chinese National Excellent Young Investigator Award in 2014 and the Youth in Chemistry Award from the Chinese Chemical Society in 2016. Her current research is focused particularly on molecular recognition, microfluidics, and point-of-care testing.

Chao Lu

Chao Lu received his PhD degree in Materials Science from the Chinese Academy of Sciences. He is currently a full Professor at the State Key Laboratory of Chemical Resource Engineering, Beijing University of Chemical Technology. In 2011, he was selected to participate in the New Century Outstanding Talent scheme of the Ministry of Education. His research interests focus on the design, synthesis, and functional study of luminescent molecules and composites. He is responsible for national and international research projects and has published more than 80 papers in international peer-reviewed journals.

Rui Tian

Rui Tian received her PhD degree at the College of Science, Beijing University of Chemical and Technology under the supervision of Prof. Dr Xue Duan. She now works in the State Key Laboratory of Chemical Resource Engineering, Beijing University of Chemical Technology. Her research interests are focused on the structural design, assembly, and functional study of inorganic-organic composite materials. She is responsible for national research projects and has published more than 20 papers in national and international journals.

Youjun Yang

Youjun Yang is a Professor of pharmacy at the East China University of Science and Technology since 2010. He was trained as a physical organic chemist and a supramolecular chemist in the groups of Robert M. Strongin (PhD, LSU, 2002-2007) and Eric V. Anslyn (Postdoc, UT Austin, 2007-2010). His research interests broadly fall within the field of synthetic dye chemistry, spectroscopy, photochemistry, bioimaging, and redox homeostasis. He developed high-performance deep-NIR absorbing/emitting dyes, Hill-type pH probes, Photo-triggered photo-calibrated NO/CO donors, Covalent-Assembly type molecular probes, and antibacterial hits. He won the Czarnik Emerging Investigator award, and the Excellent Young Scholar of NSFC.

Dechen Jiang

Dr Dechen Jiang is currently a Professor at the School of Chemistry and Chemical Engineering at Nanjing University. He obtained his BSc, MSc and PhD degrees from Nanjing University in 2000, Fudan University in 2003, and the Case Western Reserve University in 2008, respectively. After 3 years of postdoctoral training at UNC-Chapel Hill, Dr Jiang joined Nanjing University to start his independent research. Dr Jiang has authored and co-authored over 50 research publications in journals such as PNAS, JACS, Angew Chem and Anal. Chem. His research focuses on the development of methodology and is instrumental for single cell analysis.

frontiers in Chemistry

ORIGINAL RESEARCH
published: 23 August 2019
doi: 10.3389/fchem.2019.00588

Influence of Fixation and Permeabilization on the Mass Density of Single Cells: A Surface Plasmon Resonance Imaging Study

Ruoyu Cheng[1†], *Feng Zhang*[2†], *Meng Li*[1], *Xiang Wo*[1], *Yu-Wen Su*[3,4*] *and Wei Wang*[1*]

[1] State Key Laboratory of Analytical Chemistry for Life Science, School of Chemistry and Chemical Engineering, Nanjing University, Nanjing, China, [2] Department of Monoclonal Antibody Products, National Institutes for Food and Drug Control, Beijing, China, [3] School of Pharmacy, Nanjing Medical University, Nanjing, China, [4] Department of Clinical Pharmacology, Sir Run Run Hospital, Nanjing Medical University, Nanjing, China

OPEN ACCESS

Edited by:
Huangxian Ju,
Nanjing University, China

Reviewed by:
Chao Lu,
Beijing University of Chemical Technology, China
Zhaoxiang Deng,
University of Science and Technology of China, China

***Correspondence:**
Yu-Wen Su
suyuwen@njmu.edu.cn
Wei Wang
wei.wang@nju.edu.cn

[†] These authors have contributed equally to this work

Specialty section:
This article was submitted to Analytical Chemistry, a section of the journal Frontiers in Chemistry

Received: 31 January 2019
Accepted: 06 August 2019
Published: 23 August 2019

Citation:
Cheng R, Zhang F, Li M, Wo X, Su Y-W and Wang W (2019) Influence of Fixation and Permeabilization on the Mass Density of Single Cells: A Surface Plasmon Resonance Imaging Study. Front. Chem. 7:588. doi: 10.3389/fchem.2019.00588

Fixation and permeabilization of cells and tissues are essential processes in biological techniques like immunofluorescence and immunohistochemistry for cell biology studies. In typical procedures, the biological samples are treated by paraformaldehyde and Triton X-100 to achieve cellular fixation and permeabilization, respectively, prior to the incubation with specific antibodies. While it is well-known that the integrity of cell membrane has been broken during these processes, quantitative studies on the loss of cellular mass density and the enhancement of molecular accessibility at single cell level are still rare. In this study, we employed the surface plasmon resonance (SPR) imaging technique to monitor the mass density change of single cells during sequential fixation and permeabilization processes. We further utilize the osmotic responses of single cells to sugar molecules as an indicator to evaluate the integrity of cell membranes. It was found that, while fixation initially destructed the integrity of cell membranes and increased the permeability of intra- and extra-cellular molecules, it was permeabilization process that substantially induced significant loss in cellular mass density.

Keywords: surface plasmon resonance imaging, fixation, permeabilization, immunofluorescence, osmotic pressure

INTRODUCTION

Immunofluorescence is a powerful technique to visualize the distribution of specific biomolecules within biological samples such as cells and tissues (Joshi and Yu, 2017). In typical cell-based immunofluorescent assays, adherent cells were incubated with fluorescent antibody to enable specific recognition and binding between the antibody and the target molecule in the cells. After thorough rinse, the sample was placed under fluorescence microscope to obtain a fluorescence image, from which the distribution of target molecules was reported by the fluorescent tags. In order to facilitate the accessibility of antibody to the target molecules and to inhibit the inherent cellular activity, the samples were often fixed and permeabilized prior to the staining procedures. They were particularly necessary when the target molecules were located within the cytoplasm. Among many types of reagents, paraformaldehyde (PFA) and Triton X-100 are probably the most widely used ones for fixation and permeabilization, respectively.

Depolymerization of PFA produced formaldehyde molecules to create covalent chemical bonds between proteins in the sample. The mechanism of the action relied on the activation of one of the amino acid residuals lysine. PFA also dissolved some lipids in cellular membranes which slightly damaged the cell membrane integrity (Fox et al., 1985; Thavarajah et al., 2012; Kiernan, 2018). Triton X-100, as an effective non-ionic detergent, could dissolve lipids from cell membranes, so that the cell membrane became more permeable to the fluorescent antibody. The permeabilization step removed more cellular membrane lipids due to its uncharged, hydrophilic head groups that consist of polyoxyethylene moieties to allow large molecules like antibodies to get inside the cell (Jamur and Oliver, 2010; Koley and Bard, 2010). A schematic illustration of cell fixation and permeabilization process is shown in **Figure 1D**. Despite of the fact that fixation and permeabilization have become routine procedures in immunofluorescence and immunohistochemistry, pretty rare efforts have been made to quantitatively clarify their influences on the membrane integrity and cellular mass density at single cell level.

Surface plasmon resonance (SPR) has been a popular and powerful technique to determine the binding kinetics between a pair of molecules since its invention in 1980s (Liedberg et al., 1983; Cullen et al., 1987). This is attributed to its remarkable advantages, including real-time quantitative kinetic measurement with high temporal resolutions, compatibility with expanded devices, and most importantly, its intrinsic feature of label-free (Rothenhäusler and Knoll, 1988; Phillips and Cheng, 2007; Homola, 2008; Abadian et al., 2014; Méjard et al., 2014; Yanase et al., 2014; Su and Wang, 2018). Early applications mostly focused on characterizing and quantifying biomolecular interactions by immobilizing purified molecules onto SPR sensing substrates (gold-coated glass slides). Such *ex situ* studies not only required the labor-intensive purification procedures, but also led to results that may not reflect the natural interaction in living beings (Phillips and Cheng, 2007; Homola, 2008). Driven by both the technical advancement in various SPR imaging (SPRi) systems and the scientific motivation in single cell imaging and analysis, both prism and objective-based SPRi techniques have been employed to image the mass distribution of single living cells without the need of labeling (Wang et al., 2010, 2012a; Yanase et al., 2010; Yang et al., 2015; Zhang et al., 2015). Each one has its own merits. The latter has a higher spatial resolutions and the former has a better sensitivity. By monitoring the time-lapsed SPR images of single living cells during various types of physiological and biological stimulations, important spatial and dynamic information regarding the cell-substrate interactions (Giebel et al., 1999), cell migrations (Smith et al., 2004), osmotic responses (Wang et al., 2012a), ligand-receptor binding kinetics (Wang et al., 2012b, 2014), signaling pathways (Deng et al., 2016), protein activation dynamics (Peng et al., 2018), and living cancer cell drug responses (Wang et al., 2018) have been obtained. For instances, existing studies have clearly demonstrated that SPRi techniques were capable for mapping the mass density as well as the membrane integrity at single cell level (Yanase et al., 2010; Wang et al., 2012b; Yang et al., 2015). The image contrast of SPRi came from the subcellular distribution of refractive index, which was roughly determined by the local mass density. Binding of specific antibodies onto the cell membrane that expressed the corresponding antigens, or stimulating the living cells with particular chemicals, was found to alter the mass density of single cells in a heterogeneous and dynamic manner (Wang et al., 2012a,b). Exposure of single living cells to hypertonic solutions was found to induce the contraction of cells, indicating the excellent integrity of cell membranes (Wang et al., 2012a). However, how the fixation and permeabilization treatments would affect the SPR images of single cells remains unclear.

In the present work, we employed a home-built SPRi system to continuously record the time-lapsed SPR images of tens of single living cells when the cells were successively treated by 4% PFA solution and 1% Triton X-100 solution. The mass density of single cells was determined by the averaged SPRi signal. The membrane integrity was evaluated by exposing the cells to hypertonic solution. It was found that, in addition to the slightly reduced mass density by <10%, PFA treatment significantly destructed the cell integrity as indicated by the loss of osmotic response upon the exposure of sugar molecules. Subsequent treatment by Triton X-100, however, significantly reduced the mass density by another 20%, suggesting the severe destruction to the membrane integrity.

MATERIALS AND METHODS

Materials

Dulbecco's phosphate buffered saline (PBS, Gibco), Sucrose (Sinopharm Chemical Reagent Co., Ltd), Triton X-100 (Aladdin), Paraformaldehyde (Shanghai Lingfeng Chemical Reagent Co., Ltd). All of the reagents were dissolved in PBS.

Cell Culture

BT-474 cells were cultured at 37°C with 5% CO_2 and 70% relative humidity in Dubelco's Modified Eagle's Medium (DMEM, Invitrogen) with 10% fetal bovine serum (FBS, Invitrogen), 100 units/mL penicillin and 100 μg/mL streptomycin (Invitrogen). Cells was passed when they were 70–80% confluent by treating with 0.25% trypsin solution (Gibco).

Prism-Based SPR Imaging Setups

A schematic diagram and a photo of the SPRi system are presented in **Figures 1A,B**. The SPRi apparatus is mainly composed of three parts: light source, optical components and camera.

- Light source: A 670 nm light-emitting diode (L7868-01, Hamamatsu, Japan) and a temperature-controlled mounting socket (LDM21, Thorlabs, Newton, USA).
- Optical components (Edmund Optics, USA): A triangle SF-11 prism with a sensor chip on (No. 1 BK7 glass from Fisherbrand), a converging lens, a polarizer, and a tunable lens.
- Camera: Charge-coupled device camera (Pike F032B, Allied Vision Technology, Newburyport, USA).

The p-polarized light hits the bottom of the gold-coated glass slide through the prism directly and the camera captures the

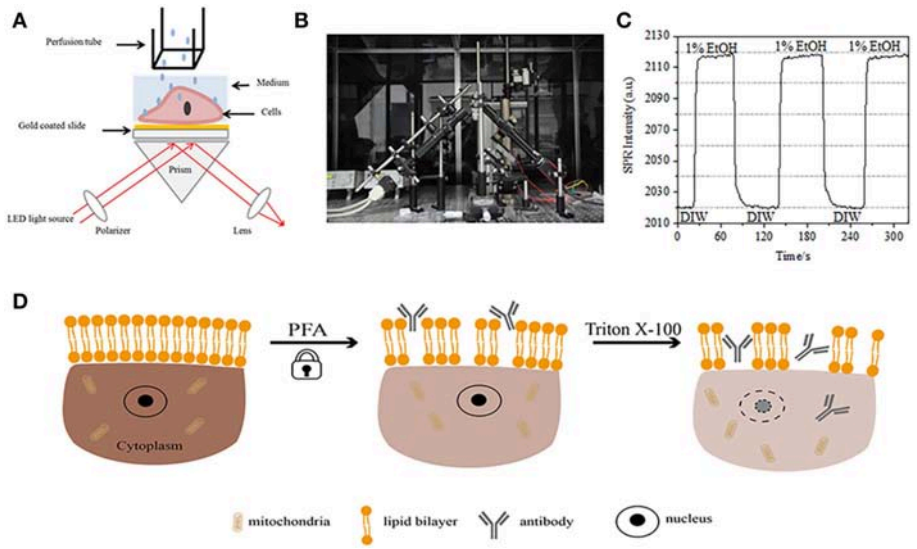

FIGURE 1 | Prism-based SPR imaging setups. **(A)** Schematic illustration of the experimental set-up. **(B)** A photograph of the apparatus. **(C)** Sensitivity calibration curve. **(D)** Schematic illustration of cell fixation and permeabilization.

reflected beam to generate SPR images at a rate of 0.828 Frame per second (fps). When choosing 4X magnification in a tunable lens, the field of view was $\sim 2 \times 2$ mm^2.

Sensor Chip Preparation

Each chip was washed with 75% ethanol and deionized water (DIW), followed by UV exposure for 30 min to remove the surface contamination and sterilize them before each experiment. A Flexi-Perm silicon chamber (Greiner Bio-One) was placed on top of the gold chip to serve as a cell culture well. To achieve the surface modification prior to cell seeding, a 100 μg/mL 150 μL collagen solution was added to the chamber and kept in an incubator for 2 h. The chip was then rinsed with deionized water twice and DMEM twice prior to cell seeding. To make the cells a good shape, the chip was incubated in the growth medium for 36 h. The growth medium was then replaced with PBS buffer solution for 10 min for cells achieving a balance.

Flow System

A gravity driven multichannel drug perfusion system was applied to injection and switch of the solution. The flow rate is 300 μL/min and the solution switching rate around the cells can reach 1–2 s.

Sensitivity Calibration

A sensor chip was prepared as described in preceding part without surface modification and cell seeding. First, DIW flowed over the chip for about 60 s. Then, it was replaced by 1% (v/v) ethanol solution for another 60 s. As one of the most commonly used calibration solution, 1% ethanol is known to increase the SPR angle of DIW by 60 mDeg. Experimental results showed that SPR intensity accordingly increased by 96 I.U. (**Figure 1C**), corresponding to a sensitivity of 1.6 ΔI.U./mDeg.

RESULTS AND DISCUSSION

The cell membrane (also known as cytoplasmic membrane), consisting of a lipid bilayer with embedded proteins, is a semi-permeable membrane that encloses the cytoplasm of a cell. The fixation and permeabilization steps of cells and tissue samples, which could alter the permeability of cell membrane, are crucial procedures that could determine the successes of immunofluorescent or immunohistochemical assays. In addition to this, the antibody quality and the immunoreaction procedure are other key determinants to these kinds of experiments. SPR has the feature that both the resonant angle and the refractive index (RI) near the sensing surface are highly sensitive to the mass density of the surface layer in the medium-metal interface. Therefore, cell's mass density variations taking place on or near the metal film (∼200 nm) could be synchronously recorded by measuring the intensity of the reflected light. By employing surface plasmon resonance imaging technique, we explored dynamic distribution of cellular mass density with high spatial and temporal resolutions and reliable sensitivity in both fixation and permeabilization processes in this study.

Initial Mass Density Loss in Cell Fixation by PFA

The first step to prepare biological samples for immunofluorescent or immunohistochemical analysis is usually fixation. And the most commonly used fixatives for these kinds of assays are crosslinking fixatives like PFA that works by generating covalent chemical bonds between proteins in cells or tissues. We therefore investigated the influence of PFA treatment on cellular mass density. Living BT-474 cells were cultured on coverslip coated by gold film with a thickness of

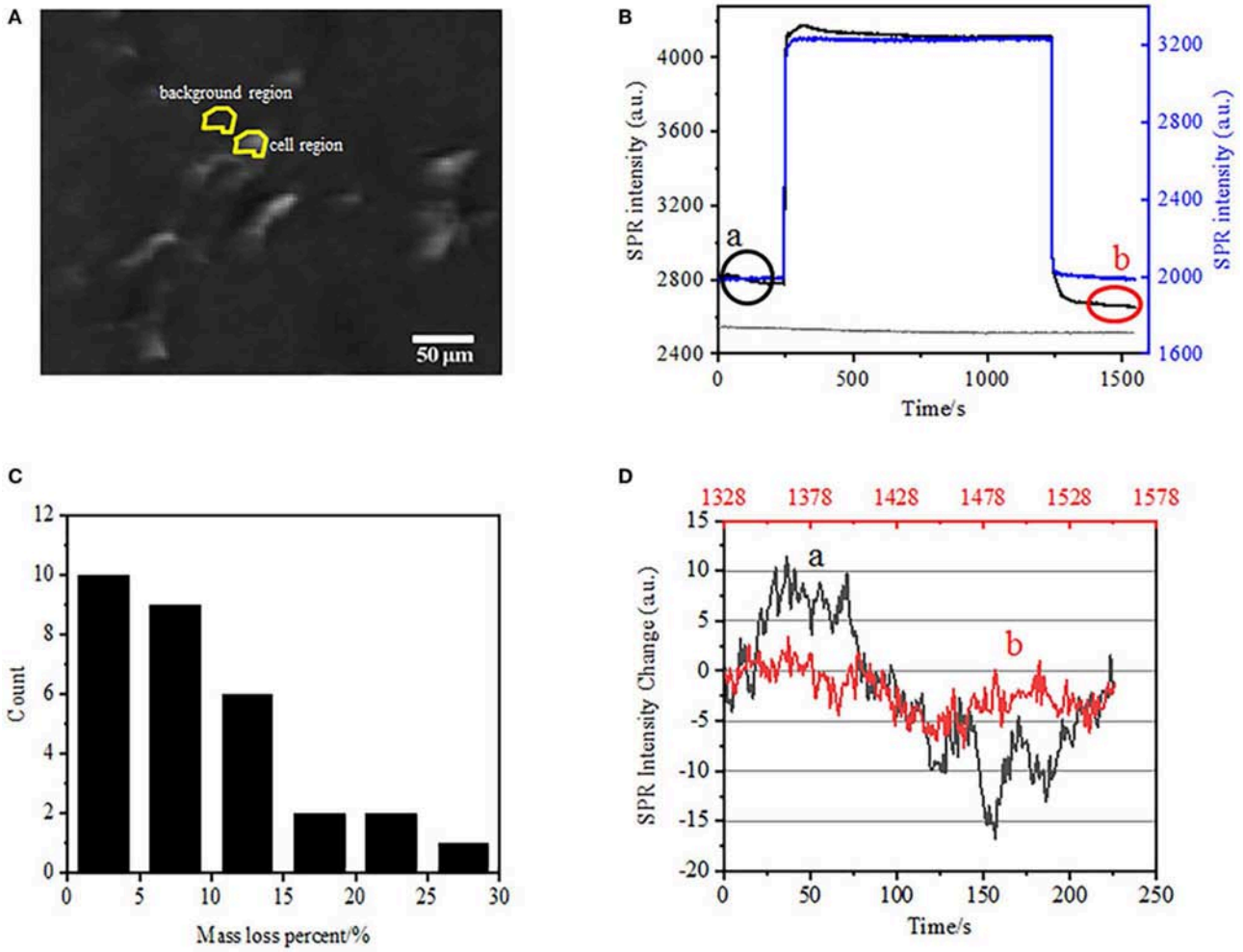

FIGURE 2 | Cell fixation process. **(A)** SPRi image of BT-474 cells. **(B)** SPR signals of single cell (black curve) and background (blue curve) undergoing a solution switching process: PBS buffer to 4% PFA to PBS buffer. SPR signal of single cell treated with PBS during 1,500 s (gray curve). **(C)** Mass loss distribution of 30 single cells. **(D)** Noise level of the cell before (a) and after (b) PFA treatment.

50 nm. A representative SPR image containing single cells is provided in **Figure 2A**. SPR signals of each cell can be obtained by choosing a region-of-interest in the SPR image that matches the morphology of the investigated cell. In a typical experiment, when solution flowed over the cells, SPR sensorgrams of the cells were obtained by analyzing each cell as shown in **Figure 2B** (black curve). In the preceding 242 s, PBS buffer without PFA was flowing over the cells and the baseline was determined by the system stability (light source and mechanical stability) and the inherent micromotion signals generated by the living cells. PFA solution was then introduced at the 242th second, which immediately increased the SPR signal because of the relatively large refractive index of 4% PFA solution (bulk effect). PFA solution ran for another 17 min to achieve sufficient fixation. At the 1237th second, PFA solution was switched back to pure PBS solution. In addition to the reduced bulk effect, a decrease in the SPR intensity of single cells was found when comparing the signals before (0–242) and after (1237–1545) the PFA treatments and the mass loss percent was obtained through dividing the decrease value to the initial value. The SPR sensongrams of the background (an adjacent region without cell adhesion, blue curve) and a single cell treated with PBS during 1,500 s (gray curve) are also shown in **Figure 2B**. Statistical analysis on 30 cells reveals an averaged mass density loss of $10 \pm 5\%$ as shown in **Figure 2C**. It was also found that, after PFA treatment, the baseline fluctuation level in SPR signal was significantly reduced by half or even two third, suggesting the loss of micromotions and fixation of the treated cells as shown in **Figure 2D**. Such micromotion signals were generated by a bunch of dynamic cellular activities from different cell components including skeleton, membranes and organelles. The fixation terminated such biological activities and therefore eliminated the micromotion signals, accompanying with a significantly reduced intensity fluctuation in the SPR sensograms of single cells.

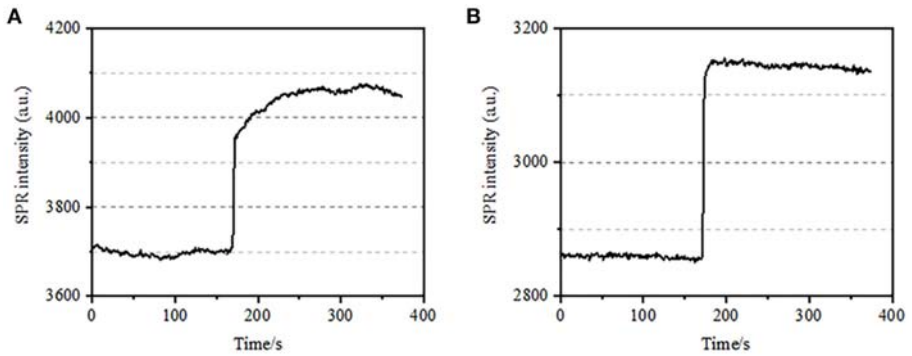

FIGURE 3 | Osmotic pressure responses of cells. **(A)** Response of a living cell to 25 mM sucrose. **(B)** Response of the same cell fixed (10 min) to 25 mM sucrose.

Osmotic Pressure Response in Cell Fixation by PFA

The integrated structure of cell membrane, a semi-permeable membrane, regulates the homeostasis of a cell to reach balance in physiological osmotic pressure. PFA treatment was also found to have the ability in destructing the membrane integrity as shown in **Figure 3**. When the buffer around the target cell changed into 25 mM sucrose solution in <1 s via a drug-perfusion system, a hypertonic cell culture environment was created. For living cells, the exposure to hypertonic solution triggered a series of physiological responses to balance the intracellular and extracellular osmotic pressure, which has been investigated in details in our previous work (Wang et al., 2012a). In this study, a typical SPR sensorgram of single physiological BT-474 cells is provided in **Figure 3A**. Upon the exposure to hypertonic sucrose solution, treated cells firstly underwent a pressing shrink, leading to a gradual increase in SPR intensity until a plateau was reached. It suggested the increased mass density as a result of cell shrink and subcellular components gathering toward the bottom of the gold culture coverslip. The gradual increase in SPR intensity by hypertonic stimulation is a kind of physiological regulation for cellular osmotic pressure, thus indicating the physiological integrity of the cell membrane. When the membrane integrity was destroyed, the introduction of hypertonic sucrose solution was found to immediately increase the SPR intensity in a much shorter time, as shown in **Figure 3B**. It is because the sugar molecules freely penetrated into the cells without resistance from the semi-permeable membrane and increased the local refractive index immediately (bulk effect). It is clear that, while the slow increase in the SPR intensity reflected the physiological osmotic regulation (**Figure 3A**), the rapid jump demonstrated the cell membrane had been damaged to allow for the free entry of small sugar molecules (**Figure 3B**).

Substantial Mass Density Loss in Cell Permeabilization by Triton

In the previous fixation stage, an initial cell mass density decreased just by ∼10% (**Figure 2C**). It is reasonable to speculate that the PFA fixation only slightly destructed the membrane integrity and increased the permeability of small molecules. Majority of the intracellular components should be still harbored within the cytoplasmic membrane. We subsequently studied the influence of a typical permeabilization detergent, 1% Triton X-100, on cells that have been fixed with PFA for 17 min previously. A representative SPR sensorgram of single cells during exposure to 1% Triton X-100 is shown in **Figure 4A**. The introduction of Triton X-100 increased the SPR intensity followed by a gradual decrease. The first increase is a consequence of increase refractive index of bulk solution, and the followed decrease indicated the gradual loss in the mass density due to the cell permeabilization. The reduced mass density was more plentiful when comparing the SPR intensity change before (0-300 s) and after the introduction of detergent (1,300–1,800 s). Analysis on 30 single cells demonstrated that the Triton X-100 treatment created a substantial mass density decrease by another 20 ± 5% after PFA fixation as shown in **Figure 4D** and **Table 1**. It is clear that the detergent Triton X-100 eliminated much more cellular membrane lipids and severely destructed the membrane integrity in this permeabilization stage. This resulted in more intracellular components, especially macromolecules, to release from the cells. And also, this allows large molecules like antibodies to get inside the cell in the next immunoreaction stage. Although SPR intensity of small molecules leaching was detected after PFA fixation, permeabilization by using Triton X-100 detergent clearly solubilized lipids and made the cells much more permeable to the movements of macromolecules in and out of the cell body.

It was found that the loss in mass density is a rather rapid process, which occurred in a few minutes in permeabilization stage (**Figure 4A**). The decrease in mass density roughly followed a monotonic decay within a time period of 126 s. The typical sensorgrams of single cells under 0.5 and 0.1% Triton X-100 are displayed in **Figures 4B,C**, respectively. The permeabilization process became much slower when reducing the concentration of detergent. It took 126, 510, 2,600 s for the three kinds of the treated cells to finish mass loss.

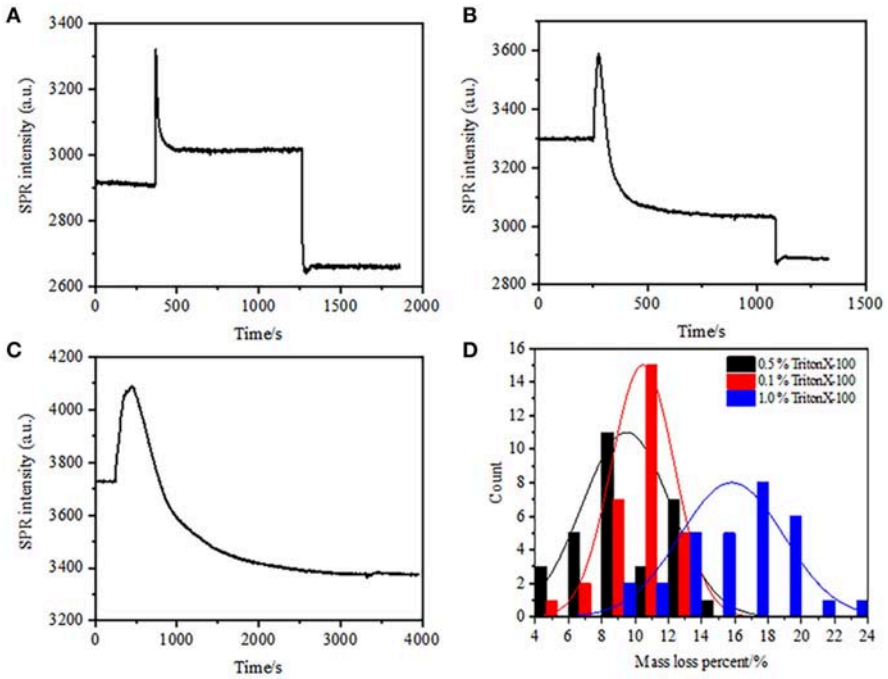

FIGURE 4 | Mass loss curves of cell treated with different concentration solutions **(A)** 1.0%, **(B)** 0.5%, **(C)** 0.1%. **(D)** Mass loss distribution of 30 single cells in different conditions.

TABLE 1 | A summary of variations in mass density loss of statistic cells in different conditions.

Concentrations / Cell counts (30) / Mass loss	1.0 % Triton X-100	0.5 % Triton X-100	0.1 % Triton X-100
4–6%	0	3	1
6–8%	0	5	2
8–10%	2	11	7
10–12%	2	3	15
12–14%	5	7	5
14–16%	5	1	0
16–18%	8	0	0
18–20%	6	0	0
20–22%	1	0	0
22–24%	1	0	0

CONCLUSION

In summary, dynamic redistribution of cellular mass density in both fixation and permeabilization processes have been explored sensitively by using prism-based SPRi setup with high spatial and temporal resolutions. Fixative PFA could initially increase the permeability of cytoplasmic membrane to some extent because its ability of fixing cellular proteins in both membrane and intra-cellular proteins. It was supported by (1) the decreased mass density by ∼10% after a 17-min fixation treatment in 4% PFA solution, and (2) the eliminated cellular response to hypertonic solution, which demonstrated the destruction of cellular integrity to small molecules like sugars. Detergent Triton X-100 is superior to fixative PFA in solubilizing lipids and therefore increasing cell membrane permeability, accompanying with the more substantial loss in the mass density due to the release of not only small molecules but also large molecules and possibly some organelles such as vesicles. Besides, the rate of mass loss is positively correlated with Triton X-100 concentration. These results provided quantitative and dynamic understandings on the influence of fixation and permeabilization on the cellular mass density and membrane integrity, with implications for optimizing the conditions for single cell biological experiments, such as immunofluorescent and immunohistochemical assays.

AUTHOR CONTRIBUTIONS

RC, Y-WS, and WW designed the experiments. RC, FZ, ML, and XW performed the experiments. RC, Y-WS, and WW wrote the paper. RC, FZ, Y-WS, and WW discussed the results and analyzed the data.

ACKNOWLEDGMENTS

We thank financial support from the National Natural Science Foundation of China (Grant No. 21522503).

REFERENCES

Abadian, P. N., Kelley, C. P., and Goluch, E. D. (2014). Cellular analysis and detection using surface plasmon resonance techniques. *Anal. Chem.* 86, 2799–2812. doi: 10.1021/ac500135s

Cullen, D. C., Brown, R. G. W., and Lowe, C. R. (1987). Detection of immuno-complex formation via surface plasmon resonance on gold-coated diffraction gratings. *Biosensors* 3, 211–225. doi: 10.1016/0265-928X(87)85002-2

Deng, S., Yu, X., Liu, R., Chen, W., and Wang, P. (2016). A two-compartment microfluidic device for long-term live cell detection based on surface plasmon resonance. *Biomicrofluidics* 10:044109. doi: 10.1063/1.4960487

Fox, C. H., Johnson, F. B., Whiting, J., and Roller, P. P. (1985). Formaldehyde fixation. *J. Histochem. Cytochem.* 33, 845–853. doi: 10.1177/33.8.3894502

Giebel, K. F., Bechinger, C., Herminghaus, S., Riedel, M., Leiderer, P., Weiland, U., et al. (1999). Imaging of cell/substrate contacts of living cells with surface plasmon resonance microscopy. *Biophys. J.* 76, 509–516. doi: 10.1016/S0006-3495(99)77219-X

Homola, J. (2008). Surface plasmon resonance sensors for detection of chemical and biological species. *Chem. Rev.* 108, 462–493. doi: 10.1021/cr068107d

Jamur, M. C., and Oliver, C. (2010). "Permeabilization of cell membranes," in *Immunocytochemical Methods and Protocols*, eds C. Oliver and M. C. Jamur (Totowa, NJ: Humana Press), 63–66. doi: 10.1007/978-1-59745-324-0_9

Joshi, S., and Yu, D. (2017). "Chapter 8-Immunofluorescence," in *Basic Science Methods for Clinical Researchers*, eds M. Jalali, F. Y. L. Saldanha, and M. Jalali (Boston, MA: Academic Press), 135–150. doi: 10.1016/B978-0-12-803077-6.00008-4

Kiernan, J. A. (2018). Formaldehyde, formalin, paraformaldehyde and glutaraldehyde: what they are and what they do. *Micros. Today* 8, 8–13. doi: 10.1017/S1551929500057060

Koley, D., and Bard, A. J. (2010). Triton X-100 concentration effects on membrane permeability of a single HeLa cell by scanning electrochemical microscopy (SECM). *Proc. Natl. Acad. Sci. U.S.A.* 107, 16783–16787. doi: 10.1073/pnas.1011614107

Liedberg, B., Nylander, C., and Lunström, I. (1983). Surface plasmon resonance for gas detection and biosensing. *Sens. Actuat.* 4, 299–304. doi: 10.1016/0250-6874(83)85036-7

Méjard, R., Griesser, H. J., and Thierry, B. (2014). Optical biosensing for label-free cellular studies. *TrAC Trends Anal. Chem.* 53, 178–186. doi: 10.1016/j.trac.2013.08.012

Peng, Z., Lu, J., Zhang, L., Liu, Y., and Li, J. (2018). Label-free imaging of epidermal growth factor receptor-induced response in single living cells. *Analyst* 143, 5264–5270. doi: 10.1039/C8AN01534A

Phillips, K. S., and Cheng, Q. (2007). Recent advances in surface plasmon resonance based techniques for bioanalysis. *Anal. Bioanal. Chem.* 387, 1831–1840. doi: 10.1007/s00216-006-1052-7

Rothenhäusler, B., and Knoll, W. (1988). Surface-plasmon microscopy. *Nature* 332, 615–617. doi: 10.1038/332615a0

Smith, J. T., Tomfohr, J. K., Wells, M. C., Beebe, T. P., Kepler, T. B., and Reichert, W. M. (2004). Measurement of cell migration on surface-bound fibronectin gradients. *Langmuir* 20, 8279–8286. doi: 10.1021/la0489763

Su, Y. W., and Wang, W. (2018). Surface plasmon resonance sensing: from purified biomolecules to intact cells. *Anal. Bioanal. Chem.* 410, 3943–3951. doi: 10.1007/s00216-018-1008-8

Thavarajah, R., Mudimbaimannar, V. K., Elizabeth, J., Rao, U. K., and Ranganathan, K. (2012). Chemical and physical basics of routine formaldehyde fixation. *J. Oral Maxillofac. Pathol.* 16, 400–405. doi: 10.4103/0973-029X.102496

Wang, S., Shan, X., Patel, U., Huang, X., Lu, J., Li, J., et al. (2010). Label-free imaging, detection, and mass measurement of single viruses by surface plasmon resonance. *Proc. Natl. Acad. Sci. U.S.A.* 107, 16028–16032. doi: 10.1073/pnas.1005264107

Wang, W., Wang, S., Liu, Q., Wu, J., and Tao, N. (2012a). Mapping single-cell–substrate interactions by surface plasmon resonance microscopy. *Langmuir* 28, 13373–13379. doi: 10.1021/la301712h

Wang, W., Yang, Y., Wang, S., Nagaraj, V. J., Liu, Q., Wu, J., et al. (2012b). Label-free measuring and mapping of binding kinetics of membrane proteins in single living cells. *Nat. Chem.* 4, 846–853. doi: 10.1038/nchem.1434

Wang, W., Yin, L., Gonzalez-Malerva, L., Wang, S., Yu, X., Eaton, S., et al. (2014). *In situ* drug-receptor binding kinetics in single cells: a quantitative label-free study of anti-tumor drug resistance. *Sci. Rep.* 4:6609. doi: 10.1038/srep06609

Wang, Y., Zhang, S., Xu, T., Zhang, T., Mo, Y., Liu, J., et al. (2018). Ultra-sensitive and ultra-fast detection of whole unlabeled living cancer cell responses to paclitaxel with a graphene-based biosensor. *Sens. Actuat. B Chem.* 263, 417–425. doi: 10.1016/j.snb.2018.02.095

Yanase, Y., Hiragun, T., Ishii, K., Kawaguchi, T., Yanase, T., Kawai, M., et al. (2014). Surface plasmon resonance for cell-based clinical diagnosis. *Sensors* 14, 4948–4959. doi: 10.3390/s140304948

Yanase, Y., Hiragun, T., Kaneko, S., Gould, H. J., Greaves, M. W., and Hide, M. (2010). Detection of refractive index changes in individual living cells by means of surface plasmon resonance imaging. *Biosens. Bioelectron.* 26, 674–681. doi: 10.1016/j.bios.2010.06.065

Yang, Y., Yu, H., Shan, X., Wang, W., Liu, X., Wang, S., et al. (2015). Label-free tracking of single organelle transportation in cells with nanometer precision using a plasmonic imaging technique. *Small* 11, 2878–2884. doi: 10.1002/smll.201403016

Zhang, F., Wang, S., Yin, L., Yang, Y., Guan, Y., Wang, W., et al. (2015). Quantification of epidermal growth factor receptor expression level and binding kinetics on cell surfaces by surface plasmon resonance imaging. *Anal. Chem.* 87, 9960–9965. doi: 10.1021/acs.analchem.5b02572

Conflict of Interest Statement: The authors declare that the research was conducted in the absence of any commercial or financial relationships that could be construed as a potential conflict of interest.

The handling editor declared a shared affiliation, though no other collaboration, with the authors WW, RC, ML, and XW at time of review.

Copyright © 2019 Cheng, Zhang, Li, Wo, Su and Wang. This is an open-access article distributed under the terms of the Creative Commons Attribution License (CC BY). The use, distribution or reproduction in other forums is permitted, provided the original author(s) and the copyright owner(s) are credited and that the original publication in this journal is cited, in accordance with accepted academic practice. No use, distribution or reproduction is permitted which does not comply with these terms.

frontiers in Chemistry

ORIGINAL RESEARCH
published: 31 October 2018
doi: 10.3389/fchem.2018.00530

ctDNA Detection Based on DNA Clutch Probes and Strand Exchange Mechanism

Huan Chang[1,2], Yiyi Zhang[2], Fan Yang[2], Changtao Wang[1] and Haifeng Dong[1,2]**

[1] *Beijing Advanced Innovation Center for Food Nutrition and Human Health, Beijing Technology and Business University (BTBU), Beijing, China,* [2] *Beijing Key Laboratory for Bioengineering and Sensing Technology, Research Center for Bioengineering and Sensing Technology, School of Chemistry and Bioengineering, University of Science and Technology Beijing, Beijing, China*

Circulating tumor DNA (ctDNA), originating directly from the tumor or circulating tumor cells, may reflect the entire tumor genom and has gained considerable attention for its potential clinical diagnosis and prognosis throughout the treatment regimen. However, the reliable and robust ctDNA detection remains a key challenge. Here, this work designs a pair of DNA clutch separation probes and an ideal discrimination probes based on toehold-mediated strand displacement reaction (TSDR) to specifically recognize ctDNA. First, the ctDNAs were denatured to form ssDNAs, the pair of DNA clutch separation probes [one of which modified onto the magnetic nanoparticles (MNPs)] are used to recognize and hybridize with the complemental chains and prevent reassociation of denatured ssDNAs. The complemental chains are removed in magnetic field and left the wild and mutant ssDNA chains in the supernatant. Then, the TSDR specificity recognizes the target mutant sequence to ensure only the mutated strands to be detection. The proposed assay exhibited good sensitivity and selectivity without any signal amplification. The proposed assay displayed a linear range from 2 to100 nM with a limit of detection (LOD) of 0.85 nM, and it was useful for ctDNA biomedical analysis and clinic theranostic.

Keywords: ctDNA, clutch probes, discrimination probes, strand displacement reaction, selectivity

OPEN ACCESS

Edited by:
Huangxian Ju,
Nanjing University, China

Reviewed by:
Xue-Mei Li,
Linyi University, China
Hua Wang,
Qufu Normal University, China

****Correspondence:***
Changtao Wang
wangct@th.btbu.edu.cn
Haifeng Dong
hfdong@ustb.edu.cn

Specialty section:
This article was submitted to Analytical Chemistry, a section of the journal Frontiers in Chemistry

Received: *20 July 2018*
Accepted: *11 October 2018*
Published: *31 October 2018*

Citation:
Chang H, Zhang Y, Yang F, Wang C and Dong H (2018) ctDNA Detection Based on DNA Clutch Probes and Strand Exchange Mechanism. Front. Chem. 6:530. doi: 10.3389/fchem.2018.00530

INTRODUCTION

In recent years, many advanced analytical methods have been established to quantify DNAs and RNAs (Schwarzenbach et al., 2011; Si et al., 2014; Li et al., 2015; Wang et al., 2018), among them, liquid biopsy has increasingly attracted intense attention due to its rapid, cost-effective and non-invasive properties. Circulating tumor DNA (ctDNA), originating directly from the tumor or circulating tumor cells, is an effective diagnostic biomarker existing as a single or double strand in peripheral blood (Zou et al., 2017). It is potential surrogate for the entire tumor genome and has gained considerable attention for cancer diagnosis and prognosis (Das et al., 2016). It is reported that ctDNA levels could reflect the tumor burden, and patients with advanced tumors showed higher concentrations of ctDNA in plasma than that with earlier stage. For example, it was demonstrated that the level of ctDNA was related to the whole body tumor load and ctDNA decreased after complete surgery (Diehl et al., 2008). It was reported that ctDNA was detected in 82 and 47% for patients with stage IV and I disease, respectively (Bettegowda et al., 2014). Additionally, the half-life of ctDNA is very short, and it was promising for monitor the status of the tumor (Bettegowda et al., 2014; Diaz and Bardelli, 2014). Therefore, the detection of specific cancer-related sequences in ctDNA is very important in clinical application.

The detection of the ctDNA is difficult since the special double helix structure and single stranded DNAs (ssDNAs) formed during the annealing process (Noh et al., 2015), which require effective methods to prevent ssDNA from re-annealing for selectively detection of ctDNA (Das et al., 2016). Currently, DNA sequencing and polymerase chain reaction (PCR) are conventional methods for monitoring ctDNA in the blood (Murtaza et al., 2013; Bettegowda et al., 2014; Newman et al., 2014). However, both of them suffer some deficiencies including the biological environment interference, time-consuming, and cost-ineffective (Dewey et al., 2012; Wang et al., 2014). Therefore, the robust, sensitive, and selective detection of ctDNA are still urgently needed.

Two significant prerequisites for ctDNA detection are separation probes effectively preventing ssDNA from re-annealing and discrimination probes specifically recognizing the target ssDNA. The hybridization specificity based on based pairing almost requires the string hybridization condition or chemically complex nucleotide modifications. Toehold-mediated strand displacement reaction (TSDR) is widely applied in the dynamic DNA assembly for biomedical application by regulating the reaction rate (Yurke and Mills, 2003; Zhang and Winfree, 2009). Rationally designed hybridization probes based on strand exchange mechanisms or strand displacement reaction is intriguing since it can effectively and robustly distinguish single-base mutation in the gene fragment in various conditions (Xiao et al., 2005; Wang and Zhou, 2008).

Herein, this work designs a pair of DNA clutch separation probes and an ideal discrimination probes based on TSDR to specifically recognize mutant ctDNA (**Figure 1**). Under annealing, the pair of DNA clutch separation probes clutch 3 and clutch 5 could recognize and hybridize with the complementary chains (red color) and prevent reassociation of denatured ssDNAs. The complementary chains were then removed in magnetic field and the wild and left the mutant ssDNA chains in the supernatant. Finally, the discrimination probes based on TSDR which could specifically recognize the target mutant ssDNA sequence to produce the fluorescence signal for detection. Thus, the specific mutant ctDNA detection has been realized, displaying a good potential in the field of ctDNA biomedical application.

MATERIALS AND METHODS

Reagents and Materials

1-(3-Dimethylaminopropyl)-3-ethylcarbodiimidehydrochloride (EDC), Tris (2-carboxy-ethyl), N-hydro-xysuccinimide (NHS), phosphine (TCEP), were obtained from Sigma-Aldrich (St. Louis, MO). The ultrapure water was from a Millipore water purification system (18 MΩ, Milli-Q, Millipore, USA). Magnetic nanoparticles (MNPs) (20 mg/mL) modified with carboxyl (-COOH) group were obtained from Zhengzhou Innosep Biosciences Co., Ltd. (Zhengzhou, China). All of the DNA sequences were from Sangon Biological Engineering

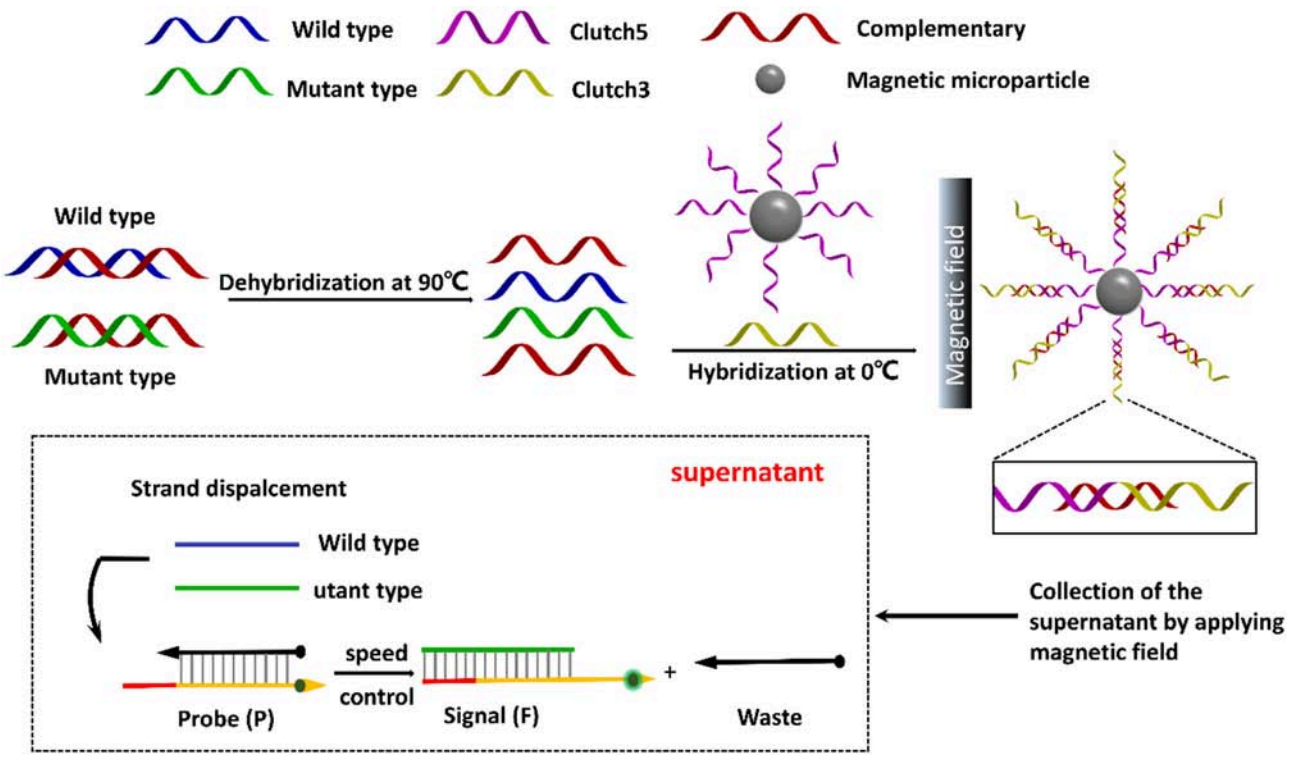

FIGURE 1 | Schematic illustration of direct detection of ctDNA based on DNA clutch separation probes and TSDR reaction.

Technology & Services Co., Ltd. (Shanghai, China) and the detailed information of sequences were presented in **Table 1**. Transmission electron microscopy (TEM; JEM2010F, JEOL, 200 kV) was used to exam the morphology of the MNPs. Dynamic light scattering (DLS) was recorded on a Zetasizer Nano S system (Malvern Instruments, Malvern, U.K.). The UV–vis absorption measurements were performed with a UV-1800 spectrometer (Shimadzu, Kyoto, Japan). All fluorescence measurements were carried out on a F-4500 fluorescence spectrometer (Hitachi, Tokyo, Japan). The agarose gel electrophoresis images were captured with an Alliance Ld2 (Uvitec, Cambridge, U.K.).

TABLE 1 | The detailed information of the DNA sequences used in the experiment.

Oligonucleotide	Sequence (5′-3′)
BRAF wild	TAGCTACAGTGAAATC
BRAF mutant	TAGCTACAGAGAAATC
Complementary sequence	GATTTCACTGTAGCTA
DNAclutch5	/NH2/(CH2)6GAAGACCTCACAGTAAAAATAGG TGATTTTGGTCTAGCTACAGT
DNA clutch3	GAAATCTCGATGGAGTGGGTCCCATCAG TTTGAAC
DNA 1	GAAATC
Probe 1	GATTTCACTGTAGCTA
DNA 2	/BHQ2/GATGTAGCTA
Probe 2	GATTTCACTGTAGCTACATC/Cy5/
DNA 3	/BHQ2/ACGATGTAGCTA
Probe 3	GATTTCACTGTAGCTACATCGT/Cy5/

The base marked red in the table is the mutation site.

Characterization of Carboxylated MNPs

10 mg/mL carboxylated MNPs were diluted into 0.5 mg/mL in phosphate buffer saline (PBS, pH = 5.1, 10 mM) and sufficiently sonicated for 2 h to obtain the dispersed solution, 2 μL of the sample was then dropped on a double networked supporting membrane fixed with small clips and dried using the heating plate for TEM analysis. 0.5 mg/mL MNPs was diluted with distilled water to 1 mL and added to a particle size cell for DLS measurement.

DNA Functionalization of MNPs

30 μL of MNPs (0.5 mg/mL, pH =5.1), 30 μL MNPs probe (100 μM) and 4 mg of EDC were mixed in a centrifugal tube and reacted for 15 min. One milligram of NHS was then injected and the mixture was further reacted for 12 h in PBS solution (10 mM, pH = 7.4). Then the MNPs-DNA were washed with PBS (10 mM, pH = 7.4) for three times and stored in 120 mL of PBS (10 mM, pH = 7.4) for further use.

Electrophoresis Gel Characterization

The hybridization of clutch probes and the ssDNA were performed at 0°C for 1 h, and verified by 4% agarose gel electrophoresis (100 V, 50 mA).

Optimization of Discrimination Probes

The ssDNA (10 μL, 1 μM) labeled with fluorescent FAM firstly hybridized with their complementary ssDNA labeled with quenching groups (BHQ2) at 37°C for 2 h to form duplex helices discrimination probes. The target ssDNA with single nucleotide mutant (10 μL, 1 μM) or its wild type ssDNA (10 μL, 1 μM) was then added to the 100 μL of solution containing discrimination probes and incubated at desired time and temperatures. Afterwards, the fluorescence intensity was detected using a fluorescence spectrometer.

ctDNA Detection

Four microliter ctDNA with different concentrations were heated at 90°C for 2 min, and then added into solution containing 7 μL MNPs probes (20 μM) and 9 μL clutch 3 probe (20 μM) and reacted at 0°C for 60 min. The mixture was separated at a magnetic field and the supernatant was collected for further use. Ten microliter supernatant was added into 4 μL discrimination probes (10 μM) and the mixture was diluted into 200 μL and reacted at 37°C for 10 min. Afterwards, the fluorescence was scanned with a fluorescence spectrometer with excitation wavelength at 488 nm and scanning emission spectra from 505 to 700 nm.

RESULTS AND DISCUSSION

Characterization of MNPs-DNA

As shown in **Figure 2A**, it was obvious that the MNPs displayed uniform spherical and showed a particle size of about 500 nm. The MNP displayed a negative zeta potential of −11.8 mV, and the introduction of negatively charged DNA led to the zeta potential decreased to −22.5 mV (**Figure 2B**). In comparison with the UV-vis spectrum of MNPs, a strong characteristic absorption peak at 258 nm was observed in that of MNPs-DNA, revealing DNA was efficiently modified on MNPs' surface (Zhu et al., 2006; **Figure 2C**). The DLS analysis demonstrated the aqueous size of MNPs was approximately distributed at about 510 nm, in agreement with the TEM analysis, and it increased to 535 nm after the modification of DNA (**Figure 2D**). These results suggested the successful modification of DNA on the surface of MNPs. The electrophoresis experiment was employed to characterize DNA assembly. As shown in **Figure S1**, the lane 1–3 was the complementary sequences (16 bp), clutch probe 3 (35 bp), and clutch probe 5 (44 bp), respectively. From the lanes 4–6 analysis, it indicated the complementary sequences could hybridize with clutch probe 3 (lane 4), clutch probe 5 (lane 5), to form sandwich structure (lane 6).

Toehold Exchange Probes

To obtain an ideal discrimination probes with high specificity, the "toehold exchange" probes were rationally designed. The length of the cohesive ends at the 3′ end of the replacement sequence in the discrimination probes influence significantly the specificity (Chen and Seelig, 2016), which was firstly optimized. Three types of DNA probes consisting of two single sequence labeled with BHQ2 quencher and FAM fluorescent dye, respectively, were employed to investigate the optimized cohesive ends. It was found that the probe 1, probe 2, and probe 3 displayed a

maximum $F/F_0$of 1.15, 1.52, and 4.1, respectively, where the F and F_0 was the fluorescence intensity of probes in response to the mutant-type and wild-type ctDNA (**Figures 3A–C**). Importantly, when the cohesive ends extended to twelve bases (probe 3), the wild-type ctDNA produced similar fluorescence intensity to the control (PBS, pH 7.4, 10 mM) group, which indicated the

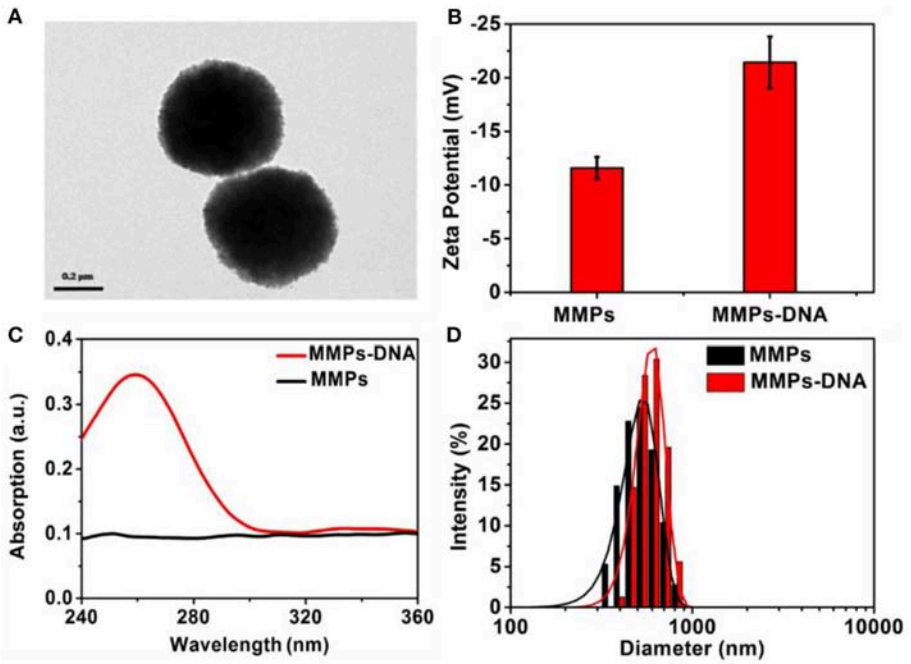

FIGURE 2 | TEM image of **(A)** MNPs, Zeta potential **(B)**, UV-visible spectra **(C),** and **(D)** DLS of MNPs and MNPs-DNA.

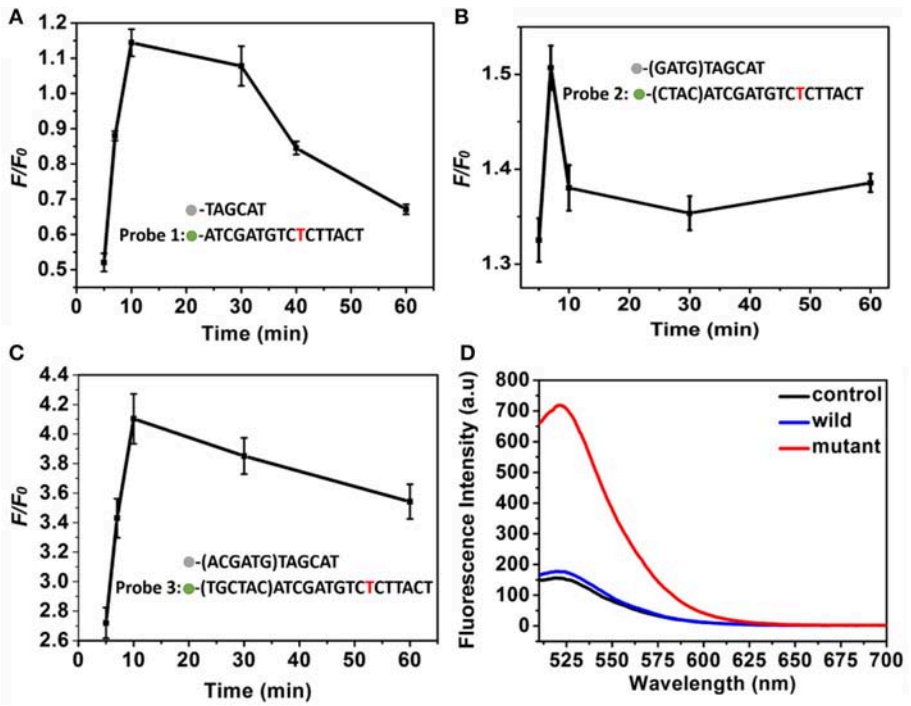

FIGURE 3 | (A–C) The F/F_0 value of **(A)** probe 1, **(B)** probe 2, and **(C)** probe 3 as a function of time. Three different discrimination probe (red is the mutant site), **(D)** Fluorescence intensity corresponding to probe 3. The concentration of the mutant type ctDNA and wild ctDNA was 100 nM.

excellent specificity of probe (**Figure 3D**). Therefore, the toehold exchange probe 3 was used in subsequent experiments.

Conditions Optimization

The experimental conditions including the ratio of volume of MNPs and DNA in the PBS (pH 7.4, 10 mM) and strand displacement reaction time were investigated to achieve the optimal signal discriminant validity. The zeta potential analysis was used to optimize the ratio of volume of MNPs and DNA. As shown in **Figure 4A**, the absolute value of zeta potential gradually increased along with the increase of the ratio of volume of MNPs and DNA, and reached to maximum at the ratio of 1:50, which was selected for the followed experiments. The displacement reaction time was a significant factor in the experiment. The short reaction time might induce insufficient displacement reaction, while long reaction time could lead to decrease of the discrimination capability for wild/mutant sequence. As shown in **Figure 4B**, the system showed a sharply increase in the discrimination capability long with the increase of reaction time increased to 10 min, and then decreased when the reaction time further increased. Thus the 10 min was selected as the optimized reaction time.

Sensitivity of the Proposed System Proposed System

Under the optimized conditions, the system was very specific that just produced fluorescence signal toward the mutant-type ctDNA, while no fluorescence signal change was observed even if the concentration of wild-type ctDNA high to 50 nM due to the TSDR probe. Furthermore, the selectivity of the method was detected by using other DNA strands with different sequences. As shown in **Figure S2**, the fluorescent intensity of mutant-type ctDNA was much higher than that produced by other DNA strands, indicating the great selectivity of the detection strategy. Motivated by the intriguing specificity, the sensitivity of the assay was further investigated for mutant-type ctDNA detection. As shown in **Figure 5A**, the fluorescence intensity increased with the increasing mutant ctDNA target concentration, and a good linear relationship between the fluorescence intensity and target concentration ranging from 2 to 50 nM was obtained (**Figure 5B**). The limit of detection

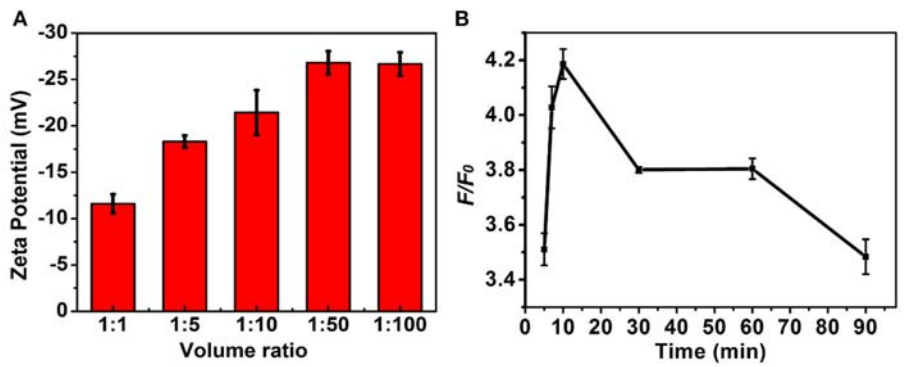

FIGURE 4 | The influence of **(A)** volume ratio of MNPs (0.5 mg/mL) to DNA (1 nM) and **(B)** strand displacement reaction temperature to the F/F_0. The concentration of the mutant type ctDNA and wild ctDNA was 100 nM.

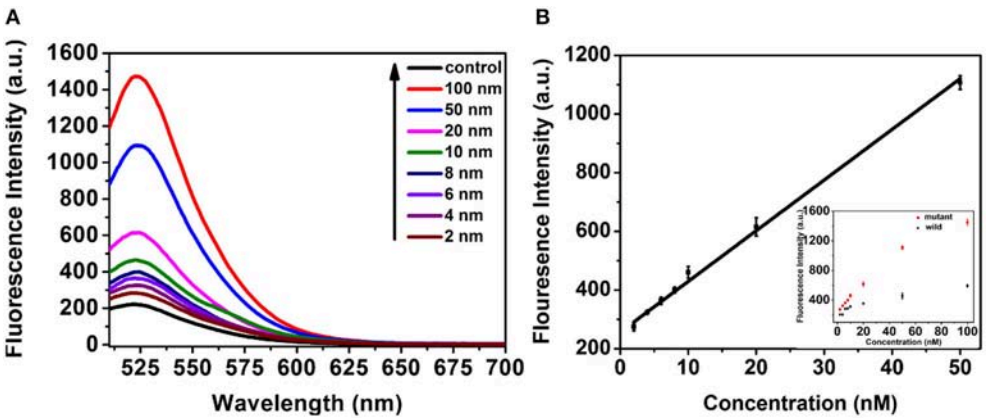

FIGURE 5 | (A) Fluorescence response of the assay to control (PBS pH 7.4, 10 mM) and mutant-type ctDNA with different concentrations. **(B)** The Linear relationship between the fluorescence intensity and concentration of mutant-type ctDNA concentration.

(LOD) was calculated to be 0.85 nM using three times of the standard deviation of the control (Wang et al., 2009). To evaluate the practical application, the serum was chosen as the biological sample to evaluate the performance of the detection system. As demonstrated in **Figure S3**, the mutant ctDNA targets were detected in serum sample solution, implying matrix effects are not a major problem on the reaction system, which indicated the promising potential for clinical application.

CONCLUSIONS

In conclusion, we develop a ctDNA specifical detection method using a pair of DNA clutch separation probes and an ideal discrimination probes based on TSDR. The clutch probes with one of which modified on the MNPs are used to hybridize the mutant ssDNA strand denatured from ctDNA, prevent it reassociation, and separate it in magnetic field to make the other ssDNA strand accessible for hybridization. The discrimination probes were carefully designed and very specific for mutant-type ctDNA, which could efficiently and specifically recognize the mutant-type ctDNA target whereas showed no response to the wild-type ctDNA. Under optimal conditions, the proposed assay displayed a good linear rang and low LOD for target mutant-type ctDNA detection, which was expected to be useful for ctDNA biomedical analysis and clinic theranostic.

AUTHOR CONTRIBUTIONS

HC designed the experiments and performed the optimization of discrimination probes, ctDNA detection, and wrote the manuscript. YZ and FY performed the characterization of carboxylated MNPs and DNA functionalization of MNPs. CW and HD contributed in project design and manuscript preparation. All authors reviewed the manuscript and approved for submission.

FUNDING

The work was supported by Special Foundation for State Major Research Program of China (Grant Nos. 2016YFC0106602 and 2016YFC0106601); National Natural Science Foundation of China (Grant No. 21645005, 21475008); the Open Research Fund Program of Beijing Advanced Innovation Center for Food Nutrition and Human Health (NO. 20171002); the Open Research Fund Program of Beijing Key Lab of Plant Resource Research and Development, Beijing Technology and Business University (PRRD-2016-YB2).

SUPPLEMENTARY MATERIAL

The Supplementary Material for this article can be found online at: https://www.frontiersin.org/articles/10.3389/fchem.2018.00530/full#supplementary-material

REFERENCES

Bettegowda, C., Sausen, M., Leary, R. J., Kinde, I., Wang, Y., Agrawal, N., et al. (2014). Detection of circulating tumor DNA in early- and late-stage human malignancies. *Sci. Transl. Med.* 6:224ra224. doi: 10.1126/scitranslmed.3007094

Chen, S. X., and Seelig, G. (2016). An engineered kinetic amplification mechanism for single nucleotide variant discrimination by DNA hybridization probes. *J. Am. Chem. Soc.* 138, 5076–5086. doi: 10.1021/jacs.6b00277

Das, J., Ivanov, I., Sargent, E. H., and Kelley, S. O. (2016). DNA clutch probes for circulating tumor DNA analysis. *J. Am. Chem. Soc.* 138, 11009–11016. doi: 10.1021/jacs.6b05679

Dewey, F. E., Pan, S., Wheeler, M. T., Quake, S. R., and Ashley, E. A. (2012). DNA sequencing clinical applications of new DNA sequencing technologies. *Circulation* 125, 931–944. doi: 10.1161/CIRCULATIONAHA.110.972828

Diaz, L. A., and Bardelli, A. (2014). Liquid biopsies: genotyping circulating tumor DNA. *J. Clin. Oncol.* 32, 579–586. doi: 10.1200/JCO.2012.45.2011

Diehl, F., Schmidt, K., Choti, M. A., Romans, K., Goodman, S., Li, M., et al. (2008). Circulating mutant DNA to assess tumor dynamics. *Nat. Med.* 14, 985–990. doi: 10.1038/nm.1789

Li, R., Li, S., Dong, M., Zhang, L., Qiao, Y., Jiang, Y., et al. (2015). A highly specific and sensitive electroanalytical strategy for microRNAs based on amplified silver deposition by the synergic TiO2 photocatalysis and guanine photoreduction using charge-neutral probes. *Chem. Commun.* 51, 16131–16134. doi: 10.1039/C5CC07277H

Murtaza, M., Dawson, S. J., Tsui, D. W., Gale, D., Forshew, T., Piskorz, A. M., et al. (2013). Non-invasive analysis of acquired resistance to cancer therapy by sequencing of plasma DNA. *Nature* 497, 108–112. doi: 10.1038/nature12065

Newman, A. M., Bratman, S. V., To, J., Wynne, J. F., Eclov, N. C., Modlin, L. A., et al. (2014). An ultrasensitive method for quantitating circulating tumor DNA with broad patient coverage. *Nat. Med.* 20, 552–558. doi: 10.1038/nm.3519

Noh, S., Ha, D. T., Yang, H., and Kim, M. S. (2015). Sensitive and direct electrochemical detection of double-stranded DNA utilizing alkaline phosphatase-labelled zinc finger proteins. *Analyst* 140, 3947–3952. doi: 10.1039/C5AN00623F

Schwarzenbach, H., Hoon, D. S., and Pantel, K. (2011). Cell-free nucleic acids as biomarkers in cancer patients. *Nat. Rev. Cancer* 11, 426–437. doi: 10.1038/nrc3066

Si, Y., Sun, Z., Zhang, N., Qi, W., Li, S., Chen, L., et al. (2014). Ultrasensitive electroanalysis of low-level free microRNAs in blood by maximum signal amplification of catalytic silver deposition using alkaline phosphatase-incorporated gold nanoclusters. *Anal. Chem.* 86, 10406–10414. doi: 10.1021/ac5028885

Wang, H., Zhang, L., Jiang, Y., Chen, L., Duan, Z., Lv, X., et al. (2018). A sandwiched electroanalysis method for probing Anthrax DNAs based on glucose-induced gold growth and catalytic coupling of tyramine using gold-mineralized glucose oxidase. *Sens. Actuator B Chem.* 261, 441–450. doi: 10.1016/j.snb.2018.01.171

Wang, J., and Zhou, H. S. (2008). Aptamer-based Au nanoparticles-enhanced surface plasmon resonance detection of small molecules. *Anal. Chem.* 80, 7174–7178. doi: 10.1021/ac801281c

Wang, X., Lim, H. J., and Son, A. (2014). Characterization of denaturation and renaturation of DNA for DNA hybridization. *Environ Health Toxicol.* 29:e2014007. doi: 10.5620/eht.2014.29.e2014007

Wang, Y., Li, J., Jin, J., Wang, H., Tang, H., Yang, R., et al. (2009). Strategy for molecular beacon binding readout: separating molecular recognition element and signal reporter. *Anal. Chem.* 81, 9703–9709. doi: 10.1021/ac901906w

Xiao, Y., Lubin, A. A., Heeger, A. J., and Plaxco, K. W. (2005). Label-free electronic detection of thrombin in blood serum by using an aptamer-based sensor. *Angew. Chem. Int. Edit.* 44, 5456–5459. doi: 10.1002/anie.200500989

Yurke, B., Mills, A. P. Jr. (2003). Using DNA to power nanostructures. *Genet. Program. Evol. Mach.* 4, 111–122. doi: 10.1023/A:1023928811651

Zhang, D. Y., and Winfree, E. (2009). Control of DNA strand displacement kinetics using toehold exchange. *J. Am. Chem. Soc.* 131, 17303–17314. doi: 10.1021/ja906987s

Zhu, X. L., Han, K., and Li, G. (2006). Magnetic nanoparticles applied in electrochemical detection of controllable DNA hybridization. *Anal. Chem.* 78, 2447–2449. doi: 10.1021/ac051962x

Zou, Z., Qi, P., Qing, Z., Zheng, J., Yang, S., Chen, W., et al. (2017). Technologies for analysis of circulating tumour DNA: progress and promise. *Trends Anal. Chem.* 97, 36–49. doi: 10.1016/j.trac.2017.08.004

Conflict of Interest Statement: The authors declare that the research was conducted in the absence of any commercial or financial relationships that could be construed as a potential conflict of interest.

Copyright © 2018 Chang, Zhang, Yang, Wang and Dong. This is an open-access article distributed under the terms of the Creative Commons Attribution License (CC BY). The use, distribution or reproduction in other forums is permitted, provided the original author(s) and the copyright owner(s) are credited and that the original publication in this journal is cited, in accordance with accepted academic practice. No use, distribution or reproduction is permitted which does not comply with these terms.

frontiers in Chemistry

REVIEW
published: 07 May 2019
doi: 10.3389/fchem.2019.00313

Biological Applications of Organic Electrochemical Transistors: Electrochemical Biosensors and Electrophysiology Recording

Liming Bai[1,2], *Cristina García Elósegui*[2,3], *Weiqi Li*[2,3], *Ping Yu*[2,3]*, *Junjie Fei*[1]* and *Lanqun Mao*[2,3]

[1] Key Laboratory of Environmentally Friendly Chemistry and Applications of Ministry of Education, College of Chemistry, Xiangtan University, Xiangtan, China , [2] Beijing National Laboratory for Molecular Sciences, Key Laboratory of Analytical Chemistry for Living Biosystems, Institute of Chemistry, The Chinese Academy of Sciences, Beijing, China, [3] School of Chemical Sciences, University of Chinese Academy of Sciences, Beijing, China

Organic electrochemical transistors (OECTs) are recently developed high-efficient transducers not only for electrochemical biosensor but also for cell electrophysiological recording due to the separation of gate electrode from the transistor device. The efficient integration of OECTs with electrochemical gate electrode makes the as-prepared sensors with improved performance, such as sensitivity, limit of detection, and selectivity. We herein reviewed the recent progress of OECTs-based biosensors and cell electrophysiology recording, mainly focusing on the principle and chemical design of gate electrode and the channel. First, the configuration, work principle, semiconductor of OECT are briefly introduced. Then different kinds of sensing modes are reviewed, especially for the biosensing and electrophysiological recording. Finally, the challenges and opportunities of this research field are discussed.

Keywords: organic electrochemical transistors, biosensing, electrochemical sensing, electrophysiology recording, conducting polymer

OPEN ACCESS

Edited by:
Huangxian Ju,
Nanjing University, China

Reviewed by:
Huawen Wu,
Lam Research, United States
Feng Gao,
Anhui Normal University, China

***Correspondence:**
Ping Yu
yuping@iccas.ac.cn
Junjie Fei
fei_junjie@xtu.edu.cn

Specialty section:
This article was submitted to Analytical Chemistry, a section of the journal Frontiers in Chemistry

Received: *06 December 2018*
Accepted: *18 April 2019*
Published: *07 May 2019*

Citation:
Bai L, Elósegui CG, Li W, Yu P, Fei J and Mao L (2019) Biological Applications of Organic Electrochemical Transistors: Electrochemical Biosensors and Electrophysiology Recording. Front. Chem. 7:313. doi: 10.3389/fchem.2019.00313

INTRODUCTION

Transistors were invented by William Shockley and his coagent in 1947 for the precluded amplification efficiency and reliability of vacuum tubes. With the discovery of conducting conjugated polymers in the late 1970s, organic conducting polymer-based transistors have been widely investigated. Among of them, organic thin-film transistors have attracted much attention due to their broad range of applications, especially in biological system, which includes two types of transistors, i.e., organic field effect transistors (OFETs) and organic electrochemical transistors (OECTs). OFETs always use small organic molecules and organic conjugated macromolecules as semiconductor, in which the gate voltage is applied across the gate insulator and through field effect doping the gate electrode modulate the channel current. Differently, OECTs use the electrolyte medium between the channel and the gate electrode rather an insulator layer. When applying gate voltages, electrochemical doping or de-doping from the electrolyte modulate the channel current. In this case, the OECTs is easier to be used in biological system since most of biological reaction or species are occurred in an electrolyte medium. More importantly, compared with other kinds of OFETs, OECTs always bear low working voltages (below 1 V), essentially evaluating its potential application in biological system.

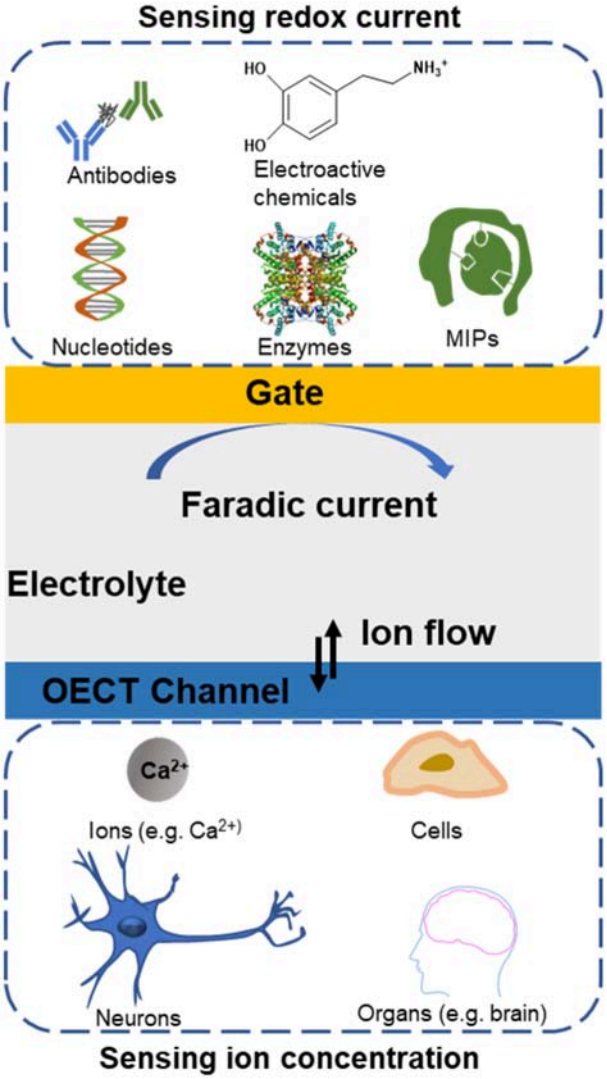

FIGURE 1 | Overview of biological systems applications based on organic electrochemical transistors.

Based on these unique properties of OECTs, various applications have been explored during the last two decades (**Figure 1**), including neural interfaces (Khodagholy et al., 2013a, 2015, 2016; Campana et al., 2014; Yan et al., 2015), chemical and biological sensors (Nakatsuka et al., 2018), printed circuits (Zakhidov et al., 2011; Kim et al., 2013; Lee et al., 2017), neuromorphic devices (Uguz et al., 2016; Gkoupidenis et al., 2017), and clinical or biomedical researches (Berggren and Richter-Dahlfors, 2007; Rivnay et al., 2013; Someya et al., 2016). In electrophysiological signals, OECTs are used both as the recording and stimulation devices (Williamson et al., 2015; Braendlein et al., 2017a). OECTs can also be applied to measure cell coverage (Lin et al., 2010), barrier tissue arrangement and cellular environment for non-electrogenic epithelial cells (Jimison et al., 2012; Yao et al., 2013; Ramuz et al., 2015; Romeo et al., 2015). Assessment protocols have been established, applying white noise at the gate (Rivnay et al., 2015b), showing that OECTs have better performance comparing with impedance sensing (Rivnay et al., 2015b,c). The ability to work in complicated environments, such as blood and milk, paves the way for multi-analyte assay in complex environments (Tria et al., 2014). As for OECT-based biosensors, the detection of metabolites in electrolytes or body fluid are valuable for early prediction of human disease (Zhu et al., 2004; Macaya et al., 2007; Bernards et al., 2008). OECTs were easily to be coupled with various fabrication techniques (ElMahmoudy et al., 2017), resulting in different formative factors with flexible and wearable applications (Fan et al., 2018; Yang et al., 2018). The characteristics of ultrahigh transconductance (Khodagholy et al., 2013b), stability in electrolytes (Lee et al., 2018), cytocompatibility (Inal et al., 2016), and biofunctional modification (Someya et al., 2016; Curto et al., 2017; Pappa et al., 2017) result in their specially appropriate for bioelectronics fabrication. OECTs can also be prepared by conducting polymers compatible with cellular platforms, offering the possibility to modulate the bio-chemical, mechanical, and electrochemical microenvironment of cells and cell health where cells behavior can be concurrently monitored.

Some of previous reviews have summarized the physics and principles of OECTs (Rivnay et al., 2018), and the applications of OECTs on the organic bioelectronics (Simon et al., 2016; Someya et al., 2016), neural monitoring (Yan et al., 2015; Rivnay et al., 2017), and other biological applications (Xenofon et al., 2015). In this review, we mainly emphasize on the recent progress of OECT-based biological applications. Firstly, we would briefly introduce the configuration of OECT, working principle and general conducting polymer for OCET. Then, the biological applications, including biosensors and cell electrophysiological recording, would be discussed in detail. In each part, we will critically demonstrate the working mechanism and evaluate the unique properties for OECTs that facilitate the application progress for special requirements. Finally, challenges and opportunities still exist toward the biofunctional OECTs and the forthcoming studies are envisioned.

BRIEF INTRODUCTION OF OECTS

Typical Configuration of OECTs

The OECTs were firstly built by White et al. (1984), in which they reported a device with a microelectrode array that can work as a transistor to amplify the tiny current when it was immersed in an electrolyte solution (**Figure 2A**). In this work, they for the first time separated the gate electrode and the semiconductor channel with electrolyte, so that both the gate and the channel interfaces can be functionally modified. It is worth to note that the gate electrode was controlled by a traditional three-electrode electrochemical system in White's configuration as shown in **Figure 2A** (White et al., 1984; Nishizawa et al., 1992). In this configuration, the counter and reference electrodes are the essential components and they, respectively, establish the current circuits and ensure the stability of the potential especially for the cyclic potential scanning. If the gate potentials kept at constant value, the gate electrodes could be simplified

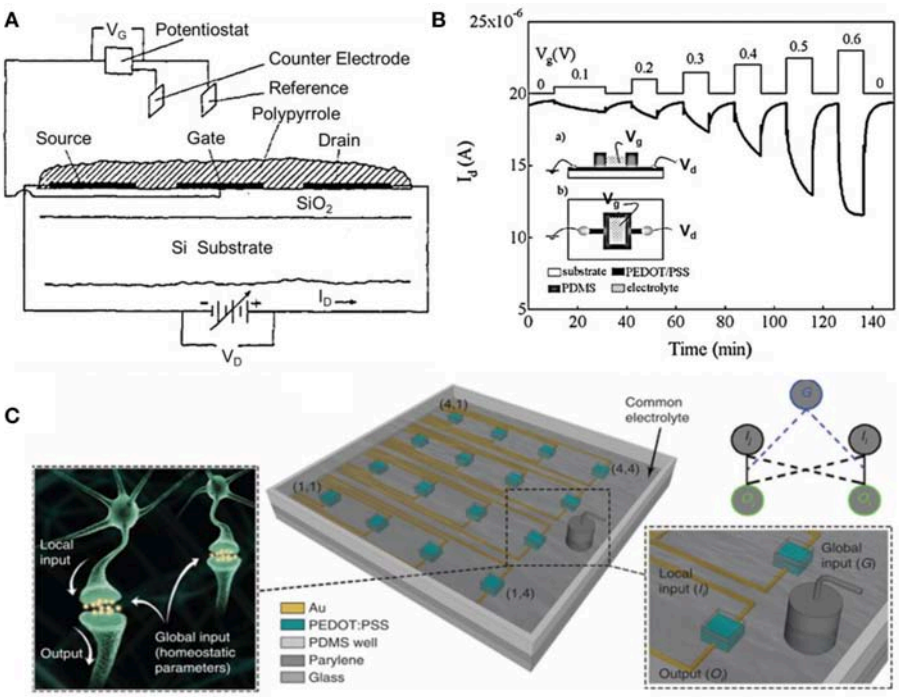

FIGURE 2 | (A) Cross-section view of the array of three gold microelectrodes with polypyrrole fabricated transistor (White et al., 1984). Reproduced with permission (White et al., 1984). Copyright© 1984 American Chemical Society. **(B)** Drain current-time response of PEDOT: PSS device. (Inset: the side view (a), and is top view (b) of the device) (Zhu et al., 2004). Reproduced with permission (Zhu et al., 2004). Copyright© 2004 The Royal Society of Chemistry. **(C)** Illustration of PEDOT: PSS array, neurons are immersed in the same electrolyte and the analogy diagram of the device grid (Gkoupidenis et al., 2017). Reproduced with permission (Gkoupidenis et al., 2017). Copyright© 2017 Nature Publishing Group.

into only one electrode because the voltage bias applied on the gate relative to the source electrode is constant, which would not influence the transfer or transconductance curve (Zhu et al., 2004). From then on, various devices based on the configuration of separated gate and channel with electrochemical and biological applications have sprung up. The most typical configuration of OECTs were constructed with one electrode (gate) immersing in the electrolyte and one channel connected by the semiconducting film with two metal electrodes (source and drain), the applied bias on the channel modulates holes or electrons moving in the semiconducting film (**Figure 2B**). In addition to the configuration of gate electrode, the development of the integration and printing technologies with OECTs enable large area computing and integration arrays of OECTs (van de Burgt et al., 2018) (**Figure 2C**).

Principle of OECTs

Bernards and Malliaras (2007) systematically demonstrated the steady-state and transient behavior of OECTs, which provided the initial view of the basic principle of OECTs. The principle was based on the ions in electrolyte transferred into the organic films, then its doping state and accordingly the conductivity of channel were changed. To operating the OECTs, the gate (gate voltage, V_G) and the drain (drain voltage, V_D) are controlled by applying constant voltages, which are referenced to the source electrode (**Figures 3A,B**). The potentials applied on gate electrode are related to the ions injecting into the channel and consequently controlling the doping state (i.e., redox state) of the conducting film. The drain current (I_D), reveals the channel's doping state, which is proportionable to the quantity of mobile holes or electrons in the channel.

To qualitatively describe the working principle of OECT, The Bernards et al. postulates that there are two circuits of the OECTs: an ionic circuit and an electronic circuit, which separately describe the ions flow in the gate/electrolyte/channel system and the charges flow in the source/channel/drain system according to Ohm's law (**Figure 3C**). In the ionic circuit, ions flowing in the electrolyte is regarded as a resistor, and the ions volume in the channel is treated as a capacitor; while the electronic circuit is seen as a resistor. This model provides a prototype of the OECTs working principle, but there are still many significant properties that need to be taken into consideration. In this case, the influences of more factors to the efficiency of OECTs are conducted, such as, the thickness of the channel (Rivnay et al., 2015a), the mixed ion-electron transport (Rivnay et al., 2016; D'Angelo et al., 2018; Berggren et al., 2019; Onorato and Luscombe, 2019), and the double-layer (Tybrandt et al., 2017) coupling of conjugated polymers (Fan et al., 2019).

In addition, the Bernards' model demonstrates that both the ionic and the electronic circuit limit the response time. On the other hand, the efficiency of transduction, from small voltage signals on the gate to large current signals in the channel, is

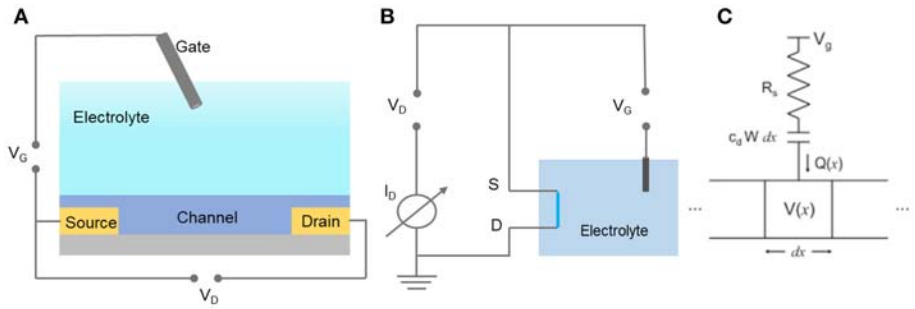

FIGURE 3 | The schematic configuration of OECT sensor **(A)** and it's equivalent circuit **(B)**. **(C)** The typical ionic and elctronic circuit (Bernards and Malliaras, 2007). Reproduced with permission (Bernards and Malliaras, 2007). Copyright© 2007 Wiley-VCH Verlag GmbH & Co. KGaA, Weinheim.

characterized with the first derivation of the transfer curve, called transconductance ($g_m = \partial I_D/\partial V_G$). High transconductance values reflects the effective gating but leads to the slow operation of OECTs (Khodagholy et al., 2013b; Rivnay et al., 2013). In general, OECTs with the liquid electrolyte have the response time about tens of microseconds, which is suitable for most biosensor and for electrophysiological recordings (Rivnay et al., 2015c; Onorato and Luscombe, 2019). While the OECT with gel or solid electrolytes as ion transportation matrix is slower than that in liquid electrolytes (Bongo et al., 2013; Yi et al., 2015), which is more appropriate for the applications where a rapid response is not necessary.

With respect to the effective gating, the geometry of OECTs sensor plays an essential role (Cicoira et al., 2010; Lee and Someya, 2019). The geometry of the OECT includes the area ratio of channel and gate, the thickness of channel, and the distance between the gate and channel electrodes. OECTs with different area ratios of channel and gate will result in the following properties: (1) OECTs with small gates have smaller background noise; (2) devices show better sensitivity with small gates; (3) $\Delta I/I_0$ always becomes unchangeable at the same substrate concentration but not depend on channel/gate area; (4) the channel/gate area ratio is irrelevant to the detection linear (Hütter et al., 2013). The redox reactions produced by redox enzymatic active molecules, such as H_2O_2, control the potential drop at the interface of metal electrolyte/channel and gate/electrolyte (Bernards et al., 2008). Therefore, if the gate area for sensing application was small, the potential drop would be mainly on the interface of gate/electrolyte. And the reactions on the gate can be effectively amplified through the nature of transistor, and vice versa (Bernards et al., 2008).

Conducting Polymers for OECTs

The channel for OECTs is always constructed by organic semiconducting polymers which always bears excellent redox activity. So far, several kinds of conjugated conducting polymers of p-type (polythiophenes, polyfluorene, donor-receptor copolymer, etc.) and n-type (commonly based on copolymers of thiophene and fluorene) has been used for constructing OECTs. Among of them, the PEDOT: PSS (**Figure 4A**) is most common polymer as the semiconducting channel of OECTs. The PEDOT is p-type doped (oxidation state), therefore holes can hop among chains, so that applied positive bias on drain will produce the hole current. The sulfonate anions of PSS are added to stabilize the oxidized polymer PEDOT, to compensate for the shortage of negative charges. The p-type conducting polymers based OECTs always perform the depletion modes (ON state at the zero gate-source bias). While the n-type polymers working in accumulation modes are lagged behind the p-type, they are significant for preparing PN-junction and logic circuits, which is crucial for neuromorphic computing and bioelectronic applications. Most recently, n-type copolymer p(gNDI-T2) and p(gNDI-gT2) (**Figure 4B**) have been developed for OECT fabrication in aqueous electrolyte (Giovannitti et al., 2016), and P-90 (**Figure 4C**) is applied to detect lactate (Pappa et al., 2018). In addition, organic small molecule materials, such as pentacene, rubrene, fullerene, octa hydroxyquinoline, was also used as the semiconductor channel. However, the conjugated polymers always possess long strip and conjugated π or p-π structure, which will facilitate the preparation and readily built the thin film with low condition requirements. Therefore, the conjugated polymers are superior to organic small molecules not only for the excellent ability to conduct carriers (holes and electrons), but also their low-cost property and accessible fabrication (Flagg et al., 2019).

The particular identification of OECTs is the doping reactions appear among the whole volume of the organic film, which is different from FETs occur on a thin interfacial region. Therefore, low-gate voltages can achieve large modulations in the drain current, herein, OECTs are effective switches, and powerful amplifiers. In addition, compared with the solid dielectric layers, the electrolyte solutions are more applicable for larger flexible devices and various substrates' integration (Volkov et al., 2017; Fidanovski and Mawad, 2019). Moreover the intrinsic quality of the tunable organic molecules will further optimize the transport of ions and electrons and simplify the bio-interfaces (Giovannitti et al., 2016; Inal et al., 2016; Pappa et al., 2018; Sun et al., 2018). All these unique properties of OECTs essentially guaranty its wide applications in biological systems as demonstrated below.

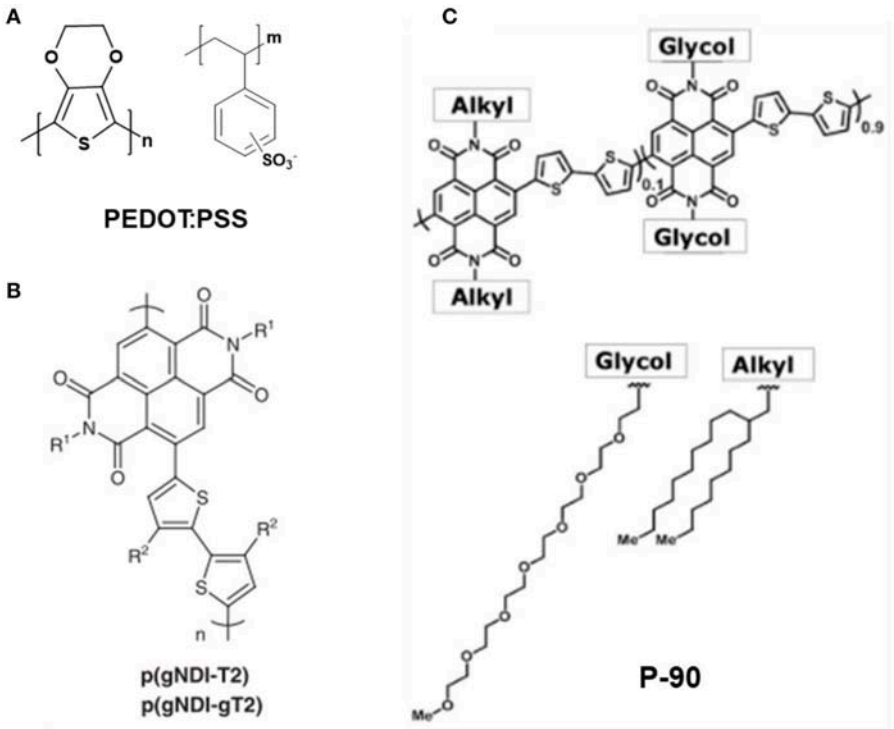

FIGURE 4 | Chemical structure of typical conducting polymer: **(A)** PEDOT: PSS. **(B)** p(gNDI-T2) and p(gNDI-gT2) (Giovannitti et al., 2016). Reproduced with permission (Giovannitti et al., 2016). Copyright© 2016 Nature Publishing Group. **(C)** P-90 (Pappa et al., 2018). Reproduced with permission (Pappa et al., 2018). Copyright© 2018 American Association for the Advancement of Science.

BIOLOGICAL APPLICATIONS OF OECTS

Biological Sensing

In this section, we mainly introduced the operating mechanisms and reviewed recent applications of the OECT-based biological sensors. For electrochemical sensors, biomolecules in biological system could be classified into electroactive and electro-inactive species (Wu et al., 2017). The electroactive molecules (e.g., norepinephrine (NE), dopamine (DA), serotonin (5-HT), histamine, ascorbic acid (AA), uric acid (UA), CO, NO, H_2S, etc.) can be directly oxidized or reduced on the electrode. While the electro-inactive molecules (e.g., glucose, glutamate, lactate, ATP, small molecule proteins, nucleic acid) can be detected by electrochemical technique through bio-recognition methods. Guided by changes of the potential drop on the gate and channel, the biosensors can generally be subdivided into the enzymatic sensing, immune-sensing, and aptamer sensing (Gentili et al., 2018). Other kinds of OECT-based sensors utilizing the changes of doping state of the conducting polymer altered by the factors, such as ions concentration and pH, are essential to advocate the progress of OECTs biological sensing (Qing et al., 2019).

The electroactive chemicals (e.g., DA, E, NE, 5-HT) in biological system, can be directly oxidized or reduced on the electrodes. For example, DA can be oxidized to o-Dopamine quinone (**Figures 5A,B**) at a certain voltage. The OECTs as a kind of transistors possesses the characteristics of amplifying in-put signals, while coupling with the nanomaterials technology, the OECT-based sensors will result in significant sensitivity improvement (Liao et al., 2014; Mak et al., 2015). In this case, the construction of the high-performance gate electrode is crucial for high-sensitive sensing. Tang et al. (2011) built a dopamine OECT sensor by comparing five kinds of gate electrodes (including graphite, Au and Pt electrode, etc), and found that the Pt gate bears the highest sensitivity as to detect 5 nM DA at the potential of 0.6 V. The synergistic effect of gate and channel for redox signals transduction will further increase the sensitivity. Gualandi et al. built an all-PEDOT: PSS OECT to sensing AA (Gualandi et al., 2015), in which by modulating the V_G and film thickness, the detection limit can be reach to 10^{-8} M level.

Selectivity is another important parameter for OECT-based sensors, especially for complicated samples. Gualandi et al. (2016) constructed an all-PEDOT: PSS-based OECT, which got the separated transconductance (g_m) linear calibration of DA without the interference from AA and UA, through changing the scan rates and gate voltages, in which case, the scan rate is an essential property for sensitivity. Classic electrochemical methods cooperate with OECT will promote the development of biosensing: fast scan cyclic voltammetry (FSCV) is widely used to detect electroactive chemicals, especially DA in neuro system, (Tybrandt et al., 2014)

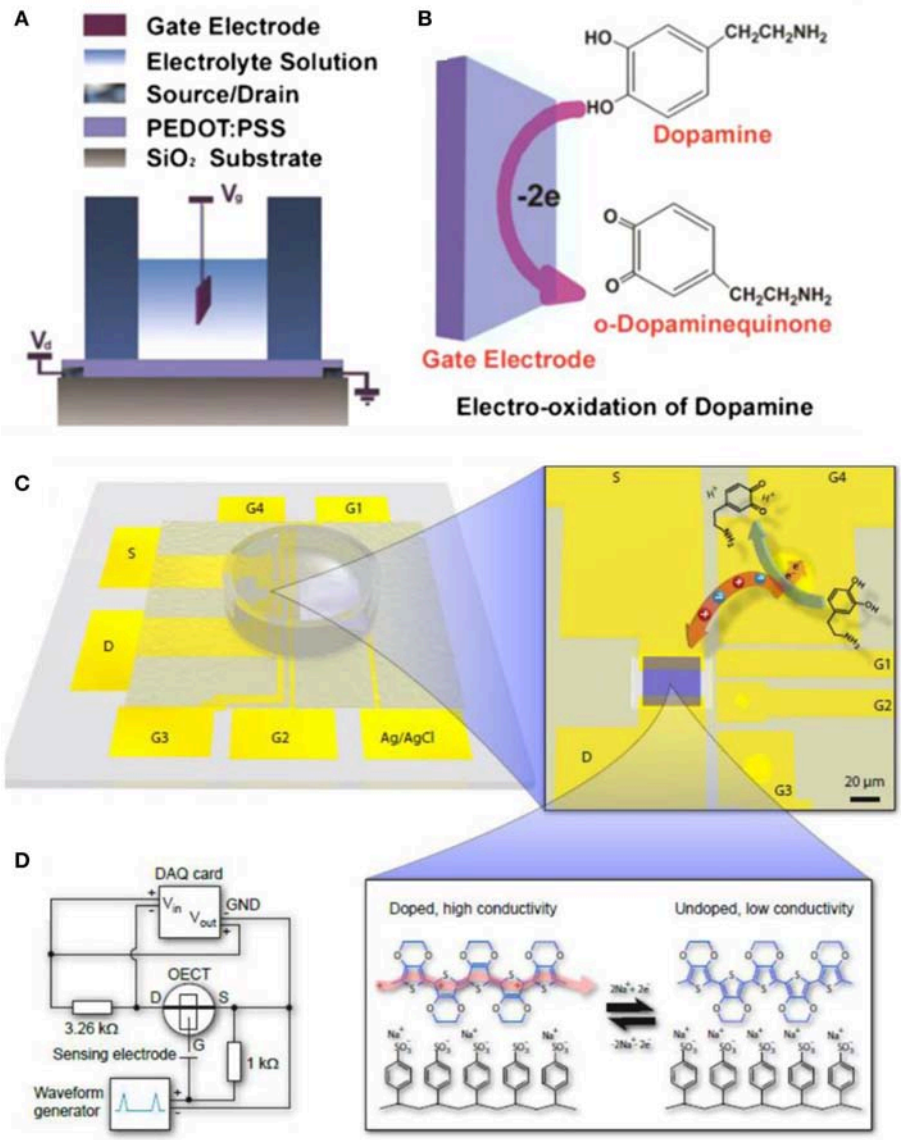

FIGURE 5 | (A) Illustration of OECT-based dopamine biosensor that PEDOT: PSS act as the conducting channel. **(B)** The oxidization of dopamine on the surface of the gate electrode (Tang et al., 2011). **(A,B)** reproduced with permission (Tang et al., 2011). Copyright© 2011 Elsevier B.V. All rights reserved. **(C)** The OECT device and gate electrodes built by patterned gold. And the illustration of dopamine oxidized on the Au gate shifting the doping state of the PEDOT: PSS channel **(D)** Experimental device circuit used for the OECT-amplified FSCV (Tybrandt et al., 2014). **(C,D)** reproduced with permission (Tybrandt et al., 2014). Copyright© 2014 Elsevier.

combined the FSCV technology and OECT (**Figures 5C,D**) successfully amplified the small detected signals under no shielding environment. This integration paves the way for multifunctional bioelectronics applying in various devices (Sivakumarasamy et al., 2018).

OECTs Based Enzymatic Biosensors

The most widely used OECTs biosensors are coupled with enzymes. The first application of the OECTs interfacing with enzymes was based on the device model developed by Nishizawa et al. (1992). They detected the conductivity of the polypyrrole channel on account of the film's responsiveness to pH induced by the penicillinase enzyme reaction. However, the polypyrrole film is pH-dependent and the linearity range is limited by the thickness of polymers, losing the regulating ability in neural pH environments. Zhu et al. (2004) illustrated a PEDOT: PSS-based transistor for glucose sensing in neutral pH electrolytes. Since PEDOT: PSS is stable in a wide pH range, it is applicable in the enzymatic sensing under neutral environment. Moreover, the bias potentials between gate and channel are small so there exists no hydrolysis of electrolyte, and the known initial properties of the transistor are enough

to meet the need for detecting several analytes, from then on, PEDOT: PSS plays an important role in the OECTs enzymic sensors.

The sensing mechanism of the typical enzymatic OECTs sensors is shown in (**Figures 6A,B**): Enzymes are immobilized on the gate electrode and catalyze the substrates into enzymatic product, through which they obtain or lose electrons on the electrode, the electrical signals are transferred to the gate electrode and further leading to channel current changes simultaneously. To maintain the charge neutrality in the whole circuit, including the ionic circuit and electronic circuit, a cation penetrates into the conducting polymer film and replaces the

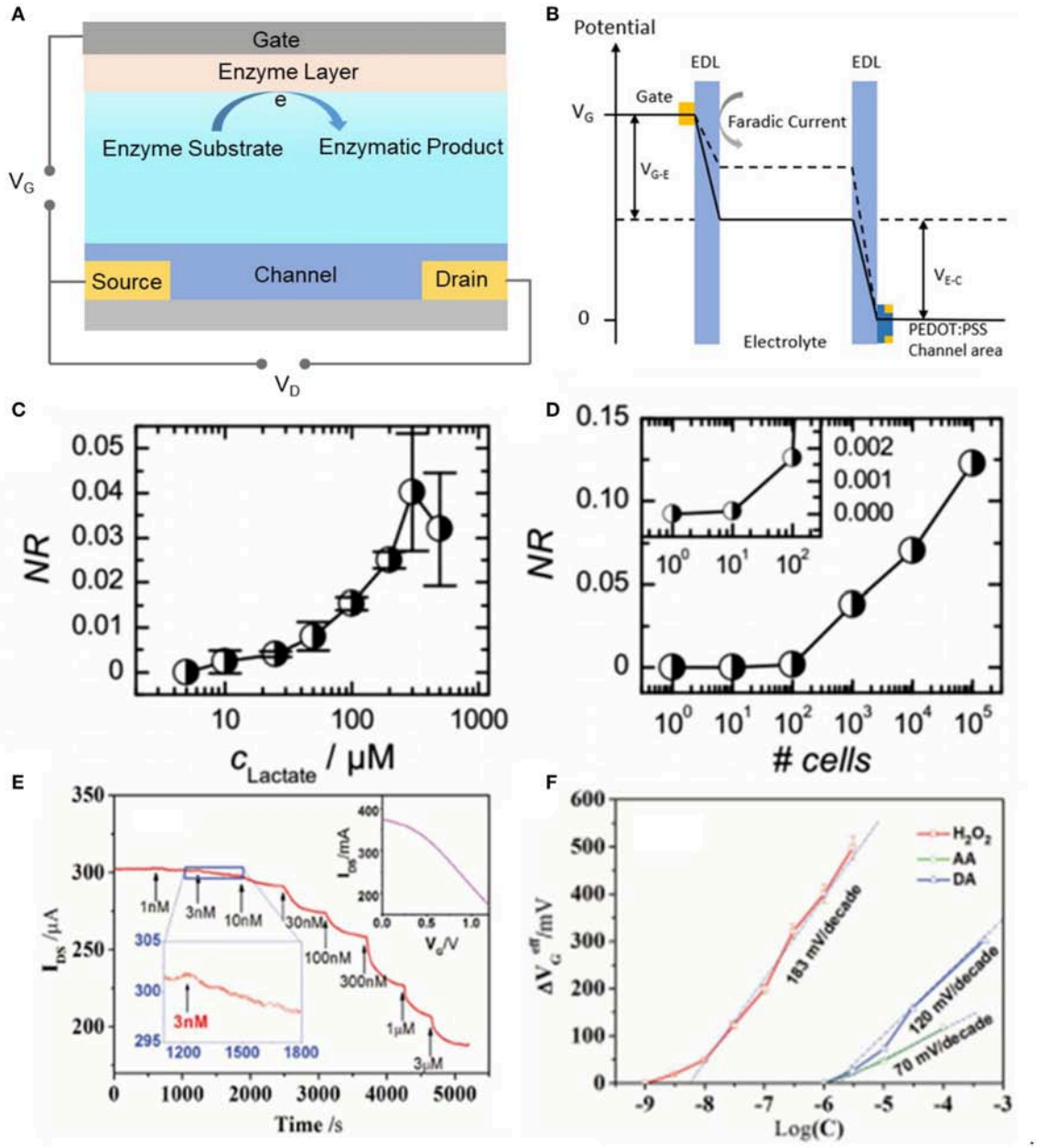

FIGURE 6 | Schematic working principle of an enzyme modified OECT sensor of **(A)** the reaction on the enzymatic gate electrode and **(B)** typical potential drop between the channel and gate with the addition of substrate. Characteristics of the sensitivity **(C)** of lactate sensor of three devices [NR (normalized response) = $\Delta V_{out}/\Delta V_{out,max}$] and **(D)** titration curve of one selected device with consecutive addition of substrate collected from cells culture of different concentrations (Braendlein et al., 2017b). Reproduced with permission (Braendlein et al., 2017b). Copyright© 2017 WILEY-VCH Verlag GmbH & Co. KGaA, Weinheim. **(E)** Titration curve of an OECT modified with PANI/Nafion-graphene/Pt as gate electrode to the additions of H_2O_2. Inset: transfer curve of the device (Liao et al., 2015). **(F)** The effective gate voltage (ΔV_G^{eff}) vs. different concentrations of H_2O_2, AA, and DA (Liao et al., 2015). Reproduced with permission (Liao et al., 2015). Copyright© 2014 WILEY-VCH Verlag GmbH & Co. KGaA, Weinheim.

role of the cationic polymer (e.g., $PEDOT^+$) compensating the anionic polymer (e.g., PSS^-), which leads to a change of the V_g ^{eff}, then a decrease of the channel current which is logarithmically proportional to concentration of enzymatic substrates.

The sensitivity of OECTs devices, lies on the nature of amplification provided by the optimized geometry and the sensitive enzymatic modification. After optimization using new materials and different modification technology, the detection levels of bioactive molecules can be promoted to a large extent. Apart from the mostly used p-type conjugated polymer, Pappa et al. (2016) demonstrated a new kind of OECTs enzymatic sensor by using an n-type conducting polymer in accumulation mode. The n-type conjugated polymer is based on the NDI-T2 polymer (also called P-90). The side glycol chains ensure the solubility of the polymer in an electrolyte and enable the enzymes anchored on the polymer and strengthen polymer's water absorbability. By modifying LOx on both channel and gate, the detection concentration of lactate can low to 10 μM, while still can't overmatch with nM level of PEDOT: PSS modified OECTs.

In addition to the high sensitivity, selectivity is another key role for the biological sensors. So far, there are several methods to improve the selectivity by rationally designing the surface chemistry of gate electrode (e.g., modifying special materials and/or modulating the interaction of ions (Yu et al., 2015). Liao et al.(**Figures 6E,F**) (Liao et al., 2015), reported a highly selective OECTs-based enzyme sensors. By modifying a bilayer film on the gate electrode, the interference of charged molecules coexisting in the solution with the analytes effectively decreased. The high selectivity of the device in this work is accomplished by firstly covering a thin layer of the compound graphene flakes and Nafion, then a thin layer of polyaniline (PANI) polymer on the gate electrode. The graphene flakes in the film are used to enhance the electrochemical catalytic performance and the conductance of gate electrode, the PANI film carrying positive charge can repel the positively charged bioactive molecules as NE, and Nafion film that is negatively charged can hinder the anionic electroactive molecules like AA and UA.

The outstanding performance of the biosensors compromise the reaction both on the gate and the channel, thus they have equivalent ability to tune the potential drop on the electrode-electrolyte interfaces, receiving the amplified signal. Wang's group (Wang et al., 2017), successfully built an OECTs glucose biosensor based on a novel woven fiber composed of polypyrrole (PPy) nanowires and reduced graphene oxide (rGO). They reported that the addition of rGO nanosheets will enhance the electronic performance of the fiber electrodes. The composites-based transistors exhibit high switch capability, fast switch speed, and long durability under electrical experiments. The transistor exhibits remarkably sensitivity for glucose sensing, the NCR/decade can be reach to 0.773. Besides, the sensors show the fast response time (i.e.g,0.5 s), good reversibility, wide linear range of glucose concentration and a lower detection limit compared with conventional methods.

Moreover, the OECTs can be used for multianalyte detections by combination with the array techniques. Pappa et al. (2016), developed a multianalyte biosensing platform using the OECTs array. The device is able to sense three typical clinically related molecules, such as glucose, lactate, and cholesterol by immobilizing relative glucose oxidase (GOx), lactate oxidase (LOx), and cholesterol oxidase (ChOx) on the PEDOT: PSS coated gate electrodes, without the electrical and chemical cross-talk over different transistors. This biosensor could be used for real sample analysis in saliva. Braendlein et al. (2017b), introduced a reference-based sensor circuit, through compromising two OECTs functionally differently, used the popular p-type semiconductor PEDOT: PSS, toward a Wheatstone bridge design. One of the two OECTs is used as the reference (immobilized with BSA) and the other is functionalized (immobilized with lactate oxidase) as the indicator. The sensor shows a low limit of detection generated by cells, estimated to be $\approx 10 \times 10^{-6}$ M, and the reference lactate concentration of fresh cells is assessed to be 50×10^{-6} M (**Figures 6C,D**). Such a circuit was firstly applied to clinically relevant testing and significantly help to accurately diagnose preliminary tumor treatment.

Disposability and stability are another key performance for the biosensors, which are benefit from the application of multifunctional materials and simple configuration techniques. Shim et al. (2009), demonstrated an all-PEDOT: PSS OECT-based glucose biosensor by introducing the mediator (e.g., ferrocene) to transfer generated electrons of redox reactions to the gate. This facile fabrication of OECT-based enzymatic biosensors realizes the character of low-cost. Khodagholy et al. (2012), incorporating ionic liquids and conjugated polymers, constructed an OECTs-based lactate biosensor by solid state gel, which contains: lactate oxidase and the mediator ferrocene for shuttling the electron transfer. This type of device is a promising wearable sensor for continuously monitoring lactate levels in athletes. Bihar et al. (2016), built an OECT-breathalyzer, with the conducting polymer PEDOT: PSS printed on paper, and the enzymatic reaction occurred in the electrolyte gel. This device is easy to use for the low-cost and disposable portable sensors to facilitate blood alcohol content sensing.

OECTs Immunosensors

Immunoassay is crucial in clinical analysis (cancer cells, biomarkers, pharmaceuticals), toxins, and microbials in the environments (Wen et al., 2017). Antibodies of the immune system are regarded as the biorecognition element, and lead to the high specificity and sensitivity of the immunosensors. As to the immune sensing, the competitive and sandwich types are widely accepted. For competition reactions, the immobilized biorecognition molecule can be either an antibody or an antigen. The sandwich-type immunosensor consists of a fundamental antibody fixed on the platform of a sensor, and the specific antigen marker in a sample solution, the secondary antibody reacts with the antigen bound, then the detectable and low noise signal are generated via enzymes (Zhang and Heller, 2005; Yu et al., 2006), redox substrates (Viswanathan et al., 2009), or nanomaterials (Liu and Lin, 2007; Kerman et al., 2008). Based on this principle, Kim et al. (2010) demonstrated an immunosensor based on OECT to sense prostate specific antigen (PSA), through conjugating AuNPs with PSA specific

antibody on the conducting channel. The limit of detection was low to 1 pg/mL compared with the maximum detection value of 4 ng/mL. Torsi's group has developed various OECT-based immunosensors transistors. In their recent study, they developed the anti-human Immunoglobulin G (anti-IgG) sensor at the detecting limit of femto-molar (Macchia et al., 2017). The anti-IgG OECT sensors have the ability to detect IgG with high biomolecular interaction in the femtomolar (fM) range by immobilizing the anti-IgG on the gold gate. They also showed a plastic OECT sensor (Macchia et al., 2018) by the gate modification, which possess the low-cost, ultra-sensitive properties, and further paves the way for application of immunoassay technology. Fu et al. (2017) have successfully applied OECTs to the sensing of protein by detecting protein cancer biomarkers in cells. The gate is modified with antibodies and catalytic nanoprobes so that the gate electrode can capture the target and output the current response for the product of catalytic reaction (i.e., electroactive H_2O_2). For the amplification nature of organic electrochemical transistors, the biosensor that detect the cancer marker HER2 has the detection limit low to 10^{-14}g mL^{-1}, which is several magnitudes lower than original electrochemical methods. Moreover, the OECTs based HER2 biosensors have a detecting concentration range from 10^{-14} to 10^{-7}g ml^{-1}, which covers the detect amount of HER2 in normal and breast cancer cells. Additionally, these protein sensors can distinguish the cancer cells from the breast cancer cells attribute to the specificity of the modified antibody.

OECTs Aptamer Sensors

Aptamer-based technology bearing the high specificity or even superior to antibodies, that has the potential for applications of diagnostics and therapy. DNA sensor based on OECT has been fabricated by Lin et al. (2011), they integrated the OECT with a flexible microfluidic device. The label-free DNA sensor was fabricated with single stranded DNA which was immobilized on the gate as the DNA probe to detect the complementary DNA targets, and the detection limit was 1 nM. More importantly, the detection limit could be extended to 10 pM if an electric pulse was applied to the gate to increase the hybridization of DNA. The modulation mechanism is the changes of surface charge on the gate electrode generated by hybridizing DNA. They hypothesized that the thickness of the electrolyte double layer is much thicker than the DNA layer, therefore, the potential of gate is not affected by the concentration of ions in the electrolyte. Peng et al. (2018) have built an OECT sensor for detecting microRNA21 by using the Au NPs and capturing probe protein to modify gate electrode. The amplification effect of OECTs and the immobilized Au NPs, leading to the high sensitivity, selectivity, and acceptable applicability of microRNA21 assay in total RNA sample, which provides potential application in the future microRNA analysis.

OECTs Coupled With Artificial Receptors

Artificial receptors possess comparatively higher chemical stability than natural receptors under physical environments, consequently they provide possible alternatives on widespread biological applications (Labib et al., 2016). Very recently, molecularly imprinted polymers (MIPs) shows great potential for the development of biotechnology, diagnostics, and stretchable devices. Parlak et al. developed an artificial receptor based wearable OECT device by preparing the molecularly selective membrane for cortisol detection (Parlak et al., 2018). The artificial receptors can overcome the instability of natural biomolecules, such as enzymes and antibodies. The biomimetic membrane based OECT was configured with wearable substrates and sample reservoirs, this device can readily get the stable signals reading-out by collecting enough sweat about 10 to 50 μL. The MIP were entrapped into a plasticized poly (vinyl chloride) (PVC), which acts as an ionic barrier to decrease the g_m but

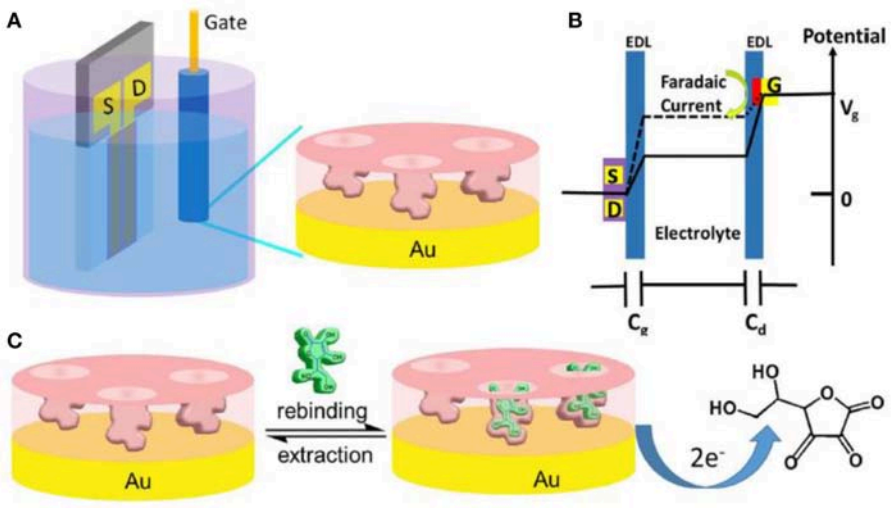

FIGURE 7 | (A) Schematic diagram of an AA sensor based on the MIP modified OECT. **(B)** Potential drop between the channel and gate of the OECT. **(C)** Schematic for the sensing of AA by MIP film modified gate (Zhang et al., 2018). Reproduced with permission (Zhang et al., 2018). Copyright© 2017 Elsevier B.V. All rights reserved.

still maintain the efficient OECT capability. And the device was applied *in vitro* and on body to conduct the cortisol changes by measuring electrochemical performance. It's meaningful that the device was used in exercising human to detect the cortisol concentration. Zhang et al. (2018) combined the molecularly imprinted polymers (MIP) with OECT-based sensor to detect ascorbic acid (AA) (**Figure 7**). The selectivity of the MIP films on the gate was conducted by the preparation of the polymer with AA removal and rebinding on the surface, then the polymer film acted as the recognition unit of the sensor. They found various species, such as H_2O_2, Gly, GSH, UA, Glu, Na^+, K^+, Fe^{2+}, Mg^{2+}, Ca^{2+}, and ASP, that has almost no interferences for AA detection. The sensors could be used for the AA analysis of vitamin C beverages.

OECTs Ion Sensing

The OECTs can be used for ion detection due to the ions transfer freely in the whole bulk of electrolyte, which includes not only aqueous solution but also other ionic and electronic media, such as gel and ionic liquid (Duc et al., 2017; Dai et al., 2018). Recently, Gentili et al. (2018) demonstrated a new principle of current-driven inverter-like, low-voltage, high-sensitivity ion detection OECT. Differently with the voltage-driven OECTs, the current-driven OECT configuration provides, low-voltage operation and high sensitivity, where the sensitivity depends on the large g_m and load resistor. However, the applied voltage should consistent with the physiological environment. So that the trade-off among sensitivity, operating range, and applied voltage are needed. The current-driven OECT configuration is based on the recording of the changing voltage generated by the ions concentration, differentiating it from the usual ion sensors where the changing of ion concentration transferred as the output voltage. Consequently, the current-driven OECT study take advantage of the large g_m of OECTs in an absolutely different way in relative to regular voltage amplifier structures, which introduce a new kind of trade-off between sensitivity and working voltage. While (Del Agua et al., 2018) introduced a PEG-based Na^+ conducting hydrogel as OECT electrolyte. The hydrogel is prepared by fast photopolymerization with commercial monomer. And the hydrogel has high ionic conductivity and can be contained during the fabrication of photolithography device. With the high performances at room temperature, this hydrogel has the possibility to replace liquid electrolytes in versatile OECTs and accomplish print integrated into flexible OECT devices.

OECTs Cell Monitoring

The coupling of OECTs with live mammalian cells for monitoring toxicology/diagnostics and other properties was developed in the past decade. Bolin et al. (2009) firstly coupled the OECTs with cells and detected the gradients of cells on the OECT channel. They seeded Madin Darby canine kidney (MDCK) epithelial cells on an OECT channel and the channel bias added and produced a potential gradient. The gate potential controls and modulates the potential gradient of channel. Therefore, the MDCK cell quantity gradient on the channel depended on the gate and source voltages. Lin et al. (2010) reported sensors based on OECTs combined with cancer cells and fibroblasts for sensing *in-vitro* cell activities. The sensing principle is the electrostatic actions on the interfaces of the cells and the OECT reactive layer. Since the device is sensitive to the surface charge changes induced by the adhesion of cells, it's applicable for solution processing to miniature and integrate cell-based sensors can further promote the cell relevant testing, such as screening drugs and testing toxic

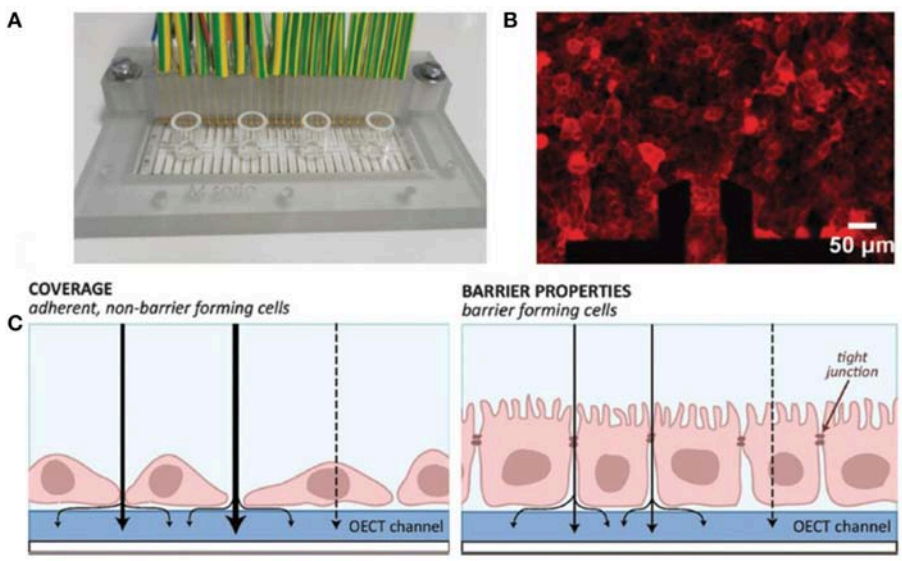

FIGURE 8 | The OECT device for monitoring adherent cells. **(A)** Measurement platform consisting of 24 OECTs divided between four glass wells. **(B)** MDCK II cells transfected with RFP actin construct seeded on device for fluorescence imaging. **(C)** Schematic diagram of the cell coverage with low ion flow through barrier (right) or high ion flow through non-barrier (left) (Ramuz et al., 2015). Reproduced with permission (Ramuz et al., 2015). Copyright© 2015 The Royal Society of Chemistry.

substances. The potential can predict the adhesion of cell and formation of epithelium (Gu et al., 2019). Ramuz et al. (2015) found that barrier tissue cells adhered on the polymer surface can be deprived of function in calcium switch assay, and re-addition of calcium lead to improvement of the cells function. The process is monitored both electronically and optically, enabling the capture of cells images while simultaneously recording electronic information (**Figure 8**).

Wei et al. (2017) presented the first report to apply OECTs for detecting the microalgae H. pluvialis cell. The constructed OECT array is a platform with advantages of convenience, and efficiency, and is able to monitor the real-time signals induced by settling H. pluvialis cells on the active conducting polymers. The results can help to estimate the time point approximately for producing the maximum astaxanthin in the commercial fermentation. Rivnay et al. (2015c), combined OECT with the impedance sensing technique by applying gate current to generate complicate low error impedance signals. They applied the method *in vitro* to sense a layer of epithelial tissue and concluded that the data is suitable to an equivalent circuit, allowing the resistance of trans-epithelial, and capacitance values of cell layer in accordance with literatures. Very recently, Chen et al. (2018) reported sensitive glycan sensors based on OECTs to detect the glycan on cells surface. PEDOT: PSS as the channel and the concanavalin A (Con A) loaded by poly dimethyl diallyl ammonium chloride (PDDA)–multiwall carbon nanotube (MWCNTs) modified the gate, which can correctly connect mannose by capturing the cancer cell. Specialized mannose nanoprobes are equipped by binding horseradish peroxidase (HRP) and aptamers on gold nanoparticles, then HRP-aptamer-Au NPs can be used to identify the human-breast cancer (MCF-7) cells, the prepared OECT-based glycan sensor leverage the electrochemical reaction on the gate electrode with the mannose on surface of captured cells. The HRP-catalyzed reduction to MCF-7 cells on the gate induced channel current responses, which generated H_2O_2 even when the cell concentration is low to 10 cells μL^{-1}. To prove the specific recognition reaction, they added N-glycan inhibitor stimulation and the signal is dramatically decreased for the decrease of mannose on cells. Furthermore, the as-formed device can be applied to analyze other glycans and cancer cells by simply altering the binding lectins and aptamer sequences. This strategy paves the way for various glycans analysis on a cell surface.

Neural Recording and Stimulation With OECTs

Recording electric signals of brain has been the most important but tough challenge in the past few decades since many kinds of diseases are strongly related to the change of signals between neurons. With the flourishing of semiconducting polymers and electrochemical transistors in the recent years, neural recording and stimulation get more opportunities to detect more precisely and applicable for more complicated *in vivo* sensing. This section focuses on the recent progress on the neural recording and stimulation based on OECTs, mainly including the development history, working mechanisms, and recent applications, and illustrate the enhanced performance for the multifunctional transistors.

Brief Introduction

In the brain, information transfer is achieved by the adjoining neurons generating bioelectrical signals, named action potential, propagating over the synapses. In the last decade, electric recording and stimulation based on metal electrodes have extremely conductive to our fundamental cognizing of real neural activities (Gilletti and Muthuswamy, 2006; Rivnay et al., 2017; Xiao et al., 2017). Conventional small metal or carbon-based microelectrodes are able to probe and stimulate neural activities with high resolution at the level of single-cell (Jasper et al., 1961). The metal microelectrode arrays can record the activities of a large population of neurons at the same time (Lee et al., 2017). Nowadays, implanting stimulating electrodes into the brain is progressively applied to deal with neurological disorders (Leleux et al., 2014; Lee et al., 2018). To compensate for available methods, the bioelectronics can be implanted into deep brain and conduct high temporal resolution, capable of directly communicating with the neuro net through electronics, and transduce neuron's electronic signals from bioelectronic signals (Jonsson et al., 2015). However, transformation presently challenged by the matching ability and electrons transfer on neural interfaces. For that metals transmit electrons signals while neural systems transmit ionic signals, the signal-to-noise signals (SNR) recorded and stimulated by bioelectronics are almost depended on the coupling transmission of electrons and ions on the metal/neural interfaces. Generally used metal electrode arrays are made of hard materials, such as gold, with their elastic module distinctly exceed the neural tissue in the range of kPa to MPa (Gilletti and Muthuswamy, 2006). The implanted electrodes in the neural tissues will cause inflammatory response results from the mechanical incompatibility, which will eventually result in electrode failure in long-term studies. In order to obtain favorable neuron/electrode interfaces, novel materials, organic conducting polymers-based bioelectronics, has exhibit strengthen neural recording and stimulation characteristics along with their merits of biocompatibility and low mechanical strength.

Mechanisms

The mechanisms of neural recording by metal electrodes or transistors is explained hereunder: the active potential of a neuron, contributes to ionic currents flux over the cell membrane, which changes the cell membrane potential, then the potential results in an electrochemical signal on the interface of metal/electrolyte or changes potential-drop of the conducting polymer. While in the brain, an enormous neural network system, the total neural electric currents generated from numerous neurons in a small bulk at a specified area will generate local field potential (LFP). This LFP called the electrocorticography (ECoG) when using the electrode on the cortical surface, and when recording with the electrode inserted deep into the brain called stereoelectroencephalography (SEEG). The longer

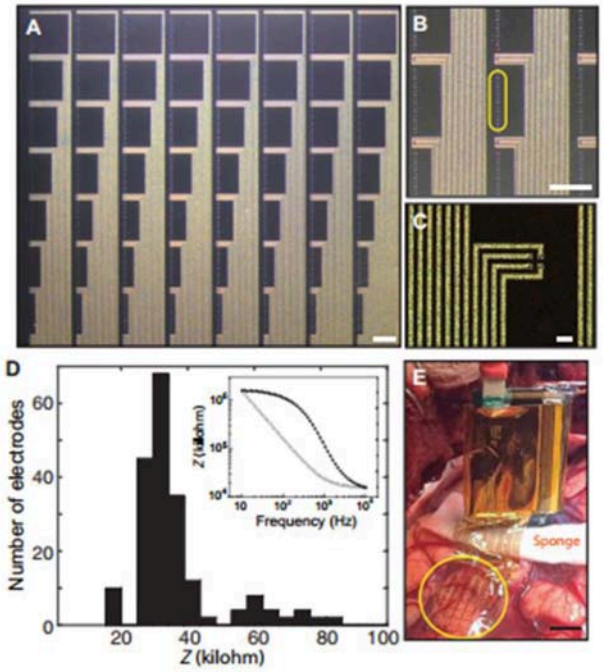

FIGURE 9 | Device structure and characterization of NeuroGrid for intraoperative recording. **(A)** Photo of NeuroGrid (240 channel, scale bar, 1 mm). **(B)** Amplified picture of electrodes arranged in 2 × 2 tetrodes (2 mm spacing between each tetrode, scale bar, 1 mm). **(C)** Structure of electrodes coated by conducting polymer involving a single tetrode (scale bar, 20 mm). **(D)** Histogram displaying impedance of a single NeuroGrid: yield = 87.5% (240 electrodes involved). Inset: electrochemical impedance phase and magnitude of a single electrode at the level of physiological frequencies. **(E)** Photograph of intraoperation by putting NeuroGrid (240-channel, yellow circle, scale bar, 1 cm) on the surface of the cortex (Khodagholy et al., 2016). Copyright© 2016 American Association for the Advancement of Science.

distance between the recording electrode and the location leads to useless signals for understanding the processes of neuropathology, hence the SEEG conduct the most informative signals. Conducting polymer-based electrode has extensively enhanced the electrical performances and biocompatibility of mental inserted intracortical electrodes. However, compared with the SEEG, the ECoG is non-invasive, the characteristics of ECoG have been significantly improved by using more stable polymers and rational building of devices (Khodagholy et al., 2016) (**Figure 9**).

As for the neural stimulation, charges flow from electrodes to neurons, and the charge injection ability on the electrode/neural interfaces is regarded as the parameters to be measured (Lee and Someya, 2019). The neural stimulation generated charges have the quantity that many orders of magnitude higher than the electrodes recorded signals, which mostly because of the meaningless coupling on the electrode/neuron interface. The ideal stimulation electrodes would be small enough to selectively put on the target. However, the small electrode requires high potential which leads to undesirable reactions and confuses the recording signals. Therefore, organic conducting polymers advanced the neural recording and stimulation, promoted OECTs application in the field of neural recording (Green et al., 2013).

Recent Advances

Implantable ECoG electrodes with flexibility and biocompatibility are of great importance in conforming stable neural interfaces (Campana et al., 2014). Green et al. (2013) examined the long-term stability and injecting limit of PEDOT-coated Pt electrode arrays stimulated under

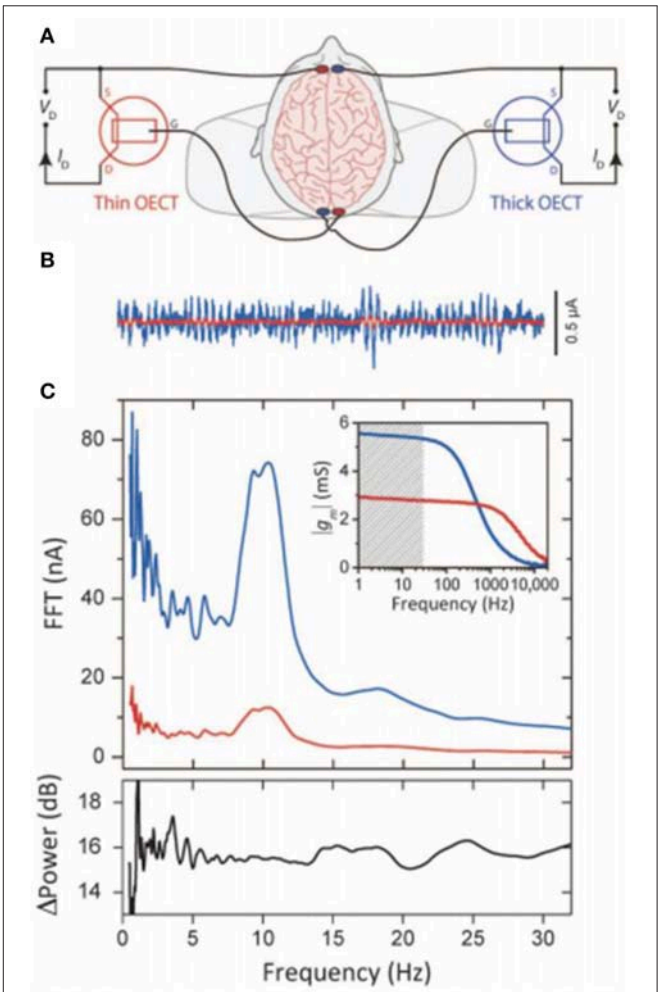

FIGURE 10 | High-transconductance OECTs enhanced EEG recordings. **(A)** Schematic wiring of simultaneously recording human EEG signals by two OECTs. **(B)** The rhythm from a thin (red) and thick (blue) 6-s recordings of OECT. **(C)** Top: fast Fourier transform (FFT) of simultaneous 60 s EEG recordings (inset: response of transconductance frequency, shaded band is the EEG-relevant frequencies). Bottom: the power enhancement recording from the thick compared to the thin device, showing the richer spectral content below the α band and using the thick device leading to the enhanced low-frequency signal (Rivnay et al., 2015a). Reproduced with permission (Rivnay et al., 2015a). Copyright© 2015 American Association for the Advancement of Science.

biological electrolytes. The PEDOT-coated Pt electrodes have the charge injection limit of 30 times larger in physiological relevant media and 20 times larger in protein supplemented media compared with bare Pt electrodes. Additionally, the PEDOT-coated electrode that has lower potential excursion can read out signals in the visual cortex in *in-vivo* studies and electrically stimulated potentials. Concerning the continual stimulation, the PEDOT electrodes perform high duration and amplification. The high frequency pulsing of 2,000 Hz stimulation rate, didn't induce loss in stimulation performance, so that the electrodes could be applied to evoke the neural response of injected charge at the average of 76.0 nC (67.0 $\mu C\ cm^{-2}$), which has no obviously difference with the Pt electrodes, with the average threshold response of 84.5 nC (74.5 $\mu C\ cm^{-2}$). Tunable channel thickness can result in tunable transconductance (Rivnay et al., 2015a), which relatively demonstrate a novel high-performance method for human brain rhythms using the organic transistors (**Figure 10**).

Information transfer within the brain occurs in the network where neurons are associated with each other by enormous synapses and immersed in the same physiological environments (George et al., 2019). The electrolyte builds complex connections between different synapses, and the global regulations would induce the overall behavior of a large neuro population (Bettinger, 2018). Gkoupidenis et al. (2017) firstly demonstrated the concept of global regulation through the electrolyte gating with neuromorphic devices, they established an array device based on PEDOT: PSS to access the global control characteristics of neurons in a common electrolyte. The array of two-terminal devices immersed in 100 mM electrolyte and the PEDOT: PSS channels of each device serves as the hard connection between the input and output wire. The voltage bias applied on the electrolyte and concentration of ions globally modulate the hard connections. To make use of this effect, they proved synchronism of I/O transmission and the behavior of global clock, similar with the coupling of individual neuron activity and global oscillation in neural networks. These results show the electrolyte gating is advantageous to realize the neuromorphic devices with higher precision and complexity. Khodagholy et al. (2016) introduced a neural interface device (NeuroGrid) (**Figure 10**) that can simultaneously recording LFP and the action potential from brain surface. The recording signals with the PEDOT: PSS-based NeuroGrids between mid-γ waves (75 to 90 Hz) decreased correctly to the distance on separate electrodes, demonstrating NeuroGrids have high–spatial resolution when representing activities of small populations of neurons.

Coupling of OECTs with *in vivo* electrophysiological recordings is necessary and beneficial for brain-machine interfaces (Won et al., 2018; Gu et al., 2019). Because the organic transistors with conducting channels can connect both electronics and ions within the electrolyte. Ions can penetrate into the volume of the polymer channel and compensate the semiconductor, which will consequently change the conducting ability and thus modulate the current density of the channel. There are many factors can be tuned to obtain the ideal devices, such as channel thickness and the geometry of the channel. van de Burgt et al. (2018), demonstrated the ECoG recording of OECTs. The device, with an organic electrochemical transistor embedded on a thin organic film, recording *in vivo* epileptiform discharge, and performing great signal-to-noise ratio compared with state-of-the-art surface electrode. In addition, the OECTs can record the low-amplitude activities on the surface of the brain, which was superior to the traditional surface electrodes (Martin and Malliaras, 2016). Finally, the biocompatible, mechanical flexible devices for recording brain activities with superior signal-to-noise ratio hold promising future for medical applications.

CONCLUSIONS

Organic bioelectronics, as a promising popular interdisciplinary subject, targets to interface electronics and biology so that improve present biomedical technologies. The OECT lies in the center of this field mainly due to its initial nature of interfacing with biological components and has been proven to exceed general devices such as traditional electrochemical method. Moreover, various biological applications have been explored, including detecting metabolite and monitoring physiological signals since the OECTs bear the following advantages: (i) Stability is an extremely valued performance for biosensing. The OECT has been proven to work stably in various electrolytes, such as cerebrospinal fluid, cell media, sweat, and tears. The durability in these complex electrolytes can last; (ii) Sensitivity could be largely improved by OECT. Since small changes on the input will lead to enormous changes on the output. OECTs display high transconductance values, characteristically high gain, and the time response can be improved by tuning the geometry and size of the channel; (iii) OECTs could be easily integrated with biological system, such as individual cells, tissues, and even whole organs. Moreover, the gate electrode and conducting polymers could be easily modified by various recognition molecules; (iv) Compatibility with photo lithographical techniques also promote the microscale devices construction, especially interesting for monitoring activities of *in vitro* or *in vivo* cells.

In the past decade there has been noticeable progress on the advancing of OECTs for biological applications, however, numerous challenges still remain. These including: (i) The discovery and implementation of innovative active conducting polymers with enhanced properties with regard to conductivity, stability, patterning and restorability; (ii) The fabrication of devices for integrating multiplexed miniaturized arrays on versatile sensors, which may possibly power, record, or transmit the signals; (iii) The selectivity remains a big challenge for multi-chemicals and molecules sensing, especially for complicated samples (e.g., micro dialysate from brain); (iv) The response time was slow for the OECT devices due to the ions of electrolyte moving into or out of the volume of channel. The solution of these questions would largely accelerate the wide application of OECT in biological system, especially for the development of wearable device and brain-machine interface.

AUTHOR CONTRIBUTIONS

LB, CE, and WL collected the publications related to this review article, wrote the first draft of the manuscript and made subsequent corrections. PY, JF, and LM completed critical literature analysis and checked subsequent manuscript drafts.

FUNDING

The authors are grateful for financial support from the National Science Foundation of China (Grant Nos. 21475138, 21775151, and 21790053 for PY and 21790390, 21790391, 21435007, 21621062 for LM), the Strategic Priority Research Program of Chinese Academy of Sciences (Grant No. XDB30000000), and the Chinese Academy of Sciences (QYZDJ-SSWSLH030).

REFERENCES

Berggren, M., Crispin, X., Fabiano, S., Jonsson, M. P., Simon, D. T., Stavrinidou, E., et al. (2019). Ion electron-coupled functionality in materials and devices based on conjugated polymers. *Adv. Mater.* 2019:e1805813. doi: 10.1002/adma.201805813

Berggren, M., and Richter-Dahlfors, A. (2007). Organic bioelectronics. *Adv. Mater.* 19, 3201–3213. doi: 10.1002/adma.200700419

Bernards, D. A., Macaya, D. J., Nikolou, M., DeFranco, J. A., Takamatsu, S., and Malliaras, G. G. (2008). Enzymatic sensing with organic electrochemical transistors. *J. Mater. Chem.* 18, 116–120. doi: 10.1039/b713122d

Bernards, D. A., and Malliaras, G. G. (2007). Steady-state and transient behavior of organic electrochemical transistors. *Adv. Funct. Mater.* 17, 3538–3544. doi: 10.1002/adfm.200601239

Bettinger, C. J. (2018). Advances in materials and structures for ingestible electromechanical medical devices. *Angew. Chem.* 57, 16946–16958. doi: 10.1002/anie.201806470

Bihar, E., Deng, Y., Miyake, T., Saadaoui, M., Malliaras, G. G., and Rolandi, M. (2016). A disposable paper breathalyzer with an alcohol sensing organic electrochemical transistor. *Sci. Rep.* 6:e27582. doi: 10.1038/srep27582

Bolin, M. H., Svennersten, K., Nilsson, D., Sawatdee, A., Jager, E. W., Richter-Dahlfors, A., et al. (2009). Active control of epithelial cell-density gradients grown along the channel of an organic electrochemical transistor. *Adv. Mater.* 21, 4379–4382. doi: 10.1002/adma.200901191

Bongo, M., Winther-Jensen, O., Himmelberger, S., Strakosas, X., Ramuz, M., Hama, A., et al. (2013). PEDOT:gelatin composites mediate brain endothelial cell adhesion. *J. Mater. Chem.* 1, 3860–3867. doi: 10.1039/c3tb20374c

Braendlein, M., Lonjaret, T., Leleux, P., Badier, J. M., and Malliaras, G. G. (2017a). Voltage amplifier based on organic electrochemical transistor. *Adv. Sci.* 4:1600247. doi: 10.1002/advs.201600247

Braendlein, M., Pappa, A. M., Ferro, M., Lopresti, A., Acquaviva, C., Mamessier, E., et al. (2017b). Lactate detection in tumor cell cultures using organic transistor circuits. *Adv. Mater.* 29:1605744. doi: 10.1002/adma.201605744

Campana, A., Cramer, T., Simon, D. T., Berggren, M., and Biscarini, F. (2014). Electrocardiographic recording with conformable organic electrochemical transistor fabricated on resorbable bioscaffold. *Adv. Mater.* 26, 3874–3878. doi: 10.1002/adma.201400263

Chen, L., Fu, Y., Wang, N., Yang, A., Li, Y., Wu, J., et al. (2018). Organic electrochemical transistors for the detection of cell surface glycans. *ACS Appl. Mater. Interfaces.* 10, 18470–18477. doi: 10.1021/acsami.8b01987

Cicoira, F., Sessolo, M., Yaghmazadeh, O., DeFranco, J. A., Yang, S. Y., and Malliaras, G. G. (2010). Influence of device geometry on sensor characteristics of planar organic electrochemical transistors. *Adv. Mater.* 22, 1012–1016. doi: 10.1002/adma.200902329

Curto, V. F., Marchiori, B., Hama, A., Pappa, A.-M., Ferro, M. P., Braendlein, M., et al. (2017). Organic transistor platform with integrated microfluidics for in-line multi-parametric *in vitro* cell monitoring. *Micro. Nano.* 3:17028. doi: 10.1038/micronano.2017.28

Dai, S., Chu, Y., Liu, D., Cao, F., Wu, X., Zhou, J., et al. (2018). Intrinsically ionic conductive cellulose nanopapers applied as all solid dielectrics for low voltage organic transistors. *Nat. Commun.* 9:2737. doi: 10.1038/s41467-018-05155-y

D'Angelo, P., Tarabella, G., Romeo, A., Marasso, S. L., Verna, A., Cocuzza, M., et al. (2018). PEDOT:PSS morphostructure and ion-to-electron transduction and amplification mechanisms in organic electrochemical transistors. *MDPI Mater.* 12:9. doi: 10.3390/ma12010009

Del Agua, I., Porcarelli, L., Curto, V. F., Sanchez-Sanchez, A., Ismailova, E., Malliaras, G. G., et al. (2018). A Na+ conducting hydrogel for protection of organic electrochemical transistors. *J. Mater. Chem. B.* 6, 2901–2906. doi: 10.1039/C8TB00201K

Duc, C., Vlandas, A., Malliaras, G. G., and Senez, V. (2017). Electrowetting on immersed conducting hydrogel. *J. Phys. Chem. B.* 121, 9947–9956. doi: 10.1021/acs.jpcb.7b07971

ElMahmoudy, M., Charrier, A., Uguz, I., Malliaras, G. G., and Sanaur, S. (2017). Tailoring the electrochemical and mechanical properties of PEDOT:PSS films for bioelectronics. *Macromol. Mater. Eng.* 302:1600497. doi: 10.1002/mame.201600497

Fan, J., Rezaie, S. S., Facchini-Rakovich, M., Gudi, D., Montemagno, C., and Gupta, M. (2019). Tuning PEDOT:PSS conductivity to obtain complementary organic electrochemical transistor. *Org. Electron.* 66, 148–155. doi: 10.1016/j.orgel.2018.12.013

Fan, X., Wang, N., Wang, J., Xu, B., and Yan, F. (2018). Highly sensitive, durable and stretchable plastic strain sensors using sandwich structures of PEDOT:PSS and an elastomer. *Mater. Chem. Front.* 2, 355–361. doi: 10.1039/c7qm00497d

Fidanovski, K., and Mawad, D. (2019). Conjugated polymers in bioelectronics: addressing the interface challenge. *Adv. Healthc. Mater.* 2019:e1900053. doi: 10.1002/adhm.201900053

Flagg, L. Q., Bischak, C. G., Onorato, J. W., Rashid, R. B., Luscombe, C. K., and Ginger, D. S. (2019). Polymer crystallinity controls water uptake in glycol side-chain polymer organic electrochemical transistors. *J. Am. Chem. Soc.* 141, 4345–4354. doi: 10.1021/jacs.8b12640

Fu, Y., Wang, N., Yang, A., Law, H. K., Li, L., and Yan, F. (2017). Highly sensitive detection of protein biomarkers with organic electrochemical transistors. *Adv. Mater.* 29:e1703787. doi: 10.1002/adma.201703787

Gentili, D., D'Angelo, P., Militano, F., and Mazzei, R. (2018). Integration of organic electrochemical transistors and immuno-affinity membranes for label-free detection of interleukin-6 in the physiological concentration range through antibody–antigen recognition. *J. Mater. Chem. B.* 6, 5400–5406. doi: 10.1039/c8tb01697f

George, D. S., Jennifer, N. G., and Dion, K. (2019). Internal ion-gated organic electrochemical transistor: a building block for integrated bioelectronics. *Sci. Adv.* 5:eaau7378. doi: 10.1126/sciadv.aau7378

Gilletti, A., and Muthuswamy, J. (2006). Brain micromotion around implants in the rodent somatosensory cortex. *J. Neural Eng.* 3, 189–195. doi: 10.1088/1741-2560/3/3/001

Giovannitti, A., Nielsen, C. B., Sbircea, D.-T., Inal, S., Donahue, M., Niazi, M. R., et al. (2016). N-type organic electrochemical transistors with stability in water. *Nat. Commun.* 7:13066 doi: 10.1038/ncomms13066

Gkoupidenis, P., Koutsouras, D. A., and Malliaras, G. G. (2017). Neuromorphic device architectures with global connectivity through electrolyte gating. *Nat. Commun.* 8:15448. doi: 10.1038/ncomms15448

Green, R. A., Matteucci, P. B., Hassarati, R. T., Giraud, B., Dodds, C. W., Chen, S., et al. (2013). Performance of conducting polymer electrodes for stimulating neuroprosthetics. *J. Neural. Eng.* 10:016009. doi: 10.1088/1741-2560/10/1/016009

Gu, X., Yeung, S. Y., Chadda, A., Poon, E. N. Y., Boheler, K. R., and Hsing, I. M. (2019). Organic electrochemical transistor arrays for *in vitro* electrophysiology monitoring of 2D and 3D cardiac tissues. *Adv. Biosys.* 3:1800248. doi: 10.1002/adbi.201800248

Gualandi, I., Marzocchi, M., Scavetta, E., Calienni, M., Bonfiglioc, A., and Frabonia, B. (2015). A simple all-PEDOT:PSS electrochemical transistor for ascorbic acid sensing. *J. Mater. Chem. B.* 3, 6753–6762. doi: 10.1039/C5tb00916b

Gualandi, I., Tonelli, D., Mariani, F., Scavetta, E., Marzocchi, M., and Fraboni, B. (2016). Selective detection of dopamine with an all PEDOT:PSS organic electrochemical transistor. *Sci. Rep.* 6:35419. doi: 10.1038/srep35419

Hütter, P. C., Rothländer, T., Haase, A., Trimmel, G., and Stadlober, B. (2013). Influence of geometry variations on the response of organic electrochemical transistors. *Appl. Phys. Lett.* 103, 133–131. doi: 10.1063/1.4816781

Inal, S., Rivnay, J., Hofmann, A. I., Uguz, I., Mumtaz, M., Katsigiannopoulos, D., et al. (2016). Organic electrochemical transistors based on PEDOT with different anionic polyelectrolyte dopants. *J. Polym. Sci. Part B.* 54, 147–151. doi: 10.1002/polb.23938

Jasper, H. H., Arfel-Capdeville, G., and Rasmussen, T. (1961). Evaluation of EEG and cortical electrographic studies for prognosis ofseizures following surgical excision of epileptogenic lesions. *Epilepsia.* 2, 130–137. doi: 10.1111/j.1528-1157.1942.tb03224.x

Jimison, L. H., Tria, S. A., Khodagholy, D., Gurfinkel, M., Lanzarini, E., Hama, A., et al. (2012). Measurement of barrier tissue integrity with an organic electrochemical transistor. *Adv. Mater.* 24, 5919–5923. doi: 10.1002/adma.201202612

Jonsson, A., Song, Z., Nilsson, D., Meyerson, B. A., Simon, D. T., Linderoth, B., et al. (2015). Therapy using implanted organic bioelec. *Sci. Adv.* 1:e1500039. doi: 10.1126/sciadv.1500039

Kerman, K., Saito, M., Tamiya, E., Yamamura, S., and Takamura, Y. (2008). Nanomaterial-based electrochemical biosensors for medical applications. *Tren. Anal. Chem.* 27, 585–592. doi: 10.1016/j.trac.2008.05.004

Khodagholy, D., Curto, V. F., Fraser, K. J., Gurfinkel, M., Byrne, R., Diamond, D., et al. (2012). Organic electrochemical transistor incorporating an ionogel as a solid state electrolyte for lactate sensing. *J. Mater. Chem.* 22, 4440–4443. doi: 10.1039/c2jm15716k

Khodagholy, D., Doublet, T., Quilichini, P., Gurfinkel, M., Leleux, P., Ghestem, A., et al. (2013a). *In vivo* recordings of brain activity using organic transistors. *Nat. Commun.* 4:1575. doi: 10.1038/ncomms2573

Khodagholy, D., Gelinas, J. N., Thesen, T., Doyle, W., Devinsky, O., Malliaras, G. G., et al. (2015). NeuroGrid: recording action potentials from the surface of the brain. *Nat. Neurosci.* 18, 310–315. doi: 10.1038/nn.3905

Khodagholy, D., Gelinas, J. N., Zhao, Z., Yeh, M., Long, M., Greenlee, J. D., et al. (2016). Organic electronics for high-resolution electrocorticography of the human brain. *Sci. Adv.* 2:e1601027. doi: 10.1126/sciadv.1601027

Khodagholy, D., Rivnay, J., Sessolo, M., Gurfinkel, M., Leleux, P., Jimison, L. H., et al. (2013b). High transconductance organic electrochemical transistors. *Nat. Commun.* 4:2133. doi: 10.1038/ncomms3133

Kim, D. J., Lee, N. E., Park, J. S., Park, I. J., Kim, J. G., and Cho, H. J. (2010). Organic electrochemical transistor based immunosensor for prostate specific antigen (PSA) detection using gold nanoparticles for signal amplification. *Biosens. Bioelectron.* 25, 2477–2482. doi: 10.1016/j.bios.2010.04.013

Kim, S. H., Hong, K., Xie, W., Lee, K. H., Zhang, S., Lodge, T. P., et al. (2013). Electrolyte-gated transistors for organic and printed electronics. *Adv. Mater.* 25, 1822–1846. doi: 10.1002/adma.201202790

Labib, M., Sargent, E. H., and Kelley, S. O. (2016). Electrochemical methods for the analysis of clinically relevant biomolecules. *Chem. Rev.* 116, 9001–9090. doi: 10.1021/acs.chemrev.6b00220

Lee, W., Kim, D., Matsuhisa, N., Nagase, M., Sekino, M., Malliaras, G. G., et al. (2017). Transparent, conformable, active multielectrode array using organic electrochemical transistors. *PNAS.* 114, 10554–10559. doi: 10.1073/pnas.1703886114

Lee, W., and Someya, T. (2019). Emerging trends in flexible active multielectrode arrays. *Chem. Mater.* doi: 10.1021/acs.chemmater.9b00165

Lee, Y. H., Kweon, O. Y., Kim, H., Yoo, J. H., Han, S. G., and Oh, J. H. (2018). Recent advances in organic sensors for health self-monitoring systems. *J. Mater. Chem. C.* 6, 8569–8612. doi: 10.1039/c8tc02230e

Leleux, P., Badier, J. M., Rivnay, J., Bénar, C., Hervé, T., Chauvel, P., et al. (2014). Conducting polymer electrodes for electroencephalography. *Adv. Healthc. Mater.* 3, 490–493. doi: 10.1002/adhm.201300311

Liao, C., Mak, C., Zhang, M., Chan, H. L., and Yan, F. (2015). Flexible organic electrochemical transistors for highly selective enzyme biosensors and used for saliva testing. *Adv. Mater.* 27, 676–681. doi: 10.1002/adma.201404378

Liao, C., Zhang, M., Niu, L., Zheng, Z., and Yan, F. (2014). Organic electrochemical transistors with graphene-modified gate electrodes for highly sensitive and selective dopamine sensors. *J. Mater. Chem. B.* 2, 191–200. doi: 10.1039/c3tb21079k

Lin, P., Luo, X., Hsing, I. M., and Yan, F. (2011). Organic electrochemical transistors integrated in flexible microfluidic systems and used for label-free DNA sensing. *Adv. Mater.* 23, 4035–4040. doi: 10.1002/adma.201102017

Lin, P., Yan, F., Yu, J., Chan, H. L., and Yang, M. (2010). The application of organic electrochemical transistors in cell-based biosensors. *Adv. Mater.* 22, 3655–3660. doi: 10.1002/adma.201000971

Liu, G., and Lin, Y. (2007). Nanomaterial labels in electrochemical immunosensors and immunoassays. *Talanta*. 74, 308–317. doi: 10.1016/j.talanta.2007.10.014

Macaya, D. J., Nikolou, M., Takamatsu, S., Mabeck, J. T., Owens, R. M., and Malliaras, G. G. (2007). Simple glucose sensors with micromolar sensitivity based on organic electrochemical transistors. *Sens. Actuators B.* 123, 374–378. doi: 10.1016/j.snb.2006.08.038

Macchia, E., Ghittorelli, M., Tomcelli, F., and Torsi, L. (2017). "Organic electrochemical transistor immuno-sensor operating at the femto-molar limit of detection," in *2017 7th IEEE International Workshop on Advances in Sensors and Interfaces (IWASI)* (Vieste: IEEE), 68–72.

Macchia, E., Romele, P., Manoli, K., Ghittorelli, M., Magliulo, M., Kovàcs-Vajna, Z.-M., et al. (2018). Ultra-sensitive protein detection with organic electrochemical transistors printed on plastic substrate. *Flex. Print. Electron.* 3:034002. doi: 10.1088/2058-8585/aad0cb

Mak, C., Liao, C., Fu, Y., Zhang, M., Tang, C. Y., et al. (2015). Highly-sensitive epinephrine sensors based on organic electrochemical transistors with carbon nanomaterial modified gate electrodes. *J. Mater. Chem. C,.* 3, 6532–6538. doi: 10.1039/c5tc01100k

Martin, D. C., and Malliaras, G. G. (2016). Interfacing electronic and ionic charge transport in bioelectronics. *ChemElectroChem.* 3, 686–688. doi: 10.1002/celc.201500555

Nakatsuka, N., Yang, K. A., Abendroth, J. M., Cheung, K. M., Xu, X., Yang, H., et al. (2018). Aptamer–field-effect transistors overcome Debye length limitations for small-molecule sensing. *Science* 362, 319–324. doi: 10.1126/science.aao6750

Nishizawa, M., Matsue, T., and Uchida, I. (1992). Penicillin sensor based on a microarray electrode coated with pH-responsive polypyrrole. *Anal. Chem.* 64, 2642–2644. doi: 10.1021/ac00045a030

Onorato, J. W., and Luscombe, C. K. (2019). Morphological effects on polymeric mixed ionic/electronic conductors. *Mol. Syst. Des. Eng.* 4, 310–324. doi: 10.1039/c8me00093j

Pappa, A. M., Curto, V. F., Braendlein, M., Strakosas, X., Donahue, M. J., Fiocchi, M., et al. (2016). Organic transistor arrays integrated with finger-powered microfluidics for multianalyte saliva testing. *Adv. Healthc. Mater.* 5, 2295–2302. doi: 10.1002/adhm.201600494

Pappa, A. M., Inal, S., Roy, K., Zhang, Y., Pitsalidis, C., Hama, A., et al. (2017). Polyelectrolyte layer-by-layer assembly on organic electrochemical transistors. *ACS Appl. Mater. Interfaces*. 9, 10427–10434. doi: 10.1021/acsami.6b15522

Pappa, A. M., Ohayon, D., Giovannitti, A., Maria, I. P., Savva, A., Uguz, I., et al. (2018). Direct metabolite detection with an n-type accumulation mode organic electrochemical transistor. *Sci. Adv.* 4:eaat0911. doi: 10.1126/sciadv.aat0911

Parlak, O., Keene, S. T., Marais, A., F., C. V., and Salleo, A. (2018). Molecularly selective nanoporous membrane-based wearable organic electrochemical device for noninvasive cortisol sensing. *Sci. Adv.* 4:eaar2904. doi: 10.1126/sciadv.aar2904

Peng, J., He, T., Sun, Y., Liu, Y., Cao, Q., Wang, Q., et al. (2018). An organic electrochemical transistor for determination of microRNA21 using gold nanoparticles and a capture DNA probe. *Mikrochim Acta.* 185:408. doi: 10.1007/s00604-018-2944-x

Qing, X., Wang, Y., Zhang, Y., Ding, X., Zhong, W., Wang, D., et al. (2019). Wearable fiber-based organic electrochemical transistors as a platform for highly sensitive dopamine monitoring. *ACS Appl. Mater. Interfaces* 11, 13105–13113. doi: 10.1021/acsami.9b00115

Ramuz, M., Hama, A., Rivnay, J., Leleux, P., and Owens, R. M. (2015). Monitoring of cell layer coverage and differentiation with the organic electrochemical transistor. *J. Mater. Chem. B.* 3, 5971–5977. doi: 10.1039/c5tb00922g

Rivnay, J., Inal, S., Collins, B. A., Sessolo, M., Stavrinidou, E., Strakosas, X., et al. (2016). Structural control of mixed ionic and electronic transport in conducting polymers. *Nat. Commun.* 7:11287. doi: 10.1038/ncomms11287

Rivnay, J., Inal, S., Salleo, A., Owens, R. M., Berggren, M., and Malliaras, G. G. (2018). Organic electrochemical transistors. *Nat. Rev. Mater.* 3:17086. doi: 10.1038/natrevmats.2017.86

Rivnay, J., Leleux, P., Ferro, M., Sessolo, M., Williamson, A., Koutsouras, D., et al. (2015a). High-performance transistors for bioelectronics through tuning of channel thickness. *Sci. Adv.* 1:e1400251. doi: 10.1126/sciadv.1400251

Rivnay, J., Leleux, P., Hama, A., Ramuz, M., Huerta, M., Malliaras, G. G., et al. (2015b). Using white noise to gate organic transistors for dynamic monitoring of cultured cell layers. *Sci. Rep.* 5:11613. doi: 10.1038/srep11613

Rivnay, J., Owens, R. M., and Malliaras, G. G. (2013). The rise of organic bioelectronics. *Chem. Mater.* 26, 679–685. doi: 10.1021/cm4022003

Rivnay, J., Ramuz, M., Leleux, P., Hama, A., Huerta, M., and Owens, R. M. (2015c). Organic electrochemical transistors for cell-based impedance sensing. *Appl. Phys. Lett.* 106:043301. doi: 10.1063/1.4906872

Rivnay, J., Wang, H., Fanno, L., Deisseroth, K., and Malliaras, G. G. (2017). Next-generation probes, particles, and proteins for neural interfacing. *Sci. Adv.* 3:e1601649. doi: 10.1126/sciadv.1601649

Romeo, A., Tarabella, G., D'Angelo, P., Caffarra, C., Cretella, D., Alfieri, R., et al. (2015). Drug-induced cellular death dynamics monitored by a highly sensitive organic electrochemical system. *Biosens. Bioelectron.* 68, 791–797. doi: 10.1016/j.bios.2015.01.073

Shim, N. Y., Bernards, D. A., Macaya, D. J., Defranco, J. A., Nikolou, M., Owens, R. M., et al. (2009). All-plastic electrochemical transistor for glucose sensing using a ferrocene mediator. *mdpi Sens.* 9, 9896–9902. doi: 10.3390/s91209896

Simon, D. T., Gabrielsson, E. O., Tybrandt, K., and Berggren, M. (2016). Organic bioelectronics: bridging the signaling gap between biology and technology. *Chem. Rev.* 116, 13009–13041. doi: 10.1021/acs.chemrev.6b00146

Sivakumarasamy, R., Hartkamp, R., Siboulet, B., Dufrêche, J. F., Nishiguchi, K., Fujiwara, A., et al. (2018). Selective layer-free blood serum ionogram based on ion-specific interactions with a nanotransistor. *Nat. Mater.* 17, 464–470. doi: 10.1038/s41563-017-0016-y

Someya, T., Bao, Z., and Malliaras, G. G. (2016). The rise of plastic bioelectronics. *Nature*. 540, 379–385. doi: 10.1038/nature21004

Sun, H., Vagin, M., Wang, S., Crispin, X., Forchheimer, R., Berggren, M., et al. (2018). Complementary logic circuits based on high-performance n-type organic electrochemical transistors. *Adv. Mater.* 30:e1704916. doi: 10.1002/adma.201704916

Tang, H., Lin, P., Chan, H. L., and Yan, F. (2011). Highly sensitive dopamine biosensors based on organic electrochemical transistors. *Biosens. Bioelectron.* 26, 4559–4563. doi: 10.1016/j.bios.2011.05.025

Tria, S. A., Ramuz, M., Huerta, M., Leleux, P., Rivnay, J., Jimison, L. H., et al. (2014). Dynamic monitoring of Salmonella typhimurium infection of polarized epithelia using organic transistors. *Adv. Healthc. Mater.* 3, 1053–1060. doi: 10.1002/adhm.201300632

Tybrandt, K., Kollipara, S. B., and Berggren, M. (2014). Organic electrochemical transistors for signal amplification in fast scan cyclic voltammetry. *Sens. Actuators B.* 195, 651–656. doi: 10.1016/j.snb.2014.01.097

Tybrandt, K., Zozoulenko, I. V., and Berggren, M. (2017). Chemical potential–electric double layer coupling in conjugated polymer–polyelectrolyte blends. *Sci. Adv.* 3;eaao3659. doi: 10.1126/sciadv.aao3659

Uguz, I., Ganji, M., Hama, A., Tanaka, A., Inal, S., Youssef, A., et al. (2016). Autoclave sterilization of PEDOT:PSS electrophysiology devices. *Adv. Healthc. Mater.* 5, 3094–3098. doi: 10.1002/adhm.201600870

van de Burgt, Y., Melianas, A., Keene, S. T., Malliaras, G., and Salleo, A. (2018). Organic electronics for neuromorphic computing. *Nat. Electron.* 1, 386–397. doi: 10.1038/s41928-018-0103-3

Viswanathan, S., Rani, C., Vijay Anand, A., and Ho, J. A. (2009). Disposable electrochemical immunosensor for carcinoembryonic antigen using ferrocene liposomes and MWCNT screen-printed electrode. *Biosens. Bioelectron.* 24, 1984–1989. doi: 10.1016/j.bios.2008.10.006

Volkov, A. V., Wijeratne, K., Mitraka, E., Ail, U., Zhao, D., Tybrandt, K., et al. (2017). Understanding the capacitance of PEDOT:PSS. *Adv. Funct. Mater.* 27:1700329. doi: 10.1002/adfm.201700329

Wang, Y., Qing, X., Zhou, Q., Zhang, Y., Liu, Q., Liu, K., et al. (2017). The woven fiber organic electrochemical transistors based on polypyrrole nanowires/reduced graphene oxide composites for glucose sensing. *Biosens. Bioelectron.* 95, 138–145. doi: 10.1016/j.bios.2017.04.018

Wei, W., Xiao, K., Tao, M., Nie, L., Liu, D., Ke, S., et al. (2017). A novel organic electrochemical transistor-based platform for monitoring the senescent green vegetative phase of haematococcus pluvialis cells. *MDPI Sensors*. 17:1997. doi: 10.3390/s17091997

Wen, W., Yan, X., Zhu, C., Du, D., and Lin, Y. (2017). Recent advances in electrochemical immunosensors. *Anal. Chem.* 89, 138–156. doi: 10.1021/acs.analchem.6b04281

White, H. S., Kittlesen, G. P., and Wrighton, M. S. (1984). Chemical derivatization of an array of three gold microelectrodes with polypyrrole: fabrication of a molecule-based transistor. *J. Am. Chem. Soc.* 106, 5375–5377. doi: 10.1021/ja00330a070

Williamson, A., Ferro, M., Leleux, P., Ismailova, E., Kaszas, A., Doublet, T., et al. (2015). Localized neuron stimulation with organic electrochemical transistors on delaminating depth probes. *Adv. Mater.* 27, 4405–4410. doi: 10.1002/adma.201500218

Won, S. M., Song, E., Zhao, J., Li, J., Rivnay, J., and Rogers, J. A. (2018). Recent advances in materials, devices, and systems for neural interfaces. *Adv. Mater.* 30:e1800534. doi: 10.1002/adma.201800534

Wu, F., Yu, P., and Mao, L. (2017). Self-powered electrochemical systems as neurochemical sensors: toward self-triggered *in vivo* analysis of brain chemistry. *Chem. Soc. Rev.* 46, 2692–2704. doi: 10.1039/c7cs00148g

Xenofon, S., Bongo, M., and M., O. R. (2015). The organic electrochemical transistor for biological applications. *J. Appl. Polym. Sci.* 132:41735. doi: 10.1002/app.41735

Xiao, T., Wu, F., Hao, J., Zhang, M., Yu, P., and Mao, L. (2017). *In vivo* analysis with electrochemical sensors and biosensors. *Anal. Chem.* 89, 300–313. doi: 10.1021/acs.analchem.6b04308

Yan, F., Li, X., and Fang, Y. (2015). Organic bioelectronics for neural interfaces. *J. Mater. Chem. C.* 3, 6424–6430. doi: 10.1039/c5tc00569h

Yang, K., Yuan, S., Huan, Y., Wang, J., Tu, L., Xu, J., et al. (2018). Tunable flexible artificial synapses: a new path toward a wearable electronic system. *npj. Flex. Electron.* 2:20. doi: 10.1038/s41528-018-0033-1

Yao, C., Xie, C., Lin, P., Yan, F., Huang, P., and Hsing, I. M. (2013). Organic electrochemical transistor array for recording transepithelial ion transport of human airway epithelial cells. *Adv. Mater.* 25, 6575–6580. doi: 10.1002/adma.201302615

Yi, Z., Natale, G., Kumar, P., Di Mauro, E., Heuzey, M., Perepichka, I., et al. (2015). Ionic liquid–water mixtures and ion gels as electrolytes for organic electrochemical transistors. *J. Mater. Chem. C.* 3, 6549–6553. doi: 10.1039/c5tc00712g

Yu, P., He, X., and Mao, L. (2015). Tuning interionic interaction for highly selective *in vivo* analysis. *Chem. Soc. Rev.* 44, 5959–5968. doi: 10.1039/c5cs00082c

Yu, X., Munge, B., Patel, V., Jensen, G., Bhirde, A., Gong, J. D., et al. (2006). Carbon nanotube amplification strategies for highly sensitive immunodetection of cancer biomarkers. *J. Am. Chem. Soc.* 128, 11199–11205. doi: 10.1021/ja062117e

Zakhidov, A. A., Fong, H. H., DeFranco, J. A., Lee, J. K., Taylor, P. G., Ober, C. K., et al. (2011). Fabrication of polymer-based electronic circuits using photolithography. *Appl. Phys. Lett.* 99:183308. doi: 10.1063/1.3650474

Zhang, L., Wang, G., Wu, D., Xiong, C., Zheng, L., Ding, Y., et al. (2018). Highly selective and sensitive sensor based on an organic electrochemical transistor for the detection of ascorbic acid. *Biosens. Bioelectron.* 100, 235–241. doi: 10.1016/j.bios.2017.09.006

Zhang, Y., and Heller, A. (2005). Reduction of the nonspecific binding of a target antibody and of its enzyme-labeled detection probe enabling electrochemical immunoassay of an antibody through the 7 pg/mL-100 ng/mL (40 fM-400 pM) range. *Anal. Chem.* 77, 7758–7762. doi: 10.1021/ac051218

Zhu, Z. T., Mabeck, J. T., Zhu, C., Cady, N. C., Batt, C. A., and Malliaras, G. G. (2004). A simple poly(3,4-ethylene dioxythiophene)/poly(styrene sulfonic acid) transistor for glucose sensing at neutral pH. *Chem. Commun.* 2004, 1556–1557. doi: 10.1039/b403327m

Conflict of Interest Statement: The authors declare that the research was conducted in the absence of any commercial or financial relationships that could be construed as a potential conflict of interest.

Copyright © 2019 Bai, Elósegui, Li, Yu, Fei and Mao. This is an open-access article distributed under the terms of the Creative Commons Attribution License (CC BY). The use, distribution or reproduction in other forums is permitted, provided the original author(s) and the copyright owner(s) are credited and that the original publication in this journal is cited, in accordance with accepted academic practice. No use, distribution or reproduction is permitted which does not comply with these terms.

frontiers in Chemistry

ORIGINAL RESEARCH
published: 12 December 2018
doi: 10.3389/fchem.2018.00618

An Allosteric-Probe for Detection of Alkaline Phosphatase Activity and Its Application in Immunoassay

Jingjing Guo[1], Mingxuan Gao[1], Yanling Song[2], Li Lin[1], Kaifeng Zhao[1], Tian Tian[1], Dan Liu[1], Zhi Zhu[1]* and Chaoyong James Yang[1,2]*

[1] MOE Key Laboratory of Spectrochemical Analysis and Instrumentation, Key Laboratory for Chemical Biology of Fujian Province, State Key Laboratory of Physical Chemistry of Solid Surfaces, Collaborative Innovation Center of Chemistry for Energy Materials, College of Chemistry and Chemical Engineering, Xiamen University, Xiamen, China, [2] Institute of Molecular Medicine, Renji Hospital, School of Medicine, Shanghai Jiao Tong University, Shanghai, China

A fluorescence strategy for alkaline phosphatase (ALP) assay in complicated samples with high sensitivity and strong stability is developed based on an allosteric probe (AP). This probe consists of two DNA strands, a streptavidin (SA) aptamer labeled by fluorophore and its totally complementary DNA (cDNA) with a phosphate group on the 5′ end. Upon ALP introduction, the phosphate group on the cDNA is hydrolyzed, leaving the unhydrolyzed cDNA sequence for lambda exonuclease (λ exo) digestion and releasing SA aptamer for binding to SA beads, which results in fluorescence enhancement of SA beads that can be detected by flow cytometry or microscopy. We have achieved a detection limit of 0.012 U/mL with a detection range of 0.02∼0.15 U/mL in buffer and human serum. These figures of merit are better than or comparable to those of other methods. Because the fluorescence signal is localized on the beads, they can be separated to remove fluorescence background from complicated biological systems. Notably, the new strategy not only applies to ALP detection with simple design, easy operation, high sensitivity, and good compatibility in complex solution, but also can be utilized in ALP-linked immunosorbent assays for the detection of a wide range of targets.

Keywords: aptamer, alkaline phosphatase, allosteric-probes, complex sample, immunoassay

OPEN ACCESS

Edited by:
Huangxian Ju,
Nanjing University, China

Reviewed by:
Chih-Ching Huang,
National Taiwan Ocean University, Taiwan
Xiliang Luo,
Qingdao University of Science and Technology, China

***Correspondence:**
Yanling Song
songyanling2012@hotmail.com
Zhi Zhu
zhuzhi@xmu.edu.cn

Specialty section:
This article was submitted to Analytical Chemistry, a section of the journal Frontiers in Chemistry

Received: *20 September 2018*
Accepted: *30 November 2018*
Published: *12 December 2018*

Citation:
Guo J, Gao M, Song Y, Lin L, Zhao K, Tian T, Liu D, Zhu Z and Yang CJ (2018) An Allosteric-Probe for Detection of Alkaline Phosphatase Activity and Its Application in Immunoassay. Front. Chem. 6:618. doi: 10.3389/fchem.2018.00618

INTRODUCTION

Alkaline phosphatase (ALP), a type of hydrolase enzyme, is widespread in nature for removing phosphate groups from various biomolecules like nucleic acids, proteins, and carbohydrates. ALP is present in all tissues in the human body. Due to ALP's important role in metabolism in the liver and development of the skeleton, an abnormal level of ALP is often related to bone disease (Garnero and Delmas, 1993), liver dysfunction (Ooi et al., 2007), diabetes (Berberoglu et al., 2007), and breast cancer (Brar et al., 1993). Hence, development of ALP detection methods is important for clinical diagnosis and cancer screening. In addition, like horseradish peroxidase (HRP), ALP can conjugate to streptavidin (Zhou et al., 2016) or a detection antibody for signal amplification and output in enzyme-linked immunosorbent assay (ELISA) (Porstmann et al., 1985). Therefore, development of new assays for ALP not only satisfies clinical diagnostic requirements but also improves the performance of ALP-labeled ELISAs.

Because ALP catalyzes the dephosphorylation processes of various substrates, many methods have been applied to quantify ALP's enzymatic activity, including fluorescence (Liang et al., 2013; Qian et al., 2015; Hu et al., 2016), colorimetry (Jiao et al., 2014; Yang et al., 2016), electrochemistry (Barroso et al., 2016), chemiluminescence (Jiang and Wang, 2012), and surface-enhanced Raman spectroscopy (Ruan et al., 2006). Most assays employ small molecules as substrates, including pyrophosphate (PPi), ascorbic acid 2–phosphate (AAP), p-nitrophenyl phosphate (PNPP), and p-aminophenyl phosphate (PAPP). Due to the easy labeling with a signal molecule and digestion by nuclease, nucleic acids are ideal phosphorylation substrates. Lambda exonuclease (λ exo) is a highly processive 5'-3' double-stranded DNA (dsDNA) exodeoxyribonuclease, which can selectively digest the 5'-phosphorylated strand of dsDNA, while work inefficiently on single-stranded DNA (ssDNA) and non-phosphorylated DNA. Miao et al. reported an electrochemical strategy to detect ALP by using dsDNA probes, and λ exo was employed for enzyme-mediated signal amplification (Miao et al., 2011). However, the complex preparation steps for electrochemical sensors make the workload heavier and test time longer. In addition, the poor limit of detection (LOD) (100 U/L) still needs improvement. Colorimetric strategies exploiting nucleic acids as the substrates coordinating with λ exo for ALP detection have also been developed. For example, a perylene probe can induce the aggregation of gold nanoparticles, which causes a color change from pink red to dark blue (Jiao et al., 2014). Disadvantages include preparation difficulty and poor LOD (32 U/L), limiting the practical applications in biological samples. More recently, Liu et al. developed a new fluorescent ALP assay using prior binding of graphene oxide (GO) to ssDNA over dsDNA (Liu et al., 2016), resulting in a lower LOD (0.19 U/L), but performance of this method may be compromised in human serum without a separation step. Overall, it is apparent that these sensors often suffer from complicated probe preparation and detrimental effects of the biological matrix, such as the influence of sample autofluorescence. So far, the detection of ALP in complicated samples in these methods is mostly performed in 1% human serum (Ma et al., 2016) or cell extracts (Jiao et al., 2014). Higher concentrations of complicated samples may affect the probes, leading to failure of the biological assay. To solve these problems, new signaling strategies with high sensitivity and strong stability in complicated samples are highly desired for ALP detection.

In our previous work, we proposed the design and application of allosteric molecular beacons (aMBs) (Song et al., 2011, 2012; Zhang et al., 2016; Gao et al., 2017) for highly sensitive and selective detection of nucleic acids, proteins and small molecules in complicated biological systems. Briefly, an aMB is an ssDNA labeled by fluorophore containing a molecular recognition sequence, streptavidin (SA) aptamer and its cDNA. The hybridization allows the probe to form a stable hairpin structure, preventing the probe from binding to SA beads. When the target is present, the recognition sequence binds to the target, which opens the hairpin structure to release SA aptamer, allowing the probe to bind to SA beads, consequently leading to fluorescent signal readout. The bead-based separation (Huang and Liu, 2010) and the single-fluorophore-labeled reporter contribute to the low background and little influence of matrix effects.

Herein, we report the design of an allosteric probe (AP) based on an aMB to improve the ALP detection performance in complex environments. The AP contains two complementary sequences, an SA aptamer labeled by fluorophore and its total cDNA modified with a 5'-phosphoryl terminus. In the absence of ALP, the cDNA is promptly cleaved by λ exo to release the SA aptamer, which binds to SA beads within 5 min incubation, resulting in fluorescence enhancement of SA beads that can be detected by microscopy or flow cytometry. In contrast, ALP catalyzes hydrolysis of the 5'-phosphoryl terminus from the cDNA, producing a 5'-hydroxyl end product that prevents λ exo cleavage. As a consequence, no SA aptamers bind to SA beads yielding weak fluorescence. Compared to the reported ALP detection methods, interfering autofluorescence from species in the complex biological system can be easily isolated by a bead-based separation, such as simple centrifugation or filtration, to reduce non-specific adsorption-induced background. Besides, a large surface-to-volume ratio enriches the fluorescent signals on the beads which improves the signal-background-ratio (SBR). Without the need for nucleic acid amplification, the developed AP avoids the use of multiple enzymes and consequent complicated operation and cross-contamination, thereby decreasing operational difficulty and time-consumption for signal readout. The results show a detection limit of 0.012 U/mL and a linear response over the range of 0.02–0.15 U/mL in buffer and human serum with high sensitivity and selectivity. Furthermore, the method can be applied to the inhibitor screening of ALP and ALP-labeled ELISA, expanding the scope of practical applications. This strategy introduces a new way to detect ALP and shows the potential for applications in drug discovery and cancer diagnosis.

MATERIALS AND METHODS

Materials

Alkaline phosphatase (ALP, 1000 U/mL) and p-nitrophenyl phosphate (PNPP) were purchased from Thermo Fisher Scientific Inc (Shanghai, China). Lambda exonuclease (λ exo, 5000 U/mL) and T4 ligase were obtained from New England Biolabs (Ipswich, MA, USA). Thrombin was supplied from Haematologic Technologies (Essex Junction, VT, USA). Lysozyme was purchased from R&D Systems (Minneapolis, MN, USA). Human serum albumin (HSA) was bought from Tagene Biotechnology Co., Ltd. (Xiamen, China). Proteinase K was purchased from BBI Science (Shanghai, China). Trypsin was purchased from Biofroxx (Einhausen, Germany). Na_3VO_4, human IgG and anti-human IgG-coated ELISA plates were purchased from Sigma-Aldrich (St. Louis, MO, USA). L-cysteine was bought from Sinopharm Chemical Reagent Co. Ltd (Shanghai, China). Human serum was obtained from Affiliated Chenggong Hospital (Xiamen University). Streptavidin (SA) Sepharose beads were purchased from GE Healthcare (Chicago, IL, USA). ALP-labeled goat anti-human IgG was purchased

from Abcam (Cambridge, MA, USA). RIPA and PMSF were bought from Solarbio life sciences (Beijing, China). All other chemicals were analytical reagent grade and used without further purification. All oligonucleotides used in this study were synthesized and HPLC purified by Sangon Biotechnology Co., Ltd. (Shanghai, China) and sequences are listed in **Table S1**.

Optimization of the AP

To obtain the best SBR, the SA aptamer sequences were optimized. To prepare the DNA for hybridization, 10 μM AP (including the SA aptamer and its total cDNA) was heated to 95°C for 5 min and then held at 37°C for 30 min. In a typical ALP assay, 200 nM AP in 100 μL buffer (70 mM Tris-HCl, 10 mM $MgCl_2$, pH = 8.0) with 10 U/mL ALP was incubated at 37°C for 10 min. Then 100 U/mL λ exo was added to the solution and incubated at 37°C for 30 min to digest the 5'-phosphorylated cDNA. After incubation, the enzyme was inactivated at 75°C for 10 min. The mixture was cooled to room temperature, and 3 μL SA beads was added and rotated slowly for 5 min to interact with the free SA aptamers. After washing 3 times with buffer, the fluorescence of SA beads was quantitatively characterized by flow cytometry or fluorescence microscopy.

Quantitative Assay of ALP Activity

To achieve quantitative detection of ALP activity, a series of different concentrations of ALP was added to the reaction system. For complex biological systems, 10% human serum was utilized as the reaction buffer with different concentrations of ALP. After the enzyme-deactivation step, the precipitate was removed by centrifugation. The subsequent steps were the same as those described in the previous section.

Selectivity Study

The selectivity of the ALP assay was investigated by using other enzymes or proteins, including thrombin, T4 ligase, lysozyme, HSA, proteinase K, trypsin and de-activated ALP. The concentration of ALP was 2 U/mL, and the concentrations of other enzymes and proteins were 20 U/mL or 10 nM. Other procedures were the same as those stated above.

ALP Inhibitor Screening

The ALP inhibitor screening was performed by utilizing Na_3VO_4 and L-cysteine. Different concentrations of inhibitors were mixed with 2 U/mL ALP, and the mixture was added to 200 nM AP in 100 μL buffer. The remaining steps were the same as those stated above.

ALP-Linked Immunosorbent Assay

To achieve quantitative detection for human IgG activity, each well of an anti-human IgG coated ELISA plate was filled with human IgG (100 μL, 30–960 ng/mL) at ambient temperature for 2.5 h with gentle shaking and then washed 4 times with washing buffer (300 μL). Detection antibody, ALP-labeled goat anti-human IgG (100 μL, 1:1000) was added to each well, and incubated for 1 h at room temperature with gentle shaking and then washed 4 times with washing buffer (300 μL). Then, 200 nM AP in 100 μL buffer was added to each well and incubated at 37°C for 10 min. After incubation, all the solutions were transferred to centrifuge tubes, and the remaining steps were the same as those stated above.

Preparation of Cell Lysates

Hela cells were cultured in DMEM medium with 10% fetal bovine serum (FBS). The cells were washed three times with PBS, and treated with 1 mL RIPA and 10 μL PMSF for 1 h on ice. A suspension of 10^5 cells/mL was centrifuged at 10,000 rpm for 30 min at 4°C, and the supernatant was used as complex matrix and spiked with ALP for detection.

ALP Detection Using PNPP Substrate

Four microgram per microliter PNPP substrate dispersed in diethanolamine was prepared and added to 96-well plate. A series concentration of ALP was added to each well and incubated for 30 min at 37°C. Then the stop solution of 2 M NaOH was added for stopping reaction. Finally, the absorbance of 405 nm was recorded by microplate reader.

RESULTS AND DISCUSSION

Working Principle

As illustrated in **Figure 1**, the AP holds its duplex conformation with ALP and changes to single-stranded form without ALP, which means allosteric effect, resulting in the fluorescence readout for the detection. An AP is composed of two complementary sequences, including an SA aptamer labeled by fluorophore and its total cDNA modified with a 5'-phosphoryl terminus. When ALP is present, the 5'-phosphoryl terminus of cDNA would be hydrolyzed, thus avoiding cleavage by λ exo and blocking the SA aptamer binding affinity, resulting in low fluorescence. Without ALP, the terminus of the cDNA would remain phosphorylated, leading to degradation by λ exo to release the fluorophore-labeled SA aptamer for binding to SA beads. The decreased fluorescence of SA beads in the presence of ALP is quantitatively detected by fluorescence microscopy or flow cytometry.

Optimization of the AP and Reaction Conditions

To achieve highly sensitive detection of ALP, we designed the AP by imitating the allosteric effect in nature and optimized the SA aptamer sequences, ALP incubation time, and the concentrations of lambda exo. The sensitivity of the method relies heavily on the allosteric effect of the AP, which depends on the relative binding affinities of SA aptamer to streptavidin vs. cDNA. As shown in **Figure S1** (A), we chose three SA aptamers from the literature (Bing et al., 2010), named SA1, SA2, and SA3, with different compositions of the stem and bulge. We equilibrated SA aptamers and their cDNAs in buffer with or without ALP, then added λ exo and SA beads in succession, and finally calculated the SBR (F_0/F, where F_0 and F are fluorescence intensities without and with ALP, respectively). As shown in **Figure S1** (B), SA3 provided best SBR among all three aptamers. Since the binding affinities of SA1 and SA2 to streptavidin are higher than that of SA3, when ALP is present, SA1 and SA2 are more inclined to

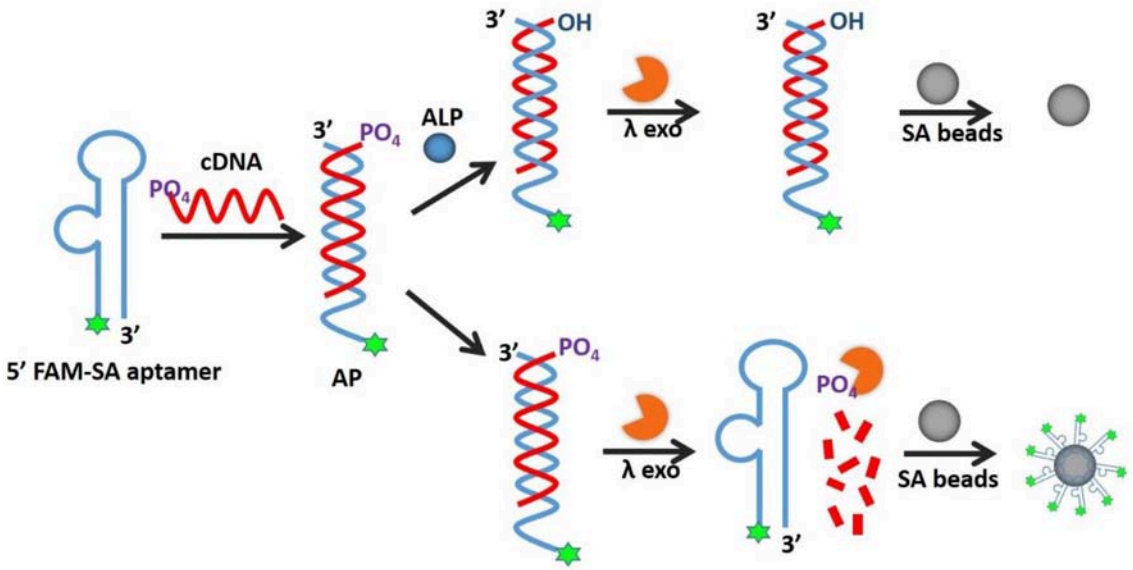

FIGURE 1 | Schematic illustration of AP for detection of alkaline phosphatase activity.

dissociate from duplex sequences and bind to SA beads, resulting in false positive signals which decreased their SBRs. Thus, SA3 was chosen for subsequent experiments.

Furthermore, as shown in **Figure S2**, we optimized the ALP incubation time from 10 to 60 min, and chose the shortest one of 10 min, since the reaction efficiency is similar for all time durations. Considering that λ exo plays an important role in sequence degradation, we optimized λ exo concentrations including 25, 50, 100, and 150 U/mL. With insufficient λ exo, the degradation efficiency on the 5'-phosphoryl terminus of cDNA3 decreases clearly. While excessive λ exo also causes non-specific degradation and waste of reagents. As shown in **Figure S3**, 100 U/mL λ exo was chosen for subsequent experiments. We also optimized λ exo incubation time ranging from 15 to 90 min (**Figure S4**). There was little difference for all tested incubation time. We chose 30 min for further experiments just to be sure the complete reaction. Fluorescence enhancement is also affected by the amount of beads present, thus we optimized the SA beads volume with 0.5–5 μL for binding to 200 nM SA3. As shown in **Figure S5**, 0.5 and 1 μL SA beads exhibited higher fluorescence intensity, but they are easy to lose during washing steps. For 3 and 5 μL SA beads, it seems that fluorescence intensity is a little lower but still noticeable. Finally, 3 μL beads were chosen as the optimal beads volume for further experiments.

Feasibility of the AP

We designed the AP consisting of SA3 and cDNA3 to test the feasibility for ALP activity detection. As shown in **Figure 2A**, the blue peak showed a low fluorescent signal, demonstrating the successful formation of the double-stranded structure to inhibit the aptamer's binding affinity. The pink peak had a higher fluorescence intensity compared to the blue peak, confirming the cleavage of cDNA3 by λ exo. Simultaneously, the fluorescence of the green peak was much lower than that of the pink one, indicating the hydroxylation of the AP by ALP. We also utilized 15% native PAGE to prove the feasibility (**Figure 2B**). Lane 1 was SA3 for comparison. For lane 2 and 3, in the absence of λ exo, SA3, and cDNA3 remained good hybridization with or without ALP. For lane 4, without ALP, cDNA3 was degraded so that the upper band was decreased as well as SA3 band recovered. For lane 5, ALP dephosphorylated the AP and protected it from λ exo cleavage, leaving the AP intact. Therefore, gel electrophoresis verifies the good hybridization between SA3 and cDNA3, dephosphorylation of 5'-phosphoryl terminus by ALP and specific digestion of phosphorylated ssDNA by λ exo. Furthermore, with the fluorescence microscope (**Figure 2C**), there was no fluorescence of the AP in the presence of 10 U/mL ALP, while the beads remained highly fluorescent in the absence of ALP. Therefore, the consistent results of flow cytometry, gel electrophoresis, and fluorescence microscopy indicate the feasibility of the AP design.

Quantitative Measurement of ALP in Buffer and Biological Samples

The quantitative detection of ALP was conducted with a series of concentrations of ALP by flow cytometry. As shown in **Figure 3A** and **Figure S6**, $(F_0\text{-}F)/F_0$ increased with the growing concentration of ALP in buffer, where F_0 and F are fluorescence intensities without and with ALP, respectively. From the fitting curve in **Figure 3A**, the LOD was 0.012 U/mL (3σ/S) and the linear range was 0.02–0.15 U/mL ($R^2 = 0.9902$), which are both superior or comparable to those of other reported methods (**Table S2**) (Dong et al., 2015; Xing et al., 2016). For clinical applications, the normal range of ALP in human serum is from 0.04 to 0.11 U/mL. In this case, the proposed method covers the normal detection range of ALP in clinical applications and

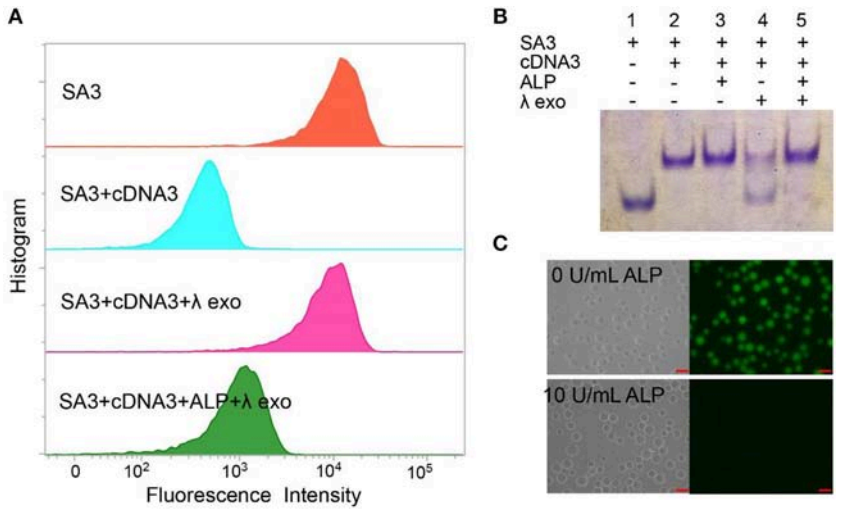

FIGURE 2 | Different methods for proving the feasibility of AP with 10 U/mL ALP: **(A)** flow cytometry, **(B)** 15% native PAGE. Lane 1, SA3; Lane 2, SA3, and cDNA3; Lane 3, SA3, cDNA3, and ALP; Lane 4, SA3, cDNA3, and λ exo; Lane 5, SA3, cDNA3, ALP, and λ exo. **(C)** fluorescence microscope.

meets the need for clinical diagnosis (Wolf, 1978). As further evidence of the effect of added ALP, fluorescence microscopy was also used for ALP screening. As shown in **Figure 3C**, distinct fluorescence decrease was observed with an incremental introduction of ALP from 0.02 to 0.15 U/mL, which is consistent with the result of flow cytometry. Therefore, based on the enrichment of fluorescence on beads with no or low levels of ALP, the signal output of the assay could be achieved by different detection methods, including flow cytometry and fluorescence microscope, providing multiple choices for ALP activity screening.

The localization of SA3 on the microbeads made it possible to separate signal generation from the interfering autofluorescence from species in the complicated biological matrix, making the AP applicable to biological samples. To verify this advantage, 10% human serum was chosen as a model complex system for our assay. Since human serum contains multiple components with autofluorescence, including amino acids, vitamins, lipids, and nucleic acid derivatives, as well as growth factor, which added to the background signal and increased homogeneous detection difficulty (Wolfbeis and Leiner, 1985). In our experiment, bead-based separation integrated the signal collection and interfering species separation, leading to highly sensitive and selective detection in complex samples. As shown in **Figure 3B**, $(F_0\text{-}F)/F_0$ increased with increasing concentrations of ALP in 10% human serum. Based on the fitting curve in **Figure 3B**, the LOD was found to be 0.019 U/mL (3σ/S) and the linear range was 0.02–0.15 U/mL ($R^2 = 0.9768$), both of which are comparable to those in buffer. In addition, 20% human serum sample was also tested (**Figure S7**), and similar results were obtained with LOD of 0.021 U/mL (3σ/S) and the linear range of 0.025–0.15 U/mL. Moreover, the AP was also spiked in Hela cell lysate of 10^5 cells/mL. As shown in **Figure S8**, the linear range was obtained as 0.05–0.20 U/mL and the LOD was 0.014 U/mL (3σ/S). Therefore, the result indicates that our proposed method is promising for detection in complex biological matrix and clinical sample.

To compare with traditional methods, we also conducted the ALP detection using PNPP substrate. As shown in **Figure S9**, the linear range was 0.15–0.35 U/mL and the LOD was 0.13 U/mL (3σ/S), which is nearly ten times higher than that of the AP. Therefore, the AP strategy outweighs the traditional method with higher sensitivity.

Selectivity Study

Selectivity of the AP assay was studied with six non-related enzymes or proteins, including thrombin, T4 ligase, lysozyme, HSA, proteinase K, trypsin, and de-activated ALP. As shown in **Figure 4**, $(F_0\text{-}F)/F_0$ was enhanced only in the presence of ALP, while negligible fluorescence change was observed for other enzymes or proteins with concentrations 10 times that of ALP. The results indicate that our proposed method exhibits good selectivity and enables distinguishing ALP from other interfering species, including other hydrolases such as proteinase K and trypsin.

Inhibitor Study

As a crucial index for clinical medicine, excess ALP in the human body can induce serious diseases (Hosking et al., 1998). Thus, it is important to study the inhibitor of ALP for medical treatment, drug development and cancer therapy. We chose sodium orthovanadate (Na_3VO_4) as a model for ALP inhibitor screening. Sodium orthovanadate is an inorganic compound that exhibits a variety of biological activities, commonly used in inhibition of phosphatases and ATPases for preventing proteins from phosphorylation or promoting phosphorylation of activation (Gordon, 1991). In principle, it is orthovanadate's resemblance to a transition-state analog of phosphate through hydration or chelation that is key to the mechanism of

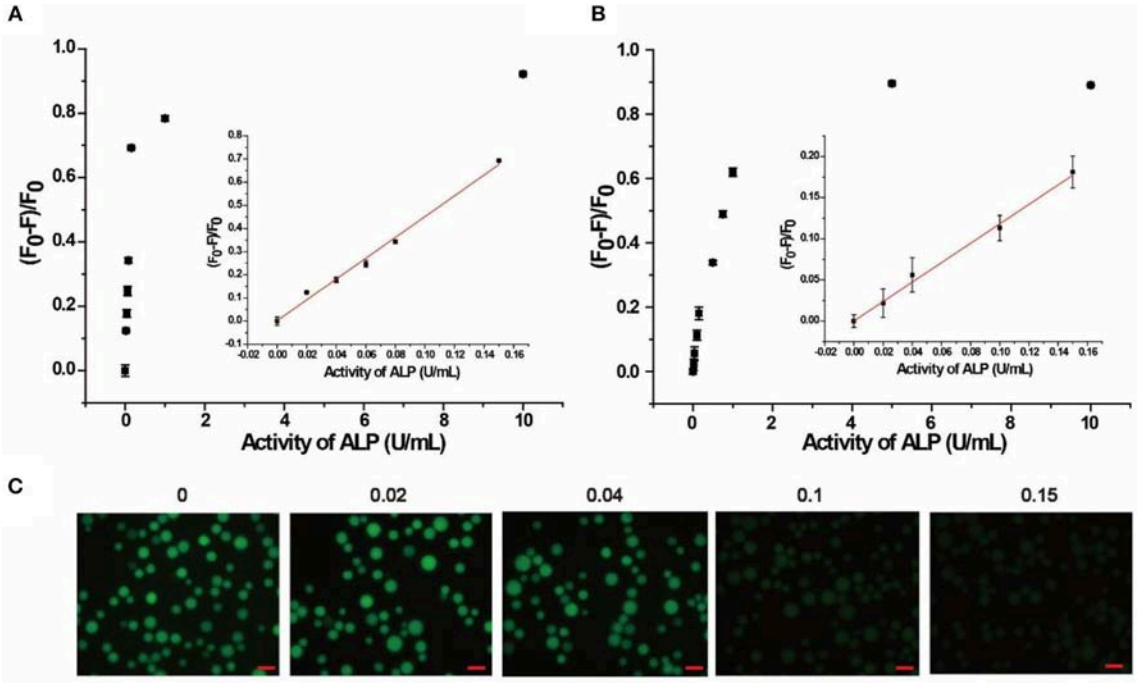

FIGURE 3 | Response of quantitative detection of ALP range from 0 to 10 U/mL in **(A)** buffer solution, **(B)** in 10% human serum monitored by flow cytometry. Inset is the calibration curve ranging from 0.02 to 0.15 U/mL. **(C)** Response of the AP to different concentrations of ALP in buffer solution monitored by fluorescence microscope. Error bars indicate the standard deviations of three samples. Scale bars are 50 μm.

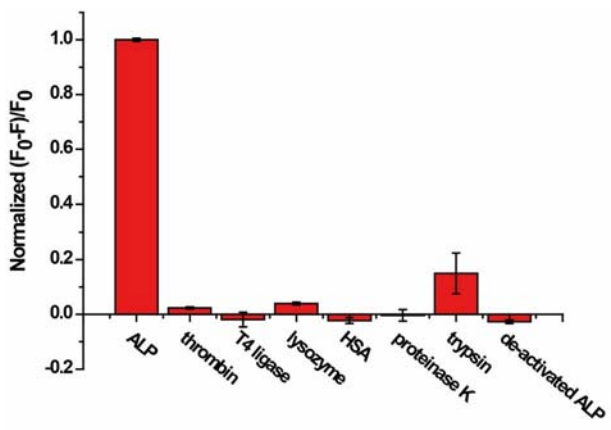

FIGURE 4 | Response of the AP to ALP, thrombin, T4 ligase, lysozyme, HSA, proteinase K, trypsin, and de-activated ALP for specificity study. The concentration of ALP is 2 U/mL, and the concentration of other enzymes and proteins are 20 U/mL or 10 nM. Error bars indicate the standard deviations of three samples.

inhibition of ALP by orthovanadate (Seargeant and Stinson, 1979).

As shown in **Figures 5A,B**, fluorescence intensities of beads read by flow cytometry exhibited gradual enhancement with increasing concentrations of Na_3VO_4. The IC50 (half maximal inhibitory concentration) value was found to be 400 μM (±150 μM), which is in good accordance with other reported work (Chen et al., 2014; Wang et al., 2014). Besides, we have studied another inhibitor L-cysteine (**Figure S10**), the corresponding IC50 was estimated to be 125 μM (±50 μM), which is close to the values obtained by using other methods (Van, 1972), indicating that our method has general applicability in inhibitor screening. Hence, the AP strategy has the potential not only to detect ALP activity, but also to investigate ALP inhibitors and develop new anticancer drugs.

Quantification of IgG Based on ALP-Linked Immunosorbent Assay

Considering its low cost, good stability, high sensitivity, and wide substrate applicability, ALP is generally used to conjugate to streptavidin or a detection antibody for signal amplification in immunoassay (Gao et al., 2014). Since we have demonstrated the feasibility of ALP analysis of the AP, the probe was further applied into an ALP-linked ELISA, taking human IgG as a model. **Figure 6A** illustrates the integration of the quantification of human IgG through a sandwich immunoassay, ALP enzymatic hydrolysis of the AP and separation of the detection signal on SA beads. In the sandwich immunoassay, capture antibody of anti-human IgG was coated on a 96-well plate. After capture of target human IgG, the detection antibody of ALP-labeled goat anti-human IgG was added to form immune complexes. Then AP was added to react with ALP, resulting in hydrolysis of the 5'-phosphoryl terminus of cDNA3. The λ

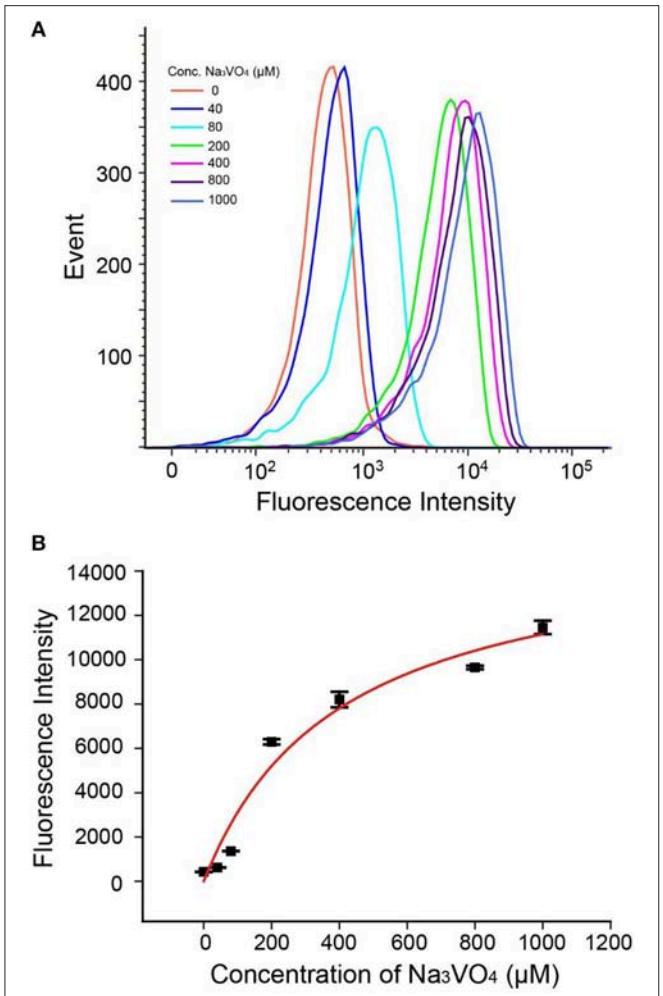

FIGURE 5 | (A) Flow cytometry data of Na_3VO_4 inhibition efficiency. **(B)** Response of the AP to 2 U/mL ALP with inhibitor Na_3VO_4. Error bars indicate the standard deviations of three samples.

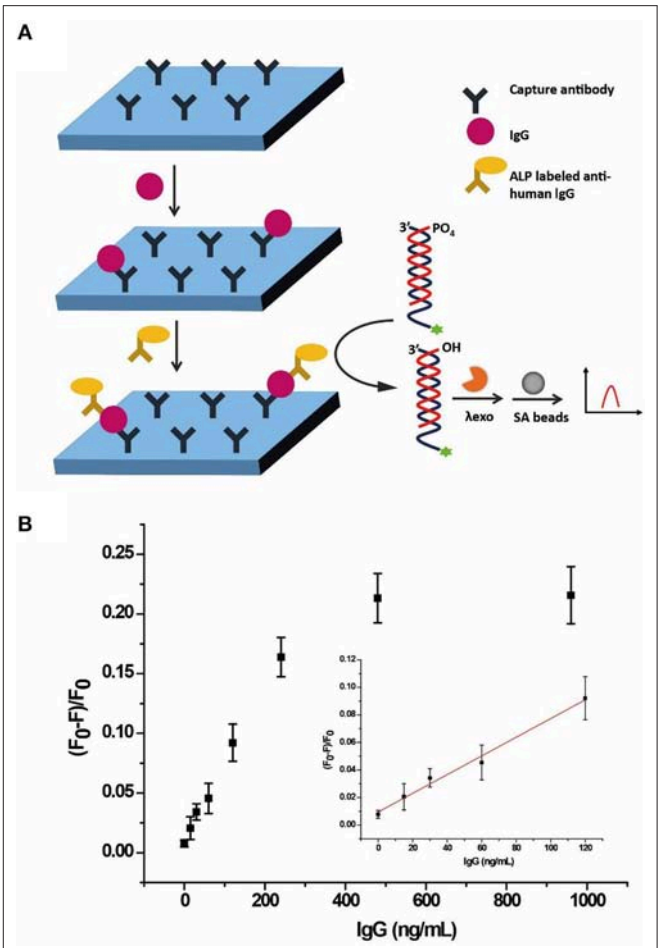

FIGURE 6 | (A) Schematic illustration of the allosteric probe for detection of IgG through ALP-labeled immunoassay. **(B)** Response of the AP to different concentrations of human IgG through ALP-linked ELISA in buffer solution monitored by flow cytometry. Error bars indicate the standard deviations of three samples.

exo digested the unhydrolyzed AP, releasing the single strand SA3 to be captured by SA beads. As a result, the fluorescence of SA3 was enriched on the beads and monitored by flow cytometry.

As shown in **Figure 6B**, $(F_0\text{-}F)/F_0$ gradually increased with the increasing concentration of human IgG from 0 to 960 ng/mL in buffer. The LOD was 12.9 ng/mL ($3\sigma/S$) and the linear range was 15–120 ng/mL ($R^2 = 0.9882$), where F_0 and F are fluorescence intensities without and with ALP, respectively. Since the normal range of IgG for healthy adults is 7–16 g/L (Dati et al., 1996), the result clearly showed that the AP with an adequate detection range and sensitivity could be applied to the quantification of human IgG.

CONCLUSIONS

In summary, we have developed a new class of probes based on the allosteric effect, called allosteric probes or AP, which can be applied for ALP activity detection. In AP assay, the single fluorophore-labeled design makes the probe simpler and cheaper than molecular beacons, which requires labeling by both fluorescence and quenching groups. Besides, only one exonuclease is used for cutting DNA sequences, avoiding the need for other assistant enzymes. In addition, the excellent binding affinity and specificity between SA aptamer and SA shortens the binding time to 5 min, and the bead-based enrichment enables a detection limit of 0.012 U/mL without the use of any nucleic acid amplification, especially avoiding complicated manipulations and cross contamination. Furthermore, due to the bead-based separation, the probe can be used in complex biological samples, averting interference from background fluorescence. Moreover, the extending applications of inhibitor study of ALP and analysis of human IgG were also explored. With the advantages of simple design, high sensitivity, easy operation, and good compatibility in complex solutions and in ALP-linked immunosorbent assays, our AP assay has great

potential for further applications in ALP inhibitor screening, drug discovery and early diagnosis of cancer. With further research to optimize the probe sequences, the AP could serve as an excellent probe for detection of other kinds of phosphatases and kinases.

AUTHOR CONTRIBUTIONS

ZZ, YS, and CY conceived and guided the study. JG performed the experiments and analyzed the data with help from MG, LL, and KZ. JG wrote the first draft of the manuscript. ZZ, YS, DL, and TT contributed to manuscript revision, read, and approved the submitted version.

ACKNOWLEDGMENTS

We thank the National Natural Science Foundation of China (21735004, 21435004, 21775128, 21705024, 21521004), Program for Changjiang Scholars and Innovative Research Teams in University (IRT13036) and the National Science Fund for Fostering Talents in Basic Science (NFFTBS, J1310024) for financial support.

SUPPLEMENTARY MATERIAL

The Supplementary Material for this article can be found online at: https://www.frontiersin.org/articles/10.3389/fchem.2018.00618/full#supplementary-material

REFERENCES

Barroso, J., Saa, L., Grinyte, R., and Pavlov, V. (2016). Photoelectrochemical detection of enzymatically generated CdS nanoparticles: application to development of immunoassay. *Biosens. Bioelectron.* 77, 323–329. doi: 10.1016/j.bios.2015.09.043

Berberoglu, Z., Gursoy, A., Bayraktar, N., Yazici, A. C., Bascil Tutuncu, N., and Demirag, N. (2007). Rosiglitazone decreases serum bone-specific alkaline phosphatase activity in postmenopausal diabetic women. *J. Clin. Endocrinol. Metab.* 92, 3523–3530. doi: 10.1210/jc.2007-0431

Bing, T., Yang, X., Mei, H., Cao, Z., and Shangguan, D. (2010). Conservative secondary structure motif of streptavidin-binding aptamers generated by different laboratories. *Bioorg. Med. Chem.* 18, 1798–1805. doi: 10.1016/j.bmc.2010.01.054

Brar, H. S., Sisley, J. F., and Johnson, R. H. (1993). Value of preoperative bone and liver scans and alkaline-phosphatase levels in the evaluation of breast-cancer patients. *Am. J. Surg.* 165, 221–223. doi: 10.1016/S0002-9610(05)80512-4

Chen, Y., Li, W., Wang, Y., Yang, X., Chen, J., Jiang, Y., et al. (2014). Cysteine-directed fluorescent gold nanoclusters for the sensing of pyrophosphate and alkaline phosphatase. *J. Mater. Chem. C* 2, 4080–4085. doi: 10.1039/c4tc00173g

Dati, F., Schumann, G., Thomas, L., Aguzzi, F., Baudner, S., Bienvenu, J., et al. (1996). Consensus of a group of professional societies and diagnostic companies on guidelines for interim reference ranges for 14 proteins in serum based on the standardization against the IFCC/BCR/CAP Reference Material (CRM 470). International Federation of Clinical Chemistry. Community Bureau of Reference of the Commission of the European Communities. College of American Pathologists. *Eur. J. Clin. Chem. Clin. Biochem.* 34, 517–520.

Dong, L., Miao, Q., Hai, Z., Yuan, Y., and Liang, G. (2015). Enzymatic hydrogelation-induced fluorescence turn-off for sensing alkaline phosphatase *in vitro* and in living cells. *Anal. Chem.* 87, 6475–6478. doi: 10.1021/acs.analchem.5b01657

Gao, M., Guo, J., Song, Y., Zhu, Z., and Yang, C. J. (2017). Detection of T4 polynucleotide kinase via allosteric aptamer probe platform. *ACS Appl. Mater. Interfaces* 9, 38356–38363. doi: 10.1021/acsami.7b14185

Gao, Z., Hou, L., Xu, M., and Tang, D. (2014). Enhanced colorimetric immunoassay accompanying with enzyme cascade amplification strategy for ultrasensitive detection of low-abundance protein. *Sci. Rep.* 4:3966. doi: 10.1038/srep03966

Garnero, P., and Delmas, P. D. (1993). Assessment of the serum levels of bone alkaline-phosphatase with a new immunoradiometric assay in patients with metabolic bone-disease. *J. Clin. Endocrinol. Metabol.* 77, 1046–1053.

Gordon, J. A. (1991). Use of vanadate as protein-phosphotyrosine phosphatase inhibitor. *Meth. Enzymol.* 201, 477–482. doi: 10.1016/0076-6879(91)01043-2

Hosking, D. J., Eusebio, R. A., and Chines, A. A. (1998). Paget's disease of bone: reduction of disease activity with oral risedronate. *Bone* 22, 51–55. doi: 10.1016/S8756-3282(97)00222-6

Hu, X. L., Wu, X. M., Fang, X., Li, Z.J., and Wang, G. L. (2016). Switchable fluorescence of gold nanoclusters for probing the activity of alkaline phosphatase and its application in immunoassay. *Biosens. Bioelectron.* 77, 666–672. doi: 10.1016/j.bios.2015.10.046

Huang, P. J. J., and Liu, J. (2010). Flow cytometry-assisted detection of adenosine in serum with an immobilized aptamer sensor. *Anal. Chem.* 82, 4020–4026. doi: 10.1021/ac9028505

Jiang, H., and Wang, X. (2012). Alkaline phosphatase-responsive anodic electrochemiluminescence of CdSe nanoparticles. *Anal. Chem.* 84, 6986–6993. doi: 10.1021/ac300983t

Jiao, H., Chen, J., Li, W., Wang, F., Zhou, H., Li, Y., et al. (2014). Nucleic acid-regulated perylene probe-induced gold nanoparticle aggregation: a new strategy for colorimetric sensing of alkaline phosphatase activity and inhibitor screening. *ACS Appl. Mater. Interfaces* 6, 1979–1985. doi: 10.1021/am405020b

Liang, J., Kwok, R. T., Shi, H., Tang, B. Z., and Liu, B. (2013). Fluorescent light-up probe with aggregation-induced emission characteristics for alkaline phosphatase sensing and activity study. *ACS Appl. Mater. Interfaces* 5, 8784–8789. doi: 10.1021/am4026517

Liu, X. G., Xing, X. J., Li, B., Guo, Y. M., Zhang, Y. Z., Yang, Y., et al. (2016). Fluorescent assay for alkaline phosphatase activity based on graphene oxide integrating with lambda exonuclease. *Biosens. Bioelectron.* 81, 460–464. doi: 10.1016/j.bios.2016.03.030

Ma, J. L., Yin, B. C., Wu, X., and Ye, B.C. (2016). Copper-mediated DNA-scaffolded silver nanocluster On-Off switch for detection of pyrophosphate and alkaline phosphatase. *Anal. Chem.* 88, 9219–9225. doi: 10.1021/acs.analchem.6b02465

Miao, P., Ning, L., Li, X., Shu, Y., and Li, G. (2011). An electrochemical alkaline phosphatase biosensor fabricated with two DNA probes coupled with lambda exonuclease. *Biosens. Bioelectron.* 27, 178–182. doi: 10.1016/j.bios.2011.06.047

Ooi, K., Shiraki, K., Morishita, Y., and Nobori, T. (2007). High-molecular intestinal alkaline phosphatase in chronic liver diseases. *J. Clin. Lab. Anal.* 21, 133–139. doi: 10.1002/jcla.20178

Porstmann, B., Porstmann, T., Nugel, E., and Evers, U. (1985). Which of the commonly used marker enzymes gives the best results in colorimetric and fluorimetric enzyme immunoassays - horseradish-peroxidase, alkaline-phosphatase or beta-galactosidase. *J. Immunol. Methods* 79, 27–37. doi: 10.1016/0022-1759(85)90388-6

Qian, Z., Chai, L., Tang, C., Huang, Y., Chen, J., and Feng, H. (2015). Carbon quantum dots-based recyclable real-time fluorescence assay for alkaline phosphatase with adenosine triphosphate as substrate. *Anal. Chem.* 87, 2966–2973. doi: 10.1021/ac504519b

Ruan, C., Wang, W., and Gu, B. (2006). Detection of alkaline phosphatase using surface-enhanced Raman spectroscopy. *Anal. Chem.* 78, 3379–3384. doi: 10.1021/ac0522106

Seargeant, L. E., and Stinson, R. A. (1979). Inhibition of human alkaline phosphatases by vanadate. *Biochem. J.* 181, 247–250. doi: 10.1042/bj1810247

Song, Y., Cui, L., Wu, J., Zhang, W., Zhang, W. Y., Kang, H., et al. (2011). Allosteric molecular beacons for sensitive detection of nucleic acids, proteins, and small molecules in complex biological samples. *Chemistry* 17, 9042–9046. doi: 10.1002/chem.201101353

Song, Y., Zhang, W., An, Y., Cui, L., Yu, C., Zhu, Z., et al. (2012). Label-free visual detection of nucleic acids in biological samples with single-base mismatch detection capability. *Chem. Commun.* 48, 576–578. doi: 10.1039/C1CC15777A

Van, B. H. (1972). Kinetics and inhibition of alkaline phosphatases from canine tissues. *Biochim. Biophys. Acta* 289, 158–168. doi: 10.1016/0005-2744(72)90118-0

Wang, F., Li, Y., Li, W., Zhang, Q., Chen, J., Zhou, H., et al. (2014). A facile method for detection of alkaline phosphatase activity based on the turn-on fluorescence of resorufin. *Anal. Methods* 6, 6105–6109. doi: 10.1039/C4AY00634H

Wolf, P. L. (1978). Clinical significance of an increased or decreased serum alkaline phosphatase level. *Arch. Pathol. Lab. Med.* 102, 497–501.

Wolfbeis, O. S., and Leiner, M. (1985). Mapping of the total fluorescence of human-blood serum as a new method for its characterization. *Anal. Chim. Acta* 167, 203–215. doi: 10.1016/S0003-2670(00)84422-0

Xing, X., Liu, X., Zhou, Y., Xu, D., Pang, D., and Tang, H. (2016). Graphene oxide enhanced specificity at aptamer and its application to multiplexed enzymatic activity sensing. *RSC Adv.* 6, 11815–11821. doi: 10.1039/C5RA25481G

Yang, J., Zheng, L., Wang, Y., Li, W., Zhang, J., Gu, J., et al. (2016). Guanine-rich DNA-based peroxidase mimetics for colorimetric assays of alkaline phosphatase. *Biosens. Bioelectron.* 77, 549–556. doi: 10.1016/j.bios.2015.10.003

Zhang, W., Zu, X., Song, Y., Zhu, Z., and Yang, C. J. (2016). Detection of DNA methyltransferase activity using allosteric molecular beacons. *Analyst* 141, 579–584. doi: 10.1039/C5AN01763G

Zhou, B., Yang, H., Deng, Y., Liu, M., Liu, B., He, N., et al. (2016). Ultrasensitive quantitation of MicroRNAs via magnetic beads-based chemiluminesent assay. *Sci. China Chem.* 59, 1051–1058. doi: 10.1007/s11426-015-0504-0

Conflict of Interest Statement: The authors declare that the research was conducted in the absence of any commercial or financial relationships that could be construed as a potential conflict of interest.

Copyright © 2018 Guo, Gao, Song, Lin, Zhao, Tian, Liu, Zhu and Yang. This is an open-access article distributed under the terms of the Creative Commons Attribution License (CC BY). The use, distribution or reproduction in other forums is permitted, provided the original author(s) and the copyright owner(s) are credited and that the original publication in this journal is cited, in accordance with accepted academic practice. No use, distribution or reproduction is permitted which does not comply with these terms.

frontiers in Chemistry

ORIGINAL RESEARCH
published: 11 April 2019
doi: 10.3389/fchem.2019.00242

Substrate-Assisted Visualization of Surfactant Micelles via Transmission Electron Microscopy

Zekun Zhang, Kaitao Li, Rui Tian and Chao Lu**

State Key Laboratory of Chemical Resource Engineering, Beijing University of Chemical Technology, Beijing, China

The visualization of the micellar morphological evolution for surfactant has drawn much attention due to its self-assemble ability to fold into various structures. However, the direct observation of the soft materials with low atomic number has been hampered because of the poor scattering contrast and complex staining process by the traditional transmission electron microscopy (TEM) techniques. Herein, we reported a novel strategy to the visualization of surfactant micelles with the assistance of layered double hydroxides (LDHs) via TEM. Owing to the uniformly distributed metal ions and positive charges in the LDHs, the surfactant at the micelle-water interface reacted with LDHs to form a stabilized architecture through electrostatic and hydrogen-bond interactions. The morphologies of the surfactant can be clearly observed through the surfactant-LDHs architectures, exhibiting high contrast by TEM techniques. Significantly, the micellar evolutions involving the spherical, rodlike, and wormlike shapes were successfully distinguished. Our results may provide great possibilities and inspirations for the visualization for morphology of soft matters.

Keywords: transmission electron microscopy, visualization, surfactant micelles, layered double hydroxides, morphological evolution

OPEN ACCESS

Edited by:
Huangxian Ju,
Nanjing University, China

Reviewed by:
Chih-Ching Huang,
National Taiwan Ocean University, Taiwan
Xia Guan,
Louisiana State University, United States

****Correspondence:***
Rui Tian
tianrui@mail.buct.edu.cn
Chao Lu
luchao@mail.buct.edu.cn

Specialty section:
This article was submitted to Analytical Chemistry, a section of the journal Frontiers in Chemistry

Received: *06 December 2018*
Accepted: *26 March 2019*
Published: *11 April 2019*

Citation:
Zhang Z, Li K, Tian R and Lu C (2019) Substrate-Assisted Visualization of Surfactant Micelles via Transmission Electron Microscopy. Front. Chem. 7:242. doi: 10.3389/fchem.2019.00242

INTRODUCTION

Surfactant is a widely applied soft material which exhibits self-assemble ability to fold into micelles with various structures (Jain and Bates, 2003; Stano and Luisi, 2010; Liu et al., 2018). The studies of the morphology and structure for micelles have drawn increasing attention due to their great significance in biological and material science (Landsmann et al., 2010; Wang et al., 2013; Hu and Chou, 2014). Transmission electron microscopy (TEM) is a valid technique widely applied to provide morphological aspects for visualization (Jung et al., 2003; O'Reilly et al., 2005; Honda et al., 2010). However, the observation for the surfactant micelles has been hampered due to the poor scattering contrast of the constituent elements with low atomic number (Egerton, 2013; Proetto et al., 2014). Although the supplemented attachments of TEM (such as liquid-cell and cryo-TEM) can provide supports for the morphological studies, this method suffered from sophisticated operation and sampling procedure (Geng and Discher, 2005; Parent et al., 2017; Zeng et al., 2017; Creatto et al., 2018; Stawski et al., 2018; Zhao et al., 2018; Suys et al., 2019). Therefore, it is a topic of significance to realize the visualization for the morphological evolution of the micelles during the formation process.

Staining is commonly done with heavy metal oxides (e.g., OsO_4 and RuO_4) for improving TEM contrast (Trent et al., 1983; Serizawa et al., 2000; Humphrey, 2009; Aramaki et al., 2017; Xu et al., 2017; Parker et al., 2018). Unsatisfactorily, the staining process usually comes along with inhomogeneity for staining segment, which might affect the true representation of the samples (Smith and Bryg, 2006). Moreover, the toxicity of the heavy metals has largely limited the application of staining. The fact has motivated us to explore an environmentally friendly alternative to enhance the scattering contrast and assist the visualization of micelles (Claypool et al., 1997; Aso et al., 2013).

Layered double hydroxides (LDHs) are a class of 2D inorganic metallic layered materials composed of edge-sharing metal-hydroxide octahedral structure (Abellan et al., 2012; Tian et al., 2018). The versatile di- and trivalent metal cations distributed uniformly in the host layer with the tunable electropositivity derived from the trivalent metal ions (Wang and O'Hare, 2012; Tian et al., 2015). The constituent metal elements, positively-charged layers and the abundant active sites of LDHs provided great possibilities for the construction of functional composites through electrostatic interaction and hydrogen bonds (Rogez et al., 2011; Fan et al., 2014). These superiorities inspired us to explore the potential of LDHs to assist the visualization of surfactant micelles by TEM technique.

In this study, we demonstrated the visualization of surfactant micelles with the assist of LDHs via traditional TEM. An amphoteric surfactant *N*-hexadecyl-*N,N*-dimethyl-3-ammonio-1-propanesulfonate (SHDAB) with sulfonate anion in the head was employed. The functional groups at the micelle-water interface could react with LDHs to form a stabilized SHDAB@LDHs architecture by electrostatic and hydrogen-bond interactions (**Figure 1**). Owing to the capillary-compensated flow during droplet evaporation process, the LDHs nanoplates deposited at the edge of the droplet as "coffee-ring" (Deegan et al., 1997; Parneix et al., 2010; Cui et al., 2012) (**Scheme S1**). Visualization images with excellent contrast were achieved for SHDAB@LDHs architecture through TEM techniques. More importantly, the whole micellar morphological transition involving the spherical, rodlike and wormlike shapes could be effectively recognized with the continuously increased concentration of SHDAB (**Scheme S2**). The sizes of the micelles in the evolution identified with the data obtained from atomic force microscope (AFM). Therefore, it is anticipated that LDHs-assisted visualization of surfactant micelles may open new possibilities of TEM applications, especially for the soft materials.

METHODS

Materials, Reagents, and Instruments

All reagents in experiments are of analytical grade and used without further purification. NaOH, $Al(NO_3)_3{\cdot}9H_2O$, $Mg(NO_3)_2{\cdot}6H_2O$ are purchased from Beijing Chemical Reagent Company (Beijing, China). SHDAB is purchased from Tokyo Chemical Industry Co. Ltd (Tokyo, Japan). Ultra-pure water was obtained from the Milli-Q purification system (Barnstead, CA, USA).

Surface tension measurements of the SHDAB surfactant were measured on a Force Tensiometer (K100) by the Wilhelmy plate technique (Kruss, Germany). Electrical conductivity measurements were accomplished using an EC 215 conductivity meter (Shanghai Jingmi Instrumental Co., China). The ultrasonic treatment was implemented in an ultrasonic cleaning machine (Kunshan Ultrasonic Instrument Co. Ltd., China) with the frequency of 100%. TEM images were measured by the Tecnai $G^2$20 (FEI Company, USA) with the accelerating voltage of 200 kV. The morphological studies of the LDHs were implemented on a scanning electron microscope (SEM Hitachi S-4700). The morphology data of SHDAB micelles were acquired on AFM by the NanoScope 9.1 (Bruker, Germany) instrument. X-ray diffraction (XRD) patterns of SHDAB, LDHs and SHDAB@LDHs architectures were measured on a D8 ADVANCE X-ray diffractometer (Bruker, Germany). FT-IR spectra were performed on a Nicolet 6700 (Thermo Electron). Zeta potentials of all the samples were recorded on a Malvern Zetasizer 3000HS nano-granularity analyzer. Isothermal titration calorimeter (ITC) was employed to study the interaction between SHDAB and LDHs on a Nano ITC (TA Instruments Waters, LLC, UT). 1.0 mL SHDAB aqueous (3.69×10^{-4} mol·L^{-1}) was titrated into 0.25 mL LDHs (2.00×10^{-3} mol·L^{-1}) in the measurement which was periodically calibrated with an internal electric heater. The heats of interaction during each injection were measured by integration of each titration peak using the ORIGIN software delivered with the ITC.

Synthesis of MgAl-CO_3-LDHs

According to the reported method (Gao et al., 2017; Tian et al., 2018), the LDHs were prepared with a few modifications. A mixed salt solution of $Mg(NO_3)_2{\cdot}6H_2O$ (19.200 g, 0.075 mol) and $Al(NO_3)_3{\cdot}9H_2O$ (9.375g, 0.025 mol) was dissolved in 150 mL water in a 250 mL flask. Subsequently, the prepared alkaline liquor of NaOH (8.000 g, 0.200 mol) was added to keep a constant pH value of 8.5. Then, the suspension was stirred for another 20 min, followed by transfer to a furnace tube at 110°C for 24 h. Finally, the precipitate was centrifuged, washed with water and stored at 4°C for further use.

Preparation of Surfactant Micelles

The stock solution was prepared by dissolving SHDAB (0.017 g, 0.044 mol) in 30 mL ultra-pure water. Then, the SHDAB solution with different concentration (0.0295 mM, 0.059 mM, 0.295 mM, 1.48 mM) was prepared. After the ultrasonic treatment at 50°C for 4 h, the micelles with different morphologies were acquired.

Synthesis of SHDAB@LDHs Architecture

Firstly, the LDHs suspensions were treated under ultrasonic to obtain a uniformly dispersed colloidal solution. Then, the as-prepared LDHs with different volumes (3.53, 7.06, 35.29, 176.45 μL) were added into the SHDAB surfactant micelles solution of different concentration (0.04 mM, 0.08 mM, 0.40 mM, 2.00 mM), respectively. Finally, the mixtures were treated under ultrasonic irradiation at 50°C for 4 h to prepare the SHDAB@LDHs architectures. In order to evaluate the morphological evolution of SHDAB micelles, *m*-SHDAB@LDHs architectures were prepared

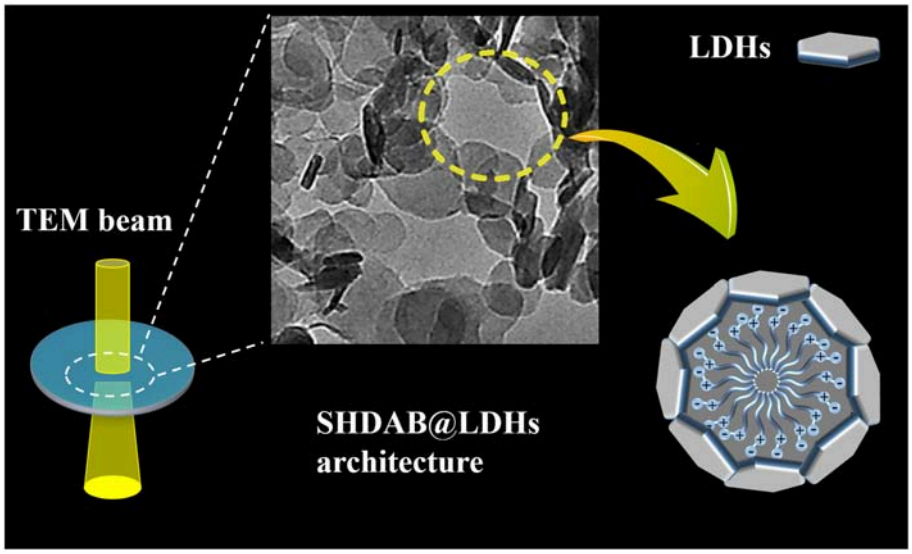

FIGURE 1 | Schematic representation of visualization for surfactant micelles with the assist of LDHs via TEM imaging.

TABLE 1 | The concentrations of SHDAB and LDHs in samples *m*-SHDAB@LDHs architectures.

Samples	SHDAB/mM	LDHs/mM
$m = 0.0295$	0.0295	0.04
$m = 0.0590$	0.0590	0.08
$m = 0.295$	0.295	0.40
$m = 1.48$	1.48	2.00

with the molecular ratio of SHDAB to LDHs determined as 0.295 to 0.400. The detailed compositions in *m*-SHDAB@LDHs architectures were listed in **Table 1**.

RESULTS AND DISCUSSION

Characterizations of the Surfactant

N-hexadecyl-*N,N*-dimethyl-3-ammonio-1-propanesulfonate (SHDAB) is a kind of betaine surfactant with negatively charged sulfonic acid in headgroup (**Figure S1**). To study the morphological transitions of SHDAB, the critical micelle concentration (CMC) has been investigated through the surface activities study (Claussen, 1967). The surface tension (γ) was plotted with the logarithm value of concentration for SHDAB. With the increased logarithm value of concentration for SHDAB, the surface tension of SHDAB decreased sharply at first and reached a relatively constant value after a marked change at 0.0295 mM for SHDAB (**Figure 2A**). The phenomenon was attributed to the presence of SHDAB monomers which preferred to adsorb at the water-air interface when the concentrations were below the CMC. When the adsorption at the water-air interface got saturated with the increased SHDAB monomers, the SHDAB tended to form micelles in the solution, exhibiting an almost constant surface tension. The inflection point from **Figure 2A** demonstrated that the CMC of SHDAB was 0.0295 mM. Moreover, the value of CMC was also investigated by conductivity measurements (Guégan et al., 2016). **Figure 2B** showed that the conductivity (κ) grew linearly with the logarithm value of concentration for SHDAB increased. Then, a slow growth was observed when the concentration of SHDAB was larger than 0.0295 mM. Such a turning point manifested the formation of micelles was determined as CMC for SHDAB, in agreement with that obtained by surface tension measurement. Notably, the CMC value of 0.0295 mM for SHDAB accorded with previous work (Liu et al., 2013).

Visualization of Surfactant Assisted by LDHs

To observe the morphological evolution of SHDAB micelles in different concentrations, MgAl-LDHs nanoplates were prepared via a hydrothermal method (**Figure S2**) (Gao et al., 2017; Tian et al., 2018). As shown in **Figure 3A**, the LDH particles were well-dispersed after ultrasonic irradiation. High contrast of inherent LDHs can be observed, as a result of the presence of metal elements (Mg and Al) in the host layers. On the contrary, TEM image of SHDAB micelles (0.295 mM) showed the blurred boundaries on account of weak scattering contrast by the constituent light elements (**Figure 3B**). In order to distinguish the SHDAB micelles, LDH particles were added into SHDAB to construct the SHDAB@LDHs architecture for visualization. Significantly, uniformly-distributed porous structure surrounded by continuous LDHs could be observed (**Figure S3**). The reason for the formation of the porous structure may be due to the fact that the positively charged LDHs were attached at the edges of the SHDAB micelles. During the evaporation process, the LDHs nanoparticles fell apart to the edge and accumulated at the border of the SHDAB@LDHs composites, and a "coffee-ring"

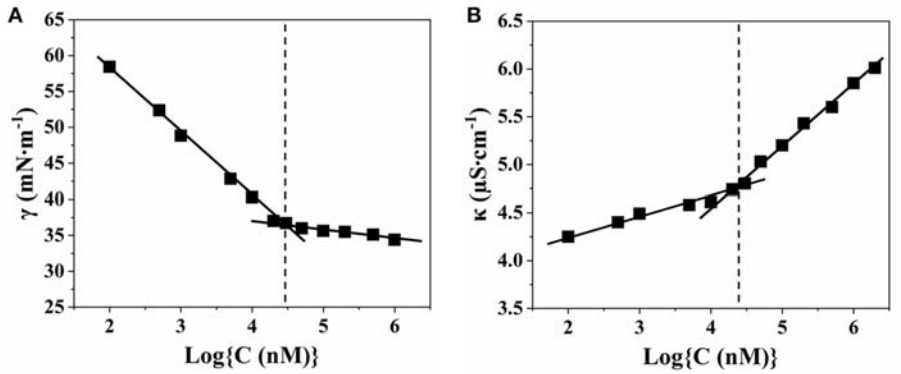

FIGURE 2 | Relationship between the concentration of SHDAB with **(A)** surface tension (γ) and **(B)** conductivity (κ), respectively.

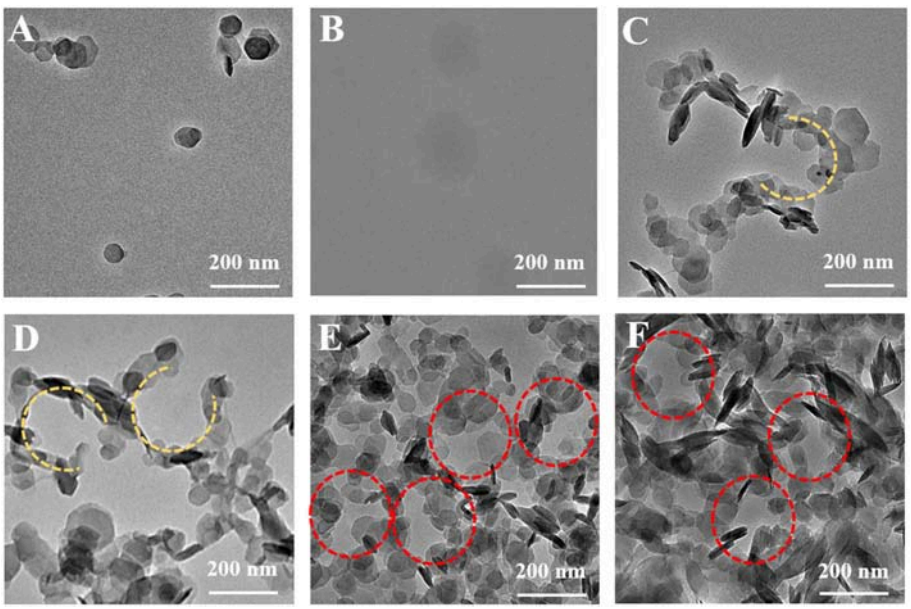

FIGURE 3 | TEM images of **(A)** the LDHs, **(B)** the SHDAB micelles and **(C–F)** the SHDAB@LDHs architectures with increased concentration of LDHs in SHDAB aqueous solution (0.295 mM); from C to F: 0.04 mM, 0.08 mM, 0.40 mM and 2.00 mM, respectively.

was observed (**Scheme S1**) (Deegan et al., 1997; Parneix et al., 2010; Cui et al., 2012). The results demonstrated the success of LDH-assisted visualization of SHDAB by TEM technique.

The optimum conditions for the visualization of SHDAB micelles were carried out. Firstly, the LDHs and SHDAB micelles were mixed and treated under continuous stirring. However, the LDH particles aggregated randomly (**Figure S3A**), which failed to give a description for SHDAB micelles. With the assistance of heat treatment at 50°C to accelerate the interaction, porous structures were gradually formed (**Figure S3B**). The irregular morphology indicated the insufficient combination between LDHs and SHDAB micelles. It has been reported that the ultrasonic irradiation is a powerful strategy for the improvement of the reaction efficiency due to the active energy of ultrasound waves (Hasaninejed et al., 2013). Herein, the porous structure appeared under the condition of ultrasonic irradiation (**Figure S3C**). Moreover, heating treatment (50°C) was taken to optimize the conditions. The 0.295-SHDAB@LDHs architecture was successfully formed and stabilized with well-organized morphologies under ultrasonic irradiation along with thermal treatment (**Figure S3D**).

The quantities of LDHs in the visualization process were evaluated. LDHs with different concentrations (0.04 mM, 0.08 mM, 0.40 mM, 2.00 mM) were added into the SHDAB micelles (0.295 mM) under ultrasonic irradiation and thermal treatment. It can be observed that the LDHs nanoparticles accumulated around the SHDAB micelles gradually to form the SHDAB@LDH architecture (**Figure 3**). The porous structure was subsequently formed with the increased content of LDHs (**Figures 3C,D**), and a complete porous structures can be

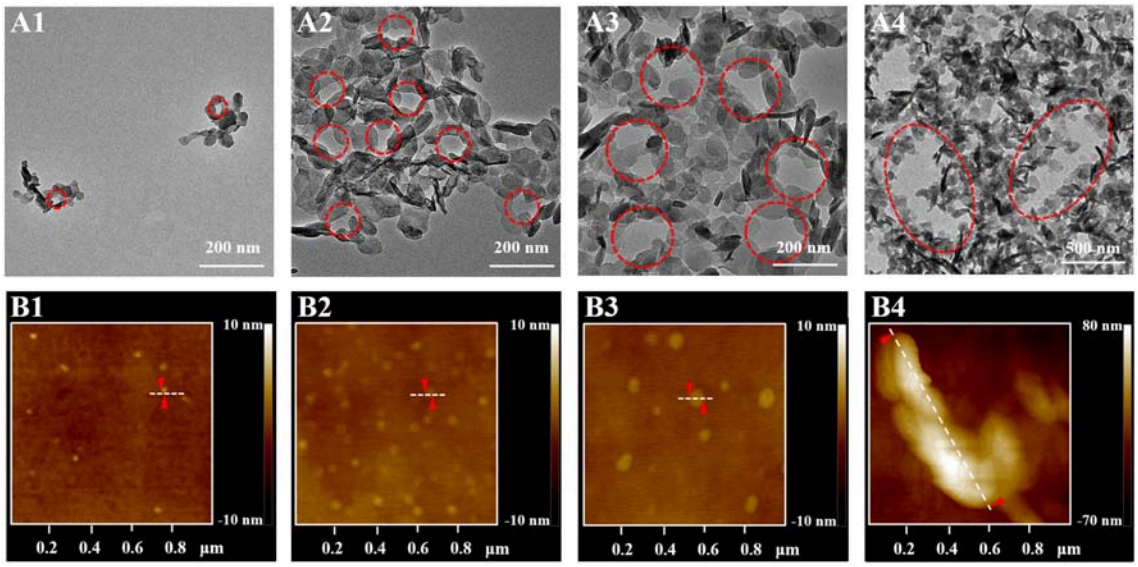

FIGURE 4 | (A) TEM images of the proposed LDHs-assisted visualization of SHDAB, and **(B)** AFM investigations of SHDAB micelles; the concentration of SHDAB varied from 0.0295 mM (CMC), 0.0590 mM, 0.295 mM to 1.48 mM, respectively.

formed with the LDHs content of 0.40 mM (**Figure 3E**). Moreover, the excess increase of LDHs (up to 2.00 mM) led to the aggregated LDHs overlapped with the SHDAB@LDH architecture (**Figure 3F**). Therefore, to achieve the visualization of micelles, the molecular ratio of SHDAB to LDHs was determined as 0.295 to 0.400. In addition, the time of ultrasonic irradiation also exerted an influence on the SHDAB@LDHs architectures. With the prolonged time, LDHs got adjacent to electrical double layers formed at the micelle-water interface. As depicted in **Figure S4**, the 0.295-SHDAB@LDHs architecture exhibited excellent morphology until 4 h' treatment and achieved an equilibrium state afterwards. Therefore, a finely tuned visualization strategy for micelles has been successfully established, which showed high contrast and distinguished imaging effect.

Visualization of the Morphological Evolution for the Surfactant

It has been reported that surfactants could be assembled into varied shapes when the concentrations of surfactant were larger than the CMC value (Shah et al., 2016). The SHDAB@LDHs architectures with increased concentration of SHDAB were prepared at the optimized ratio of SHDAB to LDHs (**Table 1**). With the concentration of SHDAB at the CMC value (0.0295 mM), a near-spherical porous structure was formed with an approximate radius of 26 nm, and the surfactant micelles were labeled with red dash line (**Figure 4A1**). The results indicated that the SHDAB micelles were surrounded by LDH nanoparticles. Interestingly, the porous architecture grew up to 58 nm with the concentration of SHDAB increased to 0.0590 mM (**Figure 4A2**). For the tenfold concentration of CMC value (0.295 mM), the SHDAB transformed from spherical to rodlike architecture with the size of 169 nm (**Figure 4A3**). Moreover, closely packed LDHs nanoplates around a lanky wormlike shape (length of 879 nm) can be observed with growing concentration of SHDAB to fiftyfold concentration of CMC (1.48 mM, **Figure 4A4**). It is noteworthy that the regulated activities of SHDAB from spherical, rodlike and wormlike structures can be visualized with the assist of LDHs by TEM imaging technique.

The dimensional and morphological properties of micelles in the transition process were testified by AFM. **Figure 4B** showed the AFM profile images of the pure SHDAB in the different concentrations from one to fifty times of CMC value. It was obvious that the micelles grew up from spherical to wormlike shape along with the increased concentrations. The section analysis was implemented to acquire the size of the micelles. The micelles changed from 30 nm, 62 nm and 178 nm of spherical shape to oval with the length of 903 nm when the concentration of LDHs changed from 0.0295 mM to 1.48 mM (**Figure S5**). The AFM data were in good conformity with the TEM images assisted by LDHs (**Table S1**). Moreover, the SHDAB@LDHs architectures can also be constructed by LDHs nanoparticles with smaller size (∼25 nm, **Figure S6**), and the transformation of the micelles morphology can be visualized (**Figure S7**). These results demonstrated that the size of LDHs did not influence the visualization of SHDAB, and the proposed method showed good accuracy by the assistance of LDHs.

Mechanism Studies

In order to study the mechanism for the formation of SHDAB@LDHs architectures, several experiments were carried out. As illustrated from the structure of SHDAB in **Figure S1**, the SHDAB surfactant can self-assemble into micelles by the synergetic functions of the hydrophobic interaction between

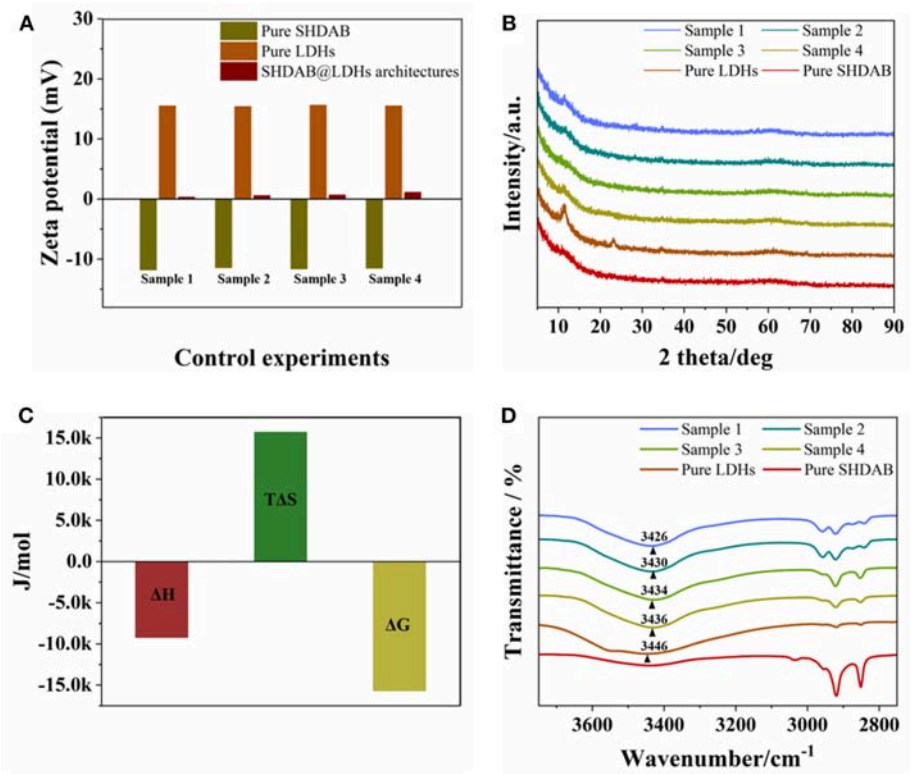

FIGURE 5 | (A) Zeta potentials, **(B)** XRD patterns, **(C)** ITC, and **(D)** FT-IR measurements of SHDAB, LDHs and SHDAB@LDHs architectures. Sample 1 to 4 represented the 0.0295-SHDAB@LDHs, 0.0590-SHDAB@LDHs, 0.295-SHDAB@LDHs and 1.48-SHDAB@LDHs architectures, respectively.

the alkane tail groups and electrostatic repulsion between the anionic head groups. As a result, the zeta potential value at the micelle-water interface of electrical double layer was −11.5 mV, indicating the stability of the SHDAB micelles with the negatively-charged groups exposed in solution (**Figure 5A**). Notably, the zeta potential of 15.5 mV for LDHs was beneficial for the electrostatic attraction toward the adjacent SHDAB micelles. The stabilized SHDAB@LDHs architecture with slight positive charge (0.3 mV) was obtained. The XRD measurements were implemented to study the structure of LDHs. The results demonstrated the unchanged interlayer space of LDHs, indicating that the SHDAB micelles were only attached at the surface of LDHs for the SHDAB@LDHs architectures (**Figure 5B**). To take a deep insight into the interaction between SHDAB micelles and LDHs, ITC measurement was carried out (**Figure S8**). The data indicated the simultaneous process for self-assembly of SHDAB micelles and the formation of the SHDAB@LDHs architectures (Kroflic et al., 2012). As shown in **Figure 5C**, the negative value of the free enthalpy showed the autonomous formation process of SHDAB@LDHs architectures (Zheng et al., 2016). Furthermore, the obvious vibration peaks in the range 3,650–3,200 cm^{-1} can be observed for the SHDAB@LDHs architectures. The peaks were blue-shifted in comparison with the FT-IR spectra for the pristine LDHs (**Figure 5D**). These results demonstrated the hydrogen bond interactions between quaternary ammonium cations of SHDAB and hydroxyl groups of LDHs. Therefore, both electrostatic and hydrogen bond interactions contributed to the formation of SHDAB@LDHs architectures for the visualization of SHDAB.

CONCLUSION

In summary, we have presented an attractive approach for the visualization of surfactant SHDAB with the assist of LDHs via TEM imaging. Based on the electrostatic and hydrogen bond interactions between LDHs and SHDAB, well-organized SHDAB@LDHs architectures were formed. The morphologies of SHDAB surfactant can be distinguished with high scattering contrast and clear boundary, as a result of the environmentally friendly staining by LDHs. Notably, the morphological evolution involving spherical, rodlike and wormlike shapes can be witnessed, in accordance with AFM measurements. Therefore, our facile strategy opens up viable possibilities for the direct visualization of soft materials.

AUTHOR CONTRIBUTIONS

ZZ, RT, and CL conceived the experiments. ZZ and KL carried out the experiments. ZZ, RT, and CL contributed to data analysis

and writing of this manuscript. All the authors have reviewed the manuscript and agreed to its publication.

FUNDING

This work was supported by National Basic Research Program of China (973 Program, 2014CB932103), the National Natural Science Foundation of China (21656001, 21521005, 21575010 and 21701004), and Innovation and Promotion Project of Beijing University of Chemical Technology.

SUPPLEMENTARY MATERIAL

The Supplementary Material for this article can be found online at: https://www.frontiersin.org/articles/10.3389/fchem.2019.00242/full#supplementary-material

REFERENCES

Abellan, G., Coronado, E., Manti-Gastaldo, C., Ribera, A., and Sanchez-Royo, J. F. (2012). Layered double hydroxide (LDH)–organic hybrids as precursors for low-temperature chemical synthesis of carbon nanoforms. *Chem. Sci.* 3, 1481–1485. doi: 10.1039/c2sc01064j

Aramaki, K., Iwata, C., Mata, J., Maehara, T., Aburano, D., Sakanishi, Y., et al. (2017). One-step formulation of nonionic surfactant bicelles (NSBs) by a double-tailed polyglycerol-type nonionic surfactant. *Phys. Chem. Chem. Phys.* 19, 23802–23808. doi: 10.1039/c7cp02585h

Aso, R., Kurata, H., Namikoshi, T., Hashimoto, T., Kuo, S. W., Chang, F. C., et al. (2013). Quantitative imaging of T_g in block copolymers by low-angle annular dark-field scanning transmission electron microscopy. *Macromolecules* 46, 8589–8595. doi: 10.1021/ma4014934

Claussen, W. F. (1967). Surface tension and surface structure of water. *Science* 156, 1226–1227. doi: 10.1126/science.156.3779.1226

Claypool, C. L., Faglioni, F., Goddard, W. A., Gray, H. B., Lewis, N. S., and Marcus, R. A. (1997). Source of image contrast in STM images of functionalized alkanes on graphite: a systematic functional group approach. *J. Phys. Chem. B.* 101, 5978–5995. doi: 10.1021/jp9701799

Creatto, E. J., Ceccacci, F., Mancini, G., and Sabadini, E. (2018). Effect of the hydrophobic tail of a chiral surfactant on the chirality of aggregates and on the formation of wormlike micelles. *Langmuir* 34, 13288–13295. doi: 10.1021/acs.langmuir.8b02556

Cui, L., Zhang, J., Zhang, X., Huang, L., Wang, Z., Li, Y., et al. (2012). Suppression of the coffee ring effect by hydrosoluble polymer additives. *ACS Appl. Mater. Interfaces* 4, 2775–2780. doi: 10.1021/am300423p

Deegan, R. D., Bakajin, O., Dupont, T. F., Huber, G., Nagel, S. R., and Witten, T. A. (1997). Capillary flow as the cause of ring stains from dried liquid drops. *Nature* 389, 827–829. doi: 10.1038/39827

Egerton, R. F. (2013). Control of radiation damage in the TEM. *Ultramicroscopy* 127, 100–108. doi: 10.1016/j.ultramic.2012.07.006

Fan, G. L., Li, F., Evans, D. G., and Duan, X. (2014). Catalytic applications of layered double hydroxides: recent advances and perspectives. *Chem. Soc. Rev.* 43, 7040–7066. doi: 10.1039/c4cs00160e

Gao, R., Yan, D., Evans, D. G., and Duan, X. (2017). Layer-by-layer assembly of long-afterglow self-supporting thin films with dual-stimuli-responsive phosphorescence and antiforgery applications. *Nano Res.* 10, 3606–3617. doi: 10.1007/s12274-017-1571-x

Geng, Y., and Discher, D. E. (2005). Hydrolytic degradation of poly(ethylene oxide)-block-polycaprolactone worm micelles. *J. Am. Chem. Soc.* 127, 12780–12781. doi: 10.1021/ja053902e

Guégan, R., Sueyoshi, K., Anraku, S., Yamamoto, S., and Miyamito, N. (2016). Sandwich organization of non-ionic surfactant liquid crystalline phases as induced by large inorganic K4Nb6O17 nanosheets. *Chem. Commun.* 52, 1594–1597. doi: 10.1039/c5cc08948d

Hasaninejed, A., Kazerooni, M. R., and Zare, A. (2013). Room-temperature, catalyst-free, one-pot pseudo-five-component synthesis of 4,4-(arylmethylene)bis(3-methyl-1-phenyl-1H-pyrazol-5-ol)s under ultrasonic irradiation. *ACS Sustainable Chem. Eng.* 1, 679–684. doi: 10.1021/sc400081c

Honda, S., Yamamoto, T., and Tezuka, Y. (2010). Topology-directed control on thermal stability: micelles formed from linear and cyclized amphiphilic block copolymers. *J. Am. Chem. Soc.* 132, 10251–10253. doi: 10.1021/ja104691j

Hu, D., and Chou, K. C. (2014). Re-evaluating the surface tension analysis of polyelectrolyte-surfactant mixtures using phase-sensitive sum frequency generation spectroscopy. *J. Am. Chem. Soc.* 136, 15114–15117. doi: 10.1021/ja5049175

Humphrey, C. D. (2009). Negative stain transmission electron microscopy of viruses and virus-like particles. *Microsc. Microanal.* 15, 376–377. doi: 10.1017/S1431927609094446

Jain, S., and Bates, F. S. (2003). On the origins of morphological complexity in block copolymer surfactants. *Science* 300, 460–464. doi: 10.1126/science.1082193

Jung, H. M., Price, K. E., and McQuade, D. T. (2003). Synthesis and characterization of cross-linked reverse micelles. *J. Am. Chem. Soc.* 125, 5351–5355. doi: 10.1021/ja0271983

Kroflic, A., Sarac, B., and Rogac, M. B. (2012). Thermodynamic characterization of 3-[(3-cholamidopropyl)-dimethylammonium]-1-propanesulfonate (CHAPS) micellization using isothermal titration calorimetry: temperature, salt, and pH dependence. *Langmuir* 28, 10363–10371. doi: 10.1021/la302133q

Landsmann, S., Lizandara-Pueyo, C., and Polarz, S. (2010). A new class of surfactants with multinuclear, inorganic head groups. *J. Am. Chem. Soc.* 132, 5315–5321. doi: 10.1021/ja1011178

Liu, F., Xiao, J. W., Garamus, V. M., Almásy, L., Willumeit, R., Mu, B., et al. (2013). Interaction of the biosurfactant, surfactin with betaines in aqueous solution. *Langmuir* 29, 10648–10657. doi: 10.1021/la400683u

Liu, H., Wang, R., Wei, J., Cheng, C., Zheng, Y., Pan, Y., et al. (2018). Conformation-directed micelle-to-vesicle transition of cholesterol-decorated polypeptide triggered by oxidation. *J. Am. Chem. Soc.* 140, 6604–6610. doi: 10.1021/jacs.8b01873

O'Reilly, R. K., Joralemon, M. J., Wooley, K. L., and Hawker, C. J. (2005). Functionalization of micelles and shell cross-linked nanoparticles using click chemistry. *Chem. Mater.* 17, 5976–5988. doi: 10.1021/cm051047s

Parent, L. R., Bakalis, E., Ramírez-Hernández, A., Kammeyer, J. K., Park, C., Pablo, J., et al. (2017). Directly observing micelle fusion and growth in solution by liquid-cell transmission electron microscopy. *J. Am. Chem. Soc.* 139, 17140–17151. doi: 10.1021/jacs.7b09060

Parker, K. A., Li, Y., Eshein, A., Zhu, S., Hampton, C. M., Drummy, L. F., et al. (2018). Positive staining for improved contrast of macromolecules in transmission electron microscopy. *Microsc. Microanal.* 24, 1730–1731. doi: 10.1017/S1431927618009133

Parneix, C., Vandoolaeghe, P., Nikolayev, V. S., Quéré, D., Li, J., and Cabane, B. (2010). Dips and rims in dried colloidal films. *Phys. Rev. Lett.* 105, 266103. doi: 10.1103/PhysRevLett.105.266103

Proetto, M. T., Rush, A. M., Chien, M. P., Baeza, P. A., Patterson, J. P., Thompson, M. P., et al. (2014). Dynamics of soft nanomaterials captured by transmission electron microscopy in liquid water. *J. Am. Chem. Soc.* 136, 1162–1165. doi: 10.1021/ja408513m

Rogez, G., Massobrio, C., Rabu, P., and Drillon, M. (2011). Layered hydroxide hybrid nanostructures: a route to multifunctionality. *Chem. Soc. Rev.* 40, 1031–1058. doi: 10.1039/c0cs00159g

Serizawa, T., Takehara, S., and Akashi, M. (2000). Transmission electron microscopic study of cross-sectional morphologies of core-corona polymeric nanospheres. *Macromolecules* 33, 1759–1764. doi: 10.1021/ma9907486

Shah, A., Shahzad, S., Munir, A., Nadagouda, M. N., Khan, G. S., Shams, D. F., et al. (2016). Micelles as soil and water decontamination agents. *Chem. Rev.* 116, 6042–6074. doi: 10.1021/acs.chemrev.6b00132

Smith, R. W., and Bryg, V. (2006). Staining polymers for microscopical examination. *Rubber Chem. Technol.* 79, 520–540. doi: 10.5254/1.3547949

Stano, P., and Luisi, P. L. (2010). Achievements and open questions in the self-reproduction of vesicles and synthetic minimal cells. *Chem. Commun.* 46, 3639–3653. doi: 10.1039/B913997D

Stawski, T. M., Roncal-Herrero, T., Fernandez-Martinez, A., Matamoros-Veloza, A., Kröger, R., and Benning, L. G. (2018). "On demand" triggered crystallization of $CaCO_3$ from solute precursor species stabilized by the water-in-oil microemulsion. *Phys. Chem. Chem. Phys.* 20, 13825–13835. doi: 10.1039/C8CP00540K

Suys, E. J. A., Warren, D. B., Pham, A. C., Nowell,. C. J., Clulow, A. J., Benameur, H., et al. (2019). A nonionic polyethylene oxide (PEO) surfactant model: experimental and molecular dynamics studies of Kolliphor EL. *J. Pharm. Sci.* 108, 193–204. doi: 10.1016/j.xphs.2018.11.028

Tian, R., Zhang, S. T., Li, M. W., Zhou, Y. Q., Lu, B., Yan, D. P., et al. (2015). Localization of Au nanoclusters on Layered Double Hydroxides nanosheets: confinement-induced emission enhancement and temperature-responsive luminescence. *Adv. Funct. Mater.* 25, 5006–5015. doi: 10.1002/adfm.201501433

Tian, R., Zhong, J. P., Lu, C., and Duan, X. (2018). Hydroxyl-triggered fluorescence for location of inorganic materials in polymer-matrix composites. *Chem. Sci.* 9, 218–222. doi: 10.1039/c7sc03897f

Trent, J. S., Scheinbeim, J. I., and Couchman, P. R. (1983). Ruthenium tetraoxide staining of polymers for electron microscopy. *Macromolecules* 16, 589–598. doi: 10.1021/ma00238a021

Wang, H. Y., Zhang, L. M., Wang, J. J., Li, Z. Y., and Zhang, S. J. (2013). The first evidence for unilamellar vesicle formation of ionic liquids in aqueous solutions. *Chem. Commun.* 49, 5222–5224. doi: 10.1039/c3cc41908h

Wang, Q., and O'Hare, D. (2012). Recent advances in the synthesis and application of Layered Double Hydroxide (LDH) nanosheets. *Chem. Rev.* 112, 4124–4155. doi: 10.1021/cr200434v

Xu, H., Du, N., Song, Y., Song, S., and Hou, W. (2017). Vesicles of 2-ketooctanoic acid in water. *Soft Matter* 13, 2246–2252. doi: 10.1039/c6sm02665f

Zeng, Z. Y., Zheng, W. J., and Zheng, H. M. (2017). Visualization of colloidal nanocrystal formation and electrode-electrolyte interfaces in liquids using TEM. *Acc. Chem. Res.* 50, 1808–1817. doi: 10.1021/acs.accounts.7b00161

Zhao, M., Gao, Z., Dai, C., Zhang,. Y., Sun, X., Gao, M., et al. (2018). Investigation of active-inactive material interdigitated aggregates formed by wormlike micelles and cellulose nanofiber. *J. Phys. Chem. B.* 122, 10371–10376. doi: 10.1021/acs.jpcb.8b06440

Zheng, Y., You, S. S., Ji, C. D., Yin, M. Z., Yang, W. T., and Shen, J. (2016). Development of an amino acid-functionalized fluorescent nanocarrier to deliver a toxin to kill insect pests. *Adv Mater.* 28, 1375–1380. doi: 10.1002/adma.201504993

Conflict of Interest Statement: The authors declare that the research was conducted in the absence of any commercial or financial relationships that could be construed as a potential conflict of interest.

Copyright © 2019 Zhang, Li, Tian and Lu. This is an open-access article distributed under the terms of the Creative Commons Attribution License (CC BY). The use, distribution or reproduction in other forums is permitted, provided the original author(s) and the copyright owner(s) are credited and that the original publication in this journal is cited, in accordance with accepted academic practice. No use, distribution or reproduction is permitted which does not comply with these terms.

frontiers in Chemistry

METHODS
published: 14 May 2019
doi: 10.3389/fchem.2019.00342

A Threshold-Limited Fluorescence Probe for Viscosity

Zuhai Lei[1,2], Kai Xin[1], Shaobing Qiu[1], Liling Hou[3], Xiangming Meng[3] and Youjun Yang[1]**

[1] State Key Laboratory of Bioreactor Engineering, Shanghai Key Laboratory of Chemical Biology, School of Pharmacy, East China University of Science and Technology, Shanghai, China, [2] Shanghai Key Laboratory of Molecular Catalysis and Innovative Materials, State Key Laboratory of Molecular Engineering of Polymers and iChem, Department of Chemistry, Fudan University, Shanghai, China, [3] Department of Chemistry, Anhui University, Hefei, China

Viscosity of body fluid is an established biomarker of pathological conditions. Abnormality of cellular viscosity occurs when cells are challenged with external stresses. Small molecule probes to assess the viscosity are sought after for both disease diagnostics and basic studies. Fluorescence based probes are particular attractive due to their potentials for convenient and high spatiotemporal resolution microscopic monitoring of biological samples. The dyes with a floppy push-pull backbone or dyes with a rotatable substituent exhibits a viscosity responsive fluorescence enhancement and therefore viable viscosity probes. The scaffold of the existing viscosity probes contains typically one such floppy site. Therefore, they typically linearly respond to log(viscosity). We argue that minor viscosity fluctuation could potentially be physiological as the biological system is dynamic. We wish to develop a type of conceptually-new, threshold-limited viscosity probes, to complement the existing probes. Such probes do not exhibit a fluorescence enhancement when challenged with minor and presumably physiological enhancement of viscosity. When the viscosity is higher than a certain threshold, their fluorescence turns on. We hypothesize that a dye with two far-apart floppy sites could potentially yield such a threshold-limited signal and designed **VPZ2** and **VPZ3**. Through spectral titration, **VPZ3** was found to yield the desired threshold-limited signal. **VPZ3** was suitable for *in vitro* bioimaging of viscosity under one-photon or two-photon excitation. **VPZ3** is potentially useful in many downstream applications. Future work includes fine-tune of the threshold to allow tailored limit for fluorescence turn-on to better meet the need of different applications. Besides the implications in the real-world applications, the design concept could also be translated to design of alternative substrates.

Keywords: threshold-limited, probe, viscosity, two-photon, fluorescence

OPEN ACCESS

Edited by:
Huangxian Ju,
Nanjing University, China

Reviewed by:
Juyoung Yoon,
Ewha Womans University, South Korea
Yun Lu,
Nanjing University, China

***Correspondence:**
Youjun Yang
youjunyang@ecust.edu.cn
Xiangming Meng
mengxm@ahu.edu.cn

Specialty section:
This article was submitted to Analytical Chemistry, a section of the journal Frontiers in Chemistry

Received: *28 February 2019*
Accepted: *25 April 2019*
Published: *14 May 2019*

Citation:
Lei Z, Xin K, Qiu S, Hou L, Meng X and Yang Y (2019) A Threshold-Limited Fluorescence Probe for Viscosity. Front. Chem. 7:342. doi: 10.3389/fchem.2019.00342

INTRODUCTION

Viscosity is a biophysical parameter of homeostasis (Tsien, 1989; Balkwill et al., 2012; Wang et al., 2017). By altering the molecular diffusion kinetics, biomolecular trafficking, lipid fluidity, and protein conformational rate, all physiological processes including enzymatic activity, energy metabolism, and signal transduction are affected (Miyamoto et al., 1990; Uribe and Smpedro, 2003; Boric et al., 2012; Liu et al., 2014; Sekhar et al., 2014). Abnormal fluctuation of microenvironmental viscosity is found to be reliable biomarker of underlying diseases or stresses

(Aydemir et al., 2008; Harisa, 2014; Kasperczyk et al., 2014; Herranz et al., 2018). Oxidative burst can alter the membrane fluidity through lipid peroxidation and hence disrupts its function (Richter, 1987; Hormel et al., 2013). Lysosome storage disorders are associated with increased local viscosity (Platt et al., 2012; Devany et al., 2018). Viscosity is also vital to maintain the mitochondrial network organization and energy metabolism (Mecocci et al., 1997). Hyperviscosity, or macroscopic high blood viscosity, is found with patients of many blood diseases, such as myeloma, leukemia, anemia, and sepsis (Gustine et al., 2016). Therefore, fluorescent probes for viscosity are in need for both basic biomedical studies and disease diagnosis to monitor the viscosity of complex biological systems (Haidekker and Theodorakis, 2007; Kuimova et al., 2008; Sutharsan et al., 2010;

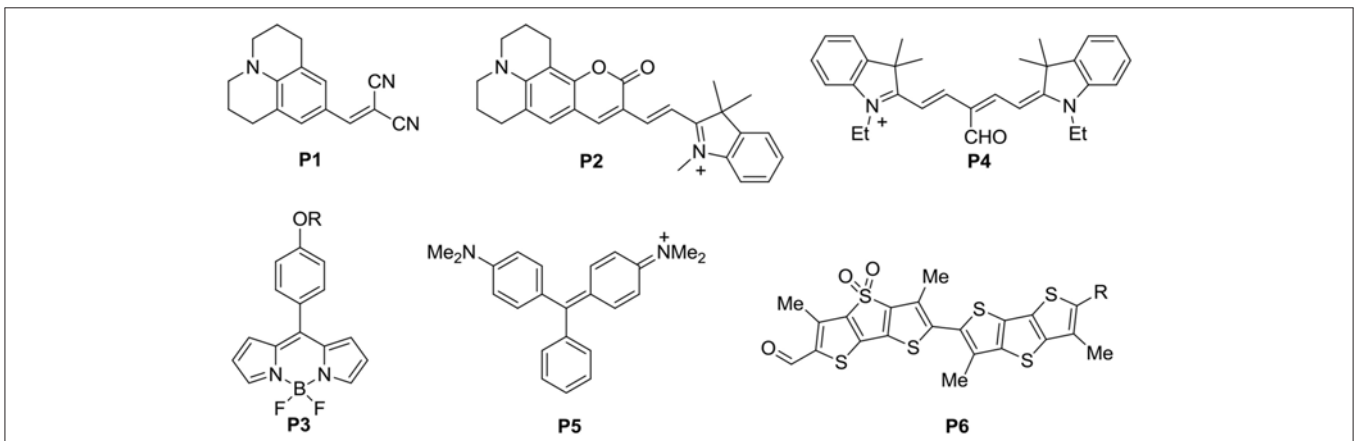

FIGURE 1 | Structures of a number of classic molecular rotors (**1**–**6**).

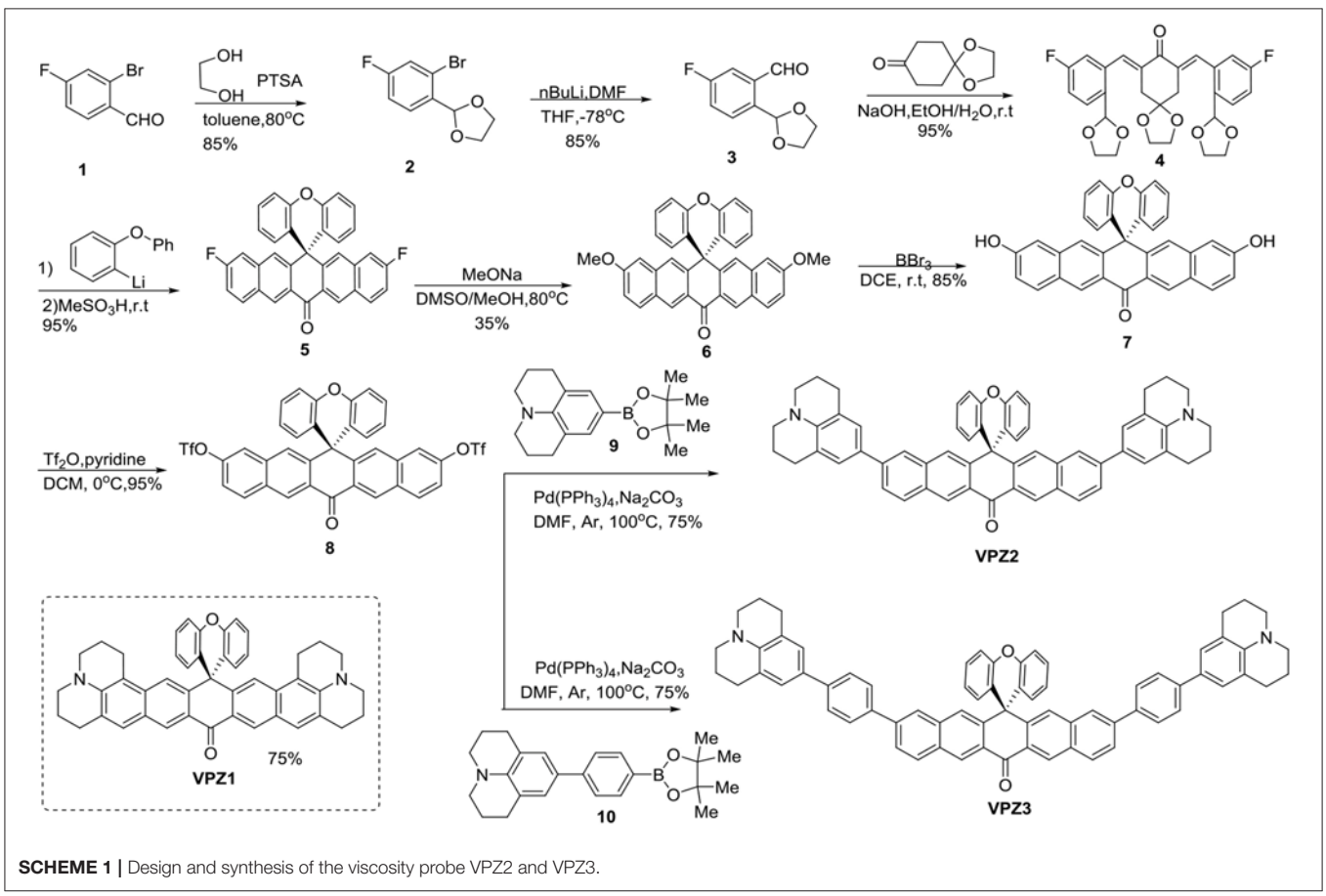

SCHEME 1 | Design and synthesis of the viscosity probe VPZ2 and VPZ3.

Kuimova, 2012; Wang et al., 2013; López-Duarte et al., 2014; Yang et al., 2014; Chen et al., 2015; Vyšniauskas et al., 2015, 2016; Lee et al., 2016; Ren et al., 2016; Su et al., 2016; Zhu et al., 2016; Klymchenko, 2017; Lyubov et al., 2017; Ning et al., 2017; Song et al., 2017).

The capability of a dye to sense environmental viscosity originates from its excited state dynamics, including non-radiative rotational deactivation and radiative deactivation (Klymchenko, 2017). For a fluorophore exhibiting a high degree of rotational freedom, it is typically non-fluorescent. When the rotational freedom is restricted, possibility of radiative deactivation enhances. The structural freedom of the fluorophore may come from rotatable bonds of the push-pull backbone, as seen in **P1** (Loutfy and Arnold, 1982), and **P2** (Cui et al., 2019) (**Figure 1**). Or, a group may be installed to a rigid push-pull backbone via a single bond to construct a molecular rotor, e.g., **P3** (Kuimova et al., 2008). Or, it could be a flexible push-pull backbone installed with a rotatable group, e.g., **P4** (Peng et al., 2011), **P5** (Babendure et al., 2003), and **P6** (Colom et al., 2018) (**Figure 1**). Typically, these molecular rotors respond linearly to log(viscosity). Minor enhancement of microscopic viscosity could be physiological considering the dynamic nature of a biological system. Therefore, we are interested in development of a new class of molecular rotors which does not respond to minor enhancement of viscosity, until the viscosity surpasses a certain threshold limit. Such threshold-limited molecular rotors could potentially be very useful in disease diagnostics. The existence of one site of high rotational freedom in the scaffold of a fluorophore is required to yield a viscosity-sensitive fluorescence enhancement. We propose that two such sites are warranted to exhibit threshold-limited response to viscosity. Intuitively, minor enhancement of viscosity may restrict the rotational freedom of one site, leaving the other site unaffected to quench the fluorescence of the fluorophore. When the viscosity is higher than a certain limit, the chances of simultaneous restriction of both sites becomes possible and fluorescence enhancement should be noticeable. Also, sterics should be present in the scaffold of such a probe to minimize unintended fluorescence turn-on by aggregation or unselective binding with native biomacromolecules (Lei et al., 2017).

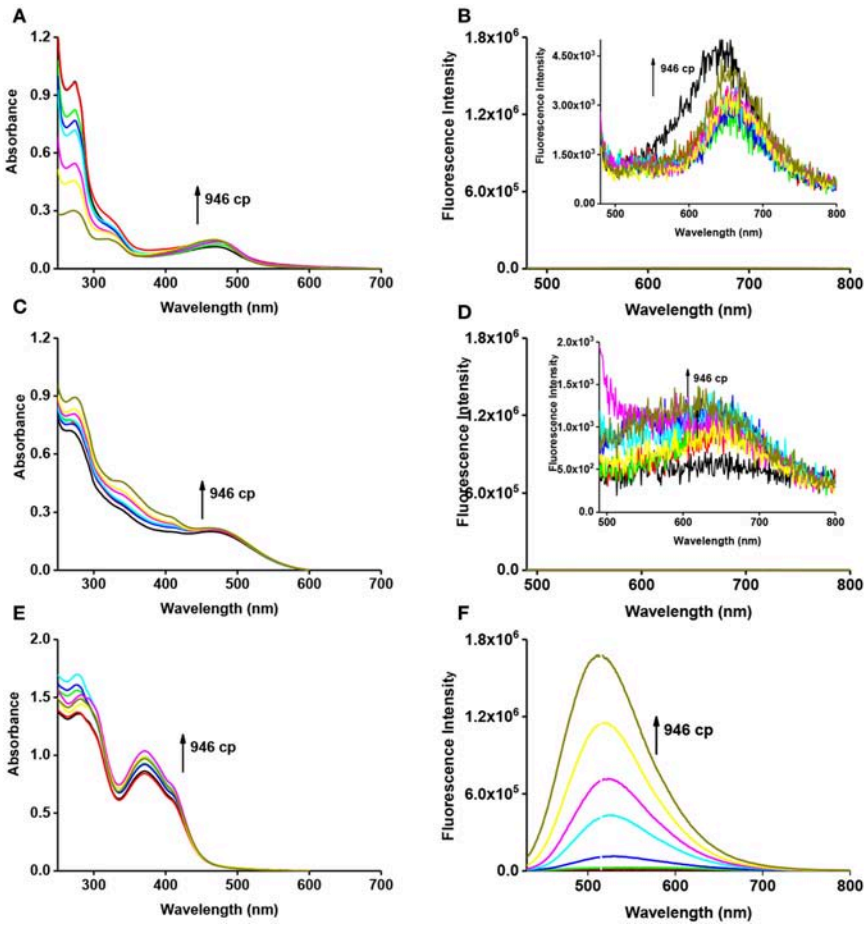

FIGURE 2 | Absorption (**A**, **VPZ1**; **C**, **VPZ2**; **E**, **VPZ3**) and emission (**B**, **VPZ1**; **D**, **VPZ2**; **F**, **VPZ3**) spectra of **VPZ** probes in different viscosity (glycerol and water), concentration: 10 μM.

Herein, we report the synthesis, spectral titrations and proof-of-concept bioimaging of threshold-limited fluorescent probe (**VPZ1-3**) for microscopic viscosity.

RESULTS AND DISCUSSIONS

Compound Synthesis

VPZ1 is a known compound and synthesized according to the reported method (Lei et al., 2017). The synthesis **VPZ2** and **VPZ3** are displayed in **Scheme 1** 2-Bromo-4-fluorobenzaldehyde (**1**) was condensed with ethylene glycol in the presence of p-toluene-sulfonic acid to the corresponding 1,3-dioxolane derivative (**2**) in an 85% yield. Then **2** was treated with nBuLi at −78°C to generate the nucleophilic intermediate phenyllithium reagent *in situ*, which was quenched with DMF to yield the benzaldehyde derivative (**3**) in good yield. Through aldol condensation of **3** and 1,4-cyclohexanedione monoacetal under basic conditions, **4** was obtained in an 95% yield. (2-Phenoxyphenyl) lithium was added into a solution of 4 in THF. The resulting carbinol product was isolated and treated with methylsulfonic acid without further purification to afford **5** through a cascade of reactions. The crystal structure of the compound 5 was obtained and the diphenylether moiety and the bottom dinaphthylmethanone unit are perpendicular. Replacement of fluorine atoms of **5** with methoxide gave **6** in an 35% yield. Then the two methoxys groups of **6** was demethylated by BBr_3 to get **7,** the hydroxyls of which were converted to triflate by treatment of triflic anhydride to obtain the key intermediate **8**. The viscosity probes (**VPZ2** and **VPZ3**) were furnished by the Suzuki–Miyaura cross coupling reactions with **9** and **10**, respectively. The NMR and the HRMS spectra of all new compounds are provided in the SI (**Figures S1**–**S25**). The crystal structure of compound 5 was obtained (**Figure S26**).

Spectral Titrations

With the probes in hand, we firstly tested the photophysical properties of these probes (**Figure 2**, glycerol and water). The maximum absorption wavelength of **VPZ1**, **VPZ2,** and **VPZ3** in pure water is about 470, 465, and 373 nm, respectively. Their fluorescence is very weak but still observable. The emission wavelength of **VPZ1**, **VPZ2,** and **VPZ3** is about 650, 650, and 515 nm, respectively. With their symmetric D-A-D structure, the **VPZ** probes typically exhibit a Stokes shift of ca. 140–190 nm, much larger than that of a list of common fluorophores, such as fluorescein (24 nm), tetramethylrhodamine (25 nm), BODIPY (20 nm), Cy5 (20 nm), Cy7 (23 nm), which is desirable for imaging-based applications. We tested the viscosity related spectral responses (**Figure 2**). **VPZ** probes were added into solvent mixtures of water and glycerol exhibiting different viscosity values, their absorption and emission spectra were recorded. As shown in **Figure 2**, the absorption of **VPZ** probes exhibited only very subtle changes with respect to the increase of the solvent viscosity. The fluorescence emission intensity of **VPZ1** and **VPZ2** remained essentially unchanged with respect to the increase of the solvent viscosity. Notably, **VPZ3** show a strong increase in fluorescence (ca.126-fold) with the increase of viscosity. Very interestingly, the fluorescence intensity of **VPZ3** did not immediately increase when the solvent viscosity increased (**Figure 3**). Instead, the fluorescence intensity remained unchanged until the Log(viscosity) of the solution was higher than 10. After that, the fluorescence of **VPZ3** enhanced linearly with respect to Log(viscosity). This is in good agreement with the design rational of the **VPZ** series of probes. The fluorescence life-time decay of VPZ3 in different solvent mixtures of H2O and glycerol was acquired (**Figure S27**). Since **VPZ3** has the best performance against different viscosity, we chosen **VPZ3** as the viscosity probe for the cell imaging study. The fact that **VPZ1** and **VPZ2** do not fluoresce in this solvent mixture is intriguing and subject to further in-depth photophysical studies.

Cell Images

The short absorption wavelength of **VPZ3** limits its usage in imaging-based application *in vivo* with one photon excitation.

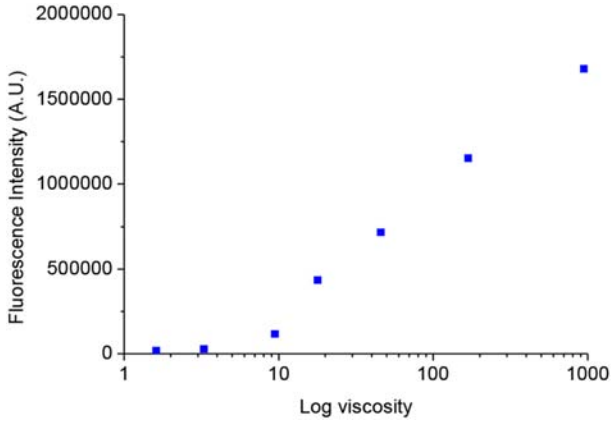

FIGURE 3 | The relationship of the fluorescence intensity of **VPZ3** at varying solvent viscosity.

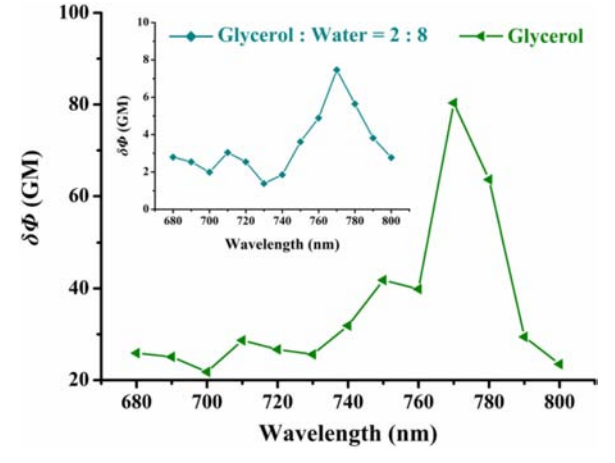

FIGURE 4 | Two-photon excitation action cross-section of **VPZ3** in the glycerol–water system with different viscosities (20% glycerol and 100% glycerol). Two-photon excitation wavelength range: 680–880 nm ($\Delta\lambda = 10$ nm).

To apply **VPZ3** in cell study, we firstly performed the two-photon cross-section (δ) test (**Figure 4**) since the short one photon excitation problem can be circumvented by two-photon excitation. The maximum δ is about 80 GM at 770 nm in glycerol. Therefore, 770 nm was used for the cell imaging study.

The cytotoxicity of **VPZ3** was determined by MTT. In short, HepG2 cells were incubated with **VPZ3** with different concentration for 24 h. The cell viability remained 85% at up to 25 μM (**Figure S28**). The low cytotoxicity of **VPZ3** promotes us to further explore the possibility of **VPZ3** as a fluorescence probe for the detection of cell viscosity. In order to demonstrate the imaging ability of **VPZ3** in living cells, the HepG2 cells were incubated with **VPZ3** (10 μM) at 37 and 25°C for 30 min separately. The ptimages of the cells were collected under two-photon excitation. As we known, lower temperature means higher viscosity for the cells. The fluorescence intensity of cells incubated at 25°C was higher than those at 37°C significantly (**Figure 5**). The imaging results supported that the **VPZ3** could be used for monitoring the viscosity in the cytoplasm of living cells.

To further demonstrate the potentials of **VPZ3** in monitoring the micro-viscosity change of cells, **VPZ3** was used to monitor the real-time viscosity change during cell apoptosis. Because etoposide (a chemotherapy drug used to treat many types of cancer) can cause cell death, the micro-viscosity of the cells will change greatly during the apoptosis process. HepG2 cells were incubated with etoposide. The two-photon fluorescence images were collected at different times during the apoptosis process. As shown in **Figure 6**, the fluorescence intensity of the cells increased greatly during the apoptosis upon addition of etoposide. In contrast, the fluorescence of the cells without the addition of etoposide kept unchanged (**Figure S29**). These results clearly show that **VPZ3** could be used to monitor the viscosity changes during the apoptosis process.

CONCLUSION

In summary, we have developed a series of new fluorescence probes (**VPZ**) for viscosity monitoring based on a symmetric D-A-D framework. Among the three **VPZ** probes, **VPZ3**

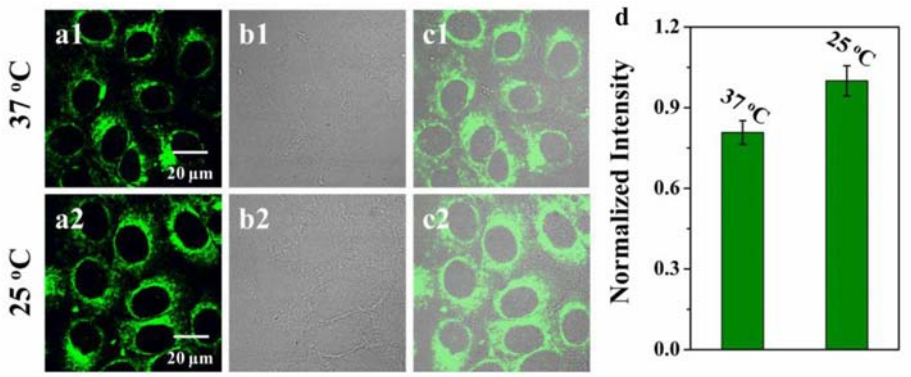

FIGURE 5 | Two-photon confocal images of HepG2 cells incubated with **VPZ3** (10 μM) after 30 min of incubation at **(a1)** 37°C and **(a2)** 25°C, respectively and then washed with 10 mM PBS buffer. λ_{ex} = 770 nm, emission wavelength from 500 to 540 nm; **(b1,b2)** bright-field images of HepG2 cells; **(c1)** the overlay of panels **(a1,b1)**; **(c2)** the overlay of **(a2,b2)**. **(d)** Normalized intensity analysis of the probe at 37 and 25°C, respectively. Scale bars: 20 μm.

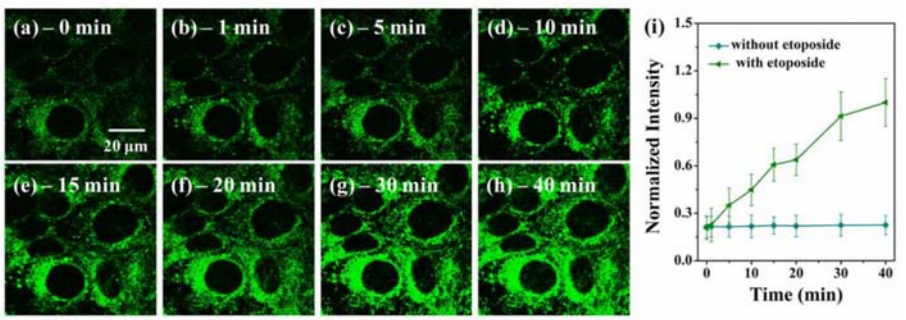

FIGURE 6 | (a–h) Two-photon confocal images of HepG2 cells incubated with **VP3** (10 μM) at different time points after the addition of 2.0 μM etoposide, λ_{ex} = 770 nm, emission wavelength from 500 to 540 nm. **(i)** Plot of normalized intensities of **the probe** against time with (triangle, green line) and without (circle, blue line) etoposide. Scale bars: 20 μm.

showed a great "off-on" fluorescence response (ca. 126-fold) with increasing viscosity in the glycerol-water system. **VPZ3** shows low cytotoxicity and could be used to monitor the real-time viscosity change during the cell apoptosis process. We expect **VPZ3** to find applications in basic biological studies related cell apoptosis and disease diagnostics.

DATA AVAILABILITY

All datasets generated for this study are included in the manuscript and/or the **Supplementary Files**.

AUTHOR CONTRIBUTIONS

ZL prepared the compound synthesis. KX and SQ involved in the synthesis and carried spectral titrations. LH carried out biological studies. YY and XM conceived the project. Everyone contributed to manuscript preparation.

SUPPLEMENTARY MATERIAL

The Supplementary Material for this article can be found online at: https://www.frontiersin.org/articles/10.3389/fchem.2019.00342/full#supplementary-material

REFERENCES

Aydemir, B., Onaran, I., Kiziler, A. R., Alici, B., and Akyolcu, M. C. (2008). The influence of oxidative damage on viscosity of seminal fluid in infertile men. *J. Androl.* 29, 41–46. doi: 10.2164/jandrol.107.003046

Babendure, J. R., Adams, S. R., and Tsien, R. Y. (2003). Aptamers switch on fluorescence of triphenylmethane dyes. *J. Am. Chem. Soc.* 125, 14716–14717. doi: 10.1021/ja037994o

Balkwill, F. R., Capasso, M., and Hagemann, T. (2012). The tumor microenvironment at a glance. *J. Cell Sci.* 125, 5591–5596. doi: 10.1242/jcs.116392

Boric, M., Danevcic, T., and Stopar, D. (2012). Viscosity dictates metabolic activity of Vibrio ruber. *Front. Microbiol.* 3:255. doi: 10.3389/fmicb.2012.00255

Chen, S., Hong, Y., Zeng, Y., Sun, Q., Liu, Y., Zhao, E., et al. (2015). Mapping live cell viscosity with an aggregation-induced emission fluorogen by means of two-photon fluorescence lifetime imaging. *Chem. A Eur. J.* 21, 4315–4320. doi: 10.1002/chem.201405658

Colom, A., Derivery, E., Soleimanpour, S., Tomba, C., Molin, M. D., Sakai, N., et al. (2018). A fluorescent membrane tension probe. *Nat. Chem.* 10, 1118–1125. doi: 10.1038/s41557-018-0127-3

Cui, J., Yao, Y., Chen, C., Huang, R., Zhang, W., and Qian, J. (2019). Mitochondria-targeted ratiometric fluorescent probes for micropolarity and microviscosity and their applications. *Chin. Chem. Lett.* doi: 10.1016/j.cclet.2018.12.031. [Epub ahead of print].

Devany, J., Chakraborty, K., and Krishnan, Y. (2018). Subcellular nanorheology reveals lysosomal viscosity as a reporter for lysosomal storage diseases. *Nano Lett.* 18, 1351–1359. doi: 10.1021/acs.nanolett.7b05040

Gustine, J., Meid, K., Manning, R. R., Dubeau, T., Ghobrial, I. M., Treon, S. P., et al. (2016). The high risk for symptomatic hyperviscosity in patients with high serum IgM levels can be used to support initiation of treatment in waldenström macroglobulinemia. *Blood* 128:2983. Available online at: http://www.bloodjournal.org/content/128/22/2983/tab-article-info

Haidekker, M. A., and Theodorakis, E. A. (2007). Molecular rotors—fluorescent biosensors for viscosity and flow. *Organ. Biomol. Chem.* 5, 1669–1678. doi: 10.1039/B618415D

Harisa, G. I. (2014). Blood viscosity as a sensitive indicator for paclitaxel induced oxidative stress in human whole blood. *J. Androl.* 23, 48–54. doi: 10.1016/j.jsps.2014.04.006

Herranz, B., Alvarez, M. D., and Perez-Jimenez, J. (2018). Association of plasma and urine viscosity with cardiometabolic risk factors and oxidative status. A pilot study in subjects with abdominal obesity. *PLoS ONE* 13:e0204075. doi: 10.1371/journal.pone.0204075

Hormel, T. T., Kurihara, S. Q., Brennan, M. K., and Parthasarathy, R. (2013). Measuring lipid membrane viscosity using rotational and translational particle diffusion. *Biophys. J.* 104, 426A−427A. doi: 10.1016/j.bpj.2012.11.2374

Kasperczyk, A., Słowinska-Łozynska, L., Dobrakowski, M., Zalejska-Fiolka, J., and Kasperczyk, S. (2014). The effect of lead-induced oxidative stress on blood viscosity and rheological properties of erythrocytes in lead exposed humans. *Clin. Hemorheol. Microcirc.* 56, 187–195. doi: 10.3233/CH-131678

Klymchenko, A. S. (2017). Solvatochromic and fluorogenic dyes as environment-sensitive probes: design and biological applications. *Acc. Chem. Res.* 50, 366–375. doi: 10.1021/acs.accounts.6b00517

Kuimova, M. K. (2012). Mapping viscosity in cells using molecular rotors. *Phys. Chem. Chem. Phys.* 14, 12671–12686. doi: 10.1039/C2CP41674C

Kuimova, M. K., Yahioglu, G., Levitt, J. A., and Suhling, K. (2008). Molecular rotor measures viscosity of live cells via fluorescence lifetime imaging. *J. Am. Chem. Soc.* 130, 6672–6673. doi: 10.1021/ja800570d

Lee, S. C., Heo, J., Ryu, J. W., Lee, C. L., Kim, S., Tae, J. S., et al. (2016). Pyrrolic molecular rotors acting as viscosity sensors with high fluorescence contrast. *Chem. Commun.* 52, 13695–13698. doi: 10.1039/C6CC06521J

Lei, Z., Li, X., Luo, X., He, H., Zheng, J., Qian, X., et al. (2017), Bright, stable, and biocompatible organic fluorophores absorbing/emitting in the deep near-infrared spectral region. *Angew. Chem. Int. Ed.* 56, 2979–2983. doi: 10.1002/anie.201612301

Liu, T., Liu, X., Spring, D. R., Qian, X., Cui, J., and Xu, Z. (2014). Quantitatively mapping cellular viscosity with detailed organelle information via a designed PET fluorescent probe. *Sci. Rep.* 4:5418. doi: 10.1038/srep05418

López-Duarte, I., Vu, T. T., Izquierdo, M. A., Bull, J. A., and Kuimova, M. K. (2014). A molecular rotor for measuring viscosity in plasma membranes of live cells. *Chem. Commun.* 50, 5282–5284. doi: 10.1039/C3CC47530A

Loutfy, R. O., and Arnold, B. A. (1982). Effect of viscosity and temperature on torsional relaxation of molecular rotors. *J. Phys. Chem.* 86, 4205–4211. doi: 10.1021/j100218a023

Lyubov, 'E., S., Izquierdo, M. A., López-Duarte, I., Bull, J. A., Shirmanova, M. V., Klapshina, L. G., et al. (2017). Imaging tumor microscopic viscosity *in vivo* using molecular rotors. *Sci. Rep.* 7:41097. doi: 10.1038/srep41097

Mecocci, P., Beal, M. F., Cecchetti, R., Polidori, M. C., Cherubini, A., Chionne, F., et al. (1997). Mitochondrial membrane fluidity and oxidative damage to mitochondrial DNA in aged and AD human brain. *Mol. Chem. Neuropathol.* 31, 53–64. doi: 10.1007/BF02815160

Miyamoto, A., Araiso, T., Koyama, T., and Ohshika, H. (1990). Membrane viscosity correlates with α1-adrenergic signal transduction of the aged rat cerebral cortex. *J. Neurochem.* 55, 70–75. doi: 10.1111/j.1471-4159.1990.tb08822.x

Ning, P., Dong, P., Geng, Q., Bai, L., Ding, Y., Tian, X., et al. (2017). A two-photon fluorescent probe for viscosity imaging *in vivo*. *J. Mater. Chem. B* 5, 2743–2749. doi: 10.1039/c7tb00136c

Peng, X., Yang, Z., Wang, J., Fan, J., He, Y., Song, F., et al. (2011). Fluorescence ratiometry and fluorescence lifetime imaging: using a single molecular sensor for dual mode imaging of cellular viscosity. *J. Am. Chem. Soc.* 133, 6626–6635. doi: 10.1021/ja1104014

Platt, F. M., Boland, B., and van der Spoel, A. C. (2012). Lysosomal storage disorders: the cellular impact of lysosomal dysfunction. *J. Cell Biol.* 199, 723–734. doi: 10.1083/jcb.201208152

Ren, M., Deng, B., Zhou, K., Kong, X., Wang, J. Y., and Lin, W. (2016). Single fluorescent probe for dual-imaging viscosity and H2O2 in mitochondria with different fluorescence signals in living cells. *Anal. Chem.* 89, 552–555. doi: 10.1021/acs.analchem.6b04385

Richter, C. (1987). Biophysical consequences of lipid peroxidation in membranes. *Chem. Phys. Lipids* 44, 175–189. doi: 10.1016/0009-308490049-1

Sekhar, A., Latham, M. P., Vallurupalli, P., and Kay, L. E. (2014). Viscosity-dependent kinetics of protein conformational exchange: microviscosity effects and the need for a small viscogen. *J. Phys. Chem. B* 118, 4546–4551. doi: 10.1021/jp501583t

Song, X., Li, N., Wang, C., and Xiao, Y. (2017). Targetable and fixable rotor for quantifying mitochondrial viscosity of living cells by fluorescence lifetime imaging. *J. Mater. Chem. B* 5, 360–368. doi: 10.1039/C6TB02524B

Su, D., Teoh, C., Gao, N., Xu, Q. H., and Chang, Y. T. (2016). A simple BODIPY-based viscosity probe for imaging of cellular viscosity in live cells. *Sensors* 16:1397. doi: 10.3390/s16091397

Sutharsan, J., Lichlyter, D., Wright, N. E., Dakanali, M., Haidekker, M. A., and Theodorakis, E. A. (2010). Molecular rotors: synthesis and evaluation as viscosity sensors. *Tetrahedron* 66, 2582–2588. doi: 10.1016/j.tet.2010.01.093

Tsien, R. Y. (1989). Fluorescent probes of cell signaling. 12, 227–253

Uribe, S., and Smpedro, J. G. (2003). Measuring solution viscosity and its effect on enzyme activity. 5, 108–115. doi: 10.1251/bpo52

Vyšniauskas, A., Qurashi, M., Gallop, N., Balaz, M., Anderson, H. L., and Kuimova, M. K. (2015). Unravelling the effect of temperature on viscosity-sensitive fluorescent molecular rotors. *Chem. Sci.* 6, 5773–5778. doi: 10.1039/C5SC02248G

Vyšniauskas, A., Qurashi, M., and Kuimova, M. K. (2016). A molecular rotor that measures dynamic changes of lipid bilayer viscosity caused by oxidative stress. *Chem. A Eur. J.* 22, 13210–13217. doi: 10.1002/chem.201601925

Wang, L., Xiao, Y., Tian, W., and Deng, L. (2013). Activatable rotor for quantifying lysosomal viscosity in living cells. *J. Am. Chem. Soc.* 135, 2903–2906. doi: 10.1021/ja311688g

Wang, M., Zhao, J., Zhang, L., Wei, F., Lian, Y., Wu, Y., et al. (2017). Role of tumor microenvironment in tumorigenesis. *J. Cancer* 8, 761–773. doi: 10.7150/jca.17648

Yang, Z., Cao, J., He, Y., Yang, J. H., Kim, T., Peng, X., et al. (2014). Macro-/micro-environment-sensitive chemosensing and biological imaging. *Chem. Soc. Rev.* 43, 4563–4601. doi: 10.1039/c4cs00051j

Zhu, H., Fan, J., Du, J., and Peng, X. (2016). Fluorescent probes for sensing and imaging within specific cellular organelles. *Acc. Chem. Res.* 49, 2115–2126. doi: 10.1021/acs.accounts.6b00292

Conflict of Interest Statement: The authors declare that the research was conducted in the absence of any commercial or financial relationships that could be construed as a potential conflict of interest.

Copyright © 2019 Lei, Xin, Qiu, Hou, Meng and Yang. This is an open-access article distributed under the terms of the Creative Commons Attribution License (CC BY). The use, distribution or reproduction in other forums is permitted, provided the original author(s) and the copyright owner(s) are credited and that the original publication in this journal is cited, in accordance with accepted academic practice. No use, distribution or reproduction is permitted which does not comply with these terms.

frontiers in Chemistry

ORIGINAL RESEARCH
published: 24 May 2019
doi: 10.3389/fchem.2019.00360

Phosphate Assay Kit in One Cell for Electrochemical Detection of Intracellular Phosphate Ions at Single Cells

Haiyan Xu†, Dandan Yang†, Dechen Jiang and Hong-Yuan Chen*

State Key Laboratory of Analytical Chemistry for Life Science, School of Chemistry and Chemical Engineering, Nanjing University, Nanjing, China

In this paper, phosphate assay kit in one cell is realized for the electrochemical detection of intracellular phosphate ions at single cells. The components of the phosphate assay kit, including maltose phosphorylase, maltose, mutarotase, and glucose oxidase, are electrochemically injected into a living cell through a nanometer-sized capillary with the ring electrode at the tip. These components react with phosphate ions inside the cell to generate hydrogen peroxide that is electrochemically oxidized at the ring electrode for the qualification of intracellular phosphate ions. An average 1.7 nA charge was collected from eight individual cells, suggesting an intracellular phosphate concentration of 2.1 mM. The establishment in the electrochemical measurement of phosphate ions provides a special strategy to monitor the fluctuation of intracellular phosphate at single cells, which is significant for the future investigation of phosphate signal transduction pathway.

Keywords: nanocapillary, phosphate ions, single cells, electrochemistry, phosphate assay kit

OPEN ACCESS

Edited by:
Huangxian Ju,
Nanjing University, China

Reviewed by:
Juewen Liu,
University of Waterloo, Canada
Dhammanand Jagdeo Shirale,
North Maharashtra University, India

****Correspondence:***
Dechen Jiang
dechenjiang@nju.edu.cn

†These authors have contributed equally to this work

Specialty section:
This article was submitted to Analytical Chemistry, a section of the journal Frontiers in Chemistry

Received: *08 February 2019*
Accepted: *01 May 2019*
Published: *24 May 2019*

Citation:
Xu H, Yang D, Jiang D and Chen H-Y (2019) Phosphate Assay Kit in One Cell for Electrochemical Detection of Intracellular Phosphate Ions at Single Cells. Front. Chem. 7:360. doi: 10.3389/fchem.2019.00360

INTRODUCTION

Inorganic phosphate ions are the most abundant anions inside the cells that are essential for nucleic acid and phospholipid biosynthesis, as well as for energy metabolism (Bevington et al., 1992). The concentration of intracellular phosphate is tightly maintained by membrane transporters, and the disorder of intracellular phosphate level is known to be related with multiple pathological conditions (Bun-Ya et al., 1991). For example, elevated phosphate is reported to be associated with ischemia and hypoxia, while less phosphate is related with skeletal muscle fatigue and hypophosphatemia (Bergwitz and Jüppner, 2011). Therefore, monitoring the fluctuation of intracellular phosphate is important for the biological study of phosphate signal transduction pathways. Considering the significant cellular heterogeneity, the ability to measure the phosphate level at single cells will provide more elegant information to elucidate these pathways (Wang and Bodovitz, 2010).

Many techniques, such as the colorimetry (Dickman and Bray, 1940; Cogan et al., 1999), ion chromatography (Galceran et al., 1993), fluorescence (Huang et al., 2008; Saeed et al., 2010), electrochemistry (Forano et al., 2018), and flow injection analysis (Pérez-Ruiz et al., 2001), have been well developed for the measurement of phosphate ions in the solution. The detection limit using these classical instrumental methods in the laboratories is between 20 and 150 nM (Lawal and Adeloju, 2013). To measure phosphate ions in the biological samples, a series of chemosensors

were synthesized that are capable of detecting inorganic phosphates at a physiological pH (Hatai et al., 2012; Liu et al., 2016). However, very few fluorescent probes have been synthesized to recognize phosphate ions inside the cells, which are partially due to the poor selectivity for phosphate in presence of structurally similar anions in cells (Guo et al., 2015; Zhang et al., 2018).

The phosphate assay kit includes the biologically specific maltose phosphorylase that converts maltose (in the presence of phosphate) into glucose 1-phosphate and glucose. Then, glucose oxidase included in the kit reacts with glucose to generate gluconolactone and hydrogen peroxide for the colorimetric or fluorescent determination of phosphate (McDermott et al., 2006). Due to good selectivity of the enzymes in the assay, this kit has been widely applied for the specific analysis of phosphate ions in the solution (Mousty et al., 2001) and cellular lysate (Zhang et al., 2015). Accordingly, the loading of these kit components into one cell to initialize the reaction with intracellular phosphate and the immediate detection of the product (e.g., hydrogen peroxide) should provide an alternative strategy to detect phosphate ions at single cells.

Nanoelectrochemistry is a robust tool for the detection of intracellular species at single cells that positions a nanometer-sized electrode into a living cell and collects the current or charge after the electrochemical conversion of the target molecules at the electrode surface (Wightman, 2006; Wang et al., 2012; Li et al., 2014). Previously, our group designs a nanometer-sized capillary with a ring electrode at the tip that is filled with the kit components. Upon the position of the capillary inside one living cell, a voltage is applied at a metal wire in the capillary to induce electroosmotic flow (EOF) that results in the electrochemical pumping of these components into the cell (Pan et al., 2016). After the reaction between the kit components and the target molecule for a certain time, the hydrogen peroxide generated could be electrochemically detected at the ring electrode. As a result, intracellular glucose and the activity of sphingomyelinase have been successfully quantified without the significant interruption of cellular activity. Using this approach, the loading of the phosphate assay kit in one cell is feasible, and thus, the detection of phosphate ions at single cells could be realized. As compared with the previously reported approach using the synthesized probes, this kit-based method uses the commercially available kit components that avoid the complicated structural design of the probe and guarantee the specific recognition of phosphate ions.

In this paper, the components of the phosphate assay kit, including maltose phosphorylase, maltose, mutarotase, and glucose oxidase, are filled into the nanocapillary, which is electrochemically loaded into the cell, as demonstrated in **Figure 1A**. Intracellular phosphate reacts with maltose phosphorylase and maltose to form α-glucose, which is transformed into β-glucose for the following oxidation by glucose oxidase (**Figure 1B**). The hydrogen peroxide generated is then electrochemically oxidized at the ring electrode for the quantification of phosphate ions inside the cells. The detection ability of this approach for phosphate ions in aqueous solution and inside the cells is investigated.

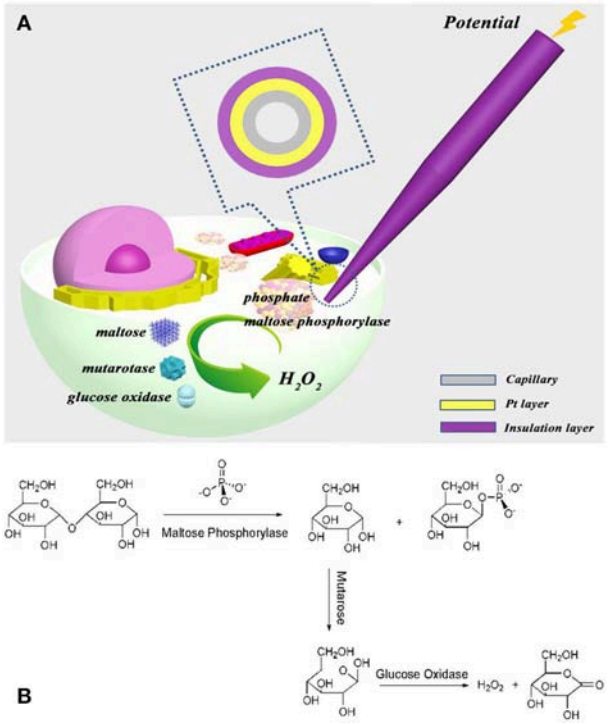

FIGURE 1 | (A) Schematic illustration to show the electrochemical loading of the phosphate assay kit in one cell and the following electrochemical detection of intracellular phosphate ions at single cells; **(B)** the reaction of kit components (maltose phosphorylase, maltose, mutarotase, and glucose oxidase) with phosphate ions.

EXPERIMENTAL SECTION

Chemical and Cells

The phosphate assay kit (P22061) is obtained from Molecular Probes, Inc. (OR, USA). All the other chemicals are purchased from Sigma Chemical Co. (MO, USA). HeLa cells were obtained from the Institute of Biochemistry and Cell Biology, Shanghai Institute for Biological Science of Chinese Academy of Science (Shanghai, China). HeLa cells were cultured in DMEM/high glucose medium supplemented with 10% fetal bovine serum and 1% penicillin/streptomycin at 37°C under a humidified atmosphere containing 5% CO_2.

Apparatus and Measurement

The nanocapillaries with a Pt layer at the tip opening (∼130 nm in diameter) are fabricated following our previously reported protocol (Pan et al., 2016). The kit components, including maltose phosphorylase (50 U/ml), maltose (40 mM), glucose oxidase (10 mg/ml), and mutarotase (50 U/ml), are filled into the capillary. A Pt wire is inserted into the capillary that is applied with a voltage of 1 V to electrochemically pump the kit components outside the capillary. Immediately after the egression and the following reaction with phosphate ions, a voltage of 0.6 V is applied at the Pt layer at the nanocapillary for

the electrochemical detection using a CHI 660E electrochemical station (CH Instruments) at room temperature.

Single-Cell Analysis

Single-cell analysis is performed under a microscope (Nikon ECLIPSE Ti-U, Nikon, Japan). Prior to each measurement, the cells are washed and re-cultured in extracellular buffer (ECB buffer: 135 mM NaCl, 5 mM KCl, 10 mM HEPES, 2 mM $MgCl_2$, and 2 mM $CaCl_2$) in the absence of extracellular phosphate ions. The nanocapillary is mounted on a 3D translation stage to achieve the penetration into the target cell.

RESULTS AND DISCUSSION

Analysis of Phosphate Ions in the Buffer

To validate our approach for the measurement of phosphate ions, the initial experiment is conducted in ECB buffer with different concentrations of phosphate ions. As compared with 1× phosphate buffer saline (PBS), ECB buffer has almost the same ion strength and viscosity, resulting in similar EOF rate in the capillary. Therefore, the electrochemical loading condition optimized in the previous work, including a voltage of 1 V and an application time of 30 s, is used to egress femtoliter (fl) volume of kit components outside the capillary (Pan et al., 2016). The non-faradic (or charging) charge from the Pt layer at the tip of the capillary is collected in the buffer without any phosphate ions after the electrochemical egression (**Figure 2A**, trace a). Once 0.1 mM phosphate ions are added into the buffer, an increase in the charge is observed (trace b) after the egression of fresh kit components. When one kit component (maltose phosphorylase, maltose, or glucose oxidase) is removed from the mixed solution inside the capillary, this charge increase disappears. Both of the results suggest the occurrence of chemical reactions of kit components and phosphate ions outside the tip that generates hydrogen peroxide and the following charge increase.

The addition of more phosphate ions in the buffer elevates the concentration from 0.1 to 3 mM. Consequently, the gradual increases in the charge are observed (**Figure 2A**, traces c–f), which are correlated with the concentration of phosphate ions. After subtracting the background charge, the charge increases at the time of 250 s from three independent experiments are measured and plotted with the concentrations of phosphate ions, as shown in **Figure 2B**. The coefficient of determination in the fitting curve is 0.98, exhibiting a near-linear relationship between the charge increase and the concentrations of phosphate ions. The relative standard deviation in this detection range is less than 16.8%. Accordingly, the charge collected in our approach could be applied to quantify the phosphate ions.

To characterize the conversion of phosphate ions by the kit components, these charge increases are compared with those collected from the measurement of glucose. Experimentally, the nanocapillaries loaded with glucose oxidase are applied to collect the charge increases in the presence of aqueous glucose, as shown in **Figure S1** (supporting information). These

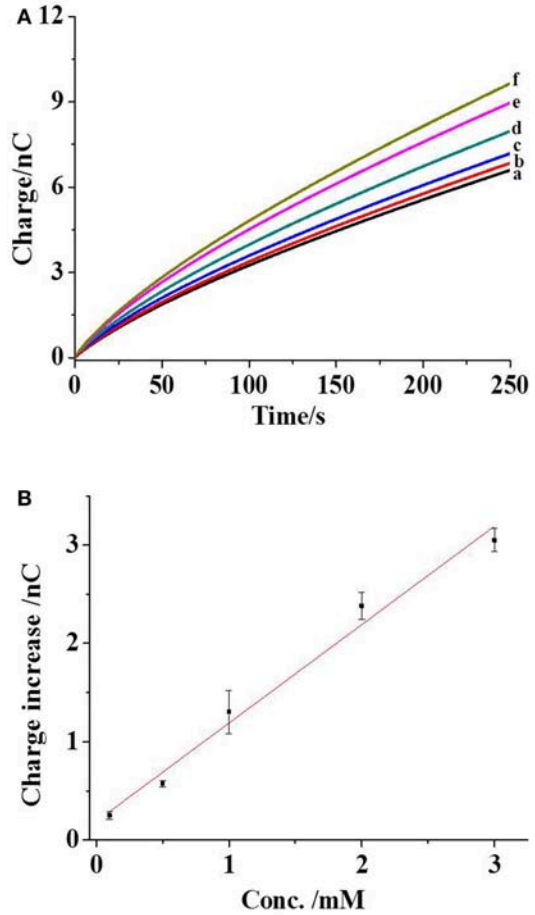

FIGURE 2 | (A) The charges of capillary exposed to the ECB buffer (curve a), with 0.1 (curve b), 0.5 (curve c), 1 (curve d), 2 (curve e), and 3 mM phosphate ions (curve f). The capillary is filled with maltose phosphorylase (50 U/ml), maltose (40 mM), glucose oxidase (10 mg/ml), and mutarotase (50 U/ml). The condition for the electrochemical loading is 1 V for 30 s. **(B)** The correlation between the charge increase and the concentration of phosphate ions. The error bars present the standard deviations from three independent measurements. The line is the linear fitting curve.

charge increases are rationed with those from the measurement of phosphate ions, which are in the range of 20 and 56%. These values exhibit the limited conversion of phosphate ions by multiple enzymes, and thus, the control of the egression and the following detection time are critical to obtain the reproducible result. For the specificity of our measurement, various phosphate-containing species, such as pyrophosphate, hexametaphosphate, tripolyphosphate, and ATP, are measured successively using the nanocapillaries (Wang et al., 2018). As shown in **Figure S2** (supporting information), no significant charge increase is observed at all these species, exhibiting good specificity of our assay.

Single-Cell Analysis

The same measurement process is conducted after the insertion of a nanocapillary into a living cell, as imaged in **Figure 3A**.

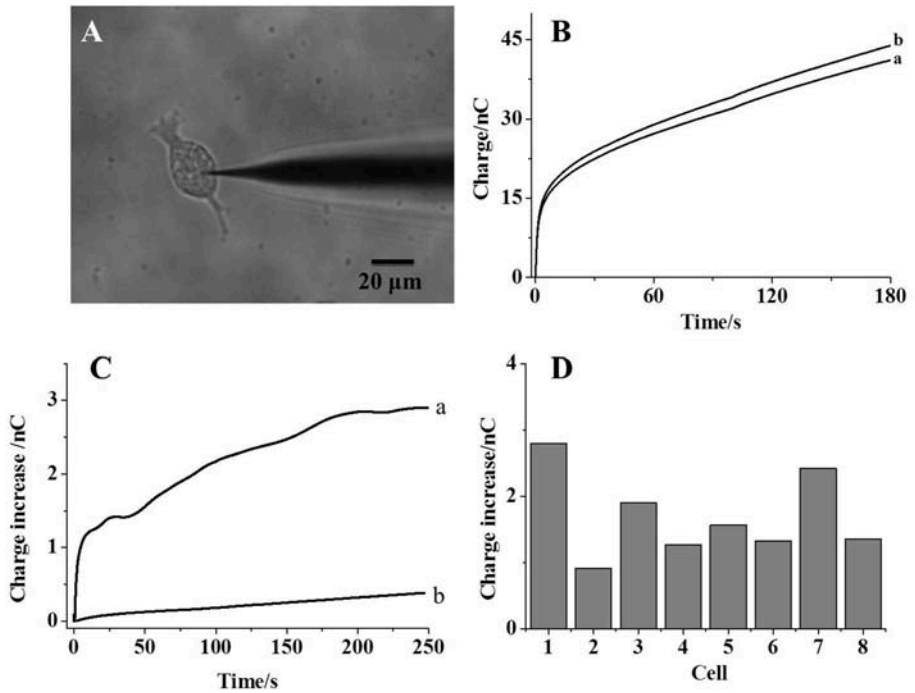

FIGURE 3 | (A) The bright-field image of a nanocapillary inserted into a living HeLa cell; **(B)** the charges collected before (curve a) and after (curve b) the electrochemical loading of kit components into the cells; **(C)** trace a: the charge difference between curve a and b in **(B)**; trace b: the charge difference before and after the electrochemical loading of maltose, mutarotase, and glucose oxidase only into the cells; **(D)** the charge increases collected from eight individual cells.

Because the reaction of kit components with phosphate ions generates glucose, intracellular glucose needs to be minimized to reduce the additional contribution on the charge. Therefore, the cells are starved overnight prior to each measurement, and the intracellular glucose was reported to be ∼0.12 mM (Zhang et al., 2014). After the collection of the background charge (**Figure 3B**, trace a), a voltage of 1 V is applied at the Pt wire inside the capillary for 30 s to egress the kit components into the cell. Intracellular calcium concentration is continuously monitored using the Fluo-3 probe under the fluorescence microscope (Gobet et al., 1995). As shown in **Figure S3** (supporting information), no significant increase in the calcium concentration suggests minor interruption of cellular activity during the penetration and the following electrochemical loading. After the egression of the kit components and the recording of the charge, an increase in the charge is observed (**Figure 3B**, trace b), which should be ascribed to hydrogen peroxide generated from the reaction with intracellular phosphate ions. To exclude the possible contribution from intracellular glucose or reactive oxygen species on the charge increase, the control experiment is performed by the introduction of the solution with glucose oxidase only. No charge increase obtained suggests that the charge increase in **Figure 3B** is mainly contributed by intracellular phosphate ions.

The charge difference before and after the introduction of kit components (trace a and b) is calculated and plotted in **Figure 3C** (trace a). An initially fast increase in the charge clearly exhibits a fast reaction between the kit components and phosphate ions. After the reaction for 200 s, the charge difference reaches the steady state, which should be attributed to the depletion of phosphate ions inside the cells. Thus, this steady-state charge increase could be used to estimate the amount of intracellular phosphate ions. Eight cells are analyzed individually and the steady-state charge increase is listed in **Figure 3D**. An averaged 1.7 nC is calculated from these cells with a relative standard deviation of 35.3%. According to Faraday's law, 8.5 fmol phosphate ions are detected in one cell. Because the size of a single cell is 20 μm and the cellular volume is estimated to be 4 pl, 2.1 mM phosphate ions are determined in one cell, which is consistent to the literature result (Bevington et al., 1986). Since some glucose is still present inside the starved cells, the control experiment is conducted using the nanocapillary loaded with maltose, mutarotase, and glucose oxidase only. The absence of maltose phosphorylase should not initialize the generation of glucose from phosphate ions. The charge difference before and after the introduction of these components into one cell is shown in **Figure 3C** (trace b). Only a slight increase in the charge supports the minor contribution of intracellular glucose on the measurement of phosphate ions inside the cells. The successful detection of intracellular phosphate ions at individual cells supports the accuracy of our approach to determine intracellular phosphate ions at single cells.

CONCLUSION

In summary, the electrochemical detection of intracellular phosphate ions at single cells is realized by the loading of phosphate assay kit into one cell. This approach utilizes the commercially available kit to react with phosphate ions and, thus, avoids the design and preparation of the recognition probe. This simplification facilitates the detection of phosphate ions at single living cells. The future development will focus on the application of this approach to analyze the activity of phosphatase that releases a phosphate group from its substrate. The qualification of the activity of phosphatase, especially phosphatase and tensin homolog (PTEN), at single cells could provide the important information for the drug development. To realize this aim, the detection limit of our assay should be improved, which is undergoing in the lab.

AUTHOR CONTRIBUTIONS

HX and DY performed the experiments and analyzed the data. DJ and H-YC designed the project and wrote the paper.

ACKNOWLEDGMENTS

This work was supported by Key Laboratory of Analytical Chemistry for Life Science (no. 5431ZZXM1803).

SUPPLEMENTARY MATERIAL

The Supplementary Material for this article can be found online at: https://www.frontiersin.org/articles/10.3389/fchem.2019.00360/full#supplementary-material

REFERENCES

Bergwitz, C., and Jüppner, H. (2011). Phosphate sensing. *Adv. Chron. Kidney Dis.* 18, 132–144. doi: 10.1053/j.ackd.2011.01.004

Bevington, A., Kemp, G. J., Graham, R., and Russell, G. (1992). Phosphate-sensitive enzymes: possible molecular basis for cellular disorders of phosphate metabolism. *Clin. Chem. Enzym. Comms.* 4, 235–257.

Bevington, A., Mundy, K. I., Yates, A. J., Kanis, J. A., Russell, R. G., Taylor, D. J., et al. (1986). A study of intracellular orthophosphate concentration in human muscle and erythrocytes by 31P nuclear magnetic resonance spectroscopy and selective chemical assay. *Clin. Sci.* 71, 729–735. doi: 10.1042/cs0710729

Bun-Ya, M., Nishimura, M., Harashima, S., and Oshima, Y. (1991). The PHO84 gene of *Saccharomyces cerevisiae* encodes an inorganic phosphate transporter. *Mol. Cell Biol.* 11, 3229–3238. doi: 10.1128/MCB.11.6.3229

Cogan, E. B., Birrell, G. B., and Griffith, O. H. (1999). A robotics-based automated assay for inorganic and organic phosphates. *Anal. Biochem.* 271, 29–35. doi: 10.1006/abio.1999.4100

Dickman, S. R., and Bray, R. H. (1940). Colorimetric determination of phosphate. *Ind. Eng. Chem. Anal. Ed.* 12, 665–668. doi: 10.1021/ac50151a013

Forano, C., Farhat, H., and Mousty, C. (2018). Recent trends in electrochemical detection of phosphate in actual waters. *Curr. Opin. Electrochem.* 11, 55–61. doi: 10.1016/j.coelec.2018.07.008

Galceran, M. T., Diez, M., and Paniagua, L. (1993). Determination of phosphate in samples with high levels of sulphate by ion chromatography. *J. Chromatogr. A.* 657, 77–85. doi: 10.1016/0021-9673(93)83037-S

Gobet, I., Lippai, M., Tomkowiak, M., Durocher, Y., Leclerc, C., and Moreau, M., et al (1995). 4-Aminopyridine acts as a weak base and a Ca2+ mobilizing agent in triggering oocyte meiosis reinitiation and activation in the Japanese clam *Ruditapes philippinarum*. *Int. J. Dev. Biol.* 39, 485–491. doi: 10.1016/0248-4900(96)81407-9

Guo, L. E., Zhang, J. F., Liu, X. Y., Zhang, L. M., Zhang, H. L., Chen, J. H., et al. (2015). Phosphate ion targeted colorimetric and fluorescent probe and its use to monitor endogeneous phosphate ion in a hemichannel-closed cell. *Anal. Chem.* 87, 1196–1201. doi: 10.1021/ac503818p

Hatai, J., Pal, S., and Bandyopadhyay, S. (2012). An inorganic phosphate (Pi) sensor triggers 'turn-on' fluorescence response by removal of a Cu2+ ion from a Cu2+-ligand sensor: determination of Pi in biological samples. *Tetrahedron. Lett.* 53, 4357–4360. doi: 10.1016/j.tetlet.2012.06.014

Huang, X., Guo, Z. Q., Zhu, W. H., Xie, Y. S., and Tian, H. (2008). A colorimetric and fluorescent turn-on sensor for pyrophosphate anion based on a dicyanomethylene-4H-chromene framework. *Chem. Commun.* 5143–5145. doi: 10.1039/b809983a

Lawal, A. T., and Adeloju, S. B. (2013). Progress and recent advances in phosphate sensors: a review *Talanta* 114, 191–203. doi: 10.1016/j.talanta.2013.03.031

Li, Y. T., Zhang, S. H., Wang, L., Xiao, R. R., Liu, W., Zhang, X. W., et al. (2014). Nanoelectrode for amperometric monitoring of individual vesicular exocytosis inside single synapses. *Angew. Chem. Int. Ed.* 53, 12456–12460. doi: 10.1002/anie.201404744

Liu, B., Wang, H., Yang, D., Tan, R., Zhao, R. R., Xu, R., et al. (2016). A cyanine-based colorimetric and fluorescent probe for highly selective sensing and bioimaging of phosphate ions. *Dyes Pigments.* 133, 127–131. doi: 10.1016/j.dyepig.2016.04.032

McDermott, M. I., Sigal, Y. J., Crump, J. S., and Morris, A. J. (2006). Enzymatic analysis of lipid phosphate phosphatases. *Methods* 39, 169–179. doi: 10.1016/j.ymeth.2006.05.010

Mousty, C., Cosnier, S., Shan, D., and Mu, S. (2001). Trienzymatic biosensor for the determination of inorganic phosphate. *Anal. Chim. Acta* 443, 1–8. doi: 10.1016/S0003-2670(01)01188-6

Pan, R., Xu, M. C., Jiang, D. C., Burgess, J. D., and Chen, H. Y. (2016). Nanokit for single-cell electrochemical analyses. *Proc. Natl. Acad. Sci. U.S.A.* 113, 11436–11440. doi: 10.1073/pnas.1609618113

Pérez-Ruiz, T., Martínez-Lozano, Tomás, C. V., and Martín, J. (2001). Flow-injection spectrofluorimetric determination of dissolved inorganic and organic phosphorus in waters using on-line photo-oxidation. *Anal. Chim. Acta* 442, 147–153. doi: 10.1016/S0003-2670(01)01080-7

Saeed, M. A., Powell, D. R., and Hossaina, M. A. (2010). Fluorescent detection of phosphate anion by a highly selective chemosensor in water. *Tetrahedron Lett.* 51, 4904–4907. doi: 10.1016/j.tetlet.2010.07.078

Wang, D., and Bodovitz, S. (2010). Single cell analysis: the new frontier in 'omics'. *Trends Biotechnol.* 28, 281–290. doi: 10.1016/j.tibtech.2010.03.002

Wang, X., Lopez, A., and Liu, J. W. (2018). Adsorption of phosphate and polyphosphate on nanoceria probed by DNA oligonucleotides. *Langmuir.* 34, 7899–7905. doi: 10.1021/acs.langmuir.8b01482

Wang, Y., Noël, J. M., Velmurugan, J., Nogala, W., Mirkin, M. V., Lu, C., et al. (2012). Nanoelectrodes for determination of reactive oxygen and nitrogen species inside murine macrophages. *Proc. Natl. Acad. Sci. U.S.A.* 109, 11534–11539. doi: 10.1073/pnas.1201552109

Wightman, R. M. (2006). Detection technologies. Probing cellular chemistry in biological systems with microelectrodes. *Science* 311, 1570–1574. doi: 10.1126/science.1120027

Zhang, J., Sassen, T., ten Pierick, A., Ras, C., Heijnen, J. J., and Wahl, S. A. (2015). A fast sensor for *in vivo* quantification of cytosolic phosphate in *Saccharomyces cerevisiae*. *Biotechnol. Bioeng.* 112, 1033–1046. doi: 10.1002/bit.25516

Zhang, J., Wang, S., Liu, C. H., He, G. W., and Peng, T. Y. (2018). A novel turn-on fluorescent probe for highly selective detection of phosphate ion in living cell. *Chin. J. Chem.* 36, 1179–1181. doi: 10.1002/cjoc.201800376

Zhang, L., Su, F., Buizer, S., Kong, X., Lee, F., Day, K., et al. (2014). A polymer-based ratiometric intracellular glucose sensor. *Chem. Commun.* 50, 6920–6922. doi: 10.1039/C4CC01110D

Conflict of Interest Statement: The authors declare that the research was conducted in the absence of any commercial or financial relationships that could be construed as a potential conflict of interest.

The handling editor declared a shared affiliation, though no other collaboration, with the authors HX, DY, DJ, and H-YC at time of review.

Copyright © 2019 Xu, Yang, Jiang and Chen. This is an open-access article distributed under the terms of the Creative Commons Attribution License (CC BY). The use, distribution or reproduction in other forums is permitted, provided the original author(s) and the copyright owner(s) are credited and that the original publication in this journal is cited, in accordance with accepted academic practice. No use, distribution or reproduction is permitted which does not comply with these terms.

Catalysis and Photocatalysis

Maylis Orio

Maylis Orio is a theoretical chemist specializing in quantum chemistry applied to bioinorganic systems. After obtaining a PhD studying the structure and properties of polynuclear iron complexes, her three-year postdoctoral work was dedicated to the theoretical study of metalloprotein active sites. She has acquired expertise in EPR spectroscopy while appointed as a CNRS researcher. She eventually joined an experimental laboratory with the aim to reinforce her skills toward mechanistic investigation in biocatalysis. She has an important background in computational chemistry and can handle sophisticated theoretical methods to study structures, properties, and reactivity of bioinorganic systems at the molecular level.

Shinya Furukawa

Shinya Furukawa obtained his BEng, MEng, and PhD at Kyoto University in March 2012. He joined the Tokyo Institute of Technology as an Assistant Professor in April 2012. He then moved to Hokkaido University as an Associate Professor in June 2016. His research is focused on the catalytic chemistry of metallic materials, metal complexes, and semiconductor photocatalysts. His current interest is focused on catalysis over the surface of bimetallic materials such as alloys and intermetallics. He likes not only to develop highly efficient catalytic systems but also to deeply clarify the reaction mechanism in an atomic scale using experimental and theoretical approaches.

Gufeng Wang

Gufeng Wang holds BSc and MSc degrees from Nanjing University, and a PhD degree from the University of Iowa. He then worked as a postdoc associate in Iowa State University and US DOE for 5 years. Afterwards, he joined the faculty of the Chemistry Department at North Carolina State University in 2011. His research interests are focused on developing novel nanoparticles that have unique optical and chemical properties, super resolution optical imaging techniques, and light-actuated molecular machines, to solve problems relevant to human health and renewable energy.

Jonathan Zacharias Bloh

Dr Jonathan Zacharias Bloh studied Life Science and later obtained his PhD in Technical Chemistry in 2012 at Leibniz University, Hannover. Thereafter he spent one and a half years as a postdoc at the University of Aberdeen in Scotland. Since 2014, he is the head of the Chemical Technology group at the DECHEMA Research Institute in Frankfurt am Main, Germany. His current research covers photocatalysis, reaction engineering, and chemo-enzymatic processes.

Ljiljana Fruk

Ljiljana studied chemistry at the University of Zagreb, obtained a PhD in biospectroscopy from the University of Strathclyde, Glasgow, and worked on DNA structuring and enzyme reconstitution as a postdoctoral fellow at the University of Dortmund. She established her own research group at Karlsruhe Institute of Technology in 2009 to focus on the nanomaterial biofunctionalization and design of light-triggered nanodevices. Since 2015 she is a lecturer at the Department of Chemical Engineering and Biotechnology, University of Cambridge. Her research is focused on the design of biocompatible hybrid materials for nanomedicine and catalysis, and the development of mild strategies for nanomaterial biofunctionalization. She is also a well-known science popularizer and co-author of the field-establishing Molecular Aesthetics book.

frontiers in Chemistry

ORIGINAL RESEARCH
published: 27 June 2019
doi: 10.3389/fchem.2019.00405

Efficient Light-Driven Hydrogen Evolution Using a Thiosemicarbazone-Nickel (II) Complex

Stylianos Panagiotakis[1], *Georgios Landrou*[1], *Vasilis Nikolaou*[1], *Anisa Putri*[2], *Renaud Hardré*[2], *Julien Massin*[2], *Georgios Charalambidis*[1]*, *Athanassios G. Coutsolelos*[1]* *and Maylis Orio*[2]*

[1] *Laboratory of Bioinorganic Chemistry, Department of Chemistry, University of Crete, Heraklion, Greece,* [2] *Aix Marseille Université, CNRS, Centrale Marseille, iSm2, Marseille, France*

In the following work, we carried out a systematic study investigating the behavior of a thiosemicarbazone-nickel (II) complex (**NiTSC-OMe**) as a molecular catalyst for photo-induced hydrogen production. A comprehensive comparison regarding the combination of three different chromophores with this catalyst has been performed, using **[Ir(ppy)$_2$(bpy)]PF$_6$**, **[Ru(bpy)$_3$]Cl$_2$** and **[ZnTMePy]PCl$_4$** as photosensitizers. Thorough evaluation of the parameters affecting the hydrogen evolution experiments (i.e., concentration, pH, solvent nature, and ratio), has been performed in order to probe the most efficient photocatalytic system, which was comprised by **NiTSC-OMe** and **[Ir(ppy)$_2$(bpy)]PF$_6$** as catalyst and chromophore, respectively. The electrochemical together with the photophysical investigation clarified the properties of this photocatalytic system and allowed us to propose a possible reaction mechanism for hydrogen production.

Keywords: light-driven hydrogen production, catalyst, nickel, molecular photosensitizer, photophysics

OPEN ACCESS

Edited by:
Bunsho Ohtani,
Hokkaido University, Japan

Reviewed by:
Marco Armandi,
Polytechnic University of Turin, Italy
Mirco Natali,
University of Ferrara, Italy

***Correspondence:**
Georgios Charalambidis
gcharal@uoc.gr
Athanassios G. Coutsolelos
acoutsol@uoc.gr
Maylis Orio
maylis.orio@univ-amu.fr

Specialty section:
This article was submitted to Catalysis and Photocatalysis, a section of the journal Frontiers in Chemistry

Received: *17 December 2018*
Accepted: *20 May 2019*
Published: *27 June 2019*

Citation:
Panagiotakis S, Landrou G, Nikolaou V, Putri A, Hardré R, Massin J, Charalambidis G, Coutsolelos AG and Orio M (2019) Efficient Light-Driven Hydrogen Evolution Using a Thiosemicarbazone-Nickel (II) Complex. Front. Chem. 7:405. doi: 10.3389/fchem.2019.00405

INTRODUCTION

One of the most important challenges of our society, that still lie ahead, is to discover renewable and abundant energy sources (Hosenuzzaman et al., 2015; Hosseini and Wahid, 2016). Solar energy is indeed an attractive and unlimited energy source which nonetheless requires the development of novel as well as efficient storage technologies (Styring, 2012; Tachibana et al., 2012; Faunce et al., 2013). Interestingly, hydrogen could unquestionably be applied for such a purpose: (i) it is the simplest and the most plentiful element on earth, (ii) the energy of the hydrogen-hydrogen bond is high, and (iii) it is considered as a non-polluting fuel (Peel, 2003). Hence, photocatalytic water splitting leading to hydrogen production is a method that without any doubt could be proved as an auspicious solution (Lewis and Nocera, 2006). Photocatalytic hydrogen production can be accomplished by systems containing a photosensitizer, a sacrificial electron donor and a catalyst (Ladomenou et al., 2015; Yuan et al., 2017). Nevertheless, there are plenty unsolved issues that still rest in the field of photocatalytic hydrogen production. Specifically, the development of systems utilizing earth-abundant materials with enhanced efficiency and durability (Wang and Sun, 2010; Du and Eisenberg, 2012). To that end, numerous hydrogen evolution catalysts along with a great number of different photosensitizers have been extensively examined over the last years (Tran et al., 2010, 2012; Du and Eisenberg, 2012; Wang et al., 2012; Sartorel et al., 2013).

Photocatalytic systems involving low-cost molecular catalysts and compounds prepared through easy synthetic approaches have been widely studied over the past decade (Artero et al., 2011; Eckenhoff et al., 2013; Ladomenou et al., 2015). Specifically, cobaloximes (Fihri et al., 2008; Lazarides et al., 2009, 2014; Du and Eisenberg, 2012; Landrou et al., 2016; Panagiotopoulos et al., 2016), and other polypyridine cobalt complexes have been applied as noble-metal-free catalysts (Eckenhoff et al., 2013; Yin et al., 2015; Zee et al., 2015). Although, several of these catalysts are efficient for photocatalytic hydrogen evolution reaction (HER), their stability was greatly limited upon visible light irradiation. Moreover, many researches draw inspiration from Nature trying to replicate the function of the hydrogenase enzymes (Lubitz et al., 2014; Brazzolotto et al., 2016), leading to the design of nickel complexes that were evaluated as molecular catalysts for HER. As a result, plenty nickel catalysts such as nickel bis(diphosphine) (DuBois and DuBois, 2009a,b; Helm et al., 2011; McLaughlin et al., 2011), and pyridinethiolate (Han et al., 2012, 2013; Rao et al., 2016) have been applied in such schemes, since they reproduce the structure of the active site of hydrogenase. Due to the effect of non-innocent ligands, (Han et al., 2012, 2013; Rao et al., 2015, 2016; Inoue et al., 2017) such nickel complexes have displayed excellent efficiency as catalyst reaching around 7,500 TON (Han et al., 2013; Rao et al., 2016). Thiosemicarbazone metal complexes are an emerging class of new HER electrocatalysts (Haddad et al., 2016, 2017; Straistari et al., 2017, 2018a,b) that have already been proved to be redox active (Blanchard et al., 2005; Haddad et al., 2017; Straistari et al., 2017) The presence of S-donors as well as N-atoms in thiosemicarbazone allows the protonation of the ligand and serve as proton relays (Campbell, 1975; DuBois, 2014; Coutard et al., 2016). One of the most essential aspect of light-driven proton reduction is the appropriate choice of the light-harvesting unit (i.e., photosensitizer, Ps). Despite the fact that $[Ru(bpy)_3]Cl_2$ remains the most widely employed chromophore in such systems (Khnayzer et al., 2014; Lo et al., 2016), iridium complexes are still the most efficient entities found in several photocatalytic systems (Goldsmith et al., 2005; Andreiadis et al., 2011). Additionally, porphyrins and other tetrapyrrolic derivatives can be effective candidates for HER due to their unique stability, electrochemical properties, and appropriate energy levels (Ladomenou et al., 2015). For this reason, various metalloporphyrins such as Zn(II) or Sn(IV), have been utilized as photosensitizers for photocatalytic HER over the years (Lazarides et al., 2014; Koposova et al., 2016; Landrou et al., 2016; Queyriaux et al., 2018).

Here we will discuss the implications of our findings regarding a novel photoinduced HER scheme using a noble-metal-free *bis*-thiosemicarbazone nickel (II) complex (Straistari et al., 2017), namely **NiTSC-OMe**. In this study, three different light harvesting complexes, **$[Ir(ppy)_2(bpy)]PF_6$ (Ps1)**, **$[Ru(bpy)_3]Cl_2$ (Ps2)**, and **$[ZnTMePy]PCl_4$ (Ps3)** (Andreiadis et al., 2011; Lazarides et al., 2014; Natali et al., 2014) were used as photosensitizers and trimethylamine (TEA) as the sacrificial electron donor (**Figure 1**). The efficiency of the resulting photocatalytic system was optimized by studying different concentrations of the catalyst, the effect of solvent mixture, the solvent ratio, and the influence of pH in the buffer solution. The electron transfer processes that occur were examined through fluorescence spectroscopic techniques. To solidify the photochemical stability of our system, regeneration experiments were conducted and the homogeneous nature of our catalytic system was proved using poisoning experiments. Based on the results gathered from these studies we were finally able to propose a possible reaction mechanism for light-driven hydrogen production with our photocatalytic system.

EXPERIMENTAL SECTION

Materials and Methods

Reagents and solvents were purchased as reagent grade from usual commercial sources and were used without further purification, unless otherwise stated. **$[Ir(ppy)_2(bpy)]PF_6$** and **$[Ru(bpy)_3]Cl_2$** were purchased from commercial sources and used without further purification. The nickel thiosemicarbazone complex (**NiTSC-OMe**) (Straistari et al., 2017) and the Zinc (II) *meso*-tetrakis (1-methylpyridinium-4-yl) porphyrin tetrachloride (**$[ZnTMePy]PCl_4$**) (Lazarides et al., 2014) were prepared as previously reported.

Photophysical Measurements

UV-Vis absorption spectra were measured on a Shimadzu UV-1700 spectrophotometer using 10 mm path-length cuvettes (**Figure S1**). The emission spectra were measured by exciting the samples at 337 nm using a JASCO FP-6500 fluorescence spectrophotometer equipped with a red sensitive WRE-343 photomultiplier tube (wavelength range 200–850 nm).

Photocatalytic HER Experiments

For the photoinduced HER studies, each sample was prepared in a 42 mL glass vial with silicone septum. The buffer solutions were prepared by dissolving the sacrificial electron donor [triethylamine (TEA) or ascorbic acid (AA)] in water. It was necessary to add a small amount of acetonitrile in order to obtain a homogeneous solution. The pH was adjusted to the required value using concentrated HCl or NaOH solutions. Then the organic solvent (CH_3CN or EtOH) was added in order to obtain the desired ratio. For the sample preparation, the chromophore was dissolved in the buffer solution and consequently a solution of the catalyst in CH_3CN or EtOH was added. The final volume of the sample was 5 mL and the mixture was degassed for 10 min using nitrogen. The vials were sealed and the samples irradiated with a white LED lamp (power of 40 W, color temperature of 6,400 K and lumen of 3,800 LM, **Figure S2**). The amounts of produced hydrogen were determined by gas chromatography (external standard technique) using a Shimadzu GC-2010 plus chromatograph with a TCD detector and a molecular sieve 5 Å column (30–0.53 mm). Gas samples of 100 μL were taken from the headspace and injected immediately into the GC. In all cases, the reported results are the average of three independent experiments. The TONs were calculated using the produced moles of hydrogen vs. the moles of the catalyst. Control experiments were performed under the same conditions after the removal of the catalyst from the hydrogen generating system.

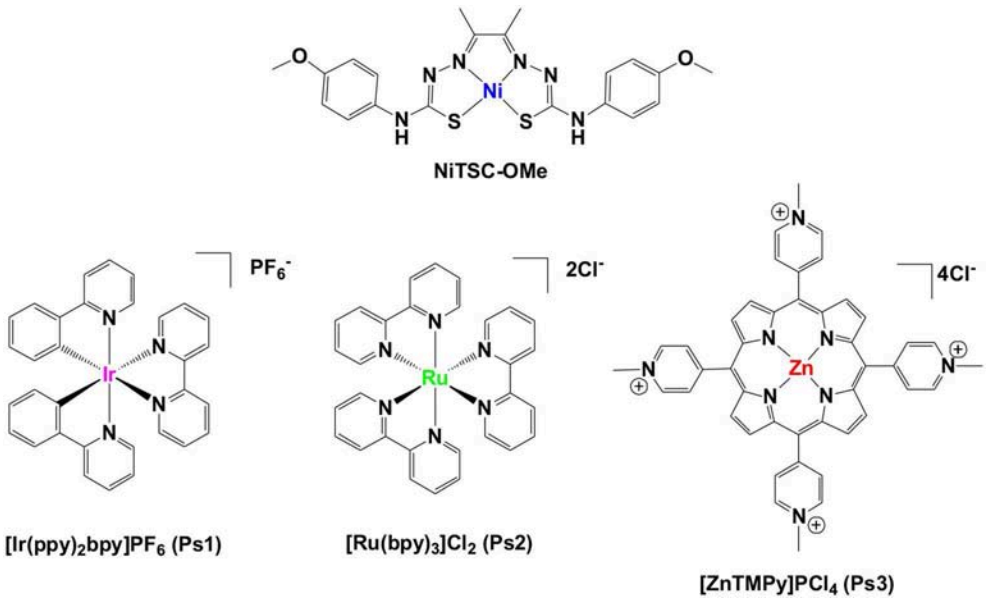

FIGURE 1 | Structures of the molecular catalyst and the photosensitizers used in this work.

Mercury poisoning experiments were performed, in order to examine the possible formation of metallic nanoparticles or colloids during the hydrogen evolution process. In these studies, an excess of mercury (ca. 40 equiv.) was added to the hydrogen evolution solutions (prepared with the above mentioned procedure).

RESULTS AND DISCUSSION

In our recent work, we reported the synthesis of a novel nickel catalyst (**NiTSC-OMe**, **Figure 1**) that exhibits high electrocatalytic activity for proton reduction to dihydrogen (Straistari et al., 2017). Based on these encouraging results we wanted to examine the capability of this catalyst toward photochemical hydrogen production. Thus, in the present study three different chromophores (**Figure 2**) were tested as photosensitizers and combined with the **NiTSC-OMe** catalyst to determine its ability as an effective photocatalytic system to reduce protons into hydrogen. We have analyzed various parameters, such as the concentration of the catalyst (10^{-5} – 5×10^{-8} M), the pH of the buffer solution, the effect of the solvent ratio in the photocatalytic mixture and the stability of our system. We carried out several experiments using TEA [5% (v/v)] or AA (0.2 M) as the sacrificial electron donors in various pH buffers (from pH = 2.5 to pH = 10). In addition, different concentrations of the catalyst and the chromophore were tested using varied solvent mixtures. Notably, in all cases no hydrogen production was observed using $[\mathbf{Ru(bpy)_3}]^{2+}$ (**Ps2**) or $[\mathbf{ZnTMePy}]^{+}$ (**Ps3**) as photosensitizers. However, when $[\mathbf{Ir(ppy)_2(bpy)}]^{+}$ (**Ps1**) was used as photosensitizer and TEA [5% (v/v)] as sacrificial electron donor, a photocatalytic hydrogen evolution of 140 μL from 1 ml of H_2O was recorded, highlighting once more that the photosensitizer is an essential component in such photocatalytic HER systems.

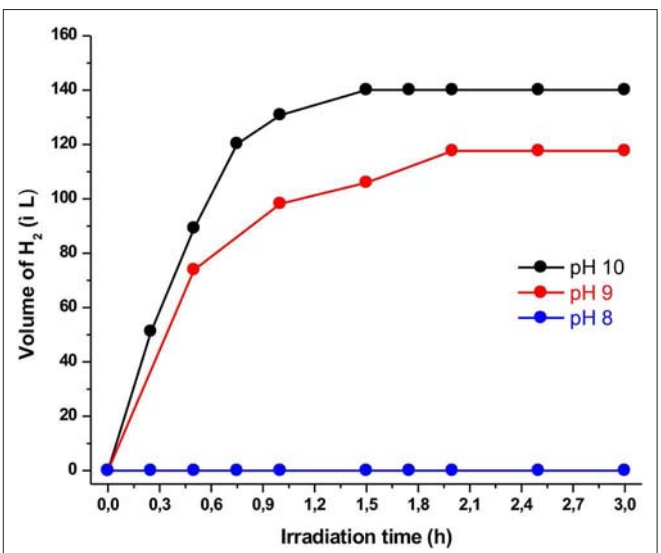

FIGURE 2 | Plot of hydrogen production upon irradiation of solutions (4:1 CH_3CN/H_2O) containing **Ps1** (5×10^{-4} M), **NiTSC-OMe** (10^{-5} M), and TEA [5% (v/v)] at different pH values.

In the above mentioned system, the first parameter that we examined was the effect of the protons concentration (pH). In detail, we used three different buffer solutions with pH values of 8, 9, and 10, concluding that the optimum one was at pH = 10. As presented in **Figure 2** using the solution with pH = 8, no hydrogen production was observed after 3 h of irradiation. On the contrary, using buffer solutions of pH = 9

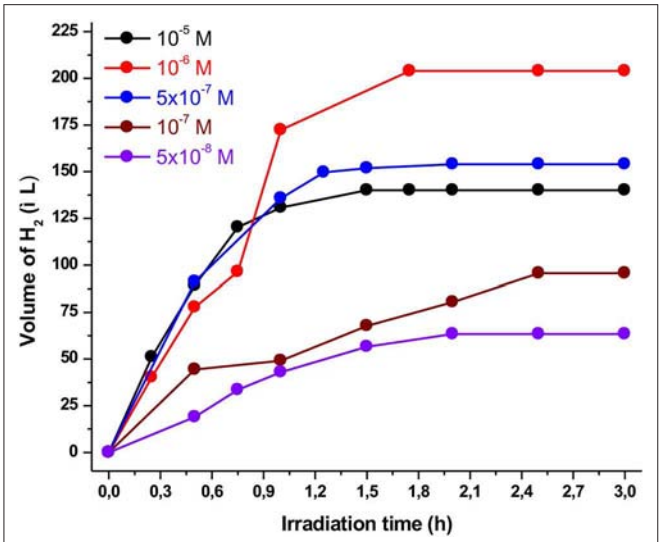

FIGURE 3 | Plot of hydrogen production upon irradiation of different **NiTSC-OMe** concentrations containing **Ps1** (5×10^{-4} M), TEA [5% (v/v)] in a 4:1 CH_3CN/H_2O solution at pH 10.

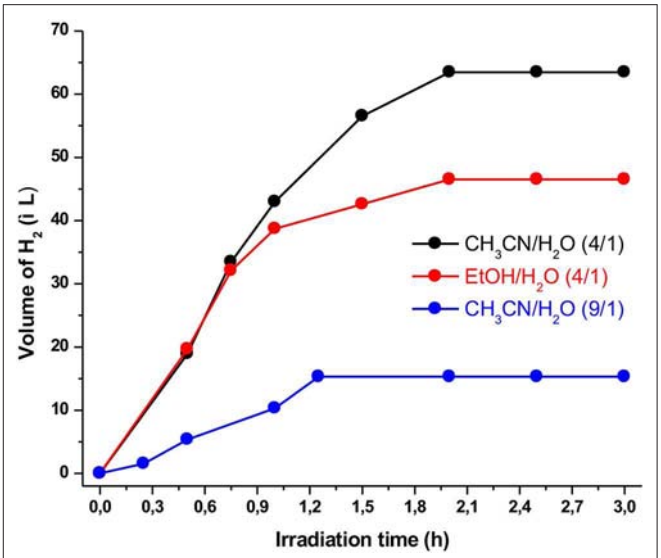

FIGURE 4 | Effect of various solvent mixtures on hydrogen production using the photocatalytic system containing **Ps1** (5×10^{-4} M), **NiTSC-OMe** (5×10^{-8} M), and TEA [5% (v/v)] at pH 10.

and pH = 10 we detected hydrogen production of 105 and 125 TONs, respectively. These findings are consistent with results derived from similar systems in which the optimum pH value is close to the pKa value of the sacrificial electron donor. Namely, in our case since the pKa of TEA is 10.7, the optimum pH of the buffer solution was expected at pH = 10 (Pellegrin and Odobel, 2017). Moreover, at pH values lower than its pKa value TEA is protonated and loses its electron donating ability (Rao et al., 2016).

Furthermore, the performances of the photocatalytic HER systems strongly depend on the catalyst concentration as well as the relative ratio between the photosensitizer and the catalyst. Accordingly, we kept the concentration of the **Ps1** photosensitizer constant (5×10^{-4} M), while the concentration of the catalyst varied from 10^{-5} to 5×10^{-8} M. As illustrated in **Figure 3**, the volume of the produced H_2 was increased when the concentration of the catalyst decreased from 10^{-5} to 10^{-6} M, reaching a maximum of 204 μL. In addition, further decrease in the concentration of the catalyst (5×10^{-7}–5×10^{-8}) resulted in lower catalytic efficiency. On the other hand, the catalytic activity of the system (TON) was increased when the concentration of the catalyst decreased from 10^{-5} to 5×10^{-8} M (**Figure S4**). Notably, when the concentration of the **NiTSC-OMe** was 5×10^{-8} M the system displayed the maximum TON and TOF values, namely 11,333 and 7,971, respectively (see **Table S1**). These results are in contrast with our previous work (Lazarides et al., 2014; Panagiotopoulos et al., 2016), where the maximum photocatalytic activity was observed when the concentration of the catalyst was in excess compared to that of the photosensitizer. This behavior can be attributed to two possible reasons: (i) the quenching of the excited state of the **Ps1** by the **NiTSC-OMe** complex and (ii) the great difference in the molecular absorptivity (ε) of complexes. Concerning the first hypothesis, since the reductive quenching process of photosensitizer by the catalyst is in competition with the expected reaction with TEA, decreasing the catalyst concentration will possibly favor the suggested reductive pathway. Moreover, regarding the second probable assumption, in our previous work the photosensitizer $[\mathbf{ZnTMePy}]^+$ exhibited an absorption coefficient of $\varepsilon = 1{,}80{,}000\ M^{-1}.cm^{-1}$. In the present study though, the **Ps1** exhibits an absorption coefficient of $\varepsilon = 6000\ M^{-1}.cm^{-1}$ (Andreiadis et al., 2011), and the catalyst (**NiTSC-OMe**) displays an absorption band at 470 nm with an epsilon value of $\varepsilon = 17{,}000\ M^{-1}cm^{-1}$ (Straistari et al., 2017). Consequently, the absorption properties of the catalyst can reduce the available photons for the photosensitizer, thus the catalyst concentration should be lower than that of the photosensitizer in order for the system to be more efficient.

The nature as well as the ratio of the solvents definitely plays a significant role in the HER. As a result, we examined two different solvent mixtures, i.e., CH_3CN/H_2O and Ethanol/H_2O, using also different ratio (from 4:1 to 9:1). As shown in **Figure 4**, the best solvent mixture was found to be CH_3CN/H_2O in a 4:1 ratio producing a maximum volume of hydrogen of 63 μL after almost 2 h of irradiation. We concluded that the solvent ratio induced critical changes on the hydrogen production, most likely because affecting the solubility properties. These solubility properties can be altered via the dielectric constant and the diffusion coefficient of each solvent (Rao et al., 2015; Pellegrin and Odobel, 2017). When CH_3CN/H_2O in a 9:1 ratio was utilized as the solvent mixture, the photocatalytic performance dramatically decreased. The smaller water concentration probably leads to lower solubility with direct impact on the photocatalytic activity of the system.

In all presented photocatalytic experiments, H_2 production stops after almost 2 h of irradiation. Therefore, regeneration

and photolysis experiments have been performed in order to examine the stability of our system (**Figure 5** and **Figure S3**). As illustrated in **Figure 5** (right part), we performed UV-Vis absorption photolysis experiment in a solution containing **Ps1** and **NiTSC-OMe**. The characteristic absorption bands of our system (416 for **Ps1** and 460 nm for **NiTSC-OMe**) were significantly decreased after 15 min of irradiation, suggesting bleaching of the photolysis solutions. After the addition of either the catalyst or the photosensitizer we didn't observed any hydrogen evolution. However, when both components were added to the reaction mixture, the catalytic system was effectively regenerated, leading to 3,067 TON (**Figure 5**, left), suggesting that both these components undergo concomitant decomposition after almost 2 h of irradiation.

The degraded compounds can form metallic nanoparticles, which can act as the catalytic species during HER (Lazarides et al., 2014). In order to exclude this possibility we performed mercury poisoning experiments. Photocatalytic experiments in the presence of mercury showed no significant change in the amount of the produced H_2 (11,787 TONs), thus confirming the homogeneous nature of our photocatalytic system.

To shed light into the mechanism of photocatalytic system, fluorescence spectroscopy was used. Specifically, emission spectroscopy experiments were carried out using **Ps1** (4×10^{-5} M) as photosensitizer upon its excitation at 337 nm in CH_3CN solution. While the photocatalytic measurements were performed in a CH_3CN/H_2O mixture, the photophysical studies were carried out using CH_3CN as a solvent. This is due to the fact that TEA was not soluble enough in the high concentrations needed for the Stern Volmer plots in the CH_3CN/H_2O mixture. Firstly, we examined the quenching process on **Ps1** by increasing the concentration of either TEA ($0 \rightarrow 0.36$ M)] (**Figure S5**, left) or **NiTSC-OMe** ($0 \rightarrow 4.1 \times 10^{-5}$ M) (**Figure S6**, left). In addition, we have calculated the Stern-Volmer constant (K_{SV}) based on Stern-Volmer plot (**Figures S4, S5**, right), using the equation $I_o/I = 1 + K_{SV}[Q]$, where I_o and I are the fluorescence intensities observed in the absence and in the presence of each quencher, respectively, and [Q] is defined as the quencher concentration (Keizer, 1983). In perfect agreement with previous publications, the K_{SV} constant was higher in the case of the catalyst ($K_{SV} = 13{,}419.5\ M^{-1}$) compared to the TEA ($K_{SV} = 11.7\ M^{-1}$). Moreover, we calculated the quenching constant for

TABLE 1 | Redox potentials (V vs. NHE) of the different compounds employed in this study (Ps* represents the excited state of Ps: Ps^+ and Ps^-, its oxidized and reduced forms, respectively) together with the thermodynamic driving forces for the different electron transfer processes (ΔG^1(PS/Cat), ΔG^2(PS/Cat), and ΔG(SED/PS), eV).

Photosensitizers	$E(Ps^+/Ps^*)$	$E(Ps/Ps^-)$	$E(Ps^+/Ps)$	$E(Ps^*/Ps^-)$
Ps1	−0.60	−1.17	+1.50	+0.93
ΔG^1(PS/Cat)	+0.44	−0.13		
ΔG^2(PS/Cat)	+1.07	+0.50		
ΔG(SED/PS)			−0.57	0
Ps2	−0.86	−1.28	+1.26	+0.84
ΔG^1(PS/Cat)	+0.18	−0.24		
ΔG^2(PS/Cat)	+0.81	+0.39		
ΔG(SED/PS)			−0.33	+0.09
Ps3	−0.45	−0.85	+1.18	+0.78
ΔG^1(PS/Cat)	+0.26	+0.20		
ΔG^2(PS/Cat)	+1.22	+0.82		
ΔG(SED/PS)			−0.25	+0.15
Catalyst	$E(Ni^{II}/Ni^{I})$	$E(Ni^{I}/L^{\cdot -})$	**SED**	E_{Ox}
NiTSC-OMe	−1.04	−1.67	**TEA**	0.93

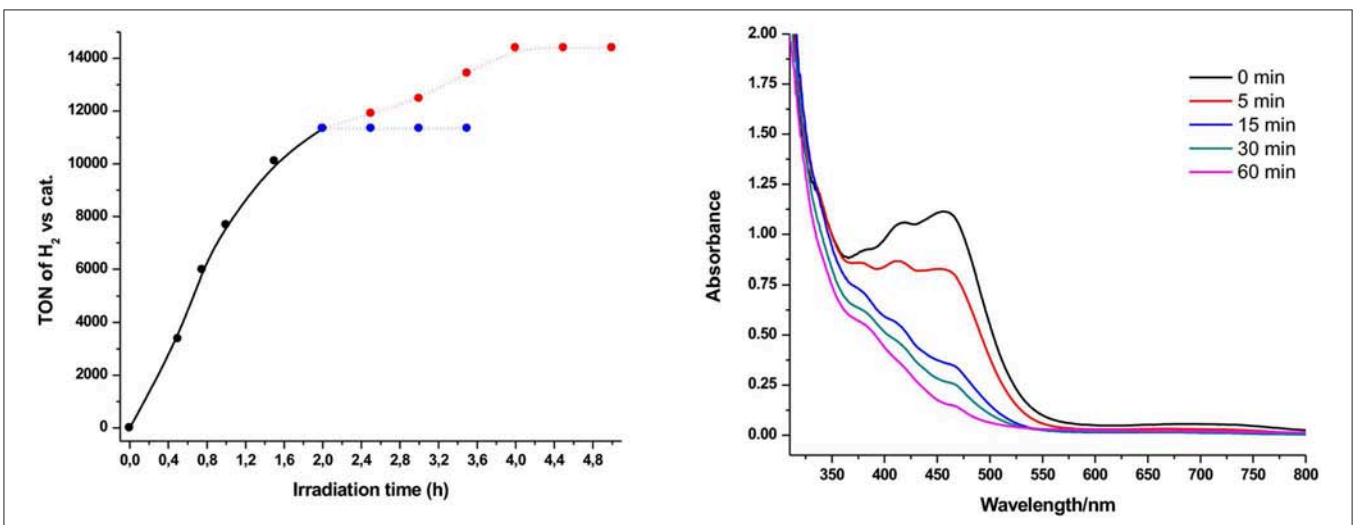

FIGURE 5 | Hydrogen production upon irradiation of solutions (4:1 CH_3CN/H_2O) containing **Ps1** (5×10^{-4} M), **NiTSC-OMe** (5×10^{-8} M), and TEA [5% (v/v)] at pH = 10. Regeneration of **Ps1** and **NiTSC-OMe** (red dot line). Regeneration of **Ps1** or **NiTSC-OMe** (blue dot line) **(left)**. UV-vis absorption spectra recorded during the course of the photolysis experiment in 10 mm cuvette, containing **Ps1** (7×10^{-5} M), **NiTSC-OMe** (5×10^{-5} M), and TEA [5% (v/v)] at pH = 10 **(right)**.

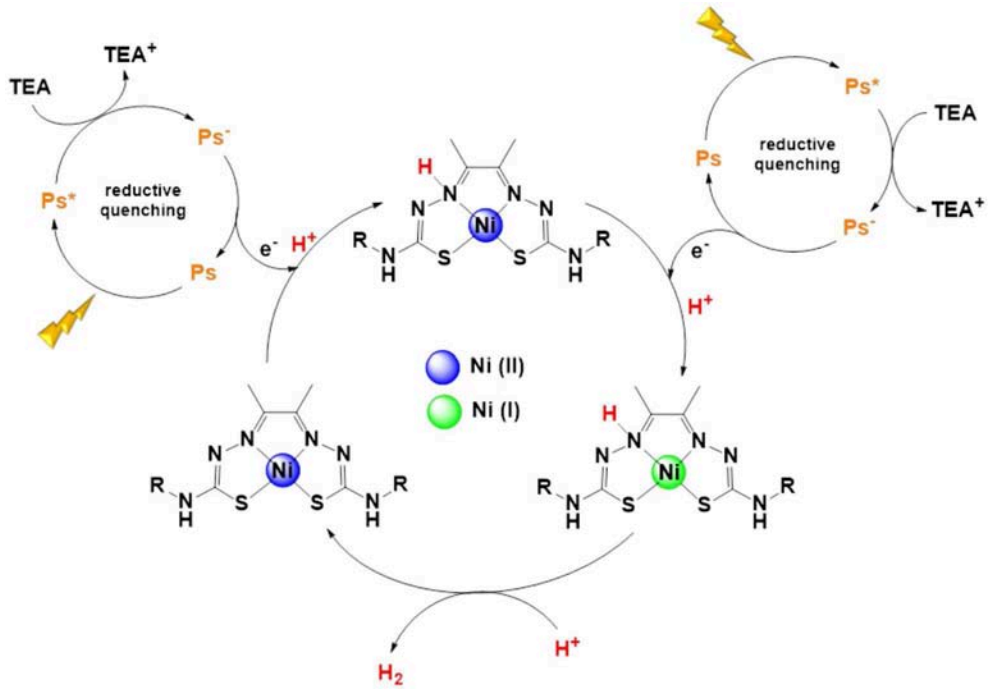

SCHEME 1 | Proposed mechanism of hydrogen photogeneration.

NiTSC-OMe ($K_Q = 4.99 \times 10^{10}\ M^{-1}s^{-1}$) and for TEA ($K_Q = 4.35 \times 10^{7}\ M^{-1}s^{-1}$) as well, which are derived from the equation: $K_{SV} = K_Q\ \tau$, where τ stands for the excited state lifetime in the absence of the quencher (Han et al., 2013; Yuan et al., 2016). However, under similar conditions to the H_2 production experiments in the emission spectra of **Ps1**, we observe that the characteristic fluorescence peak of the photosensitizer (at 590 nm) decreases only when the sacrificial electron donor (TEA) is added (**Figure S7**). What is more, there is a great difference in the quenching process, namely 50% in case of TEA and 1% in case of the catalyst. Therefore, even though, the rate constant by the **NiTSC-OMe** is greater than the rate constant by TEA, the major electron transfer pathway occurs from the excited photosensitizer to TEA, since the concentration of electron donor is bigger than that of the catalyst in the system (Han et al., 2013). In summary, hydrogen production in our system is initiated via reductive quenching of the photosensitizer.

The redox potentials of the reported compounds used in this study are listed in **Table 1**. Based on these values the thermodynamic driving forces for the different electron transfer processes, ΔG^i(PS/Cat), were calculated [(Queyriaux et al., 2017) and references herein, Goldsmith et al., 2005]. The resulting ΔG^1(PS/Cat) values turn out to be in agreement with the fluorescence quenching measurements which seems to indicate that the initial step is the reductive quenching of the photosensitizer. Indeed, the calculated ΔG^1(PS/Cat) values are positive for a reduction from Ps^+/Ps^* for **Ps1** and **Ps2** (+0.44 and +0.18, respectively) whereas they are negative for a reduction from Ps/Ps^- (−0.13 and −0.24, respectively). It is also possible to find that whatever the mechanism is, the **Ps3** potentials are not negative enough to reduce the nickel catalyst, which would explain the observed lack of photocatalytic activity. The double reduction of the catalyst is also unlikely since the values of ΔG^2(PS/Cat) are largely positive (> +0.40 eV) which would not be in favor an EECC mechanism (E corresponds to an electron transfer step and C to a chemical reaction, here protonation). Finally, the difference in activity between **Ps1** and **Ps2** does not seem to be rationalized by the little difference in driving force of injection (respectively, −0.13 and −0.24 eV), but rather by the difference of driving regeneration force ΔG(SED/PS) which is larger in the case of **Ps2** than for **Ps1** (respectively, +0.09 and 0 eV).

Taking into consideration all studies reported in this work, we propose a possible H_2 production mechanism as illustrated in **Scheme 1**. First, $[Ir(ppy)_2(bpy)]^+$ (Ps) is excited by visible light irradiation to form the excited state of the photosensitizer (Ps*). Subsequently, the sacrificial electron donor (TEA) transfers an electron to the excited photosensitizer via reductive quenching process forming its oxidized state (TEA^+) and the reduced state of the photosensitizer (Ps^-) (**Scheme 1**).

Then, a protonation of coordinated *N*-atom of the ligand on nickel complex takes place (Straistari et al., 2017) followed by an electron transfer process from the photosensitizer (Ps^-) to the nickel catalyst, creating the nickel (I) complex and forming an hydride intermediate as presented in the scheme bellow. Finally, H_2 production from the system through the nickel catalyst occurs together with its regeneration.

CONCLUSIONS

In summary, a systematic photocatalytic study toward light-driven hydrogen production is presented herein, using three different chromophores and one bis-thiosemicarbazone nickel complex. When **NiTSC-OMe** was combined with either **Ps2** or **Ps3**, no hydrogen production was observed under various experimental conditions. However, when Ps1 was utilized as a chromophore, H_2 production was detected. In order to estimate the optimal conditions we examined the influence of various parameters: the concentration of the catalyst, the pH value of the buffer solution and the ratio as well as the nature of the solvent mixture. Overall, the highest amount of H_2 (204 μL,) was attained using a 4:1 CH_3CN/H_2O solution containing **NiTSC-OMe** (10^{-6} M), **Ps1** (5×10^{-4} M), TEA [5% (v/v)] at pH 10. The maximum catalytic activity of the system though, with the highest TON and TOF values (11,333 and 7,971) were observed using **NiTSC-OMe** (5×10^{-8} M), **Ps1** (5×10^{-4} M), TEA [5% (v/v)] at pH 10 in 4:1 CH_3CN/H_2O solution. All the promising results displayed in this study offer new aspects regarding the combination of chromophores with nickel catalysts for hydrogen production. In addition, such efforts could in general provide new perspectives improving the efficiency and the function of catalytic systems developed for photoinduced hydrogen evolution using water.

AUTHOR CONTRIBUTIONS

MO and AC designed and directed the study. AP synthesized the catalyst. SP, GL, and VN performed the experiments. RH, JM, GC, AC, and MO analyzed the data. GC, AC, and MO wrote the paper with input from all authors. All authors contributed to the design and implementation of the research, to the analysis of the results and to the writing of the manuscript.

ACKNOWLEDGMENTS

General Secretariat for Research and Technology (GSRT) and Hellenic Foundation for Research and Innovation (HFRI) (project code: 508) are gratefully acknowledged for the financial support of this research. Also, the European Commission's Seventh Framework Program (FP7/2007-2013) under grant agreement no. 229927 (FP7-REGPOT-2008-1, Project BIO-SOLENUTI), and the Special Research Account of the University of Crete.

SUPPLEMENTARY MATERIAL

The Supplementary Material for this article can be found online at: https://www.frontiersin.org/articles/10.3389/fchem.2019.00405/full#supplementary-material

REFERENCES

Andreiadis, E. S., Chavarot-Kerlidou, M., Fontecave, M., and Artero, V. (2011). Artificial photosynthesis: from molecular catalysts for light-driven water splitting to photoelectrochemical cells. *Photochem. Photobiol.* 87, 946–964. doi: 10.1111/j.1751-1097.2011.00966.x

Artero, V., Chavarot-Kerlidou, M., and Fontecave, M. (2011). Splitting water with cobalt. *Angewandte Chemie* 50, 7238–7266. doi: 10.1002/anie.201007987

Blanchard, S., Neese, F., Bothe, E., Bill, E., Weyhermüller, T., and Wieghardt, K. (2005). Square planar vs tetrahedral coordination in diamagnetic complexes of nickel(II) containing two bidentate pi-radical monoanions. *Inorg. Chem.* 44, 3636–3656. doi: 10.1021/ic040117e

Brazzolotto, D., Gennari, M., Queyriaux, N., Simmons, T. R., Pecaut, J., Demeshko, S., et al. (2016). Nickel-centred proton reduction catalysis in a model of [NiFe] hydrogenase. *Nat. Chem.* 8, 1054–1060. doi: 10.1038/nchem.2575

Campbell, M. J. M. (1975). Transition-metal complexes of thiosemicarbazide and thiosemicarbazones. *Coord. Chem. Rev.* 15, 279–319. doi: 10.1016/S0010-8545(00)80276-3

Coutard, N., Kaeffer, N., and Artero, V. (2016). Molecular engineered nanomaterials for catalytic hydrogen evolution and oxidation. *Chem. Commun.* 52, 13728–13748. doi: 10.1039/C6CC06311J

Du, P. W., and Eisenberg, R. (2012). Catalysts made of earth-abundant elements (Co, Ni, Fe) for water splitting: Recent progress and future challenges. *Energy Environ. Sci.* 5, 6012–6021. doi: 10.1039/c2ee03250c

DuBois, D. L. (2014). Development of molecular electrocatalysts for energy storage. *Inorg. Chem.* 53, 3935–3960. doi: 10.1021/ic4026969

DuBois, M. R., and DuBois, D. L. (2009a). Development of molecular electrocatalysts for CO_2 reduction and H-2 production/oxidation. *Acc. Chem. Res.* 42, 1974–1982. doi: 10.1021/ar900110c

DuBois, M. R., and DuBois, D. L. (2009b). The roles of the first and second coordination spheres in the design of molecular catalysts for H-2 production and oxidation. *Chem. Soc. Rev.* 38, 62–72. doi: 10.1039/B801197B

Eckenhoff, W. T., Mcnamara, W. R., Du, P. W., and Eisenberg, R. (2013). Cobalt complexes as artificial hydrogenases for the reductive side of water splitting. *Biochim. Biophys. Acta* 1827, 958–973. doi: 10.1016/j.bbabio.2013.05.003

Faunce, T. A., Lubitz, W., Rutherford, A. W., Macfarlane, D. R., Moore, G. F., Yang, P. D., et al. (2013). Energy and environment policy case for a global project on artificial photosynthesis. *Energy Environ. Sci.* 6, 695–698. doi: 10.1039/c3ee00063j

Fihri, A., Artero, V., Razavet, M., Baffert, C., Leibl, W., and Fontecave, M. (2008). Cobaloxime-based photocatalytic devices for hydrogen production. *Angewandte Chemie* 47, 564–567. doi: 10.1002/anie.200702953

Goldsmith, J. I., Hudson, W. R., Lowry, M. S., Anderson, T. H., and Bernhard, S. (2005). Discovery and high-throughput screening of heteroleptic iridium complexes for photoinduced hydrogen production. *J. Am. Chem. Soc.* 127, 7502–7510. doi: 10.1021/ja0427101

Haddad, A. Z., Cronin, S. P., Mashuta, M. S., Buchanan, R. M., and Grapperhaus, C. A. (2017). Metal-assisted ligand-centered electrocatalytic hydrogen evolution upon reduction of a Bis(thiosemicarbazonato)Cu(II) complex. *Inorg. Chem.* 56, 11254–11265. doi: 10.1021/acs.inorgchem.7b01608

Haddad, A. Z., Garabato, B. D., Kozlowski, P. M., Buchanan, R. M., and Grapperhaus, C. A. (2016). Beyond metal-hydrides: non-transition-metal and metal-free ligand-centered electrocatalytic hydrogen evolution and hydrogen oxidation. *J. Am. Chem. Soc.* 138, 7844–7847. doi: 10.1021/jacs.6b04441

Han, Z., Mcnamara, W. R., Eum, M. S., Holland, P. L., and Eisenberg, R. (2012). A nickel thiolate catalyst for the long-lived photocatalytic production of hydrogen in a noble-metal-free system. *Angewandte Chemie* 51, 1667–1670. doi: 10.1002/anie.201107329

Han, Z., Shen, L., Brennessel, W. W., Holland, P. L., and Eisenberg, R. (2013). Nickel pyridinethiolate complexes as catalysts for the light-driven production of hydrogen from aqueous solutions in noble-metal-free systems. *J. Am. Chem. Soc.* 135, 14659–14669. doi: 10.1021/ja405257s

Helm, M. L., Stewart, M. P., Bullock, R. M., DuBois, M. R., and DuBois, D. L. (2011). A synthetic nickel electrocatalyst with a turnover frequency above 100,000 s(-1) for H-2 production. *Science* 333, 863–866. doi: 10.1126/science.1205864

Hosenuzzaman, M., Rahim, N. A., Selvaraj, J., Hasanuzzaman, M., Malek, A. B. M. A., and Nahar, A. (2015). Global prospects, progress, policies, and environmental impact of solar photovoltaic power generation. *Renew. Sust. Energy Rev.* 41, 284–297. doi: 10.1016/j.rser.2014.08.046

Hosseini, S. E., and Wahid, M. A. (2016). Hydrogen production from renewable and sustainable energy resources: Promising green energy carrier for clean development. *Renew. Sust. Energy Rev.* 57, 850–866. doi: 10.1016/j.rser.2015.12.112

Inoue, S., Mitsuhashi, M., Ono, T., Yan, Y. N., Kataoka, Y., Handa, M., et al. (2017). Photo- and electrocatalytic hydrogen production using valence isomers of N2S2-type nickel complexes. *Inorg. Chem.* 56, 12129–12138. doi: 10.1021/acs.inorgchem.7b01244

Keizer, J. (1983). Non-linear fluorescence quenching and the origin of positive curvature in Stern-Volmer plots. *J. Am. Chem. Soc.* 105, 1494–1498. doi: 10.1021/ja00344a013

Khnayzer, R. S., Thoi, V. S., Nippe, M., King, A. E., Jurss, J. W., El Roz, K. A., et al. (2014). Towards a comprehensive understanding of visible-light photogeneration of hydrogen from water using cobalt(II) polypyridyl catalysts. *Energy Environ. Sci.* 7, 1477–1488. doi: 10.1039/C3EE43982H

Koposova, E., Liu, X., Pendin, A., Thiele, B., Shumilova, G., Ermolenko, Y., et al. (2016). Influence of meso-substitution of the porphyrin ring on enhanced hydrogen evolution in a photochemical system. *J. Phys. Chem. C* 120, 13873–13890. doi: 10.1021/acs.jpcc.6b01467

Ladomenou, K., Natali, M., Iengo, E., Charalampidis, G., Scandola, F., and Coutsolelos, A. G. (2015). Photochemical hydrogen generation with porphyrin-based systems. *Coord. Chem. Rev.* 304, 38–54. doi: 10.1016/j.ccr.2014.10.001

Landrou, G., Panagiotopoulos, A. A., Ladomenou, K., and Coutsolelos, A. G. (2016). Photochemical hydrogen evolution using Sn-porphyrin as photosensitizer and a series of Cobaloximes as catalysts. *J. Porphyr. Phthalocyanines* 20, 534–541. doi: 10.1142/S1088424616500243

Lazarides, T., Delor, M., Sazanovich, I. V., Mccormick, T. M., Georgakaki, I., Charalambidis, G., et al. (2014). Photocatalytic hydrogen production from a noble metal free system based on a water soluble porphyrin derivative and a cobaloxime catalyst. *Chem. Commun.* 50, 521–523. doi: 10.1039/C3CC45025B

Lazarides, T., Mccormick, T., Du, P., Luo, G., Lindley, B., and Eisenberg, R. (2009). Making hydrogen from water using a homogeneous system without noble metals. *J. Am. Chem. Soc.* 131, 9192–9194. doi: 10.1021/ja903044n

Lewis, N. S., and Nocera, D. G. (2006). Powering the planet: Chemical challenges in solar energy utilization. *Proc. Natl. Acad. Sci. U. S. A,* 103, 15729–15735. doi: 10.1073/pnas.0603395103

Lo, W. K. C., Castillo, C. E., Gueret, R., Fortage, J., Rebarz, M., Sliwa, M., et al. (2016). Synthesis, characterization, and photocatalytic H-2-evolving activity of a family of [Co(N4Py)(X)](n+) complexes in aqueous solution. *Inorg. Chem.* 55, 4564–4581. doi: 10.1021/acs.inorgchem.6b00391

Lubitz, W., Ogata, H., Rudiger, O., and Reijerse, E. (2014). Hydrogenases. *Chem. Rev.* 114, 4081–4148. doi: 10.1021/cr4005814

McLaughlin, M. P., Mccormick, T. M., Eisenberg, R., and Holland, P. L. (2011). A stable molecular nickel catalyst for the homogeneous photogeneration of hydrogen in aqueous solution. *Chem. Commun.* 47, 7989–7991. doi: 10.1039/c1cc12347e

Natali, M., Luisa, A., Lengo, E., and Scandola, F. (2014). Efficient photocatalytic hydrogen generation from water by a cationic cobalt(II) porphyrin. *Chem. Commun.* 50, 1842–1844. doi: 10.1039/c3cc48882a

Panagiotopoulos, A., Ladomenou, K., Sun, D., Artero, V., and Coutsolelos, A. G. (2016). Photochemical hydrogen production and cobaloximes: the influence of the cobalt axial N-ligand on the system stability. *Dalton Transact.* 45, 6732–6738. doi: 10.1039/C5DT04502A

Peel, M. (2003). *The Hydrogen Economy: The Creation of the Worldwide Energy Web and the Redistribution of Power on Earth*. Tls-the Times Literary Supplement, 5227 29–29.

Pellegrin, Y., and Odobel, F. (2017). Sacrificial electron donor reagents for solar fuel production. *Comptes Rendus Chimie* 20, 283–295. doi: 10.1016/j.crci.2015.11.026

Queyriaux, N., Giannoudis, E., Windle, C. D., Roy, S., Pecaut, J., Coutsolelos, A. G., et al. (2018). A noble metal-free photocatalytic system based on a novel cobalt tetrapyridyl catalyst for hydrogen production in fully aqueous medium. *Sustain. Energy Fuels* 2, 553–557. doi: 10.1039/C7SE00428A

Queyriaux, N., Wahyuono, R. A., Fize, J., Gablin, C., Wächtler, M., Martinez, E., et al. (2017). Aqueous photocurrent measurements correlated to ultrafast electron transfer dynamics at ruthenium tris diimine sensitized NiO photocathodes. *J. Phys. Chem. C* 121, 5891–5904. doi: 10.1021/acs.jpcc.6b12536

Rao, H., Wang, Z. Y., Zheng, H. Q., Wang, X. B., Pan, C. M., Fan, Y. T., et al. (2015). Photocatalytic hydrogen evolution from a cobalt/nickel complex with dithiolene ligands under irradiation with visible light. *Catal. Sci. Technol.* 5, 2332–2339. doi: 10.1039/C4CY01574F

Rao, H., Yu, W. Q., Zheng, H. Q., Bonin, J., Fan, Y. T., and Hou, H. W. (2016). Highly efficient photocatalytic hydrogen evolution from nickel quinolinethiolate complexes under visible light irradiation. *J. Power Sourc.* 324, 253–260. doi: 10.1016/j.jpowsour.2016.05.095

Sartorel, A., Bonchio, M., Campagna, S., and Scandola, F. (2013). Tetrametallic molecular catalysts for photochemical water oxidation. *Chem. Soc. Rev.* 42, 2262–2280. doi: 10.1039/C2CS35287G

Straistari, T., Fize, J., Shova, S., Reglier, M., Artero, V., and Orio, M. (2017). A Thiosemicarbazone-nickel(II) complex as efficient electrocatalyst for hydrogen evolution. *Chemcatchem* 9, 2262–2268. doi: 10.1002/cctc.201600967

Straistari, T., Hardré, R., Fize, J., Shova, S., Giorgi, M., Réglier, M., et al. (2018a). Hydrogen evolution reactions catalyzed by a bis(thiosemicarbazone) cobalt complex: an experimental and theoretical study. *Chem. Euro. J.* 24, 8779–8786. doi: 10.1002/chem.201801155

Straistari, T., Hardre, R., Massin, J., Attolini, M., Faure, B., Giorgi, M., et al. (2018b). Influence of the metal ion on the electrocatalytic hydrogen production by a thiosemicarbazone palladium complex. *Euro. J. Inorg. Chem.* 2259–2266. doi: 10.1002/ejic.201800120

Styring, S. (2012). Artificial photosynthesis for solar fuels. *Faraday Discus.* 155, 357–376. doi: 10.1039/C1FD00113B

Tachibana, Y., Vayssieres, L., and Durrant, J. R. (2012). Artificial photosynthesis for solar water-splitting. *Nat. Photonics* 6, 511–518. doi: 10.1038/nphoton.2012.175

Tran, P. D., Artero, V., and Fontecave, M. (2010). Water electrolysis and photoelectrolysis on electrodes engineered using biological and bio-inspired molecular systems. *Energy Environ. Sci.* 3, 727–747. doi: 10.1039/b926749b

Tran, P. D., Wong, L. H., Barber, J., and Loo, J. S. C. (2012). Recent advances in hybrid photocatalysts for solar fuel production. *Energy Environ. Sci.* 5, 5902–5918. doi: 10.1039/c2ee02849b

Wang, M., Chen, L., and Sun, L. C. (2012). Recent progress in electrochemical hydrogen production with earth-abundant metal complexes as catalysts. *Energy Environ. Sci.* 5, 6763–6778. doi: 10.1039/c2ee03309g

Wang, M., and Sun, L. C. (2010). Hydrogen production by noble-metal-free molecular catalysts and related nanomaterials. *Chemsuschem* 3, 551–554. doi: 10.1002/cssc.201000062

Yin, M. C., Ma, S., Wu, C. J., and Fan, Y. T. (2015). A noble-metal-free photocatalytic hydrogen production system based on cobalt(III) complex and eosin Y-sensitized TiO2. *Rsc Adv.* 5, 1852–1858. doi: 10.1039/C4RA10767E

Yuan, Y. J., Tu, J. R., Lu, H. W., Yu, Z. T., Fan, X. X., and Zou, Z. G. (2016). Neutral nickel(II) phthalocyanine as a stable catalyst for visible-light-driven hydrogen evolution from water. *Dalton Transact.* 45, 1359–1363. doi: 10.1039/C5DT04311E

Yuan, Y. J., Yu, Z. T., Chen, D. Q., and Zou, Z. G. (2017). Metal-complex chromophores for solar hydrogen generation. *Chem. Soc. Rev.* 46, 603–631. doi: 10.1039/C6CS00436A

Zee, D. Z., Chantarojsiri, T., Long, J. R., and Chang, C. J. (2015). Metal-polypyridyl catalysts for electro- and photochemical reduction of water to hydrogen. *Acc. Chem. Res.* 48, 2027–2036. doi: 10.1021/acs.accounts.5b00082

Conflict of Interest Statement: The authors declare that the research was conducted in the absence of any commercial or financial relationships that could be construed as a potential conflict of interest.

Copyright © 2019 Panagiotakis, Landrou, Nikolaou, Putri, Hardré, Massin, Charalambidis, Coutsolelos and Orio. This is an open-access article distributed under the terms of the Creative Commons Attribution License (CC BY). The use, distribution or reproduction in other forums is permitted, provided the original author(s) and the copyright owner(s) are credited and that the original publication in this journal is cited, in accordance with accepted academic practice. No use, distribution or reproduction is permitted which does not comply with these terms.

frontiers in Chemistry

ORIGINAL RESEARCH
published: 20 March 2019
doi: 10.3389/fchem.2019.00138

Highly Active Ni- and Co-Based Bimetallic Catalysts for Hydrogen Production From Ammonia-Borane

Shinya Furukawa[1,2]*, *Genki Nishimura*[3], *Tomoaki Takayama*[3] and *Takayuki Komatsu*[3]*

[1] Institute for Catalysis, Hokkaido University, Sapporo, Japan, [2] Elements Strategy Initiative for Catalysts and Batteries, Kyoto University, Kyoto, Japan, [3] Department of Chemistry, School of Science, Tokyo Institute of Technology, Tokyo, Japan

Ammonia-borane is one of the most promising candidates for hydrogen carriers. A series of Ni- and Co-based bimetallic catalysts supported on SiO_2 (Ni–M/SiO_2 and Co–M/SiO_2; M = Ga, Ge, Sn, Zn) was prepared and tested as catalysts for hydrogen production from ammonia-borane (AB) in water or methanol. Ni–Zn/SiO_2 and Co–Ge/SiO_2 exhibited catalytic activities much higher than those of monometallic Ni/SiO_2 and Co/SiO_2, respectively. Ni–Zn/SiO_2 showed a high catalytic activity when water was used as a solvent, where the reaction was completed within 6 min at room temperature with a specific reaction rate of 4.3 ml min^{-1} mmol-cat^{-1} mM-AB^{-1}. To the best of our knowledge, this is the highest value among those reported using 3d metal-based catalysts. Co–Ge/SiO_2 afforded a five-fold higher reaction rate than that of the corresponding monometallic Co/SiO_2. XRD, TEM, and HAADF-STEM-EDS analyses revealed that $Ni_{0.75}Zn_{0.25}$ and $Co_{0.8}Ge_{0.2}$ solid-solution alloys were formed with high phase purities. An XPS study showed that Co atoms in $Co_{0.8}Ge_{0.2}$ were electron-enriched due to electron transfer from Ge to Co, which may be the origin of the improved catalytic activity.

Keywords: hydrogen production, ammonia borane, hydrolysis, alloy, catalyst

OPEN ACCESS

Edited by:
Steve Suib,
University of Connecticut,
United States

Reviewed by:
Balaraman Ekambaram,
National Chemical Laboratory (CSIR),
India
Liwu Zhang,
Fudan University, China
Guohong Wang,
Hubei Normal University, China

***Correspondence:**
Shinya Furukawa
furukawa@cat.hokudai.ac.jp
Takayuki Komatsu
komatsu.t.ad@m.titech.ac.jp

Specialty section:
This article was submitted to Catalysis and Photocatalysis, a section of the journal Frontiers in Chemistry

Received: *27 November 2018*
Accepted: *25 February 2019*
Published: *20 March 2019*

Citation:
Furukawa S, Nishimura G, Takayama T and Komatsu T (2019) Highly Active Ni- and Co-Based Bimetallic Catalysts for Hydrogen Production From Ammonia-Borane. Front. Chem. 7:138. doi: 10.3389/fchem.2019.00138

INTRODUCTION

Hydrogen has been considered as one of the best energy carrier alternatives to fossil fuels because of its high energy density, clean combustion product (only water), and environmental friendliness (Schlapbach and Züttel, 2011). Hydrogen is currently produced by steam reforming of methane contained in natural gas (Heinzel et al., 2002), which is not renewable and sustainable. Therefore, alternative methodologies such as photocatalytic (Moniz et al., 2015; Chen et al., 2017; Wang et al., 2017) and photoelectrochemical (Zhang et al., 2014; Zheng and Zhang, 2016; Han et al., 2017) water splitting have recently attracted increasing attention. On the other hand, storage, transport, and release of hydrogen are known as technological barriers to practical application in view of cost and safety (Züttel, 2003). Ammonia–borane ($H_3N{\cdot}BH_3$, hereafter AB) is one of the more promising candidates as a hydrogen carrier or source (Landge et al., 2018) owing to its high hydrogen content (19.6 wt%), high thermal stability, and low toxicity (Marder, 2007). AB can release three equimolar amounts of hydrogen at ambient temperatures using an appropriate catalyst through solvolysis

with protic solvents such as water and methanol. Using noble metals such as Pt, Rh, Ir enables the achievement of rapid hydrogen release typically within several minutes (Chandra and Xu, 2007; Xu and Chandra, 2007). Recently, development of non-noble 3d transition metal-based catalysts that are active for hydrogen production from AB has been increasingly focused (Xu and Chandra, 2006; Yan et al., 2008, 2009; Kalidindi et al., 2009; Metin et al., 2010; Patel et al., 2010; Ozay et al., 2011; Peng et al., 2015). To develop highly efficient catalytic systems using base metal elements, the catalytic activity of these metals should be greatly enhanced by appropriate catalyst design such as the modification of morphology, the addition of some cocatalysts, or the formation of alloy phases (Furukawa and Komatsu, 2017).

In this study, a series of Ni- and Co-based bimetallic catalysts was prepared (Ni–M/SiO_2 and Co–M/SiO_2; M = Ga, Ge, Sn, and Zn) and tested as catalysts for hydrogen production from AB in water or methanol as a solvent. The observed catalytic performances were discussed in view of the reaction mechanism. Herein, we report a novel and highly efficient catalytic system for hydrogen production from AB using non-noble metal catalysts.

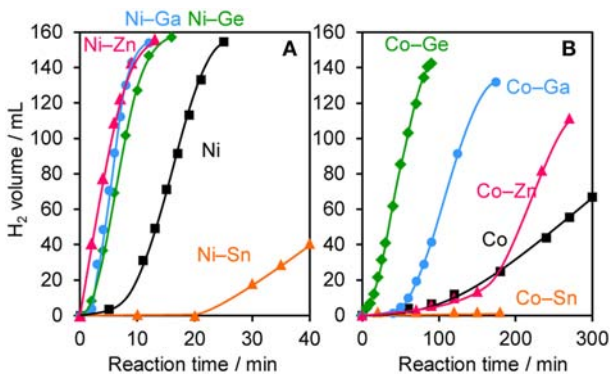

FIGURE 1 | Time course of H_2 evolution during catalytic methanolysis of AB using **(A)** Ni- and **(B)** Co-based catalysts.

MATERIALS AND METHODS

Catalyst Preparation

Monometallic Ni and Co catalysts were prepared by pore-filling impregnation using silica as a support. Aqueous solutions of $Ni(NO_3)_2{\cdot}6H_2O$ (Wako, 99%) or $Co(NO_3)_2{\cdot}3H_2O$ (Sigma Aldrich, 99%) were added to dried silica gel (CARiACT G-6, Fuji Silysia, S_{BET} = 470 m^2 g^{-1}) so that the solutions filled the silica pores. The mixtures were sealed overnight at room temperature and dried over a hot plate, followed by reduction under flowing H_2 at 600°C for 1 h. Silica-supported Ni- and Co-based catalysts (Ni–M/SiO_2 and Co–M/SiO_2; M = Ga, Ge, Sn, and Zn) were prepared by pore-filling co-impregnation. Mixed aqueous solutions of $Ni(NO_3)_2{\cdot}6H_2O$ or $Co(NO_3)_2{\cdot}3H_2O$ and a second metal salt, $Ga(NO_3)_3{\cdot}nH_2O$ (Wako, 99.9%), $(NH_4)_2GeF_6$ (Sigma Aldrich, 99.99%), $SnCl_2$ (Kanto, 97%), and $Zn(NO_3)_2{\cdot}6H_2O$ (Kanto, 99%) were used in a manner similar to that of the monometallic catalyst. The metal loading of Ni or Co, the atomic ratio of Ni/M or Co/M, and the reduction temperature during the catalyst preparation were set to 3 wt%, 3.0, and 600°C except for Ni–Ge and Co–Ge, which had a reduction temperature of 800°C, and Co–Sn with an atomic ratio of 1.0.

Characterizations

The crystal structures of the catalysts were determined by powder X-ray diffraction (XRD) with a Rigaku RINT2400 diffractometer using a Cu Kα X-ray source. Difference XRD patterns were obtained by subtracting the pattern for the SiO_2 support from those of the supported catalysts. Transmission electron microscopy (TEM) was conducted using a JEOL JEM-2010F microscope at an accelerating voltage of 200 kV. To prepare the TEM specimen, all samples were sonicated in tetrachloromethane and then dispersed on a Cu grid supported by an ultrathin carbon film. X-ray photoelectron spectra (XPS) of the bimetallic compounds were measured with an ULVAC PHI 5000 VersaProbe spectrometer. The catalyst was pressed into a pellet and placed into a quartz reactor, where it was reduced under flowing hydrogen (60 ml min^{-1}) at 450°C for 0.5 h prior to the measurement. The sample was put into a transfer vessel in a

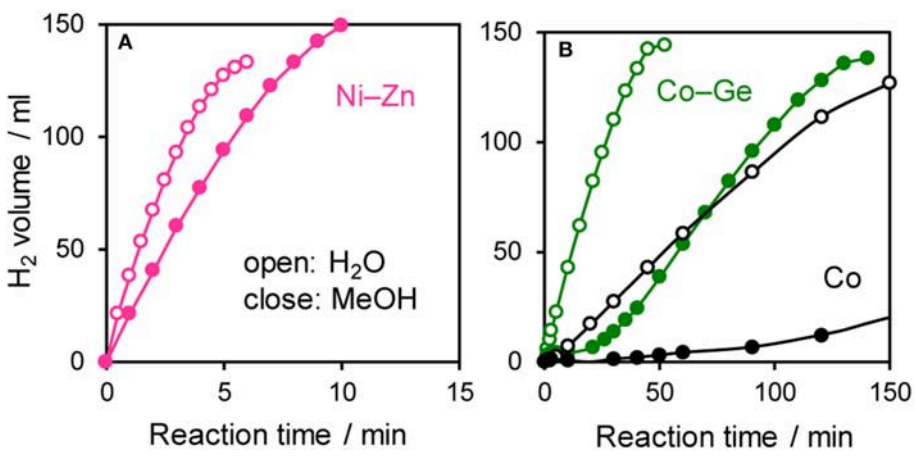

FIGURE 2 | Time course of H_2 evolution during catalytic hydrolysis (H_2O) and methanolysis (MeOH) of AB using **(A)** Ni–Zn, **(B)** Co–Ge, and Co catalyst.

grove box (O_2 concentration: <1 ppm) and then introduced into the spectrometer without exposure to air. Spectra were obtained with an Al Kα X-ray source, using C 1s as a reference for binding energy (284.8 eV). The reduction behavior of the catalyst was examined by temperature-programmed reduction (TPR). Under flowing H_2 (5%)/Ar, the temperature of the sample bed was raised from room temperature to 900°C at a heating rate of 10°C·min^{-1} and the consumption of hydrogen was continuously measured by a thermal conductivity detector (TCD).

Catalytic Reaction

A catalyst (100 mg) was placed into a 50 mL three-necked round-bottom flask equipped with a silicone rubber septum and a gas burette and pretreated under an H_2 stream (60 mL·min^{-1}) at 450°C for 0.5 h using a mantle heater. After the pretreatment, dry Ar (20 mL·min^{-1}) was passed into the flask to replace the residual H_2, and the flask was cooled to room temperature. A reaction mixture containing a solvent (deionized water or dehydrated methanol, Kanto 99.8%, 10 mL) and AB (Sigma-Aldrich, 97%, 2.0 mmol) was added into the flask through the septum at 25°C. The volume of the evolved H_2 was measured using the gas burette. The total volume of H_2 is expected to be 147 ml (6.0 mmol) at 25°C for the complete conversion of AB (2.0 mmol).

RESULTS AND DISCUSSION

The prepared Ni- and Co-based catalysts were tested for H_2 production from AB using methanol as a solvent (**Figure 1**). The monometallic Ni catalyst showed moderate catalytic activity with a short induction period. The Ni–Sn catalyst showed a very low catalytic activity with a long induction period. On the other hand, the Ni–Zn, Ni–Ga, and Ni–Ge catalysts exhibited high catalytic activities without an induction period. Particularly for the Ni–Zn catalyst, the reaction was completed within ca. 10 min. Co-based catalysts generally gave catalytic activities lower than those of Ni-based catalysts, which reflects the intrinsic difference of catalytic activity between Ni and Co for this reaction. Moreover, the catalytic activities were quite different depending on the second metal (Co–Ge > Co–Ga >> Co >> Co–Sn). Induction periods were observed for some catalysts (Ni, Ni–Sn, Co, Co–Ga, and Co–Zn), indicating that, for these catalysts, some real active species (probably, zero-valent Ni or Co species) were formed or increased during the catalytic reaction. A remarkable

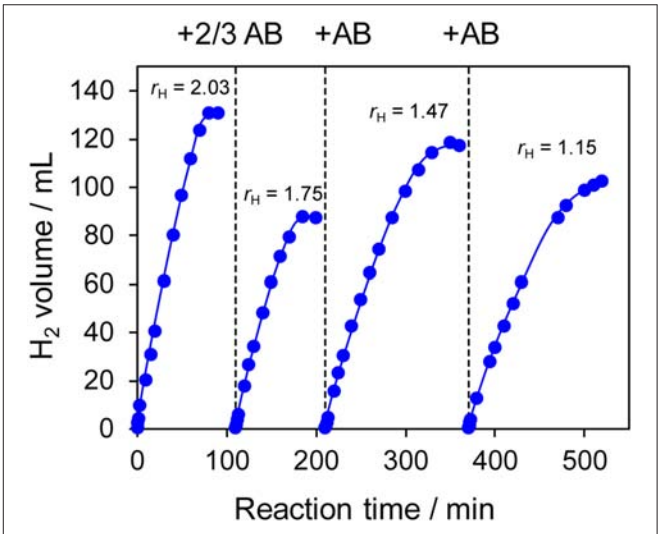

FIGURE 3 | Reuse tests for H_2 production in methanol using Co–Ge/SiO_2 catalyst. For the first reuse at 110 min, the amount of AB was reduced to 2/3 (1.33 mmol).

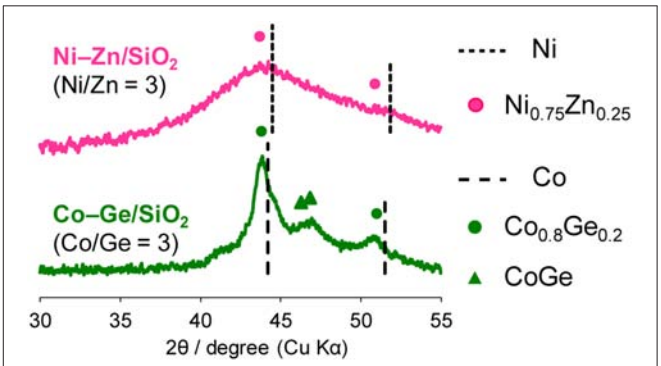

FIGURE 4 | XRD patterns of Ni–Zn/SiO_2 (Ni/Zn = 3) and Co–Ge/SiO_2 (Co/Ge = 3).

TABLE 1 | Summary of reaction condition and rate of AB hydrolysis at 25°C using various catalysts.

Catalyst	Cat (mmol)	AB (mmol)	AB/Cat	r_{H2} (ml min^{-1})	r_{cat} (ml min^{-1} mmol-cat^{-1})	$r_{cat[AB]}$ (ml min^{-1} mmol-cat^{-1} mM-AB^{-1})	Duration (min)[a]	References
Fe	0.192	1.6	8.3	15	79	0.50	10	Yan et al., 2008
Co/C	0.058	3.2	56	3.6	61	0.20	50	Xu and Chandra, 2006
Co–B	0.2	15.0	75	29	145	1.45	–	Patel et al., 2010
Ni	0.025	2.0	80	5.0	200	1.00	50	Metin et al., 2010
Ni_2P	0.054	2.08	38	46	852	2.05	6	Peng et al., 2015
Ni–Zn	0.050	2.0	40	43	860	4.30	6	This work
Co–Ge	0.051	2.0	39	4.5	88	0.44	50	
Co	0.051	2.0	39	0.9	18	0.09	>150	

[a] *Time needed for completion of H_2 evolution.*

enhancement in the reaction rate was achieved by addition of Ge to Co, suggesting the contribution of a specific effect of Ge on the catalysis. The discovered active catalysts, Ni–Zn and Co–Ge, were also tested in hydrogen production from AB in water as a solvent (**Figure 2**). For each catalyst, H_2 evolution in water was much faster than that in methanol as reported for Ni- and Co-based catalysts in the literature. Note that the reaction was completed within 6 min when the Ni–Zn catalyst was used. This is one of the best performances in AB hydrolysis reported to this day. The obtained catalytic performance was listed in **Table 1** with those of reported catalysts. Because the reaction conditions were different depending on each study, we quantitatively compared them based on the specific H_2 formation rates ($r_{cat[AB]}$) calculated by dividing H_2 formation rates (r_{H2}) by the amount of catalyst (mmol) and concentration of AB (mM). Since the number of active sites, such as metal atoms on the surface, was not clearly mentioned, the total number of metal atoms was used for this calculation. The difference in AB concentration was compensated for by assuming the first-order dependence of the formation rate on AB concentration. The Ni–Zn catalyst exhibited an $r_{cat[AB]}$ value higher than that of Ni_2P, which was reported to be the most active base-metal catalyst for AB hydrolysis (Peng et al., 2015). Therefore, the Ni–Zn catalyst is the most active 3d metal-based catalyst for H_2 production by hydrolysis of AB. We also examined the reusability of the catalysts. **Figure 3** shows the result of the reuse test for

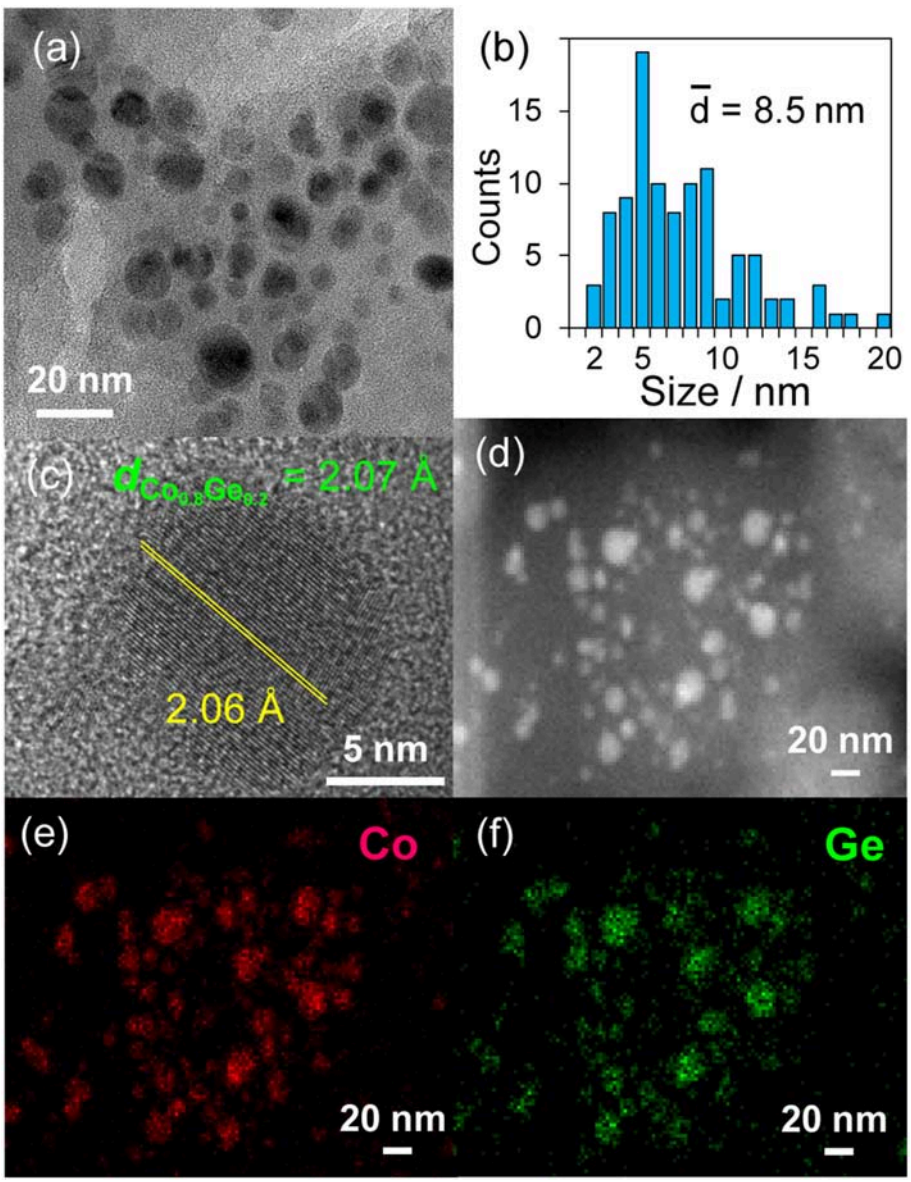

FIGURE 5 | (a) TEM image and the **(b)** size distribution of Co–Ge/SiO_2 catalyst. **(c)** High resolution TEM image of a single nanoparticle of Co–Ge. **(d)** HAAF-STEM image of Co–Ge/SiO_2 catalyst and elemental maps of **(e)** Co, and **(f)** Ge for the nanoparticles acquired using EDS.

the Co–Ge/SiO_2 catalyst in H_2 production in methanol. At the first reuse at 110 min, we added 1.33 mol of AB (2/3 equivalent to the standard condition). The total volume H_2 evolved decreased from 130.5 to 87 ml, showing complete conversion of AB at reuse. The reaction rate also became approximately two-thirds of the original (2.03–1.75), indicating that r_{H2} strongly depends on AB concentration. Although the reaction rate was slightly decreased at the second and third reuse, the Co–Ge/SiO_2 catalyst could be reused without any regeneration procedure. Thus, it was found that the Co–Ge/SiO_2 was a recyclable heterogeneous catalyst for H_2 production from AB.

Then, the discovered active catalysts were characterized to clarify their structures. **Figure 4** shows XRD patterns of the Ni–Zn/SiO_2 and Co–Ge/SiO_2 catalysts. For Ni–Zn/SiO_2, a solid-solution alloy between Ni and Zn with a 3: 1 ratio, namely $Ni_{0.75}Zn_{0.25}$ phase (Vassilev, 1992), was observed as single phase. A similar alloy phase ($Co_{0.8}Ge_{0.2}$) (Ishida and Nishizawa, 1991) was also observed as a main species for Co–Ge/SiO_2. One-to-one intermetallic phase of CoGe was also detected as a minor species. Thus, XRD analysis confirmed the formation of alloy phases with high purities. The crystallite sizes of Ni–Zn and Co–Ge were estimated using Scherrer equation as <3 and 9 nm, respectively. The larger crystallite size of Co–Ge may stem from the higher reduction temperature (800°C) during the catalyst preparation. **Figure 5** shows TEM and STEM images of Co–Ge/SiO_2, size distribution of nanoparticles, and the elemental map of Co and Ge acquired using EDS. Particle size ranged from 2 to 20 nm with a mean diameter of 8.5 nm (**Figures 5a,b**), which is consistent with the crystallite size estimated by the Scherrer equation (9 nm). **Figure 5c** displays the high-resolution TEM image of a single Co–Ge nanoparticle. Lattice fringes with 2.06 Å spacing were clearly observed, which agrees finely with the interplanar distance of the (111) plane of $Co_{0.8}Ge_{0.2}$ solid-solution alloy with an fcc structure (2.07 Å) (Ishida and Nishizawa, 1991). The elemental maps of Co and Ge that were acquired using the EDS analysis revealed that the Co and Ge atoms comprising the nanoparticles were homogeneously dispersed (**Figures 5d–f**). These results strongly suggest that the $Co_{0.8}Ge_{0.2}$ alloy nanoparticles were formed with high phase purities. Thus, the results obtained from the STEM-EDS analysis were consistent with that of XRD.

We then studied the reason why the catalytic activity was significantly enhanced by the formation of the alloy phase. Because the Co–Ge system exhibited a remarkable increase in the reaction rate (five times higher) compared to pure Co, we focused on the difference between the Co and Co–Ge systems.

Figure 6 shows the TPR profiles of the Co/SiO_2 and Co–Ge/SiO_2 catalysts. To evaluate the reduction temperatures of the component metals, as-impregnated catalysts were used for the TPR experiments. For both catalysts, intense peaks were observed at 150 and 200°C, which may be attributed to the reduction of O_2 or NO_2 derived from the decomposition of the $Co(NO_3)_2$ (van Steen et al., 1996). For Co/SiO_2, two reduction peaks were observed at 260 and 760°C, which are assigned to the reduction of Co^{2+} species that weakly and strongly interact with the silica surface, respectively (van Steen et al., 1996). On the contrary, for Co–Ge/SiO_2, three different reduction peaks were observed at 370, 550, and 740°C, which could be assigned to the reduction of Co^{2+}, Co^{3+}, and Ge^{4+} species. We previously reported a TPR profile of Ge/SiO_2, with reduction peaks appearing at temperatures higher than 650°C (Komatsu et al., 1997). Therefore, the reduction peak at 740°C can be attributed to the reduction of Ge^{4+}. The other reduction peaks assignable for Co species appeared at much higher temperatures than that for Co/SiO_2, suggesting that the strong interaction between Co and Ge inhibits the reduction of Co^{2+}. It can be said that Co species in Co/SiO_2 were not completely reduced because the reduction temperature for the preparation of Co/SiO_2 (600°C) is not sufficient to completely reduce all the Co species. This

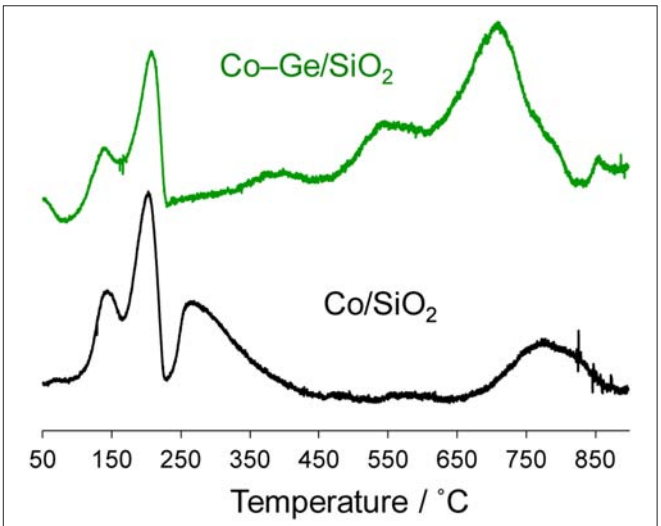

FIGURE 6 | TPR profiles for as-impregnated $Co(NO_3)_2/SiO_2$ and $Co(NO_3)_2$-$(NH_4)_2GeF_6/SiO_2$ catalysts.

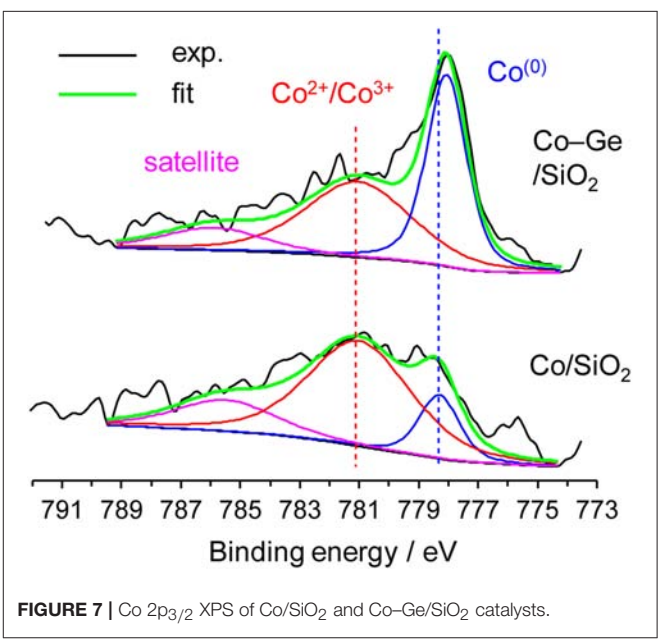

FIGURE 7 | Co $2p_{3/2}$ XPS of Co/SiO_2 and Co–Ge/SiO_2 catalysts.

may be one of the reasons why the Co/SiO_2 catalysts showed low catalytic activity. On the contrary, for $Co–Ge/SiO_2$, the reduction temperature for the preparation (800°C) is enough to reduce all the Co^{2+} and Ge^{4+} species.

We also investigated the electronic states of the Co/SiO_2 and $Co–Ge/SiO_2$ catalysts by XPS (**Figure 7**). For Co/SiO_2, the fraction of Co^{2+} or Co^{3+} species (Sexton et al., 1986) was much higher than that of $Co^{(0)}$, suggesting that a large part of the catalyst surface is oxidized. By contrast, for $Co–Ge/SiO_2$, $Co^{(0)}$ (Sexton et al., 1986) was detected as a main species. These results are consistent with the expectation derived from TPR mentioned above. It is also likely that Co atoms on the $Co–Ge/SiO_2$ catalyst are more resistant to aerobic oxidation than those on Co/SiO_2. Jagirdar et al. reported that Co^{2+} or Ni^{2+} ions could be reduced by the evolved H_2 during hydrolysis of AB to form Ni or Co nanoparticles (Kalidindi et al., 2008). Therefore, it is likely that similar *in situ* reduction of Co^{2+} could occur to completely reduce the catalyst surface in our system. This may be the reason why the induction period was observed in H_2 production from AB over Co/SiO_2. The binding energies of Co^{2+} or Co^{3+} for Co/SiO_2 and $Co–Ge/SiO_2$ were almost same, suggesting that Ge species do not affect the electronic state of Co cations. However, a different trend was observed for $Co^{(0)}$ species: $Co–Ge/SiO_2$ exhibited a lower binding energy than Co/SiO_2, indicating that Co atoms in Co–Ge are electron-enriched compared with pure Co. This is probably because electron transfer from Ge to Co occurs due to alloy formation. Similar electron transfer has also been reported for the relevant systems such as Pt–Ge alloys (Komatsu et al., 1997). Thus, XPS analysis revealed that the formation of Co–Ge alloy drastically changed the electronic state of Co. On the basis of these results, we considered that the difference in the electron density of $Co^{(0)}$ species, namely, electron-enrich Co by Ge via alloying, is the key factor for the remarkable enhancement in the catalytic activity.

The reaction mechanism of AB hydrolysis has been reported as follows: (1) the formation of an activated complex between AB and the metal surface, (2) B–N bond scission assisted by H_2O attack, and (3) hydrolysis of the resulting BH_3 moiety to form H_2 and BO_2^- (Xu and Chandra, 2006; Mahyari and Shaabani, 2014). It is also known that H atoms bound to the B and N atoms are slightly electropositive and electronegative, respectively, due to the different electronegativities of B and N. Therefore, it is likely that the alloy surface with polar active sites ($Co^{\delta-}$–$Ge^{\delta+}$) facilitates the formation of the active complex (1), thus enhancing the following steps and the overall reaction rate. A similar reaction mechanism has also been reported in the system of $Ru^{\delta-}$–$Ni^{\delta+}$ bimetallic catalysts for AB hydrolysis (Mori et al., 2016).

CONCLUSION

In this study, we prepared a series of Ni- and Co-based bimetallic catalysts ($Ni–M/SiO_2$ and $Co–M/SiO_2$; M = Ga, Ge, Sn, and Zn) and tested them in H_2 production from AB in water or methanol. Catalytic activity for hydrogen production is enhanced by the addition of second metals except Sn. Particularly, the addition of Ge to Co enables great enhancement in the catalytic activity, namely a five-fold higher r_{H2} than the monometallic Co/SiO_2 catalyst. The active species is electron-enriched Co atoms constituting the $Co_{0.8}Ge_{0.2}$ solid solution alloy phase. The $Ni–Zn/SiO_2$ catalyst exhibited an $r_{cat[AB]}$ value higher than those ever reported for hydrolysis of AB to the best of our knowledge. The $Ni_{0.75}Zn_{0.25}$ solid solution alloy phase acts as the active species.

AUTHOR CONTRIBUTIONS

SF designed the research and experiments. GN performed all the experiments. TT managed the HAADF-STEM-EDS analysis. SF and TK prepared the manuscript.

FUNDING

This work was supported by JSPS KAKENHI grant numbers 26820350 and 17H0496508.

ACKNOWLEDGMENTS

We deeply appreciate the Center for Advanced Materials Analysis of the Tokyo Institute of Technology for the aid of TEM and STEM observation.

REFERENCES

Chandra, M., and Xu, Q. (2007). Room temperature hydrogen generation from aqueous ammonia-borane using noble metal nano-clusters as highly active catalysts. *J. Power Sources* 168, 135–142. doi: 10.1016/j.jpowsour.2007.03.015

Chen, S. S., Takata, T., and Domen, K. (2017). Particulate photocatalysts for overall water splitting. *Nat. Rev. Mater.* 2:17050. doi: 10.1038/Natrevmats.2017.50

Furukawa, S., and Komatsu, T. (2017). Intermetallic compounds: promising inorganic materials for well-structured and electronically modified reaction environments for efficient catalysis. *ACS Catalysis* 7, 735–765. doi: 10.1021/acscatal.6b02603

Han, J., Zheng, X., Zhang, L., Fu, H., and Chen, J. (2017). Removal of SO_2 on a nanoporous photoelectrode with simultaneous H_2 production. *Environ. Sci. Nano* 4, 834–842. doi: 10.1039/C6EN00638H

Heinzel, A., Vogel, B., and Hübner, P. (2002). Reforming of natural gas—hydrogen generation for small scale stationary fuel cell systems. *J. Power Sources* 105, 202–207. doi: 10.1016/S0378-7753(01)00940-5

Ishida, K., and Nishizawa, T. (1991). The Co-Ge (cobalt-germanium) system. *J. Phase Equilibria* 12, 77–83. doi: 10.1007/BF02663679

Kalidindi, S. B., Indirani, M., and Jagirdar, B. R. (2008). First row transition metal ion-assisted ammonia-borane hydrolysis for hydrogen generation. *Inorgan. Chem.* 47, 7424–7429. doi: 10.1021/ic800805r

Kalidindi, S. B., Vernekar, A. A., and Jagirdar, B. R. (2009). Co-Co2B, Ni-Ni3B and Co-Ni-B nanocomposites catalyzed ammonia-borane methanolysis for hydrogen generation. *Phys. Chem. Chem. Phys.* 11, 770–775. doi: 10.1039/b814216e

Komatsu, T., Hyodo, S., and Yashima, T. (1997). Catalytic properties of Pt-Ge intermetallic compounds in the hydrogenation of 1,3-butadiene. *J. Phys. Chem. B* 101, 5565–5572. doi: 10.1021/Jp971117l

Landge, V. G., Pitchaimani, J., Midya, S. P., Subaramanian, M., Madhu, V., and Balaraman, E. (2018). Phosphine-free cobalt pincer complex catalyzed Z-selective semi-hydrogenation of unbiased alkynes. *Catalysis Sci. Technol.* 8, 428–433. doi: 10.1039/c7cy01994g

Mahyari, M., and Shaabani, A. (2014). Nickel nanoparticles immobilized on three-dimensional nitrogen-doped graphene as a superb catalyst for the generation of hydrogen from the hydrolysis of ammonia borane. *J. Mater. Chem. A* 2, 16652–16659. doi: 10.1039/c4ta03940h

Marder, T. B. (2007). Will we soon be fueling our automobiles with ammonia–borane? *Angew. Chem. Int. Ed.* 46, 8116–8118. doi: 10.1002/anie.200703150

Metin, O., Mazumder, V., Ozkar, S., and Sun, S. S. (2010). Monodisperse nickel nanoparticles; and their catalysis in hydrolytic dehydrogenation of ammonia borane. *J. Am. Chem. Soc.* 132, 1468–1469. doi: 10.1021/ja909243z

Moniz, S. J. A., Shevlin, S. A., Martin, D. J., Guo, Z. X., and Tang, J. W. (2015). Visible-light driven heterojunction photocatalysts for water splitting—a critical review. *Energy Environ. Sci.* 8, 731–759. doi: 10.1039/c4ee03271c

Mori, K., Miyawaki, K., and Yamashita, H. (2016). Ru and Ru-Ni nanoparticles on TiO_2 support as extremely active catalysts for hydrogen production from ammonia-borane. *ACS Catalysis* 6, 3128–3135. doi: 10.1021/acscatal.6b00715

Ozay, O., Inger, E., Aktas, N., and Sahiner, N. (2011). Hydrogen production from ammonia borane via hydrogel template synthesized Cu, Ni, Co composites. *Int. J. Hydrogen Energy* 36, 8209–8216. doi: 10.1016/j.ijhydene.2011.04.140

Patel, N., Fernandes, R., Guella, G., and Miotello, A. (2010). Nanoparticle-assembled Co-B thin film for the hydrolysis of ammonia borane: a highly active catalyst for hydrogen production. *Appl. Catalysis B Environ.* 95, 137–143. doi: 10.1016/j.apcatb.2009.12.020

Peng, C. Y., Kang, L., Cao, S., Chen, Y., Lin, Z. S., and Fu, W. F. (2015). Nanostructured Ni_2P as a robust catalyst for the hydrolytic dehydrogenation of ammonia-borane. *Angew. Chem. Int. Ed.* 54, 15725–15729. doi: 10.1002/anie.201508113

Schlapbach, L., and Züttel, A. (2011). "Hydrogen-storage materials for mobile applications," in *Materials for Sustainable Energy: A Collection of Peer-Reviewed Research and Review Articles from Nature Publishing Group*, ed V. Dusastre (London: World Scientific), 265–270.

Sexton, B., Hughes, A., and Turney, T. (1986). An XPS and TPR study of the reduction of promoted cobalt-kieselguhr Fischer-Tropsch catalysts. *J. Catalysis* 97, 390–406. doi: 10.1016/0021-9517(86)90011-4

van Steen, E., Sewell, G. S., Makhothe, R. A., Micklethwaite, C., Manstein, H., de Lange, M., et al. (1996). TPR study on the preparation of impregnated Co/SiO_2 catalysts. *J. Catalysis* 162, 220–229. doi: 10.1006/jcat.1996.0279

Vassilev, G. P. (1992). Thermodynamic evaluation of the Ni-Zn system. *J. Alloys Compounds* 190, 107–112. doi: 10.1016/0925-8388(92)90184-B

Wang, Q., Hisatomi, T., Suzuk, Y., Pan, Z. H., Seo, J., Katayama, M., et al. (2017). Particulate photocatalyst sheets based on carbon conductor layer for efficient Z-scheme pure-water splitting at ambient pressure. *J. Am. Chem. Soc.* 139, 1675–1683. doi: 10.1021/jacs.6b12164

Xu, Q., and Chandra, M. (2006). Catalytic activities of non-noble metals for hydrogen generation from aqueous ammonia-borane at room temperature. *J. Power Sources* 163, 364–370. doi: 10.1016/j.jpowsour.2006.09.043

Xu, Q., and Chandra, M. (2007). A portable hydrogen generation system: catalytic hydrolysis of ammonia–borane. *J. Alloys Compounds* 446, 729–732. doi: 10.1016/j.jallcom.2007.01.040

Yan, J. M., Zhang, X. B., Han, S., Shioyama, H., and Xu, Q. (2008). Iron-nanoparticle-catalyzed hydrolytic dehydrogenation of ammonia borane for chemical hydrogen storage. *Angew. Chem. Int. Ed.* 47, 2287–2289. doi: 10.1002/anie.200704943

Yan, J. M., Zhang, X. B., Han, S., Shioyama, H., and Xu, Q. (2009). Synthesis of longtime water/air-stable ni nanoparticles and their high catalytic activity for hydrolysis of ammonia-borane for hydrogen generation. *Inorgan. Chem.* 48, 7389–7393. doi: 10.1021/ic900921m

Zhang, L., Reisner, E., and Baumberg, J. J. (2014). Al-doped ZnO inverse opal networks as efficient electron collectors in $BiVO_4$ photoanodes for solar water oxidation. *Energy Environ. Sci.* 7, 1402–1408. doi: 10.1039/C3EE44031A

Zheng, X. Z., and Zhang, L. W. (2016). Photonic nanostructures for solar energy conversion. *Energy Environ. Sci.* 9, 2511–2532. doi: 10.1039/c6ee01182a

Züttel, A. (2003). Materials for hydrogen storage. *Mater. Today* 6, 24–33. doi: 10.1016/S1369-7021(03)00922-2

Conflict of Interest Statement: The authors declare that the research was conducted in the absence of any commercial or financial relationships that could be construed as a potential conflict of interest.

Copyright © 2019 Furukawa, Nishimura, Takayama and Komatsu. This is an open-access article distributed under the terms of the Creative Commons Attribution License (CC BY). The use, distribution or reproduction in other forums is permitted, provided the original author(s) and the copyright owner(s) are credited and that the original publication in this journal is cited, in accordance with accepted academic practice. No use, distribution or reproduction is permitted which does not comply with these terms.

frontiers in Chemistry

REVIEW
published: 14 May 2019
doi: 10.3389/fchem.2019.00299

Harnessing Plasmon-Induced Hot Carriers at the Interfaces With Ferroelectrics

Vineet Kumar, Shaun C. O'Donnell, Daniel L. Sang, Paul A. Maggard and Gufeng Wang**

Department of Chemistry, North Carolina State University, Raleigh, NC, United States

This article reviews the scientific understanding and progress of interfacing plasmonic particles with ferroelectrics in order to facilitate the absorption of low-energy photons and their conversion to chemical fuels. The fundamental principles of hot carrier generation and charge injection are described for semiconductors interfaced with metallic nanoparticles and immersed in aqueous solutions, forming a synergistic juncture between the growing fields of plasmonically-driven photochemistry and semiconductor photocatalysis. The underlying mechanistic advantages of a metal-ferroelectric vs. metal-nonferroelectric interface are presented with respect to achieving a more optimal and efficient control over the Schottky barrier height and charge separation. Notable recent examples of using ferroelectric-interfaced plasmonic particles have demonstrated their roles in yielding significantly enhanced photocurrents as well as in the photon-driven production of molecular hydrogen. Notably, plasmonically-driven photocatalysis has been shown to occur for photon wavelengths in the infrared range, which is at lower energies than typically possible for conventional semiconductor photocatalysts. Recent results thus demonstrate that integrated ferroelectric-plasmonic systems represent a potentially transformative concept for use in the field of solar energy conversion.

Keywords: ferroelectrics, surface plasmon resonance, Schottky barrier, spontaneous polarization, hot electrons, charge injection, photocatalysis

OPEN ACCESS

Edited by:
Bunsho Ohtani,
Hokkaido University, Japan

Reviewed by:
Ying Dai,
Shandong University, China
Yun Hau Ng,
University of New South Wales, Australia

****Correspondence:***
Paul A. Maggard
pamaggar@ncsu.edu
Gufeng Wang
gufeng_wang@ncsu.edu

Specialty section:
This article was submitted to Catalysis and Photocatalysis, a section of the journal Frontiers in Chemistry

Received: *25 February 2019*
Accepted: *12 April 2019*
Published: *14 May 2019*

Citation:
Kumar V, O'Donnell SC, Sang DL, Maggard PA and Wang G (2019) Harnessing Plasmon-Induced Hot Carriers at the Interfaces With Ferroelectrics. Front. Chem. 7:299. doi: 10.3389/fchem.2019.00299

BACKGROUND

Generation of Hot Carriers in Plasmonic Nanoparticles

The transformation of solar energy into chemical potential energy, e.g., such that which is stored in molecular hydrogen, represents a sustainable and favorable pathway to eventually displacing fossil fuels as the predominant energy resource. Noble metals have been drawing increasing attention as a component of efficient light-harvesting systems arising from the collective oscillation of their conduction electrons, i.e., surface plasmon resonances (SPR), that can be excited by photons over a very wide range of infrared to ultraviolet wavelengths (Brongersma et al., 2015; Linic et al., 2015; Moskovits, 2015). Within a metallic nanoparticle, localized surface plasmons are produced that are confined to an area that is similar to or smaller than the wavelength of light excitation. Subsequent to the absorption of light, a number of competing elementary processes and potential outcomes can occur (**Figure 1**), with timescales that are dependent upon the nanoparticle size, shape, and electronic structure. The basic features of these competing processes have been the focus of reviews.

Briefly, when a metal particle is irradiated by light, the electromagnetic field induces the polarization of the conduction electrons with respect to the positive ionic cores, creating an

electric dipole (**Figure 1A**). The Columbic interaction between the opposite charges acts as a restoring force, which leads to electronic oscillations, where the collective electronic oscillations are named plasmons. When the electronic oscillations occur locally at the nanoparticle as shown in **Figure 1A**, the corresponding surface oscillation is known as localized SPR (LSPR). Under resonance conditions, the particle absorption cross section is greatly enhanced, e.g., up to five orders of magnitude larger than those of typical dye molecules (Jain et al., 2006). The SPR wavelengths of the plasmonic nanoparticles are tunable, by varying size and shape, across the entire visible spectrum. The confined electronic oscillations in the particle enhance the local electric field distribution at the surface of the nanostructures. This leads to several interesting phenomena such as Surface-Enhanced Raman Scattering (SERS), etc., which is beyond the scope of this review article.

The plasmon resonances can decay radiatively by re-emission of photons or non-radiatively by Landau damping with the creation of electron-hole pairs, on the timescale of ∼1–100 fs. For small nanoparticles (∼10–25 nm) and sub-radiant plasmon modes, the branching ratio is predominated by the creation of electron-hole pairs. An example of the non-thermalized distribution of charged carriers is illustrated in **Figure 1B**, showing "hot" electrons and holes that are energetically above and below the Fermi level of the metal particle, respectively (Mukherjee et al., 2013; Linic et al., 2015). The resulting distribution is a sensitive function of the plasmon energy, particle size, and the electronic structure of the metallic nanoparticle, as described previously. These hot carriers will adiabatically re-equilibrate via electron scattering and Auger transitions on the order of 100 fs to 1 ps (**Figure 1C**) to produce a Fermi-Dirac like distribution with a high effective electron temperature of several thousand degrees. Thus, *high energy hot electrons* can be produced in the process even when the particle is excited by relatively low energy photons (Moskovits, 2015).

Shown in **Figure 2**, for example, a recent investigation into 15 nm Ag nanoparticles shows a wide calculated distribution of hot carriers for a continuously-irradiated particle and lifetimes that varied between 0.05 and 1.0 ps. Thus, the energetic distribution of the hot carriers, i.e., both their densities and energies, is a highly sensitive function of their re-equilibration lifetimes. For a photon energy of 3.65 eV, a wide range of excited states is ultimately achieved that ranges from 3 to 4 eV both above and below the Fermi level for the hot electron and hot hole states, respectively, as shown in **Figure 2**. These represent electrochemical potentials for both electrons and holes that exceed the band energy requirements for the water-splitting half reactions, as will be described below. For a larger particle size of 25 nm, a significantly smaller hot-carrier density (∼50%) results because of the higher number of allowable electronic states. Lastly, the thermal re-equilibration with the lattice requires on the order of several picoseconds (**Figure 1D**), followed by heat transfer to the surroundings in ∼10 ps to 10 ns.

Critical to solar energy conversion, high-energy hot electrons and holes are generated in plasmonic nanoparticles during the light absorption processes, with lifetimes on the order of 10 ps before thermal equilibration with the surroundings (Hoggard et al., 2013; Major et al., 2014; Linic et al., 2015). This realization has led to a surge of recent studies that have demonstrated that the excitation of the SPR of particle-based catalysts can be used to facilitate or greatly amplify their catalytic activities (Adleman et al., 2009; Bueno Alejo et al., 2011; Christopher et al., 2011; Liu et al., 2011; Warren and Thimsen, 2012; Hoggard et al., 2013; Mubeen et al., 2013; Mukherjee et al., 2013; Major et al., 2014; Marchuk and Willets, 2014; Linic et al., 2015). How specific catalytic reactions are impacted by excitation of the plasmonic nanoparticle is still under intense investigation and likely varies case-by-case. Generally, it is viewed that SPR can enhance photon-driven chemical reactions through two possible mechanisms. These include the local photothermal effect, i.e., the reaction is thermally activated or expedited by the hot lattice produced by thermal re-equilibration, and more interestingly, by hot charge transfer across interfaces to molecular absorbates to electrochemically induce reactivity. In the latter pathway, the excitation of the SPR causes the formation of hot electron-hole pairs that can then be transferred to the metal surface and the adsorbate molecules directly or indirectly, inducing the chemical reactions (Major et al., 2014; Brandt et al., 2016).

Prominent early examples of hot electron transfer include the dissociation of H_2 molecules on the surface of ∼10–20 nm Au particles, or the oxidation of ethylene by O_2 using 60 nm Ag nanocubes (Mukherjee et al., 2014). For the room-temperature dissociation of H_2 molecules, the study found that hot electrons transferred most effectively across a nanoshell of SiO_2 and less effectively across a nanoshell of TiO_2, owing to the lower-energy conduction band of TiO_2 that functions as a highly effective electron acceptor. Conversely, hot hole transfer has been demonstrated in the growth of Ag nanoprisms via oxidation of citrate anions in solution (Jin et al., 2003). The plasmon-induced growth of the Ag nanoprisms was found to be more sensitively dependent on the incident photon energy rather than the photon flux, owing to the increasing oxidizing power of the hot holes. Many other remarkable studies in this field have proven that the energies and lifetimes of the hot electron and holes can be sensitively manipulated and used to enable their facile transfer to adsorbates and/or through interfaces. These can be utilized to drive reactions that have significant activation energies, or alternatively, reactions that are thermodynamically uphill in energy.

Light-Driven Reactivity at Semiconductor Surfaces

The realization that light-absorption by semiconductors could be used to drive chemical reactions occurred in the early 1970s with the seminal research on *n*-type TiO_2 that demonstrated that water could be oxidized at its surfaces to molecular oxygen (Fujishima and Honda, 1972; Kawai and Sakata, 1980; Hoffmann et al., 1995; Kato et al., 2003; Maeda et al., 2005; Linic et al., 2011; Sivula et al., 2011; Ohno et al., 2012; Huang et al., 2017; Suzuki et al., 2018). Since that time, semiconductors from among many different chemical systems have been investigated for their ability to function at high solar-to-chemical efficiencies and stabilities, including in the oxides, chalcogenides, and nitrides. These have

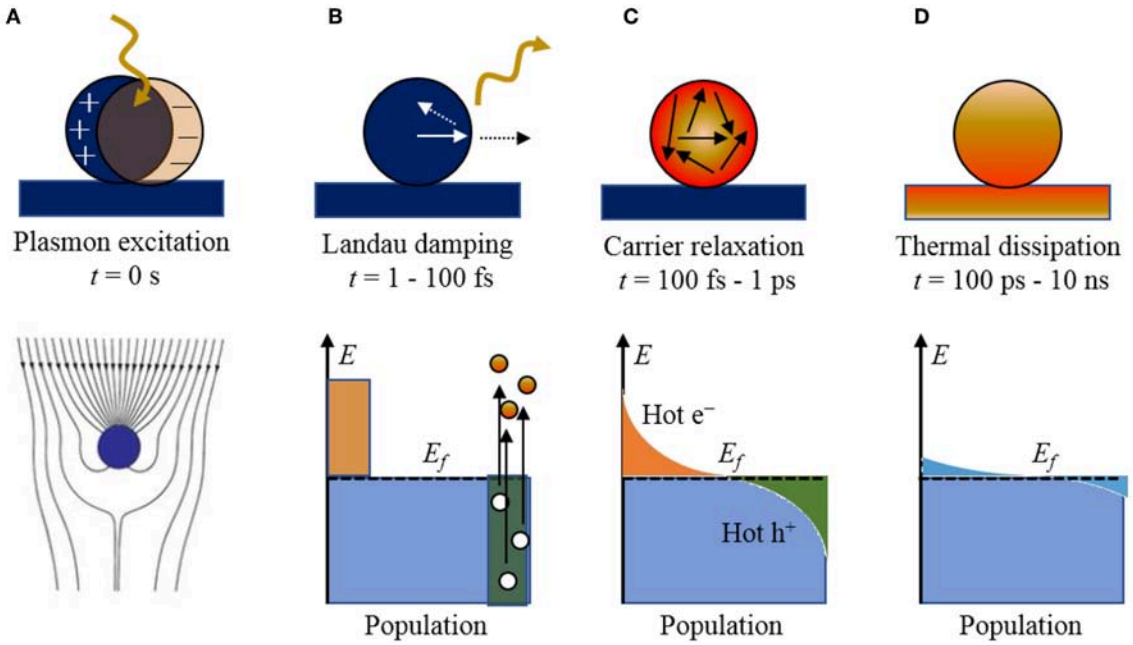

FIGURE 1 | The stepwise processes of photoexcitation and electronic relaxation for a metallic nanoparticle with the characteristic timescales and population of electronic states: **(A)** excitation of a localized surface plasmon, **(B)** Landau damping and the creation of electron-hole pairs, **(C)** carrier relaxation and thermalized "hot" distribution of carriers, and **(D)** thermal dissipation to the surroundings. The Fermi level is labeled by E_f. Adapted with permission from Brongersma et al. (2015). Copyright 2015 Spring Nature.

included in applications such as in thin-film photovoltaics and photoelectrodes, as well as in the form of photocatalyst particles. However, the anatase polymorph of TiO_2 has been among the most highly investigated materials for the water splitting reactions to produce molecular hydrogen and oxygen (Kawai and Sakata, 1980; Hoffmann et al., 1995).

Shown in **Figure 3A**, a photocatalytic reaction consists of three basic steps, including the absorption of bandgap photons with the generation of electron (e^-) and hole (h^+) pairs, charge separation and transport to the surfaces via their diffusion and drift, and then electron transfer at the surfaces to drive redox reactions, e.g., such as for water splitting. A key element to the charge separation is the space charge layer that forms at the semiconductor surface as a result of its equilibration with the chemical potential of the solution. In an *n*-type semiconductor, this results in an upward band bending with a depth given by W_{sc} that is a function of the dopant density, dielectric constant, and space charge height. The electron-hole pairs will be separated if they are produced within this layer or if they can diffuse to it before recombining. In this case, the oxidation reaction occurs at the semiconductor surface and the reduction reaction occurs at a counter-electrode or at a surface cocatalyst island such as Pt.

The production of molecular hydrogen from the splitting of water is a thermodynamically uphill process with a Gibbs' free energy change of ∼238 KJ/mol, thus requiring the equivalent of >1.23 eV (<1,008 nm) per photon (Maeda et al., 2006; Ingram and Linic, 2011; Sivula et al., 2011; Wang and Astruc, 2014). A semiconductor with a bandgap size of >1.23 eV and suitable band energies that straddle the water redox couples can be used to drive the water splitting reaction at its surfaces from solar irradiation. A consideration of the required overpotentials at its surface catalyst sites increases the optimal photon energy to ∼1.6–2.0 eV, or to wavelengths less than about ∼600–775 nm for a single junction photoelectrode or photocatalyst particle. Considering that the solar irradiation, i.e., AM 1.5 G light, includes a large (>50%) contribution in the infrared energy range with wavelengths of >800 nm, there is a significant fraction of solar energy that cannot be utilized in single-junction semiconductor systems for photocatalysis (Navarro et al., 2009; Long et al., 2015). Other factors that negatively impact the light-driven reactions at the surfaces include the efficiency of charge separation, charge carrier lifetimes, and surface reaction rates and stability. Owing to these limitations, their practical efficiency in converting sunlight to chemical energy remains low (<1% for total solar energy) compared to the minimum solar-to-hydrogen efficiency of ∼10% that is required for commercial viability (Lewerenz and Peter, 2013).

Under ultraviolet irradiation, many large bandgap semiconductors show a high quantum efficiency and outstanding stability, e.g., La-doped $NaTaO_3$ and TiO_2 with bandgap sizes of ∼3–4.5 eV. This has led to numerous studies aimed at their sensitization to visible-light wavelengths, such as using molecular dyes via charge injection of their excited electrons. However, most molecular dyes degrade rapidly over time or cannot be used to drive the overall water splitting reaction. Plasmonic nanoparticles, either bare or combined with a semiconductor,

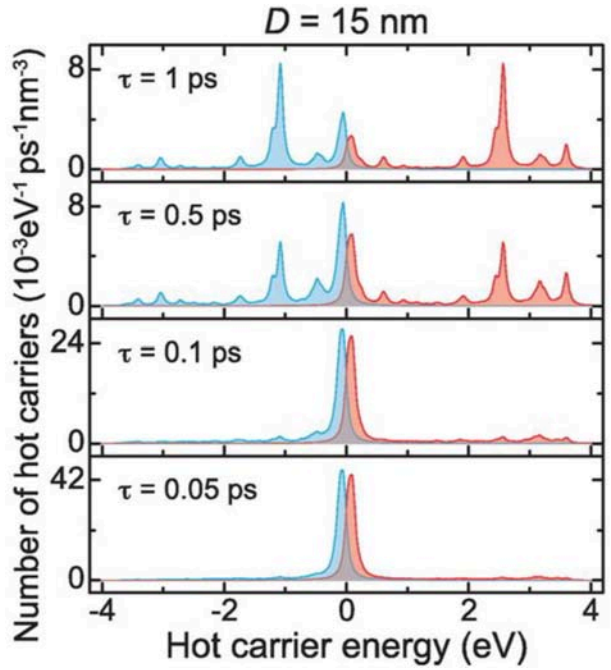

FIGURE 2 | Hot carrier distributions per unit time and volume as a function of energy, calculated for a 15 nm diameter Ag nanoparticle. Hot electrons and hot holes are plotted as the blue and red lines, respectively, with the Fermi level set at the zero energy. The stacked plots show the changes in the hot carrier distributions for relaxation lifetimes from 0.05 to 1.0 ps. An incident photon energy of 3.65 eV was used. Adapted with permission from Manjavacas et al. (2014). Copyright 2014 American Chemical Society.

have most recently been the subject of several key investigations for use in light-driven reactions (Zhu, 1994; Wang et al., 2008; Li et al., 2015; Ma, X. et al., 2016; Ortiz et al., 2017). The placement of a plasmonic particle and a semiconductor surface in close vicinity can have a remarkable impact on their catalytic activity. For example, Ma et al. found that the photocatalytic activity in a combined plasmonic-semiconductor particle can be increased through local electric field enhancement of photo-induced charge carrier generation at the semiconductor surface (Ma et al., 2014a). The photo-degradation of methyl orange under visible-light irradiation was investigated for Ag@AgCl, where AgCl is a wide band gap material (>3 eV). It was proposed that energy transfer from the Ag nanoparticle to the semiconductor AgCl required the presence of mid-gap defect states. In this case, the SPR of the Ag nanoparticles was found to enhance the excitations of AgCl involving these defect states.

More generally, photogenerated hot charge carrier injection from the plasmonic particles to the semiconductors has been found to play a dominant role in modulating semiconductor reactivity. Hot electron injection from plasmonic particles to semiconductors has been demonstrated, and hybrid plasmonic-semiconductor materials have been utilized in a growing number of investigations of photovoltaic devices (Atwater and Polman, 2010; Linic et al., 2011; Thomann et al., 2011; Mubeen et al., 2013; Clavero, 2014) and photocatalysts (Zhao et al., 1996; Christopher et al., 2011; Marimuthu et al., 2013; Mukherjee et al., 2013). Combining plasmonic nanoparticles with a semiconductor photocatalyst can significantly boost the efficiency of light absorption as well as induce high local electric fields for charge separation. More importantly, the semiconductor can serve as a sink for hot electrons generated in the SPR process, extending their lifetimes to be in the nanosecond time scale (Zhu, 1994). Many of these investigations have shown enhancements of the photocatalytic rates at their surfaces. As illustrated in **Figure 3B**, the concept is that the excitation of the localized SPR of nanoparticles will generate hot electrons and hot holes that can be injected into the conduction band or the valence band, respectively, of the metal oxide. Thus, the oxidation and reduction reactions can occur separately over the plasmonic nanoparticle and metal oxide. In addition, the operational wavelength range of such systems can be tuned by controlling the SPR resonance frequency from the infrared to ultraviolet photon energies.

However, the efficient utilization of the hot electrons has been a formidable challenge because of the extremely short relaxation lifetimes, on the order of a few picoseconds, owing to the multiple fast relaxation processes including electron-electron scattering, electron-interface scattering, electron–phonon interaction, photoluminescence, etc. (Linic et al., 2011; Manjavacas et al., 2014; Ma, X. C. et al., 2016). When combining the plasmonic particles with conventional semiconductors, the hot electron injection efficiency (HEIE) is usually low. The Schottky barrier (i.e., the energy barrier across the metal and the semiconductor interface, described later) is the main hurdle for the low efficiency. Practical factors, e.g., the occupation of surface oxygen vacancies of titania oxide by Au atoms during the synthetic process, may increase the barrier and expand the space charge region, which significantly decreases the HEIE (Ma et al., 2014b). Strategies to most efficiently use the hot charge carriers generated in an SPR process are currently under intensive investigation (Ma, X. C. et al., 2016). Current efforts to improve the hot electron injection efficiency include designing composite structures so that the hot electrons have sufficient momentum to cross the interface (Giugni et al., 2013), chemically modifying the surfaces so that efficient electronic coupling between the plasmonic particle and the semiconductor occurs (Tamura et al., 2009), and applying pressure, which shifts the positions of the valence/conduction bands and favors lowering the barrier height (Ma, X. et al., 2016; Lv et al., 2018). However, these efforts have so far not yielded an adequately efficient design to capture and harness the hot electrons.

Ferroelectric Surfaces for Extracting Hot Carriers of Plasmonic Nanoparticles

Ferroelectric materials have been extensively used in microelectronics, memory storage devices, temperature sensors and switches, thin film capacitors, and more (Daniel and Astruc, 2004). They are characterized as possessing a large, reversible electric polarization within their crystalline grains owing to a displacement of the centroid of positive and negative charges, as illustrated in **Figures 4A–C** for $BaTiO_3$ in the symmetric cubic

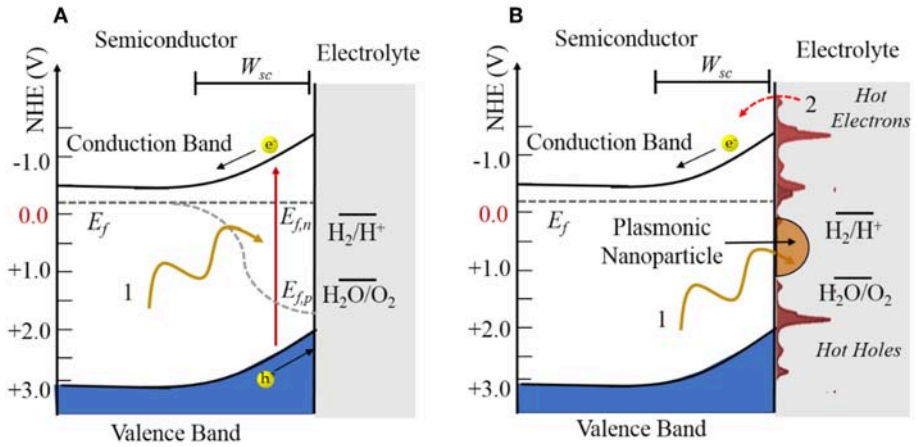

FIGURE 3 | Illustration of **(A)** an *n*-type semiconductor-electrolyte interface under irradiation and **(B)** an *n*-type semiconductor with a plasmonic nanoparticle attached at the surface. The quasi-Fermi levels in **(A)** are labeled by $E_{f,n}$ and $E_{f,p}$ and the Fermi level in **(B)** labeled by E_f. The space charge width is labeled by W_{sc}.

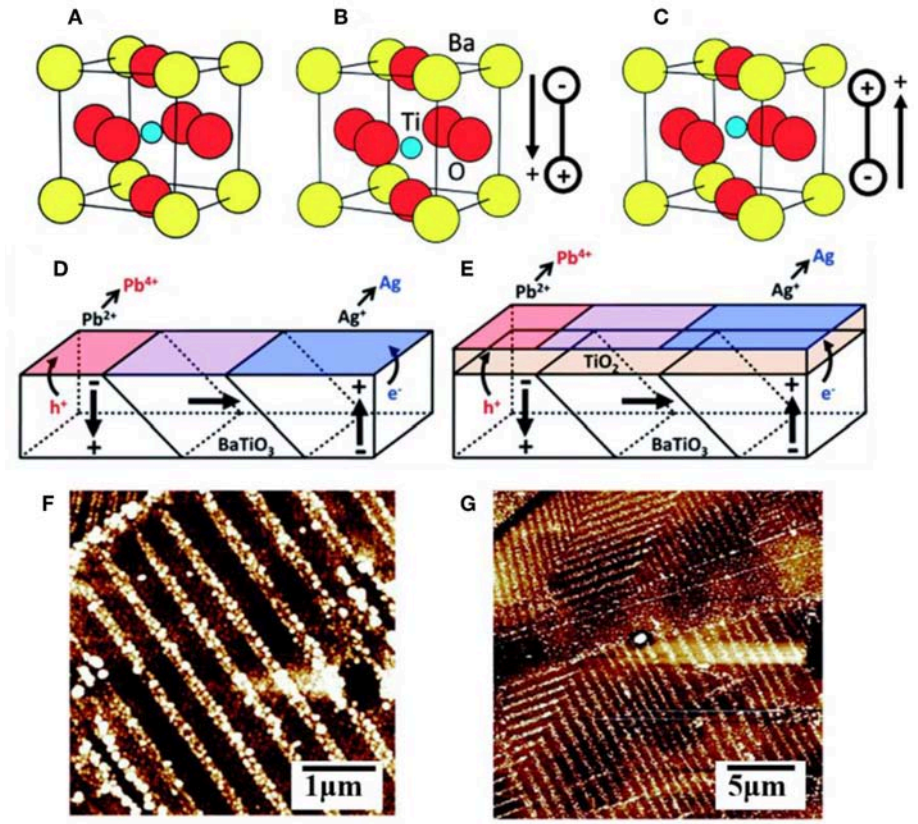

FIGURE 4 | The unit cell of $BaTiO_3$ in the **(A)** cubic form and **(B,C)** in its ferroelectric polymorph showing two different polar orientations. A multidomain surface with multiple polar orientations without **(D)** and with **(E)** a TiO_2 layer coating. AFM images of a (100) oriented $BaTiO_3$ surface after photochemical deposition of metallic Ag (white contrast) without **(F)** and with **(G)** the TiO_2 layer coating. Adapted with permission from Giocondi and Rohrer (2001). Copyright 2001 American Chemical Society.

(*Pm-3m*) or distorted tetragonal (*P4mm*) polymorphs of the perovskite structure type. Many ferroelectrics with the common ABO_3 composition crystallize in perovskite-type structures that exhibit polar distortions. For example, ferroelectric $PbTiO_3$ exhibits a tetragonal structural distortion below a Curie temperature of ∼495°C and with a large, spontaneous

ferroelectric polarization of ∼80 μC cm^{-2} that persists even in the absence of an applied electric field (Qin et al., 2007; Arney et al., 2011; Cao et al., 2012b; Kakekhani and Ismail-Beigi, 2016; Kakekhani et al., 2016; Wang et al., 2016). A freshly prepared sample will have a large number of individual grains, or domains, with random orientations that are separated by domain walls, shown in **Figures 4D,E** for $BaTiO_3$. Unit cells within the domain have a shared polarization direction, labeled with arrows, owing to the collective displacements of the cations in the same directions. However, changes to the displacement of the cations around the oxygen anions can be induced by application of an external electric field, causing the polarization of individual grains to eventually be aligned with the external field in a process known as poling. This process is reversible, and thus ferroelectrics have a switchable polarization (Kalinin and Bonnell, 2001; Bonnell and Kalinin, 2002; Streiffer et al., 2002; Daniel and Astruc, 2004; Cai et al., 2007).

Many recent studies have suggested that the surfaces of a ferroelectric (FE) can yield potentially optimal configurations for achieving significant efficiency enhancements of charge separation and charge injection across interfaces. The spontaneous polarization can facilitate electron-hole separation within the ferroelectrics through coulombic interactions (Yun and Altman, 2007), and also where the domain walls can act as charge trapping centers or as reactive surface sites (Qin et al., 2007; Sakar et al., 2016; Zhu et al., 2018). Many prior studies have demonstrated that the internal polarization of a ferroelectric can result in the spatial segregation of oxidation and reduction reactions over its oppositely polarized surfaces. For example, photochemical deposition studies on $BaTiO_3$, $BiFeO_3$, and other ferroelectrics have shown spatial separation of the light-driven oxidation of Pb^{2+}(aq) to PbO_2(s) and the light-driven reduction of Ag^{+}(aq) to Ag(s) (Li et al., 2014). An illustrative case is depicted in **Figure 4** for $BaTiO_3$, wherein atomic force microscopy shows that its positively polarized surfaces are preferentially the sites for reductive reactivity and its negatively polarized surfaces are the preferential sites for oxidative reactivity. Recent calculations have shown that positively and negatively polarized domains, which are separated by 180°, lead to the highly efficient separation of the charged carriers to the oppositely polarized surfaces with internal quantum efficiencies that can exceed 90% (Glickstein et al., 2016). The advantage is that both types of carriers, i.e., majority and minority carriers, can be separated and reacted over adjacent surfaces without the need for extended diffusion pathways through a film, external circuit, or via redox shuttles in solution. Efficient charge separation within ferroelectrics is thus an attractive feature for photocatalytic reactions such as water splitting. For example, using the ferroelectric $PbTiO_3$, Maggard et al. investigated its photocatalytic activity for the reduction and oxidation of water and showed that high activities for both reactions occur for nanoparticles as well as micron-sized particles (Arney et al., 2011). A limiting feature of ferroelectrics is that, with a few rare exceptions, they usually have large bandgap sizes that fall within the ultraviolet energy range. For example, $PbTiO_3$ has a bandgap that falls at the edge of the visible range at ∼2.7 eV and does not absorb light with a wavelength longer than ∼460 nm. Thus, the many recent investigations into ferroelectrics have focused on their capabilities to increase charge separation or charge extraction when combined with semiconductors with smaller bandgap sizes (Bowen et al., 2014).

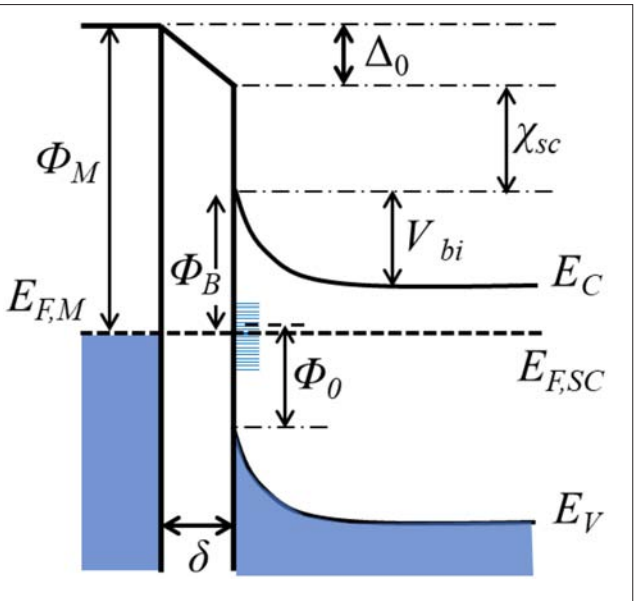

FIGURE 5 | Energy diagram of a metal-semiconductor(*n*-type) contact with an interfacial layer. Φ_M, metal work function; $E_{F,M}$ and $E_{F,SC}$, Fermi levels of the metal and semiconductor. χ_{SC}: semiconductor electron affinity. E_C, E_V: Energy levels at the edges of the conduction and valence bands. Φ_B: Schottky barrier height. V_{bi}: built-in potential. δ: interfacial thickness. Δ_0: voltage drop across the interface. Φ_0: energy change between the valence band edge and charge neutrality level.

Recent results, described below, have suggested that the tethering of plasmonic nanoparticles to the surfaces of a ferroelectric can lead to an optimal configuration for achieving an enhanced extraction of hot carriers from them. The basic idea is that a ferroelectric with a large surface polarization can facilitate the fast charge extraction of hot carriers from plasmonic nanoparticles. The unique advantages of this combined system include the capability to independently manipulate the electric polarization of the ferroelectrics as well as the local SPR wavelengths of the nanoparticles in order to achieve synergistic energetic conditions at their interface to optimize the injection of the hot charge carriers. In addition, better charge separation can be achieved in this combined system in which the domain walls of the ferroelectrics can serve as the charge trapping centers or as reactive surface sites (Qin et al., 2007; Sakar et al., 2016; Zhu et al., 2018). Furthermore, all potential advantages of an interfaced metal-semiconductor system are inherited, e.g., enhanced optical excitation of the semiconductor due to the local field effect (Ma et al., 2014b). The underlying mechanism for the enhanced charge injection involves a tuning of the band bending and the Schottky barrier height at the semiconductor-metal interface, which has also represented a long-standing

problem in the physics and chemistry of electronic materials. The impacts of the ferroelectric polarization and the composition of the metallic particles are described below, together with recent experimental results that have demonstrated that the hot charge carriers can be injected into ferroelectrics (Atwater and Polman, 2010; Grinberg et al., 2013).

MODELS OF METAL-FERROELECTRIC INTERFACES AND THE SCHOTTKY BARRIER

Currently very little is known, either theoretically or experimentally, about the hot charge injection from plasmonic particles to ferroelectric materials from a perspective of light-driven catalysis, e.g., such as for water splitting reactions. Investigations of the interfaces between metals and ferroelectrics have focused on their potential applications in solid-state photovoltaic devices, wherein the ferroelectric both functions as the light-absorbing component as well as the underlying driving force for charge separation. A model of the electronic structure and band bending at semiconductor surfaces interfaced with a metal is described first, followed by the impact of the ferroelectric polarization at this interface. This is critical to understanding the experimental photocurrents and photocatalytic properties in recent investigations.

Schottky Barrier Height at Semiconductor-Metal Interfaces

At the surface of a crystalline semiconductor, the periodic pattern of chemical bonds is interrupted and leads to the formation of dangling bonds from the incomplete atomic coordination environments. These dangling bonds can be responsible for the formation of localized surface states with energies that fall within the band gap of the semiconductor. An inversion layer, or depletion region, is formed near the surfaces, which results from a flow of its majority carriers, i.e., either *n*-type or *p*-type, either toward or away from the surfaces to fill the surface states and reach electrochemical equilibrium (Sze and Ng, 2006). The interface states are filled up to the charge neutrality level (CNL), above which these states are empty (Tersoff, 1986; Robertson and Chen, 1999). The charge transfer between the surface states and the bulk of the semiconductor causes the bands to bend at the interface (McCaldin et al., 1976; Spicer et al., 1980).

When a semiconductor is in contact with a metal, the difference in their work functions causes electrons to transfer between them. For example, if the metal work function is larger than that of the semiconductor, the electrons will flow from

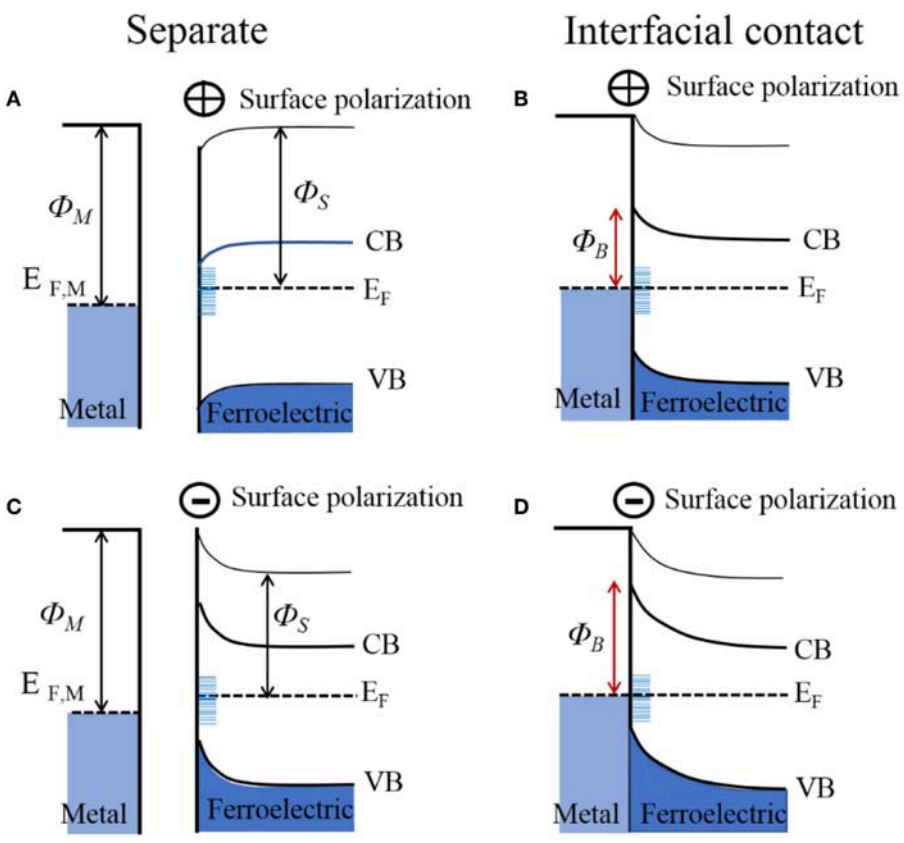

FIGURE 6 | Electronic energy levels of an *n*-type ferroelectric for its surfaces that are positively charged (upper; **A,B**) and negatively charged (lower; **C,D**), shown before and after interfacial contact with a metal. Φ_M, metal work function; Φ_S, semiconductor work function; Φ_B, Schottky barrier height; E_F, Fermi level; CB, conduction band; VB, valence band.

the semiconductor to the metal until the Fermi levels have equilibrated. Electron transfer from semiconductor to the metal (for $\Phi_M > \Phi_{SC}$) or from metal to semiconductor (for $\Phi_M < \Phi_{SC}$) will cause band bending upward or downward, respectively, at their interfacial region (Zhang and Yates, 2012). For example, **Figure 5** shows an example whereby Φ_M is larger than Φ_{SC} and upward band-bending has resulted. This junction, known as a Schottky junction, represents a potential energy barrier that manifests as a rectifying electrical contact between the metal and the semiconductor, i.e., the flow of electrons in this case occurs most easily from the semiconductor to the metal. The energy barrier for electrons to flow in the reverse direction from the metal and into the conduction band (CB) of the semiconductor is known as the Schottky barrier (Φ_B). The flow or injection of electrons across this barrier depends in an exponential manner on the height of the Schottky barrier and is thus one of the most critical properties of a metal-semiconductor interface. In the simplest case, the energetic height of the Schottky barrier follows the Schottky-Mott relationship, which for an *n*-type semiconductor is given by Equation (1):

$$\Phi_B = \Phi_M - \chi_{SC} \tag{1}$$

where χ_{SC} is semiconductor electron affinity. It can be taken that the voltage drop arising from the formation of an interface dipole, i.e., Δ_0, is considered to be zero for this simplified case. The band bending at the surface of the semiconductor functions as the driving force for charge separation, and is given by the built-in potential (V_{bi}) in Equation (2):

$$V_{bi} = \Phi_B - (E_C - E_{F,SC}) \tag{2}$$

where $E_{F,SC}$ is the Fermi level of the semiconductor, and E_C is the conduction band edge of the semiconductor. Hot electron injection will be favored when $\Phi_{SC} < \Phi_M$ and the semiconductor bands bend up, while hot hole injection will be favored when $\Phi_{SC} > \Phi_M$ and the bands bend down. Thus, in both cases, the unidirectional injection of hot carriers across the interface leads to their efficient separation via a drift current in the semiconductor that flows away from the metallic nanoparticle. Note that in this review article, the focus is exclusively on the injection of hot electrons, which are relatively better characterized and typically have high mobility. For a *p*-type semiconductor, the bands typically bend downward due to its low-lying Fermi level. In this case, the potential barrier (V_{bi}) will be nil and instead an accumulation layer will form. Thus, the interfaces between plasmonic metals and *p*-type semiconductors will not be favorable for hot electron injection. Hence, only *n*-type semiconductors are covered in this review.

With rare exceptions, however, the Schottky barrier height has been found to show a relatively weak correlation with the metal work function as predicted by Equation 1 (Tung, 2000; Dimoulas et al., 2006). The cause of this is known as Fermi level pinning and is driven by a large concentration of mid-gap states that form at the metal-semiconductor interface arising from metal-induced gap states, disorder-induced gap states, defect states, and other surface defects. These states become filled by charge flow from the semiconductor and result in an interface dipole and a voltage drop across the interface. Different models have been proposed to account for this phenomenon, including the most popular Cowley-Sze model, which takes semiconductor surface states and Fermi level pinning into consideration. The revised form of the Schottky barrier height is defined by the following Equation (3) (Bardeen, 1947; Cowley and Sze, 1965):

$$\Phi_B = S(\Phi_M - \chi_{SC}) + (1 - S)(E_g - \Phi_0) \tag{3}$$

Here, E_g represents the band gap of the semiconductor; Φ_0 is the energy difference between the CNL and the valence band edge of the semiconductor at the surface, and *S* is the pinning parameter depending on the surface state density of the semiconductor. Practically, *S* has been found to fall between 0 and 1, where "0" stands for maximum and "1" stands for minimum pinning, respectively (Cohen, 1979). Monch empirically found that the pinning parameter, *S*, follows a linear approximation (Mönch, 1987):

$$S = 1/(1 + 0.1(\varepsilon - 1)^2) \tag{4}$$

where the dielectric constant ε is taken as the square of the refractive index of the semiconductor. For ionic semiconductors such as ZnO or ZnSe, *S* approaches 1 (Schottky limit) and the Cowley–Sze model reduces to Schottky–Mott model (Equation 1). For covalent semiconductors, *S* approaches 0 (Bardeen limit). When the interface state density approaches infinity, then the Cowley-Sze model takes the form of Equation (5):

$$\Phi_B = E_g - \Phi_0 \tag{5}$$

In this case, the Fermi level of the metal is pinned to CNL, and hence the Schottky barrier height is independent of the metal work function (Bardeen, 1947; Kurtin et al., 1969). This relationship was found by Dimoulas et al. to be consistently followed at metal/Ge interfaces (Dimoulas et al., 2006). However, the Schottky barrier height is known to be intricately dependent upon the specific interfacial bonding, i.e., sensitive to surface orientation, surface relaxation, and other factors (Tung, 2014). It has been reported in many cases to typically vary by amounts of ± 0.2 to 0.8 eV for even the same metal and semiconductor combinations. Thus, the formation and height of the Schottky barrier must be investigated for each specific metal-semiconductor combination and under identical conditions of their preparation.

Ferroelectric Control Over the Schottky Barrier Height

At metal-ferroelectric interfaces, the spontaneous surface polarization must also be accounted for when considering the band bending and Schottky barrier height. This is a consequence of the fact that the ferroelectric polarization at the surface will establish an additional interface potential and, depending on its orientation, will modify the surface binding energies and Schottky barier height with the metal. The effect of the surface polarization has been observed in the photocatalytic reactivity of multi-domain ferroelectrics, notably including

$PbTiO_3$, $Pb(Ti_{1-x}Zr_x)O_3$ (PZT), $BaTiO_3$, and $BaBiFeO_3$ (Inoue et al., 1989; Apostol et al., 2013). In these cases, the different orientations of the surface polarization, e.g., represented as P(+), P(−), or P(0), can cause light-driven reduction reactions at P(+) surfaces and oxidation reactions at P(−) surfaces, as shown in **Figures 4F,G** for $BaTiO_3$ (Schultz et al., 2011). When P(−) and P(+) surface polarizations occur at the surface of the ferroelectric, the interface dipole leads to a negative and positive impact on the band bending, respectively, illustrated in **Figures 6A,C**. Thus, with bandgap excitation of electron-hole pairs in the depletion region, the electrons are separated and driven to P(+) surfaces and the holes to the P(−) surfaces. For a ferroelectric in contact with a metal, the difference in the work function of the metal and semiconductor will equilibrate with the flow of charged carriers between them, and either strengthen or weaken the surface ferroelectric polarization, thus modifying the Schottky barrier height. Shown in **Figures 6B,D** is the example of a metal in interfacial contact with the P(+) and P(−) of a ferroelectric, e.g., Au in contact with PZT. Pintilie and Alexe quantitatively expressed the band-bending of ferroelectric semiconductors by introducing the surface polarization as a sheet of surface charge located at a finite distance from the electrode interface, with a modified built-in potential V_{bi}' at the ferroelectric surface given by Equation (6) (Jones et al., 2008):

$$V_{\mathrm{bi}}' = V_{bi} \pm P\delta/\varepsilon_0\varepsilon_{\mathrm{st}} \tag{6}$$

where P is the component of the polarization that is perpendicular to the sample surface, ε_0 is the permittivity of free space, ε_{st} is the low-frequency (or static) dielectric constant, and δ is the interface thickness layer which is typically assumed to be on the order of a single unit cell. This gives a quantitative estimate of the degree of band-bending at polarized ferroelectric surfaces, as has been confirmed by recent investigations on PZT, $BaTiO_3$, and $BiFeO_3$ (Pintilie and Alexe, 2005; Pintilie et al., 2005, 2014). For *n*-type ferroelectric semiconductors interfaced to metals, the P(−) polarized surface will cause the Schottky barrier to be higher as compared to the unpolarized P(0), shown in **Figure 6D**. Correspondingly, the P(+) polarized surfaces will serve to either lower or completely reverse the Schottky barrier, shown in **Figure 6B**. Whether the bands on the P(+) surface bend downward or upward depends on the magnitude of the

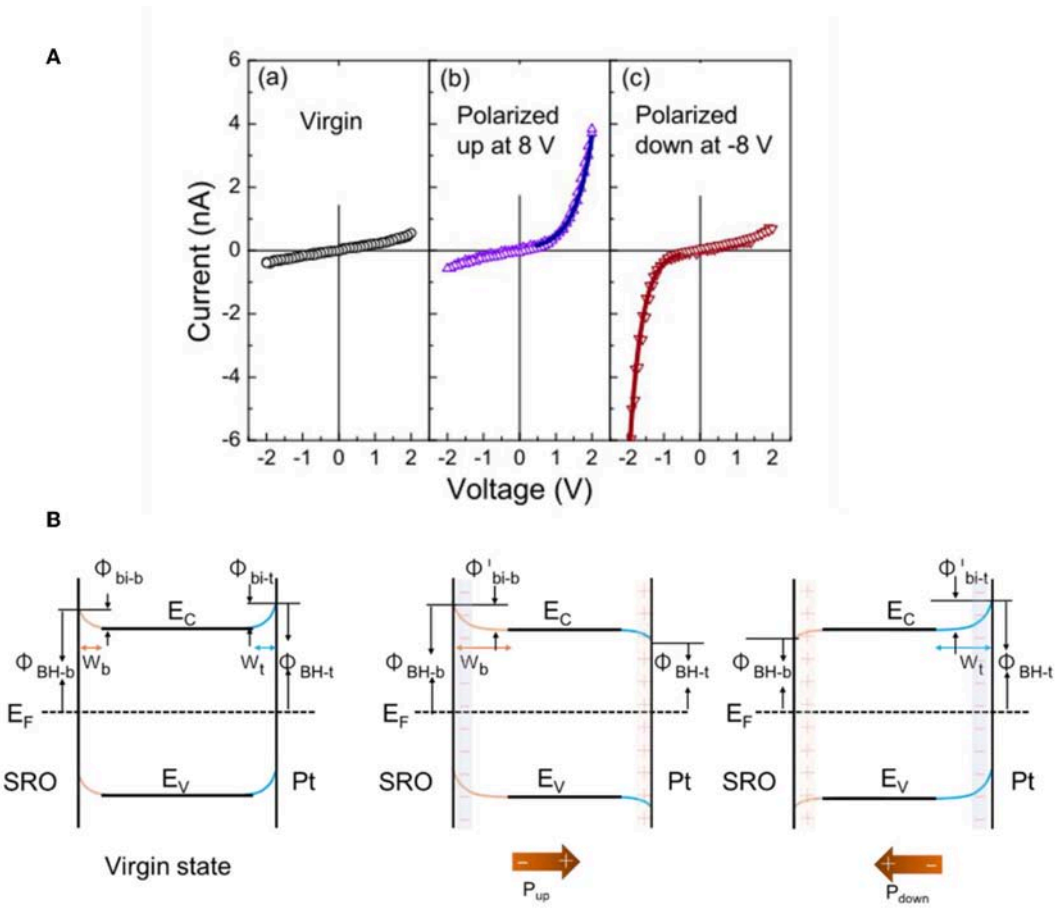

FIGURE 7 | Band-bending at SRO/BFO/Pt heterojunctions. **(A)** I–V characteristics at left: virgin state, middle: polarized up state, and right: polarized down state. **(B)** Proposed energy band diagrams at different ferroelectric polarization states. Left: virgin state. Middle: polarization up state. Right: polarization down state. Figures adapted from Wang et al. (2011). Copyright 2011 AIP Publishing.

band-bending introduced by the spontaneous polarization, as determined by Equation (6). However, the surface polarization of many strong ferroelectrics can have a predominating impact, e.g., changes to the Schottky barrier heights of up to ∼1.1 eV for $BaTiO_3$ and up to ∼0.9 eV for PZT (Pintilie et al., 2014).

EXPERIMENTAL INVESTIGATIONS OF SCHOTTKY BARRIER HEIGHTS AND BAND BENDING AT FERROELECTRIC-METAL INTERFACE

Manipulation of Interfacial Electrical Transport and Charge Separation

The strong polarization-dependent manipulation of the Schottky barrier at ferroelectric-metal interfaces has been investigated in several recent studies, such as has been typically characterized by current-voltage (I–V) curves or X-ray photoelectron spectroscopy (Yang et al., 2010; Alexe and Hesse, 2011; Cao et al., 2012a). For example, recent studies have focused on their rectifying electrical behavior, such as to yield switchable diodes, or in facilitating charge separation and transport in solar cells with the ferroelectric as the light absorber. It has been shown that by reversing the polarization of the ferroelectric the Schottky barrier can be reversed and induce a switchable diode behavior at the interface (Wang et al., 2011). For example, Wang et al. characterized the interfacial Schottky barrier between platinum/$BiFeO_3$ (BFO) using current-voltage hysteresis, shown in **Figure 7A**. A thin film of ferroelectric BFO was grown over a $SrTiO_3$ (001) (SRO) single crystal and ∼100 μm platinum dots were deposited over the BFO film. The Pt and SRO acted as the two electrodes to measure the electrical current and exhibited distinct hysteresis behavior that indicated large resistive switching between −6 and +6 V. Both the positive and negative polarization were characterized independently. First, the SRO/BFO/Pt heterojunction was polarized to induce upward and downward polarization, shown in **Figure 7B** with the two polarization directions. The I-V curves show that for the virgin state without poling, the current is very small and increases linearly with voltage at both positive and negative bias. For the polarized-up state, the current increases exponentially with the positive applied voltage, i.e., SRO as the anode and Pt as the cathode, but increases much more slowly with negative applied voltage. This shows a forward diode-like behavior. For the polarized down state, the current shows a reverse diode behavior. This switchable diode behavior demonstrated that the Schottky barriers between the *n*-type semiconductor ferroelectric BFO and metallic electrodes have been changed by the polarization switching. Changes in the interfacial band structure with the two different polarizations for the SRO/BFO/Pt sandwich are illustrated in **Figure 7B**. In the virgin state, the Schottky barrier heights at both interfaces are sufficiently large owing to the larger

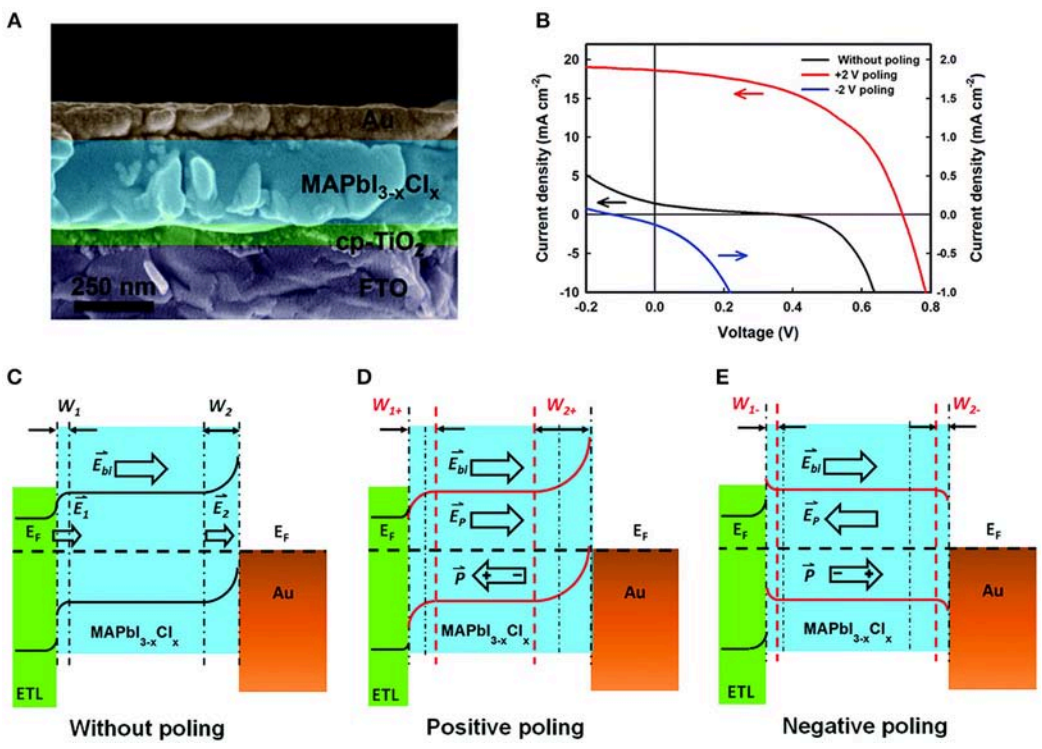

FIGURE 8 | Band-bending at TiO_2/$MAPbI_{3-x}Cl_x$/Au heterojunctions. **(A)** SEM of the ferroelectrics-based solar cell (left) and J–V plot (right). **(B)** Proposed electronic band structure under different polarization conditions. **(C)** Without poling. **(D)** Positive poling. **(E)** Negative poling. Figures adapted from Chen et al. (2015). Copyright 2015 Royal Society of Chemistry.

work functions of the SRO and Pt contacts compared to that for BFO. This is consistent with the very small currents. For positive polarization, the Schottky barrier becomes reversed on the Pt side, forming an Ohmic contact, with the cell behaving like a forward diode as shown in **Figure 7B** (middle). For the opposite ferroelectric polarization, the Schottky barrier becomes reversed to form an Ohmic contact on the SRO side, and the cell behaves like a reverse diode [**Figure 7B** (right)]. These observations are consistent with Equation 6 and demonstrate the modulation of the Schottky barrier using the ferroelectric polarization at the interfaces.

Ferroelectric-based solar cells have been the subject of many recent investigations owing to their switchable photocurrents and higher-than-bandgap open circuit photovoltages, including for $BiFeO_3$, PZT, $BaTiO_3$, and Bi_2FeCrO_6 (Moubah et al., 2012; Zenkevich et al., 2014; Zheng et al., 2014; Nechache et al., 2015). For example, modification of the Schottky barrier height and depletion region at a ferroelectric-metal interface were investigated by Chen et al. and found to achieve solar cells with power conversion efficiencies of up to 6.7% and photocurrents of $\sim$19 mA cm^{-2} on electrically-poled samples (Chen et al., 2015). The ferroelectric methylammonium lead trihalide ($MAPbX_3$) (FE-MAP) was used with a configuration of TiO_2/FE-MAP/Au, shown in **Figure 8A**. Electric poling of $\pm$5 V DC voltage was used to switch the domain alignments (**Figure 8B**). The proposed band structure of all three subunits of the solar cell is illustrated in **Figures 8C–E**. In the pristine state, i.e., no poling, a Schottky barrier forms at the ferroelectric/Au interface owing to the greater work function of Au. At the other side, a compact TiO_2 thin layer serves as the *n*-type electron transport layer (ETL). The bands in $MAPbX_3$ are bent downward and upward at the TiO_2/ferroelectric and the ferroelectric/Au interfaces, respectively, shown in **Figure 8C**. Upon irradiation of the cell the two depletion regions drive the separation of the electron-hole pairs, with larger depletion regions favoring a more efficient charge separation. With no electrical poling, the solar cell gives a power conversion efficiency of only $\sim$0.09%, a photocurrent of 1.47 mA cm^{-2} and an open circuit photovoltage of 0.37 V. However, a positive electric poling of the ferroelectric at +0.2 V leads to significantly enhanced band bending, i.e., a higher Schottky barrier height at the ferroelectric-Au interface that widens the depletion region for more efficient charge separation, illustrated in **Figure 8D**. This gives a dramatically higher power conversion efficiency of 6.7%, a photocurrent of 18.5 mA cm^{-2} and an open circuit voltage of 0.72 V. Thus, the direction and magnitude of the surface polarization can be effectively used to manipulate the interfacial barrier heights, which for solar cell designs can yield a more efficient charge separation and higher open circuit voltage.

Facilitating Hot Carrier Extraction Using Ferroelectrics

While there are many recent investigations into the utility of ferroelectric-metal interfaces for charge separation in solar cells, currently very few studies have focused on the effects of the photo-excitation of the localized SPR of the metallic nanoparticles. The excitation of the localized SPR can lead to the efficient absorption of photons and the generation of hot carriers with sufficiently high energies compared to the Schottky barrier in order to facilitate injection. For example, Schottky barrier heights for several metal-ferroelectric combinations have been measured to fall within the range of $\sim$0.1 to 0.9 eV, such as those found for PZT-Au interfaces of $\sim$0.3 eV and $BaTiO_3$-Cu interfaces at 0.2 eV (Pintilie et al., 2014). Thus, the excitation of the localized SPR and the generation of hot carriers at energies only a few hundred millielectron volts above the Fermi level are sufficient for injection over the Schottky barrier and into the ferroelectric in many cases. The critical role of the barrier height in the injection of electrons from metals into semiconductors was first modeled by Fowler in the early 1900s, as given in Equation (7) (Fowler, 1931):

$$Y_{Fow}(h\nu) \approx \frac{1}{8E_F}\frac{(h\nu - \phi_b)^2}{h\nu} \tag{7}$$

where Y_{Fow} is the Fowler yield, h is Planck's constant; ν is the incident light frequency; ϕ_B is the barrier height at the interface, and E_F is the Fermi energy of the metal. This is a semiclassical model with the basic assumption that the kinetic energy of the hot electrons normal to the barrier must be greater than the barrier height. This equation shows that injection of hot carriers is proportional to the square of the barrier height and can be manipulated by interfacial ferroelectric polarization. Theoretical calculations have been used to determine the optimal energetic structure at the interface and have suggested efficiency limits of about 1–10% under the most optimistic conditions (Leenheer et al., 2014). Further studies, however, which take into account anisotropic particle shapes that impact the electron-phonon scattering events and diffuse reflections, have shown that these factors can significantly increase the hot electron injection efficiency up to a higher efficiency limit of about 20% (Blandre et al., 2018), which is a factor of four greater than Fowler's limiting efficiency. Only a few recent investigations have reported the use of metal-ferroelectric interfaces to further enhance the hot carrier injection efficiency, as described below.

Hot Charge Injection at Buried Nano-Au/PZT Interfaces

The earliest research efforts focused on extracting hot charge carriers using non-ferroelectric semiconducting oxides, especially TiO_2, as described above. Despite the intense surge of interest in this area, the resulting efficiencies are usually very low, and a detailed understanding of the hot carrier process has remained unclear. Ferroelectric-interfaced plasmonic nanoparticles represent a relatively unexplored and fertile research ground, wherein by contrast, the ferroelectric polarization can be used to systematically manipulate the Schottky barrier height and the extent of the depletion region as a function of the ferroelectric surface polarization and applied poling field. In the first reported study by Wang et al., solar cells were constructed using a ferroelectric $Pb(Ti_{1-x}Zr_x)O_3$ (PZT) film that was patterned with an array of Au nanoparticles with lateral dimensions of 270 $\times$ 270 nm^2 and a thickness of $\sim$60 nm.

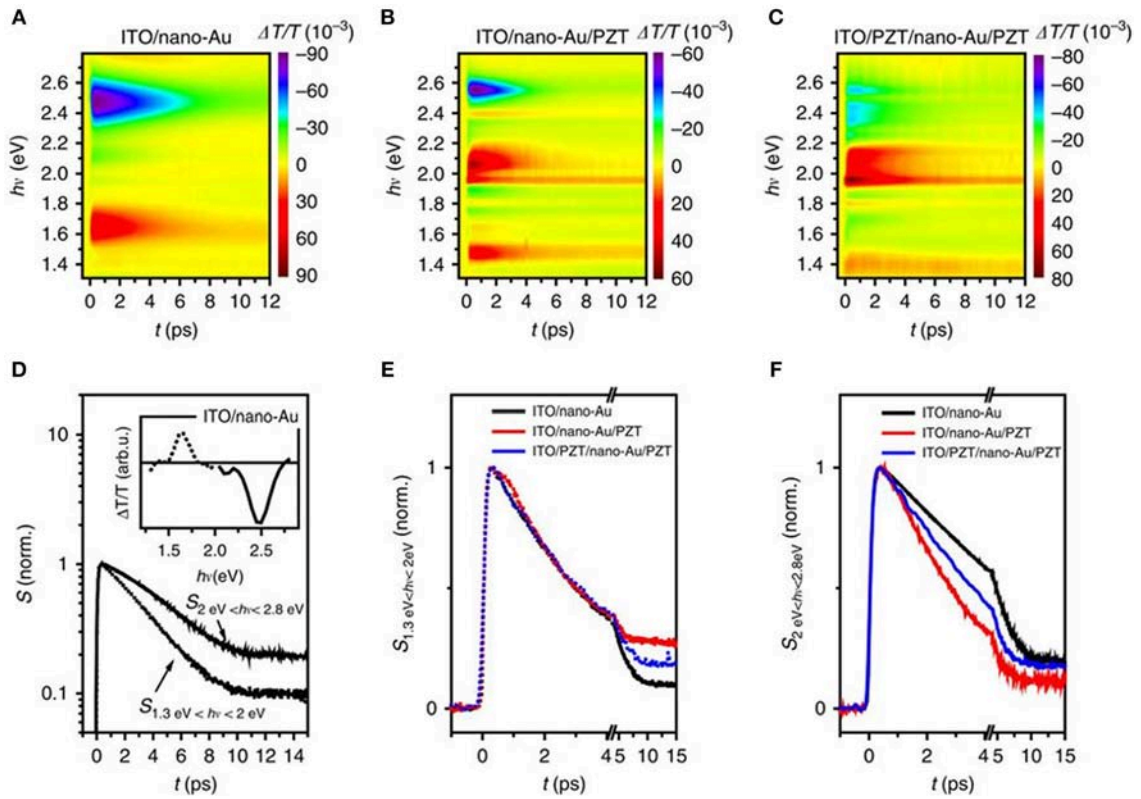

FIGURE 9 | Transient absorbance spectroscopy of the plasmonic-ferroelectric hybrids. Time evolution of ΔT/T for **(A)** ITO/nano-Au, **(B)** ITO/nano-Au/PZT, and **(C)** ITO/PZT/nano-Au/PZT, following photoexcitation with 70 fs ultraviolet pulses at 400 nm. **(D)** The time evolution of the response for ITO/nano-Au in the low and high frequencies, respectively. Comparison of the **(E)** low-frequency and **(F)** high-frequency dynamics between the three nano-Au hybrids. Figure adapted from Wang et al. (2016). Copyright 2016 Nature Publishing Group.

For this relatively large size of Au nanoparticles, the radiative re-emission of photons significantly predominates compared to hot carrier generation, as described in the Background section. Further, the distribution of hot carriers is calculated to be only on the order of a few tenths of an eV different than the Fermi energy. However, prior studies have found the Schottky barrier of PZT-Au interfaces to be as low as ∼0.1 eV (Pintilie et al., 2014). The photocurrent was still boosted by nearly an order of magnitude when aligning the polarization direction in PZT and reversing the Schottky barrier with the electrolyte. This increased the external quantum efficiency from ∼0.1 to 0.3% at 600 nm, which is at significantly lower energies than the PZT band gap of ∼3.6 eV.

Broadband transient absorbance (TA) measurements were used to characterize the hot charge transfer between the Au nanoparticles and PZT. Femtosecond optical pulses centered at a wavelength of 400 nm were used for excitation, i.e., at photon energies below the PZT band gap. The nano-Au array on ITO/glass showed two distinct, spectrally well-separated components in the transient spectra, shown in **Figures 9A,D**: one increased transmission peak (ΔT/T, or decreased absorption peak) at 1.65 eV and the other reduced transmission peak at 2.5 eV. The former was linked to the photoinduced changes in the localized SPR absorption at 1.5 eV, and the latter was attributed to the bulk-like response of Au, governed by the photoinduced changes in the density of states for the d-band to Fermi level transition. A reduced transmission indicates the increased density of states after photo-excitation.

For devices of ITO/nano-Au/PZT and ITO/PZT/nano-Au/PZT, shown in **Figures 9B,C**, the time evolution of the low energy (1.3–2 eV) and the high energy (2.0–2.8 eV) responses were analyzed (**Figures 9E,F**). The relaxation dynamics of the low-energy part are similar for all three devices and can all be fitted with a single exponential decay. However, the high energy component shows a non-exponential relaxation, with the following trend in rates $k_{ITO/nano-Au/PZT} > k_{ITO/PZT/nano-Au/PZT} > k_{ITO/nano-Au}$. These results suggested that: (1) there are additional decay channels for the relaxation of the photo-excited density of states for nano-Au/PZT, and (2) nano-Au to PZT charge transfer yielded the accelerated relaxation of the bulk-like Au density of states. However, the photoinduced transmission on the poled ITO/PZT/nano-Au/PZT samples, i.e., at fields of +10 and −10 V, resulted in only minor changes in the relaxation dynamics. The conclusion suggested that the polarization at the PZT surface had little impact on the band bending and charge injection efficiency, in

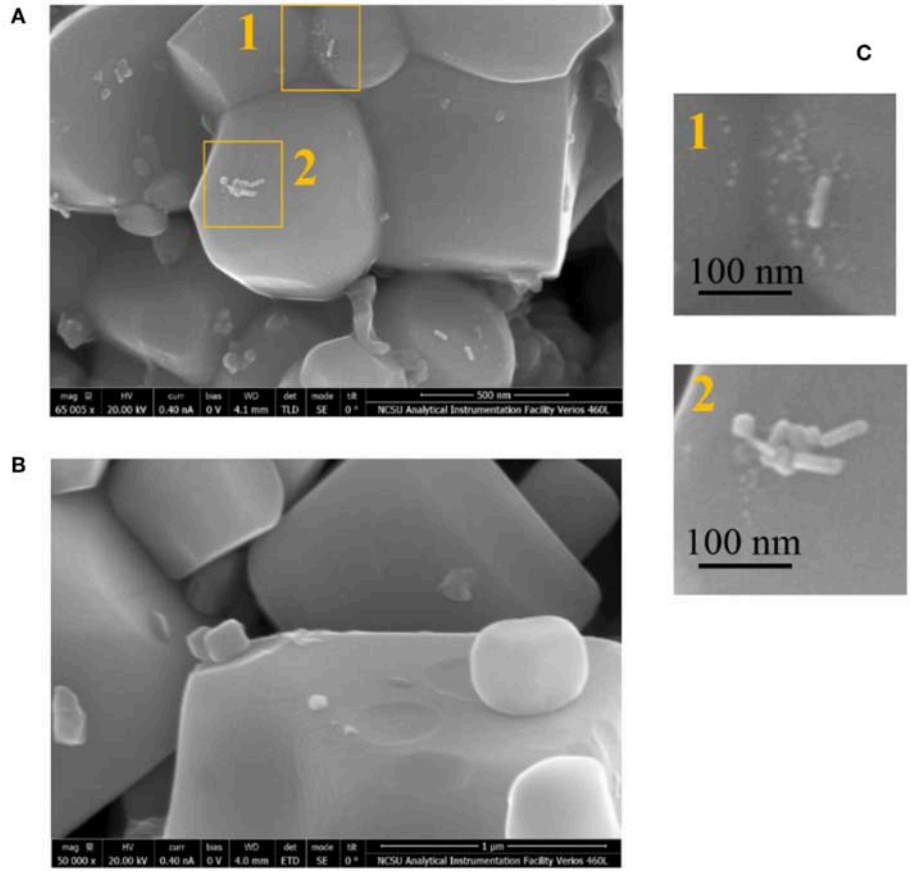

FIGURE 10 | SEM images of $PbTiO_3$ particles impregnated with and without AuNRs (**A,B**, respectively; Scale bar: 1 μm). The insets, 1 and 2 in **(C)**, show higher magnification SEM images of the $PbTiO_3$ surfaces after the photochemical reduction of Pt driven by light excitation of the localized SPR of the AuNRs and hot carrier injection. The Pt islands are confirmed by EDS scanning and are visible as white dots near the deposited AuNRs to within ∼100 nm on the surfaces. Figure adapted from Ortiz et al. (2018). Copyright 2018 American Chemical Society.

surprising contradiction to prior studies on ferroelectric-based solar cells. Independent characterization of the Schottky barrier heights could help elucidate their role in impacting the injection of hot carriers.

Hot Charge Injection From Au Nanoparticles to $PbTiO_3$: Photochemical Reactions

Direct evidence of hot carrier injection from metal to ferroelectric $PbTiO_3$ (PT) particles was first reported by Ortiz et al. via the photochemical reduction of Pt on composite AuNRs/PT particles (Ortiz et al., 2018). The AuNR particles were synthesized as long nanorods with high aspect ratios of ∼5:1 and impregnated onto micron-sized ferroelectric PT particles. The AuNRs/PT particles were suspended in an aqueous solution of H_2PtCl_6 with methanol as a sacrificial agent. The light-driven reaction proceeds by the photochemical reduction of the Pt(IV) cations in solution to form Pt(s) islands on the PT surfaces, together with the concomitant oxidation of methanol to carbon dioxide. The AuNRs/PT particles were irradiated by photons from 976 nm near IR light (NIR, 2.0 W/cm^2), thus exciting the localized SPR and excluding the direct bandgap excitation of the ferroelectric PT. After irradiation under 976 nm light for 30 min, the AuNR/PT particles were then characterized by SEM to exhibit photochemically deposited Pt islands over the surfaces. The Pt islands were localized within a region about <100 nm from the AuNRs on the PT surfaces, as shown in **Figure 10A** (regions 1 and 2, see **Figure 10C**) and confirmed using EDX scans. As a control, no Pt islands were found to grow on the ferroelectric PT particles in the absence of AuNRs (**Figure 10B**). These results demonstrated that hot carrier injection occurs from the AuNR to ferroelectric particles, which drove the photochemical reduction of the Pt at the surfaces.

As $PbTiO_3$ is a known photocatalyst for water reduction when excited by bandgap light, it is anticipated that the hot carrier injection at the Au-PT interface should also lead to the light-driven production of molecular hydrogen at its surfaces, but with the use of photons lower than bandgap energies. In a study by Wang et al., the first example of water reduction to molecular hydrogen driven by hot carrier injection was demonstrated for the combination of Pt-end-capped AuNRs, i.e., Pt-AuNRs, and ferroelectric PT. Similar conditions were employed for the photochemical deposition of Pt, which involved

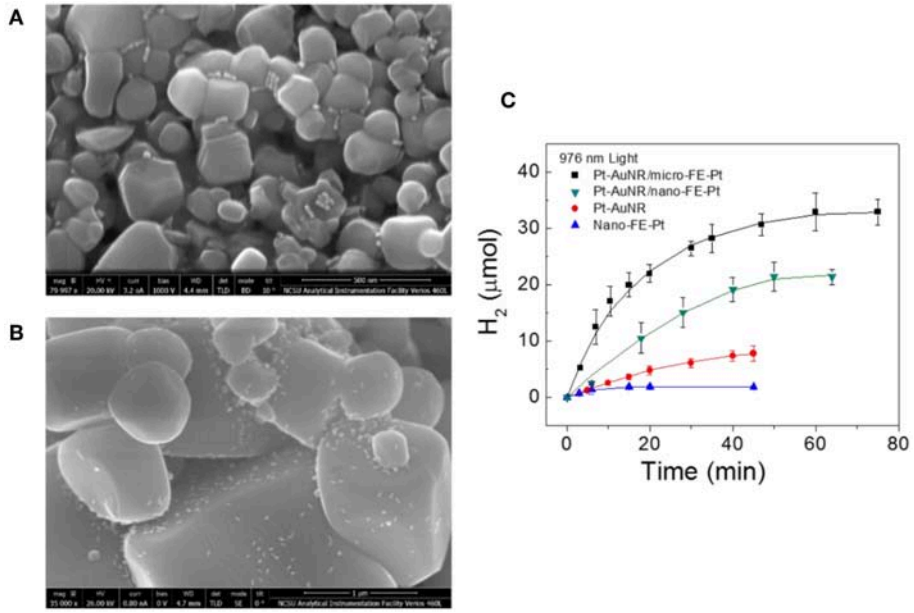

FIGURE 11 | SEM images of ferroelectric PT particles impregnated with Pt-end-capped AuNRs, for the **(A)** nano-PT particles with dimensions of ∼125 nm and for the **(B)** micro-PT particles with dimensions of ∼1 μm. The AuNRs appear as white dots, with scale bars of 500 nm. **(C)** Hydrogen production vs. time for the Pt-AuNR/micro-FE-Pt and Pt-AuNR/nano-FE-Pt particles under near-IR irradiation. For comparison, photocatalytic hydrogen production for Pt-AuNRs and nano-PT particles are also plotted. Figure adapted from Ortiz et al. (2018). Copyright 2018 American Chemical Society.

irradiating the samples with near IR light at a wavelength of 976 nm and methanol as a sacrificial reagent. For the ferroelectric PT, both micron-sized (micro-PT; average diameter of ∼1 μm) and nanosized (nano-PT; average diameter of ∼125 nm) particles were used to determine the relative impacts of the surface area and loading with AuNRs. Shown in **Figures 11A,B**, the SEM images show that the AuNRs are distributed evenly over the nano-PT and micro-PT surfaces. The average loading of the AuNRs on the particles were ∼0.60 (AuNRs:PT) for nano-PT and ∼280 for 1 μm micro-PT. As the AuNRs are relatively sparsely deposited on the PT surfaces, the net "effective PT surface area," i.e., the area beneath the AuNR and in its vicinity that the hot electrons can diffuse (∼100 nm), is nearly a constant, enabling a direct comparison of the hydrogen production rates. Using sub-bandgap photons with a wavelength of 976 nm and a power density of 2.0 W cm^{-1}, molecular hydrogen was produced with the AuNRs/PT particles at initial rates of 1.41 ± 0.40 μmol H_2 min^{-1} for nano-PT particles and 0.88 ± 0.27 μmol H_2 min^{-1} for micro-PT particles, as shown in **Figure 11C**. As controls, the ferroelectric PT particles alone showed little detectable activity, while the Pt-end-capped AuNRs alone exhibited a low initial photocatalytic rate of ∼0.25 μmol H_2 min^{-1}. For equal amounts of plasmonic Au nanorods, the initial photocatalytic rates for hydrogen production were thus increased by a factor of ∼5.6 when interfaced with the ferroelectric PT particles. A photon efficiency of up to ∼0.28% for near-infrared light was measured, significantly higher than for previously reported metal-semiconductor combinations (0.01–0.1%) (Pu et al., 2013; Robatjazi et al., 2015).

The photocatalysis experiments have demonstrated that AuNRs can inject hot electrons into the ferroelectric particles upon irradiation of their localized SPR, and that the injected electrons are driving reduction reactions at the ferroelectric surfaces. It is notable that the interfaces between the plasmonic and the ferroelectric particles were not controlled in terms of positive or negative surface polarization. The natural randomization of the surface sites over which the AuNRs are deposited will lead to these making interfacial contact over a fraction of surfaces with suitable polarization directions, which favors hot electron injection over a Schottky barrier, i.e., the P(+) surfaces. Yet, a significant enhancement of the photocatalytic rates is found.

To further probe how the SPR-generated hot electrons are involved in the photocatalytic reaction, the initial hydrogen production rates were measured as a function of the near-IR irradiation power, plotted in **Figure 12**. Interestingly, a non-linearly increasing rate ∼ power relationship is observed, in contrast to the linear relationship for the same reaction usually observed on metal-only particle surfaces. The non-linear relationship is possibly introduced during the charge injection process: only when the hot electrons have an energy higher than the interfacial energy barrier can they be transferred to ferroelectric particles and participate in the chemical reaction. The photo-excited electron energy, i.e., shown in **Figure 1C**, follows Fermi-Dirac distribution:

$$f(E) = \frac{1}{\exp[(E - E_F)/k_B T] + 1} \tag{8}$$

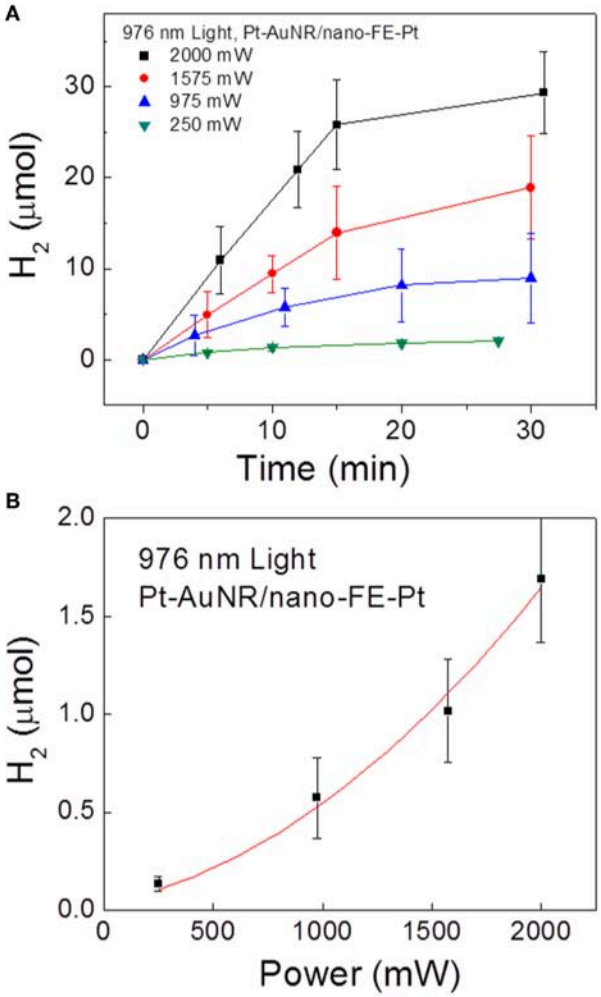

FIGURE 12 | Photocatalytic H_2 gas production on Pt-AuNR/nano-PT particles under 976 nm light at power densities of 250, 975, 1,575, and 2,000 mW. **(A)** Measured H_2 production vs. time at the different irradiation powers, and **(B)** initial reaction rate vs. irradiation power. Figure adapted from Ortiz et al. (2018). Copyright 2018 American Chemical Society.

where f is the probability an energy level is filled, E_F is the Fermi level, k_B is the Boltzmann constant, and T is the effective temperature. Given that recent models show that the effective electron temperature increases linearly with respect to the fluency of the photon flux, the total number of "high energy" hot electrons exceeding a large threshold value increases non-linearly, as described previously (Manjavacas et al., 2014). This is consistent with the observed non-linear reaction rate ~ irradiation power relationship.

In these studies using Au nanoparticle interfaced with ferroelectrics, the Au nanoparticles were utilized to generate hot electrons because of their efficiency in harvesting solar energies down into the infrared wavelengths (Hartland, 2011; Ye et al., 2012; Jing et al., 2014; Kakekhani and Ismail-Beigi, 2016). The ferroelectrics, PT and PZT, were selected owing to their large and stable ferroelectric polarization, and they have been investigated in several prior studies that demonstrated a strong polarization-dependent modulation of the Schottky barrier height with the surface Au nanoparticles. For example, the ferroelectric PT has been characterized as an *n*-type semiconductor with a bandgap of ~2.7 eV (Reddy and Parida, 2013) and an electron affinity χ of ~3.5 eV (Pintilie et al., 2008; Li et al., 2012; Suriyaprakash et al., 2017). When Au (work function $\Phi_M = 5.1$ eV) is in contact with a normal semiconductor with a similar electron affinity as that of PT, the semiconductor bands bend upward at their surface, leading to a low-energy Schottky barrier on the order of ~0.1–0.3 eV (Zhang and Yates, 2012; Pintilie et al., 2014). On the P(+) oriented surfaces of PT, the band bending is decreased or even reversed, while on the P(–) surfaces of PT the band bending will be further increased. It is conjectured that the lower energy barrier would favor the charge injection from Au to ferroelectric particles, leading to a higher efficiency in hot charge injection. In addition, it is also proposed that the surface polarization in the ferroelectric particles could trap the injected electrons at the domain boundaries (Wu et al., 2012; Sluka et al., 2013), which prevents them from flowing back to the metal (being quenched) and extending their lifetimes.

CONCLUSIONS

In summary, the synergistic combination of plasmonic and ferroelectric particles represents a novel pathway for harnessing the efficient production and injection of hot carriers generated by the excitation of localized SPR. The energetic distribution of hot carrier generation in plasmonic nanoparticles is a sensitive function of the particle sizes and chemical compositions, and under optimal conditions, can result in the generation of hot carriers with energies that are from ~0.1 to 1.5 eV above and below the Fermi level. Concomitantly, a detailed understanding of the energetic structure at metal-ferroelectric interfaces is emerging and demonstrating that the modulation of the Schottky barrier height and band bending can be manipulated by the ferroelectric surface polarization. The Schottky barrier height, for example, typically varies from ~0.1 to 0.4 eV for common metal-ferroelectric interfaces and is thereby compatible with the energetic distribution of hot carrier generation in plasmonic nanoparticles. These synergistic features of their electronic properties have resulted in several novel studies involving the use of metal-ferroelectric interfaces for investigating switchable diode behavior as well as solar cells with high power conversion efficiencies. Most promisingly, these results show that by combining plasmonic and ferroelectric particles, novel photoelectrochemical and photocatalyst designs are possible for solar energy conversion.

FUTURE PROSPECTS

Currently, the field of ferroelectric-interfaced plasmonic nanoparticles is still in its infancy, with only a very limited number of studies in this novel direction. Future

investigations will aid in more deeply understanding the underlying mechanisms of hot electron generation and injection at metal-ferroelectric interfaces, designing more optimal integrated systems, and using these catalysts to efficiently drive photocatalytic reactions at the surfaces using solar energy. Among the prominent current challenges, the quantitative relationship between the charge injection/reaction rate and the ferroelectric polarization needs to be elucidated, such as via characterization of the band banding using I–V curves and X-ray photoelectron spectroscopy (XPS) (Chen and Klein, 2012). Second, the reactive sites, including both reductive and oxidative sites, need to be mapped out over these integrated systems. Third, the ferroelectric-plasmonic systems can be further tuned through changes in composition, e.g., in order to tune the bandgap of the ferroelectric or its surface polarization to facilitate changes in interfacial band-bending and charge injection. Fourth, the exposed facets of the ferroelectrics may play an important role in the Schottky barrier height. For example, facet-dependent photocatalytic activity is a common feature of photocatalyst particles, such as what has been reported for Cu_2O (Yuan et al., 2016). Controlling the anisotropic growth of ferroelectric particles can also serve as a means in tuning the photocatalytic activity. Finally, alternative plasmonic materials can also be investigated which are less expensive, such as silver or copper. It can be anticipated that the optimization of interfacial metal-ferroelectric systems will offer remarkable new capabilities to achieve high solar conversion efficiencies at low-energy wavelengths, i.e., extending into the infrared wavelengths, and which is not possible in conventional semiconductor-based systems.

AUTHOR CONTRIBUTIONS

VK, PM, and GW wrote the manuscript. All authors have intellectual contributions to this work.

FUNDING

This work was supported by the Chemistry Department, North Carolina State University.

REFERENCES

Adleman, J. R., Boyd, D. A., Goodwin, D. G., and Psaltis, D. (2009). Heterogenous catalysis mediated by plasmon heating. *Nano Lett.* 9, 4417–4423. doi: 10.1021/nl902711n

Alexe, M., and Hesse, D. (2011). Tip-enhanced photovoltaic effects in bismuth ferrite. *Nat. Commun.* 2:256. doi: 10.1038/ncomms1261

Apostol, N. G., Stoflea, L. E., Lungu, G. A., Chirila, C., Trupina, L., Negrea, R. F., et al. (2013). Charge transfer and band bending at Au/Pb(Zr0.2Ti0.8)O_3 interfaces investigated by photoelectron spectroscopy. *Appl. Surf. Sci.* 273, 415–425. doi: 10.1016/j.apsusc.2013.02.056

Arney, D., Watkins, T., and Maggard, P. A. (2011). Effects of particle surface areas and microstructures on photocatalytic H_2 and O_2 production over $PbTiO_3$. *J. Am. Ceram. Soc.* 94, 1483–1489. doi: 10.1111/j.1551-2916.2010.04262.x

Atwater, H. A., and Polman, A. (2010). Plasmonics for improved photovoltaic devices. *Nat. Mater.* 9, 205–213. doi: 10.1038/nmat2629

Bardeen, J. (1947). Surface states and rectification at a metal semi-conductor contact. *Phys. Rev.* 71, 717–727. doi: 10.1103/PhysRev.71.717

Blandre, E., Jalas, D., Petrov, A. Y., and Eich, M. (2018). Limit of efficiency of generation of hot electrons in metals and their injection inside a semiconductor using a semiclassical approach. *ACS Photonics* 5, 3613–3620. doi: 10.1021/acsphotonics.8b00473

Bonnell, D. A., and Kalinin, S. V. (2002). "Local polarization, charge compensation, and chemical interactions on ferroelectric surfaces: a route toward new nanostructures," in *Ferroelectric Thin Films X*, eds S. R. Gilbert, S. TrolierMcKinstry, Y. Miyasaka, and D. J. Wouters (New York, NY: Cambridge University Press), 317–328. doi: 10.1557/PROC-688-C9.5.1

Bowen, C. R., Kim, H. A., Weaver, P. M., and Dunn, S. (2014). Piezoelectric and ferroelectric materials and structures for energy harvesting applications. *Energy Environ. Sci.* 7, 25–44. doi: 10.1039/C3EE42454E

Brandt, N. C., Keller, E. L., and Frontiera, R. R. (2016). Ultrafast surface-enhanced raman probing of the role of hot electrons in plasmon-driven chemistry. *J. Phys. Chem. Lett.* 7, 3179–3185. doi: 10.1021/acs.jpclett.6b01453

Brongersma, M. L., Halas, N. J., and Nordlander, P. (2015). Plasmon-induced hot carrier science and technology. *Nat. Nanotechnol.* 10, 25–34. doi: 10.1038/nnano.2014.311

Bueno Alejo, C. J., Fasciani, C., Grenier, M., Netto-Ferreira, J. C., and Scaiano, J. C. (2011). Reduction of resazurin to resorufin catalyzed by gold nanoparticles: dramatic reaction acceleration by laser or LED plasmon excitation. *Catal. Sci. Technol.* 1, 1506–1511. doi: 10.1039/c1cy00236h

Cai, Z. Y., Xing, X. R., Yu, R. B., and Sun, X. Y. (2007). Morphology-controlled synthesis of lead titanate powders. *Inorg. Chem.* 46, 7423–7427. doi: 10.1021/ic700966n

Cao, D., Wang, C., Zheng, F., Dong, W., Fang, L., and Shen, M. (2012a). High-efficiency ferroelectric-film solar cells with an n-type Cu_2O cathode buffer layer. *Nano Lett.* 12, 2803–2809. doi: 10.1021/nl300009z

Cao, D., Wang, C., Zheng, F., Fang, L., Dong, W., and Shen, M. (2012b). Understanding the nature of remnant polarization enhancement, coercive voltage offset and time-dependent photocurrent in ferroelectric films irradiated by ultraviolet light. *J. Mater. Chem.* 22, 12592–12598. doi: 10.1039/c2jm32102e

Chen, B., Shi, J., Zheng, X., Zhou, Y., Zhu, K., and Priya, S. (2015). Ferroelectric solar cells based on inorganic-organic hybrid perovskites. *J. Mater. Chem. A* 3, 7699–7705. doi: 10.1039/C5TA01325A

Chen, F., and Klein, A. (2012). Polarization dependence of Schottky barrier heights at interfaces of ferroelectrics determined by photoelectron spectroscopy. *Phys. Rev. B* 86:094105. doi: 10.1103/PhysRevB.86.094105

Christopher, P., Xin, H. L., and Linic, S. (2011). Visible-light-enhanced catalytic oxidation reactions on plasmonic silver nanostructures. *Nat. Chem.* 3, 467–472. doi: 10.1038/nchem.1032

Clavero, C. (2014). Plasmon-induced hot-electron generation at nanoparticle/metal-oxide interfaces for photovoltaic and photocatalytic devices. *Nat. Photonics* 8, 95–103. doi: 10.1038/nphoton.2013.238

Cohen, M. L. (1979). Schottky and Bardeen limits for Schottky barriers. *J. Vacuum Sci. Technol.* 16, 1135–1136. doi: 10.1116/1.570176

Cowley, A. M., and Sze, S. M. (1965). Surface states and barrier height of metal-semiconductor systems. *J. Appl. Phys.* 36, 3212–3220. doi: 10.1063/1.1702952

Daniel, M. C., and Astruc, D. (2004). Gold nanoparticles: assembly, supramolecular chemistry, quantum-size-related properties, and applications toward biology, catalysis, and nanotechnology. *Chem. Rev.* 104, 293–346. doi: 10.1021/cr030698+

Dimoulas, A., Tsipas, P., Sotiropoulos, A., and Evangelou, E. K. (2006). Fermi-level pinning and charge neutrality level in germanium. *Appl. Phys. Lett.* 89:252110. doi: 10.1063/1.2410241

Fowler, R. H. (1931). The analysis of photoelectric sensitivity curves for clean metals at various temperatures. *Phys. Rev.* 38, 45–56. doi: 10.1103/PhysRev.38.45

Fujishima, A., and Honda, K. (1972). Electrochemical photolysis of water at a semiconductor electrode. *Nature* 238:37. doi: 10.1038/238037a0

Giocondi, J. L., and Rohrer, G. S. (2001). Spatial separation of photochemical oxidation and reduction reactions on the surface of ferroelectric $BaTiO_3$. *J. Phys. Chem. B* 105, 8275–8277. doi: 10.1021/jp011804j

Giugni, A., Torre, B., Toma, A., Francardi, M., Malerba, M., Alabastri, A., et al. (2013). Hot-electron nanoscopy using adiabatic compression of surface plasmons. *Nat. Nanotechnol.* 8, 845–852. doi: 10.1038/nnano.2013.207

Glickstein, J. J., Salvador, P. A., and Rohrer, G. S. (2016). Multidomain simulations of coated ferroelectrics exhibiting spatially selective photocatalytic activity with high internal quantum efficiencies. *J. Mater. Chem. A* 4, 16085–16093. doi: 10.1039/C6TA07083C

Grinberg, I., West, D. V., Torres, M., Gou, G., Stein, D. M., Wu, L., et al. (2013). Perovskite oxides for visible-light-absorbing ferroelectric and photovoltaic materials. *Nature* 503:509. doi: 10.1038/nature12622

Hartland, G. V. (2011). Optical studies of dynamics in noble metal nanostructures. *Chem. Rev.* 111, 3858–3887. doi: 10.1021/cr1002547

Hoffmann, M. R., Martin, S. T., Choi, W. Y., and Bahnemann, D. W. (1995). Environmental applications of semiconductor photocatalysis. *Chem. Rev.* 95, 69–96. doi: 10.1021/cr00033a004

Hoggard, A., Wang, L.-Y., Ma, L., Fang, Y., You, G., Olson, J., et al. (2013). Using the plasmon linewidth to calculate the time and efficiency of electron transfer between gold nanorods and graphene. *ACS Nano* 7, 11209–11217. doi: 10.1021/nn404985h

Huang, Y.-C., Chang, S.-Y., and Jehng, J.-M. (2017). Photocatalytic H2 generation efficiencies of TiO_2 nanotube-based heterostructures grafted with ZnO nanorods, Ag nanoparticles, or Pd nanodendrites. *J. Phys. Chem. C* 121, 19063–19068. doi: 10.1021/acs.jpcc.7b05806

Ingram, D. B., and Linic, S. (2011). Water splitting on composite plasmonic-metal/semiconductor photoelectrodes: evidence for selective plasmon-induced formation of charge carriers near the semiconductor surface. *J. Am. Chem. Soc.* 133, 5202–5205. doi: 10.1021/ja200086g

Inoue, Y., Sato, K., and Sato, K. (1989). Photovoltaic and photocatalytic behaviour of a ferroelectric semiconductor, lead strontium zirconate titanate, with a polarization axis perpendicular to the surface. *J. Chem. Soc. Farad. Trans. 1* 85, 1765–1774. doi: 10.1039/f19898501765

Jain, P. K., Lee, K. S., El-Sayed, I. H., and El-Sayed, M. A. (2006). Calculated absorption and scattering properties of gold nanoparticles of different size, shape, and composition: applications in biological imaging and biomedicine. *J. Phys. Chem. B* 110, 7238–7248. doi: 10.1021/jp057170o

Jin, R. C., Cao, Y. C., Hao, E. C., Metraux, G. S., Schatz, G. C., and Mirkin, C. A. (2003). Controlling anisotropic nanoparticle growth through plasmon excitation. *Nature* 425, 487–490. doi: 10.1038/nature02020

Jing, H., Zhang, Q., Large, N., Yu, C., Blom, D. A., Nordlander, P., et al. (2014). Tunable plasmonic nanoparticles with catalytically active high-index facets. *Nano Lett.* 14, 3674–3682. doi: 10.1021/nl5015734

Jones, P. M., Gallardo, D. E., and Dunn, S. (2008). Photochemical investigation of a polarizable semiconductor, lead-zirconate-titanate. *Chem. Mater.* 20, 5901–5906. doi: 10.1021/cm8015116

Kakekhani, A., and Ismail-Beigi, S. (2016). Ferroelectric oxide surface chemistry: water splitting via pyroelectricity. *J. Mater. Chem. A* 4, 5235–5246. doi: 10.1039/C6TA00513F

Kakekhani, A., Ismail-Beigi, S., and Altman, E. I. (2016). Ferroelectrics: a pathway to switchable surface chemistry and catalysis. *Surf. Sci.* 650, 302–316. doi: 10.1016/j.susc.2015.10.055

Kalinin, S. V., and Bonnell, D. A. (2001). Local potential and polarization screening on ferroelectric surfaces. *Phys. Rev. B* 63:125411. doi: 10.1103/PhysRevB.63.125411

Kato, H., Asakura, K., and Kudo, A. (2003). Highly efficient water splitting into H_2 and O_2 over lanthanum-doped $NaTaO_3$ photocatalysts with high crystallinity and surface nanostructure. *J. Am. Chem. Soc.* 125, 3082–3089. doi: 10.1021/ja027751g

Kawai, T., and Sakata, T. (1980). Photocatalytic hydrogen-production from liquid methanol and water. *J. Chem. Soc. Chem. Comm.* 694–695. doi: 10.1039/c39800000694

Kurtin, S., McGill, T. C., and Mead, C. A. (1969). Fundamental transition in the electronic nature of solids. *Phys. Rev. Lett.* 22, 1433–1436. doi: 10.1103/PhysRevLett.22.1433

Leenheer, A. J., Narang, P., Lewis, N. S., and Atwater, H. A. (2014). Solar energy conversion via hot electron internal photoemission in metallic nanostructures: efficiency estimates. *J. Appl. Phys.* 115:134301. doi: 10.1063/1.4870040

Lewerenz, H.-J., and Peter, L. (2013). Photoelectrochemical water splitting: materials, processes and architectures. *R. Soc. Chem.* doi: 10.1039/9781849737739

Li, L., Salvador, P. A., and Rohrer, G. S. (2014). Photocatalysts with internal electric fields. *Nanoscale* 6, 24–42. doi: 10.1039/C3NR03998F

Li, L., Zhang, Y. L., Schultz, A. M., Liu, X., Salvador, P. A., and Rohrer, G. S. (2012). Visible light photochemical activity of heterostructured $PbTiO_3$-TiO_2 core-shell particles. *Cat. Sci. Technol.* 2, 1945–1952. doi: 10.1039/c2cy20202f

Li, X., Yu, J. G., Low, J. X., Fang, Y. P., Xiao, J., and Chen, X. B. (2015). Engineering heterogeneous semiconductors for solar water splitting. *J. Mater. Chem. A* 3, 2485–2534. doi: 10.1039/C4TA04461D

Linic, S., Aslam, U., Boerigter, C., and Morabito, M. (2015). Photochemical transformations on plasmonic metal nanoparticles. *Nat. Mater.* 14, 567–576. doi: 10.1038/nmat4281

Linic, S., Christopher, P., and Ingram, D. B. (2011). Plasmonic-metal nanostructures for efficient conversion of solar to chemical energy. *Nat. Mater.* 10, 911–921. doi: 10.1038/nmat3151

Liu, Z. W., Hou, W. B., Pavaskar, P., Aykol, M., and Cronin, S. B. (2011). Plasmon resonant enhancement of photocatalytic water splitting under visible illumination. *Nano Lett.* 11, 1111–1116. doi: 10.1021/nl104005n

Long, R., Li, Y., Song, L., and Xiong, Y. J. (2015). Coupling solar energy into reactions: materials design for surface plasmon-mediated catalysis. *Small* 11, 3873–3889. doi: 10.1002/smll.201403777

Lv, X., Wei, W., Zhao, P., Li, J., Huang, B., and Dai, Y. (2018). Tunable Schottky contacts in MSe_2/$NbSe_2$ (M = Mo and W) heterostructures and promising application potential in field-effect transistors. *Phys. Chem. Chem. Phys.* 20, 1897–1903. doi: 10.1039/C7CP07546D

Ma, X., Dai, Y., Yu, L., and Huang, B. (2014a). New basic insights into the low hot electron injection efficiency of gold-nanoparticle-photosensitized titanium dioxide. *ACS Appl. Mater. Interfaces* 6, 12388–12394. doi: 10.1021/am502251j

Ma, X., Dai, Y., Yu, L., and Huang, B. (2016). Interface Schottky barrier engineering via strain in metal-semiconductor composites. *Nanoscale* 8, 1352–1359. doi: 10.1039/C5NR05583K

Ma, X., Dai, Y., Yu, L., Lou, Z., Huang, B., and Whangbo, M.-H. (2014b). Electron-hole pair generation of the visible-light plasmonic photocatalyst Ag@AgCl: enhanced optical transitions involving midgap defect states of AgCl. *J. Phys. Chem. C* 118, 12133–12140. doi: 10.1021/jp5023604

Ma, X. C., Dai, Y., Yu, L., and Huang, B. B. (2016). Energy transfer in plasmonic photocatalytic composites. *LightSci. Appl.* 5:e16017. doi: 10.1038/lsa.2016.17

Maeda, K., Takata, T., Hara, M., Saito, N., Inoue, Y., Kobayashi, H., et al. (2005). GaN:ZnO solid solution as a photocatalyst for visible-light-driven overall water splitting. *J. Am. Chem. Soc.* 127, 8286–8287. doi: 10.1021/ja0518777

Maeda, K., Teramura, K., Lu, D. L., Takata, T., Saito, N., Inoue, Y., et al. (2006). Photocatalyst releasing hydrogen from water - enhancing catalytic performance holds promise for hydrogen production by water splitting in sunlight. *Nature* 440, 295–295. doi: 10.1038/440295a

Major, T. A., Lo, S. S., Yu, K., and Hartland, G. V. (2014). Time-resolved studies of the acoustic vibrational modes of metal and semiconductor nano-objects. *J. Phys. Chem. Lett.* 5, 866–874. doi: 10.1021/jz4027248

Manjavacas, A., Liu, J. G., Kulkarni, V., and Nordlander, P. (2014). Plasmon-induced hot carriers in metallic nanoparticles. *ACS Nano* 8, 7630–7638. doi: 10.1021/nn502445f

Marchuk, K., and Willets, K. A. (2014). Localized surface plasmons and hot electrons. *Chem. Phys.*. 445, 95–104. doi: 10.1016/j.chemphys.2014.10.016

Marimuthu, A., Zhang, J., and Linic, S. (2013). Tuning selectivity in propylene epoxidation by plasmon mediated photo-switching of Cu oxidation state. *Science* 339, 1590–1593. doi: 10.1126/science.1231631

McCaldin, J., McGill, T., and Mead, C. (1976). Correlation for III-V and II-VI semiconductors of the Au Schottky barrier energy with anion electronegativity. *Phys. Rev. Lett.* 36:56. doi: 10.1103/PhysRevLett.36.56

Mönch, W. (1987). Role of virtual gap states and defects in metal-semiconductor contacts. *Phys. Rev. Lett.* 58, 1260–1263. doi: 10.1103/PhysRevLett.58.1260

Moskovits, M. (2015). The case for plasmon-derived hot carrier devices. *Nat. Nanotechnol.* 10, 6–8. doi: 10.1038/nnano.2014.280

Moubah, R., Rousseau, O., Colson, D., Artemenko, A., Maglione, M., and Viret, M. (2012). Photoelectric effects in single domain $BiFeO_3$ crystals. *Adv. Funct. Mater.* 22, 4814–4818. doi: 10.1002/adfm.201201150

Mubeen, S., Lee, J., Singh, N., Kraemer, S., Stucky, G. D., and Moskovits, M. (2013). An autonomous photosynthetic device in which all charge carriers derive from surface plasmons. *Nat. Nanotechnol.* 8, 247–251. doi: 10.1038/nnano.2013.18

Mukherjee, S., Libisch, F., Large, N., Neumann, O., Brown, L. V., Cheng, J., et al. (2013). Hot electrons do the impossible: plasmon-induced dissociation of H_2 on Au. *Nano Lett.* 13, 240–247. doi: 10.1021/nl303940z

Mukherjee, S., Zhou, L. A., Goodman, A. M., Large, N., Ayala-Orozco, C., Zhang, Y., et al. (2014). Hot-electron-induced dissociation of H-2 on gold nanoparticles supported on SiO_2. *J. Am. Chem. Soc.* 136, 64–67. doi: 10.1021/ja411017b

Navarro, R. M., del Valle, F., de la Mano, J. A. V., Alvarez-Galvan, M. C., and Fierro, J. L. G. (2009). "Photocatalytic water splitting under visible light: concept and catalysts development," in *Photocatalytic Technologies*, eds H. I. DeLasa and B. S. Rosales (Madrid: Elsevier), 111–143. doi: 10.1016/S0065-2377(09)00404-9

Nechache, R., Harnagea, C., Li, S., Cardenas, L., Huang, W., Chakrabartty, J., et al. (2015). Bandgap tuning of multiferroic oxide solar cells. *Nat. Photonics* 9, 61–67. doi: 10.1038/nphoton.2014.255

Ohno, T., Bai, L., Hisatomi, T., Maeda, K., and Domen, K. (2012). Photocatalytic water splitting using modified GaN:ZnO Solid solution under visible light: long-time operation and regeneration of activity. *J. Am. Chem. Soc.* 134, 8254–8259. doi: 10.1021/ja302479f

Ortiz, N., Zoellner, B., Hong, S. J., Hoang, K., Ji, Y., Liu, Y., et al. (2017). Harnessing hot electrons from near IR light for hydrogen production using Pt-end-capped-AuNRs. *ACS Appl. Mater. Interf.* 9, 25962–25969. doi: 10.1021/acsami.7b05064

Ortiz, N., Zoellner, B., Kumar, V., Janelli, T., Tang, S., Maggard, P. A., et al. (2018). Composite ferroelectric and plasmonic particles for hot charge separation and photocatalytic hydrogen gas production. *ACS Appl. Energy Mater.* 1, 4606–4616. doi: 10.1021/acsaem.8b00772

Pintilie, I., Teodorescu, C. M., Ghica, C., Chirila, C., Boni, A. G., Hrib, L., et al. (2014). Polarization-control of the potential barrier at the electrode interfaces in epitaxial ferroelectric thin films. *ACS Appl. Mater. Interfaces* 6, 2929–2939. doi: 10.1021/am405508k

Pintilie, L., and Alexe, M. (2005). Metal-ferroelectric-metal heterostructures with Schottky contacts. I. Influence of the ferroelectric properties. *J. Appl. Phys.* 98:124103. doi: 10.1063/1.2148622

Pintilie, L., Boerasu, I., Gomes, M. J. M., Zhao, T., Ramesh, R., and Alexe, M. (2005). Metal-ferroelectric-metal structures with Schottky contacts. II. Analysis of the experimental current-voltage and capacitance-voltage characteristics of $Pb(Zr,Ti)O_3$ thin films - art. no. 123104. *J. Appl. Phys.* 98:124104. doi: 10.1063/1.2148623

Pintilie, L., Vrejoiu, I., Hesse, D., and Alexe, M. (2008). The influence of the top-contact metal on the ferroelectric properties of epitaxial ferroelectric Pb(Zr0.2Ti0.8)O3 thin films. *J. Appl. Phys.* 104:114101. doi: 10.1063/1.3021293

Pu, Y.-C., Wang, G., Chang, K.-D., Ling, Y., Lin, Y.-K., Fitzmorris, B. C., et al. (2013). Au nanostructure-decorated TiO_2 nanowires exhibiting photoactivity across entire UV-visible region for photoelectrochemical water splitting. *Nano Lett.* 13, 3817–3823. doi: 10.1021/nl4018385

Qin, M., Yao, K., Liang, Y. C., and Gan, B. K. (2007). Stability of photovoltage and trap of light-induced charges in ferroelectric WO_3-doped $(Pb_{0.97}La_{0.03})(Zr0.52Ti0.48)O_3$ thin films. *Appl. Phys. Lett.* 91:092904. doi: 10.1063/1.2776855

Reddy, K. H., and Parida, K. (2013). Fabrication, characterization, and photoelectrochemical properties of Cu-Doped $PbTiO_3$ and its hydrogen production activity. *ChemCatChem* 5, 3812–3820. doi: 10.1002/cctc.201300462

Robatjazi, H., Bahauddin, S. M., Doiron, C., and Thomann, I. (2015). Direct plasmon-driven photoelectrocatalysis. *Nano Lett.* 15, 6155–6161. doi: 10.1021/acs.nanolett.5b02453

Robertson, J., and Chen, C. W. (1999). Schottky barrier heights of tantalum oxide, barium strontium titanate, lead titanate, and strontium bismuth tantalate. *Appl. Phys. Lett.* 74, 1168–1170. doi: 10.1063/1.123476

Sakar, M., Balakumar, S., Saravanan, P., and Bharathkumar, S. (2016). Particulates vs. fibers: dimension featured magnetic and visible light driven photocatalytic properties of Sc modified multiferroic bismuth ferrite nanostructures. *Nanoscale* 8, 1147–1160. doi: 10.1039/C5NR06655G

Schultz, A. M., Zhang, Y., Salvador, P. A., and Rohrer, G. S. (2011). Effect of crystal and domain orientation on the visible-light photochemical reduction of Ag on $BiFeO_3$. *ACS Appl. Mater. Interf.* 3, 1562–1567. doi: 10.1021/am200127c

Sivula, K., Le Formal, F., and Graetzel, M. (2011). Solar water splitting: progress using hematite (alpha-Fe_2O_3) photoelectrodes. *Chemsuschem* 4, 432–449. doi: 10.1002/cssc.201000416

Sluka, T., Tagantsev, A. K., Bednyakov, P., and Setter, N. (2013). Free-electron gas at charged domain walls in insulating $BaTiO_3$. *Nat. Commun.* 4:1808. doi: 10.1038/ncomms2839

Spicer, W. E., Lindau, I., Skeath, P., Su, C. Y., and Chye, P. (1980). Unified mechanism for schottky-barrier formation and III-V oxide interface states. *Phys. Rev. Lett.* 44, 420–423. doi: 10.1103/PhysRevLett.44.420

Streiffer, S. K., Eastman, J. A., Fong, D. D., Thompson, C., Munkholm, A., Murty, M. V. R., et al. (2002). Observation of nanoscale 180 degrees stripe domains in ferroelectric $PbTiO_3$ thin films. *Phys. Rev. Lett.* 89:067601. doi: 10.1103/PhysRevLett.89.067601

Suriyaprakash, J., Xu, Y. B., Zhu, Y. L., Yang, L. X., Tang, Y. L., Wang, Y. J., et al. (2017). Designing of metallic nanocrystals embedded in non-stoichiometric perovskite nanomaterial and its surface-electronic characteristics. *Sci. Rep.* 7:8343. doi: 10.1038/s41598-017-09031-5

Suzuki, H., Kunioku, H., Higashi, M., Tomita, O., Kato, D., Kageyama, H., et al. (2018). Lead bismuth oxyhalides $PbBiO_2X$ (X = Cl, Br) as visible-light-responsive photocatalysts for water oxidation: role of lone-pair electrons in valence band engineering. *Chem. Mater.* 30, 5862–5869. doi: 10.1021/acs.chemmater.8b01385

Sze, S. M., and Ng, K. K. (2006). *Physics of Semiconductor Devices*. Hoboken, NJ: John Wiley & Sons. doi: 10.1002/0470068329

Tamura, T., Ishibashi, S., Terakura, K., and Weng, H. M. (2009). First-principles study of the rectifying properties of Pt/TiO_2 interface. *Phys. Rev. B* 80:195302. doi: 10.1103/PhysRevB.80.195302

Tersoff, J. (1986). Band lineups at II-VI heterojunctions: failure of the common-anion rule. *Phys. Rev. Lett.* 56, 2755–2758. doi: 10.1103/PhysRevLett.56.2755

Thomann, I., Pinaud, B. A., Chen, Z., Clemens, B. M., Jaramillo, T. F., and Brongersma, M. L. (2011). Plasmon enhanced solar-to-fuel energy conversion. *Nano Lett.* 11, 3440–3446. doi: 10.1021/nl201908s

Tung, R. T. (2000). Chemical bonding and fermi level pinning at metal-semiconductor interfaces. *Phys. Rev. Lett.* 84, 6078–6081. doi: 10.1103/PhysRevLett.84.6078

Tung, R. T. (2014). The physics and chemistry of the Schottky barrier height. *Appl. Phys. Rev.* 1:011304. doi: 10.1063/1.4858400

Wang, C., Jin, K., Xu, Z., Wang, L., Ge, C., Lu, H., et al. (2011). Switchable diode effect and ferroelectric resistive switching in epitaxial $BiFeO_3$ thin films. *Appl. Phys. Lett.* 98:192901. doi: 10.1063/1.3589814

Wang, C. L., and Astruc, D. (2014). Nanogold plasmonic photocatalysis for organic synthesis and clean energy conversion. *Chem. Soc. Rev.* 43, 7188–7216. doi: 10.1039/C4CS00145A

Wang, P., Huang, B. B., Qin, X. Y., Zhang, X. Y., Dai, Y., Wei, J. Y., et al. (2008). Ag@AgCl: a highly efficient and stable photocatalyst active under visible light. *Angew. Chem. Int. Edn.* 47, 7931–7933. doi: 10.1002/anie.200802483

Wang, Z. J., Cao, D. W., Wen, L. Y., Xu, R., Obergfell, M., Mi, Y., et al. (2016). Manipulation of charge transfer and transport in plasmonic-ferroelectric hybrids for photoelectrochemical applications. *Nat. Commun.* 7:10348. doi: 10.1038/ncomms10348

Warren, S. C., and Thimsen, E. (2012). Plasmonic solar water splitting. *Energy Environ. Sci.* 5, 5133–5146. doi: 10.1039/C1EE02875H

Wu, W. D., Horibe, Y., Lee, N., Cheong, S. W., and Guest, J. R. (2012). Conduction of topologically protected charged ferroelectric domain walls. *Phys. Rev. Lett.* 108:077203. doi: 10.1103/PhysRevLett.108.077203

Yang, S. Y., Seidel, J., Byrnes, S. J., Shafer, P., Yang, C. H., Rossell, M. D., et al. (2010). Above-bandgap voltages from ferroelectric photovoltaic devices. *Nat. Nanotechnol.* 5:143. doi: 10.1038/nnano.2009.451

Ye, X., Jin, L., Caglayan, H., Chen, J., Xing, G., Zheng, C., et al. (2012). Improved size-tunable synthesis of monodisperse gold nanorods through the use of aromatic additives. *ACS Nano* 6, 2804–2817. doi: 10.1021/nn300315j

Yuan, G. Z., Hsia, C. F., Lin, Z. W., Chiang, C., Chiang, Y. W., and Huang, M. H. (2016). Highly facet-dependent photocatalytic properties of Cu2O crystals established through the formation of Au-decorated Cu_2O heterostructures. *Chem. Eur. J.* 22, 12548–12556. doi: 10.1002/chem.201602173

Yun, Y., and Altman, E. I. (2007). Using ferroelectric poling to change adsorption on oxide surfaces. *J. Am. Chem. Soc.* 129, 15684–15689. doi: 10.1021/ja0762644

Zenkevich, A., Matveyev, Y., Maksimova, K., Gaynutdinov, R., Tolstikhina, A., and Fridkin, V. (2014). Giant bulk photovoltaic effect in thin ferroelectric $BaTiO_3$ films. *Phys. Rev. B* 90:161409. doi: 10.1103/PhysRevB.90.161409

Zhang, Z., and Yates, J. T. (2012). Band bending in semiconductors: chemical and physical consequences at surfaces and interfaces. *Chem. Rev.* 112, 5520–5551. doi: 10.1021/cr3000626

Zhao, G., Kozuka, H., and Yoko, T. (1996). Sol-gel preparation and photoelectrochemical properties of TiO_2 films containing Au and Ag metal particles. *Thin Solid Films* 277, 147–154. doi: 10.1016/0040-6090(95)08006-6

Zheng, F. G., Zhang, P., Wang, X. F., Huang, W., Zhang, J. X., Shen, M. R., et al. (2014). Photovoltaic enhancement due to surface-plasmon assisted visible-light absorption at the inartificial surface of lead zirconate-titanate film. *Nanoscale* 6, 2915–2921. doi: 10.1039/C3NR05757G

Zhu, W., Luo, W., Akkopru-Akgun, B., Lanagan, M., Randall, C. A., and Trolier-McKinstry, S. (2018). Ultraviolet-assisted cold poling of $Pb(Zr_{0.52}Ti_{0.48})O_3$ films. *J. Mater. Sci.* 53, 7180–7186. doi: 10.1007/s10853-018-2069-y

Zhu, X. (1994). Surface photochemistry. *Annu. Rev. Phys. Chem.* 45, 113–144. doi: 10.1146/annurev.pc.45.100194.000553

Conflict of Interest Statement: The authors declare that the research was conducted in the absence of any commercial or financial relationships that could be construed as a potential conflict of interest.

Copyright © 2019 Kumar, O'Donnell, Sang, Maggard and Wang. This is an open-access article distributed under the terms of the Creative Commons Attribution License (CC BY). The use, distribution or reproduction in other forums is permitted, provided the original author(s) and the copyright owner(s) are credited and that the original publication in this journal is cited, in accordance with accepted academic practice. No use, distribution or reproduction is permitted which does not comply with these terms.

frontiers in Chemistry

ORIGINAL RESEARCH
published: 14 March 2019
doi: 10.3389/fchem.2019.00128

A Holistic Approach to Model the Kinetics of Photocatalytic Reactions

*Jonathan Z. Bloh**

DECHEMA-Forschungsinstitut, Frankfurt am Main, Germany

Understanding and modeling kinetics is an essential part of the optimization and implementation of chemical reactions. In the case of photocatalytic reactions this is mostly done one-dimensionally, i.e., only considering the effect of one parameter at the same time. However, as discussed in this study, many of the relevant reaction parameters have mutual interdependencies that call for a holistic multi-dimensional approach to accurately model and understand their influence. Such an approach is described herein, and all the relevant equations given so that researchers can readily implement it to analyze and model their reactions.

Keywords: photocatalysis, kinetic analysis, high light intensity, temperature effects, heterogeneous photocatalysis, molecular photocatalysis, photoredox catalysis

1. INTRODUCTION

The importance of photocatalysis in fundamental and applied science has expanded tremendously over the last decades (Schneider et al., 2014; Augugliaro et al., 2015; Balzani et al., 2015; Romero and Nicewicz, 2016). Next to applications of heterogeneous photocatalysis in the removal of air pollutants (Ballari and Brouwers, 2013; Patzsch et al., 2018) and waste-water treatment (Alfano et al., 2000; Malato et al., 2009), a variety of applications in the field of organic synthesis (Friedmann et al., 2016; Bloh and Marschall, 2017) have emerged, particularly using molecular photoredox catalysts (Zeitler, 2009; Romero and Nicewicz, 2016).

In the latter field, this interest is in part due to the need of more efficient, sustainable and eco-friendly reactions as photons are essentially traceless reagents, but also partly due to the emergence of LEDs as very affordable and efficient high-power light sources which have made it very easy to perform photocatalytic reactions with appreciable rates. However, if these reactions are to be implemented in industrially relevant processes, they need to be both efficient and productive, i.e., and have both high quantum yield and reaction rates at the same time. This requires a precise knowledge about kinetics and the influence of all relevant reaction parameters. Yet, relatively little is known about the behavior of these reactions at the very high photon fluxes required to reach molar conversions within hours. Generally, at least for heterogeneous reactions, the observation is that at some point the response of the reaction rate to the light intensity becomes non-linear and yields increasingly diminishing returns (Dillert et al., 2013; Dilla et al., 2017; Deng, 2018).

Kinetic modeling and analysis of heterogeneous photocatalysis is mostly based on relatively simple Langmuir-Hinshelwood type kinetics, with linear or mixed linear and square root dependence on the light intensity (Mills et al., 2015; Camera-Roda et al., 2016). The major problem with this approach is that using this rate law, with an average light intensity, is only a valid approach if the reaction rate scales linearly with the light intensity at every point in the reaction vessel. Considering the distribution of the light intensity and absorption inside the reactor and calculating local reaction rates to integrate into a global average, is only done in a select few and very specific cases (Camera-Roda et al., 2016; Grčić and Li Puma, 2017).

OPEN ACCESS

Edited by:
Bunsho Ohtani,
Hokkaido University, Japan

Reviewed by:
Libor Čapek,
University of Pardubice, Czechia
Leny Yuliati,
Universitas Ma Chung, Indonesia

***Correspondence:**
Jonathan Z. Bloh
bloh@dechema.de

Specialty section:
This article was submitted to Catalysis and Photocatalysis, a section of the journal Frontiers in Chemistry

Received: *03 December 2018*
Accepted: *18 February 2019*
Published: *14 March 2019*

Citation:
Bloh JZ (2019) A Holistic Approach to Model the Kinetics of Photocatalytic Reactions. Front. Chem. 7:128. doi: 10.3389/fchem.2019.00128

In photoredox catalysis, kinetic analysis is almost exclusively based on fluorescence methods such as Stern-Volmer analysis (Arias-Rotondo and McCusker, 2016; Pitre et al., 2016).

As shown recently, most reaction parameters show a mutual interdependence on each other and therefore cannot be properly studied in one-dimensional approaches, where just one parameter is varied (Burek et al., 2019). Instead, a holistic approach is needed to take the light intensity and distribution, catalyst and substrate concentration and the temperature into account at the same time. This contribution describes this approach in detail.

2. HETEROGENEOUS PHOTOCATALYTIC REACTIONS

The model used herein to describe heterogeneous photocatalytic reactions is based on three elementary steps (*R*1-3), which are illustrated in **Figure 1**. While in the overall reactions, reduction and oxidation always have to take place, we only consider one of those half-reactions, whichever one is slower and rate-determining. The other half-reaction is consequently assumed to be much faster and has no effect on the overall observed reaction rate. It should also be considered that contrary to molecular systems, reduction and oxidation neither have to take place in a set sequence, nor necessarily at the same time, as the photocatalyst particle has a certain capacity to store excess charges over short time-frames (Mohamed et al., 2011).

The first reaction step (*R*1, Equation 1) is the generation of reactive surface sites (c_R^*) which are essentially charge carriers (electrons or holes, depending on whichever reaction is rate-limiting) trapped at surface sites. The rate of this reaction is dependent on the local volumetric rate of photon absorption (LVRPA, L_p^a), the quantum yield (ϕ) and is normalized to the fraction of available surface trap sites that are not already filled. This is based on the assumption that a trap already filled cannot take up additional charges.

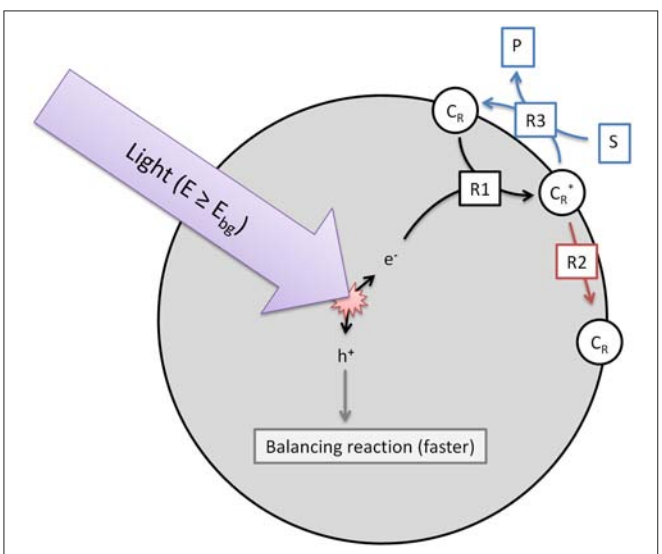

FIGURE 1 | Illustration of the three elementary reactions which are the basis of the kinetic model. Shown are the generation of reactive surface sites (*R*1), the recombination (*R*2) and the charge transfer to the target substrate (*R*3).

Many kinetic models assume that the reaction rate is dependent on the concentration of conduction band electrons (or valence band holes). However, this approach is flawed since the electrons and the substrate molecules are present in separate phases and can therefore not freely interact with each other. Since the reaction happens *via* the surface, only electrons present (or trapped) at the surface matter for the reaction rate. We simply consider the whole process of photon absorption, electron/hole pair generation and migration and trapping at surface sites as one process. Consequently, the respective quantum yield (ϕ) already comprises all loss processes along this pathway, e.g., bulk recombination. The efficiency of this process should theoretically be a property of the photocatalyst and be independent of the reaction studied. Additionally, the normalization to the total number of available surface trap sites is necessary, otherwise, given a high enough light intensity the model could theoretically create an infinite number of reactive active sites, which will never be the case for a limited number of catalyst particles.

$$R1(c_R \rightarrow c_R^*): \phi \cdot L_p^a \cdot \frac{c_R}{c_{R,0}} \tag{1}$$

These reactive surface sites can relax back to the ground state by recombining with their respective charge-carrier counterpart (*R*2, Equation 2). Note that this represents only the (relatively slow) decay of surface traps, as bulk recombination is already accounted for in *R*1. We model this as a simple first-order reaction, dependent on the recombination rate (k_r) and the density of trapped charges, given here by the fraction of filled surface traps to total surface traps.

Often, the recombination rate is modeled as a second-order reaction with respect to the concentration of electrons or holes (Zhang et al., 2012). This is a problematic approach, as the concentration (in electrons per reaction volume unit) of charges is not an appropriate measure since the electrons cannot freely move inside the reaction medium, only inside their photocatalyst (nano)particle. If for instance, in a given volume element there are 10 photocatalyst particles each containing a single charge, the recombination rate should be different than if it is just one particle containing 10 charges. It is for this reason that we chose to model the recombination rate as a function of density of trapped charges (in the photocatalyst particles) rather than a concentration of charge carriers. It should be noted however, that for an invariant catalyst concentration this is still proportional to the concentration of charges.

There is considerable disagreement in the literature about whether the decay of charge carriers follows first- or second-order kinetics (Zhang et al., 2012). In this case, while *R*2 models this as a first-order decay, the total rate of recombination (factoring in the contribution of bulk recombination from *R*1) is actually predominantly second-order with respect to the light intensity,

cf. Burek et al. (2019), SI.

$$R2(c_R^* \rightarrow c_R) : k_r \cdot \frac{c_R^*}{c_{R,0}} \tag{2}$$

Finally, the charge transfer to the target substrate can be considered (*R*3, Equation 3). This is dependent on the concentration of reactive surface sites, the surface coverage (θ) of the photocatalyst with the target substrate and a monomolecular kinetic constant (k). The surface coverage can simply be modeled as a function of substrate concentration ([*S*]) and adsorption constant (K_{ads}) using a Langmuir isotherm, Equation (4).

$$R3(c_R^* + S \rightarrow c_R + P) : k \cdot \theta \cdot c_R^* \tag{3}$$

$$\theta = \frac{K_{ads} \cdot [S]}{1 + K_{ads} \cdot [S]} \tag{4}$$

Under the assumption that these processes (*R*1-3) happen on a timescale much faster than macroscopic mixing and changes in the substrate concentration, a pseudo-steady-state approach ($c_R, c_R^* = const.$, $R1 = R2 + R3$) yields an explicit equation for the concentration of reactive surface sites, Equation (5), and the target (observed) reaction rate ($r = R3$), Equation (6).

$$c_R^* = \frac{\phi \cdot L_p^a \cdot c_{R,0}}{\phi \cdot L_p^a + k_r + k \cdot \theta \cdot c_{R,0}} \tag{5}$$

$$r = R3 = \frac{\phi \cdot L_p^a \cdot c_{R,0} \cdot k \cdot \theta}{\phi \cdot L_p^a + k_r + k \cdot \theta \cdot c_{R,0}} \tag{6}$$

Since the concentration of reactive sites is difficult to determine and typically unknown, it is more practical to normalize the rate constant to the catalyst mass (c_0), Equation (7), which leads to Equation (8), which represents the general case for calculating the *local* reaction rate. It is important to understand that this equation cannot be directly used to calculate observed *average* reaction rates unless certain criteria are met (*vide infra*), since the local reaction rate dramatically varies throughout the reaction medium.

$$k^* = \frac{k \cdot c_{R,0}}{c_0} \tag{7}$$

$$r = \frac{\phi \cdot L_p^a \cdot k^* \cdot \theta \cdot c_0}{\phi \cdot L_p^a + k_r + k^* \cdot \theta \cdot c_0} \tag{8}$$

2.1. Effect of Catalyst Concentration and Light Intensity

This general rate law (Equation 8) can be simplified if one of the limiting cases implies that the light intensity is either very high or very low in relation to the reaction's kinetic limit, Equations (9) and (10), these limiting cases can also be seen in **Figure 2**. At low light intensity, the reaction is purely governed by the flux of absorbed photons, in this regime, the observed overall photonic efficiency is constant. Parameters affecting the rate of electron transfer from the photocatalyst to the substrate have only negligible effect here. If on the contrary, the local light intensity is very high, the reaction is completely limited by the intrinsic kinetics of the reaction. In this case, the photocatalyst effectively behaves like an ordinary heterogeneous catalyst, since all of the reactive sites are permanently active due to the high photon flux.

$$(\phi \cdot L_p^a) \gg (k_r + k^* \cdot \theta \cdot c_0) : r = k^* \cdot \theta \cdot c_0 \tag{9}$$

$$(\phi \cdot L_p^a) \ll (k_r + k^* \cdot \theta \cdot c_0) : r = \phi \cdot L_p^a \cdot \frac{k^* \cdot \theta \cdot c_0}{k_r + k^* \cdot \theta \cdot c_0} \tag{10}$$

It is very important to understand that only if the former case of low light intensity and constant photonic efficiency is fulfilled in the whole reaction medium (i.e., even at the point of highest absorbed photon flux), the local reaction rate equals the average (observed) reaction rate $\langle r \rangle$ when using the average volumetric rate of photon absorption (AVRPA, $\left\langle L_p^a \right\rangle$) instead of the LVRPA, Equation (11). However, particularly for reactions with bad kinetics this will often not be the case even for moderate light intensities (*vide infra*).

$$(\phi \cdot L_{p,max}^a) \ll (k_r + k^* \cdot \theta \cdot c_0) : \langle r \rangle = \phi \cdot \left\langle L_p^a \right\rangle \cdot \frac{k^* \cdot \theta \cdot c_0}{k_r + k^* \cdot \theta \cdot c_0} \tag{11}$$

Furthermore, the rate equation (Equation 8) shows a saturation-curve behavior with respect to both the light intensity and the catalyst concentration. Interestingly, the value of one of those parameters needed to achieve saturation increases with higher values of the other. This is illustrated in **Figure 3**, where it is obvious that the catalyst concentration needed for saturation increases linearly with the light intensity. Likewise, if the reaction rate is considered as a function of light intensity, one can see that the higher the catalyst concentrations is, the longer the linear regime and the more light is needed to be fully saturated with photons, *cf.* **Figure 2**. This inter-dependency of catalyst concentration and light intensity was recently observed by us for the first time in the case of photocatalytic hydrogen peroxide formation by reduction of molecular oxygen (Burek et al., 2019). Since typically, the two parameters are not studied in depth at the same time, this effect has been largely invisible up to now. The conclusion here is that the higher the employed light intensity is, the higher should also be the catalyst concentration in order to keep the same efficiency. Since there are obvious limits to this in terms of solubility/dispersibility of the photocatalyst in the reaction medium, other measures should also be taken at very high light intensities (*vide infra*).

2.2. Effect of Substrate Concentration

The local reaction rate equation (Equation 8) can be rewritten into a pseudo-Langmuir-Hinshelwood form, Equation (12). Consequently, if the substrate concentration is the only parameter varied, the behavior might look like classical Langmuir-Hinshelwood and can be modeled and analyzed this way. This approach, however, might lead to false conclusions,

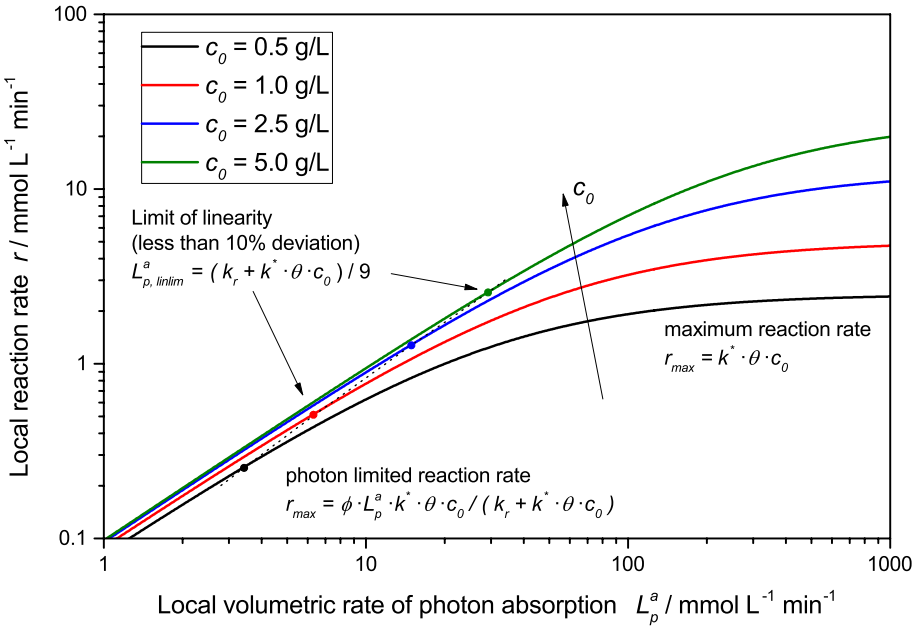

FIGURE 2 | Exemplary dependency of the local reaction rate (Equation 8) on the light intensity for different catalyst concentrations in a double logarithmic plot. Parameters used: $\phi = 0.1, k_r = 500\,\mu\text{mol}\,\text{L}^{-1}\,\text{min}^{-1}, k^* = 5.000\,\mu\text{mol}\,\text{g}^{-1}\,\text{min}^{-1}, \theta = 1$.

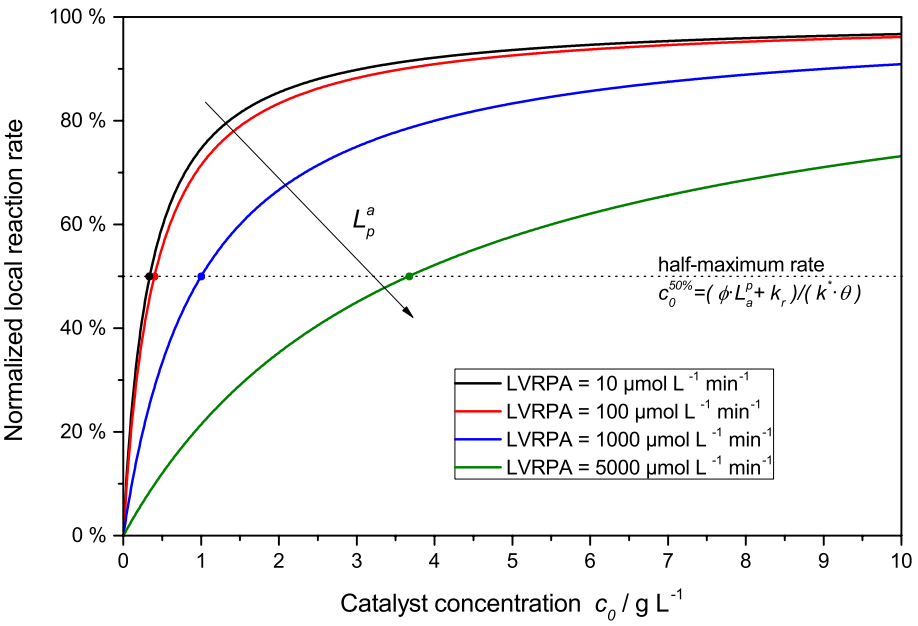

FIGURE 3 | Exemplary dependency of the (normalized) local reaction rate (Equation 8 divided by L_p^a) in dependence of the catalyst concentration for various LVRPA. Parameters used: $\phi = 1, k_r = 500\,\mu\text{mol}\,\text{L}^{-1}\,\text{min}^{-1}, k^* = 1.500\,\mu\text{mol}\,\text{g}^{-1}\,\text{min}^{-1}, \theta = 1$.

as the respective parameters k' and K'_{ads} do not resemble their classical physical meaning and are, in fact, influenced by a number of other parameters, *cf.* Equation (13).

$$r = \frac{k' \cdot K'_{ads} \cdot [S]}{1 + K'_{ads} \cdot [S]} \tag{12}$$

$$k' = \frac{\phi \cdot L_p^a \cdot k^* \cdot c_0}{\phi \cdot L_p^a + k_r + k^* \cdot c_0}; K'_{ads} = K_{ads} \cdot \left(1 + \frac{k^* \cdot c_0}{\phi \cdot L_p^a + k_r}\right) \tag{13}$$

The fact these pseudo-Langmuir-Hinshelwood parameters are dependent on the light intensity for instance, has already

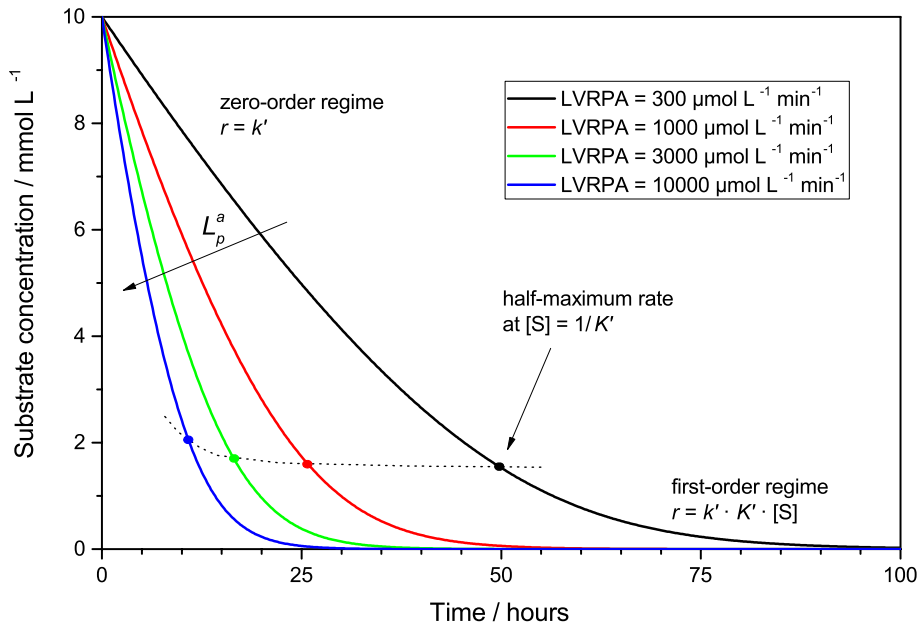

FIGURE 4 | Exemplary course of the substrate concentration (starting from $10\,\mathrm{mmol\,L^{-1}}$) over time in a given volume element for different LVRPA according to Equation (12). Parameters used: $\phi = 0.026$, $c_0 = 2.5\,\mathrm{g\,L^{-1}}$, $k_r = 653\,\mu\mathrm{mol\,L^{-1}\,min^{-1}}$, $k^* = 1358\,\mu\mathrm{mol\,g^{-1}\,min^{-1}}$, $K_{ads} = 0.1\,\mathrm{L\,mmol^{-1}}$.

been suggested and experimentally observed by other authors (Ollis, 2005; Dillert et al., 2012; Mills et al., 2015; Camera-Roda et al., 2016).

Consequently, the observed reaction is rate mixed zero- and first-order at high and low substrate concentration, respectively, *cf.* **Figure 4**. Interestingly, due to the light intensity dependence of the pseudo-adsorption constant, the inflection points between the zero- and first-order regimes given by the half-maximum rate gradually shifts to higher substrate concentration with higher light intensity. If concentration-time profiles for a given reaction are recorded, they can be modeled and analyzed using Equations (8) or (12), to extract useful information about the respective parameters. Since integration of this rate law does not yield an explicit equation, modeling has to be done numerically using for instance the Euler-Cauchy method. While the possibility to analyze these kinetics using a linearized approach exits, the author advises against that and to use the numerical approach instead, since linearization suffers from error inversion and weighting problems.

2.3. Average Reaction Rates

In many cases, rate laws similar to the ones presented above are applied to analyze the concentration-time profiles of photocatalytic reactions. However, this completely ignores the fact that these are *local* reaction rates, depending on the *local* absorbed photon flux, which varies dramatically throughout the reaction medium. As mentioned above, using the average photon flux to calculate the average reaction rate is only valid if the reaction rate is linearly dependent on the light intensity even at the "brightest spot" of the reaction, i.e., where the absorbed photon flux is at its maximum, Equation (11). In a linear light path, by ignoring scattering and calculating the light absorption behavior using the Lambert-Beer law, Equation (14), the LVRPA can be approximated using the negative derivative of the intensity attenuation, Equation (15), with the irradiance (I_0, given in photons, not energy) and the extinction coefficient (ϵ). From this, the maximum locally absorbed light intensity at the very beginning of the light path ($z = 0$) can be calculated using Equation (16).

$$I(z) = I_0 \cdot 10^{-\epsilon \cdot c_0 \cdot z} \tag{14}$$

$$L_p^a(z) = \frac{-dI(z)}{dz} = \epsilon \cdot c_0 \cdot ln(10) \cdot I_0 \cdot 10^{-\epsilon \cdot c_0 \cdot z} \tag{15}$$

$$L_{p,max}^a = L_p^a(0) = \epsilon \cdot c_0 \cdot ln(10) \cdot I_0 \tag{16}$$

With this equation it becomes apparent that the maximum locally absorbed photon flux can easily be 2 to 3 orders of magnitude higher than the average. Consequently, only if the condition given by Equation (17) is met, the above mentioned simplification of using Equation (11) is valid. Experimentally this can be checked by studying the reaction rate's response to a varied light intensity. If the response is completely linear across the studied range, the simplified approach is allowed.

$$(\phi \cdot \epsilon \cdot c_0 \cdot ln(10) \cdot I_0) \ll (k_r + k^* \cdot \theta \cdot c_0) \tag{17}$$

However, if this not the case, then the local reaction rate needs to be integrated over the whole reaction medium, taking the LVRPA distribution into account to obtain the average observed reaction rate. Particularly for complex light source and reactor geometries, this can be a quite challenging and time-consuming task which involves calculating the LVRPA across

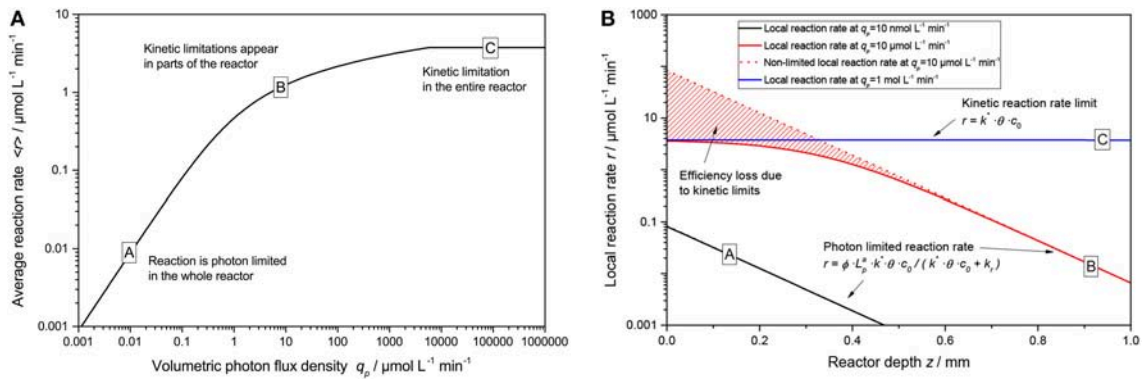

FIGURE 5 | (A) Exemplary course of the average reaction rate $\langle r \rangle$ in dependence of the volumetric photon flux density q_p according to Equation (19). **(B)** Locally resolved reaction rate as a function of reactor depth z according to Equation (8) with Equation (15) for the three cases marked A–C in **(A)**. Parameters used: $\phi = 1, c_0 = 2.5\,\mathrm{g\,L^{-1}}, k_r = 500\,\mathrm{\mu mol\,L^{-1}\,min^{-1}}, k^* = 1.500\,\mathrm{\mu mol\,g^{-1}\,min^{-1}}, \theta = 1, \epsilon = 16.4\,\mathrm{L\,g^{-1}\,cm^{-1}}, d = 0.1\,\mathrm{cm}$.

the three-dimensional reaction volume with numerical methods. However, under certain conditions this can be vastly simplified: If the light path from the lamp is collimated and is only attenuated along one dimension of the reactor. This is for instance the case when using a tubular reactor that is irradiated from its circular base or top, for instance when using a standard cylindrical beaker and irradiating it from above. In this case, the LVRPA can be approximated to only vary alongside the direction of the beam (z) with the other two directions following rotational symmetry. This allows to estimate the LVRPA using Equation (15) and to calculate the average reaction rate by integrating the local reaction rate over the whole reactor volume, Equation (18), yielding Equation (19).

$$\langle r \rangle = \frac{1}{d} \cdot \int_0^d \frac{\phi \cdot L_p^a(z) \cdot k^* \cdot \theta \cdot c_0}{\phi \cdot L_p^a(z) + k_r + k^* \cdot \theta \cdot c_0} dz \tag{18}$$

$$\langle r \rangle = k^* \cdot \theta \cdot c_0 + \frac{k^* \cdot \theta}{d \cdot \epsilon \cdot ln(10)} \cdot ln \left(\frac{\phi \cdot I_0 \cdot \epsilon \cdot c_0 \cdot ln(10) + k^* \cdot \theta \cdot c_0 + k_r}{\phi \cdot I_0 \cdot \epsilon \cdot c_0 \cdot ln(10) + (k^* \cdot \theta \cdot c_0 + k_r) \cdot 10^{\epsilon \cdot c_0 \cdot d}} \right) \tag{19}$$

Unless very optically dilute solutions are used, the condition expressed by Equation (20) is true and a simplified version of the rate equation can be used, Equation (21).

$$10^{\epsilon \cdot c_0 \cdot d} \gg \frac{\phi \cdot I_0 \cdot \epsilon \cdot c_0 \cdot ln(10)}{k^* \cdot \theta \cdot c_0 + k_r} \tag{20}$$

$$\langle r \rangle = \frac{k^* \cdot \theta}{d \cdot \epsilon \cdot ln(10)} \cdot ln \left(\frac{\phi \cdot I_0 \cdot \epsilon \cdot c_0 \cdot ln(10)}{k^* \cdot \theta \cdot c_0 + k_r} + 1 \right) \tag{21}$$

Furthermore, by defining the optical density (α) and using the volumetric photon flux density (q_p) instead of the irradiance, Equation (22), the sometimes more practical variant Equation (23) is obtained.

$$I_0 = q_p \cdot d; \alpha = \epsilon \cdot d \cdot ln(10) \tag{22}$$

$$\langle r \rangle = \frac{k^* \cdot \theta}{\alpha} \cdot ln \left(\frac{\phi \cdot q_p \cdot \alpha \cdot c_0}{k^* \cdot \theta \cdot c_0 + k_r} + 1 \right) \tag{23}$$

An exemplary plot of Equation (19) is shown in **Figure 5A**. Here, three regimes are apparent: At low light intensity, the reaction scales linearly with the light intensity across the whole reaction medium (A), in this case the simplified rate law given by Equation (11) is applicable. At some point, non-linearities start to appear in some parts of the reactor (the "bright" zone) and the average reaction rate starts to show diminishing returns (B). This corresponds to the non-linear response (approximately following a square root dependence) that was often reported for photocatalytic reactions at higher light intensities. If extremely high light intensities are used, the reaction will be limited at every point in the reactor and the average reaction rate is given by Equation (9) (C). However, the latter case is practically impossible to achieve with conventional light sources unless very small reactors with dilute photocatalyst are used.

Recently, we could show on the basis of the photocatalytic reduction of molecular oxygen to hydrogen peroxide, that this approach yields very good results in describing the complex behavior of the reaction rate in dependence of both catalyst concentration and light intensity, *cf.* **Figure 6** (Burek et al., 2019).

Figure 5B nicely illustrates the fundamental problem of intensifying photocatalytic reactions. In order to avoid kinetic limitations, the light intensity needs to be so low that even at the beginning of the reactor, no limitations manifest. This in turn means that in the rest of the reactor, the reaction only proceeds with orders of magnitude lower rates. One way to circumvent that is by using very dilute solutions or small dimensions that the light falloff through the reactor is only small (e.g., $< 50\,\%$). In that case, the reaction rate would not vary so much in the reactor and the average reaction rate is almost equal to the maximum local reaction rate, vastly increasing catalyst efficiency. However, this would also mean that a significant portion of the light is transmitted though the reactor and not used, dramatically reducing the overall photonic efficiency. Another possible solution is to use delocalized internal illumination so that the light distribution in the medium is more homogeneous (Burek et al., 2017).

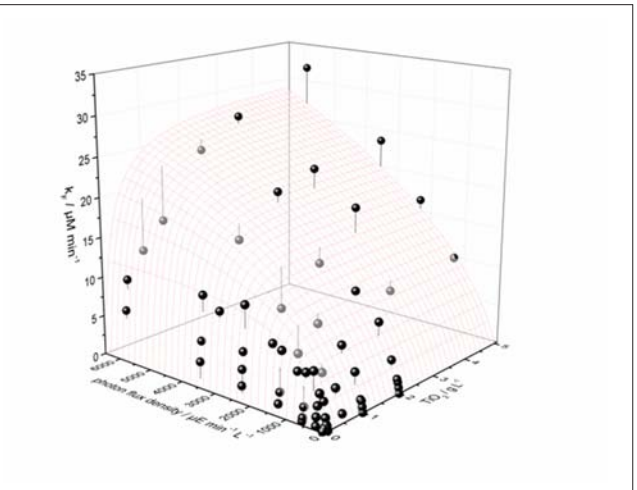

FIGURE 6 | Interdependence of the measured H_2O_2 formation rate constant k_F on the amount of catalyst and the photon flux density shown as black and dark gray dots. Also shown is the calculated best fit to the proposed model (Equation 23) as a surface plot; the vertical lines attached to the data points show their respective difference to the calculation. Data points that are black mean they are on or above the surface plot, and dark gray data points signify they are below the surface. Parameters used: $\phi = 0.02623, k_r = 653\,\mu mol\,L^{-1}\,min^{-1}, k^* \cdot \theta = 1358\,\mu mol\,g^{-1}\,min^{-1}, \epsilon = 16.4\,L\,g^{-1}\,cm^{-1}, d = 4\,cm$. Reprinted with permission from Burek et al. (2019), ©2018 American Chemical Society.

2.4. Effects of Temperature

Another important parameter of the reaction is the temperature. While this is one of the most important parameters in thermally activated catalysis and typically described via the Arrhenius law, Equation (24), this parameter is only studied in few photocatalytic systems. The rationale behind this seems to be that the reaction is initiated by the massive energy provided by the photons, so room temperature is sufficient to drive the reactions (Herrmann, 1999; Carp et al., 2004; Gaya and Abdullah, 2008; Malato et al., 2009). Yet, there are many publications which clearly show a temperature dependence of the photocatalytic reactions and use the Arrhenius law to calculate apparent activation energies (E_A^*) of 5 to 28 kJ mol^{-1} (Al-Sayyed et al., 1991; Hirakawa et al., 2004; Soares et al., 2007; Costacurta et al., 2010; Hu et al., 2010). While these are modest values in comparison with typical catalytic processes, they should not be neglected either. For instance, with these values, increasing the reaction temperature from 25 to 80 °C corresponds to an increase of 37 to 481 % in the kinetic constant.

$$k^* = A \cdot e^{\frac{-E_A}{R \cdot T}} \tag{24}$$

The Arrhenius law can easily be integrated into the present kinetic model by modulating the kinetic constant k^* by the temperature according to Equation (24). As shown in exemplary **Figure 7**, the temperature effects are strongly masked at lower light intensities, as improving the kinetics in that regime has negligible impact on the overall reaction, which is limited by the available photons here. However, at high light intensities, the temperature effect becomes much more prominent as it presents a way to overcome kinetic limitation there and to extend the linear regime. Consequently, using higher temperatures is a promising approach to combine high productivity and high quantum yield.

Interestingly, attempts to calculate the apparent activation energies (E_A^*) from the reaction rates obtained at a given light intensity, through Arrhenius plots (they mostly show acceptable fits), yields dramatically differing results with changing light intensity and range from 4.0 to 24.4 kJ mol^{-1}. The true activation energy (30 kJ mol^{-1}) is only revealed at very high light intensity, when the reaction is entirely kinetically limited. This would explain why authors in the past have reported vastly different apparent activation energies for the same reactions. Consequently, temperature effects of photocatalytic reaction cannot be properly studied at low reaction rates and will only yield misleading results.

Coincidentally, as at very high light intensities the energy input into the solution by the photons will be quite significant, achieving those higher temperatures will often be possible without additional heating. Researchers also need make sure to accurately control and measure the temperature in their reaction media, as to not mistake high light intensity effects for temperature effects that occur through unintentional radiative heating.

As pointed out by some authors, the solubility and adsorption of reactants is also strongly dependent on the temperature and this can significantly contribute to the observed overall temperature effects (Herrmann, 2005; Malato et al., 2009).

2.5. Limitations

It should be noted that while the above-mentioned approach has the advantage that it is very easy to implement given the low number of parameters and explicit equations, it also suffers from several drawbacks. The first is that here, a steady-state is assumed and therefore, dynamic processes are not taken into account. For instance, mass transport, adsorption and desorption rates are supposed to be much faster than the reaction are therefore have no effect, only their equilibrium state is modeled. This will obviously not be true in all cases, particularly for very intensified reactions and reagents with sluggish mobility. In those cases, dynamic models have to be used which will unfortunately make complex numerical simulation mandatory.

Furthermore, in the model we consider all photocatalytic reactions as one-electron transfers. If true concerted multi-electron transfers, not consecutive one-electron transfer events, drive the reaction (which typically requires a co-catalyst) this approach likely has to be modified accordingly.

Another potential problem is that scattering is completely neglected in the model (at least in the integrated form). Heterogeneous catalysts suspended in the reaction medium will scatter some of the incident light back out of the reactor, diminishing the actual available photon flux. This will lead to an underestimation of the LVRPA and consequently the quantum yield in the model. However, if the scattered-out light is determined either experimentally or computationally, the

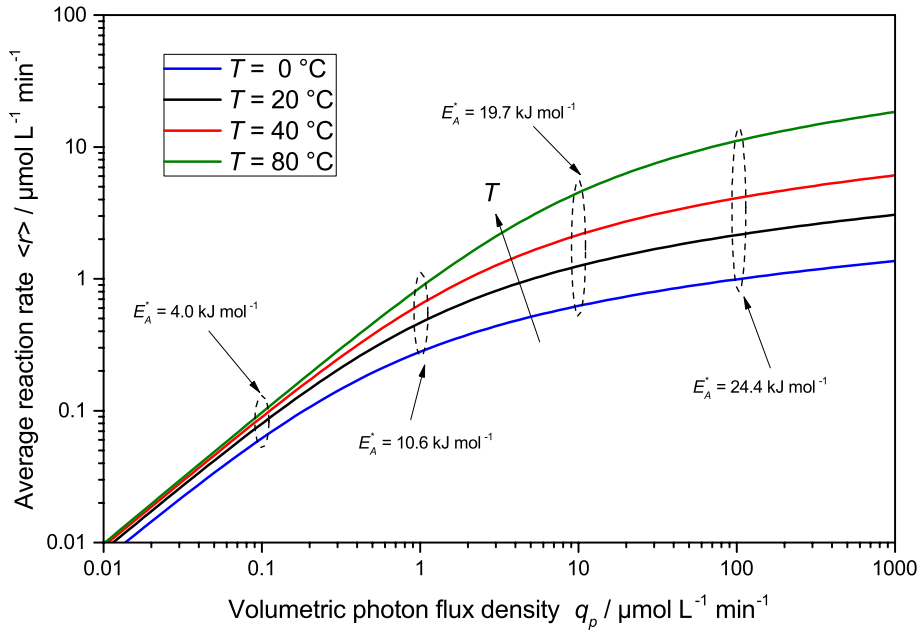

FIGURE 7 | The change in average reaction rate is a function of light intensity for different temperatures calculated according to Equation (23) with Equation (24). Also shown are the apparent activation energies E_A^* obtained from Arrhenius plots at a given light intensity. Parameters used: $\phi = 1, c_0 = 2.5\,\mathrm{g\,L^{-1}}$, $k_r = 500\,\mu\mathrm{mol\,L^{-1}\,min^{-1}}, A = 3.325 \times 10^8\,\mu\mathrm{mol\,g^{-1}\,min^{-1}}, E_A = 30\,\mathrm{kJ\,mol^{-1}}, \theta = 1, \epsilon = 16.4\,\mathrm{L\,g^{-1}\,cm^{-1}}, d = 0.1\,\mathrm{cm}$.

incident photon flux can be corrected for it and the model should be accurate with respect to this aspect.

The model also cannot account for changes in the solution properties such as solvent or pH. Since these parameters have very reaction-specific effects, they need to be studied on a case-by-case basis. However, it should be noted that theoretically, changes in the solvent or pH should only affect the rate constant, not the quantum yield or recombination rate.

If different photocatalysts are studied (different materials, surface area, synthesis routes, doping, etc.), this will most likely affect all three primary parameters (rate constant, quantum yield and recombination rate). Since this model requires a substantial amount of data points to deliver fairly accurate parameters, it will be quite time-consuming to compare different catalysts based on the kinetic model. However, doing so would likely provide interesting insight into their properties as changes in the kinetics (rate constant) and photophysical properties (quantum yield, recombination rate) can be separately attributed.

2.6. Application of the Model

Despite the limitations stated above, the model presented herein should be readily applicable to most standard photocatalytic reactions. Since most experimental setups feature illumination only from one direction, they are already compatible with the model. Ideally the light source should be collimated, and the beam should hit the reactor at a flat surface, although deviations from that likely only lead to small errors due to higher reflection losses. In almost all cases, Equation (23) can be directly used to model the observed reaction rates. For extremely high light intensities or very low photocatalyst concentrations, it should be checked if Equation (19) yields different values, in that case it has to be used instead.

$$\langle r \rangle = \frac{k^* \cdot \theta}{\alpha} \cdot ln\left(\frac{\phi \cdot q_p \cdot \alpha \cdot c_0}{k^* \cdot \theta \cdot c_0 + k_r} + 1\right) \tag{23}$$

This equation features the typically known parameters catalyst concentration (c_0) and incident light intensity (I_0, measurable for instance with physical probes at the reactor position) or volumetric photon flux density (q_p, measurable with chemical actinometry, see Equation (22) about how to interconvert these quantities). The optical density α can also be calculated using Equation (22) and determining the extinction coefficient (ϵ) by a simple transmission measurement. The surface coverage θ can be obtained using Equation (4) which adds the (known) substrate concentration and adsorption constant to the variables. If the substrate concentration is not varied, a constant, e.g., $\theta = 1$, may be used instead but this will scale the rate constant accordingly.

$$\theta = \frac{K_{ads} \cdot [S]}{1 + K_{ads} \cdot [S]} \tag{4}$$

This only leaves the rate constant (k^*), quantum yield (ϕ) and recombination rate (k_r) as unknown variables. These can be obtained by fitting the model to experimental data using non-linear optimization. Since there are three unknown parameters (four if the adsorption constant is unknown as well) the number of data points with varied light intensity and catalyst concentration should be significantly higher than that number to achieve good accuracy for the parameters. The rate equation can also be used to simulate concentration-time-profiles

of individual experiments by numerical methods such as the Euler-Cauchy algorithm.

If the effect of changing temperature should be accounted for as well, Equation (24) can be used to replace k^* in Equation (23). This adds the known parameter temperature and allows to determine the unknown pre-exponential factor A and activation energy E_A.

$$k^* = A \cdot e^{\frac{-E_A}{R \cdot T}} \tag{24}$$

Thorough analysis of the model parameters will reveal ways to optimize the reaction with respect to both high reaction rates and photonic efficiency. Typically, this will involve increasing substrate and photocatalyst concentrations to their saturation point as well as the temperature. However, these measures all have physical constraints due to solubility/dispersibility limits and in case of temperature, boiling point of the solvent. So, at a certain point, the reaction cannot be further improved by just tuning the reaction conditions and other measures have to be taken. This can either be improvements of the catalyst itself (which can directly increase the reaction rate kinetics, i.e., k^*) for instance by using co-catalysts which improve the charge transfer to the substrate. Another way is to improve the reactor used in order to reduce inhomogeneities in the light distribution. For instance, a shorter average light path will lead to a lower optical thickness and thereby allow higher average reaction rates at the same apparent quantum yield, *cf.* Equation (17).

3. MOLECULAR PHOTOCATALYTIC REACTIONS

The methodology used in the model, described above, can also be adapted to molecular (homogeneous) photocatalytic reactions. As shown in **Figure 8**, the first step of the catalytic cycle ($R1$) is again the excitation of the photocatalyst (PC) to its reactive state (PC^*), in dependence of the local volumetric rate of photon absorption (L_p^a). Since the reactive state is typically the triplet state, this reaction summarizes photon absorption and inter-system crossing. The quantum yield of this reaction (ϕ) consequently represents the yield of reactive (triplet) states that are generated upon photon absorption. The reaction rate is normalized to the fraction of unexcited photocatalyst to total photocatalyst. This is done under the assumption that multi-photon absorption does not lead to additional or faster reaction events, i.e., an already excited, oxidized or reduced photocatalyst may absorb additional photons, but this does not lead to an altered reactivity. This normalization is also needed, since if otherwise, given a sufficiently high light intensity, the model could mathematically create more excited photocatalysts than total photocatalysts.

The next step of the catalytic cycle is either relaxation of the excited state ($R2$) back to the ground state or reductive/oxidative quenching ($R3$). The former is usually accompanied by fluorescence and a first-order reaction with respect to concentration of the excited state. The rate of this reaction is usually expressed as the half-life-time (τ). The

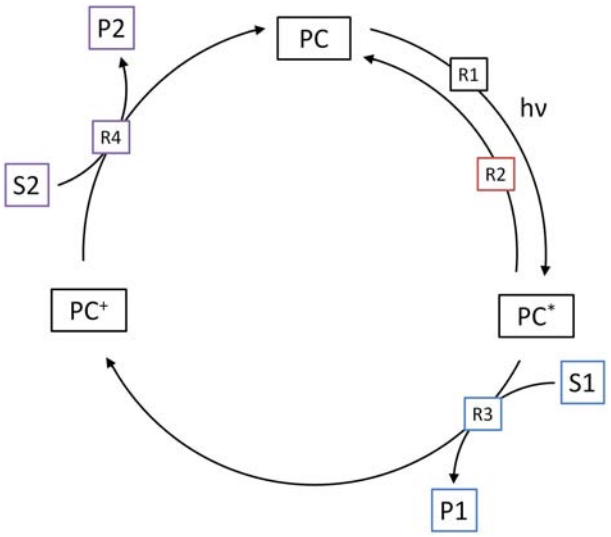

FIGURE 8 | Illustration of the four elementary reactions which are the basis of the kinetic model for molecular photocatalytic reactions. Shown are the generation of the excited state ($R1$), the relaxation ($R2$), oxidative quenching ($R3$) and regeneration of the photocatalyst ($R4$).

competing reaction is the electron transfer to or from one of the substrates. Since from a modeling perspective, oxidative and reductive quenching are identical, here only oxidative quenching ($R3$) is considered. This is typically a second-order reaction and therefore dependent on both the concentration of the excited state photocatalyst and the target substrate (S_1). The rate of this reaction is further described by the corresponding bimolecular rate constant (k_1).

In the last step, the cycle needs to be closed by regenerating (reducing) the oxidized photocatalyst (PC^+) back to the ground state ($R4$). This is done by reaction with the second substrate (S_2), again in a second-order reaction with the corresponding bimolecular rate constant (k_2). Note that either the first, second or both substrates might represent the target reaction.

$$R1(PC \rightarrow PC^*) : \phi \cdot L_p^a \cdot \frac{[PC]}{[PC_0]} \tag{25}$$

$$R2(PC^* \rightarrow PC) : \frac{[PC^*]}{\tau} \tag{26}$$

$$R3(PC^* + S_1 \rightarrow PC^+ + P_1) : k_1 \cdot [S_1] \cdot [PC^*] \tag{27}$$

$$R4(PC^+ + S_2 \rightarrow PC + P_2) : k_2 \cdot [S_2] \cdot [PC^+] \tag{28}$$

Since these reactions are usually significantly faster (ns to ms time-scale) than macroscopic mixing and changes in the substrate concentrations, it is assumed that a steady state is also present with respect to the local light intensity and substrate concentration. A steady-state approximation ($[PC], [PC^*], [PC^+] = const.$, $R1 = R2 + R3$, $R3 = R4$) yields Equation (29) for $[PC^*]$ and Equation (30) for $R3/4$.

$$[PC^*] = \frac{\phi \cdot L_p^a}{\frac{\phi \cdot L_p^a}{[PC_0]}\left(1 + \frac{k_1 \cdot [S_1]}{k_2 \cdot [S_2]}\right) + \frac{1}{\tau} + k_1 \cdot [S_1]} \tag{29}$$

$$r = R3 = R4 = \frac{k_1 \cdot [S_1] \cdot \phi \cdot L_p^a}{\frac{\phi \cdot L_p^a}{[PC_0]}(1 + \frac{k_1 \cdot [S_1]}{k_2 \cdot [S_2]}) + \frac{1}{\tau} + k_1 \cdot [S_1]} \quad (30)$$

This rate equation has the following limiting case which represents low light intensity. Note that contrary to heterogeneous systems, in molecular photocatalysis practically all cases fall into this category (*vide infra*).

$$L_p^a \ll \frac{[PC_0] \cdot (\frac{1}{\tau} + k_1 \cdot [S_1])}{1 + \frac{k_1 \cdot [S_1]}{k_2 \cdot [S_2]}} : \langle r \rangle = \phi \cdot \left\langle L_p^a \right\rangle \cdot \frac{k_1 \cdot [S_1] \cdot \tau}{1 + k_1 \cdot [S_1] \cdot \tau} \quad (31)$$

As stated above for heterogeneous systems, in cases when the response of the reaction rate to light intensity is linear in the entire reaction medium (low light intensity), the local volumetric rate of photon absorption may be replaced by the average volumetric rate of photon absorption ($\left\langle L_p^a \right\rangle$, AVRPA), to calculate the observed average reaction rate $\langle r \rangle$. The AVRPA can easily be measured using actinometry or calculated from the incident photon flux and the extinction of the photocatalyst. In this linear case, the well-known Stern-Volmer equation, Equation (33), can also be derived from the relaxation rate (*R*2), Equation (32), which it is proportional to the fluorescence intensity (*F*).

$$R2 = \frac{\phi \cdot \left\langle L_p^a \right\rangle}{1 + k_1 \cdot [S_1] \cdot \tau} \propto F \quad (32)$$

$$\frac{F_0}{F} = 1 + k_1 \cdot [S_1] \cdot \tau \quad (33)$$

As long as the light intensity is sufficiently small and the reaction rate increases linearly with the light intensity, the reaction kinetics can easily be described by Equation (31). This represents a mixed zero- and first-order reaction similar to Langmuir-Hinshelwood or Michaelis-Menten kinetics. At a high substrate concentration, the reaction is zero-order and the reaction rate is only dependent on the light intensity and quantum yield, Equation (34).

$$[S_1] \cdot \tau \cdot k_1 \gg 1 : r = \phi \cdot \left\langle L_p^a \right\rangle = r_{max} \quad (34)$$

At lower substrate concentration the reaction rate gradually shifts to first-order kinetics, where it is linearly dependent on the substrate concentration, quantum yield, light intensity, bimolecular rate constant and excited state life-time of the photocatalyst, Equation (35). A pseudo-inflection point between both regimes is given by the half-maximum reaction rate which is reached when $[S_1] \cdot k_1 \cdot \tau = 1$. This is exactly the behavior that is often observed if kinetics of photoredox catalysis are studied (Gazi et al., 2017; Le et al., 2017).

$$[S_1] \cdot \tau \cdot k_1 \ll 1 : r = \phi \cdot \left\langle L_p^a \right\rangle \cdot k_1 \cdot [S_1] \cdot \tau \quad (35)$$

Unfortunately, integration of this rate law (Equation 31) does not yield an explicit equation for the substrate concentration change over time, but it can readily be modeled and fitted using a numerical simulation (e.g., Euler-Cauchy method). Fitting this equation to a sufficiently detailed concentration-time-profile will also directly allow to extract both the quantum yield and bimolecular rate constant if τ and $\left\langle L_p^a \right\rangle$ are known, rendering Stern-Volmer analysis superfluous.

All of these simplifications are only applicable when the light intensity is so small, that the majority of the photocatalyst is always in its ground state. At higher light intensity, the reaction rate would yield increasingly diminishing returns with respect to the light intensity. Given the limits of linearity, it seems rather unlikely to actually reach the non-linear part in practical applications. Using the same method described above for heterogeneous systems, the maximum local absorbed light intensity present at the very beginning of the light path ($z = 0$) can again be calculated using Equation (16).

$$\epsilon \cdot ln(10) \cdot I_0 \ll \frac{(\frac{1}{\tau} + k_1 \cdot [S_1]) \cdot (k_2 \cdot [S_2])}{k_1 \cdot [S_1] + k_2 \cdot [S_2]} \quad (36)$$

This reduces the limiting case to Equation (36). Neglecting concentrated light sources such as lasers, irradiances of up to about $10\,W\,cm^{-2}$ are possible with current technology. This equals a photon flux of about $35\,\mu mol\,cm^{-2}\,s^{-1}$ in the UVA to blue light region. With $\epsilon = 15.000\,L\,mol^{-1}\,cm^{-1}$ and assuming the substrates are present in $10\,mmol\,L^{-1}$ concentration, this means that both bimolecular rate constants need to be much larger than $1.2 \times 10^5\,L\,mol^{-1}\,s^{-1}$, or in case of k_1, the half-life time of the photocatalyst's excited state may instead be much shorter than 0.8 ms. Given that both, rate constants are typically reported in the range of 10^6 to $10^8\,L\,mol^{-1}\,s^{-1}$ and the half-life time of the photocatalysts are often in the low µs regime, the limiting case seems to be fulfilled in practically all cases relevant today. However, if strongly absorbing photocatalysts are used in combination with high light intensity, slow kinetics and low substrate concentration, this limiting case needs to be revisited in order to make sure no non-linearities occur. The authors note that if a kinetic limitation takes place it is most likely caused by a slow regeneration reaction (*R*4). In those cases, similar measures defined for the heterogeneous reactions can be taken to accurately model the system and to overcome the limitations.

Similar considerations that were made for heterogeneous systems, concerning the temperature, can also be made for photoredox catalysis, however, one has to keep in mind that not just the target kinetic constant, but all the reaction constants will vary with temperature.

4. CONCLUSION

The vast majority of reports of photocatalytic reactions are one-dimensional studies that only look at the effect of one parameter. This very easily leads to misinterpretations as correlations of different parameters are invisible in this case. Moreover, the effect of some reaction parameters such as temperature are strongly masked under a variety of conditions and can therefore only be properly studied using a holistic multi-dimensional approach.

Using the average volumetric rate of photon absorption or any figure proportional to it, such as lamp power or irradiance, to

analyze the kinetics of photocatalytic reactions is only a valid approach if the light intensity is so low that the reaction rate is linearly proportional to the light intensity at every point in the reaction vessel. In that case it is also possible to use pseudo Langmuir-Hinshelwood kinetics to simulate and analyze the reaction rate, as long as the substrate concentration is the only parameter varied in a set of experiments. However, in this case care need to be taken not to misinterpret the corresponding parameters (k' and K'_{ads}) for their actual physical meaning, as they are in fact modulated by a number of other parameters such as the light intensity.

In case of moderate to high light intensities, the abovementioned simplification does not hold true and the reaction rate instead has to be integrated over the whole reaction volume, taking the light distribution into account. However, herein we could show that for some experimental setups there exist relatively simple explicit equations to solve this rather complex problem. These can easily be fit to the experimental data to obtain the underlying physically meaningful parameters. First examples already show that this approach yields very good results and can account for the effect of light intensity, catalyst and substrate concentration as well as temperature as well as their respective inter-dependencies (Burek et al., 2019).

Temperature is mostly neglected as a parameter in photocatalytic reactions as typically no significant influence is observed. However, this is only true as long as the intrinsic reaction kinetics are not rate-limiting and the reaction is purely governed by the number of available photons. At higher light intensities, the reaction kinetics play an ever-increasing role and here, temperature effects become apparent. In fact, we could show that a classical Arrhenius approach to modulate the rate constant yields very good results here. Similarly, the effect of other parameters affecting the reaction kinetics such as substrate concentration and catalyst concentration is much more prominent at high light intensities.

From a reaction engineering point of view, it would be desirable to work at the highest technically achievable light intensity, while still maintaining high photonic efficiency. Unfortunately, the reaction rate's response to light intensity becomes increasingly non-linear with increased intensity, which led several researchers to believe that high productivity and high efficiency are contradictory. However, the non-linearity can be compensated by increasing the reaction kinetics accordingly, e.g., by using a higher temperature, substrate or catalyst concentration. Yet, there are still limits to what extent this can be done to, so the ultimate goal should be to improve the employed catalyst or to reduce the inhomogeneity of the light distribution in the reaction vessel, e.g., by using delocalized internal illumination (Burek et al., 2017).

If the aim is only to achieve a maximum apparent quantum yield, the reaction should be run at low light intensity. Under these conditions, the reaction kinetics are also much more forgiving and using lower substrate/photocatalyst concentration and temperature should not have a significant negative impact on the observed reaction rate.

Similar considerations can be applied for molecular photocatalytic reactions and the respective equations, to simulate and analyze the mixed zero- and first-order kinetics of these reactions are given herein. However, integration over the reaction volume is likely not necessary in these cases, because, due to generally better kinetics, it is unlikely that non-linearities will appear when considering the technical limits of the current non-focused light sources.

DATA AVAILABILITY

All datasets generated for this study are included in the manuscript.

AUTHOR CONTRIBUTIONS

The author confirms being the sole contributor of this work and has approved it for publication.

FUNDING

The author is grateful to the German Research Foundation (DFG) for financial support within the project no. BL 1425/1-1 and the German Ministry of Economics (BMWi) for funding the AiF/IGF project *QuinoLight*, grant no. 18904 N/1.

REFERENCES

Alfano, O., Bahnemann, D., Cassano, A., Dillert, R., and Goslich, R. (2000). Photocatalysis in water environments using artificial and solar light. *Catal. Today* 58, 199–230. doi: 10.1016/S0920-5861(00)00252-2

Al-Sayyed, G., D'Oliveira, J. C., and Pichat, P. (1991). Semiconductor-sensitized photodegradation of 4-chlorophenol in water. *J. Photochem. Photobiol. A Chem.* 58, 99–114. doi: 10.1016/1010-6030(91)87101-Z

Arias-Rotondo, D. M., and McCusker, J. K. (2016). The photophysics of photoredox catalysis: a roadmap for catalyst design. *Chem. Soc. Rev.* 45, 5803–5820. doi: 10.1039/C6CS00526H

Augugliaro, V., Camera-Roda, G., Loddo, V., Palmisano, G., Palmisano, L., Soria, J., et al. (2015). Heterogeneous photocatalysis and photoelectrocatalysis: from unselective abatement of noxious species to selective production of high-value chemicals. *J. Phys. Chem. Lett.* 6, 1968–1981. doi: 10.1021/acs.jpclett.5b00294

Ballari, M., and Brouwers, H. (2013). Full scale demonstration of air-purifying pavement. *J. Hazard. Mater.* 254–255, 406–414. doi: 10.1016/j.jhazmat.2013.02.012

Balzani, V., Bergamini, G., and Ceroni, P. (2015). Light: a very peculiar reactant and product. *Angew. Chemie Int. Ed.* 54, 11320–11337. doi: 10.1002/anie.201502325

Bloh, J. Z., and Marschall, R. (2017). Heterogeneous photoredox catalysis: reactions, materials, and reaction engineering. *Eur. J. Org. Chem.* 2017, 2085–2094. doi: 10.1002/ejoc.201601591

Burek, B., Bahnemann, D. W., and Bloh, J. Z. (2019). Modeling and optimization of the photocatalytic reduction of molecular oxygen to hydrogen peroxide over titanium dioxide. *ACS Catal.* 9, 25–37. doi: 10.1021/acscatal.8b03638

Burek, B. O., Sutor, A., Bahnemann, D. W., and Bloh, J. Z. (2017). Completely integrated wirelessly-powered photocatalyst-coated spheres as a novel means to perform heterogeneous photocatalytic reactions. *Catal. Sci. Technol.* 7, 4977–4983. doi: 10.1039/C7CY01537B

Camera-Roda, G., Loddo, V., Palmisano, L., and Parrino, F. (2016). Guidelines for the assessment of the rate law of slurry photocatalytic reactions. *Catal. Today* 281, 221–230. doi: 10.1016/j.cattod.2016.06.050

Carp, O., Huisman, C., and Reller, A. (2004). Photoinduced reactivity of titanium dioxide. *Prog. Solid State Chem.* 32, 33–177. doi: 10.1016/j.progsolidstchem.2004.08.001

Costacurta, S., Maso, G. D., Gallo, R., Guglielmi, M., Brusatin, G., and Falcaro, P. (2010). Influence of temperature on the photocatalytic activity of sol-gel TiO 2 films. *ACS Appl. Mater. Interfaces* 2, 1294–1298. doi: 10.1021/am100149e

Deng, Y. (2018). Developing a Langmuir-type excitation equilibrium equation to describe the effect of light intensity on the kinetics of the photocatalytic oxidation. *Chem. Eng. J.* 337, 220–227. doi: 10.1016/j.cej.2017.12.059

Dilla, M., Mateblowski, A., Ristig, S., and Strunk, J. (2017). Photocatalytic CO2 reduction under continuous flow high-purity conditions: influence of light intensity and H2O concentration. *ChemCatChem* 9, 4345–4352. doi: 10.1002/cctc.201701189

Dillert, R., Engel, A., Große, J., Lindner, P., and Bahnemann, D. W. (2013). Light intensity dependence of the kinetics of the photocatalytic oxidation of nitrogen(ii) oxide at the surface of TiO2. *Phys. Chem. Chem. Phys.* 15:20876. doi: 10.1039/c3cp54469a

Dillert, R., Stötzner, J., Engel, A., and Bahnemann, D. W. (2012). Influence of inlet concentration and light intensity on the photocatalytic oxidation of nitrogen(II) oxide at the surface of Aeroxide® TiO2 P25. *J. Hazard. Mater.* 211–212, 240–246. doi: 10.1016/j.jhazmat.2011.11.041

Friedmann, D., Hakki, A., Kim, H., Choi, W., and Bahnemann, D. (2016). Heterogeneous photocatalytic organic synthesis: state-of-the-art and future perspectives. *Green Chem.* 18, 5391–5411. doi: 10.1039/C6GC01582D

Gaya, U., and Abdullah, A. (2008). Heterogeneous photocatalytic degradation of organic contaminants over titanium dioxide: a review of fundamentals, progress and problems. *J. Photochem. Photobiol. C Photochem. Rev.* 9, 1–12. doi: 10.1016/j.jphotochemrev.2007.12.003

Gazi, S., Dokić, M., Moeljadi, A. M. P., Ganguly, R., Hirao, H., and Soo, H. S. (2017). Kinetics and DFT studies of photoredox carbon-carbon bond cleavage reactions by molecular vanadium catalysts under ambient conditions. *ACS Catal.* 7, 4682–4691. doi: 10.1021/acscatal.7b01036

Grčić, I., and Li Puma, G. (2017). Six-flux absorption-scattering models for photocatalysis under wide-spectrum irradiation sources in annular and flat reactors using catalysts with different optical properties. *Appl. Catal. B Environ.* 211, 222–234. doi: 10.1016/j.apcatb.2017.04.014

Herrmann, J. (1999). Heterogeneous photocatalysis: fundamentals and applications to the removal of various types of aqueous pollutants. *Catal. Today* 53, 115–129. doi: 10.1016/S0920-5861(99)00107-8

Herrmann, J. M. (2005). Heterogeneous photocatalysis: state of the art and present applications. *Top. Catal.* 34, 49–65. doi: 10.1007/s11244-005-3788-2

Hirakawa, T., Whitesell, J. K., and Fox, M. A. (2004). Effect of temperature and pressure in the photocatalytic oxidation of n-octanol on partially desilanized hydrophobic TiO2suspended in aerated supercritical CO2. *J. Phys. Chem. B* 108, 10213–10218. doi: 10.1021/jp0364957

Hu, Q., Liu, B., Zhang, Z., Song, M., and Zhao, X. (2010). Temperature effect on the photocatalytic degradation of methyl orange under UV-vis light irradiation. *J. Wuhan Univ. Technol. Sci. Ed.* 25, 210–213. doi: 10.1007/s11595-010-2210-5

Le, C. C., Wismer, M. K., Shi, Z. C., Zhang, R., Conway, D. V., Li, G., et al. (2017). A general small-scale reactor to enable standardization and acceleration of photocatalytic reactions. *ACS Cent. Sci.* 3, 647–653. doi: 10.1021/acscentsci.7b00159

Malato, S., Fernández-Ibáñez, P., Maldonado, M., Blanco, J., and Gernjak, W. (2009). Decontamination and disinfection of water by solar photocatalysis: recent overview and trends. *Catal. Today* 147, 1–59. doi: 10.1016/j.cattod.2009.06.018

Mills, A., O'Rourke, C., and Moore, K. (2015). Powder semiconductor photocatalysis in aqueous solution: an overview of kinetics-based reaction mechanisms. *J. Photochem. Photobiol. A Chem.* 310, 66–105. doi: 10.1016/j.jphotochem.2015.04.011

Mohamed, H. H., Dillert, R., and Bahnemann, D. W. (2011). Reaction dynamics of the transfer of stored electrons on TiO2 nanoparticles: a stopped flow study. *J. Photochem. Photobiol. A Chem.* 217, 271–274. doi: 10.1016/j.jphotochem.2010.09.024

Ollis, D. F. (2005). Kinetics of liquid phase photocatalyzed reactions: an illuminating approach. *J. Phys. Chem. B* 109, 2439–2444. doi: 10.1021/jp04 0236f

Patzsch, J., Spencer, J. N., Folli, A., and Bloh, J. Z. (2018). Grafted iron(III) ions significantly enhance NO2 oxidation rate and selectivity of TiO2 for photocatalytic NOx abatement. *RSC Adv.* 8, 27674–27685. doi: 10.1039/C8RA05017A

Pitre, S. P., McTiernan, C. D., and Scaiano, J. C. (2016). Understanding the kinetics and spectroscopy of photoredox catalysis and transition-metal-free alternatives. *Acc. Chem. Res.* 49, 1320–1330. doi: 10.1021/acs.accounts.6b00012

Romero, N. A., and Nicewicz, D. A. (2016). Organic photoredox catalysis. *Chem. Rev.* 116, 10075–10166. doi: 10.1021/acs.chemrev.6b00057

Schneider, J., Matsuoka, M., Takeuchi, M., Zhang, J., Horiuchi, Y., Anpo, M., et al. (2014). Understanding TiO 2 photocatalysis: mechanisms and materials. *Chem. Rev.* 114, 9919–9986. doi: 10.1021/cr5001892

Soares, E. T., Lansarin, M. A., and Moro, C. C. (2007). A study of process variables for the photocatalytic degradation of rhodamine B. *Brazi. J. Chem. Eng.* 24, 29–36. doi: 10.1590/S0104-66322007000100003

Zeitler, K. (2009). Photoredox catalysis with visible light. *Angew. Chem. Int. Ed. Engl.* 48, 9785–9789. doi: 10.1002/anie.200904056

Zhang, L., Mohamed, H. H., Dillert, R., and Bahnemann, D. (2012). Kinetics and mechanisms of charge transfer processes in photocatalytic systems: a review. *J. Photochem. Photobiol. C Photochem. Rev.* 13, 263–276. doi: 10.1016/j.jphotochemrev.2012.07.002

Conflict of Interest Statement: The author declares that the research was conducted in the absence of any commercial or financial relationships that could be construed as a potential conflict of interest.

Copyright © 2019 Bloh. This is an open-access article distributed under the terms of the Creative Commons Attribution License (CC BY). The use, distribution or reproduction in other forums is permitted, provided the original author(s) and the copyright owner(s) are credited and that the original publication in this journal is cited, in accordance with accepted academic practice. No use, distribution or reproduction is permitted which does not comply with these terms.

NOMENCLATURE

Symbol	*Unit*	*Description*
α	-	*Optical thickness*
ϵ	$\mathrm{L\,g^{-1}\,cm^{-1}}$	*Mass extinction coefficient (of heterogeneous photocatalyst)*
ϵ	$\mathrm{L\,mol^{-1}\,cm^{-1}}$	*Molar extinction coefficient (of molecular photocatalyst)*
ϕ	-	*Intrinsic quantum yield*
θ	-	*Surface coverage of the catalyst with the substrate*
τ	s	*Half-life time of the photocatalyst's excited state*
A	$\mathrm{mol\,g^{-1}\,s^{-1}}$	*Pre-exponential factor*
c_0	$\mathrm{g\,L^{-1}}$	*Catalyst concentration*
c_R	$\mathrm{mol\,L^{-1}}$	*Concentration of unexcited reactive centers*
$c_{R,0}$	$\mathrm{mol\,L^{-1}}$	*Concentration of total reactive centers*
c_R^*	$\mathrm{mol\,L^{-1}}$	*Concentration of excited reactive centers*
d	cm	*Total length of the reactor alongside the beam direction (z)*
E_A	$\mathrm{kJ\,mol^{-1}}$	*Activation energy*
E_A^*	$\mathrm{kJ\,mol^{-1}}$	*Apparent activation energy*
F	-	*Fluorescence intensity*
F_0	-	*Fluorescence intensity in the absence of a quencher*
I_0	$\mathrm{mol\,m^{-2}\,s^{-1}}$	*Photon irradiance incident at the reactor surface*
$I(z)$	$\mathrm{mol\,m^{-2}\,s^{-1}}$	*Photon irradiance at a specific position alongside the beam direction (z)*
k	$\mathrm{s^{-1}}$	*First-order rate constant for the conversion of the substrate to the product*
k^*	$\mathrm{mol\,g^{-1}\,s^{-1}}$	*Rate constant k_1 normalized to the catalyst concentration*
k'	$\mathrm{mol\,L^{-1}\,s^{-1}}$	*Pseudo Langmuir-Hinshelwood rate constant*
k_1	$\mathrm{L\,mol^{-1}\,s^{-1}}$	*Second-order rate constant for the conversion of the substrate to the product*
k_2	$\mathrm{L\,mol^{-1}\,s^{-1}}$	*Second-order rate constant for the regeneration of the photocatalyst*
k_r	$\mathrm{mol\,L^{-1}\,s^{-1}}$	*Recombination rate constant*
K_{ads}	$\mathrm{L\,mol^{-1}}$	*Adsorption constant for the substrate on the photocatalyst*
K'_{ads}	$\mathrm{L\,mol^{-1}}$	*Pseudo Langmuir-Hinshelwood adsorption constant*
L_p^a	$\mathrm{mol\,L^{-1}\,s^{-1}}$	*Local volumetric rate of photon absorption (LVRPA)*
$L_p^a(z)$	$\mathrm{mol\,L^{-1}\,s^{-1}}$	*LVRPA at a specific depth of reactor alongside the beam direction (z)*
$L_{p,max}^a$	$\mathrm{mol\,L^{-1}\,s^{-1}}$	*Maximum LVRPA at any position in the reactor*
$\langle L_p^a \rangle$	$\mathrm{mol\,L^{-1}\,s^{-1}}$	*Average volumetric rate of photon absorption (AVRPA)*
$[PC]$	$\mathrm{mol\,L^{-1}}$	*Concentration of the photocatalyst in the ground state*
$[PC_0]$	$\mathrm{mol\,L^{-1}}$	*Total concentration of the photocatalyst in all states*
$[PC^*]$	$\mathrm{mol\,L^{-1}}$	*Concentration of the photocatalyst in the excited state*
$[PC^+]$	$\mathrm{mol\,L^{-1}}$	*Concentration of the photocatalyst in the oxidized state*
q_p	$\mathrm{mol\,L^{-1}\,s^{-1}}$	*Volumetric photon flux density*
r	$\mathrm{mol\,L^{-1}\,s^{-1}}$	*Local reaction rate*
r_{max}	$\mathrm{mol\,L^{-1}\,s^{-1}}$	*Maximum local reaction rate*
$\langle r \rangle$	$\mathrm{mol\,L^{-1}\,s^{-1}}$	*Average reaction rate*
R	$\mathrm{J\,mol^{-1}\,K^{-1}}$	*Universal gas constant*
$[S]$	$\mathrm{mol\,L^{-1}}$	*Concentration of the substrate*
$[S_1]$	$\mathrm{mol\,L^{-1}}$	*Concentration of substrate 1*
$[S_2]$	$\mathrm{mol\,L^{-1}}$	*Concentration of substrate 2*
T	K	*Absolute temperature*
z	cm	*Depth into in the reactor alongside the beam direction*

frontiers in Chemistry

ORIGINAL RESEARCH
published: 26 April 2019
doi: 10.3389/fchem.2019.00278

Flavin Conjugated Polydopamine Nanoparticles Displaying Light-Driven Monooxygenase Activity

*Leander Crocker and Ljiljana Fruk**

Department of Chemical Engineering and Biotechnology, University of Cambridge, Cambridge, United Kingdom

A hybrid of flavin and polydopamine (PDA) has been explored as a photocatalyst, drawing inspiration from natural flavoenzymes. Light-driven monoxygenase activity has been demonstrated through the oxidation of indole under blue light irradiation in ambient conditions, to afford indigo and indirubin dyes. Compared to riboflavin, a flavin-polydopamine hybrid is shown to be more resistant to photobleaching and more selective toward dye production. In addition, it has been demonstrated that it can be recycled from the solution and used for up to four cycles without a marked loss of activity, which is a significant improvement compared to other heterogenous flavin catalysts. The mechanism of action has been explored, indicating that the PDA shell plays an important role in the stabilization of the intermediate flavin-peroxy species, an active component of the catalytic system rather than acting only as a passive nanocarrier of active centers.

Keywords: flavin, polydopamine, light-driven reaction, monooxygenase, indole

OPEN ACCESS

Edited by:
Bunsho Ohtani,
Hokkaido University, Japan

Reviewed by:
Dirk Tischler,
Ruhr University Bochum, Germany
Yasushi Imada,
Tokushima University, Japan

****Correspondence:***
Ljiljana Fruk
lf389@cam.ac.uk

Specialty section:
This article was submitted to Catalysis and Photocatalysis, a section of the journal Frontiers in Chemistry

Received: *30 January 2019*
Accepted: *04 April 2019*
Published: *26 April 2019*

Citation:
Crocker L and Fruk L (2019) Flavin Conjugated Polydopamine Nanoparticles Displaying Light-Driven Monooxygenase Activity. Front. Chem. 7:278. doi: 10.3389/fchem.2019.00278

INTRODUCTION

Flavin-containing monooxygenases (FMOs) are an important class of xenobiotic-degrading enzymes present in both eukaryotic and prokaryotic organisms. For example, they are able to add molecular oxygen to the lipophilic xenobiotic compounds, thereby increasing their solubility enough to allow excretion. As a result, organisms are protected from potentially toxic exogenous compounds derived from natural sources and, particularly important for humans, the metabolism of drugs and pollutants (Krueger and Williams, 2005; Zhou and Shephard, 2006; Hodgson, 2010). One of the substrates for FMOs, which is also widespread in nature is the *N*-heterocycle indole. It is considered to be an aromatic pollutant due to its toxicity and potential mutagenicity (Sullivan and Gad, 2014), but it is also a versatile intermediate species and signaling molecule across families of organisms (Lee and Lee, 2010; Erb et al., 2015; Lee et al., 2015a,b). Indigo dyes are currently commercially produced by chemical synthesis using aniline, formaldehyde, and hydrogen cyanide to form phenylglycinonitrile, subsequently hydrolyzed to yield phenylglycine, which is finally converted to indigotin. This process involves use of toxic chemicals and extensive purification steps, limiting the environmental viability and prompting the design of more green-chemistry oriented strategies (Blackburn et al., 2009).

FMOs, as well as the other xenobiotic-degrading enzymes such as cytochrome P450s, have been shown to convert indole to the blue indigo dye through initial oxidation to indoxyl and subsequent dimerization to form the dye as shown in **Scheme 1**. This transformation has been utilized as an enzymatic assay to screen for oxygenases (O'Connor et al., 1997; Singh et al., 2010; Lin et al., 2012; Nagayama et al., 2015), but also as a greener alternative to the industrial manufacturing of indigo and related indigoid dyes. To achieve that, a whole cell biocatalysis relying on the cellular FMO's

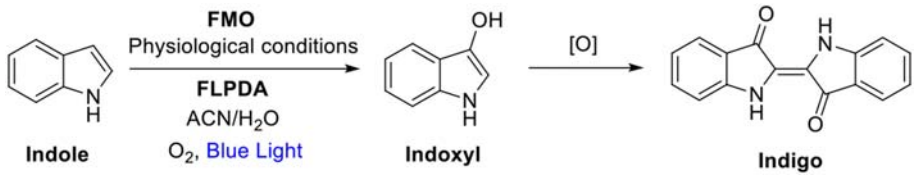

SCHEME 1 | Indole oxidation to indoxyl and further oxidation and dimerization to indigo where FMO, Flavin-containing monooxygenases; **FLPDA**, flavin-polydopamine; CAN, acetonitrile; [O], further oxidation processes by O_2 (Mermod et al., 1986; Meyer et al., 2002).

is utilized to achieve that since the current industrial manufacturing of these dyes is highly energy demanding, results in large amounts of toxic waste products, and requires number of purification steps (Han et al., 2012; Hsu et al., 2018; Ma et al., 2018). However, a whole-cell biocatalysis is also faced with complex product separation and catalyst inhibition, which incurs large costs and reactor downtime periods (Lin and Tao, 2017). Alternatives such as the use of the isolated enzymes suffer from limited enzyme quantities, low stability under non-physiological conditions, sensitivity to organic solvents, as well as challenging post-reaction isolation, hence limiting large scale industrial applications (Reetz, 2002; Li et al., 2012).

Taken out of a protein environment, flavin analogs derived from cofactors flavin mononucleotide (FMN), flavin adenine dinucleotide (FAD) and riboflavin have shown huge potential for catalytic applications, especially in photocatalytic processes (de Gonzalo and Fraaije, 2013; König et al., 2013; Cibulka, 2015). Despite the relative ease of visible-light driven flavin photocatalysis, high yielding reactions, and low toxicity, there are still challenges related to their long-term stability and photobleaching, as well as the separation of the catalyst from the products and subsequent catalyst reuse. To address these issues, attempts have been made to immobilize flavins onto various solid carriers such as silica beads or resins to achieve a heterogeneous catalytic systems, although limited success has been reported in relation to recyclability and activity (Schmaderer et al., 2009; Špačková et al., 2017; Arakawa et al., 2018). Taking this into account, we have rationalized that the use of solid, polymeric carrier, which not only permits immobilization of flavin but also displays some intrinsic properties similar to protein shells such as H-bonding and electron transfer, could significantly improve both the activity and post-reaction recovery of the hybrid catalytic system.

Herein, we present a new strategy to design a versatile enzyme-inspired photocatalytic system by embedding flavin within an active polymer matrix. We have chosen polydopamine (PDA) as the carrier polymer due to its reported biocompatibility (Hong et al., 2011; D'Ischia et al., 2014) and structural and electronic properties (Liu et al., 2014). Composed of a sequence of extended π-systems, PDA is considered to be an amorphous organic semiconductor, and has been used to improve various nanoparticle catalysts (Ma et al., 2015; Kunfi et al., 2017; Zhou et al., 2017), enhance the efficiency and stability of whole cell biocatalytic systems (Wang et al., 2017), and act as an electron gate for artificial photosynthesis due to its excellent electron accepting ability (Kim et al., 2014). Although PDA's main application has been to act as a molecular adhesive, due to its capability to form coatings on virtually any surface (Lee et al., 2007), an ability equally as interesting is its intrinsic catalytic activity (Mrõwczynski et al., 2014; Yang et al., 2014; Du et al., 2015), which has not yet been explored to afford hybrid organic systems with photocatalytic activity.

We hypothesized that monooxygenase activity of the flavin-polydopamine (**FLPDA**) system could be initiated through blue light irradiation to excite the flavin moieties, bypassing the use of external reducing agents or cofactors such as NADH. At the same time, PDA can be utilized as an active solid support enabling both the electron transfer and the stabilization of reactive intermediates. The latter was inspired by BLUF (blue light sensors using FAD) photoreceptors, in which an electron transfer between flavin cofactor and tyrosine in the protein shell is the key process enabling the stabilization of intermediates and switching from dark-adapted to light-adapted state, which guides biological signaling pathways (Mathes et al., 2012). In addition, the photoinduced electron transfer from tryptophan to flavin has been shown to be a crucial step in the control of CRY protein's activity, which is responsible for control of the light dependent circadian clocks in plants and animals (Lin et al., 2018). As shown in **Scheme 2**, the structure of PDA mimics both the tyrosine and tryptophan residues, indicating that the polymer could actively engage in electron transfer processes and impact the catalytic activity of embedded flavin. With this in mind, we focused our efforts to synthesize **FLPDA** nanoparticles through the co-polymerization of a flavin-dopamine monomer, **FLDA**, and dopamine. We then investigated the light-driven monooxygenase activity of the particles through blue light irradiation in the presence of indole under ambient conditions.

EXPERIMENTAL

General

All materials were purchased from either Acros Organics, Alfa Aeser, Sigma-Aldrich, or TCI Chemicals in the highest purity available and used without further purification. ^{1}H and ^{13}C NMR measurements were carried out using a 500 MHz DCH Cryoprobe Spectrometer. HRMS was recorded on a ThermoFinnigan Orbitrap Classic (Fisher Scientific). UV-Vis absorption spectra were obtained with an Agilent Cary 300 Spectrophotometer. Fluorescence emission spectra were obtained using a Varian Cary Eclipse Fluorescence

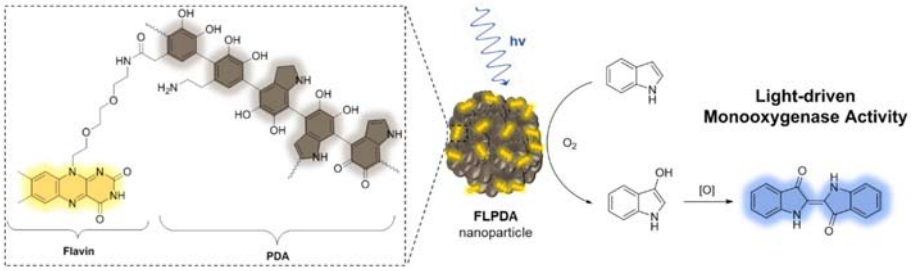

SCHEME 2 | Structure of flavin-polydopamine (FLPDA) units (left) and the reaction scheme illustrating explored light-driven oxidation of indole to indigo in presence of **FLPDA** nanoparticles (right).

Spectrophotometer using excitation and emission slits of 10 nm. DLS and Zeta Potential measurements were recorded using a Zetasizer Nano Range instrument (Malvern Panalytical). FTIR spectroscopy was carried out using a Bruker Tensor 27 spectrometer with samples pressed into KBr pellets. STEM images were obtained using a Hitachi S-5500 In-Lens FE STEM (2009) at an acceleration voltage of 1.0 kV. Samples were suspended in water and drop cast on lacey carbon copper grids (Agar Scientific). HPLC was carried out on an Agilent 1260 Infinity Quaternary LC equipped with a Zorbax Eclipse Plus C18 column (5 μm, 4.6 × 1.5 mm, Agilent) and diode array detector (monitoring at 270 nm). The mobile phase consisted of Solvent A (water + 0.1% formic acid) and solvent B (ACN/MeOH, 50:50, v/v) running along the following gradient: 0–8 min 85% A and 15% B at a flow rate of 1 mL/min, 8–15 min 65% A and 35% B at a flow rate of 2 mL/min. Indole (99%), isatin (97%), and oxindole (98%) were purchased from Sigma-Aldrich and calibration curves were obtained from 0 to 1.0 mM stock solutions in order to estimate product concentrations and % conversions. LC-MS was performed on an Agilent G6550 QTof mass spectrometer coupled to an Agilent 1200 Series Infinity LC system using a Zorbax Eclipse Plus C18 column (5 μm, 4.6 × 1.5 mm, Agilent). The mobile phase consisted of Solvent A (water + 0.1% formic acid) and solvent B (ACN + 0.1% formic acid) running along the following gradient: 0–14 min 85% A and 15% B to 5% A and 95% B at a flow rate of 0.8 mL/min. The electrospray source was operated with a capillary voltage of 3.0 kV and a nozzle voltage of 1.0 kV. Nitrogen was used as the desolvation gas at a total flow of 14 L/min. All *m/z* values stated are that of the $[M+H]^+$ molecular ion.

Synthesis of FLDA Monomer

See section Synthesis of Flavin-Dopamine Monomer in **Supplementary Information** for full synthetic details.

Synthesis of FLPDA

A mixture of ammonia solution (0.1 mL, 28%), ethanol (1.5 mL), and Milli Q water (4.5 mL) was stirred at room temperature for 30 min in reaction vessels protected from direct sunlight. Dopamine hydrochloride (15.80 mg, 0.083 mmol) dissolved in Milli-Q water (0.5 mL) and FLDA (8.73 mg, 0.017 mmol) dissolved in ethanol (0.5 mL) were mixed before being added dropwise to the reaction mixture. The resulting dark brown/black mixture was left to stir in the presence of air for 24 h. The mixture was then centrifuged at 25,000 × g for 30 min and the supernatant was removed. The precipitate was washed with Milli-Q water (3 × 40 mL) and then suspended in Milli-Q water (20 mL), frozen in liquid N_2 and lyophilized to yield a dark brown/black powder (5.5 mg, ρ = 22% where ρ is the percent weight conversion of monomers) (Jiang et al., 2014).

Photooxidation of Indole

FLPDA (0.01–0.1 mg/mL) and indole (0.2 μmol—0.05 mmol) were added to a 50:50 acetonitrile/water (2 mL) solvent system and the mixture was saturated with O_2 gas for 10 min before irradiating with a custom-made blue LED strips setup (12 V) with a cooling fan to maintain a temperature of ∼25°C (see **Figure S1** for setup). For small scale reactions, 100 μL aliquots were taken from the reaction mixture and diluted to 1 mL (50:50 acetonitrile/water) for analysis by UV-Vis absorption spectroscopy. Post-irradiation (2–6 h), the reaction mixture was either diluted in 50:50 acetonitrile/water (10 mL) and the catalyst removed by centrifugation and washed with water (3 × 12 mL) for further use, or the catalyst was removed by centrifugation and the supernatant analyzed by HPLC-UV and LC-MS. For larger scale reactions the resulting supernatant was concentrated under reduced pressure and residue analyzed by ESI-MS and UV-Vis absorption spectroscopy.

RESULTS AND DISCUSSION

Synthesis of Flavin-Polydopamine

FLPDA nanoparticles were formed by the copolymerization of dopamine (**DA**) with the flavin derivative, **FLDA** that was synthesized according to the route shown in **Scheme 3**. First, the functionalized triethylene glycol species, **1** (Deng et al., 2011) was used in a mono-substitution reaction with 4,5-dimethylbenzene-1,2-diamine to form N^1-(2-(2-(2-azidoethoxy)ethoxy)ethyl)-4,5-dimethylbenzene-1,2-diamine, **2**.

Isoalloxazine formation was achieved through the double condensation reaction with alloxan monohydrate to obtain flavin derivative **3**. The azide functionality was then reduced *via* catalytic hydrogenation to yield the amine-bearing flavin derivative **4**. Conjugation of this compound to the activated

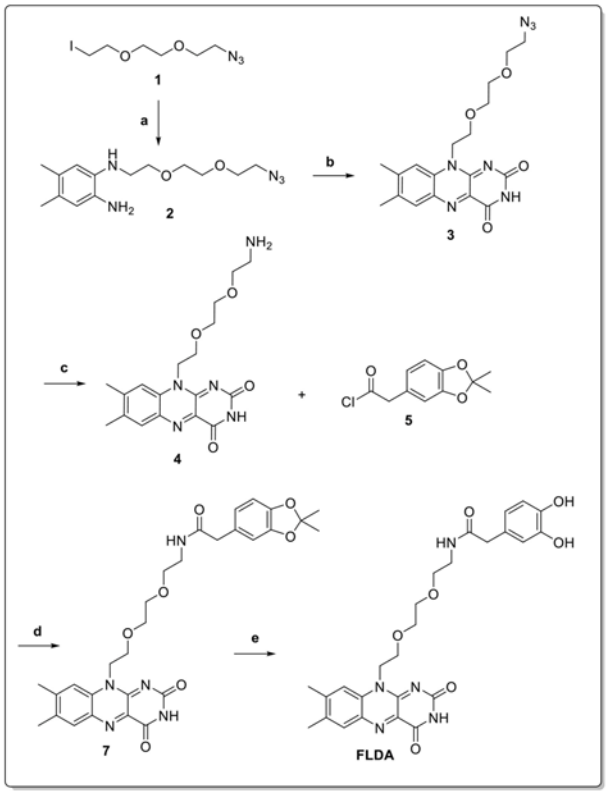

SCHEME 3 | Reaction conditions: (a) 4,5-dimethylbenzene-1,2-diamine, K_2CO_3, DMF, 50 °C, 12 h (70%); (b) alloxan monohydrate, B_2O_3, AcOH, RT, dark, 48 h (69%); (c) Pd/C, H_2, AcOH, RT, dark, 18 h (84%); (d) TEA, DMF, RT, dark, 18 h (62%); (e) TFA/DCM, RT, dark, 2 h (99%).

catechol-protected dopamine analog **6** resulted in protected **FLDA** derivative **7**, which was subsequently deprotected to afford the target **FLDA** monomer. Co-polymerization of dopamine and **FLDA** was carried out following a room temperature procedure adapted from Ai et al. (2013), and using ammonia addition to a water/ethanol solvent system in the presence of air. It should be noted that the reaction vessels were protected from direct light exposure to avoid any possible side reactions through the excitation of flavin moieties.

To validate the presence of flavin moieties, **FLPDA** was first analyzed by UV-Vis absorption and fluorescence spectroscopy. UV-Vis spectra of **FLDA** monomer shows absorption bands at λ_{max} = 445 nm and 373 nm (**Figure 1A**) corresponding to the transitions from the ground state (S_0) to the S_1 (λ_{max} ∼ 442–450 nm) and S_2 (λ_{max} ∼ 360–375 nm) excited states (Heelis, 1982). These bands are red-shifted to ∼ 456 nm for the $S_0 \rightarrow S_1$ transition and ∼ 376 nm for the $S_0 \rightarrow S_2$ transition in **FLPDA** (**Figure 1B**), which can be explained by an increase in proton donation from PDA (Kotaki et al., 1970) and by electron-withdrawing inductive effects on the flavin moieties due to incorporation into the highly conjugated PDA system (Mataranga-Popa et al., 2015). The fluorescence emission spectra of **FLDA** and **FLPDA** are characterized by emission maxima at 527 nm (λ_{ex} = 450 nm), which correlates well to other known flavin compounds (Kotaki and Yagi, 1970), and confirms the presence of flavin moieties in **FLPDA** NPs (see **Figures 1C,D**). An earlier study in which flavin compounds were complexed with eumelanin showed that the fluorescent properties of flavins did not change upon binding and there is no significant fluorescence quenching by the polymer (Kozik et al., 1990). We have used this fact to approximate flavin concentration within **FLPDA** by means of a calibration curve comparison (see **Figure S2** and **Table S2**). This gave an approximate concentration of flavin within **FLPDA** at 279.7 nmol/mg. It is worth noting that the amounts of flavin do not exactly match the monomer ratio used to synthesize the particles. The reason for this could be either the engulfing of the flavin moieties within particles or the base catalyzed cleavage/hydrolysis of flavin moieties during the polymerization, which results in the loss of characteristic flavin fluorescence (Smith and Bruice, 1975; Harayama et al., 1984).

FTIR spectroscopy was additionally employed to confirm **FLPDA** composition. The spectrum of PDA (**Figure 2A**) shows characteristic bands at 3,356 cm^{-1} relating to O-H and N-H stretching vibrations. In **FLDA** spectrum the bands corresponding to these vibrations broadens into one band at 3,414 cm^{-1}, which is also the case for **FLPDA**. Unlike for PDA, in the spectra of **FLPDA** bands at 2,924 and 2,855 cm^{-1} corresponding to C-H stretching vibration can be clearly identified and correlated well to the spectrum of **FLDA**. As seen in the zoomed spectra in **Figure 2B**, bonds characteristic for flavins such as the sharp bands at 1,545 cm^{-1} and 1,580 cm^{-1} relating to ν(C = N) modes in the isoalloxazine ring (Rieff et al., 2011) can clearly be observed in FLPDA, This is also true for the contributions from flavin carbonyl ν(C = O) (1,711 and 1,680 cm^{-1}) and ν(C = C). In addition, there are C = O and C-O vibrational modes of PDA, seen at 1,610 and 1,512 cm^{-1}, respectively, which are not observed in FLDA. Further C = N and C = C combined contributions can also be seen at shifted wavenumbers in the spectrum of **FLPDA** (1,292 cm^{-1}).

Finally, the size and morphology of **FLPDA** were investigated using STEM. As shown in **Figure 3** FLPDA solution is made up of spherical particles of similar size (∼200 nm) with relatively large size distribution (± ∼50 nm) (see **Table S1**). In contrast, PDA synthesized under the same conditions displays a narrower size distribution with an average size of 110 ± 18 nm (see **Table S1**), clearly indicating that the presence of flavin moieties affects the polymerization mechanism and oligomer aggregation to form particles with less defined shape and size. This is most likely due to H-bonding and electrostatic interactions between the flavin group and oligomeric units, and our ongoing work is focused on optimizing the polymerization procedure.

Indole Photooxidation

Having successfully prepared and characterized the **FLPDA** nanoparticles, we set out to investigate their catalytic activity in the presence of indole under blue light irradiation and explored their resemblance to the FMO enzyme activity. At first, small scale reactions were carried out using 1.0 mM indole with 50 μg/mL **FLPDA** and monitored by UV-Vis absorption spectroscopy. As shown in **Figure 4A** the absorption spectrum of indole (0 h) has a characteristic absorbance band at λ_{max} = 287 nm. After 0.5 h irradiation, this peak decreases in intensity and a new band appears at λ_{max} ∼ 380 nm which is consistent

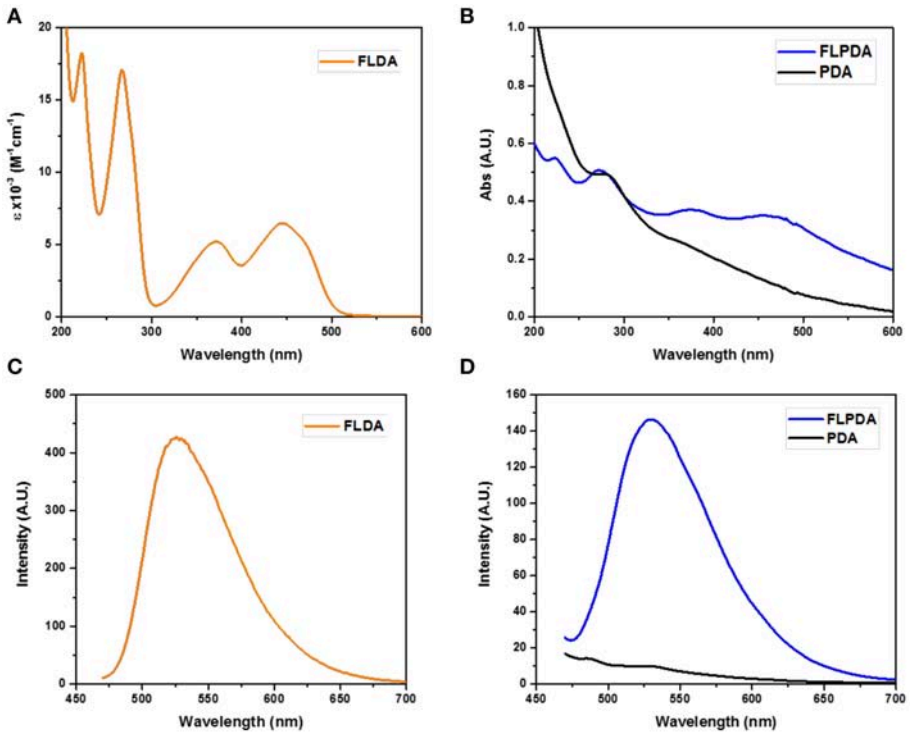

FIGURE 1 | UV-Vis spectra of **FLDA** (80 μM, 0.04 mg/mL in water **(A)**, and **FLPDA** and PDA (0.1 mg/mL in water **(B)**, and corresponding fluorescence spectra **(C,D)**.

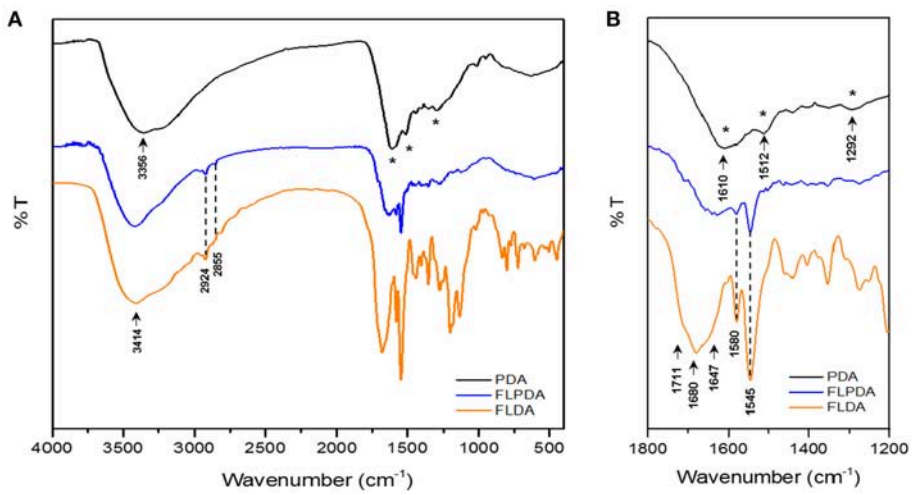

FIGURE 2 | Full-scale FTIR **(A)** and zoomed **(B)** spectra of **PDA**, **FLPDA**, and **FLDA**.

with the consumption of indole and the production of 2 and 3-position hydroxylated indole species (Kumar and Kumar, 1998; Kuo and Mauk, 2012; Linhares et al., 2014). These bands increase in intensity with time and a shoulder replacing the characteristic band belonging to indole at 2 h indicates its consumption (Kuo and Mauk, 2012). We also monitored the fluorescence emission (λ_{ex} = 365 nm) of the reaction as shown in **Figure 4B** and observed the formation of fluorescent indoxyl species (λ_{em} = 465 nm) at 0.5 h and 1 h (Gehauf and Goldenson, 1957; Woo et al., 2000). After 1 h the signal disappears most likely due to indoxyl dimerization into the fluorescent, water-soluble leuco-indigo (λ_{em} = 523 nm) (Gehauf and Goldenson, 1957; Seixas De Melo et al., 2004). Control experiments were carried out in the dark showing no reaction after 18 h, and by irradiating indole alone, indole in the presence of pure PDA particles, and indole in the presence of **FLPDA** under inert Ar atmosphere; all of which

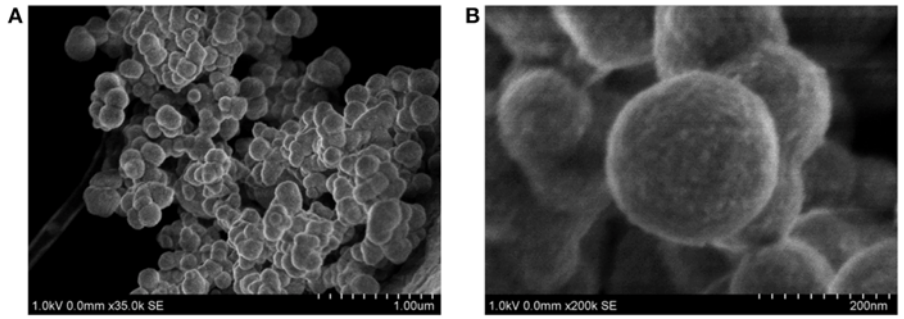

FIGURE 3 | STEM images of **FLPDA** at different scales **(A)** scale bar = 1.00 μm and **(B)** scale bar = 200 nm.

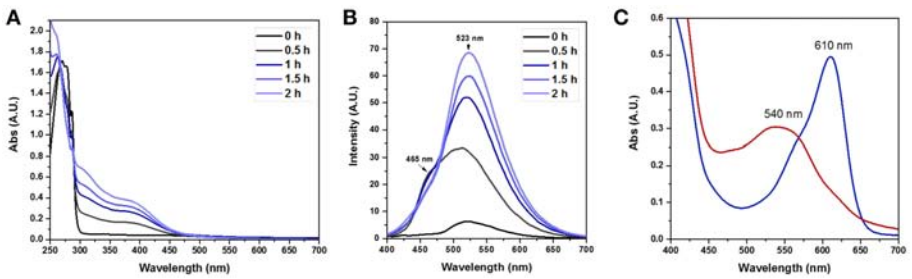

FIGURE 4 | (A) UV-Vis absorption spectra of the photooxidation of indole (1.0 mM) in the presence of **FLPDA** (50 μg/mL) in O_2 saturated ACN/H_2O (1:1, v/v). **(B)** Fluorescence emission spectra (λ_{ex} = 380 nm) of indole (1.0 mM) photooxidation in the presence of **FLPDA** (50 μg/mL) in O_2 saturated ACN/H_2O (1:1, v/v). All spectra are 10× dilutions of reaction mixture. **(C)** UV-Vis absorption spectra of produced indirubin (λ_{max} = 540 nm) and indigo (λ_{max} = 610 nm) in DMF.

showed negligible changes in indole's characteristic absorption band (see **Figure S3**).

Several oxidation products were obtained from the **FLPDA** catalyzed photooxidation of indole and three major products were identified by LC-MS (**Figure 5**) and compared to the commercial reagents. These were isatin **11** (7.07 min, *m/z*: 148), 2-oxindole **9** (7.69 min, *m/z*: 134), and indoxyl **10** observed as its more stable keto-form **10a** (4.23 min, *m/z*: 132). Other products with higher *m/z* values were also identified *via* LC-MS of the reaction mixture, including indigo/indirubin (two signals with *m/z*: 263) and two others with m/z values of 249 and 281. Their structures are proposed in **Scheme 4** and **Figure S5** as products **12** and **13**, and their production is particularly interesting as they were observed in reactions catalyzed by enzymes such as laccases and P450s that contain inorganic cofactors (Gillam et al., 2000; Ganachaud et al., 2008; Linhares et al., 2014).

The formation of indigo and indirubin were initially observed by TLC analysis of the reaction mixture and were then isolated after reaction workup and characterized by UV-Vis (indirubin λ_{max} = 540 nm and indigo λ_{max} = 610 nm as seen in **Figure 4C**). It should be noted that theses dyes were not observed to form during the reaction itself, but only upon removal of the solvent to initiate precipitation or with the addition of weak acid to the reaction mixture or supernatant which catalyzed their formation (Zelentskii et al., 1970). Yields of the dyes were measured by UV-Vis spectroscopy using published extinction coefficients (Seixas De Melo et al., 2004) and were generally low (<4%) when precipitated out of solution after solvent removal however this is comparable to other biomimetic systems using Fe(II) and Mn(III) porphyrin complexes in the presence of H_2O_2 (Linhares et al., 2014; Rebelo et al., 2014) indicating that low yields are the consequence of the non-specific binding sites, as the active site of FMO alters the product selectivity (Han et al., 2012). We noticed that adding weak acid to the reaction mixture after irradiation provided better yields of dye, however, primarily favored the formation of indirubin (see **Table 1**).The light-driven oxidation of indole by **FLPDA** is clearly non-specific due to the range of identified oxidation products, however, these main products resemble those formed by FMOs and other xenobiotic degrading enzymes. To our knowledge, this is the only reported example of an organic nanoparticle-based photocatalyst that shows this activity. In addition, the only other example of photocatalytic oxidation of indole to form indigo and related compounds are CdS quantum dots, the use of which has serious implications in terms of toxicity (Tsoi et al., 2013; Yong et al., 2013).

We also compared the activity of our hybrid catalyst to homogenous flavin, riboflavin (**RF**), under the same reaction conditions. To make an experimentally valid comparison, we used the same effective flavin concentration for both **FLPDA** and **RF** based on the fluorescence calibration curve utilized to characterize **FLPDA**, namely 20 μM for **RF** (2 mol%) and 36 μg/mL **FLPDA**. UV-Vis analysis of the reaction mixture containing **RF** showed an increased rate of indole consumption (shoulder formation at ∼280 nm as shown in **Figure 7A**) after

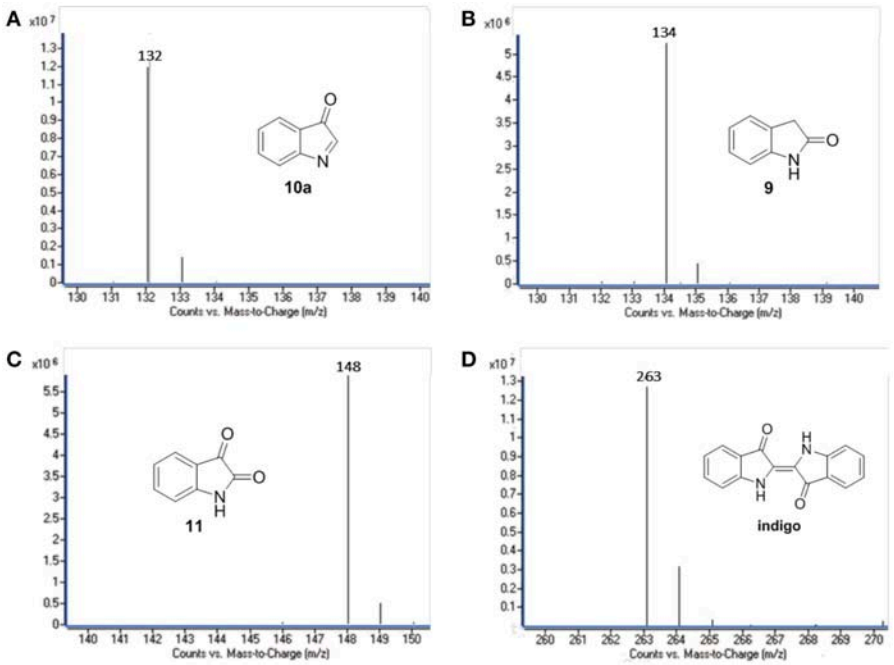

FIGURE 5 | LC-MS chromatograms of the major oxidation products: **(A) 9**, **(B) 10a**, **(C) 11**, and **(D)** indigo.

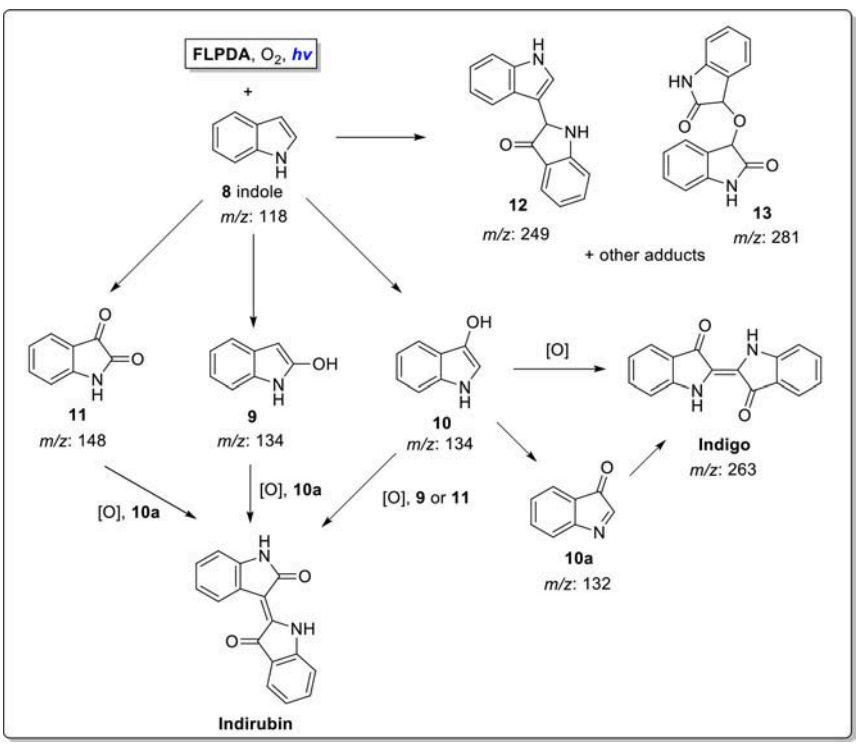

SCHEME 4 | Proposed reaction scheme for indole photooxidation in presence of enzyme mimicking **FLPDA**.

0.5 h. HPLC analysis indicated that there is a greater conversion of indole in presence of RF compared to **FLPDA,** and similar products although in different yields, were observed as shown in **Figure 6** and **Table 1**. We next compared the yield of dyes after the reactions through the addition of 2 drops of 1M HCl to each reaction mixture to initiate dimerization of hydroxylated

TABLE 1 | Amounts and conversions of major compounds identified by HPLC after acidification of reaction mixture using commercial standards as a calibration reference.

Catalyst	Indole (μM)	Oxindole (9) (μM)	Isatin (11) (μM)	Indole conversion	Indigoid yield*
FLPDA (36 ug/mL)	213	22	60	79%	5%
RF (20 μM)	24	16	80	97%	1%

*([*indigoid*] × 2/[*consumed indole*]) *(Xu et al., 2012) with [indigoid] being determined by UV-Vis spectroscopy.*

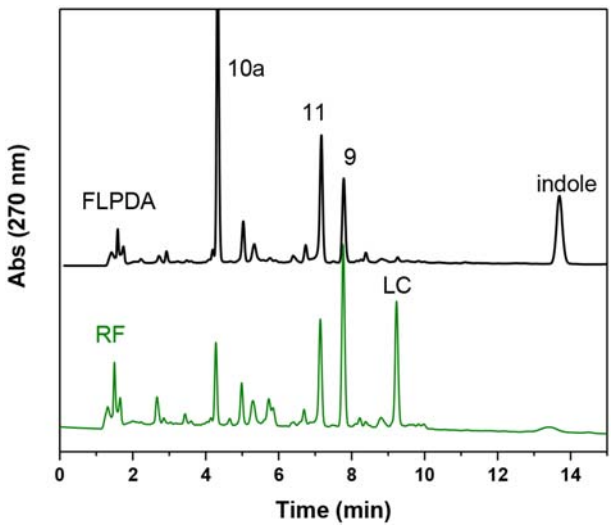

FIGURE 6 | HPLC chromatograms of the reaction mixture after 2 h blue light irradiation of indole (1.0 mM) in the presence of **FLPDA** (36 μg/mL) in ACN/H_2O (1:1, v/v) and riboflavin **RF** (20 μM).

indole species to form the indigoid dyes. As shown in **Figure 7B**, there was more indirubin obtained from the reaction conducted in the presence of **FLPDA** than **RF**, which was expected as 2.5 times more precursor **10a** can be detected in HPLC profile shown in **Figure 6**. Clearly, despite the decreased indole conversion, **FLPDA** appears to be more selective than its homogeneous counterpart toward dye conversion.

It is also worth noting that after the irradiation, **RF** could no longer be identified by TLC analysis within the reaction mixture and had degraded to lumichrome (LC), which was confirmed both by HPLC and LC-MS (9.22 min, *m/z*: 243) (**Figure 6**). Although there was some photodecomposition observed in **FLPDA**, the concentration of lumichrome was five times lower compared to **RF** (based on HPLC integration), indicating that the hybrid catalyst offers more protection toward photodecomposition of active flavin centers, and mitigates the loss of catalysis observed in homogenous systems.

Further Control Experiments and Possible Mechanism of Action

As this is a novel hybrid system, we were also interested in unveiling the photocatalytic mechanism of **FLPDA.** To achieve this we employed a superoxide radical scavenger TEMPO and the singlet oxygen scavenger DABCO to quench these prominent reactive oxygen species (ROS) that may be liberated from reduced and/or photoexcited flavin species (Massey et al., 1969; Müller and Ahmad, 2011). As can be seen from the HPLC chromatograms of the reactions shown in **Figure 8**, the addition of these quenchers did not appear to inhibit the reaction completely. In fact, we observed that in the case of DABCO, the basic character of the species may have played a role in lowering the activity of **FLPDA** as flavins and PDA are less stable within a basic environment (Song et al., 1965; Yang et al., 2018). In terms of product selectivity, **10a** was not detected most likely due to direct oxidization to isatin **11** in basic condition (**Table 2**). Based on these observations it could be assumed that singlet oxygen plays a minimal role in **FLPDA** activity as both compounds **9** and **11** are obtained in the presence of singlet oxygen quencher.

The addition to the superoxide scavenger, TEMPO had no deleterious effect on **FLPDA** activity either and in fact, it enhanced the production of **9, 10a**, and **11**. In fact, TEMPO most probably acts as a redox mediator and co-catalyst in the reaction, as previously shown for the synthesis of isatin derivatives in the presence of hypervalent iodine (Sai Prathima et al., 2015). TEMPO's participation in the reactions was additionally proved by appearance of the by-product 2,2,6,6-tetramethylpiperidine (TMP) at a retention time of 2.49 min, *m/z*: 142 (LC-MS analysis). It should be noted that pigment melanin, composed of PDA units, is capable of superoxide quenching (Tada et al., 2010), and it is safe to assume that any superoxide radical generated by flavin would be quickly quenched by PDA in its immediate proximity.

We further investigated the mechanism of **FLPDA**'s photocatalytic activity by using a fluorescence-based assay to monitor the release of H_2O_2 liberated from the unstable 4a-hydroperoxy-flavin species formed when reduced flavin moieties interact with oxygen (Usselman et al., 2014). We reasoned that the lower amount of H_2O_2 obtained in photo-reaction in presence of **FLPDA** compared to free flavin (riboflavin **RF**), would indicate potential stabilization of 4a-hydroperoxy-flavin species, and its interaction with indole (**Scheme 5**) instead of direct transformation into reactive oxygen species. To minimize the loss of photons due to the scattering effect of a colloidal heterogeneous catalyst, low concentration of **FLPDA** (10 μg/mL) was used, and the concentration of indole and effective concentration of free flavin were adjusted accordingly. The amount of H_2O_2 released after 1 h of irradiation was 3.62 ± 0.18 nmol for **FLPDA** and 5.13 ± 0.04 nmol for **RF** (see **Figure S4**). The lower value obtained for **FLPDA** suggest that the stabilization of 4a-hydroperoxy flavin species in **FLPDA** may occur, although this hypothesis can only be fully confirmed after the completion of already initiated EPR study.

Based on current data, we propose the mechanism shown in **Scheme 5**, which includes the formation of the 4a-hydroperoxy species as a result of indole and/or PDA photoreduction, and subsequent interaction with oxygen. This species could be stabilized by H-bonding with neighboring PDA moieties and be stable long enough to interact with the indole substrate. In addition, the appearance of compounds **12** and **13** indicates Type 1 photosensitization of indole through electron transfer to excited flavin moieties similar to that previously observed for riboflavin

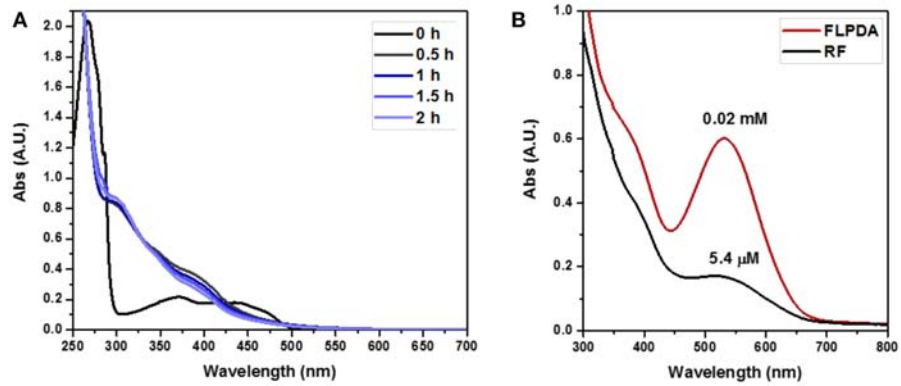

FIGURE 7 | (A) UV-Vis absorption spectra of the photooxidation of indole (1.0 mM) in the presence of **RF** (20 μM) in O_2 saturated ACN/H_2O (1:1, v/v). **(B)** Plot comparing the reactions post acid workup (3× dilutions of reaction mixtures).

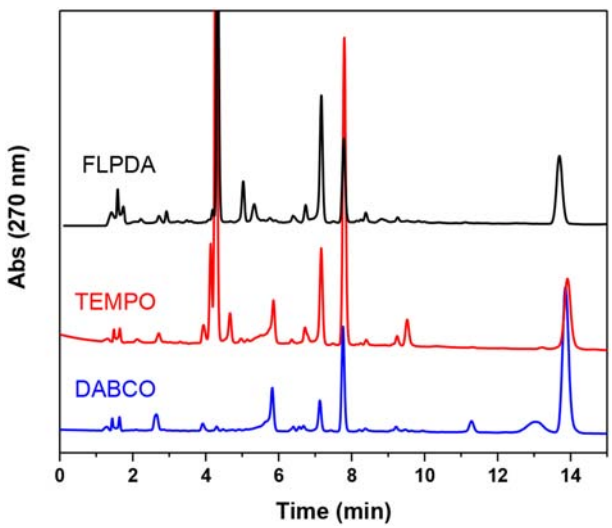

FIGURE 8 | HPLC chromatograms of control experiments in which **FLPDA** (50 μg/mL) and indole (1.0 mM) were irradiated in presence of radical scavengers DABCO (1.0 mM) and TEMPO (1.0 mM).

TABLE 2 | Amounts and conversions of major compounds identified by HPLC after acidification of reaction mixture using commercial standards as a calibration reference.

Quencher	Indole (μM)	Oxindole (9) (μM)	Isatin (11) (μM)	Indole conversion
TEMPO	177	278	121	82%
DABCO	326	143	252	67%

and tryptophan (Silva et al., 2019). However, as stated above further studies using EPR spectroscopy are being undertaken to confirm our theory.

Although some "dark" reactions in the presence of flavin species have resulted in excellent yields of desired products (Arakawa et al., 2017; Chevalier et al., 2018), use of light to trigger the reaction cascade that leads to complex dye formation would have multiple advantages in an industrial setting, including temporal and spatial control, ultimately leading to the design of more efficient reactors.

Recyclability

Finally, we were interested to estimate the reusability of **FLPDA** in this light-driven reaction as this is a desirable property for scaling up and industrial applications enhancing the green potential of the system. Previous work on a heterogeneous flavin-based photocatalytic system using mesoporous silica to immobilize flavin moieties suffered from a severe loss of activity after the first reuse, and a complete inactivation upon second and third attempt (Špačková et al., 2017). For our nanoparticle-based system, the catalyst was easily removed from the reaction mixture *via* centrifugation and maintained activity for 4 cycles. As a proof of concept study, activity was monitored by irradiation of **FLPDA** particles (50 μg/ml) with indole (1.0 mM) for 1.5 h and measuring the changes in absorption of the reaction mixture between 300 and 600 nm as shown in **Figure 9A**. The area within this region was integrated and used as a measure for oxidized indole species production. The first run showed a decrease in relative activity compared to the initial run only by a factor of 1.36 (**Figure 9B**) and the subsequent three runs stayed within a similar range before minimum activity, although not a complete loss, was observed by run 6.

The enhanced stability of our system could be explained by the electron transfer from PDA to flavin moieties upon irradiation as proposed in our mechanism (**Scheme 5**). It has already been shown that an addition of an electron donor, such as 2-(*N*-morpholino)ethanesulfonic acid (MES) buffer, limits photo-induced decomposition reactions that curtail flavin activity upon irradiation (Alonso-De Castro et al., 2017). However, during the recycling steps, the number of retrieved particles decreased with each run. Loss of particles and the catalytic activity could point toward the photo-degradation of PDA moieties similar to what was previously observed in melanin samples (Ito et al., 2018). However, we did not notice any difference in the particle size and morphology after 2 h of irradiation (**Figures 9C,D**), which

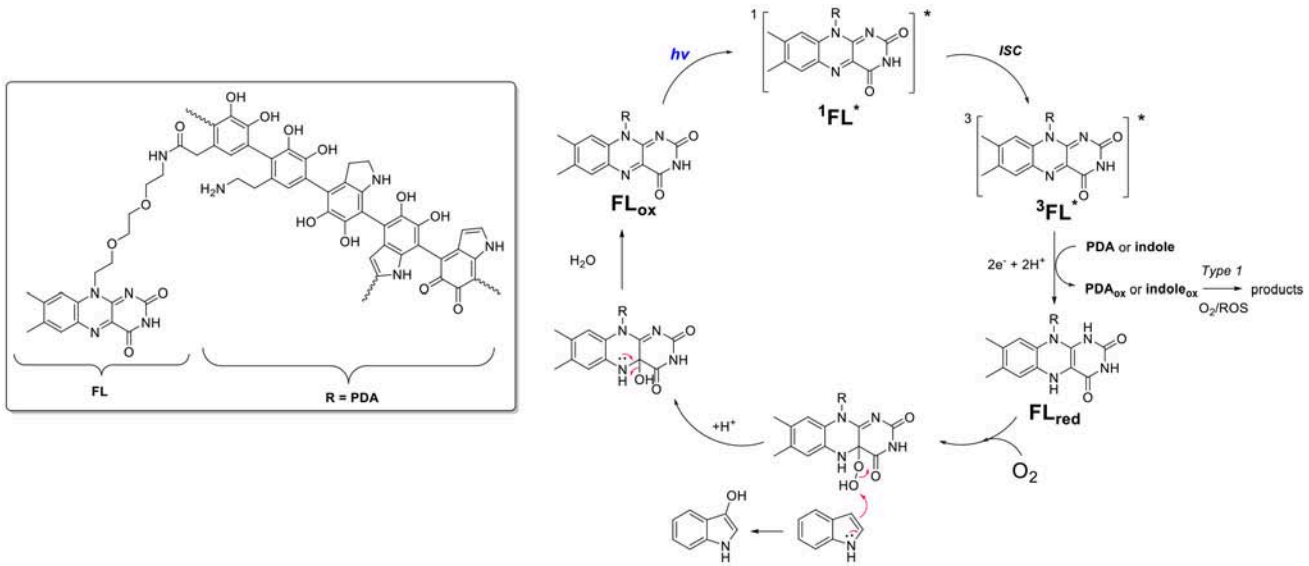

SCHEME 5 | Proposed mechanism of action involving electron transfer process between flavin (FL) and PDA moieties within **FLPDA** hybrid catalyst.

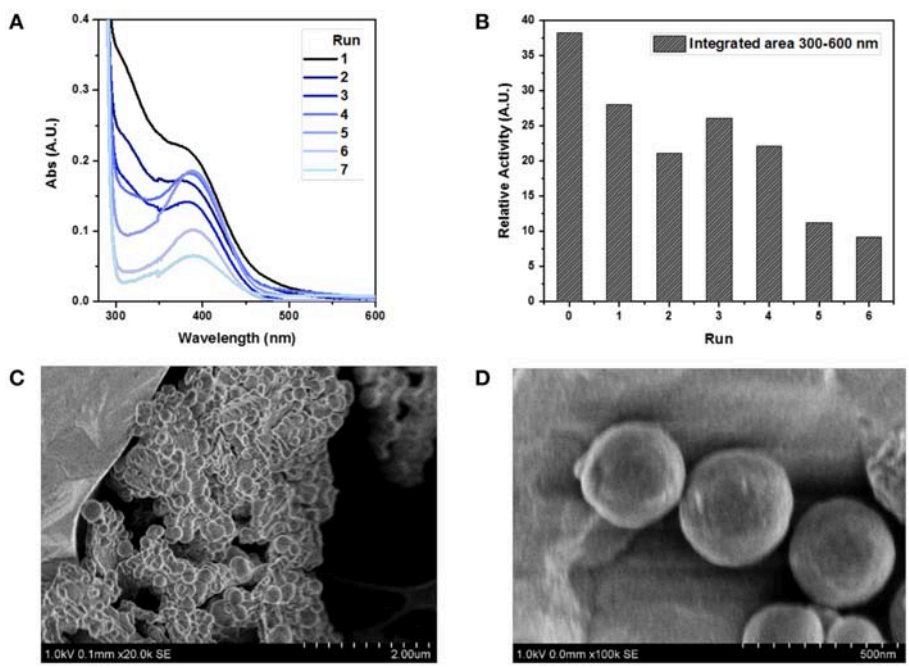

FIGURE 9 | Study of FLPDA catalyst recyclability. UV-Vis absorption spectra of different runs using a recycled catalyst **(A)** and the relative activity plot using the integrated area between 300 and 600 nm of each run **(B)**. STEM image of FLPDA particles after 2 h irradiation shown at different scales **(C)** scale bar = 2.00 μm, and **(D)** scale bar = 500 nm. Reaction conditions: indole (1.0 mM), **FLPDA** (50 μg/mL) in O_2 saturated ACN/H_2O (1:1, v/v) and irradiation for 1.5 h.

disputes this argument, and indicates a mere physical loss of particles during recovery procedures.

Our ongoing work is focused on exploring the long-term stability and photo-degradation of **FLPDA**, as well as establishing a detailed mechanism using EPR studies. We believe this information will allow us to rationally design better catalytic systems with enantio-selective potential. We are also currently working on improving the reusability of **FLPDA** by addition of magnetic Fe_3O_4 nanoparticles during co-polymerization to enable magnetically aided retrieval, which has already proven effective in various application using PDA (Liu et al., 2013, 2017; Xie et al., 2014; Yu et al., 2016).

CONCLUSION

We have developed a novel photocatalytic organic nanoparticle system made from flavin conjugated polydopamine. This was achieved through a convenient co-polymerization method involving dopamine and a flavin-dopamine analog, **FLDA**, to form **FLPDA**. The system effectively displays activity analogous to xenobiotic-degrading enzymes such as FMO, shown, using the oxidation reaction of indole, to form the indigo dye. In addition, it employs irradiation with visible light rather than an external cofactor for catalyst activation. The products observed in the reaction; indigo, indirubin, and related compounds, clearly indicated FMO-like activity of **FLPDA**. Additional ROS scavenging studies as well as the nature of some products, further confirmed that **FLPDA** displays mechanistic similarities to natural FMO, which is characterized by the formation of 4a-hydroperoxy flavin as a reactive intermediate. In contrast to our heterogeneous hybrid flavin, free flavin in a solution was characterized with higher photo-degradation and lower dye yields. In addition, **FLPDA** can easily be recovered from the reaction mixture and displays recyclable activity up to four cycles. We hope that this initial work sets the foundation to enable the design of more elaborate photocatalytic biopolymer hybrids comprising of flavin, PDA and additional functional moieties, to be applied in heterogeneous catalysis and artificial photosynthesis.

AUTHOR CONTRIBUTIONS

LC carried out all the synthesis, characterization and analyses, and wrote the draft manuscript. LF was involved in the experimental planning and manuscript proofreading and corrections. LF was the academic lead of the project in charge of experimental planning and funding.

FUNDING

The project was funded by the Department of Chemical Engineering and Biotechnology Start-up grant awarded to LF. LC would like to acknowledge support for DTP-EPSRC doctoral programme (EP/N509620/1).

ACKNOWLEDGMENTS

We would like to thank Dijana Matak, as well as Rhian Preece, Nitin Rustogi, and Sabine Bahn for their help with LC-MS analysis.

SUPPLEMENTARY MATERIAL

The Supplementary Material for this article can be found online at: https://www.frontiersin.org/articles/10.3389/fchem.2019.00278/full#supplementary-material

REFERENCES

Ai, K., Liu, Y., Ruan, C., Lu, L., and Lu, G. (2013). Sp2 C-dominant N-doped carbon sub-micrometer spheres with a tunable size: a versatile platform for highly efficient oxygen-reduction catalysts. *Adv. Mater.* 25, 998–1003. doi: 10.1002/adma.201203923

Alonso-De Castro, S., Ruggiero, E., Ruiz-De-Angulo, A., Rezabal, E., Mareque-Rivas, J. C., Lopez, X., et al. (2017). Riboflavin as a bioorthogonal photocatalyst for the activation of a PtIV prodrug. *Chem. Sci.* 8, 4619–4625. doi: 10.1039/c7sc01109a

Arakawa, Y., Minagawa, K., and Imada, Y. (2018). Advanced flavin catalysts elaborated with polymers. *Polym. J.* 50, 941–949. doi: 10.1038/s41428-018-0089-8

Arakawa, Y., Yamanomoto, K., Kita, H., Minagawa, K., Tanaka, M., Haraguchi, N., et al. (2017). Design of peptide-containing: N 5-unmodified neutral flavins that catalyze aerobic oxygenations. *Chem. Sci.* 8, 5468–5475. doi: 10.1039/c7sc01933e

Blackburn, R. S., Bechtold, T., and John, P. (2009). The development of indigo reduction methods and pre-reduced indigo products. *Color. Technol.* 125, 193–207. doi: 10.1111/j.1478-4408.2009.00197.x

Chevalier, Y., Lock Toy Ki, Y., le Nouen, D., Mahy, J. P., Goddard, J. P., and Avenier, F. (2018). Aerobic Baeyer–Villiger oxidation catalyzed by a flavin-containing enzyme mimic in water. *Angew. Chem. Int. Ed.* 57, 16412–16415. doi: 10.1002/anie.201810124

Cibulka, R. (2015). Artificial flavin systems for chemoselective and stereoselective oxidations. *European J. Org. Chem.* 2015, 915–932. doi: 10.1002/ejoc.201403275

de Gonzalo, G., and Fraaije, M. W. (2013). Recent developments in Flavin-based catalysis. *ChemCatChem* 5, 403–415. doi: 10.1002/cctc.201200466

Deng, L., Norberg, O., Uppalapati, S., Yan, M., and Ramström, O. (2011). Stereoselective synthesis of light-activatable perfluorophenylazide- conjugated carbohydrates for glycoarray fabrication and evaluation of structural effects on protein binding by SPR imaging. *Org. Biomol. Chem.* 9, 3188–3198. doi: 10.1039/c1ob05040k

D'Ischia, M., Napolitano, A., Ball, V., Chen, C. T., and Buehler, M. J. (2014). Polydopamine and eumelanin: from structure-property relationships to a unified tailoring strategy. *Acc. Chem. Res.* 47, 3541–3550. doi: 10.1021/ar500273y

Du, Y., Yang, H. C., Xu, X. L., Wu, J., and Xu, Z. K. (2015). Polydopamine as a catalyst for thiol coupling. *ChemCatChem* 7, 3822–3825. doi: 10.1002/cctc.201500643

Erb, M., Veyrat, N., Robert, C. A. M., Xu, H., Frey, M., Ton, J., et al. (2015). Indole is an essential herbivore-induced volatile priming signal in maize. *Nat. Commun.* 6:6273. doi: 10.1038/ncomms7273

Ganachaud, C., Garfagnoli, V., Tron, T., and Iacazio, G. (2008). Trimerisation of indole through laccase catalysis. *Tetrahedron Lett.* 49, 2476–2478. doi: 10.1016/j.tetlet.2008.02.021

Gehauf, B., and Goldenson, J. (1957). Detection and estimation of nerve gases by fluorescence reaction. *Anal. Chem.* 29, 276–278. doi: 10.1021/ac60122a029

Gillam, E. M. J., Notley, L. M., Cai, H., De Voss, J. J., and Guengerich, F. P. (2000). Oxidation of indole by cytochrome P450 enzymes. *Biochemistry* 39, 13817–13824. doi: 10.1021/bi001229u

Han, G. H., Gim, G. H., Kim, W., Seo, S., Il, and Kim, S. W. (2012). Enhanced indirubin production in recombinant *Escherichia coli* harboring a flavin-containing monooxygenase gene by cysteine supplementation. *J. Biotechnol.* 164, 179–187. doi: 10.1016/j.jbiotec.2012.08.015

Harayama, T., Tezuka, Y., Taga, T., and Yoneda, F. (1984). Hydrolysis products of flavins (isoalloxazines). *Tetrahedron Lett.* 25, 4015–4018. doi: 10.1016/0040-4039(84)80054-4

Heelis, P. F. (1982). The photophysical and photochemical properties of flavins (isoalloxazines). *Chem. Soc. Rev.* 11:15. doi: 10.1039/cs9821100015

Hodgson, E. (2010). Introduction to biotransformation (metabolism). *Hayes Handb. Pestic. Toxicol.* 2010, 865–875. doi: 10.1016/B978-0-12-374367-1.00036-7

Hong, S., Kim, K. Y., Wook, H. J., Park, S. Y., Lee, K. D., Lee, D. Y., et al. (2011). Attenuation of the *in vivo* toxicity of biomaterials by polydopamine surface modification. *Nanomedicine* 6, 793–801. doi: 10.2217/nnm.11.76

Hsu, T. M., Welner, D. H., Russ, Z. N., Cervantes, B., Prathuri, R. L., Adams, P. D., et al. (2018). Employing a biochemical protecting group for a sustainable indigo dyeing strategy. *Nat. Chem. Biol.* 14, 256–261. doi: 10.1038/nchembio.2552

Ito, S., Wakamatsu, K., and Sarna, T. (2018). Photodegradation of eumelanin and pheomelanin and its pathophysiological implications. *Photochem. Photobiol.* 94, 409–420. doi: 10.1111/php.12837

Jiang, X., Wang, Y., and Li, M. (2014). Selecting water-alcohol mixed solvent for synthesis of polydopamine nano-spheres using solubility parameter. *Sci. Rep.* 4:6070. doi: 10.1038/srep06070

Kim, J. H., Lee, M., and Park, C. B. (2014). Polydopamine as a biomimetic electron gate for artificial photosynthesis. *Angew. Chem. Int. Ed.* 53, 6364–6368. doi: 10.1002/anie.201402608

König, B., Kümmel, S., and Cibulka, R. (2013). Flavin photocatalysis. *Chem. Photocatal.* 3, 45–66. doi: 10.1515/9783110269246.45

Kotaki, A., Naoi, M., and Yagi, K. (1970). Effect of proton donors on the absorption spectrum of flavin compounds in apolar media. *J. Biochem.* 68, 287–292. doi: 10.1093/oxfordjournals.jbchem.a129358

Kotaki, A., and Yagi, K. (1970). Fluorescence properties of flavins in various solvents. *J. Biochem.* 68, 509–516. doi: 10.1093/oxfordjournals.jbchem.a129381

Kozik, A., Korytowski, W., Sarna, T., and Bloom, A. S. (1990). Interactions of flavins with melanin. Studies on equilibrium binding of riboflavin to DOPA-melanin and some spectroscopic characteristics of flavin-melanin complex. *Biophys. Chem.* 38, 39–48. doi: 10.1016/0301-4622(90)80038-9

Krueger, S. K., and Williams, D. E. (2005). Mammalian flavin-containing monooxygenases: structure/function, genetic polymorphisms and role in drug metabolism. *Pharmacol. Ther.* 106, 357–387. doi: 10.1016/j.pharmthera.2005.01.001

Kumar, A., and Kumar, S. (1998). Colloidal CdS-induced photocatalytic reaction of 2-methyl-indole—mechanistic analysis of oxidation of indoles. *J. Phys. Org. Chem.* 11, 277–282. doi: 10.1002/(SICI)1099-1395(199804)11:4<277::AID-POC3>3.0.CO;2-T

Kunfi, A., Szabó, V., Mastalir, Á., Bucsi, I., Mohai, M., Németh, P., et al. (2017). Palladium on polydopamine: its true potential in catalytic transfer hydrogenations and heck coupling reactions. *ChemCatChem* 9, 3236–3244. doi: 10.1002/cctc.201700609

Kuo, H. H., and Mauk, A. G. (2012). Indole peroxygenase activity of indoleamine 2,3-dioxygenase. *Proc. Natl. Acad. Sci. U.S.A.* 109, 13966–13971. doi: 10.1073/pnas.1207191109

Lee, H., Dellatore, S. M., Miller, W. M., and Messersmith, P. B. (2007). Mussel-inspired surface chemistry for multifunctional coatings. *Science* 318, 426–430. doi: 10.1126/science.1147241

Lee, J. H., Kim, Y. G., Baek, K. H., Cho, M. H., and Lee, J. (2015a). The multifaceted roles of the interspecies signalling molecule indole in Agrobacterium tumefaciens. *Environ. Microbiol.* 17, 1234–1244. doi: 10.1111/1462-2920.12560

Lee, J. H., and Lee, J. (2010). Indole as an intercellular signal in microbial communities. *FEMS Microbiol. Rev.* 34, 426–444. doi: 10.1111/j.1574-6976.2009.00204.x

Lee, J. H., Wood, T. K., and Lee, J. (2015b). Roles of indole as an interspecies and interkingdom signaling molecule. *Trends Microbiol.* 23, 707–718. doi: 10.1016/j.tim.2015.08.001

Li, S., Yang, X., Yang, S., Zhu, M., and Wang, X. (2012). Technology prospecting on enzymes: application, marketing and engineering. *Comput. Struct. Biotechnol. J.* 2:e201209017. doi: 10.5936/csbj.201209017

Lin, B., and Tao, Y. (2017). Whole-cell biocatalysts by design. *Microb. Cell Fact.* 16:106. doi: 10.1186/s12934-017-0724-7

Lin, C., Top, D., Manahan, C. C., Young, M. W., and Crane, B. R. (2018). Circadian clock activity of cryptochrome relies on tryptophan-mediated photoreduction. *Proc. Natl. Acad. Sci. U.S.A.* 115, 3822–3827. doi: 10.1073/pnas.1719376115

Lin, G. H., Chen, H. P., Huang, J. H., Liu, T. T., Lin, T. K., Wang, S. J., et al. (2012). Identification and characterization of an indigo-producing oxygenase involved in indole 3-acetic acid utilization by *Acinetobacter baumannii*. *Antonie van Leeuwenhoek* 101, 881–890. doi: 10.1007/s10482-012-9704-4

Linhares, M., Rebelo, S. L. H., Simões, M. M. Q., Silva, A. M. S., Neves, M. G. P. M. S., Cavaleiro, J. A. S., et al. (2014). Biomimetic oxidation of indole by Mn(III)porphyrins. *Appl. Catal. A Gen.* 470, 427–433. doi: 10.1016/j.apcata.2013.11.023

Liu, R., Guo, Y., Odusote, G., Qu, F., and Priestley, R. D. (2013). Core-shell Fe3O4 polydopamine nanoparticles serve multipurpose as drug carrier, catalyst support and carbon adsorbent. *ACS Appl. Mater. Interfaces* 5, 9167–9171. doi: 10.1021/am402585y

Liu, S., Qileng, A., Huang, J., Gao, Q., and Liu, Y. (2017). Polydopamine as a bridge to decorate monodisperse gold nanoparticles on Fe_3O_4 nanoclusters for the catalytic reduction of 4-nitrophenol. *RSC Adv.* 7, 45545–45551. doi: 10.1039/c7ra09373j

Liu, Y., Ai, K., and Lu, L. (2014). Polydopamine and its derivative materials: synthesis and promising applications in energy, environmental, and biomedical fields. *Chem. Rev.* 114, 5057–5115. doi: 10.1021/cr400407a

Ma, A., Xie, Y., Xu, J., Zeng, H., and Xu, H. (2015). The significant impact of polydopamine on the catalytic performance of the carried Au nanoparticles. *Chem. Commun.* 51, 1469–1471. doi: 10.1039/C4CC08489F

Ma, Q., Zhang, X., and Qu, Y. (2018). Biodegradation and biotransformation of indole: advances and perspectives. *Front. Microbiol.* 9, 2625. doi: 10.3389/fmicb.2018.02625

Massey, V., Strickland, S., Mayhew, S. G., Howell, L. G., Engel, P. C., Matthews, R. G., et al. (1969). The production of superoxide anion radicals in the reaction of reduced flavins and flavoproteins with molecular oxygen. *Biochem. Biophys. Res. Commun.* 36, 891–897. doi: 10.1016/0006-291X(69)90287-3

Mataranga-Popa, L. N., Torje, I., Ghosh, T., Leitl, M. J., Späth, A., Novianti, M. L., et al. (2015). Synthesis and electronic properties of π-extended flavins. *Org. Biomol. Chem.* 13, 10198–10204. doi: 10.1039/c5ob01418b

Mathes, T., Van Stokkum, I. H. M., Stierl, M., and Kennis, J. T. M. (2012). Redox modulation of flavin and tyrosine determines photoinduced proton-coupled electron transfer and photoactivation of BLUF photoreceptors. *J. Biol. Chem.* 287, 31725–31738. doi: 10.1074/jbc.M112.391896

Mermod, N., Harayama, S., and Timmis, K. N. (1986). New route to bacterial production of indigo. *Bio/Technology* 4, 321–324. doi: 10.1038/nbt0486-321

Meyer, A., Würsten, M., Schmid, A., Kohler, HP„ and Witholt, B. (2002). Hydroxylation of Indole by laboratory-evolved 2-hydroxybiphenyl 3-monooxygenase. *J. Biol. Chem.* 277, 34161–34167. doi: 10.1074/jbc.m205621200

Mrõwczynski, R., Bunge, A., and Liebscher, J. (2014). Polydopamine—an organocatalyst rather than an innocent polymer. *Chem. A Eur. J.* 20, 8647–8653. doi: 10.1002/chem.201402532

Müller, P., and Ahmad, M. (2011). Light-activated cryptochrome reacts with molecular oxygen to form a flavin-superoxide radical pair consistent with magnetoreception. *J. Biol. Chem.* 286, 21033–21040. doi: 10.1074/jbc.M111.228940

Nagayama, H., Sugawara, T., Endo, R., Ono, A., Kato, H., Ohtsubo, Y., et al. (2015). Isolation of oxygenase genes for indigo-forming activity from an artificially polluted soil metagenome by functional screening using *Pseudomonas putida* strains as hosts. *Appl. Microbiol. Biotechnol.* 99, 4453–4470. doi: 10.1007/s00253-014-6322-2

O'Connor, K. E., Dobson, A. D. W., and Hartmans, S. (1997). Indigo formation by microorganisms expressing styrene monooxygenase activity. *Appl. Environ. Microbiol.* 63, 4287–4291.

Rebelo, S. L. H., Linhares, M., Simões, M. M. Q., Silva, A. M. S., Neves, M. G. P. M. S., Cavaleiro, J. A. S., et al. (2014). Indigo dye production by enzymatic mimicking based on an iron(III)porphyrin. *J. Catal.* 315, 33–40. doi: 10.1016/j.jcat.2014.04.012

Reetz, M. T. (2002). Directed evolution of selective enzymes and hybrid catalysts. *Tetrahedron* 58, 6595–6602. doi: 10.1016/S0040-4020(02)00668-3

Rieff, B., Bauer, S., Mathias, G., and Tavan, P. (2011). IR spectra of flavins in solution: DFT/MM description of redox effects. *J. Phys. Chem. B* 115, 2117–2123. doi: 10.1021/jp111334z

Sai Prathima, P., Bikshapathi, R., and Rao, V. J. (2015). Synthesis of isatin derivatives under metal free conditions using hypervalent iodine. *Tetrahedron Lett.* 56, 6385–6388. doi: 10.1016/j.tetlet.2015.09.124

Schmaderer, H., Hilgers, P., Lechner, R., and König, B. (2009). Photooxidation of benzyl alcohols with immobilized flavins. *Adv. Synth. Catal.* 351, 163–174. doi: 10.1002/adsc.200800576

Seixas De Melo, J., Moura, A. P., and Melo, M. J. (2004). Photophysical and spectroscopic studies of indigo derivatives in their keto and leuco forms. *J. Phys. Chem. A* 108, 6975–6981. doi: 10.1021/jp049076y

Silva, E., Barrias, P., Fuentes-Lemus, E., Tirapegui, C., Aspee, A., Carroll, L., et al. (2019). Riboflavin-induced Type 1 photo-oxidation of tryptophan using a high

intensity 365 nm light emitting diode. *Free Radic. Biol. Med.* 131, 133–143. doi: 10.1016/J.FREERADBIOMED.2018.11.026

Singh, A., Singh Chauhan, N., Thulasiram, H. V., Taneja, V., and Sharma, R. (2010). Identification of two flavin monooxygenases from an effluent treatment plant sludge metagenomic library. *Bioresour. Technol.* 101, 8481–8484. doi: 10.1016/j.biortech.2010.06.025

Smith, S. B., and Bruice, T. C. (1975). Mechanisms of isoalloxazine (flavine) hydrolysis. *J. Am. Chem. Soc.* 97, 2875–2881. doi: 10.1021/ja00843a043

Song, P. S., Smith, E. C., and Metzler, D. E. (1965). Photochemical degradation of flavins. II. The mechanism of alkaline hydrolysis of 6,7-dimethyl-9-formylmethylisoalloxazine1,2. *J. Am. Chem. Soc.* 87, 4181–4184. doi: 10.1021/ja01096a031

Špačková, J., Svobodová, E., Hartman, T., Stibor, I., Kopecká, J., Cibulková, J., et al. (2017). Visible light [2+2] photocycloaddition mediated by Flavin derivative immobilized on mesoporous silica. *ChemCatChem* 9, 1177–1181. doi: 10.1002/cctc.201601654

Sullivan, D. W., and Gad, S. E. (2014). "Indole," in *Encyclopedia of Toxicology, 3rd edn*, ed P. Wexler (Cambridge, MA: Acadmeic Press), 1030–1031. doi: 10.1016/B978-0-12-609386454-3.00860-5

Tada, M., Kohno, M., and Niwano, Y. (2010). Scavenging or quenching effect of melanin on superoxide anion and singlet oxygen. *J. Clin. Biochem. Nutr.* 46, 224–228. doi: 10.3164/jcbn.09-84

Tsoi, K. M., Dai, Q., Alman, B. A., and Chan, W. C. W. (2013). Are quantum dots toxic? Exploring the discrepancy between cell culture and animal studies. *Acc. Chem. Res.* 46, 662–671. doi: 10.1021/ar300040z

Usselman, R. J., Hill, I., Singel, D. J., and Martino, C. F. (2014). Spin biochemistry modulates reactive oxygen species (ROS) production by radio frequency magnetic fields. *PLoS ONE* 9:e93065. doi: 10.1371/journal.pone.0093065

Wang, L., Hu, Z.-Y., Yang, X.-Y., Zhang, B.-B., Geng, W., Van Tendeloo, G., et al. (2017). Polydopamine nanocoated whole-cell asymmetric biocatalysts. *Chem. Commun.* 53, 6617–6620. doi: 10.1039/C7CC01283G

Woo, H. J., Sanseverino, J., Cox, C. D., Robinson, K. G., and Sayler, G. S. (2000). The measurement of toluene dioxygenase activity in biofilm culture of *Pseudomonas putida* F1. *J. Microbiol. Methods* 40, 181–191. doi: 10.1016/S0167-7012(00)00123-8

Xie, Y., Yan, B., Xu, H., Chen, J., Liu, Q., Deng, Y., et al. (2014). Highly regenerable mussel-inspired Fe_3O_4@polydopamine-Ag core-shell microspheres as catalyst and adsorbent for methylene blue removal. *ACS Appl. Mater. Interfaces* 6, 8845–8852. doi: 10.1021/am501632f

Xu, J., Shoji, O., Fujishiro, T., Ohki, T., Ueno, T., and Watanabe, Y. (2012). Construction of biocatalysts using the myoglobin scaffold for the synthesis of indigo from indole. *Catal. Sci. Technol.* 2, 739–744. doi: 10.1039/c2cy00427e

Yang, W., Liu, C., and Chen, Y. (2018). Stability of polydopamine coatings on gold substrates inspected by surface plasmon resonance imaging. *Langmuir* 34, 3565–3571. doi: 10.1021/acs.langmuir.7b03143

Yang, Z., Sun, J., Liu, X., Su, Q., Liu, Y., Li, Q., et al. (2014). Nano-sized polydopamine-based biomimetic catalyst for the efficient synthesis of cyclic carbonates. *Tetrahedron Lett.* 55, 3239–3243. doi: 10.1016/j.tetlet.2014.04.033

Yong, K. T., Law, W. C., Hu, R., Ye, L., Liu, L., Swihart, M. T., et al. (2013). Nanotoxicity assessment of quantum dots: from cellular to primate studies. *Chem. Soc. Rev.* 42, 1236–1250. doi: 10.1039/c2cs35392j

Yu, X., Cheng, G., and Zheng, S. Y. (2016). Synthesis of self-assembled multifunctional nanocomposite catalysts with highly stabilized reactivity and magnetic recyclability. *Sci. Rep.* 6:25459. doi: 10.1038/srep25459

Zelentskii, A. N., Fomin, G. V., Kutafina, N. V., and Berlin, A. A. (1970). The mechanism of oxidation of indoxyl and its analogs to indigo and indigoides. *Bull. Acad. Sci. USSR Div. Chem. Sci.* 19, 1105–1107. doi: 10.1007/BF01084331

Zhou, J., and Shephard, E. A. (2006). Mutation, polymorphism and perspectives for the future of human flavin-containing monooxygenase 3. *Mutat. Res. Rev. Mutat. Res.* 612, 165–171. doi: 10.1016/j.mrrev.2005.09.001

Zhou, X., Jin, B., Luo, J., Gu, X., and Zhang, S. (2017). Photoreduction preparation of Cu_2O@polydopamine nanospheres with enhanced photocatalytic activity under visible light irradiation. *J. Solid State Chem.* 254, 55–61. doi: 10.1016/j.jssc.2017.07.007

Conflict of Interest Statement: The authors declare that the research was conducted in the absence of any commercial or financial relationships that could be construed as a potential conflict of interest.

Copyright © 2019 Crocker and Fruk. This is an open-access article distributed under the terms of the Creative Commons Attribution License (CC BY). The use, distribution or reproduction in other forums is permitted, provided the original author(s) and the copyright owner(s) are credited and that the original publication in this journal is cited, in accordance with accepted academic practice. No use, distribution or reproduction is permitted which does not comply with these terms.

Chemical and Process Engineering (formerly Chemical Engineering)

Camille Petit

Dr Camille Petit is a Reader in the Chemical Engineering Department at Imperial College London. She leads the Multifunctional Materials Laboratory. She was a postdoctoral researcher at Columbia University and obtained her PhD in Chemistry from the City University of New York. Her research interests encompass the development of porous materials for energy and environmental applications. She focuses on metal-organic frameworks and nitride-based materials for molecular separations and solar energy conversion. She received the 2017 AIChE's 35 under 35 award, the 2017 ExxonMobil European Science & Engineering Program Award, the 2017 IOM3 Silver Medal, and the 2015 IChemE Sir Frederick Warner medal.

Kelly M. Schultz

Dr Kelly M. Schultz is an Associate Professor in the Department of Chemical and Biomolecular Engineering at Lehigh University. She obtained her PhD in Chemical Engineering advised by Eric Furst from the University of Delaware. She was a Howard Hughes Medical Institute postdoctoral research associate at the University of Colorado at Boulder working for Kristi Anseth. She began her position at Lehigh in 2013. She was named a TA Instruments Distinguished Young Rheologists in 2014, received an NSF CAREER Award in 2018, and a Libsch Early Career Research Award in 2019. Her group studies emerging hydrogel materials developed for consumer products and biological applications.

Florent Allais

Florent Allais is a Professor in Chemistry at AgroParisTech, Paris, France and the Director of the URD ABI in Pomacle, France. He obtained his PhD from the University of Florida in 2004 and his postdocs at ESPCI, Paris, France and ICSN, Gif-sur-Yvette, France. He has published approximately 80 papers and filed 16 patents. His multidisciplinary research team combine biotechnologies, green chemistry, and downstream processing approaches to develop durable processes to turn agro-resources into platform molecules as well as valuable chemicals that can be used in chemistry, in food/feed or cosmetics to name a few.

Tsuguyuki Saito

Dr Tsuguyuki Saito is an Associate Professor of the University of Tokyo, Japan. He obtained his PhD degree in 2008 from the University of Tokyo for his study on TEMPO-mediated oxidation of cellulosic fibers. He has further developed this oxidation as a tool to produce the finest type of cellulose nanofibers (CNF) with a width of approximately 3 nm from wood pulp in an energy-efficient way. For his ground-breaking discovery on CNF production, he was awarded the Marcus Wallenberg Prize by the Marcus Wallenberg Foundation in 2015, and the JSPS prize by the Japan Society for the Promotion of Science in 2019.

frontiers in Chemistry

ORIGINAL RESEARCH
published: 26 March 2019
doi: 10.3389/fchem.2019.00160

Porous Boron Nitride Materials: Influence of Structure, Chemistry and Stability on the Adsorption of Organics

*Sofia Marchesini, Xiyu Wang and Camille Petit**

Department of Chemical Engineering, Barrer Centre, Imperial College London, London, United Kingdom

Porous boron nitride (BN) is structurally analogous to activated carbon. This material is gaining increasing attention for its potential in a range of adsorption and chemical separation applications, with a number of recent proof-of-concept studies on the removal of organics from water. Today though, the properties of porous BN—i.e., surface area, pore network, chemistry—that dictate adsorption of specific organics remain vastly unknown. Yet, they will need to be optimized to realize the full potential of the material in the envisioned applications. Here, a selection of porous BN materials with varied pore structures and chemistries were studied for the adsorption of different organic molecules, either directly, through vapor sorption analyses or as part of a water/organic mixture in the liquid phase. These separations are relevant to the industrial and environmental sectors and are envisioned to take advantage of the hydrophobic character of the BN sheets. The materials were tested and regenerated and their physical and chemical features were characterized before and after testing. This study allowed identifying the adsorption mechanisms, assessing the performance of porous BN compared to benchmarks in the field and outlining ways to improve the adsorption performance further.

Keywords: boron nitride, vapor sorption, adsorption, separations, water stability

OPEN ACCESS

Edited by:
Gil Garnier,
Bioresource Processing Institute of Australia (BioPRIA), Australia

Reviewed by:
Petra Foerst,
Technische Universität München, Germany
Xiao-Yu Wu,
Massachusetts Institute of Technology, United States

****Correspondence:***
Camille Petit
camille.petit@imperial.ac.uk

Specialty section:
This article was submitted to Chemical Engineering, a section of the journal Frontiers in Chemistry

Received: *28 November 2018*
Accepted: *04 March 2019*
Published: *26 March 2019*

Citation:
Marchesini S, Wang X and Petit C (2019) Porous Boron Nitride Materials: Influence of Structure, Chemistry and Stability on the Adsorption of Organics. Front. Chem. 7:160. doi: 10.3389/fchem.2019.00160

INTRODUCTION

Chemical separations account for more than half of the total energy consumed in industry owing to the many separation processes performed *via* distillation (Sholl and Lively, 2016). Adsorbent materials or membranes, which are able to separate molecules based on size exclusion principles and/or chemistries, offer a possibly less energy intensive and hence more sustainable route to separations (Sholl and Lively, 2016). Realizing the potential of adsorption and membrane separation requires the production of porous materials with tailorable properties and porosities. Today, research in this area primarily focuses on materials such as metal-organic frameworks (James, 2003), zeolites (Misaelides, 2011), carbon-based materials (Dias et al., 2007), covalent organic frameworks (Côté et al., 2005), and polymer of intrinsic microporosity (McKeown and Budd, 2006). A recent addition to this list is porous boron nitride (BN). Owing to its high thermal stability, "rich" chemistry, and high surface area [up to ~2,000 m^2 g^{-1} reported so far (Li et al., 2013b; Marchesini et al., 2017b)], porous BN has been tested for a range of different applications such as catalysis (Venegas et al., 2017), CO_2 capture, oil spill clean-up (Lei et al., 2013), hydrogen storage

(Portehault et al., 2010; Lei et al., 2014; Weng et al., 2014), and water cleaning (Zhang et al., 2012; Li et al., 2013a,b; Lei et al., 2015). Porous BN is somewhat analogous to activated carbon in terms of its turbostratic to amorphous structure with 6-member rings of alternating B and N atoms. Yet, its chemistry is obviously different from that of carbonaceous materials as the material is made of polar B-N bonds. BN materials are typically hydrophobic. Such a feature can be particularly advantageous for the adsorption of organics, either in the vapor phase or as part of a water/organic mixture in the liquid phase. In fact, a number of studies report the use of porous BN for the removal of organic molecules (e.g., dyes, pharmaceutical molecules, oils) from water Zhang et al., 2012; Li et al., 2013a,b; Lei et al., 2015. The sorption mechanisms are typically associated to: (i) π-π stacking interactions between the BN sheets and aromatic dye molecules (Zhang et al., 2012; Liu et al., 2014, 2015); (ii) electrostatic dipole-dipole interactions between the polar B-N bond and the polar dyes (Liu et al., 2014; Lin et al., 2016); (iii) physisorption in the micropores of BN (Liu et al., 2014; Lin et al., 2016), and (iv) hydrophobic interactions (Yu et al., 2018). The adsorption capacity can be highly dependent upon the pH of the solution in the case of dye sorption, due to electrostatic interactions with the polar dyes, which are weakened by competitive adsorption of protons or hydroxides (Singla et al., 2015; Li et al., 2016). For a similar reason, OH-functionalised BN adsorbs more cationic dyes (e.g., methylene blue) than its pristine counterpart (Li et al., 2015). Porous BN materials exhibit competitive sorption capacities of selected organics compared to other common adsorbents such as activated carbons (Yu et al., 2018). Interestingly, many studies on the removal of organics from water using porous BN, report multiple adsorption and desorption cycles with minimal (5–15%) decrease in performance (Li et al., 2013b, 2015; Lei et al., 2015; Zhao et al., 2015; Liu et al., 2016). This behavior is surprising given the demonstrated instability of some porous BN structures in the presence of water, which causes a decrease in porosity (Shankar et al., 2018). This raises a question around the effect of BN porosity in these applications. Overall, the studies above serve as proof-of-concept for the use of porous BN as adsorbent for a given organic. Today though, the materials parameters—i.e., surface area, pore network, chemistry—that dictate adsorption of specific organics remain vastly unknown.

Herein, we synthesized BN samples exhibiting a range of pore structures and crystallinity as well as distinct chemistries (Marchesini et al., 2017a; Shankar et al., 2018) The pore structure of the materials was controlled *via* manipulation of the precursor type and ratio used to synthesized BN (see our previous study Marchesini et al., 2017a). We tuned the crystallinity and chemistry—particularly the amount of O groups—using the synthesis temperature (Shankar et al., 2018). We tested all the porous BN samples for the adsorption of different organic molecules, either directly, through vapor sorption analyses or as part of a water/organic mixture in the liquid phase. The organics selected for this study cover different classes of chemicals in terms of polarity and molecular size: alkanes (linear and branched), cycloalkanes, aromatics alcohols, and dyes. We characterized the samples before and after adsorption and linked their materials features to the adsorption behaviors.

Materials Synthesis

We synthesized porous BN materials following a procedure previously developed by our group Marchesini et al., 2017b. Boron- and nitrogen- containing precursors were mixed and ground in different molar ratios. The precursors were placed in an alumina boat crucible and heated up to the 1050 or 1500°C for 3.5 h (10°C/min ramp rate) under nitrogen gas flow (50 cc/min during analysis, 3 h at 250 cc/min to purge). The furnace was cooled while flowing nitrogen until ambient temperature. We refer to porous BN samples synthesized at 1050°C as "low temperature BN" samples, and to porous BN samples synthesized at 1500°C as "high temperature BN" samples. We used three different sample formulations as follows:

- BN-U5: molecular ratio of urea:boric acid = 5:1;
- BN-MU0.25:5: molecular ratio of melamine:urea:boric acid = 0.25:5:1;
- BN-MU1:5: molecular ratio of melamine:urea:boric acid = 1:5:1.

Materials Characterization

Materials characterization techniques were used to: (i) verify that the synthesized samples cover a range of porosity, crystallinity and chemistry as envisioned initially and (ii) assess the impact of adsorption on the materials features and (iii) extract information of the adsorption mechanisms.

Structural Properties and Morphology

Nitrogen physisorption isotherms were measured using a porosity analyser (Micromeritics 3Flex) at −196 °C. Prior to nitrogen sorption analysis, the samples were degassed overnight at 120 °C at roughly 0.2 mbar pressure and degassed again *in-situ* on the porosity analyser for 4 h down to around 0.003 mbar at 120 °C. From the nitrogen isotherms, we derived the surface areas, total pore volumes, micro- and mesopore volumes of BN samples and pore size distributions (Rouquerol et al., 2013). The surface areas of the samples were calculated using the Brunauer-Emmett-Teller (BET) method (Brunauer et al., 1938). The total volume of pores was calculated from the volume of N_2 adsorbed at $P/P_0 = 0.97$. The micropore volume was determined using the Dubinin Radushkevich method (Chen and Yang, 1994). The pore size distributions were calculated using a DFT model for carbons with slit-shape pores using the Micromerics software.[1] We assessed the crystallinity (or lack of) of our samples *via* powder X-ray diffraction (XRD) using an X-ray diffractometer (PANalytical X'Pert PRO) in reflection mode. The operating conditions included an anode voltage of 40 kV and an emission current of 40 mA using monochromatic Cu Kα radiation (λ = 1.54178 Å).

Chemical Properties

The porous BN samples were characterized by Fourier Transform Infrared (FT-IR) spectroscopy. The samples were first ground in

[1] http://www.nldft.com

an agate mortar and spectra were collected in the range of 600–4000 cm^{-1} using a Perkin-Elmer Spectrum 100 Spectrometer equipped with an attenuated total reflectance (ATR) accessory. X-ray Photoelectron Spectroscopy (XPS) was performed using a Thermo Scientific K-Alpha$^+$ X-ray Photoelectron Spectrometer equipped with a MXR3 Al Kα monochromated X-ray source ($h\nu = 1486.6$ eV). X-ray gun power was set to 72 W (6 mA and 12 kV). All high resolution spectra (B 1*s*, N 1*s*, C 1*s*, and O 1*s*) were acquired using 20 eV pass energy and 0.1 eV step size. The samples were ground and mounted on the XPS sample holder using conductive carbon tape. Thermo Avantage software (ThermoFisher Scientific) was used to analyse the data. The XPS spectra were shifted to align the peak for adventitious carbon (C-C) at 285.0 eV.

Materials Testing

Organic Vapor Sorption

We conducted these analyses to assess the "idealized" (i.e., single adsorbate, no competitive adsorption) adsorption of several molecules with different polarities and molecular sizes. We performed vapor sorption experiments on an IGA gravimetrical analyser (Hiden Isochema). The IGA analyser is equipped with a microbalance with ± 1 μg resolution. The samples (∼30 mg) were degassed *in-situ* at 120 °C for 4 h using a furnace attachment, prior to analysis. An ultra-high vacuum of up to 10^{-6} mbar could be created inside the chamber. Solvents were purified by cycles of evacuation followed by vapor equilibrium, repeated for at least 10 times. The solvents were vaporized and dosed up to 90 % of their saturation pressures at 25 °C: n-heptane (P_0: 61.12 mbar), 2,3-dymethylpentane (P_0: 91.82 mbar), toluene (P_0: 37.93 mbar), methylcyclohexane (P_0: 61.79 mbar), 1-butanol (P_0: 9.22 mbar), methanol (P_0: 169.24 mbar). The temperature was controlled using an external water bath equipped with a thermocouple which maintained a temperature stability of ± 0.3 °C. Equilibrium for each pressure point was predicted by the IGA software after a minimum wait of 20 min, by checking for weight changes using the least squares regression to extrapolate the asymptote (tolerance of 99 %). Pressure increase/decrease was performed with a rate of ∼0.25–1 of the step pressure change. All solvents were of analytical grade. We performed *in situ*-degas in between each experiment at 250 °C to regenerate porous BN. Solvent selectivity was calculated as the ratio of quantity adsorbed of two pure solvents measured under the same conditions, assuming equal partial pressures.

Water Vapor Sorption

Prior to testing the removal of organics from water, we assessed water sorption to evaluate the affinity of the samples with water and quantify their water adsorption capacity. Porous BN samples were degassed at 120 °C at roughly 0.2 mbar pressure and again *in-situ* on the porosity analyser (Micromeritics 3Flex) for 4 h down to around 0.003 mbar. We collected water vapor isotherms at 30 °C for porous BN samples at up to 90% relative humidity in a gas/vapor volumetric analyser.

Organics Removal From Water

We used a dye [Rhodamine B, RhB (HPLC, Sigma Aldrich)] as a representative organic molecule owing to the ease of monitoring dye sorption using UV-vis spectroscopy. In a typical test, 250 mL of stock solution (of 40 mg/L in deionized water) were vigorously stirred and 100 mg of porous BN powder were added to the solution while stirring. At 0, 5, 10, 30, 60, 120, 240 min, about 2 mL of solution were collected with a syringe and filtered with a syringe filter (0.45 μm) to remove BN powder. We then analyzed these solutions using UV-vis spectrophotometry to determine the dye concentration. UV-vis spectra were collected between 400 and 650 nm ($\lambda_{maxRhodamine} = 554$ nm) at a scan speed of 480 nm/min using a Perkin Elmer Lambda 35 spectrophotometer with quartz cuvettes. Calibration was performed by preparing solutions with decreasing dye concentrations (see calibration curve in **Supplementary Figure 1**, $R^2 > 0.99$). After 240 min, BN samples were filtered using a Buchner filtration system, dried in the oven at 120 °C and then heated at 600 °C (10 °C/min) for 3 h in a tubular furnace under air gas flow (50 mL/min) before being reused for a second adsorption cycle. We selected this regeneration temperature based on the decomposition temperature of the dye, as determined by TGA analysis (Netzsch TG209 F1 Libra, 10 °C/min ramp rate, under air gas flow at 0.1 L/min; **Supplementary Figure 2A**).

RESULTS AND DISCUSSION

First, we confirmed the "profiles" of the materials synthesized using a number of characterization techniques to assess the range of porosity, crystallinity, and functionalization. As expected, the porous BN materials were all micro/mesoporous but displayed different pore volumes and BET surface areas (**Table 1**; **Figure 1A**). The samples covered a range going from 734 to 1650 m^2g^{-1} in terms of surface area and 31 to 62% in terms of microporosity volume compared to total porosity. For all samples, the surface area and porosity decreased upon thermal treatment, as expected (Shankar et al., 2018). All samples contained oxygen atoms as part of their structure, as determined from XPS analyses (**Table 1**) and high temperature porous BN samples generally exhibited a lower oxygen content compared to low temperature porous BN samples. All porous BN samples displayed very similar XRD patterns with the same peak position for the (002) peak between the different samples, indicating similar d (002)-spacing (∼0.35 nm) (**Supplementary Figures 3A,B**). The absence of other reflections other than the (002) and (100) and the large width and low intensity of the peaks confirmed that all samples were turbostratic. Despite a similar lack of crystallinity in the bulk phase between the low and high temperature BN samples, our prior work identified localized regions of increased crystallinity and thereby hydrophobicity in the high temperature BN sample (Shankar et al., 2018). We assessed the effect of these crystalline and hydrophobic regions on the adsorption behavior below.

We then tested the low temperature porous BN materials (different pore structures and similar chemistries) for adsorption of C-7 hydrocarbons exhibiting different sizes/shapes (e.g., linear n-heptane or branched 2,3-dimethylpentane) and/or chemistries (e.g., aromatic toluene or non-aromatic methylcyclohexane) and two different alcohols (methanol and 1-butanol). Through this study, we intended to identify links between the materials physical properties, including porosity, and the adsorption

TABLE 1 | Overview of the porosity and chemistry of the porous BN samples: textural parameters derived from nitrogen sorption isotherms at −196 °C and relative atomic percentages derived from XPS analysis.

Sample	S_{BET} (m^2/g)	V_{tot} (cm^3/g)	V_{micro} (cm^3/g)	V_{meso} (cm^3/g)	V_{micro}/V_{tot} (%)	O 1*s* (at %)	N 1*s* (at %)	B 1*s* (at %)
LOW TEMPERATURE BN								
BN-U5	1,092	0.927	0.444	0.483	48	7	41	52
BN-MU0.25:5	1,339	1.026	0.545	0.481	53	8	40	52
BN-MU1:5	1,650	1.120	0.660	0.460	41	9	39	52
HIGH TEMPERATURE BN								
BN-U5	734	0.999	0.305	0.694	31	6	42	52
BN-MU0.25:5	940	1.095	0.409	0.686	62	6	42	52
BN-MU1:5	980	1.005	0.460	0.545	54	4	43	53

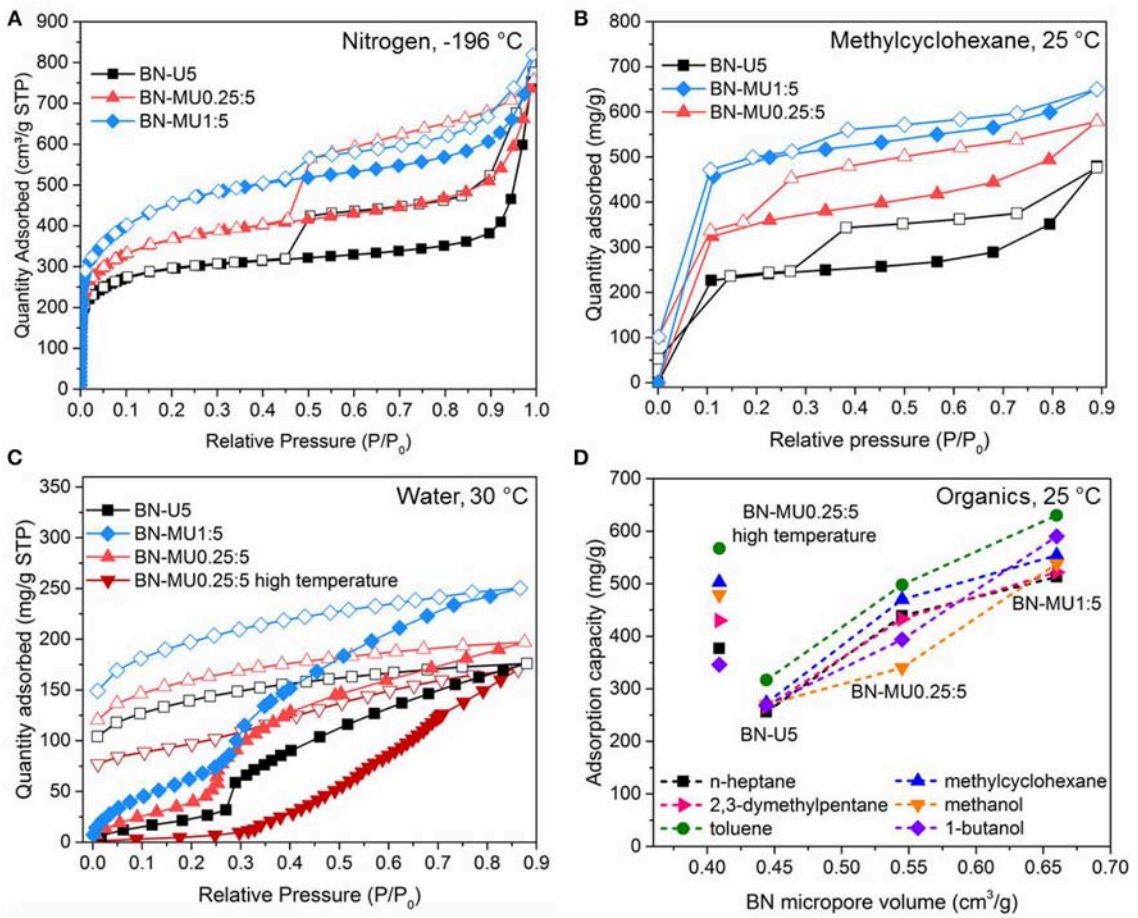

FIGURE 1 | Organics and water sorption behaviors of porous BN samples of varying pore structures: **(A)** N_2 sorption isotherms at −196 °C for three low temperature porous BN samples, **(B)** methylcyclohexane vapor sorption isotherms for the same three low temperature porous BN samples at 25 °C, **(C)** water vapor sorption isotherms for low temperature porous BN and one high temperature porous BN sample at 30 °C, **(D)** organic vapor sorption capacity at 0.6 P/P_0 vs. micropore volume of porous BN for three low temperature samples and a high temperature BN. Open symbols in the figures represent desorption.

performance. The results are presented in **Figure 1B** for methylcyclohexane and in **Supplementary Figure 4** for all other chemicals. The three samples exhibited different sorption isotherms. Given that their chemical composition was similar, the differences are attributed to differences in physisorption dictated by the pore structure of the materials. In fact, the organic vapor sorption isotherms followed the same patterns as the nitrogen sorption at −196 °C (compare **Figures 1A**,**B**). The total vapor sorption capacity increased with increasing surface areas and most of the vapors were adsorbed at low relative pressures,

in the microporous regions. The presence of mesopores caused capillary condensation (e.g., see BN-MU0.25:5) as indicated by the presence of hystereses in the desorption curves. Most of the vapors desorbed (**Figure 1B**) as the pressure was lowered, confirming that little/no chemisorption occurred.

We also evaluated water sorption for different low temperature porous BN samples at 30 °C (**Figure 1C**). Water uptake increased with the surface areas. Importantly, the water did not completely desorb upon reducing the pressure as observed from the "open" hystereses. As highlighted in a previous study (Shankar et al., 2018), this behavior originates from the hydrolysis of the BN materials through the following reaction: $2BN + 3H_2O \rightarrow B_2O_3 + 2NH_3$. The hydrolysis of porous BN takes place due to the presence of defects in the structure (Motojima et al., 1982; Alkoy et al., 1997; Streletskii et al., 2009; Cao et al., 2012; Shankar et al., 2018). Upon thermal treatment, as mentioned above, we form localized regions of increased crystallinity and hydrophobicity. Hence, the high temperature porous BN showed a reduced water uptake capacity, especially at low relative pressures (**Figure 1C**). At higher pressures, the remaining defects sites react with water leading to decomposition of the material (Shankar et al., 2018).

From the organic vapor sorption isotherms, we calculated the sorption capacity at 0.6 P/P_0 (**Figure 1D**). At this relative pressure, organic vapor uptake had ceased and BN materials were saturated. Sorption capacities of low temperature porous BN samples increased with increasing micropore volumes for all organics considered (**Figure 1D**). We found a linear trend between BN micropore volume and sorption capacity for porous BN materials with similar chemistries. This aligns with the behavior observed in activated carbons (Lillo-Ródenas et al., 2005). All porous BN materials adsorbed more toluene than any of the other tested adsorbates. We hypothesized that this is due to the presence of π-π interactions between the *h*-BN rings in porous BN and the aromatic rings in toluene, which contribute to improved physisorption. To put the results in perspective, porous BN exhibited toluene and methanol sorption capacities of the same order of magnitude to activated carbons with similar surface areas (toluene: 700 vs. 950 mg g^{-1}; methanol: 600 vs. 800 mg g^{-1}) (Xu et al., 2015). While the materials absorbed large amounts of organics, they were not selective (**Supplementary Figure 5**; linear n-heptane vs. branched 2,3-dimethylpentane; aromatic toluene vs. non-aromatic methylcyclohexane). This is related to the multimodal pore size distribution of the material—i.e., no narrow pore size distribution—that prevent size exclusion (**Supplementary Figure 6**). Similarly, we tested a high temperature porous BN sample for organic vapor sorption to evaluate the effect of the localized hydrophobic regions of the material (**Figure 1D**). Despite its lower porosity compared to the low temperature BN samples, the high temperature BN sample exhibited increased uptake of all organics. Further support for this observation is provided below when investigating dye sorption.

The adsorption potential of all porous BN materials was finally evaluated for a practical application. We employed

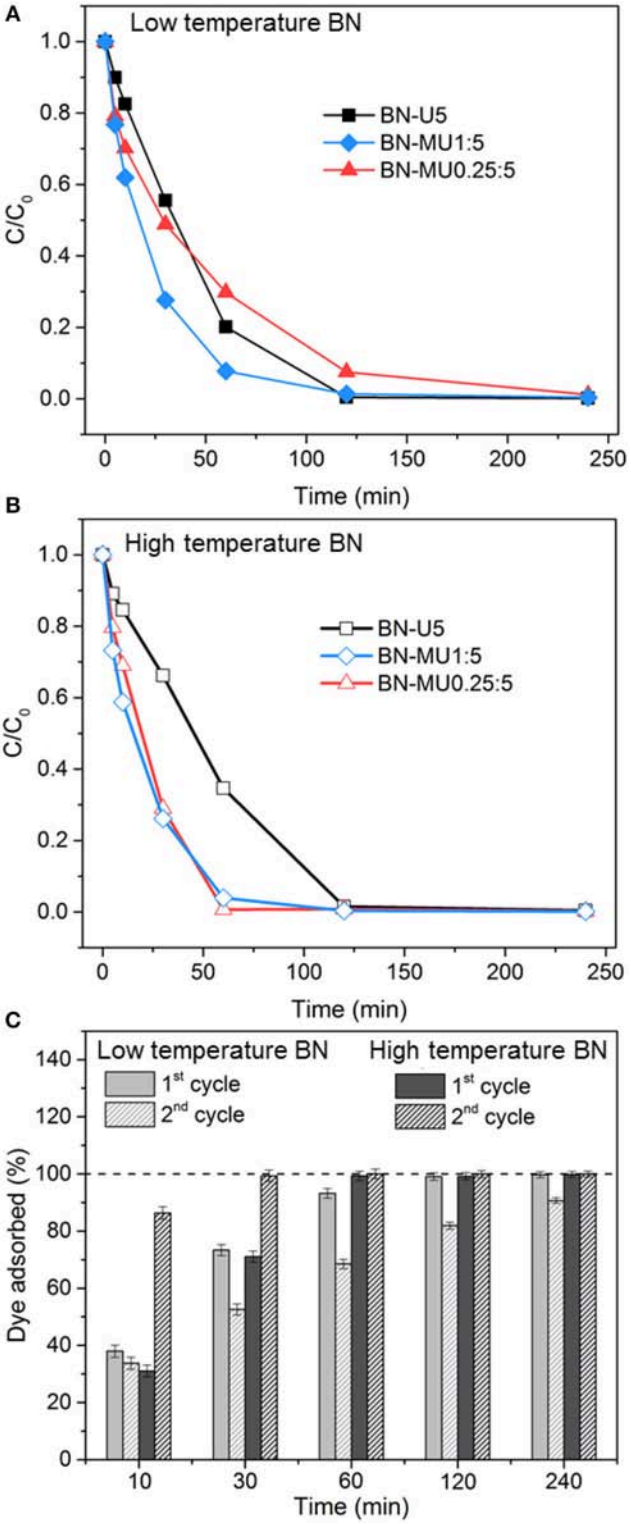

FIGURE 2 | Removal of an organic (Rhodamine B) from water using porous BN samples: **(A)** RhB sorption over time for the low temperature porous BN samples, **(B)** RhB sorption over time for the high temperature porous BN samples, **(C)** evaluation of the recyclability of the best performing porous BN samples at low (BN-MU1:5) and high (BN-MU0.25:5) temperature after regeneration in air at 600 °C.

the porous BN samples (low and high temperatures) for the removal of organics (here Rhodamine B, RhB) from water. The results are presented in **Figure 2**. All samples achieved complete removal of the dye within 4 h or less (**Figures 2A,B**). The time needed to reach complete removal reduced or remained unchanged (for BN-U5) when using the high temperature samples despite their initially lower surface area. Again, high temperature porous BN materials displayed a higher adsorption capacity for organics. We attribute this observation to the increased hydrophobicity and water stability of the high temperature BN samples, as well as to the presence of a larger quantity of π electrons, which allowed greater affinity for the adsorbate while preventing *in-situ* collapse of the material.

We regenerated the better performing low and high temperature samples (BN-MU1:5 and BN-MU0.25:5, respectively) at 600 °C in air and tested them for a second adsorption cycle. The results are reported in **Figure 2C**. While the low temperature BN sample exhibited a decreased capacity after regeneration (10 % decrease at 4 h), the high temperature BN sample maintained its original capacity. This is related to the greater stability of the high temperature sample in the aqueous environment compared to the low temperature sample. Analyses are presented below to confirm this aspect. Interestingly, the high temperature porous BN sample adsorbed more dye in the 2nd cycle than in the 1st cycle for the same exposure time. We explain this by the greater dispersibility of regenerated sample. Indeed, after regeneration and prior to the second sorption run, the sample exhibited finer particles.

We characterized the BN samples after the 1st cycle of dye removal from water and subsequent regeneration in air at 600 °C. This was done to confirm whether a collapse (partial or complete) of the porosity occurred and influenced the adsorption in the 2nd cycle as observed above. To quantify the impact of this potential collapse on the adsorption behavior, both the low and high temperature BN samples were analyzed—the high temperature BN samples being *a priori* less prone to collapse. We note that TGA and XPS analyses confirmed that the dye was completely removed upon regeneration in air at 600 °C (**Supplementary Figure 2**): no carbon residues were observed after regeneration.

First, we analyzed the changes in porosities of the BN samples before testing and after regeneration (**Figure 3**). All low temperature porous BN samples showed a significant decrease in surface area and micropore volume after regeneration pointing to a collapse of the structure *via* hydrolysis (Shankar et al., 2018). Interestingly, the percentage of micropores decreased significantly in all porous BN samples, indicating that the

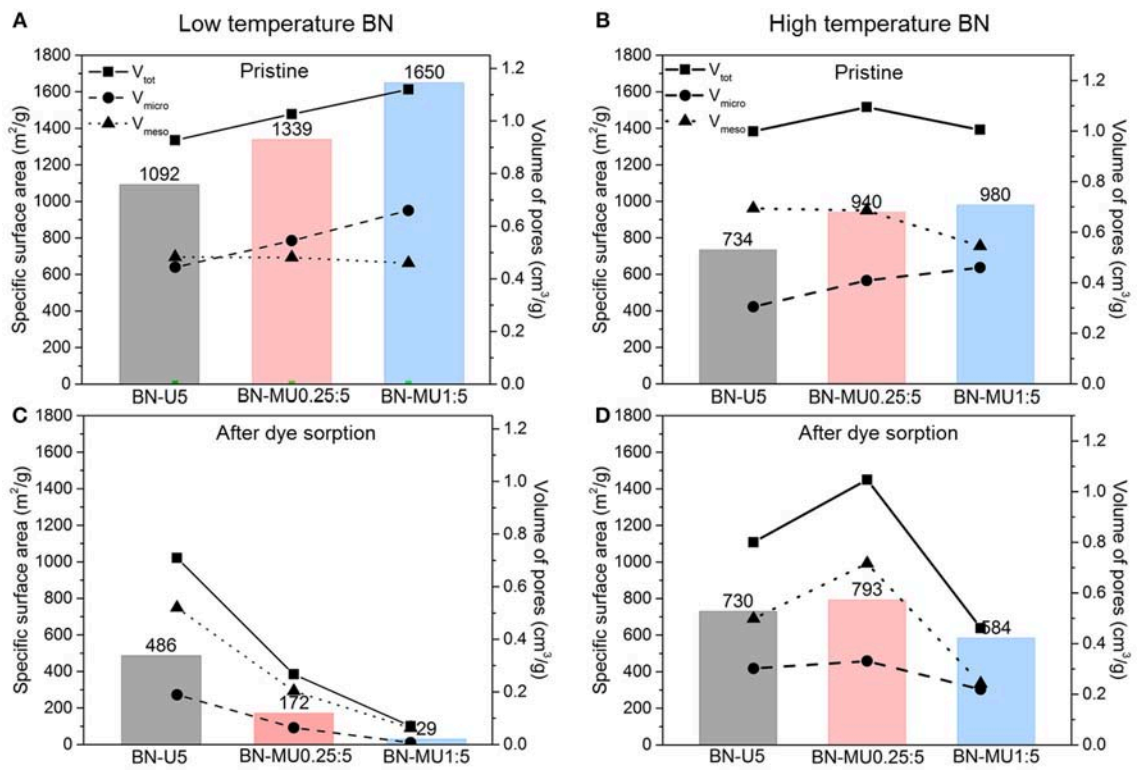

FIGURE 3 | Changes in the porosity of the BN samples upon adsorption and regeneration at 600 °C in air. Textural parameters derived from N_2 sorption isotherms at −196 °C for porous BN samples: **(A)** synthesized at low temperature, **(B)** synthesized at high temperature, **(C)** synthesized at low temperature after dye sorption and regeneration, **(D)** synthesized at high temperature after dye sorption and regeneration.

micropores were initially most susceptible to hydrolysis. This hypothesis is supported by the fact that porous BN samples with higher micropore volumes (BN-MU1:5 > BN-MU0.25:5 > BN-U5), were more unstable, as indicated by a larger decrease in surface area and pore volume. For instance, highly microporous BN-MU1:5 exhibited a significant decrease in surface area from 1650 to 29 m^2g^{-1}, while the surface area of less microporous BN-U5 decreased from 1092 to 486 m^2g^{-1}. This is not surprising as the more porous samples are probably more defective and therefore more prone to hydrolysis. Despite the large decrease in surface area after regeneration, the RhB adsorption capacity only decreased by about 10 %. We hypothesized that the RhB concentration used was not high enough to saturate the adsorbent. Therefore, despite a reduced surface area after regeneration, the adsorption capacity was not significantly affected. The high temperature BN samples exhibited higher stability than the low temperature BN samples after testing and regeneration. Indeed, the samples maintained a high porosity after testing and regeneration. This aligns with the better performance of the high temperature BN samples observed before (**Figure 2**).

Continuing on the characterization of the materials post testing and regeneration, all samples showed a higher relative intensity of the (002)/(100) peaks, possibly indicating a preferred orientation of the crystals along the (002) plane (**Supplementary Figure 3**). In addition, the peak position for the (002) peak (∼25°) shifted to higher angles, indicative of a decrease of the d(002)-spacing and the full width at half maximum (FWHM) decreased, demonstrating an increase in crystallite size (larger number of 2D layers). These three factors together showed that the samples exhibited higher crystallinity after exposure to water, probably as amorphous BN was more readily decomposed in water, resulting in an apparent increase in crystallinity.

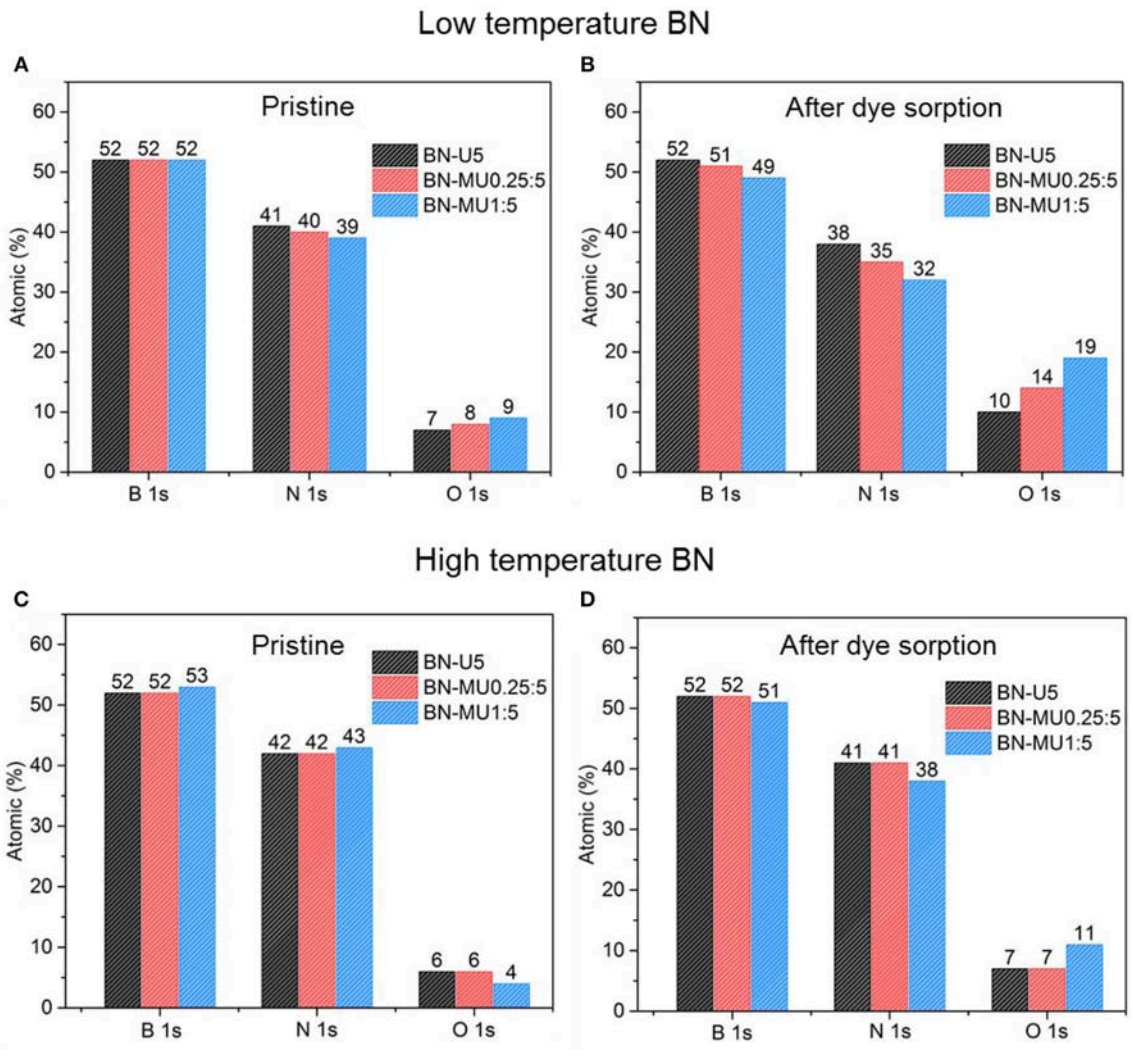

FIGURE 4 | Changes in the chemistry of the BN samples upon adsorption and regeneration at 600 °C in air: **(A,B)** low temperature porous BN samples and **(C,D)** high temperature porous BN samples.

After demonstrating that the porosity of the high temperature BN samples was maintained upon adsorption testing and regeneration, we investigated any potential changes in the chemistry of the materials using XPS analyses. The relative atomic percentages derived from XPS confirmed that the oxygen content increased in all low temperature porous BN samples after adsorption testing and regeneration (**Figures 4A,B**). This further supports the hydrolysis of the low temperature BN samples, causing the oxidation of BN and formation of a larger quantity of boronoxynitride and B-OH groups (Lin et al., 2011). Samples with higher micropore volumes and surface areas (BN-MU1:5 > BN-MU0.25:5 > BN-U5) showed higher increases in oxygen content, indicative of more extensive hydrolysis, in line with the previously described structural changes. The relative nitrogen content decreased in all samples after exposure to water, confirming that a decomposition reaction is occurring, in which water reacts with BN to release ammonia: $3H_2O + 2BN \rightarrow B_2O_3 + 2NH_3$ (Lin et al., 2011). On the other hand, the high temperature porous BN samples did not show any major variations in oxygen content from XPS analysis for two of the samples (**Figures 4C,D**) (BN-U5-1500C and BN-MU0.25:5-1500C).

CONCLUSIONS

We presented here a study on the adsorption behavior of porous boron nitride. For this, we synthesized porous BN samples with varied porosity, crystallinity and chemistry in order to identify the effect of these materials features on the adsorption of different organics. The main conclusions of this work are summarized below:

- Porous BN materials exhibit high sorption capacities for organics, as shown *via* gravimetrical vapor sorption analysis. The organic sorption capacity for toluene on porous BN (∼650 mg/g at 25 °C and 0.6 P/P_0) is comparable to the capacity of activated carbons previously reported in the literature;
- Porous BN materials exhibit low selectivity between the different organics tested here, as highlighted from similar adsorption capacities of organic vapors. This is attributed to their multimodal pore size distribution and amorphous nature, which prevent size exclusion separation.
- Porous BN materials demonstrate higher adsorption capacity of aromatic toluene compared to non-aromatic counterpart, methylcyclohexane. The enhanced toluene adsorption capacity is hypothesized to be due to π-π stacking interactions between the aromatic solvent and the B-N hexagonal rings.
- The adsorption of organics increases with the porosity when the chemistries of the materials are similar. Yet, porosity is not the dominating adsorption parameter. Increasing the crystallinity and hydrophobicity of porous BN materials *via* a heat treatment further allows enhanced organic removal from water, water stability and recyclability (2 cycles tested). The enhanced removal capacity was demonstrated from higher and more efficient removal of Rhodamine B dye from water. High temperature BN was also able to retain better the porosity and chemistry after regeneration. This is attributed to the reduced amount of defect sites that causes hydrolysis of the material and impairs its adsorption performance.
- Porous BN material can be used for organic adsorption from water, such as aromatic dyes (Rhodamine B) and shows complete removal and potentially good recyclability.

DATA AVAILABILITY

All datasets generated for this study are included in the manuscript and the **Supplementary Files**.

AUTHOR CONTRIBUTIONS

SM and CP designed the experiments. SM and XW carried out the experiments. SM, XW, and CP analyzed the data. SM and CP wrote the manuscript. All authors have read and agreed the submission of the manuscript.

ACKNOWLEDGMENTS

The authors would like to thank Dr. Les Bolton and Prof. Glenn Sunley from BP for their technical input. The authors would also like to acknowledge the funding and technical support from BP through the BP International Center for Advanced Materials (BP-ICAM), which made this research possible, as well as EPSRC for the funding through the CDT in Advanced Characterization of Materials (CDT-ACM) (EP/L015277/1). We also acknowledge support from the Department of Chemical Engineering at Imperial College London.

SUPPLEMENTARY MATERIAL

The Supplementary Material for this article can be found online at: https://www.frontiersin.org/articles/10.3389/fchem.2019.00160/full#supplementary-material

REFERENCES

Alkoy, S., Toy, C., Gönül, T., and Tekin, A. (1997). Crystallization behavior and characterization of turbostratic boron nitride. *J. Eur. Ceramic Soc.* 17, 1415–1422. doi: 10.1016/S0955-2219(97)00040-X

Brunauer, S., Emmett, P. H., and Teller, E. (1938). Adsorption of gases in multimolecular layers. *J. Am. Chem. Soc.* 60, 309–319. doi: 10.1021/ja01269a023

Côté, A. P., Benin, A. I., Ockwig, N. W., O'Keeffe, M., Matzger, A. J., Yaghi O. M. (2005). Porous, crystalline, covalent organic frameworks. *Science* 310, 1166–1170. doi: 10.1126/science.1120411

Cao, F., Liu, K., Fang, Z., and Wang, S. (2012). Hydrolysis mechanism of borazine-derived boron nitride pyrolysized below 1200 C. *J. Mater. Sci. Technol.* 28, 956–960. doi: 10.1016/S1005-0302(12)60158-3

Chen, S., and Yang, R. (1994). Theoretical basis for the potential theory adsorption isotherms. The dubinin-radushkevich and dubinin-astakhov equations. *Langmuir* 10, 4244–4249. doi: 10.1021/la00023a054

Dias, J. M., Alvim-Ferraz, M. C., Almeida, M. F., Rivera-Utrilla, J., and Sánchez-Polo, M. (2007). Waste materials for activated carbon preparation and its use in aqueous-phase treatment: a review. *J. Environ. Manage.* 85, 833–846. doi: 10.1016/j.jenvman.2007.07.031

James, S. L. (2003). Metal-organic frameworks. *Chem. Soc. Rev.* 32, 276–288. doi: 10.1039/b200393g

Lei, W., Liu, D., and Chen, Y. (2015). Highly crumpled boron nitride nanosheets as adsorbents: scalable solvent-less production. *Adv. Mater. Interfaces* 2:1400529. doi: 10.1002/admi.201400529

Lei, W., Portehault, D., Liu, D., Qin, S., and Chen, Y. (2013). Porous boron nitride nanosheets for effective water cleaning. *Nat. Commun.* 4:1777. doi: 10.1038/ncomms2818

Lei, W., Zhang, H., Wu, Y., Zhang, B., Liu, D., Qin, S., et al. (2014). Oxygen-doped boron nitride nanosheets with excellent performance in hydrogen storage. *Nano Energy* 6, 219–224. doi: 10.1016/j.nanoen.2014.04.004

Li, J., Huang, Y., Liu, Z., Zhang, J., Liu, X., Luo, H., et al. (2015). Chemical activation of boron nitride fibers for improved cationic dye removal performance. *J. Mater. Chem. A* 3, 8185–8193. doi: 10.1039/C5TA00601E

Li, J., Lin, J., Xu, X., Zhang, X., Xue, Y., Mi, J., et al. (2013a). Porous boron nitride with a high surface area: hydrogen storage and water treatment. *Nanotechnology* 24:155603. doi: 10.1088/0957-4484/24/15/155603

Li, J., Xiao, X., Xu, X., Lin, J., Huang, Y., Xue, Y., et al. (2013b). Activated boron nitride as an effective adsorbent for metal ions and organic pollutants. *Scient. Rep.* 3:3208. doi: 10.1038/srep03208

Li, Q., Yang, T., Yang, Q., Wang, F., Chou, K.-C., and Hou, X. (2016). Porous hexagonal boron nitride whiskers fabricated at low temperature for effective removal of organic pollutants from water. *Ceramics Int.* 42, 8754–8762. doi: 10.1016/j.ceramint.2016.02.114

Lillo-Ródenas, M., Cazorla-Amorós, D., and Linares-Solano, A. (2005). Behaviour of activated carbons with different pore size distributions and surface oxygen groups for benzene and toluene adsorption at low concentrations. *Carbon* 43, 1758–1767. doi: 10.1016/j.carbon.2005.02.023

Lin, J., Xu, L., Huang, Y., Li, J., Wang, W., Feng, C., et al. (2016). Ultrafine porous boron nitride nanofibers synthesized via a freeze-drying and pyrolysis process and their adsorption properties. *RSC Adv.* 6, 1253–1259. doi: 10.1039/C5RA23426C

Lin, Y., Williams, T. V., Xu, T.-B., Cao, W., Elsayed-Ali, H. E., and Connell, J. W. (2011). Aqueous dispersions of few-layered and monolayered hexagonal boron nitride nanosheets from sonication-assisted hydrolysis: critical role of water. *J. Phys. Chem. C* 115, 2679–2685. doi: 10.1021/jp110985w

Liu, D., He, L., Lei, W., Klika, K. D., Kong, L., and Chen, Y. (2015). Multifunctional polymer/porous boron nitride nanosheet membranes for superior trapping emulsified oils and organic molecules. *Adv. Mater. Interfaces* 2:1500228. doi: 10.1002/admi.201500228

Liu, D., Lei, W., Qin, S., and Chen, Y. (2014). Template-free synthesis of functional 3D BN architecture for removal of dyes from water. *Scient. Rep.* 4:4453. doi: 10.1038/srep04453

Liu, D., Lei, W., Qin, S., Klika, K. D., and Chen, Y. (2016). Superior adsorption of pharmaceutical molecules by highly porous BN nanosheets. *Phys. Chem. Chem. Phys.* 18, 84–88. doi: 10.1039/C5CP06399J

Marchesini, S., McGilvery, C. M., Bailey, J., and Petit, C. (2017a). Template-free synthesis of highly porous boron nitride: insights into pore network design and impact on gas sorption. *ACS Nano* 11, 10003–10011. doi: 10.1021/acsnano.7b04219

Marchesini, S., Regoutz, A., Payne, D., and Petit, C. (2017b). Tunable porous boron nitride: Investigating its formation and its application for gas adsorption. *Microporous Mesoporous Mater.* 243, 154–163. doi: 10.1016/j.micromeso.2017.02.010

McKeown, N. B., and Budd, P. M. (2006). Polymers of intrinsic microporosity (PIMs): organic materials for membrane separations, heterogeneous catalysis and hydrogen storage. *Chem. Soc. Rev.* 35, 675–683. doi: 10.1039/b600349d

Misaelides, P. (2011). Application of natural zeolites in environmental remediation: A short review. *Microporous Mesoporous Mater.* 144, 15–18. doi: 10.1016/j.micromeso.2011.03.024

Motojima, S., Tamura, Y., and Sugiyama, K. (1982). Low temperature deposition of hexagonal BN films by chemical vapour deposition. *Thin Solid Films* 88, 269–274. doi: 10.1016/0040-6090(82)90056-6

Portehault, D., Giordano, C., Gervais, C., Senkovska, I., Kaskel, S., Sanchez, C., et al. (2010). High-surface-area nanoporous boron carbon nitrides for hydrogen storage. *Adv. Funct. Mater.* 20, 1827–1833. doi: 10.1002/adfm.201000281

Rouquerol, J., Rouquerol, F., Llewellyn, P., Maurin, G., and Sing, K. S. (2013). *Adsorption by Powders and Porous Solids: Principles, Methodology and Applications*. London: Academic Press.

Shankar, R., Marchesini, S., and Petit, C. (2018). Enhanced hydrolytic stability of porous boron nitride via the control of crystallinity, porosity and chemical composition. *J. Phys. Chem. C* 123. doi: 10.1021/acs.jpcc.8b11731

Sholl, D. S., and Lively, R. P. (2016). Seven chemical separations: to change the world: purifying mixtures without using heat would lower global energy use, emissions and pollution–and open up new routes to resources. *Nature* 532, 435–438. doi: 10.1038/532435a

Singla, P., Goel, N., and Singhal, S. (2015). Boron nitride nanomaterials with different morphologies: synthesis, characterization and efficient application in dye adsorption. *Ceramics Int.* 41, 10565–10577. doi: 10.1016/j.ceramint.2015.04.151

Streletskii, A., Permenov, D., Bokhonov, B., Kolbanev, I., Leonov, A., Berestetskaya, I., et al. (2009). Destruction, amorphization and reactivity of nano-BN under ball milling. *J. Alloys Compounds* 483, 313–316. doi: 10.1016/j.jallcom.2008.08.088

Venegas, J. M., Grant, J. T., McDermott, W. P., Burt, S. P., Micka, J., Carrero, C. A., et al. (2017). Selective oxidation of n-butane and isobutane catalyzed by boron nitride. *ChemCatChem*. 9, 2118–2127. doi: 10.1002/cctc.201601686

Weng, Q., Wang, X., Bando, Y., and Golberg, D. (2014). One-step template-free synthesis of highly porous boron nitride microsponges for hydrogen storage. *Adv. Energy Mater.* 4:1301525. doi: 10.1002/aenm.201301525

Xu, F., Tang, Z., Huang, S., Chen, L., Liang, Y., Mai, W., et al. (2015). Facile synthesis of ultrahigh-surface-area hollow carbon nanospheres for enhanced adsorption and energy storage. *Nat. Commun.* 6:7221. doi: 10.1038/ncomms8221

Yu, S., Wang, X., Pang, H., Zhang, R., Song, W., Fu, D., et al. (2018). Boron nitridebased materials for the removal of pollutants from aqueous solutions: a review. *Chem. Eng. J.* 333, 343–360. doi: 10.1016/j.cej.2017.09.163

Zhang, X., Lian, G., Zhang, S., Cui, D., and Wang, Q. (2012). Boron nitride nanocarpets: controllable synthesis and their adsorption performance to organic pollutants. *CrystEngComm*. 14, 4670–4676. doi: 10.1039/c2ce06748j

Zhao, H., Song, X., and Zeng, H. (2015). 3D white graphene foam scavengers: vesicant-assisted foaming boosts the gram-level yield and forms hierarchical pores for superstrong pollutant removal applications. *NPG Asia Materials*. 7:e168.

Conflict of Interest Statement: The authors declare that the research was conducted in the absence of any commercial or financial relationships that could be construed as a potential conflict of interest.

Copyright © 2019 Marchesini, Wang and Petit. This is an open-access article distributed under the terms of the Creative Commons Attribution License (CC BY). The use, distribution or reproduction in other forums is permitted, provided the original author(s) and the copyright owner(s) are credited and that the original publication in this journal is cited, in accordance with accepted academic practice. No use, distribution or reproduction is permitted which does not comply with these terms.

frontiers in Chemistry

ORIGINAL RESEARCH
published: 08 May 2019
doi: 10.3389/fchem.2019.00317

Structural Changes in Polymeric Gel Scaffolds Around the Overlap Concentration

*Han Zhang, Matthew D. Wehrman and Kelly M. Schultz**

Department of Chemical and Biomolecular Engineering, Lehigh University, Bethlehem, PA, United States

Cross-linked polymeric gels are an important class of materials with applications that broadly range from synthetic wound healing scaffolds to materials used in enhanced oil recovery. To effectively design these materials for each unique applications a deeper understanding of the structure and rheological properties as a function of polymeric interactions is required. Increasing the concentration of polymer in each scaffold increases physical interactions between the molecules that can be reflected in the material structure. To characterize the structure and material properties, we use multiple particle tracking microrheology (MPT) to measure scaffolds during gelation. In MPT, fluorescently labeled probe particles are embedded in the material and the Brownian motion of these particles is captured using video microscopy. Particle motion is related to rheological properties using the Generalized Stokes-Einstein Relation. In this work, we characterize gelation of a photopolymerized scaffold composed of a poly(ethylene glycol) (PEG)-acrylate backbone and a PEG-dithiol cross-linker. Scaffolds with backbone concentrations below and above the overlap concentration, concentration where polymer pervaded volume begins to overlap, are characterized. Using time-cure superposition (TCS) we determine the critical relaxation exponent, n, of each scaffold. The critical relaxation exponent is a quantitative measure of the scaffold structure and is similar to a complex modulus, G^*, which is a measure of energy storage and dissipation. Our results show that below the overlap concentration the scaffold is a tightly cross-linked network, $n_{avg} = 0.40 \pm 0.03$, which stores energy but can also dissipate energy. As polymeric interactions increase, we measure a step change in the critical relaxation exponent above the overlap concentration to $n_{avg} = 0.20 \pm 0.03$. After the overlap concentration the scaffold has transitioned to a more tightly cross-linked network that primarily stores energy. Additionally, continuing to increase concentration results in no change in the scaffold structure. Therefore, we determined that the properties of this scaffold can be tuned above and below the overlap concentration by changing the polymer concentration but the structure will remain the same in each concentration regime. This is advantageous for a wide range of applications that require scaffolds with varying stiffness and the same scaffold architecture.

Keywords: multiple particle tracking microrheology, hydrogel scaffolds, poly(ethylene glycol), photopolymerization, time-cure superposition

OPEN ACCESS

Edited by:
Gil Garnier,
Bioresource Processing Institute of Australia (BioPRIA), Australia

Reviewed by:
Erica Wanless,
University of Newcastle, Australia
Eric Furst,
University of Delaware, United States

****Correspondence:***
Kelly M. Schultz
kes513@lehigh.edu

Specialty section:
This article was submitted to Chemical Engineering, a section of the journal Frontiers in Chemistry

Received: *05 December 2018*
Accepted: *23 April 2019*
Published: *08 May 2019*

Citation:
Zhang H, Wehrman MD and Schultz KM (2019) Structural Changes in Polymeric Gel Scaffolds Around the Overlap Concentration. Front. Chem. 7:317. doi: 10.3389/fchem.2019.00317

INTRODUCTION

Synthetic gels are designed with unprecedented complexity from the bulk material properties down to the scaffold microstructure (Stauffer et al., 1982; Moradi-Araghi et al., 1988; Scanlan and Winter, 1991; Lutolf et al., 2003; Engler et al., 2006; Serra et al., 2006; Zolfaghari et al., 2006; Yamaguchi et al., 2007; He et al., 2009; Schultz et al., 2009a; Schwartz et al., 2010; Tse and Engler, 2010; Zustiak and Leach, 2010; Wylie et al., 2011; Tirrell, 2012; Jung et al., 2013; Tongwa et al., 2013; Purcell et al., 2014; Wang and Heilshorn, 2015; Escobar et al., 2017). This complexity grows out of the vast array of applications and high demand on gel versatility. Gels are part of everyday life from commonly used personal, fabric and home care products to exotic biomaterials designed to mimic the extracellular matrix (ECM) (Winter and Chambon, 1986; Scanlan and Winter, 1991; West and Hubbell, 1999; Raeber et al., 2005, 2007; Yamaguchi et al., 2007; Benton et al., 2009; Fairbanks et al., 2009b; Zustiak and Leach, 2010; Wylie et al., 2011; Wehrman et al., 2018). Cross-linked gels have also played a significant role in enhanced oil recovery (Moradi-Araghi et al., 1988; Zolfaghari et al., 2006; He et al., 2009; Jung et al., 2013; Tongwa et al., 2013). These materials are used to decrease permeability in high permeability zones near naturally fractured carbonates that require water shutoff but cannot be permanently plugged. Rheological measurement is a critical means for characterizing and validating gelation strategies and gaining insight into their structure and properties. Quantitatively identifying dynamic scaffold structure and properties and the relation to material function is crucial in advancing the design of these materials. These history-dependent systems are characterized during gelation to establish a quantitative framework to understand how polymeric interactions, i.e. overlap and entanglement, within macromer solutions change the gelation reaction and influence final material properties in a chain-growth system. We characterize the scaffold structure and rheological properties of a well-defined photopolymerized hydrogel scaffold with increasing polymeric interactions due to an increase in the concentration of the polymer backbone. This work can be leveraged to design gels with highly-engineered microstructures and properties that can be tailored throughout the phase transition.

In this work, polymeric interactions are varied to determine the change in the gelation reaction and final material properties. We are using a neutral polymer, poly(ethylene glycol) (PEG). Due to this, polymeric interactions are defined as only physical interactions between the macromolecules in solution. Polymeric solutions have three regimes in the concentration-viscosity curve: dilute, semi-dilute and entangled (Graessley, 1980; Doi and Edwards, 1988; Pavlov et al., 2003; Rubinstein and Colby, 2003; Wehrman et al., 2018). In the dilute regime, polymers do not interact. In the semi-dilute regime, the pervaded volume of the polymers begin to overlap. In the entangled regime, polymer molecules physically interact and entangle (Graessley, 1980; Doi and Edwards, 1988; Pavlov et al., 2003; Rubinstein and Colby, 2003; Wehrman et al., 2018). The overlap concentration, c^*, is defined in a good solvent as

$$c^* = \frac{M}{\frac{4}{3}\pi R_g^3 N_A} \tag{1}$$

where M is the molecular weight, N_A is Avogadro's number and R_g is the radius of gyration defined for a star polymer as $R_g^{star} = R_g^{arm}\left[\frac{3f-2}{f}\right]^{\frac{1}{2}}$ where R_g^{arm} is the radius of gyration of a single arm and f is the number of functional groups on the polymer. The entanglement concentration, c^{**}, is defined as

$$c^{**} = \frac{\nu\,(M_s/N_A)}{b^6} \tag{2}$$

where ν is the excluded volume parameter, M_s is the monomer molecular weight and b is the Kuhn length (Graessley, 1980; Doi and Edwards, 1988; Larson, 1999; Pavlov et al., 2003; Rubinstein and Colby, 2003). The gel characterized in this work is a four-arm star PEG-acrylate cross-linked with a linear PEG-dithiol. This is a photopolymerization reaction that uses lithium phenyl-2,4,6-trimethylbenzoylphosphinate (LAP) as a photoinitiator. PEG is chosen due to the versatility of this molecule. PEG is a hydrophilic molecule that can be functionalized with many different chemistries (Bhat and Timasheff, 1992; Iza et al., 1998; Kienberger et al., 2000; Bryant and Anseth, 2002; Hansen et al., 2003; Rubinstein and Colby, 2003; Lee et al., 2007; Aimetti et al., 2009; Fairbanks et al., 2009a). Due to this versatility, PEG has been widely used as the basis for polymeric gel scaffolds that are used in applications from consumer care products to implantable biomaterials. With the development of each new chemistry, the change in the rheology and structure must be understood to design these materials for each application.

Bulk rheological measurements have been the classic way to characterize gelling materials and polymeric solutions (Muthukumar and Winter, 1986; Winter and Chambon, 1986; Chambon and Winter, 1987; Winter, 1987; Adolf and Martin, 1990; Scanlan and Winter, 1991; Izuka et al., 1992; Winter and Mours, 1997; Larson, 1999; Rubinstein and Colby, 2003; Larsen, 2008; Larsen and Furst, 2008; Larsen et al., 2008). In these measurements the viscous, G'', and elastic component, G', of the complex modulus, G^*, is measured. When a material gels the viscous component decreases as the elastic component simultaneously increases. At the gel point, G' and G'' are parallel over all frequencies (Muthukumar and Winter, 1986; Winter and Chambon, 1986; Chambon and Winter, 1987; Winter, 1987; Adolf and Martin, 1990; Scanlan and Winter, 1991; Winter and Mours, 1997; Larson, 1999). To determine the point at which a material gels, which is defined as the first sample-spanning network cluster, time-cure superposition (TCS) is used. Time-cure superposition is the superposition of viscoelastic functions at different extents of reaction (Muthukumar and Winter, 1986; Winter and Chambon, 1986; Chambon and Winter, 1987; Winter, 1987; Adolf and Martin, 1990; Scanlan and Winter, 1991; Winter and Mours, 1997; Larson, 1999). TCS is used to determine the critical gel time, t_c, and critical relaxation exponent, n. The critical relaxation exponent indicates the structure of the scaffold

and is a measure similar to a complex modulus, indicating how much energy the scaffold can store and dissipate. Although bulk rheology has been the classic way to collect data of gelling systems, microrheological characterization can also be used.

Microrheological characterization has been used extensively to characterize gelling materials (Freundlich and Seifriz, 1922; Heilbronn, 1922; Seifriz, 1924; Valentine et al., 1996, 2001; Crocker et al., 2000; Gardel et al., 2005; Panorchan et al., 2006; Slopek et al., 2006; Veerman et al., 2006; Caggioni et al., 2007; Wong Po Foo et al., 2009; Corrigan and Donald, 2009a; Mulyasasmita et al., 2011; Schultz and Furst, 2012; Schultz and Anseth, 2013; Furst and Squires, 2017). Our work focuses on passive microrheological characterization of gelling scaffolds. Multiple particle tracking microrheology (MPT), a passive microrheological technique, measures the Brownian motion of probe particles embedded in a material which is related to rheological properties using the Generalized Stokes-Einstein Relation (GSER) (Mason and Weitz, 1995; Crocker and Grier, 1996; Mason, 2000; Valentine et al., 2004; Savin and Doyle, 2005; Squires and Mason, 2010; Furst and Squires, 2017). Advantages of MPT that make it ideal for characterization of gelling scaffolds are: small sample size ($1 - 50\ \mu$L), measurement of a large frequency range (up to MHz), short acquisition time enabling measurement of steady state properties of an evolving material and sensitivity in the low moduli range enabling characterization of the fragile microstructure of a gel at the sol-gel transition (Mason et al., 1997; Waigh, 2005, 2016; Squires and Mason, 2010; Schultz and Furst, 2012; Wehrman et al., 2016; Furst and Squires, 2017; Daviran et al., 2018). Additionally, TCS has been adapted to determine the critical gelation time and critical relaxation exponent using MPT measurements (Larsen and Furst, 2008; Larsen et al., 2008; Corrigan and Donald, 2009a,b; Schultz et al., 2009a). Due to these advantages, we use MPT to characterize the critical transitions of PEG-acrylate gels as polymeric interactions are increased.

Previous work determined the overlap concentration, $c^* = 13 \pm 4$ wt%, of the PEG-acrylate backbone using bulk rheology (Wehrman et al., 2018). This previous investigation also characterized the change in material properties and structure when the PEG-acrylate backbone is below (3 wt%) and above (10 and 18 wt%) the overlap concentration. This work characterized a change in structure to a more tightly cross-linked scaffold as PEG-acrylate concentration is increased (Wehrman et al., 2018). The present work expands upon this work to determine if there is a gradual or step change in the structure of the material below and above c^*. Scaffolds are characterized changing the PEG-acrylate concentration below c^* from $4 - 9$ wt% and above c^* at 13 and 15 wt%. Data from the previous study is also included for comparison. First, the kinetics of gelation are measured with MPT. The logarithmic slope of the mean-squared displacement, α, quantifies the change in material properties during scaffold gelation. For this chain-growth gel, there is an initial step when polymers are adding to growing chains and there is no measurable change in the rheology. Once chains begin to cross-link and form the gel network, rapid gelation is measured. Normalization of the UV exposure time with the final time of gelation, defined as the time when $\alpha \approx 0.02$, results in all curves collapsing onto a master curve indicating that polymeric interactions do not change the kinetics of gelation. TCS is used to analyze MPT data at PEG-acrylate backbone concentrations above and below c^*. We calculate a critical relaxation exponent, n, and critical gelation time, t_c, for each scaffold. The critical relaxation exponent is constant above and below c^* with a step change at c^*. The normalized critical gelation time has no change as a function of PEG-acrylate concentration. Together, these results characterize a change in scaffold structure that is only dependent on the overlap concentration. This will enable the scaffold rheological properties to be tailored without changing the structure. This work provides additional information about scaffold properties and structure which can be used to tailor these materials for applications that include decreasing permeability during enhanced oil recovery, rheological modification of fabric and home care products and as synthetic implantable materials for wound healing.

MATERIALS AND METHODS

Hydrogel Scaffold

The hydrogel scaffold is composed of a four-arm star PEG-acrylate which is cross-linked with PEG-dithiol. PEG-acrylate has a molecular weight of $M_n = 20,000$ g mol^{-1} (JenKem Technology) and is end-functionalized with acrylates ($f = 4$ where f is functionality). The cross-linker is a PEG end-functionalized with thiols ($M_n = 1,500$ g mol^{-1}, $f = 2$, Aldrich). These two molecules undergo a chain-growth polymerization upon exposure to ultraviolet (UV) light (PhotoFluor LM-75, output range $340 - 800$ nm, 89 North, Inc.). The reaction is initiated by lithium phenyl-2,4,6 trimethylbenzoylphosphinate (LAP). LAP is synthesized using previously published protocols (Fairbanks et al., 2009a). Carboxylated polystyrene probe particles ($2a = 0.97 \pm 0.01\ \mu$m where a is the particle radius, Polysciences, Inc.) are added to the polymer precursor solution to enable multiple particle tracking microrheological measurements.

Hydrogel samples maintain an acrylate:thiol ratio of 1.4 : 1. The concentration of PEG-acrylate is changed by 1 wt% from $4 -$ 9 wt%. Higher PEG-acrylate concentrated samples are measured and are 13 and 15 wt%. Data from 3, 10 and 18 wt% are included from a previous study for comparison (Wehrman et al., 2018). During sample preparation, all concentrated stock solutions are kept on ice for 30 min prior to addition to the polymer precursor solution. This ensures that there are no reactions in the solutions, especially thiol-thiol reactions in the PEG-dithiol stock solution. The polymer precursor solutions consist of PEG-acrylate, PEG-dithiol, 1.5 mM LAP, 0.052% solids per volume probe particles and water. Solutions are well-mixed prior to injection into the sample chamber. Hydrogel samples are gelled by exposure to UV light and MPT data are collected.

Multiple Particle Tracking Microrheology

Multiple particle tracking microrheology (MPT) measures the change in rheological properties during scaffold gelation. In MPT, the Brownian motion of 1 μm fluorescently labeled probe particles (carboxylated polystyrene particles, $2a = 0.97 \pm$

0.01 μm, Polysciences, Inc.) is measured. Data are collected using video microscopy on an inverted fluorescent microscope (Zeiss Observer Z1, Carl Zeiss AG). A high numerical aperture water-immersion objective is used to capture data, which maximizes the pixels per probe particle (63× water-immersion objective, N.A. 1.3, 1× optovar, Carl Zeiss AG). Our equipment is calibrated to minimize static and dynamic particle tracking errors (Savin and Doyle, 2005). Data are collected at 30 frames per second and an exposure time of 1000 μs (Phantom Miro M120, 1024 × 1024 pixels, Vision Research Inc.).

After data acquisition, the brightness-weighted centroid of each probe particle is determined using classical tracking algorithms (Crocker and Grier, 1996; Crocker and Weeks, 2011; Furst and Squires, 2017). These algorithms determine the center of each particle in each frame. Those particle centers are linked together into trajectories using a probability distribution function that accounts for Brownian motion (Crocker and Grier, 1996; Crocker and Weeks, 2011; Furst and Squires, 2017). From the particle positions, the ensemble-averaged mean-squared displacement (MSD, $\langle \Delta r^2(\tau) \rangle$) is calculated from the two-dimensional data using $\langle \Delta r^2(\tau) \rangle = \langle \Delta x^2(\tau) \rangle + \langle \Delta y^2(\tau) \rangle$. From the MSD, rheological properties can be calculated using the Generalized Stokes-Einstein Relation

$$\langle \Delta r^2(\tau) \rangle = \frac{k_B T}{\pi a} J(\tau) \tag{3}$$

where k_B is the Boltzmann constant, T is the temperature, a is the particle radius and $J(\tau)$ is the creep compliance.

To measure gelation using MPT we first add probe particles into the polymer precursor solution. Briefly, 1 μm probe particles are washed 3× by dilution and centrifugation at 5,000 RPM for 5 min (Centrifuge 5425, Eppendrof) to remove any excess dye. Probe particles are then sonicated (40 kHz, Emerson Industrial Automation) for 15 min to ensure that there are no particle aggregates. We add probes at a final concentration of 0.052% solids per volume to the polymer precursor solution. We then inject our polymer precursor solution into a sample chamber. Sample chambers are made on a standard glass slide (75 × 25 × 1 mm, Thermo Fisher Scientific), with 0.16 mm thick spacers and a coverglass (22 × 22 × 0.16 mm) as the top of the chamber. After the polymer precursor solution has filled the sample chamber it is sealed with an air-curing epoxy (Gorilla Glue Company). During curing, sample chambers are kept in the dark and allowed to cure for 15 min.

Each sample is exposed to UV light and MPT data are collected. This is repeated until ≈30 min after complete gelation is measured. Neutral density filters (Chroma Technology) are used to lower the intensity of the UV light. This is done to slow the gelation reaction enabling acquisition of MPT data during the sol-gel transition. The neutral density filters used are 32 and 10% transmission (Chroma Technologies) for 4−15 and 18 wt% PEG-acrylate, respectively. Due to the arbitrary time of UV exposure, data are reported as a normalized UV exposure time which is UV exposure time divided by final time of gelation. The final time of gelation is the time when the logarithmic slope of the MSD, α, is ≤0.02. All MPT experiments are repeated at least 3× to ensure repeatability and critical values are reported as the average ± the standard deviation.

RESULTS AND DISCUSSION

This work characterizes the change in rheological properties and scaffold structure as polymeric interactions are increased. Previous work determined the overlap concentration, c^*, of this PEG-acrylate backbone using bulk rheology and MPT. The value of $c^* = 13 \pm 4$ wt% (Wehrman et al., 2018). We consider scaffolds with PEG-acrylate concentrations $c \leq 9$ wt% to be below c^* and $c > 9$ wt% to be above c^*. This uses the lower limit of c^* as the transition point. This value is chosen not only from the measurements of c^* but also from the characterization of scaffold properties presented here. We measure the same trend in gelation kinetics as a function of UV exposure, regardless of PEG-acrylate concentration. Previous work found that below the overlap concentration the material had a more open structure than samples at and above the overlap concentration. This work expands this initial study determining that there is a step change in the scaffold structure when the overlap concentration is reached. In the previous study, we hypothesized that there would be a gradual decrease in the value of n below the overlap concentration and a constant value above c^*. The gradual decrease in n below c^* would have indicated a more densely cross-linked structure as the concentration is increased. Instead, we measure no change in the dilute, $c < c^*$, and semi-dilute, $c > c^*$, concentration regimes, but there is a step change in the structure of the scaffold at the transition. This result indicates that the structure remains constant above and below the overlap concentration regardless of PEG-acrylate concentration. This information can lead to the design of new materials, where the moduli of the material can be tailored for applications, such as the mimic of a tissue or a material to reduce permeability in enhanced oil recovery without changing the scaffold structure.

Scaffold Gelation

Multiple particle tracking microrheology measures the scaffold properties during gelation. After UV exposure, MPT data are collected. From the MPT data, the ensemble-averaged mean-squared displacement is calculated for all the measured probe particles. Previous work that used MPT to measure this hydrogel scaffold determined that the scaffold evolves homogeneous during gelation with each particle probing the same material properties (Wehrman et al., 2018). The logarithmic slope of the MSD, $\alpha = \frac{d \log \langle \Delta r^2(\tau) \rangle}{d \log \tau}$, is a measure of the state of the material (Stauffer et al., 1982; Winter and Chambon, 1986; Adolf and Martin, 1990; Larsen and Furst, 2008; Corrigan and Donald, 2009a,b; Schultz et al., 2009a, 2012; Schultz and Furst, 2012; Wehrman et al., 2016; Daviran et al., 2018). When $\alpha = 1$ probe particles are freely diffusing and the material is a liquid. When $\alpha \to 0$ probe particles are completely arrested in the gel scaffold. This occurs at a low moduli value, $G' \approx 4$ Pa (Waigh, 2005; Schultz and Furst, 2011, 2012; Furst and Squires, 2017). Due to the low maximum moduli value, bulk rheology should be used to supplement MPT to measure the

equilibrated material properties. Finally, when $0 < \alpha < 1$ the material is a viscoelastic sol or gel and probe particle movement is restricted.

To quantitatively determine when the sol-gel transition occurs, time-cure superposition (TCS) is used to analyze the critical transition and will be discussed in detail below. From TCS, the critical relaxation exponent is determined, n. $\alpha = n$ is the sol-gel transition (Larsen and Furst, 2008; Corrigan and Donald, 2009a,b; Schultz et al., 2009a,b; Schultz and Anseth, 2013; Adibnia and Hill, 2016; Wehrman et al., 2016; Escobar et al., 2017; Daviran et al., 2018). This is when the first sample-spanning network cluster has formed and is the definition of a gel (Stauffer et al., 1982; Muthukumar and Winter, 1986; Winter and Chambon, 1986; Chambon and Winter, 1987; Winter, 1987; Adolf and Martin, 1990; Larsen and Furst, 2008; Corrigan and Donald, 2009a,b; Schultz et al., 2009a,b; Schultz and Anseth, 2013; Adibnia and Hill, 2016; Wehrman et al., 2016; Escobar et al., 2017; Daviran et al., 2018). To determine the state of the material α is compared to n. When $\alpha < n$ the material is a gel and when $\alpha > n$ the material is a sol (Larsen and Furst, 2008; Corrigan and Donald, 2009a,b; Schultz et al., 2009a,b; Schultz and Anseth, 2013; Adibnia and Hill, 2016; Wehrman et al., 2016; Escobar et al., 2017) ; (Daviran et al., 2018).

Figures 1A,B show the change in α as the polymer precursor solution is exposed to UV light. Upon initial exposure to UV light there is lag prior to scaffold gelation. This lag is due to radicals being formed in the polymer precursor solution and the growth of polymeric chains that are not cross-linking into a network structure. During chain-growth, cross-linking occurs by the addition of polymers to growing network chains. Those chains then cross-link together to form the scaffold network structure (Rubinstein and Colby, 2003; Tibbitt et al., 2013; Payamyar et al., 2016). This cross-linking of chains leads to the steep slope in α vs. normalized UV exposure. Prior to the decrease in α, probe particles are freely diffusing. During this time polymer chains are forming but are not large enough to restrict probe particle motion. When these chains start to cross-link, the network structure is forming and probe particle movement becomes restricted and, eventually, arrested in the gel scaffold. At the point of probe particle arrest, the network structure will continue to grow, but MPT can no longer measure the change in material properties.

For all PEG-acrylate samples the kinetics of gelation follow the same trend that is described above. **Figure 1A** shows PEG-acrylate samples with concentrations below c^* and **Figure 1B** are concentrations above c^*. This is further illustrated in **Figure S1**, where all concentrations are plotted together. In **Figures 1A,B**, UV exposure time is normalized by the UV exposure when complete gelation is measured, defined as $\alpha \leq 0.02$. This value is used because it is a slope where no probe particle movement is measured. Upon normalization, all data sets collapse and have a lag in gelation and then a steep slope, where the value of α decreases rapidly with time. Therefore, from these experiments, we can conclude that there is no change in the mechanism of gelation when polymeric interactions are added into the system by concentrating the PEG-acrylate backbone over c^*.

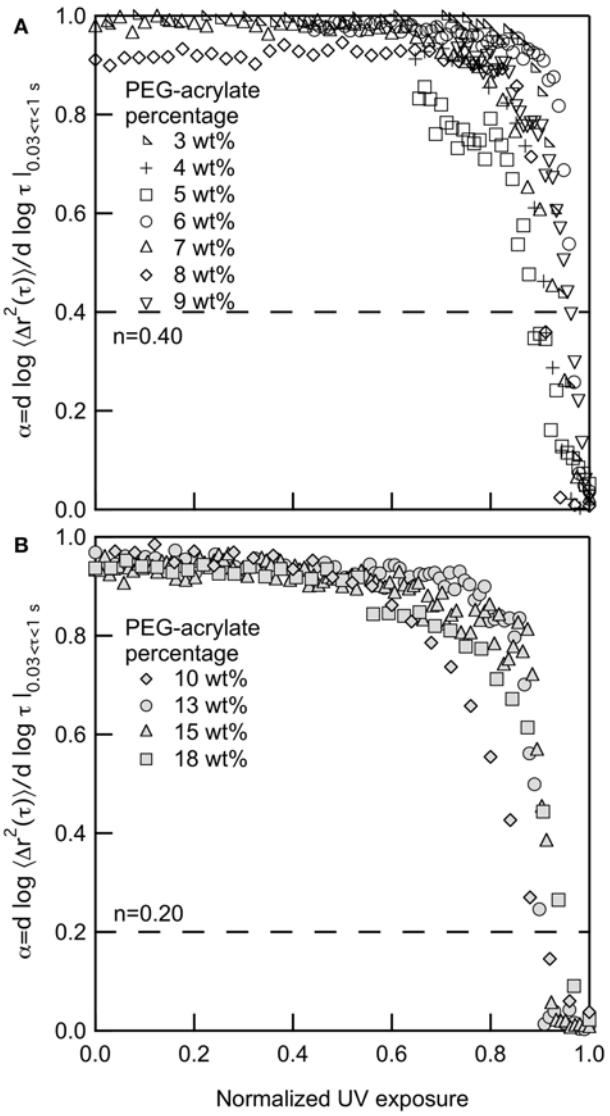

FIGURE 1 | Logarithmic slope of the MSD, α, for gelation of PEG-acrylate gels when the backbone concentrations is **(A)** below and **(B)** above the overlap concentration, c^*. The dotted line in both graphs is the critical relaxation exponent, n. 3, 10 and 18 PEG-acrylate wt% data originally appeared in Wehrman et al. (2018).

Time-Cure Superposition

Time-cure superposition (TCS) is used to analyze each scaffold gelation reaction and determine the critical relaxation exponent, n, and the critical gelation time, t_c. TCS is the superposition of viscoelastic functions at different extents of reaction (Muthukumar and Winter, 1986; Winter and Chambon, 1986; Chambon and Winter, 1987; Winter, 1987; Adolf and Martin, 1990; Larsen and Furst, 2008; Corrigan and Donald, 2009a,b; Schultz et al., 2009a,b; Schultz and Anseth, 2013; Adibnia and Hill, 2016; Wehrman et al., 2016; Escobar et al., 2017;

Daviran et al., 2018). This analysis exploits the self-similarity of measurements of the scaffold material properties prior to and after gelation to shift data onto master curves. In MPT, the shortest lag times, $0.03 \leq \tau \leq 1$s, measure the longest relaxation times, τ_R, of the material. This is because the short lag times are equivalent to high frequency measurements in bulk rheology. The longest relaxation times in the pre- and post-gel give distinct curvature to MSDs measured with MPT. In the pre-gel, the longest relaxation time of the polymers are measured. In the post-gel, the longest relaxation time of the gel network is being probed (Muthukumar and Winter, 1986; Winter and Chambon, 1986; Chambon and Winter, 1987; Winter, 1987; Adolf and Martin, 1990; Larsen and Furst, 2008; Corrigan and Donald, 2009a,b; Schultz et al., 2009a,b; Schultz and Anseth, 2013; Adibnia and Hill, 2016; Wehrman et al., 2016; Escobar et al., 2017; Daviran et al., 2018). Since these measurements are probing the same relaxation time, over a large time scale, the data can be shifted into pre- and post-gel master curves by shifting along the lag time and MSD axes.

The shift factors determine the critical values, namely the critical relaxation exponent and critical gelation time (Muthukumar and Winter, 1986; Winter and Chambon, 1986; Chambon and Winter, 1987; Winter, 1987; Adolf and Martin, 1990; Larsen and Furst, 2008; Corrigan and Donald, 2009a,b; Schultz et al., 2009a,b; Schultz and Anseth, 2013; Adibnia and Hill, 2016; Wehrman et al., 2016; Escobar et al., 2017; Daviran et al., 2018). The lag time shift factor, a, is related to the inverse of the longest relaxation time, τ_R, and the distance away from the critical gelation time, $\frac{|t-t_c|}{t_c}$, by a scaling factor y by

$$a \sim \tau_R^{-1} \sim \left(\frac{|t-t_c|}{t_c}\right)^y. \tag{4}$$

Similarly the MSD shift factor, b, is related to the inverse of the steady state creep compliance, J_e, and the distance away from the critical gelation time by a scaling factor z by

$$b \sim J_e^{-1} \sim \left(\frac{|t-t_c|}{t_c}\right)^z. \tag{5}$$

The critical relaxation exponent is the ratio of the two scaling exponent

$$n = \frac{z}{y}. \tag{6}$$

The critical relaxation exponent determines the state of the material as described in detail above. This is the value of α where the first sample-spanning network cluster forms during gelation. Additionally, n can be thought of as a complex modulus, G^*, with both a viscous and elastic component. When $n > 0.5$ the material is an open porous network which dissipates more energy than it stores. When $n < 0.5$ the scaffold is a tightly cross-linked network that stores more energy. When $n = 0.5$ the scaffold is a percolated network which stores and dissipates equal amounts of energy (Stauffer et al., 1982; Schultz et al., 2009a; Wehrman et al., 2018).

All data taken of PEG-acrylate gelation is analyzed with TCS to determine the value of the critical relaxation exponent, n, and the critical gelation time, t_c. TCS for a 4 wt% PEG-acrylate gelation is shown in **Figure 2**. An example of TCS for all other PEG-acrylate concentrations are in the Supplementary Material, **Figures S2–S8**. The ensemble-averaged MSD is calculated from MPT data, **Figure 2A**. The MSDs decrease in both magnitude and α as UV exposure time is increased. Initially, probe particles are freely diffusing in the polymer solution. As UV exposure increases the scaffold network grows and probe particle movement decreases. As mentioned above, at the sol-gel transition there is a change in the shape of MSD curves due to the change in the relaxation times measured from the relaxation of polymers to the relaxation of a network. This change in shape enables the MSD curves to be shifted into two master curves, a pre- and post-gel master curve, **Figure 2B**. The start of the pre-gel master curve is the polymeric solution with $\alpha = 1$. As the value of $a \cdot \tau$ decreases the value of α also decreases which is due to the growing polymer chains restricting the movement of the probe particles. Additionally, the curvature of the pre-gel curve shows that at short lag times the MSD curves up slightly, which is the measure of the polymeric longest relaxation time, τ_R (Furst and Squires, 2017; Wehrman et al., 2018). At $\alpha = n$ the pre- and post-gel master curves meet. In the pre-gel curve this is the last measurement before the sample-spanning network cluster forms and in the post-gel curve this is the first measurement after the sample-spanning network cluster has formed. In the post-gel master curve as $a \cdot \tau$ increases, there is a decrease in α until $\alpha \to 0$ and probe particles are completely arrested in the polymerized network scaffold. In the post-gel master curve, the curvature is reversed and at short lag times, the MSDs curve down, indicative of measurements of the longest relaxation time of a network.

The shift factors are used to determine the critical relaxation exponent and critical gelation time. In **Figure 2C** both the lag time and MSD shift factors diverge at the sol-gel transition. This is the divergence of the viscosity upon network formation and the emergence of the elastic modulus, $G^{'}$, as the network continues to grow. This divergence happens at the critical gelation time, which is $t_c = 11.6$ min for this 4 wt% PEG-acrylate network. The critical relaxation exponent is the ratio of scaling exponents. Scaling exponents y and z are calculated by fitting the $\log a$ and $\log b$ vs. the $\log \frac{|t-t_c|}{t_c}$, **Figure 2D**. The ratio of the scaling exponents determine the critical relaxation exponent, which is $n = 0.26 \pm 0.08$ for this hydrogel scaffold.

This analysis is done for all MSD data collected both above and below c^*. Since the absolute value of UV exposure can be dependent on the size of the sample, we normalize the critical gelation time by the final time of gelation $\left(t_{c,norm} = \frac{t_c}{t_{final}}\right)$. The critical gelation time, t_c, is defined as the time when the first sample-spanning network cluster is formed in the material. The final time of gelation, t_{final}, is again defined as the time when $\alpha \leq 0.02$. The normalized critical gelation time is $t_{c,norm} = 0.86 \pm 0.17$ and $t_{c,norm} = 0.96 \pm 0.06$ for PEG-acrylate concentrations below and above c^*, respectively. A plot of these values is provided in the Supplementary Material, **Figure S9**. These values are within error of each other, indicating that the critical gelation time

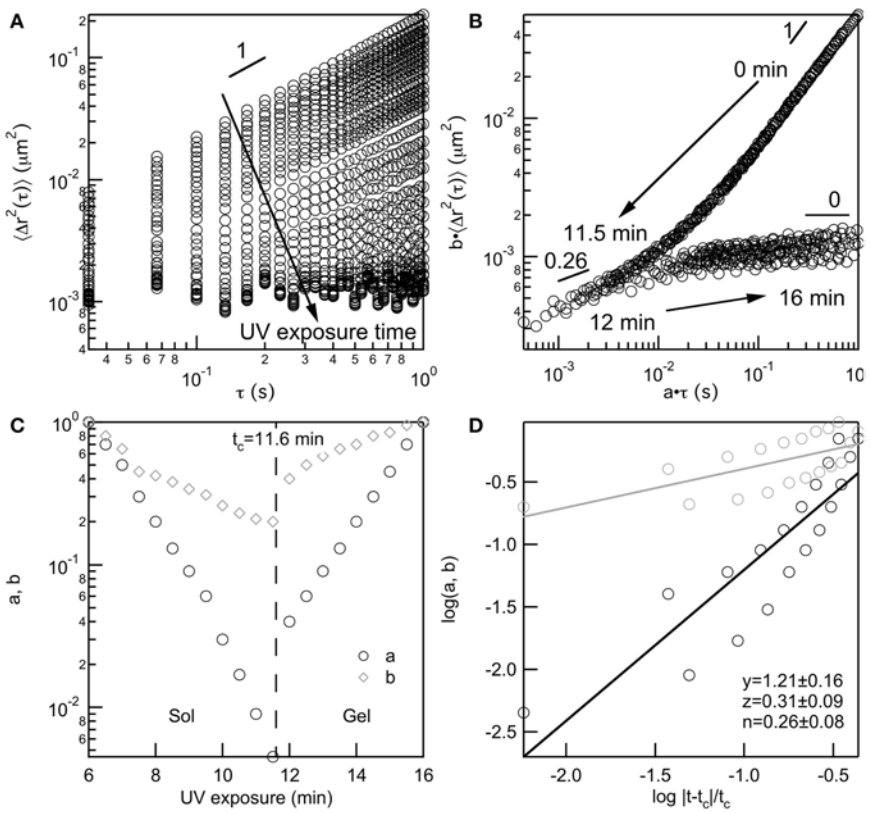

FIGURE 2 | Four wt% PEG-acrylate scaffold gelation analyzed using time-cure superposition. **(A)** Ensemble-averaged MSD data collected as UV exposure time is increased. **(B)** MSD curves shifted into pre- and post-gel master curves using shifting factors *a* and *b*, which **(C)** diverge at the critical gelation time, t_C, at the sol-gel transition. **(D)** The scaling exponents *y* and *z* are determined from the slope of $\log a$ and $\log b$ vs. the logarithm of the distance away from the critical gelation time, $\log \frac{|t-t_C|}{t_C}$. The critical relaxation exponent, *n* is calculated from the scaling factors.

occurs at the same point within the scaffold gelation reaction regardless of the backbone concentration. The first sample-spanning cluster will require a similar amount of cross-links regardless of polymeric interactions and, therefore, occurs at a similar point in the gelation process. This is also supported by the collapse of MPT measurements throughout gelation in **Figures 1A,B**. These results show that scaffold gelation proceeds through the same reaction mechanism regardless of polymeric interactions in the precursor solution.

Finally, the critical relaxation exponent is calculated for scaffolds above and below the overlap concentration of PEG-acrylate. **Figure 3** is a plot of the average value of *n* vs. PEG-acrylate concentration. As described previously, scaffold with $c \leq 9$ wt% are considered below c^* and $c > 9$ wt% are considered above c^*. The critical relaxation exponent indicates the scaffold structure and is a measure similar to a complex modulus, indicating how much energy the scaffold can store and dissipate. The value of *n* has a step change at the overlap concentration. Below c^* $n_{avg} = 0.40 \pm 0.03$ and above c^* $n_{avg} = 0.20 \pm 0.03$. This step change in the value of *n* indicates that there is a change in structure below and above the overlap concentration, but within the dilute and semi-dilute concentration regimes there is no structural change. For all concentrations, a tightly cross-linked network that stores more energy than it dissipates is measured.

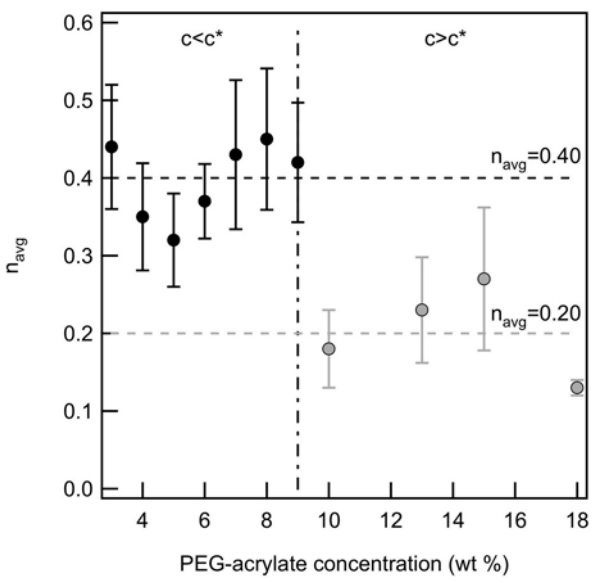

FIGURE 3 | The critical relaxation exponent below and above c^* for a PEG-acrylate:PEG-dithiol scaffold by increasing the backbone concentration above c^*. There is a step change in the value of *n* when the concentration is above c^*.

When $c > c^*$ the network is more tightly cross-linked with a smaller pore structure than when $c < c^*$. This is due to polymeric interactions. When $c > c^*$, polymers are interacting and are able to enter into the pervaded volume of other chains. Due to the polymers being physically closer during network formation there is a high likelihood of arm interpenetration during network formation. This leads to a scaffold with a smaller porous structure that can store energy. This result indicates that the scaffold structure is unchanged by the change in backbone concentration. The only factor that changes scaffold structure is whether the backbone concentration is above or below c^*. Therefore, this scaffold can be tailored to change the elastic moduli of the material without changing the structure of the scaffold enabling the material to be tailored for desired applications.

CONCLUSIONS

This work characterizes the change in rheological properties and scaffold structure during the photopolymerization of a four-arm star PEG-acrylate:PEG-dithiol hydrogel scaffold as polymeric interactions are added to the system. MPT is used to measure the change in scaffold properties as UV exposure time is increased. The gelation mechanism is the same for all scaffolds, regardless of polymeric interactions. The rheology of all scaffolds indicate that they follow a typical chain-growth polymerization. Upon UV exposure, chains of polymers begin to grow in the system and gelation is measured when these chains begin to cross-link into a network. Measured mean-squared displacements are further analyzed using time-cure superposition. The critical relaxation exponent and critical gelation time are determined. The normalized critical gelation time is independent of polymeric interactions. This result supports measurements that all scaffolds follow the same gelation mechanism. The critical relaxation exponent is sensitive to polymeric interactions. A step change in the value of the critical relaxation exponent is measured when polymeric interactions increase above the overlap concentration. This decrease in the value of n indicates that scaffolds made with backbone concentrations above c^* have a smaller porous network which stores more energy than scaffold made with PEG-acrylate concentrations below c^*. This is due to the increased physical interactions, which likely lead to an interpenetrated network structure when $c > c^*$.

The results of this work provide a predictability of material properties, structure and kinetics during gelation. This information can be used to determine the feasibility of these scaffolds for desired applications, particularly when these materials are made in a new environment and require a specific modulus and structure. A stable structure below and above c^* enables properties of the material to be tailored while the structure remains constant. The wide applicability of hydrogel scaffolds has lead to the need to more precisely design these materials. This work informs this design by building a knowledge base which can be exploited to minimize trial-and-error when a scaffold is used in a new application.

AUTHOR CONTRIBUTIONS

HZ was responsible for design of experiments and collection and analysis of data. MW was responsible for design of experiments. KS was responsible for design of experiments, data analysis and writing the manuscript.

FUNDING

Funding for this work was provided by the American Chemical Society Petroleum Research Fund (54462-DNI7). Acknowledgment is made to the Donors of the American Chemical Society Petroleum Research Fund for support of this research.

ACKNOWLEDGMENTS

The authors would like to acknowledge Stephanie Cook, Melissa J. Milstrey, and Danielle Rafanelli for their help with experiments. The authors would also like to acknowledge Nan Wu for carefully reading the manuscript.

SUPPLEMENTARY MATERIAL

The Supplementary Material for this article can be found online at: https://www.frontiersin.org/articles/10.3389/fchem.2019.00317/full#supplementary-material

Additional graphs for α vs. normalized UV exposure for all PEG-acrylate concentrations, TCS of each PEG-acrylate concentration and $t_{c,norm}$ for all PEG-acrylate concentrations are provided. Additionally, a table with the values of n and $t_{c,norm}$ are provided for each PEG-acrylate concentration and can be found in the Supplemental data.

REFERENCES

Adibnia, V., and Hill, R. J. (2016). Universal aspects of hydrogel gelation kinetics, percolation and viscoelasticity from PA-hydrogel rheology. *J. Rheol.* 60, 541–548. doi: 10.1122/1.4948428

Adolf, D., and Martin, J. E. (1990). Time-cure superposition during crosslinking. *Macromolecules.* 23, 3700–3704.

Aimetti, A. A., Machen, A. J., and Anseth, K. S. (2009). Poly(ethylene glycol) hydrogels formed by thiol-ene photopolymerization for enzyme-responsive protein delivery. *Biomaterials.* 30, 6048–6054. doi: 10.1016/j.biomaterials.2009.07.043

Benton, J. A., Fairbanks, B. D., and Anseth, K. S. (2009). Characterization of valvular interstitial cell function in three dimensional matrix metalloproteinase degradable PEG hydrogels. *Biomaterials.* 30, 6593–6603. doi: 10.1016/j.biomaterials.2009.08.031

Bhat, R., and Timasheff, S. N. (1992). Steric exclusion is the principal source of the preferential hydration of proteins in the presence of polyethylene glycols. *Protein Sci.* 1, 1133–1143.

Bryant, S. J., and Anseth, K. S. (2002). Hydrogel properties influence ECM production by chondrocytes photoencapsulated in poly(ethylene glycol) hydrogels. *J. Biomed. Mater. Res.* 59, 63–72. doi: 10.1002/jbm.1217

Caggioni, M., Spicer, P. T., Blair, D. L., Lindberg, S. E., and Weitz, D. A. (2007). Rheology and microrheology of a microstructured fluid: The gellan gum case. *J. Rheol.* 51, 851–865. doi: 10.1122/1.2751385

Chambon, F., and Winter, H. H. (1987). Linear viscoelasticity at the gel point of a crosslinking PDMS with imbalanced stoichiometry. *J. Rheol.* 31, 683–697.

Corrigan, A. M., and Donald, A. M. (2009a). Particle tracking microrheology of gel-forming amyloid fibril networks. *Eur. Phys. J. E.* 28, 457–462. doi: 10.1140/epje/i2008-10439-7

Corrigan, A. M., and Donald, A. M. (2009b). Passive microrheology of solvent-induced fibrillar protein networks. *Langmuir.* 25, 8599–8605. doi: 10.1021/la804208q

Crocker, J. C., and Grier, D. G. (1996). Methods of digital video microscopy for colloidal studies. *J. Colloid Interface Sci.* 179, 298–310.

Crocker, J. C., Valentine, M. T., Weeks, E. R., Gisler, T., Kaplan, P. D., Yodh, A. G., et al. (2000). Two-point microrheology of inhomogeneous soft materials. *Phys. Rev. Lett.* 85, 888–891. doi: 10.1103/PhysRevLett.85.888

Crocker, J. C., and Weeks, E. R. (2011). *Particle Tracking Using idl*. Available online at: http://www.physics.emory.edu/faculty/weeks//idl/

Daviran, M., Caram, H. S., and Schultz, K. M. (2018). Role of cell-mediated enzymatic degradation and cytoskeletal tension on dynamic changes in the rheology of the pericellular region prior to human mesenchymal stem cell motility. *ACS Biomater. Sci. Eng.* 4, 468–472. doi: 10.1021/acsbiomaterials.7b01005

Doi, M., and Edwards, S. F. (1988). *The Theory of Polymer Dynamics*. New York, NY: Oxford University Press.

Engler, A. J., Sen, S., Lee Sweeney, H., and Discher, D. E. (2006). Matrix elasticity directs stem cell lineage specification. *Cell.* 126, 677–689. doi: 10.1016/j.cell.2006.06.044

Escobar, F., Anseth, K. S., and Schultz, K. M. (2017). Dynamic changes in material properties and degradation of poly(ethylene glycol)-hydrazone gels as a function of pH. *Macromolecules.* 50, 7351–7360. doi: 10.1021/acs.macromol.7b01246

Fairbanks, B. D., Schwartz, M. P., Bowman, C. N., and Anseth, K. S. (2009a). Photoinitiated polymerization of PEG-diacrylate with lithium phenyl-2,4,6-trimethylbezoylphosphinate: polymerization rate and cytocompatibility. *Biomaterials.* 30, 6702–6707. doi: 10.1016/j.biomaterials.2009.08.055

Fairbanks, B. D., Schwartz, M. P., Halevi, A. E., Nuttelman, C. R., Bowman, C. N., and Anseth, K. S. (2009b). A versatile synthetic extracellular matrix mimic via thiol-norbornene photopolymerization. *Adv. Mater.* 10, 3114–3121. doi: 10.1002/adma.200901808

Freundlich, H., and Seifriz, W. (1922). Ober die elastizitat von solen und gelen. *Z. Phys. Chem.* 104, 232–261.

Furst, E. M., and Squires, T. M. (2017). *Microrheology. 1st Edn.* New York, NY: Oxford University Press.

Gardel, M. L., Valentine, M. T., and Weitz, D. A. (2005). *Microscale Diagnostic Techniques*. Heidelberg; New York, NY: Springer.

Graessley, W. W. (1980). Polymer chain dimensions and the dependence of viscoelastic properties on concentration, molecular weight and solvent power. *Polymer.* 21, 258–262.

Hansen, P. L., Cohen, J. A., Podgotnik, R., and Parsegian, V. A. (2003). Osmotic properties of poly (ethylene glycols): quantitative features of brush and bulk scaling laws. *Biophys. J.* 84, 350–355. doi: 10.1016/S0006-3495(03)74855-3

He, Y., Xiong, S., Yang, Z., Ruan, X., and Gong, Y. (2009). The research on cross-linking gel as in-depth profile control agent. *Petrol. Sci. Technol.* 27, 1300–1311. doi: 10.1080/10916460802455236

Heilbronn, A. (1922). Eine neue methode zur bestimmung der viskositat lebender protoplasten. *Jahrb. Wiss. Bot.* 61, 284–338.

Iza, M., Stoianovici, G., Viora, L., Grossiord, J. L., and Couarraze, G. J. (1998). Hydrogels of poly(ethylene glycol): mechanical characterization and release of a model drug. *J. Control. Release.* 52, 41–51.

Izuka, A., Winter, H. H., and Hashimoto, T. (1992). Molecular weight dependence of viscoelasticity of polycaprolactone critical gels. *Macromolecules.* 25, 2422–2428.

Jung, J. C., Zhang, K., Chon, B. H., and Choi, H. J. (2013). Rheology and polymer flooding characteristics of partially hydrolyzed polyacrylamide for enhanced heavy oil recovery. *J. Appl. Polym. Sci.* 127, 4833–4839. doi: 10.1002/app.38070

Kienberger, F., Pastushenko, V. P., Kada, G., Gruber, H. J., Riener, C., Schindler, H., et al. (2000). Static and dynamical properties of single poly (ethylene glycol) molecules investigated by force spectroscopy. *Single Mol.* 1, 123–128. doi: 10.1002/1438-5171(200006)1:2<123::AID-SIMO123>3.0.CO;2-3

Larsen, T. H. (2008). *Microrheology of Responsive Hydrogels*. Ph.D. thesis, University of Delaware.

Larsen, T. H., and Furst, E. M. (2008). Microrheology of the liquid-solid transition during gelation. *Phys. Rev. Lett.* 100:146001. doi: 10.1103/PhysRevLett.100.146001

Larsen, T. H., Schultz, K. M., and Furst, E. M. (2008). Hydrogel microrheology near the liquid-solid transition. *Korea-Aust. Rheol. J.* 20, 165–173. Available online at: https://www.rheology.or.kr/home/kor/journal/karj_list.aspx?journalid=22&volume=20&journalno=3

Larson, R. G. (1999). *The Structure and Rheology of Complex Fluids*. New York, NY: Oxford University Press.

Lee, S. H., Moon, J. J., Miller, J. S., and West, J. L. (2007). Poly(ethylene glycol) hydrogels conjugated with a collagenase-sensitive fluorogenic substrate to visualize collagenase activity during three-dimensional cell migration. *Biomaterials.* 28, 3163–3170. doi: 10.1016/j.biomaterials.2007.03.004

Lutolf, M. P., Weber, F. E., Schmoekel, H. G., Schense, J. C., Kohler, T., Muller, R., et al. (2003). Repair of bone defects using synthetic mimetics of collagenous extracellular matrices. *Nat. Biotech.* 21, 513–518. doi: 10.1038/nbt818

Mason, T. G. (2000). Estimating the viscoelastic moduli of complex fluids using the Generalized Stokes–Einstein equation. *Rheol. Actac.* 39, 371–378. doi: 10.1007/s003970000094

Mason, T. G., Ganesan, K., van Zanten, J. H., Wirtz, D., and Kuo, S. C. (1997). Particle tracking microrheology of complex fluids. *Phys. Rev. Lett.* 79, 3282–3285.

Mason, T. G., and Weitz, D. A. (1995). Optical measurements of frequency-dependent linear viscoelastic moduli of complex fluids. *Phys. Rev. Lett.* 74, 1250–1253.

Moradi-Araghi, A., Beardmore, D. H., and Stahl, G. A. (1988). *The Application of Gels in Enhanced Oil Recovery; Theory, Polymers and Crosslinker Systems*. Boston, MA: Springer.

Mulyasasmita, W., Lee, J. S., and Heilshorn, S. C. (2011). Molecular-level engineering of protein physical hydrogels for predictive sol–gel phase behavior. *Biomacromolecules.* 12, 3406–3411. doi: 10.1021/bm200959e

Muthukumar, M., and Winter, H. H. (1986). Fractal dimension of a crosslinking polymer at the gel point. *Macromolecules.* 19, 1284–1285.

Panorchan, P., Lee, J. S. H., Kole, T. P., Tseng, Y., and Wirtz, D. (2006). Microrheology and ROCK signaling of human endothelial cells embedded in a 3D matrix. *Biophys. J.* 91, 3499–3507. doi: 10.1529/biophysj.106.084988

Pavlov, G., Finet, S., Tatarenko, K., Korneeva, E., and Ebel, C. (2003). Conformation of heparin studied with macromolecular hydrodynamic methods and X-ray scattering. *Eur. Biophys. J.* 32, 437–449. doi: 10.1007/s00249-003-0316-9

Payamyar, P., King, B. T., Ottinger, H. C., and Schluter, A. (2016). Two-dimensional polymers: concepts and perspectives. *Chem. Commun.* 52, 18–34. doi: 10.1039/C5CC07381B

Purcell, B. P., Lobb, D., Charati, M. B., Dorsey, S. M., Wade, R. J., Zellars, K. N., et al. (2014). Injectable and bioresponsive hydrogels for on-demand matrix metalloproteinase inhibition. *Nat. Mater.* 13, 653–661. doi: 10.1038/nmat3922

Raeber, G. P., Lutolf, M. P., and Hubbell, J. A. (2005). Molecularly engineered PEG hydrogels: a novel model system for proteolytically mediated cell migration. *Biophys. J.* 89, 1374–1388. doi: 10.1529/biophysj.104.050682

Raeber, G. P., Lutolf, M. P., and Hubbell, J. A. (2007). Mechanisms of 3-D migration and matrix remodeling of fibroblasts within artificial ECMs. *Acta Biomater.* 3, 615–629. doi: 10.1016/j.actbio.2007.03.013

Rubinstein, M., and Colby, R. H. (2003). *Polymer Physics. 1st Edn.* New York, NY: Oxford University Press.

Savin, T., and Doyle, P. S. (2005). Static and dynamic errors in particle tracking microrheology. *Biophys. J.* 88, 623–638. doi: 10.1529/biophysj.104.042457

Scanlan, J. C., and Winter, H. H. (1991). Composition dependence of the viscoelasticity of end-linked poly(dimethylsiloxane) at the gel point. *Macromolecules.* 24, 47–54.

Schultz, K. M., and Anseth, K. S. (2013). Monitoring degradation of matrix metalloproteinases- cleavable PEG hydrogels via multiple particle tracking microrheology. *Soft Matter.* 9, 1570–1579. doi: 10.1039/C2SM27303A

Schultz, K. M., Baldwin, A. D., Kiick, K. L., and Furst, E. M. (2009a). Gelation of covalently cross-linked PEG-heparin hydrogels. *Macromolecules.* 42, 5310–5316. doi: 10.1021/ma900766u

Schultz, K. M., Baldwin, A. D., Kiick, K. L., and Furst, E. M. (2009b). Rapid rheological screening to identify conditions of biomaterial hydrogelation. *Soft Matter.* 5, 740–742. doi: 10.1039/b818178k

Schultz, K. M., Baldwin, A. D., Kiick, K. L., and Furst, E. M. (2012). Capturing the comprehensive modulus profile and reverse percolation transition of a degrading hydrogel. *Macro Lett.* 1, 706–708. doi: 10.1021/mz300106y

Schultz, K. M., and Furst, E. M. (2011). High-throughput rheology in a microfluidic device. *Lab Chip.* 11, 3802–3809. doi: 10.1039/c1lc20376b

Schultz, K. M., and Furst, E. M. (2012). Microrheology of biomaterial hydrogelators. *Soft Matter.* 8, 6198–6205. doi: 10.1039/C2SM25187F

Schwartz, M. P., Fairbanks, B. D., Rogers, R. E., Rangarajan, R., Zaman, M. H., and Anseth, K. S. (2010). A synthetic strategy for mimicking the extracellular matrix provides insight about tumor cell migration. *Integr. Biol.* 2, 32–40. doi: 10.1039/b912438a

Seifriz, W. (1924). The structure of protoplasm and of inorganic gels: an analogy. *J. Exp. Biol.* 1, 431–443.

Serra, L., Domenech, J., and Peppas, N. A. (2006). Drug transport mechanisms and release kinetics from molecularly designed poly(acrylic acid-g-ethylene glycol) hydrogels. *Biomaterials.* 27, 5440–5451. doi: 10.1016/j.biomaterials.2006.06.011

Slopek, R. P., McKinley, H. K., Henderson, C. L., and Breedveld, V. (2006). *In situ* monitoring of mechanical properties during photopolymerization with particle tracking microrheology. *Polymer.* 47, 2263–2268. doi: 10.1016/j.polymer.2006.01.095

Squires, T. M., and Mason, T. G. (2010). Fluid mechanics of microrheology. *Annu. Rev. Fluid Mech.* 42, 413–438. doi: 10.1146/annurev-fluid-121108-145608

Stauffer, D., Coniglio, A., and Adam, M. (1982). Gelation and critical phenomena. *Adv. Polym. Sci.* 44, 103–158.

Tibbitt, M. W., Kloxin, A. M., Sawicki, L. A., and Anseth, K. S. (2013). Mechanical properties and degradation of chain and step-polymerized photodegradable hydrogels. *Macromolecules.* 46, 2785–2792. doi: 10.1021/ma302522x

Tirrell, D. A. (Ed.). (2012). *Biomaterials: Important Areas for Future Investment*. National Science Foundation.

Tongwa, P., Nygaard, R., and Bai, B. (2013). Evaluation of a nanocomposite hydrogel for water shut-off in enhanced oil recovery applications: design, synthesis, and characterization. *J. Appl. Polym. Sci.* 128, 787–794. doi: 10.1002/app.38258

Tse, J. R., and Engler, A. J. (2010). Preparation of hydrogel substrates with tunable mechanical properties. *Curr. Protoc. Cell Biol.* 10.16, 1–10. doi: 10.1002/0471143030.cb1016s47

Valentine, M. T., Dewalt, L. E., and Ou-Yang, H. D. (1996). Forces on a colloidal particle in a polymer solution: a study using optical tweezers. *J. Phys. Condes. Matter.* 8, 9477–9482.

Valentine, M. T., Kaplan, P. D., Crocker, J. C., Gisler, T., Prud'homme, R. K., Beck, M., et al. (2001). Investigating the microenvironments of inhomogeneous soft materials with multiple particle tracking. *Phys. Rev. E.* 64:061506. doi: 10.1103/PhysRevE.64.061506

Valentine, M. T., Perlman, Z. E., Gardel, M. L., Shin, J. H., Matsudaira, P., Mitchison, T. J., et al. (2004). Colloid surface chemistry critically affects multiple particle tracking measurements of biomaterials. *Biophys. J.* 86, 4004–4014. doi: 10.1529/biophysj.103.037812

Veerman, C., Rajagopal, K., Palla, C. S., Pochan, D. J., Schneider, J. P., and Furst, E. M. (2006). Gelation kinetics of beta-hairpin peptide hydrogel networks. *Macromolecules.* 39, 6608–6614. doi: 10.1021/ma0609331

Waigh, T. A. (2005). Microrheology of complex fluids. *Rep. Prog. Phys.* 68, 685–742. doi: 10.1088/0034-4885/68/3/R04/pdf

Waigh, T. A. (2016). Advances in the microrheology of complex fluids. *Rep. Prog. Phys.* 79:074601. doi: 10.1088/0034-4885/79/7/074601

Wang, H., and Heilshorn, S. C. (2015). Adaptable hydrogel networks with reversible linkages for tissue engineering. *Adv. Mater.* 27, 3717–3736. doi: 10.1002/adma.201501558

Wehrman, M. D., Leduc, A., Callahan, H. E., Mazzeo, M. S., Schumm, M., and Schultz, K. M. (2018). Rheological properties and structure of step- and chain-growth gels concentrated above the overlap concentration. *AIChE J.* 64, 3168–3176. doi: 10.1002/aic.16062

Wehrman, M. D., Lindberg, S., and Schultz, K. M. (2016). Quantifying the dynamic transition of hydrogenated castor oil gels measured via multiple particle tracking microrheology. *Soft Matter.* 12, 6463–6472. doi: 10.1039/C6SM00978F

West, J. L., and Hubbell, J. A. (1999). Polymeric biomaterials with degradation sites for proteases involved in cell migration. *Macromolecules.* 32, 241–244.

Winter, H. H. (1987). Can the gel point of a cross-linking polymer be detected by the G'-G" crossover? *Polym. Eng. Sci.* 27, 1698–1702.

Winter, H. H., and Chambon, F. (1986). Analysis of linear viscoelasticity of a crosslinking polymer at the gel point. *J. Rheol.* 30, 367–382.

Winter, H. H., and Mours, M. (1997). Rheology of polymers near liquid-solid transitions. *Adv. Polym. Sci.* 134, 165–234.

Wong Po Foo, C. T. S., Lee, J. S., Mulyasasmita, W., Parisi-Amin, A., and Heilshorn, S. C. (2009). Two-component protein-engineered physical hydrogels for cell encapsulation. *PNAS.* 106, 22067–22072. doi: 10.1073/pnas.0904851106

Wylie, R. G., Ahsan, S., Aizawa, Y., Maxwell, K. L., Morshead, C. M., and Shoichet, M. S. (2011). Spatially controlled simultaneous patterning of multiple growth factors in three-dimensional hydrogels. *Nat. Mater.* 10, 799–806. doi: 10.1038/nmat3101

Yamaguchi, N., Zhang, L., Chae, B.-S., Palla, C. S., Furst, E. M., and Kiick, K. L. (2007). Growth factor mediated assembly of cell receptor-responsive hydrogels. *J. Am. Chem. Soc.* 129, 3040–3041. doi: 10.1021/ja0680358

Zolfaghari, R., Katbab, A. A., Nabavizadeh, J., Yousefzadeh Tabasi, R., and Hossein Nejad, M. (2006). Preparation and characterization of nanocomposite hydrogels based on polyacrylamide for enhanced oil recovery applications. *J. Appl. Polym. Sci.* 100, 1096–2103. doi: 10.1002/app.23193

Zustiak, S. P., and Leach, J. B. (2010). Hydrolytically degradable poly(ethylene glycol) hydrogel scaffolds with tunable degradation and mechanical properties. *Biomacromolecules.* 11, 1348–1357. doi: 10.1021/bm100137q

Conflict of Interest Statement: The authors declare that the research was conducted in the absence of any commercial or financial relationships that could be construed as a potential conflict of interest.

Copyright © 2019 Zhang, Wehrman and Schultz. This is an open-access article distributed under the terms of the Creative Commons Attribution License (CC BY). The use, distribution or reproduction in other forums is permitted, provided the original author(s) and the copyright owner(s) are credited and that the original publication in this journal is cited, in accordance with accepted academic practice. No use, distribution or reproduction is permitted which does not comply with these terms.

frontiers in Chemistry

ORIGINAL RESEARCH
published: 27 March 2019
doi: 10.3389/fchem.2019.00159

Preparation of Renewable Epoxy-Amine Resins With Tunable Thermo-Mechanical Properties, Wettability and Degradation Abilities From Lignocellulose- and Plant Oils-Derived Components

*Louis Hollande[1,2], Izia Do Marcolino[1], Patrick Balaguer[3], Sandra Domenek[2], Richard A. Gross[4] and Florent Allais[1]**

[1] URD ABI, CEBB, AgroParisTech, Pomacle, France, [2] UMR GENIAL, AgroParisTech, INRA, Université Paris-Saclay, Massy, France, [3] Institut de Recherche en Cancérologie de Montpellier, Val d'Aurelle, Montpellier, France, [4] Department of Chemistry and Chemical Biology, Rensselaer Polytechnic Institute, Troy, NY, United States

OPEN ACCESS

Edited by:
Gil Garnier, Bioresource Processing Institute of Australia (BioPRIA), Australia

Reviewed by:
Guillermo Javier Copello, Consejo Nacional de Investigaciones Científicas y Técnicas (CONICET), Argentina
Juan Carlos Serrano-Ruiz, Universidad Loyola Andalucía, Spain

***Correspondence:**
Florent Allais
florent.allais@agroparistech.fr

Specialty section:
This article was submitted to Chemical Engineering, a section of the journal Frontiers in Chemistry

Received: *28 November 2018*
Accepted: *04 March 2019*
Published: *27 March 2019*

Citation:
Hollande L, Do Marcolino I, Balaguer P, Domenek S, Gross RA and Allais F (2019) Preparation of Renewable Epoxy-Amine Resins With Tunable Thermo-Mechanical Properties, Wettability and Degradation Abilities From Lignocellulose- and Plant Oils-Derived Components. Front. Chem. 7:159. doi: 10.3389/fchem.2019.00159

One-hundred percent renewable triphenol—GTF—(glycerol trihydroferulate) and novel bisphenols—GDF_x–(glycerol dihydroferulate) were prepared from lignocellulose-derived ferulic acid and vegetal oil components (fatty acids and glycerol) using highly selective lipase-catalyzed transesterifications. Estrogenic activity tests revealed no endocrine disruption for GDF_x bisphenols. Triethyl-benzyl-ammonium chloride (TEBAC) mediated glycidylation of all bis/triphenols, afforded innocuous bio-based epoxy precursors GDF_xEPO and GTF-EPO. GDF_xEPO were then cured with conventional and renewable diamines, and some of them in presence of GTF-EPO. Thermo-mechanical analyses (TGA, DSC, and DMA) and degradation studies in acidic aqueous solutions of the resulting epoxy-amine resins showed excellent thermal stabilities ($T_d5\% = 282–310°C$), glass transition temperatures (T_g) ranging from 3 to 62°C, tunable tan α, and tunable degradability, respectively. It has been shown that the thermo-mechanical properties, wettability, and degradability of these epoxy-amine resins, can be finely tailored by judiciously selecting the diamine nature, the GTF-EPO content, and the fatty acid chain length.

Keywords: ferulic acid, glycerol, lipase, bio-based thermosets, wettability, degradability

INTRODUCTION

Thermoset polymers are widely used in industrial applications thanks to their versatile performance, good durability, and excellent chemical resistance provided by their highly cross-linked structure (Ellis, 1993; Auvergne et al., 2014; Ramon et al., 2018). It is therefore very common to find these polymers in a broad range of applications such as maintenance coating, adhesives for aerospace (Prolongo et al., 2009) and automobile (Holbery and Houston, 2006) industries, or binders in composites (Gojny et al., 2006). Epoxy resins are one of the most important thermoset materials and are usually synthesized by reacting (poly)phenolic compounds with epichlorohydrin under basic conditions (Bruins, 1968).

The thermoset polymers sector, and more generally the polymer industry, has adopted the current trend which consists in developing greener and more sustainable chemicals and technologies. For instance, Solvay or Dow Chemical have already initiated the transition with the commercialization of bio-based epichlorohydrin prepared from the chlorination of bio-based glycerol, a by-product of biodiesel production (Strebelle et al., 2001; Freddy, 2006). Furthermore, a number of renewable resources—including fatty acids (Biermann et al., 2000; Maisonneuve et al., 2013; Laurichesse et al., 2014), lignocellulosic biomass (Isikgor and Becer, 2015), and enzymatic products—have been reported as alternative feedstocks in polymers synthesis.

Bisphenol A (BPA) is commonly used to prepare commercial high-performance epoxy resins (aka DGEBA, DiGlycidylEther of Bisphenol A). Although DGEBA, upon curing with diamines, leads to cross-linked materials with exceptional properties such as strong adhesion, mechanical integrity and chemical resistance, BPA is recognized as an endocrine disruptive chemical and many studies have been conducted to replace it by innocuous bio-based chemicals. Lignans and lignin-derived chemicals that can be obtained through pyrolysis (Celikbag et al., 2017; Barde et al., 2018) or controlled depolymerization (Pandey and Kim, 2011; Shuai et al., 2016) are the most used biomass-derived chemical platforms for the design of bio-based BPA-substitutes, for the preparation of sustainable thermosets with high thermo-mechanical properties. Indeed, the aromatic moieties present in these bio-based chemicals confer rigidity to the resulting polymers (Wang et al., 2017; Feghali et al., 2018). For example, there have been many reports on epoxy resins from eugenol (Wan et al., 2016), vanillin (Fache et al., 2015a,b; Hernandez et al., 2016; Mauck et al., 2017; Nicastro et al., 2018; Savonnet et al., 2018; Zhao et al., 2018), ferulic and sinapic acids (Maiorana et al., 2016; Janvier et al., 2017; Ménard et al., 2017), guaiacols (Maiorana et al., 2015), and creosol (Meylemans et al., 2011) with promising performances capable of competing with current DGEBA-based materials. However, few researchers have considered the potential toxicity of these BPA substitutes, especially endocrine disruption, which remains a crucial health issue for both plastic sector workers and consumers (Jiang et al., 2018). The degradability of the resulting materials and their behavior regarding water are two other aspects that are also under-investigated. In fact, in most of the studies described above, the thermo-mechanical (e.g., T_g) and physico-chemical (e.g., wettability) properties of the materials cannot be finely tuned because of the lack of apolar moieties in the bio-based aromatic-epoxies.

Plant oil-derived fatty acids are highly valuable building blocks and are frequently used as renewable resources for the synthesis of thermoplastics/thermosets (Meier, 2018). Their long aliphatic chain and their double bond(s) allow a wide number of chemical modifications and provide materials with tunable properties, such as glass transition temperature (T_g), chemical resistance, (bio)degradability, and adhesion strength. Combining the rigidity of bio-based aromatic building blocks and the apolar moiety of the alkyl chain of a fatty acid in a single BPA-substitute thus appears as an interesting approach to finely tune the T_g, the wettability and the degradability of the resulting epoxy-amine resins, after curing with diamines.

In this present work, we aim at developing a series of bio-based epoxy resins, from naturally occurring ferulic acid and plant oils-derived components (i.e., glycerol and fatty acids), to access epoxy-amine thermoset materials with tunable thermo-mechanical properties, wettability and chemical degradation ability. Through highly selective chemo-enzymatic pathways, several polyphenolic compounds, named GDF_x and GTF, have been prepared with tunable flexibility and degree of functionality (i.e., 2 or 3). The determination of the toxicity of these compounds has been carried out by determining their binding to human hormone receptors (ERα, PXR, and AR) and was benchmarked against that of commercial and controversial BPA. GDF_x and GTF were then converted to their corresponding glycidyl ether by TEBAC-mediated glycidylation in presence of epichlorohydrin. Characterization studies were then performed on the corresponding epoxy resins formulations (i.e., molecular weight distribution and EEW). The latter were finally cured with three crosslinkers (i.e., IPDA, DA10, and DIFFA) and the thermo-mechanical properties as well as wettability and chemical degradation abilities of the resulting epoxy-amine resins were investigated.

EXPERIMENTAL

Material

Ferulic acid, lauric acid, palmitic acid, stearic acid, benzyl bromide, *N*,*N*-Dimethylpyridin-4-amine (DMAP), *N*,*N*-Diisopropylcarbodiimide (DIC), benzyltriethyl ammonium chloride (TEBAC), and palladium supported on carbon, were supplied by Sigma-Aldrich. Glycerol was purchased from Alfa Aesar. Epichlorohydrin was purchased from Acros Organics. Isophorone diamine (IPDA) and Decane diamine (DA10) were purchased from TCI. *Candida antarctica* Lipase B (CAL-B) immobilized on resin (LC200291, 10,000 propyl laurate units.g^{-1}) was obtained from Novozyme. All reactants were used as received. All solvents were bought either from ThermoFisher Scientific or VWR. Deuterated chloroform ($CDCl_3$) was purchased from Euriso-top.

Methods

Purification

Column chromatographies were carried out with an automated flash chromatography (PuriFlash 4100, Interchim) and pre-packed INTERCHIM PF-30SI-HP (30 μm silica gel) columns using a gradient of cyclohexane and ethyl acetate for the elution.

Characterization

FT-IR analyses were performed on Cary 630 FT-IR with ATR. NMR analyses were recorded on a Bruker Fourier 300. ^{1}H NMR spectra of samples were recorded in $CDCl_3$ at 300 MHz, chemicals shifts were reported in parts per million ($CDCl_3$ residual signal at $\delta = 7.26$ ppm). ^{13}C NMR spectra of samples were recorded at 75 MHz ($CDCl_3$ signal at $\delta = 77.16$ ppm). HRMS were recorded by the PLANET platform at URCA on a Micromass GC-TOF.

Gel Permeation Chromatography (GPC)

Gel permeation chromatography (GPC) was performed at 40°C on an Infinity 1260 system from Agilent Technologies with PL-gel 5 μM MIXED-D column in THF (flow rate 1 mL.min^{-1}) using conventional PS calibration and UV detection at 280 nm.

Thermo-Gravimetric Analyses (TGA)

Thermo-gravimetric analyses (TGA) were recorded on a Q500, from TA. About 10 mg of each sample was heated at 10°C.min^{-1} from 30 to 500°C under nitrogen or oxygen flow (60 mL.min^{-1}).

Differential Scanning Calorimetry (DSC)

Differential scanning calorimetry (DSC) thermograms were obtained using a DSC TA Q20, under inert atmosphere (N_2), with a calibration using indium, *n*-octadecane and *n*-octane standards. For each sample, about 10 mg was weighed in a pan which was then sealed and submitted to three heat/cool/heat cycles: heating from 30 to 200°C at 10°C.min^{-1}, cooling from 200°C to −50°C at 20°C.min^{-1}. Glass transition temperatures (T_g) were determined at the inflection value in the heat capacity jump.

Dynamical Mechanical Analyses (DMA)

Dynamical Mechanical Analyses (DMA) were performed on a DMA Q800 from the TA Instrument. The DMA samples had a rectangular geometry (length: 40 mm, width: 8 mm, thickness: 1.5 mm). Uniaxial stretching of samples was performed while heating at a rate of 3°C.min^{-1} from 30 to 200°C, keeping frequency at 1 Hz. Deformation was kept at 0.001% (amplitude of 7 μm) to stay in the linear viscoelastic region. The storage modulus (E') and tan δ curves as a function of the temperature, were recorded and analyzed using the TA Instruments Universal Analysis 2000 software. The temperatures T_α *(°C)* were determined as the temperatures at the peak maximum of the tan δ curves.

Synthesis of Resin Epoxy Precursors

Scheme 1 presents the complete synthetic pathway using the following molecules: ferulic acid (**a**), ethyl dihydroferulate (**b**), benzylated ethyl ferulate (**c**), benzylated glycerol diferulate (GDFoBn) (**d**), glycerol tri-dihydroferulate (GTF) (**e**) and lipophilic glycerol dihydroferulates (GDF_x) (**f**, **g** and **h**). Compound syntheses were carried out following procedures previously described in the literature (Ménard et al., 2017; Hollande and Domenek, 2018). Full characterizations and detailed procedures for new compounds are given in the **Electronic Supplementary Information** (ESI). ^{1}H & ^{13}C NMR spectra, FTIR spectrum as well as TGA trace of GTF-EPO can be found in a previous published work (Ménard et al., 2017).

Glycidylation

Phenolic precursors (GDF_x or GTF; 1 eq) were dissolved in epichlorohydrin (10 eq/OH). Triethyl benzyl chloride (TEBAC) (0.2 eq) was added and the suspension was stirred for 2 h at 80°C. The reaction medium was cooled down to room temperature and NaOH (5M, 2 eq/OH) was added. The biphasic solution was vigorously stirred for 4 h at room temperature then extracted with ethyl acetate (3 × 100 mL). The organic layers were washed with brine (80 mL), dried over anhydrous $MgSO_4$, filtered and concentrated *in vacuo*.

Epoxide Equivalent Weight (EEW)

Experimental values of EEW for the epoxide resins synthesized herein were determined by ASTM D1652. Samples were dissolved in dichloromethane (DCM) with tetraethylammonium bromide and titrated in triplicate, using perchloric acid solution in acetic acid (1 N). Crystal violet was used as an indicator and the end point was determined when the solution turned from blue to green for longer than 30 s. Detailed results are provided in the ESI.

Preparation of Cured Epoxy Materials

This method considers that the epoxy resins prepared herein contained small amounts of higher molecular weights fractions. The weight of the resins and cross-linkers were determined by using the EEW values and amine hydrogen equivalent weight (AHEW). Weights of reaction components for the formulated resin systems were determined using equation (1). Equations (2) and (3) were used to calculate the AHEW and to obtain the parts by weight of diamine per hundred parts resin (phr).

$$EEW\ of\ mix = \frac{Total\ Weight}{\frac{Weight\ of\ resin\ A}{EEW\ of\ resin\ A} + \frac{Weight\ of\ resin\ B}{EEW\ of\ resin\ B}} \quad (1)$$

$$AHEW = \frac{molecular\ weight\ of\ amine}{number\ of\ active\ hydrogens} \quad (2)$$

$$phr = \frac{AHEW\ x\ 100}{EEW} \quad (3)$$

For instance, if phr = 20, then 20 g of diamine would be needed for 100 g of epoxy resin. Epoxy resins were vigorously mixed with the appropriate amount of crosslinker at room temperature in a disposable aluminum pan. In the case of the solid diamine DA10, an additional stirring time at 120°C was necessary to obtain a complete dissolution of the amine in the epoxy precursor. Mixtures were then transferred into rectangular stainless steel molds (length: 40 mm, width: 8 mm, thickness: 1.5 mm). The method of curing was adapted from a literature procedure (Janvier et al., 2017). In summary, the resins were maintained under ambient conditions in the molds for 2 h and then for 2 h at 60°C, for 20 h at 110°C and for 1 h at 150°C.

Hydrolytic Degradation Assays

Cured resin samples with dimensions about 4 × 8 × 1.5 mm, with weights ranging from 75 to 95 mg, were placed in a 10 mL sealed tube. An aqueous solution of HCl (3M) was added. The vials were heated at 60°C for 40 min for equilibration. Incubations were then continued for 5, 20, 26, 43, and 50 h. The residual solid was then washed with deionized water, dried then weighed to determine the mass loss.

Measurement of Contact Angle

The contact angle (θ) of liquid water against the cured epoxy resins was measured by the sessile drop method at room

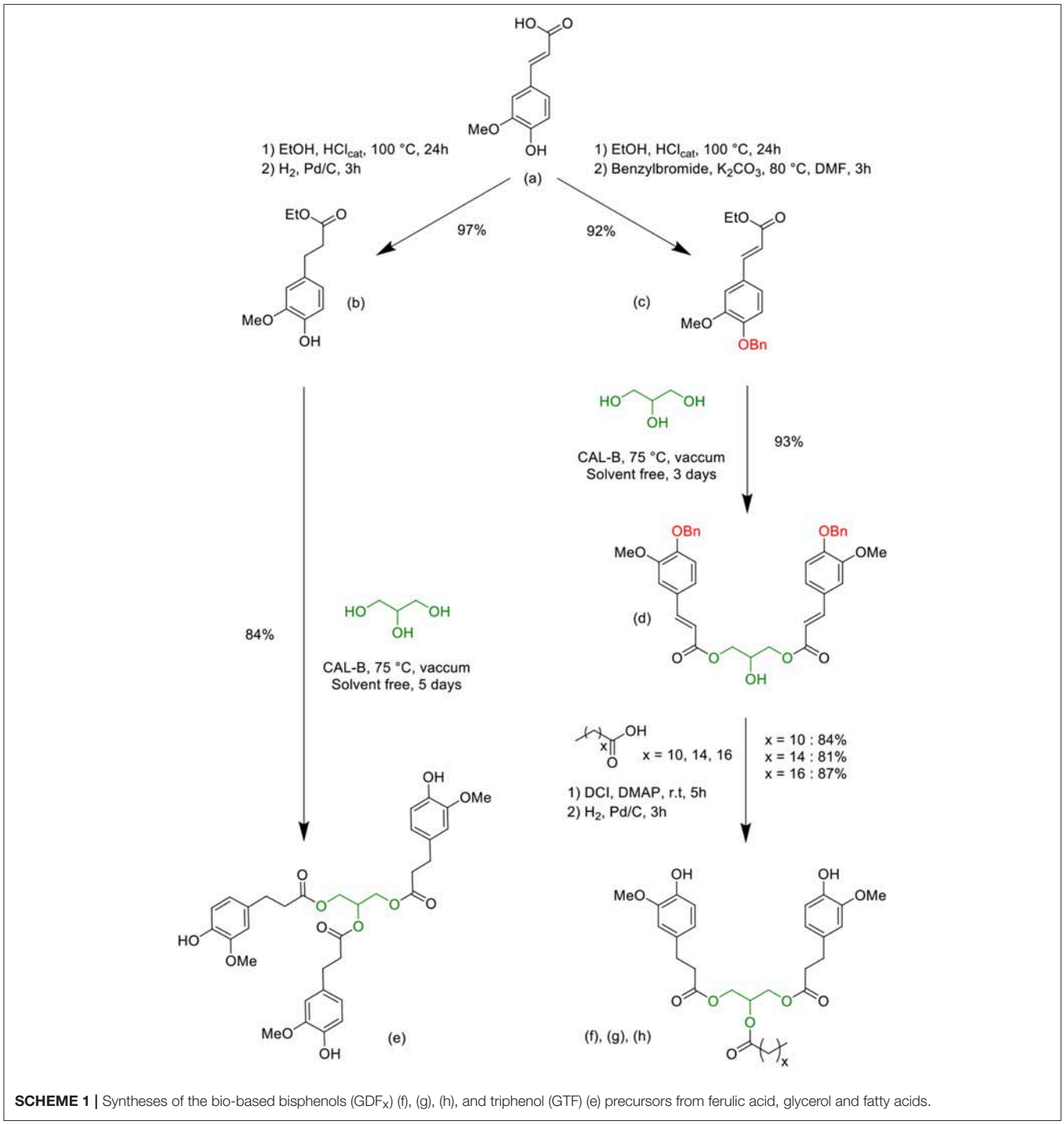

SCHEME 1 | Syntheses of the bio-based bisphenols (GDF$_X$) (f), (g), (h), and triphenol (GTF) (e) precursors from ferulic acid, glycerol and fatty acids.

temperature with a drop shape analysis system (DIGIDROP and Visiodrop software). The contact angle was measured at three different locations for each thermoset and the average value was reported.

Estrogen Binding Affinity Testing

The agonistic and antagonistic potentials of bisphenols were analyzed following a literature method (Delfosse et al., 2012) in which ERα, PXR, and AR transcriptional activities were monitored by using corresponding reporter cells HELN ERα, U2OS AR, and HG5LN PXR cells, respectively. Activities were measured in relative light units (RLU) and 100% activities were assigned to the RLU value obtained with 10 nM agonist control (estradiol (E_2), R 1881, SR 12813). The vehicle (DMSO) was tested as a control without any compound.

RESULTS AND DISCUSSION

Synthesis of the Bio-Based Epoxy Resin

Chemo-Enzymatic Synthesis

Chemical esterification of *p*-hydroxycinnamic acids with alcohol is unselective and side reactions generally lead to an unwanted product that needs to be removed by purification steps, generating waste to dispose of. In opposition, the lipase-mediated enzymatic synthesis offers some advantages for synthesizing esters, such as milder reaction conditions and selectivity. Hence, the selective synthesis of the bis/tri-ferulate resin epoxy precursors **e**, **f**, **g** and **h**, involving glycerol linker group, was based on chemo-enzymatic methods recently published (**Scheme 1**) (Pion et al., 2013; Hollande and Domenek, 2018).

Ferulic acid was first transformed either in ethyl dihydroferulate (**Scheme 1**, b) or in benzylated ethyl ferulate (**Scheme 1**, c), through a two-step one-pot process. Afterwards, a specific affinity of *Candida antarctica* Lipase B (CAL-B) toward glycerol allowed controlling the degree of functionalization of the latter, giving access to the symmetric bisphenol (**Scheme 1**, d) or to the fully functionalized glycerol triferulate (**Scheme 1**, e) in excellent yields and purities. Fatty acids were then grafted onto the available secondary alcohol of the intermediary compound d, immediately followed by a palladium-catalyzed hydrogenation to simultaneously reduce unsaturation and cleave the benzyl group, thus providing the GDF_x compounds (**Scheme 1**, f, g, h. It is noteworthy to mention that all the syntheses described in **Scheme 1** have been performed at the multi-gram scale. Moreover, in a recent work, we have not only demonstrated the feasibility of the lipase-mediated transesterification of dihydroferulate ethyl ester at the kilo-scale (Teixeira et al., 2017), but also devised a sustainable and industrially relevant membrane-based technique, allowing both the purification of the targets and the recycling of solvents and unreacted reagents.

Endocrine Receptor Activities of GDF_x Bisphenols

Nowadays, the development of new platform chemicals is deeply regulated, especially for bisphenolic compounds—such as BPA—and other controversial endocrine disrupting chemicals (EDCs). Herein, endocrine activities of newly created GDF_x bisphenols were investigated by evaluating their ability to interact with three types of receptors ERα, PXR, and AR. ERα is a member of the nuclear hormone receptors family, and its activity is regulated by the steroid estrogen sex hormone 17β-estradiol (E2). PXR is a member of the steroid and xenobiotic sensing nuclear receptors family and AR is a nuclear type androgen receptor that is activated by binding with any of the androgenic hormones. In **Figure 1A**, sex hormone E2 induces a 100% ERα activity at 5.10^{-10} M, which plateaus at higher concentrations. For BPA, estrogenic activity was observed at molarities of 10^{-7} and slightly above 60% at concentrations of 10^{-5}. In contrast, all newly created GDF_x bisphenols, GDF_{10}, GDF_{14}, and GDF_{16}, exhibited an activity similar to that of the control, even with increasing concentrations. In addition, **Figure 1B** reveals that the highest concentration tested for GDF_x family (i.e., 10^{-5} M) did not induce any abnormal receptor activities on both PXR and AR. Finally, an endocrine disruption assay (ESI p22) indicated that phenolic structures were neither agonist nor antagonist ligands. Based on these results, that demonstrated the innocuousness of these newly created GDF_x bisphenols, we were encouraged to further explore their use for the production of epoxies and epoxy-amine resins.

Glycidylation

Epoxy resins synthesis consists in the glycidylation of the different GDF_x bisphenols, using the classical procedure, i.e., large excess of epichlorohydrin under alkaline conditions. However, to prevent the partial hydrolysis of the internal ester moieties observed by Maiorana et al. (2016) during classical glycidylation of bisferulate esters, milder temperatures, and shorter reaction times were applied. Thus, to offset this restriction, a catalytic amount of triethylbenzyl ammonium chloride (TEBAC) as phase transfer catalyst—well known for allowing higher epoxy functionality—was used (Fache et al., 2015a). Under such conditions, the phenolate formed is able to attack each one of the carbons of epichlorohydrin (**Scheme 2**), two of them, (b) and (c), leading to the epoxy ring opening. Thus, a basic treatment is necessary to close the open forms. Yet, not all the resulting species are diepoxies resins. Side reactions can occur, the most important being (b) the oxetane formation or (d) the formation of branched molecules due to the oligomerization of chlorinated intermediate (Ellis, 1993).

Resulting crude di/triglycidyl ether bis/triferulate epoxy resins, named GDF_xEPO, and GTF-EPO, respectively, were obtained in high isolated yields (>85%). All the resins prepared herein (see ESI, p18) showed the appearance of an epoxy vibrational band at 912 cm^{-1} characteristic of oxirane C-O group on their FT-IR spectra. ^{1}H NMR analyses showed the expected chemical shifts for the proton on the tertiary carbon of the oxirane ring at 3.40 ppm (see ESI, p17). However, signals were also observed between 3.75 and 3.95 ppm, which could be attributed to the oxetane or the oligomeric production epoxies pictured in **Scheme 2** (b) and (d). In order to investigate the potential side formation of such oligomeric epoxies, molecular weight distributions of GDF_xEPO and GTF-EPO resins were measured by gel permeation chromatography. The results are shown in **Figure 2** and the ESI (p20-21).

The distribution of molecular species (M_n) in epoxy resins was analogous for each sample. Experimentally determined values (GPC) described the normalized weight distribution of epoxy systems in two monodisperse fractions according to the M_w/M_n values closed to 1.0. The first corresponds to the monomeric glycidyl ether of GDF_{10}, GDF_{14}, GDF_{16}, and GTF, with M_n *of* 840, 970, 1,070, and 860 g/mol, respectively, whereas the second corresponds to M_n above 2,000 g/mol, suggesting the formation of oligomeric by-products through the dimerization of chlorinated intermediate depicted in **Scheme 2**. Nevertheless, the contribution of the high molecular weight tail to the cumulative molecular weight distribution is <5%. Considering the relatively low concentration of by-products estimated through ^{1}H NRM and GPC analyses, we decided to use these epoxy resins directly without further purification. **Table 1** displays values of experimental and theoretical epoxide

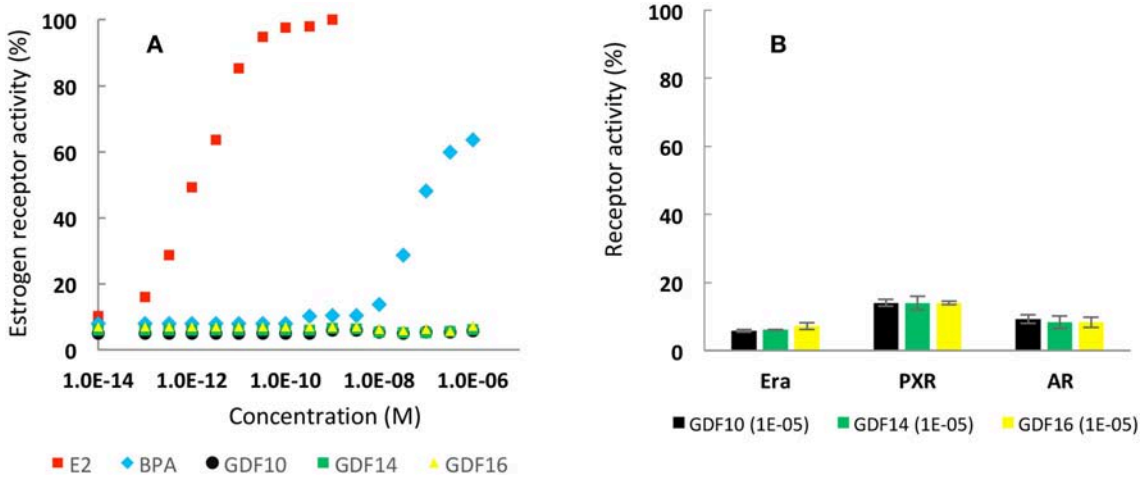

FIGURE 1 | (A) Estrogenic activity (%) as function of concentration of E2, BPA and synthesized bisphenols. **(B)** Activities (%) of Erα, PXR and AR induced by synthesized bisphenol at 10^{-5} molarity.

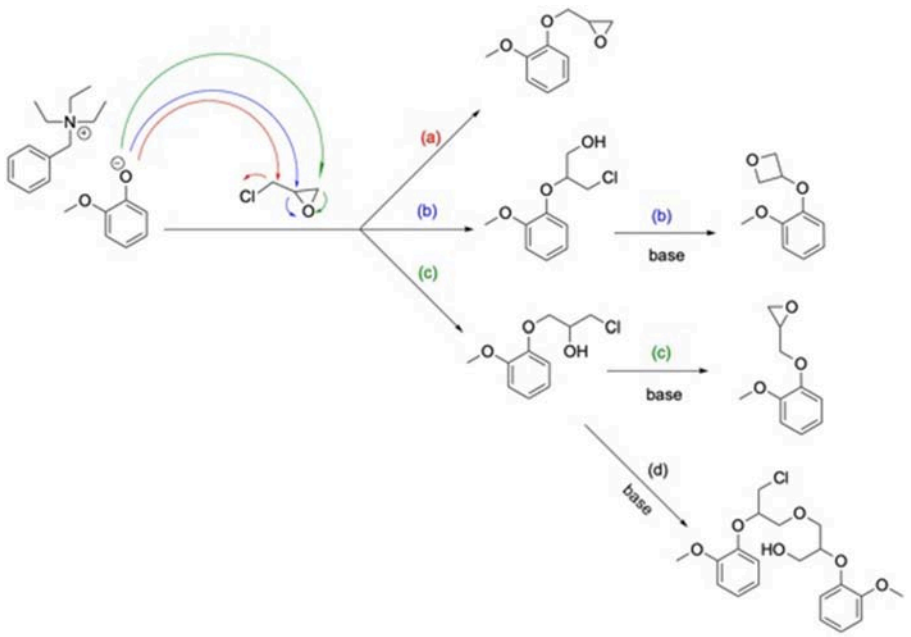

SCHEME 2 | Glycidylation mechanism by SN_2 (a) or epoxy ring opening (c) and oxetane (b) or oligomeric product (d) formation consequent to a basic treatment.

equivalent weights (EEW) where the latter assumes 100% conversion to the corresponding monomeric glycidyl ferulate structures. Experimental EEWs values are 11 to 15% greater than that of the corresponding theoretical values. This result is attributed to the formation of dimers which results in the increase of the EEW of the synthesized resins above the theoretical value. Finally, **Table 1** also reports on the thermal behaviors of uncured resins. TGA analysis revealed thermostability (T_d 5%) in the range of 311–340°C under an inert atmosphere, and 304–321°C under an oxidative atmosphere. Furthermore, the alkyl chain length does not significantly impact the degradation temperature.

Thermosets Synthesis

The chemical structures of all amine hardeners or curing agents are reported in **Figure 3**. Two bio-based (DA10 and DIFFA) and one extensively used fossil-based (IPDA), presenting different rigidities, were selected.

To ensure that epoxy resin has a good reactivity toward diamines, a DSC analysis of an equimolar mixture of resins and diamines was carried out (**Figure 4**). An exothermic peak was observed around 100°C corresponding to the epoxy ring-opening reaction to form the crosslinked polymer. In order to ensure chain mobility during gelation and to obtain optimal crosslinking content, a multistep temperature program was

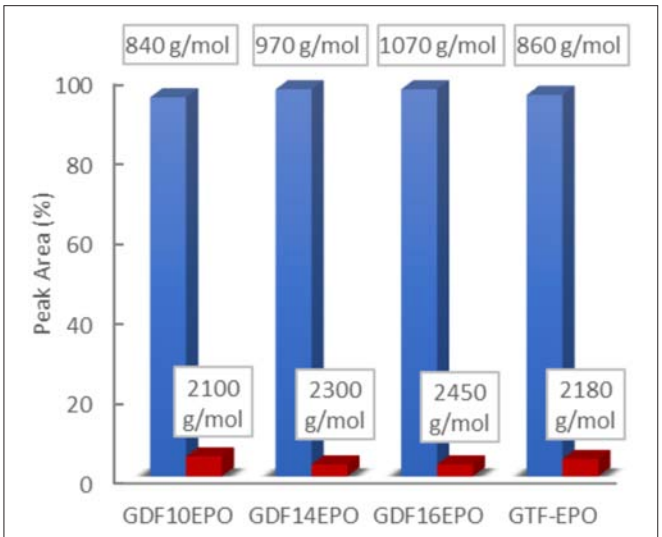

FIGURE 2 | Relative molecular weight distribution (%) of epoxy resins determined by GPC.

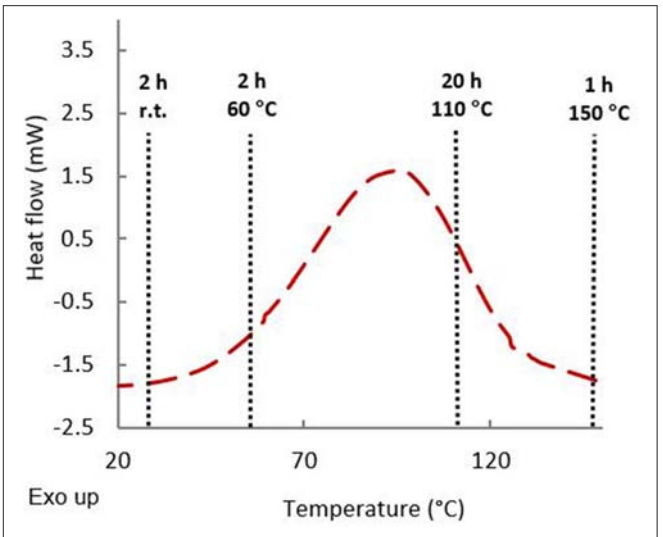

FIGURE 4 | DSC analysis of an equimolar mixture of $GDF_{10}EPO$ and curing agent (IPDA).

TABLE 1 | Epoxy resins characterization.

Resin type	Epoxy content			Thermal analysis*		
	EEW_{exp}	EEW_{theore}	Increase (%)	T_d 5% (°C)[a]	T_d max (°C)[a]	T_o 5% (°C)[b]
$GDF_{10}EPO$	426 ± 6	371	13	317	369	314
$GDF_{14}EPO$	471 ± 5	400	15	311	396	304
$GDF_{16}EPO$	463 ± 9	414	11	340	371	321
GTF-EPO	303 ± 5	265	13	x	x	x

*Determined by TGA (10°C.min^{-1}).
[a]Under N_2 flow.
[b]Under O_2 flow.

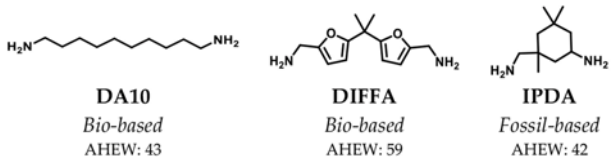

FIGURE 3 | Chemical structures of the curing agents used for thermoset formulation.

elaborated. Mixtures were first left for 2 h at room temperature followed by two additional hours at 60°C. Formulations were then cured at $T \approx T_{DSCcrosslinkingpeak}$ (20 h at 110°C), then at $T > T_{DSCcrosslinkingpeak}$ (1 h at 150°C). Each difunctionalized GDF_xEPO epoxy precursor was cured in presence of each curing agent leading to 9 formulations (**Table 2**, thermosets 1–9). In order to tune the properties of these thermosets, and as the formulations with diamines and difunctionalized GDF_xEPO (i.e., thermosets 1–9) did not provide materials rigid enough to perform DMA analyses, 1 formulation with GTF-EPO (**Table 2**, thermoset 15) as well as 5 co-formulations with IPDA, in variable ratios of difunctionalized ($GDF_{14}EPO$) and tri-functionalized (GTF-EPO) epoxy resin (**Table 2**, thermosets 10–14) were also prepared.

Characterization of the Thermosets

Thermogravimetric Analyses (TGA)

The thermal stability of cured thermosets was studied by thermal gravimetric analysis (TGA) under nitrogen flow. $T_d5\%$ was defined as the temperature at which the thermosets lost 5% of its initial mass, Td_{max} as the temperature at which the kinetic degradation of the thermoset occurs at the maximum rate and $W\%_{char}$ corresponds to the relative amount of stable residue at a high temperature. **Table 2** sums up the values for the thermosets prepared and all thermograms are displayed in ESI p23-25. The lowest $T_d5\%$ was obtained with DIFFA (**Table 2**; thermosets 4–6), which might be explained by the initiation of the degradation by rupture of the curing agent segment, as reported by Ménard et al. (2017). Overall, higher $T_d5\%$ and Td_{max}were measured with IPDA- and DA10-containing resins. Concerning the high temperature stable char content ($W\%_{char}$), values were around 10% for GDF_xEPO resins; moreover, the higher the GTF-EPO ratio in epoxy resin system, the higher the char content. This parameter would be particularly interesting for the development of flame-retardant materials.

Differential Scanning Calorimetric Analyses (DSC)

The degree of cure of the resins and glass transition temperatures were both determined through DSC. Analyses of post-cured resins showed no residual exothermic peak above or below the glass transition corresponding to further curing reactions (ESI, p26-28). These results indicate that if additional cure ever occurred during DSC heating, it is below the instrument level of detection. Therefore, consumption of epoxy moieties and concurrent events of cross-linking during the curing cycle

TABLE 2 | Results of the analyses of thermosets (ATG, DSC, DMA).

Thermoset	Curing agent	Resin type	$T_d5\%$ (°C)[a]	Td_{max} (°C)[a]	w% char[a]	T_g(°C)[b]	T_α (°C)[c]	E′ glassy (Mpa)[c]	E′ elastic (Mpa)[c]
1	DA10	$GDF_{10}EPO$	296	356	9.9	5	x	x	X
2	DA10	$GDF_{14}EPO$	299	356	7.7	4	x	x	x
3	DA10	$GDF_{16}EPO$	306	365	8.6	3	x	x	x
4	DIFFA	$GDF_{10}EPO$	282	368	16.9	15	x	x	x
5	DIFFA	$GDF_{14}EPO$	286	378	13.6	11	x	x	x
6	DIFFA	$GDF_{16}EPO$	282	376	15.9	16	x	x	x
7	IPDA	$GDF_{10}EPO$	310	369	9.0	21	x	x	x
8	IPDA	$GDF_{14}EPO$	298	352	10.9	23	x	x	x
9	IPDA	$GDF_{16}EPO$	297	367	10.0	18	x	x	x
10	IPDA	87%-$GDF_{14}EPO$ 13%-GTF-EPO	290	378	10.1	25	x	x	x
11	IPDA	75%-$GDF_{14}EPO$ 25%-GTF-EPO	287	373	9.7	28	x	x	x
12	IPDA	50%-$GDF_{14}EPO$ 50%-GTF-EPO	289	371	14.2	45	61	678	3.5
13	IPDA	25%-$GDF_{14}EPO$ 75%-GTF-EPO	282	372	15.9	54	63	1,985	7.5
14	IPDA	10%-$GDF_{14}EPO$ 90%-GTF-EPO	266	371	18.7	60	71	2,523	9.7
15	IPDA	GFT-EPO	279	372	17.5	62	72	1,685	8.8

[a]*Determined by TGA (10°C.min^{-1}, N_2 flow).*
[b]*Determined by DSC on the second heat-cool-heat cycle (10°C.min^{-1}, N_2 flow).*
[c]*Determined by DMA (frequency 1 Hz, amplitude 7 μm, 3°C.min^{-1}). E'_{glassy} at 30°C, $E'_{elastic}$ at 150°C.*

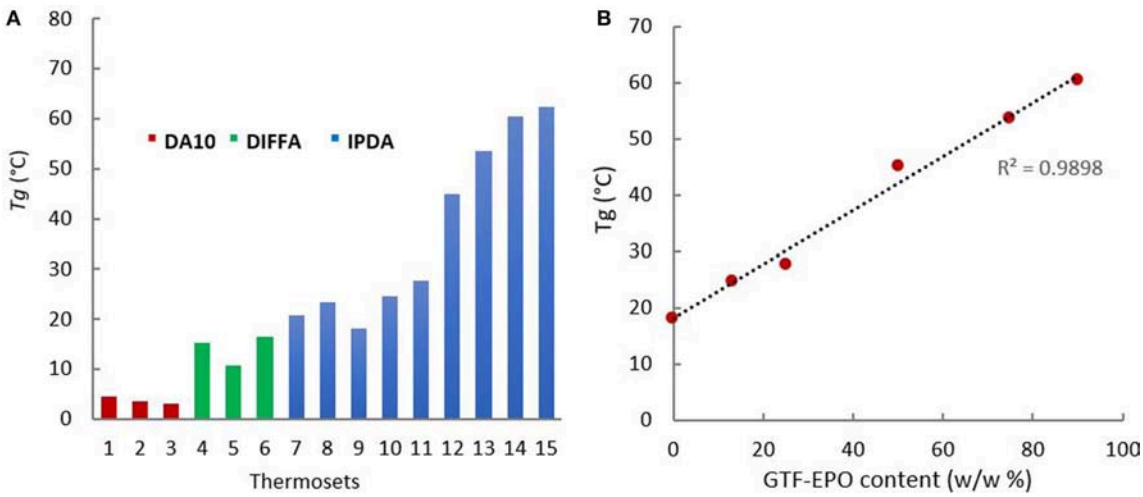

FIGURE 5 | (A) T_g for thermosets formulated with (red) DA10, (green) DIFFA, and (blue) IPDA; **(B)** *Tg* as a function of GTF-EPO resin content.

adopted herein results in a degree of cure that closely approaches its upper limit. Furthermore, the curing of difunctionalized resins (**Table 2**, entries 1–9 and 15) with hardeners presenting various rigidities (DA10 < DIFFA < IPDA due to their aliphatic, aromatic, and cyclic configuration), respectively, lead to a restricted range of T_g values (from 3 to 23°C). Hence, the most flexible amine (DA10) provided the lowest T_g values, while the IPDA-containing thermosets led to the highest T_g. Nevertheless, for a given diamine, thermosets exhibit quite similar T_g, meaning that the impact of the diamine on the rigidity of the network outweighs that of the alkyl chain length (**Figure 5A**), Entries 1–3; 4–6; 7–9).

When IPDA reacted with tri-functionalized resins, i.e., GTF-EPO, the T_g value increased up to 60°C due to the higher epoxy functionally (2 vs. 3) and higher cross-link density (**Figure 5A**, 15). Moreover, as shown in **Figure 5B**, it is noteworthy to

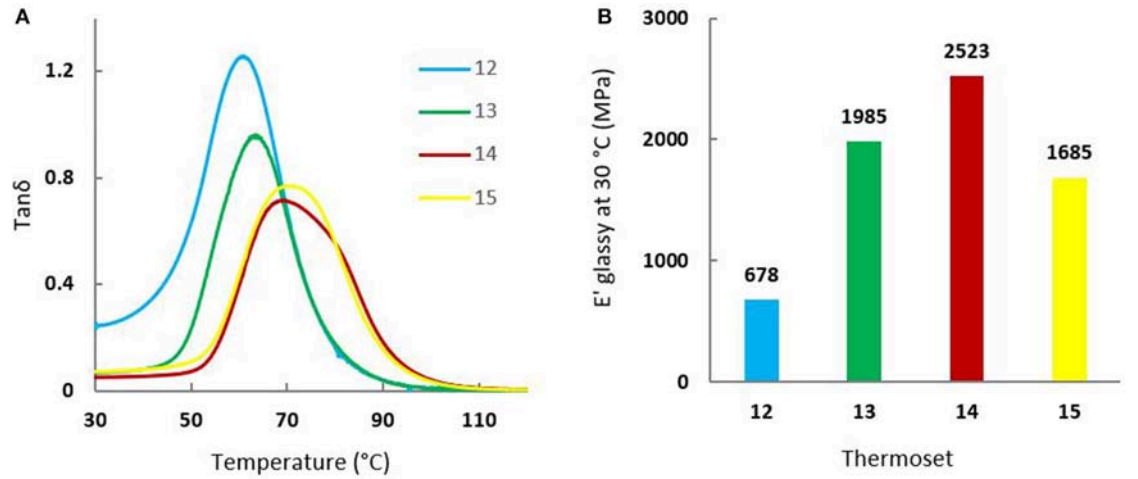

FIGURE 6 | (A) Tan δ curves of (blue) 12, (green) 13, (red) 14, and (yellow) 15 thermosets; **(B)** Storage modulus (E'_{glassy}) at 30°C of (blue) 12, (green) 13, (red) 14, and (yellow) 15 thermosets.

mention that the T_g increased linearly with the tri-functionalized resin GTF-EPO content ($R^2 = 0.9898$).

Dynamic Mechanical Analyses (DMA)

Mechanical properties of the cured resins were evaluated by DMA on each sample with a glass transition upwards of 30°C (thermoset 12–15). **Figure 6** and **Table 2** provide (a) tan δ values as a function of temperature and (b) storage modulus values at the glassy state at 30°C. Similar to the previous linear relationship observed for T_g and GTF-$EPO_{wt\%}$, the same trend was observed for tan δ that increased with the increasing incorporation of the GTF-EPO to the $GDF_{14}EPO$ system. As discussed previously, the thermal behaviors observed with the addition of GTF-EPO was a consequence of the decrease of EEWs of the co-formulated systems relative to the GDF_xEPO resin. In other words, co-formulated resins will lead to thermosets with relatively higher crosslink densities. On the other hand, when the ratio of $GDF_{14}EPO$ in GTF-EPO does not exceed 25 wt%, thermosets exhibit a higher storage modulus than that of the GTF-EPO resin (**Figure 6B**; entries 13 and 14 vs. 15). It is worth mentioning that the storage modulus at 30°C of epoxy systems which contain 10 wt% of $GDF_{14}EPO$ is 50% higher than that of the GTF-EPO thermoset (2,523 vs. 1,685 MPa). This rather unexpected outcome may be explained by the more efficient interaction/distribution of lipophilic GTFxEPO epoxies during the gelation/curing induced by their "surfactant" properties.

Degradation and Wettability Behavior

To gain further insight on how surface hydrophobicity varies as a function of the alkyl chain length, contact angles were measured (**Table 3**). Whatever the curing agent, increasing the alkyl chain length from 12 to 18 carbons (i.e., lauric acid -> palmitic acid -> stearic acid) resulted in an increase of the contact angle (**Table 3**; thermosets 1 vs. 3, 4 vs. 6, and 7 vs. 9). However, it is worth mentioning that the nature of the curing agent does not significantly impact the hydrophilicity of thermosets as for a same resin GDF_xEPO cured with the three different curing agents (i.e., DA10, DIFFA, and IPDA) contact angles differ by $< \pm 7°$.

TABLE 3 | Characterization of weight loss plots and contact angle.

Thermoset	Resin type	Curing agent	Weight loss/hour 10^{-3} ($mg.h^{-1}$)	Least squares fitting value for weight loss plots (R^2)	Contact angle (°)
1	$GDF_{10}EPO$	DA10	−17.1	0.965	66 ± 2
2	$GDF_{14}EPO$	DA10	−15.8	0.997	75 ± 5
3	$GDF_{16}EPO$	DA10	−2.2	0.990	82 ± 6
4	$GDF_{10}EPO$	DIFFA	−17.3	0.997	63 ± 8
5	$GDF_{14}EPO$	DIFFA	−12.8	0.983	76 ± 6
6	$GDF_{16}EPO$	DIFFA	−5.2	0.939	83 ± 5
7	$GDF_{10}EPO$	IPDA	−20.1	0.981	79 ± 3
8	$GDF_{14}EPO$	IPDA	−14.7	0.854	82 ± 1
9	$GDF_{16}EPO$	IPDA	−10.6	0.947	88 ± 4

In addition, thermosets weight loss, determined as a function of the incubation time in acidic aqueous solutions, was plotted (**Figure 7**). Data showed a decrease in mass upon incubation with linear behavior, according to the R^2 values for weight loss plots (**Table 3**). Finally, it is noteworthy to mention that the length of the fatty acid chain grafted onto GDF_x epoxies had a significant effect on the hydrolytic degradation rate of cured thermosets. Indeed, an increase in hydrophobicity of the thermoset, by increasing the length of the fatty acids graft, was consistent with a corresponding decrease of the degradation rate measured in $mg.h^{-1}$ and the susceptibility of that surface to hydrolysis.

CONCLUSION

Herein, the chemo-enzymatic synthesis, thermo-mechanical properties, wettability and acidic hydrolysis of 100% renewable

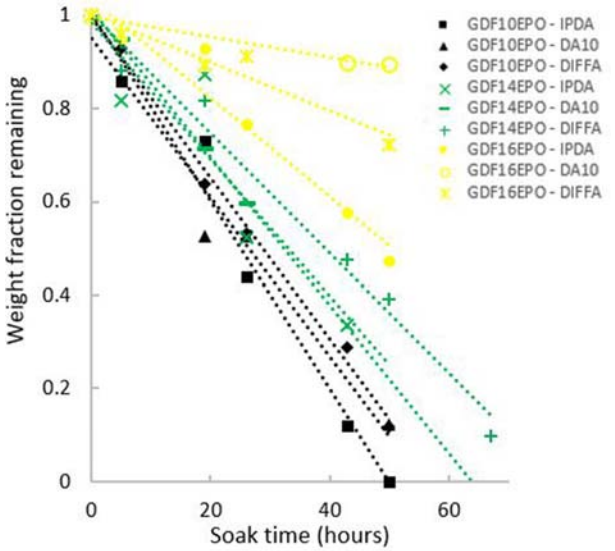

FIGURE 7 | Analyses of thermoset weight loss as function of incubation time at 60°C in acid aqueous solutions.

ferulic-, glycerol- and fatty acids-based bis- and triphenols - GDF_x and GTF - are described. The estrogenic activity of GDF_x with fatty acid chain lengths of 12, 16, and 18-carbons was quantified and compared to bisphenol A and 17β-estradiol and showed no significant activity for ERα, PXR, and AR receptors. Bio-based GDF_x and GTF bis/triphenols were then successfully converted to their corresponding di- and triglycidyl ether epoxy resins (i.e., GDF_xEPO and GTF-EPO, respectively) through a TEBAC-mediated glycidylation. GDF_xEPO was then cured with DIFFA, DA10 and IPDA diamines; GDF_{14}EPO was also co-formulated with tri-functionalized GTF-EPO and IPDA. All the resulting epoxy-amines exhibited relatively high thermostability with $T_d5\%$ ranging from 282 to 310°C and T_g between 3 and 62°C. Surprisingly, in the case of GDF_xEPO-diamine resins, for a given diamine, the chain length of the fatty acid moiety did not significantly impact the T_g. However, one can tailor the T_g by playing with the diamine nature and achieve T_g up to 23°C with IPDA and GDF_{14}EPO. To further tailor the T_g and to reach higher values, GTF-EPO must be added to the formulation. In such formulations, DSC and DMA analyses showed that the T_g and the storage modulus can also be modulated by finely adjusting the GTF-EPO content. Finally, with regards to wettability and degradability, the chain length of the fatty acid was found to provide a simple but powerful approach to tailor the wettability and the susceptibility to hydrolysis of the GDF_xEPO-based epoxy-amine resins. Indeed, the shortest fatty acid provided the highest wetting and hydrolysis rate, and *vice-versa*. This study therefore demonstrates the great potential of combining ferulic acid, glycerol and fatty acids using chemo-enzymatic processes for the preparation of epoxies and epoxy-amine networks with tunable properties.

AUTHOR CONTRIBUTIONS

FA and RG conceived the research. FA and SD managed the research. LH and ID performed the chemo-enzymatic reactions and the characterizations. PB performed the endocrine disruption assays. FA and LH provided the technical guidelines, reviewed the results, wrote, and drafted the article. FA, RG, and SD reviewed and approved the article.

ACKNOWLEDGMENTS

The authors are grateful to Région Grand Est, Conseil Départemental de la Marne and Grand Reims for financial support.

SUPPLEMENTARY MATERIAL

The Supplementary Material for this article can be found online at: https://www.frontiersin.org/articles/10.3389/fchem.2019.00159/full#supplementary-material

REFERENCES

Auvergne, R., Caillol, S., David, G., Boutevin, B., and Pascault, J.-P. (2014). Biobased thermosetting epoxy: present and future. *Chem. Rev.* 114, 1082–1115. doi: 10.1021/cr3001274

Barde, M., Adhikari, S., Via, B. K., and Auad, M. L. (2018). Synthesis and characterization of epoxy resins from fast pyrolysis bio-oil. *Green Mater.* 6, 76–84. doi: 10.1680/jgrma.17.00038

Biermann, U., Friedt, W., Lang, S., Lühs, W., Machmüller, G., Metzger, J. O., et al. (2000). New syntheses with oils and fats as renewable raw materials for the chemical industry. *Angew. Chemie Int. Ed.* 39, 2206–2224. doi: 10.1002/1521-3773(20000703)39:13<2206::AID-ANIE2206>3.0.CO;2-P

Bruins, P. F. (1968). "Epoxy resin technology," in *Interscience*, ed P. F. Bruins (New York, NY), 275.

Celikbag, Y., Meadows, S., Barde, M., Adhikari, S., Buschle-Diller, G., Auad, M. L., et al. (2017). Synthesis and characterization of bio-oil-based self-curing epoxy resin. *Ind. Eng. Chem. Res.* 56, 9389–9400. doi: 10.1021/acs.iecr.7b02123

Delfosse, V., Grimaldi, M., Pons, J.-L., Boulahtouf, A., le Maire, A., Cavailles, V., et al. (2012). Structural and mechanistic insights into bisphenols action provide guidelines for risk assessment and discovery of bisphenol A substitutes. *Proc. Natl. Acad. Sci. U.S.A.* 109, 14930–14935. doi: 10.1073/pnas.1203574109

Ellis, B. (1993). *Chemistry and Technology of Epoxy Resins*. Dordrecht: Springer.

Fache, M., Auvergne, R., Boutevin, B., and Caillol, S. (2015a). New vanillin-derived diepoxy monomers for the synthesis of biobased thermosets. *Eur. Polym. J.* 67, 527–538. doi: 10.1016/j.eurpolymj.2014.10.011

Fache, M., Boutevin, B., and Caillol, S. (2015b). Vanillin production from lignin and its use as a renewable chemical. *ACS Sustain. Chem. Eng.* 4, 35–46. doi: 10.1021/acssuschemeng.5b01344

Feghali, E., Torr, K. M., van de Pas, D. J., Ortiz, P., Vanbroekhoven, K., Eevers, W., et al. (2018). Thermosetting polymers from lignin model compounds and depolymerized lignins. *Top. Curr. Chem.* 376, 1–25. doi: 10.1007/s41061-018-0211-6

Freddy, G. (2006). Solvay will make epichlorohydrin from glycerol. *Ind Bioprocess* 28, 8–9.

Gojny, F. H., Wichmann, M. H. G., Fiedler, B., Kinloch, I. A., Bauhofer, W., Windle, A. H., et al. (2006). Evaluation and identification of electrical and thermal conduction mechanisms in carbon nanotube/epoxy composites. *Polymer* 47, 2036–2045. doi: 10.1016/j.polymer.2006.01.029

Hernandez, E. D., Bassett, A. W., Sadler, J. M., La Scala, J. J., and Stanzione, J. F. (2016). synthesis and characterization of bio-based epoxy resins derived from vanillyl alcohol. *ACS Sustain. Chem. Eng.* 4, 4328–4339. doi: 10.1021/acssuschemeng.6b00835

Holbery, J., and Houston, D. (2006). Natural-fiber-reinforced polymer composites in automotive applications. *JOM* 58, 80–86. doi: 10.1007/s11837-006-0234-2

Hollande, L., and Domenek, S. (2018). Chemo-enzymatic synthesis of renewable sterically-hindered phenolic antioxidants with tunable polarity from lignocellulose and vegetal oil components. *Int. J. Mol. Sci.* 19:3358. doi: 10.3390/ijms19113358

Isikgor, F. H., and Becer, C. R. (2015). Lignocellulosic biomass: a sustainable platform for the production of bio-based chemicals and polymers. *Polym. Chem.* 6, 4497–4559. doi: 10.1039/C5PY00263J

Janvier, M., Hollande, L., Jaufurally, A. S., Pernes, M., Ménard, R., Grimaldi, M., et al. (2017). Syringaresinol: a renewable and safer alternative to bisphenol A for epoxy-amine resins. *ChemSusChem* 10, 738–746. doi: 10.1002/cssc.201601595

Jiang, H., Sun, L., Zhang, Y., Meng, F., Zhang, W., and Zhao, C. (2018). Estrogenic activity research of a novel fluorinated bisphenol and preparation of an epoxy resin as alternative to bisphenol A epoxy resin. *Eur. Polym. J.* 108, 507–516. doi: 10.1016/j.eurpolymj.2018.09.020

Laurichesse, S., Huillet, C., and Avérous, L. (2014). Original polyols based on organosolv lignin and fatty acids: new bio-based building blocks for segmented polyurethane synthesis. *Green Chem.* 16, 3958–3970. doi: 10.1039/C4GC00596A

Maiorana, A., Reano, A. F., Centore, R., Grimaldi, M., Balaguer, P., Allais, F., et al. (2016). Structure property relationships of biobased: N -alkyl bisferulate epoxy resins. *Green Chem.* 18, 4961–4973. doi: 10.1039/C6GC01308B

Maiorana, A., Spinella, S., and Gross, R. A. (2015). Bio-based alternative to the diglycidyl ether of bisphenol A with controlled materials properties. *Biomacromolecules* 16, 1021–1031. doi: 10.1021/acs.biomac.5b00014

Maisonneuve, L., Lebarbé, T., Grau, E., and Cramail, H. (2013). Structure–properties relationship of fatty acid-based thermoplastics as synthetic polymer mimics. *Polym. Chem.* 4, 5472–5517. doi: 10.1039/c3py00791j

Mauck, J. R., Yadav, S. K., Sadler, J. M., La Scala, J. J., Palmese, G. R., Schmalbach, K. M., et al. (2017). Preparation and characterization of highly bio-based epoxy amine thermosets derived from lignocellulosics. *Macromol. Chem. Phys.* 218:1700013. doi: 10.1002/macp.201700013

Meier, M. A. R. (2018). Plant-oil-based polyamides and polyurethanes: toward sustainable nitrogen-containing thermoplastic materials. *Macromol. Rapid Commun.* 40:1800524. doi: 10.1002/marc.201800524

Ménard, R., Caillol, S., and Allais, F. (2017). Ferulic acid-based renewable esters and amides-containing epoxy thermosets from wheat bran and beetroot pulp: chemo-enzymatic synthesis and thermo-mechanical properties characterization. *Ind. Crops Prod.* 95, 83–95. doi: 10.1016/j.indcrop.2016.10.016

Meylemans, H. A., Groshens, T. J., and Harvey, B. G. (2011). Synthesis of renewable bisphenols from creosol. *ChemSusChem* 5, 206–210. doi: 10.1002/cssc.201100402

Nicastro, K. H., Kloxin, C. J., and Epps, T. H. (2018). Potential lignin-derived alternatives to bisphenol a in diamine-hardened epoxy resins. *ACS Sustain. Chem. Eng.* 6, 14812–14819. doi: 10.1021/acssuschemeng.8b03340

Pandey, M. P., and Kim, C. S. (2011). Lignin depolymerization and conversion: a review of thermochemical methods. *Chem. Eng. Technol.* 34, 29–41. doi: 10.1002/ceat.201000270

Pion, F., Reano, A. F., Ducrot, P.-H., and Allais, F. (2013). Chemo-enzymatic preparation of new bio-based bis- and trisphenols: new versatile building blocks for polymer chemistry. *RSC Adv.* 3:8988. doi: 10.1039/c3ra41247d

Prolongo, S. G., Gude, M. R., Sanchez, J., and Ureña, A. (2009). Nanoreinforced epoxy adhesives for aerospace industry. *J. Adhes.* 85, 180–199. doi: 10.1080/00218460902881766

Ramon, E., Sguazzo, C., and Moreira, P. (2018). A review of recent research on bio-based epoxy systems for engineering applications and potentialities in the aviation sector. *Aerospace* 5:110. doi: 10.3390/aerospace5040110

Savonnet, E., Grau, E., Grelier, S., Defoort, B., and Cramail, H. (2018). Divanillin-based epoxy precursors as DGEBA substitutes for biobased epoxy thermosets. *ACS Sustain. Chem. Eng.* 6, 11008–11017. doi: 10.1021/acssuschemeng.8b02419

Shuai, L., Amiri, M. T., Questell-Santiago, Y. M., Héroguel, F., Li, Y., Kim, H., et al. (2016). Formaldehyde stabilization facilitates lignin monomer production during biomass depolymerization. *Science* 354, 329–333. doi: 10.1126/science.aaf7810

Strebelle, M., Gilbeau, P., and Catinat, J.-P. (2001). Epichlorohydrin-*Based Product* and *Process* for *Manufacturing This Product*.

Teixeira, A. R. S., Willig, G., Couvreur, J., Flourat, A. L., Peru, A. A. M., Ferchaud, P., et al. (2017). From bench scale to kilolab production of renewable ferulic acid-based bsiphenols: optimisation and evaluation of different purification approaches towards a technical feasibility and process environmental sustainability. *React. Chem. Eng.* 2, 406–419. doi: 10.1039/C7RE00017K

Wan, J., Gan, B., Li, C., Molina-Aldareguia, J., Kalali, E. N., Wang, X., et al. (2016). A sustainable, eugenol-derived epoxy resin with high biobased content, modulus, hardness and low flammability: synthesis, curing kinetics and structure–property relationship. *Chem. Eng. J.* 284, 1080–1093. doi: 10.1016/j.cej.2015.09.031

Wang, S., Bassett, A. W., Wieber, G. V., Stanzione, J. F., and Epps, T. H. (2017). Effect of methoxy substituent position on thermal properties and solvent resistance of lignin-inspired poly(dimethoxyphenyl methacrylate)s. *ACS Macro Lett.* 6, 802–807. doi: 10.1021/acsmacrolett.7b00381

Zhao, S., Huang, X., Whelton, A. J., and Abu-Omar, M. M. (2018). Renewable epoxy thermosets from fully lignin-derived triphenols. *ACS Sustain. Chem. Eng.* 6, 7600–7608. doi: 10.1021/acssuschemeng.8b00443

Conflict of Interest Statement: The authors declare that the research was conducted in the absence of any commercial or financial relationships that could be construed as a potential conflict of interest.

Copyright © 2019 Hollande, Do Marcolino, Balaguer, Domenek, Gross and Allais. This is an open-access article distributed under the terms of the Creative Commons Attribution License (CC BY). The use, distribution or reproduction in other forums is permitted, provided the original author(s) and the copyright owner(s) are credited and that the original publication in this journal is cited, in accordance with accepted academic practice. No use, distribution or reproduction is permitted which does not comply with these terms.

frontiers in Chemistry

ORIGINAL RESEARCH
published: 07 May 2019
doi: 10.3389/fchem.2019.00316

Nanocellulose Xerogels With High Porosities and Large Specific Surface Areas

Shunsuke Yamasaki[1], *Wataru Sakuma*[1], *Hiroaki Yasui*[1], *Kazuho Daicho*[1], *Tsuguyuki Saito*[1]*, *Shuji Fujisawa*[1], *Akira Isogai*[1] and *Kazuyoshi Kanamori*[2]

[1] Department of Biomaterial Sciences, Graduate School of Agricultural and Life Sciences, The University of Tokyo, Tokyo, Japan, [2] Department of Chemistry, Graduate School of Science, Kyoto University, Kyoto, Japan

Xerogels are defined as porous structures that are obtained by evaporative drying of wet gels. One challenge is producing xerogels with high porosity and large specific surface areas, which are structurally comparable to supercritical-dried aerogels. Herein, we report on cellulose xerogels with a truly aerogel-like porous structure. These xerogels have a monolithic form with porosities and specific surface areas in the ranges of 71–76% and 340–411 m^2/g, respectively. Our strategy is based on combining three concepts: (1) the use of a very fine type of cellulose nanofibers (CNFs) with a width of ∼3 nm as the skeletal component of the xerogel; (2) increasing the stiffness of wet CNF gels by reinforcing the inter-CNF interactions to sustain their dry shrinkage; and (3) solvent-exchange of wet gels with low-polarity solvents, such as hexane and pentane, to reduce the capillary force on drying. The synergistic effects of combining these approaches lead to improvements in the porous structure in the CNF xerogels.

Keywords: cellulose nanofiber, xerogel, aerogel, porous material, ambient pressure drying

OPEN ACCESS

Edited by:
Gil Garnier,
Bioresource Processing Institute of Australia (BioPRIA), Australia

Reviewed by:
Dong Gu,
Wuhan University, China
Makoto Tabata,
Chiba University, Japan
Lorenz Ratke,
Institute of Materials Research, German Aerospace Center, Germany

***Correspondence:**
Tsuguyuki Saito
asaitot@mail.ecc.u-tokyo.ac.jp

Specialty section:
This article was submitted to Chemical Engineering, a section of the journal Frontiers in Chemistry

Received: *22 February 2019*
Accepted: *23 April 2019*
Published: *07 May 2019*

Citation:
Yamasaki S, Sakuma W, Yasui H, Daicho K, Saito T, Fujisawa S, Isogai A and Kanamori K (2019) Nanocellulose Xerogels With High Porosities and Large Specific Surface Areas. Front. Chem. 7:316. doi: 10.3389/fchem.2019.00316

INTRODUCTION

Aerogels are defined from a processing perspective as porous structures that are obtained by supercritical drying of wet gels (Hüsing and Schubert, 1998). In general, aerogels are mesoporous and combine a high porosity and large specific surface area (SSA). Owing to their specific porous structure, aerogels can excellently function as thermal, acoustic, and electrical insulators as well as catalyst supports, separators, and adsorbents. Some aerogels can be optically transparent yet thermally insulating, and have drawn interest as transparent insulators that might reduce thermal energy loses from windows in offices and automobiles (Hayase et al., 2014; Zu et al., 2018). Aerogels were first reported in 1931 (Kistler, 1931); however, it remains difficult to put aerogels to practical use because of two problems: one is the mechanical brittleness of aerogels; and the other is the process of supercritical drying, which limits productivity and scalability. Therefore, much effort has recently been made to overcome these problems.

In terms of the brittleness, one approach is to use cellulose nanofibers (CNFs) as the skeletal units of aerogels. CNFs are wood-derived emerging materials, which have excellent mechanical strength (∼3 GPa) (Saito et al., 2013) and solvent tolerance. CNFs are thus suitable building blocks for aerogels. Pääkkö et al. (2008) demonstrated the flexibility of structurally aerogel-like CNF cryogels, and Kobayashi et al. (2014) have reported on mechanically tough aerogels with good optical transparency and thermal insulating properties, based on a very fine type of CNFs with a width of ∼3 nm.

One approach to addressing the processing problem is to switch focus from aerogels to xerogels. Xerogels are defined as porous structures that are obtained by evaporative drying of wet gels. However, producing structurally aerogel-like xerogels under ambient conditions remains particularly challenging. Even thick block-like hydrogels shrink considerably during evaporative drying owing to capillary forces; hence, the resulting xerogels inevitably become thin films with a very low porosity. One approach is to exchange the solvent of the wet gels, which is typically water, to a solvent of lower polarity, such as hexane and pentane, to reduce the capillary force. This concept was reported in a paper by Prakash et al. (1995), in which aerogel-like silica xerogels were formed as a thin film with a high porosity (∼99%) through solvent exchange after chemically modifying the silica skeleton to be hydrophobic. Later, Kanamori et al. (2007) further developed the idea and reported that monolithic xerogels can be optically transparent and even exhibit rubbery compression with the use of organosilicons as the skeletal precursor.

In the field of cellulose science, Toivonen et al. (2015) reported a landmark study of CNF xerogels, which were similarly produced through a solvent exchange process. Here CNFs were formed into a wet cake by vacuum filtration of their water dispersion, followed by drying under ambient conditions after solvent exchange with octane. The resulting xerogels were mesoporous and in a film form with a thickness of ∼25 μm. Their porosity and SSA were ∼60% and 200 m^2/g, respectively, which are high characteristics among xerogels but still not within the structural range of supercritical-dried CNF aerogels (porosity 60–99%, SSA 300–600 m^2/g) (Sehaqui et al., 2011; Kobayashi et al., 2014; Sakai et al., 2016). In another route to xerogel formation, freeze-thawing of aqueous CNF dispersions has been used to form block-like hydrogels, followed by solvent exchange. The resulting xerogels were monolithic with a high porosity of over 98% but were macroporous. Their SSA values were ∼30 m^2/g (Li et al., 2017; Erlandsson et al., 2018). Furthermore, a non-CNF skeletal, different type of cellulosic xerogels with a high porosity (∼90%) has been produced by a molecular dissolution-regeneration process; however, the SSA values of these materials were ∼10–30 m^2/g (Pour et al., 2016).

Here we report on CNF xerogels with a truly aerogel-like porous structure. The xerogels are in a monolithic form with high porosities and SSA in the ranges of 71–76% and 340–411 m^2/g, respectively. Our strategy is based on three ideas: (1) the use of a very fine type of CNFs with a width of ∼3 nm; (2) increasing the stiffness of precursor hydrogels by reinforcing inter-CNF interactions; and (3) solvent exchange as described above. To our knowledge, these ideas have not yet been combined, and the synergistic effects of these factors lead to the development of porous structure in CNF xerogels.

MATERIALS AND METHODS

Materials

A softwood bleached kraft pulp (Nippon Paper Industries, Japan) was used as the starting sample. The pulp was maintained in an undried state after bleaching. Before use, the pulp was demineralized by stirring in an aqueous HCl solution at pH 2 for 1 h, followed by washing with deionized water. All chemicals and solvents were of laboratory grade (Wako Pure Chemicals, Japan) and used as received.

Preparation of CNFs

CNF dispersions were prepared according to our previous reports (Saito et al., 2006; Sakai et al., 2016). In brief, the pulp was oxidized by a TEMPO/NaBr/NaClO system with 10 mmol of NaClO added per gram of pulp. The carboxylate content of the oxidized pulp was ∼1.6 mmol/g. The oxidized pulp was then suspended in water at a concentration of 0.5% w/w, and disintegrated into CNFs by passing the suspension through a high-pressure water jet system (HJP-25005X, Sugino Machine) five times.

Xerogel Formation via Acid-Induced Gelation

The 0.5% w/w CNF dispersion (20 g) was poured into a plastic mold with an inner dimension of 6 × 5.5 × 1 cm^3. A 1 M HCl solution (6 mL) was spread over the dispersion and allowed to stand for 1 h. The resulting hydrogel was removed from the mold and cut into pieces of ∼10 × 10 × 5 mm^3 in size with a sharp blade. Some pieces were immersed into 0.01 M HCl (150 mL) and shaken at ambient conditions for 1 day using an orbital shaker at 50 rpm, followed by rinsing out the HCl with distilled water over 2 days. The hydrogels were then dried at 23°C under ambient pressure. The resulting xerogels are denoted as *w*-xerogels. For reference, supercritical-dried CNF aerogels were also prepared from the same lot of hydrogel according to our previous report (Sakai et al., 2016).

The remaining pieces of the hydrogel were immersed in a mixed solution of 0.01 M HCl (75 mL) and ethanol (75 mL) and shaken under ambient conditions for 1 day using an orbital shaker at 50 rpm. The gel pieces were then shaken in an ethanol bath (280 mL) at 40°C for 3 days, accompanied by replacement of the bath with fresh ethanol twice a day. Some of the alcogel pieces were further shaken in a bath of acetone, hexane or pentane (280 mL) at 40°C for 3 days, accompanied by replacement of the bath with each fresh solvent twice a day. Each of the ethanol-, acetone-, hexane-, and pentane-exchanged gels was dried at 23°C under ambient pressure in an airtight desiccator containing silica gel at the bottom; the resulting xerogels are denoted as *e*-, *a*-, *h*- and *p*-xerogels, respectively.

Xerogel Formation via Metal Ion-Induced Gelation

The 0.5% w/w CNF dispersion (20 g) was poured into the same plastic mold as for that used for the acid-induced gelation (see section Xerogel Formation via Acid-Induced Gelation). A 0.1 M solution of $MgCl_2$, $CaCl_2$, or $AlCl_3$ (6 mL) was spread over the dispersions, which were then allowed to stand for 24 h. Similar to the case of the acid-induced gelation, the resulting hydrogel was cut into pieces with dimensions of ∼10 × 10 × 6 mm^3. The gel pieces were shaken in a 0.01 M solution of $CaCl_2$, $MgCl_2$, or $AlCl_3$ (150 mL) for 1 day and then successively in a mixed solution of water (75 mL) and ethanol (75 mL) for 1 day each. The subsequent processing after solvent exchange with the mixed

solutions involved the same steps as for the acid-induced gelation with ethanol and hexane. The xerogels resulting from evaporative drying of hexane are denoted as *h-Mg-*, *h-Ca-*, and *h-Al-*xerogels.

Membrane Xerogel Formation

An 0.5% w/w CNF dispersion (27 g) was poured into a glass dish with an inner diameter of 7 cm. A 0.1 M $AlCl_3$ solution (8 mL) was spread over the dispersion, which was then allowed to stand for 24 h. The originally air-exposed, top surface of the resulting hydrogel was cut off using a sharp blade to obtain a columnar gel with a thickness of ∼6 mm. The shaped gel was shaken in a 0.01 M $AlCl_3$ solution (150 mL) for 1 day and successively in a mixed solution of water (75 mL) and ethanol (75 mL) for 1 day each. The subsequent process involved the same solvent-exchange steps with the use of ethanol and hexane for the acid-induced gelation. The hexane-exchanged gel was then sandwiched with flat PTFE plates and allowed to dry at 23°C under ambient pressure in an airtight desiccator containing silica gel at its bottom. The top PTFE plate was 34 g in weight.

Analyses

Scanning electron microscope (SEM) images were acquired with a Hitachi S-4800 field-emission microscope operated at 1 kV. Prior to SEM observations, the xerogels were split using tweezers, and the exposed cross-sections were thinly coated with osmium with the use of a Meiwafosis Neo osmium coater at 5 mA for 10 s. Nitrogen adsorption–desorption isotherms were measured with a Quantachrome NOVA 4200e at −196°C after degassing of the samples in the system at 105°C for 3 h. The SSA values and pore size distributions of the xerogels were estimated from the isotherms following Brunauer–Emmett–Teller (BET) theory and the Barrett–Joyner–Halenda (BJH) model, respectively. The porosity values (%) of the xerogels were calculated using the

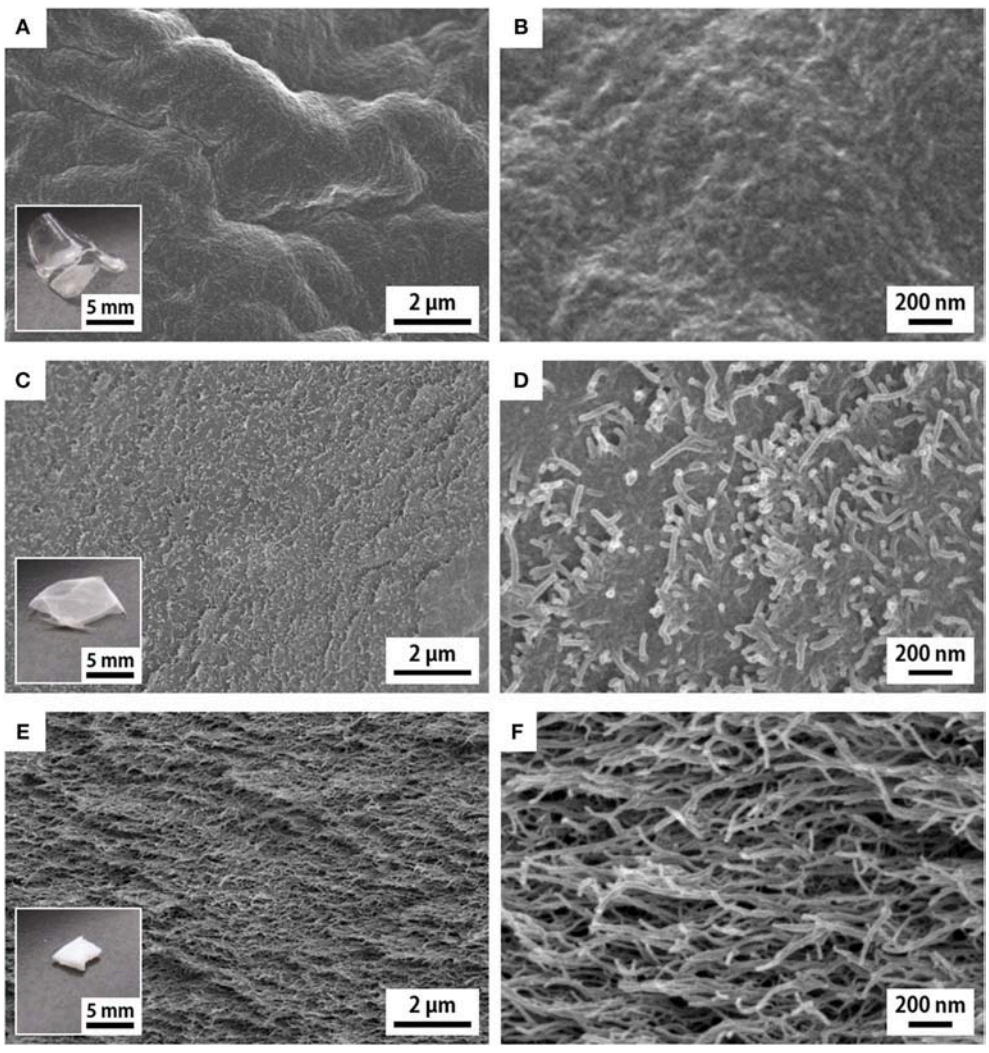

FIGURE 1 | SEM images of the cross sections of the **(A,B)** *w*-xerogel, **(C,D)** *a*-xerogel, and **(E,F)** *h*-xerogel. Insets show the appearances of the respective xerogels.

following equation,

$$Porosity = \frac{V_p}{V_p + 1/\rho_t} \times 100,$$

where V_p is the pore volume (cm^3/g) of the corresponding xerogel, and ρ_t is the true density of the CNF (1.64 g/cm^3). The pore volumes V_p of the xerogels were estimated from the maximum amounts of N_2 adsorbed into the respective xerogels by converting the adsorbed amount expressed as a gas volume at 273 K and 1 atm into pore-filling volumes as liquid nitrogen at −196°C. The porosity of the reference aerogel was calculated in the usual manner from its apparent volume and weight. Fourier transform infrared (FTIR) spectra of the xerogels were obtained with a JASCO FT/IR-6100. Tensile testing of the membranous xerogel was performed at 23°C and 50% relative humidity with the use of a Shimadzu EZ-TEST equipped with a 500 N load cell. The specimens were ∼2 mm wide and 20 mm long. Ten specimens were measured with a span length of 10 mm at a rate of 1.0 mm/min. The thermal conductivity k of the membranous xerogel was estimated based on the following equation,

$$k = \rho\alpha c,$$

where ρ, α and c are the bulk density, thermal diffusivity, and specific heat capacity of the xerogel, respectively. The thermal diffusivity α (9.02×10^{-8} m^2/s) was measured at 23°C and 50% relative humidity using an ai-Phase Mobile 1U device. The specific heat capacity c at 23°C (1.23 J/g·K) was measured using a Perkin-Elmer DSC 8500 instrument.

RESULTS AND DISCUSSION

The CNF in the present study was chemically modified by a TEMPO-oxidation process (see section Materials and Methods). The TEMPO-oxidized CNFs are characterized by a uniform width of ∼3 nm (Daicho et al., 2018), and by a high density of surface carboxyl groups (1–1.7 groups/nm^2). The carboxyl groups are in the form of sodium salts and are well-dissociated in water. Accordingly, electric double layer repulsion is induced between the CNFs in water, and these CNFs are stably dispersed. Their dispersibility strongly depends on the pH of the system and the presence of co-existing salts (Tanaka et al., 2014, 2016). The CNFs start to attractively interact by lowering of the pH below the pK_a value 3.6 for the carboxyl group and form a stiff hydrogel (Saito et al., 2011). Here, the sodium carboxylates (-COO^-Na^+) turn into carboxylic acids (-COOH). The inter-CNF repulsion is lost, and the CNFs are partially assembled or networked through hydrogen bonding and other van der Waals interactions. For this sol-gel transition, the storage modulus G′ of the system increases by several orders of magnitude. Similar behavior is observed when multivalent metal ions, such as Ca^{2+} and Al^{3+}, are added into the system (Goi et al., 2018). The inter-CNF interactions are dominated by ionic bonds in this case, such that the resulting hydrogels are thereby stiffer than the acid-type gels.

Xerogels via Acid-Induced Gelation

Initially, the acid type hydrogels were solvent-exchanged with ethanol, acetone, hexane, and pentane, followed by evaporative drying at 23°C under ambient pressure. For reference, some of the hydrogel samples were directly subjected to evaporative drying. Although all the hydrogels were shaped

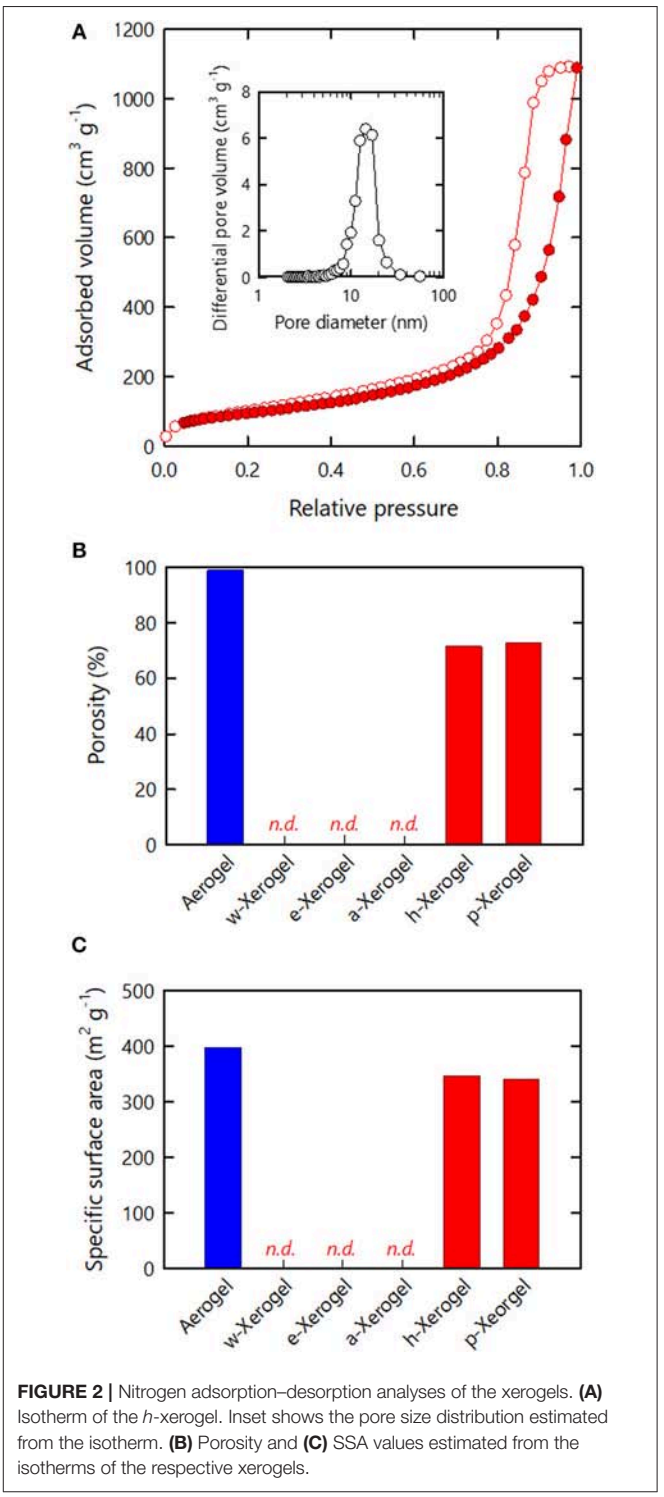

FIGURE 2 | Nitrogen adsorption–desorption analyses of the xerogels. **(A)** Isotherm of the *h*-xerogel. Inset shows the pore size distribution estimated from the isotherm. **(B)** Porosity and **(C)** SSA values estimated from the isotherms of the respective xerogels.

in block-like pieces with a size of ~10 × 10 × 6 mm^3 (**Supplementary Figure S1**), the resulting xerogels through solvent exchange differed from each other in both appearance and skeletal structure (**Figure 1**).

The reference *w*-xerogels, obtained by evaporation of water, formed thin and optically transparent films (the inset of **Figure 1A**). The CNF morphology was invisible at the cross sections of the *w*-xerogel films by SEM (**Figures 1A,B**). We explain this result by the close assembly of CNFs, which was induced by the strong capillary force of water (surface tension $\gamma \approx 72$ mN/m). The *e*- and *a*-xerogels obtained by evaporation of ethanol ($\gamma \approx 22$ mN/m) and acetone ($\gamma \approx 24$ mN/m) also formed thin films but had a hazy appearance (the inset of **Figure 1C**). The CNF morphology at their cross sections became visible, although the CNFs remained closely assembled (**Figures 1C,D**). Ethanol and acetone are also likely to interact strongly with the polar groups on the CNF surfaces, such as hydroxyl and carboxyl groups, resulting in the close assembly of CNFs at a meniscus on the solvent evaporation. Notable cases were found for the *h*- and *p*-xerogels, which were obtained by evaporation of hexane ($\gamma \approx 18$ mN/m) and pentane ($\gamma \approx 16$ mN/m), respectively. These xerogels had a block-like, monolithic shape (~1 mm thick) and were optically opaque (the inset of **Figure 1E**). The CNF assembly on drying was sufficiently suppressed, such that a network-like CNF skeleton was formed within the xerogels (**Figures 1E,F**). There might exist a threshold at $\gamma \approx 20$ mN/m for the solvent developing a porous structure within the xerogels, in the case when no further hydrophobization or stronger cross-linking was applied to the TEMPO-oxidized CNFs.

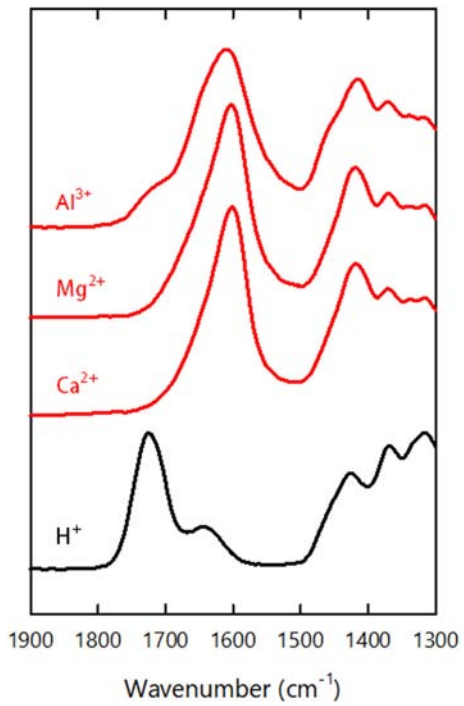

FIGURE 3 | FTIR spectra of the *h*-xerogel, *h-Ca*-xerogel, *h-Mg*-xerogel, and *h-Al*-xerogel.

Nitrogen adsorption–desorption analyses were performed on the series of xerogels (**Figure 2**). For reference, we also analyzed aerogels obtained from the acid type CNF hydrogels via supercritical drying (**Supplementary Figure S2**). Although the *w*-, *e*- and *a*-xerogels were non-porous, as shown in **Figure 1**, and could not be analyzed, both the *h*- and *p*-xerogels exhibited typical isotherms of mesoporous structures (**Figure 2A**). The isotherms were characterized by hysteresis at a high relative pressure, caused by capillary condensation of nitrogen gas in pores. The pore sizes estimated from the isotherms of the *h*- and *p*-xerogels ranged from a few nm to ~30 nm (the inset of **Figure 2A**). Note that the capillary pressures on nitrogen sorption can be of order 1 MPa (Reichenauer and Scherer, 2001) and thus shrinkage of the xerogels should be inevitable at a high relative pressure; the pore sizes in the present study are lower estimates.

The porosity values of the xerogels were also estimated from the isotherms (**Figure 2B**), where the maximum amounts of nitrogen adsorbed were regarded as the pore filling volumes of liquefied nitrogen through capillary condensation (see section Materials and Methods). The resulting values thus reflect the lower limit of the porosity. Although the porosity of materials

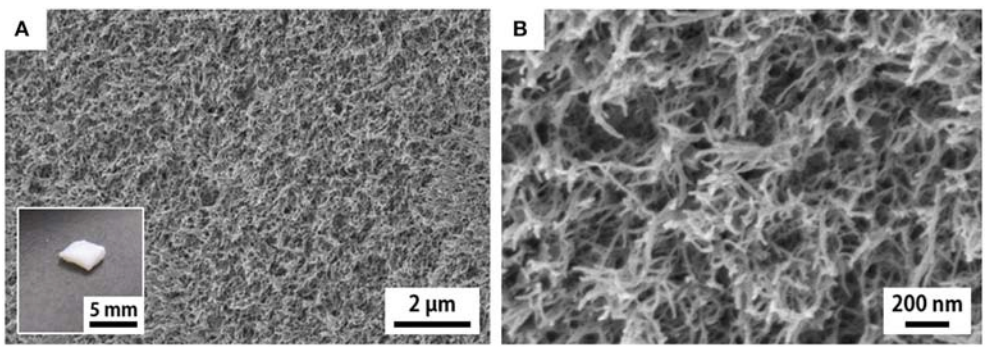

FIGURE 4 | SEM images of the cross section of the *h-Al*-xerogel. **(A,B)** show the images taken at low and high magnifications, respectively. Inset shows appearance of the *h-Al*-xerogel.

is commonly evaluated from their dimensions, mass, and true density, in the present study it was difficult to reliably measure the dimensions of the series of xerogels, which had distorted shapes and rough surfaces. The porosities of the *w*-, *e*-, and *a*-xerogels, evaluated on this basis, were below the limit of detection. The porosity values of the *h*- and *p*-xerogels were found to be as high as 70%. A value of 70% is within the porosity range of CNF aerogels reported to date (>60%) (Sehaqui et al., 2011; Sakai et al., 2016), but was lower than the porosity of the reference aerogel, as shown in **Figure 2B** (∼99%). Note that the reference aerogels in the present study were prepared by acid-induced gelation of TEMPO-oxidized CNFs; their structural profiles as porous materials, including porosity and SSA, are among the highest reported for cellulosic porous structures (Kobayashi et al., 2014).

The SSA results of the xerogels are shown in **Figure 2C**. Similar to the porosity, the SSA values of the *w*-, *e*- and *a*-xerogels were below the limit of detection (∼2 m^2/g). The SSA values of both the *h*- and *p*-xerogels were as high as 340 m^2/g. Although the value of 340 m^2/g was lower than the SSA of the reference aerogels (∼400 m^2/g), it is the highest SSA value ever reported for an ambient pressure-dried xerogel of cellulose or its derivatives. These results justify our combined strategy of: 1) the use of 3 nm-wide TEMPO-oxidized CNFs; 2) stiffening the inter-CNF interaction; and 3) solvent exchange.

Xerogels via Metal Ion-Induced Gelation

We examined further reinforcing the inter-CNF interactions by ionically cross-linking carboxylate groups via multivalent metal ions, namely Mg^{2+}, Ca^{2+}, and Al^{3+} (Goi et al., 2018). The resulting hydrogels were solvent-exchanged with hexane based on the results in the previous section, followed by evaporative drying at 23°C under ambient pressure.

Figure 3 shows FTIR spectra of the xerogels formed through metal ion-induced gelation (*h-Mg*-, *h-Ca*-, and *h-Al*-xerogels). For reference, the spectrum of the acid-type one (*h*-xerogel) is also shown. In the spectra, the carboxyl-related IR adsorptions were as follows (Fujisawa et al., 2011): the C=O stretch of the carboxylic acid groups was at 1,720 cm^{-1}, the C=O stretch of carboxylate groups was at 1,600 cm^{-1}, and the C–O symmetric stretching of carboxylate groups was at 1,410 cm^{-1}. An adsorption peak was also present from bending of adsorbed water molecules at 1,630 cm^{-1}. The reference *h*-xerogel showed no peaks at 1,600 and 1,410 cm^{-1} but had a clear adsorption at 1,720 cm^{-1}. Meanwhile, the *h-Mg*-, *h-Ca*-, and *h-Al*-xerogels showed little or no adsorption at 1,720 cm^{-1} but had distinct peaks at 1,600 and 1,410 cm^{-1}, regardless of the ionic species present. The small adsorption at 1,720 cm^{-1} for the *h-Al*-xerogel indicated the presence of carboxylic acid groups. This result is explained by the pH of the gelling agent; a 0.01 M $AlCl_3$ solution that has a pH value of 3.8 was used in the gelation process for the *h-Al*-xerogel, and some of the carboxyl groups will be protonated because their pK_a value is 3.6. We estimated the ratio of the carboxylic acid groups to the total carboxylate content to be ∼15% based on the peak area. For *h-Mg*- and *h-Ca*-xerogels, $MgCl_2$ and $CaCl_2$ solutions with pH values of ∼6 were used, such that no protonation occurred in the gelation process. Furthermore, neither Na^+ ions in the starting CNF dispersion nor Cl^- ions in the gelling agents were detected by energy-dispersive X-ray (EDX) spectroscopy (data not shown). In fact, each multivalent metal ion in the xerogel electrostatically interacted with two or three carboxylate anions on the same or two different CNF surfaces. Otherwise, hydroxide ions would be coupled to electrically neutralize the remaining charges of the metal salts of carboxyl groups, for example, $-COO^- Al(OH)_2^+$.

As for the case of the *h*-xerogels, all the *h-Mg*-, *h-Ca*-, and *h-Al*-xerogels possessed a monolithic shape (roughly 1 mm in thickness), and a network-like CNF skeleton formed within the xerogels (**Figure 4**, **Supplementary Figure S3**). These xerogels showed similar nitrogen adsorption–desorption isotherms to those for the *h*-xerogels (see **Figure 2A**). The porosity values,

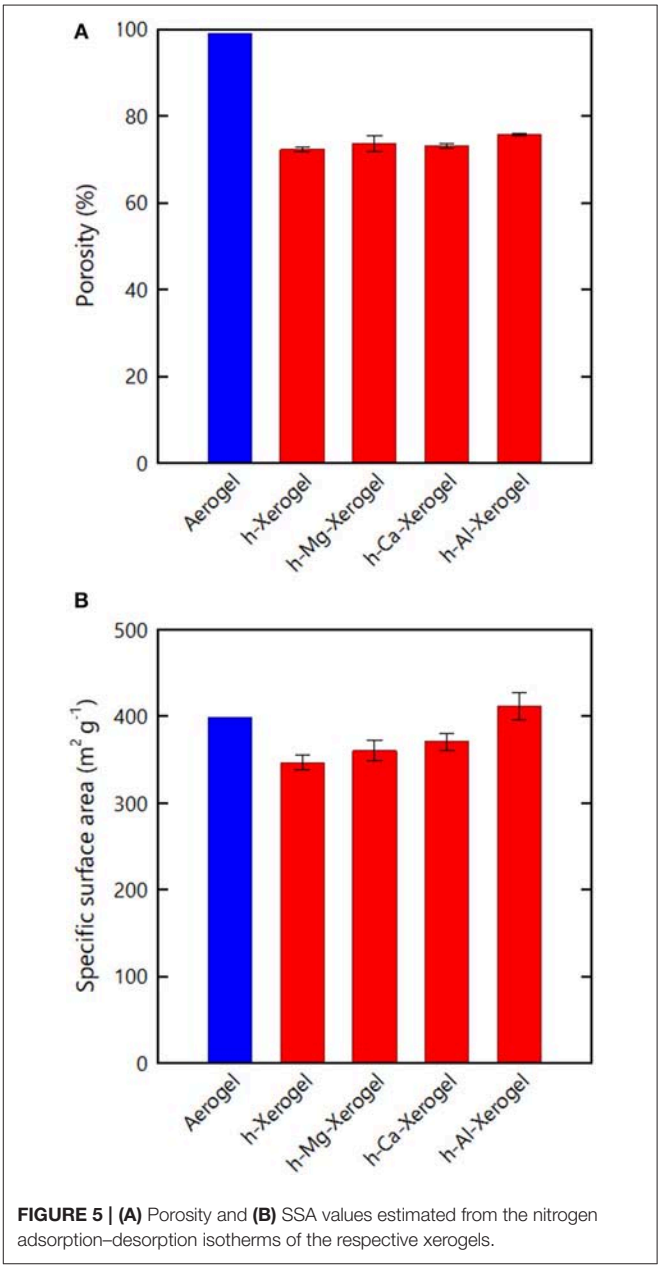

FIGURE 5 | (A) Porosity and **(B)** SSA values estimated from the nitrogen adsorption–desorption isotherms of the respective xerogels.

which were estimated from the isotherms, increased slightly from 71% for the *h*-xerogel to 76% for the *h-Al*-xerogel (**Figure 5A**). The SSA significantly increased from a high value of ∼340 m^2/g for the *h*-xerogel to 410 m^2/g for the *h-Al*-xerogel (**Figure 5B**). This value of 410 m^2/g is truly comparable to the SSA of the reference aerogels (∼400 m^2/g). Considering the electrostatic interactions with the carboxylate anions, the trivalent ions of Al^{3+} were likely more effective than the divalent ions of Mg^{2+} and Ca^{2+}, in improving the porosity and SSA.

Membrane Xerogels

The *h-Al*-xerogels were optically opaque as shown in **Figure 4**, despite their high porosity and SSA. We attribute this result to their surface roughness. Thus, we tried to reduce the surface roughness of the *h-Al*-xerogels by sandwiching the precursor organogels with flat PTFE plates during drying (see section Materials and Methods). The compression force imposed on the organogels by sandwiching was estimated to be ∼87 Pa. Although the resulting *h-Al*-xerogels formed films (∼74 μm), their optical transmittance improved greatly (**Figure 6A**) (see **Supplementary Figure S4** for a light transmittance spectrum). In addition, the nitrogen adsorption–desorption isotherms of the film-like *h-Al*-xerogels were as categorized as type IV IUPAC physisorption, similar to the monolithic *h*- and *h-Al*-xerogels (**Figure 6B**). The porosity and SSA values were then estimated from the isotherm to be ∼60% and 270 m^2/g, respectively. These values are lower than those of the *h-Al*-xerogels but still high as those of cellulosic xerogels.

Unlike the other xerogels in the present study, the film-like *h-Al*-xerogels had sufficiently flat surfaces that their specimen sizes could be reliably measured. Next, we analyzed the tensile properties and thermal conductivity of the film-like *h-Al*-xerogels. In the tensile tests, the film-like xerogels exhibited a high Young's modulus E and tensile strength σ of ∼3 and 49 MPa, respectively (see **Supplementary Figure S5** for a typical stress–strain curve). These values are within the range of the E and σ values of practically applicable plastic films (Ashby et al., 2009), which is surprising because of the high porosity and a large SSA of the xerogels. We explain this result by the high strength of the CNFs and their strong interactions at the contacting surfaces. The thermal conductivity k of the film-like xerogels was measured to be 0.095 W/m·K in the out-of-plain direction. This value is intermediate between those of highly-compacted CNF films (0.11–0.14 W/m·K) (Zhao et al., 2018) and insulating CNF aerogels (0.02–0.04 W/m·K) (Sakai et al., 2016). The porosity and SSA of the xerogels (∼60% and 270 m^2/g) were both higher than those of the compacted films (10–18% and < 2 m^2/g) but lower than those of the insulating aerogels (>97% and > 300 m^2/g). Therefore, the drying conditions should be further explored to obtain heat-insulating yet optically-transparent CNF xerogels with a truly aerogel-like porous structure.

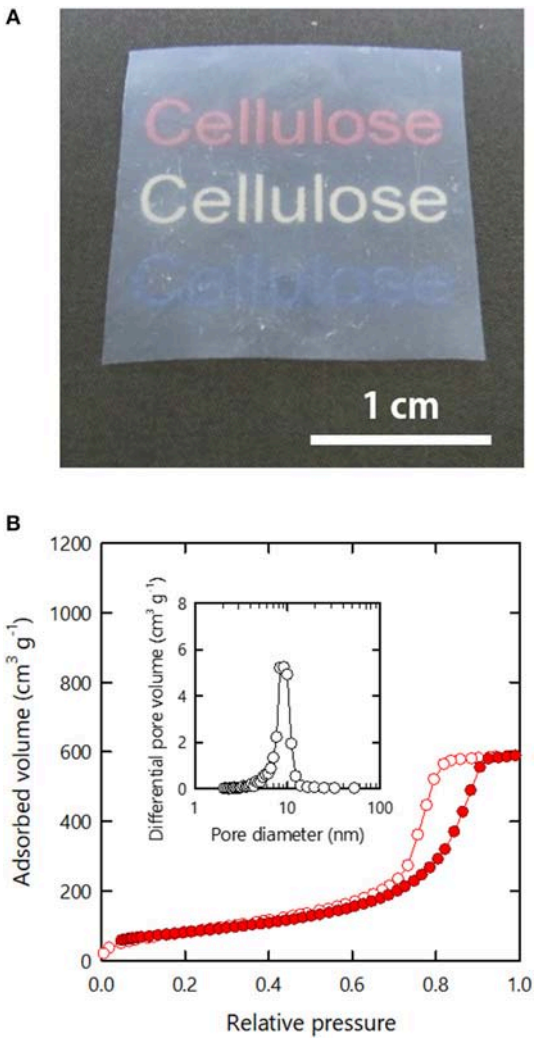

FIGURE 6 | (A) Appearance and **(B)** nitrogen adsorption–desorption isotherm of the membranous *h-Al*-xerogel. Inset in **(B)** shows the pore size distribution estimated from the isotherm.

CONCLUSIONS

Monolithic CNF xerogels with high porosities and large SSAs in the ranges of 71–76% and 340–411 m^2/g, respectively, were prepared via evaporative drying under ambient conditions. These characteristics fall within the structural range of supercritical-dried CNF aerogels reported to date. These materials were achieved by a combination of three concepts: (1) the use of TEMPO-oxidized CNFs with a uniform width of ∼3 nm to exploit the potential SSA of CNFs; (2) stiffening the inter-CNF interactions in the hydrogels by, for example, ionic cross-linking to withstand their dry shrinkage; and (3) solvent exchange with low-polarity solvents such as hexane and pentane to reduce the capillary forces during drying. All the monolithic xerogels had distorted shapes and rough surfaces. Accordingly, these materials were opaque despite having high porosity and SSA. Therefore, further exploration of the drying conditions might enable monolithic yet optically-transparent CNF xerogels. Such trials should also look to optimize the inter-CNF interactions and make the CNF surfaces more hydrophobic.

DATA AVAILABILITY

The datasets for this manuscript are not publicly available because the raw data supporting the conclusions of this manuscript will be made available by the authors, without undue reservation, to any qualified researcher. Requests to access the datasets should be directed to TS, asaitot@mail.ecc.u-tokyo.ac.jp.

AUTHOR CONTRIBUTIONS

TS conceived the concept of the study. SY and TS designed the experiments with the help of KK. SY performed most of the experiments with the help of WS, HY, and KD. All the authors analyzed the data. SY and TS mainly wrote the manuscript with the contributions of all the authors.

FUNDING

This research was supported by the JST-Mirai R&D Program (JPMJMI17ED) and in part by the JSPS Grant-in-Aid for Young Scientists B (17K15298).

SUPPLEMENTARY MATERIAL

The Supplementary Material for this article can be found online at: https://www.frontiersin.org/articles/10.3389/fchem.2019.00316/full#supplementary-material

REFERENCES

Ashby, M. F., Shercliff, H., and Cebon, D. (2009). *Materials: Engineering, Science, Processing and Design, 2nd Ed*. Oxford: Butterworth-Heinemann.

Daicho, K., Saito, T., Fujisawa, S., and Isogai, A. (2018). The crystallinity of nanocellulose: dispersion-induced disordering of the grain boundary in biologically structured cellulose. *ACS Appl. Nano Mater.* 1, 5774–5785. doi: 10.1021/acsanm.8b01438

Erlandsson, J., Pettersson, T., Ingverud, T., Granberg, H., Larsson, P. A., Malkoch, M., et al. (2018). On the mechanism behind freezing-induced chemical crosslinking in ice-templated cellulose nanofibril aerogels. *J. Mater. Chem. A* 6, 19371–19380. doi: 10.1039/c8ta06319b

Fujisawa, S., Okita, Y., Fukuzumi, H., Saito, T., and Isogai, A. (2011). Preparation and characterization of TEMPO-oxidized cellulose nanofibril films with free carboxyl groups. *Carbohydr. Polym.* 84, 579–583. doi: 10.1016/j.carbpol.2010.12.029

Goi, Y., Saito, T., and Isogai, A. (2018). Mechanical properties and preparing processes of the TEMPO-oxidized cellulose nanofibers hydrogels. *J. Fiber Sci. Technol.* 74, 24–29. doi: 10.2115/fiberst.2017-0038

Hayase, G., Kugimiya, K., Ogawa, M., Kodera, Y., Kanamori, K., and Nakanishi, K. (2014). The thermal conductivity of polymethylsilsesquioxane aerogels and xerogels with varied pore sizes for practical application as thermal superinsulators. *J. Mater. Chem. A* 2, 6525–6531. doi: 10.1039/C3TA15094A

Hüsing, N., and Schubert, U. (1998). Aerogels-airy materials: chemistry, structure, and properties. *Angew. Chem. Int. Ed.* 37, 22–45. doi: 10.1002/(SICI)1521-3773(19980202)37:1/2<22::AID-ANIE22>3.0.CO;2-I

Kanamori, K., Aizawa, M., Nakanishi, K., and Hanada, T. (2007). New transparent methylsilsesquioxane aerogels and xerogels with improved mechanical properties. *Adv. Mater.* 19, 1589–1593. doi: 10.1002/adma.200602457

Kistler, S. S. (1931). Coherent expanded aerogels and jellies. *Nature* 127, 741. doi: 10.1038/127741a0

Kobayashi, Y., Saito, T., and Isogai, A. (2014). Aerogels with 3D ordered nanofiber skeletons of liquid-crystalline nanocellulose derivatives as tough and transparent insulators. *Angew. Chem. Int. Ed.* 53, 10394–10397. doi: 10.1002/anie.201405123

Li, Y., Tanna, V. A., Zhou, Y., Winter, H. H., Watkins, J. J., and Carter, K. R. (2017). Nanocellulose aerogels inspired by frozen tofu. *ACS Sustain. Chem. Eng.* 5, 6387–6391. doi: 10.1021/acssuschemeng.7b01608

Pääkkö, M., Vapaavuori, J., Silvennoinen, R., Kosonen, H., Ankerfors, M., Lindström, T., et al. (2008). Long and entangled native cellulose I nanofibers allow flexible aerogels and hierarchically porous templates for functionalities. *Soft Matter* 4, 2492–2499. doi: 10.1039/B810371B

Pour, G., Beauger, C., Rigacci, A., and Budtova, T. (2016). Xerocellulose: lightweight, porous and hydrophobic cellulose prepared via ambient drying. *J. Mater. Sci.* 50, 4526–4535. doi: 10.1007/s10853-015-9002-4

Prakash, S. S., Brinker, C. J., Hurd, A. J., and Rao, S. M. (1995). Silica aerogel films prepared at ambient pressure by using surface derivatization to induce reversible drying shrinkage. *Nature* 374, 439. doi: 10.1038/374439a0

Reichenauer, G., and Scherer, G. W. (2001). Extracting the pore size distribution of compliant materials from nitrogen adsorption. *Colloids Surf. A* 187–188, 41–50. doi: 10.1016/S0927-7757(01)00619-7

Saito, T., Kuramae, R., Wohlert, J., Berglund, L. A., and Isogai, A. (2013). An ultrastrong nanofibrillar biomaterial: the strength of single cellulose nanofibrils revealed via sonication-induced fragmentation. *Biomacromolecules* 14, 248–253. doi: 10.1021/bm301674e

Saito, T., Nishiyama, Y., Putaux, J. L., Vignon, M., and Isogai, A. (2006). Homogeneous suspensions of individualized microfibrils from TEMPO-catalyzed oxidation of native cellulose. *Biomacromolecules* 7, 1687–1691. doi: 10.1021/bm060154s

Saito, T., Uematsu, T., Kimura, S., Enomae, T., and Isogai, A. (2011). Self-aligned integration of native cellulose nanofibrils towards producing diverse bulk materials. *Soft Matter* 7, 8804–8809. doi: 10.1039/C1SM06050C

Sakai, K., Kobayashi, Y., Saito, T., and Isogai, A. (2016). Partitioned airs at microscale and nanoscale: thermal diffusivity in ultrahigh porosity solids of nanocellulose. *Sci. Rep.* 6:20434. doi: 10.1038/srep20434

Sehaqui, H., Zhou, Q., Ikkala, O., and Berglund, L. A. (2011). Strong and tough cellulose nanopaper with high specific surface area and porosity. *Biomacromolecules* 12, 3638–3644. doi: 10.1021/bm2008907

Tanaka, R., Saito, T., Hänninen, T., Ono, Y., Hakalahti, M., Tammelin, T., et al. (2016). Viscoelastic properties of core-shell-structured, hemicellulose-rich nanofibrillated cellulose in dispersion and wet-film states. *Biomacromolecules* 17, 2104–2111. doi: 10.1021/acs.biomac.6b00316

Tanaka, R., Saito, T., Ishii, D., and Isogai, A. (2014). Determination of nanocellulose fibril length by shear viscosity measurement. *Cellulose* 21, 1581–1589. doi: 10.1007/s10570-014-0196-4

Toivonen, M. S., Kaskela, A., Rojas, O. J., Kauppinen, E. I., and Ikkala, O. (2015). Ambient-dried cellulose nanofibril aerogel membranes with high tensile strength and their use for aerosol collection and templates for transparent, flexible devices. *Adv. Funct. Mater.* 25, 6618–6626. doi: 10.1002/adfm.201502566

Zhao, M., Ansari, F., Takeuchi, M., Shimizu, M., Saito, T., Berglund, L. A., et al. (2018). Nematic structuring of transparent and multifunctional nanocellulose papers. *Nanoscale Horiz.* 3, 28–34. doi: 10.1039/c7nh00104e

Zu, G., Shimizu, T., Kanamori, K., Zhu, Y., Maeno, A., Kaji, H., et al. (2018). Transparent, superflexible doubly cross-linked polyvinylpolymethylsiloxane aerogel superinsulators via ambient pressure drying. *ACS Nano* 12, 521–532. doi: 10.1021/acsnano.7b07117

Conflict of Interest Statement: The authors declare that the research was conducted in the absence of any commercial or financial relationships that could be construed as a potential conflict of interest.

Copyright © 2019 Yamasaki, Sakuma, Yasui, Daicho, Saito, Fujisawa, Isogai and Kanamori. This is an open-access article distributed under the terms of the Creative Commons Attribution License (CC BY). The use, distribution or reproduction in other forums is permitted, provided the original author(s) and the copyright owner(s) are credited and that the original publication in this journal is cited, in accordance with accepted academic practice. No use, distribution or reproduction is permitted which does not comply with these terms.

Chemical Biology

Ryo Okamoto

Ryo Okamoto received his BSc in 2004, MSc in 2006 and his PhD in 2009 from Yokohama City University under the supervision of Prof. Yasuhiro Kajihara. From 2009, he joined the Stephen B. H. Kent lab at the University of Chicago as a Postdoctoral Fellow for research abroad as part of the Japan Society for the Promotion of Science (JSPS). He joined Kajihara's group at Osaka University as an Assistant Professor in 2010 and was promoted to Associate Professor in 2017. His current research interest is the chemical synthesis of artificial proteins that surpass the functions of native proteins.

Xiaojun Peng

Xiaojun Peng obtained his PhD from Dalian University of Technology in 1989, after which he was a postdoctoral researcher in organic chemistry at Nankai University from 1990 to 1992. In 1992, he returned to the School of Chemical Engineering of Dalian University of Technology, and also held positions as a visiting scholar at Stockholm University and Northwestern University. He has received several prestigious awards including the Cross-Century Excellent Talents award, awarded by the Ministry of Education in 2000. He was also noted as one of the leading talents in Liaoning Province in 2010.

Jiangli Fan

Jiangli Fan obtained her PhD from Dalian University of Technology in 2005 in China. In 2010 she attended the University of South Carolina as a visiting scholar. She is currently a Professor at the State Key Laboratory of Fine Chemicals at Dalian University of Technology. Her research interests focus on small-molecule fluorescent probes for bioimaging and sensing, photosensitizers based photodynamic therapy, and targeted nanodrug delivery.

Zhiqian Guo

Prof. Zhiqian Guo obtained his BSc degree in Fine Chemicals from Zheng Zhou University in 2002. He then obtained his PhD degree in Applied Chemistry from East China University of Science & Technology (ECUST) in 2010. (Advisor: Professor Wei-Hong ZHU). From 2011 to 2012, he worked with Prof. Dr Juyoung Yoon (Ewha Woman's University/Korea) on organic chemistry. He became a full Professor at the School of Chemistry and Molecular Engineering at ECUST in 2017. He was a recipient of NSFC for Excellent Young Grants (2016), and Cheung Kong Young Scholar (Younger Project) (2017). His current research interests focus on functional chromophores, including fluorescent sensors, molecular imaging, drug delivery systems, and molecular logic devices.

Yimon Aye

Born and raised in Burma, Yimon Aye obtained her undergraduate and PhD degrees in Chemistry at Oxford (UK) and Harvard (USA), respectively. She received her postdoctoral training in Biochemistry at MIT (USA). In her independent career that began in mid-2012, she set out to understand the detailed mechanisms of electrophile signaling. This impetus culminated in the development of "REX" technologies (T-REX™ delivery and G-REX™ profiling). In a parallel research program, she studies pathways involved in genome maintenance, including the mechanisms of anticancer drugs in clinical use. In mid-2018, she established the Laboratory of Electrophiles And Genome Operation (LEAGO) at EPFL (Switzerland).

Mehdi Mobli

Associate Prof. Mehdi Mobli (PhD 2004, University of Liverpool) is a Principal Research Fellow at the University of Queensland's Centre for Advanced Imaging. His research involves understanding the mechanisms of ion-channel function in health and disease, and his group is well known for fundamental contributions to the field of nuclear magnetic resonance (NMR) spectroscopy. He has over 100 publications including 13 book chapters and two books. His research has been recognized through a number of awards including the Sir Paul Callaghan Medal (ANZMAG - NMR research), the Tregear Award (Australian Peptide Society - peptide research), and the MERCK medal (ASBMB - biochemistry).

frontiers in Chemistry

ORIGINAL RESEARCH
published: 28 March 2019
doi: 10.3389/fchem.2019.00173

N,N-Dimethylaminoxy Carbonyl, a Polar Protecting Group for Efficient Peptide Synthesis

Ryo Okamoto, Emiko Ono, Masayuki Izumi and Yasuhiro Kajihara*

Department of Chemistry, Osaka University, Toyonaka, Japan

Peptide coupling with minimal protection is one of the desired methods for the synthesis of peptides and proteins. To achieve regioselective amide bond formation, side chain protection is often essential; however, protecting groups potentially diminish peptide solubility and render the polar polyamide chain amphipathic due to their apolar nature. In this manuscript, we describe a new protecting group, *N,N*-dimethylaminoxy carbonyl (Dmaoc), and its use in peptide coupling reactions. The Dmaoc group has a relatively polar character compared to the Boc group, which is a conventional protecting group for the N^{ε}-amine of Lys residues. This polar protecting group is removable by reduction in the buffer containing (±)-dithiothreitol (DTT). Furthermore, the Dmaoc group proved compatible with peptide ligation strategies featuring the activation of *N*-acyl diaminobenzamides (Dbz) with sodium nitrate to generate the respective benzotriazole leaving group. The Dmaoc/Dbz strategy described in this manuscript provides a new method for the chemical synthesis of peptides.

Keywords: *N,N*-dimethylaminoxy carbonyl, Dmaoc, Dbz, peptide coupling, solid phase peptide synthesis, chemical ligation, thioester, protecting group

OPEN ACCESS

Edited by:
John D. Wade,
Florey Institute of Neuroscience and Mental Health, Australia

Reviewed by:
William D. Lubell,
Université de Montréal, Canada
Knud J. Jensen,
University of Copenhagen, Denmark

****Correspondence:***
Ryo Okamoto
rokamoto@chem.sci.osaka-u.ac.jp

Specialty section:
This article was submitted to Chemical Biology, a section of the journal Frontiers in Chemistry

Received: *08 January 2019*
Accepted: *05 March 2019*
Published: *28 March 2019*

Citation:
Okamoto R, Ono E, Izumi M and Kajihara Y (2019) N,N-Dimethylaminoxy Carbonyl, a Polar Protecting Group for Efficient Peptide Synthesis. Front. Chem. 7:173. doi: 10.3389/fchem.2019.00173

INTRODUCTION

Peptide coupling reactions are essential for the chemical synthesis of polypeptides and proteins (Kricheldorf, 2006; Kent, 2017). Considerable efforts have been devoted to the development of chemical ligation for the chemoselective coupling of unprotected peptides. Many proteins have been synthesized using a variety of chemical ligation techniques, including native chemical ligation (Bode, 2011, 2017; Jin and Li, 2018; Liu and Li, 2018). These methodologies are generally based on site-specificity, which limits the amino acid sites for ligations. Consequently, chemical ligation often requires the preparation of suitable building blocks for peptide coupling at desired sites, depending on the amino acid sequence of target polypeptides.

Strategies are desired for the coupling of peptide fragments possessing diverse chemical structures using minimal functional group protection (Aimoto, 1999; Hojo, 2014). To achieve regioselective amide bond formation, side chain protection is often essential; however, many protecting groups diminish peptide solubility and render the polar polyamide chain amphipathic due to their nonpolar nature. A strategy involving minimal use of protection on the N^{ε}-amine of Lys residues and the *N*-terminal α-amine may circumvent the solubility problem and avoid undesirable amide bond formation. The utility of the minimum protection strategy for peptide coupling was demonstrated in the chemical synthesis of proteins using the thioester leaving group (Aimoto, 1999). However, this strategy used Boc protection on the N^{ε}-amine of Lys, which increases the risk of poor solubility, depending on the number of protecting groups in the target peptide sequence.

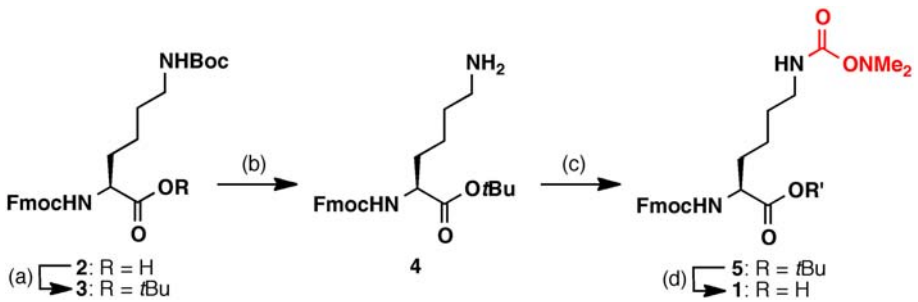

FIGURE 1 | Synthesis of Fmoc-Lys(Dmaoc)-OH **1**. Reagents and conditions: **(a)** Boron trifluoride diethyl ether complex, *tert*-butyl 2,2,2-trichloroacetimidate; **(b)** TFA, dichrolomethane (y = 86%, over 2 steps); **(c)** *N,N'*-carbonyldiimidazole, *N,N*-dimethyl hydroxylamine hydrochloride (y = 46%); **(d)** 6 M hydrochloric acid, 1,4-dioxane (y = 91%).

The isonicotinyloxycarbonyl (iNoc) group has been used to circumvent the intrinsic low solubility of protected peptides (Veber et al., 1977). Recently, the protection of the N^{ε}-amine of Lys residues with the iNoc group has also demonstrated its utility during peptide synthesis (Asahina et al., 2015). These reports suggest the potential of polar protecting groups for the chemical synthesis of peptides. However, much effort has not been paid to the development of new polar protecting groups that are stable but efficiently removable under mild reaction conditions.

Herein, we present a polar protecting group *N,N*-dimethylaminooxy carbonyl (Dmaoc) for the N^{ε}-amine of Lys and its use in peptide synthesis. This protecting group can be removed by reduction in a buffer containing thiol. The Dmaoc group proved compatible with peptide ligation strategies featuring the activation of *N*-acyl diaminobenzamides (Dbz) with sodium nitrate to generate the respective benzotriazole (Bt) leaving group (Wang et al., 2015; Weidmann et al., 2016), as further demonstrated by the synthesis of Sunflower trypsin inhibitor.

RESULTS AND DISCUSSION

Firstly, Fmoc-Lys(Dmaoc)-OH **1** was synthesized from commercially available Fmoc-Lys(Boc)-OH **2** for the preparation of Dmaoc protected peptide by Fmoc solid phase peptide synthesis (SPPS) (**Figure 1**). The Lys derivative **2** was esterified using *tert*-butyl trichloroacetimidate. The Boc group was removed selectively by treatment with trifluoroacetic acid (TFA)/dichloromethane solution. The Dmaoc group was then incorporated onto the N^{ε}-amine of Lys of **4** by treatment with *N,N'*-carbonyldiimidazole, followed by the addition of *N,N*-dimethylhydroxylamine. After optimizing the conditions for removing the *t*Bu ester moiety, we found that the treatment of the fully protected Lys derivative **5** with the mixed solution of 6 M HCl and 1,4-dioxane (1: 1 vol/vol) afforded Fmoc-Lys(Dmaoc)-OH **1** in good yield.

In order to perform a peptide coupling reaction, we focused on the Dbz group that was known as a precursor of the Bt group. Thioesters have been utilized as an efficient leaving group for peptide coupling reactions. However, the synthesis of peptide-thioesters is still difficult in Fmoc SPPS, and thus several thioester surrogates have been developed. Recently, the Dawson and Liu groups have independently reported the synthesis of peptide-thioester from peptide-Dbz through the formation of peptide-Bt (Wang et al., 2015; Weidmann et al., 2016). These synthetic methodologies were based on previous studies by Katritzky et al. (1992, 2000, 2004), in which *N*-acyl-Bt was used as an efficient acylating agent. We envisaged that peptide-Bt, prepared from peptide-Dbz, could be used as a *C*-terminal activated peptide for peptide coupling reactions.

The Dmaoc-protected peptide having the Dbz group was synthesized by standard Fmoc SPPS (**Figure 2**). The synthesis was performed on the commercially available Fmoc-Dbz-polystyrene resin, according to the protocol reported by Dawson et al. (Blanco-Canosa and Dawson, 2008). Coupling of Fmoc-amino acids including **1** was performed by using standard coupling reagents such as HATU or HBTU, together with *N,N*-diisopropylethylamine (DIEA) (see **Supplementary Material** for the detail). Removal of the Fmoc group was also performed under standard conditions using 20% piperidine/*N,N*-dimethylformamide (DMF). After complete assembly, the peptide was detached from the solid support by use of a TFA cocktail. This Fmoc SPPS successfully yielded the Dmaoc-protected peptide-Dbz (peptide(Dmaoc)-Dbz **6**, 66% isolated yield).

The Dmaoc group includes the dimethylamino moiety that can be a proton acceptor and this structural property allowed us to anticipate the polar nature of the Dmaoc group. The polarity of the Dmaoc group was compared with the Boc group, a conventional protecting group for the N^{ε}-amine of Lys. The peptide(Dmaoc)-Dbz **6** and corresponding Boc-protected peptide **7** were subjected to reversed-phase high-performance liquid chromatography (**Figure 3**). This analysis revealed that the retention time for the peptide(Dmaoc)-Dbz **6** was shorter than that of the peptide(Boc)-Dbz **7**. This result indicates that the Dmaoc group has essentially higher polarity than that of Boc group.

We found that the Dmaoc group could be removed under reductive conditions (**Figure 4**). The removal of

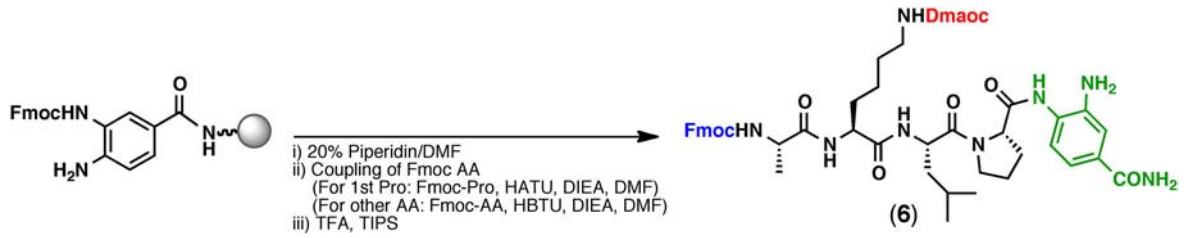

FIGURE 2 | Fmoc SPPS of Dmaoc-protected peptide (**6**).

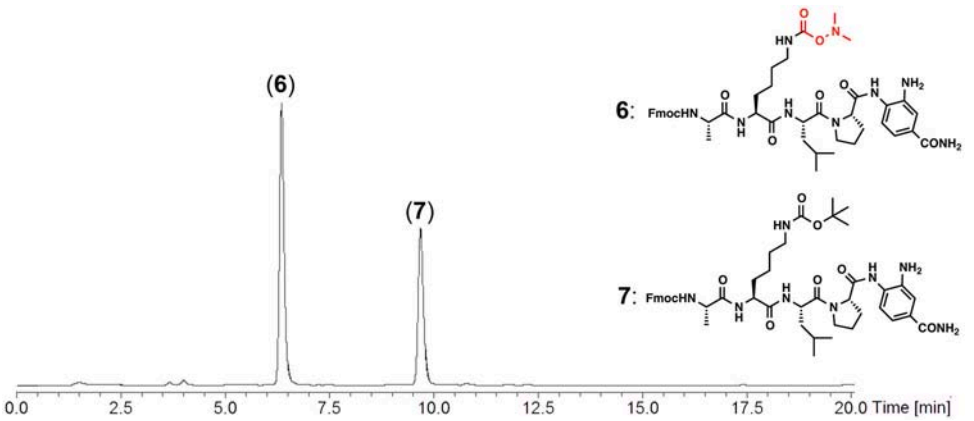

FIGURE 3 | RP-HPLC chromatogram for the analysis of Dmaoc-protected peptide (**6**) and Boc-protected peptide (**7**). Chromatographic separation was performed by using a linear gradient of 0.1% HCOOH aq.: 90% acetonitrile aq. containing 0.09% HCOOH from 60:40 to 30:70 over 20 min at a flow rate of 0.3 mL/min. C4 silica gel with column dimension 2.0 × 150 mm was used for this analysis. The eluent was monitoring by UV-absorbance at 280 nm with on-line ESI-MS.

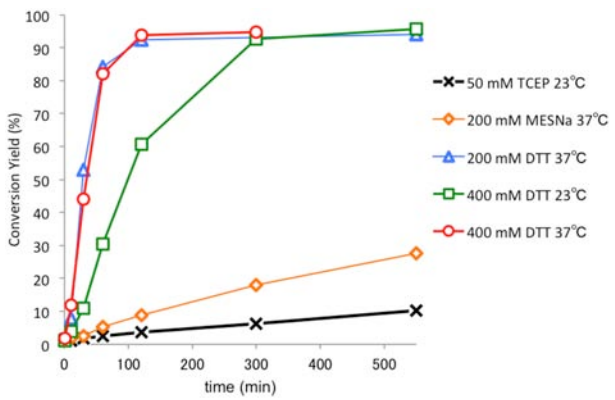

FIGURE 4 | Investigation of the reaction rate for the removal of Dmaoc group of peptide **6**. The reaction was performed using 4 mM of the peptide (0.5 mg) in 0.1 M sodium phosphate buffer containing 6 M guanidine hydrochloride and reducing agents at pH 7.0. At each time point, the fraction conversion was determined by HPLC peak area intensities.

the Dmaoc group on peptide **6** was conducted in a buffer at pH 7.0 in the presence of reducing agents such as sodium 2-mercaptosulfonate (MESNa), (±)-dithiothreitol (DTT) or tris(2-carboxyethyl)phosphine (TCEP). Consequently, the Dmaoc group was efficiently removed within a few hours in the presence of DTT. In contrast, the deprotection rate was slow in the presence of MESNa or TCEP, and no deprotection was observed without reducing agents. These results suggested that a suitable reducing potency as well as the nucleophilicity of the thiol group contributed to the removal of Dmaoc group; however, a detailed investigation of the reaction mechanism is still underway.

We then tested the peptide coupling between the peptide(Dmaoc)-Dbz **6** and the heptapeptide **8** (**Figure 5A**, **Figures S-1**,**S-4**). The Dbz group was converted into Bt by treatment with sodium nitrate ($NaNO_2$) in acidic DMF at −17°C (**Figure 5B**a). Subsequently, peptide **8**, 3-hydroxy-1,2,3-benzotriazine-4(3*H*)-one (HOOBt) and DIEA were added to initiate the peptide coupling via the conversion of peptide-Bt (**9**) into an active peptide-ester. This reaction gave Dmaoc-protected undecapeptide **10** within 14 h (**Figure 5B**c). After separating the crude peptide **10** from DMF by ether precipitation, the resultant material was dissolved in phosphate buffer (pH 7.0) containing DTT to remove the Dmaoc group. This reaction proceeded to completion within 2 h and gave peptide **11** (**Figure 5B**d). To remove the *N*-terminal Fmoc group, piperidine was subsequently added to the reaction mixture (**Figures 5B**e,f). As a result, these sequential reactions efficiently yielded undecapeptide **12** (60% isolated yield over four steps).

Encouraged by the result of the peptide coupling reaction, we conducted the synthesis of a cyclic peptide using the Dmaoc/Dbz

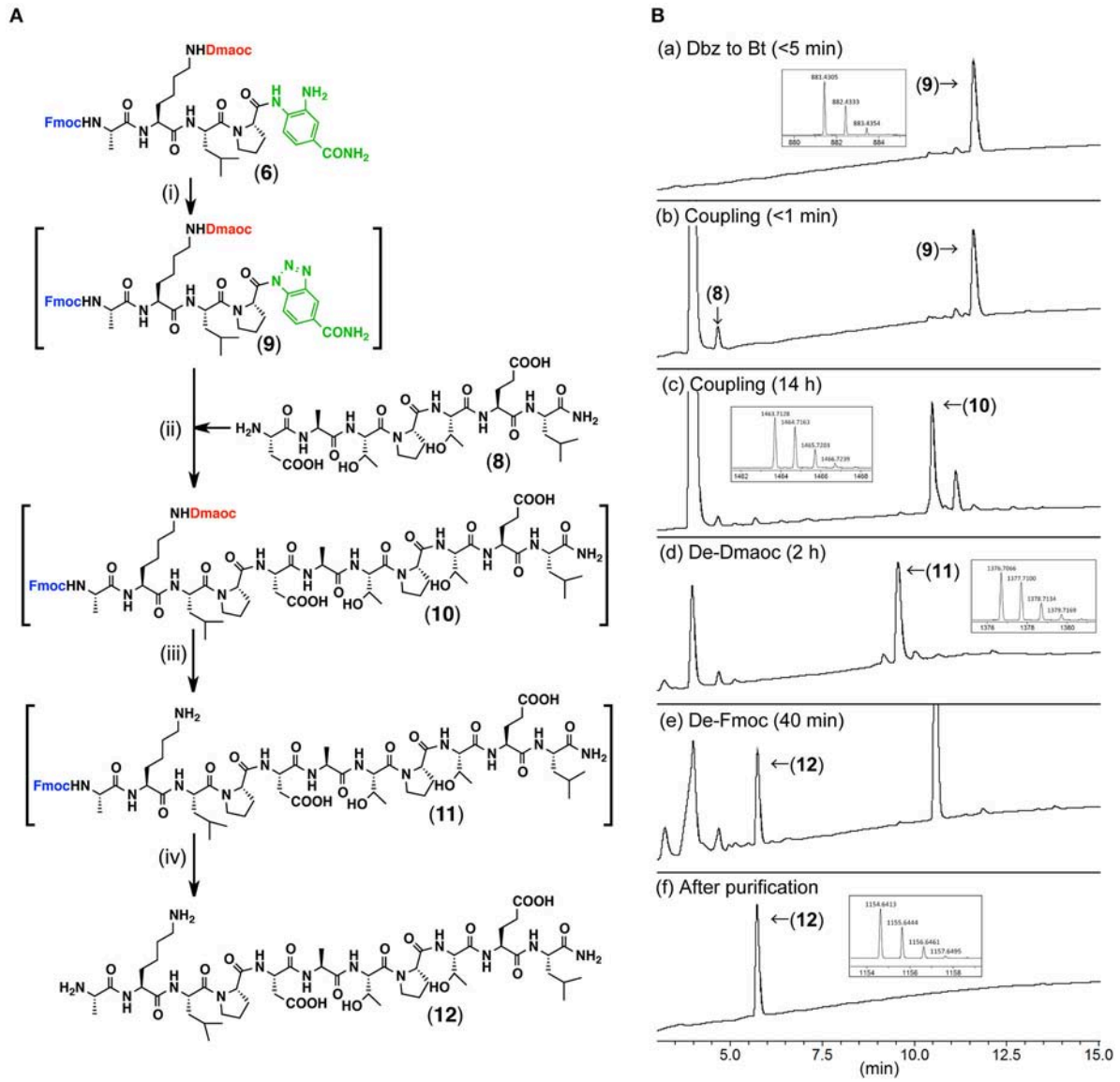

FIGURE 5 | The coupling of the Dmaoc-protected peptide-Dbz **6** and the heptapeptide **8**. **(A)** Reaction scheme for the peptide coupling followed by the deprotections; Reagents and conditions: (i) $NaNO_2$, DMF/4 M HCl in 1,4-dioxane (39: 1 vol/vol); (ii) DIEA, HOOBt, DMF; (iii) Ether precipitation then 0.1 M sodium phosphate buffer containing 6 M guanidine-hydrochloride and 0.2 M DTT (pH 7.0) at 37°C; (iv) piperidine. **(B)** LC data for the monitoring of the sequential reactions. Analytical condition: Linear gradient of 0.1% HCOOH aq.: 90% acetonitrile aq. containing 0.09% HCOOH from 90:10 to 30:70 over 15 min at a flow rate of 0.3 ml/min. The eluent was monitoring by UV-absorbance at 218 nm with on-line ESI-MS. Insets are expanded view of $[M+H]^+$ ion peak acquired by on-line ESI-HRMS from each UV peak labeled with compound number. m/z calculated mono isotopic $[M+H]^+$ for compound **9** $C_{45}H_{57}N_{10}O_9^+$ 881.4304; for compound **10** $C_{69}H_{103}N_{14}O_{21}^+$ 1463.7417; for compound **11** $C_{66}H_{98}N_{13}O_{19}^+$ 1376.7096; for compound **12** $C_{51}H_{88}N_{13}O_{17}^+$ 1154.6416.

strategy. Sunflower trypsin inhibitor (SFTI) is one of the smallest cyclic peptides that has a head-to-tail ring structure consisting of 14 amino acids, including one Lys residue. The chemical synthesis of SFTI has been achieved using native chemical ligation, which requires an *N*-terminal cysteine residue (Daly et al., 2006). In our present research, the Dmaoc/Dbz strategy was applied to the construction of the cyclic-structure of SFTI. We expected that this result would provide us with a new synthetic route for cyclic peptides that do not have Cys residues.

Linear Dmaoc-protected SFTI-Dbz prepared by Fmoc SPPS was subjected to an intramolecular peptide bond formation followed by the removal of the Dmaoc group (**Figure 6**, **Figures S-2**,**S-3**). The sequential reactions in the conversion of Dbz to Bt and the subsequent coupling steps resulted in the formation of disulfide bonded cyclic SFTI(Dmaoc) **15** and a cyclic SFTI(Dmaoc)-NO adduct **16**. These products were afforded because the starting peptide **13** had free thiols, which could be oxidized by $NaNO_2$. We expected that the NO group

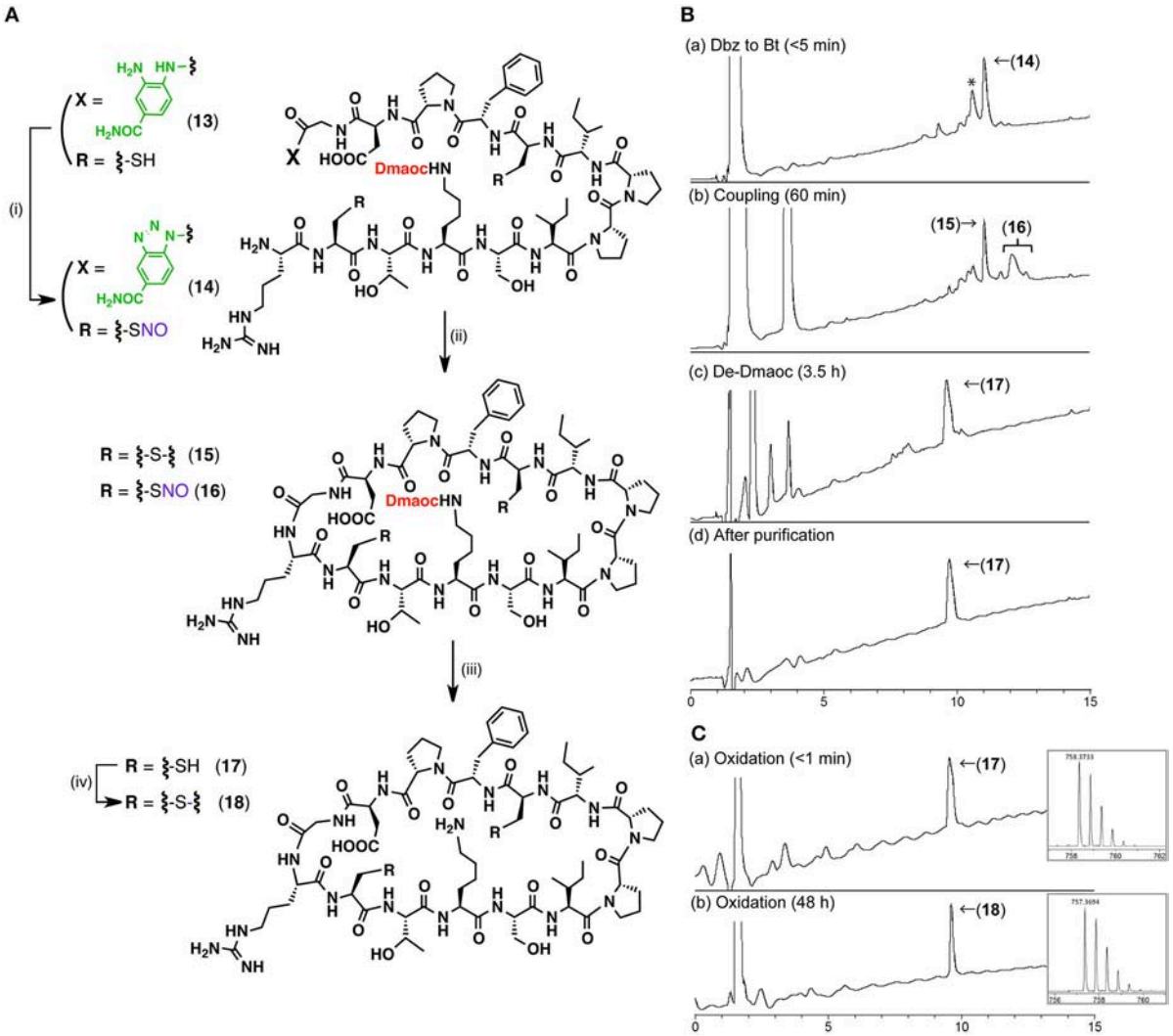

FIGURE 6 | The synthesis of cyclic peptide, SFTI using the Dmaoc protected peptide-Dbz (**13**). **(A)** Reaction scheme for the synthesis of SFTI; Reagents and conditions: (i) $NaNO_2$, DMF / 4 M HCl in dioxane (39: 1, vol/vol); (ii) DIEA, HOOBt, DMF; (iii) Ether precipitation then 0.1 M sodium phosphate buffer containing 6 M guanidine-hydrochloride and 0.2 M DTT (pH 7.0) at 37°C; (iv) 20 % DMSO aq. **(B)** LC data for the monitoring of the sequential reactions and **(C)** LC data for the formation of disulfide bond; Analytical condition: Linear gradient of 0.1% HCOOH aq.: 90% acetonitrile aq. containing 0.09% HCOOH from 90:10 to 30:70 over 15 min at a flow rate of 0.3 ml/min. The eluent was monitoring by UV-absorbance at 218 nm with on-line ESI-MS. Peak labeled with asterisk in the chromatogram of **(Ba)**, was corresponding to the hydrolyzed form of peptide **14** judged by on-line MS analysis (see **Supplementary Material**). This was plausibly afforded in LC-MS analysis and not from reaction mixture, since this product was not observed in the following coupling step; Insets are expanded view of $[M+H]^+$ ion peak acquired by on-line ESI-HRMS from each peak labeled with compound number. m/z calculated mono isotopic $[M+2H]^{2+}$ for **17** $C_{67}H_{108}N_{18}O_{18}S_2$ 758.3760 and oxidized form **18** $C_{67}H_{108}N_{18}O_{18}S_2$ 758.3760.

would be removed simultaneously during the deprotection of the Dmaoc group with thiol. The subsequent deprotection of Dmaoc using DTT successfully yielded the reduced form of cyclic SFTI **17** (43% isolated yield over three steps). This product was converted into the corresponding oxidized form of SFTI **18** quantitatively by treatment with DMSO (**Figure 6C**, **Figure S-3**). The synthesis of cyclic peptide SFTI demonstrated the utility of our peptide coupling strategy using the Dmaoc and Dbz groups for the chemical synthesis of peptide derivatives.

CONCLUSION

We reported the Dmaoc as a polar protecting group and its use in peptide coupling reactions. The polarity of Dmaoc is higher than that of the Boc group, which is a conventional protecting group of the N^{ε}-amines of Lys. The Dmaoc-protected peptides could be synthesized by standard Fmoc-SPPS straightforwardly and were successfully used for the synthesis of Sunflower trypsin inhibitor peptide. The Dmaoc group was stable during the synthesis but

removable in a buffer containing thiol, thereby achieving the facile deprotection of Dmaoc after the peptide coupling reactions. The unique character of the Dmaoc group would expand the chemical toolbox for the synthesis of peptides and proteins, which would contribute to the development of next-generation drugs.

DATA AVAILABILITY

All datasets generated for this study are included in the manuscript and/or the **Supplementary Files**.

AUTHOR CONTRIBUTIONS

All experiments and data analysis were carried out by RO and EO. The experiment design and manuscript preparation were done by RO. MI assisted with the experiment design. YK assisted with experiment design and the preparation of manuscript. All authors were involved in the discussion and have approved the submitted manuscript.

FUNDING

This work was supported by JSPS KAKENHI (26810092): Grant-in-Aid-for Young Scientists (B).

SUPPLEMENTARY MATERIAL

The Supplementary Material for this article can be found online at: https://www.frontiersin.org/articles/10.3389/fchem.2019.00173/full#supplementary-material

REFERENCES

Aimoto, S. (1999). Polypeptide synthesis by the thioester method. *Pept. Sci.* 51, 247–265. doi: 10.1002/(SICI)1097-0282(1999)51:4<247::AID-BIP2>3.0.CO;2-W

Asahina, Y., Komiya, S., Ohagi, A., Fujimoto, R., Tamagaki, H., Nakagawa, K., et al. (2015). Chemical synthesis of O-glycosylated human interleukin-2 by the reverse polarity protection strategy. *Angew. Chem. Int. Ed.* 54, 8226–8230. doi: 10.1002/anie.201501847

Blanco-Canosa, J. B., and Dawson, P. E. (2008). An efficient Fmoc-SPPS approach for the generation of thioester peptide precursors for use in native chemical ligation. *Angew. Chem. Int. Ed.* 47, 6851–6855. doi: 10.1002/anie.200705471

Bode, J. W. (2011). Rethinking amide bond synthesis. *Nature* 480, 471–479 doi: 10.1038/nature10702

Bode, J. W. (2017). Chemical protein synthesis with the α-Ketoacid–Hydroxylamine ligation. *Acc. Chem. Res.* 50, 2104–2115. doi: 10.1021/acs.accounts.7b00277

Daly, N. L., Chen, Y.-K., Foley, F. M., Bansal, P. S., Bharathi, R., Clark, R. J., et al. (2006). The absolute structural requirement for a proline in the P3'-position of bowman-birk protease inhibitors is surmounted in the minimized SFTI-1 scaffold. *J. Biol. Chem.* 281, 23668–23675. doi: 10.1074/jbc.M601426200

Hojo, H. (2014). Recent progress in the chemical synthesis of proteins. *Curr. Opin. Struct. Biol.* 26, 16–23. doi: 10.1016/j.sbi.2014.03.002

Jin, K., and Li, X. (2018). Advances in native chemical ligation–desulfurization: a powerful strategy for peptide and protein synthesis. *Chem. Eur. J.* 24, 17397–17404. doi: 10.1002/chem.201802067

Katritzky, A. R., He, H.-Y., and Suzuki, K. (2000). N-acylbenzotriazoles: neutral acylating reagents for the preparation of primary, secondary, and tertiary amides. *J. Org. Chem.* 65, 8210–8213. doi: 10.1021/jo000792f

Katritzky, A. R., Ji, F.-B., Fan, W.-Q., Beretta, P., and Bertoldi, M. (1992). Syntheses of triazolo[6,7-d]phthalide and triazolo[6,7-d]dihydrocoumarin. *J. Heterocyclic Chem.* 29, 1519–1523. doi: 10.1002/jhet.5570290624

Katritzky, A. R., Shestopalov, A. A., and Suzuki, K. (2004). A new convenient preparation of thiol esters utilizing N-Acylbenzotriazoles. *Synthesis* 2004, 1806–1813. doi: 10.1055/s-2004-829126

Kent, S. (2017). Chemical protein synthesis: Inventing synthetic methods to decipher how proteins work. *Bioorg. Med. Chem.* 25, 4926–4937. doi: 10.1016/j.bmc.2017.06.020

Kricheldorf, H. R. (2006). Polypeptides and 100 years of chemistry of α-Amino acid N-carboxyanhydrides. *Angew. Chem. Int. Ed.* 45, 5752–5784. doi: 10.1002/anie.200600693

Liu, H., and Li, X. (2018). Serine/threonine ligation: origin, mechanistic aspects, and applications. *Acc. Chem. Res.* 51, 1643–1655. doi: 10.1021/acs.accounts.8b00151

Veber, D. F., Paleveda, W. J., Lee, Y. C., and Hirschmann, R. (1977). Isonicotinyloxycarbonyl a novel amino protecting group for peptide synthesis. *J. Org. Chem.* 42, 3286–3288. doi: 10.1021/jo00440a018

Wang, J.-X., Fang, G.-M., He, Y., Qu, D.-L., Yu, M., Hong, Z.-Y., et al. (2015). Peptide o-aminoanilides as crypto-thioesters for protein chemical synthesis. *Angew. Chem. Int. Ed.* 54, 2194–2198. doi: 10.1002/anie.201408078

Weidmann, J., Dimitrijević, E., Hoheisel, J. D., and Dawson, P. E. (2016). Boc-SPPS: compatible linker for the synthesis of peptide o-aminoanilides. *Org. Lett.* 18, 164–167. doi: 10.1021/acs.orglett.5b03111

Conflict of Interest Statement: The authors declare that the research was conducted in the absence of any commercial or financial relationships that could be construed as a potential conflict of interest.

Copyright © 2019 Okamoto, Ono, Izumi and Kajihara. This is an open-access article distributed under the terms of the Creative Commons Attribution License (CC BY). The use, distribution or reproduction in other forums is permitted, provided the original author(s) and the copyright owner(s) are credited and that the original publication in this journal is cited, in accordance with accepted academic practice. No use, distribution or reproduction is permitted which does not comply with these terms.

frontiers in Chemistry

ORIGINAL RESEARCH
published: 12 October 2018
doi: 10.3389/fchem.2018.00485

Lighting-Up Tumor for Assisting Resection via Spraying NIR Fluorescent Probe of γ-Glutamyltranspeptidas

*Haidong Li[1], Qichao Yao[1], Feng Xu[1], Ning Xu[1], Wen Sun[1], Saran Long[1], Jianjun Du[1], Jiangli Fan[1], Jingyun Wang[2] and Xiaojun Peng[1]**

[1] State Key Laboratory of Fine Chemicals, Dalian University of Technology, Dalian, China, [2] Department School of Life Science and Biotechnology, Dalian University of Technology, Dalian, China

For the precision resection, development of near-infrared (NIR) fluorescent probe based on specificity identification tumor-associated enzyme for lighting-up the tumor area, is urgent in the field of diagnosis and treatment. Overexpression of γ-glutamyltranspeptidase, one of the cell-membrane enzymes, known as a biomarker is concerned with the growth and progression of ovarian, liver, colon and breast cancer compared to normal tissue. In this work, a remarkable enzyme-activated NIR fluorescent probe NIR-SN-GGT was proposed and synthesized including two moieties: a NIR dicyanoisophorone core as signal reporter unit; γ-glutamyl group as the specificity identification site. In the presence of γ-GGT, probe NIR-SN-GGT was transformed into NIR-SN-NH_2, the recovery of Intramolecular Charge Transfer (ICT), liberating the NIR fluorescence signal, which was firstly employed to distinguish tumor tissue and normal tissues *via* simple "spraying" manner, greatly promoting the possibility of precise excision. Furthermore, combined with magnetic resonance imaging by T2 weight mode, tumor transplanted BABL/c mice could be also lit up for first time by NIR fluorescence probe having a large stokes, which demonstrated that probe NIR-SN-GGT would be a useful tool for assisting surgeon to diagnose and remove tumor in clinical practice.

Keywords: enzyme-activated, NIR fluorescent probe, spraying, large stokes shift, diagnose, clinical practice, tumor, γ-Glutamyltranspeptidase

OPEN ACCESS

Edited by:
Tony D. James,
University of Bath, United Kingdom

Reviewed by:
John Stephen Fossey,
University of Birmingham,
United Kingdom
Suying Xu,
Beijing University of Chemical Technology, China

****Correspondence:***
Xiaojun Peng
pengxj@dlut.edu.cn

Specialty section:
This article was submitted to Chemical Biology, a section of the journal Frontiers in Chemistry

Received: *17 August 2018*
Accepted: *24 September 2018*
Published: *12 October 2018*

Citation:
Li H, Yao Q, Xu F, Xu N, Sun W, Long S, Du J, Fan J, Wang J and Peng X (2018) Lighting-Up Tumor for Assisting Resection via Spraying NIR Fluorescent Probe of γ-Glutamyltranspeptidas. Front. Chem. 6:485. doi: 10.3389/fchem.2018.00485

INTRODUCTION

With the improvement of economic level, diagnose and treatment of cancer is getting more and more attention (Cheng et al., 2011; Chen et al., 2016, 2018; Cong et al., 2018; Jung et al., 2018; Lee et al., 2018; Yang et al., 2018; Zhang et al., 2018). The traditional clinical detection techniques, such as positron emission tomography (PET) (Mileshkin et al., 2011; Xiao et al., 2012), magnetic resonance imaging (MRI) (Sardanelli et al., 2010; Pinto et al., 2011) and X-ray imaging (Huang et al., 2011; Shi et al., 2014), are widely used to the medical examination of humans. Unfortunately, the fatal flaw in these techniques is the inability to diagnose early tumors, especially for flat or depressed lesions (Park et al., 2018). Although histopathological biopsy could provide the accurate diagnose result, it is suffered from the possibility of real-time diagnosis *in situ* due to the complex

processing and time-consuming of the sample separation (Kozlowski et al., 2006). Indeed, surgical specialists urgent need an effective tool to easily distinguish between tumor and normal tissue during surgery. Fluorescence technology has been paid unprecedented attention (Blum et al., 2007; Paulick and Bogyo, 2008; Asanuma et al., 2015; Ofori et al., 2015; Cheng et al., 2016; Gu et al., 2016a,b; Hu et al., 2016; Chen et al., 2017; He et al., 2017; Liu et al., 2017a,b,c; Wang et al., 2017a, 2018; Yin et al., 2017; Kuriki et al., 2018; Li et al., 2018b; Llancalahuen et al., 2018; Miao et al., 2018; Sedgwick et al., 2018; Shang et al., 2018; Verwilst et al., 2018), especially for medical diagnosis and treatment system (Kim et al., 2017; Li et al., 2017b; Verwilst et al., 2017), owing to efficient identification without destructive *in vivo*. Thus, it is of great medical significance to develop fluorescent probe that can assist clinician for imaging and resection of tumor.

γ-glutamyltranspeptidase (γ-GGT; EC 2.3.2.2), an over-expression enzyme associated with the growth and progression of ovarian, liver, colon and breast cancer compared to normal tissue (De Young et al., 1978; Shinozuka et al., 1979; Rao et al., 1986), plays important roles in many physiological and pathological processes (Pompella et al., 2006; Strasak et al., 2010), which is regarded as an important target for analysis and imaging *in vitro* or *in vivo* (Li et al., 2015b, 2016c; Wang et al., 2015, 2017b; Park et al., 2016a,b; Zhang et al., 2016a,b; Liu et al., 2018). However, rarely related fluorescent probe could be qualified for the identification tumor by tracking the activity of γ-GGT enzyme *in vivo* (Urano et al., 2011), especially for NIR emission property, possessing good performances of avoiding auto-fluorescence and deeper tissue penetration (Gu et al., 2016a). In addition, large stokes shift could effectively avoid self-absorbing for beneficial to fluorescence imaging. Till to now, there is no fluorescence probe visualized tracking the activity of γ-GGT enzyme in various organs. More importantly, by "spraying" manner, tumor tissue could be conveniently and efficiently lighted up from normal tissue, which is urgent need for precision medicine.

In this work, based on our previous research (Li et al., 2018a), through installing γ-GGT enzyme-activable unit on photo-stability; large stokes shift and controllable NIR chromophore, probe NIR-SN-GGT was successfully proposed and synthesized for monitoring the activity of γ-GGT *in vitro* and *in vivo*. NIR fluorescence emission was strictly modulated through the electron donor capability of amino. Upon addition γ-GGT into solution, obvious NIR fluorescence emission signal was observed after activable group cut off, which attributed to the enhancement of electronic capacity of product NIR-SN-NH_2. By layer scanning and 3D imaging construction of tissue slices, the probe NIR-SN-GGT was breakthrough employed to evaluate the content of γ-GGT enzyme in different organs. To the best of our knowledge, tumor tissue could be distinguished from normal through "spraying" NIR fluorescence probe style for the first time.

Experimental Section

General Information and Materials

All reagents used were obtained from commercial suppliers and were used without further purification unless otherwise stated. Solvents used were purified *via* standard methods. Twice-distilled purified water used in all experiments was from Milli-Q systems. ^{1}H-NMR and ^{13}C-NMR spectra were recorded on a Bruker Avance II 400 MHz spectrometer. Chemical shifts (δ) were reported as ppm (in MeOD or DMSO-d_6, with TMS as the internal standard). Fluorescence spectra were performed on a VARIAN CARY Eclipse fluorescence spectrophotometer (Serial No.MY15210003) in 10 × 10 mm quartz cell. Excitation and emission slit widths were modified to adjust the fluorescence intensity to a suitable range. Absorption spectra were measured on Agilent Technologies CARY 60 UV-Vis spectrophotometer (Serial No.MY1523004) in 10 × 10 mm quartz cell. Mass spectrometric data were achieved with HP1100LC/MSD MS and an LC/Q-TOF-MS instruments. Mito-Tracker Green, Lyso-Tracker Green and Hoechst 33342 were purchased from Life Technologies Co. (USA). Nitroreductase, transglutaminase, γ-glutamyltranspeptidase, and 6-Diazo-5-oxo-L-norleucine (DON) were purchased from Sigma-Aldrich. All pH measurements were performed using the Ohaus Starter 2100 pH meter. The fluorescence quantum yields for compounds with Absolute PL Quantum Yield Spectrometer (HAMAMATSU C11347). Instruments used in cell imaging tests were carried out on Olympus FV1000 and FV1000-IX81 confocal microscopy (Olympus, Japan). Slight pH variations in the solutions were achieved by adding the minimum volumes of HCl or NaOH (1 M). Flash column chromatography was performed using silica gel (200–300 mesh) obtained from Qingdao Ocean Chemicals. Flow cytometry analysis was carried out on cytometer (Attune NxT). MRI imaging of mice was carried out on NIUMAG analytical instrument (MesoMR23-060H-I). Tumor tissue slices were prepared from freezing microtome (LEICA CM1860 UV). All the interferential reagents were prepared based on published literatures (Li et al., 2015a, 2016a,b, 2018a; Fan et al., 2017).

Detection Limit

The detection limit (DL) was calculated based on the fluorescence titration of probe NIR-SN-GGT (10 μM) in the presence of γ-GGT (0-10 mU/mL). The fluorescence intensity of probe NIR-SN-GGT was measured and standard deviation of the blank measurement was achieved. The detection limit was calculated with the following equation: Detection limit $= 3\sigma/k$. Where σ is the standard deviation of the blank measurement, k is the slope between the fluorescence intensity (F_{650} nm) versus various γ-GGT concentrations.

Determination of the Quantum Yield

The fluorescence quantum yields for compounds with Absolute PL Quantum Yield Spectrometer (HAMAMATSU C11347). Operating this system is simple. Load a sample and press the start button to measure the photoluminescence quantum yields, excitation wavelength dependence, PL excitation spectrum and other properties in a short time. The PL Quantum Yield (Φ) is expressed as the ratio of the number of photons emitted from molecules (PNem) to that absorbed by molecules (PNabs). As following equation: Φ = PNem/PNabs.

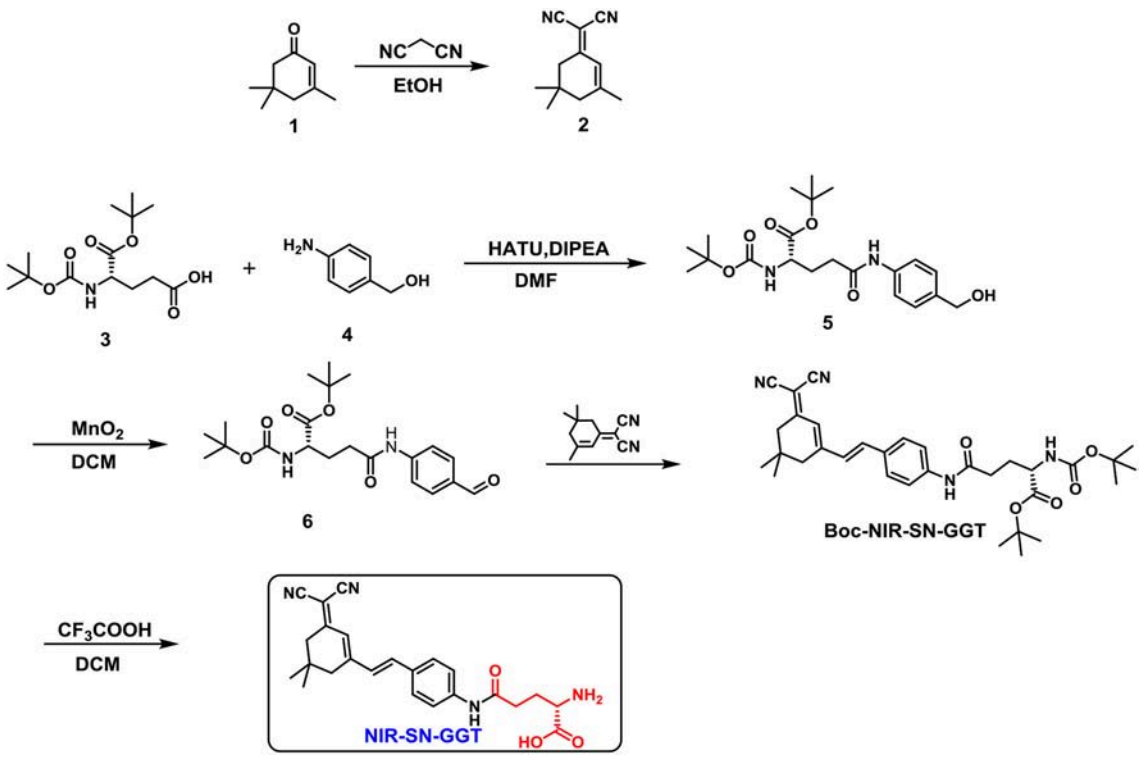

SCHEME 1 | The synthesis route of probe NIR-SN-GGT.

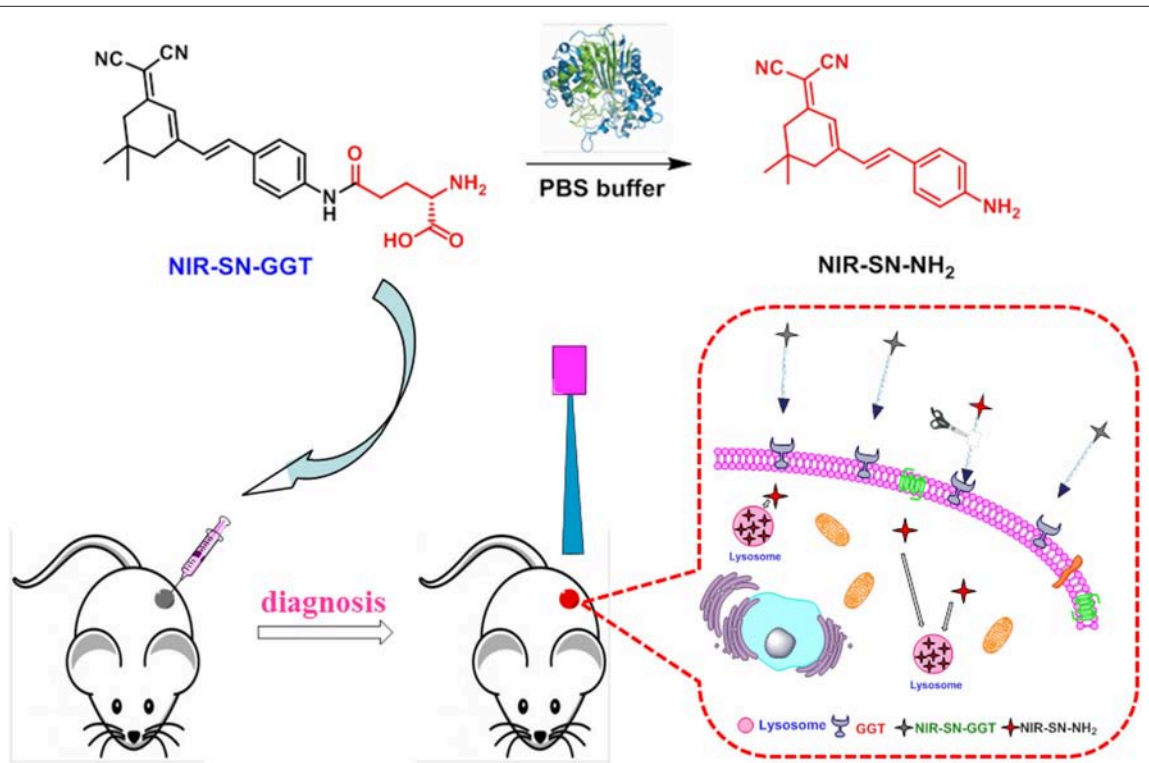

SCHEME 2 | Recognition mechanism of probe NIR-SN-GGT for γ-GGT enzyme *in vivo*.

Cell Incubation

Ovarian cancer cells (A2780 cells), breast cancer 4T1 cells (4T1 cells) and human umbilical vein endothelial cells (HUVEC cells) were purchased from Institute of Basic Medical Sciences (IBMS) of the Chinese Academy of Medical Sciences. Except for A2780 cells treated with Dulbecco's modified Eagle's medium (DMEM, Invitrogen), others cells were cultured in RPMI medium 1640 supplemented with 10% fetal bovine serum (Invitrogen). The cells were seeded in confocal culture dishes and then incubated for 24 h at 37°C under a humidified atmosphere containing 5% CO_2.

Cytotoxicity Assays

Measurement of cell viability was measured by reducing of MTT (3-(4, 5)-dimethylthiahiazo (-2-yl)-3, 5-diphenytetrazoliumromide) to formazan crystals using mitochondrial dehydrogenases. A2780 and HUVEC cells were seeded in 96-well microplates (Nunc, Denmark) at a density of 1×10^5 cells/mL in 100 μL medium containing 10% FBS. After 24 h of cell attachment, the plates were then washed with 100 μL/well PBS buffer. The cells were then cultured in medium with 0, 1, 2, 5, and 10 μM of probe NIR-SN-GGT for 24 h. Cells in culture medium without probe NIR-SN-GGT were used as the control. Six replicate wells were used for each control and test concentration. 10 μL of MTT (5 mg/mL) prepared in PBS was added to each well and the plates were incubated at 37°C for another 4 h in a 5% CO_2 humidified incubator. The medium was then carefully removed, and the purple crystals were lysed in 200 μL DMSO. Optical density of solutions was determined on a microplate reader (Thermo Fisher Scientific) at 490 nm. Cell viability was expressed as a percent of the control culture value, and it was calculated using the following equation: Cells viability (%) = $(OD_{dye} - OD_{blank})/(OD_{control} - OD_{blank}) \times 100$

Imaging Endogenous γ-GGT Activity in Living Cells

A2780 and HUVEC cells were seeded in glass-bottom culture dishes at approximately concentration of 2×10^4 cells/mL and allowed to culture for 24 h at 37°C in a 5% CO_2 humidified incubator. For the detection of endogenous γ-GGT activity, A2780 and HUVEC cells were incubated with probe NIR-SN-GGT (10 μM) 37°C for 30 min, followed by washing thrice with free DMEM. Under the confocal fluorescence microscope (Olympus FV1000-IX81) with a 60 × objective lens, probe NIR-SN-GGT was excited at 488 nm (one-photon) and 800 (two-photon), next, fluorescence emission at 655–755 nm channel and 575–630 nm channel were gathered, respectively.

Time-Dependent Cell Imaging

The time-dependent cell imaging of probe NIR-SN-GGT (10 μM) monitoring endogenous γ-GGT activity in A2780 cells and HUVEC cells were investigated on Olympus FV1000-IX81 with the excitation at 488 nm. Fluorescent signals were recorded as time went on. After that, quantitative image analysis of the

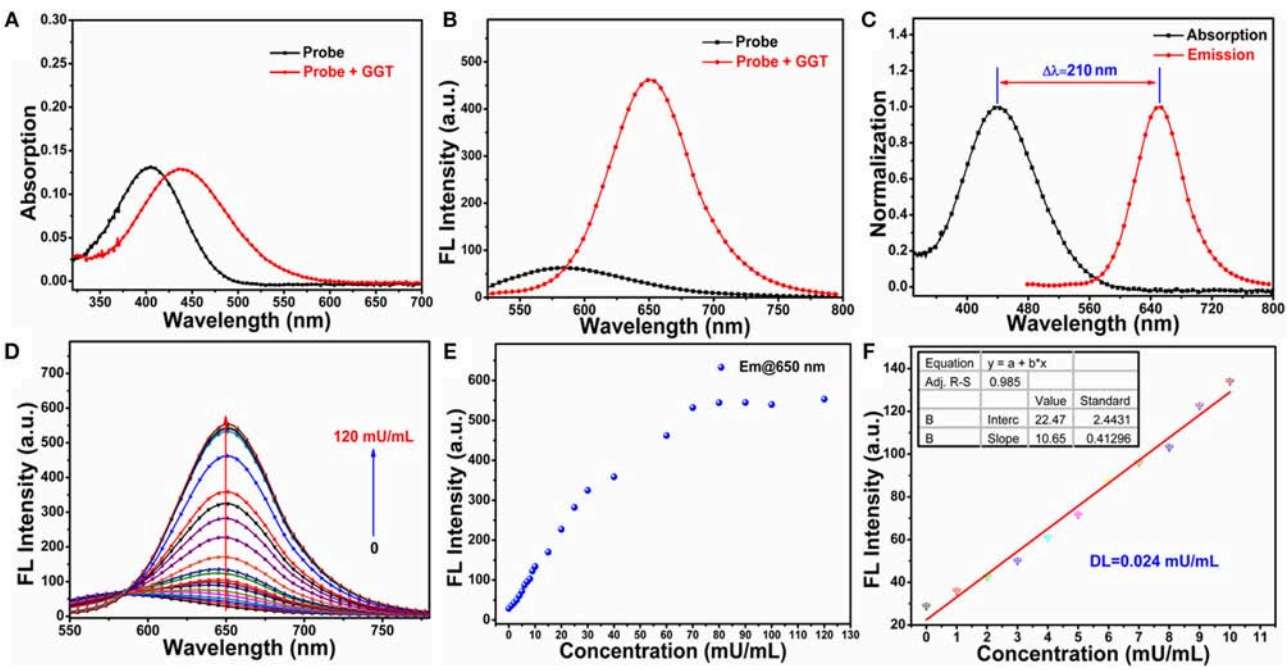

FIGURE 1 | (A) UV-Vis and **(B)** fluorescence spectra changes of probe NIR-SN-GGT (10 μM) toward adding 60 mU/mL γ-GGT enzyme in PBS buffer solution (0.01 M, pH 7.4). **(C)** Normalization UV-Vis (blank line) and fluorescence spectrum (red line) of NIR-SN-NH_2 in PBS buffer solution (0.01 M, pH 7.4). **(D)** Fluorescence titration experiments of probe NIR-SN-GGT (10 μM) toward different concentrations of γ-GGT enzyme (titration concentrations: 0, 1, 2, 3, 4, 5, 6, 7, 8, 9, 10, 15, 20, 25, 30, 40, 60, 70, 80, 90, 100, 120 mU/mL). **(E)** Fluorescence intensities of probe NIR-SN-GGT (10 μM) around 650 nm toward various concentrations of γ-GGT enzyme (0-120 mU/mL). **(F)** The linearity of F_{650nm} vs. low concentration of γ-GGT ranging from 0 to 10 mU/mL. The experiments were repeated three times and the data were shown as mean (±S.D.). λ_{ex} = 445 nm, slit: 10/10 nm.

average fluorescence intensity of cells, determined from analysis of 9 regions of interest (ROIs) across cells.

Concentration-Dependent Cell Imaging

The concentration-dependent cell imaging of probe NIR-SN-GGT for monitoring endogenous γ-GGT activity in A2780 cells was investigated on Olympus FV1000-IX81 with the excitation at 488 nm. In the experiment, the concentration of probe NIR-SN-GGT was set 0, 5, 10, and 15 μM, respectively. Before cell imaging, A2780 cells were pre-treated with probe NIR-SN-GGT for 30 min at 37°C in the incubator. After that, quantitative image analysis of the average fluorescence intensity of cells, determined from analysis of 9 regions of interest (ROIs) across cells.

Flow Cytometry Analysis

A2780 cells and HUVEC cells gathered in logarithmic growth phase were incubated in 6-well with DMEM medium or RPMI 1640 medium at 37°C in a 5% CO_2 humidified incubator. The density of 1×10^5-5×10^5 was cultured and dilution with 500 μL PBS buffer. A2780 cells and HUVEC cells were pre-treated with probe NIR-SN-GGT (10 μM) 37°C for 30 min, followed by centrifugation (1000 r/min, 5 min) and dispersion with PBS buffer solution for twice. After that, cells were finally suspended in 0.5 ml PBS buffer and analyzed through flow cytometer (Attune NxT), and each sample was terminated with 10,000 target cells.

Visualization of γ-GGT Activity in Tissue and Mice Xenograft Tumor Model

All procedures were carried out in compliance with the guide for the care and use of laboratory animal resources and the national research council, and were approved by the institutional animal care and use committee of the NIH. For establishing a mouse tumor model, the 4T1 mammary carcinoma cells were chose to transplant under the armpit of approximately 15–20 g male BABL/c mice. After 10 days inoculation, the xenograft tumor mice were given with 50 μM 100 μL probe NIR-SN-GGT through *in-situ* injection within the period of mice anesthesia. After that, the imaging of mice was carried out on the NightOWL II LB983 small animal *in vivo* imaging system (Germany) with a 475 nm excitation and a 665 nm emission filter. Tumor tissue slices of 100 or 500 μm were prepared from freezing microtome (LEICA CM1860 UV). As a comparison, normal slices were chose from muscle tissue of hind legs. Next, these tissues were incubated with probe NIR-SN-GGT (10 μM) at 37°C for 45 min, followed by washing thrice with phosphate buffer saline (0.01 M, pH 7.4). Under the confocal fluorescence microscope (Olympus

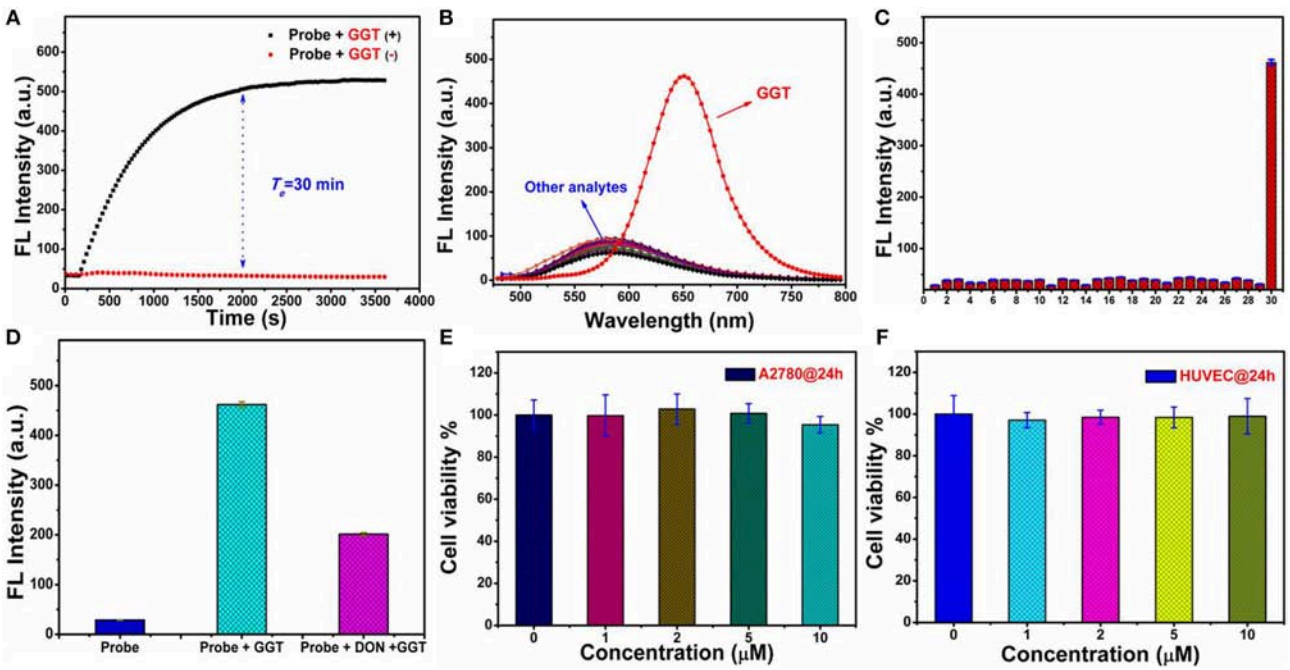

FIGURE 2 | (A) Time responses on the fluorescence intensity (F_{650nm}) of probe NIR-SN-GGT (10 μM) in the absence (red) and presence (blank) of 100 mU/mL γ-GGT enzyme. **(B)** Fluorescent spectra and **(C)** fluorescent intensity (F_{650nm}) changes of probe NIR-SN-GGT (10 μM) for different analytes in PBS buffer solution (0.01 M, pH 7.4). Insert 1: balnk; 2: Na^+ (500 μM); 3: K^+ (500 μM); 4: Ca^{2+} (500 μM); 5: Ni^{2+} (500 μM); 6: Mg^{2+} (500 μM); 7: NH_4^+ (500 μM); 8: F^- (500 μM); 9: Cl^- (500 μM); 10: Br^- (500 μM); 11: I^- (500 μM); 12: CH_3COO^- (500 μM); 13: HCO_3^- (500 μM); 14: CO_3^{2-} (500 μM); 15: S^{2-} (500 μM); 16: HPO_4^- (500 μM); 17: NO_3^- (500 μM); 18: SO_4^{2-} (500 μM); 19: SCN^- (500 μM); 20: NO_2^- (500 μM); 21: Glutathione (GSH, 500 μM); 22: Cysteine (Cys, 500 μM); 23: Homocysteine (Hcy, 500 μM); 24: Ascorbic acid (AA, 500 μM); 25: NO (500 μM); 26: NaClO (100 μM); 27: H_2O_2 (100 μM); 28: nitroreductase (10 μg/mL); 29 transglutaminase (60 mU/mL); 30: γ-GGT (60 mU/mL). **(D)** Inhibition experiments of probe NIR-SN-GGT (10 μM) for γ-GGT enzyme. **(E,F)** The cytotoxicity of probe NIR-SN-GGT in living A2780 cells and HUVEC cells, respectively. The experiments were repeated three times (cytotoxicity tests for six times) and the data were shown as mean (±S.D.). λ_{ex} = 445 nm, slit: 10/10 nm.

FV1000-IX81) with a 60 × objective lens, probe TCF-GGT was excited at 800 (two-photon), next, fluorescence emissions at 575–630 nm of red channel were gathered. In tissue depth imaging, the 3D images were constructed *via* every 5 μm as a step under the same condition. Quantitative image analysis of the average fluorescence intensity of cells, determined from analysis of 9 regions of interest (ROIs) across cells.

Synthesis of Probe NIR-SN-GGT

Synthesis of compound 2

Compound **1** (2.76 g, 20 mmol), malononitrile (3.30 g, 50 mmol) and catalytic dose of piperidine (0.05 mL) were dissolved in 50 mL dry ethanol. The mixture was stirred at 80°C for 6 h. After removing the solvent by reduced pressure distillation, fuscous solid was obtained finally. The solid was with ethyl acetate three times. The organic phase was dried with anhydrous Na_2SO_4 for overnight and vacuum filter. Following, the crude product was purified through silica gel column chromatography to obtain 1.93 g white crystal compound **2** (yield 52%). ^{1}H NMR (400 MHz, DMSO-d_6) δ 6.56 (d, J = 1.3 Hz, 1H), 2.54 (s, 2H), 2.24 (s, 2H), 2.05 (s, 3H), 0.96 (s, 6H). ^{13}C NMR (100 MHz, DMSO-d_6) δ 171.91, 162.98, 119.87, 113.92, 113.12, 76.48, 45.28, 42.43, 32.42, 27.74, 25.43, ESI-MS: m/z calculated for $C_{12}H_{13}N_2^-$ $[M\text{-}H]^-$: 185.25, found: 185.12.

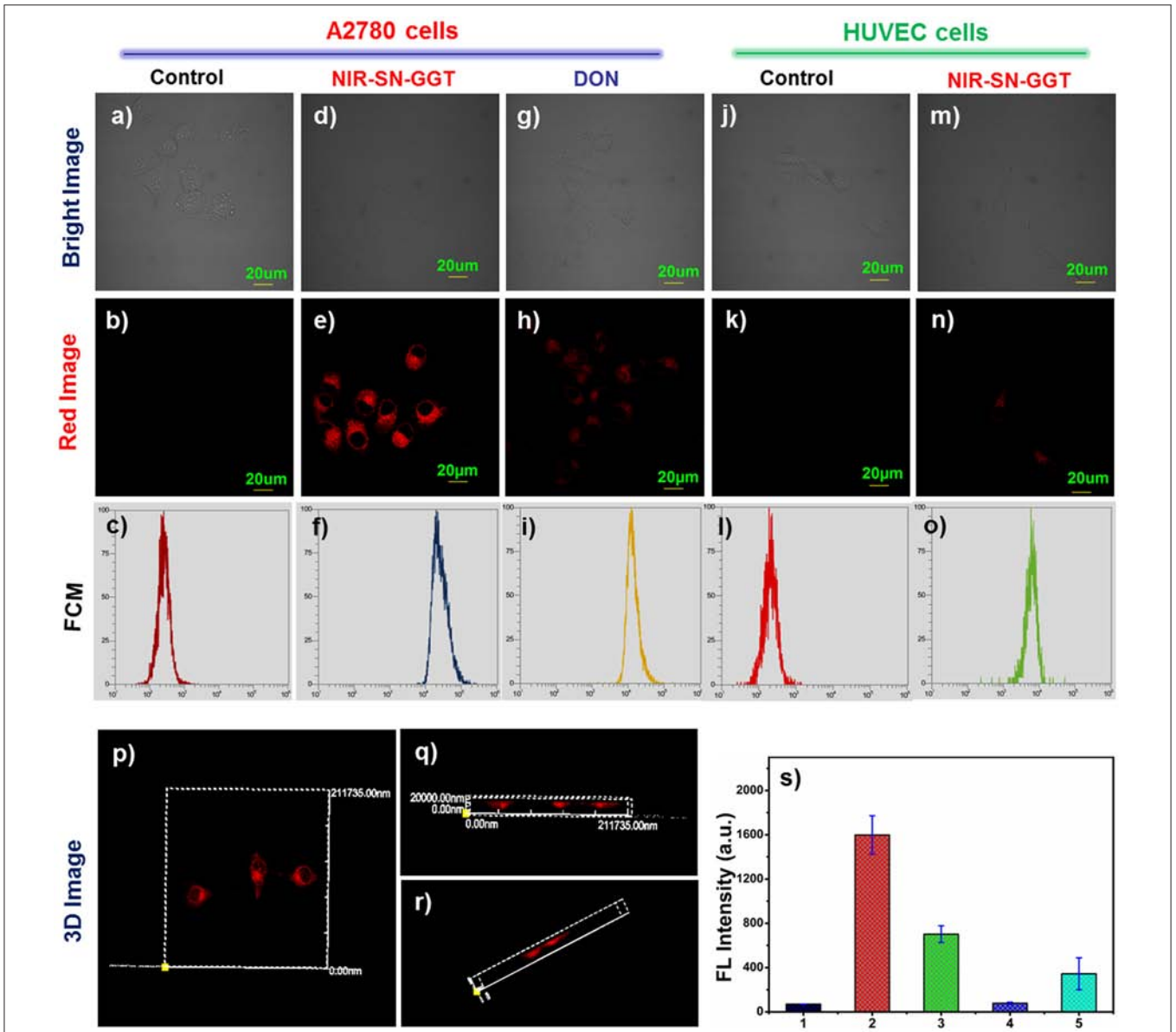

FIGURE 3 | Confocal fluorescence imaging of living cells. **(a,b)** A2780 cells; **(d,e)** A2780 cells incubated with 5 μM probe NIR-SN-GGT; **(g,h)** A2780 cells pretreated with 30 μM DON (inhibitor) and adding 5 μM probe NIR-SN-GGT; **(j,k)** HUVEC cells; **(m-n)** HUVEC cells treated with 5 μM probe NIR-SN-GGT; **(c,f,i,l,o)** represent the corresponding flow cytometry (FCM); **(p,q,r)** 3D fluorescence imaging of A2780 cells; **(s)** fluorescence emission intensities of red channel were measured as averages of 9 regions of interest (ROIs) from different treated cells (**b,e,h,k,n**). Error bar = RSD (n = 9). λex = 488 nm and λem = 655–755 nm. Scale bar = 20 μm.

Synthesis of compound 5 and 6

The synthesis of compound **5** and **6** were referred from the reported literature (Li et al., 2018a).

Synthesis of compound Boc-NIR-SN-GGT

Compound **6** (406 mg, 1 mmol) and compound **2** (186 mg, 1 mmol) were dissolved in 5 mL dry EtOH solution. Then, catalytic dose of piperidine (0.05 mL) was added into the above solution. The reaction system was stirred at 80°C for overnight under N_2 protection. After removing the solvent by reduced pressure distillation, crude jacinth solid was obtained finally without further purification for the next step. ESI-MS: *m/z* calculated for $C_{33}H_{42}N_4NaO_5^+$ $[M+Na]^+$: 597.30, found: 597.32.

Synthesis of probe NIR-SN-GGT

Compound **Boc-NIR-SN-GGT** (56 mg, 0.1 mmol) was dissolved in 2 mL dry CH_2Cl_2 and stirred at room temperature for 10 min. Next, 2 mL CH_2Cl_2-TFA (v/v 1:1) was added into above mixture *via* drop by drop style. When add was completed, the mixture system continued to stir overnight. After that, the crude product was purified through silica gel column chromatography to obtain 23 mg bright red probe **NIR-SN-GGT** (yield 54%)0.1H NMR (400 MHz, MeOD/TFA, 0.60 mL/0.05 mL) δ 7.62 (d, J = 8.7 Hz, 2H), 7.56 (d, J = 8.8 Hz, 2H), 7.17 (d, J = 16.1 Hz, 1H), 7.07 (d, J = 16.1 Hz, 1H), 6.81 (s, 1H), 4.07 (t, J = 6.5 Hz, 1H), 2.71 (t, J = 7.0 Hz, 2H), 2.60 (s, 2H), 2.53 (s, 2H), 2.27 (m, 2H), 1.06 (s, 6H). ^{13}C NMR (125 MHz, MeOD-TFA) δ 171.19, 170.11, 169.85, 155.21, 139.67, 136.70, 131.90, 128.13, 122.47, 119.77, 116.62, 113.78, 112.46, 76.98, 52.07, 42.52, 38.45, 31.47, 26.63, 25.48. ESI-HRMS: *m/z* calculated for $C_{24}H_{27}N_4O_3^+$ $[M+H]^+$: 419.2078, found: 419.2074.

RESULTS AND DISCUSSION

Design Probe NIR-SN-GGT

The synthetic procedure of probe NIR-SN-GGT was described in **Scheme 1**, which was fully validated through ^{1}H, ^{13}C-NMR and ESI-HRMS in the Supplementary Data (**Figures S20–S22**). In consideration of γ-glutamyl group as the recognition, it was installed on the framework of near-infrared emission. When γ-GGT encounter probe NIR-SN-GGT, it is cut off by specificity, liberating bare amino in the D-π-A structure. Then, NIR fluorescence signal of around 650 nm was observed through the modulation of Intermolecular Charge Transfer (ICT), where the recognition procedure of probe NIR-SN-GGT for target was shown in **Scheme 2**.

Spectroscopic Characteristics of Probe NIR-SN-GGT

With probe NIR-SN-GGT in hand, firstly, we studied the basic spectral properties of probe NIR-SN-GGT in different solvents

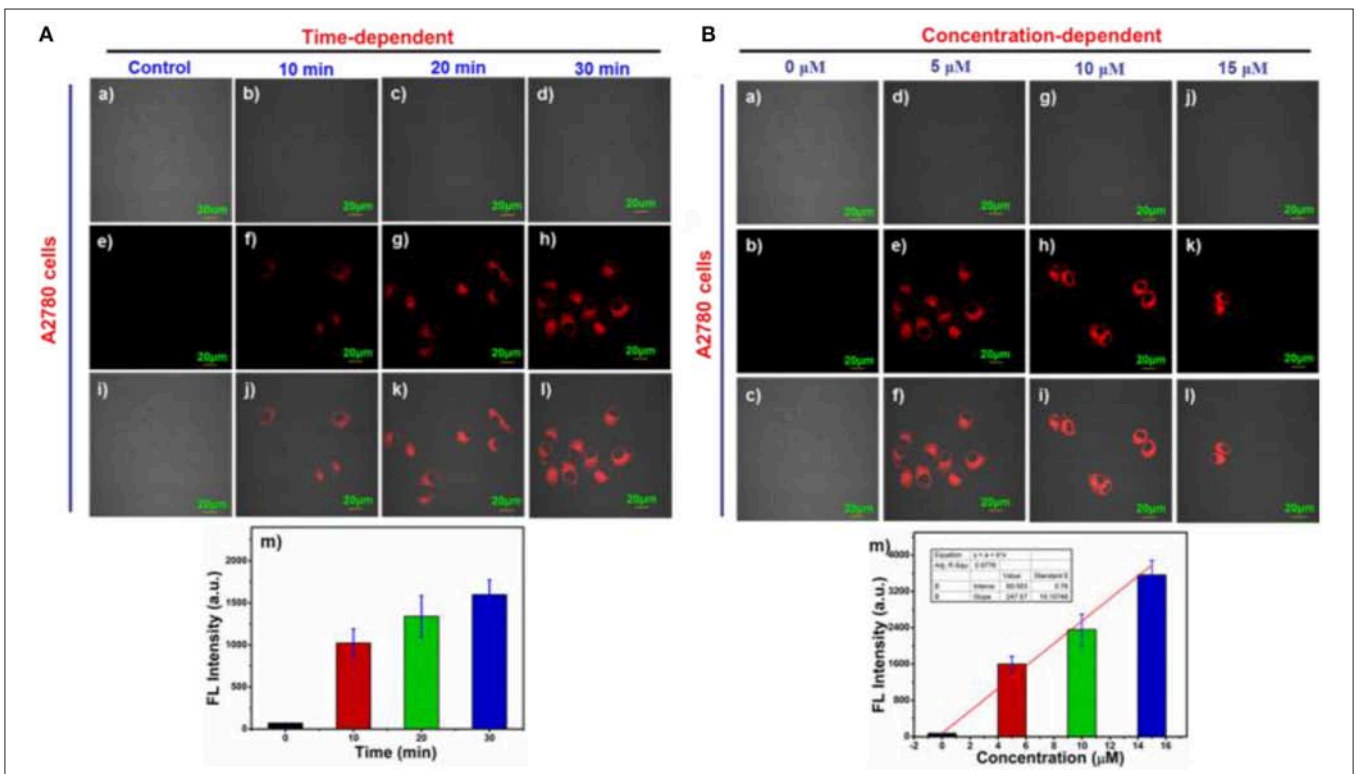

FIGURE 4 | (A) Time and **(B)** Concentration-dependent imaging of probe NIR-SN-GGT in A2780 cells. (a–d) bright imaging; (e–h) fluorescence imaging; (i–l) merged imaging; (m) fluorescence emission intensities of NIR channel were measured as averages of 9 regions of interest (ROIs) from different treated A2780 cells. Error bar = RSD (n = 9). λex = 488 nm and λem = 655–755 nm. Scale bar = 20 μm.

(**Figures S1, S2**). UV-Vis titration experiments of probe NIR-SN-GGT in PBS buffer solution (0.01 M, pH 7.4) demonstrated that probe had considerable solubility in aqueous solution (**Figure S3**). In addition, probe NIR-SN-GGT showed good stability (**Figure S4**), which laid the foundation for practical application of biology. As is seen in **Figure 1A**, adding 60 mU/mL γ-GGT enzyme in PBS buffer solution, and the absorption peak around 405 nm of probe NIR-SN-GGT (10 μM) reduced accompanied by the appearance of new absorption peak around 440 nm. The color of solution ranging from light green to yellowish-brown (**Figure S5**), which made the recognition of γ-GGT enzyme, was through the naked eyes. In the fluorescent spectra, obvious NIR signal emission was gathered (**Figure 1B**) accompanied by the quantum yield varying from 0.012 to 0.038 in PBS buffer solution. Notably, such a large stokes shift of $\Delta\lambda = 210$ nm effectively avoiding self-absorption is more conducive to fluorescence imaging (**Figure 1C**). With the increase of γ-GGT concentration (0-120 mU/mL), the fluorescence intensity around 650 nm of probe NIR-SN-GGT (10 μM) gradually enhanced (**Figure 1D**) and reached a plateau needing 70 mU/mL γ-GGT with a remarkable 21.84-fold enhancement (**Figure 1E**). In order to explore the sensitivity of probe NIR-SN-GGT, the low concentration (0–10 mU/mL) titration experiments were carried out in PBS buffer solution (0.01 M, pH 7.4). As is depicted in **Figure 1F**, there was an excellent linear relationship ($R^2 = 0.9851$) between the fluorescence intensity of 650 nm and various concentrations. Subsequently, the detection limit (DL) of probe NIR-SN-GGT versus γ-GGT was calculated to be 0.024 mU/mL, and proved that probe had the ability to quantitatively detect trace γ-GGT *in vitro*.

Response Speed and Selectivity

The reaction speed of probe NIR-SN-GGT toward γ-GGT is an important indicator for evaluating the availability of probe. As is seen in **Figure 2A**, it took approximately 30 min to reach equilibrium which showed that probe NIR-SN-GGT possessed the ability to recognize γ-GGT activity in real-time. Next, biological interferences including ions, amino acid, reductive species, reactive oxygen and enzymes were also investigated the influence on probe. To our delight, except for γ-GGT, none of the others interfered with probe NIR-SN-GGT (**Figures 2B,C**); clearly indicating that probe NIR-SN-GGT has outstanding selectivity in a variety of biologically related species.

Effects on Micro-Environment and Sensing Mechanism

The influences of micro-environment factors (e.g., pH and temperature) on the recognition of probe NIR-SN-GGT toward γ-GGT were performed. As is demonstrated in **Figures S6, S7**,

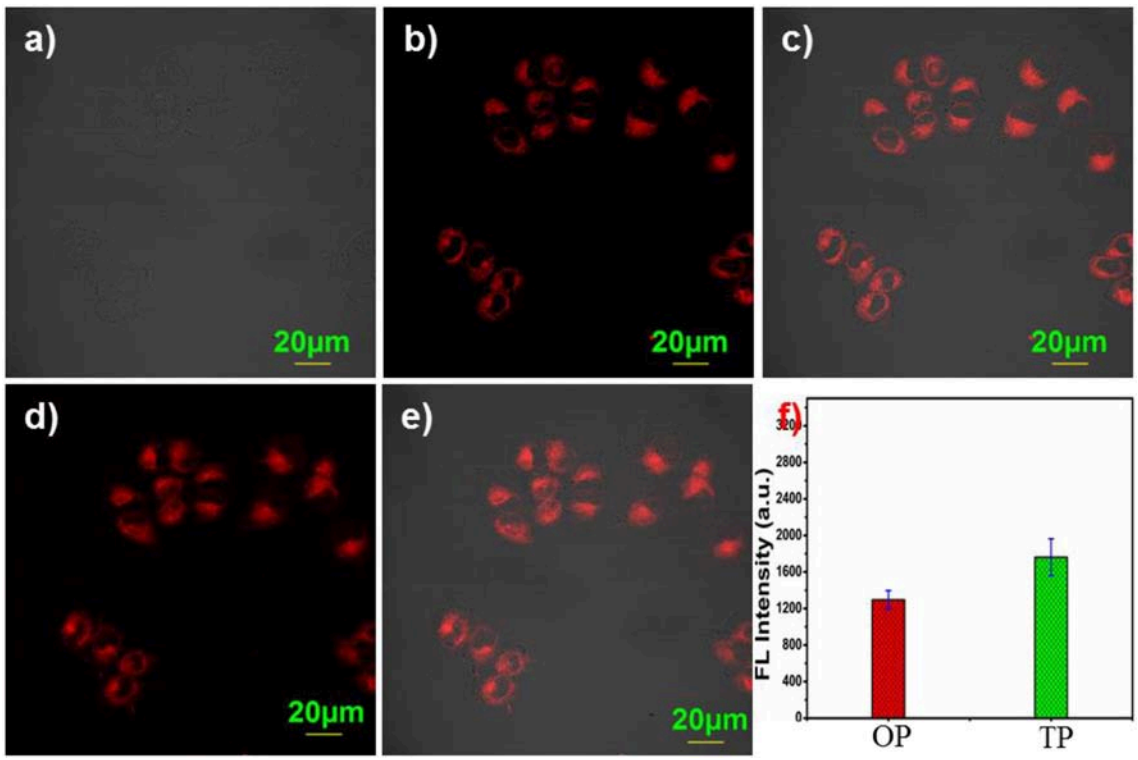

FIGURE 5 | Two-photon fluorescence imaging of probe NIR-SN-GGT in A2780 cells. **(a)** bright imaging; **(b)** one-photon imaging; **(c)** merged imaging from **(a,b)**; **(d)** two-photon imaging; **(e)** merged imaging between **(a)** and **(d)**; **(f)** fluorescence emission intensities of NIR channel were measured as averages of 9 regions of interest (ROIs) from different treated A2780 cells. Error bar = RSD ($n = 9$). (OP mode) λex = 488 nm and λem = 655-755 nm; (TP mode) λex = 800 nm and λem = 575–630 nm. Scale bar = 20 μm.

the related-parameters (pH = 7.4 and T = 37°C) are especially suitable for probe NIR-SN-GGT to track the activity of γ-GGT *in vivo*. Subsequently, we explored the enzyme-activation mechanism of probe for γ-GGT through HPLC and ESI-HRMS experiments. Only probe showed an obvious signal peak with retention time at 13.426 min (**Figure S8**, blue line). Upon addition γ-GGT into solution for incubation 30 min, a new distinct signal peak appeared at 18.018 min (**Figure S8**, red line), and the corresponding ESI-HRMS spectra was shown in **Figure S9**. There was an obvious peak at m/z 290.1658 corresponding to the positive ion mode of product NIR-SN-NH_2 (calcd. 290.1652 for $[M+H]^+$). Besides, the ability catalytic of γ-GGT for probe was largely suppressed (**Figure 2D** and **Figure S10**) after adding 30 μM 6-Diazo-5-oxo-L-norleucine (DON, an inhibitor for γ-GGT enzyme). Based on above results, γ-GGT-intervened enzymatic reactions at specific site of probe NIR-SN-GGT was verified shown in **Scheme 2**.

MTT Assays and Cell Imaging

In order to study the biocompatibility of probe NIR-SN-GGT, standard 5-diphenyltetrazolium bromide (MTT) assays in A2780 cells and HUVEC cells were carried out, respectively. As is observed in **Figures 2E,F**, experimental results indicated that probe NIR-SN-GGT was almost no cytotoxicity toward living cells.

Ovarian cancer cells (cancer cells) were selected as research object because of γ-GGT overexpression on the surface of its membrane. After A2780 cells incubated with 5 μM probe NIR-SN-GGT for 30 min, NIR fluorescence signal (655–755 nm) was obtained from **Figure 3e**. By contrast, no-treated A2780 cells were basically no fluorescence signal (**Figures 3a–c**). In addition, pre-treated A2780 cells with 30 μM DON (inhibitor) for 1 h, and then incubated with 5 μM probe NIR-SN-GGT for 30 min, we found that the intensity of NIR fluorescence signal became very weaker (**Figures 3g–i**) compared to **Figures 3d,e**. Hence, based on the above experiments confirmed that probe

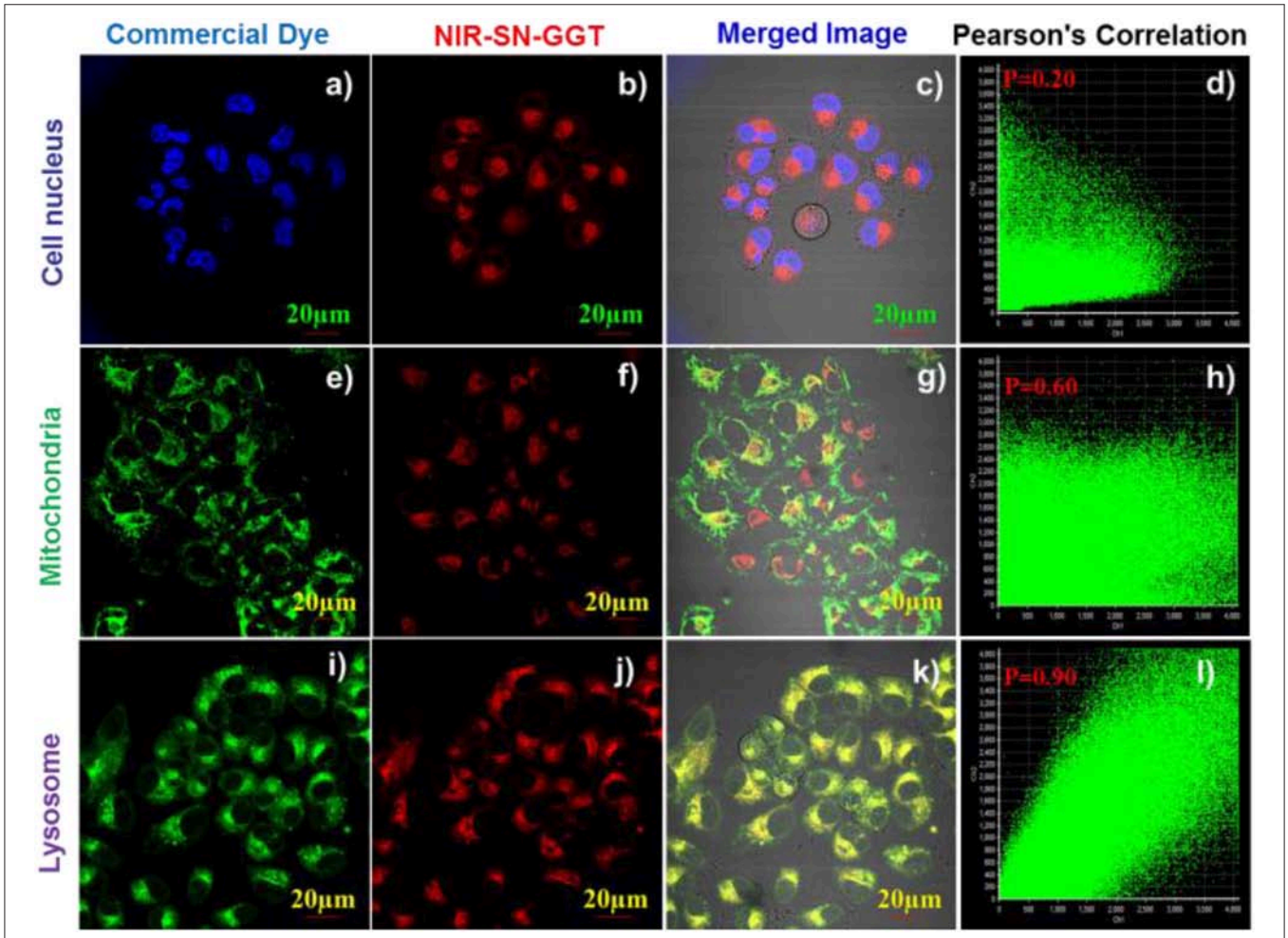

FIGURE 6 | Fluorescence imaging of subcellular localization in living A2780 cells. A2780 cells were treated with 5 μM probe NIR-SN-GGT for 20 min and the co-incubated 0.1 μM Hoechst 33342 **(a–d)**, 0.5 μM Mito-Tracker **(e–h)**, 0.5 μM Lyso-Tracker **(i–l)** for another 15 min at 37 °C. The blue channel of Hoechst 33342 dye was collected at 410-480 nm with the excitation at 405 nm. The green channel of Mito-Tracker and Lyso-Tracker dyes were collected at 500-560 nm with the excitation at 488 nm. The red channel of probe NIR-SN-GGT was collected at 655-755 nm with the excitation at 488 nm. Scale bar = 20 μm.

NIR-SN-GGT was used to monitor the activity of γ-GGT through NIR channel. Moreover, the ability of probe for differentiating tumor cells from normal cells was further confirmed. HUVEC cells (normal cells, **Figures 3j–l**) were used as negative control owing to low expression of γ-GGT. Upon addition 5 μM probe NIR-SN-GGT, negligible fluorescence signal was observed, as expected in **Figures 3m,n**. Subsequently, flow cytometry assays (FCM) demonstrated that HUVEC cells (**Figure 3o**) were distinguishable from A2780 cells (**Figure 3f**) through high throughput data analysis. So, this probe was successfully employed to track γ-GGT enzyme for the identification cancer cells. Besides, three-dimensional (3D) imaging of A2780 cells and HUVEC cells treated with probe NIR-SN-GGT was also investigated *via* *z*-scan (**Figures 3p–r**, and **Figures S11a–c**). Fluorescence emission intensities of NIR channel were measured as averages of 9 regions of interest (ROIs) from different treated cells (**Figure 3s**). Above results undoubtedly verified that probe NIR-SN-GGT possessed the ability for distinguishing cancer cells from normal cells through 2D&3D imaging, which was beneficial for clinician to the early diagnosis and resection operation of the tumor.

Time/Concentration-Dependent Imaging

Time-dependent response of 5 μM probe NIR-SN-GGT in living A2780 cells was carried out. As is seen in **Figure 4A**, after incubating for 10 min with this probe, there was obvious fluorescence signal from **Figures 4Af**. As time went on, the fluorescence intensity of NIR channel gradually increased (**Figures 4Ae–h,m**). By comparison, weak fluorescence signal of HUVEC cells pretreated with 5 μM probe NIR-SN-GGT for 30 min was observed (**Figures S12a–i**). In addition, concentration-dependent experiments of ovarian cancer

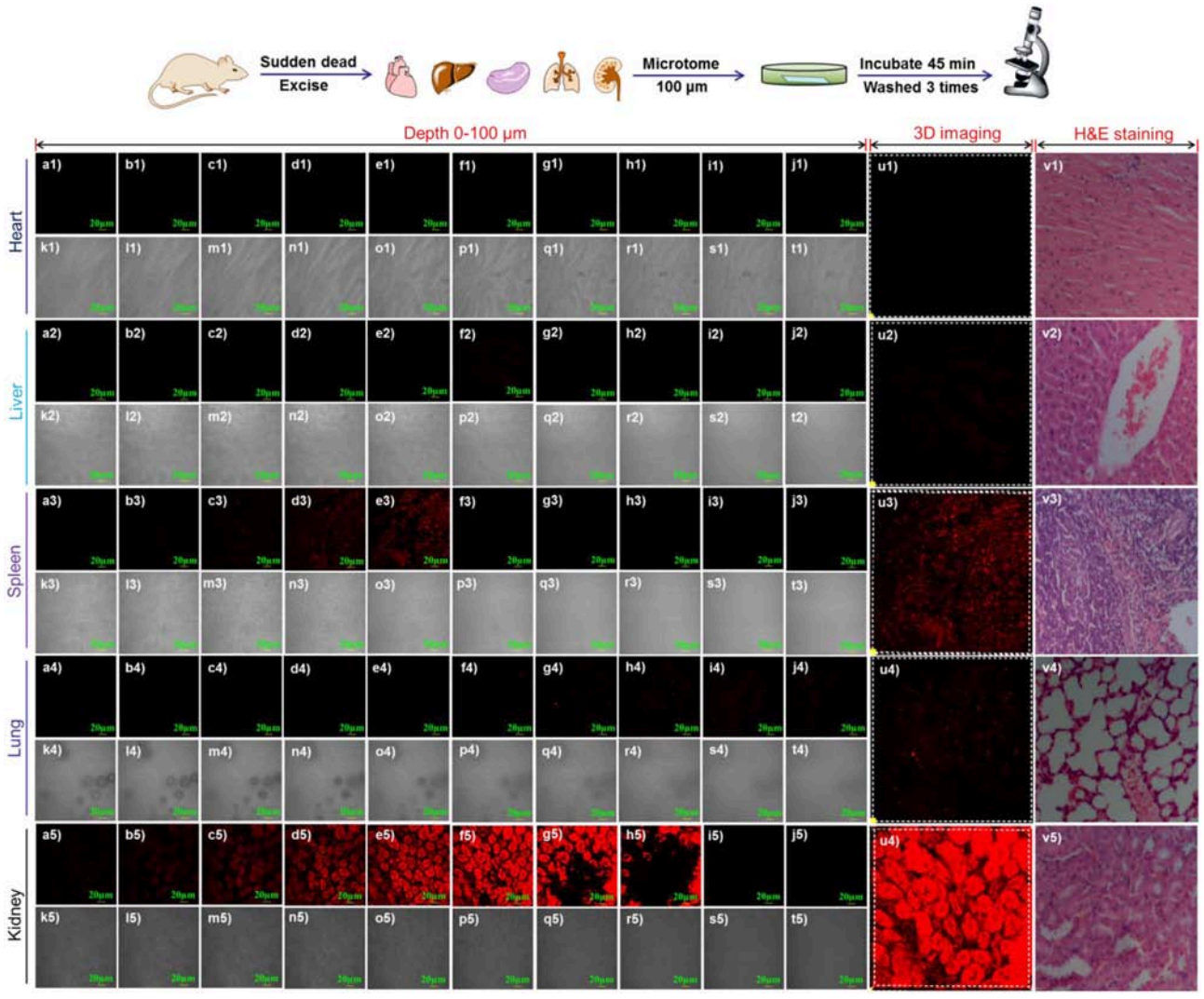

FIGURE 7 | Confocal fluorescence imaging of endogenous γ-GGT activity in various organs including heart, liver, spleen, lung and kidney. Tissue slices of 100 μm were prepared by freezing microtome (LEICA CM1860 UV). 3D-depth images of different tissue were obtained through *z*-scan pattern with step size 10 μm. (a-j) fluorescence channel; k-t bright channel; u) 3D-restruction imaging; v) HandE staining. λex = 488 nm and λem = 655-755 nm. Scale bar = 20 μm.

cells were also investigated (**Figure 4B**). With the increase of probe concentration, the fluorescence intensity increased (**Figures 4Bb–k**) and showed a good linear relationship (R^2 = 0.9776, **Figure 4Bm**), which verified that probe NIR-SN-GGT could be used to detect the endogenous γ-GGT activity with semi-quantitative detection.

Two-Photon Imaging Evaluation

Considering the advantages of two-photon fluorescence probes, such as long excitation wavelength, deep tissue penetration, and less photo-bleaching etc., are widely used in the field of chemical biology (Li et al., 2017a). Therefore, two-photon (TP) imaging experiments were performed in living A2780

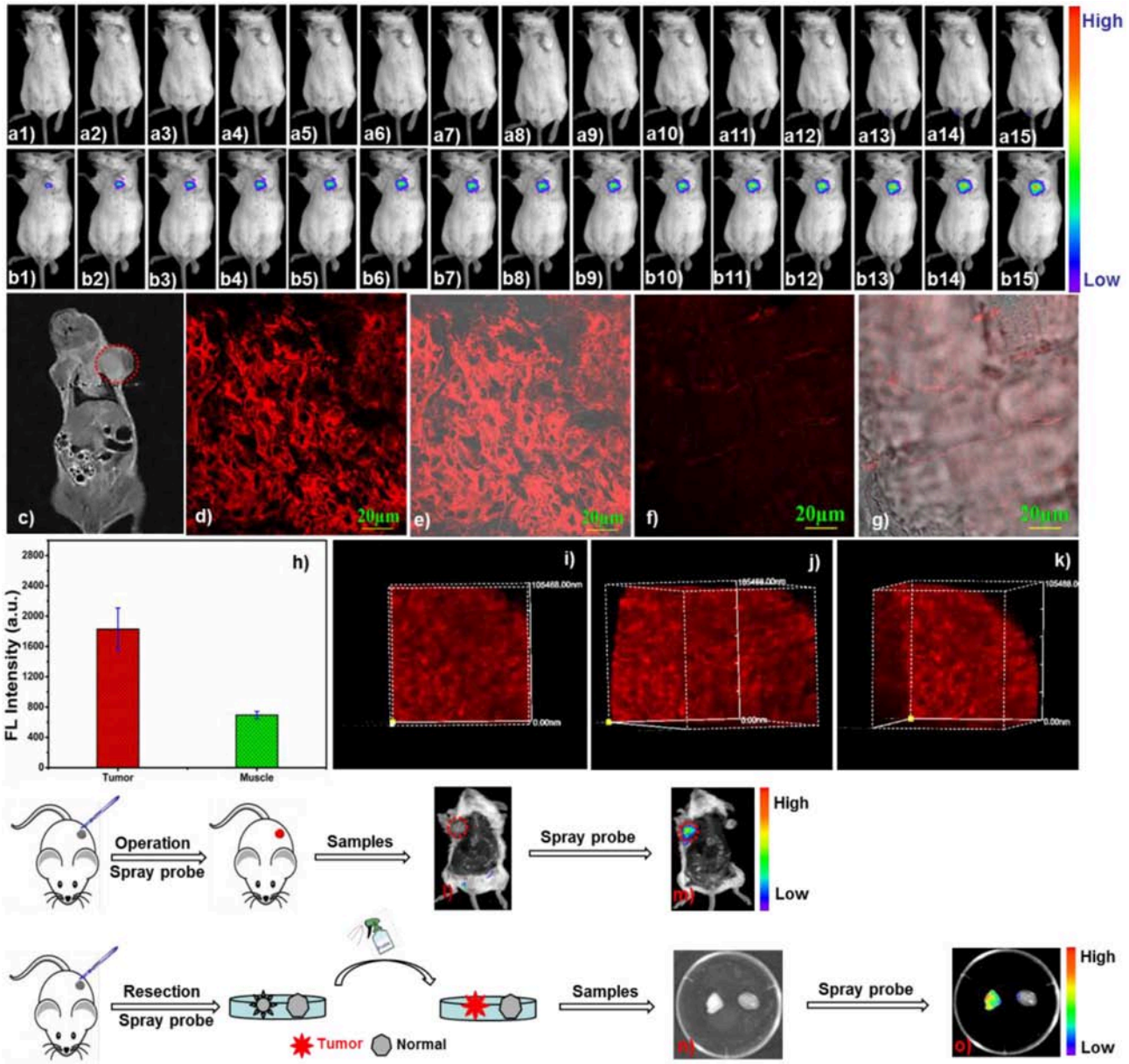

FIGURE 8 | (a,b) *In vivo* fluorescence imaging of γ-GGT activity in BABL/c mice bearing xenograft tumor. Probe NIR-SN-GGT (50 μM, 100 μL) was intratumoral injected, subsequently, fluorescent photographs (insert: b1) 2 min; (b2) 5 min; (b3) 10 min; (b4) 15 min; (b5) 20 min; (b6) 25 min; (b7) 30 min; (b8) 40 min; (b9) 50 min; (b10) 60 min; (b11) 70 min; b12 80 min; b13) 90 min; (b14) 100 min; (b15) 120 min) were gathered with excitation at 475 nm (fwhm 20 nm) and emission at 655 nm (fwhm 20 nm). (a1–a15) the corresponding control group was injected equivalent PBS buffer (pH 7.4, 0.01 M) solution. **(c)** MRI imaging (MesoMR23-060H-I) *via* T2 weighted imaging (red dotted line represents the tumor). **(d–g)** Tissue imaging of tumor tissue (**d**-fluorescence channel, **e**-merged channel) and normal (**f**-fluorescence channel, **g**-merged channel) pre-incubated with 10 μM probe NIR-SN-GGT in PBS buffer solution, and washed thirce by PBS buffer. **(h)** The fluorescence intensities of tumor and normal were gathered as averages of 21 regions of interest (ROIs) from NIR channel. **(i–k)** 3D-depth imaging (500 μm) of tumor tissue under the two-photon excitation at 800 nm. Fluorescence imaging of mouse (before **l**) and after **(m)** was sprayed with probe NIR-SN-GGT (100 μM, 150 μL). Fluorescence imaging of tumor tissue (left side) and normal tissue (right side) *via* "spraying" style (**n**: bright image; **o**: fluorescence image). λex = 488 nm, λem = 655–755 nm. Scale bar = 20 μm.

cells. Upon addition 5 μM probe NIR-SN-GGT, obvious two-photon fluorescence signal was obtained (**Figures 5d,e**) as well as one-photon (OP) imaging (**Figures 5a–c,f**), indicating that probe NIR-SN-GGT had a two-photon recognition capability for γ-GGT enzyme. Photo-stability is one of the important factors in biological imaging. To our satisfaction, the NIR fluorescence intensity of probe was not apparent changes under continuous two-photon of 800 nm irradiation (**Figure S13**). Taken together, probe NIR-SN-GGT is an excellent two-photon tool for monitoring the activity of γ-GGT enzyme in living cells with outstanding photo-stability, as we expected.

Subcellular Localization

To research the distribution of probe NIR-SN-GGT triggered by γ-GGT in living A2780 cells, thus, co-location experiments were carried out. As is observed in **Figure 6**, the red signal of probe NIR-SN-GGT (**Figure 6j**) and the green signal of Lyso-Tracker (**Figure 6i**) overlay well (**Figure 6k**) with the outstanding Pearson's correlation of 0.90 (**Figure 6l**), which showed that the product of enzyme catalytic probe was mainly clustered in lysosomes rather than nucleus ($P = 0.20$, **Figure 6d**) and mitochondria ($P = 0.60$, **Figure 6h**). Faced the above results, we speculated that this distribution was caused by the alkalization effect of the exposed amino products (**Scheme 2**).

Imaging of Endogenous γ-GGT Activity in Various Organs

Endogenous γ-GGT enzyme (Crystal structure, **Figure S14**) generated from the precursor protein *via* posttranslational processing, catalyzing the cleavage of the γ-glutamyl unit in the important biological species (Okada et al., 2006). Thus, it indicated that γ-GGT plays a very vital role in different tissues and organs. Until now, to the best of our knowledge, there is no literature report to use visualization tool for monitoring the activity of γ-GGT enzyme in various organs. Based on it, we had tried to investigate the applicability of probe NIR-SN-GGT for meeting the above requirements. Tissue sections of the experiment were immediately prepared from isolated organs including heart (**Figures 7a1–u1**), liver (**Figures 7a2–u2**), spleen (**Figures 7a3–u3**), lung (**Figures 7a4–u4**), and kidney (**Figures 7a5–u5**) through freezing microtome (LEICA CM1860 UV), and the above organizations biopsy were confirmed through H&E staining (**Figures 7v1–v5**). Each tissue of 100 μm was pre-treated with 10 μM probe NIR-SN-GGT for 45 min at indoor environment, and washed thrice by PBS buffer to removing excess probe. As shown in **Figure 7**, the confocal fluorescence imaging of step size 10 μm of tissue slice was performed. Apparent fluorescence signal of nephridial tissue was observed (**Figures 7a5–t5**), and 3D-reconstructed imaging was shown in **Figure 7u5**, which clearly visual displayed the content of γ-GGT enzyme more than other organs (heart, liver, spleen, and lung). According to medical research reported glomerulonephritis could increase the γ-GGT enzyme level (Malyszko, 2010). Thus, probe NIR-SN-GGT can be employed for helping secretory doctor to diagnose acute glomerulonephritis. In addition, the content of γ-GGT enzyme in spleen was also abundant (**Figures 7a3–u3**). Various fluorescence intensity of tissues represented different the content of γ-GGT *in situ*. As far as we know, this is the first NIR fluorescence probe for visualizing the contents of different organs by monitoring the activity of γ-GGT enzyme, which is useful for the detection of γ-GGT-related diseases.

In vivo Fluorescence and MRI Imaging of γ-GGT Activity in Xenograft Tumor Mode

In view of its high selectivity, sensitivity, photo-stability as well as NIR fluorescence emission, avoiding background interference and reducing light scattering, has been laid the foundation for *in vivo* application. Then, we explored the availability of probe NIR-SN-GGT in the transplanted tumor of BABL/c mice. As demonstrated in **Figure 8b**, after probe NIR-SN-GGT (50 μM, 100 μL) was directly *in-situ* injected, the NIR fluorescence signal of 655-755 nm on the tumor area enhanced gradually (**Figures 8b1–b15**), which attributed to the tracking over-expression γ-GGT on tumor site. In comparison, fluorescence intensity of control group injected equivalent PBS buffer solution was not gathered up to 2 h (**Figures 8a1–a15**). Combined with magnetic resonance imaging (MRI) through T2 weighted imaging (**Figure 8c**), probe NIR-SN-GGT could light up tumor relying on tracking endogenous γ-GGT enzymes, which would help surgeon real-time to the diagnosis *in situ* and treatment of cancer. Besides, tissues imaging of probe NIR-SN-GGT were also performed on laser confocal fluorescence microscopy (FV1000-IX81). Various tissues samples were prepared by freezing-microtome (Leica CM1860 UV), and pretreated with 10 μM probe NIR-SN-GGT for 45 min at room temperature. Obvious NIR fluorescence signal of 655-755 nm was gathered from tumor tissue, as we expected in **Figures 8d,e**. By comparison, weak fluorescence signal of normal tissue was observed due to lacking of γ-GGT overexpression (**Figures 8f,g** and **Figure S16b**). Their fluorescence intensity statistics were shown in **Figure 8h**, which were consistent with layer scanning of tissue imaging (**Figure S15**). In consideration of its excellent two-photon performance, 3D imaging of 500 μm was also studied under the excitation 800 nm by *z*-scan pattern with step size 5 μm. As depicted in **Figures 8i–k**, remarkable 3D-imaging clearly demonstrated probe NIR-SN-GGT had excellent deep tissue permeability. More interestingly, tumor could be lighted up (**Figures 8l,m**) after "spraying" probe NIR-SN-GGT (100 μM, 150 μL) 30 min, greatly promoting the possibility of precise excision. In addition, compared to normal tissue (**Figures 8n,o**, right side), isolated tumor tissue (**Figure S16a**, H&E staining) was also easily lighted up through "spraying" probe NIR-SN-GGT (100 μM, 50 μL) on the surface (**Figures 8l,m**, left side). Based on above results, to our satisfaction, probe NIR-SN-GGT was used to the identification tumor transplanted in BABL/c mice and deep tissue (up to 500 μm) accompanied by MRI imaging, which would be in favor of early diagnosis and treatment of tumor in clinical practice.

CONCLUSION

In summary, a smart fluorescent probe NIR-SN-GGT was successfully developed through rational design. After γ-GGT

accurately cleaving activated unit, liberating bare amino, NIR fluorescence emission signal of 650 nm strengthen gradually, which attributed to the recovery of Intramolecular Charge Transfer (ICT) mechanism. Only γ-GGT made the probe fluorescence spectrum clear change, and low detection limit of probe was calculated to be 0.024 mU/mL, undoubtedly verified that probe NIR-SN-GGT would employed to detect trace γ-GGT in complex system. Owing to its good biocompatibility and photo-stability, probe NIR-SN-GGT was also used to the identification cancer cells (A2780 cells) from normal cells (HUVEC cells) by fluorescence imaging and high throughput flow cytometry. Through "spraying" manner, to the best of our knowledge, tumor tissue could be lighted up compared to normal tissue for first time. We hope that enzyme-activated NIR fluorescent probe NIR-SN-GGT can be a potential functional molecular tool for inhibitor development, early diagnosis and resection of cancer.

ETHICS STATEMENT

This study was carried out in accordance with the recommendations of Dalian Medical University Animal Care and Use Committee. The protocol was approved by the Dalian Medical University Animal Care and Use Committee.

AUTHOR CONTRIBUTIONS

HL was responsible for performing the experiments and writing manuscript. QY was responsible for carrying out animal experiments. FX and NX were responsible for providing cells. WS, SL, JD, and JF were responsible for discussing experimental results. JW and XP were responsible for designing experiments and revising the paper.

FUNDING

This work was financially supported by National Natural Science Foundation of China (project 21421005, 21576037, and U1608222).

SUPPLEMENTARY MATERIAL

The Supplementary Material for this article can be found online at: https://www.frontiersin.org/articles/10.3389/fchem.2018.00485/full#supplementary-material

REFERENCES

Asanuma, D., Sakabe, M., Kamiya, M., Yamamoto, K., Hiratake, J., Ogawa, M., et al. (2015). Sensitive β-galactosidase-targeting fluorescence probe for visualizing small peritoneal metastatic tumours *in vivo*. *Nat. Commun.* 6:6463. doi: 10.1038/ncomms7463

Blum, G., von Degenfeld, G., Merchant, M. J., Blau, H. M., Bogyo, M. (2007). Noninvasive optical imaging of cysteine protease activity using fluorescently quenched activity-based probes. *Nat. Chem. Biol.* 3, 668–677. doi: 10.1038/nchembio.2007.26

Chen, J., Liu, L., Motevalli, S. M., Wu, X., Yang, X.-H., Li, X., et al. (2018). Light-triggered retention and cascaded therapy of albumin-based theranostic nanomedicines to alleviate tumor adaptive treatment tolerance. *Adv. Funct. Mater.* 28:1707291. doi: 10.1002/adfm.201707291

Chen, W., Zheng, R., Baade, P. D., Zhang, S., Zeng, H., Bray, F., et al. (2016). Cancer statistics in China, 2015. *CA- Cancer J. Clin.* 66, 115–132. doi: 10.3322/caac.21338

Chen, X., Lee, D., Yu, S., Kim, G., Lee, S., Cho, Y., et al. (2017). *In vivo* near-infrared imaging and phototherapy of tumors using a cathepsin B-activated fluorescent probe. *Biomaterials* 122, 130–140. doi: 10.1016/j.biomaterials.2017.01.020

Cheng, D., Pan, Y., Wang, L., Zeng, Z., Yuan, L., Zhang, X., et al. (2016). Selective visualization of the endogenous peroxynitrite in an inflamed mouse model by a mitochondria-targetable two-photon ratiometric fluorescent probe. *J. Am. Chem. Soc.* 139, 285–292. doi: 10.1021/jacs.6b10508

Cheng, L., Yang, K., Li, Y., Chen, J., Wang, C., Shao, M., et al. (2011). Facile preparation of multifunctional upconversion nanoprobes for multimodal imaging and dual-targeted photothermal therapy. *Angew. Chem. Int. Ed.* 50, 7385–7390. doi: 10.1002/anie.201101447

Cong, Y., Xiao, H., Xiong, H., Wang, Z., Ding, J., Li, C., et al. (2018). Dual drug backboned shattering polymeric theranostic nanomedicine for synergistic eradication of patient-derived lung cancer. *Adv. Mater.* 30:1706220. doi: 10.1002/adma.201706220

De Young, L. M., Richards, W., Bonzelet, W., Tsai, L., and Boutwell, R. (1978). Localization and significance of γ-glutamyltranspeptidase in normal and neoplastic mouse skin. *Cancer Res.* 38, 3697–3701.

Fan, J., Guo, S., Wang, S., Kang, Y., Yao, Q., Wang, J., et al. (2017). Lighting-up breast cancer cells by a near-infrared fluorescent probe based on KIAA1363 enzyme-targeting. *Chem. Commun.* 53, 4857–4860. doi: 10.1039/c7cc01798g

Gu, K., Liu, Y., Guo, Z., Lian, C., Yan, C., Shi, P., et al. (2016a). *In situ* ratiometric quantitative tracing of intracellular leucine aminopeptidase activity via an activatable near-infrared fluorescent probe. *ACS Appl. Mater. Interfaces*. 8, 26622–26629. doi: 10.1021/acsami.6b10238

Gu, K., Xu, Y., Li, H., Guo, Z., Zhu, S., Zhu, S., et al. (2016b). Real-time tracking and *in vivo* visualization of β-Galactosidase activity in colorectal tumor with a ratiometric NIR fluorescent probe. *J. Am. Chem. Soc.* 138, 5334–5340. doi: 10.1021/jacs.6b01705

He, X., Li, L., Fang, Y., Shi, W., Li, X., and Ma, H. (2017). *In vivo* imaging of leucine aminopeptidase activity in drug-induced liver injury and liver cancer via a near-infrared fluorescent probe. *Chem. Sci.* 8, 3479–3483. doi: 10.1039/c6sc05712h

Hu, Y., Chen, L., Jung, H., Zeng, Y., Lee, S., Swamy, K. M., et al. (2016). Effective strategy for colorimetric and fluorescence sensing of phosgene based on small organic dyes and nanofiber platforms. *ACS Appl. Mater. Interfaces* 8, 22246–22252. doi: 10.1021/acsami.6b07138

Huang, P., Bao, L., Zhang, C., Lin, J., Luo, T., Yang, D., et al. (2011). Folic acid-conjugated silica-modified gold nanorods for X-ray/CT imaging-guided dual-mode radiation and photo-thermal therapy. *Biomaterials* 32, 9796–9809. doi: 10.1016/j.biomaterials.2011.08.086

Jung, H. S., Verwilst, P., Sharma, A., Shin, J., Sessler, J. L., and Kim, J. S. (2018). Organic molecule-based photothermal agents: an expanding photothermal therapy universe. *Chem. Soc. Rev.* 47, 2280–2297. doi: 10.1039/c7cs00522a

Kim, E.-J., Kumar, R., Sharma, A., Yoon, B., Kim, H. M., Lee, H., et al. (2017). *In vivo* imaging of β-galactosidase stimulated activity in hepatocellular carcinoma using ligand-targeted fluorescent probe. *Biomaterials* 122, 83–90. doi: 10.1016/j.biomaterials.2017.01.009

Kozlowski, P., Chang, S. D., Jones, E. C., Berean, K. W., Chen, H., and Goldenberg, S. L. (2006). Combined diffusion-weighted and dynamic contrast-enhanced MRI for prostate cancer diagnosis-correlation with biopsy and histopathology. *J. Magn. Reson. Imaging* 24, 108–113. doi: 10.1002/jmri.20626

Kuriki, Y., Kamiya, M., Kubo, H., Komatsu, T., Ueno, T., Tachibana, R., et al. (2018). Establishment of molecular design strategy to obtain activatable fluorescent probes for carboxypeptidases. *J. Am. Chem. Soc.*140, 1767–1773. doi: 10.1021/jacs.7b11014

Lee, M. H., Sharma, A., Chang, M. J., Lee, J., Son, S., Sessler, J. L., et al. (2018). Fluorogenic reaction-based prodrug conjugates as targeted cancer theranostics. *Chem. Soc. Rev.* 47, 28–52. doi: 10.1039/c7cs00557a

Li, H., Yao, Q., Fan, J., Du, J., Wang, J., and Peng, X. (2016a). An NIR fluorescent probe of uric HSA for renal diseases warning. *Dyes Pigments* 133, 79–85. doi: 10.1016/j.dyepig.2016.05.039

Li, H., Yao, Q., Fan, J., Du, J., Wang, J., and Peng, X. (2017a). A two-photon NIR-to-NIR fluorescent probe for imaging hydrogen peroxide in living cells. *Biosens. Bioelectron.* 94, 536–543. doi: 10.1016/j.bios.2017.03.039

Li, H., Yao, Q., Fan, J., Hu, C., Xu, F., Du, J., et al. (2016b). A fluorescent probe for ratiometric imaging of SO_2 derivatives in mitochondria of living cells. *Ind. Eng. Chem. Res.* 55, 1477–1483. doi: 10.1021/acs.iecr.5b04530

Li, H., Yao, Q., Xu, F., Xu, N., Duan, R., Long, S., et al. (2018a). Imaging gamma-glutamyltranspeptidase for tumor identification and resection guidance via enzyme-triggered fluorescent probe. *Biomaterials* 179, 1–14. doi: 10.1016/j.biomaterials.2018.06.028

Li, H., Yao, Q., Xu, F., Xu, N., Ma, X., Fan, J., et al. (2018b). Recognition of exogenous and endogenous nitroxyl in living cells via a two-photon fluorescent probe. *Anal. Chem.* 90, 4641–4648. doi: 10.1021/acs.analchem.7b05172

Li, H. D., Yao, Q. C., Fan, J. L., Jiang, N., Wang, J. Y., Xia, J., et al. (2015a). A fluorescent probe for H_2S *in vivo* with fast response and high sensitivity. *Chem. Commun.* 51, 16225–16228. doi: 10.1039/c5cc06612c

Li, L., Shi, W., Wang, Z., Gong, Q., and Ma, H. (2015b). Sensitive fluorescence probe with long analytical wavelengths for γ-Glutamyl transpeptidase detection in human serum and living cells. *Anal. Chem.* 87, 8353–8359. doi: 10.1021/acs.analchem.5b01535

Li, L., Shi, W., Wu, X., Gong, Q., Li, X., and Ma, H. (2016c). Monitoring γ-glutamyl transpeptidase activity and evaluating its inhibitors by a water-soluble near-infrared fluorescent probe. *Biosens. Bioelectron.* 81, 395–400. doi: 10.1016/j.bios.2016.03.021

Li, X., Kim, C. Y., Lee, S., Lee, D., Chung, H.-M., Kim, G., et al. (2017b). Nanostructured phthalocyanine assemblies with protein-driven switchable photoactivities for biophotonic imaging and therapy. *J. Am. Chem. Soc.* 139, 10880–10886. doi: 10.1021/jacs.7b05916

Liu, H.-W., Hu, X.-X., Li, K., Liu, Y., Rong, Q., Zhu, L., et al. (2017a). A mitochondrial-targeted prodrug for NIR imaging guided and synergetic NIR photodynamic-chemo cancer therapy. *Chem. Sci.* 8, 7689–7695. doi: 10.1039/c7sc03454g

Liu, K., Kong, X., Ma, Y., and Lin, W. (2017b). Rational design of a robust fluorescent probe for the detection of endogenous carbon monoxide in living zebrafish embryos and mouse tissue. *Angew. Chem. Int.Ed.* 56, 13489–13492. doi: 10.1002/anie.201707518

Liu, T., Yan, Q., Feng, L., Ma, X., Tian, X., Yu, Z., et al. (2018). Isolation of γ-glutamyl-transferase rich-bacteria from mouse gut by a near-infrared fluorescent probe with large stokes shift. *Anal. Chem.* 90, 9921–9928. doi: 10.1021/acs.analchem.8b02118

Liu, Y., Zhu, S., Gu, K., Guo, Z., Huang, X., Wang, M., et al. (2017c). GSH-activated NIR fluorescent prodrug for podophyllotoxin delivery. *ACS Appl. Mater. Inter.* 9, 29496–29504. doi: 10.1021/acsami.7b07091

Llancalahuen, F. M., Fuentes, J. A., Carreño, A., Zúñiga, C., Páez-Hernández, D., Gacitúa, M., et al. (2018). New properties of a bioinspired pyridine benzimidazole compound as a novel differential staining agent for endoplasmic reticulum and golgi apparatus in fluorescence live cell imaging. *Front. Chem.* 6:345. doi: 10.3389/fchem.2018.00345

Malyszko, J. (2010). Biomarkers of acute kidney injury in different clinical settings: a time to change the paradigm? *Kidney Blood Press. Res.* 33, 368–382. doi: 10.1159/000319505

Miao, Q., Yeo, D. C., Wiraja, C., Zhang, J., Ning, X., Xu, C., et al. (2018). Near-infrared fluorescent molecular probe for sensitive imaging of keloid. *Angew. Chem. Int. Ed.* 57, 1256–1260. doi: 10.1002/anie.201710727

Mileshkin, L., Hicks, R. J., Hughes, B. G., Mitchell, P. L., Charu, V., Gitlitz, B. J., et al. (2011). Changes in ^{18}F-fluorodeoxyglucose and ^{18}F-fluorodeoxythymidine positron emission tomography imaging in patients with non-small cell lung cancer treated with erlotinib. *Clin. Cancer Res.* 17, 3304–3315. doi: 10.1158/1078-0432.ccr-10-2763

Ofori, L. O., Withana, N. P., Prestwood, T. R., Verdoes, M. V., Brady, J. J., Winslow, M. M., et al. (2015). Design of protease activated optical contrast agents that exploit a latent lysosomotropic effect for use in fluorescence-guided surgery. *ACS Chem. Biol.* 10, 1977–1988. doi: 10.1021/acschembio.5b00205

Okada, T., Suzuki, H., Wada, K., Kumagai, H., and Fukuyama, K. (2006). Crystal structures of gamma-glutamyltranspeptidase from *Escherichia coli*, a key enzyme in glutathione metabolism, and its reaction intermediate. *Proc. Natl. Acad. Sci. U.S.A.* 103, 6471–6476. doi: 10.1073/pnas.0511020103

Park, S., Bae, D. J., Ryu, Y.-M., Kim, S.-Y., Myung, S.-J., and Kim, H.-J. (2016a). Mitochondria-targeting ratiometric fluorescent probe for γ-glutamyltranspeptidase and its application to colon cancer. *Chem. Commun.* 52, 10400–10402. doi: 10.1039/c6cc05573g

Park, S., Lim, S.-Y., Bae, S. M., Kim, S.-Y., Myung, S.-J., and Kim, H.-J. (2016b). Indocyanine-based activatable fluorescence turn-on probe for γ-glutamyltranspeptidase and its application to the mouse model of colon cancer. *ACS Sensors* 1, 579–583. doi: 10.1021/acssensors.5b00249

Park, Y., Ryu, Y.-M., Wang, T., Jung, Y., Kim, S., Hwang, S., et al. (2018). Colorectal cancer diagnosis using enzyme-sensitive ratiometric fluorescence dye and antibody-quantum dot conjugates for multiplexed detection. *Adv. Funct. Mater.* 28:1703450. doi: 10.1002/adfm.201703450

Paulick, M. G., and Bogyo, M. (2008). Application of activity-based probes to the study of enzymes involved in cancer progression. *Curr. Opin. Genet. Dev.* 18, 97–106. doi: 10.1016/j.gde.2007.12.001

Pinto, P. A., Chung, P. H., Rastinehad, A. R., Baccala, A. A., Kruecker, J., Benjamin, C. J., et al. (2011). Magnetic resonance imaging/ultrasound fusion guided prostate biopsy improves cancer detection following transrectal ultrasound biopsy and correlates with multiparametric magnetic resonance imaging. *J. Urol.* 186, 1281–1285. doi: 10.1016/j.juro.2011.05.078

Pompella, A., De Tata, V., Paolicchi, A., and Zunino, F. (2006). Expression of γ-glutamyltransferase in cancer cells and its significance in drug resistance. *Biochem. Pharmacol.* 71, 231–238. doi: 10.1016/j.bcp.2005.10.005

Rao, M. S., Tatematsu, M., Subbarao, V., Ito, N., and Reddy, J. K. (1986). Analysis of peroxisome proliferator-induced preneoplastic and neoplastic lesions of rat liver for placental form of glutathione S-transferase and γ-glutamyltranspeptidase. *Cancer Res.* 46, 5287–5290.

Sardanelli, F., Boetes, C., Borisch, B., Decker, T., Federico, M., Gilbert, F. J., et al. (2010). Magnetic resonance imaging of the breast: recommendations from the EUSOMA working group. *Eur. J. Cancer* 46, 1296–1316. doi: 10.1016/j.ejca.2010.02.015

Sedgwick, A. C., Han, H.-H., Gardiner, J. E., Bull, S. D., He, X.-P., and James, T. D. (2018). The development of a novel AND logic based fluorescence probe for the detection of peroxynitrite and GSH. *Chem. Sci.* 9, 3672–3676. doi: 10.1039/c8sc00733k

Shang, X., Li, J., Feng, Y., Chen, H., Guo, W., Zhang, J., et al. (2018). Low-cytotoxicity fluorescent probes based on anthracene derivatives for hydrogen sulfide detection. *Front. Chem.* 6:202. doi: 10.3389/fchem.2018.00202

Shi, J., Wang, L., Zhang, J., Ma, R., Gao, J., Liu, Y., et al. (2014). A tumor-targeting near-infrared laser-triggered drug delivery system based on GO@Ag nanoparticles for chemo-photothermal therapy and X-ray imaging. *Biomaterials* 35, 5847–5861. doi: 10.1016/j.biomaterials.2014.03.042

Shinozuka, H., Sells, M. A., Katyal, S. L., Sell, S., and Lombardi, B. (1979). Effects of a choline-devoid diet on the emergence of γ-glutamyltranspeptidase-positive foci in the liver of carcinogen-treated rats. *Cancer Res.* 39, 2515–2521.

Strasak, A. M., Goebel, G., Concin, H., Pfeiffer, R. M., Brant, L. J., Nagel, G., et al. (2010). Prospective study of the association of serum γ-glutamyltransferase with cervical intraepithelial neoplasia III and invasive cervical cancer. *Cancer Res.* 70, 3586–3593.

Urano, Y., Sakabe, M., Kosaka, N., Ogawa, M., Mitsunaga, M., Asanuma, D., et al. (2011). Rapid cancer detection by topically spraying a γ-glutamyltranspeptidase-activated fluorescent probe. *Sci. Transl. Med.* 3:110ra119. doi: 10.1126/scitranslmed.3002823

Verwilst, P., Han, J., Lee, J., Mun, S., Kang, H. G., and Kim, J. S. (2017). Reconsidering azobenzene as a component of small-molecule hypoxia-mediated cancer drugs: a theranostic case study. *Biomaterials* 115, 104–114. doi: 10.1016/j.biomaterials.2016.11.023

Verwilst, P., Kim, H. S., Kim, S., Kang, C., and Kim, J. S. (2018). Shedding light on tau protein aggregation: the progress in developing highly selective fluorophores. *Chem. Soc. Rev.* 47, 2249–2265. doi: 10.1039/c7cs00706j

Wang, F., Xu, G., Gu, X., Wang, Z., Wang, Z., Shi, B., et al. (2018). Realizing highly chemoselective detection of H_2S *in vitro* and *in vivo* with fluorescent probes inside core-shell silica nanoparticles. *Biomaterials* 159, 82–90. doi: 10.1016/j.biomaterials.2018.01.009

Wang, F., Zhu, Y., Zhou, L., Pan, L., Cui, Z., Fei, Q., et al. (2015). Fluorescent *In Situ* targeting probes for rapid imaging of ovarian-cancer-specific γ-glutamyltranspeptidase. *Angew. Chem. Int. Ed.* 54, 7349–7353. doi: 10.1002/anie.201502899

Wang, P., Zhang, C., Liu, H. W., Xiong, M., Yin, S. Y., Yang, Y., et al. (2017a). Supramolecular assembly affording a ratiometric two-photon fluorescent nanoprobe for quantitative detection and bioimaging. *Chem. Sci.* 8, 8214–8220. doi: 10.1039/c7sc03977h

Wang, P., Zhang, J., Liu, H.-W., Hu, X.-X., Feng, L.-L., Yin, X., et al. (2017b). An efficient two-photon fluorescent probe for measuring γ-glutamyltranspeptidase activity during the oxidative stress process in tumor cells and tissues. *Analyst* 142, 1813–1820. doi: 10.1039/c7an00229g

Xiao, Y., Hong, H., Javadi, A., Engle, J. W., Xu, W., Yang, Y., et al. (2012). Multifunctional unimolecular micelles for cancer-targeted drug delivery and positron emission tomography imaging. *Biomaterials* 33, 3071–3082. doi: 10.1016/j.biomaterials.2011.12.030

Yang, K., Liu, Y., Liu, Y., Zhang, Q., Kong, C., Yi, C., et al. (2018). Cooperative assembly of magneto-nanovesicles with tunable wall thickness and permeability for MRI-guided drug delivery..*J Am. Chem. Soc.* 140, 4666–4677. doi: 10.1021/jacs.8b00884

Yin, C.-X., Xiong, K.-M., Huo, F.-J., Salamanca, J. C., and Strongin, R. M. (2017). Fluoreszenzsonden mit mehreren Bindungsstellen unterscheiden zwischen Cys, Hcy und GSH. *Angew. Chem. Int. Ed.* 129, 13368–13379. doi: 10.1002/ange.201704084

Zhang, H., Wang, K., Xuan, X., Lv, Q., Nie, Y., and Guo, H. (2016a). Cancer cell-targeted two-photon fluorescence probe for the real-time ratiometric imaging of DNA damage. *Chem. Commun.* 52, 6308–6311. doi: 10.1039/c6cc02290a

Zhang, P., Jiang, X.-,f., Nie, X., Huang, Y., Zeng, F., Xia, X., et al. (2016b). A two-photon fluorescent sensor revealing drug-induced liver injury via tracking γ-glutamyltranspeptidase (GGT) level *in vivo*. *Biomaterials* 80, 46–56. doi: 10.1016/j.biomaterials.2015.11.047

Zhang, R., Feng, L., Dong, Z., Wang, L., Liang, C., Chen, J., et al. (2018). Glucose and oxygen exhausting liposomes for combined cancer starvation and hypoxia-activated therapy. *Biomaterials* 162, 123–131. doi: 10.1016/j.biomaterials.2018.02.004

Conflict of Interest Statement: The authors declare that the research was conducted in the absence of any commercial or financial relationships that could be construed as a potential conflict of interest.

Copyright © 2018 Li, Yao, Xu, Xu, Sun, Long, Du, Fan, Wang and Peng. This is an open-access article distributed under the terms of the Creative Commons Attribution License (CC BY). The use, distribution or reproduction in other forums is permitted, provided the original author(s) and the copyright owner(s) are credited and that the original publication in this journal is cited, in accordance with accepted academic practice. No use, distribution or reproduction is permitted which does not comply with these terms.

frontiers in Chemistry

ORIGINAL RESEARCH
published: 15 October 2018
doi: 10.3389/fchem.2018.00488

Imaging of Formaldehyde in Live Cells and *Daphnia magna* via Aza-Cope Reaction Utilizing Fluorescence Probe With Large Stokes Shifts

Mingwang Yang[1], Jiangli Fan[1], Jianjun Du[1], Saran Long[1], Jia Wang[2]* and Xiaojun Peng[1]*

[1] State Key Laboratory of Fine Chemicals, Dalian University of Technology, Dalian, China, [2] Department of Breast Surgery, Institute of Breast Disease, Second Hospital of Dalian Medical University, Dalian, China

OPEN ACCESS

Edited by:
Tony D. James,
University of Bath, United Kingdom

Reviewed by:
Xiao-Peng He,
East China University of Science and Technology, China
Suying Xu,
Beijing University of Chemical Technology, China
Xiao-Yu Hu,
Nanjing University of Aeronautics and Astronautics, China

***Correspondence:**
Jiangli Fan
fanjl@dlut.edu.cn
Jia Wang
wangjia0829jp@yahoo.co.jp

Specialty section:
This article was submitted to Chemical Biology, a section of the journal Frontiers in Chemistry

Received: *14 August 2018*
Accepted: *25 September 2018*
Published: *15 October 2018*

Citation:
Yang M, Fan J, Du J, Long S, Wang J and Peng X (2018) Imaging of Formaldehyde in Live Cells and Daphnia magna via Aza-Cope Reaction Utilizing Fluorescence Probe With Large Stokes Shifts. Front. Chem. 6:488. doi: 10.3389/fchem.2018.00488

Formaldehyde (FA), a highly reactive carbonyl species, plays significant role in physiological and pathological functions. However, elevated FA will lead to cognitive impairments, memory loss and various neurodegenerative diseases due to its potent DNA and protein cross-linking mechanisms. In this work, a fluorescence probe, **BD-CHO**, based on benz-2-oxa-1, 3- diazole (**BD**) skeleton, was designed and synthesized for detection of FA via Aza-Cope reaction with high selectivity and large Stokes shifts (about 118 nm). **BD-CHO** was successfully applied to monitor the changes FA level in living cells, and kidney tissues of mice. Importantly it was the first time that **BD-CHO** was used for visualizing exogenous FA changes in *Daphnia magna* through fluorescence microscopy, demonstrating its potential application for studies of biological processes associated with FA.

Keywords: fluorescence probe, formaldehyde, *Daphnia magna*, large Stokes shifts, Aza-Cope reaction, bioimaging

INTRODUCTION

Formaldehyde (FA) is a common environmental toxin but also endogenously produced through metabolism of amino acids or xenobiotics catalyzed by demethylases and oxidases, such as lysine-specific demethylase 1 (LDS1) (Shi et al., 2004) and semicarbazide-sensitive amine oxidase (SSAO) (O'Sullivan, 2004). The physiological FA levels ranging from 0.1 mM in blood to 0.4 mM intracellular (Andersen et al., 2010; Tong et al., 2013b) and is a well-established neurotoxin that affects memory, learning, and behavior (Tong et al., 2013a; Tulpule and Dringen, 2013). However, due to the rapidly growing list of modified DNA (Jones, 2012; Kohli and Zhang, 2013) and RNA (Jia et al., 2011) bases, elevated of FA are implicated in numerous disease pathologies, including neurodegenerative diseases, (Tong et al., 2011, 2013b) diabetes, heart disorders (Tulpule and Dringen, 2013), and Alzheimer's disease (Unzeta et al., 2007). Hence, the development of effective method for detecting FA in biosystem is urgent to understand the roles and metabolism process of FA.

Comparing to conventional detection approach, including colormetric assays (Luo et al., 2001), GC analyses (Bagheri et al., 2009; Chen et al., 2009), HPLC (Nash, 1953; Soman et al., 2008), fluorescence probes are considered as one of the most powerful tools due to their simplified operation, high selectivity and sensitivity, real-time detectability, and biocompatibility

(Tang et al., 2015; Zhou et al., 2015; Bruemmer et al., 2017a; Xu et al., 2017). To date, a number of fluorescent probes for FA visualization have been reported based on the fluorophores of silicon rhodol, 1,8-naphthalimide, resorufin and so forth (Brewer and Chang, 2015; Roth et al., 2015; He et al., 2016; Bruemmer et al., 2017b; Liu et al., 2017; Xie et al., 2017a,b; Bi et al., 2018; Zhou et al., 2018). However, some of them suffered from disadvantages including time-consuming and rigorous synthetic procedure, high background fluorescence and small Stokes shifts which restricted their widely applications in biological system. In the presence of FA, partial probes encounter relatively small Stokes shifts which is not conducive to separating excitation and emission bands, in turn, cannot effectively minimize the interferences caused by self-absorption or auto-fluorescence (Abeywickrama et al., 2017; Chen et al., 2017). Meanwhile, low background fluorescence is beneficial for improving signal to noise ratio (SNR), facilitating to clearly visualize FA in complex biological environment. Hence, it is urgent to develop a FA-selective fluorescence probe with large Stokes shifts and low basal fluorescence.

Herein, we report an Aza-Cope reaction-based fluorescence probe (**BD-CHO**) for FA (**Figure 1**). The core structure of the probe was benz-2-oxa-1, 3- diazole (**BD**), an excellent fluorophore with facile modified and good stability which has been widely used to design fluorescence sensors (Taliani et al., 2007; Liu et al., 2011; Chen et al., 2012; Jiang et al., 2017), and homoallylic amine as FA-recognized group. **BD-CHO** shows good selectivity and sensitivity toward FA over other reactive carbonyl species (RCS) *in vitro* and is subsequently applied to visualize endogenous or exogenous FA in living cells and tissues. Significantly, to the best of our knowledge, **BD-CHO** is the first fluorescence probe for imaging FA in *Daphnia magna*.

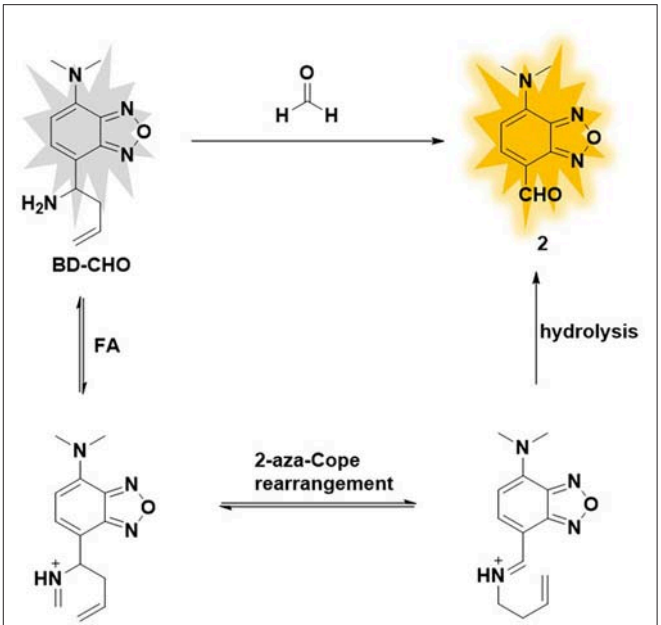

FIGURE 1 | Design of formaldehyde probe BD-CHO.

EXPERIMENTAL SECTION

Materials and Instruments

Unless otherwise stated, all chemicals were purchased from commercial suppliers and used without further purification. The solvents were purified by conventional methods before used. All analytes were obtained by traditional methods. 4-Chloro-2, 1, 3-benzoxadiazole was purchased from TCI chemical. Silica gel (200–300 mesh) used for flash column chromatography was purchased from Qingdao Haiyang Chemical Co., Ltd. ^{1}HNMR and ^{13}CNMR spectra were determined by 400 MHz and 100 MHz using Bruker NMR spectrometers. Chemical shifts (δ) were expressed as parts per million (ppm, in $CDCl_3$ or DMSO, with TMS as the internal standard). Meanwhile, high-resolution mass spectrometry was achieved with ESI-TOF and FTMS-ESI instrument. Fluorescence measurements were performed on an Agilent Technologies CARY Eclipse fluorescence spectrophotometer, and absorption spectra were measured on a PerkinElmer Lambda 35 UV–vis spectrophotometer. The pH values of sample solutions were measured with a precise pH-meter pHS-3C. Fluorescence quantum yield was achieved from a C11347-11 Absolute PL Quantum Yield Spectrometer. MTT assays were conducted on the Varioskan LUX Multimode Microplate Reader. The instrument used for imaging living cells and tissues of mice was an Olympus FV 1000 confocal microscopy purchased from Olympus.

Determination of Detection Limits

According to the fluorescence titration data, a linear relationship between the fluorescence intensity ($F_{578\ nm}$) and FA concentrations was observed, the detection limit was calculated with the following equation: Detection limit = 3σ/k. Where σ is the standard deviation of blank measurements ($n = 10$), k is the slop between the fluorescence intensity vs. the concentrations of FA.

Cytotoxicity Assays

The MTT method was employed to assess the cellular cytotoxicity of **BD-CHO**. Before experiments, MCF-7 cells at a density of 1×10^4 cells/well were seeded into 96-well plates and cultured for 24 h. Then the fresh culture contained **BD-CHO** over a range of concentrations (0–30 μM) ($n = 6$) to substitute the previous media, and further incubation for 24 h. After that, 10 μL of MTT (5 mg/mL in PBS) was added into per well and incubated another 4 h. Finally, 100 μL of DMSO was then added to dissolve formazan. The absorbance at 490 and 570 nm was measured in a microplate reader, and the cell viability (%) was calculated according to the following equation: Cells viability (%) = [OD570 (sample)—OD490 (sample)] / [OD570 (control)—OD490 (control)] × 100.

Living Cells Incubation and Imaging

MCF-7 cells, HepG2 cells and HeLa cells were purchased form Institute of Basic Medical Sciences (IBMS) of the Chinese Academy of Medical Sciences. MCF-7 cells were cultured in

90% Dulbecco's Modified Eagle Medium (DMEM, Gibico) supplemented with 10% FBS (Gibico) and 1% antibiotics (100 U/mL penicillin and 100 μg/mL streptomycin, Hyclone) in an atmosphere of 37°C and 5% CO_2. One day before imaging, the cells were detached and were replanted on glass-bottomed dishes and allowed to adhere for 24 h. For imaging exogenous FA, the culture media of HepG2 cells was replaced with 2 mL of serum-free DMEM containing 10 μM fluorescent probe (from 2 mM stock in DMSO) and the cells were incubated for 30 min. Cells were then washed once with 2 mL PBS and then incubated further with FA (0.5 mM) for 3 h prior to imaging. For inhibition tests, FA-treated cells were incubated with DMEM containing sodium bisulfite (1 mM) and washed with PBS, then incubated with 10 μM fluorescent probe for 3 h before imaging. For imaging endogenous, MCF-7 cells were pretreated with or without (control) the inhibitor tranylcypromine (TCP) or GSK-LSD 1 for 20 h, followed by exchange into serum-free DMEM containing 10 μM fluorescent probe for 3 h.

Fluorescence Imaging of in Kidney Slices

Kidney slices were surgically exposed in Balb/c mice, which was approved by the Dalian Medical University Animal Care and Use Committee. The fresh kidney tissues were incubated with 10 μM **BD-CHO** for 30 min, and then, 1 mM FA was added for another 3 h. Before imaging, the tissues were washed with PBS three times. Olympus FV 1000 confocal microscopy with 20× objective lens was used for fluorescence imaging. All of these experiments were carried out in accordance with the relevant laws and guidelines.

Fluorescence Imaging in *Daphnia magna*

The *D. magna* (age < 72 h) were cultured in clean non-chlorinated tap water under cool-white fluorescence light with light (14 h)-dark (10 h) photoperiod (Du et al., 2018). The animals were incubated with **BD-CHO** (10 μM) for 1 h, followed by washing twice with PBS and then incubated further with or without FA for 3 h. Olympus FV 1000 confocal microscopy with 4× objective lens was used for fluorescence imaging.

Synthesis of BD-CHO

The synthetic procedure was illuminated in **Figure 2**. Compound **1**: 4-Chloro-2,1,3-benzoxadiazole (1.0 g, 6.5 mmol), ethanol (10 mL), dimethylamine hydrochloride (3.0 g, 36.7 mmol), and triethylamine (6.0 mL) were mixed in a 25 mL autoclave at room temperature and followed by quick closure. Then, the bomb was heated with stirring at 150°C for 48 h. The mixture was cooled to room temperature and the solvent was removed under reduced pressure. After the addition of NaOH solution (2 M, 20 mL) to the residue, the mixture was extracted with ethyl acetate (30 Ml × 3). The combined organic layer was dried with anhydrous magnesium sulfate. After the removal of solvent, the product was purified by silica gel column chromatography with dichloromethane: petroleum ether (1:1) as the eluent to afford the desire product to yield red solid (965 mg, 91.0%). ^{1}H NMR (400 MHz, $CDCl_3$) δ (ppm): δ 7.18 (d, J = 7.3 Hz, 1H), 7.02 (s, 1H), 6.06 (s, 1H), 3.25 (s, 6H). ^{13}C NMR (101 MHz, $CDCl_3$) δ (ppm): 150.87, 145.72, 139.87, 133.36, 104.86, 102.13, 41.99, 1.01. MS (ESI-TOF): calculated for $C_8H_{10}N_3O^+$, $[M+H]^+$, m/z, 164.08, found: 164.05.

Compound **2:** $POCl_3$ (2 mL, 21 mmol) and anhydrous DMF (10 mL, 128 mmol) are mixed slowly with stirring in a round-bottomed flask at 0°C. Then, an anhydrous DMF (5 mL) containing compound **1** (960 mg, 5.9 mmol) was added into the mixture. Finally, the obtained mixture was stirred at room temperature about 6 h. The reaction was quenched by pouring the mixture into the ice water (50 mL). After pH was adjusted to pH ∼ 9 by 10% NaOH, the mixture was extracted by ethyl acetate (30 mL × 3). The combined organic layer was dried with anhydrous magnesium sulfate. After the removal of solvent, the product was purified by silica gel column chromatography with petroleum ether: ethyl acetate (1:1) as the eluent to afford

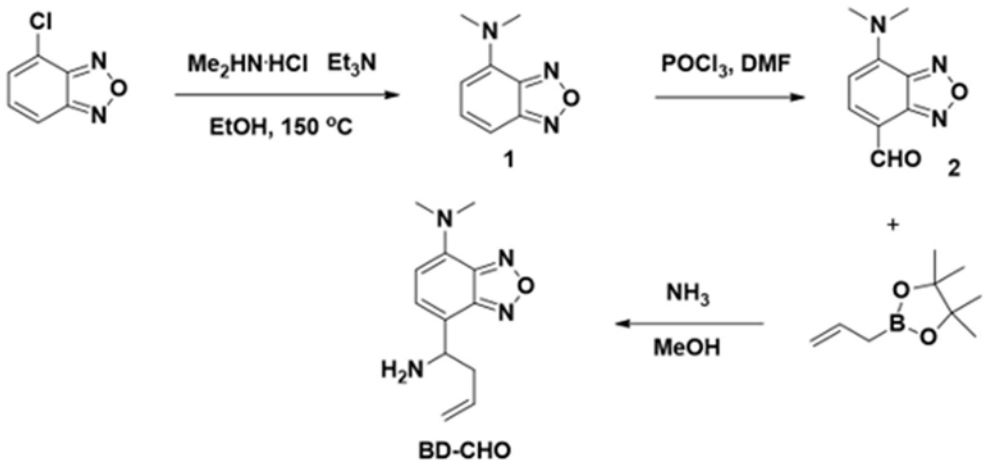

FIGURE 2 | Synthetic procedure of BD-CHO.

the desired product to yield red solid (743 mg, 65.8%). ^{1}H NMR (400 MHz, $CDCl_3$) δ (ppm): 10.03 (s, 1H), 7.89 (d, J = 8.2 Hz, 1H), 6.15 (d, J = 8.2 Hz, 1H), 3.58 (s, 6H). ^{13}C NMR (101 MHz, $CDCl_3$) δ (ppm): 185.93, 147.71, 145.08, 144.87, 142.15, 111.46, 102.35, 42.90, 1.01. HRMS (ESI-TOF): calculated for $C_9H_{10}N_3O_2^+$, $[M+H]^+$, m/z, 192.0773, found: 192.0767.

BD-CHO

To a solution containing compound **2** (192 mg, 1.0 mmol) in 20 mL of CH_3OH, 6 mL of NH_3 solution (7.0 M in CH_3OH, 42 mmol) was added at 0°C under argon atmosphere and stirred 30 min. After that, allylboronic acid pinacol ester (0.48 mL, 2.5 mmol) was added, the mixture was warmed to ambient temperature and stirred overnight. The solvent was removed

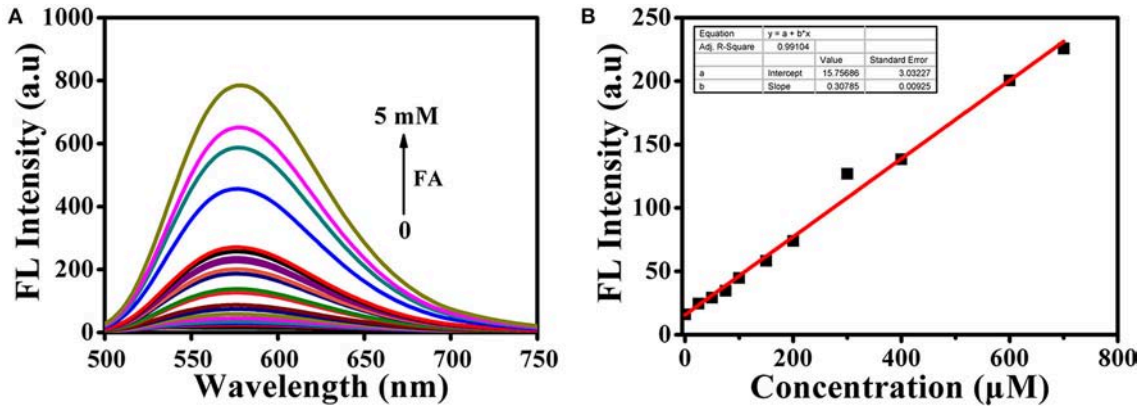

FIGURE 3 | (A) Fluorescence spectra of 10 μM BD-CHO after addition of FA in HEPES buffer (20 mM, pH 7.4, 50% DMSO). **(B)** Linear relationship between the fluorescence intensity of BD-CHO (10 μM) and FA concentration (0–800 μM) in HEPES buffer (20 mM, pH 7.4, 50% DMSO). λ_{ex} = 460 nm, slit: 10/10 nm.

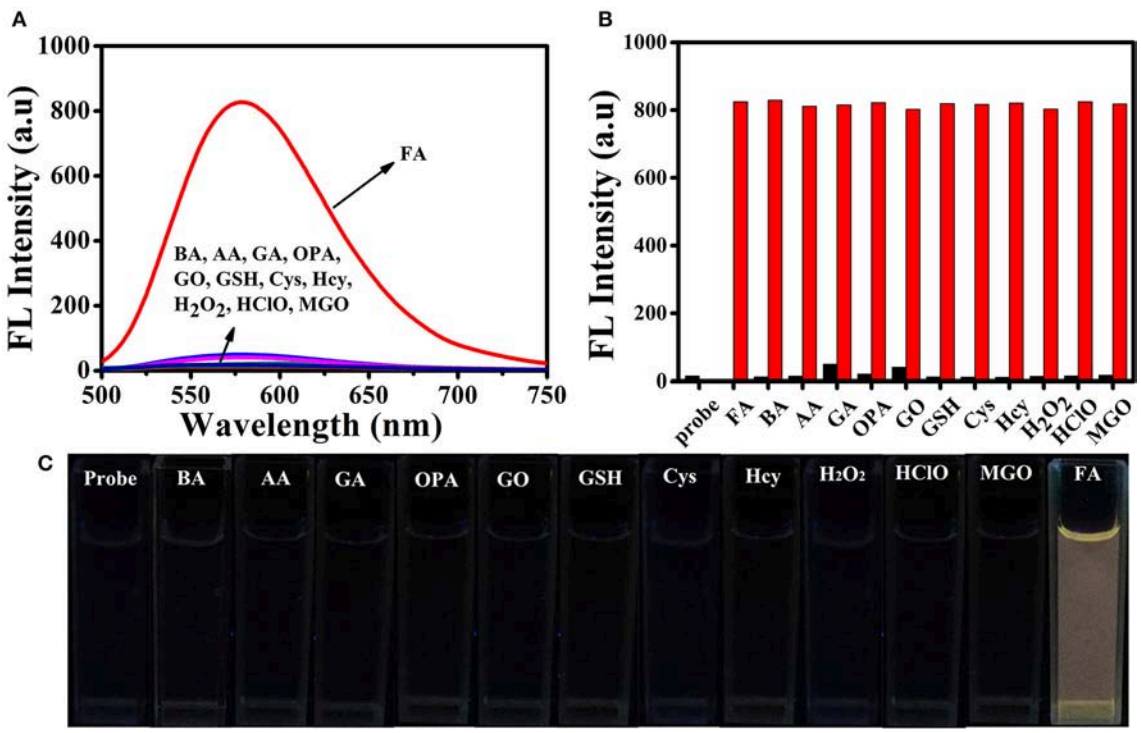

FIGURE 4 | (A) Fluorescence spectra of 10 μM BD-CHO in the presence of FA (5 mM) and other various analytes (5 mM) in HEPES buffer (20 mM, pH 7.4, 50% DMSO). **(B)** Fluorescence intensity of BD-CHO (at 578 nm) in the presence of various analytes (black) or in the presence of both FA and the corresponding analyte (red): Formaldehyde (FA), benzaldehyde (BA), acetaldehyde (AA), glutaraldehyde (GA), *o*-phthalaldehyde (OPA), glyoxal (GO), Glutathione (GSH), Cysteine (Cys), Homo cysteine (Hcy), H_2O_2, HClO, Methylglyoxal (MGO) in HEPES buffer (20 mM, pH 7.4, 50% DMSO). λ_{ex} = 460 nm, slit: 10/10 nm. **(C)** The color fluorescence images of BD-CHO in FA and other analytes under illumination with a 365 nm UV lamp.

under reduced pressure, and the residue was purified by silica gel column chromatography with dichloromethane: methanol (50:1) as the eluent to afford probe **BD-CHO** as yellow solid (101 mg, 43.4%). ^{1}H NMR (400 MHz, $CDCl_3$) δ (ppm): 7.06 (d, J = 7.5 Hz, 1H), 5.94 (d, J = 7.6 Hz, 1H), 5.68 (dd, J = 17.0, 9.7 Hz, 1H), 4.99 (dd, J = 19.8, 13.8 Hz, 2H), 4.20 (t, J = 6.6 Hz, 1H), 3.19 (s, 6H), 2.71–2.54 (m, 1H), 2.48 (dd, J = 14.2, 7.2 Hz, 1H), 2.09 (s, 2H). ^{13}C NMR (101 MHz, $CDCl_3$) δ (ppm) 149.25, 146.08, 138.78, 135.27, 129.21, 120.35, 117.72, 105.15, 52.63, 41.94, 41.81. HRMS (ESI-TOF): calculated for $C_{12}H_{12}N_3O^-$, $[M\text{-}NH_2]^-$, m/z, 216.1137, found: 216.1134.

RESULTS AND DISCUSSION

Design and Synthesis of BD-CHO

To design selective and sensitive fluorescence probe for the FA detection, we focus on homoallylamine trigger which can specially react with FA and produce an electron-withdrawing aldehyde group via an Aza-Cope rearrangement reaction. Benz-2-oxa-1, 3- diazole (**BD**) was chosen as fluorophore core due to easily regulated intramolecular charge transfer (ICT) and excellent photophysical property. In this probe, dimethylamine group was introduced as an electron-donating group (EDG) and homoallylic amine as FA-recognized group. The original **BD-CHO** exhibits almost no fluorescence due to the poor electron withdrawing ability of the homoallylamine moiety. After addition of FA, the amine reacts selectively with FA to form an imine intermediate, which simultaneously undergoes 2-Aza-Cope rearrangement and final hydrolysis to produce an aldehyde group with power electron withdrawing ability (**Figure 1**) (Brewer et al., 2017; Dou et al., 2017). As a result, the intramolecular charge transfer (ICT) process from π-conjugated electron donor (dimethylamine group) to the aldehyde group is opened, showing a "turn-on" fluorescence response.

The probe **BD-CHO** was readily prepared by coupling compound **2** with allylboronic acid pinacol ester in the presence of NH_3 solution. The intermediates and target compound were well characterized by ^{1}H NMR, ^{13}C NMR, HR-MS (**Figures S11–S16**).

Spectral Properties of BD-CHO

All the spectra of **BD-CHO** were investigated in HEPES buffer containing DMSO (V/V = 1:1, 20 mM, pH 7.4). Upon addition of FA, the maximum absorption wavelength shifted from 450 to 460 nm (**Figure S1**). The probe exhibited almost no fluorescence in the absence of FA, which made **BD-CHO** more favorable probe for highly sensitive detecting FA. In the presence of 5 mM FA, however, the fluorescence intensity sharp enhanced about 55-fold at 578 nm with excited at 460 nm (**Figure 3A**)

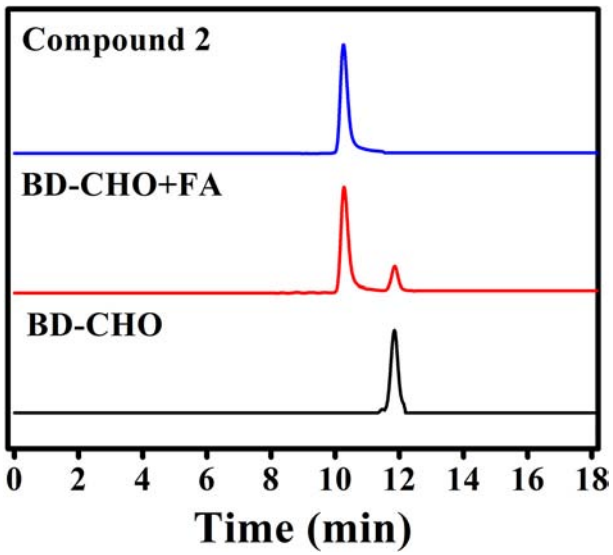

FIGURE 6 | HPLC analysis of compound 2, probe BD-CHO before (black) and after (red) incubation with FA (5 mM) at 37°C for 2 h.

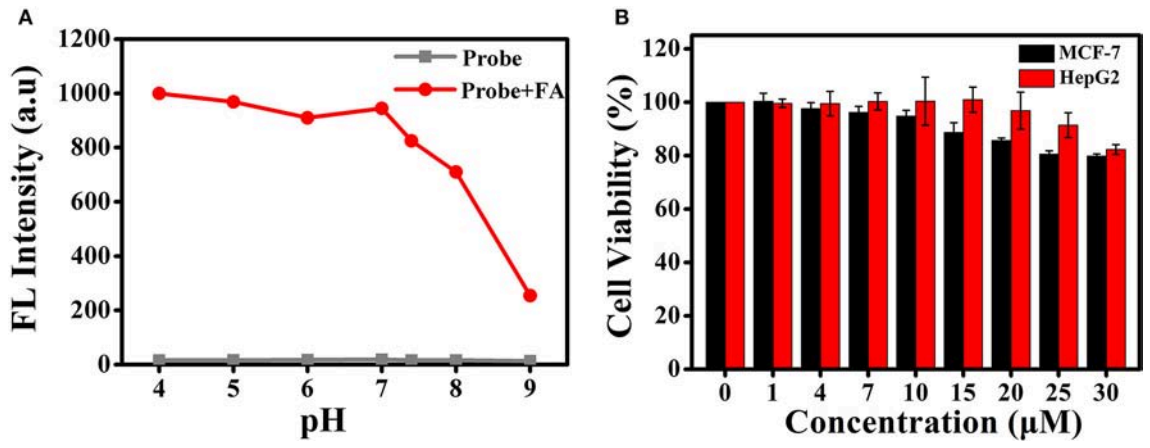

FIGURE 5 | (A) Fluorescence responses of BD-CHO (10 μM) in the presence (red) and absence (blank) of FA in HEPES buffer (20 mM, pH 7.4, 50% DMSO) with different pH values. λ_{ex} = 460 nm, slit: 10/10 nm **(B)** The cell cytotoxicity of BD-CHO in MCF-7 and HepG2 cells.

and the fluorescence quantum yield increased from 0.015 to 0.080. Importantly, **BD-CHO** displayed a large Stokes shifts (118 nm) in response to FA (**Figure S2**), which is beneficial for fluorescent detection in view of reduction of self-absorption. Upon addition of 5 mM FA, the fluorescence intensity of **BD-CHO** increased dramatically over 50 min and reaches a plateau after approximately 3 h (**Figure S3**). There was a linear concentration-dependent fluorescent response with **BD-CHO** toward FA ranging from 0 to 0.8 mM, with a high correlation coefficient $R^2 = 0.991$ (**Figure 3B**). Thus, the detection limit was calculated to be around 9.7 μM, allowing its applicability for the detection of the intracellular FA (100–400 μM) (Andersen et al., 2010).

Selectivity and pH Influence

High selectivity is necessary and crucial for evaluating the applicability of the fluorescent probe. Therefore, we investigated the ability of **BD-CHO** to distinguish FA from various relevant species, including benzaldehyde (BA), acetaldehyde (AA), glutaraldehyde (GA), *o*-phthalaldehyde (OPA), glyoxal (GO), methylglyoxal (MGO), biothiols (Cys, Hcy, and GSH), H_2O_2, HClO. As shown in **Figure 4A**, negligible fluorescence intensity changes of **BD-CHO** were obtained in the presence of possible interfering analytes but a 55-fold fluorescence enhancement with FA. The fluorescence change can also be observed with naked eyes under illumination with a 365 nm UV lamp (**Figure 4C**). To further evaluate the selectivity, competitive experiments were performed in the presence of 5 mM FA and various other species (**Figure 4B**). **BD-CHO** still responded to FA with turn-on fluorescence signal in the presence of competitive species. These results demonstrate that the ability of **BD-CHO** to specifically recognize FA over others relative analytes in complexed biological system. Subsequently, we investigated the effect of pH on the recognition of FA. As shown in **Figure 5A**, fluorescence response of **BD-CHO** to FA is independent of pH in the range 5.0–8.0, indicating its suitability for imaging under physiological conditions.

Recognized Mechanism

The possible sensing mechanism was shown in **Figure 1**. Firstly, homoallylamine moiety in **BD-CHO** reacted with FA to afford 2-aza-1,5-dienes, and then the 2-Aza-Cope rearrangement occurred via [3,3]-migration to form α, β-ene, which was hydrolyzed in aqueous solution to release highly fluorescent compound **2**. In order to verify the proposed hypothesis, we compared the absorption and fluorescence spectra of **BD-CHO** in the presence of FA with that of the compound 2. As shown in **Figure S4**, the absorption and fluorescence spectra of **BD-CHO** + FA were almost identical to that of compound **2**, indicating that compound **2** might be the final reaction product of the **BD-CHO** with FA. Meanwhile, HPLC analysis was used to further confirm the detected product. As shown in **Figure 6**, the chromatographic peak of compound **2** and **BD-CHO** were found at 10.27 and 11.85 min, respectively. Additionally, upon addition of FA (5 mM) and incubation with **BD-CHO** for 2 h, the reaction product exhibited a chromatographic peak at 10.27 min, which matched

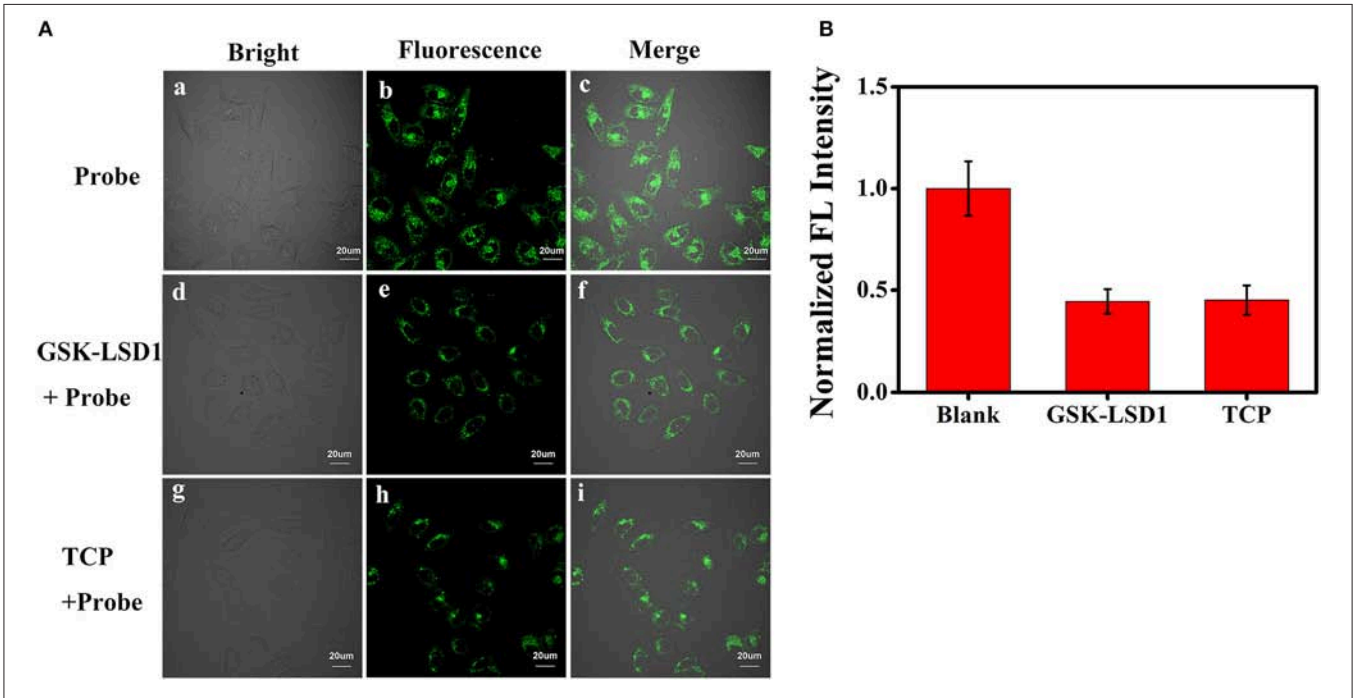

FIGURE 7 | (A) Fluorescence image for BD-CHO in GSK-LSD1 and TCP treated MCF-7 cells. (a-c) blank, (d-f) Cells were pre-treated with 1 μM GSK-LSD1 for 20 h and then with BD-CHO (10 μM) for 3 h, (g-i) Cells were pre-treated with 20 μM TCP for 20 h and then with BD-CHO (10 μM) for 3 h. $\lambda_{ex} = 488$ nm, collected 550–600 nm. **(B)** Mean fluorescence intensity of MCF-7 cells treated with blank, GSK-LSD1 and TCP. Scale bar: 20 μm.

perfectly with compound 2; a weak peak was also observed at 11.85 min, corresponding to probe **BD-CHO**. Furthermore, HR-MS confirmed this result, where a noticeable signal peak at m/z = 214.0584 was assigned to $[M + Na]^+$ (compound **2**, calculated for 214.0592) (**Figure S5**). This is consistent with the previously reported mechanism (Xu et al., 2016; Yang et al., 2018).

Fluorescence Imaging of Exogenous and Endogenous FA in Living Cells

Encouraged by the excellent photophysical properties of **BD-CHO** and its selective response to FA *in vitro*, we attempted to assess the suitability of **BD-CHO** for monitoring FA in living cells. Accordingly, the cytotoxicity of **BD-CHO** was established using MTT assays with MCF-7 cells and HepG 2 cells. It was found that the cell viabilities exceed 94% when incubated cells for 24 h with 10 μM **BD-CHO**, demonstrating the low cytotoxicity of **BD-CHO** (**Figure 5B**). The probe has good stability in biological medium (**Figure S6**).

Subsequently, we evaluated the ability of **BD-CHO** to visualize changes of FA in living cells using confocal microscopy. HepG2 cells were treated with 10 μM **BD-CHO** for 30 min at 37°C, it showed almost invisible fluorescence signal when excited at 488 nm (**Figures S7a–c**). When probe loaded cells were treated with 0.5 mM FA for another 3 h, obvious green fluorescence signal was observed (**Figures S7d–f**). $NaHSO_3$ was used for negative experiments, because it can efficiently react with FA to destroy the central carbonyl group (Tang et al., 2016). When the cells were pre-treated with 0.5 mM FA and 1 mM $NaHSO_3$ for 30 min, and then cultured with **BD-CHO** for 3 h, the green fluorescence became faint (**Figures S7g–i**). Owing to overexpression of LSD1, MCF-7 cells were known to showed elevated FA levels (Liu et al., 2013). When the LSD1 was pharmacological inhibited, the FA levels significantly decreased (Brewer and Chang, 2015). The MCF-7 cells were treated with **BD-CHO** and the cells exhibited strong green fluorescence signal (**Figure 7Ab**), which indicated a high level of FA in MCF-7 cells. However, when MCF-7 cells were incubated with 1 μM GSK-LSD1 (Munoz, 2015) (an LSD1 inhibitor with an IC_{50} of 42 nM) and then with **BD-CHO**, a decrease in **BD-CHO** fluorescence signal compared to control cells was observed (**Figure 7Ae**). Additionally, treatment with 20 μM tranylcypromine (Lee et al., 2006) (TCP, an LSD1 inhibitor

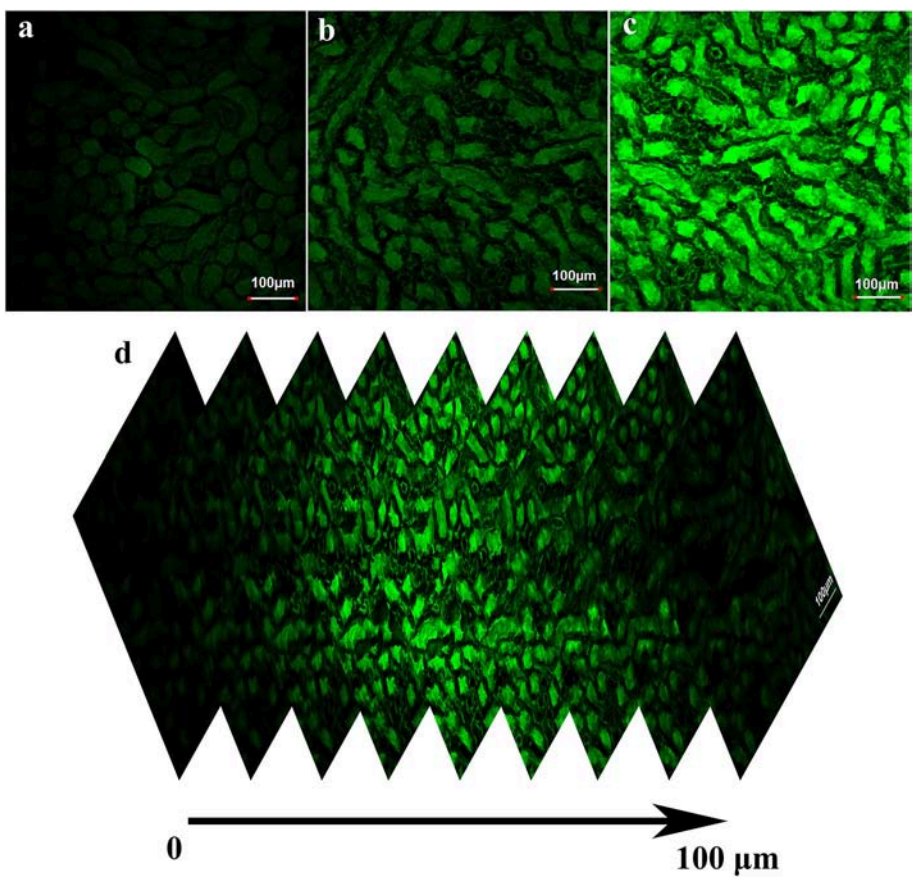

FIGURE 8 | Fluorescence image of fresh kidney tissue slices stained with 10 μM BD-CHO for 1 h and then treated without **(a)** and with **(b)** 0.5 mM **(c)** 1 mM FA for further 3 h. **(d)** Fluorescence image of kidney tissue slices incubated with BD-CHO and FA at different depths (0–100 μm). λ_{ex} = 488 nm, collected 550–600 nm. Scale bar: 100 μm.

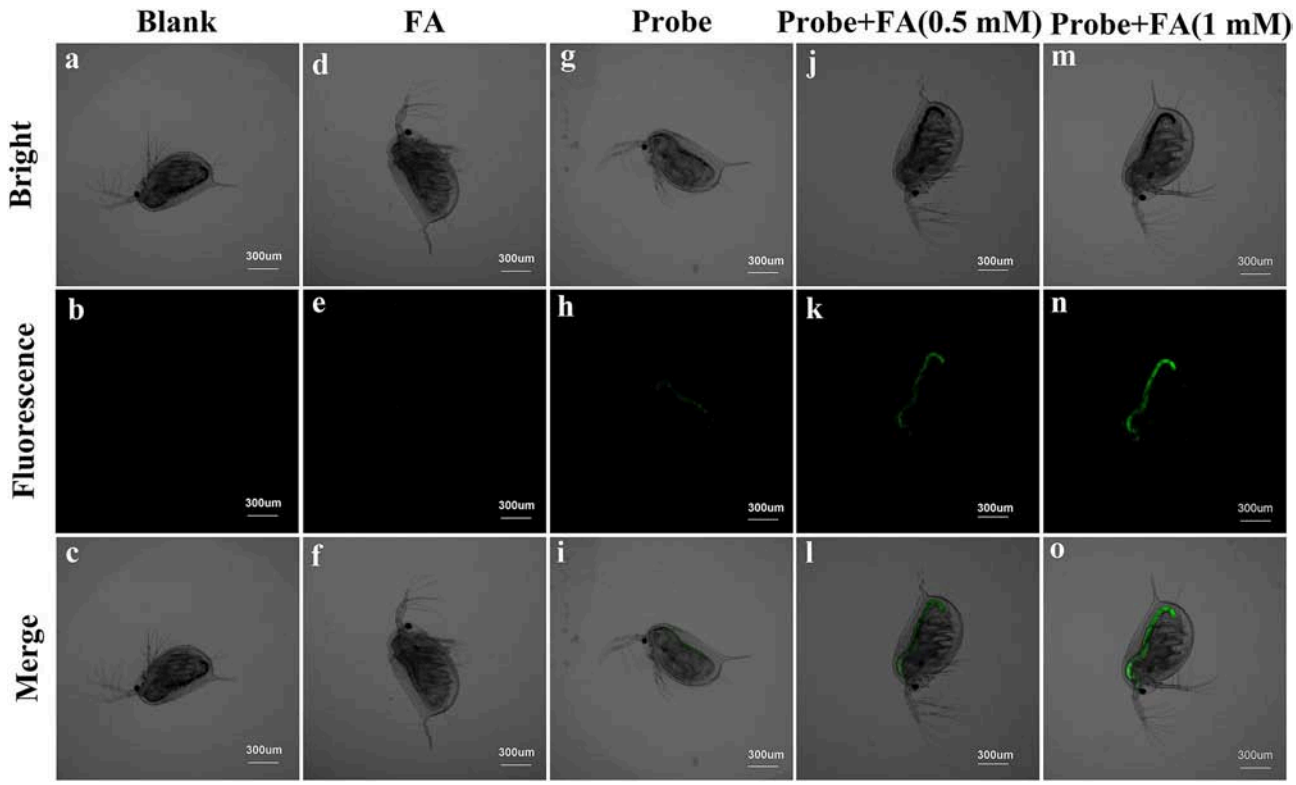

FIGURE 9 | Fluorescence imaging of living *Daphnia magna*. *Daphnia magna* treated with PBS **(a–c)**, FA **(d–f)** and probe **(g–i)** independently. *Daphnia magna* were incubated with 10 μM BD-CHO for 1 h and then with 0.5 mM **(j–l)** and 1 mM **(m–o)** FA for another 3 h before imaging. $\lambda_{ex} = 488$ nm, collected 550–600 nm. Scale bar: 300 μm.

with an IC_{50} of 2 μM), also attenuated **BD-CHO** fluorescence (**Figures 7Ah,B**). Meantime, the detection of endogenous FA changes in HeLa cells were also carried out (**Figure S8**). Take together, the data showed that **BD-CHO** is capable of detecting exogenous and endogenous produced FA in living cells.

Fluorescence Imaging in Kidney Tissues

We further investigated whether **BD-CHO** could image FA in living kidney tissue slices. The kidney tissue slices only soaked in 10 μM **BD-CHO** solution for 3 h showed negligible fluorescence signal (**Figure 8a**, **Figure S9**). By contrast, when the mice kidney tissue slices were soaked in 10 μM **BD-CHO** solution for 30 min, and then soaked in the FA solution for another 3 h, the strong green fluorescence signals were observed (**Figures 8b,c**) with the penetration depth of up to about 100 μm (**Figure 8d**, **Figure S10**). These results indicated that **BD-CHO** was capable of imaging FA in the kidney tissue slices.

Fluorescence Imaging in *Daphnia magna*

The ability of **BD-CHO** for detecting FA *in vivo* was evaluated in living *Daphnia magna*, a widely used animal as a standard Environmental Protection Agency test organism (Lovern and Klaper, 2006), using fluorescence imaging. The untreated and FA-treated *Daphnia magna* showed no fluorescence signal (**Figures 9a–f**). It exhibits faint green fluorescence signal when the *Daphnia magna* were incubated with 10 μM **BD-CHO** for 3 h at 25°C (**Figures 9g–i**). By contrast, upon in the succession treated with **BD-CHO** and different concentration FA, the *Daphnia magna* displays noticeable fluorescence enhancement in green channel (**Figures 9j–o**), indicating that **BD-CHO** could be used for the fluorescence imaging of FA in living *Daphnia magna*.

CONCLUSIONS

In summary, an efficient fluorescent probe, **BD-CHO**, for selective detection of FA via 2-Aza-Cope reaction with large Stokes shifts has been designed and synthesized. In the presence of FA, the fluorescence intensity was significantly increased (about 55-fold) and exhibited large Stokes shifts (about 118 nm). The recognition mechanism of **BD-CHO** to FA was confirmed by HPLC and MS analysis. The probe was used for the fluorescence imaging of exogenous and endogenous FA in living cells with low cytotoxicity and autofluorescence. In addition, **BD-CHO** could also detect FA in living kidney tissue slices with a penetration depth of up to about 100 μm. More importantly, **BD-CHO** was successfully applied to monitor exogenous FA changes in *Daphnia magna* for the first time. All the results indicated that **BD-CHO** could potentially serve as a useful tool

for studying the pathology and physiology role of FA in complex biosystem.

ETHICS STATEMENT

This study was carried out in accordance with the recommendations of Dalian Medical University Animal Care and Use Committee. The protocol was approved by the Dalian Medical University Animal Care and Use Committee.

AUTHOR CONTRIBUTIONS

MY was responsible for designing and performing the experiments. JD and SL were responsible for the characterization of compounds. JF, JW, and XP were responsible for discussing and revising the paper.

FUNDING

This work was financially supported by National Science Foundation of China (21576037, 21676047, 21421005, 21703025), NSFC-Liaoning United Fund (U1608222).

SUPPLEMENTARY MATERIAL

The Supplementary Material for this article can be found online at: https://www.frontiersin.org/articles/10.3389/fchem.2018.00488/full#supplementary-material

REFERENCES

Abeywickrama, C. S., Wijesinghe, K. J., Stahelin, R. V., and Pang, Y. (2017). Bright red-emitting pyrene derivatives with a large Stokes shift for nucleus staining. *Chem. Commun.* 53, 5886–5889. doi: 10.1039/c7cc03417b

Andersen, M. E., Clewell, H. J. III, Bermudez, E., Dodd, D. E., Willson, G. A., Campbell, J. L., et al. (2010). Formaldehyde: integrating dosimetry, cytotoxicity, and genomics to understand dose-dependent transitions for an endogenous compound. *Toxicol. Sci.* 118, 716–731. doi: 10.1093/toxsci/kfq303

Bagheri, H., Ghambarian, M., Salemi, A., and Es-Haghi, A. (2009). Trace determination of free formaldehyde in DTP and DT vaccines and diphtheria-tetanus antigen by single drop microextraction and gas chromatography-mass spectrometry. *J. Pharm. Biomed. Anal.* 50, 287–292. doi: 10.1016/j.jpba.2009.04.039

Bi, A., Gao, T., Cao, X., Dong, J., Liu, M., Ding, N., et al. (2018). A novel naphthalimide-based probe for ultrafast, highly selective and sensitive detection of formaldehyde. *Sens. Actuators B Chem.* 255, 3292–3297. doi: 10.1016/j.snb.2017.09.156

Brewer, T. F., Burgos-Barragan, G., Wit, N., Patel, K. J., and Chang, C. J. (2017). A 2-aza-Cope reactivity-based platform for ratiometric fluorescence imaging of formaldehyde in living cells. *Chem. Sci.* 8, 4073–4081. doi: 10.1039/c7sc00748e

Brewer, T. F., and Chang, C. J. (2015). An aza-cope reactivity-based fluorescent probe for imaging formaldehyde in living cells. *J. Am. Chem. Soc.* 137, 10886–10889. doi: 10.1021/jacs.5b05340

Bruemmer, K. J., Brewer, T. F., and Chang, C. J. (2017a). Fluorescent probes for imaging formaldehyde in biological systems. *Curr. Opin. Chem. Biol.* 39, 17–23. doi: 10.1016/j.cbpa.2017.04.010

Bruemmer, K. J., Walvoord, R. R., Brewer, T. F., Burgos-Barragan, G., Wit, N., Pontel, L. B., et al. (2017b). Development of a general aza-cope reaction trigger applied to fluorescence imaging of formaldehyde in living cells. *J. Am. Chem. Soc.* 139, 5338–5350. doi: 10.1021/jacs.6b12460

Chen, M. L., Ye, M. L., Zeng, X. L., Fan, Y. C., and Yan, Z. (2009). Determination of sulfur anions by ion chromatography–postcolumn derivation and UV detection. *Chin. Chem. Lett.* 20, 1241–1244. doi: 10.1016/j.cclet.2009.05.003

Chen, W., Yue, X., Li, W., Hao, Y., Zhang, L., Zhu, L., et al. (2017). A phenothiazine coumarin-based red emitting fluorescent probe for nanomolar detection of thiophenol with a large Stokes shift. *Sens. Actuators B Chem.* 245, 702–710. doi: 10.1016/j.snb.2017.01.167

Chen, Y., Zhu, C., Yang, Z., Li, J., Jiao, Y., He, W., et al. (2012). A new "turn-on" chemodosimeter for Hg2+: ICT fluorophore formation via Hg(2+)-induced carbaldehyde recovery from 1,3-dithiane. *Chem. Commun.* 48, 5094–5096. doi: 10.1039/c2cc31217d

Dou, K., Chen, G., Yu, F., Liu, Y., Chen, L., Cao, Z., et al. (2017). Bright and sensitive ratiometric fluorescent probe enabling endogenous FA imaging and mechanistic exploration of indirect oxidative damage due to FA in various living systems. *Chem. Sci.* 8, 7851–7861. doi: 10.1039/c7sc03719h

Du, Z., Song, B., Zhang, W., Duan, C., Wang, Y. L., Liu, C., et al. (2018). Quantitative monitoring and visualization of hydrogen sulfide *in vivo* using a luminescent probe based on a ruthenium(II) complex. *Angew. Chem. Int. Ed Engl.* 57, 3999–4004. doi: 10.1002/anie.201800540

He, L., Yang, X., Ren, M., Kong, X., Liu, Y., and Lin, W. (2016). An ultra-fast illuminating fluorescent probe for monitoring formaldehyde in living cells, shiitake mushrooms, and indoors. *Chem. Commun.* 52, 9582–9585. doi: 10.1039/c6cc04254f

Jia, G., Fu, Y., Zhao, X., Dai, Q., Zheng, G., Yang, Y., et al. (2011). N6-methyladenosine in nuclear RNA is a major substrate of the obesity-associated FTO. *Nat. Chem. Biol.* 7, 885–887. doi: 10.1038/nchembio.687

Jiang, Y., Zheng, G., Cai, N., Zhang, H., Tan, Y., Huang, M., et al. (2017). A fast-response fluorescent probe for hypochlorous acid detection and its application in exogenous and endogenous HOCl imaging of living cells. *Chem. Commun.* 53, 12349–12352. doi: 10.1039/c7cc07373a

Jones, P. A. (2012). Functions of DNA methylation: islands, start sites, gene bodies and beyond. *Nat. Rev. Genet.* 13, 484–492. doi: 10.1038/nrg3230

Kohli, R. M., and Zhang, Y. (2013). TET enzymes, TDG and the dynamics of DNA demethylation. *Nature* 502, 472–479. doi: 10.1038/nature12750

Lee, M. G., Wynder, C., Schmidt, D. M., McCafferty, D. G., and Shiekhattar, R. (2006). Histone H3 lysine 4 demethylation is a target of nonselective antidepressive medications. *Chem. Biol.* 13, 563–567. doi: 10.1016/j.chembiol.2006.05.004

Liu, C., Jiao, X., He, S., Zhao, L., and Zeng, X. (2017). A reaction-based fluorescent probe for the selective detection of formaldehyde and methylglyoxal via distinct emission patterns. *Dyes Pigments* 138, 23–29. doi: 10.1016/j.dyepig.2016.11.020

Liu, J., Liu, F. Y., Tong, Z. Q., Li, Z. H., Chen, W., Luo, W. H., et al. (2013). Lysine-specific demethylase 1 in breast cancer cells contributes to the production of endogenous formaldehyde in the metastatic bone cancer pain model of rats. *PLoS ONE* 8:e58957. doi: 10.1371/journal.pone.0058957

Liu, Z., Wang, X., Yang, Z., and He, W. (2011). Rational design of a dual chemosensor for cyanide anion sensing based on dicyanovinyl-substituted benzofurazan. *J. Org. Chem.* 76, 10286–10290. doi: 10.1021/jo201878k

Lovern, S. B., and Klaper, R. (2006). Daphnia magna mortality when exposed to titanium dioxide and fullerene (C-60) nanoparticles. *Environ. Toxicol. Chem.* 25, 1132–1137. doi: 10.1897/05-278r.1

Luo, W., Li, H., Zhang, Y., and Ang, C. (2001). Determination of formaldehyde in blood plasma by high performance liquid chromatography with fluorescence detection. *J. Chromatogr. B* 753, 253–257. doi: 10.1016/S0378-4347(00)00552-1

Munoz, O. (2015). *(Hetero)aryl Cyclopropylamine Compounds as LSD1 Inhibitors. U.S. Pat.* 20150025054.

Nash, T. (1953). The colorimetric estimation of formaldehyde by means of the hantzsch reaction. *Biochem. J.* 55, 416–421. doi: 10.1042/bj0550416

O'Sullivan, J. (2004). Semicarbazide-sensitive amine oxidases: enzymes with quite a lot to do. *Neurotoxicology* 25, 303–315. doi: 10.1016/s0161-813x(03)00117-7

Roth, A., Li, H., Anorma, C., and Chan, J. (2015). A reaction-based fluorescent probe for imaging of formaldehyde in living cells. *J. Am. Chem. Soc.* 137, 10890–10893. doi: 10.1021/jacs.5b05339

Shi, Y., Lan, F., Matson, C., Mulligan, P., Whetstine, J. R., Cole, P. A., et al. (2004). Histone demethylation mediated by the nuclear amine oxidase homolog LSD1. *Cell* 119, 941–953. doi: 10.1016/j.cell.2004.12.012

Soman, A., Qiu, Y., and Li, Q. (2008). HPLC-UV method development and validation for the determination of low level formaldehyde in a drug substance. *J. Chromatogr. Sci.* 46, 461–465. doi: 10.1093/chromsci/46.6.461

Taliani, S., Simorini, F., Sergianni, V., La Motta, C., Da Settimo, F., Cosimelli, B., et al. (2007). New fluorescent 2-phenylindolglyoxylamide derivatives as probes targeting the peripheral-type benzodiazepine receptor: design, synthesis, and biological evaluation. *J. Med. Chem.* 50, 404–407. doi: 10.1021/jm061137o

Tang, Y., Kong, X., Xu, A., Dong, B., and Lin, W. (2016). Development of a two-photon fluorescent probe for imaging of endogenous formaldehyde in living tissues. *Angew. Chem. Int. Ed Engl.* 55, 3356–3359. doi: 10.1002/anie.201510373

Tang, Y., Lee, D., Wang, J., Li, G., Yu, J., Lin, W., et al. (2015). Development of fluorescent probes based on protection-deprotection of the key functional groups for biological imaging. *Chem. Soc. Rev.* 44, 5003–5015. doi: 10.1039/c5cs00103j

Tong, Z., Han, C., Luo, W., Li, H., Luo, H., Qiang, M., et al. (2013a). Aging-associated excess formaldehyde leads to spatial memory deficits. *Sci. Rep.* 3:1807. doi: 10.1038/srep01807

Tong, Z., Han, C., Luo, W., Wang, X., Li, H., Luo, H., et al. (2013b). Accumulated hippocampal formaldehyde induces age-dependent memory decline. *Age* 35, 583–596. doi: 10.1007/s11357-012-9388-8

Tong, Z., Zhang, J., Luo, W., Wang, W., Li, F., Li, H., et al. (2011). Urine formaldehyde level is inversely correlated to mini mental state examination scores in senile dementia. *Neurobiol. Aging* 32, 31–41. doi: 10.1016/j.neurobiolaging.2009.07.013

Tulpule, K., and Dringen, R. (2013). Formaldehyde in brain: an overlooked player in neurodegeneration? *J. Neurochem.* 127, 7–21. doi: 10.1111/jnc.12356

Unzeta, M., Solé, M., Boada, M., and Hernández, M. (2007). Semicarbazide-sensitive amine oxidase (SSAO) and its possible contribution to vascular damage in Alzheimer's disease. *J. Neural. Transm.* 114, 857–862. doi: 10.1007/s00702-007-0701-0

Xie, X., Tang, F., Shangguan, X., Che, S., Niu, J., Xiao, Y., et al. (2017a). Two-photon imaging of formaldehyde in live cells and animals utilizing a lysosome-targetable and acidic pH-activatable fluorescent probe. *Chem. Commun.* 53, 6520–6523. doi: 10.1039/c7cc03050a

Xie, Z., Ge, J., Zhang, H., Bai, T., He, S., Ling, J., et al. (2017b). A highly selective two-photon fluorogenic probe for formaldehyde and its bioimaging application in cells and zebrafish. *Sens. Actuators B Chem.* 241, 1050–1056. doi: 10.1016/j.snb.2016.10.039

Xu, J., Zhang, Y., Zeng, L., Liu, J., Kinsella, J. M., and Sheng, R. (2016). A simple naphthalene-based fluorescent probe for high selective detection of formaldehyde in toffees and HeLa cells via aza-Cope reaction. *Talanta* 160, 645–652. doi: 10.1016/j.talanta.2016.08.010

Xu, Z., Chen, J., Hu, L.-L., Tan, Y., Liu, S.-H., and Yin, J. (2017). Recent advances in formaldehyde-responsive fluorescent probes. *Chinese Chem. Lett.* 28, 1935–1942. doi: 10.1016/j.cclet.2017.07.018

Yang, H., Fang, G., Guo, M., Ning, P., Feng, Y., Yu, H., et al. (2018). A ratiometric two-photon fluorescent probe for selective detection of endogenous formaldehyde via Aza-Cope reaction. *Sens. Actuators B Chem.* 270, 318–326. doi: 10.1016/j.snb.2018.05.069

Zhou, X., Lee, S., Xu, Z., and Yoon, J. (2015). Recent progress on the development of chemosensors for gases. *Chem. Rev.* 115, 7944–8000. doi: 10.1021/cr500567r

Zhou, Y., Yan, J., Zhang, N., Li, D., Xiao, S., and Zheng, K. (2018). A ratiometric fluorescent probe for formaldehyde in aqueous solution, serum and air using aza-cope reaction. *Sens. Actuators B Chem.* 258, 156–162. doi: 10.1016/j.snb.2017.11.043

Conflict of Interest Statement: The authors declare that the research was conducted in the absence of any commercial or financial relationships that could be construed as a potential conflict of interest.

Copyright © 2018 Yang, Fan, Du, Long, Wang and Peng. This is an open-access article distributed under the terms of the Creative Commons Attribution License (CC BY). The use, distribution or reproduction in other forums is permitted, provided the original author(s) and the copyright owner(s) are credited and that the original publication in this journal is cited, in accordance with accepted academic practice. No use, distribution or reproduction is permitted which does not comply with these terms.

frontiers in Chemistry

ORIGINAL RESEARCH
published: 14 May 2019
doi: 10.3389/fchem.2019.00291

Near-Infrared Aggregation-Induced Emission-Active Probe Enables *in situ* and Long-Term Tracking of Endogenous β-Galactosidase Activity

Wei Fu[†], *Chenxu Yan*[†], *Yutao Zhang, Yiyu Ma, Zhiqian Guo* and Wei-Hong Zhu*

State Key Laboratory of Bioreactor Engineering, Shanghai Key Laboratory of Functional Materials Chemistry, School of Chemistry and Molecular Engineering, Institute of Fine Chemicals, East China University of Science and Technology, Shanghai, China

High-fidelity tracking of specific enzyme activities is critical for the early diagnosis of diseases such as cancers. However, most of the available fluorescent probes are difficult to obtain *in situ* information because of tending to facile diffusion or inevitably suffering from aggregation-caused quenching (ACQ) effect. In this work, we developed an elaborated near-infrared (NIR) aggregation-induced emission (AIE)-active fluorescent probe, which is composed of a hydrophobic 2-(2-hydroxyphenyl) benzothiazole (HBT) moiety for extending into the NIR wavelength, and a hydrophilic β-galactosidase (β-gal) triggered unit for improving miscibility and guaranteeing its non-emission in aqueous media. This probe is virtually activated by β-gal, and then specific enzymatic turnover would liberate hydrophobic AIE luminogen (AIEgen) QM-HBT-OH. Simultaneously, brightness NIR fluorescent nanoaggregates are *in situ* generated as a result of the AIE-active process, making on-site the detection of endogenous β-gal activity in living cells. By virtue of the NIR AIE-active performance of enzyme-catalyzed nanoaggregates, QM-HBT-βgal is capable of affording a localizable fluorescence signal and long-term tracking of endogenous β-gal activity. All results demonstrate that the probe QM-HBT-βgal has potential to be a powerful molecular tool to evaluate the biological activity of β-gal, attaining high-fidelity information in preclinical applications.

Keywords: fluorescent probe, near-infrared, aggregation-induced emission, β-galactosidase, *in situ*, long-term tracking

OPEN ACCESS

Edited by:
Tony D. James,
University of Bath, United Kingdom

Reviewed by:
Wenjing Tian,
Jilin University, China
Jingzhi Sun,
Zhejiang University, China

****Correspondence:***
Zhiqian Guo
guozq@ecust.edu.cn

[†]These authors have contributed equally to this work

Specialty section:
This article was submitted to Chemical Biology, a section of the journal Frontiers in Chemistry

Received: *31 January 2019*
Accepted: *09 April 2019*
Published: *14 May 2019*

Citation:
Fu W, Yan C, Zhang Y, Ma Y, Guo Z and Zhu W-H (2019) Near-Infrared Aggregation-Induced Emission-Active Probe Enables in situ and Long-Term Tracking of Endogenous β-Galactosidase Activity. Front. Chem. 7:291. doi: 10.3389/fchem.2019.00291

INTRODUCTION

Specific enzymes play vital roles in a wide range of biological processes. Among them, β-galactosidase (β-gal) is overexpressed in primary ovarian cancers, which has been regarded as an important biomarker for cell senescence and ovarian cancer diagnosis (Dimri et al., 1995; Spergel et al., 2001). In view of this importance, real-time tracking of β-gal activity has become a powerful tool for accurate disease diagnostics. Recently, fluorescent probes have gained ever-increasing attention owing to its noninvasiveness to tissue and high sensitivity (Sun et al., 2016; Xu K. et al., 2016). However, current strategy for enzyme probes is generally based on fluorophores that are soluble in the cytoplasm (Bhuniya et al., 2014; Li X. et al., 2014; Zhang et al., 2014, 2018; Wang F. et al., 2015; Xu et al., 2015; Makukhin et al., 2016; Wu et al., 2016; Chen X. et al., 2017). These responsive probes

largely suffer from inaccurate *in situ* information about biocatalytic activity, because the products of small molecules by enzyme conversion quickly diffuse away from the site of their generation (Kamiya et al., 2011; Yang et al., 2013; Li L. et al., 2014; Yin et al., 2014; Xu Q. et al., 2016; Zhou et al., 2016; Zhu et al., 2016; Wu et al., 2017). These released fluorophores even tend to translocate out of cells, thus making long-term tracking in living subjects difficult (Taylor et al., 2012; Wang et al., 2013; Liu H. W. et al., 2017). On the other hand, it is still far from achieving *in situ* accurate information, owing to the distorted signal from inevitable aggregation-caused quenching (ACQ) effect (Sun et al., 2014; Wu et al., 2014; Li et al., 2015; Gu et al., 2016; Liu Z. et al., 2017; Qi et al., 2018). Therefore, it is an urgent demand to overcome the dilemma of the released fluorophores between aggregation requirement for diffusion-resistant and ACQ effect resulting from aggregation.

With this in mind, we envisioned that near-infrared (NIR) aggregation-induced emission (AIE) probes (Qin et al., 2012; Leung et al., 2013; Mei et al., 2015; Guo et al., 2016; Wang et al., 2016; Yan et al., 2016; Liu L. et al., 2017; Shi et al., 2017; Yang et al., 2017; Zhang F. et al., 2017; Feng and Liu, 2018; Wang Y.-L. et al., 2018; Xie et al., 2018) can provide reliable opportunities to address the aforementioned intractable dilemma. The design of the AIE fluorophores extending into NIR wavelength for decreased autofluorescence and high penetration depth is essentially required for attaching additionally a hydrophobic π-conjugated bridge (Guo et al., 2014; Lim et al., 2014; Chevalier et al., 2016; Andreasson and Pischel, 2018; Li et al., 2018; Yan et al., 2018a,b,c). Impressively, nanoaggregates of the released fluorophores ideally meet the hydrophobic requirements for long-term tracking, and the AIE character of the aggregates can well solve the notorious ACQ effect. Furthermore, we anticipate that AIE-active β-gal probes integrating light-up NIR characteristic in synergy with tunable aggregation behavior could make a breakthrough to detect endogenous β-gal with high-fidelity imaging in living subjects. During the response to β-gal, the aggregation behavior of the AIE probe altered from the molecular dissolved state into the aggregated state, achieving AIE-active NIR mode. In this case, the more AIEgens aggregate, the brighter their NIR emission becomes, making them suitable for *in situ* sensing and long-term tracking of biomolecules in living systems (Kwok et al., 2015; Peng et al., 2015; Yuan et al., 2016; Nicol et al., 2017). However, as far as we know, AIE-active β-gal probes possessing the characteristics of both localizable NIR fluorescence signal and long-term tracking mode are scarcely reported.

Herein, we developed an elaborated NIR AIE-active β-gal probe for enabling *in situ* and long-term tracking of endogenous enzyme activity (**Scheme 1**). Firstly, we focus on our group-developed AIE building block of quinoline-malononitrile (QM) to overcome the enrichment quenching effect (Shi et al., 2013; Shao et al., 2014, 2015; Wang M. et al., 2018). Then, the lipophilic 2-(2-hydroxyphenyl) benzothiazole (HBT) moiety is covalently attached as an external π-conjugated backbone for extending the NIR emission. Furthermore, the masking of the phenolic hydroxyl group prohibits the excited-state intramolecular proton transfer (ESIPT) process and thus largely suppresses fluorescence (Kwon and Park, 2011; Thorn-Seshold et al., 2012; Hu et al., 2014; Zhou et al., 2015; Cui et al., 2016; Chen L. et al., 2017; Chen Y. H. et al., 2017; Zhang P. et al., 2017; Sedgwick et al., 2018a,b; Zhou and Han, 2018). Finally, we utilized the hydrophilic galactose moiety as the β-gal-triggered unit for keeping probes in the fluorescence-*off* state with minimal background. When converted by β-gal, the probe releases free QM-HBT-OH, which is found to be nearly insoluble and aggregated in water and shows bright NIR fluorescence owing to the AIE building block with extended π-conjugated structure. By virtue of the NIR AIE-active performance of enzyme-catalyzed nanoaggregates, QM-HBT-βgal is capable of affording a localizable fluorescence signal and long-term tracking of endogenous β-gal activity. Our results demonstrate that the probe QM-HBT-βgal has potential to be a powerful molecular tool to evaluate the biological activity of β-gal.

EXPERIMENTAL SECTION

Materials and General Methods

Unless especially stated, all solvents and chemicals were purchased from commercial suppliers in analytical grade and used without further purification. β-Galactosidase (β-gal) was supplied by *J&K* Scientific Ltd (Beijing, China). The ^{1}H and ^{13}C NMR spectra were recorded on a Bruker AM 400 spectrometer, using TMS as an internal standard. High-resolution mass spectrometry data were obtained with a Waters LCT Premier XE spectrometer. Absorption spectra were collected on a Varian Cary 500 spectrophotometer, and fluorescence spectra measurements were performed on a Varian Cary Eclipse fluorescence spectrophotometer. The time-dependent fluorescence measurements were conducted upon continuous illumination (Hamamatsu, LC8 Lightningcure, 300 W). Dynamic light scattering (DLS) experiments were conducted with Zetasizer Nano-ZS (Malvern Instruments, Worcestershire, UK), and scanning electron microscope (SEM) images were operated on a JEOL JSM-6360 scanning electron microscope. Confocal fluorescence images were taken on a confocal laser scanning microscope (CLSM, Leica confocal microscope TCS SPS CFSMP).

General Procedure for *in vitro* Monitoring β-gal Activity

Probes were dissolved in dimethyl sulfoxide (DMSO, AR) to obtain 1-mM stock solutions. All UV–vis absorption and fluorescence spectra measurements were carried out in PBS/DMSO buffer solution (7:3, v/v, pH = 7.4, 50 mM). In a 3-mL tube, PBS buffer (2.1 mL) and DMSO (900 μL) solution were mixed, and then the probe (30 μL) was added to obtain a final concentration of 10 μM. β-Gal was dissolved in a PBS buffer, and an appropriate volume was added to the sample solution. After rapid mixing of the solution, it was transferred to a 10 × 10-mm quartz cuvette and incubated at 37°C for *in vitro* detection.

Cell Experiment

Cell Lines

This study was performed in strict accordance with ethical standards including ethics committee approval and consent procedure, and adhered to standard biosecurity and institutional safety procedures. This study was performed in strict accordance with the NIH *Guidelines for the Care and Use of Laboratory Animals* (NIH Publication No. 85-23 Rev. 1985) and was approved by the Institutional Animal Care and Use Committee of National Tissue Engineering Center (Shanghai, China).

The human ovarian adenocarcinoma cell line SKOV-3 cells and the human epithelioid cervical carcinoma cell line HeLa cells were purchased from the Institute of Cell Biology (Shanghai, China). Cells were all propagated in T-75 flasks cultured at 37°C under a humidified 5% CO_2 atmosphere in RPMI-1640 medium or DMEM medium (GIBCO/Invitrogen, Camarillo, CA, USA), which were supplemented with 10% fetal bovine serum (FBS, Biological Industry, Kibbutz Beit Haemek, Israel) and 1% penicillin–streptomycin (10,000 U mL^{-1} penicillin and 10 mg mL^{-1} streptomycin, Solarbio Life Science, Beijing, China).

In vitro Cytotoxicity Assay

The cell cytotoxicity of QM-HBT-βgal to SKOV-3 cells and HeLa cells was measured by 3-(4,5-dimethylthiazol-2-yl)-2,5-diphenyltetrazolium bromide (MTT) assay. Cytotoxicity was evaluated by Cell Counting Kit-8 (Dojindo, Tokyo, Japan) according to the factory's instruction. Cells were plated in 96-well plates in 0.1-mL volume of DMEM or RPMI-1640 medium with 10% FBS, at a density of 1×10^4 cells/well, and added with desired concentrations of SKOV-3. After incubation for 24 h, absorbance was measured at 595 nm with a Tecan GENios Pro Multifunction Reader (Tecan Group Ltd., Maennedorf, Switzerland). Each concentration was measured in triplicate and used in three independent experiments. The relative cell viability was calculated by the following equation: cell viability (%) = $(OD_{treated}/OD_{control}) \times 100\%$.

Cells Imaging

Cells were seeded onto glass-bottom petri dishes in culture medium (1.5 mL) and allowed to adhere for 12 h before imaging. Probe QM-HBT-βgal at a final concentration of 10 μM (containing 0.1% DMSO) was added into culture medium and incubated for different times at 37°C under a humidified 5% CO_2 atmosphere. Cells imaging was captured by using a confocal laser scanning microscope (Leica confocal microscope TCS SPS CFSMP) with a 60 × oil immersion objective lens. The fluorescence signals of cells incubated with probes were collected at 650–700 nm under excitation wavelength at 460 nm.

Synthesis of Probe QM-HBT-βgal

Synthesis of Compound 1

A mixture of 2-aminobenzenethiol (2 g, 16.0 mmol) and 2-hydroxy-3-methylbenzoic acid (2 g, 16.0 mmol) in polyphosphoric acid (15 mL) was heated in an oil bath at 180°C for 10 h under an argon atmosphere and then was cooled at room temperature. The mixture was then poured into ice, filtered, and the resulting solid product was washed with water, dried in air, and finally purified by column chromatography using dichloromethane/petroleum ether (v/v, 2:1) as the eluent to afford a white solid product (1 g): yield 26%. ^{1}H NMR (400 MHz, $CDCl_3$, ppm): $\delta = 2.36$ (s, 3H, C***H***$_3$-H), 6.87 (t, $J = 8.0$ Hz, 1H, phenyl-H), 7.27 (s, 1H, phenyl-H), 7.41 (t, $J = 8.0$ Hz, 1H, phenyl-H), 7.50 (t, $J = 8.0$ Hz, 1H, phenyl-H), 7.56 (d, $J = 8.0$ Hz, 1H, phenyl-H), 7.90 (d, $J = 8.0$ Hz, 1H, phenyl-H), 7.97 (d, $J = 8.0$ Hz, 1H, phenyl-H), 12.8 (s, 1H, -O***H***). ^{13}C NMR (100 MHz, $CDCl_3$, ppm): δ 169.81, 156.29, 151.83, 133.69, 132.71, 126.63, 126.07, 125.43, 122.07, 121.49, 119.00, 116.02, 16.08. Mass spectrometry (ESI-MS, *m/z*): $[M + H]^+$ calcd. for $[C_{14}H_{11}NOS + H]^+$ 242.0640; found 242.0636.

Synthesis of Compound 2

Compound 1 (200 mg, 0.83 mmol) was dissolved in 10 mL of trifluoroacetic acid, and then, hexamethylenetetramine (174.5 mg, 1.25 mmol) was added. The mixture was heated in an oil bath at 90°C for 20 h under an argon atmosphere. The reaction mixture was then cooled to room temperature and poured into 6 M HCl (30 mL) and extracted with CH_2Cl_2. The combined organic extracts were washed with saturated brine. Next, purification was done by column chromatography using dichloromethane as the eluent to afford the pure product as a whiteness solid (100 mg): yield 45%.^{1}H NMR (400 MHz, $CDCl_3$, ppm): δ 2.42 (s, 3H, C***H***$_3$-H), 7.47 (t, $J = 8.0$ Hz, 1H, phenyl-H), 7.55 (t, $J = 8.0$ Hz, 1H, phenyl-H), 7.80 (s, 1H, phenyl-H), 7.95 (d, $J = 8.0$ Hz, 1H, phenyl-H), 8.01 (d, $J = 8.0$ Hz, 1H, phenyl-H), 8.11 (d, $J = 8.0$ Hz, 1H, phenyl-H), 9.92 (s, 1H, C***H***O-H), 13.6 (s, 1H, -O***H***). ^{13}C NMR (100 MHz, $CDCl_3$, ppm): δ 190.29, 168.63, 161.12, 151.27, 133.98, 132.62, 128.95, 128.18, 126.98, 126.02, 122.20, 121.67, 116.17, 16.06. Mass spectrometry (ESI-MS, *m/z*): $[M - H]^-$ calcd. for $[C_{15}H_{11}NO_2S - H]^-$ 268.0432; found 268.0436.

Synthesis of QM-HBT-OH

Compound 2 (100 mg, 0.37 mmol) and 2-(1-ethyl-2-methylquinolin-4(1*H*)-ylidene)malononitrile (132 mg, 0.56 mmol) were dissolved in acetonitrile (20 ml) with piperidine (0.5 ml). Then, the mixture was refluxed for 10 h under an argon atmosphere. The solvent was removed under reduced pressure, and then, the crude product was purified by silica gel chromatography using dichloromethane as the eluent to afford QM-HBT-OH as a red solid (50 mg): yield 28%. ^{1}H NMR (400 MHz, DMSO-d_6, ppm) δ1.45 (t, $J = 8.0$ Hz, 3H, NCH_2C***H***$_3$-H), 2.18 (s, 3H, C***H***$_3$-H), 4.59 (q, $J = 8.0$ Hz, 2H, NC***H***$_2CH_3$-H), 7.09 (d, $J = 16.0$ Hz, 1H, alkene-H), 7.15 (s, 1H, phenyl-H), 7.29 (t, $J = 8.0$ Hz, 1H, phenyl-H), 7.42 (d, $J = 8.0$ Hz, 1H, phenyl-H), 7.50 (d, $J = 16.0$ Hz, 1H, alkene-H), 7.56 (d, $J = 8.0$ Hz, 1H, phenyl-H), 7.73(s, 1H, phenyl-H), 7.87 (t, $J = 8.0$ Hz, 1H, phenyl-H), 7.92 (d, $J = 8.0$ Hz, 1H, phenyl-H), 8.00 (d, $J = 8.0$ Hz, 1H, phenyl-H), 8.04 (t, $J = 8.0$ Hz, 1H, phenyl-H), 8.24 (d, $J = 8.0$ Hz, 1H, phenyl-H), 8.90 (d, $J = 8.0$ Hz, 1H, phenyl-H). ^{13}C NMR (100 MHz, DMSO-d_6, ppm): δ 165.84, 151.86, 150.47, 150.34, 143.33, 138.18, 135.37, 132.98, 130.47, 128.51, 124.97, 124.23, 122.31, 121.25, 120.70, 120.40, 117.76, 104.59, 43.02, 17.53, 13.63. Mass spectrometry (ESI-MS, *m/z*): $[M - H]^-$ calcd. for $[C_{30}H_{22}N_4OS - H]^-$ 485.1436; found 485.1439.

Synthesis of QM-HBT-βgalAc

QM-HBT-OH (100 mg, 0.21 mmol) and tetra-O-acetyl-α-D-galactopyranosyl-1-bromide (150 mg, 0.36 mmol) were dissolved in acetonitrile (15 ml) with Cs_2CO_3 (359 mg, 1.10 mmol) and Na_2SO_4 (125 mg, 0.88 mmol) under argon protection at room temperature. The mixture then was stirred at room temperature for 4 h. After filtration, the solvent was removed under reduced pressure. The residue was taken up in sat.NH_4Cl and extracted with CH_2Cl_2. Next, the solution was dried over anhydrous Na_2SO_4, and the solvent was removed by evaporation again. Finally, the crude product was purified by silica gel chromatography using dichloromethane/methanol (100:1) to afford the desired product QM-HBT-βgalAc as a red solid (30 mg): yield 18%. ^{1}H NMR (400 MHz, DMSO-d_6, ppm) δ 1.41 (t, J = 8.0 Hz, 3H, $NCH_2C\boldsymbol{H}_3$-H), 1.76 (s, 3H, acetyl-H), 1.94 (s, 3H, acetyl-H), 1.99 (s, 3H, acetyl-H), 2.08 (s, 3H, acetyl-H), 2.46 (s, 3H, $C\boldsymbol{H}_3$-H), 3.56 (m, 2H, $C\boldsymbol{H}_2OCOCH_3$), 4.06 (t, J = 8.0 Hz, 1H, galactose-H), 4.62 (q, J = 8.0 Hz, 2H, $NC\boldsymbol{H}_2CH_3$-H), 5.16 (s, 1H, galactose-H), 5.24 (s, 1H, galactose-H), 5.34 (s, 1H, galactose-H), 5.48 (m, 1H, galactose-H), 7.06 (s, 1H, phenyl-H), 7.47 (t, J = 8.0 Hz, 1H, phenyl-H), 7.54 (t, J = 8.0 Hz, 1H, phenyl-H), 7.60 (d, J = 16.0 Hz, 2H, alkene-H), 7.65 (d, J = 8.0 Hz, 1H, phenyl-H), 7.95 (t, J = 8.0 Hz, 1H, phenyl-H), 8.01(s, 1H, phenyl-H), 8.11 (m, 2H, phenyl-H), 8.19 (d, J = 8.0 Hz, 1H, phenyl-H), 8.37(s, 1H, phenyl-H), 8.95 (d, J = 8.0 Hz, 1H, phenyl-H). ^{13}C NMR (100 MHz, DMSO-d_6, ppm): δ 169.67, 169.45, 163.39, 167.27, 152.34, 151.67, 149.11, 138.43, 137.75, 135.94, 133.74, 132.40, 132.29, 129.09, 127.67, 126.03, 125.12, 122.78, 121.61, 120.61, 118.12, 107.28, 99.94, 91.56, 70.10, 69.77, 69.18, 68.22, 67.00, 64.11, 61.19, 60.60, 47.20, 43.84, 20.52, 20.11, 16.21, 13.69. Mass spectrometry (ESI-MS, m/z): $[M + H]^+$ calcd. for $[C_{44}H_{40}N_4O_{10}S + H]^+$ 817.2543; found 817.2548.

Synthesis of QM-HBT-βgal

QM-HBT-βgalAc (50 mg, 0.06 mmol) was added to MeONa (70 mg, 1.3 mmol) in methanol (10 ml), and the mixture was stirred at room temperature for 4 h. Then, the reaction mixture was neutralized with Amberlite IR-120 plus (H^+). After Amberlite IR-120 plus (H^+) was filtered off, the solvent was removed by evaporation. Finally, the crude product was purified by silica gel chromatography using dichloromethane/methanol (40:1) to afford the desired product QM-HBT-βgal (16 mg): ^{1}H NMR (400 MHz, DMSO-d_6, ppm) δ 1.41 (t, J = 8.0 Hz, 3H, $NCH_2C\boldsymbol{H}_3$-H), 2.53 (s, 3H, $C\boldsymbol{H}_3$-H), 3.07-3.26 (m, 4H, -O$\boldsymbol{H}$), 3.27(m, 2H, -$C\boldsymbol{H}_2$OH), 3.28 (m, 2H, galactose-H), 3.61 (d, J = 8.0 Hz, 1H, galactose-H), 3.87 (d, J = 8.0 Hz, 1H, galactose-H), 4.62 (q, J = 8.0 Hz, 2H, $NC\boldsymbol{H}_2CH_3$-H), 4.77 (d, J = 8.0 Hz, 1H, galactose-H), 7.07 (s, 1H, phenyl-H), 7.44 (t, J = 8.0 Hz, 1H, phenyl-H), 7.52 (d, J = 8.0 Hz, 1H, phenyl-H), 7.58 (d, J = 16.0 Hz, 2H, phenyl-H), 7.64 (d, J = 8.0 Hz, 1H, phenyl-H), 7.95 (d, J = 8.0 Hz, 1H, phenyl-H), 7.97 (s, 1H, phenyl-H), 8.09 (d, J = 16.0 Hz, 1H, alkene-H), 8.11 (d, J = 8.0 Hz, 1H, phenyl-H), 8.12 (d, J = 16.0 Hz, 1H, alkene-H), 8.39 (d, J = 8.0 Hz, 1H, phenyl-H), 8.95 (d, J = 8.0 Hz, 1H, phenyl-H). ^{13}C NMR (100 MHz, DMSO-d_6, ppm): δ 163.97, 153.87, 152.25, 151.58, 149.12, 138.67, 137.72, 136.00, 133.68, 132.49, 132.05, 131.29, 128.18, 127.56, 125.08, 125.01, 124.95, 122.52, 121.71, 120.89, 120.58, 119.15, 118.07, 107.19, 104.47, 75.48, 73.11, 71.11, 67.66, 59.79, 47.10, 43.85, 16.81, 13.71. Mass spectrometry (ESI-MS, m/z): $[M + H]^+$ calcd. for $[C_{36}H_{32}N_4O_6S + H]^+$649.2121; found 649.2123.

RESULTS AND DISCUSSION

Design and Synthesis

In our strategy, QM is employed as the AIE building block along with generating modifiable sites for functionalization, which could perform controllable NIR emission via tuning electron–donor ability (Shi et al., 2013; Shao et al., 2014, 2015; Wang M. et al., 2018). Particularly, neighboring HBT moiety is covalent attached as hydrophobic π-conjugated backbone, efficiently extending emission wavelength to the NIR region. Finally, a β-gal activatable unit is grafted at the position of phenolic hydroxyl group, blocking the ESIPT process and endowing the elaborated probe QM-HBT-βgal with moderate water solubility. In consequence, the molecular dissolved state in the aqueous system renders the probe almost non-fluorescent. After being specifically hydrolyzed by β-gal, hydrophobic QM-HBT-OH can be released and aggregated with a remarkable light-up AIE-active fluorescent signal, which could be well retained in the reaction site and emit strong fluorescence for long-term tracking endogenous β-gal activity. The synthetic route for the probe is depicted in the Materials and General Methods (**Scheme S1**), which was fully characterized by ^{1}H and ^{13}C NMR and high-resolution mass spectrometry (HRMS) (**Figures S10–S24**).

Aggregation-Induced Emission Properties of QM-HBT-βgal and QM-HBT-OH

Initially, the AIE properties of QM-HBT-βgal and QM-HBT-OH were investigated in the water/THF mixed solvents with different water volume fractions (f_w = 0–90%) in **Figure 1**. Actually, both compounds showed two absorption peaks at 360 and 440 nm, respectively. The absorption spectrum of QM-HBT-βgal displayed only slight changes with the increasing f_w (**Figure 1A**), but that of QM-HBT-OH significantly descended when the f_w exceeded 70% (**Figure 1D**), resulting from the light scattering effect of the well-formed nanoaggregates. As expected, the hydrophilic galactose group makes QM-HBT-βgal in the molecular dissolved state in water, which exhibits non-emission in various water/THF mixtures (**Figures 1B**,**C**), with a quantum yield (Φ) of 0.1 using Rhodamine B as a reference compound. In contrast, QM-HBT-OH showed distinct light-up AIE characteristics. By increasing the f_w from 0 to 60%, the emission intensity increased slowly, accompanied by an obvious bathochromic shift (**Figure 1E**). Further addition of water leads to a sharp and dramatic enhancement in fluorescence intensity (Φ = 3.6%), which correlates well with the formation of nanoaggregates in poorer solvents (**Figure 1F**). Here, the initial fluorescence-*off* state of QM-HBT-βgal and significant AIE-active NIR fluorescence of QM-HBT-OH in aggregated state made it as an ideal candidate for tracking β-gal.

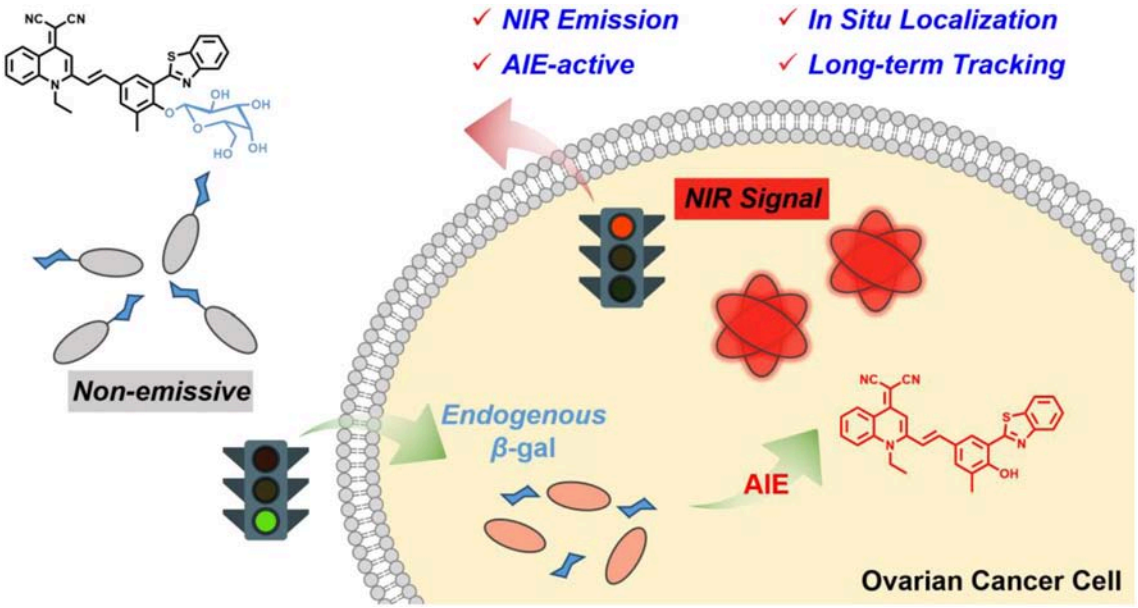

SCHEME 1 | Schematic illustration of an enzyme β-gal-regulated liberation strategy for on-site sensing and long-term tracking.

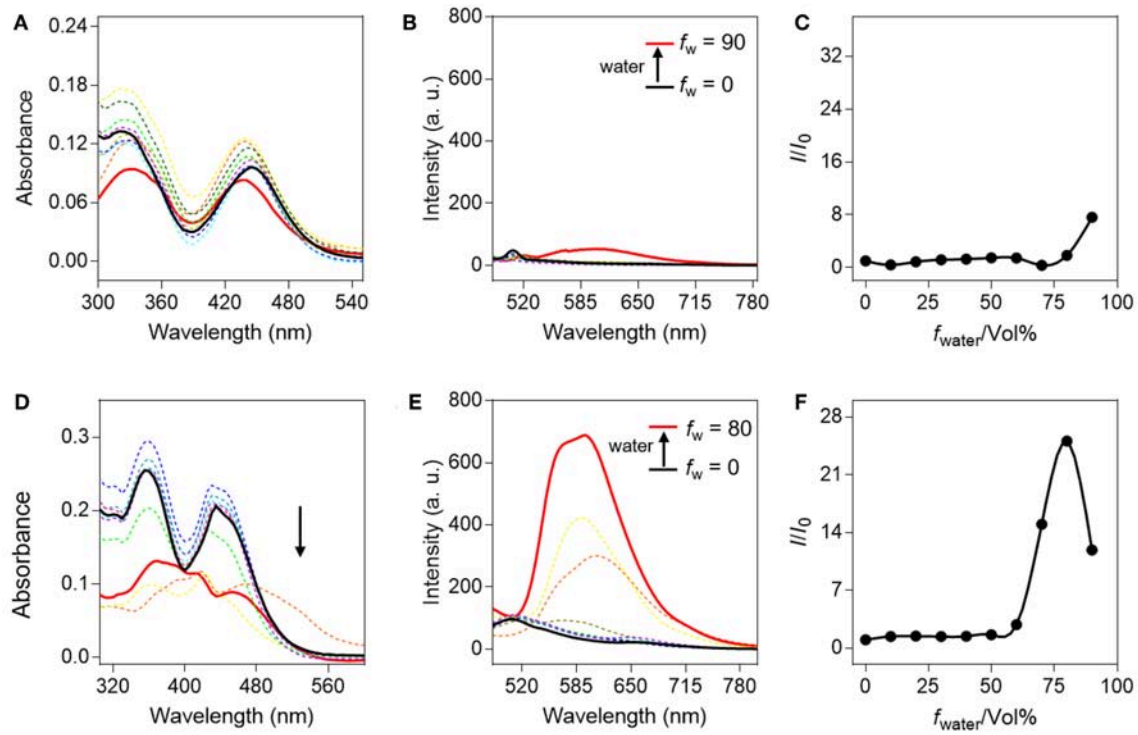

FIGURE 1 | Spectral properties of QM-HBT-βgal and QM-HBT-OH with different water fractions (f_w) in a mixture of water/tetrahydrofuran. **(A)** Absorption spectra, **(B)** emission spectra, and **(C)** I/I_0 plots of QM-HBT-βgal (10 μM); **(D)** absorption spectra, **(E)** emission spectra, and **(F)** I/I_0 plots of QM-HBT-OH (10 μM), where I is the fluorescence intensity at 620 nm and I_0 is the fluorescence intensity of QM-HBT-βgal or QM-HBT-OH in 0% water, λ_{ex} = 460 nm.

Spectroscopic Properties and Optical Response to β-gal

A smart AIE-active β-gal NIR fluorescent probe should significantly alter its fluorescence characteristic upon response to β-gal. With the probe QM-HBT-βgal in hand, we investigated the optical response of the probe to β-gal in the aqueous solution (PBS/DMSO = 7:3, v/v, 50 mM, pH = 7.4) at 37°C. QM-HBT-βgal has a broad absorption band at 440 nm, and the absorbance peak decreased gradually with the addition of β-gal (**Figure S1**). As shown in **Figures 2A**,**B**, a distinct NIR fluorescence enhancement at 650 nm was observed from QM-HBT-βgal upon the addition of 10 U β-gal, accompanied by a significant bathochromic shift in emission spectra. It could be interpreted that the QM-HBT-βgal can be specifically hydrolyzed by β-gal and then spontaneously form nanoaggregates QM-HBT-OH with a remarkable AIE-active fluorescent signal, which is confirmed by **Figures S2, S3**, and we observe *in situ* generation of about 200-nm nanoaggregates by DLS and SEM characterization. In addition, the enhancement of fluorescence intensity is dependent on the incubation time with β-gal, leveling off at around 6 h. In contrast, negligible fluorescence intensity change of QM-HBT-βgal was observed without the addition of β-gal, indicative of the moderate and efficient enzyme response rate toward β-gal. Further, we performed the titration to study the enzymatic fluorescence response of QM-HBT-βgal (**Figure 2C**). With the increase of β-gal concentration (0–12 U),

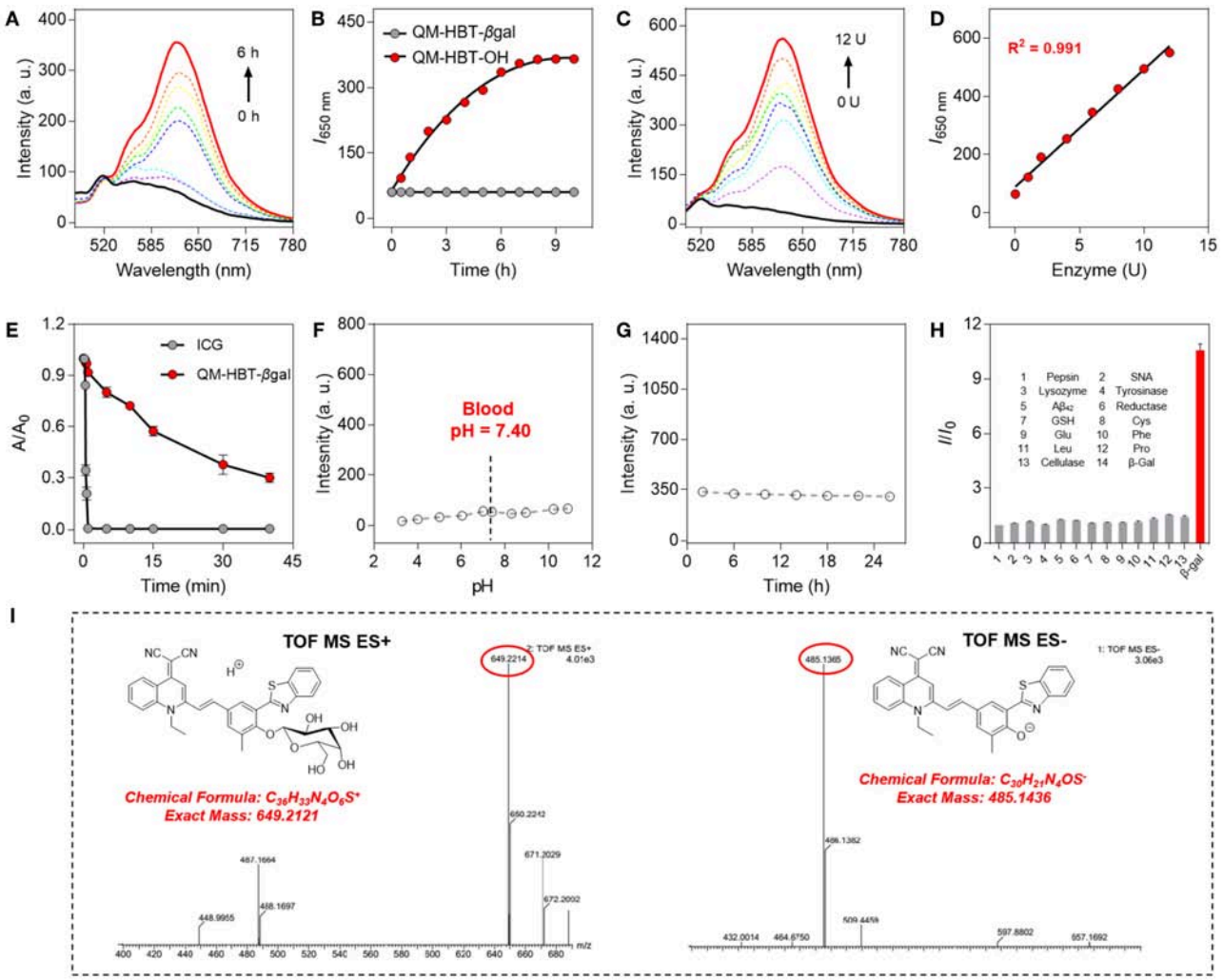

FIGURE 2 | (A) Time-dependent fluorescence spectra of QM-HBT-βgal (10 μM) with 10 U β-gal in aqueous solution (PBS/DMSO = 7:3, v/v, 50 mM, pH = 7.4) at 37°C. **(B)** Time dependence of I_{650} nm for QM-HBT-βgal before (black) and after (red) adding β-gal, λ_{ex} = 460 nm. **(C)** Fluorescence spectra of QM-HBT-βgal (10 μM) upon treatment with increasing concentrations of β-gal (0–12 U) after incubation for 6 h. **(D)** Fluorescence intensity I_{650} nm as a function of β-gal concentration after incubation for 6 h. **(E)** Time-dependent fluorescence intensity of ICG (10 μM, monitored at 812 nm, and λ_{ex} = 780 nm) and QM-HBT-βgal (10 μM, monitored at 650 nm, and λ_{ex} = 460 nm) under sustained illumination. **(F)** Fluorescence intensity at 650 nm of QM-HBT-βgal remaining stable in various pH values and **(G)** fresh mouse serum over 24 h at 37°C. **(H)** Fluorescence responses of QM-HBT-βgal (10 μM) upon incubation with β-gal (10 U) and various other analytes (100 equiv.) in aqueous solution (PBS/DMSO = 7:3, v/v, 50 mM, pH = 7.4) at 37°C, λ_{ex} = 460 nm. **(I)** High-resolution mass spectrometry (HRMS) demonstrating the enzyme-activatable mechanism and showing the cleavage product QM-HBT-OH.

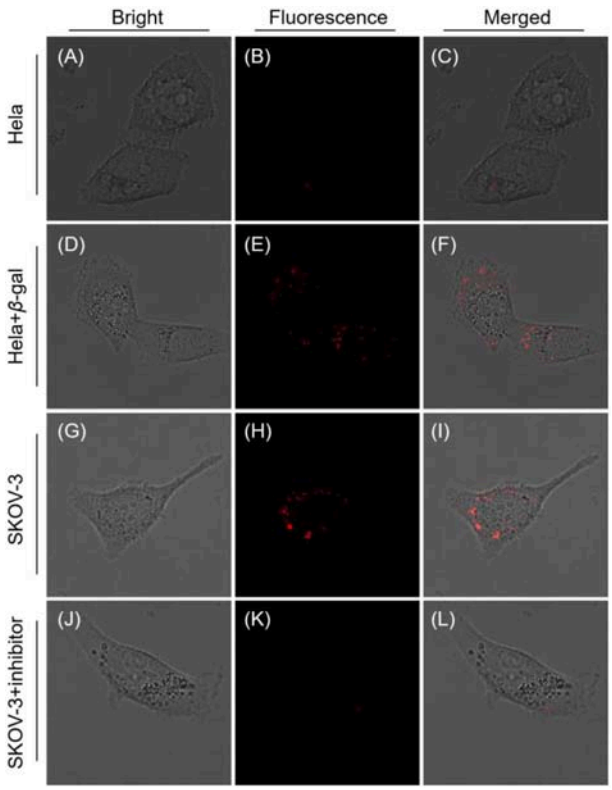

FIGURE 3 | Confocal laser scanning microscopy (CLSM) images of Hela and SKOV-3 cells incubated with QM-HBT-βgal (10 μM) for 4 h: **(A–C)** Hela cells, **(D–F)** Hela cells pretreated with 1 mM β-gal for 0.5 h. **(G–I)** SKOV-3 cells, and **(J–L)** SKOV-3 cells pretreated with 1 mM inhibitor for 0.5 h. The window of fluorescence emission collection is 650–700 nm, $\lambda_{ex} = 460$ nm.

the fluorescence intensity around 650 nm of QM-HBT-βgal gradually enhanced and showed a linear correlation vs. the concentration of β-gal in the range of 0–12 U with a correlation coefficient of 0.991 (**Figure 2D**). Obviously, these remarkable characteristics of QM-HBT-βgal indicated that it could be capable of detecting β-gal activity.

Photostability and Selectivity

The high photostability of QM-HBT-βgal is very crucial to perform long-term tracking and high-fidelity imaging of enzyme activity in preclinical applications. Compared with the commercial FDA-approved NIR contrast agent ICG, the time-dependent absorbance measurements were also conducted to evaluate the photostability of QM-HBT-βgal upon continuous illumination (Hamamatsu, LC8 Lightningcure, 300 W) in aqueous solution (**Figure 2E**). As calculated, the half-life of QM-HBT-βgal (∼1,500 s) is 60-fold longer than that of ICG (∼25 s), suggestive of excellent photostability of QM-HBT-βgal, which further confirmed its potential application in long-term tracking.

We further study the stability of the probe QM-HBT-βgal in different pH values. **Figure 2F** indicates excellent stability of QM-HBT-βgal in various pH values (3–11), and its excellent stability remained in fresh mouse serum over 24 h (**Figure 2G**). In addition, the probe QM-HBT-βgal exhibits excellent pH stability in the medium of FBS (**Figures S4, S8** and **S9**). Furthermore, prior to investigating endogenous β-gal activity in living cells, the specificity of QM-HBT-βgal toward β-gal was also evaluated with potential competitive species including amino acids, enzymes, serum markers, and metabolic substances. As shown in **Figure 2H**, compared with β-gal, nearly negligible fluorescence change of QM-HBT-βgal makes it a promising candidate to achieve accurate detection under practical applications.

Sensing Mechanism

For gaining insight into the activation mechanism of probe QM-HBT-βgal for enzyme β-gal, and then *in situ* release of QM-HBT-OH as NIR AIEgens, we acquired high-resolution mass spectrometry to confirm this proposed mechanism. In the electrospray ionization (ESI)-MS spectra of QM-HBT-βgal with β-gal, the peaks of QM-HBT-βgal and QM-HBT-O^- were found at *m/z* 649.2214 and 485.1365 (**Figure 2I**), respectively. The result clearly indicated that QM-HBT-βgal could be specifically activated by enzyme β-gal, and release QM-HBT-OH as NIR AIEgens.

Imaging of Endogenous β-gal in Living Cells

In order to study the biocompatibility of probe QM-HBT-βgal, standard 5-diphenyltetrazolium bromide (MTT) assays in human ovarian carcinoma cells (SKOV-3 cells) and human epithelioid cervical carcinoma cells (Hela cells) were carried out, respectively. As is observed in **Figure S5**, experimental results verified that probe QM-HBT-βgal has almost no cytotoxicity toward living cells.

Taken all together, the probe QM-HBT-βgal is anticipated to be capable of accurately detecting the endogenous enzyme activity in living cells with *in situ* formation of AIEgen nanoaggregates. To demonstrate this potential, SKOV-3 cells were used as a model, because they overexpress β-gal (Asanuma et al., 2015), while Hela cells without expressed β-gal were used as a negative control model. As depicted in **Figures 3A–C**, no fluorescence was observed at the Hela cells, in accordance with the weak fluorescence spectrum of QM-HBT-βgal. In contrast, by adding an exogenous 10 U β-gal to Hela cells, a significant enhancement of fluorescence (**Figures 3D–F**) was observed due to further the enzyme conversion process. As demonstrated, the enzyme-catalyzed AIE-active NIR fluorescent probe QM-HBT-βgal can be used to detect β-gal in cancer cells. Impressively, SKOV-3 cells, which were treated with QM-HBT-βgal for 3 h, exhibit strong fluorescence in its NIR fluorescent channel (**Figures 3G–I**), suggesting its possible reaction with endogenous β-gal in the cells. These AIE-active signals were interpreted as being insoluble aggregates of released QM-HBT-OH, only occurring at the site where the probe is reacted with β-gal. To verify that the fluorescence change was caused by endogenous β-gal, 1 mM D-galactose (an inhibitor of β-gal; Portaccio et al., 1998) was used to pretreat the cells for 0.5 h. Negligible fluorescence signal was observed in the NIR channel (**Figures 3J–L**), indicating that the enhancement in SKOV-3 cells indeed results from the endogenous β-gal activity.

To establish the precise intracellular localization, co-staining experiments of QM-HBT-βgal were performed with SKOV-3 cells. The AIE-active probe QM-HBT-βgal co-staining with commercially available Golgi-Tracker Green, LysoTracker Red, ER-Tracker Red, and Mito-Tracker Red shows an obvious co-localization characteristic (**Figure 4**). Specifically, the red channel

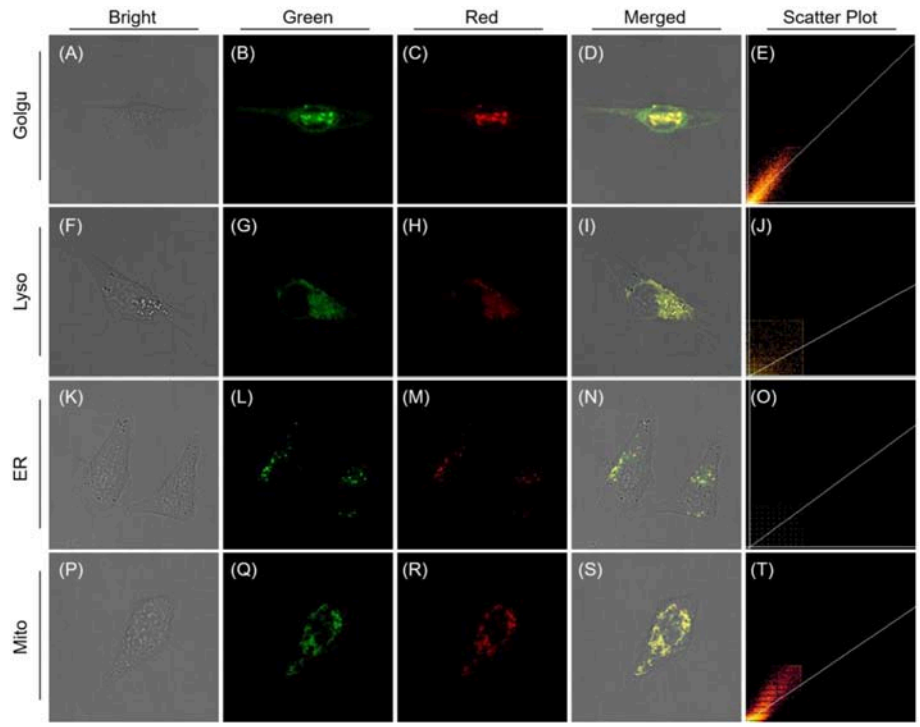

FIGURE 4 | CLSM images for intracellular localization of QM-HBT-βgal in SKOV-3 cells. Cells were incubated with QM-HBT–βgal (10 μM) for 2 h and then co-stained with 1 μM Golgi-Tracker Green (BODIPY FL C5-Ceramide) **(A–E)**, 100 nM Lyso-Tracker Red DND-99 **(F–J)**, 1 μM ER-Tracker Red (BODIPY TR Glibenclamide) **(K–O)**, and 200 nM Mito-Tracker Red for 30 min **(P–T)**, respectively. The green channel at 510–530 nm for Golgi-Tracker Green **(B)**, λ_{ex} = 505 nm; 610–630 nm for ER-Tracker Red **(L)**, 590–610 nm for Lyso-Tracker Red DND-99 **(G)** and Mito-Tracker Red **(Q)**, λ_{ex} = 561 nm. The red channel at 650–700 nm, λ_{ex} = 460 nm.

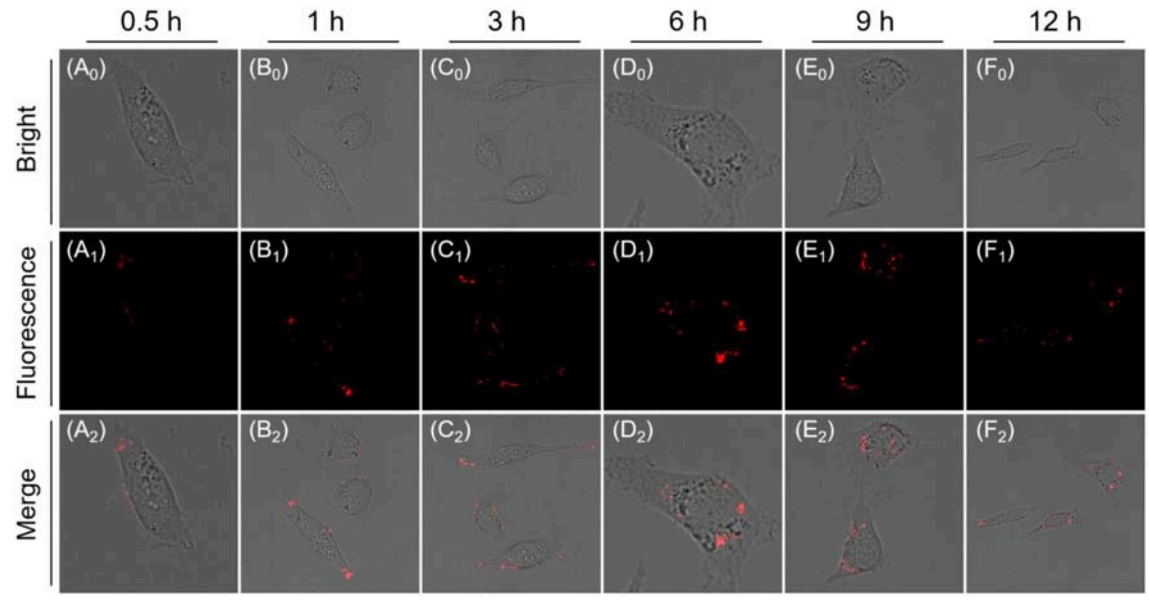

FIGURE 5 | Time-dependent CLSM images of SKOV-3 cells incubated with QM-HBT-βgal (10 μM) (**A_0-F_0**: Bright field, **A_1-F_1**: Fluorescence channel) and (**A_2-F_2**: Merge channel). The window of fluorescence emission collection is 650–700 nm (λ_{ex} = 460 nm).

from AIEgen nanoaggregates largely overlaps with the green channel from Mito-Tracker Red and Golgi-Tracker Red, with Pearson's correlation coefficients of 0.8977 and 0.8522 (**Table S1**). These results indicate that enzyme-catalyzed AIEgen QM-HBT-OH tends to mainly accumulate in the mitochondria and Golgi body.

Furthermore, long-term tracking of endogenous β-gal experiments also conducted in living cells. Indeed, its fluorescence intensity slowly increases and reaches a plateau at 3 h, which does not change significantly over the next 3 h ($t = 6$ h; **Figure 5**), suggesting the AIE-active NIR fluorescent signal is ascribed to nanoaggregate formation, which could amplify the fidelity signals because of emitting stronger during concentration enrichment of AIEgen nanoaggregates. Most importantly, AIEgen nanoaggregates do not easily leak out of cells during prolonged incubation, due to its lipophilicity of extending π-conjugated backbone. When the incubation time was increased to 12 h, the intracellular fluorescence intensity was slightly attenuated and was fixed in the local region (**Figure 5**). In addition, we use the commercial non-*in situ* fluorescent probe (ICG) and the reported probe DCM-βgal by introducing ACQ fluorophore dicyanomethylene-4*H*-pyran (DCM) as control compounds (**Figures S6, S7**), demonstrating the long-term tracking capability of NIR AIE-active QM-HBT-βgal.

Altogether, all these experiment results verified that the AIE-active NIR probe QM-HBT-βgal can overcome intracellular diffusion and attain high-fidelity enzyme information, enabling *in situ* and long-term tracking of β-gal in SKOV-3 cells.

CONCLUSIONS

In summary, we have developed an enzyme-responsive NIR AIE-active probe QM-HBT-βgal for *in situ* and long-term tracking of endogenous β-gal activity, overcoming the dilemma of the requirement for released molecular fluorophores between diffusion-resistant and ACQ effect. Notably, QM-HBT-βgal is almost non-emissive in aqueous media, and upon the addition of β-gal, the masking groups at the hydroxyl moieties of QM-HBT-βgal were removed, thus recovering ESIPT and strong AIE-active NIR fluorescent signal in the aggregate states. Compared with other available β-gal probes, the AIE-active NIR probe QM-HBT-βgal not only provides localization signal of the β-gal at the reaction site but also avoids self-quenching when accumulated in cells, making obvious the advance in high-fidelity detection of endogenous enzyme activity. This study provides a promising strategy for the design of NIR AIE-active probes, paving a new pathway for *in situ* and long-term tracking of enzyme activity in preclinical applications.

AUTHOR CONTRIBUTIONS

WF and CY contributed equally. WF and CY was responsible for performing the experiments and writing manuscript. YZ and YM were responsible for providing cells. W-HZ were responsible for discussing experimental results. ZG was responsible for designing experiments and revising the paper.

FUNDING

This work was supported by NSFC/China (21788102, 21622602, 21636002, and 81522045), the National Key Research and Development Program (2017YFC0906902 and 2016YFA0200300), the Shanghai Municipal Science and Technology Major Project (grant no. 2018SHZDZX03), the Shuguang Program of Shanghai Education Development Foundation and Shanghai Municipal Education Commission (18SG27), and the Scientific Committee of Shanghai (15XD1501400).

SUPPLEMENTARY MATERIAL

The Supplementary Material for this article can be found online at: https://www.frontiersin.org/articles/10.3389/fchem.2019.00291/full#supplementary-material

REFERENCES

Andreasson, J., and Pischel, U. (2018). Molecules for security measures: from keypad locks to advanced communication protocols. *Chem. Soc. Rev.* 47, 2266–2279. doi: 10.1039/c7cs00287d

Asanuma, D., Sakabe, M., Kamiya, M., Yamamoto, K., Hiratake, J., Ogawa, M., et al. (2015). Sensitive β-galactosidase-targeting fluorescence probe for visualizing small peritoneal metastatic tumours *in vivo*. *Nat. Commun.* 6:6463. doi: 10.1038/ncomms7463

Bhuniya, S., Maiti, S., Kim, E. J., Lee, H., Sessler, J. L., Hong, K. S., et al. (2014). An activatable theranostic for targeted cancer therapy and imaging. *Angew. Chem. Int. Ed.* 53, 4469–4474. doi: 10.1002/anie.201311133

Chen, L., Wu, D., Kim, J. M., and Yoon, J. (2017). An ESIPT-based fluorescence probe for colorimetric, ratiometric, and selective detection of phosgene in solutions and the gas phase. *Anal. Chem.* 89, 12596–12601. doi: 10.1021/acs.analchem.7b03988

Chen, X., Lee, D., Yu, S., Kim, G., Lee, S., Cho, Y., et al. (2017). *In vivo* near-infrared imaging and phototherapy of tumors using a cathepsin B-activated fluorescent probe. *Biomaterials* 122, 130–140. doi: 10.1016/j.biomaterials.2017.01.020

Chen, Y. H., Wei, T. W., Zhang, Z. J., Chen, T. T., Li, J., Qiang, J., et al. (2017). A benzothiazole-based fluorescent probe for ratiometric detection of Al^{3+} in aqueous medium and living cells. *Ind. Eng. Chem. Res.* 56, 12267–12275. doi: 10.1021/acs.iecr.7b02979

Chevalier, A., Zhang, Y., Khdour, O. M., Kaye, J. B., and Hecht, S. M. (2016). Mitochondrial nitroreductase activity enables selective imaging and therapeutic targeting. *J. Am. Chem. Soc.* 138, 12009–12012. doi: 10.1021/jacs.6b06229

Cui, L., Baek, Y., Lee, S., Kwon, N., and Yoon, J. (2016). An AIE and ESIPT based kinetically resolved fluorescent probe for biothiols. *J. Mater. Chem. C* 4, 2909–2914. doi: 10.1039/c5tc03272e

Dimri, G. P., Lee, X., Basile, G., Acosta, M., Scott, G., Roskelley, C., et al. (1995). A biomarker that identifies senescent human cells in culture and in aging skin *in vivo*. *Proc. Natl. Acad. Sci. U.S.A.* 92, 9363–9367.

Feng, G., and Liu, B. (2018). Aggregation-induced emission (AIE) dots: emerging theranostic nanolights. *Acc. Chem. Res.* 51, 1404–1414. doi: 10.1021/acs.accounts.8b00060

Gu, K., Xu, Y., Li, H., Guo, Z., Zhu, S., Zhu, S., et al. (2016). Real-time tracking and *in vivo* visualization of β-galactosidase activity in colorectal tumor with a

ratiometric near-infrared fluorescent probe. *J. Am. Chem. Soc.* 138, 5334–5340. doi: 10.1021/jacs.6b01705

Guo, Z., Park, S., Yoon, J., and Shin, I. (2014). Recent progress in the development of near-infrared fluorescent probes for bioimaging applications. *Chem. Soc. Rev*. 43, 16–29. doi: 10.1039/c3cs60271k

Guo, Z. Q., Shao, A. D., and Zhu, W. H. (2016). Long wavelength AIEgen of quinoline-malononitrile. *J. Mater. Chem. C* 4, 2640–2646. doi: 10.1039/c5tc03369a

Hu, Q., Gao, M., Feng, G., and Liu, B. (2014). Mitochondria-targeted cancer therapy using a light-up probe with aggregation-induced-emission characteristics. *Angew. Chem. Int. Ed.* 53, 14225–14229. doi: 10.1002/anie.201408897

Kamiya, M., Asanuma, D., Kuranaga, E., Takeishi, A., Sakabe, M., Miura, M., et al. (2011). β-Galactosidase fluorescence probe with improved cellular accumulation based on a spirocyclized rhodol scaffold. *J. Am. Chem. Soc.* 133, 12960–12963. doi: 10.1021/ja204781t

Kwok, R. T., Leung, C. W., Lam, J. W., and Tang, B. Z. (2015). Biosensing by luminogens with aggregation-induced emission characteristics. *Chem. Soc. Rev.* 44, 4228–4238. doi: 10.1039/c4cs00325j

Kwon, J. E., and Park, S. Y. (2011). Advanced organic optoelectronic materials: harnessing excited-state intramolecular proton transfer (ESIPT) process. *Adv. Mater*. 23, 3615–3642. doi: 10.1002/adma.201102046

Leung, C. W., Hong, Y., Chen, S., Zhao, E., Lam, J. W., and Tang, B. Z. (2013). A photostable AIE luminogen for specific mitochondrial imaging and tracking. *J. Am. Chem. Soc.* 135, 62–65. doi: 10.1021/ja310324q

Li, L., Zhang, C. W., Chen, G. Y., Zhu, B., Chai, C., Xu, Q. H., et al. (2014). A sensitive two-photon probe to selectively detect monoamine oxidase B activity in Parkinson's disease models. *Nat. Commun.* 5:3276. doi: 10.1038/ncomms4276

Li, X., Gao, X., Shi, W., and Ma, H. (2014). Design strategies for water-soluble small molecular chromogenic and fluorogenic probes. *Chem. Rev.* 114, 590–659. doi: 10.1021/cr300508p

Li, X., Kwon, N., Guo, T., Liu, Z., and Yoon, J. (2018). Innovative strategies for hypoxic-tumor photodynamic therapy. *Angew. Chem. Int. Ed.* 57, 11522–11531. doi: 10.1002/anie.201805138

Li, Y., Sun, Y., Li, J., Su, Q., Yuan, W., Dai, Y., et al. (2015). Ultrasensitive near-infrared fluorescence-enhanced probe for *in vivo* nitroreductase imaging. *J. Am. Chem. Soc.* 137, 6407–6416. doi: 10.1021/jacs.5b04097

Lim, S. Y., Hong, K. H., Kim, D. I., Kwon, H., and Kim, H. J. (2014). Tunable heptamethine-azo dye conjugate as an NIR fluorescent probe for the selective detection of mitochondrial glutathione over cysteine and homocysteine. *J. Am. Chem. Soc.* 136, 7018–7025. doi: 10.1021/ja500962u

Liu, H. W., Li, K., Hu, X. X., Zhu, L., Rong, Q., Liu, Y., et al. (2017). *In situ* localization of enzyme activity in live cells by a molecular probe releasing a precipitating fluorochrome. *Angew. Chem. Int. Ed.* 56, 11788–11792. doi: 10.1002/anie.201705747

Liu, L., Zhang, F., Xu, B., and Tian, W. (2017). Silica nanoparticles based on an AIE-active molecule for ratiometric detection of RNS *in vitro*. *J. Mater. Chem. B* 5, 9197–9203. doi: 10.1039/c7tb02734f

Liu, Z., Zhou, X., Miao, Y., Hu, Y., Kwon, N., Wu, X., et al. (2017). A reversible fluorescent probe for real-time quantitative monitoring of cellular glutathione. *Angew. Chem. Int. Ed.* 56, 5812–5816. doi: 10.1002/anie.201702114

Makukhin, N., Tretyachenko, V., Moskovitz, J., and Misek, J. (2016). A ratiometric fluorescent probe for imaging of the activity of methionine sulfoxide reductase A in cells. *Angew. Chem. Int. Ed.* 55, 12727–12730. doi: 10.1002/anie.201605833

Mei, J., Leung, N. L., Kwok, R. T., Lam, J. W., and Tang, B. Z. (2015). Aggregation-induced emission: together we shine, united we soar! *Chem. Rev.* 115, 11718–11940. doi: 10.1021/acs.chemrev.5b00263

Nicol, A., Kwok, R. T. K., Chen, C., Zhao, W., Chen, M., Qu, J., et al. (2017). Ultrafast delivery of aggregation-induced emission nanoparticles and pure organic phosphorescent nanocrystals by saponin encapsulation. *J. Am. Chem. Soc.* 139, 14792–14799. doi: 10.1021/jacs.7b08710

Peng, L., Gao, M., Cai, X., Zhang, R., Li, K., Feng, G., et al. (2015). A fluorescent light-up probe based on AIE and ESIPT processes for β-galactosidase activity detection and visualization in living cells. *J. Mater. Chem. B* 3, 9168–9172. doi: 10.1039/c5tb01938a

Portaccio, M., Stellato, S., Rossi, S., Bencivenga, U., Mohy Eldin, M. S., Gaeta, F. S., et al. (1998). Galactose competitive inhibition of β-galactosidase (*Aspergillus oryzae*) immobilized on chitosan and nylon supports. *Enzyme Microb. Technol.* 23, 101–106.

Qi, Y., Huang, Y., Li, B., Zeng, F., and Wu, S. (2018). Real-time monitoring of endogenous cysteine levels *in vivo* by near-infrared turn-on fluorescent probe with large stokes shift. *Anal. Chem.* 90, 1014–1020. doi: 10.1021/acs.analchem.7b04407

Qin, W., Ding, D., Liu, J., Yuan, W. Z., Hu, Y., Liu, B., et al. (2012). Biocompatible nanoparticles with aggregation-induced emission characteristics as far-red/near-infrared fluorescent bioprobes for *in vitro* and *in vivo* imaging applications. *Adv. Funct. Mater.* 22, 771–779. doi: 10.1002/adfm.201102191

Sedgwick, A. C., Dou, W. T., Jiao, J. B., Wu, L., Williams, G. T., Jenkins, A. T. A., et al. (2018a). An ESIPT probe for the ratiometric imaging of peroxynitrite facilitated by binding to β-aggregates. *J. Am. Chem. Soc.* 140, 14267–14271. doi: 10.1021/jacs.8b08457

Sedgwick, A. C., Wu, L., Han, H. H., Bull, S. D., He, X. P., James, T. D., et al. (2018b). Excited-state intramolecular proton-transfer (ESIPT) based fluorescence sensors and imaging agents. *Chem. Soc. Rev.* 47, 8842–8880. doi: 10.1039/c8cs00185e

Shao, A., Xie, Y., Zhu, S., Guo, Z., Zhu, S., Guo, J., et al. (2015). Far-red and near-IR AIE-active fluorescent organic nanoprobes with enhanced tumor-targeting efficacy: shape-specific effects. *Angew. Chem. Int. Ed.* 54, 7275–7280. doi: 10.1002/anie.201501478

Shao, A. D., Guo, Z. Q., Zhu, S. J., Zhu, S. Q., Shi, P., Tian, H., et al. (2014). Insight into aggregation-induced emission characteristics of red-emissive quinoline-malononitrile by cell tracking and real-time trypsin detection. *Chem. Sci.* 5, 1383–1389. doi: 10.1039/c3sc52783b

Shi, C., Guo, Z., Yan, Y., Zhu, S., Xie, Y., Zhao, Y. S., et al. (2013). Self-assembly solid-state enhanced red emission of quinolinemalononitrile: optical waveguides and stimuli response. *ACS Appl. Mater. Interfaces* 5, 192–198. doi: 10.1021/am302466m

Shi, X., Yu, C. Y. Y., Su, H., Kwok, R. T. K., Jiang, M., He, Z., et al. (2017). A red-emissive antibody-AIEgen conjugate for turn-on and wash-free imaging of specific cancer cells. *Chem. Sci.* 8, 7014–7024. doi: 10.1039/c7sc01054k

Spergel, D. J., Krüth, U., Shimshek, D. R., Sprengel, R., and Seeburg, P. H. (2001). Using reporter genes to label selected neuronal populations in transgenic mice for gene promoter, anatomical, and physiological studies. *Prog. Neurobiol.* 63, 673–686. doi: 10.1016/s0301-0082(00)00038-1

Sun, W., Guo, S., Hu, C., Fan, J., and Peng, X. (2016). Recent development of chemosensors based on cyanine platforms. *Chem. Rev.* 116, 7768–7817. doi: 10.1021/acs.chemrev.6b00001

Sun, X., Xu, Q., Kim, G., Flower, S. E., Lowe, J. P., Yoon, J., et al. (2014). A water-soluble boronate-based fluorescent probe for the selective detection of peroxynitrite and imaging in living cells. *Chem. Sci.* 5, 3368–3373. doi: 10.1039/c4sc01417k

Taylor, A., Wilson, K. M., Murray, P., Fernig, D. G., and Levy, R. (2012). Long-term tracking of cells using inorganic nanoparticles as contrast agents: are we there yet? *Chem. Soc. Rev.* 41, 2707–2717. doi: 10.1039/c2cs35031a

Thorn-Seshold, O., Vargas-Sanchez, M., McKeon, S., and Hasserodt, J. (2012). A robust, high-sensitivity stealth probe for peptidases. *Chem. Commun.* 48, 6253–6255. doi: 10.1039/c2cc32227g

Wang, F., Zhu, Y., Zhou, L., Pan, L., Cui, Z., Fei, Q., et al. (2015). Fluorescent *in situ* targeting probes for rapid imaging of ovarian-cancer-specific gamma-glutamyltranspeptidase. *Angew. Chem. Int. Ed.* 54, 7349–7353. doi: 10.1002/anie.201502899

Wang, H., Ma, K., Xu, B., and Tian, W. (2016). Tunable supramolecular interactions of aggregation-induced emission probe and graphene oxide with biomolecules: an approach toward ultrasensitive label-free and "turn-on" DNA sensing. *Small* 12, 6613–6622. doi: 10.1002/smll.201601544

Wang, M., Xu, Y., Liu, Y., Gu, K., Tan, J., Shi, P., et al. (2018). Morphology tuning of aggregation-induced emission probes by flash nanoprecipitation: shape and size effects on *in vivo* imaging. *ACS Appl. Mater. Interfaces* 10, 25186–25193. doi: 10.1021/acsami.8b08159

Wang, Y.-L., Fan, C., Xin, B., Zhang, J.-P., Luo, T., Chen, Z.-Q., et al. (2018). AIE-based super-resolution imaging probes for β-amyloid plaques in mouse brains. *Mater. Chem. Front.* 2, 1554–1562. doi: 10.1039/c8qm00209f

Wang, Z., Chen, S., Lam, J. W., Qin, W., Kwok, R. T., Xie, N., et al. (2013). Long-term fluorescent cellular tracing by the aggregates of AIE bioconjugates. *J. Am. Chem. Soc.* 135, 8238–8245. doi: 10.1021/ja312581r

Wu, D., Sedgwick, A. C., Gunnlaugsson, T., Akkaya, E. U., Yoon, J., and James, T. D. (2017). Fluorescent chemosensors: the past, present and future. *Chem. Soc. Rev.* 46, 7105–7123. doi: 10.1039/c7cs00240h

Wu, X., Li, L., Shi, W., Gong, Q., and Ma, H. (2016). Near-infrared fluorescent probe with new recognition moiety for specific detection of tyrosinase activity: design, synthesis, and application in living cells and zebrafish. *Angew. Chem. Int. Ed.* 55, 14728–14732. doi: 10.1002/anie.201609895

Wu, X., Sun, X., Guo, Z., Tang, J., Shen, Y., James, T. D., et al. (2014). *In vivo* and *in situ* tracking cancer chemotherapy by highly photostable NIR fluorescent theranostic prodrug. *J. Am. Chem. Soc.* 136, 3579–3588. doi: 10.1021/ja412380j

Xie, S., Wong, A. Y. H., Kwok, R. T. K., Li, Y., Su, H., Lam, J. W. Y., et al. (2018). Fluorogenic Ag(+) -tetrazolate aggregation enables efficient fluorescent biological silver staining. *Angew. Chem. Int. Ed.* 57, 5750–5753. doi: 10.1002/anie.201801653

Xu, K., Luan, D., Wang, X., Hu, B., Liu, X., Kong, F., et al. (2016). An ultrasensitive cyclization-based fluorescent probe for imaging native HOBr in live cells and zebrafish. *Angew. Chem. Int. Ed.* 55 , 12751–12754. doi: 10.1002/anie.201606285

Xu, Q., Heo, C. H., Kim, G., Lee, H. W., Kim, H. M., and Yoon, J. (2015). Development of imidazoline-2-thiones based two-photon fluorescence probes for imaging hypochlorite generation in a co-culture system. *Angew. Chem. Int. Ed.* 54, 4890–4894. doi: 10.1002/anie.201500537

Xu, Q., Heo, C. H., Kim, J. A., Lee, H. S., Hu, Y., Kim, D., et al. (2016). A selective imidazoline-2-thione-bearing two-photon fluorescent probe for hypochlorous acid in mitochondria. *Anal. Chem.* 88, 6615–6620. doi: 10.1021/acs.analchem.6b01738

Yan, C., Guo, Z., Liu, Y., Shi, P., Tian, H., and Zhu, W. H. (2018a). A sequence-activated AND logic dual-channel fluorescent probe for tracking programmable drug release. *Chem. Sci.* 9, 6176–6182. doi: 10.1039/c8sc02079e

Yan, C., Guo, Z., Shen, Y., Chen, Y., Tian, H., and Zhu, W. H. (2018b). Molecularly precise self-assembly of theranostic nanoprobes within a single-molecular framework for *in vivo* tracking of tumor-specific chemotherapy. *Chem. Sci.* 9, 4959–4969. doi: 10.1039/c8sc01069b

Yan, J., Lee, S., Zhang, A., and Yoon, J. (2018c). Self-immolative colorimetric, fluorescent and chemiluminescent chemosensors. *Chem. Soc. Rev.* 47, 6900–6916. doi: 10.1039/c7cs00841d

Yan, L., Zhang, Y., Xu, B., and Tian, W. (2016). Fluorescent nanoparticles based on AIE fluorogens for bioimaging. *Nanoscale* 8, 2471–2487. doi: 10.1039/c5nr05051k

Yang, J., Ren, Z., Xie, Z., Liu, Y., Wang, C., Xie, Y., et al. (2017). AIEgen with fluorescence-phosphorescence dual mechanoluminescence at room temperature. *Angew. Chem. Int. Ed.* 56, 880–884. doi: 10.1002/anie.201610453

Yang, Y., Zhao, Q., Feng, W., and Li, F. (2013). Luminescent chemodosimeters for bioimaging. *Chem. Rev.* 113, 192–270. doi: 10.1021/cr2004103

Yin, J., Kwon, Y., Kim, D., Lee, D., Kim, G., Hu, Y., et al. (2014). Cyanine-based fluorescent probe for highly selective detection of glutathione in cell cultures and live mouse tissues. *J. Am. Chem. Soc.* 136, 5351–5358. doi: 10.1021/ja412628z

Yuan, Y., Zhang, C. J., Xu, S., and Liu, B. (2016). A self-reporting AIE probe with a built-in singlet oxygen sensor for targeted photodynamic ablation of cancer cells. *Chem. Sci.* 7, 1862–1866. doi: 10.1039/c5sc03583j

Zhang, F., Di, Y., Li, Y., Qi, Q., Qian, J., Fu, X., et al. (2017). Highly efficient far red/near-infrared fluorophores with aggregation-induced emission for bioimaging. *Dyes Pigm.* 142, 491–498. doi: 10.1016/j.dyepig.2017.04.004

Zhang, J., Chai, X., He, X. P., Kim, H. J., Yoon, J., and Tian, H. (2018). Fluorogenic probes for disease-relevant enzymes. *Chem. Soc. Rev.* 48, 683–722. doi: 10.1039/c7cs00907k

Zhang, L., Duan, D., Liu, Y., Ge, C., Cui, X., Sun, J., et al. (2014). Highly selective off-on fluorescent probe for imaging thioredoxin reductase in living cells. *J. Am. Chem. Soc.* 136, 226–233. doi: 10.1021/ja408792k

Zhang, P., Nie, X., Gao, M., Zeng, F., Qin, A., Wu, S., et al. (2017). A highly selective fluorescent nanoprobe based on AIE and ESIPT for imaging hydrogen sulfide in live cells and zebrafish. *Mater. Chem. Front.* 1, 838–845. doi: 10.1039/c6qm00223d

Zhou, J., Shi, W., Li, L., Gong, Q., Wu, X., Li, X., et al. (2016). Detection of misdistribution of tyrosinase from melanosomes to lysosomes and its upregulation under psoralen/ultraviolet a with a melanosome-targeting tyrosinase fluorescent probe. *Anal. Chem.* 88, 4557–4564. doi: 10.1021/acs.analchem.6b00742

Zhou, L., Zhang, X., Lv, Y., Yang, C., Lu, D., Wu, Y., et al. (2015). Localizable and photoactivatable fluorophore for spatiotemporal two-photon bioimaging. *Anal. Chem.* 87, 5626–5631. doi: 10.1021/acs.analchem.5b00691

Zhou, P., and Han, K. (2018). Unraveling the detailed mechanism of excited-state proton transfer. *Acc. Chem. Res.* 51, 1681–1690. doi: 10.1021/acs.accounts.8b00172

Zhu, H., Fan, J., Du, J., and Peng, X. (2016). Fluorescent probes for sensing and imaging within specific cellular organelles. *Acc. Chem. Res.* 49, 2115–2126. doi: 10.1021/acs.accounts.6b00292

Conflict of Interest Statement: The authors declare that the research was conducted in the absence of any commercial or financial relationships that could be construed as a potential conflict of interest.

Copyright © 2019 Fu, Yan, Zhang, Ma, Guo and Zhu. This is an open-access article distributed under the terms of the Creative Commons Attribution License (CC BY). The use, distribution or reproduction in other forums is permitted, provided the original author(s) and the copyright owner(s) are credited and that the original publication in this journal is cited, in accordance with accepted academic practice. No use, distribution or reproduction is permitted which does not comply with these terms.

frontiers in Chemistry

REVIEW
published: 21 March 2019
doi: 10.3389/fchem.2019.00125

Chemical Biology Gateways to Mapping Location, Association, and Pathway Responsivity

Marcus J. C. Long[1†], *Xuyu Liu*[2†] *and Yimon Aye*[2*]

[1] *Independent Researcher, Beverley, United Kingdom,* [2] *École Polytechnique Fédérale de Lausanne, Institute of Chemical Sciences and Engineering, Lausanne, Switzerland*

Here we discuss, how by applying chemical concepts to biological problems, methods have been developed to map spatiotemporal regulation of proteins and small-molecule modulation of proteome signaling responses. We outline why chemical-biology platforms are ideal for such purposes. We further discuss strengths and weaknesses of chemical-biology protocols, contrasting them against classical genetic and biochemical approaches. We make these evaluations based on three parameters: occupancy; functional information; and spatial restriction. We demonstrate how the specific choice of chemical reagent and experimental set-up unite to resolve biological problems. Potential improvements/extensions as well as specific controls that in our opinion are often overlooked or employed incorrectly are also considered. Finally, we discuss some of the latest emerging methods to illuminate how chemical-biology innovations provide a gateway toward information hitherto inaccessible by conventional genetic/biochemical means. Finally, we also caution against solely relying on chemical-biology strategies and urge the field to undertake orthogonal validations to ensure robustness of results.

Keywords: chemical biology methods, T-REX, G-REX, APEX, Bio-ID, PUP-IT, Model organisms

OPEN ACCESS

Edited by:
John D. Wade,
Florey Institute of Neuroscience and Mental Health, Australia

Reviewed by:
Martin D. Witte,
University of Groningen, Netherlands
Giovanni Signore,
Scuola Normale Superiore di Pisa, Italy

***Correspondence:**
Yimon Aye
yimon.aye@epfl.ch

[†]*These authors have contributed equally to this work*

Specialty section:
This article was submitted to Chemical Biology, a section of the journal Frontiers in Chemistry

Received: *16 December 2018*
Accepted: *18 February 2019*
Published: *21 March 2019*

Citation:
Long MJC, Liu X and Aye Y (2019) Chemical Biology Gateways to Mapping Location, Association, and Pathway Responsivity. Front. Chem. 7:125. doi: 10.3389/fchem.2019.00125

This article is intended to be a primer for the use of chemical biology. We focus on processes that are limited kinetically by reactive chemistry or that use reactive short-lived molecules to perturb and/or monitor individual-protein- or locale-specific function in living systems. We begin by discussing the need for chemical biology and the underlying design/execution of chemical-biology experiments, including ways to avoid pitfalls. We subsequently highlight some of the latest, and what we consider most interesting, chemical-biology approaches and evaluate their benefits and limitations. These methods are contrasted against classical genetic and chemical/biochemical techniques.

THE NEED FOR CHEMICAL BIOLOGY: *BEYOND GENETICS AND BIOCHEMISTRY*

Chemical biology occupies a niche that is not adequately filled by traditional biological sciences. Biochemistry/enzymology are suited to understand proteins in isolation, or in lysates. Using these methods, functions of individual proteins have been divined (Knowles and Albery, 1977), rates of specific steps of enzyme-catalyzed reactions have been elucidated, and development of tools to modulate a specific enzymatic process has been established. For instance, inhibition experiments directly impact physiological studies because inhibitors can downregulate specific enzymatic

function expediently. Such events can in turn impact cellular pathways/processes rapidly, without the system being given the chance to compensate for the signaling changes incurred upon activity loss (as can occur during genetics experiments, *vide infra*). By measuring time-dependent effects, one can observe how the system responds to loss of the target protein's function. Such inhibition studies are of course also directly applicable to drug design and discovery. Perhaps Daniel Bovet's award of the 1957 Nobel Prize for physiology or medicine is the best example of the use of inhibitors for both academic and industrial pursuits[1]. The Nobel Prize in Physiology or Medicine 1957 was awarded to Daniel Bovet "for his discoveries relating to synthetic compounds that inhibit the action of certain body substances, and especially their action on the vascular system and the skeletal muscles." Inhibitors continue to be used to study age- or context-specific loss of protein function for comparison to genetic knockout studies or to better model diseases (Ogasawara et al., 2018). Of equal importance, since knockout and chemical inhibition are not necessarily the same in terms of percentage of loss of function and the effect on global protein function, such chemical-biology experiments require careful consideration and data interpretation (Hedstrom, 2017).

Biochemistry/enzymology also are often used to study *robust complexes or* individual protein function, such as by immunoprecipitation, or activity assays. However, these experiments are typically carried out in lysates or on purified proteins. Cellular compartmentalization is lost under these conditions, and several other contextual factors are also perturbed. Such biochemistry experiments were instrumental in unraveling many fundamental processes, like the nature of triplet codons (Matthaei et al., 1962). But in many instances, the loss of context that occurs upon lysis or upon isolation incurs artifacts or loss of activity/structure, due to, for example, incorrect preparation techniques (Darling and Reid, 1979; Wang et al., 2011), or expression conditions (Osz-Papai et al., 2015). Furthermore, these assays also require large amounts of protein, thereby losing track of information on cell-to-cell variation, for example. Small-molecule bulk-exposure regimens tend to lack resolution at the sub-cellular and organ/tissue scales, unless cell-surface behaviors are investigated using cell-impermeable molecules, or deploying, as we see below, chemical-biological tricks. It is worth noting that the intracellular concentration of a small molecule is not necessarily the concentration of the molecule in the media. Especially for reactive small molecules (Liu et al., 2019), there is often a concentration gradient across the cell.

On the other hand, genetic tools have proven powerful for studying the functions and necessities of genes, pathways, and specific-protein functions. Such studies can often be carried out in the subcellular locale or organ/tissue of choice. High-throughput screening approaches to find specific genetic associations, that are difficult to identify otherwise, have been applied to global analysis of protein stability (Yen et al., 2008), cell-to-cell variation (Livet et al., 2007), and pathway intersections. Genetics—often guided through biochemical/structural studies, random mutation of putatively-important mutants, or genomic sequencing of selected mutants showing resistance to an inhibitor, or rescue of a specific phenotype—offers ways to manipulate *steady-state* information flow. Oftentimes, these experiments can be carried out at the single-cell level. However, genetic techniques often lack dynamic range and precise temporal control, especially in higher eukaryotes, in all but a few instances. Thus, new methods were required to deliver high-resolution information on transient associations, to enable investigations of rapid gain of function, to effect localized perturbation, or to zoom-in on the signaling behavior of individual proteins/pathways.

These questions above have all been tackled to varying success by chemical biology. Chemical biology offers the ability to generate reactive chemical signals at will, or modulate chemical properties of specific proteins at a preordained time, often in specific locales for a specific duration. In many of the most pertinent and informative scenarios, chemical-biology methods offer insight because they can generate "on demand" highly-reactive small molecules, whose half-lives and diffusion distances are short (Parvez et al., 2018). Localization or duration control are often achieved in conjunction with genetically-encodable elements that can serve as frameworks for biocompatible processes. Thus, although a simplification, chemical biology exists to some extent to: (1) bring the power of *in vitro* analysis to the cell, and ideally to the whole organism; and to (2) extend genetically-encodable functions beyond those accessible through the use of canonical amino acids. Indeed, much of the advances of chemical biology have been made by researchers that seek to perform work on questions at a "triple point," i.e., the intersection of multiple fields, such as chemistry, enzymology, and cell signaling; or enzymology, bioinorganic chemistry, and genetics.

As chemical biology straddles several spheres of life sciences, we begin by discussing some intrinsic issues with chemical biology, and how they can be limited. We further discuss pitfalls and how to surmount them and aspects of good experimental design.

UTILITY TO MODEL ORGANISMS

One key benefit of genetic methods/analysis is applicability to model organisms and humans (e.g., through heredity maps, lineage information). Indeed, simply examining if a mutant or disease is dominant vs. recessive, and other simple hereditary patterns, can give clues to disease mechanisms that are informative (Wilkie, 1994). Most enzymology/biochemistry techniques are less applicable to model-organism studies. Ultimately many inhibitors/small-molecule-probes are either too toxic, metabolically unstable, or administered in cell/tissue-penetrable "prodrug" forms, yielding limited information to link a precise chemotype/target-engagement to phenotype. Of course, there are some excellent small-molecule modulators/probes applicable to numerous model organisms. Indeed, 92% of approved drugs targeting the human proteome are small molecule-derived as opposed to biologics (Santos et al., 2017). Ideal chemical-biology methods should be applicable to model

[1]https://www.nobelprize.org/prizes/medicine/1957/summary/

organisms; however, at the moment, few are generally applicable to much beyond cell culture. This limitation is in part because many methods require non-biocompatible chemical manipulations and/or use reagents either too toxic and/or impermeable to live models on the order of the experiment, thereby limiting the experiments to cultured cells or isolated organelles. Studies in lysates also remain a go-to strategy in proof-of-concept chemical-biology methods development, although these conditions provide little or no information on subcellular regulation or reflect close-to "real-world" conditions with respect to intracellular concentrations/assemblies/activities of specific macromolecules or metabolites. It is our hope that more model organism-based investigations with precise control in space, time, and context will surface in the future.

DEFINING ON-TARGET SPECIFICITY: NECESSITATING ORTHOGONAL VALIDATIONS

Generally, a small molecule used for chemical biology should be as non-invasive as possible. Thus, it should not ideally cause cell death, cell-cycle stall, or adversely affect relevant pathways. Thus, changes in the aforementioned parameters induced by the small molecule should all be assessed. Such assessments should be made early in methods development. Since most cells in culture are grown in high-serum media, ideally the compound should not interact strongly with serum. Should serum be an issue, low-serum media is available, or cells can be switched to serum-free conditions during compound exposure. Ideally, in model organisms, the molecule should also not affect growth, development, or fecundity, among other easily-measurable parameters. Should a molecule/regimen satisfy the above criteria, one can consider it biocompatible. However, it should be noted that most genes are in excess and are not absolutely required for growth/survival, especially in the rich conditions that we culture cells and organisms. These rich conditions may mask negative effects that could be observed under the intended experimental conditions, or when other stresses are added to the system. This is an ongoing issue for all research that is not easily addressable. We will elaborate on some ways chemical biologists have practically obviated these issues below.

Based on our current understanding of the number of proteins, protein-modified states, and protein-protein/protein–nucleic acid interactions, as well as the sheer number of non-protein molecules in cells, it seems highly unlikely that any molecule is "100% selective." Thus, there should always be concerns levied regarding off-target or artefactual effects arising due to use of small molecules, regardless of methods used to evaluate binding promiscuity 1962; Feldwisch-Drentrup, 2017. How binding promiscuity could impact a chemical-biology process depends on what the intended measurements are. Furthermore, observation of binding/labeling alone does not necessitate changes in enzyme activity/protein function, protein—protein/nucleic-acid interactions, or any process relevant to the intended experiment. Since the scope of this review does not warrant an extended discussion on IDing small-molecule targets, we focus here on methods aimed at assessing to what extent a specific output measured following a small-molecule treatment can be ascribed to a specific protein under study.

Integrating siRNA/shRNA-Knockdowns to Small-Molecule Experiments

One of the most common ways to use small molecules for mechanistic analysis is to assess whether a specific protein's activity is required for a process. Proteasome inhibitors are, for instance, commonly used to investigate degradation mechanisms (Goldberg, 2012). When using small-molecule inhibitors that are well characterized to validate if the activity of protein of interest (POI) or pathway is required for a specific function, it is responsible to assay more than one inhibitor targeting the POI or pathway (Zhang et al., 2013; Coffey et al., 2016; Conciatori et al., 2018; Smith et al., 2019) (**Figure 1A**). The use of inactive structural/regioisomeric analogs of a single inhibitor to verify "on-target" effects is inadequate, since if a modification manifested within the analog silences an on-target binding event, it may also silence off-target binding events, or affect permeation/stability, and overall negative data could be misinterpreted as "proving" on-target specificity (**Figure 1B**). However, in cases where there is high enantiospecificity shown by a chiral ligand, inactive epimers of the inhibitor that are inactive are useful (Bondeson et al., 2015).

An alternative way to validate inhibition assays is siRNA, or knockout technologies. Knockdown/knockout and inhibition are not necessarily identical to small molecules in terms of overall effect (Weiss et al., 2007). However, if the POI's chemical activity is required for a specific process, the effects of knockdown/knockout and inhibition should often be similar. To rule out off-target effects of the siRNA, at least two siRNAs are best deployed, separately per experiment. If all conditions, or the majority of conditions, agree with the postulate, this is good evidence that the POI is involved in the pathway. The logic of such experiments runs that the off-target binding of structurally-dissimilar inhibitors, or sequence-dissimilar siRNAs, is unlikely to converge at a point other than the desired target. As the number of different components of the comparison, and indeed the chemical difference across the different comparisons, increases, the robustness of such a conclusion also increases.

Finally, we note that cell-line validation is critical for genetic processes. This process must include both antibody validation and functional validation of knockdown, but may need to be extended to genotyping genes of interest, especially in cultured cells (Long et al., 2017a). Rigorous literature searches are also helpful to uncover other known issues surrounding generated/evolved lines (Princiotta et al., 2001), or species-specific effects (Gupta et al., 1986) that can potentially cause confounding results.

Integrating Resistant Cell Lines

If the mode of action of a compound is unknown, target-specificity validations are not as simple. One classic method to assess on-target effects of toxic drugs is to develop resistant cell

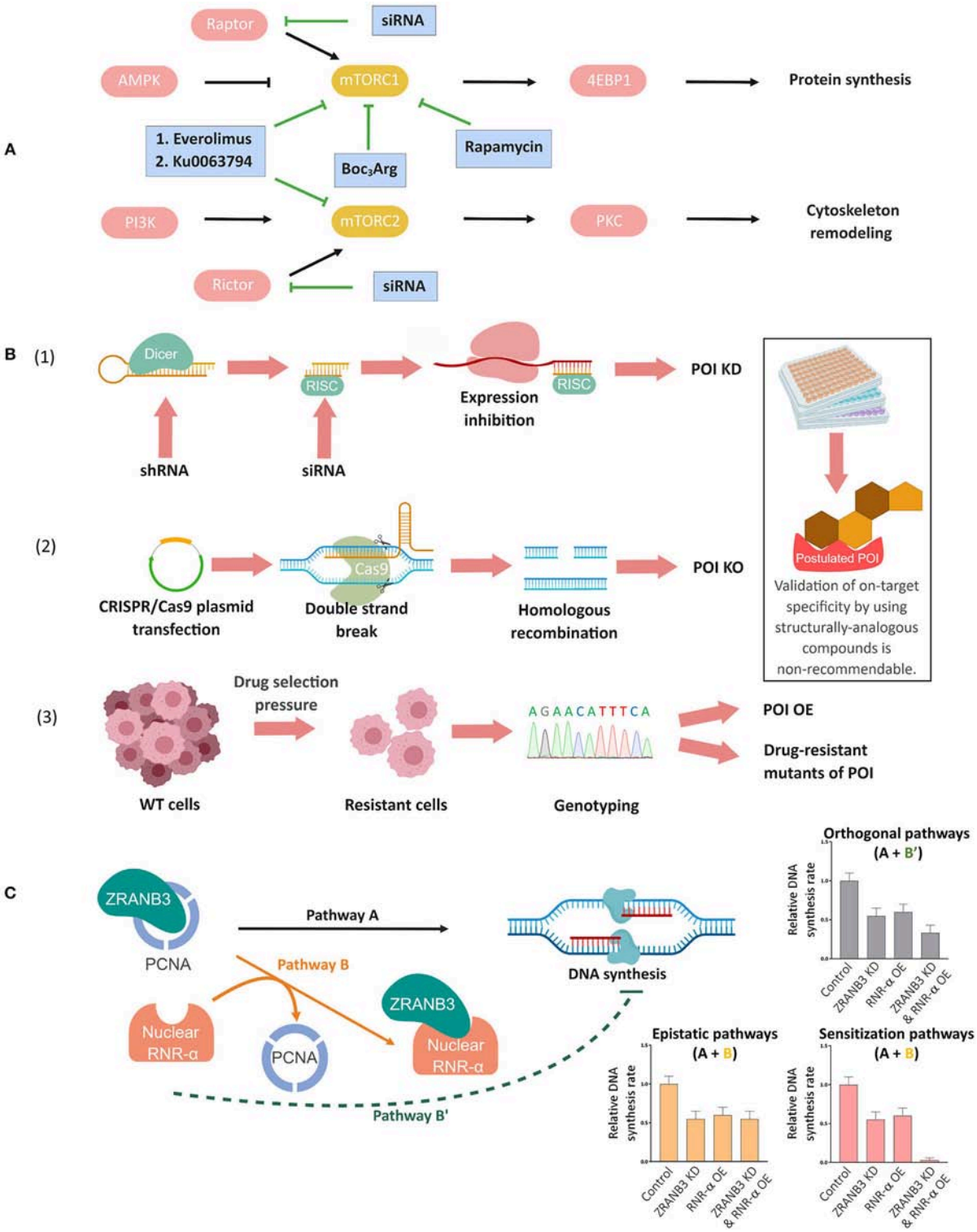

FIGURE 1 | Complementary genetic methods to validate chemical biology outcomes. **(A)** Deconvolution of mammalian target of rapamycin complex (mTORC)-1 and-2 signaling pathways using mTORC-1 selective small-molecule inhibitors, dual inhibitors of mTORC-1 and-2, and specific knockdown of the respective companion (Raptor or Rictor) of each mTORC (Conciatori et al., 2018). **(B)** Orthogonal validations to confirm on-target specificity of small-molecule probes/inhibitors. (1) siRNA/shRNA knockdown (KD), (2) targeted knockout (KO) through CRISPR/Cas9 or other gene-editing techniques, and (3) genotyping in resistant cell lines. In (1), Dicer, a ribonuclease-(RNase)-III converts shRNAs into siRNAs. The cleaved double-stranded RNA is incorporated into the RNA-induced silencing complex (RISC) and the resulting strand complementary to mRNA subsequently inhibits mRNA expression. In (2), mammalian cells are transfected with a plasmid containing desired

(Continued)

FIGURE 1 | sgRNA/Cas-9 combination, which results in the formation of a ribonucleoprotein complex of the Cas9 protein and the sgRNA upon expression. Upon the complementation between sgRNA and the target sequence, the Cas9 protein undergoes allosteric activation and cleaves the double-stranded DNA. This double-strand break (DSB) will lead to either non-homologous end joining (not shown, but the most commonly employed strategy to make a genetic knockout) or homologous recombination with an ectopic DNA repair template containing a deletion sequence (shown in figure). Upon cell colony selection, the desired KO will be confirmed experimentally**.** In (3) continued exposure, typically to escalating concentrations of a drug, can lead to selection of resistant cells that may overexpress the target protein (POI OE), or express drug resistant mutants, amongst other possibilities discussed in the text and elsewhere. Inset: Note that on-target validation using different analogs of the compounds is non-recommendable (see text). **(C)** *Concept of epistasis exemplified by nuclear RNR-α and ZRANB3 in DNA synthesis.* RNR-α, once inside nucleus, binds to ZRANB3 nuclear protein, displacing ZRANB3's cognate binding partner, PCNA, *in vitro* and in cell lysates. But this data alone does not prove that such a mechanism occurs in an intact cell. Cells deficient of ZRANB3 (i.e., ZRANB3-KD) suppresses DNA-synthesis by ∼30−40%, supporting the previous data on ZRANB3—PCNA binding-dependent DNA-synthesis (Pathway A). Overexpression (OE) of nuclear RNR-α suppresses DNA-synthesis to a similar extent but this result does not prove that ZRANB3 is a target of nuclear RNR-α in DNA-synthesis downregulation. By examining how nuclear RNR-α affects DNA-synthesis in ZRANB3-KD cells, the requirement of ZRANB3 for nuclear-RNR-α-dependent effects on DNA synthesis can be assessed. Indeed, in the absence of ZRANB3, nuclear-RNR-α-promoted DNA-synthesis suppression is ablated, supporting Pathway B (epistatic regulation via ZRANB3) over Pathway B'(direct downregulation, independent of ZRANB3), and also indicating that ZRANB3 is only a promoter of DNA synthesis (otherwise, the combination treatment would likely lead to a synergistic suppression of DNA synthesis). This analysis was also backed up by the fact that expression of RNR-α-binding-defective but otherwise functional ZRANB3-mutants renders cells resistant to nuclear-RNR-α-driven DNA-synthesis inhibition (Fu et al., 2018).

lines, as these may overexpress the drug target (**Figure 1B**). Thus, there are known lines resistant to inhibitors such as hydroxyurea, MK2206, and methotrexate overexpressing their target protein, namely, ribonucleotide reductase(RNR)-subunit-β (Eriksson et al., 1984; Aye et al., 2015), Akt3 (Stottrup et al., 2016), and dihydrofolate reductase (Schimke, 1988), respectively.

However, it should be noted that there are multiple mechanisms to effect resistance, aside from direct upregulation of the target. Examining methotrexate resistance as an example, beyond target-gene upregulation, upregulation of efflux and altered drug metabolism are common routes to resistance (Bertino et al., 1996; Ercikan-Abali et al., 1997; van der Heijden et al., 2007). Indeed, transcription and translation of specific genes are often responsive to their products inhibition, meaning that cells actively work to countermand suppression of activity, and also that protein-upregulation often accompanies small-molecule inhibition. Thus, assessment of protein expression of the intended target following inhibition should be routine.

Protein overexpression itself can have unexpected consequences. An overexpressed protein can achieve micro-molar concentrations in mammalian cells (Zhao et al., 2018). Thus, particularly in instances where binding efficacy is moderate-to-high (a situation that can easily render concentrations of compound administered similar to, or significantly lower than, the overexpressed protein), the overexpressed protein could significantly reduce concentrations of active compound, sacrificially protecting other important targets, without it actually ever being a biologically-relevant target. Furthermore, protein overexpression can rewire signaling networks such that a drug may no longer be effective due to hyper-stimulation of a compensatory pathway.

Integrating Functional Mutants

In some instances, overexpression of a resistant mutant—ideally with kinetic properties similar to that of the wild-type-protein—can also occur upon drug exposure. For instance, the discovery of RNR-α(D57N) mutant of the enzyme RNR that has similar *in vitro* kinetic activity (Aye and Stubbe, 2011) but is not inhibited by the native nucleotide dATP was discovered through such experiments (Ullman et al., 1980; Weinberg et al., 1981; Caras and Martin, 1988). These mutants can also be used to evaluate on-target specificity through overexpression, or better yet, through close-to-endogenous expression (**Figure 1B**; Wisitpitthaya et al., 2016). Under these conditions, mass action effects discussed above are much less likely, rendering the conclusions more incontestable.

Integrating Epistasis Concepts

Modern approaches toward on-target specificity have focused on knockdown or knockout of the postulated target. Knockdown of a target typically sensitizes cells to a drug, because one can consider that some of the drug's "work" has been done for it, so it is easier for the drug to take effect. This sort of sensitization is most-commonly observed under conditions where there is little phenotypic output due to the knockdown. In some instances, knockdown of the protein is so acute that there is essentially a knockout of protein function. Under these conditions (or with true knockouts), one may expect there to be essentially no impact of the drug, as there is no target. This condition is termed *epistasis* (Cordell, 2002; Miko, 2008). If the drug functions through processes not associated with the proposed target, then similar fold effects will still be seen in the knockdown/knockout line. This sort of analysis applies equally to protein-based inhibitors and small molecules.

Our laboratory recently used such arguments to elucidate the pathway through which nuclear-translocated RNR-subunit-α suppresses DNA synthesis (Fu et al., 2018; **Figure 1C**). Our data showed that RNR-α is able to bind to a nuclear-localized protein called ZRANB3. We hypothesized that this interaction may inhibit ZRANB3-function because ZRANB3—RNR-α interaction also led to disruption of PCNA binding to ZRANB3, and it is known that the ZRANB3—PCNA complex plays a role in DNA damage response (Poole and Cortez, 2017). Our data revealed that robust (∼85%) knockdown of ZRANB3 by three different siRNAs suppressed DNA-synthesis rate by 30–40% (Fu et al., 2018), showing that ZRANB3 is a promoter (although not necessarily required) for DNA synthesis, and that in the knockdown states, ZRANB3's activity is significantly depleted. Overexpression of RNR-α (which raises nuclear RNR-α levels, allowing ZRANB3 to bind RNR-α) also suppressed DNA-synthesis rate. Thus, there were several possible scenarios: (assuming ZRANB3 were a promoter of DNA

synthesis and RNR-α inhibits ZRANB3) we would see that ZRANB3-knockdown cells (that have significantly lost ZRANB3's DNA synthesis promoting function) are resistant to RNR-α overexpression; (assuming ZRANB3 were *required* for DNA synthesis and RNR-α inhibits ZRANB3) we would see a large fold increase in fold suppression of DNA synthesis upon RNR-α overexpression in the knockdown lines as the minimal ZRANB3 remaining would be overwhelmed by the influx of the inhibitor RNR-α; (assuming ZRANB3 does not mediate the nuclear-RNR-α-promoted DNA-synthesis suppression) there would be a drop in DNA-synthesis rate when RNR-α was overexpressed in the ZRANB3-knockdown cells of the same fold to what was seen in the control cells. The first of these outcomes was observed (Fu et al., 2018), consistent with nuclear-RNR-α acting as an inhibitor of ZRANB3-function and ZRANB3 being a promoter of DNA synthesis. We validated these experiments by showing similar outcomes upon dATP treatment, a situation that causes RNR-α to translocate into the nucleus. We were also able to derive a functional point mutant of ZRANB3 (that cannot bind RNR-α but can promote DNA synthesis), and this mutant was resistant to RNR-α-overexpression (Fu et al., 2018).

Of course, one must be careful to interpret how knockdown, and especially knockout, affects cells. For instance, in some cases even 85% knockdown of the target protein is not sufficient to observe significant pathway flux change (Lew and Tolan, 2012), thus it may not be possible to obtain significant sensitization using siRNA. Furthermore, since knockout of a target protein should ideally mimic saturating drug behavior, knockout may not be tolerated. Thus derived knockout lines can suffer from change of flux through necessary pathways, likely suppressing growth rates, or selecting for cells with modified survival responses, etc. Such residual knockout cells can appear resistant, solely because a few outliers from the population have been selected. However, the observance of resistance in knockout lines still remains good evidence for an on-target mechanism (Chauhan et al., 2012). Accordingly, the use/derivation of resistant point mutants as performed above are highly useful for mechanistic studies.

DEALING WITH ECTOPIC PROTEINS: JUDICIOUS CHOICES FOR MINIMAL INTERFERENCE

Aside from employing ectopic small molecules, many chemical-biology methods employ unnatural (often fusion) proteins ectopically expressed in the system under study. The effect of these non-native elements must be considered when evaluating each specific method and the data each method produces. Any perturbation imposed by the ectopic protein on the basal levels of pathway signal and the responsivity of the pathway must be assessed.

Transient Expression vs. Stable Integration

Considerations should also be made on how such transgenes will be introduced (**Figure 2A**). For cell culture, transient transfection is common. This procedure tends to give high levels of expression that are significantly variable across individual cells. Thus, single-cell analysis must be performed carefully such that expression of transgene is normalized, or at least accounted for. Furthermore, bulk phenotypic outputs could be derived from a subset of cells from the transfected pool (Parvez et al., 2016). Transfection also requires large amounts of plasmid, and chemical treatment of cells with lipid or other reagents.

An alternative is the use of cells containing integrated copies of the plasmid, or integrated ectopic DNA. Integration can be achieved under conditions of prolonged selection post transfection (Lin et al., 2015), through viral integration, or through transposases, all of which typically give "random" incorporation usually at multiple loci. Targeted integration (which limits chances of integration incurring off-target effects) using FLIP-recombinase (Schlake and Bode, 1994; Fu et al., 2018) or similar setups has also become popular (**Figure 2A**). Overall benefits of integration approaches include: obviating the need to transfect, which gives increased reliability, and reduced variations across experiments. Furthermore, single clones of lines can be chosen to ensure uniform expression of the transgene. If several clones are picked, a range of expressions can be chosen. Alternatively, inducible lines can be used that give calibrated expression.

Model organisms vary in their analogies to cell culture in these respects. Some are routinely manipulated transiently or through modification at the genome level during experiments. Zebrafish is a good example of such a system (**Figure 2B**). Others are almost exclusively manipulated through heritable manipulations, such as *C. elegans*. There are also some species-specific quirks, such as the ability of worms to form stable extrachromosomal arrays. We have shown that this system can prove very useful for chemical biology as the array-containing worms can be selected using a visual marker (e.g., fluorescence), and give a predictable percentage of transgenic progeny vs. wildtype progeny (Hall-Beauvais et al., 2018; Long et al., 2018a). Thus, experiments ultimately contain both wildtype and transgenic animals derived from the same founders that have been exposed to identical experimental conditions.

Knock-Out/Knock-In Lines

There are several issues that need to be considered when planning to derive knockout or knock-in lines. There are important differences between implementing these approaches in cancer cell lines vs. model organisms. Indeed, the aneuploidy of cancer cells renders knock-in generation difficult to achieve currently. Some cancer cells lines are "near diploid," such as HCT116, which has enabled homozygous and heterozygous knock-ins to be made by several methods we describe below (Duncan et al., 2012). The issue of aneuploidy in cancer cell lines could also potentially contribute to difficulty in generating knockout lines in cancer cells, although this does not appear to be a huge factor for CRISPR-Cas9 technologies (Yuen et al., 2017). Notably, the on- vs. off-target effects of all genetic manipulation strategies are hotly debated (Gallagher and Haber, 2018; Wang et al., 2018). These issues in whole organisms can be overcome by outcrossing, but this issue is not possible to "fix" in cultured cells.

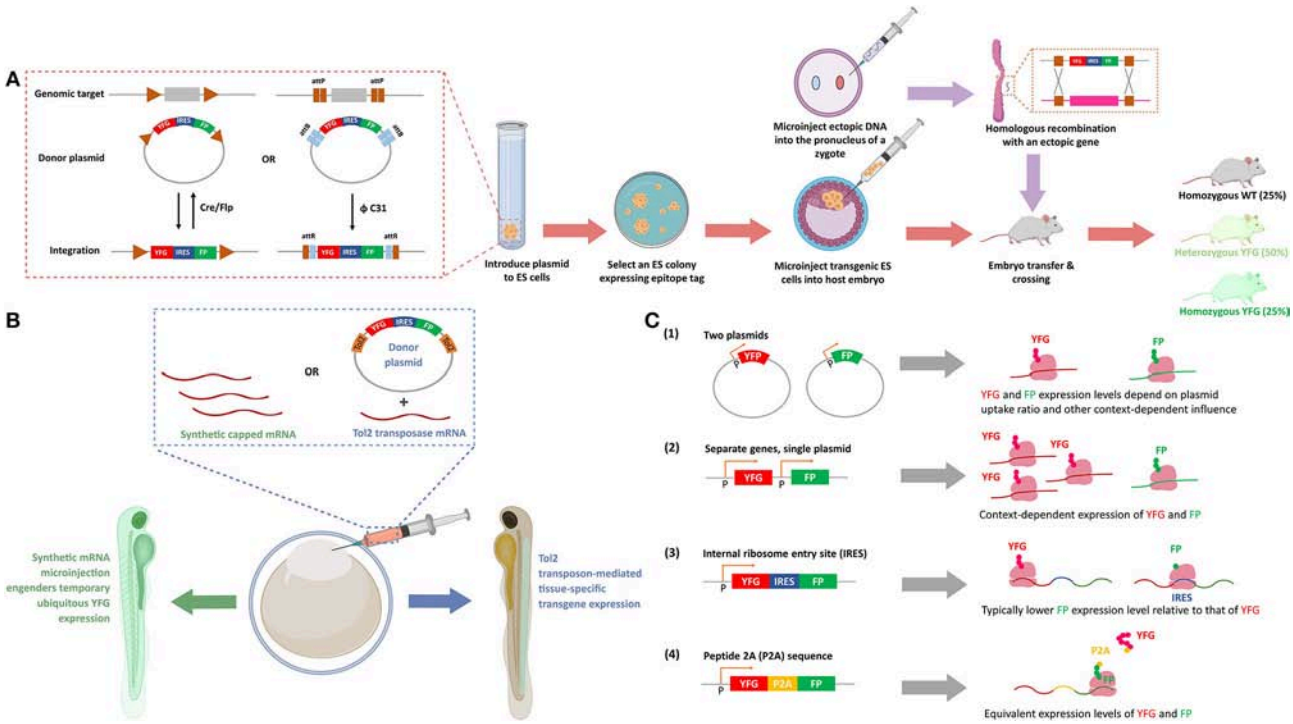

FIGURE 2 | Methods to express ectopic protein through introduction of ectopic nucleic acids. **(A)** Genetic integration of POI in cell lines and transgenic (Tg) mice. Inset: The recombinases [Cre and Flipase (Flp)] can be used to exchange genomic DNA with plasmid DNA to promote targeted integration of your favorite gene (YFG) into specific cell lines, or a suitable host. The bacteriophage ΦC31 integrase can perform a similar function in mouse. ΦC31 enables site-specific integration of the genes flanking phage attB-sites into the locus of host genome that is pre-engineered with up- and down-stream phage attP-sites. This recombination is irreversible because the resultant attR-flanked genes in host genome is not recognized by ΦC31 integrase. (FP, fluorescence protein; IRES, internal ribosomal entry site, that enables bicistronic expression of, in this figure, YFG and FP). To create a Tg mouse, a suitable embryonic stem (ES) cell line is prepared, and post integration of YFG-IRES-FP, colonies that have undergone insertion are selected and subsequently injected into a fertilized cell, giving rise to mosaic progeny that can be further manipulated. After multiple crossing with wild-type (WT) mice, 25% and 50% of the progeny have homozygous and heterozygous YFG knock-in, respectively (lower row, arrows in salmon). Alternatively, DNA with homology arms overlapping with the target site of interest can be injected into the pro-nuclei of fertilized embryos, and post-recombination, targeted-knock-in of the specific allele is created (top row, arrows in purple). **(B)** Transient expression and stable integration of POI in zebrafish. The eggs of zebrafish, which undergo external fertilization, can be injected with synthetic mRNA, to give ubiquitous, transient expression of YFG. Alternatively, a number of other random- or targeted-insertion protocols can be used. In this case, the transposon Tol2 is shown that gives random-integration of YFG—IRES—FP construct. Depending on the promoter driving the transgene (here, YFP and FP), locale-specific or ubiquitous expression can be achieved. **(C)** Different methods of POI expression in cultured cells. (1) Transfection of two plasmids gives a population of cells that express both genes (YFG and FP), with expression levels of each gene varying widely from cell to cell, with little correlation in the relative expression levels of each gene. (2) Separate genes on single plasmids can give standardized amounts of each protein, although the ratio of each protein is context-dependent, as transcription, mRNA stability and translation are independent between each protein (YFG and FP). (3) In IRES-driven bicistronic expression systems, transcription and mRNA stability of each protein are the same, but translation of the two genes (YFG and FP) can be considerably different. Typically, the protein downstream to IRES is expressed to a lower level than the one upstream to IRES. (4) In P2A-driven systems, transcription, mRNA stability, and translation are all the same (see text for details). (P designates promoter-binding site in **B,C**).

In general, targeted genome modification involves introducing a specific targeted DNA double-stranded break (DSB), which is then fixed either by homologous recombination (HR) or through non-homologous end joining (NHEJ). Indeed, the ability to induce specific DSBs is a critical factor of these experiments, explaining why targeted nucleases are such "big news." DSB can be achieved by expression of a nuclease that will specifically cut at an intended locus. In the modern era, DSB is most-readily introduced using CRISPR-Cas9, although other nucleases, including TALENs (Joung and Sander, 2013), have been and are still used. If there is no DNA with which to undergo recombination, the cell can repair the damage through NHEJ. This is an error-prone method that leads to formation of an "indel" (insertion/deletion polymorphism). Ideally, the indel creates a premature stop codon in the protein of interest (POI), yielding a truncated POI, although clearly frameshifts often also occur. It is important to appreciate that such systems create a "non-functional" protein, although typically mRNA-production still occurs and a gene product is often still generated, which could retain some bioactivity.

Knock-in is a particularly useful method to study the consequences of unnatural gene-products. Classic methods involve injection of linearized ectopic DNA into pro-nuclei of zygotes, and rely upon spontaneous HR (an error-free process) to introduce the gene of interest. Often times, the ectopic DNA contains a selection cassette, which can

be removed post selection by standard methods. In more modern approaches, a DSB is induced consequentially with the introduction of the DNA (either short single-stranded DNA with short overlapping regions, or longer double-stranded DNA) to promote recombination. Thus, the ectopic DNA can be incorporated into the locus of the break more efficiently.

Recently, CRISPR-Cas9 has become a method of choice for generation of DSBs to assist in generation of knock-in lines (Platt et al., 2014), in a range of organisms including mice (Singh et al., 2015), worms (Dickinson and Goldstein, 2016), and parasites (Cui and Yu, 2016). This requires the expression of Cas9, which can be achieved through the injection of protein, DNA, or mRNA. Although numerous factors intrinsic to the protein affect protein expression (such as protein stability), typically, a knock-in line is the most likely to lead to a set-up where protein expression (and protein translational/transcriptional regulation) are unperturbed compared to wild type. Unfortunately, as alluded to above, we currently lack the ability to generate knock-in lines of most cancer cells. Thus, knock-in cell lines are derived from genetically-engineered organisms, whose cells are harvested and then adapted into cell lines. This approach can work well, even if the knock-in is unable to survive to adulthood, as all that is required are relatively early embryos (Fu et al., 2018).

Cre-Lox has been used to perform context- or stage-specific manipulation of numerous organisms (**Figure 2A**), and similar concepts using CRISPR-Cas9 are also being introduced (Katigbak et al., 2018). Critically, CRISPR-Cas9 editing can be conducted in adult mice, under correct conditions. Such strategies are particularly relevant to knockout/mutation of essential genes and generation of targeted disease models.

Fluorescent Proteins and Epitope Tags

Regardless of the model system and expression system, ideally, all non-canonical/ectopic sequences, or protein domains should be removed from the expressed POI. For instance, it is common to express ectopic POIs as fusions with fluorescent proteins (FPs) or other chemically reactive domains, like Halo or SNAP, etc. Our subsequent discussion focuses on FPs, which are arguably most commonly used and for which several issues have been raised. However, protein-specific caveats likely apply to all ectopic protein domains and to a lesser extend linker regions and epitope tags. Efforts to assess validity (e.g. activity, localization, response)/rule out artifacts (unexpected effects on critical pathways, unexpected growth defects, etc.) in the specific system of use should always be made. FPs are certainly not bio-inert (Koelsch et al., 2013; Coumans et al., 2014; Ansari et al., 2016; Ganini et al., 2017); their use should be restricted where possible, especially in cell culture, unless, for instance, single live cell analysis is required. If FPs are required, whenever possible, fusion of FP to the POI can be circumvented through the use of separate promoters, plasmids, or, more reliably, through the use of bicistronic systems, such as IRES, or self-splicing peptides, like P2A. IRES/P2A also allow relative protein expression to be assessed across different cells (Jang et al., 1988; Pelletier and Sonenberg, 1988; Trichas et al., 2008; **Figure 2C**). It is important to note that IRES and P2A, are cell-type and organism dependent in terms of their effectiveness. Furthermore, P2A gives similar levels of each protein post translation (assuming each protein has similar stabilities Liu et al., 2017), but IRES biases expression against the protein downstream of the IRES (Mizuguchi et al., 2000). These nuances have been judiciously employed in experimental designs (Wang et al., 2015). The excitation and emission wavelength of the FP should be chosen to be as far away from background fluorescence and from any other photochemistry/redox-chemistry that is being conducted. Typically, red fluorescence gives better signal to noise.

In model organisms, such as *C. elegans* and *D. melanogaster*, the use of FPs as reporters of transgenicity are common, although dominant phenotypic markers, such as *rol-6* ("roller") or *ro+* ("rough"), are also used (Lockett et al., 1992). These phenotypic markers tend to be derived from known dominant mutants, leading to obvious physical deformities, and hence are "hard-wired," and as they affect, for instance, motility, they may pose undesired impacts on physiology. By contrast, for FP's, the locale of expression can be defined by the user. One can consider restricting fluorescence to a small number of cells (e.g., touch neurons, via the *C. elegans* promoter *Mec7*, in worms), or to cells that are not intended for the specific chemical-biology experiments (such as pharynx expression, via the *C. elegans* promoter *Myo2*, and gut expression of the key transgene, via the *C. elegans* promoter, *Ges-1*). If it is necessary to mark the specific transgenic cells with FPs, IRES, or likely better P2A fusions of the required gene with an FP, are best deployed (**Figure 2C**).

Furthermore, directing subcellular localization of the FP to a region that is not intended to be studied can also be useful, such as fusing the FP to a nuclear-localization sequence (NLS), if studying cytosolic processes with the specific POI. Finally, expressing POIs with epitope tags (FLAG, HA, V5, etc.) is often useful in cell culture for enrichment of specific proteins, but it is almost essential in model organisms, especially those for which homology with humans is only moderate, e.g., *C. elegans*. If the POI is fused to another protein-tag, such as Halo-Tag, for which highly-specific, low cross-reactivity antibodies are available (*vide infra*), such antibodies can often substitute. However, the background labeling of the antibody for the proteome from the species of interest should be evaluated, prior to design of the fusion construct, and the requirements of the whole experiment should be considered.

Additional Considerations

Ideally, activity/function of any fusion-POI expressed should be compared against the non-fused/non-tagged POI. This assessment can be done *in vitro*, or by measuring expected phenotypes/responses in cells/organisms in which the native protein has been depleted (by RNAi, or genetic knock out) and the fusion-POI exogenously supplemented. Knock-in lines are ideal, especially when the gene in question is essential, although for most purposes, simultaneous knockdown of a specific gene and plasmid transfection is operationally similar (provided the knockdown leads to a measurable effect on the cells that can be rescued). In cases where simultaneous siRNA knockdown and re-expression of the modified target POI is performed, the ectopic POI typically should have a synonymous mutation of the siRNA

target sequence. The re-expressed protein should be shown to occur at close to endogenous levels.

Because most chemical-biology approaches are multi-parameter, and these parameters often interact to make a new state that is not a simple "sum" of the individual parts, it can be argued that there is no "ideal" chemical-biology method. Hence, we emphasize that all chemical-biology approaches should be validated orthogonally. However, we also stress that close-to-ideal chemical-biology methods lend themselves to the development of as careful-and-as-close-to-"real" controls as possible. For our purposes, this means that assay conditions can be modulated such that *a single variable* is changed at a time (e.g., using a point mutant that does not process the chemistry/signal-propagation as intended). In fact, when such controls are available or built into the design, results tend to transpose well to real-life and any small-molecule-induced perturbations to the resting state of the cell can usually be tolerated.

PERTURBATION STRATEGIES: *COMPLEMENTING BIOSENSORS*

Most chemical-biology perturbation methods begin with the system at a "basal state" followed by a rapid jump to a new state induced by some form of chemical perturbation. The time taken to reach the new state/or the reactivity of the molecules generated, is often a key parameter that must be optimized such that genuine dynamics of cell responses can be measured on their relevant timescales. Thus, just as in classic kinetics experiments, the speed of the perturbation must be faster than other ensuing processes intended to be measured, so that a true readout of the chronology of the responses is established. In many instances, chemical-biology perturbations can elicit a shift to a "new state," or generate a reactive small molecule in minutes or even seconds.

By contrast, the length of time required to synthesize RNA and protein, and indeed the half-lives of most proteins are typically hours (Vogel and Marcotte, 2012; Liu et al., 2016; Mathieson et al., 2018) in higher eukaryotes, although precise values are species- and protein-dependent. Indeed, genetic techniques, like LOX/tet/RNAi/Flip/CRISPR-Cas9, also have a long latency. Arguably the "fastest-responding" genetically-encodable element is modulation of protein degradation (either positive or negative). The fastest responding of these strategies are mostly chemical genetic in nature. Such perturbation methods include: SHIELD (Banaszynski et al., 2006), auxin-initiated decay (Nishimura et al., 2009), HyT (and derivative stress induction methods) (Neklesa et al., 2011), Boc3Arg (Shi et al., 2016) and PROTACs (Lai and Crews, 2017). There are also some systems based on heat-shock that can be applied to organisms such as yeast (Dohmen et al., 1994), but one must consider the pleiotropic effects of temperature on the system in these instances as well. Despite these methods being considered rapid, 1–3 h is still required to have a significant effect (assumed to occur around 50% protein depletion, although much greater degradation than that can be required Lew and Tolan, 2012), and the slow step is almost certainly the change in stability of the protein target, not the engagement of the small molecule with its protein target, or the thermal unfolding of the protein (further underlining the relative slowness of biological recognition processes; Shamir et al., 2016).

Recently, photoactivatable cell signaling has also become common. This overall strategy represents another rapid response genetic unit. Importantly, this strategy has proven applicable to multiple different biological problems (Zhang and Cui, 2015), often (although not always) where oligomerization, dimerization, or recruitment are required for changes of cellular protein activity. In many instances, the system is also reversible, rendering these systems ideal for measuring signal-induced changes. Another group of rapid genetically-encodable methods involves chemical-induced dimerization (Stanton et al., 2018), a strategy that dates back to the earliest years of chemical biology (Spencer et al., 1993), but has found applications to modern genetic approaches, such as split-Cas9 (Zetsche et al., 2015). Using Cas9 as a specific example, intended outputs (e.g., transcriptional regulation, gene "deletion" or DNA damage) occur post Cas9 binding to its target DNA-sequence, meaning they are inherently controlled by factors with relatively long latency, such as mRNA stability or recruitment of transcriptional apparatus. Furthermore, Cas9 target engagement can take hours (Jones et al., 2017), even in *E. coli*. Finally, genetically-encodable sensors: such as the ROS-sensors: HYPER (Belousov et al., 2006) and roGFP (Meyer and Dick, 2010), the calcium sensor: m-GECO (Zhao et al., 2011); as well as the fleet of biosensors for kinase-activity (Mo et al., 2017) or metabolite sensing (Litke et al., 2016; Tao et al., 2017), are also rapidly-responsive elements, although these are not perturbation/labeling tools. However, use of these established visualization/activity-monitoring methods in conjunction with perturbation strategies—such as inhibition, integration of dominant-negative or gain-of-function alleles, or other targeted chemical-biology perturbation approaches that we outline below—offers a gateway to study cell responsivity and pathway architecture.

PARAMETERS

In this section, we discuss a few representative chemical-biology techniques (chosen for illustrative purposes from the much larger armory of methods these days available to researchers) in terms of the following parameters: (1) occupancy, i.e., whether these techniques are intended to saturate their targets or label only a subset of available targets based on some parameter; (2) spatial restriction, i.e., how constrained the techniques can be to a specific macromolecule, organelle, or interactome; and (3) functional information, i.e., what can we learn about the consequences of localization/reactivity/labeling using the technique. We further discuss the overall invasiveness of the methods and controls that are built in to the methods and orthogonal validation of the data. We will also evaluate how compatible and comparable these methods are with genetic/biochemical techniques.

Target Saturation Methods to Probe Protein Localization and Associations

These methods are not strictly direct perturbation methods. However, they ideally employ reactive small molecules, generated

on demand to chemically tag a specific set of proteins present in a chosen locale, or interactome, at a specific time (**Table 1**). These tagging processes thus reveal proteins either localized within a specific region or associating with a specific protein, even if they are present in low amounts, or if the interactions occur for a short period of time. Optimal parameters for these methods typically involve minimizing diffusion distance of the reactive molecule (Parvez et al., 2018), restricting membrane permeability (Yang and Hinner, 2015), and controlling the exposure time of the reactive entity to the native environment (Long et al., 2017c; Parvez et al., 2018).

APEX

APEX is an extremely useful method to profile protein localizations and associations. The key to this method is deployment of an engineered soybean ascorbate peroxidase protein that creates a reactive biotinylated phenoxyl radical, which has a short half-life (1 ms), giving APEX a labeling range of around 40 nm (Rhee et al., 2013; **Figure 3A**). The generation of this molecule within a defined compartment/region gives high resolution for assigning localizations and associations, which can be carried out in a multiplex manner (Cruz-Lopez et al., 2018). For instance, novel mitochondrial-associating proteins have been identified using APEX. Recent successes of APEX include profiling of associations at specific genomic loci (Myers et al., 2018) (through fusion to a binding-competent but catalytically-inactive mutant of Cas9, dCas9) and identifying new protein-protein associations (Xue et al., 2017). APEX has also recently been applied to RNA immuno-precipitation (Kaewsapsak et al., 2017). Thus, APEX was one of the most-widely used chemical biology methods in 2017–2018. Soybean peroxidase, from which both APEX-based probes are derived, is also known to be relatively robust to pH and temperature (Henriksen et al., 2001), although it does require a metallocofactor, and hence activity is dependent on correct loading of the cofactor, which could be context dependent.

Because of the short half-life and ectopic nature of the phenoxyradical (Rhee et al., 2013), APEX is unable to probe, for instance, downstream signaling. It is noteworthy that APEX outputs, although internally subject to not much more than 20% variability run to run, are subject to significant variability dependent upon the comparison used (Markmiller et al., 2018). Thus, multiple cross comparisons may be required to build up a complete picture of the interactome. Furthermore, APEX tends to favor labeling of unfolded proteins (Minde et al., 2018), so there is certainly the possibility for biased outcomes. Soybean peroxidase is known to generate spontaneous reactive oxygen species under certain conditions, and hence APEX could confer context specific changes to cellular redox levels that are difficult to address (Kimura and Kawano, 2015). How the ectopic overexpression of peroxidase may alter signaling/interactome architectures and redox homeostasis, etc., has not yet been assessed. Furthermore, APEX requires stimulation with peroxide (∼1 mM) to form the phenoxy radical. This requirement likely restricts the use of this technique to 2D-cell culture/isolated organs (Chen et al., 2015), as it is unlikely whole organisms will take up peroxide equally. Peroxide treatment is only for a relatively short time (minutes), but even brief pulses of peroxide can alter signaling pathways, elicit translocation, and affect protein stability/integrity (Parvez et al., 2018). Many small molecules can also be inactivated/compromised by peroxide treatment. APEX has, however, proven to be compatible with some important methods, including EM (Martell et al., 2017; Mavlyutov et al., 2017). Control for the peroxide is an intrinsic challenge of the peroxidase-based platform. The bioactivity of the phenoxy-radical-precursor that cells are treated with for significant dose (0.5 mM) and exposure-time (0.5 h) prior to oxidation as well as the post-treatment quenching regimen (5 mM Trolox and 10 mM ascorbate performed 3 times), also remains untested.

BioID

BioID uses an engineered promiscuous *E. coli* biotin ligase. This protein generates a reactive biotinylated molecule, biotin-AMP, *in situ* (**Figure 3B**). Biotin-AMP is a type of acyl phosphate, which are short-lived species whose hydrolysis liberates around as much energy as ATP hydrolysis (Meyerhof and Shatas, 1952; Di Sabato and Jencks, 1961). Acylphosphates are kinetically

TABLE 1 | Comparison of the representative chemical-biology techniques discussed in this review.

	PROTAC	APEX	BioID	(mini) Turbo ID	si/shRNA knockdown[a]	T-REX	G-REX
Effective time ($t_{1/2}$)	1–3 h	1 min	∼18 h	10 min−2 h	Variable (hours to days)	1 min	1 min
Occupancy	High	Proximity-dependent	Proximity-dependent	Proximity-dependent	Time-dependent	Target-dependent	Low
Spatio-temporal control	Low	High	Medium	Medium	Low	High	n.d.[b]
POI-specific functional information	High	Low	Low	Low	Variable (dependent on target intrinsic stability)	High	Low
Organismal applications	High	Low	Medium	Medium	Medium	Medium	Medium

[a] *RNAi is highly species dependent. It is extremely efficacious in worms, where effects can also be heritable. In higher eukaryotes, RNAi delivery is a significant challenge, although there are some drugs that have entered trials. Yeast and other lower eukaryotes and prokaryotes lack RNAi machinery.*
[b] *Not yet determined.*

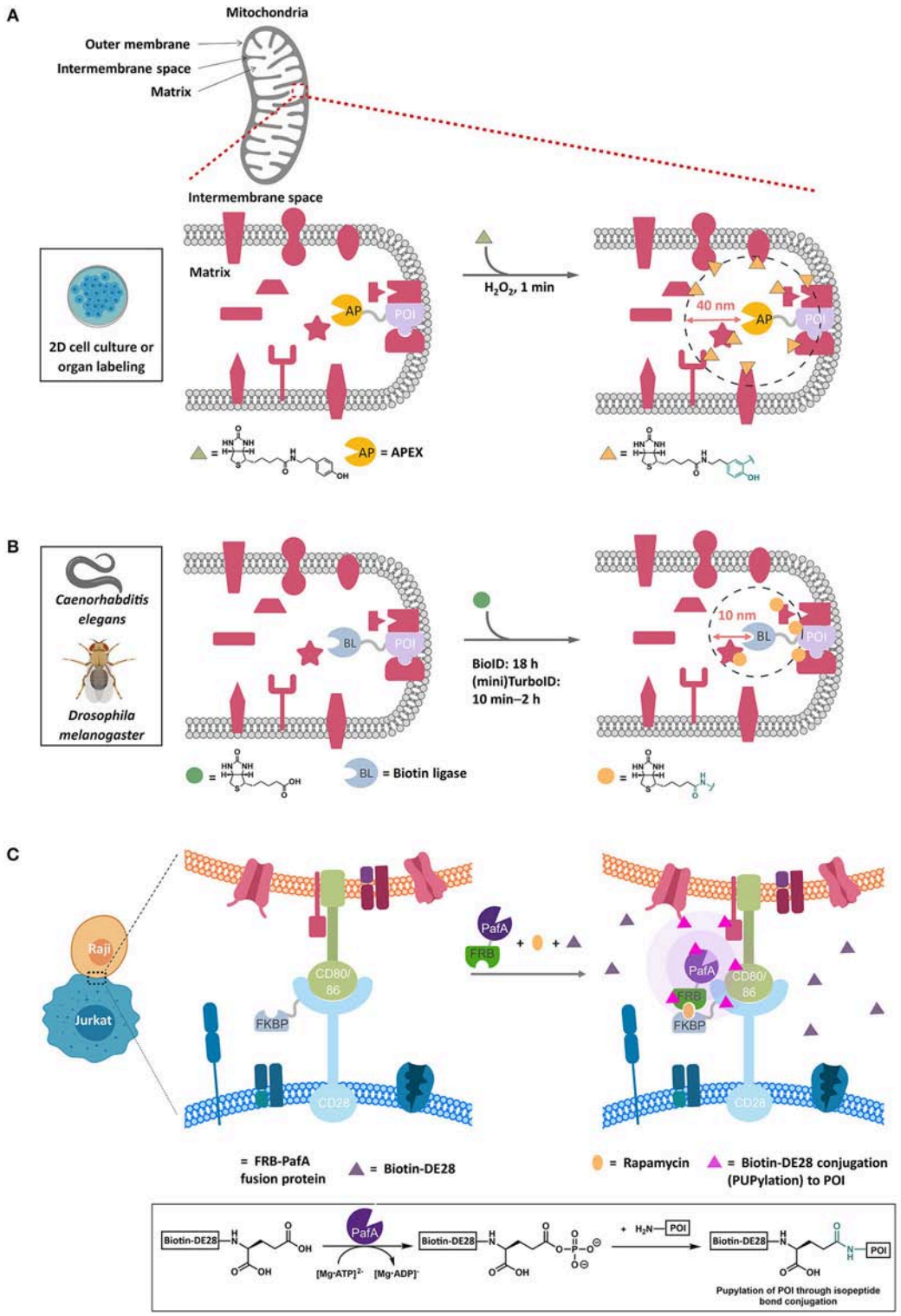

FIGURE 3 | Representative proximity-based target ID platforms. **(A)** APEX method. APEX-fused POI is overexpressed in live cells and targeted to the compartment of interest, such as the mitochondrial intermembrane in this example. The typical experimental procedure involves incubating cells with biotin-phenol (30 min, 0.5 mM) followed by a brief exposure to H_2O_2 (1 min, 1 mM) to initiate the biotinylation of the proteins proximal to the POI (within ~40 nm). After quenching the oxidants, cell lysis and streptavidin enrichment, the biotinylated proteins can be ID'ed by trypsin-digest and LC-MS/MS analysis. Currently, APEX's application is limited to 2D-cell culture and isolated organs. **(B)** BioID method. In this proximity-biotinylation catalyzed by promiscuous biotin ligases (BLs), various forms of BirA mutants have been employed, with TurboID and miniTurboID as the latest, leading to biotinylation of proteins spatially close to the POI (fused to BL). These biotin ligases catalyze the

(Continued)

FIGURE 3 | formation of biotin-5′-AMP ester, which diffuses out of the active site and is captured by the accessible nucleophilic residues (primarily lysine) of the POI and those of the proteins within 10 nm on average from the POI. BioID experiment typically requires 18 h or longer periods of time to achieve significant biotinylation of the proteins. TurboID and miniTurboID have significantly improved the biotinylation efficiency (10 min – 2 h) with little difference in labeling output. TurboID and miniTurboID have been successfully applied to tissue-specific protein ID using *D. melanogaster* and *C. elegans* as model organisms, although the optimized biotinylation conditions of TurboID and miniTurbo in human cells may not be transposable to these organisms, owing to the differences in growth temperature and time scale. **(C)** PUP-IT method. This method IDs protein–protein interactions through proximity-PUPylation on cell surface; e.g., PUP-IT has been applied to mark the cell–cell recognition events between Raji and Jurkat cells. The FKBP fusion of CD28 is stably expressed on cell-surface membrane in Jurkat cells. Upon addition of rapamycin (orange oval) and PafA(PUP ligase)-FRB fusion protein to the growth media, a functional PUP-IT complex proximal to CD28 receptor is formed. The addition of biotin-DE28 (purple triangle)—the truncated PUP protein that remains active in PUPylation reaction catalyzed by PafA—enables PUPylation of Raji cell-surface proteins CD80 and CD86 rapidly (magenta triangle), which are known to interact with the CD28 receptor in Jurkat cells. Inset shows the underlying chemistry. FKBP, FK506 binding protein. FRB, FKBP-rapamycin binding domain.

less stable than ATP, although they are more stable than the phenoxy radical generated by APEX in water (Long et al., 2016). However, in the biological milieu, biotin-AMP is ephemeral and has a diffusion distance of around 10 nm (Kim et al., 2014) (i.e., is likely more spatially restricted than APEX and may ultimately give protein-level resolution Rees et al., 2015), and is capable of labeling proximal lysines. One critical difference between APEX and BioID is that BioID does not require stimulation with peroxide to generate the intermediate, and as such BioID has been applied to multiple model organisms including mice, *Toxoplasma gondi* (Long et al., 2018b), and slime molds. Recently, there have been some extensions to this method to improve the context dependence, including split-BioID (De Munter et al., 2017; Schopp et al., 2017). Critically, two different split proteins have been reported, testifying to the versatility of BioID. Finally, BioID has recently been coupled with affinity purification MS, using Strep-II tag to allow more quantitative analysis of interaction distances across large complexes (Liu et al., 2018b).

One of the major issues with BioID is the slow kinetics of formation of biotin-AMP, which can particularly restrict use in organisms that are not grown at 37°C. This issue was recently overcome by engineering ligases with heightened kinetic proficiencies. TurboID and miniTurbo (a truncated version of TurboID) allow substantial biotinylation of the proteome in a few hours, as opposed to the typical 18 h in BioID (Branon et al., 2018). Although, little difference in the labeled proteins detected was observed between the two conditions in cultured cells, several important applications were shown in model organisms. For instance, the embryonic development of *C. elegans* is approximately 14 h and its optimal development temperature is 16–20°C (Zhang et al., 2015). Thus, a rapid labeling strategy is required to enable sufficient build-up of labeled protein in the embryonic stages. As may have been predicted, BioID did not label embryos well, but TurboID and miniTurbo yielded robust labeling.

BioID requires ATP to generate the reactive species. Thus, one could consider BioID to be more cellular context-dependent than APEX. Although this question has not been systematically addressed, and despite ATP being a critical component of the cell, it is known that ATP levels are fluxional (Imamura et al., 2009; Tantama et al., 2013) and time-(Schneider and Gourse, 2004) and locale-dependent (Suzuki et al., 2015) and variable cell-to-cell (Yaginuma et al., 2014). Furthermore, although many of the issues of BioID were solved by Turbo/miniTurbo-ID, it is worth noting that these proteins are not inert and can potentially stress cells/deplete cellular resources. Evidence for this was provided as TurboID-expressing worms were developmentally delayed, although this was not observed in miniTurboID-expressing worms; the reasons for these differences are unknown. It is possible that split TurboID would obviate some of these issues.

Reactive Ubiquitin Analogs

Another recent innovation aimed at mapping the cellular interactome exploits the enzymatic formation of acylphosphate intermediates on ubiquitin-like small protein domains, namely, prokaryotic ubiquitin-like protein (PUP) (Pearce et al., 2008) and Nedd8 in eukaryotes (Kamitani et al., 1997). PUP and Nedd8, upon activation by specific enzymes, PafA and Ubc12, respectively, form acylphosphates. By fusing proteins capable of forming PUP-acylphosphate or Nedd8-acylphosphate to a POI, proteins that associate with the POI have been identified. Since Nedd8 is an endogenous modification process in cultured mammalian cells, evaluation of the specificity of the tagging process is more complex than PUP. Furthermore, it remains unknown how elevated Nedd8-modification of individual proteins may impinge on native signaling/protein-association networks.

An extension to the Nedd8 approach has also been applied to identification of ligand—protein interactions. In this case, SNAP tag, an epitope tag that reacts irreversibly with a benzyl guanidine (Hill et al., 2016), was fused to an engineered Nedd8-conjugating enzyme Ubc12 that is capable of conjugating a biotinylated Nedd8 to proximal proteins. When a benzyl guanidine tag was fused to a small molecule of interest, such as Dasatinib, a Bcr-Abl/Src kinase inhibitor, known binders of Dasatinib were modified by Nedd8.

The PUP-based method can identify interactions that are very low affinity *in vitro* (maximum $K_d \sim 250\,\mu M$). Cell-based studies focused on the interactome of membrane proteins including CD28 (Liu et al., 2018a). Critically, modification by PUP was exclusively at lysine. Furthermore, several new interactions were identified, and these interactors were dependent on the presence of the CD28 C-terminal tail (**Figure 3C**). The experiments were carried out over a period of 24–36 h, timescale to similar to those used in Bio-ID.

The PUP/Nedd8 methods have strengths and weaknesses similar to Bio-ID as the intermediate formed is an acylphosphate (similar to the acyl-AMP intermediate Di Sabato and Jencks, 1961) and the protein turnover mechanism and kinetics may be similar. However, it is noteworthy that acylphosphate half-lives are variable in solution and biological systems (being dependent

likely on enzymatic and metal-catalyzed hydrolysis, to name two variables Di Sabato and Jencks, 1961; Parvez et al., 2018). Thus, careful considerations must be placed on the cellular backgrounds used when comparing the half-lives/diffusion distances of these systems. Although a similar concern applies to phenoxy radicals, such as are generated by APEX, the interaction preferences and modes of interaction/destabilization are different between acyl phosphates and radicals (Parvez et al., 2018). Thus, factors affecting longevity, diffusivity and off-target interactions are likely different between the methods. Interestingly, although both Bio-ID and PafA are ATP-hydrolyzing proteins whose kinetics are readily assessable *in vitro*, these have not been quantitatively compared. It has been shown that PafA is more readily auto PUPylated than BirA is auto-biotinylated (Liu et al., 2018a), but these outputs could be dependent on multiple factors not necessarily intrinsically linked to the activities of the enzymes.

There is also a significant difference in sizes between Nedd8/PUP and biotin. These differences clearly affect several biophysical aspects of the reactive intermediates, including: (1) the diffusion properties of the two molecules (diffusion distances decrease rapidly in cells as a function of size Parvez et al., 2018); (2) how the modified proteins may behave, in terms of association and stability over the long duration required for the experiment; (3) how the cell is affected; (4) the intrinsic reactivity biases of each probe; and yet (5) mean that for Nedd8/PUP both the activating protein AND the substrate's locale can be controlled to zero-in on associations/effects in specific locales.

Finally, it is noteworthy that immediately post synthesis, PafA is able to activate PUP and label interacting proteins. Maturation of T cells (and T-cell receptors, such as CD28) is complex (Wucherpfennig et al., 2010), and it is unknown precisely where upon this maturation process PUP is most readily able to label the CD28 interactome. Almost certainly, PUP is available at the membrane surface where CD28 ultimately resides, but it is unknown if PUP is present at points along the CD28 maturation process. Furthermore, because the dwell time of CD28 is relatively short during its maturation compared to its final localization (Stoops et al., 2015), and PUP-IT is relatively slow to label proteins, it is likely some chaperones are missed even if PUP were to be available at all points along the maturation pathway. APEX, with its faster labeling kinetics and small molecule substrate would likely be able to ID more potential interacting proteins (especially from locales where CD28 does not ultimately reside), especially if used in conjunction with inhibitors. Of course, unlike the small molecule substrate of APEX, PUP can be specifically targeted to specific locales along the CD28 maturation pathway. For instance, attempting to ID CD28 associating proteins using cells expressing ER-localized PUP, would illuminate "only" ER-specific interactors, provided PafA and PUP are functional in the ER.

Other Reactive-Molecule-Based Methods and Extensions

Other reactive-molecule-generation methods have recently been disclosed that function similarly to those discussed above, such as reactive N-arylation by N-acyl transferases (Kleinpenning et al., 2018). Although, so far these new techniques have not particularly expanded the repertoire of reactive molecule-based probes, they do have different requirements/cofactors needed for activity. Thus conditions where deployment of these probes is more informative than APEX and BioID may thus not yet have been discovered/assayed. Extensions to APEX and BioID have focused on trying to extract more data from the labeling reactions than simple protein ID using BioID and APEX (Udeshi et al., 2017; Kim et al., 2018). The logic of these extensions goes that a more detailed idea of the interaction region can be gained using such strategies. However, in order for such experiments to work well, the resolution would have to be less than the size of a protein domain 2–5 nm—a scenario unlikely to be easily achievable based on reported diffusion distances (Parvez et al., 2018). There would also have to be assumptions that all residues react equally with these high-energy probes.

COMPARISON WITH CLASSICAL METHODS TO UNDERSTAND LOCALIZATION AND ASSOCIATION

Protein localization is a critical parameter governing protein function. For instance, many proteins gain new associations, or functions upon translocation leading to important cellular responses. In some cases, the amount of translocation or partitioning of a protein between different organelles can be minimal. For instance, only a 2- to 3-fold *increase* in nuclear RNR-α levels can elicit suppression in DNA synthesis (Fu et al., 2018). Whether such small fold changes could be reliably detected by APEX localization studies and similar methods, in our opinion, remains to be conclusively proven.

The question of where proteins localize has been studied traditionally by immunofluorescence (IF) and fractionation. Both methods are powerful and often give consistent outcomes. These methods are ostensibly quantitative and so in principal can give an idea of relative amounts of protein in one locale over another and can measure even quite small changes.

However, it is worth remembering that traditional methods tend to suffer from limited spatial resolution and low sensitivity. This is for a number of reasons. First, both readouts are typically made by antibodies, so validating specificity through the use of clear controls (knockout/siRNA) are important and in reality in IF and western blotting, background labeling can limit signal to noise. Both methods suffer from intrinsic artifacts: for IF fixing can affect protein localization antigen presentation, whereas use of fluorescent proteins can affect target protein localization; during fractionation proteins can leak from membranes or there can be contamination from unintended structures. Thus, in our opinion at least, perhaps the biggest improvement that reactive labeling methods bring to localization studies is the ability to couple an unambiguous readout (MS) to stringent tagging protocol that is strongly spatially restricted.

There is estimated to be 650,000 protein-protein interactions (PPIs) in human cells, although this number reflects only a fraction of a percent of the total number of possible pairwise interactions (Stumpf et al., 2008). There are likely many more

possible associations when one considers protein-DNA/protein-RNA interactions and non-degenerate higher order complexes. Many of these PPIs are robust, with relatively long half-lives and K_d's in the nanomolar range. Such interactions can be readily assessed by classic methods such as co-IP, native gel, or 2D-PAGE gels. These methods have benefits in that they can be carried out in native cells, tissue, etc. However, requirement for lysing of the cells can introduce artifacts due to dysregulation of cellular compartmentalization, allowing interactions that do not happen in the cell to occur (Fu et al., 2018), or loosing weaker interactions (French et al., 2016). Weaker/more transient associations can be studied by semi-classical methods such as cross-linking (either chemical or UV). Crosslinking methods have the benefit of "trapping" the complex in the cell, prior to lysis, giving more confidence of cellular relevance, and eliminating the possibility of post lysis association. However, the use of reactive cross-linkers also potentially brings in possibilities of off-target cross-linking, can perturb cellular homeostasis, can mask epitopes, and may not be compatible with other transformations/experimental protocols. The reaction products of cross-linking experiments are also complex aggregates that require extensive verification and (typically) excellent antibodies that have been rigorously validated. However, oftentimes protein complexes/aggregates can be resolved using SDS-PAGE, allowing for identification of hetero/homo-dimers and/or higher-order aggregates to be assigned with reasonable accuracy (Aye et al., 2012).

Even though post-lysis associations are minimized by cross linking, there is little information offered concerning where in the cell this association occurs. This can be addressed by imaging experiments. Fluorescence colocalization of FP, or otherwise tagged proteins, or immunofluorescence has been used to visualize associations in live cells (Pedley and Benkovic, 2017), as has FRET (Kenworthy, 2001) and similar methods (Coffey et al., 2016). The use of proximity ligation (Fredriksson et al., 2002; Bellucci et al., 2014), which is read out via immunofluorescence on fixed cells, is also increasing. This method uses DNA-tagged antibodies that when in "close" proximity (40 nm) can template a rolling PCR reaction, allowing for puncta to be observed in specific cellular compartments where an association occurs. This method is signal amplifying, and hence very sensitive. However, since the distance covered (40 nm) by this method is much larger than most proteins, resolution is likely insufficient to "prove" a "direct" interaction.

There are numerous genetic methods to probe PPIs. The most commonly investigated method is the yeast-2-hybrid (Y2H) assay (Vidal and Fields, 2014). This method uses a split transcription factor one terminus of which is fused to a bait protein, and the other terminus of which is typically fused to a series of test proteins. Pairwise combinations of the bait and each test construct are expressed in yeast. When the bait and a test protein interact, the split transcription factor is able to form a viable protein, and typically drives transcription of a gene required for survival, such that only cells expressing proteins that interact with the test protein survive. Aside from the requirement to use ectopic protein and the fact that the native proteins are not used, criticism has been levied at this method because yeast is not a similar environment to human cells in terms of complexity, organelle structure and the posttranslational modifications it is capable of. Interactions must also happen in the nucleus. Furthermore, many Y2H methods are based off a 2 micron-plasmid system (Chan et al., 2013) that gives high expression of each protein, which "may" provide false positives. However, false positives are clearly not as detrimental as false negative, which are also abundant due to incomplete coverage of screening libraries, incomplete expression and poor folding. The use of autosomally replicating sequence-containing plasmids can also alleviate the issue of high protein expression/high copy number (Newlon and Theis, 1993).

Y2H has been extended to mammalian cells, where more complex modifications are possible, but many of the same issues remained, and the library generations are arguably more complex. Non-allelic non-complementation is a screening method that looks for unexpected non-complementation (i.e., where a cross of two strains with mutations to different genes do not give viable offspring) and can be carried out in numerous organisms (Firmenich et al., 1995; Rancourt et al., 1995; Yook et al., 2001). The likely explanation for such an effect is that proteins reside in the same pathway, and commonly these proteins form a complex that is so depleted in the double heterozygote complementation is not possible. Although this is clearly an indirect assay, it has proven very informative and variations of this assay have been used to uncover interesting aspects of cancer biology (Davoli et al., 2013). Aside from these in-cell-relevant experiments, phage display has also been used for HT-protein protein interaction screening (Gibney et al., 2018). This method is of course sensitive and accurate. However, it lacks the ability to be employed in cells (Kokoszka and Kay, 2015).

Chemotype Specific Sensing and Signaling: REX Technologies

REX technologies developed by our laboratory were ultimately aimed at studying the signaling function of reactive electrophilic species (RES) in living systems with individual-protein specificity and in precise space and time (**Figure 4**) (Fang et al., 2013; Lin et al., 2015; Parvez et al., 2015, 2016; Long et al., 2017a,b, 2018a; Hall-Beauvais et al., 2018; Surya et al., 2018; Zhao et al., 2018). The method uses custom-designed bi-functional small-molecule probes [such as Ht-PreHNE for controlled release of a native electrophile 4-hydroxynonenal (HNE)]. One terminus of the probe binds HaloTag irreversibly by virtue of a pendant alkylchloride function. The other end of the bi-functional probe delivers a payload of a specific reactive electrophilic species, e.g., HNE, upon light illumination ($t_{1/2}$ of release for various enals/enone-derived electrophiles, < 1 min) (Lin et al., 2015). Upon RES liberation, sensor proteins responsive to a given RES have to rapidly intercept the RES prior to diffusion and/or degradation/metabolism (Liu et al., 2019). Thus, the concept underlying REX technologies is unusual in that it harnesses intrinsic "reactivity/affinity-matching" between the released ligand and (a) POI(s) (Long and Aye, 2016, 2017; Long et al., 2016, 2017c; Parvez et al., 2018; Poganik et al., 2018; Liu et al., 2019). HaloTag-targetable photocaged probes such as Ht-PreHNE (1–20 μM)

are tolerated by cells for > 2 h, and worms/developing fish for several days (Parvez et al., 2016; Long et al., 2017a,b, 2018a; Hall-Beauvais et al., 2018; Surya et al., 2018; Zhao et al., 2018). Ht-PreHNE does not affect DNA damage response, ubiquitination, and several other essential processes in cells and fish (Parvez et al., 2016; Long et al., 2017a,b; Zhao et al., 2018).

We discuss below two different REX technologies, as well as potential or yet-unnoticed shortcomings of the method.

T-REX: Target-Specific Reactive Small-Molecule Sensing and Signaling

T-REX (**Figure 4A**) uses a HaloTag-POI fusion to give the specific POI first refusal for the RES (e.g., HNE) photouncaged from Halo (Fang et al., 2013; Lin et al., 2015; Parvez et al., 2015, 2016; Long et al., 2017a,b, 2018a; Hall-Beauvais et al., 2018; Surya et al., 2018; Zhao et al., 2018). In this way, a specific POI, providing it is HNE-sensitive, can be HNEylated in the backdrop of a largely unperturbed cell. T-REX gives relatively high RES-occupancy of a specific POI, but incurs very little RES-modification/stress of the total proteome (Parvez et al., 2016; Long et al., 2017a,b; Zhao et al., 2018). Thus, T-REX is also a highly spatially-restricted method and has proven to be compatible with numerous other chemical biology/genetic techniques. Finally, because individual POIs are modified, functional downstream responses elicited as a consequence of specific POI—RES interaction can be read out. Interestingly, proteins that are appreciably modified by HNE under T-REX tend to undergo phenotypically-dominant effects as a consequence of substoichiometric-HNEylation (Lin et al., 2015; Parvez et al., 2015, 2016; Long and Aye, 2017; Long et al., 2017b; Zhao et al., 2018). Thus, T-REX has established that some proteins are wired to react rapidly with HNE and to modulate signaling at fractional occupancy. We have dubbed such proteins privileged first responders (PFRs) (Long and Aye, 2017; Parvez et al., 2018; Poganik et al., 2018; Zhao et al., 2018; Liu et al., 2019). Using T-REX, HNEylation, at individual protein-specific levels, has been shown to impact numerous critical signaling subsystems and pathway intersections, including ubiquitination (Zhao et al., 2018) and phosphorylation (Long et al., 2017b).

The POI-specific nature of T-REX renders the method not particularly high-throughput. G-REX (vide infra) (Zhao et al., 2018) can assume this role if it is needed. Critically, because T-REX uses ectopic expression, RES-labeling and downstream signaling require the HaloTag protein to be fused to POI; and expressing the POI and HaloTag separately and replicating T-REX in this "split" control system ablates both the POI RES-modification and signal propagation downstream (Lin et al., 2015; Parvez et al., 2015, 2016; Long et al., 2017b). Similar controls were recently introduced and shown to be effective for APEX2 (Ariotti et al., 2015, 2018). We have also identified point mutants that are enzymatically or functionally active but do not sense the RES delivered under T-REX conditions (Long et al., 2017b; Surya et al., 2018; Zhao et al., 2018). Notably, these mutants are also refractory to downstream signaling changes induced upon T-REX (Long et al., 2017b; Surya et al., 2018; Zhao et al., 2018).

T-REX has found application to several model organisms, such as *C. elegans* and larval zebrafish (Long et al., 2017b, 2018a; Hall-Beauvais et al., 2018; Zhao et al., 2018). G-REX has as yet not been so applied. T-REX was used in fish embryos to study the effects of HNEylation of two different sensor proteins, Ube2V2 (Poganik et al., 2018; Zhao et al., 2018) and Akt3 (Long and Aye, 2017; Long et al., 2017b). It was noted that in these systems, expression of the transgenes was similar to that of the endogenous proteins (Long et al., 2017b; Zhao et al., 2018), rendering the systems more "natural" than that in cultured cells where the level of Halo-POI-overexpression was significant. Satisfyingly in both cases, delivery and downstream signaling was observed in zebrafish similarly to cell culture. However, because of the implicit requirement of UV-light that is poorly tissue-penetratable, whole organism studies with T-REX on, for instance, mice or adult fish, are not yet possible. This current limitation would not restrict use in certain organs like the brain or blood, however. Two-photon-based photocages would render REX technologies more broadly compatible and would also lower the overall impact of the method on UV-sensitive molecules/processes, such as DNA-synthesis/repair and RNA regulation.

G-REX: Genome-Wide Assay for Protein Reactivity With Specific Electrophiles

G-REX (**Figure 4B**) was established to address limitations underlying with the existing RES-sensor profiling strategies, which rely upon high doses of reactive covalent chemicals for long periods of time. Such flooding strategies tend to incur significant off-target effects due to mass action. These approaches, although they likely achieve high occupancy and modification of multiple potential targets, also affect physiology through, for instance, perturbing cellular redox environment, and inducing stress and apoptosis. RES-permeability, intracellular distribution, metabolism, and specific subcellular redox environments, etc., altogether render the consequences of cell treatment by a reactive molecule such as HNE highly context dependent.

G-REX is designed to release a small, defined pulse of (alkyne-functionalized) RES [e.g., ∼5 μM of HNE over 2–5 min in HEK293T cells with ubiquitous Halo expression (Zhao et al., 2018)]. Under these controlled conditions, PFRs to HNE are identified. HNEylated proteins are biotinylated by Click coupling with azido-biotin, precipitation, resolubilization, and streptavidin enrichment followed by mass spectrometry. Using this approach, several PFRs to HNE, including Ube2V2 and Ube2V1, were identified as well as numerous known HNE sensors. Importantly, any enriched hits from G-REX can be validated for HNE-sensing and HNEylation-specific signaling function using T-REX. By contrast, G-REX is not intended to study downstream signaling.

Using G-REX—T-REX coupled strategy, Ube2V2 and Ube2V1 were validated to be HNE-sensitive and modification impact respective signal propagation downstream (Zhao et al., 2018). Several biochemical methods further document these findings. Thus G-REX is an unusual strategy in that it is a global method that aims to achieve only low-occupancy on-target proteins (Liu et al., 2019). Its spatial resolution is currently unknown, although HaloTag itself has been successfully localized

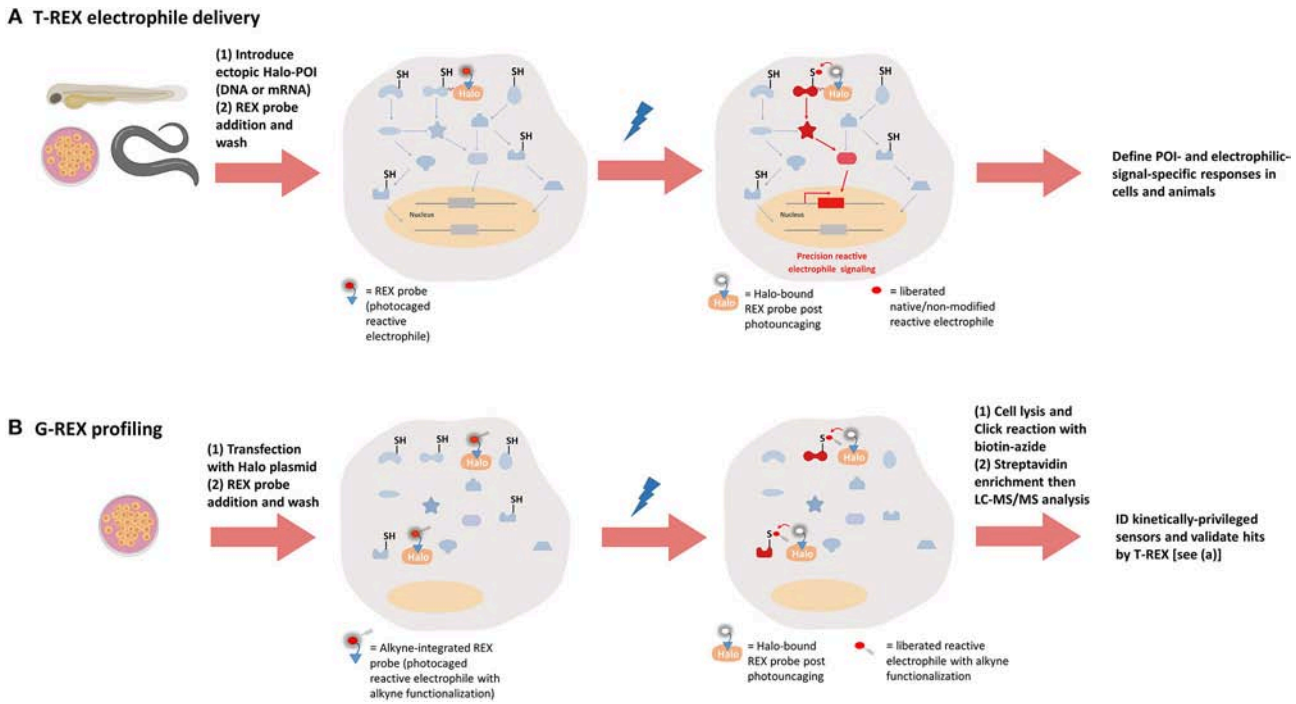

FIGURE 4 | REX technologies to interrogate precision electrophile signaling (T-REX) and mine kinetically-privileged sensors (KPSs) to specific reactive electrophilic species (RES) (G-REX). **(A)** T-REX electrophile delivery. A functional Halo-POI fusion protein is expressed either transiently or stably in live cells, worms, or larval fish. Treatment of these living models with a bio-inert REX probe [photocaged-RES (with or without alkyne functionalization)] (1–25 μM, 1–2.5 h, depending on the system) results in stoichiometric covalent binding of the probe to Halo. After several rounds of exchange with fresh growth media/buffer containing no probe (to washout the unbound REX probe), light exposure (1–3 min, 365 nm, 0.3–5 mW/cm^2, depending on the system) liberates a specific RES of choice (with or without alkyne-modification) within the microenvironment of Halo-POI, thereby giving the POI the first refusal to the RES. Labeling occurs provided the POI is a KPS of this RES. Provided the resulting substoichiometric RES-modification of the POI is sufficient to elicit either gain-of-function or dominant-loss-of-function signaling responses, T-REX presents a unique means to directly link target-engagement to function. [We define such sensors that can elicit dominant responses at low-occupancy as privileged first responders (PFRs)]. When the alkyne-modified version of the probe is used, the magnitude of measured responses can be quantitatively correlated with the POI-target-occupancy (by fluorescence-gel-based analysis following Click coupling of the alkyne-functionalized-RES-modified-POI with an azido-fluorophore). **(B)** *G-REX profiling.* G-REX enables genome-wide direct ID of KPSs under controlled and RES-limited conditions. Cells ectopically expressing HaloTag-protein are treated with the same REX probe used in T-REX (but the alkyne-modified version) under conditions similar to those deployed in T-REX. Without fusing Halo to any proteins, G-REX approach that allows for user-defined time-, dose-, and locale-controlled release of a specific RES is set to directly capture (localized) native sensors (i.e., KPSs) most responsive to the liberated RES, at low-occupancy covalent RES-modifications. Cell lysis and click coupling with biotin-azide followed by streptavidin enrichment engender RES-bound KPS(s) to be ID'ed by digest LC-MS/MS. The resultant top hits can be functionally validated using T-REX **(A)**.

to specific subcellular compartments. It remains unknown how diffusive/reactive HNE is, which may intrinsically limit this method's utility to organelle-specific release.

G-REX has several method-specific limitations. First, G-REX only releases a brief and low concentration pulse of RES. Thus, G-REX is a "target-poor" strategy and could potentially miss some privileged sensors. Such issues can be circumvented by repeating experiments numerous (3 or more) times and further integrating quantitative proteomics such as SILAC (Ong et al., 2002) or TMT-labeling (Thompson et al., 2003). However, MS analysis is costly and time consuming and these constraints should be considered when planning/choosing G-REX. To enable target ID, an alkyne-functionalized variant of native RES is used in G-REX. For lipid-derived electrophiles (LDEs), alkyne tagging is minimally (if at all) invasive, although alkynylated versions of many drugs have been successfully deployed for successful target ID (Wright and Sieber, 2016; Parker et al., 2017). Radioisotope tagging or antibody affinity methods present alternatives to alkyne. However, antibodies are much lower sensitivity than alkyne-based Click coupling/enrichment, and radioisotope incorporation may still prove difficult to apply to highly reactive electrophiles, where there is significant background radioactivity, especially given the low occupancy of RES-modification that underlies G-REX. To users' benefit, biotin/streptavidin-based enrichment permits the non-alkynylated electrophile to be used as an "ideal" control for comparison.

VALIDATIONS AND CURRENT LIMITATIONS

REX-probes currently rely on UV-illumination to liberate RES, admittedly for a short period of time and at low-power light sources that the data show does not affect the cell/animal in any appreciable way (Parvez et al., 2016; Long et al., 2017a,b; Zhao et al., 2018). Second, REX-platforms require ectopic expression

of HaloTagged-POI (in T-REX) or HaloTag alone (in G-REX) to enable localization and concentration of probe (e.g., Ht-PreHNE) [and liberated RES (e.g., HNE)]. The effects of HaloTag protein on cellular functions are not clearly known, although HaloTag has been applied to numerous systems with little negative effects reported (England et al., 2015).

Notably, identical modification/signaling outcomes are achieved irrespective of N- vs. C-terminal HaloTagging on the POI in T-REX (Lin et al., 2015; Parvez et al., 2016). This outcome indicates that the origin of HNE-liberation is not particularly relevant to sensing. Thus, it can be inferred that T-REX is mimicking genuinely what happens post entry of the liberated RES into the solvent cage of POI fused to Halo. However, we are still unsure whether solvent cage entry is rate-limiting for POI-modification, and if reorganization may cause unanticipated issues that affect efficacy of for instance, POI RES-sensing, or conformational properties of ligand and POI. These concerns have been partially addressed by assaying *in vitro* relative rates of HNEylation of POIs identified to be highly RES-reactive by T-REX in cells/animals (Long et al., 2017b; Surya et al., 2018; Zhao et al., 2018). All sensors assayed were found to be uniquely HNE-sensitive. T-REX assays on POIs identified through G-REX agree with these conclusions (vide infra).

Third, photocaged probes, such as Ht-PreHNE, may be subject to inherent biases (intrinsic concern for any small-molecule probe). Beyond deploying various REX-technical controls and hypomorphic sensing-defective functional mutants (Long et al., 2017b; Zhao et al., 2018), the *in vitro* and other RES bolus dosing experiments in cells discussed above help assuage this worry (Surya et al., 2018). Improved photocaging strategies are presently being undertaken to further limit the possibility of artifacts.

NON-TETHERED APPROACHES

All the above methods share the unifying theme that a "minor" perturbation to typical signaling pathways occurs. Critically, T-REX and G-REX use an ectopic protein anchor to ensure such a system is maintained as much as possible, i.e., the Halo protein serves in part to allow washout of excess probe, ensuring any probe-specific perturbations of the system (due to the lipid fragment of the probe, for instance) can be removed. Similar techniques using non-localized/tethered probes have been applied to mechanistic analysis and target ID, using dual photocaging (Höglinger et al., 2017). However, in these methods, the photocaged cannot be completely washed away, due to having no probe-anchoring device, such as Halo. Organelle specificity has been instead achieved by chemical means, such as fusing triphenylphosphine to direct the probe to the mitochondria (Wagner et al., 2018), and many pioneering contributions have been made in this arena. The probe concentrations and those of the released lipids are difficult to normalize under these systems, and are likely not readily tunable or comparable between different cells. When using an ectopic protein, as the ectopic protein expression can be calculated, and the amount of precursor on the protein can also be assessed, these values are much more readily normalized. To some extent, the adverse effects of the excess probe and the uncaged species can be circumvented by irradiating specific sections of a cell. However, this approach is restricted to single or a few cell-based analyses.

OUTLOOK

Our aim in this review is 2-fold: to stimulate discussion on the fundamentals of chemical biology methods; and to highlight methods development at the boundary of chemistry and biology with the focus on emerging chemistry-driven perturbation methods that shed light on the biological locale/interactome and signaling consequences. It is at this intersection of biochemical/enzymological and organic chemistry disciplines where we feel chemical biology is most useful and where as a field we need to go. Improvement and further expansion should be built on our better understanding and appreciation of where the field currently is in terms of limitations that it faces and successes it has had, on our conscious and responsible use of methods and understanding of systems to apply them, and on having a firm idea of where the field is going. We strongly believe that chemical biology has the ability to deeply probe complex biological questions but our progress is hampered by reliance on unrealistic models and analogy to former biochemical studies. Using the most relevant model systems will be an enabling step forward in successfully tackling the important problems unsolvable by traditional genetics and biochemistry.

AUTHOR CONTRIBUTIONS

MJCL and XL contributed equally to this work. XL contributed to the creation of all figures and tables as well as manuscript editing and formatting. MJCL drafted the manuscript. YA oversaw the manuscript outline, overall direction and planning. All authors contributed to reference collection, selection and final proof.

ACKNOWLEDGMENTS

Novartis Foundation for Medical-Biological Research (Switzerland); National Centre of Competence in Research (NCCR): Chemical Biology (Swiss National Science Foundation), NIH innovator award (1DP2GM114850), and Swiss Federal Institute of Technology Lausanne (EPFL) are acknowledged for research support. G-REX technology had been filed for patent application by Cornell University (USA). BioRender is used for all figures.

REFERENCES

(1962). Withdrawal of thalidomide from the market. *Can. Med. Assoc. J.* 86, 664–664.

Ansari, A. M., Ahmed, A. K., Matsangos, A. E., Lay, F., Born, L. J., Marti, G., et al. (2016). Cellular GFP toxicity and immunogenicity: potential confounders in *in vivo* cell tracking experiments. *Stem Cell Rev. Reports* 12, 553–559. doi: 10.1007/s12015-016-9670-8

Ariotti, N., Hall, T. E., Rae, J., Ferguson, C., McMahon, K.-A., Martel, N., et al. (2015). Modular detection of GFP-labeled proteins for rapid screening by electron microscopy in cells and organisms. *Dev. Cell* 35, 513–525. doi: 10.1016/j.devcel.2015.10.016

Ariotti, N., Rae, J., Giles, N., Martel, N., Sierecki, E., Gambin, Y., et al. (2018). Ultrastructural localisation of protein interactions using conditionally stable nanobodies. *PLoS Biol.* 16:e2005473. doi: 10.1371/journal.pbio.2005473

Aye, Y., Brignole, E. J., Long, M. J. C., Chittuluru, J., Drennan, C. L., Asturias, F. J., et al. (2012). Clofarabine targets the large subunit (α) of human ribonucleotide reductase in live cells by assembly into persistent hexamers. *Chem. Biol.* 19, 799–805. doi: 10.1016/j.chembiol.2012.05.015

Aye, Y., Li, M., Long, M. J. C., and Weiss, R. S. (2015). Ribonucleotide reductase and cancer: biological mechanisms and targeted therapies. *Oncogene* 34, 2011–2021. doi: 10.1038/onc.2014.155

Aye, Y., and Stubbe, J. (2011). Clofarabine 5′-di and -triphosphates inhibit human ribonucleotide reductase by altering the quaternary structure of its large subunit. *Proc. Natl. Acad. Sci. U.S.A.* 108:9815. doi: 10.1073/pnas.1013274108

Banaszynski, L. A., Chen, L.-C., Maynard-Smith, L. A., Ooi, A. G., and Wandless, T. J. (2006). A rapid, reversible, and tunable method to regulate protein function in living cells using synthetic small molecules. *Cell* 126, 995–1004. doi: 10.1016/j.cell.2006.07.025

Bellucci, A., Fiorentini, C., Zaltieri, M., Missale, C., and Spano, P. (2014). "The "*in situ*" proximity ligation assay to probe protein–protein interactions in intact tissues," in *Exocytosis and Endocytosis*, ed A.I. Ivanov. (New York, NY: Springer), 397–405.

Belousov, V. V., Fradkov, A. F., Lukyanov, K. A., Staroverov, D. B., Shakhbazov, K. S., Terskikh, A. V., et al. (2006). Genetically encoded fluorescent indicator for intracellular hydrogen peroxide. *Nat. Methods* 3, 281–286. doi: 10.1038/nmeth866

Bertino, J. R., Göker, E., Gorlick, R., Li, W. W., and Banerjee, D. (1996). Resistance mechanisms to methotrexate in tumors. *Oncologist* 1, 223–226.

Bondeson, D. P., Mares, A., Smith, I. E. D., Ko, E., Campos, S., Miah, A. H., et al. (2015). Catalytic *in vivo* protein knockdown by small-molecule PROTACs. *Nat. Chem. Biol.* 11, 611–617. doi: 10.1038/nchembio.1858

Branon, T. C., Bosch, J. A., Sanchez, A. D., Udeshi, N. D., Svinkina, T., Carr, S. A., et al. (2018). Efficient proximity labeling in living cells and organisms with TurboID. *Nat. Biotechnol.* 36:880. doi: 10.1038/nbt.4201

Caras, I. W., and Martin, D. W. Jr. (1988). Molecular cloning of the cDNA for a mutant mouse ribonucleotide reductase M1 that produces a dominant mutator phenotype in mammalian cells. *Mol. Cell. Biol.* 8, 2698–2704. doi: 10.1128/MCB.8.7.2698

Chan, K.-M., Liu, Y.-T., Ma, C.-H., Jayaram, M., and Sau, S. (2013). The 2 micron plasmid of Saccharomyces cerevisiae: a miniaturized selfish genome with optimized functional competence. *Plasmid* 70, 2–17. doi: 10.1016/j.plasmid.2013.03.001

Chauhan, D., Tian, Z., Nicholson, B., Kumar, K. G. S., Zhou, B., Carrasco, R., et al. (2012). A small molecule inhibitor of ubiquitin-specific protease-7 induces apoptosis in multiple myeloma cells and overcomes bortezomib resistance. *Cancer Cell* 22, 345–358. doi: 10.1016/j.ccr.2012.08.007

Chen, C.-L., Hu, Y., Udeshi, N. D., Lau, T. Y., Wirtz-Peitz, F., He, L., et al. (2015). Proteomic mapping in live Drosophila tissues using an engineered ascorbate peroxidase. *Proc. Natl. Acad. Sci.U.S.A.* 112, 12093–12098. doi: 10.1073/pnas.1515623112

Coffey, R. T., Shi, Y., Long, M. J., Marr, M. T., and Hedstrom, L. (2016). Ubiquilin mediated small molecule inhibition of mammalian target of rapamycin complex 1 (mTORC1) signaling. *J. Biol. Chem.* M115:691584. 291, 5221–5223. doi: 10.1074/jbc.M115.691584

Conciatori, F., Bazzichetto, C., Falcone, I., Pilotto, S., Bria, E., Cognetti, F., et al. (2018). Role of mTOR Signaling in tumor microenvironment: an overview. *Int. J. Mol. Sci.* 19:2453. doi: 10.3390/ijms19082453

Cordell, H. J. (2002). Epistasis: what it means, what it doesn't mean, and statistical methods to detect it in humans. *Hum. Mol. Genet.* 11, 2463–2468. doi: 10.1093/hmg/11.20.2463

Coumans, J. V. F., Gau, D., Poljak, A., Wasinger, V., Roy, P., and Moens, P. (2014). Green fluorescent protein expression triggers proteome changes in breast cancer cells. *Exp. Cell Res.* 320, 33–45. doi: 10.1016/j.yexcr.2013.07.019

Cruz-Lopez, D., Ramos, D., Castilloveitia, G., and Schikorski, T. (2018). Quintuple labeling in the electron microscope with genetically encoded enhanced horseradish peroxidase. *PLoS ONE* 13:e0200693. doi: 10.1371/journal.pone.0200693

Cui, Y., and Yu, L. (2016). Application of the CRISPR/Cas9 gene editing technique to research on functional genomes of parasites. *Parasitol. Int.* 65(6, Part A), 641–644. doi: 10.1016/j.parint.2016.08.011

Darling, T. L., and Reid, T. W. (1979). Apparent allosterism by avian myeloblastosis virus reverse transcriptase and *E. coli* DNA polymerase I. *Nucleic Acids Res.* 6, 1189–1201. doi: 10.1093/nar/6.3.1189

Davoli, T., Xu, A. W., Mengwasser, K. E., Sack, L. M., Yoon, J. C., Park, P. J., et al. (2013). Cumulative haploinsufficiency and triplosensitivity drive aneuploidy patterns and shape the cancer genome. *Cell* 155, 948–962. doi: 10.1016/j.cell.2013.10.011

De Munter, S., Görnemann, J., Derua, R., Lesage, B., Qian, J., Heroes, E., et al. (2017). Split-BioID: a proximity biotinylation assay for dimerization-dependent protein interactions. *FEBS Lett.* 591, 415–424. doi: 10.1002/1873-3468.12548

Di Sabato, G., and Jencks, W. P. (1961). Mechanism and catalysis of reactions of acyl phosphates. II. Hydrolysis1. *J. Am. Chem. Soc.* 83, 4400–4405. doi: 10.1021/ja01482a025

Dickinson, D. J., and Goldstein, B. (2016). CRISPR-based methods for Caenorhabditis elegans genome engineering. *Genetics* 202, 885–901. doi: 10.1534/genetics.115.182162

Dohmen, R., Wu, P., and Varshavsky, A. (1994). Heat-inducible degron: a method for constructing temperature-sensitive mutants. *Science* 263, 1273–1276. doi: 10.1126/science.8122109

Duncan, C. G., Barwick, B. G., Jin, G., Rago, C., Kapoor-Vazirani, P., Powell, D. R., et al. (2012). A heterozygous IDH1R132H/WT mutation induces genome-wide alterations in DNA methylation. *Genome Res.* 22, 2339–2355. doi: 10.1101/gr.132738.111

England, C. G., Luo, H., and Cai, W. (2015). HaloTag technology: a versatile platform for biomedical applications. *Bioconjug. Chem.* 26, 975–986. doi: 10.1021/acs.bioconjchem.5b00191

Ercikan-Abali, E. A., Banerjee, D., Waltham, M. C., Skacel, N., Scotto, K. W., and Bertino, J. R. (1997). Dihydrofolate reductase protein inhibits its own translation by binding to dihydrofolate reductase mRNA sequences within the coding region. *Biochemistry* 36, 12317–12322. doi: 10.1021/bi971026e

Eriksson, S., Gräslund, A., Skog, S., Thelander, L., and Tribukait, B. (1984). Cell cycle-dependent regulation of mammalian ribonucleotide reductase. The S phase-correlated increase in subunit M2 is regulated by *de novo* protein synthesis. *J. Biol. Chem.* 259, 11695–11700.

Fang, X., Fu, Y., Long, M. J. C., Haegele, J. A., Ge, E. J., Parvez, S., et al. (2013). Temporally controlled targeting of 4-hydroxynonenal to specific proteins in living cells. *J. Am. Chem. Soc.* 135, 14496–14499. doi: 10.1021/ja405400k

Feldwisch-Drentrup, H. (2017). New clues to why a French drug trial went horribly wrong. *Science* doi: 10.1126/science.aan6949

Firmenich, A. A., Elias-Arnanz, M., and Berg, P. (1995). A novel allele of Saccharomyces cerevisiae RFA1 that is deficient in recombination and repair and suppressible by RAD52. *Mol. Cell. Biol.* 15, 1620. doi: 10.1128/MCB.15.3.1620

Fredriksson, S., Gullberg, M., Jarvius, J., Olsson, C., Pietras, K., Gústafsdóttir, S. M., et al. (2002). Protein detection using proximity-dependent DNA ligation assays. *Nat. Biotechnol.* 20:473. doi: 10.1038/nbt0502-473

French, J. B., Jones, S. A., Deng, H., Pedley, A. M., Kim, D., Chan, C. Y., et al. (2016). Spatial colocalization and functional link of purinosomes with mitochondria. *Science* 351:733. doi: 10.1126/science.aac6054

Fu, Y., Long, M. J. C., Wisitpitthaya, S., Inayat, H., Pierpont, T. M., Elsaid, I. M., et al. (2018). Nuclear RNR-α antagonizes cell proliferation by directly inhibiting ZRANB3. *Nat. Chem. Biol.* 14, 943–954. doi: 10.1038/s41589-018-0113-5

Gallagher, D. N., and Haber, J. E. (2018). Repair of a site-specific DNA cleavage: old-school lessons for Cas9-mediated gene editing. *ACS Chem. Biol.* 13, 397–405. doi: 10.1021/acschembio.7b00760

Ganini, D., Leinisch, F., Kumar, A., Jiang, J., Tokar, E. J., Malone, C. C., et al. (2017). Fluorescent proteins such as eGFP lead to catalytic oxidative stress in cells. *Redox Biol.* 12, 462–468. doi: 10.1016/j.redox.2017.03.002

Gibney, E., Van Noorden, R., Ledford, H., Castelvecchi, D., and Warren, M. (2018). 'Test-tube' evolution wins Chemistry Nobel Prize. *Nature* 562, 176–176. doi: 10.1038/d41586-018-06753-y

Goldberg, A. L. (2012). Development of proteasome inhibitors as research tools and cancer drugs. *J. Cell Biol.* 199, 583–588. doi: 10.1083/jcb.201210077

Gupta, R. S., Chopra, A., and Stetsko, D. K. (1986). Cellular basis for the species differences in sensitivity to cardiac glycosides (digitalis). *J. Cell. Physiol.* 127, 197–206. doi: 10.1002/jcp.1041270202

Hall-Beauvais, A., Zhao, Y., Urul, D. A., Long, M. J. C., and Aye, Y. (2018). Single-protein-specific redox targeting in live mammalian cells and C. elegans. *Curr. Protocols Chem. Biol.* 10:e43. doi: 10.1002/cpch.43

Hedstrom, L. (2017). The bare essentials of antibiotic target validation. *ACS Infect. Dis.* 3, 2–4. doi: 10.1021/acsinfecdis.6b00185

Henriksen, A., Mirza, O., Indiani, C., Teilum, K., Smulevich, G., Welinder, K. G., et al. (2001). Structure of soybean seed coat peroxidase: a plant peroxidase with unusual stability and haem-apoprotein interactions. *Protein Sci.* 10, 108–115. doi: 10.1110/ps.37301

Hill, Z. B., Pollock, S. B., Zhuang, M., and Wells, J. A. (2016). Direct proximity tagging of small Molecule protein targets using an engineered NEDD8 Ligase. *J. Am. Chem. Soc.* 138, 13123–13126. doi: 10.1021/jacs.6b06828

Höglinger, D., Nadler, A., Haberkant, P., Kirkpatrick, J., Schifferer, M., Stein, F., et al. (2017). Trifunctional lipid probes for comprehensive studies of single lipid species in living cells. *Proc. Natl. Acad. Sci. U.S.A.* 114, 1566–1571. doi: 10.1073/pnas.1611096114

Imamura, H., Huynh Nhat, K. P., Togawa, H., Saito, K., Iino, R., Kato-Yamada, Y., et al. (2009). Visualization of ATP levels inside single living cells with fluorescence resonance energy transfer-based genetically encoded indicators. *Proc. Natl. Acad. Sci. U.S.A.* 106, 15651–15656. doi: 10.1073/pnas.0904764106

Jang, S. K., Kräusslich, H. G., Nicklin, M. J., Duke, G. M., Palmenberg, A. C., and Wimmer, E. (1988). A segment of the 5' nontranslated region of encephalomyocarditis virus RNA directs internal entry of ribosomes during *in vitro* translation. *J. Virol.* 62, 2636–2643.

Jones, D. L., Leroy, P., Unoson, C., Fange, D., Curić, V., Lawson, M. J., et al. (2017). Kinetics of dCas9 target search in *Escherichia coli*. *Science* 357, 1420–1424. doi: 10.1126/science.aah7084

Joung, J. K., and Sander, J. D. (2013). TALENs: a widely applicable technology for targeted genome editing. *Nat. Rev. Mol. Cell Biol.* 14, 49–55. doi: 10.1038/nrm3486

Kaewsapsak, P., Shechner, D. M., Mallard, W., Rinn, J. L., and Ting, A. Y. (2017). Live-cell mapping of organelle-associated RNAs via proximity biotinylation combined with protein-RNA crosslinking. *Elife* 6:e29224. doi: 10.7554/eLife.29224

Kamitani, T., Kito, K., Nguyen, H. P., and Yeh, E. T. (1997). Characterization of NEDD8, a developmentally down-regulated ubiquitin-like protein. *J. Biol. Chem.* 272, 28557–28562. doi: 10.1074/jbc.272.45.28557

Katigbak, A., Robert, F., Paquet, M., and Pelletier, J. (2018). Inducible genome editing with conditional CRISPR/Cas9 mice. *G3: Genes Genomes Genet.* 8, 1627–1635. doi: 10.1534/g3.117.300327

Kenworthy, A. K. (2001). Imaging protein-protein interactions using fluorescence resonance energy transfer microscopy. *Methods* 24, 289–296. doi: 10.1006/meth.2001.1189

Kim, D. I., Birendra, K. C., Zhu, W., Motamedchaboki, K., Doye, V., and Roux, K. J. (2014). Probing nuclear pore complex architecture with proximity-dependent biotinylation. *Proc. Natl. Acad. Sci. U.S.A.* 111, E2453–E2461. doi: 10.1073/pnas.1406459111

Kim, D. I., Cutler, J. A., Na, C. H., Reckel, S., Renuse, S., Madugundu, A. K., et al. (2018). BioSITe: a method for direct detection and quantitation of site-specific biotinylation. *J. Proteome Res.* 17, 759–769. doi: 10.1021/acs.jproteome.7b00775

Kimura, M., and Kawano, T. (2015). Hydrogen peroxide-independent generation of superoxide catalyzed by soybean peroxidase in response to ferrous ion. *Plant Signal. Behav.* 10:e1010917. doi: 10.1080/15592324.2015.1010917

Kleinpenning, F., Eising, S., Berkenbosch, T., Garzero, V., Schaart, J. M., and Bonger, K. M. (2018). Subcellular protein labeling by a spatially restricted arylamine N-acetyltransferase. *ACS Chem. Biol.* 13, 1932–1937. doi: 10.1021/acschembio.8b00178

Knowles, J. R., and Albery, W. J. (1977). Perfection in enzyme catalysis: the energetics of triosephosphate isomerase. *Acc. Chem. Res.* 10, 105–111. doi: 10.1021/ar50112a001

Koelsch, K. A., Wang, Y., Maier-Moore, J. S., Sawalha, A. H., and Wren, J. D. (2013). GFP affects human T cell activation and cytokine production following *in vitro* stimulation. *PLoS ONE* 8:e50068. doi: 10.1371/journal.pone.0050068

Kokoszka, M. E., and Kay, B. K. (2015). "Mapping protein–protein interactions with phage-displayed combinatorial peptide libraries and alanine scanning," in *Peptide Libraries: Methods and Protocols*, ed R. Derda (New York, NY: Springer), 173–188. doi: 10.1007/978-1-4939-2020-4_12

Lai, A. C., and Crews, C. M. (2017). Induced protein degradation: an emerging drug discovery paradigm. *Nat. Rev. Drug Disc.* 16, 101–114. doi: 10.1038/nrd.2016.211

Lew, C. R., and Tolan, D. R. (2012). Targeting of several glycolytic enzymes using RNA interference reveals aldolase affects cancer cell proliferation through a non-glycolytic mechanism. *J. Biol. Chem.* 287, 42554–42563. doi: 10.1074/jbc.M112.405969

Lin, H.-Y., Haegele, J. A., Disare, M. T., Lin, Q., and Aye, Y. (2015). A generalizable platform for interrogating target- and signal-specific consequences of electrophilic modifications in redox-dependent cell signaling. *J. Am. Chem. Soc.* 137, 6232–6244. doi: 10.1021/ja5132648

Litke, J. L., You, M., and Jaffrey, S. R. (2016). Developing fluorogenic riboswitches for imaging metabolite concentration dynamics in bacterial cells. *Meth. Enzymol.* 572, 315–333. doi: 10.1016/bs.mie.2016.03.021

Liu, Q., Zheng, J., Sun, W., Huo, Y., Zhang, L., Hao, P., et al. (2018a). A proximity-tagging system to identify membrane protein–protein interactions. *Nat. Methods* 15, 715–722. doi: 10.1038/s41592-018-0100-5

Liu, X., Long, M. J., and Aye, Y. (2019). Proteomics and beyond: cell decision-making shaped by reactive electrophiles. *Trends Biochem. Sci.* 44, 75–89. doi: 10.1016/j.tibs.2018.09.014

Liu, X., Salokas, K., Tamene, F., Jiu, Y., Weldatsadik, R. G., Öhman, T., et al. (2018b). An AP-MS- and BioID-compatible MAC-tag enables comprehensive mapping of protein interactions and subcellular localizations. *Nat. Commun.* 9:1188. doi: 10.1038/s41467-018-03523-2

Liu, Y., Beyer, A., and Aebersold, R. (2016). On the dependency of cellular protein levels on mRNA abundance. *Cell* 165, 535–550. doi: 10.1016/j.cell.2016.03.014

Liu, Z., Chen, O., Wall, J. B. J., Zheng, M., Zhou, Y., Wang, L., et al. (2017). Systematic comparison of 2A peptides for cloning multi-genes in a polycistronic vector. *Sci. Rep.* 7:2193. doi: 10.1038/s41598-017-02460-2

Livet, J., Weissman, T. A., Kang, H., Draft, R. W., Lu, J., Bennis, R. A., et al. (2007). Transgenic strategies for combinatorial expression of fluorescent proteins in the nervous system. *Nature* 450, 56–62. doi: 10.1038/nature06293

Lockett, T. J., Lewy, D., Holmes, P., Medveczky, K., and Saint, R. (1992). The rough (*ro+*) gene as a dominant P-element marker in germ line transformation of *Drosophila melanogaster*. *Gene* 114, 187–193. doi: 10.1016/0378-1119(92)90573-8

Long, M. J., Lin, H.-Y., Parvez, S., Zhao, Y., Poganik, J. R., Huang, P., et al. (2017a). β-TrCP1 is a vacillatory regulator of Wnt signaling. *Cell Chem. Biol.* 24, 944–957.e947. doi: 10.1016/j.chembiol.2017.06.009

Long, M. J. C., and Aye, Y. (2016). The die is cast: precision electrophilic modifications contribute to cellular decision making. *Chem. Res. Toxicol.* 29, 1575–1582. doi: 10.1021/acs.chemrestox.6b00261

Long, M. J. C., and Aye, Y. (2017). Privileged electrophile sensors: a resource for covalent drug development. *Cell Chem. Biol.* 24, 787–800. doi: 10.1016/j.chembiol.2017.05.023

Long, M. J. C., Parvez, S., Zhao, Y., Surya, S. L., Wang, Y., Zhang, S., et al. (2017b). Akt3 is a privileged first responder in isozyme-specific electrophile response. *Nat. Chem. Biol.* 13:333. doi: 10.1038/nchembio.2284

Long, M. J. C., Poganik, J. R., and Aye, Y. (2016). On-demand targeting: investigating biology with proximity-directed chemistry. *J. Am. Chem. Soc.* 138, 3610–3622. doi: 10.1021/jacs.5b12608

Long, M. J. C., Poganik, J. R., Ghosh, S., and Aye, Y. (2017c). Subcellular redox targeting: bridging *in vitro* and *in vivo* chemical biology. *ACS Chem. Biol.* 12, 586–600. doi: 10.1021/acschembio.6b01148

Long, M. J. C., Urul, D. A., Chawla, S., Lin, H.-Y., Zhao, Y., Haegele, J. A., et al. (2018a). Precision electrophile tagging in *Caenorhabditis elegans*. *Biochemistry* 57, 216–220. doi: 10.1021/acs.biochem.7b00642

Long, S., Brown, K. M., and Sibley, L. D. (2018b). CRISPR-mediated tagging with BirA allows proximity labeling in Toxoplasma gondii. *Bio Protocol* 8:e2768. doi: 10.21769/BioProtoc.2768

Markmiller, S., Soltanieh, S., Server, K. L., Mak, R., Jin, W., Fang, M. Y., et al. (2018). Context-dependent and disease-specific diversity in protein interactions within stress granules. *Cell* 172, 590–604.e513. doi: 10.1016/j.cell.2017.12.032

Martell, J. D., Deerinck, T. J., Lam, S. S., Ellisman, M. H., and Ting, A. Y. (2017). Electron microscopy using the genetically encoded APEX2 tag in cultured mammalian cells. *Nat. Protoc.* 12, 1792–1816. doi: 10.1038/nprot.2017.065

Mathieson, T., Franken, H., Kosinski, J., Kurzawa, N., Zinn, N., Sweetman, G., et al. (2018). Systematic analysis of protein turnover in primary cells. *Nat. Commun.* 9:689. doi: 10.1038/s41467-018-03106-1

Matthaei, J. H., Jones, O. W., Martin, R. G., and Nirenberg, M. W. (1962). Characteristics and composition of RNA coding units. *Proc. Natl. Acad. Sci. U.S.A.* 48, 666–677. doi: 10.1073/pnas.48.4.666

Mavlyutov, T. A., Yang, H., Epstein, M. L., Ruoho, A. E., Yang, J., and Guo, L.-W. (2017). APEX2-enhanced electron microscopy distinguishes sigma-1 receptor localization in the nucleoplasmic reticulum. *Oncotarget* 8, 51317–51330. doi: 10.18632/oncotarget.17906

Meyer, A. J., and Dick, T. P. (2010). Fluorescent protein-based redox probes. *Antioxid. Redox Signal.* 13, 621–650. doi: 10.1089/ars.2009.2948

Meyerhof, O., and Shatas, R. (1952). Heat of hydrolysis of acetyl phosphate. *Arch. Biochem. Biophys.* 40, 253–262. doi: 10.1016/0003-9861(52)90109-4

Miko, I. (2008). Epistasis: gene interactions and phenotypic effects. *Nat. Educ.* 1, 197.

Minde, D.-P., Ramakrishna, M., and Lilley, K. S. (2018). Cellular labelling favours unfolded proteins. *bioRxiv*. doi: 10.1101/274761

Mizuguchi, H., Xu, Z., Ishii-Watabe, A., Uchida, E., and Hayakawa, T. (2000). IRES-dependent second gene expression is significantly lower than cap-dependent first gene expression in a bicistronic vector. *Mol. Ther.* 1, 376–382. doi: 10.1006/mthe.2000.0050

Mo, G. C. H., Ross, B., Hertel, F., Manna, P., Yang, X., Greenwald, E., et al. (2017). Genetically encoded biosensors for visualizing live-cell biochemical activity at super-resolution. *Nat. Methods* 14, 427–434. doi: 10.1038/nmeth.4221

Myers, S. A., Wright, J., Peckner, R., Kalish, B. T., Zhang, F., and Carr, S. A. (2018). Discovery of proteins associated with a predefined genomic locus via dCas9–APEX-mediated proximity labeling. *Nat. Methods* 15, 437–439. doi: 10.1038/s41592-018-0007-1

Neklesa, T. K., Tae, H. S., Schneekloth, A. R., Stulberg, M. J., Corson, T. W., Sundberg, T. B., et al. (2011). Small-molecule hydrophobic tagging–induced degradation of HaloTag fusion proteins. *Nat. Chem. Biol.* 7, 538–543. doi: 10.1038/nchembio.597

Newlon, C. S., and Theis, J. F. (1993). The structure and function of yeast ARS elements. *Curr. Opin. Genet. Dev.* 3, 752–758. doi: 10.1016/S0959-437X(05)80094-2

Nishimura, K., Fukagawa, T., Takisawa, H., Kakimoto, T., and Kanemaki, M. (2009). An auxin-based degron system for the rapid depletion of proteins in nonplant cells. *Nat. Methods* 6, 917–922. doi: 10.1038/nmeth.1401

Ogasawara, D., Ichu, T.-A., Vartabedian, V. F., Benthuysen, J., Jing, H., Reed, A., et al. (2018). Selective blockade of the lyso-PS lipase ABHD12 stimulates immune responses *in vivo*. *Nat. Chem. Biol.* 14, 1099–1108. doi: 10.1038/s41589-018-0155-8

Ong, S.-E., Blagoev, B., Kratchmarova, I., Kristensen, D. B., Steen, H., Pandey, A., et al. (2002). Stable isotope labeling by amino acids in cell culture, SILAC, as a simple and accurate approach to expression proteomics. *Mol. Cell. Proteom.* 1:376. doi: 10.1074/mcp.M200025-MCP200

Osz-Papai, J., Radu, L., Abdulrahman, W., Kolb-Cheynel, I., Troffer-Charlier, N., Birck, C., et al. (2015). "Insect cells–baculovirus system for the production of difficult to express proteins," in *Insoluble Proteins: Methods and Protocols*, ed E. García-Fruitós (New York, NY: Springer), 181–205.

Parker, C. G., Kuttruff, C. A., Galmozzi, A., Jørgensen, L., Yeh, C.-H., Hermanson, D. J., et al. (2017). Chemical proteomics identifies SLC25A20 as a functional target of the ingenol class of actinic keratosis drugs. *ACS Central Sci.* 3, 1276–1285. doi: 10.1021/acscentsci.7b00420

Parvez, S., Fu, Y., Li, J., Long, M. J. C., Lin, H.-Y., Lee, D. K., et al. (2015). Substoichiometric hydroxynonenylation of a single protein recapitulates whole-cell-stimulated antioxidant response. *J. Am. Chem. Soc.* 137, 10–13. doi: 10.1021/ja5084249

Parvez, S., Long, M. J. C., Lin, H.-Y., Zhao, Y., Haegele, J. A., Pham, V. N., et al. (2016). T-REX on-demand redox targeting in live cells. *Nat. Protoc.* 11, 2328–2356. doi: 10.1038/nprot.2016.114

Parvez, S., Long, M. J. C., Poganik, J. R., and Aye, Y. (2018). Redox signaling by reactive electrophiles and oxidants. *Chem. Rev.* 118, 8798–8888. doi: 10.1021/acs.chemrev.7b00698

Pearce, M. J., Mintseris, J., Ferreyra, J., Gygi, S. P., and Darwin, K. H. (2008). Ubiquitin-like protein involved in the proteasome pathway of *Mycobacterium tuberculosis*. *Science* 322, 1104–1107. doi: 10.1126/science.1163885

Pedley, A. M., and Benkovic, S. J. (2017). A new view into the regulation of purine metabolism: the purinosome. *Trends Biochem. Sci.* 42, 141–154. doi: 10.1016/j.tibs.2016.09.009

Pelletier, J., and Sonenberg, N. (1988). Internal initiation of translation of eukaryotic mRNA directed by a sequence derived from poliovirus RNA. *Nature* 334:320. doi: 10.1038/334320a0

Platt, R. J., Chen, S., Zhou, Y., Yim, M. J., Swiech, L., Kempton, H. R., et al. (2014). CRISPR-Cas9 knockin mice for genome editing and cancer modeling. *Cell* 159, 440–455. doi: 10.1016/j.cell.2014.09.014

Poganik, J. R., Long, M. J. C., and Aye, Y. (2018). Getting the message? Native reactive electrophiles pass two out of three thresholds to be bona fide signaling mediators. *BioEssays* 40:1700240. doi: 10.1002/bies.201700240

Poole, L. A., and Cortez, D. (2017). Functions of SMARCAL1, ZRANB3, and HLTF in maintaining genome stability. *Crit. Rev. Biochem. Mol. Biol.* 52, 696–714. doi: 10.1080/10409238.2017.1380597

Princiotta, M. F., Schubert, U., Chen, W., Bennink, J. R., Myung, J., Crews, C. M., et al. (2001). Cells adapted to the proteasome inhibitor 4-hydroxy- 5-iodo-3-nitrophenylacetyl-Leu-Leu-leucinal-vinyl sulfone require enzymatically active proteasomes for continued survival. *Proc. Natl. Acad. Scie. U.S.A.* 98, 513–518. doi: 10.1073/pnas.98.2.513

Rancourt, D. E., Tsuzuki, T., and Capecchi, M. R. (1995). Genetic interaction between hoxb-5 and hoxb-6 is revealed by nonallelic noncomplementation. *Genes Dev.* 9, 108–122. doi: 10.1101/gad.9.1.108

Rees, J. S., Li, X.-W., Perrett, S., Lilley, K. S., and Jackson, A. P. (2015). Protein neighbors and proximity proteomics. *Mol. Cell. Proteomics* 14, 2848–2856. doi: 10.1074/mcp.R115.052902

Rhee, H.-W., Zou, P., Udeshi, N. D., Martell, J. D., Mootha, V. K., Carr, S. A., et al. (2013). Proteomic mapping of mitochondria in living cells via spatially restricted enzymatic tagging. *Science* 339, 1328–1331. doi: 10.1126/science.1230593

Santos, R., Ursu, O., Gaulton, A., Bento, A. P., Donadi, R. S., Bologa, C. G., et al. (2017). A comprehensive map of molecular drug targets. *Nat. Rev. Drug Disc.* 16:19. doi: 10.1038/nrd.2016.230

Schimke, R. T. (1988). Gene amplification in cultured cells. *J. Biol. Chem.* 263, 5989–5992.

Schlake, T., and Bode, J. (1994). Use of Mutated FLP Recognition Target (FRT) sites for the exchange of expression cassettes at defined chromosomal loci. *Biochemistry* 33, 12746–12751. doi: 10.1021/bi00209a003

Schneider, D. A., and Gourse, R. L. (2004). Relationship between growth rate and ATP concentration in *Escherichia coli*: a bioassay for available cellular ATP. *J. Biol. Chem.* 279, 8262–8268. doi: 10.1074/jbc.M311996200

Schopp, I. M., Amaya Ramirez, C. C., Debeljak, J., Kreibich, E., Skribbe, M., Wild, K., et al. (2017). Split-BioID a conditional proteomics approach to monitor the composition of spatiotemporally defined protein complexes. *Nat. Commun.* 8:15690. doi: 10.1038/ncomms15690

Shamir, M., Bar-On, Y., Phillips, R., and Milo, R. (2016). SnapShot: timescales in cell biology. *Cell* 164:1302. doi: 10.1016/j.cell.2016.02.058

Shi, Y., Long, M. J. C., Rosenberg, M. M., Li, S., Kobjack, A., Lessans, P., et al. (2016). Boc(3)Arg-linked ligands induce degradation by localizing target proteins to the 20S proteasome. *ACS Chem. Biol.* 11, 3328–3337. doi: 10.1021/acschembio.6b00656

Singh, P., Schimenti, J. C., and Bolcun-Filas, E. (2015). A mouse geneticist's practical guide to CRISPR applications. *Genetics* 199, 1–15. doi: 10.1534/genetics.114.169771

Smith, B. E., Wang, S. L., Jaime-Figueroa, S., Harbin, A., Wang, J., Hamman, B. D., et al. (2019). Differential PROTAC substrate specificity dictated by orientation of recruited E3 ligase. *Nat. Commun.* 10:131. doi: 10.1038/s41467-018-08027-7

Spencer, D., Wandless, T., Schreiber, S., and Crabtree, G. (1993). Controlling signal transduction with synthetic ligands. *Science* 262, 1019–1024. doi: 10.1126/science.7694365

Stanton, B. Z., Chory, E. J., and Crabtree, G. R. (2018). Chemically induced proximity in biology and medicine. *Science* 359:eaao5902. doi: 10.1126/science.aao5902

Stoops, E. H., Hull, M., Olesen, C., Mistry, K., Harder, J. L., Rivera-Molina, F., et al. (2015). The periciliary ring in polarized epithelial cells is a hot spot for delivery of the apical protein gp135. *J. Cell Biol.* 211:287. doi: 10.1083/jcb.201502045

Stottrup, C., Tsang, T., and Chin, Y. R. (2016). Upregulation of AKT3 confers resistance to the AKT inhibitor MK2206 in breast cancer. *Mol. Cancer Ther.* 15, 1964–1974. doi: 10.1158/1535-7163.MCT-15-0748

Stumpf, M. P. H., Thorne, T., de Silva, E., Stewart, R., An, H. J., Lappe, M., et al. (2008). Estimating the size of the human interactome. *Proc. Natl. Acad. Sci. U.S.A.* 105, 6959–6964. doi: 10.1073/pnas.0708078105

Surya, S. L., Long, M. J. C., Urul, D. A., Zhao, Y., Mercer, E. J., Eisaid, I. M., et al. (2018). Cardiovascular small heat shock protein HSPB7 is a kinetically privileged reactive electrophilic species (RES) sensor. *ACS Chem. Biol.* 13, 1824–1831. doi: 10.1021/acschembio.7b00925

Suzuki, R., Hotta, K., and Oka, K. (2015). Spatiotemporal quantification of subcellular ATP levels in a single HeLa cell during changes in morphology. *Sci. Rep.* 5:16874. doi: 10.1038/srep16874

Tantama, M., Martínez-François, J. R., Mongeon, R., and Yellen, G. (2013). Imaging energy status in live cells with a fluorescent biosensor of the intracellular ATP-to-ADP ratio. *Nat. Commun.* 4:2550. doi: 10.1038/ncomms3550

Tao, R., Zhao, Y., Chu, H., Wang, A., Zhu, J., Chen, X., et al. (2017). Genetically encoded fluorescent sensors reveal dynamic regulation of NADPH metabolism. *Nat. Methods* 14, 720–728. doi: 10.1038/nmeth.4306

Thompson, A., Schäfer, J., Kuhn, K., Kienle, S., Schwarz, J., Schmidt, G., et al. (2003). Tandem mass tags: a novel quantification strategy for comparative analysis of complex protein mixtures by MS/MS. *Anal. Chem.* 75, 1895–1904. doi: 10.1021/ac0262560

Trichas, G., Begbie, J., and Srinivas, S. (2008). Use of the viral 2A peptide for bicistronic expression in transgenic mice. *BMC Biol.* 6:40. doi: 10.1186/1741-7007-6-40

Udeshi, N. D., Pedram, K., Svinkina, T., Fereshetian, S., Myers, S. A., Aygun, O., et al. (2017). Antibodies to biotin enable large-scale detection of biotinylation sites on proteins. *Nat. Methods* 14, 1167. doi: 10.1038/nmeth.4465

Ullman, B., Clift, S., Gudas, L., Levinson, B., Wormsted, M., and Martin, D. (1980). Alterations in deoxyribonucleotide metabolism in cultured cells with ribonucleotide reductase activities refractory to feedback inhibition by 2'-deoxyadenosine triphosphate. *J. Biol. Chem.* 255, 8308–8314.

van der Heijden, J. W., Dijkmans, B. A. C., Scheper, R. J., and Jansen, G. (2007). Drug Insight: resistance to methotrexate and other disease-modifying antirheumatic drugs—from bench to bedside. *Nat. Clin. Pract. Rheumatol.* 3:26. doi: 10.1038/ncprheum0380

Vidal, M., and Fields, S. (2014). The yeast two-hybrid assay: still finding connections after 25 years. *Nat. Methods* 11:1203. doi: 10.1038/nmeth.3182

Vogel, C., and Marcotte, E. M. (2012). Insights into the regulation of protein abundance from proteomic and transcriptomic analyses. *Nat. Rev. Genet.* 13, 227–232. doi: 10.1038/nrg3185

Wagner, N., Stephan, M., Höglinger, D., and Nadler, A. (2018). A click cage: organelle-specific uncaging of lipid messengers. *Angewandte Chem. Int. Edit.* 57, 13339–13343. doi: 10.1002/anie.201807497

Wang, G., Du, M., Wang, J., and Zhu, T. F. (2018). Genetic variation may confound analysis of CRISPR-Cas9 off-target mutations. *Cell Disc.* 4:18. doi: 10.1038/s41421-018-0025-2

Wang, W., Perovic, I., Chittuluru, J., Kaganovich, A., Nguyen, L. T. T., Liao, J., et al. (2011). A soluble α-synuclein construct forms a dynamic tetramer. *Proc. Natl. Acad. Sci. U.S.A.* 108, 17797–17802. doi: 10.1073/pnas.1113260108

Wang, X., Zhao, B. S., Roundtree, I. A., Lu, Z., Han, D., Ma, H., et al. (2015). N(6)-methyladenosine modulates messenger RNA translation efficiency. *Cell* 161, 1388–1399. doi: 10.1016/j.cell.2015.05.014

Weinberg, G., Ullman, B., and Martin, D. W. Jr. (1981). Mutator phenotypes in mammalian cell mutants with distinct biochemical defects and abnormal deoxyribonucleoside triphosphate pools. *Proc. Natl. Acad. Sci. U.S.A.* 78, 2447–2451. doi: 10.1073/pnas.78.4.2447

Weiss, W. A., Taylor, S. S., and Shokat, K. M. (2007). Recognizing and exploiting differences between RNAi and small-molecule inhibitors. *Nat. Chem. Biol.* 3:739. doi: 10.1038/nchembio1207-739

Wilkie, A. O. (1994). The molecular basis of genetic dominance. *J. Med. Genet.* 31, 89–98. doi: 10.1136/jmg.31.2.89

Wisitpitthaya, S., Zhao, Y., Long, M. J. C., Li, M., Fletcher, E. A., Blessing, W. A., et al. (2016). Cladribine and fludarabine nucleotides induce distinct hexamers defining a common mode of reversible RNR inhibition. *ACS Chem. Biol.* 11, 2021–2032. doi: 10.1021/acschembio.6b00303

Wright, M. H., and Sieber, S. A. (2016). Chemical proteomics approaches for identifying the cellular targets of natural products. *Nat. Prod. Rep.* 33, 681–708. doi: 10.1039/C6NP00001K

Wucherpfennig, K. W., Gagnon, E., Call, M. J., Huseby, E. S., and Call, M. E. (2010). Structural biology of the T-cell receptor: insights into receptor assembly, ligand recognition, and initiation of signaling. *Cold Spring Harb. Perspect. Biol.* 2:a005140. doi: 10.1101/cshperspect.a005140

Xue, M., Hou, J., Wang, L., Cheng, D., Lu, J., Zheng, L., et al. (2017). Optimizing the fragment complementation of APEX2 for detection of specific protein-protein interactions in live cells. *Sci. Rep.* 7:12039. doi: 10.1038/s41598-017-12365-9

Yaginuma, H., Kawai, S., Tabata, K. V., Tomiyama, K., Kakizuka, A., Komatsuzaki, T., et al. (2014). Diversity in ATP concentrations in a single bacterial cell population revealed by quantitative single-cell imaging. *Sci. Rep.* 4:6522. doi: 10.1038/srep06522

Yang, N. J., and Hinner, M. J. (2015). Getting across the cell membrane: an overview for small molecules, peptides, and proteins. *Methods Mol. Biol.* 1266, 29–53. doi: 10.1007/978-1-4939-2272-7_3

Yen, H.-C. S., Xu, Q., Chou, D. M., Zhao, Z., and Elledge, S. J. (2008). Global protein stability profiling in mammalian cells. *Science* 322, 918–923. doi: 10.1126/science.1160489

Yook, K. J., Proulx, S. R., and Jorgensen, E. M. (2001). Rules of nonallelic noncomplementation at the synapse in *Caenorhabditis elegans*. *Genetics* 158, 209–220.

Yuen, G., Khan, F. J., Gao, S., Stommel, J. M., Batchelor, E., Wu, X., et al. (2017). CRISPR/Cas9-mediated gene knockout is insensitive to target copy number but is dependent on guide RNA potency and Cas9/sgRNA threshold expression level. *Nucleic Acids Res.* 45, 12039–12053. doi: 10.1093/nar/gkx843

Zetsche, B., Volz, S. E., and Zhang, F. (2015). A split-Cas9 architecture for inducible genome editing and transcription modulation. *Nat. Biotechnol.* 33, 139–142. doi: 10.1038/nbt.3149

Zhang, B., Xiao, R., Ronan, E. A., He, Y., Hsu, A.-L., Liu, J., et al. (2015). Environmental temperature differentially modulates C. elegans longevity through a thermosensitive TRP channel. *Cell Reports* 11, 1414–1424. doi: 10.1016/j.celrep.2015.04.066

Zhang, H., Berel, D., Wang, Y., Li, P., Bhowmick, N. A., Figlin, R. A., et al. (2013). A comparison of Ku0063794, a dual mTORC1 and mTORC2 inhibitor, and temsirolimus in preclinical renal cell carcinoma models. *PLoS ONE* 8:e54918. doi: 10.1371/journal.pone.0054918

Zhang, K., and Cui, B. (2015). Optogenetic control of intracellular signaling pathways. *Trends Biotechnol.* 33, 92–100. doi: 10.1016/j.tibtech.2014.11.007

Zhao, Y., Araki, S., Wu, J., Teramoto, T., Chang, Y.-F., Nakano, M., et al. (2011). An expanded palette of genetically encoded Ca^{2+} indicators. *Science* 333, 1888–1891. doi: 10.1126/science.1208592

Zhao, Y., Long, M. J. C., Wang, Y., Zhang, S., and Aye, Y. (2018). Ube2V2 is a rosetta stone bridging redox and ubiquitin codes, coordinating DNA damage responses. *ACS Central Sci.* 4, 246–259. doi: 10.1021/acscentsci.7b00556

Conflict of Interest Statement: G-REX technology had been filed for patent application by Cornell University (USA).

Copyright © 2019 Long, Liu and Aye. This is an open-access article distributed under the terms of the Creative Commons Attribution License (CC BY). The use, distribution or reproduction in other forums is permitted, provided the original author(s) and the copyright owner(s) are credited and that the original publication in this journal is cited, in accordance with accepted academic practice. No use, distribution or reproduction is permitted which does not comply with these terms.

frontiers in Chemistry

ORIGINAL RESEARCH
published: 16 April 2019
doi: 10.3389/fchem.2019.00238

Elucidating the Lipid Binding Properties of Membrane-Active Peptides Using Cyclised Nanodiscs

*Alan H. Zhang[1†], Ingrid A. Edwards[2†], Biswa P. Mishra[1], Gagan Sharma[1], Michael D. Healy[2], Alysha G. Elliott[2], Mark A. T. Blaskovich[2], Matthew A. Cooper[2], Brett M. Collins[2], Xinying Jia[1] and Mehdi Mobli[1]**

[1] Centre for Advanced Imaging, The University of Queensland, Brisbane, QLD, Australia, [2] Institute for Molecular Bioscience, The University of Queensland, Brisbane, QLD, Australia

OPEN ACCESS

Edited by:
John D. Wade,
Florey Institute of Neuroscience and Mental Health, Australia

Reviewed by:
Thorsten Wohland,
National University of Singapore, Singapore
Stefan W. Vetter,
North Dakota State University, United States

***Correspondence:**
Mehdi Mobli
m.mobli@uq.edu.au

[†] These authors have contributed equally to this work

Specialty section:
This article was submitted to Chemical Biology, a section of the journal Frontiers in Chemistry

Received: 28 January 2019
Accepted: 26 March 2019
Published: 16 April 2019

Citation:
Zhang AH, Edwards IA, Mishra BP, Sharma G, Healy MD, Elliott AG, Blaskovich MAT, Cooper MA, Collins BM, Jia X and Mobli M (2019) Elucidating the Lipid Binding Properties of Membrane-Active Peptides Using Cyclised Nanodiscs. Front. Chem. 7:238. doi: 10.3389/fchem.2019.00238

The lipid composition of the cellular membrane plays an important role in a number of biological processes including the binding of membrane-active peptides. Characterization of membrane binding remains challenging, due to the technical limitations associated with the use of standard biophysical techniques and available membrane models. Here, we investigate the lipid binding properties of two membrane-active peptides, VSTx1, a well characterized ion-channel inhibitor, identified from spider venom, that preferentially binds to anionic lipid mixtures, and AA139 an antimicrobial β-hairpin peptide with uncharacterised lipid binding properties, currently in pre-clinical development. The lipid binding properties of these peptides are elucidated using nanodiscs formed by both linear and circularized (sortase-mediated) forms of a membrane scaffold protein (MSP1D1ΔH5). We find that nanodiscs formed by circularized MSPs—in contrast to those formed by linear MSPs—are sufficiently stable under sample conditions typically used for biophysical measurements (including lipid composition, a range of buffers, temperatures and concentrations). Using these circularized nanodiscs, we are able to extract detailed thermodynamic data using isothermal titration calorimetry (ITC) as well as atomic resolution mapping of the lipid binding interfaces of our isotope labeled peptides using solution-state, heteronuclear, nuclear magnetic resonance (NMR) spectroscopy. This represents a novel and general approach for elucidating the thermodynamics and molecular interface of membrane-active peptides toward flat lipid bilayers of variable composition. Our approach is validated by first determining the thermodynamic parameters and binding interface of VSTx1 toward the lipid bilayer, which shows good agreement with previous studies using lipid micelles and liposomes. The method is then applied to AA139, where the membrane binding properties are unknown. This characterization, involved solving the high-resolution structure of AA139 in solution using NMR spectroscopy and the development of a suitable expression system for isotope labeling. AA139 was found to bind exclusively to anionic membranes with moderate affinity (K_d∼low μM), and was found to have a lipid binding interface involving the termini of the β-hairpin structure.

The preference of AA139 for anionic lipids supports a role for membrane binding in the mode-of-action of this peptide, which is also consistent with its higher inhibitory activity against bacterial cells compared to mammalian cells. The described approach is a powerful method for investigation of the membrane binding properties of this important class of molecules.

Keywords: arenicin, VSTx1, nanodiscs, POPC, POPG, cNW9, membrane-active peptide

INTRODUCTION

The composition of the lipid bilayer can have a significant impact on a number of biological processes including the trafficking of soluble proteins, the structure, dynamics and function of integral membrane proteins and the action of membrane-active peptides (Escriba et al., 2008). The latter have emerged as an important class of molecules in the search for novel antimicrobials and ion-channel inhibitors (Zhang et al., 2018). A major limitation in the characterization of membrane-active peptides is the lack of detailed thermodynamic, kinetic and structural information regarding their lipid interactions. Such information can usually be facilitated by biophysical studies in solution (Lee, 2018). Structural characterization of peptides is traditionally conducted using nuclear magnetic resonance (NMR) spectroscopy (Klint et al., 2013), while membrane-binding assays are most commonly conducted using a combinations of chromatography and fluorescence methods (Deuis et al., 2016) or surface plasmon resonance analysis (Hodnik and Anderluh, 2013). Thus, structural details of the binding of membrane-active peptides to lipid bilayers is often only available at very low resolution, hampering efforts to elucidate their mode-of-action. High-resolution structural data is often difficult to obtain by X-ray diffraction methods due to difficulties in crystallization of peptide-lipid complexes. Solid-state NMR is often the only method to study these systems at atomic resolution, although the analysis of such data is often challenging and time-consuming (Mani et al., 2006). Solution-state NMR experiments can with relative ease provide high-resolution information about binding interfaces, although such studies have been limited to use of detergent and/or lipid micelles or bicelles as membrane mimetics (Warschawski et al., 2011; Lau et al., 2016). These models do not accurately reflect the geometry of the cell membrane, in particular they have a significantly higher curvature, which can cause peptides to adopt non-native conformations, or to aggregate (Catoire et al., 2014).

Lipid bilayer nanodiscs (ND) have been developed to solubilize and reconstitute membrane proteins in lipid bilayers, and their use is rapidly expanding (Bayburt et al., 2002; Shaw et al., 2004). NDs are self-assembled soluble particles (from ∼10 to 50 nm in diameter), where each particle consists of two membrane scaffold proteins (MSPs), derived from human apo-lipoprotein I that is wrapped around a flat phospholipid bilayer. NDs are increasingly being used in biophysical studies, typically for structural studies of membrane proteins and binding interaction studies of lipophilic ligands or ligands that interact with membrane proteins (Hagn et al., 2013; Shenkarev et al., 2014). Recently, a variant of NDs has been described where the *N*- and *C*-termini are ligated via a peptide bond using sortase enzymes (Nasr et al., 2017; Yusuf et al., 2018)–circularized nanodiscs referred to as cNDs hereafter.

A significant advantage of (c)NDs is in their modularity. Different compositions of synthetic phospholipids can be encapsulated, and these soluble discs can then be studied under a range of solution conditions (pH, temperature, salt etc.). It is often possible to incorporate specific lipid compositions and obtain homogeneous NDs (Lee et al., 2015; Yeh et al., 2016). In particular, we are here interested in studying the binding of membrane-active peptides that have shown activity against anionic lipid bilayers mimicking those of Gram-negative bacteria. We employ heteronuclear NMR experiments using isotope labeled peptides to map the lipid binding interface of these peptides at atomic resolution. In these experiments, the nanodisc is unlabelled and therefore remains undetected. To ensure that these discs remain stable under the conditions of typical NMR experiments we have conducted a detailed study of the solution characteristics and stability of linear and circularized NDs containing mixtures of POPC and POPG.

The stability of the NDs were evaluated by size-exclusion chromatography (SEC), electron microscopy (EM) and mass spectrometry (MS), under different storage conditions with variable buffer (pH), temperature and concentration. While non-circularized NDs containing anionic lipids were shown to be poorly stable, excellent stability was found when using the cNDs. The latter was then used for solution-state biophysical studies to investigate the lipid binding interactions of two peptides that are known to exert their function in anionic lipid bilayer environments.

To determine the binding of these membrane-active peptides to model membranes of Gram-negative bacteria in NDs, we first studied the well characterized spider toxin, VSTx1, isolated from the venom of *Grammostola spatulata*. In previous studies using centrifugation coupled with chromatography, the peptide has been shown to partition into liposomes containing mixtures of POPC and POPG, but these studies did not find partitioning of the peptide into liposomes containing only zwitterionic POPC

Abbreviations: Nanodisc, ND; circular MSP1D1ΔH5, cNW9; linear MSP1D1ΔH5, dH5; antimicrobial peptides, AMPs; membrane scaffold protein, MSP; protein databank, PDB; dodecylphosphocholine, DPC; 1,2-dimyristoyl-sn-glycero-3-phosphocholine, dodecyl-β-D-maltoside (DDM), decyl-β-D-maltoside (DM), DMPC; 1,2-Dimyristoyl-sn-glycero-3-phosphorylglycerol, DMPG; palmitoyloleoyl-phosphatidylcholine, POPC; palmitoyloleoyl-phosphatidylglycerol, POPG; size exclusion chromatography, SEC; electron microscope, EM; mass spectrometry, MS; chemical shift perturbation, CSP; polymerase chain reaction, PCR.

lipids (Jung et al., 2005; Ozawa et al., 2015; Lau et al., 2016). The peptide was, however, found to bind to zwitterionic DHPC (and DM) micelles in NMR studies (Lee and Mackinnon, 2004; Wang et al., 2018).

Here, we first measured the thermodynamics of the binding of the peptide against cNDs using isothermal titrations calorimetry (ITC) experiments. We then mapped the lipid binding interface of the peptide using chemical shift mapping experiments by analysis of, 2D ^{1}H-^{15}N-HSQC, solution-state NMR experiments. Our results show very weak binding of the peptide to POPC bilayers in cNDs–much weaker than that observed when using DHPC micelles. In contrast, the peptide binds very strongly to anionic cNDs, consistent with the previous liposome experiments, suggesting that the binding of the peptide to micelles is different than to bilayers.

Next, the described approach was applied to an antimicrobial peptide, AA139, currently undergoing preclinical trials for the treatment of Gram-negative bacterial infections. AA139 is an analog of arenicin-3, a peptide antibiotic that was originally identified as part of a group of broad-spectrum antimicrobial peptides isolated from the lugworm *Arenicola marina* by *Novozymes* (Novozymes A/S Copenhagen). The mode-of-action of this peptide remains unknown; however, the related arenicin-2 peptide was shown to form pores in planar lipid bilayers, suggesting a cytotoxic mode-of-action (Shenkarev et al., 2011). A bacterial expression system was developed for recombinant expression and labeling of the peptide. To map the binding interface of the peptide, the structure of the peptide was also solved in solution by standard NMR methods, revealing a twisted β-hairpin fold, common in this family of peptides. The biophysical data (EM/NMR/ITC) show that AA139 does bind to anionic cNDs but does not form pores, suggesting a different mode-of-action to arenicin-2 (Shenkarev et al., 2011).

The presented approach provides a platform for measurement of both thermodynamic and structural data for membrane-active peptides using a planar bilayer system, using standard NMR experiments. The flexibility and stability of the cNDs as a model system promises to improve our understanding of this important class of molecules.

MATERIALS AND METHODS

Materials

The construct for the evolved pentamutant of Sortase A in a pET29 vector was a gift from Prof. David R. Liu's laboratory (Harvard University). Expression and purification of the pentamutant Sortase A from *Escherichia coli* BL21(DE3) cells was performed as previously described (Chen et al., 2011). The construct for MSP1D1ΔH5 (dH5 hereafter) in a pET28a vector was a gift from Prof. Gerhard Wagner at the Harvard Medical School. Using NEB Q5 Site-Directed Mutagenesis Kit (New England BioLabs, NEB), a DNA sequence encoding LPGTGAAALEHHHHHH was appended into the end of the encoding sequence for MSP1D1ΔH5 construct to create the NW9 construct. Synthetic lipids, palmitoyloleoyl-phosphatidylcholine (POPC) and palmitoyloleoyl-phosphatidylglycerol (POPG), in powder form were purchased from Avanti Polar Lipids (Alabaster, AL). These were resuspended in chloroform and dried by nitrogen flow and vacuum overnight to a thin layer in glass tubes. Lipid stocks were sealed and left at −80°C for long-term storage.

Peptide Expression and Purification

Isotopically single labeled ^{15}N-VSTx1 was expressed and purified as previously described (Lau et al., 2016). A synthetic AA139 gene was introduced into both a pOPINE vector (Berrow et al., 2007) and a pLIC vector (Klint et al., 2013), containing a SUMO and MBP fusion tag, respectively. Initial expression tests show that soluble AA139 was only overexpressed when using the pOPINE expression vector with a SUMO tag. Subsequently we also screened the expression of VSTx1 in a similar N-terminal SUMO-tagged fusion expression vector (unpublished), which also produced high soluble protein yields (∼0.5 mg per liter of culture). Recombinant ^{15}N-AA139 was expressed as a His_6-tagged SUMO fusion protein in *E. coli* (SHuffle T7 strain cells–NEB cat. C3029J) using standard biochemical methods. Details of the expression and purification methods are provided in the **Supplementary Information**.

NMR Structure of AA139

1D ^{1}H NMR experiments were recorded at different pHs and at pH 3.3 all non-exchangeable backbone amide protons could be observed. The spectra at pH 3.3 and 6.5 were superimposable indicating that the structure is unaffected by the change in pH. Subsequently, 2.5 mM synthetic AA139 (provided by Adenium) was analyzed in 20 mM phosphate buffer at pH 3.3 containing 5% D_2O. All NMR experiments were performed on a Bruker Avance III spectrometer equipped with a cryogenically cooled triple resonance probe operating at a nominal ^{1}H frequency of 700 or 900 MHz. The excitation sculpting sequence was used to suppress the solvent (H_2O) resonance. Two-dimensional TOCSY [t_m (MLEV17 spin-lock mixing pulses) = 80 ms], NOESY [t_m (mixing time) = 300 ms], ^{15}N-HSQC and ^{13}C-HSQC were recorded at 25°C. Chemical shifts were directly (for ^{1}H) or indirectly (for ^{13}C, ^{15}N) referenced relative to the 2, 2-dimethylsilapentane-5-sulfonic acid (DSS) signal at 0 ppm. The assignment of proton resonances was carried out using TOCSY and NOESY data using the CCPNMR software (Skinner et al., 2015). Torsion angles constraints were obtained using the TALOS+ software (Shen et al., 2009), and structure calculations were performed using CYANA 3.0 (Guntert, 2004).

Hydrogen-Deuterium Exchange Studies

All NMR spectra for the hydrogen-deuterium exchange studies were recorded on the spectrometer described above at 25°C. Spectra were referenced to DSS at 0 ppm. Lyophilized peptide was initially solubilized in 20 mM phosphate buffer at pH 3.3. The peptide was then lyophilized and subsequently dissolved in 100% D_2O followed by immediate transfer to the spectrometer for measurement. 1D ^{1}H and 2D TOCSY spectra were recorded at specific time points over a 24 h period. Hydrogen-deuterium exchange rates were measured by integrating each exchangeable amide resonance separately.

Amide Temperature Coefficient Studies

The temperature dependence of amide proton resonances was derived from 1D ^{1}H to 2D TOCSY spectra recorded on a Bruker ARX 500 MHz spectrometer. Spectra were measured between 15° and 35°C, in 5°C increments, and referenced to DSS at 0 ppm. Assignment of the spectra was performed using the CCPNMR software (Skinner et al., 2015).

NW9 Circularization

NW9 protein expression and purification followed standard procedures and is described in detail in the **Supplementary Information**, yielding 20 ± 5 mg of NW9 per liter of LB media. NW9 after TEV protease cleavage was buffer exchanged into the reaction buffer (20 mM Tris·HCl pH 7.5 and 150 mM NaCl) and then supplemented with 1 mM dodecyl-β-D-maltoside (DDM), 1 mM 2-mercaptoethanol and 10 mM $CaCl_2$. 1:2 molar equivalents of evolved 5'-1' pentamutant Sortase A and NW9 were mixed and diluted to a total protein concentration of 15 μM. The reaction was left stirring for > 3 h at room temperature, for complete cyclisation of NW9 to cNW9. Subsequently, SM-2 Biobeads (Bio-rad) at 1 g/100 ml of reaction mixture were added to remove the detergent DDM from the reaction mixture. After incubation of 1 h of detergent absorption, the reaction mixture was filtered on a 0.45 μm polyethersulfone (PES) membrane and loaded into two 5 mL HisTrap Fast Flow Ni(II) columns (GE Healthcare) pre-equilibrated with reaction buffer to remove histidine tagged products including Sortase A, TEV protease and cleaved histidine tags. The flow-through containing cNW9 was collected and buffer exchanged to buffer A_{ex} (20 mM Tris·HCl pH 7.5, 1 mM DDM). The sample was purified and fractionated by anion-exchange chromatography using a HiScreen Q HP Column (GE Healthcare) using liquid chromatography (AKTAPurifier, GE Healthcare). After sample loading a linear gradient from 0 to 80% buffer B_{ex} (20 mM Tris·HCl pH 7.5, 500 mM NaCl, 1 mM DDM) was applied for 40 column-volumes.

ND Production

To assemble NDs, dH5 or cNW9 and lipids were co-dissolved at [lipid]:[MSP] ratio of 50:1 in reconstitution buffer (20 mM Tris·HCl pH 7.4, 100 mM NaCl, 0.5 mM EDTA and 100 mM cholate) and mixed for 1 h at 4°C. A molar ratio of 1:50 (MSP:lipids) was calculated using the equation: $N_L \times S = (0.423 \times M\text{-}9.75)^2$, where N_L is the number of lipids per ND, M is the number of amino acids in the scaffold protein and S is the mean surface area per lipid used to form the lipid-nanodisc, measured in Å^2 (Ritchie et al., 2009)–POPC and POPG have been estimated to have a similar mean surface area of around 70 Å^2 (Janosi and Gorfe, 2010). Nevertheless, to confirm these calculations for the anionic lipid mixtures a range of MSP:lipid ratios (1:10, 1:30, 1:40, 1:50, and 1:80) were screened to monitor aggregation behavior. SEC chromatography of the assembled discs, showed high monodispersity in the 1:30–1:50 range, while 1:10 and 1:80 ratios produced chromatograms with evidence of high levels of inhomogeneity. Finally, the homogeneity of the lipid mixtures within the discs, was monitored by anion exchange chromatography and the elution profile was found to consist of a single peak, confirming efficient mixing of the lipids within the nanodiscs.

0.6 g of Bio-Beads SM-2 (Bio-rad) was added per mL of reaction volume, to absorb the detergent (cholate), and thus initiating ND assembly. The mixture was gently stirred for 4 h at 4°C for complete detergent removal. The solution was filtered through a 0.45 μm PES membrane to remove the Bio-Beads and then concentrated using centrifugal filtration (Amicon Centricon with a 10 kDa MW cut-off). The sample was buffer exchanged using a PD-10 column (GE Healthcare) into three different buffers: (i) 20 mM Tris·HCl pH 7.5, 50 mM NaCl, 1 mM EDTA; (ii) 20 mM $NaPO_4$ pH 6.5, 50 mM NaCl, 1 mM EDTA; (iii) 20 mM Bis·Tris pH 6.5, 50 mM NaCl, 1 mM EDTA. After buffer exchange of NDs into one of three buffers, samples were concentrated by centrifugal filtration to ∼5 mg/mL (unless otherwise stated) and stored at 4 °C.

Electron Microscopy (EM)

Lipid NDs were diluted to a final concentration of 200 nM in 20 mM Tris–HCl, pH 7.5, 50 mM NaCl and adsorbed to glow-discharged and carbon-coated EM grids. Samples were prepared by conventional negative staining with 1 % (w/v) uranyl acetate. EM images were collected with a Tecnai 12 electron microscope operated at an acceleration voltage of 120 kV.

Liquid Chromatography–Mass Spectrometry (LC-MS)

LC-MS analysis was conducted on lipid nanodiscs using Agilent Technologies 1200 Series Instrument with a G1316A variable wavelength detector set at λ = 210 nm, 1200 Series ELSD, 6110 quadrupole ESI-MS, using an Agilent Zorbax Eclipse XDB-Phenyl column (3 × 100 mm, 3.5 μm particle size, flow rate 1 mL/min, the mobile phases 0.05% formic acid in water and 0.05% formic acid in acetonitrile).

Isothermal Titration Calorimetry (ITC)

The affinities of AA139 and VSTx1 for cNDs (both POPC and POPC:POPG mixtures) were determined using a Microcal iTC200 instrument (Malvern, UK). Experiments were performed in 20 mM Bis·Tris (pH 6.5), 50 mM NaCl and 1 mM EDTA. The peptides (at 350 μM) were titrated into 25 μM cNDs in 15× 2.8 μl (AA139) and 19× 2.2 μl (VSTx1) injections at 25 °C. Considering the symmetry of the cNDs the stoichiometry (n) was fixed at an even integer value (2, 4, 6 etc.). The concentration of the peptide was fixed and the effective concentration of the nanodisc allowed to vary together with the remaining variables. The effective nanodisc concentration was then fixed to the above determined value and all other parameters (including n) allowed to vary in order to determine the dissociation constants (K_d) and enthalpy of binding (ΔH). During the fitting procedure the ITC response was integrated and normalized to a single-site binding model. The apparent binding free energy (ΔG) and entropy (ΔS) were calculated from the relationships $\Delta G = RT\ln(K_d)$ and $\Delta G = \Delta H\text{-}T\Delta S$. All experiments were performed at least in triplicate to ensure reproducibility of the data.

NMR Titration

Solution NMR titration experiments between ^{15}N-VSTx1 and ^{15}N-AA139 and unlabelled cNDs [cNW9 (POPC/POPG (4:1))] were performed on a Bruker Avance III spectrometer equipped with a cryogenically cooled triple resonance probe operating at a nominal ^{1}H frequency of 700 MHz. ^{15}N-HSQC spectra were recorded at 25 °C. The concentration of ^{15}N-VSTx1 or ^{15}N-AA139 were kept constant at 20 and 40 μM respectively, while the concentration of cNDs [cNW9 (POPC/POPG (4:1))] was increased from 0 to 20 μM, with a total of up to six concentrations. A second titration of ^{15}N-VSTx1 against cNDs [cNW9 (POPC)] was conducted under identical conditions to those noted above for this peptide. Each 2D experiment was acquired for ∼ 45 min (16 scans and 75 complex points for AA139, and 32 scans and 37 complex points for VSTx1). All titrations were performed in 20 mM Bis·Tris buffer (pH 6.5), 50 mM NaCl and 1 mM EDTA.

NMR titration experiments between unlabelled VSTx1 or AA139 and ^{15}N-cNDs [^{15}N-cNW9 (POPC/POPG(4:1))] were performed on a Bruker Neo spectrometer equipped with a cryogenically cooled, triple resonance probe, operating at a nominal ^{1}H frequency of 900 MHz, at 50°C. Three experiments were performed, the concentration of cNDs [^{15}N-cNW9 (POPC/POPG (4:1))] was kept constant at 100 μM, while the concentration of VSTx1 or AA139 was increased from 0 to 50 then 100 μM. Each experiment was acquired over 4 h (128 scans and 50 increments).

NMR Data Analysis

All spectra were processed using Topspin (Bruker Biospin) and the Rowland NMR toolkit (University of Connecticut). CCPNMR was used for spectral analysis. The change in peak intensity between titration points is the product of several dynamic processes that occur due to the binding event (for further details see **Supplemental Discussion**). The intensity of the signal is thus attenuated according to the weighted average of the free and bound states of the peptide:

$$I_{obs} = f_F I_F + f_B I_B \tag{1}$$

The change in signal intensity due to this process I_{obs} can be related to the fraction of the peptide bound to the cND:

$$\Delta I_{obs} = f_B \Delta I_{\max} \tag{2}$$

f_B (fraction of the concentration of ligand bound to cNDs over the total ligand concentration- $\frac{[L_B]}{[L_T]}$) can then be fitted to a quadratic equation to obtain estimates of the dissociation constant, K_d, and the number of equivalent binding sites on the cND, n, available for peptide binding (Granot, 1983; Williamson, 2013):

$$f_B = \frac{(n \times [cND_T] + [L_T] + K_d) - \sqrt{\left((n \times [cND_T] + [L_T] + K_d)^2 - 4\,[L_T] \times (n \times [cND_T]\right)}}{2\,[L_T]} \tag{3}$$

where $[L_T]$ is the total ligand concentration (^{15}N labeled peptide), $[cND_T]$ is the total concentration of cND at each titration point, $I_{\max}$ is the normalized maximum intensity change and I_{obs} is the normalized change in signal intensity for a given spin pair and correlates with the mole fraction of peptide bound to the cND. It is assumed that (i) the signal observed is due to free ligand in addition to any residual signal from the bound ligand, due to fast local motion; (ii) at the highest concentration of nanodisc the binding is saturated (i.e., any signal remaining at highest cND conc. belongs to residues having fast local motion). Given the preceding conditions, normalization of the maximum-intensity-change ensures that the change in intensity observed is bounded between the free and saturated state (accounting for fast local motion). This allows us to fit data from all of the HSQC signals simultaneously. However, prior to this global fitting, each residue was fitted individually, those residues that yielded poor fits to the equation (i.e., produced very large fitting errors or negative K_d values) were excluded on the basis that additional processes were dominating the observed signal intensity change (other than chemical exchange due to binding). At this step residues with insufficient valid titration points (i.e., low initial intensity or very rapid decay, yielding fewer than three titration points above the noise level) and those from overlapping residues were removed. For all of the remaining residues a nearly constant value of n was found. The value of n was found to be close to an even integer, which agreed with the symmetry of the nanodisc, and the value of n was subsequently fixed to this nearest even integer value. Once this value was fixed a global fit of all of the data to equations 2/3 was performed. The fitting was performed using a Levenberg-Marquardt iterative non-linear least squares method (in Gnuplot v.3.5).

RESULTS

cNW9 Production

MSP circularization following standard Sortase A reaction conditions (Tris·HCl, NaCl and $CaCl_2$ conditions) (Nasr et al., 2017), led to a low yield of monomeric, cyclised, cNW9 (∼3 mg/l of LB, corresponding to 15% of total NW9 produced). We observed that a large proportion of the reaction products were multimeric by-products (Mei and Atkinson, 2015; Henrich et al., 2017). To improve the yield of monomeric cNW9, we conducted a screen of reaction conditions including (i) temperature, (ii) total protein concentrations and (iii) different detergents/supplements added. Under optimized conditions, the reactions at 4 °C, room temperature and at 37°C were mostly complete in >24, ∼3, and <1 h, respectively. Lowering the total protein concentrations from 30 to 5 μM led to detectable improvements in the fraction of monomeric products. A screening of detergents showed that non-ionic detergents such DM or DDM significantly improved the yield of monomeric cNW9 formed (from ∼3 to ∼6 mg/l of LB; or equivalently from 15 to 30% yield), while ionic detergents such as cholate had minimal effects on the final yield (see **Figure S1A**). Similar improvements in yields (doubling of the yield in presence of detergents) has been independently observed elsewhere using

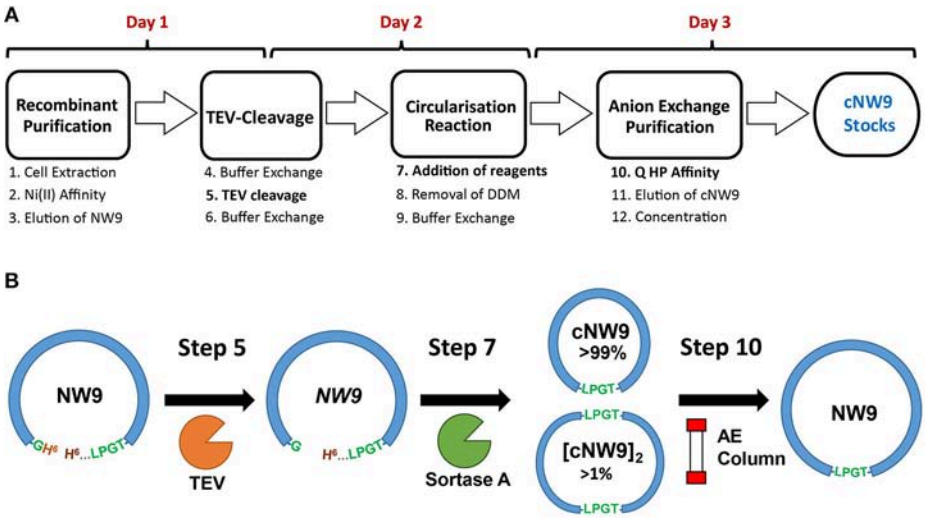

FIGURE 1 | Production and circularization of cNW9. **(A)** Cell extraction of recombinant, noncircular cNW9 (NW9) followed by affinity purification (Ni Sepharose resin) and TEV cleavage (day 1 and overnight). TEV-cleaved NW9 circularization to a circular monomeric product (cNW9) and multimeric by-products ($[cNW9]_n$) mediated by sortase A and assisted with lipid-detergents (day 2). Purification of cNW9 by anion exchange chromatography (Q HP resin) and concentration of protein stocks (day 3). **(B)** Reaction scheme for circularizing NW9 to cNW9 is illustrated with the key components/variants as designated in **(A)** (NW9, TEV, sortase A, anion-exchange column) and annotated with the key reaction steps in **(A)**.

the non-ionic detergent Triton X-100 (Yusuf et al., 2018). In both cases the presence of detergents leads to near-complete removal of multimeric by-products. Following circularization, reverse nickel affinity and anion exchange chromatography, cNW9 is obtained at >99% purity (**Figure 1** and **Figure S1B**). The assembly of the lipid cNDs routinely resulted in a yield of > 80% of pure lipid nanodiscs, regardless of the lipid composition.

Nanodisc Stability Study

Three buffer conditions were chosen for the study of lipid-nanodiscs (ND) following the literature (Shenkarev et al., 2014; Susac et al., 2014) and NMR titration requirements:

(i) 20 mM Tris·HCl pH 7.5, 50 mM NaCl, 1 mM EDTA, a standard buffer-salt condition;
(ii) 20 mM $NaPO_4$ pH 6.5, 50 mM NaCl, 1 mM EDTA, a common NMR condition at a relatively low pH; and
(iii) 20 mM Bis-Tris pH 6.5, 50 mM NaCl, 1 mM EDTA, where the low pH is retained while the favorable conductivity of the Tris based buffer is also retained.

Size-exclusion chromatography (SEC) was performed on ND samples at 5 mg/mL concentration, using a Superdex S200 5/150 *Increase* gel filtration column, pre-equilibrated in 20 mM Tris·HCl pH 7.5, 150 mM NaCl. Samples run over SEC were monitored and assessed for stability (all SEC traces can be found in **Figures S2**–**S5**).

To start, samples were stored at 4°C and monitored by SEC over intervals from day 1 to 30. The SEC profiles for circular cNW9 NDs were always sharper, indicating greater homogeneity of the sample. With the lipid composition consisting solely of POPC lipids, virtually no change in sample profiles was observed for cNW9 or dH5 NDs up to 30 days in the standard buffer condition (i).

cNDs were stable up to 30 days in all buffers tested. However, dH5 NDs in the lower pH conditions of (ii) and (iii) resulted in SEC profiles having an asymmetric peak, with a shoulder at shorter elution times (indicating either unassembled MSP or aggregates) after only 3 days of storage. It should be noted that unassembled MSP elutes earlier than the assembled NDs, indicating a larger effective molecular radius. Under these conditions the phosphate buffer condition (ii) seemed to be slightly worse for stability than the Bis-Tris buffer condition (iii).

The introduction of 20% POPG into the NDs did not affect the stability of cNW9 ND samples at 4°C. However, significant changes in the profile were observed in all buffer conditions for dH5 NDs at 4°C, with the observed effect getting worse from Tris (i) to Bis-Tris (iii) to phosphate (ii) buffer conditions. In the Bis-Tris buffer condition (iii), significant changes in the profile were observed for dH5 NDs at storage temperatures of 25° and 37°C. However, for cNW9 NDs, no changes were observed at either of these temperatures. **Table 1** summarizes our observations, where the sample is deemed unstable if a clear change in the SEC profile can be seen, in particular noting the presence of shoulders or peaks at elution times earlier than that of the main ND peak.

A detailed study was conducted for both constructs of NDs containing POPC/POPG (4:1) in 20 mM Bis-Tris pH 6.5, 50 mM NaCl, 1 mM EDTA using an analytical Supderdex S200 10/300 *Increase* column. Note that this column provides a higher resolution than the smaller S200 5/150 column used in our screening experiments described above (i.e., traces in **Figures S2**–**S5**). At assembly time (day 0), both constructs were analyzed by SEC, using the 10/300 column pre-equilibrated in 20 mM Tris-HCl pH 7.5, 150 mM NaCl (**Figures 2A,B**). The NDs were

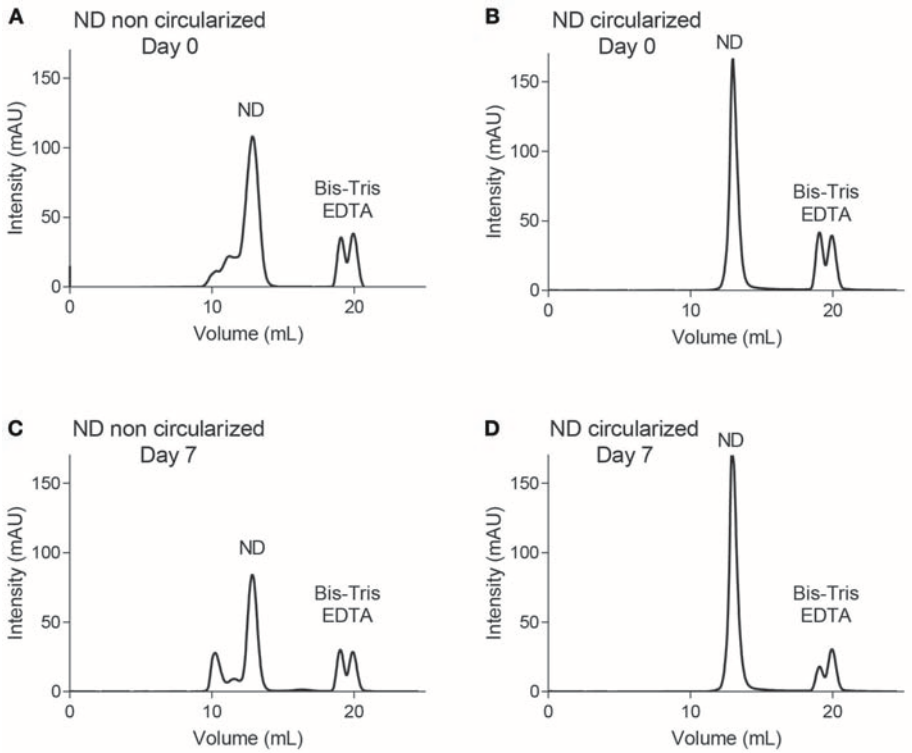

FIGURE 2 | Size exclusion chromatography using an S200 Increase 10/300 column. Traces of NDs containing POPC/POPG (4:1) lipids using membrane scaffold proteins dH5 **(A,C)** and cNW9 **(B,D)** at day 0 **(A,B)** and day 7 **(C,D)** after storage at room temperature.

TABLE 1 | Summary of nanodisc stability under different storage conditions.

Buffer	Temperature (°C)	Days stable/ total days			
		NDs with POPC		NDs with POPC:POPG (4:1)	
		dH5	cNW9	dH5	cNW9
i. 20 mM Tris pH 7.5 *50 mM NaCl and 1 mM EDTA*	4	30/30	30/30	1/30	30/30
ii. 20 mM PO_4 pH6.5 *50 mM NaCl and 1 mM EDTA*	4	3/30	30/30	1/30	30/30
iii. 20 mM Bis-Tris pH6.5 *50 mM NaCl and 1 mM EDTA*	4	3/30	30/30	1/30	30/30
	25	–	–	1/2	2/2
	37	–	–	0/2	2/2
	−20	–	–	2/2	2/2

Circular and linear (cNW9 and dH5) nanodiscs containing either zwitterionic (POPC) or anionic [POPC:POPG (4:1)] lipid mixtures were stored at different temperatures in different buffers (all including 50 mM NaCl and 1 mM EDTA). The stability of the discs was monitored by size-exclusion chromatography using an S200 Increase 5/150 column (GE Healthcare), at daily intervals.

left at room temperature for seven days and reanalyzed via SEC (**Figures 2C,D**). Each fraction was subjected to LC-MS (**Figures S6**–**S7**). Negative stain EM was also performed for selected fractions of NDs [dH5 (POPC/POPG (4:1))], confirming the presence of NDs of increased diameter after 7 days of storage (**Figure S8**). The dH5 ND samples aggregated over time, while no degradation was observed for cNW9 NDs.

Recombinant Peptide Production and Solution Structure Determination

VSTx1 was produced using an MBP-fusion construct as previously described, where the structure of this peptide is also reported (Lau et al., 2016)–yielding ∼1 mg of peptide per liter of bacterial culture. VSTx1 was also produced using a SUMO-fusion construct. The smaller fusion partner further simplified the purification step by HPLC, where MBP would often be present as a significant and difficult to remove contaminant. The SUMO fusion of VSTx1 yielded ∼0.5 mg of pure peptide per liter of culture.

AA139 was expressed in *E. coli* SHuffle cells transformed with a pOPINE-His_6-SUMO-AA139 plasmid vector. The transformed cells were cultivated in minimal medium containing ^{15}N-NH_4Cl. The His_6-SUMO-AA139 fusion protein was obtained in the soluble fraction after cell lysis. Following Ni^{2+} affinity chromatography and cleavage with SUMO protease, AA139 was purified via reversed-phase HPLC. The final yield was approximately 1 mg of ^{15}N-AA139 per liter of culture. The purity and mass were analyzed by LC-MS. The mass of the peptide is 2548.1 g/mol. The experimentally measured m/z values of ^{15}N-AA139 (647.9 [+4], 518.6 [+5] and 432.3 [+6]), match the calculated values (647.8, 518.4 and 432.2). The purity of both peptides was >99% (as measured by HPLC).

TABLE 2 | Thermodynamic parameters for VSTx1 and AA139 binding to cNDs.

Peptide	K_d	ΔH	−TΔS	ΔG	*n*
	μM	*kcal/mol*	*kcal/mol*	*kcal/mol*	
VSTx1	2.02 ± 0.81	−1.92 ± 0.73	−5.88 ± 0.94	−7.80 ± 0.22	2.00 ± 0.20
AA139	1.16 ± 0.28	−6.29 ± 0.61	−1.83 ± 0.75	−8.12 ± 0.16	4.09 ± 0.09

The average and standard deviation of three replicates are presented. Fitted values of the dissociation constant (K_d), enthalpy (ΔH) of binding and stoichiometry (n), as well as the calculated binding free energy (ΔG) and entropy (-TΔS) are reported.

Chemical shifts of the protons of AA139 were measured from 2D ^{1}H–^{1}H TOCSY and NOESY NMR spectra. ^{13}C and ^{15}N shifts were obtained from 2D HSQC spectra (**Table S1** – BMRB ID: 30260). Secondary Hα shifts (**Figure S9**) show that AA139 is composed of two β-strands and a turn forming a β-hairpin structure (Wishart et al., 1995), further supported by hydrogen bonds (see **Tables S2**, **S3**), The chemical shifts were used to predict backbone dihedral angles (TALOS), and were subsequently used in structure calculations. The peptide structure is further stabilized by two disulfide bridges Cys^{3}-Cys^{20} and Cys^{7}-Cys^{16}, these were defined by three upper and three lower distance restraints between the heteroatoms, and included in the structure calculations. The above restraints were supplemented with NOE based distance restraints and the NMR solution structure of AA139 (PDB 5V11), was calculated by torsion angle dynamics (CYANA–see also **Figure S10** and **Table S4**). The two β-strands cover residues Cys^{3}-Arg^{10} and Arg^{13}-Cys^{20}. The β-strands are intervened by a type I' β-turn (Asn^{11}/Gly^{12}) forming slightly twisted anti-parallel β-strands in the β-hairpin structure. The distortion created by the right-handed twist of the two-stranded β-sheet results in an amphipathic structure, commonly observed in membrane interacting peptides.

Peptide-Lipid Interactions by ITC and NMR

cNDs containing a zwitterionic (POPC) or an anionic lipid mixture [POPC:POPG (4:1)] in the above described Tris-Bis buffer (20 mM BisTris (pH 6.5), 50 mM NaCl and 1 mM EDTA–used in all subsequent experiments) were used to study the interactions between the cNDs and the membrane-active peptides (VSTx1 or AA139) by isothermal titration calorimetry (ITC) and NMR. Neither peptide showed binding to zwitterionic cNDs by ITC.

Initial NMR experiments were conducted to find concentration ranges where clear intensity changes could be observed (data not shown). Based on these concentrations, a titration was conducted where the concentrations of uniformly isotopically labeled ^{15}N-VSTx1 or ^{15}N-AA139 was fixed at 20 and 40 μM, respectively, and NMR spectra were acquired in the presence of increasing concentrations of cNDs.

ITC Results

The ITC binding isotherms using anionic cNDs produced results consistent with weak binding in the μM range (**Figure S11**). During the fitting, first the stoichiometry for the binding of VSTx1 to cNDs was determined to be 2 peptides per disc [i.e., other even integer values used produced larger errors, see also Materials and Methods section Isothermal Titration Calorimetry (ITC)]. Using this information, the effective concentration of cNDs in the ITC experiment was determined (4.54 μM). This is roughly 1/5 of the concentration determined by measurement of absorbance at 280 nm from the MSPs, and consistent with the POPG ratio within the discs. The experiment was repeated with different starting concentrations of peptides and nanodiscs, in all cases yielding the same fitted parameters (data not shown). The effective cND concentration determined by the fitting procedure was used for all subsequent modeling, where, instead the stoichiometry was allowed to vary. This yielded a stoichiometry of 4 AA139 peptides to each cND. The ITC data are shown in **Figure S11** and the fitting of these data to the binding isotherm summarized in **Table 2** (see also **Table S5**).

^{15}N HSQC Titrations of VSTx1

^{15}N-VSTx1 at a concentration of 20 μM was titrated in a series against anionic cNDs [POPC:POPG (4:1)] with increasing concentration: 0, 5, 10, and 20 μM (20 mM BisTris (pH 6.5), 50 mM NaCl and 1 mM EDTA). Each of the four samples was then used to acquire a 2D ^{1}H-^{15}N-HSQC experiment. A concentration dependent broadening of the signals was observed (see **Figure 3**). There were also minor chemical shift changes in a concentration dependent manner for signals that experienced significant line-broadening. The fitting was performed as described (see Materials and methods), where the backbone amide of Leu31 was excluded due to a very sharp signal loss leading to insufficient points for fitting (only 2 points above the noise–taken as 3 times the noise level). Glu2, Lys5, Ser13, and Ser24 were completely undetectable under conditions tested. Resonances of Cys10 and Asn12 were removed due to overlap.

The initial fit of individual residues to Equations (2) and (3) showed that residues Cys3, Asn14, Asp15, Cys16, and Phe35 as well as the sidechain resonance of Asn14 did not produce reliable fits to the model. The remaining residues fit the binding isotherm having, $n = 2.3 \pm 0.7$ (equivalent binding sites). The resonances of Gly4, Met7, Trp8, Ser23, Arg25, Trp26 and the sidechain of Trp28 all decayed rapidly with increased cND concentration, and these only had three valid titration points (missing a signal above noise level at the highest concentration of nanodisc). The value of, *n*, was subsequently fixed to 2 (even integer) for a global fit of all remaining resonances containing four valid data points after normalization, i.e., Phe6, Lys9, Lys11, Cys17, Lys18, Asp19, Leu20, V21, Cys22, Lys27, Trp28, Cys29, Val30, Ala32, Ser33, and sidechain NH resonances of Trp8, Asn12 and Trp26. This yielded

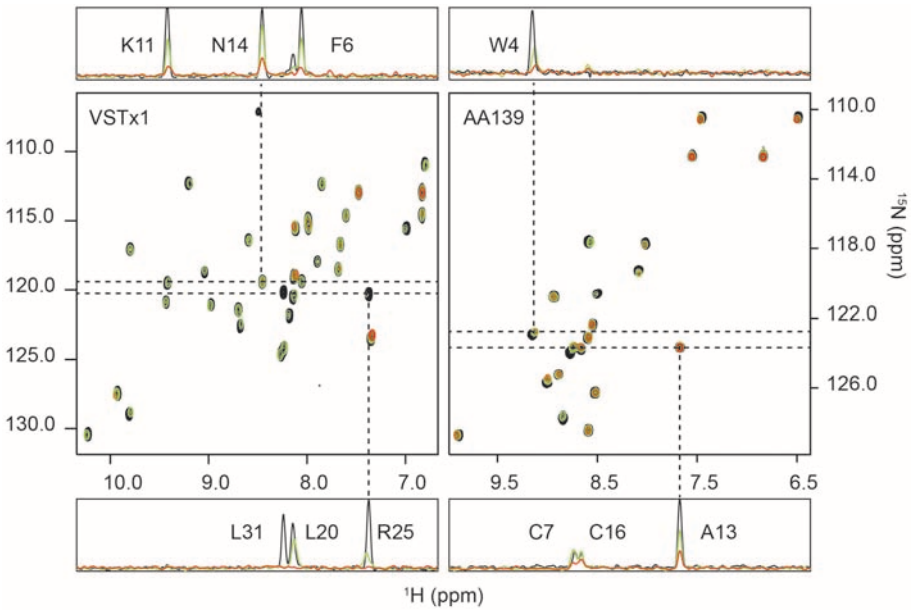

FIGURE 3 | ^{1}H-^{15}N HSQC titrations of membrane-active peptides against nanodiscs containing bacterial model membranes. (Left) The titration of ion-channel inhibitor VSTx1 (20 μM) against increasing concentration of nanodiscs [POPC:POPG (4:1)]. The three superimposed spectra correspond to a [peptide]:[nanodisc] ratio of 1:0 (black), 1:0.25 (green) and 1:1 (red). (Right) The titration of antimicrobial peptide AA139 (40 μM) against increasing concentration of nanodiscs [POPC:POPG (4:1)]. The three superimposed spectra correspond to a [peptide]:[nanodisc] ratio of 1:0 (black), 1:0.25 (green) and 1:0.375 (red). In both cases 1D traces are shown at ^{15}N frequencies corresponding to peaks that show a small change in intensity that does not fit to the binding isotherm (N14 for VSTx1 and Ala13 for AA139), and a signal (Arg25 for VSTx1 and Trp4 for AA139) having a strong intensity change that fits the binding isotherm. The latter also display an observable chemical shift and linewidth change consistent with intermediate exchange due to binding. Assignments are provided in 1D traces.

an equilibrium dissociation constant, K_d, of 1.11 ± 0.13 μM– using a constant value of 2 equivalent binding sites (**Figure S12**).

Further to the above titration, a second series of experiments were conducted with cNDs containing zwitterionic lipids. It had previously been observed that VSTx1: 1) binds to zwitterionic micelles, and 2) binds to the MSP of NDs (Shenkarev et al., 2014; Lau et al., 2016). The titrations were conducted under identical conditions as those described above for the anionic lipid NDs. This approach allows us to isolate the effect of the anionic lipids from any binding to zwitterionic lipids and MSP as well as potentially providing insights into the binding of the peptide to neutral lipids. The results show a significantly weaker binding than that observed for the anionic lipids (note that this binding was undetectable using ITC). The average change in peak height between the control experiments and the lowest concentration of added nanodisc (5 μM) is 38% (standard deviation of 15%) for the anionic lipid mixture and only 5% (standard deviation of 10%) for the zwitterionic mixture (in both cases removing L31 as an outlier). Only a few peaks displayed significant intensity changes (>10%) in the zwitterionic lipid mixture at this concentration of cNDs (backbone amides of Gly4, Phe6, Lys9, Lys11, Arg25, Trp26, Leu31, Ala32 as well as the sidechain amides of Trp8 and Trp26). Interestingly, the pattern of peak intensity changes remains similar in both cases, indicating that the binding mode is conserved. We also note that the majority of these amino acids could be fitted to the binding isotherm in the previous titration.

^{15}N HSQC Titrations of AA139

^{15}N-AA139 (40 μM) was titrated in the presence of cNDs [POPC:POPG (4:1)] at 0, 5, 7.5, 10, 12.5, 15 and 20 μM. For each sample a 2D ^{1}H-^{15}N HSQC spectrum was acquired. The increasing concentration of the ND added did not result in any significant chemical shift changes, however, significant broadening of the signals was observed in a concentration dependent manner (see **Figure 3**). The change in intensity was modeled using a quadratic equation to obtain estimates of the stoichiometry and dissociation constant of the interaction (Equations 2, 3). As noted in the methods section, several residues were removed for either yielding too few data points (backbone amides of Phe2, Asn11 and Gly12) or due to overlap (Val6 and Cys7). The initial fitting led to the exclusion of residues that did not fit to the model (Cys3, Ala8, Arg9, Arg10, Ala13, Arg14, Cys16, and Cys20). The line-broadening in these residues cannot be modeled by equations (2) and (3), either due to an insufficient change in intensity across the concentration range tested or the presence of other exchange processes. The remaining seven residues all fit the model well and produced values of equivalent binding sites, n, of 3.9 with a standard deviation of 0.3. This value was then fixed to 4, and after normalization of the observed maximum height change, a global fit of the data for all residues was performed, yielding an equilibrium dissociation constant, K_d, of 0.41 ± 0.13 μM (**Figure S12**).

Further, a qualitative analysis of the likely binding interface of the peptide was performed by comparing the intensity of the signals at the first two titration points (in the absence of cNDs and in the presence of 5 μM of cND). Residues that are most strongly affected at this low concentration of ND, are most likely to be at the binding interface. These residues include the hydrophobic and acidic residues at the termini of the β-hairpin loop (see also **Figure 4**).

Peptide-MSP Interactions by NMR

As noted above it had previously been suggested that there is an interaction between the anionic MSP and cationic peptides such as VSTx1 and AA139 (Shenkarev et al., 2014). A titration series of unlabeled peptides at 0, 50 and 100 μM against cNDs [^{15}N-cNW9: (POPC)] at 100 μM was conducted in the Tris-Bis buffer (iii) described above. The titration was followed by 2D ^{1}H-^{15}N TROSY experiments acquired at 50 °C for 4 h. The spectra featured well dispersed peaks for ^{15}N-cNDs at this temperature (at 25 °C the signals were unresolvable). In both cases, there were no peptide-concentration dependent chemical shift or intensity changes, suggesting that there is little or no interaction between the MSP and the peptides (**Figure S13**). The sample stability was monitored before and after each experiment by SEC and 1D ^{1}H NMR (not shown), and the NDs were found to be intact in all cases (see also **Figure S14**).

DISCUSSION

Production and Stability of Anionic NDs

The procedure described here for production of cNDs, departs from the original protocol described (Nasr et al., 2017). Here, a sortase inhibitor was not required and lipid-detergents (1 mM DDM) were used in the cyclisation reaction, which not only allows for higher protein concentrations in the circularization reaction but also leads to improved yields of the monomeric product, likely due to disruption of the formation of dimeric MSPs in solution. Our results are consistent with the independently developed protocol by Yusuf et al. where introduction of Triton X-100 (1 mM) was shown to significantly reduce multimeric by-products when trying to cyclise small MSP constructs through the same sortase-mediated reaction (Yusuf et al., 2018). The convergence of these methods on the optimal concentration of detergents during cyclisation is an encouraging sign of arrival at a general approach to generating high yields of cNDs.

In this work, we investigated the stability of NDs containing anionic lipid mixtures commonly used to model the bacterial membrane [POPC:POPG (4:1)], and compare this to NDs containing zwitterionic lipids (POPC). The stability of the NDs is evaluated based on EM images and SEC profiles, where in the latter aggregation or disassembly results in asymmetric elution profiles with increased absorbance at early elution times. For the linear NDs there is a general trend that the lower pH buffers result in higher heterogeneity of the NDs (**Figures S2–S3**). The level of heterogeneity increases over time and after ∼ 3 days we find that in the lower pH buffers (Bis-tris and phosphate at pH 6.5) the shoulders of the ND elution peaks increase in intensity sufficiently to be observed as distinct peaks. These trends are exacerbated in the presence of anionic lipid mixtures (in linear NDs), where at low pH there is clear evidence of aggregation/disassembly even at day 0 (**Figure S3**), in all buffers tested (result of all observations summarized in **Table 1** based on data in **Figures S2–S5**). We note that the observed heterogeneity would render most biophysical measurements unfeasible.

Fortunately, the introduction of head-to-tail cyclisation of the MSP resulted in excellent (c)ND stability regardless of the lipid composition or sample conditions–i.e., no changes were observed to the SEC elution profiles or EM images. Our conclusion based on these results is that small linear NDs are unsuitable for studies of anionic lipid bilayers. We further note that, although it is known that the presence of anionic lipids does not alter the membrane thickness or its fluidity, it has a very significant effect on the stability of lipid nanodiscs in solution. This conclusion may shed some light into previous work on the use of anionic NDs for studies of membrane-active peptides, where it was found that VSTx1 binds very effectively to anionic NDs, and based on analysis of NMR titration data a stoichiometry of ∼35 peptides to each ND was found (Shenkarev et al., 2014). This value appears physically unlikely considering that the peptide diameter can be estimated to be ∼20 Å (measured from the pdb structure 2N1N across the orange region in **Figure 4A**) and the ND used in the reported study has an available lipid diameter of ∼ 58 or 35 Å when excluding one or two shells of MSP bound lipids, respectively (Hagn et al., 2018). Based on our findings (although using a smaller ND) the apparently high stoichiometry may have been a consequence of aggregation due to instability of the linear NDs used. Indeed, despite the inherent experimental limitations at the observed binding affinities, our NMR and ITC data are both consistent with two independent binding sites for VSTx1 on cNW9 (available lipid diameter of cNW9 estimated to be 43 or 26 Å when excluding one or two shells of MSP bound lipids, respectively; Hagn et al., 2018), which provides a physically more realistic binding mode.

Although protein interactions with NDs have been studied previously by ITC (Agamasu et al., 2017), to our knowledge, ITC has not previously been utilized to quantify interactions between membrane-active peptides and NDs, and our results demonstrate that it may prove to be a valuable tool in future studies of such peptides. Finally, we also acquired dynamic light scattering (DLS) data for our samples to determine if this could be used to distinguish assembled and unassembled NDs. However, for these small NDs, the size difference between the MSP and the ND was too small to generate a reliable difference in scattering (data not shown).

Expression and Binding of Membrane-Active Peptides to Bacterial Model Membranes

Isotope labeling of both membrane-active peptides was achieved through recombinant protein expression in bacteria. In the case of AA139, a SUMO-fusion tag produced high soluble

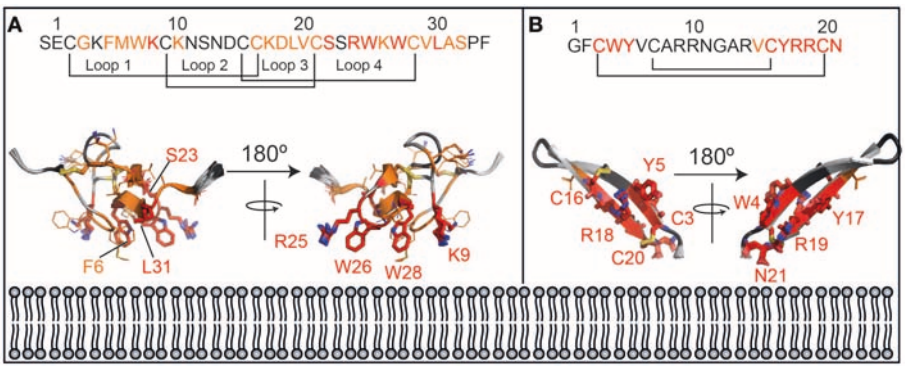

FIGURE 4 | Lipid interaction of membrane-active peptides. Cartoon representation of the peptides [**A** = VSTx1 (PDBID: 2N1N), **B** = AA139 (PDID: 5V11)] are oriented to show the likely binding orientation with respect to the lipid bilayer (bottom) based on the NMR titration data (180° rotation also shown). Disulfide bonds are shown as sticks. The peptide sequences and numbering are shown above the peptides. The residues in red (sidechains as sticks and labeled) are those that show the strongest perturbation upon addition of nanodiscs, those in orange show an intensity change consistent with the binding isotherm (sidechains as sticks) and residues in dark gray show smaller perturbation that do not fit the binding isotherm. Residues that were not included in the analysis (missing/overlapped) are shown in light gray. Structures in panels **(A)** and **(B)** are not to the same scale.

yields (∼1 mg per liter of culture) when expressed in SHuffle cells, in contrast to the MBP fusion expressed in the BL21 strain, where no soluble protein was found. It is worth noting the inherent challenge in finding a suitable bacterial expression system for an antimicrobial peptide. In this case it appears that the SUMO-fusion may have reduced the toxicity of the peptide. Although the bacterial expression of VSTx1 had previously been described, we also found that VSTx1 could be produced in relatively high yields using this strategy (SUMO-fusion in SHuffle cells–yielding 0.5 mg per liter of culture).

Transferring the results of the analysis of the NMR data (see discussion in **Supplementary Information**), onto the structure of the two peptides, allows us to gain some insights in the likely binding pose of the two molecules (**Figure 4**). In particular, those residues that show large intensity changes and fit the binding isotherm [fall into category (c or d) in **Supplemental Discussion**] are most likely to be in the binding interface and are shown in red with their sidechains displayed as sticks. These residues also show the highest intensity changes at the lowest concentration of NDs added.

Those that fit the binding isotherm but show smaller changes in their intensity [category (a) in **Supplemental Discussion**] are likely to experience membrane binding to some extent, and these are shown in orange with sidechains as lines. Those that show relatively small intensity changes, and do not fit the binding isotherm [category (b) in **Supplemental Discussion**] are least likely to be close to the binding interface and are shown in dark gray without sidechains indicated. Residues that were not included in the analysis are shown in light gray. This data is consistent with the interpretation that the red residues are inserting into the membrane while the orange residues are at the lipid/water interface.

The lipid binding data for VSTx1 are consistent with previous findings, and show, perhaps unsurprisingly, that the positively charged peptide binds more strongly to lipids containing negative head-groups. What is surprising, however, is that the same amino acids show the strongest perturbations in both titrations (against anionic and zwitterionic bilayers). This would suggest that the binding is driven by the hydrophobic patch of the peptide (loops 1 and 4) and that the affinity is enhanced by the basic residues in these loops in the presence of acidic moieties at the bilayer surface. This is particularly interesting as this peptide has been found to interact with acidic residues on its ion-channel receptor, in what appears to be a conserved mode-of-action in the inhibitory function of gating-modifier toxins (Lau et al., 2016; Zhang et al., 2018). It is also worth noting that the peptide had previously been found to bind zwitterionic micelles with moderate affinity by NMR spectroscopy (Ozawa et al., 2015; Lau et al., 2016). In contrast, we find that the peptide binds very weakly to zwitterionic lipids in cNDs and that this binding is undetectable by ITC. These results are more consistent with the centrifugation assays performed using liposomes (where no partitioning into zwitterionic liposomes is observed). Taken together, this suggests that the peptide has a stronger affinity for micelles than for bilayers–it remains to be seen if this is a general finding for membrane-active peptides or a property of VSTx1. Interestingly, however, the micelle binding interface identified by NMR (Ozawa et al., 2015; Lau et al., 2016) is the same as the cND interface identified here. Thus, although in this case, we find that the peptide has a stronger affinity for micelles than lipid bilayers, it appears that the binding mode is conserved.

The structure of AA139 reveals a twisted β-hairpin structure similar to other members of this family of antimicrobial peptides (Edwards et al., 2016). In contrast to the related arenicin-2 peptide, however, we do not observe any evidence of the peptide disrupting lipid membranes (from EM data–**Figure S14**). The NMR data suggest that the termini of the peptide are the likely interface with the lipid bilayer. This segment of the protein

contains a hydrophobic N-terminus and a basic C-terminus, which are both likely to contribute to its interaction with the anionic lipid bilayer. An interesting observation is that the negatively charged C-terminus is likely to form unfavorable interaction with both the head-groups and the tails of the lipids, and that amidation of this residue may enhance its affinity toward bacterial membranes. The binding pose also suggests that the long axis of the peptide is likely to be closer to being perpendicular to the plane of the bilayer, than in the plane. This may provide some support for the higher stoichiometry (of peptide to disc) derived for this peptide from the NMR data when compared to VSTx1.

The ITC experiments revealed that both peptides had binding affinities in the low μM range. Interestingly, although the binding free energy (ΔG) is similar in both cases (∼-8 kcal/mol), the relative contribution of entropic and enthalpic terms is different. The binding of VSTx1 appears to be largely driven by an entropic component (∼-6 kcal/mol) rather than an enthalpic component (∼-2 kcal/mol). The larger entropic term is consistent with increased disorder either in the peptide or the lipid bilayer upon binding. Although it is difficult to deduce the relative contributions of each of these components, we do see a very significant broadening of residue L31 of VSTx1 even in the presence of small concentrations of cNDs. This is consistent with a conformational change upon binding, and is likely to account for some of the observed gain in entropy. The change in conformation of a leucine residue is likely to occur in a highly apolar environment and the data would suggest that this face of the molecule partitions into the lipid bilayer.

In contrast to VSTx1, the ITC results for AA139 reveal a reversal of the relative thermodynamic terms, with a greater enthalpic term (∼-6 kcal/mol). AA139 has a net charge of +5 which is due to the presence of five arginine residues accounting for almost a quarter of the total amino acid composition. This would suggest that the binding of the peptide is driven by charge-charge interactions at the lipid interface, involving some of these residues. As noted above the masking of the C-terminal charge through amidation would increase the net charge to +6 which may further strengthen the enthalpic contribution to the binding energy.

In general, there is good qualitative agreement between the ITC and the NMR data. The binding constants derived from the NMR data were as expected exaggerated when compared to the ITC data, thus, although not quantitative provide a reasonable estimate of the binding. The stoichiometry was consistent when comparing data from the two methods. We note that in both cases the relatively weak binding observed, required careful analysis of the data, where a priori knowledge regarding the symmetry of the disc was used to improve the fitting of the data. Thus, although there is good agreement in the values derived, we note that these data are near the limits of binding interactions that can be detected by the two methods and some uncertainties are likely associated with the inherent sensitivity of these techniques in this binding regime.

CONCLUSION

We present a method to obtain high yields of cNDs in 3 days and assess their suitability for biophysical studies in solution. We performed size-exclusion chromatography (SEC) of linear and cyclised NDs of different compositions under varying conditions. The cNDs consistently displayed significantly improved stability over their noncircular counterparts. The study revealed that linear NDs can be unstable under common experimental conditions, particularly in phosphate buffers at a low pH and when containing anionic lipids. In contrast, cNDs were stable at all solution conditions and lipid compositions tested. In addition, the sharper peaks observed in the SEC profiles indicate greater homogeneity. Finally, we describe a method for high-yield (∼mg per liter of culture) recombinant production of two membrane-active peptides, notably including an antimicrobial peptide–AA139.

These materials are then used to evaluate the use of biophysical methods to study the membrane binding properties of membrane-active peptides against cNDs containing anionic lipid mixtures, that approximate the charge distribution of bacterial membranes. We use ITC to measure the binding thermodynamics, and heteronuclear 2D NMR to characterized the binding of ^{15}N-labeled peptides against cNDs. We first study the well characterized VSTx1 peptide to validate the proposed approach, and find good agreement with previous reports while revealing new information regarding the thermodynamics of the binding event. We then apply our method to gain insights into the activity of AA139, an antimicrobial peptide with an unknown mode-of-action. ITC and NMR data show that AA139 binds to the cNDs with low μM affinity, which is driven by a significant enthalpic contribution (−6 kcal/mol) and a stoichiometry of 4 peptides per disc. We further solved the structure of AA139 by NMR, which revealed a twisted β-hairpin fold, and allowed us to determine the likely lipid-binding interface of the peptide, which included the tails of the antiparallel β-sheets. These results establish the use of cNDs in combination with ITC and solution-state NMR as a novel and general method for investigating the membrane binding properties of membrane-active peptides.

AUTHOR CONTRIBUTIONS

AZ, IE, and MM conceived the study. AZ, IE, BM, GS, MH, and XJ performed the experiments. AZ, IE, BM, MH, BC, and MM analyzed the data. IE, AZ, and MM wrote the paper with input from all authors. All authors contributed to different components of the study design.

ACKNOWLEDGMENTS

This project was supported by the Australian Research Council (ARC grants: DP140101098, FTl10100925) and the National Health and Medical Research Council (NHMRC grants: APP1102267, APP1080405, APP1106590 and APP1136021). IE and AZ are supported by an International Postgraduate

Award and an Australian Postgraduate Award Ph.D. scholarship, respectively. We thank Adenium Biotech for allowing this work using AA139 and Dr. Frank Sainsbury for his technical assistance. We are also grateful to Dr. Mahmoud L. Nasr and Prof. Gerhard Wagner for MSP1D1ΔH5 expression plasmid and Prof. David R. Liu for sortase A pentamutant expression plasmid. Finally, we thank Dr. Zhenling Cui and Prof. Kirill Alexandrov for the advice and reagents regarding SUMO-tag cleavage by SUMO protease.

SUPPLEMENTARY MATERIAL

The Supplementary Material for this article can be found online at: https://www.frontiersin.org/articles/10.3389/fchem.2019.00238/full#supplementary-material

The supporting information include further details on the NMR analysis, ITC data, size exclusion chromatography profiles, thin layer chromatography images, EM negative staining images and LC-MS traces.

REFERENCES

Agamasu, C., Ghanam, R. H., Xu, F., Sun, Y., Chen, Y., and Saad, J. S. (2017). The interplay between calmodulin and membrane interactions with the pleckstrin homology domain of akt. *J. Biol. Chem.* 292, 251–263. doi: 10.1074/jbc.M116.752816

Bayburt, T. H., Grinkova, Y. V., and Sligar, S. G. (2002). Self-assembly of discoidal phospholipid bilayer nanoparticles with membrane scaffold proteins. *Nano Lett.* 2, 853–856. doi: 10.1021/nl025623k

Berrow, N. S., Alderton, D., Sainsbury, S., Nettleship, J., Assenberg, R., Rahman, N., et al. (2007). A versatile ligation-independent cloning method suitable for high-throughput expression screening applications. *Nucleic Acids Res.* 35:e45. doi: 10.1093/nar/gkm047

Catoire, L. J., Warnet, X. L., and Warschawski, D. E. (2014). "Micelles, bicelles, amphipols, nanodiscs, liposomes, or intact cells: the hitchhiker's guide to the study of membrane proteins by NMR," in *Membrane Proteins Production for Structural Analysis,* eds I. Mus-Veteau (New York, NY: Springer New York), 315–345.

Chen, I., Dorr, B. M., and Liu, D. R. (2011). A general strategy for the evolution of bond-forming enzymes using yeast display. *Proc. Natl. Acad. Sci. U.S.A.* 108, 11399–11404. doi: 10.1073/pnas.1101046108

Deuis, J. R., Dekan, Z., Inserra, M. C., Lee, T. H., Aguilar, M. I., Craik, D. J., et al. (2016). Development of a muO-conotoxin analogue with improved lipid membrane Interactions and potency for the analgesic sodium channel NaV1.8. *J. Biol. Chem.* 291, 11829–11842. doi: 10.1074/jbc.M116.721662

Edwards, I. A., Elliott, A. G., Kavanagh, A. M., Zuegg, J., Blaskovich, M. A. T., et al. (2016). Contribution of amphipathicity and hydrophobicity to the antimicrobial activity and cytotoxicity of β-hairpin peptides. *ACS Infect. Dis.* 2, 442–450. doi: 10.1021/acsinfecdis.6b00045

Escriba, P. V., Gonzalez-Ros, J. M., Goni, F. M., Kinnunen, P. K., Vigh, L., Sanchez-Magraner, L., et al. (2008). Membranes: a meeting point for lipids, proteins and therapies. *J. Cell. Mol. Med.* 12, 829–875. doi: 10.1111/j.1582-4934.2008.00281.x

Granot, J. (1983). Determination of dissociation-constants of 1-1 complexes from nmr data - optimization of the experimental setup by statistical-analysis of simulated experiments. *J. Magnet. Resonance* 55, 216–224.

Guntert, P. (2004). Automated NMR structure calculation with CYANA. *Methods Mol. Biol.* 278, 353–378. doi: 10.1385/1-59259-809-9:353

Hagn, F., Etzkorn, M., Raschle, T., and Wagner, G. (2013). Optimized phospholipid bilayer nanodiscs facilitate high-resolution structure determination of membrane proteins. *J. Am. Chem. Soc.* 135, 1919–1925. doi: 10.1021/ja310901f

Hagn, F., Nasr, M. L., and Wagner, G. (2018). Assembly of phospholipid nanodiscs of controlled size for structural studies of membrane proteins by NMR. *Nat. Protoc.* 13, 79–98. doi: 10.1038/nprot.2017.094

Henrich, E., Peetz, O., Hein, C., Laguerre, A., Hoffmann, B., Hoffmann, J., et al. (2017). Analyzing native membrane protein assembly in nanodiscs by combined non-covalent mass spectrometry and synthetic biology. *Elife* 6:e20954. doi: 10.7554/eLife.20954

Hodnik, V., and Anderluh, G. (2013). "Surface plasmon resonance for measuring interactions of proteins with lipid membranes," in *Lipid-Protein Interactions: Methods and Protocols,* eds J. H. Kleinschmidt (Totowa, NJ: Humana Press), 23–36.

Janosi, L., and Gorfe, A. A. (2010). Simulating POPC and POPC/POPG bilayers: conserved packing and altered surface reactivity. *J. Chem. Theory Comput.* 6, 3267–3273. doi: 10.1021/ct100381g

Jung, H. J., Lee, J. Y., Kim, S. H., Eu, Y. J., Shin, S. Y., Milescu, M., et al. (2005). Solution structure and lipid membrane partitioning of VSTx1, an inhibitor of the KvAP potassium channel. *Biochemistry* 44, 6015–6023. doi: 10.1021/bi0477034

Klint, J. K., Senff, S., Saez, N. J., Seshadri, R., Lau, H. Y., Bende, N. S., et al. (2013). Production of recombinant disulfide-rich venom peptides for structural and functional analysis via expression in the periplasm of *E. coli*. *PLoS ONE* 8:e63865. doi: 10.1371/journal.pone.0063865

Lau, C. H. Y., King, G. F., and Mobli, M. (2016). Molecular basis of the interaction between gating modifier spider toxins and the voltage sensor of voltage-gated ion channels. *Sci. Rep.* 6:34333. doi: 10.1038/srep34333

Lee, M. T. (2018). Biophysical characterization of peptide-membrane interactions. *Adv. Phys. X* 3, 145–164. doi: 10.1080/23746149.2017.1408428

Lee, S. Y., and Mackinnon, R. (2004). A membrane-access mechanism of ion channel inhibition by voltage sensor toxins from spider venom. *Nature* 430, 232–235. doi: 10.1038/nature02632

Lee, T. Y., Yeh, V., Chuang, J., Chung Chan, J. C., Chu, L. K., and Yu, T. Y. (2015). Tuning the photocycle kinetics of *Bacteriorhodopsin* in lipid nanodiscs. *Biophys. J.* 109, 1899–1906. doi: 10.1016/j.bpj.2015.09.012

Mani, R., Cady, S. D., Tang, M., Waring, A. J., Lehrer, R. I., and Hong, M. (2006). Membrane-dependent oligomeric structure and pore formation of a beta-hairpin antimicrobial peptide in lipid bilayers from solid-state NMR. *Proc. Natl. Acad. Sci. USA.* 103, 16242–16247. doi: 10.1073/pnas.0605079103

Mei, X., and Atkinson, D. (2015). Lipid-free apolipoprotein A-I structure: insights into HDL formation and atherosclerosis development. *Arch. Med. Res.* 46, 351–360. doi: 10.1016/j.arcmed.2015.05.012

Nasr, M. L., Baptista, D., Strauss, M., Sun, Z. J., Grigoriu, S., Huser, S., et al. (2017). Covalently circularized nanodiscs for studying membrane proteins and viral entry. *Nat. Methods* 14, 49–52. doi: 10.1038/nmeth.4079

Ozawa, S., Kimura, T., Nozaki, T., Harada, H., Shimada, I., and Osawa, M. (2015). Structural basis for the inhibition of voltage-dependent K+ channel by gating modifier toxin. *Sci. Rep.* 5:14226. doi: 10.1038/srep14226

Ritchie, T. K., Grinkova, Y. V., Bayburt, T. H., Denisov, I. G., Zolnerciks, J. K., Atkins, W. M., et al. (2009). Chapter 11 - reconstitution of membrane proteins in phospholipid bilayer nanodiscs. *Meth. Enzymol.* 464, 211–231. doi: 10.1016/S0076-6879(09)64011-8

Shaw, A. W., Mclean, M. A., and Sligar, S. G. (2004). Phospholipid phase transitions in homogeneous nanometer scale bilayer discs. *FEBS Lett.* 556, 260–264. doi: 10.1016/S0014-5793(03)01400-5

Shen, Y., Delaglio, F., Cornilescu, G., and Bax, A. (2009). TALOS+: a hybrid method for predicting protein backbone torsion angles from NMR chemical shifts. *J. Biomol. NMR* 44, 213–223. doi: 10.1007/s10858-009-9333-z

Shenkarev, Z. O., Balandin, S. V., Trunov, K. I., Paramonov, A. S., Sukhanov, S. V., Barsukov, L. I., et al. (2011). Molecular mechanism of action of beta-hairpin antimicrobial peptide arenicin: oligomeric structure in dodecylphosphocholine micelles and pore formation in planar lipid bilayers. *Biochemistry* 50, 6255–6265. doi: 10.1021/bi200746t

Shenkarev, Z. O., Lyukmanova, E. N., Paramonov, A. S., Panteleev, P. V., Balandin, S. V., Shulepko, M. A., et al. (2014). Lipid-protein nanodiscs offer new perspectives for structural and functional studies of water-soluble membrane-active peptides. *Acta Naturae* 6, 84–94.

Skinner, S. P., Goult, B. T., Fogh, R. H., Boucher, W., Stevens, T. J., Laue, E. D., et al. (2015). Structure calculation, refinement and validation using CcpNmr analysis. *Acta Crystallogr. D Biol. Crystallogr.* 71, 154–161. doi: 10.1107/S1399004714026662

Susac, L., Horst, R., and Wuthrich, K. (2014). Solution-NMR characterization of outer-membrane protein A from *E. coli* in lipid bilayer nanodiscs and detergent micelles. *Chembiochem* 15, 995–1000. doi: 10.1002/cbic.201300729

Wang, Z., Wang, X., and Wang, J. (2018). Recent advances in antibacterial and antiendotoxic peptides or proteins from marine resources. *Mar. Drugs* 16:e57. doi: 10.3390/md16020057

Warschawski, D. E., Arnold, A. A., Beaugrand, M., Gravel, A., Chartrand, E., and Marcotte, I. (2011). Choosing membrane mimetics for NMR structural studies of transmembrane proteins. *Biochim. Biophys. Acta* 1808, 1957–1974. doi: 10.1016/j.bbamem.2011.03.016

Williamson, M. P. (2013). Using chemical shift perturbation to characterise ligand binding. *Prog. Nucl. Magn. Reson. Spectrosc.* 73, 1–16. doi: 10.1016/j.pnmrs.2013.02.001

Wishart, D. S., Bigam, C. G., Holm, A., Hodges, R. S., and Sykes, B. D. (1995). (1)H, (13)C and (15)N random coil NMR chemical shifts of the common amino acids. I. investigations of nearest-neighbor effects. *J. Biomol. NMR* 5:332. doi: 10.1007/BF00227471

Yeh, V., Hsin, Y., Lee, T. Y., Chan, J. C. C., Yu, T. Y., and Chu, L. K. (2016). Lipids influence the proton pump activity of photosynthetic protein embedded in nanodiscs. *RSC Adv.* 6, 88300–88305. doi: 10.1039/C6RA13650H

Yusuf, Y., Massiot, J., Chang, Y. T., Wu, P. H., Yeh, V., Kuo, P. C., et al. (2018). Optimization of the production of covalently circularized nanodiscs and their characterization in physiological conditions. *Langmuir* 34, 3525–3532. doi: 10.1021/acs.langmuir.8b00025

Zhang, A. H., Sharma, G., Undheim, E. A. B., Jia, X., and Mobli, M. (2018). A complicated complex: ion channels, voltage sensing, cell membranes and peptide inhibitors. *Neurosci. Lett.* 679, 35–47. doi: 10.1016/j.neulet.2018.04.030

Conflict of Interest Statement: The authors declare that the research was conducted in the absence of any commercial or financial relationships that could be construed as a potential conflict of interest.

Copyright © 2019 Zhang, Edwards, Mishra, Sharma, Healy, Elliott, Blaskovich, Cooper, Collins, Jia and Mobli. This is an open-access article distributed under the terms of the Creative Commons Attribution License (CC BY). The use, distribution or reproduction in other forums is permitted, provided the original author(s) and the copyright owner(s) are credited and that the original publication in this journal is cited, in accordance with accepted academic practice. No use, distribution or reproduction is permitted which does not comply with these terms.

Electrochemistry

Ruoxue Yan

Dr Ruoxue Yan is an Assistant Professor at the Department of Chemical and Environmental Engineering. She obtained her PhD degree in Chemistry from UC Berkeley in 2010 with a designated emphasis on nanoscience and nanotechnology, a MSc degree in 2005 and a BSc degree in 2002)in Chemistry from Tsinghua University. Her research is focused on the synthesis, processing, and fabrication of high performance nanomaterials for advanced electronics, photonics, and biological applications. Her lab is currently engaged in research concerning optical biosensing, flexible electronics, surface and tip enhanced Raman spectroscopy, and the development of advanced nanoscale chemical imaging tools.

Syed Mubeen

Syed Mubeen attended the Central Electrochemical Research Institute to complete his undergraduate education in Chemical and Electrochemical Engineering. After his doctoral studies at the University of California, Riverside and postdoctoral research at the University of California, Santa Barbara, he moved to the Midwest in 2014 to assume a position of Assistant Professor at the University of Iowa in the Chemical and Biochemical Engineering Department. His group are interested in several problems related to energy and water research, including solar fuels and chemicals, electrochemical energy conversion, desalination and water purification, and engineering novel materials (including plasmonic nanostructures), and systems for energy applications. Mubeen has co-authored over 30 publications and has one issued and four pending US patents on gas sensors, photoelectrocatalysis, and batteries. He is also Lead Scientist at HyperSolar, Inc, a public company developing solar technologies for water purification.

Juchen Guo

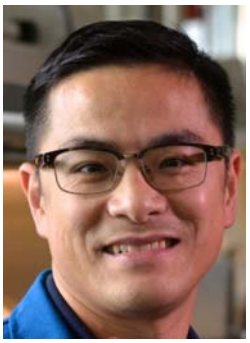

Juchen Guo is an Associate Professor at University of California Riverside. He earned his Bachelor's degree in chemical engineering from Zhejiang University in 1999 and his PhD in chemical engineering from the University of Maryland in 2007 under the supervision of Prof. Timothy A. Barbari. From 2007 to 2011, he performed his postdoctoral studies at the University of Maryland under the direction of Profs. F. Joseph Schork and Chunsheng Wang. He also performed postdoctoral studies at Cornell University from 2011 to 2012 under the direction of Prof. Lynden A. Archer prior to joining the Department of Chemical and Environmental Engineering at UC Riverside in 2012. He was the recipient of the 2014 Hellman Fellowship and the 2018 NSF CAREER Award. His research interests include interfacial phenomena and material properties in electrochemical energy storage systems.

Su Ha

Su Ha is a Professor in the Gene and Linda Voiland School of Chemical Engineering and Bioengineering at Washington State University. His research has been cited over 4,500 times and he has an h-index of 29. In 2014, he was named as Highly Cited Researcher by Thomson Reuters. His research focuses on generating hydrogen gas from bio-fuels and abundant natural gases, developing fuel cells that directly convert the chemical energy of small organic molecules (e.g., formic acid) or logistic fuels (e.g., gasoline) to electrical power, working with natural enzymes to produce electrical power from sugars, and developing electric field assisted fuel reforming systems.

Jungbae Kim

Jungbae Kim is a Professor in the Department of Chemical and Biological Engineering at Korea University. He completed his Bachelor's and Master's in Chemical Engineering at Seoul National University, before completing his PhD and a post-doctoral position in Biochemical Engineering at the University of Iowa. Prior to his position at Korea University, Junbae Kim held positions at Rensselaer Polytechnic Institute and the Pacific Northwest National Laboratory. His research expertise includes but is not limited to nanobiocatalysis, single enzyme nanoparticles, enzyme coatings, nanoscale enzyme reactors, biosensors, and biofuel cells.

Jennifer L. Schaefer

Jennifer L. Schaefer is an Assistant Professor in the Department of Chemical and Biomolecular Engineering at the University of Notre Dame. Dr Schaefer obtained MEng and BChE degrees in chemical engineering and a BSc in chemistry from Widener University in 2008. She obtained a PhD in chemical engineering at Cornell University in January 2014. She then held a NRC Postdoctoral Research Associateship in the Materials Science and Engineering Division at the National Institute of Standards and Technology, until moving to the University of Notre Dame in July 2015. Her research group studies ion transport, interfacial phenomena, and applied polymer materials in electrochemical and electroactive devices.

Ekaterina V. Skorb

Ekaterina V. Skorb obtained her PhD, summa cum laude, in physical chemistry in 2008. Subsequently, she was the Alexander von Humboldt Fellow at the Max Planck Institute of Colloids and Interfaces (MPIKG, Germany) with Prof. Möhwald. Since 2013 she has been group leader at the Biomaterials Department (MPIKG, Germany). She was a Visiting Scholar at Harvard in Prof. Whitesides group (2016-2017). Since 2017 she is a Professor at the ITMO University leading the Infochemistry group. Her current scientific interests are broad and include the synthetic cell, smart dynamic materials, and systems for personal diagnostics, study, and the modeling of nonlinear chemical processes.

Abhishek Lahiri

Abhishek Lahiri is a senior scientist at the Institute of Electrochemistry, Clausthal University of Technology, Germany. He obtained his PhD degree from the Institute of Materials Research, University of Leeds, UK in 2008. He worked as a postdoctoral researcher at the University of Alabama, USA and Tohoku University, Japan from 2008 to 2011. His research interest includes electrochemical synthesis of functional materials for batteries and catalysis, interfacial electrochemistry in ionic liquids, and understanding the battery interface in ionic liquid electrolytes.

frontiers in Chemistry

ORIGINAL RESEARCH
published: 13 June 2019
doi: 10.3389/fchem.2019.00442

Photochemically Induced Phase Change in Monolayer Molybdenum Disulfide

Peter Byrley[1], *Ming Liu*[2] *and Ruoxue Yan*[1,3]*

[1] Department of Chemical and Environmental Engineering, University of California, Riverside, Riverside, CA, United States,
[2] Department of Electrical and Computer Engineering, University of California, Riverside, Riverside, CA, United States,
[3] Material Science and Engineering Program, Bourns College of Engineering, University of California, Riverside, Riverside, CA, United States

Monolayer transition metal dichalcogenide (TMDs) are promising candidates for two-dimensional (2D) ultrathin, flexible, low-power, and transparent electronics and optoelectronics. However, the performance of TMD-based devices is still limited by the relatively low carrier mobility and the large contact resistance between the semiconducting 2D channel material and the contact metal electrodes. Phase-engineering in monolayer TMDs showed great promise in enabling the fabrication of high-quality hetero-phase structures with controlled carrier mobilities and heterojunction materials with reduced contact resistance. However, to date, general methods to induce phase-change in monolayer TMDs either employ highly-hostile organometallic compounds, or have limited compatibility with large-scale, cost-effective device fabrication. In this paper, we report a new photochemical method to induce semiconductor to metallic phase transition in monolayer MoS_2 in a benign chemical environment, through a bench-top, cost-effective solution phase process that is compatible with large-scale device fabrication. It was demonstrated that photoelectrons produced by the band-gap absorption of monolayer MoS2 have enough chemical potential to activate the phase transition in the presence of an electron-donating solvent. This novel photochemical phase-transition mechanism advances our fundamental understanding of the phase transformation in 2D transition metal dichalcogenides (TMDs), and will open new revenues in the fabrication of atomically-thick metal-semiconductor heterostructures for improved carrier mobility and reduced contact resistance in TMD-based electronic and optoelectronic devices.

Keywords: phase transition, photochemical, molybdenum disulfide (MoS_2) , transition metal dichacogenide, *in situ* spectroscopic characterization, XPS, Raman

OPEN ACCESS

Edited by:
Nosang Vincent Myung, University of California, Riverside, United States

Reviewed by:
Gwan-Hyoung Lee, Yonsei University, South Korea
Ying Dai, Shandong University, China

***Correspondence:**
Ruoxue Yan
rxyan@engr.ucr.edu

Specialty section:
This article was submitted to Electrochemistry, a section of the journal Frontiers in Chemistry

Received: *21 February 2019*
Accepted: *29 May 2019*
Published: *13 June 2019*

Citation:
Byrley P, Liu M and Yan R (2019) Photochemically Induced Phase Change in Monolayer Molybdenum Disulfide. Front. Chem. 7:442. doi: 10.3389/fchem.2019.00442

INTRODUCTION

Layered transition metal dichalcogenides (TMDs) have attracted major research interests in recent years because of their special two-dimensional layer structures and potential as high-performance functional nano-materials. The presence of a finite band gap, photo-responsivity, and outstanding electronic and optical properties make them promising candidates for optoelectronics and nanoelectronics.

Field effect transistors (FET) based on monolayer TMDs, in particular, MoS_2 and WSe_2, have been widely studied due to their excellent properties including high on/off ratios (exceeding 10^8), immunity to short channel effects, and abrupt subthreshold switching (Yoon et al., 2011; Song et al., 2013; Kappera et al., 2014a; Pradhan et al., 2014; Liu et al., 2015). To further improve the device performance, research efforts have been focused on enhancing the carrier mobilities, investigating the contact mechanisms, and limitations in carrier transport (Radisavljevic et al., 2011; Kim et al., 2012; Das et al., 2013; Gong et al., 2013; Radisavljevic and Kis, 2013; Sangwan et al., 2013; Li et al., 2017; Lv et al., 2018). Currently, the reported carrier mobilities have a wide range of variations from 1 to 400 $cm^2V^{-1}s^{-1}$, depending on the fabrication method, contact resistance, and it was recently found out that they also depend on the phase of the TMD layer (Kappera et al., 2014a,b; Guo et al., 2015; Ma et al., 2015). TMDs have several different phases, including the most common 2H phase (semiconducting) and 1T phase (metallic) (van der Zande et al., 2013; Voiry et al., 2013; Zhou et al., 2013; Kappera et al., 2014a; Acerce et al., 2015; Tang and Jiang, 2015). These two phases have different electronic band structures and other properties such as carrier mobility and optical absorption efficiency in the visible range (Guo et al., 2015; Xiong et al., 2015). Theoretical studies have put the electron and hole mobilities in 1T-MoS_2 at 6.4×10^4 cm^2 V^{-1} s^{-1} and 5.7×10^4 cm^2 V^{-1} s^{-1}, respectively, which are about two orders of magnitude higher than in 1H-MoS_2 (1.2×10^2 cm^2 V^{-1} s^{-1} for electrons and 3.8×10^2 cm^2 V^{-1} s^{-1} for holes) (Kan et al., 2014). This large enhancement was attributed to the reduction of the electron (hole) effective mass from 0.49 m_e (0.60 m_h) to 0.12 m_e (0.05 m_h) when the 2H-MoS_2 is converted to 1T-MoS_2 (Kan et al., 2014). It has also been shown that the 1T-phase MoS_2 can significantly decrease the contact resistance of monolayer-MoS_2-based transistors to ∼200–300 Ω-μm at the room temperature from ∼1,000 Ω-μm in devices using pure 2H-MoS_2 (Kappera et al., 2014a), an impressive level that is getting close to the best contact resistance between graphene and palladium reported by IBM ($110 \pm 20\,\Omega\,\mu m$ at 6 K) (Xia et al., 2011). Phase-engineering in monolayer TMDs has offered an extra handle in performance optimization of TMDs-based nano-electronics and optoelectronic by enabling the preparation of novel structures, such as high-quality mix-phase material with controllable carrier mobility and patternable heterojunction materials (Duan et al., 2014; Duesberg, 2014; Gong et al., 2014; Huang et al., 2014; Mahjouri-Samani et al., 2015; Zeng et al., 2015; Zheng et al., 2015).

Traditionally, 2H to 1T phase transition is realized through alkali metal (Li^+, Na^+, or K^+) intercalation using highly reductive organometallic compounds, such as n- or t-butylithium, and has been studied for about three decades in bulk MoS_2 (Py and Haering, 1983; Zheng et al., 2014; Mahjouri-Samani et al., 2015; Tan and Zhang, 2015). In a typical synthesis, MoS_2 is intercalated with lithium to form the reduced Li_xMoS_n phase with expanded lattice, which can be exfoliated into monolayer films by ultrasound-assisted hydration process. The reduced Li_xMoS_n phase has the same octahedral symmetry as 1T-MoS_2, and the subsequent deintercalation preserves the octahedral structure, yielding a metastable 1T metallic phase. Recently, this method has been extended to the preparation of mono- or few layer TMDs (Eda et al., 2011; Zeng et al., 2011; Cheng et al., 2014; Dong et al., 2014; Eng et al., 2014; Knirsch et al., 2015). The major drawback of this technique is the long lithiation time (e.g., a range of 2 h to 3 days soaking at 100°C), and the poor film quality due to the damage due to the violent reaction between lithium and water. The use of expensive and hostile organometallic compounds requires an oxygen- and water-free processing environment and is highly explosive, which leads to cost and safety concerns as the phase-engineering process is scaled up. Thus, there is a lot of interest in developing a method to induce phase change in monolayer MoS_2 that is safer, more time efficient and lower cost. Several alternative methods have been proposed to induce the 2H to 1T phase transition in monolayer MoS_2, including strain, electron beam, plasma bombardment, and plasmonic hot electron induction (Enyashin et al., 2011; Kang et al., 2014; Lin et al., 2014; Katagiri et al., 2016; Zhu et al., 2017). However, in general, a clean, low cost and scalable phase engineering technique is still not available.

In this paper, we report a new photochemical route to induce 2H to 1T phase transition in MoS_2 monolayers in a benign chemical environment. We find that photoelectrons produced by the band-gap absorption of monolayer MoS_2 have enough chemical potential to activate the phase transition in the presence of a hole scavenger. This novel photochemical phase-transition mechanism was systematically investigated by *in-situ* 2D photoluminescence (PL) mapping, *in-situ* Raman, atomic force microscopy (AFM), and X-ray photoelectron spectroscopy (XPS) and control experiments demonstrating the dependence of the phase-change process on the redox environment.

RESULTS AND DISCUSSION

Figure 1 shows the mechanistic illustration of the photochemical phase-transition mechanism. As shown in **Figure 1A**, the 2H-MoS_2 has the D_{3h} symmetry, and its crystal field splits the five Mo 4d orbitals into three groups (**Figure 1B,** left): an *a* orbital ($4d_{z^2}$), which is the most stable of all, followed by two degenerate *e'* orbitals ($4d_{xz}$ and $4d_{yz}$) and two degenerate *e"* ($4d_{x^2-y^2}$ and $4d_{yz}$) orbitals. The Mo ion is in the +4 oxidation state and has two 4d electrons, both residing in the lowest lying $4d_{z^2}$ and leaving the higher energy 4d orbitals empty. The complete occupation of the $4d_{z^2}$, which correspond to the valance band in its electronic band structure, renders 2H semiconducting. On the contrary, 1T-MoS_2 has a centrosymmetric O_h symmetry (**Figure 1A**, right), which splits the Mo 4d orbitals into 2 groups (**Figure 1B**, right): the lower energy t_{2g} orbitals ($4d_{xy}$, $4d_{xz}$, and $4d_{yz}$) and the higher energy e^*_g orbitals ($4d_{z^2}$ and $4d_{x^2-y^2}$). At the ground state, the two Mo 4d-electrons has to fill in 2 of the 3 degenerate t_{2g} orbitals instead. The incomplete occupation of the 1T t_{2g} orbitals indicates partially occupied valence band, making 1T phase metallic (Chhowalla et al., 2015). The S 3p states do not influence the electronic structure of the materials, as they are located approximately 3 eV away from the Fermi level. Since the $4d_{z^2}$ orbital in 2H-MoS_2 is slightly more stable than the t_{2g}

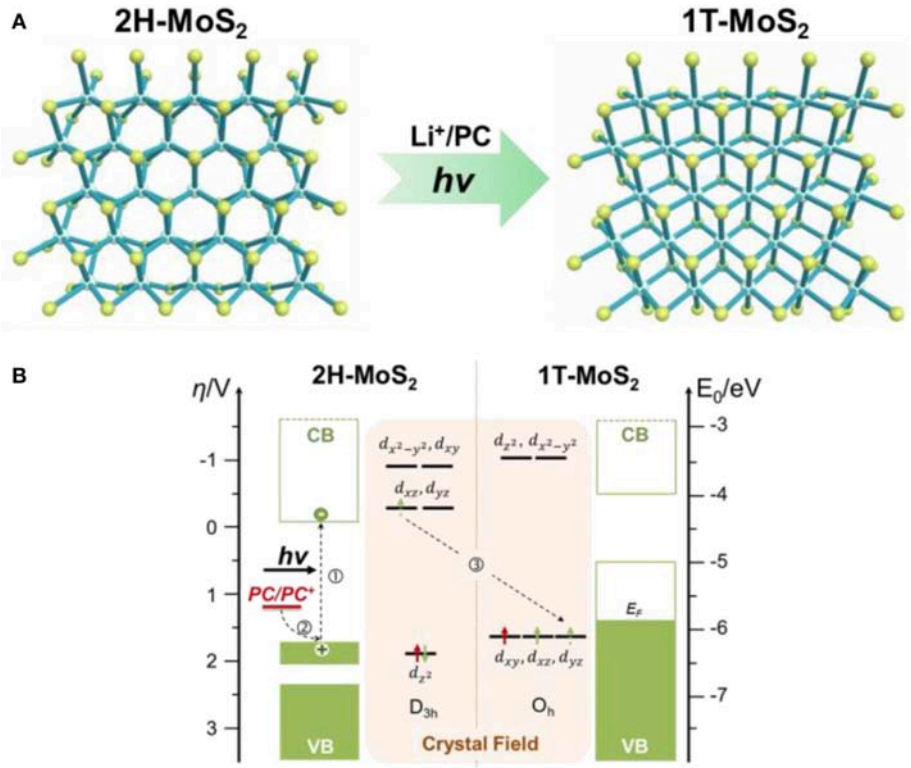

FIGURE 1 | Mechanistic illustration of the photochemical 2H to 1T phase transition in monolayer MoS_2. **(A)** Atomic structures of 2H- and 1T-MoS2. **(B)** Energy diagram of 2H- and 1T-MoS_2 and the corresponding crystal fields of Mo 4d orbitals. The proposed route of photochemical phase transition is marked by dotted arrows. Step 1, photo absorption to generate photo electrons in the conduction band (CB) and photo holes in the valence band (VB) of 2H-MoS_2 (left). Step 2, electron donation from the hole scavenger, propylene carbonate (PC), whose redox potential falls above the valence band of the 2H-MoS_2. The photo-assisted electron injection to the conduction band of 2H-MoS_2 destabilizes the 2H phase. Step 3, phase transition from the destabilized 2H phase to the thermodynamically more stable 1T phase (for d^3 configuration). The green arrows on the 4d orbitals represent the original 4d electrons on the Mo atom, while the red arrows represent the extra electron donated by the hole scavenger molecule.

orbitals in 1T-MoS_2, the total energy of Mo 4d-electrons are also lower, rendering 2H phase thermodynamically favored.

When the 2H-MoS_2 accept an extra electron, that electron is forced into the high energy *e*' orbitals, which is much higher than $4d_{z^2}$ due to the large crystal field stabilization energy in D_{3h} symmetry, destabilizing 2H phase. On the contrary, the triply degenerate t_{2g} orbitals in 1T phase would be able to accommodate all three Mo 4d electrons and reach the stable half-filled configuration. Since t_{2g} in 1T-MoS_2 is much lower in energy than *e*' orbitals in 2H-MoS_2, the total energy of the d^3 configuration is considerably lower in 1T phase, thus allowing phase conversion to occur (Enyashin and Seifert, 2012; Cheng et al., 2014; Kan et al., 2014). This forms the foundation of electron-injection-induced MoS_2 phase transition. Instead of using the hostile reductant like butylithium in the chemical intercalation method, or direct physical electron injections using high-energy electron beams or plasmonic hot-electrons, in the photochemical route, low energy visible light was used to provide the extra electron by generating photoelectrons in 2H-MoS_2.

As shown in **Figure 1B**, visible light with a photon energy beyond the bandgap of monolayer 2H-MoS_2 (∼1.8eV) excites a valence band ($4d_{z^2}$) electron into the conduction band, which corresponds to the degenerate *e*' orbitals ($4d_{xz}$ and $4d_{yz}$). The photo-generated hole left behind in the $4d_{z^2}$ state is filled by an electron transferred from a hole scavenging molecule, whose oxidation potential is higher than $4d_{z^2}$, or the top of the valence band. Effectively, this is a photo-reduction process, in which the electron injected into MoS_2 is supplied by the hole scavenger and the activation energy is provided by a visible photon. In our demonstration, the hole scavenger used is propylene carbonate (PC), the oxidation potential of which is 1.2V vs. NHE (Kanamura et al., 1995), which converts to −5.6 eV vs. vacuum. This is slightly above the valence band of monolayer 2H-MoS_2, which is roughly around −6.5 eV below vacuum (Schlaf et al., 1999; Choi et al., 2013; Furchi et al., 2014). The reduced MoS2 goes through phase-transition to the more-stable 1T structure, which was then stabilized by Li^+ ions, which balance the negative charges on reduced 1T-MoS_2. The Li^+ ion here is not from harsh organolithium, but is from a mild lithium salt ($LiPF_6$) dissolved in PC.

Figure 2 shows the *in situ* 2D photoluminescence mapping that follows the photochemical phase transition of 2H-MoS_2 monolayer flakes grown with chemical vapor deposition (CVD) on a SiO_2 substrate. The substrate was encapsulated in a liquid

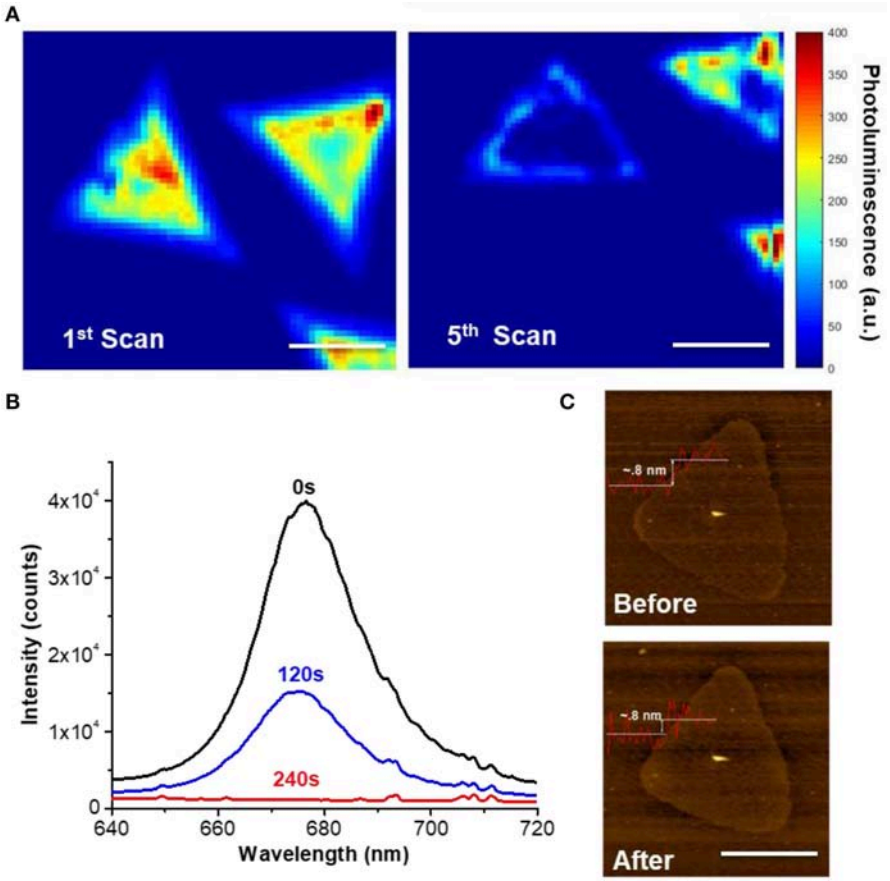

FIGURE 2 | Optical and morphological characterization of the photochemical phase change of monolayer CVD MoS_2. **(A)** *in-situ* 2D photoluminescence (PL) imaging following the photochemical phase change of a single MoS_2 monolayer flake (left). The left image shows the initial scanning and the right image shows the 5th consecutive scan after 2 h of imaging with a laser power of 0.76 mW/μm^2 at 532 nm and 1 s/pixel. The right image was slightly drifted/rotated with respect to the right image during alignment and slight distortion was also observed due to piezo hysteresis. Scale bar: 10 μm. **(B)** Time dependent PL spectra of a MoS_2 flake during illumination showing clear PL quenching (5 s accumulation time). **(C)** AFM image of the same MoS_2 monolayer flake before and after the photochemical phase change showing no sign of photodamage to the structure integrity. Scale bar: 10 μm.

chamber with 1M PC solution of $LiPF_6$ and sealed to prevent evaporation. The MoS_2 monolayer flakes were then scanned with a tightly-focused 532 nm laser. With a photon energy higher than the band gap of monolayer MoS_2, the laser served dual purposes: providing activation energy for the photo-reduction and exciting MoS_2 photoluminescence, the quenching of which serves an *in-situ* indicator of the formation of the 1T metallic phase (Eda et al., 2011). The laser power was maintained at 0.76 mW/μm^2 (1.2 μm spot size) to prevent photodamage and an accumulation time of 1 s per pixel was used for all 2D scanning. **Figures 2A,B** show the result of the 1st and 5th laser scan of the same MoS_2 flake (on the left), which shows a clear PL quenching which suggests the increase of the metallic 1T-phase component. The entire 5 scans were compiled in **Figure S1**, which shows the gradual PL quenching of the left domain with time evolution. It is worth mentioning that scan 3 and 4 was stopped early so the total illumination times of the two MoS_2 flakes on the right are shorter than the domain on the left. The different degrees of PL quenching among the MoS_2 flakes clearly demonstrates the correlation between the PL intensity and the duration of light exposure. **Figure 2B** shows the PL spectra of another MoS_2 flake, collected at different times during continued illumination, also showing a clear time-dependence in PL quenching on light exposure. **Figure S2** further shows that the PL intensity decays exponentially with the illumination time. AFM images taken before and after laser exposure (0.76 mW/μm^2, 240 s) in $LiPF_5$/PC solution (**Figure 2C**) indicate that the sample was not damaged by laser ablation. This is consistent with previous reports that the thermal effect is insignificant at such low power densities and laser thinning requires at least 20 mW/μm^2 in laser power (Najmaei et al., 2012; Hu et al., 2017).

We have observed considerable variations in different CVD MoS_2 samples. The CVD grown MoS_2 flakes are highly prone to chalcogen deficiency because of the high volatility of chalcogenides, and therefore contain an abundance of chalcogen vacancies inherently creates structural defects that affect carrier diffusion and activate non-radiative recombination channels (Zhou et al., 2013; Hong et al., 2015). Depending on the

growth parameter, such as the amount and distance of solid precursors, growth temperature and duration, the film quality can vary significantly from batch to batch and even at different positions on the same substrate (Zafar et al., 2017). These variations affect the optical behavior of the sample as well as any photo-induced processes, however, there have been increasing research attentions directed on the defect-controlled growth of high-quality MoS_2 films (Chen et al., 2015; Tao et al., 2017). The continued improvement in MoS_2 synthesis will provide more precision in the optimization of the photochemical phase transition method.

In-situ confocal Raman spectroscopy was carried out to examine the structure evolution of the MoS_2 flakes. The Raman spectra (**Figure 3**) show characteristic peaks at 382 and 402 cm^{-1}, which can be assigned to the E^1_{2g} and A_{1g} phonon modes, respectively (Sun et al., 2014). Chemically exfoliated 1T-MoS_2 using butyllithium solution shows distinct Raman signature of superlattices at 150 cm^{-1} (J_1), 226 cm^{-1} (J_2), and 333 cm^{-1} (J_3)(Yang et al., 1991). The appearance of these superlattice peaks has been used as the indication of the 1T phase (Kang et al., 2014; Kappera et al., 2014b; Zhu et al., 2017), however, it is also worth noting that their relative intensities, and even whether or not they appear together in mixed phase monolayer MoS_2 samples are not in agreement across the literature. For example, 1T-MoS_{-2} flakes produced with 40 s Ar plasma treatment has 40% 1T phase, but J_1 and J_2 intensities are both quite similar to the pristine sample before treatment, leaving J_3 is the most prominent peak (Zhu et al., 2017). In a separate case, 48 hours of n-butyl lithium treatment yields 70% of 1T phase and its Raman spectra shows a very prominent J_2 peak, a very weak J_3, and no J_1(Kappera et al., 2014b). In our case, the lowest frequency J_1 peak is too weak to be discerned from the residue laser background which takes off quickly below 175 cm^{-1}. The J_2 peak is very close to LA mode of MoS_2 at 227 cm^{-1}, which also makes it difficult to stand out. However, with the increasing illumination time, a new J_3 peak was clearly observed after 20 min under a laser illumination power of 0.14 mW/μm^2, clearly indicative of a 1T phase formation. We have also observed a new peak at ~370 cm^{-1}, which was also seen in chemically exfoliated 1T-MoS_2 together with the superlattice peaks, however, its structural origin was not clear (Yang et al., 1991). The broadening and intensity attenuation of E^1_{2g} peak was not obvious, indicating a partial phase-change under this illumination condition, without the significant loss of the D_{3h} symmetry (Yang et al., 1991). We want to point out here that the degree of phase change is limited in the *in-situ* confocal Raman measurement because of a limited illumination power attainable at the sample surface and the stage drifting of the confocal Raman. However, the presence of characteristic 1T-MoS_2 Raman peaks at the low frequency region supports the PL measurement result.

X-ray photoelectron spectroscopy (XPS) provides additional evidence of the formation of 1T phase through the photochemical phase transition process. **Figure 4** shows the select-area XPS spectra of the as-synthesized CVD monolayer MoS_2 flake (top) and a CVD MoS_2 sample phase-modified with the photochemical method. The MoS_2 flake was illuminated with a 532 nm laser

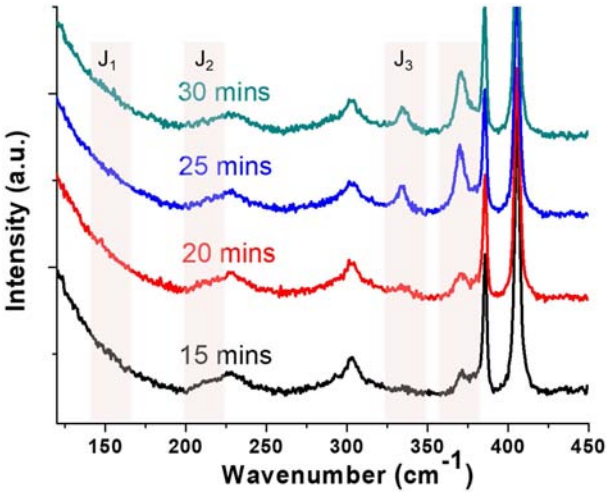

FIGURE 3 | *In-situ* Raman spectra following the time evolution of a monolayer MoS_2 flake during photochemical phase change. Two new peaks (330 and 370 cm^{-1}) indicative of the 1T phase appeared with increasing illumination time (532 nm, 0.14 mW/μm^2). The 19.8 cm^{-1} distance between the E^1_{2g} and A_{1g} peaks indicates that the sample is a MoS_2 monolayer.

(~0.2 mW/μm^2, 1.2 μm spot size) for 30 min in the presence of 1M $LiPF_4$/PC solution. The XPS measurement was performed with an AXIS Supra (Kratos Instruments) using a 500 mm Rowland circle monochromated Al Ka x-ray source and an aperture of 20 μm diameter for select area measurement. All spectra were calibrated by the C 1 s peak at 284.5 eV (see **Figure S3**). The peaks around 230 and 233 eV, corresponding to the Mo^{4+} $3d_{5/2}$ and Mo^{4+} $3d_{3/2}$ components in 2H-MoS_2, shifted slightly but distinctly to lower energies after the photochemical process, important evidence of the presence of the 1T phase (Eda et al., 2011; Cai et al., 2015). For the as-made 2H-MoS_2, the XPS intensity goes back to the baseline between peaks (234 eV and 231 eV), whereas the phase-modified sample shows clear peak broadening on the low energy side and the intensity no longer goes back to the baseline at these locations, also indicating the presence of additional peaks. The deconvolution of Mo and S XPS peaks reveals 1T peaks at lower energy along with the original 2H peaks, and the relative content of 1T phase is estimated to be ~15% for this particular MoS_2 flake. Considering the laser spot size of 1.2 μm and the XPS aperture of 20 μm, the illuminated region accounts for only a tiny fraction (0.3%) of the XPS probed area. The measured spectrum represents the averaged results over the entire probed area, which indicates that the photochemical phase-modification can go far beyond the illuminated region, possibly due to exciton/charge carrier diffusion and laser scattering in the liquid chamber.

In order to further validate the proposed mechanism, the effect of different experimental parameters, such as the presence of Li^+ ion, the illumination wavelength, the redox potentials of hole scavengers, were studied. **Figure 5** summarized the

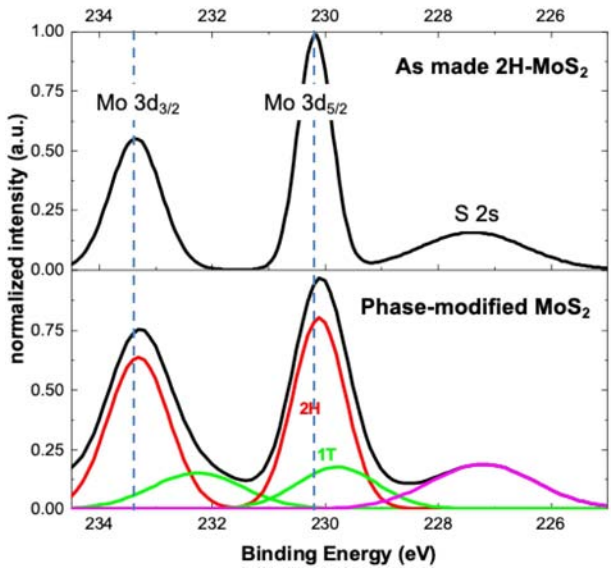

FIGURE 4 | XPS spectra of as-synthesized and phase-modified monolayer MoS_2. The phase-modified MoS_2 sample (bottom black curve) shows a distinct shift and peak broadening in the Mo $3d_{3/2}$ and $3d_{5/2}$ binding energies, indicating the presence of 1T phases.

photoluminescence (PL) spectra measured on single CVD-MoS_2 monolayer flakes before and after 1 h of laser illumination under different conditions. The powers of the illumination laser and the excitation laser used for PL measurement, as well as the accumulation time of the PL spectra, was kept the constant for all control experiments. **Figure 5A** shows the expected PL quenching on a single MoS_2 flake induced by 532 nm laser illumination in 1M $LiPF_6$-PC solution, indicative of the semiconductor to metal phase transition. As illustrated in **Figure 5E**, the 532 nm laser has a photo-energy of 2.33 eV, large enough to bridge the 1.8 eV bandgap of monolayer MoS_2 and excite photoelectrons that destabilize the 2H phase. The photogenerated holes left behind in the valence band were filled by electrons transferred from the PC, whose redox potential sits above the top of the MoS_2 valence band. On the contrary, if the photon energy of the illumination laser is lower than the MoS_2 bandgap or the redox potential of the hole scavenger sits below the top of the MoS_2 valence band, no significant PL quenching was observed, as shown in **Figures 5B,C.** The 785 nm laser has a photon energy of 1.58 eV, not enough excite photoelectrons into the conduction band of monolayer 2H-MoS_2. The acetonitrile (AN) solvent, which is more stable against oxidation than PC, has an oxidation potential of >2.6 V vs. NHE (Portis et al., 1972), which converts to −7.0 eV vs. vacuum, lower than the valence band top of the monolayer 2H-MoS_2 (−6.5 eV below vacuum), and unable to function as an efficiency electron donator (e.g., hole scavenger). We have also observed that the Li^+ also plays a critical role in the photochemical phase transition mechanism. As shown in **Figure 5D**, PL quenching was not observed with pure PC and no Li^+ to stabilize the photoreduced MoS_2. The role of Li^+ is similar to that of the chemical exfoliation method, where the chemically reduced MoS_2 (by butylithium) is intercalated with Li^+ ions to form a stable Li_xMoS_n phase that has the same O_h symmetry as 1T-MoS_2. After deintercalation, the octahedral structure is preserved to yield the 1T-MoS_2 phase. The absorption of Li^+ on photoreduced monolayer MoS_2 stabilizes the negative charges and facilitates the D_{3h} (2H) to O_h (1T) structural transition. The results of these control experiments support the proposed photochemical phase transition mechanism illustrated in **Figure 1**.

CONCLUSION

In summary, we have demonstrated a new photochemical route to induce 2H to 1T phase transition in MoS_2 monolayers in a benign chemical environment. Photoelectrons generated by the band-gap absorption of monolayer MoS_2 provide the chemical potential necessary to activate the phase transition in the presence of a proper electron-donating solvent and stabilizing metal ion. Clear evidence of phase transition was seen with a combination of characterization methods including *in-situ* 2D PL mapping, *in-situ* Raman, AFM, and XPS. This benchtop solution-based photochemical phase engineering method does not rely on glove box or any expensive clean-room technique, and is compatible with photolithography for phase-patterning on wafer-scale CVD sample. It demonstrates great promises as a clean, low cost and scalable alternative of the monolayer TMD phase engineering, and further advances the optimization and commercialization of TMD-based electronic components.

EXPERIMENTAL

Preparation of Monolayer MoS_2 Sample

Monolayer MoS_2 was synthesized on a thermal oxide (300 nm SiO_2/Si) substrate at a growth temperature of 650°C in a custom CVD system using sulfur (99.98%, Sigma Aldrich) and MoO_3 (99.99%, Sigma Aldrich) powder as solid precursors and Argon as carrier gas (20 sccm). After growth, the silica substrate was placed in a custom microscope liquid cell filled with 5 microliters of $LiPF_6$: PC solution (1.0M, battery grade, Sigma Aldrich) and sealed to prevent liquid evaporation.

Photoluminescence Measurement

The PL was measured with an inverted microscope with a HORIBA iHR550 spectrophotometer and a Synapse EM CCD. A green laser (GEM 532, $\lambda = 532$ nm, Laser Quantum) was used to excite the MoS_2 PL and to induce photochemical phase change. The power density of the laser is tuned by optical density filters and the reported values in the paper was measured at the sample plane. *In-situ* 2D mapping was conducted at 1 s/pixel using a custom LabView program. The PL spectra were measured with a 20 μm slit and 5 s accumulation time.

AFM Measurement

The topological images of the MoS_2 monolayer flake before and after illumination were collected with a commercial AFM (SmartSPM, AIST-NT). The before image was measured on as-synthesized sample. After the illumination in $LiPF_6$/PC solution, the sample was removed from the liquid cell

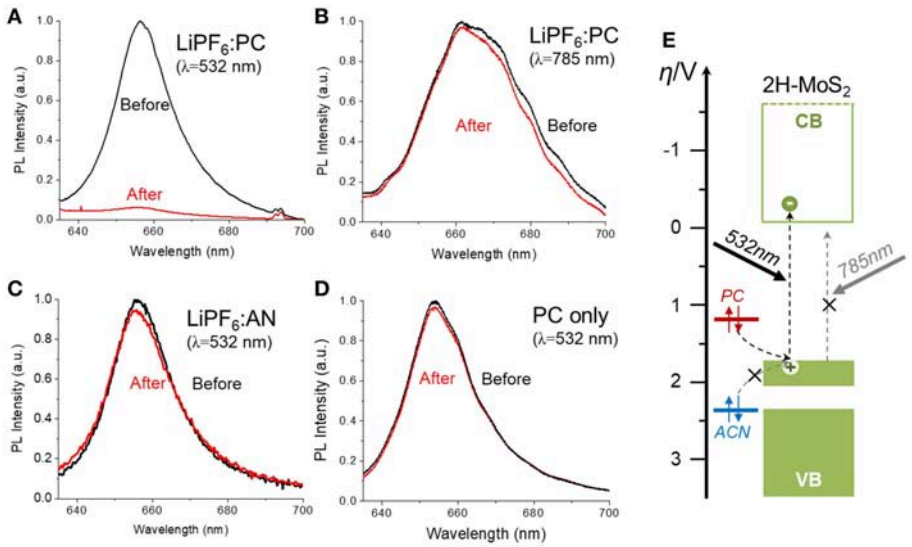

FIGURE 5 | Measured MoS_2 Photoluminescence (PL) spectra before and after 1 h of laser illumination under different conditions: **(A)** 1M PC solution of $LiPF_6$ with 532 nm illumination, **(B)** 1M PC solution of $LiPF_6$ with 785 nm illumination. The 785 nm laser correspond to 1.58 eV in photon energy, **(C)** 1M acetonitrile (AN) solution of $LiPF_6$ with 532 nm illumination, **(D)** Pure PC (no Li^+ ion) with 532 nm illumination. The power density of the illumination lasers in different control experiments were kept constant. Each PL spectrum was measured under 532 nm excitation for the same accumulation time (5 s), **(E)** The energy diagram illustrating the alignment of the 2H-MoS_2 bands with redox potentials of the hole scavengers (PC and AN).

and washed with pure propylene carbonate solvent and ethanol several times to remove excess $LiPF_6$ on the surface. The sample was then dried and characterized by AFM immediately.

In-situ Raman Measurements

The Raman spectra were measured with a commercial confocal Raman system (LabRAM, Horiba). A green Raman laser (532 nm, 0.14 mW/μm^2 measured at the sample surface) was used to excite the Raman spectra and induce the photochemical phase transition. Each Raman spectra was taken with 10 s exposure time and three accumulations.

Preparation of 1M $LiPF_6$ in Acetonitrile

Pure $LiPF_6$ powder (99.9%, Sigma Aldrich) was mixed in acetonitrile under an inert atmosphere for two days at high spin speed.

XPS Analysis

XPS analysis was done using a Kratos Instruments AXIS Supra with a 500 mm Rowland circle monochromated Al Ka X-ray 1486.6 eV source at the University of California, Irvine Materials Research Institute.

DATA AVAILABILITY

All datasets generated for this study are included the manuscript and/or the **Supplementary Files**.

AUTHOR CONTRIBUTIONS

RY and ML conceived the idea and designed the experiment. PB carried out the experiment and analyzed data. PB and RY wrote the manuscript with input from all authors.

FUNDING

Funding for this research was provided by the National Science Foundation under Award DMR-1649795. Work by PB was partially supported by the GAANN Fellowship.

SUPPLEMENTARY MATERIAL

The Supplementary Material for this article can be found online at: https://www.frontiersin.org/articles/10.3389/fchem.2019.00442/full#supplementary-material

REFERENCES

Acerce, M., Voiry, D., and Chhowalla, M. (2015). Metallic 1T phase MoS2 nanosheets as supercapacitor electrode materials. *Nat. Nanotechnol.* 10, 313–318. doi: 10.1038/nnano.2015.40

Cai, L., He, J., Liu, Q., Yao, T., Chen, L., Yan, W., et al. (2015). Vacancy-induced ferromagnetism of MoS2 nanosheets. *J. Am. Chem. Soc.* 137, 2622–2627. doi: 10.1021/ja5120908

Chen, W., Zhao, J., Zhang, J., Gu, L., Yang, Z., Li, X., et al. (2015). Oxygen-assisted chemical vapor deposition growth of large single-crystal and high-quality monolayer MoS2. *J. Am. Chem. Soc.* 137, 15632–15635. doi: 10.1021/jacs.5b10519

Cheng, Y., Nie, A., Zhang, Q., Gan, L. Y., Shahbazian-Yassar, R., and Schwingenschlogl, U. (2014). Origin of the phase transition in lithiated molybdenum disulfide. *Acs Nano* 8, 11447–11453. doi: 10.1021/nn505668c

Chhowalla, M., Voiry, D., Yang, J. E., Shin, H. S., and Loh, K. P. (2015). Phase-engineered transition-metal dichalcogenides for energy and electronics. *MRS Bull.* 40, 585–591. doi: 10.1557/mrs.2015.142

Choi, M. S., Lee, G. H., Yu, Y. J., Lee, D. Y., Lee, S. H., Kim, P., et al. (2013). Controlled charge trapping by molybdenum disulphide and graphene in ultrathin heterostructured memory devices. *Nat. Commun.* 4:1624. doi: 10.1038/ncomms2652

Das, S., Chen, H. Y., Penumatcha, A. V., and Appenzeller, J. (2013). High performance multilayer MoS2 transistors with scandium contacts. *Nano Lett.* 13, 100–105. doi: 10.1021/nl303583v

Dong, L., Lin, S., Yang, L., Zhang, J., Yang, C., Yang, D., et al. (2014). Spontaneous exfoliation and tailoring of MoS2 in mixed solvents. *Chem. Commun.* 50, 15936–15939. doi: 10.1039/C4CC07238C

Duan, X., Wang, C., Shaw, J. C., Cheng, R., Chen, Y., Li, H., et al. (2014). Lateral epitaxial growth of two-dimensional layered semiconductor heterojunctions. *Nat. Nanotechnol.* 9, 1024–1030. doi: 10.1038/nnano.2014.222

Duesberg, G. S. (2014). Heterojunctions in 2d semiconductors a perfect match. *Nat. Mater.* 13, 1075–1076. doi: 10.1038/nmat4127

Eda, G., Yamaguchi, H., Voiry, D., Fujita, T., Chen, M., and Chhowalla, M. (2011). Photoluminescence from chemically exfoliated MoS2. *Nano Lett.* 11, 5111–5116. doi: 10.1021/nl201874w

Eng, A. Y., Ambrosi, A., Sofer, Z., Šimek, P., and Pumera, M. (2014). Electrochemistry of transition metal dichalcogenides: strong dependence on the metal-to-chalcogen composition and exfoliation method. *Acs Nano* 8, 12185–12198. doi: 10.1021/nn503832j

Enyashin, A. N., and Seifert, G. (2012). Density-functional study of LixMoS2 intercalates (0 <= x <= 1). *Comput. Theor. Chem.* 999, 13–20. doi: 10.1016/j.comptc.2012.08.005

Enyashin, A. N., Yadgarov, L., Houben, L., Popov, I., Weidenbach, M., Tenne, R., et al. (2011). New route for stabilization of 1T-WS2 and MoS2 phases. *J. Phys. Chem. C* 115, 24586–24591. doi: 10.1021/jp2076325

Furchi, M. M., Pospischil, A., Libisch, F., Burgdörfer, J., and Mueller, T. (2014). Photovoltaic effect in an electrically tunable van der Waals heterojunction. *Nano Lett.* 14, 4785–4791. doi: 10.1021/nl501962c

Gong, C., Huang, C., Miller, J., Cheng, L., Hao, Y., Cobden, D., et al. (2013). Metal contacts on physical vapor deposited monolayer MoS. *Acs Nano* 7, 11350–11357. doi: 10.1021/nn4052138

Gong, Y., Lin, J., Wang, X., Shi, G., Lei, S., Lin, Z., et al. (2014). Vertical and in-plane heterostructures from WS2/MoS2 monolayers. *Nat. Mater.* 13, 1135–1142. doi: 10.1038/nmat4091

Guo, Y., Sun, D., Ouyang, B., Raja, A., Song, J., Heinz, T. F., et al. (2015). Probing the dynamics of the metallic-to-semiconducting structural phase transformation in MoS2 crystals. *Nano Lett.* 15, 5081–5088. doi: 10.1021/acs.nanolett.5b01196

Hong, J., Hu, Z., Probert, M., Li, K., Lv, D., Yang, X., et al. (2015). Exploring atomic defects in molybdenum disulphide monolayers. *Nat. Commun.* 6:6293. doi: 10.1038/ncomms7293

Hu, L., Shan, X., Wu, Y., Zhao, J., and Lu, X. (2017). Laser thinning and patterning of MoS2 with layer-by-layer precision. *Sci. Rep.* 7:15538. doi: 10.1038/s41598-017-15350-4

Huang, C., Wu, S., Sanchez, A. M., Peters, J. J., Beanland, R., Ross, J. S., et al. (2014). Lateral heterojunctions within monolayer MoSe2-WSe2 semiconductors. *Nat. Mater.* 13, 1096–1101. doi: 10.1038/nmat4064

Kan, M., Wang, J. Y., Li, X. W., Zhang, S. H., Li, Y. W., Kawazoe, Y., et al. (2014). Structures and phase transition of a MoS2 monolayer. *J. Phys. Chem. C* 118, 1515–1522. doi: 10.1021/jp4076355

Kanamura, K., Toriyama, S., Shiraishi, S., and Takehara, Z. (1995). Studies on electrochemical oxidation of nonaqueous electrolytes using *in-situ* ftir spectroscopy .1. The effect of type of electrode on on-set potential for electrochemical oxidation of propylene carbonate containing 1.0 Mol Dm(-3) Liclo4. *J. Electrochem. Soc.* 142, 1383–1389. doi: 10.1149/1.2048586

Kang, Y., Najmaei, S., Liu, Z., Bao, Y., Wang, Y., Zhu, X., et al. (2014). Plasmonic hot electron induced structural phase transition in a MoS2 monolayer. *Adv. Mater.* 26, 6467–6471. doi: 10.1002/adma.201401802

Kappera, R., Voiry, D., Yalcin, S. E., Branch, B., Gupta, G., Mohite, A. D., et al. (2014a). Phase-engineered low-resistance contacts for ultrathin MoS2 transistors. *Nat. Mater.* 13, 1128–1134. doi: 10.1038/nmat4080

Kappera, R., Voiry, D., Yalcin, S. E., Jen, W., Acerce, M., Torrel, S., et al. (2014b). Metallic 1T phase source/drain electrodes for field effect transistors from chemical vapor deposited MoS2. *Apl. Mater.* 2:092516. doi: 10.1063/1.4896077

Katagiri, Y., Nakamura, T., Ishii, A., Ohata, C., Hasegawa, M., Katsumoto, S., et al. (2016). Gate-tunable atomically thin lateral MoS2 schottky junction patterned by electron beam. *Nano Lett.* 16, 3788–3794. doi: 10.1021/acs.nanolett.6b01186

Kim, S., Konar, A., Hwang, W. S., Lee, J. H., Lee, J., Yang, J., et al. (2012). High-mobility and low-power thin-film transistors based on multilayer MoS2 crystals. *Nat. Commun.* 3:1011. doi: 10.1038/ncomms2018

Knirsch, K. C., Berner, N. C., Nerl, H. C., Cucinotta, C. S., Gholamvand, Z., McEvoy, N., et al. (2015). Basal-plane functionalization of chemically exfoliated molybdenum disulfide by diazonium salts. *Acs Nano* 9, 6018–6030. doi: 10.1021/acsnano.5b00965

Li, F., Wei, W., Zhao, P., Huang, B., and Dai, Y. (2017). Electronic and optical properties of pristine and vertical and lateral heterostructures of Janus MoSSe and WSSe. *J. Phys. Chem. Lett.* 8, 5959–5965. doi: 10.1021/acs.jpclett.7b02841

Lin, Y. C., Dumcenco, D. O., Huang, Y. S., and Suenaga, K. (2014). Atomic mechanism of the semiconducting-to-metallic phase transition in single-layered MoS2. *Nat. Nanotechnol.* 9, 391–396. doi: 10.1038/nnano.2014.64

Liu, E., Fu, Y., Wang, Y., Feng, Y., Liu, H., Wan, X., et al. (2015). Integrated digital inverters based on two-dimensional anisotropic ReS2 field-effect transistors. *Nat. Commun.* 6:6991. doi: 10.1038/ncomms7991

Lv, X., Wei, W., Zhao, P., Li, J., Huang, B., Dai, Y. (2018). Tunable Schottky contacts in MSe 2/NbSe 2 (M= Mo and W) heterostructures and promising application potential in field-effect transistors. *Phys. Chem. Chem. Phys.* 20, 1897–1903. doi: 10.1039/C7CP07546D

Ma, Y., Liu, B., Zhang, A., Chen, L., Fathi, M., Shen, C., et al. (2015). Reversible semiconducting-to-metallic phase transition in chemical vapor deposition grown mono layer WSe2 and applications for devices. *Acs Nano* 9, 7383–7391. doi: 10.1021/acsnano.5b02399

Mahjouri-Samani, M., Lin, M. W., Wang, K., Lupini, A. R., Lee, J., Basile, L., et al. (2015). Patterned arrays of lateral heterojunctions within monolayer two-dimensional semiconductors. *Nat. Commun.* 6:7749. doi: 10.1038/ncomms8749

Najmaei, S., Liu, Z., Ajayan, P. M., and Lou, J. (2012). Thermal effects on the characteristic Raman spectrum of molybdenum disulfide (MoS2) of varying thicknesses. *Appl. Phys. Lett.* 100:013106. doi: 10.1063/1.3673907

Portis, L. C., Mann, C. K., and Roberson, J. C. (1972). Anodic background reaction in moist acetonitrile. *Anal. Chem.* 44, 294–297. doi: 10.1021/ac60310a018

Pradhan, N. R., Rhodes, D., Feng, S., Xin, Y., Memaran, S., Moon, B.-H., et al. (2014). Field-effect transistors based on few-layered alpha-MoTe2. *Acs Nano* 8, 5911–5920. doi: 10.1021/nn501013c

Py, M. A., and Haering, R. R. (1983). Structural destabilization induced by lithium intercalation in Mos2 and related-compounds. *Can. J. Phys.* 61, 76–84. doi: 10.1139/p83-013

Radisavljevic, B., and Kis, A. (2013). Mobility engineering and a metal-insulator transition in monolayer MoS2. *Nat Mater.* 12, 815–820. doi: 10.1038/nmat3687

Radisavljevic, B., Radenovic, A., Brivio, J., Giacometti, V., and Kis, A. (2011). Single-layer MoS2 transistors. *Nat. Nanotechnol.* 6, 147–150. doi: 10.1038/nnano.2010.279

Sangwan, V. K., Arnold, H. N., Jariwala, D., Marks, T. J., Lauhon, L. J., and Hersam, M. C. (2013). Low-frequency electronic noise in single-layer MoS2 transistors. *Nano Lett.* 13, 4351–4355. doi: 10.1021/nl402150r

Schlaf, R., Lang, O., Pettenkofer, C., and Jaegermann, W. (1999). Band lineup of layered semiconductor heterointerfaces prepared by van der Waals epitaxy: charge transfer correction term for the electron affinity rule. *J. Appl. Phys.* 85, 2732–2753. doi: 10.1063/1.369590

Song, J. G., Park, J., Lee, W., Choi, T., Jung, H., Lee, C. W., et al. (2013). Layer-controlled, wafer-scale, and conformal synthesis of tungsten disulfide nanosheets using atomic layer deposition. *Acs Nano* 7, 11333–11340. doi: 10.1021/nn405194e

Sun, Y., Liu, K., Hong, X., Chen, M., Kim, J., Shi, S., et al. (2014). Probing local strain at MX2–metal boundaries with surface plasmon-enhanced raman scattering. *Nano Lett.* 14, 5329–5334. doi: 10.1021/nl5023767

Tan, C., and Zhang, H. (2015). Wet-chemical synthesis and applications of non-layer structured two-dimensional nanomaterials. *Nat. Commun.* 6:7873. doi: 10.1038/ncomms8873

Tang, Q., and Jiang, D. E. (2015). Stabilization and band-gap tuning of the 1T-MoS2 monolayer by covalent functionalization. *Chem. Mater.* 27, 3743–3748. doi: 10.1021/acs.chemmater.5b00986

Tao, L., Chen, K., Chen, Z., Chen, W., Gui, X., Chen, H., et al. (2017). Centimeter-scale CVD growth of highly crystalline single-layer MoS2 film with spatial homogeneity and the visualization of grain boundaries. *ACS Appl. Mater. Interfaces* 9, 12073–12081. doi: 10.1021/acsami.7b00420

van der Zande, A. M., Huang, P. Y., Chenet, D. A., Berkelbach, T. C., You, Y., Lee, G. H., et al. (2013). Grains and grain boundaries in highly crystalline monolayer molybdenum disulphide. *Nat. Mater.* 12, 554–561. doi: 10.1038/nmat3633

Voiry, D., Yamaguchi, H., Li, J., Silva, R., Alves, D. C., Fujita, T., et al. (2013). Enhanced catalytic activity in strained chemically exfoliated WS2 nanosheets for hydrogen evolution. *Nat Mater.* 12, 850–855. doi: 10.1038/nmat3700

Xia, F., Perebeinos, V., Lin, Y. M., Wu, Y., and Avouris, P. (2011). The origins and limits of metal-graphene junction resistance. *Nat. Nanotechnol.* 6, 179–184. doi: 10.1038/nnano.2011.6

Xiong, F., Wang, H., Liu, X., Sun, J., Brongersma, M., Pop, E., et al. (2015). Li intercalation in MoS2: *in situ* observation of its dynamics and tuning optical and electrical properties. *Nano Lett.* 15, 6777–6784. doi: 10.1021/acs.nanolett.5b02619

Yang, D., Sandoval, S. J., Divigalpitiya, W. M., Irwin, J. C., and Frindt, R. F. (1991). Structure of single-molecular-layer MoS_2. *Phys. Rev. B* 43, 12053–12056. doi: 10.1103/PhysRevB.43.12053

Yoon, Y., Ganapathi, K., and Salahuddin, S. (2011). How good can monolayer MoS2 transistors Be? *Nano Lett.* 11, 3768–3773. doi: 10.1021/nl2018178

Zafar, A., Nan, H., Zafar, Z., Wu, Z., Jiang, J., You, Y., et al. (2017). Probing the intrinsic optical quality of CVD grown MoS2. *Nano Res.* 10, 1608–1617. doi: 10.1007/s12274-016-1319-z

Zeng, Q., Wang, H., Fu, W., Gong, Y., Zhou, W., Ajayan, P. M., et al. (2015). Band engineering for novel two-dimensional atomic layers. *Small* 11, 1868–1884. doi: 10.1002/smll.201402380

Zeng, Z., Yin, Z., Huang, X., Li, H., He, Q., Lu, G., et al. (2011). Single-layer semiconducting nanosheets: high-yield preparation and device fabrication. *Angew. Chem. Int. Edit.* 50, 11093–11097. doi: 10.1002/anie.201106004

Zheng, J., Zhang, H., Dong, S., Liu, Y., Nai, C. T., Shin, H. S., et al. (2014). High yield exfoliation of two-dimensional chalcogenides using sodium naphthalenide. *Nat. Commun.* 5:2995. doi: 10.1038/ncomms3995

Zheng, S. J., Sun, L., Yin, T., Dubrovkin, A. M., Liu, F., Liu, Z., et al. (2015). Monolayers of WxMo1-xS2 alloy heterostructure with in-plane composition variations. *Appl. Phys. Lett.* 106:063113. doi: 10.1063/1.4908256

Zhou, W., Zou, X., Najmaei, S., Liu, Z., Shi, Y., Kong, J., et al. (2013). Intrinsic structural defects in monolayer molybdenum disulfide. *Nano Lett.* 13, 2615–2622. doi: 10.1021/nl4007479

Zhu, J., Wang, Z., Yu, H., Li, N., Zhang, J., Meng, J., et al. (2017). Argon plasma induced phase transition in monolayer MoS2. *J. Am. Chem. Soc.* 139, 10216–10219. doi: 10.1021/jacs.7b05765

Conflict of Interest Statement: The authors declare that the research was conducted in the absence of any commercial or financial relationships that could be construed as a potential conflict of interest.

The handling editor declared a shared affiliation, though no other collaboration, with the authors PB, ML, and RY at time of review.

Copyright © 2019 Byrley, Liu and Yan. This is an open-access article distributed under the terms of the Creative Commons Attribution License (CC BY). The use, distribution or reproduction in other forums is permitted, provided the original author(s) and the copyright owner(s) are credited and that the original publication in this journal is cited, in accordance with accepted academic practice. No use, distribution or reproduction is permitted which does not comply with these terms.

frontiers in Chemistry

ORIGINAL RESEARCH
published: 06 November 2018
doi: 10.3389/fchem.2018.00523

Low-Loading of Pt Nanoparticles on 3D Carbon Foam Support for Highly Active and Stable Hydrogen Production

Abdulsattar H. Ghanim[1†], Jonathan G. Koonce[1†], Bjorn Hasa[2], Alan M. Rassoolkhani[1], Wei Cheng[1], David W. Peate[3], Joun Lee[1] and Syed Mubeen[1]*

[1] Department of Chemical and Biochemical Engineering, University of Iowa, Iowa, IA, United States, [2] Department of Chemical Engineering, University of Patras, Patras, Greece, [3] Department of Earth and Environmental Sciences, University of Iowa, Iowa, IA, United States

OPEN ACCESS

Edited by:
Nosang Vincent Myung,
University of California, Riverside,
United States

Reviewed by:
Min Ho Seo,
Korea Institute of Energy Research,
South Korea
Sung Mook Choi,
Korea Institute of Materials Science,
South Korea

***Correspondence:**
Syed Mubeen
syed-mubeen@uiowa.edu

[†]These authors have contributed equally to this work

Specialty section:
This article was submitted to Electrochemistry, a section of the journal Frontiers in Chemistry

Received: 28 June 2018
Accepted: 10 October 2018
Published: 06 November 2018

Citation:
Ghanim AH, Koonce JG, Hasa B, Rassoolkhani AM, Cheng W, Peate DW, Lee J and Mubeen S (2018) Low-Loading of Pt Nanoparticles on 3D Carbon Foam Support for Highly Active and Stable Hydrogen Production. Front. Chem. 6:523. doi: 10.3389/fchem.2018.00523

Minimizing Pt loading is essential for designing cost-effective water electrolyzers and fuel cell systems. Recently, three-dimensional macroporous open-pore electroactive supports have been widely regarded as promising architectures to lower loading amounts of Pt because of its large surface area, easy electrolyte access to Pt sites, and superior gas diffusion properties to accelerate diffusion of H_2 bubbles from the Pt surface. However, studies to date have mainly focused on Pt loading on Ni-based 3D open pore supports which are prone to corrosion in highly acidic and alkaline conditions. Here, we investigate electrodeposition of Pt nanoparticles in low-loading amounts on commercially available, inexpensive, 3D carbon foam (CF) support and benchmark their activity and stability for electrolytic hydrogen production. We first elucidate the effect of deposition potential on the Pt nanoparticle size, density and subsequently its coverage on 3D CF. Analysis of the Pt deposit using scanning electron microscopy images reveal that for a given deposition charge density, the particle density increases (with cubic power) and particle size decreases (linearly) with deposition overpotential. A deposition potential of −0.4 V vs. standard calomel electrode (SCE) provided the highest Pt nanoparticle coverage on 3D CF surface. Different loading amounts of Pt (0.0075–0.1 mg_{Pt}/cm^2) was then deposited on CF at −0.4 V vs. SCE and subsequently studied for its hydrogen evolution reaction (HER) activity in acidic 1M H_2SO_4 electrolyte. The Pt/CF catalyst with loading amounts as low as 0.06 mg_{Pt}/cm^2 (10-fold lower than state-of-the-art commercial electrodes) demonstrated a mass activity of 2.6 ampere per milligram Pt at 200 mV overpotential, nearly 6-fold greater than the commercial Pt/C catalyst tested under similar conditions. The 3D architectured electrode also demonstrated excellent stability, showing <7% loss in activity after 60 h of constant current water electrolysis at 100 mA/cm^2.

Keywords: hydrogen evolution reaction, electrocatalyst, platinum nanoparticle, carbon foam, 3D support

INTRODUCTION

Water electrolysis offers the potential to produce clean H_2 sustainably from renewable electricity and water (Esposito et al., 2012; Chen et al., 2016; Jia et al., 2016). To design high-efficiency electrolyzers, highly active stable electrocatalysts are needed that can operate without corrosion in either strong acids or strong bases (Chen et al., 2018; Fu et al., 2018). To date, only electrocatalysts made of expensive platinum group metals (PGMs), specifically Pt, Ir, and Rh can deliver these needs (Angelo, 2007; Li et al., 2015; Zhang et al., 2015; Cheng et al., 2016; Tymoczko et al., 2016). Current practices to minimize mass loading of precious metals rely on constructing catalysts in the form of nanoparticles on low-cost 2D carbon supports (e.g., carbon cloth or carbon paper), with state-of-the-art commercial catalysts having a PGM mass loading of ∼0.1–1 mg_{PGM}/cm^2 (Friedrich et al., 2004; Tymoczko et al., 2016; Park et al., 2018). However, for wide-spread practical applications, the target PGM loading level should be <0.125 mg_{PGM}/cm^2 (Benjamin et al., 2017). It is to be noted that considerable amount of revolutionary work has been dedicated to the development of earth-abundant catalysts for water electrolysis for some years (Cabán-Acevedo et al., 2015; Callejas et al., 2016; Liu et al., 2016; Tang et al., 2017). However, their activity and stability at present state are not sufficiently advanced to be performance-competitive (Faber et al., 2014).

Use of macroporous open-pore 3D catalyst supports (e.g., foam architecture; **Figure 1**) has been recommended to improve catalyst utilization efficiency and lower the PGM metal loadings (Li et al., 2015; Pierozynski and Mikolajczyk, 2016). These foams have pore sizes ranging from 0.2 to 5 mm and can serve as both current collectors and as supports to load catalysts (Xing et al., 2011; Huang et al., 2017). Compared to traditional 2D supports, 3D open-pore foam architecture provides large surface area, enhanced electrolyte penetration, and gas diffusion, excellent structural integrity, and fast 3D electron transfer pathways (Friedrich et al., 2004; Aldalbahi et al., 2018). Additionally, the continuous, open-pore architecture of the 3D foams, is expected to provide excellent mass and ion-transport to and from the catalyst site, significantly improving the bubble convection when operated at high water electrolysis current densities. Recently, several approaches have been demonstrated to load PGMs on 3D open-pore metallic foams. For example, van Drunen et al. (2014) deposited platinum nanoparticles electrolessly on Ni foam and evaluated its performance for different electrocatalytic reactions. Li et al. (2015) demonstrated successful deposition of complete-monolayer of Pt on a 3D nickel foam substrate using Au or Ag buffer layer for hydrogen evolution reaction.

While many possible 3D foams are amenable to loading electrocatalyst, for large-scale cost-effective production of catalyst/support assemblies, the support should be made of low-cost materials and should be highly resistant to chemical and electrochemical corrosion. In this regard, carbon foam supports are of particular interest due to their low-cost and excellent chemical stability. In fact, 3D carbon foams (CF) have been used successfully as current collectors for microbatteries (Johns et al., 2011), metal ion removal (Friedrich et al., 2004), supercapacitors (Fischer et al., 1997), and enzymatic fuel cells (Kizling et al., 2017). However, to the best of our knowledge, no report exists on optimizing PGM loading on 3D carbon foams and benchmarking its electrocatalytic activity for important reactions such as hydrogen evolution reaction (HER).

In the present work, we synthesize uniformly dispersed Pt nanoparticles on inexpensive 3D open-pore carbon foam support using electrodeposition and optimize its catalytic activity for HER reaction. We elucidate the dependence of Pt nanoparticle diameter, density, and mass loading on electrodeposition potential and deposition charge density. The Pt/CF catalyst with loading as low as 0.06 mg/cm^2 (∼10-fold lower than state-of-the-art commercial electrodes) yield the highest mass and surface area specific activity that is six and 67 times the activity of commercial Pt/C catalyst tested under similar conditions. Moreover, the Pt/CF catalyst also demonstrate highly stable HER activity in acidic conditions after a continuous long-term chronopotentiometry run at high current density (@100 mA/cm^2).

MATERIALS AND METHODS

Materials

Reticulated vitreous carbon (RVC) foam substrates with 100 pores per inch (PPI) and a specific surface area of 2×10^3 square feet per cubic foot, and 1.96×10^{-2} ohms sq^{-1} electrical surface resistance were purchased from McMaster-Carr (Duocell RVC Foam, ERG Aerospace). Commercial Pt/C cloth (0.5 mg/cm^2, 67 m^2/g_{Pt}, 20 wt%, E-TEK; Muthuswamy et al., 2013) and bare carbon cloth were purchased from Fuel Cell Store. All chemicals were purchased from Fisher Scientific (sodium chloride (NaCl, 99%), potassium hydroxide (KOH, 86.3%), sulfuric acid (H_2SO_4, 96.3%), hydrochloric acid (HCl, 36.5%), nitric acid (HNO_3, 69%), potassium tetrachloroplatinate (K_2PtCl_4, 99.9%), and copper sulfate pentahydrate ($CuSO_4 \bullet 5H_2O$, 98%). The standard solutions for Pt and Rh detection using ICP-MS (1,000 ppm platinum and 1,000 ppm rhenium) were purchased from Inorganic Ventures. All solutions for deposition and catalyst testing were prepared using ultrapure water (18 $M\Omega$/cm).

Pt Nanoparticle Deposition on Carbon Foam Surface

A room temperature three-electrode electrochemical set-up was used for Pt electrodeposition with carbon foam as the working electrode, Pt wire as the counter electrode and a Saturated Calomel Electrode (SCE) as the reference electrode. The plating solution was made of 0.5 M sodium chloride and 3 mM potassium tetrachloroplatinate (K_2PtCl_4) with pH adjusted to 4 using dilute HCl. All depositions were carried out on a new carbon foam substrate with dimensions cut to $2 \times 1 \times 0.3$ cm. The Pt nanoparticles were deposition following a potentiostatic double pulse deposition technique (**Figure S1**). In this technique, each pulse consisted of a constant potential deposition period (till 15 mC of charge was passed) and a constant potential surface activation period (5 s). The target deposition potentials were chosen from linear sweep voltammetry curves (**Figure S2**). The target deposition charge density was obtained by controlling the

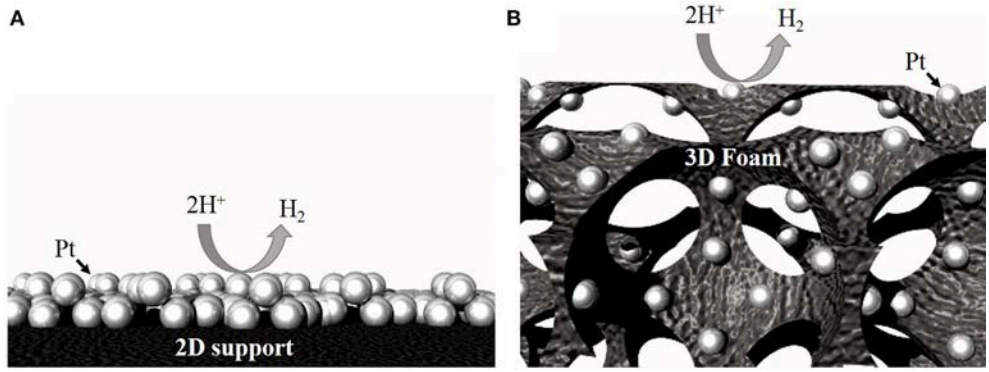

FIGURE 1 | Schematic showing higher accessibility for the same number of particles on a 3D support **(B)** compared to a 2D support **(A)**.

total number of pulses. Four different deposition potentials [-0.2,−0.3,−0.4, and−0.5 V vs. SCE (V_{SCE})] and four different deposition charge densities (50, 100, 150, and 300 mC/cm^2) were investigated for this study. A potential of 0 V_{SCE} was chosen as the surface activation potential for all depositions to remove any adsorbed chloride and hydrogen atoms from the deposited Pt surface.

Characterization

Scanning Electron Microscopy (SEM) was done by using a field emission SEM (Hitachi S-4800), and the particles size and density were determined by using Image-J software. For each sample, three separate areas were analyzed with Image-J to give an average for the particles diameter and density. A low-magnification SEM image of carbon foam loaded with Pt nanoparticles is shown in **Figure S3**.

Mass loading of Pt was determined using inductively coupled plasma mass spectrometry (ICP-MS). One square centimeter area of the carbon foam with deposited Pt particles was digested in 1 mL of aqua regia. The aqua regia was prepared from concentrated hydrochloric acid and concentrated nitric acid that was combined in a molar ratio of 3:1 HCl:HNO_3. This was diluted by a factor of 10,000 to bring the concentration to the ppb range. Samples were analyzed on a Thermo X-series II ICP-MS instrument. All samples were doped with a known amount of Re to correct for instrumental drift. Multiple Pt isotopes were measured to verify that polyatomic interferences were not an issue with these samples. Calibration curves were made for each isotope (^{194}Pt, ^{195}Pt, ^{196}Pt) (**Figure S4**). All resulted in consistent concentrations, and the final values were calculated from a weighted average using the natural abundances of the three major platinum isotopes.

Electrochemical active surface area (ECSA) of Pt nanoparticles on carbon foam was calculated using copper underpotential deposition method (Cu-UPD) technique. The Pt loaded carbon foam served as the working electrode, Pt wire served as the counter electrode and Ag/AgCl as the reference electrode. The Cu-UPD experiments were carried out in 0.001 M $CuSO_4$in 0.5 M H_2SO_4 solution. The electrodes were cycled between the potential limits of 0.15–0.8 vs. $V_{Ag/AgCl}$ at a scan rate of 20 mV/s until the charges associated with Cu stripping remained constant for each cycle (**Figure S5**). By comparing this value to the charge of the formed Cu monolayer on polycrystalline Pt (410 μC/cm^2), and by knowing the total mass loading of Pt, the ECSA can be calculated using the following equation:

$$ECSA_{Pt}\left(\frac{cm^2}{mg_{Pt}}\right) = \left[\frac{Q_{Cu-UPD\ (\mu C)}}{410\frac{\mu C}{cm^2}\ X\ mg_{Pt}}\right]$$

Hydrogen Evolution Reaction Experiments

Platinum nanoparticle-loaded carbon foam samples were tested for hydrogen evolution reaction (HER) in acid (1 M H_2SO_4) and alkaline (1 M KOH) electrolyte. A three-electrode electrochemical set-up was used for all HER studies. The carbon foam with Pt loading was used as the working electrode, pure platinum wire as the counter electrode, Ag/AgCl as a reference electrode for the acidic electrolyte, and Hg/HgO as the reference electrode for the alkaline electrolyte. Cyclic voltammetry (CV) runs were done at a scan rate of 100 mV/s. For all representative CV curves shown in this study, the electrodes were cycled for at least 30+ times (totaling 50–70 C/cm^2) which allowed for a stable and repeatable curve. The overpotential values were calculated from the final cycle of the CV graphs. All CV runs were compensated for iR losses. For stability tests, a constant cathodic current density of 100 mA/cm^2 was applied and the potential was monitored as a function of time (chronopotentiometry technique). Similar strategy of cycling the electrodes as explained above was practiced prior to all stability tests.

RESULTS AND DISCUSSION

Effect of Deposition Potential on Pt Nanoparticle Size and Density

Figures 2A–D shows representative top-down scanning electron microscopy (SEM) images of Pt nanoparticles deposited on carbon foam for different deposition potential pulses. Four different deposition potentials,−0.2,−0.3,−0.4, and−0.5 V vs. Standard Calomel Electrode (V_{SCE}) (from linear sweep voltammetry; **Figure S2**) were chosen for this study. As shown

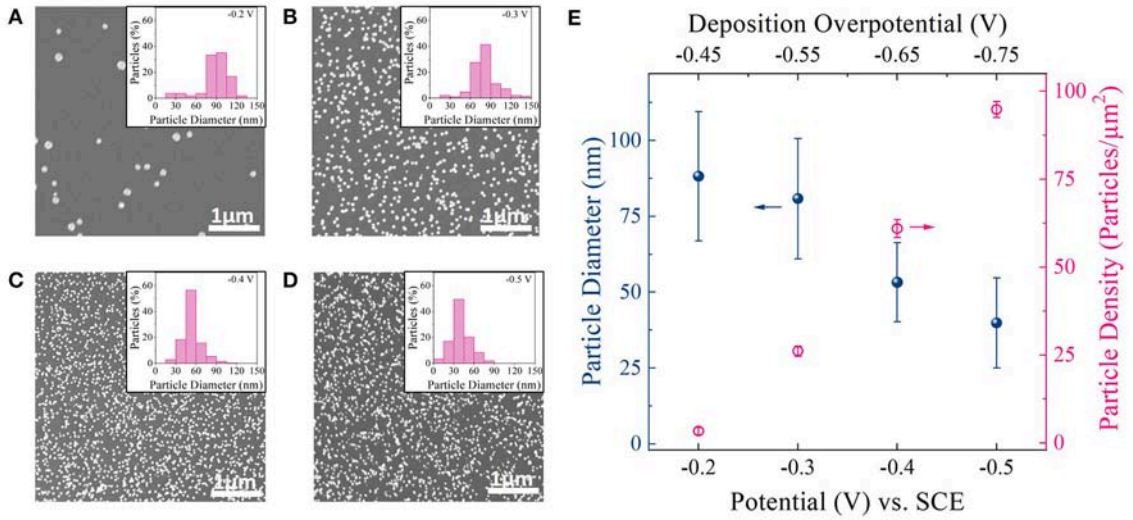

FIGURE 2 | (A–D) SEM images of Pt particles on carbon foam supports deposited at -0.2 V_{SCE}, -0.3 V_{SCE}, -0.4 V_{SCE}, and -0.5 V_{SCE}. Inset: Histogram showing particle size distribution for each deposition potential. **(E)** Average diameter and density of Pt nanoparticles deposited at different deposition potential pulses. Top x-axis: Deposition overpotential (η) value for Pt deposition.

in **Figure S2**, these deposition potentials are well negative to the equilibrium potential for Pt deposition ($+0.25$ V_{SCE}) (Liu et al., 2012). Deposition potentials more negative than -0.5 V_{SCE} resulted in hydrogen evolution ($E^0_{H+/H2,pH=4} = -0.48$ V_{SCE}) during Pt deposition and consequently was not chosen. All depositions were carried for an equivalent deposition charge density of 150 mC/cm^2. Corresponding i-t deposition transients for each deposition potential is shown in **Figure S6**.

The SEM images (**Figures 2A–D**) revealed well dispersed Pt nanoparticles on the carbon surface for all deposition potentials. **Figure 2E** shows a plot of particle diameter and density as a function of deposition potential as measured from ImageJ software. Corresponding histogram plots are shown in the inset of SEM images. From the SEM images, histogram plots, and **Figure 2E** one could observe a clear decrease in particle size and increase in particle density as the deposition overpotential increased. This suggests that at low electrodeposition overpotential (-0.2 V_{SCE}), the nucleation rate is slower than the rate of the nucleus growth on the carbon foam surface (Hussain et al., 2017). That is, it is more favorable for Pt to deposit on the existing nuclei and grow before the next nucleus is formed on carbon surface (heterogeneous reduction), resulting in larger and fewer number of Pt nanoparticles (**Figure 2A**). With the increase in deposition overpotentials (-0.3, -0.4, and -0.5 V_{SCE}), the rate of nucleation increases resulting in densely distributed smaller Pt nanoparticles (**Figures 2B–D**). In fact both particle diameter and particle density follows classical heterogeneous nucleation and growth mechanism (Pei et al., 2017), with particle diameter decreasing linearly with deposition overpotential and particle density increasing to the cube power with increasing deposition overpotential (**Figure S7**).

Since for electrocatalysis application, high surface coverage of smaller Pt nanoparticles on a given support surface directly translates to high geometric activity, we chose to work with higher deposition overpotentials for further catalyst optimization studies. Particularly -0.4 V_{SCE} was chosen as our optimal deposition potential, since it provided the highest Pt surface area to support surface area among the deposition potentials chosen for this study (**Figure S8**).

Effect of Deposition Charge on Pt Mass Loading

To address the challenging cost targets associated with Pt, it is very important to significantly reduce Pt mass loading without compromising its geometric and specific activity. Mass loading of Pt on CF was controlled by simply tuning the deposition time (mass deposited is directly proportional to the charge passed). Four different charge densities were chosen to electrodeposit Pt on CF surface (50, 100, 150, and 300 mC/cm^2; denoted hereafter as Pt/CF_{50}, Pt/CF_{100}, Pt/CF_{150}, and Pt/CF_{300}). These deposition charge densities were selected such that the Pt mass loading for the highest deposition charge (Pt/CF_{300}) was lower than the recommended target Pt loading level of <0.125 mg_{Pt}/cm^2 for electrocatalytic applications. As discussed above, a deposition potential pulse of -0.4 V_{SCE} was selected for all these studies.

Table 1 column 2 summarizes Pt mass loading (mg_{Pt}/cm^2) results measured using inductively coupled plasma mass spectrometry (ICP-MS; see Materials and Methods section) for different deposition charge densities. As expected, the Pt mass loading increased with increasing deposition charge density, varying from 0.0075 mg_{Pt}/cm^2 for Pt/CF_{50} to 0.1015 mg_{Pt}/cm^2 for Pt/CF_{300} sample.

Figures 3B–E shows SEM images of Pt deposition progression as a function of deposition charge density. **Figure 3A** is a plot of particle density and diameter as a function of mass loading. For Pt/CF_{50}, the particle density on average was 66 particles/μm^2 (**Figure 3A** red trace), and the particles remained sparsely distributed on the carbon foam surface. Doubling

the deposition charge density increased the particle density by ~27% to 84 particles/μm^2 while effectively keeping the average particle diameter constant (43 nm; **Figure 3A** black blue trace). This observed increase in particle density with deposition charge signifies that the Pt deposition on 3D foam follows a progressive nucleation and growth process. That is, as deposition time increases, more and more Pt nuclei are formed at the carbon surface, increasing the surface area of Pt per unit volume of the catalyst support. This is consistent with the trend observed for measured surface area (cm^2_{Pt}) of the catalyst which shows an increase with increasing deposition charge density (**Table 1** Column 4). For an instantaneous nucleation and growth mechanism, the particle density should remain relatively constant as the deposition charge increases (Grujicic and Pesic, 2002).

The histogram plots for the particle diameter (**Figures 3F–I**) further elucidates the Pt deposition mechanism with increasing deposition charge. A log-normal distribution was observed for each loading level. A log-normal distribution is expected when nucleation dominates growth, which increases the number of small particles with time with simultaneous growth of larger particles deposited initially. The above observation is very similar to what was observed by Teran et al. (2010) who calculated the grain size distribution for a random nucleation and growth process. However, with further increase in mass loading (Pt/CF_{300}) the particle density starts to decrease (**Figure 3A**, red trace), possibly due to coalescence of the neighboring particles as evidenced by the increase in average particle diameter from 43 to 70 nm (**Figure 3A**, blue trace). The coalescence of the particles observed for Pt/CF_{300} is also evident from the histogram plot **Figure 3H**, where the peak of the distribution shifts to the right with a larger spread.

TABLE 1 | Tabulated data of each platinum loading level using a 1 cm^2 geometric area of Pt/CF.

Sample	Mass Pt (mg_{Pt}/cm^2)	Electrochemical active surface area		Pt surface area (cm^2_{Pt})
		(m^2_{Pt}/g_{Pt})	(cm^2_{Pt}/mg_{Pt})	
Pt/CF_{50}	0.0075	11.066	110.66	0.83
Pt/CF_{100}	0.0325	5.877	58.77	1.91
Pt/CF_{150}	0.059	6.322	63.22	3.73
Pt/CF_{300}	0.1015	6.732	67.32	6.80

HER Activity

The effect of Pt mass loading on HER activity in acidic and alkaline conditions was evaluated using a standard three-electrode electrochemical cell. **Figure 4A** shows geometric HER current densities (mA/cm^2_{geo}) obtained in 1 M H_2SO_4 for Pt/CF samples by sweeping voltages from 0.1 V vs. reversible

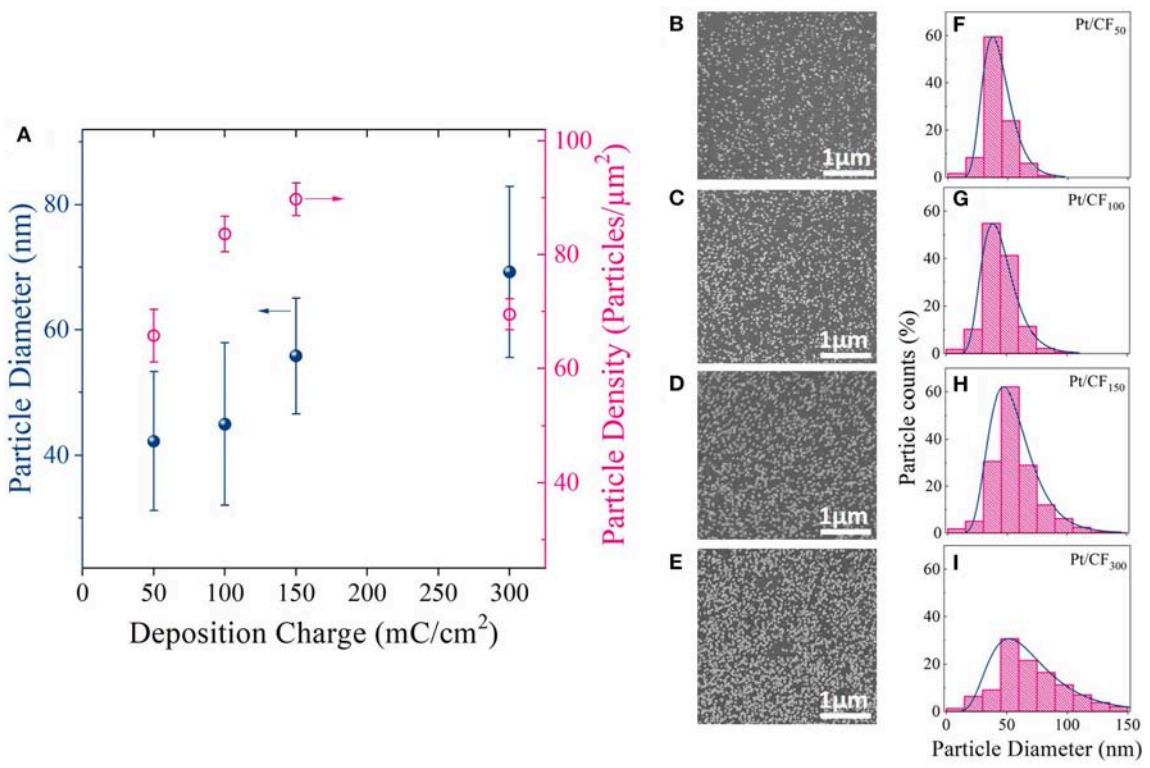

FIGURE 3 | (A) Average Pt particle diameter and density for different deposition charge densities (50, 100, 150, and 300 mC/cm^2). The deposition potential was kept constant at −0.4 V_{SCE}. **(B–E)** SEM images and **(F–I)** corresponding histogram plots showing the particle diameter distribution for each charge density.

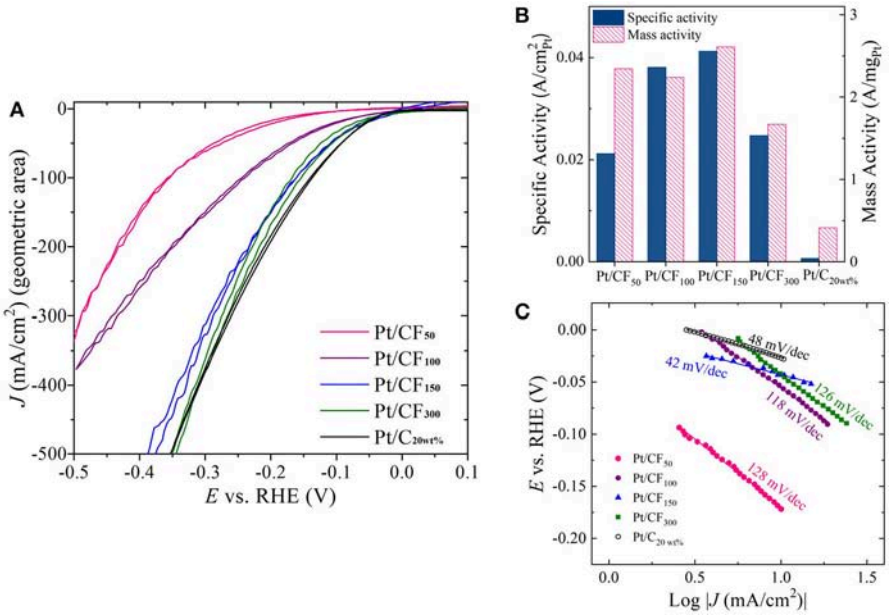

FIGURE 4 | (A) Cyclic voltammetry (CV) sweeps showing HER activity in 1 M H_2SO_4 for four Pt loading levels (50, 100, 150, and 300 mC/cm^2) as well as commercial Pt-loaded carbon cloth. **(B)** Plot of specific activity and mass activity of each catalyst at $\eta = 200$ mV. **(C)** Tafel slope plots constructed for each Pt loading level.

hydrogen electrode (V_{RHE}) to −0.5 V_{RHE} at a rate of 100 mV/s (see the Materials and Methods section for more details). All Pt/CF electrodeposited samples were directly used as working electrodes for the HER tests. Commercial Pt/carbon cloth with 20 wt. % Pt and mass loading of 0.5 mg_{Pt}/cm^2 (denoted hereafter as $Pt/C_{20wt\%}$) was also selected as a reference point and studied under the same conditions. For all measurements, the HER currents were measured as a function of ohmic-corrected potential. As shown in **Figure 4A**, the Pt/CF catalysts demonstrated increasing HER currents with increase in Pt mass loading. Particularly, Pt/CF_{150} and Pt/CF_{300} catalyst showed excellent HER activity, as evidenced by the very small overpotential (η) of 370 and 340 mV needed to deliver a high current density of 500 mA/cm^2. **Figure S10** provides cyclic voltammograms from the 10th CV cycle for each Pt loading with its corresponding Tafel slope analysis. These values are comparable to state-of-the-art commercial 2D $Pt/C_{20wt\%}$ sample (**Figure 4A**, black trace). It should be noted that the Pt/CF_{150} and Pt/CF_{300} samples had Pt mass loading 10- and 5-fold lower than the commercial $Pt/C_{20wt\%}$electrode and HER results were obtained under quiescent electrode/electrolyte conditions (no vigorous stirring and/or electrolyte flow).

Although geometric current density serves as a practical metric to compare catalyst performance, for optimal catalyst design it is important to compare mass activity (A/mg_{Pt}) and specific activity (A/cm^2_{Pt}) as a function of Pt loading. **Figure 4B**, red bars show mass activity measured at $\eta = 200$ mV for different deposition charge densities. The mass activity of Pt/CF samples remained more or less independent to initial deposition charge density, with the highest mass activity of 2.61 A/mg_{Pt} obtained for Pt/CF_{150}, which is 6.3 times higher than that of the state-of-the-art commercial $Pt/C_{20wt\%}$ (0.41 A/mg_{Pt}). The mass activity decreased with further Pt mass loading (Pt/CF_{300}; 1.67 A/mg_{Pt}), possibly due to the reduction in Pt mass utilization due to coalescence of smaller particles as discussed above (**Figures 3E,I**). However, we note that the lowest mass activity obtained for Pt/CF_{300} (1.67 A/mg_{Pt}) is still four times higher than that of the commercial catalyst.

The specific activity (A/cm^2_{Pt}) for each catalyst was determined from its mass activity (A/mg_{Pt}) and electrochemical active surface area (ECSA; cm^2_{Pt}/mg_{Pt}). The measured ECSA for different mass loading (in cm^2_{Pt}/mg_{Pt} and $m^2_{Pt}/g_{Pt)}$ is summarized in **Table 1** Column 3. Cu-underpotential (Cu-UPD) deposition was used to determine the ECSA assuming a specific charge of 420 $\mu C/cm^2_{Pt}$ per monolayer Cu deposited on the Pt surface (see Materials and Methods Section). No Cu-UPD was observed on bare carbon foam substrate. The specific activity of the catalyst increased with Pt loading with Pt/CF_{150} catalyst showing nearly 67 times greater specific activity compared to commercial $Pt/C_{20wt\%}$ catalyst (**Figure 4B**, blue bars). The specific activity decreased with further increase in deposition charge density (Pt/CF_{300}) likely due to decreased Pt mass utilization caused by nanostructure/morphology changes as discussed above. The Tafel analysis (**Figure 4C**) gave Tafel slope values of 128, 118, 42, and 126 mV/dec for Pt/CF_{50}, Pt/CF_{100}, Pt/CF_{150}, and Pt/CF_{300} when plotted for current density ranges 3–30 mA/cm^2. The Tafel slope for Pt/CF_{150} was lower than commercial $Pt/C_{20wt\%}$ (48 mV/dec), which is consistent with this catalyst having the highest mass and specific activity. When tested in alkali media (1M KOH), the Pt/CF catalysts exhibited similar trends to that observed in acidic electrolyte (**Figures S9, S11**). The Pt/CF_{150} catalyst exhibited the best catalytic performance with a specific activity of 0.126 A/cm^2_{Pt} (@$\eta = 400$ mV) with a reasonably small Tafel slope (105 mV/dec) for alkaline conditions. XRD Data

for different Pt loading levels is provided in **Figures S12, S13** provides current density-volage profile for Pt/CF_{150} sample with Graphite as the counter electrode.

To better understand the role of 3D carbon foam substrates on observed HER enhancement, electrochemical tests were carried out on 2D carbon cloth with Pt mass loading similar to the best performing Pt/CF electrode (Pt/CF_{150}). The Pt was loaded on the 2D carbon cloth following the exact electrodeposition protocols. The amount of Pt deposited was controlled by tuning the deposition charge and HER tests were carried out using the same electrochemical set-up with similar reactor volume and electrode positioning. As shown in **Figure 5A**, for the same mass loading, the Pt/C and Pt/CF electrode (represented as Pt/C_{150} and Pt/CF_{150}) have similar overpotential values up to current densities of 75 mA/cm^2 (see **Figure S14** for Tafel slope analysis). However, with increasing current densities, the Pt/CF_{150} behaved superior compared to its 2D counterpart. For example, to achieve 400 mA/cm^2, the Pt/CF_{150} required a modest overpotential of 350 mV compared to 500 mV for Pt/C_{150} electrode. No significant HER currents were observed on bare carbon cloth (C_{Bare}). The observed superior performance for Pt/CF_{150} at higher current densities further corroborates that 3D CF substrate provides better bubble convection and access to catalyst sites compared to 2D carbon cloth. We also normalized the performance of both Pt/C_{150} and Pt/CF_{150} electrode by their corresponding actual catalyst loadings and found that the difference in mass activity between Pt/CF_{150} and Pt/C_{150} increases with increasing HER overpotential (**Figure 5B**). At an overpotential of 400 mV ($-0.4V_{RHE}$), the mass activity of Pt/CF was 8.75 A/mg_{Pt}, almost 70% higher than that of Pt/C electrode.

Long-Term Stability

To evaluate the long-term stability of the Pt/CF catalysts, accelerated degradation studies were performed for the best performing Pt/CF_{150} catalyst in acidic conditions. The stability was assessed by monitoring the increase in overpotential in 1 M H_2SO_4 for an applied current density of 100 mA/cm^2. No *iR* compensation was carried out for the stability runs. **Figure 6** shows that after 60 hours of continuous operation the overpotential increased by less than 16 mV (7%) in acid. It is to be noted that the current density used here for stability measurement is 10-fold higher than that of the most reported literature values for low PGM loaded materials (Li et al., 2015). The catalysts after stability testing were characterized by SEM images, which showed no obvious change to the structural morphology (particle diameter and density), indicating that the Pt nanoparticles are extremely stable and bound strongly to the carbon foam support even under high current density operation.

In conclusion, we demonstrated a simple solution-processed electrodeposition technique to load low amounts of Pt nanoparticles on low-cost, high surface area 3D carbon foam support for HER reaction. We established the dependence of particle diameter and density as a function of deposition potential and charge density and investigated the HER activity

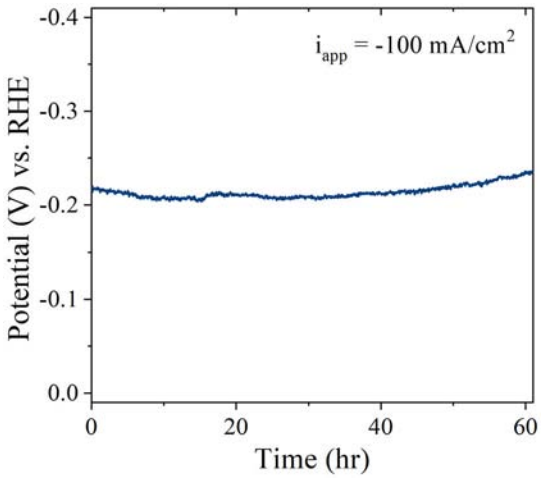

FIGURE 6 | Stability of Pt/CF_{150} operating at−100 mA/cm^2 in 1 M H_2SO4.

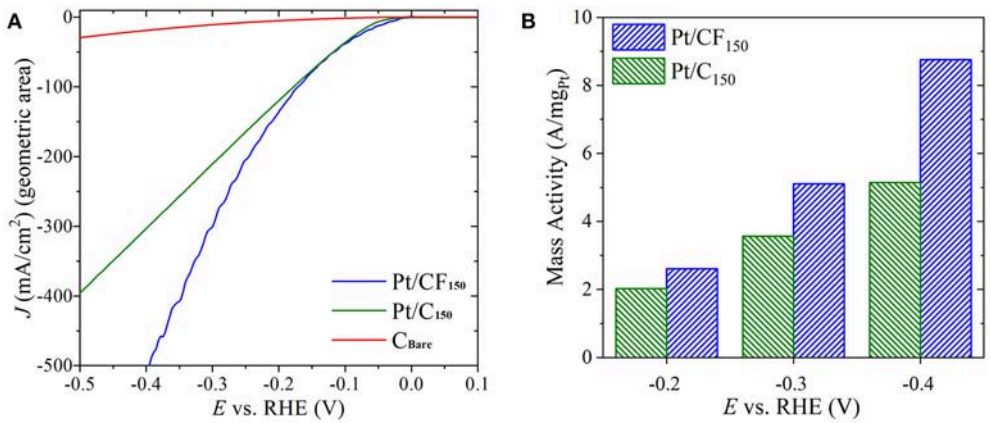

FIGURE 5 | (A) Forward scan from cyclic voltammetry (CV) sweeps showing HER activity in 1 M H_2SO_4 for Pt loaded on 3D carbon foam with 150 mC/cm^2 loading (Pt/CF_{150}), Pt loaded on carbon cloth with 150 mC/cm^2 loading (Pt/C_{150}), and bare carbon cloth (C_{Bare}). The potential is iR-compensated. **(B)** Mass activity of Pt/CF_{150} and Pt/C_{150} at three overpotentials.

of the Pt-loaded carbon foams. All synthesized Pt/CF catalysts exhibited excellent mass activities that are superior to the state-of-the-art commercial Pt/C catalyst. For the best performing Pt/CF catalyst, the mass and specific activity were 6.3 and 67 times higher than commercial Pt/C catalysts. Also, the best performing catalyst showed excellent stability with minimal degradation when operated at high current densities. We attribute this significant improvement in catalytic activity observed for Pt/CF samples to the following reasons. (i) The electrodeposition technique allows binder-free deposition of Pt directly on the electroactive site of the support facilitating efficient charge transport across support/catalyst interface. (ii) Enhanced mass transport: the 3D open-pore foam architecture provides enhanced electrolyte penetration and improved diffusion of H^+ ions and H_2 to and from the Pt nanoparticle surface. (iii) Increased surface area of the 3D carbon foam providing easy access to the catalytic sites.

AUTHOR CONTRIBUTIONS

AG and JK designed and carried out all the synthesis, characterization, and data analysis. BH performed Tafel analysis. AR, WC, and JL assisted AG and JK with material synthesis and microscopy characterization. DP performed ICPMS measurements. SM supervised the work, designed experiments with AG and JK. All authors were involved in manuscript writing.

ACKNOWLEDGMENTS

This work was partially supported by Desalination and Water Purification Research and Development Program, Bureau of Reclamation under Agreement No. R16AC00126. JK and WC are grateful for the support by The University of Iowa through Sponsored Research Agreement with HyperSolar Inc., under grant number 18786500. SM and AR also acknowledge the support of the University of Iowa startup funds.

SUPPLEMENTARY MATERIAL

The Supplementary Material for this article can be found online at: https://www.frontiersin.org/articles/10.3389/fchem.2018.00523/full#supplementary-material

REFERENCES

Aldalbahi, A., Rahaman, M., Almoigli, M., Meriey, A. Y., and Alharbi, K. N. (2018). Improvement in electrode performance of novel SWCNT loaded three-dimensional porous RVC composite electrodes by electrochemical deposition method. *Nanomaterials* 8:19. doi: 10.3390/nano8010019

Angelo, A. C. D. (2007). Electrocatalysis of hydrogen evolution reaction on Pt electrode surface-modified by S-2 chemisorption. *Int. J. Hydrogen Energy* 32, 542–547. doi: 10.1016/j.ijhydene.2006.06.052

Benjamin, T., Borup, R., Garland, N., Gittleman, C., Habibzadeh, B., Hirano, S., et al. (2017). *Fuel Cell Technical Team Roadmap*. Energy.gov (Office of Energy Efficiency & Renewable Energy).

Cabán-Acevedo, M., Stone, M. L., Schmidt, J. R., Thomas, J. G., Ding, Q., Chang, H. C., et al. (2015). Efficient hydrogen evolution catalysis using ternary pyrite-type cobalt phosphosulphide. *Nat. Mater.* 14, 1245–1251. doi: 10.1038/Nmat4410

Callejas, J. F., Read, C. G., Roske, C. W., Lewis, N. S., and Schaak, R. E. (2016). Synthesis, characterization, and properties of metal phosphide catalysts for the hydrogen-evolution reaction. *Chem. Mater.* 28, 6017–6044. doi: 10.1021/acs.chemmater.6b02148

Chen, G. F., Luo, Y. R., Ding, L. X., and Wang, H. H. (2018). Low-voltage electrolytic hydrogen production derived from efficient water and ethanol oxidation on fluorine-modified FeOOH anode. *ACS Catal.* 8, 526–530. doi: 10.1021/acscatal.7b03319

Chen, L., Dong, X., Wang, Y., and Xia, Y. (2016). Separating hydrogen and oxygen evolution in alkaline water electrolysis using nickel hydroxide. *Nat. Commun.* 7:11741. doi: 10.1038/ncomms11741

Cheng, N., Stambula, S., Wang, D., Banis, M. N., Liu, J., Riese, A., et al. (2016). Platinum single-atom and cluster catalysis of the hydrogen evolution reaction. *Nat. Commun.* 7:13638. doi: 10.1038/ncomms13638

Esposito, D. V., Hunt, S. T., Kimmel, Y. C., and Chen, J. G. (2012). A new class of electrocatalysts for hydrogen production from water electrolysis: metal monolayers supported on low-cost transition metal carbides. *J. Am. Chem. Soc.* 134, 3025–3033. doi: 10.1021/ja208656v

Faber, M. S., Lukowski, M. A., Ding, Q., Kaiser, N. S., and Jin, S. (2014). Earth-abundant metal pyrites (FeS2, CoS2, NiS2, and their alloys) for highly efficient hydrogen evolution and polysulfide reduction electrocatalysis. *J. Phys. Chem. C* 118, 21347–21356. doi: 10.1021/jp506288w

Fischer, U., Saliger, R., Bock, V., Petricevic, R., and Fricke, J. (1997). Carbon aerogels as electrode material in supercapacitors. *J. Porous Mater.* 4, 281–285. doi: 10.1023/A:1009629423578

Friedrich, J. M., Ponce-De-Leon, C., Reade, G. W., and Walsh, F. C. (2004). Reticulated vitreous carbon as an electrode material. *J. Electroanal. Chem.* 561, 203–217. doi: 10.1016/j.jelechem.2003.07.019

Fu, L., Yang, F., Cheng, G., and Luo, W. (2018). Ultrathin Ir nanowires as high-performance electrocatalysts for efficient water splitting in acidic media. *Nanoscale* 10, 1892–1897. doi: 10.1039/c7nr09377b

Grujicic, D., and Pesic, B. (2002). Electrodeposition of copper: the nucleation mechanisms. *Electrochim. Acta* 47, 2901–2912. doi: 10.1016/S0013-4686(02)00161-5

Huang, L. R., Hou, Y. P., Yu, Z. B., Peng, Z. B., Wang, L., Huang, J., et al. (2017). Pt/Fe-NF electrode with high double-layer capacitance for efficient hydrogen evolution reaction in alkaline media. *Int. J. Hydrogen Energy* 42, 9458–9466. doi: 10.1016/j.ijhydene.2017.02.055

Hussain, S., Erikson, H., Kongi, N., Merisalu, M., Rahn, M., Sammelselg, V., et al. (2017). Platinum particles electrochemically deposited on multiwalled carbon nanotubes for oxygen reduction reaction in acid media. *J. Electrochem. Soc.* 164, F1014–F1021. doi: 10.1149/2.0091712jes

Jia, J., Seitz, L. C., Benck, J. D., Huo, Y., Chen, Y., Ng, J. W., et al. (2016). Solar water splitting by photovoltaic-electrolysis with a solar-to-hydrogen efficiency over 30. *Nat. Commun.* 7:13237. doi: 10.1038/ncomms13237

Johns, P., Roberts, M., and Owen, J. (2011). Conformal electrodeposition of manganese dioxide onto reticulated vitreous carbon for 3D microbattery applications. *J. Mater. Chem.* 21, 10153–10159. doi: 10.1039/c0jm04357e

Kizling, M., Dzwonek, M., Olszewski, B., Bacal, P., Tymecki, Ł., Wieckowska, A., et al. (2017). Reticulated vitreous carbon as a scaffold for enzymatic fuel cell designing. *Biosens. Bioelectron.* 95, 1–7. doi: 10.1016/j.bios.2017.03.070

Li, M., Ma, Q., Zi, W., Liu, X., Zhu, X., and Liu, S. F. (2015). Pt monolayer coating on complex network substrate with high catalytic activity for the hydrogen evolution reaction. *Sci. Adv.* 1:e1400268. doi: 10.1126/sciadv.1400268

Liu, W., Hu, E., Jiang, H., Xiang, Y., Weng, Z., Li, M., et al. (2016). A highly active and stable hydrogen evolution catalyst based on pyrite-structured cobalt phosphosulfide. *Nat. Commun.* 7:10771. doi: 10.1038/ncomms10771

Liu, Y., Gokcen, D., Bertocci, U., and Moffat, T. P. (2012). Self-terminating growth of platinum films by electrochemical deposition. *Science* 338, 1327–1330. doi: 10.1126/science.1228925

Muthuswamy, N., de la Fuente, J. L., Ochal, P., Giri, R., Raaen, S., Sunde, S., et al. (2013). Towards a highly-efficient fuel-cell catalyst: optimization of Pt particle size, supports and surface-oxygen group concentration. *Phys. Chem. Chem. Phys.* 15, 3803–3813. doi: 10.1039/C3CP43659D

Park, H., Choe, S., Kim, H., Kim, D. K., Cho, G., Park, Y., et al. (2018). Direct fabrication of gas diffusion cathode by pulse electrodeposition for proton exchange membrane water electrolysis. *Appl. Surf. Sci.* 444, 303–311. doi: 10.1016/j.apsusc.2018.03.071

Pei, A., Zheng, G., Shi, F., Li, Y., and Cui, Y. (2017). Nanoscale nucleation and growth of electrodeposited lithium metal. *Nano Lett.* 17, 1132–1139. doi: 10.1021/acs.nanolett.6b04755

Pierozynski, B., and Mikolajczyk, T. (2016). Cathodic evolution of hydrogen on platinum-modified nickel foam catalyst. *Electrocatalysis* 7, 121–126. doi: 10.1007/s12678-015-0290-x

Tang, Y., Fang, X., Zhang, X., Fernandes, G., Yan, Y., Yan, D., et al. (2017). Space-confined earth-abundant bifunctional electrocatalyst for high-efficiency water splitting. *ACS Appl. Mater. Interfaces* 9, 36762–36771. doi: 10.1021/acsami.7b10338

Teran, A. V., Bill, A., and Bergmann, R. B. (2010). Time-evolution of grain size distributions in random nucleation and growth crystallization processes. *Phys. Rev. B* 81:075319. doi: 10.1103/PhysRevB.81.075319

Tymoczko, J., Calle-Vallejo, F., Schuhmann, W., and Bandarenka, A. S. (2016). Making the hydrogen evolution reaction in polymer electrolyte membrane electrolysers even faster. *Nat. Commun.* 7:10990. doi: 10.1038/ncomms10990

van Drunen, J., Pilapil, B. K., Makonnen, Y., Beauchemin, D., Gates, B. D., and Jerkiewicz, G. (2014). Electrochemically active nickel foams as support materials for nanoscopic platinum electrocatalysts. *ACS Appl. Mater. Interfaces* 6, 12046–12061. doi: 10.1021/am501097t

Xing, W., Qiao, S. Z., Wu, X. Z., Gao, X. L., Zhou, J., Zhuo, S. P., et al., (2011). Exaggerated capacitance using electrochemically active nickel foam as current collector in electrochemical measurement. *J. Pow. Sources* 196, 4123–4127. doi: 10.1016/j.jpowsour.2010.12.003

Zhang, C., Hong, Y., Dai, R., Lin, X., Long, L. S., Wang, C., et al., (2015). Highly active hydrogen evolution electrodes via co-deposition of platinum and polyoxometalates. *ACS Appl. Mater. Interfaces* 7, 11648–11653. doi: 10.1021/acsami.5b02899

Conflict of Interest Statement: The authors declare that the research was conducted in the absence of any commercial or financial relationships that could be construed as a potential conflict of interest.

Copyright © 2018 Ghanim, Koonce, Hasa, Rassoolkhani, Cheng, Peate, Lee and Mubeen. This is an open-access article distributed under the terms of the Creative Commons Attribution License (CC BY). The use, distribution or reproduction in other forums is permitted, provided the original author(s) and the copyright owner(s) are credited and that the original publication in this journal is cited, in accordance with accepted academic practice. No use, distribution or reproduction is permitted which does not comply with these terms.

frontiers in Chemistry

ORIGINAL RESEARCH
published: 09 October 2018
doi: 10.3389/fchem.2018.00476

Lithium Sulfide–Carbon Composites via Aerosol Spray Pyrolysis as Cathode Materials for Lithium–Sulfur Batteries

Noam Hart[1], *Jiayan Shi*[1], *Jian Zhang*[2], *Chengyin Fu*[1] *and Juchen Guo*[1,2*]

[1] *Department of Chemical and Environmental Engineering, University of California, Riverside, Riverside, CA, United States,*
[2] *Materials Science and Engineering Program, University of California, Riverside, Riverside, CA, United States*

We demonstrate a new technique to produce lithium sulfide-carbon composite (Li_2S-C) cathodes for lithium-sulfur batteries *via* aerosol spray pyrolysis (ASP) followed by sulfurization. Specifically, lithium carbonate-carbon (Li_2CO_3-C) composite nanoparticles are first synthesized via ASP from aqueous solutions of sucrose and lithium salts including nitrate ($LiNO_3$), acetate (CH_3COOLi), and Li_2CO_3, respectively. The obtained Li_2CO_3-C composites are subsequently converted to Li_2S-C through sulfurization by reaction to H_2S. Electrochemical characterizations show excellent overall capacity and cycle stability of the Li_2S-C composites with relatively high areal loading of Li_2S and low electrolyte/Li_2S ratio. The Li_2S-C nanocomposites also demonstrate clear structure-property relationships.

Keywords: aerosol spray pyrolysis, nanocomposites, lithium-sulfur batteries, lithium sulfide, sulfurization

OPEN ACCESS

Edited by:
Fan Zhang,
Fudan University, China

Reviewed by:
Piercarlo Mustarelli,
University of Pavia, Italy
Yuan Yang,
Columbia University, United States

***Correspondence:**
Juchen Guo
jguo@engr.ucr.edu

Specialty section:
This article was submitted to Electrochemistry, a section of the journal Frontiers in Chemistry

Received: *20 July 2018*
Accepted: *20 September 2018*
Published: *09 October 2018*

Citation:
Hart N, Shi J, Zhang J, Fu C and Guo J (2018) Lithium Sulfide–Carbon Composites via Aerosol Spray Pyrolysis as Cathode Materials for Lithium–Sulfur Batteries. Front. Chem. 6:476. doi: 10.3389/fchem.2018.00476

INTRODUCTION

Lithium-sulfur (Li-S) batteries are regarded as one of the most promising electrochemical energy storage technologies due to their low cost, environmental benignity, and outstanding theoretical capacity (Wang et al., 2013; Son et al., 2015). However, despite tremendous research and development efforts, there are still a number of challenges hindering their commercialization. Among these key challenges are the polysulfides shuttle effect and high electrolyte/sulfur ratio, which are significantly magnified by the instability of the Li metal anode (Chen J. et al., 2017; Chen S. et al., 2017; Pan et al., 2018; Wu et al., 2018). Therefore, high capacity non-Li anodes, particularly those comprised of silicon-based materials, have been proposed as replacements for Li metal in Li-S batteries (Yang et al., 2010). The use of silicon anode materials would require a pre-lithiated sulfur cathode, i.e., lithium sulfide (Li_2S). In recent years, various methods to synthesize Li_2S-carbon composite materials have been reported, including high-energy mixing Li_2S with carbon (Cai et al., 2012; Jha et al., 2015), chemical lithiation of S-C composites (Hwa et al., 2015), Li_2S-C composites synthesis *via* dissolving and precipitating Li_2S in ethanol (Wu et al., 2014a,b,c, 2015, 2016), embedding Li_2S in carbon matrix *via* Li-nitrogen interaction (Guo et al., 2013), reaction between Li metal and carbon disulfide (Tan et al., 2017), converting LiOH to Li_2S *via* sulfurization with H_2S (Dressel et al., 2016), and thermal reduction of Li_2SO_4 by carbon (Yang et al., 2013; Kohl et al., 2015; Li et al., 2015; Yu et al., 2017; Zhang et al., 2017; Ye et al., 2018). In addition, the mechanism studies on Li_2S activation and capacity degradation were also reported (Vizintin et al., 2017; Piwko et al., 2018). In this work, we report a new scalable method for synthesizing Li_2S-C composites via aerosol spray pyrolysis (ASP) followed by sulfurization.

MATERIALS AND METHODS

Materials Synthesis

Three lithium salts including lithium nitrate ($LiNO_3$), lithium acetate (CH_3COOLi) and lithium carbonate (Li_2CO_3) were used as the precursors for Li_2S with sucrose as the precursor for carbon. Each Li salt was dissolved in deionized water with sucrose at different concentrations as listed in **Table S1**. The obtained solutions were used in the ASP process.

The ASP system in this study is illustrated in **Figure S1**. The commercial aerosol generator (TSI, Model 3076) consisting of a nebulizer and a solution reservoir is attached to a diffusion dryer followed by a tubular furnace and a filter collector. The diffusion dryer was composed by two concentric tubes: The outer tube is made of 3-inch inner diameter PVC tubing and the inner tube is made of 0.5-inch diameter steel mesh with the annular space filled with porous silica gel. The aerosol of the precursor solution was generated by the nebulizer and carried through the diffusion dryer by argon gas to desiccate the water content. The resultant dry particles were continuously carried into the tube furnace heated at 850°C to produce the Li_2CO_3-C nanoparticles, which are collected with a stainless-steel filter down stream outside the tube furnace.

The synthesized Li_2CO_3-C composite is placed in an alumina boat in a tubular furnace, followed by purging with argon for an hour. The furnace was then heated to 725°C and maintained at this temperature for 5 h under a flow of 5 vol.% H_2S and 95 vol.% argon. After 5 h the flow gas was switched to pure argon and the furnace was cooled naturally to room temperature. The product was collected in an argon-filled glovebox due to the sensitivity of Li_2S to moisture.

Materials Characterization

The nitrogen adsorption-desorption isotherms of the produced composite materials were obtained with a surface area and porosity analyzer (Micromeritics ASAP2020). For a particular analysis, approximately 200 mg sample was first degassed at 150°C for 3 h, then the nitrogen adsorption-desorption isotherms were measured from 0 to 1 relative pressure. The surface area was obtained with the Brunauer-Emmett-Teller (BET) method. The crystalline species in the composites were characterized by powder X-Ray diffraction (XRD, PANalytical) with a CuKα source and a scan rate of $0.11^\circ\ s^{-1}$. Kapton tape was used to seal the Li_2S-C composites to protect Li_2S from reacting with the moisture in ambient environment during measurement. The morphology and microstructure of the composites were characterized by scanning electron microscopy (SEM) and transmission electron microscopy (TEM, Tecnai T12). Carbon content in the Li_2CO_3-C composites was measured with thermogravimetric analysis (TGA, TA Instruments). The TGA samples were held at 120°C for 30 min to remove the moisture absorbed from environment, followed by heating to 600°C at a rate of $10°C\ min^{-1}$ with an isothermal step in dry air. The carbon contents in Li_2CO_3-C_{NitS}, Li_2CO_3-C_{AceS} and Li_2CO_3-C_{CarS} (**Figure S2**) are very consistent at 20.7, 22.8, and 21.2 wt.%, respectively. Assuming complete conversion from Li_2CO_3 to Li_2S without carbon loss, the Li_2S content in Li_2S-C_{NitS}, Li_2S-C_{AceS} and Li_2S-C_{CarS} can be estimated as 70.4, 67.8, and 69.8 wt.%, respectively. The accurate Li_2S content in the Li_2S-C composites is determined as follows: 100 mg Li_2S-C was thoroughly washed 4 times using 15 mL ethanol each time in the glovebox to remove Li_2S. The obtained carbon was weighed after dried at 120°C for 8 h in the glovebox. The Li_2S content is 71.3 wt.% in Li_2S-C_{NitS}, 69.1 wt.% in Li_2S-C_{AceS}, and 71.6 wt.% in Li_2S-C_{CarS}, which all agree very well with the estimated values.

Electrode Preparation and Cell Testing

The electrode is composed of 80 wt.% of Li_2S-C composite, 10 wt.% of carbon black additive, and 10 wt.% of polystyrene as the binder. Polystyrene was selected as the binder to avoid the use of polar solvents (both protic and aprotic), most of which dissolve Li_2S to some extent. Instead, mesitylene (Sigma-Aldrich) was used as the solvent for polystyrene in the electrode slurry. The electrodes were coated on carbon-coated aluminum current collector (MTI Corporation) in the argon-filled glovebox, with the average loading of Li_2S-C composite at $2\ mg\ cm^{-2}$. The electrodes were dried overnight in argon glovebox at room temperature, followed by drying at 120°C for 4 h. The dried electrodes are assembled into 2032-type coin cells with lithium foil anode (99.9%, Alfa Aesar) and Celgard® 2,500 separator. The electrolyte used in this study is 1M lithium bis(trifluoromethanesulfonyl)imide (LiTFSI) solution in a mixture of 1,3-dioxolane (DOL), dimethoxyethane (DME) and 1-butyl-1-methylpyrrolidinium bis(trifluoromethanesulfonyl)imide (Pyr14TFSI) (1:3:1 by vol.) with 1.5 wt.% of $LiNO_3$. The electrolyte to Li_2S ratio (μL/mg) was kept at 10 in all coin cells testing. To activate the Li_2S-C electrode, the first anodic scan in the cyclic voltammetry (CV) was to 3.9 V vs. Li^+/Li, and the anodic limit in the following scans was 2.6 V vs. Li^+/Li. Similarly, the first charge was run at a rate of $50\ mA\ g^{-1}$ (with respect to Li_2S) to a charge cutoff of 3.5 V. Subsequent cycles are run at $117\ mA\ g^{-1}$ between 2.6 V and 1.8 V vs. Li^+/Li.

RESULTS AND DISCUSSION

During ASP synthesis, three aqueous solutions containing sucrose (as carbon precursor) and either lithium nitrate ($LiNO_3$), lithium acetate (CH_3COOLi), or lithium carbonate (Li_2CO_3), denoted as NitS, AceS, and CarS, respectively, were atomized into aerosols with a pressure-enabled atomizer. The aerosols were subsequently carried by argon gas through a diffusion dryer and a tubular furnace for pyrolysis within an inert environment. The powder X-ray diffraction (XRD) patterns in **Figure 1A** clearly indicate that the obtained composites from all three lithium salts are Li_2CO_3-C composite with comparable carbon content (20.7 wt.% in Li_2CO_3-C_{NitS}, 22.8 wt.% in Li_2CO_3-C_{AceS} and 21.2 wt.% in Li_2CO_3-C_{CarS} *via* thermalgravimetric analysis, **Figure S2**). It is worth noting that sucrose solution without the lithium salts (i.e., precursors of Li_2CO_3) completely decomposes during the same ASP without any carbon formation. This observation reveals that Li_2CO_3 serves as the nucleation sites for carbonization of sucrose in ASP (Skrabalak and Suslick, 2006). However, the formation mechanisms of Li_2CO_3 from these three Li salts are clearly

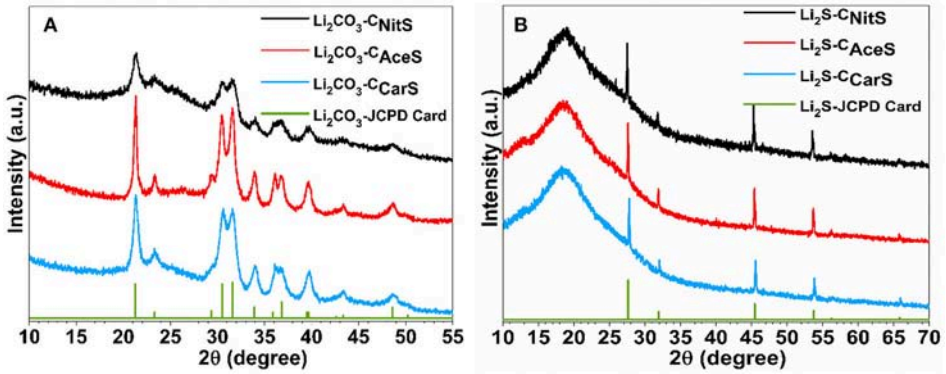

FIGURE 1 | XRD patterns of **(A)** the Li_2CO_3-C composites obtained from ASP and **(B)** the Li_2S-C composites after sulfurization.

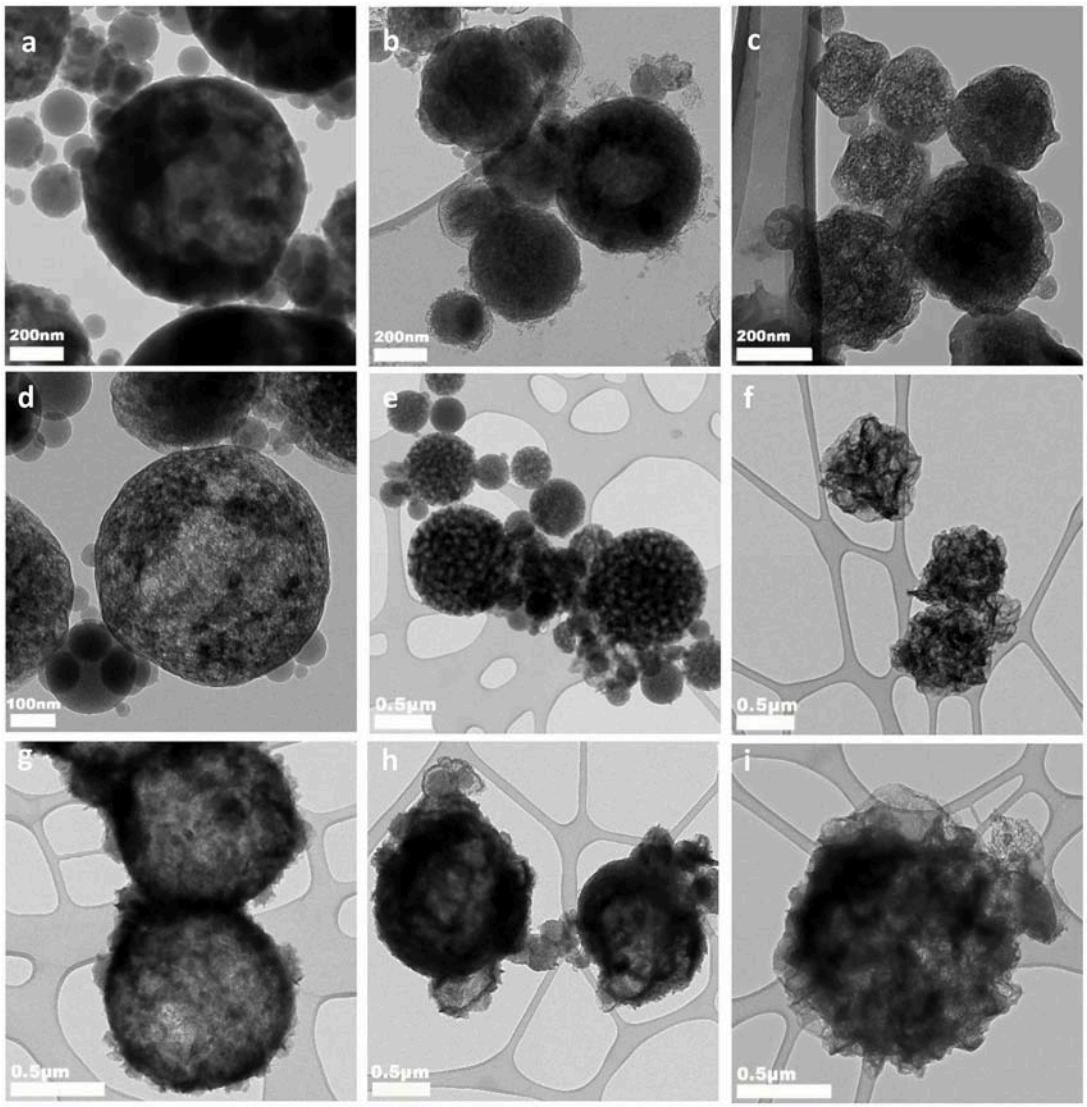

FIGURE 2 | TEM images of **(a)** Li_2CO_3-C_{NitS}, **(b)** Li_2CO_3-C_{AceS}, **(c)** Li_2CO_3-C_{CarS}; TEM images of the carbon matrix of **(d)** Li_2CO_3-C_{NitS}, **(e)** Li_2CO_3-C_{AceS}, **(f)** Li_2CO_3-C_{CarS} after Li_2CO_3 removed; and TEM images of **(g)** Li_2S-C_{NitS}, **(h)** Li_2S-C_{AceS}, **(i)** Li_2S-C_{CarS}.

different. For $LiNO_3$, its thermal decomposition is known to proceed according to **Reaction 1**: (Stern and Weise, 1969)

$$\mathbf{2LiNO_3 \rightarrow Li_2O + 2NO_x + (2.5 - x)O_2} \quad (1)$$

Based on the XRD evidence of Li_2CO_3 with the absence of crystalline Li_2O, it can be speculated that carbon dioxide (CO_2) released from pyrolysis of sucrose further reacts with Li_2O to generate Li_2CO_3 according to **Reaction 2**:

$$\mathbf{Li_2O + CO_2 \rightarrow Li_2CO_3} \quad (2)$$

CH_3COOLi undergoes thermal decomposition to generate Li_2CO_3 and acetone according to **Reaction 3**: (Roe and Finlay, 1952)

$$\mathbf{2CH_3COOLi \rightarrow Li_2CO_3 + C_3H_6O} \quad (3)$$

For the CarS precursor, Li_2CO_3 undergoes precipitation during ASP without decomposition, thus becoming directly embedded into the carbon matrix formed by the carbonization of sucrose.

Although the obtained Li_2CO_3-C composites have consistent composition and carbon content, they have distinctively different microstructures as displayed by the transmission electron microscopy (TEM) images in **Figure 2** (scanning electron microscopy images in **Figure S3**). The Li_2CO_3-C_{NitS} nanoparticles in **Figure 2A** have a hollow-shell structure with irregular-shaped interior voids due to the release of NO_x and O_2 gases during pyrolysis. The high solubility of $LiNO_3$ in water also contributes to the formation of this hollow structure. When water evaporates during ASP, $LiNO_3$ precipitates at the outer surface of the aerosol droplets following the surface precipitation mechanism (Messing et al., 1993). The microstructure of the Li_2CO_3-C_{NitS} nanoparticles is further revealed by the TEM image in **Figure 2D**, after the removal of Li_2CO_3 using diluted hydrochloric acid (HCl). The carbon matrix of Li_2CO_3-C_{NitS} has a highly porous structure after Li_2CO_3 removal, indicating that Li_2CO_3 occupies the majority of the volume in the Li_2CO_3-C_{NitS} nanoparticles. The specific surface area of Li_2CO_3-C_{NitS} before and after Li_2CO_3 removal obtained from the nitrogen adsorption-desorption isotherms (**Figure 3** and **Table S2**) is consistent with this observation: the specific surface area of Li_2CO_3-C_{NitS} is significantly increased from 26.8 to 608.2 $m^2\ g^{-1}$ after Li_2CO_3 removal.

On the other hand, Li_2CO_3-C_{AceS} nanoparticles show a denser spherical structure in **Figure 2B**. It is worth noting that the AceS precursor solution has a significantly lower sucrose/lithium salt molar ratio at 1:15 compared to 1:1.5 in NitS and 1:1.18 in CarS. Given the 22.8 wt.% carbon content in Li_2CO_3-C_{AceS}, it is believed the generated acetone during the pyrolysis of CH_3COOLi must function as the major source for carbon formation. The TEM image of the carbon matrix after Li_2CO_3 removal in **Figure 2E** reveals the distribution of Li_2CO_3 in the Li_2CO_3-C_{AceS} nanoparticles is not as uniform as in Li_2CO_3-C_{NitS}. The carbon matrix has a golf ball-like structure with relatively large pores, previously occupied by Li_2CO_3, distributed within. The specific surface area of Li_2CO_3-C_{AceS} is 76.3 $m^2\ g^{-1}$, which increases to 184.9 $m^2\ g^{-1}$ after Li_2CO_3 removal. This modest increase of surface area also indicates the relatively larger size of Li_2CO_3 compared to that of Li_2CO_3-C_{NitS}.

As shown in **Figure 2C**, the Li_2CO_3-C_{CarS} nanoparticles clearly have a different structure resembling crumpled spheres, which is due to the much lower solubility of Li_2CO_3 in water than those of $LiNO_3$ and CH_3COOLi. The concentration of Li_2CO_3 in the CarS precursor solution is 0.1 M, which is close to saturation (Zou et al., 2013). Therefore, Li_2CO_3 undergoes fast and uniform precipitation from the aerosol droplets' evaporation in ASP according to the volume precipitation mechanism (Messing et al., 1993). In addition, the ASP of CarS precursor also releases fewer gaseous species without decomposition of Li_2CO_3. Both factors contribute to better confinement and more uniform distribution of Li_2CO_3. After Li_2CO_3 removal, the carbon matrix retains its original structure with apparently higher porosity as shown in **Figure 2F**. The specific surface area of Li_2CO_3-C_{CarS} nanoparticles is 43.7 $m^2\ g^{-1}$, which increases to 443.6 $m^2\ g^{-1}$ after Li_2CO_3 removal.

The Li_2CO_3-C nanoparticles obtained *via* ASP were subsequently reacted with mixed hydrogen sulfide and argon gas (H_2S/Ar at 5/95 vol.%) at 725°C to yield the Li_2S-C composites

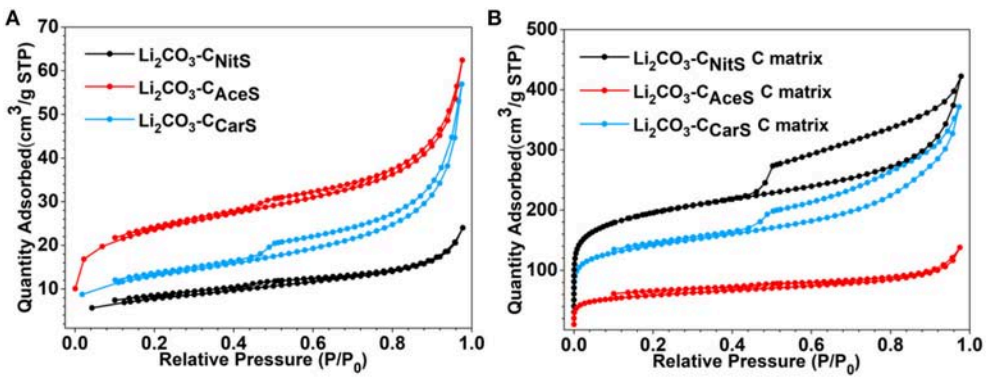

FIGURE 3 | N_2 adsorption-desorption isotherms of **(A)** Li_2CO_3-C nanoparticles and **(B)** the carbon matrix after Li_2CO_3 removal.

according to **Reaction 4**, confirmed by the XRD patterns shown in **Figure 1B**.

$$Li_2CO_3 + H_2S \rightarrow Li_2S + H_2O + CO_2 \quad (4)$$

The TEM images of the Li_2S-C composites in **Figures 2G–I** (scanning electron microscopy images in **Figure S4**) demonstrate that these nanoparticles sustain their original structures after the conversion to Li_2S from Li_2CO_3.

Figure 4 shows the first three CV cycles of the Li_2S-C vs. Li counter/reference electrode in two-electrode cells. The cathodic peak in the first delithiation scan of Li_2S-C_{NitS} is centered at 3.5 V with a small shoulder at 3.4 V. The Li_2S-C_{AceS} composite demonstrates a broader delithiation peak at the same potential.

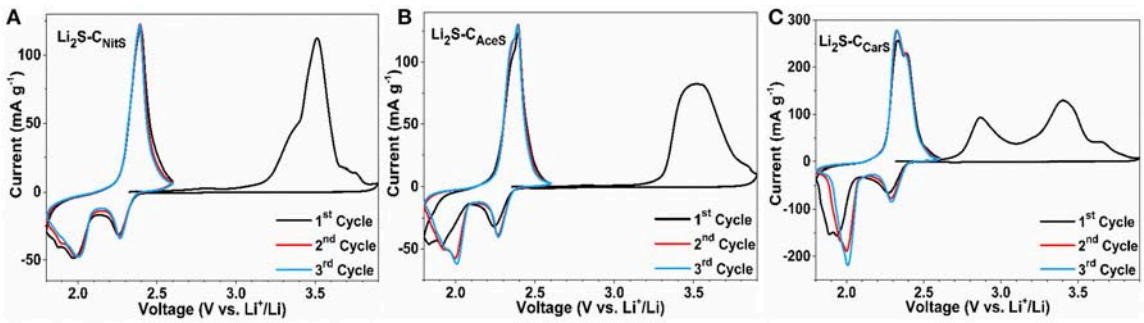

FIGURE 4 | CV scans of **(A)** Li_2S-C_{NitS}, **(B)** Li_2S-C_{AceS}, **(C)** Li_2S-C_{CarS} using 0.2 mV s^{-1} scan rate.

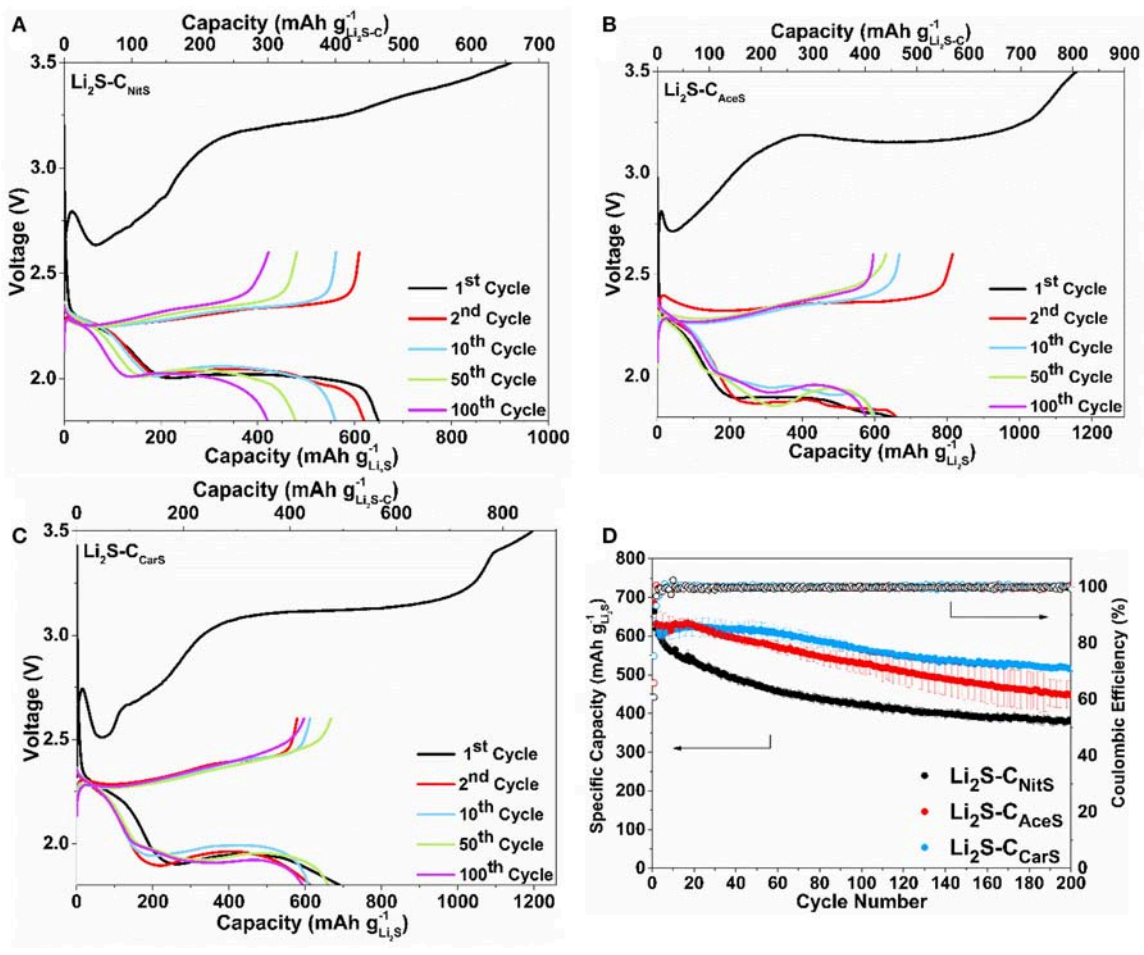

FIGURE 5 | Representative charge-discharge curves of **(A)** Li_2S-C_{NitS}, **(B)** Li_2S-C_{AceS}, **(C)** Li_2S-C_{CarS} at the 1st, 2nd, 10th, 50th, and 100th cycle, and **(D)** the cycle stability of these composites at 117 mA g^{-1}.

In contrast, Li_2S-C_{CarS} shows two distinct cathodic peaks at 2.75 and 3.4 V vs. Li^+/Li. The lower cathodic peak of the Li_2S-C_{CarS} composite at 2.75 V indicates a lower energy barrier for the delithiation reaction (Zhou et al., 2017). The Li_2S-C_{CarS} composite also demonstrates the highest peak current in the consecutive lithiation-delithiation scans. The superior performance of Li_2S-C_{CarS} may be reflective of the intimate contact of Li_2S and the carbon matrix. **Figure 5** displays the representative charge-discharge curves and the cycle stability of the Li_2S-C composites. The electrolyte/Li_2S ratio is 10:1 (μL/mg), and all Li_2S-C composites are first charged to 3.5 V (activation) vs. Li^+/Li with a current density of 50 mA g^{-1}. The charge-discharge curves demonstrate similar cycling behavior of these three Li_2S-C composites. However, Li_2S-C_{AceS} shows the highest charge-discharge hysteresis, which is consistent with the lowest surface area of its carbon matrix. On the other hand, although Li_2S-C_{NitS} shows the lowest voltage hysteresis due to the highest surface area of its carbon matrix, its capacity rapidly fades. As a composite with the balanced microstructure, Li_2S-C_{CarS} demonstrates the best overall performance: After 200 cycles, Li_2S-C_{CarS} can retain a capacity of 540 mAh g^{-1}, superior to 385 mAh g^{-1} of Li_2S-C_{NitS} and 460 mAh g^{-1} of Li_2S-C_{AceS}, indicating the effectiveness of the Li_2S-C_{CarS} composite architecture in sequestrating polysulfides. The overall performance demonstrated by Li_2S-$C_{CarS,}$ in terms of areal loading, E/Li_2S ratio, overall capacity, and cycle stability, is on par with the best performance reported to date (**Table S3**).

In summary, we examined a new synthetic route for the production of Li_2S-C composite materials for Li-S batteries. The combination of aerosol spray pyrolysis and sulfurization has been shown to be a robust method for the conversion of various lithium salts including nitrate, acetate, and carbonate to Li_2S-C nanocomposites using sucrose as the carbon precursor. Furthermore, the cycling performance of the Li_2S-C composite has been found to be closely correlated to its precursor-derived microstructure. The combination of Li_2CO_3 and sucrose results in the Li_2S-C composite with the best electrochemical performance, which has a non-hollow composite structure with Li_2S uniformly embedded in the carbon matrix. The detailed mechanism of aerosol spray pyrolysis and the optimization of the composite's structure and electrochemical performance will be further investigated in our future studies.

AUTHOR CONTRIBUTIONS

NH completed most of the experiments. JS, JZ, and CF helped with the experiments and data analysis. JG designed the experiments. All authors co-wrote the manuscript.

ACKNOWLEDGMENTS

We gratefully acknowledge the financial support from Power Energy Solutions Inc.

SUPPLEMENTARY MATERIAL

The Supplementary Material for this article can be found online at: https://www.frontiersin.org/articles/10.3389/fchem.2018.00476/full#supplementary-material

REFERENCES

Cai, K., Song, M., Cairns, J. E., Zhang, Y. (2012). Nanostructured Li_2S-C composites as cathode material for high-energy Lithium/Sulfur batteries. *Nano Lett*. 12, 6474–6479. doi: 10.1021/nl303965a

Chen, J., Henderson, W. A., Pan, H., Perdue, R. B., Cao, R., Hu, J. Z., et al. (2017). Improving Lithium–Sulfur battery performance under lean electrolyte through nanoscale confinement in soft swellable gels. *Nano Lett*. 17, 3061–3067. doi: 10.1021/acs.nanolett.7b00417

Chen, S., Gao, Y., Yu, Z., Gordin, L. M., Song, J., and Wang, D. (2017). High capacity of Lithium-Sulfur batteries at low electrolyte/Sulfur ratio enabled by an Organosulfide containing electrolyte. *Nano Energy* 31, 418–423. doi: 10.1016/j.nanoen.2016.11.057

Dressel, B. C., Jha, H., Eberle, A., Gasteiger, A. H., and Fassler, F. T. (2016). Electrochemical performance of Lithium-Sulfur batteries based on a Sulfur cathode obtained by H_2S gas treatment of a Lithium salt. *J. Power Sour*. 307, 844–848. doi: 10.1016/j.jpowsour.2015.12.140

Guo, J., Yang, Z., Yu, Y., Abruña, H. D., and Archer, L. A. (2013). Lithium–Sulfur battery cathode enabled by Lithium–Nitrile interaction. *J. Am. Chem. Soc*. 135, 763–767. doi: 10.1021/ja309435f

Hwa, Y., Zhao, J., and Cairns, E. J. (2015)Lithium Sulfide (Li2S)/Graphene Oxide nanospheres with conformal carbon coating as a high-rate, long-life cathode for Li/S cells. *Nano Lett*. 15, 3479–3486. doi: 10.1021/acs.nanolett.5b00820

Jha, H., Buchberger, I., Cui, X., Meini, S., and Gasteiger, H. A. (2015). Li-S batteries with Li2S cathodes and Si/C anodes. *J. Electochem. Soc*. 162, 1829–1835. doi: 10.1149/2.0681509jes

Kohl, M., Bruckner, J., Bauer, I., Althues, H., and Kaskel, S. (2015). Synthesis of highly electrochemically active Li2S nanoparticles for Lithium–Sulfur-batteries. *J. Mater. Chem. A* 3, 16307–16312. doi: 10.1039/C5TA04504E

Li, Z., Zhang, S., Zhang, C., Ueno, K., Yasuda, T., Tatara, R., et al. (2015). One-pot pyrolysis of Lithium Sulfate and graphene nanoplatelet aggregates: *in situ* formed Li2S/ graphene composite for Lithium–Sulfur batteries. *Nanoscale* 7, 14385–14392. doi: 10.1039/C5NR03201F

Messing, G., Zhang, S., and Jayanthi, G. (1993). Ceramic powder synthesis by spray pyrolysis. *J. Am. Ceram. Soc*. 76, 2707–2726.

Pan, H., Han, S. K., Engelhard, H. M., Cao, R., Chen, J., Zhang, J., et al. (2018). Addressing passivation in Lithium–Sulfur battery under lean electrolyte condition. *Adv. Funct. Mater*. 28:1707234. doi: 10.1002/adfm.201707234

Piwko, M., Weller, C., Hippauf, F., Dorfler, S., Althues, H., and Kaskel, S. (2018). Symmetric Lithium Sulfide-Sulfur cells: a method to study degradation mechanisms of cathode, separator and electrolyte concepts for Lithium-Sulfur batteries. *J. Electrochem. Soc*. 165, A1084–A1091. doi: 10.1149/2.1131805jes

Roe, A., and Finlay, J. B. (1952). The isotope effect II, pyrolysis of Lithium Acetate 1-C14. *J. Am. Chem. Soc*. 74, 2442–2443.

Skrabalak, S. E., and Suslick, K. S. (2006). Porous carbon powders prepared by ultrasonic spray pyrolysis. *J. Am. Chem. Soc*. 128, 12642–12643. doi: 10.1021/ja064899h

Son, Y., Son, Y., Lee, J., Jang, J., and Cho, J. (2015). Recent advances in Lithium Sulfide cathode materials and their use in Lithium Sulfur batteries. *Adv. Energy Mat*. 5:1500110. doi: 10.1002/aenm.201500110

Stern, K. H., and Weise, E. L. (1969). *High Temperature Properties and Decomposition of Inorganic Salts; Part 2. Carbonates*. Washington, DC: United States Dept of Commerce.

Tan, G., Xu, R., Xing, Z., Yuan, Y., Lu, J., Wen, J., et al. (2017). Burning lithium in CS2 for high-performing compact Li2 S–graphene nanocapsules for Li–S batteries. *Nat. Energy* 2:17090. doi: 10.1038/nenergy.2017.90

Vizintin, A., Chabanne, L., Tchernychova, E., Arcon, I., Stievano, L., Aquilanti, G., et al. (2017). The mechanism of Li_2S activation in Lithium-sulfur batteries: can we avoid the Polysulfide formation? *J. Power Sour*. 344, 208–217. doi: 10.1016/j.jpowsour.2017.01.112

Wang, D., Zeng, Q., Zhou, G., Yin, L., Li, F., Cheng, H., et al. (2013). Carbon-Sulfur composites for Li-S batteries: status and prospects. *J. Mat. Chem. A* 1, 9382–9394. doi: 10.1039/C3TA11045A

Wu, F., Kim, H., Magasinski, A., Lee, J., Lin, H., and Yushin, G. (2014a). Harnessing steric separation of freshly nucleated Li2S nanoparticles for bottom-up assembly of high-performance cathodes for Lithium-Sulfur and Lithium-Ion batteries. *Adv. Energy Mater*. 4:1400196. doi: 10.1002/aenm.201400196

Wu, F., Lee, J., Magasinski, A., Kim, H., and Yushin, G. (2014b). Solution-based processing of graphene-Li2S composite cathodes for Lithium-Ion and Lithium-Sulfur batteries. *Part. Part. Syst. Charact*. 31, 639–644. doi: 10.1002/ppsc.201300358

Wu, F., Lee, J., Zhao, E., Zhang, B., and Yushin, G. (2016). Graphene–Li2S–carbon nanocomposite for Lithium–Sulfur batteries. *ACS Nano* 10, 1333–1340. doi: 10.1021/acsnano.5b06716

Wu, F., Lee, J. E., Fan, F., Nitta, N., Kim, H., Zhu, T., et al. (2015). A hierarchical particle–shell architecture for long-term cycle stability of Li2S cathodes. *Adv. Mater*. 27, 5579–5586. doi: 10.1002/adma.201502289

Wu, F., Magasinski, A., and Yushin, G. (2014c). Nanoporous Li2S and MWCNT-linked Li2S powder cathodes for Lithium-Sulfur and Lithium-ion battery chemistries. *J. Mater. Chem. A* 2, 6064–6070. doi: 10.1039/C3TA14161F

Wu, S. D., Shi, F., Zhou, G., Zu, C., Liu, C., Liu, K., et al. (2018). Quantitative investigation of Polysulfide adsorption capability of candidate materials for Li-S batteries. *Energy Storage Mater*. 13, 241–246. doi: 10.1016/j.ensm.2018.01.020

Yang, Y., McDowell, M. T., Jackson, A., Cha, J. J., Hong, S. S., and Cui, Y. (2010). New nanostructured Li2S/Silicon rechargeable battery with high specific energy. *Nano Lett*. 10, 1486–1491. doi: 10.1021/nl100504q

Yang, Z., Guo, J., Das, K. S., Yu, Y., Zhou, Z., Abruna, D. H., et al. (2013). *In situ* synthesis of Lithium Sulfide–carbon composites as cathode materials for rechargeable Lithium batteries. *J. Mater. Chem. A* 1, 1433–1440. doi: 10.1039/C2TA00779G

Ye, F., Noh, H., Lee, J., Lee, H., and Kim, H. (2018). Li_2S/carbon nanocomposite strips from a low-temperature conversion of Li_2SO_4 as high-performance Lithium-Sulfur cathodes. *J. Mater. Chem. A* 6, 6617–6624. doi: 10.1039/C8TA00515J

Yu, M., Wang, Z., Wang, Y., Dong, Y., and Qiu, J. (2017). Freestanding flexible Li2S paper electrode with high mass and capacity loading for high-energy Li-S batteries. *Adv. Energy Mater*. 7:1700018. doi: 10.1002/aenm.201700018

Zhang, J., Shi, Y., Ding, Y., Peng, L., Zhang, W., and Yu, G. (2017). A conductive molecular framework derived Li2S/N,P-codoped carbon cathode for advanced Lithium–Sulfur Batteries. *Adv. Energy Mater*. 7:1602876. doi: 10.1002/aenm.201602876

Zhou, G., Tian, H., Jin, Y., Tao, X., Liu, B., Zhang, R., et al. (2017). Catalytic oxidation of Li2S on the surface of metal Sulfides for Li–S batteries. *Proc. Natl. Acad. Sci. U.S.A*. 114, 840–845. doi: 10.1073/pnas.1615837114

Zou, H., Gratz, E., Apelian, D., and Wang, Y. (2013). A novel method to recycle mixed cathode materials for Lithium Ion batteries. *Green Chem*. 15, 1183–1191. doi: 10.1039/C3GC40182K

Conflict of Interest Statement: The authors declare that the research was conducted in the absence of any commercial or financial relationships that could be construed as a potential conflict of interest.

Copyright © 2018 Hart, Shi, Zhang, Fu and Guo. This is an open-access article distributed under the terms of the Creative Commons Attribution License (CC BY). The use, distribution or reproduction in other forums is permitted, provided the original author(s) and the copyright owner(s) are credited and that the original publication in this journal is cited, in accordance with accepted academic practice. No use, distribution or reproduction is permitted which does not comply with these terms.

frontiers in Chemistry

ORIGINAL RESEARCH
published: 19 February 2019
doi: 10.3389/fchem.2019.00084

Effect of Surface and Bulk Properties of Mesoporous Carbons on the Electrochemical Behavior of GOx-Nanocomposites

Tsai Garcia-Perez[1], Shouzhen Hu[1], Youngho Wee[2], Louis Scudiero[3], Conrad Hoffstater[1], Jungbae Kim[2] and Su Ha[1]**

[1] School of Chemical Engineering and Bioengineering, Washington State University, Pullman, WA, United States, [2] Department of Chemical and Biological Engineering, Korea University, Seoul, South Korea, [3] Department of Chemistry and Materials Science and Engineering Program, Washington State University, Pullman, WA, United States

OPEN ACCESS

Edited by:
Nosang Vincent Myung, University of California, Riverside, United States

Reviewed by:
Aihua Liu, Qingdao University, China
Dunfeng Gao, Fritz-Haber-Institut, Germany
Wook Ahn, Soonchunhyang University, South Korea

***Correspondence:**
Jungbae Kim
jbkim3@korea.ac.kr
Su Ha
suha@wsu.edu

Specialty section:
This article was submitted to Electrochemistry, a section of the journal Frontiers in Chemistry

Received: 12 October 2018
Accepted: 31 January 2019
Published: 19 February 2019

Citation:
Garcia-Perez T, Hu S, Wee Y, Scudiero L, Hoffstater C, Kim J and Ha S (2019) Effect of Surface and Bulk Properties of Mesoporous Carbons on the Electrochemical Behavior of GOx-Nanocomposites. Front. Chem. 7:84. doi: 10.3389/fchem.2019.00084

Biofuel cell (BFC) electrodes are typically manufactured by combining enzymes that act as catalysts with conductive carbon nanomaterials in a form of enzyme-nanocomposite. However, a little attention has been paid to effects of the carbon nanomaterials' structural properties on the electrochemical performances of the enzyme-nanocomposites. This work aims at studying the effects of surface and bulk properties of carbon nanomaterials with different degrees of graphitization on the electrochemical performances of glucose oxidase (GOx)-nanocomposites produced by immobilizing GOx within a network of carbon nanopaticles. Two types of carbon nanomaterials were used: graphitized mesoporous carbon (GMC) and purified mesoporous carbon (PMC). Graphitization index, surface functional groups, hydrophobic properties, and rate of aggregation were measured for as-received and acid-treated GMC and PMC samples by using Raman spectrometry, *X-ray photoelectron spectroscopy (*XPS), contact angle measurement, and dynamic light scattering (DLS), respectively. In addition to these physical property characterizations, the enzyme loading and electrochemical performances of the GOx-nanocomposites were studied via elemental analysis and cyclic voltammetry tests, respectively. We also fabricated BFCs using our GOx-nanocomposite materials as the enzyme anodes, and tested their performances by obtaining current-voltage (IV) plots. Our findings suggest that the electrochemical performance of GOx-nanocomposite material is determined by the combined effects of graphitization index, electrical conductivity and surface chemistry of carbon nanomaterials.

Keywords: graphitized mesoporous carbon, graphitization index, hydrophobic properties, biofuel cells, glucose oxidase, enzymatic nanocomposites

INTRODUCTION

Self-powered implantable devices such as deep brain neurostimulators, pacemakers, and biosensors for environmental monitoring have enormous potential in medical, agricultural or even military applications (Falk et al., 2012; Katz, 2013). Biofuel cells (BFCs) can be an alternative portable power solution to batteries for powering these devices, due to their capability to continuously convert the chemical energy from organic fuels, such as glucose in fruits or human blood, into electricity

(Katz, 2013; MacVittie et al., 2015). Enzymatic BFCs use (1) enzymes to catalyze both oxidation of organic fuels and reduction of oxidizing agents, and (2) conductive materials (such as carbon nanomaterials) to transmit the electrons between the enzymes' active sites and the electrodes. Thus, the physical properties of both materials—enzymes and nanomaterials—play a key role in the BFC's electrochemical performances. However, to the best of our knowledge, little attention has been paid to the effects of the carbon nanoparticle's surface and bulk properties on the overall electrochemical performance of the enzyme electrodes.

Graphitized mesoporous carbons (GMC) and purified mesoporous carbons (PMC) are two types of mesoporous carbon materials with similar chemical composition and morphological properties, but different surface and structural properties. This contrast on the properties of GMC and PMC makes them the ideal carbon nanomaterials for investigating the effects of carbon nanomaterials' properties on the electrochemical performances of BFCs.

Graphitized and non-graphitized carbons are structurally different (Franklin, 1951). The graphitization process of the carbon is a method to produce well-organized graphite (Mattia et al., 2006). Non-graphitized carbons exhibit a cross-linked structure where graphitic structures are randomly oriented in a rigid mass. Conversely, graphitized carbons present a compact structure where the graphite layers have a nearly parallel orientation. Graphite layers play a major role in both the surface and bulk properties of these materials. The hydrophobicity and electrical conductivity of the carbon materials, for example, are directly related to the level of graphitization of the carbon materials (Pantea et al., 2003). Hydrophobicity also affects the nanoparticle aggregation process (Nel et al., 2009). It is known that the surface of graphitized materials presents smaller amounts of oxygen functionalities compared to that of non-graphitized materials, which strongly repels water molecules (due to their hydrophobic nature) and decreases electrostatic repulsion among the nanoparticles. Consequently, these nanomaterials can form a compact carbon network with low dispersion in an aqueous medium. These unique properties of nanomaterials have been used to physically entrap large enzyme aggregates within the carbon networks and to form protein-nanocomposite materials (Garcia-Perez et al., 2016). This observation suggests that the performance of this hybrid protein-nanoparticle composite structure highly depends on the graphitization index of the carbon nanomaterial used as the enzyme support. Literature shows that the GMC sample can be used to entrap enzymes to build bioelectrodes (Garcia-Perez et al., 2016; Walcarius, 2017), although no information has been reported in the literature on employing the PMC sample for electrochemical applications.

This work aims to study the effects of the bulk and the surface properties of different carbon nanomaterials on the electrochemical performances of glucose oxidase (GOx)-nanocomposite bioanode materials under the BFC operation mode. For the present study, a homemade Proton Exchange Membrane (PEM) fuel cell was used to test the enzymatic BFC performances. Four different bioanodes were manufactured using GOx as catalysts and (a) GMC, (b) PMC, (c) acid treated GMC, and (d) acid treated PMC as carbon supports.

MATERIALS AND METHODS

Materials

Graphitized mesoporous carbons (GMC) (specific surface area of 70 m^2/g and average pore diameter of 13.7 nm, purity >99.95%) and purified mesoporous carbons (PMC) (specific surface area of 200 m^2/g and average pore diameter of 6.4 nm, purity >99.95%) were purchased from Sigma Aldrich. Glucose oxidase (GOx) Type VII from *Aspergillus niger,* glutaraldehyde (8% in water), ammonium sulfate (molecular biology grade), Nafion® (5 wt% in a mixture of water and lower aliphatic alcohols), D-glucose, o-Dianisidine dihydrochloride, and Peroxidase Type II from *Horseradish* were also obtained from Sigma Aldrich. Nanopure water (>18 MΩ-cm) was used to prepare sodium phosphate buffer (hereafter referred to as PB) and Tris-buffer solutions. The glucose solutions used during the electrochemical tests were prepared 1 day in advance to allow mutarotation of α-glucose to β-glucose.

Methods

GOx-Nanocomposites Preparation

The GOx-nanocomposites were prepared using cross-linked GOx aggregates as the catalyst and the GMC or the PMC as the carbon supports. The carbon materials were first acid treated using 25 ml of a mixture of nitric acid and sulfuric acid in a volume ratio of 1:3. The acids were mixed in a 50 ml bottle and allowed to cool down to room temperature. Then, 0.25 g of the carbon nanoparticles were added into the acid mixture, as they were stirred with a magnetic bar. The suspension was then shaken for 24 h. Following the acid treatment, the samples were washed with nanopure water and vacuum filtered. The GOx-nanocomposites were prepared by adding 5 ml of ammonium sulfate solution (0.5 mg/ml) to 2.5 ml of GOx solution (1 mg of GOx/ml) to precipitate the enzymes. Then, 0.13 vol% of glutaraldehyde was added to the solution in order to obtain the cross-linked GOx aggregates. Next, 5 ml of nanocarbon solutions (1 mg/ml) was added and stirred for 30 min using a shaker (Max Q 2,000) to form the GOx-nanocomposites. These nanocarbon solutions included the GMC, PMC, acid treated GMC (herein referred to as GMCac), and acid treated PMC (herein referred to as PMCac) dispersed into the buffer solution. The nanocomposites were washed 6 times: 2 times with Tris-buffer solution (pH 7.2) to cap the underreacted glutaraldehyde and 4 times with sodium phosphate buffer (PB, 100 mM, pH 7.0) to remove the free GOx. Each washing process consisted of adding 10 ml of buffer to each suspension and then vortexing, shaking, and centrifuging. The supernatant was then removed. Finally, the PB solution was added to the GOx-nanocomposites to reach a final volume of 5 ml. The nanocomposite suspension in PB was stored at 4°C. The prepared samples will be referred to as: the GOx-GMC for cross-linked GOx aggregates-GMC; the GOx-GMCac for cross-linked GOx aggregates-GMC acid treated; the GOx-PMC for cross-linked

GOx aggregates-PM; and the GOx-PMCa for cross-linked GOx aggregates-PMCac.

Elemental analysis and surface characterization

The ratio of enzyme to carbon material (mg of enzyme/mg of mesoporous carbon) present in each nanocomposite was estimated by determining the elemental composition (C, H, N) of the GOx-nanocomposites, GOx and carbon nanomaterials. The tests were conducted by Intertek Pharmaceutical Services (Intertek.com). For the elemental analysis, the GOx-nanocomposites samples were washed with PB only, skipping the Tris-buffer washing step for the elemental analysis tests to guarantee the enzymes are the only major source of nitrogen (Kim et al., 2011). Before sending the GOx-nanocomposite samples to Intertek Pharmaceutical Services, the samples were freeze-dried to remove water from the system. Both the GOx enzyme and nanomaterial samples were sent to the company for the elemental analysis without any special treatments. The residual water contents of the carbon nanomaterial samples were determined (prior to the elemental analysis) through thermogravimetric analysis (TGA) (García et al., 2013). Based on our TGA analysis, the water contents for the nanomaterial samples were negligible (i.e., there was no water content for both the GMC and GMCac samples, while the PMC and PMCac samples contained 2.4 and 5.9 weight% of water content, respectively).

The elemental composition of the GOx-nanocomposites, GOx, and the carbon nanomaterials was measured and reported in terms of weight%. The GMC, GMCac, and PMC contained no nitrogen. Unlike the GMC, GMCac, and PMC, the elemental analysis of the PMCac showed a trace of nitrogen element. However, its amount was insignificant and we can ignore its contribution for estimating the GOx amount presented in the GOx-PMCac nanocomposite sample. Since every GOx contains a fixed number of nitrogen element and GOx is the only major source of nitrogen element, we can easily approximate the total amount of GOx presented in each GOx-nanocomposite sample using the nitrogen weight% information obtained from the elemental analysis. Based on the carbon weight% information, we can also estimate the total amount of carbon nanomaterials presented in each GOx-nanocomposite sample. Based on this total amount information of both GOx and carbon nanomaterials, we can determine the ratio of enzyme to carbon nanomaterial (weight% of enzyme/weight% of carbon nanomaterial) for each GOx-nanocomposite sample.

The aggregation process of the carbon nanoparticles was studied by conducting dynamic light scattering (DLS) measurements. The size of the carbon nanoparticles aggregates was determined every 1 min. In addition, the interaction between the carbon nanomaterials and water was visualized by creating a thin film of each carbon nanomaterial and placing 20 μl of nanopure water on the top of it.

The graphitization index of the samples was determined via Raman Spectrometry. The Raman tests were carried out using a Jobin–Yvon Horiba LabRAM-HR spectrometer at 532 nm excitation wavelength. Prior to the tests, the samples were diluted 10 times in KBr. Each sample was scanned at least 6 times. All Raman measurements were conducted at room temperature. In addition, the functional groups on the surfaces of the samples were studied by means of X-ray photoelectron spectroscopy (XPS). The XPS spectra were recorded on a Kratos AXIS-165 XPS spectrometer using a monochromatized AlKα X-ray anode (1,486.6 eV) in an ultra-high vacuum system. The spectrometer was calibrated against both the Au $4f_{7/2}$ peak at 84.0 eV and the Ag $3d_{5/2}$ peak at 368.3 eV. Survey scans were recorded at 80 eV pass energy with a step size of 1 eV. C 1s core level spectra were recorded at 40 eV pass energy with a step size of 0.1 eV. CasaXPS software was used to analyze the XPS spectra of C 1s for all samples. The full width at half maximum (FWHM) were set to 0.8 eV for C-C bond, 1.2 eV for C-OH bond, 1.5 eV for C=O, O-C=O and carbonate bonds, and 2 eV for the $\pi \rightarrow \pi^*$ transition. Finally, all the spectra curves were smoothed using the Sawitzki-Golay algorithm with a kernel of five points.

Carbon nanoparticle's morphological characterization

Microscopy techniques were performed to visualize the structure of the carbon nanoparticles and the GOx-nanocomposites. A Zeiss 510 Confocal Microscope was used to conduct confocal analysis. In addition to confocal analysis, transmission electron microscopy (TEM) was carried out to visualize the distribution of

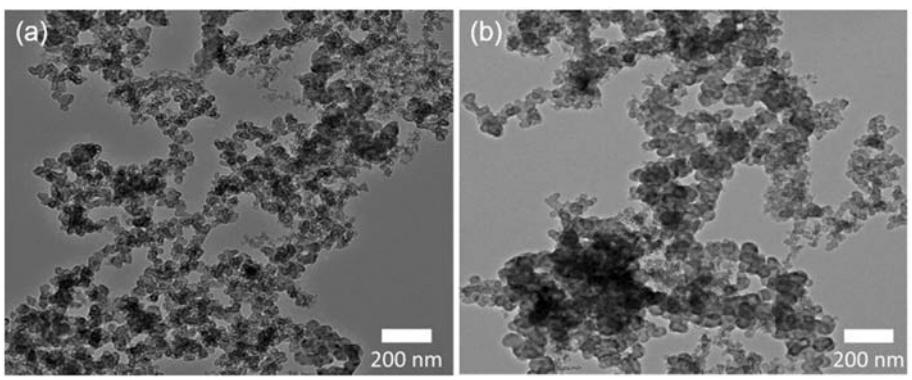

FIGURE 1 | TEM images of as-received carbon nanomaterials: **(a)** GMC and **(b)** PMC.

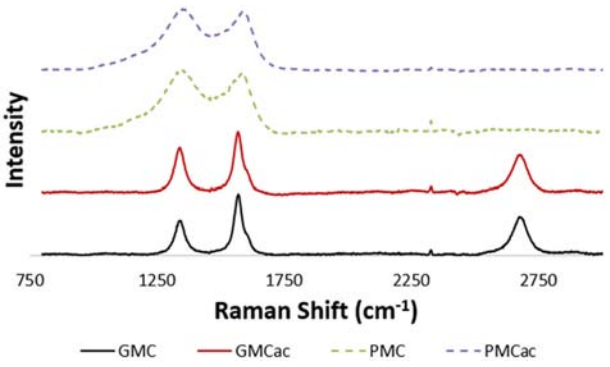

FIGURE 2 | Raman spectra of GMC, GMCac, PMC, and PMCac.

the enzymes within the carbon nanoparticle network at a smaller scale. The TEM tests were conducted using a FEI TEM T20 microscopy at least in 5 different spots. The preparation of the samples was conducted using a similar step reported in a previous work (Garcia-Perez et al., 2016).

Electrochemical properties

Cyclic voltammetry (CV) was conducted using a conventional three electrode setup. Pt mesh and Ag/AgCl (KCl saturated) electrode were used as a counter electrode and a reference electrode, respectively. In addition, the working electrodes were prepared by placing 10 μl of the GOx-nanocomposites suspension (∼1.5 mg of GOx-nanocomposite/ml of suspension) on a glassy carbon electrode using Nafion® binder (0.5% of the total volume). All of the CV tests were carried out using N_2-saturated PB (100 mM, pH of 7.0) at room temperature, while the working electrode was rotated at 500 rpm. The N_2-saturated PB solutions were prepared by bubbling high purity N_2 into the solutions for 30 min before the test, followed by blanketing the solutions with N_2 during the tests.

The enzyme anodes were prepared by physically absorbing the GOx-nanocomposites onto carbon paper disk with a geometric area of 0.332 cm^2. A concentrated solution of GOx-nanocomposites was prepared by centrifuging an aliquot of 0.6 ml of GOx-nanocomposite from the main stoke for 5 min, removing 410 μl of supernatant, and adding 10 μl of 5% Nafion® solution into the remaining pellet. After that, the carbon disks were added one by one to the suspension and shaken for 10 min. The electrodes were then removed and dried for 1 h under hood conditions. Finally, the electrodes were washed three times with 100 mM PB buffer (pH 7.0) and stored at 4°C before use.

The electrochemical properties of the GMC, GMCac, PMC, and PMCac samples were studied by using CV tests. The electrodes were prepared by placing 40 μl of a nanoparticle suspension (1 mg of carbon nanoparticle/ml of ethanol) on the glassy carbon electrode and let it dry at room temperature. The ferrocyanide/ferricyanide couple is a benchmark used in our electrochemical measurements to determine the electron transfer characteristics of each electrode. The CV plots were obtained in the presence of 1 mM of potassium ferricyanide in PB (100 mM, pH 7.0) at scan rate of 10 mV s^{-1}. The current density (μA/cm^2) was determined by dividing the current obtained in the CV test with the total surface area of carbon nanomaterial (see Materials).

A homemade PEM fuel cell was used to evaluate the electrochemical performance of the GOx-nanocomposites under the enzymatic biofuel cell (BFC) operating mode as presented in previous papers (Fischback et al., 2006; Garcia-Perez et al., 2016).

TABLE 1 | A summary of Raman spectra for the GMC, GMCac, PMC and PMCac samples.

Samples	FWHM (G band)	FWHM (D band)	I_G/I_D	$1/(I_G/I_D)$
GMC	39.05	45.95	1.87	0.54
GMCac	44.73	47.91	1.45	0.69
PMC	111.24	206.22	–	–
PMCac	112.73	212.74	–	–

RESULTS AND DISCUSSION

Morphology, Graphitization Index, Surface Chemistry, and Wettability of GMC and PMC

Figure 1 presents the TEM images of as-received GMC and as-received PMC. Both carbon nanomaterials present similar polygonal conformations and dimensions in the nanoscale range, but they offer different specific surface areas (200 m^2/g for PMC and 70 m^2/g for GMC) according to their vendor information. **Figure 2** presents the Raman spectra of the four carbon nanomaterials used in this work (GMC, PMC, GMCac, and PMCac). The GMC sample presents large G and D peaks at around 1,582 cm^{-1} and 1,350 cm^{-1}, respectively. The GMC sample also shows a strong D′ peak at around 2,700 cm^{-1}. These sharp G peak and strong G′ peak shown in the Raman spectrum of the GMC sample indicate that the GMC is consisted of a multilayer of graphene and, consequently, it presents a very organized bulk structure. Furthermore, the *full width half maximum* (FWHM) of the G and D peaks for the GMC and PMC samples show different values: around 39–45 cm^{-1} (G-D peak) for the GMC and 111–206 cm^{-1} (G-D peak) for the PMC (see **Table 1**). The higher FWHM values for the PMC's G and D peaks as well as the disappearance of its G′ peak at around 2,700 cm^{-1} indicate a lack of three-dimensional order of PMC materials, which is probably due to its turbostratic conformation (Ferrari, 2007). In summary, the GMC sample presents a highly graphitized structure, while the PMC sample mainly consists of turbostratic carbon structures with a low degree of bulk organization.

The graphitization index was calculated as an intensity ratio between the G peak and the D peak (*IG/ID*) of Raman spectra, and their inverse values (*ID/IG*) were used to quantify the defects in the carbon structure (**Table 1**). The high graphitization index of the as-received GMC (1.87) and GMCac (1.45) confirms that these materials present a well-organized bulk structure. However, the graphitization index of GMCac is lower than that of the

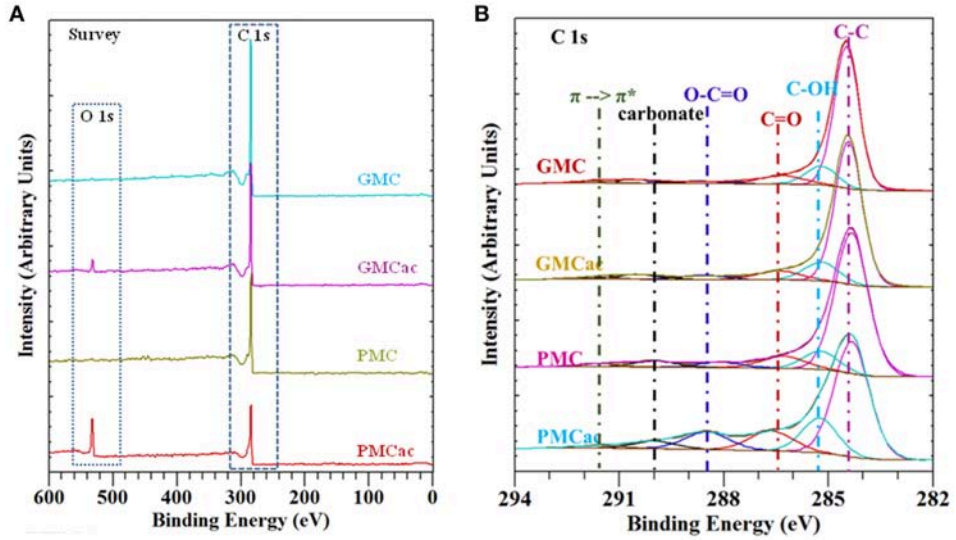

FIGURE 3 | (A) XPS survey spectra and **(B)** curve fitted XPS C 1s peaks for GMC, GMCac, PMC, and PMCac.

as-received GMC (a reduction of ∼22%), suggesting that the acid treatment creates defects on the GMC. For amorphous materials, this G peak can be attributed to the presence of benzene rings that are condensed into the amorphous structure (Schwan et al., 1996). Therefore, the intensity of this G peak (I_G) and *IG/ID* peak ratios cannot be used to quantify the graphitization index of PMC materials. Thus, both the *IG/ID* and *ID/IG* peak ratios of both the PMC and PMCac samples are not included in **Table 1**.

The functional groups present on the surface of the GMC, GMCac, PMC, and PMCac nanomaterials were determined by XPS measurements. The XPS spectra are presented in **Figure 3**. As shown in **Figure 3A**, a main peak at around 284 eV for C 1s in the XPS survey scan was detected for all four samples. New peaks around 532 eV are observed in the XPS survey scans for both the GMCac and the PMCac samples. Such new peaks were identified as O 1s, which indicate that the surface of GMC and PMC nanomaterials are functionalized after the acid treatment. The effect of the acid treatment can be analyzed from the ratio between the amount of O and C elements obtained from the XPS spectra. The O/C ratios for the as-received GMC and as-received PMC samples were 0.004 and 0.001, respectively. These results indicate that both as-received nanomaterials present a low percentage of oxygen functionalities on their surfaces. After the treatment with H_2SO_4/HNO_3, the O/C ratio increased to 0.045 and 0.218 for the GMCac and PMCac samples, respectively. This increase in the O/C atomic ratio indicates that the acid treatment has effectively introduced oxygen functional groups on the surface of both materials. The higher increase in the oxygen functionalities content of the PMC sample after the acid treatment (PMCac; 17.90%) than that of the GMC sample (GMCac; 4.39%) indicates that the PMC sample is more easily oxidized than the GMC sample, probably due to its larger number of surface defects.

TABLE 2 | Atomic percentages of the oxygen functional groups on the surface of the carbon nanoparticles obtained by XPS.

Sample	Atomic %					
	C-OH	C=O	O-C=O	Carbonate	C	O
GMC	12.21	8.12	2.40	3.40	99.60	0.40
GMCac	12.31	7.58	3.33	3.75	95.61	4.39
PMC	9.97	8.27	3.84	4.44	99.90	0.10
PMCac	16.74	11.99	10.62	4.47	82.10	17.90

The XPS C 1s high resolution spectra for the GMC, GMCac, PMC, and PMCac nanomaterials are shown in **Figure 3B**. Six main peaks were derived from curve fitting. The peaks obtained at 284.4 eV, 285.4 eV, 286.7 eV, 288.5 eV, and 290.1 eV are attributed to C-C, C-OH (phenol or alcohol), C=O (carbonyl or quinone groups), O-C=O (carboxyl, lactone, or ester groups), and carbonate groups, respectively (Chiang and Lee, 2009). The percentages of carbon and oxygen functionalities obtained from the deconvolution of the XPS spectra in the C 1s region is presented in **Table 2**. It is known that the oxidation reaction of carbon nanostructures occurs in two steps. The first step consists of the oxidant attack on the graphene structure by electrophilic reactions to generate active sites. The actives sites are sites on the nanoparticle surface where chemical functionalities are introduced, for instance C–OH groups (Santangelo et al., 2012). In fact, the C-OH groups are the oxygen functional groups that are present in higher percentage on the surface of all the carbon samples. The increase of the atomic % of C-OH groups observed for the PMC sample after the acid treatment (from 9.97 atomic% in the PMC to 16.74 atomic% in the PMCac) indicates that a significant amount of active sites were created on its surfaces during the oxidation process (Chiang and Lee, 2009).

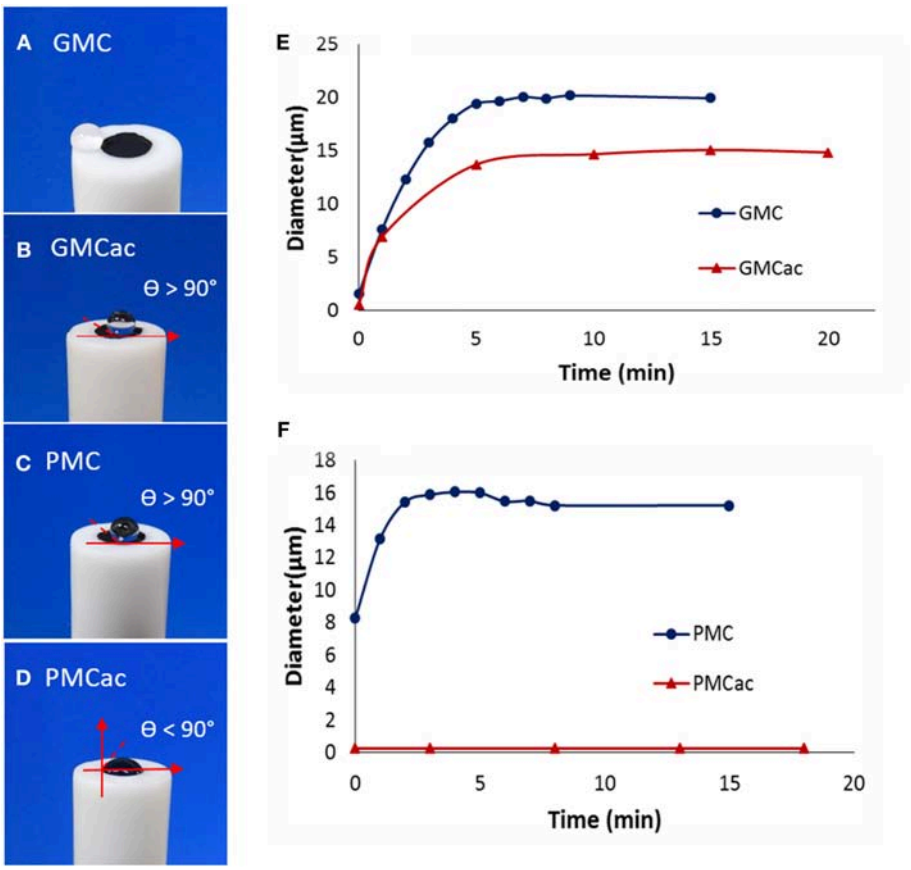

FIGURE 4 | Images of a drop of water (20 μm) placed on films of **(A)** GMC, **(B)** GMCac, **(C)** PMC, and **(D)** PMCac. Dynamic light scattering measurements for the aggregation of **(E)** GMC/GMCac and **(F)** PMC/PMCac as a function of time.

Meanwhile, only a small increase in the number of C-OH groups was observed after the acid treatment for the GMC sample. Thus, the generated surface defects on the GMC sample by the acid treatment is lower than that of the PMC sample, probably due to its higher graphitization index compared to that of the PMC sample. The second oxidation step consists of a process where the active sites generated in the first step are further oxidized and the aromatic rings are opened (Santangelo et al., 2012). During this process, some of the C-OH groups generated in the first oxidation step are consumed to produce O-C=O. In fact, the surface concentration of O-C=O functional group increases in both samples after the acid treatment, but in different proportions. The atomic percentage of O-C=O increases by 176.6% in the case of the PMC sample but only by 37.5% in the case of the GMC sample, which is in agreement with the fact that carbon nanomaterials with the lower graphitization index are easier to oxidize (Bi et al., 2008).

Figure 4A shows that GMC presents a super-hydrophobic surface, where a drop of water jumps away from the carbon nanomaterial due to their lack of affinity. The acid treatment of this material increases its affinity for water, but the surface is still hydrophobic since a drop of water deposited on its surface has a contact angle higher than 90° (shown as $\theta > 90°$ in **Figure 4B**). **Figure 4C** shows that the as-received PMC is also a hydrophobic material. However, it has lower hydrophobicity than the as-received GMC (**Figure 4A**). This is in an agreement with the fact that the hydrophobicity of carbon materials decreases as the degree of graphitization decreases (Mattia et al., 2006). In contrast, the PMCac nanomaterial is hydrophilic, which shows a contact angle of <90° (**Figure 4D**). A high affinity of the PMCac nanomaterial for water is related to the large percentage of oxygen functionalities on its surface after the acid treatment.

The DLS measurements presented in **Figure 4E** indicate that the GMC and GMCac nanomaterials aggregate very quickly and form the aggregates with a diameter around 21 μm and 14 μm, respectively. The high aggregation rate for the GMC nanomaterial probably results from a combination of its high hydrophobic forces and low electrostatic repulsion among the individual GMC nanoparticles. The presence of oxygen functionalities on the surface of the GMCac nanomaterial would lead to a decrease of the hydrophobic forces and an increase of the electrostatic repulsions, producing a decrease in its aggregation rate. Meanwhile, the DLS measurements of the PMCac nanomaterial (**Figure 4F**) indicate its low tendency to form the carbon aggregates, which is probably due to "hydrophilic repulsions" between the

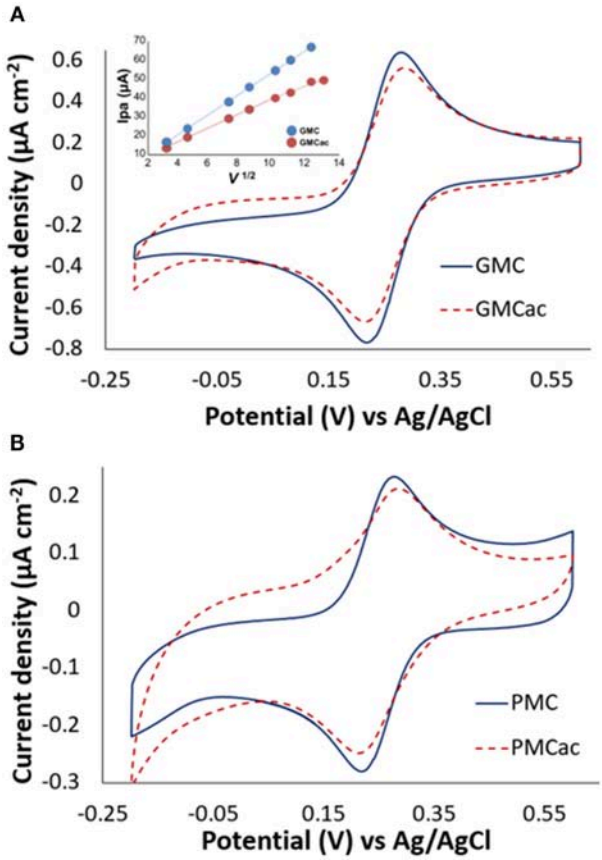

FIGURE 5 | Cyclic voltammograms of **(A)** GMC/GMCac and **(B)** PMC/PMCac obtained in 1 mM of $K_3[Fe(CN)_6]$ at 10 mV s^{-1}. The inset in A shows the plot of i_{pa} *vs.* $v^{1/2}$ *for GMC and GMCac*.

individual PMCac nanoparticles. It has been reported that water molecules can adhere to hydrophilic particles (solvation phenomena) with enough energy to create a layer on its surface that prevents the nanoparticles from aggregating with each other (Nel et al., 2009).

Electrochemical Characterization of GMC and PMC

Figure 5 presents the CV plots for the GMC, GMCac, PMC, and PMCac nanomaterials obtained in the presence of 1 mM of potassium ferricyanide in PB (100 mM, pH 7.0) at the scan rate of 10 mV s^{-1}. The CVs of the GMC and PMC show well-defined redox peaks at $E_{pc} = +0.22$ V (cathodic peak) and $E_{pa} = +0.27$ V (anodic peak). The separation between the peaks ($\Delta E_p = E_{pa} - E_{pc}$) in both cases is around 50 mV and the calculated formal potential was $E^\circ = +0.25$ V vs. Ag/AgCl. This value is close to the formal potential calculated for the $[Fe(CN)_6]^{3-/4-}$ redox reaction for a glassy carbon electrode ($E^\circ = +0.24$ V vs. Ag/AgCl), indicating the high electron transfer rate.

The effect of the acid treatment on the electrical conductivity of the carbon nanomaterials is also presented in **Figure 5**. The GMCac nanomaterial presents a 16.80% higher value of ΔE_p than that of the GMC nanomaterial (**Figure 5A**), while the PMCac nanomaterial presents a 27.20 % higher value of ΔE_p than that of the PMC nanomaterial at 10 mV s^{-1} (**Figure 5B**). This result suggests that the electron transfer capabilities of both the GMC and PMC samples have been negatively affected by the acid treatment, which may be due to the damage of their graphitic structures produced by its chemical oxidation in the H_2SO_4/HNO_3 solution. The CV tests were also conducted at different scan rates. Based on these CV data, a plot of i_{pa} vs. $v^{1/2}$ for the GMC and GMCac nanomaterials is constructed as shown in **Figure 5A**. The GMC sample presents a linear behavior with a slope of 5.53 μA $mV^{-1/2}$ $s^{1/2}$ for the entire scan range. Therefore, the GMC sample is able to efficiently transfer electrons (i.e., reversible electron transfer) with the high electron transfer rates. Meanwhile, the GMCac sample presents a linear behavior with a slope of 3.86 μA $mV^{-1/2}$ $s^{1/2}$, but only till 100 mV s^{-1}, indicating that the redox reaction deviates from the behavior proposed by the Randles-Sevcik equation at the high scan rates. This suggests that the GMCac sample experiences an irreversible electron transfer at high scan rates, confirming that the GMCac sample is less electrically conductive than the GMC sample.

The peak-to-peak potentials (ΔE_p) for the GMC and PMC samples at 100 mV-s are a) GMC: $\Delta E_p = 59.62mV$ and b) PMC: $\Delta E_p = 63.20\ mV$. Since higher values of ΔE_p are associated with lower electron transfer rates, these results indicate that the electron transfer rate of the PMC sample is smaller than that of the GMC sample. This difference is more important when the scan rate is increased (GMC: $\Delta E_p = 64.9\ mV$; PMC: $\Delta E_p = 75.25\ mV$ at 200 mV-s). The presence of an ordered graphitic layer for the GMC sample is responsible for its enhanced electrical conductivity due to the localization of the π electrons (Portet et al., 2007; Lu et al., 2009). In summary, in terms of the electrical conductivity, the GMC nanomaterial is the best selection for making the high performance GOx-nanocomposite anode material.

Morphology and Enzyme Loading of the GOx-Nanocomposites

Confocal microscopy was used to visualize the GOx-nanocomposites at higher magnifications (**Figure 6**). The locations of GOx aggregates in the confocal images were identified as bright spots due to the fluorescent property of the enzymes, while the carbon nanomaterials appear as black spots. **Figures 6a–c** show that the GOx-nanocomposites produced with the GMC, GMCac, and PMC samples present large enzyme aggregates. Thus, the physically entrapped enzyme aggregates are in a close contact with a large network of carbon nanomaterials. However, the GOx-PMCac nanocomposites are highly dispersed within the PB solution as shown in **Figure 6d**. This is in an agreement with the low aggregation tendency of PMCac observed in the DLS measurements. TEM tests were conducted in order to obtain a more detailed visualization of the small GOx-PMCac nanocomposites. The TEM image presented in **Figure 6e** shows the presence of GOx-aggregates within the PMCac network. This image suggests that the PMCac

nanomaterial is able to entrap the smaller enzyme aggregates along with a much less compact carbon network structure compared to that of the GMC, GMCac, and PMC nanomaterials.

Our elemental analyses results showed that the nanocomposites contain 0.54 ± 0.05, 0.47 ± 0.01, 0.55 ± 0.11, and 0.45 ± 0.07 mg enzyme/mg of mesoporous carbon for the GOx-GMCac, GOx-GMC, GOx-PMCac, and GOx-PMC samples, respectively. These enzyme loading results suggest that the carbon nanomaterials are able to entrap similar amounts of enzymes per amount of carbon nanomaterials. Thus, any differences observed in their electrochemical performances cannot be attributed to differences in the enzyme loading but to the differences of carbon nanoparticles' physical properties.

Electrochemical Behavior of GOx-Nanocomposites

The electrochemical performances of the GOx-nanocomposites were studied using CV tests. **Figure 7** shows the CV plots obtained for the GOx-GMC, GOx-GMCac, GOx-PMC, and GOx-PMCac samples at 100 mV s^{-1} under the N_2-saturated PB condition. **Figure 7A** presents the CV plots for the GOx-GMC sample, while the GOx aggregates and the GMC nanomaterial are shown as control. The CV plot for the GMC nanomaterial is featureless, indicating that the carbon nanoparticle by itself is not able to produce any electrochemical responses under the N_2-saturated PB condition. The CV plot corresponding to the GOx aggregates shows a small redox peak. Meanwhile, the CV test for the GOx-GMC (**Figure 7A**) shows two well-defined redox peaks: an anodic peak at −0.437 V and a cathodic peak located at −0.419 V. The fact that an improved electrochemical activity is observed for the GOx-GMC sample when compared with the GOx aggregates and the GMC nanomaterial, suggest that the compact carbon network of the GOx-GMC sample provides the enhanced electron transfer process.

The formal potential (E_o') calculated as $E_0^{'} = \frac{E_{pa} + E_{pc}}{2}$ was −0.429 V vs. Ag/AgCl, which is close to the formal potential of FAD/$FADH_2$ (Guiseppi-Elie and Baughman, 2002; Liu et al., 2007; Vogt et al., 2014; Wilson, 2016). The origin of this peak is still not clear (Luong et al., 2016; Milton and Minteer, 2017). It is currently accepted that the direct electron transfer is very difficult to occur for GOx-based enzyme electrodes because the active site of GOx is buried inside its protein structure and the surface of GOx is covered by non-conductive glycosylation layer (Wilson, 2016). This peak has been ascribed to adsorbed free FAD (flavin adenine dinucleotide) on the carbon nanomaterials or the presence of impurities in the commercial GOx (Vogt et al., 2014; Wilson, 2016). Some authors also suggested that small traces of O_2 in the solution can also promote pseudo-direct electron transfer (pseudo-DET) (Milton and Minteer, 2017). Determining the electron transfer mechanism between the active site of GOx and the electrode surface requires further study and is beyond the scope of this paper. The CV curves obtained for the GOx-GMCac and GOx-PMC nanocomposites also exhibit two redox peaks at around −0.429 V vs. Ag/AgCl (**Figures 7B,C**). Conversely, the GOx-PMCac sample shows a featureless CV plot indicating its low electrochemical activity.

According to **Figure 7**, the redox peaks of the GOx-GMC sample show higher current peak intensities than that of the GOx-GMCac and GOx-PMC samples (Ipa = 6.63 μA for the GOx-GMC vs. Ipa = 4.23 μA for the GOx-GMCac and 3.13 μA for the GOx-PMC). This may result from the enhanced electrical conductivity of the GMC sample, which arises from its high graphitization index and low concentration of oxygen functionalities on its surface (Datsyuk et al., 2008). The peak-to-peak potentials (ΔE_p) were 19.8, 27.06, and 39.72 mV for the GOx-GMC, GOx-GMCac, and GOx-PMC samples, respectively. It is known that this parameter is directly related to the electron transfer rate constant (k_s) (i.e., the decreased separation between the redox peaks indicates the faster electron transfer rate during the charge transfer reaction).

The electron transfer rate constant (k_s) for each sample was also determined by using the Laviron method for ΔE_p is $<200/n$ mV (n is the number of electrons transferred during the reaction) and the transfer coefficient value varies between 0.3 and 0.7 (Laviron, 1979). The k_s for the GOx-GMC, GOx-GMCac, and GOx-PMC nanocomposites were 6.63, 4.57, and 2.74 s^{-1}, respectively. Therefore, the GOx-GMC nanocomposite displayed the highest electron transfer rate, confirming that the as-received GMC is the best electron transfer promoting carbon nanomaterial. The value of k_s cannot be estimated for the GOx-PMCac sample since it does not show any distinctive redox peak. This result indicates that the PMCac sample doesn't facilitate the efficient electron transfer process in the system due to its low conductivity and lack of continuous carbon network.

The mechanism governing the electron transfer process in the GOx-based enzyme electrodes has been subjected to intense research with various interpretations (Vogt et al., 2014; Luong et al., 2016). This paper doesn't aim to determine the electron transfer mechanism in our GOx-nanocomposite materials. Instead, we intend to show the effect of employing different mesoporous carbons with various surface and bulk properties on the electrochemical performances of the GOx-nanocomposites.

Figure 8 shows the power density of the GOx-nanocomposites obtained in the BFC, using 10 mM glucose solution as the fuel. The values of maximum power density for the BFCs with the GOx-GMCac, GOx-GMC, GOx-PMC and GOx-PMCac bioanodes are 22.40, 15.80, 7.06, and 6.89 μW/cm^2, respectively. Because the enzyme loadings in all cases are similar, any differences observed in their maximum power density would be attributed to differences in carbon nanoparticles' properties.

The BFC with the GOx-GMC bioanode produces 2.2 times the power density of the BFC with the GOx-PMC bioanode (15.80 vs. 7.06 μW/cm^2). Furthermore, the BFC with the GOx-GMCac bioanode produces 3.2 times the power density of the BFC with the GOx-PMCac bioanode (22.40 vs. 6.89 μW/cm^2). As described in the earlier section, the GMC sample offers a more ordered carbon bulk structure and higher electrical conductivity than that of the PMC sample. Hence, our BFC results can be attributed to the higher electrical conductivity offered by the GMC nanomaterial than the PMC nanomaterial.

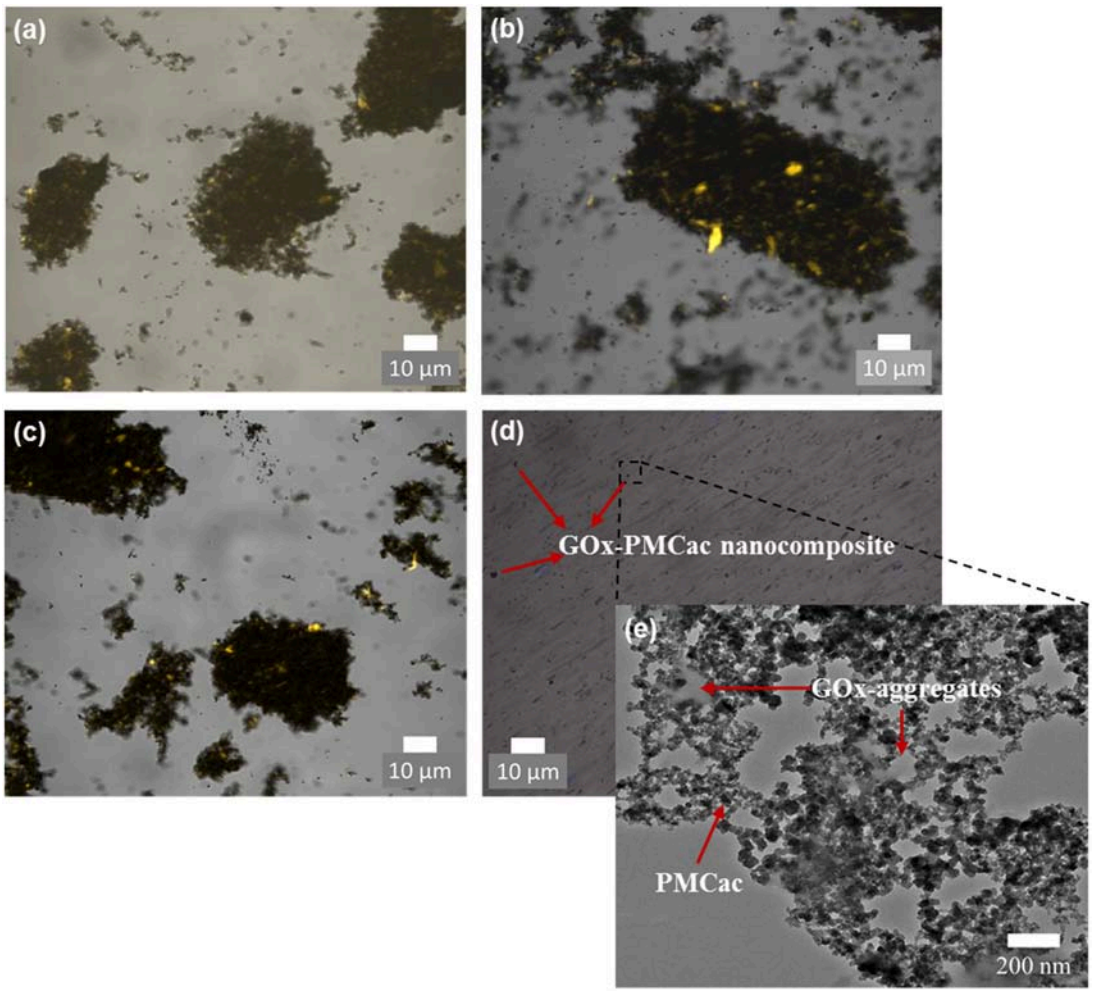

FIGURE 6 | Confocal images of **(a)** GOx-GMC, **(b)** GOx-GMCac, **(c)** GOx-PMC, and **(d)** GOx-PMCac nanocomposites; and **(e)** TEM image of the GOx-PMCac nanocomposites.

However, if the electrical conductivity of nanomaterials is the only key parameter that determines the power density of the BFC, the BFC with the GOx-GMC bioanode should provide the highest power density because the GOx-GMC offers the highest electrochemical properties and highest electron transfer rate constant (k_s) as shown in their CV tests (**Figure 5**). Nevertheless, according to **Figure 8**, the highest power density output was obtained from the BFC with the GOx-GMCac bioanode. This result suggests that the power density of the BFC does not solely depended on the electrical conductivity of the nanomaterials.

To understand this unexpected result, we need to consider the differences in the morphology of the carbon nanomaterial aggregates used. According to TEM images shown in **Figure 6**, the bright spots indicate the enzyme aggregates. It seems that the GOx-GMC sample offers a higher degree of carbon packing than that of the GOx-GMCac sample. Thus, a smaller number of bright spots (i.e., the enzyme aggregates) are exposed to the surface for the GOx-GMC sample than the GOx-GMCac sample. According to **Figure 4**, the GOx-GMC sample possesses the super hydrophobic surface property where the GOx-GMCac sample shows the decreased surface hydrophobicity due to the increased number of the surface functional group. Since the dispersion of the carbon nanomaterial in the aqueous media decreases as its surface hydrophobicity increases, the GOx-GMC sample with the higher surface hydrophobicity leads to the GOx nanocomposite material with the more compact carbon network structure than that of the GOx-GMCac sample. For the GOx-GMC sample, it seems that the carbon packing is too high where the carbon nanomaterials cover much of the enzyme aggregates at its surface and it would prevent the efficient mass transport of the fuel to the enzymes. Addition to the poor mass transport of the fuel over the surface of the GOx-GMC sample, it could also produce a very tight carbon network structure with low available internal void spaces for the efficient fuel transportation within the nanocomposite structure (Catalano et al., 2015). Consequently, the BFC with the GOx-GMCac bioanode produces the higher power density

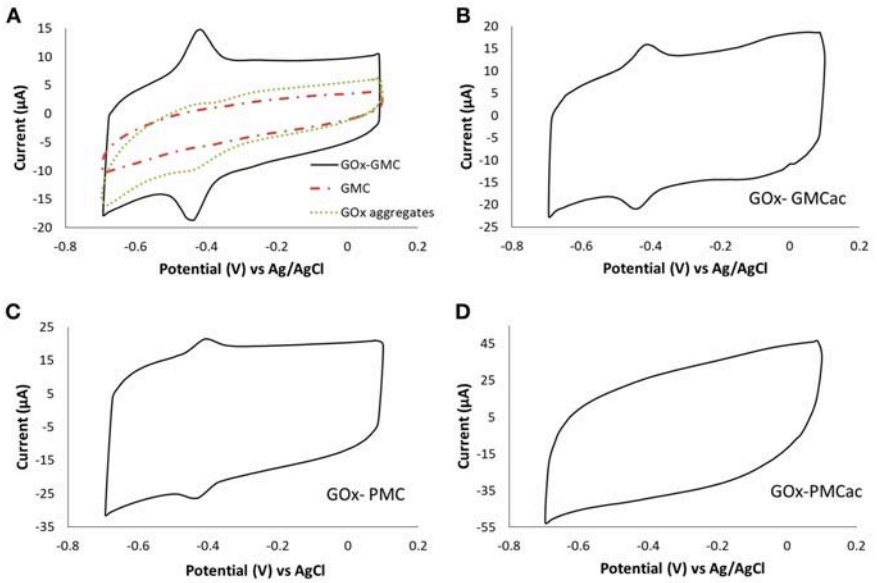

FIGURE 7 | Cyclic voltammograms of **(A)** GOx-GMC, **(B)** GOx-GMCac, **(C)** GOx-PMC, and **(D)** GOx-PMCac nanocomposites. They are obtained in a N_2 saturated PB electrolyte at a scan rate of 100 mV s^{-1}.

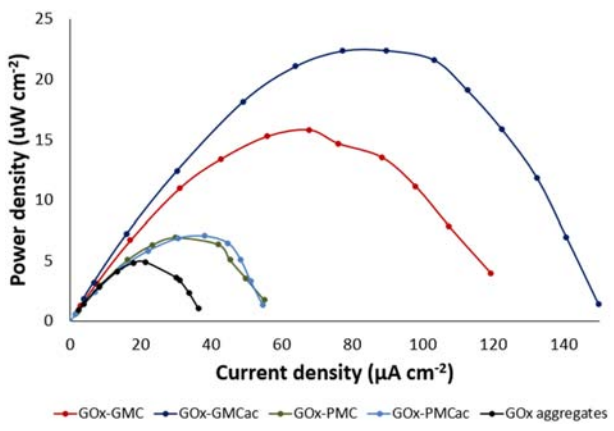

FIGURE 8 | Biofuel cell power densities, measured in 10 mM glucose solution at room temperature for GOx-GMC, GOx-GMCac, GOx-PMC, GOx-PMCac nanocomposites and GOx-aggregates anodes.

than that of the GOx-GMC bioanode where it offers both the high electrical conductivity and the efficient mass transport of the fuel.

In contrast to the GOx-GMC sample, the GOx-PMCac sample shows the most open carbon network structures with a greater number of enzyme aggregates that are exposed to the surface (**Figure 6**). Such structure would allow the high mass transport of the fuel, but it would lead to a very poor electrical conductivity because it is unable to form a continuous carbon network for the electrons to efficiently move through the system. Consequently, the BFC with the GOx-PMCac produces the one of the worst power density outputs as shown in **Figure 8**. This finding suggests that the electrochemical performance of the GOx-bioanodes is not only depended on the bulk properties (e.g., graphitization index and electrical conductivity) of the carbon nanomaterials, but it is also depended on the surface properties (e.g., concentration of surface functional group and degree of surface hydrophobicity) of the carbon nanomaterials to form the continuous carbon network structure.

CONCLUSIONS

The electrochemical performances of four GOx-nanocomposites manufactured by using four different carbon nanomaterials as the supports were studied. Our findings indicate that the physical properties of carbon nanomaterials significantly affect the electrochemical performances of the GOx-nanocomposites produced by immobilizing GOx-aggregates within a network of these carbon nanomaterials. The GOx-GMC sample offers the most efficient electron transfer rate due to its highly ordered crystalline structure and compacted carbon network structure. On the other hand, the GOx-PMCac sample offers the least efficient electron transfer rate due to its turbostratic carbon structures with a low degree of bulk organization and its inability to form the continuous carbon network (i.e., its high dispersion nature) in the aqueous media. Consequently, the BFC with the GOx-GMC bioanode produces the higher power density output than that of the GOx-PMCac bioanode. However, the highest power density of the BFC can be obtained when both the high electrical conductivity and efficient mass transport of the fuel were achieved. To this regard, the GOx-GMC sample is not the best bioanode material because its TEM image suggests that its resulted carbon network is too tight

and degree of carbon aggregate is too high for achieving the efficient mass transport of the fuel. When the GMC sample is acid treated to form the GMCac, additional surface defects were introduced decreasing both the surface hydrophobicity and the electron transport efficiency, while improving the mass transport of the fuel by reducing its tendency to form the tight carbon network. The BFC with the GOx-GMCac bioanode produced the highest maximum power density output of 22.40 $\mu W/cm^2$, which is about 42 % higher than that of the GOx-GMC bioanode. This result suggests that the positive effect of the acid treatment for the GMC material (i.e., improving the mass transport of the fuel) outweighs its negative effect (i.e., decreasing the electrical conductivity). Therefore, the GOx-nanocomposites as the effective enzyme anodes for various electrochemical applications should achieve both the high electronical conductivity and efficient mass transport of the fuel by optimizing not only its bulk property (e.g., electrical conductivity) but also optimizing its surface property (e.g., surface hydrophobicity).

AUTHOR CONTRIBUTIONS

TG-P gave significant efforts to obtain **Figures 1**, **2**, **4**–**7**. SH and LS gave significant efforts to obtain **Figure 3**. CH gave significant efforts to obtain **Figure 8**. YW gave significant efforts to develop the procedure for creating the protein aggregates for this manuscript. JK supervised our efforts to create the enzyme anode using the protein-nanocomposites. SuH supervised our efforts to conduct the physical and electrochemical property measurements of protein-nanocomposite-based enzyme anode and its biofuel cells.

FUNDING

This work was supported by the Global Research Laboratory Program (2014K1A1A2043032) and Nano-Material Technology Development Program (2014M3A7B4052193) through the National Research Foundation of Korea (NRF) funded by the Ministry of Science and ICT.

REFERENCES

Bi, H., Kou, K.-C., and Ostrikov, K., Zhang, J.-Q. (2008). Graphitization of nanocrystalline carbon microcoils synthesized by catalytic chemical vapor deposition. *J. Appl. Phys.* 104:033510. doi: 10.1063/1.2963712

Catalano, P. N., Wolosiuk, A., Soler-Illia, G. J., and Bellino, M. G. (2015). Wired enzymes in mesoporous materials: a benchmark for fabricating biofuel cells. *Bioelectrochemistry* 106(Pt A), 14–21. doi: 10.1016/j.bioelechem.2015.06.006

Chiang, Y.-C., and Lee, C.-Y. (2009). Changes in material properties and surface fractality of multi-walled carbon nanotubes modified by heat and acid treatments. *J. Mater. Sci.* 44, 2780–2791. doi: 10.1007/s10853-009-3366-2

Datsyuk, V., Kalyva, M., Papagelis, K., Parthenios, J., Tasis, D., Siokou, A., et al. (2008). Chemical oxidation of multiwalled carbon nanotubes. *Carbon* 46, 833–840. doi: 10.1016/j.carbon.2008.02.012

Falk, M., Blum, Z., and Shleev, S. (2012). Direct electron transfer based enzymatic fuel cells. *Electrochim. Acta* 82, 191–202. doi: 10.1016/j.electacta.2011.12.133

Ferrari, A. C. (2007). Raman spectroscopy of graphene and graphite: Disorder, electron–phonon coupling, doping and nonadiabatic effects. *Solid State Commun.* 143, 47–57. doi: 10.1016/j.ssc.2007.03.052

Fischback, M. B., Youn, J. K., Zhao, X., Wang, P., Park, H. G., Chang, H. N., et al. (2006). Miniature biofuel cells with improved stability under continuous operation. *Electroanalysis* 18, 2016–2022. doi: 10.1002/elan.200603626

Franklin, R. R. (1951). Crystallite growth in graphitized and non graphitized carbons. *Proc. R. Soc. Lond. Ser. A. Math. Phys. Sci.* 209, 196–218.

García, R., Pizarro, C., Lavín, A. G., and Bueno, J. L. (2013). Biomass proximate analysis using thermogravimetry. *Bioresour. Technol.* 139, 1–4. doi: 10.1016/j.biortech.2013.03.197

Garcia-Perez, T., Hong, S. G., Kim, J., and Ha, S. (2016). Entrapping cross-linked glucose oxidase aggregates within a graphitized mesoporous carbon network for enzymatic biofuel cells. *Enzyme Microb. Technol.* 90, 26–34. doi: 10.1016/j.enzmictec.2016.04.010

Guiseppi-Elie, L. C. A., and Baughman, R. (2002). Direct electron transfer of glucose oxidase on carbon nanotubes. *Nanotechnology* 13, 559–564. doi: 10.1088/0957-4484/13/5/303

Katz, E. K. (2013). Implanted biofuel cells operating *in vivo* – methods, applications and perspectives – feature article. *Energy Environ. Sci.* 6, 2791–2803. doi: 10.1039/c3ee42126k

Kim, B. C., Zhao, X., Ahn, H. K., Kim, J. H., Lee, H. J., Kim, K. W., et al. (2011). Highly stable enzyme precipitate coatings and their electrochemical applications. *Biosens. Bioelectron.* 26, 1980–1986. doi: 10.1016/j.bios.2010.08.068

Laviron, E. (1979). General expression of the linear potential sweep voltammogram in the case of diffusionless electrochemical systems. *J. Electroanal. Chem.* 101, 19–28. doi: 10.1016/S0022-0728(79)80075-3

Liu, Q., Lu, X., Li, J., Yao, X., and Li, J. (2007). Direct electrochemistry of glucose oxidase and electrochemical biosensing of glucose on quantum dots/carbon nanotubes electrodes. *Biosens. Bioelectron.* 22, 3203–3209. doi: 10.1016/j.bios.2007.02.013

Lu, X., Xiao, Y., Lei, Z., Chen, J., Zhang, H., Ni, Y., et al. (2009). A promising electrochemical biosensing platform based on graphitized ordered mesoporous carbon. *J. Mater. Chem.* 19:4707. doi: 10.1039/b903179k

Luong, J. H. T., Glennon, J. D., Gedanken, A., and Vashist, S. K. (2016). Achievement and assessment of direct electron transfer of glucose oxidase in electrochemical biosensing using carbon nanotubes, graphene, and their nanocomposites. *Microchim. Acta* 184, 369–388. doi: 10.1007/s00604-016-2049-3

MacVittie, K., Conlon, T., and Katz, E. (2015). A wireless transmission system powered by an enzyme biofuel cell implanted in an orange. *Bioelectrochem. A* 106, 28–33. doi: 10.1016/j.bioelechem.2014.10.005

Mattia, D., Rossi, M. P., Kim, B. M., Korneva, G., Bau, H. H., and Gogotsi, Y. (2006). Effect of graphitization on the wettability and electrical conductivity of CVD-carbon nanotubes and films. *J. Phys. Chem. B* 110, 9850–9855. doi: 10.1021/jp061138s

Milton, R. D., and Minteer, S. D. (2017). Direct enzymatic bioelectrocatalysis: differentiating between myth and reality. *J. R. Soc. Interface* 14:20170253. doi: 10.1098/rsif.2017.0253

Nel, A. E., Mädler, L., Velegol, D., Xia, T., Hoek, E. M., Somasundaran, P., et al. (2009). Understanding biophysicochemical interactions at the nano-bio interface. *Nat. Mater.* 8, 543–557. doi: 10.1038/nmat2442

Pantea, D., Darmstadt, H., Kaliaguine, S., and Roy, C. (2003). Electrical conductivity of conductive carbon blacks: influence of surface chemistry and topology. *Appl. Surf. Sci.* 217, 181–193. doi: 10.1016/S0169-4332(03)00550-6

Portet, C., Yushin, G., and Gogotsi, Y. (2007). Electrochemical performance of carbon onions, nanodiamonds, carbon black and multiwalled nanotubes in electrical double layer capacitors. *Carbon* 45, 2511–2518. doi: 10.1016/j.carbon.2007.08.024

Santangelo, S., Messina, G., Faggio, G., Abdul Rahim, S. H., and Milone, C. (2012). Effect of sulphuric-nitric acid mixture composition on surface chemistry and structural evolution of liquid-phase oxidised carbon nanotubes. *J. Raman Spectrosc.* 43, 1432–1442. doi: 10.1002/jrs.4097

Schwan, S. U. J., Batori, V., Ehrhardt, H., and Silva, S. R. P. (1996). Raman spectroscopy on amorphous carbon films. *J. Appl. Phys.* 80, 440–447.

Vogt, S., Schneider, M., Schäfer-Eberwein, H., and Nöll, G. (2014). Determination of the pH dependent redox potential of glucose oxidase by spectroelectrochemistry. *Anal. Chem.* 86, 7530–7535. doi: 10.1021/ac501289x

Walcarius, A. (2017). Recent trends on electrochemical sensors based on ordered mesoporous carbon. *Sensors* 17:E1863. doi: 10.3390/s17081863

Wilson, G. S. (2016). Native glucose oxidase does not undergo direct electron transfer. *Biosens. Bioelectron.* 82, vii–viii. doi: 10.1016/j.bios.2016.04.083

Conflict of Interest Statement: The authors declare that the research was conducted in the absence of any commercial or financial relationships that could be construed as a potential conflict of interest.

Copyright © 2019 Garcia-Perez, Hu, Wee, Scudiero, Hoffstater, Kim and Ha. This is an open-access article distributed under the terms of the Creative Commons Attribution License (CC BY). The use, distribution or reproduction in other forums is permitted, provided the original author(s) and the copyright owner(s) are credited and that the original publication in this journal is cited, in accordance with accepted academic practice. No use, distribution or reproduction is permitted which does not comply with these terms.

frontiers in Chemistry

ORIGINAL RESEARCH
published: 03 April 2019
doi: 10.3389/fchem.2019.00194

The Influence of Interfacial Chemistry on Magnesium Electrodeposition in Non-nucleophilic Electrolytes Using Sulfone-Ether Mixtures

*Laura C. Merrill and Jennifer L. Schaefer**

Department of Chemical and Biomolecular Engineering, University of Notre Dame, Notre Dame, IN, United States

One of the limiting factors in the development of magnesium batteries is the reversibility of magnesium electrodeposition and dissolution at the anode. Often irreversibility is related to impurities and decomposition. Herein we report on the cycling behavior of magnesium metal anodes in different electrolytes, $Mg(HMDS)_2$ – 4 $MgCl_2$ in tetrahydrofuran (THF) and a butyl sulfone/THF mixture. The deposition morphology and anode-electrolyte interface is studied and related to Mg/Mg cell cycling performance. It is found that adding the sulfone caused the formation of a boundary layer at the electrode-electrolyte interface, which, in turn, resulted in a particle-like deposition morphology. This type of deposition has a high surface area, which alters the effective local current density and results in electronically isolated deposits. Extended cycling resulted in magnesium growth through a separator. Electrolyte decomposition is observed with and without the addition of the sulfone, however the addition of the sulfone increased the degree of decomposition.

Keywords: magnesium battery, electrodeposition, electrolyte, sulfones, interface, dendrite

OPEN ACCESS

Edited by:
Nosang Vincent Myung, University of California, Riverside, United States

Reviewed by:
Juchen Guo, University of California, Riverside, United States
Abhishek Lahiri, Clausthal University of Technology, Germany

****Correspondence:***
Jennifer L. Schaefer
jennifer.l.schaefer.43@nd.edu

Specialty section:
This article was submitted to Electrochemistry, a section of the journal Frontiers in Chemistry

Received: *31 January 2019*
Accepted: *14 March 2019*
Published: *03 April 2019*

Citation:
Merrill LC and Schaefer JL (2019) The Influence of Interfacial Chemistry on Magnesium Electrodeposition in Non-nucleophilic Electrolytes Using Sulfone-Ether Mixtures. Front. Chem. 7:194. doi: 10.3389/fchem.2019.00194

INTRODUCTION

Demands for high performance batteries have increased with the use of portable electronic devices and electric vehicles, leading to growth in research of post lithium-ion batteries. The use of metallic anodes, as opposed to intercalation anodes, creates an opportunity to meet these high performance metrics. A metallic anode is entirely comprised of active material, thus the theoretical energy density is inherently greater than traditional lithium-ion anodes that use host matrices. Magnesium is a viable anode option as it has large theoretical volumetric and gravimetric capacities (3,800 mAh/cm^3 and 2,200 mAh/g respectively), relatively low electrodeposition potential (−2.4 V vs. SHE), and is widely abundant in the Earth's crust.

Magnesium has gained attention as a post lithium-ion anode material following the first magnesium battery prototype developed in the early 2000s (Aurbach et al., 2000). This prototype used an electrolyte composed of a Grignard reagent complexed with a Lewis acid to achieve highly reversible electrodeposition (Aurbach et al., 2000; Amir et al., 2007; Viestfrid et al., 2007). Recent progress has focused on non-Grignard chemistries through use of alternative electrolytes, such as magnesium alkoxides or magnesium bis(hexamethyldisilizide) ($Mg(HMDS)_2$) complexed with a chloride salt ($MgCl_2$ or $AlCl_3$) in tetrahydrofuran (THF) (Kim et al., 2011; Herb et al., 2015; Liao et al., 2015; Pan et al., 2015), and $Mg(TFSI)_2$, or $Mg(BH_4)_2$ in dimethoxyethane (DME) or higher order glymes (Mohtadi et al., 2012; Ha et al., 2014). Despite this progress, magnesium battery research has been hindered by low electrodeposition/dissolution efficiencies; the use of a

metallic anode requires Coulombic efficiencies >99% for practical application (Wang et al., 2018). In the presence of trace impurities and certain salts and solvents, the metal is able to form a stable passivating layer that prevents the magnesium ions from reaching the active magnesium metal surface, thus not allowing electron transfer to occur. Because of this, only certain salt and solvent combinations have resulted in reversible magnesium electrodeposition.

Recently there has been interest in magnesium deposition and how deposition kinetics can influence the resultant morphology (Viestfrid et al., 2005; Matsui, 2011; Wetzel et al., 2015; Crowe et al., 2017). Early magnesium battery research suggested that it is unfavorable for magnesium to form dendrites, unlike lithium metal; this is attributed to differences in the crystal structures of each metal (Ling et al., 2012; Jäckle and Groß, 2014; Lautar et al., 2019). Although magnesium is less likely to form dendrites compared to lithium, dendritic magnesium deposits been observed with both complex and simple salt electrolytes (Ding et al., 2018; Davidson et al., 2019). In particular, $Mg(TFSI)_2$ systems were found to short circuit cells due to the formation of an unstable solid electrolyte interphase (SEI), resultant from the partial decomposition of $Mg(TFSI)_2$ (Ding et al., 2018; Kang et al., 2019).

Previously, we reported that the addition of sulfones to an electrolyte could increase the thermal stability, however electronically isolated deposits upon continued cycling were also observed (Merrill and Schaefer, 2018). Here, we report on the crystallinity and morphology of the magnesium deposits from electrolytes with and without the sulfone as a function of current density and substrate. We also probe the interfacial impedances throughout galvanostatic cycling and relate these findings to the morphologies observed. It was found that the sulfone based electrolytes result in high surface area deposition morphologies, such a hemispheres, compared to the electrolyte containing only THF; this is attributed to the influence of a boundary layer at the electrode that forms with the addition of the sulfone.

MATERIALS AND METHODS

Materials and Electrolyte Solutions

Tetrahydrofuran (99.9%, THF), magnesium bis(hexamethyldisilazide) (97%, $Mg(HMDS)_2$), di-n-butylsulfone (99%, BS), and magnesium chloride (99.99%, $MgCl_2$) were purchased from Sigma Aldrich, and ethyl methyl sulfone (98%, EMS) was purchased from TCI. All solvents were distilled under nitrogen flow on a Schlenk line. $Mg(HMDS)_2$ was recrystallized from anhydrous n-heptane (Sigma Aldrich) in a glovebox prior to use. All solvents and solvent mixtures were dried using molecular sieves for at least 48 h before making the electrolytes. Only new or acid washed glassware was used, and all glassware was dried in a 120°C convection oven. The electrolyte formulations were $Mg(HMDS)_2$ – 4 $MgCl_2$ (nominally 1.25 M Mg) in THF, 50 THF/50 BS (v/v), and 50 THF/50 EMS (v/v). Electrolytes were prepared as described in previous work (Liao et al., 2015; Merrill and Schaefer, 2018).

Magnesium (99.95%, Solution Materials, LLC), copper (McMaster Carr), and platinum (Alfa Aesar) were used as electrode materials for this study. Platinum was cleaned with concentrated nitric acid, then washed with MilliQ water, and dried in a 120°C convection. Copper was sonicated in isopropanol and then dried. Magnesium was scraped to remove its native oxide layer, then polished with 1,200, 2,000, and 3,000 grit sand paper, washed with anhydrous THF, then scraped again to further smooth the surface. **Supplementary Figure 1** shows electron micrographs of the bulk magnesium surface before and after the final scraping step.

All electrolytes and electrochemical cells were prepared in an argon filled glovebox with <5 ppm oxygen and moisture. Coin cell measurements were completed outside of the glovebox.

Electrochemical Measurements

All electrochemical measurements were taken using a PARSTAT MC1000 from Princeton Applied Research.

Galvanostatic electrodeposition was carried out in a 2 electrode solution cell. The working electrode was either magnesium, copper, or platinum and a magnesium strip was used as the counter/reference electrode. Currents of 1 and 0.5 mA/cm^2 were applied until the total charge passed was 1 C/cm^2 for microscopy characterization or 10 C/cm^2 for X-ray diffraction (XRD) measurements.

Chronoamperometry measurements were completed using a 2 electrode solution cell. The working electrode was copper and the counter/reference electrode was magnesium. The cell was held at open circuit for 10 s followed by a potential step for 10 s. Overpotentials used include −250, −375, and −500 mV vs. Mg^0/Mg^{2+}.

Galvanostatic cycling and impedance were carried out in symmetric Mg/Mg CR2032 coin cells. The cells were assembled in an argon filled glovebox. A dried glass fiber separator was used to support the electrolyte. A current of −0.5 mA/cm^2 was applied for 1,000 s followed by +0.5 mA/cm^2 for 1,000 s. Impedance measurements were taken every five cycles, with an amplitude of 10 mV RMS and a frequency range of 10 kHz to 1 Hz.

X-ray Diffraction (XRD)

XRD measurements were obtained using a Bruker D8 Advance Davinci with a SOL-XE energy dispersive x-ray detector. Measurements were taken in the range of 20 and 70°, with a step size of 0.004°, and a step time of 2.5 s. Only copper was used as the substrate for magnesium deposition for XRD measurements. Measurements were taken on a silicon crystal zero diffraction plate from MTI Corporation.

Scanning Electron Microscopy (SEM)

SEM images were taken using an FEI Magellan 400 microscope with a voltage of 10 kV and a current of 50 pA at a working distance of 4.3 mm. Elemental analysis was completed using a Bruker energy dispersive x-ray spectrometer (EDS) at a working distance of 4.7 mm with an increased current to achieve adequate signal (>1,000 cps). Samples were washed with anhydrous THF then put under vacuum prior to characterization. A Pelco SEM pin stub vacuum desiccator was used to transfer samples from the lab to the microscope to minimize air exposure.

X-ray Photoelectron Spectroscopy (XPS)

XPS measurements were taken using a PHI VersaProbe II. Point scans were taken with a 50 W power X-ray. Prior to measurements, samples were sputtered for 2 min with 2 kV Ar^+ to clean the surface. Survey measurements were taken with a 187.85 eV pass energy over 7 scans. Each individual binding energy measurement was taken with a 23.5 eV pass energy for 12 scans. A 100 ms time step was used for all scans. Samples were washed with THF and dried under vacuum prior to analysis, then transferred to the instrument using the Pelco pin stub holder, however air exposure could not be completely avoided upon transfer into the machine's sample holder.

RESULTS AND DISCUSSION

Morphologies of Magnesium Deposits

Magnesium was deposited from each electrolyte at different current densities onto copper, platinum, and magnesium. Previous reports of magnesium deposition showed that for a Grignard based electrolyte, increasing the current density will bring it into a mass transport limited regime. Once the system is mass transport limited, the magnesium will not be able to optimize its direction of growth (Viestfrid et al., 2005; Matsui, 2011). This can then result in the magnesium crystal growing in the perpendicular direction to the substrate or growing in the same direction as the crystal facets within the substrate. Low current results in operation in the charge transport limited regime. This allows the magnesium to nucleate on the substrate and grow in a thermodynamically controlled manner, often resulting in high surface area deposits. As shown in **Supplementary Figure 2**, the formation of spherical magnesium deposits can ultimately increase the effective local current density, leading to decomposition that is evident from the charging on the deposits in the SEM images. In this work, we focus on magnesium electrodeposition at moderate (0.5 mA/cm^2) and high (1 mA/cm^2) current densities.

At 0.5 mA/cm^2, there are significant differences in the morphology of the deposits from the 50 BS/50 THF electrolyte and THF electrolyte, as depicted in **Figure 1**. This is particularly evident on the copper and platinum substrates. The deposition from the 50 BS/50 THF electrolyte consists of deposits that are spaced apart, suggesting that the magnesium was able to nucleate at different points on the substrate, but the clusters of magnesium did not merge together. Areas of charging (apparent from areas of brightness on the SEM image), caused by non-conductive materials, are present around the edges of the spherical deposits. This non-metallic material could be produced due to electrolyte decomposition or a disruption in the electric field. The THF electrolyte exhibits very flat deposition composed of small, uniform crystals; an increased magnification of the SEM image is shown in **Supplementary Figure 3**. The magnesium clusters deposited from the THF electrolyte were able to merge after the initial nucleation. For both electrolytes, the deposition is more disperse on the bulk magnesium sheet metal, and appears to grow along the ridges of the bulk material; the deposits will typically form at imperfections on the metal that generated during the removal of the passivation layer by mechanical scraping. The deposit from the THF electrolyte has a greater degree of agglomeration compared to the deposit from the 50 BS/50 THF electrolyte.

When the current density was increased to 1 mA/cm^2, the deposits became flatter and more uniform, as shown in **Figure 2**. This is likely because the increased current density does not allow for the magnesium deposits to optimize the crystal orientation, like at lower currents. However, as shown in **Supplementary Figure 4**, the morphology of the magnesium deposit varies throughout the copper substrate, likely due to the influence of different crystal facets throughout the copper. The deposits from the 50 BS/50 THF electrolyte are more uniform and flat on the platinum substrate, compared to the copper, confirming that the substrate used will alter the interfacial chemistry. Again, the deposit from the THF electrolyte resulted in smooth deposition, in particular on copper. The deposition on the magnesium substrate resulted from the agglomeration of islands, however at the higher current each cluster is smaller, which is characteristic of the increased current density.

As shown in **Figure 3**, the magnesium deposited at 0.5 mA/cm^2 on copper preferentially grows along the (1 0 1) crystal plane for both electrolytes, which is the plane with the highest surface area fraction (Lautar et al., 2019). This observation suggests that the interactions between the electrolyte and the metal are more favorable. If the electrolyte-metal interface is thermodynamically preferred, then the deposit will grow such to maximize the surface area in contact with the electrolyte. The deposit from the 50 BS/50 THF electrolyte is less crystalline, evident from both decreased peak intensity and an increased full width half maximum, compared with the signal of the deposit from the THF electrolyte. The amorphous nature may be due to the high surface area nature of the deposits or due to a greater degree of decomposition.

The corresponding XRD of the deposits grown at 1 mA/cm^2 show that different magnesium crystal orientations result from electrodeposition from each electrolyte, shown in **Figure 4**. The deposit from the THF electrolyte has increased crystallinity and a higher fraction of (0 0 2) orientation. This change in crystal orientation with current density suggests that the system with the THF electrolyte reached a transport limited regime at 1 mA/cm^2. As shown in **Supplementary Figure 5**, the (0 0 2) plane is the primary plane in the copper substrate. The deposit from the 50 BS/50 THF electrolyte continues to deposit preferentially in the (1 0 1) plane, again with a lower degree of crystallinity. Because the 50 BS/50 THF electrolyte has a lower ionic conductivity (0.8 vs. 1.5 mS/cm at 30°C), it is unlikely that the THF electrolyte would enter a mass transport limited regime at a lower current than the 50 BS/50 THF electrolyte (Merrill and Schaefer, 2018). This suggests that the interfacial chemistry between the 50 BS/50 THF electrolyte and the substrate drives the resultant morphology, and that the interfacial chemistry with the THF electrolyte is different.

It is noted that the deposits from each electrolyte look different to the naked eye. The deposits from the THF electrolyte are a silvery-white color whereas the deposits from the 50 BS/50 THF electrolyte are black (see **Supplementary Figure 6**). As shown in our previous work, there is minimal decomposition therefore

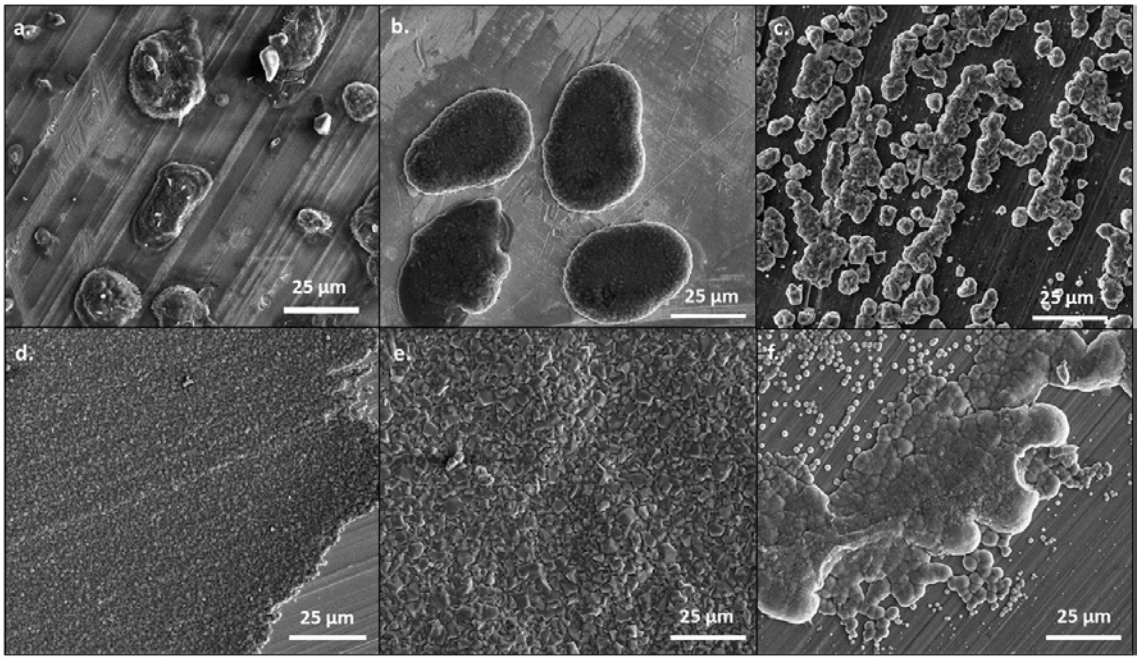

FIGURE 1 | SEM images of magnesium plated at 0.5 mA/cm^2. A total of 1 C of charge was passed for each sample. Magnesium metal was plated from the 50 BS/50 THF electrolyte on **(A)** copper, **(B)** platinum, and **(C)** magnesium; and from the THF electrolyte on **(D)** copper, **(E)** platinum, and **(F)** magnesium. All images are shown at a magnification of 1000x.

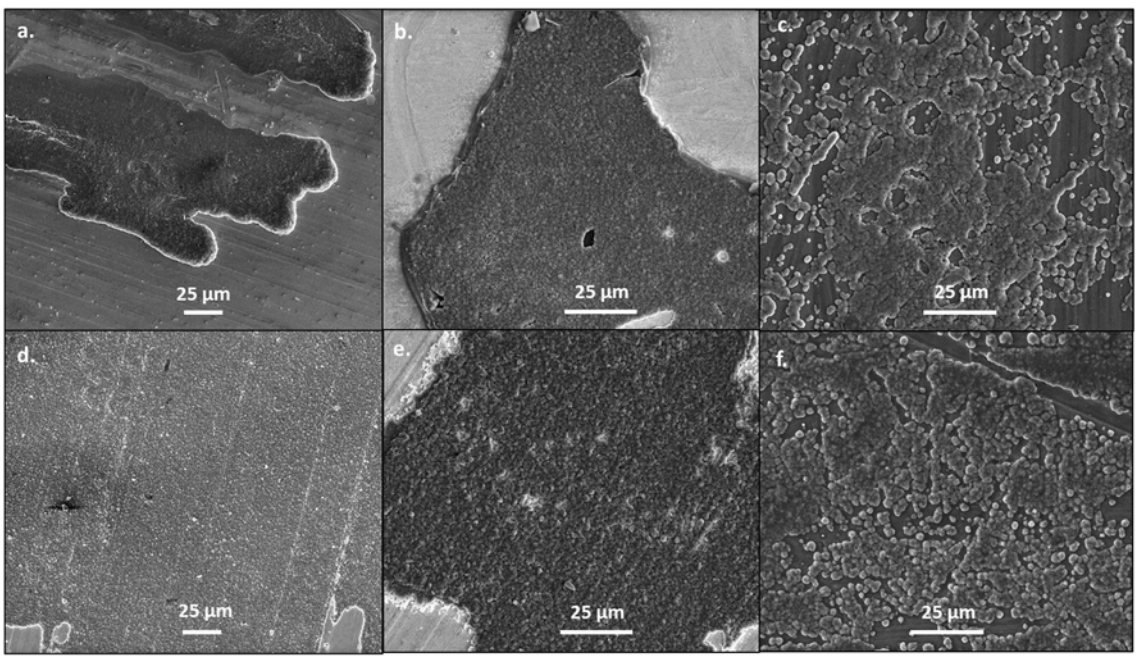

FIGURE 2 | SEM images of magnesium plated at 1 mA/cm^2. A total of 1 C of charge was passed for each sample. Magnesium metal was plated from the 50 BS/50 THF electrolyte on **(A)** copper, **(B)** platinum, and **(C)** magnesium; and from the THF electrolyte on **(D)** copper, **(E)** platinum, and **(F)** magnesium. All images are shown at a magnification of 1000x.

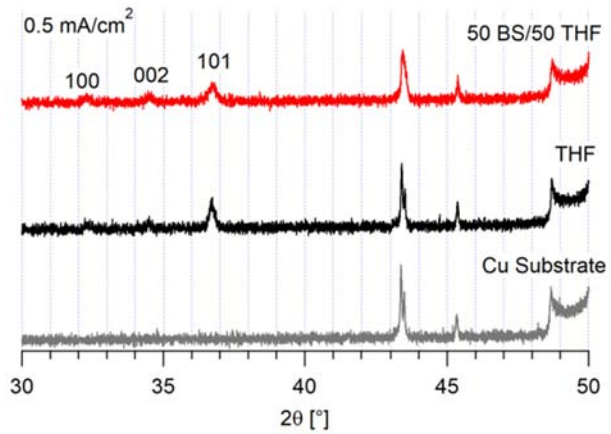

FIGURE 3 | XRD of magnesium deposits on a copper substrate. 10 C of charge was passed at 0.5 mA/cm^2.

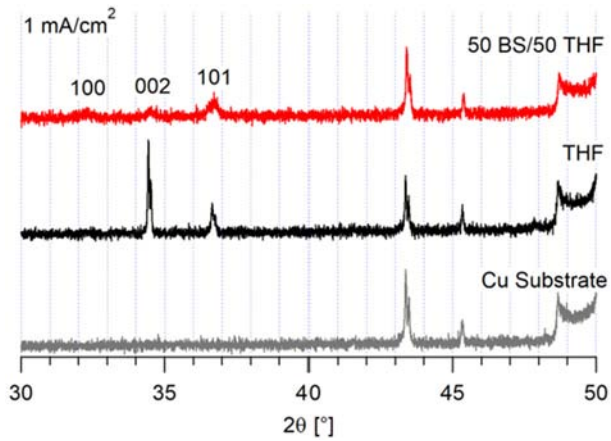

FIGURE 4 | XRD of magnesium deposits on a copper substrate. 10 C of charge was passed at 1 mA/cm^2.

the resultant black color is likely related to the particle-like morphology (Merrill and Schaefer, 2018).

Chronoamperometry experiments were completed to further interrogate the deposition and nucleation processes for each electrolyte. The current response to a potential step is different for the two electrolytes, as shown in **Supplementary Figure 7**. The 50 BS/50 THF electrolyte begins with a large current, which immediately drops, followed by a slow increase and the beginnings of a plateau. This initial large current may be attributed to polarization of ions in the boundary layer at the electrode/electrolyte interface; this large current obscures the current due to the initial nucleation process in the 50 BS/50 THF electrolyte. In the transient for the THF electrolyte, a small local maximum is present, followed by similar behavior to the mixed solvent electrolyte. The local maximum is likely representative of the initial magnesium nucleation. Because the electron transfer reaction is hypothesized to be preceded by a chemical equilibrium step (Ta et al., 2018), it is likely that the chemical equilibrium step causes the initial decrease in current for each electrolyte. The Cottrell equation could not be fit to either electrolyte; therefore, the Scharifker and Hill models for instantaneous and progressive nucleation could not be directly applied to this system (Scharifker and Hills, 1983). Nevertheless, the local maxima in the THF electrolyte were used to plot a dimensionless graph of i^2/i_m^2 vs. t/t_m (**Supplementary Figure 8**), and suggest the formation of nucleation sites at short time scales. The complexity of the magnesium electrolytes are attributed to the changes from the ideal behavior, as previously derived to describe other systems (Scharifker and Hills, 1983); the magnesium electrolytes likely contain multiple electrochemically active complex cations with varying diffusivities. Additionally, the magnesium electrolytes facilitate boundary layer formation at the electrode/electrolyte interface when the system is at rest, as described below.

Impedance and Cycling

Symmetric magnesium coin cells were cycled 100 times at 0.5 mA/cm^2, starting with a negative current. Impedance measurements were taken every 5 cycles after the positive current. This was done to learn about the interfacial impedances throughout cycling and to determine if either passivation, or soft short circuiting, would be observed throughout extended cycling. Soft short circuiting is a phenomenon where the magnesium deposit is partially passivated and slowly grows through the separator, eventually making contact with the counter electrode, therefore short circuiting the cell. This has been observed with $Mg(TFSI)_2$ electrolytes, which are unstable in the presence of magnesium metal (Ding et al., 2018; Kang et al., 2019).

As shown in **Figure 5**, there are very large differences in resistance for each electrolyte during galvanostatic cycling. The THF electrolyte initially starts with a high overpotential of ~0.4 V vs. Mg, which then decreases throughout cycling. The 50 BS/50 THF electrolyte shows a similar decrease in overpotential during the first few cycles, however a much greater overpotential is maintained throughout cycling (about 200 vs. 75 mV). This is in part due to the greater bulk resistance caused by the lower conductivity of the 50 BS/50 THF electrolyte. Therefore, to maintain the same current, a higher overpotential is required. Over extended cycling, there is a gradual increase in overpotential for the case with the 50 BS/50 THF electrolyte; indicating an increase in resistance. The cycling behavior of a wet THF electrolyte (40–60 ppm moisture) was similar to that of an electrolyte made with dried THF. This confirms that the large over potentials present in the chronopotentiogram are unique to the sulfone electrolyte, and not related to the existence of residual water or passivation of magnesium due to residual water.

The corresponding Nyquist plots give more information about the impedances within the cells. For the THF electrolyte, there is a decrease in interfacial impedance throughout cycling until the cells appear to reach a steady state (around cycle 60), shown in **Figure 6A**. This is represented by the initial high overpotential, which then decreases and plateaus throughout cycling. The bulk impedance stays fairly constant throughout cycling. The decreasing interfacial impedance in the first 60 cycles is possibly due to a combination of two phenomena: one being the removal of trace water in the electrolyte, and the

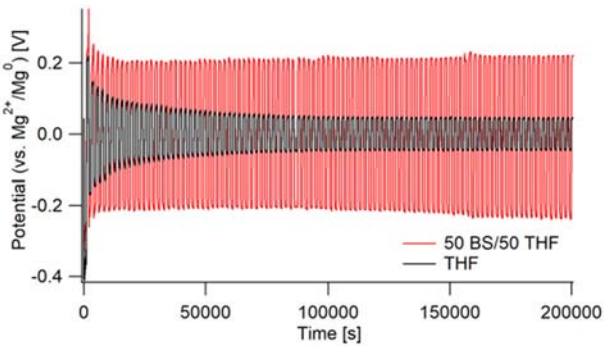

FIGURE 5 | Galvanostatic cycling of Mg/Mg cells in 50 BS/50 THF (red) and THF (black). Cells were cycled at a current of 0.5 mA/cm^2 for 1,000 s, starting with a negative current, then switching to a positive. This was repeated for 100 cycles with impedance measurements taken every 5 cycles.

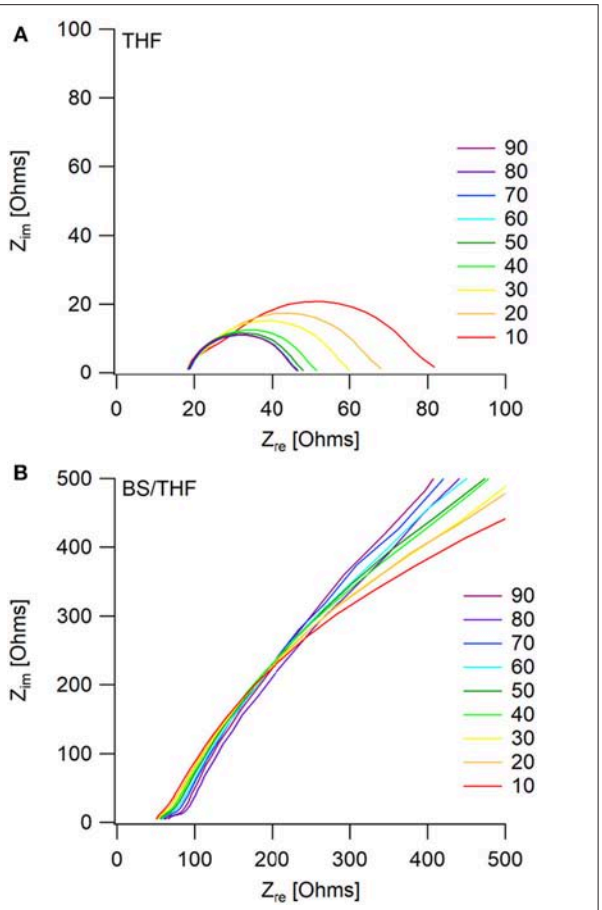

FIGURE 6 | Impedance measurements taken every 5th cycle (only multiples of 10 are shown for visual clarity) after the positive current step, during galvanostatic cycling. Mg/Mg cells were cycled in **(A)** the THF electrolyte and **(B)** the 50 BS/50 THF electrolyte.

other due to a native surface layer that forms on the electrodes as previously described by the Aurbach group (Lu et al., 1999; Doron Aurbach et al., 2003; Viestfrid et al., 2005; Attias et al., 2019). **Supplementary Figure 9** shows that the interfacial impedances for the wet THF and the dry THF electrolytes are comparable.

The similar decrease in overpotential during the first couple cycles of the 50 BS/50 THF electrolyte is likely due to the same phenomena as described with the THF electrolyte, however, a decrease in interfacial impedance is not observed, as shown in **Figure 6B**. Instead, there is a very large interfacial impedance present throughout cycling. A similar impedance is observed in the pristine cells for both electrolytes (**Supplementary Figure 10**), however after the application of a current, the interfacial impedance greatly decreases in the THF electrolyte. This impedance is caused by the formation of a boundary layer at the electrodes; because the sulfone group is polarizable and the alkane chains are able to stack, it is plausible that this boundary layer is stabilized. This boundary layer could be the cause of the high surface area deposition morphology by altering the interface. Provided the interaction between the metal and the boundary layer is more thermodynamically favorable, the deposit would grow to maximize its surface area to allow more of the metal to be in contact with the boundary layer.

The bulk resistance does increase with continued cycling, likely due to solvent loss via decomposition. As previously reported, the 50 BS/50 THF electrolyte is able to maintain Coulombic efficiencies around 90–95%, suggesting that there is a small amount of electrolyte decomposition (Merrill and Schaefer, 2018). Therefore, the gradual increase in bulk resistance and overpotential throughout cycling is related to the gradual buildup of a passivating surface layer. Over extended cycling the impedance continues to grow, suggesting that the cell will become fully passivated.

Post Mortem Analysis

SEM/EDS

Upon post-mortem analysis of the cells, the cycling of the 50 BS/50 THF electrolyte caused the separator to turn black whereas the separator used with the THF electrolyte had minimal discoloration in it (**Supplementary Figure 11**). This suggests decomposition of the 50 BS/50 THF electrolyte and/or the growth of the magnesium through the separator. The electrode used with the THF electrolyte was silvery-white whereas the electrode used with the 50 BS/50 THF electrolyte remained gray with large amounts of the glass fiber separator sticking to it, evidence that the magnesium began to grow through the separator. The SEM images in **Figures 7A**,**B** show the magnesium electrodes after a final stripping step. The electrode cycled with the 50 BS/50 THF electrolyte had areas of charging indicating partial decomposition. The electrode cycled with the THF electrolyte was more compact with the appearance of a higher degree of crystallinity. Because the resultant deposits from the 50 BS/50 THF electrolyte prefer a particle-like morphology, it is likely that the deposits are able to grow through the separator. Furthermore, as discussed earlier, this type of deposition can result in high local current densities which can lead to solvent decomposition.

Elemental analysis of the SEM-imaged surfaces are presented in **Figure 7C**. Increased proportions of elements other than

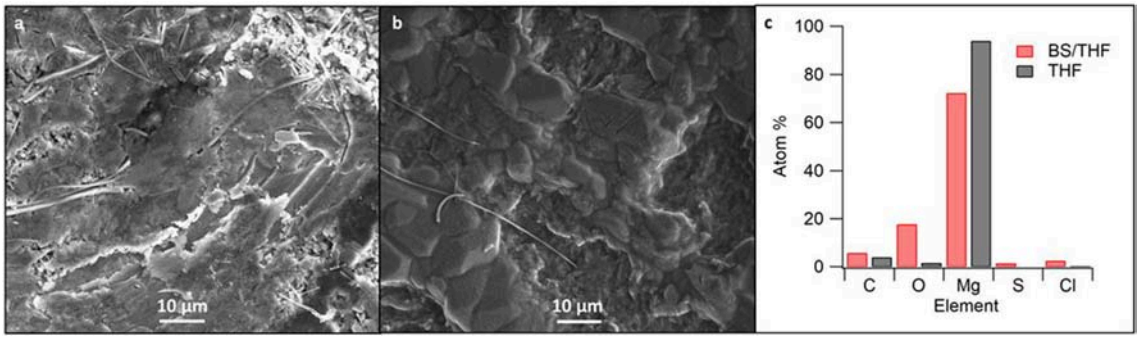

FIGURE 7 | SEM images of cycled magnesium in **(A)** the 50 BS/50 THF electrolyte and **(B)** the THF electrolyte. SEM images were taken at 1000x magnification; **(C)** shows the corresponding elemental composition as detected by EDS measurements.

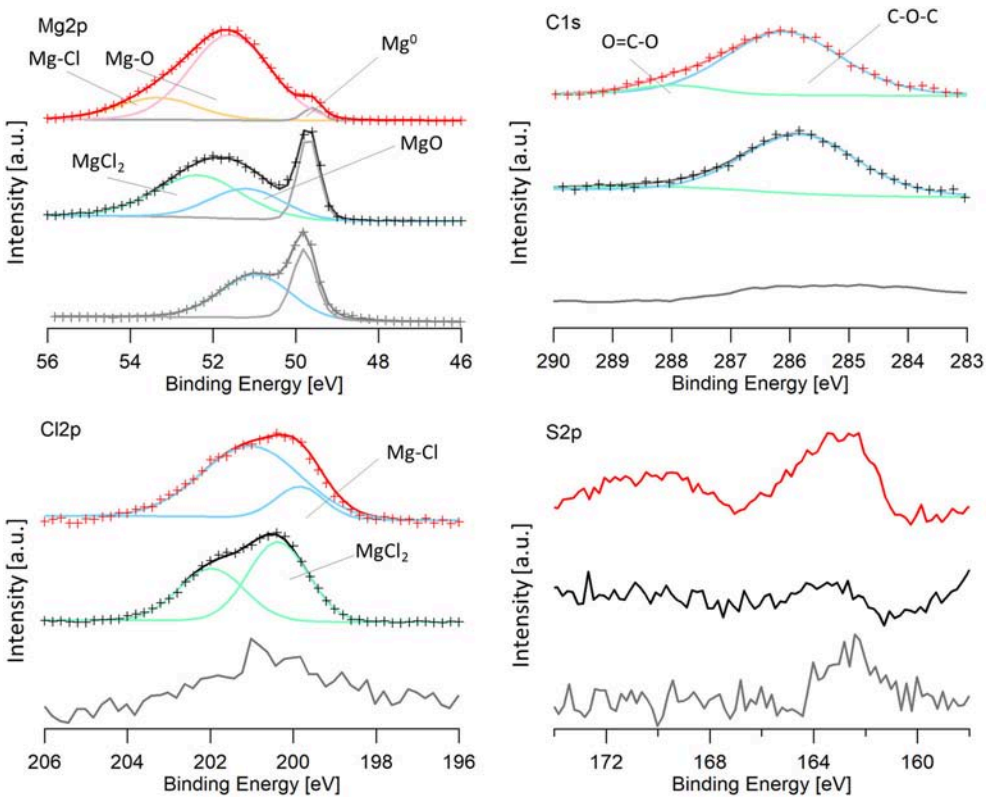

FIGURE 8 | XPS spectra of an Mg electrode cycled in the 50 BS/50 THF electrolyte (red), an Mg electrode cycled in the THF electrolyte (black), and a pristine magnesium electrode (gray). For data that is fit: the experimental data is shown by the crosses and the line with the same color is the calculated fit. Peaks are shown by blue, green, pink, orange, and gray lines and are labeled on the image. Mg-Cl and Mg-O labels on the graph refer to a magnesium-chloride species (such as RMgCl or adsorbed MgCl) and a magnesium-oxygen species (such as $Mg(OR)_2$ or $Mg(OH)_2$) and are a different from $MgCl_2$ and MgO.

magnesium are present in the deposit from the sulfone-ether electrolyte. Given that the Coulombic efficiency is <100%, the non-magnesium species are likely due to a decomposition product, such as solvent decomposition during deposition. This is further discussed with the XPS data. Alternatively, it is possible that the mixed solvent electrolyte contains a higher degree of impurities; although the butyl sulfone was distilled, its purity has not been determined.

XPS of Cycled Electrodes

Magnesium electrodes were characterized via XPS after the last dissolution step in the 100 cycles. The spectra from a pristine magnesium metal foil was included for a baseline comparison. Because oxidation was unable to be avoided upon transfer, as described in the experimental section, samples were sputtered for 2 min with Ar^+. The spectra were calibrated to the lowest energy magnesium peak, assumed to be Mg^0 (49.6 eV), because of the

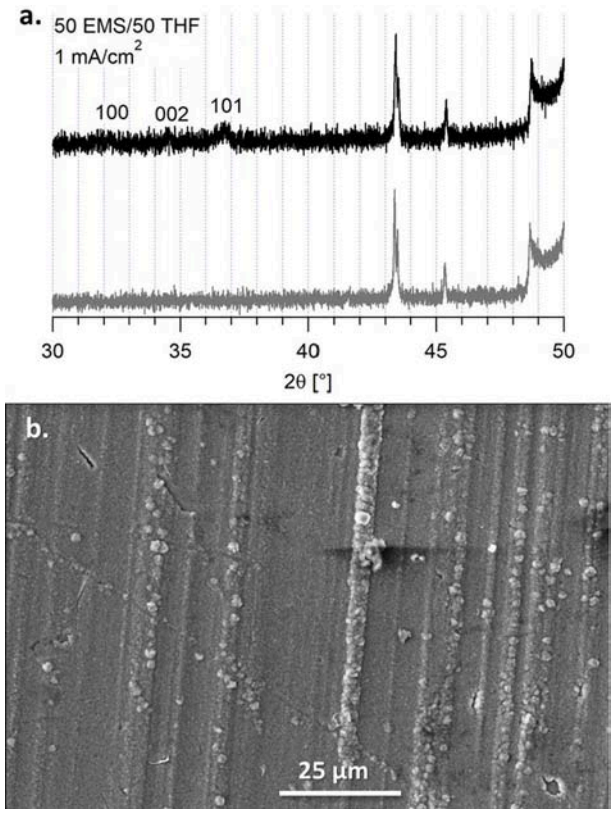

FIGURE 9 | (A) XRD of the deposit from the 50 EMS/50 THF electrolyte on a copper substrate (black) and the copper substrate (gray). **(B)** SEM image of the deposit from the 50 EMS/50 THF electrolyte on a copper substrate at a current density of 1 mA/cm^2, taken at a magnification of 1000x.

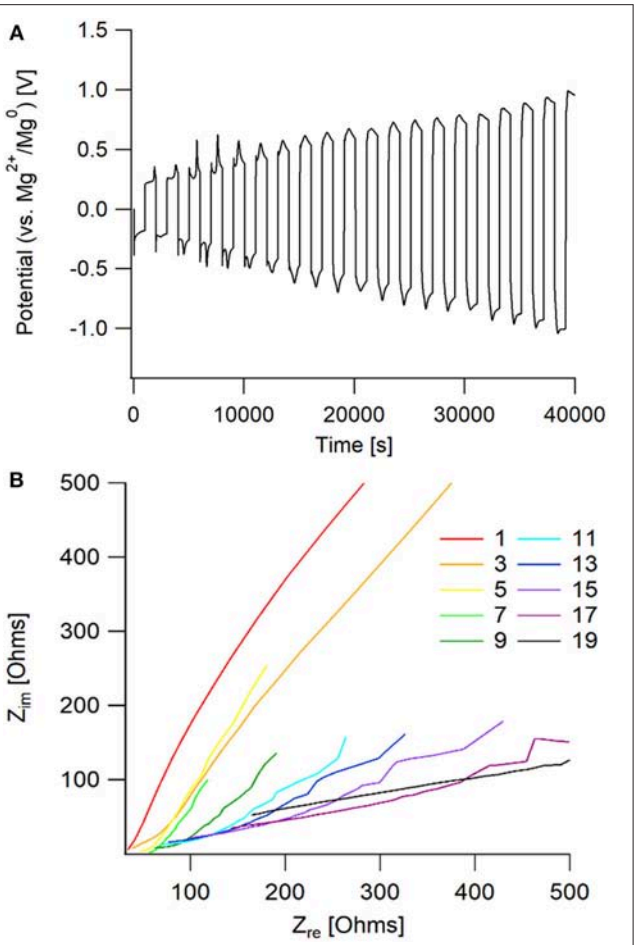

FIGURE 10 | (A) Potential vs. time graph of galvanostatic cycling of an Mg/Mg cell with the 50 EMS/50 THF electrolyte. **(B)** Nyquist plot of the impedance taken every other cycle for the galvanostatic cycling. Impedance measurements were taken after completion of the full cycle, following the positive current step.

low carbon signal. The Mg2p, Cl2p, S2p, and C1s regions are shown in **Figure 8**, for the cycled electrodes.

It is immediately evident that both cycled electrodes have a higher degree of oxidation compared to the pristine magnesium. However, the sample cycled in the 50 BS/50 THF electrolyte has a larger amount of decomposition products present, evident from the smaller metallic magnesium peak. Some oxidation may be attributed to transfer, considering the pristine magnesium metal is partly oxidized. The electrode cycled in the THF electrolyte has an oxidation peak with the same binding energy as the oxidation of the pristine electrode, shown in blue, and it is likely due to the formation of magnesium oxide. This peak is shifted to a slightly higher binding energy for the electrode cycled in the 50 BS/50 THF electrolyte. This is likely due to an Mg-O bond as well, but is attributed to a different species (ex. $Mg(OR)_2$ or $Mg(OH)_2$), resultant from decomposition.

Both of the cycled electrodes show a higher binding energy peak in the magnesium XPS spectra that is due to an Mg-Cl bond, also identified in the Cl2p region. The active species is a magnesium chloride cation and an adsorption step precedes the electron transfer, which can cause the Mg-Cl peak to be present (Doron Aurbach et al., 2003; Viestfrid et al., 2005; Attias et al., 2019). For the magnesium electrode cycled in the THF only electrolyte, the Cl2p region contains $MgCl_2$, evident from its binding energy around 200 eV (Magni and Somorjai, 1996). The residual $MgCl_2$ on the cycled electrode is due to its low solubility in THF; similar reports have been shown for $MgBr_2$ (Wetzel et al., 2015). The Cl2p peak for the electrode cycled in the mixed solvent electrolyte was shifted slightly lower (199.6 eV) (Moulder et al., 1992). This binding energy is evident of a metal-chloride (ex. RMgCl, or adsorbed MgCl), suggesting the formation of a different Mg-Cl species. This species may be resultant from the adsorption step as discussed above or a decomposition product. The Cl2p spectra for both electrodes show the presence of a secondary peak, which is due to the spin orbit splitting (Moulder et al., 1992).

The carbon spectra for magnesium electrodes cycled in each electrolyte features a major peak at 286 eV and a smaller peak at 288 eV which is characteristic of C-O-C and O-C=O, respectively. Because the XPS is carried out under high vacuum, it is unlikely that the major peak at 286 eV is due to THF solvent, but rather THF decomposition products, such as poly(ether). The O-C=O peak is also attributed to the decomposition of

THF. Although THF-based electrolytes are reported to have high reversibility, THF has been shown to decompose on magnesium electrodes upon cycling in Grignard based electrolytes (Wetzel et al., 2015).

Unique to the 50 BS/50 THF electrolyte is the presence of sulfur compounds. In the S2p region, there is a small peak at 162 eV present in the 50 BS/50 THF sample. Because the intensities of these peaks are low, the peaks could not be properly fit, and the presence of a second sulfur species could not be verified. The peak at 162 eV is representative of a metal-sulfide bond, indicating that the sulfone, or a trace sulfur-containing impurity present in the electrolyte, reacted with magnesium to form an Mg-S bond.

Other Sulfones

An alternative to butyl sulfone was studied to determine if the boundary layer effect observed in the EIS and the morphology of the magnesium deposits was due to incorporating a higher dielectric media or due to the stacking nature of the alkane chains. We previously compared the $Mg(HMDS)_2$ – 4 $MgCl_2$ electrolyte in 50 BS/50 THF to the electrolyte in sulfolane (SL)/THF (50/50, v/v), but this electrolyte was unable to support reversible magnesium deposition (Merrill and Schaefer, 2018). However, the electrolyte in a 50 EMS/50 THF mixture was able to support quasi-reversible magnesium electrodeposition. This electrolyte has a lower Coulombic efficiency, compared to the 50 BS/50 THF electrolyte, around 80% from cyclic voltammetry measurements (**Supplementary Figure 12**). Despite the flat, orderly deposition observed in the SEM image, **Figure 9**, the XRD still shows that the deposits are primarily amorphous. Because of the lower efficiency, decomposition may be causing the amorphous behavior of the magnesium deposit upon the extended potential hold. However, like with the 50 BS/50 THF electrolyte, the presence of a boundary layer can influence the deposition morphology.

This particular electrolyte was not able to maintain extended cycling in a symmetric cell, shown in **Figure 10**. The passivation layer that grew on the magnesium metal caused an increasing resistance, that lead to the system reaching the voltage threshold of $\pm$ 1.5 V vs. Mg^{2+}/Mg^0. From the Nyquist plot, it is observed that there is a large increase in bulk impedance within the first 20 cycles, indicating that there was significant solvent decomposition. However, prior to the bulk resistance increase, the same impedance behavior to the 50 BS/50 THF electrolyte is observed in the early cycles. This confirms that the sulfone group is responsible for boundary layer formation at the electrode surface.

CONCLUSIONS

It was determined that both substrate and current density have an influence on the microscopic properties of magnesium electrodeposits. More importantly, it was shown that the use of a sulfone/THF solvent mixture dramatically affects the deposition quality by changing the interfacial chemistry, leading to thermodynamically controlled deposition. It is hypothesized that the addition of sulfones to the electrolyte creates a boundary layer at the electrode-electrolyte interface due to the adsorption of the sulfone groups to the metal. It is likely that this boundary layer is what influences the formation of spherical deposits, due to the surface energies between the metal and the sulfone boundary layer.

The aforementioned particle-like deposition can be caused by the application of low current densities, prior to entering a mass transport limited regime. Increasing the current density can lessen the extent of spherical deposits, provided the interfacial chemistry, or thermodynamics, does not drive the deposition morphology—as is the case with the electrolytes containing sulfones. The high surface area deposits can change the effective current density, which results in areas of decomposition. Furthermore, upon extended cycling, non-uniform deposition into the pores of the separator is facilitated.

DATA AVAILABILITY

All datasets generated for this study are included in the manuscript and/or the **Supplementary Files**.

AUTHOR CONTRIBUTIONS

JS conceived and guided the study. LM planned and conducted the experiments and data analysis. Both authors contributed to the writing of this paper.

FUNDING

LM gratefully acknowledges the ND Center for Environmental Science and Technology and ND Energy for funding. Partial financial support was provided by the National Science Foundation through grant number CBET-1706370.

ACKNOWLEDGMENTS

We acknowledge the ND Energy Materials Characterization Facility and the Notre Dame Integrated Imaging Facility for use of their instrumentation and facilities.

SUPPLEMENTARY MATERIAL

The Supplementary Material for this article can be found online at: https://www.frontiersin.org/articles/10.3389/fchem.2019.00194/full#supplementary-material

REFERENCES

Amir, N., Vestfrid, Y., Chusid, O., Gofer, Y., and Aurbach, D. (2007). Progress in nonaqueous magnesium electrochemistry. *J. Power Sourc.* 174, 1234–1240. doi: 10.1016/j.jpowsour.2007.06.206

Attias, R., Salama, M., Hirsch, B., Goffer, Y., and Aurbach, D. (2019). Anode-electrolyte interface in secondary magnesium batteries. *Joule.* 3, 27–52. doi: 10.1016/j.joule.2018.10.028

Aurbach, D., Lu, Z., Schechter, A., Gofer, Y., Gizbar, H., Turgeman, R., et al. (2000). Prototype systems for rechargeable magnesium batteries. *Nature.* 407, 724–727. doi: 10.1038/35037553

Aurbach, D., Weissman, I., Gofer, Y., and Levi, E. (2003). Non-aqueous magnesium electrochemistry and its application in secondary batteries. *Chem. Rec.* 3, 61–73. doi: 10.1002/tcr.10051

Crowe, A. J., DiMeglio, J. L., Stringham, K. K., and Bartlett, B. M. (2017). Kinetics of magnesium deposition and stripping from non-aqueous electrolytes. *J. Phys. Chem. C* 121, 20613–20620. doi: 10.1021/acs.jpcc.7b06068

Davidson, R., Verma, A., Santos, D., Hao, F., Fincher, C., Xiang, S. et al. (2019). Formation of magnesium dendrites during electrodeposition. *ACS Energy Lett.* 4, 375–376. doi: 10.1021/acsenergylett.8b02470

Ding, M. S., Diemant, T., Behm, R. J., Passerini, S., and Giffin, G. A. (2018). Dendrite growth in Mg metal cells containing MgTFSI2/glyme electrolytes. *J. Electrochem. Soc.* 165, A1983–A1990. doi: 10.1149/2.1471809jes

Ha, S. Y., Lee, Y. W., Woo, S. W., Koo, B., Kim, J. S., Cho, J., et al. (2014). Magnesium(II) bis(trifluoromethane sulfonyl imide-based electrolytes with wide electrochemical windows for rechargeable magnesium batteries. *ACS Appl. Mater. Interfaces.* 6, 4063–4073. doi: 10.1021/am405619v

Herb, J. T., Nist-Lund, C., Schwartz, J., and Arnold, C. B. (2015). Structural effects of magnesium dialkoxides as precursors for magnesium-ion electrolytes. *ECS Electrochem. Lett.* 4, A49–A52. doi: 10.1149/2.0031506eel

Jäckle, M., and Groß, A. (2014). Microscopic properties of lithium, sodium, and magnesium battery anode materials related to possible dendrite growth. *J. Chem. Phys.* 141, 174710–117417. doi: 10.1063/1.4901055

Kang, S., Kim, H., Hwang, S., Jo, M., Jang, M., Park, C., et al. (2019). Electrolyte additive enabling conditioning-free electrolytes for magnesium batteries. *ACS Appl. Mater. Interfaces.* 11, 517–524. doi: 10.1021/acsami.8b13588

Kim, H. S., Arthur, T. S., Allred, G. D., Zajicek, J., Newman, J. G., Rodnyansky, A. E., et al. (2011). Structure and compatibility of a magnesium electrolyte with a sulphur cathode. *Nat. Commun.* 2, 1–6. doi: 10.1038/ncomms1435

Lautar, A. K., Kopac, D., Rejec, T., Bancic, T., and Dominko, R. (2019). Morphology evolution of magnesium facets: DFT and KMC simulations. *Phys. Chem. Chem. Phys.* 29, 2434–2442. doi: 10.1039/C8CP06171H

Liao, C., Sa, N., Key, B., Burrell, A. K., Cheng, L., Curtiss, L. A., et al. (2015). The unexpected discovery of the Mg(HMDS)2/MgCl2 complex as a magnesium electrolyte for rechargeable magnesium batteries. *J. Mater. Chem. A* 3, 6082–6087. doi: 10.1039/C5TA00118H

Ling, C., Banerjee, D., and Matsui, M. (2012). Study of the electrochemical deposition of Mg in the atomic level: why it prefers the non-dendritic morphology. *Electrochim. Acta.* 76, 270–274. doi: 10.1016/j.electacta.2012.05.001

Lu, Z., Schechter, A., Moshkovich, M., and Aurbach, D. (1999). On the electrochemical behavior of magnesium electrodes in polar aprotic electrolyte solutions. *J. Electroanal. Chem.* 466, 203–217. doi: 10.1016/S0022-0728(99)00146-1

Magni, E., and Somorjai, G. A. (1996). Preparation of a model Ziegler-Natta catalyst: electron irradiation induced titanium chloride deposition on magnesium chloride thin films grown on gold. *Surf. Sci.* 345, 1–16. doi: 10.1016/0039-6028(95)07393-0

Matsui, M. (2011). Study on electrochemically deposited Mg metal. *J. Power Sourc.* 196, 7048–7055. doi: 10.1016/j.jpowsour.2010.11.141

Merrill, L. C., and Schaefer, J. L. (2018). Conditioning-free electrolytes for magnesium batteries using sufone–ether mixtures with increased thermal stability. *Chem. Mater.* 30, 3971–3974. doi: 10.1021/acs.chemmater.8b00483

Mohtadi, R., Matsui, M., Arthur, T. S., and Hwang, S. J. (2012). Magnesium borohydride: from hydrogen storage to magnesium battery. *Angew. Chem. Int. Ed.* 51, 9780–9783. doi: 10.1002/anie.201204913

Moulder, J. F., Stickle, W. F., Sobol, P. E., and Bomben, K. D. (1992). *Handbook of X-ray Photoelectron Spectroscopy: A Reference Book of Standard Spectra for Identification and Interpretation of XPS Data*. Minnesota: Perkin-Elmer Corporation.

Pan, B., Zhang, J., Huang, J., Vaughey, J. T., Zhang, L., Han, S. D., et al. (2015). A lewis acid-free and phenolate-based magnesium electrolyte for rechargeable magnesium batteries. *Chem. Commun.* 51, 6214–6217. doi: 10.1039/c5cc01225b

Scharifker, B., and Hills, G. (1983). Theoretical and experimental studies of multiple nucleation. *Electrochim. Acta.* 28, 879–889. doi: 10.1016/0013-4686(83)85163-9

Ta, K., See, K. A., and Gewirth, A. A. (2018). Elucidating Zn and Mg electrodeposition mechanism in nonaqueous electrolytes for next-generation metal batteries. *J. Phys. Chem. C* 122, 13790–13796. doi: 10.1021/acs.jpcc.8b00835

Viestfrid, Y., Chusid, O., Goffer, Y., Aped, P., and Aurbach, D. (2007). Structural analysis of electrolyte solutions comprising magnesium-aluminate chloro-organic complexes by Raman spectroscopy. *Organometallics.* 26, 3130–3137. doi: 10.1021/om061076s

Viestfrid, Y., Levi, M. D., Gofer, Y., and Aurbach, D. (2005). Microelectrode studies of reversible Mg deposition in THF solutions containing complexes of alkylaluminum chlorides and dialkylmagnesium. *J. Electroanal. Chem.* 576, 183–195. doi: 10.1016/j.jelechem.2004.09.034

Wang, D., Gao, X., Chen, Y., Jin, L., Kuss, C., and Bruce, P. G. (2018). Plating and stripping calcium in an organic electrolyte. *Nat. Mater.* 17, 16–20. doi: 10.1038/NMAT5036

Wetzel, D. J., Malone, M. A., Haasch, R. T., Meng, Y., Vieker, H., Hahn, N. T., et al. (2015). Passivation dynamics in the anisotropic deposition and stripping of bulk magnesium electrodes during electrochemical cycling. *ACS Appl. Mater. Interfaces.* 7, 18406–18414. doi: 10.1021/acsami.5b04487

Conflict of Interest Statement: The authors declare that the research was conducted in the absence of any commercial or financial relationships that could be construed as a potential conflict of interest.

Copyright © 2019 Merrill and Schaefer. This is an open-access article distributed under the terms of the Creative Commons Attribution License (CC BY). The use, distribution or reproduction in other forums is permitted, provided the original author(s) and the copyright owner(s) are credited and that the original publication in this journal is cited, in accordance with accepted academic practice. No use, distribution or reproduction is permitted which does not comply with these terms.

frontiers in Chemistry

PERSPECTIVE
published: 06 June 2019
doi: 10.3389/fchem.2019.00419

Localization of Ion Concentration Gradients for Logic Operation

Nikolay V. Ryzhkov[1], *Pavel Nesterov*[1], *Natalia A. Mamchik*[1], *Stanislav O. Yurchenko*[2] *and Ekaterina V. Skorb*[1]*

[1] *Laboratory of Solution Chemistry of Advanced Materials and Technologies, ITMO University, Saint Petersburg, Russia,*
[2] *Terahertz Technology Lab, Bauman Moscow State Technical University, Moscow, Russia*

Adjustment of the environmental acidity is a powerful method for fine-tuning the outcome of many chemical processes. Numerous strategies have been developed for the modification of pH in bulk as well as locally. Electrochemical and photochemical processes provide a powerful approach for on-demand generation of ion concentration gradients locally at solid-liquid interfaces. Spatially organized in individual way electrodes provide a particular pattern of proton distribution in solution. It opens perspectives to iontronics which is a bioinspired approach to signaling, information processing, and storing by spatial and temporal distribution of ions. We prove here that soft layers allow to control of ion mobility over the surface as well as processes of self-organization are closely related to change in entropy. In this work, we summarize the achievements and discuss perspectives of ion gradients in solution for information processing.

Keywords: interface, polyelectrolyte multilayers, pH-gradient, logic gates, iontronics

OPEN ACCESS

Edited by:
Luís D. Carlos,
University of Aveiro, Portugal

Reviewed by:
Carlos D. S. Brites,
University of Aveiro, Portugal
Ryuji Kawano,
Tokyo University of Agriculture and Technology, Japan

***Correspondence:**
Ekaterina V. Skorb
skorb@corp.ifmo.ru

Specialty section:
This article was submitted to Electrochemistry, a section of the journal Frontiers in Chemistry

Received: *07 February 2019*
Accepted: *21 May 2019*
Published: *06 June 2019*

Citation:
Ryzhkov NV, Nesterov P, Mamchik NA, Yurchenko SO and Skorb EV (2019) Localization of Ion Concentration Gradients for Logic Operation. Front. Chem. 7:419. doi: 10.3389/fchem.2019.00419

INTRODUCTION

Nobel laureate Herbert Kroemer stated that "the interface is the device" in reference to heterogeneous semiconductor structures. But this idea also inspired the development of interfacial science beyond the physics of heterostructures. Interfaces play a significant role in many physical and chemical processes. There is a wide variety of procedures for surface treatment and the modification of functional interfaces. Decher et al. (1992) described alternately exposing of charged substrates to positively and negatively charged macromolecules in order to obtain functional multilayered coatings. Layer-by-layer (LbL) assembled coatings and capsules have found various applications due to the versatility of multilayer formation technique and a variety of charged compounds which may be incorporated into it (Decher et al., 1998; Ryzhkov et al., 2019a). Polyelectrolyte multilayers are traditional components of biomaterial surface coatings (Zhukova et al., 2017), membranes for separation (Rmaile et al., 2003), as well as cargoes for drug encapsulation and delivery (Nikitina et al., 2018).

Polyelectrolyte multilayers are also considered to be an appropriate model mimicking the structure and properties of biological membranes (Zhu and Szostak, 2009). A lipid bilayer supported by a polyelectrolyte cushion provides a platform for modeling and investigating many cellular processes. Nowadays, transport processes in polyelectrolyte layers has garnered much attention. Due to their selective ionic permeability (Tanaka and Sackmann, 2005), one may perform dynamic polarization across the membrane. This process simulates neuron polarization during nerve conduction, thereby modeling information processing in living systems.

Development of a reliable model infallibly mimicking biological way of information processing is still a challenge. A lot of efforts are put to mimic biological way of computation by artificial

matter. The simplest example of information operations is switching functions following Boolean logic—logic gates. Logic gates use binary inputs and produce a single binary output. By now, several systems based on polyelectrolytes that perform information processing according to Boolean logic and using ionic signals (particularly protons) have been developed. Motornov et al. (2008) designed an enzyme-based hybrid system of pH-responsive nanoparticles assembling and disassembling following AND/OR Boolean logic. Motornov et al. (2009) also developed a pH-responsive Pickering emulsion coupled with specific enzymatic reactions performing AND and OR logic. Han et al. (2009) developed microchip polyelectrolyte diodes representing AND, OR, and NAND logic based on ion transportation through the polyelectrolyte interface. Thus, applicability of iontronic devices were demonstrated.

Reversible conformational changes of polymer brushes atop an electrode modulated by pH and influencing charge transport behavior are wifely exploited for designing biomimetic iontronic calculating devices. A more detailed mechanism is described as follows. For example, sucrose in the presence of both invertase (Input A) and glucose oxidase (Input B) results in a decrease in pH, transforming into gluconic acid (AB). The described system performs AND Boolean logic. OR logic can be designed using an ethyl butyrate-glucose mixture. Acidification of the medium (A+B) in this case can be achieved either by the oxidation of ethyl butyrate to butyric acid by esterase (Input A) or by the oxidation of glucose to gluconic acid by glucose oxidase (Input B). In brief, enzymatic inputs run a cascade of reactions leading to a pH shift to acidic values. The electrode surface with grafted shrunk poly-4-vinyl pyrrolidone (P4VP) at neutral pH is not electrochemically active because of the blocking effect of the polymer film. Output "1" of the logic operations yielded a pH drop to acidic conditions, resulting in the protonation and swelling of the P4VP polymer allowing penetration of a soluble redox probe to the conducting support. Thus, one may perform amperometry or impedance spectroscopy study for output detection. Wang et al. (2009) designed the system described above. Different groups employed a large variety of enzymes and electrode coatings for realizing a similar approach to designing biochemical logic gates. Privman et al. (2008), Katz and Minko (2015), and Poghossian et al. (2015) developed enzyme-based biocomputing systems coupled with pH-responsive membranes and electrodes. As a result, they obtained bioelectronic devices switchable by logically processed biomolecular signals. Reversible pH-responsive on-off behavior performing Boolean logic was suggested for designing novel multi switchable electrochemical biosensors based on electrodes covered by polymer network (Liu et al., 2012) or polymer brushes (Li et al., 2014) and electrodes made of inorganic-polymer composites (Wang et al., 2015).

Significant progress in DNA and molecular logic operations was made in recent years. However, various issues remain unresolved. For example, information transfer through live-machine interfaces: living matter conducts electricity mostly using ions, while machines conduct electricity mostly using electrons (Yang and Suo, 2018). It's of high importance nowadays because technologies at the interface between natural and artificial plays a central role in science. We suggest here a strategy for performing iontronic logic operations at interfaces in solutions and present it's modeling by the electrochemical and photochemical system and how they can be related to Shannon's entropy. Having an array of electrodes and applying potential bias according to some program, one may realize the spatial distribution of acidic and basic areas in water solutions close to an electrode in a unique pattern with micrometer resolution. It's key to iontronic information processing. Designating current density higher than some value as logic input "1" and pH lower than some cut-off as logic output "1," we may design different logic gates varying the geometry of input electrodes, the position of response point and cut-off values. We present here the simplest AND logic gate performed by a couple of microelectrodes and discuss assembling of individual logic gates in concatenated logic cascades and complex branching networks by multielectrode arrays.

Having an array of electrodes and applying potential, oxidation, and reduction processes may be localized at particular electrodes and hence spatially separated. Protons propagating from parental electrode serve as information transmitters. Moreover, we have demonstrated that polyelectrolyte modification of electrode surface may lead to amplification and better localization of ion fluxes and hence signal amplification and can be related to self-organization *vs*. Shannon's entropy. All this discussion is also extrapolated to polyelectrolyte modified photoelectrodes under irradiation.

ENHANCING ELECTROCHEMICALLY PRODUCED IONIC SIGNALS BY POLYELECTROLYTE ASSEMBLIES

Electrochemistry provides one with a powerful approach for the on-demand local generation of ionic signals. For example, proton fluxes may be produced by electrochemical hydroquinone oxidation (Fomina et al., 2016). Due to their proton-coupled electron transfer, low redox potential, and relative chemical stability, quinones are widely used as the electroactive species for the controlled generation/consumption of protons (Dochter et al., 2015; Garnier et al., 2015). Naturally occurring hydroquinone compounds play a significant role in electron/proton transfer of many biological processes (Jeyanthi et al., 2016). Thus, the quinone/hydroquinone transition serves as an essential electrochemical model for the development of biomimetic systems. Its changing molecular structure allows for its electrochemical properties to be tuned (Peduto et al., 2017). But characteristics of an electrode reaction are highly affected by the microstructure of the electrode surface, since the fact that electrochemical systems under investigation are heterogeneous and electrode reaction is related to electron transfer through the electrode-electrolyte interface.

Electrode surface influences diffusion of electrochemical reactants and products as well as Faradaic process. In case of hydroquinone oxidation, horizontal and vertical proton propagation is supposed to be a three-dimensional pH wave. It originates from the ion source and weakens as it moves

away. Fick's laws describe diffusion and postulate that ionic flux goes from regions of higher concentration to areas with a lower one. Furthermore, the magnitude of the driving force determining ion movement is proportional to the concentration gradient. Ion fluxes and the concentration of a particular ion close to the surface of the electrodes were investigated using Scanning Vibrating Electrode Technique (SVET) and Scanning Ion-Selective Electrode Technique (SIET), unique tools for the characterization of local ionic currents in solution and ion concentration gradient measurement, respectively (Souto et al., 2010). SVET allows the electric field in a solution to be measured for the visualization of anodic and cathodic areas on surfaces with nA precision and μm spatial resolution (**Figure 1a**). During SVET-analysis, a vibrating Pt-probe (**Figure 1b**) scans the surface, estimating its electrical potential in amplitude points of its vibration and then recalculates it in ionic currents. SIET is based on potentiometric principles. A glass capillary microelectrode with the ion-selective membrane in the tip scans the surface, measuring the concentration of a particular ion.

We have studied the effect of polyelectrolyte assembly on top of an electrode on the propagation of electrochemically generated protons. The system under investigation is a working electrode (WE) gold or platinum wire embedded in an epoxy resin so that its round section was brought into contact with a solution (**Figure 1c**). System may be also extended to several electrodes (**Figures 1d,e**). Electrochemical reaction is coupled with proton release. The pH-wave propagation is driven by a concentration gradient. Further, the surface of the noble metal electrode (WE) was subsequently modified with nanometer-thin layers of the polycation polyethyleneimine (PEI) and the polyanion poly(sodium 4-styrenesulfonate) (PSS). PEI is considered to be a proton sponge that stores electrochemically generated protons while the PSS layer serves as a cation exchange layer. The electrode was first covered by branched PEI to provide secure anchoring to the surface and to act as a positively charged terminating layer. Deposition of PSS was then carried out via electrostatic interaction with the underlying layer. Although polymer multilayer assembly leads to no change in redox processes at electrode/electrolyte interface, both the anodic and cathodic activity of the Pt electrode measured by SVET is higher for one that is polyelectrolyte coated than for a bare one (**Figures 1f,g**). It is worth noting that a terminating PEI layer resulted in more pronounced anodic/cathodic activity. However, if this polyelectrolyte membrane is thick enough, ion flux from the surface is suppressed (Ryzhkov et al., 2019b).

Since LbL polyelectrolyte assemblies contain many uncompensated charges, ions cannot freely pass through the membrane. Although it is still passive transport down their concentration gradient, ion movement pathways are more complex and cannot be explained by simple diffusion. We consider polyelectrolyte LbL assemblies as a convenient tool for controlling the transmission of the ion signal. Strong and weak polyelectrolyte assemblies, including charged biopolymers and hydrogels, can regulate charge carrier generation, the diffusion of ions at interfaces, lifetime and storage (Ryzhkov et al., 2019a). There is still no general theory precisely predicting electrode response to polyelectrolyte modification. Until now, multicomponent coatings formed by multilayers of different polyelectrolyte compositions (strong–strong, strong–weak, weak–weak) have been analyzed as nanolayers for corrosion protection. The mechanism of multilayer protective action is based on pH buffering polybasic and polyacid complexes (Andreeva et al., 2010; Skorb and Andreeva, 2015). It has also been demonstrated that polyelectrolyte layers can be used as an efficient pH-buffering protective layer for pH-sensitive soft materials (Skorb and Andreeva, 2013). It is expected that by combining polyelectrolytes of different molecular weights, strengths, and with different specific functional moieties, one can flexibly tune spatial and temporal distribution of ionic fluxes through the membrane and perform independent handling by cations and anions. That fact opens up prospects for developing futuristic biomimetic information processing using ions as signal carriers.

DISCUSSION OF SOFT MATTER ASSEMBLIES FOR CONTROLLING ION FLUXES

LbL deposition of polyelectrolyte multilayers is a universal approach to designing interfaces with unique properties. Its impact is not limited by enhancement of ion fluxes described above. Different effects may be achieved by polyelectrolytes of different nature. Recent progress in science provides an understanding of polyelectrolyte complexation principles. Despite the apparent simplicity of the assembly procedure, the processes occurring in the multilayers are incredibly complex. Polyelectrolyte layers in multilayered structures are not perfectly stratified, and polymer chains of polycations and polyanions are significantly interpenetrated (Schönhoff, 2003). Much attention is drawn to the dynamics and internal structure of polyelectrolyte multilayers and studying of internal diffusion (Fares and Schlenoff, 2017; Selin et al., 2017). Various parameters such as ionic strength (Steitz et al., 2000), charge density (Steitz et al., 2001), pH, and temperature (Karg et al., 2008) influence the internal structure of polyelectrolyte film. Several models of diffusion in ultrathin polyelectrolyte films were suggested (Klitzing and Möhwald, 1996; Farhat and Schlenoff, 2001). Three different modes of interaction of polyelectrolyte multilayers and small ionic species were observed—permeability, non-permeability, and ions accumulation. It was also found that the permeability of polyelectrolyte membranes depends mostly on film composition rather than its thickness (Hoshi et al., 2003). The outermost layer of polyelectrolyte LbL assembly carry out excess non-compensated charge and plays a crucial role in permeability properties blocking penetration of similarly charged small species (Rmaile et al., 2003). Fu et al. (2017) demonstrated that pairs of weak polyelectrolytes tend to transport small molecules or ions more, whereas multilayers assembled from strong polyelectrolytes are less permeable. Kelly et al. (2018) demonstrated that ion flux through the membrane is significantly affected by the stoichiometry of the polyelectrolyte multilayer. An excess of some component, polycation, or polyanion, changes diffusion

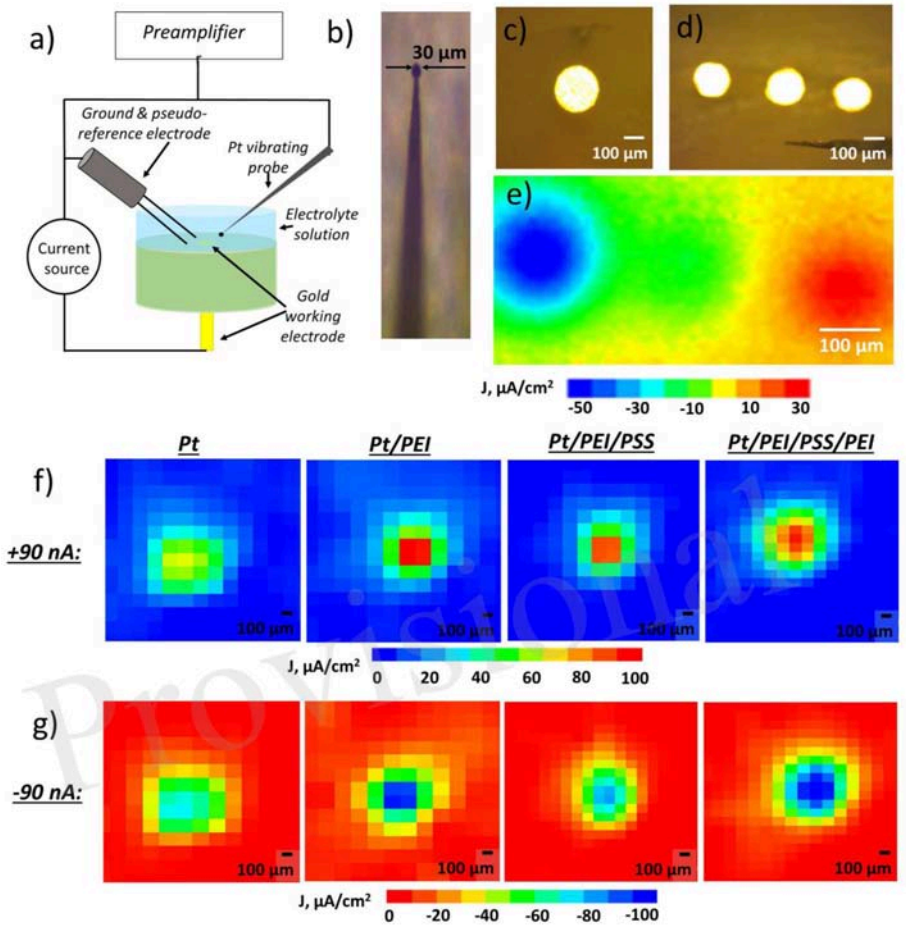

FIGURE 1 | (a) Schematic of scanning vibrating electrode technique (SVET) for determining an ionic current that can be used together with scanning ion selective electrode (SIET). **(b)** Pt-Ir vibrating probe for SVET, **(c)** top view of gold electrode embedded in epoxy resin, **(d)** top view of working electrodes (WE) embedded in epoxy resin **(e)** ion currents mapped by SVET in solution over three WEs, left electrode is negatively polarized (−90 nA), right one—positively (+90 nA), red demonstrates areas of positive ionic current in solution related to anodic activity and blue—areas of negative ionic current in solution and cathodic activity on the surface, **(f,g)** ionic current over one WE under either positively [in **(f)**] or negatively [in **(g)**] on pristine Pt or Pt covered with different polyelectrolyte multilayers—Pt/polyethylenimine (Pt/PEI), Pt/PEI/ poly(sodium 4-styrenesulfonate) (Pt/PEI/PSS), and Pt/PEI/PSS/PEI—number of layers affects drastically on the ionic current.

and permeability of ions through the polyelectrolyte multilayer. Ion transportation through polyelectrolyte multilayers can be described similarly to solid matter permeability. Thus, the action of surrounding polyelectrolyte chains affects diffusion through polyelectrolyte assemblies significantly and diffusion is thermoactivated (Spruijt et al., 2008). Internal interfaces predetermine the properties of polyelectrolyte multilayers, and one should therefore keep in mind the composition and structure of the multilayer, the internal layer chemistry, and interactions between components when designing functional polyelectrolyte multilayers (Brezhneva et al., 2019). The means of changing the permeability of polymer layers mentioned above have already found extensive use in the development of semipermeable separating membranes and electrochemical sensors with improved selectivity, sensitivity, and response time.

Thus, polyelectrolyte multilayers are a powerful instrument for the regulation of ion-fluxes. By varying membrane composition, enhanced ion transport, accumulation, and delayed release can be realized.

PH-WAVE PROPAGATION AS A BASIS FOR IONTRONICS

Precise control over electrochemically generated ion fluxes open perspectives for flexible and reliable approach for transition from machine way of information processing (via electrons) to biological one (via ions) and developing technologies at the interface between natural and artificial (wearable and implantable devices, for example).

Our interest is focused on information transfer in aqueous solutions and the prospective for communication with living matter. Here, we demonstrate a proof of concept of basic logic operations that use ions as input and/or output signals which allows unequivocal output reading. The system under

investigation is presented by an array of gold or platinum electrodes particularly embedded in an epoxy resin and immersed in the electrolyte solution. The simplest model systems containing two electrodes are shown in **Figure 2**.

By applying positive and negative potentials to the electrodes one is able to carry out a pH coupled redox process (e.g., hydroquinone oxidation). Herewith, oxidation and reduction processes may be spatially separated. As a result, the distribution of acidic and basic areas in a solution adjusted to an electrode surface may be realized particularly. Anodic and cathodic activity are localized directly at the electrodes while the resulting pH gradient is more spatially blurred. The desired localization of the proton wave may be achieved via electrode functionalization by polymer assembly. The electrodes may be designated as inputs and the acidity of the space between the electrodes as output in terms of logic gates. Simple AND logic operations (**Figure 2a**) may be performed. The main processor of any computing device is basically a bunch of interconnected logic gates, thus performing these simple logic operations is an important step toward biomimetic iontronic calculations. The open-circuit potential applied to the input electrode (**Figure 2b**) is designated as input "0" and hydroquinone oxidation potential (0.70 vs. SHE) as input "1." The acidity of the solution between the electrodes is read as an output signal. A pH lower than some threshold, for example, 5.0, is designated as output "1" with anything lower being "0." Two "0" inputs provide "0" output (**Figure 2c**). If only one of the electrodes is polarized, the resulting pH wave does not reach the output area, and pH $>$ 5.0. Therefore, the output signal is "0" (**Figure 2d**). Otherwise, if both input electrodes are polarized, generated protons propagate to the output area, making the pH there significantly acidic, $<$5.0, giving signal "1" in output area (**Figure 2e**).

In general, the model system described above may be extended to several dozen electrodes. As such, some electrodes may be assigned as inputs while others are for the reading of the electrochemical output. We started with three microelectrodes (**Figure 1d**) and, by SVET, demonstrated that the independent polarization of electrodes might be performed, while no effect of the bipolar electrode was observed in the studied potential window (**Figure 1e**).

What we plan to do next is to cover the output electrode with pH sensitive film, grafted P4VP or P2VP brushes for example (Pennakalathil et al., 2010; Ghostine and Schlenoff, 2011). This thin polymer layer in its non-protonated state is collapsed and acts as an insulator, inhibiting direct electron transfer from the electrode to the electrochemically active specimen in solution and vice versa. If only one input electrode is active, the resulting proton wave does not reach the output electrode. The polymer layer still blocks the electrode surface and no current is observed during polarization. When both inputs are "1" (applied potential of hydroquinone oxidation), then the resulting proton wave reaches the output electrode, making the surrounding media acidic enough to protonate the blocking polymer layer atop the output electrode. As a result, polymer conformation changes from collapsed to swelled, allowing penetration of hydroquinone to the electrode. Thus, an anodic current of hydroquinone oxidation may be registered at the output electrode. A Faradaic current registered at the output electrode above a certain threshold is assigned as "1" and lower as "0." Thus, switching of output electrode activity may be performed according to Boolean logic. It is worth noting that in this case some autocatalysis may be shown, and the acidification of the area close to the output electrode leads to electrochemical generation of more protons. Thus, signal amplification and signal transmission from one location to another realizing specific pathways through the electrode network may be performed.

Our future research direction will be focused on different geometries of input electrode array, varying applied potentials and passed currents, and regimes of application (constant current, pulses, etc.). Another direction is the development of novel approaches for output electrode modification for ensuring disambiguation of output response reading.

SELF-ORGANIZATION VS. SHANNON'S ENTROPY

Fundamental concept of information theory is Shannon's entropy. Entropy in this case is a measure of unpredictability of the state, or equivalently, of its average information content. We suggest here description of described above approach to designing of iontronic devices in terms of Shannon's entropy.

Idea here is a correlation of soft matter components (polyelectrolytes and lipid layers) of living cell and our biomimetic model (**Figures 3A,B**). We took photochemical system (**Figure 3C**) (Maltanava et al., 2017) shown previously as the analogy to electrochemically induced proton gradients in aqueous electrolytes and collect SIET pH maps for pristine working electrode (WE) (System I), WE covered with polyelectrolyte multilayers (System II) and WE covered with polyelectrolyte multilayers and lipid layer on top (System III).

Processes of self-organization are known to be closely related to change in entropy of the system (Haken, 2006). Typically, this occurs with spatial change in thermodynamic (as temperature, density, and pressure) as well as chemical parameters and, in particular, ion composition of the system. In our case, the changes of temperature, density, and pressure are negligible, while the local electrochemical influence affects directly the ion-distribution in the solution. Note that the spatial pH-redistribution occurs self-consistently, being accompanied by local electric potential redistribution during the free-energy minimization of the system. In result, the self-organization and the redistribution of pH-fields are directly associated with each other and, thus, the change of entropy can be illustrated using the fields of pH.

According to its definition, the Shannon's entropy is (Haken, 2006).

$$S = -\sum_i p_i \log_2 p_i \quad (1)$$

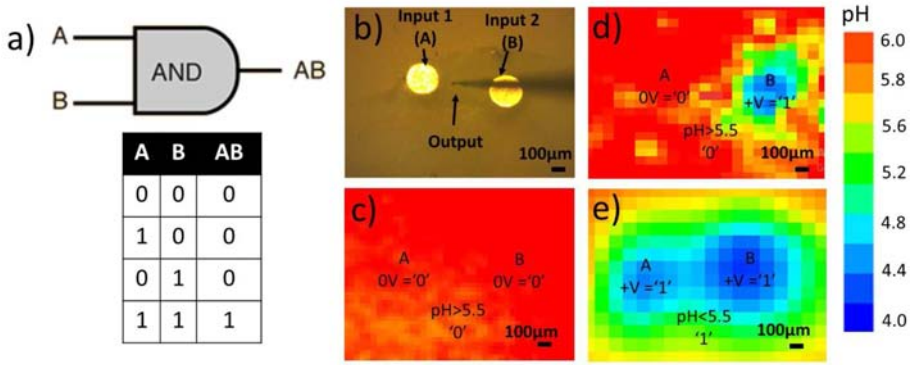

FIGURE 2 | (a) Basic AND logic gate and corresponding truth table, **(b)** system of two WEs embedded in epoxy holder, **(c–e)** 2D pH-maps via SIET of two input electrodes in hydroquinone solution during polarization of electrodes in different regimes and interpretation in terms of logic gates, positive polarization +V is determined as input "1," no polarization 0V as input "0," pH >5.0 is determined as output "0" and pH<5.0 as output "1," **(c)** no potential applied, both inputs are "0," as a result, no pH drop – output "0," **(d)** positive potential is applied to the right electrode "1," left one is not polarized "0," resulting pH drop localized on right electrode and doesn't propagate to output area "0" **(e)** positive potential applied to both electrodes "1," resulting proton wave reaches output area giving output "1".

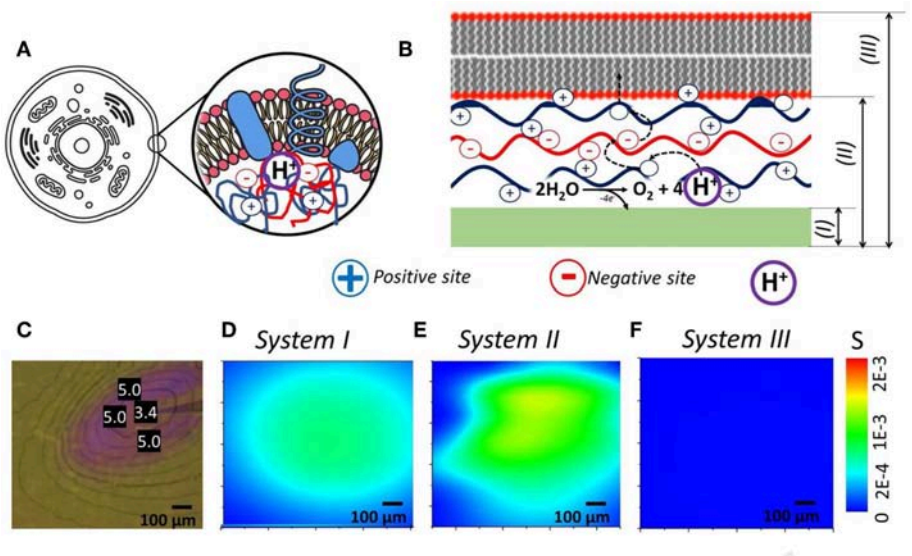

FIGURE 3 | (A,B) Idea of cell prototype system that consists of polyelectrolyte assembly or coacervates, reactions inside that are protected from environment by lipid bilayers. **(C)** System with local gradient of pH initiated by light (measured pH values are shown in units in photo). **(D–F)** Recalculated into Shannon's entropy SIET pH maps of—**(D)** pristine WE, **(E)** WE covered with polyelectrolytes, and **(F)** WE covered with polyelectrolytes and lipid bilayer—processes of self-organization are closely related to change in entropy of the system.

where $0 < p_i < 1$ is the probability to measure some observable value i. In a case of a lot of observable independent values (e.g., set of p-values at different spatial points), corresponding summation over them should be performed in the right hand side of Equation (1).

The particular physical sense of the probability p depends on the system's nature and plays an important role for interpretation of the results. For instance, p can be related to the probability of some molecular dipole orientation or electric charge in case of electric systems, an electron spin orientation or magnetic polarization in magnetic systems, a particular state of photons in optical systems, or concentration of chemicals in reacting systems (Haken, 2006). In the same manner, this approach could be naturally expanded to solutions, to consider p in sense of probability that an observed ion in the solution is an H^+ or OH^- ion (whose concentrations are related with each other). In other words, we may use the parts of H^+ and OH^- ions as the probabilities p_H and p_{OH}, to calculate corresponding contribution to the Shannon's entropy associated with the pH in a given spatial area of measurement. One should note that, generally speaking, the pH distribution provides the same information as the field of electric potential, since they are consistently related with each other in the solution.

The probability to observe H^+ cations in a solution during a measurement is simply related to the cation concentration in the system and pH of the solution as $p_H = C_H/C_0 = 10^{-pH}$, where $C_0 = 1M$ is a normalizing concentration. For OH^- anions, we have $p_{OH} = C_{OH}/C_O = 10^{pH-14}$, since $p_H\ p_{OH} = 10^{-14}$. From here, by substitution of this expression for p into Equation (1), we readily obtain the pH-related part of the Shannon's entropy as

$$\begin{aligned} S &= \log_2 10\,(pH\ 10^{-pH} + pOH\ 10^{-pOH}) \\ &= \log_2 10\,(pH\ 10^{-pH} + (14 - pH)\ 10^{\,pH-14}) \end{aligned} \quad (2)$$

Equation (2) determines the contribution to Sannon's entropy, associated with pH measured in a small volume (which we consider as a subsystem of a large system herein the pH-measurement is performed). At pH = 7, Equation (2) exhibits a local minimum. Note that Equation (2) is symmetric relatively pH = 7 and, at pH < 6.8 (pH > 7.2), the first (second) term in the parenthesizes becomes negligible.

The total entropy for given discrete spatial distribution of pH (distribution of the system states) can be calculated with summation over the *S*-values in all spatial points of the system. This situation with discrete distribution of pH field is typical for experiments we performed, since the size of a "cell" (small open volume of the solution) wherein pH is measured is determined by the electrode size.

The approach based on Equation (2) is convenient for analysis of self-organization phenomena (related to change in pH-distributions) and their interpretation in terms of entropy fields. This can be illustrated using results of our measurements of pH fields in different systems. For instance, taking spatial distribution of cations determined experimentally in cases of bare electrode, as well as for electrode covered by polyelectrolyte multilayer $(PEI/PSS)_3$ and lipid bilayer, we obtained the spatial distributions of entropy $S(x, y)$ represented in **Figures 3D–F**. Interestingly, huge difference is observed for obtained the spatial distributions of entropy that can be associated with various soft matter components for controlling ion fluxes.

CONCLUDING REMARKS AND OUTLOOK

In this perspective, we highlight information processing and signaling by spatial and temporal distribution of ions. A model electrochemical and photochemical system creating local ion-fluxes were demonstrated.

Electrodes spatially organized in a particular manner allows propagation of pH waves to be triggered and spatial distribution of H^+ according to a particular pattern to be realized. Proton diffusion from two sources is reported to model the AND logic gate. We are currently studying how the system geometry influences the pattern of proton concentration and developing a simulation that predicts pH pattern depending on the working electrode geometry and vice versa, namely suggesting electrode geometry depending on desired pH pattern.

The LbL assembly of polyelectrolyte multilayers is suggested as an instrument to control horizontal and vertical ion propagation with ability to correlate it with the spatial distributions of entropy. The experiments we have described are only a small sample of the full range of polyelectrolyte materials that can be assembled on top of electrodes and tested for ion conduction ability.

EXPERIMENTAL SECTION

Three-electrode electrochemical cells (working electrode, Pt counter electrode and Ag/AgCl reference electrode) were utilized as model electrochemical and photoelectrochemical systems. Working electrode was presented by gold or platinum wire (0.2 mm in diameter, 2–3 cm length) embedded in epoxy resin so that circular cross-section of wire exposed to outside media on flat surface of obtained holder. Anodized TiO_2 (1.5 cm^2) under low intensity light-emitted diode (365 nm) irradiation focused in spot (~0.25 cm^2) was utilized as working photoelectrode. The anodic and cathodic activity of electrode under polarization in water solution as well as photoactivity of illuminated TiO_2 was studied by SVET and generated pH gradients by SIET. To perform the SVET and SIET measurements, a system from Applicable Electronics (USA) modulated by an ASET program (Sciencewares, USA) was used. As a vibrating probe for SVET experiments, an insulated Pt-Ir microprobe (Microprobe Inc., USA) with a platinum black spherical tip 30 μm in diameter was used. The probe was made to vibrate both parallel and perpendicular to the specimen surface at a height of 150 μm. The amplitude of vibration was 30 μm, while the probe vibrated at frequencies of 136 Hz (perpendicular to surface) and 225 Hz (parallel to surface). Only the perpendicular component was used in the treatment and presentation of the data. The environmental pH measurements by SIET were carried out using glass-capillary microelectrodes filled with Hydrogen Ionophore Cocktail I (Sigma) based liquid pH-selective membrane and KCl + KH_2PO_4 internal solution. Ag/AgCl/KCl (sat) was used as the external reference electrode. The pH-selective microelectrodes were calibrated using commercially available pH buffers and demonstrated a linear Nernstian response−55 to−58 mV/pH—in a pH range from 3 to 8. The local activity of H^+ was detected 25 μm above the surface. Instrumentation allows to measure voltage with nV precision level, and measure extremely low ion concentration gradients. Step motors allow to study electrochemical activity of material with micrometer spatial resolution and high-resolution maps were obtained. Electrochemical systems were studied in 60 mM hydroquinone solution in 150 mM KNO_3, photoelectrochemical one without addition of hydroquinone.

The deposition of the polyelectrolyte multylayers onto the surface of working electrode was performed using the classical Layer-by-Layer technique. Two mg/ml each branched polyethylenimine (PEI, Mw 70 kDa, 30% water solution purchased from Alfa Aesar) and polystyrene sulfonate (PSS, Mw 500 kDa purchased from Polysciences Inc.,) were dissolved in 0.5 M aqueous NaCl to make polycation and polyanion solutions respectively. Each layer took 20 min to be deposited after which it was rinsed with excess distilled water and then steam-dried. On top of polyelectrolyte modified TiO_2 lipid bilayer was also deposited from 10 mg/ml dispersion of Lecisoy 400 vesicles for 1 h. Further electrochemical characterization

of modified electrodes and photoelectrodes were performed as described above.

SVET data presented as obtained, SIET data recalculated according to previous calibration. Mapping for each experimental condition were reproduced at least three times, one of typical maps is presented.

AUTHOR CONTRIBUTIONS

NR and ES contributed conception and design of the study. SY contributes discussion and writing of Shannon's entropy vs. H^+ concentration gradient part. NR, NM, and PN performed experimental work and treatment of the data. NR wrote the first draft of the manuscript. ES coordinated the study and helped draft the manuscript.

FUNDING

This work is supported by RSF Grant No. 17-79-20186. ES also thanks the ITMO Fellowship Professorship Program for Infrastructural Support. Contribution by SY (discussion and the entropy vs self-organization analysis) was supported by Russian Science Foundation, Grant No. 17-19-01691.

REFERENCES

Andreeva, D. V., Skorb, E. V., and Shchukin, D. G. (2010). Layer-by-layer polyelectrolyte/inhibitor nanostructures for metal corrosion protection. *ACS Appl. Mater. Interfaces* 2, 1954–1962. doi: 10.1021/am1002712

Brezhneva, N., Nikitina, A., Ryzhkov, N., Klestova, A., Vinogradov, A. V., and Skorb, E. V. (2019). Importance of buffering nanolayer position in Layer-by-Layer assembly on titania based hybrid photoactivity. *J. Sol-Gel Sci. Technol.* 89:92. doi: 10.1007/s10971-018-4728-5

Decher, G., Eckle, M., Schmitt, J., and Struth, B. (1998). Layer-by-layer assembled multicomposite films. *Curr. Opin. Colloid Interface* 3, 32–39. doi: 10.1016/S1359-0294(98)80039-3

Decher, G. H. J. D., Hong, J. D., and Schmitt, J. (1992). Buildup of ultrathin multilayer films by a self-assembly process: III. Consecutively alternating adsorption of anionic and cationic polyelectrolytes on charged surfaces. *Thin Solid Films* 210, 831–835. doi: 10.1016/0040-6090(92)90417-A

Dochter, A., Garnier, T., Pardieu, E., Chau, N. T. T., Maerten, C., Senger, B., et al. (2015). Film self-assembly of oppositely charged macromolecules triggered by electrochemistry through a morphogenic approach. *Langmuir* 31, 10208–10214. doi: 10.1021/acs.langmuir.5b02749

Fares, H. M., and Schlenoff, J. B. (2017). Diffusion of sites versus polymers in polyelectrolyte complexes and multilayers. *J. Am. Chem. Soc.* 139, 14656–14667. doi: 10.1021/jacs.7b07905

Farhat, T. R., and Schlenoff, J. B. (2001). Ion transport and equilibria in polyelectrolyte multilayers. *Langmuir* 17, 1184–1192. doi: 10.1021/la001298+

Fomina, N., Johnson, C. A., Maruniak, A., Bahrampour, S., Lang, C., Davis, R. W., et al. (2016). An electrochemical platform for localized pH control on demand. *Lab Chip* 16, 2236–2244. doi: 10.1039/C6LC00421K

Fu, J., Fares, H. M., and Schlenoff, J. B. (2017). Ion-pairing strength in polyelectrolyte complexes. *Macromolecules* 50, 1066–1074. doi: 10.1021/acs.macromol.6b02445

Garnier, T., Dochter, A., Chau, N. T. T., Schaaf, P., Jierry, L., and Boulmedais, F. (2015). Surface-confined self-assembly of polyampholytes generated from charge-shifting polymers. *Chem. Commun.* 51, 14092–14095. doi: 10.1039/C5CC04477D

Ghostine, R. A., and Schlenoff, J. B. (2011). Ion diffusion coefficients through polyelectrolyte multilayers: temperature and charge dependence. *Langmuir* 27, 8241–8247. doi: 10.1021/la2015258

Haken, H. (ed.). (2006). *Information and Self-Organization. A Macroscopic Approach to Complex Systems*. Berlin: Springer.

Han, J. H., Kim, K. B., Kim, H. C., and Chung, T. D. (2009). Ionic circuits based on polyelectrolyte diodes on a microchip. *Angew. Chem.* 121, 3888–3891. doi: 10.1002/ange.200900045

Hoshi, T., Saiki, H., and Anzai, J. I. (2003). Amperometric uric acid sensors based on polyelectrolyte multilayer films. *Talanta* 61, 363–368. doi: 10.1016/S0039-9140(03)00303-5

Jeyanthi, V., Anbu, P., Vairamani, M., and Velusamy, P. (2016). Isolation of hydroquinone (benzene-1, 4-diol) metabolite from halotolerant Bacillus methylotrophicus MHC10 and its inhibitory activity towards bacterial pathogens. *Bioprocess. Biosyst. Eng.* 39, 429–439. doi: 10.1007/s00449-015-1526-0

Karg, M., Pastoriza-Santos, I., Rodriguez-Gonzalez, B., Klitzing, R., Wellert, S., and Hellweg, T. (2008). Temperature, pH, and ionic strength induced changes of the swelling behavior of PNIPAM– poly (allylacetic acid) copolymer microgels. *Langmuir* 24, 6300–6306. doi: 10.1021/la702996p

Katz, E., and Minko, S. (2015). Enzyme-based logic systems interfaced with signal-responsive materials and electrodes. *Chem. Commun.* 51, 3493–3500. doi: 10.1039/C4CC09851J

Kelly, K. D., Fares, H. M., Abou Shaheen, S., and Schlenoff, J. B. (2018). Intrinsic properties of polyelectrolyte multilayer membranes: erasing the memory of the interface. *Langmuir* 34, 3874–3883. doi: 10.1021/acs.langmuir.8b00336

Klitzing, R. V., and Möhwald, H. (1996). A realistic diffusion model for ultrathin polyelectrolyte films. *Macromolecules* 29, 6901–6906. doi: 10.1021/ma960240s

Li, Z., Wang, H., Song, X., Yan, J., Hu, H., and Yu, B. (2014). Dual-responsive polymer brushes as an electrochemical logic gate. *J Electroanal Chem.* 719, 7–13. doi: 10.1016/j.jelechem.2014.01.030

Liu, D., Liu, H., and Hu, N. (2012). pH-, sugar-, and temperature-sensitive electrochemical switch amplified by enzymatic reaction and controlled by logic gates based on semi-interpenetrating polymer networks. *J. Phys. Chem. B* 116, 1700–1708. doi: 10.1021/jp209788g

Maltanava, H. M., Poznyak, S. K., Andreeva, D. V., Quevedo, M. C., Bastos, A. C., Tedim, J., et al. (2017). Light-induced proton pumping with a semiconductor: vision for photoproton lateral separation and robust manipulation. *ACS Appl. Mater. Interfaces* 9, 24282–24289. doi: 10.1021/acsami.7b05209

Motornov, M., Zhou, J., Pita, M., Gopishetty, V., Tokarev, I., Katz, E., et al. (2008). "Chemical transformers" from nanoparticle ensembles operated with logic. *Nano Lett.* 8, 2993–2997. doi: 10.1021/nl802059m

Motornov, M., Zhou, J., Pita, M., Tokarev, I., Gopishetty, V., Katz, E., et al. (2009). An integrated multifunctional nanosystem from command nanoparticles and enzymes. *Small* 5, 817–820. doi: 10.1002/smll.200801550

Nikitina, A. A., Ulasevich, S. A., Kassirov, I. S., Bryushkova, E. A., Koshel, E. I., and Skorb, E. V. (2018). Nanostructured layer-by-layer polyelectrolyte containers to switch biofilm fluorescence. *Bioconjug. Chem.* 29, 3793–3799. doi: 10.1021/acs.bioconjchem.8b00648

Peduto, A., Scuotto, M., Krauth, V., Roviezzo, F., Rossi, A., Temml, V., et al. (2017). Optimization of benzoquinone and hydroquinone derivatives as potent inhibitors of human 5-lipoxygenase. *Eur. J. Med. Chem.* 127, 715–726. doi: 10.1016/j.ejmech.2016.10.046

Pennakalathil, J., Kim, T. H., Kim, K., Woo, K., Park, J. K., and Hong, J. D. (2010). Ion-permselective polyelectrolyte multilayer membrane installed with a pH-sensitive oxazine switch. *Langmuir* 26, 11349–11354. doi: 10.1021/la1007044

Poghossian, A., Katz, E., and Schöning, M. J. (2015). Enzyme logic AND-Re set and OR-Reset gates based on a field-effect electronic transducer modified with multi-enzyme membrane. *Chem. Commun.* 51, 6564–6567. doi: 10.1039/C5CC01362C

Privman, M., Tam, T. K., Pita, M., and Katz, E. (2008). Switchable electrode controlled by enzyme logic network system: approaching physiologically regulated bioelectronics. *J. Am. Chem. Soc.* 131, 1314–1321. doi: 10.1021/ja8088108

Rmaile, H. H., Farhat, T. R., and Schlenoff, J. B. (2003). pH-Gated permeability of variably charged species through polyelectrolyte multilayer membranes. *J. Phys. Chem*. 107, 14401–14406. doi: 10.1021/jp035921l

Ryzhkov, N. V., Brezhneva, N., and Skorb, E. V. (2019a). Feedback mechanisms at solid/polyelectrolyte interfaces for applied materials. *Surface Innovat*. 7, 145–167. doi: 10.1680/jsuin.19.00006

Ryzhkov, N. V., Mamchik, N. A., and Skorb, E. V. (2019b). Electrochemical triggering of lipid bilayer lift-off oscillation at the electrode interface. *J. R. Soc. Interface* 16:20180626. doi: 10.1098/rsif.2018.0626

Schönhoff, M. (2003). Self-assembled polyelectrolyte multilayers. *Curr. Opin. Colloid Interface* 8, 86–95. doi: 10.1016/S1359-0294(03)00003-7

Selin, V., Ankner, J. F., and Sukhishvili, S. A. (2017). Nonlinear layer-by-layer films: effects of chain diffusivity on film structure and swelling. *Macromolecules* 50, 6192–6201. doi: 10.1021/acs.macromol.7b01218

Skorb, E. V., and Andreeva, D. V. (2013). Layer-by-Layer approaches for formation of smart self-healing materials. *Polym. Chem*. 4, 4834–4845. doi: 10.1039/c3py00088e

Skorb, E. V., and Andreeva, D. V. (2015). Self-healing properties of layer-by-layer assembled multilayers. *Polymer Int.* 64, 713–723. doi: 10.1002/pi.4899

Souto, R. M., Lamaka, S. V., and González, S. (2010). "Uses of scanning electrochemical microscopy in corrosion research," in *Microscopy: Science, Technology, Application and Education*, eds A. Mendez-Vilas and J. Diaz (Badajos: Formatex Research Center), 1769–1780.

Spruijt, E., Choi, E. Y., and Huck, W. T. (2008). Reversible electrochemical switching of polyelectrolyte brush surface energy using electroactive counterions. *Langmuir* 24, 11253–11260. doi: 10.1021/la801994b

Steitz, R., Jaeger, W., and Klitzing, R. V. (2001). Influence of charge density and ionic strength on the multilayer formation of strong polyelectrolytes. *Langmuir* 17, 4471–4474. doi: 10.1021/la010168d

Steitz, R., Leiner, V., Siebrecht, R., and Klitzing, R. V. (2000). Influence of the ionic strength on the structure of polyelectrolyte films at the solid/liquid interface. *Colloids Surf. A* 163, 63–70. doi: 10.1016/S0927-7757(99)00431-8

Tanaka, M., and Sackmann, E. (2005). Polymer-supported membranes as models of the cell surface. *Nature* 437, 656–663. doi: 10.1038/nature 04164

Wang, L., Lian, W., Yao, H., and Liu, H. (2015). Multiple-stimuli responsive bioelectrocatalysis based on reduced graphene oxide/poly (N-isopropylacrylamide) composite films and its application in the fabrication of logic gates. *ACS Appl. Mater. Interfaces* 7, 5168–5176. doi: 10.1021/am50 75002

Wang, X., Zhou, J., Tam, T. K., Katz, E., and Pita, M. (2009). Switchable electrode controlled by Boolean logic gates using enzymes as input signals. *Bioelectrochemistry* 77, 69–73. doi: 10.1016/j.bioelechem.2009.06.012

Yang, C., and Suo, Z. (2018). Hydrogel ionotronics. *Nat. Rev. Mater*. 3, 125–142. doi: 10.1038/s41578-018-0018-7

Zhu, T. F., and Szostak, J. W. (2009). Coupled growth and division of model protocell membranes. *J. Am. Chem. Soc*. 131, 5705–5713. doi: 10.1021/ja900919c

Zhukova, Y., Hiepen, C., Knaus, P., Osterland, M., Prohaska, S., Dunlop, J. W. C., et al. (2017). The role of titanium surface nanostructuring on preosteoblast morphology, adhesion and migration. *Adv. Health Mater*. 6:1601244. doi: 10.1002/adhm.201601244

Conflict of Interest Statement: The authors declare that the research was conducted in the absence of any commercial or financial relationships that could be construed as a potential conflict of interest.

Copyright © 2019 Ryzhkov, Nesterov, Mamchik, Yurchenko and Skorb. This is an open-access article distributed under the terms of the Creative Commons Attribution License (CC BY). The use, distribution or reproduction in other forums is permitted, provided the original author(s) and the copyright owner(s) are credited and that the original publication in this journal is cited, in accordance with accepted academic practice. No use, distribution or reproduction is permitted which does not comply with these terms.

frontiers in Chemistry

REVIEW
published: 20 February 2019
doi: 10.3389/fchem.2019.00085

A Review on the Electroless Deposition of Functional Materials in Ionic Liquids for Batteries and Catalysis

Abhishek Lahiri, Giridhar Pulletikurthi and Frank Endres*

Institute of Electrochemistry, Clausthal University of Technology, Clausthal-Zellerfeld, Germany

Developing functional materials via electroless deposition, without the need of external energy is a fascinating concept. Electroless deposition can be subcategorized into galvanic displacement reaction, disproportionation reaction, and deposition in presence of reducing agents. Galvanic displacement reaction is a spontaneous reduction process wherein the redox potentials of the metal/metal ion in the electrolyte govern the thermodynamic feasibility of the process. In aqueous solutions, the galvanic displacement reaction takes place according to the redox potentials of the standard electrochemical series. In comparison, in the case of ionic liquids, galvanic displacement reaction can be triggered by forming metal ion complexes with the anions of the ionic liquids. Therefore, the redox potentials in ILs can be different to those of metal complexes in aqueous solutions. In this review, we highlight the progress in the electroless deposition of metals and semiconductors nanostructures, from ionic liquids and their application toward lithium/sodium batteries, and in catalysis.

Keywords: ionic liquids, electroless deposition, catalysis, batteries, galvanic displacement

OPEN ACCESS

Edited by:
Nosang Vincent Myung, University of California, Riverside, United States

Reviewed by:
Syed Mubeen Jawahar Hussaini, The University of Iowa, United States
Giovanni Zangari, University of Virginia, United States

****Correspondence:***
Abhishek Lahiri
abhishek.lahiri@tu-clausthal.de

Specialty section:
This article was submitted to Electrochemistry, a section of the journal Frontiers in Chemistry

Received: *23 November 2018*
Accepted: *31 January 2019*
Published: *20 February 2019*

Citation:
Lahiri A, Pulletikurthi G and Endres F (2019) A Review on the Electroless Deposition of Functional Materials in Ionic Liquids for Batteries and Catalysis. Front. Chem. 7:85. doi: 10.3389/fchem.2019.00085

INTRODUCTION

A simple route for developing various metal and semiconductor nanostructures is one of the major challenges in materials research, which has a significant impact in the fields of energy storage and conversion, catalysis, sensors, photonics and optoelectronics, and biology. Electroless deposition is an elegant and versatile technique for metal plating as well as for developing various metal nanostructures. Electroless deposition can be subdivided into three categories: (1) Galvanic Displacement reaction: **Figure 1A** shows a schematic diagram of this process. In this process, when exposing a less noble metal containing solution (S) to a more noble metal (M), a spontaneous electrochemical reaction (redox reaction) takes place wherein the more noble metal is reduced by the Electrons generated from the less noble metal, as shown in Equations (1, 2). This technique is used to develop various nanostructures which can be used for different applications in batteries and catalysis.

$$S = S^{n+} + ne^- \quad (1)$$

$$M^{n+} + ne^- = \mathrm{M} \quad (2)$$

(2) Using a reducing agent: In this process, the employed reducing agent undergoes oxidation and provides electrons to the metal ions present in the electrolyte. When exposing the substrate to a

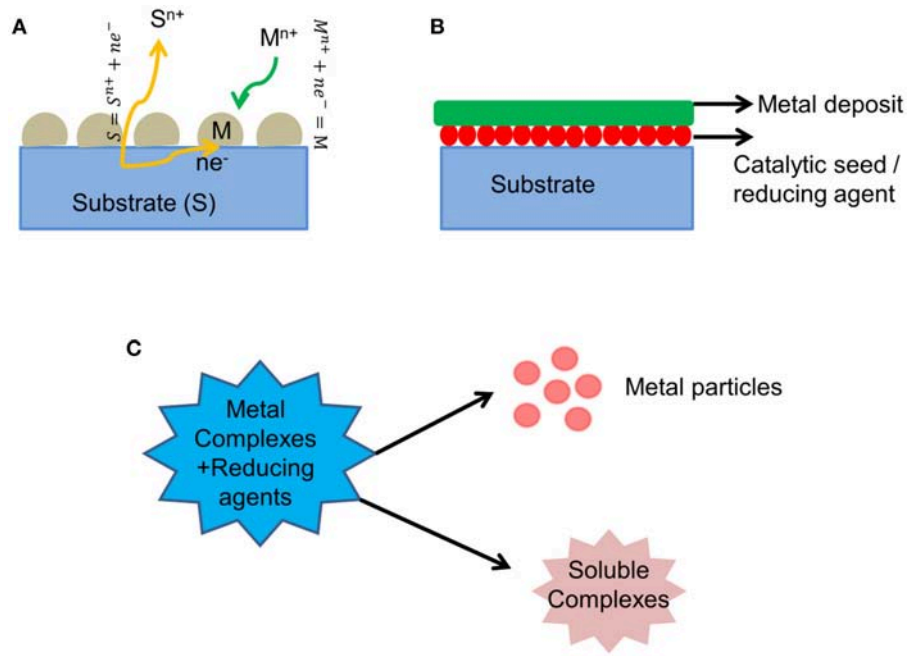

FIGURE 1 | Schematic diagram of various electroless deposition processes **(A)** Galvanic displacement reaction **(B)** Reduction using reducing agents **(C)** Disproportionation reaction.

metal ion containing electrolyte, spontaneous metal deposition occurs on the substrate as shown in the schematic diagram in **Figure 1B**. This technique is generally used for developing metal coatings over insulating or non-conductive substrates.

(3) Disproportionation reaction: In this process, the metal complex in presence of certain substances such as acids/salts or carbon monoxide, leads to the formation of metal particles, and other soluble products as shown in the schematic diagram in **Figure 1C**. This technique is usually used to generate metal nanoparticles which can be used as catalysts.

In aqueous systems, the galvanic displacement reaction occurs according to the standard electrochemical series wherein the redox reactions mainly depend on the concentration of metal ions, pH, and temperature. Furthermore, the electroless deposition is usually limited to a few monolayers without the addition of a catalyst. A change in the metal ion speciation in aqueous solutions might also result in a deviation from the standard electrochemical potentials, which has not been studied in great detail (Abbott et al., 2011, 2018), but might open up a few new opportunities for developing functional materials.

In direct comparison to aqueous solutions, ionic liquids possess advantages for favoring the galvanic displacement reaction. Ionic liquids are entirely made up of cations and anions, and can be divided into three subcategories of protic, aprotic, and deep eutectic solvents (DES) (Smith et al., 2014; Greaves and Drummond, 2015; Watanabe et al., 2017). In the last couple of years, the addition of water and molecular solvents in ionic liquids have also been explored as electrolytes for different applications and been described as the "fourth evolution in ionic liquids" (MacFarlane et al., 2018). This makes a large number of ionic liquids and its mixtures as possible electrolytes to tune the redox reactions (M/M^{n+}) and to trigger the galvanic displacement process. However, compared to aqueous electrolytes, there is no universal electrochemical series in the case of ionic liquids due to the lack of a standard reference electrode potential.

As only ions are present in ionic liquids, by changing the anions of the ionic liquids, the speciation of metals/semiconductor ions can be altered (Borisenko et al., 2018; Lahiri et al., 2018a). A change in the speciation leads to a different electrochemical behavior and has also shown to affect the morphology of the deposit (Pulletikurthi et al., 2013, 2014; Borisenko et al., 2018; Lahiri et al., 2018a). Interestingly, it was reported that changing the cations of the ionic liquids also affects the morphology of the electrodeposits (Zein El Abedin et al., 2006; Al-Salman and Endres, 2009; Ispas et al., 2010). The changes in the morphology of the electrodeposit were related to the difference in the interfacial structure of the ionic liquid at the electrode/electrolyte interface (EEI) (Endres et al., 2010). Unlike aqueous systems which form a double layer structure at the EEI, ionic liquids form a multilayered structure and the addition of metal ions affects this EEI structure (Lahiri et al., 2015a; Carstens et al., 2016), which influences the deposition kinetics. Therefore, in ionic liquids, a variation in the combination of both anions and cations can change the electrochemical behavior of metal/semiconductor deposition, which would also be the case for electroless deposition. In batteries, synthesis of various nanostructures with a high surface area and mechanical stability is important in order to develop a long-term stable battery. Electroless deposition in ionic liquids shows a promising route to

obtain such nanostructures. Furthermore, in catalysis, not only is a high surface area important, but a high number of catalytic activation sites are also necessary. Such control over morphology and tunable active sites can be achieved in ionic liquids which will be shown in the review.

Thus, based on the above brief description, it is clear that electroless deposition in ionic liquids differs from aqueous-based electrolytes. Numerous studies of electroless deposition in aqueous systems can be found in literature, yet little has been reported from ionic liquids. In this short review, we will present results on electroless deposition of metals in ionic liquids and show the application of the obtained nanostructures for batteries and catalysis. Finally, we will propose the various challenges and future prospects of electroless deposition in ionic liquids.

ELECTROLESS DEPOSITION OF NOBLE METALS

The first example of galvanic displacement reaction of silver (Ag) on Cu was shown by Abbott et al. (2007) in a DES composed of choline chloride (ChCl) and ethylene glycol (EG). Electroless deposition of Ag is an important industrial process for printed circuit boards (PCBs) to prevent degradation of the copper surface and is usually done by plating silver on copper from an $AgNO_3/HNO_3$ solution. Compared to the corrosive nature of the aqueous solution which also affects the copper in PCBs, an ionic liquid or DES does provide a safer alternative. Secondly, in aqueous solutions for the electroless deposition to prolong beyond few nanometers, a palladium catalyst is used (Shipley, 1961; Djokic, 2002). However, in the case of ionic liquids, it was shown that the galvanic displacement reaction of silver continued beyond a few nanometers without the use of any additional catalyst. In ChCl:EG eutectic ionic liquid, the galvanic displacement reaction took place according to Equation (3).

$$Ag_{IL}^{+} + Cu\,(s) = Cu_{IL}^{+} + Ag(s) \tag{3}$$

Figures 2A,B shows the AFM image of the deposit along with the height profile of Ag deposition on Cu, respectively. It is evident from **Figure 2A** that Ag electroless deposition on Cu is thick and from the height image in **Figure 2B**, the thickness was found to be ∼500 nm. This shows that electroless deposition of Ag on Cu from ionic liquids is clearly different from aqueous electrolytes where thermodynamics governs the redox potential and the reaction would stop in aqueous electrolytes once the Cu is covered with Ag. However, this was not the case for ILs as reported in Abbott et al. (2007). The authors reported from quartz crystal microbalance (QCM) investigations that during a controlled electroless deposition wherein copper was first electroplated on Au, with time, all the copper was replaced by Ag. Based on the results of scanning electron microscopy (SEM), Atomic Force Microscopy (AFM), and QCM, it was concluded that the electroless deposition of Ag on Cu might be limited by the diffusion of Cu^{+} ions. Temperature and different silver salts were also found to influence the deposition of Ag.

Different silver salts ($AgNO_3$, Ag_2SO_4, Ag(acetate), and AgCl) were investigated for silver plating. The best and most consistent result for electroless deposition of Ag on Cu was obtained from AgCl in the DES (Abbott et al., 2008). This means that the anion of the Ag salt alters the electroless deposition process which might be due to the change in speciation. However, Ag speciation studies are still lacking in DES which would have provided more information regarding the deposition quality as well as reaction kinetics. From the above studies, it appears that Cl^{-} ions can trigger the galvanic displacement reaction at the electrode/electrolyte interface. With a change in temperature from 20 to 45°C, the deposition rate was found to increase from 45 to 110 nm min^{-1} (Smith et al., 2010). Based on the results of the galvanic displacement of Ag on Cu, the authors also performed a pilot scale study for Ag plating on Cu in PCBs (Smith et al., 2010). For an industrial process, the rate of deposition must be increased to 0.2 μm min^{-1} which was achieved by increasing the Ag concentration in the liquid. **Figure 2C** shows the image of Ag coated Cu in a PCB using electroless deposition in the liquid. This clearly shows that it is possible to scale-up electrochemical processes in ILs and deep eutectic solvents with comparable/better results than the existing methods without the use of sacrificial precious metals.

Silver was also plated on Cu from a 1-butyl-3-methylimidazolium bromide (BMImBr)-AgBr electrolyte (Grishina and Ramenskaya, 2017). It was shown that the displacement reaction leads to the formation of $CuBr_2$ which dissolves in the electrolyte turning the solution to pale violet. From such a liquid, a silver coating thickness of up to 10 μm could be achieved. By studying the reaction kinetics, the authors showed that the galvanic displacement process took place in two stages. The rate constant in the first stage was found to be 5.1 × 10^{-5} s^{-1} which increased to 5.3 × 10^{-4} s^{-1} in the second stage and was related to the decrease in charge transfer resistance (Grishina and Ramenskaya, 2017). Although, compared to DES, a much thicker Ag layer could be achieved, the viscosity of BMImBr is higher than DES and therefore the removal of ionic liquids after the displacement process might be an issue. Furthermore, questions regarding the reuse of the BMImBr-AgBr electrolyte for plating silver on copper for practical applications remain unanswered.

Wang et al. studied the use of aqueous based choline chloride to study the galvanic displacement reaction of Ag on Cu with different silver salts of $AgNO_3$, AgCl, and Ag_2SO_4 (Wang et al., 2013a). It was shown that the mole ratio of ChCl and H_2O affected the deposition of Ag from $AgNO_3$. Furthermore, as observed previously by Abbott et al. with increase in temperature, the rate of deposition was shown to increase and by determining the deposition rate at various temperatures, the activation energy for Ag deposition was found to be 13 kJ mol^{-1}. However, from XRD analysis, the authors observed both Ag and Cu peaks which suggests that the thickness of Ag deposited was very low. Furthermore, the lack of adhesion tests along with limited solubility of AgCl and Ag_2SO_4 in the electrolyte questions the applicability of aqueous based electrolytes for metal plating.

The same authors also studied the electroless deposition of Pd on Ni-P coated Cu sheets using ChCl-H_2O electrolyte containing $PdCl_2$ (Wang et al., 2015a). Pd is a versatile catalyst to promote many organic reactions (Miyaura and Suzuki, 1995)

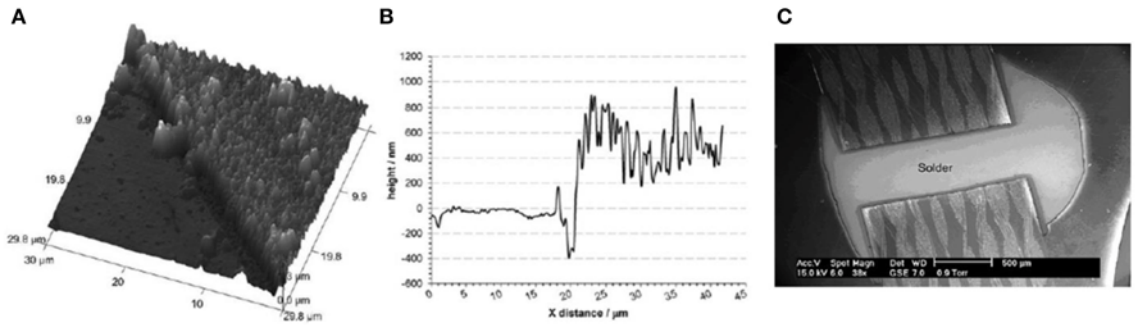

FIGURE 2 | (A) 3D AFM image of electroless deposited Ag on Cu **(B)** AFM height profile of the electroless deposited Ag on Cu shown in **Figure 1A (C)** Ag deposited on a printed circuit board. Reproduced from Abbott et al. (2007) and Abbott et al. (2008) with permission from The Royal Society of Chemistry and Elsevier.

as well as for hydrogen evolution reactions (Pentland et al., 1957) and therefore the electroless deposition becomes a simple technique to develop Pd nanostructures for catalysis applications. For electroless deposition of Pd on Ni-P coated Cu, plating parameters such as ChCl concentration, $PdCl_2$ concentration, pH, and temperature of the electrolyte were investigated. The pH of mixtures of ionic liquids and water can in principle be measured e.g., ChCl-H_2O mixtures. However, the pH of pure/neat aprotic ionic liquids cannot be defined. The galvanic displacement reaction involved the oxidation of nickel and the reduction of Pd^{2+} ions. The authors showed that as the concentration of ChCl in the electrolyte increased from 20 to 120 g L^{-1}, the deposition rate of Pd decreased from 2 to 0.6 µm h^{-1} which was attributed to the change in the coordination of Pd^{2+} ions in ChCl. Unfortunately, the speciation of Pd ions in the electrolyte was not analyzed by the authors. The microstructure of the deposit was also found to change with different immersion times. With deposition time of <5 min, spherical structures were obtained whereas with increase in time to 30 min, nanosheet like structures were observed. Increasing the electrolyte temperature from 55 to 75°C at a fixed ChCl:$PdCl_2$ ratio led to an increase in deposition rate from 1.1 to 2 µm h^{-1}. The change in pH of the electrolyte from 0.6 to 2 did not affect the deposition rate significantly. At an optimum electrolyte composition of 40 g L^{-1} ChCl, 2 g L^{-1} $PdCl_2$, and at a temperature of 60°C, Pd deposition of about 3 µm in thickness could be achieved in 90 min. Finally, the authors tested the corrosion resistance of Pd coated Ni-P/Cu in 3.5% NaCl and showed that Pd indeed improves the corrosion resistance of the material. Although, water based ionic liquids showed the possibility of galvanic displacement reaction, the applicability of the deposited Pd as catalyst was not investigated. Furthermore, the microstructure was shown to change from spherical to nanosheet like structure with deposition time. Such changes in microstructure are particularly interesting in catalytic applications. The lack of such studies makes it hard to evaluate the applicability of electroless deposition processes compared to regular electrodeposition processes.

Electroless deposition of gold was investigated from a few ionic liquids (Aldous et al., 2007; Ballantyne et al., 2015; Wang et al., 2015b). Gold deposition from chloroauric acid ($HAuCl_4$) in ChCl-H_2O was investigated on Ni-P coated Cu (Wang et al., 2015b). The authors showed that with an increase in $HAuCl_4$ concentration in the electrolyte (from 0.5 to 2 g L^{-1}), the rate of deposition increased from 5 to 22.5 nm min^{-1}. However, with higher concentration (2 g L^{-1}), the gold coating peeled off from the substrate. The change in ChCl concentration also affected the deposition rate. With decrease in ChCl concentration again the coated gold did not adhere to the surface whereas with increase in ChCl concentration, the gold deposition rate decreased. The change in the deposition rate with ChCl concentration seems to be due to a change in the coordination of $HAuCl_4$ with ChCl. However, the lack of the information regarding Au^{3+} coordination in the electrolyte makes it difficult to get a clear picture about the deposition process. The plating temperature also affected the rate of deposition. At 60°C, gold deposited at 6 nm min^{-1}, which increased to 13 nm min^{-1} at 90°C. The change in pH of the electrolyte from 0.5 to 3 did not influence the gold deposition rate. For a practical application, the authors also investigated the lifetime of the electrolyte by measuring the absorption spectra of the Au^{3+} ion as a function of time. They found that the solution was relatively stable over time and a loss in absorption of only ∼5% was observed after about 2 months. Based on this work it is clear that galvanic displacement of gold is possible from water based ionic liquids. However, the non-adhesive nature of the film rises concerns about the applicability of this electrolyte. It appears that slow rate of deposition is better for obtaining a stable gold coating. Further studies are required e.g., by preparing suitable electrode materials by surface modification to achieve good Au adhesion from the water based ionic liquid electrolyte.

A comprehensive study regarding metal-ion speciation of Au^{+} and how it influences the deposition rate and morphology was performed by Ballantyne et al. The Au^{+} speciation was studied for three different gold salts [AuCl, AuCN, and $KAu(CN)_2$] in a deep eutectic solvent composed of ChCl and 1, 2-ethanediol (Ballantyne et al., 2015). Prior to galvanic displacement reactions, the authors tested the gold electrodeposition from the three salts on Pt. The cyclic voltammetry (CV) experiments revealed that a complete

reversible process for the gold deposition and stripping occurred for AuCl whereas for both AuCN and $KAu(CN)_2$ no noticeable deposition peaks were observed.

This clearly indicated that Au speciation in the ionic liquid was different. From extended X-ray absorption fine structure (EXAFS) measurements, the authors showed that for AuCl, a coordination number of two was obtained leading to the formation of $[AuCl_2]^-$ species in the ionic liquid. However, in presence of AuCN and $KAu(CN)_2$, a mixed coordination of $[AuCl(CN)]^-$ was observed and no exchange of ligand between CN and Cl took place. Therefore, from the CV, no clear deposition and stripping peaks were obtained for the Au salts in liquids containing cyanide ions. On performing electroless deposition of Au onto nickel from the three electrolytes, the plating rate was found to be different. From AuCl, a plating rate of 1.16 nm min^{-1} was obtained whereas from AuCN and $KAu(CN)_2$ the deposition rate decreased to 0.76 and 0.37 nm min^{-1}, respectively. **Figure 3a** shows the optical image of Au plated on nickel from three different Au salts. Although, a thick gold film was obtained from AuCl (showing a dark brown color in **Figure 3a**, 1), the Au deposit did not adhere strongly to the nickel substrate, and could be easily peeled off. The best gold finish on nickel with a good adhesion property was obtained from the ionic liquid containing AuCN (**Figure 3a,** 2) whereas the deposition from $KAu(CN)_2$ did not give a good plating quality (**Figure 3a,** 3). Thus, this study clearly revealed that metal ion speciation is not only an important factor to control the deposition rate but also to develop better coating materials. Further work based on these studies can be performed to obtain different gold morphologies to be applied in catalysis.

A unique way of proton induced electroless deposition of Au was shown by Aldous et al. (2007) from the ionic liquid 1-butyl-1-methylimidazolium bis(trifluoromethylsulfonyl)amide ([BMIM]TFSA). The authors showed that gold could be deposited on glassy carbon (**Figure 3b**) without applying any potential from $H[AuCl_4]$ in [BMIM]TFSA. They argued that $[AuCl_4]^-$ gets adsorbed on specific sites of the glassy carbon electrode and the H^+ assists in the reduction of gold ions via a disproportionation reaction. It was further shown that addition of HTFSA to the electrolyte facilitated the electroless deposition process. Interestingly, the electroless deposition led to formation of triangular facet gold nanoplates as well as gold nanoparticles as shown in **Figure 3c**. However, changing the anion of IL from $TFSA^-$ to $[PF_6]^-$ or $[BF_4]^-$ did not lead to gold deposition. Although an interesting result of developing tunable gold nanoplates was demonstrated, no further studies were taken up to identify the parameters for producing only triangular shaped gold nanoplates. Gold nanoparticles and nanoplates have immense applications in biosensing (Zeng et al., 2011), plasmonic (Anderson et al., 2013), catalysis (Thompson, 2007), and so forth. Therefore, exploiting electroless deposition to directly obtain tunable plasmonic properties opens new avenues for material synthesis. Furthermore, speciation of Au might have played a key role to promote and develop different gold nanostructures which needs further investigation.

Gold deposition from $H[AuCl_4]$ in 1-butyl-1-methyl-pyrrolidinium dicyanamide ($[Py_{1,4}]DCA$) was studied on copper at different temperatures of 20–80°C (De Sá et al., 2013). The authors reported that Cu dissolves into the ionic liquid forming a copper dicyanamide complex and simultaneous deposition of gold on copper takes place. The morphology of the gold deposited on copper had a spherical structure of ∼200 nm in size and with increase in temperature, the amount of deposit was found to increase at a faster deposition rate. However, the authors neither studied the adhesive nature of gold on copper nor the speciation of Au^+ ion or the catalytic applicability of the deposit.

Electroless deposition of platinum nanoparticles was achieved from ionic liquids by a disproportionation reaction (Zhang et al., 2013). Pt was deposited onto glassy carbon from [EMIm]TFSA and $[EMIm]BF_4$ ionic liquids containing $K_2[PtCl_4]$ and HTFSA or CH_3SO_3H. It was observed that without a proton source, no reduction of Pt took place. The anion of the ionic liquid was also shown to affect the formation of Pt nanoparticles wherein it was shown that changing the anion of the ionic liquid from $TFSA^-$ to BF_4^-, a small quantity of Pt nanoparticles was obtained. This might be due to a different speciation of Pt in the employed ionic liquids which was not evaluated. Electroless deposition of Pt nanoparticles obtained from [EMIm]TFSA in presence of HTFSA is shown in **Figure 3d**, which shows Pt nanoparticles of 1.3 nm in diameter. The obtained Pt nanoparticles were used for electrocatalysis of formic acid. **Figure 3e** shows the electrocatalysis of formic acid to CO_2 on Pt nanoparticles obtained from [EMIm]TFSA containing HTFSA (solid line in **Figure 3e**) or CH_3SO_3H (dashed line in **Figure 3e**). It is evident that the oxidation current density of formic acid conversion on Pt nanoparticles deposited from HTFSA and CH_3SO_3H is different, which was related to the different facets formed in the nanoparticles. Therefore, it is possible that with proper choice of ionic liquids and reducing agents, high catalytic facet noble metal nanoparticles can be produced by electroless deposition, and exploited in catalysis.

ELECTROLESS DEPOSITION OF NON-NOBLE METALS

Tin (Sn) deposition on Cu by a galvanic displacement reaction was studied in ChCl-H_2O in the presence of thiourea (Wang et al., 2013b). From the standard electrochemical series, the Cu/Cu^+ redox potential is more positive compared to the Sn/Sn^{2+}, thus the galvanic displacement reaction should not be feasible due to a positive value for change in Gibbs energy. However, in ionic liquids, the speciation of the metal ions can be changed, and the redox potentials can favor the galvanic displacement reaction, thus making the electroless deposition of Sn on Cu feasible. Moreover, it was shown that the rate of deposition of Sn on Cu depends on temperature and concentrations of $SnCl_2$ and thiourea in ChCl-H_2O. On increasing the $SnCl_2$ concentration up to 15 g L^{-1} a deposition rate of ∼3.2 μm h^{-1} was observed. The addition of thiourea of 90 g L^{-1} marginally improved the rate of deposition to ∼3.4 μm h^{-1}. The XRD results showed that within 1 min of galvanic displacement at 40°C, prominent peaks of Sn

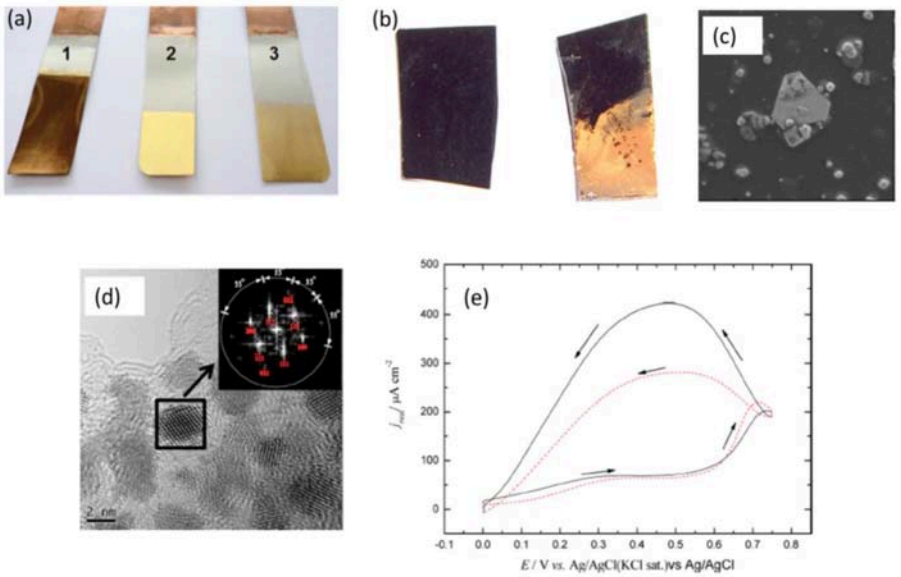

FIGURE 3 | (a) Electroless deposition of Au on nickel from (a1) AuCl (a2) AuCN (a3) $KAu(CN)_2$ in ChCl-1, 2-ethanediol **(b)** Electroless deposition of Au from $H[AuCl_4]$ in EMImTFSA in presence of HTFSA on glassy carbon **(c)** Gold nanoplates formed by electroless deposition on glassy carbon from $H[AuCl_4]$ in EMImTFSA in presence of HTFSA **(d)** Electroless deposition of Pt nanoparticles **(e)** Methanol electrooxidation on Pt nanoparticles formed by electroless deposition. Reproduced from Aldous et al. (2007), Zhang et al. (2013) and Ballantyne et al. (2015) with permission from The Royal Society of Chemistry and American Chemical Society, Copyright 2007, 2013 American Chemical Society.

could be distinguished. Sn is a promising anode material for both Li-ion and Na-ion batteries (Liu et al., 2016). However, no attempt was made to use these deposits for battery applications or to understand the mechanism of the galvanic displacement reaction.

Electroless plating of copper on Al and Al-5 wt%Si was shown to be feasible in ChCl-ethylene glycol (ChCl-EG) (Kang et al., 2014, 2015). Although the galvanic displacement reaction of Cu on Al is possible from aqueous solutions, the presence of an oxide layer on Al inhibits the formation of uniform Cu coatings. Furthermore, strong alkaline solutions or F-containing solutions are required to remove the oxide layer from Al to facilitate the electroless deposition process (Ai et al., 2011; Ye et al., 2012). However, in ionic liquids, no F-containing additive was needed. A few Cu(II) salts [$CuSO_4.5H_2O$, $CuCl_2.2H_2O$, and $Cu(CH_3COO)_2$] were tested for the electroless deposition on Al (Kang et al., 2014), among which $CuCl_2.2H_2O$ showed the highest solubility in ChCl-EG. Based on UV visible spectroscopy, formation of $[CuCl_4]^{2-}$ was identified and the galvanic displacement reaction was proposed as shown in Equations (4, 5).

$$Al + 3[CuCl_4]^{2-} \rightarrow Al^{3+} + 3[CuCl_2]^{-} + 6Cl^{-} \quad (4)$$

$$Al + 3[CuCl_2]^{-} \rightarrow Al^{3+} + 3Cu + 6Cl^{-} \quad (5)$$

Electrochemical noise analysis (ECN) was used to identify the number of stages for the electroless deposition process from the plots of current vs. time from which four stages were identified for the galvanic displacement reaction (Kang et al., 2014). In the first stage the sharp increase in current was attributed to nucleation-growth phenomena followed by a decrease in reaction rate in 2nd stage which led to decrease in current. In third and fourth stages, the current was low but almost constant and was related to galvanic displacement reactions. However, the displacement reaction on Al-5 wt%Si was found to be slightly different (Kang et al., 2015). From the microstructure and elemental map analyses, it was observed that initially Cu displaced only Al and did not form any coating on the silicon regions of the Al-Si alloy. With time, a uniform coating could be obtained both on Al and Al-Si alloy. However, there are a few open questions as to how did Cu(II) displace the Si in the Al-Si alloy which will need further investigation. Furthermore, with change in Si concentration in the Al-Si alloy, it would be interesting to evaluate the electroless deposition process.

To improve the corrosion resistance and mechanical properties of Al, Ni-P coating is usually used from aqueous solutions at temperatures of >80°C. Kang et al. showed that modifying the Al substrate with galvanic displacement of Cu or Zn followed by electroless deposition of Ni-P on the modified substrate led to a better and uniform coating with improved corrosion resistance (Kang et al., 2017). The authors argued that Cu/Zn acted as a catalytic material which improved the deposition of Ni-P. Unfortunately, the microstructural analysis was limited to understanding the surface phenomena without looking into the cross-sectional phenomena of Al-Cu/Zn-Ni-P. It is important to understand the cross-sectional behavior and the grain boundary formed between Al-Cu and Ni-P in order to improve the deposition characteristics. Therefore, further studies are needed to evaluate the complex displacement reaction mechanism.

Al coating on reactive metal surfaces, especially on steel is an attractive technique to prevent corrosion and to improve the conductivity. Al has been electrodeposited on various substrates from ionic liquids (Zein El Abedin et al., 2005; Zein El Abedin and Endres, 2006; Eiden et al., 2009; Giridhar et al., 2012a). $AlCl_3$ dissolution in ionic liquids is an exothermic process. Depending on the $AlCl_3$ concentration in the ionic liquid, Lewis acid or Lewis basic electrolytes can be formed. Aluminum can be electrodeposited from Lewis acids of 60:40 mol% of $AlCl_3$:[EMIm]Cl. The electrodeposits contain micrometer sized Al (**Figure 4A**).

When changing the electrolyte from $AlCl_3$:[EMIm]Cl to $AlCl_3$:1-butyl-1-methylpyrrolidinium chloride ($AlCl_3$:[$Py_{1,4}$]Cl) electrodeposition leads to nanocrystalline Al (**Figure 4B**). The change in the deposit morphology can be attributed to a change in interfacial structure at the EEI (Endres et al., 2010). Similar results have also been observed for the electrodeposition of Al from $AlCl_3$ dissolved in ILs containing bis(trifluoromethylsulfonyl)amide (Moustafa et al., 2007) and trifluoromethylsulfonate anions (Giridhar et al., 2012b) with either 1-butyl-1-methylpyrrolidinium or 1-ethyl-3-methylimidazolium cations. By mixing both [EMIm]Cl and [$Py_{1,4}$]Cl with $AlCl_3$, a range of different microstructures could be obtained. Al deposits have been made from various compositions of $AlCl_3$:1-ethyl-3-methylimidazolium chloride ($AlCl_3$:[EMIm]Cl) and $AlCl_3$: 1-butyl-1-methylpyrrolidinium chloride ($AlCl_3$:[$Py_{1,4}$]Cl). The deposits thus obtained possess nanostructures and/or microstructures depending on the amount of 60:40 mol% $AlCl_3$:[EMIm]Cl in the mixtures of 60:40 mol% $AlCl_3$:[$Py_{1,4}$]Cl and 60:40 mol% $AlCl_3$:[EMIm]Cl. This study clearly showed that the cation of the ionic liquid has a remarkable influence on the particle size of Al electrodeposited from the aforementioned ionic liquids.

Recent studies have shown the possibility of electroless coating of Al using reducing agents in ionic liquids. Koura et al. (2008) used reducing agents such as LiH, $LiAlH_4$, or diisobutyl aluminum hydride for the reduction of Al from $AlCl_3$-1-ethyl-3-methylimidazolium chloride. The plating time, temperature and concentration of the reducing agent were evaluated for electroless deposition of Al on copper. At 25 and 35°C, a maximum amount of 0.4 mg cm^{-2} of Al was obtained whereas on increasing the temperature to 45°C, the amount decreased to 0.25 mg cm^{-2}, which was attributed to the decomposition of the electrolyte. With increase in plating time and concentration of the reducing agent, the authors found that the Al particle size increased, and thicker deposits could be obtained. Among the three reducing agents, the authors found that the addition of diisobutyl aluminum hydride led to a much smoother surface. A comparison of electroless deposited Al (**Figure 4C**) and electrodeposited Al from the same electrolyte is shown in **Figure 4A**. It is evident that Al deposits in both cases show particle sizes of ∼2–3 μm on the electrode. This shows that electroless deposition in presence of a reducing agent is a simple route to obtain Al on different substrates without the need of additional energy. Furthermore, such a technique might be useful to coat Al on an insulating substrate as well.

A much more detailed study of electroless deposition of Al from $AlCl_3$/[EMIm]Cl in presence of diisobutyl aluminum hydride as reducing agent was investigated by Shitanda et al. (2009). The proposed reaction mechanism for the electroless deposition is shown in Equations (6, 7).

$$4Al_2Cl_7^- + 3e^- \rightarrow 7AlCl_4^- + Al \quad (6)$$

$$2\{(CH_3)_2 - CH - CH_2 - AlH - CH_2 - CH - (CH_3)_2\} \rightarrow 2\{(CH_3)_2 - CH - CH_2 - Al - CH_2 - CH - \left(CH_3\right)_2\}^+ + H_2 + 2e^- \quad (7)$$

The authors analyzed various parameters such as the influence of plating time, temperature, concentration of reducing agent and the concentration of metal ions on the electroless plating, and surface morphology of Al. With increase in plating time at temperatures of 35 and 55°C, the amount of Al deposit increased. However, on performing the experiments at 65°C, the amount of Al decreased due to decomposition of the electrolyte. With time, at lower temperature (35°C) it was shown that the Al crystals grew in size to 2–5 μm and on increasing the temperature to 65°C, a much smoother surface with a smaller grain size (<1 μm) was obtained. The change in $AlCl_3$ concentration in the electrolyte also affected the deposit morphology. When changing the mol% of $AlCl_3$ from 52 to 58 and 66.7, more Al could be deposited. However, a smoother film could be obtained for 58 mol% $AlCl_3$. Finally, with an increase in reducing agent concentration in the electrolyte with a fixed $AlCl_3$ concentration, more Al could be plated.

Using the same [EMIm]Cl/$AlCl_3$ electrolyte in the presence of diisobutyl aluminum hydride as reducing agent, electroless deposition of Al was also successfully obtained on nickel nanowires (Poges et al., 2018). Using SEM and neutron scattering measurements, the authors showed that a core-shell structure was obtained for electroless deposited Al on Ni nanowires. The Al coating thickness on the nickel nanowires was found to be between 300 and 600 nm. The ferromagnetic magnetization property was found to decrease from 43.3 to 31.4 emu g^{-1} from the magnetic measurement of nickel nanowires and Al coated nickel nanowires, respectively. Although, these studies showed a simple route for Al plating, further investigation on practical systems like steel might be more appropriate.

Al has also been used as a corrosion protection layer for uranium (Egert and Scott, 1987; Jiang et al., 2017). Recently, electroless deposition of Al from [EMIm]Cl/$AlCl_3$ on uranium was shown to be an effective method for coating uranium (Jiang et al., 2018). The galvanic displacement reaction of Al on U takes place according to Equation (8).

$$U + 4Al_2Cl_7^- \rightarrow Al + U^{3+} + 7AlCl_4^- \quad (8)$$

As uranium dissolves into the electrolyte, simultaneous Al deposition occurs. From UV-visible spectroscopy, the authors evaluated the dissolution rate of U during the displacement reaction. Within the first 20 min of the reaction, the U dissolution rate decreased from 0.03 to 0.02 mol min^{-1} m^{-2}. After 120 min of the reaction, an insignificant amount of U was found to

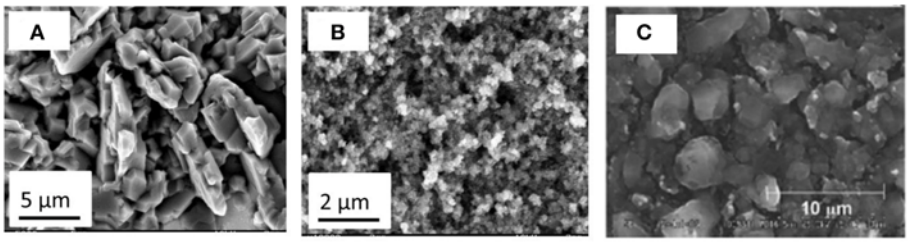

FIGURE 4 | (A) Microstructure of electrodeposited Al from [EMIm]Cl/$AlCl_3$ at −0.3 V vs. Al and **(B)** from [$Py_{1,4}$]Cl/$AlCl_3$ at −0.3 V vs. Al for 1 h **(C)** Al electroless deposited from [EMIm]Cl/$AlCl_3$ in presence of LiH as reducing agent. Reproduced from Koura et al. (2008) with permission from The Electrochemical Society.

dissolve which suggested that most of the U was covered by Al. From a cross-sectional SEM analysis, the authors showed that a 200 nm thick Al deposit was formed on U after 2 h of reaction. Although this study shows a simple route to protect U, the practical application of this process remains arguable due to cleaning procedures required after the deposition process and disposal of the U ions in the solution.

Galvanic displacement of nickel on copper was achieved using a deep eutectic solvent of ChCl and ethylene glycol mixtures (Yang et al., 2016). Nickel was shown to form $[NiCl_4]^{2-}$ ions in the electrolyte which displaced copper, forming nickel metal and $[CuCl_3]^{2-}$ ions. It was shown that the displacement reaction takes place in three stages. Initially, copper is stripped resulting in a porous structure along with progressive nucleation of nickel nanoparticles. In the second stage, more copper is dissolved leading to surface cracks along with deposition and growth of nickel. Finally, as the nickel covers the copper surface, the reaction slows down leading to the formation of a porous nickel layer. The obtained nickel was used as a catalytic material for the hydrogen evolution reaction (HER). The HER catalytic activity of nickel was shown to be better than nickel wire and required a lower overpotential of 170 mV vs. RHE for HER. A large exchange current density of 0.186 mA cm^{-2} with a relatively small Tafel slope of 98.5 mV $decade^{-1}$ could be achieved by the obtained porous nickel structures on Cu.

ELECTROLESS DEPOSITION OF ALLOYS AND COMPOSITE MATERIALS

Alloys and composite materials have been shown to be useful electrode materials for Li-ion and Na-ion batteries as they have lower volume expansion during intercalation/deintercalation processes, high theoretical capacities, and longer life time compared to carbon electrodes and to their metal counterparts (Zhang, 2011; Obrovac and Chevrier, 2014; Lahiri and Endres, 2017). Alloys and composites are in general deposited using high temperature techniques, vacuum techniques, sol-gel processes, or by electrodeposition (Zhang, 2011; Obrovac and Chevrier, 2014; Lahiri and Endres, 2017). Electroless deposition has also been used to develop alloys and composites.

A copper antimonide (Cu-Sb) alloy has been used as anode for both Li and Na-ion batteries (Lahiri and Endres, 2017). The Cu_2Sb alloy has been prepared by galvanic displacement reaction from ionic liquids (Lahiri et al., 2018b). It was observed that on exposing a copper substrate to $SbCl_3$-[EMIm]TFSA, Cu_2Sb nanoplates formed instantaneously. From mass spectroscopic analysis, it was shown that $SbCl_3$ in the electrolyte forms a $[SbCl_2(TFSA)_3]^{2-}$ complex which had a lower reduction potential compared to Cu/Cu^+ in the same electrolyte and triggered the electroless deposition to take place. The electroless deposition process was studied using *in situ* X-ray photoelectron spectroscopy (XPS), X-ray diffraction (XRD), and *in situ* atomic force microscopy (AFM). From XPS and XRD measurements, formation of CuCl was observed which suggested that a three-electron transfer process was taking place for the formation of Cu_2Sb. From *in situ* AFM, the deposition rate was estimated to be between 0.4 and 1.65 nm min^{-1}. The electroless deposited Cu_2Sb nanoplates were also tested for Li and Na ion batteries with an ionic liquid electrolyte which showed a promising battery performance. However, the question remains as to why Cu_2Sb formed a nanoplate structure by electroless deposition. Further studies using transmission electron microscopy along with selected area electron diffraction (SAED) might reveal the crystal growth mechanism.

It was interesting that Fe could also be deposited on Cu by galvanic displacement reaction from 0.15 M $FeCl_2$ dissolved in a mixture of 1-butylpyrrolidine and $AlCl_3$ (1:1.2 mol ratio) containing toluene at 60°C (Lahiri et al., 2018b). Although from aqueous standard electrochemical series, such a galvanic displacement reaction is impossible, these reactions become feasible in ionic liquids due to the difference in speciation. The electroless deposited Fe was confirmed with XRD measurements. Further studies regarding the influence of $FeCl_2$ concentration in the eutectic-based ionic liquid is required to understand the reaction mechanism of the galvanic displacement reaction process. Furthermore, such studies will be useful to improve the deposition as well as to develop different nanostructures.

Unlike Cu_2Sb, interestingly, semiconducting amorphous gallium antimonide (GaSb) was obtained by electroless deposition of Sb on Ga from ionic liquids (Lahiri et al., 2015b). Galvanic displacement of Sb on Ga was performed from two different ionic liquids with [$Py_{1,4}$]TFSA and [EMIm]TFSA. The change in the cation of the ionic liquid influenced the

morphology of GaSb deposit. The bandgap of the GaSb deposit was found to be ∼0.9 eV. From *in situ* AFM studies, the deposition rate was reported to be 2.3 nm min^{-1}. Furthermore, formation of GaSb nanowires was shown to be possible using electroless deposition. As the open circuit potential of Sb/Sb^{3+} is more positive compared to Si and Ge in the same ionic liquid, Sb modification of both electrodeposited Si and Ge was achieved (Lahiri et al., 2016, 2017). The electroless deposition of Sb on Ge from 0.1 M $SbCl_3$-$[Py_{1,4}]$TFSA led to the formation of Sb nanoparticles. **Figure 5A** shows the microstructure of the deposit wherein Ge nanoparticles of 200–300 nm are covered with Sb nanoparticles of <50 nm in size. XPS and Raman studies showed the formation of Ge_xSb_{1-x}. From Raman spectroscopy (**Figure 5B**) at room temperature, both Ge and Sb peaks are observed with a shoulder showing the formation of Ge_xSb_{1-x}. With annealing, a clear shift in the Ge peak is seen confirming the formation of Ge_xSb_{1-x}. As both Ge and Sb are possible anode materials for Na-ion batteries, Ge and Sb modified Ge were tested as battery electrodes with an ionic liquid electrolyte (Lahiri et al., 2016). **Figure 5C** compares 50 charge-discharge cycles of electrodeposited Ge and Sb modified Ge with sodium bis(fluorosulfonyl)amide (NaFSA) in $[Py_{1,4}]$FSA ionic liquid as electrolyte. It is evident that modifying the Ge with Sb led to a higher Na capacity storage even at higher current densities of 0.83 A g^{-1} compared to Ge which was cycled at a current density of 0.54 A g^{-1}. Similar to the modification of Ge with Sb, electrodeposited silicon was also modified by Ag and Sb as it was found that the open circuit potentials of both Ag/Ag^+ and Sb/Sb^{3+} are more positive to Si(IV)/Si in the ionic liquid (Lahiri et al., 2017). From quartz crystal microbalance (QCM) measurements, the rate of deposition for Sb on Si was found to be 2.7 ng sec^{-1} for the first 1,000 s which then decreases to 0.4 ng sec^{-1}. In comparison, the deposition of Ag on Si was 6.2 ng sec^{-1} which decreased to 1.8 ng sec^{-1} after 1,000 s. Although a three times increase in the deposition of Ag is expected compared to Sb deposition, it was shown that due to difference in speciation of Ag and Sb salts in an ionic liquid, the deposition rates differed. In comparison to the formation of Sb nanoparticles in the case of Ge (**Figure 5A**), a layered structure of Sb has been seen for Si (**Figure 5D**). This suggests that the nucleation-growth process of Sb on the two semiconductors is different. The electrodeposited Si and Sb modified Si was also tested as an anode for Li-ion battery.

Figure 5E shows the charge-discharge curves of the electrodeposit in 1 M LiTFSA-$[Py_{1,4}]$TFSA cycled at 0.25 C. The Sb modified Si showed a capacity of over 2,000 mAh g^{-1} for the first 10 cycles which decreased to 1,100 mAh g^{-1} at the 30th cycle. Compared to the modified Si, the electrodeposited silicon showed a lower Li storage capacity. Based on the results of Sb electroless deposition, further investigations are needed regarding long term cycling stability of the anode material. Furthermore, during battery testing, the lithiation/delithiation processes need to be evaluated in order to understand how the alloying of Sb/semiconductor changes.

CHALLENGES AND LIMITATIONS OF IONIC LIQUIDS FOR ELECTROLESS DEPOSITION

The electroless deposition process in ionic liquids has been shown to be an autocatalytic deposition process which occurs at the metal/electrolyte interface by the reduction of metallic ions/complexes in the presence or in the absence of externally added reducing agents. However, this process suffers from a few limitations such as slow ion transport/diffusion of metal ion species/complexes and slow kinetics of the deposition process at room temperature. Furthermore, issues regarding adhesion of the film, surface selectivity, control over deposit morphology, and purity of the films exist. Therefore, future efforts need to be directed toward overcoming these limitations in order to develop a successful method for material synthesis using this simple energy-free methodology.

For example, in the galvanic displacement reaction the substrate serves as a reducing agent and an electron source for the reduction of metal ion species/complexes. Here, the rate of the deposition depends on the transport of the ions to the interface and also on the rate of dissolution of the substrate. Although an increase in temperature does improve the reaction kinetics and the diffusion processes, however, adhesion of the reduced metal on the substrate might not always be sufficiently good. Therefore, an optimum condition between reaction kinetics, diffusion parameters, temperature, and adhesion of the films need to be balanced.

For better adhesion as well as to develop different nanostructures, surface selectivity plays a key role during the galvanic displacement process. A proper surface modification could lead to a good metal finish. Furthermore, it could promote development of interesting nanostructures which can then be applied in batteries and catalysis. The crystal plane of the surface will also influence the galvanic displacement reaction and deposit morphology which has not yet been studied in ionic liquids.

The grain size and growth of the deposited films for galvanic displacement reactions depend on different factors such as immersion time and temperature, rate of deposition, activation sites on the substrate and speciation in ionic liquids. Control over these factors in electroless deposition is challenging. Usually, large grains or thick films have been obtained at longer immersion times and at higher temperatures. However, by controlling the reaction kinetics and by addition of surfactants/mixture of ionic liquids, it could be possible to spatially control the grains/films which would be of interest for catalytic applications. Furthermore, it might be possible to develop various nanostructures which can then be applied as electrodes in batteries and catalysis/electrocatalysis.

One major issue with electroless deposition from ionic liquids is the cleaning process to obtain the deposited film without any contaminants. Usually, salts of the metallic substrate and trapped ionic liquid are present in the deposits which are difficult to remove. Suitable solvents are required to remove these salts/ionic liquids. It is of interest to design tuneable ionic liquids which can be used to dissolve the metal salts formed during galvanic

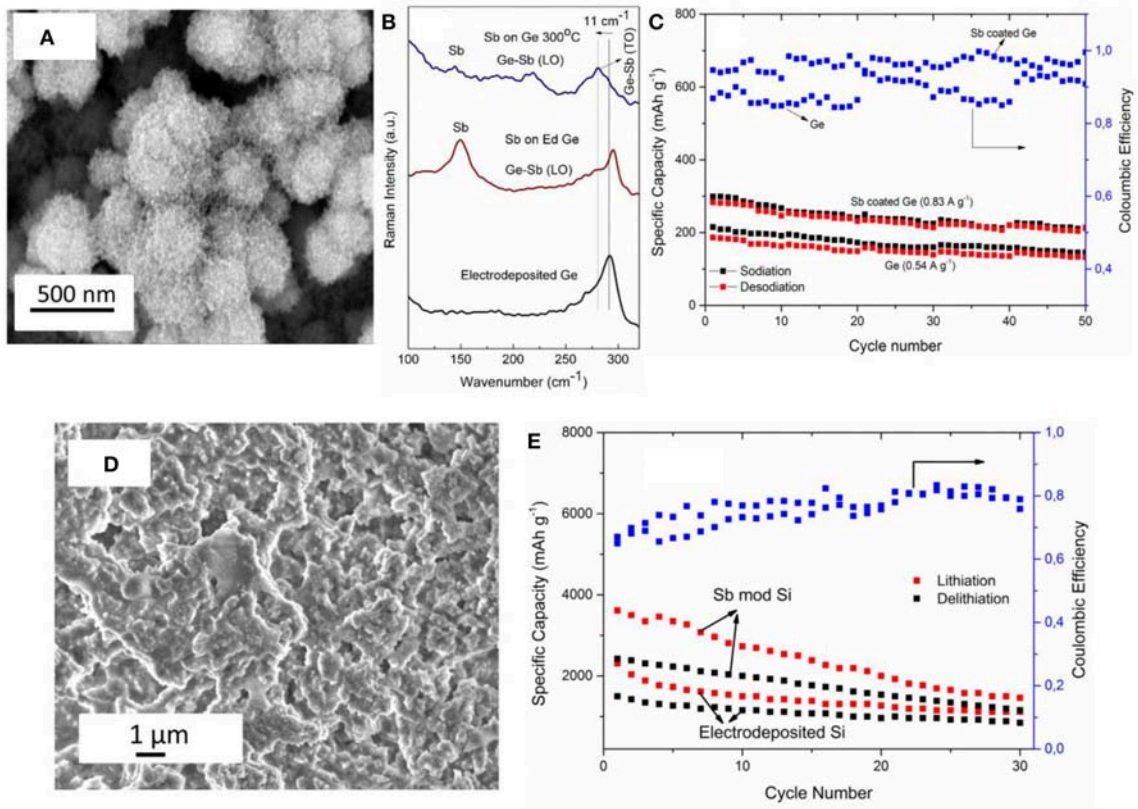

FIGURE 5 | (A) Microstructure of Sb modified Ge nanoparticles **(B)** Raman spectra of electrodeposited Ge (black line), electroless deposited Sb on Ge (red line) and after annealing to 300°C (blue line) **(C)** SEM of electroless deposition Sb on silicon **(D)** Charge-Discharge cycles of electrodeposited Ge and Sb modified Ge for Na-ion batteries in 1 M NaFSA-[$Py_{1,4}$]FSA **(E)** Charge-Discharge cycles of electrodeposited Si and Sb modified Si for Li-ion batteries in 1 M LiTFSA-[$Py_{1,4}$]TFSA. Reproduced from Lahiri et al. (2016) and Lahiri et al. (2017) with permission from The Royal Society of Chemistry and American Chemical Society. Copyright 2017 American Chemical Society.

displacement reaction and the ionic liquid itself being soluble in simple organic solvents.

Finally, the ultimate challenge is to develop an electrochemical series for ionic liquids. This would require a universal reference electrode. At present a universal reference electrode for ionic liquids does not yet exist. Depending on the individual experiment a Pt quasi-reference electrode is an acceptable compromise.

SUMMARY AND FUTURE PERSPECTIVES

In the last decade, electroless deposition from ionic liquids has been identified as a promising route for developing various metal and semiconductor nanostructures, some of which have shown to be useful in catalysis and as electrodes for batteries. Compared to aqueous solutions, the electroless deposition of noble metals from ionic liquids does not stop after a few monolayers and leads to deposits with thicknesses between 100 nm and 10 µm. Furthermore, as the speciation of metals can be modified in ionic liquids, the electroless deposition does not always follow the standard electrochemical series. Various parameters such as the metal precursors, the employed ionic liquid, temperature, and concentration were shown to affect the deposit morphology, particle size as well as the deposition rate. The presence of an ionic liquid also affected the crystallographic planes. This was exemplified in the electroless deposition of Pt nanoparticles from different ionic liquids wherein it was shown that the formic acid oxidation current differed and depended on the low index planes of the Pt nanoparticles. Similarly, it was shown that depending on the Au precursor and the ionic liquid, triangular gold nanoplates could be formed. Therefore, ionic liquids can be used as a medium to control the crystallographic facets, which turn out to be a useful approach to improve catalytic reactions. In the case of electroless plating of noble metals (e.g., Ag) for PCBs, the adhesion of these metals is an important factor for both Au and Ag deposition. The adhesion properties of the electroless coated metals have been shown to be dependent on the metal ion speciation and the ionic liquid played a vital role to obtain a good metal finish.

Besides noble metals, the possibility of coating non-noble metals especially aluminum on steel, which is an industrially important technique for corrosion prevention makes electroless deposition a lucrative technique to be exploited. For

electrodeposition, it was shown that by changing the cation of the ionic liquid, the morphology and the grain size of the deposit could be altered which will in-turn influence the corrosion properties of the coating. Such simple modifications become a useful tool to obtain better corrosion prevention materials which are yet to be investigated by an electroless deposition route from ionic liquids.

Electroless deposition in ionic liquids was also utilized for developing intermetallics and composites which have potential applications as electrode materials for batteries. Various alloy nanostructures have been obtained by electroless deposition from ionic liquids and were shown to have good Li and Na storage properties. The ease of the process for materials synthesis makes it a beneficial technique for developing other alloy nanostructures which can be tested as electrodes for batteries.

Thus, based on the above literature, it is clear that some limitations and challenges remain in the field of electroless deposition from ionic liquids. However, it is evident that electroless deposition in ionic liquids has tremendous potential for developing functional materials both for catalysis and for batteries which are yet to be exploited. New domains comprising of mixtures of ionic liquids, addition of organic solvents and water in ionic liquids for electroless deposition of metals and semiconductors are yet to be investigated which might lead to a facile synthesis technique to obtain novel nanostructures. The possibility of developing porous materials and one-dimensional nanostructures by template-assisted techniques would also bring new perspectives to electroless deposition from ionic liquids. Finally, the challenge will be to develop ionic liquid-based electrolytes with smart functionalities that could be used to develop specific functional materials.

AUTHOR CONTRIBUTIONS

All authors listed have made a substantial, direct and intellectual contribution to the work, and approved it for publication.

REFERENCES

Abbott, A., Aldous, L., Borisenko, N., Coles, S., Fontaine, O., Garcia, J. D. G., et al. (2018). Electrochemistry: general discussion. *Faraday Discuss.* 206, 405–426. doi: 10.1039/C7FD90093G

Abbott, A. P., Frisch, G., Gurman, S. J., Hillman, A. R., Hartley, J., Holyoak, F., et al. (2011). Ionometallurgy: designer redox properties for metal processing. *Chem Commun*. 47, 10031–10033. doi: 10.1039/c1cc13616j

Abbott, A. P., Griffith, J., Nandhra, S., O'Conner, C., Postlethwaite, S., Ryder, K. S., et al. (2008). Sustained electroless deposition of metallic silver from a choline chloride-based ionic liquid. *Surf. Coat. Technol.* 202, 2033–2039. doi: 10.1016/j.surfcoat.2007.08.055

Abbott, A. P., Nandhra, S., Postlethwaite, S., Smith, E. L., and Ryder, K. S. (2007). Electroless deposition of metallic silver from a choline chloride-based ionic liquids: a study using acoustic impedance spectroscopy, SEM and atomic force microscopy. *Phys. Chem. Chem. Phys.* 9, 3735–3743. doi: 10.1039/b703954a

Ai, J. H., Liu, S. P., Widharta, N. A., Adhikari, S., Anderegg, J. W., and Herbert, K. R. (2011). Copper layers deposited on aluminum by galvanic displacement. *J. Phys. Chem. C*. 115, 22354–22359. doi: 10.1021/jp2054266

Aldous, L., Silvester, D. S., Pitner, W. R., Compton, R. G., Lagunas, M. C., and Hardacre, C. (2007). Voltammetric studies of gold, protons, and $[HCl_2]^-$ in ionic liquids. *J. Phys. Chem. C*. 111, 8496–8503. doi: 10.1021/jp0709555

Al-Salman, R., and Endres, F. (2009). Template-assisted electrodeposition of Si_xGe_{1-x} nanowires with varying length and composition from two different ionic liquids. *J. Mater. Chem*. 19, 7228–7231. doi: 10.1039/b909265j

Anderson, L. J. E., Zhen, Y-R., Payne, C. M., Nordlander, P., and Hafner, J. H. (2013). Gold nanobelts as high confinement plasmonic waveguides. *Nano. Lett*. 13, 6256–6261. doi: 10.1021/nl4037356

Ballantyne, A. D., Forrest, G. C. H., Frisch, G., Hartley, J. M., and Ryder, K. S. (2015). Electrochemistry and speciation of Au+ in a deep eutectic solvent: growth and morphology of galvanic immersion coatings. *Phys. Chem. Chem. Phys*. 17, 30540–30550. doi: 10.1039/C5CP05748E

Borisenko, N., Lahiri, A., Pulletikurthi, G., Cui, T., Carstens, T., Zahlbach, J., et al. (2018). The Au(111)/IL interfacial nanostructure in the presence of precursors and its influence on the electrodeposition process. *Faraday Discuss*. 206, 459–473. doi: 10.1039/C7FD00165G

Carstens, T., Lahiri, A., Borisenko, N., and Endres, F. (2016). $[Py_{1,4}]$FSI-NaFSI-based ionic liquid electrolyte for sodium batteries: Na+ solvation and interfacial nanostructure on Au(111). *J. Phys. Chem. C*. 120, 14736–14741. doi: 10.1021/acs.jpcc.6b04729

De Sá, A. I., Eugénio, S., Quaresma, S., Rangel, C. M., and Vilar, R. (2013). Gold deposition from 1-butyl-1-methyl-pyrrolidinium dicyanamide ionic liquid at open-circuit and under potentiostatic control. *Surf. Coat. Technol*. 232, 645–651. doi: 10.1016/j.surfcoat.2013.06.061

Djokic, S. S. (2002). "Electroless deposition of metals and alloys" in *Modern Aspects of Electrochemistry*, Vol. 35, eds. E. C. Brian E. Conway and E. W. Ralph E. White (New York, NY: Springer, US), 51–133.

Egert, C. M., and Scott, D. G. (1987). A study of ion plating parameters, coating structure, and corrosion protection for aluminum coatings on uranium. *J. Vac. Technol. A*. 5, 2724–2727. doi: 10.1116/1.574728

Eiden, P., Liu, Q., Zein El Abedin, S., Endres, F., and Krossing, I. (2009). An experimental and theoretical study of the aluminium species present in mixtures of AlCl3 with the ionic liquids $[BMP]Tf_2N$ and $[EMIm]Tf_2N$. *Chem-A European Eur. J*. 15, 3426–3434. doi: 10.1002/chem.200801616

Endres, F., Höfft, O., Borisenko, N., Gasparotto, L. H., Prowald, A., Al-Salman, R., et al. (2010). Do solvation layers of ionic liquids influence electrochemical reactions? *Phys. Chem. Chem. Phys*. 12, 1724–1732. doi: 10.1039/b923527m

Giridhar, P., Zein El Abedin, S., and Endres, F. (2012a). Electrodeposition of aluminium from 1-butyl-1-methylpyrrolidinium chloride/$AlCl_3$ and mixtures with 1-ethyl-3-methylimidazolium chloride/$AlCl_3$. Electrochim. *Acta*. 70, 210–214. doi: 10.1016/j.electacta.2012.03.056

Giridhar, P., Zein El Abedin, S., and Endres, F. (2012b). Electrodeposition of nanocrystalline aluminium, copper, and copper–aluminium alloys from 1-butyl-1-methylpyrrolidinium trifluoromethyl sulfonate ionic liquid. *J. Solid State Electrochemistry*. 16, 3487–3497. doi: 10.1007/s10008-012-1800-x

Greaves, T. L., and Drummond, C. J. (2015). Protic ionic liquids: Evolving structure-property relationships and expanding applications. *Chem. Rev*. 115, 11379–11448. doi: 10.1021/acs.chemrev.5b00158

Grishina, E. P., and Ramenskaya, L. M. (2017). Silver cementation on copper in 1-butyl-3-methylimidazolium bromide-silver bromide ionic liquid medium. *J. Mol. Liquids*. 248, 963–971. doi: 10.1016/j.molliq.2017.10.118

Ispas, A., Adolphi, B., Bund, A., and Endres, F. (2010). On the electrodeposition of tantalum from three different ionic liquids with the bis(trifluoromethylsulfonyl)amide anion. *Phys. Chem. Chem. Phys*. 12, 1793–1803. doi: 10.1039/b922071m

Jiang, Y., Ding, J., Luo, L., Shi, P., and Wang, X. (2017). Electrodepositing aluminum coating on uranium from aluminum chloride-1-ethyl-3-methylimidazolium chloride ionic liquid. *Surf. Coat. Technol*. 309, 980–985. doi: 10.1016/j.surfcoat.2016.10.049

Jiang, Y., Fang, L., Luo, L., Wang, S., and Wang, X. (2018). Deposition mechanism of aluminum on uranium in AlCl3-1-ethyl-3-methylimidazolium chloride ionic liquid by galvanic displacement. *J. Appl. Electrochem*. 48, 827–834. doi: 10.1007/s10800-018-1204-4

Kang, R., Liang, J., Liu, B., and Peng, Z. (2014). Copper galvanic replacement on aluminium from a choline chloride based ionic liquid: effect of thiourea. *J. Electrochem. Soc.* 161, D534–D539. doi: 10.1149/2.08114 10jes

Kang, R., Liang, J., Qiao, Z., and Peng, Z. (2015). Growth kinetics of copper replacement deposition on Al and Al-Si from a deep eutectic solvent. *J. Electrochem. Soc.* 162, D515–D519. doi: 10.1149/2.02515 10jes

Kang, R., Peng, Z., Liu, B., Wang, D., and Liang, J. (2017). A protocol for fast electroless Ni-P on Al alloy at medium-low temperature accelerated by hierarchically structured Cu immersion layer. *Surf. Coat. Technol.* 309, 67–74. doi: 10.1016/j.surfcoat.2016.11.029

Koura, N., Nagase, H., Sato, A., Kumakura, S., Takeuchi, K., Ui, K., et al. (2008). Electroless plating of aluminum from a room-temperature ionic liquid electrolyte. *J. Electrochem. Soc.* 155, D155–D157. doi: 10.1149/1.2 817880

Lahiri, A., Borisenko, N., Olschewski, M., Gustus, R., Zahlbach, J., and Endres, F. (2015b). Electroless deposition of III-V semiconductor nanostructures from ionic liquids at room temperature. *Angew. Chem. Int. Ed.* 54, 11870–11874. doi: 10.1002/anie.201504764

Lahiri, A., Borisenko, N., Olschewski, M., Pulletikurthi, G., and Endres, F. (2018b). Anomalous electroless deposition of less noble metals on Cu in ionic liquids and its application towards battery electrodes. *Faraday Discuss.* 206, 339–351. doi: 10.1039/C7FD00121E

Lahiri, A., Carstens, T., Atkin, R., Borisenko, N., and Endres, F. (2015a). *In situ* atomic force microscopic studies on the interfacial multilayer nanostructure of LiTFSI-[$Py_{1,4}$]TFSI on Au(111): influence of Li^+ ion concentration on the Au(111)/IL interface. *J. Phys. Chem. C.* 119, 16734–16742. doi: 10.1021/acs.jpcc.5b04562

Lahiri, A., and Endres, F. (2017). Electrodeposition of nanostructured materials from aqueous, organic and ionic liquid electrolytes for Li-ion and Na-ion batteries: a comparative review. *J. Electrochem. Soc.* 164, D597–D612. doi: 10.1149/2.1011709jes

Lahiri, A., Lu, T., Behrens, N., Borisenko, N., Li, G., and Endres, F. (2017). Hydrofluoric acid-free electroless deposition of metal on silicon in ionic liquids and its enhanced performance in lithium storage. *ACS Appl. Mater. Interfaces.* 9, 11350–11355. doi: 10.1021/acsami.7b01404

Lahiri, A., Olschewski, M., Gustus, R., Borisenko, N., and Endres, F. (2016). Surface modification of battery electrodes via electroless deposition with improved performance for Na-ion batteries. *Phys. Chem. Phys.* 18, 14782–14786. doi: 10.1039/C6CP02364A

Lahiri, A., Pulletikurthi, G., Behrens, N., Cui, T., and Endres, F. (2018a). *In situ* atomic force microscopy and electrochemical quartz crystal microbalance studies on the electrodeposition and oxidation of silicon. *J. Phys. Chem. C.* 122, 14499–14510. doi: 10.1021/acs.jpcc.8b02462

Liu, L., Xie, F., Lyu, J., Zhao, T., Li, T., and Choi, B. G. (2016). Tin-based anode materials with well-designed architectures for next-generation lithium-ion batteries. *J. Power. Sources.* 321, 11–35. doi: 10.1016/j.jpowsour.2016. 04.105

MacFarlane, D. R., Chong, A. L., Forysth, M., Kar, M., Vijayaraghavan, R., Somers, A., et al. (2018). New dimensions in salt-solvent mixtures: a 4th evolution of ionic liquids. *Faraday Discuss.* 206, 9–28. doi: 10.1039/C7FD0 0189D

Miyaura, N., and Suzuki, A. (1995). Palladium-catalyzed cross-coupling reactions of organoboron compounds. *Chem. Rev.* 95, 2457–2483. doi: 10.1021/cr00039a007

Moustafa, E. M., Zein El Abedin, S., Shkurankov, A., Zschippang, E., Saad, A. Y., Bund, A., et al. (2007). Electrodeposition of Al in 1-Butyl-1-methylpyrrolidinium Bis(trifluoromethylsulfonyl)amide and 1-Ethyl-3-methylimidazolium Bis(trifluoromethylsulfonyl)amide Ionic Liquids: *in situ* STM and EQCM Studies. *J. Phys. Chem. B* 111, 4693–4704. doi: 10.1021/jp0670687

Obrovac, M. N., and Chevrier, V. L. (2014). Alloy negative electrodes for Li-ion batteries. *Chem. Rev.* 114, 11444–11502. doi: 10.1021/cr500207g

Pentland, N., Bockris, J. O. M., and Sheldon, E. (1957). Hydrogen evolution reaction on copper, gold molybdenum, palladium, rhodium and iron. *J. Electrochem. Soc.* 104, 182–194.

Poges, S., Jin, J., Guild, C., Li, W.-N., Birnkrant, M., and Suib, S. L. (2018). Preparation and characterization of aluminum coatings via electroless plating onto nickel nanowires using ionic liquid plating solution. *Mater. Chem. Phys.* 207, 303–308. doi: 10.1016/j.matchemphys.2017.12.079

Pulletikurthi, G., Elbasiony, A. M., Zein El Abedin, S., and Endres, F. (2014). A comparative study on the electrodeposition of tin from two different ionic liquids: Influence of the anion on the morphology of the tin deposits. *ChemElectroChem* 1, 1549–1556. doi: 10.1002/celc.2014 02155

Pulletikurthi, G., Lahiri, A., Carstens, T., Borisenko, N., Zein El Abedin, S., and Endres, F. (2013). Electrodeposition of silicon from three different ionic liquids: possible influence of the anion on the deposition process. *J. Solid State Electrochem.* 17, 2823–2832. doi: 10.1007/s10008-013-2 185-1

Shipley, C. R. (1961). *Method of Electroless Deposition on a Substrate and Catalyst Solution Thereof.* US Patent 3,011,920A, Washington, DC: U.S. Patent and Trademark Office.

Shitanda, I., Sato, A., Itagaki, M., Watanabe, K., and Koura, N. (2009). Electroless plating of aluminum using diisobutyl aluminum hydride as liquid reducing agent in room-temperature ionic liquid. *Electrochim Acta.* 54, 5889–5893. doi: 10.1016/j.electacta.2009.05.052

Smith, E. L., Abbott, A. P., Griffin, J., Harris, R. C., O'Conner, C., and Ryder, K. S. (2010). Pilot trials of immersion silver deposition using a choline chloride based ionic liquid. *Circuit World.* 36, 3–9. doi: 10.1108/030561210110 15031

Smith, E. L., Abbott, A. P., and Ryder, K. S. (2014). Deep eutectic solvents (DESs) and their applications. *Chem. Rev.* 114, 11060–11082. doi: 10.1021/cr300162p

Thompson, D. T. (2007). Using gold nanoparticles for catalysis. *Nano Today* 2, 40–43. doi: 10.1016/S1748-0132(07)70116-0

Wang, Y., Cao, X., Wang, W., Mitsuzak, N., and Chen, Z. (2015b). Immersion gold deposition from a chloroauric acid-choline chloride solution: deposition kinetics and coating performance. *Surf. Coat. Technol.* 265, 62–67. doi: 10.1016/j.surfcoat.2015.01.062

Wang, Y., He, J., Wang, W., Naotoshi, M., and Chen, Z. (2013b). Sustained immersion tin deposition on copper from choline chloride based aqueous solution without reducing agent. *J. Electrochem. Soc.* 160, D295–D299. doi: 10.1149/2.005308jes

Wang, Y., Li, W., Wang, W., Mitsuzak, N., Bao, W., and Chen, Z. (2015a). Thick pure palladium film with varied crystal structure electroless deposited from choline chloride-palladium chloride solution without the addition of reductant. *Thin Solid Films* 586, 35–40. doi: 10.1016/j.tsf.2015.04.038

Wang, Y., Zhou, Y., Wang, W., and Chen, Z. (2013a). Sustained deposition of silver on copper surface from choline chloride aqueous solution. *J. Electrochem. Soc.* 160, D119–D123. doi: 10.1149/2.012304jes

Watanabe, M., Thomas, M. L., Zhang, S., Ueno, K., Yasuda, T., and Dokko, K. (2017). Application of ionic liquids to energy storage and conversion materials and devices. *Chem. Rev.* 117, 7190–7239. doi: 10.1021/acs.chemrev.6b 00504

Yang, C., Zhang, Q. B., and Abbott, A. P. (2016). Facile fabrication of nickel nanostructures on a copper-based template via a galvanic displacement reaction in a deep eutectic solvent. *Electrochem. Commun.* 70, 60–64. doi: 10.1016/j.elecom.2016.07.004

Ye, W., Chen, Y., Zhou, F., Wang, C., and Li, Y. (2012). Fluoride-assisted galvanic replacement synthesis of Ag and Au dendrites on aluminium foil with enhanced SERS and catalytic activities. *J. Mater. Chem.* 22, 18327–18334. doi: 10.1039/c2jm32170j

Zein El Abedin, S., and Endres, F. (2006). Electrodeposition of metals and semiconductors in air-and water-stable ionic liquids. *ChemPhysChem* 7, 58–61. doi: 10.1002/cphc.200500288

Zein El Abedin, S., Moustafa, E. M., Hempelmann, R., Natter, H., and Endres, F. (2005). Additive free electrodeposition of nanocrystalline aluminium in a water and air stable ionic liquid. *Electrochem. Commun.* 7, 1111–1116. doi: 10.1016/j.elecom.2005.08.010

Zein El Abedin, S., Moustafa, E. M., Hempelmann, R., Natter, H., and Endres, F. (2006). Electrodeposition of nano- and microcrystalline aluminium in three different air and water stable ionic liquids. *ChemPhysChem.* 7, 1535–1543. doi: 10.1002/cphc.200600095

Zeng, S., Yong, K.-T., Roy, I., Dinh, X.-Q., Yu, X., and Luan, F. (2011). A review on functionalized gold nanoparticles for biosensing applications. *Plasmonics*. 6, 491–506. doi: 10.1007/s11468-011-9228-1

Zhang, D., Okajima, T., Lu, D., and Ohsaka, T. (2013). Electroless deposition of platinium nanoparticles in room-temperature ionic liquids. *Langmuir* 29, 11931–11940. doi: 10.1021/la402429v

Zhang, W.-J. (2011). A review of the electrochemical performance of alloy anodes for lithium-ion batteries. *J. Power. Sources*. 196, 13–24. doi: 10.1016/j.jpowsour.2010.07.020

Conflict of Interest Statement: The authors declare that the research was conducted in the absence of any commercial or financial relationships that could be construed as a potential conflict of interest.

Copyright © 2019 Lahiri, Pulletikurthi and Endres. This is an open-access article distributed under the terms of the Creative Commons Attribution License (CC BY). The use, distribution or reproduction in other forums is permitted, provided the original author(s) and the copyright owner(s) are credited and that the original publication in this journal is cited, in accordance with accepted academic practice. No use, distribution or reproduction is permitted which does not comply with these terms.

Green and Sustainable Chemistry

Fan Xia

Fan Xia's research is focused on bio-analytical chemistry. He obtained his PhD at the Chinese Academy of Sciences Institute of Chemistry (ICCAS) as part of Professor Lei Jiang's group. Following this he was a Postdoctoral Fellow in Professor Alan J. Heeger's group at the University of California Santa Barbara. Between 2012 and 2016 he was a Professor at Huazhong University of Science and Technology (HUST), and since 2016 he has been Dean and Professor of the Faculty of Materials Science and Chemistry at China University of Geosciences.

Reid C. Van Lehn

Reid Van Lehn is an Assistant Professor in the Department of Chemical and Biological Engineering and the Jay and Cynthia Ihlenfeld Faculty Scholar in the College of Engineering at the University of Wisconsin-Madison. He obtained a BSc and PhD in Materials Science and Engineering from the Massachusetts Institute of Technology under the supervision of Professor Alfredo Alexander-Katz. He performed his postdoctoral research with Professor Thomas Miller III at the California Institute of Technology before joining the faculty at UW-Madison in 2016. His research interests center on developing and applying molecular simulation methods to understand and engineer synthetic and biological soft materials.

Guanying Chen

Dr Guanying Chen obtained a PhD degree in optics in 2009 from Harbin Institute of Technology (HIT), China. He then became an Assistant professor in 2009, an Associate Professor in 2012, and a full Professor in 2013) at HIT. He completed his postdoc from 2009 to 2011 and became an affiliated adjunct research associate professor (since 2012) at the Institute for Lasers, Photonics and Biophotonics (ILPB), SUNY Buffalo. His interests include lanthanide luminescence, optical bioimaging, and solar cells. He has published more than 100 peer-reviewed papers and serves as an editorial board member for the SCI-indexed journals of *Scientific Reports, Nanomaterials, Crystals*, and as the guest editor for *Theranostics*.

Christopher J. Barile

Christopher Barile is an Assistant Professor in chemistry at the University of Nevada, Reno. His research combines electrochemistry, inorganic chemistry, and materials chemistry with an emphasis on energy conversion, storage, and efficiency. Chris earned a BSc with distinction and co-terminal MSc degrees in chemistry from Stanford University with James Collman. He then attended the University of Illinois at Urbana-Champaign and obtained his PhD working with Andrew Gewirth studying advanced battery technologies and reactions involving multiple proton and electron transfer steps. Prof. Barile then returned to Stanford as a postdoctoral scholar with Michael McGehee before starting his independent career in July 2017.

Fumiaki Amano

Fumiaki Amano is an Associate Professor at the University of Kitakyushu, Japan. His research is centered on photoelectrochemistry of oxide semiconductor materials. He was awarded the 9th Honda-Fujishima Prize by the Electrochemical Society of Japan in 2010, the Catalysis Society of Japan Award for Young Researchers in 2017, and the Young Scientists' Prize of the Commendation for Science and Technology by the MEXT in 2018. He obtained a PhD from Kyoto University in 2006. He worked as an Assistant Professor at Catalysis Research Center, Hokkaido University from 2006 to 2011 and as a Lecturer at the University of Kitakyushu from 2011 to 2014.

Jie He

Jie He received his BSc and MSc degrees in Polymer Materials Science and Engineering from Sichuan University in 2005 and 2007. He obtained his PhD in Chemistry from Universite de Sherbrooke (Quebec Canada) in 2010. He then worked as a postdoctoral fellow at the University of Maryland. In 2014, he joined the faculty of the University of Connecticut where he is currently an Assistant Professor of Chemistry. His research focuses on the design of polymer/inorganic hybrid materials for bioinspired catalysis and renewable energy conversion. He was a recipient of the 2018 AAUP Excellence Award and the 2012 Governor General of Canada's Academic Gold Medal.

frontiers in Chemistry

MINI REVIEW
published: 29 November 2019
doi: 10.3389/fchem.2019.00826

Bioinspired Slippery Lubricant-Infused Surfaces With External Stimuli Responsive Wettability: A Mini Review

Xian Yang[1], Yu Huang[1,4], Yan Zhao[2]*, Xiaoyu Zhang[1], Jinhua Wang[1], Ei Ei Sann[3], Khin Hla Mon[3], Xiaoding Lou[1] and Fan Xia[1]*

[1] Engineering Research Center of Nano-Geomaterials of Ministry of Education, Faculty of Material Science and Chemistry, China University of Geosciences, Wuhan, China, [2] Department of Materials Science, Institute of Molecular Materials and Devices, Fudan University, Shanghai, China, [3] Department of Industrial Chemistry, Dagon University, Yangon, Myanmar, [4] Key Laboratory of Bio-inspired Materials and Interfacial Science, Technical Institute of Physics and Chemistry, Chinese Academy of Science, Beijing, China

Responsive slippery lubricant-infused surfaces (SLIS) have attracted substantial attention because of the high demand of fundamental research and practical applications, such as controllable liquid-repellency, intelligent, and easy-to-implement wettability switching. In this review, advanced development of responsive slippery surfaces is briefly summarized upon various external stimuli, including stress, electrical field, magnetic field, and temperature. In addition, remaining challenge and prospect are also discussed.

Keywords: bio-inspired, liquid-infused surfaces, slippery surface, stimuli response, wettability, interfacial adhesion

OPEN ACCESS

Edited by:
Steve Suib,
University of Connecticut,
United States

Reviewed by:
Carmen Alvarez-Lorenzo,
University of Santiago de Compostela, Spain
Mingjie Liu,
Beihang University, China

***Correspondence:**
Yu Huang
yuhuang@cug.edu.cn
Yan Zhao
zhaoy@fudan.edu.cn

Specialty section:
This article was submitted to Green and Sustainable Chemistry, a section of the journal Frontiers in Chemistry

Received: *02 June 2019*
Accepted: *13 November 2019*
Published: *29 November 2019*

Citation:
Yang X, Huang Y, Zhao Y, Zhang X, Wang J, Sann EE, Mon KH, Lou X and Xia F (2019) Bioinspired Slippery Lubricant-Infused Surfaces With External Stimuli Responsive Wettability: A Mini Review. Front. Chem. 7:826. doi: 10.3389/fchem.2019.00826

INTRODUCTION

Surface's wettability is one of the most fundamental performances in numerous biological processes and industrial technologies, which attracts researchers' interest for a long time. In the past decades, owing to new understanding of species wetting mechanism, bio-inspired materials with super-wettability are flourishing through modeled after surface morphology and chemical composition of the nature species (Liu et al., 2017; Sett et al., 2017; Li et al., 2019). For example, *Nepenthes* pitcher plants fill water in the spaces among the micro structure to form a slippery liquid film, leading insects to aquaplane into their stomach. Since Wong et al. (2011) mimicked pitcher plants' slippery surface and fabricated slippery liquid-infused porous surfaces (**Figures 1A,B**), a serial of liquid-infused surfaces, or well-known as slippery lubricant-infused surfaces (SLIS), have been developed for various applications, such as liquid repellency (Hozumi et al., 2011; Huang et al., 2017), liquid or gas transportation (Chen et al., 2016; Xiao et al., 2019), water harvesting (Zhang et al., 2017), oil-water separation (Solomon et al., 2014; Wang et al., 2017a), anti-corrosion (Lee et al., 2017; Howell et al., 2018), heat transfer (Anand et al., 2012), visual biosensors (Gao et al., 2018), and so on. The two basic components of SLIS are solid substrates to hold liquid and the liquid for infiltration, as shown in **Figure 1C**. The solid substrates may have a micro/nano structural surface to infuse lubricant (Xiao et al., 2013; Dai et al., 2015), or can be swollen in lubricant (Yao et al., 2014). The liquid hold by the solid substrates acts as stable lubricant to repel any impinging immiscible fluids, and ensures the repellent fluids to slide away without any resistance. To distinguish the liquid for infused and the fluids for repellency, we refer the infused liquid as "lubricant" in this mini review from now on. No matter the substrates' surfaces are rough or

flat, the key feature of SLIS is the thin layer of lubricant cover the substrate. This lubricant layer forms a dynamic and stable lubricant/substrate interface. If this thin lubricant is removed, the film would lose its excellent liquid repellency and droplet pin on the surface as a result. This is because the interfacial adhesion of the repelling liquid/solid surface is obviously larger than that of the repelling liquid/lubricant, as shown in **Figure 1D**. Based on this mechanism, SLIS with controllable and reversible wettability were developed through stimulus-triggered switch in substrate's chemical composition or/and morphologies, lubricant's height or/and phase, repellent liquid's chemical component and so on. Meanwhile, other properties, like optical property, will also change and endow SLIS with different functionalities. The responsive SLIS have demonstrated their ability of controllable repellent droplet's motion behavior, which provides significant insight of developing devices for fog collection (Peng et al., 2015), oil-water separation (Calcagnile et al., 2012), droplets' delivery (Hou et al., 2017), complex-flow distribution (Cao et al., 2017), biomimetic tissue (Wang Y. et al., 2018), and so on.

In addition, typical response materials have been adopted for different external stimuli. Elastic and nanoporous polymers such as polydimethylsiloxane (PDMS) and polyurethane (PU) are mainstream in mechanically responsive SLIS. Electrical responsive materials are chosen primarily based on electrowetting mechanism, generally both the substrate and the repellent liquid should be conductive. Magnetic field response strategies include magnetic particles doped substrates or introduces magnetic lubricant. Traditional thermal response is mainly realized by thermosensitive lubricant such as paraffin or mixtures of solid/liquid oil.

EXTERNAL STIMULI RESPONSIVE SLIS

Mechanically Responsive SLIS

Stretching or mechanical pressing represents a simple, straightforward and effective strategy for tuning the wettability of SLIS. Generally, replacing the rigid substrate with a continuous elastic polymer is required to enable mechanical deformation. The stress would vary the surface's morphology and lubricant layer's height, resulting in the change of surface's wettability. Yao et al. (2013) adopted a nanoporous elastic PDMS substrate to support lubricant. This film would reversibly adjust the droplet's sliding behaviors on it, as shown in **Figure 2A**. When the film was stretched, the lubricant would flow into the pores. In this case, the solid surface formed a rough interface, resulting in the droplet pinned. Without stress, the lubricant came out from the porous. The film restored its liquid repellency and made the droplet slide away. In this research, graded mechanical stimulus was proved to lead to dynamic and precise regulation of optical transparency and wettability. This film provided a new idea for fuel transport pipes or microfluidic systems. Based on Yao's research, Liu et al. (2016) constructed an elastic substrate with periodical porous structure instead of atactic porous. The film was demonstrated a variable structural-color SLIS with self-reporting surface wettability. When the film was elastically deformed by stress, lubricant thickness and structural color of surface would change simultaneously along the deformation of porous. Consequently, the accompaniment of these changes made self-reporting of surface wettability a reality. Beside optical devices, SLIS with controllable wettability also demonstrated their applications in collecting water from atmosphere or water-oil mixture (Han et al., 2016; Park et al., 2016; Fu et al., 2017). Most research was focused on strengthening condensation and shedding of water, avoiding the wind-caused loss of the water captured. Wang et al. (2017b) developed a flexible SLIS by infusing perfluoropolyether into a fluorinated-copolymer-modified PU with adjustable and elastic deformability. Through controlling the droplets' sliding behavior, the stress responsive SLIS showed some adaptability of environmental and realized high efficiency of water collection.

Although the mechanical responsive SLIS have been demonstrated reversible deformation and wettability switching, their dependence on elastic substrate severally limit their practical applications. What's more, continuous stress and deformation would trigger the potential mechanical damage. Improving the inherent durability of materials or introducing self-repairing materials should be a key point for developing mechanical responsive SLIS.

Electrical Field Responsive SLIS

Electrowetting is a method of changing interfacial wettability by adjusting the potential between the liquid and solid electrodes. Due to its fast response, wide range changes, small size and good reliability, electrowetting method has been widely used in optics, biology, and microelectronics (Mugele and Baret, 2005). Generally, to achieve electrical field responsive SLIS, both the substrate and the repellent liquid should be conductive. Heng et al. firstly put forward a serial of SLIS with anisotropic and electrically responsive sliding (Guo et al., 2016; Che et al., 2017; Wang et al., 2018a,b; Han et al., 2019). Firstly, by directional freeze drying, they synthesized oriented and conductive membrane with porous structure. Then, silicone oil was introduced into the membrane. With voltage applied, the surface's chemical components and micro/nano structure won't change. However, electrostatic attraction between the repellent conductive droplet and its image charge increased under voltage. The thickness of the lubricant reduced, and droplet's wetting status changed. As a result, the droplet was pinned on the surface (**Figure 2B**). In the other hand, without voltage, the conductive droplet slid easily due to the thick layer of lubricant. Later on, Heng's group (Che et al., 2017) filled the surface with conductive lubricant. Compared with non-conductive lubricant, an electrical double layer with higher charge density was achieved with the same voltage. Therefore, the SLIS realized droplet's reversible motion control with a smaller voltage. They (Wang et al., 2018a) further researched the lubricant's viscosity effected on the electrical field responsive SLIS. The results suggested that lubricant with low viscosity would require a smaller voltage to adjust the droplet's motion behavior. Based on tuning the properties of lubricant, Heng's a serial of research provided novel insights of SLIS' wettability adjustment. In addition, they (Wang et al., 2018b) also developed a photoelectric synergetic responsive SLIS. With voltage applied in dark, there was an electrical double layer. With illumination, the photo-generated electrons would

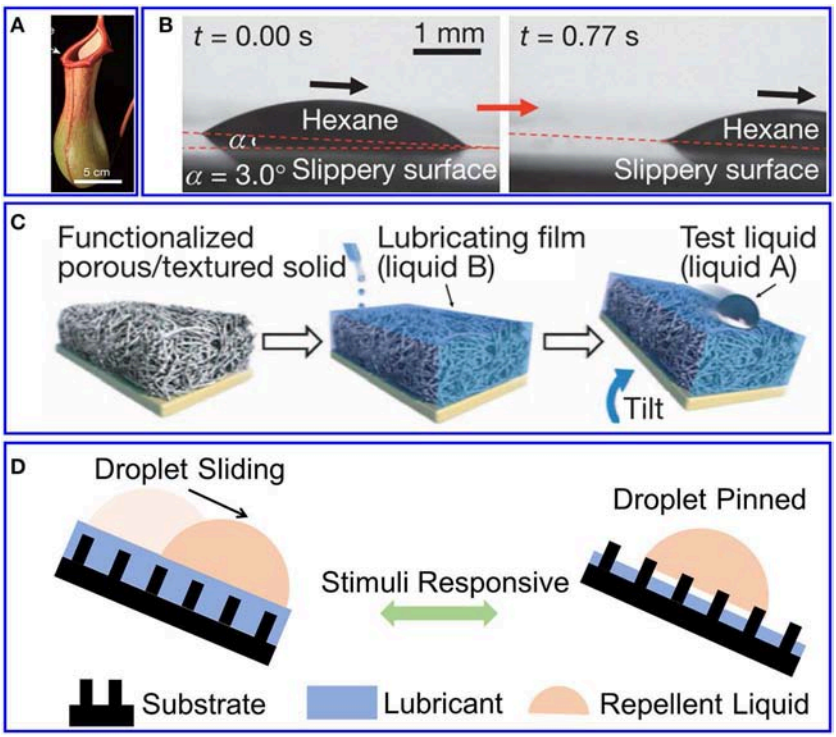

FIGURE 1 | SLIS inspired by pitch plant. **(A)** Photo of pitch plant (Chen et al., 2016). Reproduced with permission. Copyright 2016, Springer Nature. **(B)** A droplet of hexane sliding on SLIS (Wong et al., 2011). Reproduced with permission. Copyright 2011, Springer Nature. **(C)** Schematic fabrication of SLIS (Wong et al., 2011). Reproduced with permission. Copyright 2011, Springer Nature. **(D)** Schematic illustration of stimuli responsive SLIS.

increase the charge density, which results in a larger friction force to pin the droplet on the surface.

To achieve electrically responsive SLIS, relevant chemical environment is fatally necessary. For example, the repellent liquid should always contact with an electrode. The preconditions severely limit their applications in conductive surface, conductive repellent liquid, and even conductive lubricant. Therefore, there is still a long way for electrically responsive SLIS to come to real-life applications.

Magnetic Field Responsive SLIS

Magnetic field is one of the most employed methods of adjusting surface's wettability. Compared with other physical stimuli, the structure of surface can switch in a short time driven by magnetic force. Meantime, applied magnetic fields with different directions provide more possibilities for changing surface's different properties. The magnetic field responsive SLIS with switchable wettability have achieved fruitful development in fog collection (Peng et al., 2015), oil-water separation (Calcagnile et al., 2012), complex-flow distribution (Cao et al., 2017), droplets' delivery (Hou et al., 2017), and so on.

For example, Cao et al. (2017) constructed ferromagnetic microcilia with different tilted angles to realize unidirectional wetting behaviors. On this film, droplets slid easily in the opposite direction of the microcilia's tilted, due to the low the liquid-air interfacial adhesion. Later on, they further developed a magnetically responsive surface to control water-droplet from rolling to pinning (Hou et al., 2017). Distinct from Cao's surface, our group (Huang et al., 2017) designed a magnetically dynamic surface inspired by pitcher plant and lotus leaf, which could reversibly switch droplet between SLIS state and superhydrophobic state. In this research, PDMS was mixed with iron powder to form magnetically responsive micropillar array. The micropillar array could transform from fully upright (superhydrophobic state) to nearly flattened (SLIS state) morphology in different directions of external magnetic field, as shown in **Figure 2C**. The SLIS could alter liquid's repellency according to demand, which provided new opportunities of programmable fluid collection, smart waterproof clothing, adaptive drag control, and so on.

Instead of doping magnetic particles into the substrate, Tian et al. (2016) adopted magnetic fluids as lubricant and filled it into nano-structural substrate. The film's wettability could be adjusted by morphological transformation between rough and smooth in various magnetic fields, which provides new idea for designing microfluidic devices. Through magnetic lubricant, the tuning of interface's morphology could be more precise. Recently, Wang W. et al. (2018) designed a hierarchical magnetic responsive SLIS through infiltrating ferrofluids into surface with regular porous. The exiting capillary pressure induced multi-scale topographical responses and other novel functions. For example, when applied magnetic field, ferrofluid depleted from the microstructures.

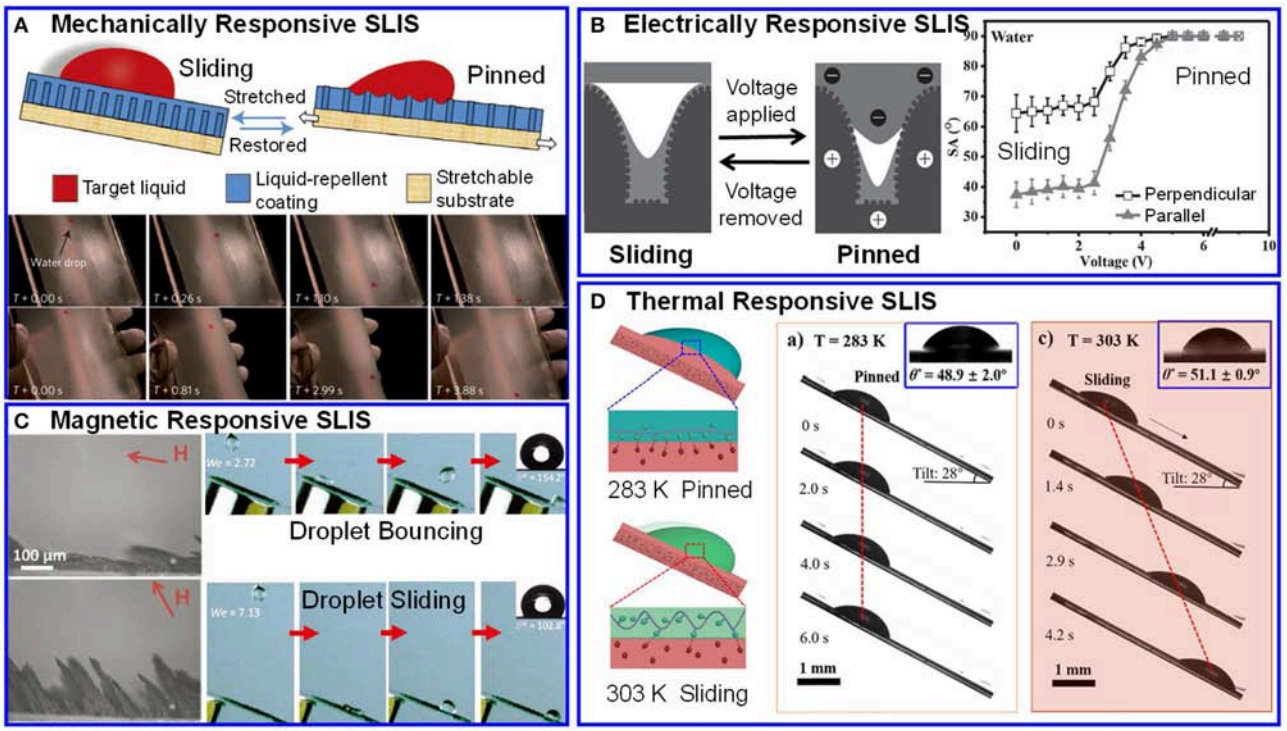

FIGURE 2 | Responsive SLIS display different wetting behaviors by different stimulus triggered. **(A)** Stress responsive SLIS (Yao et al., 2013), Reproduced with permission. Copyright 2013, Springer Nature. **(B)** Electric field responsive SLIS (Guo et al., 2016), Reproduced with permission. Copyright 2016, WILEY-VCH Verlag GmbH & Co. KGaA. **(C)** Magnetic field responsive SLIS (Huang et al., 2017), Copyright 2017, WILEY-VCH Verlag GmbH & Co. KGaA. **(D)** Temperature responsive SLIS (Wang et al., 2019). Copyright 2019, ACS.

As a result, the non-magnetic colloidal particles fell down to the solid/lubricant interface and formed specific patterns. These multi-scale reconfigurable topographies can be used as biological tissues, responsive coating, and digital microfluidics.

Although various magnetic responsive SLIS have been demonstrated fast, controllable and flexible wettability switching, magnetic responsive substrates with large-scale and well-organized micro/nano structure are still rare. Combined with lithography technology may take into consideration.

Temperature Responsive SLIS

Temperature is considered as a controllable and quantitative external stimulus, which extends widely applications *in vivo*, industrial and medical fields. Generally, for typical temperature responsive SLIS, thermo-responsive solidifiable lubricants were adopted to achieve interfacial adhesion switching (Yao et al., 2014; Manabe et al., 2016; Wang B. L. et al., 2018). In Yao et al. (2014), firstly introduced *n*-paraffin to organogel and form temperature responsive SLIS. In this work, switching of droplet's wettability occurred at the paraffin's melting temperature (T_m). When the environmental temperature was higher than T_m, paraffin was in the liquid phase, acting as lubricant filled in the PDMS network. Therefore, a droplet on SLIS was in low adhesive state. However, when the temperature dropped to lower than T_m, paraffin turned into solid phase and became a part of solid substrate. The droplet on this surface was in high adhesive Wenzel state. Later on, they (Wang B. L. et al., 2018) combined anisotropic substrate and thermo-responsive SLIS to achieve more precise control of the liquid droplet motion. According to Yao's research, Manabe et al. (2016) adopted mixtures of solid/liquid paraffin as lubricant. Through adjusting the ratios of solid/liquid paraffin and ambient temperature, the film's transparency and wettability would change. Combined with optical property's change, the film displayed potential of applications in smart windows, innovative medicine, and other bio-chemical devices. Similarly, the change of lubricant condensed phase between liquid and gel also varied surface's wetting behaviors. Zhu et al. (2016) impregnated a nanostructured surface with heated mineral oil to fabricate temperature responsive SLIS. When the mineral oil cooled down to ambient temperature, the oil turned to gel. In this case, the interfacial adhesion would increase. By taking advantage of dynamic viscoelastic property of mineral oil, the droplet motion, sliding speed, and thermal variation can be well-controlled. Zheng et al. (2017) infused lubricant with lower critical solution temperature (LCST) to porous substrate. When the environmental temperature was higher than LCST (i.e., 313 K), water droplet was slippery on the surface. In contrast, when the temperature was lower than LCST (i.e., 293 K), water droplet was miscible with

the lubricant. In their research, *in situ* wetting, dewetting, penetration and optical properties could be controlled under thermo-stimuli. Recently, combined printing method, Yao's group (He et al., 2018) adopted thermochromic inks to fabricate patterned thermo-responsive SLIS with multi-functionalities, including self-reporting wettability, and sensing the temperature of contacting liquids. This kind of slippery surface would be of great importance in sensors and medical package.

Generally, traditional smart SLIS focused on the responsive components contained in solid substrate and lubricant to vary the interface's topography, modulus, and surface energy. Modification of the repellent liquid was still rare. Recently, our group (Gao et al., 2018) approved that through adjusting the hydrophobic interactions between biological droplet and lubricant, the biological droplet's motion behavior could be easily tuned. The hydrophobic interactions mainly depended on the chain length of ssDNA in repellent droplet. To the best of our knowledge, this was the first research focused on adjusting the SLIS's interfacial adhesion through the repellent liquid. Their biosensing applications for ATP, microRNA, and thrombin detection are also demonstrated. Based on this research, very recently, we (Wang et al., 2019) put forward a temperature responsive interfacial adhesion on SLIS. When environmental temperature increased, ssDNA became more flexible and more mobile. The molecular configuration transformed to reduce the hydrophobic moieties exposure. As a result, the hydrophobic interaction between lubricant and hydrophobic moieties was weakened, leading to droplet slide, as shown in **Figure 2D**. The thermo-responsive sliding behavior of the biological droplet would offer a new strategy for advanced antifouling systems.

Although various temperature-responsive SLIS have been demonstrated, most of them are still restricted to several kinds of thermo-sensitive materials. Novel materials displaying obvious difference in wettability under small change of temperature should be explored. Additionally, besides temperature-dependent substrate and lubricant, thermo-responsive repellent liquid should be considered for particular applications, such as biological droplets in micro-biochips.

CONCLUSION

In this review, we concentrate on recent development of SLIS with external stimuli responsive wettability, including stress responsive SLIS, electrical responsive SLIS, magnetically responsive SLIS, and thermo-responsive SLIS. Through introducing stimuli responsive materials or replace some parts of SLIS, repellent droplet's wetting behaviors and other properties of the film, such as structural colors and transparency, would be reversibly changed. Based on the responsive SLIS's ability of timely control of droplets, SLIS have demonstrated their potential applications in fog collection, oil-water separation, droplets' delivery, complex-flow distribution, visual biosensors, biomimetic tissue, adaptive drag control, and so on.

Although various SLIS have been demonstrated distinctive advantages and features under external stimuli challenges still remain in their practical applications. Firstly, some responsive SLIS are limited with complex, strict or high-cost preparation processes. Economical, reproducible, and effective fabrication to achieve well-organized micro/nanostructures and integrate stimuli-responsive components into SLIS is the first and foremost challenge. Secondly, reliability and durability of responsive SLIS are needed to improve. Besides substrate's long-term durability and mechanical stability, lubricant's depletion caused by cloaking effect or volatility should be paid attention (Carlson et al., 2013; Daniel et al., 2017). Appropriate selection of materials to avoid cloaking effect are advised. Choosing lubricants with higher viscosity and lower vapor pressure, or designing intelligent materials with self-healing or self-refill are also effective methods. On the other hand, since SLIS have potential applications in biomedical areas, including antibiofouling, antithrombosis, point-of-care diagnostics, surgery, and tissue integration, constructing responsive SLIS with biocompatibility materials and bioactive functions should be taken into consideration. Thirdly, smart SLIS mainly focused on introducing responsive components as solid substrate or lubricant, through stimuli responsive repellent liquid are still rare. More responsive repellent liquid should be developed. Furthermore, through design various responsive materials as different parts of SLIS at the same time, dual- or multi-stimuli responsive SLIS with multi-functionalities could be achieved. This may be a potential development direction for responsive SLIS.

AUTHOR CONTRIBUTIONS

YH, YZ, and XY proposed the manuscript. XY, YH, XZ, and JW wrote the manuscript. All authors revised the manuscript.

FUNDING

This work was supported by the National Natural Science Foundation of China (51803194, 51903051, 21525523, 21722507, 21574048, 21874121, and 21874056), the National Basic Research Program of China (973 Program, 2015CB932600), and the National Key R&D Program of China (2017YFA0208000). Funding of Key Laboratory of Bio-inspired Materials and Interfacial Science, Technical Institute of Physics and Chemistry, Chinese Academy of Science.

REFERENCES

Anand, S., Paxson, A. T., Dhiman, R., Smith, J. D., and Varanasi, K. K. (2012). Enhanced condensation on lubricant-impregnated nanotextured surfaces. *ACS Nano* 6, 10122–10129. doi: 10.1021/nn303867y

Calcagnile, P., Fragouli, D., Bayer, I. S., Anyfantis, G. C., Martiradonna, L., Cozzoli, P. D., et al. (2012). Magnetically driven floating foams for the removal of oil contaminants from water. *ACS Nano* 6, 5413–5419. doi: 10.1021/nn3012948

Cao, M., Jin, X., Peng, Y., Yu, C., Li, K., Liu, K., et al. (2017). Unidirectional wetting properties on multi-bioinspired magnetocontrollable slippery microcilia. *Adv. Mater.* 29:1606869. doi: 10.1002/adma.201606869

Carlson, A., Kim, P., Amberg, G., and Stone, H. A. (2013). Short and long time drop dynamics on lubricated substrates. *EPL* 104:34008. doi: 10.1209/0295-5075/104/34008

Che, P., Heng, L., and Jiang, L. (2017). Lubricant-infused anisotropic porous surface design of reduced graphene oxide toward electrically driven smart control of conductive droplets' motion. *Adv. Funct. Mater.* 27:1606199. doi: 10.1002/adfm.201606199

Chen, H., Zhang, P., Zhang, L., Liu, H., Jiang, Y., Zhang, D., et al. (2016). Continuous directional water transport on the peristome surface of Nepenthes alata. *Nature* 532, 85–89. doi: 10.1038/nature17189

Dai, X., Stogin, B. B., Yang, S., and Wong, T. S. (2015). Slippery wenzel state. *ACS Nano* 9, 9260–9267. doi: 10.1021/acsnano.5b04151

Daniel, D., Timonen, J. V., Li, R., Velling, S. J., and Aizenberg, J. (2017). Oleoplaning droplets on lubricated surfaces. *Nat. Phys.* 13:1020–1025. doi: 10.1038/NPHYS4177

Fu, Y., Jin, B., Zhang, Q., Zhan, X., and Chen, F. (2017). pH-Induced switchable superwettability of efficient antibacterial fabrics for durable selective oil/water separation. *ACS Appl. Mater. Interfaces* 9, 30161–30170. doi: 10.1021/acsami.7b09159

Gao, Z. F., Liu, R., Wang, J., Dai, J., Huang, W. H., Liu, M., et al. (2018). Controlling droplet motion on an organogel surface by tuning the chain length of DNA and its biosensing application. *Chem* 4, 2929–2943. doi: 10.1016/j.chempr.2018.09.028

Guo, T., Che, P., Heng, L., Fan, L., and Jiang, L. (2016). Anisotropic slippery surfaces: electric-driven smart control of a drop's slide. *Adv. Mater.* 28, 6999–7007. doi: 10.1002/adma.201601239

Han, K., Heng, L., and Jiang, L. (2016). Multiphase media antiadhesive coatings: Hierarchical Self-Assembled porous materials generated using breath figure patterns. *ACS Nano* 10, 11087–11095. doi: 10.1021/acsnano.6b05961

Han, K., Heng, L., Zhang, Y., Liu, Y., and Jiang, L. (2019). Slippery surface based on photoelectric responsive nanoporous composites with optimal wettability region for droplets' multifunctional manipulation. *Adv. Sci.* 6:1801231. doi: 10.1002/advs.201801231

He, W., Liu, P., Jiang, J., Liu, M., Li, H., Zhang, J., et al. (2018). Development of multifunctional liquid-infused materials by printing assisted functionalization on porous nanocomposites. *J. Mater. Chem. A* 6, 4199–4208. doi: 10.1039/c7ta10780c

Hou, G., Cao, M., Yu, C., Zheng, S., Wang, D., Zhu, Z., et al. (2017). Foolproof method for fast and reversible switching of water-droplet adhesion by magnetic gradients. *ACS Appl. Mater. Interfaces* 9, 23238–23245. doi: 10.1021/acsami.7b07409

Howell, C., Grinthal, A., Sunny, S., Aizenberg, M., and Aizenberg, J. (2018). Designing liquid-infused surfaces for medical applications: a review. *Adv. Mater.* 30:1802724. doi: 10.1002/adma.201802724

Hozumi, A., Cheng, D. F., and Yagihashi, M. (2011). Hydrophobic/superhydrophobic oxidized metal surfaces showing negligible contact angle hysteresis. *J. Colloid Interface Sci.* 353, 582–587. doi: 10.1016/j.jcis.2010.09.075

Huang, Y., Stogin, B. B., Sun, N., Wang, J., Yang, S., and Wong, T. S. (2017). A switchable cross-species liquid repellent surface. *Adv. Mater.* 29:1604641. doi: 10.1002/adma.201604641

Lee, J., Shin, S., Jiang, Y., Jeong, C., Stone, H. A., and Choi, C. H. (2017). Oil-impregnated nanoporous oxide layer for corrosion protection with self-healing. *Adv. Funct. Mater.* 27:1606040. doi: 10.1002/adfm.201606040

Li, J., Ueda, E., Paulssen, D., and Levkin, P. A. (2019). Slippery lubricant-infused surfaces: properties and emerging applications. *Adv. Funct. Mater.* 29:1802317. doi: 10.1002/adfm.201802317

Liu, C., Ding, H., Wu, Z., Gao, B., Fu, F., Shang, L., et al. (2016). Tunable structural color surfaces with visually self-reporting wettability. *Adv. Funct. Mater.* 26, 7937–7942. doi: 10.1002/adfm.201602935

Liu, M., Wang, S., and Jiang, L. (2017). Nature-inspired superwettability systems. *Nat. Rev. Mater.* 2:17036. doi: 10.1038/natrevmats.2017.36

Manabe, K., Matsubayashi, T., Tenjimbayashi, M., Moriya, T., Tsuge, Y., Kyung, K. H., et al. (2016). Controllable broadband optical transparency and wettability switching of temperature-activated solid/liquid-infused nanofibrous membranes. *ACS Nano* 10, 9387–9396. doi: 10.1021/acsnano.6b04333

Mugele, F., and Baret, J. C. (2005). Electrowetting: from basics to applications. *J. Phys. Condensed Matter* 17, R705–R774. doi: 10.1088/0953-8984/17/28/R01

Park, K. C., Kim, P., Grinthal, A., He, N., Fox, D., Weaver, J. C., et al. (2016). Condensation on slippery asymmetric bumps. *Nature* 531, 78–82. doi: 10.1038/nature16956

Peng, Y., He, Y., Yang, S., Ben, S., Cao, M., Li, K., et al. (2015). Magnetically induced fog harvesting via flexible conical arrays. *Adv. Funct. Mater.* 25, 5967–5971. doi: 10.1002/adfm.201502745

Sett, S., Yan, X., Barac, G., Bolton, L. W., and Miljkovic, N. (2017). Lubricant-infused surfaces for low-surface-tension fluids: promise versus reality. *ACS Appl. Mater. Interfaces* 9, 36400–36408. doi: 10.1021/acsami.7b10756

Solomon, B. R., Hyder, M. N., and Varanasi, K. K. (2014). Separating oil-water nanoemulsions using flux-enhanced hierarchical membranes. *Sci. Rep.* 4:5504. doi: 10.1038/srep05504

Tian, D., Zhang, N., Zheng, X., Hou, G., Tian, Y., Du, Y., et al. (2016). Fast responsive and controllable liquid transport on a magnetic fluid/nanoarray composite interface. *ACS Nano* 10, 6220–6226. doi: 10.1021/acsnano.6b02318

Wang, B. L., Heng, L., and Jiang, L. (2018). Temperature-responsive anisotropic slippery surface for smart control of the droplet motion. *ACS Appl. Mater. Interfaces* 10, 7442–7450. doi: 10.1021/acsami.7b1681

Wang, J., Huang, Y., You, K., Yang, X., Song, Y., Zhu, H., et al. (2019). Temperature-driven precise control of biological droplet's adhesion on slippery surface. *ACS Appl. Mater. Interfaces* 11, 7591–7599. doi: 10.1021/acsami.8b21088

Wang, W., Timonen, J. V., Carlson, A., Drotlef, D. M., Zhang, C. T., Kolle, S., et al. (2018). Multifunctional ferrofluid-infused surfaces with reconfigurable multiscale topography. *Nature* 559, 77–82. doi: 10.1038/s41586-018-0250-8

Wang, Y., Di, J., Wang, L., Li, X., Wang, N., Wang, B., et al. (2017a). Infused-liquid-switchable porous nanofibrous membranes for multiphase liquid separation. *Nat. Commun.* 8:575. doi: 10.1038/s41467-017-00474-y

Wang, Y., Ma, K., and Xin, J. (2018). Stimuli-responsive bioinspired materials for controllable liquid manipulation: principles, fabrication, and applications. *Adv. Funct. Mater.* 28:1705128. doi: 10.1002/adfm.201705128

Wang, Y., Qian, B., Lai, C., Wang, X., Ma, K., Guo, Y., et al. (2017b). Flexible slippery surface to manipulate droplet coalescence and sliding, and its practicability in wind-resistant water collection. *ACS Appl. Mater. Interfaces* 9, 24428–24432. doi: 10.1021/acsami.7b06775

Wang, Z., Heng, L., and Jiang, L. (2018a). Effect of lubricant viscosity on the self-healing properties and electrically driven sliding of droplets on anisotropic slippery surfaces. *J. Mater. Chem. A* 6, 3414–3421. doi: 10.1039/c7ta10439a

Wang, Z., Liu, Y., Guo, P., Heng, L., and Jiang, L. (2018b). Photoelectric synergetic responsive slippery surfaces based on tailored anisotropic films generated by interfacial directional freezing. *Adv. Funct. Mater.* 28:1801310. doi: 10.1002/adfm.20180131

Wong, T. S., Kang, S. H., Tang, S. K., Smythe, E. J., Hatton, B. D., Grinthal, A., et al. (2011). Bioinspired self-repairing slippery surfaces with pressure-stable omniphobicity. *Nature* 477, 443–447. doi: 10.1038/nature10447

Xiao, L., Li, J., Mieszkin, S., Di Fino, A., Clare, A. S., Callow, M. E., et al. (2013). Slippery liquid-infused porous surfaces showing marine antibiofouling properties. *ACS Appl. Mater. Interfaces* 5, 10074–10080. doi: 10.1021/am402635p

Xiao, X., Zhang, C., Ma, H., Zhang, Y., Liu, G., Cao, M., et al. (2019). Bioinspired slippery cone for controllable manipulation of gas bubbles in low-surface-tension environment. *ACS Nano* 13, 4083–4090. doi: 10.1021/acsnano.8b08480

Yao, X., Hu, Y., Grinthal, A., Wong, T. S., Mahadevan, L., and Aizenberg, J. (2013). Adaptive fluid-infused porous films with tunable transparency and wettability. *Nat. Mater.* 12, 529–534. doi: 10.1038/nmat3598

Yao, X., Ju, J., Yang, S., Wang, J., and Jiang, L. (2014). Temperature-driven switching of water adhesion on organogel surface. *Adv. Mater.* 26, 1895–1900. doi: 10.1002/adma.201304798

Zhang, S., Huang, J., Chen, Z., and Lai, Y. (2017). Bioinspired special wettability surfaces: from fundamental research to water harvesting applications. *Small* 13:1602992. doi: 10.1002/smll.201602992

Zheng, Y., Liu, X., Xu, J., Zhao, H., Xiong, X., Hou, X., et al. (2017). Thermoresponsive mobile interfaces with switchable wettability, optical properties, and penetrability. *ACS Appl. Mater. Interfaces* 9, 35483–35491. doi: 10.1021/acsami.7b12354

Zhu, G. H., Zhang, C., Wang, C., and Zacharia, N. S. (2016). Gel-infused slippery surface with enhanced longevity and thermally controllable sliding properties. *Adv. Mater. Interfaces* 3:1600515. doi: 10.1002/admi.201600515

Conflict of Interest: The authors declare that the research was conducted in the absence of any commercial or financial relationships that could be construed as a potential conflict of interest.

Copyright © 2019 Yang, Huang, Zhao, Zhang, Wang, Sann, Mon, Lou and Xia. This is an open-access article distributed under the terms of the Creative Commons Attribution License (CC BY). The use, distribution or reproduction in other forums is permitted, provided the original author(s) and the copyright owner(s) are credited and that the original publication in this journal is cited, in accordance with accepted academic practice. No use, distribution or reproduction is permitted which does not comply with these terms.

frontiers in Chemistry

ORIGINAL RESEARCH
published: 19 June 2019
doi: 10.3389/fchem.2019.00439

Quantifying the Stability of the Hydronium Ion in Organic Solvents With Molecular Dynamics Simulations

*Alex K. Chew and Reid C. Van Lehn**

Department of Chemical and Biological Engineering, University of Wisconsin – Madison, Madison, WI, United States

The solution-phase stability of the hydronium ion catalyst significantly affects the rates of acid-catalyzed reactions, which are ubiquitously utilized to convert biomass to valuable chemicals. In this work, classical molecular dynamics simulations were performed to quantify the stability of hydronium and chloride ions by measuring their solvation free energies in water, 1,4-dioxane (DIOX), tetrahydrofuran (THF), γ-valerolactone (GVL), N-methyl-2-pyrrolidone (NMP), acetone (ACE), and dimethyl sulfoxide (DMSO). By measuring the free energy for transferring a hydronium ion from pure water to pure organic solvent, we found that the hydronium ion is destabilized in DIOX, THF, and GVL and stabilized in NMP, ACE, and DMSO relative to water. The distinction between these organic solvents can be used to predict the preference of the hydronium ion for specific regions in aqueous mixtures of organic solvents. We then incorporated the stability of the hydronium ion into a correlative model for the acid-catalyzed conversion of 1,2-propanediol to propanal. The revised model is able to predict experimental reaction rates across solvent systems with different organic solvents. These results demonstrate the ability of classical molecular dynamics simulations to screen solvent systems for improved acid-catalyzed reaction performance.

Keywords: acid-catalyzed reactions, solvent effects, biomass conversion, hydronium ion, classical molecular dynamics simulation, solvation free energy

OPEN ACCESS

Edited by:
Moisés Canle, University of A Coruña, Spain

Reviewed by:
Valerije Vrcek, University of Zagreb, Croatia
Arturo Santaballa, University of A Coruña, Spain

****Correspondence:***
Reid C. Van Lehn
vanlehn@wisc.edu

Specialty section:
This article was submitted to Green and Sustainable Chemistry, a section of the journal Frontiers in Chemistry

Received: *13 February 2019*
Accepted: *28 May 2019*
Published: *19 June 2019*

Citation:
Chew AK and Van Lehn RC (2019) Quantifying the Stability of the Hydronium Ion in Organic Solvents With Molecular Dynamics Simulations. Front. Chem. 7:439. doi: 10.3389/fchem.2019.00439

INTRODUCTION

The catalytic upgrading of biomass (e.g., wood, crops, etc.) is a promising strategy to obtain valuable chemicals from renewable resources while limiting waste products (Huber et al., 2006; Stöcker, 2008; Tock et al., 2010; Shuai and Luterbacher, 2016; Nguyen et al., 2017; Walker et al., 2019). For example, cellulose, one of the primary components of lignocellulosic biomass, can be converted through a series of dehydration and hydrolysis reactions to form 5-hydroxymethylfurfural, a platform chemical for fuels and other commodity chemicals (Chheda et al., 2007; Corma et al., 2007; Román-Leshkov et al., 2007; Pagan-Torres et al., 2012; Mellmer et al., 2015; He et al., 2017). These reactions are typically performed in aqueous solution where extensive control over reaction kinetics and selectivity is available by tuning the temperature, catalyst, and solvent composition (Huber et al., 2006; Chheda et al., 2007; Román-Leshkov et al., 2007; Mellmer et al., 2014b; Motagamwala et al., 2016; He et al., 2017; Won et al., 2017; Sener et al., 2018). Solution-phase biomass conversion reactions ubiquitously require an acidic proton catalyst (H^+), which exists

in solution as a hydronium ion (H_3O^+). In homogenous reactions, the catalyst is obtained from the addition of a Brønsted acid (He et al., 2017) and the reactions follow a specific catalysis mechanism since a protonated solvent is the catalyst. **Figure 1A** shows an example reaction for the acid-catalyzed dehydration of 1,2-propanediol to propanal, which is representative of acid-catalyzed reactions for biomass-derived model compounds (Mellmer et al., 2018; Walker et al., 2019). In these reactions, the hydronium ion catalyst (H_3O^+) protonates the reactant (R) to form a reactant/proton complex (RH^+). The reaction proceeds to a charged transition state ($[RH^+]^{TS}$) and subsequently forms the product (P) with the hydronium ion reformed (**Figure 1B**). The relative stabilities of the reactant, transition state, and catalyst in solution are thus critical for determining reaction kinetics (Shuai and Luterbacher, 2016). Understanding how these solvent effects influence reaction kinetics is necessary to guide the optimization of solvent compositions and reactor conditions and maximize the productivity of biomass conversion reactions.

Previous studies have found that mixtures of water and organic, polar aprotic cosolvents (i.e., mixed-solvent environments) can increase or decrease the rates of Brønsted acid-catalyzed reactions depending on the stability of the acid catalyst (Mellmer et al., 2014b, 2018; Shuai and Luterbacher, 2016; Sener et al., 2018). One mechanism by which the solvent composition affects catalyst stability is by shifting the acid dissociation equilibrium, which is quantified by the acid disassociation constant (K_a). For example, weak acids with small K_a values, such as formic acid or acetic acid, were found to decrease acid-catalyzed reaction rates in mixed-solvent environments compared to pure water due to the reduced availability of catalytic hydronium ions (Mellmer et al., 2014b). Conversely, strong acids with large K_a values, such as triflic acid, dissociate in a small fraction of water and were found to improve xylose conversion reaction rates by 40-fold in 90 wt% γ-valerolactone (Mellmer et al., 2014b), suggesting an alternative role for the solvent. Based on combined classical and *ab initio* molecular dynamics (MD) simulations, Mellmer et al. found that the hydronium ion catalyst in mixed-solvent systems is destabilized in the bulk solvent relative to the local solvent domain of the reactant due to unfavorable interactions between the hydronium ion and the cosolvent (Mellmer et al., 2018). As a result, the acid catalyst is thermodynamically driven to water-enriched local solvent domains formed by hydrophilic reactants when a high mass fraction of the organic phase is present, effectively lowering activation energy barriers and increasing reaction rates relative to pure water (**Figure 1B**). Together, these results indicate that the solvent composition can modulate reaction kinetics by both modulating catalyst availability and the interactions of the catalyst with the reactant.

Building upon these studies, we hypothesized that acid-catalyzed reaction rates correlate with the formation of water-enriched local solvent domains because the catalyst is assumed to be stabilized by interactions with water and thus the formation of water-enriched local solvent domains would drive the partitioning of the catalyst to the reactant (Mellmer et al., 2018; Walker et al., 2019). We derived a correlative model that used descriptors derived from classical MD simulations

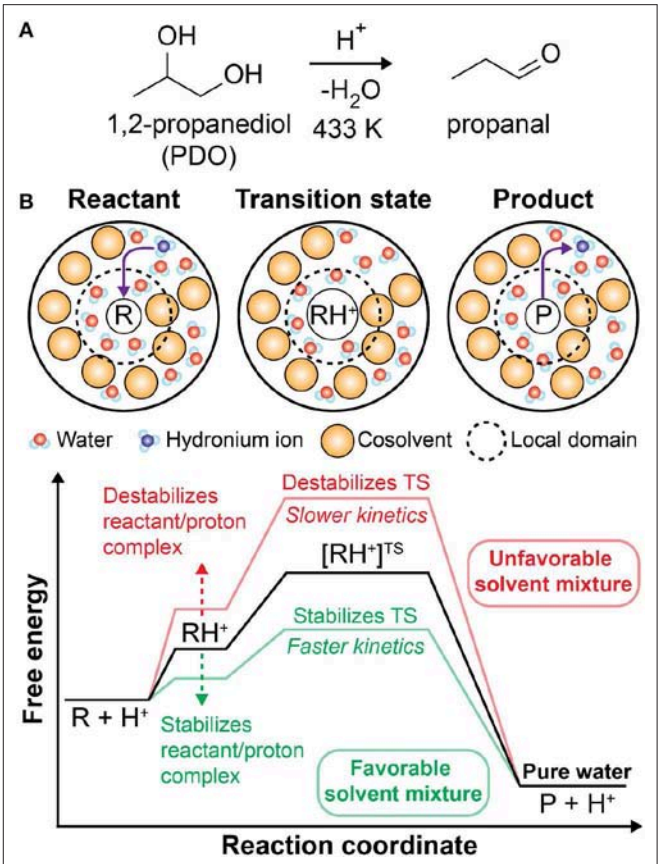

FIGURE 1 | (A) Brønsted acid-catalyzed reaction of 1,2-propanediol (PDO) to propanal. **(B)** Schematic of acid-catalyzed reactions in mixed-solvent environments. The reaction proceeds through a charged transition state (TS) formed from the protonation of the reactant by a hydronium ion catalyst. The corresponding free energy diagram schematically depicts the influence of mixed-solvent environments (red and green lines) on acid-catalyzed reactions relative to pure water (black line). This free energy landscape is representative of 1,2-propanediol dehydration based on prior computational findings (Mellmer et al., 2018). For different acid-catalyzed reactions, the relative free energies of the various states may differ (Mellmer et al., 2018), but general features should be similar.

to predict experimental reaction kinetics for seven biomass-derived model compounds in aqueous mixtures of dioxane and γ-valerolactone (Walker et al., 2019). While reaction free energies are typically determined from *ab initio* level studies (Caratzoulas and Vlachos, 2011; Mellmer et al., 2018), this hypothesis allowed us to use classical MD simulations to more rapidly screen through multiple solvent compositions and reactions. However, the assumption that the hydronium ion preferentially interacts with water is not always true. For instance, more basic organic solvents, such as dimethyl sulfoxide (DMSO), have been shown to participate in the reaction mechanism by stabilizing the proton (Mellmer et al., 2018). The addition of DMSO has also been shown to diminish acid-catalyzed conversion of *tert*-butanol (Mellmer et al., 2018), indicating that addition of organic solvents can also destabilize the reactant/proton complex, raise energy barriers, and consequently slow reaction kinetics relative to pure

water (**Figure 1B**). Therefore, understanding and quantifying the thermodynamic stability of the hydronium ion in mixed-solvent environments is essential to accurate predictions of acid-catalyzed reaction kinetics.

It is experimentally difficult to directly measure the free energy of an isolated hydronium ion in solution since electroneutrality must be maintained (Reif and Hünenberger, 2011). To obtain single-ion thermodynamics, non-classical techniques such as atomic and molecular spectroscopy combined with statistical mechanics are utilized (Hunenberger and Reif, 2011). To broaden the range of possible systems, computational tools have been developed to model the hydronium ion and isolate the role of the solvent on the acid catalyst (Varghese and Mushrif, 2019). For solution-phase reactions, we quantify the stability of the acid catalyst in terms of its solvation free energy, or the free energy for introducing the catalyst in solution. The solvation free energy accounts for interactions between the catalyst and solvent (e.g., hydrogen bonding, ion-dipole interactions, and van der Waals forces) and the solvent reorganization necessary to accommodate the catalyst. Solvation free energies are also important in determining the partitioning of ions between different phases (Duignan et al., 2017). Typically, *ab initio* level simulations are performed to accurately compute solvation free energies of the acid catalyst (Tunon et al., 1993; Tawa et al., 1998; Mejias and Lago, 2000; Pliego and Riveros, 2001; Kelly et al., 2007). However, these simulations are computationally expensive and thus challenging to perform for multiple solvent compositions. Recently, Bonthuis et al. developed a classical hydronium ion model that accurately reproduces experimental solvation free energies in pure water (Bonthuis et al., 2016). We thus hypothesize that this classical hydronium ion model can be used to compute solvation free energies of the acid catalyst and leverage the computational efficiency of MD simulations to screen stability in different solvent compositions, assuming that the hydronium ion maintains its structure in these solvents. These calculations can then be used to predict the relationship between solvent composition and reaction kinetics for acid-catalyzed reactions.

Herein, we use classical MD simulations to study the stability of a hydronium ion in six organic polar aprotic cosolvents: dioxane (DIOX), tetrahydrofuran (THF), γ-valerolactone (GVL), N-methyl pyrrolidine (NMP), acetone (ACE), and dimethyl sulfoxide (DMSO). We also study the stability of a chloride ion in the same solvents to calculate the effect of the conjugate base. We use previous literature values for the reaction rates of the acid-catalyzed conversion of 1,2-propandiol (PDO) as a model reaction to study the influence of the different cosolvents. Since our previous work found favorable agreement between MD simulation-derived descriptors with experimental reaction rates without mechanistic details of the reaction (Walker et al., 2019), we focus on studying how water-enrichment (or cosolvent-enrichment) can improve reaction performance by favorably facilitating a hydronium ion. We then quantify the stabilities of the hydronium and chloride ions in pure and mixed-solvent environments by computing the solvation free energies. We find that the free energy for transferring a hydronium ion from pure water to organic solvent can distinguish between solvents that favorably (NMP, ACE, DMSO) and unfavorably (DIOX, THF, GVL) solvate the acid catalyst. With this information, we improve our previously developed correlative model for the conversion of PDO (Walker et al., 2019) by including a cosolvent-specific descriptor that incorporates information about the stability of the hydronium ion in the solvent system.

METHODS

Classical MD simulations were performed using GROMACS 2016 (Páll et al., 2015). We used the classical hydronium and chloride ion models parameterized by Bonthuis et al. (2016), which have been found to reproduce experimental solvation free energies in pure water systems modeled using the Single Point Charge/Extended (SPC/E) water model (Berendsen et al., 1987). Bond constraints for the hydronium ion were modified to improve simulation performance by using the more efficient LINCS constraint algorithm (Hess et al., 1997) instead of the SHAKE constraint algorithm (Ryckaert et al., 1977) (**Supplementary Section 1**, Supplementary Material). PDO and all cosolvents were parameterized using the CGenFF/CHARMM36 forcefields (Vanommeslaeghe et al., 2009; Yu et al., 2012; Best et al., 2013), while water was modeled using the SPC/E model (Berendsen et al., 1987). For all simulations, Verlet lists were generated using a 1.2 nm neighbor list cutoff. Van der Waals interactions were modeled with a Lennard-Jones (LJ) potential with a 1.2 nm cutoff that was smoothly shifted to zero between 1.0 and 1.2 nm. Electrostatic interactions were calculated using the smooth Particle Mesh Ewald method with a short-range cutoff of 1.2 nm, grid spacing of 0.12 nm, and 4th order interpolation. Bonds were constrained using the LINCS algorithm. All thermostats used a 1.0 ps time constant and all barostats used a 5.0 ps time constant with an isothermal compressibility of 5.0×10^{-5} bar^{-1}.

We initialized simulation configurations using the protocol schematically depicted in **Figure 2A**. The initial simulation box containing water and cosolvent (if applicable) had dimensions of $(6\,\text{nm})^3$ in all simulations and was equilibrated in a *NPT* simulation for 5 ns at $T = 300\,\text{K}$ and $P = 1$ bar with a velocity-rescale thermostat and Berendsen barostat. A single reactant or ion molecule (designated as "M" in **Figure 2A**) was then added to the system and equilibrated with the same barostat and thermostat for 500 ps. *NPT* production simulations were performed for all systems for 200 ns with a Parrinello-Rahman barostat and Nose-Hoover thermostat; simulations of the reactant, PDO, were performed at $T = 433.15\,\text{K}$ to match the experimental reaction temperature (Mellmer et al., 2018) while simulations of the hydronium/chloride ions were performed at $T = 300\,\text{K}$. Simulation configurations were output every 10 ps and the final 190 ns of each production trajectory were used for analysis. Simulation analysis was performed using the *MDTraj* library (McGibbon et al., 2015) and analysis tools developed in-house. MD simulations were performed using a leapfrog integrator with a 2-fs time step. **Figure 2B** shows simulation snapshots of the nearby solvent environment around a hydronium ion in 90 wt% DIOX, 90 wt% DMSO, and pure water.

Each solvation free energy was computed from a series of stochastic dynamics simulations (**Figure 2A**). Simulations were

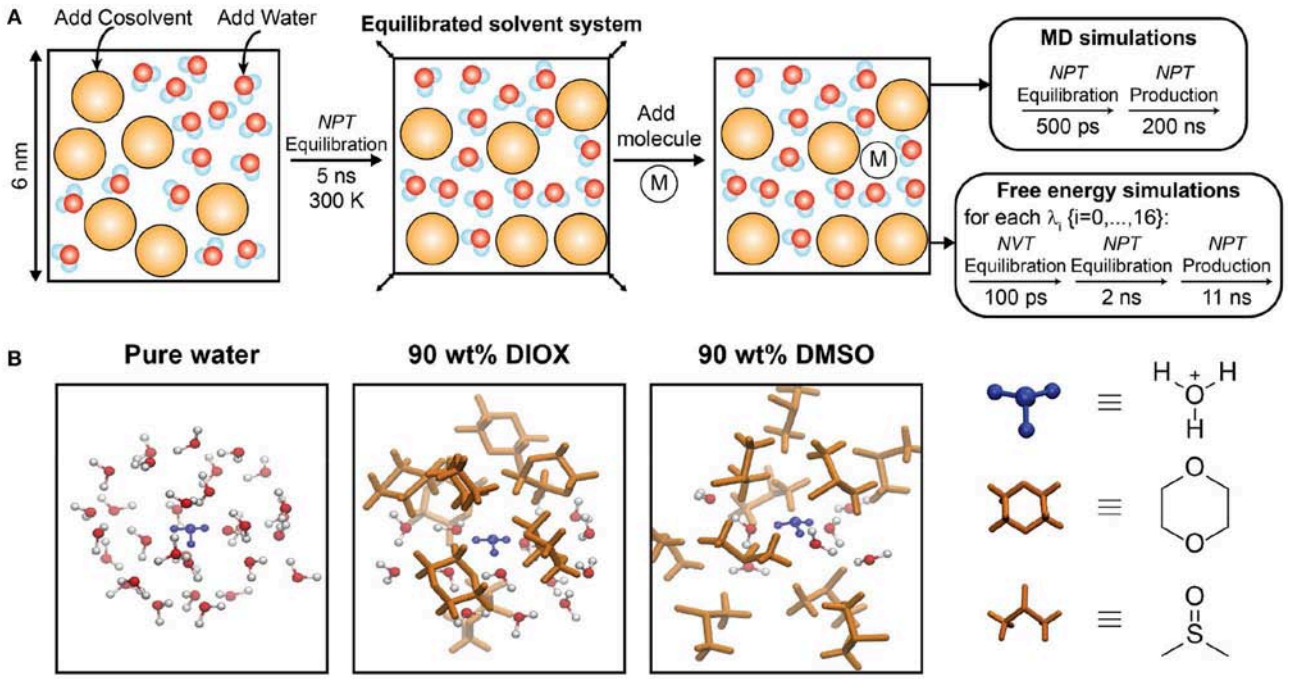

FIGURE 2 | (A) Schematic representation of simulation workflow for molecular dynamics and free energy simulations. *M* denotes either 1,2-propanediol, a hydronium ion, or a chloride ion. **(B)** Simulation snapshots of hydronium ion in pure water, 90 wt% DIOX, and 90 wt% DMSO. The hydronium ion is located at the center and only solvent molecules within a 5 Å radius is shown.

initialized using an equilibrated solvent system (as described above) with a hydronium or chloride ion added to the system. The total potential of the system was defined as a function of two parameters, λ_{LJ} and λ_{elec}, which scale the LJ and electrostatic potentials between the solute and solvent, as shown in Equation 1:

$$U\left(\lambda_{LJ},\lambda_{elec}\right) = U^{LJ}_{M,\,solv}\left(\lambda_{LJ}\right) + U^{elec}_{M,\,solv}\left(\lambda_{elec}\right) + U^{bonded}_{M} + U^{nonbonded}_{M} + U^{bonded}_{solv} + U^{nonbonded}_{solv} \quad (1)$$

$U^{LJ}_{M,\,solv}$ and $U^{elec}_{M,\,solv}$ are the LJ and electrostatic potentials between solute and solvent, U^{bonded}_{M} and $U^{nonbonded}_{M}$ are intramolecular bonded and non-bonded potentials of the solute, and U^{bonded}_{solv} and $U^{nonbonded}_{solv}$ are the bonded and non-bonded potentials between all solvent molecules (Shivakumar et al., 2010). We performed 17 independent simulations for each solvation free energy: fourteen in which $\lambda_{elec} = 0.00$ and $\lambda_{LJ} = 0.00$, 0.00922, 0.04794, 0.11505, 0.260634, 0.31608, 0.43738, 0.56262, 0.68392, 0.79366, 0.88495, 0.95206, 0.99078, or 1.00, and three in which $\lambda_{LJ} = 1.00$ and $\lambda_{elec} = 0.25$, 0.75, or 1.00. The LJ coupling parameters represent a 12-point Gaussian sequence, used previously to verify ion model parameters (Horinek et al., 2009; Bonthuis et al., 2016). All free energy simulations used a soft-core LJ potential as described in the **Supplementary Section 2.1**, Supplementary Material (Beutler et al., 1994). For each simulation, the system was energy minimized with the steepest descent algorithm and equilibrated with a 100 ps *NVT* simulation followed by a 2 ns *NPT* simulation with the Berendsen barostat. An 11 ns *NPT* production simulation was then performed with the Parrinello-Rahman barostat. All simulations were performed at $T = 300$ K and $P = 1$ bar. Energy differences computed between all pairs of windows were collected every 0.2 ps and solvation free energies were computed with the Multistate Bennett Acceptance Ratio (Shirts and Chodera, 2008) method using the python alchemical-analysis tool (Klimovich et al., 2015). The 11 ns of each *NPT* production simulation were split into two 5.5 ns trajectories and treated as two independent trials. All solvation free energy results and error bars are reported as the average and standard deviation of the two trials, respectively. We further calculated three analytical correction terms to account for: (1) finite-size effects due to system interactions with periodic images, (2) the compression free energy for transferring an ion from a 1 atm ideal gas phase to 1 mol/L ideal solution, and (3) the electrostatic energy required to pass through an interfacial potential when the ion transfers from vacuum to bulk solution. These correction terms are included to account for differences between simulation and experiments as described in **Supplementary Section 2.2**, Supplementary Material.

RESULTS

Comparison Between Experimental Reaction Rates and Preferential Exclusion Coefficient

In our previous study of solution-phase acid-catalyzed reactions (Walker et al., 2019), we hypothesized that the transition state is lower in free energy relative to the initial reactant state in

mixed-solvent environments due to two reasons: (1) the catalyst is destabilized in bulk solvent relative to a water-enriched local domain near the reactant, leading to a thermodynamic driving force for the transfer of catalytic protons to the local domain, and (2) the transition state is stabilized by water confined within this domain. We then developed a correlative model for experimental reaction rates by quantifying water enrichment in the vicinity of the reactant, supporting the hypothesis for aqueous mixtures of DIOX and GVL. This hypothesis assumes that the hydronium ion catalyst has a higher affinity for water than the cosolvent. However, this assumption may not be accurate for more basic cosolvents, such as DMSO, which can favorably stabilize the acid catalyst in bulk solution (Mellmer et al., 2018). We thus test the validity of this assumption by determining if experimental reaction rates correlate with water enrichment for a model reaction, the Brønsted acid-catalyzed conversion of 1,2-propanediol (PDO) to propanal (**Figure 1A**), in DIOX and DMSO mixed-solvent environments. These cosolvents represent extremes in polarity: the dielectric constant of DIOX is 2.20, whereas the dielectric constant of DMSO is 48.90 (Fowler et al., 1971).

We first analyze the solvent environment around PDO by calculating the radial distribution function (RDF). The RDF quantifies the solvent density, normalized by the bulk solvent density, at a distance r away from a central point. **Figure 3** shows the RDF between the center of mass of PDO and water for 90 wt% DIOX, 90 wt% DMSO, and pure water. In 90 wt% DIOX, the peak of the RDF is significantly higher than in pure water, indicating that water preferentially partitions to the local solvent domain around PDO in high concentrations of DIOX. Conversely, in 90 wt% DMSO, the first peak of the RDF is almost the same as in pure water and the RDF then drops below unity at $\sim$ 0.60 nm, indicating the local depletion of water. The diminished water content near PDO in aqueous mixtures of DMSO is due to the cosolvent's high affinity for oxygen groups, resulting in a competition between water and DMSO for the hydroxyl groups of PDO (Vishnyakov et al., 2001). These findings confirm that DMSO and DIOX significantly influence the extent to which the reactant preferentially recruits water to the local domain.

Since RDFs are difficult to compare across different cosolvent concentrations, we previously computed the preferential exclusion coefficient (Γ), a molecular descriptor that quantifies the local domain composition around the reactant (Walker et al., 2019). Γ is defined as the excess number of cosolvent molecules within the local solvent domain of the reactant relative to the bulk solvent domain, computed using Equation 2 (Kang and Smith, 2007; Shulgin and Ruckenstein, 2007; Schneider and Trout, 2009; Shukla and Trout, 2011):

$$\Gamma = -\left\langle n_C^L - n_W^L \left(\frac{n_C^B}{n_W^B} \right) \right\rangle \tag{2}$$

n_C and n_W denote the number of cosolvent and water molecules, and superscripts L and B indicate molecules within the local and bulk domains, respectively. We define the boundary between local and bulk solvent domains as the value of r at which the RDF reaches unity (**Figure 3**), which occurs at $r = 1.59$ nm for both

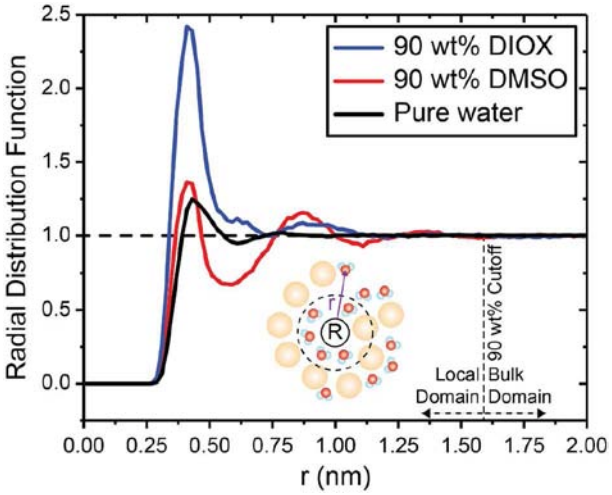

FIGURE 3 | Radial distribution function between the center of mass of PDO and water in 90 wt% DIOX, 90 wt% DMSO, and pure water. Local and bulk domain cutoffs were determined as the value of r for which the RDF reaches unity. Bin widths for the RDFs were set to 0.02 nm.

solvent systems. Positive Γ values indicate lower concentrations of cosolvent in the local solvent domain of the reactant compared to the bulk solvent domain. Therefore, positive Γ indicates the reactant has a higher affinity for water. Conversely, negative values of Γ indicate that the reactant has a higher affinity for the cosolvent.

We previously found that simulation-derived Γ correlates with experimental reaction rates quantified by the kinetic solvent parameter (σ) defined in Equation (3) (Walker et al., 2019):

$$\sigma_{org,j}^{i} = \left(\frac{k_{org,j}^{i}}{k_{H_2O}^{i}} \right) \tag{3}$$

$\sigma_{org,j}^{i}$ is the kinetic solvent parameter for the ith reaction and the subscript denotes the identity and composition (in jth mass fraction) of the organic solvent, $k_{org,j}^{i}$ is the apparent rate constant in aqueous mixtures with the organic phase, and $k_{H_2O}^{i}$ is the apparent rate constant in pure water. For simplicity, we denote $\sigma_{org,j}^{i}$ as σ. Positive σ values indicate that the reaction occurs more favorably in aqueous mixtures with organic solvents compared to pure water. Negative σ values indicate the converse. We take experimental reaction rates from Mellmer et al. (2018), which are tabulated in **Supplementary Section 3**, Supplementary Material.

Figure 4A compares values of simulation-derived Γ (filled lines) and experimentally measured σ (Mellmer et al., 2018) (dashed lines) for aqueous mixtures of DIOX and DMSO for the PDO dehydration reaction. In each separate mixed-solvent environment, Γ and σ are correlated across the solvent composition range as shown in **Figure 4B**. We report the Pearson correlation coefficient (Pearson's r) as an indicator of linear correlation: values close to 1 indicate total positive linear correlation, values close to -1 indicate total negative linear

correlation, and values close to 0 indicate no linear correlation. We find $r = 0.97$ for aqueous mixtures of DIOX, indicating strong positive linear correlation. However, we find $r = -0.97$ for aqueous mixtures of DMSO, indicating strong negative correlation and that the depletion of water around PDO in DMSO mixtures still leads to enhanced reaction kinetics. These results indicate that in either solvent system the preferential exclusion coefficient can predict reaction kinetics; however, the negative correlation between Γ and σ in DMSO suggests that increased reaction rates are not due to water enrichment. This finding suggests that the assumption that the acid catalyst preferentially partitions to water-enriched regions of the system is not valid for all cosolvents and must be revised to derive a correlative model for reaction rates that can be broadly applied to any cosolvent of interest.

Solvation Free Energy of the Hydronium Ion in Pure Solvent Systems

Previous studies have found that the hydronium ion is more stable in DMSO than water based on lower solvation free energies (Kelly et al., 2007). Since our simulations show that PDO preferentially interacts with DMSO rather than water and PDO reaction rates are increased in high concentrations of DMSO, the reactant/proton complex may be stabilized in the organic phase compared to the water phase, leading to increased reaction rates. Therefore, we hypothesize that the solvation free energy of the hydronium ion catalyst in the organic solvent can be used to classify the preference for the catalyst for either water or organic phase and develop an updated correlative model between Γ and σ for a range of cosolvents.

We calculated the solvation free energy of the hydronium ion in six organic, polar aprotic solvents (**Figure 5A**) and performed the same calculations for a chloride ion to determine the solvation free energy for a conjugate base. We selected polar aprotic solvents due to their relevance to acid-catalyzed biomass conversion processes, in which inclusion of these solvents has been found to enhance reaction performance (Mellmer et al., 2014b, 2018; Walker et al., 2019). To test the simulation approach, we first calculated solvation free energies in pure water as −465.1 kJ/mol [experimentally measured as −453.2 kJ/mol (Pliego, 2003)] for the hydronium ion and −286.4 kJ/mol [experimentally measured as −304.6 kJ/mol (Pliego and Riveros, 2000)] for the chloride ion; their sum of −751.5 kJ/mol is comparable to the estimated experimental value of −757.8 kJ/mol (Pliego and Riveros, 2000; Pliego, 2003). The experimental values reproduced from Pliego (2003) and Pliego and Riveros (2000) are modified to include the 7.9 kJ/mol correction term associated with transferring an ion from 1 atm ideal gas phase to 1 mol/L ideal solution to compare with our results (**Supplementary Section 2.2**, Supplementary Material). The relative differences between solvation free energies are more important than absolute values (Horinek et al., 2009) for inferring the behavior of the ions in different solvents; therefore, we focus on relative transfer free energies between pure water and organic solvents.

We computed the free energy of transferring the hydronium or chloride ion from water to solvent systems with organic solvents using Equation 4 (schematically illustrated in **Figure 5B**):

$$\Delta G_j^{H_2O \to k} = \Delta G_j^k - \Delta G_j^{H_2O} \tag{4}$$

k denotes the solvent system of interest and j denotes either a hydronium or chloride ion. A negative value of $\Delta G_j^{H_2O \to k}$ indicates that the ion is thermodynamically stabilized in the kth solvent system compared to pure water. **Figure 5C** shows $\Delta G_j^{H_2O \to k}$ of the hydronium and chloride ions in each pure solvent. For the hydronium ion (cyan bars), $\Delta G_{H_3O^+}^{H_2O \to k}$ is positive for DIOX, GVL, and THF, indicating that the hydronium ion is unfavorable in these solvents. These results support our prior assumption that the hydronium ion prefers water rather than the organic phase in these solvents, allowing us to correlate the formation of water-enriched local domains to reaction kinetics (Walker et al., 2019). Conversely, $\Delta G_{H_3O^+}^{H_2O \to k}$ is negative for NMP, ACE and DMSO, indicating that the hydronium ion is favorable in these solvents. Notably, these solvents are more basic than water (Fawcett, 1993) based on several solvent scales (e.g., B parameter of Koppel and Palm, 1972, or Kamlet-Taft β scale, Kamlet and Taft, 1976; Fawcett, 1993) (discussed below and in **Table 1**). The negative free energy for transferring a hydronium ion from water to DMSO agrees with prior results (Kelly et al., 2007; Mellmer et al., 2018) and supports the hypothesis that the sign of this free energy change determines the relationship between Γ and σ for DIOX and DMSO mixtures (**Figure 4**). In a similar fashion, we suspect that ACE and DMSO would exhibit similar solvent effects.

Solvation Free Energy of the Chloride Ion in Pure Solvent Systems

While the solvation free energy of the hydronium ion alone quantifies catalyst stability, the effect of the solvent on acid dissociation equilibrium depends on the solvation free energy of the hydronium ion and its conjugate base (i.e., the chloride ion). **Figure 5C** shows that $\Delta G_{Cl^-}^{H_2O \to k}$ is positive for all pure organic solvent systems (purple bars), indicating that the chloride ion thermodynamically prefers water over each of these solvents. Furthermore, the solvation free energies for the chloride ion do not vary significantly for the different organic solvents, with the exception of DIOX and THF. The difference in the solvation of the hydronium and chloride ions is likely due to differences in hydrogen bonding capabilities: the hydronium ion can donate and accept hydrogen bonds while the chloride ion can only accept hydrogen bonds. Since water is the only solvent in this study that can donate hydrogen bonds, it is expected that the chloride ion is most stable in water.

The effect of the solvent on the solvation free energies of the hydronium and chloride ions relative to their solvation free energies in water is quantified via the term $\sum \Delta G$, which we define in Equation 5 as:

$$\sum \Delta G = \sum \Delta G_{H_3O^+Cl^-}^{k \to H_2O} = \Delta G_{H_3O^+}^{H_2O \to k} + \Delta G_{Cl^-}^{H_2O \to k} \tag{5}$$

We expect that positive values of $\sum \Delta G$ would reduce acid dissociation relative to pure water due to the decreased stability of the dissociated ions in the pure organic solvent. **Figure 5C** shows

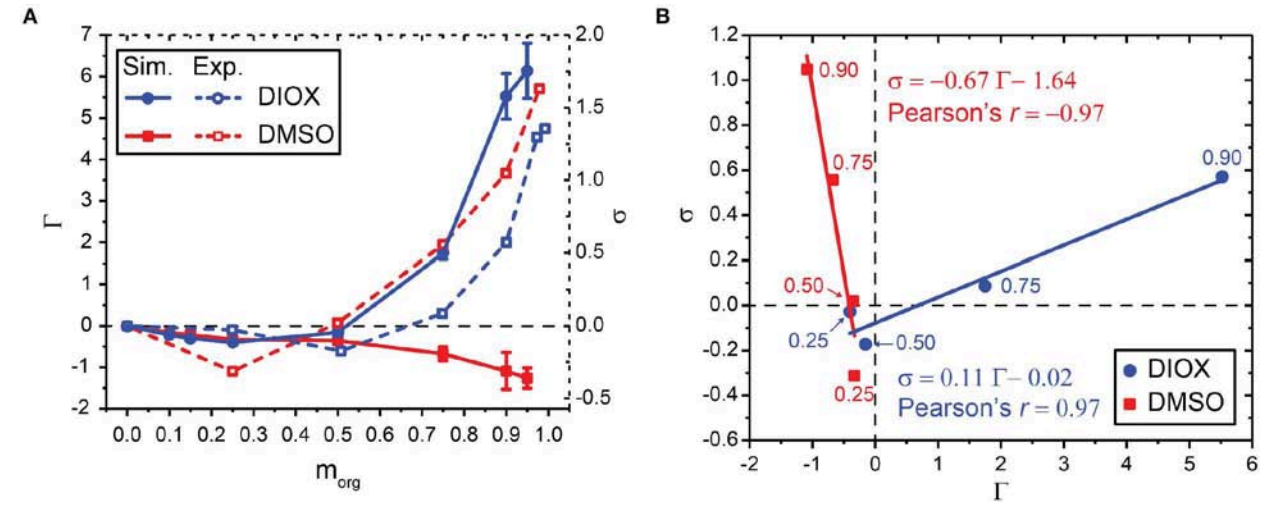

FIGURE 4 | (A) Relationship between simulated preferential exclusion coefficient (Γ) and experimentally determined kinetic solvent parameters (σ) for aqueous mixtures of DIOX and DMSO. Experimental values were taken from Mellmer et al. (2018). **(B)** Correlation between Γ and σ for aqueous mixtures of DIOX and DMSO. Data points are labeled with the wt% of the organic solvent. 25, 50, 75, and 90 wt% organic solvent was used to correlate Γ and σ as indicated for each point. The best-fit line is drawn and labeled with the corresponding equation and Pearson's *r*.

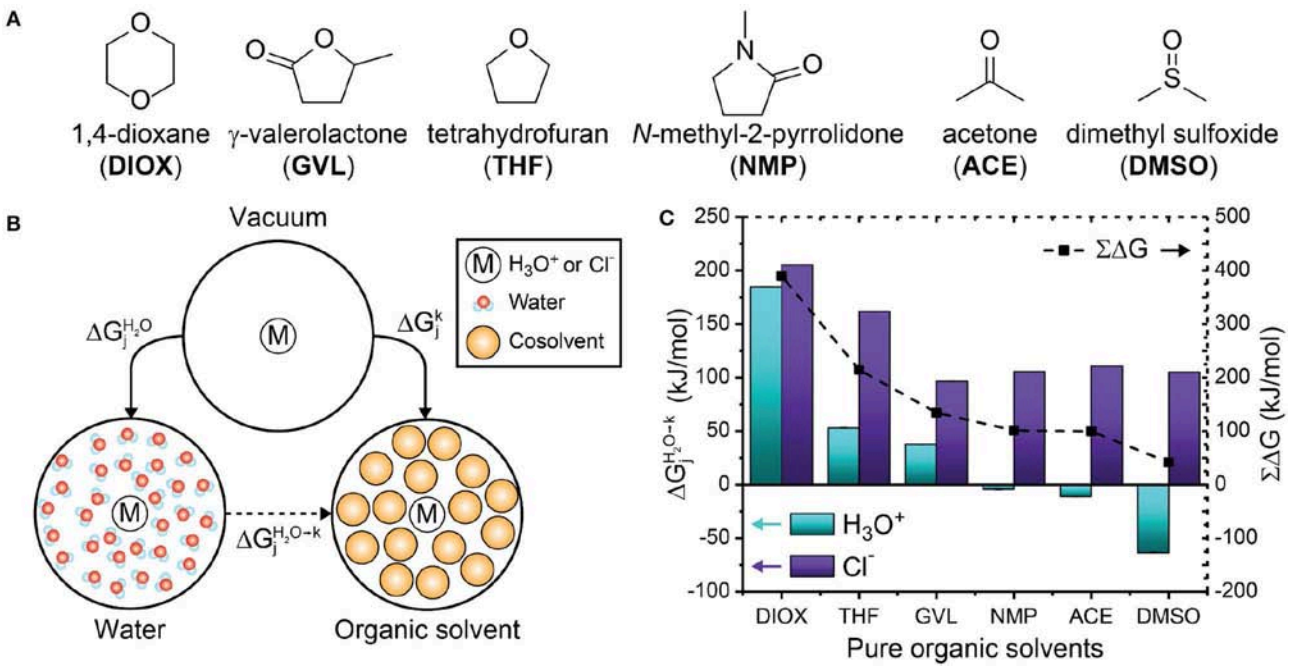

FIGURE 5 | (A) Chemical structures of the organic solvents used in this study. **(B)** Thermodynamic cycle used to compute the free energy for transferring a hydronium or chloride ion from pure water to pure organic solvent. ΔG_j^k and $\Delta G_j^{H_2O}$ are solvation free energies while $\Delta G_j^{H_2O \to k}$ is the transfer free energy computed from Equation 4. **(C)** Transfer free energies for six pure organic solvents. Cyan and purple bars indicate hydronium (H_3O^+) and chloride (Cl^-) ion transfer free energies, respectively. Dashed lines indicate the sum of the transfer energies. Error bars were computed from the standard deviation of two trials; the error is <1 kJ/mol and is not visible in the plot. The error is tabulated in **Supplementary Table 4**.

that $\sum \Delta G$ is positive for each organic solvent (black dashed lines). This result suggests that all of the polar aprotic solvents would decrease acid dissociation, leading to the reduced catalyst availability associated with weak acids based on experiments (Mellmer et al., 2014b). The sign of $\sum \Delta G$ is largely dictated by the solvation free energies of the chloride ion, indicating that the selection of the conjugate base is important for acid disassociation (Mellmer et al., 2014b), although the choice of

conjugate base would not affect the solvation free energies of the hydronium ion itself.

Relationship Between Solvation Free Energies and Solvent Parameters

Given the computational expense of free energy calculations, we next sought to relate the transfer free energy results ($\Delta G_{H_3O^+}^{k\rightarrow H_2O}$ and $\sum \Delta G$) to tabulated solvent properties to determine if these properties could accelerate solvent screening. **Table 1** compares transfer free energy values to solvent dielectric constants and Kamlet-Taft parameters (α, β, π^*). We use the dielectric constant to quantify the polarizability of the solvents and the Kamlet-Taft parameters to quantify hydrogen-bond donating ability (acidity, α), hydrogen-bond accepting ability (basicity, β), and polarity/polarizability (π^*) (Kamlet and Taft, 1976; Taft and Kamlet, 1976; Kamlet et al., 1977, 1983). Each of the Kamlet-Taft parameters are scaled from 0 to 1 based on two reference solvents. For instance, π^* uses cyclohexane and DMSO as a reference for 0 and 1, respectively (Kamlet et al., 1977; Laurence et al., 1994). We expect that the stability of a hydronium ion can be influenced by the polarity of the solvent; however, neither dielectric constant nor π^* quantitatively correlate with $\Delta G_{H_3O^+}^{k\rightarrow H_2O}$ or $\sum \Delta G$. Furthermore, basicity is expected to be an important metric of whether a hydronium ion is favored in a solvent environment, with larger β values indicating more basic solvents that would favorably solvate the acidic hydronium ion, but there is no clear correlation between β and the free energy results. We also do not find a correlation between α and the free energy results, which is expected since acidity does not directly relate to the stability of a hydronium ion in a solvent system.

These data suggest that typical solvent-specific parameters cannot easily describe the interplay of solute-solvent interactions and solvent reorganization that dictate the measured transfer free energies. We further computed the RDF between the hydronium ion and pure solvents (**Supplementary Figure 7**, Supplementary Material) to determine if solvent structure correlated with the transfer free energies, but we do not find a clear trend to explain the results found in **Figure 5C**. This data thus suggests that the free energy calculations are providing new information that can be used to predict the preference of the hydronium ion for either water or an organic solvent and quantify the effect of solvent composition on acid dissociation. It is also possible that the MD workflow is insufficiently accurate to predict these values, particularly given the classical model of the hydronium ion. However, the good agreement between the calculated solvation free energies of the hydronium and chloride ions in water with experimental data suggests that the model is reasonable. We also emphasize that DIOX, THF, and GVL have positive values of $\Delta G_{H_3O^+}^{k\rightarrow H_2O}$ and lead to increased reaction rates in mixed-solvent systems when water is enriched near the reactant, while DMSO has a negative value of $\Delta G_{H_3O^+}^{k\rightarrow H_2O}$ and leads to increased reaction rates in mixed-solvent systems when the cosolvent is enriched near the reactant. The distinct behavior of these cosolvents mirrors the difference in the sign of the calculated transfer free energies, suggesting that the transfer free energies are correctly capturing differences in the preference of the hydronium ion for bulk organic solvent.

TABLE 1 | Dielectric constants and Kamlet-Taft parameters (α, β, π^*) for pure solvents, tabulated according to decreasing transfer free energy of a hydronium ion ($\Delta G_{H_3O^+}^{k\rightarrow H_2O}$) in these solvents. $\sum \Delta G$ was computed with Equation 5.

Solvent	Dielectric constant[a]	Kamlet-taft Parameters			$\Delta G_{H_3O^+}^{k\rightarrow H_2O}$	$\sum \Delta G$
		α[b]	β[b]	π^*[c]		
DIOX	2.20	0.00	0.37	0.49	184.6	389.85
THF	7.40	0.00	0.55	0.55	53.0	214.91
GVL	36.47	0.00	0.60	0.83	37.8	134.36
Water	78.50	1.17	0.47	1.14	0.0	0.00
NMP	32.16	0.00	0.77	0.92	−4.3	101.25
ACE	20.70	0.08	0.43	0.62	−11.2	99.55
DMSO	48.90	0.00	0.76	1.00	−63.5	41.69

All solvation free energies are in units of kJ/mol.

[a] *Values are from Fowler et al. (1971), except for GVL (Wohlfarth, 2015), and NMP (Uosaki et al., 1996).*

[b] *Values from Marcus (1993), except for GVL (Jessop et al., 2012).*

[c] *Values from Laurence et al. (1994), except for GVL (Jessop et al., 2012), and water (Buhvestov et al., 1998).*

Transfer Free Energies of the Hydronium and Chloride Ion in Mixed-Solvent Systems

Figure 6A shows the free energies for transferring either a hydronium or chloride ion to aqueous mixtures of DMSO and DIOX from pure water; these solvents represent extrema of low and high affinity cosolvents for the hydronium ion. In aqueous mixtures of DMSO, **Figure 6A** shows a monotonic decrease in the hydronium ion transfer free energy (i.e., an increase in hydronium ion stability relative to pure water) as the mass fraction of the organic phase increases. Since the free energy calculations in pure organic solvents (**Figure 5C**) show that pure DMSO stabilizes the hydronium ion more than water, these results agree with the expectation that increasing concentrations of DMSO results in improved stability of the hydronium ion. **Figure 6B** shows RDFs between the hydronium ion and both water and DMSO in 90 wt% DMSO. The peak of the ion-water RDF in 90 wt% DMSO is higher than in pure water, showing a local enrichment of water around the ion; however, there is also a cosolvent peak at ∼0.38 nm, showing an enrichment in DMSO. Therefore, water and DMSO both favorable solvate the hydronium ion (visually shown in **Figure 2C**), leading to its increased stability relative to pure water. These results are consistent with experimental trends that find that increasing the concentration of DMSO monotonically increases basicity (Catalán et al., 2001). The results further suggest that there should be a driving force to partition the hydronium ion to regions of the solvent system that have the highest concentration of DMSO to reduce its free energy to the greatest extent, agreeing with the hypothesis that local enrichment of DMSO around a reactant leads to an increase in acid-catalyzed reaction rates.

In aqueous mixtures of DIOX, **Figure 6A** shows a non-monotonic trend in the hydronium ion transfer free energy as

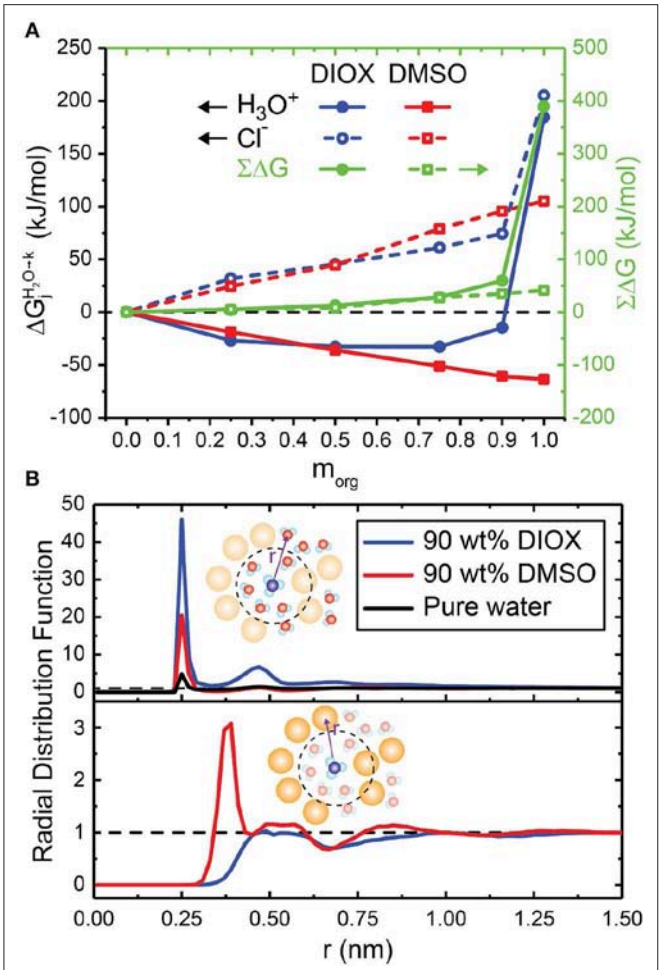

FIGURE 6 | (A) Transfer free energies for transferring hydronium (H_3O^+, filled lines) and chloride (Cl^-, dashed lines) ions from pure water to aqueous mixtures of dioxane (DIOX, blue lines) and dimethyl sulfoxide (DMSO, red lines). The sums of the transfer free energies ($\sum \Delta G$) are shown as green lines. Error bars are not shown; they range from 0 to 2.5 kJ/mol when averaging two trials and tabulated in **Supplementary Table 5**. **(B)** Radial distribution function (RDF) between the center of mass of the hydronium ion to water (top) and the organic solvent (bottom) in 90 wt% DIOX, 90 wt% DMSO, and pure water. Bin widths for the RDFs were set to 0.02 nm.

the mass fraction of the organic phase increases. The transfer free energy is negative for all mixed compositions indicating that the hydronium ion is more stable than in either pure solvent. In the RDFs presented in **Figure 6B**, the peak of the ion-water RDF in 90 wt% DIOX is almost 10-fold larger than the peak in pure water, indicating a significant enrichment of water around the hydronium ion (visually shown in **Figure 2B**). In addition, the cosolvent RDF (**Figure 6B**, bottom) shows that DIOX is depleted near the hydronium ion up to distances of about 1 nm. These results together indicate that the hydronium ion nucleates a local domain of water molecules confined within the vicinity of the ion by the surrounding cosolvent. We attribute the decreased free energy of the hydronium ion in the mixed-solvent environment to the formation of this domain, which effectively sequesters water molecules to eliminate unfavorable water-cosolvent interactions that are not present in either pure solvent. Surprisingly, this data suggests that there should not be a driving force for hydronium ions to partition from bulk mixed-solvent environments to water-enriched domains near hydrophilic reactants as previously hypothesized because the solvation free energy of the ion in pure water is higher than in the mixed-solvent environment. This finding suggests that the stabilization of the charged transition state by confined water molecules in the water-enriched local domain might be the dominant factor leading to increased reaction rates. However, these calculations omit explicit modeling of the reactant, which could affect partitioning thermodynamics.

Finally, **Figure 6A** shows that the chloride ion is not favored in any mixed-solvent composition, resulting in positive $\Delta G_j^{H_2O\to k}$ and $\sum \Delta G$ values for all DIOX and DMSO mass fractions. These data again indicate that acid dissociation is preferred in pure water rather than any mixed-solvent environment and thus weak acids are less likely to dissociate, diminishing reaction performance.

DISCUSSION

Screening Solvent Properties Using a Classical Hydronium Ion Model

Recent studies of acid-catalyzed biomass conversion reactions have illustrated that the stability of the hydronium ion catalyst in various mixed-solvent environments can dramatically affect reaction rates (Mellmer et al., 2014a,b, 2018; Shuai and Luterbacher, 2016; He et al., 2017; Walker et al., 2018, 2019; Varghese and Mushrif, 2019). Computational tools have been developed to study the hydronium ion in different solvent systems (Tawa et al., 1998; Bonthuis et al., 2016; Varghese and Mushrif, 2019), with *ab initio* molecular dynamics emerging as a powerful method to study interactions between the hydronium ion and solvent molecules due to the method's accuracy and ability to capture quantum mechanical effects (Tuckerman et al., 1994, 1995a,b, 1997; Sagnella et al., 1996; Marx et al., 1999; Morrone and Tuckerman, 2002; Izvekov and Voth, 2005; Marx, 2006). However, *ab initio* simulations are computationally expensive and difficult to expand across multiple solvent systems. Therefore, we used a classical hydronium ion model (Bonthuis et al., 2016) to compute the stability of the hydronium ion by measuring its solvation free energy in solvent systems with organic, polar aprotic solvents. Our findings suggest that the hydronium ion is unfavorable in DIOX, THF, and GVL solvents but favorable in NMP, ACE, and DMSO solvents (**Figure 5C**). These results can classify whether a solvent favorably facilitates a hydronium ion to help determine which phase the acid catalyst prefers in mixed-solvent systems. Furthermore, we could not identify a tabulated cosolvent-specific descriptor (e.g., dielectric constant, Kamlet-Taft parameters) that correlates with the hydronium ion solvation free energies, although the solvation free energies qualitatively capture features of solvent scales, such as the large distinction between DIOX and DMSO solvents. The lack of correlation suggests that the solvation free

energy calculated from a MD simulation may provide unique information on proton-solvent interactions and can act as a cosolvent-specific descriptor for the stability of the acid catalyst.

In mixed-solvent environments, the solvation structure around the hydronium ion show that water-enriched local domains are formed, analogous to water-enrichment around hydrophilic reactants (Mellmer et al., 2018; Walker et al., 2019), but the magnitude of enrichment is dependent on the choice of organic solvent. DMSO molecules compete with water for binding sites around the hydronium ion, whereas DIOX molecules are depleted around the hydronium ion. The hydronium ion solvation free energies in aqueous mixtures of DIOX suggest that small amounts of water can stabilize the hydronium ion to a greater degree than pure water or DIOX. This stabilization originates from the hydronium ion being confined by water, a solvent environment also found in water-enriched local domains formed by hydrophilic reactants. This finding suggests that stabilization of charged transition states by confined water in mixed-solvent environments may contribute to the increased reaction rates observed experimentally.

In all solvent environments studied, the sum of the transfer free energies of the hydronium and chloride ions from water was positive. This result indicates that non-aqueous environments tend to suppress acid dissociation, leading to lower catalyst availability for weak acids that translates to lower reaction rates (Mellmer et al., 2014b). However, in this work we only studied the solvation free energy of a chloride ion conjugate base, and thus investigating the effect of alternative conjugate bases on acid dissociation could yield different effects on acid dissociation. For example, triflic acid is known to readily disassociate even in high concentrations of DMSO (Mellmer et al., 2018). Future work will thus extend the framework developed here to further screen conjugate bases to determine the effect on acid dissociation, enabling the incorporation of these values into correlative models for reaction optimization.

Incorporation of Hydronium Ion Stability Into the Correlative Model of Reaction Rates

Figure 4 showed that the acid-catalyzed dehydration of PDO depends on the choice of cosolvent, with the experimentally measured kinetic solvent parameter (σ) correlating with the simulation-derived preferential exclusion parameter (Γ) in aqueous mixtures of DIOX and DMSO. This correlation is based on the physical understanding that catalytic hydronium ions preferentially partition to the water-enriched local domain around the reactant, increasing reaction performance and leading to a positive correlation between σ and Γ (**Figure 4B**). However, the correlation between σ and Γ is negative in DMSO, a solvent for which water depletion around the reactant is observed while reaction rates still increase. We hypothesized that the negative correlation may be because the hydronium ion preferentially interacts with DMSO rather than water and thus partitions to the water-depleted, DMSO-enriched local domain. This hypothesis is supported by the negative free energy for transferring a hydronium ion from water to DMSO as shown in **Figure 5B**. Thus, the correlation between Γ and σ must be adjusted to account for the stability of the hydronium ion in the local domain.

We include the sign of the hydronium ion transfer free energy between pure organic solvent to water, $\Delta G_{H_3O^+}^{H_2O\rightarrow pure\ org.}$, as a correction term in the preferential exclusion coefficient (Γ') by using Equation 6:

$$\Gamma' = \Gamma^* \text{sign}\left(\Delta G_{H_3O^+}^{H_2O\rightarrow pure\ org.}\right) \tag{6}$$

Equation 6 ensures that Γ' and σ are positively correlated for aqueous mixtures of DMSO as shown in **Figure 7A**. We interpret Γ' as quantifying the enrichment of the solvent (water or cosolvent) that preferentially stabilizes the hydronium ion, such that larger values of Γ' suggest higher catalyst availability in the local domain of the reactant. Since Γ' and σ are positively correlated for both aqueous mixtures of DIOX and DMSO, we can then write a correlative model for σ_{pred} that bridges these distinct solvents using Equation 7:

$$\sigma_{pred} = A\left(\Gamma'\right) \tag{7}$$

A is a constant. **Supplementary Figure 8** shows the correlation between σ_{pred} and σ_{exp} when combining results from both DIOX-water and DMSO-water mixtures, resulting in a best-fit slope of 0.25 (ideally this value should be unity), and a root-mean-square error (RMSE) between predicted and experimental values of 0.39. Similar to our previous work (Walker et al., 2019), we next explored the use of multiple descriptors in combination to improve this correlation. In particular, we define $\Delta G_{H_3O^+}^{k/H_2O}$ as the ratio of the solvation free energy of the hydronium ion in the kth solvent system ($\Delta G_{H_3O^+}^{k}$) to the solvation free energy of hydronium ion in pure water ($\Delta G_{H_3O^+}^{H_2O}$).

$$\Delta G_{H_3O^+}^{k/H_2O} = \frac{\Delta G_{H_3O^+}^{k}}{\Delta G_{H_3O^+}^{H_2O}} \tag{8}$$

Since acid-catalyzed reactions generally form a charged transition state after protonation of the reactant (**Figure 1B**), we interpret $\Delta G_{H_3O^+}^{k/H_2O}$ as a unitless metric that estimates transition state stability in mixed-solvent systems compared to pure water. In our prior work, the reactant-water hydrogen bonding lifetime was identified as a descriptor that quantified transition state stability (Walker et al., 2019); here, $\Delta G_{H_3O^+}^{k/H_2O}$ generalizes this prior finding to account for non-hydrogen bonding interactions. **Supplementary Figure 9** shows $\Delta G_{H_3O^+}^{k/H_2O}$ as a function of solvent composition for aqueous mixtures of DIOX and DMSO. For these cosolvents, $\Delta G_{H_3O^+}^{k/H_2O}$ is greater than unity.

We combined Γ' and $\Delta G_{H_3O^+}^{k/H_2O}$ using the multilinear regression model shown in Equation 9, where A, B, and C are coefficients. To enable comparison between the coefficients, we standardized Γ' and $\Delta G_{H_3O^+}^{k/H_2O}$ by subtracting their mean

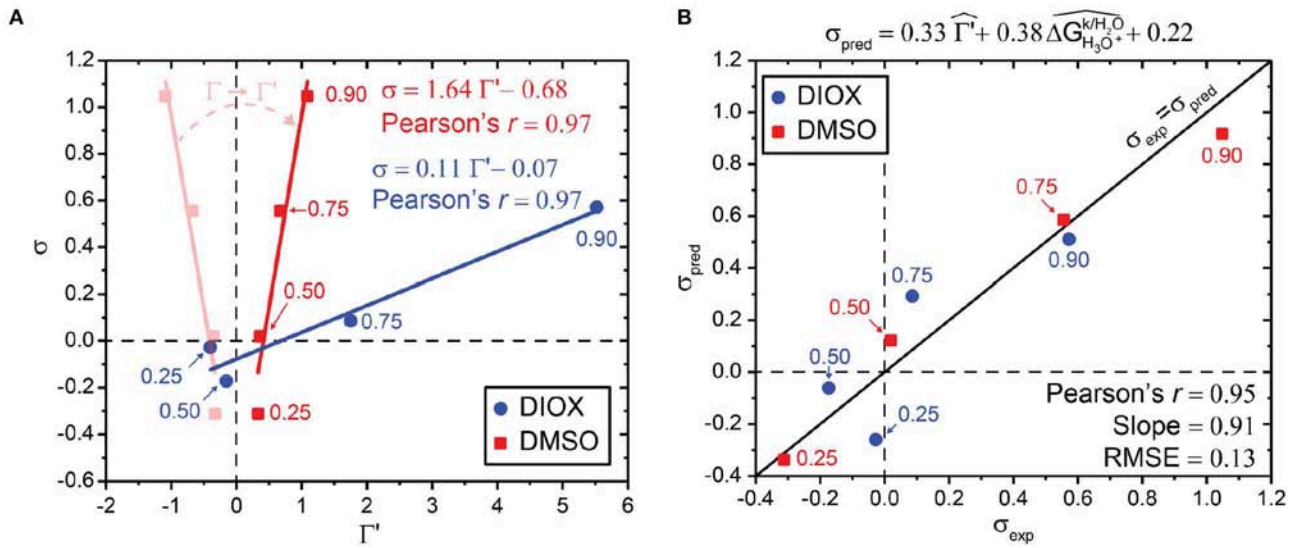

FIGURE 7 | (A) Correlation between simulated preferential exclusion coefficient with solvation free energy correction term (Γ′), as expressed in Equation 7, and experimentally determined kinetic solvent parameters (σ) for aqueous mixtures of DIOX and DMSO. Experimental values were taken from Mellmer et al. (2018). Transparent red points and lines show how Γ relates to Γ′. **(B)** Parity plot between predicted kinetic solvent parameter (σ_{pred}) and experimental kinetic solvent parameter (σ_{exp}) using results from aqueous mixtures of DIOX and DMSO. The correlative model is based on Equation 9 as shown above the plot. Data points are labeled with the wt% of the organic solvent.

and dividing by their standard deviations as described in **Supplementary Section 5.2**. All standardized variables are denoted by a hat accent.

$$\sigma_{pred} = A\left(\hat{\Gamma}'\right) + B\left(\widehat{\Delta G^{k/H_2O}_{H_3O^+}}\right) + C \tag{9}$$

Figure 7B shows the correlation between σ_{pred} and $\sigma_{\exp}$ when using Equation 9 and combining results from both DIOX-water and DMSO-water mixtures. The best-fit slope is 0.91, close to the ideal value of unity, and the RMSE between predicted and experimental values is 0.13, which is comparable to experimental error (Walker et al., 2019). Furthermore, the coefficients for $\hat{\Gamma}'$ and $\Delta G^{k/H_2O}_{H_3O^+}$ are comparable (0.33 vs. 0.38), suggesting that solvent enrichment around the reactant that favors the hydronium ion catalyst and the transition state stability are important variables for the prediction of acid-catalyzed reaction kinetics. We thus find that including information on the hydronium ion solvation free energy in an organic solvent can improve the correlation between Γ and σ when considering aqueous mixtures with different polar aprotic cosolvents. We note that additional solvent-specific descriptors (e.g., hydrogen bonding between water and the organic phase, etc.) may improve the correlation between different solvent systems and is a subject of future research.

CONCLUSIONS

We performed classical molecular dynamics simulations and solvation free energy calculations to quantify the stability of hydronium and chloride ions in six organic, polar aprotic solvents. We found that the hydronium ion is favorably solvated in pure NMP, ACE, and DMSO solvents, but unfavorably solvated in pure DIOX, THF, and GVL solvents. In mixed-solvent environments, the inclusion of water with DIOX stabilizes the hydronium ion more than their pure solvent counterparts. We attribute this increased stabilization to the formation of water-enriched local solvent domains around the hydronium ion. In aqueous mixtures of DMSO, the hydronium ion is further stabilized with increasing concentration of the organic phase. Conversely, the chloride ion is destabilized in all pure organic solvents and mixed solvent systems, inhibiting acid dissociation. By quantifying the stability of the hydronium ion in organic solvents, we obtained a new cosolvent-specific descriptor that quantifies acid catalyst stability. We incorporated this descriptor into a correlative model for 1,2-propanediol dehydration reaction rates to demonstrate that the solvation free energy results can be used to bridge reaction rate predictions across different cosolvent systems. Incorporating information about the acid catalyst stability in different solvent mixtures represents an important step toward the rational design of mixed-solvent environments for acid-catalyzed reaction schemes and has the potential to alleviate time-intensive experimentation that accompanies the optimization of biomass conversion reactions for maximum productivity.

DATA AVAILABILITY

All datasets generated for this study are included in the manuscript and/or the **Supplementary Files**.

AUTHOR CONTRIBUTIONS

AC designed, performed, and analyzed the molecular dynamics simulations. AC and RV conceived of the simulations, interpreted the results, and wrote the manuscript.

FUNDING

The authors acknowledge support from the Department of Chemical and Biological Engineering at the University of Wisconsin-Madison and the Wisconsin Alumni Research Fund. This work used the Extreme Science and Engineering Discovery Environment (XSEDE), which is supported by National Science Foundation grant number ACI-1549562. This work also used the computing resources and assistance of the UW-Madison Center for High Throughput Computing (CHTC) in the Department of Computer Sciences. The CHTC is supported by UW-Madison, the Advanced Computing Initiative, the Wisconsin Alumni Research Foundation, the Wisconsin Institutes for Discovery, and the National Science Foundation, and is an active member of the Open Science Grid, which is supported by the National Science Foundation and the U.S. Department of Energy's Office of Science.

ACKNOWLEDGMENTS

The authors would like to thank Benginur Demir for sharing the 1,2-propanediol dehydration experimental data.

SUPPLEMENTARY MATERIAL

The Supplementary Material for this article can be found online at: https://www.frontiersin.org/articles/10.3389/fchem.2019.00439/full#supplementary-material

REFERENCES

Berendsen, H. J. C., Grigera, J. R., and Straatsma, T. P. (1987). The missing term in effective pair potentials. *J. Phys. Chem.* 91, 6269–6271. doi: 10.1021/j100308a038

Best, R. B., Zhu, X., Shim, J., Lopes, P. E., Mittal, J., Feig, M.,et al. (2013). Optimization of the additive CHARMM all-atom protein force field targeting improved sampling from the backbone and side chain and dihedral angles. *J. Chem. Theory Comput.* 8, 3257–3273. doi: 10.1021/ct300400x

Beutler, T. C., Mark, A. E., Vanschaik, R. C., Gerber, P. R., and Vangunsteren, W. F. (1994). Avoiding singularities and numerical instabilities in free-energy calculations based on molecular simulations. *Chem. Phys. Lett.* 222, 529–539. doi: 10.1016/0009-2614(94)00397-1

Bonthuis, D. J., Mamatkulov, S. I., and Netz, R. R. (2016). Optimization of classical nonpolarizable force fields for OH- and H3O+. *J. Chem. Phys.* 144:104503. doi: 10.1063/1.4942771

Buhvestov, U., Rived, F., Rafols, C., Bosch, E., and Roses, M. (1998). Solute-solvent and solvent-solvent interactions in binary solvent mixtures. Part 7. Comparison of the enhancement of the water structure in alcohol-water mixtures measured by solvatochromic indicators. *J. Phys. Org. Chem.* 11, 185–192.

Caratzoulas, S., and Vlachos, D. G. (2011). Converting fructose to 5-hydroxymethylfurfural: a quantum mechanics/molecular mechanics study of the mechanism and energetics. *Carbohydr. Res.* 346, 664–672. doi: 10.1016/j.carres.2011.01.029

Catalán, J., Díaz, C., and García-Blanco, F. (2001). Characterization of binary solvent mixtures of DMSO with water and other cosolvents. *J. Org. Chem.* 66, 5846–5852. doi: 10.1021/jo010415i

Chheda, J. N., Huber, G. W., and Dumesic, J. A. (2007). Liquid-phase catalytic processing of biomass-derived oxygenated hydrocarbons to fuels and chemicals. *Angew. Chem. Int. Ed.* 46, 7164–7183. doi: 10.1002/anie.200604274

Corma, A., Iborra, S., and Velty, A. (2007). Chemical routes for the transformation of biomass into chemicals. *Chem. Rev.* 107, 2411–2502. doi: 10.1021/cr050989d

Duignan, T. T., Baer, M. D., Schenter, G. K., and Mundy, C. J. (2017). Real single ion solvation free energies with quantum mechanical simulation. *Chem. Sci.* 8, 6131–6140. doi: 10.1039/C7SC02138K

Fawcett, W. R. (1993). Acidity and basicity scales for polar-solvents. *J. Phys. Chem.* 97, 9540–9546. doi: 10.1021/j100139a045

Fowler, F. W., Katritzky, A. R., and Rutherford, R. J. (1971). Correlation of solvent effects on physical and chemical properties. *Chem. Soc. B Phys. Org.* 460–469. doi: 10.1039/j29710000460

He, J. Y., Liu, M. J., Huang, K. F., Walker, T. W., Maravelias, C. T., Dumesic, J. A., et al. (2017). Production of levoglucosenone and 5-hydroxymethylfurfural from cellulose in polar aprotic solvent-water mixtures. *Green Chem.* 19, 3642–3653. doi: 10.1039/C7GC01688C

Hess, B., Bekker, H., Berendsen, H. J. C., and, Fraaije, J. G., E. M. (1997). LINCS: a linear constraint solver for molecular simulations. *J. Comput. Chem.* 18, 1463–1472.

Horinek, D., Mamatkulov, S. I., and Netz, R. R. (2009). Rational design of ion force fields based on thermodynamic solvation properties. *J Chem. Phys.* 130:124507. doi: 10.1063/1.3081142

Huber, G. W., Iborra, S., and Corma, A. (2006). Synthesis of transportation fuels from biomass: chemistry, catalysts, and engineering. *Chem. Rev.* 106, 4044–4098. doi: 10.1021/cr068360d

Hunenberger, P., and Reif, M. (2011). Single-ion solvation: experimental and theoretical approaches to elusive thermodynamic quantities. *Single-Ion Solvation: Experimental and Theoretical Approaches to Elusive Thermodynamic Quantities* (Cambridge: Royal Society of Chemistry), 1–664.

Izvekov, S., and Voth, G. A. (2005). *Ab initio* molecular-dynamics simulation of aqueous proton solvation and transport revisited. *J. Chem. Phys.* 123:044505. doi: 10.1063/1.1961443

Jessop, P. G., Jessop, D. A., Fu, D. B., and Phan, L. (2012). Solvatochromic parameters for solvents of interest in green chemistry. *Green Chem.* 14, 1245–1259. doi: 10.1039/c2gc16670d

Kamlet, M. J., Abboud, J. L., and Taft, R. W. (1977). The solvatochromic comparison method. 6. The.pi.* scale of solvent polarities. *J. Am. Chem. Soc.* 99, 6027–6038. doi: 10.1021/ja00460a031

Kamlet, M. J., Abboud, J. L. M., Abraham, M. H., and Taft, R. W. (1983). Linear solvation energy relationships. 23. A comprehensive collection of the solvatochromic parameters, pi-star, alpha and beta, and some methods for simplifying the generalized solvatochromic equation. *J. Org. Chem.* 48, 2877–2887. doi: 10.1021/jo00165a018

Kamlet, M. J., and Taft, R. W. (1976). The solvatochromic comparison method. I. The.beta.-scale of solvent hydrogen-bond acceptor (HBA) basicities. *J. Am. Chem. Soc.* 98, 377–383. doi: 10.1021/ja00418a009

Kang, M., and Smith, P. E. (2007). Preferential interaction parameters in biological systems by Kirkwood-Buff theory and computer simulation. *Fluid Phase Equilib.* 256, 14–19. doi: 10.1016/j.fluid.2006.11.003

Kelly, C. P., Cramer, C. J., and Truhlar, D. G. (2007). Single-ion solvation free energies and the normal hydrogen electrode potential in methanol, acetonitrile, and dimethyl sulfoxide. *J. Phys. Chem. B* 111, 408–422. doi: 10.1021/jp065403l

Klimovich, P. V., Shirts, M. R., and Mobley, D. L. (2015). Guidelines for the analysis of free energy calculations. *J. Comput. Aided Mol. Des.* 29, 397–411. doi: 10.1007/s10822-015-9840-9

Koppel, I. A., and Palm, V. A. (1972). "The influence of the solvent on organic reactivity," in *Advances in Linear Free Energy Relationships,* eds N. B.

Chapman and J. Shorter (Boston, MA: Springer US: Boston, MA). p., 203–280. doi: 10.1007/978-1-4615-8660-9_5

Laurence, C., Nicolet, P., Dalati, M. T., Abboud, J. L. M., and Notario, R. (1994). The empirical-treatment of solvent solute interactions - 15 years of Pi. *J. Phys. Chem.* 98, 5807–5816. doi: 10.1021/j100074a003

Marcus, Y. (1993). The properties of organic liquids that are relevant to their use as solvating solvents. *Chem. Soc. Rev.* 22, 409–416. doi: 10.1039/cs9932200409

Marx, D. (2006). Proton transfer 200 years after von Grotthuss: insights from *ab initio* simulations. *Chemphyschem* 7, 1848–1870. doi: 10.1002/cphc.200600128

Marx, D., Tuckerman, M. E., Hutter, J., and Parrinello, M. (1999). The nature of the hydrated excess proton in water. *Nature* 397, 601–604. doi: 10.1038/17579

McGibbon, R. T., Beauchamp, K. A., Harrigan, M. P., Klein, C., Swails, J. M., Hernández, C. X., et al. (2015). MDTraj: a modern open library for the analysis of molecular dynamics trajectories. *Biophys. J.* 109, 1528–1532. doi: 10.1016/j.bpj.2015.08.015

Mejias, J. A., and Lago, S. (2000). Calculation of the absolute hydration enthalpy and free energy of H+ and OH-. *J. Chem. Phys.* 113, 7306–7316. doi: 10.1063/1.1313793

Mellmer, M. A., Alonso, D. M., Luterbacher, J. S., Gallo, J. M. R., and Dumesic, J. A. (2014a). Effects of gamma-valerolactone in hydrolysis of lignocellulosic biomass to monosaccharides. *Green Chem.* 16, 4659–4662. doi: 10.1039/C4GC01768D

Mellmer, M. A., Gallo, J. M. R., Alonso, D. M., and Dumesic, J. A. (2015). Selective production of levulinic acid from furfuryl alcohol in THF solvent systems over H-ZSM-5. *ACS Catal.* 5, 3354–3359. doi: 10.1021/acscatal.5b00274

Mellmer, M. A., Sanpitakseree, C., Demir, B., Bai, P., Ma, K. W., Neurock, M., et al. (2018). Solvent-enabled control of reactivity for liquid-phase reactions of biomass-derived compounds. *Nat. Catal.* 1, 199–207. doi: 10.1038/s41929-018-0027-3

Mellmer, M. A., Sener, C., Gallo, J. M. R., Luterbacher, J. S., Alonso, D. M., and Dumesic, J. A. (2014b). Solvent effects in acid-catalyzed biomass conversion reactions. *Angew. Chem. Int. Ed.* 53, 11872–11875. doi: 10.1002/anie.201408359

Morrone, J. A., and Tuckerman, M. E. (2002). *Ab initio* molecular dynamics study of proton mobility in liquid methanol. *J. Chem. Phys.* 117, 4403–4413. doi: 10.1063/1.1496457

Motagamwala, A. H., Won, W. Y., Maravelias, C. T., and Dumesic, J. A. (2016). An engineered solvent system for sugar production from lignocellulosic biomass using biomass derived gamma-valerolactone. *Green Chem.* 18, 5756–5763. doi: 10.1039/C6GC02297A

Nguyen, T. Y., Cai, C. M., Kumar, R., and Wyman, C. E. (2017). Overcoming factors limiting high-solids fermentation of lignocellulosic biomass to ethanol. *Proc. Natl. Acad. Sci. U.S.A.* 114, 11673–11678. doi: 10.1073/pnas.1704652114

Pagan-Torres, Y. J., Wang, T. F., Gallo, J. M. R., Shanks, B. H., and Dumesic, J. A. (2012). Production of 5-Hydroxymethylfurfural from glucose using a combination of lewis and bronsted acid catalysts in water in a biphasic reactor with an alkylphenol solvent. *ACS Catal.* 2, 930–934. doi: 10.1021/cs300192z

Páll, S., Abraham, M. J., Kutzner, C., Hess, B., and Lindahl, E. (2015). "Tackling exascale software challenges in molecular dynamics simulations with GROMACS," in *Solving Software Challenges for Exascale: International Conference on Exascale Applications and Software, EASC 2014*, eds S Markidis, and E. Laure (Cham; Stockholm: Springer International Publishing: Cham). *p.* 3–27. doi: 10.1007/978-3-319-15976-8_1

Pliego, J. R. (2003). Thermodynamic cycles and the calculation of pK(a). *Chem. Phys. Lett.* 367, 145–149. doi: 10.1016/S0009-2614(02)01686-X

Pliego, J. R., and Riveros, J. M. (2000). New values for the absolute solvation free energy of univalent ions in aqueous solution. *Chem. Phys. Lett.* 332, 597–602. doi: 10.1016/S0009-2614(00)01305-1

Pliego, J. R., and Riveros, J. M. (2001). The cluster-continuum model for the calculation of the solvation free energy of ionic species. *J. Phys Phys. Chem. A* 105, 7241–7247. doi: 10.1021/jp004192w

Reif, M. M., and Hünenberger, P. H. (2011). Computation of methodology-independent single-ion solvation properties from molecular simulations. IV. Optimized Lennard-Jones interaction parameter sets for the alkali and halide ions in water. *J. Chem. Phys.* 134:144104. doi: 10.1063/1.3567022

Román-Leshkov, Y., Barrett, C. J., Liu, Z. Y., and Dumesic, J. A. (2007). Production of dimethylfuran for liquid fuels from biomass-derived carbohydrates. *Nature* 447, 982–U5985. doi: 10.1038/nature05923

Ryckaert, J. P., Ciccotti, G., and, Berendsen, H. J. C. (1977). Numerical-integration of cartesian equations of motion of a system with constraints - molecular-dynamics of N-alkanes. *J. Comput. Phys.* 23, 327–341. doi: 10.1016/0021-9991(77)90098-5

Sagnella, D. E., Laasonen, K., and Klein, M. L. (1996). *Ab initio* molecular dynamics study of proton transfer in a polyglycine analog of the ion channel gramicidin A. *Biophys. J.* 71, 1172–1178. doi: 10.1016/S0006-3495(96)79321-9

Schneider, C. P., and Trout, B. L. (2009). Investigation of cosolute - protein preferential interaction coefficients: new insight into the mechanism by which arginine inhibits aggregation investigation of cosolute - protein preferential interaction coefficients: new insight into the mechanism by. *J. Phys. Chem. B* 113, 2050–2058. doi: 10.1021/jp808042w

Sener, C., Motagamwala, A. H., Alonso, D. M., and Dumesic, J. A. (2018). Enhanced furfural yields from xylose dehydration in the gamma-valerolactone/water solvent system at elevated temperatures. *ChemSusChem* 11, 2321–2331. doi: 10.1002/cssc.201800730

Shirts, M. R., and Chodera, J. D. (2008). Statistically optimal analysis of samples from multiple equilibrium states. *J. Chem. Phys.* 129:124105. doi: 10.1063/1.2978177

Shivakumar, D., Williams, J., Wu, Y., Damm, W., Shelley, J., and Sherman, W. (2010). Prediction of absolute solvation free energies using molecular dynamics free energy perturbation and the OPLS force field. *J. Chem. Theory Comput.* 6, 1509–1519. doi: 10.1021/ct900587b

Shuai, L., and Luterbacher, J. (2016). Organic solvent effects in biomass conversion reactions. *ChemSusChem* 9, 133–155. doi: 10.1002/cssc.201501148

Shukla, D., and Trout, B. L. (2011). Preferential interaction coefficients of proteins in aqueous arginine solutions and their molecular origins. *J. Phys. Chem. B* 115, 1243–1253. doi: 10.1021/jp108586b

Shulgin, I. L., and Ruckenstein, E. (2007). Local composition in the vicinity of a protein molecule in an aqueous mixed solvent. *J. Phys. Chem. B* 111, 3990–3998. doi: 10.1021/jp066353n

Stöcker, M. (2008). Biofuels and biomass-to-liquid fuels in the biorefinery: catalytic conversion of lignocellulosic biomass using porous materials. *Angew. Chem. Int. Ed* 47, 9200–9211. doi: 10.1002/anie.200801476

Taft, R. W., and Kamlet, M. J. (1976). The solvatochromic comparison method. 2. The.alpha.-scale of solvent hydrogen-bond donor (HBD) acidities. *J. Am. Chem. Soc.* 98, 2886–2894. doi: 10.1021/ja00426a036

Tawa, G. J., Topol, I. A., Burt, S. K., Caldwell, R. A., and Rashin, A. A. (1998). Calculation of the aqueous solvation free energy of the proton. *J. Chem. Phys.* 109, 4852–4863. doi: 10.1063/1.477096

Tock, L., Gassner, M., and Marechal, F. (2010). Thermochemical production of liquid fuels from biomass: thermo-economic modeling, process design and process integration analysis. *Biomass Bioenergy* 34, 1838–1854. doi: 10.1016/j.biombioe.2010.07.018

Tuckerman, M., Laasonen, K., Sprik, M., and Parrinello, M. (1995a). *Ab-initio* molecular-dynamics simulation of the solvation and transport of hydronium and hydroxyl ions in water. *J. Chem. Phys.* 103, 150–161. doi: 10.1063/1.469654

Tuckerman, M., Laasonen, K., Sprik, M., and Parrinello, M. (1995b). *Ab-Initio* molecular-dynamics simulation of the solvation and transport Of H3o+ and Oh- ions in water. *J. Phys. Chem.* 99, 5749–5752. doi: 10.1021/j100016a003

Tuckerman, M. E., Laasonen, K., Sprik, M., and Parrinello, M. (1994). *Ab-initio* simulations of water and water ions. *J. Phys. Cond. Matter* 6, A93–A100. doi: 10.1088/0953-8984/6/23A/010

Tuckerman, M. E., Marx, D., Klein, M. L., and Parrinello, M. (1997). On the quantum nature of the shared proton in hydrogen bonds. *Science* 275, 817–820. doi: 10.1126/science.275.5301.817

Tunon, I., Silla, E., and Bertran, J. (1993). Proton solvation in liquid water - an abinitio study using the continuum model. *J. Phys. Chem.* 97, 5547–5552. doi: 10.1021/j100123a016

Uosaki, Y., Kawamura, K., and Moriyoshi, T. (1996). Static relative permittivities of water plus 1-methyl-2-pyrrolidinone and water plus 1,3-dimethyl-2-imidazolidinone mixtures under pressures up to 300 MPa at 298.15 K. *J. Chem. Eng. Data* 41, 1525–1528. doi: 10.1021/je960236b

Vanommeslaeghe, K., Hatcher, E., Acharya, C., Kundu, S., Zhong, S., Shim, J., et al. (2009). CHARMM general force field: a force field for drug-like molecules compatible with the CHARMM all-atom additive biological force fields. *J. Comput. Chem.* 31, 671–690. doi: 10.1002/jcc.21367

Varghese, J. J., and Mushrif, S. H. (2019). Origins of complex solvent effects on chemical reactivity and computational tools to investigate them: a review. *React. Chem. Eng.* 4, 165–206. doi: 10.1039/C8RE00226F

Vishnyakov, A., Lyubartsev, A. P., and Laaksonen, A. (2001). Molecular dynamics simulations of dimethyl sulfoxide and dimethyl sulfoxide-water mixture. *J. Phys. Chem. A* 105, 1702–1710. doi: 10.1021/jp0007336

Walker, T. W., Chew, A. K., Li, H. X., Demir, B., Zhang, Z. C., Huber, G. W., et al. (2018). Universal kinetic solvent effects in acid-catalyzed reactions of biomass-derived oxygenates. *Energy Environ. Sci.* 11, 617–628. doi: 10.1039/C7EE03432F

Walker, T. W., Motagamwala, A. H., Dumesic, J. A., and Huber, G. W. (2019). Fundamental catalytic challenges to design improved biomass conversion technologies. *J. Catal*, 369, 518–525. doi: 10.1016/j.jcat.2018.11.028

Wohlfarth, C. (2015). "Static dielectric constant of γ-valerolactone," in *Static Dielectric Constants of Pure Liquids and Binary Liquid Mixtures: Supplement to Volume IV/17*, ed M. D. Lechner (Berlin: Springer Berlin Heidelberg), 91–91. doi: 10.1007/978-3-662-48168-4

Won, W. Y., Motagamwala, A. H., Dumesic, J. A., and Maravelias, C. T. (2017). A co-solvent hydrolysis strategy for the production of biofuels: process synthesis and technoeconomic analysis. *React. Chem. Eng.* 2, 397–405. doi: 10.1039/C6RE00227G

Yu, W., He, X., Vanommeslaeghe, K., and MacKernell, A. D. (2012). Extension of the CHARMM general force field to sulfonyl- containing compounds and its utility in biomolecular simulations. *J. Comput. Chem.* 33, 2451–2468. doi: 10.1002/jcc.23067

Conflict of Interest Statement: The authors declare that the research was conducted in the absence of any commercial or financial relationships that could be construed as a potential conflict of interest.

Copyright © 2019 Chew and Van Lehn. This is an open-access article distributed under the terms of the Creative Commons Attribution License (CC BY). The use, distribution or reproduction in other forums is permitted, provided the original author(s) and the copyright owner(s) are credited and that the original publication in this journal is cited, in accordance with accepted academic practice. No use, distribution or reproduction is permitted which does not comply with these terms.

frontiers in Chemistry

ORIGINAL RESEARCH
published: 27 March 2019
doi: 10.3389/fchem.2019.00161

A Strategy for Prompt Phase Transfer of Upconverting Nanoparticles Through Surface Oleate-Mediated Supramolecular Assembly of Amino-β-Cyclodextrin

*Xindong Wang and Guanying Chen**

MIIT Key Laboratory of Critical Materials Technology for New Energy Conversion and Storage, Key Laboratory of Micro-systems and Micro-structures, School of Chemistry and Chemical Engineering, Harbin Institute of Technology, Ministry of Education, Harbin, China

Lanthanide-doped upconverting nanoparticles (UCNPs) are promising for applications as wide as biosensing, bioimaging, controlled drug release, and cancer therapy. These applications require surface engineering of as-prepared nanocrystals, commonly coated with hydrophobic ligand of oleic acid, to enable an aqueous dispersion. However, literature-reported approaches often require a long time and/or multiple step treatment, along with several fold upconversion luminescence (UCL) intensity decrease. Here, we describe a strategy allowing oleate-capped UCNPs to become water-soluble and open-modified, with almost undiminished UCL, through ultrasonication of minutes. The prompt phase transfer was enabled by oleate-mediated supramolecular self-assembly of amino modified β-cyclodextrin (amino-β-CD) onto UCNPs surface. We showed that this method is valid for a wide range of UCNPs with quite different sizes (6–400 nm), various dopant types (Er, Tm, and Ho), and hierarchical structures (core, core-shell). Importantly, the amino group of amino-β-CD on the surface of treated UCNPs provide possibilities to introduce entities for biotargeting or functionalization, as exemplified here, a carboxylic-containing near infrared dye (Cy 7.5) that sensitizes UCNPs to enhance their UCL by ~4,820 fold when excited at ~808 nm. The described method has implications for all types of oleate-capped inorganic nanocrystals, facilitating their myriad bioapplications.

Keywords: lanthanides, upconverting, phase transfer, amino-β-cyclodextrin, supramolecular self-assembly

OPEN ACCESS

Edited by:
Steve Suib,
University of Connecticut,
United States

Reviewed by:
Huibiao Liu,
Institute of Chemistry (CAS), China
Gang Han,
University of Massachusetts Medical School, United States

***Correspondence:**
Guanying Chen
chenguanying@hit.edu.cn

Specialty section:
This article was submitted to Green and Sustainable Chemistry, a section of the journal Frontiers in Chemistry

Received: *25 November 2018*
Accepted: *04 March 2019*
Published: *27 March 2019*

Citation:
Wang X and Chen G (2019) A Strategy for Prompt Phase Transfer of Upconverting Nanoparticles Through Surface Oleate-Mediated Supramolecular Assembly of Amino-β-Cyclodextrin. Front. Chem. 7:161. doi: 10.3389/fchem.2019.00161

INTRODUCTION

Lanthanide-doped upconverting nanoparticles (UCNPs) are a new type of luminescent materials, which can produce visible or ultraviolet luminescence upon near infrared (NIR) excitation. They possess superior advantages over commonly seen luminescent materials (i.e., organic dyes, fluorescent proteins, and quantum dots), such as large anti-stoke shift, low imaging background, good colloidal stability, and deep tissue light activation (Chen et al., 2015; Wang et al., 2017). These merits empower them for uses in a comprehensive range of photonic and biophotonic applications, including solar cells, security encoding, and in particular, bio-imaging, biosensing, and light-activated cancer therapy. Most of these applications demand nanocrystal surface with critical

engineered constituents, such as functional small molecule dyes, polymers, peptides, proteins, and nucleic acids, which, however, is generally unavailable from as-prepared UCNPs surface (Liu et al., 2011b; Wang et al., 2011; Chen et al., 2014, 2016).

The pristine ligands on the as-prepared UCNPs surface constitute the basic structure for surface engineering, which have an anchoring head group to coordinate to surface exposed metallic ions and an end group that points outside when dispersed. These ligands play a significant role in controlling the process of nanocrystal growth in solution as well as nanocrystal colloidal dispensability in solvents. Until now, commonly seen UCNPs with controlled and uniform sizes, shapes, crystal phases, are often synthesized with a high boiling point ligand of oleic acid (OA) (and sometimes together with oleylamine). The head group of OA is a carboxylic group, while the end group is a long alky chain, rendering them dispersible in non-polar organic solvents such as hexane. However, the hydrophobicity of the long alky chain prevents UCNPs for uses in aqueous media as well as for introduction of groups for biotargeting and functionalization. To solve this problem, a number of approaches have been developed and reported, such as ligand exchange (Wu et al., 2009; Shao et al., 2016; Wei et al., 2016; Lee et al., 2017), silica coating (Liu et al., 2013; Li et al., 2014b; Gnanasammandhan et al., 2016), oxidation of the C=C bond in the OA ligand (Chen et al., 2008; Zhou et al., 2009; Dai et al., 2012), assembly of amphiphilic polymers (Camli et al., 2010; Danhier et al., 2012; Zou et al., 2016), and other available methods (Salinas et al., 2015; Liu et al., 2017). However, most of these literature-reported methods typically either require a long time and multiple step treatment to render UCNPs water-soluble, or the obtained aqueous nanocrystals often lack open-modified groups, such as -NH_2 and -COOH, for grafting needed functionalities (Li et al., 2014a, 2018). Moreover, these reported phase transfer processes are often in company with several fold UCL intensity decrease in UCNPs. It is still of importance to develop a simple and rapid approach to make OA-capped UCNPs hydrophilic and be open-modified for further functionalization.

Since the 1987 Nobel Prize in supramolecular chemistry, supramolecular recognition and self-assembly have been paid increased attentions in both scientific and technological developments (Yang et al., 2014; Mattia and Otto, 2015; Lehn, 2017). Cyclodextrin (CD), a water-soluble cyclic supramolecule, has a rigid well-defined ring structure and is able to firmly bind to some particular low-molecular-weight compounds, endowing these compounds new physiochemical properties (Harada, 2001; Descalzo et al., 2006). Indeed, recent results show that CD and its derivatives are able to form supramolecular complexes with OA molecules, providing possibilities for nanocrystal surface treatment to control their dispersibility properties (Wang et al., 2003; Liu et al., 2011a; Omer et al., 2011). Compared with commonly used surface treatment methods, the method of CD modification is simple and prompt (only needs ultrasonication for several minutes), leaving the pristine ligands anchored on UCNPs surface intact. As a result, this surface treatment method could avoid the formation of surface defects for energy trapping that typically leads to the decrease of UCL quantum yield.

In this work, we synthesized amino modified β-cyclodextrin (amino-β-CD) and then applied it to OA-capped UCNPs of varying type (different sizes, various types of lanthanide dopants, and core-shell structure), enabling them water-soluble and open-modified for functionalization. The interaction between the host molecule of amino-β-CD and the guest surface molecule of OA allowed a prompt, stable, and straightforward self-assembly of amino-β-CD onto the surface of UCNPs through ultrasonication of 2–4 min. Experimental results showed that the morphology, crystallographic phase, and UCL intensity of UCNPs are retained to a maximum. Importantly, the amino groups contained in the surface CD molecules allow to introduce a carboxylic-containing dye (Cy 7.5) onto the nanocrystal surface that can sensitize the nanocrystal to enhance its UCL by ∼4,820 fold when excited at ∼808 nm.

MATERIALS AND METHODS

Reagents And Apparatus

Oleic acid (OA) and 1-octadecene (ODE) were purchased from Sigma Aldrich (USA). Rare earth chloride hexahydrate ($YCl_3{\cdot}6H_2O$ 99.9%, $YbCl_3{\cdot}6H_2O$ 99.9%, $ErCl_3{\cdot}6H_2O$ 99.9%, $TmCl_3{\cdot}6H_2O$ 99.9%, and $HoCl_3{\cdot}6H_2O$ 99.9%), rare earth nitrates ($Y(NO_3)_3{\cdot}6H_2O$ 99.9%, $Yb(NO_3)_3{\cdot}5H_2O$ 99.9%, and $Er(NO_3)_3{\cdot}5H_2O$ 99.9%), sodium oleate, ammonium hydroxide, β-CD, epoxy chloropropane, neutral alumina (100–200 mesh), and sodium fluoride (NaF) were from Aladdin (Shanghai, China). Hexane, methanol, ethanol, sodium hydroxide (NaOH), and ammonium fluoride (NH_4F) were purchased from Xilong Scientific Co., Ltd (Guangdong, China). Yttrium oleate was prepared according to a method in a literature (Park et al., 2004). All the reagents were used without further purification.

The transmission electron microscope (TEM) images were acquired with a 100 CX II TEM microscope (JEM, Japan). Fourier transform infrared (FTIR) spectra were recorded on a Nicolet AVATAR360 FTIR spectrometer (Thermo Nicolet Corporation, USA). Luminescence spectra were obtained at a FLAME-T-VIS-NIR Spectrometer Assembly (Ocean Optics, USA) with an excitation from a ∼980 or 808 nm diode laser (CNI, Changchun). The integration time for the spectrometer was set to 600 ms, while the power of 980 and 808 nm laser was set to 400 and 300 mW, respectively, for all pertinent optical experiments. ^1H nuclear magnetic resonance (NMR) spectra were recorded on Bruker Avance 500 (500 MHz, USA). Luminescence lifetimes were recorded on the FLS 980 transient fluorescence spectrometer (Edinburgh Instruments, England).

Preparation of $NaYF_4$: Yb, Er UCNPs

Preparation of Small Size (6 nm) $NaYF_4$: 30%Yb, 2%Er UCNPs

Small size $NaYF_4$: 30%Yb, 2%Er UCNPs (6 nm) were synthesized according to a previous procedure with modifications (Rinkel et al., 2016). Typically, 1.59 g of rare earth oleates (Y, Yb and Er oleates with a molar ratio of 0.68: 0.3: 0.02) and 4.06 g of sodium oleate were firstly combined with 20 mL OA and 20 mL octadecene in a 100 mL three neck flask. The mixture was degassed for 1 h at 100°C under Ar atmosphere and vigorous

stirring. Then, 0.68 g of NH_4F was added to the solution, which maintained at 100°C for 30 min with Ar atmosphere protection. Subsequently, the reaction mixture containing sodium oleate, rare-earth oleates and NH_4F in a molar ratio of 8:1:11 was heated to 300°C with a heating rate of 16°C/min, and then kept at this temperature for 30 min. After cooling to room temperature, excess ethanol was added to the solution to precipitate the nanocrystals, followed by centrifugation at 10,000 rpm/min for 5 min. The collected precipitate was redispersed in a small amount of hexane, and then precipitated again with ethanol. Finally, the resultant UCNPs were collected with centrifugation and redispersed in 10 mL hexane.

Preparation of Middle Size (42 nm) $NaYF_4$: 30%Yb, 2%Er UCNPs

Middle size $NaYF_4$: 30%Yb, 2%Er particles (42 nm) were synthesized as follows: 0.2063 g $YCl_3.6H_2O$, 0.1162 g $YbCl_3.6H_2O$, and 0.0076 g $ErCl_3.6H_2O$ (Y, Yb and Er chlorides in a molar ratio of 0.68: 0.3: 0.02) were mixed with 9 mL OA and 15 mL octadecene in a 100 mL three neck flask. The slurry mixture was heated to 150°C and kept for 30 min to form a transparent solution under Ar flow protection. Then the mixture was cooled down to 50°C, followed by addition of 10 mL methanol containing 0.1482 g NH_4F and 0.1000 g NaOH, and then stirred for 30 min. Subsequently, the mixture was heated to 80°C and kept at this temperature for 30 min in order to evaporate methanol. Then the mixture was heated to 300°C with a rate of 15°C/min under Ar flow, and maintained at 300°C for 60 min. After cooling to room temperature, excess ethanol was added to the solution to precipitate the nanocrystals, followed by centrifugation at 6,000 rpm/min for 5 min. The precipitate was collected and redispersed in a small amount of hexane, and then precipitated again with ethanol. Finally, the particles were separated by centrifugation and redispersed in 10 mL hexane.

Preparation of Large Size (400 nm) $NaYF_4$: 30%Yb, 2%Er UCNPs

Firstly, 1.0846 g NaOH was mixed with 4 mL H_2O, 12 mL OA, and 6 mL ethanol, and stirred for 30 min. Then, a certain amount of rare earth nitrates (Y, Yb, and Er nitrates in a molar ratio of 0.68: 0.3: 0.02) were added into the mixture and stirred for another 10 min. Subsequently, 4 mL NaF (1.25 M) solution was added and stirred for 30 min. Finally, the solution was transferred to a stainless Teflon autoclave (50 mL), sealed, and heated at 180°C for 24 h. After cooling to room temperature, excess ethanol was added to the solution to precipitate UCNPs, followed by centrifugation at 6,000 rpm/min for 5 min. The precipitate was then redispersed in a small amount of hexane, and precipitated again with ethanol. Finally, the resultant particles were separated by centrifugation and redispersed in 10 mL hexane.

Preparation of Middle Size (42 nm) $NaYF_4$: Yb, X (X = Er, Tm, and Ho) UCNPs

The synthesis procedures are similar with the one of middle size $NaYF_4$: Yb, Er particle. A total amount of 1 mmol rare earth chloride hexahydrate (Y+Yb+X, X = Er, Tm, and Ho) were mixed with 9 mL OA and 15 mL octadecene. The slurry mixture was heated to 150°C and kept for 30 min to form a transparent solution under Ar flow. Then the mixture was cooled down to 50°C, followed by addition of 10 mL methanol containing 0.1482 g NH_4F and 0.1000 g NaOH, and stirred for 30 min. The mixture was then heated to 80°C and kept for 30 min in order to evaporate methanol. Subsequently, the solution was heated to 300°C with a rate of 15°C/min under Ar flow, and maintained at 300°C for 60 min. After naturally cooling to room temperature, excess ethanol was added to precipitate the nanocrystals followed by centrifugation at 6,000 rpm/min for 5 min. The precipitate was then redispersed in a small amount of hexane and precipitated again with ethanol. Finally, the particles were separated by centrifugation and redispersed in 10 mL hexane.

Preparation of Middle Size Core-Shell (64 nm) $NaYF_4$: Yb, Er@$NaYF_4$ UCNPs

The middle size core particles (42 nm) of $NaYF_4$: Yb, Er were synthesized using the above-mentioned procedure. The coating procedure of the inert shell layer of $NaYF_4$ was described as follows. First, 0.5 mmol of yttrium hexhydrate chloride was mixed with 9 mL OA and 15 mL octadecene in a 100 mL three necked flask. The slurry mixture was then heated to 150°C and kept at this temperature for 30 min to form a transparent solution under Ar atmosphere protection. Subsequently, the mixture was cooled down to 50°C, followed by addition of 10 mL methanol containing 0.0741 g NH_4F and 0.0500 g NaOH, and 10 mL hexane containing the 42 nm core $NaYF_4$:Yb, Er particles. After magnetic stirring at this temperature for 30 min, the mixture was heated to 80°C and kept at this temperature for 30 min to evaporate methanol. The mixture was then heated to 300°C with a rate of 15°C/min under Ar atmosphere protection, and maintained at this temperature for 60 min. After cooling to room temperature, excess ethanol was added to precipitate the nanocrystals from the mixture, followed by centrifugation at 6,000 rpm/min for 5 min. The precipitate was redispersed in a small amount of hexane and then precipitated with addition of excessive ethanol. Finally, the particles were collected by centrifugation and redispersed in 10 mL hexane.

Preparation Of Amino-β-CD

As shown in **Figure 1a**, the epoxy chloropropane was used to crosslink the amino group and the β-CD in a dilute alkali solution. The procedure to prepare amino modified β-CD is described as follows. Firstly, 8.1 g β-CD and 6.7 g KOH were added into 70 mL H_2O, which was kept stirring until β-CD was completely dissolved. The resultant mixture was then heated to 50°C, to which 3.4 g ammonium hydroxide and 10.2 g epoxy chloropropane were added in order. Subsequently, the mixture solution was heated to 60°C and maintained at this temperature for 1 h. When completing the reaction, the pH of the solution was first adjusted to 5–6, and then 150 mL ethanol was poured into the solution at room temperature. The final product was purified via neutral alumina column, using an eluent of 60% ethanol. The resultant mixture was concentrated to 30 mL by evaporating redundant ethanol, followed by adding a large amount of absolute

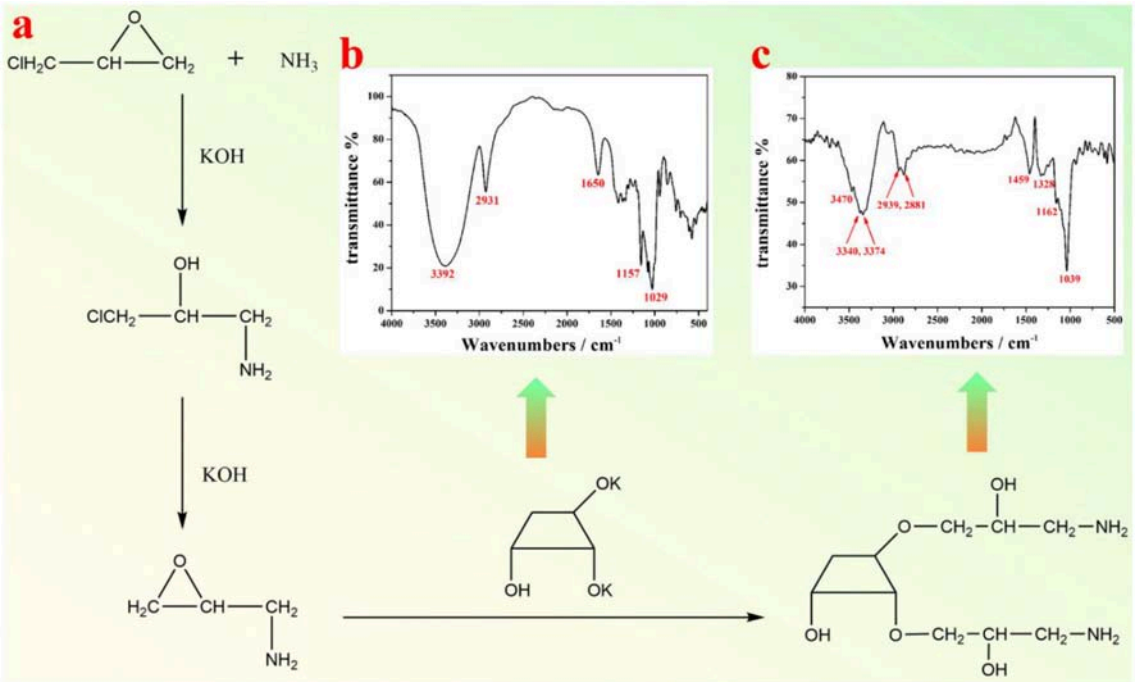

FIGURE 1 | (a) A schematic illustration of synthesis of amino-β-CD; FTIR spectra of **(b)** β-CD, and **(c)** amino-β-CD.

methanol and placed overnight. Finally, the amino-β-CD product was filtrated and dried in vacuum.

FTIR spectra of pristine β-CD (**Figure 1b**) and amino functionalized β-CD (**Figure 1c**) were both measured. As shown in **Figure 1b**, the bands at 2,931 cm^{-1} and 1,334–1,440 cm^{-1} represent the stretching and bending vibration of alkane (C-H). The bands at 3,392 and 1,650 cm^{-1} represent the stretching and bending vibration of O-H, and the bands at 1,029 and 1,157 cm^{-1} are both from the stretching vibration of C-O. After amino group modification, the vibration bands of O-H and C-H are both changed (move or split, **Figure 1c**), which are possibly due to the influence of linked amino alkane. Furthermore, the bending vibrations of O-H at 1,650 cm^{-1} and the stretching vibration of C-O at 1,157 cm^{-1} almost disappear, since the -OH group has been replaced by the amino alkane group. The appearance of the stretching vibration of the N-H group at 3,470 cm^{-1} clearly indicates the presence of amino group, and thus the successful preparation of amino-β-CD. The NMR spectrum of amino functionalized β-CD was shown in **Figure S1**. ^{1}H NMR of amino-β-CD (500 MHz, DMSO-d_6) δ 8.84 (s, 4H), 7.49 (s, 1H), 7.39 (s, 1H), 7.28 (s, 1H), 5.78–5.71 (m, 4H), 5.59 (s, 2H), 5.03 (s, 6H), 4.84 (s, 3H), 4.58 (s, 6H), 4.03 (s, 2H), 3.99–3.94 (m, 1H), 3.87 (s, 2H), 3.69 (s, 15H), 3.63 (s, 12H), 3.56 (s, 3H), 3.36 (ddt, J = 31.8, 15.0, 6.9 Hz, 14H), 3.23–3.16 (m, 21H), 3.00 (s, 1H), 2.87 (s, 2H).

Surface Modification of OA-Capped UCNPs With Amino-β-CD

Surface treatment of OA-capped UCNPs was realized through an OA-targeting supermolecular self-assembly of amino-β-CD on to the nanoparticle surface (consult **Figure 2a**). In a typical procedure, a certain amount (1 mL) of as-prepared UCNPs in hexane (concentration of 10 mg/mL) were dispersed in 10 mL water solution containing amino-β-CD (10 mg/mL) and 0.06 M hydrochloric acid. The mixture was ultrasonically treated for 2–4 min at room temperature. Note that, longer ultrasound time is needed for smaller sized particles (6 nm). Finally, the resultant mixture was centrifugally separated to collect the product, which was then washed three more times with 10 mL deionized water, and finally stored in 5 mL deionized water.

Attachment of Cy 7.5 to Amino-β-CD Modified $NaYF_4$: Yb, Er UCNPs

The attachment of near infrared Cy 7.5 dye to the surface of amino β-CD modified $NaYF_4$: Yb, Er UCNPs was realized through direct formation of a covalent amide bond between the carboxyl group of Cy 7.5 dye and the amino moiety of amino β-CD, with presence of cross-linking reagents (EDC/NHS) (consult **Figure 5A**). Specifically, 100 μL of Cy 7.5 dye water solution (2 mg/mL) was added into 1 mL water solution containing EDC (400 mM) and NHS (100 mM), which was freshly prepared before the use for activation of the carboxyl group for 2 h. Then, 2 mL of amino-β-CD modified UCNPs (10 mg/mL) water solution were added to the activated Cy 7.5 solution, and stirred for 4 h at room temperature. Finally, the resultant mixture was centrifugally separated to collect the product, followed by washing three times with 10 mL dimethyl formamide (DMF), and then stored in 5 mL DMF for measurements.

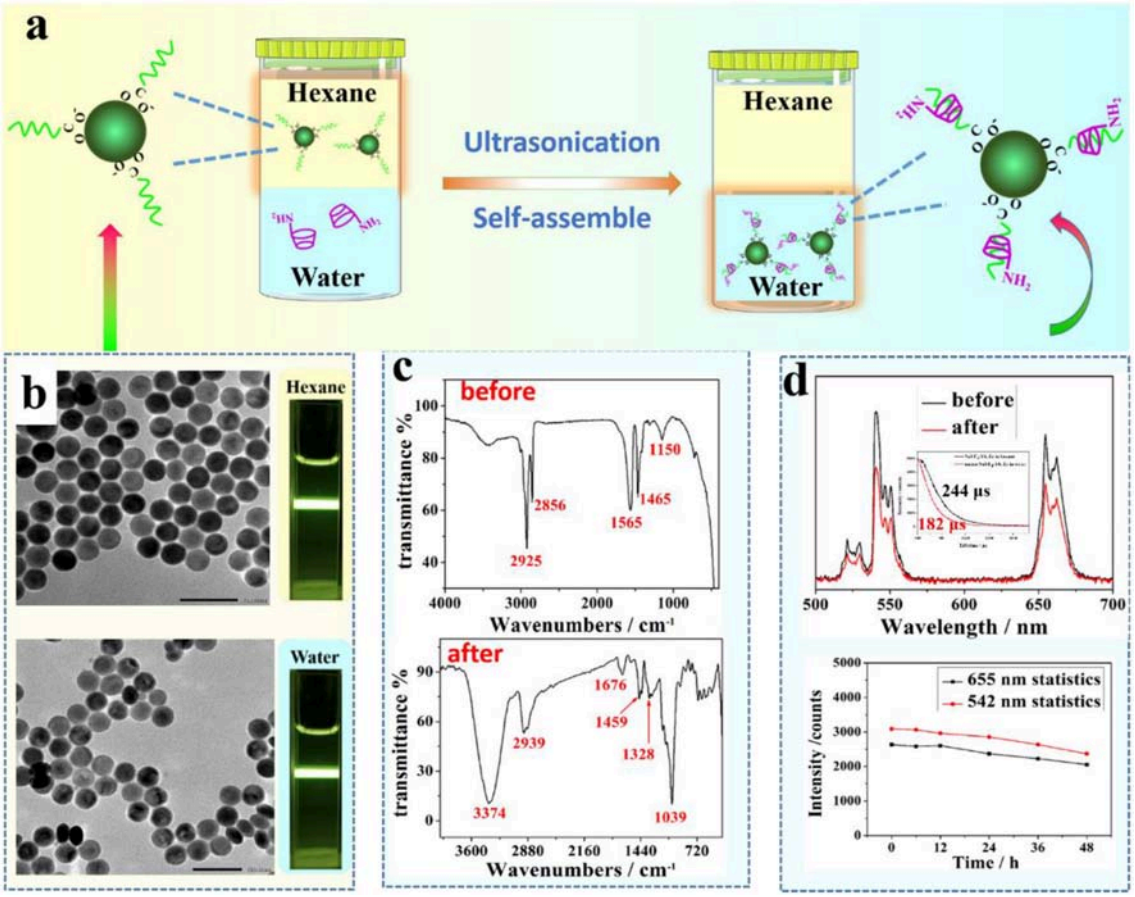

FIGURE 2 | (a) A schematic illustration of the phase transfer process of UCNPs from hexane to water; **(b)** TEM images of $NaYF_4$:Yb, Er UCNPs before (upper figure) and after (bottom figure) surface treatment, **(c)** FTIR spectra of UCNPs before (upper figure) and after (bottom figure) surface treatment with amino-β-CD; **(d)** A comparison of UCL spectra of $NaYF_4$:Yb, Er UCNPs before and after surface treatment (upper figure); The inert is the relevant lifetime changes. an evaluation of water stability of amino-β-CD modified UCNPs through monitoring UCL peak change at 655 and 542 nm over a period of time (bottom figure).

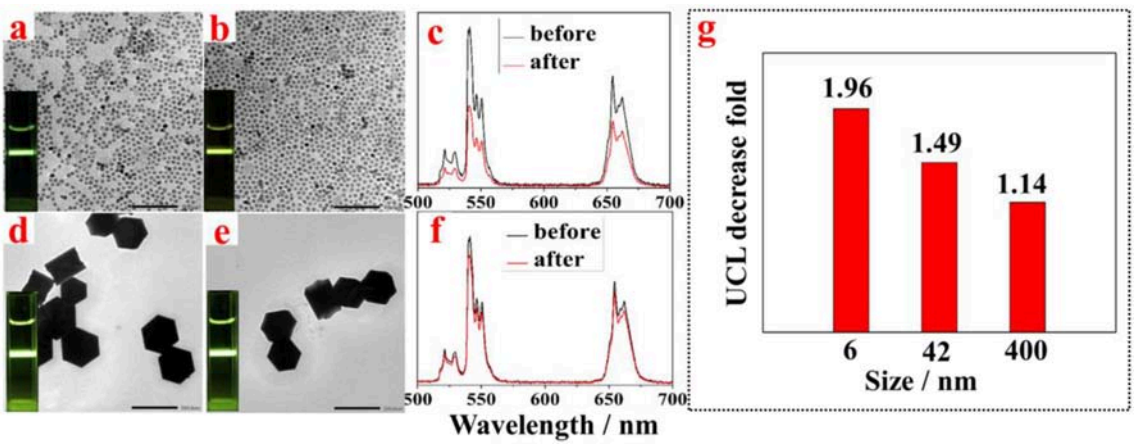

FIGURE 3 | TEM images of $NaYF_4$:Yb, Er UCNPs with small size before **(a)** and after **(b)** surface treatment, and with large size before **(d)** and after **(e)** surface treatment; the corresponding UCL spectra from $NaYF_4$:Yb, Er UCNPs with **(c)** small size and **(f)** before and after surface treatment; **(g)** The observed UCL decrease fold vs. the size of $NaYF_4$:Yb, Er UCNPs after surface treatment with amino-β-CD.

RESULTS AND DISCUSSION

Figure 2 shows the result of surface treatment of middle size $NaYF_4$:Yb, Er UCNPs (42 nm) with amino-β-CD through ultrasonication of two min. An intercalation of the long alky chain of OA molecules with the rigid ring of β-CD allows a stable attachment of amino-β-CD molecules to the nanocrystal surface (**Figure 2a**). The hydrophilicity of amino-β-CD, therefore, imparts a phase transfer of hydrophobic OA-capped UCNPs from organic phase (hexane) in the upper layer to aqueous phase at the bottom. A successful phase transfer can be indicated by an observation of strong UCL from surface-treated UCNPs in an aqueous dispersion (**Figure 2b**). To further demonstrate the successful phase transfer, we acquired FTIR spectra of UCNPs before and after amino-β-CD surface treatment (**Figure 2c**). Before surface treatment, the bands at 2,856/2,925 cm^{-1} and 1,465 cm^{-1} are from the stretching and bending vibration of alkane (C-H), while the bands at 1,150 and 1,565 cm^{-1} represent the stretching vibration of C-O and C=O groups, arising from the OA ligand molecule on the surface. After surface modification, the vibration bands of OA at both 1,150 and 1,565 cm^{-1} nearly disappear, being attributed to the host-guest intercalation of the amino-β-CD and the OA molecule. In addition, the characteristic vibration bands at 1,039, 1,328, 1,459, 2,939, and 3,374 cm^{-1} of amino-β-CD molecule (**Figure 1**), emerges after surface treatment, which indicates the successful attachment of amino-β-CD molecules onto the surface of OA-capped UCNPs.

The amino-β-CD surface treatment procedure does not produce overt effects on UCNPs size and morphology, as the $NaYF_4$:Yb, Er UCNPs, before and after treatment, are both shown to be spherical with a narrow size distribution of about 42 nm (**Figure 2b**). In addition, UCL spectra of the middle size UCNPs before (dispersed in hexane) and after (dispersed in water) amino-β-CD treatment were acquired and shown in **Figure 2d**. The UCL peaks at 525/542 and 655 nm, located in the visible spectral region, correspond to the $^2H_{11/2}/^4S_{3/2} \rightarrow {}^4I_{15/2}$, and $^4F_{9/2} \rightarrow {}^4I_{15/2}$ transitions of Er^{3+} ions, respectively, in good agreement with previously reported results (Chen et al., 2014). In addition, after phase transfer to water, the lifetime of $NaYF_4$:Yb, Er UCNPs slightly decreases from 244 to 182 μs, implying that the integrity of prestine surface was largely retained (**Figure 2d**). The UCL intensity remain almost undiminished after the phase conversion from hexane to water, showing a slight decrease of 1.5 fold. This conclusion can also be suggested from a direct comparison of UCL photographic images in both hexane and water (**Figure 2b**). To investigate the stability of amino-β-CD modified UCNPs, room temperature UCL spectra of these surface-treated UCNPs were measured at different time points (0, 6, 12, 24, 36, and 48 h) over a period of 2 days. As shown in the bottom of **Figure 2d**, the luminescence intensities of Er at 542 and 655 nm were merely slightly decreased with an increase of time, and retained about 90% of UCL intensity for up to 2 days, demonstrating the good stability of amino-β-CD surface-treated UCNPs. The amino-CD modified nanoparticles also showed good photostability using 400 mW 980 nm laser illuminated for 30 min (**Figure S2**),

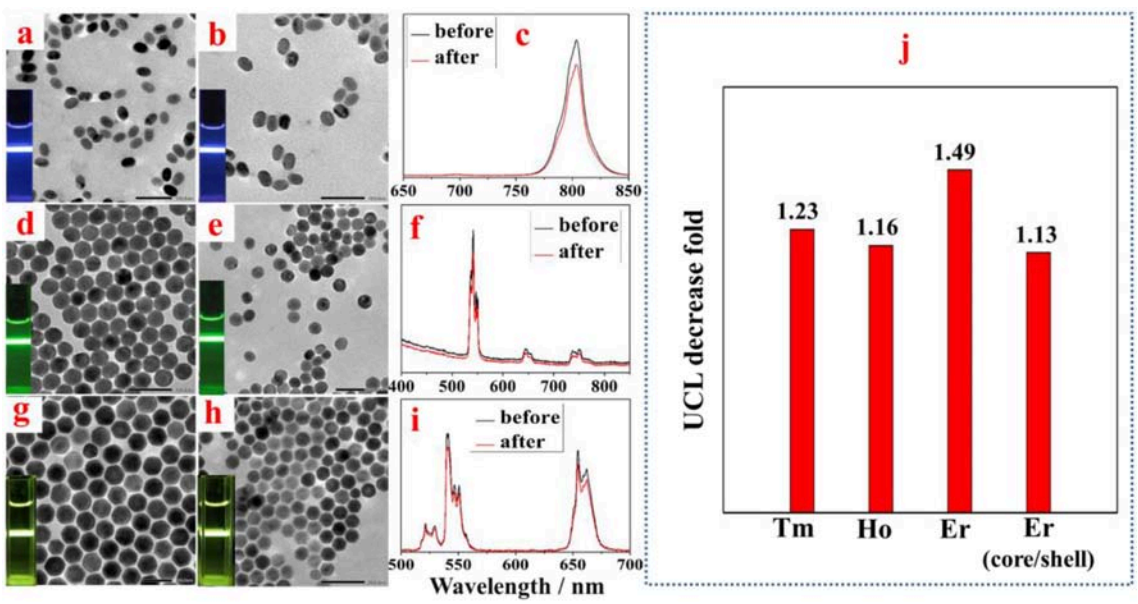

FIGURE 4 | TEM images of middle size $NaYF_4$:Yb,Tm **(a,b)**, $NaYF_4$:Yb, Ho **(d,e)**, and core-shell $NaYF_4$:Yb, Er@$NaYF_4$ UCNPs **(g,h)** before and after surface treatment. The corresponding UCL spectra from $NaYF_4$:Yb,Tm **(c)**, $NaYF_4$:Yb, Ho **(f)**, and core-shell $NaYF_4$:Yb, Er@$NaYF_4$ UCNPs **(i)**, respectively. The column graph data in **(j)** depicts a comparison of surface treatment induced UCL decrease fold for UCNPs doped with different activators (Tm, Ho, and Er) or with core/shell structure.

and great chemical stability when aged in water for 12 h (**Figure S3**).

To test whether the described approach can be valid for small and large OA-capped UCNPs, we synthesized UCNPs of small size (6 nm) and large size (400 nm) and implemented the phase transfer procedure. TEM images of the $NaYF_4$:Yb, Er UCNPs of small and large size UCNPs before and after amino-β-CD modification are correspondingly shown in **Figures 3a,b,d,e**, respectively. As expected, no overt changes of morphology and size were observed. UCNPs of both small and large sizes were successfully transferred into aqueous phase, displaying intense UCL in water (small size, the inset of **Figure 3b**; large size, the inset of **Figure 3e**). The UCL intensity from UCNPs of both sizes (small size, **Figure 3c**; large size, **Figure 3f**) were almost retained. This can also be seen from a comparison of UCL photographic images before and after phase transfer (small size, the inset of **Figure 3a** vs. **Figure 3b**; large size, the inset of **Figure 3d** vs. **Figure 3e**). Note that the fold of surface treatment induced UCL decrease diminishes with an increase of the size of UCNPs, from ∼2 fold for 6 nm UCNPs to ∼1.1 fold for 400 nm UCNPs (**Figure 3g**). This observation possibly stems from the decreased surface to volume ratio with an increase of particle size. It is known that the large surface to volume ratio can produce pronounced UCL quenching effect, as a large number of rare earth ions will be exposed to surrounding quenching centers (surface defects, high energy vibrations from ligands and solvents) (Chen et al., 2014). As a result, after phase transfer, smaller size UCNPs with larger surface to volume ratio are more prone to be quenched by water molecules from solvent, thus resulting in higher UCL decrease. However, it should be noted that the observed maximum UCL decrease is merely 2 fold for small size UCNPs (6 nm). This result indicates that the intercalation of amino-β-CD to the surface of OA-capped UCNPs is able to retain the integrity of pristine particles, without creating noticeable surface defects for substantial UCL quenching that were commonly seen in literature- reported phase transfer methods.

To investigate the effect of amino-β-CD treatment on the UCL of other types of UCNPs, we prepared a set of middle size (42 nm) UCNPs with different emission bands and with a core/shell structure (core 42 nm, core-shell 64 nm). As shown in **Figure 4**, TEM images of $NaYF_4$:Yb, X (X = Tm, or Ho) UCNPs (42 nm) and $NaYF_4$:Yb, Er@$NaYF_4$ core-shell UCNPs (64 nm) before and after amino-β-CD modification present no identifiable changes on the morphologies and sizes, as expected. In addition, no spectral and relative intensities changes were observed for both $NaYF_4$:Yb, X (X = Tm, or Ho) UCNPs and $NaYF_4$:Yb, Er@$NaYF_4$ core-shell UCNPs after surface modification with amino-β-CD. The UCL intensities show a slight decrease after the conversion from hexane to water, which can be ascribed to the quenching effect induced by energetic hydroxyl (-OH) group of water molecules. However, it should be noted that the UCL quenching fold for middle size (42 nm) $NaYF_4$:Yb, Tm and $NaYF_4$:Yb, Ho are both about 1.2, a little smaller than the 1.5 fold for middle size (42 nm) $NaYF_4$:Yb, Er, presenting negligible quenching effect (**Figure 4j**). Importantly, the UCL quenching fold for the $NaYF_4$:Yb, Er@$NaYF_4$ core-shell UCNPs is just 1.1 fold, displaying almost identical UCL intensity before and after amino-β-CD treatment. This indicates that the aqueous environment produces no quenching effect for UCL from the core/shell structure UCNPs, which can possibly be due to the spatial isolation of the core from the surrounding environment.

The amino group on the surface of lanthanide-doped nanocrystals provide numerous open-modified opportunities for further functionalizations through a covalent linkage of functional molecules, such as dye, protein, and ribonucleic acid. As a proof-of-concept experiment, a type of carboxyl group functionalized near infrared dye (Cy 7.5) was linked onto the surface of $NaYF_4$:Yb, Er UCNPs through formation of an amide bond with the amino group contained in amino-β-CD on the nanocrystal surface (**Figure 5a**). It has been shown that organic dye sensitization is promising to solve the weak and narrow absorption problem of lanthanide-doped UCNPs, as the absorption of an organic dye is three orders of magnitude higher than that of a lanthanide ion. After light absorption, efficient nonradative energy transfer from organic dyes to the ytterbiurm (Yb) ions on the nanocrystal surface can empower an efficient photon upconversion through well-established Yb-X (X = Er, Ho, Tm) interactions, here X = Er (Chen et al., 2015; Wang et al., 2017). The β-CD modified $NaYF_4$:Yb, Er UCNPs without Cy 7.5 dyes served as a control sample. As shown in **Figure 5b**, under an excitation at 808 nm, the Cy 7.5 linked-$NaYF_4$:Yb, Er UCNPs exhibit intense UCL with characteristic peaks of Er at 542 and 655 nm, in marked contrast

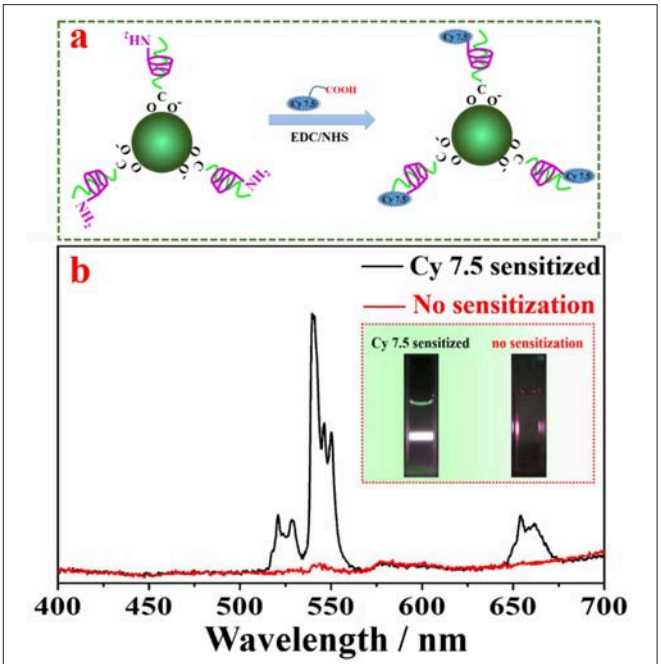

FIGURE 5 | (a) A schematic illustration of grafting Cy 7.5 dyes to the surface of UCNPs; **(b)** UCL spectra of $NaYF_4$:Yb, Er UCNPs with and without Cy 7.5 dyes on the nanocrystal surface, showing UCL enhancement of ∼4,820 fold due to the antenna effect of the grafted dye.

to none UCL from the control sample. The sensitization effect can take place through either covalently linked dyes or non-covalently linked dyes. We estimated about 80% sensitization enhancement originates from the covalent linkage of Cy 7.5 dyes (**Figure S4**). In addition, we calculated that the integrated UCL from Cy 7.5 dye-modified UCNPs in the spectral range of 400–700 nm was about ∼4,820 fold higher than that of UCL from the control sample. This significant UCL enhancement can be clearly discerned from the photographic UCL images (the inset of **Figure 5b**), which unambiguously originated from the sensitization of the $NaYF_4$:Yb, Er UCNPs by the linked Cy 7.5 dye on the UCNPs surface.

CONCLUSIONS

In summary, we have developed a simple approach for prompt conversion of hydrophobic lanthanide-doped UCNPs, commonly capped with OA ligand, to be water-soluble and open-modified for functionalization, based on OA-targeting supramolecular self-assembly of amino-β-CD. This method was shown to be valid for UCNPs with a broad spectrum of sizes (6–400 nm), a set of rare earth dopants (Yb/Er, Yb/Ho, and Yb/Tm), as well as core-shell structure through ultrasonication of 2–4 min. Importantly, UCL intensities from surface treated UCNPs were almost identical to their parent OA-capped UCNPs. Moreover, these amino-β-CD modified UCNPs were found to be stable over 48 h without overt diminishment of their UCL intensities. The amino group on the surface of resultant amino-β-CD modified UCNPs creates opportunities to graft other functionalities, as exemplified here, by a covalent linkage of the carboxylic-containing dye (Cy 7.5) to the surface, which sensitizes 42 nm $NaYF_4$:Yb/Er UCNPs, enhancing their UCL by ∼4,820 fold (when excited at 808 nm). The described approach here holds great promise for surface treatment of other kinds of OA or OA-analogs capped inorganic nanocrystals, fostering their applications in nanomedicine and theranostics.

AUTHOR CONTRIBUTIONS

XW and GC conceived the idea and designed the investigation. XW contributed to the synthesis and characterization of the materials. XW and GC analyzed the data and wrote the manuscript. All authors approved the submitted version.

ACKNOWLEDGMENTS

This work was supported in part by the grants from the National Natural Science Foundation of China (51672061), and the Fundamental Research Funds for the Central Universities, China (HIT. BRETIV.201503).

SUPPLEMENTARY MATERIAL

The Supplementary Material for this article can be found online at: https://www.frontiersin.org/articles/10.3389/fchem.2019.00161/full#supplementary-material

REFERENCES

Camli, S. T., Buyukserin, F., Balci, O., and Budak, G. G. (2010). Size controlled synthesis of sub-100 nm monodisperse poly(methylmethacrylate) nanoparticles using surfactant-free emulsion polymerization. *J. Colloid Interface Sci.* 344, 528–532. doi: 10.1016/j.jcis.2010.01.041

Chen, G., Damasco, J., Qiu, H., Shao, W., Ohulchanskyy, T. Y., Valiev, R. R., et al. (2015). Energy-cascaded upconversion in an organic dye-sensitized core/shell fluoride nanocrystal. *Nano Lett.* 15, 7400–7407. doi: 10.1021/acs.nanolett.5b02830

Chen, G., Qiu, H., Prasad, P. N., and Chen, X. (2014). Upconversion nanoparticles: design, nanochemistry, and applications in theranostics. *Chem. Rev.* 114, 5161–5214. doi: 10.1021/cr400425h

Chen, G., Roy, I., Yang, C., and Prasad, P. N. (2016). Nanochemistry and nanomedicine for nanoparticle-based diagnostics and therapy. *Chem. Rev.* 116, 2826–2885. doi: 10.1021/acs.chemrev.5b00148

Chen, Z., Chen, H., Hu, H., Yu, M., Li, F., Zhang, Q., et al. (2008). Versatile synthesis strategy for carboxylic acid–functionalized upconverting nanophosphors as biological Labels. *J. Am. Chem. Soc.* 130, 3023–3029. doi: 10.1021/ja076151k

Dai, Y., Yang, D., Ma, P. A., Kang, X., Zhang, X., Li, C., et al. (2012). Doxorubicin conjugated NaYF4:Yb^{3+}/Tm^{3+} nanoparticles for therapy and sensing of drug delivery by luminescence resonance energy transfer. *Biomaterials* 33, 8704–8713. doi: 10.1016/j.biomaterials.2012.08.029

Danhier, F., Ansorena, E., Silva, J. M., Coco, R., Le Breton, A., and Préat, V. (2012). PLGA-based nanoparticles: an overview of biomedical applications. *J. Control. Release* 161, 505–522. doi: 10.1016/j.jconrel.2012.01.043

Descalzo, A. B., Martínez-Máñez, R., Sancenón, F., Hoffmann, K., and Rurack, K. (2006). The supramolecular chemistry of organic-inorganic hybrid materials. *Angew. Chem. Int. Ed.* 45, 5924–5948. doi: 10.1002/anie.200600734

Gnanasammandhan, M. K., Idris, N. M., Bansal, A., Huang, K., and Zhang, Y. (2016). Near-IR photoactivation using mesoporous silica-coated NaY[F.sub.4]:Yb,Er/Tm upconversion nanoparticles. *Nat. Protoc.* 11, 688–713. doi: 10.1038/nprot.2016.035

Harada, A. (2001). Cyclodextrin-based molecular machines. *Acc. Chem. Res.* 34, 456–464. doi: 10.1021/ar000174l

Lee, J., Yoo, B., Lee, H., Cha, G. D., Lee, H.-S., Cho, Y., et al. (2017). Ultra-wideband multi-dye-sensitized upconverting nanoparticles for information security application. *Adv. Mater.* 29:1603169-n/a. doi: 10.1002/adma.201603169

Lehn, J.-M. (2017). Supramolecular chemistry: where from? Where to? *Chem. Soc. Rev.* 46, 2378–2379. doi: 10.1039/C7CS00115K

Li, J., Jiu, T., Tao, G. H., Wang, G., Sun, C., Li, P., et al. (2014a) Manipulating surface ligands of Copper Sulfide nanocrystals: synthesis, characterization, and application to organic solar cells. *J. Colloid Interface Sci.* 419, 142–147. doi: 10.1016/j.jcis.2013.12.057

Li, J., Kuang, C., Zhao, M., Zhao, C., Liu, L., Lu, F., et al. (2018). Ternary CuZnS nanocrystals: synthesis, characterization, and interfacial application in perovskite solar cells. *Inorg. Chem.* 57, 8375–8381. doi: 10.1021/acs.inorgchem.8b01030

Li, X., Zhou, L., Wei, Y., El-Toni, A. M., Zhang, F., and Zhao, D. (2014b). Anisotropic growth-induced synthesis of dual-compartment janus mesoporous silica nanoparticles for bimodal triggered drugs delivery. *J. Am. Chem. Soc.* 136, 15086–15092. doi: 10.1021/ja508733r

Liu, B., Deng, X., Xie, Z., Cheng, Z., Yang, P., and Lin, J. (2017). Thiol-ene click reaction as a facile and general approach for surface functionalization of colloidal nanocrystals. *Adv. Mater.* 29:1604878-n/a. doi: 10.1002/adma.201604878

Liu, J., Bu, W., Pan, L., and Shi, J. (2013). NIR-triggered anticancer drug delivery by upconverting nanoparticles with integrated azobenzene-modified mesoporous silica. *Angew. Chem. Int. Ed.* 52, 4375–4379. doi: 10.1002/anie.201300183

Liu, Q., Chen, M., Sun, Y., Chen, G., Yang, T., Gao, Y., et al. (2011a). Multifunctional rare-earth self-assembled nanosystem for tri-modal upconversion luminescence/fluorescence/positron emission tomography imaging. *Biomaterials* 32, 8243–8253. doi: 10.1016/j.biomaterials.2011.07.053

Liu, Q., Sun, Y., Yang, T., Feng, W., Li, C., and Li, F. (2011b). Sub-10 nm hexagonal lanthanide-doped NaLuF4 upconversion nanocrystals for sensitive bioimaging *in vivo*. *J. Am. Chem. Soc.* 133, 17122–17125. doi: 10.1021/ja207078s

Mattia, E., and Otto, S. (2015). Supramolecular systems chemistry. *Nat. Nano*. 10, 111–119. doi: 10.1038/nnano.2014.337

Omer, M., Haider, S., and Park, S.-Y. (2011). A novel route for the preparation of thermally sensitive core-shell magnetic nanoparticles. *Polymer* 52, 91–97. doi: 10.1016/j.polymer.2010.11.011

Park, J., An, K., Hwang, Y., Park, J.-G., Noh, H.-J., Kim, J.-Y., et al. (2004). Ultra-large-scale syntheses of monodisperse nanocrystals. *Nat. Mater.* 3, 891–895. doi: 10.1038/nmat1251

Rinkel, T., Raj, A. N., Dühnen, S., and Haase, M. (2016). Synthesis of 10 nm β. SyF_4:Yb,Er/$NaYF_4$ core/shell upconversion nanocrystals with 5 nm particle cores. *Angew. Chem. Int. Ed. Engl.* 55, 1164–1167. doi: 10.1002/anie.201508838

Salinas, B., Ruiz-Cabello, J., Lechuga-Vieco, A. V., Benito, M., and Herranz, F. (2015). Surface-functionalized nanoparticles by olefin metathesis: a chemoselective approach for *in vivo* characterization of atherosclerosis plaque. *Chem. A Eur. J.* 21, 10450–10456. doi: 10.1002/chem.201500458

Shao, W., Chen, G., Kuzmin, A., Kutscher, H. L., Pliss, A., Ohulchanskyy, T. Y., et al. (2016). Tunable narrow band emissions from dye-sensitized core/shell/shell nanocrystals in the second near-infrared biological window. *J. Am. Chem. Soc.* 138, 16192–16195. doi: 10.1021/jacs.6b08973

Wang, G., Peng, Q., and Li, Y. (2011). Lanthanide-doped nanocrystals: synthesis, optical-magnetic properties, and applications. *Acc. Chem. Res.* 44, 322–332. doi: 10.1021/ar100129p

Wang, X., Valiev, R. R., Ohulchanskyy, T. Y., Agren, H., Yang, C., and Chen, G. (2017). Dye-sensitized lanthanide-doped upconversion nanoparticles. *Chem. Soc. Rev.* 46, 4150–4167. doi: 10.1039/C7CS00053G

Wang, Y., Wong, J. F., Teng, X., Lin, X. Z., and Yang, H. (2003). "Pulling" nanoparticles into water: phase transfer of oleic acid stabilized monodisperse nanoparticles into aqueous solutions of α-cyclodextrin. *Nano Lett.* 3, 1555–1559. doi: 10.1021/nl034731j

Wei, W., Chen, G., Baev, A., He, G. S., Shao, W., Damasco, J., et al. (2016). Alleviating luminescence concentration quenching in upconversion nanoparticles through organic dye sensitization. *J. Am. Chem. Soc.* 138, 15130–15133. doi: 10.1021/jacs.6b09474

Wu, S., Han, G., Milliron, D. J., Aloni, S., Altoe, V., Talapin, D. V., et al (2009). Non-blinking and photostable upconverted luminescence from single lanthanide-doped nanocrystals. *Proc. Natl. Acad. Sci.* 106, 10917–10921. doi: 10.1073/pnas.0904792106

Yang, Y.-W., Sun, Y.-L., and Song, N. (2014). Switchable host-guest systems on surfaces. *Acc. Chem. Res.* 47, 1950–1960. doi: 10.1021/ar500022f

Zhou, H.-P., Xu, C.-H., Sun, W., and Yan, C.-H. (2009). Clean and flexible modification strategy for carboxyl/aldehyde-functionalized upconversion nanoparticles and their optical applications. *Adv. Funct. Mater.* 19, 3892–3900. doi: 10.1002/adfm.200901458

Zou, X., Xu, M., Yuan, W., Wang, Q., Shi, Y., Feng, W., et al. (2016). A water-dispersible dye-sensitized upconversion nanocomposite modified with phosphatidylcholine for lymphatic imaging. *Chem. Commun.* 52, 13389–13392. doi: 10.1039/C6CC07180E

Conflict of Interest Statement: The authors declare that the research was conducted in the absence of any commercial or financial relationships that could be construed as a potential conflict of interest.

Copyright © 2019 Wang and Chen. This is an open-access article distributed under the terms of the Creative Commons Attribution License (CC BY). The use, distribution or reproduction in other forums is permitted, provided the original author(s) and the copyright owner(s) are credited and that the original publication in this journal is cited, in accordance with accepted academic practice. No use, distribution or reproduction is permitted which does not comply with these terms.

frontiers in Chemistry

ORIGINAL RESEARCH
published: 06 November 2018
doi: 10.3389/fchem.2018.00543

Membrane-Modified Metal Triazole Complexes for the Electrocatalytic Reduction of Oxygen and Carbon Dioxide

*Skye N. Supakul and Christopher J. Barile**

Department of Chemistry, University of Nevada, Reno, NV, United States

In this manuscript, an electrochemical architecture is designed that controls the kinetics of proton transfer to metal triazole complexes for electrocatalytic O_2 and CO_2 reduction. Self-assembled monolayers of these catalysts are attached to a glassy carbon electrode and covered with a lipid monolayer containing proton carriers, which acts as a proton-permeable membrane. The O_2 reduction voltammograms on carbon are similar to those obtained on membrane-modified Au electrodes, which through the control of proton transfer rates, can be used to improve the selectivity of O_2 reduction. The improved voltage stability of the carbon platforms allows for the investigation of a CO_2 reduction catalyst inside a membrane. By controlling proton transfer kinetics across the lipid membrane, it is found that the relative rates of H_2, CO, and HCOOH production can be modulated. It is envisioned that the use of these membrane-modified carbon electrodes will aid in understanding catalytic reactions involving the transfer of multiple protons and electrons.

Keywords: electrocatalysis, carbon dioxide reduction, oxygen reduction, self-assembled monolayer, flip-flop diffusion, lipid monolayer

OPEN ACCESS

Edited by:
Nosang Vincent Myung, University of California, Riverside, United States

Reviewed by:
Syed Mubeen Jawahar Hussaini, University of Iowa, United States
Federica Valentini, Università di Roma Tor Vergata, Italy

****Correspondence:***
Christopher J. Barile
cbarile@unr.edu

Specialty section:
This article was submitted to Green and Sustainable Chemistry, a section of the journal Frontiers in Chemistry

Received: *26 July 2018*
Accepted: *19 October 2018*
Published: *06 November 2018*

Citation:
Supakul SN and Barile CJ (2018) Membrane-Modified Metal Triazole Complexes for the Electrocatalytic Reduction of Oxygen and Carbon Dioxide. Front. Chem. 6:543. doi: 10.3389/fchem.2018.00543

INTRODUCTION

The electrocatalysis of small molecules is important in a wide range of renewable energy devices (Duan et al., 2015; Zeng and Li, 2015; Zhang et al., 2017). Many of these conversion processes involve multiple proton and electron transfer steps (Mayer, 2004; Huynh and Meyer, 2007; Dai et al., 2015). For example, the electrocatalytic reduction of O_2 to water, which occurs in the cathode of fuel cells, requires the transfer of four protons and four electrons (Gewirth and Thorum, 2010). Similarly, the CO_2 reduction reaction, which can produce sustainable fuels, also requires multiple proton and electron transfer steps (Hori et al., 1985; Hori, 2008). These two reactions, along with most others requiring multiproton and multielectron transfer, are therefore mechanistically complex, both in terms of the reaction intermediates and in the range of products that are ultimately generated.

In both CO_2 reduction and the O_2 reduction reaction (ORR), the dynamics of proton transfer to catalytic sites are instrumental in dictating catalyst selectivity and performance (Hammes-Schiffer and Soudackov, 2008; Hammes-Schiffer, 2009). For small molecule electrocatalysts, several approaches have been used to interrogate the effect of proton transfer on catalysis. The most common methodology is to synthesize a group of ligands with pendant proton relays, which tune proton availability to a metal-centered catalytic core (Sjödin et al., 2005; Rosenthal and Nocera, 2007; Wenger, 2013). However, the incorporation of these proton relays often changes the steric

and electronic environment of the catalyst, which in turn alters its redox properties (McCrory et al., 2007; Thorseth et al., 2013). An alternative strategy is to bury electrocatalysts inside lipid membranes with embedded proton carriers (Hosseini et al., 2011). This approach allows for proton transfer dynamics to the catalyst to be controlled without changing the molecular identity of the catalyst (Barile et al., 2014). These electrode platforms consist of a thiol-based self-assembled monolayer (SAM) on Au electrodes that are covered by a lipid monolayer appended via Van der Waals interactions (Tse et al., 2015).

Previous results demonstrate that the incorporation of alkyl proton carriers inside the lipid layer of these electrodes can be used to control the kinetics of proton transfer to catalysts (Tse et al., 2016). In particular, the selectivity of a Cu triazole ORR catalyst can be improved using this platform such that adequately tuned proton transfer rates cause water to be the sole product generated. Unfortunately, the extension of membrane-modified thiol-based Au SAMs to other catalytic systems is limited by their narrow electrochemical stability. Thiol-based Au SAMs are not stable at highly negative potentials (Srisombat et al., 2011), which means they cannot be used to study reduction reactions with high overpotentials such as CO_2 reduction.

In this manuscript, membrane-modified carbon electrodes are designed that allow for proton transfer dynamics to electrocatalysts to be controlled and that exhibit greater electrochemical stability than their Au counterparts. The architecture developed here enables the interrogation of the membrane-modified ORR, and also the study of reactions such as the CO_2 reduction reaction, which occurs at high overpotentials.

MATERIALS AND METHODOLOGY

Chemicals were obtained from commercial sources and were not subjected to additional purification. 1,2-dimyristoyl-*sn*-glycero-3-phosphocholine (DMPC) lipid was obtained from Avanti Polar Lipids, and the proton carriers dodecylboronic acid (DBA) and mono-n-dodecylphosphate (MDP) were obtained from Alfa Aesar. Triazole ligands were synthesized following a literature procedure (Li et al., 2015). For experiments under controlled temperatures, the temperature was maintained within 3 degrees of the reported value. Electrochemical analysis and attachments were conducted using a VSP-300 Biologic Potentiostat utilizing a three-electrode arrangement consisting of a leakless Ag/AgCl (3M KCl, eDaq, Inc.) reference electrode that is stable in both aqueous and ethanolic solutions, a Pt wire counter electrode, and a Au or glassy carbon working electrode. Previously reported procedures for experiments on Au electrodes were followed (Tse et al., 2016).

For experiments with carbon, a 5 mm diameter glassy carbon electrode was used as the working electrode. The working electrode was cleaned before each experiment by rinsing the electrode surface using de-ionized water, followed by manual polishing with 0.3 μm alumina particles suspended in de-ionized water on a polishing pad for approximately 6 min. After polishing, the electrode was sonicated in de-ionized water, followed by sonication in acetone, and finally sonication in isopropyl alcohol for 3 min each before being dried under a stream of air. For the electrochemical attachment of the amino-terminated triazole onto the glassy carbon electrode, cyclic voltammograms were conducted with the cleaned electrode in a 10 mL ethanolic solution containing 5 mM amino-terminated triazole and 100 mM $LiClO_4$ from a potential of 2 V to −0.01 V at a scan rate of 10 mV/s for 10 cycles. Following the attachment, the electrode was sonicated in pH 7 potassium phosphate buffer for 10 min to remove excess, unattached triazole molecules. After sonication, the amino-terminated triazole surface was immersed in a 10 mL de-ionized water solution containing 10 mM $CuSO_4$ or 10 mM $AgNO_3$ for 1 hr to form the Cu-triazole or Ag-triazole complex, respectively. For the attachment of the lipid membrane containing a proton carrier, the glassy carbon electrode modified with the Cu-triazole complex was immersed in a 1 mL $CHCl_3$ solution containing 7.4 mM DMPC and 5.6 mM proton carrier for 20 s followed by a brief submersion into 3 mL de-ionized water containing 100 mM KCl until excess $CHCl_3$ solution separated away from the electrode surface. Finally, the membrane-modified electrode was rinsed with pH 7 phosphate buffer before electrochemical analyses were performed.

To test the catalytic activity of the membrane-modified glassy carbon electrode, O_2 reduction and CO_2 reduction reactions were performed. A pH 7 phosphate buffer solution was sparged with air or CO_2 for a minimum of 20 min to ensure the solution was saturated with the specific gas. Electrocatalytic activity was evaluated using linear sweep voltammetry from 0.3 V to −0.7 V for O_2 reduction or 0.3 V to −2.0 V for CO_2 reduction at a scan rate of 10 mV/s. A blocking test to assess the integrity of the membrane-covered electrode was performed after each reduction reaction using a CV from 0.5 V to −0.5 V at a scan rate of 50 mV/s in a de-ionized water solution containing 1.5 mM $K_3Fe(CN)_6$ and 100 mM NaCl. The products of the CO_2 reduction reaction were identified using protocols modified from the literature (Tornow et al., 2012). ^{1}H NMR spectroscopy was used to quantify HCOOH production. ^{1}H NMR spectra were obtained using a Varian 400 MHz NMR Spectrometer in the Shared Instrument Laboratory (SIL) in the Department of Chemistry at the University of Nevada, Reno (UNR). CO production was quantified using a colorimetric assay based on $K_2Pd(SO_3)_2$ (Lin et al., 2018). GC-MS (Agilent 7890A) was used to identify any possible >2 e^- CO_2 reduction products such as C_2H_4 and CH_4.

RESULTS AND DISCUSSION

Ligand Design

To construct membrane-modified electrodes for electrocatalysis, two triazole molecules were first synthesized following literature protocols (Li et al., 2015). The structure of these molecules can be divided into three different sections, each with a specific function. First, the molecules contain a diaminotriazole core (**Figure 1**, blue), which upon metal binding serves as the active electrocatalytic site. This catalyst core was studied because the dinuclear Cu complex of 3,5-diamino-1,2,4-triazole has previously been demonstrated to be an efficient and stable ORR catalyst (Thorum et al., 2009). Second, the molecules contain

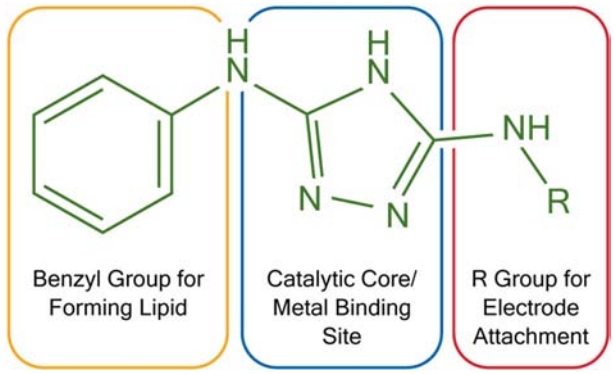

FIGURE 1 | Functional and structural features of two triazoles used in electrocatalysis. $R = -(CH_2)_6SH$ for Au electrodes and $R = -H$ for carbon electrodes.

either an alkyl thiol or a primary amine arm (**Figure 1**, red). These functional groups allow the molecules to be covalently attached to either Au or carbon electrodes, respectively. Lastly, both molecules contain a hydrophobic benzyl group (**Figure 1**, orange) so that lipid layers can be appended on top of the catalysts via Van der Waals interactions.

Electrocatalytic O_2 Reduction on Membrane-Modified Au Electrodes

After synthesizing these triazole ligands, the electrocatalytic activity of the Cu triazole complex on Au electrodes was first analyzed with and without lipid membranes. First, the Cu catalyst was attached to Au electrodes by forming a SAM of the thiol-modified triazole and subsequently immersing the SAM in a solution of $CuSO_4$ (**Figure 2**, green, $R_1 = -(CH_2)_6SH$). A linear sweep voltammogram (LSV) of the Cu catalyst in air-saturated pH 7 phosphate buffer displays an ORR onset potential of about 0 V and a diffusion-limited peak current density of about −0.062 mA/cm^2 (**Figure 3**, black line). Upon covering the catalyst with a lipid monolayer (**Figure 2**, blue, $R_1 = -(CH_2)_6SH$), the activity of the catalyst diminishes substantially due to slow proton transport through the hydrophobic lipid membrane (Barile et al., 2014; **Figure 3**, blue line). Strikingly, the incorporation of dodecylboronic acid (DBA) into the lipid layer (**Figure 2**, red, $R_1 = -(CH_2)_6SH$) revives much of the catalytic activity (**Figure 3**, red line). These observations on Au match previous results and as discussed (Tse et al., 2016), the presence of lipid-bound proton carriers accelerates proton transfer to the ORR catalyst. In particular, the proton carrier enhances the current of the ORR, but does not significantly change the ORR onset potential as compared to the lipid-only case (Hosseini et al., 2011).

The enhancement of current elicited by the proton carrier is due to a change in the ORR mechanism as demonstrated in previous work (Tse et al., 2016; Gautam et al., 2018). In the presence of lipid layer without proton carrier, the hydrophobic nature of the lipid impedes proton transfer to the catalyst, which causes the ORR to proceed primarily via a 1 e^- pathway to yield superoxide. With the incorporation of proton carrier, the proton transfer rate to the catalyst is increased, which favors the 4 e^- reduction of O_2 to water. In the absence of a lipid layer, the Cu catalyst reduces O_2 by both 2 e^- and 4 e^- pathways to produce a mixture of H_2O_2 and water. The mechanistic details for all of these electrochemical environments are illustrated in **Figure S1**.

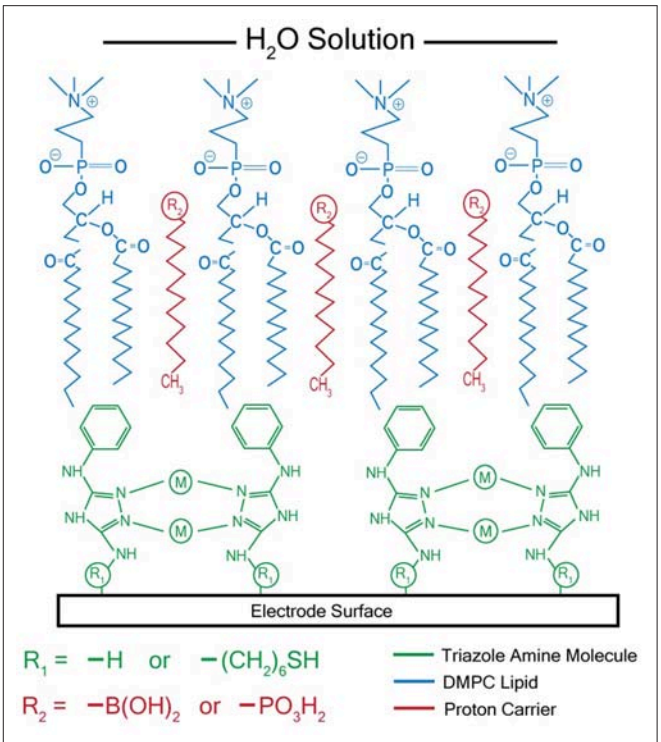

FIGURE 2 | Schematic of membrane-modified electrode consisting of a metal triazole catalyst (green) and a lipid monolayer (blue) with proton carrier (red). M = Cu^{2+} or Ag^+ for catalysts that reduce O_2 or CO_2, respectively.

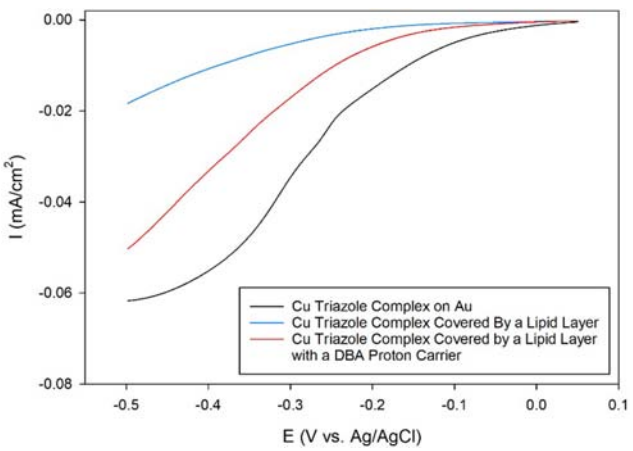

FIGURE 3 | Linear sweep voltammograms of O_2 reduction by a Au electrode modified with the Cu complex of the thiol-terminated triazole (black line) covered by a lipid membrane (blue line) with DBA proton carrier (red line) in pH 7 phosphate buffer at a scan rate of 10 mV/s.

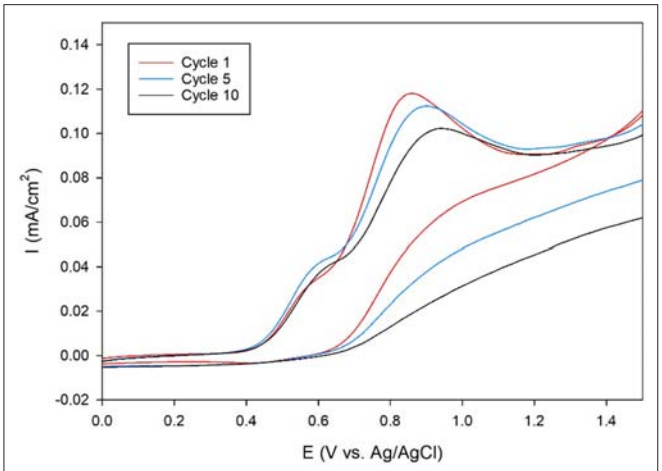

FIGURE 4 | Cyclic voltammogram cycles 1 (red line), 5 (blue line), and 10 (black line) of a glassy carbon electrode in an ethanolic solution of 5 mM amino-terminated triazole and 100 mM $LiClO_4$ at a scan rate of 10 mV/s.

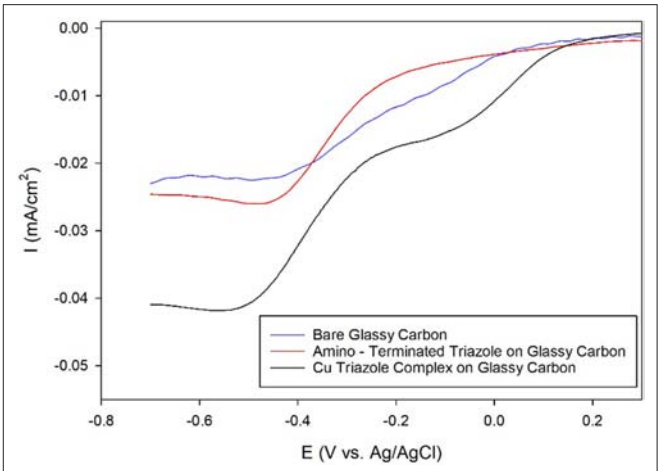

FIGURE 5 | Linear sweep voltammograms of O_2 reduction by a glassy carbon electrode (blue line) modified with the amino-terminated triazole (red line) and the Cu complex of the amino-terminated triazole (black line) in pH 7 phosphate buffer at a scan rate of 10 mV/s.

Electrocatalytic O_2 Reduction on Membrane-Modified Glassy Carbon Electrodes

Next, the ORR catalytic activity on carbon electrodes was analyzed since carbon is more durable and inexpensive than Au, making it the electrode of choice for commercial fuel cells. Toward this end, membrane-modified glassy carbon electrodes were designed. First, the amino-terminated triazole was covalently attached to the electrode surface through the oxidation of the primary amine group using cyclic voltammetry (CV). The CVs recorded during the attachment process display anodic peaks at around 0.8–0.9 V, which indicate that the amine is oxidized at the carbon surface (**Figure 4**). These results are similar to previous studies, which use CV to electrochemically attach primary alkyl amines to carbon electrodes (Deinhammer et al., 1994).

After electrochemical attachment of the amino-terminated triazole to the carbon electrode, the Cu-triazole complex was formed by soaking the electrode in a solution of $CuSO_4$ (**Figure 2**, green, R_1 = –H). The presence of a Cu(I)/Cu(II) redox couple in a CV of the Cu-modified electrode indicates that Cu was successfully incorporated into the electrode architecture (**Figure S2**). The Cu complex catalyzes the reduction of O_2 with an onset potential of about +0.1 V and a diffusion-limited current density of about −0.04 mA/cm^2 (**Figure 5**, black line). The onset potential for this catalyst is fairly similar to what is observed for O_2 reduction by the Cu triazole complex immobilized on a Au electrode (**Figure 3**, black line). LSVs of O_2 reduction by a bare glassy carbon electrode and an electrode modified with triazole in the absence of Cu exhibit more negative onset potentials and less diffusion-limited current as compared to catalysis by the Cu triazole complex (**Figure 5**, blue and red lines, respectively). These experiments indicate that the Cu triazole complex is a more active ORR catalyst than the controls.

Having established the electrocatalytic activity of the Cu triazole complex on a carbon electrode, the surface was next modified with a lipid membrane to control proton transfer to the catalyst. The lipid membrane was formed by soaking the electrode in a solution containing DMPC using a method adapted from a previously reported procedure (Han et al., 2003; **Figure 2**, blue, R_1 = –H). The incorporation of a lipid layer on top of the Cu catalyst shifts the onset potential for the ORR significantly negative and also decreases the diffusion-limited current density (**Figure 6**, blue line). This result indicates that the ORR is inhibited by the presence of the lipid layer due to impeded proton transfer to the catalyst by the hydrophobic membrane in a manner similar to the lipid-covered catalyst on Au. The addition of DBA, a boronic acid proton carrier, to the lipid layer (**Figure 2**, red, R_1 = –H) increases the ORR diffusion-limited current density, but does not significantly alter the ORR onset potential (compare **Figure 6**, red line to blue line). The presence of a proton carrier accelerates proton transfer to the Cu catalyst, which results in the increased catalytic current density observed. The finding that the proton carrier enhances the current of the ORR, but does not significantly change the ORR onset potential as compared to the lipid-only case, suggests that the proton carrier increases the kinetics of the ORR without significantly affecting the reaction thermodynamics. Taken together, these results indicate that membrane-modified electrodes can be successfully formed on glassy carbon substrates and that the general electrochemical behavior of these systems is similar to those constructed on Au.

To assess the integrity of the lipid layer during the ORR, blocking experiments were performed using $K_3Fe(CN)_6$ in bulk solution after the ORR as described in other systems (Barile et al., 2016). A decrease in the current density observed from the Fe(II)/Fe(III) redox couple using lipid-modified electrodes as compared to membrane-free electrodes indicates that the lipid layer remains intact during the ORR process (**Figure S3**). In fact, the blocking data show that the Fe(II)/Fe(III) redox couple is less pronounced when the proton carrier is incorporated in the lipid layer (**Figure S3**, red line) as compared to lipid only

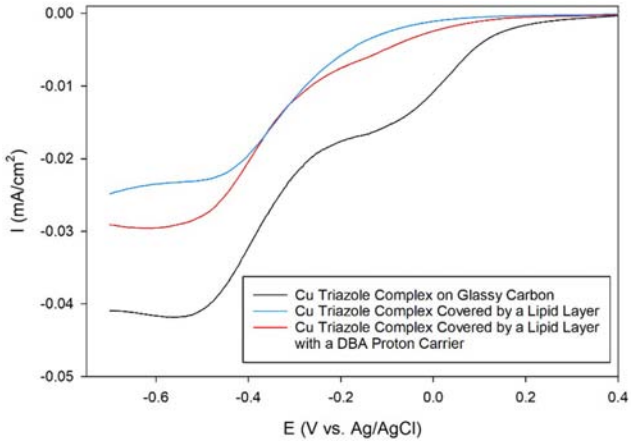

FIGURE 6 | Linear sweep voltammograms of O_2 reduction by a glassy carbon electrode modified with the Cu complex of the amino-terminated triazole (black line) covered by a lipid membrane (blue line) with DBA proton carrier (red line) in pH 7 phosphate buffer at a scan rate of 10 mV/s.

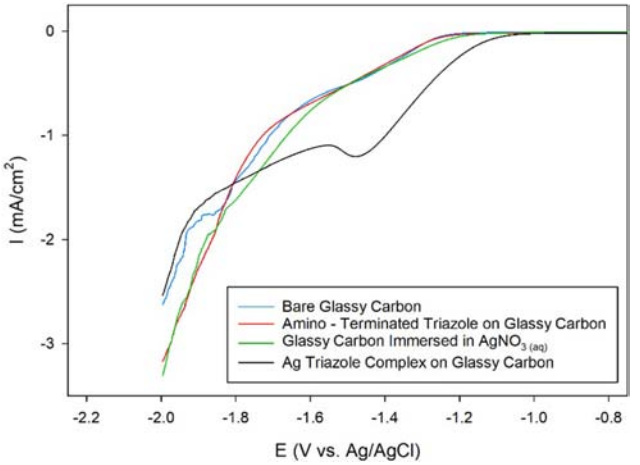

FIGURE 7 | Linear sweep voltammograms of CO_2 reduction by a glassy carbon electrode (blue line) modified with the amino-terminated triazole (red line) and the Ag complex of the amino-terminated triazole (black line) in pH 7 phosphate buffer at a scan rate of 10 mV/s. CO_2 reduction by a glassy carbon electrode immersed only in $AgNO_{3(aq)}$ and subsequently rinsed with water was also evaluated as a control experiment (green line).

case (**Figure S3**, blue line). These results demonstrate that the incorporation of the proton carrier into the lipid membrane does not adversely affect the integrity of the lipid layer and instead actually enhances lipid formation. Therefore, the increase in ORR current density elicited by the proton carrier is not caused by a disruption in the integrity of the lipid membrane. Instead, the proton carrier causes an increase in the electrocatalytic O_2 reduction current density by the Cu catalyst because it accelerates the proton transfer rate to the catalyst. The origin of this current enhancement was further confirmed by averaging results obtained across eight experimental trials (**Figure S4**). This analysis demonstrates that the proton carrier enhances the kinetics of the ORR even when taking into account the integrity of the lipid layer as determined from subsequent blocking experiments.

Electrocatalytic CO_2 Reduction on Membrane-Modified Glassy Carbon Electrodes

Electrocatalytic CO_2 reduction typically occurs at high overpotentials (Qiao et al., 2014). Hence, it is difficult to study CO_2 reduction using membrane-modified Au electrodes because Au SAMs degrade at potentials more negative than about −0.5 V (Srisombat et al., 2011). To overcome this issue, a CO_2 reduction catalyst was prepared on a membrane-modified glassy carbon electrode because carbon electrodes are more electrochemically stable. Furthermore, the majority of previous studies of CO_2 reduction catalysts on carbon electrodes utilize a binder, most commonly Nafion, to adhere the catalyst to the electrode (Tornow et al., 2012; Thorson et al., 2013; Weng et al., 2018). Inks containing carbon, Nafion, and the catalyst are usually dropcast on a glassy carbon electrode to form a porous multilayer catalyst structure that is useful for practical high current density devices, but complicates catalyst surface structure and hinders fundamental electrochemical analysis.

In contrast to a multilayer architecture, we electrochemically attach a monolayer of catalyst to glassy carbon electrodes that do not require the use of a binder. This method of surface modification allows for a more direct assessment of the activity of molecular CO_2 catalysts. Moreover, binders such as Nafion dramatically alter the proton transfer rates to embedded catalysts. The binder-free system devised here enables us to systematically analyze the effect of proton transfer on catalyst performance. In a manner similar to the previously described Cu triazole ORR catalyst, the kinetics of proton transfer to a CO_2 reduction catalyst can be tuned by covering the catalyst with a lipid monolayer.

Ag complexes containing N-based heterocycles form one class of molecular CO_2 reduction catalysts (Tornow et al., 2012). Therefore, a Ag triazole catalyst was synthesized by soaking a glassy carbon electrode modified with the amino-terminated triazole in a solution of $AgNO_3$ (**Figure 2**, green, $R_1 = -H$). A LSV of the Ag triazole complex in the presence of CO_2 displays a peak around −1.5 V and a onset potential of about −1.1 V, indicating that the complex electrocatalytically reduces CO_2 (**Figure 7**, black line). Control experiments performed using a bare glassy carbon electrode, an electrode only immersed in $AgNO_3$, or an electrode modified with only the triazole ligand do not exhibit this peak and have a more negative onset potential of about −1.25 V (**Figure 7**, blue, green, and red lines, respectively). These experiments demonstrate that the Ag triazole complex is a more effective CO_2 reduction catalyst than any of its individual components.

A further control experiment of a LSV of the Ag triazole complex conducted in a N_2 environment shows a similar onset potential of about −1.25 V and also does not exhibit a peak at −1.5 V (**Figure 8**, red line). This experiment provides two important insights into the catalytic behavior of these systems.

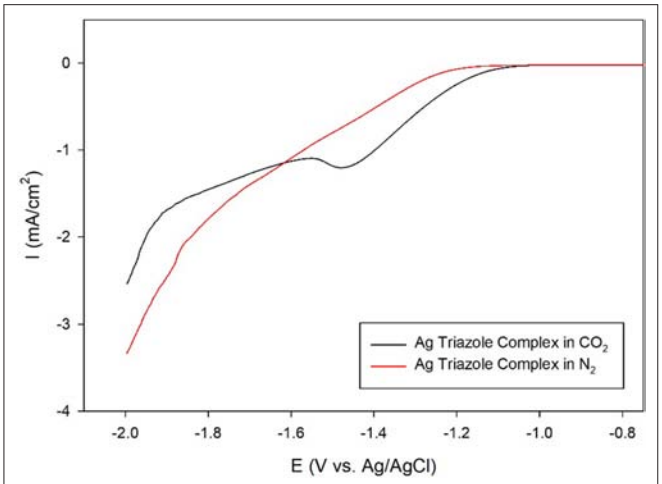

FIGURE 8 | Linear sweep voltammograms by a glassy carbon electrode modified with the Ag complex of the amino-terminated triazole in CO_2-saturated (black line) and N_2-saturated (red line) pH 7 phosphate buffer at a scan rate of 10 mV/s.

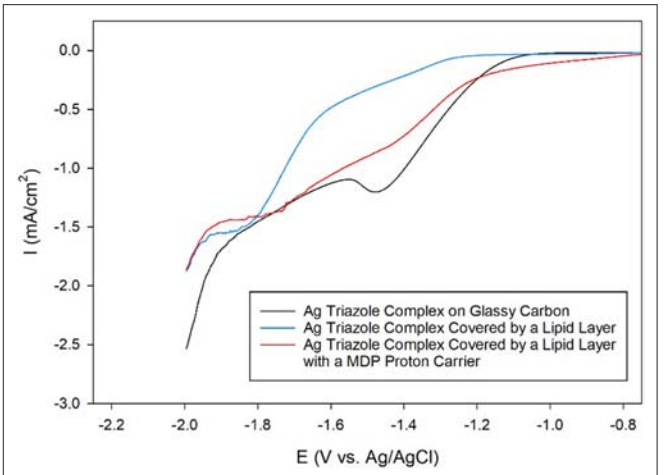

FIGURE 9 | Linear sweep voltammograms of CO_2 reduction by a glassy carbon electrode modified with the Ag complex of the amino-terminated triazole (black line) covered by a lipid membrane (blue line) with MDP proton carrier (red line) in pH 7 phosphate buffer at a scan rate of 10 mV/s.

First, the lack of a peak in the LSV under N_2 further confirms that the Ag triazole complex catalyzes CO_2 reduction. Second, the similarity of the LSV of the Ag triazole complex in N_2 to the other control experiments presented in **Figure 7** suggests that the cathodic current observed in these cases is due to the H_2 evolution reaction. In other words, a bare glassy carbon electrode or an electrode modified with only the triazole ligand does not significantly reduce CO_2 under these conditions.

Having established that the Ag triazole complex catalyzes CO_2 reduction, its catalytic performance was next measured using a membrane-modified electrode. When the catalyst is covered by a lipid monolayer (**Figure 2**, blue, $R_1 = -H$), the onset potential for catalysis shifts negative and the CO_2 reduction peak is not present (**Figure 9**, blue line), indicating that CO_2 reduction is significantly inhibited in this case. The lipid impedes access of protons to the catalyst, which are necessary for most CO_2 reduction processes (Costentin et al., 2013). Furthermore, the current density in the LSV with lipid only reaches about -1.9 mA/cm^2 at -2.0 V as compared to about -3.4 mA/cm^2 at -2.0 V for the Ag triazole complex without lipid in N_2 (**Figure 8**, red line). Since the Ag triazole complex without lipid in N_2 catalyzes the H_2 evolution reaction as discussed in the preceding paragraph, the decrease in the magnitude of current density observed for the lipid-modified catalyst indicates that the H_2 evolution reaction is suppressed. This finding is consistent with the idea that the lipid layer slows down proton transfer to the catalyst since the H_2 evolution reaction requires protons.

The addition of a proton carrier, either an alkyl phosphate, MDP, or an alkyl boronic acid, DBA, into the lipid layer (**Figure 2**, red, $R_1 = -H$) produces significant changes in the voltammetry of the Ag catalyst (**Figure 9**, red line and **Figure S5**, red line). For both proton carriers, there is more catalytic current in the regime of -1.2 to -1.8 V compared to the lipid-only case, and there are not significant differences in the integrity of the lipid layer as determined by blocking experiments (**Figure S6**). These results suggest that, compared to the lipid-only case, the activity of the CO_2 reduction catalyst is altered by the presence of the proton carrier, likely due to the enhancement of proton transfer rates to the catalytic active site. The amount of current enhancement observed depends upon the quantity of proton carrier added to the lipid layer (**Figure S7**), which dictates the rate of proton transfer to the catalyst. The LSVs of the Ag catalyst in the presence of proton carrier also depend upon temperature with greater current densities for CO_2 reduction observed as the temperature is increased (**Figure S8**).

The CO_2 reduction products obtained using the Ag triazole catalyst in different electrode environments at -1.75 V were quantified (**Figure 10**). The unmodified Ag triazole complex on glassy carbon produces nearly equal amounts of CO and HCOOH (∼15% Faradaic efficiency each) along with substantial quantities of H_2. These results confirm that the Ag triazole complex is an active CO_2 reduction catalyst. However, the catalyst also produces a larger amount of H_2 than is observed with Nafion-bound Ag triazole complexes (Tornow et al., 2012). The greater quantity of H_2 produced likely originates from exposed portions of the carbon surface that are not modified by the Ag triazole monolayer.

Covering the Ag triazole catalyst with a lipid layer decreases the Faradaic efficiency of H_2 production from ∼71 to ∼56%. The decreased quantity of H_2 produced is attributed to the hydrophobic nature of the lipid environment, which decreases the rate of proton transfer to the catalyst. With an impeded proton transfer rate, the catalyst has more time to bind and reduce CO_2 to either CO or HCOOH. This alteration in mechanism with a change in proton transfer rate is displayed schematically in **Figure S9**. The results indicate that the catalyst preferentially reduces CO_2 to CO (∼32%) over HCOOH (∼12%). Again, the hydrophobic nature of the lipid environment likely dictates product selectivity. Water is formed as a coproduct with CO, but not with HCOOH. We

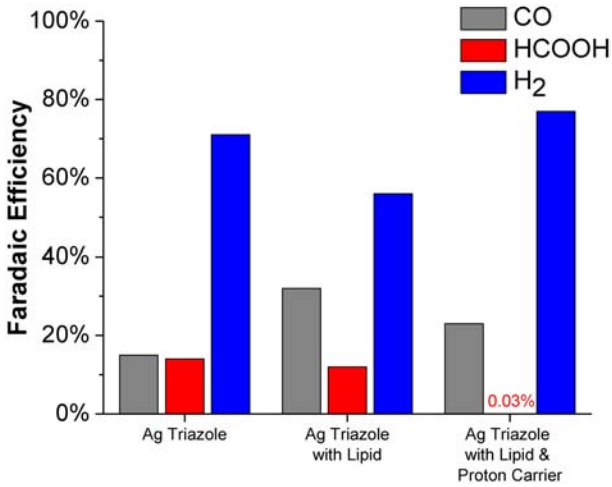

FIGURE 10 | Faradaic efficiencies for CO (gray), HCOOH (red), and H_2 (blue) production from the Ag triazole complex (left) with lipid (middle) and DBA proton carrier (right) obtained from chronoamperometry experiments at −1.75 V vs. Ag/AgCl.

hypothesize that the preference for CO formation is due to the favorable elimination of water out of the hydrophobic lipid interior, which shifts the reaction equilibria toward CO production.

The product selectively is further altered when a proton carrier is incorporated in the lipid layer. Specifically, the Faradaic efficiency for H_2 increases from ∼56 to ∼77% upon adding the proton carrier. The proton carrier increases proton transfer kinetics to the catalyst, which favors the production of H_2. Interestingly, the proton carrier drastically increases the ratio of CO to HCOOH generated and almost completely eliminates HCOOH production (∼0.03% Faradaic efficiency). The exact origin of this change in product selectivity is unknown, but possibly originates from interactions between the proton carrier and CO_2 reduction intermediates. The CO_2 reduction products of this system were also quantified as a function of temperature (**Figure S10**). Decreasing the reaction temperature to 1°C increases the Faradaic efficiency for HCOOH production to ∼3%. At this low temperature, previous studies have demonstrated that proton carriers cannot undergo flip-flop diffusion because the lipid layer is below its gel-phase transition temperature (Barile et al., 2014). Therefore, we anticipate that at 1°C, the Ag catalyst behaves as if there is no proton carrier. This hypothesis is supported by the observation that the ratio of CO to HCOOH production with proton carrier in the cold is similar to the lipid-only case at room temperature.

Lastly, the effect of voltage on the CO_2 product speciation was tested. The CO_2 products generated at −2 V are displayed in **Figure S11**. At this higher overpotential, the Ag triazole catalyst in the absence of lipid produces similar quantities of CO, HCOOH, and H_2 as compared to the −1.75 V case. However, when the catalyst contains a lipid layer with or without the proton carrier, the Faradaic efficiencies for CO and HCOOH both decrease to ∼2%, suggesting that the lipid layer inhibits CO_2 reduction at this higher overpotential.

CONCLUSIONS

We designed membrane-modified electrodes containing metal triazole complexes that electrocatalyze the reduction of O_2 and CO_2. For the O_2 reduction reaction, the complexes were anchored using SAMs on both Au and glassy carbon electrodes. By covering the catalysts in a lipid layer containing proton carriers, the kinetics of proton transfer to the complexes can be controlled on both substrates. The membrane-modified electrocatalytic systems developed on glassy carbon electrodes have a wider electrochemical window than those using Au, which enable the study of CO_2 reduction by lipid-covered catalysts. The results suggest that the relative rates of H_2, CO, and HCOOH production can be altered through the use of membranes.

AUTHOR CONTRIBUTIONS

SS performed experiments. Both SS and CB designed experiments, interpreted the data, and wrote the paper.

FUNDING

Acknowledgment is made to the donors of The American Chemical Society Petroleum Research Fund for partial support of this research. We thank Research and Innovation at the University of Nevada, Reno for partial support of this research.

ACKNOWLEDGMENTS

We acknowledge the Shared Instrumentation Laboratory in the Department of Chemistry at the University of Nevada, Reno. We thank Dr. Edmund Tse for useful discussions.

SUPPLEMENTARY MATERIAL

The Supplementary Material for this article can be found online at: https://www.frontiersin.org/articles/10.3389/fchem.2018.00543/full#supplementary-material

REFERENCES

Barile, C. J., Tse, E. C. M., Li, Y., Gewargis, J. P., Kirchschlager, N. A., Zimmerman, S. C. et al. (2016). The flip-flop diffusion mechanism across lipids in a hybrid bilayer membrane. *Biophys. J.* 110. 2451–2462. doi: 10.1016/j.bpj.2016.04.041

Barile, C. J., Tse, E. C. M., Li, Y., Sobyra, T. B., Zimmerman, S. C., Hosseini, A. et al. (2014). Proton switch for modulating oxygen reduction by a copper electrocatalyst embedded in a hybrid bilayer membrane. *Nat. Mater.* 13, 619–623. doi: 10.1038/nmat3974

Costentin, C., Robert, M., and Savéant, J. (2013). Catalysis of the electrochemical reduction of carbon dioxide. *Chem. Soc. Rev.* 42, 2423–2436. doi: 10.1039/C2CS35360A

Dai, L., Xue, Y., Qu, L., Choi, H., and Baek, J. (2015). Metal-free catalysts for oxygen reduction reaction. *Chem. Rev.* 115, 4823–4892. doi: 10.1021/cr5003563

Deinhammer, R. S., Ho, M., Anderegg, J. W., and Porter, M. D. (1994). Electrochemical oxidation of amine-containing compounds: a route to the surface modification of glassy carbon electrodes. *Langmuir*. 10, 1306–1313. doi: 10.1021/la00016a054

Duan, J., Chen, S., Jaroniec, M., and Qiao, S. Z. (2015). Heteroatom-doped graphene-based materials for energy-relevant electrocatalytic processes. *ACS Catal.* 5, 5207–5234. doi: 10.1021/acscatal.5b00991

Gautam, R., Lee, Y. T., Herman, G. L., Moreno, C. M., Tse, E. C. M., and Barile, C. J. (2018). Controlling proton and electron transfer rates enhances the activity of an oxygen reduction electrocatalyst. *Angew. Chem. Int. Edit.* 57, 13480–13483. doi: 10.1002/anie.201806795

Gewirth, A. A., and Thorum, M. S. (2010). Electroreduction of dioxygen for fuel-cell applications: materials and challenges. *Inorg. Chem.* 49, 3557–3566. doi: 10.1021/ic9022486

Hammes-Schiffer, S. (2009). Theory of proton-coupled electron transfer in energy conversion processes. *Acc. Chem. Res.* 42, 1881–1889. doi: 10.1021/ar9001284

Hammes-Schiffer, S., and Soudackov, A. V. (2008). Proton-coupled electron transfer in solution, proteins, and electrochemistry. *J. Phys. Chem. B.* 112, 14108–14123. doi: 10.1021/jp805876e

Han, X., Wang, L., Qi, B., Yang, X., and Wang, E. (2003). A strategy for constructing a hybrid bilayer membrane based on a carbon substrate. *Anal. Chem.* 75, 6566–6570. doi: 10.1021/ac034592q

Hori, Y. (2008). "Electrochemical CO2 reduction on metal electrodes," in *Modern Aspects of Electrochemistry*, eds C. G. Vayenas, R. E. White, M. E. Gamboa-Aldeco (New York, NY: Springer), 89–189.

Hori, Y., Kikuchi, K., and Suzuki, S. (1985). Production of CO and CH_4 in electrochemical reduction of CO_2 at metal electrodes in aqueous hydrogencarbonate solution. *Chem. Lett.* 14, 1695–1698. doi: 10.1246/cl.1985.1695

Hosseini, A., Barile, C. J., Devadoss, A., Eberspacher, T. A., Decreau, R. A., and Collman, J. P. (2011). Hybrid bilayer membrane: a platform to study the role of proton flux on the efficiency of oxygen reduction by a molecular electrocatalyst. *J. Am. Chem. Soc.* 133, 11100–11102. doi: 10.1021/ja204418j

Huynh, M. H., and Meyer, T. J. (2007). Proton-coupled electron transfer. *Chem. Rev.* 107, 5004–5064. doi: 10.1021/cr0500030

Li, Y., Tse, E. C., Barile, C. J., Gewirth, A. A., and Zimmerman, S. C. (2015). Photoresponsive molecular switch for regulating transmembrane proton-transfer kinetics. *J. Am. Chem. Soc.* 137, 14059–14062. doi: 10.1021/jacs.5b10016

Lin, C., Xian, X., Qin, X., Wang, D., Tsow, F., Forzani, E., et al. (2018). High performance colorimetric carbon monoxide sensor for continous personal exposure monitoring. *ACS Sens.* 3, 327–333. doi: 10.1021/acssensors.7b00722

Mayer, J. M. (2004). Proton-coupled electron transfer: a reaction chemist's view. *Annu. Rev. Phys. Chem.* 55, 363–390. doi: 10.1146/annurev.physchem.55.091602.094446

McCrory, C. C., Ottenwaelder, X., Stack, T. D., and Chidsey, C. E. (2007). Kinetic and mechanistic studies of the electrocatalytic reduction of O_2 to H_2O with mononuclear Cu Complexes of Substituted 1,10-Phenanthrolines. *J. Phys. Chem. A.* 111, 12641–12650. doi: 10.1021/jp076106z

Qiao, J., Liu, Y., Hong, F., and Zhang, J. (2014). A review of catalysts for the electroreduction of carbon dioxide to produce low-carbon fuels. *Chem. Soc. Rev.* 43, 631–675. doi: 10.1039/C3CS60323G

Rosenthal, J., and Nocera, D. G. (2007). Role of proton-coupled electron transfer in O–O bond activation. *Acc. Chem. Res.* 40, 543–553. doi: 10.1021/ar7000638

Sjödin, M., Styring, S., Wolpher, H., Xu, Y., Sun, L., and Hammarström, L. (2005). Switching the redox mechanism: models for proton-coupled electron transfer from tyrosine and tryptophan. *J. Am. Chem. Soc.* 127, 3855–3863. doi: 10.1021/ja044395o

Srisombat, L., Jamison, A. C., and Lee, T. R. (2011). Stability: a key issue for self-assembled monolayers on gold as thin-film coatings and nanoparticle protectants. *Coll. Surf. A* 390, 1–19. doi: 10.1016/j.colsurfa.2011.09.020

Thorseth, M. A., Letko, C. S., Tse, E. C. M., Rauchfuss, T. B., and Gewirth, A. A. (2013). Ligand effects on the overpotential for dioxygen reduction by Tris(2-pyridylmethyl)amine derivatives. *Inorg. Chem.* 52, 628–634. doi: 10.1021/ic301656x

Thorson, M. R., Siil, K. I., and Kenis, P. J. A. (2013). Effect of cations on the electrochemical conversion of CO_2 to CO. *J. Electrochem. Soc.* 160, F69–F74.

Thorum, M. S., Yadav, J., and Gewirth, A. A. (2009). Oxygen reduction activity of a copper complex of 3,5-diamino-1,2,4-triazole supported on carbon black. *Angew. Chem. Int. Ed.* 48, 165–167. doi: 10.1002/anie.200803554

Tornow, C. E., Thorson, M. R., Ma, S., Gewirth, A. A., and Kenis, P. J. (2012). Nitrogen-based catalysts for the electrochemical reduction of CO_2 to CO. *J. Am. Chem. Soc.* 134, 19520–19523. doi: 10.1021/ja308217w

Tse, E. C., Barile, C. J., Gewargis, J. P., Li, Y., Zimmerman, S. C., and Gewirth, A. A. (2015). Anion transport through lipids in a hybrid bilayer membrane. *Anal. Chem.* 87, 2403–2409. doi: 10.1021/ac5043544

Tse, E. C., Barile, C. J., Kirchschlager, N. A., Li, Y., Gewargis, J. P., Zimmerman, S. C. et al. (2016). Proton transfer dynamics control the mechanism of O_2 reduction by a non-precious metal electrocatalyst. *Nat. Mater.* 15, 754–759. doi: 10.1038/nmat4636

Weng, Z., Wu, Y., Wang, M., Jiang, J., Yang, K., Huo, S. et al. (2018). Active sites of copper-complex catalytic materials for electrochemical carbon dioxide reduction. *Nat. Commun.* 9:415.

Wenger, O. S. (2013). Proton-coupled electron transfer with photoexcited metal complexes. *Acc. Chem. Res.* 46, 1517–1526. doi: 10.1021/ar300289x

Zeng, M., and Li, Y. (2015). recent advances in heterogeneous electrocatalysts for the hydrogen evolution reaction. *J. Mater. Chem. A.* 3, 14942–14962. doi: 10.1039/C5TA02974K

Zhang, W., Lai, W., and Cao, R. (2017). Energy-related small molecule activation reactions: oxygen reduction and hydrogen and oxygen evolution reactions catalyzed by porphyrin- and corrole-based systems. *Chem. Rev.* 117, 3717–3797. doi: 10.1021/acs.chemrev.6b00299

Conflict of Interest Statement: The authors declare that the research was conducted in the absence of any commercial or financial relationships that could be construed as a potential conflict of interest.

Copyright © 2018 Supakul and Barile. This is an open-access article distributed under the terms of the Creative Commons Attribution License (CC BY). The use, distribution or reproduction in other forums is permitted, provided the original author(s) and the copyright owner(s) are credited and that the original publication in this journal is cited, in accordance with accepted academic practice. No use, distribution or reproduction is permitted which does not comply with these terms.

frontiers in Chemistry

ORIGINAL RESEARCH
published: 03 December 2018
doi: 10.3389/fchem.2018.00598

Photoelectrochemical Gas–Electrolyte–Solid Phase Boundary for Hydrogen Production From Water Vapor

Fumiaki Amano[1,2]*, *Ayami Shintani*[1], *Hyosuke Mukohara*[1], *Young-Min Hwang*[1] and *Kenyou Tsurui*[1]

[1] Department of Chemical and Environmental Engineering, The University of Kitakyushu, Kitakyushu, Japan, [2] Precursory Research for Embryonic Science and Technology (PRESTO), Japan Science and Technology Agency (JST), Kawaguchi, Japan

Hydrogen production from humidity in the ambient air reduces the maintenance costs for sustainable solar-driven water splitting. We report a gas-diffusion porous photoelectrode consisting of tungsten trioxide (WO_3) nanoparticles coated with a proton-conducting polymer electrolyte thin film for visible-light-driven photoelectrochemical water vapor splitting. The gas–electrolyte–solid triple phase boundary enhanced not only the incident photon-to-current conversion efficiency (IPCE) of the WO_3 photoanode but also the Faraday efficiency (FE) of oxygen evolution in the gas-phase water oxidation process. The IPCE was 7.5% at an applied voltage of 1.2 V under 453 nm blue light irradiation. The FE of hydrogen evolution in the proton exchange membrane photoelectrochemical cell was close to 100%, and the produced hydrogen was separated from the photoanode reaction by the membrane. A comparison of the gas-phase photoelectrochemical reaction with that in liquid-phase aqueous media confirmed the importance of the triple phase boundary for realizing water vapor splitting.

Keywords: gas-phase water splitting, solar H_2 production, visible-light-driven photoelectrode, tungsten oxide photoanode, proton exchange membrane

OPEN ACCESS

Edited by:
Steve Suib, University of Connecticut, United States

Reviewed by:
Chang-Yong Nam, Brookhaven National Laboratory (DOE), United States
Christoph Richter, Deutsches Zentrum für Luft- und Raumfahrt, Helmholtz-Gemeinschaft Deutscher Forschungszentren (HZ), Germany

***Correspondence:**
Fumiaki Amano
amano@kitakyu-u.ac.jp

Specialty section:
This article was submitted to Green and Sustainable Chemistry, a section of the journal Frontiers in Chemistry

Received: *13 October 2018*
Accepted: *19 November 2018*
Published: *03 December 2018*

Citation:
Amano F, Shintani A, Mukohara H, Hwang Y-M and Tsurui K (2018) Photoelectrochemical Gas–Electrolyte–Solid Phase Boundary for Hydrogen Production From Water Vapor. Front. Chem. 6:598. doi: 10.3389/fchem.2018.00598

INTRODUCTION

Large-scale deployment of photocatalytic and photoelectrochemical (PEC) water-splitting technologies, accompanied by fuel cells and energy carrier technologies, will allow the realization of the hydrogen (H_2) economy (Maeda and Domen, 2010). Separation of H_2 and oxygen (O_2) is easily achieved in PEC systems that use solid polymer electrolyte membranes (Pinaud et al., 2013; McKone et al., 2014). Laboratory-scale PEC studies are usually performed in aqueous electrolyte solutions using purified water without contamination. However, in practice, water resources are an issue for solar H_2 production. Stable supply of water might be problematic for large-scale solar H_2 production owing to limited rainfall in areas with low-cost land and abundant solar radiation such as deserts (Kumari et al., 2016). Another possible feedstock is seawater, but its use requires purification to avoid problems such as corrosion, poisoning, fouling, and byproduct formation. In contrast, gaseous water has been proposed as an attractive alternative to liquid water because an inexhaustible supply of water vapor from the ambient humid air is available at sea with high relative humidity (~80%) (Kumari et al., 2016). Gas-phase operations can significantly decrease maintenance costs because the natural convection of air can be used to feed the water vapor and

systems to purify and pump liquid water are not required (Rongé et al., 2014; Modestino et al., 2015).

Gas-phase water splitting by all-solid PEC systems has been studied using proton exchange membranes (PEMs) as a solid polymer electrolyte and n-type semiconductor electrodes as a photoanode (Georgieva et al., 2009, 2010; Iwu et al., 2013; Rong et al., 2013; Tsui et al., 2013; Rongé et al., 2014; Stoll et al., 2016, 2017; Verbruggen et al., 2017). PEC water oxidation is induced by photogenerated holes on the photoanode, which is in contact with the membrane, whereas the H_2 evolution reaction occurs on the cathode, which is located on the opposite side of the membrane. The PEM-based photoelectrolyzer (PEM-PEC cell) can be operated using gas-phase reactants such as water vapor and volatile organic compounds in air. However, the photon-to-current conversion efficiencies of the photoanodes are frequently low owing to the difficulties associated with designing electrodes for "gas–solid" PEC systems in contrast to those for conventional "liquid–solid" systems in aqueous electrolytes. The photoelectrode for a gas-phase reaction should exhibit gas diffusion properties for mass transport and proton conductivity for ion transport toward the membrane. It has been proposed that high-surface-area photoanodes need to be covered with a polymer electrolyte thin film to maximize the gas–electrolyte–solid phase contact area (Spurgeon and Lewis, 2011; Xiang et al., 2016). However, the effect of such a triple phase boundary has not been elucidated for gas–solid PEC systems. In addition, most studies have focused on TiO_2-based photoanodes under UV irradiation, and there are only a few reports on visible-light-responsive photoelectrodes for gas-phase reactions (Georgieva et al., 2009; Stoll et al., 2017). The use of narrow band gap semiconductors is necessary to achieve high solar-to-hydrogen efficiency because the number of photons is limited in the UV range. The maximum solar-to-hydrogen efficiency is only 1.7% even if all the UV light with wavelength shorter than 400 nm is utilized for water splitting reaction under AM1.5G spectrum (Abe, 2010; Hisatomi et al., 2015).

The aim of this study was to develop an all-solid PEC system with a triple phase boundary for water vapor splitting under visible-light irradiation. We selected tungsten trioxide (WO_3) as a blue-light responsive semiconductor with a narrow band gap of 2.6–2.7 eV (Amano et al., 2013). High-surface-area WO_3 nanoparticles were deposited on porous titanium microfiber felt (WO_3/Ti fiber), which was then covered with a perfluorosulfonic acid ionomer electrolyte thin film to improve its proton transport properties. The perfluorosulfonate ionomer, DuPont Nafion®, exhibits good proton conductivity at room temperature in hydrous conditions (Kusoglu and Weber, 2017). The Nafion ionomer thin film also has high chemical stability, moderate gas permeability, and moisture absorbency, which allows it to capture humidity in the gas phase (Modestino et al., 2015). We fabricated a membrane electrode assembly (MEA) by hot pressing the WO_3/Ti-fiber electrode onto a PEM with a platinum catalyst film on the opposite side. The effect of the ionomer thin film loading on the PEC performances of the WO_3/Ti fiber electrode was investigated in both humidified argon and liquid water using two-electrode and conventional three-electrode configurations.

MATERIALS AND METHODS

Preparation of WO_3 Gas Diffusion Electrode

Sintered Ti microfiber felt (thickness: 0.1 mm, Nikko Techno, Japan) was used as a macroporous conductive substrate to prepare a gas diffusion electrode composed of WO_3 nanoparticles (Homura et al., 2014; Amano et al., 2017). Ammonium metatungstate hydrate (20.4 g, Nippon Inorganic Colour & Chemical, Japan) and PEG 20,000 (10.0 g, Wako Pure Chemical, Japan) were dissolved in deionized water (40.0 g) as a solution for dip coating of the Ti microfiber felt. The dip coating process was performed three times. The precursor-coated Ti microfiber felt was dried at 353 K and calcined in air at 923 K for 2 h to achieve crystallization of WO_3. If required, the obtained WO_3/Ti fiber electrode was treated with a Nafion® perfluorosulfonic acid (PFSA) ionomer dispersion (5 wt% in mixture of lower aliphatic alcohols and water, contains 45% water, Sigma-Aldrich Japan, Japan) as a proton-conducting polymer. The dispersion was dropped on the electrode (10 μL cm^{-2}), and the wetted electrode was dried at 353 K. The loading amount of the Nafion ionomer was ∼0.6 mg cm^{-2}.

Preparation of Membrane Electrode Assembly

A carbon black-supported platinum nanoparticles (Pt/CB) was used as a cathode catalyst for H_2 evolution. A cathode catalyst ink was prepared by ultrasonication of a mixture of a Pt/CB (TEC10E50E, Pt loading: 46.6 wt%, Tanaka Kikinzoku Kogyo, Japan) and the Nafion ionomer dispersion. The weight ratio of the Nafion ionomer to Pt was adjusted to 1.0, and the loading amount of platinum was ∼0.1 mg cm^{-2}. The ionomer-mixed Pt/CB film and the WO_3/Ti fiber electrode were hot pressed onto a Nafion membrane N117 (thickness: 183 μm, DuPont, USA) at 15 kN and 413 K. The composition of the MEA was "WO_3/Ti fiber | Nafion membrane | ionomer-mixed Pt/CB."

Characterization

Scanning electron microscopy (SEM) observation and energy dispersive X-ray spectroscopy (EDS) analysis were performed on a JSM-7800F microscope (JEOL, Japan). The electrode was directly deposited on carbon tape. High-magnification SEM observation was performed on S-5200 microscope (Hitachi, Japan) with an operating voltage of 5 kV. Before the high-magnification observation, the sample deposited on carbon tape was coated with gold using an E-1030 ion sputter coater (Hitachi, Japan).

Nitrogen adsorption isotherms were recorded at 77 K in the relative pressure range between 0.05 and 0.30 with a BELSORP-mini system (MicrotracBEL, Japan). Before the measurements, the electrode was outgassed at 473 K for 2 h. The Brunauer–Emmett–Teller (BET) equation was used to calculate the surface area of WO_3/Ti fiber electrode. The BET specific surface area of the WO_3 particles was estimated from the measured surface area of the electrode and the loading amount of the WO_3 particles. The BET specific surface area of Ti microfibers was smaller than the measurement limit.

Photoelectrochemical Measurements

The PEC reaction was conducted at room temperature (298 K) and atmospheric pressure (0.1 MPa). The gas-phase water splitting reaction was performed using a dual compartment stainless-steel PEC reactor with an optical window, as shown in **Figure 1**. The compartments were separated by the Nafion membrane. Water vapor (3 vol%) was introduced into each compartment by passing argon at a flow rate of 20 mL min^{-1} through a bubbler filled with deionized water. The electrode area was 25 cm^2, but the light irradiation area was 16 cm^2 owing to the presence of a gold-coated copper plate as the current collector. Photoirradiation was performed using 3 W blue light-emitting diode lamps. The emission was centered at a wavelength (λ) of 453 nm with a full width at half maximum of 22 nm. The optical power was measured to be ~7 mW cm^{-2}. A 300 W xenon lamp with bandpass filters (bandwidth ~10 nm) was used to obtain the action spectrum for the incident photon-to-current conversion efficiency (IPCE), which is the ratio of the number of electric charges to the number of incident photons, as shown in equation (1).

$$\mathrm{IPCE} = (i_{\mathrm{photo}} \times 1240/\lambda)/I_0 \quad (1)$$

where i_{photo} is the steady-state photocurrent density [mA cm^{-2}], $1240/\lambda$ is the monochromatic photon energy [eV], and I_0 is the power of the incident monochromatic light [mW cm^{-2}]. The Faraday efficiency (FE), also known as the current efficiency, was calculated from the ratio of the electric current required for the formation of a product to the total electric current, as shown in equation (2).

$$\mathrm{FE} = (n_{\mathrm{e}} \times F \times r(x))/i_{\mathrm{photo}} \quad (2)$$

where n_{e} is the number of electrons required to form a product, F is the Faraday constant, and $r(x)$ is the formation rate of product x. The amounts of evolved O_2 and H_2 were analyzed using an online gas chromatograph equipped with a thermal conductivity detector and an MS-5A column with argon as the carrier gas. The n_{e} values of H_2 and O_2 are 2 and 4, respectively.

An H-type dual compartment glass reactor was used for the PEC measurements of small area electrodes (light irradiation area: 1 cm^2). The compartment separated by the Nafion membrane was filled with 3 vol% H_2O vapor in argon or an aqueous electrolyte of 0.1 mol L^{-1} sulfuric acid (pH = 1). A silver/silver chloride (Ag/AgCl) reference electrode (+195 mV vs. the standard hydrogen electrode) was used in the three-electrode configuration. The Nernst equation [equation (3)] can be used to convert the electrode potential vs. Ag/AgCl ($E_{\mathrm{Ag/AgCl}}$) to the potential vs. the reversible hydrogen electrode (E_{RHE}).

$$E_{\mathrm{RHE}} = E_{\mathrm{Ag/AgCl}} + 0.059\mathrm{pH} + 0.195 \quad (3)$$

RESULTS

Preparation of the Ionomer-Coated WO_3 Photoelectrode

To allow for gas diffusion and ion transport, the PEM-based PEC cell for gaseous reactants requires a three-dimensional porous electrode rather than a conventional planar dense electrode. We used a titanium microfiber felt that has a high porosity (67%) owing to its three-dimensional fibrous structures with diameters of 20 μm (Amano et al., 2017). The specific surface area of the Ti microfiber felt with a thickness of 0.1 mm was ~450 cm^2 g^{-1}, which is 90 times larger than that of a conventional two-dimensional Ti sheet with a thickness of 1.0 mm (5 cm^2 g^{-1}). The formation of a highly crystalline monoclinic WO_3 phase was confirmed by X-ray diffraction and Raman spectroscopy (Amano et al., submitted). The loading amount of WO_3 was 13 mg cm^{-2}, which corresponds to 27 wt% in the WO_3/Ti fiber electrode. SEM images of the WO_3/Ti fiber after gold sputtering (**Figure 2A**) revealed that monoclinic WO_3 formed nanoparticles with particle diameters of ~100 nm. The BET specific surface area of the WO_3 particles was measured to be 7.5 m^2 g^{-1}, which corresponds to the average diameter of 110 nm assuming that each particle was a sphere. The estimated particle size was similar to that of the WO_3 particles observed in SEM images. The PEC performance for water oxidation was tested in a conventional aqueous electrolyte solution (phosphate buffer, pH = 2.2). The performance of the WO_3/Ti fiber electrode was superior to that of a WO_3 particle electrode obtained by deposition of WO_3 nanoparticles on a two-dimensional substrate such as transparent conductive oxide-coated glass and a titanium sheet (Amano et al., 2017). The IPCE of the WO_3/Ti fiber electrode was ~60% at 1.0 V vs. Ag/AgCl under UV irradiation, and the FE of O_2 evolution was higher than 70%.

A Nafion ionomer dispersion was cast on the high-surface-area WO_3 nanoparticle electrode. **Figure 2B** shows a high-magnification SEM image of the WO_3/Ti fiber electrode after gold sputtering. The sputtered gold nanoparticles were clearly observed in the case of the ionomer-coated WO_3/Ti fiber, suggesting that the Nafion ionomer thin film induced the heterogeneous nucleation of the gold nanoparticles. This phenomenon would be a useful method to visualize the Nafion ionomer thin film in SEM observation. We found that the thin film covered the WO_3 particles, with some of the ionomer aggregated at the grain boundary. The thickness of the ionomer thin film was estimated to be ~3 nm by using the specific gravity of the Nafion membrane (1.98) assuming that the thin layer uniformly covers the surface of the WO_3 nanoparticles. EDS elemental analysis confirmed an increase in the content of carbon and fluorine after ionomer coating. The fluorine mapping shows that the ionomer was dispersed on the macroporous electrode, with some of the ionomer segregated in the void spaces of the Ti microfibers (**Figure 2C**). The ionomer-coated WO_3/Ti fiber photoanode (5 × 5 cm^2) and an ionomer-mixed Pt/CB cathode (5 × 5 cm^2) were pressed on both sides of a Nafion membrane (8 × 8 cm^2) to fabricate an MEA for a large stainless-steel PEC reactor (irradiated area: 16 cm^2).

Gas-Phase Water Splitting in the PEM-PEC Reactor

Figure 3A shows the photoresponse of the WO_3/Ti fiber photoanode with and without the ionomer in an argon flow with 3 vol% H_2O vapor (relative humidity: ~90%) under chopped

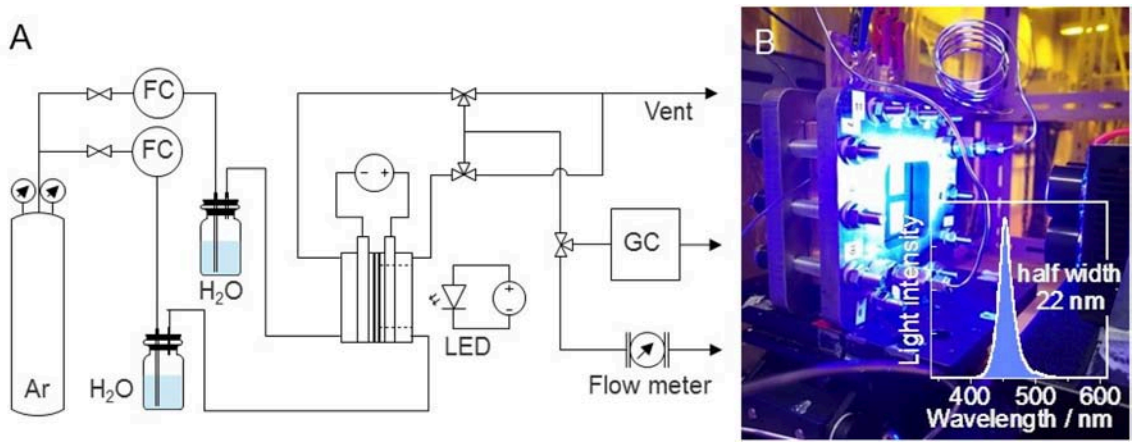

FIGURE 1 | Process flow for photoelectrolysis of water vapor (FC, flow controller; LED, light-emitting diode; GC, gas chromatograph). **(B)** Photograph of the photoelectrolyzer and blue LED (inset: spectrum of the blue light, centered at 453 nm).

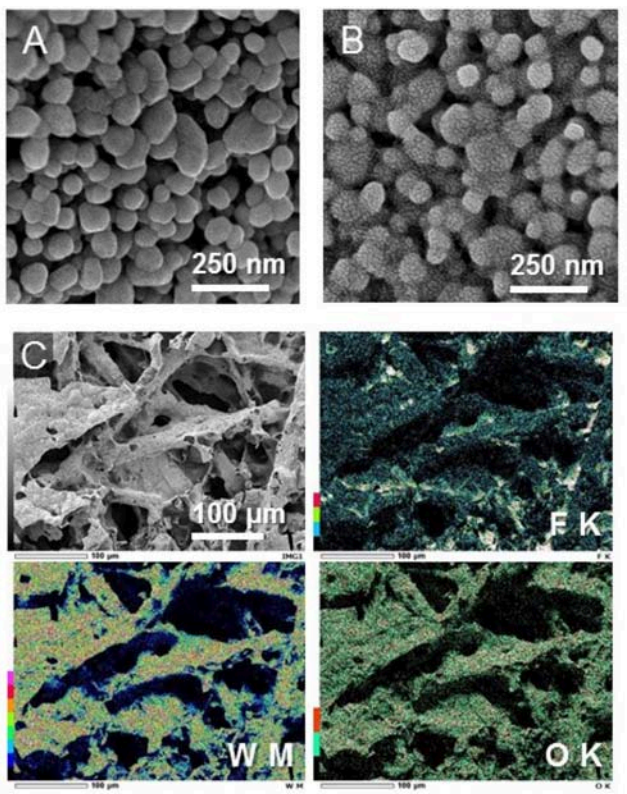

FIGURE 2 | SEM images of **(A)** the bare WO_3/Ti fiber electrode and **(B)** the ionomer-coated WO_3/Ti fiber electrode. The images were obtained after sputtering with gold. **(C)** EDS mapping images for F, W, and O elements of the ionomer-coated WO_3/Ti fiber electrode.

visible-light irradiation ($\lambda = 453$ nm). The two compartments of the large PEM-PEC cell were pre-purged with water vapor for more than 1 h. The applied voltage corresponds to the potential difference between the WO_3/Ti fiber photoanode and the ionomer-mixed Pt/CB cathode. The WO_3/Ti fiber electrode without the ionomer coating exhibited small photocurrent and a slow photoresponse during the gas-phase PEC measurements. The photocurrent was significantly decreased compared with that observed for the PEC performance test in a conventional aqueous electrolyte solution. In contrast, the ionomer-coated WO_3/Ti fiber electrode showed an increased photocurrent response in the gas-phase PEC measurements. The photocurrent at applied voltages higher than 0.2 V quickly increased when the UV light was turned on, and quickly decayed to the dark current level when the light was turned off. Thus, we found that the photoresponse of the WO_3/Ti fiber photoanode was accelerated by the Nafion ionomer coating, indicating that the electron transfer from water to WO_3 was accelerated. **Figure 3B** shows the time course of the photocurrent at 1.2 V. A Faraday current was not observed at steady state in the dark. The IPCE at 1.2 V was 7.6% for the ionomer-coated WO_3/Ti fiber photoanode, but the IPCE was only 3.8% in the absence of the ionomer coating. Moreover, an anodic current owing to water vapor oxidation was observed only under photoirradiation. Thus, the Nafion ionomer coating enhanced the steady-state photocurrent of the WO_3/Ti fiber electrode.

Figure 4 shows the outcome of the visible-light-induced gas-phase water-splitting reaction in the PEM-PEC reactor. The applied voltage was set to 1.2 V, which is less than the thermodynamic minimum voltage required for water electrolysis at room temperature (1.23 V). The reaction was repeated twice to check the evolved gasses in the photoanode and cathode compartments individually. In the first run, we analyzed the gas evolved from the cathode compartment. We detected continuous H_2 formation over the ionomer-mixed Pt/CB catalyst cathode when the photoanode was irradiated with blue light. The H_2 production rate in the cathode compartment was consistent with half of the electron flow in the outer circuit ($e^-/2$). The FE of H_2 evolution was close to 100%, assuming a two-electron reaction ($2H^+ + 2e^- \rightarrow H_2$). This result indicates that the photoexcited

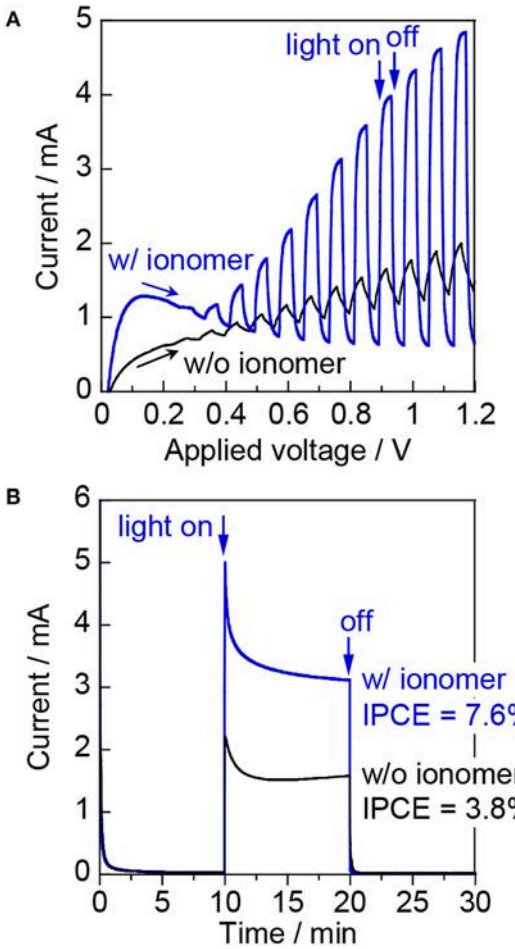

FIGURE 3 | (A) Linear sweep voltammetry curves at a scan rate of 20 mV s^{-1} under chopped irradiation (2 s intervals) and **(B)** current–time curves at an applied voltage of 1.2 V for WO_3/Ti fiber electrodes with and without the Nafion ionomer coating. Reaction conditions: 453 nm blue light, irradiance: 6.8 mW cm^{-2}, photoirradiation area: 16 cm^2, Ar/H_2O = 97/3, flow rate to each electrode: 20 mL min^{-1}.

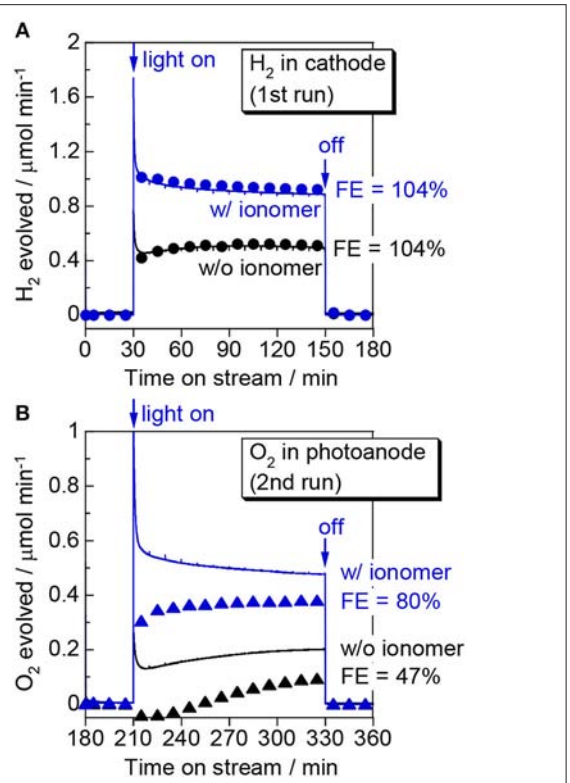

FIGURE 4 | Time course of **(A)** H_2 evolution in the first run and **(B)** O_2 evolution in the second run during gas-phase water splitting over WO_3/Ti fiber photoelectrodes with and without a Nafion ionomer coating. We measured the H_2 evolved in the cathode compartment in the first run and the O_2 evolved in the photoanode compartment in the second run. The symbols show the product formation rate determined by gas chromatography and the curves show the electron flow passing through the outer circuit ($e^-/2$ for H_2 and $e^-/4$ for O_2). Reaction conditions: 453 nm blue light, irradiance: 6.8 mW cm^{-2}, photoirradiation area: 16 cm^2, applied voltage: 1.2 V, Ar/H_2O = 97/3, flow rate to each electrode: 20 mL min^{-1}, temperature: 298 K, pressure: 0.1 MPa.

electrons in the conduction band of WO_3 are transported via the outer circuit to the counter electrode to reduce protons and evolve H_2. The visible-light-induced H_2 production rate was ~1.0 μmol min^{-1}.

In the second run, we analyzed the gas in the photoanode compartment. Although we confirmed that O_2 evolution occurred under photoirradiation, the O_2 formation rate was less than a quarter of the electron flow ($e^-/4$). It should be noted that the formation rate shows a net increase of O_2 because a small amount of O_2 was mixed in the flow from the ambient air. When the light was turned on, we observed an initial decrease in the O_2 concentration for the bare WO_3/Ti fiber photoanode, likely because the O_2 contaminant was consumed by a process such as photoabsorption under photoirradiation. The O_2 evolution rate gradually increased with the PEC reaction, but the FE of O_2 evolution was only 47%, even just before turning off the light. As the FE was calculated by assuming that four electrons are required for the O_2 evolution reaction, an FE of <100% indicates the presence of byproducts such as hydrogen peroxide in the photoanode compartment. The formation of hydrogen peroxide via a reaction requiring two electrons was reported for a PEC reaction over a WO_3 photoanode in an aqueous electrolyte (Santato et al., 2001). In contrast, the Nafion ionomer coating significantly enhanced the FE of O_2 evolution up to 80%. This result suggests that the proton-conducting thin film promoted the four-electron water oxidation reaction to evolve O_2. The visible-light-induced O_2 production rate with this electrode was ~0.4 μmol min^{-1} at an IPCE of 7.5% at 1.2 V.

Figure 5 shows a proposed schematic mechanism for water vapor oxidation over the ionomer-coated WO_3/Ti fiber photoanode. The O_2 evolution reaction ($2H_2O \rightarrow O_2 + 4H^+ + 4e^-$) is recognized as a proton-coupled electron transfer process (Surendranath et al., 2010; Warren et al., 2010). Photocatalysis processes over TiO_2 and ZnO have also been confirmed as proton-coupled electron transfer reactions (Schrauben et al., 2012). The photogenerated holes in the valence band induce

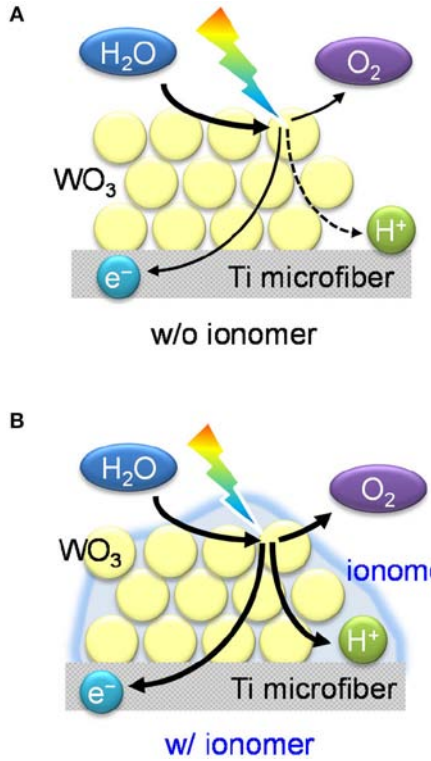

FIGURE 5 | Schematic illustrations of **(A)** the interfaces of the WO_3/Ti fiber electrode without the ionomer coating and **(B)** the photoelectrochemical triple phase boundary of the ionomer-coated WO_3/Ti fiber electrode.

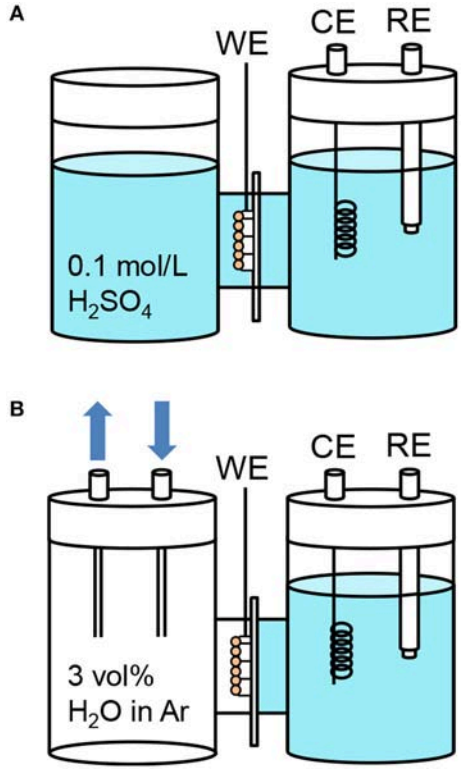

FIGURE 6 | Schematic illustrations of the H-type dual compartment glass reactors used for testing the PEC performance of **(A)** "liquid | solid | liquid" interfaces and **(B)** "gas | solid | liquid" interfaces in the three-electrode configuration. (WE: 1 cm^2 working electrode pressed on a Nafion membrane, CE: Pt counter electrode, RE, Ag/AgCl reference electrode). The gas flow was argon with 3 vol% water vapor. The aqueous electrolyte was 0.1 mol L^{-1} sulfuric acid (pH =1).

four-electron oxidation of water to evolve O_2. The concerted transfer process enhances the reaction rate because the transfer of multiple electrons and protons at the same time avoids the formation of the high-energy intermediates obtained during stepwise reactions. However, proton transfer at the gas–solid interface will be difficult in the absence of an aqueous electrolyte, which acts as an ion conductor. Therefore, the proton-coupled electron transfer is the rate-determining step of water vapor oxidation over the bare WO_3/Ti fiber electrode. However, we found that the proton-conducting ionomer thin film promotes the gas-phase PEC reaction over the WO_3/Ti fiber electrode. These results clearly indicate the importance of the gas–electrolyte–solid triple phase boundary for the PEC water vapor splitting reaction.

PEC Measurements in the Three-Electrode Configuration

We aimed to investigate the role of the triple phase boundary on the gas-phase PEC reactions. A small H-type glass cell (irradiated area: 1.0 cm^2) was used to compare the PEC performance under different conditions. **Figure 6** shows the setup for the PEC measurements in the three-electrode configuration using a platinum wire counter electrode and a Ag/AgCl reference electrode. The two compartments were separated by a Nafion membrane. We filled the cathode compartment with an aqueous electrolyte to maintain electrical neutrality between the membrane, the counter electrode, and the reference electrode. The WO_3/Ti fiber photoanode, which was in contact with the Nafion membrane, was exposed to the other compartment. We investigated two different photoanode conditions. In the first, the photoanode was immersed in an aqueous electrolyte (**Figure 6A**), whereas in the second, the photoanode was exposed to an argon flow with 3 vol% water vapor (**Figure 6B**). These setups are denoted as "liquid | solid | liquid" and "gas | solid | liquid" interfaces, respectively.

Figure 7A shows the photocurrent density at 1.0 V vs. Ag/AgCl for the "liquid | solid | liquid" interfaces. The photocurrent exhibited by the bare electrode was higher than that of the ionomer-coated electrode during the liquid-phase water splitting reaction. This observation indicates that the Nafion ionomer coating retards the oxidation of water, probably by interrupting water adsorption and/or O_2 desorption on the WO_3 surface. **Figure 7B** shows the photocurrent density at 1.0 V vs. Ag/AgCl for the "gas | solid | liquid" interfaces. The IPCE decreased from 28.1 to 10.7% when the photoanode cell was changed from the liquid phase to the two-phase environment. This decrease indicates that the penetration of

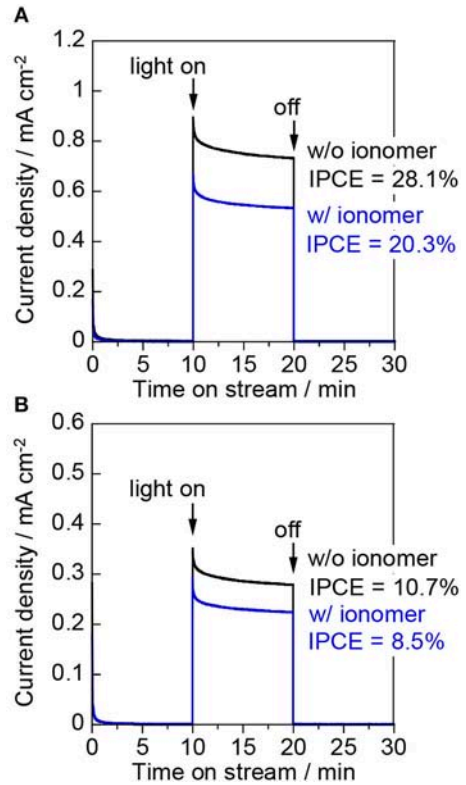

FIGURE 7 | Current–time curves of **(A)** the "liquid | solid | liquid" interfaces and **(B)** the "gas | solid | liquid" interfaces at an applied potential of 1.0 V vs. Ag/AgCl in a three-electrode configuration. The working electrodes were WO_3/Ti fiber electrodes with and without a Nafion ionomer coating. The irradiation source was 453 nm blue light.

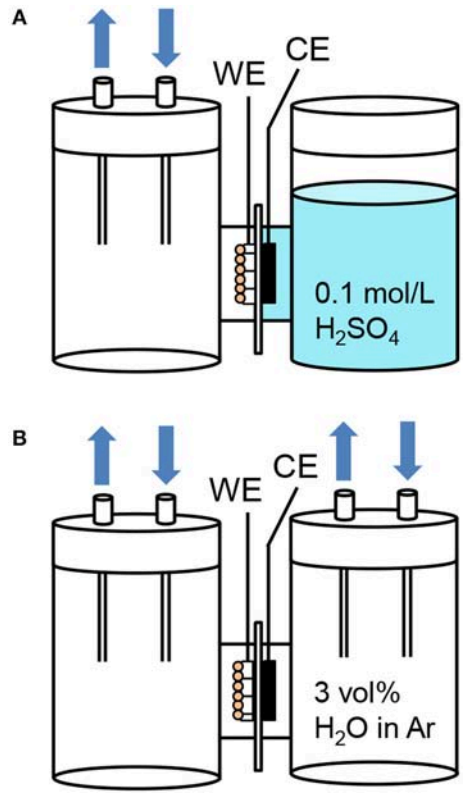

FIGURE 8 | Schematic illustrations of the H-type dual compartment glass reactors using for testing the PEC performance of **(A)** "gas | solid | liquid" interfaces and **(B)** "gas | solid | gas" interfaces in the two-electrode configuration. (WE: 1 cm^2 working electrode pressed on a Nafion membrane, CE: ionomer-mixed Pt/CB electrode on the opposite side of the membrane).

the aqueous electrolyte into the interconnected mesopores of the WO_3 nanoparticles is very important for enhancing the proton-coupled electron transfer process during water oxidation. The photocurrent of the bare electrode decreased more than that of the ionomer-coated electrode when the liquid phase was changed for the two-phase environment. However, the photocurrent of the bare electrode was still higher than that of the ionomer-coated electrode. This is because the Nafion membrane remained fully hydrated when one part of it was in contact with the aqueous electrolyte in the other compartment. Therefore, the bare WO_3 electrode was also coated with a thin layer of the aqueous electrolyte because it was in contact with the wetted Nafion membrane.

PEC Measurements in the Two-Electrode Configuration

We further investigated the PEC performance of the WO_3/Ti fiber photoanodes in the two-electrode configuration to compare two different cathode conditions as shown in **Figure 8**. The ionomer-mixed Pt/CB film was used as a counter electrode in place of the platinum wire in the three-electrode configuration. The WO_3/Ti fiber and the ionomer-mixed Pt/CB film were in contact with a Nafion membrane. For the "gas | solid | liquid" interfaces, the WO_3/Ti fiber photoanode was exposed to the gas phase and the ionomer-mixed Pt/CB cathode was immersed in an aqueous electrolyte (**Figure 8A**). For the "gas | solid | gas" interfaces, both the photoanode and the cathode were exposed to the gas phase (**Figure 8B**). The electrode potential of 1.0 V vs. Ag/AgCl at pH = 1 corresponds to 1.25 V vs. RHE. Therefore, we set the applied voltage to 1.20 V in the two-electrode configuration.

Figure 9A shows the results for the "gas | solid | liquid" interfaces in the two-electrode system. The photocurrent densities at an applied voltage of 1.2 V were similar to those at 1.0 V vs. Ag/AgCl in the three-electrode configuration. This result indicates that the cathodic polarization distributed from the applied voltage was small on the ionomer-mixed Pt/CB catalyst electrode owing to the low overpotential for the H_2 evolution reaction. The performance of a polymer electrolyte fuel cell is significantly increased by a good network of the perfluorosulfonate ionomers contacting with Pt nanoparticles (Uchida et al., 1995). The ionomer is also necessary to prepare the viscous catalyst ink for the Pt/CB catalyst layer with good bonding. **Figure 9B** shows the photocurrent density at the "gas | solid | gas" interfaces in the two-electrode system. The IPCE of the bare WO_3/Ti fiber decreased from 8.2 to

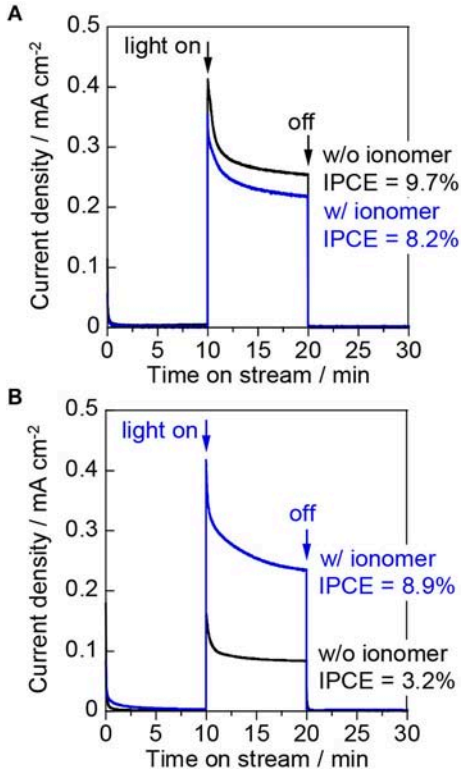

FIGURE 9 | Current–time curves of **(A)** the "gas | solid | liquid" interfaces and **(B)** the "gas | solid | gas" interfaces at an applied voltage of 1.2 V in the two-electrode configuration. The working electrodes were WO_3/Ti fiber electrodes with and without a Nafion ionomer coating. The irradiation source was 453 nm blue light.

3.2% by changing from the two-phase condition to the gas-phase condition. In contrast, the photocurrent densities of the ionomer-coated WO_3/Ti fiber were the same for the "gas | solid | liquid" and the "gas | solid | gas" interfaces. As a result, the IPCE of the ionomer-coated WO_3/Ti fiber was 180% higher than that of the bare WO_3/Ti fiber electrode in the gas-phase PEC reaction.

Figure 10 shows the IPCE action spectrum of the ionomer-coated WO_3/Ti fiber electrode in the "gas | solid | liquid" interfaces. A visible-light response was observed at ∼460 nm, which is consistent with the optical band gap of monoclinic WO_3 nanoparticles (2.67 eV) estimated from the Tauc plot of the diffuse reflectance spectrum (Amano et al., 2017). In this study, the photocurrent response was investigated under blue light irradiation at 453 nm, which is very close to the threshold wavelength. This is the reason for the relatively low IPCE values under blue light. We found that the IPCE at 1.0 V vs. Ag/AgCl was higher than 40% under UV irradiation at wavelengths <400 nm. Moreover, the IPCE value was much higher than that of an ionomer-coated TiO_2/Ti fiber (IPCE = 26% at 1.2 V under 365 nm UV irradiation) for gas-phase water oxidation (Amano et al., in press). To the best of our knowledge, this IPCE value is the highest among those reported for photoanodes in PEM-PEC systems.

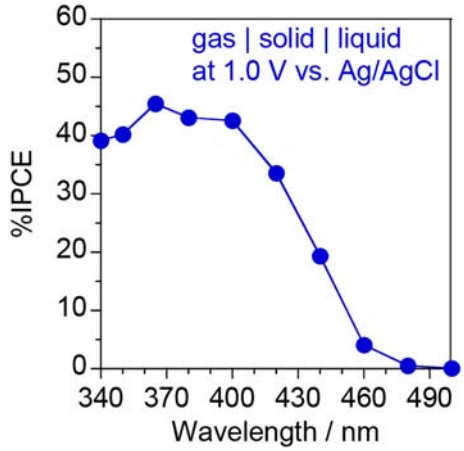

FIGURE 10 | IPCE action spectrum of the ionomer-coated WO_3/Ti fiber photoanode at 1.0 V vs. Ag/AgCl using the "gas | solid | liquid" interfaces shown in **Figure 8A**.

DISCUSSION

We found that a proton-conducting ionomer coating enhanced the PEC oxidation of water in the gas phase, although this effect was not observed in aqueous media. The IPCE of the bare WO_3/Ti fiber decreased from 28.1% in the liquid phase to 9.7–10.7% in the two-phase system and to 3.2% in the gas phase. This behavior indicates that an aqueous electrolyte is essential for PEC reactions that involve proton-coupled electron transfer. In the case of the gas-phase PEC reaction, the hydrated Nafion ionomer thin film plays the role of a solid electrolyte with good proton conductivity at room temperature. The ionomer coating also can absorb water molecules from the gas phase to enhance the hydration of the electrode surface. The Nafion ionomer membrane must be hydrated to maintain the high proton conductivity (Spurgeon and Lewis, 2011). The investigation of the PEC reaction in aqueous media revealed that the ionomer thin film slightly retards the transport of materials, which affects water adsorption and/or O_2 desorption on the WO_3 surface. However, the gas permeability of the thin film is sufficient to create a gas–electrolyte–solid triple phase boundary, where gaseous reactants and products are accessible.

Recently, we found that TiO_2 electrodes without a Nafion ionomer coating exhibit negligible photocurrents for the PEC oxidation of gas-phase water vapor (Amano et al., in press). In contrast, the bare WO_3/Ti fiber electrode exhibited a moderate photocurrent density during the gas-phase PEC reaction. This difference in behavior can be attributed to the proton conductivity of the oxide surfaces. The Nafion ionomer is a perfluorosulfonic acid with strong acidity, and WO_3 is an acidic oxide with an isoelectric point at pH 1.5 (Anik and Cansizoglu, 2006). In contrast, TiO_2 is a neutral oxide with an isoelectric point at pH 5–7 (Maeda and Domen, 2010). Thus, the acidic nature of the WO_3 surface can slightly promote proton transport at room temperature. However, the proton conductivity of the bare electrode was not sufficient for the gas-phase PEC reaction.

The Nafion ionomer coating enhanced the photocurrent density for the oxidation of water vapor to evolve O_2. The FE of O_2 evolution was enhanced to 80%, suggesting that the majority of the photogenerated holes were consumed by a four-electron reaction involving proton-coupled electron transfer.

The fabricated PEM-PEC cell shows a H_2 evolution rate of $\sim$1.0 μmol min^{-1} at 1.2 V under visible-light irradiation (λ = 453 nm, $I_0 = 6.8$ mW cm^{-2}). The rate of H_2 evolution was much higher than that of the previously reported PEM-PEC systems (Stoll et al., 2016, 2017). The IPCE of 40% in the UV range was also the highest value in the gas-phase water photoelectrolysis reaction. This work highlights that the gas–electrolyte–solid triple phase boundary sustained by solid polymer electrolyte plays a significant role in enhancing the photocurrent in the absence of liquid water. To implement solar water splitting technologies, it is necessary to decrease the applied bias voltage and increase the IPCE in the visible light region.

In conclusion, we have successfully fabricated a PEC system consisting of WO_3 nanoparticles for water vapor splitting under visible-light irradiation. A high-surface-area WO_3/Ti fiber gas diffusion electrode was coated with a perfluorosulfonate electrolyte thin film to improve the proton conductivity. Under gas-phase conditions, the ionomer coating significantly enhanced the IPCE as well as the current efficiency of the O_2 evolution reaction by four-electron oxidation of water vapor. The gas–electrolyte–solid triple phase boundary on the high-surface-area photoanode enhanced the extent of proton-coupled electron transfer between the photogenerated holes and the adsorbed water, which was fed from the gas phase. The concept provides insights into the features necessary for successful gas-phase operation, which is a promising approach for low-cost, large-scale H_2 production under solar irradiation.

AUTHOR CONTRIBUTIONS

FA designed and guided the study and wrote the paper; AS, HM, Y-MH, and KT carried out experiments and analyzed the data.

ACKNOWLEDGMENTS

This work was supported by the JST, Precursory Research for Embryonic Science and Technology (PRESTO), grant number JPMJPR15S1 and JPMJPR18T1.

REFERENCES

Abe, R. (2010). Recent progress on photocatalytic and photoelectrochemical water splitting under visible light irradiation. *J. Photochem. Photobiol. C* 11, 179–209. doi: 10.1016/j.jphotochemrev.2011.02.003

Amano, F., Ishinaga, E., and Yamakata, A. (2013). Effect of particle size on the photocatalytic activity of WO_3 particles for water oxidation. *J. Phys. Chem. C* 117, 22584–22590. doi: 10.1021/jp408446u

Amano, F., Mukohara, H., Shintani, A., and Tsurui, K. (in press). Solid polymer electrolyte-coated titania nanotube macroporous photoelectrode for gas-phase water splitting. *ChemSusChem*. doi: 10.1002/cssc.201802178

Amano, F., Shintani, A., Tsurui, K., and Hwang, Y.-M. (2017). Fabrication of tungsten trioxide photoanode with titanium microfibers as a three dimensional conductive back contact. *Mater. Lett.* 199, 68–71. doi: 10.1016/j.matlet.2017.04.051

Anik, M., and Cansizoglu, T. (2006). Dissolution kinetics of WO_3 in acidic solutions. *J. Appl. Electrochem.* 36, 603–608. doi: 10.1007/s10800-006-9113-3

Georgieva, J., Armyanov, S., Poulios, I., Jannakoudakis, A. D., and Sotiropoulos, S. (2010). Gas phase photoelectrochemistry in a polymer electrolyte cell with a titanium dioxide/carbon/nafion photoanode. *Electrochem. Solid State Lett.* 13, P11–P13. doi: 10.1149/1.3465306

Georgieva, J., Armyanov, S., Poulios, I., and Sotiropoulos, S. (2009). An all-solid photoelectrochemical cell for the photooxidation of organic vapours under ultraviolet and visible light illumination. *Electrochem. Commun.* 11, 1643–1646. doi: 10.1016/j.elecom.2009.06.019

Hisatomi, T., Takanabe, K., and Domen, K. (2015). Photocatalytic water-splitting reaction from catalytic and kinetic perspectives. *Catal. Lett.* 145, 95–108. doi: 10.1007/s10562-014-1397-z

Homura, H., Ohtani, B., and Abe, R. (2014). Facile fabrication of photoanodes of tungsten(VI) oxide on carbon microfiber felts for efficient water oxidation under visible light. *Chem. Lett.* 43, 1195–1197. doi: 10.1246/cl.140320

Iwu, K. O., Galeckas, A., Kuznetsov, A. Y., and Naorby, T. (2013). Solid-state photoelectrochemical H2 generation with gaseous reactants. *Electrochim. Acta* 97, 320–325. doi: 10.1016/j.electacta.2013.03.013

Kumari, S., Turner White, R., Kumar, B., and Spurgeon, J. M. (2016). Solar hydrogen production from seawater vapor electrolysis. *Energy Environ. Sci.* 9, 1725–1733. doi: 10.1039/c5ee03568f

Kusoglu, A., and Weber, A. Z. (2017). New insights into perfluorinated sulfonic-acid ionomers. *Chem. Rev.* 117, 987–1104. doi: 10.1021/acs.chemrev.6b00159

Maeda, K., and Domen, K. (2010). Photocatalytic water splitting: recent progress and future challenges. *J. Phys. Chem. Lett.* 1, 2655–2661. doi: 10.1021/jz1007966

McKone, J. R., Lewis, N. S., and Gray, H. B. (2014). Will solar-driven water-splitting devices see the light of day? *Chem. Mater.* 26, 407–414. doi: 10.1021/cm4021518

Modestino, M. A., Dumortier, M., Hosseini Hashemi, S. M., Haussener, S., Moser, C., and Psaltis, D. (2015). Vapor-fed microfluidic hydrogen generator. *Lab Chip* 15, 2287–2296. doi: 10.1039/c5lc00259a

Pinaud, B. A., Benck, J. D., Seitz, L. C., Forman, A. J., Chen, Z., Deutsch, T. G., et al. (2013). Technical and economic feasibility of centralized facilities for solar hydrogen production via photocatalysis and photoelectrochemistry. *Energy Environ. Sci.* 6, 1983–2002. doi: 10.1039/c3ee40831k

Rongé, J., Deng, S., Pulinthanathu Sree, S., Bosserez, T., Verbruggen, S. W., Kumar Singh, N., et al. (2014). Air-based photoelectrochemical cell capturing water molecules from ambient air for hydrogen production. *RSC Adv.* 4, 29286–29290. doi: 10.1039/c4ra05371k

Rongé, J., Nijs, D., Kerkhofs, S., Masschaele, K., and Martens, J. A. (2013). Chronoamperometric study of membrane electrode assembly operation in continuous flow photoelectrochemical water splitting. *Phys. Chem. Chem. Phys.* 15, 9315–9325. doi: 10.1039/c3cp50890k

Santato, C., Ulmann, M., and Àugustynski, J. (2001). Photoelectrochemical properties of nanostructured tungsten trioxide films. *J. Phys. Chem. B* 105, 936–940. doi: 10.1021/jp002232q

Schrauben, J. N., Hayoun, R., Valdez, C. N., Braten, M., Fridley, L., and Mayer, J. M. (2012). Titanium and zinc oxide nanoparticles are proton-coupled electron transfer agents. *Science* 336, 1298–1301. doi: 10.1126/science.1220234

Spurgeon, J. M., and Lewis, N. S. (2011). Proton exchange membrane electrolysis sustained by water vapor. *Energy Environ. Sci.* 4, 2993–2998. doi: 10.1039/c1ee01203g

Stoll, T., Zafeiropoulos, G., Dogan, I., Genuit, H., Lavrijsen, R., Koopmans, B., et al. (2017). Visible-light-promoted gas-phase water splitting using porous WO_3/$BiVO_4$ photoanodes. *Electrochem. Commun.* 82, 47–51. doi: 10.1016/j.elecom.2017.07.019

Stoll, T., Zafeiropoulos, G., and Tsampas, M. N. (2016). Solar fuel production in a novel polymeric electrolyte membrane photoelectrochemical (PEM-PEC) cell with a web of titania nanotube arrays as photoanode and gaseous reactants. *Int. J. Hydrogen Energy* 41, 17807–17817. doi: 10.1016/j.ijhydene.2016.07.230

Surendranath, Y., Kanan, M. W., and Nocera, D. G. (2010). Mechanistic studies of the oxygen evolution reaction by a cobalt-phosphate catalyst at neutral pH. *J. Am. Chem. Soc.* 132, 16501–16509. doi: 10.1021/ja106102b

Tsui, L.-K., Homma, T., and Zangari, G. (2013). Photocurrent conversion in anodized TiO_2 nanotube arrays: effect of the water content in anodizing solutions. *J. Phys. Chem. C* 117, 6979–6989. doi: 10.1021/jp400318n

Uchida, M., Aoyama, Y., Eda, N., and Ohta, A. (1995). Investigation of the microstructure in the catalyst layer and effects of both perfluorosulfonate lonomer and PTFE-loaded carbon on the catalyst layer of polymer electrolyte fuel cells. *J. Electrochem. Soc.* 142, 4143–4149. doi: 10.1149/1.2048477

Verbruggen, S. W., Van Hal, M., Bosserez, T., Rongé, J., Hauchecorne, B., Martens, J. A., et al. (2017). Harvesting hydrogen gas from air pollutants with an unbiased gas phase photoelectrochemical cell. *ChemSusChem* 10, 1413–1418. doi: 10.1002/cssc.201601806

Warren, J. J., Tronic, T. A., and Mayer, J. M. (2010). Thermochemistry of proton-coupled electron transfer reagents and its implications. *Chem. Rev.* 110, 6961–7001. doi: 10.1021/cr100085k

Xiang, C., Weber, A. Z., Ardo, S., Berger, A., Chen, Y., Coridan, R., et al. (2016). Modeling, simulation, and implementation of solar-driven water-splitting devices. *Angew. Chem. Int. Ed.* 55, 12974–12988. doi: 10.1002/anie.201510463

Conflict of Interest Statement: The authors declare that the research was conducted in the absence of any commercial or financial relationships that could be construed as a potential conflict of interest.

Copyright © 2018 Amano, Shintani, Mukohara, Hwang and Tsurui. This is an open-access article distributed under the terms of the Creative Commons Attribution License (CC BY). The use, distribution or reproduction in other forums is permitted, provided the original author(s) and the copyright owner(s) are credited and that the original publication in this journal is cited, in accordance with accepted academic practice. No use, distribution or reproduction is permitted which does not comply with these terms.

frontiers in Chemistry

REVIEW
published: 30 January 2019
doi: 10.3389/fchem.2019.00022

Templated Growth of Crystalline Mesoporous Materials: From Soft/Hard Templates to Colloidal Templates

Lei Zhang[1,2], *Lei Jin*[2], *Ben Liu*[1]* and *Jie He*[2,3]*

[1] Jiangsu Key Laboratory of New Power Batteries, Collaborative Innovation Center of Biomedical Functional Materials, School of Chemistry and Materials Science, Nanjing Normal University, Nanjing, China, [2] Department of Chemistry, University of Connecticut, Mansfield, CT, United States, [3] Institute of Materials Science, University of Connecticut, Mansfield, CT, United States

Mesoporous non-siliceous materials, in particular mesoporous transition metal oxides (*m*-TMOs), are of interest due to their fascinating electronic, redox, and magnetic properties for a wide range of applications in catalysis and energy storage. Control of the porosity (e.g., pore size, wall thickness, and surface area) and the crystalline degree (e.g., phase composition, crystallinity, and crystal grain size) of *m*-TMOs are critical for those applications. To crystallize TMOs, high temperature annealing is often needed to remove the amorphous defects and/or tune the compositions of different crystalline phases. This has brought many challenges to surfactant or block copolymer templates used in the process of evaporation-induced-self-assembly to prepare *m*-TMOs. In this review, we summarize the most recent achievements including the findings in our own laboratory on the use of organosilicate-containing colloids for the templated growth of mesoporous materials. We review a few key examples of preparing crystalline mesoporous oxides using different templating methods. The colloidal templating method by which mesoporous nanostructures can be stabilized up to 1,000°C is highlighted. The applications of *m*-TMOs and meso metal-oxide hybrids synthesized using organosilicate-containing colloidal templates in photocatalysis and high-temperature catalysis are also discussed.

Keywords: mesoporous materials, templates, transition metal oxides, nanoconfinement, polymer micelles, organosilicate

OPEN ACCESS

Edited by:
Steve Suib,
University of Connecticut,
United States

Reviewed by:
Roberto Millini,
Eni (Italy), Italy
Matteo Guidotti,
Italian National Research Council (CNR), Italy
Miguel Angel Centeno,
Instituto de Ciencia de Materiales de Sevilla (ICMS), Spain

***Correspondence:**
Ben Liu
ben.liu@njnu.edu.cn
Jie He
jie.he@uconn.edu

Specialty section:
This article was submitted to Green and Sustainable Chemistry, a section of the journal Frontiers in Chemistry

Received: *28 November 2018*
Accepted: *10 January 2019*
Published: *30 January 2019*

Citation:
Zhang L, Jin L, Liu B and He J (2019) Templated Growth of Crystalline Mesoporous Materials: From Soft/Hard Templates to Colloidal Templates. Front. Chem. 7:22. doi: 10.3389/fchem.2019.00022

INTRODUCTION

Mesoporous materials are porous materials with periodically ordered pores in the range of 2∼50 nm. They have large accessible surface areas and tunable pore sizes, which are of particular benefit for mass transport and dispersion of electrons/reactants. Therefore, mesoporous materials show great potential in electrocatalysis (Wu et al., 2012; Ren et al., 2013; Xin et al., 2018), photocatalysis (Li et al., 2007; Onozuka et al., 2012; Joo et al., 2013; Liu et al., 2015b) and energy storage, and conversion (Li et al., 2015, 2016; Fang et al., 2016; Le et al., 2017). Since ordered mesoporous silica such as MCM-41 were discovered in 1992 (Kresge et al., 1992), extensive efforts have been devoted to the development of many other mesoporous silica such as SBA-15/16 (Zhao et al., 1998a,b; Sakamoto et al., 2000), KIT-6 (Kleitz et al., 2003), AMS (Qiu and Che, 2011; Han and Che, 2013), and FDU-12 (Fan et al., 2003, 2005). These mesoporous silica with ordered and

interconnected nanopores as well as excellent thermal stability have been broadly used as support for metal nanocatalysts. Other than mesoporous silica, there has been a substantial amount of interest in mesoporous transition metal oxides (*m*-TMOs) due to their unique *d*-shell electrons, resulting in a redox active surface on top of the nanosized pores (Schüth, 2001). Compared to amorphous mesoporous silica, *m*-TMOs exhibit enhanced electronic and optical properties (Kondo and Domen, 2008), which have been proven to be essential in the applications such as photocatalysis (Kuo et al., 2015; Liu et al., 2015b), electrocatalysis (Burke et al., 2015; Song et al., 2018), and battery materials (Su et al., 2016; Zheng et al., 2018).

The crystallinity of *m*-TMOs is of critical importance for some of their applications. Since high-temperature annealing is the most common way to increase the crystallinity and tune the crystalline phases of *m*-TMOs (Lee et al., 2008; Zhang et al., 2010; Liu et al., 2015b), how to stabilize porous frameworks under high temperature is the key to producing highly crystalline *m*-TMOs. Using photocatalysis as an example, TiO_2 is one of the most well-studied photocatalysts. The low-crystalline TiO_2 with amorphous domains is known to effectively trap photo-excited electrons and holes that lower the overall utilization of photoexcitation (Ohtani et al., 1997). TiO_2 has two common crystalline structures, including rutile and anatase. As a photocatalyst, anatase shows much better activity compared to rutile. Interestingly, TiO_2 with mixed phases outperforms both pure phases (Cong and Xu, 2011; Zhao et al., 2013; Siah et al., 2016). P25 (Degussa) consisting of ∼80% of anatase and ∼20% of rutile has often been used as a benchmark TiO_2 photocatalyst. Since there is a type II band alignment of ∼0.4 eV (the energy of valance band) (Scanlon et al., 2013), TiO_2 with a mixture of phases shows enhanced charge separation efficiency at the interface of rutile and anatase (Kawahara et al., 2002; Miyagi et al., 2004). Converting anatase or non-crystalline to rutile TiO_2 requires high-temperature annealing, e.g., at 800°C, although the rutile TiO_2 is more stable. When the annealing is carried out in a mesoporous TiO_2, the collapse of the porous framework occurs before the phase transition due to the overgrowth of crystal grains (Schüth, 2001; Yun et al., 2001). Another example is the formation of crystalline mixed oxides in order to control the optical properties. Carter et al. have proposed the MnO:ZnO alloys that potentially shift the band energy of MnO dramatically (Kanan and Carter, 2012, 2013). MnO as an n-type semiconductor has a large bandgap of 4.0 eV but, when forming alloys with ZnO, its band energy can be shifted largely to a bandgap of 2.6 eV, which is potentially useful for photocatalytic water splitting or CO_2 reduction. The formation of mixed oxides of MnO:ZnO needs high-temperature treatment at 700°C (Song et al., 2015). The synthesis of such binary or ternary oxides (e.g., copper tungstate and perovskites) in mesoporous form will be very difficult because of the poor thermal stability of porous frameworks. Overall, the control of crystallinity and crystal phases is critical in tuning the physicochemical properties of *m*-TMOs.

In this review, we summarize the synthetic methods in recent years for the preparation of highly crystalline *m*-TMOs. The synthesis will be discussed by classifying the synthetic methods based on the templates (**Figure 1**), including hard templates, soft templates, and colloidal templates. There are a number of excellent review papers on the synthesis of mesoporous materials such as TiO_2 (Li et al., 2013), non-siliceous oxides (Gu and Schuth, 2014), and metal oxides (Ren et al., 2012) by mainly soft-templating and hard-templating methods. We intend to highlight a few key examples in control of the crystallinity of *m*-TMOs by different methods, with a focus on the findings in our own laboratory on the use of organosilicate-containing colloids for the templated growth of mesoporous materials. The applications of colloidal-templated porous oxides and metal-oxide hybrids in photocatalysis will be included. At the end of this review, we include a short perspective in this area. We hope that this review will help readers to understand the challenges and solutions in the rational design and application of crystalline *m*-TMOs.

HARD-TEMPLATING METHOD

The hard-templating method, also known as nanocasting, provides the most accessible strategy to synthesize crystalline mesoporous materials. Nanocasting is to make use of a rigid mold with defined porous structures on the nanometer scale where the target materials or their precursors are added to fill the pore of the mode, and the primary mold is subsequently removed after the formation of target materials (Lu and Schüth, 2006). In detail, nanocasting of *m*-TMO includes three steps: (1) synthesis of mesoporous replicas (e.g., silica, carbons, and aluminates); (2) infiltration of metal precursors and further decomposition to form crystalline materials; and (3) removal of the hard template to release the pores. Upon removal of the mold, the yielded *m*-TMO will replicate the complementary mesostructures of the hard template. For instance, silica templates equipped with ordered cylindrical channels can produce nanowires or nanoarrays (Lu and Schüth, 2005), while the template with spherical pores can prepare the nanosphere arrays (Lu and Schüth, 2006), and the template with bicontinuous pores results in bicontinuous mesostructured duplicates with periodically and helically twisted nanowires (Yang and Zhao, 2005). The framework thickness of the mesoporous silica is usually in the range of 2–11 nm; thus, the pore size of derived replicas of *m*-TMO is also in the same range (Schüth, 2001).

Ideally, all crystalline mesoporous materials can be synthesized using the hard-templating method if the corresponding metal precursors can be filled into the pore of the mold. So far, among numerous hard templates, mesoporous silica (e.g., SBA-15 and KIT-6) are commonly used for the preparation of mesoporous materials due to their diverse pore architectures and extremely uniform pore size/size distribution. SBA-15 has uniform hexagonal pores with the pore diameter in the range of 5–15 nm (Zhao et al., 1998a,b; Sakamoto et al., 2000). KIT-6 shows a bicontinuous structure as a gyroid cubic symmetry Ia3d with a pore diameter in the range of 4–12 nm (Kleitz et al., 2003). When using mesoporous silica as a template, the removal of silica to release the pore usually relies on the etching by concentrated NaOH or HF. One can also consider the use of mesoporous carbon as a template to prepare *m*-TMO, where the carbon template can simply be oxidized by low-temperature annealing

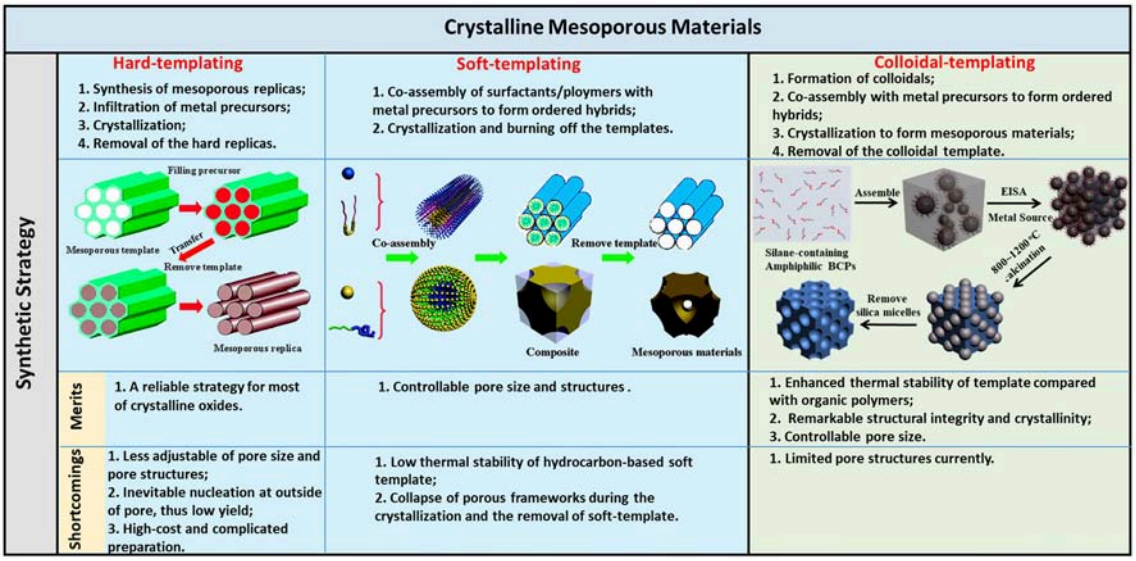

FIGURE 1 | Illustration of the synthetic methods/procedures of crystalline mesoporous materials and the merits/shortcomings of the three methods. Reprinted with permission from Gu and Schuth (2014) and Liu et al. (2015b). Copyright 2015 American Chemical Society and Copyright 2014 Royal Society of Chemistry.

in air (Lu et al., 2002; Roggenbuck and Tiemann, 2005; Polarz et al., 2007; Liang et al., 2008).

Given the hard templates that can support and confine the grain growth of TMOs, the crystalline phases and pore features of metal oxides can be rationally designed. Taking manganese oxides as an example, Bruce's group synthesized mesoporous β-MnO_2, Mn_2O_3, and Mn_3O_4 by high-temperature calcination at different temperatures or in the assistance of H_2, using KIT-6 as the hard template (Jiao and Bruce, 2007; Jiao et al., 2007). All the materials possessed similar mesoporous frameworks and well-controlled crystalline phases of Mn oxides (**Figures 2A–C**). Similarly, iron oxides (Jiao et al., 2006) and cobalt oxides (Jiao et al., 2005a) with different crystalline phases were also obtained using the same strategy (Ren et al., 2009). Furthermore, bicontinuous mesoporous nanochannels of KIT-6 can also be utilized to tailor the final porosity of the materials. By selectively filling in different sets of nanochannels, mesoporous oxides with different pore sizes and even pore hierarchies (macropore, mesopore, and micropore) were successfully synthesized (**Figures 2D–F**) (Ren et al., 2013). The hard-templating synthesis of mesoporous materials is also extendable to metal sulfides and phosphides (Fu et al., 2016; Jin et al., 2017).

The hard-templating method shows limited control over the mesoporous structures but, in KIT-6 template, the distribution, and adjustable ratio of the two different pores can be achieved by hydrothermal synthetic conditions (**Figure 3**) (Jiao et al., 2008; Ren et al., 2010). Using mesoporous NiO as an example, an alcoholic solution of $Ni(NO_3)_2$ was mixed with KIT-6 and then redispersed in hexane to achieve a very high degree of pore filling. Followed by calcination at 550°C and removal of KIT-6 via etching with NaOH, mesoporous NiO with a specific surface area of 108.6 m^2 g^{-1} can be synthesized. KIT-6 has two sets of pores

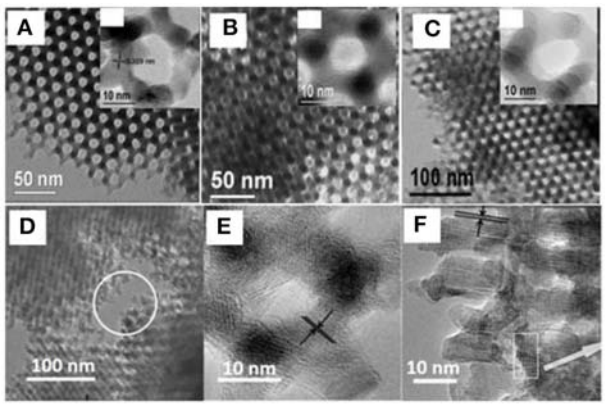

FIGURE 2 | Control of crystallinity and mesostructures of Mn oxides. TEM images of **(A)** mesoporous β-MnO_2, **(B)** Mn_2O_3, and **(C)** Mn_3O_4, and TEM images of **(D–F)** hierarchical porous MnO_2 templated by KIT-6. Reprinted with permission from Jiao and Bruce (2007), Jiao et al. (2007) and Ren et al. (2013) Copyright 2013 Nature Publishing Group and Copyright 2007 Willey VCH.

with bicontinous channels and the development of these channels varies along with the hydrothermal synthetic conditions of KIT-6. At a higher hydrothermal temperature (>130°C), the existence of interconnected porous channels in KIT-6 favors complete growth of NiO across both sets of mesopores, leading to the formation of mesoporous NiO with a pore diameter (∼3.3 nm) similar to the wall thickness of KIT-6 (**Figure 3**). On the other hand, with less interconnected pores at a lower hydrothermal temperature, the growth of mesoporous NiO within only one set of mesopores was observed. The resultant mesoporous NiO has a pore size of ∼11 nm, equivalent to the dimension of two walls plus the pore

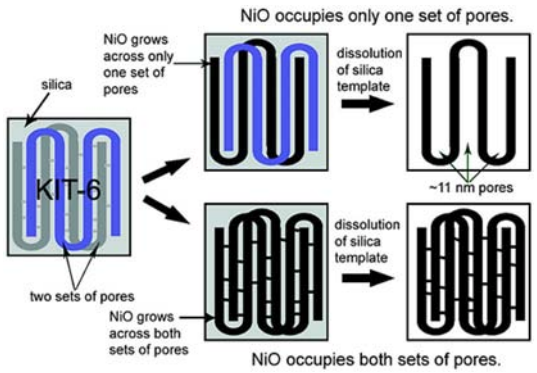

FIGURE 3 | Scheme illustrating the synthesis of *m*-TMO with two pore size distributions by using KIT-6 as the template. Reprinted with permission from Jiao et al. (2008). Copyright 2008 American Chemical Society.

size of KIT-6. Through this method, mesoporous β-MnO_2 and NiO with large (∼11 nm) and small (∼3.3 nm) controllable pore sizes can be prepared.

Using SBA-15 as a template, *m*-TMO with ordered cylindrical channels can be prepared. Zhu et al. reported the highly crystalline Cr_2O_3 using aminopropyl-triethoxysilane (APTS)-modified SBA-15 (Zhu et al., 2003). The formation of crystalline Cr_2O_3 needs calcination of the Cr_2O_3@SBA above 350°C. After the removal of SBA-15, the mesoporous Cr_2O_3 possesses a specific surface area of 58.1 m^2 g^{-1} and an average pore size of 3.4 nm. Other mesoporous *m*-TMOs with cylindrical pores can be prepared through a similar route (Chen et al., 2003; Jiao et al., 2005b; Yue et al., 2005). Our group also demonstrated mesoporous Co_3O_4, NiO, and their binary oxides by using bicontinuous KIT-6 as the template. Through a solid-phase sulfurization method based on sulfur, bicontinuous mesoporous CoS_2, NiS_2, and their binary sulfides can be further synthesized (Jin et al., 2017). When using the double templates, more sophisticated nanostructures can be designed. For example, if coated with thin carbon on the SBA channels first, the further growth of metal oxides will be confined in the hollow carbon nanotubes within SBA-15. Zhao et al. showed the synthesis of a mesoporous Co_3O_4@ carbon nanotube using double templates of silica and carbon. The resultant oxide-in-tube nanostructures possess a specific surface area up to 750 m^2 g^{-1} and a controllable size of Co_3O_4 between 3 and 7 nm.

The synthetic challenge of the hard-templating method is to completely fill the pores of the template due to the slow mass transfer at nanoscale (Yang and Zhao, 2005). Mostly, only small pieces of mesoporous replicas can be yielded. Despite functionalized mesoporous templates with binding groups (e.g., $-NH_2$, -OH, $-CH=CH_2$) (Zhu et al., 2003; Tian et al., 2004; Wang et al., 2005), metal precursors still inevitably nucleate and grow in the outside of template pores, in particular under high temperature. Additionally, the pore size of resultant replicas that is determined by the thickness of the framework is usually small and less adjustable in both SBA series and KIT-6. Meanwhile, the nanocasting method is high-cost and time-consuming (Lu and Schüth, 2005, 2006; Yang and Zhao, 2005).

SOFT-TEMPLATING METHOD

The soft-templating method usually uses unrigid nanostructures formed by intermolecular interaction force as templates. Followed by the deposition of inorganic sources on the surface and interior of the unrigid soft templates, the formation of mesostructures with defined pore structures and sizes can occur. Generally, soft templates include soft matter, including organic surfactants and/or block copolymers, that can interact with metal ions and self-assemble into liquid crystal phases to template the sol-gel process. The assembled process between metal ions and soft matter is driven by weak non-covalent bonds, such as hydrogen bonds, van der Waals forces, and electrostatic interaction. In addition, cooperative assembly between metal ions and soft matter is mostly involved in facilitating this process. Mesostructures with open pores can be obtained after the removal of soft template through calcination. The soft-templating method offers a large room of controllability in terms of the pore structures and pore sizes compared to the hard-templating method. The key of the soft-templating method is the control over the sol-gel transition of precursors along the self-assembly of soft templates, i.e., surfactants/block copolymers (Meng et al., 2005; Li et al., 2013; Lokupitiya et al., 2016). By rationally tuning the cooperative assembly between precursors and templates, mesoporous materials can be obtained through either a solution-phase synthesis or evaporation-induced self-assembly (EISA) process. The first report on solution-phase synthesis of mesoporous oxides and phosphates by a similar route for MCM silica was in Huo et al. (1994). Due to the straightforwardness of tunability in size and self-assembled mesophases of surfactants/block copolymer, the soft-templating method has been widely used to tailor the mesoporous sizes and framework nanostructures of *m*-TMOs.

However, it is difficult to release mesopores by removing the surfactant because of the disruption and collapse of these porous frameworks during the crystallization of *m*-TMOs. Ying et al. first reported the ordered mesoporous TiO_2 with open pores using titanium acetylacetonate tri-isopropoxide as Ti precursor and tetradecylphosphate as the template (Antonelli and Ying, 1995). The presence of acetylacetone slowed down the sol-gel transition, which allowed further interaction and co-assembly with Ti and the template. The resultant mesoporous TiO_2 had a surface area of 200 m^2 g^{-1} after calcination. Her group has extended this solution synthetic method to synthesize the ordered mesoporous Nb_2O_5 (Antonelli et al., 1996), VO_x (Liu et al., 1997), and ZrO_2 (Wong et al., 1997; Antonelli, 1999).

Yang and Zhao creatively developed Pluronic polymers (commercial PEO-PPO-PEO triblock copolymers) as soft templates in non-aqueous solution to synthesize a series of mesoporous silica and metal oxide, including TiO_2, ZrO_2, Al_2O_3, Nb_2O_5, Ta_2O_5, WO_3, HfO_2, SnO_2, and mixed oxides $SiAlO_{3.5}$, $SiTiO_4$, $ZrTiO_4$, Al_2TiO_5, and ZrW_2O_8 (Yang et al., 1998, 1999). Pluronic polymers have a long flexible poly(ethylene oxide)

(PEO) chain that can coordinate with transitional metal ions via weak coordination bonds. The absence of water enabled a controllable sol-gel, i.e., hydrolysis and condensation of metal precursors. These resulted in the optimal co-assembly at inorganic/organic interfaces; therefore, Pluronic polymers further templated the growth of a number of *m*-TMOs with periodically ordered mesoporous nanostructures. Through EISA, Sanchez et al. used PEO-based surfactants (e.g., Pluronic F127, Pluronic P123, Brij 56, and Brij 58) as templates to synthesize highly ordered *m*-TMOs (Grosso et al., 2001; Crepaldi et al., 2003). However, since the conventional EISA method usually employed Pluronic polymers as templates, the pore size of *m*-TMOs is usually <15 nm owing to the short hydrophobic PPO segments (Yang et al., 1998). Furthermore, both PEO and PPO polymers are thermally unstable. When annealing those *m*-TMOs to remove the template, the mesoporous nanostructures ineluctably undergo structural reconstruction for crystallization, leading to the overgrowth of crystal grains, and even collapse of mesoporous frameworks (Schüth, 2001; Yun et al., 2001).

More recently, Suib's group has developed a universal strategy to synthesize the thermally stable and crystalline *m*-TMOs (Poyraz et al., 2013). As illustrated in **Figure 4A**, the inverse micelle formed by Pluronic P123 served as a nanoreactor where the positively charged transition metal-oxo clusters were confined via hydrogen bonding interaction. As stabilized by P123, the uncontrolled aggregation of the clusters was reduced and hindered. The addition of 1-butanol, the solvent and interface modifier, further enhanced the physical barrier between the oxo-clusters and prevented condensation. The essential presence of nitric acid in this system enabled the penetration of the positively charged metal-oxo clusters into the micelles, simultaneously increasing the solubility of P123 and hydrating the core. Interestingly, the decomposition of the nitrate ions into nitric oxides (NO_x) played a critical role in the consecutive heat treatment by adsorption onto metal oxo-clusters, therefore impeding the uncontrolled condensation. After the removal of P123 by calcination at different temperatures ranging from 150 to 550°, the *m*-TMOs were readily obtained with tunable pore size distribution. For example, the mesoporous MnO_2 evolved from amorphous materials with higher specific surface area (255 $m^2\ g^{-1}$) and smaller pore size (2 nm) at a low temperature of 150° (**Figures 4B,C**), to the ordered crystalline Mn_2O_3 with lower specific surface area (35 $m^2\ g^{-1}$), and enlarged pore size (12.3 nm) at an elevated temperature of 550° (**Figures 4D,E**). This method allows the general syntheses to a range of *m*-TMOs including nickel, cobalt, iron oxides etc (Poyraz et al., 2013, 2014; Song et al., 2014; Jiang et al., 2015; Wasalathanthri et al., 2015). It is worth mentioning that the series of the *m*-TMOs are highly resistant to elevated temperatures up to 400∼550°, showing superior thermal stability. This unique stable mesoporous structure affords the development of more efficient and heat-tolerant catalysts in high-temperature reactions (Poyraz et al., 2013; Lu et al., 2015; Vovchok et al., 2018).

As mentioned above, the crystallinity of TiO_2 determines the surface amorphous defects that plays a critical role in photocatalysis. The high temperature treatment for a typical *m*-TiO_2 obtained using Pluronic polymers as templates, usually causes structural collapse of the ordered mesoporous frameworks (Schüth, 2001; Yun et al., 2001). To solve the thermal stability challenges in soft-templating, Wiesner's group developed the combined assembly by soft and hard chemistries (so-called CASH, **Figure 5a**) method to fabricate mesoporous metal oxides (*m*-TiO_2 and *m*-Nb_2O_5) with excellent thermal stability and crystallinity (Lee et al., 2008). In the CASH method for the synthesis of *m*-TiO_2 (**Figure 5a**), titanium chloride firstly reacted with titanium isopropoxide to form the metal oxide clusters and corresponding alkyl halide, which was added into the tetrahydrofuran (THF) solution of the block copolymer of poly(isoprene-block-ethylene oxide) (PI-*b*-PEO, $M_n = 27{,}220\ g\ mol^{-1}$). The hydrophilic PEO selectively bound the metal oxide sol, which generated an amorphous hybrid material under evaporation of a PI-*b*-PEO/metal oxide solution in air (the obtained hybrid in **Figure 5b**). Secondly, the as-made PI-*b*-PEO/metal oxide hybrids were annealed at 700°C in argon to achieve the highly crystalline materials. The metal oxide crystals nucleate, grow, and sinter into porous frameworks and PEO was removed by thermal decomposition, while the PI segments can be transformed *in situ* into a carbon scaffold inside the pore channels due to the existence of sp^2 hybridized carbon atoms in the PI segments of PI-*b*-PEO (the TiO_2-C composite in **Figure 5c**). The generated carbon scaffold acts as a hard template *in situ* to prevent the collapse of mesoporous frameworks while crystallizing under high temperature treatment (700°C). Thus this generated highly crystalline TiO_2 (Lee et al., 2008). Finally, the carbon inside TiO_2-C composite could be removed by heating in air, yielding a well-organized, highly crystalline mesoporous TiO_2 (**Figure 5d**) with a pore size of 23.6 nm and a specific surface area of 75 $m^2\ g^{-1}$. Other polymers, like poly(ethylene oxide)-*b*-polystyrene (PEO-*b*-PS), which includes sp^2 hybridized carbon atoms and can be carbonized under inert atmosphere, potentially are useful to obtain highly crystalline *m*-TMOs using the CASH method (Zhang et al., 2011).

Other than carbonization thermally, Zhao's group developed a simple sulfuric acid (H_2SO_4) carbonization method to generate a highly crystalline, ultra-stable ordered *m*-TiO_2 by using Pluronic polymers (P123, F127, and F10) as templates (**Figure 6A**) (Zhang et al., 2010). In the process of EISA with titanium isopropoxide (TIPO), a mixture of HCl, and H_2SO_4 as the acidic catalyst carbonized the polymer template to form amorphous carbon in the original pore channels. The *in situ*-formed carbon templates can stabilize the mesoporous structures during crystallization (650°C) in N_2. After burning off the carbon at 450°C in air, the resultant *m*-TiO_2 with a specific surface area of 193 $m^2\ g^{-1}$ and a pore size of 4.6 nm was generated, which also possessed a high crystallinity of anatase and thermal stability (**Figures 6B,C**). To keep the structural order of *m*-TMOs, Zhou et al. synthesized the well-ordered mesoporous *m*-TiO_2 with improved crystallinity and remarkably thermal stability through the EISA method assisted with encircling ethylenediamine (EN) protectors to retain the mesoporous structure (Zhou et al., 2011). The EN species could tightly interact and bind on the surface of TiO_2 while prohibiting undesirable grain growth and structure transformation during calcination. Thus, the

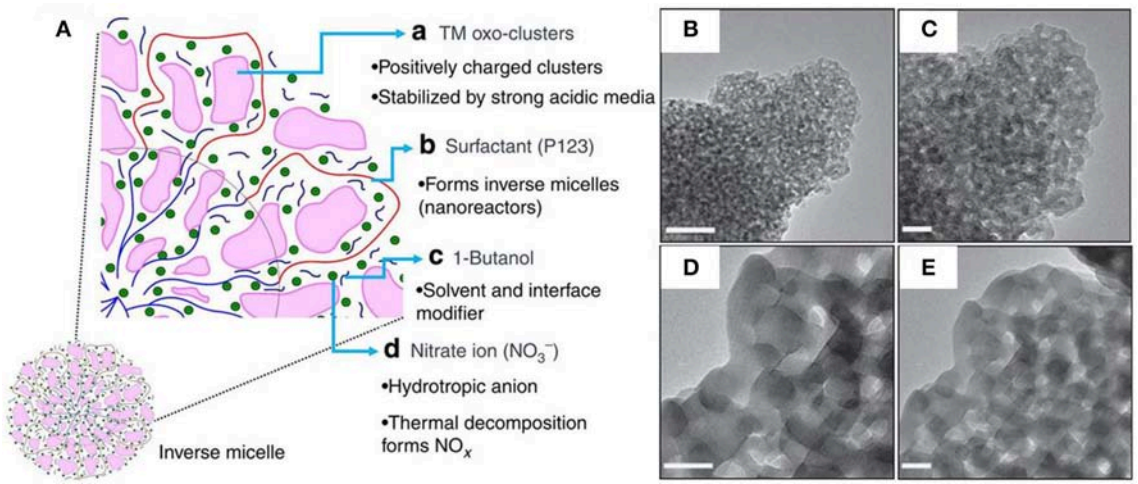

FIGURE 4 | (A) The synthetic mechanism scheme of *m*-TMOs using the inverse sol-gel method. **(B–E)** HR-TEM images of mesoporous MnO_2 at different calcination temperature: **(B,C)** 150°C and **(D,E)** 550°C. Scale bars are 20 nm. Reprinted with permission from Poyraz et al. (2013) Copyright 2013 Nature Publishing Group.

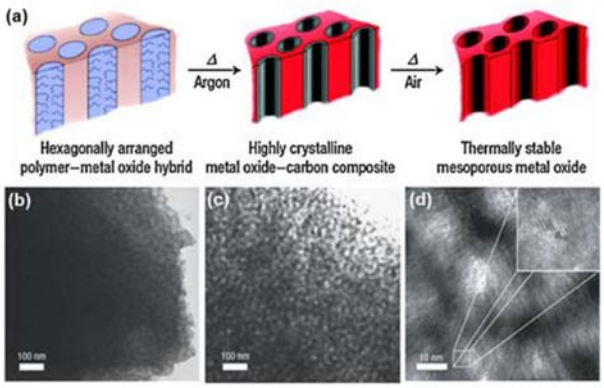

FIGURE 5 | (a) Schematic illustration of combined assembly by soft and hard (CASH) method. TEM images of **(b)** as-made PI-*b*-PEO/TiO_2 hybrids, **(c)** the TiO_2-C composite after heat treatment under argon, and **(d)** the resultant *m*-TiO_2 after removal of the carbon after calcination in air. Reprinted with permission from Lee et al. (2008). Copyright 2008 Nature Publishing Group.

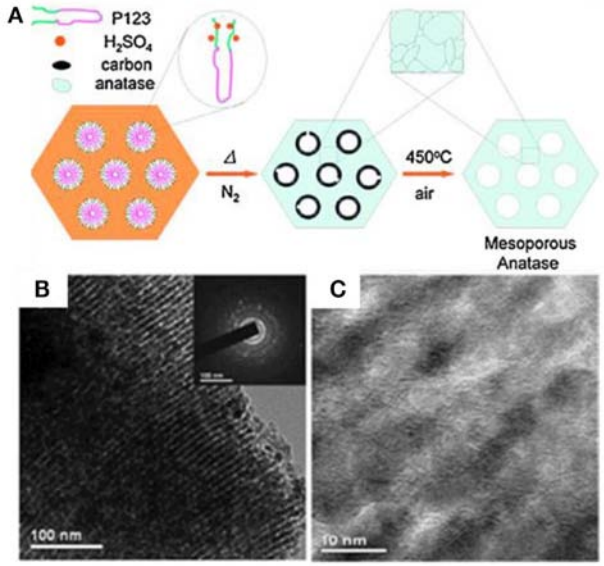

FIGURE 6 | (A) Scheme showing the sulfuric acid carbonization method for the synthesis of *m*-TiO_2. **(B,C)** TEM images of *m*-TiO_2 prepared by the surfactant sulfuric acid carbonization method after calcinating at 650°C in N_2. Reprinted with permission from Zhang et al. (2010). Copyright 20 Willey VCH.

mesoporous TiO_2 obtained in this method is stable up to 700°C; and it has a specific surface area of 122 m^2 g^{-1} and a pore size of 10 nm.

COLLOIDAL-TEMPLATING METHOD

The examples highlighted in the soft-templating method share a key idea, i.e., to improve the stability of hydrocarbon-based polymer templates and to confine the crystal growth during thermal treatment. Even though the carbonization of polymer templates enhances thermal stability, it is limited to some extent. The carbonized polymer templates require the thermal annealing with extra caution, for example, under inert gas atmosphere and without extremely long annealing time. Otherwise, the carbonized polymer templates can be oxidized, further resulting in the collapse of porous frameworks.

One ultimate solution to the thermal stability of templates is to introduce inorganic components, including inorganic nanoparticles (NPs) or non-hydrocarbon-based elements to polymer templates. Inorganic NPs have an inherently much higher thermal stability compared to organic polymers, while some of non-hydrocarbon-based elements, e.g., Si, can convert into inorganic oxides that are known to be thermally stable

as well. By coupling inorganic templates with polymers, the advantages from soft-templating and hard-templating methods can be said to emerge as the "colloidal-templating" method. Colloidal templates are composed of an inorganic NP core tethered with flexible polymer tails. In view of the topology of colloidal templates, they are extremely like polymer micelles, which have been used in the soft-templating method to grow mesoporous materials (Bastakoti et al., 2014, 2016; Jiang et al., 2017, 2018; Tanaka et al., 2018). In the colloidal-templating method, polymers as soft templates are responsible for coordinating inorganic metal ions to self-assemble into nanostructures, similar to that of the soft-templating method. The inorganic NPs, on the other hand, serve as hard templates to offer thermal stability and nanoconfinement to crystallize the framework under high-temperature annealing. Colloidal templates similar to the surfactants/block copolymers can form periodically ordered nanostructures in the course of sol-gel to fabricate mesoporous materials.

One example of colloidal templates by Dong et al. is to synthesize mesoporous graphene using oleic acid (OA)-capped Fe_3O_4 nanocrystals (Jiao et al., 2015). The self-assembled OA-capped Fe_3O_4 first formed the ordered 3D Fe_3O_4 nanocrystal superlattices. The superlattices were further calcined at 1,000°C under argon. As inorganic components, Fe_3O_4 nanocrystals are thermally very stable with respect to annealing, while OA can be carbonized to form continuous carbon frameworks. Followed by the removal of Fe_3O_4 nanocrystals using HCl, the ordered mesoporous carbon was derived and then transformed into highly ordered mesoporous graphene with *fcc* symmetric mesoporosity. However, such a colloidal template is difficult to extend to the synthesis of *m*-TMO, since mixed metal oxides can be formed under high-temperature annealing.

Organosilicate-containing colloidal templates are also utilized as soft-hard templates to synthesize highly crystalline mesoporous materials, which is largely beyond the capacity of the traditional soft-templating method. It is worth noting that the phase transition of TiO_2 requires high temperature calcination (>800°C). Traditional carbon-based soft templates are unlikely to be stable at such a high temperature to support the mesoporous frameworks. Our group recently developed a new series of colloidal templates consisting of a silica-containing inorganic core and PEO shell (Liu et al., 2015b). The synthesis of such colloidal templates is based on the self-assembly of amphiphilic block copolymers in water (**Figure 7**). Briefly, a diblock copolymer of poly(ethylene oxide)-*block*-poly[3-(trimethoxysilyl)propyl methacrylate] (PEO-*b*-PTMSPMA) can form polymer micelles in the mixture solvent of water and ethanol. The micelles are highly uniform with an average diameter of 25 ± 2 nm. The hydrophobic PTMSPMA block contains trimethoxysilyl moieties that can hydrolyze to form polysilsesquioxane. Upon the addition of transition metal precursors, the coordination interaction between PEO and metal ions, similar to that in the soft-templating method, can result in the co-assembly of colloidal templates with metal precursors along with sol-gel transition during EISA. When annealing at high temperature, the polysilsesquioxane cores of colloidal templates further convert into rigid silica nanoparticles to support the structural integrity of the mesoporous framework, while the PEO will be burned off. Since silica is stable up to an air temperature of 1,000°C, the porous materials can be directly annealed at 1,000°C without disrupting their mesostructures. Therefore, the colloidal-templating method offers an ideal solution to the disadvantages of traditional soft templates, having poor thermal stability, and low mechanical strength.

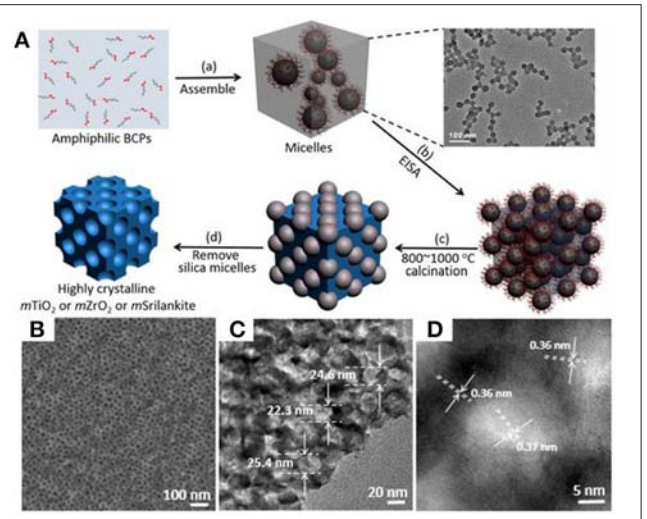

FIGURE 7 | (A) Schematic illustration of highly crystalline *m*-TMOs based on the colloidal amphiphile-templating method. **(B)** SEM, and **(C,D)** TEM images of as-resultant *m*-TiO_2 with uniform mesopores. Reprinted with permission from Liu et al. (2015b). Copyright 2015 American Chemical Society.

Using *m*-TiO_2 as an example, our group demonstrated that *m*-TiO_2 synthesized with colloidal templates could be recrystallized at 900°C under air without further pretreatment (**Figure 7B**). *m*-TiO_2 has a pore size of 21 nm and a specific surface area of 54.5 $m^2\ g^{-1}$. Importantly, calcination at 900°C can lead to the formation of TiO_2 with mixed anatase and rutile, similar to that of P25. Crystallization of mesoporous TiO_2 is rationally tailored by calcination temperature or time, which exhibit dramatically enhanced activity toward photocatalysis (discussed below). In addition, the colloidal-templating method can be extended to synthesize the other *m*-TMOs, such as group-V *m*-ZrO_2 and group-IV/group-V mixed transition-metal oxide, $Zr_{0.33}Ti_{0.67}O_2$ (*m*-Srilankite). In particular, highly crystalline *m*-ZrO_2 and *m*-Srilankite with uniform pore sizes can be obtained at 800°C.

Following the similar synthetic strategy, the colloidal templating method can used to prepare mesoporous carbon or TMO supported on carbon. To do so, the colloidal templates can template the oxidative self-polymerization of dopamine to polydopamine (PDA) nanospheres Liu et al. (2017b). In this case, the hydrogen bonds between dopamine with the PEO shell of colloidal templates drive the co-assembly. Since there are abundant functional groups (e.g., catechol and amine) of PDA to strongly coordinate metal ions (e.g., Co^{2+}), the hybrids of PDA, and colloidal templates can physically absorb Co^{2+} ions. When annealing at 650°C under N_2, the PDA backbone could be transformed into hierarchical porous

carbon frameworks by pyrolysis while Co^{2+} ions were reduced metallic Co nanoparticles (2–7 nm) (Liu et al., 2017b). Here, the mechanically strong colloidal templates not only supported the porous carbon frameworks, but also confined the growth of Co NPs to restrain their overgrowth. Our group also extended this universal colloidal-templating method to develop a series of mesoporous hybrid nanostructures of metal-oxides and metal-carbons (Liu et al., 2016, 2017a,b, 2018).

In addition, the use of colloidal templates can bring unexpected functionalities of inorganic NP to oxides, e.g., optical and/or catalytic properties, when replacing the silica cores of the colloidal template with noble metal NPs (Joo et al., 2009). One intriguing report from Mirkin's group shows that DNA-modified Au NPs as colloidal templates can guide the synthesis of mesoporous silica (**Figure 8a**) (Auyeung et al., 2015). To do so, the citrate-capped 5 nm Au NPs were first modified by thiolated DNA sequences (∼25 dsDNA per NP). Other DNA strands complementary to the DNA ligands on Au NPs were added into the mixture solution (1:1 ratio) of Au to initiate rapid aggregation. The disordered aggregates were subsequently slow-cooled from 60 to 25°C at a rate of 0.1°C/10 min to get spatially organized Au superlattices. The Au superlattices were further utilized as templates to grow silica in the DNA domain. Upon the removal of DNA by calcination, Au NP superlattices within porous silica supports could be synthesized. Due to the confinement of silica, Au NPs have high thermal stability without sintering. The obtained hybrids show a typical Type-IV isotherm with a specific surface area of 210 $m^2 g^{-1}$ (**Figures 8b,c**). The porous Au NP superlattices with available channels are catalytically active in alcohol oxidation.

Co-assembly of two sets of colloidal templates into mesoporous materials also provides a new strategy to encapsulate functional NPs, especially noble metal NPs, within mesoporous frameworks of TMOs. Recently, two sets of colloids, including PS-*b*-PEO-tethered Au (Au-PS-PEO) and spherical colloidal of self-assembled PS-*b*-PEO, were utilized as co-templates for the growth of Au/*m*WO_3 hybrid materials (Liu et al., 2015a). The two sets of colloidal templates share similar structural and chemical features and can co-assemble during the growth and crystallization of WO_3, thus resulting in the homogeneous dispersion of Au NPs within *m*WO_3. The porous frameworks can limit the mobility of Au NPs to enhance thermal stability, while the Au NPs confined by *m*-TMOs essentially exert plasmonic enhancement for the photocatalytic performance of *m*-TMOs. More importantly, because Au NPs are pre-synthesized, this method thus paves the first way to rationally control loading sizes and amounts of noble metal NPs within mesoporous oxides. The same strategy is also extendable to encapsulate noble metal NPs within *m*TiO_2m (Liu et al., 2017a). Furthermore, two sets of the colloidal templates with different structural features are also successful in the formation of noble metal-oxide hybrid materials. For example, Au-PEO colloids and P123 have been used as co-templates to disperse Au NPs with mesoporous silica, which exhibited dramatically enhanced thermal stability of Au NPs for the high-temperature reaction (discussed later).

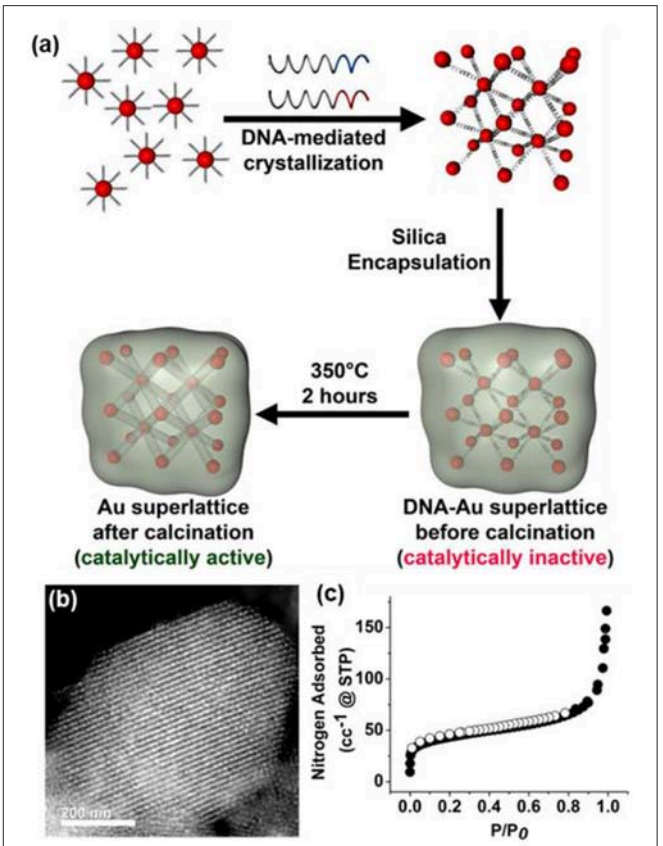

FIGURE 8 | (a) Synthesis of the catalytically active DNA-NP superlattices. **(b)** The TEM image of silica-encapsulated Au superlattices after the removal of DNA. **(c)** Nitrogen sorption isotherms of porous silica. Reprinted with permission from Auyeung et al. (2015). Copyright 2015 American Chemical Society.

APPLICATIONS

Crystalline *m*-TMOs with high surface areas, uniform pore sizes, and accessible interspaces exhibited great potential in many applications. We highlight a few examples on the applications of *m*-TMOs synthesized via the colloidal-templating method. The first example of the application is *m*-TiO_2 synthesized by organosilane-containing colloids for photocatalytic degradation of organic dye (Liu et al., 2015b). As discussed above, having thermally stable colloidals as the soft-hard templates renders the resultant *m*-TiO_2 with the precisely tunable crystalline phase of anatase and rutile by tuning the calcination temperature. The percentage of anatase and rutile can be controlled by calcination temperature and annealing time. The mesoporous TiO_2 obtained at 1,000°C for 1 h has ∼39% of rutile and ∼61% of anatase. In contrast, the mesoporous TiO_2 obtained below 800°C has almost 100% anatase phase. Both crystallinity and controllable anatase/rutile interface play an important role in the enhancement of photocatalytic activity. We used the photo decomposition of organic dye (Rhodamine B, RhB) to evaluate the photocatalytic performance of different *m*-TiO_2 obtained from different calcination conditions. The

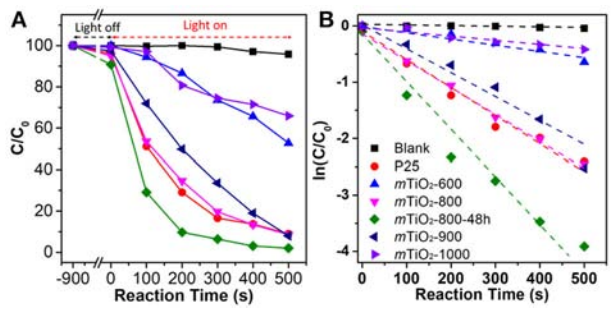

FIGURE 9 | Photocatalytic activity of *m*-TiO_2. **(A)** Photocatalytic degradation of RhB and **(B)** the fitting of the rate constant by using different mesoporous TiO_2 (*m*TiO_2) obtained at different calcination temperatures. Reprinted with permission from Liu et al. (2015b) Copyright 2015 American Chemical Society.

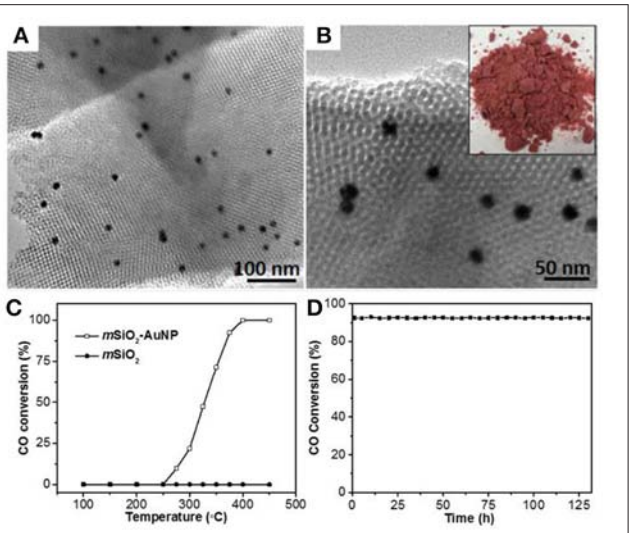

FIGURE 10 | (A,B) TEM images of Au@*m*SiO_2. The size of Au NPs is 14 nm. **(C)** High-temperature CO oxidation performance of mesoporous SiO_2 (*m*SiO_2) and mesoporous SiO_2 with 1% loading of 14 nm Au NPs (*m*SiO_2-AuNP14-1%). **(D)** Durability test of CO oxidation with *m*SiO_2-AuNP14-1% at 375°C over 130 h. Reprinted with permission from Liu et al. (2017a). Copyright 2010 Royal Society of Chemistry.

photocatalytic decomposition results of RhB were obtained from the change of absorption intensity in the corresponding UV-vis spectra (**Figure 9A**). In addition, **Figure 9B** displays the kinetic fitting results by plotting ln (C/C_0) against the reaction time. The control experiment without a catalyst showed a very slow decomposition rate of RhB, with a rate constant of 9 $\times$ 10^{-5} s^{-1}. *m*-TiO_2 obtained at 800 and 900°C exhibited an increased photocatalytic activity with rate constant of 5.1 $\times$ 10^{-3} s^{-1} and 4.4 $\times$ 10^{-3} s^{-1}, respectively. The photo-decomposition activity of *m*-TiO_2 obtained at 800°C for 48 h with the highest activity showed 1.7 times higher than that of commercial P25. The above results indicate that the importance of mesoporous nanostructures and the interface of anatase and rutile phases for their photocatalytic activity. The change of photocatalytic activity is closely related to the crystallinity and controllable interface of anatase/rutile. The highly crystalline *m*-TMOs also can be prepared by using the CASH method (Lee et al., 2008), which decreased the defects to improve performance in photocatalysis.

The colloidal-templating method provides a new avenue to stabilize the noble metal NPs within a mesoporous framework, especially with amorphous SiO_2 as the support. Using KIT-6-typed SiO_2 with the framework and mesochannels smaller than the size of Au NPs could dramatically enhance the thermal stability of Au under high temperature, while Au NPs confined by mesoporous frameworks remain accessible and catalytically active (Liu et al., 2017a). We evaluated the high temperature catalytic performance of Au@*m*SiO_2 (**Figures 10A,B**) for CO oxidation. As shown in **Figure 10C**, when the catalytic temperature reached 275°C (light-off temperature), the CO conversion of *m*SiO_2-AuNP hybrids show catalytic activity for CO oxidation and achieved 100% of CO conversion at 400°C. In contrast, *m*SiO_2 without Au NPs showed no CO oxidation activity even at 450°C. The high temperature stability of *m*SiO_2-AuNP hybrids is further investigated in **Figure 10D**. No decrease in activity was observed for more than 130 h of continuous operation, indicating that *m*SiO_2-AuNP hybrid catalysts have outstanding stability under high temperature. Not only the mesoporous structure of Au@*m*SiO_2, but also Au NPs displayed extraordinary stability after CO oxidation for 130 h, further indicating the superior thermal stability of Au endowed by the nanoconfinement effect of mesoporous oxide supports. Moreover, these mesoporous metal-oxide hybrids are also potentially useful for other high temperature catalysis such as the oxidation of methane to methanol (Agarwal et al., 2017; Williams et al., 2018).

SUMMARY AND PERSPECTIVES

Advances in the rational design and formation of highly crystalline *m*-TMOs with controlled crystallinity and functions largely broaden their practical applications in catalysis and energy storage/conversion. The development of new synthetic methods is the key for all those applications. In this review, we summarize the current synthetic methodologies of *m*-TMOs, including soft-templating, hard-templating, and colloidal-templating methods, and briefly discuss their advantages/disadvantages for the synthesis of *m*-TMOs. Special focus is given to the colloidal-templating synthesis of *m*-TMOs and hybrid materials of porous metal-oxides, beyond the capability of other traditional synthetic methods. Several typical examples are provided to highlight the potential applications of *m*-TMOs and porous metal-oxides synthesized by colloidal-templating method.

Despite much progress made in the synthesis of crystalline *m*-TMOs, there are still unmet synthetic challenges, particularly for the colloidal-templating method. First, no example has been documented on crystalline perovskites using soft-templating or

colloidal-templating methods. Perovskites, as a complex oxide consisting of two or more simple oxides, have a cubic structure with a general formula of ABO_3; and they have been studied extensively due to the interesting electronic and catalytic activity, e.g., as a solid electrolyte (Zhou et al., 2016) and cathode materials for fuel cells (Skinner, 2001; Suntivich et al., 2011). The synthesis of perovskites usually relies on the solid-state annealing of the mixture of oxides at >700°C (Zhu et al., 2014). Because of the slow diffusion in solid states, the synthesis of perovskites can take a few hours to days to anneal the oxide mixtures. With the new CASH or organosilicate-containing colloidal-templating methods, it will be of interest to extend the current synthetic capacity to crystalline perovskites. Secondly, encapsulating noble metal NPs within highly crystalline *m*-TMOs is also unresolved. There is an extensive literature on the strong metal-oxide interaction (Tauster, 1987; Farmer and Campbell, 2010), known to be critical for catalytic activity of metal-oxide hybrids. The formation of the strong metal-oxide interaction (or strong metal-support interaction, SMSI) requires the annealing under reductive atmosphere. Control of metal-oxide interaction in the context of mesoporous hybrids has rarely been reported in previous research. In addition, we expect that more achievements from other fields, including macromolecules, electronics, and biomedical, can be incorporated in further developments of the synthesis and applications of *m*-TMOs. For example, new colloidal templates with different topologies assembled from different amphiphilic block copolymers (Yao et al., 2015) can add more structural hierarchies to crystalline *m*-TMOs. The interdisciplinary aspects that bring the new knowledge across fields will create new opportunities in solving those synthetic challenges.

AUTHOR CONTRIBUTIONS

All authors listed have made a substantial, direct and intellectual contribution to the work, and approved it for publication.

ACKNOWLEDGMENTS

JH is grateful for financial support from the National Science Foundation (CBET-1705566) and the University of Connecticut. BL is grateful for support from the Jiangsu Specially Appointed Professor plan and the Natural Science Foundation of Jiangsu Province (No. BK20180723).

REFERENCES

Agarwal, N., Freakley, S. J., Mcvicker, R. U., Althahban, S. M., Dimitratos, N., He, Q., et al. (2017). Aqueous Au-Pd colloids catalyze selective CH4 oxidation to CH3OH with O2 under mild conditions. *Science* 358, 223–227. doi: 10.1126/science.aan6515

Antonelli, D. M. (1999). Synthesis and mechanistic studies of sulfated meso- and microporous zirconias with chelating carboxylate surfactants. *Adv. Mater.* 11, 487–492. doi: 10.1002/(SICI)1521-4095(199904)11:6<487::AID-ADMA487>3.0.CO;2-2

Antonelli, D. M., Nakahira, A., and Ying, J. Y. (1996). Ligand-assisted liquid crystal templating in mesoporous niobium oxide molecular sieves. *Inorg. Chem.* 35, 3126–3136. doi: 10.1021/ic951533p

Antonelli, D. M., and Ying, J. Y. (1995). Synthesis of hexagonally packed mesoporous TiO_2 by a modified sol–gel method. *Angew. Chem. Int. Ed.* 34, 2014–2017. doi: 10.1002/anie.199520141

Auyeung, E., Morris, W., Mondloch, J. E., Hupp, J. T., Farha, O. K., and Mirkin, C. A. (2015). Controlling structure and porosity in catalytic nanoparticle superlattices with DNA. *J. Am. Chem. Soc.* 137, 1658–1662. doi: 10.1021/ja512116p

Bastakoti, B. P., Ishihara, S., Leo, S. Y., Ariga, K., Wu, K. C., and Yamauchi, Y. (2014). Polymeric micelle assembly for preparation of large-sized mesoporous metal oxides with various compositions. *Langmuir* 30, 651–659. doi: 10.1021/la403901x

Bastakoti, B. P., Li, Y., Guragain, S., Pramanik, M., Alshehri, S. M., Ahamad, T., et al. (2016). Synthesis of mesoporous transition-metal phosphates by polymeric micelle assembly. *Chem. Eur. J.* 22, 7463–7467. doi: 10.1002/chem.201600435

Burke, M. S., Enman, L. J., Batchellor, A. S., Zou, S., and Boettcher, S. W. (2015). Oxygen evolution reaction electrocatalysis on transition metal oxides and (Oxy)hydroxides: activity trends and design principles. *Chem. Mater.* 27, 7549–7558. doi: 10.1021/acs.chemmater.5b03148

Chen, S.-J., Li, L.-H., Chen, X.-T., Xue, Z., Hong, J.-M., and You, X.-Z. (2003). Preparation and characterization of nanocrystalline zinc oxide by a novel solvothermal oxidation route. *J. Cryst. Growth.* 252, 184–189. doi: 10.1016/S0022-0248(02)02495-8

Cong, S., and Xu, Y. (2011). Explaining the high photocatalytic activity of a mixed phase TiO_2: a combined effect of O_2 and crystallinity. *J. Phys. Chem. C* 115, 21161–21168. doi: 10.1021/jp2055206

Crepaldi, E. L., Soler-Illia, G. J., Grosso, D., Cagnol, F., Ribot, F., and Sanchez, C. (2003). Controlled formation of highly organized mesoporous titania thin films: from mesostructured hybrids to mesoporous nanoanatase TiO_2. *J. Am. Chem. Soc.* 125, 9770–9786. doi: 10.1021/ja030070g

Fan, J., Yu, C., Gao, F., Lei, J., Tian, B., Wang, L., et al. (2003). Cubic mesoporous silica with large controllable entrance sizes and advanced adsorption properties. *Angew. Chem. In. Ed.* 42, 3146–3150. doi: 10.1002/anie.200351027

Fan, J., Yu, C., Lei, J., Zhang, Q., Li, T., Tu, B., et al. (2005). Low-temperature strategy to synthesize highly ordered mesoporous silicas with very large pores. *J. Am. Chem. Soc.* 127, 10794–10795. doi: 10.1021/ja052619c

Fang, Y., Lv, Y., Gong, F., Elzatahry, A. A., Zheng, G., and Zhao, D. (2016). Synthesis of 2D-mesoporous-carbon/MoS2 heterostructures with well-defined interfaces for high-performance lithium-ion batteries. *Adv. Mater.* 28, 9385–9390. doi: 10.1002/adma.201602210

Farmer, J. A., and Campbell, C. T. (2010). Ceria maintains smaller metal catalyst particles by strong metal-support bonding. *Science* 329, 933–936. doi: 10.1126/science.1191778

Fu, S., Zhu, C., Song, J., Engelhard, M. H., Li, X., Du, D., et al. (2016). Highly ordered mesoporous bimetallic phosphides as efficient oxygen evolution electrocatalysts. *ACS Ener. Lett.* 1, 792–796. doi: 10.1021/acsenergylett.6b00408

Grosso, D., De, A. A., Soler-Illia, G. J., Babonneau, F., Sanchez, C., Albouy, P.-A., et al. (2001). Highly organized mesoporous titania thin films showing mono-oriented 2D hexagonal channels. *Adv. Mater.* 13, 1085–1090. doi: 10.1002/1521-4095(200107)13:14<1085::AID-ADMA1085>3.0.CO;2-Q

Gu, D., and Schuth, F. (2014). Synthesis of non-siliceous mesoporous oxides. *Chem. Soc. Rev.* 43, 313–344. doi: 10.1039/C3CS60155B

Han, L., and Che, S. (2013). Anionic surfactant templated mesoporous silicas (AMSs). *Chem. Soc. Rev.* 42, 3740–3752. doi: 10.1039/C2CS35297D

Huo, Q., Margolese, D. I., Ciesla, U., Feng, P., Gier, T. E., Sieger, P., et al. (1994). Generalized synthesis of periodic surfactant/inorganic composite materials. *Nature* 368:317–321. doi: 10.1038/368317a0

Jiang, B., Guo, Y., Kim, J., Whitten, A. E., Wood, K., Kani, K., et al. (2018). Mesoporous metallic iridium nanosheets. *J. Am. Chem. Soc.* 140, 12434–12441. doi: 10.1021/jacs.8b05206

Jiang, B., Li, C., Dag, O., Abe, H., Takei, T., Imai, T., et al. (2017). Mesoporous metallic rhodium nanoparticles. *Nat. Commun.* 8:15581. doi: 10.1038/ncomms15581

Jiang, T., Poyraz, A. S., Iyer, A., Zhang, Y., Luo, Z., Zhong, W., et al. (2015). Synthesis of mesoporous iron oxides by an inverse micelle method and their application in the degradation of orange II under visible light at neutral pH. *J. Phys. Chem. C* 119, 10454–10468. doi: 10.1021/acs.jpcc.5b02057

Jiao, F., and Bruce, P. G. (2007). Mesoporous crystalline β-MnO_2–a reversible positive electrode for rechargeable lithium batteries. *Adv. Mater.* 19, 657–660. doi: 10.1002/adma.200602499

Jiao, F., Harrison, A., Hill, A. H., and Bruce, P. G. (2007). Mesoporous Mn_2O_3 and Mn_3O_4 with crystalline walls. *Adv. Mater.* 19, 4063–4066. doi: 10.1002/adma.200700336

Jiao, F., Harrison, A., Jumas, J.-C., Chadwick, A. V., Kockelmann, W., and Bruce, P. G. (2006). Ordered mesoporous Fe_2O_3 with crystalline walls. *J. Am. Chem. Soc.* 128, 5468–5474. doi: 10.1021/ja0584774

Jiao, F., Hill, A. H., Harrison, A., Berko, A., Chadwick, A. V., and Bruce, P. G. (2008). Synthesis of ordered mesoporous NiO with crystalline walls and a bimodal pore size distribution. *J. Am. Chem. Soc.* 130, 5262–5266. doi: 10.1021/ja710849r

Jiao, F., Shaju, K. M., and Bruce, P. G. (2005a). Synthesis of nanowire and mesoporous low-temperature LiCoO2 by a post-templating reaction. *Angew. Chem. Int. Ed.* 44, 6550–6553. doi: 10.1002/anie.200501663

Jiao, K., Zhang, B., Yue, B., Ren, Y., Liu, S., Yan, S., et al. (2005b). Growth of porous single-crystal Cr_2O_3 in a 3-D mesopore system. *Chem. Commun.* 5618–5620. doi: 10.1039/b512080b

Jiao, Y., Han, D., Liu, L., Ji, L., Guo, G., Hu, J., et al. (2015). Highly ordered mesoporous few-layer graphene frameworks enabled by Fe_3O_4 nanocrystal superlattices. *Angew. Chem. Int. Ed.* 54, 5727–5731. doi: 10.1002/anie.201501398

Jin, L., Liu, B., Wu, Y., Thanneeru, S., and He, J. (2017). Synthesis of mesoporous CoS_2 and $Ni_xCo_{1-x}S_2$ with superior supercapacitive performance using a facile solid-phase sulfurization. *ACS App. Mater. Interfaces* 9, 36837–36848. doi: 10.1021/acsami.7b11453

Joo, J. B., Dahl, M., Li, N., Zaera, F., and Yin, Y. (2013). Tailored synthesis of mesoporous TiO_2 hollow nanostructures for catalytic applications. *Energy Environ. Sci.* 6, 2082–2092. doi: 10.1039/c3ee41155a

Joo, S. H., Park, J. Y., Tsung, C. K., Yamada, Y., Yang, P., and Somorjai, G. A. (2009). Thermally stable Pt/mesoporous silica core-shell nanocatalysts for high-temperature reactions. *Nat. Mater.* 8, 126–131. doi: 10.1038/nmat2329

Kanan, D. K., and Carter, E. A. (2012). Band gap engineering of MnO via ZnO alloying: a potential new visible-light photocatalyst. *J. Phys. Chem. C* 116, 9876–9887. doi: 10.1021/jp300590d

Kanan, D. K., and Carter, E. A. (2013). Ab initio study of electron and hole transport in pure and doped MnO and MnO:ZnO alloy. *J. Mater. Chem. A* 1:9246. doi: 10.1039/c3ta11265a

Kawahara, T., Konishi, Y., Tada, H., Tohge, N., Nishii, J., and Ito, S. (2002). A patterned TiO_2(Anatase)/TiO_2(Rutile) bilayer-type photocatalyst: effect of the anatase/rutile junction on the photocatalytic activity. *Angew. Chem. Int. Ed.* 41, 2811–2813. doi: 10.1002/1521-3773(20020802)41:15<2811::AID-ANIE2811>3.0.CO;2-#

Kleitz, F., Hei Choi, S., and Ryoo, R. (2003). Cubic Ia3d large mesoporous silica: synthesis and replication to platinum nanowires, carbon nanorods and carbon nanotubesElectronic supplementary information (ESI) available: TEM images of mesoporous cubic silica and Pt networks, XRD patterns during formation of the cubic phase. *Chem. Commun.* 2136–2137. doi: 10.1039/b306504a

Kondo, J. N., and Domen, K. (2008). Crystallization of mesoporous metal oxides. *Chem. Mater.* 20, 835–847. doi: 10.1021/cm702176m

Kresge, C. T., Leonowicz, M. E., Roth, W. J., Vartuli, J. C., and Beck, J. S. (1992). Ordered mesoporous molecular sieves synthesized by a liquid-crystal template mechanism. *Nature* 359:710–712. doi: 10.1038/359710a0

Kuo, C.-H., Mosa, I. M., Poyraz, A. S., Biswas, S., El-Sawy, A. M., Song, W., et al. (2015). Robust mesoporous manganese oxide catalysts for water oxidation. *ACS Catal.* 5, 1693–1699. doi: 10.1021/cs501739e

Le, Z., Liu, F., Nie, P., Li, X., Liu, X., Bian, Z., et al. (2017). Pseudocapacitive sodium storage in mesoporous single-crystal-like TiO2-graphene nanocomposite enables high-performance sodium-ion capacitors. *ACS Nano* 11, 2952–2960. doi: 10.1021/acsnano.6b08332

Lee, J., Orilall, M. C., Warren, S. C., Kamperman, M., Disalvo, F. J., and Wiesner, U. (2008). Direct access to thermally stable and highly crystalline mesoporous transition-metal oxides with uniform pores. *Nat. Mater.* 7, 222–228. doi: 10.1038/nmat2111

Li, H., Bian, Z., Zhu, J., Huo, Y., Li, H., and Lu, Y. (2007). Mesoporous Au/TiO2 nanocomposites with enhanced photocatalytic activity. *J. Am. Chem. Soc.* 129, 4538–4539. doi: 10.1021/ja069113u

Li, J., Wang, Y., Tang, J., Wang, Y., Wang, T., Zhang, L., et al. (2015). Direct growth of mesoporous carbon-coated Ni nanoparticles on carbon fibers for flexible supercapacitors. *J. Mater. Chem. A* 3, 2876–2882. doi: 10.1039/C4TA05668J

Li, W., Liu, J., and Zhao, D. (2016). Mesoporous materials for energy conversion and storage devices. *Nat. Rev. Mater.* 1:16023. doi: 10.1038/natrevmats.2016.23

Li, W., Wu, Z., Wang, J., Elzatahry, A. A., and Zhao, D. (2013). A perspective on mesoporous TiO2 materials. *Chem. Mater.* 26, 287–298. doi: 10.1021/cm4014859

Liang, C., Li, Z., and Dai, S. (2008). Mesoporous carbon materials: synthesis and modification. *Angew. Chem.* 47, 3696–3717. doi: 10.1002/anie.200702046

Liu, B., Jiang, T., Zheng, H., Dissanayke, S., Song, W., Federico, A., et al. (2017a). Nanoengineering of aggregation-free and thermally-stable gold nanoparticles in mesoporous frameworks. *Nanoscale* 9, 6380–6390. doi: 10.1039/C7NR01988B

Liu, B., Jin, L., Zheng, H., Yao, H., Wu, Y., Lopes, A., et al. (2017b). Ultrafine co-based nanoparticle@mesoporous carbon nanospheres toward high-performance supercapacitors. *ACS App. Mater. Interfaces* 9, 1746–1758. doi: 10.1021/acsami.6b11958

Liu, B., Kuo, C. H., Chen, J., Luo, Z., Thanneeru, S., Li, W., et al. (2015a). Ligand-assisted co-assembly approach toward mesoporous hybrid catalysts of transition-metal oxides and noble metals: photochemical water splitting. *Angew. Chem. Int. Ed.* 54, 9061–9065. doi: 10.1002/anie.201502892

Liu, B., Louis, M., Jin, L., Li, G., and He, J. (2018). Co-template directed synthesis of gold nanoparticles in mesoporous titanium dioxide. *Chem. Eur. J.* 24, 9651–9657. doi: 10.1002/chem.201801223

Liu, B., Luo, Z., Federico, A., Song, W., Suib, S. L., and He, J. (2015b). Colloidal amphiphile-templated growth of highly crystalline mesoporous nonsiliceous oxides. *Chem. Mater.* 27, 6173–6176. doi: 10.1021/acs.chemmater.5b02248

Liu, B., Yao, H., Daniels, R. A., Song, W., Zheng, H., Jin, L., et al. (2016). A facile synthesis of Fe3C@mesoporous carbon nitride nanospheres with superior electrocatalytic activity. *Nanoscale* 8, 5441–5445. doi: 10.1039/C6NR00604C

Liu, P., Moudrakovski, I. L., Liu, J., and Sayari, A. (1997). Mesostructured vanadium oxide containing dodecylamine. *Chem. Mater.* 9, 2513–2520. doi: 10.1021/cm970067u

Lokupitiya, H. N., Jones, A., Reid, B., Guldin, S., and Stefik, M. (2016). Ordered mesoporous to macroporous oxides with tunable isomorphic architectures: solution criteria for persistent micelle templates. *Chem. Mater.* 28, 1653–1667. doi: 10.1021/acs.chemmater.5b04407

Lu, A.-H., Schmidt, W., Taguchi, A., Spliethoff, B., Tesche, B., and Schüth, F. (2002). Taking nanocasting one step further: replicating CMK-3 as a silica material. *Angew. Chem. Int. Ed.* 41, 3489–3492. doi: 10.1002/1521-3773(20020916)41:18<3489::AID-ANIE3489>3.0.CO;2-M

Lu, A.-H., and Schüth, F. (2005). Nanocasting pathways to create ordered mesoporous solids. *C. R. Chim.* 8, 609–620. doi: 10.1016/j.crci.2004.10.020

Lu, A. H., and Schüth, F. (2006). Nanocasting: a versatile strategy for creating nanostructured porous materials. *Adv. Mater.* 18, 1793–1805. doi: 10.1002/adma.200600148

Lu, H., Zhang, P., Qiao, Z. A., Zhang, J., Zhu, H., Chen, J., et al. (2015). Ionic liquid-mediated synthesis of meso-scale porous lanthanum-transition-metal perovskites with high CO oxidation performance. *Chem. Commun.* 51, 5910–5913. doi: 10.1039/C5CC00534E

Meng, Y., Gu, D., Zhang, F., Shi, Y., Yang, H., Li, Z., et al. (2005). Ordered mesoporous polymers and homologous carbon frameworks: amphiphilic surfactant templating and direct transformation. *Angew. Chem. Int. Ed.* 44, 7053–7059. doi: 10.1002/anie.200501561

Miyagi, T., Kamei, M., Mitsuhashi, T., Ishigaki, T., and Yamazaki, A. (2004). Charge separation at the rutile/anatase interface: a dominant factor of photocatalytic activity. *Chem. Phys. Lett.* 390, 399–402. doi: 10.1016/j.cplett.2004.04.042

Ohtani, B., Ogawa, Y., and Nishimoto, S.-I. (1997). Photocatalytic activity of amorphous–anatase mixture of titanium(IV) oxide particles suspended in aqueous solutions. *J. Phys. Chem. C* 101, 3746–3752. doi: 10.1021/jp962702+

Onozuka, K., Kawakami, Y., Imai, H., Yokoi, T., Tatsumi, T., and Kondo, J. N. (2012). Perovskite-type La2Ti2O7 mesoporous photocatalyst. *J. Solid States Chem.* 192, 87–92. doi: 10.1016/j.jssc.2012.03.055

Polarz, S., Orlov, A. V., Schuth, F., and Lu, A. H. (2007). Preparation of high-surface-area zinc oxide with ordered porosity, different pore sizes, and nanocrystalline walls. *Chem. Eur. J.* 13, 592–597. doi: 10.1002/chem.200600428

Poyraz, A. S., Kuo, C.-H., Kim, E., Meng, Y., Seraji, M. S., and Suib, S. L. (2014). Tungsten-promoted mesoporous group 4 (Ti, Zr, and Hf) transition-metal oxides for room-temperature solvent-free acetalization and ketalization reactions. *Chem. Mater.* 26, 2803–2813. doi: 10.1021/cm501216c

Poyraz, A. S., Kuo, C. H., Biswas, S., King'ondu, C. K., and Suib, S. L. (2013). A general approach to crystalline and monomodal pore size mesoporous materials. *Nat. Commun.* 4:2952. doi: 10.1038/ncomms3952

Qiu, H., and Che, S. (2011). Chiral mesoporous silica: chiral construction and imprinting via cooperative self-assembly of amphiphiles and silica precursors. *Chem. Soc. Rev.* 40, 1259–1268. doi: 10.1039/C0CS00002G

Ren, Y., Armstrong, A. R., Jiao, F., and Bruce, P. G. (2010). Influence of size on the rate of mesoporous electrodes for lithium batteries. *J. Am. Chem. Soc.* 132, 996–1004. doi: 10.1021/ja905488x

Ren, Y., Ma, Z., and Bruce, P. G. (2012). Ordered mesoporous metal oxides: synthesis and applications. *Chem. Soc. Rev.* 41, 4909–4927. doi: 10.1039/c2cs35086f

Ren, Y., Ma, Z., Morris, R. E., Liu, Z., Jiao, F., Dai, S., et al. (2013). A solid with a hierarchical tetramodal micro-meso-macro pore size distribution. *Nat. Commun.* 4:2015. doi: 10.1038/ncomms3015

Ren, Y., Ma, Z., Qian, L., Dai, S., He, H., and Bruce, P. G. (2009). Ordered crystalline mesoporous oxides as catalysts for CO oxidation. *Catal. Lett.* 131, 146–154. doi: 10.1007/s10562-009-9931-0

Roggenbuck, J., and Tiemann, M. (2005). Ordered mesoporous magnesium oxide with high thermal stability synthesized by exotemplating using CMK-3 carbon. *J. Am. Chem. Soc.* 127, 1096–1097. doi: 10.1021/ja043605u

Sakamoto, Y., Kaneda, M., Terasaki, O., Zhao, D. Y., Kim, J. M., Stucky, G., et al. (2000). Direct imaging of the pores and cages of three-dimensional mesoporous materials. *Nature* 408,449–453. doi: 10.1038/35044040

Scanlon, D. O., Dunnill, C. W., Buckeridge, J., Shevlin, S. A., Logsdail, A. J., Woodley, S. M., et al. (2013). Band alignment of rutile and anatase TiO(2). *Nat. Mater.* 12, 798–801. doi: 10.1038/nmat3697

Schüth, F. (2001). Non-siliceous mesostructured and mesoporous materials. *Chem. Mater.* 13, 3184–3195. doi: 10.1021/cm011030j

Siah, W. R., Lintang, H. O., Shamsuddin, M., and Yuliati, L. (2016). High photocatalytic activity of mixed anatase-rutile phases on commercial TiO2nanoparticles. *Mater. Sci. Eng.* 107:012005. doi: 10.1088/1757-899X/107/1/012005

Skinner, S. J. (2001). Recent advances in Perovskite-type materials for solid oxide fuel cell cathodes. *J. Inorg. Mater.* 3, 113–121. doi: 10.1016/S1466-6049(01)00004-6

Song, F., Bai, L., Moysiadou, A., Lee, S., Hu, C., Liardet, L., et al. (2018). Transition metal oxides as electrocatalysts for the oxygen evolution reaction in alkaline solutions: an application-inspired renaissance. *J. Am. Chem. Soc.* 140, 7748–7759. doi: 10.1021/jacs.8b04546

Song, M. S., Nahm, S., Cho, W. I., and Lee, C. (2015). Enhanced electrochemical performance of a ZnO-MnO composite as an anode material for lithium ion batteries. *Phys. Chem. Chem. Phys.* 17, 23496–23502. doi: 10.1039/C5CP03375F

Song, W., Poyraz, A. S., Meng, Y., Ren, Z., Chen, S.-Y., and Suib, S. L. (2014). Mesoporous Co3O4 with controlled porosity: inverse micelle synthesis and high-performance catalytic CO oxidation at −60°C. *Chem. Mater.* 26, 4629–4639. doi: 10.1021/cm502106v

Su, H., Jaffer, S., and Yu, H. (2016). Transition metal oxides for sodium-ion batteries. *Energy Storg. Mater.* 5, 116–131. doi: 10.1016/j.ensm.2016.06.005

Suntivich, J., May, K. J., Gasteiger, H. A., Goodenough, J. B., and Shao-Horn, Y. (2011). A perovskite oxide optimized for oxygen evolution catalysis from molecular orbital principles. *Science* 334, 1383–1385. doi: 10.1126/science.1212858

Tanaka, S., Kaneti, Y. V., Bhattacharjee, R., Islam, M. N., Nakahata, R., Abdullah, N., et al. (2018). Mesoporous iron oxide synthesized using poly(styrene-b-acrylic acid-b-ethylene glycol) block copolymer micelles as templates for colorimetric and electrochemical detection of glucose. *ACS App. Mater. Interfaces* 10, 1039–1049. doi: 10.1021/acsami.7b13835

Tauster, S. J. (1987). Strong metal-support interactions. *Acc. Chem. Res.* 20, 389–394. doi: 10.1021/ar00143a001

Tian, B., Liu, X., Solovyov, L. A., Liu, Z., Yang, H., Zhang, Z., et al. (2004). Facile synthesis and characterization of novel mesoporous and mesorelief oxides with gyroidal structures. *J. Am. Chem. Soc.* 126, 865–875. doi: 10.1021/ja037877t

Vovchok, D., Guild, C. J., Dissanayake, S., Llorca, J., Stavitski, E., Liu, Z., et al. (2018). *In situ* characterization of mesoporous Co/CeO2 catalysts for the high-temperature water-gas shift. *J. Phys. Chem. C* 122, 8998–9008. doi: 10.1021/acs.jpcc.8b01271

Wang, Y., Yang, C.-M., Schmidt, W., Spliethoff, B., Bill, E., and Schüth, F. (2005). Weakly ferromagnetic ordered mesoporous Co3O4 synthesized by nanocasting from vinyl-functionalized cubic Ia3d mesoporous silica. *Adv. Mater.* 17, 53–56. doi: 10.1002/adma.200400777

Wasalathanthri, N. D., Poyraz, A. S., Biswas, S., Meng, Y., Kuo, C.-H., Kriz, D. A., et al. (2015). High-performance catalytic CH4 oxidation at low temperatures: inverse micelle synthesis of amorphous mesoporous manganese oxides and mild transformation to K2–xMn8O16 and ϵ-MnO2. *J. Phys. Chem. C* 119, 1473–1482. doi: 10.1021/jp5108558

Williams, C., Carter, J. H., Dummer, N. F., Chow, Y. K., Morgan, D. J., Yacob, S., et al. (2018). Selective oxidation of methane to methanol using supported AuPd catalysts prepared by stabilizer-free sol-immobilization. *ACS Catal.* 8, 2567–2576. doi: 10.1021/acscatal.7b04417

Wong, M. S., Antonelli, D. M., and Ying, J. Y. (1997). Synthesis and characterization of phosphated mesoporous zirconium oxide. *Nanostruct. Mater.* 9, 165–168. doi: 10.1016/S0965-9773(97)00044-5

Wu, Z., Lv, Y., Xia, Y., Webley, P. A., and Zhao, D. (2012). Ordered mesoporous platinum@graphitic carbon embedded nanophase as a highly active, stable, and methanol-tolerant oxygen reduction electrocatalyst. *J. Am. Chem. Soc.* 134, 2236–2245. doi: 10.1021/ja209753w

Xin, X., Qin, H., Cong, H. P., and Yu, S. H. (2018). Templating synthesis of mesoporous Fe3C-encapsulated Fe-N-doped carbon hollow nanospindles for electrocatalysis. *Langmuir* 34, 4952–4961. doi: 10.1021/acs.langmuir.8b00548

Yang, H., and Zhao, D. (2005). Synthesis of replica mesostructures by the nanocasting strategy. *J. Mater. Chem. A* 15, 1217–1231. doi: 10.1039/b414402c

Yang, P., Zhao, D., Margolese, D. I., Chmelka, B. F., and Stucky, G. D. (1998). Generalized syntheses of large-pore mesoporous metal oxides with semicrystalline frameworks. *Nature* 396:152–155. doi: 10.1038/24132

Yang, P., Zhao, D., Margolese, D. I., Chmelka, B. F., and Stucky, G. D. (1999). Block copolymer templating syntheses of mesoporous metal oxides with large ordering lengths and semicrystalline framework. *Chem. Mater.* 11, 2813–2826. doi: 10.1021/cm990185c

Yao, D., Chen, Y., and Jin, R. (2015). Different dimensional silica materials prepared using shaped block copolymer nanoobjects as catalytic templates. *J. Mater. Chem. B* 3, 5786–5794. doi: 10.1039/C5TB00589B

Yue, B., Tang, H., Kong, Z., Zhu, K., Dickinson, C., Zhou, W., et al. (2005). Preparation and characterization of three-dimensional mesoporous crystals of tungsten oxide. *Chem. Phys. Lett.* 407, 83–86. doi: 10.1016/j.cplett.2005.03.066

Yun, H.-S., Miyazawa, K., Zhou, H. S., Honma, I., and Kuwabara, M. (2001). Synthesis of mesoporous thin TiO2 films with hexagonal pore structures using triblock copolymer templates. *Adv. Mater.* 13, 1377–1380. doi: 10.1002/1521-4095(200109)13:18<1377::AID-ADMA1377>3.0.CO;2-T

Zhang, J., Deng, Y., Gu, D., Wang, S., She, L., Che, R., et al. (2011). Ligand-assisted assembly approach to synthesize large-pore ordered mesoporous titania with thermally stable and crystalline framework. *Adv. Energy Mater.* 1, 241–248. doi: 10.1002/aenm.201000004

Zhang, R., Tu, B., and Zhao, D. (2010). Synthesis of highly stable and crystalline mesoporous anatase by using a simple surfactant sulfuric acid carbonization method. *Chem. Eur. J.* 16, 9977–9981. doi: 10.1002/chem.201001241

Zhao, D., Feng, J., Huo, Q., Melosh, N., Fredrickson, G. H., Chmelka, B. F., et al. (1998a). Triblock copolymer syntheses of mesoporous silica with periodic 50 to 300 angstrom pores. *Science* 279, 548–552. doi: 10.1126/science.279.5350.548

Zhao, D., Huo, Q., Feng, J., Chmelka, B. F., and Stucky, G. D. (1998b). Nonionic triblock and star diblock copolymer and oligomeric surfactant syntheses of

highly ordered, hydrothermally stable, mesoporous silica structures. *J. Am. Chem. Soc.* 120, 6024–6036. doi: 10.1021/ja974025i

Zhao, H., Liu, L., Andino, J. M., and Li, Y. (2013). Bicrystalline TiO2 with controllable anatase–brookite phase content for enhanced CO2 photoreduction to fuels. *J. Mater. Chem. A* 1,8209–8216.doi: 10.1039/C3TA11226H

Zheng, M., Tang, H., Li, L., Hu, Q., Zhang, L., Xue, H., et al. (2018). Hierarchically nanostructured transition metal oxides for lithium-ion batteries. *Adv. Sci.* 5:1700592. doi: 10.1002/advs.201700592

Zhou, W., Sun, F., Pan, K., Tian, G., Jiang, B., Ren, Z., et al. (2011). Well-ordered large-pore mesoporous anatase TiO2 with remarkably high thermal stability and improved crystallinity: preparation, characterization, and photocatalytic performance. *Adv. Funct. Mater.* 21, 1922–1930. doi: 10.1002/adfm.201002535

Zhou, Y., Guan, X., Zhou, H., Ramadoss, K., Adam, S., Liu, H., et al. (2016). Strongly correlated perovskite fuel cells. *Nature* 534, 231–234. doi: 10.1038/nature17653

Zhu, J., Li, H., Zhong, L., Xiao, P., Xu, X., Yang, X., et al. (2014). Perovskite oxides: preparation, characterizations, and applications in heterogeneous catalysis. *ACS Catal.* 4, 2917–2940. doi: 10.1021/cs500606g

Zhu, K., Yue, B., Zhou, W., and He, H. (2003). Preparation of three-dimensional chromium oxide porous single crystals templated by SBA-15. *Chem. Commun.* 98–99. doi: 10.1039/b210065g

Conflict of Interest Statement: The handling editor declared a shared affiliation, though no other collaboration, with the authors JH, LJ, and LZ at the time of review.

The remaining author declares that the research was conducted in the absence of any commercial or financial relationships that could be construed as a potential conflict of interest.

Copyright © 2019 Zhang, Jin, Liu and He. This is an open-access article distributed under the terms of the Creative Commons Attribution License (CC BY). The use, distribution or reproduction in other forums is permitted, provided the original author(s) and the copyright owner(s) are credited and that the original publication in this journal is cited, in accordance with accepted academic practice. No use, distribution or reproduction is permitted which does not comply with these terms.

Inorganic Chemistry

Timothy R. Cook

Timothy R. Cook is an Assistant Professor at the University of Buffalo's Department of Chemistry. His research focuses on several aspects of materials science, including self-assembly and characterization of discrete inorganic metallacycles and cages, energy harvesting, transport and storage in photo- and redox-active molecular materials, as well as polynuclear catalysts for small molecule activations of relevance to renewable energy schemes. Professor Cook completed his PhD at the Massachusetts Institute of Technology (MIT), followed by postdoctoral and Research Assistant Professor positions at the University of Utah.

Bo Zhou

Prof. Bo Zhou obtained his PhD degree in Optics from the City University of Hong Kong in 2011, and then worked as a postdoctoral researcher at the Hong Kong Polytechnic University and Institute of Materials Research and Engineering, A*STAR, Singapore. Since 2017, he has been a full Professor at South China University of Technology. His research interests focus on luminescence mechanism of lanthanides, upconversion nanomaterials, glass materials and fibers, and nanophotonics. He has authored and co-authored over 50 peer-reviewed papers in journals including Nature Nanotechnology, Advanced Materials, Angewandte Chemie, Advanced Functional Materials, Advanced Science, and Progress in Materials Science.

Oleksandr A. Savchuk

Oleksandr Savchuk has a Master's degree in physics of semiconductors and nanostructures at Chernivtsi National University, Ukraine. His Master's thesis was focused on the synthesis of ZnO nanoparticles by pulsed laser ablation technique in liquid media. In 2016, he finished his doctorate studies at the University Rovira i Virgili, Tarragona, Spain, where he completed his thesis work conducted in the Physics and Crystalography of Materials and Nanomaterials laboratories, at the Department of Physical and Inorganic Chemistry. Currently, Oleksandr is a research fellow at the International Iberian Nanotechnology Laboratory (INL) Braga, Portugal, working on intracellular temperature measurements using luminescence nanothermometry for hyperthermia treatment.

Xiaoji Xie

Xiaoji Xie earned his BSc degree in Chemistry from Nanjing University in 2009. He obtained his PhD in 2013 at the National University of Singapore with Prof. X. Liu. He then became a postdoctoral researcher working in collaboration with Prof. X. Liu. He joined the Institute of Advanced Materials (IAM) at Nanjing Tech University, China in 2014. His current research involves the investigation of inorganic functional nanomaterials such as upconversion nanoparticles for bioapplications, catalysis ,and sensing.

Eduardo D. Martínez

Eduardo D. Martínez is an assistant researcher at the Institute of Nanoscience and Nanotechnology-CONICET located in the city of Bariloche, Argentina. He has a degree in materials engineering and a PhD in chemistry from the University of San Martín, Argentina. He performed a postdoctoral fellowship in his present institution developing nanocomposite materials for microfabrication and a second postdoc at the Universidad Estadual de Campinas, (UNICAMP), Brazil, devoted to upconverting nanoparticles. His expertise lies in the field of nanomaterials and nanocomposites, focused on plasmonics and photonics. Specifically, he works in the chemical synthesis of nanoparticles and their assembly into nanostructures and devices by combining bottom-up and top-down approaches.

Jérôme Long

Jérôme Long received his PhD from Pierre and Marie Curie University (Paris VI) in 2009 under the supervision of Dr Valérie Marvaud. He undertook postdoctoral research at the University of Ottawa with Prof. M. Murugesu before joining the University of Montpellier as an Assistant Professor in 2010. His current research is oriented towards the design and characterization of multifunctional molecular materials at bulk and nano-scales.

Laleh Tahsini

Dr Laleh Tahsini completed her PhD work at Sharif University of Technology (SUT), Iran, and the University of Manchester, UK. In 2009, She joined the MOBIC group in Ewha Woman's University, South Korea and worked as a postdoctoral researcher with Professors Kenneth D. Karlin (Johns Hopkins University) and Shunichi Fukuzumi (Osaka University). In 2011, she joined Prof. Linda Doerrer's group at Boston University, where she worked on electrocatalytic water oxidation. Dr Tahsini became an Assistant Professor at the chemistry department of Oklahoma State University in Fall 2014. The research theme of her group is inorganic and organometallic chemistry: synthesis, reactivity, and application.

Carlos D. S. Brites

Carlos DS Brites completed his PhD in Physics in the MAP-FIS joint program in 2012 at CICECO (University of Aveiro, Portugal) and at ICMA (University of Zaragoza, Spain), within the groups of Prof. F. Palacio and Dr A. Millan. His research interests focus on the luminescent properties of trivalent lanthanide as sensors and as functional molecular devices. He has authored 40 publications (h index 20, >2000 citations) and holds three international patents. He is currently a Researcher at CICECO as a member of the PHANTOM-G group, headed by prof. L. D. Carlos.

Kevin R. Kittilstved

Kevin Kittilstved was born in Spokane, Washington and graduated with degrees in chemistry from Gonzaga University (BSc) and the University of Washington (PhD). He held postdoctoral positions at the Université de Genève and the University of Washington prior to joining the University of Massachusetts Amherst as an Assistant Professor. Kevin is the recipient of the NSF CAREER Award and was recently promoted to Associate Professor. His research program focuses on understanding and exploiting the defect chemistry of inorganic materials to control physical properties and electronic structures from the molecular to the bulk.

Thomas L. Gianetti

Dr Gianetti is an Assistant Professor at the University of Arizona since September 2017. He was born in Marseille, south of France, where he completed his initial education. He graduated in 2009 from CPE Lyon, an engineering school in France, with a BSc and MSc degree in chemistry and chemical engineering. He then pursued his PhD studies at the University of California, Berkeley under the guidance of Profs Arnold and Bergman, followed by a post-doctoral position at the ETH Zürich with Prof. Grützmacher. His current work focuses on developing new catalytic systems for energy conversion and the removal of environmentally dangerous chemicals.

frontiers in Chemistry

ORIGINAL RESEARCH
published: 13 August 2019
doi: 10.3389/fchem.2019.00567

Coordination-Driven Self-Assembly of Silver(I) and Gold(I) Rings: Synthesis, Characterization, and Photophysical Studies

Cressa Ria P. Fulong[1], *Sewon Kim*[1], *Alan E. Friedman*[2] *and Timothy R. Cook*[1]*

[1] *Department of Chemistry, University at Buffalo, The State University of New York, Buffalo, NY, United States,* [2] *Department of Materials Design and Innovation, University at Buffalo, The State University of New York, Buffalo, NY, United States*

In this work, we investigate the self-assembly between Ag(I) and Au(I) centers and pyridyl donors to form hexagonal metallacycles and related linear complexes. The precipitation of hexagonal metallacycles upon assembly in chloroform/methanol mixtures results in high solid-state photo-stability. Whereas, the Ag(I) species have fast kinetics and high formation constants in acetone, this solvent interferes in the formation of the analogous Au(I) complexes. The photophysical properties of this suite of metallacycles was investigated including steady-state absorption, emission, and time-resolved lifetime measurements. All ligands and hexagons exhibited ligand-centered singlet emissions with ground-state absorption and emission perturbed upon coordination. The ligand-based fluorescent photoluminescence was affected by the heavy-atom effect when halide or metals are present, attenuating quantum yields as evidenced by increases in the experimentally measured non-radiative rate constants. The formation of group 11 metallacycles is motivated by their potential applications in mixed-matrix materials wherein metal ions can interact with substrate to facilitate separations chemistry with reduced energy requirements, in particular the isolation of ethylene and light olefins. Existing processes involve cryogenic distillation, an energy intensive and inefficient method.

Keywords: self-assembly, coordination, metallacycle, silver hexagon, gold hexagon

OPEN ACCESS

Edited by:
Luís D. Carlos,
University of Aveiro, Portugal

Reviewed by:
Fernando Novio,
Catalan Institute of Nanoscience and Nanotechnology (CIN2), Spain
Lin Xu,
East China Normal University, China

***Correspondence:**
Timothy R. Cook
trcook@buffalo.edu

Specialty section:
This article was submitted to Inorganic Chemistry, a section of the journal Frontiers in Chemistry

Received: *28 February 2019*
Accepted: *26 July 2019*
Published: *13 August 2019*

Citation:
Fulong CRP, Kim S, Friedman AE and Cook TR (2019) Coordination-Driven Self-Assembly of Silver(I) and Gold(I) Rings: Synthesis, Characterization, and Photophysical Studies. Front. Chem. 7:567. doi: 10.3389/fchem.2019.00567

INTRODUCTION

Coordination-driven self-assembly (Leininger et al., 2000) is a valuable strategy for the design and synthesis of discrete molecular complexes such as metallacycles and metallacages for biomedical (Cook et al., 2013; Casini et al., 2017) catalytic (Ito et al., 2000; Brown et al., 2009; Smulders and Nitschke, 2012; Vardhan and Verpoort, 2015; Kuijpers et al., 2016), molecular sensing (Tashiro et al., 2005; Kim and Ahn, 2008; Wang et al., 2011; Zwijnenburg et al., 2016; Cao et al., 2017), and small molecule adsorption and separation applications (Sudik et al., 2005; Zhao et al., 2010; Riddell et al., 2011; Amayuelas et al., 2016). This strategy exploits pre-programmed directionality information on metal acceptor and ligand donor building blocks to form complex architectures driven by metal-ligand coordination (Cook and Stang, 2015). A careful design of building blocks coupled with thermodynamic driving forces favors the convergent formation of discrete molecular

complexes over divergent coordination polymers a.k.a. metal-organic frameworks (MOFs) (Fujita et al., 2001).

Inspired by previous reports on hexagonal self-assemblies from *trans*-capped Pt(II) precursors (Yang et al., 2007) and 120° bidentate pyridine-type ligands, which are known for their luminescent properties, and other luminescent Pt(II)-based metallacycles (Huang et al., 2017; Tang et al., 2018), we now report the self-assembly of hexagonal metallacycles from the same class of ligand donors and Ag(I) and Au(I) metal acceptors. There have been few reports on linear Ag(I) (Del Piero et al., 2008) and Au(I) (Fernández et al., 2007) complexes, and Ag(I) metallacycles (Shin et al., 2003; Chen and Mak, 2005; Fromm et al., 2005; Ren et al., 2006; Kim et al., 2009; Wan and Mak, 2011; Kole et al., 2012; Wei et al., 2012; Chevrier et al., 2013) with pyridine-type ligands, but these are the first Ag(I) and Au(I) hexagonal rings. We also synthesized Ag(I) and Au(I) monomeric complexes using analogous monodentate pyridine-type ligands. Having both linear monomeric complexes and hexagonal metallacycles enables the comparison of solid- and solution-state structures, organic solvent solubilities, photophysical properties, as well as light-stabilities. These self-assembled Ag(I) and Au(I) hexagons have limited solubility in organic solvents. Efforts are ongoing to improve the solubilities of these metallacycles including but not limited to pre- and post-assembly ligand modification.

We have an ongoing interest in incorporating these metallacycles and metallacages as filler materials in mixed-matrix materials (MMMs) (Fulong et al., 2018). MMMs are a type of thin-film composite material typically composed of a highly porous inorganic/organic filler and an organic polymer binder. The significance of MMMs in the medical and small molecule purification industries has been steadily increasing in the past decade and contemporary research is largely focused on MOFs as a filler material (Dechnik et al., 2017). We have previously shown the importance of solubilizing the filler material into the polymer solution to fabricate thin, flexible, homogeneous, and highly permeable MMMs (Fulong et al., 2018). Along these lines, we highlighted the advantage and ease of using discrete coordination cages over MOFs as MMMs filler material due to the former's solubility in a range of solvents. For certain separations the filler material introduces sites for intermolecular interactions with substrate, which enables active separation rather than just size-selective sieving. As a result, the design of fillers with unsaturated metals or other binding sites enables the fabrication of MMMs with improved permeability and selectivity. Since a variety of metal centers may be used as nodes in coordination-driven self-assembly, properly matching metal ions to a separation of interest is an important first-principle in the design of new metal-organic materials (Dechnik et al., 2017).

The incorporation of silver salts has been identified as an effective strategy for increasing the selectivity of olefin/paraffin membranes based on the ability of electron-rich olefins to interact with metal ions, an attractive technology given the scope of the petrochemical industry wherein ethylene is used a primary building block (Eldridge, 1993). These materials suffer from the instability of Ag(I) ions that react with oxygen and leach from the material. We hypothesized that Ag(I) ions may be stabilized by a linear L–Ag(I)–L environment that still enables equatorial interactions with substrate (Fox et al., 2002; Gimeno, 2009). Other transition metals with coordination numbers of three or more require capping ligands to prevent divergent framework formation (Fujita, 1998; Fujita et al., 2001). For Ag(I) and Au(I), with linear coordination environments, capping ligands are not required and coordination with bent ditopic donors may furnish discrete metallacycles.

MATERIALS AND METHODS

All reagents and solvents were reagent grade and used as received without further purification unless noted. Methanol (CH_3OH), acetone, dichloromethane (DCM), ethyl acetate (EtOAc), n-hexanes, toluene, diethyl ether, petroleum ether, potassium hydroxide (KOH), sodium sulfate (Na_2SO_4) and potassium carbonate (K_2CO_3) were purchased from Fisher Scientific. N,N-dimethylformamide (DMF) was purchased from Macron Fine Chemicals. Tetrahydrofuran (THF), triethylamine (NEt_3), and chloroform ($CHCl_3$) were purchased from EMD Millipore. Ethanol (EtOH, 200 proof) was purchased from Decon Labs, Inc. Tetrakis(triphenylphosphine)palladium(0) ($Pd(PPh_3)_4$), and bis(triphenylphosphine)palladium(II) chloride ($Pd(PPh_3)_2Cl_2$), and 1,3-dibromobenzene were purchased from Matrix Scientific. 4-pyridinylboronic acid ($pyB(OH)_2$) was purchased from AK Scientific. Copper (I) iodide (CuI) was purchased from Strem Chemicals. Tetrahydrothiophene (tht) was purchased from Aldrich. Silver(I) hexafluorophosphate ($AgPF_6$) was purchased from Oakwood Chemical. Hydrogen tetrachloroaurate(III) trihydrate ($HAuCl_4{\cdot}3H_2O$) was purchased from J&J Materials Inc. 4-ethynylpyridine hydrochloride and 1,3,5-tribromobenzene were purchased from Ark Pharm Inc. Deionized water was used whenever water was needed. THF was purified and dried through a Pure Process Technology free standing solvent purification system. NEt_3 was purified and dried by distillation in KOH. DMF was filtered and dried using activated molecular sieves under N_2 and freeze-pump-thawed with water before use for synthesis.

^{1}H Nuclear Magnetic Resonance (NMR) spectra were recorded on either Varian 300 or 400 MHz spectrometer. Chemical shifts (δ) are reported in parts per million (ppm) referenced using the residual protio-solvent peaks as internal standards. Coupling constants (J) are quoted in Hertz (Hz), and the following abbreviations are used to describe the signal multiplicities: s (singlet); d (doublet); t (triplet); q (quartet); m (multiplet). Fourier Transform-Ion Cyclotron Resonance (FT-ICR) mass spectra were acquired using a Bruker Daltonics SolariX 12T FT-ICR Mass Spectrometer that was calibrated with > 90% Angiotensin I purchased from Sigma Aldrich under either Electrospray Ionization (ESI) or Laser Desorption Ionization (LDI) modes. Single Crystal X-ray Diffraction (SC-XRD) Crystallography was performed using a Bruker D8 Venture diffractometer in a fixed-chi geometry, equipped with a Photon-100 CMOS area detector, Oxford Cryosystems cryostat, a molybdenum

source (Mo, λ = 0.71073 Å), and a graphite monochromator. Fourier Transform Infrared Resonance (FT-IR) spectra were collected from a Perkin Elmer 1760 FT-IR spectrometer equipped with horizontal attenuated total reflectance (HATR) from 4,000 to 500 cm^{-1} wavenumbers (ν). The following abbreviations are used to describe signal intensities: w (weak); m (medium); s (strong). All UV-Vis absorption spectra were acquired from an Agilent Cary 8454 UV-Vis Diode Array system. Blank spectra with pure solvents were acquired before each run. All emission spectra were collected using a Horiba Scientific FluoroMax-4 Spectrofluorometer equipped with Quanta-φ Integrating light sphere with Spectralon coating for quantum yield (Φ) measurements and Delta-Hub DH-HT High Throughput Time-correlated Single Photon Counting (TCSPC) Controller and Nano-LED NL-C2 pulsed-diode controller with N-350 NanoLED Source for lifetime measurements. All solution-state absorbance and emission spectra were collected using a 10-mm rectangular quartz cuvette from Starna Cells Inc.

Synthesis of Ag(I) Complex ($AgL1_2$)

Ag**L1**$_2$ complex was self-assembled using a modified literature procedure (Chen et al., 2013). In a foil-covered 200-mL round-bottom flask, 0.800 g (3.1 mmol) **L1** was dissolved in 80.0 mL $CHCl_3$. In another foil-covered 100-mL round-bottom flask, 0.720 g (2.85 mmol) $AgPF_6$ was dissolved in 80.0 mL MeOH then layered over the **L1** solution. After 48 h, white needle-like crystals form. These crystals were filtered and washed with 10-mL portions of $CHCl_3$ (3x) to afford 1.19 g (100% yield) isolated product. ^{1}H NMR (400 MHz, acetone-d_6, 25°C): δ (ppm) = 8.81 (d, ^3J = 5.2 Hz, 4H, pyridyl H_α), 7.82 (s, 2H, phenyl H), 7.77 (d, ^3J = 6.3 Hz, 4H, pyridyl H_β), 7.71 (d, ^3J = 8.1 Hz, 2H, phenyl H), 7.65 (d, ^3J = 7.8 Hz, 2H, phenyl H), 7.46 (t, ^3J = 7.9 Hz, 2H, phenyl H). FT-IR (ATR, cm^{-1}): 3069 (w), 2235 (w), 2187 (w), 1609 (m), 1558 (w), 1506 (w), 1470 (w), 1433 (w), 1405 (w), 1223 (w), 1152 (w), 1070 (w), 1031 (w), 991 (w), 915 (w), 881 (m), 815 (m), 775 (m), 757 (m), 743 (m), 678 (m), 663 (m), 553 (m), 531 (m).

Synthesis of ({AgL2}$_6$) Ag(I) Hexagon

{Ag**L2**}$_6$ hexagon, was self-assembled using a modified literature procedure (Chen et al., 2013). In a foil-covered 20-mL scintillation vial, 0.050 g (0.14 mmol) **L2** was dissolved in 5.0 mL $CHCl_3$. In another foil-covered 20-mL scintillation vial, 0.035 g (0.14 mmol) $AgPF_6$ was dissolved in 5.0 mL MeOH then layered over the **L2** solution. After 48 h, white powdered product formed which was filtered and washed with 10-mL portions of $CHCl_3$ (3x) to afford 0.062 g (73% yield) isolated product. ^{1}H NMR (400 MHz, acetone-d_6, 25°C): δ (ppm) = 8.72 (d, ^3J = 5.9 Hz, 24H, pyridyl H_α), 7.90 (s, 11H, phenyl H), 7.83 (s, 6H, phenyl H), 7.62 (d, ^3J = 6.0 Hz, 24H, pyridyl H_β). FT-IR (ATR, cm^{-1}): 3076 (w), 2219 (w), 1613 (m), 1557 (w), 1507 (w), 1435 (m), 1338 (w), 1291 (w), 1221 (m), 1174 (w), 1162 (w), 1136 (w), 1107 (w), 1066 (w), 1028 (w), 993 (w), 964 (w), 864 (m), 821 (s), 748 (w), 736 (w), 663 (m), 573 (w), 552 (s).

Synthesis of ({AgL3}$_6$) Ag(I) Hexagon

{Ag**L3**}$_6$ hexagon, was self-assembled using a modified literature procedure (Chen et al., 2013). In a foil-covered 20-mL scintillation vial, 0.050 g (0.18 mmol) **L3** was dissolved in 5.0 mL $CHCl_3$. In another foil-covered 20-mL scintillation vial, 0.045 g (0.18 mmol) $AgPF_6$ was dissolved in 5.0 mL MeOH then layered over the **L3** solution. After 48 h, white powdered product formed which was filtered and washed with 10-mL portions of $CHCl_3$ (3x) to afford 0.096 g (100% yield) isolated product. ^{1}H NMR (400 MHz, acetone-d_6, 25°C): δ (ppm) = 8.74 (d, ^3J = 6.0 Hz, 24H, pyridyl H_α), 7.86 (s, 6H, phenyl H), 7.74 (d, ^3J = 9.3 Hz, 12H, phenyl H), 7.66 (d, ^3J = 6.1 Hz, 23H, pyridyl H_β), 7.63 – 7.56 (m, 7H, phenyl H). FT-IR (ATR, cm^{-1}): 3107 (w), 2203 (w), 1615 (m), 1543 (w), 1501 (w), 1431 (w), 1227 (w), 1167 (w), 1064 (w), 1025 (w), 878 (w), 821 (m), 752 (w), 733 (w), 682 (w), 556 (m), 541 (m).

Synthesis of ({AgL4}$_6$) Ag(I) Hexagon

{Ag**L4**}$_6$ hexagon, was self-assembled using a modified literature procedure (Chen et al., 2013). In a foil-covered 20-mL scintillation vial, 0.025 g (0.11 mmol) **L4** was dissolved in 2.0 mL $CHCl_3$. In another foil-covered 20-mL scintillation vial, 0.027 g (0.11 mmol) $AgPF_6$ was dissolved in 2.0 mL MeOH then layered over the **L4** solution. After 48 h, white powdered product formed which was filtered and washed with 10-mL portions of $CHCl_3$

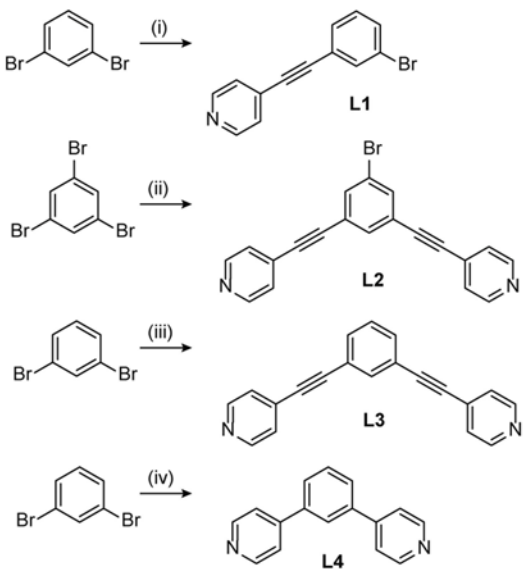

(i) 1 eq. 4-ethynylpyridine hydrochloride, CuI, $Pd(PPh_3)_4$, dry THF/NEt_3, reflux under N_2 at 60°C for 48 h,
(ii) 2 eq. 4-ethynylpyridine hydrochloride, CuI, $Pd(PPh_3)_2Cl_2$, dry $toluene/NEt_3$, reflux under N_2 at 90°C for 48 h,
(iii) 2 eq. 4-ethynylpyridine hydrochloride, CuI, $Pd(PPh_3)_2Cl_2$, dry $toluene/NEt_3$, reflux under N_2 at 90°C for 48 h, and
(iv) 2 eq. $pyB(OH)^2$, K^2CO_3, $Pd(PPh_3)_4$, 98:2 dry DMF/H_2O, reflux under N_2 at 100°C for 48 h

SCHEME 1 | Coupling reactions to form **L1**, **L2**, **L3**, and **L4**.

(3x) to afford 0.052 g (92% yield) isolated product. ^{1}H NMR (400 MHz, acetone-d_6, 25°C): δ (ppm) = 8.76 (d, ^{3}J = 6.7 Hz, 24H, pyridyl H_α), 8.25 (s, 5H, phenyl H), 8.00–7.87 (m, 36H, pyridyl H_β and phenyl H), 7.80–7.71 (m, 5H, phenyl H). FT-IR (ATR, cm^{-1}): 3092 (w), 1618 (m), 1545 (w), 1513 (w), 1478 (w), 1431 (w), 1411 (w), 1314 (w), 1230 (w), 1069 (w), 1031 (w), 1019 (w), 873 (m), 818 (s), 791 (s), 736 (m), 695 (m), 663 (w), 637 (m), 613 (w), 555 (s).

Synthesis of Au(I) Complex (Au$L1_2$)

Au**L1**$_2$ complex was self-assembled using a modified literature procedure (Lin et al., 2008). In a foil-covered 2-dram vial, 0.020 g (0.078 mmol) **L1**, 0.025 g (0.078 mmol) Au(tht)Cl were dissolved in 6.0 mL acetone. After 6 h, the solution was concentrated in vacuo and the collected solid was washed with 6-mL portions of $CHCl_3$ (3x) to afford 0.007 g (20% yield) isolated product. ^{1}H NMR (300 MHz, acetone-d_6, 25°C): δ (ppm) = 8.84 (d, ^{3}J = 6.0 Hz, 4H, pyridyl H_α), 7.89 (d, ^{3}J = 7.0 Hz, 5H, pyridyl H_β), 7.80 (s, 2H, phenyl H), 7.68 (td, ^{3}J = 16.3, 15.7, 7.8 Hz, 10H), 7.50 – 7.40 (m, 3H, phenyl H). FT-IR (ATR, cm^{-1}): 3044 (w), 2918 (w), 2856 (w), 2218 (m), 2187 (w), 1943 (w), 1801 (w), 1614 (m), 1588 (m), 1558 (w), 1496 (w), 1463 (w), 1429 (w), 1404 (w), 1261 (w), 1234 (w), 1217 (w), 1158 (w), 1105 (w), 1088 (w), 1060 (w), 1038 (w), 987 (w), 906 (w), 876 (w), 836 (m), 814 (w), 789 (m), 747 (w), 713 (w), 691 (w), 680 (m), 655 (m), 565 (w), 535 (m).

Synthesis of Au(I) Hexagons ({AuL2}$_6$)

{Au**L2**}$_6$ hexagon was self-assembled using a modified literature procedure (Lin et al., 2008). In a foil-covered 2-dram vial, 0.028 g (0.078 mmol) **L2**, 0.025 g (0.078 mmol) Au(tht)Cl were dissolved in 6.0 mL $CHCl_3$. After 24 h, the solution was concentrated in vacuo and the collected yellow solid was washed with 6-mL portions of $CHCl_3$ (3x) to afford 0.025 g (78% yield) isolated product. ^{1}H NMR (400 MHz, CD_3NO_3, 25°C): δ (ppm) = 8.84–8.71 (m, 24H, pyridyl H_α), 8.09 – 7.82 (m, 40H, pyridyl H_β and phenyl H). FT-IR (ATR, cm^{-1}): 3100 (w), 3044 (w), 2210 (m), 1615 (s), 1553 (w), 1496 (w), 1430 (m), 1336 (w), 1288 (w), 1211 (m), 1171 (w), 1134 (w), 1105 (w), 1063 (m), 1046 (w), 992 (w), 966 (w), 863 (m), 826 (m), 761 (w), 721 (w), 672 (m), 587 (w), 574 (m), 527 (w).

Synthesis of Au(I) Hexagons ({AuL3}$_6$)

{Au**L3**}$_6$ hexagon was self-assembled using a modified literature procedure (Lin et al., 2008). In a foil-covered 2-dram vial, 0.022 g (0.078 mmol) **L3**, 0.025 g (0.078 mmol) Au(tht)Cl were dissolved in 6.0 mL $CHCl_3$. After 24 h, the solution was concentrated in vacuo and the collected yellow solid was washed with 6-mL portions of $CHCl_3$ (3x) to afford 0.026 g (89% yield) isolated product. ^{1}H NMR (400 MHz, CD_3NO_3, 25°C): δ (ppm) = 8.76 (d, ^{3}J = 5.0 Hz, 24H, pyridyl H_α), 8.08 – 7.70 (m, 41H, pyridyl H_β and phenyl H), 7.66–7.57 (m, 7H, phenyl H). FT-IR (ATR, cm^{-1}): 3092 (w), 3029 (w), 2203 (m), 1943 (w), 1609 (s), 1529 (w), 1492 (w), 1427 (w), 1324 (w), 1213 (w), 1162 (w), 1150 (w), 1125 (w), 1093 (w), 1065 (w), 1042 (w), 991 (w), 942 (w), 902 (w), 831 (m), 792 (w), 754 (w), 729 (w), 666 (w), 569 (w), 544 (w).

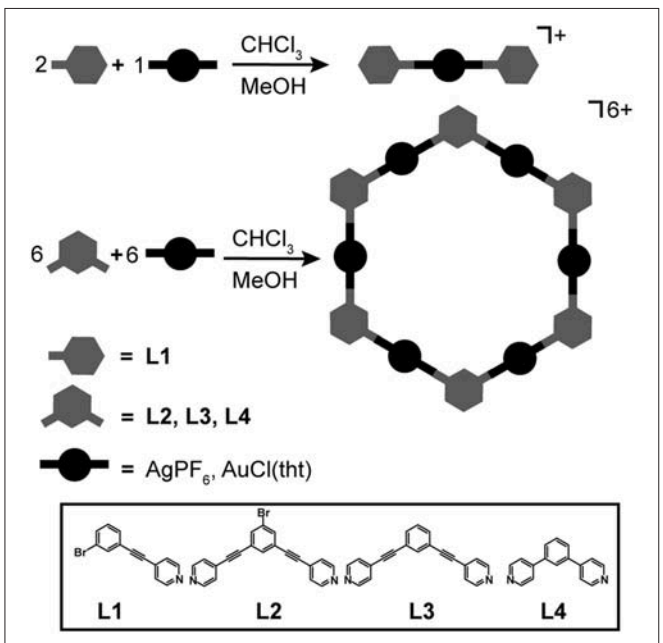

FIGURE 1 | Self-assembly of Ag(I) and Au(I) hexagons and mononuclear homoleptic complexes.

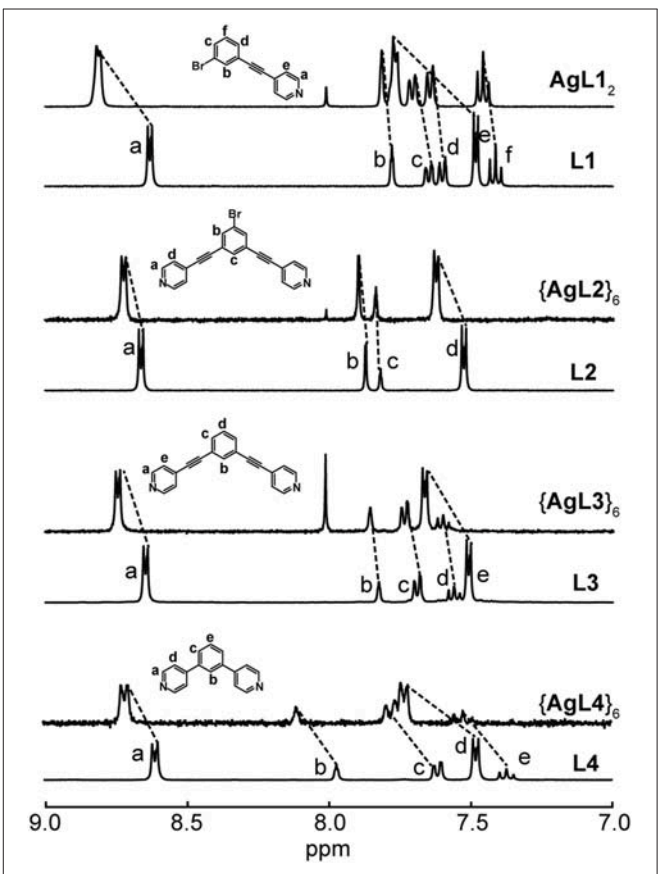

FIGURE 2 | ^{1}H NMR spectra of **L1** and Ag**L1**$_2$, **L2** and {Ag**L2**}$_6$, **L3** and {Ag**L3**}$_6$ and **L4** and {Ag**L4**}$_6$ in acetone-d_6.

Synthesis of Au(I) Hexagons ({AuL4}$_6$)

{Au**L4**}$_6$ hexagon was self-assembled using a modified literature procedure (Lin et al., 2008). In a foil-covered 2-dram vial, 0.018 g (0.078 mmol) **L4**, 0.025 g (0.078 mmol) Au(tht)Cl were dissolved in 6.0 mL $CHCl_3$. After 24 h, the solution was concentrated in vacuo and the collected white solid was washed with 6-mL portions of $CHCl_3$ (3x) to afford 0.027 g (100% yield) isolated product. ^{1}H NMR (400 MHz, CD_3NO_3, 25°C): δ (ppm) = 8.82 (d, ^{3}J = 6.7 Hz, 24H, pyridyl H$_\alpha$), 8.35 (s, 7H, phenyl H), 8.22 (d, ^{3}J = 6.3 Hz, 22H, pyridyl H$_\beta$), 8.11 (d, ^{3}J = 9.4 Hz, 14H, phenyl H), 7.86 (t, ^{3}J = 7.6 Hz, 7H, phenyl H). FT-IR (ATR, cm^{-1}): 3060 (w), 1611 (s), 1546 (w), 1508 (w), 1472 (w), 1443 (w), 1427 (w), 1398 (m), 1340 (w), 1318 (w), 1266 (w), 1231 (m), 1186 (w), 1109 (w), 1076 (m), 1034 (w), 970 (w), 935 (w), 915 (w), 857 (w), 832 (m), 786 (s), 761 (w), 732 (m), 687 (w), 667 (w), 645 (m), 632 (w), 606 (w), 535 (s).

RESULTS AND DISCUSSION

Self-Assembly of Ag(I) and Au(I) Complexes and Hexagons

Four pyridyl ligands, 1-bromo-3(4-ethynylpyridyl)benzene (**L1**), 5-bromo-1,3-bis(4-ethynylpyridyl)benzene (**L2**), 1,3-bis(4-ethynylpyridyl)benzene (**L3**), and 1,3-bis(4-pyridyl)benzene (**L4**), were prepared as donors for self-assembly reactions. As illustrated in **Scheme 1**, **L1**, **L2**, and **L3** were prepared following a typical Sonogashira coupling reaction while **L4** was prepared following a typical Suzuki coupling reaction. The ^{1}H NMR spectra of **L1**, **L2**, **L3**, and **L4** in acetone-d$_6$ are summarized in **Supplementary Figures 1A–D**, respectively. The **L1** ^{1}H spectrum shows the pyridyl-H doublets at 8.63 and 7.49 ppm and the benzyl-H singlet at 7.78 ppm, two doublets at 7.65 and 7.60 ppm, and triplet at 7.42 ppm. The **L2** spectrum shows the pyridyl-H doublets at 8.66 and 7.53 ppm and the benzyl-H singlets at 7.87 and 7.82 ppm. The **L3** spectrum shows the pyridyl-H doublets at 8.65 and 7.51 ppm and the benzyl-H singlet at 7.83 ppm, doublet at 7.69 ppm, and triplet at 7.56 ppm. The **L4** spectrum shows the pyridyl-H doublets at 8.68 and 7.78 ppm and the benzyl-H singlet at 8.17 ppm, doublet at 7.89 ppm, and triplet at 7.70 ppm.

L1 was used to synthesize linear Ag(I) and Au(I) complexes, while **L2**, **L3**, and **L4** were used to self-assemble Ag(I) and Au(I) hexagonal metallacycles. The general method used to self-assemble the complexes and hexagons is shown in **Figure 1**. All self-assembly reactions were performed in the absence of light to ensure no loss in Ag(I) and Au(I) precursors. The monomeric Ag(I) complex, Ag**L1**$_2$, was prepared by layering one equivalent of $AgPF_6$ in MeOH over two equivalents of **L1** in $CHCl_3$. This resulted in the crystallization of Ag**L1**$_2$ after 48 h. Ag(I) hexagons, {Ag**L**}$_6$ where **L** = **L2**, **L3**, and **L4**, were prepared by layering one equivalent of $AgPF_6$ in MeOH over one equivalent of **L** in $CHCl_3$. The hexagons precipitated at almost quantitative yields as white powders after 48 h. The gold analogs, Au(I) hexagons, {Au**L**}$_6$ where **L** = **L2**, **L3**, and **L4**, were prepared by mixing 1:1 equivalents of Au(tht)Cl and **L** in $CHCl_3$. After 24 h, powdered metallacycles were isolated upon solvent removal and $CHCl_3$ washing. In the case of the monomeric Au(I) complex, Au**L1**$_2$, previous attempts using pure $CHCl_3$ or 1:1 (v/v) $CHCl_3$/MeOH did not result in any complex formation. However, the complex was isolated at a relatively low yield by mixing 1:1 equivalents of Au(tht)Cl and **L1** in acetone.

^{1}H NMR of Ag(I) and Au(I) Complexes and Hexagons

A notable challenge in characterizing these self-assembled Ag(I) and Au(I) complex and hexagons is their limited solubilities. Coordinating solvents such as acetonitrile (MeCN) and *N,N*'-dimethylsulfoxide (DMSO), which are typically used in solution-state structural analyses of Ag(I) and Ag(I) complexes proved to be unsuitable for our complexes and hexagons (Laye, 2007; Lin et al., 2008). In all cases, we observed ligand dissociation upon addition of MeCN or DMSO.

Nonetheless, we were able to detect the intact Ag(I) complexes and hexagons (**Figure 2**) as well as Au(I) complex (**Figure 3**) in acetone. The coordination of the pyridyl ligands to Ag(I) and Au(I) is exemplified by the characteristic downfield shifts in ^{1}H NMR peaks as well as peak integration agreements (**Supplementary Figures 2, 3A**). In addition, the same peak splitting patterns between

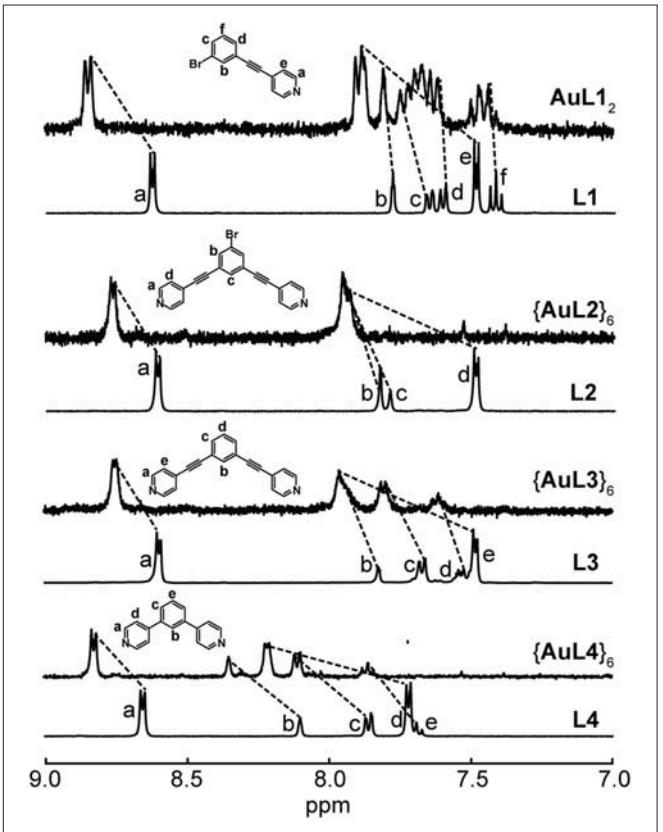

FIGURE 3 | ^{1}H NMR spectra of **L1** and Au**L1**$_2$ in acetone-d$_6$, **L2** and {Au**L2**}$_6$, **L3** and {Au**L3**}$_6$ and **L4** and {Au**L4**}$_6$ in nitromethane-d$_3$.

the ligand and the complex/hexagon were expected due to the C_{2v} symmetry of both Ag**L1**$_2$ and Au**L1**$_2$ complexes and the D_{6h} symmetry of all {Ag**L**}$_6$ hexagonal metallacycles.

For the Au(I) hexagons, ligand dissociation occurs when MeCN, DMSO, and acetone were used as solvents. These hexagons are insoluble in all other solvents except for nitromethane, in which we were able to observe intact Au(I) hexagons. **Figure 3** summarizes the ^{1}H NMR spectra of {Au**L2**}$_6$, {Au**L3**}$_6$, and {Au**L4**}$_6$. The full spectra of each Au(I) hexagon are shown in **Supplementary Figures 3B–D**. Similar to the Ag(I) hexagons, the downfield shifts of all ^{1}H NMR peaks, the peak integration agreements, and the similarity in peak splitting patterns indicate the formation of pure Au(I) hexagonal metallacycles. Although the solubility of these species is limited, our identification of NMR-suitable solvents rules out the formation of polymeric species as such coordination polymers are fully insoluble. ESI-MS (see below) further confirms the stoichiometries of self-assembly.

Formation of Ag(I) and Au(I) Complexes and Hexagons in Acetone

All of these complexes were synthesized in pure $CHCl_3$ or in $CHCl_3$ mixtures with MeOH. MeCN and DMSO competitively coordinate with the Ag(I) and Au(I) resulting in ligand dissociation. Acetone was a suitable solvent for the building blocks, as well as the final assemblies, enabling the study of complex formation. Using ^{1}H NMR methods, we initially acquired a series of spectra for a solution containing 1:1 equivalents of Ag:**L** in acetone upon mixing and after 24 h (**Supplementary Figure 4**). We observed that the thermodynamic products formed immediately upon mixing with no significant changes observed after 24 h. This suggests a fast

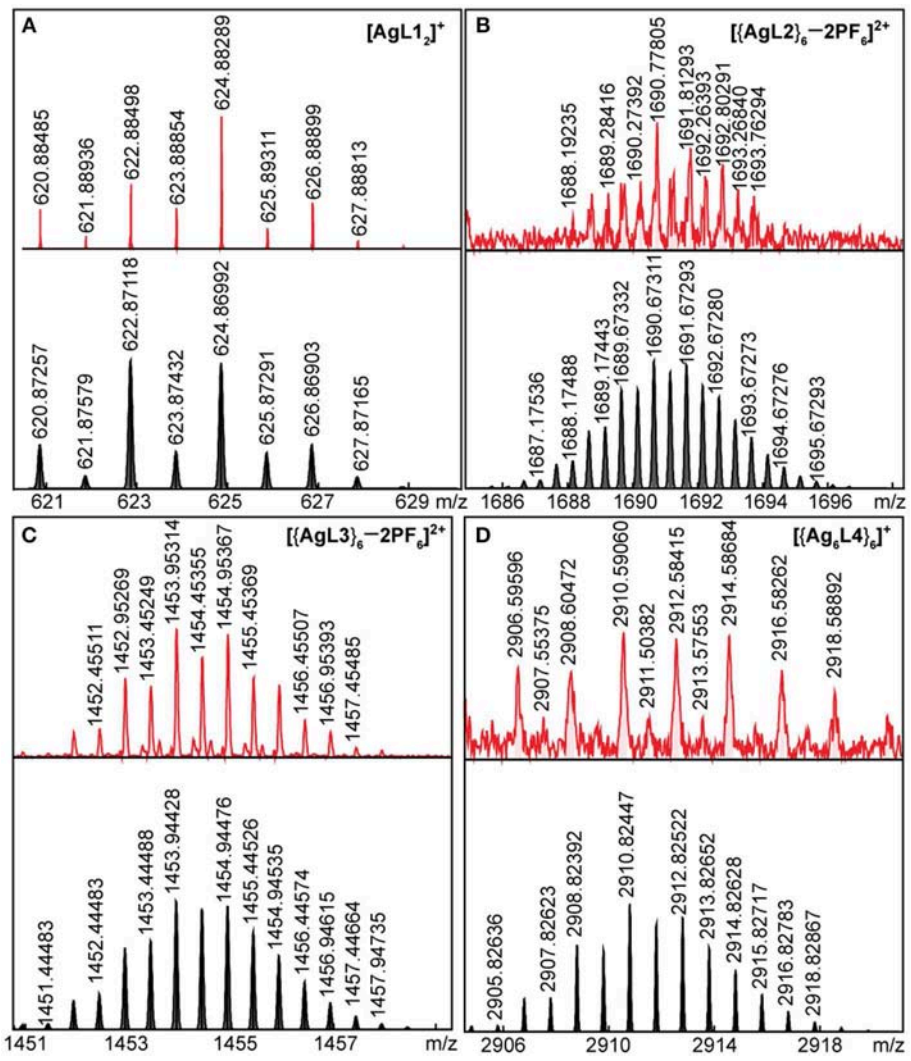

FIGURE 4 | ESI-FT-ICR MS spectrograms of intact **(A)** Ag**L1**$_2$, **(B)** {Ag**L2**}$_6$, **(C)** {Ag**L3**}$_6$, and **(D)** LDI-FT-ICR MS spectrum of intact {Ag**L4**}$_6$ (top = experimental, bottom = simulated).

kinetics with a large formation constant for all Ag(I) complex and hexagons in acetone.

Similarly, we wanted to study the solution formation of the Au(I) complex and hexagons. In this case, we prepared solutions containing 1:1, 2:1, and 3:1 equivalents of Au:**L** in acetone to ensure complete ligand coordination. The acquired ^{1}H NMR spectra at 0 (upon mixing), 6, 24, and 48 h were summarized in **Supplementary Figures 5–7** for 1:1, 2:1, and 3:1 solutions, respectively. It was observed that the Au**L1**$_2$ complex self-assembles within 6 h then partially dissociates thereafter. In the case of both {Au**L2**}$_6$ and {Au**L3**}$_6$, an equilibrium was established immediately upon mixing that stays up to at least 48 h. Products of {Au**L4**}$_6$ hexagon assembly crash out of solution immediately upon mixing such that we only observe uncoordinated **L4** and partially dissolved products. In all cases, the initial coordination is fast; however, quantitative analyses of the NMR peaks is not straightforward using a one-step metal-ligand binding model. There are reports on the mechanism and reducing ability of acetone to form Au nanoparticles from Au(III) and Au(I) (Marin et al., 2008). Thus, we think that there is a possibility of either Au(I) slowly being released as Au(0) from the hexagonal metallacycle into the acetone solution or acetone competitively coordinating to Au(I) to form other products.

FT-ICR MS of Ag(I) and Au(I) Complexes and Hexagons

High-resolution mass spectrometry (HRMS) was used to probe the stoichiometry of our self-assemblies. We used Fourier transform-ion cyclotron mass spectrometry (FT-ICR MS) with electrospray ionization (ESI) for soluble complexes and hexagons, while laser desorption ionization (LDI) was used for hexagons that are unstable in acetone. ESI, as a soft

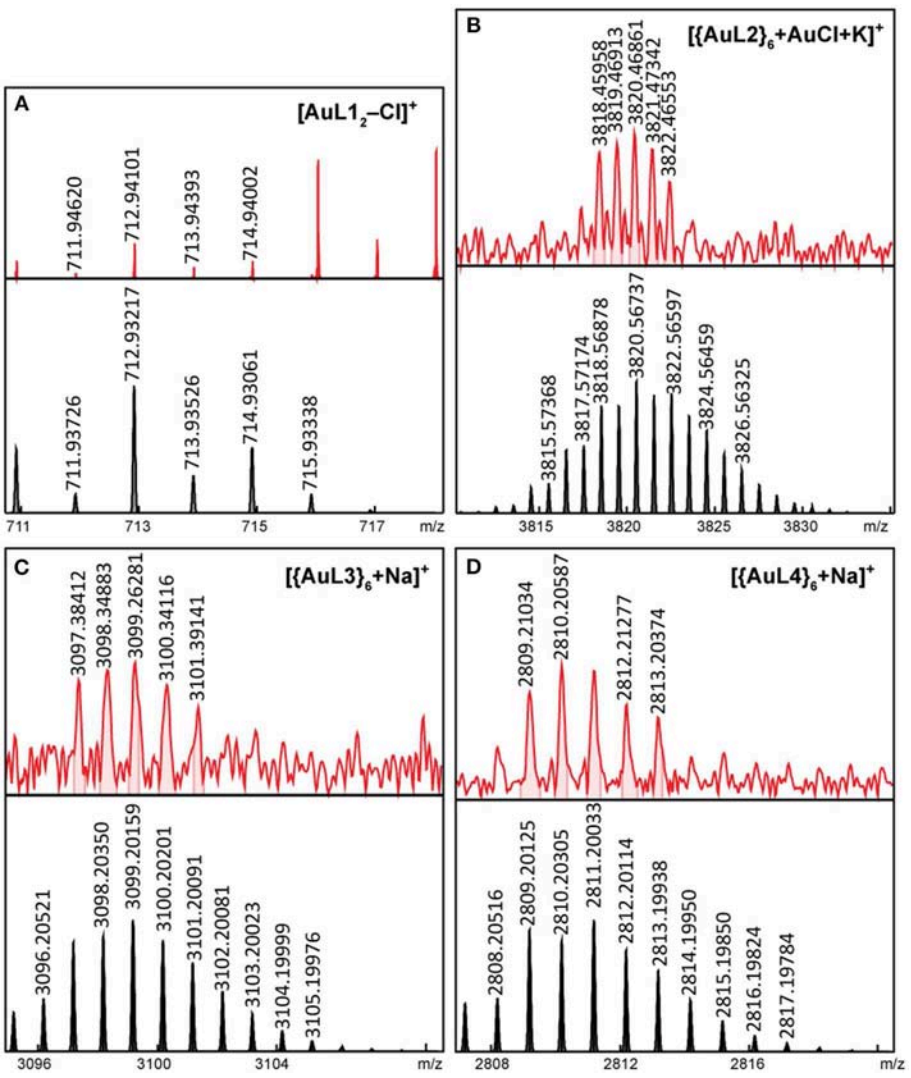

FIGURE 5 | ESI-FT-ICR MS spectrogram of intact **(A)** Au**L1**$_2$ and LDI-FT-ICR MS spectrograms of intact **(B)** {Au**L2**}$_6$, **(C)** {Au**L3**}$_6$, and **(D)** {Au**L4**}$_6$ (top = experimental, bottom = simulated).

ionization technique, is advantageous and popularly used in detection of intact coordination complexes and cages with high molar masses (Vikse and Scott McIndoe, 2018). Typical of soft ionization methods, molecules are ionized by either loss of ions or association with low-valent ions. In the case of our Ag(I) and Au(I) complexes and hexagons, loss of counter-ions results in multiply-charged compounds that are easily detectable by HR-MS at lower m/z. In cases wherein the hexagon is not stable in acetone, we opted to use matrix-free LDI, which uses high-energy lasers to ionize samples in the solid state. LDI is not popularly used in coordination chemistry due to formation of singly-charged fragment ions (Mandal et al., 2019). We, nonetheless, successfully identified intact hexagons in their solid state.

The mass spectrograms for Ag(I) complex and hexagons and for Au(I) complex and hexagons are shown in **Figures 4**, **5**, respectively. For the Ag(I) complex and hexagons, we were able to detect the intact $[Ag\mathbf{L1}_2]^+$ complex (**Figure 4A**) as well as $[\{Ag\mathbf{L2}\}_6 - 2PF_6]^{2+}$ hexagon (**Figure 4B**) and $[\{Ag\mathbf{L3}\}_6 - 2PF_6]^{2+}$ hexagon (**Figure 4C**) by ESI-FT-ICR MS. A loss of one PF_6^- counter-ion was observed for the complex and two PF_6^- were observed for both hexagons. $[\{Ag\mathbf{L4}\}_6]^+$ hexagon (**Figure 4D**), which has low solubility in acetone, was detected by LDI-FT-ICR MS.

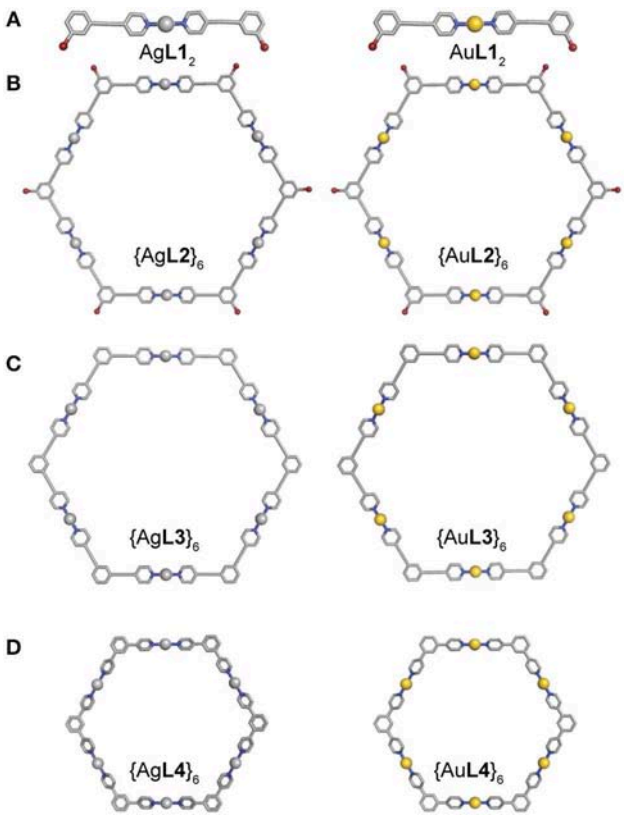

FIGURE 6 | Molecular models from crystal structure of **(A)** Ag**L1**$_2$ (CCDC 1879931) and Universal Force Field (UFF) optimized structures of Au**L1**$_2$, **(B)** {Ag**L2**}$_6$ and {Au**L2**}$_6$, **(C)** {Ag**L3**}$_6$ and {Au**L3**}$_6$, and **(D)** {Ag**L4**}$_6$ and {Au**L4**}$_6$ (C = gray, N = blue, Br = maroon, Ag = silver, and Au = gold).

For the Au(I) complex and hexagons, we were able to detect the intact $[Au\mathbf{L1}_2]^+$ complex (**Figure 5A**) with a loss of Cl^- counter-ion by ESI-FT-ICR MS. The Au(I) hexagons, which are unstable is acetone were detected by LDI-FT-ICR MS. We were able to detect singly-charged intact $[\{Au\mathbf{L2}\}_6+AuCl+K]^+$ hexagon (**Figure 5B**), $[\{Au\mathbf{L3}\}_6+Na]^+$ hexagon (**Figure 5C**), and $[\{Au\mathbf{L4}\}_6+Na]^+$ hexagon (**Figure 5D**). Each of these hexagons have six chloride counter-ions. We also observed $\{Au\mathbf{L}\}_6$ fragments (**Supplementary Figures 12–15**) with chloride counter-ions by ESI-FT-ICR MS, which further confirms the presence of chloride counter-ions in the Au(I) hexagons.

In all cases, we were able to confirm the presence of intact complexes and cages from the agreement of molecular ion m/z and isotopic distribution pattern between the simulated and experimental spectrograms. The presence of complex and hexagon fragmentation (**Supplementary Figures 8–11** for Ag(I) and **Supplementary Figures 12–15** for Au(I) complexes and hexagons) in the mass spectra further confirmed the structure and counter-ions of the linear complex and hexagonal self-assemblies since these fragments were not detected in the NMR studies.

Structures of Ag(I) and Au(I) Complexes and Hexagons

Single-crystal X-ray diffraction was attempted to further elucidate the structures of the Ag(I) and Au(I) complexes and hexagons. Slow evaporation of acetone solutions resulted in very fine needle-like crystals. Only crystals of Ag**L1**$_2$ gave a tractable data set. The asymmetric unit contains two formula units ($Z' = 2$) held in a cofacial conformation as well as a single chloroform molecule. Each Ag(I) center possess a coordination number of 2 with near ideal 180° geometries (**Figure 6A** and **Supplementary Figure 16** and **Table S1**). The PF_6- counter ion is outer sphere with a closest contact of approximately 3 Å. It is apparent that non-covalent interactions are a strong driving force in the resulting crystal structure of this compound. An apparent argentophilic Ag(I)—Ag(I) interaction leads to the interesting cofacial conformation (∼3.5 Å). Furthermore, interaction between the electron-rich Br atoms and the H atoms (average separation 3.60(9) Å) of the corresponding formula unit further contribute to the observed structure.

Molecular mechanics geometry optimizations were carried out on the Au(I) complex and the Ag(I) and Au(I) hexagons (**Figures 6B–D**). These structures were optimized using Universal Force Field (UFF) as implemented in ArgusLab. All hexagons formed from **L2** and **L3** preserved ligand planarity. In contrast, the hexagons from **L4** have pyridyl groups that are rotated by 40° from the central phenyl due to the steric strain of the protons on neighboring aromatic rings.

Solid-State Light Stability of Ag(I) and Au(I) Complexes and Hexagons

Solid-state IR spectroscopy is another useful tool to confirm the coordination of the pyridyl ligands to Ag(I) and Au(I) metal acceptors and study the solid-state photostability of the complexes and hexagons. We acquired FT-IR spectra of the

ligands, complexes and hexagons as synthesized. After a week of storing the complexes and hexagons under room light at ambient conditions, we re-acquired the FT-IR spectra of each compound. The ligand IR spectra are shown in both **Figures 7**, **8**, where the characteristic aromatic -CH stretching at 3,000–3,100 cm^{-1}, aromatic -CC- stretching at 1,400–1,600 cm^{-1}, and aromatic -CN- stretching at 1,600 cm^{-1} are present in all ligands (Katritzky and Hands, 1958; Schrader, 2007). The characteristic alkyne -CC- stretching at 2,100 cm^{-1} are also present in **L1**, **L2**, and **L3**.

In all cases, there is a slight shift to higher wavenumbers upon Ag(I) or Au(I) coordination, most notably for the -CN- stretching peaks at 1,600 cm^{-1}. We observe no change in both the functional group and the fingerprint regions after exposure of the complexes and hexagons to room light for one week, which confirms the improved photo-stability of Ag(I) and Au(I) upon coordination into both linear complex and hexagonal metallacycle.

Photophysical Properties of Ag(I) and Au(I) Complexes and Hexagons

The photophysical properties of these self-assembled complexes and hexagons were studied using steady-state and time-resolved methods. Studies of Ag(I) (Zhou et al., 2006; Laye, 2007; Yeşilel et al., 2012; Mei et al., 2015a; Jenkins and Assefa, 2017) and Au(I) (Lin et al., 2008; Langdon-Jones and Pope, 2014; Shakirova et al., 2017) complexes and metallacycles with N-donor heterocyclic ligands demonstrate interesting luminescent properties, which assigned to metal-to-ligand charge transfers (MLCT), ligand-based charge transfers, or metal-perturbed ligand-based charge transfers in part due to argentophilic or aurophilic interactions.

We studied both the solution- and solid-state photoluminescence of all Ag(I) and Au(I) complexes and hexagons; however, the acetone instability of some compounds limited our solution-state studies to the photoluminescence of Ag(I) complexes and hexagons and the mononuclear Au(I) complex in acetone. The solution-state absorption and emission of the free ligands, Ag(I) and Au(I) complexes, and Ag(I) hexagons are summarized in **Figure 9**. Several UV-vis absorption features were masked by the UV-cutoff of acetone. Nonetheless, the high energy band due to $\pi \rightarrow \pi^*$ ligand-centered transitions that is typical of aromatic and alkynyl-containing ligands (Shakirova et al., 2017) were prominent in **L1**, **L2**, and **L3** and less so in **L4** due to the absence of ethynyl spacer in this ligand. We see a slight red-shift in the absorption of Ag**L1**$_2$ (**Figure 9A**) but not in Au**L1**$_2$ (**Figure 9E**) or any of the Ag(I) hexagons (**Figures 9B–D**) suggesting ligand-centered transitions for the Au(I) complex and Ag(I) hexagons and metal-perturbed ligand-centered transition for the Ag(I) complex, which is supported by the presence of argentophilic interactions in the crystal structure (**Figure 6**).

Table 1 shows the summary of all measured quantum yields (Φ, **Supplementary Figures 17–22**) and lifetimes (τ, **Supplementary Figures 23–25**) and all calculated radiative (k_r) and non-radiative (k_{nr}) decay rate constants. At 330 nm

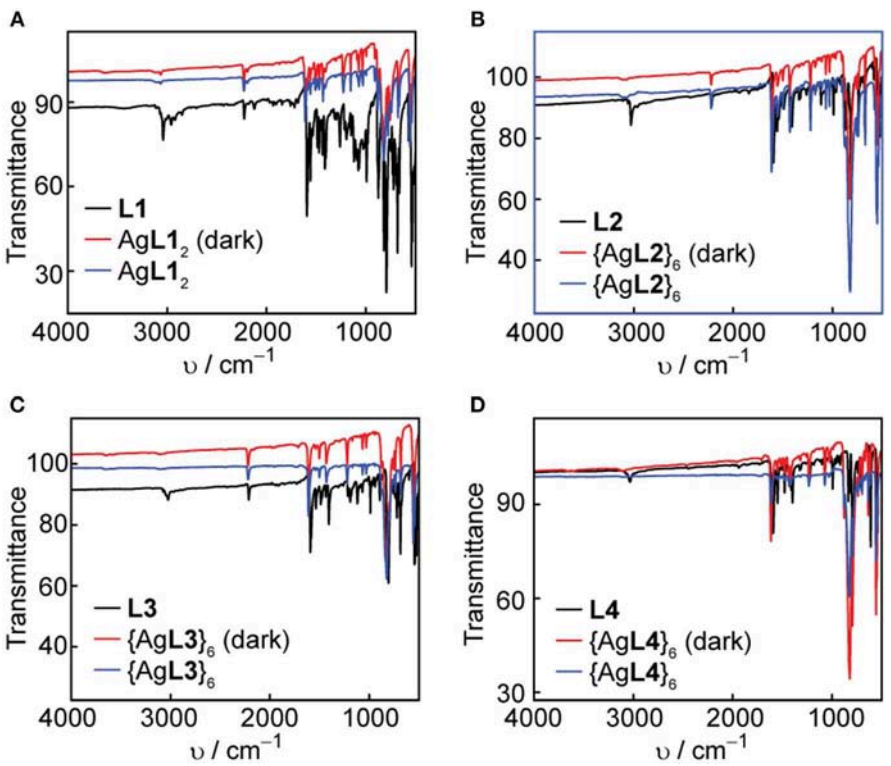

FIGURE 7 | Comparison of FT-IR spectra in the dark and under room light conditions for **(A) L1** and Ag**L1**$_2$, **(B) L2** and {Ag**L2**}$_6$, **(C) L3** and {Ag**L3**}$_6$, and **(D) L4** and {Ag**L4**}$_6$.

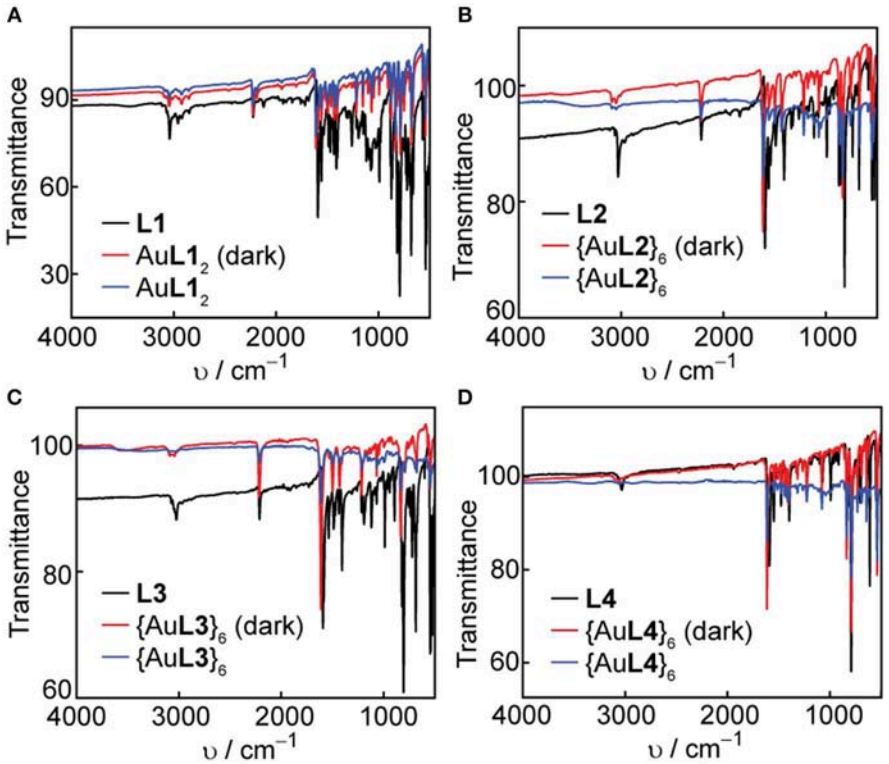

FIGURE 8 | Comparison of FT-IR spectra in the dark and under room light conditions for **(A) L1** and Au**L1**$_2$, **(B) L2** and {Au**L2**}$_6$, **(C) L3** and {Au**L3**}$_6$, and **(D) L4** and {Au**L4**}$_6$.

excitation, fluorescence emission bands centered at 375 nm (**Figures 9A–C**) were observed for **L1**, **L2**, and **L3** in acetone at 3.82, 0.800, and 7.76% quantum yields and 0.11, 0.12, 0.49 ns lifetimes, respectively (**Table 1**). These ligands have ethynyl spacers that connect the central phenyl group to the pyridyl group/s, which helps rigidify the structure and enhance emission. The highest quantum yield and longest lifetime was observed in **L3**, which is not affected by heavy-atom effects, unlike **L1** and **L2** wherein bromide was present. In addition, the four-fold increase in k_{nr} for **L1** (8.91×10^9 s^{-1}) and **L2** (8.00×10^9 s^{-1}) as compared to **L3** (1.89×10^9 s^{-1}), further supports the enhancement of inter-system crossing (ISC) for the bromine-containing ligands. On the other hand, a weak fluorescence band centered at 400 nm (**Figure 9D**) was observed for **L4** but has a quantum yield and lifetime below the limit of our instrumental detection. By placing an upper bound on quantum yield and lifetime of **L4** based on instrumental detection limits, we estimated an upper limit to k_r and a lower limit to k_{nr} as shown in **Table 1**. The absence of the ethynyl spacer in **L4** introduces rotational freedom that enhances internal conversion resulting in very weak emission of the ligand.

Similar to the absorption profiles, we also observe a red-shift in the emission band of Ag**L1**$_2$ centered at 400 nm (**Figure 9A**) but not in Au**L1**$_2$ (375 nm, **Figure 9E**) or any of the Ag(I) hexagons, {Ag**L2**}$_6$ (375 nm, **Figure 9B**), {Ag**L3**}$_6$ (375 nm, **Figure 9C**), and {Ag**L4**}$_6$ (400 nm, **Figure 9D**). These emission profiles are similar to that of the ligand with significant reduction in quantum yields and lifetimes upon ligand coordination to Ag(I) and Au(I) suggesting ligand-centered singlet emissions with some perturbations from Ag(I) argentophilic interactions for the Ag(I) complex. Although not as common, fluorescent transition metal complexes are known (Chia and Tay, 2014). The lack of triplet emissions in these complexes can be attributed to either lack of metal-ligand interaction resulting in small metal contribution at the excited state or larger rate constant for fluorescence compared to that of ISC, which is reasonable given the fluorescence emission of the free ligand. Based on our decay rate constant calculations for the Ag(I) and Au(I) complexes and Ag(I) hexagons, k_{nr} is always higher than k_r which implies poor metal-ligand interaction as the main reason for lack of phosphorescence in these compounds.

We also reported the solid-state quantum yields of all ligands, Ag(I) and Au(I) complexes, and hexagons in **Table 1**. Similar to the solution-state quantum yields, the highest and lowest quantum yields are observed for **L3** are **L4**, respectively. Upon ligand coordination to either Ag(I) and Au(I), we see a general decrease in quantum yields except for {Ag**L2**}$_6$, {Ag**L4**}$_6$, and {Ag**L4**}$_6$. These quantum yield enhancement may be due to aggregation induced emission (Fan et al., 2015; Mei et al., 2015b), particularly in metallacycles containing **L4**, which in itself is weakly emissive, wherein

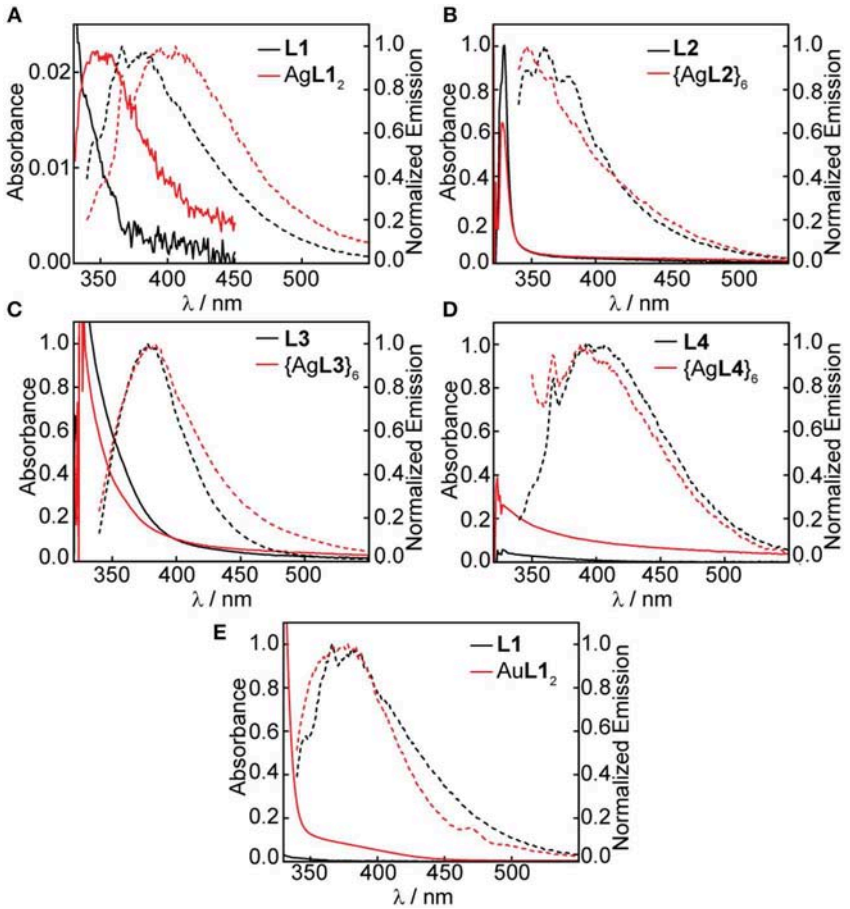

FIGURE 9 | UV-vis absorbance and emission spectra in acetone of **(A)** 0.10 mM **L1** and saturated Ag**L1**$_2$, **(B)** 0.10 mM **L2** and saturated {Ag**L2**}$_6$, **(C)** 0.10 mM **L3** and saturated {Ag**L3**}$_6$, and **(D)** 1.0 mM **L4** and saturated {Ag**L4**}$_6$, **(E)** 0.10 mM **L1** and 0.10 mM Ag**L1**$_2$.

TABLE 1 | Solution- and solid-state quantum yields and lifetimes of ligands, Ag and Au complexes and hexagons.

Compound	$\Phi_{solid\text{-}state}$, %	$\Phi_{solution\text{-}state}$,[a] %	τ, ns	k_r, s^{-1}	k_{nr}, s^{-1}
L1	0.480	3.82	0.11	3.54×10^8	8.91×10^9
L2	0.180	0.800	0.12	6.45×10^7	8.00×10^9
L3	1.190	7.76	0.49	1.59×10^8	1.89×10^9
L4	0.010	~0.01*	0.10**	$<1.00 \times 10^6$	$>1.00 \times 10^{10}$
AgL1$_2$	0.200	2.32	0.10**	$>2.32 \times 10^8$	$>9.77 \times 10^9$
{AgL2}$_6$	0.340	0.300	0.10**	$>3.00 \times 10^7$	$>9.97 \times 10^9$
{AgL3}$_6$	0.130	4.70	0.17	2.83×10^8	5.74×10^9
{AgL4}$_6$	0.510	~0.01*	0.10**	$<1.00 \times 10^6$	$>1.00 \times 10^{10}$
AuL1$_2$	0.06	1.12	0.11	1.04×10^8	9.19×10^9
{AuL2}$_6$	0.170	***	***	***	***
{AuL3}$_6$	0.010	***	***	***	***
{AuL4}$_6$	0.110	***	***	***	***

[a]*solution-state quantum yield all measured in acetone.*
**measured QY is below the instrumental limit of detection of 0.01%.*
***measured lifetime is below the instrumental limit of detection of 0.10 ns.*
****QY not measured due to instability in acetone.*

non-radiative pathways are attenuated when intramolecular motions are reduced.

CONCLUSION

Silver(I) and gold(I) mononuclear complexes and hexagonal rings were self-assembled from $AgPF_6$ and Au(tht)Cl precursors and mono- and bidentate pyridyl ligands. These coordination resulting in self-assembly and complex formation was evidenced by the downfield ^{1}H NMR peak shifts of the ligand pyridyl H peaks and FT-ICR MS peaks with isotopic distributions and mass-to-charge ratios consistent with intact [6 + 6] cores that ionized by the loss of counterions.

Longer-term photostability of all complexes and hexagons in the solid-state were confirmed by FT-IR. Significant peak shifts to higher wavenumbers were observed upon coordination of the ligands to either Ag(I) or Au(I). No changes to the spectra were observed after storing the compounds at ambient conditions under room light for one week.

Ligand-centered fluorescence emission was observed for many of these complexes. In both the solid- and solution-state, **L3** and **L4** were the most and least emissive ligands, respectively. In the solid-state, all complexes and hexagons have diminished emission except for $\{Ag\mathbf{L2}\}_6$, $\{Ag\mathbf{L4}\}_6$, and $\{Au\mathbf{L4}\}_6$ wherein aggregation-induced emission was observed. In the solution-state, all ligands and hexagons exhibited ligand-centered singlet emissions while $Ag\mathbf{L1}_2$ and $Au\mathbf{L1}_2$ both exhibited metal-perturbed ligand-centered singlet emissions.

This work establishes that Ag(I) and Au(I) centers are effective linear nodes for self-assembly reactions with dipyridyl ligands and that the resultant materials stabilize these ions with respect to oxidation and photodecomposition. Due to the modular nature of coordination-driven self-assembly, efforts are ongoing to exploit ligand-tuning to incorporate functional groups that will enhance metallacycle solubility to improve their processability for incorporation into mixed-matrix materials.

DATA AVAILABILITY

The dataset $Ag\mathbf{L1}_2$ (CCDC No. 1879931) for this study can be found in the Cambridge Crystallographic Data Centre https://www.ccdc.cam.ac.uk/solutions/csd-system/components/csd/.

AUTHOR CONTRIBUTIONS

CF designed and carried out the experiments and wrote the manuscript. SK assisted in ligand synthesis. AF carried out the mass spec characterization. TC designed the project and wrote the manuscript.

FUNDING

The project described was supported by Award Number S10RR029517 from the National Center For Research Resources.

ACKNOWLEDGMENTS

TC thanks the University at Buffalo for startup support resources. This work was completed using the resources of the Chemistry Instrument Center (CIC), University at Buffalo, SUNY, Buffalo, NY.

SUPPLEMENTARY MATERIAL

The Supplementary Material for this article can be found online at: https://www.frontiersin.org/articles/10.3389/fchem.2019.00567/full#supplementary-material

REFERENCES

Amayuelas, E., Fidalgo-Marijuan, A., Bazan, B., Urtiaga, M. K., Barandika, G., and Arriortua, M.-I. (2016). CuII-based metal-organic nanoballs for very rapid adsorption of dyes and iodine. *Cryst. Eng. Comm.* 18, 1709–1712. doi: 10.1039/C5CE02511G

Brown, C. J., Bergman, R. G., and Raymond, K. N. (2009). Enantioselective catalysis of the aza-cope rearrangement by a chiral supramolecular assembly. *J. Am. Chem. Soc.* 131, 17530–17531. doi: 10.1021/ja906386w

Cao, A., Zhu, W., Shang, J., Klootwijk, J. H., Sudhölter, E. J. R., Huskens, J., et al. (2017). Metal–organic polyhedra-coated Si nanowires for the sensitive detection of trace explosives. *Nano Lett.* 17, 1–7. doi: 10.1021/acs.nanolett.6b02360.

Casini, A., Woods, B., and Wenzel, M. (2017). The promise of self-assembled 3D supramolecular coordination complexes for biomedical applications. *Inorg. Chem.* 56, 14715–14729. doi: 10.1021/acs.inorgchem.7b02599

Chen, Q., Jiang, F., Yuan, D., Chen, L., Lyu, G., and Hong, M. (2013). Anion-driven self-assembly: from discrete cages to infinite polycatenanes step by step. *Chem. Commun.* 49, 719–721. doi: 10.1039/C2CC36921D

Chen, X.-D., and Mak, T. C. W. (2005). Order of the coordinating ability of polyatomic monoanions established from their interaction with a disilver(i) metallacyclophane skeleton. *Chem. Commun.* 3529–3531. doi: 10.1039/B505919D.

Chevrier, I., Sagu,é, J. L., Brunetto, P. S., Khanna, N., Rajacic, Z., and Fromm, K. M. (2013). Rings, chains and helices: new antimicrobial silver coordination compounds with (iso-)nicotinic acid derivatives. *Dalton Trans.* 42, 217–231. doi: 10.1039/C2DT31259J

Chia, Y. Y., and Tay, M. G. (2014). An insight into fluorescent transition metal complexes. *Dalton Trans.* 43, 13159–13168. doi: 10.1039/C4DT01098A

Cook, T. R., and Stang, P. J. (2015). Recent developments in the preparation and chemistry of metallacycles and metallacages via coordination. *Chem. Rev.* 115:7001–45. doi: 10.1021/cr5005666.

Cook, T. R., Vajpayee, V., Lee, M. H., Stang, P. J., and Chi, K.-W. (2013). Biomedical and biochemical applications of self-assembled metallacycles and metallacages. *Acc. Chem. Res.* 46, 2464–2474. doi: 10.1021/ar400010v

Dechnik, J., Gascon, J., Doonan, C. J., Janiak, C., and Sumby, C. J. (2017). Mixed-matrix membranes. *Angew. Chem. Int. Ed.* 56, 9292–9310. doi: 10.1002/anie.201701109

Del Piero, S., Fedele, R., Melchior, A., Portanova, R., Tolazzi, M., and Zangrando, E. (2008). Solvation effects on the stability of silver(I) complexes with pyridine-containing ligands studied by thermodynamics and DFT methods. *Inorg. Chem.* 47, 1406–1406. doi: 10.1021/ic800010g

Eldridge, R. B. (1993). Olefin/paraffin separation technology: a review. *Ind. Eng. Chem. Res.* 32, 2208–2212. doi: 10.1021/ie00022a002

Fan, W.-J., Sun, B., Ma, J., Li, X., Tan, H., and Xu, L. (2015). Coordination-driven self-assembly of carbazole-based metallodendrimers with generation-dependent aggregation-induced emission behavior. *Chem. Eur. J.* 21, 12947–12959. doi: 10.1002/chem.201501282

Fernández, E. J., Laguna, A., López-de-Luzuriaga, J. M., Monge, M., Montiel, M., Olmos, M. E., et al. (2007). Pyridine gold complexes. an emerging class of luminescent materials. *Gold Bull.* 40, 172–183. doi: 10.1007/bf03215578

Fox, B. S., Beyer, M. K., and Bondybey, V. E. (2002). Coordination chemistry of silver cations. *J. Am. Chem. Soc.* 124, 13613–13623. doi: 10.1021/ja0176604

Fromm, K. M., Doimeadios, J. L. S., and Robin, A. Y. (2005). Concomitant crystallization of two polymorphs—a ring and a helix: concentration effect on supramolecular isomerism. *Chem. Commun.* 2005, 4548–4550. doi: 10.1039/B506389B

Fujita, M. (1998). Metal-directed self-assembly of two- and three-dimensional synthetic receptors. *Chem. Soc. Rev.* 27, 417–425. doi: 10.1039/A827417Z

Fujita, M., Umemoto, K., Yoshizawa, M., Fujita, N., Kusukawa, T., and Biradha, K. (2001). Molecular paneling coordination. *Chem. Commun.* 509–518. doi: 10.1039/B008684N

Fulong, C. R. P., Liu, J., Pastore, V. J., Lin, H., and Cook, T. R. (2018). Mixed-matrix materials using metal-organic polyhedra with enhanced compatibility for membrane gas separation. *Dalton Trans.* 47, 7905–7915. doi: 10.1039/C8DT00082D

Gimeno, M. C. (2009). "The chemistry of gold," in *Modern Supramolecular Gold Chemistry*, ed A. Laguna (Wiley-VCH Verlag GmbH & Co. KGaA), 10–14. doi: 10.1002/9783527623778.ch1

Huang, C.-B., Xu, L., Zhu, J.-L., Wang, Y.-X., Sun, B., Li, X., et al. (2017). Real-time monitoring the dynamics of coordination-driven self-assembly by

fluorescence-resonance energy transfer. *J. Am. Chem. Soc.* 139, 9459–9462. doi: 10.1021/jacs.7b04659

Ito, H., Kusukawa, T., and Fujita, M. (2000). Wacker oxidation in an aqueous phase through the reverse phase-transfer catalysis of a self-assembled nanocage. *Chem. Lett.* 29, 598–599. doi: 10.1246/cl.2000.598

Jenkins, D. E., and Assefa, Z. (2017). Structural, photoluminescence, and theoretical DFT studies of gold(I) and silver(I) metallacycle dinuclear complexes of 1-methylbenzimidazolediphenyl phosphine (MBDP) ligand. *J. Mol. Struct.* 1133, 374–383. doi: 10.1016/j.molstruc.2016.11.070

Katritzky, A. R., and Hands, A. R. (1958). 448. Infrared studies of heterocyclic compounds. Part II. 2-Monosubstituted pyridines. *J. Chem. Soc.* 1958, 2202-2204. doi: 10.1039/JR9580002202

Kim, C. W., Kim, C.-R., Noh, T. H., and Jung, O.-S. (2009). Ring-conformations via the competition of electrostatic interaction and argentophilic interaction. cyclodimeric structures of silver trifluoromethanesulfonate containing isonicotinate ester Ligands. *Bull. Kor. Chem. Soc.* 30:2341. doi: 10.5012/BKCS.2009.30.10.2341

Kim, D.-S., and Ahn, K. H. (2008). Fluorescence "Turn-On" sensing of carboxylate anions with oligothiophene-based o-(Carboxamido)trifluoroacetophenones. *J. Org. Chem.* 73, 6831–6834. doi: 10.1021/jo801178y

Kole, G. K., Tan, G. K., and Vittal, J. J. (2012). Photoreactivity of Ag(I) complexes and coordination polymers of pyridyl acrylic acids. *Crystal Growth Des.* 12, 326–332. doi: 10.1021/cg201119c

Kuijpers, P. F., Otte, M., Dürr, M., Ivanović-Burmazovi,ć, I., Reek, J. N. H., and de Bruin, B. (2016). A self-assembled molecular cage for substrate-selective epoxidation reactions in aqueous media. *ACS Catal.* 6, 3106–3112. doi: 10.1021/acscatal.6b00283.

Langdon-Jones, E. E., and Pope, S. J. A. (2014). Recent developments in gold(i) coordination chemistry: luminescence properties and bioimaging opportunities. *Chem. Commun.* 50, 10343–10354. doi: 10.1039/C4CC03259D

Laye, R. H. (2007). Syntheses and photophysical properties of a series of [2:2] silver(I) metallocycles. *Inorg. Chim. Acta.* 360, 439–447. doi: 10.1016/j.ica.2006.07.068

Leininger, S., Olenyuk, B., and Stang, P. J. (2000). Self-assembly of discrete cyclic nanostructures mediated by transition metals. *Chem. Rev.* 100, 853–908. doi: 10.1021/cr9601324

Lin, J. C. Y., Tang, S. S., Vasam, C. S., You, W. C., Ho, T. W., Huang, C. H., et al. (2008). Structural, photophysical, and catalytic properties of Au(I) complexes with 4-substituted pyridines. *Inorg. Chem.* 47, 2543–2551. doi: 10.1021/ic701872f

Mandal, A., Singha, M., Addy, P. S., and Basak, A. (2019). Laser desorption ionization mass spectrometry: Recent progress in matrix-free and label-assisted techniques. *Mass Spectrometry Rev.* 38, 3–21. doi: 10.1002/mas.21545

Marin, M. L., McGilvray, K. L., and Scaiano, J. C. (2008). Photochemical strategies for the synthesis of gold nanoparticles from Au(III) and Au(I) using photoinduced free radical generation. *J. Am. Chem. Soc.* 130, 16572–16584. doi: 10.1021/ja803490n

Mei, H.-X., Zhang, T., Wang, D.-F., Huang, R.-B., and Zheng, L.-S. (2015a). Metallacycles or coexistence of isomeric metallacycle and chain: Anion-dependent luminescent Ag complexes of a flexible diaminotriazine–imidazole ligand. *J. Mol. Struct.* 1091, 57–64. doi: 10.1016/j.molstruc.2015.02.030

Mei, J., Leung, N. L. C., Kwok, R. T. K., Lam, J. W. Y., and Tang, B. Z. (2015b). Aggregation-induced emission: together we shine, united we soar! *Chem. Rev.* 115, 11718–11940. doi: 10.1021/acs.chemrev.5b00263

Ren, Y. P., Kong, X.-J., Long, L.-S., Huang, R.-B., and Zheng, L.-S. (2006). Anion-dependent assembly of cyclic structure. *Crystal Growth Des.* 6, 572–576. doi: 10.1021/cg050459a

Riddell, I. A., Smulders, M. M. J., Clegg, J. K., and Nitschke, J. R. (2011). Encapsulation, storage and controlled release of sulfur hexafluoride from a metal–organic capsule. *Chem. Commun.* 47, 457–459. doi: 10.1039/C0CC02573A

Schrader, B. (2007). "Infrared and Raman spectroscopy: methods and applications," in *Infrared and Raman Spectroscopy*, ed B. Schrader (Wiley-VCH Verlag GmbH), 711–764. doi: 10.1002/9783527615438.refs

Shakirova, J. R., Tomashenko, O. A., Grachova, E. V., Starova, G. L., Sizov, V. V., Khlebnikov, A. F., et al. (2017). Gold(I)–alkynyl complexes with an N-donor heterocyclic ligand: synthesis and photophysical properties. *Eur. J. Inorg. Chem.* 2017, 4180–4186. doi: 10.1002/ejic.201700731

Shin, D. M., Lee, I. S., Lee, Y.-A., and Chung, Y. K. (2003). Self-assembly between silver(I) and Di- and Tri-2-pyridines with flexible spacer: formation of discrete metallocycle versus coordination polymer. *Inorg. Chem.* 42, 2977–2982. doi: 10.1021/ic0260163

Smulders, M. M. J., and Nitschke, J. R. (2012). Supramolecular control over Diels–Alder reactivity by encapsulation and competitive displacement. *Chem. Sci.* 3, 785–788. doi: 10.1039/C1SC00847A

Sudik, A. C., Millward, A. R., Ockwig, N. W., Côté, A. P., Kim, J., and Yaghi, O. M. (2005). Design, synthesis, structure, and gas (N2, Ar, CO2, CH4, and H2) sorption properties of porous metal-organic tetrahedral and heterocuboidal polyhedra. *J. Am. Chem. Soc.* 127, 7110–7118. doi: 10.1021/ja042802q

Tang, J.-H., Sun, Y., Gong, Z.-L., Li, Z.-Y., Zhou, Z., Wang, H., et al. (2018). Temperature-responsive fluorescent organoplatinum(II) metallacycles. *J. Am. Chem. Soc.* 140, 7723–7729. doi: 10.1021/jacs.8b04452

Tashiro, S., Tominaga, M., Kawano, M., Therrien, B., Ozeki, T., and Fujita, M. (2005). Sequence-selective recognition of peptides within the single binding pocket of a self-assembled coordination cage. *J. Am. Chem. Soc.* 127, 4546–4547. doi: 10.1021/ja044782y

Vardhan, H., and Verpoort, F. (2015). Metal-organic polyhedra: catalysis and reactive intermediates. *Adv. Synt. Catal.* 357, 1351–1368. doi: 10.1002/adsc.201400778

Vikse, K. L., and Scott McIndoe, J. (2018). Ionization methods for the mass spectrometry of organometallic compounds. *J. Mass Spectromet.* 53, 1026–1034. doi: 10.1002/jms.4286

Wan, C.-Q., and Mak, T. C. W. (2011). Unusual carbonyl···carbonyl interaction in supramolecular structures of silver(I) complexes with 2,6-Pyridinediylbis(4-pyridinyl)methanone. *Crystal Growth Des.* 11, 832–842. doi: 10.1021/cg101490a

Wang, J., He, C., Wu, P., Wang, J., and Duan, C. (2011). An amide-containing metal–organic tetrahedron responding to a spin-trapping reaction in a fluorescent enhancement manner for biological imaging of NO in living cells. *J. Am. Chem. Soc.* 133, 12402–12405. doi: 10.1021/ja2048489

Wei, W., Yu, H., Jiang, F., Liu, B., Ma, J., and Hong, M. (2012). Anion-controlled conformational variation: structural modulation and anion exchange of Ag(i) coordination networks. *Cryst. Eng. Comm.* 14, 1693–1700. doi: 10.1039/C1CE06141K

Yang, H.-B., Ghosh, K., Northrop, B. H., Zheng, Y.-R., Lyndon, M. M., Muddiman, D. C., et al. (2007). A highly efficient approach to the self-assembly of hexagonal cavity-cored Tris[2]pseudorotaxanes from several components via multiple noncovalent interactions. *J. Am. Chem. Soc.* 129, 14187–14189. doi: 10.1021/ja073744m

Yeşilel, O. Z., Karamahmut, B., Semerci, F., and Yeşilöz, Y. (2012). Synthesis, crystal structures, spectroscopic and thermal properties of silver(I) saccharinate complexes with N-donor ligands. *Polyhedron* 42, 307–314. doi: 10.1016/j.poly.2012.05.034

Zhao, D., Yuan, D., Krishna, R., van Baten, J. M., and Zhou, H.-C. (2010). Thermosensitive gating effect and selective gas adsorption in a porous coordination nanocage. *Chem. Commun.* 46, 7352–7354. doi: 10.1039/C0CC02771E

Zhou, J., Liu, X., Zhang, Y., Li, B., and Zhang, Y. (2006). Synthesis, structures and luminescent properties of two silver supramolecular isomers with one-dimensional concavo-convex chain and dimer metallacycle. *Inorg. Chem. Commun.* 9, 216–219. doi: 10.1016/j.inoche.2005.11.001

Zwijnenburg, M. A., Berardo, E., Peveler, W. J., and Jelfs, K. E. (2016). Amine molecular cages as supramolecular fluorescent explosive sensors: a computational perspective. *J. Phy. Chem. B* 120, 5063–5072. doi: 10.1021/acs.jpcb.6b03059

Conflict of Interest Statement: The authors declare that the research was conducted in the absence of any commercial or financial relationships that could be construed as a potential conflict of interest.

Copyright © 2019 Fulong, Kim, Friedman and Cook. This is an open-access article distributed under the terms of the Creative Commons Attribution License (CC BY). The use, distribution or reproduction in other forums is permitted, provided the original author(s) and the copyright owner(s) are credited and that the original publication in this journal is cited, in accordance with accepted academic practice. No use, distribution or reproduction is permitted which does not comply with these terms.

frontiers in Chemistry

ORIGINAL RESEARCH
published: 25 January 2019
doi: 10.3389/fchem.2018.00673

Understanding the Role of Yb^{3+} in the Nd/Yb Coupled 808-nm-Responsive Upconversion

Nan Song, Bo Zhou, Long Yan, Jinshu Huang and Qinyuan Zhang**

State Key Laboratory of Luminescent Materials and Devices, Guangdong Provincial Key Laboratory of Fiber Laser Materials and Applied Techniques, Institute of Optical Communication Materials, South China University of Technology, Guangzhou, China

The realization of upconversion at 808 nm excitation has shown great advantages in advancing the broad bioapplications of lanthanide-doped nanomaterials. In an 808 nm responsive system, Nd^{3+} and Yb^{3+} are both needed where Nd^{3+} acts as a sensitizer through absorbing the excitation irradiation. However, few studies have been dedicated to the role of Yb^{3+}. Here, we report a systemic investigation on the role of Yb^{3+} by designing a set of core-shell-based nanostructures. We find that energy migration over the ytterbium sublattice plays a key role in facilitating the energy transportation, and moreover, we show that the interfacial energy transfer occurring at the core-shell interface also has a contribution to the upconversion. By optimizing the dopant concentration and surface anchoring the infrared indocyanine green dye, the 808 nm responsive upconversion is markedly enhanced. These results present an in-depth understanding of the fundamental interactions among lanthanides, and more importantly, they offer new possibilities to tune and control the upconversion of lanthanide-based luminescent materials.

Keywords: upconversion, energy migration, interfacial energy transfer, Nd/Yb coupled system, mechanistic study

OPEN ACCESS

Edited by:
Luís António Dias Carlos, University of Aveiro, Portugal

Reviewed by:
Xiaoji Xie, Nanjing Tech University, China
Jean-Claude Georges Bunzli, École Polytechnique Fédérale de Lausanne, Switzerland

****Correspondence:***
Bo Zhou
zhoubo@scut.edu.cn
Qinyuan Zhang
qyzhang@scut.edu.cn

Specialty section:
This article was submitted to Inorganic Chemistry, a section of the journal Frontiers in Chemistry

Received: *30 October 2018*
Accepted: *24 December 2018*
Published: *25 January 2019*

Citation:
Song N, Zhou B, Yan L, Huang J and Zhang Q (2019) Understanding the Role of Yb^{3+} in the Nd/Yb Coupled 808-nm-Responsive Upconversion. Front. Chem. 6:673. doi: 10.3389/fchem.2018.00673

INTRODUCTION

Recently, substantial attention has been devoted to the lanthanide-doped nanoparticles due to their great infrared-to-visible photon upconversion performance (Auzel, 2004; Haase and Schafer, 2011; Zhou et al., 2015), which shows potential applications ranging from bioimaging (Zhu et al., 2017) to photodynamic therapy (Xu et al., 2017), 3D display (Deng et al., 2015), security (Lu et al., 2014), anti-counterfeiting (Li et al., 2016), and super-resolution nanoscopy (Liu et al., 2017). The unique 4f electronic configuration with abundant energy levels allows us to easily realize multi-wavelength upconversion emission bands upon infrared excitations (Chen et al., 2014; Dong et al., 2015; Zheng et al., 2015). By taking advantage of strategies including development of new host materials (Lei et al., 2017), control of local structure (Fischer et al., 2016), mechanistic exploration of new pathways using energy migration (Wang et al., 2011; Chen et al., 2017), cross-relaxation (Liu et al., 2017) and interfacial energy transfer (Zhou et al., 2016, 2018), efficient upconversion from a set of lanthanides such as Er^{3+}, Tm^{3+}, Ho^{3+}, Tb^{3+}, and Eu^{3+} was obtained. However, the most used upconversion systems are based on a Yb-sensitized design with 980 nm excitation, which makes the upconversion nanoparticles unsuitable for biological application because of the strong absorption

of water at this wavelength region (Weissleder, 2001; Kobayashi et al., 2011; Zhu et al., 2017). Therefore, developing new classes of upconversion materials would be of great importance for their biomedical applications.

Interestingly, recent works suggest that Nd^{3+} is a possible sensitizer to move the excitation wavelength from 980 to 808 nm due to its $^4F_{5/2} \leftarrow {}^4I_{9/2}$ absorption transition at this wavelength region (Liu et al., 2017; Xie et al., 2017) together with efficient energy transfer from Nd^{3+} to Yb^{3+} (Parent et al., 1986). More importantly, the absorption of excitation energy by water in biological tissues can be effectively minimized. To date, the 808 nm pumped upconversion from a series of lanthanides (e.g., Er and Tb) has been realized (Zhong et al., 2014; Zhou et al., 2018). In the Nd-sensitized upconversion system, Yb^{3+} is also employed to facilitate the energy transfer from Nd^{3+} to the lanthanide emitter, and the typical processes involved in this system can be schematically illustrated in **Figure 1A**. So far, there are four typical core-shell schemes can be used to obtain the upconversion, and typical sample forms for Er^{3+} are $NaYF_4$:Yb/Er/Nd(20/2/1 mol%)@$NaYF_4$, $NaYF_4$:Yb/Er/Nd(20/2/1 mol%)@$NaYF_4$:Nd(30 mol%), $NaYF_4$:Yb/Er@$NaYF_4$:Nd(30 mol%), and $NaYF_4$:Yb/Er(20/2 mol%)@$NaYF_4$:Nd/Yb(30/10 mol%), among which the last one shows the best upconversion behavior (**Figure 1B**). However, few studies have explored the role of Yb^{3+}, which is necessary in the 808 nm pumped upconversion systems, and the mechanism of the luminescence physics occurring in the Nd/Yb coupled upconversion is still not clear.

In this study, we performed a mechanistic investigation on the role of Yb^{3+} in the Nd/Yb coupled 808 nm responsive upconversion. We demonstrated that energy migration over the Yb-sublattice plays a key role in facilitating the energy transportation from the Nd^{3+} sensitizer to the lanthanide emitter. More importantly, we showed that the interfacial energy transfer from Yb^{3+} in the shell to the lanthanide emitter in the core across the core-shell interface also contributes to the upconversion. Such an 808 nm responsive upconversion can be markedly enhanced by optimizing the sample structure together with surface anchoring the infrared indocyanine green (ICG) dye. Our results present an in-depth understanding of the luminescence mechanism involving the Nd/Yb coupled upconversion nanomaterials, which would contribute to both fundamental research and practical applications of lanthanide-doped luminescent materials.

EXPERIMENTAL

Materials

The materials including yttrium(III) acetate hydrate (99.9%), erbium(III) acetate hydrate (99.9%), ytterbium(III) acetate hydrate (99.99%), thulium(III) acetate hydrate (99.9%), holmium(III) acetate hydrate (99.9%), neodymium(III) acetate hydrate (99.9%), oleic acid (90%), 1-octadecene (90%), sodium hydroxide (NaOH; >98%), and ammonium fluoride (NH_4F; >98%) were all purchased from *Sigma-Aldrich*. The nitrosonium tetrafluoroborate ($NOBF_4$; 98%) was purchased from *Alfa Aesar* and indocyanine green ($C_{43}H_{47}N_2NaO_6S_2$), N,N-dimethylformamide (DMF; anhydrous, 99.8%) were purchased from *Energy Chemical*. All these materials were used as received unless otherwise noted.

Sample Synthesis

The core-shell based nanoparticles were synthesized using a coprecipitation chemical method, which was shown to be a good way for the preparation of core only and core-shell based nanoparticles (Wang et al., 2011). The core nanoparticle samples were pre-synthesized as the seeds for growth of the core-shell structure. In a typical procedure for the synthesis of $NaYF_4$:Yb/Er core nanoparticles, to a 50-mL flask containing oleic acid (3 mL) and 1-octadecene (7 mL) was added a water solution containing $Y(CH_3CO_2)_3$, $Yb(CH_3CO_2)_3$, and $Er(CH_3CO_2)_3$ at designed ratios (e.g., 78:20:2 mol%) with a total amount of 0.4 mmol. The resulting mixture was heated at 150°C for 1 h and then cooled down to room temperature. Subsequently, a methanol solution containing NaOH (1 mmol) and NH_4F (1.6 mmol) was added and stirred at 50°C for 0.5 h, and then heated at 290°C under an argon flow for 1.5 h before cooling down to room temperature. The resulting core nanoparticles were collected by centrifugation, washed with ethanol, and finally dispersed in cyclohexane. Other control core nanoparticles were synthesized using a similar procedure except for the use of different lanthanide precursors.

Next, the core-shell nanoparticles were prepared with a two-step coprecipitation method using the pre-synthesized core nanoparticles as seeds for shell layer growth. Typically, for the synthesis of $NaYF_4$:Yb/Er@$NaYF_4$:Nd/Yb core-shell nanoparticles, to a 50-mL flask containing oleic acid (3 mL) and 1-octadecene (7 mL) was added a water solution containing $Y(CH_3CO_2)_3$, $Nd(CH_3CO_2)_3$, and $Yb(CH_3CO_2)_3$ at designed ratios (e.g., 40:50:10 mol%) with a total amount of 0.4 mmol. The resulting mixture was heated at 150°C for 1 h and then cooled down to room temperature. Subsequently, the pre-synthesized $NaYF_4$:Yb/Er particles were added as seeds along with a methanol solution containing NaOH (1 mmol) and NH_4F (1.6 mmol) was added and stirred at 50°C for 0.5 h, and then heated at 290°C under an argon flow for 1.5 h before cooling down to room temperature. The resulting nanoparticles were collected by centrifugation, washed with ethanol, and finally dispersed in cyclohexane. The core-shell-shell nanoparticles were prepared through a three-step coprecipitation method with a similar procedure except for using pre-synthesized core-shell particles as the seeds for the outermost shell layer growth.

The following synthetic procedure was used to prepare dye-decorated nanoparticles. Firstly, the sub-nanometer ligands of $NOBF_4$ were used to exchange the oleic acid ligands for the nanoparticles by coprecipatition method. The nanoparticles despersed in cyclohexane were mixed with the DMF solution of $NOBF_4$ (0.1 M) at room temperature, and the mixture was shaken gently for minutes to extract nanoparticles from upper cyclohexane layer into the bottom DMF layer. The bottom layer solution was then centrifuged at 11,000 rpm for 25 min, and the precipitated nanoparticles were weighted and re-dispersed in DMF (~60 mg/mL) for NIR dye sensitization experiment. Subsequently, a suitable amount of the ICG dyes dissolved DMF

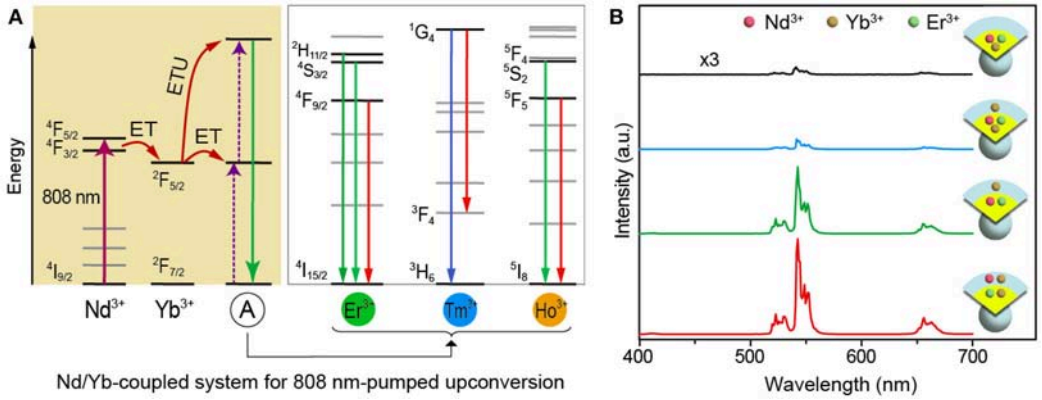

FIGURE 1 | (A) Schematic illustration of energy transportation processes involving the Nd/Yb coupled upconversion system. The typical upconverted visible transitions from Er^{3+}, Tm^{3+}, and Ho^{3+} are marked in the right panel. ET and ETU stand for energy transfer and energy transfer upconversion, respectively. **(B)** Upconversion emission spectra from the four types of core-shell samples of $NaYF_4$:Yb/Er/Nd(20/2/1 mol%)@$NaYF_4$, $NaYF_4$:Yb/Er/Nd(20/2/1 mol%)@$NaYF_4$:Nd(30 mol%), $NaYF_4$:Yb/Er(20/2 mol%)@$NaYF_4$:Nd(30 mol%), and $NaYF_4$:Yb/Er(20/2 mol%)@$NaYF_4$:Nd/Yb(30/10 mol%) under 808 nm excitation.

solution (1 μg/mL) was added to the nanoparticle dispersed DMF solution. This mixture was stirred overnight at room temperature to produce the ICG dyes sensitized nanoparticles in DMF solution.

Characterization

The powder X-ray diffraction (XRD) data were recorded on a Philips Model PW1830 X-ray powder diffractometer with Cu Kα radiation (λ = 1.5406 Å). The upconversion emission spectra and infrared emission spectra were measured by a Jobin-Yvon Triax 320 spectrofluorometer equipped with an 808-nm laser diode with power density of 27.9 W/cm^2. A 980-nm laser diode with identical power density was also used for the excitation of control samples. The decay curves were measured with the same spectrofluorometer using the pulsed lasers as excitation sources. The low- and high-resolution transmission electron microscopy (TEM) measurements, together with elements mappings, were performed on a JEM 2100F with an acceleration voltage of 200 kV. The upconversion emission photographs were taken with a digital camera.

RESULTS AND DISCUSSION

We firstly made an optimization of the upconversion from the $NaYF_4$:Yb/Er@$NaYF_4$:Nd/Yb core-shell nanoparticles at 808 nm excitation. Here the typical $NaYF_4$:Yb/Er(20/2 mol%) nanoparticles were used as core seeds because of their good upconverted luminescence (**Figure S1**). The as-synthesized core-shell nanoparticles showed good monodispersive characteristic (**Figures 2A,B**) and are in hexagonal phase according to the XRD diffraction profile (**Figure S2**). As shown in **Figure 2C**, the increment of Nd^{3+} concentration in the shell layer contributes to an enhancement of the visible upconversion of Er^{3+} and the optimal concentration of Nd^{3+} is found to be 50 mol%. It is easily understood that heavier dopant concentration of sensitizer can result in a higher absorption of the incident excitation irradiation. The upconversion as a function of Yb^{3+} concentration in the shell was also investigated, and the result is shown in **Figure 2D**. The presence of Yb^{3+} in the shell layer indeed leads to the enhancement of upconversion; however, a higher dopant concentration can cause a serious luminescence quenching, and a concentration of 10 mol% is found to be the optimized value with 12.3 times enhancement (**Table S1**). Thus, the optimal concentration of dopants in the shell layer for Nd-Yb pair is determined to be 50 and 10 mol%, respectively. The upconversion performance from Tm^{3+} and Ho^{3+} was also measured by preparing the $NaYF_4$:Yb/A(A=Tm,Ho)@$NaYF_4$:Nd/Yb core-shell samples, and typical upconversion emission profiles were obtained (**Figure S3**). Because Er^{3+} exhibits the most intensive upconversion emission, it was used in the following experiments.

In order to investigate the possible energy migration involving the Nd/Yb coupled upconversion system, we propose a core-shell-shell trilayer nanostructure by inserting the Yb-doped interlayer into the $NaYF_4$:Yb/Er(20/2 mol%)@$NaYF_4$:Nd/Yb(50/10 mol%) core-shell nanostructure, as schematically shown in **Figure 3A**. In this case, the upconversion of Er^{3+} from the core should be closely dependent on the content of Yb^{3+} in the interlayer since it acts as a bridge to facilitate the energy transportation from the outermost shell layer to the core under 808 nm irradiation. These nanoparticles were successfully prepared using the three-step co-precipitation method (**Figure 3B**) and their upconversion emission spectra are shown in **Figure 3C**. It is clearly observed that the upconverted emission from Er^{3+} produces an initial increase and then a decline with the increase of Yb^{3+} content. More importantly, almost no Er^{3+} upconversion is observed for the sample without Yb^{3+} doping in the interlayer. These results clearly confirmed the occurrence of energy migration among Yb-sublattice, and the optimal Yb^{3+} content is at around 20 mol%. On the other hand, intense infrared emission bands of Yb^{3+} were also recorded, see **Figure 3D**. This indicates that the spontaneous $^2F_{5/2} \rightarrow {}^2F_{7/2}$

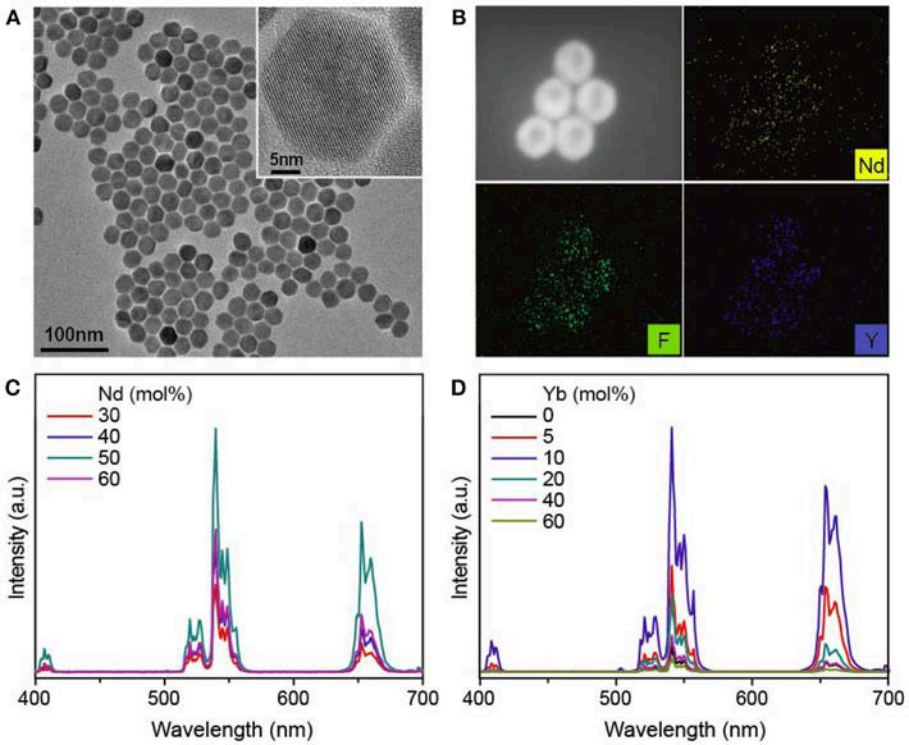

FIGURE 2 | (A) TEM image of the as-synthesized $NaYF_4$:Yb/Er(20/2 mol%)@$NaYF_4$:Nd/Yb(50/10 mol%) core-shell nanoparticles. Inset shows the high-resolution TEM image of a single nanoparticle. **(B)** STEM image of the **(A)** sample and the element mappings of Y, Nd, and F. **(C,D)** Upconversion emission spectra from **(C)** $NaYF_4$:Yb/Er(20/2 mol%)@$NaYF_4$:Nd/Yb(x/10; $x =$ 30∼60 mol%) and **(D)** $NaYF_4$:Yb/Er(20/2 mol%)@$NaYF_4$:Nd/Yb(40/y; $y =$ 0∼60 mol%) core-shell nanoparticles under 808 nm excitation.

transition is also a leading de-excitation channel for Yb^{3+} ions apart from energy migration.

We recently discovered that Yb-mediated interfacial energy transfer is an efficient process for enabling the upconversion from lanthanides (Zhou et al., 2018). Thus, there might exist a channel to activate the lanthanide emitter through a way of interfacial energy transfer in addition to the energy migration involving Yb-sublattice, as schematically illustrated in **Figure 4A**. Then two control core-shell samples of $NaYF_4$:Er@$NaYF_4$:Nd/Yb and $NaYF_4$:Er@$NaYF_4$:Nd were synthesized to check the role of Yb^{3+} in the shell layer. Note that no Yb^{3+} was incorporated into the core aiming to remove the possible interference of Yb^{3+} from the core on the resultant upconversion. Interestingly, the upconverted emission of Er^{3+} was markedly enhanced for the core-shell sample after the presence of Yb^{3+} in the shell layer (**Figure 4B**). This observation confirmed that the Yb^{3+} in the shell layer plays a key role in transporting the excitation energy from the shell layer to the core, and more importantly, it verified that the interfacial energy transfer from the Yb^{3+} in the shell to the Er^{3+} in the core indeed occur. Therefore, it can be concluded that both processes of energy migration and interfacial energy transfer contribute to the observation of efficient upconversion from the Nd/Yb coupled nanosystem.

Such an 808 nm enabled upconversion allows for a further enhancement of the upconversion by introducing the infrared dyes which have much higher absorption ability than Nd^{3+} at 808 nm wavelength region (**Figure 5A**), and the subsequent energy transfer from dye to Nd^{3+} could help greatly enhance the upconversion in this system (Zou et al., 2012; Wu et al., 2016; Wang et al., 2017). Considering the high absorption cross section ($\sim 6 \times 10^{-16}$ cm^2) of indocyanine green (ICG) dye which is ∼5,000 times higher than that of Nd^{3+} (1.2×10^{-19} cm^2) at around 800 nm (Kushida et al., 1968; De Boni and Mendonca, 2011), here we used it to sensitize the upconversion from the present $NaYF_4$:Yb/Er@$NaYF_4$:Nd/Yb core-shell nanoparticles (Wang et al., 2018). As shown in **Figures 5B,C**, the emission intensity is markedly enhanced when using the ICG dye amount of 150 μL (1 μg/mL), confirming the effectiveness of the construction in **Figure 5A**. The detail of energy transportation was shown in **Figure S4**. It should be pointed out that this dye-sensitized upconversion is 210 times more enhanced than that from $NaYF_4$:Yb/Er/Nd@$NaYF_4$:Nd core-shell nanoparticles (**Figure 5D**) when ICG used is 150 μL, at which the number of ICG per particle is estimated to be 32.8 given a full attachment of them at the surface. This result would greatly contribute to the diversity of frontier biological applications.

On the other hand, recent studies showed that a control of energy migration involving Yb-sublattice present a novel and efficient approach to tuning and enhancing upconversion

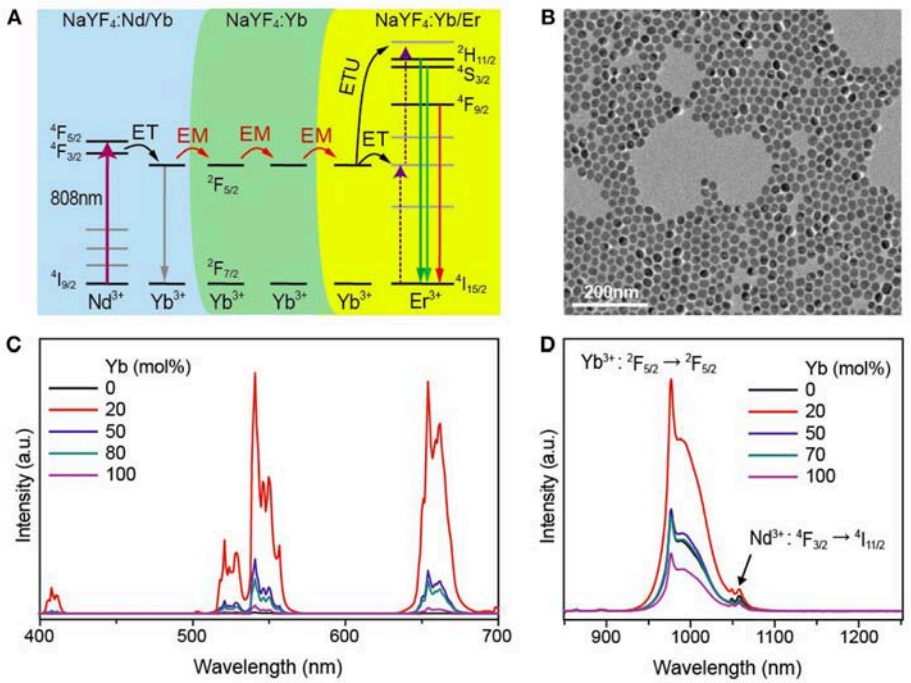

FIGURE 3 | (A) Schematic of proposed $NaYF_4$:Yb/Er@$NaYF_4$:Yb@$NaYF_4$:Nd/Yb core-shell-shell nanostructure for investigating the role of energy migration involving Yb-sublattice. **(B)** TEM image of the as-synthesized $NaYF_4$:Yb/Er(20/2 mol%)@$NaYF_4$:Yb(20 mol%)@$NaYF_4$:Nd/Yb(50/10 mol%) core-shell-shell nanoparticles. **(C)** Upconversion emission spectra from the **(A)** samples with a fine tuning of Yb^{3+} concentration under 808 nm excitation. **(D)** Near infrared emission spectra from **(C)** samples under 808 nm excitation.

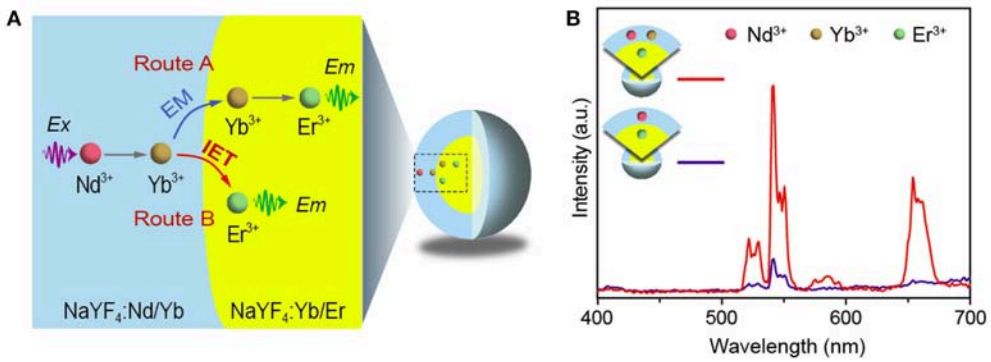

FIGURE 4 | (A) Schematic of possible energy migration (EM; Route A) and interfacial energy transfer (IET; Route B) in the design of $NaYF_4$:Yb/Er@$NaYF_4$:Nd/Yb core-shell nanostructure. Ex and Em stand for excitation and emission, respectively. **(B)** Upconversion emission spectra from control samples of $NaYF_4$:Er(2 mol%)@$NaYF_4$:Nd/Yb(50/10 mol%) and $NaYF_4$:Er(2 mol%)@$NaYF_4$:Nd(50 mol%) under 808 nm excitation.

performance of lanthanides (Chen et al., 2016; Liu et al., 2018). In the present work, the presence of Yb^{3+} into the shell layer indeed leads to a decline of the upconversion (**Figure S5**). We then designed a $NaYF_4$:Yb/Er@$NaNdF_4$:Yb@$NaYF_4$:Nd core-shell-shell nanostructure to improve the upconversion at 808 nm irradiation by making a fine tuning of the Yb^{3+} concentration in the Nd-sublattice (**Figure 6A**). It was found that 50 mol% Yb^{3+} in the $NaNdF_4$ interlayer is the optimal value for balancing the absorption and further transportation of the incident 808 nm excitation energy. Note that this Yb^{3+} content (50 mol%) in the interlayer is much higher than that from the $NaYF_4$:Yb/Er@$NaYF_4$:Nd/Yb core-shell nanostructure (10 mol%), revealing that there might exist a possibility of energy migration over to the surface which can quench the upconversion. In this case, the designs with high doping of migratory lanthanides need an optically inert shell layer to isolate the interactions between lanthanide emitter and surface quencher (Liu et al., 2018; Yan et al., 2018). Notably, the

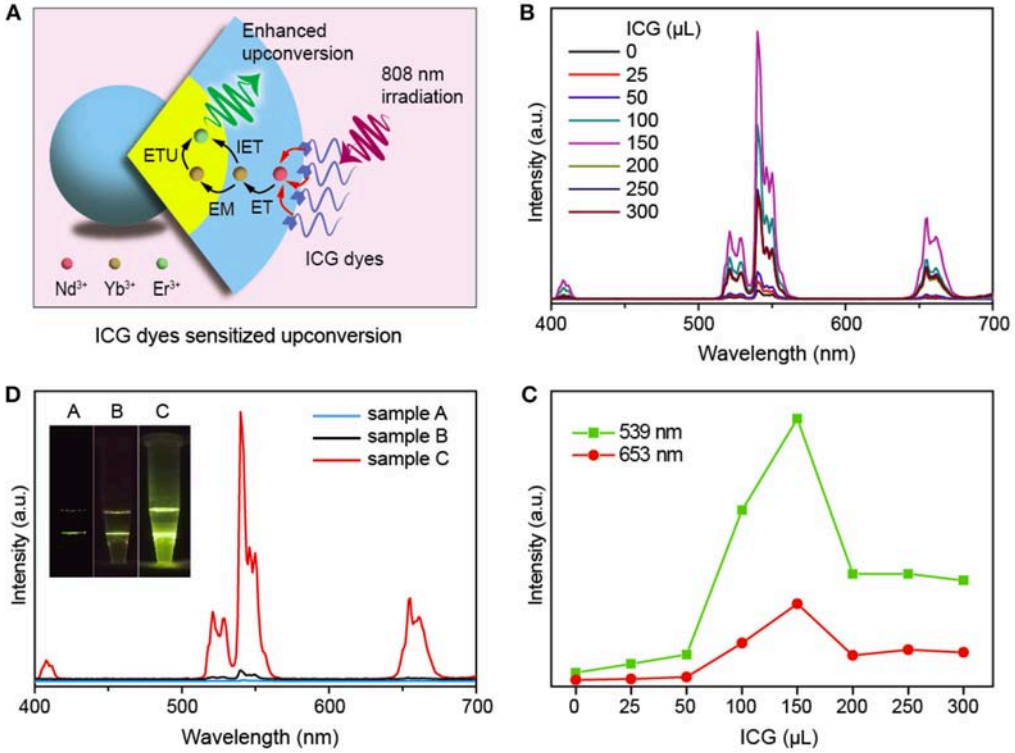

FIGURE 5 | (A) Schematic of enhancing upconversion through using the infrared ICG dye. **(B)** Upconversion emission spectra from the **(B)** $NaYF_4$:Yb/Er(20/2 mol%)@$NaYF_4$:Nd/Yb(50/10 mol%) core-shell nanoparticles sensitized with different amount of ICG dyes (1 μg/mL) under 808 nm excitation. **(C)** Dependence of upconversion emission intensity on the content of ICG. **(D)** A comparison of the upconversion from the $NaYF_4$:Yb/Er/Nd(20/2/1 mol%)@$NaYF_4$:Nd(30 mol%) (sample A) and $NaYF_4$:Yb/Er(20/2 mol%)@$NaYF_4$:Nd/Yb(50/10 mol%) (sample B), and the ICG dye sensitized $NaYF_4$:Yb/Er(20/2 mol%)@$NaYF_4$:Nd/Yb(50/10 mol%) (sample C) core-shell-shell nanoparticles. Inset shows their emission photographs under 808 nm irradiation.

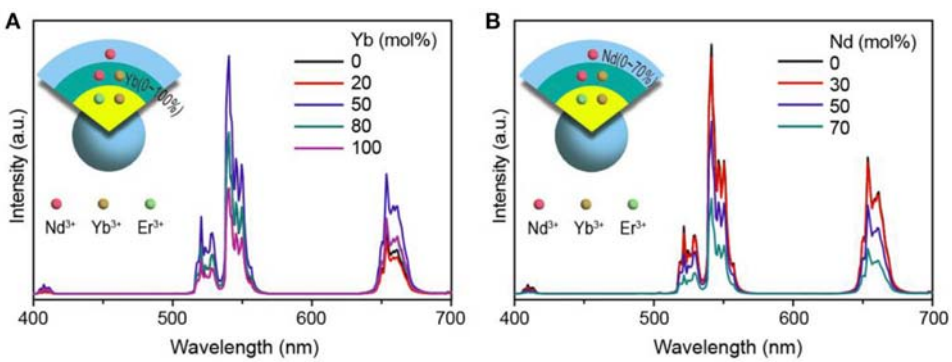

FIGURE 6 | Upconversion emission spectra from the **(A)** $NaYF_4$:Yb/Er(20/2 mol%)@$NaNdF_4$:Yb(0~100 mol%)@$NaYF_4$:Nd(50 mol%) and **(B)** $NaYF_4$:Yb/Er(20/2 mol%)@$NaNdF_4$:Yb(50 mol%)@$NaYF_4$:Nd(0~70 mol%) core-shell-shell samples under 808 nm excitation. Insets show the structure of the trilayer samples.

upconversion emission intensity is much weaker for these samples without the outermost shell layer (**Figure S6**). We further investigated the role of Nd^{3+} in the outermost shell layer. And the spectral result shows that a doping of it in the shell layer caused a slight decline in the upconversion intensity (**Figure 6B**) and lifetime (**Figure S7**). It should be noted that the near infrared emission from Yb^{3+} can be well improved (**Figure S8**).

CONCLUSIONS

In conclusion, the role of Yb^{3+} in the Nd/Yb coupled upconversion system was mechanistically investigated. By designing a $NaYF_4$:Yb/Er@$NaYF_4$:Yb@$NaYF_4$:Nd/Yb core-shell-shell nanostructure with a Yb^{3+} content tuneable interlayer, we have confirmed that the energy migration over the ytterbium sublattice plays a critical role in facilitating the energy transportation from the sensitizer in the shell to the lanthanide emitter in the core. Interestingly, the direct interfacial energy transfer from Yb^{3+} in the shell to the emitter in the core also contributes to the upconversion. By further sensitization through using the infrared dyes, the upconversion luminescence intensity was markedly enhanced. These results on dynamics in the 808 nm pumped upconversion systems provide an in-depth mechanistic understanding of the energy interactions occurred in lanthanides, and more importantly, the markedly enhanced upconversion performance shows great promise in the diversity of biological applications.

AUTHOR CONTRIBUTIONS

BZ conceived and designed the experiments. NS, LY, and JH performed the experiments. BZ and QZ supervised the project. BZ wrote the manuscript with input from all authors.

FUNDING

This work is supported by the National Natural Science Foundation of China (51702101 and 51472088), the Local Innovative and Research Teams Project of Guangdong Pearl River Talents Program (2017BT01X137), and the Fundamental Research Funds for the Central Universities (2017MS001, SCUT).

SUPPLEMENTARY MATERIAL

The Supplementary Material for this article can be found online at: https://www.frontiersin.org/articles/10.3389/fchem.2018.00673/full#supplementary-material

REFERENCES

Auzel, F. (2004). Upconversion and anti-stokes processes with f and d ions in solids. *Chem. Rev.* 104, 139–173. doi: 10.1021/cr020357g

Chen, G., Qiu, H., Prasad, P. N., and Chen, X. (2014). Upconversion nanoparticles: design, nanochemistry, and applications in theranostics. *Chem. Rev.* 114, 5161–5214. doi: 10.1021/cr400425h

Chen, X., Jin, L., Kong, W., Sun, T., Zhang, W., Liu, X., et al. (2016). Confining energy migration in upconversion nanoparticles towards deep ultraviolet lasing. *Nat. Commun.* 7:10304. doi: 10.1038/ncomms10304

Chen, X., Jin, L., Sun, T., Kong, W., Yu, S., and Wang, F. (2017). Energy migration upconversion in Ce(III)-doped heterogeneous core–shell–shell nanoparticles. *Small* 13:1701479. doi: 10.1002/smll.201701479

De Boni, L., and Mendonca, C. R. (2011). Study of absorption spectrum and dynamics evaluation of the indocyanine-green first singlet excited state. *J. Phys. Org. Chem.* 24, 630–634. doi: 10.1002/poc.1800

Deng, R., Qin, F., Chen, R., Huang, W., Hong, M., and Liu, X. (2015). Temporal full-colour tuning through non-steady-state upconversion. *Nat. Nanotech.* 10, 237–242. doi: 10.1038/nnano.2014.317

Dong, H., Du, S., Zheng, X., Lyu, G., Sun, L., Li, L., et al. (2015). Lanthanide nanoparticles: from design toward bioimaging and therapy. *Chem. Rev.* 115, 10725–10815. doi: 10.1021/acs.chemrev.5b00091

Fischer, S.T., Bronstein, N. D., Swabeck, J. K., Chan, E. M., and Alivisatos, A. P. (2016). Precise tuning of surface quenching for luminescence enhancement in core-shell lanthanide-doped nanocrystals. *Nano Lett.* 16, 7241–7247. doi: 10.1021/acs.nanolett.6b03683

Haase, M., and Schafer, H. (2011). Upconverting nanoparticles. *Angew. Chem. Int. Ed.* 50, 5808–5829. doi: 10.1002/anie.201005159

Kobayashi, H., Longmire, M. R., Ogawa, M., and Choykea, P. L. (2011). Rational chemical design of the next generation of molecular imaging probes based on physics and biology: mixing modalities, colors and signals. *Chem. Soc. Rev.* 40, 4626–4648. doi: 10.1039/c1cs15077d

Kushida, T., Marcos, H. M., and Geusic, J. E., (1968). Laser transition cross section and fluorescence branching ratio for Nd^{3+} in yttrium aluminum garnet. *Phys. Rev.* 167, 289–291.

Lei, P., An, R., Yao, R. S., Wang, Q., Dong, L., Xu, X., et al. (2017). Ultrafast synthesis of novel hexagonal phase $NaBiF_4$ upconversion nanoparticles at room temperature. *Adv. Mater.* 29:1700505. doi: 10.1002/adma.201700505

Li, X., Guo, Z., Zhao, T., Lu, Y., Zhou, L., Zhao, D., et al. (2016). Filtration shell mediated power density independent orthogonal excitations-emissions upconversion luminescence. *Angew. Chem., Int. Ed.* 55, 2464–2469. doi: 10.1002/anie.201510609

Liu, B., Li, C., Yang, P., Hou, Z., and Lin, J. (2017). 808-nm-light-excited lanthanide-doped nanoparticles: rational design, luminescence control and theranostic applications. *Adv. Mater.* 29:1605434. doi: 10.1002/adma.201605434

Liu, Q., Zhang, Y., Peng, C. S., Yang, T., Joubert, L.-M., and Chu, S. (2018). Single upconversion nanoparticle imaging at sub-10 W cm^{-2} irradiance. *Nat. Photon.* 12, 548–553. doi: 10.1038/s41566-018-0217-1

Liu, Y., Lu, Y., Yang, X., Zheng, X., Wen, S., Wang, F., et al. (2017). Amplified stimulated emission in upconversion nanoparticles for super-resolution nanoscopy. *Nature* 543, 229–233. doi: 10.1038/nature21366

Lu, Y., Lu, J., Zhao, J., Cusido, J., Raymo, F. M., Yuan, J., et al. (2014). On-the-fly decoding luminescence lifetimes in the microsecond region for lanthanide-encoded suspension arrays. *Nat. Commun.* 5:3741. doi: 10.1038/ncomms4741

Parent, C., Lurin, C., Flem, G. L., and Hagenmuller, P. (1986). $Nd^{3+} \rightarrow Yb^{3+}$ energy transfer in glasses with composition close to $LiLnP_4O_{12}$ metaphosphate (Ln = La, Nd, Yb). *J. Lumin.* 36, 49–55. doi: 10.1016/0022-2313(86)90030-X

Wang, D., Wang, D., Kuzmin, A., Pliss, A., Shao, W., Xia, J., et al. (2018). ICG-sensitized $NaYF_4$:Er nanostructure for theranostics. *Adv. Opt. Mater.* 6:1701142. doi: 10.1002/adom.201701142

Wang, F., Deng, R., Wang, J., Wang, Q., Han, Y., Zhu, H., et al. (2011). Tuning upconversion through energy migration in core-shell nanoparticles. *Nat. Mater.* 10, 968–973. doi: 10.1038/nmat3149

Wang, X., Valiev, R. R., Ohulchanskyy, T. Y., Ågren, H., Yang, C., and Chen, G. (2017). Dye-sensitized lanthanide-doped upconversion nanoparticles. *Chem. Soc. Rev.* 46, 4150–4167. doi: 10.1039/C7CS00053G

Weissleder, R. (2001). A clearer vision for *in vivo* imaging. *Nat. Biotechnol.* 19, 316–317. doi: 10.1038/86684

Wu, X., Zhang, Y., Takle, K., Bilsel, O., Li, Z., Lee, H., et al. (2016). Dye-sensitized core/active shell upconversion nanoparticles for optogenetics and bioimaging applications. *ACS Nano* 10, 1060–1066. doi: 10.1021/acsnano.5b06383

Xie, X., Li, Z., Zhang, Y., Guo, S., Pendharkar, A. I., Lu, M., et al. (2017). Emerging ≈800 nm excited lanthanide-doped upconversion nanoparticles. *Small.* 13:1602843. doi: 10.1002/smll.201602843

Xu, J., Yang, P., Sun, M., Bi, H., Liu, B., Yang, D., et al. (2017). Highly emissive dye-sensitized upconversion nanostructure for dual-photosensitizer photodynamic therapy and bioimaging. *ACS Nano* 11, 4133–4144. doi: 10.1021/acsnano.7b00944

Yan, L., Zhou, B., Song, N., Liu, X., Huang, J., Wang, T., et al. (2018). Self-sensitization induced upconversion of Er^{3+} in core–shell nanoparticles. *Nano* 10, 17949–17957. doi: 10.1039/C8NR04816A

Zheng, W., Huang, P., Tu, D., Ma, E., Zhu, H., and Chen, X. (2015). Lanthanide-doped upconversion nano-bioprobes: electronic structures, optical properties, and biodetection. *Chem. Soc. Rev.* 44, 1379–1415. doi: 10.1039/C4CS00178H

Zhong, Y., Tian, G., Gu, Z., Yang, Y., Gu, L., Zhao, Y., et al. (2014). Elimination of photon quenching by a transition layer to fabricate a quenching-shield sandwich structure for 800 nm excited upconversion luminescence of Nd^{3+}-sensitized nanoparticles. *Adv. Mater.* 26, 2831–2837. doi: 10.1002/adma.201304903

Zhou, B., Shi, B., Jin, D., and Liu, X. (2015). Controlling upconversion nanocrystals for emerging applications. *Nat. Nanotechnol.* 10, 924–936. doi: 10.1038/nnano.2015.251

Zhou, B., Tao, L., Chai, Y., Lau, P. S., Zhang, Q. Y., and Tsang, Y. H. (2016). Constructing interfacial energy transfer for photon up- and down-conversion from lanthanides in a core-shell nanostructure. *Angew. Chem. Int. Ed.* 55, 12356–12360. doi: 10.1002/anie.201604682

Zhou, B., Yan, L., Tao, L., Song, N., Wu, M., Wang, T., et al. (2018). Enabling photon upconversion and precise control of donor-acceptor interaction through interfacial energy transfer. *Adv. Sci.* 5:1700667. doi: 10.1002/advs.201700667

Zhu, X., Su, Q., Feng, W., and Li, F. (2017). Anti-Stokes shift luminescent materials for bio-applications. *Chem. Soc. Rev.* 46, 1025–1039. doi: 10.1039/C6CS00415F

Zou, W., Visser, C., Maduro, J. A., Pshenichnikov, M. S., and Hummelen, J. C. (2012). Broadband dye-sensitized upconversion of near-infrared light. *Nat. Photon.* 6, 560–564.doi: 10.1038/nphoton.2012.158

Conflict of Interest Statement: The authors declare that the research was conducted in the absence of any commercial or financial relationships that could be construed as a potential conflict of interest.

Copyright © 2019 Song, Zhou, Yan, Huang and Zhang. This is an open-access article distributed under the terms of the Creative Commons Attribution License (CC BY). The use, distribution or reproduction in other forums is permitted, provided the original author(s) and the copyright owner(s) are credited and that the original publication in this journal is cited, in accordance with accepted academic practice. No use, distribution or reproduction is permitted which does not comply with these terms.

frontiers in Chemistry

ORIGINAL RESEARCH
published: 25 February 2019
doi: 10.3389/fchem.2019.00088

Mapping Temperature Distribution Generated by Photothermal Conversion in Graphene Film Using Er,Yb:$NaYF_4$ Nanoparticles Prepared by Microwave-Assisted Solvothermal Method

Oleksandr A. Savchuk[1,2], Joan J. Carvajal[1], Yolanda Cesteros[3], Pilar Salagre[3], Huu Dat Nguyen[1], Airan Rodenas[1], Jaume Massons[1], Magdalena Aguiló[1] and Franscesc Díaz[1]*

[1] Universitat Rovira i Virgili, Departament de Química Física i Inorgànica, Física i Cristal·lografia de Materials i Nanomaterials (FiCMA-FiCNA) and EMaS, Tarragona, Spain, [2] Ultrafast Bio- and Nanophotonics Group, INL - International Iberian Nanotechnology Laboratory, Nanophotonics Department, Braga, Portugal, [3] Universitat Rovira i Virgili, Departament de Química Física i Inorgànica, Catalytic Materials in Green Chemistry (GreenCat), Tarragona, Spain

OPEN ACCESS

Edited by:
Luís António Dias Carlos, University of Aveiro, Portugal

Reviewed by:
Helene Serier-Brault, UMR6502 Institut des Matériaux Jean Rouxel (IMN), France
Andrew Nattestad, University of Wollongong, Australia

***Correspondence:**
Oleksandr A. Savchuk
oleksandr.savchuk@inl.int

Specialty section:
This article was submitted to Inorganic Chemistry, a section of the journal Frontiers in Chemistry

Received: *30 November 2018*
Accepted: *01 February 2019*
Published: *25 February 2019*

Citation:
Savchuk OA, Carvajal JJ, Cesteros Y, Salagre P, Nguyen HD, Rodenas A, Massons J, Aguiló M and Díaz F (2019) Mapping Temperature Distribution Generated by Photothermal Conversion in Graphene Film Using Er,Yb:$NaYF_4$ Nanoparticles Prepared by Microwave-Assisted Solvothermal Method. Front. Chem. 7:88. doi: 10.3389/fchem.2019.00088

This study analyzes the mapping of temperature distribution generated by graphene in a glass slide cover after illumination at 808 nm with a good thermal resolution. For this purpose, Er,Yb:$NaYF_4$ nanoparticles prepared by a microwave-assisted solvothermal method were used as upconversion luminescent nanothermometers. By tuning the basic parameters of the synthesis procedure, such as the time and temperature of reaction and the concentration of ethanol and water, we were able to control the size and the crystalline phase of the nanoparticles, and to have the right conditions to obtain 100% of the β hexagonal phase, the most efficient spectroscopically. We observed that the thermal sensitivity that can be achieved with these particles is a function of the size of the nanoparticles and the crystalline phase in which they crystallize. We believe that, with suitable changes, these nanoparticles might be used in the future to map temperature gradients in living cells while maintaining a good thermal resolution.

Keywords: green synthesis, upconversion nanoparticles, graphene, nanothermometry, thermal mapping

INTRODUCTION

Carbon-based materials have emerged as promising photothermal agents due to their wideband optical absorption that allows the absorption of light at various wavelengths leading to an efficient heat conversion (Han et al., 2018). The extraordinary properties of graphene propelled its application in many fields of science, including its use as photothermal conversion agent (Savchuk et al., 2016). The excellent performance of graphene as a photothermal conversion material has allowed its use in photothermal therapy, usually in combination with other functional materials with complementary properties (Zhu et al., 2010). However, we are not aware of the existence of studies on the thermal mapping of graphene films.

With the development of nanotechnology, the determination of temperature in a given system with submicrometric spatial resolution became possible. This has led to the development of a new

subfield of thermometry, named nanothermometry, which studies the measurement of temperature at the nanoscale level (Lee and Kotov, 2007). Luminescence thermometry is considered to be one of the most promising non-contact techniques for temperature determination at the sub-micrometer and nanometer scale due to its very high spatial, thermal, and temporal resolutions, large measurement ranges and affordable costs (Brites et al., 2012; Jaque and Vetrone, 2012). A big number of materials has been studied for luminescence nanothermometry applications, including quantum dots (Maestro et al., 2010, 2014; Vlaskin et al., 2010; Benayas et al., 2015), organic dyes (Peterman et al., 2003; Steinegger et al., 2017; Xie et al., 2017), gold nanoparticles (Bomm et al., 2012; Shang et al., 2013), polymers (Graham et al., 2010; Okabe et al., 2012; Hannecart et al., 2015), and lanthanide doped materials (Cheng et al., 2013; Zheng et al., 2014; Cerón et al., 2015; Piñol et al., 2015; Zhu et al., 2016; Balabhadra et al., 2017). The different measurement techniques used, and based on changes in radiative lifetimes, intensity variations, spectral position shifting, and broadening of emission lines induced by temperature, have proved to be potential tools for temperature determination even in biosystems (Vetrone et al., 2010; Fischer et al., 2011; Du et al., 2014; Zhu et al., 2016; Li et al., 2017).

However, some of these materials attracted more attention because of their interesting advantages for luminescent nanothermometry. These materials are the Ln^{3+}-doped upconversion nanoparticles (Ln^{3+}-UCNPs). This kind of material absorbs light in the near-infrared (NIR) region of the electromagnetic spectrum, while emitting light in the visible range (Haase and Schäfer, 2011). Pumping in the NIR allows to overcome problems related to the background fluorescence arising from biological tissues, and the potential damage that ultraviolet (UV) light can generate in them (Diao et al., 2015), for instance. Finally, the use of NIR radiation also preserves the operative lifetime of the phosphors used in comparison with those illuminated with UV light, usually damaged by this radiation, that shortens their operational lifetimes (Rapaport et al., 2006).

Er^{3+} is the most used lanthanide ion for luminescence thermometry purposes in UCNPs because of its intense green emission that consists of two luminescence bands centered at 520 and 540 nm and assigned to the $^2H_{11/2} \rightarrow {}^4I_{15/2}$ and $^4S_{3/2} \rightarrow {}^4I_{15/2}$ radiative transitions, respectively. These two energy levels, from which the emission arises, are thermally coupled and, thus, the relative emission intensity of these two luminescence bands shows a strong temperature dependence (Vetrone et al., 2010; Fischer et al., 2011; Du et al., 2014; Zhu et al., 2016; Li et al., 2017). Among the potential crystalline matrices that can host Er^{3+}, $NaYF_4$ emerged as the most promising one (Krämer et al., 2004; Wang et al., 2010).

However, $NaYF_4$ can crystallize in two polymorphic phases: the α-$NaYF_4$ phase with $Fm\bar{3}m$ space group and the hexagonal β-$NaYF_4$ phase with $P\frac{6_3}{m}$ space group (Wang et al., 2010). High reaction temperatures and long reaction times can induce the phase transformation from the metastable α phase to the thermodynamically stable β phase (Zhou et al., 2013). Thus, the synthesis of $NaYF_4$ phosphors has been extensively studied, especially to explore the best conditions to obtain the pure β phase with a high production yield. Microwave-assisted hydrothermal synthesis emerged as an efficient method for the synthesis of monodispersed and highly luminescent $NaYF_4$ nanoparticles (Wang and Nann, 2009), since it allows for a fast and uniform heating in an eco-friendly and energy-efficient way. However, those procedures still suffer from poor yields (Wang and Nann, 2009), production of mixtures of α and β phases (Mi et al., 2011), limited to microtubes (Chen et al., 2009; Tong et al., 2017), and nanowires (Wawrzynczyk et al., 2015), as well as micron-size particles (Som et al., 2016).

Here, we report the synthesis of Er,Yb:$NaYF_4$ nanoparticles by a microwave-assisted solvothermal method which allowed us to obtain these nanoparticles in short times and at low temperatures. Furthermore, by tuning the basic parameters of the synthesis process, such as temperature and time of reaction, we succeeded in obtaining nanoparticles with different sizes and in isolating the different crystalline phases. We have been able to get the right conditions to obtain 100% of the pure β-$NaYF_4$ phase with a production yield ranging from 64 to 98%. We also analyzed the temperature dependence of the luminescence of these nanoparticles. Nanoparticles with bigger sizes belonging to the hexagonal β phase showed a higher relative sensitivity than those with smaller sizes or those belonging to the cubic α phase. Finally, we used these nanoparticles to map the temperature distribution generated by the laser-induced heating of graphene deposited on a glass cover slide generated by a photothermal conversion process.

EXPERIMENTAL SECTION

Synthesis of Er,Yb:$NaYF_4$ Nanoparticles

Yb (20 mol. %), Er (2 mol. %) co-doped $NaYF_4$ nanoparticles were synthesized by a microwave-assisted solvothermal method. High purity Y_2O_3, Yb_2O_3, and Er_2O_3, analytical reagents, trisodium citrate ($Na_3C_6H_5O_7$), sodium fluoride (NaF), and ammonium fluoride (NH_4F) were used as raw starting reagents. $RE(NO_3)_3$ (RE = Y, Yb, Er) were prepared by dissolving the corresponding RE_2O_3 in 10 ml of hot nitric acid (HNO_3). After the evaporation of the nitric acid, 15–65.5 ml of ethanol (depending on the experiment) in which 8.1–24.7 g of trisodium citrate (depending on the experiment) were dissolved, were added and stirred for 60 min. In another vessel, 0.08–0.36 g of NaF and 0.45–3.62 g of NaH_4F were dissolved in 7.5–60 ml of hot water, depending on the experiment. Then, the two solutions were mixed together. After a vigorous stirring for 2 h, the solution was transferred to a Teflon reactor with a total volume of 70 ml. This reactor was placed in a Milestone ETHOS-TOUCH CONTROL laboratory microwave autoclave, where it was maintained at a temperature between 393 and 453 K under continuous stirring during a period of time ranging from 3 to 6 h, depending on the experiment. Finally, the solution was cooled down naturally, and the precipitated nanoparticles were washed with ethanol and deionized water three times. **Table 1** summarizes the synthesis conditions for the different experiments we performed.

TABLE 1 | Synthesis conditions and main characteristics of the Er,Yb:$NaYF_4$ nanoparticles obtained by the microwave-assisted solvothermal method.

Temperature (K)	Time (h)	[Ethanol/Water] (Volume %)	Crystalline phase	Crystallite size (nm)	Shape	Production yield (%)
453	6	70/30	β	63	Long rods	77
		60/40		74	Long rods	67
		50/50		55	Long rods	67
		40/60		68	Long rods	67
		30/70	α + β	48	Long rods	65
		20/80		42	Short rods	64
453	3	90/10	β	52	Spheres	98
		80/20		58	Spheres	97
		70/30		29	Irregular	97
		60/40		40	Spheres + short rods	96
		50/50		26	Irregular	86
		40/60		28	Irregular	71
423	3	90/10	α	22	Spheres	98
		80/20	β	128	Spheres	97
		70/30		60	Short rods	98
		60/40		57	Short rods	98
		50/50		37	short rods	75
		40/60		65	Short rods	69
393	3	80/20	β	62	Short rods	98
		70/30		55	Short rods	98
		60/40		72	Short rods	97
		50/50		72	Short rods	81
		40/60		58	Short rods	64

Structural and Morphological Characterization

The crystalline structure of the obtained Er,Yb:$NaYF_4$ nanoparticles was investigated by means of X-ray powder diffraction analysis using a Bruker-AXS D8-Discover diffractometer using Cu Kα radiation. The crystallite size was calculated with the data corresponding to all the reflections in the diffraction pattern using the Scherrer equation. The crystallite size is also listed in **Table 1**.

The morphology of the Er,Yb:$NaYF_4$ nanoparticles obtained by the microwave-assisted solvothermal method was investigated using an environmental scanning electron microscope (ESEM) FEI Quanta 600 and a transmission electron microscope (TEM) JEOL 1011.

Temperature-Dependent Luminescence Measurements

For temperature dependent luminescence measurements, the Er,Yb:$NaYF_4$ nanoparticles were placed in a Linkam THMS 600 heating stage equipped with a BN disk that allowed an improved temperature distribution in the chamber. The nanoparticles were excited by a fiber-coupled diode laser emitting at 980 nm with a power of 10 mW, so that the contribution of the excitation laser to the heating of the nanoparticles is negligible. The laser beam was focused on the sample with a 40× microscope objective with a numerical aperture N.A. = 0.6, providing a spot size of around 100 μm on the sample. The visible emission arising from the nanoparticles was registered by the same microscope objective, and after passing a dichroic filter to eliminate the excitation radiation, it was fiber coupled to an AVANTES AVS-USB2000 spectrometer for the recording of the emission spectra. These spectra were recorded at temperatures between RT and 333 K.

Thermal Mapping of Heat Transfer Through a Graphene-Coated Glass

Hundred microliters of a graphene solution in dymethylformamide (DMF) with a concentration of 1 mg ml^{-1} were deposited on a microscope slide cover glass with a thickness of 100 μm. The solvent was evaporated letting it dry at 353 K, generating a film with a thickness ranging between 700 nm and 1.2 μm, determined with a SENSOFAR PLμ 2300 confocal microscope. On the other side of the same microscope slide cover glass 100 μl of a dispersion of the Er,Yb:$NaYF_4$ nanoparticles in ethanol with a concentration of 10 mg ml^{-1} was deposited. A fiber-coupled diode laser emitting at 808 nm with powers ranging from 20 to 200 mW, depending on experiments, was focused on the graphene-coated cover glass using a 60× microscope objective (N. A. = 0.7), generating a beam with a diameter of 9 μm on the sample. Graphene efficiently absorbs the 808 nm laser light and converts it into heat (Savchuk et al., 2016). The temperature generated was then determined

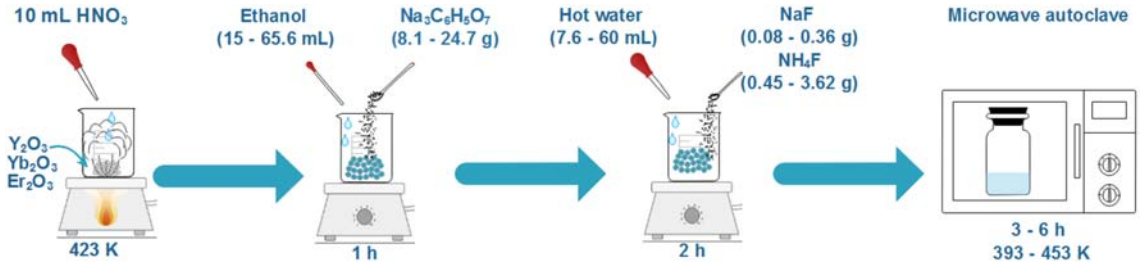

SCHEME 1 | Schematic illustration of the microwave-assisted solvothermal method for Er,Yb:$NaYF_4$ nanoparticles used.

through the analysis of the upconversion emission spectra of Er,Yb:$NaYF_4$ nanoparticles.

RESULTS AND DISCUSSION

Microwave-Assisted Solvothermal Synthesis of Er,Yb:$NaYF_4$ Nanoparticles

Er,Yb:$NaYF_4$ nanoparticles were synthesized with the microwave-assisted solvothermal method. The scheme of the synthesis process is shown in **Scheme 1**. Compared to other conventionally heated hydrothermal methods, microwave heating is a greener approach to the synthesis of materials, since it allows for a shortening of the reaction times, a reduction of the reaction temperature and thus, for a reduction of the energy consumption (Komarneni et al., 1992; Sánchez et al., 2013; Granados-Reyes et al., 2014). By changing the reaction temperature, the reaction time and the ethanol and water volumes, we obtained nanoparticles with different sizes and crystallizing in different crystalline phases, as listed in **Table 1**, identifying the conditions to obtain pure α- and β-$NaYF_4$ nanoparticles. TEM and ESEM images of all the nanoparticles obtained are presented in **Figure S1**.

Since the β phase allows to obtain a higher up-conversion emission intensity, we focused our efforts in maximizing the production of this phase.

In the case of nanoparticles synthesized at 453 K for 6 h, the pure β-$NaYF_4$ phase was obtained for solutions containing ethanol concentrations between 40 and 70%, while a mixture of the α and β phases (α phase with a lower concentration than the β phase) was obtained in solutions with a lower ethanol content. These solutions with a lower ethanol content were avoided in the remaining experiments. When the reaction time was reduced to 3 h, while keeping the reaction temperature at 453 K, the pure β phase was obtained for all the solutions analyzed. When the temperature was reduced to 423 K, the pure β phase was obtained for all the solutions analyzed, expect for the one formed by 90% ethanol and 10% water, in which we obtained the pure α phase. This solution composition was not used in the last experiment, in which the temperature was reduced to 393 K, while the reaction time was kept at 3 h. Under these conditions, we were able to obtain the pure β phase again for all the solutions analyzed.

The yields of production of the β phase were high in all cases, between 64 and 98%, as listed in **Table 1**. The production yields are higher for the samples prepared in solutions containing a higher ethanol content, and this does not seem to depend on the synthesis temperature. However, as the reaction time increased, the production yields decreased, which would indicate that the products formed tend to dissolve again with a long exposure to the solution.

The crystallite size of these nanoparticles was calculated using the Scherrer equation (Patterson, 1939). The results are listed in **Table 1**. Comparing the crystallite size of the nanoparticles obtained from solutions containing the same ethanol concentrations at different temperatures and reaction times, we observed that the smallest crystallite sizes were obtained for the nanoparticles synthesized at 453 K for 3 h, while, even when the temperature was reduced to 423 or 393 K, the crystallite size increased again.

If we take a look to the shape of the nanoparticles obtained, we can observe that at low synthesis temperatures we obtained short rods, but as the temperature increased these rods tended to transform toward more irregular or spherical shapes. However, the surfaces of these nanoparticles are not smooth, indicating that probably they are formed by the agglomeration of the smaller short rod units. Also, when the reaction time was increased from 3 to 6 h, sub-micrometric size particles exhibiting a long rod shape were obtained. Finally, comparing the shape of the nanoparticles obtained using different ethanol concentrations, we observed that as the ethanol concentration increased, the nanoparticles tended to show more irregular, spherical or long rod shapes, depending on the synthesis temperature and the reaction time used.

As explained in the Introduction of this article, microwave-assisted hydrothermal methods have been previously used for the synthesis of $NaYF_4$ phosphors. Wang and Nann used sodium trifluoroacetate (TFA), yttrium-TFA, ytterbium-TFA, and erbium-TFA as initial reagents dissolved in oleic acid and 1-octadecene to obtain $NaYF_4$ nanocrystals. They used a microwave-assisted process at 563 K for 5 min, obtaining cubic α-$NaYF_4$ nanoparticles with very small sizes (11 nm in diameter) with a poor yield (Wang and Nann, 2009). Chen et al. (2009) used NaF, NH_4HF_2, and Y, Yb, and Tm nitrates as initial reagents dissolved in water to obtain $NaYF_4$, adjusting the pH with HF, and heating the solution at 453 K for 4 h in a microwave synthesizer. They obtained β-$NaYF_4$ microtubes, 0.5 μm in diameter and 2–3 μm long. Similar microtubes were obtained

by Tong et al. (2017) using a similar methodology. Later, Mi et al. (2011) used rare earth acetates, such as NH_4F and NaCl, and fluorine and sodium sources, respectively, dissolved in a mixture of water and ethylene glycol, and treated thermally in a microwave autoclave at 433 K for 1 h. Under these conditions they obtained a mixture of the α and β phases with average sizes of around 40 nm. More recently, Wawrzynczyk et al. (2015), using a microwave flash-heating method, obtained $NaYF_4$ nanowires 1.5 mm long and 100 nm in diameter. On the other hand, Som et al. (2016) prepared Er,Yb:$NaYF_4$ phosphors using rare earth nitrates and NaF dissolved in water, and adding ethylenediamine tetra acetic acid (EDTA) as chelating agent. They adjusted the pH of the solution with NaOH in a microwave digestion unit at 453 K for different time periods extending from 10 min to 2 h. The samples obtained at shorter times crystallized in the α metastable phase with small amounts of YF_3, indicating that the reaction was not complete. For intermediate times they obtained mixtures of the α and β phases, while the samples obtained at longer times exhibited only the pure β-$NaYF_4$ phase with a hexagonal prism shape, with a mean diameter of 1.0 μm and a length of 5.5 μm. More recently, Palo and co-workers obtained $NaYF_4$ nanoparticles using a microwave-assisted solvothermal method at relatively low temperatures (413–458 K) and long times (4–12 h) (Palo et al., 2016). However, the resulting nanoparticles are a mixture of the two phases with different morphologies (spherical, large cubes, and rods). Wang et al., in their study, synthesized β-$NaYF_4$ nanoparticles uniform in size and with s strong fluorescence using a solvothermal method. The nanoparticles prepared using the synthesis optimal conditions (453 K, 24 h, and 5 ml of oleic acid) were used as fluorescent labels for fingerprint applications (Wang et al., 2015).

Thus, when comparing the results previously reported with the ones we obtained, we can conclude that the microwave-assisted solvothermal method we developed allows obtaining pure β-$NaYF_4$ nanoparticles with smaller sizes and at lower temperatures and shorter reaction times. Also, we avoided the appearance of microtubes or nanowires. Furthermore, the synthesis procedure we present here avoids the use of organic ligands like oleic acid (Wang and Nann, 2009; Wang et al., 2015) or EDTA (Som et al., 2016), which confer a hydrophobic character to the nanoparticles obtained and are difficult to eliminate at the end of the reaction. With our synthesis procedure, the production yields obtained ranged from 64 to 98%, as can be seen in **Table 1**. Thus, the methodology presented here shows several advantages over the technologies previously reported in the literature, such as the use of lower temperatures, the production of pure α and β phases, the possibility to avoid mixtures of both phases, or the use of cheaper solvents avoiding organic ligands that have to be removed at the end of the synthesis process. Furthermore, the nanoparticles obtained are already dispersible in water and biological compatible fluids, without requiring any post-growth treatment, which is a clear advantage when one expects to use such nanoparticles for biological applications.

We selected three representative sets of nanoparticles from the experiments performed: NP1, synthesized at 453 K for 6 h with an ethanol/water volume ratio 70/30; NP2, synthesized at 453 K for 3 h with an ethanol/water volume ratio 80/20; and NP3, synthesized at 423 K for 3 h with an ethanol/water volume ratio 90/10. An ESEM image of the NP1 nanoparticles is shown in **Figure 1a**. They show a prismatic shape with a hexagonal base, 300 nm in diameter and 600 nm long. This is the morphology we labeled as long rods in **Table 1**. Instead, samples NP2 and NP3 show nanoparticles with an almost spherical shape with average sizes of 50–70 and 20 nm, respectively, as observed in the TEM pictures shown in **Figures 1b,c**. They correspond to the morphologies labeled as irregular and spherical, respectively, in **Table 1**. The sizes of the nanoparticles corresponding to NP2 and NP3 samples, determined from the TEM pictures, match the crystallite sizes determined using the Scherrer equation. In the case of the NP1 sample, however, a large discrepancy was observed. This can be due to the fact that the size of these sub-micrometer particles is at the limit of the validity range for size determination using this equation, established at around 500 nm, and also to the fact that the Scherrer equation only accounts for one of the dimensions of the particles, that in this case were constituted by hexagonal prisms (Muniz et al., 2016). **Figure 1d** shows the X-ray diffraction (XRD) patterns recorded for these samples. We observed that samples NP1 and NP2 crystallize in the hexagonal system, with space group $P6_3/m$ corresponding to the β-$NaYF_4$ phase, as confirmed by the comparison with the JCPDS reference pattern 16–334, also included in the figure. In contrast, the nanoparticles in sample NP3, which were synthesized at a lower temperature and for a shorter time, crystallize in the cubic system, with space group Fm3m corresponding to the α-$NaYF_4$ phase, as confirmed by the comparison with the JCPDS reference pattern 39–723, also included in the figure. Additionally, we confirmed that the β-$NaYF_4$ nanoparticles obtained with this procedure were highly crystalline, as confirmed by the SAED pattern obtained by electron diffraction of one of these nanoparticles included in the inset of **Figure 1b**.

Temperature-Dependent Luminescence Measurements

The emission spectra of these nanoparticles after excitation at 980 nm are shown at room temperature and at 333 K in **Figure 2**. These spectra consist of two green bands centered at 520 and 540 nm, assigned to the $^2H_{11/2} \rightarrow {}^4I_{15/2}$ and $^4S_{3/2} \rightarrow {}^4I_{15/2}$ transitions of the Er^{3+} ion, respectively. An additional red band was observed at 630–670 nm, assigned to the $^4F_{9/2} \rightarrow {}^4I_{15/2}$ transition of Er^{3+}. While this red band shows a lower intensity than the green bands in samples NP1 and NP2, it is the main band in sample NP3, associated with the different crystalline phases of these nanoparticles.

The pathways for the generation of these emission lines through an upconversion process are well-known and have been previously used for luminescence thermometric applications (Vetrone et al., 2010; Dong et al., 2014; Jiang et al., 2014). Excitation at 980 nm promotes electrons of Yb^{3+} from the $^2F_{7/2}$ fundamental state to the $^2F_{5/2}$ excited state, from where an energy transfer process to Er^{3+} occurs, populating its $^4I_{11/2}$ energy

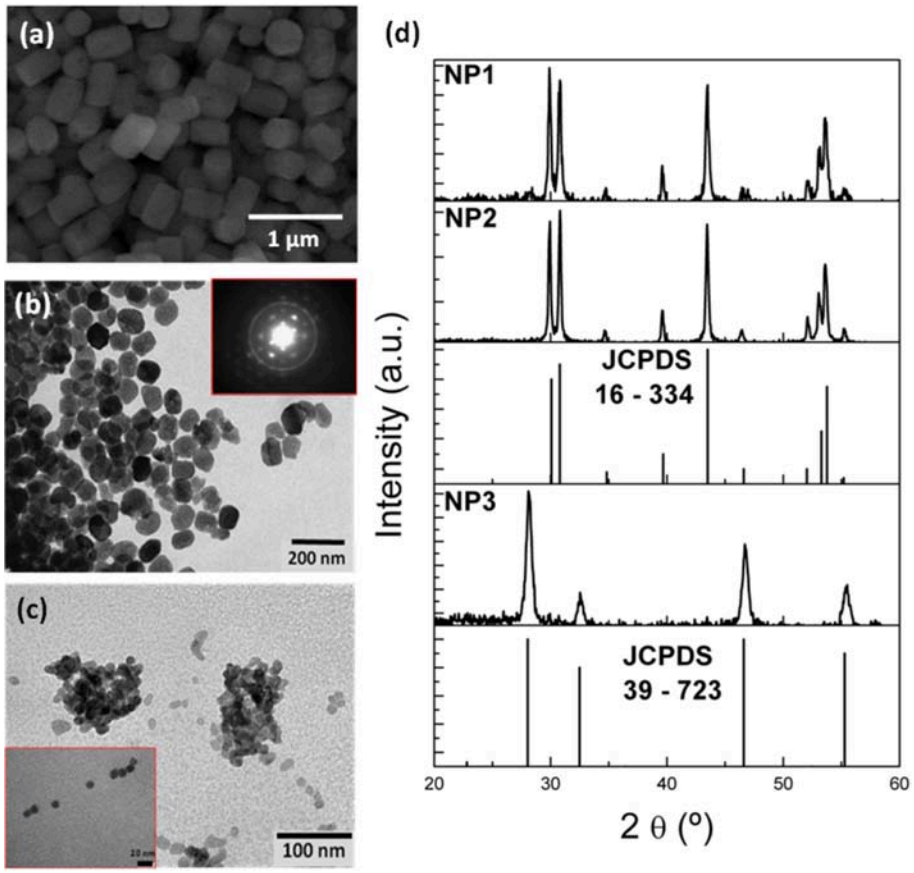

FIGURE 1 | (a) ESEM image of the nanoparticles obtained in the NP1 sample. TEM images of the nanoparticles obtained in the **(b)** NP2 and **(c)** NP3 samples. **(d)** X-ray diffraction patterns of the samples, together with the reference diffraction patterns for the α- and β-$NaYF_4$ crystalline phases.

level. A second energy transfer process from Yb^{3+} promotes the electrons of Er^{3+} from the $^4I_{11/2}$ to the $^4F_{7/2}$ level. Then, non-radiative relaxation processes populate the $^2H_{11/2}$ and $^4S_{3/2}$ states, which results in the $^2H_{11/2} \rightarrow {}^4I_{15/2}$ and $^4S_{3/2} \rightarrow {}^4I_{15/2}$ radiative decays, emitting photons at 520 and 540 nm, respectively. The $^4F_{9/2}$ energy level is populated by a new energy transfer process from Yb^{3+} to Er^{3+} that occurs after a non-radiative relaxation process from the $^4I_{11/2}$ to the $^4I_{13/2}$ energy level.

As observed in **Figure 2A**, the intensity of the visible emissions decreased when the temperature increased for all samples.

The fluorescence intensity ratio (FIR) technique has proven to be an efficient tool to evaluate the luminescence thermometry properties of the green emissions generated by Er^{3+} in several materials, including Er,Yb:$NaYF_4$ nanoparticles (Vetrone et al., 2010; Dong et al., 2014; Jiang et al., 2014). This technique is based on the comparison of the intensities of two emission bands arising from two closely spaced energy levels, the $^4S_{3/2}$ and $^2H_{11/2}$ levels of Er^{3+} in this case, whose populations are in thermal equilibrium governed by a Boltzmann distribution. **Figure 2B** shows the evolution of the FIR with temperature. FIR can be calculated based on a Boltzmann distribution equation defined as (Wade et al., 2003):

$$FIR\left(\frac{I_{520}}{I_{540}}\right) = \frac{g_1\gamma_1\sigma_1}{g_2\gamma_2\sigma_2}e^{\left(-\frac{\Delta E}{kT}\right)} \quad (1)$$

where I_{520} and I_{540} are the intensities of the emission bands located at 520 and 540 nm, respectively, g_i are the degeneracy of levels, γ_i are the spontaneous emission rates, σ_i are the absorption rates, ΔE is the energy difference between the two thermally coupled energy levels involved in the radiative transitions, k is the Boltzmann constant, and T is the absolute temperature.

Experimental points for the different samples were fitted to Equation 1, and the obtained expressions are included in **Figure 2B**. The nanoparticles that show the highest slope are those corresponding to the NP1 sample.

The qualitative performance of these nanoparticles to sense small changes in temperature was obtained by calculating the relative thermal sensitivity as the first derivative of FIR with respect to temperature divided by the FIR (Brites et al., 2012). The relative thermal sensitivities of the analyzed samples are included in **Figure 2C**. The NP1 sample, with nanoparticles exhibiting bigger sizes, possesses the highest thermal sensitivity

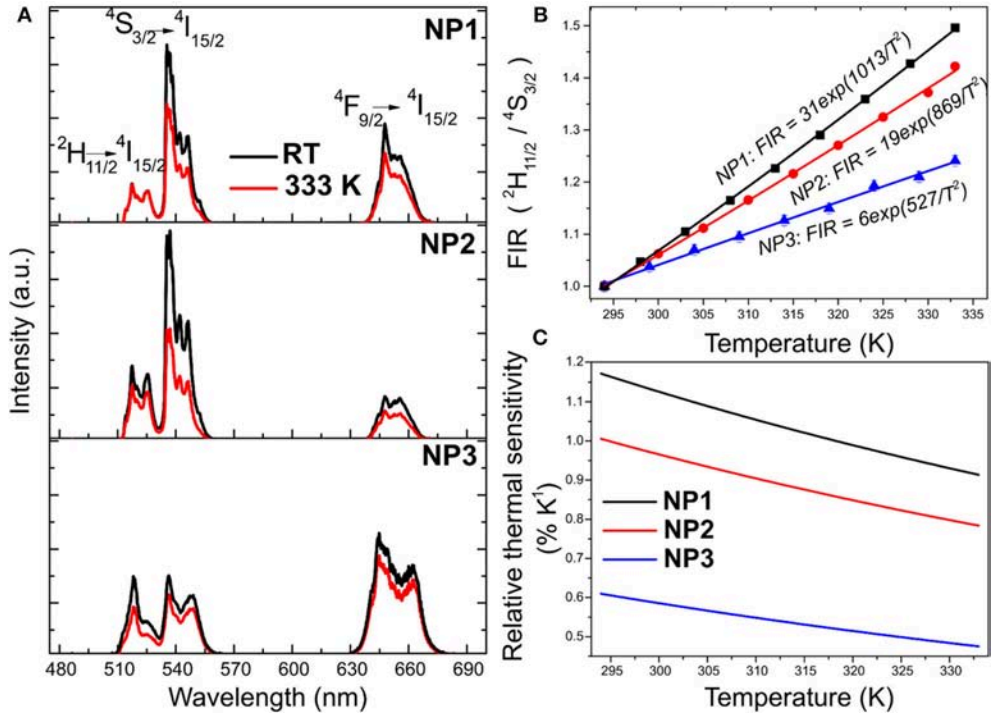

FIGURE 2 | (A) Upconversion emission spectra at room temperature (black) and 333 K (red) for NP1, NP2, and NP3 samples. **(B)** Normalized FIR as a function of temperature for NP1 (black), NP2 (red) and NP3 (blue) samples with the corresponding fitting following a Bolzmann thermal distribution. **(C)** Relative thermal sensitivity as a function of temperature for the three samples [NP1 (black), NP2 (red), and NP3 (blue)].

with a maximum of around 1.2% K^{-1} at 333 K. The thermal sensitivity of the NP2 sample is smaller than that of NP1. Thus, based on the presented results we can conclude that at the sub-micron and nanoscale, smaller β-Er,Yb:$NaYF_4$ nanoparticles would show smaller thermal sensitivities. This can be explained by the presence of a higher concentration of luminescent active ions close to the surface of smaller nanoparticles due to their higher surface to volume ratio. These ions would interact with the ligands attached to the surface of the nanoparticles, leading to concentration quenching processes that would affect negatively their thermal sensitivity. This might seem at odds with the data reported by Dong et al. (2014), since they reported that β-Er,Yb:$NaYF_4$ particles with smaller sizes presented a higher thermal sensitivity. However, they analyzed micron-size particles, while the nanoparticles here presented lay in the sub-micron and nanoscale. Nevertheless, the thermal sensitivity of the β-Er,Yb:$NaYF_4$ nanoparticles synthesized by this microwave-assisted solvothermal method is similar, or even slightly higher, than that reported for the same nanoparticles synthesized with other methods, in the range 0.21–1.24% K^{-1} (Vetrone et al., 2010; Fischer et al., 2011; Wu et al., 2011; Sedlmeier et al., 2012; Dong et al., 2014). Finally, α-Er,Yb:$NaYF_4$ nanoparticles in the NP3 sample showed the smallest thermal sensitivity. This is not surprising since the luminescence efficiency of the α-phase has been reported to be smaller than that of the β-phase, despite its thermal efficiency for luminescence thermometry has not been reported before. The thermal resolution that can be achieved with these nanoparticles, calculated by dividing the precision of the detection system (0.5% in our case) by the relative thermal sensitivity, is presented in **Figure S2**.

Temperature Distribution Mapping in Graphene by Luminescence Thermometry

In order to prove the potentiality of the Er,Yb:$NaYF_4$ nanoparticles synthesized through the microwave-assisted solvothermal method, we used them to map the temperature distribution generated on a glass coated with graphene when illuminated with a laser beam. In order to do this, we took a 100 μm thick microscope slide cover glass and we coated it with graphene flakes on one side, generating a continuous film with a thickness varying from 700 nm to 1.2 μm, and Er,Yb:$NaYF_4$ nanoparticles (corresponding to the NP1 sample) on the other side. Two spatially overlapped lasers were focused on both sides of the slide cover glass. A fiber-coupled diode laser emitting at 808 nm with a beam diameter of 9 μm was focused on the face of the cover glass coated with graphene. Graphene efficiently absorbs the 808 nm laser light and converts it into heat (Savchuk et al., 2016). The propagation of the heat generated by graphene on the opposite side of the cover glass was measured by determining the temperature through the spectra generated by the Er,Yb:$NaYF_4$ nanoparticles when excited with a fiber-coupled diode laser emitting at 980 nm with a beam diameter of 10 μm and by using the calibration curve shown in **Figure 2B**. The scheme of this experimental setup is shown in **Figure 3A**.

First, we measured the temperature that can be achieved in the system when the power of the 808 nm laser focused on

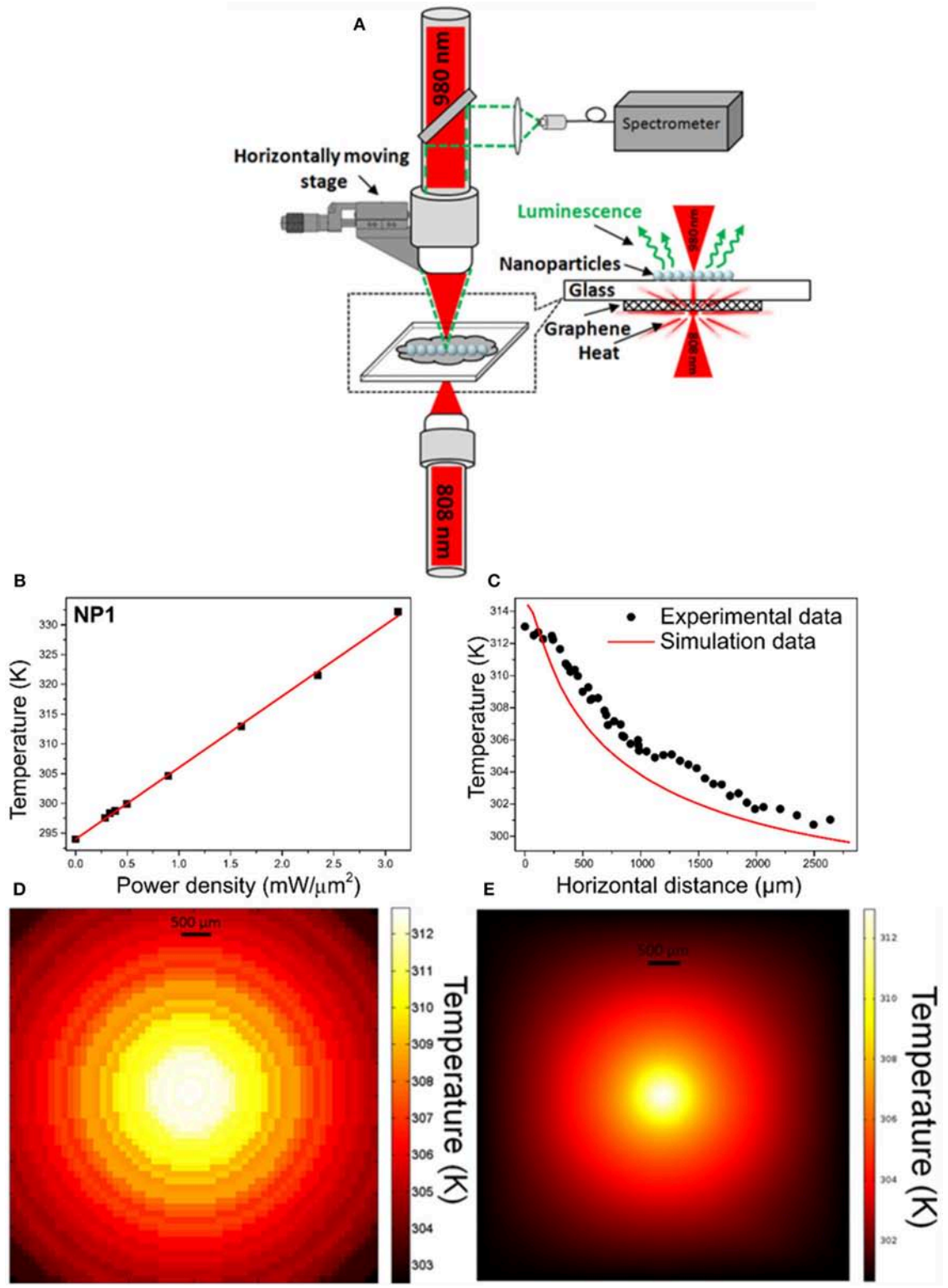

FIGURE 3 | (A) Scheme of the setup used to map the temperature distribution generated by graphene when illuminated with a 808 nm laser on a microscope slide cover glass. **(B)** Temperature achieved on the surface of the graphene-coated glass as a function of the power of the irradiating laser at 808 nm. **(C)** Temperature distribution generated by graphene on the slide cover glass determined from the luminescence spectra of the Er,Yb:$NaYF_4$ nanoparticles and comparison with the temperature distribution calculated from a heat transfer model in a 3D geometry. 2D temperature contour map generated from the data obtained **(D)** experimentally, and **(E)** with the 3D model.

graphene was increased. The results are shown in **Figure 3B**. We observed that the temperature increased linearly with the power of the laser. Based on these results, we decided to set the power of the laser at 100 mW, which allows for the temperature to achieve ∼312 K on the opposite side of the glass in order to get a constant heating and generate a thermal gradient high enough on the surface of the cover glass coated with the Er,Yb:$NaYF_4$ nanoparticles to be easily detected with them. The 980 nm excitation laser with a fixed excitation power of 100 mW was attached to a motorized stage that allowed to scan the sample below the microscope setup. We recorded the spectra of the Er,Yb:$NaYF_4$ nanoparticles in 50 μm steps. It took 60 s to record each spectrum, and the total scan duration was of 1 h. We did not observe any reduction of the emission intensity during the excitation with the 980 nm laser at a particular position of the setup, and this could be attributed to a possible heating of the nanoparticles. Thus, the power of the excitation laser we used was low enough to avoid the introduction of any artifact on the mapping of the temperature distribution in graphene. **Figure 3C** shows the temperature profile measured from the heating spot (corresponding to the 0 position) to the external part of the film along the horizontal direction and **Figure 3D** represents 2D temperature contour map of experimental data. The temperature decreased slowly along this direction, dropping down from 313.0 to 300.5 K. We were able to detect temperature changes as small as 0.2 K, smaller than the one predicted by the thermal resolution calculated from the thermal sensitivity (see **Figure S2**).

To contrast these results, the temperature distribution on the glass substrate was numerically analyzed by a finite element method (FEM) based on the commercial software COMSOL Multiphysics. The simulation was performed in a three-dimensional (3D) geometry using the heat transfer model for a steady-state study. To model the experiment, the computational domains were defined by two attached blocks which represent the glass substrate and the deposited graphene layer. The glass block used had an area of 10 × 10 mm^2, and a height of 100 μm. The graphene block was constructed with an area of 10 × 10 mm^2, and a height of 1 μm, based on the mean thickness value determined for the graphene film. In order to assign the laser beam as a heating source, a cylindrical domain (9 μm diameter, 1 μm height) was additionally created in the middle of the graphene domain corresponding to the waist of the pumping laser. A triangular mesh was defined with a well-defined size (minimum 1 μm) within the small domain (the cylindrical heat source domain) and a coarser size (maximum 1 mm) within the big domains (glass and graphene domains). To solve the heat transfer problem in the stationary state, the following thermal conductivity values of the materials were assigned to the corresponding domains: $k = 3{,}100$ W m^{-1} K^{-1} for graphene (Pop et al., 2012), and $k = 1.38$ W m^{-1} K^{-1} for the silica glass (Bansal and Doremus, 2013). The heating source was introduced to the cylindrical graphene domain with an overall heat transfer rate of 100 mW. The boundary conditions were specified with a convective heat flux in all the boundaries in which a convection coefficient (h) was determined from the best fit to the measured temperature distribution. The value of h obtained was 80 W/m^2 K, which is reasonable for the natural convection conditions taking place in the experiment.

Figure 3E shows the heat gradient calculated within the approximate range of 300 and 314 K, which closely matches the experimental results. The exponential decay trend deduced from this model is followed by the temperature profile determined experimentally with the luminescent nanoparticles. The small discrepancies that can be observed between the two profiles might be attributed to the fact that the thickness of the deposited graphene layer was not homogeneous, and also to the grain boundaries generated in this kind of films, as well as to the poor bonding between the graphene film and the glass slide, parameters that are critical in a heat transfer process, while these factors were idealized in the simulation. Also, in the model, the thermal conductivity of graphene was assumed to be isotropic whereas this might have an anisotropic behavior. Finally, by switching on the 980 nm emitting laser only during the time required to record the luminescence in each point, it would produce even more precise values of temperature. Nevertheless, and despite these considerations, the thermal gradient we measured using the Er,Yb:$NaYF_4$ nanoparticles followed the same trend than the simulated one.

As previously reported in the literature (Vetrone et al., 2010; Fischer et al., 2011), we believe that, by internalizing these luminescent nanoparticles on living cells, with the required suitable chemical functionalization of their surfaces as prior steps, thermal contour maps would also be obtained by *in vitro* procedures with the same thermal sensitivity, allowing for the illustration of the internal temperature gradients in the cells.

CONCLUSION

In summary, we synthesized Er,Yb:$NaYF_4$ nanoparticles with a microwave-assisted solvothermal method at lower temperatures and reaction times than previously reported methods. Furthermore, this synthesis method allowed to produce the α- and β phases of Er,Yb:$NaYF_4$ separately, avoiding the production of mixtures and avoiding also the use of organic solvents and ligands not miscible with water or difficult to eliminate after the reaction. An additional advantage of this synthesis method is that the produced nanoparticles are hydrophilic and can be dispersed in water or other biological compatible fluids without requiring any post-growth chemical functionalization procedure.

We analyzed the temperature dependence of the upconversion emission of these nanoparticles for their use as luminescent nanothermometers. We observed that nanoparticles with bigger sizes possess higher thermal sensitivities. Their thermal sensing capabilities were proved by determining the temperature distribution induced by the light to heat conversion generated by a graphene layer deposited on a microscope slide cover glass when illuminated with a laser emitting at 808 nm. With this experiment we wanted to show that these nanoparticles can be used to monitor the temperature increase generated by graphene and derivatives when illuminated with a laser, one of the most promising techniques nowadays for tumor

treatment by hyperthermia. We believe that by using the suitable chemical functionalization steps, these nanoparticles can be internalized in living cells to visualize their internal temperature distribution maps through *in vitro* procedures with a similar thermal resolution.

AUTHOR CONTRIBUTIONS

All authors listed have made a substantial, direct and intellectual contribution to the work, and approved it for publication.

FUNDING

This work was supported by the Spanish Government under Projects No. MAT2013-47395-C4-4-R, and TEC2014-55948-R, by Catalan Authority under Project No. 2014SGR1358, and by CMST COST Action CM1403. OS is supported by Catalan Government through the fellowship 2015FI_B2 00136.

ACKNOWLEDGMENTS

FD acknowledges additional support through the ICREA Academia awards 2010ICREA-02 for excellence in research.

SUPPLEMENTARY MATERIAL

The Supplementary Material for this article can be found online at: https://www.frontiersin.org/articles/10.3389/fchem.2019.00088/full#supplementary-material

REFERENCES

Balabhadra, S., Debasu, M. L., Brites, C. D. S., Ferreira, R. A. S., and Carlos, L. D. (2017). Upconverting nanoparticles working as primary thermometers in different media. *J. Phys. Chem. C* 121, 13962–13968. doi: 10.1021/acs.jpcc.7b04827

Bansal, N. P., and Doremus, R. H. (2013). *Handbook of Glass Properties*. Orlando, FL: Academic Press Inc.

Benayas, A., Ren, F., Carrasco, E., Marzal, V., del Rosal, B., Gonfa, B. A., et al. (2015). PbS/CdS/ZnS quantum dots: a multifunctional platform for *in vivo* near-infrared low-dose fluorescence imaging. *Adv. Funct. Mater.* 25, 6650–6659. doi: 10.1002/adfm.201502632

Bomm, J., Günter, C., and Stumpe, J. (2012). Synthesis and optical characterization of thermosensitive, luminescent gold nanodots. *J. Phys. Chem. C* 116, 81–85. doi: 10.1021/jp206260r

Brites, C. D., Lima, P. P., Silva, N. J., Millán, A., Amaral, V. S., Palacio, F., et al. (2012). Thermometry at the nanoscale. *Nanoscale* 4:4799. doi: 10.1039/c2nr30663h

Cerón, E. N., Ortgies, D. H., Del Rosal, B., Ren, F., Benayas, A., Vetrone, F., et al. (2015). Hybrid nanostructures for high-sensitivity luminescence nanothermometry in the second biological window. *Adv. Mater.* 27, 4781–4787. doi: 10.1002/adma.201501014

Chen, X., Wang, W., Chen, X., Bi, J., Wu, L., Li, Z., et al. (2009). Microwave hydrothermal synthesis and upconversion properties of $NaYF_4$:Yb^{3+}, Tm^{3+} with microtube morphology. *Mater. Lett.* 63, 1023–1026. doi: 10.1016/j.matlet.2009.01.075

Cheng, L., Wang, C., and Liu, Z. (2013). Upconversion nanoparticles and their composite nanostructures for biomedical imaging and cancer therapy. *Nanoscale* 5, 23–37. doi: 10.1039/C2NR32311G

Diao, S., Hong, H., Antaris, A. L., Blackburn, J. L., Cheng, K., Cheng, Z., et al. (2015). Biological imaging without autofluorescence in the second near-infrared region. *Nano Res.* 8, 3027–3034. doi: 10.1007/s12274-015-0808-9

Dong, B., Hua, R. N., Cao, B. S., Li, Z. P., He, Y. Y., Zhang, Z. Y., et al. (2014). Size dependence of the upconverted luminescence of NaYF4:Er,Yb microspheres for use in ratiometric thermometry. *Phys. Chem. Chem. Phys.* 16, 20009–20012. doi: 10.1039/C4CP01966K

Du, P., Luo, L., Li, W., Yue, Q., and Chen, H. (2014). Optical temperature sensor based on upconversion emission in Er-doped ferroelectric $0.5Ba(Zr_{0.2}Ti_{0.8})O_3$-$0.5(Ba_{0.7}Ca_{0.3})TiO_3$ ceramic. *Appl. Phys. Lett.* 104, 2–6. doi: 10.1063/1.4871378

Fischer, L. H., Harms, G. S., and Wolfbeis, O. S. (2011). Upconverting nanoparticles for nanoscale thermometry. *Angew. Chem. Int. Ed.* 50, 4546–4551. doi: 10.1002/anie.201006835

Graham, E. M., Iwai, K., Uchiyama, S., de Silva, A. P., Magennis, S. W., and Jones, A. C. (2010). Quantitative mapping of aqueous microfluidic temperature with sub-degree resolution using fluorescence lifetime imaging microscopy. *Lab Chip* 10, 1267–1273. doi: 10.1039/b924151e

Granados-Reyes, J., Salagre, P., and Cesteros, Y. (2014). Effect of microwaves, ultrasounds and interlayer anion on the hydrocalumites synthesis. *Microporous Mesoporous Mater.* 199, 117–124. doi: 10.1016/j.micromeso.2014.08.004

Haase, M., and Schäfer, H. (2011). Upconverting nanoparticles. *Angew. Chem. Int. Ed.* 50, 5808–5829. doi: 10.1002/anie.201005159

Han, B., Zhang, Y. L., Chen, Q. D., and Sun, H. B. (2018). Carbon-based photothermal actuators. *Adv. Funct. Mater.* 1802235, 1–23. doi: 10.1002/adfm.201802235

Hannecart, A., Stanicki, D., Vander Elst, L., Muller, R. N., Lecommandoux, S., Thévenot, J., et al. (2015). Nano-thermometers with thermo-sensitive polymer grafted USPIOs behaving as positive contrast agents in low-field MRI. *Nanoscale* 7, 3754–3767. doi: 10.1039/C4NR07064J

Jaque, D., and Vetrone, F. (2012). Luminescence nanothermometry. *Nanoscale* 4:4301. doi: 10.1039/c2nr30764b

Jiang, S., Zeng, P., Liao, L., Tian, S., Guo, H., Chen, Y., et al. (2014). Optical thermometry based on upconverted luminescence in transparent glass ceramics containing $NaYF_4$:Yb^{3+}/Er^{3+} nanocrystals. *J Alloys Compounds* 617, 538–541. doi: 10.1016/j.jallcom.2014.08.080

Komarneni, S., Roy, R., and Li, Q. H. (1992). Microwave-hydrothermal synthesis of ceramic powders. *Mater. Res. Bull.* 27, 1393–1405. doi: 10.1016/0025-5408(92)90004-J

Krämer, K. W., Biner, D., Frei, G., Güdel, H. U., Hehlen, M. P., and Lüthi, S. R. (2004). Hexagonal sodium yttrium fluoride based green and blue emitting upconversion phosphors. *Chem. Mater.* 16, 1244–1251. doi: 10.1021/cm031124o

Lee, J., and Kotov, N. A. (2007). Thermometer design at the nanoscale. *Nano Today* 2, 48–51. doi: 10.1016/S1748-0132(07)70019-1

Li, H., Dong, H., Yu, M., Liu, C., Li, Z., Wei, L., et al. (2017). NIR ratiometric luminescence detection of pH fluctuation in living cells with hemicyanine derivative-assembled upconversion nanophosphors. *Anal. Chem.* 89, 8863–8869. doi: 10.1021/acs.analchem.7b01324

Maestro, L. M., Haro-González, P., Sánchez-Iglesias, A., Liz-Marzán, L. M., García Solé, J., and Jaque, D. (2014). Quantum dot thermometry evaluation of geometry dependent heating efficiency in gold nanoparticles. *Langmuir* 30, 1650–1658. doi: 10.1021/la403435v

Maestro, L. M., Rodríguez, E. M., Rodríguez, F. S., la Cruz, M. C., Juarranz, A., Naccache, R., et al. (2010). CdSe quantum dots for two-photon fluorescence thermal imaging. *Nano Lett.* 10, 5109–5115. doi: 10.1021/nl1036098

Mi, C., Tian, Z., Cao, C., Wang, Z., Mao, C., and Xu, S. (2011). Novel microwave-assisted solvothermal synthesis of $NaYF_4$: Yb,Er upconversion nanoparticles and their application in cancer cell imaging. *Langmuir* 27:14632–14637. doi: 10.1021/la204015m

Muniz, F. T., Miranda, M. A., Morilla Dos Santos, C., and Sasaki, J. M. (2016). The Scherrer equation and the dynamical theory of X-ray diffraction. *Acta Crystallograph. A Found Adv.* 72, 385–390. doi: 10.1107/S205327331600365X

Okabe, K., Inada, N., Gota, C., Harada, Y., Funatsu, T., and Uchiyama, S. (2012). Intracellular temperature mapping with a fluorescent polymeric thermometer

and fluorescence lifetime imaging microscopy. *Nat. Commun.* 3, 705–709. doi: 10.1038/ncomms1714

Palo, E., Pihlgren, L., Tuomisto, M., Laihinen, T., Hyppänen, I., Kankare, J., et al. (2016). Up-conversion luminescence of the $NaYF_4$: Yb^{3+}, Er^{3+} nanomaterials prepared with the solvothermal synthesis. *Opt. Mater.* 59, 4–9. doi: 10.1016/j.optmat.2016.02.043

Patterson, A. L. (1939). The Scherrer formula for X-ray particle size determination. *Phys. Rev.* 56, 978–982. doi: 10.1103/PhysRev.56.978

Peterman, E. J., Gittes, F., and Schmidt, C. F. (2003). Laser-induced heating in optical traps. *Biophys. J.* 84, 1308–1316. doi: 10.1016/S0006-3495(03)74946-7

Piñol, R., Brites, C. D., Bustamante, R., Martínez, A., Silva, N. J., Murillo, J. L., et al. (2015). Joining time-resolved thermometry and magnetic-induced heating in a single nanoparticle unveils intriguing thermal properties. *ACS Nano* 9, 3134–3142. doi: 10.1021/acsnano.5b00059

Pop, E., Varshney, V., and Roy, A. K. (2012). Thermal properties of graphene: fundamentals and applications. *MRS Bull.* 37, 1273–1281. doi: 10.1557/mrs.2012.203

Rapaport, A., Milliez, J., Bass, M., Cassanho, A., and Jenssen, H. (2006). Review of the properties of up-conversion phosphors for new emissive displays. *IEEE/OSA J. Display Technol.* 2, 68–78. doi: 10.1109/JDT.2005.863781

Sánchez, S., Salagre, P., and Cesteros, Y. (2013). Ultrasounds and microwave-assisted synthesis of mesoporous hectorites. *Microporous Mesoporous Mater.* 171, 24–34. doi: 10.1016/j.micromeso.2013.01.001

Savchuk, O. A., Carvajal, J., Massons, J., Aguiló, M., and Díaz, F. (2016). Determination of photothermal conversion efficiency of graphene and graphene oxide through an integrating sphere method. *Carbon* 103, 134–141. doi: 10.1016/j.carbon.2016.02.075

Sedlmeier, A., Achatz, D. E., Fischer, L. H., Gorris, H. H., and Wolfbeis, O. S. (2012). Photon upconverting nanoparticles for luminescent sensing of temperature. *Nanoscale* 4, 7090–7096. doi: 10.1039/c2nr32314a

Shang, L., Stockmar, F., Azadfar, N., and Nienhaus, G. U. (2013). Intracellular thermometry by using fluorescent gold nanoclusters. *Angew. Chem. Int. Ed.* 52, 11154–11157. doi: 10.1002/anie.201306366

Som, S., Das, S., Yang, C.-Y., and Lu, C.-H. (2016). Enhanced upconversion of $NaYF_4$:Er^{3+}/Yb^{3+} phosphors prepared via the rapid microwave-assisted hydrothermal route at low temperature: phase and morphology control. *Opt. Lett.* 41:464. doi: 10.1364/OL.41.000464

Steinegger, A., Klimant, I., and Borisov, S. M. (2017). Purely organic dyes with thermally activated delayed fluorescence—a versatile class of indicators for optical temperature sensing. *Adv. Opt. Mater.* 5, 1–13. doi: 10.1002/adom.201700372

Tong, L., Li, X., Zhang, J., Xu, S., Sun, J., Cheng, L., et al. (2017). Microwave-assisted hydrothermal synthesis, temperature quenching and laser-induced heating effect of hexagonal microplate -$NaYF_4$: Er^{3+}/Yb^{3+} microcrystals under 1550 Nm. *Sensors Actuators B Chem.* 246, 175–180. doi: 10.1016/j.snb.2017.02.030

Vetrone, F., Naccache, R., Zamarrón, A., Juarranz de la Fuente, A., Sanz-Rodríguez, F., Martinez Maestro, L., et al. (2010). Temperature sensing using fluorescent nanothermometers. *ACS Nano* 4, 3254–3258. doi: 10.1021/nn100244a

Vlaskin, V. A., Janssen, N., van Rijssel, J., Beaulac, R., and Gamelin, D. R. (2010). Tunable dual emission in doped semiconductor nanocrystals. *Nano Lett.* 10, 3670–3674. doi: 10.1021/nl102135k

Wade, S. A., Collins, S. F., and Baxter, G. W. (2003). Fluorescence intensity ratio technique for optical fiber point temperature sensing. *J. Appl. Phys.* 94, 4743–4756. doi: 10.1063/1.1606526

Wang, F., Han, Y., Lim, C. S., Lu, Y., Wang, J., Xu, J., et al. (2010). Simultaneous phase and size control of upconversion nanocrystals through lanthanide doping. *Nature* 463, 1061–1065. doi: 10.1038/nature08777

Wang, H. Q., and Nann, T. (2009). Monodisperse upconverting nanocrystals by microwave-assisted synthesis. *ACS Nano* 3, 3804–3808. doi: 10.1021/nn9012093

Wang, M., Zhu, Y., and Mao, C. (2015). Synthesis of NIR-responsive $NaYF_4$:Yb,Er upconversion fluorescent nanoparticles using an optimized solvothermal method and their applications in enhanced development of latent fingerprints on various smooth substrates. *Langmuir* 31, 7084–7090. doi: 10.1021/acs.langmuir.5b01151

Wawrzynczyk, D., Piatkowski, D., Mackowski, S., Samoc, M., and Nyk, M. (2015). Microwave-assisted synthesis and single particle spectroscopy of infrared down- and visible up-conversion in Er^{3+} and Yb^{3+} co-doped fluoride nanowires. *J. Mater. Chem. C* 3, 5332–5338. doi: 10.1039/C5TC00468C

Wu, K., Cui, J., Kong, X., and Wang, Y. (2011). Temperature dependent upconversion luminescence of YbEr codoped $NaYF_4$ nanocrystals. *J. Appl. Phys.* 110, 3–9. doi: 10.1063/1.3631822

Xie, T. R., Liu, C. F., and Kang, J. S. (2017). Dye-based mito-thermometry and its application in thermogenesis of brown adipocytes. *Biophys. Rep.* 3, 85–91. doi: 10.1007/s41048-017-0039-6

Zheng, S., Chen, W., Tan, D., Zhou, J., Guo, Q., Jiang, W., et al. (2014). Lanthanide-doped $NaGdF_4$ core–shell nanoparticles for non-contact self-referencing temperature sensors. *Nanoscale* 6, 5675–5679. doi: 10.1039/C4NR00432A

Zhou, J., Chen, G., Wu, E., Bi, G., Wu, B., Teng, Y., et al. (2013). Ultrasensitive polarized up-conversion of Tm^{3+}-Yb^{3+} doped β-$NaYF_4$ single nanorod. *Nano Lett.* 13, 2241–2246. doi: 10.1021/nl400807m

Zhu, X., Feng, W., Chang, J., Tan, Y. W., Li, J., Chen, M., et al. (2016). Temperature-feedback upconversion nanocomposite for accurate photothermal therapy at facile temperature. *Nat. Commun.* 7, 1–10. doi: 10.1038/ncomms10437

Zhu, Y., Murali, S., Cai, W., Li, X., Suk, J. W., Potts, J. R., et al. (2010). Graphene and graphene oxide: synthesis, properties, and applications. *Adv. Mater.* 22, 3906–3924. doi: 10.1002/adma.201001068

Conflict of Interest Statement: The authors declare that the research was conducted in the absence of any commercial or financial relationships that could be construed as a potential conflict of interest.

Copyright © 2019 Savchuk, Carvajal, Cesteros, Salagre, Nguyen, Rodenas, Massons, Aguiló and Díaz. This is an open-access article distributed under the terms of the Creative Commons Attribution License (CC BY). The use, distribution or reproduction in other forums is permitted, provided the original author(s) and the copyright owner(s) are credited and that the original publication in this journal is cited, in accordance with accepted academic practice. No use, distribution or reproduction is permitted which does not comply with these terms.

frontiers in Chemistry

ORIGINAL RESEARCH
published: 28 January 2019
doi: 10.3389/fchem.2019.00021

Revisiting the Growth of Black Phosphorus in Sn-I Assisted Reactions

Dongya Wang[1], Peng Yi[1], Lin Wang[1], Lu Zhang[1], Hai Li[1], Min Lu[1], Xiaoji Xie[1]*, Ling Huang[1] and Wei Huang[1,2]*

[1] Key Laboratory of Flexible Electronics (KLOFE), Institute of Advanced Materials, Nanjing Tech University, Nanjing, China, [2] Shaanxi Institute of Flexible Electronics, Northwestern Polytechnical University, Xi'an, China

Black phosphorus, an emerging layered material, exhibits promising applications in diverse fields, ranging from electronics to optics. However, controlled synthesis of black phosphorus, particularly its few-layered counterparts, is still challenging, which should be due to the unclear growth mechanism of black phosphorus. Here, taking the most commonly used Sn-I assisted synthesis of black phosphorus as an example, we propose a growth mechanism of black phosphorus crystals by monitoring the reactions and analyzing the as-synthesized products. In the proposed mechanism, $Sn_{24}P_{19.3}I_8$ is the active site for the growth of black phosphorus, and the black phosphorus crystals are formed with the assistance of SnI_2, following a polymerization-like process. In addition, we suggest that all Sn-I assisted synthesis of black phosphorus should share the same reaction mechanism despite the differences among Sn-I containing additives. Our results shown here should shed light on the controlled synthesis of black phosphorus and facilitate further applications of black phosphorus.

Keywords: black phosphorus, growth mechanism, tin iodide, chemical vapor transport, 2D materials

OPEN ACCESS

Edited by:
Luís António Dias Carlos, University of Aveiro, Portugal

Reviewed by:
Amir Pakdel, Trinity College Dublin, Ireland
Zhong Jin, Nanjing University, China

****Correspondence:***
Min Lu
iammlv@njtech.edu.cn
Xiaoji Xie
iamxjxie@njtech.edu.cn

Specialty section:
This article was submitted to Inorganic Chemistry, a section of the journal Frontiers in Chemistry

Received: *04 December 2018*
Accepted: *10 January 2019*
Published: *28 January 2019*

Citation:
Wang D, Yi P, Wang L, Zhang L, Li H, Lu M, Xie X, Huang L and Huang W (2019) Revisiting the Growth of Black Phosphorus in Sn-I Assisted Reactions. Front. Chem. 7:21. doi: 10.3389/fchem.2019.00021

INTRODUCTION

With the rapid development of two-dimensional materials, orthorhombic black phosphorus (BP), assembled by puckered phosphorus layers of interlinked six-membered rings via van der Waals interactions, recently has attracted much research enthusiasm due to its layer-number-dependent properties (Hirsch and Hauke, 2018; Liu H. et al., 2018; Liu Y. et al., 2018). Specifically, few-layered BP possesses tunable band gap, ranging from 0.3 to 2.0 eV (Xia et al., 2014), and high carrier mobility ($\sim$1,000 $cm^2V^{-1}s^{-1}$) (Li et al., 2014), which makes it promising for diverse applications, including field effect transistor, battery, sensor, and electrocatalyst (Liu et al., 2015; Zhang Y. et al., 2017; Hu et al., 2018). Despite the outstanding properties of BP and the recent inspiring studies, the exploration of the properties of BP and corresponding applications are still constrained to some extent because of the difficulties in synthesizing BP and its layered counterparts (Hu et al., 2018; Zhang et al., 2018).

In fact, BP is a thermodynamically stable form of phosphorus but does not exist naturally. Formerly, BP was synthesized by transforming red phosphorus or white phosphorus under harsh conditions (Bridgman, 1914, 1935, 1948). It was until 2007 that a simple synthetic approach based on Sn-I assisted chemical vapor transport reactions was developed for producing BP crystals in high quality and high yield (Lange et al., 2007). In this method, BP is synthesized, in an evacuated ampoule, by programmed heating of red phosphorus with the

mineralizers (e.g., Sn/SnI_4). It should be emphasized that the mineralizers, particularly Sn and I elements, are decisive in this chemical vapor transport based method. Currently, this Sn-I assisted method is the most commonly used strategy for the large-scale preparation of high quality BP crystals, which indeed boosts both the scientific research and technological development of BP (Nilges et al., 2008; Köpf et al., 2014). Nevertheless, controlled synthesis of BP, particularly the synthesis of uniform thin BP film (few-layered BP), has not been achieved by chemical vapor transport based methods yet (Yang et al., 2015; Smith et al., 2016).

In order to realize controlled synthesis of BP, it is crucial to fully understand the corresponding formation mechanisms. Unfortunately, the formation mechanisms of BP in the Sn-I assisted method are still unclear, although several efforts have been devoted to revealing the detailed formation processes (Zhao et al., 2016a,b; Li et al., 2017; Zhang Z. et al., 2017; Shriber et al., 2018). Furthermore, the currently proposed formation mechanisms are different from each other, although they share some opinions. For example, in 2016, a molten alloy based mechanism was proposed (Zhao et al., 2016a). In this mechanism, BP crystals were believed to precipitate from the molten alloy of red phosphorus and metallic Sn when the temperature decreased. At almost the same time, a phase-transfer mechanism was proposed, in which BP crystals were proposed to be transformed from Hittorf's phosphorus with the assistance of a certain P-Sn-I ternary compound (Zhang Z. et al., 2017). Later on, BP crystals were suggested to grow, obeying a vapor-solid-solid mechanism, through the diffusion of excess P atoms from a $Sn_{24}P_{22-x}I_8$ ($x \approx 2.7$) intermediate compound (Li et al., 2017). In addition to the studies based on experimental observations, another BP formation pathway was advised recently according to first-principle calculations (Shriber et al., 2018). According to the density functional theory calculations, BP is favorably formed, in the presence of Sn-I containing mineralizer at high temperature and pressure, by a series of additions of P_4 molecules in a polymerization-like process. Collectively, more efforts are desired to elucidate the formation mechanisms of BP crystals in the Sn-I assisted synthetic method.

In this study, taking the previous studies into account, we propose a new formation mechanism of BP crystals in the Sn-I assisted reaction according to a series of reaction observations and product characterization. In our proposed mechanism, the Sn and I containing mineralizers first decompose, forming SnI_2 and Sn, and then the decomposed compounds react with phosphorus vapor at elevated temperature to form $Sn_{24}P_{19.3}I_8$. Subsequently, the $Sn_{24}P_{19.3}I_8$ molecules transport to and partially deposit at the zone with slightly low temperature (∼550–500°C) during the cooling stage, generating the growth sites for BP crystals. The $Sn_{24}P_{19.3}I_8$ molecules at the deposition zone can decompose to release SnI_2, P_4, and even P_2 at the temperature of ∼550–500°C, and thus are highly active. Meanwhile, the remaining SnI_2 in the gas phase, functioning as a mineralizer, can transport P_4 molecules to the growth sites by forming a Sn-P-I intermediate compound, yielding BP crystals in a polymerization-like process. In addition, we suggest that the Sn-I assisted synthesis of BP crystals should have the same growth processes, although different Sn and I containing additives can be used as mineralizers. We believe that this study can improve the understanding of BP synthesis, and facilitate controlled synthesis of BP for future applications.

EXPERIMENTAL SECTION

Materials

Tin powder (Sn, 99.99%) and iodine granule (I_2, AR, 99.8%) were purchased from Aladdin (Shanghai, China). Red phosphorus (99.999%, metals basis) was purchased from Alfa Aesar. Acetic acid (AR), acetic anhydride (AR), toluene (AR), and other chemicals were purchased from Shanghai Lingfeng Chemical Reagent Co., Ltd. All chemicals were used as received without further purification unless otherwise noted.

Synthesis of SnI_4, SnI_2, Sn_4P_3, $Sn_{24}P_{19.3}I_8$, SnIP, and Black Phosphorus (BP)

Synthesis of SnI_4 (Köpf et al., 2014)

To a mixture of acetic acid (25 mL) and acetic anhydride (25 mL), 0.5 g Sn powder and 2 g I_2 were added. The resulting mixture was refluxed at 120°C for 90 min, during which the Sn powder completely disappeared. After the mixture was cooled to room temperature, orange-colored SnI_4 crystals appeared and were collected. The obtained SnI_4 crystals were recrystallized in chloroform for further use.

Synthesis of SnI_2

Typically, a mixture of SnI_4 (1.2956 g) and Sn (246.2 mg) powders (molar ratio: 1:1) was loaded in an evacuated silica ampoule (∼10 cm in length and ∼10 mm in inner diameter). Subsequently, the ampoule was heated to 400°C within 1 h in a muffle furnace, annealed for 5 h, and cooled down to room temperature naturally. The SnI_2 powders, on the wall of the silica ampoule, were collected for further use.

Synthesis of Sn_4P_3

A mixture of grounded red phosphorus powder (72 mg) and tin powder (364 mg) was sealed in an evacuated silica ampoule (∼10 cm in length and ∼10 mm in inner diameter). The sealed ampoule was then annealed at 400°C for 8 h in a muffle furnace, and cooled to 200°C in 2 h. Finally, the ampoule was naturally cooled down to room temperature and the resulting Sn_4P_3 was collected.

Synthesis of $Sn_{24}P_{19.3}I_8$ and SnIP

A mixture of tin powder, red phosphorus powder, and I_2, with stoichiometric ratio, was sealed in an evacuated silica ampoule. Subsequently, the sealed ampoule was heated to 400°C within 40 min, kept for 10 h, and slowly cooled down to room temperature in 75 h. The ternary compounds were then collected from the silica ampoule.

Synthesis of Black Phosphorus (BP)

In a typical experiment, a mixture of red phosphorus (300 mg) and mineralizers (SnI_4: 6 mg, Sn: 12 mg) was sealed in an evacuated silica ampoule (∼10 cm in length and ∼10 mm in inner diameter). The ampoule was placed horizontally in the center zone of a muffle box furnace with a viewing window. It

should be noted that the temperature at the center of the furnace is slightly different from that near the wall. The temperature of the furnace was increased from room temperature to 650°C in 1 h, and then decreased to 550°C within 1 h. Afterwards, the temperature was further decreased to 500°C in 8 h, and then to 200°C in 4 h. Finally, the furnace was turned off for natural cooling to room temperature. After the reaction, BP crystals were collected from the ampoule, washed with hot toluene (∼60°C) for three times until the toluene was colorless, dried at N_2 atmosphere and stored at ambient environment.

BP crystals were also prepared in the presence of different mineralizers, such as $Sn_{24}P_{19.3}I_8$ (21.6 mg), SnIP (10.6 mg), a mixture of Sn and I_2 (Sn: 4.5–14 mg, I_2: 4.8 mg) and a mixture of SnI_2 and Sn (SnI_2: 7.1 mg, Sn: 11.2 mg), by keeping other conditions identical. Notably, despite the differences among varied mineralizers, the molar amount of I element was kept the same (0.038 mmol) when different mineralizers were used. All synthesis reactions, including the control experiments, were carried out under the same temperature program unless otherwise noted. To record the reaction processes, photographs were taken from the viewing window of the furnace at different stages during the reaction.

CHARACTERIZATION

Powder X-ray diffraction (XRD) patterns were recorded using a Rigaku Smartlab (9 kW) X-ray diffractometer with Cu Kα radiation (λ = 1.5406 Å). Raman spectra were acquired on a HR Evaluation spectrometer (Horiba, Confocal Raman Microscope) with a 532 nm laser. Thermogravimetric (TG) analysis was performed on a METTLER TGA2 under the N_2 atmosphere at a heating rate of 10°C/min. Scanning electron microscopy (SEM) image and corresponding energy dispersive X-Ray spectroscopy (EDX) analysis were carried out in a JSM-7800F (JEOL) scanning electron microscope. Low resolution transmission electron microscopy (TEM) measurements were carried out on a JEM-1400 transmission electron microscope at an acceleration voltage of 120 kV. High resolution TEM, dark-field scanning transmission electron microscopy (STEM), and corresponding EDX measurements were conducted on a 2100F transmission electron microscope at an acceleration voltage of 200 kV. Photographs were taken by a digital camera.

RESULTS AND DISCUSSION

Characterization of BP Crystals

Prior to studying the growth process of BP crystals, we first confirmed that high quality BP crystals can be obtained under our synthetic conditions. On a separate note, considering that the mixture of SnI_4 and Sn is one of the most commonly used mineralizers, we here chose the SnI_4/Sn mixture as a representative mineralizer in the following sets of experiments. As shown in **Figure 1A**, the obtained bulk BP crystals present a flower-like (radial) shape, with many sheetlike branches, on a centimeter scale and black color with metallic luster. Meanwhile, as revealed by the scanning electron microscopy (SEM) image, the BP crystal has a layered structure (**Figure 1B**), exhibiting the essential feature as a layered material (**Figure 1C**, upper panel). Further powder X-ray diffraction (XRD) analysis shows that the as-synthesized BP crystals give three main diffraction peaks at ∼16, 34, and 52° (**Figure 1D**). The XRD pattern reveals that the BP crystals are in orthorhombic phase with excellent crystallinity, while the three diffraction peaks indicate that the crystals grow in a highly oriented manner. Consistently, in the Raman spectrum, three characteristic peaks, at ∼361, 438, and 466 cm^{-1}, were observed (**Figure 1E**), which can be attributed to the characteristic A_g^1, B_{2g}, and A_g^2 modes in the orthorhombic BP lattice (**Figure 1C**, lower panel) (Guo et al., 2015; Ribeiro et al., 2018; Wang et al., 2018). In addition, high resolution transmission electron microscopy analysis of the exfoliated BP sheets, together with the energy dispersive X-Ray spectroscopy (EDX) analysis, shows the good crystallinity and purity of the as-synthesized BP crystals (**Figure S1**). Collectively, orthorhombic BP crystals, with excellent quality, can be successfully synthesized in the presence of the SnI_4/Sn mineralizer under our reaction conditions.

Influence of Mineralizer Composition on the Synthesis of BP Crystals

In order to understand the functions of the Sn-I containing mineralizers in the reactions, we first systematically tuned the molar ratio of Sn and I elements in the mineralizer by changing the amount of Sn. We found that the molar ratio of Sn:I had a threshold at ∼0.9:1, below which almost no BP crystals can be synthesized (**Figure 2A** and **Figure S2**). It should be mentioned that a similar threshold of the Sn:I molar ratio (2:1) was also observed by a previous report (Li et al., 2017), although the reported ratio is slightly different from that we found here. The difference may be due to variations in reaction conditions, including heating process, silica tube, and furnace. In particular, BP crystals with high quality can be obtained in high yield (∼90%) when the molar ratio of Sn:I is in the range from ∼0.9:1 to 3:1 (**Figures 2A,B**). Further increase of the Sn:I ratio can also produce BP crystals, but the yield of BP crystals declines in most cases. For example, when the Sn:I ratio was set at ∼10:1, small-sized BP crystals, scattered on the inner wall of the ampoule, were observed with a large number of side products (**Figure 2B**). These results indicate that the optimal molar element ratio of Sn and I, for preparing high quality BP crystals in high yield under our conditions, is in the range from ∼0.9:1 to 3:1, when the SnI_4/Sn mineralizer is used.

To check whether the Sn:I ratio for BP synthesis is dependent on the types of the Sn-I containing mineralizers, we then employed other commonly used Sn-I containing mineralizers, such as Sn/I_2 and SnI_2/Sn (**Figure S3**), to synthesize BP crystals under the same reaction conditions. As expected, high quality BP crystals can be successfully prepared in the presence of Sn/I_2 or SnI_2/Sn mineralizer if the Sn:I ratio was kept in the range from ∼0.9:1 to 3:1 (**Figure 2B** and **Figure S4**). If the Sn:I ratio was set smaller than ∼0.9:1, the reproducibility of the reaction became poor and few BP crystals were obtained in most cases (**Figure S5**). To further verify the Sn:I ratio, two ternary Sn-P-I compounds, SnIP (**Figure S6**) and $Sn_{24}P_{19.3}I_8$ (**Figure S7**), were

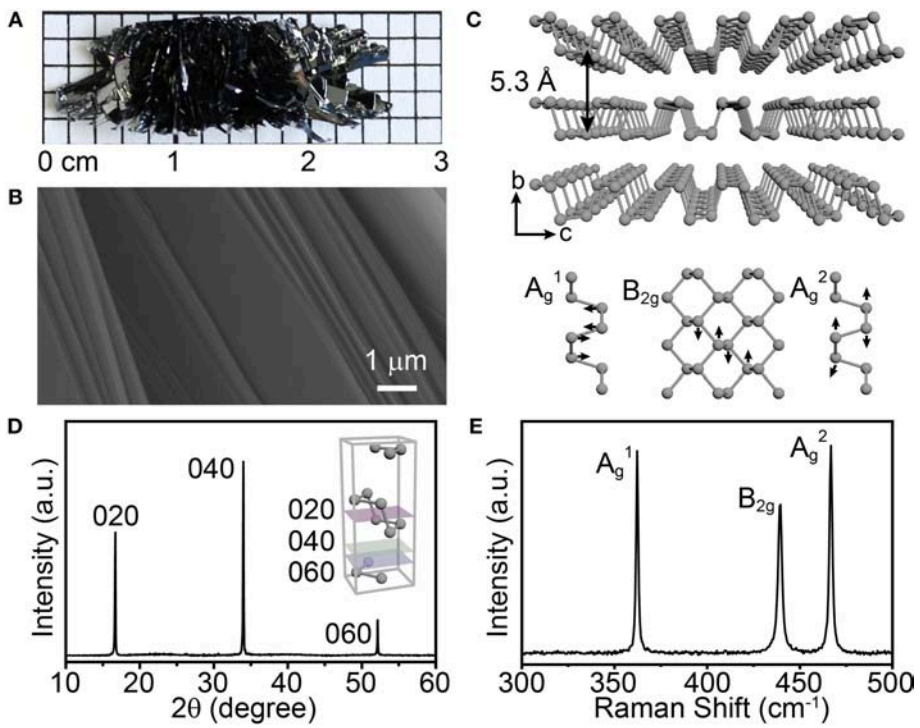

FIGURE 1 | (A) Photo of the as-prepared bulk BP crystals. **(B)** SEM image showing the layered structure of the BP crystal. **(C)** Schematic illustrations of the atomic structure of orthorhombic BP and corresponding vibrational modes in Raman spectroscopy. **(D)** Powder XRD pattern of the obtained BP crystals. Inset: schematic illustration of a crystal cell of orthorhombic BP and its crystal planes. **(E)** Raman spectrum of the as-prepared BP.

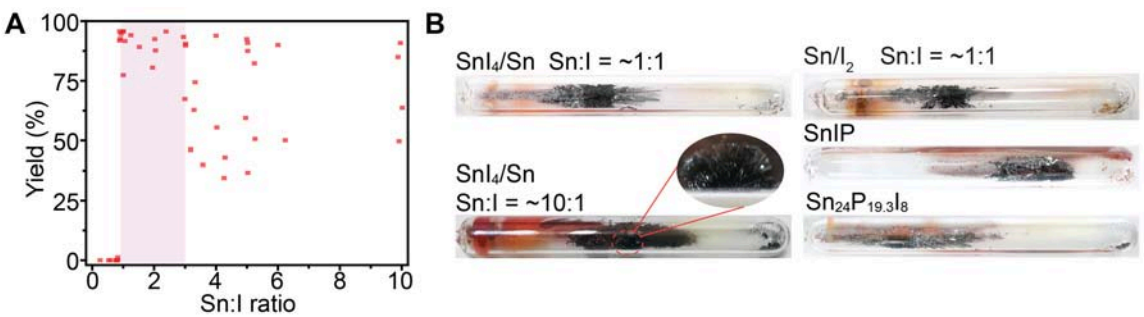

FIGURE 2 | (A) Distribution of the synthetic yield of BP crystals against Sn:I ratio in the SnI_4/Sn assisted reaction. **(B)** Photos of BP crystals in ampoules obtained in the presence of different mineralizers.

applied as mineralizers (Shatruk et al., 1999; Pfister et al., 2016). It should be mentioned that the Sn:I ratio of each Sn-P-I compound is near either the upper or lower limit of the determined range. Similar to other mineralizers, both SnIP and $Sn_{24}P_{19.3}I_8$ can yield centimeter-sized high quality BP crystals (**Figure 2B**) under the same reaction conditions, validating the determined optimum range of Sn:I ratio.

Collectively, these results reveal that the mineralizers, despite the different chemical compositions such as SnI_4/Sn, Sn/I_2, SnI_2/Sn, SnIP, and $Sn_{24}P_{19.3}I_8$, can facilitate the growth of BP crystals if a proper molar ratio of Sn and I elements is applied. Furthermore, according to these results, we can suppose that all Sn-I containing mineralizers should facilitate the formation of BP crystals through the same way.

Growth of BP Crystals and Transformation of Mineralizer

Next, we monitored the synthesis of BP crystals (**Figure 3** and **Figure S8**), by taking *in situ* photos at different stages during the reaction as marked in **Figure 3A**, to reveal the functions of the mineralizer. For comparison, pure red phosphorus and the SnI_4/Sn mineralizer were also sealed solely in ampoules and monitored under the same conditions. As shown in **Figure 3B1**, the solid reactants initially were placed at the right side of

the sealed ampoules. With the increase of the temperature, the SnI_4/Sn mineralizer began to react with red phosphorus, exhibiting some mineralization effects at ∼350°C (**Figure 3B2**, dotted box). When the temperature reached 650°C, almost all reactants including the mineralizer became vapor, leaving small amount of reactants at the original zone, and the whole ampoule exhibited orange color (**Figure 3B3**). Notably, the same orange color was also observed in the ampoule containing only the SnI_4/Sn mineralizer, indicating the orange color comes from the vapor of mineralizer. Finally, the BP crystals appeared at the other side of the ampoule during the decrease of temperature, while some solid remained at the zone where the initial reactants were placed (**Figures 3B5,B6**). Interestingly, in the ampoules containing only the SnI_4/Sn mineralizer, some orange-red colored solid appeared at almost the same position where BP crystals grew (**Figure 3B6**, dotted boxes). In stark contrast, in the absence of the mineralizer, the red phosphorus finally deposited randomly in the ampoules. Furthermore, we observed similar growth processes, with slight differences, when different types of mineralizers, such as Sn/I_2, SnIP, and $Sn_{24}P_{19.3}I_8$, were used (**Figures S9–S11**). These results show that the Sn-I containing mineralizer may first undergo transformation to form certain compounds and then react with phosphorus vapor to help the formation of BP crystals during the reaction.

To gain more insights into the growth process of BP crystals, we then tried to identify the transformation of mineralizer during the reaction. According to the thermogravimetric (TG) analysis (**Figure 3C**) and *in situ* photos (**Figure 3B**), all reactants, except Sn, should become vapor or decompose at 650°C. Comparing the status of pure I_2, SnI_4, and SnI_2 at 650°C (**Figure S12**) with the observation shown in **Figure 3B**, we can deduce that the mineralizer should decompose to form gaseous SnI_2 that exhibits orange color during the reaction. This deduction is also consistent with the previous report in which SnI_2 is believed to be the most thermodynamically stable species in the reaction system at 650°C (Li et al., 2017). Regarding the material remaining at the zone where the initial reactants are placed at 650°C, we believe that it is liquid Sn because the boiling point of Sn is ∼2,600°C (Dean, 1999). In addition, other compounds, including the common Sn-P and Sn-P-I compounds, cannot remain intact at such high temperature (∼650°C) according to the TG analysis (**Figure 3C** and **Figure S13**). Accordingly, in the Sn-I assisted synthesis of BP crystals, we suggest that the Sn-I containing mineralizer should form SnI_2 and Sn during the reaction.

To further verify the transformation of the mineralizer, we heated the SnIP and $Sn_{24}P_{19.3}I_8$ compounds under the same reaction conditions and then analyzed the final compounds (**Figure S14**). As expected, SnI_2 was observed at the place away from the zone where initial compounds were placed. Meanwhile, Sn_4P_3, formed by the reaction of Sn and P during the cooling process, appeared at the zone which originally contains the Sn-I-P compounds. In addition, we also found the presence of SnI_2 on the as-prepared BP crystals. In this set of experiments, the BP crystals, prepared with the assistance of various mineralizers, were collected from the ampoule and then immersed into hot toluene. The toluene, with light yellow color (**Figure S15**), was then distilled, producing a few powders. As characterized by Raman spectroscopy, the powders can be identified as SnI_2 (**Figure S15**).

Taken together, in the Sn-I assisted synthesis of BP crystals, the Sn-I containing mineralizer should first form sufficient SnI_2. Subsequently, the gaseous SnI_2 can react with gaseous phosphorus, forming a certain active Sn-P-I intermediate, and assist the formation of BP crystals.

Active Site Identification and Characterization

In the following set of experiments, we intended to figure out the gaseous Sn-P-I intermediate and growth details of BP crystals by both monitoring the reaction and characterizing the as-synthesized BP crystals. Actually, we observed that BP crystals grew from the bottom of the ampoule at the cooling stage (mainly from 550 to 500°C) in reactions (**Figure 3** and **Figures S8–S11**), and the growth of the crystals apparently exhibited an epitaxial manner. After the reaction, we collected the BP crystals from the ampoule tube and checked their back side which formerly attached on the wall of the ampoule. As shown in **Figures 4A,B**, a distinct intersection point with clear trails can be typically observed, indicating that the point is the starting point for growing BP crystals. Thus, we here suggest that the intersection point should be the active site for the growth of BP crystals. It should be mentioned that similar intersection points were also observed and considered as the nucleation sites for BP growth in previous studies (Zhao et al., 2016b).

Consequently, we analyzed the composition of the intersection point by energy dispersive X-Ray spectroscopy (EDX). At the intersection point of the as-prepared BP crystal, the molar ratio of Sn:I was determined as ∼0.6:1 by EDX (**Figure S16**). After thoroughly washed by hot toluene, as exampled in **Figures 4C–F**, the Sn:I ratio at the intersection point was found as ∼3.1:1 (**Figure S17**). Similarly, for the BP crystals obtained in the presence of $Sn_{24}P_{19.3}I_8$ as a mineralizer, the Sn:I ratio at the intersection point was found as ∼2.9:1 after toluene washing (**Figure S18**). Taking previous studies into account (Zhang et al., 2016; Li et al., 2017), we believe that the $Sn_{24}P_{19.3}I_8$ compound should serve as the active site for the growth of BP crystals.

Besides, in order to find out if there were any other components at the active site, we studied the intersection point of BP by Raman spectroscopy. By comparing the obtained Raman spectra at the intersection point, the presence of Hittorf's phosphorus can be deduced (**Figure S19**). It should be pointed out that we also checked the products just near the intersection point by Raman spectroscopy. Only characteristic Raman peaks of BP crystals were observed (**Figure S19**). These results show that Hittorf's phosphorus may also play a certain role during the growth of BP crystals.

Growth Mechanism of BP Crystals

As discussed in the former parts, in the Sn-I assisted synthesis of BP crystals, SnI_2 should be a critical gaseous compound that may form gaseous intermediate to facilitate the growth of BP. Meanwhile, $Sn_{24}P_{19.3}I_8$ should be the active site on

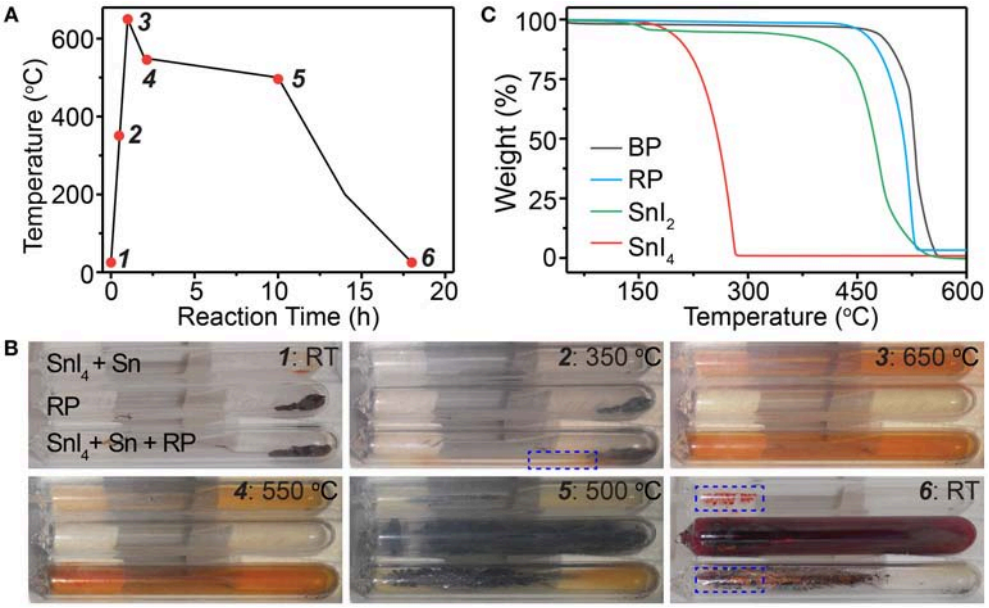

FIGURE 3 | (A) Typical time dependent temperature profile for synthesizing BP crystals and **(B)** corresponding *in situ* photos taken during the synthesis. The red dots in the profile indicate the stages when the photos are taken. **(C)** Thermogravimetric profiles of different compounds. Note that RT and RP denote room temperature and red phosphorus, respectively.

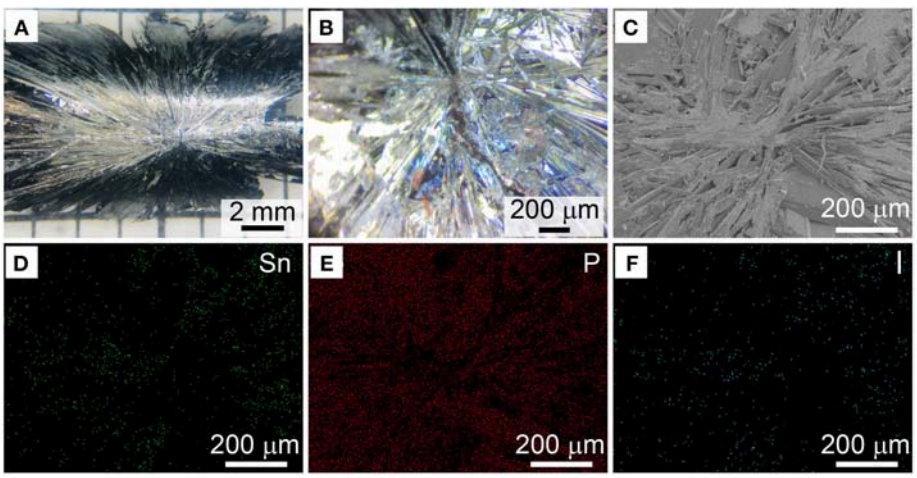

FIGURE 4 | (A) Representative photo of the as-obtained BP crystals with an intersection point. **(B)** Corresponding enlarged photo of the intersection point. **(C)** SEM image of a randomly selected intersection point. **(D–F)** Corresponding elemental mapping of the intersection point shown in **(C)**.

which the BP crystals start to grow. Combining our results, the fundamentals of chemical vapor transport reactions (Binnewies et al., 2012), and previous proposed growth mechanisms of BP crystals together (Zhao et al., 2016a,b; Li et al., 2017; Zhang Z. et al., 2017; Shriber et al., 2018), we here propose the following formation mechanism of BP crystals in the Sn-I assisted reaction (**Figure 5A**).

At the beginning of the Sn-I assisted reaction, temperature increases for reactant sublimation. At this stage, despite different mineralizers, all reactants, placed at the right side of the ampoule in our studies (**Figure 3**), sublime or decompose gradually to generate gaseous SnI_2, gaseous P_4, and liquid Sn. The resulting gaseous SnI_2, gaseous P_4, and liquid Sn can further react to form $Sn_{24}P_{19.3}I_8$ (Equation 1) and also probably some other Sn-P-I compounds at high temperature (e.g., ∼650°C in this study).

$$4SnI_2 + 20Sn + 4.825P_4 \leftrightarrow Sn_{24}P_{19.3}I_8 \quad (1)$$

Notably, in a sealed ampoule, the reaction (Equation 1), at high temperature, can be at equilibrium that is neither reactant-favored nor product-favored. Moreover, synthesis of $Sn_{24}P_{19.3}I_8$

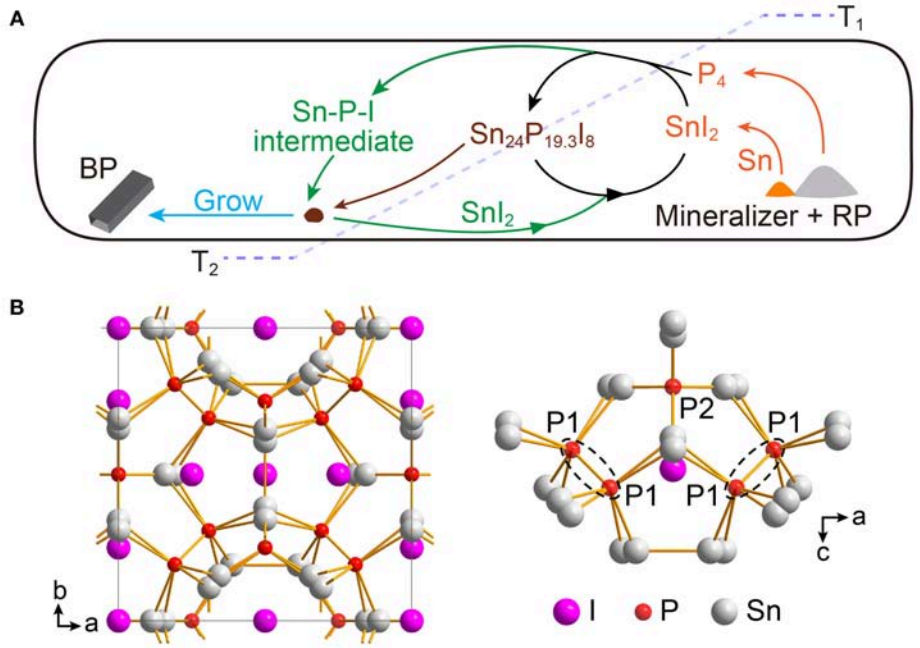

FIGURE 5 | (A) Schematic illustration of the proposed mechanism of BP growth in the Sn-I assisted reaction. The mineralizer and red phosphorus (RP) first form SnI_2, P_4, and Sn at high temperature (T_1) (orange colored arrows). The resulting SnI_2, P_4, and Sn then react to yield $Sn_{24}P_{19.3}I_8$ which can deposit at the place with relatively low temperature (T_2) (brown colored arrow). Subsequently, the BP crystals can grow with the assistance of SnI_2 (green colored arrows). **(B)** Crystal structure of $Sn_{24}P_{19.3}I_8$ where Sn and P atoms form a three dimensional framework with I atoms as guests.

typically needs much longer time than that for preparing BP crystals (Shatruk et al., 1999). Therefore, we suggest that there are still some gaseous SnI_2 in the reaction system. Regarding the liquid Sn presented at this stage, we believe that the slightly excess Sn can ensure the formation of $Sn_{24}P_{19.3}I_8$ and gaseous SnI_2.

After the temperature of the reaction system reaches 650°C, the reaction temperature starts to cool to 500°C with a low cooling rate. At this cooling stage, some $Sn_{24}P_{19.3}I_8$ molecules deposit first at the place with a bit lower temperature because of vapor oversaturation. Remarkably, we here propose that $Sn_{24}P_{19.3}I_8$, at the temperature of ∼550–500°C, should be highly active as growth sites, due to its unique structure. Structurally, $Sn_{24}P_{19.3}I_8$, with a clathrate type-I structure, is a three dimensional framework of tin and phosphorus atoms (**Figure 5B**, left panel), where I atoms are guests in the framework (Shatruk et al., 1999). There are two types of P atoms in the structure, and one type of P atoms appears in pairs with a P-P separation of 2.20 Å, similar to typical P-P bond (**Figure 5B**, right panel) (Shatruk et al., 1999). Furthermore, $Sn_{24}P_{19.3}I_8$ crystals typically can have phosphorus vacancies in their structure (Li et al., 2017). Taking the TG analysis into account (**Figure S13**), we thus reason that the positions for P atoms in the $Sn_{24}P_{19.3}I_8$ crystals, either P atoms or vacancies, can be the starting points for BP growth at the temperature of ∼550–500°C.

After the formation of growth sites, BP crystals then can continuously grow with the assistance of SnI_2, following a typical chemical vapor transportation process. More specifically, gaseous SnI_2 molecules first react with gaseous P_4 molecules at the high temperature zone, forming a Sn-P-I intermediate. The intermediate compounds then migrate to the zone with slightly lower temperature, where the growth sites are formerly formed. Subsequently, the intermediate compounds react with the active $Sn_{24}P_{19.3}I_8$, yielding BP and releasing SnI_2 for further reaction. The reaction would continue like polymerization until most of the P_4 molecules are consumed. Finally, the gaseous SnI_2 molecules are deposited randomly, mainly in the zone with lower temperature, when the temperature further decreases.

On a separate note, at the intersection points (growth sites) of the obtained BP crystals, we found Hittorf's phosphorus (**Figure S19**) which was also observed in some former studies (Chen et al., 2017; Zhang Z. et al., 2017). According to the experimental observations, Hittorf's phosphorus may function as the active sites or intermediate state for BP growth (Chen et al., 2017; Zhang Z. et al., 2017). However, considering that Hittorf's phosphorus can be directly obtained by heating red phosphorus in a vacuum container (Chen et al., 2017), we here believe that Hittorf's phosphorus should be the by-product formed at the beginning of BP growth.

CONCLUSION

In conclusion, we have successfully synthesized BP crystals with various mineralizers, including SnI_4/Sn, SnI_2/Sn, Sn/I_2, SnIP, and $Sn_{24}P_{19.3}I_8$. By monitoring the Sn-I assisted reactions and characterizing the products, together with a series of control experiments, we here propose that BP crystals grow

through a SnI_2 mineralized reaction, and the $Sn_{24}P_{19.3}I_8$ compound serves as an active site for BP growth. Although more detailed *in situ* studies are still needed, we believe that our studies shown here should provide insights into the growth mechanism of BP crystals, facilitating further manipulation of BP synthesis.

AUTHOR CONTRIBUTIONS

ML and XX conceived and designed the experiments. DW, PY, and LZ performed experiments. LW and HL contributed in the Raman analysis. ML, XX, LH, and WH supervised the research and contributed to the manuscript writing. All authors read and approved the final manuscript.

FUNDING

This work was supported by National Key R&D Program of China (2017YFA0207201), National Natural Science Foundation of China (21507059), Young Elite Scientists Sponsorship Program by CAST (2017QNRC001), Six Talent Peaks Project in Jiangsu Province (JNHB-038), and Scientific Research Foundation for the Returned Overseas Chinese Scholars, Ministry of Education.

SUPPLEMENTARY MATERIAL

The Supplementary Material for this article can be found online at: https://www.frontiersin.org/articles/10.3389/fchem.2019.00021/full#supplementary-material

REFERENCES

Binnewies, M., Glaum, R., Schmidt, M., and Schmidt, P. (2012). *Chemical Vapor Transport Reactions.* Berlin; Boston, BA: Walter de Gruyter GmbH. & Co. KG.

Bridgman, P. W. (1914). Two new modifications of phosphorus. *J. Am. Chem. Soc.* 36, 1344–1363. doi: 10.1021/ja02184a002

Bridgman, P. W. (1935). Effects of high shearing stress combined with high hydrostatic pressure. *Phys. Rev.* 48, 825–847. doi: 10.1103/PhysRev.48.825

Bridgman, P. W. (1948). The compression of 39 substances to 100,000 kg/cm^2. *Proc. Am. Acad. Arts Sci.* 76, 55–70.

Chen, Z., Zhu, Y., Lei, J., Liu, W., Xu, Y., and Feng, P. (2017). A stage-by-stage phase-induction and nucleation of black phosphorus from red phosphorus under low-pressure mineralization. *CrystEngComm* 19, 7207–7212. doi: 10.1039/C7CE01492A

Dean, J. A. (1999). *Lange's Handbook of Chemistry*, *15th edn.* New York, NY: McGraw-Hill Inc.

Guo, Z., Zhang, H., Lu, S., Wang, Z., Tang, S., Shao, J., et al. (2015). From black phosphorus to phosphorene: basic solvent exfoliation, evolution of Raman scattering, and applications to ultrafast photonics. *Adv. Funct. Mater.* 25, 6996–7002. doi: 10.1002/adfm.201502902

Hirsch, A., and Hauke, F. (2018). Post-graphene 2D. chemistry: the emerging field of molybdenum disulfide and black phosphorus functionalization. *Angew. Chem. Int. Ed. Engl.* 57, 4338–4354. doi: 10.1002/anie.201708211

Hu, Z., Niu, T., Guo, R., Zhang, J., Lai, M., He, J., et al. (2018). Two-dimensional black phosphorus: its fabrication, functionalization and applications. *Nanoscale* 10, 21575–21603. doi: 10.1039/c8nr07395c

Köpf, M., Eckstein, N., Pfister, D., Grotz, C., Krüger, I., Greiwe, M., et al. (2014). Access and *in situ* growth of phosphorene-precursor black phosphorus. *J. Cryst. Growth* 405, 6–10. doi: 10.1016/j.jcrysgro.2014.07.029

Lange, S., Schmidt, P., and Nilges, T. (2007). Au_3SnP_7@black phosphorus: an easy access to black phosphorus. *Inorg. Chem.* 46, 4028–4035. doi: 10.1021/ic062192q

Li, L., Yu, Y., Ye, G. J., Ge, Q., Ou, X., Wu, H., et al. (2014). Black phosphorus field-effect transistors. *Nat. Nanotech.* 9, 372–377. doi: 10.1038/nnano.2014.35

Li, S., Liu, X., Fan, X., Ni, Y., Miracle, J., Theodoropoulou, N., et al. (2017). New strategy for black phosphorus crystal growth through ternary clathrate. *Cryst. Growth Des.* 17, 6579–6585. doi: 10.1021/acs.cgd.7b01239

Liu, H., Du, Y., Deng, Y., and Ye, P. D. (2015). Semiconducting black phosphorus: synthesis, transport properties and electronic applications. *Chem. Soc. Rev.* 44, 2732–2743. doi: 10.1039/C4CS00257A

Liu, H., Hu, K., Yan, D., Chen, R., Zou, Y., Liu, H., et al. (2018). Recent advances on black phosphorus for energy storage, catalysis, and sensor applications. *Adv. Mater.* 30:1800295. doi: 10.1002/adma.201800295

Liu, Y., Duan, X., Huang, Y., and Duan, X. (2018). Two-dimensional transistors beyond graphene and TMDCs. *Chem. Soc. Rev.* 47, 6388–6409. doi: 10.1039/C8CS00318A

Nilges, T., Kersting, M., and Pfeifer, T. (2008). A fast low-pressure transport route to large black phosphorus single crystals. *J. Solid State Chem.* 181, 1707–1711. doi: 10.1016/j.jssc.2008.03.008

Pfister, D., Schäfer, K., Ott, C., Gerke, B., Pöttgen, R., Janka, O., et al. (2016). Inorganic double helices in semiconducting SnIP. *Adv. Mater.* 28, 9783–9791. doi: 10.1002/adma.201603135

Ribeiro, H. B., Pimenta, M. A., and de Matos, C. J. S. (2018). Raman spectroscopy in black phosphorus. *J. Raman Spectrosc.* 49, 76–90. doi: 10.1002/jrs.5238

Shatruk, M. M., Kovnir, K. A., Shevelkov, A. V., Presniakov, I. A., and Popovkin, B. A. (1999). First tin pnictide halides $Sn_{24}P_{19.3}I_8$ and $Sn_{24}As_{19.3}I_8$: synthesis and the clathrate-I type of the crystal structure. *Inorg. Chem.* 38, 3455–3457. doi: 10.1021/ic990153r

Shriber, P., Samanta, A., Nessim, G. D., and Grinberg, I. (2018). First-principles investigation of black phosphorus synthesis. *J. Phys. Chem. Lett.* 9, 1759–1764. doi: 10.1021/acs.jpclett.8b00055

Smith, J. B., Hagaman, D., and Ji, H. F. (2016). Growth of 2D. black phosphorus film from chemical vapor deposition. *Nanotechnology* 27:215602. doi: 10.1088/0957-4484/27/21/215602

Wang, C., He, Q., Halim, U., Liu, Y., Zhu, E., Lin, Z., et al. (2018). Monolayer atomic crystal molecular superlattices. *Nature* 555, 231–236. doi: 10.1038/nature25774

Xia, F., Wang, H., Xiao, D., Dubey, M., and Ramasubramaniam, A. (2014). Two-dimensional material nanophotonics. *Nat. Photon.* 8, 899–907. doi: 10.1038/nphoton.2014.271

Yang, Z., Hao, J., Yuan, S., Lin, S., Yau, H. M., Dai, J., et al. (2015). Field-effect transistors based on amorphous black phosphorus ultrathin films by pulsed laser deposition. *Adv. Mater.* 27, 3748–3754. doi: 10.1002/adma.201500990

Zhang, J. L., Han, C., Hu, Z., Wang, L., Liu, L., Wee, A. T. S., et al. (2018). 2D phosphorene: epitaxial growth and interface engineering for electronic devices. *Adv. Mater.* 30:1802207. doi: 10.1002/adma.201802207

Zhang, Y., Zheng, Y., Rui, K., Hng, H. H., Hippalgaonkar, K., Xu, J., et al. (2017). 2D black phosphorus for energy storage and thermoelectric applications. *Small* 13:1700661. doi: 10.1002/smll.201700661

Zhang, Z., Xin, X., Yan, Q., Li, Q., Yang, Y., and Ren, T. L. (2016). Two-step heating synthesis of sub,-3 millimeter-sized orthorhombic black phosphorus

single crystal by chemical vapor transport reaction method. *Sci. China Mater.* 59, 122–134. doi: 10.1007/s40843-016-0122-1

Zhang, Z., Xing, D. H., Li, J., and Yan, Q. (2017). Hittorf's phosphorus: the missing link during transformation of red phosphorus to black phosphorus. *CrystEngComm* 19, 905–909. doi: 10.1039/C6CE02550A

Zhao, M., Niu, X., Guan, L., Qian, H., Wang, W., Sha, J., et al. (2016a). Understanding the growth of black phosphorus crystals. *CrystEngComm* 18, 7737–7744. doi: 10.1039/C6CE01608A

Zhao, M., Qian, H., Niu, X., Wang, W., Guan, L., Sha, J., et al. (2016b). Growth mechanism and enhanced yield of black phosphorus microribbons. *Cryst. Growth Des.* 16, 1096–1103. doi: 10.1021/acs.cgd.5b01709

Conflict of Interest Statement: The authors declare that the research was conducted in the absence of any commercial or financial relationships that could be construed as a potential conflict of interest.

Copyright © 2019 Wang, Yi, Wang, Zhang, Li, Lu, Xie, Huang and Huang. This is an open-access article distributed under the terms of the Creative Commons Attribution License (CC BY). The use, distribution or reproduction in other forums is permitted, provided the original author(s) and the copyright owner(s) are credited and that the original publication in this journal is cited, in accordance with accepted academic practice. No use, distribution or reproduction is permitted which does not comply with these terms.

frontiers in Chemistry

ORIGINAL RESEARCH
published: 04 March 2019
doi: 10.3389/fchem.2019.00083

Upconversion Nanocomposite Materials With Designed Thermal Response for Optoelectronic Devices

Eduardo D. Martínez[1], Carlos D. S. Brites[2], Luís D. Carlos[2], Ricardo R. Urbano[1] and Carlos Rettori[1,3]*

[1] *"Gleb Wataghin" Institute of Physics (IFGW), University of Campinas (UNICAMP), Campinas, Brazil,* [2] *Physics Department and CICECO-Aveiro Institute of Materials, University of Aveiro, Aveiro, Portugal,* [3] *CCNH, Universidade Federal do ABC (UFABC), Santo André, Brazil*

Upconversion is a non-linear optical phenomenon by which low energy photons stimulate the emission of higher energy ones. Applications of upconversion materials are wide and cover diverse areas such as bio-imaging, solar cells, optical thermometry, displays, and anti-counterfeiting technologies, among others. When these materials are synthesized in the form of nanoparticles, the effect of temperature on the optical emissions depends critically on their size, creating new opportunities for innovation. However, it remains a challenge to achieve upconversion materials that can be easily processed for their direct application or for the manufacture of optoelectronic devices. In this work, we developed nanocomposite materials based on upconversion nanoparticles (UCNPs) dispersed in a polymer matrix of either polylactic acid or poly(methyl methacrylate). These materials can be processed from solution to form thin film multilayers, which can be patterned by applying soft-lithography techniques to produce the desired features in the micro-scale, and luminescent tracks when used as nanocomposite inks. The high homogeneity of the films, the uniform distribution of the UCNPs and the easygoing deposition process are the distinctive features of such an approach. Furthermore, the size-dependent thermal properties of UCNPs can be exploited by a proper formulation of the nanocomposites in order to develop materials with high thermal sensitivity and a thermochromic response. Here, we thus present different strategies for designing optical devices through patterning techniques, ink dispensing and multilayer stacking. By applying upconverting nanocomposites with unique thermal responses, local heating effects in designed nanostructures were observed.

Keywords: upconversion nanoparticles, polymer nanocomposites, luminescent coatings, optical thermometry, electrochromic devices, thermochromism, optoelectronic devices, thermoplasmonics

OPEN ACCESS

Edited by:
Federico Cesano, University of Turin, Italy

Reviewed by:
Stefanos Mourdikoudis, University College London, United Kingdom
Xiangqun Chen, Harbin Institute of Technology, China
Stefan Fischer, Stanford University, United States

****Correspondence:***
Eduardo D. Martínez
edmartin@ifi.unicamp.br

Specialty section:
This article was submitted to Inorganic Chemistry, a section of the journal Frontiers in Chemistry

Received: *29 November 2018*
Accepted: *30 January 2019*
Published: *04 March 2019*

Citation:
Martínez ED, Brites CDS, Carlos LD, Urbano RR and Rettori C (2019) Upconversion Nanocomposite Materials With Designed Thermal Response for Optoelectronic Devices. Front. Chem. 7:83. doi: 10.3389/fchem.2019.00083

INTRODUCTION

Upconversion materials are the subject of intense study both from the fundamental physics point of view and because of their potential applications in various fields of technology (Nadort et al., 2016; Zhou et al., 2018a). They can be synthesized in the form of nanoparticles with controlled composition, morphology, size, crystalline structure and surface chemistry (Wang and Liu, 2008; Bettinelli et al., 2015). The size-dependent thermal properties of upconversion nanoparticles

(UCNPs) have recently received much attention. It was shown that below a critical size of about 30 nm, the emission intensity is enhanced as the temperature increases, while thermal quenching occurs for bigger particles (Li et al., 2014). This opens up new opportunities for applications where the size-dependent thermal properties of UCNPs can act as an extra degree of freedom for controlling the optical emissions (Shao et al., 2017). However, in the attempt to apply these materials in the manufacture of optoelectronic devices, the main challenge lies in the method by which UCNPs are to be deposited and integrated into fabrication processes, ensuring a uniform distribution with controlled spatial location. Methods need to be simple, yet sufficiently versatile to be adapted to serial production or to achieve specific architectures. A common strategy to achieve this goal is the formulation of nanocomposite materials.

The topic of hybrid materials formed by inorganic nanoparticles in polymer matrices has been addressed in several review papers (Binnemans, 2009; Kango et al., 2013; Bai et al., 2016; Pastoriza-Santos et al., 2018). Luminescent NPs have already been included in polymers by polymerization of different monomers, which may or may not be attached to the NPs by covalent bonds. A common strategy for this is the polymerization of methacrylate monomers catalyzed by 2,2′-azo-bisisobutyronitrile (AIBN). This approach has successfully been applied to include QDs (Lee et al., 2000; Sun et al., 2008; Guan et al., 2009), plasmonic nanoparticles (Pastoriza-Santos et al., 2018) and upconverting crystals (Wang et al., 2007; Tabanli et al., 2017; Zhang et al., 2018). Although this strategy is well-suited for obtaining monoliths and molded pieces with excellent optical properties, it is not appropriate for direct application of the nanocomposites in forming coatings or microstructures. On the other hand, luminescent inks composed by inorganic nanoparticles dispersed in solutions with different additives (including polymers) were developed in the past by the groups of May (Blumenthal et al., 2012; Meruga et al., 2012, 2014), Xu (You et al., 2015) and others (Tan et al., 2010; Furasova et al., 2017; Ma et al., 2017).

Here, we advance the development of simple, yet reliable polymer-based nanocomposite materials as a convenient and versatile way to deposit temperature sensitive UCNPs on rigid and flexible substrates. This allows the formation of homogeneous coatings, multilayer structures and the application of soft-lithography techniques, to form luminescent patterns. We explored two different polymers to act as a matrix material: polylactic acid (PLA) and poly(methyl methacrylate) (PMMA). The former constitutes a biodegradable polymer, which is increasingly used as a feeding material for additive manufacturing (3D printing) becoming affordable and accessible; the latter, on the other hand, presents a higher thermal and mechanical stability. In addition, PMMA can be used as a positive tone resist for electron beam lithography (EBL) for fabrication of patterns in the nanoscale. Both polymers are soluble in chloroform, a fast evaporating solvent that can also act as a dispersion medium for UCNPs; therefore, the integration of both materials is straightforward. As a distinctive feature, we take advantage of the size-dependent thermal properties of UCNPs by combining particles with different sizes and compositions. The thermo-sensitive nanocomposites were tested as probes for heat dissipation in two kinds of nanostructures: first, dry deposits of gold nanostars (AuNSs) where the thermoplasmonic effect takes place. Second, by assembling an electrothermal device using percolating networks of silver nanowires (AgNWs) (Martínez et al., 2016, 2018a, 2019). In the former nanostructure, when the local surface plasmon resonance (LSPR) of AuNSs is excited, energy is dissipated via electron-phonon scattering generating heat (Baffou et al., 2010; Rodríguez-Oliveros and Sánchez-Gil, 2012). Therefore, a local increase in temperature can be triggered externally by light. In fact, the spectral position of the LSPR in AuNSs can be tuned during the synthesis to match the wavelength of the light used to excite the upconversion luminescence in UCNPs. In the case of AgNWs networks, this is a system of increasing technological interest. Among other applications, they are used in transparent electrodes (Anh Dinh et al., 2013; Ye et al., 2014), solar-cells (Langley et al., 2014), flexible and wearable electronics (Myers et al., 2015; Lee et al., 2017). Moreover, upon electrical currents flows, heat is dissipated due to the Joule effect. Therefore, AgNWs networks are also used as nanoheater films (Kim et al., 2013; Huang et al., 2015) being an ideal system for testing the thermometric nanocomposites developed here.

In this work, we show some of the potential uses of the polymer-UCNPs composite materials by performing neat examples of microfabrication, multichromatic inks and multilayers, and thermally sensitive optical coatings. We are certain that this can provide new routes for the integration of nanoparticles in the development of optoelectronic devices and luminescence-based technologies.

EXPERIMENTAL SECTION

Materials

Sodium trifluoroacetate 98% (CAS 2923-18-4), yttrium(III) trifluoroacetate >99.99% (CAS 304851-95-4), erbium(III) oxide (CAS 12061-16-4), ytterbium(III) oxide (CAS 1314-37-0), thulium(III) oxide (CAS 12036-44-1), trifluoroacetic acid 99% (CAS 76-05-1), gold(III) chloride trihydrate >99.9% (CAS 16961-25-4), $AgNO_3$ 99.9999% (CAS 7761-88-8), L-ascorbic acid, reagent grade (CAS 50-81-7), trisodium citrate dihydrate (CAS 6132-04-3), mercaptosuccinic acid 97% (CAS 70-49-5), poly(sodium 4-styrenesulfonate) MW ∼70 000 g mol^{-1} (PSS, CAS 25704-18-1), ethylene glycol (EtGOH) anhydrous (99.8%), polyvinylpyrrolidone (PVP) 360,000 mol. wt., iron(III) chloride 97% (CAS 7705-08-0), oleic acid (OA, technical grade, 90%) and 1-octadecene (ODE, technical grade, 90%) were purchased from Sigma-Aldrich Co. Gadolinium(III) acetate hydrate 99.9% (CAS 100587-93-7) and Cerium(III) chloride heptahydrate 99% (CAS 18618-55-8) were purchased from Alfa Aesar. PMMA 7% wt. in chlorobenzene resist (PMMA C7) was purchased from MicroChem Corp, USA. All commercial reagents were used without further purification. Rare-earth acetates and trifluoroacetates not listed above were prepared in our laboratory using the corresponding rare-earth oxides (X_2O_3, X = Yb, Tm, Er). In a 500 mL round bottom flask containing 30–50 mL of a 50% (v/v) aqueous solution of either acetic acid or trifluoroacetic

acid, 1–2 g of the respective oxide was added. The mixture was refluxed for 1–2 h until the complete dissolution of the oxides resulted in a clear solution. The solution was then transferred to a Pyrex open vessel and maintained at 60°C to evaporate the liquid. The dried precipitates of acetate/trifluoroacetate salts were extracted.

Synthesis of UCNPs

Large (300 nm) pure hexagonal phase $NaYF_4$ nanoparticles co-doped with ytterbium (20 mol%) and erbium (2 mol%) were synthesized by the well-established thermal decomposition method of fluoroacetates, adapting protocols described by Ye and co-workers (Ye et al., 2010). In a three neck 200 mL round bottom flask containing 15 mL of ODE and 15 mL of OA, a total of 6.2 mmol of $NaCOOCF_3$, 2.6 mmol of $Y(COOCF_3)_3$, 0.68 mmol of $Yb(COOCF_3)_3$ and 0.068 mmol of $Er(COOCF_3)_3$ were added. The flask was sealed and heated under vacuum at 125°C in order to dissolve the precursors and degas the solution. After 1 h, a condenser was mounted, and the temperature was rapidly increased (10–20°C·min^{-1}) up to 330°C under an argon flux. After 30–35 min from the beginning of the heating stage, the reaction flask was retired from the mantle and 15 mL of ODE were added to quench the reaction. Extraction of the UCNPs was performed by adding an ethanol: hexane 4:1 v/v mixture and centrifugation for 5 min at 2,400 rpm, corresponding to a relative centrifugal force (RCF) of 1,004 RCF. The washing procedure was repeated four times and the UCNPs were finally dispersed in hexane with a final concentration of about 2 g·cm^{-3}. Same method was applied for the synthesis of additional large-sized UCNPs with compositions detailed in **Table 1**.

Small size hexagonal core-UCNPs (<12 nm) were synthesized by the co-precipitation route adapting the protocols reported by Wang and co-workers (Wang et al., 2014) using rare-earth acetates as the main precursors. A total of 1 mmol of $X(COOCH_3)_3$ (X = Gd, Yb, Tm, Er) was added in a 200 mL round bottom flask containing 15 mL of ODE and 9 mL of OA. The nominal molar ratio of each system was 1:0.78:0.2:0.02 Na:Gd:Yb:Er and 1:0.695:0.3:0.005 Na:Gd:Yb:Tm. The mixture was heated up to 160°C for 1 h to dissolve the precursors and then cooled down to room temperature. At this point, a freshly prepared mixture containing 2.5 mL of a 1 M NaOH methanol solution and 10.1 mL of 0.4 M NH_4F solution in methanol was rapidly injected. The flask was heated to 50°C for 30 min and then sealed. The temperature was raised to 100°C and the vacuum pump was connected. After 15 min, the vacuum pump was shut down, a condenser was mounted, and the temperature was increased to 280°C under argon flux. The flask was retired from the mantle after 1 h and allowed to cool down to room temperature. Extraction of the UCNPs was performed by adding excess anhydrous ethanol and centrifugation using 15 mL Falcon tubes. Centrifugation was performed at 1,004 RCF (2,400 rpm) for 7 min. The precipitated UCNPs were redispersed in 4 mL of cyclohexane and ethanol was added to complete the volume. The centrifugation and washing procedure was repeated twice. Finally, the UCNPs were dispersed in 8 mL of cyclohexane. As the quantum yield of the UC process is lower for smaller particles due to surface-related quenching processes, a core–shell structure was formed by growing a thin inert layer on the surface of the pre-synthesized core UCNPs. For this, 1 mmol of $Gd(COOCH_3)_3$ was added to 8 mL of OA and 12 mL of ODE in a 200 ml three-neck round bottom flask. The mixture was heated up to 160°C for 1 h and then cooled down to room temperature. Then, 6 mL of the core UCNPs colloid in cyclohexane were added. The subsequent addition of a methanol solution of NaOH and NH_4F and the following procedures were identical to those previously described for the synthesis of core nanoparticles. The same protocol was used for the synthesis of small-sized UCNPs doped with Ce^{3+}/Ho^{3+} as detailed in **Table 1**.

TABLE 1 | Nomenclature, nominal composition and particle size ± std (determined using the TEM images) of the UCNPs employed in the formulation of the nanocomposites.

Sample	Composition	Size (nm)	Obs.
1S	$NaGd_{0.695}Yb_{0.300}Tm_{0.005}F_4$@$NaGdF_4$	8.8 ± 0.8	Small
2S	$NaGd_{0.78}Yb_{0.20}Er_{0.02}F_4$@$NaGdF_4$	11.0 ± 1.4	
3S	$NaGd_{0.63}Yb_{0.20}Ce_{0.15}Ho_{0.02}F_4$@$NaGdF_4$	8.0 ± 1.3	
1L	$NaY_{0.695}Yb_{0.300}Tm_{0.005}F_4$	(400 ± 15) × (120 ± 10)	Large
2L	$NaY_{0.78}Yb_{0.20}Er_{0.02}F_4$	(300 ± 8) × (160 ± 6)	
3L	$NaY_{0.63}Yb_{0.20}Ce_{0.15}Ho_{0.02}F_4$	(85 ± 5) × (40 ± 3)	

Synthesis of AuNSs

Gold nanostars (AuNSs) were synthesized following a seed mediated protocol at room temperature. Gold nanoparticles (AuNPs) were first synthesized to be used as seeds by adding 15 mL of a 1 wt.% trisodium citrate aqueous solution into 100 mL of a boiling solution of gold(III) chloride 1 mM and maintained at boiling temperature for 15 min. When cooled down to room temperature, the resulting colloid was filtered through a 0.22 μm PES syringe filter. For the synthesis of AuNSs, 20 μL of a 1 M HCl solution were added to 20 mL of 0.25 mM gold(III) chloride solution in Milli-Q ultrapure water. 200 μL of the seed AuNPs were added and stirred at 800 rpm for 3 min in a 100 mL round bottom flask. Immediately afterwards, 200 μL of 3.3 mM $AgNO_3$ and 100 μL of 0.1 M L-ascorbic acid solutions were added quickly and simultaneously to the reactor vessel. After 1 min, 50 μL of a 1 mM mercaptosuccinic acid solution was added followed by 1 mL of a 1 wt.% PSS solution. All steps described before were performed at ambient temperature. It is worth mentioning that by varying the ratio between the ascorbic acid, the $AgNO_3$ added and the acid concentration in the reactor, it is possible to tune the branching growth of the resulting AuNSs and therefore the spectral position of the surface plasmon resonance. Here, concentration values were tuned to produce AuNSs with a plasmon resonance in the 900–1,000 window, matching the wavelength of the excitation light used for upconversion experiments. Further details of the procedure and the influence of the synthesis parameters in the resulting AuNSs can be found in Yuan and co-workers (Yuan et al., 2012).

Synthesis of AgNWs

Silver nanowires (AgNWs) were synthesized by adapting the method described by Jiu and co-workers (Jiu et al., 2014). Briefly, 0.2 g of PVP (360,000 g·mol^{-1}) were dissolved in 15 mL of anhydrous EtGOH and a solution containing 0.25 g of $AgNO_3$ in 10 mL of EtGOH was added at room temperature simultaneously with 3.25 mg of a 0.6 mM $FeCl_3$ solution in EtGOH. The final mixture was poured into a 100 mL round flask and sealed. The flask was then placed into an oven at 130°C for 5 h without agitation. After cooling down to room temperature, extraction of the AgNWs was performed by adding excess volume of acetone. The mixture was centrifuged at 1,000 rpm and the precipitates were dispersed in isopropanol. This procedure was repeated three times until a final dispersion of AgNWs in isopropanol was prepared in a 2.5 g·L^{-1} mass concentration.

Materials Characterization

UCNPs, AuNSs and AgNWs were characterized using optical and electron microscopy. Electron microscopy was performed at LNNano, CNPEM, Campinas, Brazil. SEM images were acquired in a FEI Quanta 650 FEG microscope operated at 20 kV. Transmission electron microscopy (TEM) images were obtained with a JEM 2,100 (JEOL) equipped with a LaB_6 filament and operated at 200 kV. X-ray diffraction (XRD) was performed in a Phaser D2 diffractometer (Bruker) while dynamical light scattering (DLS) was performed in a Nanopartica SZ-100 DLS (Horiba). UV-Visible spectrophotometry was performed in a Cary 8454 Agilent Technologies. Profilometry measurements were performed at LAMULT-IFGW using a Dektak 150, Veeco stylus profilometer. Upconversion was recorded using as excitation a collimated BL976-PAG900 FBG stabilized laser (ThorLabs). All measurements were performed at a nominal power of 500 mW, except otherwise indicated. The emission was analyzed with a QEPro spectrometer (Ocean Optics) coupled to a 600 μm diameter optical fiber. A short-pass optical filter was used to avoid the spectrometer saturation by the 976 nm laser. The thermal response of UCNPs was studied by depositing the upconverting material on silicon substrates. This was carried out in two ways: the formulated nanocomposites were spin-coated at 3,000 rpm, while dry deposits of UCNPs were formed by drop-casting the colloids and evaporating the solvent (hexane or cyclohexane) at 130°C. The samples were placed in thermal contact on a Peltier plate controlled by an Arduino board. The emission spectra were acquired at varying temperatures of the plate. Spin-coating was also used to deposit nanocomposite films on glass substrates for transmittance and profilometry characterization.

RESULTS AND DISCUSSION

Two sets of UCNPs were synthesized consisting of small-sized (<20 nm) and large-sized (>50 nm) UCNPs and containing one of the following emitting ions (activators): Tm^{3+}, Er^{3+} or Ho^{3+}, with main emission lines in the blue, green or red part of the spectrum, respectively. All particles were co-doped with a certain amount of Yb^{3+} ions acting as sensitizer. The composition of each system and the nomenclature adopted here is detailed in **Table 1**. TEM images of each UCNPs system are shown in **Figure 1** and the particle size distributions resulting from the analysis of the images are presented in **Supplementary Figure 2**. In **Supplementary Figure 3**, TEM images and partcticle size analysis are shown for UCNPs of the set 2S before and after the formation of the shell layer. X-ray diffraction shows that all particles present a hexagonal (β-) crystal structure (**Supplementary Figure 1**). UCNPs containing Er^{3+} either large- and small-size (from now on 2L and 2S, respectively) are shown in **Figures 1B,F**, whereas the emission spectra obtained at calibrated temperatures using a Peltier plate are displayed in **Figures 1D,H** for each nanoparticle system. The characteristic parameters resulting from the thermal calibration are summarized in **Supplementary Table 1**. The thermal dependence of the emission spectra for additional UCNPs

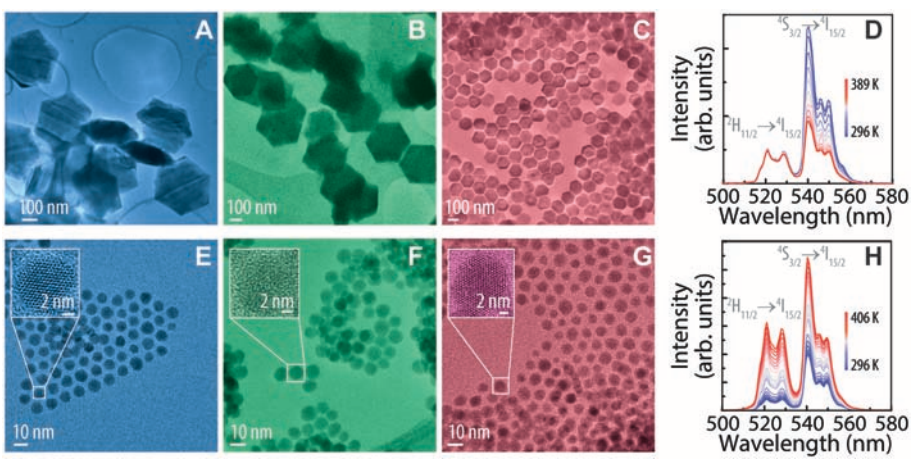

FIGURE 1 | TEM images of **(A–C)** large-size and **(E–G)** small-size UCNPs doped with **(A,E)** Tm^{3+}, **(B,F)** Er^{3+} and **(C,G)** Ce^{3+}-Ho^{3+}. Temperature dependent emission in the green spectral range of **(D)** 2L and **(H)** 2S UCNPs under 976 nm excitation.

studied in this work is presented in the **Supplementary Figure 5**. In all cases, the emission intensity is thermally quenched for large-sized UCNPs and thermally enhanced for small-sized UCNPs. This is in agreement with the size-dependent thermal response of UCNPs as already reported by Li and collaborators (Li et al., 2014). On one side, the thermal quenching effect for large-sized UCNPs is well-known and typically associated with non-radiative multiphonon relaxation (Shen et al., 2010; Yu et al., 2016). However, the thermal enhancement effect that takes place in small-size UCNPs was reported only recently and a conclusive explanation is still lacking. So far, quantum size effects affecting the phonon density of states (Li et al., 2014), thermal desorption of water molecules (Shao et al., 2017), and energy transfer between Yb^{3+} ions and anchoring groups of the capping molecules (Zhou et al., 2018b), have been proposed as an explanation for this anomalous effect. Although at this time we can not add new information to solve this issue, we can take advantage of the thermal responses by formulating nanocomposites combining both kinds of UCNPs.

UCNPs-Polymer Nanocomposites

For preparation of the nanocomposites, a certain amount of the colloids formed by UCNPs in cyclohexane was placed in a glass vial under a gentle flux of N_2 until complete evaporation of the solvent. The dried UCNPs were dispersed either in pure chloroform or in a 2 %wt. PLA solution in chloroform by means of vortex agitation and ultrasonic bath. For PMMA nanocomposites, equal amounts of the PMMA resist and the chloroform-UCNPs colloid were mixed. The approximate concentration of particles in the polymer solutions were ∼0.04 $g{\cdot}mL^{-1}$ for small-size UCNPs and ∼0.0015 $g{\cdot}mL^{-1}$ for large-size UCNPs. The prepared nanocomposite solutions were spin-coated at 3,000 rpm on glass substrates,

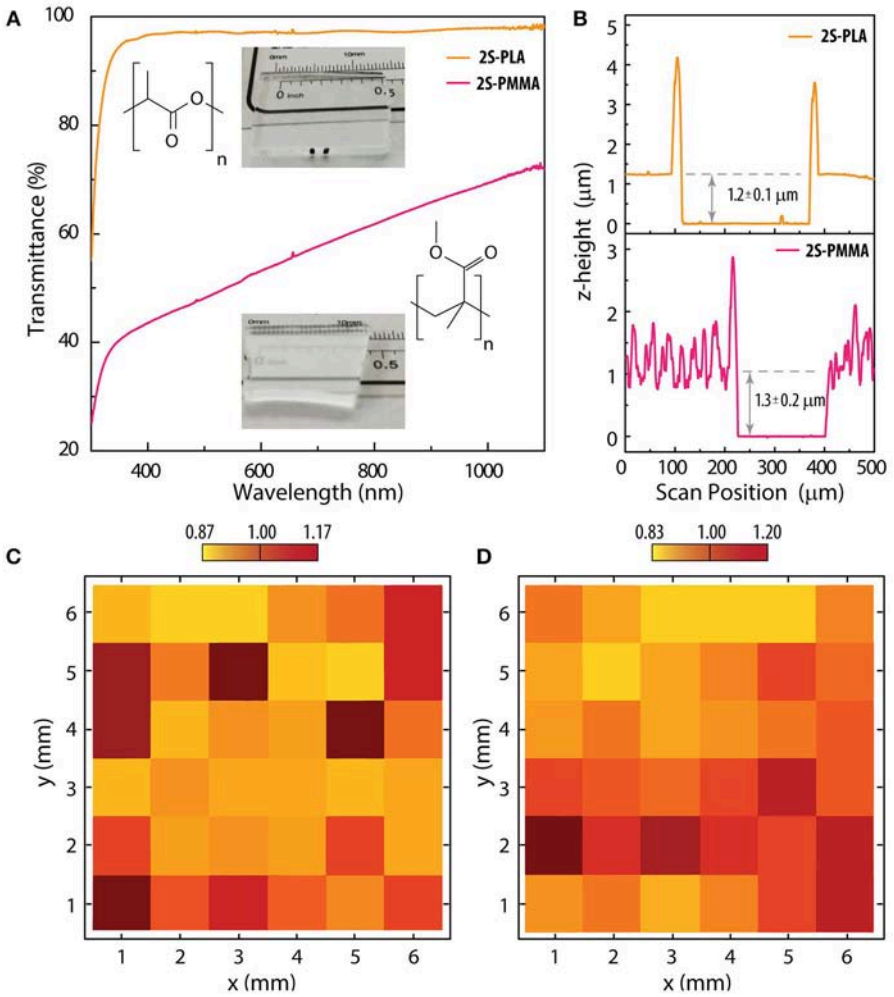

FIGURE 2 | Nanocomposites containing small-size UCNPs doped with Yb^{3+}-Er^{3+} deposited on glass substrates by spin-coating at 3,000 rpm. **(A)** Optical transmittance and pictures of 2S-PMMA and 2S-PLA samples. **(B)** Stylus profilometry performed on a scratch made on the films. Homogeneity of integrated upconversion emission spectra for nanocomposites based on **(C)** 2S-PLA and **(D)** 2S-PMMA.

forming a thin uniform layer. In order to compare the PMMA and PLA based films, the optical transmittance, the integrated intensity of the upconversion emissions and the thickness of the films were measured in samples containing 2S UCNPs. The optical transmittance was measured using a UV-visible spectrophotometer in the transmission mode (**Figure 2A**) showing a much higher transparency for the case of PLA films, while PMMA films present an opaque aspect. This could be due to the content of chlorobenzene in the PMMA resist used, which has a slower evaporation rate (1.07 compared to butyl acetate) than that of chloroform (11.6 compared to butyl acetate). The evaporation of chloroform could induce a coarse-grained deposition of the polymer. It is worth mentioning that the surface topography is not due to a clustering of the UCNPs as similar optical haze is observed for films without UCNPs. Also, it was observed that reducing the fraction of chloroform in the UCNPs-PMMA solution improves the transparency, although the viscosity is increased and therefore, the film thickness after coating is higher. The thickness of the films were characterized by stylus profilometry on a scratch made *ad-hoc* (**Figure 2B**), showing similar values for each film (∼1.2 μm for PLA and ∼1.3 μm for PMMA). The roughness was also analyzed finding values of root mean square roughness (R_q) of 0.005 μm and 0.37 μm for PLA and PMMA films, respectively. The higher R_q observed for the case of PMMA films is consistent with the lower transmittance discussed previously. The material removed from the scratches accumulated on the edges causing the peaks observed in the profilometry scans. In order to analyze the homogeneity of the coverage with UCNPs, the samples were mounted on a *x-y* micro-positioner stage. The emission spectra under excitation with a 976 nm collimated laser beam (ca. 1 mm spot size) was registered at different positions scanning a square region of 6 × 6 mm^2. A 2D map was constructed (**Figures 2C,D**) by integrating the emission spectrum at each point. Normalizing by the mean value, the emission intensity remains under a 15–20% deviation for the PLA and PMMA films, respectively.

The development of polymer-based nanocomposites is driven by the necessity of controlling the integration of nanoparticles into functional surfaces and structures. With that purpose, we tested the direct application of the formulated nanocomposites in different ways. On one side, the PLA based nanocomposite solutions containing large-size UCNPs emitting in the blue (1L, Tm^{3+} doped), green (2L, Er^{3+} doped) or red (3L, Ce^{3+}/Ho^{3+} co-doped) were used as inks to directly deposit drops and tracks with characteristic luminescent properties. Optical images of the handmade deposits are shown in **Figure 3** under white light (bright field, **Figure 3A**), dark field (**Figure 3B**) and near infrared (NIR, 976 nm) excitation (**Figures 3C,D**). Similar results (not shown) were obtained by using the UCNPs-PMMA nanocomposites. **Figure 3D** shows the use of a PLA-based nanocomposite for drawing luminescent tracks. As PLA is one of the mainstream polymer used in conventional 3D printing, this particular nanocomposite constitutes a step forward. Although

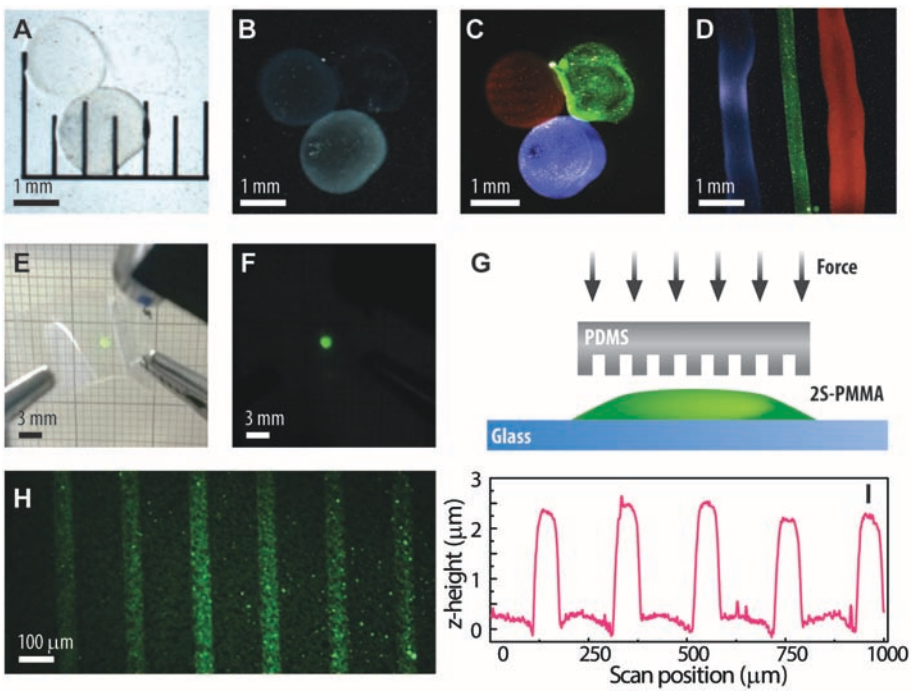

FIGURE 3 | Strategies to apply the PLA based nanocomposites as ink to directly write multicolor luminescent features. Optical images under **(A)** bright field, **(B)** dark field and **(C,D)** NIR light illumination. **(E,F)** 2L-PLA nanocomposite deposited on a flexible substrate. Scheme **(G)** of the soft lithography process to transfer micro-patterns. Luminescent tracks produced by soft lithography on 2L-UCNPs in PMMA under **(H)** NIR illumination and **(I)** height profile revealed by stylus profilometry.

we show here a proof of concept by applying the nanocomposite ink manually with a syringe, the deposition may be further improved by adopting controlled injection methods well-established in the additive manufacturing technology (Ligon et al., 2017). Additionally, the rheology of the composite inks can be optimized for a better control of the dispensing mechanism by varying the mass fraction of the polymers, while the surface tension can be adjusted by adding proper surfactants (Kumar et al., 2016).

The excellent properties of the PLA based nanocomposite can be clearly exposed by spin-coating the 2L-PLA solution into flexible substrates, in this case, a cellulose acetate sheet. The resulting film shows a high transparency and luminescence under NIR excitation as shown in **Figures 3E,F**.

By using the UCNPs-PMMA nanocomposite, we applied soft lithography methods to produce line patterns in the microscale. For that, a polydimethylsiloxane (PDMS) stamp was first prepared from a Sylgard 184 kit (Dow Chemicals®) following standard protocols (Qin et al., 2010). On a glass slide, 5 μL of the 2L-PMMA nanocomposite was poured; immediately afterwards the PDMS stamp was pressed and held in that position for 5 min, and then placed in a hot plate at 180°C for another 5 min. Once the sample was cooled down to room temperature, the stamp was carefully retired. A scheme of the method is depicted in **Figure 3G**. The resulting film presents a structure composed of the inverse pattern of the stamp, in this case, with parallel lines, ∼60 μm wide, showing a clear contrast in the luminescence under NIR excitation (**Figure 3H**). The luminescence contrast arises from the topography of the sample as revealed by the profilometry scan shown in **Figure 3I**. Each line track has a step height of 2.0–2.5 μm. It is worth mentioning that a background luminescence is detected as residual material containing UCNPs remains in the regions of contact between the PDMS and the base glass substrate.

Thermal Properties of UCNPs-Polymer Nanocomposites

The distinctive thermal properties of small- and large-sized UCNPs can be exploited to produce polymer nanocomposites with unique thermal response. We explored two approaches for the application of the polymer based UCNPs nanocomposites as thermally sensitive materials. For the first approach, depicted in **Figure 4A**, part of a glass substrate was first covered with AuNSs (**Figures 4B,C**) by drop-casting. Then, a PLA based nanocomposite containing UCNPs of the set 1L and 2S was

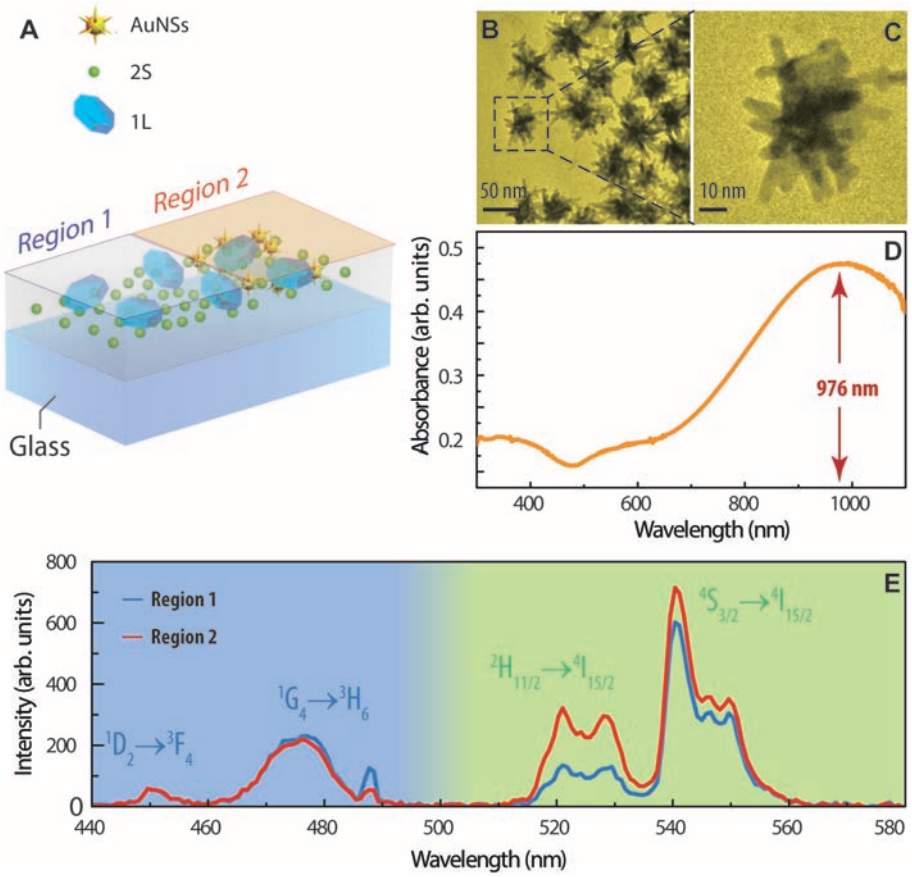

FIGURE 4 | Thermal effects on the emissions of polymer-UCNPs nanocomposites. **(A)** Scheme of samples for the study of the thermoplasmonic effect in AuNSs. **(B,C)** TEM images of AuNSs and **(D)** absorption spectra of AuNSs colloids. **(E)** Emission spectra obtained on regions without (region 1) and with (region 2) AuNSs.

spin-coated on top of it; therefore, two regions of the sample can be distinguished and compared: region 1 containing only the UCNPs and region 2 where UCNPs are deposited above AuNSs. The plasmon resonance of AuNSs (**Figure 4D**), which can be tuned by synthesis, is spectrally located at the NIR region, matching the wavelength of the light used to excite the UCNPs. The absorbed electromagnetic energy dissipates in the form of heat, which is transferred to the UCNPs located above. In the region containing AuNSs (region 2) the intensity of emissions of particles 2S (Er^{3+} doped) is enhanced compared to that measured in region 1 (**Figure 4E**). However, the emissions of UCNPs 1L is slightly reduced; therefore, the overall color of the total emission is different in both regions due to the presence of AuNSs. For UCNPs containing Er^{3+}, the local temperature can be directly calculated from the emission spectra, following the procedures described in the **Supplementary Material**. By using Equation S1 (**Supplementary Material**), the temperature in region 2 was determined to be $T = (92 \pm 4)°C$ while in region 1, $T = (25 \pm 3)°C$. It is worth noticing that by using the PLA-based nanocomposites, the homogeneous covering with UCNPs after spin-coating allows a precise comparison between both regions, being an improvement of previous methodologies in which the UCNPs were deposited by drop-casting the colloids and evaporating the solvent (Martínez et al., 2018b). This demonstrates the clear benefits of the nanocomposites formulated in this work.

In the second approach, we applied the PMMA-based nanocomposite to characterize the heat dissipation in AgNW conductive networks. A transparent thin film formed by a percolating network of AgNWs in PMMA was used as nanoheater film (**Figures 5A–C**) following previous protocols (Martínez et al., 2016, 2018a). On top of it, a PMMA based nanocomposite containing UCNPs of the set 2L and 1S was deposited by spin-coating. Again, the use of the nanocomposite presented here represents a clear improvement of our previous work (Martínez et al., 2019) by ensuring a homogeneous

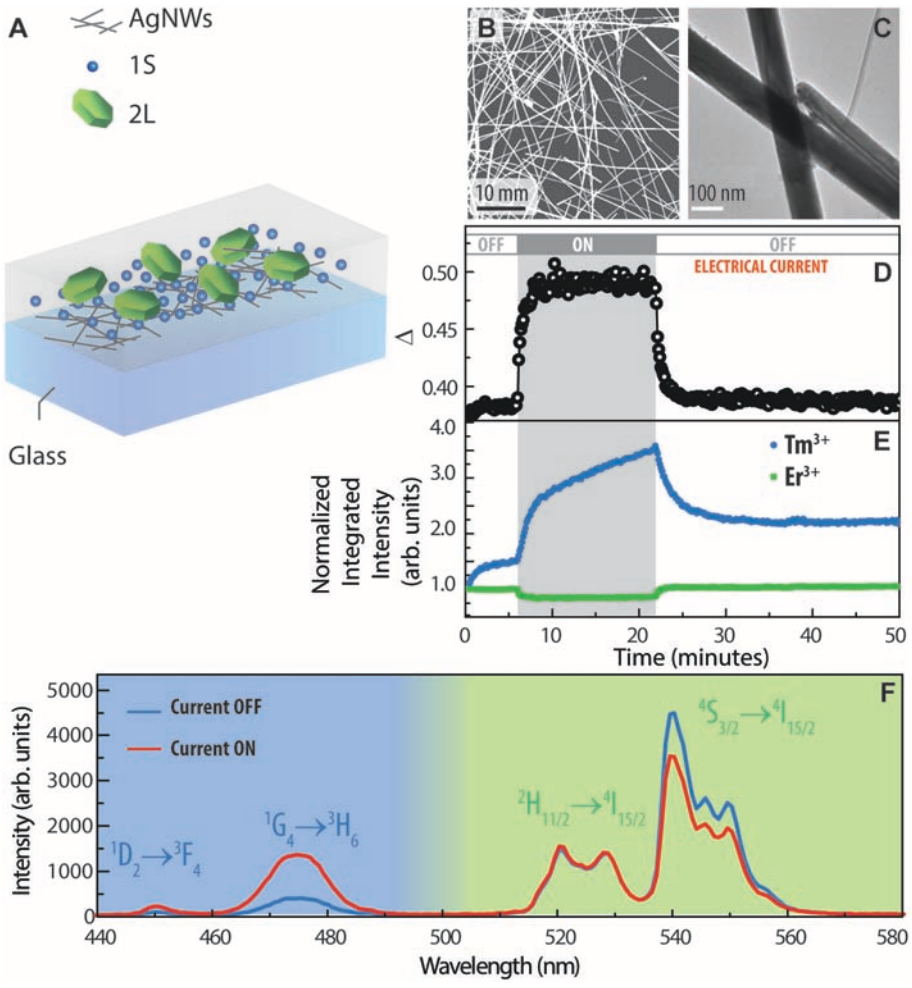

FIGURE 5 | (A) Scheme of the electrothermal devices formed by AgNWs and UCNPs nanocomposites. **(B)** SEM and **(C)** TEM images of AgNWs. **(D)** Evolution of the thermometric parameter and **(E)** integrated emissions of blue and green part of the spectrum during an electrothermal action off-on-off with an applied electrical power of 1.3 W. **(F)** Emission spectra of the electrothermal device under states on and off.

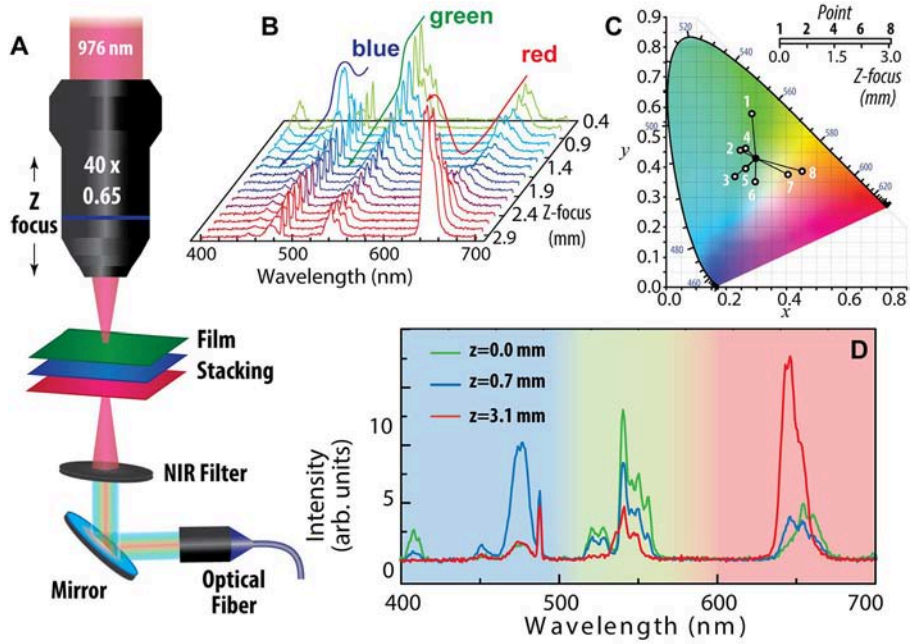

FIGURE 6 | Multicolor structure based on film stacking of UCNPs-PLA layers and z-focusing. **(A)** Scheme of the experimental set-up. **(B)** Emission spectra as a function of the z-focus position. **(C)** CIE 1931 chromaticity diagram showing the emission color obtained at selected z-focus positions. Calculations were made using ColorCalculator v7.15 OSRAM SYLVANIA, Inc. **(D)** Spectra at z-focus positions of maximum green ($z = 0$ mm), blue ($z = 0.7$ mm) and red ($z = 3.1$ mm) emission color.

covering. The resulting device, depicted in **Figure 5A**, allows for the external electrical control of the temperature of UCNPs by supplying a DC current throughout the AgNWs network, dissipating heat because of the Joule effect. When the power supply (1.3 W) was turned on, a noticeable change in the emission spectra was observed (**Figure 5F**). While the main emission line coming from the 2L UCNPs is thermally quenched, the emissions arising from UCNPs 1S are thermally enhanced. The integration of the spectra considering the blue band (440–500 nm) and the green band (500–580 nm) shows clearly that the effect of the current flow through the AgNWs film produces an augmented blue emission and a diminished green emission; furthermore, the spectral changes are reversible (**Figure 5E**). Interestingly, when considering the emissions from Er^{3+}, as discussed previously, it is possible to register the thermometric parameter (**Figure 5D**) throughout the experiment and use it to calculate the effective temperature at the emitter position. The temperature reached during the electrothermal action was $(87 \pm 3)^{\circ}$C.

Multilayer Stacking

Finally, to take advantage of the homogeneous coatings formed by spin-coating PLA-UCNPs, we built a multilayer structure formed by stacking PLA films deposited on thin glass coverslips (130–160 μm thick) containing UCNPs emitting in the green (2S), blue (1L) or red (3L) part of the spectrum. When mounting the multilayer stack under an objective lens (40x, NA 0.65), the NIR excitation laser can be focused in a spot of small volume whose position can be adjusted by micrometer screws. By using the set-up shown in **Figure 6A** we were able to register the overall emission spectra by varying the position of the z-focus (**Figure 6B**) and observing a clear shift in the emission color from green to blue, and then to red, as the characteristic emission lines of Er^{3+}, Tm^{3+}, and Ho^{3+} are successively excited. The change in the emission spectra in the blue (400–500 nm), green (500–600 nm) and red (600–700 nm) bands at each z-focus position (**Figure 6D**) modified the overall color of the emitted spectra, as shown in a chromaticity diagram Commission Internationale de l'Éclairage (CIE) 1931 on **Figure 6C**.

Notice that the multilayer stacking concept displayed in this section can be improved and adapted for other systems. For example, by forming stacking of UCNPs-nanocomposites on thin or flexible substrates, membranes can be produced whose deformation could be followed optically.

CONCLUSION

Polymer based nanocomposites containing UCNPs with different sizes and compositions were developed. Two polymers were used as matrix materials: PMMA and PLA, both of which are soluble in chloroform, forming stable suspensions upon the addition of UCNPs with oleic acid capping. The nanocomposite solutions can be deposited by spin-coating on several substrate materials, including flexible polymer sheets, producing homogeneous films (∼1 μm thick) with uniform upconversion luminescence. The nanocomposite solutions can also be applied directly, resembling an ink, providing a simple way to draw tracks and features with a precision mainly limited by the dispensing method. By using the nanocomposite inks in combination with PDMS stamps and soft lithography techniques it is possible to transfer microscale patterns forming luminescent structures.

Furthermore, we take advantage of the size-dependent thermal properties of UCNPs by formulating nanocomposites containing different combinations of small- and large-size UCNPs. We have successfully tested the thermally sensitive materials developed here by applying the nanocomposites of thermally active nanostructures. Two approaches were adopted, first, by using AuNSs with remarkable photothermal conversion efficiencies due to the thermoplasmonic effect; and second, by using conductive networks of AgNWs that can act as nanoheater films when DC currents are supplied. We successfully probed the external control of the intensity of emission lines due to the local change in the temperature, which could be directly measured by following the emissions of Er^{3+} in the green part of the spectrum or directly detected as a change in the emission color. The versatility of the nanocomposites was explored by constructing a multilayer stacking in combination with focusing optics, a simple set-up that showed to be highly sensitive to vertical displacements resulting in clear changes in the emission color. With these advances, we demonstrate that nanocomposites colloids presented in this work are extremely useful materials for direct application of UCNPs, and possibly other nanomaterials, in the assembling of novel photonic and optoelectronic devices.

DATA AVAILABILITY

The raw data supporting the conclusions of this manuscript will be made available by the authors, without undue reservation, to any qualified researcher.

AUTHOR CONTRIBUTIONS

EM conceived the project, synthesized the particles and performed all measurements. CB and LC discussed the project, analyzed the data, performed the calculations of thermometry and prepared all figures. RU and CR contributed to the experimental set-up and discussion of the project. The manuscript was written with contributions from all authors.

FUNDING

This study was financed in part by the Coordenação de Aperfeiçoamento de Pessoal de Nível Superior—Brasil (CAPES)—Finance Code 001, and by Fundação de Amparo à Pesquisa do Estado de São Paulo (FAPESP) through Grants #2011/19924-2, #2012/04870-7, #2012/05903-6, #2015/21290-2, and #2015/21289-4. Work was partially developed in the scope of the project CICECO—Aveiro Institute of Materials (Ref. FCT UID/CTM/50011/2013), financed by Portuguese funds through the Fundação para a Ciência e a Tecnologia/Ministério da Educação e Ciência (FCT/MEC) and when applicable co-financed by FEDER under the PT2020 Partnership Agreement. The financial support of FCT (PTDC/CTM-NAN/4647/2014 and POCI-01-0145-FEDER-016687) is also acknowledged. EM acknowledges, respectively, the post-doctoral FAPESP fellowship #2015/23882-4 and BEPE #2018/12489-8. CB acknowledges the grant financed by the SusPhotoSolutions project CENTRO-01-0145-FEDER-000005.

ACKNOWLEDGMENTS

We acknowledge the funding institutions and the facilities and institutions where the work was performed: Department of Quantum Electronics—Gleb Wataghin Institute of Physics (DEQ-IFGW), UNICAMP; physics department and CICECO, University of Aveiro. Electron microscopy (SEM and TEM) was performed at LNNano, Centro Nacional de Pesquisa em Energia e Materiais (CNPEM) in Campinas, SP, Brazil. Stylus profilometry was realized at LAMULT, IFGW-UNICAMP.

SUPPLEMENTARY MATERIAL

The Supplementary Material for this article can be found online at: https://www.frontiersin.org/articles/10.3389/fchem.2019.00083/full#supplementary-material

REFERENCES

Anh Dinh, D., Nam Hui, K., San Hui, K., Singh, J., Kumar, P., and Zhou, W. (2013). Silver nanowires: a promising transparent conducting electrode material for optoelectronic and electronic applications. *Rev. Adv. Sci. Eng.* 2, 324–345. doi: 10.1166/rase.2013.1048

Baffou, G., Quidant, R., and García De Abajo, F. J. (2010). Nanoscale control of optical heating in complex plasmonic systems. *ACS Nano* 4, 709–716. doi: 10.1021/nn901144d

Bai, G., Tsang, M., and Hao, J. (2016). Luminescent ions in advanced composite materials for multifunctional applications. *Adv. Funct. Mater.* 26, 6330–6350. doi: 10.1002/adfm.201602142

Bettinelli, M., Carlos, L., and Liu, X. (2015). Lanthanide-doped upconversion nanoparticles. *Phys. Today* 68, 38–44. doi: 10.1063/PT.3.2913

Binnemans, K. (2009). Lanthanide-based luminescent hybrid materials. *Chem. Rev.* 109, 4283–4374. doi: 10.1021/cr8003983

Blumenthal, T., Meruga, J., Stanley May, P., Kellar, J., Cross, W., Ankireddy, K., et al. (2012). Patterned direct-write and screen-printing of NIR-to-visible upconverting inks for security applications. *Nanotechnology* 23:185305. doi: 10.1088/0957-4484/23/18/185305

Furasova, A. D., Ivanovski, V., Yakovlev, A. V., Milichko, V. A., Vinogradov, V. V., and Vinogradov, A. V. (2017). Inkjet fabrication of highly efficient luminescent Eu-doped ZrO2nanostructures. *Nanoscale* 9, 13069–13078. doi: 10.1039/C7NR03175K

Guan, C., Lü, C., Cheng, Y., Song, S., and Yang, B. (2009). A facile one-pot route to transparent polymer nanocomposites with high ZnS nanophase contents via in situ bulk polymerization. *J. Mater. Chem.* 19, 617–621. doi: 10.1039/B818876A

Huang, Q., Shen, W., Fang, X., Chen, G., Guo, J., Xu, W., et al. (2015). Highly flexible and transparent film heaters based on polyimide films embedded with silver nanowires. *RSC Adv.* 5, 45836–45842. doi: 10.1039/C5RA06529A

Jiu, J., Araki, T., Wang, J., Nogi, M., Sugahara, T., Nagao, S., et al. (2014). Facile synthesis of very-long silver nanowires for transparent electrodes. *J. Mater. Chem. A* 2, 6326–6330. doi: 10.1039/C4TA00502C

Kango, S., Kalia, S., Celli, A., Njuguna, J., Habibi, Y., and Kumar, R. (2013). Surface modification of inorganic nanoparticles for development of organic-inorganic nanocomposites - a review. *Prog. Polym. Sci.* 38, 1232–1261. doi: 10.1016/j.progpolymsci.2013.02.003

Kim, T., Kim, Y. W., Lee, H. S., Kim, H., Yang, W. S., and Suh, K. S. (2013). Uniformly interconnected silver-nanowire networks for transparent film heaters. *Adv. Funct. Mater.* 23, 1250–1255. doi: 10.1002/adfm.201202013

Kumar, P., Singh, S., and Gupta, B. K. (2016). Future prospects of luminescent nanomaterial based security inks: From synthesis to anti-counterfeiting applications. *Nanoscale* 8, 14297–14340. doi: 10.1039/C5NR06965C

Langley, D. P., Giusti, G., Lagrange, M., Collins, R., Jiménez, C., Bréchet, Y., et al. (2014). Silver nanowire networks: physical properties and potential integration in solar cells. *Sol. Energy Mater. Sol. Cells* 125, 318–324. doi: 10.1016/j.solmat.2013.09.015

Lee, J., Sundar, V. C., Heine, J. R., Bawendi, M. G., and Jensen, K. F. (2000). Full color emission from II-VI semiconductor quantum dot-polymer composites. *Adv. Mater.* 12, 1102–1105. doi: 10.1002/1521-4095(200008)12:15<1102::AID-ADMA1102>3.0.CO;2-J

Lee, J.-G., Lee, J.-H., An, S., Kim, D.-Y., Kim, T.-G., Al-Deyab, S. S., et al. (2017). Highly flexible, stretchable, wearable, patternable and transparent heaters on complex 3D surfaces formed from supersonically sprayed silver nanowires. *J. Mater. Chem. A* 5, 6677–6685. doi: 10.1039/C6TA10997G

Li, D., Shao, Q., Dong, Y., and Jiang, J. (2014). Anomalous temperature-dependent upconversion luminescence of small-sized NaYF4 :Yb^{3+}, Er^{3+} nanoparticles. *J. Phys. Chem. C* 118, 22807–22813. doi: 10.1021/jp507804h

Ligon, S. C., Liska, R., Stampfl, J., Gurr, M., and Mülhaupt, R. (2017). Polymers for 3D printing and customized additive manufacturing. *Chem. Rev.* 117, 10212–10290. doi: 10.1021/acs.chemrev.7b00074

Ma, Q., Wang, J., Li, Z., Wang, D., Hu, X., Xu, Y., et al. (2017). Near-infrared-light-mediated high-throughput information encryption based on the inkjet printing of upconversion nanoparticles. *Inorg. Chem. Front.* 4, 1166–1172. doi: 10.1039/C7QI00194K

Martínez, E. D., Brites, C. D. S., Carlos, L. D., García-Flores, A. F., Urbano, R. R., and Rettori, C. (2019). Electrochromic switch devices mixing small- and large-sized upconverting nanocrystals. *Adv. Funct. Mater.* 29:1807758. doi: 10.1002/adfm.201807758

Martínez, E. D., Flores, A. F. G., Pastoriza, H., Urbano, R. R., and Rettori, C. (2018a). Electrothermal silver nanowire thin films for *in-situ* observation of thermally-driven chemical processes. *Sensors Actuators B* 259, 475–483. doi: 10.1016/j.snb.2017.12.021

Martínez, E. D., Lohr, J. H., Sirena, M., Sánchez, R. D., and Pastoriza, H. (2016). Silver nanowires in poly (methyl methacrylate) as a conductive nanocomposite for microfabrication. *Flex. Print. Electron.* 1, 1–10. doi: 10.1088/2058-8585/1/3/035003

Martínez, E. D., Urbano, R. R., and Rettori, C. (2018b). Thermoplasmonic enhancement of upconversion in small-size doped $NaGd(Y)F_4$ nanoparticles coupled to gold nanostars. *Nanoscale* 10, 14687–14696. doi: 10.1039/C8NR01639A

Meruga, J. M., Baride, A., Cross, W., Kellar, J. J., and May, P. S. (2014). Red-green-blue printing using luminescence-upconversion inks. *J. Mater. Chem. C* 2, 2221–2227. doi: 10.1039/c3tc32233e

Meruga, J. M., Cross, W. M., Stanley May, P., Luu, Q., Crawford, G. A., and Kellar, J. J. (2012). Security printing of covert quick response codes using upconverting nanoparticle inks. *Nanotechnology* 23, 395201. doi: 10.1088/0957-4484/23/39/395201

Myers, A. C., Huang, H., and Zhu, Y. (2015). Wearable silver nanowire dry electrodes for electrophysiological sensing. *RSC Adv.* 5, 11627–11632. doi: 10.1039/C4RA15101A

Nadort, A., Zhao, J., and Goldys, E. M. (2016). Lanthanide upconversion luminescence at the nanoscale: fundamentals and optical properties. *Nanoscale* 8, 13099–13130. doi: 10.1039/C5NR08477F

Pastoriza-Santos, I., Kinnear, C., Pérez-Juste, J., Mulvaney, P., and Liz-Marzán, L. M. (2018). Plasmonic polymer nanocomposites. *Nat. Rev. Mater.* 3, 375–391. doi: 10.1038/s41578-018-0050-7

Qin, D., Xia, Y., and Whitesides, G. M. (2010). Soft lithography for micro- and nanoscale patterning. *Nat. Protoc.* 5, 491–502. doi: 10.1038/nprot.2009.234

Rodríguez-Oliveros, R., and Sánchez-Gil, J. A. (2012). Gold nanostars as thermoplasmonic nanoparticles for optical heating. *Opt. Express* 20, 621–626. doi: 10.1364/OE.20.000621

Shao, Q., Zhang, G., Ouyang, L., Hu, Y., Dong, Y., and Jiang, J. (2017). Emission color tuning of core/shell upconversion nanoparticles through modulation of laser power or temperature. *Nanoscale* 9, 12132–12141. doi: 10.1039/C7NR03682E

Shen, X., Nie, Q., Xu, T., Dai, S., and Wang, X. (2010). Temperature dependence of upconversion luminescence in erbium-doped tellurite glasses. *J. Lumin.* 130, 1353–1356. doi: 10.1016/j.jlumin.2010.02.031

Sun, H., Zhang, H., Ju, J., Zhang, J., Qian, G., Wang, C., et al. (2008). One-step synthesis of high-quality gradient CdHgTe nanocrystals: a prerequisite to prepare CdHgTe–polymer bulk composites with intense near-infrared photoluminescence. *Chem. Mater.* 20, 6764–6769. doi: 10.1021/cm8018296

Tabanli, S., Bilir, G., and Eryurek, G. (2017). Color tunable up-conversion emission from Er3+:Y2O3nanoparticles embedded in PMMA matrix. *J. Lumin.* 182, 146–153. doi: 10.1016/j.jlumin.2016.10.009

Tan, M. C., Patil, S. D., and Riman, R. E. (2010). Transparent infrared-emitting CeF3:Yb - Er polymer nanocomposites for optical applications. *ACS Appl. Mater. Interfaces* 2, 1884–1891. doi: 10.1021/am100228j

Wang, F., Deng, R., and Liu, X. (2014). Preparation of core-shell NaGdF4 nanoparticles doped with luminescent lanthanide ions to be used as upconversion-based probes. *Nat. Protoc.* 9, 1634–1644. doi: 10.1038/nprot.2014.111

Wang, F., and Liu, X. (2008). Upconversion multicolor fine-tuning: visible to near-infrared emission from lanthanide-doped NaYF 4 nanoparticles. *J. Am. Chem. Soc.* 130, 5642–5643. doi: 10.1021/ja800868a

Wang, J., Hu, J., Tang, D., Liu, X., and Zhen, Z. (2007). Oleic acid (OA)-modified LaF3:Er,Yb nanocrystals and their polymer hybrid materials for potential optical-amplification applications. *J. Mater. Chem.* 17, 1597–1601. doi: 10.1039/B617754A

Ye, S., Rathmell, A. R., Chen, Z., Stewart, I. E., and Wiley, B. J. (2014). Metal nanowire networks: the next generation of transparent conductors. *Adv. Mater.* 26, 6670–6687. doi: 10.1002/adma.201402710

Ye, X., Collins, J. E., Kang, Y., Chen, J., Chen, D. T. N., Yodh, A. G., et al. (2010). Morphologically controlled synthesis of colloidal upconversion nanophosphors and their shape-directed self-assembly. *Proc. Natl. Acad. Sci. U.S.A.* 107, 22430–22435. doi: 10.1073/pnas.1008958107

You, M., Zhong, J., Hong, Y., Duan, Z., Lin, M., and Xu, F. (2015). Inkjet printing of upconversion nanoparticles for anti-counterfeit applications. *Nanoscale* 7, 4423–4431. doi: 10.1039/C4NR06944G

Yu, D., Ballato, J., and Riman, R. E. (2016). Temperature-dependence of multiphonon relaxation of rare-earth ions in solid-state hosts. *J. Phys. Chem. C* 120, 9958–9964. doi: 10.1021/acs.jpcc.6b01466

Yuan, H., Khoury, C. G., Hwang, H., Wilson, C. M., Grant, G. A., and Vo-Dinh, T. (2012). Gold nanostars: surfactant-free synthesis, 3D modelling, and two-photon photoluminescence imaging. *Nanotechnology* 23, 075102. doi: 10.1088/0957-4484/23/7/075102

Zhang, P., Chen, H., Yang, Y., Zhao, D., Jia, Z., Zheng, K., et al. (2018). 3D up-conversion display of NaYF4-PMMA covalent-linking nanocomposites. *J. Alloys Compd.* 753, 725–730. doi: 10.1016/j.jallcom.2018.03.225

Zhou, J., Leaño, J. L., Liu, Z., Jin, D., Wong, K.-L., Liu, R.-S., et al. (2018a). Impact of lanthanide nanomaterials on photonic devices and smart applications. *Small* 14:1801882. doi: 10.1002/smll.201801882

Zhou, J., Wen, S., Liao, J., Clarke, C., Tawfik, S. A., Ren, W., et al. (2018b). Activation of the surface dark-layer to enhance upconversion in a thermal field. *Nat. Photonics* 12, 154–158. doi: 10.1038/s41566-018-0108-5

Conflict of Interest Statement: The authors declare that the research was conducted in the absence of any commercial or financial relationships that could be construed as a potential conflict of interest.

Copyright © 2019 Martínez, Brites, Carlos, Urbano and Rettori. This is an open-access article distributed under the terms of the Creative Commons Attribution License (CC BY). The use, distribution or reproduction in other forums is permitted, provided the original author(s) and the copyright owner(s) are credited and that the original publication in this journal is cited, in accordance with accepted academic practice. No use, distribution or reproduction is permitted which does not comply with these terms.

frontiers in Chemistry

MINI REVIEW
published: 06 February 2019
doi: 10.3389/fchem.2019.00063

Luminescent Schiff-Base Lanthanide Single-Molecule Magnets: The Association Between Optical and Magnetic Properties

*Jérôme Long**

Institut Charles Gerhardt, Equipe Ingénierie Moléculaire et Nano-Objets, Université de Montpellier, ENSCM, CNRS, Montpellier, France

Luminescent Single-Molecule Magnets (SMM) belong to a new class of multifunctional molecule-materials that associate luminescence and slow relaxation of their magnetization within a single crystalline phase. We present in this mini-review the major advances that have been achieved in this new field over the last few years. More particularly, we will focus on the use of Schiff-base complexes in order to correlate magnetism and luminescence, as well as discussing the future outlooks of the field.

Keywords: lanthanides, single-molecule magnet, multifunctional molecular materials, luminescence, anisotropy, crystal-field splitting

OPEN ACCESS

Edited by:
Luís António Dias Carlos, University of Aveiro, Portugal

Reviewed by:
Jose Ramon Galan-Mascaros, Institut Català d'Investigació Química, Spain
Mahmut Özacar, Sakarya University, Turkey

***Correspondence:**
Jérôme Long
jerome.long@umontpellier.fr

Specialty section:
This article was submitted to Inorganic Chemistry, a section of the journal Frontiers in Chemistry

Received: *05 December 2018*
Accepted: *23 January 2019*
Published: *06 February 2019*

Citation:
Long J (2019) Luminescent Schiff-Base Lanthanide Single-Molecule Magnets: The Association Between Optical and Magnetic Properties. Front. Chem. 7:63. doi: 10.3389/fchem.2019.00063

INTRODUCTION

Nowadays, developing optimized molecule-based materials for future applications such as biomedicine (Horcajada et al., 2012; Long et al., 2016a), gas separation (Dechambenoit and Long, 2011), catalysis (Li et al., 2016), and quantum computing (Bogani and Wernsdorfer, 2008) frequently requires the association of different properties within a single-crystalline structure. Molecule-based materials benefit from specific assets related to their molecular nature, with respect to usual solid-state materials such as an unlimited structural diversity, weak density, optical transparency and the possibility to finely adjust and control their properties. Remarkably, coordination chemists have been at the front lines of science since the turn of the century, taking advantage of the respective intrinsic properties of metal ions and organic/inorganic ligands, to design original architectures with targeted functionalities. From a fundamental point of view, these unique molecular materials may display these properties independently, but the design of systems in which these functionalities strongly interact, constitutes the central objective for one property to control another.

Since the pioneering work of (Ishikawa et al., 2003), lanthanide-based Single-Molecule Magnets (SMM) have been investigated thoroughly because of their tremendous technological potential in high-density storage and quantum computing (Leuenberger and Loss, 2001; Woodruff et al., 2013; Liddle and van Slageren, 2015; Tang and Zhang, 2015; Ungur and Chibotaru, 2016). In such coordination complexes, an anisotropic barrier, Δ, originating from the interplay between the magnetic anisotropy and crystal-field splitting, opposes the reversal of the magnetization and leads to superparamagnetic-like behavior, comparable to that observed in magnetic nanoparticles. This feature may eventually give rise to a magnetic bistability that is strictly intrinsic to the molecular entity. Obviously, utilizing lanthanide ions constitutes a straightforward approach to implement simultaneous magnetic and luminescent properties because of their strong magnetic anisotropy and exceptional luminescence properties, dominated by f-f electronic

transitions, which results in long-lived emission, narrow bandwidth, important Stokes shifts and high quantum yields (Bunzli and Piguet, 2005). While the collection of lanthanide SMM is growing exponentially, only a small percentage of those systems exhibit lanthanide luminescence and can therefore be viewed as multifunctional. In this mini-review, we discuss the use of Schiff-base ligands and associated complexes for the design of luminescent SMM, as well as providing future outlooks and directions in the field.

CRITERIA TO DESIGN LANTHANIDE LUMINESCENT SMM

Slow relaxation of the magnetization and lanthanide luminescence, arises in both cases from the subtle association between a defined lanthanide ion and appropriate ligand(s). Therefore, the SMM behavior depends on the nature of the lanthanide ion, such as its angular momentum value, *J*, its Kramers/non-Kramers character as well as the angular dependence of the 4*f* electronic density which can be oblate (flattened spheroid) or prolate (elongated spheroid) (Rinehart and Long, 2011; Ungur and Chibotaru, 2016). On the other hand, and considering simple electrostatic considerations, the crystal-field generated by the surrounding ligands could result in the formation of m_J states largely separated in energy. Since it is mostly the single-ion anisotropy that dominates the slow relaxation, Δ is therefore directly related to crystal-field splitting, through relaxation involving the first or higher excited states. Other mechanisms involved in spin-phonon coupling (Raman and direct processes) or Quantum tunneling of Magnetization (QTM) complicate this scenario however, by creating underbarrier relaxation paths. In this sense, significant advances have been achieved in recent years, with either coordination (Chen et al., 2016; Liu et al., 2016; Meng et al., 2018) or organometallic complexes (Chen et al., 2016; Ding et al., 2016; Gregson et al., 2016; Gupta et al., 2016; Goodwin et al., 2017; Guo et al., 2017) showing for instance magnetic hysteresis higher than liquid nitrogen boiling's temperature (Guo et al., 2018). Remarkably, while the QTM affects the magnetic relaxation at a low temperature, recent studies have highlighted the decisive role of molecular vibrations (spin-phonon coupling) at a higher temperature (Goodwin et al., 2017; Escalera-Moreno et al., 2018).

With regards to lanthanide luminescence, the parity and spin forbidden character of the *f-f* transitions usually require an indirect excitation through the use of sensitizer ligands that transfers the absorbed energy to the excited state of the lanthanide ion. Consequently, the ligand is of utmost importance since it directly dictates the coordination environment suitable for the slow relaxation of the magnetization, while ensuring an efficient luminescence sensitizing toward a specific lanthanide ion. Among the lanthanide series, Dy^{3+} ion represents one of the most promising candidates to design luminescent SMM, because of its large $J = 15/2$ value, its Kramers character leading to a doubly degenerated ground state and its oblate electronic density which could be easily stabilized by usual coordination chemistry ligands. Dy^{3+} luminescence could be observed both in the visible and Near-Infra Red (NIR) (Long et al., 2018b). To a lesser extent, the NIR emissive Yb^{3+} has also been widely employed to design luminescent SMM (Pointillart et al., 2015), but optimizing the slow relaxation remains more difficult to realize with respect to Dy^{3+}. Tb^{3+} and Er^{3+} could also be employed to design luminescent SMM. Nevertheless, in practice they exhibit some drawbacks associated either to the Tb^{3+} non-Kramers nature (Ehama et al., 2013; Yamashita et al., 2013) or to the difficulty to observe Er^{3+}-based luminescence (Ren et al., 2014). Historically, the first example of SMM simultaneously exhibiting a slow relaxation of the magnetization and a weak lanthanide luminescence was reported by Bi et al. in a tetranuclear calixarene dysprosium complex in 2009 (Bi et al., 2009). Following this, various ligand families (beta-diketonates, carboxylates, aromatic amines) have been successfully explored (Long et al., 2018b; Jia et al., 2019). We will however, next focus on another class belonging to Schiff bases and describe examples that go further than the simple observation of both properties.

LUMINESCENT SCHIFF-BASE SMM: MAGNETO-LUMINESCENCE CORRELATION

Schiff-base ligands are known as simple efficient sensitizers of Ln^{3+} (Yang et al., 2014; Andruh, 2015) while benefiting from a large tunability including the denticity, rigidity/flexibility, and selective coordination sites (**Figure 1**). Several 4*f* or 3*d*/4*f* luminescent complexes based on a myriad of Schiff-base ligands and incorporating various lanthanide ions such as Eu^{3+}, Nd^{3+}, Tb^{3+}, Yb^{3+}, have been reported since the beginning of the century (Wong et al., 2002, 2006; Yang and Jones, 2005; Burrow et al., 2009; Wang et al., 2009). Nevertheless, the occurrence of slow relaxation of magnetization in these complexes was either not achieved, due to the lack of magnetic anisotropy, or was not investigated. Thus, the first example of a bifunctional Schiff-base SMM was reported by our group in 2012 in a $[Zn(NO_3)L^1Dy(NO_3)_2(H_2O)]$ complex [H_2L^1: N,N'-bis(3-methoxysalicylidene)-1,2-diaminoethane)] and based on a simple compartmentalized ligand obtained from the condensation of *o*-vanillin and ethylenediamine (Long et al., 2012). The complex could be described as a dinuclear entity in which the connections between Zn^{2+} and Dy^{3+} ions are provided by phenolate bridges (**Figure 2**). Introduction of the diamagnetic Zn^{2+} ion clearly has two benefits: it increases the negative charge (basicity) of the phenolate moieties and in turn the crystal-field splitting of the lanthanide ion (Upadhyay et al., 2014) while it does not quench the rare-earth emission in the visible spectral window. At room temperature, both a broad emission band, ascribed to the zinc complex and the typical Dy^{3+} emission lines were observed, indicating a partial energy transfer toward the lanthanide ion. Lowering the temperature (14 K) results in the exclusive observation of well-resolved Dy^{3+} emission bands. Such feature is of prime interest since the emission lines involving the electronic transitions also involve the magnetic ground state $^6H_{15/2}$ and

as a consequence directly reflects its crystal-field splitting. Remarkably, such an approach was previously utilized in the 60's, using absorption spectroscopy for ytterbium (Buchanan et al., 1967) or dysprosium garnets (Grünberg et al., 1969) and this methodology was later extended by Cucinotta et al. (2012) to correlate luminescence and magnetic properties in the archetypical SMM $Na[Dy(DOTA)(H_2O)]\cdot 4H_2O$ complex (Cucinotta et al., 2012). The emission spectrum for the complex $[Zn(NO_3)L^1Dy(NO_3)_2(H_2O)]$ shows more than eight expected transitions, resulting from the splitting of $^6H_{15/2}$ ground state into eight Kramers doublets ($J + 1/2$). This indicates the presence of "hot bands" arising from the first excited state of the emitting level $^7F_{9/2}$ (**Figure 2**). Deconvolution of the emission bands, using Gaussian functions, allows one to experimentally obtain the crystal-field splitting of the Kramers doublets. Hence, the gap between the ground and first excited doublets is estimated at 48 cm^{-1}, in line with the value of $\Delta = 35$ cm^{-1} obtained by alternate currents (ac) magnetic measurements. This suggests that the relaxation occurs *via* the first excited Kramers doublet corresponding to an Orbach process. Nevertheless, the slight discrepancy between luminescence and magnetism indicates that additional magnetic relaxation mechanisms are involved. This is further corroborated through the study of both the magnetic and luminescence properties of the aforementioned complex, diluted in a diamagnetic yttrium matrix (Long et al., 2016b). Photoluminescence confirms that: (i) the Dy^{3+} ion remains in a similar environment upon chemical dilution; (ii) as expected, the energy gap between the ground and first excited doublets is identical. The magnetic measurements for the diluted sample reveal an increased anisotropic barrier of $\Delta = 45$ cm^{-1} due to the removal of the dipolar interactions, known to enhance the QTM, that decrease the effective barrier. The value of Δ is in remarkable accordance with that obtained by luminescence, which confirms that such an approach can be used to compare the results from these two experimental techniques and further shed light on the mechanisms that govern the slow relaxation of magnetization.

Such simple methodology has been widely extended, by other groups and including our own, to numerous SMM or coordination networks that exhibit a single-ion based magnetic relaxation in order to obtain a detailed picture of the lanthanide crystal-field and therefore improves comprehension of the relaxation dynamics (Long et al., 2018b; Jia et al., 2019). We would also like to emphasize that such outcomes could also be further confirmed by the decisive input from *ab initio* calculations, especially with systems that exhibit multiple crystallographically independent sites (Long et al., 2015).

Pure 4*f* Schiff base complexes also represent another class of promising systems. However, it remains difficult to simultaneously increase the magnetic anisotropy to generate a genuine slow relaxation of magnetization, while retaining the lanthanide luminescence (Shintoyo et al., 2014; Long et al., 2018a). Therefore, one alternative strategy consists of synthesizing heterotrinuclear Zn_2Dy complexes (Oyarzabal et al., 2015; Sun et al., 2016) in which the lanthanide ion is sandwiched between two bis-phenoxide moieties. This results in

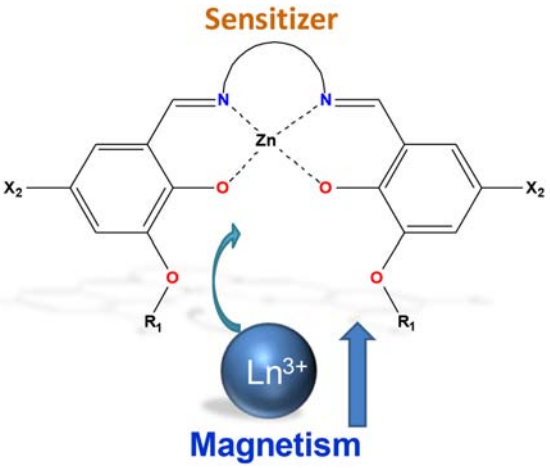

FIGURE 1 | General scheme showing the combination of compartmental Schiff-base complex and Ln^{3+} ions.

an enhancement of the axial crystal-field. The five-membered ring constituted by four methoxy oxygen and one solvate, or counter-ion, defines a basal plane (hard plane) almost perpendicular to the Zn^{2+}-Dy^{3+}-Zn^{2+} arrangement. Numerous complexes with various counter-anions and co-ligands that exhibit SMM behavior and Dy^{3+}-based luminescence associated with remanent emission from the ligands, have been reported (Costes et al., 2015, 2016). To this point, we have recently described an example of a luminescent trinuclear complex $[(ZnL^1Cl)_2Dy(H_2O)]_4[ZnCl_4]_2\cdot H_2O$ that shows a zero-field slow relaxation of magnetization that could be observed for up to 30 K (Boulkedid et al., 2018). The compound exhibits the typical Dy^{3+} emission, but the presence of four different crystallographically independent dysprosium sites precludes the extraction of the energy difference between the ground and first excited doublets. Luminescence reveals however a large total crystal-field splitting of about 1,500 cm^{-1}, indicating that such systems may have great potential if the relaxation occurs through higher excited Kramers doublets.

Schiff-base ligands could also be employed to introduce further functionalities. For instance, implementing chirality, opens the field to new properties that result from the crystallization in non-centrosymmetric structures. One can cite for instance Natural Circular Dichroism (NCD), Second-Harmonic Generation (SHG), Circular Polarized Luminescence (CPL) as well as magneto-optical cross-effects that result from the interplay with magnetism, such as magneto-chiral dichroism and Magnetized Second-Harmonic Generation (MSHG) (Train et al., 2011). In addition, the crystallization in appropriate non-centrosymmetric space groups paves the way toward advanced electrical properties such as piezo/pyroelectricity and ferroelectricity. With this in mind, we reported chiral $[ZnL^2Dy(OAc)(NO_3)_2]$ complexes based on the enantiopure Schiff base ligands *R*,*R* or *S*,*S*-HL_2 = phenol,2,2′[2,2-diphenyl-1,2-ethanediyl]bis[(E)-nitrilomethylidyne]-bis(6-methoxy) (Long et al., 2015). Each enantiomer crystallizes in the polar

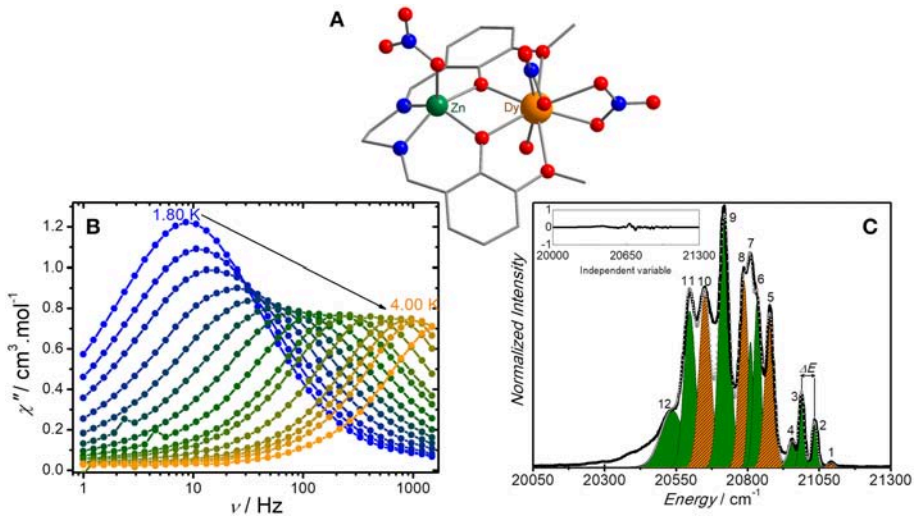

FIGURE 2 | (A) Crystal structure of the dinuclear $[Zn(NO_3)L^1Dy(NO_3)_2(H_2O)]$ complex. **(B)** Frequency dependence of the out-of-phase susceptibility (χ") obtained under a 900 dc field. **(C)** Magnification of the $^4F_{9/2} \rightarrow {}^6H_{15/2}$ emission transitions in the 20,050–21,300 cm^{-1} region (at 14 K) Multi-Gaussian function fit components arising from the first $^4F_{9/2}$ Stark sublevel to the $^6H_{15/2}$ multiplet in the energy interval. The fits regular residual plots ($R^2 > 0.98$) are shown in inset (Long et al., 2012, 2016b).

$P2_1$ space group, with two crystallographically inequivalent homochiral Zn^{2+}/Dy^{3+} complexes, in the asymmetric unit. Apart from the typical dysprosium luminescence and slow relaxation of the magnetization that have been correlated and compared with results obtained from *ab initio* calculations, the compounds exhibit a ferroelectric behavior up to the decomposition of the material at 300°C, making it the highest temperature at which a switchable polarization has been observed for a molecular ferroelectric. Such robust chiral molecular compounds may represent alternative candidates for high-temperature ferroelectrics (Hang et al., 2011).

CONCLUSIONS AND FUTURE OUTLOOK

Schiff-bases represent an interesting class of ligands from which to design luminescent lanthanide SMM. Their infinite diversity and flexibility make them ideal candidates to face the challenges in the field and to obtain air-stable luminescent SMM with high energy barriers. In a more general context, the in-depth understanding of magnetic relaxation in lanthanide-based SMM remains a challenge as this involves concepts and models in physics from the 60's, related for instance to spin-phonon coupling (Escalera-Moreno et al., 2018), which should be modernized. In this regard, photoluminescence could definitely shed light on lanthanide crystal-field splitting, to determine if the relaxation proceeds *via* the 1st or higher excited states, or involves underbarrier Raman, direct or QTM processes. Moreover, studying the vibronic coupling in high temperature SMM may be experimentally achieved by photoluminescence (emission lifetimes, *f*-*f* relative intensities…).

While the correlation between magnetism and photoluminescence should be viewed as the inception, studying the interplay between the two properties constitutes a major milestone. As both properties are intimately correlated to the electronic structure of the lanthanide ion, the coupling is expected to be strong and such a cross-effect has previously been evidenced more than 50 years ago, in paramagnetic ytterbium garnet (Buchanan et al., 1967; Grünberg et al., 1969). Thus, applying a magnetic field induces a strong modification of the emission spectrum and has been explained by the well-known Zeeman effect, that lifts the degeneracy of the Kramers doublets. Such approach was first demonstrated in lanthanide SMM, in 2016 (Bi et al., 2016) in which values of the gyromagnetic factor (that are usually difficult to experimentally obtain) were extracted, confirming the gap between the first and excited Kramers doublets. One point that needs to be addressed concerns the comprehension of the field dependence of the emission intensity as observed in others SMM (Chen et al., 2017). Such breakthroughs confirm the possibility to control both the emission intensity and wavelength by a magnetic field, which could be relevant for applications such as magnetic field sensors. However, such inductive effects may simply occur in any luminescent 4*f* paramagnetic compound, therefore, future studies should examine the existence of an interplay between the SMM property (magnetic bistability) and the luminescence. This requires circumventing synthetic issues to design systems, simultaneously exhibiting a significant magnetic remanence and coercivity at a pertinent temperature with stability over a long-time scale. This last point is of critical importance since 4*f* SMM usually shows quick relaxation of magnetization, due to the QTM. Major advances have recently been achieved in organometallic

SMM, showing magnetic bistability of up to 60–80 K (Goodwin et al., 2017; Guo et al., 2017, 2018), confirming that the design of high performing luminescent SMM with possible air-stability is within reach if suitable sensitizer ligands that are able to maximize the magnetic anisotropy, are rationally conceived.

On the other hand, introduction of chirality and other properties, resulting from the non-centrosymmetric character of the crystal structures, may be easily achieved using Schiff base ligands. Simple multifunctional molecular ferroelectrics therefore represent ideal candidates to study the coupling between the constitutive functionalities such as the magneto-electrical coupling. Designing a strong coupling between an electric and magnetic property clearly constitutes an important challenge in the field of solid-state chemistry (Fiebig et al., 2016). This indicates that molecular systems may control polarization, by applying a magnetic field and *vice versa* with prospective applications in non-volatile memories and low-consumption devices (Eerenstein et al., 2006; Cheong and Mostovoy, 2007; Mandal et al., 2015).

More generally and in order to fulfill these ambitious objectives, molecular materials also need to be integrated or shaped into more complex architectures (surfaces, films, or composites) for use in practical applications. Such strategies necessitate investigating that the considered molecular objects and their associated functionalities remain preserved. Among the characterization techniques used to investigate the latter, photo-luminescence could easily be used for this purpose. Close collaboration between chemists and photo physicists is therefore clearly necessary, in order to achieve these objectives.

AUTHOR CONTRIBUTIONS

The author confirms being the sole contributor of this work and has approved it for publication.

FUNDING

I thank the University of Montpellier, CNRS, LABEX CheMISyst ANR-10-LABX-05-01 and the Portugal-France bilateral action Program PESSOA (Hubert Curien) Multifunctional magneto-luminescent molecular architectures (33676SF) and Magneto-optical Multifunctional Nanoparticles (40773PE) for financial support.

ACKNOWLEDGMENTS

I would like to thank in particular Dr. Y. Guari and Pr. J. Larionova for their expert advice and fruitful scientific discussions. I also deeply acknowledge my colleagues Pr. R. A. S. Ferreira and Pr. Luis D. Carlos for the great collaboration. I also express my deepest acknowledgments to all my co-workers, colleagues and students.

REFERENCES

Andruh, M. (2015). The exceptionally rich coordination chemistry generated by Schiff-base ligands derived from o-vanillin. *Dalton Trans.* 44, 16633–16653. doi: 10.1039/C5DT02661J

Bi, Y., Chen, C., Zhao, Y.-F., Zhang, Y.-Q., Jiang, S.-D., Wang, B.-W., et al. (2016). Thermostability and photoluminescence of Dy(iii) single-molecule magnets under a magnetic field. *Chem. Sci.* 7, 5020–5031. doi: 10.1039/C6SC01157H

Bi, Y., Wang, X.-T., Liao, W., Wang, X., Deng, R., Zhang, H., et al. (2009). Thiacalix[4]arene-Supported planar Ln4 (Ln = TbIII, DyIII) clusters: toward luminescent and magnetic bifunctional materials. *Inorg. Chem.* 48, 11743–11747. doi: 10.1021/ic9017807

Bogani, L., and Wernsdorfer, W. (2008). Molecular spintronics using single-molecule magnets. *Nat. Mater.* 7, 179–186. doi: 10.1038/nmat2133

Boulkedid, A.-L., Long, J., Beghidja, C., Guari, Y., Beghidja, A., and Larionova, J. (2018). A luminescent Schiff-base heterotrinuclear Zn2Dy single-molecule magnet with an axial crystal field. *Dalton Trans.* 47, 1402–1406. doi: 10.1039/C7DT03842A

Buchanan, R. A., Wickersheim, K. A., Pearson, J. J., and Herrmann, G. F. (1967). Energy levels of Yb^{3+} in gallium and aluminum garnets. I. spectra. *Phys. Rev.* 159, 245–251.

Bunzli, J.-C. G., and Piguet, C. (2005). Taking advantage of luminescent lanthanide ions. *Chem. Soc. Rev.* 34, 1048–1077. doi: 10.1039/B406082M

Burrow, C. E., Burchell, T. J., Lin, P.-H., Habib, F., Wernsdorfer, W., Clérac, R., et al. (2009). Salen-Based [Zn2Ln3] complexes with fluorescence and single-molecule-magnet properties. *Inorg. Chem.* 48, 8051–8053. doi: 10.1021/ic9007944

Chen, Y.-C., Liu, J.-L., Ungur, L., Liu, J., Li, Q.-W., Wang, L.-F., et al. (2016). Symmetry-supported magnetic blocking at 20 K in pentagonal bipyramidal Dy(III) single-ion magnets. *J. Am. Chem. Soc.* 138, 2829–2837. doi: 10.1021/jacs.5b13584

Chen, Y. C., Liu, J. L., Lan, Y., Zhong, Z. Q., Mansikkamaki, A., Ungur, L., et al. (2017). Dynamic magnetic and optical insight into a high performance pentagonal bipyramidal dyIII single-ion magnet. *Chem. Eur. J.* 23, 5708–5715. doi: 10.1002/chem.201606029

Cheong, S.-W., and Mostovoy, M. (2007). Multiferroics: a magnetic twist for ferroelectricity. *Nat. Mater.* 6, 13–20. doi: 10.1038/nmat1804

Costes, J. P., Titos-Padilla, S., Oyarzabal, I., Gupta, T., Duhayon, C., Rajaraman, G., et al. (2015). Analysis of the role of peripheral ligands coordinated to znii in enhancing the energy barrier in luminescent linear trinuclear Zn-Dy-Zn single-molecule magnets. *Chem. Eur. J.* 21, 15785–15796. doi: 10.1002/chem.201501500

Costes, J. P., Titos-Padilla, S., Oyarzabal, I., Gupta, T., Duhayon, C., Rajaraman, G., et al. (2016). Effect of ligand substitution around the DyIII on the SMM properties of dual-luminescent Zn–Dy and Zn–Dy–Zn complexes with large anisotropy energy barriers: a combined theoretical and experimental magnetostructural study. *Inorg. Chem.* 55, 4428–4440. doi: 10.1021/acs.inorgchem.6b00228

Cucinotta, G., Perfetti, M., Luzon, J., Etienne, M., Car, P.-E., Caneschi, A., et al. (2012). Magnetic anisotropy in a dysprosium/DOTA single-molecule magnet: beyond simple magneto-structural correlations. *Angew. Chem. Int. Ed.* 51, 1606-1610. doi: 10.1002/anie.201107453

Dechambenoit, P., and Long, J. R. (2011). Microporous magnets. *Chem. Soc. Rev.* 40, 3249–3265. doi: 10.1039/c0cs00167h

Ding, Y.-S., Chilton, N. F., Winpenny, R. E. P., and Zheng, Y.-Z. (2016). On Approaching the Limit of molecular magnetic anisotropy: a near-perfect pentagonal bipyramidal dysprosium(III) single-molecule magnet. *Angew. Chem. Int. Ed.* 55, 16071–16074. doi: 10.1002/anie.201609685

Eerenstein, W., Mathur, N. D., and Scott, J. F. (2006). Multiferroic and magnetoelectric materials. *Nature* 442, 759–765. doi: 10.1038/nature05023

Ehama, K., Ohmichi, Y., Sakamoto, S., Fujinami, T., Matsumoto, N., Mochida, N., et al. (2013). Synthesis, structure, luminescent, and magnetic properties of carbonato-bridged ZnII2LnIII2 Complexes

[(μ4-CO3)2{ZnIILnLnIII(NO3)}2] (LnIII = GdIII, TbIII, DyIII; L1 = N,N′-Bis(3-methoxy-2-oxybenzylidene)-1,3-propanediaminato, L2 = N,N′-Bis(3-ethoxy-2-oxybenzylidene)-1,3-propanediaminato). *Inorg. Chem.* 52, 12828–12841. doi: 10.1021/ic4022273

Escalera-Moreno, L., Baldoví, J. J., Gaita-Ariño, A., and Coronado, E. (2018). Spin states, vibrations and spin relaxation in molecular nanomagnets and spin qubits: a critical perspective. *Chem. Sci.* 9, 3265–3275. doi: 10.1039/C7SC05464E

Fiebig, M., Lottermoser, T., Meier, D., and Trassin, M. (2016). The evolution of multiferroics. *Nat. Rev. Mater* 1:16046. doi: 10.1038/natrevmats.2016.46

Goodwin, C. A. P., Ortu, F., Reta, D., Chilton, N. F., and Mills, D. P. (2017). Molecular magnetic hysteresis at 60 kelvin in dysprosocenium. *Nature* 548, 439–442. doi: 10.1038/nature23447

Gregson, M., Chilton, N. F., Ariciu, A.-M., Tuna, F., Crowe, I. F., Lewis, W., et al. (2016). A monometallic lanthanide bis(methanediide) single molecule magnet with a large energy barrier and complex spin relaxation behaviour. *Chem. Sci.* 7, 155–165. doi: 10.1039/C5SC03111G

Grünberg, P., Hüfner, S., Orlich, E., and Schmitt, J. (1969). Crystal field in dysprosium garnets. *Phys. Rev.* 184, 285–293.

Guo, F.-S., Day, B. M., Chen, Y.-C., Tong, M.-L., Mansikkamäki, A., and Layfield, R. A. (2017). A dysprosium metallocene single-molecule magnet functioning at the axial limit. *Angew. Chem. Int. Ed.* 56, 11445–11449. doi: 10.1002/anie.201705426

Guo, F.-S., Day, B. M., Chen, Y.-C., Tong, M.-L., Mansikkamäki, A., and Layfield, R. A. (2018). Magnetic hysteresis up to 80 kelvin in a dysprosium metallocene single-molecule magnet. *Science* 362, 1400–1403. doi: 10.1126/science.aav0652

Gupta, S. K., Rajeshkumar, T., Rajaraman, G., and Murugavel, R. (2016). An air-stable Dy(iii) single-ion magnet with high anisotropy barrier and blocking temperature. *Chem. Sci.* 7, 5181–5191. doi: 10.1039/C6SC00279J

Hang, T., Zhang, W., Ye, H.-Y., and Xiong, R.-G. (2011). Metal-organic complex ferroelectrics. *Chem. Soc. Rev.* 40, 3577–3598. doi: 10.1039/C0CS00226G

Horcajada, P., Gref, R., Baati, T., Allan, P. K., Maurin, G., Couvreur, P., et al. (2012). Metal–organic frameworks in biomedicine. *Chem. Rev.* 112, 1232–1268. doi: 10.1021/cr200256v

Ishikawa, N., Sugita, M., Ishikawa, T., Koshihara, S.-Y., and Kaizu, Y. (2003). Lanthanide double-decker complexes functioning as magnets at the single-molecular level. *J. Am. Chem. Soc.* 125, 8694–8695. doi: 10.1021/ja029629n

Jia, J.-H., Li, Q.-W., Chen, Y.-C., Liu, J.-L., and Tong, M.-L. (2019). Luminescent single-molecule magnets based on lanthanides: design strategies, recent advances and magneto-luminescent studies. *Coord. Chem. Rev.* 378, 365–381. doi: 10.1016/j.ccr.2017.11.012

Leuenberger, M. N., and Loss, D. (2001). Quantum computing in molecular magnets. *Nature* 410, 789–793. doi: 10.1038/35071024

Li, B., Wen, H.-M., Cui, Y., Zhou, W., Qian, G., and Chen, B. (2016). Emerging multifunctional metal–organic framework materials. *Adv. Mater.* 28, 8819–8860. doi: 10.1002/adma.201601133

Liddle, S. T., and van Slageren, J. (2015). Improving f-element single molecule magnets. *Chem. Soc. Rev.* 44, 6655–6669. doi: 10.1039/C5CS00222B

Liu, J., Chen, Y.-C., Liu, J.-L., Vieru, V., Ungur, L., Jia, J.-H., et al. (2016). A stable pentagonal bipyramidal dy(iii) single-ion magnet with a record magnetization reversal barrier over 1000 K. *J. Am. Chem. Soc.* 138, 5441–5450. doi: 10.1021/jacs.6b02638

Long, J., Basalov, I. V., Forosenko, N. V., Lyssenko, K. A., Mamontova, E., Cherkasov, A. V., et al. (2018a). Dysprosium single-molecule magnets with bulky schiff-base ligands: modification of the slow relaxation of the magnetization by substituent change. *Chem. Eur. J.* 25, 474–478. doi: 10.1002/chem.201804429

Long, J., Guari, Y., Ferreira, R. A. S., Carlos, L. D., and Larionova, J. (2018b). Recent advances in luminescent lanthanide based single-molecule magnets. *Coord. Chem. Rev.* 363, 57–70. doi: 10.1016/j.ccr.2018.02.019

Long, J., Guari, Y., Guerin, C., and Larionova, J. (2016a). Prussian blue type nanoparticles for biomedical applications. *Dalton Trans.* 45, 17581–17587. doi: 10.1039/C6DT01299J

Long, J., Mamontova, E., Freitas, V., Luneau, D., Vieru, V., Chibotaru, L. F., et al. (2016b). Study of the influence of magnetic dilution over relaxation processes in a Zn/Dy single-ion magnet by correlation between luminescence and magnetism. *RSC Adv.* 6, 108810–108818. doi: 10.1039/C6RA24115H

Long, J., Rouquette, J., Thibaud, J.-M., Ferreira, R. A. S., Carlos, L. D., Donnadieu, B., et al. (2015). A high-temperature molecular ferroelectric Zn/Dy complex exhibiting single-ion-magnet behavior and lanthanide luminescence. *Angew. Chem. Int. Ed.* 54, 2236–2240. doi: 10.1002/anie.201410523

Long, J., Vallat, R., Ferreira, R. A. S., Carlos, L. D., Almeida Paz, F. A., Guari, Y., et al. (2012). A bifunctional luminescent single-ion magnet: towards correlation between luminescence studies and magnetic slow relaxation processes. *Chem. Commun.* 48, 9974–9976. doi: 10.1039/c2cc35321k

Mandal, P., Pitcher, M. J., Alaria, J., Niu, H., Borisov, P., Stamenov, P., et al. (2015). Designing switchable polarization and magnetization at room temperature in an oxide. *Nature* 525, 363–366. doi: 10.1038/nature14881

Meng, Y.-S., Xu, L., Xiong, J., Yuan, Q., Liu, T., Wang, B.-W., et al. (2018). Low-coordinate single-ion magnets by intercalation of lanthanides into a phenol matrix. *Angew. Chem. Int. Ed.* 57, 4673–4676. doi: 10.1002/anie.201801223

Oyarzabal, I., Ruiz, J., Ruiz, E., Aravena, D., Seco, J. M., and Colacio, E. (2015). Increasing the effective energy barrier promoted by the change of a counteranion in a Zn-Dy-Zn SMM: slow relaxation via the second excited state. *Chem. Commun.* 51, 12353–12356. doi: 10.1039/C5CC04495B

Pointillart, F., le Guennic, B., Cador, O., Maury, O., and Ouahab, L. (2015). Lanthanide ion and tetrathiafulvalene-based ligand as a "Magic" couple toward luminescence, single molecule magnets, and magnetostructural correlations. *ACC. Chem. Res.* 48, 2834–2842. doi: 10.1021/acs.accounts.5b00296

Ren, M., Bao, S.-S., Ferreira, R. A. S., Zheng, L.-M., and Carlos, L. D. (2014). A layered erbium phosphonate in pseudo-D5h symmetry exhibiting field-tunable magnetic relaxation and optical correlation. *Chem. Commun.* 50, 7621–7624. doi: 10.1039/C4CC02085E

Rinehart, J. D., and Long, J. R. (2011). Exploiting single-ion anisotropy in the design of f-element single-molecule magnets. *Chem. Sci.* 2, 2078–2085. doi: 10.1039/c1sc00513h

Shintoyo, S., Murakami, K., Fujinami, T., Matsumoto, N., Mochida, N., Ishida, T., et al. (2014). Crystal field splitting of the ground state of terbium(III) and dysprosium(III) complexes with a triimidazolyl tripod ligand and an acetate determined by magnetic analysis and luminescence. *Inorg. Chem.* 53, 10359–10369. doi: 10.1021/ic501453h

Sun, W.-B., Yan, P.-F., Jiang, S.-D., Wang, B.-W., Zhang, Y.-Q., Li, H.-F., et al. (2016). High symmetry or low symmetry, that is the question - high performance Dy(iii) single-ion magnets by electrostatic potential design. *Chem. Sci.* 7, 684–691. doi: 10.1039/C5SC02986D

Tang, J., and Zhang, P. (eds.). (2015). "Lanthanide single-ion molecular magnets," in *Lanthanide Single Molecule Magnets* (Berlin: Springer Berlin Heidelberg), 41–90. doi: 10.1007/978-3-662-46999-6

Train, C., Gruselle, M., and Verdaguer, M. (2011). The fruitful introduction of chirality and control of absolute configurations in molecular magnets. *Chem. Soc. Rev.* 40, 3297–3312. doi: 10.1039/c1cs15012j

Ungur, L., and Chibotaru, L. F. (2016). Strategies toward high-temperature lanthanide-based single-molecule magnets. *Inorg. Chem.* 55, 10043–10056. doi: 10.1021/acs.inorgchem.6b01353

Upadhyay, A., Singh, S. K., Das, C., Mondol, R., Langley, S. K., Murray, K. S., et al. (2014). Enhancing the effective energy barrier of a Dy(iii) SMM using a bridged diamagnetic Zn(ii) ion. *Chem. Commun.* 50, 8838–8841. doi: 10.1039/C4CC02094D

Wang, H., Zhang, D., Ni, Z.-H., Li, X., Tian, L., and Jiang, J. (2009). Synthesis, crystal structures, and luminescent properties of phenoxo-bridged heterometallic trinuclear propeller- and sandwich-like schiff-base complexes. *Inorg. Chem.* 48, 5946–5956. doi: 10.1021/ic9002862

Wong, W.-K., Liang, H., Wong, W.-Y., Cai, Z., Li, K.-F., and Cheah, K.-W. (2002). Synthesis and near-infrared luminescence of 3d-4f bi-metallic Schiff base complexes. *New. J. Chem.* 26, 275–278. doi: 10.1039/B104175B

Wong, W.-K., Yang, X., Jones, R. A., Rivers, J. H., Lynch, V., Lo, W.-K., et al. (2006). Multinuclear luminescent schiff-base Zn–Nd sandwich complexes. *Inorg. Chem.* 45, 4340–4345. doi: 10.1021/ic051866e

Woodruff, D. N., Winpenny, R. E. P., and Layfield, R. A. (2013). Lanthanide single-molecule magnets. *Chem. Rev.* 113, 5110–5148. doi: 10.1021/cr400018q

Yamashita, K., Miyazaki, R., Kataoka, Y., Nakanishi, T., Hasegawa, Y., Nakano, M., et al. (2013). A luminescent single-molecule magnet: observation of magnetic anisotropy using emission as a probe. *Dalton Trans.* 42, 1987–1990. doi: 10.1039/C2DT32785F

Yang, X., and Jones, R. A. (2005). Anion dependent self-assembly of "Tetra-Decker" and "Triple-Decker" luminescent Tb(III) salen complexes. *J. Am. Chem. Soc.* 127, 7686–7687. doi: 10.1021/ja051292c

Yang, X., Jones, R. A., and Huang, S. (2014). Luminescent 4f and d-4f polynuclear complexes and coordination polymers with flexible salen-type ligands. *Coord. Chem. Rev.* 273–274. doi: 10.1016/j.ccr.2013.11.012

Conflict of Interest Statement: The author declares that the research was conducted in the absence of any commercial or financial relationships that could be construed as a potential conflict of interest.

Copyright © 2019 Long. This is an open-access article distributed under the terms of the Creative Commons Attribution License (CC BY). The use, distribution or reproduction in other forums is permitted, provided the original author(s) and the copyright owner(s) are credited and that the original publication in this journal is cited, in accordance with accepted academic practice. No use, distribution or reproduction is permitted which does not comply with these terms.

frontiers in Chemistry

ORIGINAL RESEARCH
published: 31 January 2019
doi: 10.3389/fchem.2019.00012

C–X (X = N, O) Cross-Coupling Reactions Catalyzed by Copper-Pincer Bis(N-Heterocyclic Carbene) Complexes

*Jennifer L. Minnick, Doaa Domyati, Rachel Ammons and Laleh Tahsini**

Department of Chemistry, Oklahoma State University, Stillwater, OK, United States

Over the last two decades, N-heterocyclic carbene (NHC)–copper catalysts have received considerable attention in organic synthesis. Despite the popularity of copper complexes containing monodentate NHC ligands and recent development of poly(NHC) platforms, their application in C–C and C–heteroatom cross-coupling reactions has been limited. Recently, we reported an air-assisted Sonogashira-type cross-coupling catalyzed by well-defined cationic copper-pincer bis(NHC) complexes. Herein, we report the application of these complexes in Ullmann-type C–X (X = N, O) coupling of azoles and phenols with aryl halides in a relatively short reaction time. In contrast to other well-defined copper(I) catalysts that require an inert atmosphere for an efficient C–X coupling, the employed Cu(I)-pincer bis(NHC) complexes provide good to excellent yields in air. The air-assisted reactivity, unlike that in the Sonogashira reaction, is also affected by the base employed and the reaction time. With Cs_2CO_3 and K_2CO_3, the oxygen-generated catalyst is more reactive than the catalyst formed under argon in a short reaction time (12 h). However, the difference in reactivity is compromised after a 24 h reaction with K_2CO_3. The efficient pincer Cu-NHC/O_2/Cs_2CO_3 system provides great to excellent cross-coupling yields for electronically diverse aryl iodides and imidazole derivatives. The catalyst scope is controlled by a balance between nucleophilicity, coordinating ability, and the steric hindrance of aryl halides and N-/O-nucleophiles.

Keywords: Cu-pincer NHC complexes, Ullmann-type C–X coupling, air-assisted cross-coupling, copper-oxygen catalysts, N-aryl imidazoles, biarylethers

OPEN ACCESS

Edited by:
Luís António Dias Carlos, University of Aveiro, Portugal

Reviewed by:
Guo-Hong Tao, Sichuan University, China
Annaluisa Mariconda, University of Salerno, Italy

****Correspondence:***
Laleh Tahsini
tahsini@okstate.edu

Specialty section:
This article was submitted to Inorganic Chemistry, a section of the journal Frontiers in Chemistry

Received: *04 November 2018*
Accepted: *07 January 2019*
Published: *31 January 2019*

Citation:
Minnick JL, Domyati D, Ammons R and Tahsini L (2019) C–X (X = N, O) Cross-Coupling Reactions Catalyzed by Copper-Pincer Bis(N-Heterocyclic Carbene) Complexes. Front. Chem. 7:12. doi: 10.3389/fchem.2019.00012

INTRODUCTION

The N-arylazoles and biarylethers are among the most commonly found motifs in pharmaceuticals, biologically active molecules, crop-protection chemicals, and material science. A huge number of drugs contain N-arylimidazole moieties including cyclic AMP phosphodiesterase inhibitors (Sircar et al., 1987; Venuti et al., 1988; Güngör et al., 1992; Martinez et al., 1992; Sawanishi et al., 1997), thromboxane synthase inhibitors (Iizuka et al., 1981; Martinez et al., 1992; Cozzi et al., 1993; Nicolaï et al., 1993), topical antiglaucoma agents (Lo et al., 1992), and cardiotonic agents (Hagedorn et al., 1987; Erhardt et al., 1989; Shaw et al., 1992). In this regard, transition-metal catalyzed C-heteroatom coupling reactions have become one of the most important areas in modern chemical synthesis. Several methods have been developed for the direct coupling of azole with functionalized arenes. The most common route is nucleophilic aromatic substitution of azoles with aryl halides;

however, this approach is limited to aryl halides with strongly electron-withdrawing groups (Venuti et al., 1988; Güngör et al., 1992; Cozzi et al., 1993; Ohmori et al., 1996). A second approach to N-arylazoles is traditional Ullmann-type coupling that has a broader aryl halide scope, but requires high temperatures (>150°C), polar solvents, and often stoichiometric amounts of copper or copper salts (Ullmann and Bielecki, 1901; Ullmann, 1903; Ullmann and Sponagel, 1905). To achieve milder C–N/C–O coupling conditions, efforts have focused on the use of more activated arenes such as arylbismuth (Barton et al., 1988), -tin, (Davydov et al., 2002) -lead (Lopez-Alvarado et al., 1995), -silanes (Lam et al., 2000), and -boronic acids (Lam et al., 1998; Mederski et al., 1999; Collot et al., 2000). Some of these methods are limited in scope to certain azole and arenes or produce toxic side-products, e.g., copper-catalyzed N-phenylation of indoles by triphenylbismuth bis(trifluoroacetate) or synthesis of N-arylimidazoles using *p*-tolyllead triacetate and $Cu(OAc)_2$ catalyst (Barton et al., 1988; Lopez-Alvarado et al., 1995). A significant change to the conditions and the scope of azole N-arylation was made by Chan and Lam that reported direct coupling of arylboronic acids and azoles using stoichiometric amounts of $Cu(OAc)_2$ and pyridine (or trimethylamine) at room temperature (Lam et al., 1998). A similar approach was alternatively used to synthesize diaryl ethers from phenols and arylboronic acids (Evans et al., 1998). The shortcoming of this method, use of stoichiometric amounts of copper salts and base, was later improved in the report of a diamine-copper-catalyzed N-arylation of imidazoles (Collman and Zhong, 2000). The scope has been recently extended to heterocycles and diarylethers (Lam et al., 2001; Guillou et al., 2009; Wentzel et al., 2009; Liu et al., 2010; Wang et al., 2010).

Another approach toward milder C(aryl)–heteroatom bond formation is via a ligand-accelerated Ullmann-type coupling of aryl halides and nucleophiles at relatively lower temperatures than those used in Ullmann condensation. Buchwald reported the synthesis of various N-arylimidazoles using catalytic amounts of $Cu(OTf)_2{\cdot}C_6H_6$ and stoichiometric amounts of 1,10-phenanthroline and *trans*,*trans*-dibenzylideneacetone in xylenes at different temperatures (110–125°C) (Kiyomori et al., 1999). A vital step to this method, facilitated by soluble cuprous ions, (Paine, 1987) is ligand screening to identify the most effective platform. In this regard, systematic studies were undertaken on N-, O-, and P-donor ligands as well as copper sources which has led to the development of efficient catalysts for cross-coupling of N-heterocycles and phenols with aryl halides (Arterburn et al., 2001; Klapars et al., 2001; Antilla et al., 2002, 2004; Kelkar et al., 2002; Evano et al., 2008). In addition to the catalysts formed *in-situ* from copper salts and ligands, some well-defined copper catalysts have been identified for the N-arylation of azoles and O-arylation of phenols (Gujadhur and Venkataraman, 2001; Gujadhur et al., 2001; Choudary et al., 2005; Biffis et al., 2009). Interestingly, the reports of phosphine- and NHC-supported copper catalysts in this chemistry has been limited, unlike N- and O-donor systems. To the best of our knowledge, there has been only two reports of NHC ligands in Ullmann-type coupling wherein the catalytic activity of cationic trinuclear Cu(I)-tris(NHC) and neutral mononuclear [Cu(IPr)Cl] has been assessed (Tubaro et al., 2008; Biffis et al., 2009). The trinuclear complexes presented high reactivities in C–N, C–O, and C–C coupling reactions with a low catalyst loading.

Recently, we have developed mononuclear pyridylmethyl-linked Cu(I)-bis(NHC) complexes with alkyl wingtips, Cu-$I(R)^{C\wedge N\wedge C}$, and examined their catalytic reactivity in an air-assisted cross-coupling of terminal alkynes and aryl iodides (Domyati et al., 2016, 2018). Our interest in Ullmann-type coupling was driven partly by a need to synthesize N-arylated imidazole derivatives for our pyridine-based bis(NHC) ligands with aryl wingtips. Herein, we report based-controlled, air-assisted Ullmann-type coupling of azoles and phenols with aryl halides facilitated by pincer Cu-NHC complexes (**Figure 1**).

RESULTS AND DISCUSSION

Synthesis of Copper Catalysts

The pyridine-based pincer bis(NHC) complexes containing Me, Et, and ^{i}Pr substituents were prepared via the reaction of tetrakis(acetonitrile)copper(I) hexafluorophosphate as copper source and an *in-situ* generated carbene following our previously described procedure (Domyati et al., 2016). To compare the catalytic activity of the cationic pincer Cu-NHC complexes to one of the most efficient copper-carbene catalysts known to date, [Cu(IPr)Cl] (**4**), it was prepared by modifying a published procedure (Santoro et al., 2013; Lazreg et al., 2015). In an attempt to conduct Ullmann-type coupling of azoles under ambient conditions similar to that reported previously for primary amines and N-heterocycles (Shafir and Buchwald, 2006), an *in-situ* formed copper catalyst from CuI and 2-acetylcyclohexanone (**5**) was also utilized.

Cross-Coupling Reaction Optimization

We chose the coupling of imidazole and 4-iodoacetophenone as a model reaction to determine the optimal conditions for catalysis (**Table 1**). All reactions were carried out in a 20 mL screw-cap reaction vial that was charged with reagents and 5 mL reagent-grade solvent in air. The model reaction was initially performed using **3** as catalyst for 12 h in different solvents which provided the highest yield of N-arylimidazole in DMF at 120°C (**Table 1**, entry 5). The yield increased only to a slight extent (+4%) when the reaction time was doubled indicating an almost-completed cross-coupling in 12 h (**Table 1**, entry 6). This finding and the lack of any biaryl coupling, a potential side reaction in air, makes the pincer complexes one of the most efficient, well-defined catalysts for N-arylation of imidazole (Kiyomori et al., 1999; Biffis et al.,

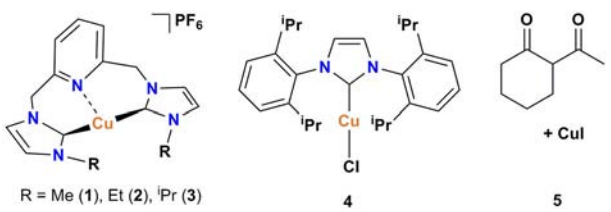

FIGURE 1 | Copper catalysts used in this study.

TABLE 1 | Reaction of imidazole with 4-iodoacetophenone catalyzed by copper complexes[a].

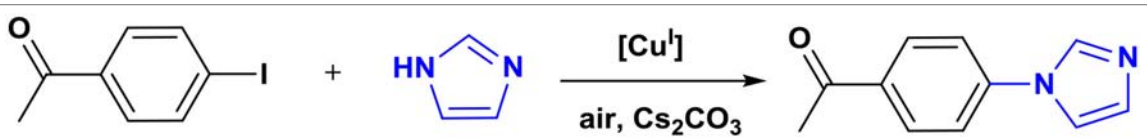

Entry	[Cu]	Solvent	Temp. (°C)	Time (h)	Yield (%)[b]
1	3	DMSO	120	12	48
2	3	p-xylene	120	12	16
3	3	Dioxane	120	12	61
4	3	Toluene	120	12	<7
5	3	DMF	120	12	78
6	3	DMF	120	24	82 (62)[c]
7	3	DMF	60	24	33
8	3	DMF	r.t.	24	0
9	2	DMF	120	24	80
10	1	DMF	120	24	71
11	4	DMF	120	24	50
12	No copper	DMF	120	24	24
13	5	DMF	r.t.	24	63
14	5	DMF	120	24	77[d] (78)[e]

[a] *Reaction conditions were as follows: 4-iodoacetophenone (0.5 mmol), imidazole (0.75 mmol), Cs_2CO_3 (1.0 mmol), [Cu] (0.05 mmol), solvent (5 mL) in air.*
[b] *Isolated yield.*
[c] ***3*** *(0.025 mmol, 5 mol%) was used.*
[d] *Under Ar and using optimized amount of reagents in (Shafir and Buchwald, 2006).*
[e] *Under air.*

2009). The catalytic activity of the pincer Cu-NHC complexes is strictly controlled by temperature. Reducing the temperature to 60°C provided a much lower yield and no conversion occurred at room temperature (**Table 1**, entries 7-8). The model reaction was then tested using **1**, **2**, and **4** as other well-defined catalysts, however, the product was isolated at lower yields than that obtained with **3**. Interestingly, **4** provided the lowest yield, even lower than that of **3** at 5 mol% loading after 24 h (**Table 1**, entries 6, 11). The reduced catalytic activity of **4** in this reaction, compared to that reported previously for the same substrates in DMSO at 100°C, is most likely due to different solvent and/or atmosphere (Biffis et al., 2009). The cross-coupling reaction in the absence of a copper catalyst provided only 24% yield under the same reaction conditions (**Table 1**, entry 12). The optimal amount of the base was determined by the highest cross-coupling yield achieved for the model reaction using various amounts of Cs_2CO_3 (**Supplementary Figure 1**).

Furthermore, we attempted to compare the pincer complexes activity to an *in-situ* formed catalyst, **5**, reported as an efficient catalyst for the Ullman-type coupling of primary amines and N-heterocycles (Shafir and Buchwald, 2006). First, the model N-arylation of imidazole was performed using **5** under the exact same conditions reported for the coupling of non-azole substrates. At room temperature, the **5**-catalyzed reaction of 4-iodoacetophenone and imidazole afforded 63% cross-coupling yield, whereas no product was formed using **3** (**Table 1**, entries 8, 13). Although this result makes **5** a more reactive catalyst than **3**, a further study revealed its limited scope due to a substrate-dependent reactivity with other aryl halides (**Supplementary Figure 2**). The coupling of imidazole with 4-iodonitrobenzene provided 67% yield at room temperature, comparable to that of the model reaction, but no cross-coupled product was isolated for 4-(trifluoromethyl)iodobenzene. Further attempts to improve the yields by conducting these reactions at a higher temperature (120°C) revealed a moderate increase for the model substrate (**Table 1**, entry 14). However, a reverse temperature effect was found with the 4-NO_2 derivative and the conversion was reduced significantly. Additionally, temperature had no improving effect on the yield of 4-CF_3 substrate and no conversion occurred even at 120°C. Unlike pincer Cu-NHC catalysts, air did not have a noticeable effect on the cross-coupling reactions catalyzed by **5** and no clear improvement of the yield was found (**Table 1**, entry 14).

Atmosphere and Base Effect

The assistant role of oxygen in Cu-NHC catalyzed Sonogashira reaction was previously shown by the greater yield of the product in air than that under argon (Domyati et al., 2018). This effect in Ullmann-type coupling was examined by conducting the model reaction under argon using the same optimized conditions found in air. After a 12 h anaerobic reaction, the N-arylimidazole was isolated at almost half of the yield obtained under air indicating the facilitating effect of oxygen in the C–N coupling reactions catalyzed by **3** as well (**Figure 2**). Interestingly, extending the reaction time to 24 h improved the yield only to a slight extent, similar to the trend observed for the aerobic reaction. To examine the effect of oxygen concentration, the model reaction

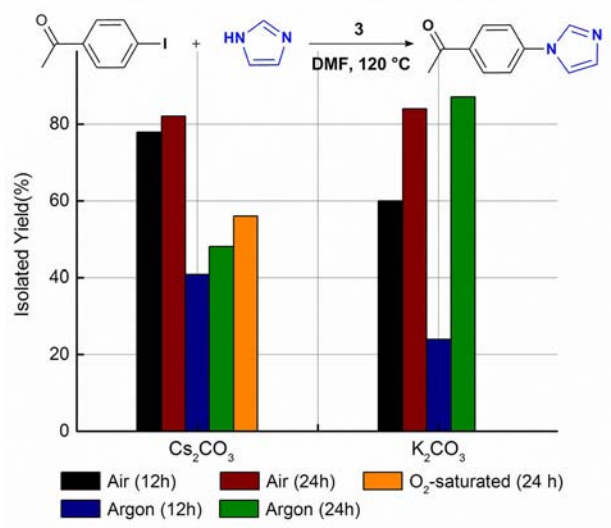

FIGURE 2 | The isolated yield of the cross-coupled product from imidazole and 4-iodoacetophenone reaction catalyzed by **3** and Cs_2CO_3 or **3** and K_2CO_3 in DMF at 120°C under an air, O_2-saturated, and argon atmosphere. Reaction conditions were as follows: aryl halide (0.5 mmol), imidazole (0.75 mmol), base (1.0 mmol), **3** (0.05 mmol), DMF (5 mL).

was performed in O_2-saturated DMF which provided a lower yield than in air but slightly more than that under argon. This indicates the significance of a certain stoichiometry of oxygen and copper to the catalytic activity, similar to that in **3**-catalyzed Sonogashira-type coupling (Domyati et al., 2018).

The oxygen-assisted cross-coupling mechanism is also controlled by the base used in the reaction. While Cs_2CO_3 provided more cross-coupled product in air than under argon in both 12 h and 24 h reaction times, the yields obtained with K_2CO_3 after 24 h were almost identical under both atmospheres. In contrast, K_2CO_3 provided a much smaller cross-coupling yield under argon in 12 h than in air supporting a slow formation of the active catalyst under anaerobic conditions. The distinct reactivity of Cu-I(R)$^{C\wedge N\wedge C}$ complexes in air from that under argon could be due to different active catalysts and potentially a different mechanism that needs to be clarified. However, the presented data support a higher cross-coupling reactivity of the air-generated catalyst in the presence of Cs_2CO_3 than that in the presence of K_2CO_3. On the other hand, the slowly-formed active catalyst under argon is more reactive in the presence of K_2CO_3 than with Cs_2CO_3. Such versatility of active catalysts controlled by simple change of the base or atmosphere is significant to the application scope of the system.

Reaction Scope

The optimized conditions were applied to a range of electronically diverse aryl halides and different N- and O-nucleophiles to explore the application scope of the pincer Cu-NHC catalysts in Ullmann-type coupling. Considering the close yields obtained for the model reaction after 12 and 24 h, most reactions were performed at both times to examine any substrate-dependent behavior in this matter. The cross-coupled products were isolated with <10% difference in yield between the two reaction times, except for the reaction of 4-iodotoluene with imidazole and 4-iodoacetophenone with pyrazole and phenol (**Scheme 1**, **3**, **13**, **16**). The coupling of *p*-substituted aryl iodides bearing electron-donating and electron-withdrawing groups with imidazole provided the corresponding N-arylimidazoles in great (82%) to excellent (>99%) yields (**Scheme 1**). An exception to this trend is the coupling of unactivated iodobenzene and imidazole that provided a moderate yield (58%) of the product in 24 h (**Scheme 1**, **2**). The less pronounced effect of the directing groups of aryl halides on the reactivity of **3** is also shown by the comparable yields of *o*-substituted substrates. While the steric hindrance of 2-iodotoluene and 2-iodonitrobenzene led to a lower cross-coupled product than their *p*-substituted analogs, their isolated yields are close with slightly higher activity of 2-iodotoluene (**Scheme 1**, **9**, **10**). The steric effects appear to play a major role in the reactivity of aryl iodides in the present system given that no product was isolated from the reaction of 2,6-dimethyliodobenzene and imidazole (**Scheme 1**, **19**). The other important parameter affecting the catalyst reactivity is the type of halide. While aryl iodides are highly reactive using **3**, the coupling of activated aryl bromides and chlorides with imidazole was achieved at moderate yields (**Scheme 1**, **11, 12**). Additionally, the coupling of imidazole with heteroaryl iodides is facilitated given the excellent yield obtained for 3-iodopyridine (**Scheme 1**, **8**). The application scope of pincer Cu-NHC complexes in Ullmann-type coupling is also controlled by the type of nucleophile used. The cross-coupling of 4-iodoacetophenone with exemplary heterocycles such as indole, pyrazole, and benzimidazole, as well as phenols provided low (18%) to moderate yields (58%) of corresponding products (**Scheme 1**, **13–18**). The reactivity pattern of nucleophiles appears to be the result of a balance between nucleophilicity and coordinating ability to the copper center controlled by steric effects in the order: imidazole > pyrazole > phenol > benzimidazole > indole. This is further confirmed by no cross-coupled product isolated from the reaction of 3,5-dimethylpyrazole and aryl iodide due to the greater steric hindrance of substituted pyrazole compared to pyrazole, despite its higher nucleophilicity (**Scheme 1**, **20**).

To clarify the scope of reactivity in O-arylation, we examined the coupling of exemplary phenol and aryl iodide derivatives bearing electron-donating and electron-withdrawing groups. Complex **3** showed good reactivity toward activated aryl iodides and phenols with moderate yields (47–57%) isolated from the phenol and p-cresol reaction with 4-iodoacetophenone and 3,5-bis(trifluoromethyl)-iodobenzene (**Scheme 1**, **16–18**). Interestingly, electron-rich aryl halide and/or electron-poor phenols shut down the reaction completely such that no cross-coupled product was isolated.

Comparison to Other Cu-NHC Catalysts

The pincer Cu-NHC complexes (**1–3**) present a new class of Ullmann-type C–heteroatom coupling catalysts with distinct structure and properties from those reported previously (**Table 2**). While complex **4** is air-stable and benefits from good solubility in less polar solvents due to charge neutrality, the

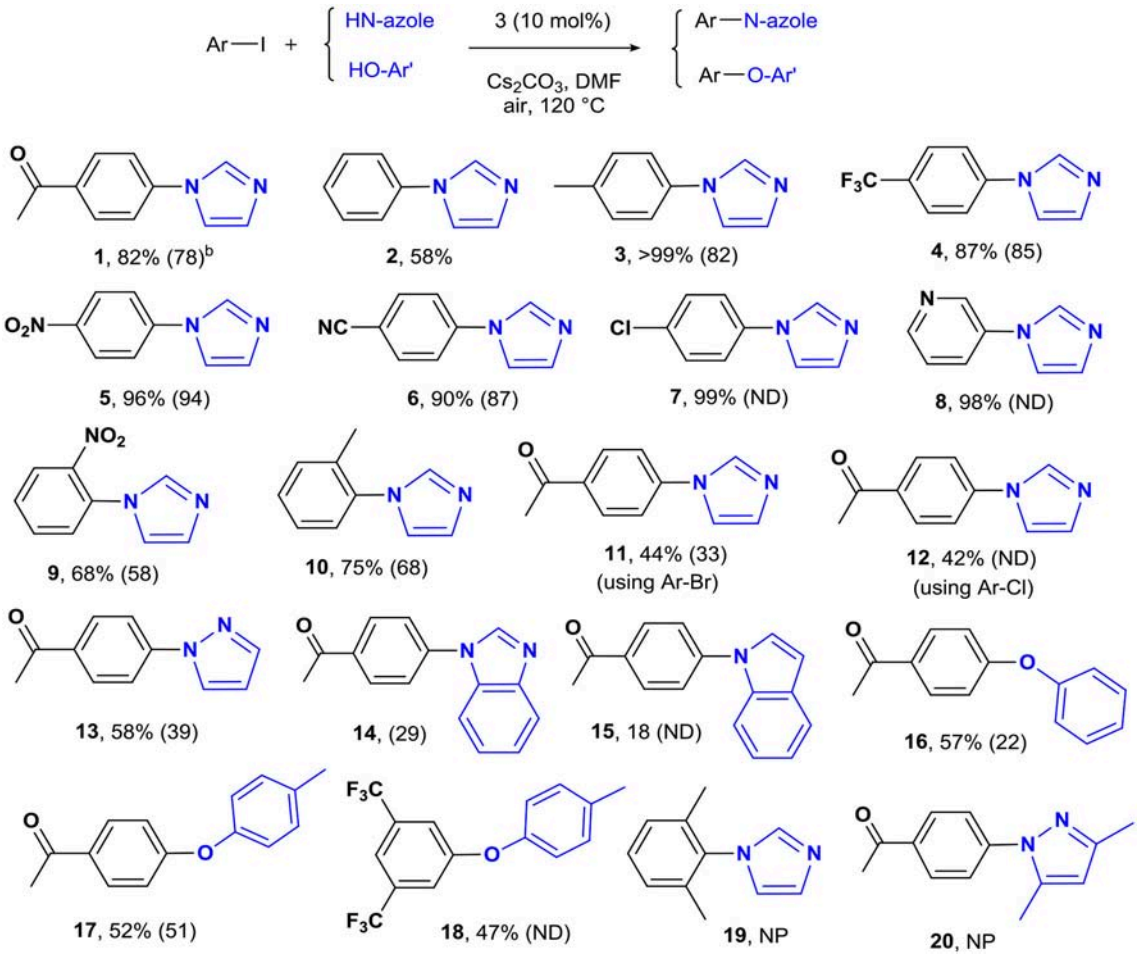

SCHEME 1 | The coupling of aryl halides and N- and O-nucleophiles catalyzed by **3**[a]. [a]Reaction conditions: aryl halide (0.5 mmol), imidazole (0.75 mmol), Cs_2CO_3 (1.0 mmol), [Cu] (0.05 mmol), solvent (5 mL), in air, 24 h. [b]Isolated yields after 24 h reaction time. The yields in parentheses are after 12 h. ND, not determined; NP, no product.

Cu-triscarbene complexes are applicable at a low catalyst loading owing to three Cu(I) ions in a molecular unit. On the other hand, pincer Cu-NHC complexes bearing small alkyl wingtips and open coordination sites can react with oxygen leading to more efficient C–X coupling systems in air than under argon. We have conducted a comparative study between pincer complex **3** and other Cu-NHC systems by taking into account the N-nucleophile substrates used in common (**Table 2**).

In contrast to **4** and the Cu-triscarbene with methyl wingtips (**Table 2**, **A**) that present a low reactivity toward aryl halides bearing weakly electron-donating groups, complex **3** is able to efficiently convert both activated, electron-poor aryl iodides and electron-rich ones (**Table 2**, entries 1, 2). In addition, **3** is able to facilitate the coupling of activated aryl bromides and chlorides with a comparable, moderate efficiency to the Cu-triscarbene complex **B**, but with a lower efficiency than that of complex **4** (**Table 2**, entries 3, 4). Regarding other azoles, **3** performs with a lower efficiency toward N-arylation of pyrazoles than other Cu-NHC complexes (**Table 2**, entry 5). To the best of our knowledge, the reactivity of other Cu-NHC complexes in cross-coupling of aryl halides with benzimidazole and indole substrates has not been reported.

MATERIALS AND METHODS

General Procedure

Imidazolium salts and Cu(I) complexes (**Figure 1**, **1–3**) were synthesized according to published procedure using standard Schlenk techniques or in an MBraun glovebox under Ar atmosphere. 1,3-Bis(diisopropylphenyl)imidazolium chloride, IPr.HCl, was obtained from TCI Chemicals. The solvents used for the syntheses were purified and distilled under N_2 atmosphere before being stored over activated molecular sieves (4 Å) in the glovebox. Tetrahydrofuran was purified by refluxing over Na/benzophenone under a N_2 atmosphere and distilled. Hexane was distilled from CaH_2 under N_2. Reagent-grade N,N-dimethylformamide (DMF), 2-acetylcyclohexanone, cesium- and potassium carbonate, and copper iodide were purchased from Sigma-Aldrich and used as received. Aryl halides were obtained from TCI Chemicals and Sigma. Flash chromatography was

TABLE 2 | Catalytic activity of different Cu-NHC complexes in selected C–N coupling reactions[a].

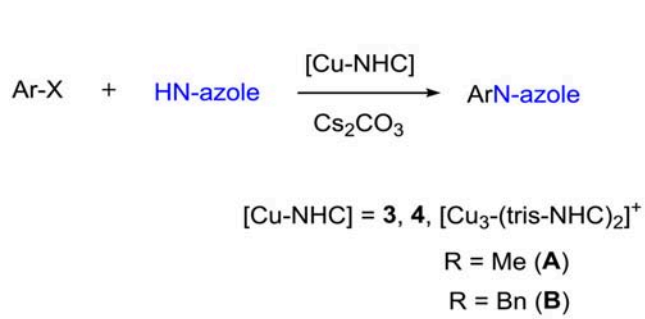

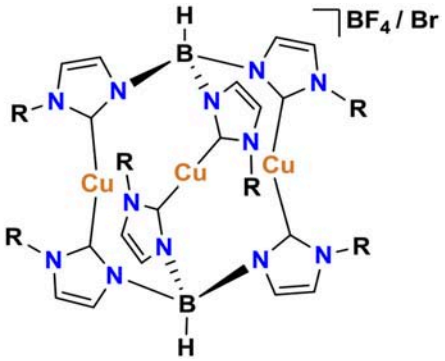

Entry	Aryl halide	Azole	Yield (%)			
			3[a]	A[b]	B[c]	4[c]
1	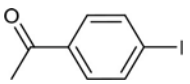	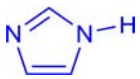	82	>99	85	86
2	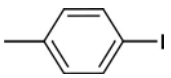	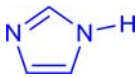	>99	20	93	ND
3	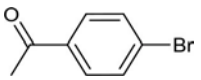	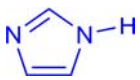	44	70	54	86
4	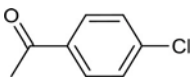	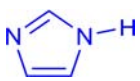	42	50	24	57
5	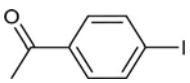	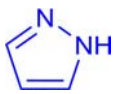	58 (62)[d]	93	ND	90

[a] *Reaction conditions were as follows: aryl halide (0.5 mmol), imidazole (0.75 mmol), Cs_2CO_3 (1.0 mmol), [Cu] (0.05 mmol), solvent (5 mL) in air, 24 h.*
[b] *Literature data (see Tubaro et al., 2008).*
[c] *Literature data (see Biffis et al., 2009).*
[d] *K_2CO_3 was used as a base.*

performed on Merck silica gel 60 (230–400 mesh) obtained from Sigma-Aldrich. NMR spectra were measured using a 400 MHz Bruker Avance III spectrometer. NMR samples were prepared in deuterated solvents, CD_3CN, $CDCl_3$, or DMSO-d_6 containing 0.05% TMS as internal standard. Chemical shifts (δ) for ^1H and ^{13}C NMR spectra were referenced to the resonance of TMS as an internal reference or the residual protio solvent. GC/MS data were collected using Shimadzu GC-MS-QP-2010S.

Synthesis of [Cu(IPr)Cl], 4

The compound was synthesized by modifying a published procedure (Santoro et al., 2013). Under an argon atmosphere, CuCl (0.105 g, 1.06 mmol), IPr.HCl (0.300 g, 0.706 mmol), and K_2CO_3 (0.293 g, 2.12 mmol) were mixed in a reaction vial, and transferred out of the glovebox. The vial was quickly charged with 4–5 mL acetone and kept under refluxing conditions for 48 h. The reaction mixture was filtered through Celite and rinsed with 10–15 mL acetone and 6–7 mL dichloromethane. The filtrate was then concentrated under vacuum and layered with hexane. The resultant white solid was then filtered and kept under vacuum to dry completely. The solid was transferred into a glovebox and recrystallized from THF and hexane affording white crystals in 78% yield (0.270 g). ^1H NMR (CD_3CN with 0.05% v/v TMS, 400 MHz): δ = 7.56 (t, 1H; J = 7.8 Hz), 7.46–7.36 (m, 3H), 2.56 (septet, 2H; J = 6.9 Hz), 1.24 (dd, 12H; J = 6.9 Hz). ^{13}C NMR (CD_3CN with 0.05% v/v TMS, 101 MHz): δ = 146.94, 135.59, 131.47, 125.12, 124.84, 29.52, 29.33, 24.98, 23.86.

Cross-Coupling Reactions Catalyzed by 3 and 4 in Air

A mixture of copper complex (0.05 mmol) and cesium carbonate (1 mmol) was added to a 20 mL vial charged with a Teflon stir bar in the glovebox. The mixture was transferred out of the glovebox and suspended in 2 mL non-anhydrous DMF. To the resulting yellow suspension, a solution of aryl halide (0.5 mmol) in 2 mL DMF followed by a solution of azole or phenol (0.75 mmol) in 1 mL DMF was added. The vial was then sealed and placed in an oil bath with pre-adjusted temperature at 120°C for 12 or 24 h. The cooled mixture was diluted with 20–30 mL ethyl acetate and filtered over a pad of silica. The silica was washed with 30–40 mL ethyl acetate and the filtrate was placed under vacuum

until dry. The residual material was loaded on a silica gel column and eluted with mixtures of hexane and ethyl acetate to afford the corresponding product. The cross-coupling reactions were repeated twice to ensure reproducibility.

Cu-Catalyzed Coupling of 4-Iodoacetophenone and Imidazole in O_2-Saturated DMF

In an argon-filled glovebox, a 20 mL scintillation vial was charged with a Teflon stir bar, copper complex (0.05 mmol), cesium carbonate (1.0 mmol), 4-Iodoacetophenone (0.5 mmol), and imidazole (0.75 mmol). The vial was sealed with a teflon cap bearing a silicone septum and transferred out of the glovebox. To this mixture, 5 mL O_2-saturated DMF prepared by bubbling dry O_2 gas through the solvent for 20 min was added. The reaction vial was then placed in an oil bath with pre-adjusted temperature at 120°C. After reaction completion, the mixture was cooled down, diluted with 20 mL ethyl acetate, and filtered through a pad of silica. The silica was washed with 30–40 mL ethyl acetate and the solvent was then removed under vacuum. The residue was purified by column chromatography to obtain analytically pure product.

Cross-Coupling Reactions Catalyzed by CuI and 2-Acetylcyclohexanone, 5

Under an argon atmosphere, a 20 mL scintillation vial was charged with a Teflon stir bar, CuI (0.05 mmol), cesium carbonate (2.0 mmol), aryl halide (1.0 mmol), imidazole (1.5 mmol), and 3.5 mL anhydrous DMF. To the mixture, 2-acetylcyclohexanone (0.2 mmol) and 0.5 mL DMF were then added. The vial was sealed, brought out of the glovebox and kept stirring at room temperature or was placed in an oil bath with pre-adjusted temperature at 110°C. The progress of the reaction was monitored by TLC at different time intervals. Upon completion of the reaction, the reaction mixture was cooled down, diluted with 20 mL ethyl acetate, and filtered through a pad of silica gel. The silica was washed with 30 mL ethyl acetate and the solvent was then removed under vacuum. The residue was diluted with 2–3 mL ethyl acetate and purified by column chromatography using varying gradients of hexane and ethyl acetate to obtain analytically pure product.

CONCLUSION

We have developed a new protocol for the Ullmann-type coupling of aryl halides with N- and O-nucleophiles catalyzed by pincer Cu-NHC complexes bearing alkyl wingtips. Unlike other well-defined Cu catalysts that are more efficient under inert atmosphere, the pincer complexes present generally a higher reactivity in air. This could be due to different active catalysts involved in the rate-determining step of the aerobic and anaerobic reactions. The oxygen-generated active catalyst was found more reactive than the catalyst formed under argon as indicated by the higher cross-coupled product obtained in air than that under argon. The air-assisted reactivity is also affected by the type of the base in the Ullman-type coupling. The catalytic reaction in air was accelerated to a greater extent using Cs_2CO_3 than K_2CO_3 as indicated by a nearly-completed reaction and a higher cross-coupling yield achieved in 12 h. Building on these findings and by taking advantage of the air-assisted reactivity of pincer complexes, an efficient cross-coupling of aryl iodides and imidazole derivatives has been developed. The catalytic system performed with a great to excellent efficiency toward the coupling of electron-poor and electron-rich aryl iodides with imidazole, but had moderate reactivity with pyrazole and aryl bromides or aryl chlorides. Further studies to clarify the reactivity of the Cu-pincer NHC complexes with nucleophiles and to improve their efficiency toward C–O coupling reactions are currently ongoing in our group.

AUTHOR CONTRIBUTIONS

JM and DD designed and completed most of the experiments and helped with data analysis. RA helped with the synthesis of copper-NHC catalysts and some of the catalytic reactions. LT and JM co-wrote the manuscript and were responsible for discussing and revising the paper.

ACKNOWLEDGMENTS

We gratefully acknowledge Oklahoma State University start-up fund (LT), NSF-BIR 9512269, Oklahoma State Regents for Higher Education, the W. M. Keck Foundation and Conoco Inc. (NMR Spectrometers in the research facility center at Oklahoma State) for financial support.

SUPPLEMENTARY MATERIAL

The Supplementary Material for this article can be found online at: https://www.frontiersin.org/articles/10.3389/fchem.2019.00012/full#supplementary-material

^{1}H and ^{13}C{^{1}H} NMR spectra for **4** and cross-coupled products (**Supplementary Figures 3–19**), catalytic performance graph of CuI/α,β-diketone catalyst (**5**), optimization graph of the base amount, and GC/MS data of cross-coupled products.

REFERENCES

Antilla, J. C., Baskin, J. M., Barder, T. E., and Buchwald, S. L. (2004). Copper–diamine-catalyzed N-arylation of pyrroles, pyrazoles, indazoles, imidazoles, triazoles. *J. Org. Chem.* 69, 5578–5587. doi: 10.1021/jo049658b

Antilla, J. C., Klapars, A., and Buchwald, S. L. (2002). The copper-catalyzed N-arylation of indoles. *J. Am. Chem. Soc.* 124, 11684–11688. doi: 10.1021/ja027433h

Arterburn, J. B., Pannala, M., and Gonzalez, A. M. (2001). Catalytic amination of 5-iodouracil derivatives. *Tetrahedron Lett.* 42, 1475–1477. doi: 10.1016/S0040-4039(00)02315-7

Barton, D. H. R., Finet, J. P., and Khamsi, J. (1988). Copper catalysed phenylation of indoles by triphenylbismuth BIS-trifluoroacetate. *Tetrahedron Lett*. 29, 1115–1118. doi: 10.1016/S0040-4039(00)86664-2

Biffis, A., Tubaro, C., Scattolin, E., Basato, M., Papini, G., Santini, C., et al. (2009). Trinuclear copper(I) complexes with triscarbene ligands: catalysis of C-N and C-C coupling reactions. *Dalton Trans*. 7223–7229. doi: 10.1039/b906730b

Choudary, B. M., Sridhar, C., Kantam, M. L., Venkanna, G. T., and Sreedhar, B. (2005). Design and evolution of copper apatite catalysts for N-arylation of heterocycles with chloro- and fluoroarenes. *J. Am. Chem. Soc*. 127, 9948–9949. doi: 10.1021/ja0436594

Collman, J. P., and Zhong, M. (2000). An efficient diamine·copper complex-catalyzed coupling of arylboronic acids with imidazoles. *Org. Lett*. 2, 1233–1236. doi: 10.1021/ol000033j

Collot, V., Bovy, P. R., and Rault, S. (2000). First combined selective N- and C-arylations with boronic acids: application to the synthesis of 1,3-diarylindazoles. *Tetrahedron Lett*. 41, 9053–9057. doi: 10.1016/S0040-4039(00)01650-6

Cozzi, P., Carganico, G., Fusar, D., Grossoni, M., Menichincheri, M., Pinciroli, V., et al. (1993). Imidazol-1-yl and pyridin-3-yl derivatives of 4-phenyl-1,4-dihydropyridines combining Ca^{2+} antagonism and thromboxane A2 synthase inhibition. *J. Med. Chem*. 36, 2964–2972. doi: 10.1021/jm00072a017

Davydov, D. V., Beletskaya, I. P., Semenov, B. B., and Smushkevich, Y. I. (2002). Regioselective arylation of N-tributylstannylated 5-substituted tetrazoles by diaryliodonium salts in the presence of $Cu(OAc)_2$. *Tetrahedron Lett*. 43, 6217–6219. doi: 10.1016/S0040-4039(02)01326-6

Domyati, D., Hope, S. L., Latifi, R., Hearns, M. D., and Tahsini, L. (2016). Cu(I) complexes of pincer pyridine-based N-heterocyclic carbenes with small wingtip substituents: synthesis and structural and spectroscopic studies. *Inorg. Chem*. 55, 11685–11693. doi: 10.1021/acs.inorgchem.6b01646

Domyati, D., Latifi, R., and Tahsini, L. (2018). Sonogashira-type cross-coupling reactions catalyzed by copper complexes of pincer N-heterocyclic carbenes. *J. Organomet. Chem*. 860, 98–105. doi: 10.1016/j.jorganchem.2018.02.028

Erhardt, P. W., Hagedorn, A. A., Davey, D., Pease, C. A., Venepalli, B. R., Griffin, C. W., et al. (1989). Cardiotonic agents. 5. Fragments from the heterocycle-phenyl-imidazole pharmacophore. *J. Med. Chem*. 32, 1173–1176. doi: 10.1021/jm00126a005

Evano, G., Blanchard, N., and Toumi, M. (2008). Copper-mediated coupling reactions and their applications in natural products and designed biomolecules synthesis. *Chem. Rev*. 108, 3054–3131. doi: 10.1021/cr8002505

Evans, D. A., Katz, J. L., and West, T. R. (1998). Synthesis of diaryl ethers through the copper-promoted arylation of phenols with arylboronic acids. An expedient synthesis of thyroxine. *Tetrahedron Lett*. 39, 2937–2940. doi: 10.1016/S0040-4039(98)00502-4

Guillou, S., Bonhomme, F. J., and Janin, Y. L. (2009). Nitrogen's reactivity of various 3-alkoxypyrazoles. *Tetrahedron* 65, 2660–2668. doi: 10.1016/j.tet.2009.01.099

Gujadhur, R., and Venkataraman, D. (2001). Synthesis of diaryl ethers using an easy-to-prepare, air-stable, soluble copper(I) catalyst. *Synth. Commun*. 31, 2865–2879. doi: 10.1081/SCC-100105338

Gujadhur, R. K., Bates, C. G., and Venkataraman, D. (2001). Formation of aryl–nitrogen, aryl–oxygen, and aryl–carbon bonds using well-defined copper(I)-based catalysts. *Org. Lett*. 3, 4315–4317. doi: 10.1021/ol0170105

Güngör, T., Fouquet, A., Teulon, J. M., Provost, D., Cazes, M., and Cloarec, A. (1992). Cardiotonic agents. Synthesis and cardiovascular properties of novel 2-arylbenzimidazoles and azabenzimidazoles. *J. Med. Chem*. 35, 4455–4463. doi: 10.1021/jm00101a024

Hagedorn, A. A., Erhardt, P. W., Lumma, W. C., Wohl, R. A., Cantor, E., Chou, Y. L., et al. (1987). Cardiotonic agents. 2. (Imidazolyl)aroylimidazolones, highly potent and selective positive inotropic agents. *J. Med. Chem*. 30, 1342–1347. doi: 10.1021/jm00391a013

Iizuka, K., Akahane, K., Momose, D., Nakazawa, M., Tanouchi, T., Kawamura, M., et al. (1981). Highly selective inhibitors of thromboxane synthetase. 1. Imidazole derivatives. *J. Med. Chem*. 24, 1139–1148. doi: 10.1021/jm00142a005

Kelkar, A. A., Patil, N. M., and Chaudhari, R. V. (2002). Copper-catalyzed amination of aryl halides: single-step synthesis of triarylamines. *Tetrahedron Lett*. 43, 7143–7146. doi: 10.1016/S0040-4039(02)01708-2

Kiyomori, A., Marcoux, J.-F., and Buchwald, S. L. (1999). An efficient copper-catalyzed coupling of aryl halides with imidazoles. *Tetrahedron Lett*. 40, 2657–2660. doi: 10.1016/S0040-4039(99)00291-9

Klapars, A., Antilla, J. C., Huang, X., and Buchwald, S. L. (2001). A general and efficient copper catalyst for the amidation of aryl halides and the N-arylation of nitrogen heterocycles. *J. Am. Chem. Soc*. 123, 7727–7729. doi: 10.1021/ja016226z

Lam, P. Y. S., Clark, C. G., Saubern, S., Adams, J., Winters, M. P., Chan, D. M. T., et al. (1998). New aryl/heteroaryl C-N bond cross-coupling reactions via arylboronic acid/cupric acetate arylation. *Tetrahedron Lett*. 39, 2941–2944. doi: 10.1016/S0040-4039(98)00504-8

Lam, P. Y. S., Deudon, S., Averill, K. M., Li, R., He, M. Y., DeShong, P., et al. (2000). Copper-promoted C–N bond cross-coupling with hypervalent aryl siloxanes and room-temperature N-arylation with aryl iodide. *J. Am. Chem. Soc*. 122, 7600–7601. doi: 10.1021/ja001305g

Lam, P. Y. S., Vincent, G., Clark, C. G., Deudon, S., and Jadhav, P. K. (2001). Copper-catalyzed general C-N and C-O bond cross-coupling with arylboronic acid. *Tetrahedron Lett*. 42, 3415–3418. doi: 10.1016/S0040-4039(01)00510-X

Lazreg, F., Nahra, F., and Cazin, C. S. J. (2015). Copper–NHC complexes in catalysis. *Coord. Chem. Rev*. 293, 48–79. doi: 10.1016/j.ccr.2014.12.019

Liu, B., Liu, B., Zhou, Y., and Chen, W. (2010). Copper(II) hydroxide complexes of N-heterocyclic carbenes and catalytic oxidative amination of arylboronic acids. *Organometallics* 29, 1457–1464. doi: 10.1021/om100009u

Lo, Y. S., Nolan, J. C., Maren, T. H., Welstead, W. J., Gripshover, D. F., and Shamblee, D. A. (1992). Synthesis and physiochemical properties of sulfamate derivatives as topical antiglaucoma agents. *J. Med. Chem*. 35, 4790–4794. doi: 10.1021/jm00104a003

Lopez-Alvarado, P., Avendano, C., and Menendez, J. C. (1995). New synthetic applications of aryllead triacetates. N-arylation of azoles. *J. Org. Chem*. 60, 5678–5682. doi: 10.1021/jo00122a060

Martinez, G. R., Walker, K. A., Hirschfeld, D. R., Bruno, J. J., Yang, D. S., and Maloney, P. J. (1992). 3,4-Dihydroquinolin-2(1H)-ones as combined inhibitors of thromboxane A2 synthase and cAMP phosphodiesterase. *J. Med. Chem*. 35, 620–628. doi: 10.1021/jm00082a002

Mederski, W. W. K. R., Lefort, M., Germann, M., and Kux, D. (1999). N-aryl heterocycles via coupling reactions with arylboronic acids. *Tetrahedron* 55, 12757–12770. doi: 10.1016/S0040-4020(99)00752-8

Nicolaï, E., Goyard, J., Benchetrit, T., Teulon, J. M., Caussade, F., Virone, A., et al. (1993). Synthesis and structure-activity relationships of novel benzimidazole and imidazo [4,5-b]pyridine acid derivatives as thromboxane A2 receptor antagonists. *J. Med. Chem*. 36, 1175–1187. doi: 10.1021/jm00061a008

Ohmori, J., Shimizu-Sasamata, M., Okada, M., and Sakamoto, S. (1996). Novel ampa receptor antagonists: synthesis and structure–activity relationships of 1-hydroxy-7-(1h-imidazol-1-yl)-6-nitro-2,3(1h,4h)- quinoxalinedione and related compounds. *J. Med. Chem*. 39, 3971–3979. doi: 10.1021/jm960387

Paine, A. J. (1987). Mechanisms and models for copper mediated nucleophilic aromatic substitution. 2. Single catalytic species from three different oxidation states of copper in an Ullmann synthesis of triarylamines. *J. Am. Chem. Soc*. 109, 1496–1502. doi: 10.1021/ja00239a032

Santoro, O., Collado, A., Slawin, A. M. Z., Nolan, S. P., and Cazin, C. S. J. (2013). A general synthetic route to [Cu(X)(NHC)] (NHC = N-heterocyclic carbene, X = Cl, Br, I) complexes. *Chem. Commun*. 49, 10483–10485. doi: 10.1039/c3cc45488f

Sawanishi, H., Suzuki, H., Yamamoto, S., Waki, Y., Kasugai, S., Ohya, K., et al. (1997). Selective inhibitors of cyclic AMP-specific phosphodiesterase: heterocycle-condensed purines. *J. Med. Chem*. 40, 3248–3253. doi: 10.1021/jm970089s

Shafir, A., and Buchwald, S. L. (2006). Highly selective room-temperature copper-catalyzed C–N coupling reactions. *J. Am. Chem. Soc*. 128, 8742–8743. doi: 10.1021/ja063063b

Shaw, K. J., Erhardt, P. W., Hagedom, A. A., Pease, C. A., Ingebretsen, W. R., and Wiggins, J. R. (1992). Cardiotonic agents. 7. Prodrug derivatives of 4-ethyl-1,3-dihydro-5-[4-(2-methyl-1H-imidazol-1-yl)benzoyl]-2H-imidazol-2-one. *J. Med. Chem*. 35, 1267–1272. doi: 10.1021/jm00085a014

Sircar, I., Weishaar, R. E., Kobylarz, D., Moos, W. H., and Bristol, J. A. (1987). Cardiotonic agents. 7. Inhibition of separated forms of cyclic nucleotide phosphodiesterase from guinea pig cardiac muscle by 4,5-dihydro-6–[4-(1H-imidazol-1-yl)phenyl]-3(2H)-pyridazinones and related compounds.

Structure-activity relationships and correlation with *in vivo* positive inotropic activity. *J. Med. Chem.* 30, 1955–1962. doi: 10.1021/jm00394a005

Tubaro, C., Biffis, A., Scattolin, E., and Basato, M. (2008). Efficient catalysis of Ullmann-type arylation reactions by a novel trinuclear copper(I) complex with a chelating tricarbene ligand. *Tetrahedron* 64, 4187–4195. doi: 10.1016/j.tet.2008.02.092

Ullmann, F. (1903). Ueber eine neue bildungsweise von diphenylaminderivaten. *Ber. Dtsch. Chem. Ges.* 36, 2382–2384. doi: 10.1002/cber.190303602174

Ullmann, F., and Bielecki, J. (1901). Ueber synthesen in der biphenylreihe. *Ber. Dtsch. Chem. Ges.* 34, 2174–2185. doi: 10.1002/cber.190103402141

Ullmann, F., and Sponagel, P. (1905). Ueber die phenylirung von phenolen. *Ber. Dtsch. Chem. Ges.* 38, 2211–2212. doi: 10.1002/cber.190503802176

Venuti, M. C., Stephenson, R. A., Alvarez, R., Bruno, J. J., and Strosberg, A. M. (1988). Inhibitors of cyclic AMP phosphodiesterase. 3. Synthesis and biological evaluation of pyrido and imidazolyl analogs of 1,2,3,5-tetrahydro-2-oxoimidazo [2,1-b]quinazoline. *J. Med. Chem.* 31, 2136–2145. doi: 10.1021/jm00119a014

Wang, L., Jiang, Z., Yu, L., Li, L., Li, Z., and Zhou, X. (2010). Cross coupling of arylboronic acids with imidazoles by sulfonatocopper(II)(salen) complex in water. *Chem. Lett*. 39, 764–765. doi: 10.1246/cl.2010.764

Wentzel, M. T., Hewgley, J. B., Kamble, R. M., Wall, P. D., and Kozlowski, M. C. (2009). Copper-catalyzed N-arylation of hindered substrates under mild conditions. *Adv. Synth. Catal.* 351, 931–937. doi: 10.1002/adsc.200800730

Conflict of Interest Statement: The authors declare that the research was conducted in the absence of any commercial or financial relationships that could be construed as a potential conflict of interest.

Copyright © 2019 Minnick, Domyati, Ammons and Tahsini. This is an open-access article distributed under the terms of the Creative Commons Attribution License (CC BY). The use, distribution or reproduction in other forums is permitted, provided the original author(s) and the copyright owner(s) are credited and that the original publication in this journal is cited, in accordance with accepted academic practice. No use, distribution or reproduction is permitted which does not comply with these terms.

frontiers in Chemistry

ORIGINAL RESEARCH
published: 18 April 2019
doi: 10.3389/fchem.2019.00267

Self-Calibrated Double Luminescent Thermometers Through Upconverting Nanoparticles

Carlos D. S. Brites[1]*, *Eduardo D. Martínez*[2], *Ricardo R. Urbano*[2], *Carlos Rettori*[2,3] and *Luís D. Carlos*[1]

[1] Physics Department and CICECO-Aveiro Institute of Materials, University of Aveiro, Aveiro, Portugal, [2] "Gleb Wataghin" Institute of Physics (IFGW), University of Campinas (UNICAMP), Campinas, Brazil, [3] Center for Natural and Human Sciences, Universidade Federal do ABC, Santo André, Brazil

Luminescent nanothermometry uses the light emission from nanostructures for temperature measuring. Non-contact temperature readout opens new possibilities of tracking thermal flows at the sub-micrometer spatial scale, that are altering our understanding of heat-transfer phenomena occurring at living cells, micro electromagnetic machines or integrated electronic circuits, bringing also challenges of calibrating the luminescent nanoparticles for covering diverse temperature ranges. In this work, we report self-calibrated double luminescent thermometers, embedding in a poly(methyl methacrylate) film Er^{3+}- and Tm^{3+}-doped upconverting nanoparticles. The Er^{3+}-based primary thermometer uses the ratio between the integrated intensities of the $^2H_{11/2} \rightarrow {}^4I_{15/2}$ and $^4S_{3/2} \rightarrow {}^4I_{15/2}$ transitions (that follows the Boltzmann equation) to determine the temperature. It is used to calibrate the Tm^{3+}/Er^{3+} secondary thermometer, which is based on the ratio between the integrated intensities of the $^1G_4 \rightarrow {}^3H_6$ (Tm^{3+}) and the $^4S_{3/2} \rightarrow {}^4I_{15/2}$ (Er^{3+}) transitions, displaying a maximum relative sensitivity of 2.96% K^{-1} and a minimum temperature uncertainty of 0.07 K. As the Tm^{3+}/Er^{3+} ratio is calibrated trough the primary thermometer it avoids recurrent calibration procedures whenever the system operates in new experimental conditions.

Keywords: luminescence, double thermometers, upconverting nanoparticles, primary thermometry, self-referenced thermometry, polymer nanocomposites

OPEN ACCESS

Edited by:
Carlos Lodeiro, Faculdade de Ciências e Tecnologia da Universidade Nova de Lisboa, Portugal

Reviewed by:
Nelsi Zaccheroni, University of Bologna, Italy
Jean-Claude Georges Bunzli, École Polytechnique Fédérale de Lausanne, Switzerland

***Correspondence:**
Carlos D. S. Brites
carlos.brites@ua.pt

Specialty section:
This article was submitted to Inorganic Chemistry, a section of the journal Frontiers in Chemistry

Received: *12 February 2019*
Accepted: *02 April 2019*
Published: *18 April 2019*

Citation:
Brites CDS, Martínez ED, Urbano RR, Rettori C and Carlos LD (2019) Self-Calibrated Double Luminescent Thermometers Through Upconverting Nanoparticles. Front. Chem. 7:267. doi: 10.3389/fchem.2019.00267

INTRODUCTION

Lanthanide-doped upconversion materials have been extensively investigated since the 1960s and displaying numerous applications due to its exceptional photophysical properties, including narrow emission lines, large anti-Stokes shift, long lifetimes, low background autofluorescence, and low toxicity (Bettinelli et al., 2015; Savchuk et al., 2018; Brites et al., 2019). The development of synthesis strategies for nanomaterials enabled a complete upconversion nanomaterials engineering, allowing the precise control of composition, morphology, size, crystalline structure, and surface chemistry (Chen et al., 2014; Wen et al., 2018).

One of the most promising applications of upconverting materials is luminescence thermometry, in which changes in photophysical properties of a material are converted into absolute temperature (Vetrone et al., 2010; Brites et al., 2012; Jaque and Vetrone, 2012). In the

last decade, inorganic compounds doped with trivalent lanthanide ions (Ln^{3+}) have been broadly studied as reliable ratiometric luminescent thermometers. The energy level structure of these ions allows to work in the so-called transparency biological windows (Hemmer et al., 2016) in which the tissues' absorption is minimized. The Yb^{3+}/Er^{3+} couple is the most investigated upconverting dopant for a wide variety of applications, being used for bioimaging (Mader et al., 2010), photothermal therapy (Cheng et al., 2012), and for fundamental studies (Brites et al., 2016b). Albeit other approaches have been reported (Rai and Rai, 2007; Gálico et al., 2017; Brites et al., 2019), it is recognized that the wise approach for upconversion nanothermometry is based on the ratio between the integrated emission intensities of two thermally-coupled transitions. Indeed, when the emission arises from two transitions ascribed to the same emitting center with integrated intensities I_1 and I_2, originated in emitting levels $|1>$ and $|2>$ separated in energy by a ΔE value between 200 and 2,000 cm^{-1} (defined as thermally-coupled levels), the levels' population is governed by Boltzmann statistics and the thermometric parameter Δ is given by:

$$\Delta = \frac{I_2}{I_1} = B \exp\left(-\frac{\Delta E}{k_B T}\right) \quad (1)$$

where k_B is the Boltzmann constant, and the pre-exponential factor B is dependent on the degeneracies, branching ratios, spontaneous absorption coefficients, and frequencies of the I_1 and I_2 transitions (Brites et al., 2019).

In terms of calibration features, the thermal probes can be sorted as secondary and primary thermometers. While for the formers a calibration procedure is mandatory, the second kind of thermometers allow the temperature determination based on an equation of state that depends only on the material's parameters (without demanding any calibration). Recently, it has been demonstrated that any upconverting thermometer based on thermally-coupled energy levels is intrinsically a primary thermometer governed by an equation of state outcoming from Equation 1 in which the pre-exponential factor B is rewritten in terms of a known temperature value (T_0) and the corresponding ratio of intensities (Δ_0) (Balabhadra et al., 2017):

$$\frac{1}{T} = \frac{1}{T_0} - \frac{k_B}{\Delta E} \ln\left(\frac{\Delta}{\Delta_0}\right) \quad (2)$$

The seminal example of an upconverting luminescent primary thermometer is based on the integrated emission intensities arising from the $^2H_{11/2} \rightarrow {}^4I_{15/2}$ (I_H) and $^4S_{3/2} \rightarrow {}^4I_{15/2}$ (I_S) Er^{3+} transitions (Balabhadra et al., 2017). If, by one hand, the self-calibration of primary thermal probes is a great benefit (see further discussion in Brites et al., 2019), on the other hand, the typical relative thermal sensitivity S_r values of primary thermometers (**Supplementary Materials**) are limited to values of the order of $1.0\%{\cdot}K^{-1}$. Contrarily, secondary thermometers can render higher values (typically $S_r > 3.0\%{\cdot}K^{-1}$) (Marciniak et al., 2017; Brites et al., 2018, 2019). However, a new calibration is mandatory whenever secondary thermometers operate in a distinct medium and this is a serious implementation bottleneck for these devices. Thus, the wisest combination should provide the possibility of predicting the temperature through a primary thermometer displaying simultaneously a performance larger than that typical of primary thermometers.

Despite the large number of reported luminescent thermometers based on a ratio of intensities from two Ln^{3+} ions (the so-called dual-center thermometers; Brites et al., 2016a, 2019), very few are examples of double thermometers, in which the temperature is extracted from two distinct thermometric parameters. Up to now, and as far as we know, double luminescent thermometers combining two different emitting centers in the same nanostructure were reported only using Ln^{3+}-doped core@shell upconverting nanoparticles (UCNPs), in all the cases through intensity ratios (Marciniak et al., 2016; Skripka et al., 2017; Martínez et al., 2019a). Marciniak et al. combined in the same UCNP one thermometer using the Er^{3+} emission in the Yb^{3+}/Er^{3+} core with a second one using the Nd^{3+} downshifting emission in the Yb^{3+}/Nd^{3+} shell. The nanostructure was excited at 808 nm, resonantly with the $^4I_{9/2} \rightarrow {}^4F_{5/2}$ Nd^{3+} transition, and a non-radiative deactivation process populated the metastable $^4F_{3/2}$ state followed by sequential Nd^{3+}-to-Yb^{3+} and Yb^{3+}-to-Er^{3+} energy transfer processes allowing Er^{3+} upconversion emission ($^4S_{3/2} \rightarrow {}^4I_{15/2}$ and $^2H_{11/2} \rightarrow {}^4I_{15/2}$) in the green spectral range (Marciniak et al., 2016). Skripka et al. further developed the same concept exciting Nd^{3+}/Ho^{3+} and Nd^{3+}/Er^{3+} ion pairs in UCNPs upon 800 nm. Like in the previous example, the system was excited through the Nd^{3+} ions followed by sequential Nd^{3+}-to-Yb^{3+} and Yb^{3+}-to-Ho^{3+} ($^5I_6$ level emitting in the 1,180–1,340 nm spectral range) or Yb^{3+}-to-Er^{3+} ($^4I_{11/2}$ and $^4I_{13/2}$ states emitting in the 1,340–1,550 nm spectral range) (Skripka et al., 2017). More recently, we described a set of electrothermal devices combining Yb^{3+}/Er^{3+} and Yb^{3+}/Tm^{3+}-doped UCNPs of distinct sizes deposited on the top of a silver nanowires network to determine the temperature using a double thermometer combining Tm^{3+} and Er^{3+} emissions (Martínez et al., 2019a).

Here we extend the concept of this later article reporting in more detail how Yb^{3+}/Er^{3+}- and Yb^{3+}/Tm^{3+}-doped UCNPs of distinct sizes embedding in poly(methyl methacrylate) (PMMA) films can be used to fabricate self-calibrated double luminescent thermometers. Moreover, the particles' dispersion is enhanced relatively to what was published in that previous work by embedding them into polymer films (see Martínez et al., 2019b for details). This permits to study the effect on the thermometers' figures of merit of combining mixtures of UCNPs with distinct sizes (e.g., large-sized Er^{3+}- and small-sized Tm^{3+}-doped UCNPs and small-sized Er^{3+}- and large-sized Tm^{3+}-doped UCNPs).

The self-referenced nanocomposites include a luminescent primary thermal probe operating based on the ratio between the integrated intensities of the $^2H_{11/2} \rightarrow {}^4I_{15/2}$ and $^4S_{3/2} \rightarrow {}^4I_{15/2}$ Er^{3+} transitions and a secondary thermometer that uses the ratio between the integrated intensities of the $^1G_4 \rightarrow {}^3H_6$ (Tm^{3+}) and the $^4S_{3/2} \rightarrow {}^4I_{15/2}$ (Er^{3+}) transitions. The primary thermometer is used to calibrate the

secondary one (that display a higher relative thermal sensitivity and a lower temperature uncertainty), avoiding recurrent and time-consuming calibration procedures whenever the system operates in new experimental conditions. The temperature prediction in primary thermometers allows to sign changes in transitions' intensity decoupling temperature-induced changes from others resulting from distinct stimuli (*viz.* pressure, stress, etc.). Moreover, our approach of incorporating a primary self-reference thermometer is a clear step-forward toward the general implementation of luminescent thermometers as it allows the systems to be calibrated even when the conventional calibration procedure cannot be executed, as for instance, when the probes are embedded in living cells (Brites et al., 2019).

EXPERIMENTAL SECTION

Materials and Synthesis

The synthesis of the UCNPs and composite films was made accordingly to the procedures presented elsewhere (Martínez et al., 2018, 2019b), as detailed in **Supplementary Materials**. **Table 1** summarizes the composition of the films.

Operating Procedure for Temperature Calibration

The composite film's temperature is controlled by a Kapton thermofoil heater (Minco) in thermal contact with the films and is determined by a thermocouple (I620–20147, VWR), also in thermal contact with the films, with an accuracy of 0.1 K. A continuous wave laser diode (980 nm, 3×10^4 W·m^{-2}) is used to excite the films and the upconversion emission is collected and guided to the detector (Maya 2000 Pro, Ocean Optics) through a QP450-1-XSR optical fiber (Ocean Optics). The emission spectra are subsequently post-processed using a MatLab® routine to calculate the Er^{3+} and Tm^{3+} transitions' integrated areas and the corresponding error values, as already reported (Brites et al., 2016a).

The intensity-to-temperature calibration procedure is done stepping the temperature in the 299–410 K range, placing the composite films in thermal contact with the temperature controller (**Figures 1A,B**) during 5 min for each temperature step, and collecting the emission spectra. The measured temperature (using the thermocouple in direct contact with the sample's surface) is compared to the predicted temperature using Equation (2). In between the temperature steps, the temperature is stabilized for 15 min and, then, all the calibration procedure takes ∼3 h per sample. The validity of the temperature measurements performed by the secondary thermometer self-referenced using the temperature calculated by the primary one (through Equation 2) was tested imposing a sharp temperature increase in the composite films (initially at room temperature), recording continuously the time-dependent upconversion emission spectra (during 200 s), and calculating the integrated areas of the Er^{3+} and Tm^{3+} transitions and the corresponding temperature values.

RESULTS AND DISCUSSION

The temperature dependent emission spectra of $\mathbf{C_1}$ and $\mathbf{C_2}$ present the characteristic narrow emission lines ascribed to the Er^{3+} and Tm^{3+} intra-4f transitions upon 980 nm excitation (power density 3×10^4 W·m^{-2}, **Figures 1C,D**). As expected, the emission intensity is thermally quenched for large-sized UCNPs and thermally enhanced for small-sized UCNPs (Martínez et al., 2019a). For the large-sized nanoparticles, the increase of temperature induces a systematic decrease of the emission intensity. All transitions suffer thermal quenching upon temperature increase, although in distinct extents. It is well-known that the thermal quenching in micro-sized particles and bulk upconverting materials has been frequently attributed to multi-phonon non-radiative relaxation mechanisms, resulting in higher decay probabilities, and, thus, the observed trends are expected (Shen et al., 2010; Yu et al., 2016). On the contrary, intensity enhancement (or reverse quenching) with the increasing temperature observed for small-sized UCNPs is in agreement with the findings firstly reported by Jiang's group (Li et al., 2014, 2015; Shao et al., 2015, 2017), and more recently by Zhou et al. (2018). The later work explained the observed thermal enhancement of the intensity for small-sized UCNPs by heat-favorable phonons existing at the surface of UCNPs that compensate the thermal quenching, favoring the energy transfer from sensitizers to activators to pump-up the intermediate excited-state upconversion process. The authors argued that the oxygen moiety chelating the Yb^{3+} ions is the key underpinning this enhancement. However, a definitive physical mechanism that fully explains this surface phonon-assisted energy transfer mechanism remains inconclusive ((Liang and Liu, 2018); Martínez et al., 2019a).

Analyzing the temperature dependence of the integrated intensities of the $^2H_{11/2} \rightarrow {}^4I_{15/2}$ (I_H), $^4S_{3/2} \rightarrow {}^4I_{15/2}$ (I_S), and $^1G_4 \rightarrow {}^3H_6$ (I_G) transitions upon increasing the temperature, we observe an increase of I_S and I_H and a marginal decrease of I_G (**Figure 2A**) for $\mathbf{C_1}$, whereas the opposite occurs for $\mathbf{C_2}$: I_S decreases, I_H is roughly constant and I_G increases (**Figure 2B**). The thermometric parameter of the Er^{3+}-based primary thermometer is defined as $\Delta_P = I_H/I_S$, whereas that of the Er^{3+}/Tm^{3+}-based secondary thermometer is defined as $\Delta_S = I_G/I_S$. Observing the temperature dependence of the intensity ratios from the primary and secondary thermometers, we notice a clear steep increase in the Δ_S ratio compared to the Δ_P one (**Figures 2C,D**). This indicates an improved in the S_r values for the dual-center secondary thermometer, in line to what is observed before, as detailed next.

The maximum relative thermal sensitivity of the primary thermometers in $\mathbf{C_1}$ and $\mathbf{C_2}$ (1.31 and 1.19%·K^{-1}, respectively) (**Figures 3A,B**) and the minimum temperature uncertainty (0.15 and 0.18 K, respectively, all at 300 K) (**Figures 3C,D**) are comparable to the values reported for Er^{3+}- based thermometers (Brites et al., 2019). Moreover, the relative thermal sensitivity of the primary thermometers (**Figures 3A,B**) is independent on nanoparticle's dimensions, in line with our previous observations (Balabhadra et al., 2017; Brites et al., 2019). The relative thermal sensitivity of the secondary

TABLE 1 | Nomenclature, nominal composition, and particle size ± std (determined using the TEM/SEM images) of the UCNPs embedded in the fabricated composite films.

Composite film	Composition (nanoparticles)	Size (nm)	Representations
C_1	$NaY_{0.695}Yb_{0.300}Tm_{0.005}F_4$	(400 ± 15) × (120 ± 10)	
	$NaGd_{0.78}Yb_{0.20}Er_{0.02}F_4$@$NaGdF_4$	11.0 ± 1.4	
C_2	$NaGd_{0.695}Yb_{0.300}Tm_{0.005}F_4$@$NaGdF_4$	8.8 ± 0.8	
	$NaY_{0.78}Yb_{0.20}Er_{0.02}F_4$	(300 ± 8) × (160 ± 6)	

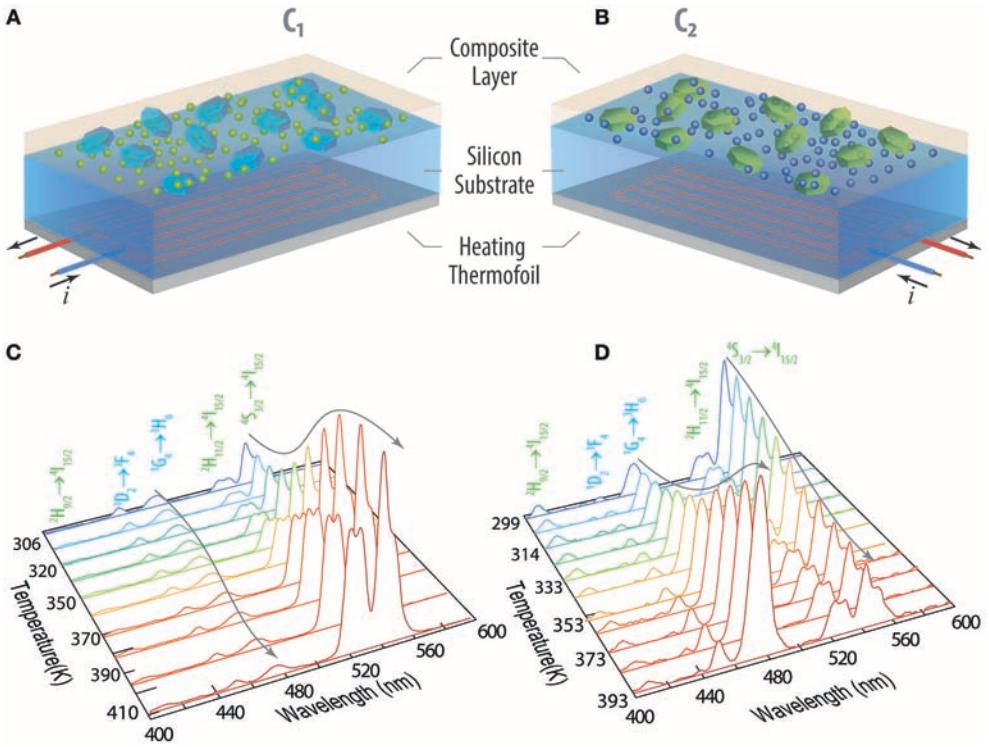

FIGURE 1 | Schematic representation of the nanocomposites **(A)** C_1 and **(B)** C_2. The electrical current flowing in the heating thermofoil is used to control the local temperature of the UCNPs in the composite layer. The temperature dependent emission spectra upon 980 nm excitation is presented for **(C)** C_1 and **(D)** C_2 within the 299–410 K range. The Er^{3+} and Tm^{3+} transitions are depicted in green and blue, respectively.

thermometers presents the typical functional forms observed for dual-center luminescent thermometers (**Figures 3A,B**) (Brites et al., 2016a) with maximum values of 2.96%·K^{-1} (C_1 at 300 K) and 2.28%·K^{-1} (C_2 at 350 K), corresponding to minimum temperature uncertainties of 0.07 K at 300 K (C_1) and 0.09 K at 350 K (C_2). There is an improvement in the relative thermal sensitivity values by a factor of up to 2.3 (in C_1), relatively to the same parameters calculated for the primary thermometer and the most advantageous combination of UCNPs is the mixture of large-sized Tm^{3+} -doped and small-sized Er^{3+} -doped UCNPs (**Figure 3**).

Comparing the performance of C_1 with those of other double luminescent thermometers in the literature, we conclude that the sensitivity values are the largest reported so far. Whereas, the system reported by Marciniak et al. presents a maximum relative sensitivity of 2.1%·K^{-1} at 370 K (Marciniak et al., 2016) that reported by Skripka et al. don't present values higher than 1.1%·K^{-1} (Skripka et al., 2017), meaning that the composite films reported here presents an increase of 40% with respect to these results. Moreover, in comparison with the system developed by us using the same design principle (Martínez et al., 2019a), the nanocomposites studied here present

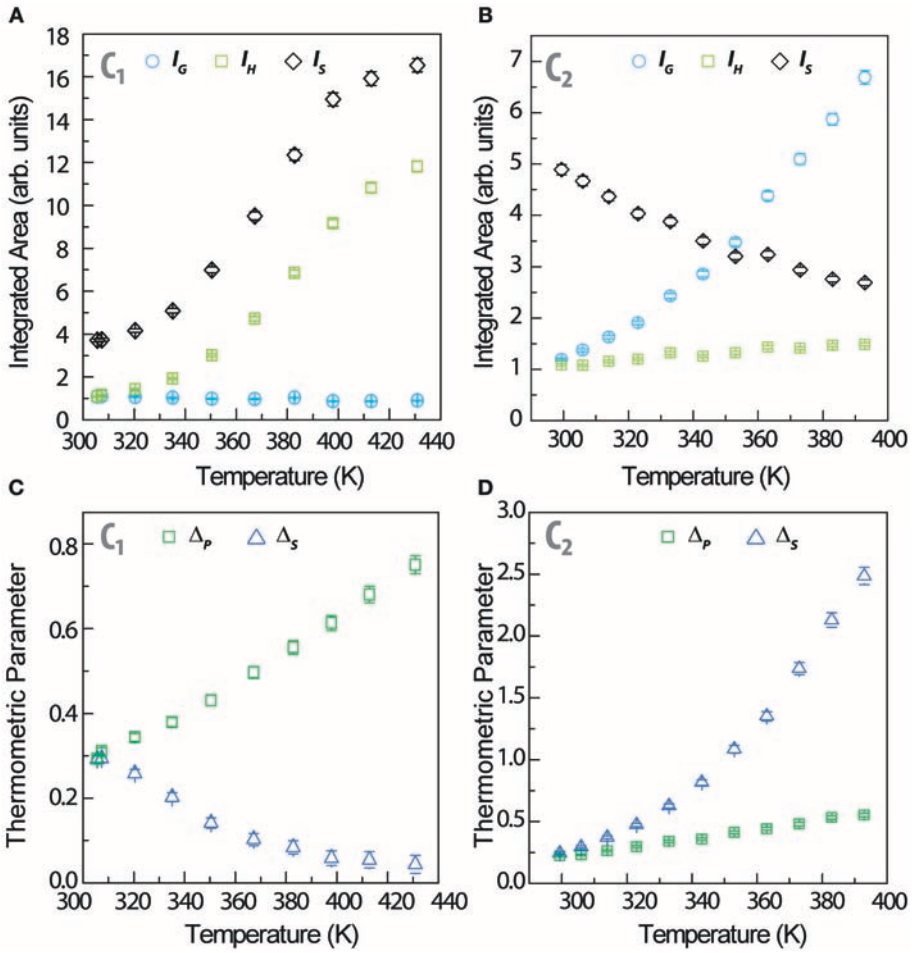

FIGURE 2 | Temperature dependence of the integrated areas of I_H, I_S (Er^{3+}) and I_G (Tm^{3+}) for **(A) C_1** and **(B) C_2**. The corresponding Δ_P and Δ_S thermometric parameters are presented in **(C)** and **(D)**, respectively.

comparable sensitivity values for the primary thermometer and about half of the sensitivity value for the secondary one. We ascribe these differences in performance to the encapsulation of the UCNPs in the PMMA that resulted in a smoother temperature enhancement of the Tm^{3+} emission of small-sized nanoparticles, in comparison with that observed previously for similar nanoparticles deposited directly on silver nanowires and exposed to the air (Martínez et al., 2019a). This is a remarkable relative thermal sensitivity tuning-up that we will exploit in a future work.

As the nanocomposite films combining the Er^{3+} and Tm^{3+} UCNPs permit to define one primary (Δ_P) and another secondary thermometric parameter (Δ_S), in what follows we show how that the first parameter (that follows Equation 2, section Er^{3+}-based primary thermometers) can be used to calibrate the secondary thermometer (section Self-referenced Er^{3+}/Tm^{3+} secondary thermometers).

Er^{3+}-Based Primary Thermometers

Despite the opposite behavior of the temperature dependence of the integrated areas of the Er^{3+} transitions for small (<10 nm) and large-sized (>100 nm) UCNPs, the ratio $\Delta_P = I_H/I_S$ always grows with the increasing temperature, irrespectively of the nanoparticle size and morphology (nanospheres or nanocrystals). To predict the temperature through Equation 2, the ΔE and Δ_0 values must be calculated for each UCNP by independent measurements (and not as fitted parameters of Equation 1). There are distinct strategies reported in the literature for extracting these parameters (Brites et al., 2019). The energy gap ΔE is evaluated deconvoluting the emission spectra at room temperature by a set of Gaussian peaks and evaluating the position of the $^2H_{11/2} \rightarrow {}^4I_{15/2}$ and $^4S_{3/2} \rightarrow {}^4I_{15/2}$ transitions' barycenter (**Supplementary Figure 1**), whereas Δ_0 is the thermometric parameter corresponding to the temperature T_0. It can be evaluated measuring the excitation power dependence of the thermometric parameter (Debasu et al., 2013), or just assuming the initial value of Δ_P at T_0 (room-temperature), when there is no excitation laser-induced heating (low excitation power density values 3×10^4 $W{\cdot}m^{-2}$). Notice the dissimilar T_0 values are consequence of distinct operating ambient conditions during the spectra acquisition. The ΔE and Δ_0 parameters for large- and small-sized Er^{3+}-doped UCNPs

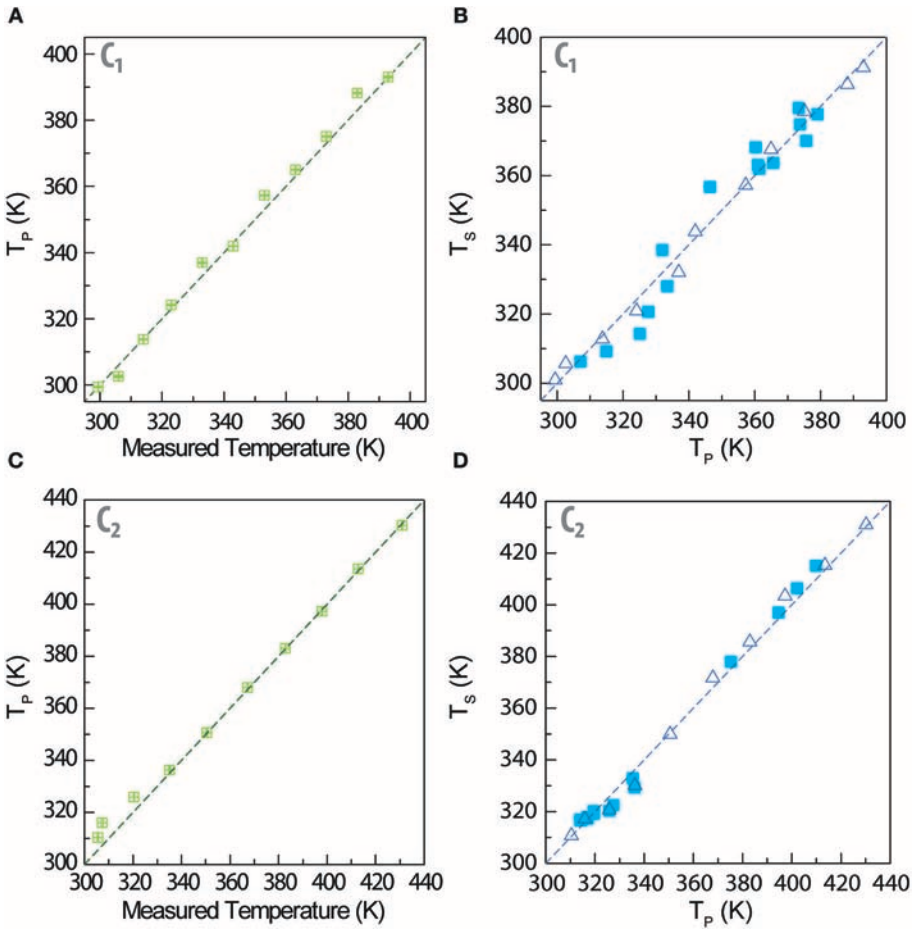

FIGURE 3 | Temperature dependence of the relative thermal sensitivity of primary and secondary thermometers for **(A)** C_1 and **(B)** C_2. **(C,D)** Temperature dependence of the corresponding temperature uncertainties, respectively.

TABLE 2 | ΔE (cm^{-1}), Δ_0 and T_0 (K) values of the primary thermometer in C_1 and C_2.

Composite film	ΔE	Δ_0	T_0
C_1	780 ± 15	0.222 ± 0.006	299.4 ± 0.1
C_2	749 ± 15	0.293 ± 0.008	305.6 ± 0.1

are presented in **Table 2**. The calculated ΔE values are similar for both composite films within the corresponding experimental errors and are in good agreement with those reported in the literature (Carnall et al., 1977).

In **Figures 4A,C** we compare the temperature calculated through Equation (2) (T_P) with that measured by a thermocouple in direct contact with the sample's surface. The remarkable agreement observed in both nanocomposites demonstrates that the primary thermometric parameter Δ_P permits to determine the temperature of the films using Equation (2), in excellent agreement with the values that are measured by a control temperature probe in contact with the nanocomposite's surface. These results validate the use of the ratio of intensities of the $^2H_{11/2} \rightarrow {}^4I_{15/2}$ and $^4S_{3/2} \rightarrow {}^4I_{15/2}$ Er^{3+} transitions for primary thermometry, as it has been systematically observed since the initial purpose of some of us (Balabhadra et al., 2017; Brites et al., 2019). Moreover, the relative thermal sensitivity of the primary thermometers in $\mathbf{C_1}$ and in $\mathbf{C_2}$ are only determined by the ΔE values (Equation 1 and **Supplementary Equation 1**) listed in **Table 2**, and that depend on the size and on the composition of the Er^{3+}-doped UCNPs. The maximum S_r values are comparable to those reported for other luminescent thermometers based on Er^{3+}-doped UCNPs (Brites et al., 2019).

Self-Referenced Er^{3+}/Tm^{3+} Secondary Thermometers

The secondary luminescent thermometer based on the Δ_S parameter determines the temperature (denoted by T_S) using the phenomenological calibration curve described by **Supplementary Equation 3** and presented in **Supplementary Figure 2**. In **Figures 3B,D** that temperature T_s is compared with that extracted from Equation (2) using the Δ_P values (T_P). It is remarkable that we calculate

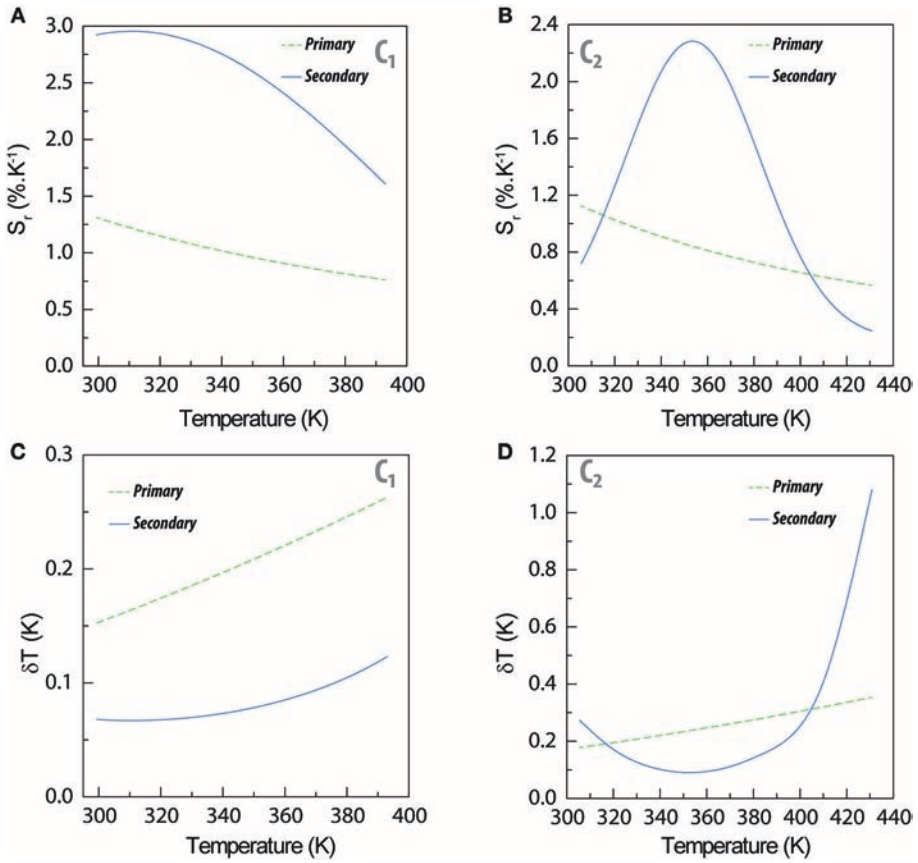

FIGURE 4 | Temperature measured by a thermocouple in contact with the composite films (*x*) vs. the temperature calculated using Equation 2 (T_P, *y*) for **(A) C_1** and **(B) C_2**. Calculated temperature T_P (*x*) vs. calculated temperature T_S (*y*) using the calibration curve of the Er^{3+}/Tm^{3+} secondary thermometer (T_S, y) for **(B) C_1** and **(D) C_2**. In (**B**,**D**), the open and solid symbols correspond to the calibration points and validity checks, respectively, as detailed in Experimental section. The straight lines correspond to $y = x$ in all the plots.

similar temperature values (T_P and T_S, based on the two thermometric parameters Δ_P and Δ_S), that agree very well with the values measured by the thermocouple in contact with the nanocomposite's surface. The temperature predicted through Equation 2 (primary thermometer) is used to calibrate the secondary thermometer (presenting a higher relative thermal sensitivity) enabling its self-referencing and not requiring the presence of an external thermocouple to set the calibration temperature during a large time period (3 h, as mentioned above).

To exemplify that the nanocomposite's temperature control can waive the record of an intensity-to-temperature calibration curve, we design a validity check experiment that consists in record the time-evolution of the emission spectra during 200 s, calculating the corresponding Δ_P and Δ_S values (the temporal evolution of the emission spectra is presented in **Supplementary Figure 2**). For each emission spectrum, we convert Δ_P into temperature using Equation (2) (**Figures 3B,D**) and Δ_S into temperature using **Supplementary Equation 3**. The results are presented as solid symbols in **Figures 3B,D**. We observe an excellent agreement between the conventional calibration and the validity check points, meaning that both calibration procedures are similar within the experimental error. Moreover, the temperature values calculated from both intensity ratios are statistically similar to those measured with the conventional calibration procedure, with an incredible gain in terms of time efficiency, because the heating ramp recording is more than 50 times faster than the conventional temperature stepping procedure.

The step forward presented in this work relatively to what was reported previously by us (Martínez et al., 2019a) is the comparison of the thermometric performances of the secondary thermometers formed by mixtures of large-sized Tm^{3+}- and small-sized Er^{3+}-doped UCNPs (**C_1**) with small-sized Tm^{3+}- and large-sized Er^{3+}-doped UCNPs (**C_2**). As expected, the functional form of S_r is the same for both composites, and for UCNPs deposited directly over a Ag-nanowires network (Martínez et al., 2019a), because it results from the phenomenological function used for fitting Δ_S, **Supplementary Equation 3** which is the same in all the three examples. Moreover, in the temperature range studied the S_r

values of $\mathbf{C_1}$ and $\mathbf{C_2}$ varies, respectively, between 1.65 and 2.93%·K^{-1} and 0.72 and 2.28%·K^{-1} (**Figures 4A,B**). These values are consistent with the changes on the integrated areas presented in **Figures 2A,B** showing that the performance of the secondary thermometer is essentially determined by the temperature enhancement observed in the integrated areas of the transitions of the small UCNPs. Furthermore, the combination of small Tm^{3+}-doped and large Er^{3+}-doped UCNPs resulted in a narrower S_r peak for $\mathbf{C_2}$ (in comparison with $\mathbf{C_1}$), that in that is comparable with that reported by us previously for UCNPs deposited directly over a Ag-nanowires network (Martínez et al., 2019a). The incorporation of the UCNPs into the PMMA film resulted in a decrease of the maximum S_r value and in the temperature at which it occurs (**Supplementary Figure 4**), in comparison with our previous work (Martínez et al., 2019a). This is consequence of the thermal dependence of the integrated area of the $^1G_4 \rightarrow {}^3H_6$ transition, that growths about seven times for $\mathbf{C_2}$ whereas in our previous work it increases about 18 times in a comparable temperature range (Martínez et al., 2019a). Thus, we conclude that the transitions originated in the small-sized Tm^{3+} particles are determining the performance of these devices (**Figure 4**). The observed changes in the integrated areas of small -sized UCNPs resulting from their embedding into PMMA are still not entirely understood, needing further experimental evidences (specially in what concerns the incorporation of UCNPs in other hosts). Work is in progress along this research line.

CONCLUSIONS

In this work, we combined a primary thermometer and a secondary thermometer rendering to self-referenced double thermometric systems in the same composite film with relative thermal sensitivity comparable with the largest ones reported yet for secondary thermometers. To illustrate this concept, Ln^{3+}-doped $NaYF_4$ and $NaGdF_4$ nanoparticles (Ln = Yb, Er, Tm) of distinct sizes were embedded in two PMMA films. The nanocomposites' inner temperature reference is the primary thermometer based on the $^2H_{11/2} \rightarrow {}^4I_{15/2}$ (I_H) and $^4S_{3/2} \rightarrow {}^4I_{15/2}$ (I_S) Er^{3+} transitions, univocally assigning each emission spectrum to the corresponding temperature using Boltzmann equation. We attest that the system is a primary thermometer comparing the predicted and measured temperature values and observing an excellent agreement between both. The secondary thermometer is based on the temperature dependence of a ratio of intensities involving one emission intensity that is thermally quenched (large-sized UCNPs) and another one that is thermally enhanced (small-sized UCNPs). The maximum relative thermal sensitivity of this thermometer is 2.96%·K^{-1} and the minimum temperature uncertainty is 0.07 K (both at 300 K), among the highest performance values reported so far for luminescent dual thermometers. Moreover, the maximum S_r value corresponds to a 2.3-fold improvement, with respect to the Er^{3+}-based primary thermometer.

This highly sensitive thermometer can be calibrated using a conventional temperature-stepping procedure, taking a total of 3 h, or using the primary thermometer to calibrate it. We validate the resulting calibration curves recording the emission spectra in a heating ramp and observing a good agreement between the temperature values calculated from the primary and the secondary thermometers independently. Although in our previous work (Martínez et al., 2019a) we adopted this faster method to calibrate the secondary thermometer, here we demonstrate that conventional and fast calibration procedures are equivalent and, thus, the external temperature control is not mandatory to calibrate the self-referenced system taking only 200 s, that constitutes a procedure more than 50 times faster than the conventional calibration.

Finally, we stress that the procedure described here of incorporating an inner self-referenced temperature probe (Er^{3+} doped UCNPs) is general and can be applied for any system that require thermal calibration. Such dual systems present the critical advantage of the secondary thermometer being more sensitive than the primary. Since the secondary thermometer can be calibrated "*in situ*," this avoids conventional methods of calibration, and opens the way for applications in biological media, particularly at the cell level. This strategy will certainly pave the road for the future routinely use of self-calibrated dual luminescent thermometers based on UCNPs, allowing to avoid long calibration procedures that require sophisticated temperature controllers, without sacrificing the temperature readout error.

DATA AVAILABILITY

The raw data supporting the conclusions of this manuscript will be made available by the authors, without undue reservation, to any qualified researcher.

AUTHOR CONTRIBUTIONS

CB, LC, and EM conceived the project. EM synthesized the particles and performed all measurements. CB, EM, and LC discussed the project, analyzed the data, performed the calculations, and prepared all figures. RU and CR contributed with the experimental set-up and discussion of the project. The manuscript was written with contributions from all authors.

FUNDING

Work was partially developed in the scope of the project CICECO–Aveiro Institute of Materials (Ref. FCT UID/CTM/50011/2019), financed by Portuguese funds through the Fundação para a Ciência e a Tecnologia/Ministério da Educação e Ciência (FCT/MEC). Financial support of FCT (PTDC/CTM-NAN/4647/2014 and POCI-01-0145-FEDER-016687) is also acknowledged. This work was supported and performed under the auspices of the Brazilian agencies CAPES, CNPq, and Fundação de Amparo à Pesquisa do Estado de São Paulo (FAPESP) through Grants #2011/19924-2, #2012/04870-7, #2012/05903-6, #2015/21290-2, and #2015/21289-4. CB

acknowledge the grant financed by the SusPhotoSolutions project CENTRO-01-0145-FEDER-000005. EM acknowledge, respectively, the post-doctoral FAPESP fellowship #2015/23882-4 and BEPE #2018/12489-8.

ACKNOWLEDGMENTS

Authors acknowledge the funding institutions and the parent institutions were the work was performed. CICECO–Aveiro Institute of Materials, University of Aveiro, and Department of Quantum Electronics, Institute of Physics Gleb Wataghin, UNICAMP.

SUPPLEMENTARY MATERIAL

The Supplementary Material for this article can be found online at: https://www.frontiersin.org/articles/10.3389/fchem.2019.00267/full#supplementary-material

REFERENCES

Balabhadra, S., Debasu, M. L., Brites, C. D. S., Ferreira, R. A. S., and Carlos, L. D. (2017). Upconverting nanoparticles working as primary thermometers in different media. *J. Phys. Chem. C* 121, 13962–13968. doi: 10.1021/acs.jpcc.7b04827

Bettinelli, M., Carlos, L. D., and Liu, X. (2015). Lanthanide-doped upconversion nanoparticles. *Phys. Today* 68, 38–44. doi: 10.1063/PT.3.2913

Brites, C. D., Lima, P. P., Silva, N. J. O., Millán, A., Amaral, V. S., Palacio, F., et al. (2012). Thermometry at the nanoscale. *Nanoscale* 4, 4799–4829. doi: 10.1039/c2nr30663h

Brites, C. D., Xie, X., Debasu, M. L., Qin, X., Chen, R., Huang, W., et al. (2016b). Instantaneous ballistic velocity of suspended brownian nanocrystals measured by upconversion nanothermometry. *Nat. Nanotechnol.* 11, 851–856. doi: 10.1038/nnano.2016.111

Brites, C. D. S., Balabhadra, S., and Carlos, L. D. (2019). Lanthanide-based thermometers: at the cutting-edge of luminescence thermometry. *Adv. Optic. Mater.* 7:1801239. doi: 10.1002/adom.201801239

Brites, C. D. S., Fiaczyk, K., Ramalho, J. F. C. B., Sojka, M., Carlos, L. D., and Zych, E. (2018). Widening the temperature range of luminescent thermometers through the intra- and interconfigurational transitions of Pr^{3+}. *Adv. Optic. Mater.* 6:1701318. doi: 10.1002/adom.201701318

Brites, C. D. S., Millán, A., and Carlos, L. D. (2016a). "Lanthanides in luminescent thermometry," in *Handbook on the Physics and Chemistry of Rare Earths*, eds J.-C. G. Bünzli and V. K. Pecharsky (Amsterdam: Elsevier Science B. V.), 339–427.

Carnall, W. T., Crosswhite, H., and Crosswhite, H. M. (1977). *Energy Level Structure and Transition Probabilities in the Spectra of the Trivalent Lanthanides in* LaF_3. Argonne Nat. Lab. 78-XX-95 Rep.

Chen, G., Qju, H. L., Prasad, P. N., and Chen, X. Y. (2014). Upconversion nanoparticles: design, nanochemistry, and applications in theranostics. *Chem. Rev.* 114, 5161–5214. doi: 10.1021/cr400425h

Cheng, L., Yang, K., Li, Y. G., Zeng, X., Shao, M. W., Lee, S. T., et al. (2012). Multifunctional nanoparticles for upconversion luminescence/MR multimodal imaging and magnetically targeted photothermal therapy. *Biomaterials* 33, 2215–2222. doi: 10.1016/j.biomaterials.2011.11.069

Debasu, M. L., Ananias, D., Pastoriza-Santos, I., Liz-Marzán, L. M., Rocha, J., and Carlos, L. D. (2013). All-in-one optical heater-thermometer nanoplatform operative from 300 to 2000 K based on Er^{3+} emission and blackbody radiation. *Adv. Mater.* 25, 4868–4874. doi: 10.1002/adma.201300892

Gálico, D. A., Mazali, I. O., and Sigoli, F. A. (2017). Nanothermometer based on intensity variation and emission lifetime of europium(III) benzoylacetonate complex. *J. Lumin.* 192, 224–230. doi: 10.1016/j.jlumin.2017.06.062

Hemmer, E., Benayas, A., Legare, F., and Vetrone, F. (2016). Exploiting the biological windows: current perspectives on fluorescent bioprobes emitting above 1000 nm. *Nanoscale Horiz.* 1, 168–184. doi: 10.1039/C5NH00073D

Jaque, D., and Vetrone, F. (2012). Luminescence nanothermometry. *Nanoscale* 4, 4301–4326. doi: 10.1039/c2nr30764b

Li, D. D., Shao, Q. Y., Dong, Y., Fang, F., and Jiang, J. Q. (2015). Ho^{3+} (or Tm^{3+})-activated upconversion nanomaterials: anomalous temperature dependence of upconversion luminescence and applications in multicolor temperature indicating and security. *Particle Particle Syst. Character.* 32, 728–733. doi: 10.1002/ppsc.201500004

Li, D. D., Shao, Q. Y., Dong, Y., and Jiang, J. Q. (2014). Anomalous temperature-dependent upconversion luminescence of small-sized $NaYF_4$:Yb^{3+},Er^{3+} nanoparticles. *J. Phys. Chem. C* 118, 22807–22813. doi: 10.1021/jp507804h

Liang, L. L., and Liu, X. G. (2018). Nanocrystals feel the heat. *Nat. Photonics* 12, 124–125. doi: 10.1038/s41566-018-0117-4

Mader, H. S., Kele, P., Saleh, S. M., and Wolfbeis, O. S. (2010). Upconverting luminescent nanoparticles for use in bioconjugation and bioimaging. *Curr. Opin. Chem. Biol.* 14, 582–596. doi: 10.1016/j.cbpa.2010.08.014

Marciniak, Ł., Prorok, K., and Bednarkiewicz, A. (2017). Size dependent sensitivity of Yb^{3+},Er^{3+} up-converting luminescent nano-thermometers. *J. Mater. Chem. C* 5, 7890–7897. doi: 10.1039/C7TC02322G

Marciniak, Ł., Prorok, K., Frances-Soriano, L., Perez-Prieto, J., and Bednarkiewicz, A. (2016). A broadening temperature sensitivity range with a core-shell YbEr@YbNd double ratiometric optical nanothermometer. *Nanoscale* 8, 5037–5042. doi: 10.1039/C5NR08223D

Martínez, E. D., Brites, C. D. S., Carlos, L. D., García-Flores, A. F., Urbano, R. R., and Rettori, C. (2019a). Electrochromic switch devices mixing small- and large-sized upconverting nanocrystals. *Adv. Funct. Mater.* 29:1807758.doi: 10.1002/adfm.201807758

Martínez, E. D., Brites, C. D. S., Carlos, L. D., Urbano, R. R., and Rettori, C. (2019b). Upconversion nanocomposite materials with designed thermal response for optoelectronic devices. *Front. Chem.* 7:83. doi: 10.3389/fchem.2019.00083

Martínez, E. D., Urbano, R. R., and Rettori, C. (2018). Thermoplasmonic enhancement of upconversion in small-size doped $NaGdYF_4$ nanoparticles coupled to gold nanostars. *Nanoscale* 10, 14687–14696. doi: 10.1039/C8NR01639A

Rai, V. K., and Rai, S. B. (2007). A comparative study of FIR and FL based temperature sensing schemes: an example of Pr^{3+}. *Appl. Phys. B Lasers Optics* 87, 323–325. doi: 10.1007/s00340-007-2592-z

Savchuk, O. A., Carvajal, J. J., Brites, C. D. S., Carlos, L. D., Aguilo, M., and Diaz, F. (2018). Upconversion thermometry: a new tool to measure the thermal resistance of nanoparticles. *Nanoscale* 10, 6602–6610. doi: 10.1039/C7NR08758F

Shao, Q. Y., Ouyang, L. L., Jin, L. F., and Jiang, J. Q. (2015). Multifunctional nanoheater based on $NaGdF_4$:Yb^{3+}, Er^{3+} upconversion nanoparticles. *Opt. Express* 23, 30057–30066. doi: 10.1364/OE.23.030057

Shao, Q. Y., Zhang, G. T., Ouyang, L. L., Hu, Y. Q., Dong, Y., and Jiang, J. Q. (2017). Emission color tuning of core/shell upconversion nanoparticles through modulation of laser power or temperature. *Nanoscale* 9, 12132–12141. doi: 10.1039/C7NR03682E

Shen, X. A., Nie, Q. H., Xu, T. F., Dai, S. X., and Wang, X. S. (2010). Temperature dependence of upconversion luminescence in erbium-doped tellurite glasses. *J. Lumin.* 130, 1353–1356. doi: 10.1016/j.jlumin.2010.02.031

Skripka, A., Benayas, A., Marin, R., Canton, P., Hemmer, E., and Vetrone, F. (2017). Double rare-earth nanothermometer in aqueous media: opening the third optical transparency window to temperature sensing. *Nanoscale* 9, 3079–3085. doi: 10.1039/C6NR08472A

Vetrone, F., Naccache, R., Zamarron, A., de la Fuente, Á. J., Sanz-Rodriguez, F., Maestro, L. M., et al. (2010). Temperature sensing using

fluorescent nanothermometers. *ACS Nano* 4, 3254–3258. doi: 10.1021/nn100244a

Wen, S., Zhou, J. J., Zheng, K. Z., Bednarkiewicz, A., Liu, X. G., and Jin, D. Y. (2018). Advances in highly doped upconversion nanoparticles. *Nat. Commun.* 9:2415. doi: 10.1038/s41467-018-04813-5

Yu, D., Ballato, J., and Riman, R. E. (2016). Temperature-dependence of multiphonon relaxation of rare-earth ions in solid-state hosts. *J. Phys. Chem. C* 120, 9958–9964. doi: 10.1021/acs.jpcc.6b01466

Zhou, J., Wen, S., Liao, J., Clarke, C., Tawfik, S. A., Ren, W., et al. (2018). Activation of the surface dark-layer to enhance upconversion in a thermal field. *Nat. Photonics* 12, 154–158. doi: 10.1038/s41566-018-0108-5

Conflict of Interest Statement: The authors declare that the research was conducted in the absence of any commercial or financial relationships that could be construed as a potential conflict of interest.

Copyright © 2019 Brites, Martínez, Urbano, Rettori and Carlos. This is an open-access article distributed under the terms of the Creative Commons Attribution License (CC BY). The use, distribution or reproduction in other forums is permitted, provided the original author(s) and the copyright owner(s) are credited and that the original publication in this journal is cited, in accordance with accepted academic practice. No use, distribution or reproduction is permitted which does not comply with these terms.

frontiers in Chemistry

ORIGINAL RESEARCH
published: 22 May 2019
doi: 10.3389/fchem.2019.00353

Reversible Control of the Mn Oxidation State in $SrTiO_3$ Bulk Powders

*Haneen Mansoor, William L. Harrigan, Keith A. Lehuta and Kevin R. Kittilstved**

Department of Chemistry, University of Massachusetts Amherst, Amherst, MA, United States

We demonstrate a low-temperature reduction method for exhibiting fine control over the oxidation state of substitutional Mn ions in strontium titanate ($SrTiO_3$) bulk powder. We employ $NaBH_4$ as the chemical reductant that causes significant changes in the oxidation state and oxygen vacancy complexation with Mn^{2+} dopants at temperatures <350°C where lattice reduction is negligible. At higher reduction temperatures, we also observe the formation of Ti^{3+} in the lattice by diffuse-reflectance and low-temperature electron paramagnetic resonance (EPR) spectroscopy. In addition to Mn^{2+}, Mn^{4+}, and the Mn^{2+} complex with an oxygen vacancy, we also observe a sharp resonance in the EPR spectrum of heavily reduced Mn-doped $SrTiO_3$. This sharp signal is tentatively assigned to surface superoxide ion that is formed by the surface electron transfer reaction between Ti^{3+} and O_2. The ability to control the relative amounts of various paramagnetic defects in $SrTiO_3$ provides many possibilities to study in a model system the impact of tunable dopant-defect interactions for spin-based electronic applications or visible-light photocatalysis.

Keywords: electron paramagnetic resonance, oxidation state, manganese, strontium titanate, inorganic materials

OPEN ACCESS

Edited by:
Luís D. Carlos,
University of Aveiro, Portugal

Reviewed by:
Emre Erdem,
Sabanci University, Turkey
Helene Serier-Brault,
UMR6502 Institut des Matériaux Jean Rouxel (IMN), France

****Correspondence:***
Kevin R. Kittilstved
kittilstved@chem.umass.edu

Specialty section:
This article was submitted to Inorganic Chemistry, a section of the journal Frontiers in Chemistry

Received: *19 February 2019*
Accepted: *29 April 2019*
Published: *22 May 2019*

Citation:
Mansoor H, Harrigan WL, Lehuta KA and Kittilstved KR (2019) Reversible Control of the Mn Oxidation State in $SrTiO_3$ Bulk Powders. Front. Chem. 7:353. doi: 10.3389/fchem.2019.00353

INTRODUCTION

The oxide $SrTiO_3$ is a classic perovskite-type member of the valuable ABO_3 semiconductor family. The promising properties such as a large tunable dielectric constant, structural phase transitions, superior charge storage capacity and tunable electronic structure have made $SrTiO_3$ an exciting candidate for a wide range of multifunctional applications (Weaver, 1959; Faughnan, 1971; Mattheiss, 1972; Müller and Burkard, 1979; Kamalasanan et al., 1993). Although in ambient conditions it exhibits a wide band gap and low electron mobility, introducing impurity dopants and intrinsic defects radically influence the conductivity and optical properties of the host material (Wild et al., 1973; Kozuka et al., 2010). The function of a semiconductor is intimately related to the chemistry and physics of native and targeted defects. The rich defect chemistry enabled by native oxygen vacancies (V_O) in semiconductors such as $SrTiO_3$, $PbTiO_3$, and $BaTiO_3$ has been correlated with numerous functions including ferroelectricity, visible-light photocatalysis, and multiferroics. These V_O defects can donate up to two electrons to the host lattice. Transition metal dopants may also impart additional functionality that result from partially-filled d-orbitals. For example, Cr^{3+} dopants, and Rh^{3+} dopants in $SrTiO_3$ can reduce protons to generate H_2 gas using visible light that creates an oxidized dopant ion and a conduction band electron, e_{cb} (Ishii et al., 2004; Sasaki et al., 2009; Kato et al., 2013). However, undesirable defects such as Cr^{6+} can form to maintain charge neutrality, but limit the photochemical efficiency by serving as a trap for the e_{cb}. These types of

high-valent defects can be removed by either post-synthetic annealing under reducing atmospheres (Zuo et al., 2010; Tan et al., 2014; Lehuta and Kittilstved, 2016), co-doping the host lattice with additional *n*-type dopants (Chan et al., 1981; Kato and Kudo, 2002; Wang et al., 2014), irradiating with UV light (Wang et al., 2006), or applying a large electrical bias (La Mattina et al., 2008). Of these, the only potentially "green" reduction source could be UV irradiation from the sun. However, we note that the reported photoreduction step using a 400 W Hg-lamp in Cr:$SrTiO_3$ powders was of the order of tens of hours. The realization of a fast, low-energy method to modulate the oxidation state of transition-metal dopants in $SrTiO_3$ and related metal oxide semiconductors could impact various fields such as visible-light photocatalysis, sensing, and spin-based electronics. To this end, recent studies on the photodoping of colloidal Cr:$SrTiO_3$ nanocrystals show promise (Harrigan and Kittilstved, 2018).

We previously studied the effect of a relatively low-temperature $NaBH_4$ reduction reaction on the oxidation state of Cr dopants in $SrTiO_3$ and related Sr_2TiO_4 bulk powders (Lehuta and Kittilstved, 2016; Lehuta et al., 2017). In those studies, we observed an order of magnitude *increase* in the Cr^{3+} concentration by EPR spectroscopy that we attributed to the reduction of EPR-silent high-valent Cr^{4+} and Cr^{6+} ions. The increase in the Cr^{3+} concentration in *n*-type $SrTiO_3$ presents an interesting scenario where the Cr^{3+} ion has a dual role of being an electron donor and a paramagnetic ion ($S = 3/2$). In addition, these observed changes are quantitatively reversible upon annealing the powders in air.

An isoelectronic analog of Cr^{3+} is Mn^{4+}, which is known to also occupy the Ti^{4+}-site in $SrTiO_3$. Although additional defects are required to maintain charge neutrality in Cr^{3+}:$SrTiO_3$, Mn^{4+} in the B-site of $SrTiO_3$ is an isovalent dopant. Amongst the transition-metal doped oxides, Mn:$SrTiO_3$ has recently received extensive attention due to its complex and unique behavior than intrinsic $SrTiO_3$. The concurrent doping of Mn and oxygen vacancies in $SrTi_{1-x}Mn_xO_{3-\delta}$ is reported to promote ferromagnetic ordering, dielectric permittivity and possible metallic behavior (Savinov et al., 2008; Choudhury et al., 2011, 2013; Middey et al., 2012; Thanh et al., 2014). These observations make nonstoichiometric Mn:$SrTiO_3$ a highly attractive candidate for spin-based electronics applications. Although not completely understood, the results are attributed to the interplay of redox-active Mn ions and the intrinsic charge compensating defects. In this regard, quantitative research is challenging due to a lack of experimental control over the interactions, and the complexity of Mn ions present in multiple oxidation states. Herein we report on the nature of the oxidation state of Mn ions and associated defect centers in bulk Mn:$SrTiO_3$ powders. We utilized various dopant-specific spectroscopic probes to elucidate the Mn oxidation state including EPR and diffuse-reflectance spectroscopies. We extend the use of $NaBH_4$ as a solid-state reductant to monitor changes in the three, unique Mn-related species as well as oxygen-related defects and "self-doped" Ti^{3+} ions. Comparison to other studies of reduced Mn:$SrTiO_3$ and noticeable absences of certain EPR-active Mn-centers is also discussed. We also observe a new signal in reduced samples that we attribute to superoxide anions, O_2^-.

MATERIALS AND METHODS

Chemicals

TiO_2 (>99.5%, Aeroxide P25 powder, Acros Organics), $Sr(NO_3)_2$ (>99%, Acros Organics), $Mn(NO_3)_2{\cdot}4H_2O$ (analytical grade, Acros Organics), $NaBH_4$ (≥98%, white powder, MP Biomedical), MgO (Fisher Science Education), and ethanol (200 proof, ACS/USP grade, Pharmco-Aaper) were used as received.

Synthesis of Bulk Mn-Doped $SrTiO_3$

Bulk powders of $SrTi_{1-x}Mn_xO_{3-\delta}$ (abbreviated Mn:$SrTiO_3$) were synthesized by a conventional solid-state reaction method, where x is the nominal concentration of Mn ($x = 0.001$) and δ is the concentration of oxygen vacancies. Briefly, $Sr(NO_3)_2$, $Mn(NO_3)_2{\cdot}4H_2O$, and TiO_2 were mixed in the desired stoichiometry and ground with a mortar and pestle for about 10 min. The mixture was then transferred to a porcelain combustion boat and placed in the center of a tube furnace inside a quartz insert. The reaction mixture was heated in air for 6 h at 1,000°C, reground for 10 min, then heated again for an additional 16 h at 1,000°C.

$NaBH_4$ Reductions and Reoxidation

Chemical reductions of the bulk powders were carried out using a modified version of reduction previously described by our group for Cr:$SrTiO_3$ (Lehuta and Kittilstved, 2016). For each reduction,

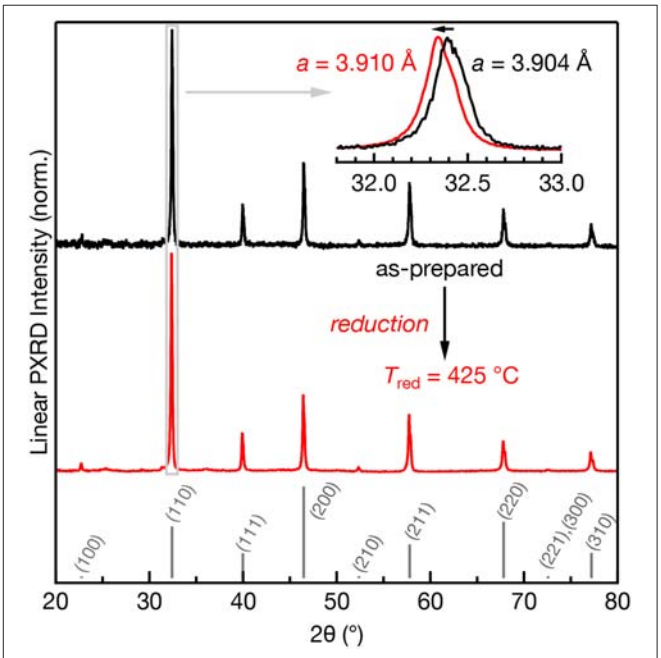

FIGURE 1 | Powder XRD patterns of 0.1% Mn:$SrTiO_3$ before (black) and after T_{red} = 425°C (red). The calculated pattern for $SrTiO_3$ (cubic phase) is shown in gray as sticks (Yamanaka et al., 2002). Inset: expanded region of the (110) diffraction peak clearly showing a shift to lower 2θ after T_{red} = 425°C.

an amount of powder was mixed in a 1:1 mole ratio with $NaBH_4$ using a mortar and pestle for 5 min and then placed in a porcelain combustion boat in the middle of a quartz insert in a tube furnace. The atmosphere in the quartz insert was continuously purged by a controlled flow of Ar gas monitored by a rotameter (Matheson 7300). The samples were heated at temperatures ranging from 300 to 425°C in 25°C increments under Ar flow for 30 min. After reducing, samples were cooled under Ar to room temperature, washed and centrifuged alternately with deionized water and ethanol to ensure complete removal of $NaBH_4$. After washing, samples were dried in an oven at 100°C for 2 h.

Reoxidation was performed by aerobically annealing the reduced samples until the physical color of the sample reversed to Mn:$SrTiO_3$ as-prepared sample.

Characterization

Powder X-ray diffraction (XRD) patterns were collected at room temperature using a Bragg-Brentano configuration with Cu K-α source (Rigaku SmartLab SE Diffraction System with cross-beam optics and D/Tex 250 Ultra 1D Si strip detector). X-band quantitative EPR spectra were collected at room temperature in 4 mm quartz EPR tubes (Wilmad-Glass) in a double rectangular resonator cavity (Bruker Elexsys E-500 with ER 4105DR cavity). Room temperature quantitative EPR spectra were collected consecutively on chemically perturbed samples (either oxidized or reduced) and an as-prepared sample using identical sample placement and instrument settings (Eaton et al., 2010). The resonance field positions in the EPR spectra for each paramagnetic Mn center were simulated using the "resfields" function in EasySpin using the reported EPR parameters from literature and referenced below (Stoll and Schweiger, 2006). Low-temperature X-band EPR spectra were measured at 77 K on powders using the perpendicular mode of a dual-mode resonator cavity with a quartz finger dewar insert (Bruker Elexsys E-500 with ER-4116 cavity) ensuring the sample height exceeded the cavity height for quantitative analysis. Diffuse-reflectance spectra were collected with an integrating

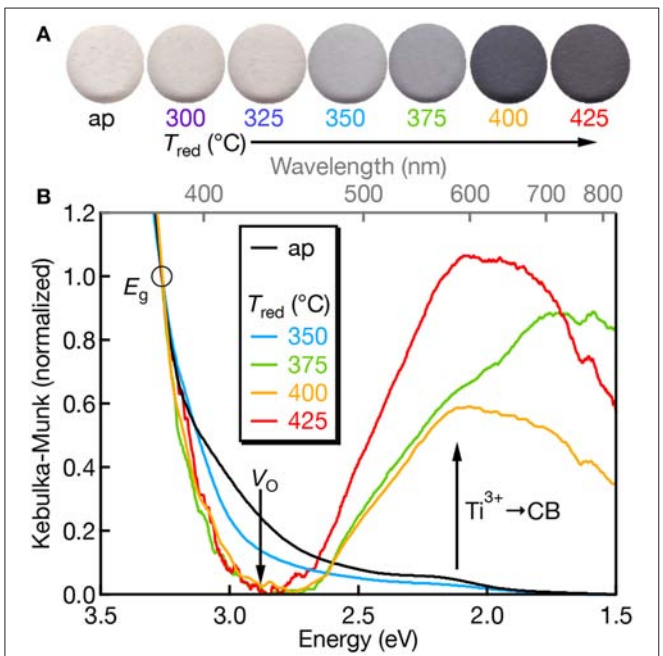

FIGURE 2 | (A) Scanned color images of Mn:$SrTiO_3$ powders as a function of T_{red}. **(B)** Diffuse-reflectance spectra of Mn:$SrTiO_3$ as a function of reduction temperature (as-prepared = black; T_{red} at 350°C (blue), 375°C (green), 400°C (orange), and 425°C (red), respectively). Data were normalized at 380 nm (3.26 eV; denoted by the circle) after setting the lowest y-value in the spectrum as the "zero." The T_{red} = 400°C spectrum was smoothed for presentation.

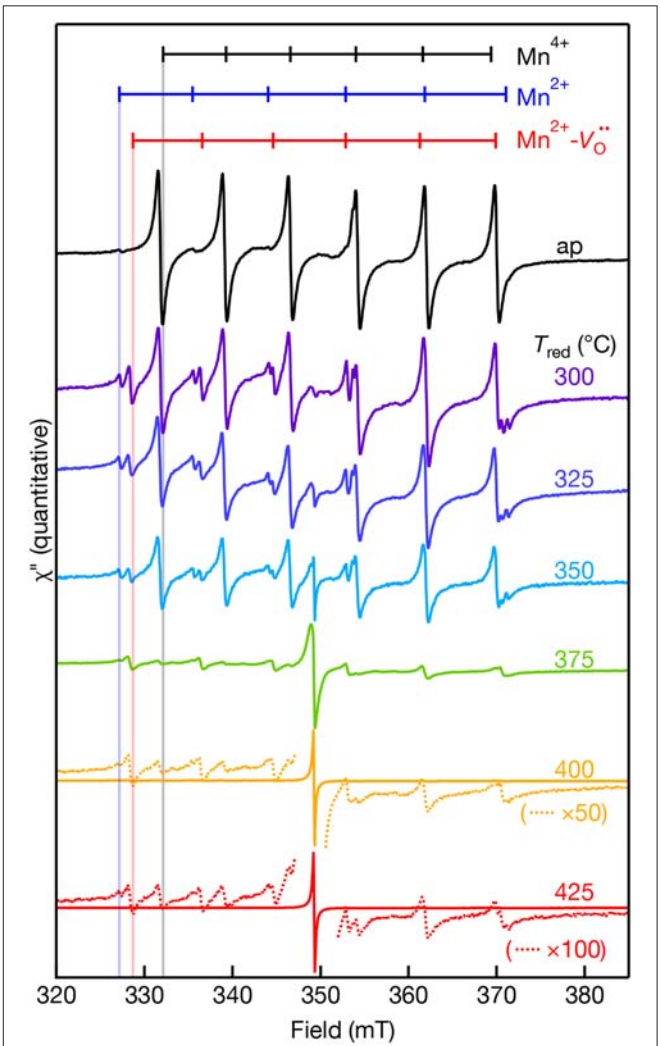

FIGURE 3 | Room temperature X-band EPR spectra of 0.1% Mn-doped $SrTiO_3$ bulk powder before (as-prepared, black) and after $NaBH_4$ reduction for 30 min at various temperatures (300–425°C). The dotted lines in the 400 and 425°C spectra are selected regions of the spectra that are multiplied (×) by 50 and 100, respectively. The calculated resonance fields for the hyperfine-split transitions of Mn^{4+} (black), Mn^{2+}-$V_O^{\cdot\cdot}$ (red), and Mn^{2+} (blue) in $SrTiO_3$ are shown as vertical markers. The calculated resonance fields were simulated for each Mn center observed in the EPR with EasySpin (see characterization). Data were collected on the same day in a double-resonator cavity equipped with an as-prepared sample in the 2nd resonator and used to standardize sample intensities.

TABLE 1 | Summary of EPR parameters for the Mn centers observed in the as-prepared and chemically treated samples reduced at various low temperatures.

EPR center	Observed in this work	*g*-value	$\|A\|$ (x10^{-4} cm^{-1})	References
Mn^{4+}	As-prepared (strong) reduced (weak)	1.994	69.4	Müller, 1959
Mn^{2+}	As-prepared (weak) reduced (strong)	2.004	82.3	Azzoni et al., 2000
[a]Mn^{2+}-$V_O^{\cdot\cdot}$	Reduced (weak)	$g_{\|\|} = 2.003$	76	Serway et al., 1977
Mn^{3+}-$V_O^{\cdot}$	Not observed	$g_{\|\|} = 7.945$ $g_{\perp} < 0.4$	37.3	Serway et al., 1977
O_2^-	Reduced (strong)	2.003	–	this work

The g-values and |A| obtained in this work are corroborated with previous reports in the literature.
[a]*An additional large axial component to the zero-field splitting was also estimated, D = 0.544 cm^{-1}.*

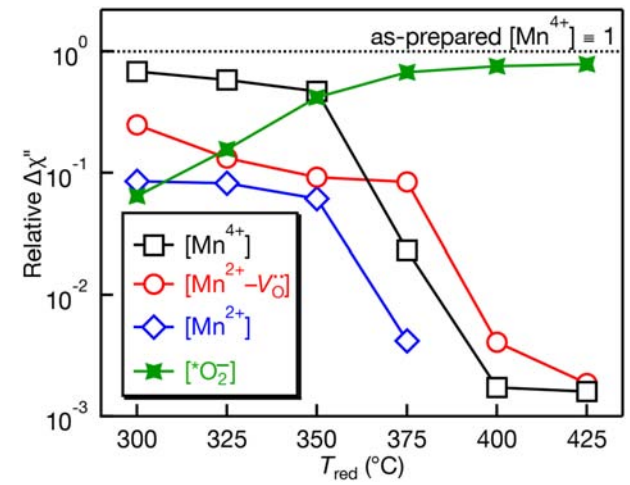

FIGURE 4 | Relative EPR peak intensities plotted on a log scale as a function of $NaBH_4$ reduction temperature (T_{red}) for Mn:$SrTiO_3$. The peak intensities are normalized vs. the intensity of the Mn^{4+} EPR signal in the as-prepared sample. Quantitative measurements performed using a dual-cavity EPR resonator (see characterization section).

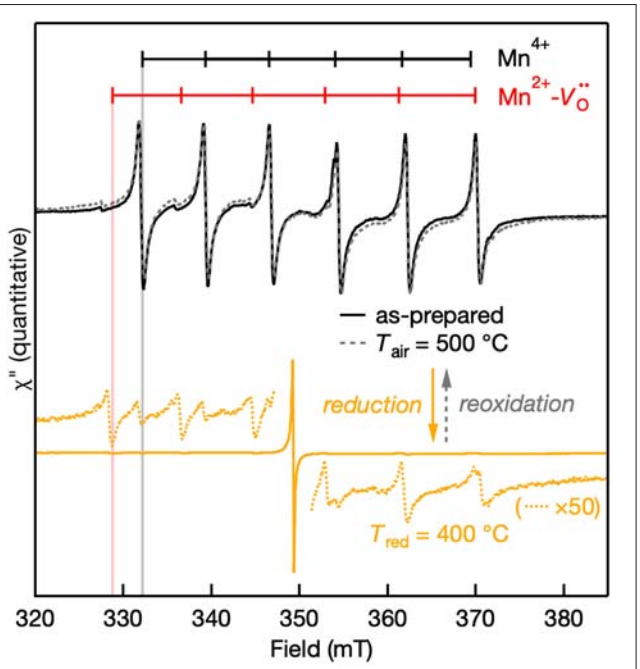

FIGURE 5 | Quantitative reversibility of the EPR signal of Mn:$SrTiO_3$ bulk powder as-prepared (solid black line), after T_{red} at 400°C (solid orange line), and after T_{air} at 500°C for ~1 h (gray dotted line). The weak Mn^{4+} and Mn^{2+} features after $NaBH_4$ reduction are still observed in the 50× scaled spectra (orange dotted lines).

sphere (Ocean Optics ISP-REF) coupled by fiber optics to a CCD-based spectrophotometer (Ocean Optics USB2000+ VIS-NIR). The optical density between the absorption minimum and the absorption at 320 nm was adjusted by diluting the powders with MgO.

RESULTS AND DISCUSSION

The room temperature powder XRD patterns of as-prepared and reduced (T_{red} = 425°C) Mn:$SrTiO_3$ are shown in **Figure 1**. All samples designated Mn:$SrTiO_3$ contain nominally 0.1% Mn content. Both the as-prepared and reduced samples indicate the presence of the cubic phase of $SrTiO_3$ (Mitchell et al., 2000). However, a clear *increase* in the lattice parameter is observed after reduction. This result is consistent with other observations and has been attributed to both changes in ionic size and electronic effects after reduction of the lattice (Janotti et al., 2012). For example, the reduction of both Mn ions ($Mn^{4+} \rightarrow Mn^{2+}$) and lattice cations ($Ti^{4+} \rightarrow Ti^{3+}$) would result in larger ions leading to lattice expansion (Shannon, 1976). No appreciable secondary phases were observed after low-temperature chemical reduction despite clear spectroscopic changes in the samples (*vide infra*).

The electronic structure of Mn:$SrTiO_3$ is dependent on the nature of the Mn-ion speciation (i.e., oxidation state(s) and first-coordination sphere). Mn^{4+} has a d^3 electronic configuration yielding a $^4A_{2g}$ ground state when substituted at the Ti^{4+}-site in $SrTiO_3$. The physical appearance of the Mn:$SrTiO_3$ as-prepared (oxidized) powders is off-white and gradually turns to black with increased reduction temperature as shown in **Figure 2A**. The black appearance of $SrTiO_3$ has been previously observed and indicates reduction in the $SrTiO_3$ lattice resulting in self-trapped electrons localized at Ti^{3+} sites (Tan et al., 2014; Lehuta and Kittilstved, 2016). The diffuse-reflectance spectra corroborates

the assignment of the black color to excitations from Ti^{3+} to conduction band states also referred to as a metal-to-metal charge transfer (MMCT) transition in the near-IR region (Khomenko et al., 1998). In the Mn:$SrTiO_3$ powder this MMCT appears at T_{red} between 350 and 375°C. The sub-bandgap tailing absorption at ∼2.9 eV has been assigned to excitations from the valence band to V_O's with different charge states (Mitra et al., 2012). With increasing T_{red}, the relative intensity of the V_O-related transitions decreases and disappears at T_{red} = 375°C and is consistent with electron accumulation in the V_O states. Both spectral changes observed here for Mn:$SrTiO_3$ with increasing T_{red} are similar to our recent study on chemically-reduced Cr:$SrTiO_3$ (Lehuta and Kittilstved, 2016).

We also do not observe Mn-centered transitions from the diffuse-reflectance spectra which we attribute to either (1) low concentrations of Mn^{3+} or Mn^{4+}, which have spin-allowed transitions in the visible, or (2) the Mn ions are primarily in their +2 oxidation state, which only has spin-forbidden transitions when the d-electrons order in the high-spin configuration (S = 5/2, $^6A_{1g}$ ground state).

EPR-active species involving Mn ions in the +2, +3, and +4 oxidation states in $SrTiO_3$ have previously been reported (Müller, 1959; Serway et al., 1977; Azamat et al., 2012). However, Mn^{3+} exhibits large zero-field splitting due to the S = 2 electronic spin state and thus, it is EPR-silent at conventional X-band frequencies (Azamat et al., 2012). The room temperature quantitative X-band EPR spectra of the Mn-doped $SrTiO_3$ samples are shown in **Figure 3** as a function of reduction temperatures ranging from T_{red} = 300–425°C. The as-prepared sample consists of two sets of sextet peaks. In accordance with the reported g-value and hyperfine splitting constant (A) of Mn^{4+} in $SrTiO_3$, the main sextet in the as-prepared sample is assigned to Mn^{4+} substituting for Ti^{4+} with an isotropic g = 1.996 and $|A|$ = 69.4 × 10^{-4} cm^{-1} (Müller, 1959). The second and much weaker set of sextets is somewhat occluded by the Mn^{4+} transitions, but the low-field resonances agree well with substitutional Mn^{2+} at the Ti^{4+} site in $SrTiO_3$ with g = 2.004 and $|A|$ = 82.30 × 10^{-4} cm^{-1} (Azzoni et al., 2000; Choudhury et al., 2013). Despite reports of both axial Mn^{2+}-$V_O^{\cdot\cdot}$ and Mn^{3+}-$V_O^{\cdot}$ complexes in Mn:$SrTiO_3$, we do not observe these complexes in the as-prepared Mn:$SrTiO_3$ sample. Hence, only the substitutional Mn^{4+} and Mn^{2+} species in an octahedral oxide crystal field co-exist in the as-prepared Mn:$SrTiO_3$ powders.

After chemical reduction with $NaBH_4$ under Ar(g) at T_{red} = 300°C, a new, third set of transitions are detected near the Mn^{2+} lines. Concomitant with the appearance of this new set of peaks is a decrease in the intensity of Mn^{4+} lines and an increase in the relative intensity of Mn^{2+}. The new set of lines agree well with the report of a substitutional Mn^{2+} center at the Ti^{4+}-site coupled to a doubly ionized oxygen vacancy (Serway et al., 1977).

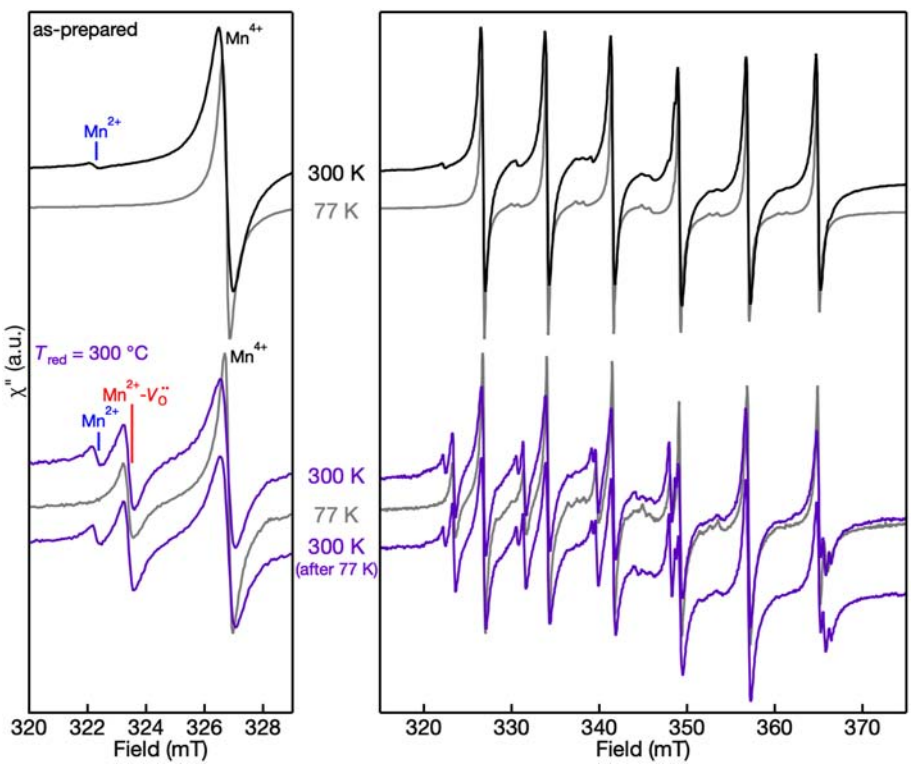

FIGURE 6 | 300 K and 77 K EPR spectra of Mn:$SrTiO_3$ powders as-prepared **(top)** and after T_{red} = 300°C **(bottom)**. **(left)** Spectra in the region of the lowest field transitions within the hyperfine structure and **(right)** full spectrum. The temperatures at which the spectra were collected are labeled in the figure. Spectra are normalized to account for the increased EPR intensity with decreasing temperature.

The reported EPR parameters of this Mn^{2+}-$V_o^{\cdot\cdot}$ complex includes a large axial component to the zero-field splitting ($D = 0.544$ cm^{-1}), $g_{||} = 2.003$, and $|A| = 76 \times 10^{-4}$ cm^{-1}. We were unable to detect any transitions at lower or higher magnetic fields likely from the low relative concentration and low nominal concentration of Mn in the lattice. The Mn^{2+}-$V_o^{\cdot\cdot}$ complex forms at low temperatures before reduction of the $SrTiO_3$ lattice at $T_{red} < 375°C$ (see **Figure 2**). One possible mechanism to explain the formation of this complex could be that oxygen vacancies may diffuse through the lattice and localize in the vicinity of Mn^{4+} substitutional sites at low temperatures. This work demonstrates that mild reduction at only $T_{red} = 300–325°C$ is sufficient to form the Mn^{2+}-$V_o^{\cdot\cdot}$ complex in bulk powders. This result contrasts with the high temperature reductions above 825°C previously used to create these centers in Mn:$SrTiO_3$ (Blazey et al., 1983; Kutty et al., 1986). In addition, we observe the co-existence of Mn^{4+} and the Mn^{2+}-$V_o^{\cdot\cdot}$ complex in the same EPR spectra at every T_{red}. This does not agree with previous single crystal studies where the Mn^{2+}-$V_o^{\cdot\cdot}$ complex was only observed when the Mn^{4+} lines were fully removed upon reduction in 5% hydrogen for 3 h at 1,000°C (Serway et al., 1977).

A new single feature centered at $B_0 \sim 350$ mT ($g \sim 2.003$) with no associated hyperfine structure was also observed in the EPR spectra after reduction. This feature increases in spectral intensity and also narrows with increasing T_{red}. This feature is similar to a feature observed in Cr:$SrTiO_3$ at $T_{red} > 375°C$ (Lehuta and Kittilstved, 2016), but has a significantly larger relative intensity compared to the dopant EPR signal in the Mn:$SrTiO_3$ sample with the same nominal dopant concentration. This feature is tentatively assigned as the EPR-active superoxide anion (O_2^-) adsorbed on the surface of $SrTiO_3$ and could form via a surface reaction between Ti^{3+} and oxygen (Bykov et al., 2013; Harrigan et al., 2016). **Table 1** below summarizes the EPR spectral parameters for previously reported Mn species in $SrTiO_3$ in the as-prepared and reduced Mn:$SrTiO_3$.

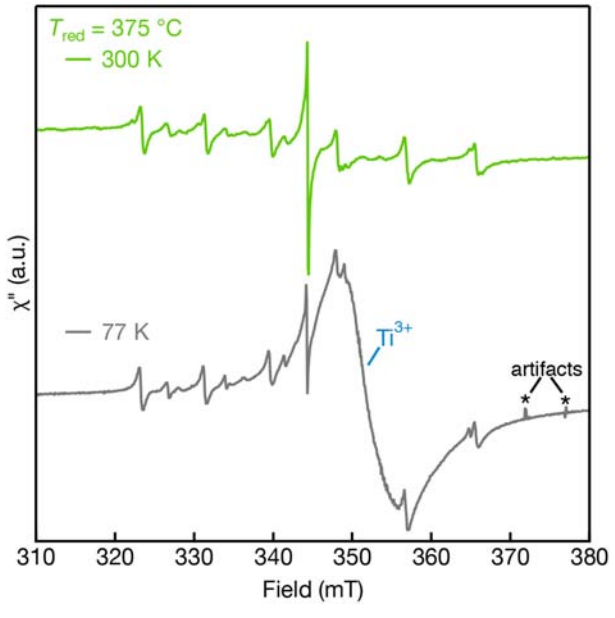

FIGURE 7 | EPR spectra of Mn:$SrTiO_3$ bulk powders reduced at $T_{red} =$ 375°C measured at 300 K (top) and 77 K (bottom). Sharp features in the 77 K spectra are attributed to artifacts resulting from bubbles that arise in the liquid nitrogen finger dewar.

The quantitative EPR spectra measured using the double resonator cavity shown in **Figure 3** was analyzed and the relative intensity of the observed EPR centers is shown in **Figure 4** as a function of T_{red}. Compared to the as-prepared Mn^{4+} signal intensity (defined as 1), a gradual decrease in the Mn^{4+} and Mn^{2+} EPR signals is observed with similar correlations in their temperature dependences. The signal for Mn^{2+} is not detected for $T_{red} \geq 375°C$. In contrast, the EPR intensity of the Mn^{2+}-$V_o^{\cdot\cdot}$ complex shows little change and is more intense than the Mn^{4+} and Mn^{2+} EPR signals for $T_{red} \geq 375°C$. The intensity of the Mn^{2+}-$V_o^{\cdot\cdot}$ complex drops by an order of magnitude after increasing T_{red} from 375 to 400°C. At the highest temperature, $T_{red} = 425°C$, the EPR intensity of the O_2^- ion is nearly 3 orders of magnitude more intense than the Mn^{2+}-$V_o^{\cdot\cdot}$ complex, indicative of substantial surface defects. Studies to identify the nature of this defect center are currently underway.

The EPR spectra of the Mn:$SrTiO_3$ powders after preparation, after $T_{red} = 400°C$, and after aerobic reoxidation at $T_{air} = 500°C$ for ~1 h are shown in **Figure 5**. The observed changes in the EPR spectra of the reduced samples revert to the as-prepared EPR spectrum by aerobically annealing the sample. The process of forming Mn^{2+}-$V_o^{\cdot\cdot}$ complex in the reduced samples is thus reversible. However, elevated temperatures and longer reoxidation times were required in contrast with the chemical reductions. Since the Mn^{2+}-$V_o^{\cdot\cdot}$ complex is a charge-neutral complex in the lattice, it is expected to be at least metastable. The apparently slower reoxidation kinetics compared to reduction kinetics suggest a metastable complex.

The 300 K (room temperature) and 77 K (liquid N_2) EPR spectra of the Mn centers in the as-prepared and $T_{red} = 300°C$ powders are shown in **Figure 6**. Two things are revealed from the EPR spectra of both as-prepared and lightly-reduced Mn:$SrTiO_3$ samples: (1) there is no evidence of self-trapped electrons at Ti^{3+} sites in the lattice based on the 77 K spectra, and (2) the EPR intensity of Mn^{2+} completely disappears at 77 K. At low temperature, the intensity of Mn^{4+} is pronounced following the typical Boltzmann statistics. In contrast, the Mn^{2+} EPR signal completely disappears at 77 K in these two samples. These results agree with a previous magnetic susceptibility and EPR study of the Mn^{2+} signal vanishing, where the behavior was attributed to increased antiferromagnetic interactions between adjacent Mn^{2+} ions with decreasing temperature (Azzoni et al., 2000). This explanation cannot be extended to describe the EPR signal of the Mn^{2+}-$V_o^{\cdot\cdot}$ complex, which does not disappear at 77 K in the $T_{red} = 300°C$ sample. To confirm the behavior of EPR signals as a function of temperature, the EPR spectrum of the reduced sample at 300 K was repeated after cooling it to 77 K and the entire spectrum is nearly identical.

The cryogenic EPR measurements were also collected for samples reduced above 350°C to reveal the effect of Ti^{3+} defects on the EPR spectra that are observed in the diffuse-reflectance spectra shown in **Figure 2**. **Figure 7** shows the 300 K

and 77 K EPR spectra of $T_{red} = 375°C$. The paramagnetic Ti^{3+} defects are not observed in the EPR performed at 300 K due to fast spin-lattice relaxation but are promptly observed at 77 K (Lehuta and Kittilstved, 2016; Harrigan and Kittilstved, 2018). At 77 K, the $T_{red} = 375°C$ sample is dominated by a broad and intense asymmetric Ti^{3+} lattice defect centered at $g = 1.94$. The appearance of this fast-relaxing defect, however, has no apparent effect on the linewidth of the Mn-centers nor the single line that we tentatively assign to surface-adsorbed O_2^- ions. We recently showed that linewidth and relaxation-dynamics of substitutional Cr^{3+} ions in $SrTiO_3$ powders and colloidal nanocrystals can be significantly altered when Ti^{3+} defects are present in the lattice through a near-resonant cross-relaxation process (Lehuta and Kittilstved, 2016; Harrigan and Kittilstved, 2018). This same behavior is not observed for any of the Mn-centers in the reduced $SrTiO_3$ powder.

CONCLUSIONS

A low-temperature chemical reduction technique has been implemented for tunability of the Mn dopant oxidation states and the related intrinsic defects in bulk Mn:$SrTiO_3$. We employed a myriad of structural and spectroscopic techniques on samples subjected to a systematic chemical reduction. Both isotropic Mn^{4+} and Mn^{2+} species were identified in the as-prepared powders. Following the thermal reduction, the samples exhibited a continuous decrease in Mn^{4+} EPR signal and an increase in the Mn^{2+} intensity, accompanied by the introduction of a Mn^{2+}-$V_o^{\cdot\cdot}$ complex. We demonstrate that our chemical treatment at merely $T_{red} = 300–325°C$ generates sufficient driving force to significantly reduce the intensity of the octahedral Mn^{4+} and Mn^{2+} dopants and form the Mn^{2+}-$V_o^{\cdot\cdot}$ complex. All the Mn peaks showed distinctive changes at low-temperature in the EPR that are readily reversible upon warming back the samples. Reductions at 375°C and above generated significant concentrations of Ti^{3+} defects that were confirmed by diffuse-reflectance and low-temperature EPR spectroscopy. All the observed perturbations in the reduced samples are entirely reversible by aerobic annealing at elevated temperatures. We also observe an intense spectral feature in the EPR spectrum in heavily-reduced Mn:$SrTiO_3$ powders that we attribute to O_2^- ions at the surface. This fast and effective strategy offers a general low-temperature reduction process that allows tunability and control over the rich dopant-defect chemistry in transition-metal doped $SrTiO_3$ materials.

DATA AVAILABILITY

The datasets generated for this study are available on request to the corresponding author.

AUTHOR CONTRIBUTIONS

HM and KL carried out the experiments, data analysis and interpretation, and edited the manuscript. WH contributed to the interpretation of the results and edited the manuscript. HM and KK contributed to the data analysis and interpretation and wrote the manuscript.

FUNDING

This work was supported by the National Science Foundation (NSF:DMR-1747593). The acquisition of the X-ray powder diffractometer was made possible through the National Science Foundation Major Research Instrumentation Program (NSF:CHE-1726578).

REFERENCES

Azamat, D. V., Badalyan, A. G., Dejneka, A., Trepakov, V. A., Jastrabik, L., and Frait, Z. (2012). High-frequency electron paramagnetic resonance investigation of Mn^{3+} centers in $SrTiO_3$. *J. Phys. Chem. Solids* 73, 822–826. doi: 10.1016/j.jpcs.2012.02.009

Azzoni, C. B., Mozzati, M. C., Paleari, A., Massarotti, V., Bini, M., and Capsoni, D. (2000). Magnetic evidence of different environments of manganese ions in Mn-substituted strontium titanate. *Solid State Commun.* 114, 617–622. doi: 10.1016/s0038-1098(00)00121-6

Blazey, K. W., Cabrera, J. M., and Müller, K. A. (1983). Oxygen vacancy-transition metal-ion impurity association in $SrTiO_3$. *Solid State Commun.* 45, 903–906. doi: 10.1016/0038-1098(83)90332-0

Bykov, I., Makarova, M., Trepakov, V., Dejneka, A., Yurchenko, L., Yurchenko, L., et al. (2013). Intrinsic and impurity defects in chromium-doped $SrTiO_3$ nanopowders: EPR and NMR study. *Phys. Status Solidi B* 250, 821–824. doi: 10.1002/pssb.201200871

Chan, N.-H., Sharma, R. K., and Smyth, D. M. (1981). Nonstoichiometry in $SrTiO_3$. *J. Electrochem. Soc.* 128, 1762–1769. doi: 10.1149/1.2127727

Choudhury, D., Mukherjee, S., Mandal, P., Sundaresan, A., Waghmare, U. V., Bhattacharjee, S., et al. (2011). Tuning of dielectric properties and magnetism of $SrTiO_3$ by site-specific doping of Mn. *Phys. Rev. B* 84:125124. doi: 10.1103/PhysRevB.84.125124

Choudhury, D., Pal, B., Sharma, A., Bhat, S. V., and Sarma, D. D. (2013). Magnetization in electron- and Mn-doped $SrTiO_3$. *Sci. Rep.* 3:1433. doi: 10.1038/srep01433

Eaton, G. R., Eaton, S. S., Barr, D. P., and Weber, R. T. (2010). *Quantitative EPR.* Vienna: Spring-Verlag/Wien. doi: 10.1007/978-3-211-92948-3

Faughnan, B. W. (1971). Photochromism in transition-metal-doped $SrTiO_3$. *Phys. Rev. B* 4, 3623–3636. doi: 10.1103/PhysRevB.4.3623

Harrigan, W. L., and Kittilstved, K. R. (2018). Reversible modulation of the Cr^{3+} spin dynamics in colloidal $SrTiO_3$ nanocrystals. *J. Phys. Chem. C* 122, 26652–26657. doi: 10.1021/acs.jpcc.8b08680

Harrigan, W. L., Michaud, S. E., Lehuta, K. A., and Kittilstved, K. R. (2016). Tunable electronic structure and surface defects in chromium-doped colloidal $SrTiO_{3-\delta}$ nanocrystals. *Chem. Mater.* 28, 430–433. doi: 10.1021/acs.chemmater.6b00049

Ishii, T., Kato, H., and Kudo, A. (2004). H_2 evolution from an aqueous methanol solution on $SrTiO_3$ photocatalysts codoped with chromium and tantalum ions under visible light irradiation. *J. Photochem. Photobiol. A Chem.* 163, 181–186. doi: 10.1016/S1010-6030(03)00442-8

Janotti, A., Jalan, B., Stemmer, S., and Van de Walle, C. G. (2012). Effects of doping on the lattice parameter of $SrTiO_3$. *Appl. Phys. Lett.* 100:262104. doi: 10.1063/1.4730998

Kamalasanan, M. N., Deepak Kumar, N., and Chandra, S. (1993). Structural, optical, and dielectric properties of sol-gel derived $SrTiO_3$ thin films. *J. Appl. Phys.* 74, 679–686. doi: 10.1063/1.355230

Kato, H., and Kudo, A. (2002). Visible-light-response and photocatalytic activities of TiO_2 and $SrTiO_3$ photocatalysts codoped with antimony and chromium. *J. Phys. Chem. B* 106, 5029–5034. doi: 10.1021/jp0255482

Kato, H., Sasaki, Y., Shirakura, N., and Kudo, A. (2013). Synthesis of highly active rhodium-doped $SrTiO_3$ powders in Z-scheme systems for visible-light-driven photocatalytic overall water splitting. *J. Mater. Chem. A* 1, 12327–12333. doi: 10.1039/c3ta12803b

Khomenko, V. M., Langer, K., Rager, H., and Fett, A. (1998). Electronic absorption by Ti^{3+} ions and electron delocalization in synthetic blue rutile. *Phys. Chem. Miner.* 25, 338–346. doi: 10.1007/s002690050124

Kozuka, Y., Hikita, Y., Bell, C., and Hwang, H. Y. (2010). Dramatic mobility enhancements in doped $SrTiO_3$ thin films by defect management. *Appl. Phys. Lett.* 97:012107. doi: 10.1063/1.3457994

Kutty, T. R. N., Gomathi Devi, L., and Murugaraj, P. (1986). The change in oxidation state of Mn ions in semiconducting $BaTiO_3$ and $SrTiO_3$ around the phase transition temperatures. *Mater. Res. Bull.* 21, 1093–1102. doi: 10.1016/0025-5408(86)90225-4

La Mattina, F., Bednorz, J. G., Alvarado, S. F., Shengelaya, A., and Keller, H. (2008). Detection of charge transfer processes in Cr-doped $SrTiO_3$ single crystals. *Appl. Phys. Lett.* 93:022102. doi: 10.1063/1.2959059

Lehuta, K. A., Haldar, A., Zhou, D., and Kittilstved, K. R. (2017). Spectroscopic study of the reversible chemical reduction and reoxidation of substitutional Cr ions in Sr_2TiO_4. *Inorg. Chem.* 56, 9177–9184. doi: 10.1021/acs.inorgchem.7b01210

Lehuta, K. A., and Kittilstved, K. R. (2016). Reversible control of the chromium valence in chemically reduced Cr-doped $SrTiO_3$ bulk powders. *Dalton. Trans.* 45, 10034–10041. doi: 10.1039/c6dt00706f

Mattheiss, L. F. (1972). Effect of the 110°K Phase transition on the $SrTiO_3$ conduction bands. *Phys. Rev. B* 6, 4740–4753. doi: 10.1103/PhysRevB.6.4740

Middey, S., Meneghini, C., and Ray, S. (2012). Evidence of oxygen-vacancy-induced ferromagnetic order in single crystal Mn-doped $SrTiO_3$. *Appl. Phys. Lett.* 101:042406. doi: 10.1063/1.4738785

Mitchell, R. H., Chakhmouradian, A. R., and Woodward, P. M. (2000). Crystal chemistry of perovskite-type compounds in the tausonite-loparite series, $(Sr_{1-2x}Na_xLa_x)TiO_3$. *Phys. Chem. Miner.* 27, 583–589. doi: 10.1007/s002690000103

Mitra, C., Lin, C., Robertson, J., and Demkov, A. A. (2012). Electronic structure of oxygen vacancies in $SrTiO_3$ and $LaAlO_3$. *Phys. Rev. B* 86:155105. doi: 10.1103/PhysRevB.86.155105

Müller, K., and Burkard, H. (1979). $SrTiO_3$: an intrinsic quantum paraelectric below 4 K. *Phys. Rev. B* 19, 3593–3602. doi: 10.1103/PhysRevB.19.3593

Müller, K. A. (1959). Electron paramagnetic resonance of manganese IV in $SrTiO_3$. *Phys. Rev. Lett.* 2, 341–343. doi: 10.1103/PhysRevLett.2.341

Sasaki, Y., Nemoto, H., Saito, K., and Kudo, A. (2009). Solar water splitting using powdered photocatalysts driven by Z-schematic interparticle electron transfer without an electron mediator. *J. Phys. Chem. C* 113, 17536–17542. doi: 10.1021/jp907128k

Savinov, M., Trepakov, V. A., Syrnikov, P. P., Železný, V., Pokorný, J., Dejneka, A., et al. (2008). Dielectric properties of Mn doped $SrTiO_3$. *J. Phys. Cond. Matter* 20:095221. doi: 10.1088/0953-8984/20/9/095221

Serway, R. A., Berlinger, W., Müller, K. A., and Collins, R. W. (1977). Electron paramagnetic resonance of three manganese centers in reduced $SrTiO_3$. *Phys. Rev. B* 16, 4761–4768. doi: 10.1103/PhysRevB.16.4761

Shannon, R. D. (1976). Revised effective ionic radii and systematic studies of interatomic distances in halides and chalcogenides. *Acta Cryst. A*32, 751–767. doi: 10.1107/S0567739476001551

Stoll, S., and Schweiger, A. (2006). EasySpin, a comprehensive software package for spectral simulation and analysis in EPR. *J. Magn. Reson.* 178, 42–55. doi: 10.1016/j.jmr.2005.08.013

Tan, H., Zhao, Z., Zhu, W. B., Coker, E. N., Li, B., Zheng, M., et al. (2014). Oxygen vacancy enhanced photocatalytic activity of pervoskite $SrTiO_3$. *ACS Appl. Mater. Interfaces* 6, 19184–19190. doi: 10.1021/am5051907

Thanh, T. D., Phan, T. L., Oanh, L. M., Minh, N. V., Lee, J. S., and Yu, S. C. (2014). Influence of Mn doping on the crystal structure, and optical and magnetic properties of $SrTiO_3$ compounds. *IEEE Trans. Magn.* 50, 1–4. doi: 10.1109/TMAG.2014.2304562

Wang, D., Ye, J., Kako, T., and Kimura, T. (2006). Photophysical and photocatalytic properties of $SrTiO_3$ doped with Cr cations on different sites. *J. Phys. Chem. B* 110, 15824–15830. doi: 10.1021/jp062487p

Wang, Q., Hisatomi, T., Ma, S. S. K., Li, Y., and Domen, K. (2014). Core/shell structured La- and Rh-codoped $SrTiO_3$ as a hydrogen evolution photocatalyst in Z-scheme overall water splitting under visible light irradiation. *Chem. Mater.* 26, 4144–4150. doi: 10.1021/cm5011983

Weaver, H. E. (1959). Dielectric properties of single crystals of $SrTiO_3$ at low temperatures. *J. Phys. Chem. Solids* 11, 274–277. doi: 10.1016/0022-3697(59)90226-4

Wild, R. L., Rockar, E. M., and Smith, J. C. (1973). Thermochromism and electrical conductivity in doped $SrTiO_3$. *Phys. Rev. B* 8, 3828–3835. doi: 10.1103/PhysRevB.8.3828

Yamanaka, T., Hirai, N., and Komatsu, Y. (2002). Structure change of $Ca_{1-x}Sr_xTiO_3$ perovskite with composition and pressure. *Am. Miner.* 87, 1183–1189. doi: 10.2138/am-2002-8-917

Zuo, F., Wang, L., Wu, T., Zhang, Z., Borchardt, D., and Feng, P. (2010). Self-doped Ti^{3+} enhanced photocatalyst for hydrogen production under visible light. *J. Am. Chem. Soc.* 132, 11856–11857. doi: 10.1021/ja103843d

Conflict of Interest Statement: The authors declare that the research was conducted in the absence of any commercial or financial relationships that could be construed as a potential conflict of interest.

Copyright © 2019 Mansoor, Harrigan, Lehuta and Kittilstved. This is an open-access article distributed under the terms of the Creative Commons Attribution License (CC BY). The use, distribution or reproduction in other forums is permitted, provided the original author(s) and the copyright owner(s) are credited and that the original publication in this journal is cited, in accordance with accepted academic practice. No use, distribution or reproduction is permitted which does not comply with these terms.

frontiers in Chemistry

REVIEW
published: 04 June 2019
doi: 10.3389/fchem.2019.00365

Molecular Orbital Insights of Transition Metal-Stabilized Carbocations

*Hannah Goodman†, Liangyong Mei† and Thomas L. Gianetti**

Department of Chemistry and Biochemistry, University of Arizona, Tucson, AZ, United States

Transition metal-stabilized carbocations are characterized by synthetically valuable interactions, yet, to date there are no comprehensive reports of the many bonding modes that can exist between a metal and carbocation. This review summarizes developments in these complexes to provide a clear picture of their properties and reactivities. In order to strategically exploit them, we propose this summary of the different bonding modes for transition metal-carbocation complexes. These models will help chemists understand the orbital interactions involved in these compounds so that they can approach their synthetic goals most effectively. Multiple transition metals and carbocations will be discussed.

Keywords: metal complexes, carbocation, bonding model, metal-carbocation interaction, molecular orbital interactions

OPEN ACCESS

Edited by:
Luís D. Carlos,
University of Aveiro, Portugal

Reviewed by:
Domenica Scarano,
University of Turin, Italy
Ahmed A. Al-Amiery,
National University of Malaysia, Malaysia

***Correspondence:**
Thomas L. Gianetti
tgianetti@email.arizona.edu

†These authors have contributed equally to this work

Specialty section:
This article was submitted to Inorganic Chemistry, a section of the journal Frontiers in Chemistry

Received: *21 February 2019*
Accepted: *02 May 2019*
Published: *04 June 2019*

Citation:
Goodman H, Mei L and Gianetti TL (2019) Molecular Orbital Insights of Transition Metal-Stabilized Carbocations. Front. Chem. 7:365. doi: 10.3389/fchem.2019.00365

INTRODUCTION

The structures, properties, and reactivities of organometallic complexes depend mostly on their ligand environment. Ligands are used to improve catalyst efficiency and accelerate the discovery of new reactivity modes. We will use M. Green's seminal model for Covalent Bond Classification (CBC method) (Green, 1995; Parkin, 2007) to define 2-center metal-ligand interactions of organometallic compounds as $ML_lX_xZ_z$, where the ligand atoms are classified as L, X, and Z ligands (**Figure 1A**). L-type ligands are Lewis bases that donate two electrons to form a dative L → M bond (e.g., PR_3, NR_3, OR). X-type ligands donate one electron, requiring oxidation of the metal center to form classical covalent M–X bonds (e.g., H^-, RO^-, Cl^-). Z-type ligands are Lewis acids that accept a pair of electrons from the metal to form a dative M ← Z bond (e.g., SO_2, BR_3). Since transition metals (TMs) are typically defined as electron-deficient species, the majority of ligands that have been developed are electron-rich Lewis-basic moieties (L- and X-types) that aim to complete the valence shell of the transition metal (also known as the 18 electron rule). However, transition metals also exhibit Lewis-basic character from metal-to-ligand back-donation from partial filling of their upper valence d shell. Organometallic chemists have recognized how this basicity can be used to promote interactions between a TM and a Lewis acid moiety, where the acid acts as a σ-acceptor (L-type) and not a σ-donor (Z-type) ligand.

The first example of Lewis acid–metal coordination was reported in 1970 (Shriver, 1970), yet the incidence of M ← Z complexes remained scarce for several decades. The scope of Lewis acids acting as σ-acceptor ligands has been significantly extended over the last two decades with the development of ambiphilic ligands—ligands that contain both electron donor (L-type) and acceptor (Z-type) groups (Amgoune and Bourissou, 2011; Braunschweig and Dewhurst, 2011; Owen, 2012, 2016; Bouhadir and Bourissou, 2016; Jones and Gabbaï, 2016). Transition metals exhibit similar ambiphilic character since they contain both filled and empty d-orbitals. When ambiphilic ligands are used, the metal center coordinates to the L-type moiety of the ligand and the degree of coordination to the Lewis acid moiety is increased (**Figure 1B**). The Z-type ligand can stabilize a

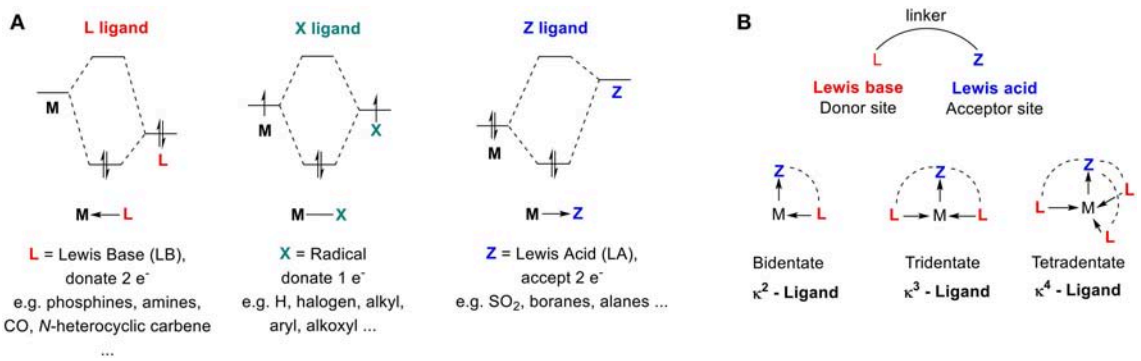

FIGURE 1 | (A) Simplified orbital diagrams associated with M—L, M—X, and M—Z interaction. **(B)** Schematic representation of ambiphilic ligands.

vacant orbital of the transition metal center while drawing electron density from the filled d-orbitals because of its σ-accepting properties. This interaction determines the electronic properties and reactivities of the metal (You et al., 2018). The synthesis, coordination chemistry, and reactivity of ambiphilic ligands and their metal complexes have been extensively studied and well-summarized in several recent reviews (Amgoune and Bourissou, 2011; Braunschweig and Dewhurst, 2011; Owen, 2012, 2016; Bouhadir and Bourissou, 2016; Jones and Gabbaï, 2016). Surprisingly, none of these reports have mentioned carbocations as Lewis acid Z-type ligands, and they neglect to examine the interactions between transition metals and persistent carbocations.

In organic chemistry, carbocations are ubiquitous. The field of carbocation chemistry has rapidly developed since its conception in 1901 when Norris discovered the first stable carbocations, triphenylmethyl ions (PH_3C^+) (Norris, 1901; Norris and Sanders, 1901) Carbocations have been identified as key intermediates in many organic reactions, including electrophilic aromatic substitutions, unimolecular nucleophilic substitutions, addition-eliminations, and many rearrangements (Olah, 2004). The significance of carbocations as reactive intermediates in acid-mediated reactions was also highlighted when Professor Olah was awarded the Nobel Prize in Chemistry to in 1994 for his contributions to carbocation chemistry (Olah, 1995). The diverse applications of carbocations in organic chemistry is outside of the scope of this review, but interested readers are encouraged to consult the many reviews published on their synthesis and applications.

This review focuses on organometallic complexes that contain a carbocation (Z-type ligand), within their first coordination sphere. In 1972, Olah proposed carbenium and carbonium ions as two distinct types of carbocations that are differentiated by their structures (Olah, 1972). The "classical" trivalent carbenium ion contains an sp^2-hybridized electron-deficient carbon atom (**Figure 2A**), while the "non-classical" carbonium ion is defined as a penta- (or higher) coordinate carbon that involves a 3-center-2-electron bond (**Figure 2B**; Winstein and Trifan, 1952; Olah, 1972). This review focuses on classical carbenium ions, which we will refer to as carbocations.

Carbocations can be transient, extremely reactive species, or they can be long-living, isolable, and storable. They gain stability from filled p orbitals or π-systems α to a sp^2 hybridized carbon, which creates resonance and delocalizes the positive charge over multiple atoms (**Figure 2A**). Their thermodynamic stability can be described in term of their pK_R^+ value, which is defined by the equilibrium between the cationic species and its corresponding carbinol (**Figure 2C**; Deno et al., 1955) A larger pK_R^+ value correlates to a more stable carbenium or, specifically, one that is resistant to nucleophilic attack by water. Examples of persistent carbenium ions and their pK_R^+ values are shown below (**Figure 2D**; Breslow and Chang, 1961; Ritchie, 1986; Amyes et al., 1992; Sørensen et al., 2014).

GENERAL BONDING CONSIDERATIONS

The bonding mode for most of the Z-type ligands described in the literature is unambiguous (Amgoune and Bourissou, 2011; Owen, 2012). In these models, there is a localized empty p orbital that acts as a σ-acceptor for a filled metal-based d orbital on either a group 13 or a hypervalent, heavy group 14 element (**Figure 1A**). However, this bonding model becomes more complicated when considering carbocation-containing species since the empty sp^2 hybridized orbital is often involved in an extended π-system that can act as an L- or X-type ligand. In order to discuss the bonding model of carbocations in depth, it is important to remind the reader about an important concept—donation and backdonation. This concept is represented by the Dewar-Chatt-Duncanson model (**Figure 3A**) with regard to metal-olefin interactions (Nelson et al., 1969; Mingos, 2001; Frenking, 2002). The filled π-orbital of the olefin donates electron density to the metal center via an interaction with an empty metal-based d orbital. This donation (L-type) is supplemented by backdonation from a filled metal-based d orbital into the empty π*-orbital (Z-type). **Figure 3A** shows how the complex can be described either as a metal-olefin adduct from modest backbonding (resulting in an L-type ligand), or as a metallacyclopropane derivative due to extensive backbonding (where the olefin serves as an LZ ligand, otherwise known as an X_2 ligand). The equivalence

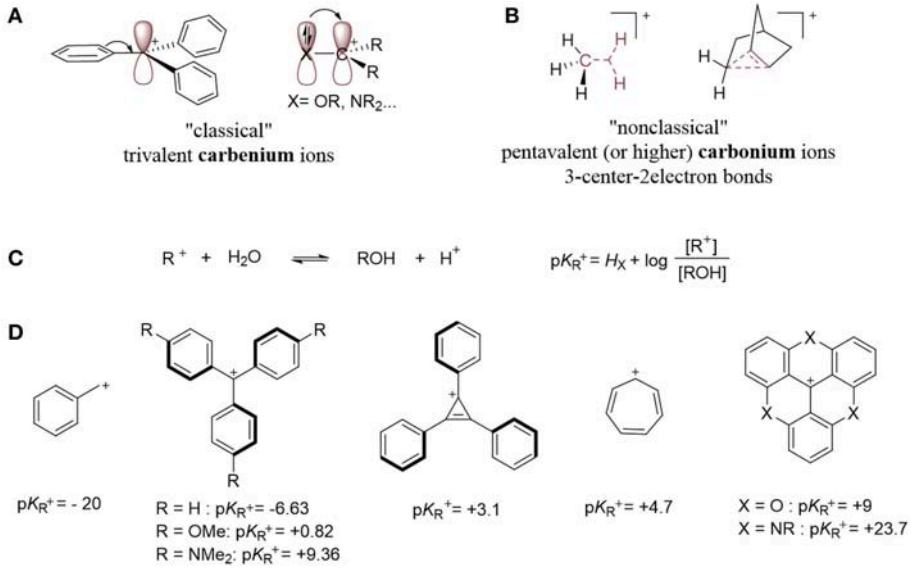

FIGURE 2 | (A) Examples of carbenium ions. **(B)** Examples of carbonium species. **(C)** Determination of carbocation stability: pK_{R+}. **(D)** Examples of carbocations and their pK_R^+ values (Breslow and Chang, 1961; Ritchie, 1986; Amyes et al., 1992; Sørensen et al., 2014).

between an LZ and X_2 system comes from the fact that both types require the involvement of two metal orbitals (**Figure 3B**; Parkin, 2007). Similar to the relationship between Fischer carbenes and Schrock alkylidenes (Fischer, 1976; Schrock, 2001, 2005; Shrock, 2002), the "triplet" state of the ligand becomes accessible only if the empty orbital is sufficiently low in energy. However, both bonding descriptions represent extreme cases of this model and most reported olefin complexes are more accurately described as a hybrid, with varying degrees of backdonation (**Figure 3A**, LZ′). The extent of backdonation strongly depends on the nature of the metal center. For example, a metal with a pair of electrons residing in a high energy orbital will favor strong backbonding interactions because of energy matching. Since it is impossible to predict which model is preferred without further spectroscopic or structural analysis, Parkin introduced the LZ′ designation, where Z′ refers to an unspecified degree of backbonding (Parkin, 2007). Examples of these types of ligands are C_2H_4 and CO. In order to describe the bonding mode for carbocation-containing ligands, we will employ this Z′ classification.

Another important concept is the equivalent neutral class (**Figure 3C**; Parkin, 2007) the classification of the ligand changes with the presence of any charge or delocalization of charge. A donor ligand with x-electrons bound to a cationic metal center is equivalent to a donor ligand (x-1)-electrons bound to a neutral metal center (i.e., $[ML]^+ \equiv [MX]$, so $X^+ \equiv Z$). Due to the cationic nature of the ligand of interest, this notation will be used to differentiate between partial backdonation (Z') and strong backdonation/charge delocalization (X^+).

Carbocation species can form either σ- or π-complexes depending on whether they are carbenylium (R_2C^+) or carbenium (R_3C^+) moieties. Carbenylium R_2C^+ ions possess a half-filled sp^2 orbital that can participate in σ-bonding with a metal center. They also have an empty p orbital, which is available for backdonation (**Figure 4A**). Using the CBC method, R_2C^+ can be described as an XZ′ ligand. These molecules are analogous to LZ′ carbenes R_2C: (vide supra, $L^+ \rightarrow X$). These carbenes can be classified in two ways, depending on the extent of π-backbonding from the metal center: either as a "Fischer carbene," which is an L-type ligand due to weak backdonation, or as a "Schrock alkylidene," which is an X_2 ligand because of strong backdonation (Parkin, 2007). A similar description for the interaction between a carbenylium R_2C^+ and a metal center can be used that also depends on the extent of π-backdonation. Stabilization of the empty p orbital by an alkyl substituent will result in no backdonation; in this case, R_2C^+ is a pure X ligand (i.e., $X = L^+$ for comparison with a Fischer carbene). On the other hand, no stabilization results in extensive backbonding so that R_2C^+ is classified as and XZ ligand (i.e., $XZ = X_2+$ for comparison with a Schrock alkylidene). Types of interactions between these extreme configurations can also be observed (XZ′ function, **Figure 3A**), as illustrated by our olefin model.

Carbenium R_3C^+ moieties only possess an empty p orbital, resulting in the formation of π-complexes (**Figure 4B**). For consistency in our discussion, we describe their bonding modes, differentiated by the extent of interaction between the metal orbitals and carbon's empty 2p orbitals. These modes of interaction range from: (1) no C^+ interaction, (2) weak interactions, and (3) full hybridization of the carbon. The persistent carbenium ions that will be discussed are stabilized by resonance with an adjacent π-system. Therefore, the ligand is considered ambiphilic, since it acts both as a σ-donor through its electron rich π-system (L-type ligand) and as a π and/or σ-acceptor through its empty π*-system and p orbital (Z-type ligand). Again, the bonding mode depends on the electron

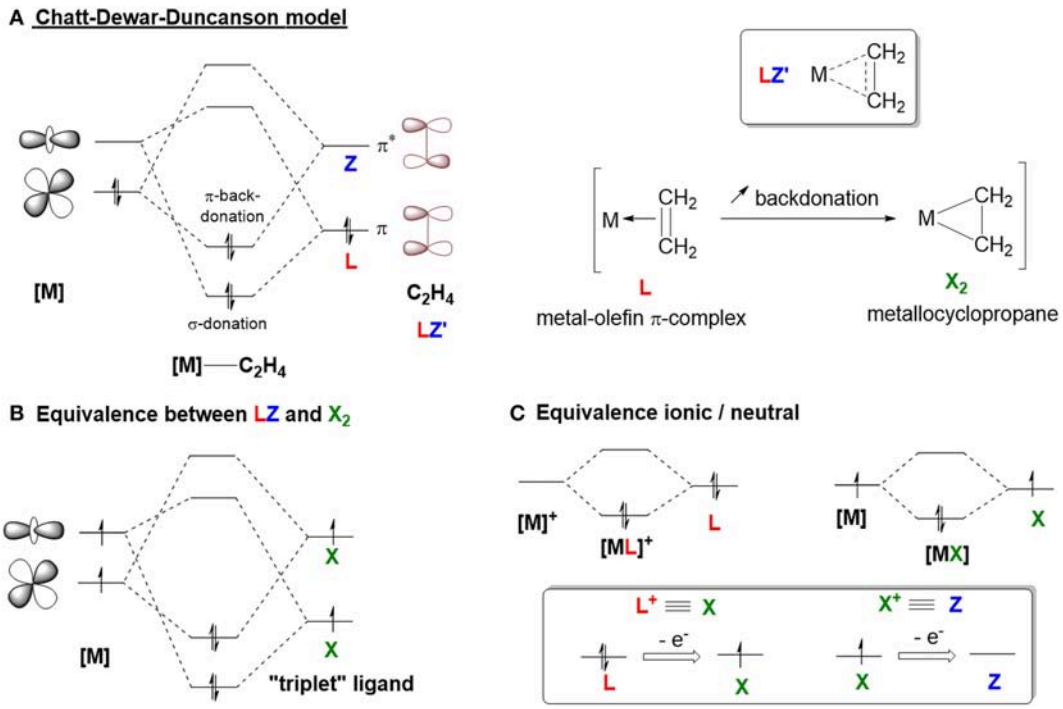

FIGURE 3 | (A) Chatt-Deward-Duncanson model. **(B,C)** Covalent bond classification equivalency.

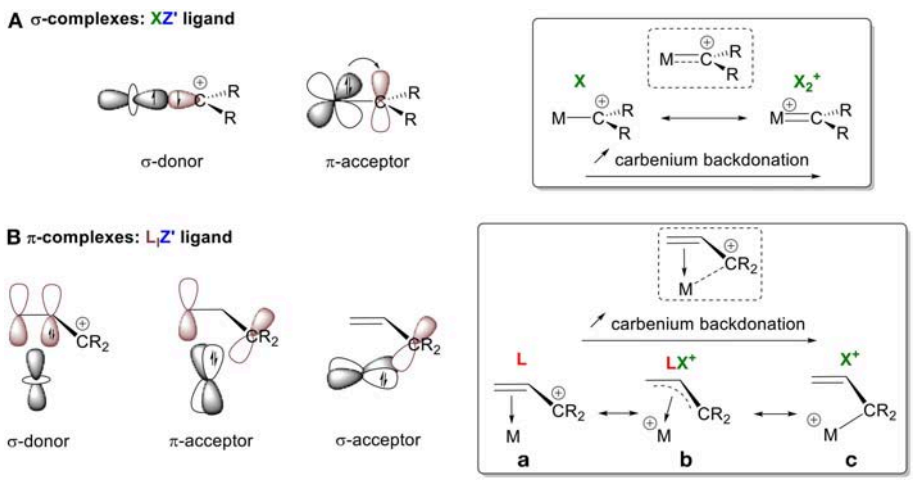

FIGURE 4 | Orbital interactions between a carbenium ion and a metal center in **(A)** σ-complexes, **(B)** π-complexes.

accepting ability of the ligand framework. In the absence of σ-backdonation from the metal, the carbenium species acts as an L-type ligand and does not interact with the metal center. In the absence of σ-backdonation from the carbenium, interactions between the filled π-system and the metal center will be the main orbital interactions, leading to a η^2 coordination mode with an L-type ligand (**Figure 4B,a**). As the interaction between the metal and the empty p orbital of the carbenium increases, the allyl cation acts as an LX^+ ligand through π- and/or σ-backdonation, resulting in η^3 bonding (**Figure 4B,b**). In the presence of extended σ-backbonding into the p orbital of R_3C^+, the M-C^+ interaction will govern the bonding mode leading to full hybridization of the carbon and a η^1 coordination mode (**Figure 4B,c**). This simplistic model is used to introduce the notion of Z′ and relative backdonation into carbenium π-complexes. A more relevant bonding view of each example system will be further discussed in their corresponding sections. This will allow us to address how the Z′ character of a carbenium

ligand is affected by the nature of the metal, its d electron count, its coordination environment, and the π-systems that stabilize the C^+ atom.

σ-COMPLEXES

As stated in the initial bonding discussion, σ-bonded carbenium complexes are in equilibrium with a carbene-bonded cationic metal. Carbenylium cations and Fisher carbenes have similar bonding modes and are considered π-acceptors. By analogy, cyclopropenylium ions are XZ'-type ligands and Fisher carbenes are LZ'-type. However, carbocations donate one electron as σ-donors while carbenes donate two electrons as σ-donors. Carbene complexes are prevalent, well-discussed species in literature so we will not focus on presenting the extensive progress in the field of carbene chemistry. Interested readers are encouraged to review articles on this subject (Ofele et al., 2009; Melaimi et al., 2010; Martin et al., 2011; Moerdyk and Bielawski, 2013). Instead, we will use selected examples to generalize bonding interactions between carbenium ions and metal centers in a σ-manner, and highlight how this bonding model is affected by the nature of the R groups on the carbenium and the metal and its ligands (L_n).

Cyclopropenylium Cations

Cyclopropenylium cation ($C_3H_3^+$) is the smallest member of the Hückel aromatic system (Breslow, 1957; Breslow and Chang, 1961). It exhibits considerable thermodynamic stability from aromaticity and resonance with 2 π-electrons delocalized over three conjugated 2p orbitals. The symmetry of its π-system imparts enormous stability relative to typical carbocations. Its protonated analog, cyclopropene, is a strained three-membered ring that is hugely thermodynamically unstable. The stability of the cation relative to the instability of the neutral species has elicited great interest in chemists and inspired synthetic and theoretical studies for decades. Cyclopropenylium cations were first synthesized by Breslow (1957) when he synthesized triphenylcyclopropenylium cation (Breslow, 1957). This was the first experimental verification of aromaticity in non-benzenoid molecules and it offered an important lesson: the energetic debt from ring strain can be compensated by aromatic stability (Breslow and Chang, 1961). Although the cation has been widely investigated since its discovery, the number of metal-bound cyclopropenylium complexes is not as abundant. A thorough review of this topic was presented by Komatsu and Kitagawa (2003).

The first isolated σ-bound cyclopropenylium-metal complexes were reported in 1978 in consecutive articles by Gompper and Bartmann (1978) and by Weiss and Priesner (1978) following two different approaches.

Approach 1: Bartmann reported the synthesis of dicarbonyl(η-cyclopentadienyl)(σ-2,3-diphenylcyclopropenyl)iron salts **2** from the nucleophilic attack of a coordinatively unsaturated metallate, sodium dicarbonyl(η-cyclopentadienyl)ferrate salt, to various cylcopropenium ions **1** (**Figure 5A**). While the formation of NaX (X = cyclopropenium counter ions) is a strong driving force for this reaction, the neutral compound **2** is highly strained and reactive from loss of aromaticity. Stability from aromaticity was easily restored by abstraction of the R_2 group (e.g., Ph, He, H, Cl) with appropriate abstracting agent E (e.g., HCl, I_2, $[(Ph)_3C^+][BF_4^-]$), resulting in the σ-bound cyclopropenylium ion complexes **3** (Gompper and Bartmann, 1978).

Approach 2: Weiss and Priesner proposed that the neutral cyclopropenylidene complex **4**, first reported by Öfele (1970), is in resonance with the Zwitterionic form **5,** where a metallate anion is bound to a cyclopropenylium moiety (**Figure 5B**; Weiss and Priesner, 1978). With the aid of a strong Lewis acid, bound anionic ligand X^- can be exchanged with a non-coordinating anion (e.g., $^-$OTf), leading to the formation of transition metal-substituted cyclopropenylium system **6**. A variety of cyclopropenylidene complexes have since been reported. Their synthesis typically follows one of three routes: (1) oxidative addition of dihalocyclypropenes followed by halide abstraction (Öfele, 1970; Konishi et al., 1978; Weiss and Priesner, 1978; Yoshida, 1982; Miki et al., 1988), (2) reaction of the cyclopropenyl salts with lithium adducts (Rees and von Angerer, 1972; Gompper and Bartmann, 1978; Konishi et al., 1978; Yoshida, 1982; Miki et al., 1988; Tamm et al., 1995; Schumann et al., 1997), or (3) cyclopropenylidene transfer (Yoshida, 1982; Gade et al., 2000; Kozma et al., 2013). These carbene species have been extensively discussed and were thoroughly reviewed by Herrmann in 2009 (Ofele et al., 2009). The bonding mode of cyclopropenylidene complexes is unambiguous and well-established by carbene chemistry and, therefore, will not be presented in this review.

As discussed, the extent of π-backdonation depends on the energies of the overlapping orbitals. Substituents on the ring alter the XZ bonding mode for this ligand because of the impact they have on the extent of electron donation and π-backdonation to the ring. In their initial report, Gompper and Bartmann synthesized complexes of substituted cyclopropenium ions with $[Fe(Cp)(CO)_2]$ (Gompper and Bartmann, 1978). They measured strength of the interaction between the iron atom and the carbon atom of the C_3 ring with IR spectroscopy and found the stretching frequencies of the CO moiety bound to iron in **3a-c** showed a clear blueshift of the $\nu_{(CO)}$ between R = Ph, R = ^{t}Bu, to R = NEt_2 (**Figure 5C**), which is consistent with a decrease in π-backdonation from the metal into the CO ligand. This decreased electron density on the metal center is a result of the increased π-accepting ability of cyclopropenylium ligand, which correlates to a lower pK_R^+ value (**Figure 5C**). These trends support the XZ-type bonding model discussed in the first part of this review (vide supra, **Figure 4A**) and is analogous to the cyclopropenylidene complexes summarized in Herrmann's review: complexes bearing cyclopropenylidene ligands with two amino substituents showed the most σ-donor/least π-acceptor ability, and those containing two phenyl groups show the least σ-donor/most π-acceptor ability (Ofele et al., 2009).

This also supports our claim that that CR_2^+ acts as an XZ′ ligand with different degrees of Z-type interactions. More precisely, complexes with $C(C(NR_2)_2)_2^+$ ligands are best described as X-type ligands with little or no π-backdonation,

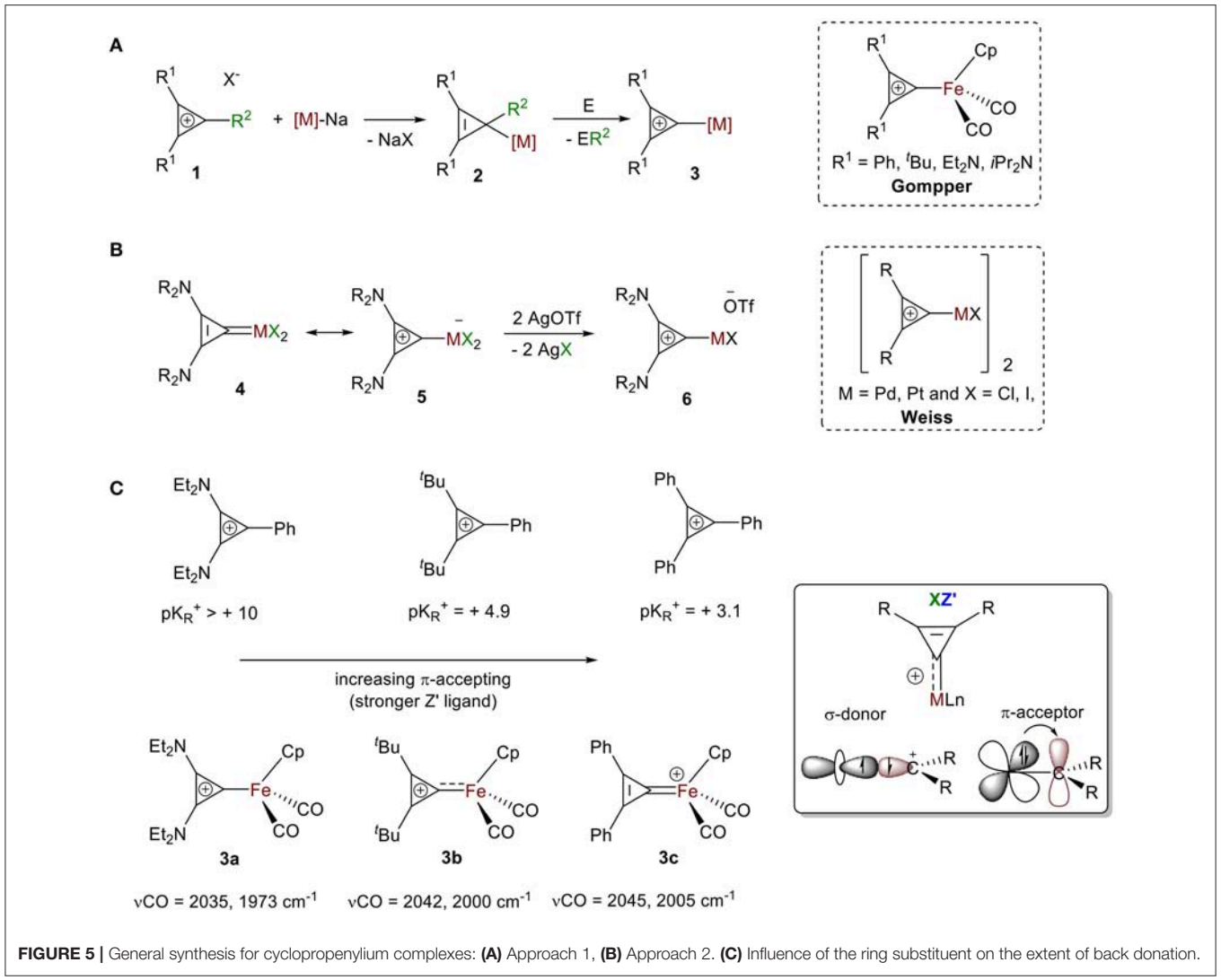

FIGURE 5 | General synthesis for cyclopropenylium complexes: **(A)** Approach 1, **(B)** Approach 2. **(C)** Influence of the ring substituent on the extent of back donation.

while complexes containing $^{+}C(CPh_2)_2$ ligands are more appropriately represented as X_2^{+} ligands because of their large Z-type interaction.

Arylenium Cations

Over the past decade, cationic gold(I) complexes have become some of the most efficient and versatile catalysts for the functionalization of C-C bonds (Echavarren and Nevado, 2004; Olah, 2004; Fürstner and Davies, 2007; Hashmi and Rudolph, 2008; Li et al., 2008; Jia and Bandini, 2015; Harris and Widenhoefer, 2016; Hopkinson et al., 2016; Zi and Toste, 2016; Shahzad et al., 2017). These complexes are typically formed from gold carbenes or from α-metallocarbenium ions. They contain a gold atom that is bound to a formally divalent carbon atom and are applied in a variety of gold-catalyzed transformations. The electronic structure of these cationic complexes is dependent on the extent of π-backbonding from the gold atom to the C_1 carbon atom (**Figure 6A**). The bonding mode of gold carbene/carbenium complexes has been extensively discussed, and much of gold carbene complexes' behavior can be understood by applying the bonding model developed by Toste and Goddard (Benitez et al., 2009). According to this model, the L–Au–C bonding network is comprised of three sets of orbital interactions: (1) a three-center, four-electron σ-hyperbond that donates electron density from filled sp^x orbitals on the carbene's carbon atom to gold's empty 6s orbital (**Figure 6A,b**), (2) two orthogonal π-bonds that donate electron density from the metal's filled 5d orbitals to the ligand's π-acceptor orbitals (**Figure 6A,a**), and (3) the carbene's π-acceptor orbitals (**Figure 6A,c**). It follows that greater σ-donation from the ligand (L) results in a weaker σ component of the Au–C_1 bond and greater π acidity of the ligand results in weaker Au-C_1 backdonation.

Cationic gold(I) complexes have been extensively studied, so this review will focus only on what we consider to be one of the most intriguing species present during gold catalysis: the *gem*-diaurated carbocation species (a carbocation that is stabilized by two gold atoms through Au-Au contacts) (Hashmi, 2014). The abundance of cationic *gem*-diaurated species discovered in gold-mediated catalysis (Harris and Widenhoefer, 2016)

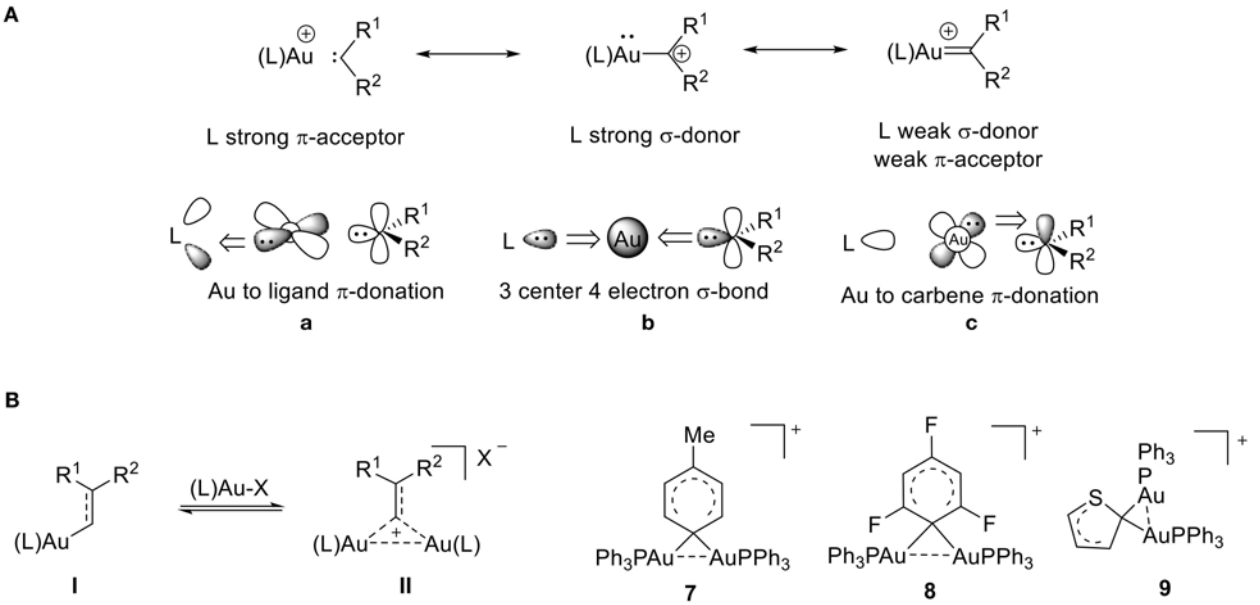

FIGURE 6 | (A) Bonding model for gold-carbene resonance structures. **(B)** *Gem*-diaurated carbocation species.

helped researchers conclude that an equilibrium exists between the vinyl gold(I) species **I** and the *gem*-diaurated species **II** (**Figure 6B**; Roithová et al., 2012; Harris and Widenhoefer, 2016). Further, the substituents R^1 and R^2 influence this equilibrium. A balance of stability and reactivity is required to observe this diaurated species **II**; otherwise, **II** can form a catalyst-poisoning thermodynamic sink, rendering the equilibrium irreversible (Roithová et al., 2012). In order for efficient catalysis to take place, the equilibrium must be reversible, and the *gem*-diaurated species **II** is actually a less reactive off-cycle species than the corresponding vinyl gold(I) species **I** (Brown et al., 2012; Zhdanko and Maier, 2013). This can be rationalized by the fact that the *gem*-diaurated species **II** is stabilized through Au-Au interactions, which makes it less reactive than the unstabilized vinyl gold(I) species **I**.

The tolyl complex **7** represents the first 1,1-diaurated carbocation derived from benzene (Nesmeyanov et al., 1974) and the cation of perchlorate salt **8** provided the first crystallographic evidence for 1,1-diauration (**Figure 6B**; Rafael et al., 1988). According to its X-ray data, complex 8 shows an Au-C-Au bond angle of 79.3°, Au-C bond lengths of 2.16 Å, and a relatively short Au···Au distance of 2.76 Å. The two [$AuPPh_3$] units in the diaurated thienyl complex **9** have identical phosphorus environments based on the ^{31}P NMR, which shows only one peak. The structure includes a short Au···Au distance of 2.81 Å and a small Au-C-Au angle of 82.5° (Porter et al., 2003), which shows a strong aurophilic interaction (Schmidbaur, 1990; Mond et al., 1995; Stephen et al., 2012), that is consistent with other reports of diaurated compounds (Osawa et al., 2008; Seidel et al., 2010). The literature range of Au-Au distances for gem-diaurated compounds is 2.72 to 2.85 Å.

π-COMPLEXES

Cyclic Carbocations

Cyclopropenium Cations

The first π-complexes with cyclopropenium cation were synthesized by Hayter (1968). His brief report included the synthesis of only one cyclopropenium-ligated complex, [(π-C_5H_5)Mo(π-C_3Ph_3)$(CO)_2$], and its characterization by ^1H NMR. The NMR spectrum showed a complex multiplet centered at $\delta = 7.2$ ppm with peak intensity ratio 5:17 for the phenyl substituents of the cyclopropenium ring (Hayter, 1968). Since Hayter's report, other isolated cyclopropenylium-metal complexes were reported; Komatsu et al. summarized these in an extensive review published in 2003 (Komatsu and Kitagawa, 2003). To the best of our knowledge, no new π-complexes of this type have since been reported.

The reactions of cyclopropenylium cations with low valent metal centers can lead to (η^3-cyclopropenyl)- (Chiang et al., 1979; Hughes et al., 1986, 1993; Lichtenberger et al., 1993; Ghilardi et al., 1995), (η^2-cyclopropenyl)- (Mealli et al., 1982), and (η^1-cyclopropenyl) (Gompper and Bartmann, 1985) metal complexes. The hapticity of the product depends on the ring's substituents, the metal, and the other ligands on the metal (**Figure 7**).

To better understand which coordination mode will be favored in each of these complex types, the molecular diagrams of C_3R_3 and the frontier orbitals for ML_n fragment ($n = 2$–5) (Jorgensen and Salem, 1973) are shown in **Figures 8A,B** respectively. The cyclopropenyl ring can either act as a: (1) σ-donor with its filled a_2'' orbital; (2) π-acceptor with its empty e'' orbital, if bound in an η^2 or η^3 coordination mode; or

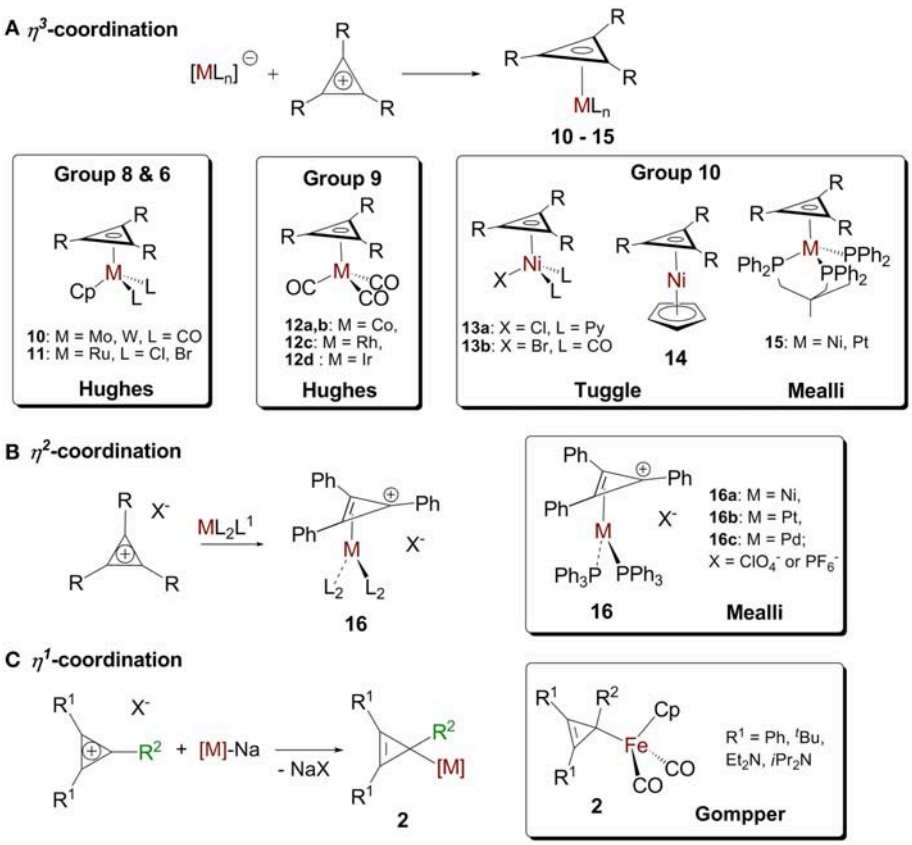

FIGURE 7 | (A) η^3-cyclopropenium complex. **(B)** d^{10} (η^2-cyclopropenium) ML_2 complex and the "Ring-whizzing" phenomenon. **(C)** η^1-cyclopropenium complex.

(3) σ-acceptor with one of the empty e″ orbitals if bound in an η^1 fashion. The coordination mode and the ring-metal interaction are determined by the d electron count of the metal and by the ligand environment of the metal fragment as established by a molecular orbital approach developed by Hoffmann et al. (Jemmis and Hoffmann, 1980). In short, the ML_n group will adopt the position that maximizes stabilizing bonding interactions. For the following discussion, the molecules will be arbitrarily split into neutral fragments, C_3R_3 and ML_n.

η^3 *coordination*

Cyclopropenium-metal complexes are prepared from the reaction between a cyclopropenium cation and a metal precursor, often a salt leading to the formation of a neutral species (**Figure 7A**; Donaldson and Hughes, 1982). We will model η^3 coordination in cyclopropenium complexes with an ML_3 d^9 fragment, $Co(CO)_3$. When the ML_3 fragment is bound to the ring in this way (**Figure 8c.1**), the a_2'' and e″ orbitals of the cyclopropenium moiety are symmetrical to the high-lying empty $2a_1$ orbital and the partially filled 2e orbital. In this case, coordination will optimize the number of metal-ring interactions, resulting in one σ- and two π-orbital interactions. If the $[Co(CO)_3]^-$ fragment moves off of the center of the ring and coordinates to it differently, part of the π-backdonation between the e orbitals will be lost. Evidence of the η^3 bonding model for $(C_3R_3)Co(CO)_3$ was confirmed experimentally by Lichtenberger et al. by photoelectron spectroscopy (Lichtenberger et al., 1993). This bonding model is applicable to complexes with the general formulas $(C_3R_3)ML_3$ (where M = Co, Rh, Ir) (Chiang et al., 1979) and $(C_3R_3)ML_2X$ (where M = Ni, Pt, Pd; X = anionic ligand; L = neutral ligand) (Mealli et al., 1981, 1983; Miki et al., 1988; Kuchenbeiser et al., 2008). Since d^9 ML_3 and d^5 ML_5 complexes are isolobal, this η^3 bonding is also appropriate for complexes with the general formula $(C_3R_3)ML_3X_2$ (where M = Ru) (Ditchfield et al., 1993; Morton and Selegue, 1999) and $(C_3R_3)ML_4X$ (where M = Mo or W) (Hayter, 1968; Drew et al., 1981; Hughes et al., 1985).

In general, the bonding mode in cyclopropenium-transition metal complexes depends on the metal involved. Strong π-backdonation from the metal to the carbocation increases the Z-type character of the ligand. It follows, then, that the distance between the metal and the C_3 ring decreases while the $\Delta G^{\ddagger}$ of rotation around their bond increases. If the metal in one of these complexes is coordinated to CO ligands, the bond between the metal and CO ligand increases in length, which results in a distinct shift in the $\upsilon_{(CO)}$ relative to that of the free CO-coordinated metal complex.

Infrared spectroscopy is the most powerful tool for monitoring reactions of metal carbonyls and for assignment of their structures, since the $\upsilon_{(CO)}$ absorptions are easily

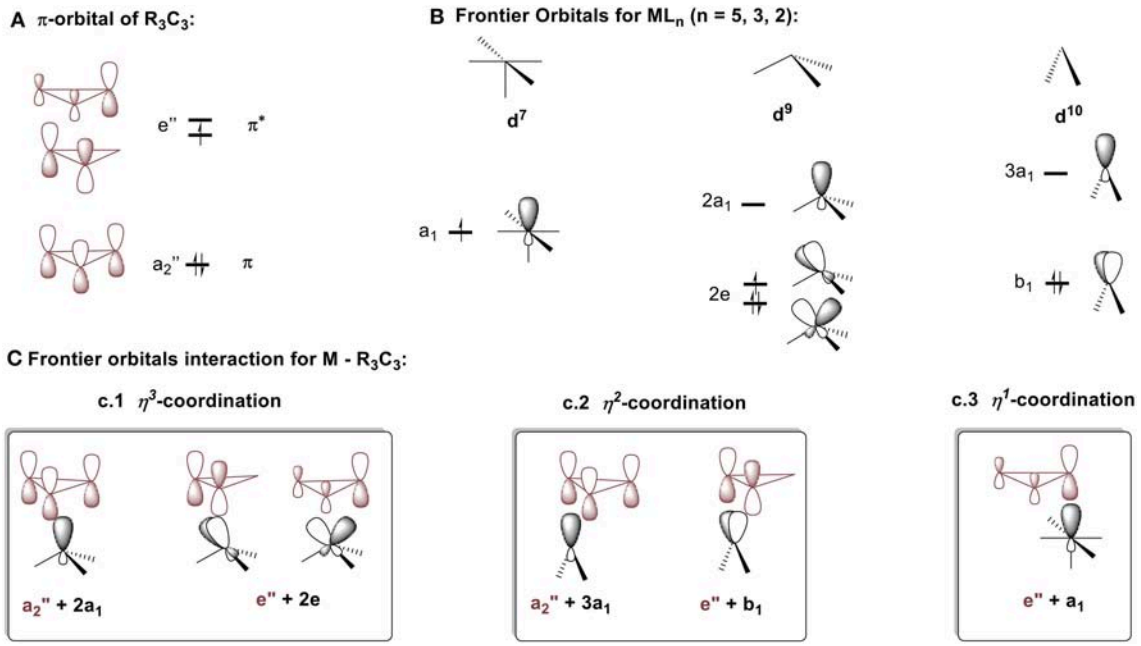

FIGURE 8 | Descritpion of bonding mode between cyclopropenium and metal fragments. **(A)** π-orbital of R_3C_3. **(B)** Frontier orbitals ML_n ($n = 5, 3, 2$). **(C)** Frontier orbitals interaction for M – R_3C_3: (c.1) η^3-coordination, (c.2) η^2-coordination, (c.3) η^1-coordination.

TABLE 1 | Compiled M-C_3 ring distance data (Churchill et al., 1984) and IR frequencies for CO in selected π-complexes.

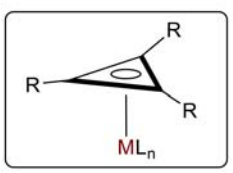

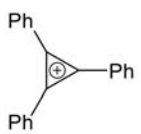

pK_R^+ = +3.1

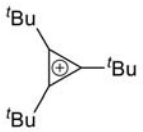

pK_R^+ = + 6.5

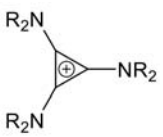

pK_R^+ > + 13

Complex	M-C_3 centroid distance (Å)	$\upsilon_{(CO)}$ cm^{-1}	Metal $\upsilon_{(CO)}$ cm^{-1} (Ellis, 2003)
12a: $Co(C_3Ph_3)(CO)_3$	2.01 (Chiang et al., 1979)	2,080, 2,040 (Hughes et al., 1993)	$[Co(CO)_4]^-$ = 1,888
12b: $Co(C_3{}^tBu_3)(CO)_3$	–	2,046, 1,976 (Hughes et al., 1993)	
12c: $Rh(C_3{}^tBu_3)(CO)_3$	–	2,055, 1,991 (Hughes et al., 1993)	$[Rh(CO)_4]^-$ = 1,895
12d: $Ir(C_3{}^tBu_3)(CO)_3$	2.02 (Hughes et al., 1993)	2,053, 1,985 (Shen et al., 1993)	$[Ir(CO)_4]^-$ = 1,895
13a: $Ni(C_3Ph_3)Cl(py)_2$	1.94 (Tuggle and Weaver, 1971a)		
14: $Ni(C_3Ph_3)(\eta^5\text{-}C_5H_5)$	1.96 (Tuggle and Weaver, 1971b)	–	–
15: $Ni(C_3Ph_3)(CH_3(CH_2PPh_2)_3)$	2.03	–	–

altered by changes to the molecular structure and charge of a carbonyl complex. It is unsurprising, then, that ion pairing between the cyclopropenium cation and a metal carbonyl anion results in significant changes in the $\upsilon_{(CO)}$ region, due to strong perturbation of the geometry of the anion. This characteristic is the result of π-backbonding, since CO is a π-acceptor ligand. When the $\upsilon_{(CO)}$ decreases as a result of decreasing bond strength, the strength of the M-C bond increases. As the M-C_3 distance decreases, the M-CO distance increases; therefore, a longer M-C_3 distance corresponds to a shorter M-CO distance and a decrease in $\upsilon_{(CO)}$ relative to free CO (2143 cm^{-1}).

The $\upsilon_{(CO)}$ of a complex is affected by the nature of the substituents on the C_3 ring (**Table 1**). When the ring substituents are changed from phenyls to t-butyls in the otherwise identical cobalt carbonyl complexes (**12a** and **12b**, respectively), the $\upsilon_{(CO)}$ decreases and the metal-centroid bond distance increase significantly as a result of the increase in electron donation from the substituent, consistent with an increase in pK_R^+ values (**Table 1**). It is worth mentioning that no metal complexes are reported with tris(amino)cyclopropenylium cations, suggesting that these are inadequately π-accepting (**Table 1**, $pK_R^+ > 10$) (Ciabattoni and Nathan, 1969; Moss et al., 1986; Bandar and

Lambert, 2013; Jiang et al., 2015). The nature of the metal also affects the electronic configuration of the complex (**Table 1**). As expected, larger metals (Co to Ir in complexes **12b−12d**) provide better orbital overlap. More π-donation between the metal and the ring is observed from Co to Ir, which is consistent with the increase in $\upsilon_{(CO)}$. Finally, the extent of the back donation from the metal to the ring is dependent on the π-accepting ability of the other ligand bound to the metal. The nickel complexes in the table below (13a, 14, and 15) illustrate this: the trisphosphine (**15**) is a stronger π-accepting ligand than either Cp or two pyridines and a chloride (**14** and **13a**, respectively), and an increase in the M-$C_{centroid}$ is observed. This suggests that the backdonation into the C_3 ring is most significant in **13a**.

Tuggle and Weaver determined an important factor of the electronic transitions in their $[(\pi\text{-}Ph_3C_3)NiCl(py)_2]\cdot py$ compound **10c** by comparing the UV-Vis spectra of their metal complex to that of the free ligand. Since the spectra showed no appreciable differences in their $\pi \rightarrow \pi^*$ transitions, they concluded the principle bonding interaction in the metal complex is not involved in the $\pi \rightarrow \pi^*$ transition (Tuggle and Weaver, 1971a). Later, they studied an analogous mixed nickel sandwich **11**, $[(\pi\text{-}Ph_3C_3)Ni(\pi\text{-}C_5H_5)_2]$, and considered the metal's interactions with each ring separately. They presented two possibilities for the cyclopropenyl moiety's interactions were presented: 1) overlap of a hybridized metal a_1 orbital (with $3d_z^2$, 4s, and $4p_z$ contributions) with the a_1 combination of the C_3 pπ orbitals; and (2) back-donation from the metal e orbitals to the e antibonding combination of the ring pπ orbitals. Importantly, they concluded that the back-donation was likely directed toward the formally positively charged C_3 ring and not toward the cyclopentadiene (Tuggle and Weaver, 1971b). This finding is consistent with our conclusions above regarding M-C_3 distance and $\upsilon_{(CO)}$.

Prior studies by Hughes et al. measured the free energy of activation ($\Delta G^{\ddagger}$) for cyclopropenium ring rotation in Mo, Ru, Co, Rh, Ir derivatives (Hughes et al., 1993), which provided quantitative correlations between electronic and steric effects of ancillary ligands. Comparison of these experimental $\Delta G^{\ddagger}$ values showed a significant increase in the rotational barrier of C_3 rotation about the metal-C_3 axis with descending group, which agreed with their prior findings in η^3 complexes (Co < Rh < Ir) (Hughes et al., 1993) and with general observations made for rotational barriers of olefin and 1,3-diene complexes of transition metals (Mann, 1982).

η^2 *coordination*

We will model η^2 coordination with a d^{10} ML_2 fragment, $Ni(PPh_3)_2$. In this case, only two frontier orbitals are suitable to interact with the ring (**Figure 8c.2**). According to Hoffmann and Mealli's calculations, the low energy levels consist of four closely spaced levels, $b_2+1a_1+a_2+2a_1$, which are identifiable with the $e_g + b_{2g} + a_{1g}$ set of typical square planar ML_4 systems (not shown in **Figure 8B**) (Jemmis and Hoffmann, 1980; Mealli et al., 1982). Higher in energy is b_1, which is hybridized out away from the L groups and toward the cyclopropenium ring. Even higher in energy is $3a_1$, which is cylindrically symmetrical and is also hybridized away from L groups. The b_1 orbital is the HOMO of a d^{10} ML_2 fragment and the $3a_1$ orbital is the LUMO. The high lying empty $3a_1$ orbital can interact with the filled a_2'' orbital of the ring and the filled b_1 metal orbital can undergoes back donation with one of orbital of e″ set of the $C_3R_3^+$ (**Figure 8A**). It is worth mentioning that π interaction between the low lying b_2 metal orbital and the other component of the e″ orbital is present but much weaker. The loss of this π interaction is compensated by the metal fragment sliding in an η^2 coordination mode to optimize the π interaction that involves the frontier b_1 orbital of the metal. This bonding type will described for complexes of the type $[(C_3R_3)ML_2]^+$ (M = Ni, Pt, Pd) and $[(C_3R_3)ML_4]^+$ with a d^8 metal due to the isolobal relationship of d^8 ML_4 and d^{10} ML_2 complexes.

The clearest indication of η^2 bonding is unequal distances between the metal atom and any of the three carbons in the ring. McClure and Weaver's platinum complex in 1973 was the first report of this unsymmetrical bonding (McClure and Weaver, 1973). In their complex, **16b** $[Pt(C_3Ph_3)(PPh_3)_2][PF_6]$ (McClure and Weaver, 1973), the Pt atom is 2.09 Å away from 2 of the cyclopropenium carbons, while it is 2.48 Å away from the third carbon. McClure concluded that his complexes are more closely related to the η^2-cyclopropene resonance form and less like the η^3 complexes Weaver synthesized earlier and that the coordination geometry and bond lengthening could be described with the bonding mode of olefins to zerovalent transition metals (McClure and Weaver, 1973).

In 1982, Mealli et al. published an important report on a phenomenon in which an ML_n unit migrates inside the periphery of a cyclic polyene. They called this unique fluxionality "ring-whizzing" (Mealli et al., 1982). Mealli compared three complexes **16** $[(Ph_3C_3)M(PPh_3)_2]X$ (where M = Ni (**16a**), Pt (**16b**)or Pd (**16c**) and X = ClO_4^- or PF_6^-) by ^{13}C NMR and by computational studies informed by their X-ray structure data. They determined that the $(Ph_3P)_2M$ unit progressively moved over the face of the cyclopropenium cation. This movement was used to chart the reaction path from one η^2 geometry, with the $(Ph_3P)_2M$ unit positioned below one C-C bond, to an equivalent η^2 geometry. They concluded that a smaller distance between the metal and one of the carbons in the ring resulted in increased tilting and twisting of the phenyl group directly connected to it. These geometric changes caused longer exocyclic C-C distances because of the decreased conjugation between the phenyl groups and the cyclopropenium ring (Gompper and Bartmann, 1985).

η^1 *coordination*

We will model the η^1 coordination mode with a d^7 ML_5 fragment, $[Fe(CO)_2Cp]^-$ (Gompper and Bartmann, 1978). The frontier orbital of this fragment has two electrons in the a_1 hybrid metal orbital that will interact with one component of the e″ cyclopropenium set. The low-lying filled e set of the metal will only have a small interaction with the e″ of the ring. The metal-ring interaction that contains only one σ molecular orbital will be strengthened if the fragment slides into an η^1 mode (**Figure 8c.3**). This type of interaction is consistent with the model C described in **Figure 4B**.

While synthesizing the first σ-complexes in 1978 (vide supra), Gompper and Bartmann synthesized a neutral intermediate (η^1-cyclopropenyl)iron $(C_3R_3)Fe(CO)_2Cp$ complex **2** (**Figure 7C**; Gompper and Bartmann, 1978). This coordination mode is rare and is mostly reported as intermediate compounds in the reaction path to the formation of cyclopropylenium σ-complexes and will not be further discussed.

To conclude, (1) d^7 ML_5 complexes interact with $C_3R_3^+$ with a single σ-type orbital, resulting in η^1 coordination for $[(C_3R_3)ML_5]$ complexes, (2) d^{10} ML_2 complexes have one σ and one π orbital interaction with $C_3R_3^+$, supporting a η^2 bonding mode in complexes with the formula $[(C_3R_3)ML_2]^+$, and (3) d^9 ML_3, and isolobal fragments (vide supra) have one σ and two π orbital interactions with the $C_3R_3^+$, resulting in an η^3 mode of coordination in complexes with the formula $[(C_3R_3)ML_3]$.

Arylenium Cations

Carbocations with conjugated π systems are one of the most common types of carbocation encountered in organic reactions, and iron was one of the earliest metals used to stabilize these carbocations (Olah et al., 2009). In general, the π orbitals of the carbocation can accept the backdonation of filled d orbitals on the metal atom, so the carbocations act as LX′ ligands. **Figure 9B** shows several representative carbocations with π-allylic systems complexed to an iron (**17** and **18**) in addition to π-allylic systems complexed to platinum (**19**), chromium, molybdenum, or tungsten (**20**) and **an** arenium cation stabilized by Os complexation **21** (Green et al., 1977; Mayr et al., 1993; Winemiller et al., 1997). All of these complexes are consistent with the orbital models in **Figure 9A**.

In addition, these metal-stabilized arylenium cations can be easily characterized by their ^{13}C NMR spectra. For example, complex **19** is featured with a typical resonance around 112 ppm for the central carbon of the η^3-C_3 system, along with two terminal carbon atoms of the allyl group around 82 ppm (Green et al., 1977). The osmium π-complex **21** was also characterized with three ^{13}C resonances in the range of 75–85 ppm, indicating that the metal binds to the arenium system in an η^3 fashion (Winemiller et al., 1997). Interestingly, studies showed that order of average reactivity of **20** toward nucleophiles was **20a**>**20b**>**20c** (Mayr et al., 1993), which can be rationalized with the orbital model in **Figure 9A**. Increasing the atomic radius leads to stronger backdonation of filled d orbitals on the metal atom (W>Mo>Cr) resulting in a metal π complex that is more stable and less reactive.

Carbocations α to Cyclic π-Systems

Another extensively studied carbocation-metal complex is α-metallocenylmethylium cation (Hill and Richards, 1961; Davis et al., 1971; Gleiter et al., 2007; Bleiholder et al., 2009; Minić et al., 2015, 2017; Espinosa Ferao and García, 2017; Muratov et al., 2017; Preethalayam et al., 2017; Fomin et al., 2018). Two different resonance structures have been proposed: (1) the cation acts as an L-type ligand by donating its filled p orbital electron density to the metal center, and (2) the cation acts as an LX^+ ligand by donating its filled p orbital electron density to the metal center through carbenium backdonation (**Figure 10A**). Consequently, some bending of the sp^2-hybridized carbocationic center toward the metal atom has always been observed, which indicates the formation of double bond.

Carbenium α to Cyclopentadienyl

α-ferrocenyl carbenium ions were first observed by Richards and Hill (1959) through solvolysis of the corresponding ferrocenyl carbinyl acetate (Richards and Hill, 1959). Since then, a wide range of α-ferrocenyl carbenium ions have been synthesized and characterized under acidic conditions through their corresponding precusors (**Figure 10B**). **Figure 10B** shows some examples of reported α-ferrocenyl carbenium ions, such as tetrafluoroborates of ferrocenyl diphenyl cyclopropenium ion **24** (Sime and Sime, 1974), α,α'-diferrocenyl methylium ion **25** (Cais et al., 1978), ferrocene-annelated allylium ion **26** (Lukasser et al., 1995), and ferrocenyl diphenyl methylium ion **27** (Behrens, 1979), along with their geometric parameters as derived from X-ray diffraction studies. There is consistent bending of the C6 atom of the fulvene ring toward the iron atom in all of these complexes, but the bending angle (α) and Fe-C6 distance (d) vary considerably.

In **24**, the positive charge of the carbenium center is delocalized into the cyclopropenylium ring, which results in a bending angle of 6.8° with an Fe-C6 bond length of 2.96 Å. In **25**-**27**, an increase of the angle (α) and a reduction of the Fe-C6 distance (d) is observed. These geometric changes can be rationalized by the orbital model in **Figure 10A**. The π acidity of the C6 center depends on the identity of R^1 and R^2. Greater electron density in the carbenium center results in less π acidity, which results in weaker π backdonation and a conformation like **23b** with a smaller bending angle. For example, the π systems in **24** and **26** increase the electron density of their C6 centers, yielding smaller bending angles.

$[(\eta^6\text{-}C_5H_4C(C_6H_5)_2)]Cr(CO_3)$ (**28b**) was the first η^6-fulvene complex studied by X-ray analysis (**Figure 11A**). This data experimentally confirmed the predicted tendency toward strong bending of C6 (Andrianov et al., 1975). The neutral complex **28b** shows a bending angle of 28.4° with a Cr-C6 bond length of 2.55 Å, which can be explained by the HOMO obtained from extended Hückel calculations is shown in **Figure 11D** (Albright et al., 1978). The bending of C6 causes a bonding interaction between C6 and the Cr-centered e_s orbital (Albright et al., 1978). X-ray studies of various fulvene-$Cr(CO)_3$ complexes with different substituent groups at C6 (**28a**-**e**, **Figure 11A**) showed the strongest bending in the unsubstituted fulvene ligand (**28a**) and only a small amount of tilt angle for **28e**, which contains a conjugated 6π-electron system at the C6 atom of the fulvene ligand (Behrens, 1979; Lubke et al., 1983). Fulvene-$Cr(CO)_3$ complexes with different groups at C6 also showed an impact on the CO chemical shift of ^{13}C NMR and stretching frequencies by IR (Lubke et al., 1983). The bending angle and C6-Cr distance changes are consistent with the above α-ferrocenylmethylium ions. In general, electron-donating groups increase the electron density of the C6 center, thereby increasing σ-donation and decreasing carbenium backdonation, resulting in smaller tilt angle (α), larger CO chemical shift (δ) and lower $\upsilon_{(CO)}$.

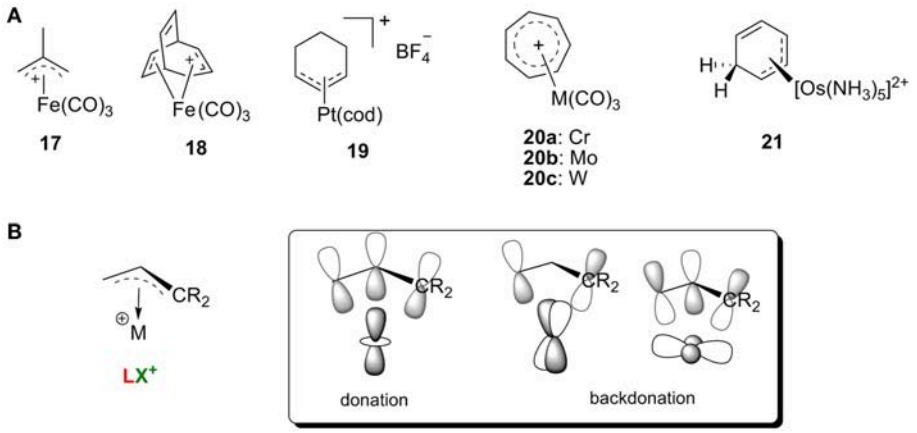

FIGURE 9 | (A) Selective transition metal-stabilized carbocations with conjugated ϕ-system, and **(B)** the correlating orbital model.

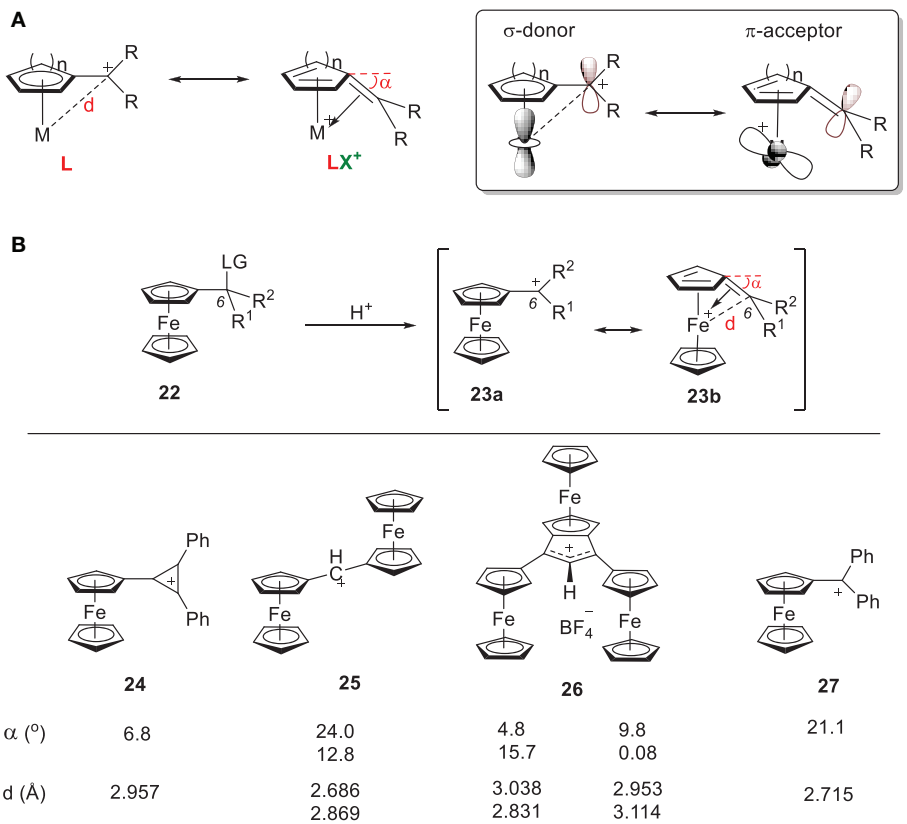

FIGURE 10 | (A) Two resonance forms of α-metallocenylmethylium cation and their orbitals. **(B)** Selected α-metallocenylmethylium cations and their general approach.

X-ray studies also showed that α-metallocenyl methylium cations show an increased metal-fulvene interaction with an increase in the metal's molecular mass. The bending angles for complexes **29a** (Kreindlin et al., 2000), **29b** (Kreindlin et al., 1987), and **29c** (Rybinskaya et al., 1989) are 22.7°, 38.2°, and 40.8°, respectively, (**Figure 11B**), which indicates a dramatic increase in metal-fulvene interactions. This is because a larger atomic radius leads to more overlap of filled metal d orbitals with the carbenium p orbital, resulting in strong carbenium backdonation and a large tilt angle (**Figure 10A**).

The effect of ligands has also been studied with DFT calculations (**Figure 11D**; Gleiter et al., 2007). We can see from MO diagrams that electron-rich ligands favor interactions with metal and carbenium centers [**Figure 11C,** Cp (**30**) > benzene (**31**) > CO (**32**)]. According to the orbital model, the electron-rich ligand can increase the electron density on the

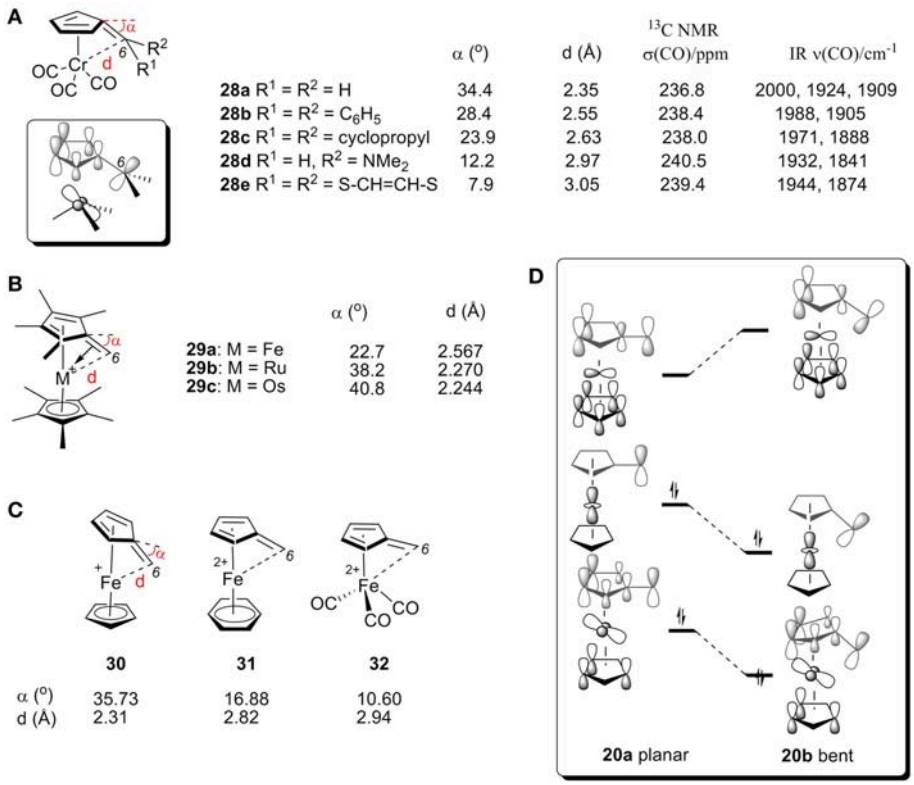

FIGURE 11 | (A) X-ray, ^{13}C NMR, and IR data for CO of complexes **28**. **(B)** Geometric parameters of complex **29** by X-ray analysis. **(C)** Geometric parameters of complexes **30-32** by DFT calculations. **(D)** Diagram between the frontier orbitals of a planar and bent α-ferrocenyl methylium ion.

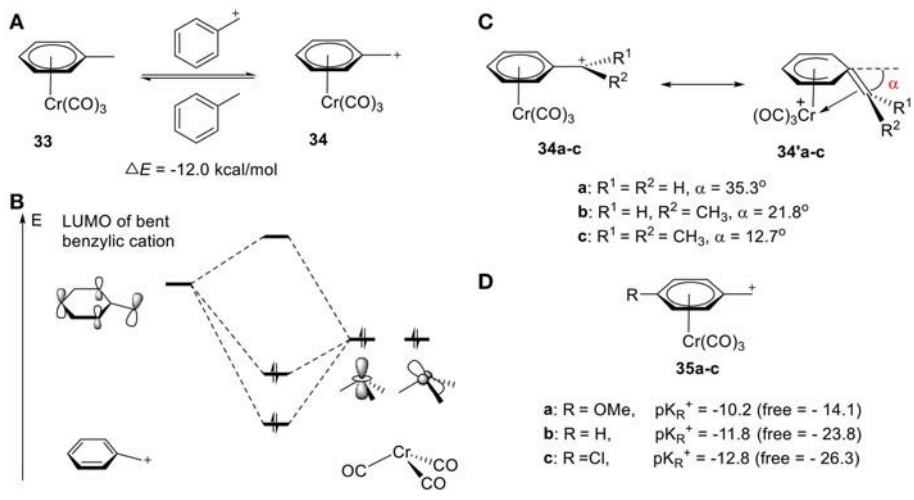

FIGURE 12 | (A) Chromium-stabilized carbocations. **(B)** Selected stabilizing orbital interactions between $Cr(CO)_3$ and benzylic cation. **(C)** Two resonance forms of Chromium-stabilized benzylic cations according to DFT calculation. **(D)** pK_R^+ values of different Cr-stabilized benzylic cations.

metal atom, resulting in carbenium backdonation and a large tilt angle.

Figure 11D shows the correlated frontier orbitals of a planar (left) and a bent structure (right) of α-ferrocenyl methylium ion (Gleiter et al., 2007; Bleiholder et al., 2009). When the bending angle increases, the LUMO is destabilized and the HOMO is stabilized, which can be rationalized by the increased bonding interaction between the C6 p orbital and the metal d-orbital of the HOMO and an increased antibonding interaction between the C6 and metal orbitals of the LUMO. As a result, electron density is transferred into an antibonding orbital between C1 and C6, resulting in a larger bending angle (α). Additionally, increasing

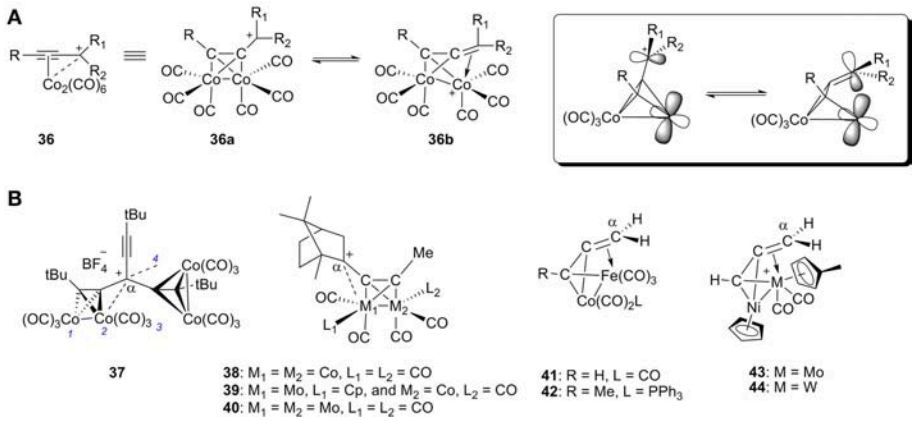

FIGURE 13 | (A) Two resonance forms of α-metallocenylmethylium cation and their orbitals. **(B)** Selected representative cationic bimetallic propargyl complexes.

the electron density of the metal center (e.g., heavier metal or electron-rich ligand) or decreasing the electron density of the carbenium center (e.g., electron-withdrawing group) will favor these interactions, leading to larger bending angle α.

Carbenium α to Aryl

Cr is well-established in its ability to stabilize carbocations, including benzylic, phenonium, and benzonorbornenyl cations (Tantillo et al., 2000; Merlic et al., 2001b; Konietzny et al., 2010; Davis et al., 2013). In 1999, the groups of Houk (Merlic et al., 1999) and Koch (Pfletschinger et al., 1999) pioneered the field through theoretical computations determining the stabilization of benzylic cations by chromium tricarbonyl. As shown in **Figure 12A**, the homodesmotic equation gives a ΔE of −12.0 kcal/mol, suggesting effective stabilization of the benzylic cation **34** by $Cr(CO)_3$ (**Figure 12A**). This stability is attributed to the other resonance form **34′**, in which the benzylic carbon bends down to coordinate to the Cr atom with an angle of 35.3°, 21.8°, and 12.7°, according to DFT calculations, for methyl, ethyl, and isopropyl cation, respectively, (**Figure 12C**; Merlic et al., 2001a). This is consistent with the substituent effects observed in **Figure 11A**. Electron-donating groups result in a smaller tilt angle (α), though steric repulsions are also likely contributive. The stability can also be rationalized in terms of orbital interactions between the hybrid fragment orbitals (Albright, 1982) of $Cr(CO)_3$ and the π molecular orbitals of benzylic cation (**Figure 12B**; Merlic et al., 2001a). In the case of the cation, the low-lying LUMO interacts strongly with the symmetric occupied hybrid metal orbitals. The overlap between the Cr and benzylic cation orbitals (especially the d_z^2-like metal orbital) is increased in two ways: (1) the distortion of the benzylic cation from planarity and, (2) shifting the chromium away from the center of the ring. Electron-donating groups can increase the electron density of C_α center and decrease carbenium backdonation, leading to a smaller tilt angle (α). These computed results are supported by the experimental pK_R^+ values of Cr-stabilized benzyl complexes **35a-c** (**Figure 12D**). The pK_R^+ increased sharply as compared to the corresponding free carbocations, indicating the stabilization of the carbocation by the Cr atom (**Figure 12D**). Additionally, more electron-deficient benzyl moieties (electron withdrawing groups) gain an even greater stabilization effect through increased π-backdonation (Trahanovsky and Wells, 1969; Cheng et al., 1993).

Carbocations α to Acyclic π-Systems (alkynyl)

Cobalt, especially cationic dicobalt propargyl complexes, have played a significant role in organic synthesis since their discovery (Nicholas and Pettit, 1971; Nicholas, 1987; McGlinchey et al., 1995; El Amouri and Gruselle, 1996; Amouri et al., 2000). In general, there are two resonance forms for this kind of propargyl cation complex **36**: (1) the cation acts as an L-type ligand by donating its filled π orbital electron density to the metal center, and (2) the cation acts as a LX^+ ligand by donating its filled π orbital electron density to the metal center with carbenium backdonation (**Figure 13A**). Both of these resonance forms provide stability to the carbocation.

A wide range of cationic dicobalt propargyl complexes or similar heterobimetallic complexes have been synthesized and characterized (**37**-**44**, **Figure 13B**; Gruselle et al., 1993; Osella et al., 1993; Melikyan et al., 1998; Chetcuti and McDonald, 2002). The propargyl cation always preferentially coordinates to one of the metal atoms in each cluster due to accumulation of positive charge. In studies of these heterobimetallic complexes, the propargyl cation prefers to coordinate to Mo and Fe instead of Co (**39**, **41,** and **42**) (Gruselle et al., 1993; Osella et al., 1993) as well as Mo and W instead of Ni (**43** and **44**) (Chetcuti and McDonald, 2002).

X-Ray Crystallography

Table 2 gives a summary of the M-C_α distance of the bimetallic complexes discussed above. In **37**, the distances between the carbocationic center and the cobalt atom are 3.07, 2.81, 3.27, and 2.89 Å, respectively, for Co1, Co2, Co3, and Co4. The 2-bornyl cation leans toward the Mo atom and the Mo-C_α distance is 2.74 Å for **39** and 2.91 Å for **40**. The preferential stabilization of the 2-bornyl cation by the molybdenum has also been rationalized with molecular orbital calculations at the

TABLE 2 | X-ray, IR, and ^{13}C NMR data for the complexes.

Complex	M-C_α distances (Å)	IR ν_{CO} (cm^{-1}) in DCM	IR ν_{CO} (cm^{-1}) in Hexane	^{13}C NMR δ(CO), ppm
37	Co1: 3.07 Co2: 2.81 Co3: 3.27 Co4: 2.89	–	–	194.4, 192.2
38	–	–	–	194.4, 192.2
39	2.74	–	–	–
40	2.91	–	–	227.1, 226.5, 223.0, 220.0
41	–	–	2,084 m, 2,041 vs. 2022 s, 2,014 m, 1,993 m, 1,981 m	210.3, $Fe(CO)_3$; 203.0, $Co(CO)_3$
42	2.20	–	2,052 vs. 2,003 s, 1,989 vs. 1,968 m	211.2, $Fe(CO)_3$; 207.3, 205.1, $Co(CO)_2$
43	–	2,049 s, 2,019 s, 1,966 m	–	–
44	–	2,047 m, 2,013 s, 1,989 w, 1,966 vw	–	–

extended Hückel level (Gruselle et al., 1993). Cations **38**-**40** do not undergo Wagner-Meerwein rearrangement as a result of their stabilization, which otherwise occurs readily for uncomplexed 2-alkynylbornyl cations. For **42**, the Fe-C_α distance is 2.195 Å. The preferential coordination of C_α with Fe has been explained by the model cluster **41** by means of extended Hückel molecular orbital calculations (Osella et al., 1993).

IR and ^{13}C NMR Spectroscopy

Table 2 also gives a summary of the IR and ^{13}C NMR data of the above bimetallic complexes. Generally, the IR ν_{CO} stretching frequencies of these cations are shifted to higher values (over 2000 cm^{-1}) compared to their corresponding neutral precusors (Osella et al., 1993; Chetcuti and McDonald, 2002). In dicobalt cation **27**, the ^{13}C NMR CO signals appear at approximately 194 ppm. Analogously, stabilization of a propargyl cation by a molybdenum center results in a shielding of the molybdenum carbonyl signals from approximately 230–220 ppm in **40** (Gruselle et al., 1993). For **41** and **42**, stabilization of a propargyl cation by an iron center shifts the carbonyl resonances to approximately 210 ppm, while the cobalt carbonyl resonances are around 203–208 ppm (Osella et al., 1993).

This stabilization can be explained in terms of orbital interactions between the metal's d orbital and the π molecular orbitals of the propargyl cation in **Figure 13A** (Gruselle et al., 1993; McGlinchey et al., 1995). The overlap between the orbitals of the metal center and of the propargyl cation (especially the d_z^2-like metal orbital) is increased by the shorter M-C_α distance, resulting from the propargyl cation bending toward the metal. The preferential coordination with a heavier metal within the heterobimetallic cations **39, 40**, and **43** is consistent with the reactivities of complex **20** and the conclusion in **Figure 9B**. However, in complexes **41**-**43**, the carbocation is bound to the lighter element, Fe. This can be explained by considering the isolobal relationship between $Co(CO)_3^+$ and $Fe(CO)_3$ (McGlinchey et al., 1995). The neutral Fe can provide more effective overlap of filled metal d orbitals with the carbenium's p orbital than Co^+, which makes the interaction with Fe more attractive. The coordination of the metal with the cation also induced higher CO stretching frequencies in IR and larger chemical shifts for CO in ^{13}C NMR.

CONCLUSION

We proposed two major bonding modes for the orbital interactions between carbeniums and metal centers in σ- and π-complexes. Most of the reported transition metal-carbocation complexes can fall into one of these two categories. In general, heavier metal atoms have larger radii, which can lead to stronger backdonation of filled d orbitals on the metal atom and greater stabilization of carbocations. In addition, electron-donating groups on the carbocations can increase the electron density of carbon center, thus increasing σ-donation while decreasing carbenium backdonation. This results in weaker transition metal-carbocation interactions. On the other hand, an electron-rich ligand can increase the electron density on the metal atom, resulting in carbenium backdonation and greater stabilization. The stabilization of carbocations by the transition metal has been unambiguously demonstrated with higher pK_R^+ values in comparison to the corresponding free carbocations.

Transition metal-stabilized carbocations have been observed and characterized throughout the last century, but there is no comprehensive summary of the bonding modes of these transition metal-carbocation complexes. To our surprise, most of this research was conducted and reported before 2000 and little attention has been given to the field during the last decades, even though much remains unknown about their properties, reactivities, and carbocation interactions with other transition metals (e.g., Pd, Rh, Ir, Ni). Because of their considerable synthetic value, it is of great importance to bring these metal-carbocation interactions back to the interest of the scientific community.

AUTHOR CONTRIBUTIONS

All authors listed have made a substantial, direct and intellectual contribution to the work, and approved it for publication.

REFERENCES

Albright, T. A. (1982). Structure adn reactivity in organometallic chemistry. An applied molecular orbital approach. *Tetrahedron* 38, 1339–1388. doi: 10.1016/0040-4020(82)80217-2

Albright, T. A., Hoffmann, R., and Hofmann, P. (1978). Cycloheptatriene and fulvene $Cr(CO)_3$complexes. *Chem. Ber.* 111, 1591–1602. doi: 10.1002/cber.19781110440

Amgoune, A., and Bourissou, D. (2011). σ-Acceptor, Z-type ligands for transition metals. *Chem. Commun.* 47, 859–871. doi: 10.1039/C0CC04109B

Amouri, H., Bégué, J. P., Chennoufi, A., Bonnet-Delpon, D., Gruselle, M., and Malézieux, B. (2000). Cobalt-induced C-N and C-C bond formation via metal-stabilized α-CF_3 carbenium ion. *Org. Lett.* 2, 807–809. doi: 10.1021/ol005554l

Amyes, T. L., Richar, J. P., and Novak, M. (1992). Experiments and calculations for determination of the stabilities of benzyl, benzhydryl, and fluorenyl carbocations: antiaromaticity revisited. *J. Am. Chem. Soc.* 114, 8032–8041. doi: 10.1021/ja00047a010

Andrianov, V. G., Struchkov, Y. T., Setkina, V. N., Zdanovich, V. I., Zhakaeva, A. Z., and Kursanov, D. N. (1975). X-ray molecular structure of tricarbonyl-(1-5,α-η-diphenylfulvene)chrornium, $[(\eta\text{-}C_5H_4CPh_2)Cr(CO)_3]$. *Chem. Commun.* 117–118. doi: 10.1039/C39750000117

Bandar, J., and Lambert, T. (2013). Aminocyclopropenium ions: synthesis, properties, and applications. *Synth.* 45, 2485–2498. doi: 10.1055/s-0033-1338516

Behrens, U. (1979). Übergangsmetall—fulven-komplexe : XIV. Kristall- und Molekülstruktur von ferrocenyldiphenylcarbenium-tetrafluoroborat, $[Cn_5H_5FeC_5H_4C(C_6H_5)_2]^+$ BF_4^-. Ein Fulven-eisen-komplex? *J. Organomet. Chem.* 182, 89–98. doi: 10.1016/S0022-328X(00)85878-7

Benitez, D., Shapiro, N. D., Tkatchouk, E., Wang, Y., Goddard, W. A., and Toste, F. D. (2009). A bonding model for gold(i) carbene complexes. *Nat. Chem.* 1, 482–486. doi: 10.1038/nchem.331

Bleiholder, C., Rominger, F., and Gleiter, R. (2009). α-metallocenylmethylium ions and their isoelectronic congeners: a comparison based on DFT calculations. *Organometallics* 28, 1014–1017. doi: 10.1021/om800573u

Bouhadir, G., and Bourissou, D. (2016). Complexes of ambiphilic ligands: reactivity and catalytic applications. *Chem. Soc. Rev.* 45, 1065–1079. doi: 10.1039/C5CS00697J

Braunschweig, H., and Dewhurst, R. D. (2011). Transition metals as Lewis bases: "Z-type" boron ligands and metal-to-boron dative bonding. *Dalt. Trans.* 40, 549–558. doi: 10.1039/C0DT01181A

Breslow, R. (1957). Synthesis of the σ-triphenylcy clopropenyl cation. *J. Am. Chem. Soc.* 79, 5318–5319. doi: 10.1021/ja01576a067

Breslow, R., and Chang, H. W. (1961). Triarylcyclopropenium ions. Synthesis and stability in the phenyl p-anisyl series. *J. Am. Chem. Soc.* 83, 2367–2375. doi: 10.1021/ja01471a031

Brown, T. J., Weber, D., Gagn,é, M. R., and Widenhoefer, R. A. (2012). Mechanistic analysis of gold(I)-catalyzed intramolecular allene hydroalkoxylation reveals an off-cycle bis(gold) vinyl species and reversible C-O bond formation. *J. Am. Chem. Soc.* 134, 9134–9137. doi: 10.1021/ja303844h

Cais, M., Dani, S., Herbstein, F., and Kapon, M. (1978). Determination of the crystal structure of α,α-diferrocenylmethylium tetrafluoroborate, a stable carbenium ion salt, and a comparison of its structure with those of other organometallic carbenium cations. *J. Am. Chem. Soc.* 100, 5554–5558. doi: 10.1021/ja00485a047

Cheng, J. P., Handoo, K. L., and Parker, V. D. (1993). Hydride affinities of carbenium ions in acetonitrile and dimethyl sulfoxide solution. *J. Am. Chem. Soc.* 115, 2655–2660. doi: 10.1021/ja00060a014

Chetcuti, M. J., and McDonald, S. R. (2002). Propargylic cations stabilized on nickel-molybdenum and nickel-tungsten bonds. *Organometallics* 21, 3162–3168. doi: 10.1021/om020155a

Chiang, T., Kerber, R. C., Kimball, S. D., and Lauher, J. W. (1979). (η^3-Triphenylcyclopropenyl) tricarbonylcobalt. *Inorg. Chem.* 18, 1687–1691. doi: 10.1021/ic50196a058

Churchill, M. R., Fettinger, J. C., McCullough, L. G., and Schrock, R. R. (1984). Transformation of a tungstenacyclobutadiene complex into a nonfluxional η^3-cyclopropenyl complex by addition of a donor ligand. The X-ray structure of $W(\eta^5\text{-}C_5H_5)[C_3(CMe_3)_2Me](PMe_3)Cl_2$. *J. Am. Chem. Soc.* 106, 3356–3357. doi: 10.1021/ja00323a051

Ciabattoni, J., and Nathan, E. C. (1969). Di-t-butylcyclopropenone and substituted Di-t-butylcyclopropenyl Cations. *J. Am. Chem. Soc.* 91, 4766–4771. doi: 10.1021/ja01045a031

Davis, R. E., Simpson, H. D., Gnce, N., and Pettit, R. (1971). The structure of α-cyclobutadienyliron tricarbonyl carbonium ions. *J. Am. Chem. Soc.* 93, 6688–6690. doi: 10.1021/ja00753a068

Davis, R. L., Lodewyk, M. W., Siebert, M. R., and Tantillo, D. J. (2013). Complex consequences: substituent effects on metala· · · arylmethylium interactions. *J. Organomet. Chem.* 748, 68–74. doi: 10.1016/j.jorganchem.2013.02.034

Deno, N. C., Jaruzelski, J. J., and Schriesheim, A. (1955). Carbonium ions. I. an acidity function (C_0) derived from arylcarbonium ion equilibria. *J. Am. Chem. Soc.* 77, 3044–3051. doi: 10.1021/ja01616a036

Ditchfield, R., Hughes, R. P., Tucker, D. S., Bierwagen, E. P., Robbins, J., Robinson, D. J., et al. (1993). Synthesis and dynamic NMR studies of η^3-triphenyl- and η^3-trimethylcyclopropenyl complexes of ruthenium, $[Ru(\eta^5\text{-}C_5R_5)(\eta^3\text{-}C_3R'_3)X_2]$ (R = H, Me; R′ = Me, Ph; X = Cl, Br, I). Extended Hückel molecular orbital study of barriers to rotation of η^3-cyclopropenyl. *Organometallics* 12, 2258–2267. doi: 10.1021/om00030a041

Donaldson, W. A., and Hughes, R. P. (1982). Mechanism of formation of (η^3-oxocyclobutenyl)cobalt compounds from $[Co(CO)_4]$- and cyclopropenium cations. *J. Am. Chem. Soc.* 104, 4846–4859. doi: 10.1021/ja00382a019

Drew, M. G. B., Brisdon, B. J., and Day, A. (1981). Cyclopropenyl and oxocyclobutenyl complexes of molybdenum. Crys- tal and molecular structures of (2,2'-bipyridine)bromodicarbonyl(1-3- η-1 ,2,3-triphenylcyclopropenyl)molybdenum(II) and (2,2'-bipyridine)-bromodicarbonyl(2-4- η-1 -oxo-2,3,4-triphenylcyclobutenyl)molybenum(II). *J. Chem. Soc., Dalt. Trans.* 1310–1316. doi: 10.1039/DT9810001310

Echavarren, A. M., and Nevado, C. (2004). Non-stabilized transition metal carbenes as intermediates in intramolecular reactions of alkynes with alkenes. *Chem. Soc. Rev.* 33, 431–436. doi: 10.1039/b308768a

El Amouri, H., and Gruselle, M. (1996). New bonding modes, fluxional behavior, and reactivity in dinuclear complexes bridged by four-electron donor unsaturated hydrocarbons. *Chem. Rev.* 96, 1077–1104. doi: 10.1021/cr9500040

Ellis, J. E. (2003). Metal carbonyl anions: from $[Fe(CO)_4]_2$-to $[Hf(CO)_6]_2$-and beyond. *Organometallics* 22, 3322–3338. doi: 10.1021/om030105l

Espinosa Ferao, A., and García, R. (2017). Fulvenization as characteristic geometric distortion in electron deficient ferrocenes. *Tetrahedron* 73, 952–956. doi: 10.1016/j.tet.2017.01.019

Fischer, E. O. (1976). On the way to carbene and carbyne complexes. *Adv. Organomet. Chem.* 14, 1–32. doi: 10.1016/S0065-3055(08)60647-4

Fomin, V. M., Kochetkova, K. S., and Klyuchevskii, K. V. (2018). Redox isomerism of α-ferrocenylcarbenium ions. *Russ. J. Gen. Chem.* 88, 948–953. doi: 10.1134/S1070363218050183

Frenking, G. (2002). "The dewar-chatt-duncanson bonding model of transition metal-olefin complexes examined by modern quantum chemical methods," in *Modern Coordination Chemistry: The Legacy of Joseph Chatt* (Royal Society of Chemistry). doi: 10.1039/9781847551481-00111

Fürstner, A., and Davies, P. W. (2007). Catalytic carbophilic activation: catalysis by platinum and gold π acids. *Angew. Chem. Int. Ed.* 46,. doi: 10.1002/anie.200604335

Gade, L. H., Memmler, H., Kauper, U., Schneider, A., Fabre, S., Bezougli, I., et al. (2000). Cooperative reactivity of early-late heterodinuclear transition metal complexes with polar organic substrates. *Chem. Eur. J.* 6, 692–708. doi: 10.1002/(SICI)1521-3765(20000218)6:4<692::AID-CHEM692>3.0.CO;2-2

Ghilardi, C. A., Innocenti, P., Midollini, S., Orlandini, A., and Vaccab, A. (1995). Dynamic nuclear magnetic resonance studies of the η^3-triphenylcyclopropenyl complexes $[M(\eta^3\text{-}C_3Ph_3)L]PF_6$ [M = Ni, Pd or Pt; L = $MeC(CH_2PPh_2)_3$]. Crystal structure of the platinum derivative. *J. Chem. Soc. Dalt. Trans.* 1109–1113. doi: 10.1039/DT9950001109

Gleiter, R., Bleiholder, C., and Rominger, F. (2007). α-Metallocenylmethylium ions and isoelectronic fulvene complexes of d6 to d9 metals. Structural considerations. *Organometallics* 26, 4850–4859. doi: 10.1021/om700272j

Gompper, R., and Bartmann, E. (1978). σ-dicarbonylcyclopentadienyliron derivatives of cyclopropenes and cyclopropenylium salts. *Angew. Chem. Int. Ed. English* 17, 456–457. doi: 10.1002/anie.197804561

Gompper, R., and Bartmann, E. (1985). σ-cyclopropenyl, dicarbonyl-η^5-cyclopentadienyl(1-cyclopropenyl)iron complexes- a new class

of σ-cyclopropenyl complexes. *Angew. Chem. Int. Ed.* 24, 209. doi: 10.1002/anie.198502091

Green, B. M., Grove, D. M., Spencer, J. L., and Stone, F. G. (1977). A. Chemistry of Bis(cyclo-octa-1,5-idene) platinum : reactions with electrophiles. *J. Chem. Soc. Dalt. Trans.* 2228–2234. doi: 10.1039/dt9770002228

Green, M. L. H. (1995). A new approach to the formal classification of covalent compounds of the elements. *J. Organomet. Chem.* 500, 127–148. doi: 10.1016/0022-328X(95)00508-N

Gruselle, M., El Hafa, H., Nikolski, M., Jaouen, G., Vaisserman, J. J., Li, L., et al. (1993). Metal cluster stabilized 2-bornyl cations: a synthetic, X-ray crystallographic, and EHMO study. *Organometallics* 12, 4917–4925. doi: 10.1021/om00036a035

Harris, R. J., and Widenhoefer, R. A. (2016). Gold carbenes, gold-stabilized carbocations, and cationic intermediates relevant to gold-catalysed enyne cycloaddition. *Chem. Soc. Rev.* 45, 4533–4551. doi: 10.1039/C6CS00171H

Hashmi, A. S. (2014). Dual gold catalysis. *Acc. Chem. Res.* 47, 864–876. doi: 10.1021/ar500015k

Hashmi, A. S., and Rudolph, M. (2008). Gold catalysis in total synthesis. *Chem. Soc. Rev.* 37, 1766–1775. doi: 10.1039/b615629k

Hayter, R. G. (1968). A new route to π-allyl complexes of molybdenum and tungsten. *J. Organomet. Chem.* 13, 4–6. doi: 10.1016/S0022-328X(00)88846-4

Hill, E. A., and Richards, J. H. (1961). Carbonium ion stabilization by metallocene nuclei. II. α-metallocenylcarbonium ions. *J. Am. Chem. Soc.* 83, 3840–3846. doi: 10.1021/ja01479a025

Hopkinson, M. N., Tlahuext-Aca, A., and Glorius, F. (2016). Merging visible light photoredox and gold catalysis. *Acc. Chem. Res.* 49, 2261–2272. doi: 10.1021/acs.accounts.6b00351

Hughes, R. P., Lambert, J. M., and Hubbard, J. L. (1986). Reactions of (η^3-Cyclopropenyl)iron Complexes With Tertiary Phosphorus Ligands. Competition between ligand substitution and cyclopropenyl migration to carbon monoxide followed by ring expansion to give oxocyclobutenyl ligands. *Organometallics* 5, 797–804. doi: 10.1021/om00135a030

Hughes, R. P., Reisch, J. W., and Rheingold, A. L. (1985). Oxidative addition of cyclopropenyl cations to zerovalent molybdenum and tungsten centers. Synthesis of η^3-cyclopropenyl and η^3-oxocyclobutenyl complexes of molybdenum(II) and tungsten(II). crystal and molecular structures of $[Mo(\eta^5\text{-}C_5H_5)(\eta^3\text{-}C_3Ph_2R)(CO)_2]$. *Organometallics* 4, 1754–1761. doi: 10.1021/om00129a012

Hughes, R. P., Tucker, D. S., and Rheingold, A. L. (1993). Preparation and dynamic behavior of η^3-cyclopropenyl complexes of cobalt, rhodium, and iridium. crystal and molecular structure of $[Ir(\eta^3\text{-}C_3^tBu_3)(CO)_3]$. *Organometallics* 12, 3069–3074. doi: 10.1021/om00032a032

Jemmis, E. D., and Hoffmann, R. (1980). Cleaving CC bonds in cyclopropenium ions. *J. Am. Chem. Soc.* 102, 2570–2575. doi: 10.1021/ja00528a009

Jia, M., and Bandini, M. (2015). Counterion effects in homogeneous gold catalysis. *ACS Catal.* 5, 1638–1652. doi: 10.1021/cs501902v

Jiang, Y., Freyer, J. L., Cotanda, P., Brucks, S. D., Killops, K. L., Bandar, J. S., et al. (2015). The evolution of cyclopropenium ions into functional polyelectrolytes. *Nat. Commun.* 6:5950. doi: 10.1038/ncomms6950

Jones, J. S., and Gabbaï, F. P. (2016). Coordination- and redox-noninnocent behavior of ambiphilic ligands containing antimony. *Acc. Chem. Res.* 49, 857–867. doi: 10.1021/acs.accounts.5b00543

Jorgensen, W. L., and Salem, L. (1973). *The Organic Chemist's Book of Orbitals*. New York, NY: Academic Press. doi: 10.1016/B978-0-12-390250-4.X5001-2

Komatsu, K., and Kitagawa, T. (2003). Cyclopropenylium cations, cyclopropenones, and heteroanalogues - recent advances. *Chem. Rev.* 103, 1371–1427. doi: 10.1021/cr010011q

Konietzny, S., Finze, M., and Rei,ß, G. J. (2010). Tricarbonyl-6,6′-dimethylfulvene chromium(0) - structural properties. *J. Organomet. Chem.* 695, 2089–2092. doi: 10.1016/j.jorganchem.2010.05.017

Konishi, H., Matsumoto, S., Kamitori, Y., Ogoshi, H., and Yoshida, Z.-I. (1978). Synthesis and properties of diaminocyclopropenylidene transition metal complexes. *Chem. Lett.* 7, 241–244. doi: 10.1246/cl.1978.241

Kozma, Á., Petuškova, J., Lehmann, C. W., and Alcarazo, M. (2013). Synthesis, structure and reactivity of cyclopropenyl-1-ylidene stabilized S(II), Se(II) and Te(II) mono- and dications. *Chem. Commun.* 49, 4145–4147. doi: 10.1039/C2CC36225B

Kreindlin, A. Z., Dolgushin, F. M., Yanovsky, A. I., Kerzina, Z. A., Petrovskii, P. V., and Rybinskaya, M. I. (2000). Synthesis, crystal and molecular structure of $[\{C_5Me_5FeC_5Me_4CH_2\}^+B\{C_6H_3(CF_3)_2\}_4^-]$, the first example of a structurally characterized primary ferrocenylcarbocation. *J. Organomet. Chem.* 616, 106–111. doi: 10.1016/S0022-328X(00)00566-0

Kreindlin, A. Z., Petrovskii, P. V., Rybinskaya, M. I., Yanovskii, A. I., and Struchkov, Y. T. (1987). Synthesis and crystal structure of nonamethylruthenocenylcarbenium hexafluorophosphate. *J. Organomet. Chem.* 319, 229–237. doi: 10.1016/0022-328X(87)83030-9

Kuchenbeiser, G., Donnadieu, B., and Bertrand, G. (2008). Stable bis(diisopropylamino)cyclopropenylidene (BAC) as ligand for transition metal complexes. *J. Organomet. Chem.* 693, 899–904. doi: 10.1016/j.jorganchem.2007.11.056

Li, Z., Brouwer, C., and He, C. (2008). Gold-catalyzed organic transformations. *Chem. Rev.* 108, 3239–3265. doi: 10.1021/cr068434l

Lichtenberger, D. L., Hoppe, M. L., Subramanian, L., Kober, E. M., Hughes, R. P., Hubbard, J. L., et al. (1993). Electron distribution and bonding in η^3-cyclopropenyl-metal complexes. *Organometallics* 12, 2025–2031. doi: 10.1021/om00030a011

Lubke, B., Edelmann, F., and Behrens, U. (1983). Synthese und Struktur von (Fulven)$Cr(CO)_3$-Komplexen. *Chem. Ber.* 116, 11–26. doi: 10.1002/cber.19831160104

Lukasser, J., Angleitner, H., Schottenberger, H., Kopacka, H., Schweiger, M., Bildstein, B., et al. (1995). Stable and crystalline allylium and allenylium salts with ferrocenyl substituents. *Organometallics* 14, 5566–5578. doi: 10.1021/om00012a025

Mann, B. L. (1982). "Comprehensive organometallic chemistry," in *Comprehensive Organometallic Chemistry*, Vol. 9, eds G. Wilkinson, F. G. A. Stone, and E. W. Abel (Oxford: Pergamon Press), 89.

Martin, D., Melaimi, M., Soleilhavoup, M., and Bertrand, G. (2011). A brief survey of our contribution to stable carbene chemistry. *Organometallics* 30, 5304–5313. doi: 10.1021/om200650x

Mayr, B. H., Müller, K.-H., and Rau, D. (1993). Comparison of the electrophilicities. *Angew. Chem. Int. Ed.* 1, 1630–1632. doi: 10.1002/anie.199316301

McClure, M. D., and Weaver, D. L. (1973). An unusual cyclopropenyl complex. The formation and structure of $[Pt\{C_3(C_6H_5)_3\}\{P(C_6H_5)_3\}_2]\ [PF_6] \cdot C_6H_6$. *J. Organomet. Chem.* 54, 59–61. doi: 10.1016/S0022-328X(00)84983-9

McGlinchey, M. J., Girard, L., and Ruffolo, R. (1995). Cluster-stabilized cations: synthesis, structures, molecular dynamics and reactivity. *Coord. Chem. Rev.* 143, 331–381. doi: 10.1016/0010-8545(95)01131-8

Mealli, C., Midollini, S., Moneti, S., and Albright, T. A. (1983). Synthesis and X-ray analysis of a nickel triphenyl-cyclopropenyl complex. A MO-interpretation of the geometry and bonding in the $(C_3H_3)ML_3$-type of complexes. *Helv. Chim. Acta* 66, 557–569. doi: 10.1002/hlca.19830660216

Mealli, C., Midollini, S., Moneti, S., and Sacconi, L. (1981). Cationic η3-Triphenylcyclopropenylnickel complexes with tridentate ligands containing N, P, As as the donor atoms. Molecular structure of η3-triphenylcyclopropenyl-1,1,1-tris(diphenylphosphinomethyl)ethanenickel perchlorate. *J. Organomet. Chem.* 205, 273–279. doi: 10.1016/S0022-328X(00)81484-9

Mealli, C., Midollini, S., Moneti, S., Sacconi, L., Silvestre, J., and Albright, T. A. (1982). Structures of $[(Ph_3C_3)M(PPh_3)_2]^+X^-$Complexes. An experimental and theoretical study of ring-whizzing. *J. Am. Chem. Soc.* 104, 95–107. doi: 10.1021/ja00365a020

Melaimi, M., Soleilhavoup, M., and Bertrand, G. (2010). Stable cyclic carbenes and related species beyond diaminocarbenes. *Angew. Chem. Int. Ed.* 49, 8810–8849. doi: 10.1002/anie.201000165

Melikyan, G. G., Bright, S., Monroe, T., Hardcastle, K. I., and Ciurash, J. (1998). Overcoming a longstanding challenge: X-ray structure of a $[Co_2(CO)_6]$-complexed propargyl cation. *Angew. Chem. Int. Ed.* doi: 10.1002/(SICI)1521-3773(19980202)37:1/2<161::AID-ANIE161>3.0.CO;2-8

Merlic, C. A., Hietbrink, B. N., and Houk, K. N. (2001a). Donor and acceptor properties of the chromium tricarbonyl substituent in benzylic and homobenzylic anions, cations, and radicals. *J. Org. Chem.* 66, 6738–6744. doi: 10.1021/jo010620y

Merlic, C. A., Miller, M. M., Hietbrink, B. N., and Houk, K. N. (2001b). Reactivity of (η^6-arene)tricarbonylchromium complexes toward additions of anions, cations, and radicals. *J. Am. Chem. Soc.* 123, 4904–4918. doi: 10.1021/ja000600y

Merlic, C. A., Walsh, J. C., Tantillo, D. J., and Houk, K. N. (1999). Chemical hermaphroditism: the potential of the $Cr(CO)_3$ moiety to stabilize transition states and intermediates with anionic, cationic, or radical character at the benzylic position. *J. Am. Chem. Soc.* 121, 3596–3606. doi: 10.1021/ja983934k

Miki, S., Ogno, T., Iwasaki, H., and Yoshida, Z. -I. (1988). Syntheses, spectroscopic characterization and electronic structure of cyclopropenylidene ligated platinum complexes. *J. Phys. Org. Chem.* 1, 333–349. doi: 10.1002/poc.610010604

Mingos, D. M. P. (2001). A historical perspective on Dewar's landmark contribution to organometallic chemistry. *J. Organomet. Chem.* 635, 1–8. doi: 10.1016/S0022-328X(01)01155-X

Minić, A., Stevaović, D., Damljanović, I., Pejović, A., Vukićević, M., Bogdaonvić, G. A., et al. (2015). Synthesis of ferrocene-containing six-membered cyclic ureas via α-ferrocenyl carbocations. *RSC Adv.* 5, 24915–24919. doi: 10.1039/C5RA01383F

Minić, A., Stevaović, D., Vukićević, M., Bogdaonvić, G. A., D'hooghe, M., Radulović, N. S., et al. (2017). Synthesis of novel 4-ferrocenyl-1,2,3,4-tetrahydroquinolines and 4-ferrocenylquinolines via α-ferrocenyl carbenium ions as key intermediates. *Tetrahedron* 73, 6268–6274. doi: 10.1016/j.tet.2017.09.014

Moerdyk, J. P., and Bielawski, C. W. (2013). Stable carbenes. *Contemp. Carbene Chem.* 40–74. doi: 10.1002/9781118730379.ch2

Mond, L., Gold, L. H., and Schmidbaur, H. (1995). Ludwig mond lecture. *High Carat Gold Compounds. Chem. Soc. Rev.* 391–400. doi: 10.1039/cs9952400391

Morton, M. S., and Selegue, J. P. (1999). The cyclo-C3ligand: trimetallic cyclopropenium complexes of Group 6-8 metals, including the X-ray crystal structure of $[\{Fe(CO)_2(Cp)\}_3(\mu_3\text{-}C_3)][SbF_6]$. *J. Organomet. Chem.* 578, 133–143. doi: 10.1016/S0022-328X(98)01115-2

Moss, R. A., Shen, S., Krogh-Jespersen, K., Potenza, J. A., Schugar, H. J., and Munjal, R. (1986). Cyclopropyl/phenylcyclopropenyl cations: studies in stabilization. *J. Am. Chem. Soc.* 108, 134–140. doi: 10.1021/ja00261a022

Muratov, D. V., Romanov, A. S., Corsinni, M., Fabrizi de Biani, F., and Siebert, W. (2017). The first triple-decker complex with a carbenium center, $[CpCo(\mu\text{-}C_3B_2Me_5)RuC_5Me_4CH_2]^+$: synthesis, reactivity, X-ray structure, and bonding. *Chem. Eur. J.* 23, 11935–11944. doi: 10.1002/chem.201702571

Nelson, J. H., Wheelock, K. S., Cusachs, L. C., and Jonassen, H. B. (1969). The nature of bonding in zerovalent platinum-acetylene complexes. *Chem. Commun*. 1019–1020. doi: 10.1039/C29690001019

Nesmeyanov, A. N., Perevalova, E. G., Grandberg, K. I., Lemenovskii, D. A., Baukova, T. V., and Afanassova, O. B. (1974). A new type of organogold compound. *J. Organomet. Chem.* 65, 131–144. doi: 10.1016/S0022-328X(00)83895-4

Nicholas, K. M. (1987). Chemistry and synthetic utility of cobalt-complexed propargyl cations. *Acc. Chem. Res.* 20, 207–214. doi: 10.1021/ar00138a001

Nicholas, K. M., and Pettit, P. (1971). An alkyne protecting group. *Tetrahedron Lett.* 3475–3478. doi: 10.1016/S0040-4039(01)97209-0

Norris, J. F. (1901). On the nonexistence of trivalent carbon. *Am. Chem. J* 25, 117–122.

Norris, J. F., and Sanders, W. W. (1901). on triphenylchloromethane. *Am. Chem. J.* 25, 54–62.

Öfele, K. (1970). Dichlor(2,3-diphenylcyclopropenyliden)palladium(II). *J. Organomet. Chem.* 22, C9–C11. doi: 10.1016/S0022-328X(00)83065-X

Ofele, K., Tosh, E., Taubmann, C., and Herrmann, W. A. (2009). Carbocyclic carbene metal complexes. *Chem. Rev.* 109, 3408–3444. doi: 10.1021/cr800516g

Olah, G. A. (1972). The general concept and structure of carbocations based on differentiation of trivalent ('classical') carbenium ions from three-center bound penta- or tetracoordinated ('nonclassical') carbonium ions. The role of carbocations in electrophilic reactions. *J. A. Chem. Soc.* 94, 808–820. doi: 10.1021/ja00758a020

Olah, G. A. (1995). My search for carbocations and their role in chemistry, nobel lecture. *Angew. Chem. Int. Ed.* 34, 1393–1405. doi: 10.1002/anie.199513931

Olah, G. A. (2004). *Carbocation Chemistry*. Hoboken, NJ: Wiley. doi: 10.1002/9780471678656

Olah, G. A., Prakash, G. K. S., Molnár, Á., and Sommer, J. (eds.). (2009). "Chapter 3: Carbocation in superacid systems," in *Superacid Chemistry* (John Wiley & Sons, Inc.), 83–310. doi: 10.1002/9780470421604

Osawa, M., Hoshino, M., and Hashizume, D. (2008). Photoluminescent properties and molecular structures of $[NaphAu(PPh_3)]$ and $[\mu\text{-Naph}\{Au(PPh_3)\}_2]\,ClO_4$ (Naph = 2-naphthyl). *Dalt. Trans.* 4, 2248–2252. doi: 10.1039/b714609d

Osella, D., Dutto, G., Jaouen, G., Vessieres, A., Raithby, P. R., De Benedetto, L., et al. (1993). Modification of estradiol at the 17-position. Effect of changing the OH group for a transition-metal carbonyl cluster on the estradiol receptor recognition. *Organometallics* 12, 4545–4552. doi: 10.1021/om00035a045

Owen, G. R. (2012). Hydrogen atom storage upon Z-class borane ligand functions: an alternative approach to ligand cooperation. *Chem. Soc. Rev.* 41, 3535–3546. doi: 10.1039/c2cs15346g

Owen, G. R. (2016). Functional group migrations between boron and metal centres within transition metal-borane and -boryl complexes and cleavage of H-H, E-H and E-E′ bonds. *Chem. Commun.* 52, 10712–10726. doi: 10.1039/C6CC03817D

Parkin, G. (2007). "Classification of organotransition metal compounds," in *Comprehensive Organometallic Chemistry III*, eds D. Mingos, P. Micheal, and R. H. Crabtree (Elsevier Ltd.), 1–57. doi: 10.1016/B0-08-045047-4/00001-7

Pfletschinger, A., Dargel, T. K., Bats, J. W., Schmalz, H. G., and Koch, W. (1999). Structural and energetical characterization of reactive intermediates derived from toluene - $Cr(CO)_3$. *Chem. Eur. J.* 5, 537–545. doi: 10.1002/(SICI)1521-3765(19990201)5:2<537::AID-CHEM537>3.0.CO;2-I

Porter, K. A., Schier, A., and Schmidbaur, H. (2003). Auration of thiophene and furan: structures of the 2-mono- and 2,2-diaurated products. *Organometallics* 22, 4922–4927. doi: 10.1021/om030575f

Preethalayam, P., Krishnan, K. S., Thulasi, S., Chand, S. S., Joseph, J., Nair, V., et al. (2017). Recent advances in the chemistry of pentafulvenes. *Chem. Rev.* 117, 3930–3989. doi: 10.1021/acs.chemrev.6b00210

Rafael, U., Laguua, A., Fernhdez, E. J., and Jones, P. G. (1988). (Polyhalophenyl)silver(I) complexes as arylating agents: crystal structure of $[(\mu\text{-}2,4,6\text{-}C_6F_3H_2)(AuPPh_3)_2]ClO_4$. *J. Organomet. Chem.* 350, 129–138. doi: 10.1016/0022-328X(88)80367-X

Rees, C. W., and von Angerer, E. (1972). Pyran-2-ylidene carbene complexes. *J. Chem. Soc. Chem. Comm*. 420. doi: 10.1039/c39720000420

Richards, J. H., and Hill, E. A. (1959). α-metallocenyl carbonium ions. *J. Am. Chem. Soc.* 81, 3484–3485. doi: 10.1021/ja01522a089

Ritchie, C. D. (1986). Cation-anion combination reactions. 26. A review. *Can. J. Chem.* 64, 2239–2256. doi: 10.1139/v86-370

Roithová, J., Janková, Š., Jašíková, L., Váňa, J., and Hybelbauerová, S. (2012). Gold-gold cooperation in the addition of methanol to alkynes. *Angew. Chem. Int. Ed.* 51, 8378–8382. doi: 10.1002/anie.201204003

Rybinskaya, M. I., Kreindlin, A. Z., Struchkov, Y. T., and Yanovsky, A. I. (1989). On the problem of the stabilization of α-metallocenylcarbocation. Synthesis, properties and crystal structure of $[C_5Me_5OsC_5Me_4CH_2^+]BPh_4^-\cdot CH_2Cl_2$. *J. Organomet. Chem.* 359, 233–243. doi: 10.1016/0022-328X(89)85433-6

Schmidbaur, H. (1990). The fascinating implications of new results in gold chemistry. *Gold Bull.* 23, 11–21. doi: 10.1007/BF03214710

Schrock, R. R. (2001). Transition metal-carbon multiple bonds. *J. Chem. Soc. Dalt. Trans.* 2541–2550. doi: 10.1039/b104609h

Schrock, R. R. (2005). High oxidation state alkylidene and alkylidyne complexes. *Chem. Commun.* 2773–2777. doi: 10.1039/b504541j

Schumann, H., Glanz, M., Girgsdies, F., Hahn, F. E., Tamm, M., and Grzegorzewski, A. (1997). Cyclopropenylidene adducts of divalent germanium, tin, and lead. *Angew. Chem. Int. Ed.* 36, 2232–2234. doi: 10.1002/anie.199722321

Seidel, G., Lehmann, C. W., and Fürstner, A. (2010). Elementary steps in gold catalysis: the significance of gem-diauration. *Angew. Chem. Int. Ed.* 49, 8466–8470. doi: 10.1002/anie.201003349

Shahzad, S. A., Sajid, M. A., Khan, Z. A., and Canseco-Gonzalez, D. (2017). Gold catalysis in organic transformations: a review. *Synth. Commun.* 47, 735–755. doi: 10.1080/00397911.2017.1280508

Shen, J. K., Basolo, F., Tucker, D. S., and Hughes, R. P. (1993). Kinetics of CO substitution in reactions of η^3-cyclopropenyl complexes of iron, cobalt, rhodium, and iridium with phosphorus ligands. First examples of a dissociative mechanism for CO substitution in the cobalt triad carbonyl complexes. *J. Am. Chem. Soc.* 115, 11312–11318. doi: 10.1021/ja00077a033

Shriver, D. F. (1970). Transition metal basicity. *Acc. Chem. Res.* 3, 231–238. doi: 10.1021/ar50031a004

Shrock, R. R. (2002). High oxidation state multiple metal-carbon bonds. *Chem. Rev.* 102, 145–179. doi: 10.1021/cr0103726

Sime, R. L., and Sime, R. J. (1974). The crystal structure of ferrocenyldiphenylcyclopropenium tetrafluoroborate, a stable carbonium ion salt. *J. Am. Chem. Soc.* 96, 892–896. doi: 10.1021/ja00810a039

Sørensen, T. J., Madsen, A. Ø., and Laursen, B. W. (2014). Synthesis and structures of N-alkyl-1,13-dimethoxychromeno-[2,3,4-kl] acridinium salts: the missing azaoxa[4]helicenium. *Chem. Eur. J.* 20, 6391–6400. doi: 10.1002/chem.201400082

Stephen, A., Hashmi, K., Braun, I., Rudolph, M., and Rominger, F. (2012). The role of gold acetylides as a selectivity trigger and the importance of gem-diaurated species in the gold-catalyzed hydroarylating-aromatization of arene-diynes. *Organometallics* 31, 644–661. doi: 10.1021/om200946m

Tamm, M., Grzegorzewski, A., and Hahn, F. E. (1995). Pentacarbonylchromium(0) and -tungsten(0) complexes with the bis(diisopropylamino) cyclopropenylidene ligand. *J. Organomet. Chem.* 501, 309–313. doi: 10.1016/0022-328X(95)05702-Q

Tantillo, D. J., Hietbrink, B. N., Merlic, C. A., and Houk, K. N. (2000). Attenuating and supplanting nonclassical stabilization: $Cr(CO)_3$-complexed benzonorbornenyl cations. *J. Am. Chem. Soc.* 122, 7136–7137. doi: 10.1021/ja000621s

Trahanovsky, W. S., and Wells, D. K. (1969). Communications to the editor: arene-metal complexes. I. Thermodynamic stabilities of substituted benzyl cations complexed with tricarbonylchromium. *J. Am. Chem. Soc.* 91, 5870–5871. doi: 10.1021/ja01049a029

Tuggle, R. M., and Weaver, D. L. (1971a). The crystal structure and properties of π-triphenylcyclopropenylchlorodipyridinenickel(0)-pyridine, a π complex of a three-membered aromatic ring. *Inorg. Chem.* 10, 2599–2603. doi: 10.1021/ic50105a046

Tuggle, R. M., and Weaver, D. L. (1971b). The crystal and molecular structure of the mixed sandwich complex π-cyclopentadienyl-π-triphenylcyclopropenylnickel, $(\pi\text{-}C_5H_5)Ni(\pi\text{-}C_3(C_6H_5)_3)$. *Inorg. Chem.* 10, 1504–1510. doi: 10.1021/ic50101a038

Weiss, R., and Priesner, C. (1978). Coordinatively unsaturated transition metal-substituted cyclopropenylium systems. *Angew. Chem. Int. Ed.* 17, 457–458. doi: 10.1002/anie.197804571

Winemiller, M. D., Kopach, M. E., and Harman, W. D. (1997). Protonation of unactivated aromatic hydrocarbons on Osmium(II): stabilization of arenium cations via unprecedented η^2 - and η^3 -coordination. *J. Am. Chem. Soc.* 119, 2096–2102. doi: 10.1021/ja963299n

Winstein, S., and Trifan, D. (1952). Neighboring carbon and hydrogen. XI. Solvolysis of exo-norbornyl p-bromobenzenesulfonate. *J. Am. Chem. Soc.* 74, 1154–1160. doi: 10.1021/ja01125a007

Yoshida, Z. (1982). Novel Pi systems possessing cyclopropenylidene moiety. *Pure Appl. Chem.* 54, 1059–1074. doi: 10.1351/pac198254051059

You, D., Yang, H., Sen, S., and Gabbaï, F. P. (2018). Modulating the σ-accepting properties of an antimony z-type ligand via anion abstraction: remote-controlled reactivity of the coordinated platinum atom. *J. Am. Chem. Soc.* 140, 9644–9651. doi: 10.1021/jacs.8b05520

Zhdanko, A., and Maier, M. E. (2013). Quantitative evaluation of the stability of gem -diaurated species in reactions with nucleophiles. *Organometallics* 32, 2000–2006. doi: 10.1021/om400083f

Zi, W., and Toste, F. D. (2016). Recent advances in enantioselective gold catalysis. *Chem. Soc. Rev.* 45, 4567–4589. doi: 10.1039/C5CS00929D

Conflict of Interest Statement: The authors declare that the research was conducted in the absence of any commercial or financial relationships that could be construed as a potential conflict of interest.

Copyright © 2019 Goodman, Mei and Gianetti. This is an open-access article distributed under the terms of the Creative Commons Attribution License (CC BY). The use, distribution or reproduction in other forums is permitted, provided the original author(s) and the copyright owner(s) are credited and that the original publication in this journal is cited, in accordance with accepted academic practice. No use, distribution or reproduction is permitted which does not comply with these terms.

Nanoscience

Ardemis A. Boghossian

Ardemis Boghossian is a tenure-track Assistant Professor at the École Polytechnique Fédérale de Lausanne (EPFL) in Switzerland. She obtained her BEng in Chemical Engineering from the University of Michigan in Ann Arbor, MI in 2007 and her PhD in Chemical Engineering from the Massachusetts Institute of Technology (MIT) in 2012 under the supervision of Michael S. Strano. She pursued her postdoctoral studies in the laboratory of Nobel Laureate Frances H. Arnold at the California Institute of Technology (Caltech) until she started her Professorship in 2015.

Farhat Nosheen

Dr Farhat Nosheen obtained her PhD degree in Chemistry from the Department of Chemistry, Tsinghua University, Beijing, China in 2016. Currently, she works as Assistant Professor at the Department of Chemistry, University of Education, Lahore, Jauharabad campus, Pakistan. Her research interests include synthesis, formation mechanisms, and electrocatalytic applications of noble metal based bi-and multimetallic nanostructures in fuel cells.

. Jianping Yang

Prof. Jianping Yang obtained the PhD degree in 2013 from Fudan University supervised by Professor Dongyuan Zhao. He then worked as a postdoctoral fellow at Tongji University, a visiting research fellow at the University of Wollongong and Monash University, and was promoted to full Professor in 2016 at Donghua University, China. His research interest include multifunctional materials *via* surface and interface controllable synthesis in the application of energy storage including Si-based lithium ion batteries, carbon-based sodium/potassium ion batteries, as well as in the application of environmental remediation such as catalytic reduction of nitrogen oxide exhaust, electrocatalytic abatement and adsorption of water pollutants.

Wei Luo

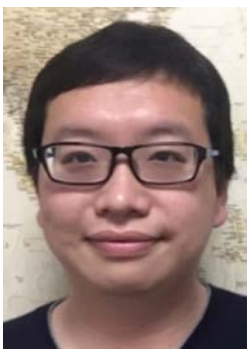

Dr Wei Luo is now a Professor at the State Key Laboratory for Modification of Chemical Fibers and Polymer Materials, College of Materials Science and Engineering at Donghua University. He obtained a Bachelor's degree in 2006 and Master's degree in 2009 from Nanjing Tech University, China. He obtained his PhD in chemistry in 2014 from Fudan University supervised by Professor Dongyuan Zhao. He received second prize of the Natural Science Award of Ministry of Education (the third awardee). His research interests mainly include the synthesis of functional mesoporous and nanomaterials for energy storage and conversion as well as sensors.

Lukasz Marciniak

Lukasz Marciniak received his MSc Eng in Physics (Photonics) from the Wroclaw University of Technology in Wroclaw, Poland, in 2009 and a PhD and habilitation in Physics from the Institute of Low Temperature and Structure Research, Polish Academy of Sciences, in 2014 and 2017, respectively. Holder of numerous awards and prizes (e.g. the Scholarship of Ministry of Science and Higher Education of Poland for Young and Outstanding Scientists 2015-2018, the START 2015 and START 2016 of Foundation for Polish Science FNP for outstanding young scientists, the gold medal of Brussels Innova 2015 and 2016, the Award of the Polish Minister of Science and Higher Education for his achievements in the international arena inventive in 2014, the Scientific Award of Wroclaw Department of Polish Academy of Sciences 'Iuvenes Wratislaviae' 2017 and the Scientific Award of "Polityka" 2018). He is the Principal Investigator in FNP First Team, NCS Opus, NCS Sonata, and the NSC Preludium. He has co-authored 90 publications and holds three patents with six patents applications. His current research focuses on nanocrystalline luminescent thermometry of lanthanide and transition metal ions doped inorganic structures.

Juewen Liu

Juewen Liu is currently a Professor of Chemistry and a University Research Chair at the University of Waterloo. Dr Liu is interested in bioanalytical chemistry, catalytic DNA and aptamers, and biointerface chemistry. He received a Fred Beamish Award from the Canadian Society for Chemistry (CSC) in 2014, and the McBryde Medal in 2018. He has published over 300 papers, receiving over 20,000 citations and has an H-index of 65. He is an Associate Editor of *Analytical Methods* and is on the Editorial Advisory Board of *Langmuir*.

Lining Sun

Lining Sun is a Professor of Chemistry and Material Science in Shanghai University. She obtained her BSc degree from Shandong Normal University in 2002 and a PhD degree from the Changchun Institute of Applied Chemistry, Chinese Academy of Sciences at the end of 2007. From 2008 to 2009, she was an Alexander-von-Humboldt Research Fellow at the University of Regensburg, Germany. In September 2009, she joined Shanghai University as an Associate Professor, and since March 2016, she has worked as a full Professor. Her research focuses on rare-earth doped upconversion luminescent nanomaterials for sensing, bioimaging, and treatment.

Qianqian Su

Qianqian Su obtained her BE degree in Materials Science and Engineering from Shandong University. She obtained her MSc degree from Guangzhou Institute of Chemistry, Chinese Academy of Sciences and completed her PhD degree under the supervision of Professor Xiaogang Liu at the National University of Singapore. She worked as a research fellow at Fudan University with Professor Fuyou Li. Shen worked as a visiting scholar at the National University of Singapore and the University of Technology Sydney. She joined the Institute of Nanochemistry and Nanobiology at Shanghai University in 2017. Her research interests focus on the development of novel luminescent nanomaterials for biomedical applications.

Renyuan Zhang

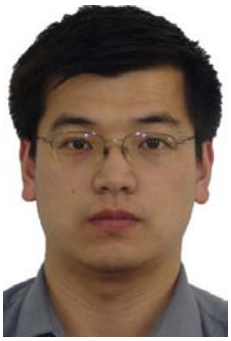

Renyuan Zhang is an Associate Professor at the Institute of New Energy for Vehicles, School of Materials Science and Engineering, Tongji University. He obtained both his Bachelor's degree in 2004, and PhD Degree in 2010 from Fudan University, supervised by of Prof. Dongyuan Zhao. He then worked as a post-doctoral researcher at the Lab of Advanced Materials, Fudan University. His current research interests include synthesis of functional nanomaterials and mesoporous materials for catalysis, energy storage and conversion.

CuiYun Yu

Dr Cui-Yun Yu is a Professor of Pharmacy and serves as the duty director of Hunan Province Cooperative Innovation Center for Molecular Target New Drug at the University of South China. She obtained her PhD degree in Polymer Science in 2009 from Wuhan University. Dr Yu is currently leading various critical national foundations including the National Key R&D Program of China and the National Natural Science Foundation of China. Her research interests focus on the design and development of novel biomaterials for tumor targeted drug delivery. Thus far, she has published more than 30 peer reviewed papers in leading journals such as ACS Applied Materials &Interface, Biomaterials Science, Molecular Pharmaceutics.

Lidan Hu

Lidan Hu obtained her PhD degree from Xiamen University in 2016. She then joined Prof. Fan Zhang's Laboratory of Nanobio in the Chemistry Department of Fudan University, as a postdoctoral fellow. In 2018, Dr Hu joined the University of South China. Her research focuses on the design, synthesis, and biomedical applications of persistent luminescence materials.

Ou Chen

Ou Chen is an Assistant Professor in the Department of Chemistry at the Brown University. He obtained his BSc degree in Chemical Physics from the University of Science and Technology of China (USTC) in 2004 and completed his PhD study in the Department of Chemistry at the University of Florida. He worked with Prof. Moungi Bawendi as a postdoctoral associate at MIT. His current research interests lie on exploring novel methodologies for generating functional nanocrystals, quantum dots and their self-assembled superstructures for energy- and bio-related applications.

Chun Xu

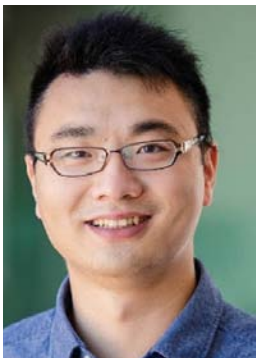

Dr Chun Xu obtained his PhD in Biomedical Engineering and Nanotechnology at The University of Queensland, Australia in 2016. Before that, he obtained a MDS in Oral and Maxillofacial Surgery and a BDS in Dentistry from Wuhan University, China. He is currently a NHMRC Senior Research Officer and C.J. Martin fellow at The University of Queensland. His research interest includes the synthesis of nanomaterials and their biomedical applications including drug delivery and tissue engineering.

frontiers in Chemistry

REVIEW
published: 19 September 2019
doi: 10.3389/fchem.2019.00612

Non-covalent Methods of Engineering Optical Sensors Based on Single-Walled Carbon Nanotubes

*Alice J. Gillen and Ardemis A. Boghossian**

École Polytechnique Fédérale de Lausanne, Lausanne, Switzerland

Optical sensors based on single-walled carbon nanotubes (SWCNTs) demonstrate tradeoffs that limit their use in *in vivo* and *in vitro* environments. Sensor characteristics are primarily governed by the non-covalent wrapping used to suspend the hydrophobic SWCNTs in aqueous solutions, and we herein review the advantages and disadvantages of several of these different wrappings. Sensors based on surfactant wrappings can show enhanced quantum efficiency, high stability, scalability, and diminished selectivity. Conversely, sensors based on synthetic and bio-polymer wrappings tend to show lower quantum efficiency, stability, and scalability, while demonstrating improved selectivity. Major efforts have focused on optimizing sensors based on DNA wrappings, which have intermediate properties that can be improved through synthetic modifications. Although SWCNT sensors have, to date, been mainly engineered using empirical approaches, herein we highlight alternative techniques based on iterative screening that offer a more guided approach to tuning sensor properties. These more rational techniques can yield new combinations that incorporate the advantages of the diverse nanotube wrappings available to create high performance optical sensors.

Keywords: optical biosensing, near-infrared sensors, single-walled carbon nanotubes (SWCNTs or SWNTs), molecular recognition, selectivity, fluorescence brightness, non-covalent solubilization

OPEN ACCESS

Edited by:
Fan Zhang,
Fudan University, China

Reviewed by:
Renren Deng,
Zhejiang University, China
Victor Alexeevich Karachevtsev,
B. Verkin Institute for Low Temperature Physics and Engineering (National Academy of Sciences Ukraine), Ukraine
Feng Long,
Renmin University of China, China

****Correspondence:***
Ardemis A. Boghossian
ardemis.boghossian@epfl.ch

Specialty section:
This article was submitted to Nanoscience, a section of the journal Frontiers in Chemistry

Received: *29 January 2019*
Accepted: *21 August 2019*
Published: *19 September 2019*

Citation:
Gillen AJ and Boghossian AA (2019) Non-covalent Methods of Engineering Optical Sensors Based on Single-Walled Carbon Nanotubes. Front. Chem. 7:612. doi: 10.3389/fchem.2019.00612

1. INTRODUCTION

Optical sensors use light as a means of contactless detection for real-time sensing. Distinct optical signals from a single device enables multimodal detection of several analytes simultaneously, a feature that is especially advantageous for remote *in vivo* biosensing applications. Fluorescence-based optical sensors require two elements for operation: a molecular recognition element that selectively interacts with the analyte of interest and an optical transducer, such as a fluorophore, that converts this interaction into a measurable optical signal.

As described in several reviews (Boghossian et al., 2011; Liu et al., 2011; Kruss et al., 2013; Pan et al., 2017), single-walled carbon nanotubes (SWCNTs) are among the most promising fluorescence-based transducers for biosensing applications. They are one-dimensional nanostructures with optoelectronic properties that are tuned by tube diameter as a result of quantum confinement. Conceptualized as cylindrically rolled sheets of graphene, SWCNTs exist with various diameters, and they can be either metallic, semi-metallic, or semiconducting, depending on the direction the sheet is rolled. In 2002, O'Connell et al. demonstrated that

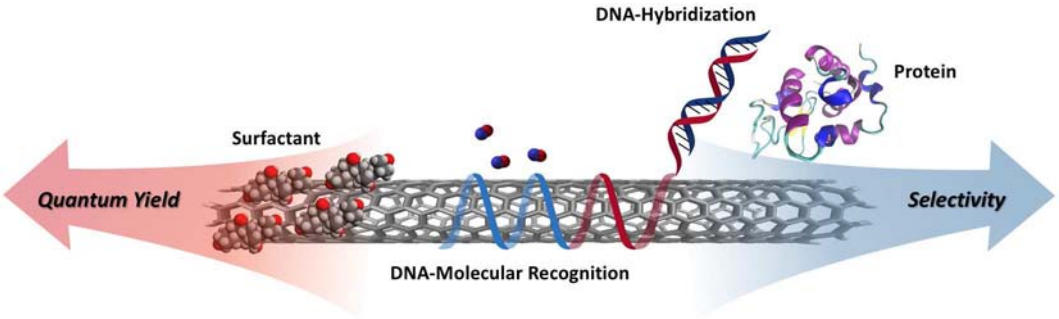

GRAPHICAL ABSTRACT | Schematic illustrating the tradeoffs between quantum yield and selectivity for various non-covalent surface functionalizations.

semiconducting forms of SWCNTs dispersed in aqueous solutions emit photoluminescence at near-infrared (near-IR) wavelengths (O'Connell et al., 2002). This emission lies within the optical transparency window for biological material (Boghossian et al., 2011) which, when coupled with the nanotube's indefinite photostability and capabilities for single-molecule detection, makes SWCNTs attractive for *in vivo* continuous monitoring applications.

The use of SWCNTs as fluorescent transducers requires surface functionalization to impart optical stability and molecular recognition. Non-functionalized SWCNTs are inherently hydrophobic and exhibit a strong tendency to aggregate into bundles in aqueous solutions. Since most SWCNT preparations contain metallic nanotubes, these bundles contribute to the fluorescence quenching of semiconducting SWCNTs through the non-radiative exciton decay channels within the bundle (O'Connell et al., 2002; Maeda et al., 2004). Therefore, the bundles need to be exfoliated to generate individually suspended nanotubes in a liquid phase for most practical applications (Coleman, 2009). Specifically, this suspension allows the semi-conducting nanotubes to fluoresce in the near-IR. In addition to enabling solubilization and fluorescence, surface functionalization can also modify the nanotube surface to promote selective interactions with particular analytes of interest (**Figure 1**). The underlying mechanism for this selectivity depends on the wrapping and remains an ongoing area of research for many wrappings (Jeng et al., 2006; Hertel et al., 2010; Bisker et al., 2016; Polo and Kruss, 2016; Antonucci et al., 2017; Kruss et al., 2017; Mann et al., 2017; Zubkovs et al., 2017; Gillen et al., 2018; Wu et al., 2018; Lambert et al., 2019).

Since covalent functionalization of the nanotube surface is known to strongly affect, or even diminish, the nanotube fluorescence, non-covalent modifications are typically used for creating optical sensors. The most common approach for non-covalently separating SWCNT bundles is liquid-phase exfoliation and stabilization (Coleman, 2009). This approach typically involves using forced dispersion (with sonication, for example) in the presence of wrappings, such as surfactants, synthetic polymers, oligonucleotides, and proteins that can stabilize the suspended SWCNTs (**Figure 2**). In addition to improving the solubility of the SWCNTs, these wrappings can also impart secondary characteristics, such as enhanced bio-compatibility and improved molecular sensitivity, overcoming problems associated with the chemical inertness of raw SWCNTs (Saifuddin et al., 2013).

In this review, we present an overview of several key methods used for the non-covalent functionalization of SWCNTs. Beginning with surfactant-coated SWCNTs, we progress toward the use of biomolecules to suspend nanotubes, highlighting key advantages and disadvantages associated with each wrapping. Finally, we conclude with a consideration of new approaches aimed at overcoming some of the limitations of both surfactant- and biomolecule-suspended SWCNTs. These examples highlight emerging methods to selectively engineer improved SWCNT-based optical sensors in complex environments.

2. SURFACTANT-COATED SWCNTS

Surfactant-coated SWCNTs represent a standard comparative benchmark for nanotube suspensions, particularly with respect to achieving scalable wrapping procedures and the high quantum yields necessary for optical sensing. Historically, the first reported suspensions of individual SWCNTs were achieved using an aqueous surfactant, sodium dodecylsulfate (SDS) (O'Connell et al., 2001, 2002; Bachilo et al., 2002). The resulting isolation of the nanotubes from surrounding bundles greatly improved the optical resolution of the absorbance spectra. Additionally, the authors were able to characterize the direct band gap of individual semiconducting SWCNTs with fluorescence spectroscopy (Bachilo et al., 2002; O'Connell et al., 2002), which was first hypothesized in the early 1990s (Dresselhaus et al., 1992; Hamada et al., 1992; Saito et al., 1992) and previously detected using Raman and STEM (Wildoer et al., 1998; Kataura et al., 1999).

To prevent re-bundling and obtain a thermodynamically stable suspension, the strong cohesion energy of the isolated tubes (~120 kT nm^{-1}) must be compensated by either tube-solvent, or in the case of surfactant-suspended SWCNTs, tube-surfactant interactions (Angelikopoulos and Bock, 2012). However, SWCNT suspensions often exist in a kinetically

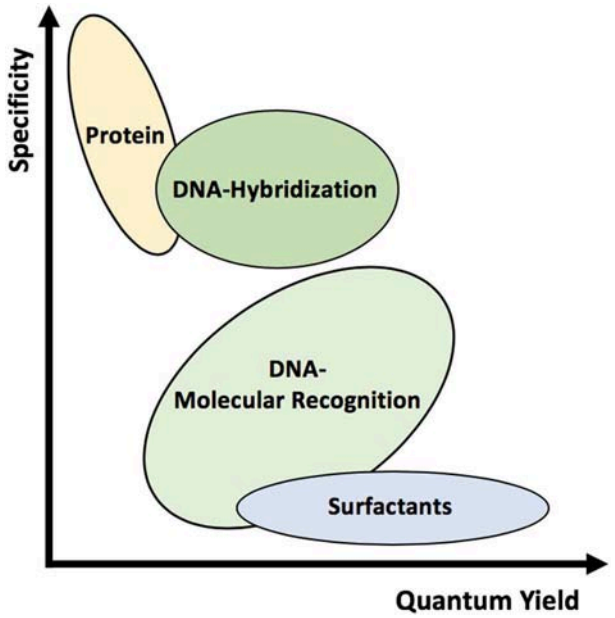

FIGURE 1 | Schematic representation of the various wrappings used to suspend SWCNTs. Different wrappings can alter the quantum yield and specificity of the complexes.

meta-stable state. Kinetic stabilization does not fully overcome the cohesion energy of the tubes; instead the surfactant creates a repulsive force between the tubes that reduces the likelihood of forming tube-tube contacts, hence slowing aggregation (Angelikopoulos and Bock, 2012). Similar to the interactions in the kinetic stabilization of colloids (Tummala and Striolo, 2008, 2009; Angelikopoulos and Bock, 2012; Kato et al., 2012; Oh et al., 2013). Previous studies hypothesized that the individual nanotubes are encased in the hydrophobic interiors of the micelle. The hydrophilic part of the surfactant molecules is believed to face outwards, creating a cylindrical micelle and a repulsive force between the nanotubes that renders a thermodynamically meta-stable suspension (**Figure 3**) (Angelikopoulos and Bock, 2008, 2012).

The use of surfactants to suspend SWCNTs has since expanded to include other anionic, cationic, and non-ionic surfactants (Hirsch, 2002; Wenseleers et al., 2004; Crochet et al., 2007; Haggenmueller et al., 2008; Blanch et al., 2010; Bergler et al., 2016; Nonoguchi et al., 2018), such as sodium cholate (SC), sodium deoxycholate (SDOC), sodium dodecylbenzenesulfonate (SDBS), lithium dodecyl sulfate (LDS), Triton X-100, and pluronic F127. Depending on the surfactant, high-quality dispersions can be achieved with large populations of individualized nanotubes (Coleman, 2009) and SWCNT concentrations >1 mg/mL. However, different surfactants have been found to vary greatly in the degree of dispersion and stability of the resulting suspensions. This variation is, in part, attributed to the interactions between the surfactant and nanotube, which result in the formation of different structures with varying degrees of surface coverage (Matarredona et al., 2003). In addition to cylindrical micelle SWCNT encapsulation, as was proposed for the SDS-suspended SWCNTs, two additional configurations include (Angelikopoulos and Bock, 2012; Xin et al., 2013) (i) Langmuir-type (random molecular adsorption) layers and (ii) adsorbed spherical and hemispherical micelles (Islam et al., 2003; Vo et al., 2016; Vo and Papavassiliou, 2017) (**Figure 3A**). The latter, spherical and hemispherical micelle formation, is adopted only by strong amphiphiles that prefer higher curvature aggregates. This formation of hemimicellar aggregates on the surface of the SWCNTs typically involves adsorption of the surfactant onto the nanotube followed by the self-assembly of the molecules, which is enabled by diffusion along the nanotube surface (Vo et al., 2016). In contrast, the former, random adsorption of the surfactant on the SWCNT surface, is adopted by weakly amphiphilic molecules [such as flavin mononucleotides (FMN)] and bile acid surfactants (including SC and SDOC) where adsorption is competitive, i.e., follows a Langmuir isotherm (Angelikopoulos and Bock, 2010, 2012; Tummala et al., 2010; Bergler et al., 2016; Xu et al., 2017).

According to both experiment and simulation, the degree of exposed SWCNT surface coverage following adsorption of surfactant molecules under all three regimes is largely dependent on surfactant concentration (Matarredona et al., 2003). Indeed, Wang et al. (2004) have shown that for Triton-X, the optimal surfactant dispersion concentration is different from the critical micelle concentration (CMC) and results from competition between maximizing surfactant adsorption on the nanotube surface and micelle-mediated depletion interactions between adjacent SWCNT bundles. Moreover, previous reports have shown vast differences in the maximum relative solubility of SWCNT complexes using the same surfactant, with an apparent dependence on the processing method and conditions. For example, suspensions made with SDBS can have maximum SWCNT concentrations of 20 mg/mL (Islam et al., 2003) or no more than ∼0.01 mg/mL (Moore et al., 2003), depending on the dispersion approach.

Another factor believed to impact the stability of surfactant-dispersed SWCNTs is the ζ-potential. When surfactant molecules adsorb onto the surface of SWCNTs, the surfactant counter-ion (commonly Na^+ or Li^+) is dissociated from the hydrophilic head group of the surfactant. These counter-ions are spatially separated from the tail group of the molecular ions, arranging in a diffuse cloud that acts as a multi-pole. As a result, surfactant-suspended nanotubes appear, from a distance, to carry an effective charge associated with this double layer, which is denoted as the ζ-potential (Coleman, 2009). This potential is equivalent to the electrostatic potential measured at the edge of the layer at the bound surfactant tail groups, and it acts as a repulsive interaction potential between neighboring SWCNTs. In a study by Sun et al. (2008), the dispersion quality of six surfactant molecules was tested. Each of the dispersion-quality metrics were found to scale well with the measured ζ-potential of the dispersion, with SDS suspending better than both SDBS and SC, corresponding to ζ-potential values of −70.0, −68.8, and −48.8 mV, respectively. These findings indicate that the dispersion quality

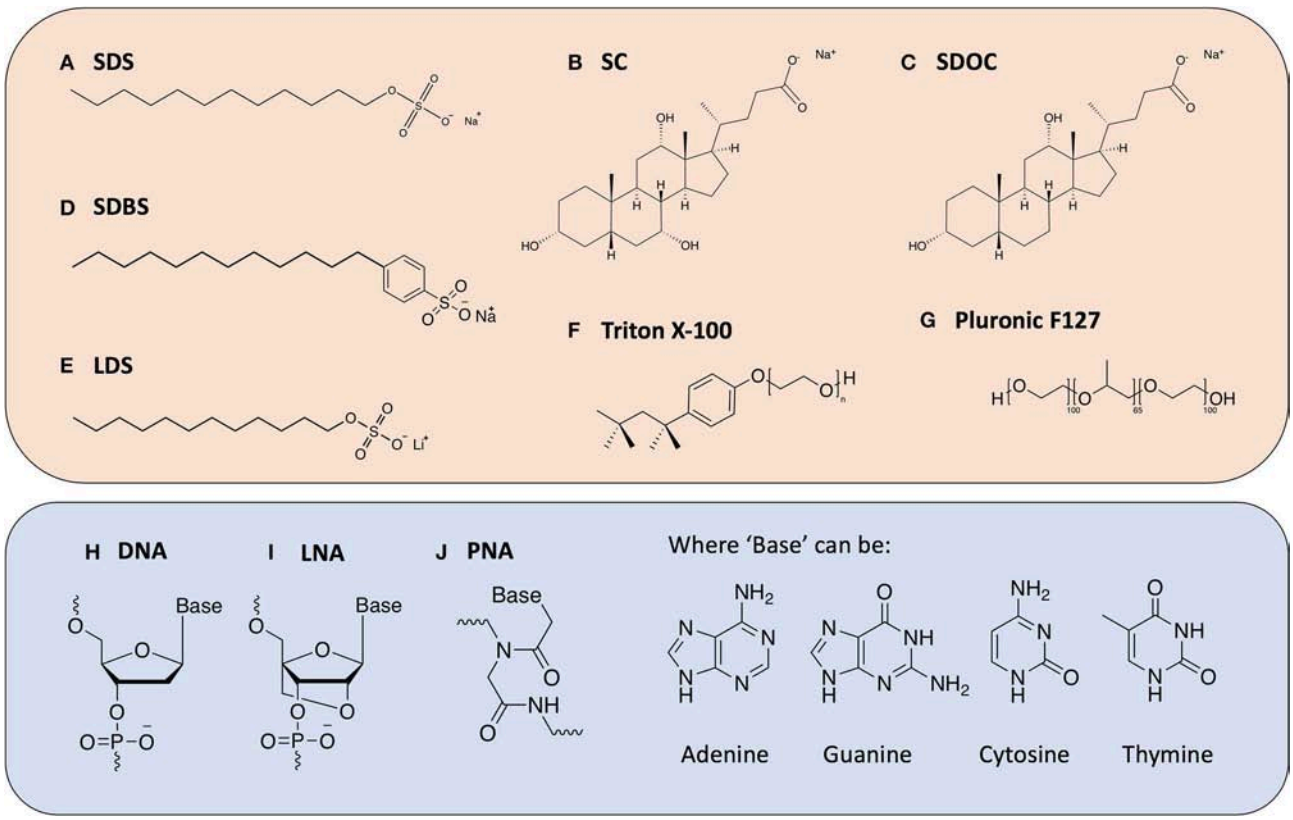

FIGURE 2 | Chemical structures of the various dispersants discussed in this review. Surfactant molecules (top box) **(A)** Sodium Dodecylsulfate (SDS); **(B)** Sodium Cholate (SC); **(C)** Sodium Deoxycholate (SDOC); **(D)** Sodium Dodecylbenzenesulfonate (SDBS); **(E)** Lithium Dodecylsulfate (LDS); **(F)** Triton X-100; **(G)** Pluronic F127; and oligonucleotide-derived molecules (bottom box); **(H)** Deoxyribo Nucleic Acid (DNA); **(I)** Locked Nucleic Acid (LNA); **(J)** Peptide Nucleic Acid (PNA).

of surfactant-SWCNTs may be controlled by the magnitude of the electrostatic repulsive forces between the coated SWCNTs (White et al., 2007; Sun et al., 2008), a property that can be tuned in order to improve the long-term stability of these solutions.

Given the dependence of maximum dispersion concentration and stability on surfactant type, we focus the remainder of our discussion on the four most commonly used surfactants for SWCNT suspension, SC, SDOC, SDS, and SDBS. These surfactants have been shown to achieve stable dispersions with suspension efficiencies above 40% (Haggenmueller et al., 2008). Despite the similar structures of SC and SDOC, which only differ by a hydroxy group, SDOC shows a marked increase in suspension yield (+17%). In addition to dispersion efficiency, the resolution of the optical absorption spectrum can be used to determine differences in the quality of SWCNT suspensions. Distinct absorption peaks are observed for both SC and SDOC, while SDS and SDBS show much broader peaks. In instances where SWCNTs are not effectively exfoliated, the van der Waals interactions between aggregated nanotubes result in broad, weak absorption peaks (Antonucci et al., 2017). This observation therefore suggests that SC and SDOC can generally yield more monodisperse SWCNTs under the studied preparation conditions. On the other hand, the broader peaks observed for SDS and SDBS indicate that these surfactants do not effectively de-bundle the nanotubes, resulting in a poorer dispersion quality despite the apparently high suspension yields.

In addition to their high dispersion efficiencies, these surfactants also benefit from a number of additional advantages. Compared to most biopolymers, these wrappings yield SWCNT suspensions that are relatively cheap and stable, and the preparation procedures are scalable enough to produce large volumes of monodisperse SWCNTs, which is an important consideration for the industrialization of nanotube sensors. Furthermore, surfactant-suspended SWCNTs typically exhibit much larger suspension (Coleman, 2009) and quantum yield values (Haggenmueller et al., 2008) compared to both protein- and DNA-suspended SWCNTs. The increased fluorescence intensity is attributed, in part, to the increased surface coverage of the surfactant on the SWCNT surface. The increased coverage results in higher levels of oxygen and water shielding, which has been shown to decrease nanotube fluorescence (Zheng et al., 2017), thereby leading to brighter SWCNT complexes. This increase in brightness is particularly important for biosensing applications, where penetration depth and sensor sensitivity have

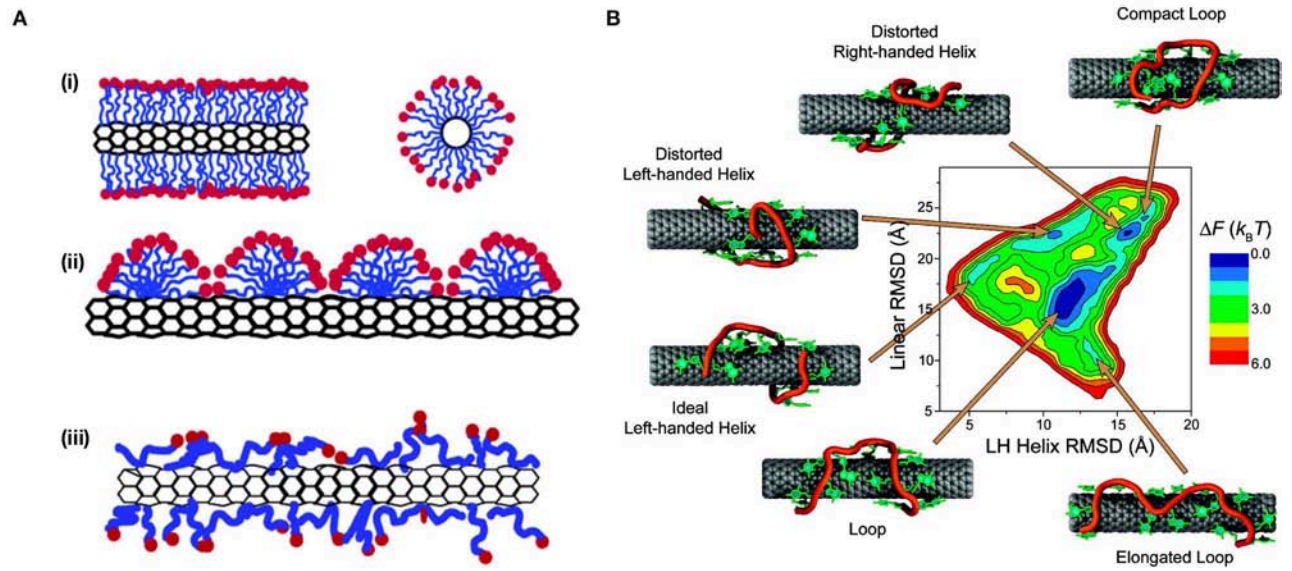

FIGURE 3 | Conformations of non-selective wrappings on SWCNT surface. **(A)** A schematic representation of the various mechanisms by which surfactant molecules interact and disperse SWCNTs. **(i)** Cylindrical micelle encapsulation; **(ii)** Hemimicellar adsorption; and **(iii)** Random adsorption. Reprinted with permission from Yurekli et al. (2004). Copyright © 2004, American Chemical Society. **(B)** Free energy landscape of $(GT)_7$-SWCNT hybrid at room temperature. Representative conformations for each local minimum are displayed. The sugar-phosphate backbone is depicted in orange, and bases are shown in green. Reprinted with permission from Johnson et al. (2009). Copyright © 2009, American Chemical Society.

been linked to quantum yield (Yum et al., 2013; Bonis-O'Donnell et al., 2017, 2019; Beyene et al., 2018).

Toxicity is an additional metric when considering surfactant-suspended SWCNTs for *in vitro* and *in vivo* biosensing applications. Surfactants allow SWCNTs to disperse in water, the universal and biological solvent, permitting researchers to flexibly carry out a variety of environmental, biocompatibility, and safety analyses (Coleman, 2009). However, certain surfactants, such as SDS and SDBS, are known to be cytotoxic to cells even at concentrations as low as 0.05 mg ml^{-1} (Dong et al., 2008), and similar effects have been observed for nanotubes suspended with these surfactants (Dong et al., 2008, 2009). In studies performed by Dong et al. (2008) and Dong et al. (2009), neither the proliferation nor viability of the cells was affected by pristine SWCNTs in the absence of surfactant. Furthermore, conjugates of SWCNTs suspended with various concentrations of SC also showed no negative impact on cell viability and growth, and proliferation was comparable to that of untreated cells. The observed cytotoxicity of the nanotube-surfactant conjugates was therefore believed to be driven by the inherent cytotoxicity of the surfactant in the suspension (Dong et al., 2008, 2009). These studies illustrate the importance surfactant selection in overcoming challenges in toxicity. Although issues such as toxicity can be mitigated through appropriate selection of surfactant type and concentration, surfactant-suspended SWCNTs are limited for biosensing applications due to their lack of inherent selectivity. As a result, current efforts focus on the use of alternative wrappings to suspend SWCNTs, including biopolymers, such as single-stranded DNA (ssDNA) and proteins.

3. BIOPOLYMER-SUSPENDED SWCNTS

DNA is one of the most extensively studied wrappings for optical sensing applications based on Raman, fluorescence, and absorption spectroscopies (Zheng et al., 2003a; Heller et al., 2006; Enyashin et al., 2007; Zhang et al., 2011; Bansal et al., 2013; Kupis-Rozmysłowicz et al., 2016; Wu et al., 2018). The non-covalent functionalization of ssDNA is based on π-stacking of the aromatic nucleotide bases with the sp^2-hybridized side-wall of carbon nanotubes (Zheng et al., 2003a). This arrangement exposes the negatively charged sugar-phosphate backbone of the DNA, which is hydrophilic and easily solvated, toward the water, enabling suspension of the DNA-SWCNT complexes in aqueous solutions (Zheng et al., 2003a). These favorable side-wall-DNA and DNA-water interactions yield suspensions that are facile and stable at room temperature for several months (Zheng et al., 2003a). Work carried out by Zheng et al. (2003a) showed that almost any ssDNA sequence could be used to successfully suspend SWCNTs in the presence of a denaturant and mild sonication. Although atomic force microscopy (AFM) measurements and simulations show DNA to helically self-assemble around the SWCNT (Zheng et al., 2003a,b), the final binding structure has been shown to be sequence-dependent, and short ssDNA strands may also assume other configurations on the nanotube surface (Zheng et al., 2003a; Johnson et al., 2008, 2009) (**Figure 3B**). The sparser surface coverage of the DNA compared to surfactants such as SC exposes a larger carbon surface to water, resulting in a decrease in the intensity and emission energy of the SWCNT fluorescence. For example, the (7,5) chirality undergoes a bathochromic shift of 17.6 meV

(15.6 nm) when wrapped in ssDNA instead of SC due to the greater water accessibility of the DNA wrapping and the resulting increase in the local dielectric constant at the nanotube surface (Jeng et al., 2006; Li and Shi, 2014). Such changes in the local dielectric have been shown to yield an expected fluorescence shift in SWCNT emission peaks (Choi and Strano, 2007).

In addition to the facile suspension procedure and stable assembly, ssDNA benefits from additional features ideal for scale-up sensor design. DNA-wrapped SWCNT suspensions can be further concentrated to achieve dispersion yields as high as 4 mg ml^{-1} (Zheng et al., 2003a). Additionally, the nearly limitless variability in sequence length and composition, as well as the well-established chemistries available for DNA functionalization, make ssDNA an incredibly malleable polymer for tuning the characteristics of the suspended SWCNTs. For example, Zheng et al. modified DNA-SWCNTs at one end with biotin that was used for immobilization onto streptavidin-coated beads (Zheng et al., 2003a). This study demonstrates one of many biochemical approaches for controlling DNA-SWCNT behavior by specifically engineering DNA-SWCNT complexes. Furthermore, both sequence length and base composition has been shown to impact the interaction potential of ssDNA with the surface of SWCNTs (Zheng et al., 2003a; Safaee et al., 2019), which has also recently been shown to vary with SWCNT chirality (Jena et al., 2017; Safaee et al., 2019).

The ability of DNA to form chirality-specific interactions has been exploited for a variety of applications, most notably, chirality separation. Chirality separation is key for multi-modal sensing applications where each chirality selectively responds to a distinct analyte in a solution mixture. Following separation, the individual chiralities can each be functionalized with a wrapping that selectively responds to a particular analyte of interest, and the analyte is detected by monitoring the corresponding wavelength. Many separation mechanisms have been devised (Chattopadhyay et al., 2003; Krupke et al., 2003, 2004; Zheng et al., 2003a,b; Heller et al., 2004; Strano et al., 2004; Huang et al., 2005; Lustig et al., 2005; Arnold et al., 2006; Peng et al., 2006; Zheng and Semke, 2007; Tu and Zheng, 2008; Tu et al., 2009; Zhang et al., 2015) with varying degrees of success; however, a facile approach for scalable, complete and total fractionation into all the single chiralities remains elusive. Aqueous two-phase polymer (ATP) separation (Khripin et al., 2013; Ao et al., 2014, 2016; Ao and Zheng, 2015; Subbaiyan et al., 2015) has emerged at the forefront of methods currently employed in chirality separation. Briefly, an ATP system consists of two separate, but permeable, water phases of slightly different compositions that is created by polymer phase separation (Ao et al., 2016). Studies have shown that the partitioning of DNA-SWCNT complexes has a strong dependence on both the DNA sequence and SWCNT structure (i.e., chirality) (Ao et al., 2014). Moreover, this partitioning can be modulated by changing the polymer compositions of the two phases in order to rescale the hydration energies. For example, the addition of dextran (DX) to a poly-(ethylene glycol)/polyacrylamide (PEG/PAM) system pulls down DNA-SWCNTs from the top to the bottom phase (due to increased hydrophilicity) while the addition of poly(vinylpyrrolidone) (PVP) has the opposite effect. The effectiveness of this method was demonstrated in work carried out by Ao et al. (Khripin et al., 2013; Ao et al., 2014, 2016; Ao and Zheng, 2015), where over 300 DNA sequences were screened using ATP separation techniques, resulting in the isolation of 23 different chiralities.

Aside from their chirality specificity and selectivity, different DNA lengths and sequences have also shown preferences toward molecular recognition with certain analytes (**Figure 4**). Small nucleotide and microRNA sequences are promising biomarkers for a variety of pathologies, including cancer (Harvey et al. , 2017). However, current methods of detection are complex and time-consuming, leading to difficulties in their implementation for point-of-care diagnostics. An advantage of DNA-SWCNT optical sensors is the ability to engineer selectivity toward target oligonucleotides by taking advantage of DNA's natural preference for specific complementary base pairing. Many studies have demonstrated the use of DNA-SWCNTs to quantitatively detect a range of both microRNA and DNA sequences (Jeng et al., 2006, 2010; Bansal et al., 2013; Harvey et al. , 2017). Work carried out by Jeng et al. and Harvey et al. have shown that these fluorescence-based sensors are even capable of detecting single nucleotide polymorphisms (SNPs) (Jeng et al., 2010) and can be multiplexed to detect several sequences simultaneously (Harvey et al. , 2017). In the study by Jeng et al., the addition of complementary DNA is believed to increase the surface coverage of the SWCNT upon hybridization, resulting in a decrease in the effective dielectric constant of the surrounding SWCNT environment and a shifting of the SWCNT fluorescence peak. Similarly, Harvey et al. propose an underlying mechanism based on changes in dielectric constant and electrostatic charge, which can modulate SWCNT emission wavelengths upon hybridization. The fluorescence shifting observed in both studies in response to complementary hybridization is particularly advantageous for detecting diseases, such as heart and kidney disease, as well as various cancers, which can be associated with different combinations of specific microRNA sequences (Etheridge et al., 2011; Hayes et al., 2014; Mishra, 2014; Bertoli et al., 2015; Wang et al., 2016; Hamam et al. , 2017).

In addition to detecting hybridization, DNA-SWCNTs can also be engineered to detect a variety of other molecules, including neurotransmitters, sugars, and peptides (Xu et al., 2007; Kruss et al., 2017; Landry et al., 2017; Bisker et al., 2018), though the underlying mechanism of these sensors remains an ongoing area of research (Bisker et al., 2015; Ulissi et al., 2015). While certain DNA-SWCNT sensors are based on oligonucleotides that act as molecular sieves, like the $(AT)_{15}$-SWCNT sensors designed to detect NO (Zhang et al., 2011), an alternative approach is based on displacement or conformational changes of the DNA wrapping (Heller et al., 2006; Landry et al., 2014, 2017; Salem et al., 2017; Beyene et al., 2018; Gillen et al., 2018). Early studies in this area screened libraries of molecules of interest against SWCNTs suspended using several different DNA sequences by monitoring the changes in the fluorescence emission of these sensors upon addition of the analyte. Through this approach, researchers were able to identify particular sequences with an enhanced affinity to certain chemicals, such as $(AT)_{15}$ toward nitric oxide (NO) (Zhang et al., 2011) (**Figure 4B**) and

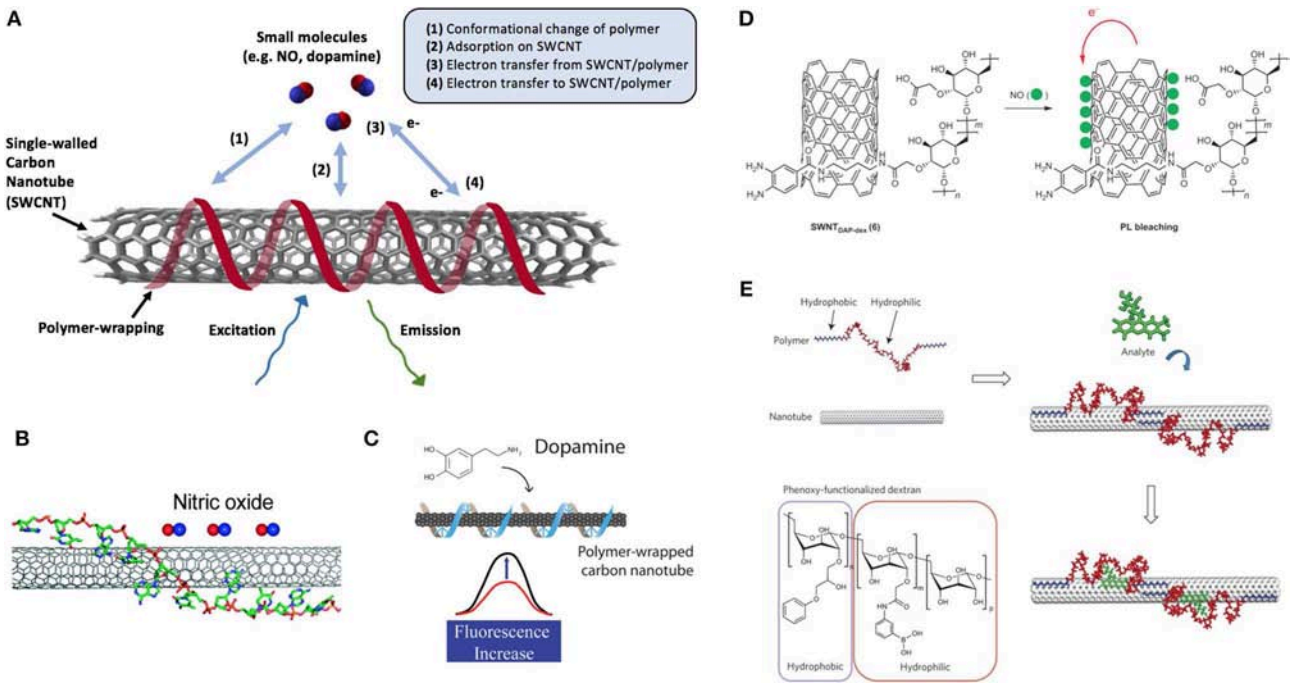

FIGURE 4 | Non-specific interactions of polymer wrappings on SWCNT surface. **(A)** Common mechanisms of interaction between small molecules and polymer-wrapped SWCNTs. **(B)** The optical response of $(AT)_{15}$ DNA oligonucleotide-wrapped SWCNT [$(AT)_{15}$-SWCNT] upon exposure to NO. A side schematic view of one of the several binding structures of $(AT)_{15}$-SCWNT simulated from a HyperChem simulation package. Bases of the DNA stack on the sidewall of the SWCNT, and the sugar-phosphate backbone extends away from the surface. Adapted with permission from Zhang et al. (2011). Copyright © 2011, American Chemical Society. **(C)** Schematic of the fluorescent turn-on sensor for dopamine. Adapted with permission from Kruss et al. (2014). Copyright © 2006, American Chemical Society. **(D)** Schematic illustration for NO detection using SWCNT-polymer hybrids, highlighting the mechanism for near-IR fluorescence bleaching by NO with SWCNT-DAP-dextran complexes. PL = photoluminescence. Reprinted with permission from Kim et al. (2009). Copyright © 2009, Nature Publishing Group. **(E)** A synthetic polymer with an alternating hydrophobic-and-hydrophilic sequence adopting a specific conformation when adsorbed to the nanotube. The polymer is pinned in place to create a favored recognition site for the molecules of interest, leading to either a wavelength or intensity change in SWCNT fluorescence. Adapted with permission from Zhang et al. (2013). Copyright © 2013, Nature Publishing Group.

$(GT)_{15}$ toward catecholamines (Zhang et al., 2011; Kruss et al., 2017; Mann et al., 2017) (**Figure 4C**). Further studies have demonstrated that DNA length can also be used to tune the fluorescence properties of DNA-SWCNT hybrids, offering a new approach to controlling the behavior of these sensors (Jena et al., 2017; Beyene et al., 2018).

Recent studies carried out by Landry et al. and Lee et al. have shown that DNA aptamers on SWCNT scaffolds can be used to detect certain biologically relevant proteins (Landry et al., 2017; Lee et al., 2018). This label-free fluorescence detection offers many advantages over conventional immunological analytical methods, such as enzyme-linked immunosorbent assays (ELISA) or mass spectroscopy, which lack temporal resolution for real-time quantification of protein levels. Furthermore, this method obviates cumbersome purification and labeling steps typically required by more classical approaches. Both RAP1 and HIV-1 (Landry et al., 2017) and platelet-derived growth factor (PDGF) (Lee et al., 2018) were successfully detected using DNA aptamer-SWCNT complexes. Moreover, the RAP1 and HIV-1 sensors were also reported to selectively respond to their target proteins in molecularly complex environments, such as crude, unpurified cell lysates (Landry et al., 2017).

Although DNA-SWCNTs have shown improved selectivity toward small molecules compared to surfactant-SWCNTs (Zhang et al., 2013), they still lag behind their protein- and peptide-based counterparts, which offer exceptional molecular recognition. Proteins are capable of not only differentiating between molecularly similar targets, but also different chiralities of the same molecule. For example, whereas proteins, such as glucose oxidase (GOX) selectively interact with D-glucose (Zubkovs et al., 2017), sensors based on the $(GT)_{15}$ DNA wrapping interact with a family of catecholamines (Kruss et al., 2014, 2017; Mann et al., 2017). Although glucose sensors based on DNA-SWCNTs have also been developed, these sensors ultimately require the addition of GOX for specificity due to the structural similarities of competing sugar molecules. Furthermore, the underlying sensing mechanisms for protein-based sensors are often more clearly identifiable. Their sensing mechanisms are quite diverse, varying from protein charge-transfer (Barone and Strano, 2006; Zubkovs et al., 2017) to exciton quenching due to protein conformational changes (Yoon et al., 2011), both of which have been shown to alter the SWCNT fluorescence intensity.

Protein-based wrappings, however, suffer from their own disadvantages; a lack of precise control during the protein

immobilization process, for example, can result in unfavorable orientations that limit access to the active site (Mohamad et al., 2015). Similarly, structural rearrangements may occur that inhibit, or in some cases destroy, the bioactivity of these molecules (Saifuddin et al., 2013; Antonucci et al., 2017). In addition, protein-based wrappings exhibit limited dispersion efficiency, which has been shown to depend on the protein and is generally less efficient than DNA- and surfactant-based suspensions. Several methods of functionalization have been proposed (Huang et al., 2002; Jiang et al., 2004; Gao and Kyratzis, 2008; Saifuddin et al., 2013; Antonucci et al., 2017) and used to create sensors based on Luciferase-suspended SWCNTs (Kim et al., 2010), AnnexinV-suspended SWCNTs (Neves et al., 2013), and anti-uPA-suspended SWCNTs (Williams et al., 2018), for example. However, these sensors require an intermediate linker or wrapping for stability, as opposed to the non-specific adsorption possible with GOX. In fact, other protein-based glucose sensors, such as those based on glucose-binding protein (Yoon et al., 2011; Yum et al., 2013), typically require more complex conjugative chemistries compared to GOX, highlighting the importance of understanding the underlying protein mechanism when determining the most appropriate method for functionalization. Although these intermediate wrappings can improve solubilization and help maintain protein structure and function on the SWCNT surface, more complex functionalization procedures with multiple conjugation steps could limit the scalability of the sensors.

Irrespective of the improved selectivity offered by DNA and especially protein-suspended SWCNTs, these sensors suffer from relatively low quantum yields compared to surfactant-suspended nanotubes (Haggenmueller et al., 2008). The low intensities restrict the depth at which these biosensors can be implanted for use *in vivo* and *in vitro*. Moreover, studies have shown that both protein- and DNA-SWCNTs are sensitive to local variations in pH (Nepal and Geckeler, 2006; Antonucci et al., 2017) and ionic strength (Heller et al., 2006; Holt et al., 2012; Salem et al., 2017; Gillen et al., 2018). The latter poses additional challenges for biosensing applications, as these ions are often involved in biological signaling pathways (such as Ca^{2+} in dopamine regulation). Therefore, fluctuations in local concentrations throughout the day would compromise the sensing capabilities of the DNA-SWCNT complexes.

4. POLYMER ENGINEERING OF SWCNT SENSOR SPECIFICITY

The tradeoffs between surfactant-suspended SWCNTs and biopolymer-suspended SWCNTs have encouraged researchers to seek an alternative means of detection based on synthetic or bioengineered polymers. *Xeno* nucleic acids (XNAs), for example, have recently been engineered to improve the sensing capabilities of DNA-SWCNTs in ionically complex systems (Gillen et al., 2018). XNAs are synthetic alternatives to naturally occurring DNA and RNA that typically benefit from greater resistivity against nuclease degradation. Due to their modularity, nucleic acids can be readily adjusted using a variety of chemical modifications (Pinheiro and Holliger, 2012; Pinheiro et al., 2013; Ghosh and Chakrabarti, 2016; Ma et al., 2016), and XNAs can contain modifications to either the nucleobase, phosphate, or sugar in an otherwise native oligonucleotide sequence (Pinheiro et al., 2013; Pinheiro and Holliger, 2014; Anosova et al., 2016). Although XNAs were initially developed to emulate the DNA replication processes found in nature, these synthetic oligomers were quickly realized for their advantages in *in vivo* stability and specificity (Wang et al., 2005; Pinheiro and Holliger, 2014; Taylor et al., 2014; Ma et al., 2016). Larger base modifications can result in altered physico-chemical properties, such as a tendency to adopt non-standard helical conformations, but certain chemical modifications to the N7 (in purines) or C5 (in pyrimidines), sites that extend into the major DNA groove, can be reasonably tolerated without significant steric impact (Pinheiro and Holliger, 2012). Backbone modifications can also alter the physico-chemical properties of oligonucleotides. One example is peptide nucleic acid (PNA), where the sugar phosphate backbone is substituted with aminoethylglycine. This substitution results in a charge-neutral polymer that is capable of strong canonical base pairing. The type and extent of the modification depends on the intended application. For example, locked nucleic acid (LNA) can greatly improve the stability of SWCNT sensors in the presence of high ionic concentrations (Gillen et al., 2018). Previous studies showed that salt cations can alter the DNA conformation on the nanotube surface, changing the emission wavelengths (Heller et al., 2006; Salem et al., 2017; Gillen et al., 2018). Since the added methyl bridge in the backbone of LNA increases the rigidity of the polymer, LNA exhibits increased conformation stability in the presence of fluctuating salt concentrations. By modifying 25% of the sequence with a "locked" base, bioengineered sensors based on LNA have been shown to withstand over two orders of magnitude higher salt concentrations without any perturbations in fluorescence. These complexes offer a strong promise for use in ionically complex media, such as blood or urine, without compromising the biocompatibility or nearly inexhaustible sequence space offered by oligonucleotide wrappings. The added chemical modifications also carry untapped potential for further narrowing selectivity through bio-conjugative chemistries that are specific to functional groups in the desired target.

Similarly, recent work by Chio et al. has employed the use of peptoids, N-substituted glycine polymers, to serve as protein molecular recognition elements for SWCNT-based sensors (Chio et al., 2019). These peptoids draw inspiration from biological peptides, with the benefit of greater resistivity against protease degradation (Anosova et al., 2016). The tunability of these sequence-defined synthetic polymers enables greater chemical diversity by providing a larger monomer space of primary amines (Sun and Zuckermann, 2013). Although the stability of the peptoid wrapping on the nanotube surface was shown to vary depending on composition, length, charge and polarity, Chio et al. demonstrated that these sensors could be used to engineer a selective sensor for the fluorescence detection of the lectin protein, wheat germ agglutinin (WGA) (Chio et al., 2019).

In addition to peptoids and oligonucleotide derivatives, purely synthetic heteropolymers have also been used to augment sensor

properties. One such platform uses Corona Phase Molecular Recognition (CoPhMoRe) and relies on SWCNT-adsorbed heteropolymers to template preferential recognition sites for target analytes. The final structures adopted by the polymer on the surface control the selectivity of the sensor toward a target. Though the mechanism for modulating SWCNT fluorescence in response to binding is likely analyte- and polymer-specific, its precise characterization remains an area of active research (Bisker et al., 2015; Ulissi et al., 2015). Typically, the heteropolymers employed contain both hydrophobic and hydrophilic segments. The former interacts with the SWCNT surface, while the latter extends into solution to suspend the complex in aqueous solutions. CoPhMoRe-based sensors have been developed to detect neurotransmitters (Kruss et al., 2013; Zhang et al., 2013; Landry et al., 2014), vitamins (Zhang et al., 2013), and steroids (Zhang et al., 2013), as well as small molecules, such as NO and H_2O_2 (Kim et al., 2009; Iverson et al., 2013; Giraldo et al., 2015) (**Figure 4**).

Furthering the development of these sensors, Bisker et al. (2016) extended the capabilities of CoPhMoRe sensors to detect larger macromolecules, such as proteins. A variant of a CoPhMoRe screening approach was used to identify polymeric wrappings that could be used to create synthetic, non-biological antibody analogs capable of recognizing biological macromolecules. This approach yielded a selective sensor for fibrinogen based on dipalmitoyl-phosphatidylethanolamine (DPPE)-PEG (5 kDa)-suspended SWCNTs. This sensor was capable of detecting fibrinogen in a competitive binding assay in the presence of albumin, which can passivate the sensor by binding to non-specific binding sites (Bisker et al., 2016). This observation suggests that CoPhMoRe is more likely due to a combination of factors related to both the specific corona phase formed by the polymer-SWCNT complex and the unique elongated conformation of the fibrinogen protein, rather than sensing mechanisms based on aggregation, molecular weight, or protein hydrophobicity.

5. CONCLUSIONS AND FUTURE PERSPECTIVE

Since the first reported aqueous suspension of individual SWCNTs with surfactant (O'Connell et al., 2001, 2002; Bachilo et al., 2002), SWCNTs have been suspended using a variety of natural and synthetic wrappings. Polymer wrappings in particular have served the dual purpose of both solubilizing SWCNTs and regulating the selectivity of SWCNTs toward specific analytes in biological media. As a result, polymers such as DNA have become standard wrappings for optical SWCNT-based biosensing, and recent efforts have focused on modifying these polymers to improve the quantum yield, stability, scalability, and selectivity of these sensors. However, with the exception of protein-based wrappings and complementary DNA-strand hybridization, the nature of the selectivity of polymer wrappings toward specific analytes remains unclear. As a result, most DNA and synthetic polymer-based SWCNT sensors are empirically engineered through random library screening and selection. These techniques evaluate the responsivity of several different polymer-wrapped SWCNTs against a variety of analytes, and the polymer-analyte combinations that yield relatively strong fluorescence responses are used to identify suitable polymer wrappings for SWCNT-based sensing (Zhang et al., 2011, 2013). Though this approach has been quite successful in identifying wrappings that can trigger a fluorescence response toward particular analytes, the sensors often show compromised selectivity. Moreover, the polymer wrappings also yield sensors with lower stability and brightness compared to surfactant wrappings.

Studies for new SWCNT optical sensors thus far screen, at most, tens of polymers at a given time (Zhang et al., 2011, 2013), meaning they have only explored a small fraction of the near-infinite polymer sequence space. One approach to overcoming the current limitations of SWCNT sensors is to screen larger polymer libraries in order to increase the chances of identifying a polymer-analyte combination with more favorable sensing properties. An alternative approach to addressing this challenge is to implement more guided techniques, such as directed evolution (Arnold, 1997). Directed evolution uses an iterative approach to improving the properties of materials that lack a defined structure-function relationship. Though the technique is conventionally used to engineer proteins, it was recently applied to engineer DNA wrappings that were shown to improve the quantum yield of an optical SWCNT-based sensor (Lambert et al., 2019). Combined with computational methods, such guided approaches can be used to identify trends between polymer sequence and sensor properties, with the goal of ultimately understanding the underlying mechanism for selectivity and designing molecular probes in a rational and predictive manner.

AUTHOR CONTRIBUTIONS

AG and AB contributed to the research and writing of this manuscript. Both authors have agreed on the final version of the manuscript submitted.

REFERENCES

Angelikopoulos, P., and Bock, H. (2008). Directed self-assembly of surfactants in carbon nanotube materials. *J. Phys. Chem. B* 112, 13793–13801. doi: 10.1021/jp804891a

Angelikopoulos, P., and Bock, H. (2010). The differences in surfactant adsorption on carbon nanotubes and their bundles. *Langmuir* 26, 899–907. doi: 10.1021/la902376b

Angelikopoulos, P., and Bock, H. (2012). The science of dispersing carbon nanotubes with surfactants. *Phys. Chem. Chem. Phys.* 14, 9546–9557. doi: 10.1039/c2cp23436j

Anosova, I., Kowal, E. A., Dunn, M. R., Chaput, J. C., Horn, W. D., and Egli, M. (2016). The structural diversity of artificial genetic polymers. *Nucleic Acids Res.* 44, 1007–1021. doi: 10.1093/nar/gkv1472

Antonucci, A., Kupis-Rozmysłowicz, J., and Boghossian, A. A. (2017). Noncovalent protein and peptide functionalization of single-walled carbon

nanotubes for biodelivery and optical sensing applications. *ACS Appl. Mater. Interfaces* 9, 11321–11331. doi: 10.1021/acsami.7b00810

Ao, G., Khripin, C. Y., and Zheng, M. (2014). DNA-controlled partition of carbon nanotubes in polymer aqueous two-phase systems. *J. Am. Chem. Soc.* 136, 10383–10392. doi: 10.1021/ja504078b

Ao, G., Streit, J. K., Fagan, J. A., and Zheng, M. (2016). Differentiating left- and right-handed carbon nanotubes by DNA. *J. Am. Chem. Soc.* 138, 16677–16685. doi: 10.1021/jacs.6b09135

Ao, G., and Zheng, M. (2015). *Current Protocols in Chemical Biology, Vol. 7*. Hoboken, NJ: John Wiley & Sons, Inc., 43–51.

Arnold, F. H. (1997). Design by directed evolution. *Acc. Chem. Res.* 31, 125–131.

Arnold, M. S., Green, A. A., Hulvat, J. F., Stupp, S. I., and Hersam, M. C. (2006). Sorting carbon nanotubes by electronic structure using density differentiation. *Nat. Nanotechnol.* 1, 60–65. doi: 10.1038/nnano.2006.52

Bachilo, S. M., Strano, M. S., Kittrell, C., Hauge, R. H., Smalley, R. E., and Weisman, R. B. (2002). Structure-assigned optical spectra of single-walled carbon nanotubes. *Science* 298, 2361–2366. doi: 10.1126/science.1078727

Bansal, J., Singh, I., Bhatnagar, P. K., and Mathur, P. C. (2013). DNA sequence detection based on raman spectroscopy using single walled carbon nanotube. *J. Biosci. Bioeng.* 115, 438–441. doi: 10.1016/j.jbiosc.2012.11.002

Barone, P. W., and Strano, M. S. (2006). Reversible control of carbon nanotube aggregation for a glucose affinity sensor. *Angew. Chem. Int. Ed.* 45, 8138–8141. doi: 10.1002/anie.200603138

Bergler, F. F., Stahl, S., Goy, A., Schöppler, F., and Hertel, T. (2016). Substrate-mediated cooperative adsorption of sodium cholate on (6,5) single-wall carbon nanotubes. *Langmuir* 32, 9598–9603. doi: 10.1021/acs.langmuir.6b02759

Bertoli, G., Cava, C., and Castiglioni, I. (2015). Micrornas: new biomarkers for diagnosis, prognosis, therapy prediction and therapeutic tools for breast cancer. *Theranostics* 5, 1122–1143. doi: 10.7150/thno.11543

Beyene, A. G., Alizadehmojarad, A. A., Dorlhiac, G., Streets, A. M., Král, P., Vuković, L., et al. (2018). Ultralarge modulation of single wall carbon nanotube fluorescence mediated by neuromodulators adsorbed on arrays of oligonucleotide rings. *Nano Lett.* 18, 6995–7003. doi: 10.1021/acs.nanolett.8b02937

Bisker, G., Ahn, J., Kruss, S., Ulissi, Z. W., Salem, D. P., and Strano, M. S. (2015). A mathematical formulation and solution of the CoPhMoRe inverse problem for helically wrapping polymer corona phases on cylindrical substrates. *J. Phys. Chem. C* 119:24. doi: 10.1021/acs.jpcc.5b01705

Bisker, G., Bakh, N. A., Lee, M. A., Ahn, J., Park, M., O'Connell, E. B., et al. (2018). Insulin detection using a corona phase molecular recognition site on single-walled carbon nanotubes. *ACS Sens.* 3, 367–377. doi: 10.1021/acssensors.7b00788

Bisker, G., Dong, J., Park, H. D., Iverson, N. M., Ahn, J., Nelson, J. T., et al. (2016). Protein-targeted corona phase molecular recognition. *Nat. Commun.* 7, 1–14. doi: 10.1038/ncomms10241

Blanch, A. J., Lenehan, C. E., and Quinton, J. S. (2010). Optimizing surfactant concentrations for dispersion of single-walled carbon nanotubes in aqueous solution. *J. Phys. Chem. B* 114, 9805–9811. doi: 10.1021/jp104113d

Boghossian, A. A., Zhang, J., Barone, P. W., Reuel, N. F., Kim, J. H., Heller, D. A., et al. (2011). Near-infrared fluorescent sensors based on single-walled carbon nanotubes for life sciences applications. *ChemSusChem* 4, 848–863. doi: 10.1002/cssc.201100070

Bonis-O'Donnell, J. T., Page, R. H., Beyene, A. G., Tindall, E. G., McFarlane, I. R., and Landry, M. P. (2017). Dual near-infrared two-photon microscopy for deep-tissue dopamine nanosensor imaging. *Adv. Funct. Mater.* 27, 1–10. doi: 10.1002/adfm.201702112

Bonis-O'Donnell, J. T. D., Pinals, R., Jeong, S., Thakrar, A., Wolfinger, R., and Landry, M. P. (2019). Chemometric approaches for developing infrared nanosensors to image anthracyclines. *Biochemistry* 58, 54–64. doi: 10.1021/acs.biochem.8b00926

Chattopadhyay, D., Galeska, I., and Papadimitrakopoulos, F. (2003). A route for bulk separation of semiconducting from metallic single-wall carbon nanotubes. *J. Am. Chem. Soc.* 125, 3370–3375. doi: 10.1021/ja028599l

Chio, L., Del Bonis-O'Donnell, J. T., Kline, M. A., Kim, J. H., McFarlane, I. R., Zuckermann, R. N., et al. (2019). Electrostatic assemblies of single-walled carbon nanotubes and sequence-tunable peptoid polymers detect a lectin protein and its target sugars. *Nano Lett.* doi: 10.1021/acs.nanolett.8b04955. [Epub ahead of print].

Choi, J. H., and Strano, M. S. (2007). Solvatochromism in single-walled carbon nanotubes. *Appl. Phys. Lett.*90, 88–91. doi: 10.1063/1.2745228

Coleman, J. N. (2009). Liquid-phase exfoliation of nanotubes and graphene. *Adv. Funct. Mater.* 19, 3680–3695. doi: 10.1002/adfm.200901640

Crochet, J., Clemens, M., and Hertel, T. (2007). Quantum yield heterogeneities of aqueous single-wall carbon nanotube suspensions. *J. Am. Chem. Soc.* 129, 8058–8059. doi: 10.1021/ja071553d

Dong, L., Joseph, K. L., Witkowski, C. M., and Craig, M. M. (2008). Cytotoxicity of single-walled carbon nanotubes suspended in various surfactants. *Nanotechnology* 19:255702. doi: 10.1088/0957-4484/19/25/255702

Dong, L., Witkowski, C. M., Craig, M. M., Greenwade, M. M., and Joseph, K. L. (2009). Cytotoxicity effects of different surfactant molecules conjugated to carbon nanotubes on human astrocytoma cells. *Nanoscale Res. Lett.* 4, 1517–1523. doi: 10.1007/s11671-009-9429-0

Dresselhaus, M. S., Dresselhaus, G., and Saito, R. (1992). Carbon fibers based on C60 and their symmetry. *Phys. Rev. B* 45, 6234–6242. doi: 10.1103/PhysRevB.45.6234

Enyashin, A. N., Gemming, S., and Seifert, G. (2007). DNA-wrapped carbon nanotubes. *Nanotechnology* 18:24. doi: 10.1088/0957-4484/18/24/245702

Etheridge, A., Lee, I., Hood, L., Galas, D., and Wang, K. (2011). Extracellular microRNA: a new source of biomarkers. *Mutat Res.* 717, 85–90. doi: 10.1016/j.mrfmmm.2011.03.004

Gao, Y., and Kyratzis, I. (2008). Covalent immobilization of proteins on carbon nanotubes using the cross-linker 1-ethyl-3-(3-dimethylaminopropyl)carbodiimide–a critical assessment. *Bioconjug. Chem.* 19, 1945–50. doi: 10.1021/bc800051c

Ghosh, S., and Chakrabarti, R. (2016). Spontaneous unzipping of xylonucleic acid assisted by a single-walled carbon nanotube: a computational study. *J. Phys. Chem. B* 120, 3642–3652. doi: 10.1021/acs.jpcb.6b02035

Gillen, A. J., Kupis-Rozmyslowicz, J., Gigli, C., Schürgers, N., and Boghossian, A. A. (2018). Xeno nucleic acid nanosensors for enhanced stability against ion-induced perturbations. *J. Phys. Chem. Lett.* 2018, 4336–4343. doi: 10.1021/acs.jpclett.8b01879

Giraldo, J. P., Landry, M. P., Kwak, S. Y., Jain, R. M., Wong, M. H., Iverson, N. M., et al. (2015). A ratiometric sensor using single chirality near-infrared fluorescent carbon nanotubes: application to *in vivo* monitoring. *Small* 11, 3973–3984. doi: 10.1002/smll.201403276

Haggenmueller, R., Rahatekar, S. S., Fagan, J. A., Chun, J., Becker, M. L., Naik, R. R., et al. (2008). Comparison of the quality of aqueous dispersions of single wall carbon nanotubes using surfactants and biomolecules. *Langmuir* 24, 5070–5078. doi: 10.1021/la703008r

Hamada, N., Sawada, S. I., and Oshiyama, A. (1992). New one-dimensional conductors: graphitic microtubules. *Phys. Rev. Lett.* 68, 1579–1581. doi: 10.1103/PhysRevLett.68.1579

Hamam, R., Hamam, D., Alsaleh, K. A., Kassem, M., Zaher, W., Alfayez, M., et al. (2017). Circulating microRNAs in breast cancer : novel diagnostic and prognostic biomarkers. *Cell Death Dis.* 8:e3045. doi: 10.1038/cddis.2017.440

Harvey, J. D., Jena, P. V., Baker, H. A., Zerze, G. H., Williams, R. M., Galassi, T. V., et al. (2017). A carbon nanotube reporter of microRNA hybridization events *in vivo*. *Nat. Biomed. Eng.* 1, 1–11. doi: 10.1038/s41551-017-0041

Hayes, J., Peruzzi, P. P., and Lawler, S. (2014). MicroRNAs in cancer: biomarkers, functions and therapy. *Trends Mol. Med.* 20, 460–469. doi: 10.1016/j.molmed.2014.06.005

Heller, D. A., Jeng, E. S., Yeung, T.-K., Martinez, B. M., Moll, A. E., Gastala, J. B., et al. (2006). Optical detection of DNA conformational polymorphism on single-walled carbon nanotubes. *Science* 311, 508–511. doi: 10.1126/science.1120792

Heller, D. A., Mayrhofer, R. M., Baik, S., Grinkova, Y. V., Usrey, M. L., and Strano, M. S. (2004). Concomitant length and diameter separation of single-walled carbon nanotubes. *J. Am. Chem. Soc.* 126, 14567–14573. doi: 10.1021/ja046450z

Hertel, T., Himmelein, S., Ackermann, T., Stich, D., and Crochet, J. (2010). Diffusion limited photoluminescence quantum yields in 1-D semiconductors : single-wall carbon nanotubes. *ACS Nano* 4, 7161–7168. doi: 10.1021/nn101612b

Hirsch, A. (2002). Functionalization of single-walled carbon nanotubes. *Angew. Chem. Int. Ed.* 41, 1853–1859. doi: 10.1002/1521-3773(20020603)41:11<1853::AID-ANIE1853>3.0.CO;2-N

Holt, B. D., McCorry, M. C., Boyer, P. D., Dahl, K. N., and Islam, M. F. (2012). Not all protein-mediated single-wall carbon nanotube dispersions are equally bioactive. *Nanoscale* 4, 7425–7434. doi: 10.1039/C2NR31928D

Huang, W., Taylor, S., Fu, K., Lin, Y., Zhang, D., Hanks, T. W., et al. (2002). Attaching proteins to carbon nanotubes via diimide-activated amidation. *Nano Lett.* 2, 311–314. doi: 10.1021/nl010095i

Huang, X., Mclean, R. S., and Zheng, M. (2005). High-resolution length sorting and purification of DNA-wrapped carbon nanotubes by size-exclusion chromatography. *Anal. Chem.* 77, 6225–6228. doi: 10.1021/ac0508954

Islam, M. F., Rojas, E., Bergey, D. M., Johnson, A. T., and Yodh, A. G. (2003). High weight fraction surfactant solubilization of single-wall carbon nanotubes in water. *Nano Lett.* 3, 269–273. doi: 10.1021/nl025924u

Iverson, N. M., Barone, P. W., Shandell, M. A., Trudel, L. J., Sen, S., Sen, F., et al. (2013). *In vivo* biosensing via tissue localizable near infrared fluorescent single walled carbon nanotubes. *Nat. Nanotechnol.* 8, 873–880. doi: 10.1038/nnano.2013.222

Jena, P. V., Safaee, M. M., Heller, D. A., and Roxbury, D. (2017). DNA-carbon nanotube complexation affinity and photoluminescence modulation are independent. *ACS Appl. Mater. Interfaces* 9, 21397–21405. doi: 10.1021/acsami.7b05678

Jeng, E. S., Moll, A. E., Roy, A. C., Gastala, J. B., and Strano, M. S. (2006). Detection of DNA hybridization using the near-infrared band-gap fluorescence of single-walled carbon nanotubes. *Nano Lett.* 6, 371–375. doi: 10.1021/nl051829k

Jeng, E. S., Nelson, J. D., Prather, K. L., and Strano, M. S. (2010). Detection of a single nucleotide polymorphism using single-walled carbon-nanotube near-infrared fluorescence. *Small* 6, 40–43. doi: 10.1002/smll.20090094

Jiang, K., Schadler, L. S., Siegel, R. W., Zhang, X., Zhang, H., and Terrones, M. (2004). Protein immobilization on carbon nanotubes via a two-step process of diimide-activated amidation. *J. Mater. Chem.* 14, 37–39. doi: 10.1039/B31 0359E

Johnson, R. R., Johnson, A. T. C., and Klein, M. L. (2008). Probing the structure of DNA-carbon nanotube hybrids with molecular dynamics. *Nano Lett.* 8, 69–75. doi: 10.1021/nl071909j

Johnson, R. R., Kohlmeyer, A., Johnson, A. T. C., and Klein, M. L. (2009). Free energy landscape of a {DNA}–carbon nanotube hybrid using replica exchange molecular dynamics. *Nano Lett.* 9, 537–541. doi: 10.1021/nl802645d

Kataura, H., Kumazawa, Y., Maniwa, Y., Umezu, I., Suzuki, S., Ohtsuka, Y., et al. (1999). Optical properties of single-wall carbon nanotubes. *Synth. Metals* 103, 2555–2558. doi: 10.1016/S0379-6779(98)00278-1

Kato, Y., Inoue, A., Niidome, Y., and Nakashima, N. (2012). Thermodynamics on soluble carbon nanotubes: how do DNA molecules replace surfactants on carbon nanotubes? *Sci. Rep.* 2, 1–7. doi: 10.1038/srep00733

Khripin, C. Y., Fagan, J. A., and Zheng, M. (2013). Spontaneous partition of carbon nanotubes in polymer-modified aqueous phases. *J. Am. Chem. Soc.* 135, 6822–6825. doi: 10.1021/ja402762e

Kim, J. H., Ahn, J. H., Barone, P. W., Jin, H., Zhang, J., Heller, D. A., et al. (2010). A luciferase/single-walled carbon nanotube conjugate for nearInfrared fluorescent detection of cellular ATP. *Angew. Chem. Int. Ed.* 49, 1456–1459. doi: 10.1002/anie.200906251

Kim, J. H., Heller, D. A., Jin, H., Barone, P. W., Song, C., Zhang, J., et al. (2009). The rational design of nitric oxide selectivity in single-walled carbon nanotube near-infrared fluorescence sensors for biological detection. *Nat. Chem.* 1, 473–481. doi: 10.1038/nchem.332

Krupke, R., Hennrich, F., Kappes, M. M., and Löhneysen, H. V. (2004). Surface conductance induced dielectrophoresis of semiconducting single-walled carbon nanotubes. *Nano Lett.* 4, 1395–1399. doi: 10.1021/nl0493794

Krupke, R., Hennrich, F., Löhneysen, H. V., and Kappes, M. M. (2003). Separation of metallic from semiconducting single-walled carbon nanotubes. *Science* 301, 344–347. doi: 10.1126/science.1086534

Kruss, S., Hilmer, A. J., Zhang, J., Reuel, N. F., Mu, B., and Strano, M. S. (2013). Carbon nanotubes as optical biomedical sensors. *Adv. Drug Deliv. Rev.* 65, 1933–1950. doi: 10.1016/j.addr.2013.07.015

Kruss, S., Landry, M. P., Vander Ende, E., Lima, B. M. A., Reuel, N. F., Zhang, J., et al. (2014). Neurotransmitter detection using corona phase molecular recognition on fluorescent single-walled carbon nanotube sensors. *J. Am. Chem. Soc.* 136, 713–724. doi: 10.1021/ja410433b

Kruss, S., Salem, D. P., Vuković, L., Lima, B., Vander Ende, E., Boyden, E. S., et al. (2017). High-resolution imaging of cellular dopamine efflux using a fluorescent nanosensor array. *Proc. Natl. Acad. Sci. U.S.A.* 114, 1789–1794. doi: 10.1073/pnas.1613541114

Kupis-Rozmysłowicz, J., Antonucci, A., and Boghossian, A. A. (2016). Review - engineering the selectivity of the DNA-SWCNT sensor. *ECS J. Solid State Sci. Technol.* 5, M3067–M3074. doi: 10.1149/2.0111608jss

Lambert, B., Gillen, A. J., Schuergers, N., Wu, S. J., and Boghossian, A. A. (2019). Directed evolution of the optoelectronic properties of synthetic nanomaterials. *Chem. Commun.* 55, 3239–3242. doi: 10.1039/C8CC08670B

Landry, M. P., Ando, H., Chen, A. Y., Cao, J., Kottadiel, V. I., Chio, L., et al. (2017). Single-molecule detection of protein efflux from microorganisms using fluorescent single-walled carbon nanotube sensor arrays. *Nat. Nanotechnol.* 12, 368–377. doi: 10.1038/nnano.2016.284

Landry, M. P., Kruss, S., Nelson, J. T., Bisker, G., Iverson, N. M., Reuel, N. F., et al. (2014). Experimental tools to study molecular recognition within the nanoparticle corona. *Sensors* 14, 16196–16211. doi: 10.3390/s140916196

Lee, K., Nojoomi, A., Jeon, J., Lee, C. Y., and Yum, K. (2018). Near-infrared fluorescence modulation of refolded DNA aptamer-functionalized single-walled carbon nanotubes for optical sensing. *ACS Appl. Nano Mater.* 1:9. doi: 10.1021/acsanm.8b01377

Li, C., and Shi, G. (2014). Carbon nanotube-based fluorescence sensors. *J. Photochem. Photobiol. C Photochem. Rev.* 19, 20–34. doi: 10.1016/j.jphotochemrev.2013.10.005

Liu, Z., Yang, K., and Lee, S.-T. (2011). Single-walled carbon nanotubes in biomedical imaging. *J. Mater. Chem.* 2011, 586–598. doi: 10.1039/C0JM 02020F

Lustig, S. R., Jagota, A., Khripin, C., and Zheng, M. (2005). Theory of structure-based carbon nanotube separations by Ion-exchange chromatography of DNA/CNT hybrids. *J. Phys. Chem. B* 109, 2559–2566. doi: 10.1021/jp0452913

Ma, Q., Lee, D., Tan, Y. Q., Wong, G., and Gao, Z. (2016). Synthetic genetic polymers: advances and applications. *Polym. Chem.* 7, 5199–5216. doi: 10.1039/C6PY01075J

Maeda, Y., Kimura, S. I., Hiroshima, Y., Kanda, M., Lian, Y., Wakahara, T., et al. (2004). Dispersion of single-walled carbon nanotube bundles in nonaqueous solution. *J. Phys. Chem. B* 108, 18395–18397. doi: 10.1021/jp0457242

Mann, F. A., Herrmann, N., Meyer, D., and Kruss, S. (2017). Tuning selectivity of fluorescent carbon nanotube-based neurotransmitter sensors. *Sensors* 17:E1521. doi: 10.3390/s17071521

Matarredona, O., Rhoads, H., Li, Z., Harwell, J. H., Balzano, L., and Resasco, D. E. (2003). Dispersion of single-walled carbon nanotubes in aqueous solutions of the anionic surfactant NaDDBS. *J. Phys. Chem. B* 107, 13357–13367. doi: 10.1021/jp0365099

Mishra, P. J. (2014). MicroRNAs as promising biomarkers in cancer diagnostics. *Biomarker Res.* 2:19. doi: 10.1186/2050-7771-2-19

Mohamad, N. R., Marzuki, N. H. C., Buang, N. A., Huyop, F., and Wahab, R. A. (2015). An overview of technologies for immobilization of enzymes and surface analysis techniques for immobilized enzymes. *Biotechnol. Biotechnol. Equip.* 29, 205–220. doi: 10.1080/13102818.2015.1008192

Moore, V. C., Strano, M. S., Haroz, E. H., Hauge, R. H., Smalley, R. E., Schmidt, J., et al. (2003). Individually suspended single-walled carbon nanotubes in various surfactants. *Nano Lett.* 3, 1379–1382. doi: 10.1021/nl03 4524j

Nepal, D., and Geckeler, K. E. (2006). pH-sensitive dispersion and debundling of single-walled carbon nanotubes: lysozyme as a tool. *Small* 2, 406–412. doi: 10.1002/smll.200500351

Neves, L. F. F., Krais, J. J., Van Rite, B. D., Ramesh, R., Resasco, D. E., and Harrison, R. G. (2013). Targeting single-walled carbon nanotubes for the treatment of breast cancer using photothermal therapy. *Nanotechnology* 24:375104. doi: 10.1088/0957-4484/24/37/375104

Nonoguchi, Y., Tani, A., Murayama, T., Uchida, H., and Kawai, T. (2018). Surfactant-driven amphoteric doping of carbon nanotubes. *Chem. Asian J.* 13, 3942–3946. doi: 10.1002/asia.201801490

O'Connell, M. J., Bachilo, S. M., Huffman, C. B., Rialon, K. L., Boul, P. J., and Noon, W. H. (2002). Band gap fluorescence from individual single-walled carbon nanotubes. *Science* 297, 593–597. doi: 10.1126/science.1072631

O'Connell, M. J., Boul, P., Ericson, L. M., Huffman, C., Wang, Y., Haroz, E., et al. (2001). Reversible water-solubilization of single-walled carbon nanotubes by polymer wrapping. *Chem. Phys. Lett.* 342, 265–271. doi: 10.1016/S0009-2614(01)00490-0

Oh, H., Sim, J., and Ju, S. Y. (2013). Binding affinities and thermodynamics of noncovalent functionalization of carbon nanotubes with surfactants. *Langmuir* 29, 11154–11162. doi: 10.1021/la4022933

Pan, J., Li, F., and Choi, J. H. (2017). Single-walled carbon nanotubes as optical probes for bio-sensing and imaging. *J. Mater. Chem. B* 2017, 6511–6522. doi: 10.1039/C7TB00748E

Peng, H., Alvarez, N. T., Kittrell, C., Hauge, R. H., and Schmidt, H. K. (2006). Dielectrophoresis field flow fractionation of single-walled carbon nanotubes. *J. Am. Chem. Soc.* 128, 8396–8397. doi: 10.1021/ja0621501

Pinheiro, V. B., and Holliger, P. (2012). The XNA world: progress towards replication and evolution of synthetic genetic polymers. *Curr. Opin. Chem. Biol.* 16, 245–252. doi: 10.1016/j.cbpa.2012.05.198

Pinheiro, V. B., and Holliger, P. (2014). Towards XNA nanotechnology: new materials from synthetic genetic polymers. *Trends Biotechnol.* 32, 321–328. doi: 10.1016/j.tibtech.2014.03.010

Pinheiro, V. B., Loakes, D., and Holliger, P. (2013). Synthetic polymers and their potential as genetic materials. *Bioessays* 35, 113–122. doi: 10.1002/bies.201200135

Polo, E., and Kruss, S. (2016). Impact of redox-active molecules on the fluorescence of polymer-wrapped carbon nanotubes. *J. Phys. Chem. C* 120, 3061–3070. doi: 10.1021/acs.jpcc.5b12183

Safaee, M. M., Gravely, M., Rocchio, C., Simmeth, M., and Roxbury, D. (2019). DNA sequence mediates apparent length distribution in single-walled carbon nanotubes. *ACS Appl. Mater. Interfaces* 11, 2225–2233. doi: 10.1021/acsami.8b16478

Saifuddin, N., Raziah, A. Z., and Junizah, A. R. (2013). Carbon nanotubes: a review on structure and their interaction with proteins. *J. Chem.* 2013:676815. doi: 10.1155/2013/676815

Saito, R., Dresselhaus, G., and Dresselhaus, M. S. (1992). Electronic structure of double-layer graphene tubules. *J. Appl. Phys.* 60, 2204–2206. doi: 10.1063/1.107080

Salem, D. P., Gong, X., Liu, A. T., Koman, V. B., Dong, J., and Strano, M. S. (2017). Ionic strength mediated phase transitions of surface adsorbed DNA on single-walled carbon nanotubes. *J. Am. Chem. Soc.* 139, 16791–16802. doi: 10.1021/jacs.7b09258

Strano, M. S., Zheng, M., Jagota, A., Onoa, G. B., Heller, D. A., Barone, P. W., et al. (2004). Understanding the nature of the DNA-assisted separation of single-walled carbon nanotubes using fluorescence and raman spectroscopy. *Nano Lett.* 4, 543–550. doi: 10.1021/nl034937k

Subbaiyan, N. K., Parra-Vasquez, A. N. G., Cambré, S., Cordoba, M. A., Yalcin, S. E., Hamilton, C. E., et al. (2015). Bench-top aqueous two-phase extraction of isolated individual single-walled carbon nanotubes. *Nano Res.* 8, 1755–1769. doi: 10.1007/s12274-014-0680-z

Sun, J., and Zuckermann, R. N. (2013). Peptoid polymers: A highly designable bioinspired material. *ACS Nano* 7, 4715–4732. doi: 10.1021/nn4015714

Sun, Z., Nicolosi, V., Rickard, D., Bergin, S. D., Aherne, D., and Coleman, J. N. (2008). Quantitative evaluation of surfactant-stabilized single-walled carbon nanotubes: Dispersion quality and its correlation with zeta potential. *J. Phys. Chem. C* 112, 10692–10699. doi: 10.1021/jp8021634

Taylor, A. I., Arangundy-Franklin, S., and Holliger, P. (2014). Towards applications of synthetic genetic polymers in diagnosis and therapy. *Curr. Opin. Chem. Biol.* 22, 79–84. doi: 10.1016/j.cbpa.2014.09.022

Tu, X., Manohar, S., Jagota, A., and Zheng, M. (2009). DNA sequence motifs for structure-specific recognition and separation of carbon nanotubes. *Nature* 460, 250–253. doi: 10.1038/nature08116

Tu, X., and Zheng, M. (2008). A DNA-based approach to the carbon nanotube sorting problem. *Nano Res.* 1, 185–194. doi: 10.1007/s12274-008-8022-7

Tummala, N. R., Morrow, B. H., Resasco, D. E., and Striolo, A. (2010). Stabilization of aqueous carbon nanotube dispersions using surfactants: insights from molecular dynamics simulations. *ACS Nano* 4, 7193–7204. doi: 10.1021/nn101929f

Tummala, N. R., and Striolo, A. (2008). Role of counterion condensation in the self-assembly of SDS surfactants at the water-graphite interface. *J. Phys. Chem. B* 112, 1987–2000. doi: 10.1021/jp077678m

Tummala, N. R., and Striolo, A. (2009). SDS surfactants on carbon nanotubes. *ACS Nano* 3, 595–602. doi: 10.1021/nn8007756

Ulissi, Z. W., Zhang, J., Sresht, V., Blankschtein, D., and Strano, M. S. (2015). 2D equation-of-state model for corona phase molecular recognition on single-walled carbon nanotube and graphene surfaces. *Langmuir* 31, 628–636. doi: 10.1021/la503899e

Vo, M. D., and Papavassiliou, D. V. (2017). Effects of temperature and shear on the adsorption of surfactants on carbon nanotubes. *J. Phys. Chem. C* 121, 14339–14348. doi: 10.1021/acs.jpcc.7b03904

Vo, M. D., Shiau, B., Harwell, J. H., and Papavassiliou, D. V. (2016). Adsorption of anionic and non-ionic surfactants on carbon nanotubes in water with dissipative particle dynamics simulation. *J. Chem. Phys.* 144:204701. doi: 10.1063/1.4949364

Wang, H., Zhou, W., Ho, D. L., Winey, K. I., Fischer, J. E., Glinka, C. J., et al. (2004). Dispersing single-walled carbon nanotubes with surfactants: a small angle neutron scattering study. *Nano Lett.* 4, 1789–1793. doi: 10.1021/nl048969z

Wang, J., Chen, J., and Sen, S. (2016). MicroRNA as biomarkers and diagnostics. *J. Cell. Physiol.* 231, 25–30. doi: 10.1002/jcp.25056

Wang, L., Yang, C. J., Medley, C. D., Benner, S. A., and Tan, W. (2005). Locked nucleic acid molecular beacons. *J. Am. Chem. Soc.* 127, 15664–15665. doi: 10.1021/ja052498g

Wenseleers, W., Vlasov, I. L., Goovaerts, E., Obraztsova, E. D., Lobach, A. S., and Bouwen, A. (2004). Efficient isolation and solubilization of pristine single-walled nanotubes in bile salt micelles. *Adv. Funct. Mater.* 14, 1105–1112. doi: 10.1002/adfm.200400130

White, B., Banerjee, S., O'Brien, S., Turro, N. J., and Herman, I. P. (2007). Zeta-potential measurements of surfactant-wrapped individual single-walled carbon nanotubes. *J. Phys. Chem. C* 111, 13684–13690. doi: 10.1021/jp070853e

Wildoer, J. W. G., Venema, L. C., Rinzler, A. G., Smalley, R. E., and Dekker, C. (1998). Electronic structure of atomically resolved carbonnanotubes. *Nature* 391, 59-62. doi: 10.1038/34139

Williams, R. M., Lee, C., and Heller, D. A. (2018). A fluorescent carbon nanotube sensor detects the metastatic prostate cancer biomarker uPA. *ACS Sens.* 3, 1838–1845. doi: 10.1021/acssensors.8b00631

Wu, S.-J., Schürgers, N., Lin, K.-H., Gillen, A. J., Corminboeuf, C., and Boghossian, A. A. (2018). Restriction enzyme analysis of double-stranded DNA on pristine single-walled carbon nanotubes. *ACS Appl. Mater. Interfaces* 10, 37386–37395. doi: 10.1021/acsami.8b12287

Xin, X., Xu, G., and Li, H. (2013). "Dispersion and property manipulation of carbon nanotubes by self-assemblies of amphiphilic molecules," in *Physical and Chemical Properties of Carbon Nanotubes*, ed S. Suzuki (IntechOpen).

Xu, J., Mueller, R., Hazelbaker, E., Zhao, Y., Bonzongo, J. C. J., Clar, J. G., et al. (2017). Strongly bound sodium dodecyl sulfate surrounding single-wall carbon nanotubes. *Langmuir* 33, 5006–5014. doi: 10.1021/acs.langmuir.7b00758

Xu, Y., Pehrsson, P. E., Chen, L., Zhang, R., and Zhao, W. (2007). Double-stranded DNA single-walled carbon nanotube hybrids for optical hydrogen peroxide and glucose sensing. *J. Phys. Chem. C* 111, 8638–8643. doi: 10.1021/jp0709611

Yoon, H., Ahn, J. H., Barone, P. W., Yum, K., Sharma, R., Boghossian, A. A., et al. (2011). Periplasmic binding proteins as optical modulators of single-walled carbon nanotube fluorescence: amplifying a nanoscale actuator. *Angew. Chem. Int. Ed.* 50, 1828–1831. doi: 10.1002/anie.201006167

Yum, K., McNicholas, T. P., Mu, B., and Strano, M. S. (2013). Single-walled carbon nanotube-based near-infrared optical glucose sensors toward *in vivo* continuous glucose monitoring. *J. Diabetes Sci. Technol.* 7, 72–87. doi: 10.1177/193229681300700109

Yurekli, K., Mitchell, C. A., and Krishnamoorti, R. (2004). Small-angle neutron scattering from surfactant-assisted aqueous dispersions of carbon nanotubes. *J. Am. Chem. Soc.*126, 9902–9903. doi: 10.1021/ja047451u

Zhang, J., Boghossian, A. A., Barone, P. W., Rwei, A., Kim, J. H., Lin, D., et al. (2011). Single molecule detection of nitric oxide enabled by d(AT)15DNA adsorbed to near infrared fluorescent single-walled carbon nanotubes. *J. Am. Chem. Soc.* 133, 567–581. doi: 10.1021/ja1084942

Zhang, J., Landry, M. P., Barone, P. W., Kim, J.-H., Lin, S., Ulissi, Z. W., et al. (2013). Molecular recognition using corona phase complexes made of synthetic polymers adsorbed on carbon nanotubes. *Nat. Nanotechnol.* 8, 959–968. doi: 10.1038/nnano.2013.236

Zhang, M., Khripin, C. Y., Fagan, J. A., McPhie, P., Ito, Y., and Zheng, M. (2015). Single-step total fractionation of single-wall carbon nanotubes

by countercurrent chromatography. *Anal. Chem.* 86, 3980–3984. doi: 10.1021/ac5003189

Zheng, M., Jagota, A., Semke, E. D., Diner, B. A., McLean, R. S., Lustig, S. R., et al. (2003a). DNA-assisted dispersion and separation of carbon nanotubes. *Nat. Mater.* 2, 338–342. doi: 10.1038/nmat877

Zheng, M., Jagota, A., Strano, M. S., Santos, A. P., Barone, P. W., Chou, S. G., et al. (2003b). Structure-based carbon nanotube sorting by sequence-dependent DNA assembly. *Science* 302, 1545–1548. doi: 10.1126/science.1091911

Zheng, M., and Semke, E. D. (2007). Enrichment of single chirality carbon nanotubes. *J. Am. Chem. Soc.* 129, 6084–6085. doi: 10.1021/ja071577k

Zheng, Y., Bachilo, S. M., and Weisman, R. B. (2017). Quenching of single-walled carbon nanotube fluorescence by dissolved oxygen reveals selective single-stranded DNA affinities. *J. Phys. Chem. Lett.* 8, 1952–1955. doi: 10.1021/acs.jpclett.7b00583

Zubkovs, V., Schuergers, N., Lambert, B., Ahunbay, E., and Boghossian, A. A. (2017). Mediatorless, reversible optical nanosensor enabled through enzymatic pocket doping. *Small* 13:1701654. doi: 10.1002/smll.201701654

Conflict of Interest Statement: The authors declare that the research was conducted in the absence of any commercial or financial relationships that could be construed as a potential conflict of interest.

Copyright © 2019 Gillen and Boghossian. This is an open-access article distributed under the terms of the Creative Commons Attribution License (CC BY). The use, distribution or reproduction in other forums is permitted, provided the original author(s) and the copyright owner(s) are credited and that the original publication in this journal is cited, in accordance with accepted academic practice. No use, distribution or reproduction is permitted which does not comply with these terms.

frontiers in Chemistry

REVIEW
published: 03 July 2019
doi: 10.3389/fchem.2019.00456

Noble Metal Based Alloy Nanoframes: Syntheses and Applications in Fuel Cells

Farhat Nosheen[1], Tauseef Anwar[2], Ayesha Siddique[3] and Naveed Hussain[4]*

[1] Department of Chemistry, University of Education, Jauharabad, Pakistan, [2] Department of Physics, The University of Lahore, Lahore, Pakistan, [3] Sulaiman bin Abdullah Aba Al-Khail-Centre for Interdisciplinary Research in Basic Sciences, International Islamic University Islamabad, Islamabad, Pakistan, [4] State Key Laboratory of New Ceramics and Fine Processing, School of Materials Science and Engineering, Tsinghua University, Beijing, China

Noble metal nanostructures are being used broadly as catalysts for energy conversion in fuel cells. To overcome the future energy crises, fuel cells are anticipated as clean energy sources because they can be operated at low temperature, their energy conversion is high and their carbon release is almost zero. However, an active and stable electrocatalyst is essential for the electrochemical reactions in fuel cells. Therefore, properties of the nanostructures greatly depend on the shape of the nanostructures. Individual as well as interaction properties are greatly affected by changes in the surface area of the nanostructures. By shape controlled synthesis, properties of the nanostructures could be further enhanced by increasing the surface area or active sites for electrocatalysts. Therefore, an efficient approach is needed for the fabrication of nanostructures to increase their efficiency, activity, or durability in fuel cells by reducing the usage of noble metals. Different types of hollow nanostructures until now have been prepared including nanoboxes, nanocages, nanoshells, nanoframes (NFs), etc. NFs are the hollow unique three-dimensional structure which have no walls—they only contain corners or edges so they have large surface area. In electrocatalytic reactions, the molecules involved in the reaction can easily reach the inner surface of the nanoframes, thus noble metals' utilization efficiency increases. NFs usually have high surface area, greater morphological and compositional stabilities, allowing them to withstand harsh environmental conditions. By considering the current challenges in fabrication of noble metal based alloy NFs as electrocatalysts, this review paper will highlight recent progress, design, and fabrication of noble metal alloy NFs through different strategies—mainly photocatalytic template, electrodeposition, Kirkendall effect, galvanic replacement, chemical/oxidative etching, combination of both and other methods. Then, electrochemical applications of NFs in fuel cells toward formic acid, methanol, ethanol, oxygen reduction reaction as well as bifunctional catalyst will also be highlighted. Finally, we will summarize different challenges in the fabrication of highly proficient nanocatalysts for the fuel cells with low cost, high efficiency and high durability, which are the major issues for the highly commercial use of fuel cells in the future.

Keywords: nanoframes, fuel cells, alloy, nanocages, multimetallic

OPEN ACCESS

Edited by:
Angang Dong,
Fudan University, China

Reviewed by:
Syed Mubeen Jawahar Hussaini,
The University of Iowa, United States
Liqiang Xu,
Shandong University, China

****Correspondence:***
Farhat Nosheen
maha.noshi@gmail.com

Specialty section:
This article was submitted to Nanoscience, a section of the journal Frontiers in Chemistry

Received: *02 February 2019*
Accepted: *07 June 2019*
Published: *03 July 2019*

Citation:
Nosheen F, Anwar T, Siddique A and Hussain N (2019) Noble Metal Based Alloy Nanoframes: Syntheses and Applications in Fuel Cells. Front. Chem. 7:456. doi: 10.3389/fchem.2019.00456

INTRODUCTION

Noble metal nanostructures are being used broadly as catalysts for energy conversion in fuel cells. To overcome the future energy crises, fuel cells are anticipated as clean energy sources. Noble metals such as platinum (Pt) as well as palladium (Pd) are the most important and effective catalysts in fuel cells, but increasing the catalyst efficiency as well as cost reduction of catalysts is a great challenge. By tuning the size, composition, and morphology, electrocatalytic activity could be enhanced (Ding et al., 2012; Wang et al., 2013, 2015a; Zhang et al., 2018b). Recent research efforts have been focused on (1) the addition of cheap transition metals to decrease the cost and improve the electronic effect of Pt, (2) tuning the morphologies with high index facets, ultrathin walls and 3D surface accessibility, (3) NF architecture which shows the 3D surface with high catalytic surface area as well as large utilization of precious metals, (4) composition segregation of Pt on the edges and corners of NFs to increase the Pt usage. Furthermore, it is very necessary to fabricate the novel nanocatalyst with both higher activity as well as stability.

Pt content could be reduced without compromising the catalytic properties by changing the solid nanostructures into hollow nanostructures with ultrathin walls and with controlled surface composition. The advantage of hollow structures over the solid particles is that Pt atoms in solid nanoparticles are unexploited because they cannot participate in electrocatalytic reactions. However, the empty interior of nanocages and nanoframe allows the reactants to interact with 3D interior and exterior surfaces in catalytic reactions (Fang et al., 2015). Moreover, atomic scale ultrathin walls below 2 nm can further improve the electrocatlytic applications. In previous studies, a lot of hollow as well as nanocage structures have been fabricated, but NF architectures—especially bi-and multimetallic NFs—have not received more attention. Attaining NFs with controlled size, highly open structure, 3D surface area, control thickness, and stable shell is a more difficult task. In recent years, some groups have been interested in the atomic scale synthesis of bi- and multimetallic NFs due to their excellent electrocatalytic activity as well as durability in fuel cells. In this review, we will highlight the state-of-the-art accomplishments on NFs and will discuss the growth mechanism, which includes the photocatalytic template method, electrodeposition, Kirkendall effect, galvanic replacement reaction, oxidative/chemical etching, and others. In previous years, researchers have fabricated the single component noble metal hollow, nanocages and NFs, but few have focused on the fabrication of noble metal based bimetallic and multimetallic NFs for fuel cells.

SYNTHETIC METHODOLOGIES FOR NANOFRAMES

Photocatalytic Template Synthesis

Template based synthesis has been widely employed for the synthesis of various hollow nanostructures (Bai et al., 2011). Photocatalytic-based hard and soft template synthesis has been used by a few groups to synthesize Pt nanocages. For example, Shi et al. developed Pt nanocages by using the liposomes as a template in which photocatalyst molecules were present. In this protocol, firstly hydrophobic Sn^{IV} octaethylporphyrin (SnOEP) has been integrated into unilamellar liposomes. After that, platinum seeds were formed due to photo-catalytic reduction of Pt salts and converted in the form of dendritic Pt-nanosheets. Then these dendritic nanosheets combined with each other inside the bilayer and evolved into nanocages. The dendritic nanosheets after combining with each other adopted the spherical structure of the liposomal template with a 2 nm thick wall and 200 nm nanocages. The synthesized Pt nanocages contain hollow voids and additional porosity, which may be beneficial for extensive applications (Shi et al., 2015). Moreover, Wang et al. developed 3D Pt nanocages by simple photocatalytic template procedure. The synthetic procedure was carried out in the presence of TiO_2 NPs that not only worked as photocatalyst but also as template. In synthesis, Pt uniform interlinked branches first formed by the increased amount of Pt precursors and reducing the intensity of light. Then, these nanobranches were photo-deposited on a TiO_2 template by irradiating the UV light without any surfactants or capping agents. After template removal, 3D Pt nanocages were attained with high surface area as well as more active sites showing them to be an active catalyst for MOR. By the photocatalytic template method, nanocages of different shapes and sizes could be synthesized by varying the exposure of light, amount of metal precursors, and size of template (Zhu et al., 2015).

Electrodeposition Method

The electrodeposition method consists of the deposition of a substance on substrate by introducing an electric current. This method is used for the fabrication of solid particles with very low porosity. However, for the creation of metal based NFs, this technique is also coupled with other strategies like chemical etching as well as electroleaching. For instance, Moghimi et al. developed FeNi NFs by the electrodeposition and electroleaching technique (Moghimi et al., 2013). The electrodeposition technique combined with chemical etching could be employed to fabricate various NFs. For example, Torimoto et al. synthesized Au NFs by the preferred electrodeposition of Au on the edges and corners of Ag cubic particles treated with the 1-octanethiol, and then chemical etchants (hydrogen peroxide and sulfuric acid) were used to chemically etch Ag particles. In this method, Ag has been used as a template, and dissolution of Ag template has not been observed during the deposition process of Au. This strategy could be used for the fabrication of NFs where simultaneous dissolution of the template needs to be avoided during electro-deposition of second material. Moreover, electrodeposition favors the formation of metal NPs irrespective of metal and their reduction potential. This method has rarely been used for synthesis of noble metal-based alloy nanoframes (Okazaki et al., 2009).

Kirkendall Effect

The Kirkendall effect is a vacancy mediated technique which is based on the net mass flow of faster diffusing species, and it is balanced by the opposing flow of vacancies. This method is useful for the synthesis of hollow and porous NCs because

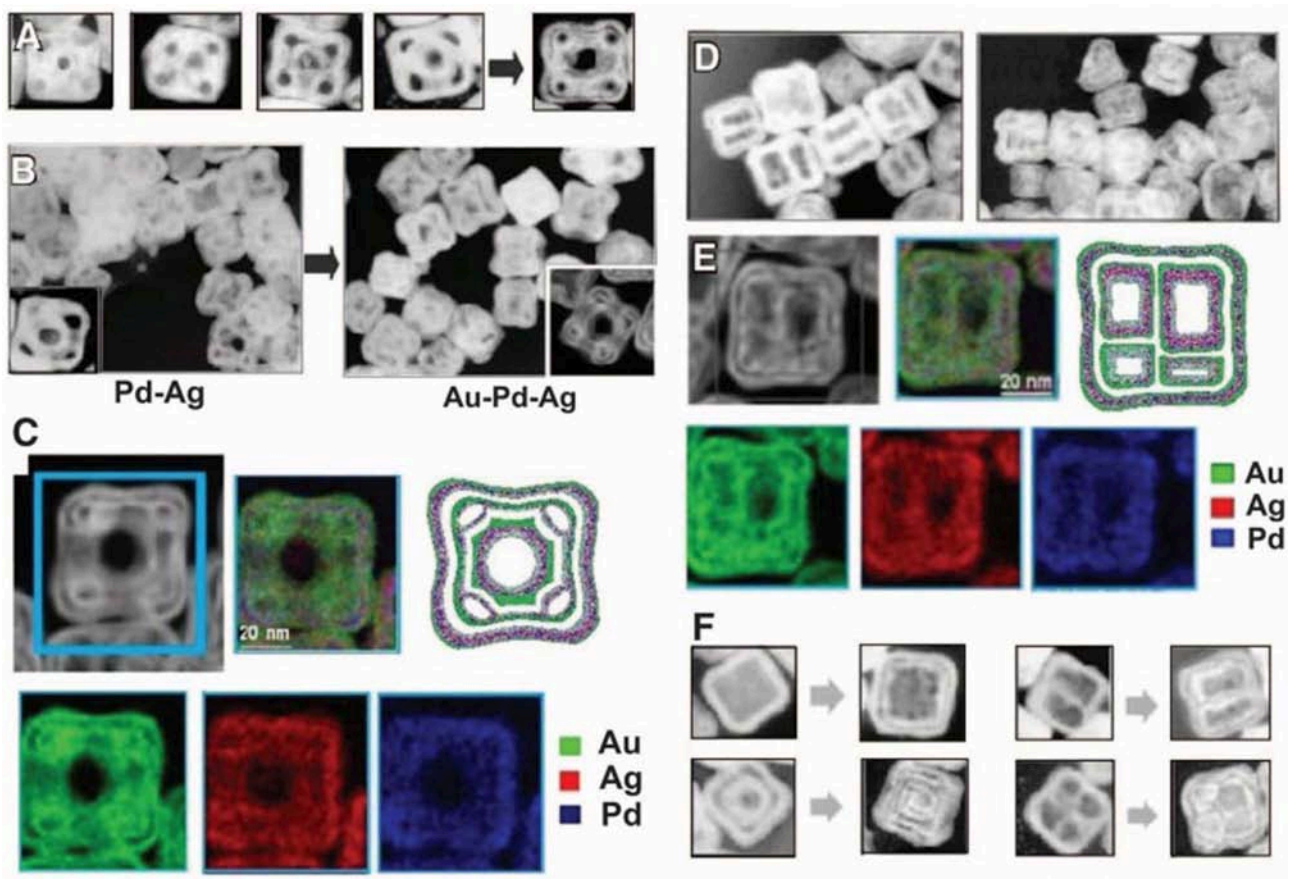

FIGURE 1 | (A) TEM images illustrating the stages of formation of hollow nanostructures by sequential action of galvanic replacement and Kirkendall effect. **(B)** TEM images showing the nanostructures dominated by galvanic replacement using palladium (left) and by Kirkendall effect using gold (right). **(C)** HAADF-STEM image and corresponding EDX elemental maps. **(D)** TEM images of multichambered NPs. **(E)** HAADF-STEM detail and corresponding EDX elemental maps. **(F)** TEM images of different structures produced by sequential action of galvanic replacement and Kirkendall effect. Adapted with permission from González et al. (2011) Copyright 2011, American Association for the Advancement of Science.

it is a diffusion procedure. González et al. used sequential galvanic replacement reaction or the Kirkendall effect at room temperature to synthesize polymetallic hollow nanocrystals (NCs) with complicated shapes and compositions such as trimetallic Pd-Au-Ag nanoboxes (González et al., 2011), as shown in **Figure 1**. Han et al. developed the Cu_3Pt NFs with unique morphology by a transformation process. The Kirkendall effect is not commonly used for noble metal alloy NFs, so we will focus more on other methods.

Galvanic Replacement Reaction

The galvanic replacement reaction is extensively employed to synthesize metal NCs with hollow interiors such as nanocages, nanoboxes, and NFs. The template oxidizes and dissolves during the galvanic replacement reaction, meanwhile metal ions reduce, and deposit on the template surface. The discrepancy of the two metals in redox potential is the driving force of the galvanic replacement. However, the structure of the NCs may be controlled by tuning the metal to salt ratio, quantity and the shape of the template. The same sacrificial template facets have the simultaneous removal of template and the deposition of atoms on all the facets. In the template containing distinct facets, the galvanic replacement reaction adopted the facet selectively. Atoms are dissolved at higher surface energy and deposited on the lower energy facets. In addition, template based, and one pot strategy are the two main methods to carry the galvanic replacement reaction (Xia et al., 2013).

Template Based Galvanic Replacement Method

Ag metal has a lower reduction potential in comparison with the other metals such as Pd, Au, etc. Due to this property, it is easy to remove the atoms by the galvanic replacement reaction, and it makes Ag the most efficient sacrificial template for the synthesis of hollow nanostructures. For instance, Mahmoud and El-Sayed have developed the double shell nanocages of different sizes with controlled thickness and used the Ag as template (Mahmoud and El-Sayed, 2012). In this protocol, the Ag template has been employed because at elevated temperatures single-crystalline Ag particles formed, which may produce the single

crystalline hollow structures in cases where the lattice of Ag and other metals match well. The size of templates was controllable from a few to 250 nm, which produced the hollow structures of different sizes. Synthesis of Ag template could be done with high yield. PVP is a good capping agent for Ag NC synthesis and it is appropriate for other metals as well, therefore the capping of the Ag template is also suitable for the synthesis of hollow structures and prevents their aggregation. In addition, the bowl-like morphology of PtAuAg nanocages was synthesized by using the seed mediated and galvanic replacement procedure (Xu et al., 2018) in which Ag seeds were used as a template. However, experiments in different optimized conditions were able to fabricate the structures which have time dependence and also depend on cetyltrimethylammonium chloride (CTAC). Due to their structure and synergetic effect of Pt, Au, and Ag, the final PtAuAg nanocatalyst exhibits higher catalytic performance. Furthermore, similar to the Ag template, Pd NCs were also used as sacrificial templates for the fabrication of PdPt hollow nanocages via the galvanic reaction as well as the co-reduction method. In another report, Xia et al. developed PdPt nanocages through a co-reduction approach along hollow centers by a combination of galvanic replacement by using Pd nanocubes as a sacrificial template and K_2PtCl_4 in presence of citric acid. Meanwhile higher concentrations of bromide and $PtCl_4^{-2}$ at elevated temperatures accelerated the galvanic replacement and produced PdPt alloy nanocages (Zhang et al., 2011). However, by replacing the citric acid with the ascorbic acid (AA), PdPt nanodendrites were gained because of the faster depletion of Pt precursors and the decreased rate of the galvanic replacement reaction. For instance, Han et al. have fabricated PdPt octahedral and cubic nanocages with hollow interiors containing porous walls by using Pd octahedra and cubic NCs as sacrificial templates. Change in the ratio of AA could control the galvanic replacement reaction and gives the PdPd alloys with distinct shapes (Hong et al., 2012a).

In addition to metal templates, metal oxide NCs have also been used as a template. Chen et al. fabricated flower shaped PdCu nanocages by utilizing the corner etched Cu_2O octaherda as a template through a facile and simple procedure. By adding the H_2PdCl_4, Cu_2O were hybridized to generate the Cu_2O@PdCu core shell, and etching of Cu_2O was done by $NH_3.H_2O$. These flower shaped nanocages of PdCu were used for the MOR that shows the higher catalytic activity, excellent stability, and more poison tolerance. These alloy nanoarchitectures were developed by the galvanic reaction and disproportionation reaction (Chen et al., 2018). Similar work is also reported by the other research group, where they used Cu_2O as a sacrificial template and distinct reducing agents to gain the cubic PtCu nanocage by redox reactions (Tian et al., 2014).

One-Pot Galvanic Replacement Method

Using the pre-synthesized templates like Pd or Ag in the synthesis of hollow nanostructures has more limitations as the synthetic procedure requires more steps such as template synthesis, shell growth as well as template removal, which limits the practical use. Use of the noble metals like Pd or Ag as sacrificial template also wastes the expensive materials and the final morphology is limited to the initial shape of the parent templates. Alternatively, to synthesize metal alloy NFs through one pot procedure is more difficult as compared to monometallic NCs because the insertion of the second metal makes the reduction more difficult. The standard reduction potential of noble metals is higher in comparison with the non-noble metals, while for the alloy NC synthesis the reduction potential difference among the two metals should be decreased. For this purpose, some ligands could be used in order to decrease the reduction rate of the two metals. Another way to reduce the reduction potential is to combine the metal cations with coordinating agents like halide ions, which more strongly coordinate with the noble metals. In one report, Huang et al. (2009) introduced iodide ions to the mixture of $Pd(acac)_2$]/[$Pt(acac)_2$] in solution of DMF, which produced $[PdI_4]^{2-}$ as the most dominating precursors, and Pd reduced the Pt ions early. Furthermore, cubic $PtCu_3$ nanocages were also developed by optimizing the reduction rate by the addition of cetyltrimethylammonium bromide (CTAB) as well as Pt and Cu species. From the above explanations, it is noticed that the CTAB in oleylamine works as a co-reductant, which tuned the Pt and Cu species reduction speed, and Cu ions are reduced before the Pt ions while the reduction rate of the Cu pair is more negative than the Pt pair (Xia et al., 2012).

Similarly, Zhang et al. reported the synthesis of PtCu yolk-cage like NCs through glycine mediated reduction kinetics. By changing the amount of glycine, morphology as well as composition of the NCs were controlled, and in this method glycine is used as a co-reductant and surface controller. Glycine may coordinate with the metal ions and when the medium is aqueous it strongly coordinates with Pt^{4+} instead of Cu^{2+}. Subsequently, platinum ions' reaction to reduced copper nanocrysrtals by galvanic replacement leads to a Pt–Cu yolk cage structure. As compared to hollow structures or nanocages, NFs are open, have 3D surface accessibility and more active sites (Zhang et al., 2013). In addition to the above examples of nanocages, we also fabricated the single crystalline octahedral PtCu NFs, which involve the synergetic effect of OH and amine groups of ethanolamine and concentration of glycine also effect the reduction rate. However, here it was also observed that the coordinating ligands changed the reduction rate of metals and make galvanic replacement reaction more feasible (Nosheen et al., 2013) (**Figures 2a,b**). The same method was also adopted by Zhang's group, and they vary the time of reaction as well as temperature to gain the multiple twinned NFs. It is very rare to fabricate the multiple twined noble metal NFs (**Figures 2c,d**). Twin defects in the metal nanoarchitecture would modulate their electronic structure as well as surface reactivity and could enhance the catalytic performance. In case of twin configuration, the decahedron is the most compact pentagonal cyclic twined shape along the D_5h symmetry and shows excellent catalytic applications. It is also observed that the twin defects act as a nucleation site which induces the generation of a highly anisotropic design and, as a result of symmetry breaking of the crystal lattice, gives more active sites for electrocatalysis. In addition, unique 5-fold twin PtCu NFs were also fabricated along nanothorn protruding from their edges. Meanwhile time dependence experimental analysis shows that

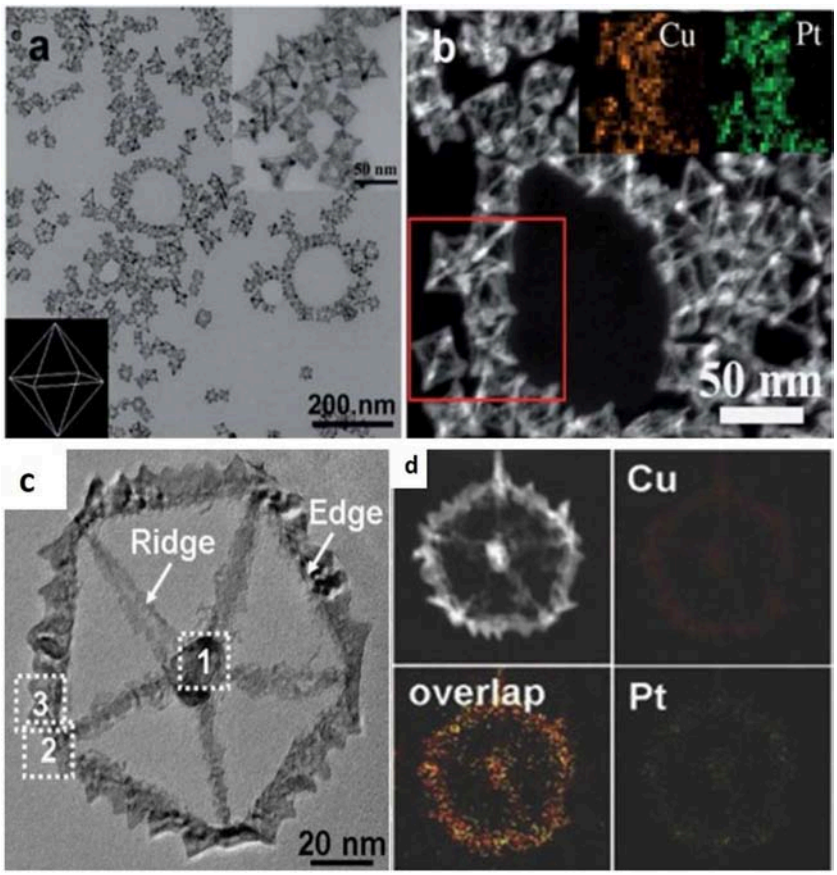

FIGURE 2 | (a) TEM image of as-prepared octahedral Pt-Cu nanoframes the top-right inset shows a high-magnification TEM image of octahedral Pt-Cu nanoframes, and the bottom-left inset shows the corresponding model image. **(b)** HAADF-STEM image of octahedral Pt–Cu nanoframes; the inset shows the selected-area (red rectangle) element analysis maps of Pt (green) and Cu (orange). Modified with permission from Nosheen et al. (2013) Copyright 2013, Royal Society of Chemistry. **(c)** TEM images of PtCu nanoframes (NFs). **(d)** HAADF-STEM image and the corresponding EDS elemental mapping of a typical PtCu NF. Modified with permission from Zhang et al. (2016) Copyright 2016, WILEY-VCH Verlag GmbH & Co. KGaA, Weinheim.

pure Cu nanooctahedra were first generated. For the fabrication of anisotropic 5-fold twin PtCu NFs, galvanic replacement reaction among the Cu nanodecahedra as well as Pt precursors in solution and site-specific co-deposition of Pt as well as Cu atoms played a key role. Interestingly, these 5-fold twin PtCu NFs showed the excellent catalytic activity in terms of ORR as well as MOR in alkaline systems (Zhang et al., 2016).

Similarly, Huang et al. (2019) have developed the 3D RD $Pt_{26}Cu_{74}$ bound with multiple index facets through a facile solvothermal strategy. In this synthetic procedure, L-proline in combination with CTAC acted as a co-structure directing agent and modulated the nucleation as well as crystal growth rate. In comparison with the $Pt_{18}Cu_{82}$, $Pt_{50}Cu_{50}$, and commercial Pt/C catalyst, these $Pt_{26}Cu_{74}$ NFs showed a more enhanced catalytic performance toward ORR and HER because of their highly open nanostructure and synergetic effect of two metals. Polyhedral NFs like catalyst shows a more active and stable performance as compared to other NFs structures. For instance, Ding et al. fabricated the rhombic dodecahedral RD PtCu NFS along a highly open nanostructure in higher yield by the facile one pot method. In the synthetic procedure, a higher concentration of cupric chloride, and the combined use of glucose and oleylamine/oleic acid are responsible for the fabrication of PtCu NFs. TEM analysis proved that the formation procedure depends on initial formation of Cu nanoarchitectures and galvanic replacement of Cu nanoarchitecture with the Pt. Because of their highly open structure, these PtCu NFs showed excellent catalytic performance for MOR in comparison with the Pt/C as well as Pt catalysts (Ding et al., 2015).

Chemical/Oxidative Etching

Etching can be defined as the selective removal of definite facets of NCs as well as less stable metals through alloys with modification of remaining atoms in order to control the shape, size, and composition. The porosity of NCs could be controlled by etchant strength and other conditions of reaction. However, most important advantage of etching process is to regulate the selectivity and rate of etching. Other parameters like the power of etchant, which consists of the chemical potential, concentration, and reaction temperature also play an important role, but selective etching includes a difficult mechanism, and it is more challenging to construct the open structure with a 3D surface by

selective etching. Chemical etching has some disadvantages like surface atoms that may be removed on haphazard positions and an etching procedure that is sometimes very strong and is difficult to stop, meaning the structure could be damaged. In previous years, a lot of etchants have been used to fabricate nanoframe and nanocage structures (Xiong et al., 2005; Au et al., 2008; Zeng et al., 2009; Zhang et al., 2010; Wu et al., 2012; Xie et al., 2012). Moreover, it is a big challenge to control the etching process, and great efforts are still required to discover the path to choose a suitable etchant for the corrosion process. In addition, NFs gained by the etching method depend on precise anisotropic elemental distribution. However, compositional anisotropy of different components on the corners, edges, or facets is linked with geometrical elemental segregation (Liu et al., 2015).

Two Step Etching

The formation of Pt and Pd based NFs is accomplished by the template-mediated growth of Pt atoms followed by the removal of template with acid etching or thermal annealing. Shape can be controlled by tuning the etching as well as regrowth rate. For instance, Wang et al. (2017b) fabricated palladium NFs by excavating the solid palladium NCs. In this synthetic procedure, etching, and regrowth steps are controlled. Different regrowth rates at corners/edges/faces and etching of Pd atoms at specific sites can be controlled by tuning the rate of etching and regrowth. Without reductant, etching rules over the process, which results in conversion of NCs with more defined structures like octahedral to cuboctahedral NCs. However, when a small quantity of reductant (HCHO) is used, the regrowth rate at corners and edge sites could be controlled, which is equivalent to the etching rate, but the regrowth rate at the face site is lower compared to the etching. So, palladium NFs can be gained if etching occurs on the faces only. By following this synthetic procedure, solid Pd cubic, octahedral, cuboctahedral, and concave cubic structures have been carved to analogous NFs. These excavated Pd NCs with a frame-like structure display excellent activity as well as durability in terms of formic acid oxidation reaction. Park and co-workers fabricated cubic Pt NFs and utilized Pd NPs as a template. Site selective coverage of bromide ions induced the selective deposition of Pt on edges/corners and Pt cubic NFs can be gained by discriminating etching of Pd cubes by using acid and H_2O_2 (Park et al., 2016).

Nanoframes With Twinned Boundaries, High Index Facets, and Ultrathin Walls

The twin defects, ultrathin shell, and composition control could increase electrocatalytic properties. Zhang et al. synthesized nanocages by depositing a small number of atom layers of Pt as shell on Pd with more regular facets and etching the Pd template. On Pd NPs, Pt atoms were grown which are tuned from 1 to 6 atom layers by the maintained reaction conditions which effect the growth, diffusion, or dissolution behavior of Pt and Pd atoms (Zhang et al., 2015a). However, in the case of many structure sensitive reactions, introducing defects like twin boundaries may reduce the activation energy and enhance the catalytic performance. Therefore, concern has been focused toward the icosahedron, which has a higher density of twins in one NC. One icosahedron has 20 tetrahedrons in it and an individual tetrahedron is linked to another along the twin boundary, which endows the icosahedral nanocage as an efficient catalyst. He et al. (2016) have deposited Pt layer that is a few layers thick on the Pd to produce the icosahedral core shell NPs, and then by discriminating etching of Pd, icosahedral Pt enriches nanocages with layers that are a few atoms thick and defects were gained. In 2016, (Wu et al., 2014) synthesized platinum-based icosahedral nanocages which had a surface bounded by [111] facets as well as twin defects/boundaries and ultrathin walls of up to six atom layers. However, nanocages were derived from $Pd@Pt_{4.5L}$ icosahedra by selective etching of the Pd core by using $FeCl_3$ as well as KBr etchants. In the etching process, the multiple twinned structure was reserved and the Pt atom in the outer layer ws restructured to keep the original twinned structure with the ultrathin wall (Wang et al., 2016).

Nanoframes With Compositional Segregation

Nanoscale compositional segregation, also called compositional anisotropy, has received more attention for the design of nanocatalysts because this procedure leads to 3D NCs with larger surface area as well as precise size and facet control. Depending on this procedure, the Pt component could be fully accessed by reactants and excellent electrocatalytic properties are obtained (Stamenkovic et al., 2006; Li et al., 2018).

In comparison to homogenous alloys, compositional segregation offers a stronger electronic effect of distinct metals, and many Pt sites are available. According to the structural as well as chemical perspective, the main benefit of the compositional segregated Pt NCs is that it allows the formation of highly open nanoarchitectures, nanocages, or NFs, which are the most promising class of nanostructure, with a 3D surface area as well as interconnected edges with high surface area and improved applications in fuel cells. Now researchers are focusing on the synthetic procedure for gaining compositional segregated Pt based nanocatalysts with distinct morphologies. Moreover, many of the previous synthesized Pt dependent NPs with hollow, cage, and frame structures are homogeneous cubic, octahedral, rhombic dodecahedral, etc. But reports on the fabrication of shape controlled with highly compositional segregated features have not been considered more. Moreover, it should be pointed out that in the previous reported analysis, compositional segregated Pt based nanomaterials have a deficiency in structure control, which is vital for the fabrication of noble metal NFs with more advanced applications. However, the synthesis of highly compositional segregated NFs with complex structures is still challenging. For the first time, Chen et al. fabricated rhombic dodecahedra Pt_3Ni NFs with 2 nm thin edges from $PtNi_3$ polyhedron by the erosion of Ni followed by annealing. In this strategy, etching was conducted by dissolved oxygen present in air instead of harsh etchants or applied voltage. The open frame structure with surface crystallinity, segregated Pt-skin and 3D structure augmented the availability of the reactants for both inner and outer surfaces. As compared to commercial Pt/C, the open framework design displayed the phase segregation Pt skin

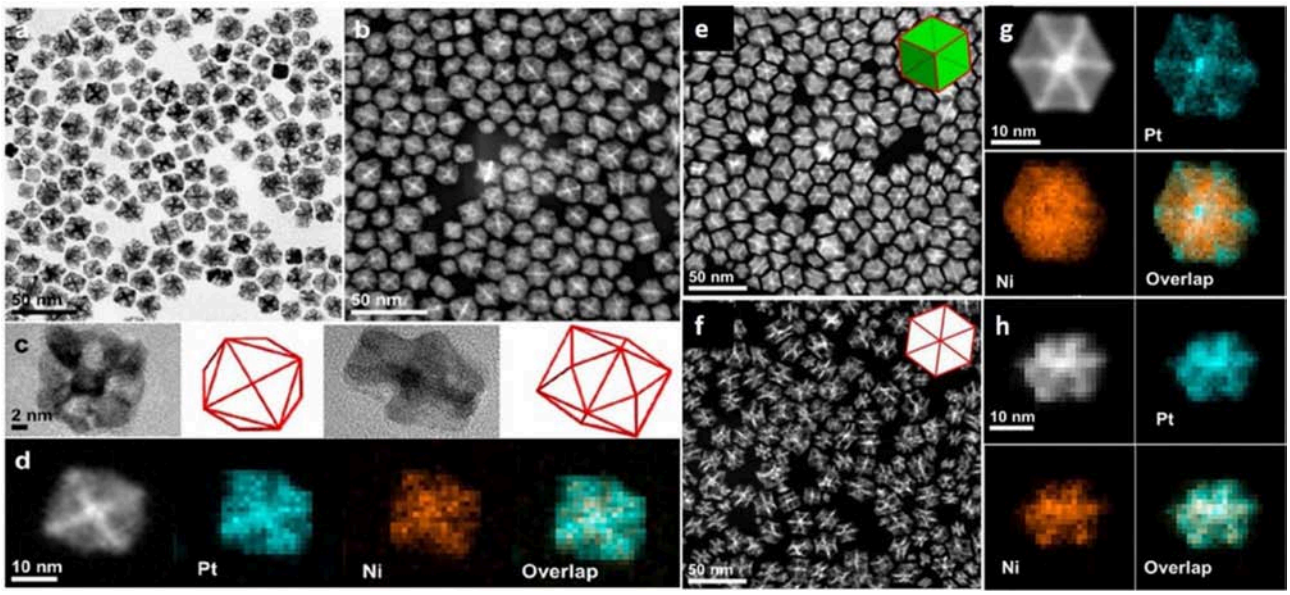

FIGURE 3 | Morphological and structural characterizations for THH Pt-Ni NFs, RDH Pt-Ni NCs, and RDH Pt-Ni NFs. **(a)** TEM image, **(b)** HAADF-STEM image, **(c)** TEM images and corresponding geometric models of THH Pt-Ni NFs oriented along two typical projections, and **(d)** HAADF-STEM-EDX elemental mapping results for individual THH Pt-Ni NF. **(e)** HAADF-STEM image and **(f)** HAADF-STEM-EDX elemental mapping results for individual RDH Pt–Ni NC. **(g)** HAADF-STEM image and **(h)** HAADF-STEM-EDX elemental mapping results for individual RDH Pt-Ni NF. Modified with permission from Ding et al. (2016) Copyright 2016, American Chemical Society.

structure, which exhibited a 36-fold enhancement in terms of ORR (Chen et al., 2014).

Another group has explained an effective procedure for the synthesis of tetrahexahedral PtNi NCS (THH PtNi NCs) as well as rhombic dodecahedral PtNi NCs (RDH PtNi NCs) with more segregated features (Ding et al., 2016). It has been reported for the first time that THH PtNi NCs have been gained in a simple organic solution system. These THH PtNi NCs as well as RDH PtNi NCS were simply obtained by tuning the ratio of oleylamine and oleic acid while keeping the other conditions constant. The synthetic procedure demonstrated that the use of dodecyltrimethylammonium chloride (DTAC) as well as changing the ratio of oleylamine, oleic acid plays important part for the synthesis of THH PtNi NCs and RDH PtNi NCs. However, by simple acetic acid treatment and removal of Ni template, the THH and RDH PtNi NFs were obtained. Due to their highly compositional segregated design, these solid PtNi NCs were transformed into the PtNi NFs which showed the more open feature. These PtNi NFs presented higher performance toward ORR and for alcohol oxidation due to enhanced consumption of Pt (**Figure 3**). Another group has proposed the synthesis of tetrahexahedral (THH) PtNi NFs by the removal of the Ni component of tetrahexahedral (THH) PtNi NPs by using carbon monoxide (CO). They demonstrated that the Ni was removed from the [100] direction by using CO molecules. However, these Pt_3Ni NFs possess a 3D open structure, high index facets and thin segregated Pt layer. Furthermore, Co could be produced from the carbon support through thermal treatment in the presence of oxygen. This approach could be used for the preparation of industrial level nanocatalysts (Wang et al., 2017a). In the same way, Luan et al. also fabricated Pt-Ni Tetrahexahedral NFs by Co etching.

Chen et al. (2019) studied the reaction procedure of seeded co-reduction for the fabrication of PtNi seeded core frame structures. By controlling the shape of seeds, rhombic dodecahedra structures were obtained by depositing the Pt on their corners and edges. Different Pt salts and the ratio of Pt and Ni salts affected the shapes of seeds as well as the final morphology. Moreover, the Ni core of these hierarchical nanoarchitectures could be etched by the acetic acid which forms the concave structure and finally hollow NFs. In addition, the morphology and composition of the product could be manipulated by controlling the rates of etching and interdiffusion between two metals. The final Pt_3Ni NFs are more stable in acidic environments and show distinct electronic properties that are different from the primary core frame nanoarchitectures because of the alloying of Pt with Ni. However, this seeded co-reduction strategy can be extended for the fabrication of other Pt-based complex core frame rhombic dodecahedral NPs. Moreover, hollow NFs used low acetic acid etching, which provides a simple means to change the phase segregation of bimetallic polyhedra for hollowing out the alloyed structure with more unique morphologies. Stamenkovic et al. explained that the 3D Pt anisotropy of PtNi rhombic dodecahedra can be controlled by changing the ratio between Pt or Ni salts; as a result, hollow, and excavated NFs can be gained after Ni corrosion. In excavated NFs, at the interior of excavated NFs Pt rich sheets were extended while hollow NFs had voids inside Pt rich edges.

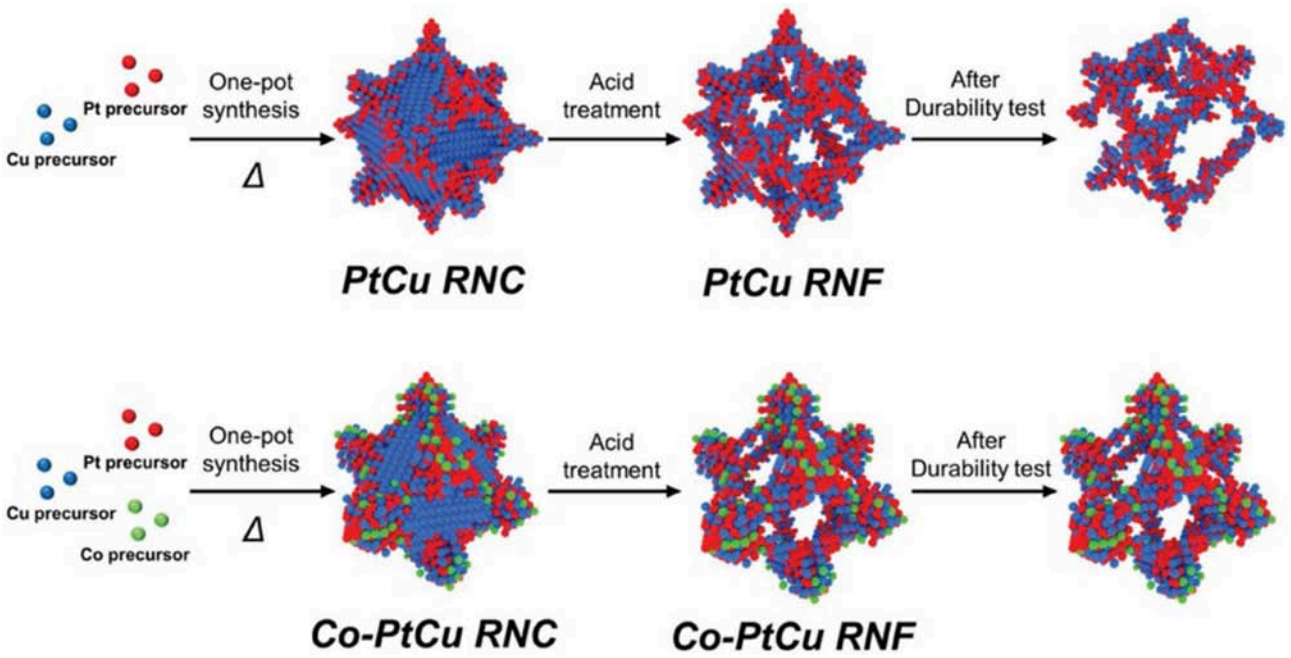

FIGURE 4 | Schematic illustration for the formation process of Cu@PtCu rhombic dodecahedral nanocrystals (PtCu RNC), PtCu rhombic dodecahedral nanoframes (PtCu RNF), Co-doped Cu@PtCu rhombic dodecahedral nanocrystals (Co-PtCu RNC), and Co-doped PtCu rhombic dodecahedral nano-frames (Co-PtCu RNF). Adapted with permission from Kwon et al. (2018b) Copyright 2018, WILEY-VCH Verlag GmbH & Co. KGaA, Weinheim.

The excavated NFs had higher ORR performance which was due to the higher Ni amount in the near surface and the stretched 2D sheet-like structure within the NFs, which exposed Pt sites (Becknell et al., 2017).

In another example, Pt was coated on the surface of Cu nanocubes in order to synthesize the rhombic dodecahedral NFs (RD NFs). Moreover, growth in the [100] direction of Cu nanocubes leads to the RD. However, with the addition of Pt salts [100], vertices of Cu-CuPt rhombic dodecahedra NCs could be stretched to the spiny CuPt RD NCs. By removing the Cu content from the seed, CuPt RD as well as spiny CuPt RD NFs were gained. Because of their open frame design, both of these NFs showed a higher catalytic performance (Lyu et al., 2017).

The additional component to the binary catalyst serves as an efficient and robust means of structural as well as compositional stability of electrocatalyst. Kwon et al. (2018b) reported that the insertion of Co to PtCu alloy NFs gives ternary PtCuCo rhombic dodecahedral NFs along the reinforced vertex of PtCuCo ternary NFs. The Pt deposited on the edges of the Cu template leads to the formation of PtCu alloy, and then this PtCu alloy enables the *in situ* decay of the third constituent, i.e., Co that penetrates into the PtCu segment to make the desired PtCuCo phase. Furthermore, the final Co-doped PtCu rhombic dodecahedral NFs (Co-PtCu rhombic nanoframe) display the vertex strengthened structure, suggesting that the deposition of Co-occurs in the region of the vertices of PtCu NFs (**Figure 4**). Similarly, Huang et al. (2018) fabricated the PtCuNi rhombic dodecahedra NFs (NFs) by a two-step etching method. Firstly, PtCuNi concave rhombic dodecahedra formed by oxidative etchant and then PtCuNi NFs formed through the acid etchant. By controlling the reaction time and Ni precursors, PtCuNi solid rhombic dodecahedra seeds' shape can be controlled. To investigate the evolution of PtCuNi NF, atomic ratios, particle size, and morphology of ternary Nfs are precisely examined. In another report, Ye and co-workers (Ye et al., 2017) synthesized the $Pt_4PdCu_{0.4}$ NFs by the Cu-assisted deposition etching process, and these NFs showed improved electrocatalytic properties due to structural and electronic effects.

One Pot Etching

Using pre-synthesized templates like Pd or Ag NPs in the synthesis of hollow nanostructures has some limitations. (1) The synthetic procedure requires more steps such as template synthesis, shell growth as well as template removal, which limits practical use. (2) Most of the synthetic procedures utilize pre-synthesized templates, which are based on the noble metals like Pd or Ag as sacrificial template and waste expensive materials. (3) The resultant shape of hollow nanocages and NF structure is limited to the initial shape of the pre-synthesized templates. So, in order to overcome these disadvantages, for the tuning of surface energies, nanoscale phase mixing or segregation, *in situ* template formation has been proposed for the fabrication of novel hollow NCs. For the synthesis of a wide variety of binary and multimetallic NPs with more defined morphology, one pot synthesis is more preferable. Moreover, binary NCs are metastable, allowing the synthesis of NCs *in situ* phase segregation or even the removal of template leads to the hollow nanoarchitectures to be accomplished in one step.

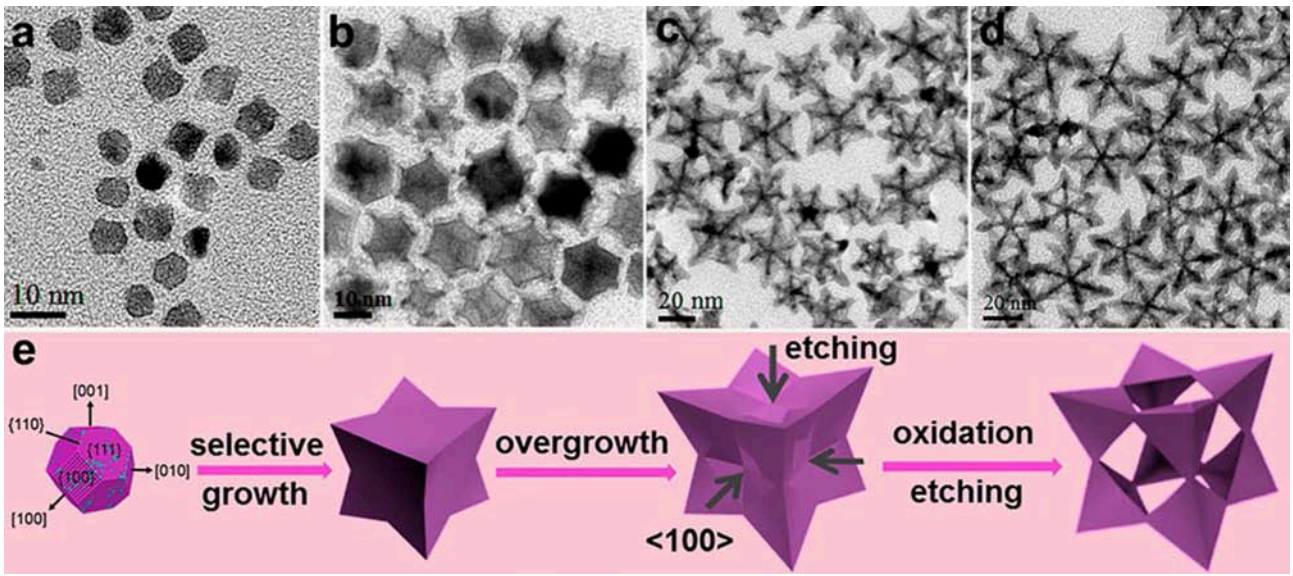

FIGURE 5 | Representative TEM images of the intermediates obtained at different reaction time during the synthesis of concave $PtCu_2$ octopod nanoframes: **(a)** 0.5, **(b)** 1, **(c)** 12, and **(d)** 18 h, respectively. **(e)** Schematic of the major steps involved in the formation of $PtCu_2$ CONFs. Adapted with permission from Luo and Shen (2017) Copyright 2017, American Chemical Society.

Carbon corrosion and leaching of transition metals during electrochemical cycling may degrade the catalyst and may decrease its durability. To overcome this problem, an active and stable catalyst is needed. Currently, polyhedral PtNi NFs have been fabricated and show the promising electrocatalytic performance for fuel cells. However, these NF catalysts have been mostly developed by the multi-step synthetic procedure, which made cost saving massive production a big challenge toward practical applications. So, engineering of self-supported as well as high-performance NF catalysts through one pot procedure is of great importance. To synthesize stable and active catalysts, Luo and Shen described a one-pot procedure for the construction of concave $PtCu_2$ octopod NFs (CONFs) with higher index facets in which CTAB is used as a structure directing agent. The CONF nanoarchitectures meet the critical design requirements for more efficient nanocatalyst-like highly open nanoarchitectures with 3D catalytic surface and a stepped surface composed of multiple index facets which showed enhanced catalytic activities. The self-supported CONFs catalyst removed the carbon erosion and facilitated the reaction by enhanced mass transport. Furthermore, CONFs are assembled by the eight symmetry feet that showed excellent physical and electrochemical stability. The evolution mechanism indicates that the octopod NFs formed from solid octapods by sequential erosion, and the overgrowth from concave cubic structure to concave octopods is comparatively slow (**Figure 5**) (Luo and Shen, 2017).

By using the one pot solvothermal strategy, Huang et al. (2018) reported 3D PtCu alloy nanocages with an open structure, large exterior and interior surfaces that are accessible for the reactants. Arginine and cetyltrimethylammonium chloride (CTAC) performed as the co-structure directing agent as well as the stabilizer. In this method, Cl^-/O_2 and oleylamine served as the etchant and co-reductant, respectively. These frame-like nanocatalysts showed greater activity and stability.

Structurally Fortified Nanoframes

More definite 3D NF design displays well-defined features like corners, edges, and facets but they degrade in harsh conditions (Park et al., 2018). However, the catalytic active surface could be preserved by the fortification of the most vulnerable sites, such as vertices through alloying and heterostructure formation, and the insertion of supported materials into NFs to maintain the overall higher surface area of the structure without losing the surface area of the exposed sites. For the formation of NFs, higher surface energies and vertices of NFs are vulnerable to the structural degradation in the chemical etching process as well as in electrocycling tests. Many groups reported the synthetic procedure in order to reduce the vulnerability of vertices by the growth of additional metals on the active vertices, which results in hetronanostructure formation at the vertices or at the alloying of vertices. However, sometimes etching and galvanic replacement reaction could take place in one process. For instance, Wu and co-workers grew Au islands on vertices of PtNi NFs. They used a protocol based on the selective galvanic replacement reaction and preferred etching, in which the role of etching was more obvious for NF synthesis. The etching was regulated by dimethylglyoxime as Pt was stable to dimethylglyoxime, therefore NFs with protected Pt edges were obtained even after etching. During MOR, the overgrowth Au sites impeded the structural deformation of PtNi NFs and the catalytic activity of Pt_3Ni NFs with the 10% Au remains unchanged after the 3,000 cycles.

Insertion of Structural Support Into the Nanoframes

The inherently weak NFs can be brutally damaged when subjected to long cycling time in electrochemical reaction, due to which a reduction in electrocatlytic performance may be observed. Hence, fabrication of NFs with strong structure support is most important and challenging. We have synthesized PtCu ultrathin NFs by the one-pot method, and these ultrathin NFs were abbreviated as hexapod backbones with thin stretchers (thinHBS). In addition to thinHBS, some other partially etched complex polyhedral hollow structures have also been synthesized. $CuCl_2$ and NaI were responsible for etching to modify the shape, whereas ethanolamine, and amino acids stabilized the [111] the domains. The combination of growth and the etching process smoothly controlled the shape. The transmission electron microscope image showed a two-dimensional picture which looks exactly like hexagonal snowflakes, and the adjacent trunks have a few stretchers which are attached to the trunks symmetrically. The trunk length was found to be 40 nm, the diameter was 5 nm and thickness of the stretchers was about 1.3 nm. The synthesized structures may be beneficial for electrocatlytic applications with enhanced activity and stability owing to ultrathin stretchers and internal trunks which provide support for stability (**Figures 6a–d**).

Moreover, trimetallic catalysts are more active and stable than bimetal alloys. In a recent study, Kwon et al. (2018a) explained the idea of a dendrite@frame-like nanostructure in which the outer PtCuNi NFs are supported by inner PtCu dendrite. Moreover, branches network as well as attached joints can reinforce the multiframe structure and could maintain the same structure during harsh conditions. In order to boost the consumption of Pt, it is necessary to have a more active PtNi alloy part for both the interior support as well as for the outer multiframes. Furthermore, the presence of nanopores in multiframes can be advantageous to entrap the gaseous reactant into nano-confined space and can show higher catalytic performance. Burst reduction and deposition of Ni after the PtNi alloying/dealloying created multiple PtNi bridges among the PtNi and superimposed interfused multiframes. By the Ni erosion, PtNi multiframes with embedded PtNi dendrites of 72 nm were gained. However, these PtNi multiframes showed a higher electrochemical active surface area and ORR performance owing to porous, more active sites, and higher index facets. Similarly, Park et al. (2017a) fabricated firm robust PtCuNi NFs, supported with an interior PtCu dendritic structure. In the formation process, first a PtCu cubic dendritic structure was formed, which evolved into PtCu@Ni dendrite@shell structures after constant deposition of Pt on the surface, and after etching process, PtCu@PtCuNi dendrite@frame (PC@PCN) formed. The detailed process showed that the morphological development into rhombic dodecahedral NCs requires Pt for the growing Ni layer (**Figures 6e–k**).

Other Uncommon Methods

In addition to the above-mentioned methodologies, a cage/frame nanostructure has been developed by the other synthetic procedures such as control decomposition kinetics, long chain alcohol (Jeyadevan et al., 2014), Ostwald ripening (Zhang et al., 2018a), etc.

Nanoframes Other Than Pt and Pd Metals

Noble metal NFs other than Pt and Pd, including gold (Au), ruthenium (Ru), iridium (Ir), and silver (Ag), have also been synthesized, but these NFs commonly have not been used for electrochemical applications in fuel cells. For their synthesis, etching, the galvanic replacement reaction and Kirkendall effect strategies were used. To cover the NFs' synthesis for all types of noble metals, we have also included a short description of noble metal NFs other than Pt and Pd.

Ultrathin triangular gold NFs have been synthesized through the etching process by Xue's group. In this strategy, Ag nanoprisms were used as the sacrificial template and $HAuCl_4$ was continuously introduced to the solution for the deposition of gold on the Ag nanoprisms. Hydroxylamine was used as the reducing agent, and after deposition of gold on the surface of Ag prism, etchants (H_2O_2+NH_4OH) were used to completely remove the Ag prism for the synthesis of ultrathin NF. H_2O_2 oxidized the Ag atoms and NH_4OH prevented the formation of other particles like AgOH and Ag_2O by dissolving the oxidized silver. Etchants were slowly added into the solution because their rapid introduction may destroy the frame structure (Shahjamali et al., 2013). In another example, ultrathin Au NFs with a thickness of 1.6 nm have been synthesized by using the Ag template with decahedral shape, twinned pentagonal rods, and icosahedra to fabricate analogous NFs. H_2O_2 was used as an etchant for the dissolution of Ag (McEachran et al., 2011).

Rhodium cubic NFs have been synthesized by Xia and co-workers, in which Pd nanocubes have been used as seeds and deposition of Rh at the edges-corners of Pd seeds occurred due to the adsorption of Br^- on facets and converted them into bimetallic Pd-Rh core-frame concave cubes. By selective etching of Pd and continuous growth of Rh, they were converted into Rh NFs (Xie et al., 2012). Another group reported the fabrication of Ru NFs by using truncated octahedal seeds, which are converted to PdRu core-frame octahedral structure that are finally converted into Ru octahedral NFs with 2 nm thick frame walls by the selective dissolution of the Pd core by etching (Ye et al., 2016). Very recently, the same group also synthesized Ru cuboctahedral NFs with the face centered cubic (fcc) phase and walls that were a few atomic layers thick by a combination of etching and the galvanic replacement method (Zhao et al., 2019). In addition to monometallic nanoframes, bimetallic nanoframes of Au, Ag, Ru, and Ir have also been synthesized. For instance, Ag/Au nanoshells with voids and pores have been fabricated by utilizing silver NPs as sacrificial templates in the presence of H_2O_2 as an etchant (Wu et al., 2012). Zhang's group fabricated Rh-based RhCu nanooctahedron frames/C, RhPdCu nanopolyhedral frames/C, and RhNi porous nanopolyhedral frames/C by using 3d metals like Cu and Ni as the sacrificial template by selective etching (Zhang et al., 2015b).

Ir-based multi-metallic double layer NFs (DNF) with NF@NF structure were developed by Lee et al. By controlling the kinetics of two types of iridium salts and salts of transition metals like

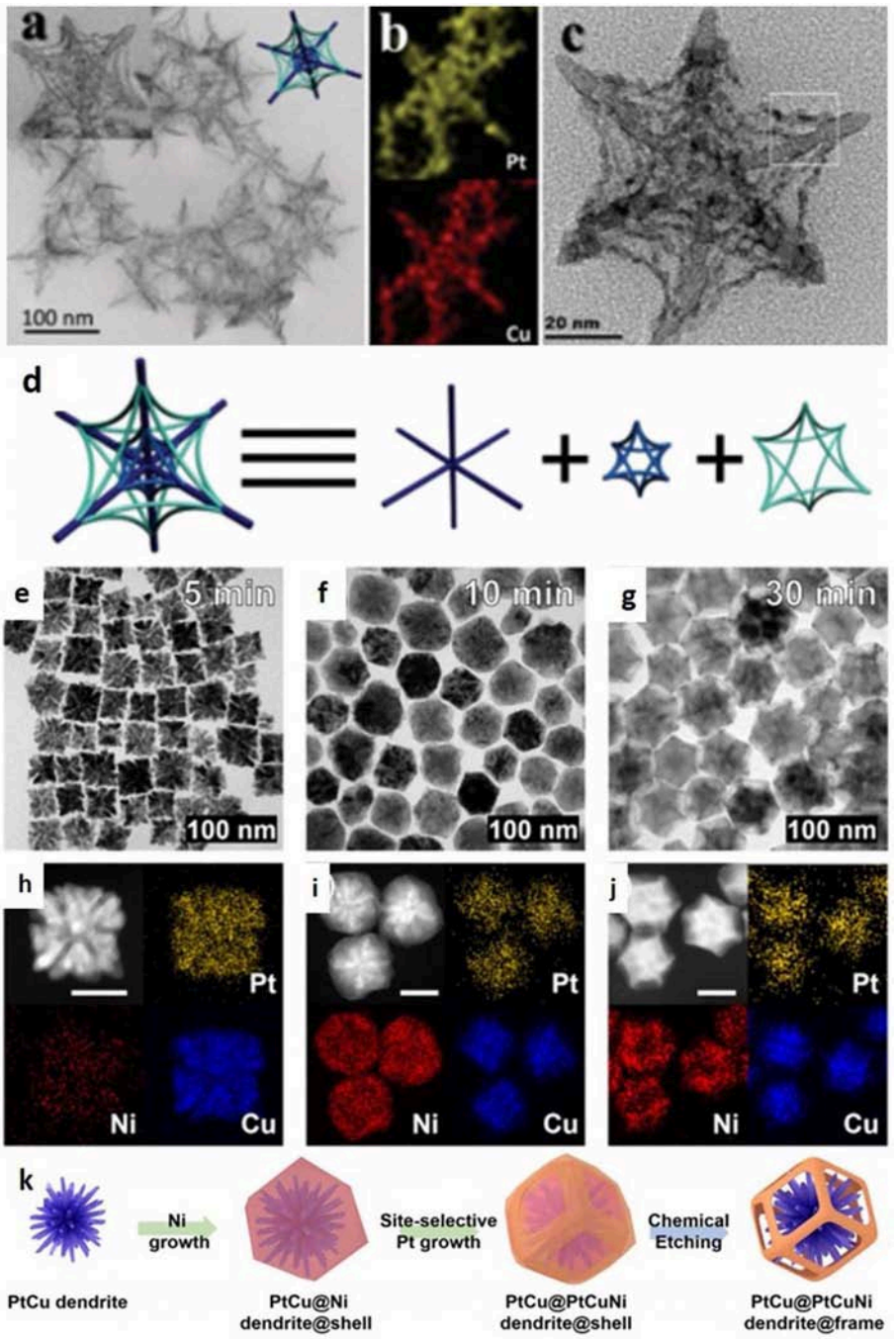

FIGURE 6 | (a) TEM images of hexapod backbones with thin stretchers (thinHBS). **(b)** Element mapping results of thinHBS. **(c)** HRTEM image of thinHBS. **(d)** The anatomic structure of thinHBS. Modified with permission from Nosheen et al. (2016) Copyright 2016, The Royal Society of Chemistry. **(e–g)** Temporal TEM images and **(h,i)** elemental mapping analysis obtained at **(e,h)** 5 min, **(f,i)** 10 min, and **(g,j)** 30 min. Scale bars in **(h–j)** are 30 nm. **(k)** Schematic illustration of formation of PC@PCN dendrite@frame. Modified with permission from Park et al. (2017a) Copyright 2017, American Chemical Society.

Ni and Cu, firstly core shell alloy@alloy formed in one step and then these structures converted into rhombic dodecahedral IrNiCu DNF by preferential etching. Single-metal NFs formed by the addition of only one type of Ir salt, which showed that for the formation of double layer NFs, two kinds of Ir-metal precursors are important. The structure of Ir-based NCs have also been converted to other double layer NF morphologies, including octahedral NFs and CuNi@Ir core-shell structures, by changing the experiment conditions. The synthesized IrNiCu double layer NFs have been used for an oxygen evolution reaction (OER) in

acid medium, which showed enhanced activity as compared to commercial Ir/C. These NFs also showed good stability toward OER that could be due to the frame which stops the growth and aggregation of NPs (Park et al., 2017b).

Galvanic replacement reaction has also been used for noble metals other than Pt and Pd by many groups to synthesize monometallic and bimetallic hollow structures, nanocages, and NFs of different morphologies by using an Ag template of desired shapes (Zeng et al., 2009; Lai et al., 2015). Colloidal gold nanorings (Au NRs) with high monodispersity were synthesized with the one pot method by galvanic replacement by Du and Wang. PVP was used as coating on the cobalt nanoparticles, and then these PVP-coated nanoparticles generated a one-dimensional assemblage of cobalt nanoparticle chains which were used as the sacrificial template and galvanically replaced by Au to form Au NRs (Hu et al., 2014). Li's group reported single crystalline octahedral AuAg alloy nanoframes by the one pot galvanic method in which polyhedral truncated Ag NPs formed in solution (Hong et al., 2012b). The same group has also developed Ru-Cu nanocages and core-shell Cu@Ru NCs by a one-step galvanic reaction (Chen et al., 2016).

An Au@Ag core-shell, Au@void@AuAg nanoshell, and Au@void@Au NF have been reported by Neretina's group. Au@Ag core-shell structures produced a noble metal rattle shape by galvanic reaction where a moveable core was present in the hollow shell. Gold, platinum and palladium templates of Wulff structures were firstly converted into core/shell structures by the reduction of silver ions, which were further converted by the replacement of silver with gold.

The Wulff-shape core could be restricted in a nanoshell/cage/frame by adjusting the shape of the shell, epitaxial correlation to substrate, and the replaced amount of shell. These structures could be considered important as there is a precise gap between the core and shell. The internal side of these structures consist of the core, shell as well as substrate, which may offer good functional potential. Furthermore, the core present in the shell may provide protection and it is also linked with the surrounding reactants due to a porous cage or frame, which may be beneficial for many applications (Hajfathalian et al., 2016). González's group used a sequential galvanic replacement reaction and the Kirkendall effect at room temperature to fabricate double-walled AuAg hollow nanoboxes (González et al., 2011).

In addition to the above-mentioned methods, some other methods have also been used to synthesize hollow structures. Hollow rutehenium (Ru) octahedral (Oh) nanocages have been developed by *in situ* formed metastable copper octahedrons. Core shell Cu-Ru NPs with meta stability formed by the co-decomposition of copper and ruthenium precursors formed, and a consequent dissolving of copper core dissolution of the core Cu produced hollow octahedron shaped Cu-doped Ru nanocages. These frame structures were also used as electrocatalysts for OER (Yoon et al., 2014). Gu et al. fabricated AuAg shells and porous AuAg NFs by using citrate capped silver nanoparticles by the galvanic replacement reaction. The AuAg nanoshells formed in the presence of $AuBr^{2-}$ and porous AuAg NFs formed in the presence of $AuCl^{4-}$. The $AuBr^{2-}$ was also used to synthesize Au@AuAg rattles (Bai et al., 2015). Qin's group reported a method to synthesize Ag@AgAu core-frame cubic structures by the co-reduction of two metals in the presence of ascorbic acid (Sun and Qin, 2015).

Electrochemical Properties

In electrocatalytic reactions, there is contact between the reaction and active sites of metal. This interaction is due to various energy levels of the outermost electrons, and the electron transfer takes place to reduce the overall energy of the system. The procedure is generally completed by bond breaking and formation, which include chemical sorption and generation of intermediate species. The metals' d band center in relation to the Fermi level is considered a significant tool for measuring the power of interaction with reaction species. The d band center of the metals could be modified by fabricating alloy nanostructures or heterogeneous atomic layers, which could improve the electrocatalytic properties. The shifts in d band center values could be ascribed to the transfer of charge or lattice change owing to the addition of more than one metal. In case of alloying, the enhancement in electrocatalytic properties could be credited to charge conversion from the transition metal atoms of less electronegativity to the more electronegative platinum atoms, and another reason is the shortening of the platinum-platinum bond distance, known as compressive strain. It may happen due to the variations in elements size of different metals. However, the charge transfer as well as strain may cause the downshifting of d-electronic states of platinum surface atoms relative to the Fermi level of alloys, and hence may reduce the poisoning effect of the oxygen reduction's intermediate species.

Moreover, it has been observed that the occurrence of different kinds of transition metals in the alloy nanostructures provide a chance for maneuvering O_2 species on different surface sites and facilitate an additional bi-functional process to accelerate the oxygen reduction kinetics. For improved electrocatalytic performance, alloy NFs with platinum-skin, platinum-skeleton, or frame have been developed as promising candidates. For example, Han and co-workers have synthesized a Pt-Cu alloy octahedral Nfs (PtCu AONFs) having spiny nano-thorns on the tops by the one-step method. The insertion of nickel ions was crucial for NF formation. The synthesized PtCu AONFs showed enhanced activity and stability for ORR. The mass and specific activities were 2.8 and 2.6 times that of commercial platinum-carbon catalysts (Zhu et al., 2019). Furthermore, these PtCu AONFs also showed better results for MOR than Pt/C. In case of PtCu alloy, the surface electronic structure of pure platinum was modified and the electrocatalytic properties enhanced toward oxygen reduction reaction because of a drop of adsorption energy between platinum and oxygen species.

Effect of Surfactants on Electrochemical Properties

For the shape control of nanoparticles, surfactants are usually used, which may also be adsorbed on the exposed crystal facets and thus affect their electrochemical performances. In short, the surface covered with surfactant may suppress the catalyst performance. To overcome this problem, removal of surfactant

is necessary. Until now, different kinds of treatments have been developed for the removal of surfactants. First, a simple washing procedure is performed, followed by separation through centrifugation, and then the following treatments:

(i) Thermal annealing: The catalysts are heated in furnace at high temperature in air.
(ii) Chemical washing: The catalysts are dispersed in acetic acid for a suitable time, followed by washing through centrifugation to remove unwanted impurities.
(iii) UV-Ozone treatment. Catalyst is deposited on the glassy carbon electrode, which is then irradiated with UV-Ozone to remove the surfactants after drying in air.
(iv) Electrochemical cyclic voltammetry is used to remove the surfactants covered on the surface of the catalysts.

APPLICATIONS IN FUEL CELLS

Liquid Fuel Oxidation Reaction

In the polyelectrolyte fuel membrane cells (PEMFCS), gaseous hydrogen fuel is replaced by liquid fuels like methanol in direct methanol fuel cells (DMFC), formic acid in the direct formic acid fuel cells (DFAFC) and ethanol in direct ethanol fuel cells (DMFC) (Park et al., 2017a). For the small portable electronic devices, liquid fuels are more suitable because of their easily exchangeable fuel cartridges, higher energy density as well as faster charging rate. Because of their higher number of advantages, which are described above, the use of liquid FCs presents more challenges. The main issue is the partial oxidation of liquid fuels which leads to the sluggish oxidation reaction kinetics, and it causes a reduction in the number of transferred electrons. In DMFC, <30% of the energy can be exploited as electricity. Another major issue is the crossover of fuel molecules from anode to cathode through diffusion by the proton exchange membrane in the cell. Due to the crossover mechanism, it not only reduces the overall cell voltage but also contaminates the cathode catalyst. Due to the partial oxidation of liquid fuel, it forms CO which adsorbs on the surface of the cathode catalyst and effects the ORR performance of the cathode in cell operation. This procedure is called CO poisoning. However, Pt-based alloys are more familiar, tolerate CO poisoning and show the excellent catalytic performance. Mostly, previous studies explained the strategies to synthesize the hollow nanoarchitectures which showed higher electrocatalytic properties.

In addition to the above electroxidation reactions, the hydrogen oxidation reaction (HOR) is also an important reaction in fuel cells. HOR is a rapid one-electron oxidation route that occurs at anode. Until now, noble metals like Pt-, Pd-, Ir-, and Rh-based monometallic and alloy structures have been used as electrocatalysts for HOR, but currently no paper is available on noble metal nanoframes, which is why we will not focus on HOR applications in fuel cells. For deeper understanding of HOR, the reader is directed to related review papers (Cong et al., 2018; Davydova et al., 2018).

Formic Acid Oxidation Reaction (FAOR)

DFAFCs are the devices which catalyze the reactions among formic acid at the anode and O_2 at the cathode and change the chemical energy into electricity (Ye et al., 2017). In recent decades, for the energy source formic acid is usually used as a fuel in DFAFCs, which have received more attention. Moreover, formic acid is liquid at room temperature and is the most promising fuel. It replaced molecular hydrogen and assisted storage as well as transportation. DFAFCs show higher power density, faster oxidation rate, and higher cell potential with mild fuel crossover.

In case of FAOR, the main limitation for the Pt catalyst is struggle among the direct dehydrogenation path and indirect oxidation path, which produce CO_2 directly and CO as an intermediate, respectively. So, enhancement of the direct pathway is necessary to assist the detachment of CO from the surface. In addition, surface as well as electronic structure play significant roles in the half reaction. However, separation of Pt atoms with others not only suppresses the indirect path but is also helpful for the CO stripping from the platinum surface. In case of alloys, atomic separation is gained, which not only tailors the surface electron densities but also stimulates direct dehydrogenation. However, synthesis of stepped atoms on the surface provides additional chance for enhanced CO stripping. Thus, fabrication of open structures and alloy formation are vital for efficient and durable catalysts for FAOR.

Wang et al. fabricated Pd NFs with more defined morphology by directly excavating the solid NCs. However, in comparison with the solid Pd catalyst, these NFs display good activity as well as durability toward FAOR because of their 3D open structure. Pd NFs displayed high activity in comparison to the Pd octahedra catalyst and a 7.5-fold increase for peak current. Because of their 3D open structure, there is a larger fraction of edges and corner atoms, which lead to good catalytic performance in terms of FAO. Moreover, the long-term stability of catalysts is estimated by the durability test as depicted in **Figure 7A**. It is noted that the nanostructure of Pd NFs were balanced and showed good stability after 1,000 cycles of durability tests (Wang et al., 2017b).

In another report, Nosheen et al. (2013) used the one pot method for the fabrication of single crystalline octahedral PtCu NFs in an aqueous system. When compared with the platinum black and platinum/carbon catalyst, these octahedral PtCu NFs showed good specific activity toward FAOR due to their exclusive frame structure and combined effect of Pt and Cu (**Figure 7B**). Furthermore, comparison of electrocatalytic properties of Pt and Pd-based nanoframes toward FAOR, MOR, EOR, ORR, and bifunctional electrocatalysis is given in **Table 1** for better understanding.

Methanol Oxidation Reaction (MOR)

In the case of DMFCs, MOR occurs at the anode with the multistep reaction, and it depends upon adsorption as well as oxidation of methanol on the catalyst. For the MOR, Pt is usually used as a catalyst due to its higher activity toward adsorption of methanol. In addition, pure Pt surface suffers from CO poisoning, which reduces the catalytic performance. Researchers

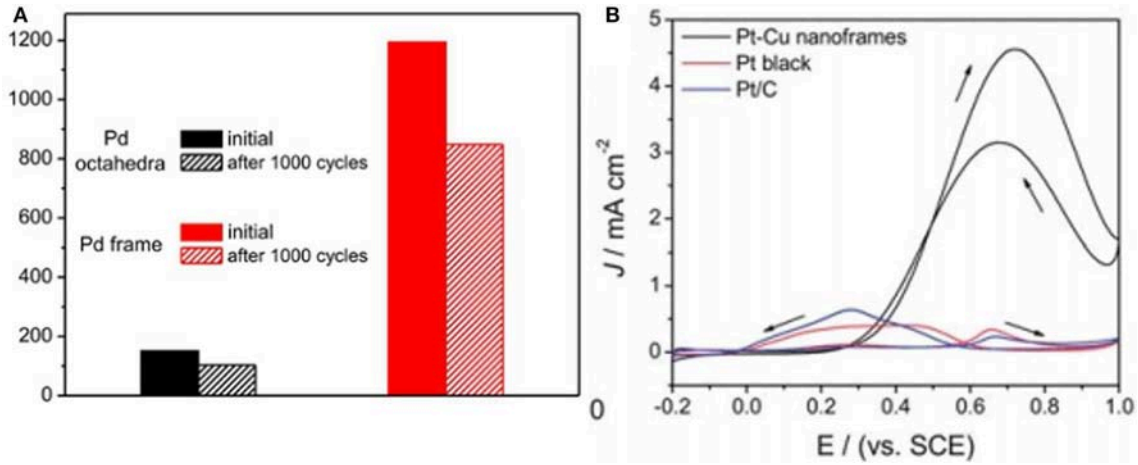

FIGURE 7 | (A) Electrochemical durability of the Pd octahedral nanoframes and solid Pd octahedra catalysts. The current density was normalized against the corresponding ECSA. Modified with permission from Wang et al. (2016) Copyright 2017, American Chemical Society. **(B)** Cyclic voltammetric CV profiles of octahedral Pt-Cu nanoframes in a 0.25 M HCOOH + 0.5 M H_2SO_4 solution (50 mV s^{-1}). The specific current density (J) was normalized to the electrochemically active surface area (ECSA). Modified with permission from Nosheen et al. (2013) Copyright 2013, Royal Society of Chemistry.

have focused on the fabrication of Pt-based nanocatalysts, which not only reduces the CO poisoning but also displays good activity and stability. For instance, Luo and Shen (2017) fabricated the PtCu NFs along higher index facets by the one pot method, which showed good catalytic performance. In addition, by tuning the ratios of Pt as well as Cu precursors, two different octopod NFs like $PtCu_2$ concave octopod NFs and ultrathin PtCu octopod NFs were synthesized. Because of their 3D surface area and higher index facets, these $PtCu_2$ concave octopod NFs displayed good catalytic performance and more CO tolerance. Regarding MOR, these $PtCu_2$ concave octopod NFs showed a 7-fold enhancement in activities as compared to the commercial Pt/C catalyst. However, in a severe environment of electrocatalytic reaction, these $PtCu_2$ concave octopod NFs are more conserved as shown in **Figures 8A,B**. In another report (Zhang et al., 2013), PtCu nanocages were developed by using the glycine mediated reaction kinetics, which showed good activity and stability for the MOR in comparison to the Pt/C and Pt black catalysts. The current density value specific activity of PtCu yolk-cage nanoalloy was 2.8 mA cm^{-2}, which was four- and 6-fold higher than Pt black and Pt/C, respectively. Similarly, Ding et al. fabricated rhombic dodecahedral PtCu NFs by using the one pot method. In comparison with the Pt/C as well as Pt black, these PtCu NFs presented good catalytic performance toward MOR due to their highly open nanostructure and synergetic effect among two metals (Ding et al., 2015). Moreover, Xia et al. (2012) synthesized the $PtCu_3$ nanocages by the one pot method in organic solution. Toward MOR, these $PtCu_3$ nanocages depicted excellent catalytic activity when compared to solid PtCu NPs as well as with single component Pt catalysts. The excellent catalytic performance was due to the special nanostructure as well as the synergetic effect among Pt as well as Cu. In addition to Pt metal, Pd alloy NFs have also been used for MOR. For instance, Chen et al. have synthesized the PdCu flower-like nanocage by using the galvanic reaction and disproportionation reaction, and in the synthetic procedure Cu_2O octahedra were used as template. These PdCu flower shaped nanocages showed more catalytic activity in comparison with the Pd NPs in terms of MOR, which was 2.7 times greater than the commercial Pd/C. The higher catalytic properties were because of their large surface area and effect of Pd and Cu metals. In addition, these PdCu nanocages have shown good stability as well as excellent poison tolerance. For MOR, the presence of 10% Au on Pt_3Ni NFs may increase the catalytic activity, and the structure was preserved even after 3,000 cycles. The Pt skinned surface of NFs that is formed via the etching process is the cause of enhanced durability, which prevented further etching of the Ni content. Furthermore, the addition of Au islands to the PtNi frame could fade the bindings of poisonous and adsorbed species on the surface, which may further enhance durability **Figures 8C,D**.

Ethanol Oxidation Reaction (EOR)

Ethanol is also a type of liquid fuel and used in direct ethanol fuel cells. For instance, Wang et al. developed 3D Pt_4Ni NFs as well as $PtNi_4$ porous octahedra by the corrosion of $PtNi_{10}$ solid nanoctahedra and compared their ethanol electrooxidation under alkaline media. Current density values at the −0.1 V in the positive scan are the 5.50 and 5.90 $mAcm^{-2}$ for the $PtNi_4$ porous $PtNi_4$ octahedra and Pt_4Ni NFs which both display a higher value as compared to the commercial Pt/C value (4.01 $mAcm^{-2}$). However, the corroded Pt_4Ni NFs as well as the $PtNi_4$ porous octahedra electrocatalyst were confirmed by mass activities, which are shown in the **Figures 9A,B**. The mass activity of Pt_4Ni NFs exhibited an improvement factor of 4.5 vs. $PtNi_{10}$ octahedra, and in the case of Pt_4Ni porous octahedra the improvement factor was 4.1, which are much better as compared to the commercial Pt/C.

According to these analyses, it is proved that ethanol electrooxidation displays improved catalytic activities after corrosion from solid $PtNi_{10}$ nanoctahedra to Pt_4Ni NFs as well

TABLE 1 | Comparison of electrocatalytic properties of Pt and Pd-based nanoframes toward FAOR, MOR, EOR, ORR, and bifunctional electrocatalysis.

Electrolyte	Types of electrocatalyst	*ECSA (H_{upd})	*Mass activity	*Mass activity enhancement vs. Pt/C	Type of electro-chemical reaction	*Specific activity	Specific activity enhancement vs. Pt/C	Stability (%) vs. Pt/C	Reference
0.5 M HCOOH + 0.5 M $HClO_4$	Pd NFs	–	–	7.5[a]	FAOR	–	–	80[b]	Wang et al., 2017b
0.25 M HCOOH+0.5 M H_2SO_4	Octaherdral PtCu NFs	4.5	–	–	FAOR	–	4.55[c]	–	Nosheen et al., 2013
0.5 M H_2SO_4 +1 M CH_3OH	$PtCu_2$ CONFs, PtCu UONFs	44.5 52.1	–	3355.6	MOR	155.9	7.5	72 53.9	Luo and Shen, 2017
0.5 M H_2SO_4+2 M CH_3OH	Pt-Cu yolk cage alloy NCs	8.3	0.7	–	MOR	–	2.8[c]	–	Zhang et al., 2013
0.1 M $HClO_4$ + 1.0 M CH_3OH	Pt-Cu NFs	41.3	0.98	1.72[c]	MOR	2.35	2.77[c]	–	Ding et al., 2015
0.1 M $HClO_4$ +1 M CH_3OH	$PtCu_3$ nanocages	35.7	–	–	MOR	–	14.1[d]	–	Xia et al., 2012
0.5 M KOH +1 M CH_3OH	PdCu Alloy Flower-like Nanocages	22.1	823	2.7[e]	MOR	–	–	–	Chen et al., 2018
0.5 M KOH + 1 M ethanol	Pt_4Ni NFs, $PtNi_4$ porous octahedra	–	–	4.5 4.1	EOR	–	5.90 5.50	–	Wang et al., 2015b
0.1 M $HClO_4$	Pt cubic NFs	–	0.45	0.82	ORR	0.53	1.17	140	Park et al., 2016
0.1 M $HClO_4$	PdPt NCs Octahedral nanocages (ONCs), Cubic nanocages (CNCs), Octahedral dendritic hollow (ODH) NCs, Cubic dendritic hollow (CDH) NCs	40.3 42.3 41.5 39.8	764.7 178.1 393.9 324.4	2.67[f] 1.39[g] 1.38[f] 2.52[g]	ORR	–	–	–	Hong et al., 2012a
0.1 M $HClO_4$	Cubic nanocage Octahedral nanocage	46.8 38.2	–	0.75	ORR	–	1.98	36[j]	Zhang et al., 2015a
0.1 M $HClO_4$	Ultrathin icosahedral Pt-enriched nanocages, octahedral nanocage, cubic nanocages	45.0	–	1.12[h] 0.75 0.38	ORR	–	2.48[h] 1.98 0.82	–	He et al., 2016
0.1 M $HClO_4$	Pt-Based Icosahedral Nanocages, Pt-based octahedral nanocages	36.5	–	–	ORR	–	3.50[i] 1.98	18[j]	Wang et al., 2016
0.1 M KOH	Cu-Pt nanocage	68	–	0.32	ORR	–	0.47	–	Dhavale and Kurungot, 2015
0.1 M $HClO_4$	Alloy Cu_3Pt NFs	30.2	–	–	ORR	–	–	–	Han et al., 2014
0.5 M KOH	PtCu hollow cubic NFs	23.4	–	0.732	ORR	–	3.12	19	Wang et al., 2018a
0.1 M $HClO_4$	Spiny rhombic dodecahedral CuPt NFs, CuPt alloy RD NFs	39.09 53.87	–	0.58 0.81	ORR	–	2.19	24.7	Lyu et al., 2017

(Continued)

TABLE 1 | Continued

Electrolyte	Types of electrocatalyst	*ECSA (H_{upd})	*Mass activity	*Mass activity enhancement vs. Pt/C	Type of electro-chemical reaction	*Specific activity	Specific activity enhancement vs. Pt/C	Stability (%) vs. Pt/C	Reference
0.5 M KOH	Cu-rich rhombic dodecahedral PtCu NFs	19.18	_	1.4[k]	ORR	_	2.7[k]	21.2	Huang et al., 2019
0.1 M $HClO_4$	Pt_3Ni NFs	1.52	_	0.9	ORR	_	1.5	40	Chen et al., 2014
0.1 M $HClO_4$	Pt-Ni multiframes	73.4	_	1.51	ORR	7.06	2.09	6.23	Kwon et al., 2018a
0.1 M $HClO_4$	Excavated NFs Hollow NFs	48.1 60.2	_	0.6 0.3	ORR	_	1.35[l] 0.55	_	Becknell et al., 2017
0.1M $HClO_4$	PtCuNi rhombic dodecahedra NFs	_	_	0.86	ORR	_	1.65	57	Huang et al., 2018
0.1 M $HClO_4$	PtPdRu dendritic nanocages	96.8	_	2.61[m]	ORR	_	1.81[m]	87	Eid et al., 2015
0.1 M $HClO_4$	PtPdNi truncated octahedral nanocages	55.7	_	1.14[n]	ORR	_	1.52[n]	85	Wang et al., 2019
M KOH 0.5 M KOH+1 M CH_3OH	PtCu NFs	12.4	_	0.211 2.26	ORR MOR	_	1.71 18.2	64.4	Zhang et al., 2016
0.1 M $HClO_4$ 0.1 M $HClO_4$ + 1 M CH_3OH	Co-PtCu rhombic dodecahedral NFs	31	_	1.56° 4.11°	ORR MOR	_	5.03[o] 13.3°	73.1 63.5	Kwon et al., 2018b
0.1M $HClO_4$, 0.1M $HClO_4$ + 0.1M HCOOH	$Pt_4PdCu_{0.4}$ Alloy NFs	_	_	1.04	ORR FAO	_	2.41 8.70	9.2 10.2	Kwon et al., 2018b
sM $HClO_4$	Pt_3Ni alloy tetrahexahedral NFs	_	_	0.47 4.2	ORR HCOOH	_	2.5	_	Wang et al., 2017a
0.5 M H_2SO_4+2 M CH_3OH 0.25M HCOOH + 0.5 M H_2SO_4	Pt-Pd-Rh-Ag NFs	_	300	3	MOR HCOOH	_	2.8	_	Saleem et al., 2016

*Units used for Pt based nanoframes are: ECSA (H_{upd}) ($m^2\ g_{Pt}^{-1}$), mass activity ($A\ mg_{Pt}^{-1}$), specific activity ($mA\ cm_{Pt}^{-2}$) While in case of PtPd NCs electrochemical values were calculated and compared with both Pt and Pd content, so units used $mA\ mg_{Pd+Pt}^{-1}$, etc. In case of Pd based NCs, electrochemical values were calculated, and compared with Pd content, so units used $mA mg_{Pd}^{-1}$, etc.

[a]Compared with Pd octahedral catalyst (unit used: $\mu A\ cm^{-2}$).

[b]Compared with the pristine Pd octahedral NCs.

[c]Also compared with Pt black.

[d]Compared with $PtCu_x$ nanoparticles and the commercial Pt electrocatalyst.

[e]Compared with commercial Pd/C.

[f]Compared with OD NCs.

[g]Compared with CD NCs.

[h]Also compared with Pd-Pt core-shell/C.

[i]Compare with Pt-based octahedral nanocages.

[j]Compared with the pristine Pt/C.

[k]Also compared with the $Pt_{18}Cu_{82}$ NCs, $Pt_{50}Cu_{50}$ NCS.

[l]Compared with hollow NFs.

[m]Also compared with PtPdRu nanodendrites.

[n]Also compared with Pd@PtPdNi MTOs.

[°]Also compared with PtCu RNF/C.

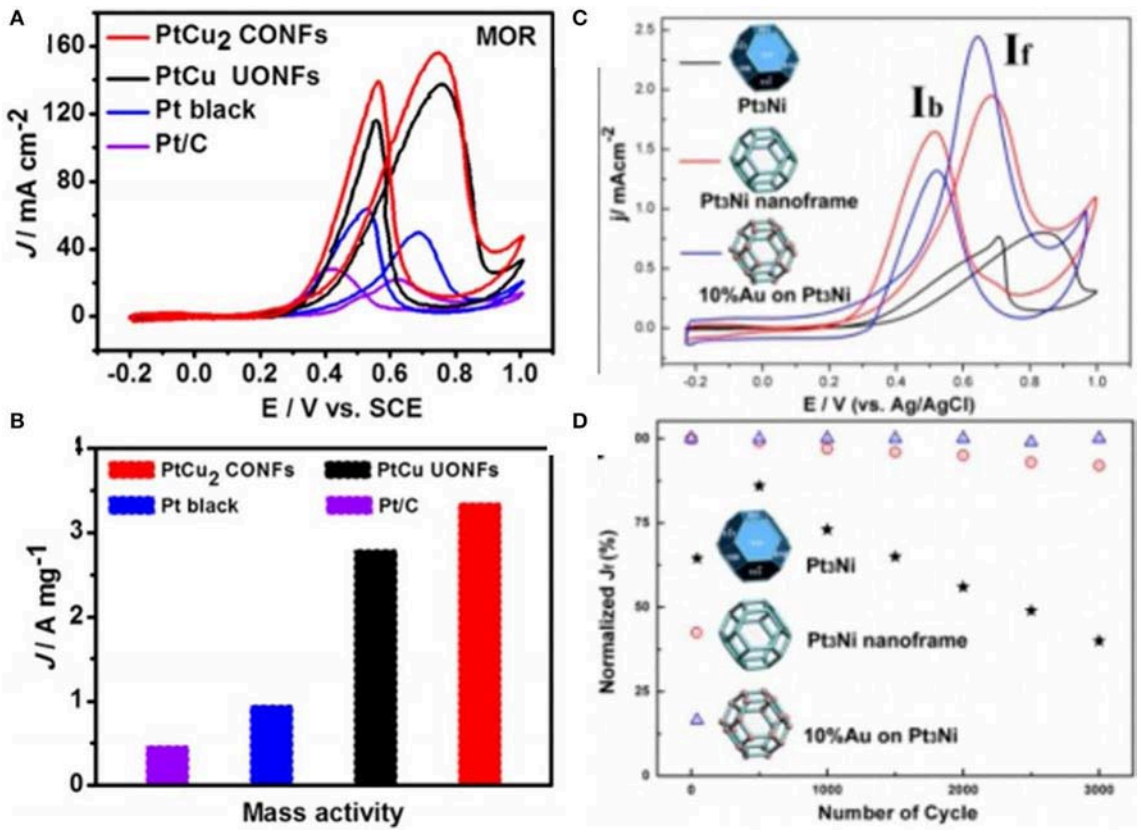

FIGURE 8 | Cyclic voltammetry (CV) curves of different electrocatalysts for methanol oxidation reaction **(A)** recorded at scanning rate of 50mV s -1 in 0.5M H2SO4+1M CH3OH solution, and formic acid oxidation reaction. **(B)** Mass activity of PtCu2 CONFs, PtCu UONFs, Pt black, and Pt/C electrocatalysts for methanol oxidation reaction. Modified with permission from Luo and Shen (2017) Copyright 2017, American Chemical Society. **(C)** Cyclic voltammograms of methanol oxidation on different catalysts in 0.1M HClO4 containing 1M MeOH. **(D)** Loss of peak current density in a forward scan as a function of cycling numbers. Modified with permission from Wu et al. (2014) Copyright 2014, American Chemical Society.

as $PtNi_4$ porous octahedra. Among these, Pt_4Ni NFs showed outstanding catalytic performance because of their higher surface area to volume ratio. In addition, $PtNi_4$ porous octahedra, a transparent structure with more voids and Pt-rich surface, shows superior catalytic activity. That is why the corroded nanocatalyst is superior to parent NCs in which mostly Pt atoms are buried inside, as shown in **Figure 9**.

Oxygen Reduction Reaction (ORR)

Pt-based nanocatalysts have been the most promising electrocatalysts toward ORR. But the main issue for platinum oxygen reduction is due to their lower abundance as well as higher price of Pt (Escudero-Escribano et al., 2018; Wang et al., 2018b). It is necessary to improve the efficacy of Pt atoms in catalysis by reducing Pt usage and to improve the ORR activity which is gained by both the surface and electronic structure. In terms of surface structure, hollow as well as open nanoarchitectures like nanocages and frames boost the number of Pt atoms on the edges and show higher activity for electrocatalysis. However, electronic effects act as another way for tuned ORR activity. As mentioned in the previous studies, the best method to tune the electronic structure is the alloying of Pt with other metals. In addition, Pt and Pd work differently, accumulate more electrons at Pt sites and may improve the catalytic performance in terms of ORR. However, noble metal-based NFs show higher catalytic activity and durability as compared to others. Park et al. (2016) reported the fabrication as well as catalytic activities of Pt cubic NFs with wall thickness <2 nm. The as synthesized Pt cubic NFs displayed a 6-fold enhancement in ORR mass activity over 20,000 cycles of repeated potential sweeping in comparison with Pt/C.

The morphology-based catalytic activities of several PdPt NCs in terms of ORR were studied, and their results have been compared with the commercial catalyst. For instance, Hong et al. synthesized nanocages of different shapes and compared them with the Pd@Pt core shell as well as NCs without hollow structure and commercial catalyst, and the as synthesized hollow structures showed enhanced ORR properties (Hong et al., 2012a). Similarly, Zhang et al. (2015a) developed Pt cubic and octahedra nanocages having [100] and [111] facets, respectively, which showed higher electrocatalytic activities in terms of ORR.

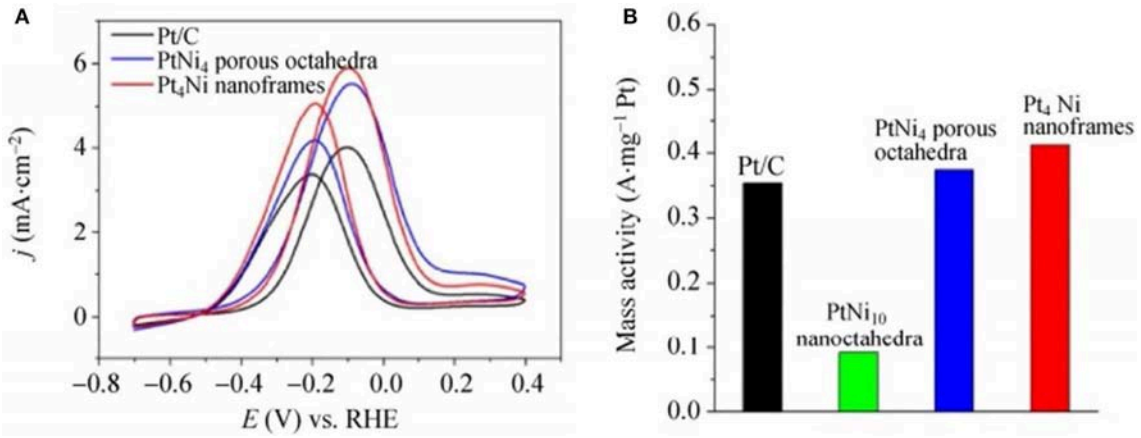

FIGURE 9 | Cyclic voltammograms of commercial Pt/C, $PtNi_4$ porous octahedra, and Pt_4 Ni nanoframes in **(A)** 0.5 M KOH + 1 M ethanol (scan rate: 50 mVs^{-1}); the current density was normalized to the ECSAs. **(B)** Mass activities measured at −0.1 V for ethanol oxidation on commercial Pt/C and three Pt-Ni catalysts; the current density was normalized to the weight of Pt loaded on the working electrode. Modified with permission from Wu et al. (2014) Copyright 2015, Tsinghua University Press and Springer-Verlag Berlin Heidelberg.

However, in case of many structure sensitive reactions, introducing defects like twin boundaries may reduce the activation energy and enhance the catalytic performance (He et al., 2016). For example, Pt-enrich few atom thick nanocages showed the mass activity 7 times larger in comparison with the Pt/C catalyst as well as 4 times larger when compared with the PdPt core shell/C catalyst. However, specific activity of Pt-enrich nanocage/C was 10 times that of the Pt/C catalyst and 3.5 times that of the PdPt core shell/C catalyst. By accelerated degradation testing, the stability of Pt-enriched nanocage/C was also studied. Pt-enriched nanocage/C displayed nearly no degradation after 10,000 cycles and icosahedral Pt-enriched nanocages were stable after accelerated degradation testing.

In addition, Wang et al. (2016) benchmarked the ORR performance of Pt based icosahedral nanocages in contrast to the Pt/C catalyst. The mass as well as specific activities of Pt icosahedral nanocage showed 6.7 and 10-fold enhancement, respectively, which is ascribed to the exposure of [111] facets, twin defects, and higher distribution of Pt. However, mass activity of Pt icosahedral nanocages was enhanced 4 times after 5,000 cycles of ADT when compared with the commercial catalyst before the durability tests.

In addition to single metal NFs, fabrication of Pt based bi-and multimetallic alloy NFs could display superior activity in terms of ORR. So, alloying of Pt with transition metals like Co, Cu, Ni, etc., could induce the compressive strain on NPs' surface because of shorter Pt-Pt distance as well as downshifting of d-band center of the Pt. Additionally, downshift of the d-band center weakens the adsorption of OH species that are intermediate to ORR, facilitates the dissociation of water molecules from catalyst surface and increases the ORR reaction rate of NPs.

Dhavale and Kurungot (2015) developed a CuPt nanocage via the galvanic displacement reaction. These CuPt NCs display 2.9-fold and 2.5-fold higher levels of mass activity as well as specific activity toward oxygen reduction reaction at 0.9 V vs. reversible hydrogen electrode. In addition, stability of CuPt nanocages was investigated by a durability test under alkaline conditions. So, CuPt NCs have higher surface area and provide additional active sites for the dissociative adsorption of oxygen and improved the ORR performance. The combination of Pt and Cu play a very important role in facilitating the dissociative adsorption of O_2. Similarly, rhombic dodecahedral Cu_3Pt NFs synthesized by the Han group are more active toward the ORR as compared to the CuPt core shell nanostructure (Han et al., 2014).

For instance, uniform PtCu alloy hollow cubic NFs were synthesized by Wang et al., and these 3D nanoarchitectures show the larger specific as well as mass activities and improved durability toward ORR in comparison with the Pt nanocubes, commercial Pt/C as well as Pt black catalyst under alkaline solution (Wang et al., 2018a).

Lyu et al. (2017) developed the CuPt alloy RD as well as spiny CuPt RD NFs. The 3D hollow structure of both sets of NFs and abundant surface defects make them active catalysts. Toward ORR, spiny RD NFs have shown the specific activity of 1.3 and 3 times as compared to the RD NFs and Pt/C catalyst. Huang et al. (2019) have fabricated 3D RD $Pt_{26}Cu_{74}$ NFs bound with multiple index facets that were synthesized by the effective facile robust solvothermal synthetic procedure. Due to exclusive morphology and the combined effect of the two metals, these $Pt_{26}Cu_{74}$ catalysts have shown higher activity as well as stability toward ORR in comparison with the $Pt_{18}Cu_{82}$, $Pt_{50}Cu_{50}$ NC, and Pt/C catalysts.

Controlling the structure at the atomic level can tune the catalytic performance of materials and may enhance the activity as well as durability. Han et al. developed highly active and durable Pt_3Ni NFs as catalysts with a 3D surface and 2 nm thin platinum skin. Both internal and external surfaces of frames are available for reactants, the and presence of segregated platinum skin demonstrate the excellent ORR activity. These Pt_3Ni NFs have exhibited enhanced mass activity and specific

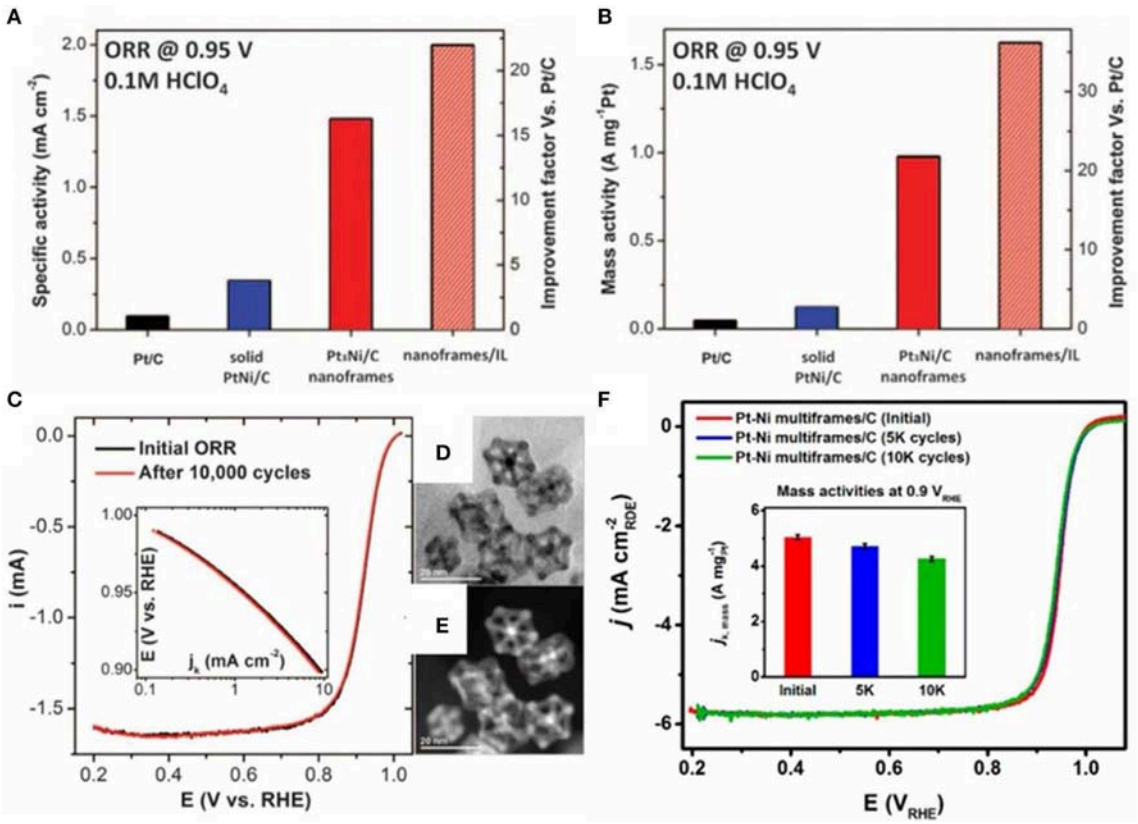

FIGURE 10 | Electrochemical properties of Pt3Ni nanoframes. **(A,B)** Specific activities **(A)** and mass activities **(B)** measured at 0.95 V, and improvement factors versus Pt/C catalysts. Because of the high intrinsic activity of the Pt3Ni nanoframes, the ORR activity values are given at 0.95 V in order to avoid the extensive error margin at 0.9 V introduced by the close proximity of current values to the diffusion-limited current. IL, ionic liquid. Electrochemical durability of Pt3Ni nanoframes. **(C)** ORR polarization curves and (inset) corresponding Tafel plots of Pt3Ni frames before and after 10,000 potential cycles between 0.6 and 1.0 V. **(C)** ORR polarization curves of the Pt-Ni multiframes/C before and after 5,000 and 10,000 cycles in an O2-saturated 0.1M HClO4 solution. The inset showing changes in mass activities of the Pt-Ni multiframes/C before and after potential cycles. **(D,E)** Bright-field STEM image **(D)** and dark-field STEM image **(E)** of Pt3Ni nanoframes/C after cycles. Modified with the permission from Chen et al. (2014) Copyright 2014, American Association for the Advancement of Science. **(F)** ORR polarization curves of the Pt-Ni multiframes/C before and after 5,000 and 10,000 cycles in an O2-saturated 0.1M HClO4 solution. The inset showing changes in mass activities of the Pt-Ni multiframes/C before and after potential cycles. Modified with permission from Kwon et al. (2018a) Copyright 2018, American Chemical Society.

activity that are 36 and 22 times those of the Pt/C, respectively. Furthermore, the frame structure was retained after 10,000 cycles, even during harsh electrochemical conditions as exhibited in **Figures 10A–E** (Chen et al., 2014). In another report, dendrite implanted PtNi multiframes display the ECSA of 73.4 m^2gPt^{-1} and mass activity of 1.51 A $mgPt^{-1}$ that is the 30 time higher than the Pt/C catalyst. It is noted that the ECSA as well as ORR performance of these dendrite embedded PtNi multiframes/C are due to their porous design, several active sites, and higher index facets **Figure 10F**.

3D Pt anisotropy of PtNi RD was tuned by controlling the ratio of Pt and Ni precursors—as a result, entire hollow NFs and excavated NFs were gained. These excavated NFs display the ∼10 times greater specific as well as ∼6 times larger mass activity in terms of ORR as compared to the Pt/C and double the mass activity of hollow NFs. However, the higher activity is due to more Ni content in the near-surface region and 2D sheet structure within the NFs, which minimized the number of buried Pt sites (Becknell et al., 2017). Wang et al. explained the preferential removal of Ni components of the tetrahexahedral (THH) PtNi NPs by using the CO. These PtNi (THH) NF structures demonstrated 8-fold higher ORR mass activity than in commercial Pt/C. In another report, PtNi NFs along (THH) and RD morphologies were used for the ORR. The as synthesized PtNi (THH) NFs display more enhanced ORR activity that shows 20.9 times larger mass activity in comparison with the commercial Pt/C.

It is observed that in addition to structure, composition also plays a very important role for the enhanced catalytic performance. For instance, RD PtCuNi NF catalysts display 6-fold higher mass activity as compared to commercial Pt/C in terms of ORR. Hollow PtPdRu dendrite nanocages with porous structure not only showed 3D surface active sites from both interior and exterior surfaces but also improved the resistance to particle aggregation. In addition, mass transfer of species inside the porous nanocages also increased. However, electronic as well as strain effect of three metal components also enhanced the activity. Therefore,

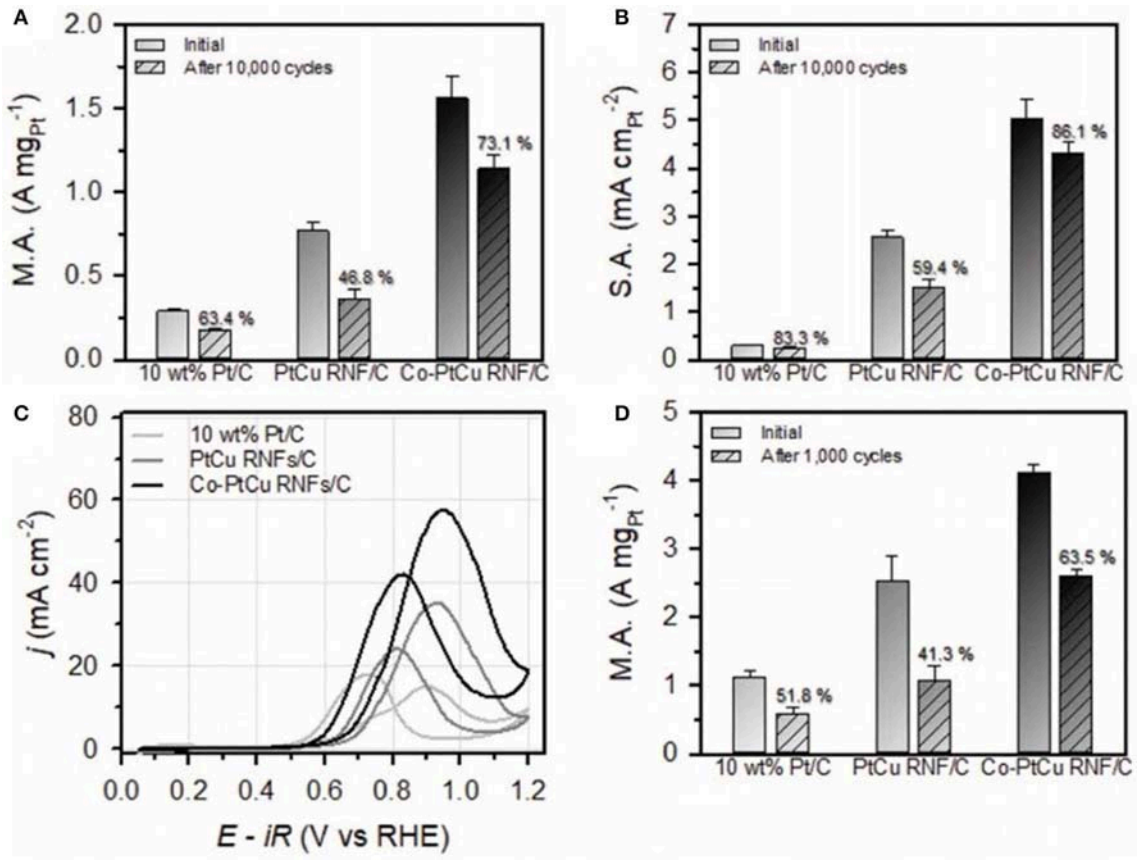

FIGURE 11 | (A,B) ORR mass and specific activities of electrocatalysts, before and after 10,000 ORR ADT cycles. **(C)** CVs of Co-PtCu RNF/C, PtCu RNF/C, and Pt/C catalysts in 0.1 M $HClO_4$+1 M CH_3 OH solution. **(D)** Mass activity of electrocatalysts for the MOR, before and after the ADTs. Modified with permission from Kwon et al. (2018b) Copyright 2018, WILEY-VCH Verlag GmbH & Co. KGaA, Weinheim.

trimetallic dendritic nanocages accelerate the kinetics of oxygen reduction. In comparison with the Pt/C, ECSA, mass activity as well as specific activity of PtPdRu dendritic nanocage were higher (Huang et al., 2018).

The PtPdNi mesoporous truncated octahedral nanocage showed higher catalytic performance toward the ORR relative to the core shell mesoporous truncated octahedra and Pt/C catalyst due to their mesoporous surface, hollow design, polyhedral shape (Wang et al., 2019).

Bifunctional Catalysts

As mentioned above, the Pt based alloy nanoarchitectures show excellent catalytic performance toward ORR and MOR. However, the bifunctional catalysts show more importance because they function as active catalysts in both anodes as well as cathodes of DMFCs. Among different hollow structures, NFs have received more attention because of their open 3D nanoframe structure. For instance, Zhang et al. (2016) synthesized the highly anisotropic 5-fold twin CuPt NFs, which shows more ORR as well as MOR activity, with a specific activity of 1.71 mA cm_{Pt}^{-2} toward ORR and 18.2 mA cm_{Pt}^{-2} for MOR. However, the rich concave site along with a higher coordination number demonstrated superior ORR activity. The most important point in this research is that the nanothorns on the edges as well as higher index facets provided extra active surface area.

In another report, Kwon et al. (2018b) fabricated Co-doped CuPt RD NFs which displayed a higher MOR specific activity of 13.3 mA cm_{Pt}^{-2} as well as a mass activity of 4.11 A mg_{Pt}^{-1}. In addition, ORR performance was also boosted with a specific activity of 5.03 mA cm_{Pt}^{-2} as well as a mass activity of 1.56 A mg_{Pt}^{-1}. However, protruded vertices also play a most important role in boosting the durability, which is confirmed by the study with the un-doped CuPt NFs (**Figure 11**). Another example is the highly composition-segregated PtNi NFs with open frame structure transformed from solid PtNi NCs. According to the catalytic results it is proven that these PtNi NFs have shown excellent catalytic performance toward ORR as well as alcohol oxidation in comparison with the commercial Pt/C catalyst. Other Pt based nanoarchitectures have been studied which are active as bifunctional catalysts in terms of ORR at the cathode as well as other fuel oxidation reactions at the anode like formic acid, ethanol, glycerol and ethylene glycol (Ye et al., 2017).

Pt_3Ni tetrahexaherdal NFs were developed by CO etching which is highly open, stable as and has a higher index microstructure which consists of a segregated Pt thin surface and downshifted d-band center, which is revealed by the

Density Functional Theory (DFT). These NFs showed excellent catalytic performance, such as higher stability in harsh reaction conditions, which promoted direct electrooxidation of formic acid to CO_2 and enhanced ORR activities. FAOR occurs on the Pt based electrode and proceeds via a dual path mechanism. In the first pathway, direct oxidation generates CO_2 and in the second pathway there is a generation of CO adsorption and then oxidation of CO_{ads} to CO_2 at higher potentials. Very recently, Wang et al. used Co etching at higher temperatures for the fabrication of Pt_3Ni tetrahexahedron NFs by using the facile as well as efficient method. So, these NFs revealed excellent stability under prolonged electrochemical potential cycles (Wang et al., 2017a).

CONCLUSION AND PERSPECTIVES

In recent years, noble metal-based NFs have received more attention because of their special structure as well as their physicochemical properties. For controlled synthesis and advanced applications of noble metal-based NFs, great efforts have been devoted in recent years. According to this review, we explained distinct methods such as the photocatalytic template method, electrodeposition, the Kirkendall effect, galvanic replacement, oxidative/chemical etching, and other methods for the fabrication of noble metal-based alloy NFs. In addition, different shapes of noble metal-based NFs have been developed and focused with ultrathin walls, high index facets, twin boundaries compositional segregation, and inner structural support. These noble metal-based NFs show excellent performance in fuel cells.

However, for the fabrication of noble metal-based NFs still more challenges are present such as tuning the porosity, voids, elemental composition as well as the thickness of ridges and atomic arrangement. For catalytic properties, controlling the ridge thickness with segregated Pt skin of metal-based NFs is of great importance and challenging. To preserve the stability of NFs after electrocatalytic cycling is a difficult task. To improve the stability of such nanostructures, the addition of dopant, or another stable structure inside NFs may secure the atomic arrangements and stability as well. The addition of a doping material can enhance the exposed atoms on the surface. NFs with more than three or four metals and other doping materials can further increase the activities and stabilities.

Furthermore, the implementation of theoretical studies must be considered to gain an understanding of the actual basis of the catalytic properties of multimetallic NFs. Additionally, theoretical studies should focus on the calculation of surface energies of the exposed atoms. It should also calculate the binding energies of reaction intermediates and surfaces of the electrocatalyst for multi-metallic structures. Density Functional Theory studies have been used for the few faceted bimetallic structures, but for the multimetallic NFs these studies are very rare. There is an urgent need to find easy calculation strategies for understanding multimetllic NFs with complex atomic arrangements, which can help to clearly identify the reasons behind their enhancement of activity and stability. Another necessity is to understand the rearrangements of atoms at atomic scale during the process of electrocatalysis. For this purpose, *in situ* study of electrochemical reactions may be a solution for the deep understanding of phase segregation and arrangement of atoms. Additionally, these catalysts should be reproducible at industrial level and should withstand the real operating environment.

Sometimes, the thermodynamic stability of alloy phases varies during synthesis and electrochemical cycling. Few efforts have been made to perform elecrocatalysis at higher potentials and temperatures to check the stability of catalysts under real operating conditions. In addition, hollow structures show a different electrochemical active surface area at different over potentials due to mass transportation and make its use limited in real applications. At low over potential, O_2 diffuses inside the inner part of hollow structures, and at high over potential, O_2 diffuses slowly inside the voids. Some groups proposed that the use of ionic liquids in place of aqueous liquids could fill the interior void of NFs and offer more O_2 solubility that could be beneficial for a real operating environment for fuel cells.

AUTHOR CONTRIBUTIONS

FN has substantial contributions to the conception, drafting and writing of this work. AS helped in writing the draft. TA contributed to the writing and revising it critically for important intellectual content. NH reviewed it and contributed in its revision. All authors read and agreed the final version of the manuscript.

REFERENCES

Au, L., Chen, Y., Zhou, F., Camargo, P. H. M., Lim, B., Li, Z. Y., et al. (2008). Synthesis and optical properties of cubic gold nanoframes. *Nano Res.* 1, 441–449. doi: 10.1007/s12274-008-8046-z

Bai, F., Sun, Z., Wu, H., Haddad, R. E., Xiao, X., and Fan, H. (2011). Templated photocatalytic synthesis of well-defined platinum hollow nanostructures with enhanced catalytic performance for methanol oxidation. *Nano Lett.* 11, 3759–3762. doi: 10.1021/nl201799x

Bai, T., Tan, Y., Zou, J., Nie, M., Guo, Z., Lu, X., et al. (2015). AuBr2—engaged galvanic replacement for citrate-capped Au–Ag alloy nanostructures and their solution-based surface-enhanced Raman scattering activity. *J. Phys. Chem. C* 119, 28597–28604. doi: 10.1021/acs.jpcc.5b10095

Becknell, N., Son, Y., Kim, D., Li, D., Yu, Y., Niu, Z., et al. (2017). Control of architecture in rhombic dodecahedral Pt-Ni nanoframe electrocatalysts. *J. Am. Chem. Soc.* 139, 11678–11681. doi: 10.1021/jacs.7b05584

Chen, C., Kang, Y., Huo, Z., Zhu, Z., Huang, W., Xin, H. L., et al. (2014). Highly crystalline multimetallic nanoframes with three-dimensional electrocatalytic surfaces. *Science* 343, 1339–1343. doi: 10.1126/science.1249061

Chen, S., Wu, H., Tao, J., Xin, H., Zhu, Y., and Chen, J. (2019). Pt–Ni seed-core-frame hierarchical nanostructures and their conversion to nanoframes for enhanced methanol electro-oxidation. *Catalysts* 9:39. doi: 10.3390/catal9010039

Chen, Y., Yu, Z., Chen, Z., Shen, R., Wang, Y., Cao, X., et al. (2016). Controlled one-pot synthesis of RuCu nanocages and Cu@Ru nanocrystals for the regioselective hydrogenation of quinoline. *Nano Res.* 9, 2632–2640. doi: 10.1007/s12274-016-1150-6

Chen, Z., He, Y. C., Chen, J. H., Fu, X. Z., Sun, R., Chen, Y. X., et al. (2018). PdCu alloy flower-like nanocages with high electrocatalytic performance for methanol oxidation. *J. Phys. Chem. C* 122, 8976–8983. doi: 10.1021/acs.jpcc.8b01095

Cong, Y., Yi, B., and Song, Y. (2018). Hydrogen oxidation reaction in alkaline media: from mechanism to recent electrocatalysts. *Nano Energy* 44, 288–303. doi: 10.1016/j.nanoen.2017.12.008

Davydova, E. S., Mukerjee, S., Jaouen, F., and Dekel, D. R. (2018). Electrocatalysts for hydrogen oxidation reaction in alkaline electrolytes. *ACS Catal.* 8, 6665–6690. doi: 10.1021/acscatal.8b00689

Dhavale, V. M., and Kurungot, S. (2015). Cu–Pt nanocage with 3-D electrocatalytic surface as an efficient oxygen reduction electrocatalyst for a primary Zn–air battery. *ACS Catal.* 5, 1445–1452. doi: 10.1021/cs501571e

Ding, J., Bu, L., Guo, S., Zhao, Z., Zhu, E., Huang, Y., et al. (2016). Morphology and phase controlled construction of Pt-Ni nanostructures for efficient electrocatalysis. *Nano Lett.* 16, 2762–2767. doi: 10.1021/acs.nanolett.6b00471

Ding, J., Zhu, X., Bu, L., Yao, J., Guo, J., Guo, S., et al. (2015). Highly open rhombic dodecahedral PtCu nanoframes. *Chem. Commun.* 51, 9722–9725. doi: 10.1039/C5CC03190G

Ding, L. X., Wang, A. L., Li, G. R., Liu, Z. Q., Zhao, W. X., Su, C. Y., et al. (2012). Porous Pt-Ni-P composite nanotube arrays: highly electroactive and durable catalysts for methanol electrooxidation. *J. Am. Chem. Soc.* 134, 5730–5733. doi: 10.1021/ja212206m

Eid, K., Wang, H., Malgras, V., Alothman, Z. A., Yamauchi, Y., and Wang, L. (2015). Trimetallic PtPdRu dendritic nanocages with three-dimensional electrocatalytic surfaces. *J. Phys. Chem. C* 119, 19947–19953. doi: 10.1021/acs.jpcc.5b05867

Escudero-Escribano, M., Jensen, K. D., and Jensen, A. W. (2018). Recent advances in bimetallic electrocatalysts for oxygen reduction: design principles, structure-function relations and active phase elucidation. *Curr. Opin. Electrochem.* 8, 135–146. doi: 10.1016/j.coelec.2018.04.013

Fang, Z., Wang, Y., Liu, C., Chen, S., Sang, W., Wang, C., et al. (2015). Rational design of metal nanoframes for catalysis and plasmonics. *Small* 11, 2593–2605. doi: 10.1002/smll.201402799

González, E., Arbiol, J., and Puntes, V. F. (2011). Carving at the nanoscale: sequential galvanic exchange and kirkendall growth at room temperature. *Science* 334, 1377–1380. doi: 10.1126/science.1212822

Hajfathalian, M., Gilroy, K. D., Golze, S. D., Yaghoubzade, A., Menumerov, E., Hughes, R. A., et al. (2016). A wulff in a cage: the confinement of substrate-based structures in plasmonic nanoshells, nanocages, and nanoframes using galvanic replacement. *ACS Nano* 10, 6354–6362. doi: 10.1021/acsnano.6b02712

Han, L., Liu, H., Cui, P., Peng, Z., Zhang, S., and Yang, J. (2014). Alloy Cu3Pt nanoframes through the structure evolution in Cu-Pt nanoparticles with a core-shell construction. *Sci. Rep.* 4:6414. doi: 10.1038/srep06414

He, D. S., He, D., Wang, J., Lin, Y., Yin, P., Hong, X., et al. (2016). Ultrathin icosahedral Pt-enriched nanocage with excellent oxygen reduction reaction activity. *J. Am. Chem. Soc.* 138, 1494–1497. doi: 10.1021/jacs.5b12530

Hong, J. W., Kang, S. W., Choi, B. S., Kim, D., Lee, S. B., and Han, S. W. (2012a). Controlled synthesis of Pd–Pt alloy hollow nanostructures with enhanced catalytic activities for oxygen reduction. *ACS Nano* 6, 2410–2419. doi: 10.1021/nn2046828

Hong, X., Wang, D., Cai, S., Rong, H., and Li, Y. (2012b). Single-crystalline octahedral Au–Ag nanoframes. *J. Am. Chem. Soc.* 134, 18165–18168. doi: 10.1021/ja3076132

Hu, Y., Chou, T., Wang, H., and Du, H. (2014). Monodisperse colloidal gold nanorings: synthesis and utility for surface-enhanced Raman scattering. *J. Phys. Chem. C* 118, 16011–16018. doi: 10.1021/jp504190d

Huang, L., Jiang, Z., Gong, W., Wang, Z., and Shen, P. K. (2018). Two-step etching fabrication of tunable ternary rhombic dodecahedral nanoframes for enhanced oxygen reduction electrocatalysis. *J. Power Sources* 406, 42–49. doi: 10.1016/j.jpowsour.2018.10.041

Huang, X., Zhang, H., Guo, C., Zhou, Z., and Zheng, N. (2009). Simplifying the creation of hollow metallic nanostructures: one-pot synthesis of hollow palladium/platinum single-crystalline nanocubes. *Angewandte Chem.* 121, 4902–4906. doi: 10.1002/ange.200900199

Huang, X. Y., You, L. X., Zhang, X. F., Feng, J. J., Zhang, L., and Wang, A. J. (2019). l-proline assisted solvothermal preparation of Cu-rich rhombic dodecahedral PtCu nanoframes as advanced electrocatalysts for oxygen reduction and hydrogen evolution reactions. *Electrochim. Acta* 299, 89–97. doi: 10.1016/j.electacta.2019.01.002

Jeyadevan, B., Cuya, J. L., Inoue, Y., Shinoda, K., Ito, T., Mott, D., et al. (2014). Novel nickel–palladium catalysts encased in a platinum nanocage. *RSC Adv.* 4, 26667–26672. doi: 10.1039/C4RA03091E

Kwon, H., Kabiraz, M. K., Park, J., Oh, A., Baik, H., Choi, S. I., et al. (2018a). Dendrite-embedded platinum–nickel multiframes as highly active and durable electrocatalyst toward the oxygen reduction reaction. *Nano Lett.* 18, 2930–2936. doi: 10.1021/acs.nanolett.8b00270

Kwon, T., Jun, M., Kim, H. Y., Oh, A., Park, J., Baik, H., et al. (2018b). Vertex-reinforced PtCuCo ternary nanoframes as efficient and stable electrocatalysts for the oxygen reduction reaction and the methanol oxidation reaction. *Adv. Funct. Mater.* 28:1706440. doi: 10.1002/adfm.201706440

Lai, W., Zhou, J., Jia, Z., Petti, L., and Mormile, P. (2015). Ag@Au hexagonal nanorings: synthesis, mechanistic analysis and structure-dependent optical characteristics. *J. Mater. Chem. C* 3, 9726–9733. doi: 10.1039/C5TC02017D

Li, J., Li, L., Wang, M. J., Wang, J., and Wei, Z. (2018). Alloys with Pt-skin or Pt-rich surface for electrocatalysis. *Curr. Opin. Chem. Eng.* 20, 60–67. doi: 10.1016/j.coche.2018.01.006

Liu, H. L., Nosheen, F., and Wang, X. (2015). Noble metal alloy complex nanostructures: controllable synthesis and their electrochemical property. *Chem. Soc. Rev.* 44, 3056–3078. doi: 10.1039/C4CS00478G

Luo, S., and Shen, P. K. (2017). Concave platinum–copper octopod nanoframes bounded with multiple high-index facets for efficient electrooxidation catalysis. *ACS Nano* 11, 11946–11953. doi: 10.1021/acsnano.6b04458

Lyu, L.-M., Kao, Y.-C., Cullen, D. A., Sneed, B. T., Chuang, Y.-C., and Kuo, C.-H. (2017). Spiny rhombic dodecahedral CuPt nanoframes with enhanced catalytic performance synthesized from Cu nanocube templates. *Chem. Mater.* 29, 5681–5692. doi: 10.1021/acs.chemmater.7b01550

Mahmoud, M. A., and El-Sayed, M. A. (2012). Metallic double shell hollow nanocages: the challenges of their synthetic techniques. *Langmuir* 28, 4051–4059. doi: 10.1021/la203982h

McEachran, M., Keogh, D., Pietrobon, B., Cathcart, N., Gourevich, I., Coombs, N., et al. (2011). Ultrathin gold nanoframes through surfactant-free templating of faceted pentagonal silver nanoparticles. *J. Am. Chem. Soc.* 133, 8066–8069. doi: 10.1021/ja111642d

Moghimi, N., Abdellah, M., Thomas, J. P., Mohapatra, M., and Leung, K. T. (2013). Bimetallic FeNi concave nanocubes and nanocages. *J. Am. Chem. Soc.* 135, 10958–10961. doi: 10.1021/ja405504q

Nosheen, F., Ni, B., Xu, X., Yang, H., Zhang, Z., and Wang, X. (2016). Facile synthesis of complex shaped Pt–Cu alloy architectures. *Nanoscale* 8, 13212–13216. doi: 10.1039/C6NR03511F

Nosheen, F., Zhang, Z. C., Zhuang, J., and Wang, X. (2013). One-pot fabrication of single-crystalline octahedral Pt-Cu nanoframes and their enhanced electrocatalytic activity. *Nanoscale* 5, 3660–3663. doi: 10.1039/c3nr00833a

Okazaki, K. I., Yasui, J. I., and Torimoto, T. (2009). Electrochemical deposition of gold frame structure on silver nanocubes. *Chem. Commun.* 28, 2917–2919. doi: 10.1039/b901469a

Park, J., Kanti Kabiraz, M., Kwon, H., Park, S., Baik, H., Choi, S.-I., et al. (2017a). Radially phase segregated PtCu@PtCuNi Dendrite@Frame Nanocatalyst for the oxygen reduction reaction. *ACS Nano* 11, 10844–10851. doi: 10.1021/acsnano.7b04097

Park, J., Kwon, T., Kim, J., Jin, H., Kim, H. Y., Kim, B., et al. (2018). Hollow nanoparticles as emerging electrocatalysts for renewable energy conversion reactions. *Chem. Soc. Rev.* 47, 8173–8202. doi: 10.1039/C8CS00336J

Park, J., Sa, Y. J., Baik, H., Kwon, T., Joo, S. H., and Lee, K. (2017b). Iridium-based multimetallic Nanoframe@Nanoframe structure: an efficient and robust electrocatalyst toward oxygen evolution reaction. *ACS Nano* 11, 5500–5509. doi: 10.1021/acsnano.7b00233

Park, J., Wang, H., Vara, M., and Xia, Y. (2016). Platinum cubic nanoframes with enhanced catalytic activity and durability toward oxygen reduction. *ChemSusChem* 9, 2855–2861. doi: 10.1002/cssc.201600984

Saleem, F., Ni, B., Yong, Y., Gu, L., and Wang, X. (2016). Ultra-small tetrametallic Pt-Pd-Rh-Ag nanoframes with tunable behavior for direct formic acid/methanol oxidation. *Small* 12, 5261–5268. doi: 10.1002/smll.201601299

Shahjamali, M. M., Bosman, M., Cao, S., Huang, X., Cao, X., Zhang, H., et al. (2013). Surfactant-free Sub-2 nm ultrathin triangular gold nanoframes. *Small* 9, 2880–2886. doi: 10.1002/smll.201300200

Shi, H., Ouyang, S., Peng, M., Wang, T., and Wang, S. (2015). Photocatalytic template synthesis of Pt nanocages with enhanced electrocatalytic performance. *ECS Electrochem. Lett.* 4, 38–42. doi: 10.1149/2.0061508eel

Stamenkovic, V. R., Mun, B. S., Mayrhofer, K. J., Ross, P. N., and Markovic, N. M. (2006). Effect of surface composition on electronic structure, stability, and electrocatalytic properties of Pt-transition metal alloys: Pt-skin versus Pt-skeleton surfaces. *J. Am. Chem. Soc.* 128, 8813–8819. doi: 10.1021/ja0600476

Sun, X., and Qin, D. (2015). Co-titration of AgNO3 and HAuCl4: a new route to the synthesis of Ag@Ag–Au core–frame nanocubes with enhanced plasmonic and catalytic properties. *J. Mater. Chem. C* 3, 11833–11841. doi: 10.1039/C5TC03002A

Tian, L., Zhong, X., Hu, W., Liu, B., and Li, Y. (2014). Fabrication of cubic PtCu nanocages and their enhanced electrocatalytic activity towards hydrogen peroxide. *Nanoscale Res. Lett.* 9:68. doi: 10.1186/1556-276X-9-68

Wang, A.-J., Zhang, X.-F., Jiang, L.-Y., Zhang, L., and Feng, J.-J. (2018a). Bimetallic alloyed ptcu nanocubic frames with three-dimensional molecular accessible surfaces for boosting oxygen reduction and glycerol oxidation reactions. *ChemCatChem* 10, 3319–3326. doi: 10.1002/cctc.201800188

Wang, A.-L., He, X.-J., Lu, X.-F., Xu, H., Tong, Y.-X., and Li, G.-R. (2015a). Palladium–cobalt nanotube arrays supported on carbon fiber cloth as high-performance flexible electrocatalysts for ethanol oxidation. *Angew. Chem. Int. Edn.* 54, 3669–3673. doi: 10.1002/anie.201410792

Wang, A.-L., Xu, H., Feng, J.-X., Ding, L.-X., Tong, Y.-X., and Li, G.-R. (2013). Design of Pd/PANI/Pd sandwich-structured nanotube array catalysts with special shape effects and synergistic effects for ethanol electrooxidation. *J. Am. Chem. Soc.* 135, 10703–10709. doi: 10.1021/ja403101r

Wang, C., Zhang, L., Yang, H., Pan, J., Liu, J., Dotse, C., et al. (2017a). High-indexed Pt3Ni alloy tetrahexahedral nanoframes evolved through preferential CO etching. *Nano Lett.* 17, 2204–2210. doi: 10.1021/acs.nanolett.6b04731

Wang, H., Li, Y., Deng, K., Li, C., Xue, H., Wang, Z., et al. (2019). Trimetallic PtPdNi-truncated octahedral nanocages with a well-defined mesoporous surface for enhanced oxygen reduction electrocatalysis. *ACS Appl. Mater. Interfaces* 11, 4252–4257. doi: 10.1021/acsami.8b18696

Wang, X., Figueroa-Cosme, L., Yang, X., Luo, M., Liu, J., Xie, Z., et al. (2016). Pt-based icosahedral nanocages: using a combination of {111} facets, twin defects, and ultrathin walls to greatly enhance their activity toward oxygen reduction. *Nano Lett.* 16, 1467–1471. doi: 10.1021/acs.nanolett.5b05140

Wang, Y., Chen, Y., Nan, C., Li, L., Wang, D., Peng, Q., et al. (2015b). Phase-transfer interface promoted corrosion from PtNi10 nanoctahedra to Pt4Ni nanoframes. *Nano Res.* 8, 140–155. doi: 10.1007/s12274-014-0603-z

Wang, Y.-J., Long, W., Wang, L., Yuan, R., Ignaszak, A., Fang, B., et al. (2018b). Unlocking the door to highly active ORR catalysts for PEMFC applications: polyhedron-engineered Pt-based nanocrystals. *Energy Environ. Sci.* 11, 258–275. doi: 10.1039/C7EE02444D

Wang, Z., Wang, H., Zhang, Z., Yang, G., He, T., Yin, Y., et al. (2017b). Synthesis of Pd nanoframes by excavating solid nanocrystals for enhanced catalytic properties. *ACS Nano* 11, 163–170. doi: 10.1021/acsnano.6b06491

Wu, H., Wang, P., He, H., and Jin, Y. (2012). Controlled synthesis of porous Ag/Au bimetallic hollow nanoshells with tunable plasmonic and catalytic properties. *Nano Res.* 5, 135–144. doi: 10.1007/s12274-012-0194-5

Wu, Y., Wang, D., Zhou, G., Yu, R., Chen, C., and Li, Y. (2014). Sophisticated construction of Au Islands on Pt–Ni: an ideal trimetallic nanoframe catalyst. *J. Am. Chem. Soc.* 136, 11594–11597. doi: 10.1021/ja5058532

Xia, B. Y., Wu, H. B., Wang, X., and Lou, X. W. (2012). One-pot synthesis of cubic PtCu3 nanocages with enhanced electrocatalytic activity for the methanol oxidation reaction. *J. Am. Chem. Soc.* 134, 13934–13937. doi: 10.1021/ja3051662

Xia, X., Wang, Y., Ruditskiy, A., and Xia, Y. (2013). 25th anniversary article: galvanic replacement: a simple and versatile route to hollow nanostructures with tunable and well-controlled properties. *Adv. Mater.* 25, 6313–6333. doi: 10.1002/adma.201302820

Xie, S., Lu, N., Xie, Z., Wang, J., Kim, M. J., and Xia, Y. (2012). Synthesis of Pd-Rh core–frame concave nanocubes and their conversion to rh cubic nanoframes by selective etching of the Pd cores. *Angew. Chem. Int. Edn.* 51, 10266–10270. doi: 10.1002/anie.201206044

Xiong, Y., Wiley, B., Chen, J., Li, Z.-Y., Yin, Y., and Xia, Y. (2005). Corrosion-based synthesis of single-crystal Pd nanoboxes and nanocages and their surface plasmon properties. *Angew. Chem. Int. Edn.* 44, 7913–7917. doi: 10.1002/anie.200502722

Xu, H., Yan, B., Li, S., Wang, J., Song, P., Wang, C., et al. (2018). Highly open bowl-like PtAuAg nanocages as robust electrocatalysts towards ethylene glycol oxidation. *J. Power Sources* 384, 42–47. doi: 10.1016/j.jpowsour.2018.02.067

Ye, H., Wang, Q., Catalano, M., Lu, N., Vermeylen, J., Kim, M. J., et al. (2016). Ru Nanoframes with an fcc structure and enhanced catalytic properties. *Nano Lett.* 16, 2812–2817. doi: 10.1021/acs.nanolett.6b00607

Ye, W., Chen, S., Ye, M., Ren, C., Ma, J., Long, R., et al. (2017). Pt4PdCu0.4 alloy nanoframes as highly efficient and robust bifunctional electrocatalysts for oxygen reduction reaction and formic acid oxidation. *Nano Energy* 39, 532–538. doi: 10.1016/j.nanoen.2017.07.025

Yoon, D., Park, S., Park, J., Kim, J., Baik, H., Yang, H., et al. (2014). One pot synthesis of hollow Cu-doped Ru octahedral nanocages via an in situ generated metastable Cu nanoparticle template. *Nanoscale* 6, 12397–12402. doi: 10.1039/C4NR03308F

Zeng, J., Zhang, Q., Chen, J., and Xia, Y. (2009). A comparison study of the catalytic properties of Au-based nanocages, nanoboxes, and nanoparticles. *Nano Lett.* 10, 30–35. doi: 10.1021/nl903062e

Zhang, H., Jin, M., Liu, H., Wang, J., Kim, M. J., Yang, D., et al. (2011). Facile synthesis of Pd-Pt Alloy nanocages and their enhanced performance for preferential oxidation of co in excess hydrogen. *ACS Nano* 5, 8212–8222. doi: 10.1021/nn202896q

Zhang, L., Roling, L. T., Wang, X., Vara, M., Chi, M., Liu, J., et al. (2015a). Platinum-based nanocages with subnanometer-thick walls and well-defined, controllable facets. *Science* 349, 412–416. doi: 10.1126/science.aab0801

Zhang, Q., Cobley, C. M., Zeng, J., Wen, L.-P., Chen, J., and Xia, Y. (2010). Dissolving Ag from Au–Ag alloy nanoboxes with H2O2: a method for both tailoring the optical properties and measuring the H2O2 concentration. *J. Phys. Chem. C* 114, 6396–6400. doi: 10.1021/jp100354z

Zhang, X.-F., Wang, A.-J., Zhang, L., Yuan, J., Li, Z., and Feng, J.-J. (2018a). Solvothermal synthesis of monodisperse PtCu dodecahedral nanoframes with enhanced catalytic activity and durability for hydrogen evolution reaction. *ACS Appl. Energy Mater.* 1, 5054–5061. doi: 10.1021/acsaem.8b01065

Zhang, Z., Liu, G., Cui, X., Chen, B., Zhu, Y., Gong, Y., et al. (2018b). Crystal phase and architecture engineering of lotus-thalamus-shaped Pt-Ni anisotropic superstructures for highly efficient electrochemical hydrogen evolution. *Adv. Mater.* 30:1801741. doi: 10.1002/adma.201801741

Zhang, Z., Luo, Z., Chen, B., Wei, C., Zhao, J., Chen, J., et al. (2016). One-pot synthesis of highly anisotropic five-fold-twinned PtCu nanoframes used as a bifunctional electrocatalyst for oxygen reduction and methanol oxidation. *Adv. Mater.* 28, 8712–8717. doi: 10.1002/adma.201603075

Zhang, Z., Yang, Y., Nosheen, F., Wang, P., Zhang, J., Zhuang, J., et al. (2013). Fine tuning of the structure of Pt–Cu alloy nanocrystals by glycine-mediated sequential reduction kinetics. *Small* 9, 3063–3069. doi: 10.1002/smll.201203200

Zhang, Z.-P., Zhu, W., Yan, C.-H., and Zhang, Y.-W. (2015b). Selective synthesis of rhodium-based nanoframe catalysts by chemical etching of 3d metals. *Chem. Commun.* 51, 3997–4000. doi: 10.1039/C4CC10050F

Zhao, M., Hood, Z. D., Vara, M., Gilroy, K. D., Chi, M., and Xia, Y. (2019). Ruthenium nanoframes in the face-centered cubic phase: facile synthesis and their enhanced catalytic performance. *ACS Nano*. doi: 10.1021/acsnano.9b02890

Zhu, C., Du, D., Eychmüller, A., and Lin, Y. (2015). Engineering ordered and nonordered porous noble metal nanostructures: synthesis, assembly, and their applications in electrochemistry. *Chem. Rev.* 115, 8896–8943. doi: 10.1021/acs.chemrev.5b00255

Zhu, G., Liu, J., Li, S., Zuo, Y., Li, D., and Han, H. (2019). Nickel-ion-oriented fabrication of Spiny PtCu alloy octahedral nanoframes with enhanced electrocatalytic performance. *ACS Appl. Energy Mater.* 4, 2862–2869. doi: 10.1021/acsaem.9b00205

Conflict of Interest Statement: The authors declare that the research was conducted in the absence of any commercial or financial relationships that could be construed as a potential conflict of interest.

Copyright © 2019 Nosheen, Anwar, Siddique and Hussain. This is an open-access article distributed under the terms of the Creative Commons Attribution License (CC BY). The use, distribution or reproduction in other forums is permitted, provided the original author(s) and the copyright owner(s) are credited and that the original publication in this journal is cited, in accordance with accepted academic practice. No use, distribution or reproduction is permitted which does not comply with these terms.

frontiers in Chemistry

REVIEW
published: 08 November 2018
doi: 10.3389/fchem.2018.00539

Big Potential From Silicon-Based Porous Nanomaterials: In Field of Energy Storage and Sensors

Rana Zafar Abbas Manj[1†], *Xinqi Chen*[1,2†], *Waheed Ur Rehman*[1], *Guanjia Zhu*[1], *Wei Luo*[1,3*] *and Jianping Yang*[1,3*]

[1] State Key Laboratory for Modification of Chemical Fibers and Polymer Materials, College of Materials Science and Engineering, Donghua University, Shanghai, China, [2] School of Physics and Mechanical and Electrical Engineering, Hubei University of Education, Wuhan, China, [3] Institute of Functional Materials, Donghua University, Shanghai, China

Silicon nanoparticles (SiNPs) are the promising materials in the various applications due to their unique properties like large surface area, biocompatibility, stability, excellent optical and electrical properties. Surface, optical and electrical properties are highly dependent on particle size, doping of different materials and so on. Porous structures in silicon nanomaterials not only improve the specific surface area, adsorption, and photoluminescence efficiency but also provide numbers of voids as well as the high surface to volume ratio and enhance the adsorption ability. In this review, we focus on the significance of porous silicon/mesoporous silicon nanoparticles (pSiNPs/mSiNPs) in the applications of energy storage, sensors and bioscience. Silicon as anode material in the lithium-ion batteries (LIBs) faces a huge change in volume during charging/discharging which leads to cracking, electrical contact loss and unstable solid electrolyte interphase. To overcome challenges of Si anode in the LIBs, mSiNPs are the promising candidates with different structures and coating of different materials to enhance electrochemical properties. On the basis of optical properties with tunable wavelength, pSiNPs are catching good results in biosensors and gas sensors. The mSiNPs with different structures and modified surfaces are playing an important role in the detection of biomarkers, drug delivery and diagnosis of cancer and tumors.

Keywords: porous structures, silicon nanomaterials, core shell, bioapplication, lithium ion battery

OPEN ACCESS

Edited by:
Fan Zhang,
Fudan University, China

Reviewed by:
Juchen Guo,
University of California, Riverside, United States
Chun Xu,
The University of Queensland, Australia

***Correspondence:**
Wei Luo
wluo@dhu.edu.cn
Jianping Yang
jianpingyang@dhu.edu.cn

†These authors have contributed equally to this work

Specialty section:
This article was submitted to Nanoscience, a section of the journal Frontiers in Chemistry

Received: *18 July 2018*
Accepted: *18 October 2018*
Published: *08 November 2018*

Citation:
Manj RZA, Chen X, Rehman WU, Zhu G, Luo W and Yang J (2018) Big Potential From Silicon-Based Porous Nanomaterials: In Field of Energy Storage and Sensors. Front. Chem. 6:539. doi: 10.3389/fchem.2018.00539

INTRODUCTION OF SILICON-BASED NANOSTRUCTURES

Silicon nanoparticles (SiNPs) have been remained a material of great interest with versatile and promising applications compared to the bulk material due to their physical and chemical properties (Dinh et al., 1996; Shiohara et al., 2009). SiNPs render a range of properties and series of functionalization (chemical and biological species), non-toxicity, biocompatibility and solubility in physiological fluid (Kang et al., 2009; Park et al., 2009; Wang et al., 2012). Electrical properties of silicon rely on temperature which is a conductor at room temperature. Electronic conductivity of SiNPs can be enhanced by doping of 3rd and 4th group elements of periodic table, functionalization and particle size (Anderson and Spear, 1977; Arora et al., 1982; Van Buuren et al., 1998; Veinot, 2006; Sivakov et al., 2009). SiNPs with different dyes also exhibit good photoluminescence (PL), fluorescent properties, tunable wavelength of excitation and emission, excellent photo and chemical stability (Chen et al., 2001; English et al., 2002; Shen et al., 2010; Intartaglia et al., 2012). Optical

properties of SiNPs strongly depend upon quantum confinement effect which varies with changes in particle size, concentration, and functionalization (Trwoga et al., 1998; Dancil et al., 1999; Ledoux et al., 2002). Due to these unique properties, SiNPs show numbers of applications in different fields like drug carriers, bioimaging, gas sensors, solar cells, electronics and energy storage devices.

In order to improve the performance in different applications, the structure of silicon has modified into the porous structure. On the basis of pores size, porous silicon is classified into microporous (pore diameter<2 nm), mesoporous (pore diameter 2–50 nm) and macro porous (pore diameter >50 nm). Because of alternation in the structure of silicon, a tremendous variation happen in optical properties of SiNPs which can attribute to the reduction in refractive index and enhancement in PL efficiency as compare to silicon at room temperature (Bsiesy et al., 1991; Astrova and Tolmachev, 2000; Chao, 2011; Min-Dianey et al., 2018). Surface properties also affected by varying the structure of silicon, the specific surface area per unit volume increase owing to pores in structure. Mesoporous structure of silicon improves surface to volume ratio, physical adsorption and electrical resistivity of silicon due to large void spaces (Karlsson et al., 2004; Hajji et al., 2006; Lasave et al., 2013; Azadeh et al., 2018). On behalf of these structural base properties, porous silicon nanomaterials have high potential to resolve challenges in different fields i.e. energy storage devices, sensors and biomedical applications (Yang et al., 2014a, 2016; Wang et al., 2015).

APPLICATIONS OF SILICON-BASED POROUS NANOMATERIALS

Lithium-Ion Batteries

Si as anode material has very high theoretical specific capacity 4,200 mA h g^{-1} as compare to graphite (Goodenough and Kim, 2009). In spite of high specific capacity of Si, Si as anode material has a major problem of volume expansion (up to 400%) during charging/discharging which lead to cracking of anode, electrical contact loss, unstable solid electrolyte interphase (SEI) film and finally fast fading of capacity (Yang et al., 2002; Jung et al., 2003; Baranchugov et al., 2007). Besides, the low intrinsic electrical conductivity (1.56×10^{-3} S m^{-1}) and lithium diffusivity of Si also limits its electrochemical performance. It has been noted that micro and nanostructure of silicon have good electrochemical performance as compare to bulk silicon as anode material (Ryu et al., 2004; Kim et al., 2008). The volume expansion of silicon anode material has been controlled by introducing nanostructure of silicon as Si micro/nanostructures, nanowires, hollow-structured and porous silicon (Li et al., 2000; Huang and Zhu, 2010; Xu et al., 2011; Wen et al., 2013; Cho et al., 2017; Kim et al., 2017). Spherical nano-particles of silicon having diameter of 150–200 nm was used as bulk silicon anode material which exhibited capacity higher than 500 mA h g^{-1} at current 0.2 A g^{-1} up to 100 cycles (Liang et al., 2018). To further enhance the electrochemical properties, silicon nanowires (SiNWs) on stainless steel was prepared by CVD process. SiNWs as anode

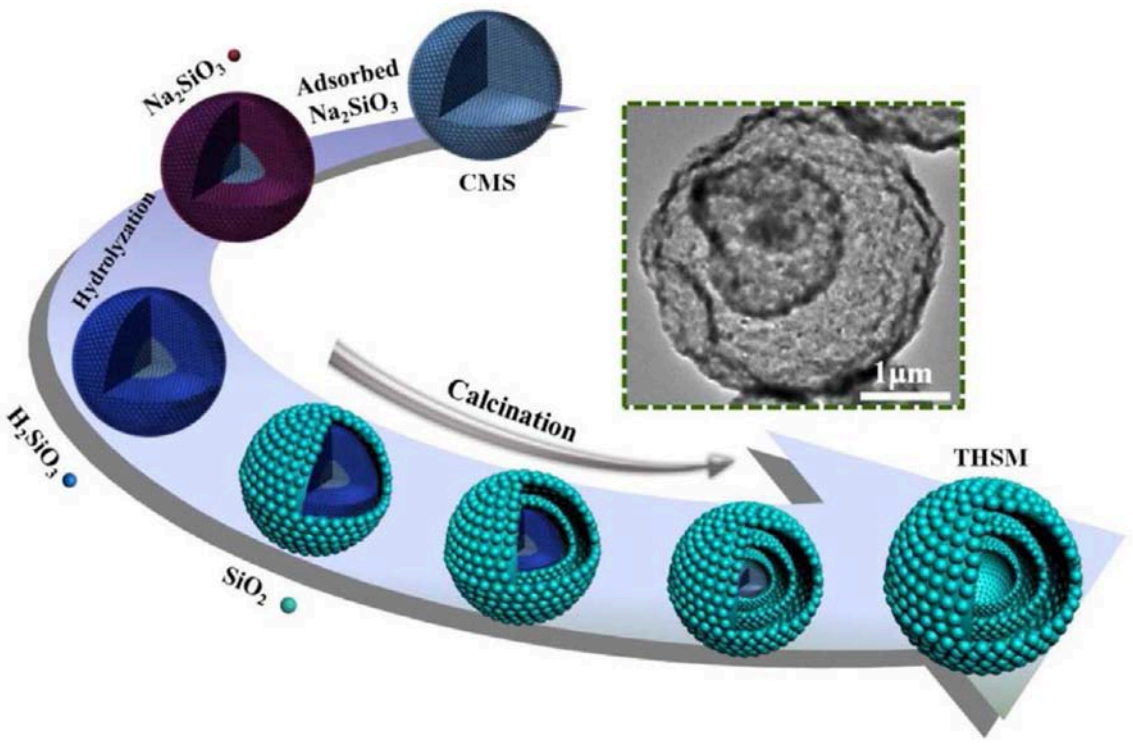

FIGURE 1 | Schematic diagram of preparation of multi-shell hollow silica sphere (Ma et al., 2017b). Copyright © 2017 Elsevier B.V. All rights reserved.

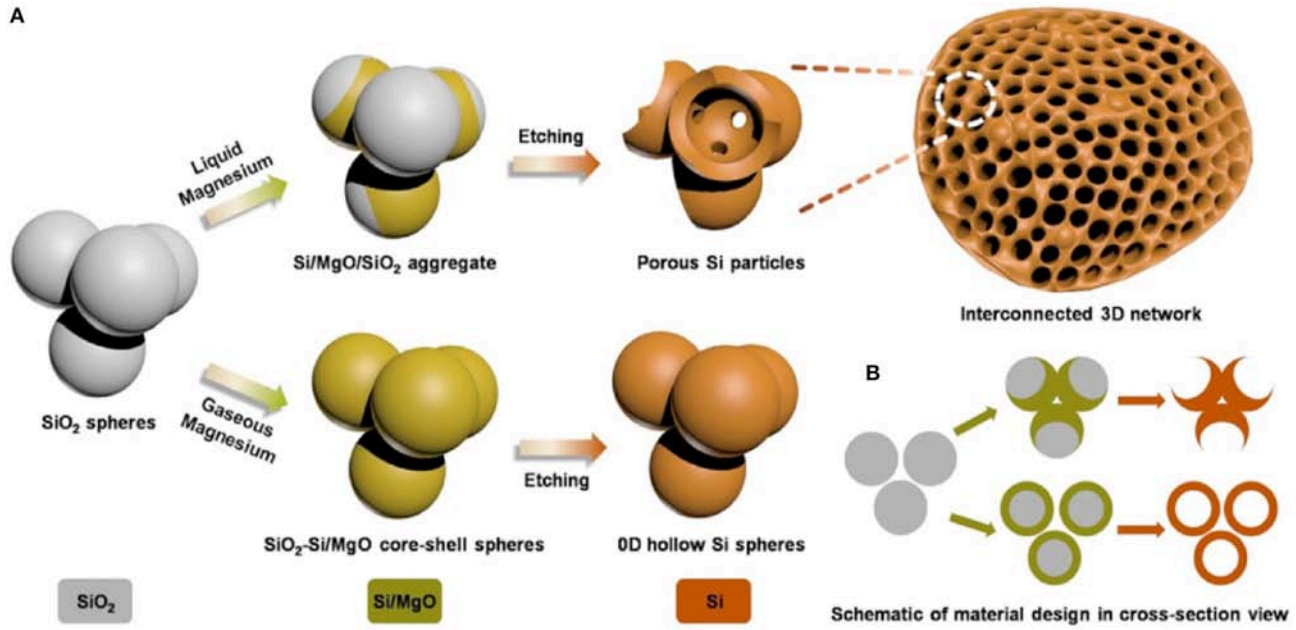

FIGURE 2 | Schematic diagram of a process of synthesis mesoporous silicon, in **(A,B)**, three-dimensional (3D) view and two-dimensional (2D) cross-sectional view (Wu et al., 2016). Copyright © 2016 Elsevier B.V. All rights reserved.

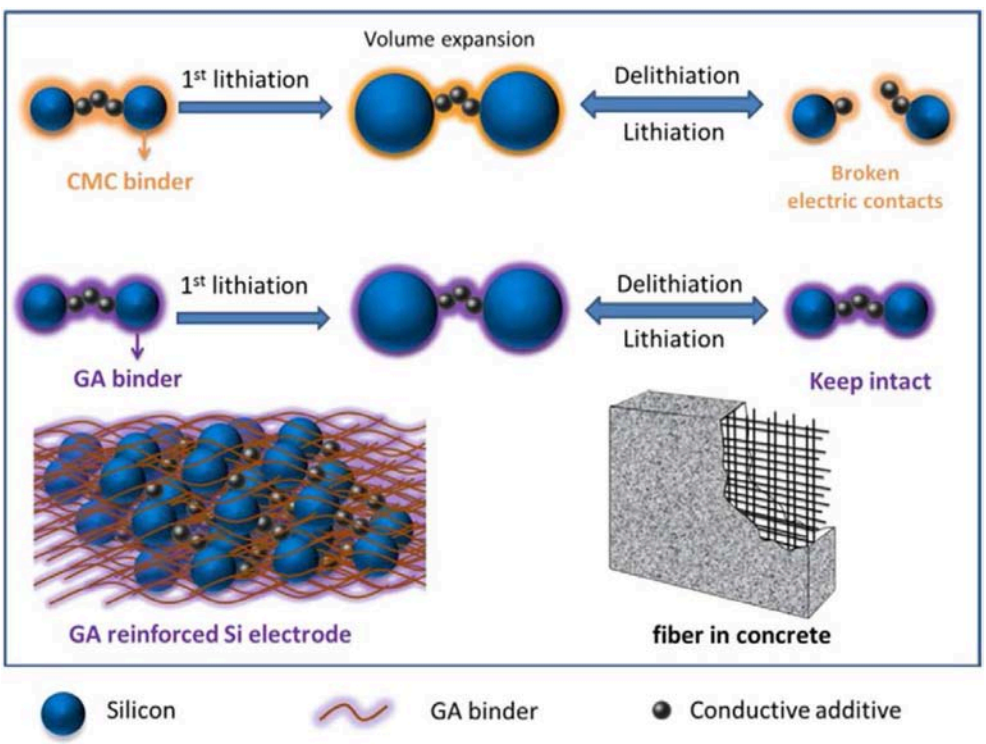

FIGURE 3 | Schematic diagram to elaborate the working of CMC and GA binder during volume change in charging/discharging (Ling et al., 2015). Copyright © 2014 Elsevier Ltd. All rights reserved.

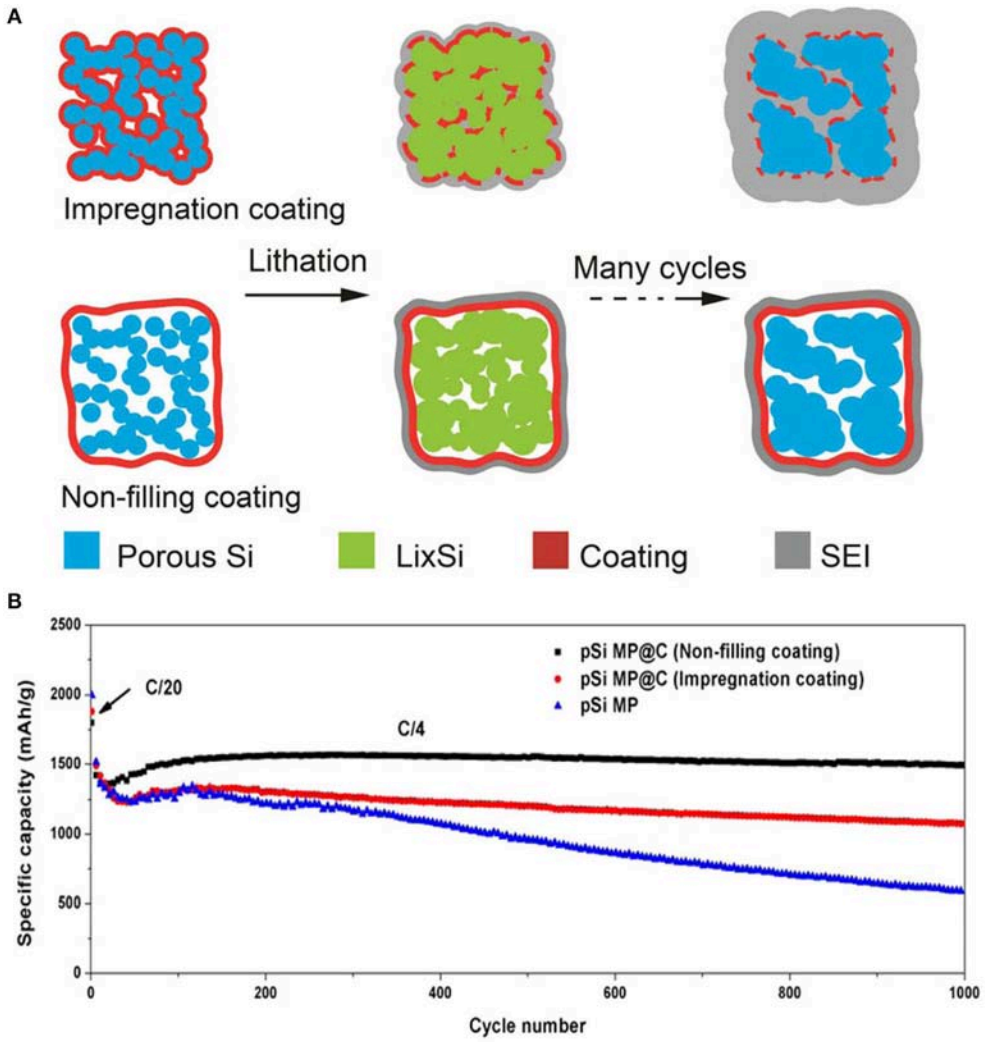

FIGURE 4 | (A) Schematic diagram of the coating process, the evolution of SEI film of impregnation and non-filling coating during cycling. **(B)** Analysis of specific capacity of non-filling, impregnation coated pSiMPs over 1,000 cycles. Reproduced with permission (Lu et al., 2015). Copyright © 2015, American Chemical Society.

material delivered great area capacity of 7.1 cm with retention 60 % at current rate C/50 and good rate performance (Leveau et al., 2016). To accommodate volume expansion of Si anode and cycling stability, the structure of silicon was modified to the spherical hollow structure of silicon as shown in **Figure 1**. The multi-shell hollow silica microsphere (MHSM) was prepared by the sacrificial template process. MHSM as anode material delivered high capacity 750 mA h g^{-1} at current 0.1 A g^{-1} after 500 cycles. MHSM exhibited excellent cycling stability because of a porous structure which provides the easy reaction among the lithium ion and anode material and reduced the reaction path (Ma et al., 2017b). Further, three-dimensional (3D) macroporous silicon was synthesized by magnesiothermic reduction to enhance structure stability, capacity and cycle life of Si anode as shown in **Figure 2**. 3D porous silicon as anode material showed high capacity with excellent retention and cycle life (1,058 mA h g^{-1} with current rate 2 A g^{-1} after 800 cycles) (Wu et al., 2016). The structural modification in silicon anode material provided a significant improvement in electrochemical performance as compared to bulk silicon anode. The large area of nano-structure and greater voids of porous structure provided a large surface to the diffusivity of lithium ions and controlled the pulverization and compensated the electrical contact loss.

Silicon Nanostructures With Binders in LIBs

The nano-structural silicon enhanced the electrochemical performance to some extent, but a modification in silicon anode was still required. Further electrical contact loss in silicon anode due to pulverization was controlled by adding conductive additives and polymer binders in Si anode (Priyono et al., 2017; Teng et al., 2018). Conductive additives provided an electronic path in charging/discharging but after some cycles failed to contact silicon particles because conductive additives could not provide binding force Si particles

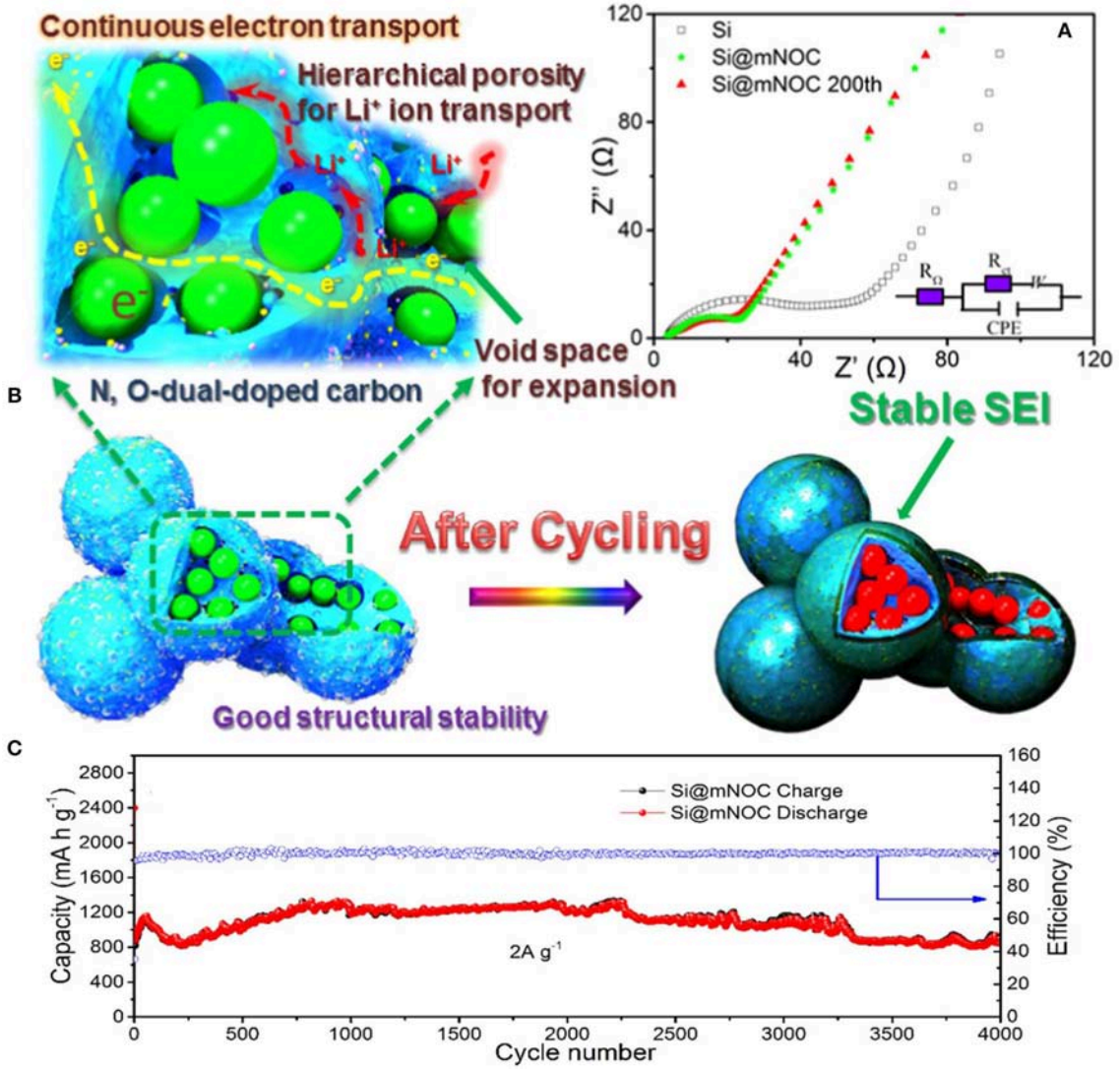

FIGURE 5 | (A) Evaluation of SEI film and surface kinetics of Si@mNOC during cycling. **(B)** Schematic representation of conductivity, stability and stable SEI film on Si@mNOC after cycling. **(C)** Cycling performance with coulombic efficiency at current 2 A g^{-1}. Reproduced with permission (Yu et al., 2016). Copyright © 2017 Elsevier Ltd. All rights reserved.

(Beattie et al., 2008; Renganathan et al., 2010). To overcome these issues, numbers of conductive binders were used to improve electronic conductivity and stability of Si anode for long cycle life (Lin et al., 2016; Sarode et al., 2018). By taking the advantages of self-healing ability of a material, a conductive binder was prepared by use of ureidopyrimidinone (UPy) and polyethylene glycol (PEG). By use UPy-PEG-UPy as a binder with SiNPs in anode material excellent electrochemical performance was achieved. SiNPs anode with UPy-PEG-UPy binder delivered high capacity 1,454 mA h g^{-1} over 400 cycles with the decay of 0.04 % per cycle. The self-healing ability of UPy-PEG-UPy binder maintained the good integrity of silicon anode as compared to the traditional binder (Yang et al., 2018). Electrical contact loss in Si anode has been tried to control by the chemically bonded conductive binder. The aqueous hybrid gel prepared with sodium carboxymethyl cellulose by cross-linker sodium borate and used with silicon as an anode material. Hybrid gel covalently bonded with silicon particles and also acted as a buffer for silicon particles. Si anode with gel exhibited good capacity and cycle life of 1211.5 mA h g^{-1} after 600 cycles with coulombic efficiency 88.95 % (Zhang et al., 2018). Furthermore, to enhance the electrochemical properties and stability of Si anode, a naturally derived gum Arabic (GA) polymer (as fiber-reinforced concrete) was used to control cracking of Si anode during charging/discharging as shown in **Figure 3**. Si anode with GA polymer binder delivered high capacity as compare to CMC binder 2,000 mA h g^{-1} at current rate 1C after 500 cycles and excellent cycle life with capacity

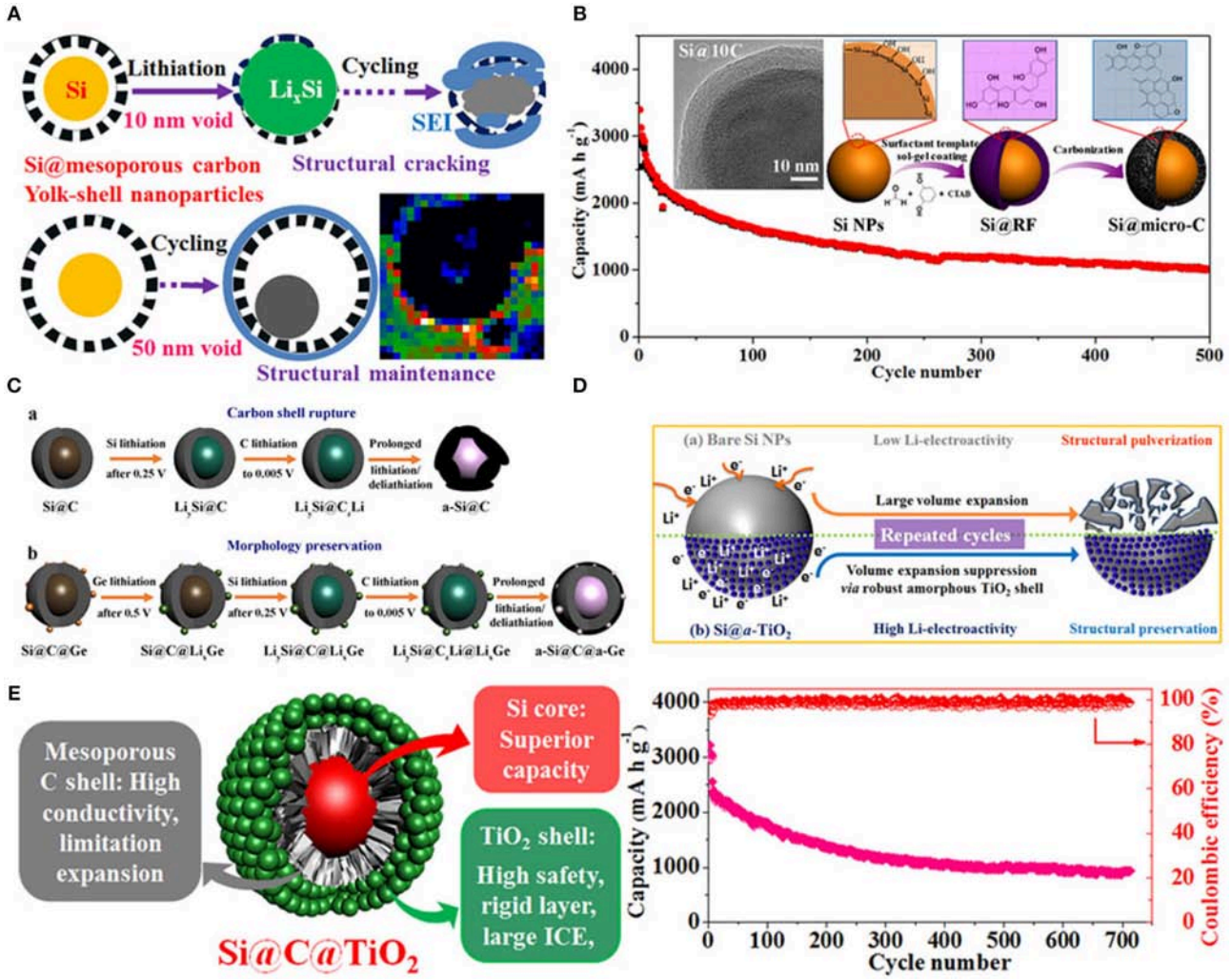

FIGURE 6 | (A) Schematic representation of charging/discharging process of the yolk-shell structured Si@mC electrode with 10 and 50 nm voids. Reproduced with permission (Yang et al., 2015). Copyright © 2015 Published by Elsevier Ltd. **(B)** Schematic diagram of synthesis process of Si@micro-C composite, surface morphology, and cycle performance. Reproduced with permission (Luo et al., 2016b). © 2016 Elsevier Ltd. All rights reserved. **(C)** Schematic representation of charging/discharging process of Si@C and Si@C@Ge. Reproduced with permission (Luo et al., 2016a). **(D)** Schematic representation of the behavior of SiNPs and Si@TiO_2 before and after cycling. Reproduced with permission (Yang et al., 2017). **(E)** Schematic illustration of conclusion and cycling performance of Si@C@TiO_2 as anode material. Reproduced with permission (Luo et al., 2016c). Copyright © 2016, American Chemical Society.

1,000 mA h g^{-1} at rate 1C over 1,000 cycles. Glycoprotein chain in GA provided good mechanical properties which behaved like a fiber in concrete and polysaccharide provided binding force due to the presence of hydroxyl groups (Ling et al., 2015). Conductive binder polymers have significantly enhanced the electrochemical properties of Si anode material and its structural integrity.

Coated-Silicon Nanostructures in LIBs

Continuous charging/discharging solid electrolyte interphase film by direct interaction between electrolyte and silicon particles is developed on silicon particles in the anode. SEI film on silicon particles acts as a barrier to further diffusion of lithium-ion and directly affects cycle life of Si anode (Yang et al., 2008; Zhou et al., 2014). Fast decay in capacity and SEI film has been controlled by a coating of different materials on silicon particles. Coating of different materials provides a barrier between direct contacts of electrolyte to active silicon which leads to decrease interfacial reaction between electrolytes to the electrode material and suppress the transformation of structure because of mechanical properties of coating materials (Kim et al., 2015). To stabilize SEI film, carbon has been used widely in the coating of silicon particles due to its good electronic and mechanical properties. Carbon coating controls the pulverization of silicon particles and prevents direct contact of the electrolyte with silicon particles (Yi et al., 2017). By leaving interior voids, unfilled pSiMPs was coated with carbon as shown in **Figure 4**. Unfilled carbon coated SiMPs as anode material delivered high capacity and excellent

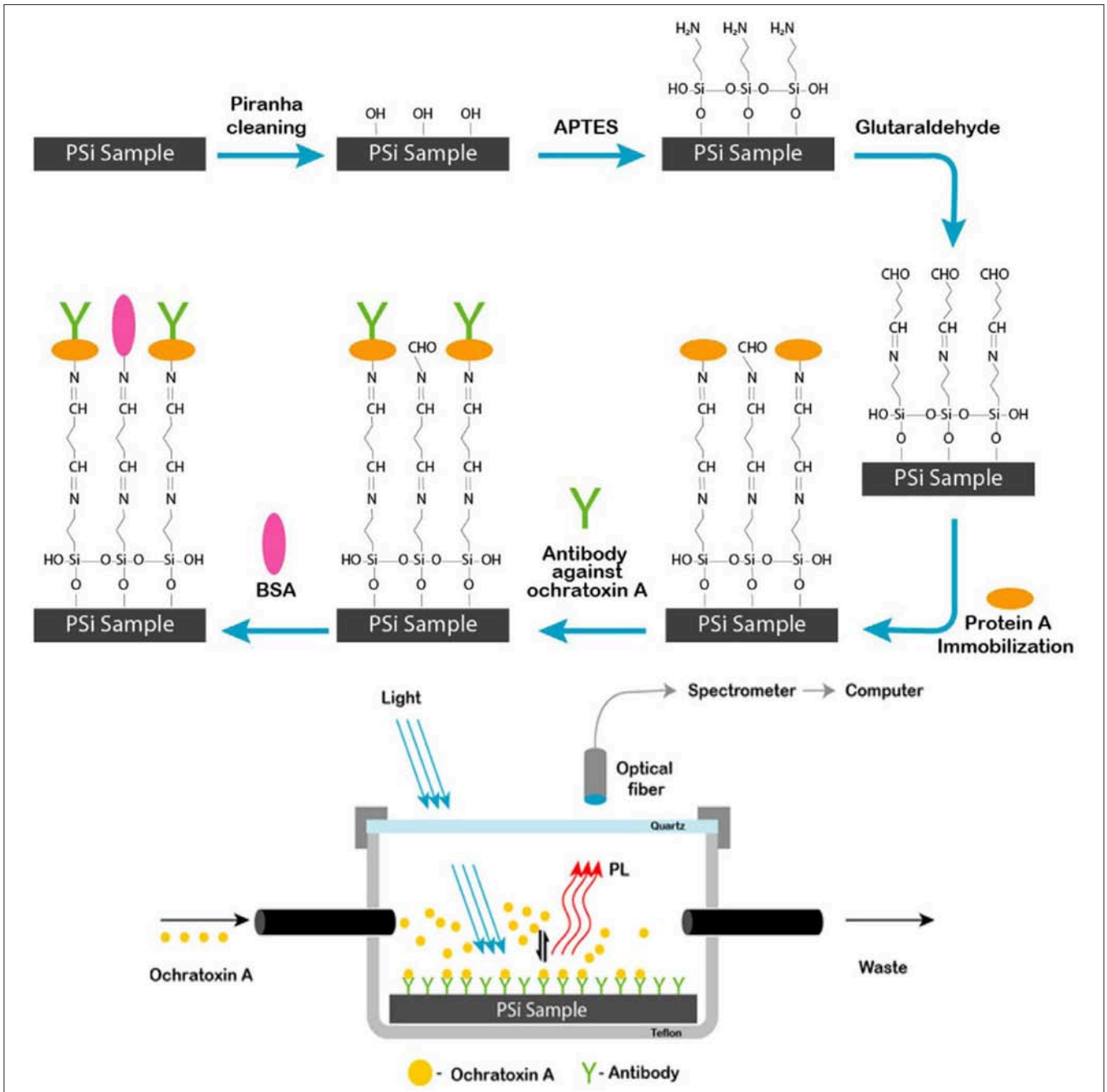

FIGURE 7 | Schematic diagram of a process of synthesis porous silicon sample and setup for range of ochratoxin (0.01–5 ng/ml) detection by using pSi immunosensor under UV Laser. Protein A covalently immobilized surface on pSiNPs further modified by anti-OTA and BSA which was sensitive toward ochratoxin (Myndrul et al., 2017). Copyright © 2017 Elsevier B.V. All rights reserved.

cycle life (1,500 mA h g^{-1} at current rate C/4 over 1,000 cycles). Exterior carbon coating prevented the direct contact electrolyte with silicon particles and interior voids provided extra space to silicon particles during volume expansion as in **Figure 4** (Lu et al., 2015). Furthermore, Apple-like silicon@nitrogen, oxygen-doped carbon hierarchical mesoporous structure was prepared and used as anode material shown in **Figure 5**. Si@mNOC as anode material delivered good capacity and long cycle life (1,203 and 900 mA h g^{-1} at current rate 2 A g^{-1} after 2,000 and 4,000 cycles in **Figure 5C**). In Si@mNOC, the void space and mesoporous structure accommodated the volume expansion and facilitated ion transport and also controlled SEI film and improved the mechanical stability of the anode material. Nitrogen and oxygen doping improved the electronic conductivity and electrochemical

performance of Si@mNOC anode shown in **Figures 5A,B** (Yu et al., 2016). Many attempts have been taken to enhance the kinetics of ionic diffusion and electrical conductivity of coating material (carbon) by doping of different atoms (oxygen, nitrogen, and sulfur) and by using hierarchical structure (Xu et al., 2015; Wang et al., 2016).

Yolk-Shell and Core-Shell Silicon Nanostructures

Furthermore, electrochemical properties of silicon anode material enhanced by the modified structure of SiNPs and by using double coating of different materials (Ensafi et al., 2017; Jang et al., 2018; Xing et al., 2018). Herein, to improve electrochemical performance of anode material in LIBs, a series of surface and interface engineering to fabricate carbon and titanium oxide coated Si with yolk and core-shell structure have been fabricated as shown in **Figure 6** (Luo et al., 2017). First, Si@mesoporous carbon yolk-shell structure was prepared which provided extra voids inside coating as shown in **Figure 6A**. This novel yolk-shell structure led to enhance rate capability, cycle life with good specific capacity and uniform stable SEI film which exhibited good electrochemical performance (Yang et al., 2015). Second, SiNPs coated with a controllable and uniform thickness of carbon coating (2–25 nm) to form a core-shell structure. This coaxial core-shell structure enhanced the stability of anode and exhibited good specific capacity over 500 cycles as shown in **Figure 6B**. (Luo et al., 2016b). Third, Si@C coated with germanium by a simple sol-gel process and formed Si@C@Ge core-satellite NPs as shown in **Figure 6C**. Coating of germanium on Si@C exhibited high electrochemical kinetic and good structural stability as compared to uncoated Si@C (Luo et al., 2016a). Fourth, to enhance initial coulombic efficiency, lithium storage safety, and structure integrity, amorphous TiO_2 coated on SiNPs and made core-shell structure by the sol-gel process. Amorphous TiO_2 shell provided high lithium storage safety by increasing lithium kinetic because of TiO_2 showed a low resistance of Li diffusion during the electrochemical process as shown in **Figure 6D**. Amorphous TiO_2 shell acted as an elastic belt on SiNPs to control volume variation during charging/discharging and stabilized the SEI film by resisting the contact of electrolyte to active silicon which has led to high cycle life (Yang et al., 2017). Last, SiNPs coated with double layer of carbon and TiO_2 (Si@C@TiO_2) via a two-step sol-gel process. Si@C@TiO_2 composite as anode material handled conductivity, volume change during lithiation/delithiation and unstable SEI film. In Si@C@TiO_2 composite carbon enhanced electrical conductivity by providing an electronic path to electron during the electrochemical process, TiO stabilized structure integrity of anode by providing mechanical properties and controlled the SEI film by stopping the direct contact of electrolyte to silicon as shown in **Figure 6E** (Luo et al., 2016c).

Sensors

On the basis of the surface, optical and electrical properties, pSiNPs have been used for detection of different atoms, gas molecules, pH and polar/non-polar organic solvent (Harraz et al., 2014; Kashyout et al., 2015; Sarkar et al., 2018). To improve the fluorescence properties of silicon oxides, these were coated with dye molecules through different functional groups. Photoluminescence intensity depends upon concentration and size of silicon particles. The doping of different particles also affected by other organic vapors which are under examinaion (Zhang et al., 2010; Huang et al., 2015; Moret et al., 2016; Nayef and Khudhair, 2018). On the basis of fluorescence quenching of pSiNPs with other atoms, pSiNPs have been used for detection of different ions and molecules (Cu^{+2}, NO_2, Hg^{2+}, NH_3, Ag^{2+}, and ethyl carbamate) (Xia et al., 2013; Luo et al., 2018; Qin et al., 2018a,b). PL immunosensor was prepared by functionalization of porous silicon with Protein-A and bovine serum albumin (BSA) for detection of Ochratoxin A under UV Laser as shown in **Figure 7**. BSA added to active sites to blocking adsorption of protein on these sites and improve sensitivity. Functionalized-pSi immunosenor was tested under the wide range of concentrations (0.01–5 ng/ml) which was exhibited high sensitivity and high-speed detection even at low level of ochratoxin A. It was observed PL-intensity decreased as concentration of Ochratoxin A increased in sample (Myndrul et al., 2017). Carbon doped silicon nanoparticles were prepared by the mild reaction and used for detection Hg^{2+}, Ag^{2+}, and latent fingerprints. SiNPs showed good sensing ability for Hg^{2+} and Ag^{2+} by highly quenched with Hg^{2+}, Ag^{2+} and provided high range wavelength of excitation and emission. SiNPs also used as fluorescence label to detect a fingerprint on different non-porous material surfaces. In the presence of ultraviolet excitation, SiNPs provided excellent fluorescent images on different surfaces as shown in **Figure 8** (Zhu et al., 2018). SiNPs are easy to synthesize and due to numbers of properties (non-toxicity, wide range fluorescence spectra, good photoluminescence peak, solubility and large surface area) remained in great interest to apply in different fields.

Other Applications

On the basis of the surface, optical, biocompatible and nontoxic properties, pSiNPs have been used in bio-applications as Nano carriers, diagnostics and for the treatment of cancer (Vaccari et al., 2006; Donnorso et al., 2012; Haidary et al., 2012; Kaasalainen et al., 2012; Tzur-Balter et al., 2013; Yang et al., 2014b; Min-Dianey et al., 2018). The mSiNPs have great potential toward drug delivery devices due to their easy functionalization, good loading/release rate, solubility, tunable porosity and a large surface area (200–800 m^2/g) (Reffitt et al., 1999; Anderson et al., 2003; Mattei and Valentini, 2003; Horcajada et al., 2004; Salonen et al., 2005; Anglin et al., 2008; Tabasi et al., 2012; Ma et al., 2017a). In bio-applications, pSiNPs exhibit good result *in vitro* and *in vivo* conditions (Ferreira et al., 2016). The pSiNPs were prepared by electrochemical etching and coated with dextran. The pSiNPs used for theranostics of cancer on the basis of photoluminescence properties and noted that excellent uptake of pSiNPs by cancer cell and also suppress the proliferation of cancer cells *in vitro* (Wang et al., 2012). SiNPs have been used for detection of microRNAs which acts as biomarkers of various diseases. The concentration of miRNAs was measured by a decrease of SiNPs fluorescence (Ding et al., 2018). Further, pSiNPs loaded with anticancer drugs and photo

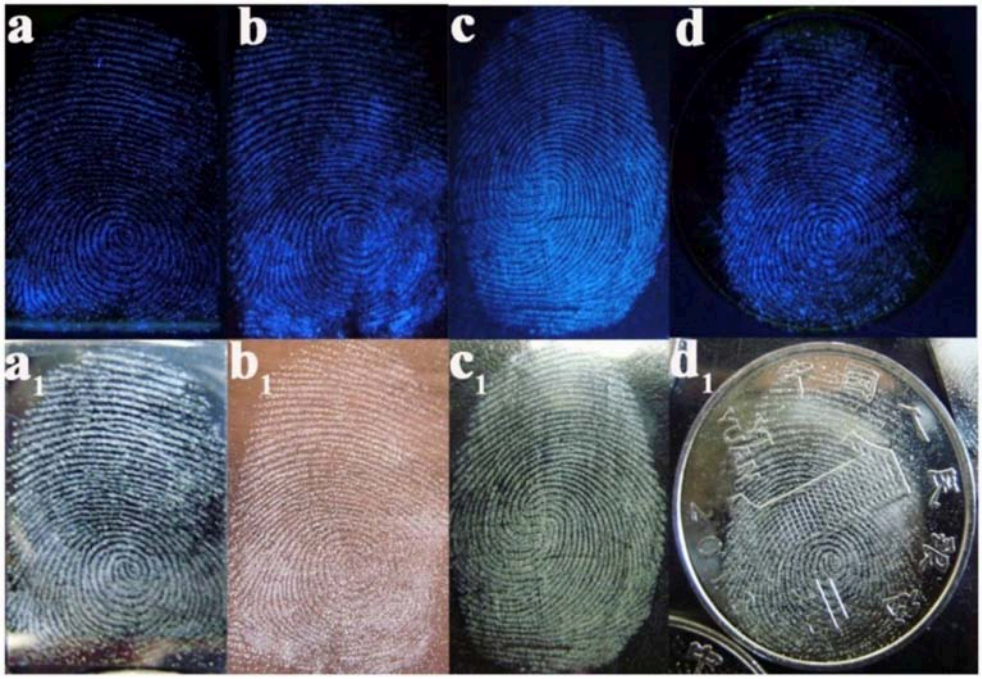

FIGURE 8 | Latent fingerprint by SiNPs on a different sheet. **(a)** Sheet of the silicon wafer, **(b)** sheet of copper, **(c)** sheet of glass, **(d)** On patterned coin (Zhu et al., 2018). Copyright © 2017 Elsevier Ltd. All rights reserved.

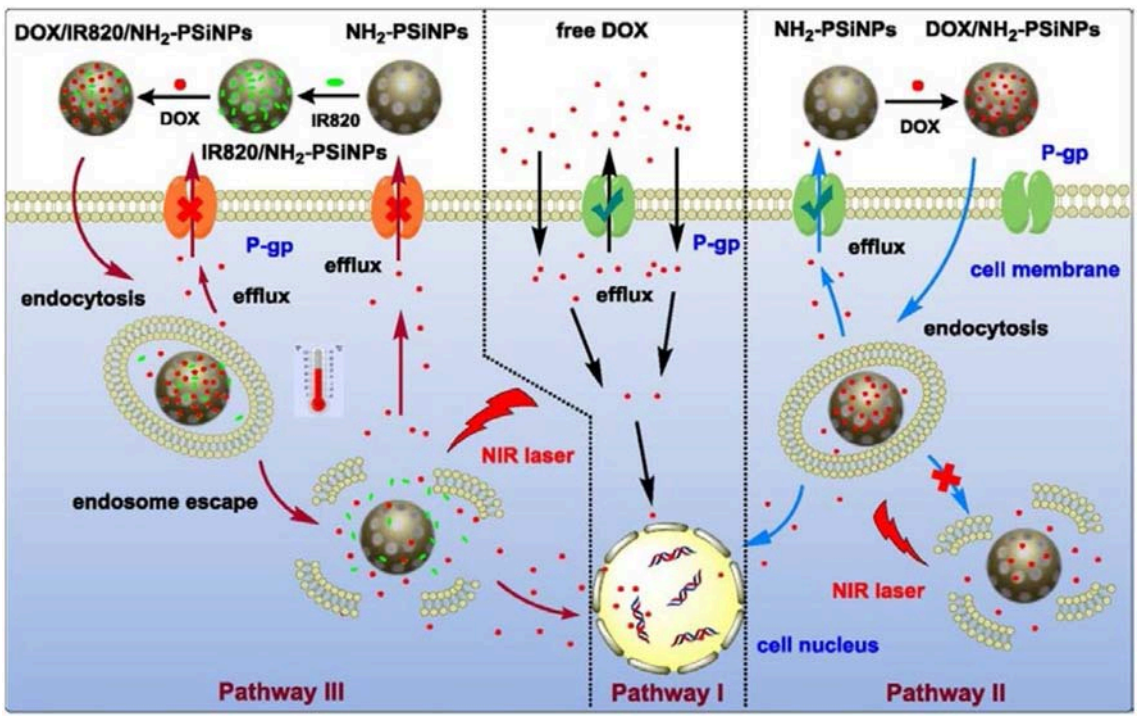

FIGURE 9 | Schematic diagram of pSiNPs based composite and process of the pathway of DOX into nuclei of MDR cancer cell with pSiNPs and without pSiNPs and with pSiNPs and dye. In pathway I, free DOX without pSiNPs carriers injected in to MDR cancer cell and efflux of DOX molecules from cell was maximum. In pathway II, DOX with pSiNPs carriers into MDR cancer cell. DOX with pSiNPs killed the cancer cell under effect of NIR Laser and efflux of DOX molecules from cell is minimum. In pathway III, DOX with dye and pSiNPs entered to MDR cancer cell and killed the cancer cells completely under effect of NIR Laser without any efflux of DOX molecules (Xia et al., 2018). Copyright © 2018 Elsevier B.V. All rights reserved.

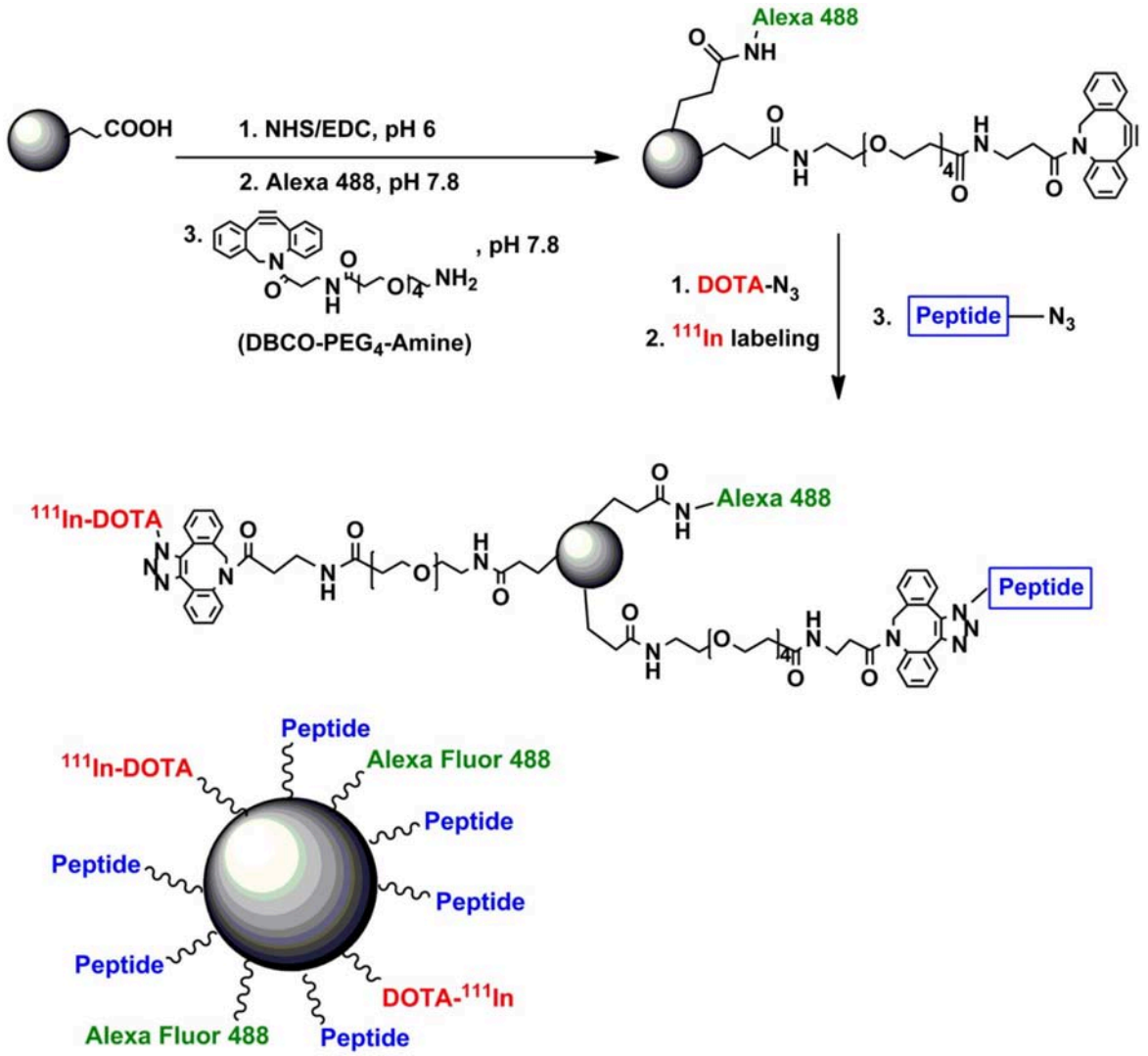

FIGURE 10 | Schematic diagram of synthesis process of multifunctional mesoporous as nanocarrier. iRGD Peptide covalently attached with pSiNPs to achieve and suppress target cancer cell. Alexa flour 488 dye bonded covalently to pSiNPs, to monitoring distribution particles in cancer cell and DOTA introduced on pSiNPs to increase hydrophilic moieties (Wang et al., 2015). Copyright © 2015 Elsevier Ltd. All rights reserved.

thermal agent by electrostatic assembly technique to treat the multidrug resistant cancer cells as shown in **Figure 9**. It is observed that pSiNPs leave the anticancer medicines 88.1% under different conditions and kill the multidrug resistant cancer cell. The pSiNPs as Nano carriers increased the efficiency of photo thermal therapy and chemotherapy (Xia et al., 2018). Furthermore, multifunctional pSiNPs were prepared by SPAAS click chemistry as shown in **Figure 10**. Multifunctional pSiNPs improved the rate of dissolution and cancer therapy. Uptake of multifunctional pSiNPs by tumors was enhanced due to the presence of iRGD peptide on the surface of pSiNPs and retained in tumors which suppressed tumors to further growth. Multifunctional pSiNPs exhibited well *in vivo* behavior and highest efficiency of drug delivery (Wang et al., 2015).

CONCLUSION AND OUTLOOK

In this review, we focus on the importance of pSiNPs with different structures in various fields. Silicon has much attractive material as an anode in LIBs due to their theoretical capacity (4,200 mA h g^{-1}), intercalated and electrical properties but after some cycles of charging/discharging volume of silicon changes. Continuous volume changes in silicon anode lead to fractures and affect the electrochemical properties. Solid electrolyte interphase developed on the particle by an electrolyte which leads to electrical contact loss. These challenges pulverization, electrical loss and stable SEI film by mesoporous silicon have been elaborated. It is observed that SiNPs play an important role to control volume changes in Si-anode as compare to silicon bulk. To control pulverization in Si anode further structure

of silicon particles has been modified to mesoporous, 3D and hollow spheres. By structural modification of SiNPs, a significant enhancement of electrochemical properties have been noted. Furthermore, to control volume change and improve electrical contact loss and stabilization of SEI film, SiNPs were coated with different materials (carbon, polymers other metals). Coating of different materials on SiNPs has significantly improved electrochemical properties and stabilize SEI films on particles. It is noted that the double coating of different material on particles enhanced electronic conductivity, capacity and control SEI film by stopping direct contact of electrolyte to particles. For future work, silicon anode material for commercial use still needs to be improved in volume change, stabilization of SEI film, high capacity, long cycle life, initial Coulombic efficiency and rate capability.

In biosensors and gas sensors, on the basis of optical and surface properties of pSiNPs have been used and exhibited good results. In sensors, porous silicon provides a number of void spaces to adsorption of different molecules, gases, drugs, and biomolecules. Structural dependent properties (optical, electrical and electrical properties) varies after adsorption of different molecules on the surface of porous silicon. This variation in properties are used to detect different materials. Further pSiNPs can be used to detect different compounds and biomarkers of different diseases which are still undetected.

Mesoporous structure of silicon provides a large surface area (200–800 m^2 g^{-1}), tunable optical properties and void spaces which act as good drug carriers. MSiNPs have been used as drug carriers, for therapy and detection of cancer cells due to their unique properties optical, non-toxicity, biocompatibility and surface properties. Detection and treatment of cancer tissues, tumors, and some biomarkers have been observed successfully by use of pSiNPs.

AUTHOR CONTRIBUTIONS

All authors listed have made a substantial, direct and intellectual contribution to the work, and approved it for publication.

ACKNOWLEDGMENTS

The authors are grateful for financial support from National Natural Science Foundation of China (No.51702046, 51702091, 51772050), Shanghai Committee of Science and Technology, China (No. 17ZR1401000), Shanghai Pujiang Program (No. 17PJ1400100), State Key Laboratory for Modification of Chemical Fibers and Polymer Materials, Donghua University. XC gratefully acknowledges the support from the Natural Science Foundation of Hubei Province, China (2017CFB192), China Postdoctoral Science Foundation (2017M621320) and the Fundamental Research Funds for the Central Universities.

REFERENCES

Anderson, D., and Spear, W. (1977). Electrical and optical properties of amorphous silicon carbide, silicon nitride and germanium carbide prepared by the glow discharge technique. *Philos. Mag.* 35, 1–16. doi: 10.1080/14786437708235967

Anderson, S., Elliott, H., Wallis, D., Canham, L., and Powell, J. (2003). Dissolution of different forms of partially porous silicon wafers under simulated physiological conditions. *Phys. Status Solidi* 197, 331–335. doi: 10.1002/pssa.200306519

Anglin, E. J., Cheng, L., Freeman, W. R., and Sailor, M. J. (2008). Porous silicon in drug delivery devices and materials. *Adv. Drug Deliv. Rev.* 60, 1266–1277. doi: 10.1016/j.addr.2008.03.017

Arora, N. D., Hauser, J. R., and Roulston, D. J. (1982). Electron and hole mobilities in silicon as a function of concentration and temperature. *IEEE Trans. Electron Devices* 29, 292–295. doi: 10.1109/T-ED.1982.20698

Astrova, E., and Tolmachev, V. (2000). Effective refractive index and composition of oxidized porous silicon films. *Mater. Sci. Eng. B* 69, 142–148. doi: 10.1016/S0921-5107(99)00236-6

Azadeh, M., Zamani, C., Ataie, A., and Morante, J. (2018). Three-dimensional rice husk-originated mesoporous silicon and its electrical properties. *Mater Today Commun*. 14, 141–150. doi: 10.1016/j.mtcomm.2018.01.003

Baranchugov, V., Markevich, E., Pollak, E., Salitra, G., and Aurbach, D. (2007). Amorphous silicon thin films as a high capacity anodes for Li-ion batteries in ionic liquid electrolytes. *Electrochem. commun.* 9, 796–800. doi: 10.1016/j.elecom.2006.11.014

Beattie, S. D., Larcher, D., Morcrette, M., Simon, B., and Tarascon, J.-M. (2008). Si electrodes for Li-ion batteries—a new way to look at an old problem. *J. Electrochem. Soc.* 155, A158–A163. doi: 10.1149/1.2817828

Bsiesy, A., Vial, J., Gaspard, F., Herino, R., Ligeon, M., Muller, F., et al. (1991). Photoluminescence of high porosity and of electrochemically oxidized porous silicon layers. *Surf. Sci.* 254, 195–200. doi: 10.1016/0039-6028(91)90652-9

Chao, Y. (2011). "Optical properties of nanostructured silicon," in *Comprehensive Nanoscience and Technology*, eds D. L. Andrews, G. D. Scholes, and G. P. Wiederrecht (Elsevier), 543–570.

Chen, H., Chiu, J., and Perng, T. (2001). On the photoluminescence of Si nanoparticles. *Mater. Phys. Mech.* 4, 62–66.

Cho, S., Jang, H. Y., Jung, I., Liu, L., and Park, S. (2017). Synthesis of embossing Si nanomesh and its application as an anode for lithium ion batteries. *J. Pow. Sources* 362, 270–277. doi: 10.1016/j.jpowsour.2017.07.048

Dancil, K.-P. S., Greiner, D. P., and Sailor, M. J. (1999). A porous silicon optical biosensor: detection of reversible binding of IgG to a protein A-modified surface. *J. Am. Chem. Soc.* 121, 7925–7930. doi: 10.1021/ja991421n

Ding, L., Liu, H., Zhang, L., Li, L., and Yu, J. (2018). Label-free detection of microRNA based on the fluorescence quenching of silicon nanoparticles induced by catalyzed hairpin assembly coupled with hybridization chain reaction. *Sens. Actuators B Chem.* 254, 370–376. doi: 10.1016/j.snb.2017.07.111

Dinh, L., Chase, L., Balooch, M., Siekhaus, W., and Wooten, F. (1996). Optical properties of passivated Si nanocrystals and SiO x nanostructures. *Phys. Rev. B* 54, 5029–5037. doi: 10.1103/PhysRevB.54.5029

Donnorso, M. P., Miele, E., De Angelis, F., La Rocca, R., Limongi, T., Zanacchi, F. C., et al. (2012). Nanoporous silicon nanoparticles for drug delivery applications. *Microelectron. Eng.* 98, 626–629. doi: 10.1016/j.mee.2012.07.095

English, D. S., Pell, L. E., Yu, Z., Barbara, P. F., and Korgel, B. A. (2002). Size tunable visible luminescence from individual organic monolayer stabilized silicon nanocrystal quantum dots. *Nano Lett.* 2, 681–685. doi: 10.1021/nl025538c

Ensafi, A. A., Abarghoui, M. M., and Rezaei, B. (2017). Metal (Ni and Bi) coated porous silicon nanostructure, high-performance anode materials for lithium ion batteries with high capacity and stability. *J. Alloys Compd.* 712, 233–240. doi: 10.1016/j.jallcom.2017.04.103

Ferreira, M. P., Ranjan, S., Correia, A. M., Mäkil,ä, E. M., Kinnunen, S. M., Zhang, H., et al. (2016). *In vitro* and *in vivo* assessment of heart-homing porous silicon nanoparticles. *Biomaterials* 94, 93–104. doi: 10.1016/j.biomaterials.2016.03.046

Goodenough, J. B., and Kim, Y. (2009). Challenges for rechargeable Li batteries. *Chem. Mater.* 22, 587–603. doi: 10.1021/cm901452z

Haidary, S. M., Corcoles, E. P., and Ali, N. K. (2012). Nanoporous silicon as drug delivery systems for cancer therapies. *J. Nanomater.* 2012:830503. doi: 10.1155/2012/830503

Hajji, M., Khardani, M., Khedher, N., Rahmouni, H., Bessaïs, B., Ezzaouia, H., et al. (2006). Structural, optical and electrical properties of quasi-monocrystalline silicon thin films obtained by rapid thermal annealing of porous silicon layers. *Thin Solid Films* 511, 235–237. doi: 10.1016/j.tsf.2005.12.044

Harraz, F. A., Ismail, A. A., Bouzid, H., Al-Sayari, S., Al-Hajry, A., and Al-Assiri, M. (2014). A capacitive chemical sensor based on porous silicon for detection of polar and non-polar organic solvents. *Appl. Surf. Sci.* 307, 704–711. doi: 10.1016/j.apsusc.2014.04.106

Horcajada, P., Ramila, A., Perez-Pariente, J., and Vallet-Reg,i, M. (2004). Influence of pore size of MCM-41 matrices on drug delivery rate. *Microporous Mesoporous Mater.* 68, 105–109. doi: 10.1016/j.micromeso.2003.12.012

Huang, R., and Zhu, J. (2010). Silicon nanowire array films as advanced anode materials for lithium-ion batteries. *Mater. Chem. Phys.* 121, 519–522. doi: 10.1016/j.matchemphys.2010.02.017

Huang, W., Li, X., Wang, H., Xu, X., Liu, H., and Wang, G. (2015). Synthesis of amphiphilic silica nanoparticles for latent fingerprint detection. *Anal. Lett.* 48, 1524–1535. doi: 10.1080/00032719.2014.984195

Intartaglia, R., Bagga, K., Scotto, M., Diaspro, A., and Brandi, F. (2012). Luminescent silicon nanoparticles prepared by ultra short pulsed laser ablation in liquid for imaging applications. *Opt. Mater. Express* 2, 510–518. doi: 10.1364/OME.2.000510

Jang, J., Kang, I., Yi, K.-W., and Cho, Y. W. (2018). Highly conducting fibrous carbon-coated silicon alloy anode for lithium ion batteries. *Appl. Surf. Sci.* doi: 10.1016/j.apsusc.2018.05.165

Jung, H., Park, M., Yoon, Y.-G., Kim, G.-B., and Joo, S.-K. (2003). Amorphous silicon anode for lithium-ion rechargeable batteries. *J. Pow. Sources* 115, 346–351. doi: 10.1016/S0378-7753(02)00707-3

Kaasalainen, M., Mäkil,ä, E., Riikonen, J., Kovalainen, M., Järvinen, K., Herzig, K. H., et al. (2012). Effect of isotonic solutions and peptide adsorption on zeta potential of porous silicon nanoparticle drug delivery formulations. *Int. J. Pharm.* 431, 230–236. doi: 10.1016/j.ijpharm.2012.04.059

Kang, Z., Liu, Y., Tsang, C. H. A., Ma, D. D. D., Fan, X., Wong, N. B., et al. (2009). Water-soluble silicon quantum dots with wavelength-tunable photoluminescence. *Adv. Mater. Weinheim.* 21, 661–664. doi: 10.1002/adma.200801642

Karlsson, L., Schubert, M., Ashkenov, N., and Arwin, H. (2004). Protein adsorption in porous silicon gradients monitored by spatially-resolved spectroscopic ellipsometry. *Thin Solid Films* 455, 726–730. doi: 10.1016/j.tsf.2004.01.062

Kashyout, A.-H., Soliman, H., Nabil, M., and Bishara, A. (2015). Impact of Congo red dye in nano-porous silicon as pH-sensor. *Sens. Actuators B Chem.* 216, 279–285. doi: 10.1016/j.snb.2015.03.099

Kim, Y.-L., Sun, Y.-K., and Lee, S.-M. (2008). Enhanced electrochemical performance of silicon-based anode material by using current collector with modified surface morphology. *Electrochim. Acta* 53, 4500–4504. doi: 10.1016/j.electacta.2008.01.050

Kim, Y.-Y., Lee, J.-H., and Kim, H.-J. (2017). Nanoporous silicon flakes as anode active material for lithium-ion batteries. *Phys. E Low Dimens. Syst. Nanostruct.* 85, 223–226. doi: 10.1016/j.physe.2016.09.007

Kim, Y. M., Ahn, J., Yu, S.-H., Chung, D. Y., Lee, K. J., Lee, J.-K., et al. (2015). Titanium silicide coated porous silicon nanospheres as anode materials for lithium ion batteries. *Electrochim. Acta* 151, 256–262. doi: 10.1016/j.electacta.2014.11.016

Lasave, L. C., Urteaga, R., Koropecki, R. R., Gonzalez, V. D., and Arce, R. D. (2013). Real-time study of protein adsorption kinetics in porous silicon. *Colloids Surf. B Biointerfaces* 111, 354–359. doi: 10.1016/j.colsurfb.2013.06.024

Ledoux, G., Gong, J., Huisken, F., Guillois, O., and Reynaud, C. (2002). Photoluminescence of size-separated silicon nanocrystals: confirmation of quantum confinement. *Appl. Phys. Lett.* 80, 4834–4836. doi: 10.1063/1.1485302

Leveau, L., Laïk, B., Pereira-Ramos, J.-P., Gohier, A., Tran-Van, P., and Cojocaru, C. S. (2016). Silicon nano-trees as high areal capacity anodes for lithium-ion batteries. *J. Pow. Sources* 316, 1–7. doi: 10.1016/j.jpowsour.2016.03.053

Li, H., Huang, X., Chen, L., Zhou, G., Zhang, Z., Yu, D., et al. (2000). The crystal structural evolution of nano-Si anode caused by lithium insertion and extraction at room temperature. *Solid State Ionics* 135, 181–191. doi: 10.1016/S0167-2738(00)00362-3

Liang, K., Yang, H., Guo, W., Du, J., Tian, L., and Wen, X. (2018). Facile preparation of nanoscale silicon as an anode material for lithium ion batteries by a mild temperature metathesis route. *J. Alloys Compd.* 735, 441–444. doi: 10.1016/j.jallcom.2017.11.119

Lin, C.-T., Huang, T.-Y., Huang, J.-J., Wu, N.-L., and Leung, M. K. (2016). Multifunctional co-poly (amic acid): a new binder for Si-based micro-composite anode of lithium-ion battery. *J. Pow. Sources* 330, 246–252. doi: 10.1016/j.jpowsour.2016.09.021

Ling, M., Xu, Y., Zhao, H., Gu, X., Qiu, J., Li, S., et al. (2015). Dual-functional gum arabic binder for silicon anodes in lithium ion batteries. *Nano Energy* 12, 178–185. doi: 10.1016/j.nanoen.2014.12.011

Lu, Z., Liu, N., Lee, H.W., Zhao, J., Li, W., Li, Y., et al. (2015). Nonfilling carbon coating of porous silicon micrometer-sized particles for high-performance lithium battery anodes. *ACS Nano* 9, 2540–2547. doi: 10.1021/nn505410q

Luo, L., Song, Y., Zhu, C., Fu, S., Shi, Q., Sun, Y.-M., et al. (2018). Fluorescent silicon nanoparticles-based ratiometric fluorescence immunoassay for sensitive detection of ethyl carbamate in red wine. *Sens. Actuators B Chem.* 255, 2742–2749. doi: 10.1016/j.snb.2017.09.088

Luo, W., Chen, X., Xia, Y., Chen, M., Wang, L., Wang, Q., et al. (2017). Surface and interface engineering of silicon-based anode materials for lithium-ion batteries. *Adv Energy Mater.* 7:1701083. doi: 10.1002/aenm.201701083

Luo, W., Shen, D., Zhang, R., Zhang, B., Wang, Y., Dou, S. X., et al. (2016a). Germanium nanograin decoration on carbon shell: boosting lithium-storage properties of silicon nanoparticles. *Adv. Funct. Mater.* 26, 7800–7806. doi: 10.1002/adfm.201603335

Luo, W., Wang, Y., Chou, S., Xu, Y., Li, W., Kong, B., et al. (2016b). Critical thickness of phenolic resin-based carbon interfacial layer for improving long cycling stability of silicon nanoparticle anodes. *Nano Energy* 27, 255–264. doi: 10.1016/j.nanoen.2016.07.006

Luo, W., Wang, Y., Wang, L., Jiang, W., Chou, S.-L., Dou, S. X., et al. (2016c). Silicon/mesoporous carbon/crystalline TiO2 nanoparticles for highly stable lithium storage. *ACS Nano* 10, 10524–10532. doi: 10.1021/acsnano.6b06517

Ma, Q., Yang, B., and Li, J. (2017a). Silicon-containing porous organic polymers: preparation, tunable porosity and carbon dioxide sorption. *J. Organomet. Chem* 830, 19–25. doi: 10.1016/j.jorganchem.2016.12.002

Ma, X., Wei, Z., Han, H., Wang, X., Cui, K., and Yang, L. (2017b). Tunable construction of multi-shell hollow SiO 2 microspheres with hierarchically porous structure as high-performance anodes for lithium-ion batteries. *Chem. Eng. J.* 323, 252–259. doi: 10.1016/j.cej.2017.04.108

Mattei, G., and Valentini, V. (2003). In situ functionalization of porous silicon during the electrochemical formation process in ethanoic hydrofluoric acid solution. *J. Am. Chem. Soc.* 125, 9608–9609. doi: 10.1021/ja036228e

Min-Dianey, K. A. A., Zhang, H.-C., M'Bouana, N. L. P., Kougblenou, K., and Xia, X. (2018). Limitation of optical properties through porous silicon photonic crystals influenced by porosity and lattice dynamic. *Opt. Mater.* 75, 150–165. doi: 10.1016/j.optmat.2017.10.023

Moret, S., Bécue, A., and Champod, C. (2016). Functionalised silicon oxide nanoparticles for fingermark detection. *Forensic Sci. Int.* 259, 10–18. doi: 10.1016/j.forsciint.2015.11.015

Myndrul, V., Viter, R., Savchuk, M., Shpyrka, N., Erts, D., Jevdokimovs, D., et al. (2017). Porous silicon based photoluminescence immunosensor for rapid and highly-sensitive detection of Ochratoxin A. *Biosens. Bioelectron.* 102:661–667. doi: 10.1016/j.bios.2017.11.048

Nayef, U. M., and Khudhair, I. M. (2018). Synthesis of gold nanoparticles chemically doped with porous silicon for organic vapor sensor by using photoluminescence. *Optik* 154, 398–404. doi: 10.1016/j.ijleo.2017.10.061

Park, J. H., Gu, L., Von Maltzahn, G., Ruoslahti, E., Bhatia, S. N., and Sailor, M. J. (2009). Biodegradable luminescent porous silicon nanoparticles for *in vivo* applications. *Nat. Mater.* 8, 331–336. doi: 10.1038/nmat2398

Priyono, B., Syahrial, A., and Subhan, A. (2017). Effect of acetylene black content to half cells Li-ion battery performance Based on $Li_4Ti_5O_{12}$ using Li_2CO_3 as lithium ion source with hydrothermal mechanochemical process. *J. Phys. Conf. Ser.* 877:012052. doi: 10.1088/1742-6596/877/1/012052

Qin, Y., Cui, Z., Zhang, T., and Liu, D. (2018a). Polypyrrole shell (nanoparticles)-functionalized silicon nanowires array with enhanced NH3-sensing response. *Sens. Actuators B Chem.* 258, 246–254. doi: 10.1016/j.snb.2017.11.089

Qin, Y., Liu, D., Wang, Z., and Jiang, Y. (2018b). Ag nanoparticles-functionalized rough silicon nanowires array and its unique response characteristics to ultrararefied NO_2. *Sens. Actuators B Chem.* 258, 730–738. doi: 10.1016/j.snb.2017.11.177

Reffitt, D. M., Jugdaohsingh, R., Thompson, R. P., and Powell, J. J. (1999). Silicic acid: its gastrointestinal uptake and urinary excretion in man and effects on aluminium excretion. *J. Inorg. Biochem.* 76, 141–147. doi: 10.1016/S0162-0134(99)00126-9

Renganathan, S., Sikha, G., Santhanagopalan, S., and White, R. E. (2010). Theoretical analysis of stresses in a lithium ion cell. *J. Electrochem. Soc.* 157, A155–A163. doi: 10.1149/1.3261809

Ryu, J. H., Kim, J. W., Sung, Y.-E., and Oh, S. M. (2004). Failure modes of silicon powder negative electrode in lithium secondary batteries. *Electrochem. Solid State Lett.* 7, A306–A309. doi: 10.1149/1.1792242

Salonen, J., Laitinen, L., Kaukonen, A., Tuura, J., Björkqvist, M., Heikkilä, T., et al. (2005). Mesoporous silicon microparticles for oral drug delivery: loading and release of five model drugs. *J. Control. Release* 108, 362–374. doi: 10.1016/j.jconrel.2005.08.017

Sarkar, T., Basu, D., Mukherjee, N., and Das, J. (2018). Comparison of glucose sensitivity of nano and macro porous silicon. *Mater. Today* 5, 9798–9803. doi: 10.1016/j.matpr.2017.10.169

Sarode, K. K., Choudhury, R., and Martha, S. K. (2018). Binder and conductive additive free silicon electrode architectures for advanced lithium-ion batteries. *J. Energy Storage* 17, 417–422. doi: 10.1016/j.est.2018.04.002

Shen, P., Uesawa, N., Inasawa, S., and Yamaguchi, Y. (2010). Stable and color-tunable fluorescence from silicon nanoparticles formed by single-step plasma assisted decomposition of SiBr4. *J. Mater. Chem.* 20, 1669–1675. doi: 10.1039/b919412f

Shiohara, A., Hanada, S., Prabakar, S., Fujioka, K., Lim, T. H., Yamamoto, K., et al. (2009). Chemical reactions on surface molecules attached to silicon quantum dots. *J. Am. Chem. Soc.* 132, 248–253. doi: 10.1021/ja906501v

Sivakov, V., Andr,ä, G., Gawlik, A., Berger, A., Plentz, J., Falk, F., et al. (2009). Silicon nanowire-based solar cells on glass: synthesis, optical properties, and cell parameters. *Nano Lett.* 9, 1549–1554. doi: 10.1021/nl803641f

Tabasi, O., Falamaki, C., and Khalaj, Z. (2012). Functionalized mesoporous silicon for targeted-drug-delivery. *Colloids Surf. B Biointerfaces* 98, 18–25. doi: 10.1016/j.colsurfb.2012.04.018

Teng, X., Xu, H.-,l., Liu, Q., Shi, L.-,l., Gai, L., Wang, L., et al. (2018). The influence of conductive additives on the performance of a SiO/C composite anode in lithium-ion batteries. *Carbon* 130:848. doi: 10.1016/j.carbon.2017.12.091

Trwoga, P., Kenyon, A., and Pitt, C. (1998). Modeling the contribution of quantum confinement to luminescence from silicon nanoclusters. *J. Appl. Phys.* 83, 3789–3794. doi: 10.1063/1.366608

Tzur-Balter, A., Gilert, A., Massad-Ivanir, N., and Segal, E. (2013). Engineering porous silicon nanostructures as tunable carriers for mitoxantrone dihydrochloride. *Acta Biomater.* 9, 6208–6217. doi: 10.1016/j.actbio.2012.12.010

Vaccari, L., Canton, D., Zaffaroni, N., Villa, R., Tormen, M., and di Fabrizio, E. (2006). Porous silicon as drug carrier for controlled delivery of doxorubicin anticancer agent. *Microelectron. Eng.* 83, 1598–1601. doi: 10.1016/j.mee.2006.01.113

Van Buuren, T., Dinh, L., Chase, L., Siekhaus, W., and Terminello, L. J. (1998). Changes in the electronic properties of Si nanocrystals as a function of particle size. *Phys. Rev. Lett.* 80, 3803. doi: 10.1103/PhysRevLett.80.3803

Veinot, J. G. (2006). Synthesis, surface functionalization, and properties of freestanding silicon nanocrystals. *Chem. comm.* 38, 4160–4168. doi: 10.1039/b607476f

Wang, C.-F., Sarparanta, M. P., Mäkil,ä, E. M., Hyvönen, M. L., Laakkonen, P. M., Salonen, J. J., et al. (2015). Multifunctional porous silicon nanoparticles for cancer theranostics. *Biomaterials* 48, 108–118. doi: 10.1016/j.biomaterials.2015.01.008

Wang, J., Liu, Y., Peng, F., Chen, C., He, Y., Ma, H., et al. (2012). A general route to efficient functionalization of silicon quantum dots for high-performance fluorescent probes. *Small* 8, 2430–2435. doi: 10.1002/smll.201102627

Wang, M., Yang, Z., Li, W., Gu, L., and Yu, Y. (2016). Superior sodium storage in 3D interconnected nitrogen and oxygen dual-doped carbon network. *Small* 12, 2559–2566. doi: 10.1002/smll.201600101

Wang, Q., Bao, Y., Zhang, X., Coxon, P. R., Jayasooriya, U. A., and Chao, Y. (2012). Uptake and toxicity studies of poly-acrylic acid functionalized silicon nanoparticles in cultured mammalian cells. *Adv. Healthc. Mater.* 1, 189–198. doi: 10.1002/adhm.201100010

Wang, Y.-X., Yang, J., Chou, S.-L., Liu, H. K., Zhang, W.-X., Zhao, D., et al. (2015). Uniform yolk-shell iron sulfide–carbon nanospheres for superior sodium–iron sulfide batteries. *Nat. Commun.* 6:8689. doi: 10.1038/ncomms9689

Wen, Z., Lu, G., Mao, S., Kim, H., Cui, S., Yu, K., et al. (2013). Silicon nanotube anode for lithium-ion batteries. *Electrochem. commun.* 29, 67–70. doi: 10.1016/j.elecom.2013.01.015

Wu, H., Du, N., Shi, X., and Yang, D. (2016). Rational design of three-dimensional macroporous silicon as high performance Li-ion battery anodes with long cycle life. *J. Pow. Sources* 331, 76–81. doi: 10.1016/j.jpowsour.2016.09.046

Xia, B., Zhang, Q., Shi, J., Li, J., Chen, Z., and Wang, B. (2018). Co-loading of photothermal agents and anticancer drugs into porous silicon nanoparticles with enhanced chemo-photothermal therapeutic efficacy to kill multidrug-resistant cancer cells. *Colloids Surf. B Biointerfaces*. 164, 291–298. doi: 10.1016/j.colsurfb.2018.01.059

Xia, B., Zhang, W., Shi, J., and Xiao, S. (2013). Fluorescence quenching in luminescent porous silicon nanoparticles for the detection of intracellular Cu 2+. *Analyst* 138, 3629–3632. doi: 10.1039/c3an00503h

Xing, Y., Shen, T., Guo, T., Wang, X., Xia, X., Gu, C., et al. (2018). A novel durable double-conductive core-shell structure applying to the synthesis of silicon anode for lithium ion batteries. *J. Pow. Sources* 384, 207–213. doi: 10.1016/j.jpowsour.2018.02.051

Xu, J., Wang, M., Wickramaratne, N. P., Jaroniec, M., Dou, S., and Dai, L. (2015). High-performance sodium ion batteries based on a 3D anode from nitrogen-doped graphene foams. *Adv. Mater. Weinheim.* 27, 2042–2048. doi: 10.1002/adma.201405370

Xu, W., Vegunta, S. S. S., and Flake, J. C. (2011). Surface-modified silicon nanowire anodes for lithium-ion batteries. *J. Pow. Sources* 196, 8583–8589. doi: 10.1016/j.jpowsour.2011.05.059

Yang, J., Shen, D., Zhou, L., Li, W., Fan, J., El-Toni, A. M., et al. (2014a). Mesoporous silica-coated plasmonic nanostructures for surface-enhanced raman scattering detection and photothermal therapy. *Adv. Healthc. Mater.* 3, 1620–1628. doi: 10.1002/adhm.201400053

Yang, J., Wang, Y., Li, W., Wang, L., Fan, Y., Jiang, W., et al. (2017). Amorphous TiO2 shells: a vital elastic buffering layer on silicon nanoparticles for high-performance and safe lithium storage. *Adv. Mater.* 29:1700523. doi: 10.1002/adma.201700523

Yang, J., Wang, Y.-X., Chou, S.-L., Zhang, R., Xu, Y., Fan, J., et al. (2015). Yolk-shell silicon-mesoporous carbon anode with compact solid electrolyte interphase film for superior lithium-ion batteries. *Nano Energy* 18, 133–142. doi: 10.1016/j.nanoen.2015.09.016

Yang, J., Zhang, F., Li, W., Gu, D., Shen, D., Fan, J., et al. (2014b). Large pore mesostructured cellular silica foam coated magnetic oxide composites with multilamellar vesicle shells for adsorption. *Chem. Comm.* 50, 713–715. doi: 10.1039/c3cc47813k

Yang, J., Zhang, L., Zhang, T., Wang, X., Gao, Y., and Fang, Q. (2018). Self-healing strategy for Si nanoparticles towards practical application as anode materials for Li-ion batteries. *Electrochem. commun.* 87, 22–26. doi: 10.1016/j.elecom.2017.12.023

Yang, J., Zhou, T., Zhu, R., Chen, X., Guo, Z., Fan, J., et al. (2016). Highly Ordered Dual Porosity Mesoporous Cobalt Oxide for Sodium-Ion Batteries. *Adv Mater Interfaces* 3(3). doi: 10.1002/admi.201500464

Yang, X., Wen, Z., Zhang, L., and You, M. (2008). Synthesis and electrochemical properties of novel silicon-based composite anode for lithium-ion batteries. *J. Alloys Compd.* 464, 265–269. doi: 10.1016/j.jallcom.2007.09.088

Yang, X.-Q., McBreen, J., Yoon, W.-S., Yoshio, M., Wang, H., Fukuda, K., et al. (2002). Structural studies of the new carbon-coated silicon anode materials using synchrotron-based in situ XRD. *Electrochem. commun.* 4, 893–897. doi: 10.1016/S1388-2481(02)00483-6

Yi, Y., Lee, G.-H., Kim, J.-C., Shim, H.-W., and Kim, D.-W. (2017). Tailored silicon hollow spheres with Micrococcus for Li ion battery electrodes. *Chem. Eng. J.* 327, 297–306. doi: 10.1016/j.cej.2017.06.103

Yu, W., Wang, H., Liu, S., Mao, N., Liu, X., Shi, J., et al. (2016). N, O-codoped hierarchical porous carbons derived from algae for high-capacity supercapacitors and battery anodes. *J. Mater. Chem. A* 4, 5973–5983. doi: 10.1039/C6TA01821A

Zhang, G. J., Luo, Z. H. H., Huang, M. J., Tay, G. K. I., and Lim, E. J. A. (2010). Morpholino-functionalized silicon nanowire biosensor for sequence-specific label-free detection of DNA. *Biosens. Bioelectron.* 25, 2447–2453. doi: 10.1016/j.bios.2010.04.001

Zhang, L., Ding, Y., and Song, J. (2018). Crosslinked carboxymethyl cellulose-sodium borate hybrid binder for advanced silicon anodes in lithium-ion batteries. *Chin. Chem. Lett.* doi: 10.1016/j.cclet.2018.03.008. [Epub ahead of print].

Zhou, Y., Jiang, X., Chen, L., Yue, J., Xu, H., Yang, J., et al. (2014). Novel mesoporous silicon nanorod as an anode material for lithium ion batteries. *Electrochim. Acta* 127, 252–258. doi: 10.1016/j.electacta.2014.01.158

Zhu, B., Ren, G., Tang, M., Chai, F., Qu, F., Wang, C., et al. (2018). Fluorescent silicon nanoparticles for sensing Hg^{2+} and Ag^{+} as well visualization of latent fingerprints. *Dyes Pigm.* 149, 686–695. doi: 10.1016/j.dyepig.2017.11.041

Conflict of Interest Statement: The authors declare that the research was conducted in the absence of any commercial or financial relationships that could be construed as a potential conflict of interest.

Copyright © 2018 Manj, Chen, Rehman, Zhu, Luo and Yang. This is an open-access article distributed under the terms of the Creative Commons Attribution License (CC BY). The use, distribution or reproduction in other forums is permitted, provided the original author(s) and the copyright owner(s) are credited and that the original publication in this journal is cited, in accordance with accepted academic practice. No use, distribution or reproduction is permitted which does not comply with these terms.

frontiers in Chemistry

ORIGINAL RESEARCH
published: 18 April 2019
doi: 10.3389/fchem.2019.00266

Mesoporous WO_3 Nanofibers With Crystalline Framework for High-Performance Acetone Sensing

Haiyun Xu[1†], Jie Gao[1†], Minhan Li[1], Yuye Zhao[1], Ming Zhang[2], Tao Zhao[1], Lianjun Wang[1], Wan Jiang[1,3,4], Guanjia Zhu[1], Xiaoyong Qian[1], Yuchi Fan[3], Jianping Yang[1,3] and Wei Luo[1,3*]*

[1] State Key Laboratory for Modification of Chemical Fibers and Polymer Materials, College of Materials Science and Engineering, Donghua University, Shanghai, China, [2] Materials Genome Institute, Shanghai University, Shanghai, China, [3] Institute of Functional Materials, Donghua University, Shanghai, China, [4] School of Materials Science and Engineering, Jingdezhen Ceramic Institute, Jingdezhen, China

OPEN ACCESS

Edited by:
Fan Zhang,
Fudan University, China

Reviewed by:
Xian Chen,
Shenzhen University, China
Jingsan Xu,
Queensland University of Technology, Australia

***Correspondence:**
Jianping Yang
jianpingyang@dhu.edu.cn
Wei Luo
wluo@dhu.edu.cn

[†]These authors have contributed equally to this work

Specialty section:
This article was submitted to Nanoscience, a section of the journal Frontiers in Chemistry

Received: *26 November 2018*
Accepted: *01 April 2019*
Published: *18 April 2019*

Citation:
Xu H, Gao J, Li M, Zhao Y, Zhang M, Zhao T, Wang L, Jiang W, Zhu G, Qian X, Fan Y, Yang J and Luo W (2019) Mesoporous WO_3 Nanofibers With Crystalline Framework for High-Performance Acetone Sensing. Front. Chem. 7:266. doi: 10.3389/fchem.2019.00266

Semiconducting metal oxides with abundant active sites are regarded as promising candidates for environmental monitoring and breath analysis because of their excellent gas sensing performance and stability. Herein, mesoporous WO_3 nanofibers with a crystalline framework and uniform pore size is successfully synthesized in an aqueous phase using an electrospinning method, with ammonium metatungstate as the tungsten sources, and SiO_2 nanoparticles and polyvinylpyrrolidone as the sacrificial templates. The obtained mesoporous WO_3 nanofibers exhibit a controllable pore size of 26.3–42.2 nm, specific surface area of 24.1–34.4 m^2g^{-1}, and a pore volume of 0.15–0.24 cm^3g^{-1}. This unique hierarchical structure, with uniform mesopores and interconnected channels, could facilitate the diffusion and transportation of gas molecules in the framework. Gas sensors, based on mesoporous WO_3 nanofibers, exhibit an excellent performance in acetone sensing with a low limit of detection (<1 ppm), short response-recovery time (24 s/27 s), a linear relationship in a broad range, and good selectivity.

Keywords: mesoporous materials, WO_3, nanofibers, electrospun, acetone, sensor

INTRODUCTION

Over the past few decades, the precise monitoring of toxic polluting gases has attracted great attention in modern society in environmental protection, industrial production, health care, and so forth (Kawano et al., 2007; Wang et al., 2007; Salehi et al., 2014). Acetone is a common type of reagent which is frequently used in manufacturing industries and laboratories (Zhang et al., 2017). As a highly toxic gas, acetone is harmful to human health, and long-term exposure to acetone may cause irritation and damage to the eyes, nose, and central nervous system (Jia et al., 2014). In addition, acetone concentrations in respiration can be characterized as a biomarker in the rapid diagnosis of diabetes, because acetone concentrations exhaled from diabetes patients (1.8 ppm) are much higher than in a healthy individual (0.3–0.9 ppm) (Singkammo et al., 2015; Zhou et al., 2018). Therefore, it is of great interest and importance to develop acetone sensors with a low detection limit, fast response recovery dynamics, high sensitivity and selectivity. Among a variety of sensing-active materials used for the detection of acetone, metal oxide semiconductors (WO_3, TiO_2, SnO_2, ZnO, Fe_2O_3, etc.) have been considered as appealing candidates due to their remarkable sensitivity,

low cost, and excellent stability (Wang et al., 2010; Luo et al., 2013; Kim and Lee, 2014; Zhu et al., 2017a; Zhou et al., 2018). The sensing mechanism of semiconducting metal oxides (SMOs)-based sensors is widely accepted to be the change in conductivity when exposed in specific gas. The adsorbed gaseous analytes may cause an increase or decrease in the resistance of semiconducting metal oxides (Barsan and Weimar, 2001; Yamazoe et al., 2003; Qiu et al., 2018; Zhang Q. et al., 2018). Given that the gas-sensing process involves the adsorption–desorption and catalytic reactions on the surface of the metal oxides, a rational design and controllable synthesis of nanomaterials with high surface areas, abundant active sites, tailor-designed nanostructures and outstanding catalytic performance, are considered as promising approaches to enhance the sensing performance of the semiconducting metal oxides.

Mesoporous semiconducting metal oxides (MSMOs), as an important category of nanostructured materials, have drawn much attention because of their high surface area, uniform pore size, highly crystalline framework, numerous active sites, interconnected pore structure and large pore size. The high surface area and abundant active sites greatly facilitates the interaction between metal oxide frameworks and gaseous molecules, as well as surface catalytic reactions. In addition, the large porosity and well-connected mesostructure favors rapid and effective diffusion of gas molecules (Li et al., 2014; Luo et al., 2016b; Ma et al., 2018). Therefore, MSMOs are regarded as promising candidates for gas sensing. To date, various MSMOs have been synthesized through different approaches, such as sol–gel processes, spray pyrolysis, chemical vapor deposition and precipitation reactions (Du et al., 2011; Luo et al., 2016a; Zhao et al., 2016; Channei et al., 2018; Jha G. et al., 2018; Zhang Y. et al., 2018). However, these methods usually give rise to an uncontrolled morphology and low porosity, which is not favorable for sensing performance. Additionally, a lot of work has been focused on the design and construction of various nanostructures of SMOs to improve the their sensing performance, including zero-dimensional nanoparticles (NPs) (Yang Z. et al., 2018; Zhang H. et al., 2018; Zhao et al., 2019), one-dimensional nanofibers (NFs) (Saha and De, 2013; Kim et al., 2016a; Ren et al., 2016; Nada et al., 2017; He et al., 2018; Jeong et al., 2018) and nanowires (NWs) (Wang et al., 2004; Rakhi et al., 2012; Dam and Lee, 2013; Chen et al., 2015; Li X. et al., 2017), two-dimensional nanosheets (Wang et al., 2016, 2017; Li F. et al., 2017; Kaneti et al., 2018) and membranes (Dasog et al., 2012; Barr et al., 2017; Jha G. et al., 2018; Wang W. Q. et al., 2018). Nanofibers have drawn particular attention due to their exceptionally high surface area-to-volume ratio, high porosity, superior surface permeability and accessibility, making them an attractive candidate for gas sensing (Guo et al., 2014; Jha R. K. et al., 2018; Yan et al., 2018). Electrospinning technology has been demonstrated as an effective approach to prepare micro-sized and nano-sized fibers. The structure, morphology and dispersion of functional components of the fibers synthesized by electrospinning can be well-tailored through well-controlled conditions and compositions (Wang and Hashimoto, 2018; Yoon et al., 2018; Zhang D. et al., 2018). Kim et al. fabricated semiconducting metal oxide nanofibers through a protein nanocage templating route, to detect trace amounts of target biomarkers in exhaled breath (Kim et al., 2016a). Nevertheless, up to now, it remains a great challenge to construct mesoporous structures in nanofibers with controllable pore size and morphologies, which is highly desirable for improved gas sensing performance.

Among various SMOs, tungsten oxide (WO_3), an *n*-type semiconductor with a band-gap of 2.5 eV, is a promising sensing material for the detection of gas due to its variable oxidation states and suitable band structure (Wang C. Y. et al., 2018). Herein, we adopt a facile approach based on electrospinning to synthesize mesoporous WO_3 nanofibers (NFs) with uniform and controllable pore sizes using SiO_2 nanoparticles and polyvinylpyrrolidone (PVP) as sacrificial templates, ammonium paratungstate as a tungsten precursor and water as a solvent. Due to the support of the rigid PVP species during electrospinning process, the interconnected porous structure and unique fiber-like morphology can be well-maintained after calcination in nitrogen and air, followed by treatment with hydrofluoric acid selectively etched silica particles, creating uniform mesopores in the nanofibers. The obtained mesoporous WO_3 NFs have crystalline frameworks, large uniform pore sizes of 26.3 nm and 42.2 nm, and their specific surface area and pore volume can be as high as 34.4 m^2/g and 24.1 cm^3/g, respectively. Moreover, the mesoporous WO_3 NFs based sensors exhibit superior gas sensing performance with a fast response (24 s) and recovery (27 s), high sensitivity of 23 (R_a/R_g) at 50 ppm when operating at 300°C, an ultralow limit of detection of 1 ppm, and good selectivity, which contributes to their good merits of suitable pore size, high surface area and abundant active sites located on the surface, and continuous and crystalline framework with open pore channels. Such an excellent sensing performance opens up the possibility for the mesoporous WO_3 NFs based sensor to be used in many fields such as environmental monitoring and in the rapid diagnosis of disease.

EXPERIMENTAL SECTION

Chemicals and Materials

Tetraethyl orthosilicate (TEOS), ethanol, NH_4OH solution and hydrofluoric acid of AR grade were purchased from Sino-Pharm Chemical Reagent Co. Ltd. Polyvinylpyrrolidone (PVP, $M_w \approx 40{,}000$ g/mol) was purchased from Aldrich. Ammonium metatungstate hydrate [$(NH_4)_6H_2W_{12}O_{40}{\cdot}xH_2O$, 99.5% metals basis] was purchased from Aladdin.

Preparation of SiO_2 NPs

The SiO_2 NPs with different diameters was prepared using a base catalyzed sol-gel method previously reported (Dasog et al., 2012). Typically, TEOS (10 mL) was dissolved in a solvent mixture of ethanol (10 mL), deionized water (20 mL) and NH_4OH solution (42 %, 5 mL). The obtained solution was further stirred for 1 or 2 h to yield different size SiO_2 NPs. The white precipitate was collected by vacuum filtration and washed with deionized water four times. The solid was transferred to an oven and was kept there for 24 h at 100°C to remove any residual water and ethanol.

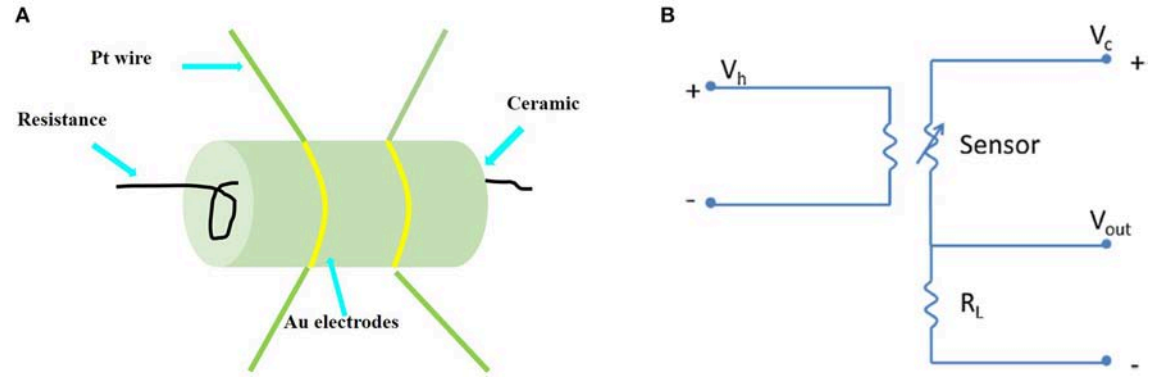

FIGURE 1 | (A) Sketch of the structure of the side-heated mesoporous WO_3 NFs based gas sensor. **(B)** Electric circuit of gas sensing measurements.

Synthesis of Mesoporous WO_3 NFs

Typically, mesoporous WO_3 NFs were synthesized through an electrospinning method as follows: $(NH_4)_6H_2W_{12}O_{40}\cdot xH_2O$ (2.7 g) and PVP (3.0 g) was dissolved in deionized water (4 mL). This was followed by the addition of SiO_2 NPs (0.035 g) with a diameter of 25 nm. Then, the solution was stirred for 20 h for further electrospinning. The as-prepared gel was loaded into a plastic syringe and connected to a high voltage power supply for electrospinning. Twenty kilovolts high voltage was applied between the spinneret and the collector in a gap of 15 cm. In this way, hybrid precursor nanofibrous membranes were obtained. Then, the as-made products were heated with a ramp of 1°C min^{-1} to 350°C for 3 h in nitrogen, resulting in the carbon-supported amorphous tungsten oxide powders. The carbon species was removed and crystallization of the amorphous tungsten oxide frameworks was carried by subsequent heat treatment with a ramp of 1°C min^{-1} to 500°C in air for another 1 h. SiO_2 NPs was completely removed from the composites by treatment with a HF solution (5 wt% aqueous solution, 8 mL) for 2 h and subsequently washed with deionized water and ethanol. Finally, the obtained sample was denoted as mesoporous WO_3-25 NFs. Through the same approach, silica NPs with larger diameters (∼40 nm) were also used as a hard template to synthesize mesoporous WO_3 NFs, and the obtained samples were denoted as mesoporous WO_3-40 NFs. Control experiments, without addition of SiO_2 NPs, were performed according to the same method and procedure, and the obtained sample was denoted as a non-mesoporous WO_3 NFs.

Measurement and Characterization

Field-emission scanning electron microscopy (FE-SEM) was operated on a Hitachi S4800 (Japan) field-emission scanning electron microscope. Transmission electron microscopy (TEM) was conducted on a JEM-2100 F at an accelerating voltage of 200 kV. Wide-angle X-ray diffraction (XRD) patterns were collected on a Rigaku D/Max-2550 PC diffractometer (Tokyo, Japan) in the 2θ range of 10–90°. Nitrogen sorption isotherms were measured at 77 K with a Micromeritics Tristar 3020 analyzer (USA). Before measurements, the samples were degassed under vacuum at 180°C for at least 6 h. The Brunauer-Emmett-Teller (BET) method was utilized to calculate the specific surface areas using the adsorption data at P/P_0 = 0.02–0.20. The pore size distribution (PSD) was calculated from the adsorption branch using the Barrett-Joyne-Halenda (BJH) model. The total pore volume (V_{total}) was estimated from the adsorbed amount at P/P_0 = 0.995. The XPS were collected on an RBD 147 upgraded PHI 5000C ESCA system with a dual X-ray source. The Mg Kα (1253.6 eV) anode and a hemispherical energy analyzer were used in the measurements. All of the binding energies were referenced to the C 1s peak at 284.8 eV of the surface adventitious carbon.

Gas Sensing Performance

Side-heated gas sensors were prepared using a similar method reported previously (Zhang et al., 2009). The mesoporous (or non-mesoporous) WO_3 NFs was mixed with deionized (DI) water and ground in an agate mortar to form a paste. The mass ratio of mesoporous (or non-mesoporous) WO_3 NFs to DI water in the paste is 7:3. The paste was coated on an alumina ceramic tube printed with a pair of Au electrodes, and the thickness of the paste membrane was about 300 μm. Subsequently, the coated alumina ceramic tube was dried at room temperature for 24 h and then annealed at 300°C for 2 h with a ramping rate of 5°C/min in air. Then, a Ni–Cr alloy wire was inserted into the tube as a heater, and the working temperature could be adjusted by changing the heating voltage. Furthermore, the obtained sensor was kept at the optimal working temperature for a week before measurement to further improve the long-term stability. The assembled sensing device is depicted in **Figure 1A**. The stationary state gas distribution method was applied for testing the gas response. In the electric circuit for measuring the gas response (**Figure 1B**), a load resistor (R_L) was connected in series with a gas sensor. The circuit voltage (V_C) was set at 5 V and the output voltage (V_{OUT}) was the terminal voltage of the load resistor. Test gases (such as acetone, methanol, ethanol, toluene, formaldehyde) were injected into a test chamber and diluted with air. The gas response of the sensor is defined as $S = R_a/R_g$ (for reducing gases) or $S = R_g/R_a$ (for oxidizing gases), where R_a is the sensor resistance in air and R_g is that in the

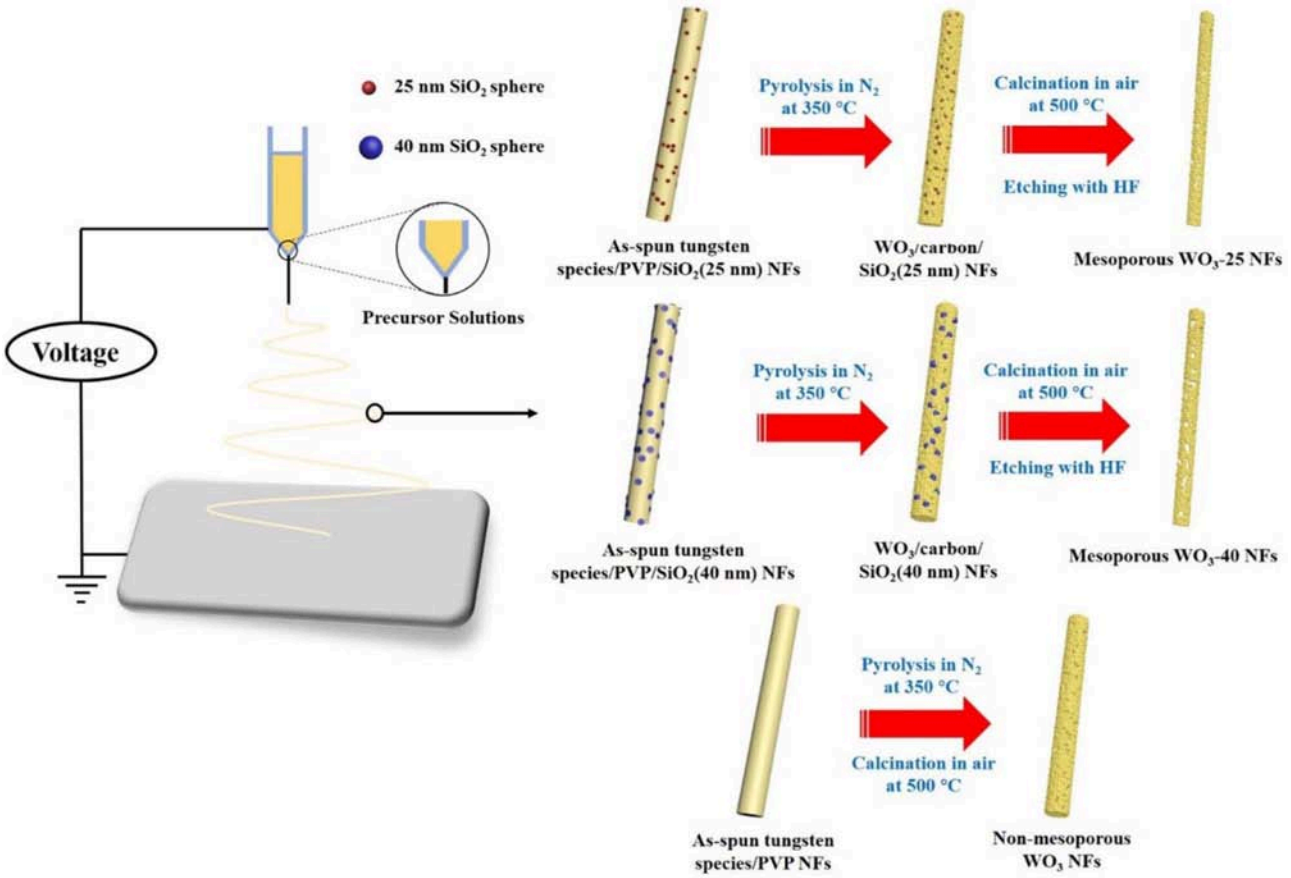

SCHEME 1 | The fabrication process of the mesoporous WO_3 NFs by electrospinning approach.

gas tested. The response time is defined as the time taken for the variation in conductance to reach 90% of the equilibrium value after a test gas was injected, and the recovery time is the time taken for the sensor to return to 10% above the original conductance in air after releasing the test gas, respectively.

RESULTS AND DISCUSSION

The diameters of the as-synthesized SiO_2 NPs are estimated to be 25 and 40 nm from the TEM images (**Figures S1A,B**). An electrospinning technique was employed to construct mesoporous WO_3 NFs from precursor solutions containing $(NH_4)_6H_2W_{12}O_{40}{\cdot}xH_2O$, PVP, SiO_2 NPs, and deionized water, as shown in **Scheme 1**. The as-spun tungsten species/PVP/SiO_2 NFs was subjected to calcination at 350°C in nitrogen, giving rise to WO_3/carbon/SiO_2 NFs owing to the partial carbonization of the PVP species. The carbonized PVP can provide carbon support inside the frameworks, which can prevent the collapse of the fiber morphology during the crystallization process of WO_3. Finally, after further pyrolysis at 500°C in air, and selective etching with hydrofluoric acid to remove the supporting carbon species and SiO_2 sacrificing templates, mesoporous WO_3 NFs is formed as a result. By using SiO_2 NPs with different diameters, two WO_3 NFs can be obtained and denoted as mesoporous WO_3-x NFs, wherein x represents the particle size of SiO_2 NPs. For comparison, non-mesoporous WO_3 NFs was also synthesized via the same approach but without SiO_2 NPs loading.

Field-emission scanning electron microscopy (FE-SEM) observation reveals that all of the as-spun composites have a uniform fiber-like morphology with a dimeter of about 450–500 nm (**Figure 2A**; **Figures S2A, S3A**) and smooth surfaces (insets in **Figure 2A**; **Figures S2A, S3A**). After pyrolysis in N_2 at 350°C, black WO_3/carbon /SiO_2 (25 nm), WO_3/carbon/SiO_2 (40 nm), and WO_3/carbon NFs can be obtained, owing to the partially carbonization of the PVP species. Compared to the as-spun NFs, the composites retained their uniform fiber morphology, and much rougher surfaces are clearly visible in the surface (**Figure 2B**; **Figures S2B, S3B**). After complete removal of carbon and silica species by further calcination in air at 500°C and etching with hydrofluoric acid, all the WO_3 NFs also retained the fiber morphology, indicating a good thermal stability, and their diameters were decreased to 250–300 nm due to the framework shrinkage at high temperature (**Figure 2C**; **Figures S2C, S3C**). It is worth noting that the WO_3 NFs consisted of large numbers of nanograins, and boundaries can be clearly observed. An FESEM image taken along the cross-section

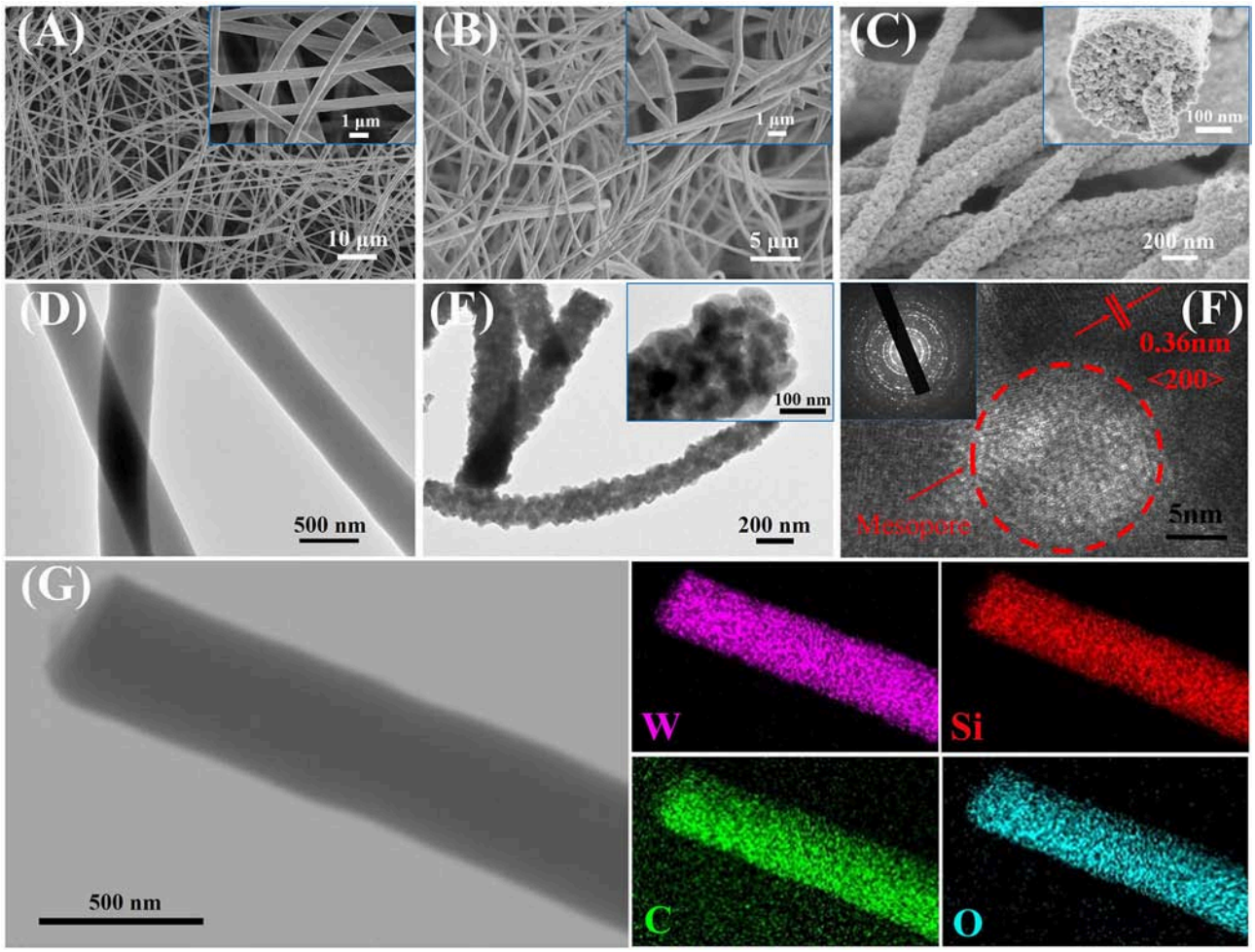

FIGURE 2 | FESEM images of **(A)** as-spun tungsten species/PVP/SiO_2 (25 nm) NFs, **(B)** WO_3/carbon/SiO_2 (25 nm) NFs, **(C)** mesoporous WO_3-25 NFs. TEM images of **(D)** WO_3/carbon/SiO_2 (25 nm) NFs, **(E)** mesoporous WO_3-25 NFs. HRTEM image of **(E)** mesoporous WO_3-25 NFs. **(F)** Scanning TEM image and the corresponding EDS mapping images **(G)** of elemental W, Si, C, and O for WO_3/carbon/SiO_2 (25 nm) NFs.

of the mesoporous WO_3-25 NFs clearly indicates the existence of mesopores around 25–30 nm (inset in **Figure 2C**), which is in good agreement with the diameter of SiO_2 nanoparticles. Due to a larger diameter of the sacrificial SiO_2 template, uniform mesopores of about 40–50 nm can be clearly visible in the SEM image of mesoporous WO_3-40 NFs (**Figure S2C**). And no obvious mesopores were observed on non-mesoporous WO_3 NFs (**Figure S3C**), attributing to the absence of the sacrificial SiO_2 template.

Transmission electron microscopy (TEM) observations further confirmed that the NFs obtained after pyrolysis at 350°C are fibrous in shape with a diameter of 400–450 nm (**Figure 2D**; **Figures S2D, S3D**). The scanning TEM (STEM) image and energy dispersive X-ray elemental mapping recorded on WO_3/carbon/SiO_2 (25 nm) NFs clearly reveals that the W, Si, C, and O elements are homogeneously distributed in entire NFs (**Figure 2G**). It suggests that the carbonized PVP molecules can provide rigid support inside the frameworks, forming a "reinforced-concrete" framework structure with WO_3 species. which can prevent the collapse of the NFs. TEM images of mesoporous WO_3-25 and mesoporous WO_3-40 NFs clearly indicate that the fiber-like morphology are well-retained, and the material consists of interconnected WO_3 nanoparticles, as well as the existence of numerous mesopores (**Figure 2E**; **Figure S2E**), which can offer abundant active sites to interact with guest molecules, greatly facilitating the diffusion of gas molecules. Additional EDS analyses of the mesoporous WO_3-25 NFs and WO_3-40 NFs were carried out as depicted in **Figures S4A,B**, respectively. The absence of peaks from Si in the EDS spectrum indicates the complete removal of SiO_2 by HF etching. Similarly, no obvious mesopores, but only WO_3 nanoparticles, were shown in the TEM image of non-mesoporous WO_3 NFs (**Figure S3E**). High resolution TEM (HR-TEM) images of mesoporous and non-mesoporous WO_3 NFs clearly show the lattice fringes of tungsten oxide with a *d*-spacing of 0.36 nm (**Figure 2F**; **Figures S2F, S3F**), corresponding

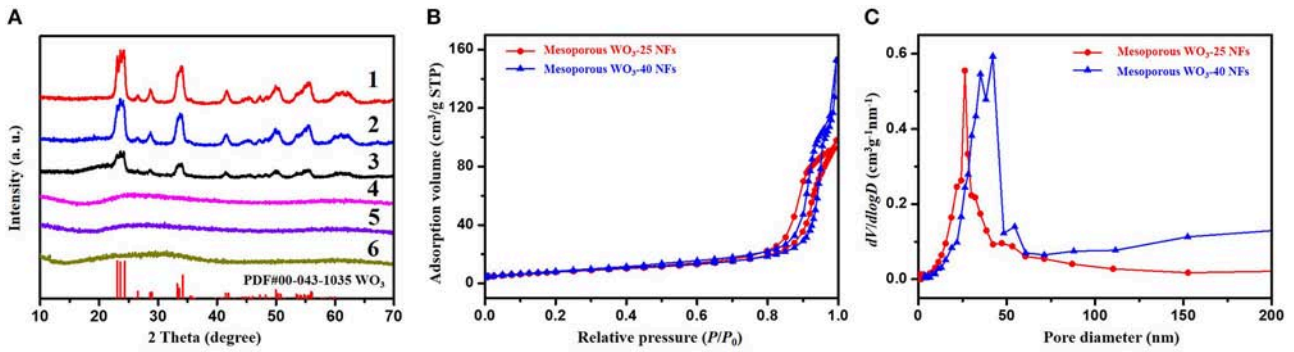

FIGURE 3 | (A) XRD patterns of (1) mesoporous WO_3-25 NFs, (2) mesoporous WO_3-40 NFs, (3) non-mesoporous WO_3 NFs, (4) WO_3/carbon/SiO_2 (25 nm) NFs, (5) WO_3/carbon/SiO_2 (40 nm) NFs, (6) WO_3/carbon NFs. **(B)** Nitrogen-sorption isotherms and **(C)** pore size distribution curves of mesoporous WO_3-25 NFs and mesoporous WO_3-40 NFs.

to the (200) planes, suggesting that the framework consists of well-crystallized and interconnected WO_3 nanoparticles. Selected-area electron diffraction (SAED), recorded on different WO_3 NFs showed well-resolved diffraction rings corresponding with the (200), (112), and (022) crystal planes of monoclinic phase WO_3 (insets in **Figure 2F**, **Figures S2F, S3F**), further confirming the crystalline feature of the scaffold.

Wide-angle X-ray diffraction (WA-XRD) patterns indicate that the WO_3/carbon/SiO_2 (25 nm), WO_3/carbon/SiO_2 (40 nm), and WO_3/carbon NFs exbibits the amorphous feature contributing to the poor crystallization (**Figure 3A**). After crystallization at 500°C, and removal of the silica nanoparticles by selective etching with hydrofluoric acid, mesoporous WO_3-25, mesoporous WO_3-40 and non-mesoporous WO_3 NFs shows well-resolved diffraction peaks in the range of 10–70°C, matching well with the crystalline monoclinic phase of WO_3 with lattice parameters of a = 0.7297, b = 0.7539, c = 0.7688 nm, and β = 90.91 (JCPDS No. 43–1,035). No diffraction peaks from other crystalline impurities are observed in the XRD patterns, indicating pure crystalline phase, which agreeing well with the HR-TEM results. The broadening of the diffraction peaks can be attributed to the small particle size of WO_3 nanocrystals (Li et al., 2014).

Nitrogen adsorption-desorption isotherms of the obtained mesoporous WO_3-25 NFs exhibit type-IV curves with H1 hysteresis loop (**Figure 3B**). The steep increase in the adsorption band at P/P_0 = 0.75–0.96 indicates mesopores with a large and uniform pore size. The pore diameter is about 26.3 nm as indicated in the pore size distributions derived from the adsorption branch of the isotherms by using Barrett-Joyner-Halenda (BJH) model (**Figure 3C**). The specific surface area and total pore volume of mesoporous WO_3-25 NFs are calculated to be as high as 34.4 m^2g^{-1} and 0.15 cm^3g^{-1}, respectively. Similarly, mesoporous WO_3-40 NFs also display type-IV curves with sharp capillary condensation steps in the relative pressure range of 0.78–0.97 (**Figure 3B**). The pore size distribution profile reveals a mesopore size of 42.2 nm (**Figure 3C**), indicating that the hard template silica nanoparticles with larger diameters result in larger mesopores. The surface area and total pore volume of mesoporous WO_3-40 NFs are approximately 24.1 m^2g^{-1} and 0.24 cm^3g^{-1}, respectively. Such a porous structure provides an amplified target-receptor interface and is beneficial for the diffusion and adsorption of large guest molecules, making it an ideal candidate for many applications involving host-guest interactions, such as catalysis and gas sensing. In addition, nitrogen adsorption–desorption isotherms of non-mesoporous WO_3-NFs show type-IV curves with H3 hysteresis loop (**Figure S5A**). The surface area and total pore volume of non-mesoporous WO_3NFs is 19.5 m^2g^{-1} and 0.17 cm^3g^{-1}, respectively. The average pore size calculated from the adsorption branch using the BJH method is about 5.3 nm (**Figure S5B**), much smaller than that of the etched samples (26.3 nm for mesoporous WO_3-25 NFs and 42.2 nm for mesoporous WO_3-40 NFs), which can be attributed to the stacked pores of small WO_3 grains.

X-ray photoelectron spectroscopy (XPS) is further used to investigate the surface composition and elemental states of the NFs before and after etching. For the WO_3/SiO_2 (25 nm) composite NFs (denoted as WO_3-25/SiO_2 NFs) before etching, four peaks corresponding to W 4f, Si 2p, W 4d and O 1s are shown in the survey spectrum (**Figure S6A**). However, after etching, the Si 2p peak at 103.3 eV disappears, indicating the complete removal of SiO_2 species by HF (Xu et al., 2015; Shi et al., 2016). The high-resolution XPS W 4d spectrum (**Figure S6B**) of the samples after etching show similar spectra and can be fitted with two peaks centering at 35.8 and 37.9 eV, which can be assigned to W^{6+} $4f_{7/2}$ and W^{6+} $4f_{5/2}$, respectively (Wang et al., 2012). These results indicate that completely oxidized W is not changed during the etching process in mesoporous WO_3-25 NFs, mesoporous WO_3-40 NFs and non-mesoporous WO_3 NFs samples. The state of O 1s indicates two types of oxygen in the surface (**Figure S6C**), lattice oxygen (O^{2-}) and adsorbed oxygen (O^- and O^{2-}). Usually, the adsorbed oxygen was more active to react with reducing gases compared with lattice oxygen, changing the concentration of main carriers (Zhu et al., 2017a).

Inspired by the unique structure of obtained mesoporous WO_3 fibers with ultra-large and controllable pore size, we tested the performance of mesoporous WO_3-25, mesoporous WO_3-40

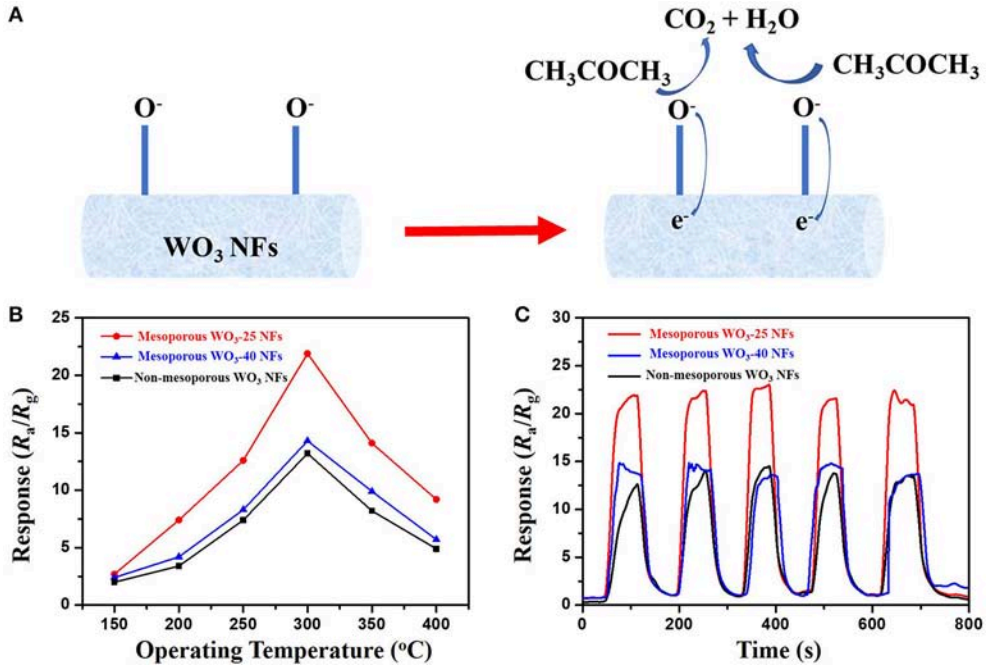

FIGURE 4 | (A) sensing mechanism of WO_3 NFs toward acetone. **(B)** responses of the mesoporous and non-mesoporous WO_3 NFs sensor to 50 ppm acetone at different operating temperatures (150–400°C). **(C)** repeating response and recovery curve of the mesoporous and non-mesoporous WO_3 NFs to 50 ppm acetone.

and non-mesoporous WO_3 NFs as sensing materials for the detection of acetone to investigate their potential application in the detection of acetone leakage and diagnosis for diabetes. The schematic diagram of sensing mechanism is shown in **Figure 4A**. In the gas sensing test, probe gases such as acetone were injected into a test chamber and mixed with air. The gas response of the sensor in this study is defined as $S = R_a/R_g$, where R_a and R_g is the resistance of the sensor in air and test gas, respectively. The response time is defined as the time required from R_a to R_a-90% × (R_a-R_g) after a test gas was injected, and the recovery time is defined as the time required from R_g to R_g + 90% × (R_a-R_g) in air after releasing the test gas, respectively. Since the sensing performances of semiconductors for a specific gas are usually dependent on the working temperature, parallel tests of mesoporous WO_3-25, mesoporous WO_3-40 and non-mesoporous WO_3 NFs based sensors were carried out toward a 50 ppm acetone gas in a range of 150–400°C to optimize the working temperature region (**Figure 4B**). It can be seen that the response of all sensors increased continuously until reaching a maximum value at 300°C and then decreased upon increase of the operating temperature. Such response behavior is due to the balance of the competition between the increase of the surface reaction rates and the decrease in the number of active sites for the adsorption of acetone at high temperatures. As a result, 300°C was adopted as the optimum working temperature for subsequent acetone detections.

In contrast, it was found that both of the mesoporous sensing materials, mesoporous WO_3-25 and WO_3-40 NFs, have shown higher responses to acetone than the non-mesoporous WO_3 NFs. Such phenomenon may contribute to the uniform mesopores and interconnected transportation channels of mesoporous WO_3 NFs resulting from the sacrificial templates including silica nanoparticles and PVP species, which provides a huge interface for the creation of active sites for acetone gas interaction, and greatly facilitates the diffusion of gas molecules in the framework. In addition, the response value increases dramatically from 13.7 for mesoporous WO_3-40 NFs to 22.1 for mesoporous WO_3-25 NFs at the same temperature, indicating that the sensitivity of the materials is closely related to its specific surface area. Mesoporous WO_3-25 NFs with a higher surface area (34.4 m^2g^{-1}) could provide more active surface sites for numerous surface reactions between guest molecules and adsorbed oxygen species on the solid-gas interface. Therefore, the response value of mesoporous WO_3-25 NFs is higher than the non-mesoporous WO_3 NFs during the operating temperature range from 150 to 400°C (**Figure 4B**), and the sensitivity of mesoporous WO_3-25 NFs is 66% higher than that of non-mesoporous WO_3 for 50 ppm at the optimal operation temperature (**Figure 4C**). Moreover, the mesoporous WO_3-25 NFs shows a response time of 24 s, much shorter than that of non-mesoporous WO_3 (67 s), as shown in the **Figure S7**. The faster response is mainly attributed to its porous structure, which could facilitate the diffusion and transport of target gas via enormous pore channels to interact with WO_3 NFs, quickly reaching the maximum sensitivity. The reversible cycles of the response curves illustrate a stable and reliable operation of acetone sensing of all the WO_3 NFs, and further confirm the consistency of mesoporous WO_3-25 NFs based sensors (**Figure 4C**). The continuous dynamic

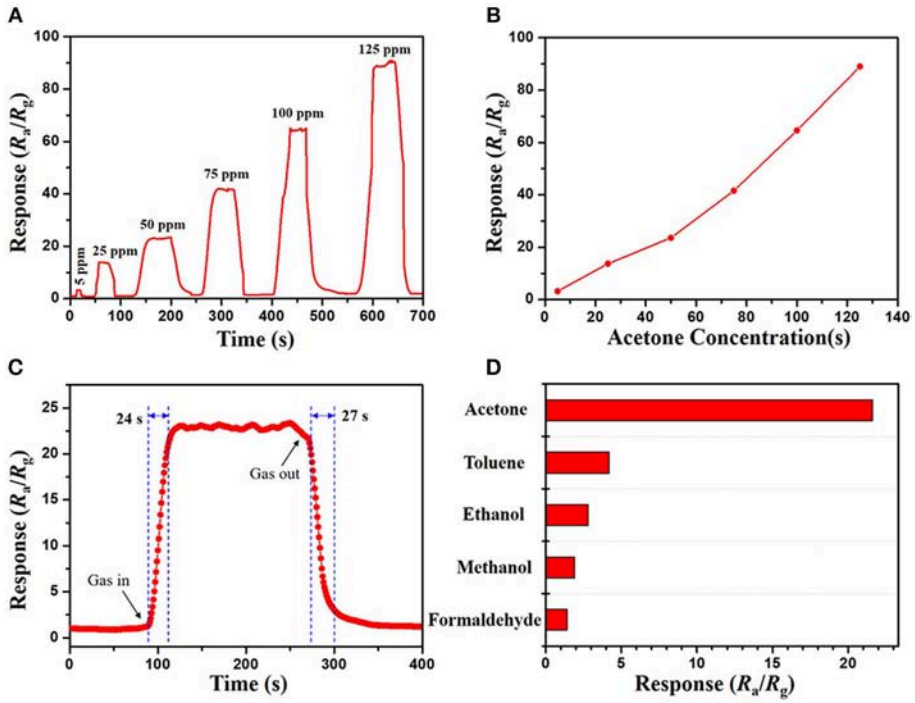

FIGURE 5 | (A) response–recovery curve and **(B)** relationships between acetone concentration and response of the mesoporous WO_3-25 NFs sensor to acetone vapors of different concentrations. **(C)** dynamic response–recovery curve of mesoporous WO_3-25 NFs sensor to 50 ppm acetone. **(D)** responses of the mesoporous WO_3-25 NFs sensor to various gases at 50 ppm.

electrical response of mesoporous WO_3-25 NFs toward different concentration of acetone (5–125 ppm) at 300°C is shown in **Figure 5A**. With the increase in acetone concentration, the response values of mesoporous WO_3-25 NFs based gas sensors rapidly increased from 3.1 at 5 ppm to 89 at 125 ppm. After aeration, the acetone molecules desorbed immediately from the surface of tungsten oxides. The response can be recovered to its initial value for all the testing concentrations, reflecting a good reversibility of the gas sensor. Surprisingly, the minimum detectable concentration can reach as low as 1 ppm (**Figure S8**). As shown in **Figure 5B**, a linear relationship between the sensing response and acetone concentrations is observed, indicating the feasibility of quantitative acetone detection by the mesoporous WO_3 NFs based sensors. As important parameters for a gas sensor, the response and recovery behaviors are also crucial for evaluating the sensing performance. The mesoporous WO_3-25 NFs based sensor exhibits a fast response of 24 s upon exposure to 50 ppm acetone and quick recovery of 27 s when acetone gas was removed (**Figure 5C**). In addition, compared with earlier reported acetone sensors, our mesoporous WO_3 NFs exhibits much better comprehensive sensing performance such as high sensitivity, low limits of detection and fast response-recovery (**Table 1**), thus becoming a promising candidate for acetone sensing in environmental monitoring and rapid medical diagnosis. Based on the aforementioned results, the predominant enhancement could mainly be explained as follows: (1) The unique hierarchical structure where uniform and controllable mesopores are well-connected with enormous transportation channels derived from PVP species, which facilitate the rapid diffusion of gas molecules. (2) The high specific surface area with abundant active sites enables the adsorption of a large amount of acetone molecules. (3) The continuous crystalline framework is also favorable for the fast transportation of charge carriers from the surface into bulk. It can therefore be concluded that the unique feature of our materials can maximize the performance of gas sensing. The selectivity of gas sensors is also an important parameter in practical applications. In this work, four kinds of typical vaporous molecules with identical concentration of 50 ppm, such as methanol, ethanol, toluene, and formaldehyde were selected as interfering gases. As illustrated in **Figure 5D**, the response value of a mesoporous WO_3-25 NFs based sensor to acetone was at least four times higher than that of interfering gases, which implies an excellent selectivity.

In summary, mesoporous WO_3 NFs with controllable pore diameters were synthesized via a facile electrospinning of an aqueous solution containing ammonium paratungstate, PVP and SiO_2 NPs sacrificing templates, followed by controlled pyrolysis at a high temperature and selective etching with hydrofluoric acid. The PVP species can provide rigid support inside frameworks, which can prevent the collapse of the unique fiber morphology and the well-connected porous structure. The decomposition of the PVP species during calcination and the etching of SiO_2 NPs was also found to contribute to the formation of interconnected transportation channels and

TABLE 1 | Comparison of acetone sensing properties of WO_3 or WO_3 based sensors with various nanostructures.

Structures	Working temperature	Acetone concentration (ppm)	Response (R_a/R_g)	Response/recovery time	References
Porous WO_3	300°C	50	12.1	4/11.7 s	Dong et al., 2016
WO_3 plate	307°C	100	~15	10/26 s	Liu et al., 2012
WO_3 nanoflowers	300°C	100	~7	Not mentioned	Wang et al., 2013
Co_3O_4-WO_3 nanocomposite	280°C	100	5.3	Not mentioned	Zhao et al., 2015
Ag-WO3 nanosheets	340°C	50	~8	28/38 s	Yin et al., 2017
MoO_3-WO_3 nanostructures	320°C	100	18.2	8/7 s	Sun et al., 2017
WO_3@CuO nanostructures	Not mentioned	50	3.4	72.2/29.4 s	Yang F. et al., 2018
cactus-like WO_3-SnO_2	360°C	100	12.1	Not mentioned	Zhu et al., 2018
Gd doped WO_3-RGO nanostructures	350°C	50	27.0	Not mentioned	Kaur et al., 2018
La_2O_3-WO_3 nanofibers	350°C	100	12.7	6/210 s	Feng et al., 2015
Mesoporous WO_3 NFs	350°C	50	22.1	24/27 s	This wok

uniform mesopores in the framework of the fibers. The obtained mesoporous WO_3 NFs possess a tunable pore size (26.3 and 42.2 nm), high surface area and pore volume (up to 34.4 m^2/g and 0.24 cm^3g^{-1}), and a well-developed hierarchical porous structure and crystalline pore walls. Sensors based on these materials were found to have an excellent acetone sensing performance with a fast response (24 s) and recovery (27 s), a low detection limit of 1 ppm, excellent selectivity and good stability, due to their high mesoporosity, abundant active sites and the continuous crystalline framework. Based on the above-mentioned results, the obtained mesoporous WO_3 NFs holds great promise for applications in various fields such as portable miniaturized devices used for environmental monitoring, and breath analysis used for disease pre-diagnosis and home security. Moreover, it is expected that the facile and effective electrospinning approach may open up new opportunities for the design of various mesoporous metal oxide NFs with high surface areas, crystalline frameworks and greatly improved mass diffusion and transportation for application in sensors, catalysis, energy storage and conversion.

AUTHOR CONTRIBUTIONS

WL and JY conceived and designed the experiments. HX, TZ, YZ and JG performed the experiments. ML, GZ, LW, WJ, YF, MZ analyzed the data. WL and HX wrote the manuscript. XQ designed the scheme. All authors reviewed the manuscript and approved the final version.

FUNDING

This work was supported by National Natural Science Foundation of China (51822202, 51772050, 51702046, 51432004, 51774096), the Shanghai Rising-Star Program (18QA1400100), the Shanghai Committee of Science and Technology, China (No. 17ZR1401000), the Shanghai Pujiang Program (No. 17PJ1400100), the Youth Top-notch Talent Support Program of Shanghai, the Program for Professor of Special Appointment (Eastern Scholar) at Shanghai Institutions of Higher Learning, the DHU Distinguished Young Professor Program and the Fundamental Research Funds for the Central Universities, the Innovation Program of Shanghai Municipal Education Commission (2017-01-07-00-03-E00025).

SUPPLEMENTARY MATERIAL

The Supplementary Material for this article can be found online at: https://www.frontiersin.org/articles/10.3389/fchem.2019.00266/full#supplementary-material

REFERENCES

Barr, T. J., Sampaio, R. N., Dimarco, B. N., James, E. M., and Meyer, G. J. (2017). Phantom electrons in mesoporous nanocrystalline SnO_2 thin films with cation-dependent reduction onsets. *Chem. Mater.* 29, 3919–3927. doi: 10.1021/acs.chemmater.6b05470

Barsan, N., and Weimar, U. (2001). Conduction model of metal oxide gas sensors. *J. Electroceram.* 7, 143–167. doi: 10.1023/A:1014405811371

Channei, D., Nakaruk, A., Khanitchaidecha, W., Jannoey, P., and Phanichphant, S. (2018). Adsorption and photocatalytic processes of mesoporous SiO_2-coated monoclinic $BiVO_4$. *Front. Chem.* 6:415. doi: 10.3389/fchem.2018.00415

Chen, P. Y., Dang, X., Klug, M. T., Courchesne, N. M. D., Qi, J., Hyder, M. N., et al. (2015). M13 Virus-enabled synthesis of titanium dioxide nanowires for tunable mesoporous semiconducting networks. *Chem. Mater.* 27, 1531–1540. doi: 10.1021/cm503803u

Dam, D. T., and Lee, J. M. (2013). Capacitive behavior of mesoporous manganese dioxide on indium–tin oxide nanowires. *Nano Energy* 2, 933–942. doi: 10.1016/j.nanoen.2013.03.014

Dasog, M., Yang, Z., and Veinot, J. G. C. (2012). Size-controlled solid state synthesis of luminescent silicon nanocrystals using Stöber silica particles. *Cryst. Eng. Comm.* 14:7576. doi: 10.1039/c2ce25950h

Dong, C., Liu, X., Guan, H., Chen, G., Xiao, X., Djerdj, I., et al. (2016). Combustion synthesized hierarchically porous WO_3 for selective acetone

sensing. *Mater. Chem. Phys.* 184, 155–161. doi: 10.1016/j.matchemphys.2016.09.036

Du, J., Lai, X., Yang, N., Zhai, J., Kisailus, D., Su, F., et al. (2011). Hierarchically ordered macro–mesoporous TiO_2-graphene composite films: improved mass transfer, reduced charge recombination, and their enhanced photocatalytic activities. *ACS Nano* 5, 590–596. doi: 10.1021/nn102767d

Feng, C., Wang, C., Cheng, P., Li, X., Wang, B., Guan, Y., et al. (2015). Facile synthesis and gas sensing properties of La_2O_3-WO_3 nanofibers. *Sensors Actuators B Chem.* 221, 434–442. doi: 10.1016/j.snb.2015.06.114

Guo, P., Zhao, G., Chen, P., Lei, B., Jiang, L., Zhang, H., et al. (2014). Porphyrin nanoassemblies via surfactant-assisted assembly and single nanofiber nanoelectronic sensors for high-performance H_2O_2 vapor sensing. *ACS Nano* 8, 3402–3411. doi: 10.1021/nn406071f

He, B., Wang, J., Fan, Y., Jiang, Y., Zhai, Y., Wang, Y., et al. (2018). Mesoporous CoO/Co–N–C nanofibers as efficient cathode catalysts for Li–O_2 batteries. *J. Mater. Chem. A* 6, 19075–19084. doi: 10.1039/C8TA07185C

Jeong, Y. J., Koo, W. T., Jang, J. S., Kim, D. H., Cho, H. J., and Kim, I. D. (2018). Chitosan-templated Pt nanocatalyst loaded mesoporous SnO_2 nanofibers: a superior chemiresistor toward acetone molecules. *Nanoscale* 10, 13713–13721. doi: 10.1039/C8NR03242D

Jha, G., Tran, T., Qiao, S., Ziegler, J. M., Ogata, A. F., Dai, S., et al. (2018). Electrophoretic deposition of mesoporous Niobium(V)oxide nanoscopic films. *Chem. Mater.* 30, 6549–6558. doi: 10.1021/acs.chemmater.8b03254

Jha, R. K., Wan, M., Jacob, C., and Guha, P. K. (2018). Ammonia vapour sensing properties of *in situ* polymerized conducting PANI-nanofiber/WS_2 nanosheet composites. *N. J. Chem.* 42, 735–745. doi: 10.1039/C7NJ03343E

Jia, Q., Ji, H., Zhang, Y., Chen, Y., Sun, X., and Jin, Z. (2014). Rapid and selective detection of acetone using hierarchical ZnO gas sensor for hazardous odor markers application. *J. Hazar. Mater.* 276, 262–270. doi: 10.1016/j.jhazmat.2014.05.044

Kaneti, Y. V., Salunkhe, R. R., Wulan Septiani, N. L., Young, C., Jiang, X., He, Y. B., et al. (2018). General template-free strategy for fabricating mesoporous two-dimensional mixed oxide nanosheets via self-deconstruction/reconstruction of monodispersed metal glycerate nanospheres. *J. Mater. Chem. A* 6, 5971–5983. doi: 10.1039/C8TA00008E

Kaur, J., Anand, K., Kaur, A., and Singh, R. C. (2018). Sensitive and selective acetone sensor based on Gd doped WO_3/reduced graphene oxide nanocomposite. *Sensors Actuators B Chem.* 258, 1022–1035. doi: 10.1016/j.snb.2017.11.159

Kawano, T., Chiamori, H. C., Suter, M., Zhou, Q., Sosnowchik, B. D., and Lin, L. (2007). An electrothermal carbon nanotube gas sensor. *Nano Lett.* 7, 3686–3690. doi: 10.1021/nl071964s

Kim, H. J., and Lee, J. H. (2014). Highly sensitive and selective gas sensors using p-type oxide semiconductors: overview. *Sensors Actuators B Chem.* 192, 607–627. doi: 10.1016/j.snb.2013.11.005

Kim, S. J., Choi, S. J., Jang, J. S., Kim, N. H., Hakim, M., Tuller, H. L., et al. (2016a). Mesoporous WO_3 nanofibers with protein-templated nanoscale catalysts for detection of trace biomarkers in exhaled breath. *ACS Nano* 10, 5891–5899. doi: 10.1021/acsnano.6b01196

Li, F., Chen, L., Knowles, G. P., Macfarlane, D. R., and Zhang, J. (2017). Hierarchical mesoporous SnO_2 nanosheets on carbon cloth: a robust and flexible electrocatalyst for CO_2 reduction with high efficiency and selectivity. *Angewandte Chem Int. Edn.* 56, 505–509. doi: 10.1002/anie.201608279

Li, X., Ding, K., Gao, B., Li, Q., Li, Y., Fu, J., et al. (2017). Freestanding carbon encapsulated mesoporous vanadium nitride nanowires enable highly stable sulfur cathodes for lithium-sulfur batteries. *Nano Energy* 40, 655–662. doi: 10.1016/j.nanoen.2017.09.018

Li, Y., Luo, W., Qin, N., Dong, J., Wei, J., Li, W., et al. (2014). Highly ordered mesoporous tungsten oxides with a large pore size and crystalline framework for H_2S sensing. *Angewandte Chem. Int. Edn.* 53, 9035–9040. doi: 10.1002/anie.201403817

Liu, S., Zhang, F., Li, H., Chen, T., and Wang, Y. (2012). Acetone detection properties of single crystalline tungsten oxide plates synthesized by hydrothermal method using cetyltrimethyl ammonium bromide supermolecular template. *Sensors Actuators B Chem.* 162, 259–268. doi: 10.1016/j.snb.2011.12.076

Luo, W., Li, Y., Dong, J., Wei, J., Xu, J., Deng, Y., et al. (2013). A resol-assisted co-assembly approach to crystalline mesoporous niobia spheres for electrochemical biosensing. *Angewandte Chem. Int. Edn.* 52, 10505–10510. doi: 10.1002/anie.201303353

Luo, W., Wang, Y., Wang, L., Jiang, W., Chou, S. L., Dou, S. X., et al. (2016a). Silicon/mesoporous carbon/crystalline TiO_2 nanoparticles for highly stable lithium storage. *ACS Nano* 10, 10524–10532. doi: 10.1021/acsnano.6b06517

Luo, W., Zhao, T., Li, Y., Wei, J., Xu, P., Li, X., et al. (2016b). A Micelle fusion-aggregation assembly approach to mesoporous carbon materials with rich active sites for ultrasensitive ammonia sensing. *J. Am. Chem. Soc.* 138, 12586–12595. doi: 10.1021/jacs.6b07355

Ma, J., Ren, Y., Zhou, X., Liu, L., Zhu, Y., Cheng, X., et al. (2018). Pt Nanoparticles sensitized ordered mesoporous WO_3 semiconductor: gas sensing performance and mechanism study. *Adv. Funct. Mater.* 28:1705268. doi: 10.1002/adfm.201705268

Nada, A. A., Nasr, M., Viter, R., Miele, P., Roualdes, S., and Bechelany, M. (2017). Mesoporous $ZnFe_2O_4$@TiO_2 nanofibers prepared by electrospinning coupled to PECVD as highly performing photocatalytic materials. *J. Phys. Chem. C* 121, 24669–24677. doi: 10.1021/acs.jpcc.7b08567

Qiu, Z., Hua, Z., Li, Y., Wang, M., Huang, D., Tian, C., et al. (2018). Acetone sensing properties and mechanism of Rh-Loaded WO_3 nanosheets. *Front. Chem.* 6, 385–385. doi: 10.3389/fchem.2018.00385

Rakhi, R. B., Chen, W., Cha, D., and Alshareef, H. N. (2012). Substrate dependent self-organization of mesoporous cobalt oxide nanowires with remarkable pseudocapacitance. *Nano Lett.* 12, 2559–2567. doi: 10.1021/nl300779a

Ren, X., Hou, H., Liu, Z., Gao, F., Zheng, J., Wang, L., et al. (2016). Shape-enhanced photocatalytic activities of thoroughly mesoporous ZnO nanofibers. *Small* 12, 4007–4017. doi: 10.1002/smll.201600991

Saha, J., and De, G. (2013). Highly ordered cubic mesoporous electrospun SiO_2 nanofibers. *Chem. Commun.* 49, 6322–6324. doi: 10.1039/c3cc42338g

Salehi, S., Nikan, E., Khodadadi, A. A., and Mortazavi, Y. (2014). Highly sensitive carbon nanotubes–SnO_2 nanocomposite sensor for acetone detection in diabetes mellitus breath. *Sensors Actuators B Chem.* 205, 261–267. doi: 10.1016/j.snb.2014.08.082

Shi, L., Wang, W., Wang, A., Yuan, K., Jin, Z., and Yang, Y. (2016). Scalable synthesis of core-shell structured SiO_x/nitrogen-doped carbon composite as a high-performance anode material for lithium-ion batteries. *J. Power Sources* 318, 184–191. doi: 10.1016/j.jpowsour.2016.03.111

Singkammo, S., Wisitsoraat, A., Sriprachuabwong, C., Tuantranont, A., Phanichphant, S., and Liewhiran, C. (2015). Electrolytically exfoliated graphene-loaded flame-made Ni-doped SnO_2 composite film for acetone sensing. *ACS Appl. Mater. Interfaces* 7, 3077–3092. doi: 10.1021/acsami.5b00161

Sun, Y., Chen, L., Wang, Y., Zhao, Z., Li, P., Zhang, W., et al. (2017). Synthesis of MoO_3/WO_3 composite nanostructures for highly sensitive ethanol and acetone detection. *J. Mater. Sci.* 52, 1561–1572. doi: 10.1007/s10853-016-0450-2

Wang, C., and Hashimoto, T. (2018). Self-organization in electrospun polymer solutions: from dissipative structures to ordered fiber structures through fluctuations. *Macromolecules* 51, 4502–4515. doi: 10.1021/acs.macromol.8b00647

Wang, C., Yin, L., Zhang, L., Xiang, D., and Gao, R. (2010). Metal oxide gas sensors: sensitivity and influencing factors. *Sensors* 10, 2088–2106. doi: 10.3390/s100302088

Wang, C. Y., Zhang, X., Rong, Q., Hou, N. N., and Yu, H. Q. (2018). Ammonia sensing by closely packed WO_3 microspheres with oxygen vacancies. *Chemosphere* 204, 202–209. doi: 10.1016/j.chemosphere.2018.04.050

Wang, G., Ling, Y., Wang, H., Yang, X., Wang, C., Zhang, J. Z., et al. (2012). Hydrogen-treated WO_3 nanoflakes show enhanced photostability. *Energy Environ. Sci.* 5, 6180–6187. doi: 10.1039/c2ee03158b

Wang, L., Bi, X., and Yang, S. (2016). Partially single-crystalline mesoporous Nb_2O_5 nanosheets in between graphene for ultrafast sodium storage. *Adv. Mater.* 28, 7672–7679. doi: 10.1002/adma.201601723

Wang, M., Fan, L., Wu, X., Tian, D., Cheng, J., Qiu, Y., et al. (2017). Hierarchical mesoporous SnO_2 nanosheets on carbon cloth toward enhancing the polysulfides redox for lithium–sulfur batteries. *J. Mater. Chem. A* 5, 19613–19618. doi: 10.1039/C7TA04937D

Wang, S., Ang, H. M., Tade, M. O. (2007). Volatile organic compounds in indoor environment and photocatalytic oxidation: state of the art. *Environ. Int.* 33, 694–705. doi: 10.1016/j.envint.2007.02.011

Wang, W. Q., Wang, X. L., Xia, X. H., Yao, Z. J., Zhong, Y., and Tu, J. P. (2018). Enhanced electrochromic and energy storage performance in mesoporous WO_3 film and its application in a bi-functional smart window. *Nanoscale* 10, 8162–8169. doi: 10.1039/C8NR00790J

Wang, X. D., Summers, C. J., and Wang, Z. L. (2004). Mesoporous single-crystal ZnO nanowires epitaxially sheathed with Zn_2SiO_4. *Adv. Mater.* 16, 1215–1218. doi: 10.1002/adma.200306505

Wang, Z., Sun, P., Yang, T., Gao, Y., Li, X., Lu, G., et al. (2013). Flower-like WO_3 architectures synthesized via a microwave-assisted method and their gas sensing properties. *Sensors Actuators B Chem.* 186, 734–740. doi: 10.1016/j.snb.2013.06.015

Xu, K., Ben, L., Li, H., and Huang, X. (2015). Silicon-based nanosheets synthesized by a topochemical reaction for use as anodes for lithium ion batteries. *Nano Res.* 8, 2654–2662. doi: 10.1007/s12274-015-0772-4

Yamazoe, N., Sakai, G., and Shimanoe, K. (2003). Oxide Semiconductor Gas Sensors. *Catalysis Surveys Asia* 7, 63–75. doi: 10.1023/A:1023436725457

Yan, S., Xue, J., and Wu, Q. (2018). Synchronous synthesis and sensing performance of α-Fe_2O_3/SnO_2 nanofiber heterostructures for conductometric C_2H_5OH detection. *Sensors Actuators B Chem.* 275, 322–331. doi: 10.1016/j.snb.2018.07.079

Yang, F., Wang, F., and Guo, Z. (2018). Characteristics of binary WO_3@CuO and ternary WO_3@PDA@CuO based on impressive sensing acetone odor. *J. Colloid Interface Sci.* 524, 32–41. doi: 10.1016/j.jcis.2018.04.013

Yang, Z., Huang, Y., Yao, F., Luo, H., and Wan, Y. (2018). Wrapping mesoporous Fe_2O_3 nanoparticles by reduced graphene oxide: enhancement of cycling stability and capacity of lithium ion batteries by mesoscopic engineering. *Ceramics Int.* 44, 20656–20663. doi: 10.1016/j.ceramint.2018.08.058

Yin, M., Yu, L., and Liu, S. (2017). Synthesis of Ag quantum dots sensitized WO_3 nanosheets and their enhanced acetone sensing properties. *Mater. Lett.* 186, 66–69. doi: 10.1016/j.matlet.2016.09.083

Yoon, J., Yang, H. S., Lee, B. S., and Yu, W. R. (2018). Recent progress in coaxial electrospinning: new parameters, various structures, and wide applications. *Adv. Mater* .30:e1704765. doi: 10.1002/adma.201704765

Zhang, D., Zhang, N., Ma, F.-F., Qi, X. D., Yang, J. H., Huang, T., et al. (2018). One-step fabrication of functionalized poly(l-lactide) porous fibers by electrospinning and the adsorption/separation abilities. *J. Hazard. Mater.* 360, 150–162. doi: 10.1016/j.jhazmat.2018.07.090

Zhang, H., Li, H., Wang, Z., Zheng, Z., Wang, P., Liu, Y., et al. (2018). Fabrication of $BiVO_4$ photoanode consisted of mesoporous nanoparticles with improved bulk charge separation efficiency. *Appl. Catalysis B Environ.* 238, 586–591. doi: 10.1016/j.apcatb.2018.07.050

Zhang, Q., Zhang, H., Xu, M., Shen, Z., and Wei, Q. (2018). A WO_3 nanorod-Cr_2O_3 nanoparticle composite for selective gas sensing of 2-butanone. *Chin. Chem. Lett.* 29, 538–542. doi: 10.1016/j.cclet.2017.09.018

Zhang, X., Dong, Z., Liu, S., Shi, Y., Dong, Y., and Feng, W. (2017). Maize straw-templated hierarchical porous ZnO:Ni with enhanced acetone gas sensing properties. *Sensors Actuators B Chem.* 243, 1224–1230. doi: 10.1016/j.snb.2016.12.076

Zhang, Y., Xu, J., Xiang, Q., Li, H., Pan, Q., and Xu, P. (2009). Brush-like hierarchical ZnO nanostructures: synthesis, photoluminescence and gas sensor properties. *J. Phys. Chem. C* 113, 3430–3435. doi: 10.1021/jp8092258

Zhang, Y., Yue, Q., Yu, L., Yang, X., Hou, X. F., Zhao, D., et al. (2018). Amphiphilic block copolymers directed interface coassembly to construct multifunctional microspheres with magnetic core and monolayer mesoporous aluminosilicate shell. *Adv. Mater.* 30:1800345. doi: 10.1002/adma.201800345

Zhao, T., Luo, W., Deng, Y., Luo, Y., Xu, P., Liu, Y., et al. (2016). Monodisperse mesoporous TiO_2 microspheres for dye sensitized solar cells. *Nano Energy* 26, 16–25. doi: 10.1016/j.nanoen.2016.04.050

Zhao, X., Ji, H., Jia, Q., and Wang, M. (2015). A nanoscale Co_3O_4-WO_3 p–n junction sensor with enhanced acetone responsivity. *J. Mater. Sci. Mater. Electron.* 26, 8217–8223. doi: 10.1007/s10854-015-3484-3

Zhao, Y., Dong, F., Han, W., Zhao, H., and Tang, Z. (2019). The synergistic catalytic effect between graphene oxide and three-dimensional ordered mesoporous Co_3O_4 nanoparticles for low-temperature CO oxidation. *Microporous Mesoporous Mater.* 273, 1–9. doi: 10.1016/j.micromeso.2018.06.042

Zhou, X., Cheng, X., Zhu, Y., Elzatahry, A. A., Alghamdi, A., Deng, Y., et al. (2018). Ordered porous metal oxide semiconductors for gas sensing. *Chin. Chem. Lett.* 29, 405–416. doi: 10.1016/j.cclet.2017.06.021

Zhu, L., Zeng, W., and Li, Y. (2018). A novel cactus-like WO_3-SnO_2 nanocomposite and its acetone gas sensing properties. *Mater. Lett.* 231, 5–7. doi: 10.1016/j.matlet.2018.08.007

Zhu, Y., Zhao, Y., Ma, J., Cheng, X., Xie, J., Xu, P., et al. (2017a). Mesoporous tungsten oxides with crystalline framework for highly sensitive and selective detection of foodborne pathogens. *J. Am. Chem. Soc.* 139, 10365–10373. doi: 10.1021/jacs.7b04221

Conflict of Interest Statement: The authors declare that the research was conducted in the absence of any commercial or financial relationships that could be construed as a potential conflict of interest.

Copyright © 2019 Xu, Gao, Li, Zhao, Zhang, Zhao, Wang, Jiang, Zhu, Qian, Fan, Yang and Luo. This is an open-access article distributed under the terms of the Creative Commons Attribution License (CC BY). The use, distribution or reproduction in other forums is permitted, provided the original author(s) and the copyright owner(s) are credited and that the original publication in this journal is cited, in accordance with accepted academic practice. No use, distribution or reproduction is permitted which does not comply with these terms.

frontiers in Chemistry

ORIGINAL RESEARCH
published: 19 September 2018
doi: 10.3389/fchem.2018.00424

The Impact of Cr^{3+} Doping on Temperature Sensitivity Modulation in Cr^{3+} Doped and Cr^{3+}, Nd^{3+} Co-doped $Y_3Al_5O_{12}$, $Y_3Al_2Ga_3O_{12}$, and $Y_3Ga_5O_{12}$ Nanothermometers

*Karolina Elzbieciak and Lukasz Marciniak**

Institute of Low Temperatures and Structure Research PAS, Wrocław, Poland

A new approach to enhance the sensitivity of transition metal ion based nanocrystalline luminescent thermometer is presented. It was shown that the increase of Cr^{3+} concentration in three types of garnet host namely $Y_3Al_5O_{12}$, $Y_3Ga_5O_{12}$, and $Y_3Al_2Ga_3O_{12}$ allows for significant enhancement of their performance in non-contact thermometry. This phenomenon is related to the weakening of the crystal field strength due to enlargement of average Cr^{3+}-O^{2-} distance at higher Cr^{3+} concentrations. By increasing Cr^{3+} concentration from 0.6 to 30%, the sensitivity increased by over one order of magnitude from $S = 0.2\%/^{\circ}C$ to $S = 2.2\%/^{\circ}C$ at 9°C in $Y_3Al_2Ga_3O_{12}$ nanocrystals. Moreover, it was found that due to the $Cr^{3+} \rightarrow Nd^{3+}$ energy transfer in the Cr^{3+}, Nd^{3+} co-doped system, the usable Cr^{3+} concentration, for which its emission can be detected, is limited to 10% while the sensitivity at −50°C was doubled (from 1.3%/°C for $Y_3Al_2Ga_3O_{12}$:10%Cr^{3+} to 2.2%/°C $Y_3Al_2Ga_3O_{12}$:10%Cr^{3+}, 1%Nd^{3+} nanocrystals).

Keywords: chromium, luminescence, luminescent thermometers, Nanocrystals (NCs), garnets

OPEN ACCESS

Edited by:
Luís António Dias Carlos, University of Aveiro, Portugal

Reviewed by:
Xiaoji Xie, Nanjing Tech University, China
Chun Xu, The University of Queensland, Australia

***Correspondence:**
Lukasz Marciniak
l.marciniak@intibs.pl

Specialty section:
This article was submitted to Nanoscience, a section of the journal Frontiers in Chemistry

Received: *21 June 2018*
Accepted: *28 August 2018*
Published: *19 September 2018*

Citation:
Elzbieciak K and Marciniak L (2018) The Impact of Cr^{3+} Doping on Temperature Sensitivity Modulation in Cr^{3+} Doped and Cr^{3+}, Nd^{3+} Co-doped $Y_3Al_5O_{12}$, $Y_3Al_2Ga_3O_{12}$, and $Y_3Ga_5O_{12}$ Nanothermometers. Front. Chem. 6:424. doi: 10.3389/fchem.2018.00424

INTRODUCTION

In response to the requirements imposed by technology, micro/nanoelectronics or photonics as well as by biomedical applications, new approaches to the luminescent nanothermometers (LNTs) have to be proposed to secure fast and accurate temperature sensing with submicrometer spatial resolution, and highly sensitive temperature readout (Brites et al., 2012; Jaque and Vetrone, 2012; Chen et al., 2016; del Rosal et al., 2016a,b; Dramićanin, 2016; Marciniak et al., 2016b; Suo et al., 2017; Wang et al., 2017; Gao et al., 2018; Liao et al., 2018; Liu et al., 2018; Malysa et al., 2018; Runowski et al., 2018; Zhong et al., 2018). One of the most promising one, relies on exploiting transition metal (TM) ions, whose highly temperature dependent emission is referred to emission of barely temperature dependent lanthanides ions (Marciniak et al., 2017a; Drabik et al., 2018; Elzbieciak et al., 2018; Kniec and Marciniak, 2018; Marciniak and Trejgis, 2018; Trejgis and Marciniak, 2018). Materials which could be applied as real time temperature sensors in biomedicine, must also accomplish some other important requirements like sufficient sensitivity to temperature changes, high stability, low cytotoxicity (Brites et al., 2012; Jaque and Vetrone, 2012; Benayas et al., 2015) and operation in spectral range of optical transparency windows of biological tissues (Anderson and Parrish, 1981; Jaque and Jacinto, 2016). Because the transition metal ions based luminescent nanothermometers meet abovementioned flagship demands, they

can be considered as distinctively attractive research area. However, in order to be applicable, the thorough understanding of the correlation between structure of the host material and the thermal quenching of luminescence has to be studied. In our previous work (Elzbieciak et al., 2018), we have shown that by appropriate adjustment of the stoichiometry of the host matrix, relative sensitivity of Cr^{3+} ions-based luminescent thermometer can be intentionally modulated. The presented tuning occurred as a result of modification of the metal-to-oxygen ionic distance, which modified the strength of the crystal field (CF) (Struve and Huber, 2000; Xu et al., 2017). Therefore, taking advantage from the fact that CF influences the position of $^4T_2$ parabola, the activation energy, responsible for determination of thermal stability of luminescence, can be deliberately reduced. Efficient thermal quenching of the luminescence intensity is beneficial for sensitive luminescent thermometry. As it was already presented (Marciniak and Bednarkiewicz, 2016; Marciniak et al., 2016a, 2017b; Azkargorta et al., 2017), significant changes of the CF strength may also result from rising the concentration of active or passive dopants. Recently, Deren et al. (2012) showed that the increase of the Cr^{3+} concentration in $Y_3Ga_5O_{12}$:Cr^{3+} causes the diminishment of $^2E \rightarrow {}^4A_2$ narrow emission band and enhancement of $^4T_2 \rightarrow {}^4A_2$ band's intensity. Lowering the CF strength by growing number of Cr^{3+} ions, which is related with the elongation of the M-O distance, should relevantly enhance the relative sensitivity to temperature changes of such Cr^{3+} based luminescent thermometer. These observations motivated us to verify this hypothesis through comprehensive investigations of the impact of Cr^{3+} concentration (0.01–50%) on the temperature sensing capability in $Y_3Al_5O_{12}$, $Y_3Al_2Ga_3O_{12}$ and $Y_3Ga_5O_{12}$ nanocrystals.

EXPERIMENTAL

Nanopowders of (0.1; 0.5; 2; 5; 10; 20; 50%) Cr^{3+} and (0.1; 0.5; 2; 5; 10; 20; 50%) Cr^{3+},1% Nd^{3+} doped $Y_3Al_5O_{12}$, $Y_3Ga_5O_{12}$ and (0.06; 0.3; 1.2; 3; 6; 9; 12; 30%) Cr^{3+}, (0.06; 0.3; 1.2; 3; 6; 9; 12; 30%) Cr^{3+}, 1%Nd^{3+} doped $Y_3Al_2Ga_3O_{12}$ garnets were synthesized by the modified Pechini method (Pechini, 1967). Whole synthesis procedure was analogous as described in our earlier work (Elzbieciak et al., 2018). In brief, in order to obtain metal nitrates, calculated amount of yttrium oxide and neodymium oxide were dissolved in deionized water with addition of ultrapure nitric acid. After triple recrystallization process, yttrium or yttrium and neodymium nitrates were mixed together with aluminum, gallium and chromium nitrates. Afterwards, aqueous solution of citric acid and PEG was added to the mixture, than it was stirred for 3 h. In order to form a resin the obtained solution was heated for 1 week at 90°C.

All the synthesized materials were annealed for 16 h at 850°C. The following starting materials were used for synthesis: yttrium oxide (Y_2O_3 with 99.995% purity from Stanford Materials Corporation), neodymium oxide (Nd_2O_3 with 99.998% purity from Stanford Materials Corporation), aluminum nitrate nonahydrate ($Al(NO_3)_3{\cdot}9H_2O$ Puratronic 99.999% purity from Alfa Aesar), gallium(III) nitrate nonahydrate ($Ga(NO_3)_3{\cdot}9H_2O$ Puratronic 99.999% purity from Alfa Aesar), chromium nitrate nonahydrate ($Cr(NO_3)_3{\cdot}9H_2O$, 99.99% purity from Alfa Aesar), citric acid ($C_6H_8O_7$ with 99.5+% purity from Alfa Aesar) and poly(ethylene glycol) (PEG $C_2H_6O_2$ BioUltra 200 from Sigma).

All of the obtained materials were examined by XRD (X-ray diffraction) measurements carried out on PANalitycal X'Pert diffractometer, equipped with an Anton Paar TCU 1000 N temperature control unit, using Ni-filtered Cu-K_α radiation ($V = 40$ kV, $I = 30$ mA). Transmission electron microscope (TEM) images were taken using FEI TECNAI G2 X-TWIN microscope equipped with EDS detector. Powders were dispersed in methanol solution in ultrasounds and applied for lacey type copper lattices. The studies were performed in conventional TEM microscope with 300 keV parallel beam electron energy. Images were digitally recorded using the Gatan Ultrascan 1000XP.

Excitation spectra were measured using FLS980 Fluorescence Spectrometer form Edinburgh Instruments. Temperature dependent emission spectra were measured using 450 nm excitation line from laser diode and recorded using a Silver-Nova Super Range TEC Spectrometer from Stellarnet of 1 nm spectral resolution. Temperature during the measurement was controlled using the THMS 600 heating stage from Linkam (0.1°C stability and 0.1°C set point resolution).

RESULTS AND DISCUSSION

The yttrium aluminum/gallium garnets, crystallize in cubic structure with Ia3-d space group. As it is known, structures of these materials ($A_3B_2C_3O_{12}$) provide three types of cation sites, namely dodecahedral Y^{3+} site and also octahedral (B) and tetrahedral (C) Al^{3+}/Ga^{3+} sites which, because of similarity in ionic radii and the same coordination number, could be occupied by lanthanide Ln^{3+} (A) and transition metal ions TM^{3+} (B, C), respectively. Representative XRD patterns of $Y_3Al_2Ga_3O_{12}$:Cr^{3+} nanocrystals with different chromium concentration are presented in **Figure 1a**. All the reflection peaks correspond to the reference patterns confirming phase purity of the synthesized materials even for high dopant concentration (see also Supporting Information, **Figures S1–S5**). It is worth noting that in case of YAG (**Figures S2, S3**) and YGG (**Figures S4, S5**) with doping above 20% of Cr^{3+} ions, additional peaks occur in the XRD pattern. The cell parameter, as it can be seen in **Figure 1b**, is strongly affected by the Cr^{3+} concentration. In the case of YAG:Cr^{3+}, parameter *a* increases from 11.99 Å for 0.1%Cr^{3+} to 12.16 Å for 50%Cr^{3+}. On the other hand for YGG:Cr^{3+} an opposite tendency can be found –the *a* parameter decreases from 12.09 Å for 0.1%Cr^{3+} to 12.05 Å for 50%Cr^{3+}. This is due to differences in ionic radius between host ions Al^{3+} (67.5 pm) and Ga^{3+}(76 pm) ions being substituted by a larger dopant Cr^{3+} ions (75.5 pm). When atom with shorter ionic radius is substituted by atom with longer one, as in the case of $Y_3Al_5O_{12}$, the volume of the unit cell increases, due to the local expansion of the structure. This was also confirmed by the increase of the microstrains in the YAG structure (calculated using Rietveld refinement, **Figure S7**). On the other hand, in the case of

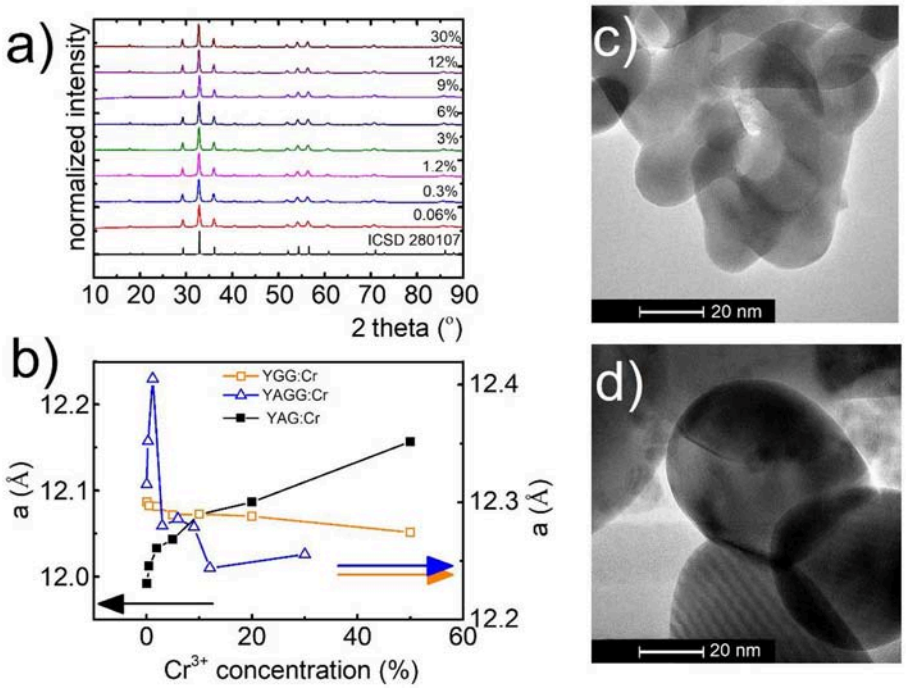

FIGURE 1 | Structural and morphological characterization of synthesized materials: XRD spectra for $Y_3Al_2Ga_3O_{12}$ **(a)** with different concentrations of Cr^{3+} ions, dependence of unit cell parameter **(a)** of YGG, YAG, and YAGG on Cr^{3+} concentration **(b)**; representative TEM images for $Y_3Al_2Ga_3O_{12}$:0.06%Cr^{3+},1%Nd^{3+} **(c)** and $Y_3Al_2Ga_3O_{12}$:30%Cr^{3+},1%Nd^{3+} **(d)** nanocrystals.

substitution of larger host ion with a smaller dopant ion, the parameter *a* and microstrains decrease likewise in the $Y_3Ga_5O_{12}$. The reduction of the cell parameter for increasing Cr^{3+} concentration observed in YAGG, is therefore a direct confirmation that Cr^{3+} ions substitute octahedral sites of Ga^{3+} ions. The average grain size of the nanocrystals, calculated using Rietveld refinement technique (around 60 nm), was in agreement with the nanoparticle size distribution determined from TEM images-70 ± 10 nm (**Figures 1c,d**, **Figure S6**). TEM images revealed good crystallization and some agglomeration of the obtained powders.

The simplified configurational coordinates diagram of Cr^{3+} is presented in **Figure 2A**. The luminescence of Cr^{3+} ions occurs through radiative depopulation of ^2E and/or $^4T_2$ states to the $^4A_2$ ground state. Due to the fact that strength of the crystal field determines the emission of Cr^{3+} ions, sharp emission line corresponding to the $^2E \rightarrow {}^4A_2$ transition and broadband emission corresponding to the $^4T_2 \rightarrow {}^4A_2$ transition can be observed in the emission spectra of Cr^{3+} ion in strong and weak crystal field, respectively. At higher temperatures, when the thermal energy is sufficient to reach the intersection point between the ^2E parabola and $^4T_2$ or $^4A_2$ parabolas, the process of nonradiative, multiphonon relaxation results in lowering of their emission intensity. Analysis of the emission spectra of $Y_3Al_2Ga_3O_{12}$:Cr^{3+} for different dopant concentration obtained upon 450 nm excitation, clearly indicates that at higher Cr^{3+} concentration the broad $^4T_2 \rightarrow {}^4A_2$ emission band localized at around 870 nm increase its intensity in respect to the $^2E \rightarrow {}^4A_2$ band at 692 nm (**Figure 2B**). Obviously, the total emission intensity decreases at higher dopant concentration due to the concentration quenching of luminescence. Nevertheless, it can be distinctly seen that $^4T_2 \rightarrow {}^4A_2$ dominates in the spectra for 30% of Cr^{3+} ions. Similar observation can be done in the emission spectra of $Y_3Al_5O_{12}$:Cr^{3+} and $Y_3Ga_5O_{12}$:Cr^{3+} nanocrystals presented in **Figures S8, S9**, respectively. However, in these cases similar trends can be observed for lower Cr^{3+} concentrations and to a lesser extent also in $Y_3Al_2Ga_3O_{12}$. Two main consequences of the lowering of $^4T_2$ state parabola can be found. First, at low dopant concentration the gradual reduction of its energy facilitates thermal depopulation of ^2E state–lowered ΔE_2 energy (the consequence of the intersection point between ^2E and $^4T_2$ parabolas). Secondly, at higher dopant concentration, when the energy $^4T_2$ state becomes lower than ^2E one, the broadband emission appears. The characteristic red-shift of the Cr^{3+} absorption bands localized around 400 nm and 575 nm, which can be attributed to the $^4A_2 \rightarrow {}^4T_1$ and $^4A_2 \rightarrow {}^4T_2$ electronic transitions, respectively, is a result of lowering of the CF strength (**Figures S12–S14**). In order to quantify the observed change of the crystal field strength in the examined nanocrystals, the Dq/B parameter was calculated for each of the samples as follows (Casalboni et al., 1994):

$$Dq = \frac{E\left({}^4A_2 \rightarrow {}^4T_2\right)}{10} \quad (1)$$

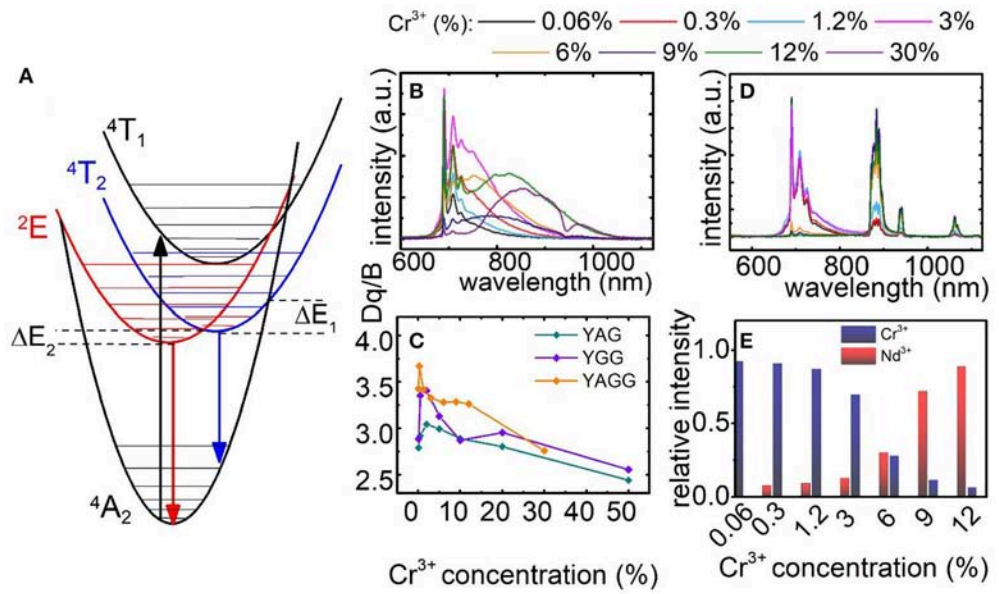

FIGURE 2 | Configurational coordinates diagram of Cr^{3+} ions **(A)**; comparison of normalized emission spectra for $Y_3Al_2Ga_3O_{12}$: xCr^{3+} **(B)** and for $Y_3Al_2Ga_3O_{12}$: xCr^{3+}, 1%Nd^{3+} nanocrystals **(D)**; dependence of Dq/B parameter **(C)** and Cr^{3+}/Nd^{3+} ratio at $T = -150°C$ **(E)** on Cr^{3+} concentration.

$$\frac{Dq}{B} = \frac{15\,(x-8)}{\left(x^2-10x\right)} \tag{2}$$

where x could be defined as (Casalboni et al., 1994):

$$x = \frac{E\left(^4A_2 \rightarrow {}^4T_1\right) - E\left(^4A_2 \rightarrow {}^4T_2\right)}{Dq} \tag{3}$$

As it can be observed in **Figure 2C** the Dq/B gradually decreases with Cr^{3+} concentration from 2.79 to 2.44 for $Y_3Al_5O_{12}$; from 2.88 to 2.55 for $Y_3Ga_5O_{12}$ and from 3.42 to 2.76 for $Y_3Al_2Ga_3O_{12}$ nanocrystals. In order to obtain self-referenced luminescent thermometer based of the Cr^{3+} emission intensity the examined nanocrystals with different Cr^{3+} concentration were co-doped with 1% Nd^{3+} ions. Emission intensity of Nd^{3+} is expected to be significantly less temperature dependent in respect to the chromium emission. Moreover, the Nd^{3+} ions emit in the first (band around 880 nm attributed to the $^4F_{3/2} \rightarrow {}^4I_{9/2}$ electronic transition) and the second (bands around 1064 nm and 1350 nm attributed to the $^4F_{3/2} \rightarrow {}^4I_{11/2}$ and $^4F_{3/2} \rightarrow {}^4I_{13/2}$ electronic transitions, respectively) optical window of the biological tissues making it well suited for biological applications.

Following excitation spectra, a 450 nm excitation line was chosen, which provides the condition of direct excitation of each individual optically active ion-Cr^{3+} ($^4A_2 \rightarrow {}^4T_1$) and independently Nd^{3+} ($^4I_{9/2} \rightarrow {}^2G_{5/2}$). As it was recently showed, this is an important condition to enhance the relative sensitivity of this kind of LTs (Marciniak et al., 2017a). In case of $Y_3Al_2Ga_3O_{12}$: Cr^{3+}, Nd^{3+} (**Figure 2D**) nanocrystals the presence of Nd^{3+} ion significantly quenched the Cr^{3+} emission intensity due to the $Cr^{3+} \rightarrow Nd^{3+}$ energy transfer. Therefore, the $^2E \rightarrow {}^4A_2$ emission band can be barely seen for $Y_3Al_2Ga_3O_{12}$: 30%Cr^{3+}, 1%Nd^{3+} while in the case of $Y_3Al_5O_{12}$ and $Y_3Ga_5O_{12}$ above 10% of Cr^{3+}, no chromium emission was detected (**Figures S10, S11**). Moreover, the presence of broad Cr^{3+} absorption bands in the excitation spectra when monitoring Nd^{3+} emission ($^4F_{3/2} \rightarrow {}^4I_{9/2}$ emission band), is an additional confirmation of the interionic energy transfer which takes place between dopants (**Figures S12–S14**). The change of contribution of the emission of particular optically active ions in the total emission intensity related with Cr^{3+} concentration is presented in **Figure 2E**. Initially, at low Cr^{3+} amount the $^2E \rightarrow {}^4A_2$ emission band dominates in the spectra. However, around 6% of Cr^{3+} its emission intensity equalize with Nd^{3+} amount. Above this value, the chromium emission intensity rapidly decreases. Therefore, this energy transfer strongly limits the usable Cr^{3+} concentration which can be applied for luminescent thermometry.

To understand the role of Cr^{3+} on the luminescence thermal quenching in the $Y_3Al_5O_{12}$ and $Y_3Ga_5O_{12}$ and $Y_3Al_2Ga_3O_{12}$ nanocrystals, their emission spectra were measured in a wide temperature range. The representative thermal evolution spectrum of $Y_3Al_2Ga_3O_{12}$:1.2%Cr^{3+} nanocrystals is presented in **Figure 3A**. It is clearly seen that sharp R-line of the $^2E \rightarrow {}^4A_2$ emission band is rapidly quenched at around 50°C in contrary to the $^4T_2 \rightarrow {}^4A_2$ emission. Therefore, due to this difference in the rates of thermal quenching of these particular emission bands, their luminescence intensity ratio was chosen as a temperature sensor LIR_1:

$$LIR_1 = \frac{Cr^{3+}(^4T_2 \rightarrow {}^4A_2)}{Cr^{3+}(^2E \rightarrow {}^4A_2)} = \frac{\int I(850-855)nm}{\int I(730-735)nm} \tag{4}$$

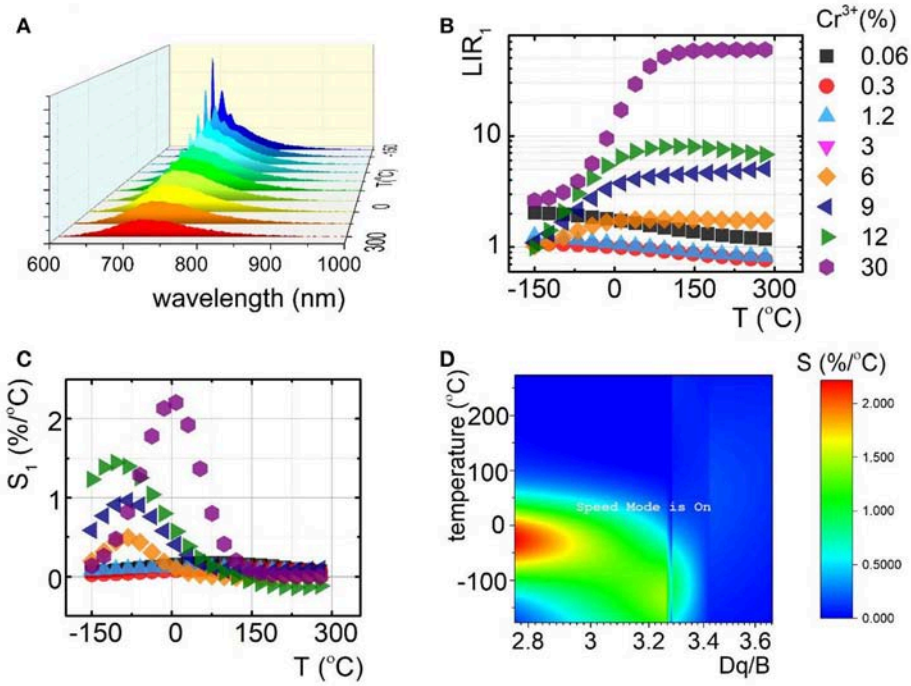

FIGURE 3 | Comparison of thermal evolution of emission spectra for $Y_3Al_2Ga_3O_{12}$:1.2%Cr^{3+} **(A)**; evolution of LIR_1 **(B)** with the corresponding relative sensitivities (S_1) **(C)** in the function of temperature; sensitivity map for different temperatures depending on Dq/B **(D)**.

At low Cr^{3+} concentration the LIR_1 decreases with temperature due to the fact that ^2E state population feeds the $^4T_2$ state at higher thermal energy. However, for higher Cr^{3+} (above 6%) different tendency can be found. Initially the LIR_1 increases up to temperatures around 100°C above which saturation of its value can be found. This effect occurs because $^4T_2 \rightarrow {}^4A_2$ band's intensity starts to play an important role in the total emission intensity. Due to the strong electron-phonon coupling, this emission band is expected to be efficiently reduced by the temperature. Therefore, its much higher rate of thermal quenching in respect to the $^2E \rightarrow {}^4A_2$ results in the enhancement of LIR_1 value. To quantitative describe the observed changes, relative sensitivity (S) of LIR_1-based luminescent thermometer was calculated according to the following formula:

$$S(T) = \frac{1}{LIR}\frac{\Delta LIR}{\Delta T}100\% \quad (5)$$

Independently from the Cr^{3+} concentration, the relative intensities reach maximal value at temperatures below 100°C. Above this value, low changes of LIR_1 are manifested as a minor value of S (**Figure 3C**). It is clearly seen that, according to our expectation, S significantly increases proportionally to Cr^{3+} content. The S_{max} at 9°C increases from 0.2%/°C for $Y_3Al_2Ga_3O_{12}$: 0.06%Cr^{3+} to 2.2%/°C for $Y_3Al_2Ga_3O_{12}$: 30%Cr^{3+} nanocrystals. Analogous tendency was found for the $Y_3Al_5O_{12}$:Cr^{3+} and $Y_3Ga_5O_{12}$:Cr^{3+} where for 10% Cr^{3+}, S_{max} equals to 2.7%/°C at −105°C and 2%/°C at −78°C respectively (**Figures S15, S16**). The observed enhancement of the rate of the thermal quenching is obviously caused by the lowering of the CF strength. The optically active ions in the heavily Cr^{3+}-doped nanocrystals are located in the lower CF sites (**Figure 3D**) which reduce the activation energy and facilitate luminescence thermal quenching. Therefore, the highest S were found for high Cr^{3+} concentration (low Dq/B values). However, above 130°C this correlation is suppressed due to the fact that above this temperature no $^2E \rightarrow {}^4A_2$ emission was observed. It is worth noting that the temperature range of high S overlaps with physiological temperature range (10–50°C) what indicates the importance of these LTs for biomedical applications.

Due to the fact that emission intensity of both $^2E \rightarrow {}^4A_2$ and $^4T_2 \rightarrow {}^4A_2$ bands decreases at higher temperatures, relative sensitivity of luminescent thermometer based on their intensity ratio is reduced. Therefore, Nd^{3+} co-dopant, whose emission intensity is expected to be less temperature dependent, were used as a luminescent reference. The luminescent properties of Nd^{3+}, Cr^{3+} co-doped nanocrystals were investigated in the analogous temperature range as in the case of singly Cr^{3+} doped counterparts. Representative thermal evolution of $Y_3Al_2Ga_3O_{12}$: 1.2%Cr^{3+}, 1%Nd^{3+} nanocrystals is presented in **Figure 4a**. According to the expectations the intensity of bands at 880 and 1,060 nm attributed to $^4F_{3/2} \rightarrow {}^4I_{9/2}$ and $^4F_{3/2} \rightarrow {}^4I_{11/2}$ electronic transition of Nd^{3+} ions, respectively, is almost independent on the temperature, while the $^2E \rightarrow {}^4A_2$ emission intensity is strongly thermally quenched. It is worth noting that at temperatures above 50°C, additional Nd^{3+} bands appears which

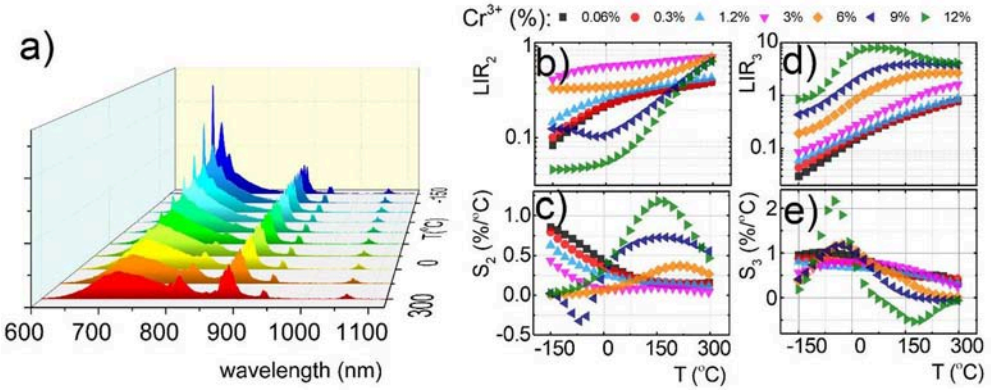

FIGURE 4 | Comparison of thermal evolution of emission spectra for $Y_3Al_2Ga_3O_{12}$:1.2%Cr^{3+}, 1%Nd^{3+} **(a)**; thermal evolution of LIR_2 **(b)**; and LIR_3 **(d)** and the corresponding relative sensitivities S_2 **(c)** and S_3 **(e)** for different Cr^{3+} concentration for $Y_3Al_2Ga_3O_{12}$:1.2%Cr^{3+}, 1%Nd^{3+} nanocrystals.

can be attributed to the $^4F_{5/2}$, $^4S_{3/2}\rightarrow{}^4I_{9/2}$ electronic transition. This band occurs at higher temperature due to the fact that population of $^4F_{5/2}$, $^4S_{3/2}$ states increases in respect to the $^4F_{3/2}$ with temperatures according to Boltzmann population. Taking advantage from these changes of the emission spectra with temperature, two types of luminescent thermometers based on the Nd^{3+}/Cr^{3+} luminescence intensity ratio have been defined as follows:

$$LIR_2 = \frac{Nd^{3+}(^4F_{3/2}\rightarrow{}^4I_{9/2})}{Cr^{3+}(^4T_2\rightarrow{}^4A_2)} = \frac{\int I(869-869.5)nm}{\int I(705-705.5)nm} \quad (6)$$

$$LIR_3 = \frac{Nd^{3+}(^4F_{5/2}\rightarrow{}^4I_{9/2})}{Cr^{3+}(^4T_2\rightarrow{}^4A_2)} = \frac{\int I(810-810.5)nm}{\int I(710-710.5)nm} \quad (7)$$

The thermal dependence of LIR_2 and LIR_3 for different concentration of Cr^{3+} ions are presented in **Figures 4b,d**, respectively. Obviously, due to the $Cr^{3+}\rightarrow Nd^{3+}$ energy transfer the usable concentration range of Cr^{3+} is strongly limited (to 12% Cr^{3+}). Independently from dopant concentration, both LIR_2 and LIR_3 increase at higher temperature due to the thermal quenching of $^4T_2\rightarrow{}^4A_2$ band of Cr^{3+} (**Figures 4b,d**). However, more rapid changes can be found for LIR_3 what is obviously related with the increase of the $^4F_{5/2}$, $^4S_{3/2}\rightarrow{}^4I_{9/2}$ emission band of Nd^{3+}. Both LIR_2 and LIR_3 are strongly modulated by the Cr^{3+} concentration. In agreement with the results obtained for singly Cr^{3+} doped systems, significant enhancement of LIR's thermal changes can be found. At heavily doped phosphors the activation energies of $^4T_2$ level is meaningfully diminished facilitating its nonradiative depopulation. Small activation energy is beneficial for enhancement of the relative sensitivity of luminescent thermometers. Therefore, these effects substantially affect the relative sensitivity of both S_2 and S_3 (**Figures 4c,e**). The highest S_2 at 150°C increases from 0.17%/°C for 0.06% of Cr^{3+} to 1.17%/°C for 12% of Cr^{3+} ions. On the other hand the S_3 at −48°C increases from 0.95%/°C for 0.06% of Cr^{3+} to 2.16%/°C for 12% of Cr^{3+} ions. Comparing these results with the **Figure 3**, evident profitable effect of the Nd^{3+} ions use as a luminescent reference can be found. The relative sensitivity for 0.06% Cr^{3+} increases from $S_1 = 0.14\%/°C$ to $S_2 = 0.17\%/°C$ and $S_3 = 0.95\%/°C$, while for 12% Cr^{3+} from $S_1 = 1.37\%/°C$ to $S_2 = 1.17\%/°C$ and $S_3 = 2.16\%/°C$. Analogous beneficial effect of high Cr^{3+} concentration can be found for $Y_3Ga_5O_{12}$:Cr^{3+}, Nd^{3+} as well as $Y_3Al_5O_{12}$:Cr^{3+}, Nd^{3+} (**Figures S10, S11**). It is also worth noting that the LIR_2 reveals high sensitivity at high temperature range (above 100°C) in contrast to LIR_3, which unveils good performance for non-contact temperature sensing at low temperatures (below 0°C). Therefore, by simultaneous employment of both of these thermometers the temperature range where high accuracy temperature readout can be achieved, is widened.

The highest recorded sensitivity ($S = 2.64\%/°C$) was found for YAG nanocrystals at −100°C for 10% of Cr^{3+} (**Figure S15B**) due to the fact of the lowest CF strength for this host material. Nevertheless, CF strength was tuned in the widest range for $Y_3Al_2Ga_3O_{12}$: Cr^{3+}, Nd^{3+} via the Cr^{3+} doping the enhancement of S_3 was the strongest in this case. The most important finding presented in this paper is that highly sensitive luminescent thermometers can be intentionally designed by the modification of the CF strength through elongation of Cr^{3+}-O^{2-} distance and enlargement of the Cr^{3+} concentration.

CONCLUSIONS

In this work, we proposed a new strategy to modulate the relative thermal sensitivity of Cr^{3+} doped nanophosphors. We considered three types of garnet matrices doped with different Cr^{3+} concentrations, with or without Nd^{3+} co-dopant. It was shown that the increase of the Cr^{3+} concentration causes elongation of the average Cr^{3+}-O^{2-} distance leading to the reduction of the crystal field strength in $Y_3Al_2Ga_3O_{12}$, $Y_3Ga_5O_{12}$ and $Y_3Al_5O_{12}$ nanocrystals. A gradual increase of the broad emission band attributed to the $^4T_2\rightarrow{}^4A_2$ spin allowed transition of Cr^{3+} is observed. Moreover, the reduction of the $^4T_2$ state energy facilitates thermal quenching of ^2E state. Therefore, the relative sensitivity of $^4T_2\rightarrow{}^4A_2$ to $^2E\rightarrow{}^4A_2$ emission intensity

increases from $S = 0.2\%/^{\circ}C$ for $0.06\%Cr^{3+}$ to $S = 2.2\%/^{\circ}C$ for $30\%Cr^{3+}$ at 9°C in $Y_3Al_2Ga_3O_{12}$ nanocrystals, from $S = 0.027\%/^{\circ}C$ for $0.5\%Cr^{3+}$ to $S = 2.7\%$ for $10\%Cr^{3+}$ at $-105^{\circ}C$ in $Y_3Al_5O_{12}$ nanocrystals, and from $S = 0.14\%/^{\circ}C$ for $0.5\%Cr^{3+}$ to $S = 2\%$ for $10\%Cr^{3+}$ at $-78^{\circ}C$ in $Y_3Ga_5O_{12}$ nanocrystals. In the case of Nd^{3+} co-doped nanocrystals, due to the $Cr^{3+} \rightarrow Nd^{3+}$ energy transfer, the usable concentration range of Cr^{3+} dopants is strongly reduced and no evidence of Cr^{3+} emission was found above 10% of Cr^{3+}. However, by taking advantage from this energy transfer and the fact that $^4F_{5/2}$, $^4S_{3/2} \rightarrow {}^4I_{9/2}$ emission intensity increases proportionally to the temperature according to the Boltzmann distribution, the relative sensitivities of luminescent thermometers defined as $^4F_{5/2}$, $^4S_{3/2} \rightarrow {}^4I_{9/2}$ to $^4T_2 \rightarrow {}^4A_2$ luminescence intensity ratio enhances from 1.3%/°C at −50°C without Nd^{3+} dopant to 2.2%/°C at −50°C for nanocrystals doped with Nd^{3+} ions $Y_3Al_2Ga_3O_{12}$: $10\%Cr^{3+}$, Nd^{3+}). The presented results confirm that the relative sensitivity of luminescent thermometers can be effectively modulated by the dopant concentration. Moreover, it was proved that the presence of Nd^{3+} dopant contributes to faster quenching of Cr^{3+} luminescence, what is favorable for highly sensitive non-contact luminescent thermometers. Our studies may be considered as a next step toward intentional designing of nanocrystalline luminescent thermometers with fully controllable thermooptical response.

AUTHOR CONTRIBUTIONS

All authors listed have made a substantial, direct and intellectual contribution to the work, and approved it for publication.

ACKNOWLEDGMENTS

The High sensitive thermal imaging for biomedical and microelectronic application project is carried out within the First Team programme of the Foundation for Polish Science co-financed by the European Union under the European Regional Development Fund.

SUPPLEMENTARY MATERIAL

The Supplementary Material for this article can be found online at: https://www.frontiersin.org/articles/10.3389/fchem.2018.00424/full#supplementary-material

REFERENCES

Anderson, R. R., and Parrish, J. A. (1981). The optics of human skin. *J. Invest. Dermatol.* 77, 13–19. doi: 10.1111/1523-1747.ep12479191

Azkargorta, J., Marciniak, L., Iparraguirre, I., Balda, R., Strek, W., Barredo-Zuriarrain, M., et al. (2017). Influence of grain size and Nd^{3+}concentration on the stimulated emission of LiLa1-xNdxP4O12crystal powders. *Opt. Mater. (Amst).* 63, 46–50. doi: 10.1016/j.optmat.2016.07.016

Benayas, A., del Rosal, B., Pérez-Delgado, A., Santacruz-Gómez, K., Jaque, D., Alonso Hirata, G., et al. (2015). Nd:YAG Near-Infrared Luminescent Nanothermometers. *Adv. Opt. Mater.* 3, 687–694. doi: 10.1002/adom.201400484

Brites, C. D., Lima, P. P., Silva, N. J., Millán, A., Amaral, V. S., Palacio, F., et al. (2012). Thermometry at the nanoscale. *Nanoscale.* 4:4799. doi: 10.1039/c2nr30663h

Casalboni, M., Luci, A., and Grassano, U. M. (1994). Optical spectroscopy of La3Ga5SiO14: Cr^{3+} crystals. *Phys. Rev. B.* 49, 3781–3790. doi: 10.1103/PhysRevB.49.3781

Chen, D., Liu, S., Zhou, Y., Wan, Z., Huang, P., and Ji, Z. (2016). Dual-activator luminescence of RE/TM:Y3Al5O12(RE = Eu^{3+}, Tb^{3+}, Dy^{3+}; TM = Mn^{4+}, Cr^{3+}) phosphors for self-referencing optical thermometry. *J. Mater. Chem. C.* 4, 9044–9051. doi: 10.1039/C6TC02934E

del Rosal, B., Carrasco, E., Ren, F., Benayas, A., Vetrone, F., Sanz-Rodríguez, F., et al. (2016a). Infrared-emitting QDs for thermal therapy with real-time subcutaneous temperature feedback. *Adv. Funct. Mater.* 26, 6060–6068. doi: 10.1002/adfm.201601953

del Rosal, B., Pérez-Delgado, A., Carrasco, E., Jovanović, D. J., Dramićanin, M. D., DraŽić, G., et al. (2016b). Neodymium-based stoichiometric ultrasmall nanoparticles for multifunctional deep-tissue photothermal therapy. *Adv. Opt. Mater.* 4, 782–789. doi: 10.1002/adom.201500726

Deren, P. J., Watras, A., Gagor, A., and Pazik, R. (2012). Weak crystal field in yttrium gallium garnet (YGG) submicrocrystals doped with Cr^{3+}. *Cryst. Growth Des.* 12, 4752–4757. doi: 10.1021/cg300435t

Drabik, J., Cichy, B., and Marciniak, L. (2018). A New Type of Nanocrystalline Luminescent Thermometers Based on Ti/Ti and Ti/Ln (Ln = Nd, Eu, Dy) Luminescence Intensity Ratio. *J. Phys. Chem. C* 122, 14928–14936. doi: 10.1021/acs.jpcc.8b02328

Dramićanin, M. D. (2016). Sensing temperature via downshifting emissions of lanthanide-doped metal oxides and salts. A review. *Methods Appl. Fluoresc.* 4:042001. doi: 10.1088/2050-6120/4/4/042001

Elzbieciak, K., Bednarkiewicz, A., and Marciniak, L. (2018). Temperature sensitivity modulation through crystal field engineering in Ga^{3+} co-doped Gd3Al5-xGaxO$_{12}$: $Cr3^{+}$, $Nd3^{+}$ nanothermometers. *Sens. Actuat. B Chem.* 269, 96–102. doi: 10.1016/j.snb.2018.04.157

Gao, Y., Cheng, Y., Huang, F., Lin, H., Xu, J., and Wang, Y. (2018). Sn^{2+}/Mn^{2+}codoped strontium phosphate ($Sr_2P_2O_7$) phosphor for high temperature optical thermometry. *J. Alloys Compd.* 735, 1546–1552. doi: 10.1016/j.jallcom.2017.11.243

Jaque, D., and Jacinto, C. (2016). Luminescent nanoprobes for thermal bio-sensing: Towards controlled photo-thermal therapies. *J. Lumin.* 169, 394–399. doi: 10.1016/j.jlumin.2015.03.037

Jaque, D., and Vetrone, F. (2012). Luminescence nanothermometry. *Nanoscale.* 4:4301. doi: 10.1039/c2nr30764b

Kniec, K., and Marciniak, L. (2018). The influence of grain size and vanadium concentration on the spectroscopic properties of YAG:V^{3+},$V^{5+}$and YAG: V, Ln3+(Ln^{3+} = Eu^{3+}, Dy^{3+}, Nd^{3+}) nanocrystalline luminescent thermometers. *Sens. Actuat. B Chem.* 264 382–390. doi: 10.1016/j.snb.2018.02.189

Liao, J., Wang, Q., Kong, L., Ming, Z., Wang, Y., Li, Y., et al. (2018). Effect of Yb3+concentration on tunable upconversion luminescence and optically temperature sensing behavior in Gd2TiO5:Yb^{3+}/Er^{3+}phosphors. *Opt. Mater. (Amst).* 75, 841–849. doi: 10.1016/j.optmat.2017.12.009

Liu, L., Sun, Z., Ma, C., Tao, R., Zhang, J., Li, H., et al. (2018). Highly sensitive and accurate optical thermometer through Er doped tellurite glasses. *Mater. Res. Bull.* 105, 306–311. doi: 10.1016/j.materresbull.2018.04.053

Malysa, B., Meijerink, A., and Jüstel, T. (2018). Temperature dependent Cr^{3+}photoluminescence in garnets of the type X3Sc2Ga3O12(X = Lu, Y, Gd, La). *J. Lumin.* 202, 523–531. doi: 10.1016/j.jlumin.2018.05.076

Marciniak, L., and Bednarkiewicz, A. (2016). The influence of dopant concentration on temperature dependent emission spectra in LiLa1–x–yEuxTbyP$_4$O$_{12}$ nanocrystals: toward rational design of highly-sensitive luminescent nanothermometers. *Phys. Chem. Chem. Phys.* 18, 15584–15592. doi: 10.1039/C6CP00898D

Marciniak, L., Bednarkiewicz, A., Drabik, J., Trejgis, K., and Strek, W. (2017a). Optimization of highly sensitive YAG:Cr^{3+}, Nd^{3+} nanocrystal-based

luminescent thermometer operating in an optical window of biological tissues. *Phys. Chem. Chem. Phys*. 19, 7343–7351. doi: 10.1039/C6CP07213E

Marciniak, Ł., Bednarkiewicz, A., Hreniak, D., and Strek, W. (2016a). The influence of Nd^{3+} concentration and alkali ions on the sensitivity of non-contact temperature measurements in $ALaP_4O_{12}$:Nd^{3+} (A = Li, K, Na, Rb) nanocrystalline luminescent thermometers. *J. Mater. Chem. C*. 4, 11284–11290. doi: 10.1039/C6TC03396B

Marciniak, L., Bednarkiewicz, A., Kowalska, D., and Strek, W. (2016b). A new generation of highly sensitive luminescent thermometers operating in the optical window of biological tissues. *J. Mater. Chem. C*. 4, 5559–5563. doi: 10.1039/C6TC01484D

Marciniak, L., Pilch, A., Arabasz, S., Jin, D., and Bednarkiewicz, A. (2017b). Heterogeneously Nd^{3+} doped single nanoparticles for NIR-induced heat conversion, luminescence, and thermometry. *Nanoscale*. 9, 8288–8297. doi: 10.1039/C7NR02630G

Marciniak, L., and Trejgis, K. (2018). Luminescence lifetime thermometry with Mn^{3+}-Mn^{4+} co-doped nanocrystals. *J. Mater. Chem. C* 6, 7092–7100. doi: 10.1039/C8TC01981A

Pechini, M. P. (1967). *US Pat*. No 3330697.

Runowski, M., Bartkowiak, A., Majewska, M., Martín, I. R., and Lis, S. (2018). Upconverting lanthanide doped fluoride NaLuF4:Yb^{3+}-Er^{3+}-Ho^{3+}- optical sensor for multi-range fluorescence intensity ratio (FIR) thermometry in visible and NIR regions. *J. Lumin*. 201, 104–109. doi: 10.1016/j.jlumin.2018.04.040

Struve, B., and Huber, G. (2000). The effect of the crystal field strength on the optical spectra of Cr^{3+} in gallium garnet laser crystals. *Appl. Phys. B*. 36, 195–201. doi: 10.1007/BF00704574

Suo, H., Hu, F., Zhao, X., Zhang, Z., Li, T., Duan, C., et al. (2017). All-in-one thermometer-heater up-converting platform YF_3 :Yb^{3+}, Tm^{3+} operating in the first biological window. *J. Mater. Chem*. C. 5, 1501–1507. doi: 10.1039/C6TC05449H

Trejgis, K., and Marciniak, L. (2018). The influence of manganese concentration on the sensitivity of bandshape and lifetime luminescent thermometers in $Y_3Al_5O_{12}$:Mn^{3+}, Mn^{4+}, Nd^{3+} nanocrystals. *Phys. Chem. Chem. Phys*. 20, 9574–9581. doi: 10.1039/C8CP00558C

Wang, C., Wadhwa, A., Cui, S., Ma, R., Qiao, X., Fan, X., et al. (2017). Dual mode temperature sensing through luminescence lifetimes of F- and O-coordinated Cr3+sites in fluorosilicate glass-ceramics. *RSC Adv*. 7, 52435–52441. doi: 10.1039/C7RA10864H

Xu, J., Ueda, J., and Tanabe, S. (2017). Toward tunable and bright deep-red persistent luminescence of Cr^{3+} in garnets. *J. Am. Ceram. Soc*. 100, 4033–4044. doi: 10.1111/jace.14942

Zhong, J., Chen, D., Peng, Y., Lu, Y., Chen, X., Li, X., et al. (2018). A review on nanostructured glass ceramics for promising application in optical thermometry. *J. Alloys Compd*. 763, 34–48. doi: 10.1016/j.jallcom.2018.05.348

Conflict of Interest Statement: The authors declare that the research was conducted in the absence of any commercial or financial relationships that could be construed as a potential conflict of interest.

Copyright © 2018 Elzbieciak and Marciniak. This is an open-access article distributed under the terms of the Creative Commons Attribution License (CC BY). The use, distribution or reproduction in other forums is permitted, provided the original author(s) and the copyright owner(s) are credited and that the original publication in this journal is cited, in accordance with accepted academic practice. No use, distribution or reproduction is permitted which does not comply with these terms.

frontiers in Chemistry

ORIGINAL RESEARCH
published: 16 April 2019
doi: 10.3389/fchem.2019.00198

Phosphorothioate DNA Mediated Sequence-Insensitive Etching and Ripening of Silver Nanoparticles

Shengqiang Hu[1,2], *Po-Jung Jimmy Huang*[2], *Jianxiu Wang*[1]* and *Juewen Liu*[2]*

[1] College of Chemistry and Chemical Engineering, Central South University, Changsha, China, [2] Department of Chemistry, Waterloo Institute for Nanotechnology, University of Waterloo, Waterloo, ON, Canada

Many DNA-functionalized nanomaterials and biosensors have been reported, but most have ignored the influence of DNA on the stability of nanoparticles. We observed that cytosine-rich DNA oligonucleotides can etch silver nanoparticles (AgNPs). In this work, we showed that phosphorothioate (PS)-modified DNA (PS-DNA) can etch AgNPs independently of DNA sequence, suggesting that the thio-modifications are playing the major role in etching. Compared to unmodified DNA (e.g., poly-cytosine DNA), the concentration of required PS DNA decreases sharply, and the reaction rate increases. Furthermore, etching by PS-DNA occurs quite independent of pH, which is also different from unmodified DNA. The PS-DNA mediated etching could also be controlled well by varying DNA length and conformation, and the number and location of PS modifications. With a higher activity of PS-DNA, the process of etching, ripening, and further etching was taken place sequentially. The etching ability is inhibited by forming duplex DNA and thus etching can be used to measure the concentration of complementary DNA.

Keywords: oligonucleotides, phosphorothioate, silver nanoparticles, plasmonics, biosensors

OPEN ACCESS

Edited by:
Huangxian Ju,
Nanjing University, China

Reviewed by:
Xiaoji Xie,
Nanjing Tech University, China
Feng Li,
Brock University, Canada

***Correspondence:**
Jianxiu Wang
jxiuwang@csu.edu.cn
Juewen Liu
liujw@uwaterloo.ca

Specialty section:
This article was submitted to Nanoscience, a section of the journal Frontiers in Chemistry

Received: *25 November 2018*
Accepted: *14 March 2019*
Published: *16 April 2019*

Citation:
Hu S, Huang P-JJ, Wang J and Liu J (2019) Phosphorothioate DNA Mediated Sequence-Insensitive Etching and Ripening of Silver Nanoparticles. Front. Chem. 7:198. doi: 10.3389/fchem.2019.00198

INTRODUCTION

Interfacing DNA with nanomaterials has resulted in many interesting hybrids for analytical (Liu and Lu, 2006; Liu et al., 2009; Zhou et al., 2017), nanotechnology (Wilner and Willner, 2012; Pu et al., 2014; Tan et al., 2014; Seeman and Sleiman, 2017; Shen C. et al., 2017; Chidchob and Sleiman, 2018; Hu et al., 2018), and biomedical applications (Qu et al., 2000; Cao et al., 2002; Liu et al., 2015; Lu et al., 2017; Sun et al., 2018). Such applied research in turn stimulated fundamental surface and biointerface studies (Herne and Tarlov, 1997; Storhoff et al., 2002; Liu, 2012; Carnerero et al., 2017). Most of previous research focused on DNA-directed assembly (Mirkin et al., 1996; Liu and Lu, 2003; Sharma et al., 2009; Chou et al., 2014; Liu and Liu, 2017; Lin et al., 2018), or DNA-templated growth of nanomaterials (Nykypanchuk et al., 2008; Surwade et al., 2013; Wu et al., 2014; Song et al., 2015), while etching or dissolution of nanoparticles by DNA was much less explored. We reason that such studies are also important for the following reasons. First, nanoparticles were always assumed to be stable during DNA conjugation or assembly. If DNA can dissolve nanoparticles, such assumptions need to be updated and care has to be taken for long-term storage of such materials. In addition, DNA-mediated etching of nanoparticles can be a way of controlled release. Finally, it can further our fundamental understanding of DNA/nanoparticle interfaces.

Using a relatively high concentration of DNA (e.g., >1 μM), we recently observed etching of silver nanoparticles (AgNPs) by DNA oligonucleotides (Hu et al., 2019). For spherical AgNPs, poly-cytosine (poly-C) was the most effective, while the other three types of homopolymers did not display an obvious effect. The base composition of DNA is critical for etching silver-based nanomaterials.

Poly-C DNA can effectively etch AgNPs, but the required high DNA concentration and specific DNA sequence restricted its applications in analytical detection and controlled release. So far, we have studied only unmodified DNA. We reason that the effect of DNA might be further improved by introducing modifications with stronger metal ligands. Phosphorothioate (PS) modification refers to replacing one of the non-bridging oxygen atoms by sulfur (**Figure 1A**) (Huang and Liu, 2014, 2015; Huang et al., 2015a,b; Liu et al., 2018). The PS sites on DNA can bind strongly to thiophilic metals (e.g., Au and Ag) and PS-modified DNA (PS-DNA) has been used for nanomaterial synthesis (Ma et al., 2008; Farlow et al., 2013; Weadick and Liu, 2015; Shen J. et al., 2017), nanostructure assembly (Jiang et al., 2005; Lee et al., 2007; Pal et al., 2009; Shen J. et al., 2017), and biosensing (Zhang et al., 2009; Huang P. J. J. et al., 2016). We previously compared adsorption of PS-DNA with normal phosphodiester DNA (PO-DNA) on AuNPs, and concluded that the PS-DNA was more strongly adsorbed (Zhou et al., 2014). PS-DNA was also used to functionalize quantum dots (Ma et al., 2008; Farlow et al., 2013). In addition, PS modifications have been used to probe the reaction mechanism of ribozymes (Cunningham et al., 1998; Huang and Liu, 2014; Huang et al., 2015a, 2019; Thaplyal et al., 2015). All these studies took advantage of the strong affinity between PS and thiophilic metals. Since silver is also strongly thiophilic, we speculate that PS-DNA may be more effective for etching AgNPs in a less DNA sequence-dependent manner.

In this work, we systematically studied the effect of PS modifications and found that it could significantly decrease the needed DNA concentration. At the same time, the sequence of DNA was less important, making DNA-mediated etching available for many more sequences. The effects of pH, DNA length, the number and location of PS modifications and DNA conformation were also systematically studied and compared with the normal DNA of the same sequences, leading to interesting multi-stage etching and ripening process and chemically controlled etching.

MATERIALS AND METHODS

Chemicals

All the DNA were purchased from Integrated DNA Technologies (IDT, Coralville, IA, USA), and their sequences are shown in **Table S1**. Commercial citrate-capped AgNPs (20 nm diameter) were purchased from Nanocomposix (San Diego, CA, USA). Trisodium citrate and 3-(N-morpholino)propanesulfonic acid (MOPS) were obtained from Sigma-Aldrich (St. Louis, MO). Sodium nitrate ($NaNO_3$) was purchased from Mandel Scientific (Guelph, ON, Canada).

Instrumentation

UV-vis absorption spectra were recorded on a spectrometer (Agilent 8453A). The morphology of AgNPs was examined by a transmission electron microscope (TEM, Philips CM10). The etching kinetics of AgNPs were monitored using a microplate reader (SpectraMax M3). Dynamic light scattering (DLS) measurements were carried out using a Zetasizer Nano 90 (Malvern) at 25°C. Circular dichroism (CD) spectra were collected on a Jasco J-715 spectrophotometer (Jasco, Japan).

Comparison of Etching by PO and PS-DNA

In a typical experiment, a 15-mer DNA (20 μM, 35 μL) was incubated with an equal volume of AgNPs (10 μg/mL) at 37°C for 1.5 h. The final concentration of DNA was 10 μM. Then, the sample was analyzed by a spectrometer.

Effect of pH on Etching Kinetics

Typically, PO-C_{15}, PS_{14}-C_{15}, or PS_{14}-T_{15} (20 μM, 50 μL) was mixed with the AgNPs (10 μg/mL, 50 μL) in a 96-well plate. Then, 10 μL of 10 mM buffer with different pH values (citrate buffer for 4.0, 5.0, and 6.0; MOPS for 7.0 and 7.9) was added and incubated at 37°C for 1.5 h. The absorbance intensity was monitored at 395 nm every 0.5 min under the kinetic mode using the plate reader.

PS-DNA Structure Dependent Etching

First, PS-R DNA (40 μM, 17.5 μL) was mixed with 17.5 μL of its cDNA of different concentrations (5.0, 10, 20, 40, 60, 80, and 100 μM), followed by the addition of $NaNO_3$ (0.25 M, 2.0 μL). Then, the mixture was heated to 95°C for 5 min and cooled slowly to room temperature. Finally, AgNPs (10 μg/mL, 35 μL) were added and incubated at 37°C for 1.5 h. The final concentrations of the cDNA were 1.25, 2.5, 5.0, 10, 15, 20, and 25 μM, respectively.

RESULTS AND DISCUSSION

PS-DNA Mediated Etching of AgNPs

To test the effect of PS modification (see **Figure 1A** for its structure), we used the four types of 15-mer DNA homopolymers both with the normal phosphodiester (PO) backbone and with full PS modifications (each bridging phosphate contained a PS modification). Our 20 nm AgNPs had a strong surface plasmon peak at 395 nm (**Figure 1C**). Adding the normal PO-A_{15} DNA had no effect and the UV-vis spectrum retained its original shape. In contrast, the PS_{14}-A_{15} (note that a 15-mer DNA has only 14 bridging phosphates) dropped the extinction peak intensity by over 80%. From this experiment, we concluded that the sulfur atoms in the PS-DNA were the reason for the decreased extinction of the AgNPs. From TEM (**Figure 2A** and **Figures S1**, **S2A**), our starting AgNPs were monodispersed ∼20 nm spheres. After adding the PS_{14}-A_{15}, overall the AgNPs became smaller (**Figures 2B,F**), indicating its etching.

Similar experiments were also performed with the other DNA sequences, and the same observations were also made with the two T_{15} DNAs from both their UV-vis spectra (**Figure 1D**) and TEM (**Figure 2C**). The lack of etching by PO-A_{15} and PO-T_{15} is in agreement with the relatively low affinity between

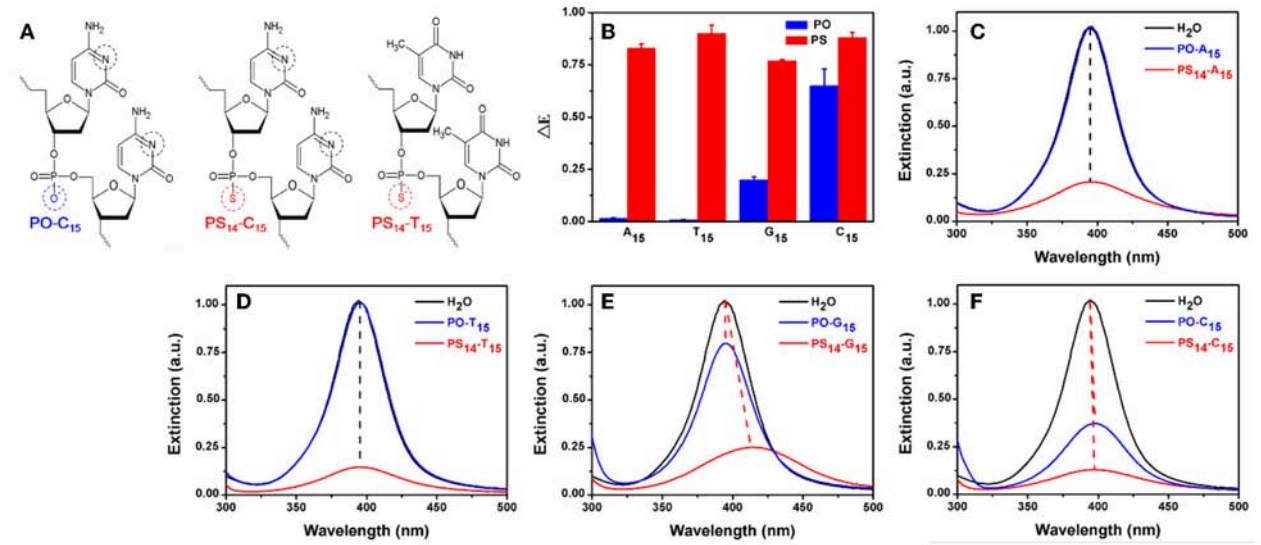

FIGURE 1 | (A) The structure of PO- and PS-DNA linkages for poly-C and poly-T DNA. The potential binding sites of DNA to AgNPs are marked in black and red circles. **(B)** The dropped extinction at 395 nm induced by 10 μM of 15-mer PO-DNA and PS-DNA. UV-vis spectra of the AgNPs treated with PO- and PS-DNA with the sequences of **(C)** A_{15}, **(D)** T_{15}, **(E)** G_{15}, and **(F)** C_{15}. The red dash lines represent red shifted spectra, while the black lines are for non-shifted spectra.

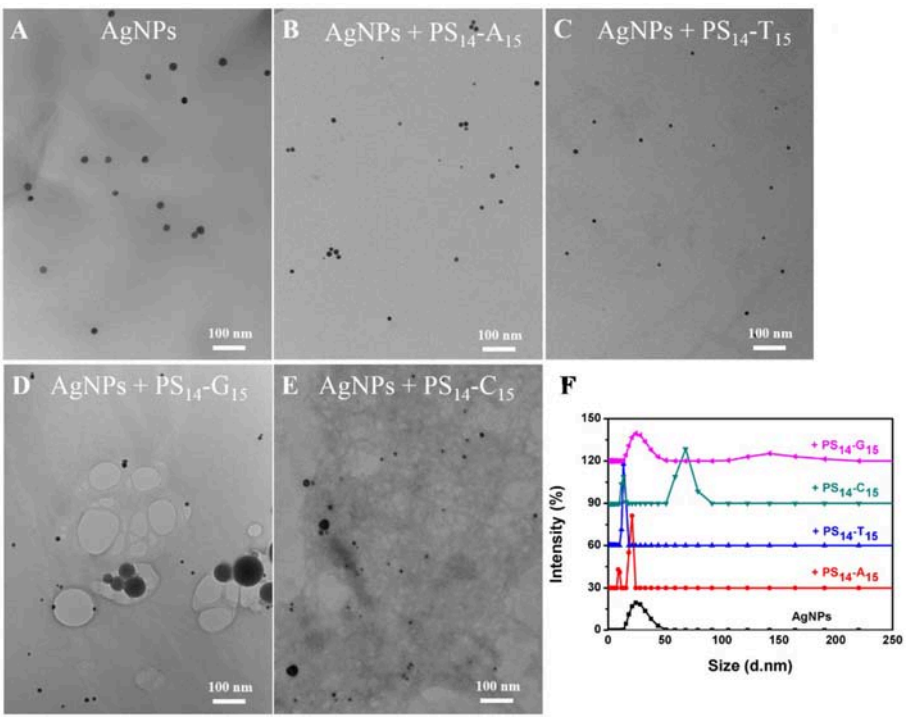

FIGURE 2 | TEM micrographs of **(A)** untreated 20 nm AgNPs, and the AgNPs treated with 10 μM **(B)** PS_{14}-A_{15}, **(C)** PS_{14}-T_{15}, **(D)** PS_{14}-G_{15}, and **(E)** PS_{14}-C_{15}. **(F)** The average hydrodynamic diameter of the AgNPs etched by 10 μM of various 15-mer PS-DNA.

these two DNA bases and silver surface (Basu et al., 2008; Wu et al., 2014).

When the PO-G_{15} was added, the extinction intensity of the AgNPs dropped by about 20% (**Figure 1E**), while a nearly 80% drop was observed when PS_{14}-G_{15} was added. At the same time, the peak red shifted by 18 nm. This suggested formation of larger AgNPs, which was confirmed by TEM (**Figure 2D**). Therefore, with this DNA concentration and reaction time, the PS_{14}-G_{15}

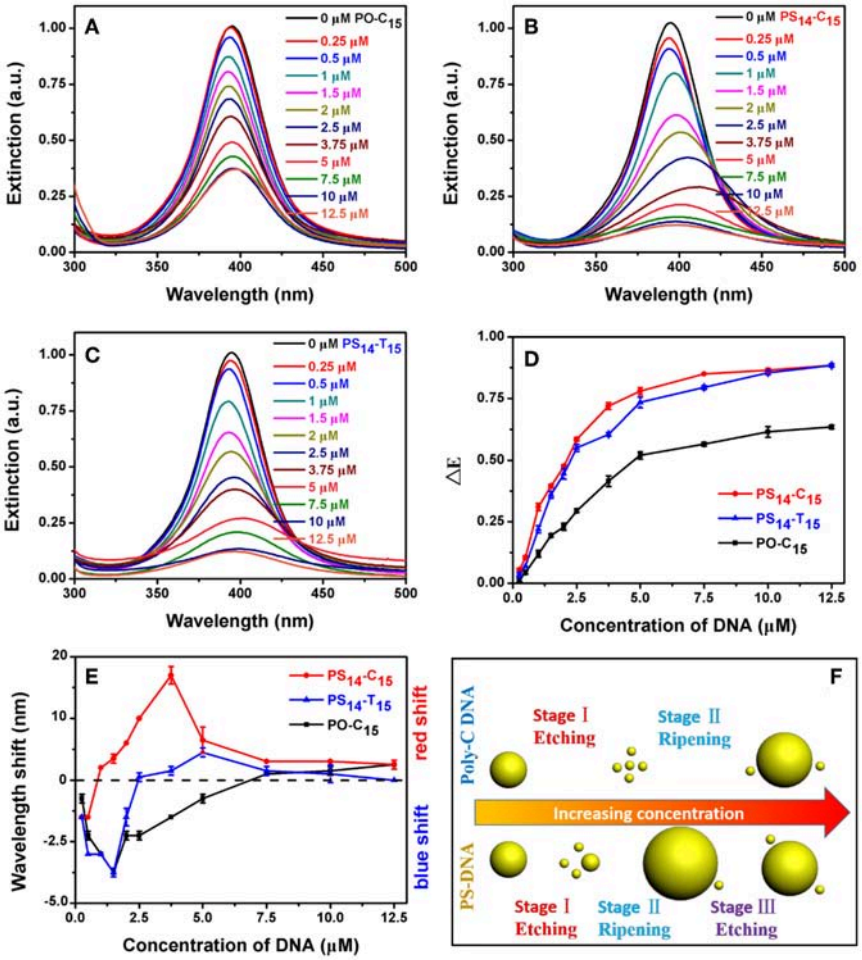

FIGURE 3 | (A) PO-C_{15}, **(B)** PS_{14}-C_{15}, and **(C)** PS_{14}-T_{15} concentration-dependent etching of the AgNPs. Relationship between DNA concentration and **(D)** dropped extinction and **(E)** wavelength shift of the AgNPs. **(F)** Comparison of the AgNPs etched by poly-C PO and PS DNA. With a stronger silver binding affinity, the PS DNA achieved the stage III reaction of further etching the larger AgNPs produced from the previous ripening stage.

helped Ostwald ripening of the AgNPs. Etching was the first step of the interaction, where the AgNPs were dissolved by the added DNA. Extensive etching and deposition of dissolved silver species on larger AgNPs (thus with lower solubility) resulted in the subsequent ripening.

The PO-C_{15} DNA was very effective in etching the AgNPs and it decreased extinction by 65% (**Figure 1F**). The extinction of the PS_{14}-C_{15}-treated sample further decreased the extinction peak to nearly 90%. Interestingly, under this condition, the ripening process caused only a 3 nm redshift, which was much smaller than that induced by PS_{14}-G_{15} (18 nm). Meanwhile, the average size of the PS_{14}-C_{15}-treated AgNPs (**Figure 2E**) was smaller than that of the PS_{14}-G_{15} treated sample (**Figure 2D**), indicating the cytosine and guanine bases also played a role on etching.

With these four pairs of DNA, we plotted the peak intensity drop in **Figure 1B**. All the PS sequences dropped the intensity by a similar value (the red bars), while a much larger difference was observed with the normal PO-DNA (blue bars). Since all the PS-DNA sequences had a significant etching effect, PS-DNA can etch the AgNPs in a less sequence-independent manner. This might be useful since etching can be general to different DNA sequences.

Comparison of PS and DNA Base Coordination

The above experiments indicated that PO-T_{15} is one of the least effective sequences for etching AgNPs. Therefore, the etching effect of PS_{14}-T_{15} should mainly come from the PS sites. PO-C_{15} is the best PO DNA and only the bases are available for etching, while PS_{14}-C_{15} is likely to be a most effective sequence overall. For PS_{14}-C_{15}, both the PS sites and the cytosine bases are likely to contribute to silver binding. Since these three sequences are representative, they were chosen for further studies. Their silver coordination sites are marked in black and red circles in **Figure 1A**.

We first studied the effect of DNA concentration. In each case, the peak intensity decreased with increase of DNA concentration (**Figures 3A–C**). At the same time, some redshifted peaks were observed at high DNA concentrations. All these experiments

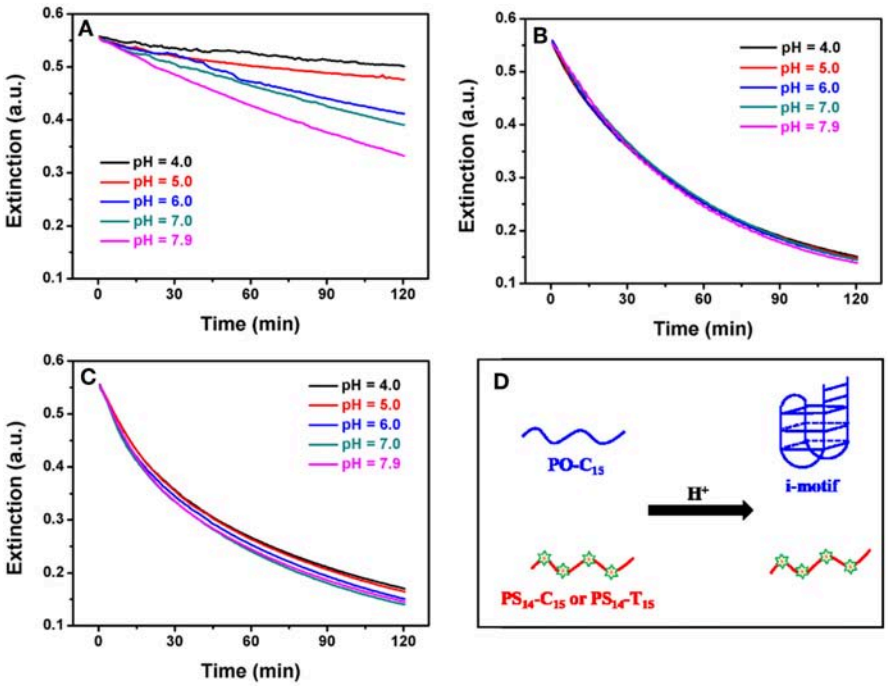

FIGURE 4 | Effect of pH on the kinetics of **(A)** PO-C_{15}, **(B)** PS_{14}-C_{15}, and **(C)** PS_{14}-T_{15} mediated AgNPs etching. Citrate buffer was used for pH 4.0, 5.0, and 6.0, and MOPS buffer was used for pH 7.0 and 7.9. **(D)** Effect of low pH on the structure of some PO and PS DNA.

were performed with an incubation time of 1.5 h, when the systems were approaching equilibrium (**Figure 4**).

By plotting the decrease of peak height against DNA concentration, we obtained their apparent binding curves (**Figure 3D**). Among these DNAs, PO-C_{15} had the lowest response with an apparent K_d of 3.87 μM. PS_{14}-C_{15} had a tighter binding with a K_d of 1.78 μM. Interestingly, PS_{14}-T_{15} had a K_d similar to that of PS_{14}-C_{15}, and thus from this standpoint, the base's contribution was minimal. Even at a relatively low DNA concentration, the base did not contribute much to etching. Adding PS modifications decreased the concentration requirement for C_{15} by 2.2-fold, while the improvement for T_{15} was close to infinity (compared to PO-T_{15}).

We then plotted the shift of peak wavelength (**Figure 3E**), where the upper half of the figure is for red shifted samples and the lower half for blue shifts. With low concentrations of PO-C_{15}, a gradual blue-shift of the AgNPs peak was observed and the maximal shift was achieved with 1.5 μM DNA, indicating etching of the AgNPs to form small particles. Then, the peak started to red shift attributable to Ostwald ripening. When the DNA concentration was more than 7.5 μM (crossing the dashed line in **Figure 3E**), the peak red-shifted relative to the original AgNPs.

For PS_{14}-C_{15}, most of their spectra were red shifted (e.g., ripening) except for the DNA concentration below 1 μM. From TEM, the overall size was indeed decreased for the 0.5 μM PS_{14}-C_{15} treated sample (**Figure S2B**). A wide size distribution with both larger and smaller AgNPs was observed for more PS_{14}-C_{15} (7.5 μM), confirming the ripening (**Figure S2C**). However, we cannot rule out slight aggregation of AgNPs occurring at the same time, which also caused the red shifted spectra. By comparing PO-C_{15} and PS_{14}-C_{15}, both showed etching at low DNA concentrations and then ripening with more DNA added. PS_{14}-C_{15} has a tighter affinity with silver allowing it to achieve the etching-to-ripening transition at a lower DNA concentration.

Interestingly, for PS_{14}-C_{15}, the red shift initially increased but later decreased when the concentration of PS_{14}-C_{15} was more than 3.75 μM (red trace in **Figure 3E**). A similar trend was also observed for PS_{14}-T_{15} despite smaller shifts compared to that of PS_{14}-C_{15}. This difference may be ascribed to their different DNA bases, suggesting that the cytosine bases of PS_{14}-C_{15} also participated in the etching process. We reason that PS_{14}-C_{15} had a complex multi-stage etching process. Low concentration of DNA contributed to AgNPs etching and further ripening (**Figures S2A–C**). Further increased PS_{14}-C_{15} DNA could further etch the larger AgNPs from the previous ripening step, which yielded the decreased red shift. The etching and thus size decrease was also confirmed by TEM (**Figure S2D**). As a result, we proposed a three-stage mechanism for PS-DNA to interact with AgNPs: etching, ripening and further etching (**Figure 3F**). For the PO-DNA, we only observed two stages (etching-ripening of AgNPs) indicating that cytosine bases alone were incapable of etching larger AgNPs, which were thermodynamically more stable than the originally used 20 nm ones. Since PS_{14}-T_{15} was also not very obvious than PS_{14}-C_{15} for this three-stage process, both cytosine bases and PS of PS_{14}-C_{15} contribute to the etching-to-ripening transition (with PS being the major contributor).

A

DNA names	Sequences (from 5′ to 3′)
PS_4-T_5	T*T*T*T*T
PS_{14}-T_{15}	T*T*T*T*T*T*T*T*T*T*T*T*T*T*T
PS_1-T_{15}	TTTTTTT*TTTTTTTT
PS_2-T_{15}	TTTTT*TTTTT*TTTTT
PS_4-T_{15}	TTT*TTT*TTT*TTT*TTT
PS_7-T_{15}	TT*TT*TT*TT*TT*TT*TT*T
PS_{7r}-T_{15}	TTTTTTT*T*T*T*T*T*T*T

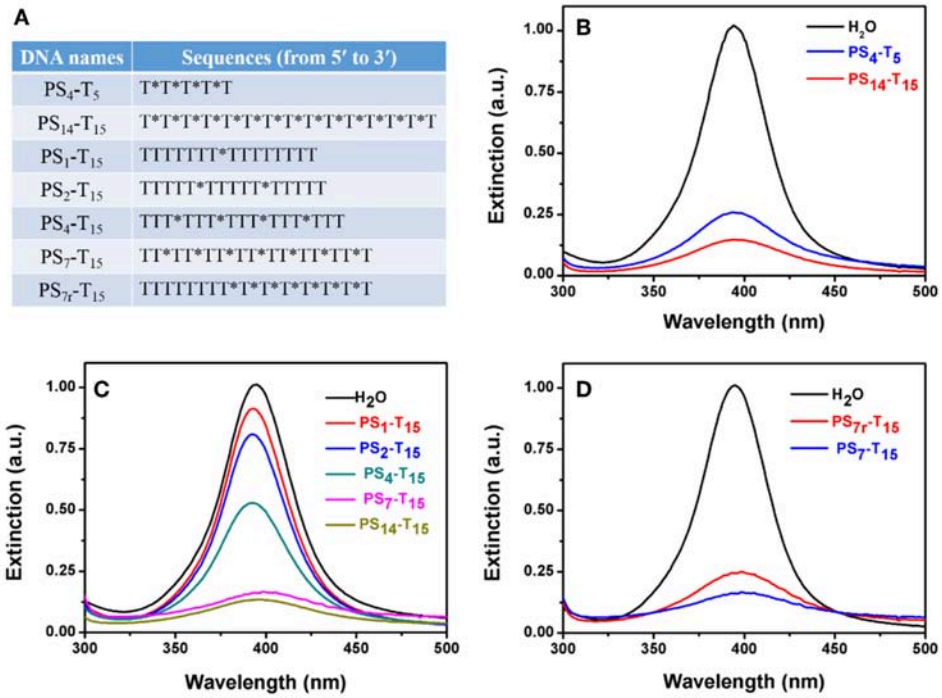

FIGURE 5 | (A) The PS-DNA sequences used for studying the number of PS modifications. PS-DNA mediated AgNP etching as a function of **(B)** poly-T DNA length, **(C)** the number, and **(D)** the location of PS modifications. The final concentration of PS_4-T_5 was 35 μM, while the concentration of all other PS-DNAs was 10 μM.

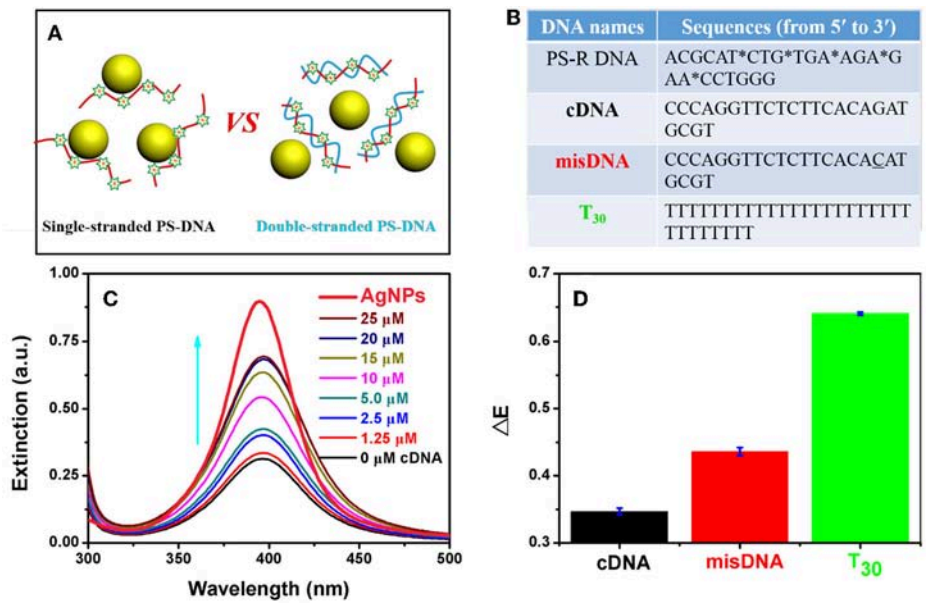

B

DNA names	Sequences (from 5′ to 3′)
PS-R DNA	ACGCAT*CTG*TGA*AGA*GAA*CCTGGG
cDNA	CCCAGGTTCTCTTCACAGATGCGT
misDNA	CCCAGGTTCTCTTCACACATGCGT
T_{30}	TTTTTTTTTTTTTTTTTTTTTTTTTTTTTT

FIGURE 6 | (A) Schematics and **(B)** DNA sequences used for PS-DNA conformation-dependent etching of AgNPs. The mistached base is underlined. **(C)** UV-vis spectra of the AgNPs mixed with the PS-R DNA in the presence of various concentrations of the cDNA. The spectrum of the AgNPs (no DNA) is in bold with red color. The arrow points increased cDNA concetnration. **(D)** Dropped extinction of the AgNPs with the PS-R DNA mixed with 25 μM of different DNA sequences.

Kinetics and Effect of pH

To further study etching, we followed the reaction kinetics. Since the conformation of poly-C DNA is strongly affected by pH (Dong et al., 2014; Huang Z. et al., 2016), we also measured the etching kinetics at different pH values. For PO-C_{15}, etching was strongly inhibited at low pH (**Figure 4A**). In particular, when

pH was at 6 or lower, etching was essentially fully inhibited. In contrast, PS_{14}-C_{15} had the same rate of etching regardless of pH from 4 to 7.9 (**Figure 4B**). We fitted the kinetic data of the PS-DNA to a first-order equation and obtained a rate constant of 41.3 h^{-1}, which was much faster than the PO kinetics of 183.4 h^{-1} at pH 7.9 (the rate of the PO samples was even slower at lower pH). Since the only difference here was the base, we reason that the inhibited PO-C_{15} etching must be related to its base protonation and formation of secondary structures such as the i-motif (**Figure 4D**).

Using circular dichroic (CD) spectroscopy, a strong positive peak at around 285 nm and a small negative peak near 260 nm were observed suggesting an intramolecular i-motif structure of PO-C_{15} at pH 4.0 (the black spectrum in **Figure S3**) (Liu and Balasubramanian, 2003). Such a folded conformation could shield the bases and inhibit their interaction with AgNPs or with Ag^+. For the PS_{14}-C_{15}-mediated etching, pH had no effect on etching. Since the PS modifications could cause a reduced melting temperature compared to the PO counterpart (Gonzalez et al., 1991), the PS_{14}-C_{15} was incapable of forming i-motif at 37°C even under acidic conditions (the red spectrum in **Figure S3**). Therefore, the exposed PS and the bases in the random-coil structured PS_{14}-C_{15} could serve as the ligand for etching the AgNPs. The pH-independent etching also appeared for PS_{14}-T_{15} (**Figure 4C**), demonstrating the generality of PS-DNA-mediated etching of AgNPs.

The Number of PS Modifications and AgNP Etching

The above experiments used 15-mer DNA with full PS modification. We then varied the number of DNA length and PS modifications (see **Figure 5A** for the DNA sequences). First, the DNA length was explored. To minimize the effect of the DNA base, PS-modified poly-T DNAs were tested. The length of DNA varied from 5-mer to 15-mer, and the total PS modification was maintained to be the same (e.g., the molar concentration of PS_4-T_5 was 3.5 times of that of PS_{14}-T_{15}). The peak of the PS_{14}-T_{15} sample dropped more than that of PS_4-T_5, suggesting that longer DNA was more effective and thus the importance of polyvalent binding (**Figure 5B**).

We then varied to the number of PS modifications, while the DNA length was maintained at 15-mer. The number of PS modifications was reduced from 14 to 7, 4, 2, and 1 (**Figure 5C**). The peak intensity gradually dropped with increased PS modifications. For the poly-T DNAs with 1–7 PS modifications, the drop in the peak intensity was linearly proportional to the number of PS (**Figure S4**), further highlighting that the PS responsible for the AgNP etching. This also provided a method to quantitatively tune the extent of etching. Further increase of the PS modifications to 14 did not bring in much more changes, suggesting that seven PS modifications could be sufficient with the 1.5 h incubation time.

Finally, we explored the effect of the location of PS modifications. Compared to the uniform distribution of PS in the whole DNA backbone of PS_7-T_{15}, the 7 PS modifications in PS_{7r}-T_{15} were concentrated on the 3′-terminus of the DNA. Interestingly, the evenly distributed PS_7-T_{15} had a stronger decrease (**Figure 5D**), implying that PS coordination is more effective when they are separated.

DNA Conformation Dependent Etching

Effective adsorption of PS-DNA on AgNPs could be important for the etching process. All the above experiments used flexible single-stranded DNA oligonucleotides, while a rigid DNA structure (e.g., duplex) may hinder the attachment of DNA to AgNPs due to restricted binding sites (**Figure 6A**). To test this hypothesis, we explored the effect of DNA conformation on etching by forming duplex DNA. However, PS modifications can weaken the stability of duplex DNA as reflected from the reduced melting temperature (T_m) (Gonzalez et al., 1991). Furthermore, the A-T base pair with a PS modification showed more decreased T_m than that of the C-G base pair (Stein et al., 1988). Therefore, we designed a PS-modified random DNA (named PS-R DNA) with a high GC content (**Figure 6B**). This DNA could etch the AgNPs (the black spectrum in **Figure 6C**), and the etching efficiency was gradually inhibited with increasing dose of the complementary DNA (cDNA). The inhibiting efficacy was sharply decreased when the misDNA with a single mismatched base was added, while a full non-complementary DNA (T_{30}) had little inhibition effect (**Figure 6D**). Therefore, we can attribute the cDNA-dependent etching to the formation of the duplex DNA. In other words, single-stranded DNA is much more effective for etching the AgNPs, although the PS backbone is still fully exposed in duplex DNA. This implies that DNA needs to fold into optimal binding structures, and etching cannot take place effectively on isolated PS sites.

CONCLUSIONS

In summary, we reported that PS modifications on DNA could improve etching of AgNPs in several aspects. First, the sequence generality is significantly expanded, and the introduced PS allows essentially any DNA sequence to etch AgNPs beyond just poly-C DNA. Furthermore, the required DNA concentration decreased clearly, and at the same DNA concentration the rate of etching was much faster than that with PS modifications. The etching process also effectively took place for PS-DNA despite the low pH, which could inhibit etching induced by normal PO-DNA (e.g., poly-C DNA). At the same time, we could control the etching efficacy through changing DNA length and the number and location of PS modifications. With stronger etching efficiency, the reaction process was found to contain three stages: etching by low concentrations of PS-DNA, followed by Ostwald ripening at medium DNA concentrations, and further etching in the presence of high DNA concentrations. This work has expanded the scope of the interaction between DNA and nanomaterials, and it might lead to interesting analytical and biomedical applications. For example, etching of various silver nanostructures may produce visible color change for colormetric biosensors. These sensors might detect multiple analytes by using aptamers and by designing strategies to target the PS sites. At the same time, it also calls for attention regarding the stability of nanomaterials when designing hybrid materials

containing silver nanoparticles (and potentially other materials) with DNA.

AUTHOR CONTRIBUTIONS

SH, JW, and JL designed the experiments and wrote the paper. SH performed the experiments. PH contributed in the DNA design. All authors read and approved the final version of the manuscript.

FUNDING

Funding for this work is from the Natural Sciences and Engineering Research Council of Canada (NSERC) and the National Natural Science Foundation of China (21575166, 21876208).

ACKNOWLEDGMENTS

SH was supported by the Chinese Scholarship Council (CSC) Scholarship (201706370185) to visit the University of Waterloo.

SUPPLEMENTARY MATERIAL

The Supplementary Material for this article can be found online at: https://www.frontiersin.org/articles/10.3389/fchem.2019.00198/full#supplementary-material

REFERENCES

Basu, S., Jana, S., Pande, S., and Pal, T. (2008). Interaction of DNA bases with silver nanoparticles: assembly quantified through SPRS and SERS. *J. Colloid Interface Sci.* 321, 288–293. doi: 10.1016/j.jcis.2008.02.015

Cao, Y. C., Jin, R., and Mirkin, C. A. (2002). Nanoparticles with raman spectroscopic fingerprints for DNA and RNA detection. *Science* 297, 1536–1540. doi: 10.1126/science.297.5586.1536

Carnerero, J. M., Jimenez-Ruiz, A., Castillo, P. M., and Prado-Gotor, R. (2017). Covalent and non-covalent DNA-gold-nanoparticle interactions: new avenues of research. *Chem. Phys. Chem.* 18, 17–33. doi: 10.1002/cphc.201601077

Chidchob, P., and Sleiman, H. F. (2018). Recent advances in DNA nanotechnology. *Curr. Opin. Chem. Biol.* 46, 63–70. doi: 10.1016/j.cbpa.2018.04.012

Chou, L. Y., Zagorovsky, K., and Chan, W. C. (2014). DNA assembly of nanoparticle superstructures for controlled biological delivery and elimination. *Nat. Nanotechnol.* 9:148. doi: 10.1038/nnano.2013.309

Cunningham, L. A., Li, J., and Lu, Y. (1998). Spectroscopic evidence for inner-sphere coordination of metal ions to the active site of a hammerhead ribozyme. *J. Am. Chem. Soc.* 120, 4518–4519. doi: 10.1021/ja973251p

Dong, Y., Yang, Z., and Liu, D. (2014). DNA nanotechnology based on i-motif structures. *Acc. Chem. Res.* 47, 1853–1860. doi: 10.1021/ar500073a

Farlow, J., Seo, D., Broaders, K. E., Taylor, M. J., Gartner, Z. J., and Jun, Y. W. (2013). Formation of targeted monovalent quantum dots by steric exclusion. *Nat. Methods* 10:1203. doi: 10.1038/nmeth.2682

Gonzalez, C., Ecker, D. J., Hoke, G. D., Draper, K., Zounes, M. C., Freier, S. M., et al. (1991). Effects of phosphorothioate capping on antivense oligonucleotide stability, hybridization and antiviral efficacy versus herpes simplex virus infection. *Nucleic Acids Res.* 19, 5743–5748. doi: 10.1093/nar/19.20.5743

Herne, T. M., and Tarlov, M. J. (1997). Characterization of DNA probes immobilized on gold surfaces. *J. Am. Chem. Soc.* 119, 8916–8920. doi: 10.1021/ja9719586

Hu, S., Ye, B., Tang, H., Wu, F., Yi, X., Yi, T., et al. (2018). Fabrication of multifunctional monometallic nanohybrids for reactive oxygen species-mediated cell apoptosis and enhanced fluorescence cell imaging. *J. Mater. Chem. B* 6, 1187–1194. doi: 10.1039/C7TB02745A

Hu, S., Yi, T., Huang, Z., Liu, B., Wang, J., Yi, X., et al. (2019). Etching silver nanoparticles using DNA. *Mater. Horiz.* 6, 155–159. doi: 10.1039/C8MH01126E

Huang, P. J., and Liu, J. (2015). Rational evolution of Cd^{2+}-specific DNAzymes with phosphorothioate modified cleavage junction and Cd^{2+} sensing. *Nucleic Acids Res.* 43, 6125–6133. doi: 10.1093/nar/gkv519

Huang, P. J. J., and Liu, J. (2014). Sensing parts-per-trillion Cd^{2+}, Hg^{2+}, and Pb^{2+} collectively and individually using phosphorothioate DNAzymes. *Anal. Chem.* 86, 5999–6005. doi: 10.1021/ac501070a

Huang, P. J. J., Moon, W. J., and Liu, J. (2019). Instantaneous iodine-assisted DNAzyme cleavage of phosphorothioate RNA. *Biochemistry* 58, 422–429. doi: 10.1021/acs.biochem.8b00900

Huang, P. J. J., van Ballegooie, C., and Liu, J. (2016). Hg^{2+} detection using a phosphorothioate RNA probe adsorbed on graphene oxide and a comparison with thymine-rich DNA. *Analyst* 141, 3788–3793. doi: 10.1039/C5AN02031J

Huang, P. J. J., Vazin, M., Matuszek, Z., and Liu, J. (2015a). A new heavy lanthanide-dependent DNAzyme displaying strong metal cooperativity and unrescuable phosphorothioate effect. *Nucleic Acids Res.* 43, 461–469. doi: 10.1093/nar/gku1296

Huang, P. J. J., Wang, F., and Liu, J. (2015b). Cleavable molecular beacon for Hg^{2+} detection based on phosphorothioate RNA modifications. *Anal. Chem.* 87, 6890–6895. doi: 10.1021/acs.analchem.5b01362

Huang, Z., Liu, B., and Liu, J. (2016). Parallel polyadenine duplex formation at low pH facilitates DNA conjugation onto gold nanoparticles. *Langmuir* 32, 11986–11992. doi: 10.1021/acs.langmuir.6b03253

Jiang, L., Zhang, H., Zhuang, J., Yang, B., Yang, W., Li, T., et al. (2005). Sterically mediated two-dimensional architectures in aggregates of Au nanoparticles directed by phosphorothioate oligonucleotide-DNA. *Adv. Mater.* 17, 2066–2070. doi: 10.1002/adma.200402004

Lee, J. H., Wernette, D. P., Yigit, M. V., Liu, J., Wang, Z., and Lu, Y. (2007). Site-specific control of distances between gold nanoparticles using phosphorothioate anchors on DNA and a short bifunctional molecular fastener. *Angew. Chem. Int. Ed.* 46, 9006–9010. doi: 10.1002/anie.200702569

Lin, Q. Y., Mason, J. A., Li, Z., Zhou, W., O'Brien, M. N., Brown, K. A., et al. (2018). Building superlattices from individual nanoparticles via template-confined DNA-mediated assembly. *Science* 359, 669–672. doi: 10.1126/science.aaq059

Liu, B., and Liu, J. (2017). Methods for preparing DNA-functionalized gold nanoparticles, a key reagent of bioanalytical chemistry. *Anal. Methods* 9, 2633–2643. doi: 10.1039/C7AY00368D

Liu, B., Sun, Z., Huang, P.-J. J., and Liu, J. (2015). Hydrogen peroxide displacing DNA from nanoceria: mechanism and detection of glucose in serum. *J. Am. Chem. Soc.* 137, 1290–1295. doi: 10.1021/ja511444e

Liu, D., and Balasubramanian, S. (2003). A proton-fuelled DNA nanomachine. *Angew. Chem. Int. Ed.* 42, 5734–5736. doi: 10.1002/anie.200352402

Liu, G., Fu, W., Zhang, Z., He, Y., Yu, H., Wang, Y., et al. (2018). Structural basis for the recognition of sulfur in phosphorothioated DNA. *Nat. Commun.* 9:4689. doi: 10.1038/s41467-018-07093-1

Liu, J. (2012). Adsorption of DNA onto gold nanoparticles and graphene oxide: surface science and applications. *Phys. Chem. Chem. Phys.* 14, 10485–10496. doi: 10.1039/c2cp41186e

Liu, J., Cao, Z., and Lu, Y. (2009). Functional nucleic acid sensors. *Chem. Rev.* 109, 1948–1998. doi: 10.1021/cr030183i

Liu, J., and Lu, Y. (2003). A colorimetric lead biosensor using DNAzyme-directed assembly of gold nanoparticles. *J. Am. Chem. Soc.* 125, 6642–6643. doi: 10.1021/ja034775u

Liu, J., and Lu, Y. (2006). Preparation of aptamer-linked gold nanoparticle purple aggregates for colorimetric sensing of analytes. *Nat. Protoc.* 1:246. doi: 10.1038/nprot.2006.38

Lu, C., Huang, Z., Liu, B., Liu, Y., Ying, Y., and Liu, J. (2017). Poly-cytosine DNA as a high-affinity ligand for inorganic nanomaterials. *Angew. Chem. Int. Ed.* 56, 6208–6212. doi: 10.1002/anie.201702998

Ma, N., Sargent, E. H., and Kelley, S. O. (2008). One-step DNA-programmed growth of luminescent and biofunctionalized nanocrystals. *Nat. Nanotechnol.* 4:121. doi: 10.1038/nnano.2008.373

Mirkin, C. A., Letsinger, R. L., Mucic, R. C., and Storhoff, J. J. (1996). A DNA-based method for rationally assembling nanoparticles into macroscopic materials. *Nature* 382, 607–609. doi: 10.1038/382607a0

Nykypanchuk, D., Maye, M. M., van der Lelie, D., and Gang, O. (2008). DNA-guided crystallization of colloidal nanoparticles. *Nature* 451:549. doi: 10.1038/nature06560

Pal, S., Sharma, J., Yan, H., and Liu, Y. (2009). Stable silver nanoparticle-DNA conjugates for directed self-assembly of core-satellite silver-gold nanoclusters. *Chem. Commun.* 2009, 6059–6061. doi: 10.1039/b911069k

Pu, F., Ren, J., and Qu, X. (2014). Nucleic acids and smart materials: advanced building blocks for logic systems. *Adv. Mater.* 26, 5742–5757. doi: 10.1002/adma.201401617

Qu, X., Trent, J. O., Fokt, I., Priebe, W., and Chaires, J. B. (2000). Allosteric, chiral-selective drug binding to DNA. *Proc. Natl. Acad. Sci. U.S.A.* 97, 12032–12037. doi: 10.1073/pnas.200221397

Seeman, N. C., and Sleiman, H. F. (2017). DNA nanotechnology. *Nat. Rev. Mater.* 3:17068. doi: 10.1038/natrevmats.2017.68

Sharma, J., Chhabra, R., Cheng, A., Brownell, J., Liu, Y., and Yan, H. (2009). Control of self-assembly of DNA tubules through integration of gold nanoparticles. *Science* 323, 112–116. doi: 10.1126/science.1165831

Shen, C., Lan, X., Zhu, C., Zhang, W., Wang, L., and Wang, Q. (2017). Spiral patterning of Au nanoparticles on Au nanorod surface to form chiral AuNR@AuNP helical superstructures templated by DNA origami. *Adv. Mater.* 29:1606533. doi: 10.1002/adma.201606533

Shen, J., Tang, Q., Li, L., Li, J., Zuo, X., Qu, X., et al. (2017). Valence-engineering of quantum dots using programmable DNA scaffolds. *Angew. Chem. Int. Ed.* 56, 16077–16081. doi: 10.1002/anie.201710309

Song, T., Tang, L., Tan, L. H., Wang, X., Satyavolu, N. S. R., Xing, H., et al. (2015). DNA-encoded tuning of geometric and plasmonic properties of nanoparticles growing from gold nanorod seeds. *Angew. Chem. Int. Ed.* 54, 8114–8118. doi: 10.1002/anie.201500838

Stein, C. A., Subasinghe, C., Shinozuka, K., and Cohen, J. S. (1988). Physicochemical properties of phospborothioate oligodeoxynucleotides. *Nucleic Acids Res.* 16, 3209–3221. doi: 10.1093/nar/16.8.3209

Storhoff, J. J., Elghanian, R., Mirkin, C. A., and Letsinger, R. L. (2002). Sequence-dependent stability of DNA-modified gold nanoparticles. *Langmuir* 18, 6666–6670. doi: 10.1021/la0202428

Sun, M., Xu, L., Qu, A., Zhao, P., Hao, T., Ma, W., et al. (2018). Site-selective photoinduced cleavage and profiling of DNA by chiral semiconductor nanoparticles. *Nat. Chem.* 10, 821–830. doi: 10.1038/s41557-018-0083-y

Surwade, S. P., Zhou, F., Wei, B., Sun, W., Powell, A., O'Donnell, C., et al. (2013). Nanoscale growth and patterning of inorganic oxides using DNA nanostructure templates. *J. Am. Chem. Soc.* 135, 6778–6781. doi: 10.1021/ja401785h

Tan, L. H., Xing, H., and Lu, Y. (2014). DNA as a powerful tool for morphology control, spatial positioning, and dynamic assembly of nanoparticles. *Acc. Chem. Res.* 47, 1881–1890. doi: 10.1021/ar500081k

Thaplyal, P., Ganguly, A., Hammes-Schiffer, S., and Bevilacqua, P. C. (2015). Inverse thio effects in the hepatitis delta virus ribozyme reveal that the reaction pathway is controlled by metal ion charge density. *Biochemistry* 54, 2160–2175. doi: 10.1021/acs.biochem.5b00190

Weadick, D., and Liu, J. (2015). Phosphorothioate DNA stabilized fluorescent gold and silver nanoclusters. *Nanomaterials* 5:804. doi: 10.3390/nano5020804

Wilner, O. I., and Willner, I. (2012). Functionalized DNA nanostructures. *Chem. Rev.* 112, 2528–2556. doi: 10.1021/cr200104q

Wu, J., Tan, L. H., Hwang, K., Xing, H., Wu, P., Li, W., et al. (2014). DNA sequence-dependent morphological evolution of silver nanoparticles and their optical and hybridization properties. *J. Am. Chem. Soc.* 136, 15195–15202. doi: 10.1021/ja506150s

Zhang, D., Deng, M., Xu, L., Zhou, Y., Yuwen, J., and Zhou, X. (2009). The sensitive and selective optical detection of mercury(II) ions by using a phosphorothioate DNAzyme strategy. *Chem. Eur. J.* 15, 8117–8120. doi: 10.1002/chem.200901268

Zhou, W., Saran, R., and Liu, J. (2017). Metal sensing by DNA. *Chem. Rev.* 117, 8272–8325. doi: 10.1021/acs.chemrev.7b00063

Zhou, W., Wang, F., Ding, J., and Liu, J. (2014). Tandem phosphorothioate modifications for DNA adsorption strength and polarity control on gold nanoparticles. *ACS Appl. Mater. Interfaces* 6, 14795–14800. doi: 10.1021/am504791b

Conflict of Interest Statement: The authors declare that the research was conducted in the absence of any commercial or financial relationships that could be construed as a potential conflict of interest.

Copyright © 2019 Hu, Huang, Wang and Liu. This is an open-access article distributed under the terms of the Creative Commons Attribution License (CC BY). The use, distribution or reproduction in other forums is permitted, provided the original author(s) and the copyright owner(s) are credited and that the original publication in this journal is cited, in accordance with accepted academic practice. No use, distribution or reproduction is permitted which does not comply with these terms.

frontiers in Chemistry

ORIGINAL RESEARCH
published: 10 April 2019
doi: 10.3389/fchem.2019.00218

The Bioavailability, Biodistribution, and Toxic Effects of Silica-Coated Upconversion Nanoparticles *in vivo*

Mingzhu Zhou[1†], *Xiaoqian Ge*[2†], *Da-Ming Ke*[1†], *Huan Tang*[3], *Jun-Zheng Zhang*[1], *Matteo Calvaresi*[4], *Bin Gao*[5], *Lining Sun*[2*], *Qianqian Su*[1*] *and Haifang Wang*[1]

[1] *Institute of Nanochemistry and Nanobiology, Shanghai University, Shanghai, China,* [2] *Research Center of Nano Science and Technology, and School of Material Science and Engineering, Shanghai University, Shanghai, China,* [3] *Beijing National Laboratory for Molecular Sciences, College of Chemistry and Molecular Engineering, Peking University, Beijing, China,* [4] *Dipartimento di Chimica "G. Ciamician," Alma Mater Studiorum–Università di Bologna, Bologna, Italy,* [5] *Cancer and Stem Cell Biology Program, Duke-NUS Medical School, Singapore, Singapore*

Lanthanide-doped upconversion nanoparticles can convert long wavelength excitation radiation to short wavelength emission. They have great potential in biomedical applications, such as bioimaging, biodetection, drug delivery, and theranostics. However, there is little information available on their bioavailability and biological effects after oral administration. In this study, we systematically investigated the bioavailability, biodistribution, and toxicity of silica-coated upconversion nanoparticles administrated by gavage. Our results demonstrate that these nanoparticles can permeate intestinal barrier and enter blood circulation by microstructure observation of Peyer's patch in the intestine. Comparing the bioavailability and the biodistribution of silica-coated upconversion nanoparticles with oral and intravenous administration routes, we found that the bioavailability and biodistribution are particularly dependent on the administration routes. After consecutive gavage for 14 days, the body weight, pathology, Zn and Cu level, serum biochemical analysis, oxidative stress, and inflammatory cytokines were studied to further evaluate the potential toxicity of the silica-coated upconversion nanoparticles. The results suggest that these nanoparticles do not show overt toxicity in mice even at a high dose of 100 mg/kg body weight.

Keywords: upconversion nanoparticle, bioavailability, distribution, toxicity, *in vivo*, gavage

OPEN ACCESS

Edited by:
Fan Zhang,
Fudan University, China

Reviewed by:
Chun Xu,
University of Queensland, Australia
Min Zhou,
Zhejiang University, China

***Correspondence:**
Lining Sun
lnsun@shu.edu.cn
Qianqian Su
chmsqq@shu.edu.cn

[†] *These authors have contributed equally to this work*

Specialty section:
This article was submitted to Nanoscience, a section of the journal Frontiers in Chemistry

Received: *30 November 2018*
Accepted: *19 March 2019*
Published: *10 April 2019*

Citation:
Zhou M, Ge X, Ke D-M, Tang H, Zhang J-Z, Calvaresi M, Gao B, Sun L, Su Q and Wang H (2019) The Bioavailability, Biodistribution, and Toxic Effects of Silica-Coated Upconversion Nanoparticles in vivo. Front. Chem. 7:218. doi: 10.3389/fchem.2019.00218

INTRODUCTION

In the last decade, lanthanide-doped upconversion nanoparticles have attracted increasing attention because of their unique advantages, such as low level of background noise, deep penetration depth, minimal photodamage, and high resistance to photobleaching (Auzel, 2004; Lu et al., 2013; Bettinelli et al., 2015; Li et al., 2015b, 2017; Jalani et al., 2018; Liu et al., 2018; Sun et al., 2018). Surface modification is typically required to make upconversion nanoparticles, UCNPs, suitable for biomedical application, which typically involves coating a hydrophilic ligand (i.e., amphiphilic polymers, proteins) or an extra hydrophilic layer (i.e., SiO_2) on their surface (Li et al., 2015a; Liu et al., 2015; Sedlmeiera and Gorris, 2015; Plohl et al., 2017). These features made UCNPs suitable for many biological and medical applications, including multimodal bioimaging, biosensing, drug delivery, photodynamic therapy, and synergetic therapy

(Lim et al., 2006; Liu et al., 2012, 2016; Yang et al., 2015; Zhou et al., 2015; Su et al., 2017; Chen et al., 2018; Green et al., 2018; Tsai et al., 2018). Despite the encouraging results that have been obtained, there are many unresolved issues relating to the biological effects of these nanomaterials.

UCNPs acting as drug carriers, contrast agents, or bioprobes have been extensively studied either in mice or in plant models (Peng et al., 2012; Liu et al., 2013; Chen et al., 2014; Wu et al., 2016). In previous studies, the majority of UCNPs toxicity assays were performed on different cell lines *in vitro* (Gnach et al., 2015; Tian et al., 2015; Wozniak et al., 2016; Wysokinska et al., 2016; Gao et al., 2017), but fewer reports focused on *in vivo* toxicity studies (Cheng et al., 2011; Wang et al., 2013; Jang et al., 2014; Lucky et al., 2016). The toxicity assays of UCNPs were routinely carried out based on the intravenous injection technique (Abdul and Zhang, 2008; Xiong et al., 2010; Zhou et al., 2011; Ramirez-Garcia et al., 2017). Very recently, Ortgies et al. developed an orally administrated lanthanide-doped UCNP for multiplexed imaging and drug delivery (Ortgies et al., 2018). It is also worth noting that oral administration of substances is a common route in scientific experiments using small animals, such as mice. However, a comprehensive study of the biodistribution and toxicity of UCNPs undergoing oral administration route was not found. Furthermore, since nanoparticles have larger sizes compared to conventional drugs, UCNPs can be poorly absorbed via the oral route. For this reason, it is important to examine whether these nanoparticles can permeate epithelial barriers, in particular the intestinal barrier. There is little information available about the bioavailability of these nanoparticles through oral exposure. Therefore, it is necessary to assess the bioavailability, distribution, and toxicity of UCNPs administrated orally.

In this study, a systematic investigation of the bioavailability, biodistribution, and toxicity of orally administered silica-coated $NaYF_4$:Yb,Er nanoparticles ($NaYF_4$:Yb,Er@SiO_2) with an average diameter of 50 nm was carried out in mice. $NaYF_4$:Yb,Er@SiO_2 nanoparticles are chosen because of their good biocompatibility, broad bioapplications, and suppression of lanthanide leakage (Liu et al., 2015). We envision that $NaYF_4$:Yb,Er@SiO_2 nanoparticles can be absorbed though Peyer's patch in intestine and then enter the blood circulation of mice. We also compare the biodistribution of orally administrated $NaYF_4$:Yb,Er@SiO_2 with that of intravenously administrated $NaYF_4$:Yb,Er@SiO_2 by TEM and inductively coupled plasma mass spectrometry (ICP-MS). The toxicity of $NaYF_4$:Yb,Er@SiO_2 is determined by several different approaches, including body weight measurement, pathology changes observation, Zn and Cu levels, serum biochemical analyses, oxidative stress, and inflammatory cytokines analysis.

MATERIALS AND METHODS

Materials

Yttrium(III) chloride hexahydrate (99.9%), ytterbium(III) chloride hexahydrate (99.9%), erbium(III) chloride hexahydrate (99.9%), oleic acid (technical grade, 90%), 1-octadecene (technical grade, 90%), Igepal CO-520 and tetraethyl orthosilicate (TEOS, 99.0%) were purchased from Sigma Aldrich. Sodium hydroxide (96%), ammonium fluoride (98%), methanol (99.5%), and ammonia solution (25–28%) were obtained from Aladdin. Nitric acid (CMOS), hydrofluoric acid (guaranteed grade), and perchloric acid (guaranteed grade) were purchased from Sinopharm Chemical Reagent Co., Ltd., Shanghai, China. All chemicals were used as received without further purification.

Characterization

The size and morphology of the nanoparticles were characterized on a low-to-high resolution transmission electron microscope (JEM-2010F, JEOL, Japan) operated at 120 kV. Powder X-ray diffraction (XRD, Nano 90ZS, Malven, Britain) measurement was performed on a 3 kW D/MAX2200 V PC diffractometer using Cu kα radiation (60 kV, 80 mA) at a step width of 8° min^{-1}. Fourier transform infrared spectroscopy (FT-IR) spectra were obtained in the spectral range from 4,000 to 400 cm^{-1} on an Avatar 370 (Nicolet, America) instrument using the pressed KBr pellet technique. The microstructure observation of Peyer's patch and liver tissue was conducted on a transmission electron microscopy (JEM-1200EX, JEOL, Japan). All biochemical assays were performed using a Hitachi 7,080 clinical automatic chemistry analyzer (Japan).

Synthesis of $NaYF_4$:Yb,Er Upconversion Nanoparticles

In a typical experiment, YCl_3 (1.56 mmol, 78%), $YbCl_3$ (0.4 mmol, 20%), and $ErCl_3$ (0.04 mmol, 2%) dissolved in deionized water were added into a 100 mL flask. The solution was then

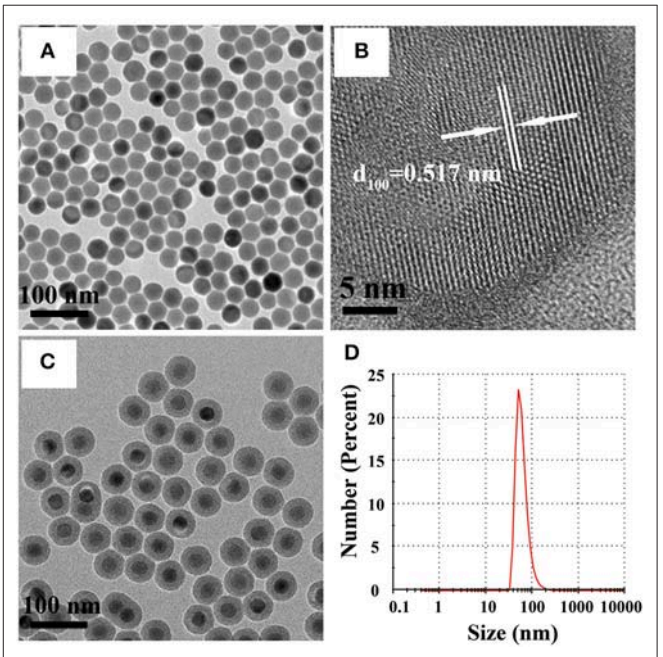

FIGURE 1 | (A,B) TEM and HRTEM images of $NaYF_4$:Yb,Er nanoparticles in cyclohexane. **(C)** TEM image of $NaYF_4$:Yb,Er@SiO_2 nanoparticles in water. **(D)** Dynamic light scattering (DLS) of $NaYF_4$:Yb,Er@SiO_2 nanoparticles in water.

heated to 110°C to evaporate water until the solution became white powder. Subsequently, 12 mL oleic acid and 30 mL 1-octadecene were added in the mixture. The mixture was then heated to 150°C and kept at this temperature for 1 h before cooling down to 50°C. Twenty milliliters of methanol solution containing NaOH (0.2 g, 1.6 mmol) and NH_4F (0.3 g, 8 mmol) was added into the flask and stirred for 30 min at 100°C to evaporate methanol. After that, the mixture was heated to 300°C and kept for 1 h under nitrogen atmosphere. The obtained mixture was precipitated by the addition of acetone, separated by centrifugation, and washed with cyclohexane. The resulting nanoparticles $NaYF_4$:Yb,Er were redispersed in 20 mL cyclohexane.

Synthesis of $NaYF_4$:Yb,Er@SiO_2 Nanoparticles

Igepal CO-520 (1 mL) was dispersed in 20 mL of cyclohexane, and then a 1.5 mL $NaYF_4$:Yb,Er nanoparticle in cyclohexane solution was added into the mixture. After stirring for 3 h, 200 μL TEOS was added and the mixture continue stirred 0.5 h. Then, 130 μL ammonia was injected into the mixture and the mixture was sealed and kept stirring for 20 h. The product was precipitated using methanol, collected by centrifugation, and washed with ethanol several times. Finally, the product was dispersed in deionized water.

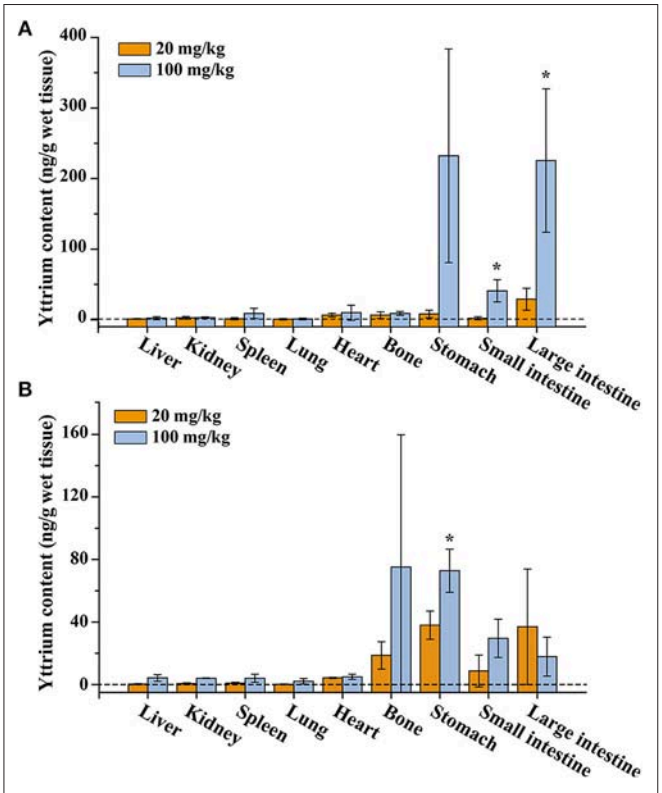

FIGURE 2 | Yttrium content in tissues of the mice after consecutive gavage administration of $NaYF_4$:Yb,Er@SiO_2 for 7 days **(A)** and 14 days **(B)**. *Significant difference between the two experimental groups ($P < 0.05$, $n = 3$).

Stability Assay

To determine the stability of $NaYF_4$:Yb,Er@SiO_2 in physiological solutions, the dissolutions of $NaYF_4$:Yb,Er@SiO_2 nanoparticles were monitored in fetal bovine serum (FBS) and simulated body fluid (SBF). SBF was prepared following the recipe in **Table S1** (Tadashi and Hiroaki, 2006). $NaYF_4$:Yb/Er@SiO_2 (0.1 mL) at a concentration of 20 mg/mL was mixed with 0.9 mL of FBS or SBF in a glass bottle. The mixture was incubated in a thermostatic shaker (150 rpm) at 37°C. After incubation for predetermined period of time, the resulting solution was centrifuged at 12,000 rpm for 15 min. The supernatant was collected and digested with 1 mL 70% HNO_3 and 0.5 mL 30% H_2O_2 at 90°C. When the solution became clear and colorless, the solution was adjusted to 8 mL by using 2% HNO_3. The content of yttrium (Y) in the solution was measured by inductively coupled plasma mass spectrometry (ICP-MS, ELAN DRC-e, PerkinElmer Co., Ltd., USA).

In vivo Experiment

All animal experiments were carried out in accordance with the guide for the animal care and use program guidelines of Shanghai University with the approval by Shanghai University. In this study, 60 mice were divided into gavage (36 mice) and intravenous administration (24 mice) groups. Six-week-old healthy male ICR mice (22–26 g) were supplied by the Experimental Animal Center, Second Military Medical University (Shanghai, China). The mice were housed in clean polypropylene cages (6 mice/cage) with the commercial pellet diet and water *ad libitum* at 22 ± 2°C and kept on a 12 h light/dark cycle. After acclimation for 1 week, four groups of mice were treated with $NaYF_4$:Yb/Er@SiO_2 (treatment group, $n = 6$) daily by gavage for 7 and 14 consecutive days with doses of 20 mg/kg bodyweight (b.w.) and 100 mg/kg (b.w.). The two corresponding control groups ($n = 6$) were treated with water daily by gavage for 7 and 14 consecutive days. In addition, four groups of mice were intravenously injected with $NaYF_4$:Yb/Er@SiO_2 (treatment group, 20 mg/kg b.w, $n = 6$) and saline (control group, $n = 6$) through mouse tail veins and sacrificed at 1 and 7 days after injection. All mice were weighed daily during the experimental period. And all experiments were repeated twice.

Biodistribution of Yttrium, Zinc, and Copper in Mice

At predetermined time points, mice were sacrificed and the contents of Y, Zn, and Cu in main organs were measured after consecutive gavage administration of $NaYF_4$:Yb/Er@SiO_2. Liver, kidneys, spleen, lungs, heart, bone, stomach, large intestine, and small intestine were collected and about 0.1–0.3 g of these organs and were digested with 70% nitric acid and hydrofluoric acid by microwave digestion system (MARS, USA). In addition, the blood samples were digested by the same method as organs. Then, perchloric acid was added into the digested solution and the mixture was heated at 200°C to remove the remaining nitric acid and hydrofluoric acid. When water was evaporated, ultrapure water was added twice. The resulting solution was

adjusted to 8 mL with 2% nitric acid solution and the metal content in solution was determined by ICP-MS.

Microstructure Observation of Peyer's Patch and Liver Tissue

Peyer's patch and liver tissue (1 mm cubes) were collected from small intestine and liver, respectively. They were subsequently fixed in 2.5% glutaraldehyde in phosphate buffer for 2 h and rinsed by 0.1 M phosphate rinsing fluid for three times. After that, the samples were post-fixed with 1% osmium tetraoxide at 4°C for 2 h and then dehydrated with ethanol and acetone as follows, 50% ethanol−15 min, 70% ethanol−15 min, 80% ethanol−15 min, 90% ethanol−15 min, 100% ethanol−20 min, and 100% acetone−20 min. Then the tissue blocks were infiltrated with embedding medium in acetone (v:v = 1:1) for 3 h, and infiltrated with embedding medium overnight. The embedded tissue blocks in embedding medium were polymerized in a dry centrifuge tube at 70°C overnight. The blocks were then cut in 50–70 nm thickness using an ultramicrotome (LKB-I, Sweden), and then counterstained with 3% uranyl acetate and lead citrate prior to TEM measurements.

Organ Index

Organ indices were calculated for major organs using the following formula: (organ weight)/(total body weight) × 100.

Histopathological Investigation

The organs including liver, kidney, lung, spleen, and small intestine were collected at each time point and fixed with formalin. The fixed organs were embedded in paraffin, sliced at a thickness of 5 μm and then placed onto glass slides. After hematoxylin–eosin (H&E) staining, the slides were investigated and photographed on an optical microscope (DM750, Leica, Germany).

Serum Biochemistry Analysis

Blood samples were collected from mice at predetermined time point and centrifuged at 3,000 rpm for 15 min. The obtained serum samples were stored at −20°C before analysis. Alanine aminotransferase (ALT), aspartate aminotransferase (AST), alkaline phosphatase (ALP), blood urea nitrogen (BUN), and creatinine (CREA) were measured using the commercial kits (The Seno Clinical Diagnostic Products Co., Japan).

Oxidative Stress Assay

The organs including liver, lung, kidney and spleen were rinsed with saline solution at 4°C and then wiped with dry filter papers. Ten or Five percent (w/v) homogenates were prepared by homogenization of tissue in saline solution at 10,000 rpm for 3 min using a homogenizer. The supernatants

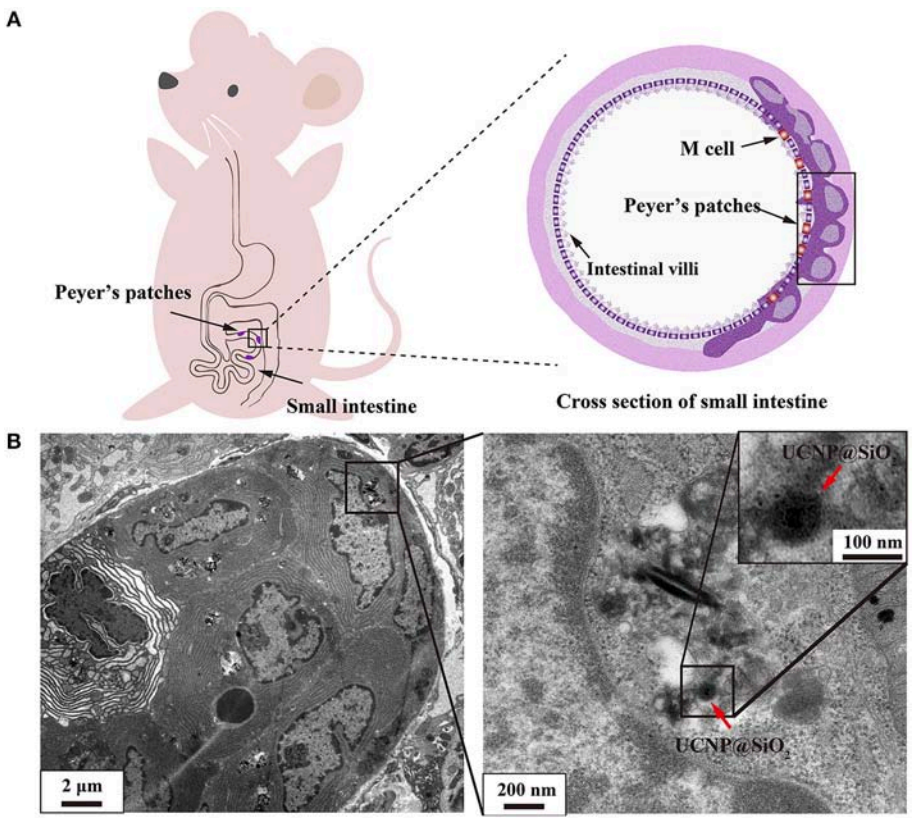

FIGURE 3 | (A) Schematic illustration of Peyer's patches in small intestine. **(B)** TEM image demonstrated that $NaYF_4$:Yb,Er@SiO_2 nanoparticles were located in Peyer's patch in small intestine of mice after 14 days' consecutive gavage administration of these nanoparticles. UCNP@SiO_2 denotes $NaYF_4$:Yb,Er@SiO_2.

were collected after centrifuging the homogenates at 3,500 rpm for 10 min. The contents of protein in the supernatants were examined by bicinchoninic acid assay (BCA protein assay kit, Nanjing Jiancheng bioengineering institute, Nanjing, China). The reduced GSH levels of the supernatants were determined by Ellman's reagent 5,5'dithiobis-(2-nitrobenzoic acid) (DTNB, Nanjing Jiancheng Biotechnology Institute, China). The lipid peroxidation indicator malondialdehyde (MDA) was estimated by the method of thiobarbituric acid reactive species (TBA, Nanjing Jiancheng Bioengineering Institute, Nanjing, China).

TNF-α, IL-6, and IL-1β Levels in Liver

The contents of TNF-α, IL-6, and IL-1β in supernatants of liver homogenates were quantified by a double-antibody sandwich ELISA commercial kit (BD Biosciences, USA). Manufacturer's protocol was followed. The absorbance was measured on a microplate reader at 450 nm (Varioskan Flash, Thermo, USA) and the contents of TNF-α, IL-6, and IL-1β were calculated based on the corresponding standard curves. The protein contents in supernatants were also determined by bicinchoninic acid assay (BCA protein assay kit, Nanjing Jiancheng bioengineering institute, Nanjing, China). The levels of TNF-α, IL-6, and IL-1β were expressed as ng/mg protein.

Statistical Analysis

All data were expressed as the mean ± standard deviation (mean ± SD) of more than three individual observations. Significance was calculated using Student's *t*-test. The difference was considered significant if $p < 0.05$. In addition, standard deviation and *p*-value were calculated by:

$$\text{Standard deviation (SD)} = \sqrt{\frac{\sum (\text{X-M})^2}{n-1}},$$

$$S = \sqrt{\frac{(n_1-1)\,SD_1^2 + (n_2-1)\,SD_2^2}{n_1+n_2-2}},$$

$$\text{p} = \frac{|M_1 - M_2|}{S}\sqrt{\frac{n_1 n_2}{n_1+n_2}}$$

X represents the data value, M refers to the average value between the data, S represents the pooled estimate of the standard deviation, n represents the number of data (Gardner and Altman, 1986).

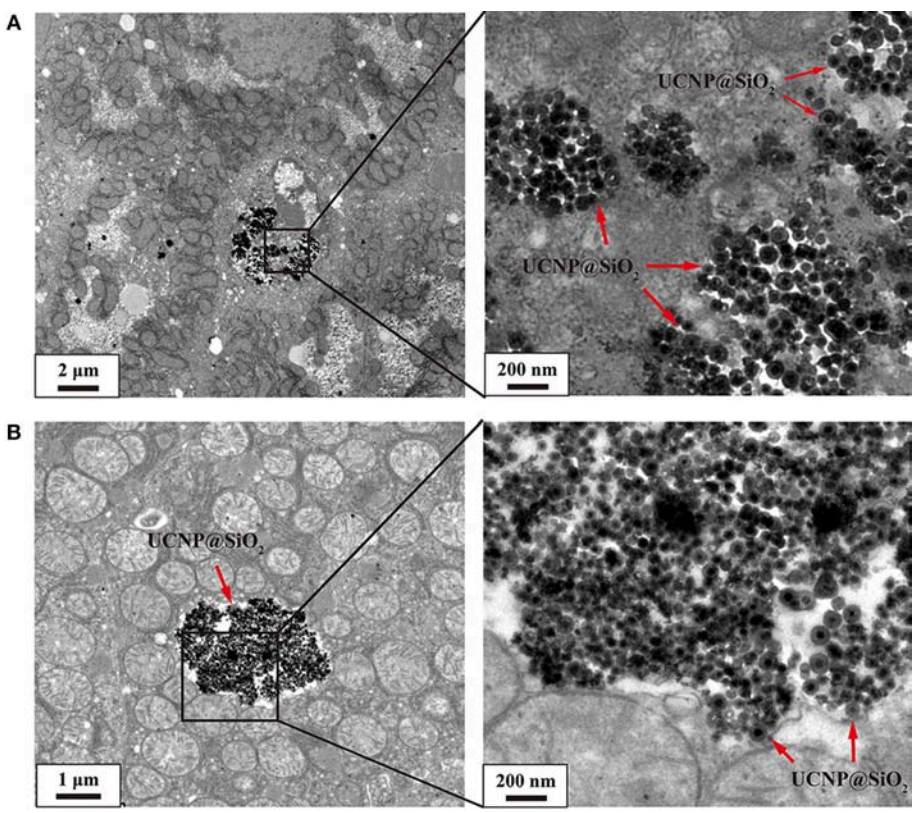

FIGURE 4 | (A) TEM image of 20 mg/kg $NaYF_4$:Yb,Er@SiO_2 intravenously treated mouse showing aggregations of these nanoparticles (red arrow) located outside of hepatocytes. **(B)** TEM image shows aggregations of $NaYF_4$:Yb,Er@SiO_2 nanoparticles (red arrow) in the cytoplasm. UCNP@SiO_2 denotes $NaYF_4$:Yb,Er@SiO_2.

RESULTS AND DISCUSSION

Characterization of $NaYF_4$:Yb,Er@SiO_2

We first characterized the morphology and size of $NaYF_4$:Yb,Er nanoparticles using a transmission electron microscope (TEM). As shown in **Figure 1A** and **Figure S1A**, uniform nanoparticles with an average diameter of around 32 nm were obtained. The obtained nanoparticles were confirmed to be single crystals with a hexagonal phase by high-resolution transmission electron microscopy (HRTEM) and X-ray powder diffraction (XRD) study (**Figure 1B** and **Figure S2**). The lattice distance of 0.517 nm corresponds to the *d* spacing for (100) plane of hexagonal $NaYF_4$. After coating with a silica layer on the surface of $NaYF_4$:Yb,Er nanoparticles, the size of the nanoparticles reached 49 nm (**Figure 1C** and **Figure S1B**). The results of dynamic light scattering (DLS) measurement show that the hydrodiameter of $NaYF_4$:Yb,Er@SiO_2 nanoparticles was around 60 nm (PDI = 0.23), confirming their mono-dispersion in aqueous solution (**Figure 1D**). The XRD pattern of $NaYF_4$:Yb/Er samples can also be indexed as a hexagonal phases of $NaYF_4$ (JCPDS file number 16-0334) (**Figure S1**). After silica coating, a broad diffraction peak at $2\theta = 22^\circ$ appeared, which can be ascribed to the peak of amorphous silica. In addition, the presence of the elements (Si, O, F, Y, Yb, Er) in the energy dispersive X-ray (EDX) spectrum also confirmed that silica shell was successfully coated onto the surface of $NaYF_4$:Yb/Er nanoparticles (**Figure S3**).

FT-IR spectra of oleic acid coated $NaYF_4$:Yb,Er and $NaYF_4$:Yb,Er@SiO_2 nanoparticles were shown in **Figure S4**. In the spectrum of oleic acid coated $NaYF_4$:Yb,Er, the peaks at 2,927 and 2,857 cm^{-1} are attributed to the asymmetric and symmetric stretching vibration of methylene (CH_2) in the long alkyl chain of oleic acid, and the 1,557 and 1,460 cm^{-1} bands are assigned to the asymmetric and symmetric stretching vibration of the carboxylic group (–COOH) in oleic acid. In the spectrum of $NaYF_4$:Yb,Er@SiO_2, the bands of Si–O–Si are located at 1,091 and 799 cm^{-1}, and the peaks at 953, 1,637, and 3,428 cm^{-1} are assigned to Si–OH, H_2O, and –OH.

Stability Assay of $NaYF_4$:Yb,Er@SiO_2 in Physiological Solution

In order to study the stability of $NaYF_4$:Yb,Er@SiO_2 under physiological conditions, the dissolved yttrium ions (Y^{3+}) of $NaYF_4$:Yb,Er@SiO_2 in FBS and SBF was monitored by ICP-MS. As shown in **Figure S5**, while the percentage of dissolved Y^{3+} in SBF was only around 0.1%, in FBS it quickly increased to around 1.2%. This result was consistent with the dissolution of Ag_2Se quantum dots, which was about 4–5% in FBS and <1% in SBF (Tang et al., 2016). Compared with naked UCNPs, these results imply that silica coating can suppress the leakage of lanthanide from nanoparticles, offering an excellent stability of $NaYF_4$:Yb,Er@SiO_2 under physiological conditions (Wang et al., 2012; Tian et al., 2015).

Stability of $NaYF_4$:Yb,Er@SiO_2 After *in vivo* Gastrointestinal Digestion

To examine the stability of $NaYF_4$:Yb,Er@SiO_2 after *in vivo* gastrointestinal digestion, we investigated the morphology and size of $NaYF_4$:Yb,Er@SiO_2 collected in feces excreted by mice orally administrated $NaYF_4$:Yb,Er@SiO_2 (100 mg/kg b.w.) by using TEM image. As shown in **Figure S6**, the morphology and size of $NaYF_4$:Yb,Er@SiO_2 was essentially not changed. This result suggest that SiO_2 coated UCNPs are also stable in the low gastric pH, which is consistent with the previous results of silica coated quantum dots (Loginova et al., 2012). This result also indicates that UCNPs with silica coating can be used to visualize the gastrointestinal tract *in vivo*.

Biodistribution of $NaYF_4$:Yb,Er@SiO_2

For the oral administration group, a relatively high concentration of Y^{3+} was detected in the gastrointestinal tract after 7 and 14 days consecutive oral exposure (**Figure 2**). In contrast, relatively low Y^{3+} concentrations were detected in several other major organs including liver, kidney, spleen, lung, heart, and bone. The concentration of yttrium in all organs

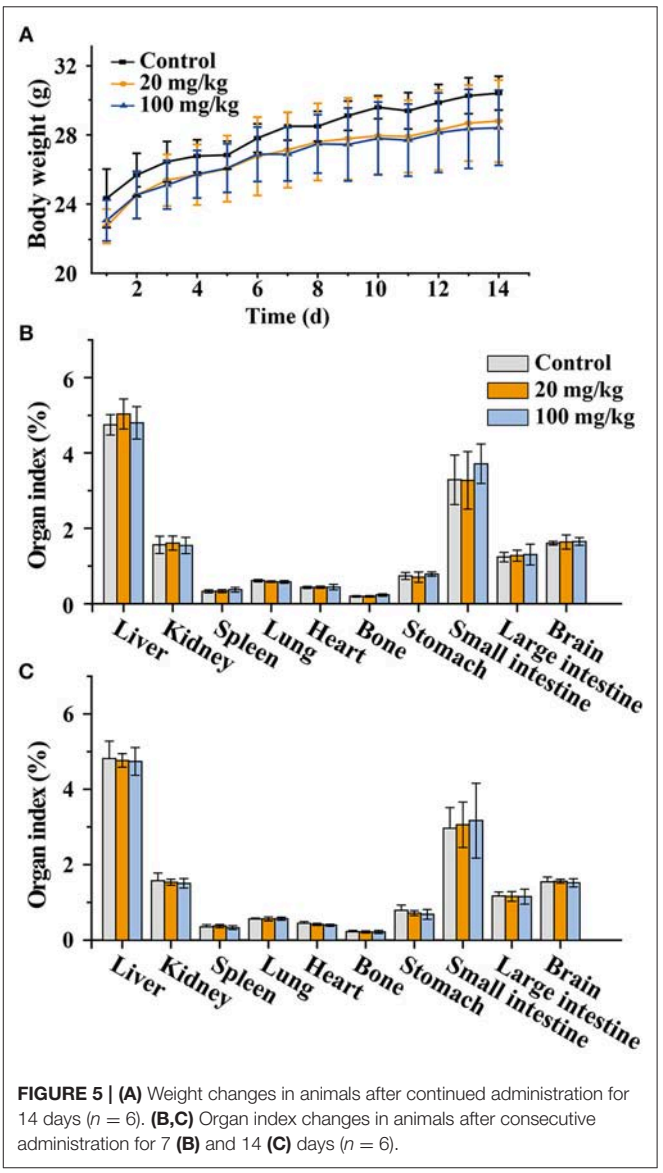

FIGURE 5 | (A) Weight changes in animals after continued administration for 14 days ($n = 6$). **(B,C)** Organ index changes in animals after consecutive administration for 7 **(B)** and 14 **(C)** days ($n = 6$).

increased to a relatively higher level at a high dose of 100 mg/kg compared with the dose of 20 mg/kg. Note that very little amount of Y^{3+} was released from $NaYF_4$:Yb,Er@SiO_2 as mentioned above, thus, it is reasonable to deduce that the Y^{3+} ion in the organs did not come from released ions of $NaYF_4$:Yb,Er@SiO_2. This may be attributed to the fact that after passing through the mouth and stomach, a small amount of $NaYF_4$:Yb,Er@SiO_2 are absorbed by the epithelium of the digestive tract and enter the blood, subsequently resulting in the accumulation of these particles in the organs.

Unlike oral administration, a very high concentration of Y^{3+} was mainly accumulated in the liver of mice after intravenous injection of these nanoparticles. With the lapse of time, the concentration of Y^{3+} decreased in liver and increased in spleen, indicating these nanoparticles follow a hepatic metabolic pathway (**Figure S7**). This result is also consistent with previous reports (Yu et al., 2017). In addition, we also examined the content of ytterbium ion (Yb^{3+}) in organs (**Figure S8**). We found that the change of Yb^{3+} content was the same as that of Y^{3+}, further indicating the good stability of those silica-coated upconversion nanoparticles *in vivo*.

Ultramicrostructure Observation of Peyer's Patch and Liver Tissue

To identify the potential uptake mechanism, we carefully examined the samples of small intestine after 14-day consecutive gavage of $NaYF_4$:Yb,Er@SiO_2 at a dose of 100 mg/kg by TEM image. It was reported that large size particles are probably absorbed by Peyer's patches through microfold (M) cells (Lundquist and Artursson, 2016). Peyer's patches are located in the mucous membrane lining of the intestine. They play a role in immunologic response (**Figure 3A**). Several studies have tested the translocation of nanoparticles in cell models (Yoshida et al., 2014; Walczak et al., 2015; Yao et al., 2015; Chen et al., 2016). However, there is no report to demonstrate this assumption *in vivo*. Here, we utilized TEM to visualize the location of the nanoparticles. As shown in **Figure 3B**, it can be clearly observed that nanoparticles are located in Peyer's patches in small intestine of mice. The size and shape of these nanoparticles were the

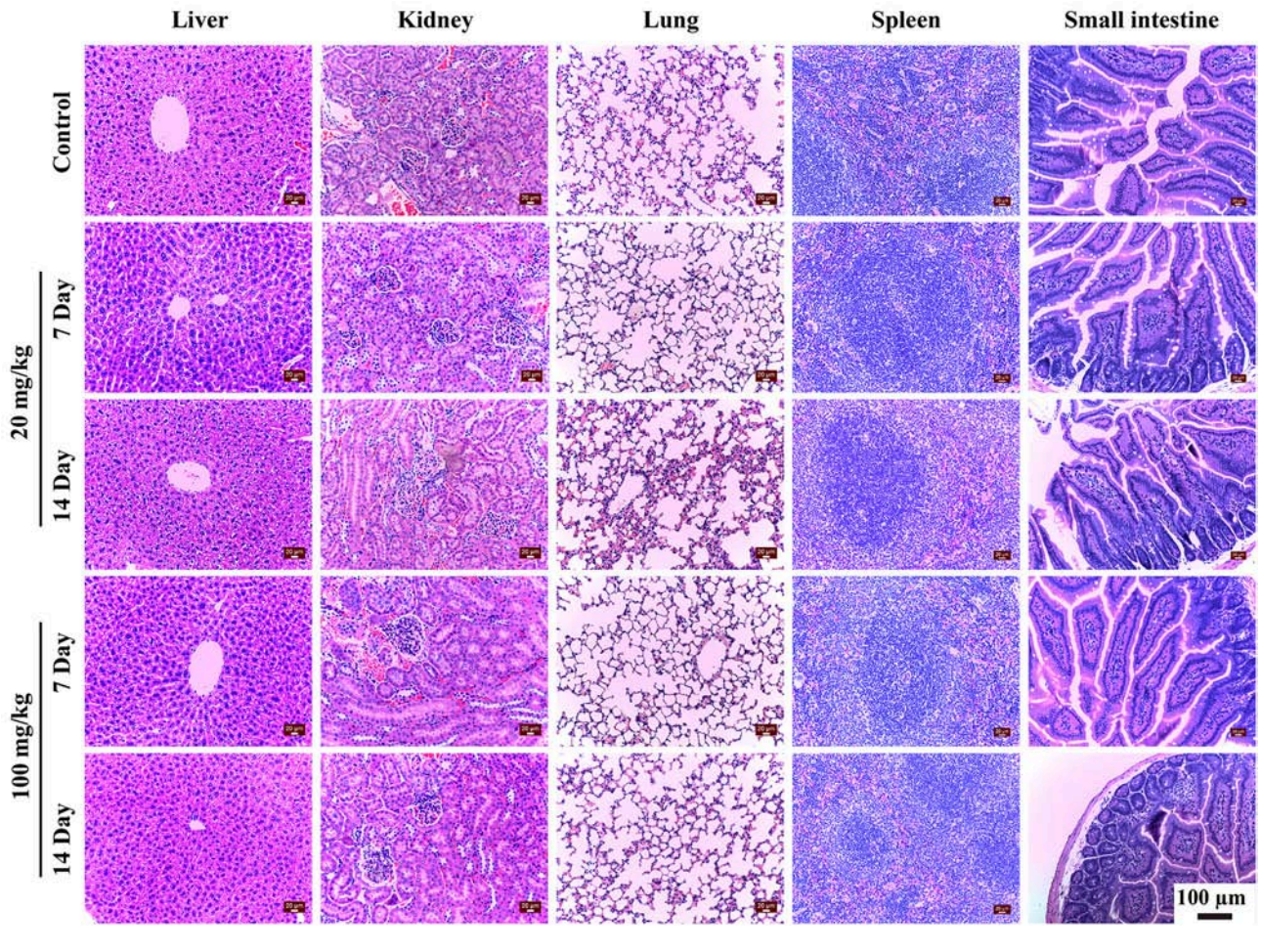

FIGURE 6 | Histopathological observation of liver, kidney, lung, spleen and small intestine of mice after 7 and 14 days' consecutive gavage administration of $NaYF_4$:Yb,Er@SiO_2 at different doses.

same as those we synthetized. This result confirms that the nanoparticles can cross small intestine through the uptake by Peyer's patches. However, due to the limited number of M cells in Peyer's patches, who compose <1 percent of the small intestine epithelial cell layer, we speculate that the bioavailability of these nanoparticles is low.

For intravenous administration, nanoparticles show a tendency to accumulate in the liver after entry into the bloodstream. As shown in **Figure 4**, a large amount of $NaYF_4$:Yb,Er@SiO_2 was observed in liver tissue at day 1 and 7 after mice were intravenously injected with these nanoparticles with dose of 20 mg/kg. This result suggests that the nanoparticles were internalized by hepatocytes.

In order to further evaluate the bioavailability of $NaYF_4$:Yb,Er@SiO_2 nanoparticles, we measured the contents of Y^{3+} in blood. For the oral administration group, the contents of Y^{3+} cannot be detected in blood after 7 and 14 days consecutive oral exposure (**Figure S9**). By comparison, relatively high concentration of Y^{3+} has been observed in blood after intravenous injection of these nanoparticles. This can be ascribed to the low bioavailability of $NaYF_4$:Yb/Er@SiO_2 nanoparticles via gavage administration route, which is consistent with the results of ultramicrostructure observation of Peyer's patch.

Body Weight and Organ Index of Mice

To evaluate the toxic effects of $NaYF_4$:Yb,Er@SiO_2 in mice, the body weights of mice were recorded every day during consecutive gavage administration. As shown in **Figure 5A**, death, obvious body weight decrease, and other signs of significant weakness were not observed in mice treated with $NaYF_4$:Yb,Er@SiO_2 over the 14-day period. The body weights of the $NaYF_4$:Yb,Er@SiO_2 treated groups increased in a pattern similar to that of the control group. Organ index is a key parameter in toxicity evaluation. Our results showed that there was no difference between the treatment group and the control group after gavage administration of $NaYF_4$:Yb,Er@SiO_2 either at a dose of 20 or 100 mg/kg (**Figures 5B,C**). These results demonstrate that $NaYF_4$:Yb,Er@SiO_2 nanoparticles have no effect on the body weight and organ index of mice.

Histological Analysis

Histological analysis of vital organs is important to evaluate whether $NaYF_4$:Yb,Er@SiO_2 could cause tissue damage, inflammation, or lesions. The analysis was performed on the liver, kidney, lung, spleen, and small intestine to investigate signs of the potential toxicity of $NaYF_4$:Yb,Er@SiO_2 at doses of 20 and

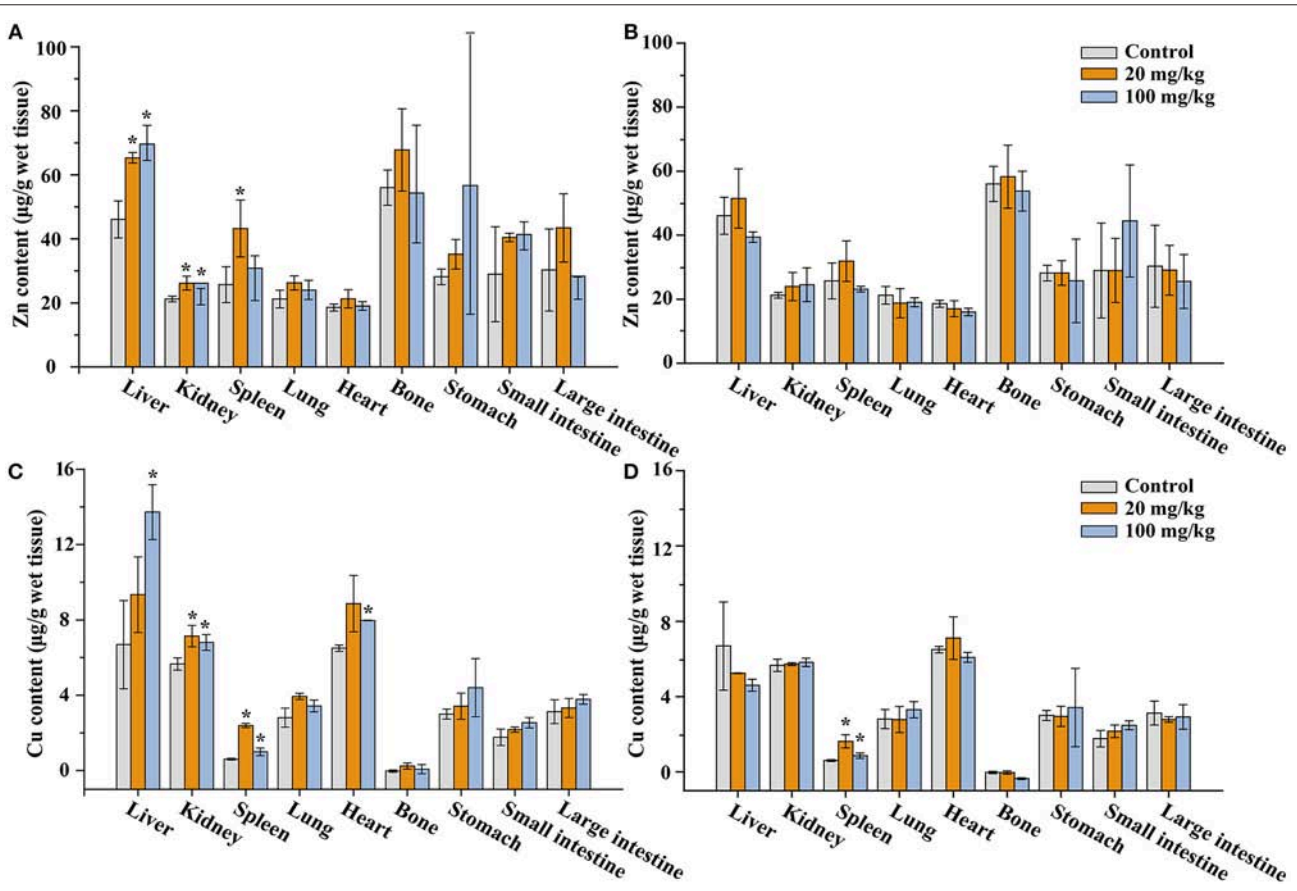

FIGURE 7 | Zinc **(A,B)** and copper **(C,D)** content in tissues of the mice after 7 **(A,C)** and 14 days' **(B,D)** consecutive gavage administration of $NaYF_4$:Yb,Er@SiO_2, respectively. *Significant difference vs. the corresponding control ($P < 0.05$, $n = 3$).

100 mg/kg for 7 and 14 days. As shown in **Figure 6**, hepatocytes were arranged in rows that radiate out from the central vein, and no inflammatory infiltrates of hepatocytes was observed in the liver samples (the first column). There was no change in the morphology of the renal corpuscles and renal tubules in the experimental and control groups (the second column). The glomerular structure was easy to distinguish and there was no sign of inflammatory infiltrates and necrosis. In addition, no pulmonary fibrosis or other abnormal phenomena was observed in the lung tissues for experimental groups (the third column). The white pulp and red pulp have normal appearance in spleen tissues (the forth column). The experimental and control mice showed normal intestine villi (the fifth column). Furthermore, the shape of the small intestine was normal, the tissue was intact, no inflammatory cells were infiltrated, and no bleeding was observed. In addition, we also conducted histological analysis on major organs (liver, kidney, lung, and spleen) after intravenous injection of $NaYF_4$:Yb,Er@SiO_2 nanoparticles into mice for 1 day. As shown in **Figure S10**, there was no obvious sign of abnormality in these major organs. Our results are also consistent with the previous study involving polyethyleneimine modified $NaYF_4$:Yb,Er nanoparticles (Yu et al., 2017). In all, these results indicate that there are no obvious difference of these organs between the experimental group and control group, and the organs of experimental group exhibited healthy structural features.

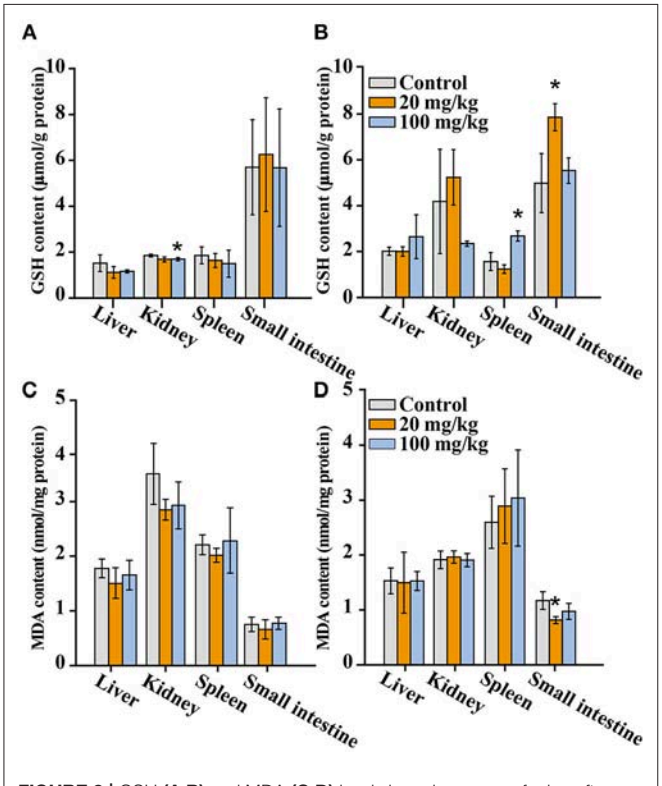

FIGURE 8 | GSH **(A,B)** and MDA **(C,D)** levels in main organs of mice after consecutive gavage administration of $NaYF_4$:Yb,Er@SiO_2 ($n = 4$). **(A,C)**: 7 days; **(B,D)**: 14 days. *Significant difference vs. the corresponding control ($P < 0.05$).

Effect of Gavage Exposure to $NaYF_4$:Yb,Er@SiO_2 on the Distribution of Zinc and Copper in Mice

The absorption of certain metal element may affect levels of essential metal elements in animals. Zinc plays a critical role in many biological functions including antioxidant defense, cell signaling, and gene expression. Copper is vital and essential to the proper functioning of organs and metabolic processes. Like all essential elements and nutrients, copper excess, or deficiency has adverse health effects.

To evaluate the influence of $NaYF_4$:Yb,Er@SiO_2 exposure, the contents of trace essential elements Zn and Cu in tissues in $NaYF_4$:Yb,Er@SiO_2-treated mice were measured by ICP-MS. Zinc levels in different organs of mice were shown in **Figures 7A,B**. After 7 days post-administration, we found that Zn concentrations significantly increase in spleen at doses of 20 mg/kg of $NaYF_4$:Yb,Er@SiO_2, and they significantly changed in liver, kidney at both doses of 20 and 100 mg/kg. However, the Zn level went back to the control level after 14-day consecutive oral exposure. In addition, copper contents in liver significantly increased at the dose of 100 mg/kg of $NaYF_4$:Yb,Er@SiO_2, while they significantly increased in kidneys, spleen and heart at both doses of 20 and 100 mg/kg $NaYF_4$:Yb,Er@SiO_2 (**Figure 7C**). Although the Cu level in spleen didn't go back to the control level, they reduced to the control level in liver, and kidney (**Figure 7D**). In addition, Zn level only significantly decreased in bone at day 1 after intravenously administration of $NaYF_4$:Yb,Er@SiO_2 at the dose of 20 mg/kg (**Figure S11A**). By contrast, Cu levels significantly increased in bone at day 1, and they significantly increased in liver, spleen, lung, heart, and stomach at day 7 (**Figure S11B**). We didn't observe the recovery in Cu level, maybe because the Cu level in mice need to take longer time to recover (i.e., 28 days) as selenium did in a previous report (Tang et al., 2016). Taken together, these results suggest that $NaYF_4$:Yb,Er@SiO_2 could slightly change the zinc and copper level of certain organs in mice. However, these changes can be recovered after a period of time.

Serum Biochemical Analyses

Serum biochemical analysis is usually used to determine whether the function of vital organs is damaged. Liver function parameters including alanine aminotransferase (ALT, IU/L), aspartate aminotransferase (AST, IU/L), alkaline phosphatase (ALP, IU/L) and kidney index blood urea nitrogen (BUN, mmol/L), and creatine (Crea mmol/L) were measured. Results showed that ALT, AST and ALP remain unchanged after consecutive administration for 7 and 14 days (**Table S2**). The BUN levels in nanoparticles treatment groups were significantly elevated at day 7, while they came back to the normal level at day 14. The Crea level in the 100 mg/kg $NaYF_4$:Yb,Er@SiO_2 group significantly declined compared with the control at day 14. In brief, $NaYF_4$:Yb,Er@SiO_2 nanoparticles induce slight

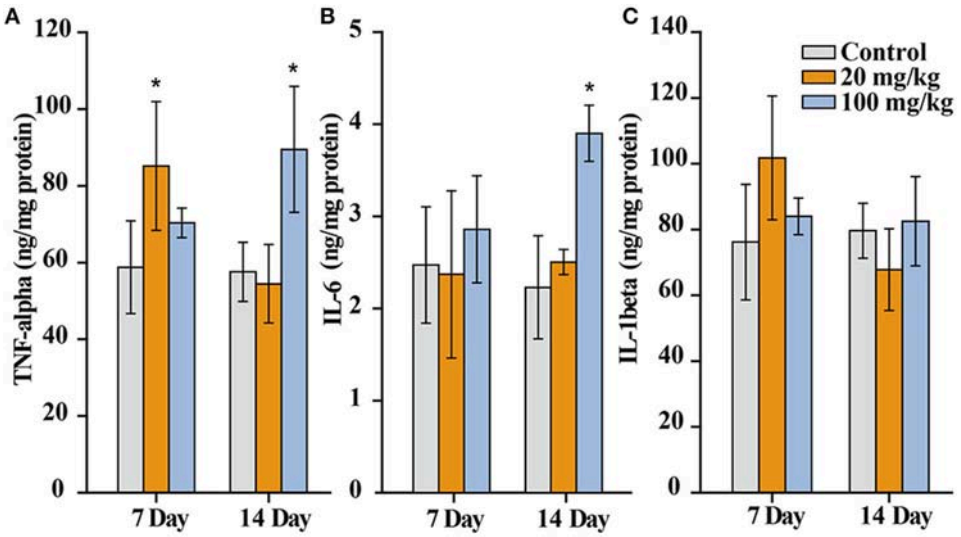

FIGURE 9 | TNF-α **(A)**, IL-6 **(B)**, and IL-1β **(C)** level in liver of mice after 7 and 14 days consecutive gavage administration of $NaYF_4$:Yb,Er@SiO_2 ($n = 5$). *Significant difference vs. the corresponding control ($P < 0.05$).

fluctuations in BUN and Crea levels after oral administration, but the levels remain in a normal range (Lu et al., 2010).

The oxidative stress is an important cause of injury or inflammation for certain organs. Therefore, we further measured the levels of glutathione (GSH) and malondialdehyde (MDA) in liver, kidneys, spleen, and small intestine. As shown in **Figure 8**, The GSH level was the highest in small intestine, reaching a value of 6 μmol/g protein, while the level in liver, kidneys, and spleen was about 2 μmol/g protein. The GSH levels in kidney (day 7), spleen and small intestine (day 14) of the 100 and 20 mg/kg $NaYF_4$:Yb,Er@SiO_2-treated group were significantly different from that of corresponding control, respectively. The MDA level in $NaYF_4$:Yb,Er@SiO_2-treated group did not show any difference with the control at day 7 after gavage administration. However, the MDA level exhibit significant difference in small intestine at day 14 with control after gavage administration of nanoparticles. In brief, it can be concluded that $NaYF_4$:Yb,Er@SiO_2 just induce slight fluctuations of GSH and MDA levels in certain organs.

Cytokines are secreted by inflammatory cells, which are involved in the immune response of the organism to foreign nanoparticles. This is the pathological basis of the occurrence and development of tissue injury. Particularly, tumor necrosis factor-alpha (TNF-alpha) is involved in inflammation and immune response. Interleukin-6 (IL-6) is involved in the pathophysiological processes of various inflammatory diseases. Interleukin-1 beta (IL-1beta) can stimulate other cytokines or inflammatory mediators, inducing the expression of immune molecules. Therefore, we detected the expression of TNF-alpha, IL-6, and IL-1beta in the liver to observe whether orally administrated $NaYF_4$:Yb,Er@SiO_2 could induce inflammation in the liver of mice. As shown in **Figure 9**, we found TNF-alpha and IL-6 are elevated in the $NaYF_4$:Yb,Er@SiO_2 (100 mg/kg) treated group compared with the control at day 14 after gavage administration, and significant difference of TNF-alpha only is observed in the 20 mg/kg treatment group at day 7. In addition, there was no difference of IL-1beta between the nanoparticles treated group and the control. Therefore, $NaYF_4$:Yb,Er@SiO_2 nanoparticles change the level of TNF-α and IL-6, while there is no influence to IL-1β after consecutive administration.

CONCLUSIONS

In this study, we systematically investigate the bioavailability, biodistribution, and toxicity of orally administered $NaYF_4$:Yb,Er@SiO_2 nanoparticles with an average diameter of 50 nm. Our results show that these nanoparticles can be absorbed by mice with oral administration and the intestinal absorption through Peyer's patch was confirmed by TEM measurement. In addition, we demonstrate that the nanoparticles with intravenous injection are trapped in hepatocytes. The biodistribution of $NaYF_4$:Yb,Er@SiO_2 is particularly dependent on the administration routes. Specifically, $NaYF_4$:Yb,Er@SiO_2 nanoparticles mainly accumulate in bone, stomach, and intestine by oral administration, while these nanoparticles mainly accumulate in liver and spleen by intravenous administration. Furthermore, our results suggest that there is no overt toxicity of $NaYF_4$:Yb,Er@SiO_2 in mice even after consecutive oral exposure for 14 days at a high dose of 100 mg/kg. Collectively, these results provide an important reference for the future medical and clinical applications of inorganic nanoparticles.

AUTHOR CONTRIBUTIONS

MZ, XG, D-MK, HT, and J-ZZ performed the experiments. HW, BG, and MC analyzed the data. QS and LS contributed to design

of the experiments and write the manuscript. All the authors discussed the results and revised the manuscript.

ACKNOWLEDGMENTS

We are thankful for financial support from the National Natural Science Foundation of China (No. 21701109, 21571125, and 31771105) and the National Basic Research Program of China (No. 2016YFA0201600).

SUPPLEMENTARY MATERIAL

The Supplementary Material for this article can be found online at: https://www.frontiersin.org/articles/10.3389/fchem.2019.00218/full#supplementary-material

REFERENCES

Abdul, J. R., and Zhang, Y. (2008). Biocompatibility of silica coated $NaYF_4$ upconversion fluorescent nanocrystals. *Biomaterials* 29, 4122–4128. doi: 10.1016/j.biomaterials.2008.07.012

Auzel, F. (2004). Upconversion and anti-stokes processes with f and d ions in solids. *Chem. Rev.* 35, 139–173. doi: 10.1021/cr020357g

Bettinelli, M., Carlos, L., and Liu, X. (2015). Lanthanide-doped upconversion nanoparticles. *Phys. Today* 68, 38–44. doi: 10.1063/pt.3.2913

Chen, B., Su, Q., Kong, W., Wang, Y., Shi, P., and Wang, F. (2018). Energy transfer-based biodetection using optical nanomaterials. *J. Mater. Chem. B* 6, 2924–2944. doi: 10.1039/c8tb00614h

Chen, G., Qiu, H., Prasad, P. N., and Chen, X. (2014). Up-conversion nanoparticles: design, nanochemistry, and applications in theranostics. *Chem. Rev.* 114, 5161–5214. doi: 10.1021/cr400425h

Chen, N., Song, Z. M., Tang, H., Xi, W. S., Cao, A., Liu, Y., et al. (2016). Toxicological effects of Caco-2 cells following short-term and long-term exposure to Ag nanoparticles. *Int. J. Mol. Sci.* 17:974. doi: 10.3390/ijms17060974

Cheng, L., Yang, K., Shao, M., Lu, X., and Liu, Z. (2011). *In vivo* pharmacokinetics, long-term biodistribution and toxicology study of functionalized upconversion nanoparticles in mice. *Nanomedicine* 6, 1327–1340. doi: 10.2217/NNM.11.56

Gao, J., Li, R., Wang, F., Liu, X., Zhang, J., Hu, L., et al. (2017). Determining the cytotoxicity of rare earth element nanoparticles in macrophages and the involvement of membrane damage. *Environ. Sci. Technol.* 51, 13938–13948. doi: 10.1021/acs.est.7b04231

Gardner, M. J., and Altman, D. G. (1986). Confidence intervals rather than P values: estimation rather than hypothesis testing. *Br. Med. J.* 292, 746–750. doi: 10.1136/bmj.292.6522.746

Gnach, A., Lipinski, T., Bednarkiewicz, A., Rybka, J., and Capobianco, J. A. (2015). Upconverting nanoparticles: assessing the toxicity. *Chem. Soc. Rev.* 44, 1561–1584. doi: 10.1039/c4cs00177j

Green, K., Huang, K., Pan, H., Han, G., and Lim, S. F. (2018). Optical temperature sensing with infrared excited upconversion nanoparticles. *Front. Chem.* 6:416. doi: 10.3389/fchem.2018.00416

Jalani, G., Tam, V., Vetrone, F., and Cerruti, M. (2018). Seeing, targeting and delivering with upconverting nanoparticles. *J. Am. Chem. Soc.* 140, 10923–10931. doi: 10.1021/jacs.8b03977

Jang, G. H., Hwang, M. P., Kim, S. Y., Jang, H. S., and Lee, K. H. (2014). A systematic *in-vivo* toxicity evaluation of nanophosphor particles via zebrafish models. *Biomaterials* 35, 440–449. doi: 10.1016/j.biomaterials.2013.09.054

Li, R., Ji, Z., Dong, J., Chang, C. H., Wang, X., Sun, B., et al. (2015a). Enhancing the imaging and biosafety of upconversion nanoparticles through phosphonate coating. *ACS Nano* 9, 3293–3306. doi: 10.1021/acsnano.5b00439

Li, X., Zhang, F., and Zhao, D. (2015b). Lab on upconversion nanoparticles: optical properties and applications engineering via designed nanostructure. *Chem. Soc. Rev.* 44, 1346–1378. doi: 10.1039/c4cs00163j

Li, Z., Yuan, H., Yuan, W., Su, Q., and Li, F. (2017). Upconversion nanoprobes for biodetections. *Coord. Chem. Rev.* 354, 155–168. doi: 10.1016/j.ccr.2017.06.025

Lim, S. F., Riehn, R., Ryu, W. S., Khanarian, N., Tung, C. K., Tank, D., et al. (2006). *In vivo* and scanning electron microscopy imaging of upconverting nanophosphors in *Caenorhabditis* elegans. *Nano Lett.* 6, 169–174. doi: 10.1021/nl0519175

Liu, J. N., Bu, W. B., and Shi, J. L. (2015). Silica coated upconversion nanoparticles: a versatile platform for the development of efficient theranostics. *Acc. Chem. Res.* 48, 1797–1805. doi: 10.1021/acs.accounts.5b00078

Liu, L., Wang, S., Zhao, B., Pei, P., Fan, Y., Li, X., et al. (2018). Er^{3+} sensitized 1530 nm to 1180 nm second near-infrared window upconversion nanocrystals for *in vivo* biosensing. *Angew. Chem. Int. Ed.* 57, 7518–7522. doi: 10.1002/anie.201802889

Liu, Y., Zhou, S., Zhuo, Z., Li, R., Chen, Z., Hong, M., et al. (2016). *In vitro* upconverting/downshifting luminescent detection of tumor markers based on Eu^{3+}-activated core-shell-shell lanthanide nanoprobes. *Chem. Sci.* 7, 5013–5019. doi: 10.1039/c6sc01195k

Liu, Z., Ju, E., Liu, J., Du, Y., Li, Z., Yuan, Q., et al. (2013). Direct visualization of gastrointestinal tract with lanthanide-doped $BaYbF_5$ upconversion nanoprobes. *Biomaterials* 34, 7444–7452. doi: 10.1016/j.biomaterials.2013.06.060

Liu, Z., Li, Z., Liu, J., Gu, S., Yuan, Q., Ren, J., et al. (2012). Long-circulating Er^{3+}-doped Yb_2O_3 up-conversion nanoparticle as an *in vivo* X-ray CT imaging contrast agent. *Biomaterials* 33, 6748–6757. doi: 10.1016/j.biomaterials.2012.06.033

Loginova, Y. F., Dezhurov, S. V., Zherdeva, V. V., Kazachkina, N. I., Wakstein, M. S., and Savitsky, A. P. (2012). Biodistribution and stability of CdSe core quantum dots in mouse digestive tract following per os administration: advantages of double polymer/silica coated nanocrystals. *Biochem. Bioph. Res. Commun.* 419, 54–59. doi: 10.1016/j.bbrc.2012.01.123

Lu, J., Liong, M., Li, Z., Zink, J. I., and Tamanoi, F. (2010). Biocompatibility, biodistribution, and drug-delivery efficiency of mesoporous silica nanoparticles for cancer therapy in animals. *Small* 6, 1794–1805. doi: 10.1002/smll.201000538

Lu, Y., Zhao, J., Zhang, R., Liu, Y., Liu, D., Goldys, E. M., et al. (2013). Tunable lifetime multiplexing using luminescent nanocrystals. *Nat. Photonics* 8, 32–36. doi: 10.1038/nphoton.2013.322

Lucky, S. S., Idris, N. M., Huang, K., Kim, J., Li, Z., Thong, P. S., et al. (2016). *In vivo* biocompatibility, biodistribution and therapeutic efficiency of titania coated upconversion nanoparticles for photodynamic therapy of solid oral cancers. *Theranostics* 6, 1844–1865. doi: 10.7150/thno.15088

Lundquist, P., and Artursson, P. (2016). Oral absorption of peptides and nanoparticles across the human intestine: opportunities, limitations and studies in human tissues. *Adv. Drug Delivery Rev.* 106, 256–276. doi: 10.1016/j.addr.2016.07.007

Ortgies, D. H., Tan, M., Ximendes, E. C., Del Rosal, B., Hu, J., Xu, L., et al. (2018). Lifetime-encoded infrared-emitting nanoparticles for *in vivo* multiplexed imaging. *ACS Nano* 12, 4362–4368. doi: 10.1021/acsnano.7b09189

Peng, J., Sun, Y., Liu, Q., Yang, Y., Zhou, J., Feng, W., et al. (2012). Upconversion nanoparticles dramatically promote plant growth without toxicity. *Nano Res.* 5, 770–782. doi: 10.1007/s12274-012-0261-y

Plohl, O., Kralj, S., Majaron, B., Frohlich, E., Ponikvar-Svet, M., Makovec, D., et al. (2017). Amphiphilic coatings for the protection of upconverting nanoparticles against dissolution in aqueous media. *Dalton Trans.* 46, 6975–6984. doi: 10.1039/c7dt00529f

Ramirez-Garcia, G., Gutierrez-Granados, S., Gallegos-Corona, M. A., Palma-Tirado, L., d'Orlye, F., Varenne, A., et al. (2017). Long-term toxicological effects of persistent luminescence nanoparticles after intravenous injection in mice. *Int. J. Pharmaceut.* 532, 686–695. doi: 10.1016/j.ijpharm.2017.07.015

Sedlmeiera, A., and Gorris, H. H. (2015). Surface modification and characterization of photon-upconverting nanoparticles for bioanalytical applications. *Chem. Soc. Rev.* 44, 1526–1560. doi: 10.1039/c4cs00186a

Su, Q., Feng, W., Yang, D., and Li, F. (2017). Resonance energy transfer in upconversion nanoplatforms for selective biodetection. *Acc. Chem. Res.* 50, 32–40. doi: 10.1021/acs.accounts.6b00382

Sun, S. K., Wang, H. F., and Yan, X. P. (2018). Engineering persistent luminescence nanoparticles for biological applications: from biosensing/bioimaging to theranostics. *Acc. Chem. Res.* 51, 1131–1143. doi: 10.1021/acs.accounts.7b00619

Tadashi, K., and Hiroaki, T. (2006). How useful is SBF in predicting *in vivo* bone bioactivity? *Biomaterials* 27, 2907–2915. doi: 10.1016/j.biomaterials.2006.01.017

Tang, H., Yang, S. T., Yang, Y. F., Ke, D. M., Liu, J. H., Chen, X., et al. (2016). Blood clearance, distribution, transformation, excretion, and toxicity of near-infrared quantum dots Ag_2Se in mice. *ACS Appl. Mater. Interfaces* 8, 17859–17869. doi: 10.1021/acsami.6b05057

Tian, J., Zeng, X., Xie, X., Han, S., Liew, O. W., Chen, Y. T., et al. (2015). Intracellular adenosine triphosphate deprivation through lanthanide-doped nanoparticles. *J. Am. Chem. Soc.* 137, 6550–6558. doi: 10.1021/jacs.5b00981

Tsai, Y. C., Vijayaraghavan, P., Chiang, W. H., Chen, H. H., Liu, T. I., Shen, M. Y., et al. (2018). Targeted delivery of functionalized upconversion nanoparticles for externally triggered photothermal/photodynamic therapies of brain glioblastoma. *Theranostics* 8, 1435–1448. doi: 10.7150/thno.22482

Walczak, A. P., Kramer, E., Hendriksen, P. J., Tromp, P., Helsper, J. P., van der Zande, M., et al. (2015). Translocation of differently sized and charged polystyrene nanoparticles in *in vitro* intestinal cell models of increasing complexity. *Nanotoxicology* 9, 453–461. doi: 10.3109/17435390.2014.944599

Wang, K., Ma, J., He, M., Gao, G., Xu, H., Sang, J., et al. (2013). Toxicity assessments of near-infrared upconversion luminescent LaF_3:Yb,Er in early development of zebrafish embryos. *Theranostics* 3, 258–266. doi: 10.7150/thno.5701

Wang, Y. F., Sun, L. D., Xiao, J. W., Feng, W., Zhou, J. C., Shen, J., et al. (2012). Rare-earth nanoparticles with enhanced upconversion emission and suppressed rare-earth-ion leakage. *Chemistry* 18, 5558–5564. doi: 10.1002/chem.201103485

Wozniak, A., Noculak, A., Gapinski, J., Kociolek, D., Boś-Liedke, A., Zalewski, T., et al. (2016). Cytotoxicity and imaging studies of β-$NaGdF_4$:$Yb^{3+}Er^{3+}$@PEG-Mo nanorods. *RSC Adv.* 6, 95633–95643. doi: 10.1039/c6ra20415e

Wu, X., Hu, P., Hu, S., Chen, Z., Yan, H., Tang, Z., et al. (2016). Upconversion nanoparticles for differential imaging of plant cells and detection of fluorescent dyes. *J. Rare Earth* 34, 208–220. doi: 10.1016/s1002-0721(16)60016-9

Wysokinska, E., Cichos, J., Ziolo, E., Bednarkiewicz, A., Strzadala, L., Karbowiak, M., et al. (2016). Cytotoxic interactions of bare and coated $NaGdF_4$:Yb^{3+}:Er^{3+} *in vivo* biodistribution imaging and toxicity of polyacrylic acid-coated upconversion nanophosphors. nanoparticles with macrophage and fibroblast cells. *Toxicol. In Vitro* 32, 16–25. doi: 10.1016/j.tiv.2015.11.021

Xiong, L., Yang, T., Yang, Y., Xu, C., and Li, F. (2010). Long-term*Biomaterials* 31, 7078–7085. doi: 10.1016/j.biomaterials.2010.05.065

Yang, D., Ma, P., Hou, Z., Cheng, Z., Li, C., and Lin, J. (2015). Current advances in lanthanide ion Ln^{3+}-based upconversion nanomaterials for drug delivery. *Chem. Soc. Rev.* 44, 1416–1448. doi: 10.1039/c4cs00155a

Yao, M., He, L., McClements, D. J., and Xiao, H. (2015). Uptake of gold nanoparticles by intestinal epithelial cells: impact of particle size on their absorption, accumulation, and toxicity. *J. Agr. Food Chem.* 63, 8044–8049. doi: 10.1021/acs.jafc.5b03242

Yoshida, T., Yoshioka, Y., Takahashi, H., Misato, K., Mori, T., Hirai, T., et al. (2014). Intestinal absorption and biological effects of orally administered amorphous silica particles. *Nanoscale Res. Lett.* 9, 532–532. doi: 10.1186/1556-276X-9-532

Yu, J., Yin, W., Peng, T., Chang, Y. N., Zu, Y., Li, J., et al. (2017). Biodistribution, excretion, and toxicity of polyethyleneimine modified $NaYF_4$:Yb,Er upconversion nanoparticles in mice via different administration routes. *Nanoscale* 9, 4497–4507. doi: 10.1039/c7nr00078b

Zhou, J. C., Yang, Z. L., Dong, W., Tang, R. J., Sun, L. D., and Yan, C. H. (2011). Bioimaging and toxicity assessments of near-infrared upconversion luminescent $NaYF_4$:Yb,Tm nanocrystals. *Biomaterials* 32, 9059–9067. doi: 10.1016/j.biomaterials.2011.08.038

Zhou, L., Wang, R., Yao, C., Li, X., Wang, C., Zhang, X., et al. (2015). Single-band upconversion nanoprobes for multiplexed simultaneous *in situ* molecular mapping of cancer biomarkers. *Nat. Commun.* 6:6938. doi: 10.1038/ncomms7938

Conflict of Interest Statement: The authors declare that the research was conducted in the absence of any commercial or financial relationships that could be construed as a potential conflict of interest.

Copyright © 2019 Zhou, Ge, Ke, Tang, Zhang, Calvaresi, Gao, Sun, Su and Wang. This is an open-access article distributed under the terms of the Creative Commons Attribution License (CC BY). The use, distribution or reproduction in other forums is permitted, provided the original author(s) and the copyright owner(s) are credited and that the original publication in this journal is cited, in accordance with accepted academic practice. No use, distribution or reproduction is permitted which does not comply with these terms.

frontiers in Chemistry

REVIEW
published: 14 May 2019
doi: 10.3389/fchem.2019.00335

Air-Stable Na_xTMO_2 Cathodes for Sodium Storage

Yi Zhang, Renyuan Zhang and Yunhui Huang*

Institute of New Energy for Vehicles, School of Materials Science and Engineering, Tongji University, Shanghai, China

Sodium-ion batteries are considered to be the most promising alternative to lithium-ion batteries for large-scale stationary energy storage applications due to the abundant sodium resource in the Earth' crust and as a result, relatively low cost. Sodium layered transition metal oxides (Na_xTMO_2) are proper Na-ion cathode materials because of low cost and high theoretical capacity. Currently most researchers focus on the improvement of electrochemical performance such as high rate capability and long cycling stability. However, for Na_xTMO_2, the structure stability against humid atmosphere is essentially important since most of them are instable in air, which is not favorable for practical application. Here we provide a comprehensive review of recent progresses on air-stable Na_xTMO_2 oxides. Several effective strategies are discussed, and further investigations on the air-stable cathodes are prospected.

Keywords: layered transition metal oxides, air-stable, cathode, sodium-ion battery, water insertion, H ion exchange

OPEN ACCESS

Edited by:
Fan Zhang,
Fudan University, China

Reviewed by:
Juchen Guo,
University of California, Riverside, United States
Jianping Yang,
Donghua University, China

****Correspondence:***
Renyuan Zhang
ryzhang@tongji.edu.cn

Specialty section:
This article was submitted to Nanoscience, a section of the journal Frontiers in Chemistry

Received: *17 February 2019*
Accepted: *25 April 2019*
Published: *14 May 2019*

Citation:
Zhang Y, Zhang R and Huang Y (2019) Air-Stable Na_xTMO_2 Cathodes for Sodium Storage. Front. Chem. 7:335. doi: 10.3389/fchem.2019.00335

INTRODUCTION

The growing demand for large-scale energy storage applications has driven the research interest into new energy storage systems with low cost. Although lithium-ion battery (LIB) can deliver high energy and power density, the limited resource and the rising cost of lithium may restrict their application in grid scale energy storage. Recently, sodium-ion battery (SIB), which owns a similar chemical storage mechanism to LIB, has been rapidly developed as a complementary technology. As the second lightest alkali metal, sodium resource is inexpensive and almost globally available. The common abundant sodium salt such as Na_2SO_4, NaCl, and Na_2CO_3 could be obtained from marine or mineral. In addition, copper foil can be replaced by cheaper aluminum foil for anode current collector since sodium has no reaction with aluminum. Therefore, SIB has received considerable attention as a promising alternative to LIB (Dunn et al., 2011; Yang et al., 2011, 2017; Palomares et al., 2013; Pan et al., 2013; Yabuuchi et al., 2014; Han et al., 2015; Kubota and Komaba, 2015; Kundu et al., 2015; Xiang et al., 2015; Hwang et al., 2017; Luo et al., 2017; Nayak et al., 2018; Zhu et al., 2019).

The SIB system consists of five parts: cathode, anode, membrane, electrolyte and current collector, which has the same structure as LIB. **Figure 1** shows typical configuration of a SIB coin cell, in which sodium layered transition metal oxide (Na_xTMO_2) and hard carbon are employed as cathode and anode, respectively. During the charge process, the Na^+ and e^- migrates to hard carbon anode with voltage increasing. During the discharge process, Na^+ and e^- return to Na_xTMO_2 cathode reversibly with voltage decreasing. The overall reaction can be described as:

$$Na_xTMO_2 + C \leftrightarrow TMO_2 + Na_xC \quad (1)$$

Numerous cathode materials such as polyanion compounds (Tripathi et al., 2013; Zhang Y. et al., 2016), layered transition metal (TM) oxides (Roger et al., 2007; Berthelot et al., 2011; Carlier et al., 2011) and Prussian blue or Metal-Organic compounds (Fang et al., 2017; Su et al., 2017;

Qian et al., 2018) have been applied as Na^+ host materials. Layered TM oxides show a high theoretical capacity among these cathode materials (Wang et al., 2018c). In addition, taking the preparation process and cost into consideration, the layered transition metal oxides are the optimal choice for practical application because they can be easily obtained by calcining the precursors in air. As a result, the layered transition metal oxides with general formula Na_xTMO_2 have attracted more and more attention since the first report by Delmas' group in the 1980s (Delmas et al., 1980, 1981).

Most of researches about Na_xTMO_2 focused on the improvement of electrochemical properties, such as: (i) eliminating Na^+ vacancy ordering to improve rate capability; (Wang et al., 2015, 2018a; Kang et al., 2018) (ii) suppressing phase transition or surface coating to achieve long cycling life; (Wang et al., 2016c; Wang P.-F. et al., 2017; You et al., 2017; Sathiya et al., 2018) (iii) exploring oxygen ion redox mechanism to achieve high energy density (Rozier et al., 2015; Kim et al., 2017; Bai et al., 2018; Maitra et al., 2018; Qiao et al., 2018; Rong et al., 2018), and so on. However, most Na_xTMO_2 materials are hygroscopic and air-instable, which limit their practical applications because huge cost will be spent on materials' storage and transportation (Blesa et al., 1993; Franger et al., 2000; Lu and Dahn, 2001b; Caballero et al., 2002; Monyoncho and Bissessur, 2013; Duffort et al., 2015; Kubota and Komaba, 2015; Boyd et al., 2018; You et al., 2018). So in recent years, the design and synthesis of air-stable Na_xTMO_2 materials have become a hot topic. In this review, we summarize the recent progress on air-stable Na_xTMO_2 materials from structure understanding to corresponding solutions, and at the same time we address the remaining problems and challenges for further development.

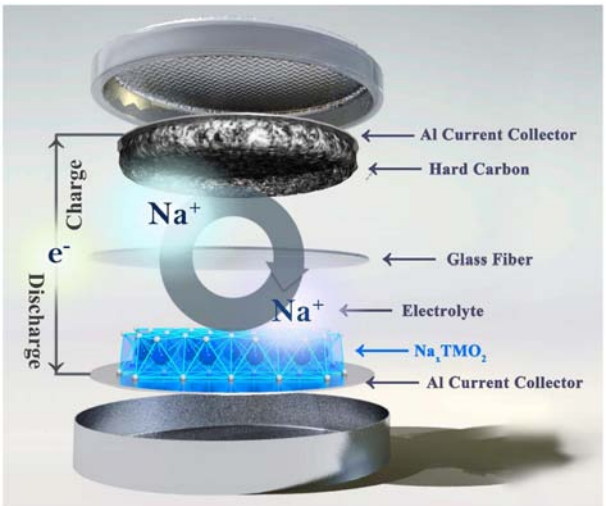

FIGURE 1 | The configuration of sodium-ion battery.

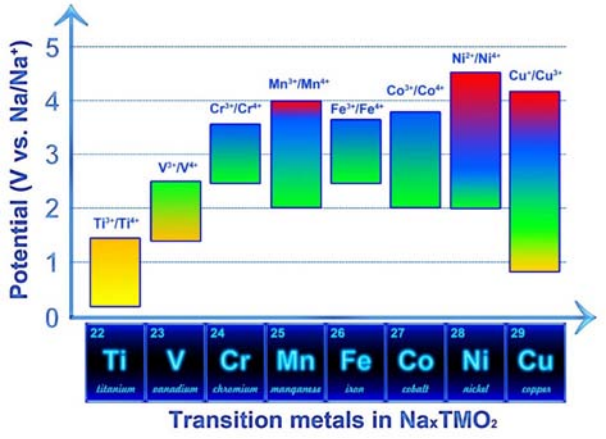

FIGURE 2 | The redox couples in Na_xTMO_2 compounds with their corresponding potential range.

STRUCTURE OF NA_XTMO_2

In Na_xTMO_2 compounds, TM layers are usually occupied by Ti, (Senguttuvan et al., 2011; Wu D. et al., 2015) V, (Hamani et al., 2011; Guignard et al., 2013; Wang et al., 2018d) Cr, (Braconnier et al., 1982; Yu et al., 2015) Mn, (Ma et al., 2011) Fe, (Blesa et al., 1993; Yabuuchi et al., 2012b) Co, (Berthelot et al., 2011; Rai et al., 2014) Ni, (Vassilaras et al., 2013; Wang et al., 2018b) Cu, (Ono et al., 2014; Jiang et al., 2018; Ono, 2018) a mixture of two (Saadoune et al., 1996; Yabuuchi et al., 2012a; Mortemard de Boisse et al., 2013; Gonzalo et al., 2014; Guo et al., 2014; Kalluri et al., 2014; Zhu et al., 2014, 2016; Chen et al., 2015; Jiang et al., 2015; Kang et al., 2015; Wang et al., 2015, 2016d; Bucher et al., 2016; Kee et al., 2016; Liu et al., 2016; Manikandan et al., 2017; Sabi et al., 2017; Song et al., 2017) or more elements (Lu and Dahn, 2001b; Buchholz et al., 2014; Li et al., 2014; Liu et al., 2015; Li Y. et al., 2015; Li Z.-Y. et al., 2015; Yue et al., 2015; Han et al., 2016a; Kang et al., 2016; Qi et al., 2016; Satyanarayana et al., 2016; Sun et al., 2016; Wang et al., 2016b; Zhang X.-H. et al., 2016; Wang L. et al., 2017; Zheng and Obrovac, 2017) The corresponding

TABLE 1 | Ionic radius of metal ions.

Metal ion	Coordination number	Ionic radius (Å)
Li^+	VI	0.76
Mg^{2+}	VI	0.72
Al^{3+}	VI	0.535
Ti^{4+}	VI	0.605
V^{5+}	VI	0.54
Cr^{3+}	VI	0.615
Mn^{4+}	VI	0.53
Fe^{3+}	VI	0.55(L); 0.645(H)*
Co^{3+}	VI	0.545(L); 0.61 (H)
Ni^{2+}	VI	0.69
Cu^{2+}	VI	0.73
Zn^{2+}	VI	0.74

**L means low spin while H means high spin.*

redox potential ranges of these TM are presented in **Figure 2**. Na_xTiO_2 compound is usually used as anode material due to its low redox potential range. $Na_x(Ni_yMn_{1-y})O_2$ compound has been thoroughly investigated as cathode material because of the relatively high redox potential and theoretical capacity. (Lu and Dahn, 2001a; Fielden and Obrovac, 2015) V, Cr and Co substitution also shows a proper potential range for cathode but it may not suitable for practical application since V, Cr, and Co are expensive and toxic. Although Fe and Cu are almost electrochemical inactive when used as $LiTMO_2$ for LIB system, (Ado et al., 1997; Arachi et al., 2012) these two elements are proven to be highly active in Na_xTMO_2 as Na-ion host. (Yabuuchi et al., 2012a; Ono, 2018) Since Ni and Co resources are mostly consumed by LIB system, the abundant Fe and Cu resources with low price are suitable for Na_xTMO_2 as sodium storage materials. (Li Y. et al., 2015; Mu et al., 2015) In addition, electrochemical inactive metal ions such as Li^+, Mg^{2+} and Zn^{2+} could also be introduced into the TM layer for the improvement of electrochemical performance (Xu et al., 2014; Wu X. et al., 2015; Wang et al., 2016c). **Table 1** lists the most common metal ions for the construction of TM layers and their corresponding ionic radii with coordination number of six (Shannon, 1976). Cations with similar ionic radius can partially substitute each other to form solid solutions, and hence various Na_xTMO_2 compounds could be designed by choosing two or more proper metal ions for the TM layer to improve electrochemical performance.ta

The crystal structure of Na_xTMO_2 can be usually classified into two types, P2 and O3 (**Figure 3**). The symbols of "P" and "O" are from the abbreviation of "prismatic" and "octahedral," "2" and "3" represents the stacking arrangement per unit of O ions. For P2 type structure (usually $x = 2/3$), Na ions occupy two different prismatic sites, one shares faces between TMO_6 octahedra called Na_f sites and another shares edges between TMO_6 octahedra called Na_e sites. TM ions are surrounded by oxygen frameworks with a stacking mode of ABBA. For O3 structure (usually x = 1), all Na ions share one edge and one face with TMO_6 octahedra. The oxygen frameworks are arranged in ABCABC pattern (Delmas et al., 1980, 1981; Shu and Chou, 2008; Morris et al., 2009; Toumar et al., 2015; Zheng C. et al., 2017).

Influence of Air on Na_xTMO_2

So far, many researches have proven that the water and CO_2 molecules from air can react with Na_xTMO_2, bringing

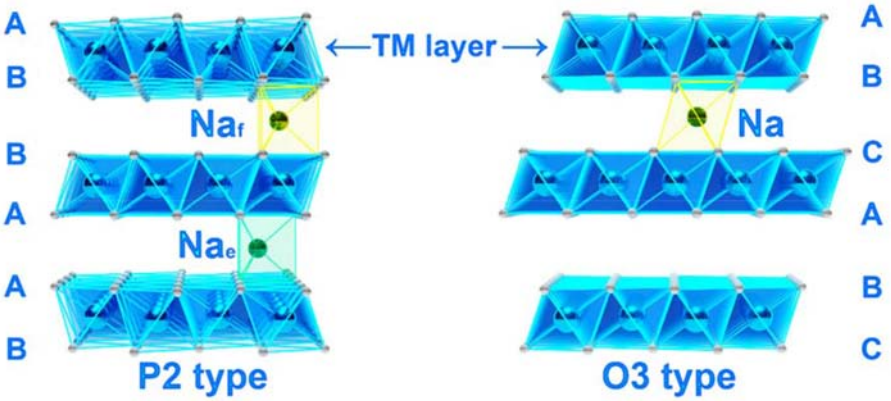

FIGURE 3 | The schematic of the crystal structure for layered sodium TM oxides, left is P2 type and right is O_3 type.

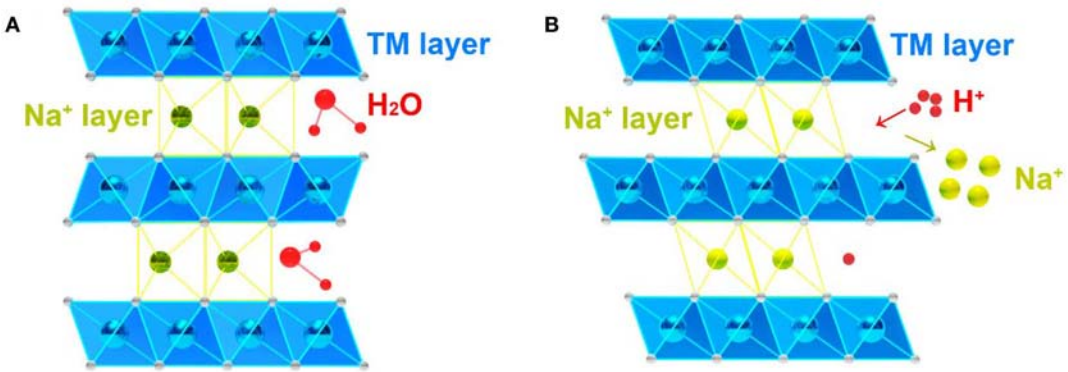

FIGURE 4 | (A) Insertion of water molecules in Na^+ layer, **(B)** Ion exchange between H^+ and Na^+ in Na^+ layer.

negative influence on its morphology, crystal structure and electrochemical performance. The water molecules are easy to react with air-instable Na_xTMO_2 by inserting into the Na layer (Le Goff et al., 1993; Paulsen and Dahn, 1999; Franger et al., 2000; Lu and Dahn, 2001b; Caballero et al., 2002; Duffort et al., 2015; Boyd et al., 2018) or exchanging Na^+ with H^+, (Blesa et al., 1993; Monyoncho and Bissessur, 2013; Kubota and Komaba, 2015; Han et al., 2016b; Yao et al., 2017) leading to the expansion of interlayer spacing and the formation of impure phase (**Figure 4**). While CO_2 can transform to CO_3^{2-} on the surface of Na_xTMO_2 (Duffort et al., 2015; You et al., 2018). These air exposed Na_xTMO_2 usually show serious capacity decay and large polarization because of: (i) the side reaction between water and electrolyte (Kawamura et al., 2006; Lux et al., 2012; Han et al., 2016b); (ii) the active-materials' surface dissolution triggered by the acid attack of proton, which is released by water molecules (Blyr et al., 1998; Thackeray et al., 1998; Benedek and van de Walle, 2008); (iii) capacity and electronic conductivity decrease caused by inactive Na_2CO_3 layer (Duffort et al., 2015; You et al., 2018). Therefore, the air-instable Na_xTMO_2 cannot maintain its original crystal structure and electrochemical property under moisture atmosphere condition.

Reaction Mechanisms of Water on Na_xTMO_2

Water molecules can insert into Na layer to form a $Na_xTMO_2{\cdot}yH_2O$ hydrate phase, which usually occurs in P2 type structure (Le Goff et al., 1993; Franger et al., 2000; Lu and Dahn, 2001b; Caballero et al., 2002; Duffort et al.,

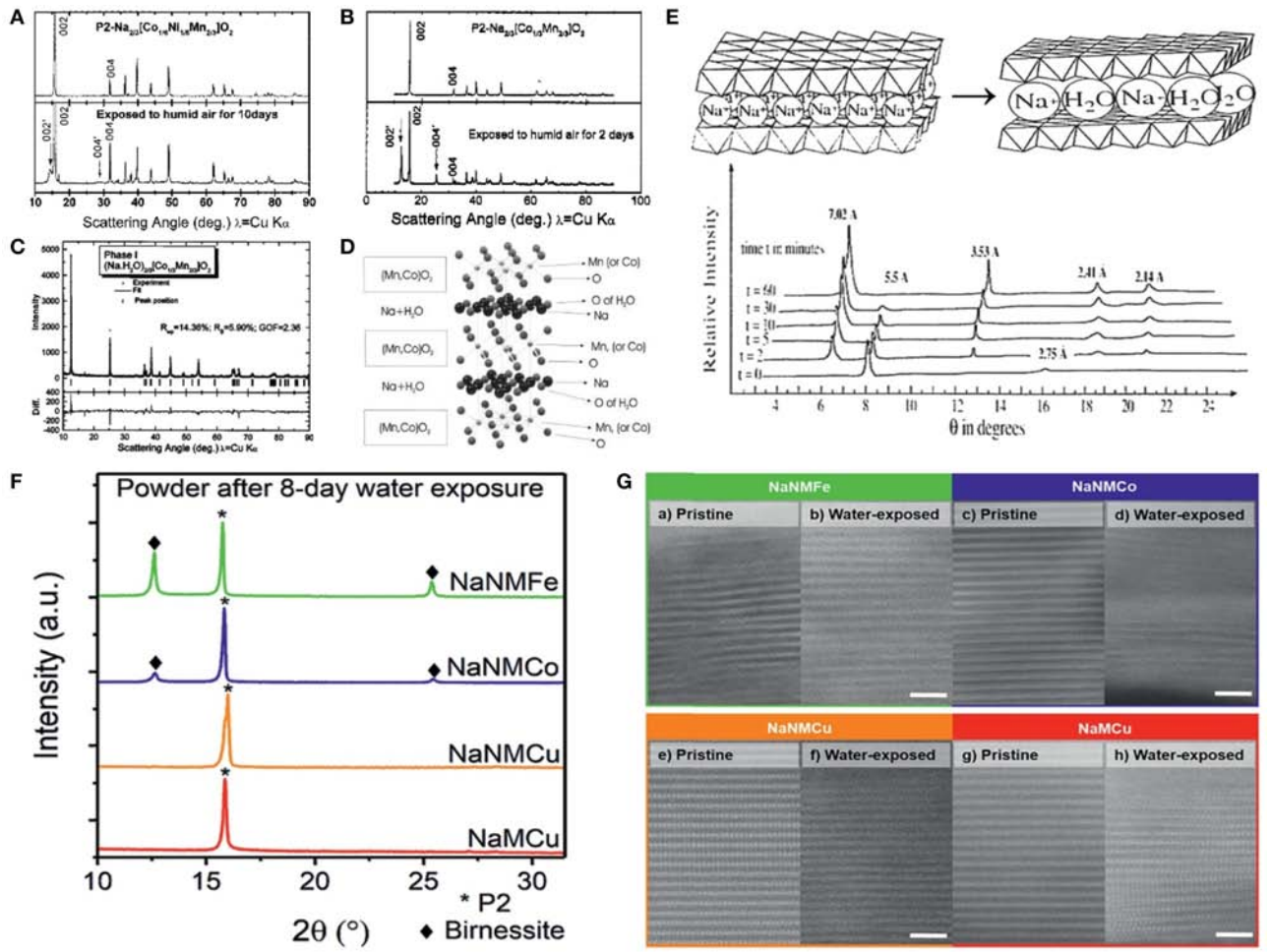

FIGURE 5 | (A) XRD patterns of pristine and air-exposed $Na_{2/3}Co_{1/6}Ni_{1/6}Mn_{2/3}O_2$ samples, **(B)** XRD patterns of pristine and air-exposed $Na_{2/3}Co_{1/3}Mn_{2/3}O_2$ samples, **(C)** Rietveld refinement of $(Na{\cdot}H_2O)_{2/3}Co_{1/3}Mn_{2/3}O_2$, **(D)** Crystal structure of $(Na{\cdot}H_2O)_{2/3}Co_{1/3}Mn_{2/3}O_2$. Reproduced with permission (Lu and Dahn, 2001b). Copyright 2001, American Chemical Society. **(E)** Water molecules insert into the Na layer of $Na_{0.7}MnO_2$ and the change of XRD patterns with the increasing time of water soaking. Reproduced with permission (Franger et al., 2000). Copyright 2000, The Electrochemical Society. **(F)** XRD patterns of P2-$Na_{0.62}Ni_{0.22}Mn_{0.66}Fe_{0.1}O_2$ (NaNMFe), P2-$Na_{0.61}Ni_{0.22}Mn_{0.66}Co_{0.1}O_2$ (NaNMCo), P2-$Na_{0.64}Ni_{0.22}Mn_{0.66}Cu_{0.11}O_2$ (NaNMCu) and P2-$Na_{0.64}Mn_{0.62}Cu_{0.31}O_2$ (NaMCu) samples after water soaking, **(G)** STEM images of pristine and water soaked NaNMFe, NaNMCo, NaNMCu and NaMCu samples. Reproduced with permission (Boyd et al., 2018). Copyright 2018, Royal Society of Chemistry.

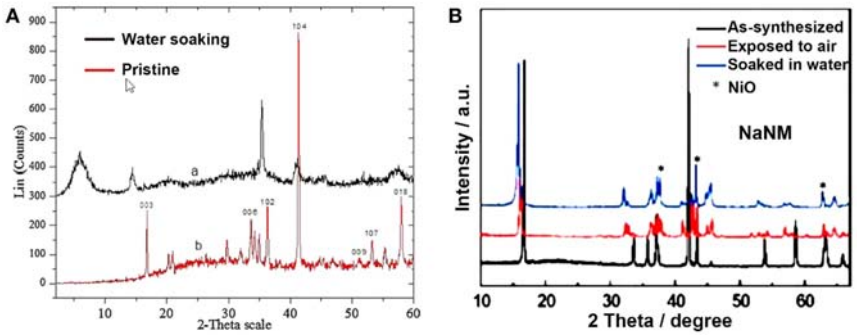

FIGURE 6 | (A) XRD patterns of pristine and water soaked $NaFeO_2$ samples. Reproduced with permission (Monyoncho and Bissessur, 2013). Copyright 2013, Elsevier. **(B)** XRD patterns of pristine, air exposed and water soaked $NaNi_{0.5}Mn_{0.5}O_2$ samples. Reproduced with permission (Yao et al., 2017). Copyright 2017, American Chemical Society.

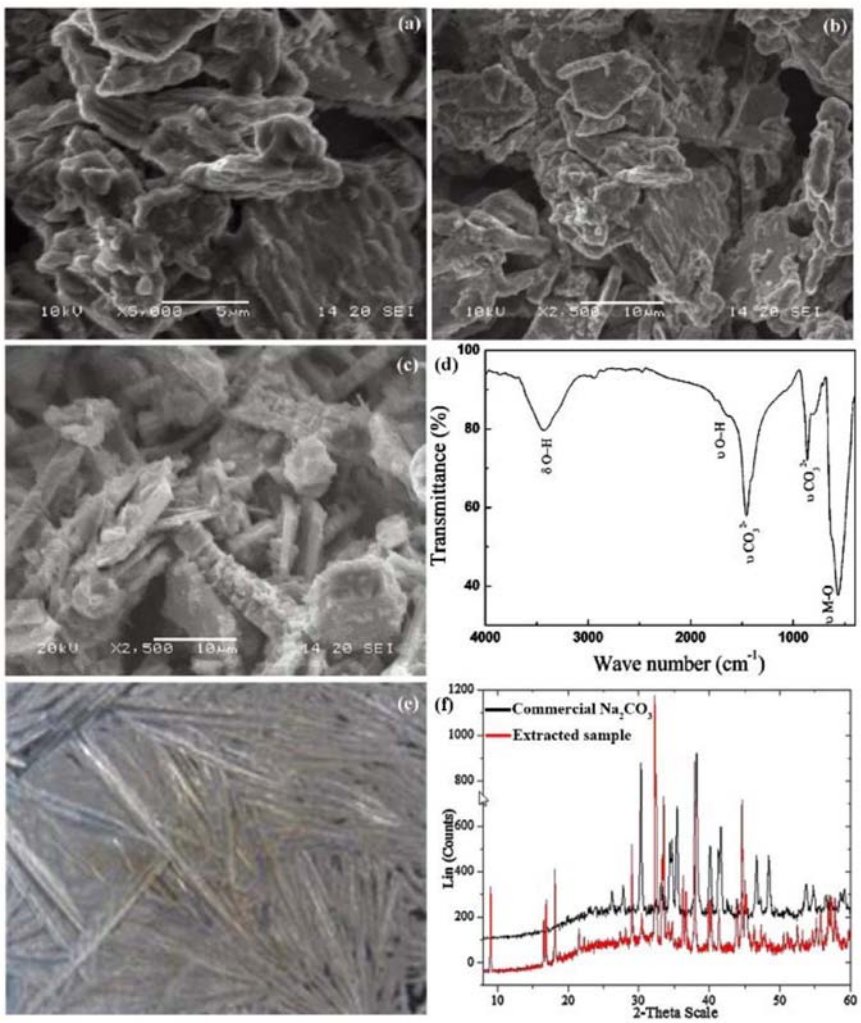

FIGURE 7 | SEM images of **(a)** pristine $NaNi_{1/3}Mn_{1/3}Co_{1/3}O_2$, **(b)** $NaNi_{1/3}Mn_{1/3}Co_{1/3}O_2$ after 15 days air-exposure, **(c)** $NaNi_{1/3}Mn_{1/3}Co_{1/3}O_2$ after 30 days air-exposure. **(d)** Infrared spectrum of $NaNi_{1/3}Mn_{1/3}Co_{1/3}O_2$ after 30 days air-exposure. Reproduced with permission (Sathiya et al., 2012). Copyright 2012, American Chemical Society. **(e)** SEM image of extracted sample, the sample is prepared by drying the aqueous solution of water-$NaFeO_2$ mixture, **(f)** XRD patterns of the extracted sample and commercial Na_2CO_3. Reproduced with permission (Monyoncho and Bissessur, 2013). Copyright 2013, Elsevier.

2015; Boyd et al., 2018). In 2001, Lu et al. (Lu and Dahn, 2001b) studied the water insertion reaction mechanism for the first time in P2-$Na_{2/3}Co_xNi_{1/3-x}Mn_{2/3}O_2$ compound ($x = 1/6$ or $1/3$). Compared with the XRD patterns of pristine $Na_{2/3}Co_xNi_{1/3-x}Mn_{2/3}O_2$, two new peaks around 14° and 28° were observed after exposing $Na_{2/3}Co_xNi_{1/3-x}Mn_{2/3}O_2$ samples in humid air environment (**Figures 5A,B**). These two peaks were assigned as hydrate phase due to the insertion of water molecules in Na layers. Rietveld refinement of hydrate $Na_{2/3}Co_{1/3}Mn_{2/3}O_2{\cdot}yH_2O$ indicated that the ratio of water/Na is close to 1:1 and the oxygen atoms from water was in the 2c site of the crystal structure (**Figures 5C,D**). Franger et al. (Franger et al., 2000) investigated the influence of water soaking on α-$Na_{0.7}MnO_2$. With the increasing of water soaking time, the two peaks around 8° and 16° were vanished and four new peaks around 6.5°, 13°, 19° and 21° appeared gradually. The α-$Na_{0.7}MnO_2$ was totally transformed to $Na_{0.45}MnO_2{\cdot}0.6H_2O$ after 60 min of water soaking treatment (**Figure 5E**). In 2018, Boyd et al. compared the air-stability of P2-$Na_{0.62}Ni_{0.22}Mn_{0.66}Fe_{0.1}O_2$ (NaNMFe), P2-$Na_{0.61}Ni_{0.22}Mn_{0.66}Co_{0.1}O_2$ (NaNMCo), P2-$Na_{0.64}Ni_{0.22}Mn_{0.66}Cu_{0.11}O_2$ (NaNMCu) and P2-$Na_{0.64}Mn_{0.62}Cu_{0.31}O_2$ (NaMCu) samples. After air-exposure treatment of these four samples for 8 days, the XRD patterns of NaNMCu and NaMCu samples remained unchanged, while two new peaks around 12.5° and 25° appeared in the patterns of NaNMFe and NaNMCo samples, indicating that water can insert in the interlayer spacing of NaNMFe and NaNMCo samples (**Figure 5F**). From the STEM images of these four samples before and after air-exposure, an obvious extension in interlayer spacing could be seen after air-exposure, proving the insertion of water molecules in the interlayer spacing (**Figure 5G**). Although water molecules can insert into the interlayer spacing of P2-Na_xTMO_2 to form a P2-$Na_xTMO_2{\cdot}yH_2O$ hydrate phase, Na_xTMO_2 phase can be regenerated by heat treatment at 200 °C to remove the water molecules (Lu and Dahn, 2001b).

For most O3-type $NaTMO_2$, water molecules can release H^+ to exchange the Na^+, (Blesa et al., 1993; Monyoncho and Bissessur, 2013; Kubota and Komaba, 2015; Han et al., 2016b; Yao et al., 2017) which could be regarded as hydrolysis reaction:

$$NaTMO_2 + xH_2O \rightarrow Na_{1-x}H_xTMO_2 + NaOH \quad (2)$$

Specially, if the TM layers contain a certain amount of Ni^{2+} ions, NiO would be emerged during the air exposure treatment:

$$NaNi_yTM_{1-y}O_2 + xH_2O \rightarrow Na_{1-x}H_xNi_{y-z}TM_{1-y}O_{2-z} + xNaOH + zNiO \quad (3)$$

This hydrolysis phenomenon has been confirmed in $NaNi_{0.5}Mn_{0.5}O_2$, $NaNi_{0.7}Mn_{0.15}Co_{0.15}O_2$ and $NaFeO_2$ compounds (Blesa et al., 1993; Monyoncho and Bissessur, 2013; Kubota and Komaba, 2015; You et al., 2018). A simple way to verify this hydrolysis reaction is to analyze the change of pH value after soaking $NaTMO_2$ in deionized water due to the release of NaOH (Blesa et al., 1993). In 2013, Monyoncho and Bissessur reported that the pH of aqueous solution was higher than 12 after mixing O3-$NaFeO_2$ sample with deionized water (Monyoncho and Bissessur, 2013). In addition, compared with the XRD patterns of pristine $NaFeO_2$ sample, the 003 peak of hydrolysis $Na_{1-x}H_xFeO_2$ sample became broader and shifted to low angle (**Figure 6A**), indicating the formation of a disordered crystal structure. Wang et al. investigated the hydrolysis reaction of O3-$NaNi_{0.5}Mn_{0.5}O_2$ sample by testing the temperature after water soaking because this reaction can release heats (Yao et al., 2017). After $NaNi_{0.5}Mn_{0.5}O_2$ was added into water, the temperature of the water was increased from 24.4 to 30.8°C. In contrast to the XRD pattern of as-synthesized sample, the 003 and 006 peaks of water soaked $NaNi_{0.5}Mn_{0.5}O_2$ shifted to low angle with the generation of NiO impurity phase (**Figure 6B**). Importantly, unlike P2 type, the hydrolysis reaction between O3 type $NaTMO_2$ and water is irreversible.

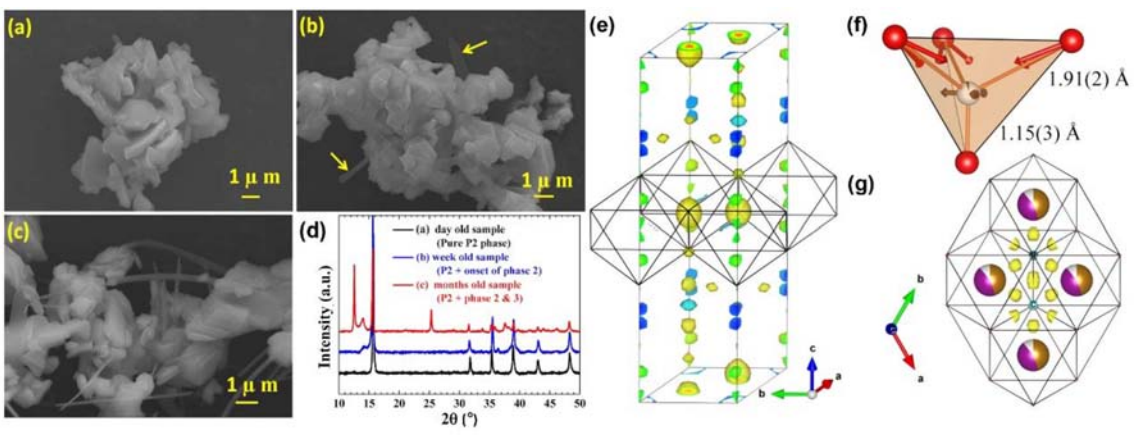

FIGURE 8 | (a) SEM images of $Na_{0.67}Mn_{0.5}Fe_{0.5}O_2$ after 1 day air-exposure, **(b)** $Na_{0.67}Mn_{0.5}Fe_{0.5}O_2$ after a couple of weeks' air-exposure, **(c)** $Na_{0.67}Mn_{0.5}Fe_{0.5}O_2$ after a couple of months' air-exposure, **(d)** XRD patterns of $Na_{0.67}Mn_{0.5}Fe_{0.5}O_2$ samples under different air-exposure time, **(e)** Nuclear Fourier difference map of $Na_{0.67}Mn_{0.5}Fe_{0.5}O_2$, **(f)** The local environment of CO, **(g)** The nuclear density around the carbon element position. Reproduced with permission (Duffort et al., 2015). Copyright 2015, American Chemical Society.

Reaction Mechanisms of CO_2 on Na_xTMO_2

As mentioned above, NaOH is generated on the surface of O3 type Na_xTMO_2 during the air exposure process, then CO_2 can further react with NaOH to form Na_2CO_3 (Sathiya et al., 2012; Monyoncho and Bissessur, 2013; You et al., 2018). This reaction can be described as:

$$NaTMO_2 + xH_2O + CO_2 \rightarrow Na_{1-x}H_xTMO_2 + Na_2CO_3 \quad (4)$$

Sathiya et al. (2012) proved the formation of Na_2CO_3 on the surface of $NaNi_{1/3}Mn_{1/3}Co_{1/3}O_2$ particles. Compared to the pristine sample (**Figure 7a**), the surface showed no obvious change after 15 days air-exposure (**Figure 7b**) but became quite rough after 30 days air-exposure (**Figure 7c**). IR spectrum revealed the bands of CO_3^{2-} at 1,450 and 863 cm^{-1}, suggesting the existence of sodium carbonates on $NaNi_{1/3}Mn_{1/3}Co_{1/3}O_2$ particles' surface (**Figure 7d**). Monyoncho and Bissessur (2013) extracted the aqueous solution from the mixture of $NaFeO_2$ and water (**Figure 7e**). The XRD pattern of extracted sample matched very well to commercial Na_2CO_3, proving the reaction of CO_2 and $NaFeO_2$ compounds (**Figure 7f**).

After the formation of Na_2CO_3 on the surface, the CO_3^{2-} can even be inserted into the TM layer, forming a "CO_4" tetrahedron. Duffort et al. elucidated the mechanism of CO_3^{2-} insertion in $Na_{0.67}Mn_{0.5}Fe_{0.5}O_2$ crystal (Duffort et al., 2015). With increasing the time of air exposure, ribbon-like particles start to appear and grow longer gradually

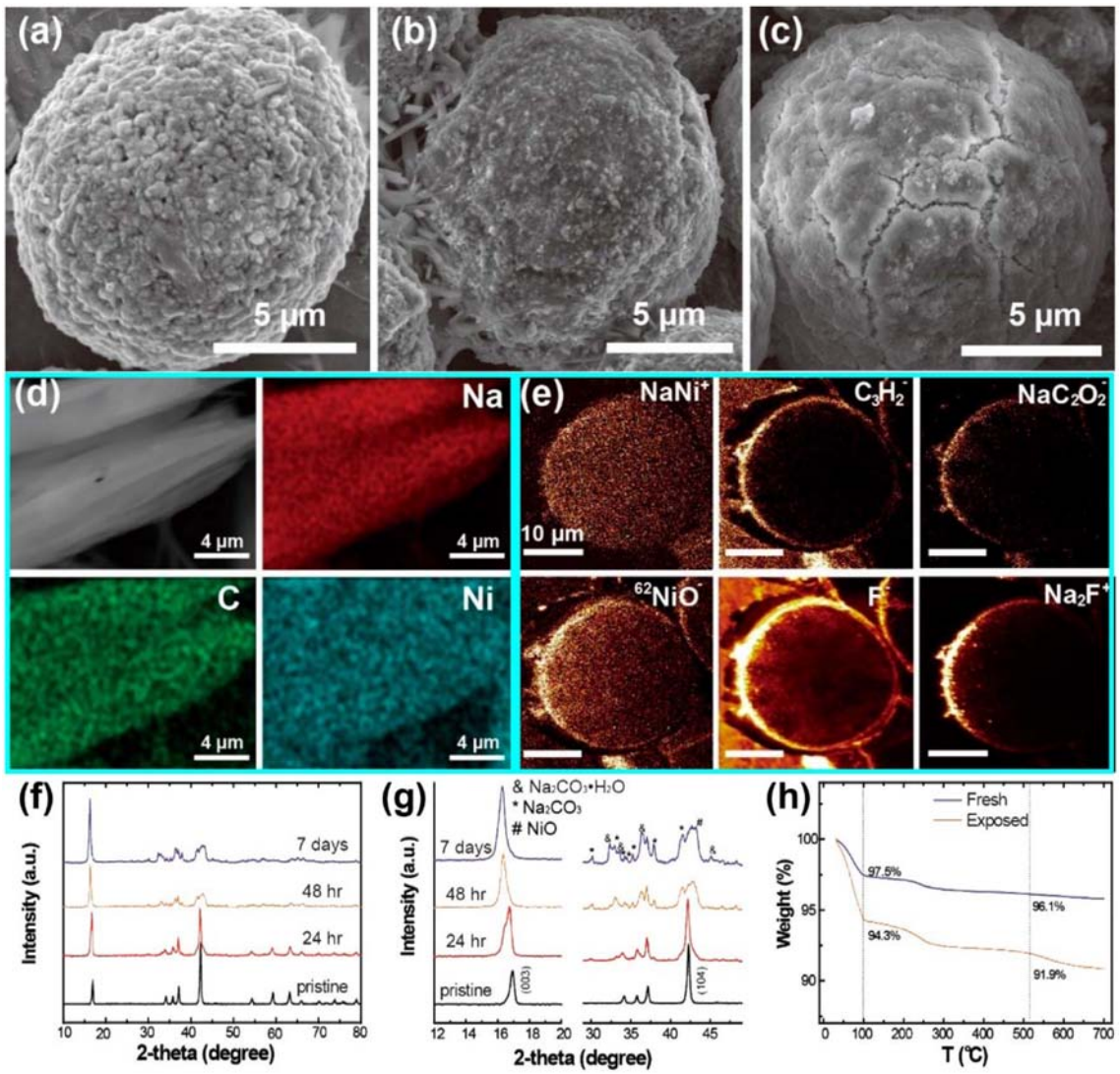

FIGURE 9 | SEM images of **(a)** pristine $NaNi_{0.7}Mn_{0.15}Co_{0.15}O_2$, **(b)** $NaNi_{0.7}Mn_{0.15}Co_{0.15}O_2$ after 24 h air-exposure, **(c)** $NaNi_{0.7}Mn_{0.15}Co_{0.15}O_2$ after 7 days air-exposure, **(d)** dendrite-like impurity in part b with the corresponding elemental mappings of Na, C and Ni, **(e)** TOF-SIMS chemical mapping of $NaNi_{0.7}Mn_{0.15}Co_{0.15}O_2$ after 24 h exposure, **(f)** XRD patterns of $NaNi_{0.7}Mn_{0.15}Co_{0.15}O_2$ samples under different air exposed time, **(g)** the enlarged peaks from part f, **(h)** TGA profiles of pristine $NaNi_{0.7}Mn_{0.15}Co_{0.15}O_2$ and 7 days exposed $NaNi_{0.7}Mn_{0.15}Co_{0.15}O_2$ samples. Reproduced with permission (You et al., 2018). Copyright 2018, American Chemical Society.

(**Figures 8a–c**). In addition, the corresponding XRD patterns of $Na_{0.67}Mn_{0.5}Fe_{0.5}O_2$ are also changed. New peak is observed around 13° after a month air exposure (**Figure 8d**), indicating the formation of hydrate phase (phase 3) and sodium-depleted P2 phase (phase 2). In Fourier difference map, the existence of large residual nuclear density is caused by the carbonate ions (**Figure 8e**) because the insertion of CO_3^{2-} leading to the changing of the nuclear density distribution (**Figure 9g**). In the TM layer, the CO_3^{2-} is combined with one C-O bond to form a CO_4 tetrahedron structure (**Figure 8f**).

Except for Na_2CO_3, other surface components are also observed. You et al. studied the surface reaction between $NaNi_{0.7}Mn_{0.15}Co_{0.15}O_2$ and air systematically by using time-of-flight secondary ion mass spectroscopy (TOF-SIMS) (You et al., 2018). The pristine sample shows a microsphere morphology, which is consisted of nanosized particles (**Figure 9a**). After 24 h air exposure treatment, the surface of this microsphere becomes smooth with the absence of nano-particles (**Figure 9b**). Finally, a thick layer of impurities is formed on the surface after 7 days air exposure (**Figure 9c**). Elements of Na, Ni, and C are distributed uniformly on the impurity surface (**Figure 9d**). The existence of $NaNi^+$, NiO, $NaC_2O_2^-$, $C_3H_2^-$, Na_2F^+, and F^- composition are confirmed by TOF-SIMS, indicating the surface degradation of $NaNi_{0.7}Mn_{0.15}Co_{0.15}O_2$ as well as the reaction between sodium carbonates and PVDF (**Figure 9e**). The 003 peak shifts to lower angles gradually because of the migration of Na^+ to the surface while the 104 peak becomes weak and vanishes after 48 h air exposure (**Figure 9f**). According to the XRD patterns in **Figure 9g**, impurities' peaks such as NiO and Na_2CO_3 are observed, indicating the surface reaction when $NaNi_{0.7}Mn_{0.15}Co_{0.15}O_2$ contacts to CO_2 and H_2O. Since the CO_2 and H_2O are absorbed and reacted with $NaNi_{0.7}Mn_{0.15}Co_{0.15}O_2$, the air-exposed sample loses more weight than the fresh sample (**Figure 9h**). All the results above can prove hat $NaNi_{0.7}Mn_{0.15}Co_{0.15}O_2$ can react with the water and carbon dioxide in the air and the impurities of $NaNi^+$, NiO, $NaC_2O_2^-$, $C_3H_2^-$, Na_2F^+ and F^- are generated on the surface.

AIR-STABLE NA_XTMO_2 COMPOUNDS

As mentioned above, $NaTMO_2$ compounds can react with water and CO_2 in air, which lead to: (i) the formation of impure phase on the surface; (ii) the insertion of H_2O and CO_3^{2-} into interlayer spacing and TM layers, respectively. On one side, the formed NaOH and Na_2CO_3 impure phase are electrochemical inactive and have low conductivity hence the rate capability of Na_xTMO_2 suffer serious decrease. On the other side, the water molecules can bring side reaction with electrolyte while the insertion of CO_3^{2-}

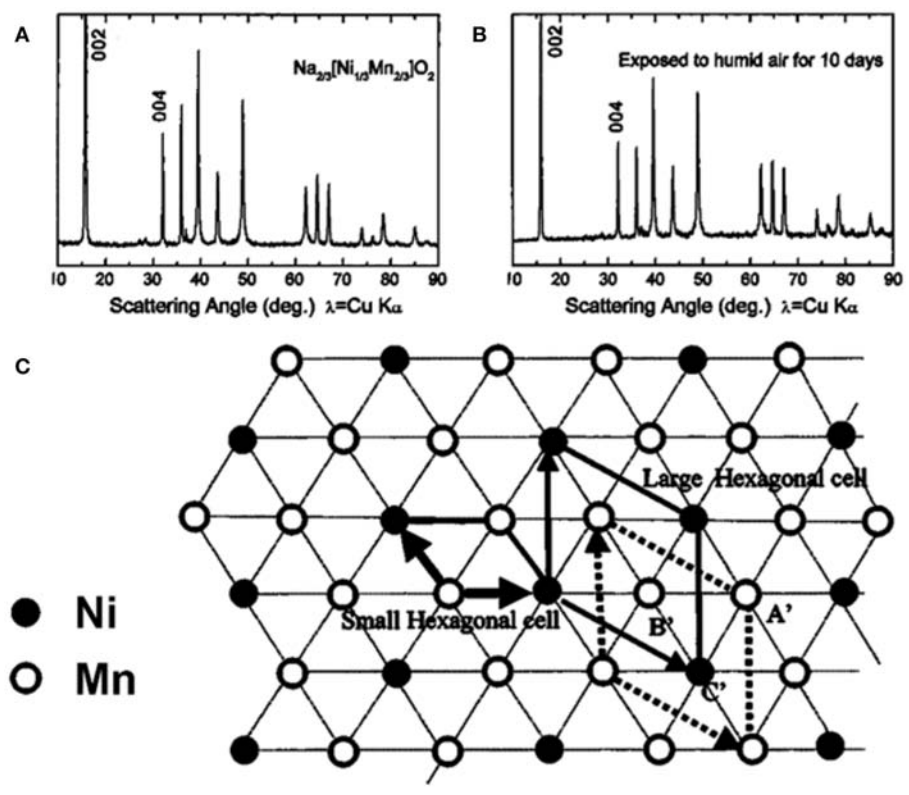

FIGURE 10 | (A) XRD pattern of pristine $Na_{2/3}Ni_{1/3}Mn_{2/3}O_2$, **(B)** XRD pattern of $Na_{2/3}Ni_{1/3}Mn_{2/3}O_2$ after 10 days air-exposure, **(C)** the Ni/Mn cationic ordering arrangement. Reproduced with permission (Lu and Dahn, 2001b). Copyright 2001, American Chemical Society.

affects the valence state of TM ions, leading to severe capacity decay. Therefore, more and more researchers are focusing on strategies to address this air-instable problems.

One strategy is to prevent the materials from contacting moisture. During the materials preparation process, once the high-temperature treatment is done, the Na_xTMO_2 products are transferred to drying room (Wang et al., 2016a) or argon-filled glove box (Yabuuchi et al., 2012a; Vassilaras et al., 2014) immediately for the cooling process and subsequent cell assembling. However, this strategy may not be suitable for the large-scale application because huge cost will rise for materials' storage. Another strategy is to design air-stable Na_xTMO_2 material. Recently, several P2 and O3 type Na_xTMO_2 materials with high stability against moisture have been reported (Lu and Dahn, 2001b; Li Y. et al., 2015; Mu et al., 2015; Guo et al., 2017; Yao et al., 2017; Zheng L. et al., 2017; Chen et al., 2018; Deng et al., 2018). Under the treatment of air exposure and water soaking, these air-stable cathodes can maintain their original crystal structure and electrochemical performance. In this part, several effective strategies for air-stable Na_xTMO_2 designing are summarized.

Constructing TM Cationic Ordering Arrangement

Lu et al. first reported an air-stable P2-$Na_{2/3}Ni_{1/3}Mn_{2/3}O_2$ with high stability under moisture condition (Lu and Dahn, 2001b). For the P2-$Na_{2/3}Ni_{1/3}Mn_{2/3}O_2$ sample, after undergoing a 10 days air-exposure treatment, no peaks shift or new peaks formation were observed in the XRD pattern, indicating that water could not be inserted into the interlayer spacing (**Figures 10A,B**). According to neutron diffraction analysis, the Ni^{2+} and Mn^{4+} ions formed an honeycomb structure with an $\sqrt{3}a \times \sqrt{3}a$ ordering arrangement in the TM layers (**Figure 10C**) (Lu et al., 2000). This Ni/Mn ordering arrangement in TM

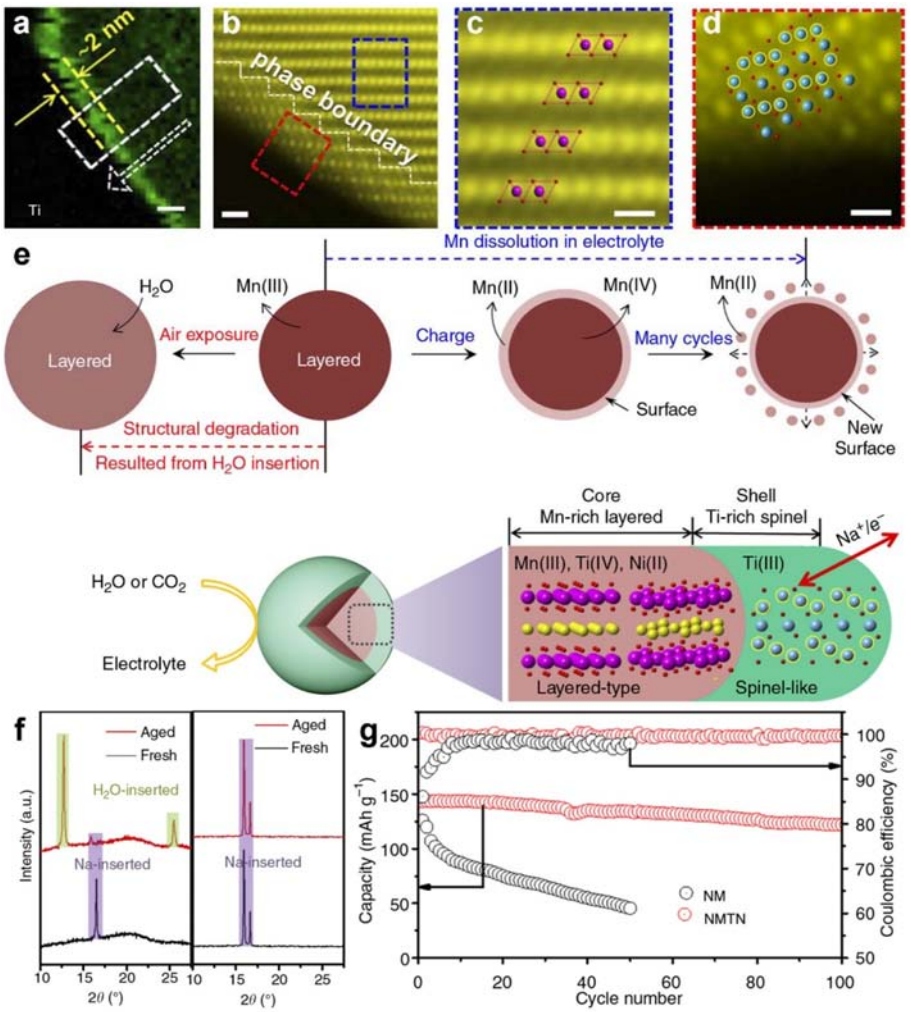

FIGURE 11 | (a) EELS chemical mapping of Ti element in NMTN sample, **(b)** STEM-HADDF image of NMTN sample, **(c)** Enlarged image extracted from the blue rectangle of part b, **(d)** Enlarged image extracted from the red rectangle of part b, **(e)** vulnerable mechanism of naked samples and protective mechanism of NMTN sample under moisture condition. **(f)** XRD patterns of naked sample (left) and NMTN sample (right) before/after air-exposure, **(g)** cycling performance of naked sample and NMTN sample. Reproduced with permission (Guo et al., 2017). Copyright 2017, Nature Publishing Group.

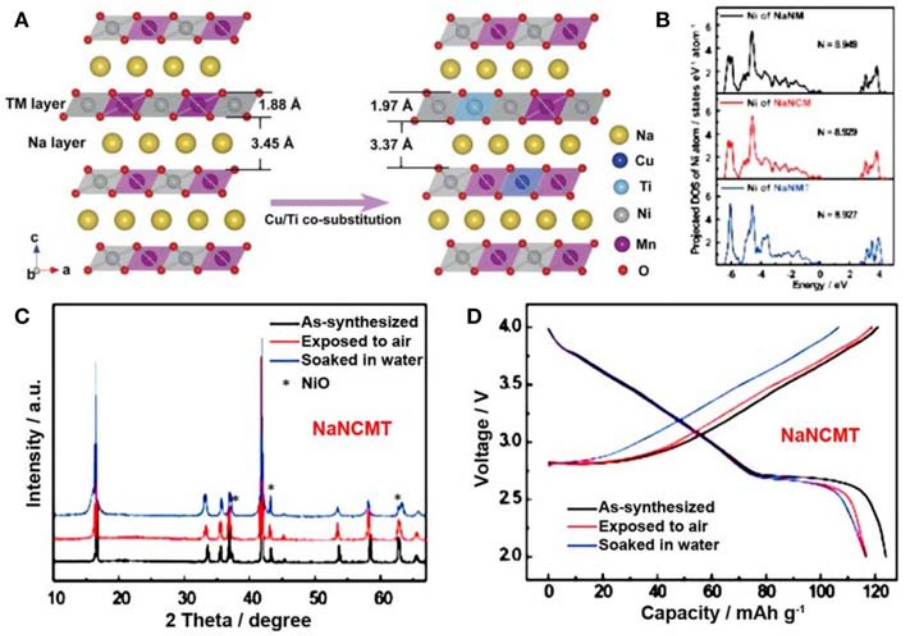

FIGURE 12 | (A) refined crystal structure of NaNM and NaNCMT samples, **(B)** Electronic density of states on Ni ion of NaNM, NaNCM, and NaNMT samples, respectively. **(C)** XRD patterns of pristine, air-exposure and water soaking NaNCMT samples. **(D)** charge/discharge curves of pristine, air-exposure and water soaking NaNCMT samples. Reproduced with permission (Yao et al., 2017). Copyright 2017, American Chemical Society.

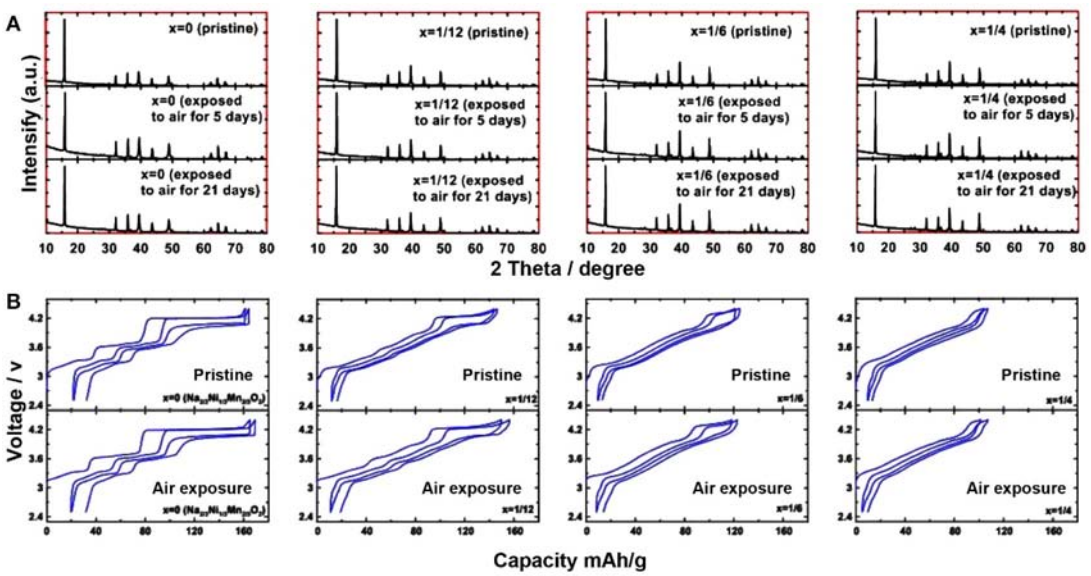

FIGURE 13 | (A) XRD patterns of $Na_{2/3}Cu_xNi_{1/3-x}Mn_{2/3}O_2$ samples ($x = 0$, 1/12, 1/6 and 1/4) before/after air-exposure, **(B)** the corresponding charge/discharge profiles. Reproduced with permission (Zheng L. et al., 2017). Copyright 2017, American Chemical Society.

layers was supposed to induce a strong interlayer interaction to prevent the water insertion. When this ordering arrangement was suppressed by the substitution of Co or Fe for Ni, water molecules could be inserted into the interlayer spacing (**Figures 5A,B,F**). However, this "interlayer interaction" between adjacent ordering TM layer has not been confirmed yet.

Coating Protective Layer

Coating a protective layer on the surface of Na_xTMO_2 is an effective method to prevent the Na_xTMO_2 from air contacting. The most common way is to coat high-voltage metal oxides with high stability against moisture. In 2017, Zhou and co-workers (Guo et al., 2017). designed an efficient

TABLE 2 | A summary of current air-stable Na_xTMO_2 cathode.

Air stable materials	Design strategies	Test conditions	Rate performance			Cycling performance			References
			Maximum rate (C)	Capacity (mAh g^{-1})	Capacity retention	Cycle rate (C)	Cycle number	Capacity retention	
$Na_{2/3}Ni_{1/3}Mn_{2/3}O_2$	Ni/Mn ordering arrangement	Air-exposure and water soaking	None	None	None	None	None	None	Lu and Dahn, 2001b
$NaMnNi_{0.1}Ti_{0.1}O_2$	titanium (III) oxides protective layer	Air-exposure	10	102	55%	5	500	81%	Guo et al., 2017
ZrO_2@$NaNi_{0.7}Mn_{0.15}Co_{0.15}O_2$	ZrO_2 protective layer	Air-exposure	10	41	37%	0.5	200	70%	You et al., 2018
$NaNi_{0.45}Cu_{0.05}Mn_{0.4}Ti_{0.1}O_2$	Cu/Ti co-substitution	Air-exposure and water soaking	4	100	80%	1	500	70.2%	Yao et al., 2017
$Na_{2/3}Cu_xNi_{1/3-x}Mn_{2/3}O_2$	Cu substitution	Air-exposure	5	80	87%	None	None	None	Zheng L. et al., 2017
$Na_{7/9}Cu_{2/9}Fe_{1/9}Mn_{2/3}O_2$	Cu substitution	Air-exposure and water soaking	2	50	52%	1	150	87%	Li Y. et al., 2015
$Na_{0.9}Cu_{0.22}Fe_{0.30}Mn_{0.48}O_2$	Cu substitution	Air-exposure	5	60	60%	0.1	100	97%	Mu et al., 2015
$NaLi_{0.05}Mn_{0.5}Ni_{0.3}Cu_{0.1}Mg_{0.05}O_2$	Cu substitution	Water soaking	1	125	71%	1	400	67.4%	Deng et al., 2018
$Na_{0.6}Mn_{0.9}Cu_{0.1}O_2$	Cu substitution	Air-exposure and water soaking	8	85	50.4%	4	250	70.4%	Chen et al., 2018

spinel-like titanium (III) oxides protective interface to improve the structure/electrochemical stability of $NaMnTi_{0.1}Ni_{0.1}O_2$. The sample surface was covered by a high Ti concentration layer with thickness of 2 nm, as shown in the electron energy-loss spectroscopy image (**Figure 11a**). Two distinct phases could be observed from the high-angle annular dark field scanning transmission electron microscopy (HAADF-STEM) image (**Figure 11b**). The bulk phase was a typical layered structure (**Figure 11c**) while the surface phase was spinel-like structure (**Figures 11d,e**). After exposing the naked bulk phase in humid air, two new peaks appeared around 12° and 25° (**Figure 11f**), indicating the insertion of water molecules. Compared to the naked bulk phase, the XRD pattern of $NaMnTi_{0.1}Ni_{0.1}O_2$ sample showed no peak change since the spinel-like titanium (III) oxides interface can act as shield to protected the bulk phase from water attacking and the electrochemical performance of bulk phase can be maintained. In half cell system, the naked bulk phase showed a dramatic decrease after 50 cycles whereas NMTN sample only showed a slight decay after 100 cycles (**Figure 11g**).

You et al. (2018) coated the surface of $NaNi_{0.7}Mn_{0.15}Co_{0.15}O_2$ with a ZrO_2 protective layer. This protective layer notably maintains the rate capability of $NaNi_{0.7}Mn_{0.15}Co_{0.15}O_2$ against moisture atmosphere. After 7 days air exposure, the ZrO_2@$NaNi_{0.7}Mn_{0.15}Co_{0.15}O_2$ sample still delivers a capacity of 96 mAh/g while $NaNi_{0.7}Mn_{0.15}Co_{0.15}O_2$ shows abnormal charge profile. The surface charge-transfer kinetics are also improved by this protective layer.

Except for Ti and Zr oxides, we suppose that other metal oxides such as MgO, ZnO, and Al_2O_3 also have the ability to work as protective layer because these high-voltage metal oxides all have high tolerance for moisture.

Cu^{2+} Substitution

The Cu^{2+} substitution is the simplest way to obtain air-stable Na_xTMO_2 compounds. The success of Cu^{2+} substitution to achieve high stability against moisture has been proven by many reports (Li Y. et al., 2015; Mu et al., 2015; Yao et al., 2017; Zheng L. et al., 2017; Chen et al., 2018; Deng et al., 2018), few references give the working mechanisms of Cu^{2+} in these air-stable Na_xTMO_2 compounds.

In, 2017, Yao et al. designed an air-stable O3-$NaNi_{0.45}Cu_{0.05}Mn_{0.4}Ti_{0.1}O_2$ (NaNCMT) cathode though cosubstitution of Cu^{2+} and Ti^{4+} in O3-$NaNi_{0.5}Mn_{0.5}O_2$ (NaNM) compound. This strategy could decrease the Na^+ interlayer distance and increase the valence state of TM ions. According to the refined crystal structure of NaNM and NaNCMT, the interlayer distance was reduced from 3.45 Å to 3.37 Å, respectively (**Figure 12A**), which was in favor of preventing the insertion of water molecules. DFT calculation revealed that Cu/Ti cosubstitution facilitated the increasing in valence state of Ni (**Figure 12B**). Compared with NaNM compound (**Figure 6B**), the XRD pattern of NaNCMT sample showed no obvious peaks change after air-exposure or water soaking (**Figure 12C**). During charge/discharge process, only slight capacity decay was observed after aging experiments (**Figure 12D**). (Yao et al., 2017) However, the explanation

about the relationship between valence state of TM ions and air-stability was not mentioned.

Zheng et al. investigated the structure stability of $Na_{2/3}Cu_xNi_{1/3-x}Mn_{2/3}O_2$ compounds ($0 \leq x \leq 1/4$) by air-exposure treatment. Compared to the XRD patterns of pristine samples, neither peaks position change nor new peaks formation were observed after exposing $Na_{2/3}Cu_xNi_{1/3-x}Mn_{2/3}O_2$ in air condition for 21 days (**Figure 13A**). According to charge/discharge profiles, all exposed electrodes had a little higher open circuit voltage than the un-exposed electrodes, but the average voltage and reversible capacity of the exposed electrodes showed no change or decay, indicating the air stability of these electrodes (**Figure 13B**). Since the radii of Cu^{2+} (0.73 Å) and Ni^{2+} (0.69 Å) were similar, replacing Ni^{2+} in $Na_{2/3}Ni_{1/3}Mn_{2/3}O_2$ by Cu^{2+} had no influence on the Ni/Mn cationic ordering arrangement. Therefore, the existence of Cu/Ni/Mn ordering arrangement could prevent the insertion of water molecules into the $Na_{2/3}Cu_xNi_{1/3-x}Mn_{2/3}O_2$ interlayer spacing because of the interlayer interaction between the adjacent Cu/Ni/Mn layer. However, no evidence was provided to prove the Cu/Ni/Mn ordering arrangement.

Other compounds such as O3-$Na_{0.9}Cu_{0.22}Fe_{0.30}Mn_{0.48}O_2$, P2-$Na_{7/9}Cu_{2/9}Fe_{1/9}Mn_{2/3}O_2$, O3-$NaLi_{0.05}Mn_{0.5}Ni_{0.3}Cu_{0.1}Mg_{0.05}O_2$, and P2-$Na_{0.6}Mn_{0.9}Cu_{0.1}O_2$ have been proved to be air-stable because all of their XRD patterns remained unchanged after air-exposure and water soaking treatment (Li Y. et al., 2015; Mu et al., 2015; Chen et al., 2018; Deng et al., 2018).

It seems that the Cu^{2+} plays an important role in maintaining the structure stability of these compounds under moisture. The reported Cu^{2+} substituted Na_xTMO_2 compounds, such as O3-$NaNi_{0.45}Cu_{0.05}Mn_{0.4}Ti_{0.1}O_2$, P2-$Na_{2/3}Cu_xNi_{1/3-x}Mn_{2/3}O_2$, O3-$Na_{0.9}Cu_{0.22}Fe_{0.30}Mn_{0.48}O_2$, O3-$NaLi_{0.05}Mn_{0.5}Ni_{0.3}Cu_{0.1}Mg_{0.05}O_2$, P2-$Na_{7/9}Cu_{2/9}Fe_{1/9}Mn_{2/3}O_2$, and P2-$Na_{0.6}Mn_{0.9}Cu_{0.1}O_2$, all show excellent structure stability under moisture condition. However, few investigations explain the working mechanism of Cu^{2+} substitution in these air-stable compounds. In O3-$NaNi_{0.45}Cu_{0.05}Mn_{0.4}Ti_{0.1}O_2$ compound system, the working mechanism of Cu^{2+} is attributed to the increase of the Ni valence state by DFT calculation, but the relationship between valence state of Ni and air-stability is not clear so far. In addition, how to explain the Ni free compound systems for their air stability after Cu^{2+} substitution still remains problems.

Table 2 lists most of the air-stable Na_xTMO_2 compounds published to date, including the design strategies and the corresponding electrochemical performance.

SUMMARY AND PROSPECTS

Air-stability is one of the key issues for practical application of Na_xTMO_2 SIB cathode materials. In recent years, with understanding the structure of Na_xTMO_2, several strategies have been developed to obtain air-stable Na_xTMO_2 compounds, including constructing TM ordering arrangement, coating protective layer and Cu^{2+} substitution. However, there still remain some challenges. For example, the reaction mechanism of the "strong interlayer interaction" for TM ordering arrangement as well as the substitution of Cu^{2+} and other cations should be further understood. In any case, we believe that the air-stable Na_xTMO_2 materials with low cost and high theoretical capacity are highly competitive as SIB cathode materials in the large-scale energy storage application.

AUTHOR CONTRIBUTIONS

RZ contributed conception and design of the manuscript. YZ organized the reference and wrote the first draft of the manuscript. All authors contributed to manuscript revision, read and approved the submitted version.

ACKNOWLEDGMENTS

We gratefully acknowledge the financial support from the National Natural Science Foundation of China (Nos. 51602221 and 51632001), Shanghai Municipal Natural Science Foundation (16ZR1438400) and the Fundamental Research Funds for the Central Universities.

REFERENCES

Ado, K., Tabuchi, M., Kobayashi, H., Kageyama, H., Nakamura, O., Inaba, Y., et al. (1997). Preparation of $LiFeO_2$ with Alpha- $NaFeO_2$-type structure using a mixed-alkaline hydrothermal method. *J. Electrochem. Soc.* 144, L177–L180.

Arachi, Y., Setsu, T., Ide, T., Hinoshita, K., and Nakata, Y. (2012). Reversible electrochemical reaction of CuO with Li in the $LiCuO_2$ system. *Solid State Ionics* 225, 611–614. doi: 10.1016/j.ssi.2011.12.006

Bai, X., Sathiya, M., Mendoza-Sánchez, B., Iadecola, A., Vergnet, J., Dedryvère, R., et al. (2018). Anionic redox activity in a newly Zn-doped sodium layered oxide P2-Na2/3Mn1–yZnyO2 ($0 < y < 0.23$). *Adv. Energy Mater.* 8:1802379. doi: 10.1002/aenm.201802379

Benedek, R., and van de Walle, A. (2008). Free energies for acid attack reactions of lithium cobaltate. *J. Electrochem. Soc.* 155, A711–A715. doi: 10.1149/1.2954958

Berthelot, R., Carlier, D., and Delmas, C. (2011). Electrochemical investigation of the P2–$NaxCoO_2$ phase diagram. *Nat. Mater.* 10, 74–80. doi: 10.1038/nmat2920

Blesa, M. C., Morán, E., Menéndez, N., Tornero, J. D., and Torrón, C. (1993). Hydrolysis of sodium orthoferrite [α-$NaFeO_2$]. *Mater. Res. Bull.* 28, 837–847. doi: 10.1016/0025-5408(93)90025-9

Blyr, A., Sigala, C., Amatucci, G., Guyomard, D., Chabre, Y., Tarascon, J., et al. (1998). Self-discharge of $LiMn_2O_4$/C Li-Ion cells in their discharged state: understanding by means of three-electrode measurements. *J. Electrochem. Soc.* 145, 194–209. doi: 10.1149/1.1838235

Boyd, S., Dhall, R., LeBeau, J., and Augustyn, V. (2018). Charge storage mechanism and degradation of P2-type sodium transition metal oxides in aqueous electrolytes. *J. Mater. Chem. A* 6, 22266–22276. doi: 10.1039/C8TA08367C

Braconnier, J. J., Delmas, C., and Hagenmuller, P. (1982). Etude par desintercalation electrochimique des systemes Na_xCrO_2 et Na_xNiO_2. *Mater. Res. Bull.* 17, 993–1000. doi: 10.1016/0025-5408(82)90124-6

Bucher, N., Hartung, S., Franklin, J. B., Wise, A. M., Lim, L. M., Chen H.-Y., et al. (2016). P2–$Na_xCo_yMn_{1-y}O_2$ ($y = 0, 0.1$) as cathode materials in sodium-ion

batteries—effects of doping and morphology to enhance cycling stability. *Chem. Mater.* 28, 2041–2051. doi: 10.1021/acs.chemmater.5b04557

Buchholz, D., Chagas, L. G., Vaalma, C., Wu, L., and Passerini, S. (2014). Water sensitivity of layered P2/P3-$Na_xNi_{0.22}Co_{0.11}Mn_{0.66}O_2$ cathode material. *J. Mater. Chem. A* 2, 13415–13421. doi: 10.1039/C4TA02627F

Caballero, A., Hernan, L., Morales, J., Sanchez, L., Pena, J. S., Aranda, M. A. G., et al. (2002). Synthesis and characterization of high-temperature hexagonal P2-$Na_{0.6}MnO_2$ and its electrochemical behaviour as cathode in sodium cells. *J. Mater. Chem.* 12, 1142–1147. doi: 10.1039/b108830k

Carlier, D., Cheng, J. H., Berthelot, R., Guignard, M., Yoncheva, M., Stoyanova, R., et al. (2011). The P2-$Na_{2/3}Co_{2/3}Mn_{1/3}O_2$ phase: structure, physical properties and electrochemical behavior as positive electrode in sodium battery. *Dalton Trans.* 40, 9306–9312. doi: 10.1039/c1dt10798d

Chen, T. R., Sheng, T., Wu, Z. G., Li, J. T., Wang, E.-H., Wu, C.-H., et al. (2018). Cu($^{2+}$) dual-doped layer-tunnel hybrid $Na_{0.6}Mn_{1-x}Cu_xO_2$ as a cathode of sodium-ion battery with enhanced structure stability, electrochemical property, and air stability. *ACS Appl. Mater. Interfaces* 10, 10147–10156. doi: 10.1021/acsami.8b00614

Chen, X., Zhou, X., Hu, M., Liang, J., Wu, D., Wei, J., et al. (2015). Stable layered P3/P2 $Na_{0.66}Co_{0.5}Mn_{0.5}O_2$ cathode materials for sodium-ion batteries. *J. Mater. Chem. A* 3, 20708–20714. doi: 10.1039/C5TA05205J

Delmas, C., Braconnier, J.-J., Fouassier, C., and Hagenmuller, P. (1981). Electrochemical intercalation of sodium in Na_xCoO_2 bronzes. *Solid State Ionics* 3, 165–169. doi: 10.1016/0167-2738(81)90076-X

Delmas, C., Fouassier, C., and Hagenmuller, P. (1980). Structural classification and properties of the layered oxides. *Physica B+C* 99, 81–85. doi: 10.1016/0378-4363(80)90214-4

Deng, J., Luo, W.-B., Lu, X., Yao, Q., Wang, Z., Liu, H.-K., et al. (2018). High energy density sodium-ion battery with industrially feasible and air-stable O3-type layered oxide cathode. *Adv. Energy Mater.* 8:1701610. doi: 10.1002/aenm.201701610

Duffort, V., Talaie, E., Black, R., and Nazar, L. F. (2015). Uptake of CO_2 in layered P2-$Na_{0.67}Mn_{0.5}Fe_{0.5}O_2$ insertion of carbonate anions. *Chem. Mater.* 27, 2515–2524. doi: 10.1021/acs.chemmater.5b00097

Dunn, B., Kamath, H., and Tarascon, J.-M. (2011). Electrical energy storage for the grid: a battery of choices. *Science* 334, 928–935. doi: 10.1126/science.1212741

Fang, C., Huang, Y., Yuan, L., Liu, Y., Chen, W., Huang, Y., et al. (2017). A metal–organic compound as cathode material with superhigh capacity achieved by reversible cationic and anionic redox chemistry for high-energy sodium-ion batteries. *Angew. Chem. Int. Ed.* 56, 6793–6797. doi: 10.1002/anie.201701213

Fielden, R., and Obrovac, M. N. (2015). Investigation of the $NaNi_xMn_{1-x}O_2$ ($0 <= x <= 1$) system for na-ion battery cathode materials. *J. Electrochem. Soc* 162, A453–A459. doi: 10.1149/2.0551503jes

Franger, S., Bach, S., Pereira-Ramos, J. P., and Baffier, N. (2000). Chemistry and electrochemistry of low-temperature manganese oxides as lithium intercalation compounds. *J. Electrochem. Soc.* 147, 3226–3230. doi: 10.1149/1.1393887

Gonzalo, E., Han, M. H., del Amo, J. M. L., Acebedo, B., Casas-Cabanas, M., Rojo, T., et al. (2014). Synthesis and characterization of pure P2-and O3-$Na_{2/3}Fe_{2/3}Mn_{1/3}O_2$ as cathode materials for Na ion batteries. *J. Mater. Chem. A* 2, 18523–18530. doi: 10.1039/C4TA03991B

Guignard, M., Didier, C., Darriet, J., Bordet, P., Elkaïm, E., and Delmas, C. (2013). P2-Na_xVO_2 system as electrodes for batteries and electron-correlated materials. *Nat Mater.* 12, 74–80. doi: 10.1038/nmat3478

Guo, S., Li, Q., Liu, P., Chen, M., and Zhou, H. (2017). Environmentally stable interface of layered oxide cathodes for sodium-ion batteries. *Nat. Commun.* 8:135. doi: 10.1038/s41467-017-00157-8

Guo, S., Yu, H., Liu, D., Tian, W., Liu, X., Hanada, N., et al. (2014). A novel tunnel $Na_{0.61}Ti_{0.48}Mn_{0.52}O_2$ cathode material for sodium-ion batteries. *Chem. Commun.* 50, 7998–8001. doi: 10.1039/c4cc02362e

Hamani, D., Ati, M., Tarascon, J.-M., and Rozier, P. (2011). Na_xVO_2 as possible electrode for Na-ion batteries. *Electrochem. Commun.* 13, 938–941. doi: 10.1016/j.elecom.2011.06.005

Han, M. H., Gonzalo, E., Sharma, N. J., López del Amo, M., Armand, M., Avdeev, M., et al. (2016a). High-performance P2-phase $Na_{2/3}Mn_{0.8}Fe_{0.1}Ti_{0.1}O_2$ cathode material for ambient-temperature sodium-ion batteries. *Chem. Mater.* 28, 106–116. doi: 10.1021/acs.chemmater.5b03276

Han, M. H., Gonzalo, E., Singh, G., and Rojo, T. (2015). A comprehensive review of sodium layered oxides: powerful cathodes for Na-ion batteries. *Energy Environ. Sci.* 8, 81–102. doi: 10.1039/C4EE03192J

Han, M. H., Sharma, N., Gonzalo, E., Pramudita, J. C., Brand, H. E., et al. (2016b). Moisture exposed layered oxide electrodes as Na-ion battery cathodes. *J. Mater. Chem. A* 4, 18963–18975. doi: 10.1039/C6TA07950D

Hwang, J.-Y., Myung, S.-T., and Sun, Y.-K. (2017). Sodium-ion batteries: present and future. *Chem. Soc. Rev.* 46, 3529–3614. doi: 10.1039/C6CS00776G

Jiang, K., Xu, S., Guo, S., Zhang, X., Zhang, X., Qiao, Y., et al. (2018). A phase-transition-free cathode for sodium-ion batteries with ultralong cycle life. *Nano Energy* 52, 88–94. doi: 10.1016/j.nanoen.2018.07.042

Jiang, X., Liu, S., Xu, H., Chen, L., Yang, J., and Qian, Y. (2015). Tunnel-structured $Na_{0.54}Mn_{0.50}Ti_{0.51}O_2$ and $Na_{0.54}Mn_{0.50}Ti_{0.51}O_2$/C nanorods as advanced cathode materials for sodium-ion batteries. *Chem. Commun.* 51, 8480–8483. doi: 10.1039/C5CC02233A

Kalluri, S., Seng, K. H., Pang, W. K., Guo, Z., Chen, Z., Liu H. K., et al. (2014). Electrospun P2-type $Na_{2/3}Fe_{1/2}Mn_{1/2}O_2$ hierarchical nanofibers as cathode material for sodium-ion batteries. *ACS Appl. Mater. Interfaces* 6, 8953–8958. doi: 10.1021/am502343s

Kang, S. M., Park, J.-H., Jin, A., Jung, Y. H., Mun, J., Sung, Y.-E. (2018). Na^+/vacancy disordered P2-$Na_{0.67}Co_{1-x}Ti_xO_2$: high-energy and high-power cathode materials for sodium ion batteries. *ACS Appl. Mater. Interfaces* 10, 3562–3570. doi: 10.1021/acsami.7b16077

Kang, W., Yu, D. Y. Lee, P.-K., Zhang, Z., Bian, H., Li, W., et al. (2016). P2-Type $Na_xCu_{0.15}Ni_{0.20}Mn_{0.65}O_2$ cathodes with high voltage for high-power and long-life sodium-ion batteries. *ACS Appl. Mater. Interfaces* 8, 31661–31668. doi: 10.1021/acsami.6b10841

Kang, W., Zhang, Z., Lee, P.-K., Ng, T.-W., Li, W., Tang, Y., et al. (2015). Copper substituted P2-type $Na_{0.67}Cu_xMn_{1-x}O_2$: a stable high-power sodium-ion battery cathode. *J. Mater. Chem. A* 3, 22846–22852. doi: 10.1039/C5TA06371J

Kawamura, T., Okada, S., and Yamaki, J.-I. (2006). Decomposition reaction of $LiPF_6$-based electrolytes for lithium ion cells. *J. Power Sources* 156, 547–554. doi: 10.1016/j.jpowsour.2005.05.084

Kee, Y., Dimov, N., Champet, S., Gregory, D. H., and Okada, S. (2016). Investigation of Al-doping effects on the $NaFe_{0.5}Mn_{0.5}O_2$ cathode for Na-ion batteries. *Ionics* 22, 2245–2248. doi: 10.1007/s11581-016-1839-2

Kim, D., Cho, M., and Cho, K. (2017). Rational design of Na(Li1/3Mn2/3)O2 operated by anionic redox reactions for advanced sodium-ion batteries. *Adv Mater* 29:1701788. doi: 10.1002/adma.201701788

Kubota, K., and Komaba, S. (2015). Review—practical issues and future perspective for Na-Ion batteries. *J. Electrochem. Soc.* 162, A2538–A2550. doi: 10.1149/2.0151514jes

Kundu, D., Talaie, E., Duffort, V., and Nazar, L. F. (2015). The emerging chemistry of sodium ion batteries for electrochemical energy storage. *Angew. Chem. Int. Ed. Engl.* 54, 3431–3448. doi: 10.1002/anie.201410376

Le Goff, P., Baffier, N., Bach, S., Pereira-Ramos, J. P., and Messina, R. (1993). Structural and electrochemical characteristics of a lamellar sodium manganese oxide synthesized via a sol-gel process. *Solid State Ionics* 61, 309–315. doi: 10.1016/0167-2738(93)90397-L

Li, X., Wu, D., Zhou, Y. N., Liu, L., Yang, X.-Q., Ceder, G., et al. (2014). O3-type $Na(Mn_{0.25}Fe_{0.25}Co_{0.25}Ni_{0.25})O_2$: a quaternary layered cathode compound for rechargeable Na ion batteries. *Electrochem. Commun.* 49, 51–54. doi: 10.1016/j.elecom.2014.10.003

Li, Y., Yang, Z., Xu, S., Mu, L., Gu, L., Hu, Y.-S., et al. (2015). Air-stable copper-based P2-$Na_{7/9}Cu_{2/9}Fe_{1/9}Mn_{2/3}O_2$ as a new positive electrode material for sodium-ion batteries. *Adv. Sci.* 2:1500031. doi: 10.1002/advs.201500031

Li, Z.-Y., Gao, R., Sun, L., Hu, Z., and Liu, X. (2015). Designing an advanced P2-$Na_{0.67}Mn_{0.65}Ni_{0.2}Co_{0.15}O_2$ layered cathode material for Na-ion batteries. *J. Mater. Chem. A* 3, 16272–16278. doi: 10.1039/C5TA02450A

Liu, L., Li, X., Bo, S.-H., Wang, Y., Chen, H., Twu, N., et al. (2015). High-performance P2-type $Na_{2/3}(Mn_{1/2}Fe_{1/4}Co_{1/4})O_2$ cathode material with superior rate capability for Na-Ion batteries. *Adv. Energy Mater.* 5:1500944. doi: 10.1002/aenm.201500944

Liu, Y., Fang, X., Zhang, A., Shen, C., Liu, Q., Enaya, H., et al. (2016). Layered P2-$Na_{2/3}[Ni_{1/3}Mn_{2/3}]O_2$ as high-voltage cathode for sodium-ion batteries: the capacity decay mechanism and Al_2O_3 surface modification. *Nano Energy* 27, 27–34. doi: 10.1016/j.nanoen.2016.06.026

Lu, Z., and Dahn, J. R. (2001a). *In situ* X-ray diffraction study of P2-$Na_{2/3}[Ni_{1/3}Mn_{2/3}]O_2$. *J. Electrochem. Soc.* 148, A1225–A1229. doi: 10.1149/1.1407247

Lu, Z., and Dahn, J. R. (2001b). Intercalation of water in P2, T2 and O2 structure $A_z[Co_xNi_{1/3-x}Mn_{2/3}]O_2$. *Chem. Mater.* 13, 1252–1257. doi: 10.1021/cm000721x

Lu, Z., Donaberger, R. A., and Dahn, J. R. (2000). Superlattice ordering of Mn, Ni, and Co in layered alkali transition metal oxides with P2, P3, and O3 structures. *Chem. Mater.* 12, 3583–3590. doi: 10.1021/cm000359m

Luo, W., Chen, X., Xia, Y., Chen, M., Wang, L., Wang, Q., et al. (2017). Surface and interface engineering of silicon-based anode materials for lithium-ion batteries. *Adv. Energy Mater.* 7:1701083. doi: 10.1002/aenm.201701083

Lux, S. F., Lucas, I. T., Pollak, E., Passerini, S., Winter, M., Kostecki, R. (2012). The mechanism of HF formation in $LiPF_6$ based organic carbonate electrolytes. *Electrochem. Commun.* 14, 47–50. doi: 10.1016/j.elecom.2011.10.026

Ma, X., Chen, H., and Ceder, G. (2011). Electrochemical properties of monoclinic $NaMnO_2$. *J. Electrochem. Soc.* 158, A1307–A1312. doi: 10.1149/2.035112jes

Maitra, U., House, R. A., Somerville, J. W., Tapia-Ruiz, N., Lozano, J. G., Guerrini, N., et al. (2018). Oxygen redox chemistry without excess alkali-metal ions in $Na_{2/3}[Mg_{0.28}Mn_{0.72}]O_2$. *Nat. Chem.* 10:288. doi: 10.1038/nchem.2923

Manikandan, P., Heo, S., Kim, H. W., Jeong, H. Y., Lee, E., and Kim, Y. (2017). Structural characterization of layered $Na_{0.5}Co_{0.5}Mn_{0.5}O_2$ material as a promising cathode for sodium-ion batteries. *J. Power Sources* 363, 442–449. doi: 10.1016/j.jpowsour.2017.07.116

Monyoncho, E., and Bissessur, R. (2013). Unique properties of α-$NaFeO_2$: De-intercalation of sodium via hydrolysis and the intercalation of guest molecules into the extract solution. *Mater. Res. Bull.* 48, 2678–2686. doi: 10.1016/j.materresbull.2013.03.027

Morris, D. J. P., Roger, M., Gutmann, M. J., Goff, J. P., Tennant, D. A., Prabhakaran, D., et al. (2009). Crystal-to-stripe reordering of sodium ions in Na_xCoO_2. *Phys. Rev. B* 79:100103. doi: 10.1103/PhysRevB.79.100103

Mortemard de Boisse, B., Carlier, D., Guignard, M., and Delmas, C. (2013). Structural and electrochemical characterizations of P2 and new O3-$Na_xMn_{1-y}Fe_yO_2$ phases prepared by auto-combustion synthesis for Na-Ion batteries. *J. Electrochem. Soc* 160, A569–A574. doi: 10.1149/2.032304jes

Mu, L., Xu, S., Li, Y., Hu, Y.-S., Li, H., Chen, L., et al. (2015). Prototype sodium-ion batteries using an air-stable and Co/Ni-Free O3-layered metal oxide cathode. *Adv. Mater.* 27, 6928–6933. doi: 10.1002/adma.201502449

Nayak, P. K., Yang, L., Brehm, W., and Adelhelm, P. (2018). From lithium-ion to sodium-ion batteries: advantages, challenges, and surprises. *Angew. Chem. Int. Ed.* 57, 102–120. doi: 10.1002/anie.201703772

Ono, Y. (2018). Structural analysis of $NaCuO_2$ cathode at various charged/discharged stages and its reaction mechanism. *Electrochemistry* 86, 309–314. doi: 10.5796/electrochemistry.18-6-E2674

Ono, Y., Yui, Y., Hayashi, M., Asakura, K., Kitabayashi, H., and Takahashi, K. I. (2014). Electrochemical properties of $NaCuO_2$ for sodium-ion secondary batteries. *ECS Trans.* 58, 33–39. doi: 10.1149/05812.0033ecst

Palomares, V., Casas-Cabanas, M., Castillo-Martínez, E., Han, M. H., and Rojo, T. (2013). Update on Na-based battery materials. A growing research path. *Energy Environ. Sci.* 6, 2312–2337. doi: 10.1039/c3ee41031e

Pan, H., Hu, Y.-S., and Chen, L. (2013). Room-temperature stationary sodium-ion batteries for large-scale electric energy storage. *Energy Environ. Sci.* 6, 2338–2360. doi: 10.1039/c3ee40847g

Paulsen, J. M., and Dahn, J. R. (1999). Studies of the layered manganese bronzes, $Na_{2/3}[Mn_{1-x}M_x]O_2$ with M=Co, Ni, Li, and $Li_{2/3}[Mn_{1-x}M_x]O_2$ prepared by ion-exchange. *Solid State Ionics* 126, 3–24. doi: 10.1016/S0167-2738(99)00147-2

Qi, X., Wang, Y., Jiang, L., Mu, L., Zhao, C., Liu, L., et al. (2016). Sodium-Deficient O3-$Na_{0.9}Ni_{0.4}Mn_xTi_{0.6-x}O_2$ Layered-Oxide Cathode Materials for Sodium-Ion Batteries. *Part. Part. Syst. Charact.* 33, 538–544. doi: 10.1002/ppsc.201500129

Qian, J., Wu, C., Cao, Y., Ma, Z., Huang, Y., Ai, X., et al. (2018). Sodium-ion batteries: prussian blue cathode materials for sodium-ion batteries and other ion batteries. *Adv. Energy Mater.* 8:1870079. doi: 10.1002/aenm.201870079

Qiao, Y., Guo, S., Zhu, K., Liu, P., Li, X., Jiang, K., et al. (2018). Reversible anionic redox activity in Na_3RuO_4 cathodes: a prototype Na-rich layered oxide. *Energy Environ. Sci.* 11, 299–305. doi: 10.1039/C7EE03554C

Rai, A. K., Anh, L. T., Gim, J., Mathew, V., and Kim, J. (2014). Electrochemical properties of Na_xCoO_2 (x∼0.71) cathode for rechargeable sodium-ion batteries. *Ceram. Int.* 40, 2411–2417. doi: 10.1016/j.ceramint.2013.08.013

Roger, M., Morris, D. J., Tennant, D., A., Gutmann, M. J., Goff, J. P., Hoffmann, J.-U., et al. (2007). Patterning of sodium ions and the control of electrons in sodium cobaltate. *Nature* 445:631. doi: 10.1038/nature05531

Rong, X., Liu, J., Hu, E., Liu, Y., Wang, Y., Wu, J., et al. (2018). Structure-induced reversible anionic redox activity in Na layered oxide cathode. *Joule* 2, 125–140. doi: 10.1016/j.joule.2017.10.008

Rozier, P., Sathiya, M., Paulraj, A.-R., Foix, D., Desaunay, T., Taberna, P.-L., et al. (2015). Anionic redox chemistry in Na-rich $Na_2Ru_{1-y}Sn_yO_3$ positive electrode material for Na-ion batteries. *Electrochem. Commun.* 53, 29–32. doi: 10.1016/j.elecom.2015.02.001

Saadoune, I., Maazaz, A., Ménétrier, M., and Delmas, C. (1996). On the $Na_xNi_{0.6}Co_{0.4}o_2$system: physical and electrochemical studies. *J. Solid State Chem.* 122, 111–117. doi: 10.1006/jssc.1996.0090

Sabi, N., Doubaji, S., Hashimoto, K., Komaba, S., Amine, K., Solhy, A., et al. (2017). Layered P2-$Na_{2/3}Co_{1/2}Ti_{1/2}O_2$ as a high-performance cathode material for sodium ion batteries. *J. Power Sources* 342, 998–1005. doi: 10.1016/j.jpowsour.2017.01.025

Sathiya, M., Hemalatha, K., Ramesha, K., Tarascon, J. M., and Prakash, A. S. (2012). Synthesis, structure, and electrochemical properties of the layered sodium insertion cathode material: $NaNi_{1/3}Mn_{1/3}Co_{1/3}O_2$. *Chem. Mater.* 24, 1846–1853. doi: 10.1021/cm300466b

Sathiya, M., Jacquet, Q., Doublet, M.-L., Karakulina, O. M., Hadermann, J.,and Tarascon, J.-M. (2018). A chemical approach to raise cell voltage and suppress phase transition in O3 sodium layered oxide electrodes. *Adv. Energy Mater.* 0, 1702599. doi: 10.1002/aenm.201702599

Satyanarayana, M., Jibin, A. K., and Varadaraju, U. V. (2016). Synthesis, structural and electrochemical study of O3-$NaNi_{0.4}Mn_{0.4}Co_{0.2}O_2$ as a cathode material for Na-ion batteries. *Rsc Adv.* 6, 61334–61340. doi: 10.1039/C6RA06785A

Senguttuvan, P., Rousse, G., Seznec, V., Tarascon, J.-M., and Palacín, M. R. (2011). $Na_2Ti_3O_7$: lowest voltage ever reported oxide insertion electrode for sodium ion batteries. *Chem. Mater.* 23, 4109–4111. doi: 10.1021/cm202076g

Shannon, R. D. (1976). Revised effective ionic-radii and systematic studies of interatomic distances in halides and chalcogenides. *Acta Crystallogr. Sect. A* 32, 751–767. doi: 10.1107/S0567739476001551

Shu, G. J., and Chou, F. C. (2008). Sodium-ion diffusion and ordering in single-crystal P2-Na_xCoO_2. *Phys. Rev. B* 78:052101. doi: 10.1103/PhysRevB.78.052101

Song, S., Kotobuki, M., Chen, Y., Manzhos, S., Xu, C., Hu, N., et al. (2017). Na-rich layered $Na_2Ti_{1-x}Cr_xO_{3-x/2}$ (x = 0, 0.06): Na-ion battery cathode materials with high capacity and long cycle life. *Sci. Rep.* 7:373. doi: 10.1038/s41598-017-00346-x

Su, D., Cortie, M., Fan, H., and Wang, G. (2017). Prussian blue nanocubes with an open framework structure coated with PEDOT as high-capacity cathodes for lithium-sulfur batteries. *Adv. Mater* 29:1700587. doi: 10.1002/adma.201700587

Sun, X., Ji, X.-Y., Xu, H.-Y., Zhang, C.-Y., Shao, Y., Zang, Y., et al. (2016). Sodium insertion cathode material $Na_{0.67}Ni_{0.4}Co_{0.2}Mn_{0.4}O_2$ with excellent electrochemical properties. *Electrochim. Acta* 208, 142–147. doi: 10.1016/j.electacta.2016.04.067

Thackeray, M. M., Shao-Horn, Y., Kahaian, A. J., Kepler, K. D., Skinner, E., Vaughey, J. T., et al. (1998). Structural fatigue in spinel electrodes in high voltage (4 V) $Li/Li_xMn_2O_4$ cells. *Electrochem. Solid-State Lett.* 1, 7–9. doi: 10.1149/1.1390617

Toumar, A. J., Ong, S. P., Richards, W. D., Dacek, S., and Cedert G. (2015). Vacancy ordering in O3-type layered metal oxide sodium-ion battery cathodes. *Phys. Rev. Appl.* 4:064002. doi: 10.1103/PhysRevApplied.4.064002

Tripathi, R., Wood, S. M., Islam, M. S., Nazar, L., and Nazar, L. F. (2013). Na-ion mobility in layered Na_2FePO_4F and olivine $Na[Fe,Mn]PO_4$. *Energy Environ. Sci.* 6, 2257–2264. doi: 10.1039/c3ee40914g

Vassilaras, P., Ma, X., Li, X., and Ceder, G. (2013). Electrochemical properties of monoclinic $NaNiO_2$. *J. Electrochem. Soc* 160, A207–A211. doi: 10.1149/2.023302jes

Vassilaras, P., Toumar, A. J., and Ceder, G. (2014). Electrochemical properties of $NaNi_{1/3}Co_{1/3}Fe_{1/3}O_2$ as a cathode material for Na-ion batteries. *Electrochem. Commun.* 38, 79–81. doi: 10.1016/j.elecom.2013.11.015

Wang, H., Gu, M., Jiang, J., Lai, C., and Ai, X. (2016a). An O3-type $NaNi_{0.5}Mn_{0.3}Ti_{0.2}O_2$ compound as new cathode material for room-temperature sodium-ion batteries. *J. Power Sources* 327, 653–657. doi: 10.1016/j.jpowsour.2016.07.109

Wang, J., He, X., Zhou, D., Schappacher, F., Zhang, X., Liu, H., et al. (2016b). O3-type $Na[Fe_{1/3}Ni_{1/3}Ti_{1/3}]O_2$ cathode material for rechargeable sodium ion batteries. *J. Mater. Chem. A* 4, 3431–3437. doi: 10.1039/C5TA10520J

Wang, L., Sun, Y.-G., Hu, L.-L., Piao, J.-Y., Guo, J., Manthiram, A., et al. (2017). Copper-substituted $Na0.67Ni_{0.3-x}Cu_xMn_{0.7}O_2$ cathode materials for sodium-ion batteries with suppressed P2-O2 phase transition. *J. Mater. Chem. A* 5, 8752–8761. doi: 10.1039/C7TA00880E

Wang, P.-F., Xin, H., Zuo, T.-T., Li, Q., Yang, X., Yin, Y.-X., et al. (2018b). An abnormal 3.7 Volt O3-type sodium-ion battery cathode. *Angew. Chem. Int. Ed.* 57, 8178–8183. doi: 10.1002/anie.201804130

Wang, P.-F., Yao, H.-R., Liu, X.-Y., Zhang, J.-N., Gu, L., Yu, X.-Q., et al. (2017). Ti-substituted $NaNi_{0.5}Mn_{0.5-x}Ti_xO_2$ cathodes with reversible O3–P3 phase transition for high-performance sodium-ion batteries. *Adv. Mater.* 29:1700210. doi: 10.1002/adma.201700210

Wang, P.-F., You, Y., Yin, Y.-X., and Guo, Y.-G. (2016d). An O3-type $NaNi_{0.5}Mn_{0.5}O_2$ cathode for sodium-ion batteries with improved rate performance and cycling stability. *J. Mater. Chem. A* 4, 17660–17664. doi: 10.1039/C6TA07589D

Wang, P.-F., You, Y., Yin, Y.-X., and Guo, Y.-G. (2018c). Layered oxide cathodes for sodium-ion batteries: phase transition, air stability, and performance. *Adv. Energy Mater.* 8:1701912. doi: 10.1002/aenm.201701912

Wang, P.-F., You, Y., Yin, Y.-X., Wang, Y.-S., Wan, L.-J., Gu, L., et al. (2016c). Suppressing the P2–O2 phase transition of $Na_{0.67}Mn_{0.67}Ni_{0.33}O_2$ by magnesium substitution for improved sodium-ion batteries. *Angew. Chem. Int. Ed. Engl.* 55, 7445–7449. doi: 10.1002/anie.201602202

Wang, P. F., Yao, H. R., Liu, X. Y., Yin, Y.-X, Zhang, J. N., Wen, Y., et al. (2018a). $Na(^+)$/vacancy disordering promises high-rate Na-ion batteries. *Sci. Adv.* 4:eaar6018. doi: 10.1126/sciadv.aar6018

Wang, Q., Xu, J., Zhang, W., Mao, M., Wei, Z., Wang, L., et al. (2018d). Research progress on vanadium-based cathode materials for sodium ion batteries. *J. Mater. Chem. A* 6, 8815–8838. doi: 10.1039/C8TA01627E

Wang, Y., Xiao, R., Hu, Y. S., Avdeev, M., and Chen, L. (2015). P2-$Na_{0.6}[Cr_{0.6}Ti_{0.4}]O_2$ cation-disordered electrode for high-rate symmetric rechargeable sodium-ion batteries. *Nat. Commun.* 6:6954. doi: 10.1038/ncomms7954

Wu, D., Li, X., Xu, B., Twu, N., Liu, L., and Ceder, G. (2015). $NaTiO_2$: a layered anode material for sodium-ion batteries. *Energy Environ. Sci.* 8, 195–202. doi: 10.1039/C4EE03045A

Wu, X., Guo, J., Wang, D., Zhong, G., McDonald, M. J., and Yang, Y. (2015). P2-type $Na_{0.66}Ni_{0.33-x}Zn_xMn_{0.67}O_2$ as new high-voltage cathode materials for sodium-ion batteries. *J. Power Sources* 281, 18–26. doi: 10.1016/j.jpowsour.2014.12.083

Xiang, X., Zhang, K., and Chen, J. (2015). Recent advances and prospects of cathode materials for sodium-ion batteries. *Adv. Mater.* 27, 5343–5364. doi: 10.1002/adma.201501527

Xu, J., Lee, D. H., Clément, R. J., Yu, X., Leskes, M., Pell, A. J., et al. (2014). Identifying the critical role of Li substitution in P2–$Na_x[Li_yNi_zMn_{1-y-z}]O_2$ ($0 < x, y, z < 1$) intercalation cathode materials for high-energy Na-Ion batteries. *Chem. Mater.* 26, 1260–1269. doi: 10.1021/cm403855t

Yabuuchi, N., Kajiyama, M., Iwatate, J., Nishikawa, H., Hitomi, S., Okuyama, R., et al. (2012a). P2-type $Na_x[Fe_{1/2}Mn_{1/2}]O_2$ made from earth-abundant elements for rechargeable Na batteries. *Nat. Mater.* 11, 512–517. doi: 10.1038/nmat3309

Yabuuchi, N., Kubota, K., Dahbi, M., and Komaba, S. (2014). Research development on sodium-ion batteries. *Chem. Rev.* 114, 11636–11682. doi: 10.1021/cr500192f

Yabuuchi, N., Yoshida, H., and Komaba, S. (2012b). Crystal structures and electrode performance of alpha-$NaFeO_2$ for rechargeable sodium batteries. *Electrochemistry* 80, 716–719. doi: 10.5796/electrochemistry.80.716

Yang, J., Wang, Y., Li, W., Wang, L., Fan, Y., Jiang, W., et al. (2017). Amorphous TiO_2 shells: a vital elastic buffering layer on silicon nanoparticles for high-performance and safe lithium storage. *Adv. Mater.* 29:1700523. doi: 10.1002/adma.201700523

Yang, Z., Zhang, J., Kintner-Meyer, M. C., Lu, X., Choi, D., Lemmon, J. P., et al. (2011). Electrochemical energy storage for green grid. *Chem. Rev.* 111, 3577–3613. doi: 10.1021/cr100290v

Yao, H.-R., Wang, P.-F., Gong, Y., Zhang, J., Yu, X., Gu, L., et al. (2017). Designing air-stable O3-type cathode materials by combined structure modulation for Na-Ion batteries. *J. Am. Chem. Soc.* 139, 8440–8443. doi: 10.1021/jacs.7b05176

You, Y., Dolocan, A., Li, W., and Manthiram, A. (2018). Understanding the air-exposure degradation chemistry at a nanoscale of layered oxide cathodes for sodium-ion batteries. *Nano Lett.* 19, 182–188 doi: 10.1021/acs.nanolett.8b03637

You, Y., Kim, S. O., and Manthiram, A. (2017). A Honeycomb-layered oxide cathode for sodium-ion batteries with suppressed P3–O1 phase transition. *Adv. Energy Mater.* 7:1601698. doi: 10.1002/aenm.201601698

Yu, C.-Y., Park, J.-S., Jung, H.-G., Chung, K.-Y., Aurbach, D., Sun, Y.-K., et al. (2015). $NaCrO_2$ cathode for high-rate sodium-ion batteries. *Energy Environ. Sci.* 8, 2019–2026. doi: 10.1039/C5EE00695C

Yue, J.-L., Yin, W.-W., Cao, M.-H., Zulipiya, S., Zhou, Y.-N., and Fu, Z.-W. (2015). A quinary layer transition metal oxide of $NaNi_{1/4}Co_{1/4}Fe_{1/4}Mn_{1/8}Ti_{1/8}O_2$ as a high-rate-capability and long-cycle-life cathode material for rechargeable sodium ion batteries. *Chem. Commun.* 51, 15712–15715. doi: 10.1039/C5CC06585B

Zhang, X.-H., Pang, W.-L., Wan, F., Guo, J.-Z., Lu, H.-Y., Li, J.-Y., et al. (2016). P2-$Na_{2/3}Ni_{1/3}Mn_{5/9}Al_{1/9}O_2$ microparticles as superior cathode material for sodium-ion batteries: enhanced properties and mechanisam via graphene connection. *ACS Appl. Mater. Interfaces* 8, 20650–20659. doi: 10.1021/acsami.6b03944

Zhang, Y., Zhao, H., and Du, Y. (2016). Symmetric full cells assembled by using self-supporting $Na_3V_2(PO_4)_3$ bipolar electrodes for superior sodium energy storage. *J. Mater. Chem. A* 4, 7155–7159. doi: 10.1039/C6TA02218A

Zheng, C., Radhakrishnan, B., Chu, I.-H., Wang, Z., and Ong, S. P. (2017). Effects of transition-metal mixing on Na ordering and kinetics in layered P2 oxides. *Phys. Rev. Appl.* 7:064003. doi: 10.1103/PhysRevApplied.7.064003

Zheng, L., Li, J., and Obrovac, M. N. (2017). Crystal structures and electrochemical performance of air-stable $Na_{2/3}Ni_{1/3-x}Cu_xMn_{2/3}O_2$ in sodium cells. *Chem. Mater.* 29, 1623–1631. doi: 10.1021/acs.chemmater.6b04769

Zheng, L., and Obrovac, M. N. (2017). Investigation of O3-type $Na_{0.9}Ni_{0.45}Mn_xTi_{0.55-x}O_2$ ($0 \leq x \leq 0.55$) as positive electrode materials for sodium-ion batteries. *Electrochim. Acta* 233, 284–291. doi: 10.1016/j.electacta.2017.03.033

Zhu, G., Zhang, F., Li, X., Luo, W., Li, L., Zhang, H., et al. (2019). Engineering the distribution of carbon *in silicon* oxide nanospheres at atomic level for highly stable anodes. *Angew Chem Int Ed Engl* 58, 1–6. doi: 10.1002/anie.201902083

Zhu, H., Lee, K. T., Hitz, G. T., Han, X., Li, Y., Wan, J., et al. (2014). Free-standing $Na_{2/3}Fe_{1/2}Mn_{1/2}O_2$@graphene film for a sodium-ion battery cathode. *ACS Appl. Mater. Interfaces* 6, 4242–4247. doi: 10.1021/am405970s

Zhu, Y.-E., Qi, X., Chen, X., Zhou, X., Zhang, X., Wei, J., et al. (2016). A P2-$Na_{0.67}Co_{0.5}Mn_{0.5}O_2$ cathode material with excellent rate capability and cycling stability for sodium ion batteries. *J. Mater. Chem. A* 4, 11103–11109. doi: 10.1039/C6TA02845D

Conflict of Interest Statement: The authors declare that the research was conducted in the absence of any commercial or financial relationships that could be construed as a potential conflict of interest.

Copyright © 2019 Zhang, Zhang and Huang. This is an open-access article distributed under the terms of the Creative Commons Attribution License (CC BY). The use, distribution or reproduction in other forums is permitted, provided the original author(s) and the copyright owner(s) are credited and that the original publication in this journal is cited, in accordance with accepted academic practice. No use, distribution or reproduction is permitted which does not comply with these terms.

frontiers in Chemistry

REVIEW
published: 31 May 2019
doi: 10.3389/fchem.2019.00387

Crucial Breakthrough of Functional Persistent Luminescence Materials for Biomedical and Information Technological Applications

Huaxin Tan, Taoyu Wang, Yaru Shao, Cuiyun Yu and Lidan Hu**

Hunan Province Cooperative Innovation Center for Molecular Target New Drug Study, Department of Biochemistry and Molecular Biology, University of South China, Hengyang, China

Persistent luminescence is a phenomenon in which luminescence is maintained for minutes to hours without an excitation source. Owing to their unique optical properties, various kinds of persistent luminescence materials (PLMs) have been developed and widely employed in numerous areas, such as bioimaging, phototherapy, data-storage, and security technologies. Due to the complete separation of two processes, —excitation and emission—, minimal tissue absorption, and negligible autofluorescence can be obtained during biomedical fluorescence imaging using PLMs. Rechargeable PLMs with super long afterglow life provide novel approaches for long-term phototherapy. Moreover, owing to the exclusion of external excitation and the optical rechargeable features, multicolor PLMs, which have higher decoding signal-to-noise ratios and high storage capability, exhibited an enormous application potential in information technology. Therefore, PLMs have significantly promoted the application of optics in the fields of multimodal bioimaging, theranostics, and information technology. In this review, we focus on the recently developed PLMs, including inorganic, organic and inorganic-organic hybrid PLMs to demonstrate their superior applications potential in biomedicine and information technology.

Keywords: persistent luminescence material, biomedical applications, information technological applications, biosensing, optical data recording, anti-counterfeiting, therapy, bioimaging

OPEN ACCESS

Edited by:
Fan Zhang,
Fudan University, China

Reviewed by:
Renren Deng,
Zhejiang University, China
Ruoxue Yan,
University of California, Riverside, United States

****Correspondence:***
Cuiyun Yu
yucuiyunusc@hotmail.com
Lidan Hu
bluebaby147@126.com

Specialty section:
This article was submitted to Nanoscience, a section of the journal Frontiers in Chemistry

Received: *05 February 2019*
Accepted: *14 May 2019*
Published: *31 May 2019*

Citation:
Tan H, Wang T, Shao Y, Yu C and Hu L (2019) Crucial Breakthrough of Functional Persistent Luminescence Materials for Biomedical and Information Technological Applications. Front. Chem. 7:387. doi: 10.3389/fchem.2019.00387

INTRODUCTION

Persistent luminescence (PL) is an optical phenomenon, in which luminescence is maintained for an appreciable time after the termination of the excitation (Hölsä, 2009). Although the origins of the PL emission are still in debate, the research, and applications of persistent luminescence materials (PLMs) have rapidly grown since the PL emission was first observed from a mineral barite (Bologna stone) in the 17th century (Lastusaari et al., 2012).

Following the enhancement in intensity, stability, and duration of PL, inorganic PLMs covering various emission colors have been fully studied and commercially applied. Since the first $SrAl_2O_4:Eu^{2+},Dy^{3+}$ green emission PLM was discovered by Matsuzawa et al. (1996), persistent luminescence phosphors (PLPs) have been rapidly developed in the last decade (Matsuzawa et al., 1996). Recently, several PLPs emitting in visual spectra have been commercialized as important night-vision materials for various innovations, owing to their sufficiently strong, and ultra-long

(>10 h) PL excited by sunlight or room light (Matsuzawa et al., 1996; Yamamoto and Matsuzawa, 1997; Wang et al., 2003). In the last few decades, visible light emitting PLPs have been widely utilized in critical applications including interior decorations, displays, signals and even certain newly-emerged technologies of anti-counterfeiting, optical recording, or biochemistry (Hölsä, 2009; Pan et al., 2012).

For biomedical applications, the PLMs can be ideal alternatives for traditional fluorescent materials, especially in bioimaging, due to the following two reasons (Lécuyer et al., 2016; Liu et al., 2018a). First, the entire fluorescence signal emitted from the PLMs *in vivo* because the tissue autofluorescence is eliminated owing to the termination of the excitation. Second, the delayed luminescence of PLMs facilitates long-time *in vitro* and *in vivo* bioimaging. In addition, the excitation and emission spectra of PLMs can be tuned conveniently to satisfy diverse demands. A typical example is near-infrared (NIR) luminescence, which is the most widely used excitation or emission wavelength in living imaging to achieve penetrability in deeper tissues (Wang et al., 2017a). However, a major limitation is the biocompatible size of PLMs. In 2007, PLM was synthesized in nanoscale in a pioneering study, initiating the research on persistent luminescence nanoparticles (PLNPs) (le Masne de Chermont et al., 2007). In addition to the above advantages, it has been verified by subsequent research in biomedical theranostics, that PLNPs have excellent dispersibility, biocompatibility and modifiability (Wang et al., 2017a; Sun et al., 2018; Xia et al., 2018).

Meanwhile, the novel generation of organic carbon-based PLMs ranging from small molecules to polymers has attracted significant attention. Compared with inorganic PLMs, the production of organic PLMs is more facile and controllable with reduced costs (Dimitrakopoulos and Malenfant, 2002; Kabe et al., 2016). The functionalization of organic PLMs with organic groups and biological ligands is more achievable. Moreover, their second level lifetime and environmental dependent feature is more suitable for demanding applications including display (Kabe et al., 2016), anti-counterfeiting (Zhou et al., 2015), bioimaging (Mikael et al., 2015), and sensors (Yang and Yan, 2016b).

With deeper understanding of the PL emission mechanism and the rapid development of synthesis technologies, more advanced applications based on PLMs have been explored. In this study, we review the crucial breakthroughs and the latest developments of research on PLMs with and without rare-element doping, to demonstrate their superior applications in biomedicine and information technology.

CLASSIFICATIONS

Inorganic PLMs

Phosphors

Since the first $SrAl_2O_4:Eu^{2+},Dy^{3+}$ PLM of green emission was discovered by Matsuzawa et al. (1996), PLPs have been rapidly developed in the last decade (Matsuzawa et al., 1996). Currently, several PL phosphors emitted in the visual spectrum, such as $CaAl_2O_4:Eu^{2+}$, Nd^{3+} (blue emission), (Yamamoto and Matsuzawa, 1997) $SrAl_2O_4:Eu^{2+},Dy^{3+}$ (green emission), (Matsuzawa et al., 1996), and $Y_2O_2S:Eu^{3+},Mg^{2+},Ti^{2+}$ (red emission) (Wang et al., 2003), have been widely commercialized as important night-vision materials. Recently, researches have mainly focused on extending the emission and excitation spectrum and prolonging the PL duration.

To achieve an unchanged white afterglow color, an effective strategy is to combine different color emission from an identical luminescence center (Liu et al., 2005; Kuang et al., 2006). For example, by doping Tb^{3+} into $Y_3\ Al_2\ Ga_3\ O_{12}$ host, three kinds of cross-relaxation energy transfer proceed: $^5D_3 \rightarrow\ ^5D_4$ and $^7F_6 \rightarrow\ ^7F_0$, $^7D_J \rightarrow\ ^5D_{1,2,3}$ and $^7F_6 \rightarrow\ ^5D_4$, and $^5D_4 \rightarrow\ ^7F_4$ and $^5D_4 \rightarrow\ ^7F_3$ in Tb^{3+}, which are blue, green and red emissions respectively. By tuning the doping concentration of Tb^{3+}, an unchanged white PL was obtained and maintained for more than 2 h (Zhang et al., 2017). In 2015, Pan and co-workers extended the PL into the ultraviolet (UV) spectral region. Using Pb^{2+} as luminescence center, the obtained $Sr_2MgGe_2\ O_7:Pb^{2+}$ phosphors exhibited strong PL emission at 370 nm for more than 12 h (**Figure 1A**) (Liang et al., 2015).

Due to the high penetration depth and low autofluorescence, NIR-emission PLMs have attracted significant interest in biomedicine applications. For the NIR emission, Cr^{3+} is the main luminescent center with a narrow-band emission (700 nm) due to the spin-forbidden $^2E \rightarrow\ ^4A_2$ transition, and a broadband emission (650–1,000 nm) due to the spin-allowed $^4T_2 \rightarrow\ ^4A_2$ transition (Struve and Huber, 1985; Forster, 1990). In 2012, Pan and co-workers developed the $Zn_3Ga_2Ge_2O_{10}:Cr^{3+}$ phosphors for the first time, which achieved an ultra-long NIR PL duration of 360 h (**Figure 1B**) (Pan et al., 2012). This breakthrough established Cr^{3+}-doped gallates, such as $ZnGa_2O_4:Cr^{3+}$ phosphors (Li et al., 2015b), $LiGa_5O_8:Cr^{3+}$ phosphors (Liu et al., 2013), and $Ca_3Ga_2Ge_3O_{12}:Nd^{3+},Cr^{3+}$ phosphors (Lin et al., 2016) as the preferred materials to obtain NIR PLMs. Meanwhile, Cr^{3+}-doped non-gallate NIR PLMs (Zn_2-xAl_2xSn_1-x$O_4:Cr^{3+}$), emitting with a strong 650–750 nm PL for more than 120s, have also been developed (Zhang et al., 2018)

To overcome the short-wavelength excitation limitation in deep tissues application, NIR-recharged PLMs were developed by introducing the upconversion concept (Chen et al., 2018). We fabricated NIR-rechargeable upconverting PL (UCPL) phosphors by combining UV-rechargeable PLPs with typical UV/blue emission upconversion materials (NaYF4:25%Yb, 0.5%Tm) (**Figure 1C**). It should be noted, that multicolor emission can also be realized by using different emission PL components. Compared with the UV excitation, no noticeable difference was found on the persistent phosphorescence properties under the NIR (980 nm) excitation (Hu et al., 2017, 2018).

Nanoparticles

While PLPs have been synthesized and maturely used for more than 20 years, their advanced development for biological application started in 2007, when Scherman et al. introduced nanoscale PLMs in their pioneering work (le Masne de Chermont et al., 2007). The conventional strategies for the preparation of PLPs typically involved high-temperature

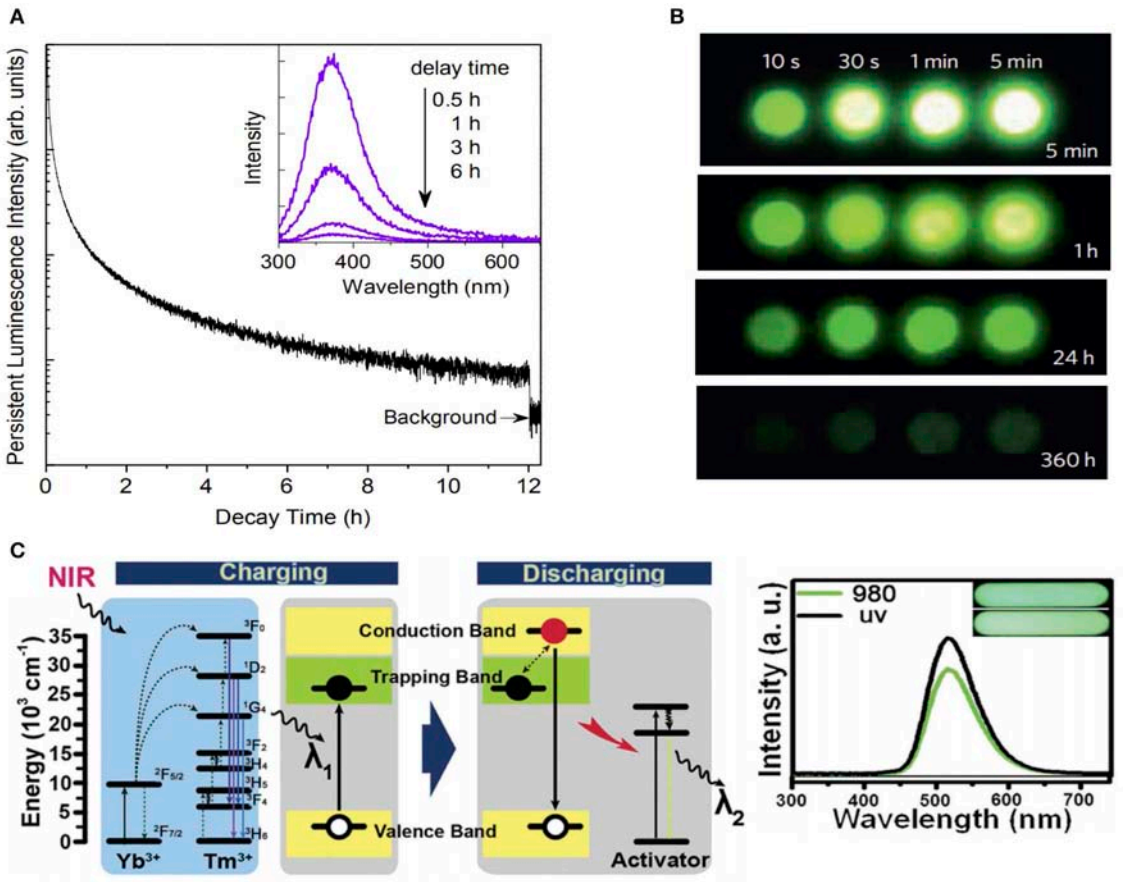

FIGURE 1 | (A) PL decay curve monitored at 370 nm after irradiation by 254-nm UV for 15 min (Liang et al., 2015). **(B)** NIR images of four $Zn_3Ga_2Ge_2O10$: 0.5%Cr^{3+} phosphor discs taken at different afterglow times after irradiation by a 365-nm lamp for durations ranging from 10 s to 5 min (Pan et al., 2012). **(C)** Energy transfer mechanism of UCPL materials (left), and the PL spectra of green emission UCPL materials taken 30 s after the excitation under 980-nm and UV lights for 15 s (right) (Hu et al., 2017). Reproduced with permission from Dalton Transactions, Nature Materials and Advanced Optical Materials.

calcination for the formation of lattice defects and trap centers, which were crucial for the afterglow property of phosphors. The inevitable costs were the large irregular size and poor dispersibility of the synthesized PLPs, which limited their biological and medical applications. To overcome the solid-state barrier, Scherman and co-workers developed a sol-gel synthesis approach for the production of the first biocompatible PLNPs ($Ca_{0.2}Zn_{0.9}Mg_{0.9}Si_2O_6$ doped with Eu^{2+}, Dy^{3+}, and Mn^{2+}) and application for *in vivo* imaging. Moreover, those nanoparticles exhibited strong persistent NIR luminescence *in vivo* for more than 1 h after being excited by UV light before injection.

In recent years, motivated by this, an increasing number of synthetic routes have been reported and summarized (Li et al., 2016). In 2017, Wang et al. outlined established techniques for PLNP preparation and classified them into two groups: the top-down and bottom-up approaches (Wang et al., 2017a). In the top-down approach, the PL of PLPs is formed in solid or sol-gel state via high-temperature combustion. From large to small, or top to down, the PLPs with large size are processed into PLNPs by certain physical methods such as grinding and pulsed laser ablation.

To achieve size- and shape-controlled building-up processes, the bottom to top methods, including hydrothermal synthesis and the template method, introduced new approaches for PLNP construction. To obtain PLNPs with diverse morphology, the synthetic processes are highly controllable by adjusting the reaction conditions. In 2015, Han et al. used a hydrothermal method for PLNP production for the first time (Li et al., 2015a). An 8-nm nanoparticle $ZnGa_2O_4Cr_{0.004}$ PLNP was synthesized in solution, which possessed renewable NIR PL and exhibited excellent monodispersity under different aqueous conditions. Yang et al. synthesized $ZnGa_2O_4$:Cr^{3+} PLNPs with specific kiwifruit-like structures using silica as templates (Lin et al., 2017). The designed morphology could be conveniently controlled by changing the size and thickness of the silica templates, which ensured the NIR PL performance during high-temperature calcination. In addition to the size and shape, the superficial geography of PLNPs, which is critical for biomedical applications,

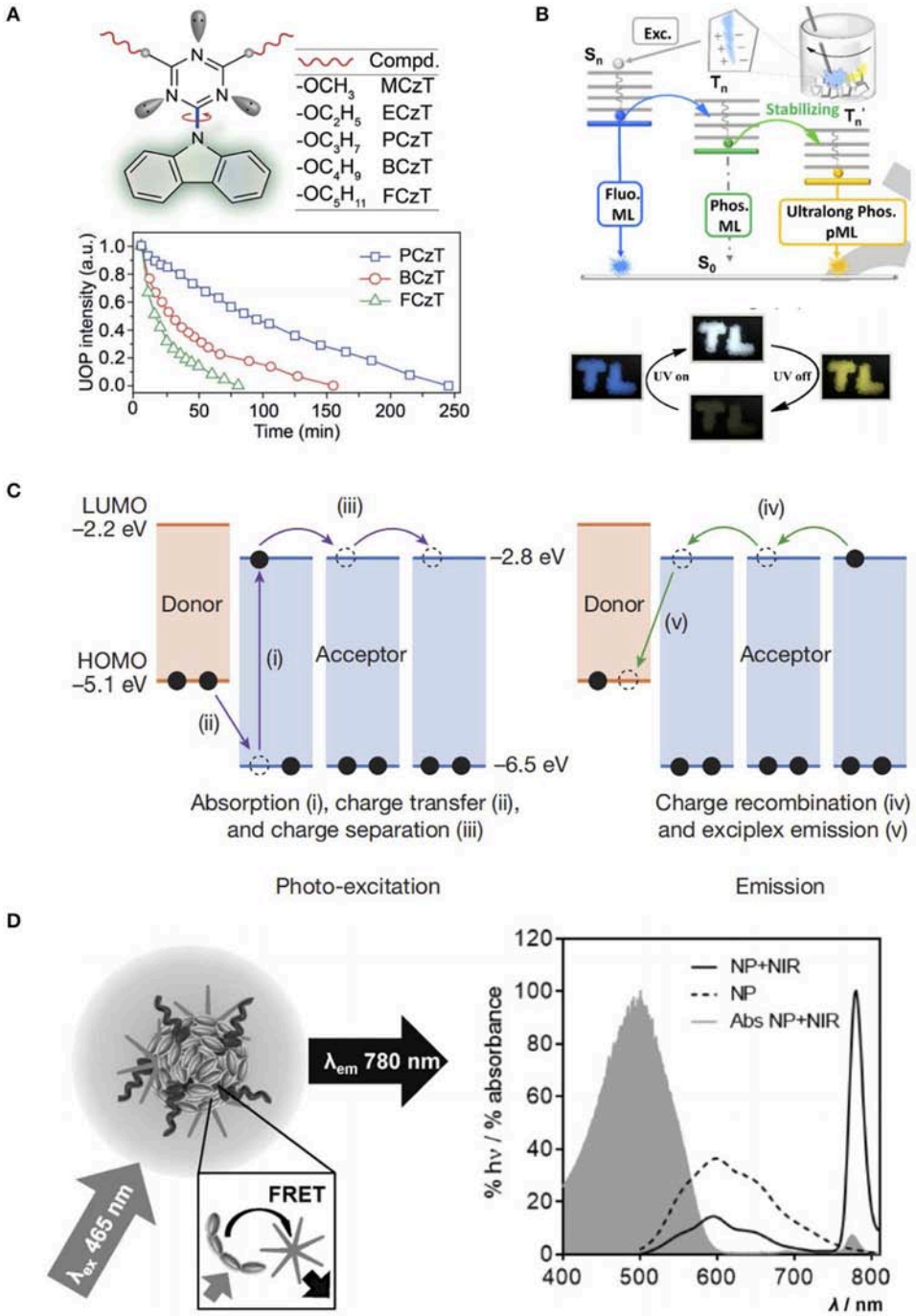

FIGURE 2 | (A) Rational design of molecular rotors (top) and ultra-long organic phosphorescence deactivation process by monitoring the emission intensities at 530 nm under ambient conditions (bottom) (Gu et al., 2018). **(B)** Energy transfer processes for transient and persistent ML of ImBr (top) and tricolor emission switching of ImB (bottom) (Li et al., 2018). **(C)** Emission mechanism of organic PL (Kabe and Adachi, 2017). **(D)** Schematic of the FRET from the MEH-PPV polymer to the NIR775 dye (left), and fluorescence spectra of the NPs with and without NIR775 dye, and absorbance spectrum of the NPs with NIR775 (right) (Mikael et al., 2015). Reproduced with permission from Angewandte Chemie International Edition, Nature, and Angewandte Chemie, respectively.

can be easily modified in the bottom-up approach. Yan et al. reported dual-modal PLNPs, functionalized with hyaluronic acid (HA) modified Gd_2O_3 via hydrothermal and biomineralization synthesis (Wang et al., 2017c). The possible application of these versatile nanoprobes can be in PL and magnetic resonance (MR) imaging, as $ZnGa_2O_4:Cr_{0.001}$ provides the NIR PL, Gd_2O_3 enhances the MR signals, and the HA can target tumor cells *in vitro* and *in vivo*.

Organic PLMs

Inorganic PLMs doped with rare-earth elements exhibit excellent optical performance with high durability and long emission. However, these systems have low dispersibility and biocompatibility, and require complex fabrication process, which limit its future applications. To overcome these limitations, several types of organic PLMs have been investigated.

Owing to the short-lived singlet exciton for fluorescence, it is a great challenge to achieve PL in purely small organic molecules, especially in single-component PL. In 2015, Huang et al. proposed that triplet excited states could be stabilized by strong coupling in H-aggregated structures. Based on this principle, a diverse array of purely organic-molecule PLMs was found with ultra-long second level luminescence lifetimes. By tailoring the molecule structures, the emission color can be tuned from green to red (An et al., 2015). In their subsequent research, a series of organic PLMs with a triazine core, carbazole unit, and alkoxy chains were designed (**Figure 2A**). The PL lifetimes were increased from ms to s by exploiting the rotor unit of carbazole and triazine, which could stabilize excited triplet excitons via the manipulation of intermolecular interactions (Gu et al., 2018). In 2018, Chi and co-workers presented a purely organic aggregation-induced emission (AIE) for the first time that exhibited transient, persistent photoluminescence, and persistent mechanoluminescence (ML) at room temperature (Li et al., 2018). As a key functional unit, N-(4-trifluoromethylphenyl)phthalimide was introduced, which was favorable to form crystals and to prevent non-radiative transitions by immobilizing the molecular conformations. Owing to its capability of promoting spin-forbidden transitions, a bromine substituent was used to enhance the intersystem crossing efficiency of the singlet-to-triplet excited state. The tricolor emission switching between blue, white, and yellow could be obtained by simply switching on and off the UV lamp (**Figure 2B**).

To achieve multi-component PL, a commonly used strategy is the host-guests system, which consists of phosphorescent guests and efficient non-radiative vibration- limiting hosts (Hirata et al., 2013). However, the practical preparation is rather complex owing to the requirement of the elaborate selection of host and guest molecules for good compatibility and the careful tuning of doping concentration to obtain the best PL performance. In 2017, Kabe and Adachi proposed a novel strategy to obtain multi-component PLMs, which only required a simple mixture of a strong electron donor N,N,N',N'-tetramethylbenzidine (TMB) with a strong electron acceptor 2,8-bis(diphenylphosphoryl)dibenzo[b,d]thiophene (PPT) (Kabe and Adachi, 2017). The gradual recombination of these two radical anions and cations provided a stable radical cation and high triplet energy, as well as a non-radiative suppressible rigid amorphous environment to generate exciplex emission (**Figure 2C**). More importantly, a breakthrough was achieved in the PL lifetime of the obtained PLMs, which was upgraded to the 1-h level. In their subsequent research, color-tuning emission from greenish-blue to red and even warm white was achieved by simply doping the organic PLMs matrix with a wide variety of emitter molecules. Due to the doped emitters, the exciplexes could generate energy via Förster resonance energy transfer (FRET), as well as prolong the emission by acting as electron trapping sites, which resulted in improved brightness and emission duration (Jinnai et al., 2018).

As important organic macromolecules, polymers were found to be suitable as PL emitters. In 2015, Rao et al. reported a certain type of fluorescent semiconducting poly[2-methoxy-5-(2-ethylhexyloxy)-1,4-phenylenevinylene] (MEH-PPV) nanoparticles, which generated NIR PL for 1-h after being excited by white light (Mikael et al., 2015). Owing to the long π-conjugation conducting bands of MEH-PPV, energy can be stored in the semiconducting layer. In the presence of NIR775, the released energy was transferred to the NIR dye encapsulated in the polymer nanoparticles and resulted in NIR PL (**Figure 2D**).

In addition to single component polymer PLMs, polymers of polylactic acid (PLA), poly-arylene ether phosphine oxide (PBPO), poly-methyl methacrylate (PMMA), poly-vinyl alcohol (PVA) and poly -vinyl-pyrrolidone (PVP) were also suitable as host materials to obtained multi-component PL by minimizing the non-radiative decay of the long-lived triplet excitons (Zhang et al., 2007; Al-Attar and Monkman, 2012; DeRosa et al., 2015; Gu et al., 2018). For example, a flexible organic PLMs system based on the engineering plastic PBPO was developed, and the PL of this system can be articles a for more than 7 min after low-power excitation. This polymer-based system exhibited excellent mechanical flexibility required for future applications such as curved products, fibers, and films (Yang and Yan, 2016b).

Inorganic-Organic Hybrid PLMs

As kind of inorganic-organic hybrids, metal–organic frameworks (MOFs) possess rigid inorganic porous structure, which can capture and stabilize emitter molecules. Therefore, the coordination of organic fluorescent units with common metal ions is effective in achieving PL in MOFs. Recently, Yan and co-workers have devoted significant efforts to explore MOFs-based PLMs. By coordinating terephthalic acid and Zn^{2+}, they developed Zn-isophthalic acid (Zn-IPA) MOFs for the first time, which exhibited green PL with a lifetime of 1.3 s (Yang and Yan, 2016b). To achieve color-tuning emission, N,N'-dimethylformamide (DMF) was introduced into the MOF nanochannels and formed a novel MOFs system [Zn(TPA)(DMF)], which exhibited tunable PL colors from green to red and cyan to yellow (Yang and Yan, 2016a). To increase the lifetime of PL emission, deuterated coronene was introduced into the zeolitic imidazolate framework (ZIF). After being encapsulated within this coronene@ZIF, the non-radiative deactivation of the emitter was proven to be significantly reduced and finally enabled a long lifetime of up to 22.4 s (Mieno et al., 2016).

In addition, metal coordination polymer (CP) materials with conveniently tunable photoactive units and photo-emissive properties were also designed for PLMs. Yan et al. developed a series of Cd-based CPs by coordinating Cd^{2+} with 1,3-benzenedicarboxylic acid (BDC), which exhibited a noticeable

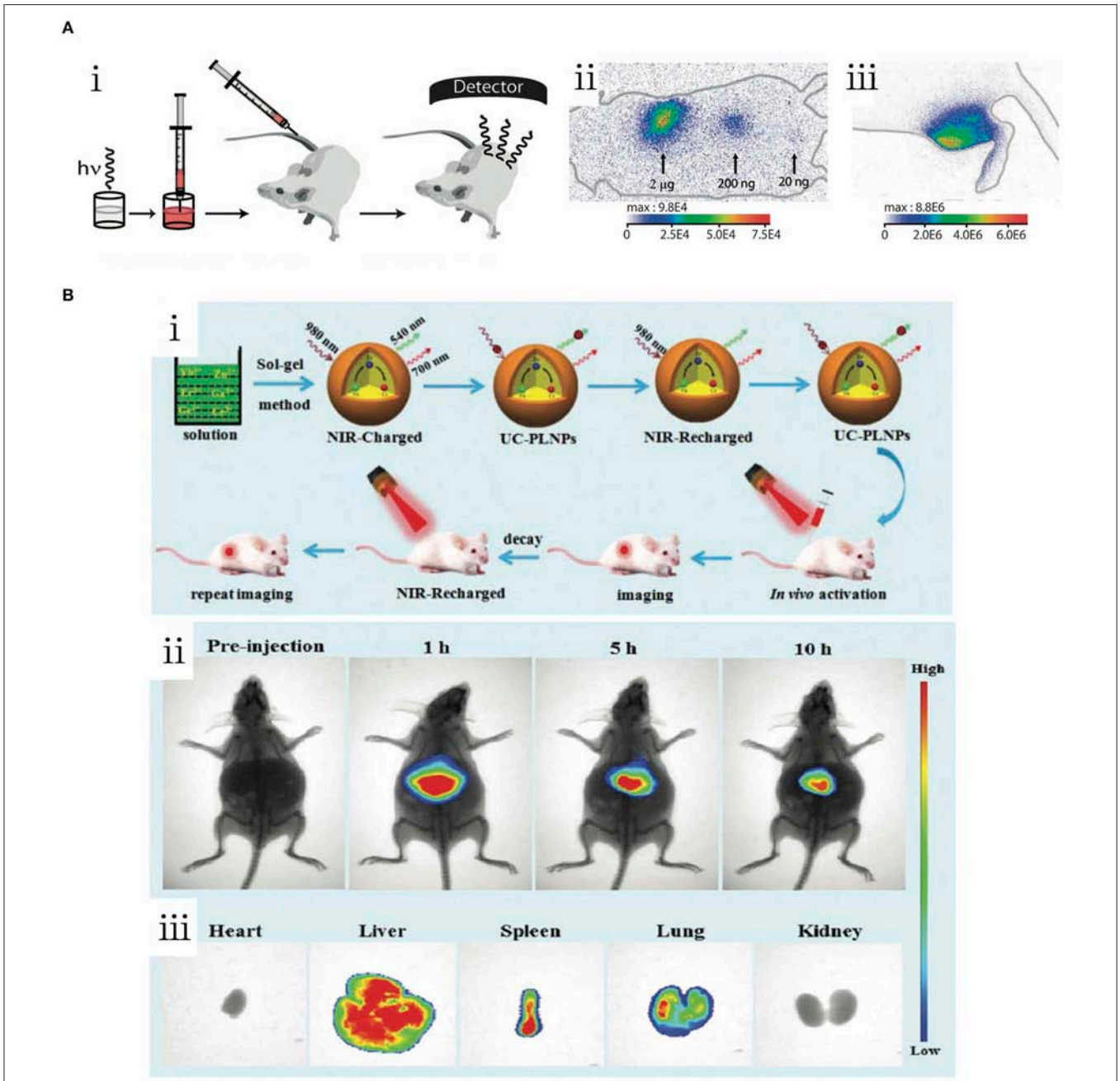

FIGURE 3 | (A) First PLNP-based *in vivo* bioimaging (le Masne de Chermont et al., 2007). (i) Schematic of the experimental procedure of the *in vivo* imaging. (ii) Living image of NPs via subcutaneous injection. (iii) Living image of NPs via intramuscular injection. **(B)** NIR-to-NIR upconverted persistent probe for *in vivo* bioimaging (Zeng et al., 2017). (i) Schematic of the preparation and experimental procedure of UC-PLNPs for *in vivo* bioimaging. (ii) *In vivo* images of UC-PLNPs under 980-nm excitation. (iii) Biodistribution of UP-PLNPs in major organs. Reproduced with permission from copyright (2007) National Academy of Sciences and Nanoscale, respectively.

ultra-long afterglow of 0.70 s (Yang et al., 2016a). To achieve color-tunable PL in CPs, a lanthanide cations doping approach was developed (Yang and Yan, 2017; Yang et al., 2017). The doped Eu^{3+} and Tb^{3+}, which have a sufficiently broad absorption band, can capture energy from CPs and show an obvious red and green PL with lifetimes of 10.54 and 57.66 ms, respectively.

APPLICATIONS

Biomedicine

Bioimaging

As mentioned in the previous section, PLNPs, especially those with NIR emission, are ideal probes in bioimaging for ultra-long PL without tissue autofluorescence background, compared

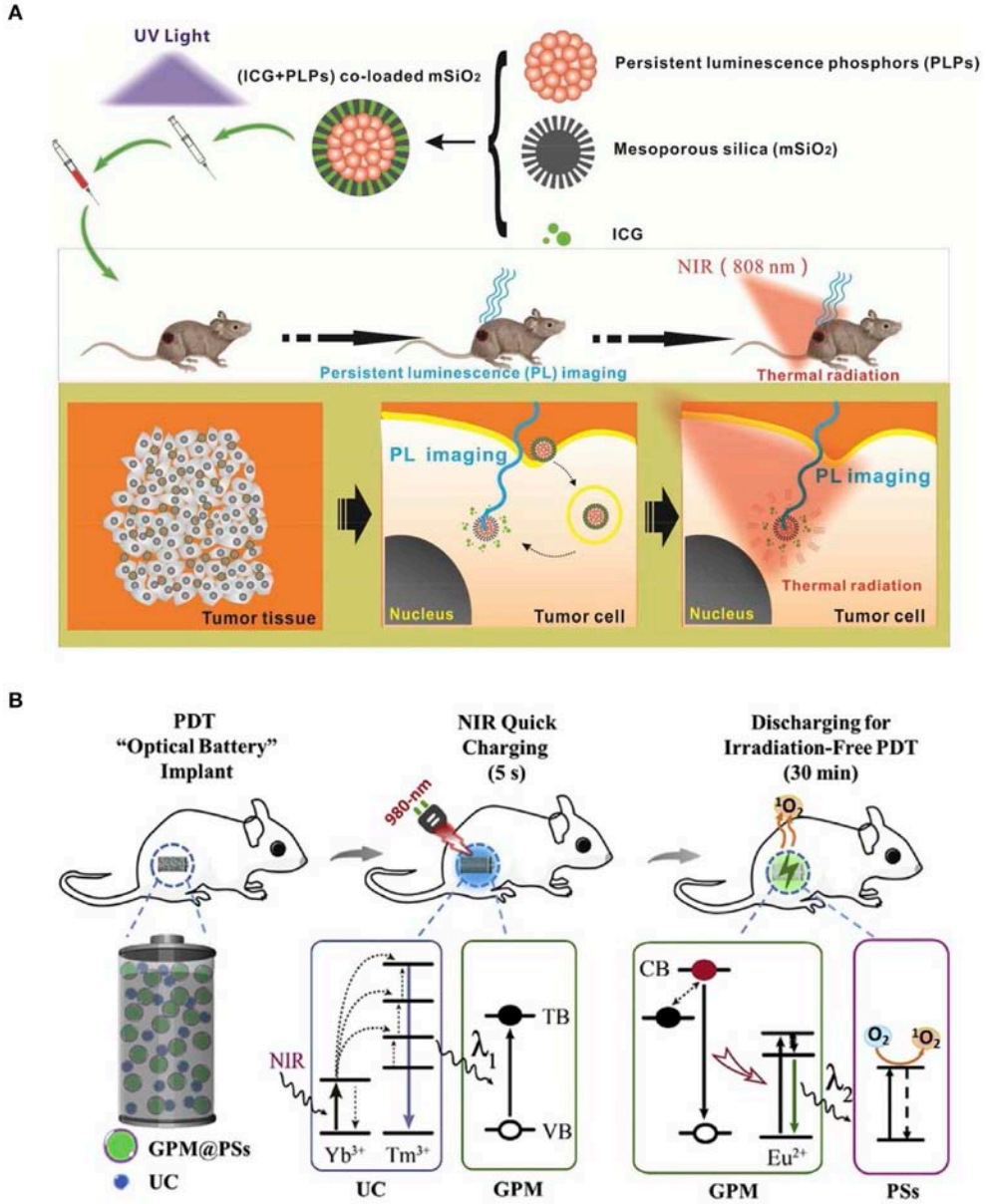

FIGURE 4 | (A) Photothermal therapy using ICG-PLPs@mSiO$_2$ (Zheng et al., 2016). **(B)** Photodynamic therapy using NIR light rechargeable UC-PLNPs (Hu et al., 2018). Reproduced with permission from ACS Applied Materials and Interfaces and Biomaterials, respectively.

with the conventional fluorescent probes such as quantum dots (Liu et al., 2018a). The first generation of PLNPs employed in *in vivo* imaging required pre-excitation by UV before being injected into the body (**Figure 3A**) (le Masne de Chermont et al., 2007). Instead of using short wavelength exciting light resources, the second generation of bioimaging PLNPs can be charged by visible lights, which enable their direct *in vivo* stimulation. Scherman et al. improved their results on living imaging by the synthesis of visible light stimulated $ZnGa_{1.995}Cr_{0.005}O_4$ PLNPs (ZGO) (Thomas et al., 2014a). The ZGO exhibited long-last NIR luminescence excited by orange/red light-emission diode (LED). Following the injection of RAW 264.7 cells with intracellular ZGO, based on the PL signals activated by LED the cells could be traced real-time *in situ* for more than 24 h. To fully exploit the tissue transparency widows in the NIR region, hybrids designs of upconversion materials and PLNPs became widely used. In 2017, Zeng and coworkers reported a combination of upconversion and PL based on the construction of upconversion-PLNPs ($Zn_3Ga_2GeO_8$:Yb/Er/Cr) (**Figure 3Bi**) (Zeng et al., 2017). Due to the upconversion effect, the nanocomposites can be excited by a 980-nm laser and emit 700 nm light, which can be absorbed and stored by PLNPs to produce NIR emission signals.

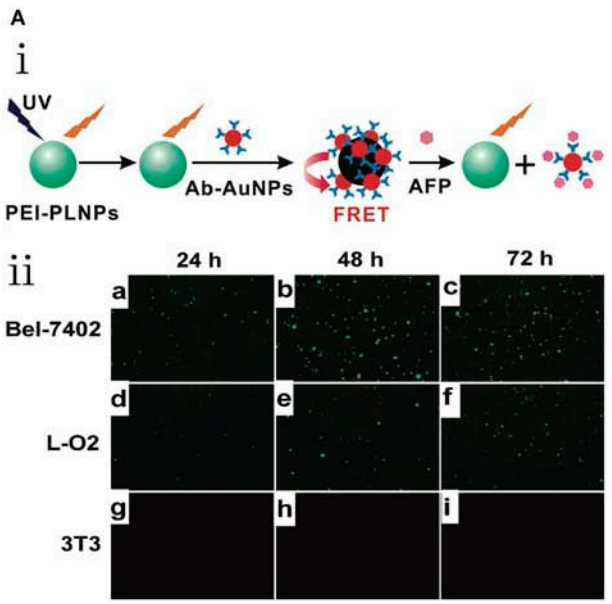

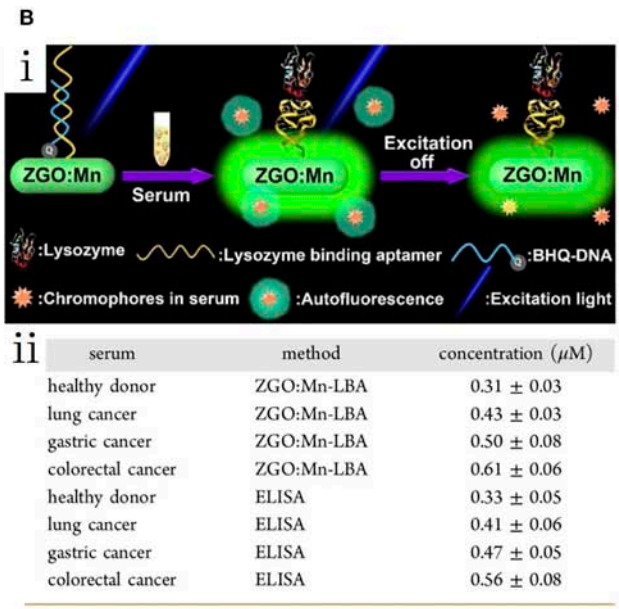

ii

serum	method	concentration (μM)
healthy donor	ZGO:Mn-LBA	0.31 ± 0.03
lung cancer	ZGO:Mn-LBA	0.43 ± 0.03
gastric cancer	ZGO:Mn-LBA	0.50 ± 0.08
colorectal cancer	ZGO:Mn-LBA	0.61 ± 0.06
healthy donor	ELISA	0.33 ± 0.05
lung cancer	ELISA	0.41 ± 0.06
gastric cancer	ELISA	0.47 ± 0.05
colorectal cancer	ELISA	0.56 ± 0.08

FIGURE 5 | (A) PLNP-based detection of AFP (Wu et al., 2011). (i) Schematic of the AFP detection of PEI-PLNPs and Ab-AuNPs. (ii) Fluorescent images of three cell lines with PLNP-based probes. **(B)** PLNR-based detection of serum lysozyme (Wang et al., 2017b). (i) Schematic of lysozyme biosensing. (ii) Detected concentrations of lysozyme by PLNRs and ELISA. Reproduced with permission from Journal of the American Chemical Society and ACS Nano, respectively.

Furthermore, studies demonstrated rechargeable *in vivo* PL for a duration of more than 10 h, which can achieve actual NIR-to-NIR bioimaging (**Figures 3B**ii,iii).

Therapy

By exploiting the PLMs irreplaceable optical nature, the PL-based theranostic applications typically combined with other therapeutic materials, can be implemented in imaging-guided chemotherapy, photothermal therapy (PTT), and photodynamic therapy (PDT) (Liu et al., 2018a; Sun et al., 2018). In 2014, Richard et al. proposed a hybrid nanostructure containing $ZnGa_{1.995}Cr_{0.005}O_4$ PLNPs and mesoporous silica as an anticancer drug delivery system (Thomas et al., 2014b). The doxorubicin-loaded ZGO@SiO_2 potently inhibited the growth of U87MG cells than the empty vectors *in vitro*. The *in vivo* transportation process was monitored in real-time. As the only FDA-approved water-soluble photothermal agent, indocyanine green (ICG) is often used in PTT systems. Chang et al. presented a novel design combining ICG and PLPs@mSiO_2 (Zheng et al., 2016). Composite materials, exhibiting both PL and photothermal conversion properties, are suitable for imaging-guided PTT (**Figure 4A**). The PL-based PDTs use a combination of PLMs and photosensitizers, which can generate cytotoxic singlet oxygen to damage the targeted cells. Zhang et al. developed a PLMs-based irradiation-free photodynamic therapeutic method by integrating the advantages of PLMs, upconversion materials, and photosensitizer (**Figure 4B**) (Hu et al., 2018). The combination of $NaYF_4$:25%Yb, 0.5%Tm upconversion materials and $SrAl_2O_4:Eu^{2+},Dy^{3+}$ PLMs enabled green PL excited by NIR. By absorbing these persistent green lights, the attached rose bengal (RB) photosensitizers were able to continuously produce singlet oxygen. Owing to the high transparency of NIR and the renewability of inner PL, the implanted material, such as an optical battery, can implement effective PDT for *in vivo* tumor suppression.

Biosensing

In 2011, Yan et al. introduced a PLNP system for biosensing (Wu et al., 2011). They combined PLNPs (Eu^{2+}- and Dy^{3+}-doped $Ca_{1.86}Mg_{0.14}ZnSi_2O_7$) and gold nanoparticles (Ab-AuNPs) modified by α-fetoprotein (AFP) antibody for the detection of AFP in tumor cells (**Figure 5A**i). The AFP is a serum glycoprotein secreted by hepatic cells in newborn period only. The abnormal increase of AFP in the serum can strongly indicate several types of cancerization. The conjugation of PLNPs and Ab-AuNPs results in an FRET attributed to the overlap of PL emission and the AuNP absorption spectra. In this process, the excited energy is captured in the FRET system, which annihilates the emitted light of the nanocomposites. While introduced to AFPs, the competing antibody-antigen bonds released the PLNPs from the AuNPs, which produces long-lasting luminescence. By avoiding the *in situ* excitation, the PLNPs-based nanosystem exhibits high signal-to-noise ratio (SNR) and excellent sensitivity for the quantitative detection of AFP in serum samples and cancer cells with a minimum detectable concentration of 0.41 μg/L (**Figure 5A**ii). Yuan et al. developed a controllable hydrothermal synthesis method to obtain PL nanorods (PLNRs) functionalized for serum lysozyme analysis (**Figure 5B**i) (Wang et al., 2017b). The further functionalization of PLNRs comprised two important parts: lysozyme-binding aptamers and a special

FIGURE 6 | (A) Pattern designed with different phosphors and demonstration of multilevel anti-counterfeiting using MCzT, PCzT, BCzT, and FCzT crystals (Gu et al., 2018). **(B)** Photographs of handwritten characters on a cigarette case under a UV lamp (254 nm) and after the lamp is switched off (Gao et al., 2017). **(C)** Typical objects stamped with orthogonal multicolor UCPL materials and the luminescence images when the 980-nm excitation is switched on and off (Hu et al., 2017). Reproduced with permission from Angewandte Chemie International Edition, Nano Research and Advanced Optical Materials, respectively.

DNA segment for luminescence quenching. The detachment of the DNA quencher together with the specific binding of lysozyme and the aptamer recovered the PL of PLNRs. The accuracy of lysozyme detection was comparable to that of ELISA in three clinical cancer samples with minimum a detectable concentration of 0.31 μM in a normal donor (**Figure 5Bii**).

Information Technology

Anti-counterfeiting

With the rapid development of science and technology, innovative anti-counterfeiting technologies are highly pursued under the situation of increasing counterfeiting activities. In recent years, anti-counterfeiting technologies based on PLMs have received significant attention owing to their properties of high emission intensities and long recognizable time.

Their direct coverage capability on various substrates enables the application of the great potential of organic PLMs in anti-counterfeiting technologies (Deng et al., 2013; An et al., 2015; Jiang et al., 2016; Yang et al., 2016b; Xue et al., 2017). In 2018, Huang and co-workers prepared a series of organic PLMs with controllable tuning of PL photoactivation and deactivation times by customizing the alkoxy chains (Gu et al., 2018). The PL of these molecular compounds can be activated by prolonged photo irradiation, and can be deactivated by thermal treatment

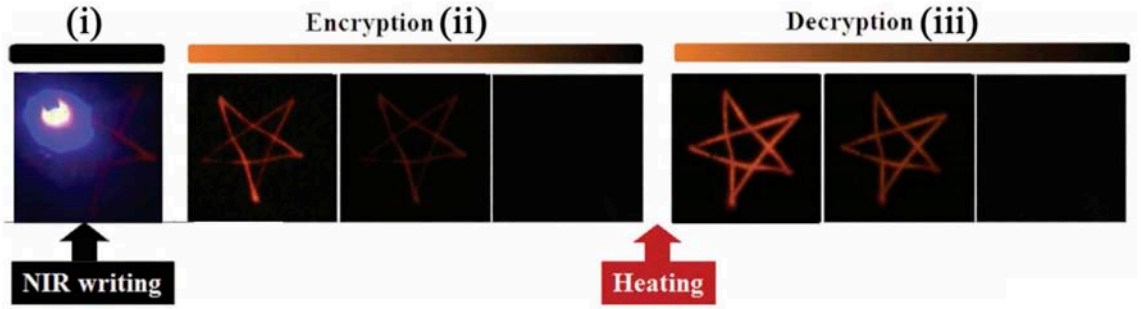

FIGURE 7 | NIR-writing encryption process and heat-induced decryption process (Hu et al., 2017). Reproduced with permission from Advanced Optical Materials.

or UV irradiation for 3 h. Considering the unique dynamic PL features of these materials, the pattern "8," which was built by different crystalline molecular compounds, could be converted into various digital numbers or letters of "8," "11," "I," "H," "E," and "C" under different irradiation or stoppage irradiation conditions (**Figure 6A**). Gao et al. developed a layered double hydroxides based polymer (PMA/LDH@PAA) thin film with a tunable PL color for anti-counterfeiting applications (Gao et al., 2017). The transparent PMA/LDH@PAA was written on a cigarette case and the writing became invisible after thorough drying (**Figure 6B**). Upon UV irradiation, the bright blue word appeared. However, the PMA/LDH@PAA anti-counterfeiting mark was still apparent after the termination of UV irradiation, whereas the proprietary markers disappeared immediately.

Compared with organic PLMs, inorganic PLMs with longer PL time and higher emission intensity are more suitable to realize anti-counterfeiting recognizable with the naked eyes. In 2018, Liu et al. synthesized a series of $NaBaScSi_2O_7$-based phosphor with photoluminescence (PhL), PL, and photostimulated luminescence (PsL) properties using co-doped $Eu^{2+}/Nd^{3+}/Pr^{3+}$ ions (Liu et al., 2018b). Under different light excitation conditions (the excited UV or 980-nm light was switched on or off), a difference in the emission colors of PhL, PL, and, PsL was represented by the different release processes of the carriers. Therefore, multiplex anti-counterfeiting was achieved by simply changing the doping of rare-earth ions in a single matrix. With the introduction of a novel NIR rechargeable orthogonal multicolor UCPL, an orthogonal anti-counterfeiting technique was developed by our research group (Hu et al., 2017). Using a simple method of stamp or modified inkjet printing, these composites enable high-speed patterned deposition on various mediums such as plastic, paper, or ceramics (**Figure 6C**). Each anti-counterfeiting letter formed has two sets of independent orthogonal emission colors recognizable with the naked eye: a multicolor upconversion luminescence when 980-nm NIR is switched on or a multicolor PL when it is switched off, which can be easily detected by a smartphone.

Optical Data Recording

Due to the energy storing capability of the deep traps, a part of the excitation energy is stored for a long time after being exposed to the light. Then, this portion of the energy can be stimulated released by optical, thermal, or mechanical force, which results in emissions and long PL. Therefore, the special phenomenon of thermo-luminescence, photostimulated luminescence, and mechanoluminescence can be applied in information write-in and read-out processes. Our research group has constructed a data-recording device based on the NIR-rechargeable upconversion PLMs (Zhuang et al., 2018). This device was fabricated by simply dispersing PLMs into polydimethylsiloxane to form a film. A 980-nm laser was used as a "pen" to encode date on the device. Following the stopping of writing, this information faded gradually and disappeared completely. However, a portion of energy obtained from the pen was stored in deep electron traps and did not discharge under normal environment for a long time. Then, under heat treatment, the recorded information could be decrypted and appeared instantly with bright PL for a duration of 1 min, due to the thermo-luminescence properties (**Figure 7**). Light-luminescence properties were also used to developed data storage devices. Recently, Xie et al. fabricated flexible phosphor films by encapsulating a series of deep-trap PLMs with multicolor emissions into silica gel (Zhuang et al., 2018). The information was conveniently encoded to the film using a 405-nm laser and the decoding process was conducted by scanning with a 980-nm laser.

CONCLUSIONS AND PROSPECTS

As promising luminescent agents, PLMs have drawn wide attentions owing to their ultra-long afterglow. In this review, we discussed the crucial breakthroughs and latest developments of different PLMs for diverse biomedical and informational applications. Inorganic PLMs with stable, potent and super-long PL were formed via effective traps and strong emitters. To overcome the low dispersibility and biocompatibility and the complexity of production, organic PLMs, consisting of purely small molecules and polymers PLMs, have been investigated.

Considering the advantages of eliminating the *in situ* excitation, PLMs exhibit enormous potential for bioimaging with super-long decay time and high SNR. Moreover, with appropriate functionalization, PLMs are ideal platforms to establish multifunctional systems in imaging-guided delivery and theranostics. Nevertheless, owing to the long reading window

provided by the PL property, PLMs also possess great potential in informational technologies, such as data storage and anti-counterfeiting.

However, for the more convenient applications of PLMs, there are still several problems need to be solved. Firstly, achieving long and strong PL synchronously poses a major challenge, because strong PL requires high radioactive decay rate at the cost of a short PL. To address this problem, the radioactive decay rate needs to be moderate and the excitation transformation needs to be sufficiently efficient. However, neither of these can be realized experimentally. Secondly, for the more efficient application in bioimaging, the stable PL of inorganic or organic PLNPs in aqueous solution is essential. In addition, the color range needs to be broadened, because various visible lights are beneficial in informational applications, and efficient excitation and emission wavelengths in NIR are favorable in biomedical applications.

In conclusion, a thorough interdisciplinary understanding of chemistry, materials science, biomedicine, and information technology is required for the breakthroughs and improvements of PLMs. This emerging and promising interdisciplinary understanding of these disciplines further promotes the application of PLMs in all fields of human society.

AUTHOR CONTRIBUTIONS

HT, CY, and LH designed and wrote the manuscript. TW and YS provided comments and helped in finalizing the manuscript. All authors reviewed the final version of the manuscript and approved it for publication.

ACKNOWLEDGMENTS

We gratefully appreciate the financial support from the National Natural Science Foundation of China (31800846), the National Key R&D Program of China (2018YFB1900200), the Hunan Provincial Natural Science Foundation of China (2019JJ50501), the Hunan Province Cooperative Innovation Center for Molecular Targeting New Drug Study (02230002000200056), and the University of South China (2016XQD43, 2018XJXZ355).

REFERENCES

Al-Attar, H. A., and Monkman, A. P. (2012). Room-temperature phosphorescence from films of isolated water-soluble conjugated polymers in hydrogen-bonded matrices. *Adv. Funct. Mater.* 22, 3824–3832. doi: 10.1002/adfm.201200814

An, Z., Zheng, C., Tao, Y., Chen, R., Shi, H., Chen, T., et al. (2015). Stabilizing triplet excited states for ultralong organic phosphorescence. *Nat. Mater.* 14:685. doi: 10.1038/nmat4259

Chen, Y., Liu, F., Liang, Y., Wang, X., Bi, J., Wang, X., et al. (2018). New up-conversion charging concept for effectively charging persistent phosphors using low-energy visible-light laser diodes. *J. Mater. Chem. C* 6, 8003–8010. doi: 10.1039/C8TC02419G

Deng, Y., Zhao, D., Chen, X., Wang, F., Song, H., and Shen, D. (2013). Long lifetime pure organic phosphorescence based on water soluble carbon dots. *Chem. Commun.* 49, 5751–5753. doi: 10.1039/c3cc42600a

DeRosa, C. A., Samonina-Kosicka, J., Fan, Z., Hendargo, H. C., Weitzel, D. H., Palmer, G. M., et al. (2015). Oxygen sensing difluoroboron dinaphthoylmethane polylactide. *Macromolecules* 48, 2967–2977. doi: 10.1021/acs.macromol.5b00394

Dimitrakopoulos, C. D., and Malenfant, P. R. L. (2002). Organic thin film transistors for large area electronics. *Adv. Mater.* 14:99.doi: 10.1002/1521-4095(20020116)14:2<99::AID-ADMA99>3.0.CO;2-9

Forster, L. S. (1990). The photophysics of chromium (III) complexes. *Chem. Rev.* 90, 331–353. doi: 10.1021/cr00100a001

Gao, R., Yan, D., Evans, D. G., and Duan, X. (2017). Layer-by-layer assembly of long-afterglow self-supporting thin films with dual-stimuli-responsive phosphorescence and antiforgery applications. *Nano Res.* 10, 3606–3617. doi: 10.1007/s12274-017-1571-x

Gu, L., Shi, H., Gu, M., Ling, K., Ma, H., Cai, S., et al. (2018). Dynamic ultralong organic phosphorescence by photo-activation. *Angewandte Chem. Int. Ed.* 57, 8425–8431. doi: 10.1002/anie.201712381

Hirata, S., Totani, K., Zhang, J., Yamashita, T., Kaji, H., Marder, S. R., et al. (2013). Efficient persistent room temperature phosphorescence in organic amorphous materials under ambient conditions. *Adv. Funct. Mater.* 23, 3386–3397. doi: 10.1002/adfm.201203706

Hölsä, J. (2009). Persistent luminescence beats the afterglow: 400 years of persistent luminescence. *Electrochem. Soc. Interface* 18, 42–45.

Hu, L., Fan, Y., Liu, L., Li, X., Zhao, B., Wang, R., et al. (2017). Orthogonal multiplexed luminescence encoding with near-infrared rechargeable upconverting persistent luminescence composites. *Adv. Opt. Mater.* 5:1700680. doi: 10.1002/adom.201700680

Hu, L., Wang, P., Zhao, M., Liu, L., Zhou, L., Li, B., et al. (2018). Near-infrared rechargeable "optical battery" implant for irradiation-free photodynamic therapy. *Biomaterials* 163, 154–162. doi: 10.1016/j.biomaterials.2018.02.029

Jiang, K., Zhang, L., Lu, J., Xu, C., Cai, C., and Lin, H. (2016). Triple-Mode Emission of Carbon Dots: Applications for Advanced Anti-Counterfeiting. *Angewandte Chem. Int. Ed.* 55, 7231–7235. doi: 10.1002/anie.201602445

Jinnai, K., Kabe, R., and Adachi, C. (2018). Wide-range tuning and enhancement of organic long-persistent luminescence using emitter dopants. *Adv. Mater.* 30:1800365. doi: 10.1002/adma.201800365

Kabe, R., and Adachi, C. (2017). Organic long persistent luminescence. *Nature* 550:384. doi: 10.1038/nature24010

Kabe, R., Notsuka, N., Yoshida, K., and Adachi, C. (2016). Afterglow organic light-emitting diode. *Adv. Mater.* 28, 655–660. doi: 10.1002/adma.201504321

Kuang, J., Liu, Y., and Zhang, J. (2006). White-light-emitting long-lasting phosphorescence in Dy^{3+}-doped $SrSiO_3$. *J. Solid State Chem.* 179, 266–269. doi: 10.1016/j.jssc.2005.10.025

Lastusaari, M., Bettinelli, M., Eskola, K. O., Höls,ä, J., and Malkamäki, M. (2012). The bologna stone: history's first persistent luminescent material. *Eur. J. Mineral.* 24, 885–890. doi: 10.1127/0935-1221/2012/0024-2224

le Masne de Chermont, Q., Corinne, C., Johanne, S., Fabienne, P., Serge, M. T., Jean-Pierre, J., et al. (2007). Nanoprobes with near-infrared persistent luminescence for *in vivo* imaging. *Proc. Natl. Acad. Sci. U.S.A.* 104, 9266–9271. doi: 10.1073/pnas.0702427104

Lécuyer, T., Teston, E., Ramirez-Garcia, G., Maldiney, T., Viana, B., Seguin, J., et al. (2016). Chemically engineered persistent luminescence nanoprobes for bioimaging. *Theranostics* 6, 2488–2523. doi: 10.7150/thno.16589

Li, J. A., Zhou, J., Mao, Z., Xie, Z., Yang, Z., Xu, B., et al. (2018). Transient and persistent room-temperature mechanoluminescence from a white-light-emitting aiegen with tricolor emission switching triggered by light. *Angewandte Chem. Int. Ed.* 57, 6449–6453. doi: 10.1002/anie.201800762

Li, Y., Gecevicius, M., and Qiu, J. (2016). Long persistent phosphors-from fundamentals to applications. *Chem. Soc. Rev.* 2016, 2090–2136. doi: 10.1039/C5CS00582E

Li, Z., Zhang, Y., Wu, X., Huang, L., Li, D., Fan, W., et al. (2015a). Direct aqueous-phase synthesis of sub-10 nm "luminous pearls" with enhanced *in vivo* renewable near-infrared persistent luminescence. *J. Am. Chem. Soc.* 137, 5304–5307. doi: 10.1021/jacs.5b00872

Li, Z., Zhang, Y., Wu, X., Wu, X., Maudgal, R., Zhang, H., et al. (2015b). *In vivo* repeatedly charging near-infrared-emitting mesoporous $SiO_2/ZnGa_2O_4:Cr^{3+}$ persistent luminescence nanocomposites. *Adv. Sci.* 2:1500001. doi: 10.1002/advs.201500001

Liang, Y., Liu, F., Chen, Y., Sun, K., and Pan, Z. (2015). Long persistent luminescence in the ultraviolet in $Pb^{(2+)}$-doped $Sr_2MgGe_2O_7$ persistent phosphor. *Dalton Transac.* 45:1322. doi: 10.1039/C5DT04588F

Lin, H., Yu, T., Bai, G., Tsang, M.-K., Zhang, Q., and Hao, J. (2016). Enhanced energy transfer in Nd^{3+}/Cr^{3+} co-doped $Ca_3Ga_2Ge_3O_{12}$ phosphors with near-infrared and long-lasting luminescence properties. *J. Mater. Chem. C* 4, 3396–3402. doi: 10.1039/C5TC04340A

Lin, X. H., Song, L., Chen, S., Chen, X. F., Wei, J. J., Li, J., et al. (2017). Kiwifruit-like persistent luminescent nanoparticles with high-performance and in situ activable near-infrared persistent luminescence for long-term *in vivo* bioimaging. *ACS Appl. Mater. Interfaces* 9, 41181–41187. doi: 10.1021/acsami.7b13920

Liu, B., Shi, C., and Qi, Z. (2005). Potential white-light long-lasting phosphor: Dy 3+-doped aluminate. *Appl. Phys. Lett.* 86:191111. doi: 10.1063/1.1925778

Liu, F., Yan, W., Chuang, Y.-J., Zhen, Z., Xie, J., and Pan, Z. (2013). Photostimulated near-infrared persistent luminescence as a new optical read-out from Cr^{3+}-doped $LiGa_5O_8$. *Sci. Rep.* 3:1554. doi: 10.1038/srep01554

Liu, J., Lécuyer, T., Séguin, J., Mignet, N., and Richard, C. (2018a). Imaging and therapeutic applications of persistent luminescence nanomaterials. *Adv. Drug Delivery Rev.* 138, 193–210. doi: 10.1016/j.addr.2018.10.015

Liu, Z., Zhao, L., Chen, W., Fan, X., Yang, X., Tian, S., et al. (2018b). Multiple anti-counterfeiting realized in $NaBaScSi_2O_7$ with a single activator of Eu^{2+}. *J. Mater. Chem. C* 6, 11137–11143. doi: 10.1039/C8TC04018D

Matsuzawa, T., Aoki, Y., Takeuchi, N., and Murayama, Y. (1996). A new long phosphorescent phosphor with high brightness, $SrAl_2O_4$: Eu^{2+},Dy^{3+}. *J. Electrochem. Soc.* 143, 2670–2673. doi: 10.1149/1.1837067

Mieno, H., Kabe, R., Notsuka, N., Allendorf, M. D., and Adachi, C. (2016). Long-lived room-temperature phosphorescence of coronene in zeolitic imidazolate framework ZIF-8. *Adv. Opt. Mater.* 4, 1015–1021. doi: 10.1002/adom.201600103

Mikael, P., Kanyi, P., Shirley, S., and Jianghong, R. (2015). Semiconducting polymer nanoparticles with persistent near-infrared luminescence for *in vivo* optical imaging. *Angewandte Chem.* 127, 11639–11642. doi: 10.1002/ange.201502736

Pan, Z., Lu, Y.-Y., and Liu, F. (2012). Sunlight-activated long-persistent luminescence in the near-infrared from Cr3+-doped zinc gallogermanates. *Nat. Mater.* 11, 58–63. doi: 10.1038/nmat3173

Struve, B., and Huber, G. (1985). The effect of the crystal field strength on the optical spectra of Cr 3+ in gallium garnet laser crystals. *Appl. Phys. B* 36, 195–201. doi: 10.1007/BF00704574

Sun, S. K., Wang, H. F., and Yan, X. P. (2018). Engineering persistent luminescence nanoparticles for biological applications: from biosensing/bioimaging to theranostics. *Acc. Chem. Res.* 51, 1131–1143. doi: 10.1021/acs.accounts.7b00619

Thomas, M., Aurélie, B., Johanne, S., Eliott, T., Sharma, S. K., Bruno, V., et al. (2014a). The in vivo activation of persistent nanophosphors for optical imaging of vascularization, tumours and grafted cells. *Nat. Mater.* 13, 418–426. doi: 10.1038/nmat3908

Thomas, M., Benoit, B., Michel, B., Daniel, S., and Cyrille, R. (2014b). Mesoporous persistent nanophosphors for *in vivo* optical bioimaging and drug-delivery. *Nanoscale* 6, 13970–13976. doi: 10.1039/C4NR03843F

Wang, J., Ma, Q., Wang, Y., Shen, H., and Yuan, Q. (2017a). Recent progress in biomedical applications of persistent luminescence nanoparticles. *Nanoscale* 9:6204. doi: 10.1039/C7NR01488K

Wang, J., Ma, Q., Zheng, W., Liu, H., Yin, C., Wang, F., et al. (2017b). One-dimensional luminous nanorods featuring tunable persistent luminescence for autofluorescence-free biosensing. *ACS Nano* 11:8185. doi: 10.1021/acsnano.7b03128

Wang, X., Zhang, Z., Tang, Z., and Lin, Y. (2003). Characterization and properties of a red and orange Y_2O_2S-based long afterglow phosphor. *Mater. Chem. Phys.* 80, 1–5. doi: 10.1016/S0254-0584(02)00097-4

Wang, Y., Yang, C. X., and Yan, X. P. (2017c). Hydrothermal and biomineralization synthesis of a dual-modal nanoprobe for targeted near-infared persistent luminescence and magnetic resonance imaging. *Nanoscale* 9, 9049–9055. doi: 10.1039/C7NR02038D

Wu, B. Y., Wang, H. F., Chen, J. T., and Yan, X. P. (2011). Fluorescence resonance energy transfer inhibition assay for α-fetoprotein excreted during cancer cell growth using functionalized persistent luminescence nanoparticles. *J. Am. Chem. Soc.* 133, 686–688. doi: 10.1021/ja108788p

Xia, S., Shi, J., Fu, X., Yi, Y., and Zhang, H. (2018). Long-term in vivo biodistribution and toxicity study of functionalized near-infrared persistent luminescence nanoparticles. *Sci. Rep.* 8:10595. doi: 10.1038/s41598-018-29019-z

Xue, P., Wang, P., Chen, P., Yao, B., Gong, P., Sun, J., et al. (2017). Bright persistent luminescence from pure organic molecules through a moderate intermolecular heavy atom effect. *Chem. Sci.* 8, 6060–6065. doi: 10.1039/C5SC03739E

Yamamoto, H., and Matsuzawa, T. (1997). Mechanism of long phosphorescence of $SrAl_2O_4$:Eu^{2+}, Dy^{3+} and $CaAl_2O_4$:Eu^{2+}, Nd^{3+}. *J. Luminescen.* 72–74, 287-289. doi: 10.1016/S0022-2313(97)00012-4

Yang, X., and Yan, D. (2016a). Long-afterglow metal-organic frameworks: reversible guest-induced phosphorescence tunability. *Chem. Sci.* 7, 4519–4526. doi: 10.1039/C6SC00563B

Yang, X., and Yan, D. (2016b). Strongly Enhanced Long-Lived Persistent Room Temperature Phosphorescence Based on the Formation of Metal-Organic Hybrids. *Advanced Optical Materials* 4, 897–905. doi: 10.1002/adom.201500666

Yang, X., and Yan, D. (2017). Long-lasting phosphorescence with a tunable color in a Mn^{2+}-doped anionic metal-organic framework. *J. Mater. Chem. C* 5, 7898–7903. doi: 10.1039/C7TC02493B

Yang, Y., Wang, K.-Z., and Yan, D. (2016a). Ultralong persistent room temperature phosphorescence of metal coordination polymers exhibiting reversible pH-responsive emission. *ACS Appl. Mater. Interfaces* 8, 15489–15496. doi: 10.1021/acsami.6b03956

Yang, Y., Wang, K.-Z., and Yan, D. (2017). Lanthanide doped coordination polymers with tunable afterglow based on phosphorescence energy transfer. *Chem. Commun.* 53, 7752–7755. doi: 10.1039/C7CC04356B

Yang, Z., Mao, Z., Zhang, X., Ou, D., Mu, Y., Zhang, Y., et al. (2016b). Intermolecular electronic coupling of organic units for efficient persistent room-temperature phosphorescence. *Angewandte Chem.* 128, 2221–2225. doi: 10.1002/ange.201509224

Zeng, S., Xue, Z., Li, X., Li, Y., Jiang, Y., Ren, G., et al.(2017). 980 nm laser-activated upconverted persistent probe for NIR-to-NIR rechargeable *in vivo* bioimaging. *Nanoscale* 9, 7276–7283. doi: 10.1039/C6NR09716B

Zhang, G., Chen, J., Payne, S. J., Kooi, S. E., Demas, J., and Fraser, C. L. (2007). Multi-emissive difluoroboron dibenzoylmethane polylactide exhibiting intense fluorescence and oxygen-sensitive room-temperature phosphorescence. *J. Am. Chem. Soc.* 129, 8942–8943. doi: 10.1021/ja0720255

Zhang, S., Mu, Z., Lv, Y., Fan, L., Li, Y., Ju, G., et al. (2017). White-light long persistent luminescence of Tb3+-doped Y3Al2Ga3O12 phosphor. *J. Alloys Compou.* 729, 418–425. doi: 10.1016/j.jallcom.2017.09.169

Zhang, Y., Huang, R., Li, H., Hou, D., Lin, Z., Song, J., et al. (2018). Germanium substitution endowing Cr^{3+}-doped Zinc aluminate phosphors with bright and super-long near-infrared persistent luminescence. *Acta Mater.* 155, 214–221. doi: 10.1016/j.actamat.2018.06.020

Zheng, B., Chen, H. B., Zhao, P. Q., Pan, H. Z., Wu, X. L., Gong, X. Q., et al. (2016). Persistent luminescent nanocarrier as an accurate tracker *in vivo* for near infrared-remote selectively triggered photothermal therapy. *ACS Appl. Mater. Interfaces* 8:21603. doi: 10.1021/acsami.6b07642

Zhou, L., Wang, R., Yao, C., Li, X., Wang, C., Zhang, X., et al. (2015). Single-band upconversion nanoprobes for multiplexed simultaneous in situ molecular mapping of cancer biomarkers. *Nat. Commun.* 6:6938. doi: 10.1038/ncomms7938

Zhuang, Y., Wang, L., Lv, Y., Zhou, T. L., and Xie, R. J. (2018). Optical data storage and multicolor emission readout on flexible films using deep-trap persistent luminescence materials. *Adv. Funct. Mater.* 28:1705769. doi: 10.1002/adfm.201705769

Conflict of Interest Statement: The authors declare that the research was conducted in the absence of any commercial or financial relationships that could be construed as a potential conflict of interest.

Copyright © 2019 Tan, Wang, Shao, Yu and Hu. This is an open-access article distributed under the terms of the Creative Commons Attribution License (CC BY). The use, distribution or reproduction in other forums is permitted, provided the original author(s) and the copyright owner(s) are credited and that the original publication in this journal is cited, in accordance with accepted academic practice. No use, distribution or reproduction is permitted which does not comply with these terms.

frontiers in Chemistry

ORIGINAL RESEARCH
published: 20 March 2019
doi: 10.3389/fchem.2019.00145

Reversible Photo-Switching of Dual-Color Fluorescent Mn-Doped CdS-ZnS Quantum Dots Modulated by Diarylethene Molecules

*Yucheng Yuan[1], Hua Zhu[1], Yasutaka Nagaoka[1], Rui Tan[1], Andrew Hunter Davis[2], Weiwei Zheng[2] and Ou Chen[1]**

[1] Department of Chemistry, Brown University, Providence, RI, United States, [2] Department of Chemistry, Syracuse University, Syracuse, NY, United States

Dynamic materials have been given an increased amount of attention in recent years with an expectation that they may exhibit properties on demand. Especially, the combination of fluorescent quantum dots (QDs) and light-responsive organic switches can generate novel photo-switchable materials for diverse applications. In this work, a highly reversible dynamic hybrid system is established by mixing dual-color emitting Mn-doped CdS-ZnS quantum dots (QDs) with photo-switchable diarylethene molecules. We show that the diarylethene 1,2-bis(5-(3,5-bis(trifluoromethyl)phenyl)-2-methylthiophen-3-yl)cyclopent-1-ene (switch molecule **1**) performs fabulous photo-switching property (between its open, **1o** and closed, **1c** forms), and high fatigue resistance in this hybrid system. The emission color switching between blue and pink of the system can be induced mainly by selective quenching/recovering of the Mn- photoluminescence (PL) of the QDs due to the switchable absorbance of the molecule **1**. Mechanistic studies show that quenching of QD emission following UV illumination was caused by both Förster resonance energy transfer (FRET) and reabsorption by surrounding **1c** molecules in the case of the Mn-PL, and solely by reabsorption in the case of badngap- (BG-)PL. This photo-switchable system could be potentially used in applications ranging from self-erasing paper to super-resolution fluorescence imaging.

Keywords: reversible photo-switching, dual-color, Mn-doped CdS-ZnS quantum dots, diarylethene switches, förster resonance energy transfer (FRET), photon reabsorption

OPEN ACCESS

Edited by:
Steve Suib, University of Connecticut, United States

Reviewed by:
Wolfram Heimbrodt, University of Marburg, Germany
Hongyou Fan, Sandia National Laboratories (SNL), United States

****Correspondence:***
Ou Chen
ouchen@brown.edu

Specialty section:
This article was submitted to Nanoscience, a section of the journal Frontiers in Chemistry

Received: *29 January 2019*
Accepted: *27 February 2019*
Published: *20 March 2019*

Citation:
Yuan Y, Zhu H, Nagaoka Y, Tan R, Davis AH, Zheng W and Chen O (2019) Reversible Photo-Switching of Dual-Color Fluorescent Mn-Doped CdS-ZnS Quantum Dots Modulated by Diarylethene Molecules. Front. Chem. 7:145. doi: 10.3389/fchem.2019.00145

INTRODUCTION

Dynamic materials have attracted attention of chemists in the past two decades owing to their potentials to be used for generating responsive materials for various applications (Kay et al., 2007; Grinthal and Aizenberg, 2013; Klajn, 2014). Meanwhile, there is comprehensive development in the syntheses of nanocrystals with controlled size, shape, structure and compositions in various material systems (Gilroy et al., 2016; Pietryga et al., 2016; Talapin and Shevchenko, 2016; Wu et al., 2016). Combining organic molecular switches with inorganic nanocrystals can therefore afford dynamic hybrid systems with switchable properties (Klajn et al., 2010; Qu et al., 2015; Bai et al., 2016; Li et al., 2017). Compared to static counterparts, dynamic materials exhibit intriguing advantages including selectively reversible properties with external stimuli, and thus potential

applications in various fields including self-erasing paper (Kundu et al., 2015), self-healing coating (Roy et al., 2015) bio-imaging etc. (Zhang et al., 2012). Among diverse stimuli, light has been favored as an external input to tune the state of materials on account of its non-chemical contaminations, convenient delivery and specificity of desired wavelengths. As a result, a variety of photo-switchable molecules such as azobenzenes (Bandara and Burdette, 2012), spiropyrans (Minkin, 2004), dithienylethenes (Irie, 2000; Irie et al., 2014), stilbene (Momotake and Arai, 2004) etc. have been employed to functionalize different nanomaterials (Yildiz et al., 2009; Klajn et al., 2010; Wang and Li, 2018) to construct light-responsive systems spanning from metal nanocrystals (Kundu et al., 2015; Manna et al., 2015; Zhao et al., 2015), metal oxide nanocrystals (Mikami et al., 2004; Min Yeo et al., 2008), to quantum dots (QDs) (Zhu et al., 2005, 2006; Díaz et al., 2011, 2015) and metal-organic frameworks (MOFs) (Dolgopolova et al., 2018).

In materials science, doping is a process that intentionally introduces impurity atoms as dopants to host lattices, thus providing unique properties inaccessible to conventional materials (Bryan and Gamelin, 2005). In this regard, doping in QDs may exhibit improved optical, magnetic and electronic properties as compared to their undoped counterparts (Yang et al., 2006; Pradhan and Peng, 2007; Bussian et al., 2008; Norris et al., 2008; Zheng and Strouse, 2011; Cai et al., 2018; Kroupa et al., 2018; Li et al., 2018). For example, when introducing transition metals or rare earth elements to the QDs, a new emission band may emerge, resulting a dual-color emission property with two tunable non-overlapping photoluminescence (PL) peaks (Wu and Yan, 2013). To this extent, Mn-doped CdS-ZnS QDs have been extensively studied as a model system for both fundamental understanding of host-to-dopant energy transfer processes and practical applications that are utilizing their dual-color emission properties (Yang et al., 2006, 2008; Chen O. et al., 2010; Chen et al., 2012; Hofman et al., 2017; Pradhan et al., 2017).

Taking advantages of the dynamic switchable absorbance of diarylethene molecules and the dual-color emission property of Mn-doped CdS-ZnS QDs, in this work, we demonstrate a photo-switchable hybrid system by selectively quenching/recovering the Mn dopant emission. The quenching process is shown to include Förster resonance energy transfer (FRET) from Mn-PL to closed isomer of diarylethenes as well as reabsorption processes. Three diarylethene switches with different electron-withdrawing groups were exploited to examine the performances of the photo-switching process. We demonstrate that the switch diarylethene molecule with substituent of 3,5-bis(trifluoromethyl)phenyl (switch **1**) afford the best fatigue-resistant performance. PL color switching between blue and pink can be obtained by sequential illumination of UV (365 nm) and visible (590 nm) light. This switchable dual-color dynamic system could be potentially useful in a broad range of applications.

MATERIALS AND METHODS

Materials

All chemicals were used without further purification. 2-Chloro-5-methylthiophene (> 96.0%) was purchased from TCI Chemicals. Tributyl borate (98%) was purchased from Strem Chemicals. 1-Bromo-3,5-bis(trifluoromethyl)benzene (99%), *n*-butyllithium (1.6 M solution in hexanes, AcroSeal), zinc dust (98+%), and tetrahydrofuran (THF, 99.9%, extra dry, stabilized, anhydrous, SC, AcroSeal) were purchased from Acros Organics. Tetrakis(triphenylphosphine) palladium(0) ($Pd(PPh_3)_4$, 99%), glutaryl chloride (97%), $TiCl_4$ (99.9% trace metals basis), sulfur powder (99.999%), 1-octadecence (ODE, tech. 90%), and oleylamine (OAm, tech. 70%) were purchased from Aldrich. Manganese acetate tetrahydrate (99%), sodium carbonate (99.8%), and all the solvents were purchased from Fisher Scientific Company. Ethyl 4-bromobenzoate (98+%), $AlCl_3$ (anhydrous, 99.985%), cadmium acetate hydrate (99.999%), cadmium oxide (99.998%), zinc stearate (count as ZnO ≈ 14%), oleic acid (OLA, 90%) and selenium (200 mesh, 99.999%) were purchased from Alfa Aesar. Nitric acid (≥69.5%, TraceSELECT) was purchased from Fluka. 4-bromo-pyridine hydrochloride (98%) was purchased from Matrix Scientific. Cadmium myristate was self-made according to the literature method (Chen et al., 2008).

Synthesis of Diarylethene Molecules

Diarylethenes were synthesized using a previous established route with minor modifications (see **Supplementary Material**) (Tam et al., 2011). The reactions were carried out using Schlenk line under dry N_2 flow. *n*-Butyllithium (1.6 M in hexane, 1.3 mL) was added to a solution of 1,2-bis(5-chloro-2-methyl-3-thienyl)cyclopentene (see **Supplementary Material** for the synthesis, 1.0 mmol) in THF (15 mL) at room temperature. After stirring for 15 min, tributyl borate (3.0 mmol) was added and followed by stirring for another 1 hr. In another flask, DMSO (25 mL) was added and degassed, then 1-bromo-3,5-bis(trifluoromethyl)benzene (2.2 mmol) and $Pd(PPh_3)_4$ (0.02 mmol) were added. After stirring for 15 min, aqueous Na_2CO_3 (2 M, 5 mL) and ethylene glycol (0.5 mL) were added. The mixture was heated up to 60°C after stirring for 15 min, then was added the above prepared solution. The resulting mixture was stirred at 80°C overnight. After cooling to room temperature, 50 mL of water was added and the mixture was extracted with 20 mL of ethyl acetate three times. The combined organic phases were washed with brine, dried over Na_2SO_4 and evaporated. Purification by flash column chromatography afforded compound 1,2-bis(5-(3,5-bis(trifluoromethyl)phenyl)-2-methylthiophen-3-yl)cyclopent-1-ene (**1o**) (32%) as a pale white solid (Herder et al., 2015). **^{1}H-NMR (400 MHz, $CDCl_3$):** δ (ppm) = 7.86 (br s, 4 H, CH_{ar}), 7.71 (br s, 2 H, CH_{ar}), 7.14 (s, 2 H, CH_{th}), 2.88 (t, $J_{H,H}$ = 7.4 Hz, 4 H, CH_2), 2.14 (p, $J_{H,H}$= 7.2 Hz, 2 H, CH_2), 2.06 (s, 6 H, CH_3). Compound 1,2-bis(2-methyl-5-(pyridin-4-yl)thiophen-3-yl)cyclopent-1-ene (**2o**, in **Supplementary Material**) was prepared by exchanging 1-bromo-3,5-bis(trifluoromethyl)benzene with 4-bromo-pyridine hydrochloride (Tam et al., 2011). ^{1}H-NMR (400 MHz, $CDCl_3$): δ (ppm) = 8.53 (d, $J_{H,H}$ = 6.0 Hz, 4H, CH_{ar}), 7.39 (d, $J_{H,H}$ = 6.4 Hz, 4H, CH_{ar}), 7.25 (s, 2H, CH_{th}), 2.86 (t, $J_{H,H}$ = 7.4 Hz, 4H, CH_2), 2.12 (m, 2H, CH_2), 2.03 (s, 6H, CH_3). Compound 4,4′-(cyclopent-1-ene-1,2-diylbis(5-methylthiophene-4,2-diyl))dibenzoic acid (**3o**, in

Supplementary Material) was obtained by switching 1-bromo-3,5-bis(trifluoromethyl)benzene to ethyl 4-bromobenzoate to perform the Suzuki reaction and followed by hydrolysis with 4 M NaOH aqueous solution in dioxane (Mulder et al., 2004; Herder et al., 2015). **^{1}H-NMR (400 MHz, $CDCl_3$):** δ (ppm) = 7.99 (d, $J_{H,H}$ = 8.8 Hz, 4 H, CH_{ar}), 7.53 (d, $J_{H,H}$ = 8.8 Hz, 4 H, CH_{ar}), 7.14 (s, 2 H, CH_{th}), 4.37 (q, $J_{H,H}$ = 7.2 Hz, 4 H, CH_3CH_2O), 2.85 (t, $J_{H,H}$ = 7.4 Hz, 4 H, CH_2), 2.10 (p, $J_{H,H}$ = 7.4 Hz, 2 H, CH_2), 2.01 (s, 6 H, CH_3), 1.39 (t, $J_{H,H}$ = 7.2 Hz, 6 H, CH_3CH_2O). **^{1}H NMR (400 MHz, DMSO-d^6):** δ (ppm) = 12.86 (s, 2H), 7.92 (d, $J_{H,H}$ = 8.0 Hz, 4 H, CH_{ar}), 7.67 (d, $J_{H,H}$ = 8.0 Hz, 4 H, CH_{ar}), 7.48 (s, 2H, CH_{th}), 2.84 (t, $J_{H,H}$ = 7.6 Hz, 4 H, CH_2), 2.07 (m, 2H), 1.92 (s, 6H).

Synthesis of Mn-Doped CdS-ZnS Core-Shell QDs

Mn-doped CdS-ZnS core-shell QDs were prepared following the reported method with minor modifications (Yang et al., 2008). First, CdS core QDs were prepared using a direct heating-up method. In a typical synthesis, cadmium myristate (1.0 mmol), sulfur (0.5 mmol), and ODE (50 mL) were added to a 100 mL-flask. The resulting mixture was degassed at room temperature for 10 min, and then was heated to 240°C under N_2 flow. The reaction was stopped by removing heating mantle and cooling to room temperature. The resulting CdS QDs were precipitated with addition of acetone, following by centrifugation and then were redispersed in hexane. A small amount of OLA can be added to assist QDs to disperse in hexane. The CdS QDs were dispersed in hexane as a stock after purified for three times. Second, ZnS shells were grown on the CdS cores using a layer by layer injection method. Typically, CdS cores (100 nmol) were mixed with ODE (3 mL) and OAm (1 mL), and the resulting mixture was degassed for 1 h at room temperature and then heat up to 220°C under N_2 flow for ZnS growth. Zinc-stearate in ODE (0.1 M) and sulfur in ODE (0.1 M) were injected simultaneously for each monolayer growth of ZnS shell. The reaction time was 10 min after each injection. The growth for first two monolayers ZnS shells was at 220°C and then was at 280°C for later growth. Third, dopant growth was performed in the same pot with ZnS shells growth. Freshly made $Mn(OAc)_2$ solution (5 mM) was injected after five monolayers of ZnS shells growth, accompanying the injection of sulfur precursor for the six monolayer. Dopant growth was allowed for 20 min and was followed by the growth of two more ZnS shells. Finally, zinc-stearate solution for the last monolayer ZnS shell growth (0.1 M, 2 mL) was injected and then the QDs were annealed at 240°C for 30 min. The resulting Mn-doped QDs were purified by three precipitation-redispersion cycles using acetone and hexane.

RESULTS AND DISCUSSIONS

We have synthesized diarylethene switch molecule featuring with electron withdrawing group of 3,5-bis(trifluoromethyl)benzene (**1**) as shown in **Figure 1A**. The ring-open isomer (**1o**) and ring-closed isomer (**1c**) can be interconverted by illumination with UV and visible light showing drastically different absorption feature. Specifically, compared to the open form (**1o**), whose π-conjugation is restricted to each half of the molecule, the

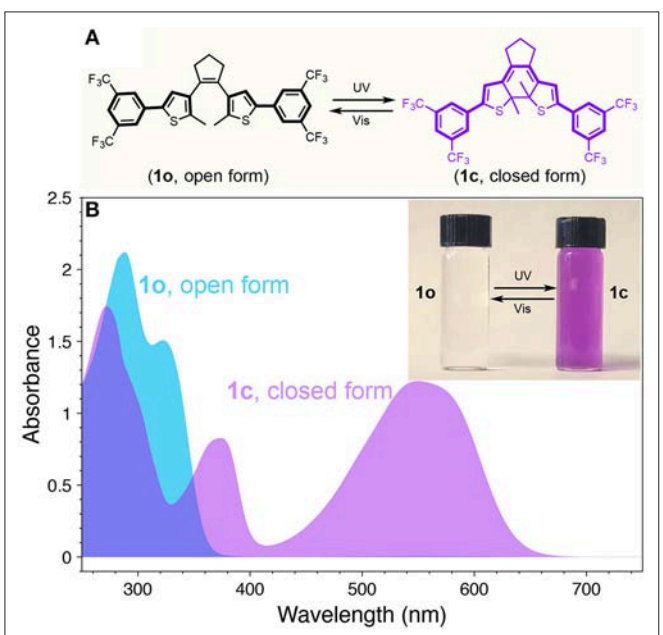

FIGURE 1 | (A) Chemical structures and photoisomerization of diarylethene **1** (Vis = visible). **(B)** UV-vis absorption spectra of **1** at open (**1o**) and closed (**1c**) forms. Inset: photograph for the THF solution of **1o** (left) and **1c** (right).

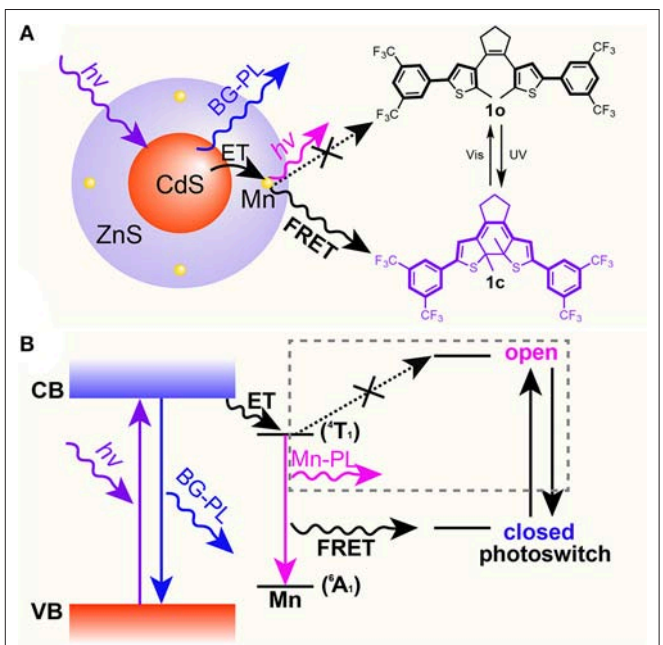

FIGURE 2 | Scheme **(A)** and energy diagram **(B)** of proposed mechanism for the selective Mn-PL quenching between Mn-doped CdS-ZnS core-shell QDs and diarylethene **1** molecules.

closed form (**1c**) possesses extended π-conjugation across the entire molecule. This extended conjugation places the highest occupied molecular orbital (HOMO) and lowest unoccupied molecular orbital (LUMO) of the molecule closer, thus allowing the absorption profile red-shift correspondingly (Kuhn, 1949). UV-visible absorption spectra of the open and closed isomers (**1o** and **1c**) of diarylethene **1** are shown in **Figure 1B**. The open form (**1o**) as prepared only shows absorbance at wavelengths shorter than 380 nm. After illumination with UV light, the molecule turns into the closed isomer (**1c**) and a pronounced absorption peak appears in the visible range (420–650 nm). It should be noted that there is minimal absorbance from both isomers (**Figure 1B**), indicating a nearly transparent window in the range of 400–420 nm. This photo-switchable absorption feature motivated us that a dynamic emitting architectural construct can be achieved when modulated with appropriate dual-color emitting fluorophores.

As mentioned above, high-quality dual-color emitters can be obtained by doping transition metals or rare earth elements in QD lattices. Among them, Mn-doped CdS-ZnS QDs have been robustly synthesized and extensively studied (Yang et al., 2006, 2008, 2009; Chen O. et al., 2010; Chen et al., 2012). When excited with high energy photons, an electron-hole pair (an "exciton") is created and confined inside the Mn-doped QD. This exciton can be radiatively deactivated through either recombination at the CdS-ZnS core-shell QD band edge to give a corresponding blue BG emission, or energy transfer to Mn dopants and subsequently emit a lower energy photon from the $^4T_1$ to $^6A_1$ states of the Mn ions (**Figure 2**) (Yang et al., 2009; Chen H.Y. et al., 2010). Most importantly, their dual-color emission bands can be adjusted to match the dynamic absorption windows of the diarylethene **1** (**Figure 1**) (Ithurria et al., 2007; Chen O. et al., 2010; Chen et al., 2012). Therefore, we hypothesize that when mixing the well-designed Mn-doped CdS-ZnS core-shell QDs and the photo-switchable diarylethene molecules together, FRET from the excited state (i.e., $^4T_1$) of Mn to the switches can be turned on and off in the closed (**1c**) and open (**1o**) forms, respectively (**Figure 2**). Thus, the system would show a combined color of both BG- and Mn-PL of the QDs while the diarylethene **1** stays at the open form (**1o**) and show the emission color mostly from BG-PL when the diarylethene **1** turns into the closed form (**1c**) (**Figure 2**). This color switching process could be simply modulated by illuminating with UV or visible light.

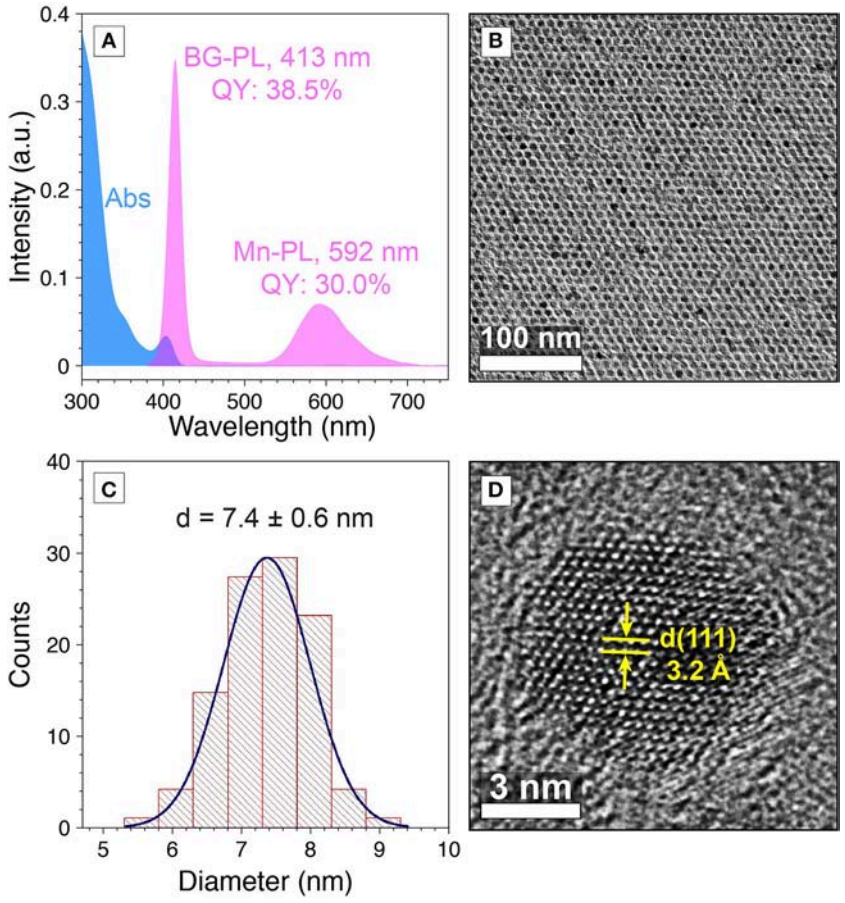

FIGURE 3 | (A) Absorption (blue) PL (pink) spectra, and **(B)** TEM image of Mn-doped CdS-ZnS core-shell QDs. **(C)** Size distribution histogram of Mn-doped CdS-ZnS core-shell QDs. **(D)** HR-TEM image for a Mn-doped CdS-ZnS core-shell QD.

To test our hypothesis, we designed and synthesized Mn-doped CdS-ZnS core-shell QDs with desired emission bands to match with the absorption profiles of the diarylethene **1**. In particular, the BG-PL centered at 413 nm with a full width at half maximum (FWHM) of 16 nm (PL QY of 38.5%) was achieved by controlling the CdS core size and ZnS shell thickness (see materials and methods for details) (**Figure 3A**). This BG-PL lays in the transmission window of the switch molecule disregarding to the open or closed form (**Figure 1B**). Meanwhile, in order to achieve a large spectral overlap between the Mn-PL and absorption feature of the **1c**, Mn-PL centered at 592 nm (PL QY of 30.0%) was accessed by doping Mn ions closer to the surface of the QDs, thus minimizing the local strain of Mn impurities (**Figure 3A**) (Ithurria et al., 2007). The Mn-to-BG PL intensity ratio was determined to be 0.24 (**Figure 3A**). Transmission electron microscopy (TEM) measurements showed the resultant QDs exhibited a spherical shape and a high morphological uniformity with an average

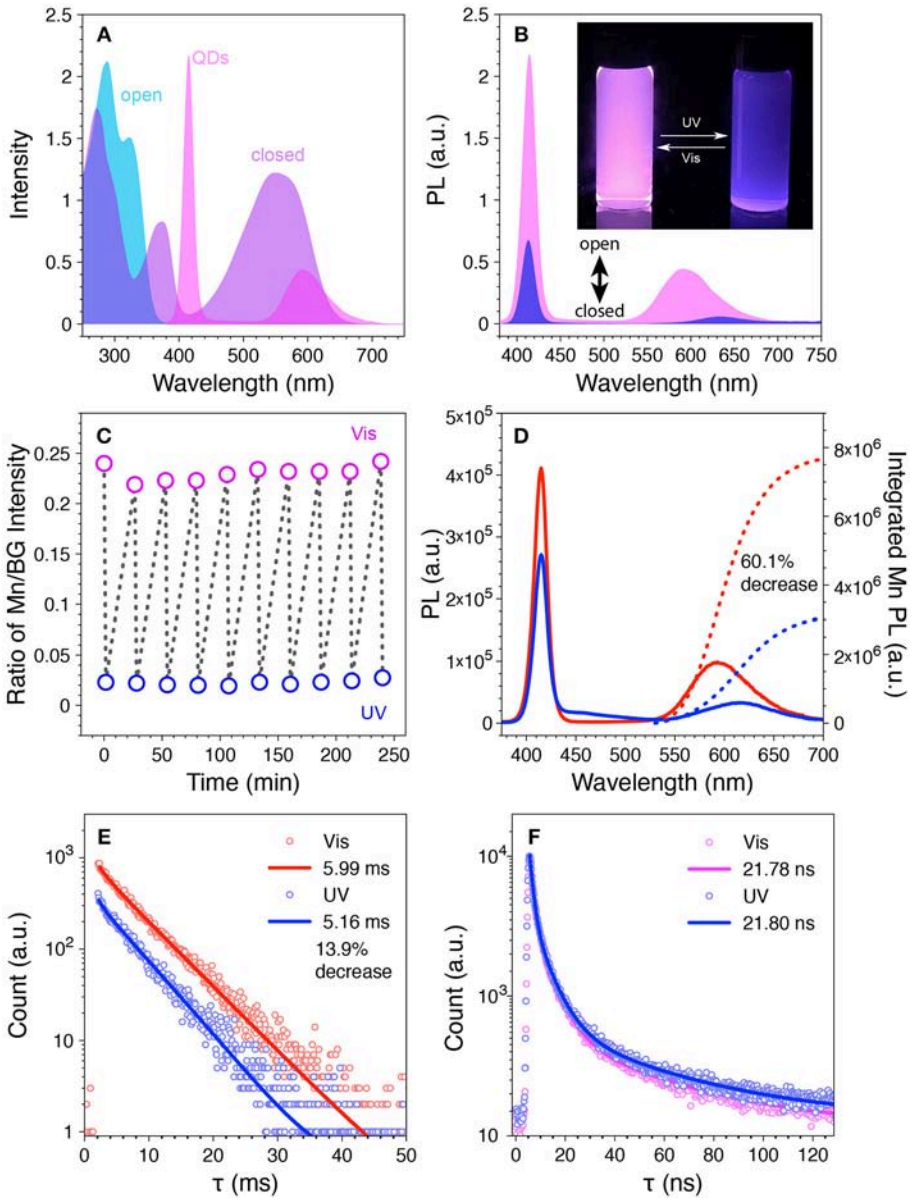

FIGURE 4 | (A) Overlay of the PL spectrum of the Mn-doped CdS-ZnS QDs with the absorption spectra of the **1o** and **1c**. **(B)** PL spectra of the mixture of Mn-doped CdS-ZnS QDs with **1o** (pink) and **1c** (blue). Inset: photograph for the mixture solution under UV light after UV (right) and visible (left) light illumination. **(C)** The ratio of Mn/BG-PL intensity during repetitive switching cycles with sequential UV (blue open circle) and visible (pink open circle) light illumination. **(D)** The PL intensity (solid lines) and integrated Mn-PL intensity (dotted lines) and **(E)** the corresponding Mn-PL lifetime changes during one switching cycle. **(F)** BG-PL lifetime decays after UV (blue) and visible (pink) light illumination.

diameter of 7.4 ± 0.6 nm (**Figures 3B, C**). High-resolution TEM (HR-TEM) image showed (111) plane with *d*-spacing of 3.2 Å (**Figure 3D**).

The prepared Mn-doped CdS-ZnS QDs and diarylethene **1** were employed to test the photo-switching property. It is shown that while both the BG- and Mn-PL are disjoint from the absorbance of **1o**, the BG-PL locates at the absorbance depression area and most of the Mn-PL overlaps with visible-range absorbance of **1c** (**Figure 4A**). We first tested the Mn-doped CdS-ZnS QDs under illumination of either UV or visible light without mixing with diarylethene **1** switches. Both BG- and Mn-PL intensities remained without any variation, indicating the robustness of the QD samples under light illumination. However, when mixing the same QDs with **1o** at a molar ratio of 1:500 in THF, the QD solution showed a pink color from the intact emission due to a minimal spectral overlap between the QD emission and the **1o** absorbance (**Figures 4A, B**). When illuminated with UV light (365 nm) for 90 s, a strong absorption feature arose in the visible range (420–650 nm, **Supplementary Figure 2a**), accompanying the decrease of the ratio of Mn/BG PL intensities from 0.24 to 0.02, corresponding to a change of the emission color from pink to blue (**Figure 4B** and **Supplementary Figure 2b**). The change of the PL intensity ratio is largely due to the dynamic Mn-PL quenching and recovering effect when the switch molecule alternates between closed (**1c**, quenching) and open (**1o**, recovering) forms (**Figure 4B**). Importantly, this observed photo-switching process is highly reversible. Ten photo-switching cycles were carried out to test the fatigue resistance of the switch molecule (i.e., diarylethene **1**), and the stability of the entire system. During these cycles, both the absorption spectra and the intensity ratios of the Mn/BG PL peaks showed excellent reversibility (**Figure 4C** and **Supplementary Figures 3, 4**), indicating a reliable photo-switching property of our designed system.

Two possible Mn-PL quenching/recovering mechanisms are attributable to the observed photo-switching property: 1) FRET from the excited state (i.e., $^4T_1$) of Mn dopant ions to the **1c** non-radiatively; 2) radiated photons of Mn-PL can be reabsorbed by the surrounding **1c**. To explore the origin of the observed Mn-PL quenching effect and their contributions, time-resolved PL lifetime measurements were carried out at different stage of the photo-switching process. When the integrated intensity of the Mn-PL decreased 60.1% of its initial value, the Mn-PL lifetime decreased from 5.99 to 5.16 ms, indicating that a 13.9% of the Mn-PL quenching can be attributed to FRET for the Mn-PL to the switch **1c** molecule in the measuring conditions (**Figures 3**, **4D,E**, see **Supplementary Material** for detailed calculation) (Medintz et al., 2003; Gu et al., 2008; Niebling et al., 2009; Tu et al., 2011; Krivenkov et al., 2019). Consequently, the rest 46.2% of Mn-PL quenching can be explained by the radiative photon reabsorption by surrounding **1c** molecule. A 31.0% of BG-PL integrated intensity decrease was also observed which again was contributed to the photon reabsorption due to the slight increase of the absorbance from the switch molecule (from **1o** to **1c**). No variance in PL lifetime (∼21 ns) of the BG-PL further confirmed the reabsorption process (**Figure 4F** and **Supplementary Figure 5**) without influencing the radiative photon recombination dynamics (Medintz et al., 2003). It is known that the efficiency of FRET process is strongly sensitive to the distance between donors and acceptors (inverse sixth power of the distance between donor and acceptor, typically within 1–10 nm) (Selvin, 2000). FRET process can happen only when the **1c** molecules reach to a close proximity (<10 nm) of the QD surface, which is in line with our experimental observation that only a small portion (13.9% of the total quenching) of the Mn-PL quenching is caused by FRET. Moreover, given the size of the QDs (i.e., 7.4 nm) and the doping radial location of the Mn dopants inside the QDs (at the interface between the 5th

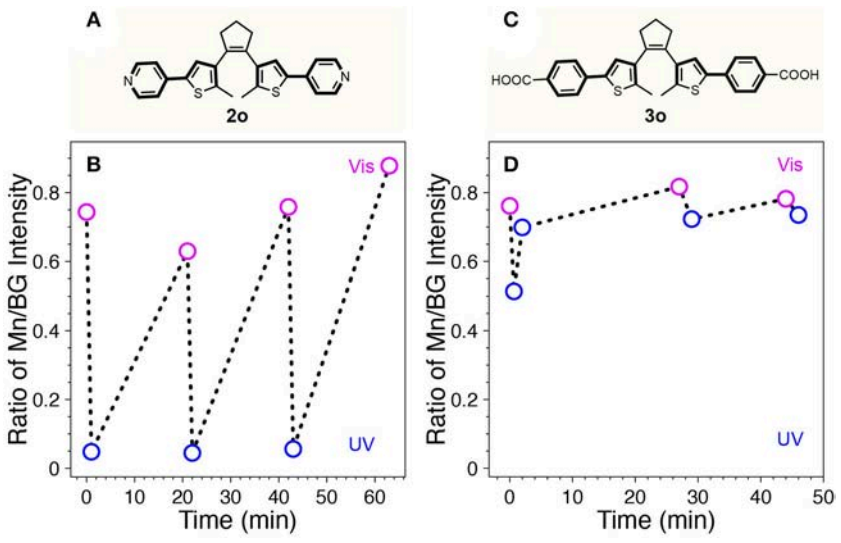

FIGURE 5 | Chemical structures of **2o (A)** and **3o (C)**. The ratio of Mn/BG-PL intensity of the mixture of Mn-doped CdS-ZnS QDs with **2o (B)** or **3o (D)** during repetitive switching cycles with sequential UV (blue open circle) and visible (pink open circle) light illumination.

and the 6th monolayer of the ZnS shell), the distances between the photo-generated exciton (electron-hole pair) center and the **1c** is 3.2 nm larger than that between the Mn ion and the **1c** the exciton center is determined at the center of core-shell QDs, (Yang et al., 2009). This larger distance will dramatically decrease the FRET efficiency between the exciton and **1c** as compared to that from Mn ion to **1c**. This again agrees well with the fact that the decrease of BG-PL is mostly attributable to the photon reabsorption process.

Recently, it was reported that a series of diarylethene switch molecules with electron withdrawing substituents on the adjacent phenyl rings could provide fatigue resistance due to minimized formation of annulated isomers (Herder et al., 2015). According to the study, two other diarylethene-based switches terminated with electron withdrawing groups of pyridine (diarylethene **2**) and 4-benzoic acid (diarylethene **3**) were synthesized and tested in our system (**Figure 5**). Diarylethene **2** was mixed with Mn-doped CdS-ZnS core-shell QDs possessing BG- and Mn-PL peaks at 414 and 600 nm, respectively. The absorption spectral evolution clearly indicated fatigue effect over only 3 cycles (**Supplementary Figure 6**). Accordingly, the BG- and Mn-PL were quenched after visible light illumination whereas the quenching effect was reduced after UV irradiation after cycles (**Supplementary Figure 7**). Since the BG-PL was more affected by the fatigue of diarylethene **2**, the ratio of Mn/BG intensity increased with 3 cycles (**Figure 5B**). Diarylethene photo-switch **3**, which possesses carboxylic groups at the para position of the phenyl rings, was expected to attach on the surface of QDs covalently. This direct attachment of the switch **3** molecules would significantly reduce the mean distance between QDs donor and switch acceptor, thus facilitate the FRET from QD to the **3** molecules. However, our result showed that while **3o** itself can be isomerized to the closed form (**3c**) under UV illumination, it irreversibly stays at its open form (**3o**) mostly after mixing with Mn-doped CdS-ZnS QDs (**Supplementary Figure 8**). It is shown that while the Mn/BG PL intensity ratio decreased with 40 s of UV illumination, it increased back with further UV illumination (**Figure 5D**). This phenomenon can be ascribed to the direct attachment of switch **3** to the surface of the QDs through the carboxylate functional group, thus leading to a close proximity of switch **3** to the QD surface constantly rather than a dynamic on-and-off process as for switches **1** and **2** cases. In this case, the visible Mn-PL of the QDs can trap the switch molecule **3** in its open form (**3o**), preventing them from turning into the closed form (**3c**). Consequently, no reversible photo-switching phenomenon can be observed as shown in **Figure 5D**, in good agreement with our experimental observations.

CONCLUSIONS

To conclude, we demonstrate a photo-switchable hybrid system with a reliable dual-color performance. This system combines photo-switchable diarylethene **1** molecule functionalized with strong electron withdrawing group of 3,5-bis(trifluoromethyl)benzene, and Mn-doped CdS-ZnS QDs with dual-emission band. Selective quenching/recovering of Mn-PL was achieved effectively, resulting in a pink and blue dual-color switching behavior under UV and visible light illumination. This photo-switching process is highly reversible and shows superior fatigue-resistance for at least 10 switching cycles. The mechanism studies using both steady-state and time-resolved PL spectroscopy reveal the PL quenching contributions from both FRET and photo-reabsorption processes. Moreover, we show that the involvements of other electron withdrawing functional groups (i.e., pyridine and carboxylate groups) limit the photo-switching property by significant molecular fatigue or irreversible optical effects. Our study sheds light on the fabrications of highly dynamic and photo-switchable hybrid systems that hold the potential in a broad range of applications spanning from self-erasing paper, biological-imaging to single molecule sensing/tracking and super-resolution imaging/localization microscopy.

DATA AVAILABILITY

The datasets for this manuscript are not publicly available because can be available upon request. Requests to access the datasets should be directed to ouchen@brown.edu.

AUTHOR CONTRIBUTIONS

YY, HZ, AD, and WZ performed experiments. YY, RT, and OC designed experiments. YY, YN, and OC interpreted the data and wrote the paper.

FUNDING

OC acknowledges the support from the Brown University startup fund.

ACKNOWLEDGMENTS

OC acknowledges support from the Senior Visiting Scholar Foundation of Key Laboratory at Fudan University. The project described was supported by Institutional Development Award Number U54GM115677 from the National Institute of General Medical Sciences of the National Institutes of Health, which funds Advance Clinical and Translational Research (Advance-CTR). The content is solely the responsibility of the authors and does not necessarily represent the official views of the National Institutes of Health. The TEM measurements were performed at the Electron Microscopy Facility in the Institute for Molecular and Nanoscale Innovation (IMNI) at Brown University.

SUPPLEMENTARY MATERIAL

The Supplementary Material for this article can be found online at: https://www.frontiersin.org/articles/10.3389/fchem.2019.00145/full#supplementary-material

REFERENCES

Bai, F., Li, B., Bian, K., Haddad, R., Wu, H., Wang, Z., et al. (2016). Pressure-tuned structure and property of optically active nanocrystals. *Adv. Mater.* 28, 1989–1993. doi: 10.1002/adma.201504819

Bandara, H. M., and Burdette, S. C. (2012). Photoisomerization in different classes of azobenzene. *Chem. Soc. Rev.* 41, 1809–1825. doi: 10.1039/C1CS15179G

Bryan, J. D., and Gamelin, D. R. (2005). Doped semiconductor nanocrystals: synthesis, characterization, physical properties, and applications. *Prog. Inorg. Chem.* 54, 47–126. doi: 10.1002/0471725560.ch2

Bussian, D. A., Crooker, S. A., Yin, M., Brynda, M., Efros, A. L., and Klimov, V. I. (2008). Tunable magnetic exchange interactions in manganese-doped inverted core–shell ZnSe–CdSe nanocrystals. *Nat. Mater.* 8:35. doi: 10.1038/nmat2342

Cai, T., Yang, H., Hills-Kimball, K., Song, J.-P., Zhu, H., Hofman, E., et al. (2018). Synthesis of all-inorganic Cd-doped $CsPbCl_3$ perovskite nanocrystals with dual-wavelength emission. *J. Phys. Chem. Lett.* 9, 7079–7084. doi: 10.1021/acs.jpclett.8b03412

Chen, H. Y., Chen, T. Y., and Son, D. H. (2010). Measurement of energy transfer time in colloidal Mn-doped semiconductor nanocrystals. *J. Phys. Chem. C* 114, 4418–4423. doi: 10.1021/jp100352m

Chen, H. Y., Maiti, S., and Son, D. H. (2012). Doping location-dependent energy transfer dynamics in Mn-doped CdS/ZnS nanocrystals. *ACS Nano* 6, 583–591. doi: 10.1021/nn204452e

Chen, O., Chen, X., Yang, Y., Lynch, J., Wu, H., Zhuang, J., et al. (2008). Synthesis of metal–selenide nanocrystals using selenium dioxide as the selenium precursor. *Angew. Chem. Int. Ed. Engl.* 120, 8766–8769. doi: 10.1002/ange.200804266

Chen, O., Shelby, D. E., Yang, Y., Zhuang, J., Wang, T., Niu, C., et al. (2010). Excitation-intensity-dependent color-tunable dual emissions from manganese-doped CdS/ZnS core/shell nanocrystals. *Angew. Chem. Int. Ed. Engl.* 122, 10330–10333. doi: 10.1002/ange.201004926

Díaz, S. A., Gillanders, F., Jares-Erijman, E. A., and Jovin, T. M. (2015). Photoswitchable semiconductor nanocrystals with self-regulating photochromic Förster resonance energy transfer acceptors. *Nat. Commun.* 6:6036. doi: 10.1038/ncomms7036

Díaz, S. A., Menéndez, G. O., Etchehon, M. H., Giordano, L., Jovin, T. M., and Jares-Erijman, E. A. (2011). Photoswitchable water-soluble quantum dots: pcFRET based on amphiphilic photochromic polymer coating. *ACS Nano* 5, 2795–2805. doi: 10.1021/nn103243c

Dolgopolova, E. A., Rice, A. M., Martin, C. R., and Shustova, N. B. (2018). Photochemistry and photophysics of MOFs: steps towards MOF-based sensing enhancements. *Chem. Soc. Rev.* 47, 4710–47128. doi: 10.1039/C7CS00861A

Gilroy, K. D., Ruditskiy, A., Peng, H. C., Qin, D., and Xia, Y. (2016). Bimetallic nanocrystals: syntheses, properties, and applications. *Chem. Rev.* 116, 10414–10472. doi: 10.1021/acs.chemrev.6b00211

Grinthal, A., and Aizenberg, J. (2013). Adaptive all the way down: building responsive materials from hierarchies of chemomechanical feedback. *Chem. Soc. Rev.* 42, 7072–7085. doi: 10.1039/C3CS60045A

Gu, J.-Q., Shen, J., Sun, L.-D., and Yan, C.-H. (2008). Resonance energy transfer in steady-state and time-decay fluoro-immunoassays for lanthanide nanoparticles based on biotin and avidin affinity. *J. Phys. Chem. C* 112, 6589–6593. doi: 10.1021/jp801203w

Herder, M., Schmidt, B. M., Grubert, L., Pätzel, M., Schwarz, J., and Hecht, S. (2015). Improving the fatigue resistance of diarylethene switches. *J. Am. Chem. Soc.* 137, 2738–2747. doi: 10.1021/ja513027s

Hofman, E., Robinson, R. J., Li, Z. J., Dzikovski, B., and Zheng, W. (2017). Controlled dopant migration in CdS/ZnS core/shell quantum dots. *J. Am. Chem. Soc.* 139, 8878–8885. doi: 10.1021/jacs.7b02320

Irie, M. (2000). Diarylethenes for memories and switches. *Chem. Rev.* 100, 1685–1716. doi: 10.1021/cr980069d

Irie, M., Fukaminato, T., Matsuda, K., and Kobatake, S. (2014). Photochromism of diarylethene molecules and crystals: memories, switches, and actuators. *Chem. Rev.* 114, 12174–12277. doi: 10.1021/cr500249p

Ithurria, S., Guyot-Sionnest, P., Mahler, B., and Dubertret, B. (2007). Mn^{2+} as a radial pressure gauge in colloidal core/shell nanocrystal's. *Phys. Rev. Lett.* 99:265501. doi: 10.1103/PhysRevLett.99.265501

Kay, E. R., Leigh, D. A., and Zerbetto, F. (2007). Synthetic molecular motors and mechanical machines. *Angew. Chem. Int. Ed.* 46, 72–191. doi: 10.1002/anie.200504313

Klajn, R. (2014). Spiropyran-based dynamic materials. *Chem. Soc. Rev.* 43, 148–184. doi: 10.1039/C3CS60181A

Klajn, R., Stoddart, J. F., and Grzybowski, B. A. (2010). Nanoparticles functionalised with reversible molecular and supramolecular switches. *Chem. Soc. Rev.* 39, 2203–2237. doi: 10.1039/B920377J

Krivenkov, V., Goncharov, S., Samokhvalov, P., Sánchez-Iglesias, A., Grzelczak, M., Nabiev, I., et al. (2019). Enhancement of biexciton emission due to long-range interaction of single quantum dots and gold nanorods in a thin-film hybrid nanostructure. *J. Phys. Chem. Lett.* 10, 481–486. doi: 10.1021/acs.jpclett.8b03549

Kroupa, D. M., Roh, J. Y., Milstein, T. J., Creutz, S. E., and Gamelin, D. R. (2018). Quantum-cutting ytterbium-doped $CsPb(Cl1–xBrx)_3$ perovskite thin films with photoluminescence quantum yields over 190%. *ACS Energy Lett.* 3, 2390–2395. doi: 10.1021/acsenergylett.8b01528

Kuhn, H. (1949). A quantum-mechanical theory of light absorption of organic dyes and similar compounds. *J. Chem. Phys.* 17, 1198–1212. doi: 10.1063/1.1747143

Kundu, P. K., Samanta, D., Leizrowice, R., Margulis, B., Zhao, H., Börner, M., et al. (2015). Light-controlled self-assembly of non-photoresponsive nanoparticles. *Nat. Chem.* 7, 646–652. doi: 10.1038/nchem.2303

Li, B., Bian, K., Zhou, X., Lu, P., Liu, S., Brener, I., et al. (2017). Pressure compression of CdSe nanoparticles into luminescent nanowires. *Sci. Adv.* 3:e1602916. doi: 10.1126/sciadv.1602916

Li, Z.-J., Hofman, E., Davis, A. H., Khammang, A., Wright, J. T., Dzikovski, B., et al. (2018). Complete dopant substitution by spinodal decomposition in Mn-doped two-dimensional CsPbCl3 nanoplatelets. *Chem. Mater.* 30, 6400–6409. doi: 10.1021/acs.chemmater.8b02657

Manna, D., Udayabhaskararao, T., Zhao, H., and Klajn, R. (2015). Orthogonal light-induced self-assembly of nanoparticles using differently substituted azobenzenes. *Angew. Chem. Int. Ed.* 54, 12394–12397. doi: 10.1002/anie.201502419

Medintz, I. L., Clapp, A. R., Mattoussi, H., Goldman, E. R., Fisher, B., and Mauro, J. M. (2003). Self-assembled nanoscale biosensors based on quantum dot FRET donors. *Nat. Mater.* 2, 630–638. doi: 10.1038/nmat961

Mikami, R., Taguchi, M., Yamada, K., Suzuki, K., Sato, O., and Einaga, Y. (2004). Reversible photo-switching of the magnetization of iron oxide nanoparticles at room temperature. *Angew. Chem. Int. Ed. Engl.* 43, 6135–6139. doi: 10.1002/anie.200460964

Min Yeo, K., Ji Gao, C., Ahn, K. H., and Su Lee, I. (2008). Superparamagnetic iron oxide nanoparticles with photoswitchable fluorescence. *Chem. Commun.* 4622–4624. doi: 10.1039/B807462C

Minkin, V. I. (2004). Photo-, thermo-, solvato-, and electrochromic spiroheterocyclic compounds. *Chem. Rev.* 104, 2751–2776. doi: 10.1021/cr020088u

Momotake, A., and Arai, T. (2004). Photochemistry and photophysics of stilbene dendrimers and related compounds. *J. Photochem. Photobiol. C* 5, 1–25. doi: 10.1016/j.jphotochemrev.2004.01.001

Mulder, A., Juković, A., Huskens, J., and Reinhoudt, D. N. (2004). Bis(phenylthienyl)ethene-tethered beta-cyclodextrin dimers as photoswitchable hosts. *Org. Biomol. Chem.* 2, 1748–1755. doi: 10.1039/b402146k

Niebling, T., Zhang, F., Ali, Z., Parak, W. J., and Heimbrodt, W. (2009). Excitation dynamics in polymer-coated semiconductor quantum dots with integrated dye molecules: the role of reabsorption. *J. Appl. Phys.* 106:104701. doi: 10.1063/1.3253762

Norris, D. J., Efros, A. L., and Erwin, S. C. (2008). Doped nanocrystals. *Science* 319, 1776–1779. doi: 10.1126/science.1143802

Pietryga, J. M., Park, Y. S., Lim, J., Fidler, A. F., Bae, W. K., Brovelli, S., et al. (2016). Spectroscopic and device aspects of nanocrystal quantum dots. *Chem. Rev.* 116, 10513–10622. doi: 10.1021/acs.chemrev.6b00169

Pradhan, N., Das Adhikari, S., Nag, A., and Sarma, D. D. (2017). Luminescence, Plasmonic, and Magnetic Properties of Doped Semiconductor Nanocrystals. *Angew. Chem. Int. Ed. Engl.* 56, 7038–7054. doi: 10.1002/anie.201611526

Pradhan, N., and Peng, X. (2007). Efficient and color-tunable Mn-doped ZnSe nanocrystal emitters: control of optical performance via greener synthetic chemistry. *J. Am. Chem. Soc.* 129, 3339–3347. doi: 10.1021/ja068360v

Qu, D. H., Wang, Q. C., Zhang, Q. W., Ma, X., and Tian, H. (2015). Photoresponsive host–guest functional systems. *Chem. Rev.* 115, 7543–7588. doi: 10.1021/cr5006342

Roy, N., Bruchmann, B., and Lehn, J. M. (2015). DYNAMERS: dynamic polymers as self-healing materials. *Chem. Soc. Rev.* 44, 3786–3807. doi: 10.1039/C5CS00194C

Selvin, P. R. (2000). The renaissance of fluorescence resonance energy transfer. *Nat. Struct. Mol. Biol.* 7:730. doi: 10.1038/78948

Talapin, D. V., and Shevchenko, E. V. (2016). Introduction: nanoparticle chemistry. *Chem. Rev.* 116, 10343–10345. doi: 10.1021/acs.chemrev.6b00566

Tam, E. S., Parks, J. J., Shum, W. W., Zhong, Y. W., Santiago-Berríos, M. B., Zheng, X., et al. (2011). Single-molecule conductance of pyridine-terminated dithienylethene Switch molecules. *ACS Nano* 5, 5115–5123. doi: 10.1021/nn201199b

Tu, D., Liu, L., Ju, Q., Liu, Y., Zhu, H., Li, R., et al. (2011). Time-Resolved FRET Biosensor Based on Amine-Functionalized Lanthanide-Doped NaYF4 Nanocrystals. *Angew. Chem. Int. Ed. Engl.* 123, 6430–6434. doi: doi: 10.1002/ange.201100303

Wang, L., and Li, Q. (2018). Photochromism into nanosystems: towards lighting up the future nanoworld. *Chem. Soc. Rev.* 47, 1044–1097. doi: 10.1039/C7CS00630F

Wu, L., Mendoza-Garcia, A., Li, Q., and Sun, S. (2016). Organic phase syntheses of magnetic nanoparticles and their applications. *Chem. Rev.* 116, 10473–10512. doi: 10.1021/acs.chemrev.5b00687

Wu, P., and Yan, X. P. (2013). Doped quantum dots for chemo/biosensing and bioimaging. *Chem. Soc. Rev.* 42, 5489–54521. doi: 10.1039/C3CS60017C

Yang, Y., Chen, O., Angerhofer, A., and Cao, Y. C. (2006). Radial-position-controlled doping in CdS/ZnS core/shell nanocrystals. *J. Am. Chem. Soc.* 128, 12428–12429. doi: 10.1021/ja064818h

Yang, Y., Chen, O., Angerhofer, A., and Cao, Y. C. (2008). On doping CdS/ZnS shell nanocrystals with Mn. *J. Am. Chem. Soc.* 130, 15649–15661. doi: 10.1021/ja805736k

Yang, Y., Chen, O., Angerhofer, A., and Cao, Y. C. (2009). Radial-position-controlled doping of CdS/ZnS core/shell nanocrystals: surface effects and position-dependent properties. *Chem. Eur. J.* 15, 3186–3197. doi: 10.1002/chem.200802295

Yildiz, I., Deniz, E., and Raymo, F. M. (2009). Fluorescence modulation with photochromic switches in nanostructured constructs. *Chem. Soc. Rev.* 38, 1859–1867. doi: 10.1039/B804151M

Zhang, J., Zou, Q., and Tian, H. (2012). Photochromic materials: more than meets the eye. *Adv. Mater.* 25, 378–399. doi: 10.1002/adma.201201521

Zhao, H., Sen, S., Udayabhaskararao, T., Sawczyk, M., Kučanda, K., Manna, D., et al. (2015). Reversible trapping and reaction acceleration within dynamically self-assembling nanoflasks. *Nat. Nanotech.* 11, 82–88. doi: 10.1038/nnano.2015.256

Zheng, W., and Strouse, G. F. (2011). Involvement of carriers in the size-dependent magnetic exchange for Mn:CdSe quantum dots. *J. Am. Chem. Soc.* 133, 7482–7489. doi: 10.1021/ja200508e

Zhu, L., Zhu, M. Q., Hurst, J. K., and Li, A. D. (2005). Light-controlled molecular switches modulate nanocrystal fluorescence. *J. Am. Chem. Soc.* 127, 8968–8970. doi: 10.1021/ja0423421

Zhu, M. Q., Zhu, L., Han, J. J., Wu, W., Hurst, J. K., and Li, A. D. (2006). Spiropyran-based photochromic polymer nanoparticles with optically switchable luminescence. *J. Am. Chem. Soc.* 128, 4303–4309. doi: 10.1021/ja0567642

Conflict of Interest Statement: The authors declare that the research was conducted in the absence of any commercial or financial relationships that could be construed as a potential conflict of interest.

Copyright © 2019 Yuan, Zhu, Nagaoka, Tan, Davis, Zheng and Chen. This is an open-access article distributed under the terms of the Creative Commons Attribution License (CC BY). The use, distribution or reproduction in other forums is permitted, provided the original author(s) and the copyright owner(s) are credited and that the original publication in this journal is cited, in accordance with accepted academic practice. No use, distribution or reproduction is permitted which does not comply with these terms.

frontiers in Chemistry

REVIEW
published: 01 May 2019
doi: 10.3389/fchem.2019.00290

Mesoporous Silica Nanoparticles for Protein Protection and Delivery

Chun Xu[1]*, *Chang Lei*[2] *and Chengzhong Yu*[2]*

[1] School of Dentistry, The University of Queensland, Brisbane, QLD, Australia, [2] Australian Institute for Bioengineering and Nanotechnology, The University of Queensland, Brisbane, QLD, Australia

Therapeutic proteins are widely used in clinic for numerous therapies such as cancer therapy, immune therapy, diabetes management and infectious diseases control. The low stability and large size of proteins generally compromise their therapeutic effects. Thus, it is a big challenge to deliver active forms of proteins into targeted place in a controlled manner. Nanoparticle based delivery systems offer a promising method to address the challenges. In particular, mesoporous silica nanoparticles (MSNs) are of special interest for protein delivery due to their excellent biocompatibility, high stability, rigid framework, well-defined pore structure, easily controllable morphology and tuneable surface chemistry. Therefore, enhanced stability, improved activity, responsive release, and intracellular delivery of proteins have been achieved using MSNs as delivery vehicles. Here, we systematically review the effects of various structural parameters of MSNs on protein loading, protection, and delivery performance. We also highlight the status of the most recent progress using MSNs for intracellular delivery, extracellular delivery, antibacterial proteins delivery, enzyme mobilization, and catalysis.

Keywords: mesoporous silica nanoparticles, mesostructure, surface modification, protein therapeutics, drug delivery

OPEN ACCESS

Edited by:
Fan Zhang,
Fudan University, China

Reviewed by:
Jianping Yang,
Donghua University, China
Paolo Saccardo,
Autonomous University of Barcelona, Spain

***Correspondence:**
Chun Xu
chun.xu@uq.edu.au
Chengzhong Yu
c.yu@uq.edu.au

Specialty section:
This article was submitted to Nanoscience, a section of the journal Frontiers in Chemistry

Received: *31 January 2019*
Accepted: *09 April 2019*
Published: *01 May 2019*

Citation:
Xu C, Lei C and Yu C (2019) Mesoporous Silica Nanoparticles for Protein Protection and Delivery. Front. Chem. 7:290. doi: 10.3389/fchem.2019.00290

INTRODUCTION OF PROTEIN THERAPEUTICS AND MSNs

In 1922 the pancreatic insulin was successfully purified and applied for Leonard Thompson, a 14 years old boy suffering type 1 diabetes, which ushered in the era of protein therapeutics (Banting et al., 1991). Since then numerous protein drugs have been developed and used in various clinical applications. By 2008, 130 protein based therapeutics had been approved by the US Food and Drug Administration (FDA) and the number of approved protein drugs soared to 239 in 2017 (Leader et al., 2008; Usmani et al., 2017). In 2018, 7 of top 10 best-selling human drugs are proteins based ones (Urquhart, 2018). Those protein therapeutics comprise enzymes, monoclonal antibodies, vaccines, hormones, growth factors, tumor necrosis factors, etc., (Usmani et al., 2017). Protein based drugs are receiving growing interest due to their specific functions, less side effects, which are also considered safer than gene therapy as no genetic change happens (Gu et al., 2011). However, the wide applications of protein drugs are hindered due to their intrinsic drawbacks especially low stability. The folded characteristic 3 dimensional structures of proteins are essential for their biological functions, but the conformation is only slightly more stable than unfolded one. From an entropic point of view proteins are easy to be denatured (Villegas et al., 2018). In addition, some therapeutic proteins need to act inside cells, thus intracellular delivery of active forms of proteins into specific cells remains the main challenge of such proteins drugs (Ghosh et al., 2010; Gu et al., 2011).

The rapid development of nanotechnology provides a revolutionary way in the design of nanoparticle based drug delivery systems to protect proteins and deliver them to desired places. New formulations based on nanoparticles or nanostructures have already been used in the clinical setting (Peer et al., 2007; Davis et al., 2008) and have demonstrated enhanced efficacy and reduced side effects, due to the properties brought on by nanoscale effects (Muller et al., 2002; Torchilin, 2005; Naseri et al., 2015). Nowadays, the clinically available delivery systems are mainly organic materials such as liposomes and other lipid formulations and polymers (Gradishar et al., 2005; Sparreboom et al., 2005; Duncan, 2006; Greco and Vicent, 2009). However, the intrinsic instability and limited drug-loading capacity inhibit their applications for protein delivery (Elsabahy and Wooley, 2012; Chen et al., 2013).

Recently, the development of inorganic materials such as MSNs, quantum dots (Gao et al., 2004; Michalet et al., 2005), carbon-based nanomaterials (Liu et al., 2011; Robinson et al., 2011), layered double hydroxides (Bao et al., 2011; Yan et al., 2013; Kura et al., 2014) and magnetic nanoparticles (Arruebo et al., 2007; Sun et al., 2008) have attracted great attention due to their remarkably high chemical stability. Among this group of carriers, MSNs are of special interest because of their excellent biocompatibility, high drug loading capacity, rigid framework, well-defined pore structure, easily controllable morphology, and tuneable surface chemistry (Lind et al., 2003; Meng et al., 2011; Chen et al., 2013; Xu et al., 2014). The delivery of proteins using traditional MSNs is usually limited by the small pores. Recent development of MSNs with large pores and novel pore structures greatly expand their applications for protein therapeutics delivery (Shen et al., 2014; Knezevic and Durand, 2015; Xiong et al., 2015; Xu et al., 2015; Yang J. P. et al., 2015). In addition, with abundant surface modification, various responsive release systems based on MSNs have been developed with numerous advantages such as improved efficacy and reduced toxicity (Zhu et al., 2017). In this review, how to design MSNs for achieving effective protein loading, protection and delivery will be comprehensively reviewed. The progress of MSNs based protein therapy for various applications including intracellular delivery, extracellular delivery, antibacterial proteins delivery, enzyme mobilization and catalysis will be highlighted.

ENGINEERING MSNs FOR PROTEIN LOADING, PROTECTION, AND DELIVERY

Encapsulation of proteins within nanocarriers can overcome the shortcomings of proteins such as poor solubility, poor stability, difficulty in crossing the cell membranes and lack of specificity. In addition, nanocarriers enable the delivery of unique drug combinations which are important for personalized medicine (Mura and Couvreur, 2012; Kim et al., 2013). Compared to current clinically used organic nanocarriers such as liposomes, MSNs can achieve higher protein loading capacity due to their large pore size, high surface area and large pore volume. In addition, it is reported that the solid frame of MSNs would protect the proteins from denaturation (Kao et al., 2014). A large number of MSNs with different structures, morphology, and surface functionalization have already been designed and applied for drug delivery (Carino et al., 2007; Vallet-Regi et al., 2007; Angelos et al., 2008; Wang, 2009; Manzano and Vallet-Regi, 2010; Yang et al., 2012; Chen et al., 2013; Shen et al., 2013; Siefker et al., 2014; Dai et al., 2017). In the following part, the effects of pore size, surface functionalization, pore structure, pore volume and surface area on the protein loading and protection ability are reviewed.

Pore Size

In order to load proteins into the mesopores, the pore sizes of MSNs usually need to be larger than the protein molecule dimensions. MSNs with larger pore sizes usually have higher drug loading amounts and faster release rates compared to the ones with small pores, which may be due to a steric hindrance effect (Vallet-Regi et al., 2008; Cirujano et al., 2017). In one study when the pore sizes of SBA-15 were varied from 8.2 to 11.4 nm, the bovine serum albumin loading ability was increased from 15 to 27% (Vallet-Regi et al., 2008). Zhang et al. (2014) prepared a series of hydrophobic silica vesicles with different entrance sizes ranging from <3.9 to 34 nm (<3.9, 6, 8, 13, 16, 24, 33, 34 nm) and tested the loading capacity of RNase A (with dimension of 2.2*2.8*3.8 nm). Silica vesicles with pore size of 6 nm exhibited the highest RNase loading amount (563 mg/g), which was almost double of that achieved by silica vesicles with small pores (<3.9 nm) or large pores (>13 nm). This effect was also observed in other mesoporous structures such as MCM-48 with a 3D cubic pore structure. MCM-48 with a pore size of 5.7 nm exhibited a higher loading capacity of ibuprofen (IBU) compared to the one with 3.6 nm pores, and a faster release rate (Izquierdo-Barba et al., 2005).

The enhanced activity and stability of proteins, once loaded inside the pores of MSNs, have been well-documented. Kao et al. (2014) studied the activity and stability of lysozyme immobilized in MSNs of various pore sizes by testing the proteins' secondary and tertiary structures with methods such as circular dichroism and activity assay. The activity of the lysozyme when immobilized in the pores of MSNs (pore size close to protein dimensions) was higher than that of native one. In addition, the enzymatic activity was also improved by MSNs from thermal denaturation (**Figure 1**, Kao et al., 2014). Kalantari also reported the immobilization of another enzyme, lipase, into MSNs with tunable pore size (from 1.6 to 13 nm). They concluded that suitable pore size (slightly larger than the size of lipase) is responsible for the loading and the performance of lipase. The MSNs with optimized pore size exhibited a high loading capacity of 711 mg g^{-1}, and an 5.23 times specific activity higher than that of the native enzyme (Kalantari et al., 2017).

Since the pore size of MSNs plays a critical role for the loading and release of protein, methods to control the pore size distribution should be briefly reviewed. Traditionally two ways have been developed to expand the pore size, utilizing polymers/surfactants with longer carbon chains/co-surfactants as template or adding suitable organic agents (swelling agents) to increase the sizes of surfactant templates (Knezevic and Durand,

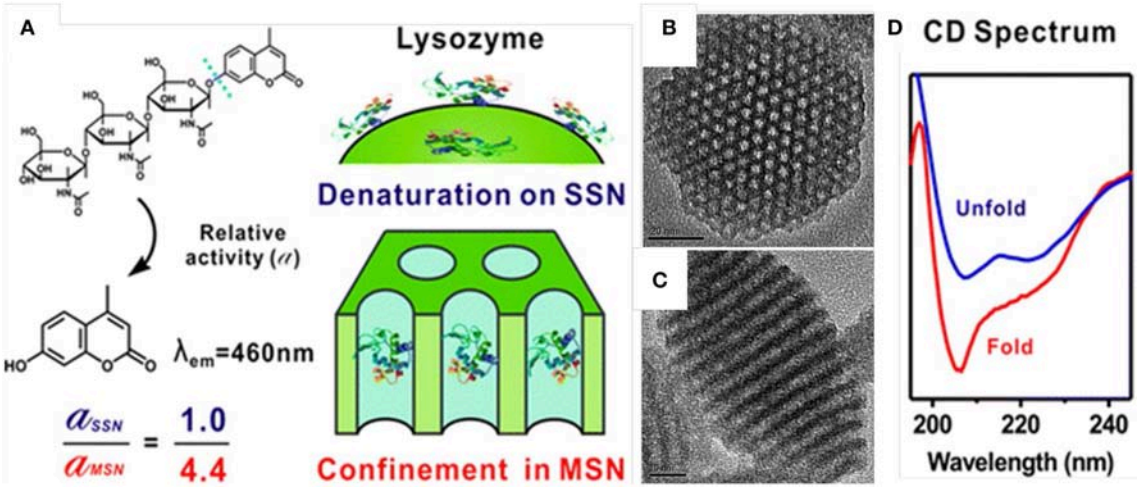

FIGURE 1 | Enhanced stability and activity of lysozyme after loaded inside the mesopores of MSNs. Schematic illustration **(A)** showed the relative activity of lysozyme loaded into MSNs was 4.4-folds higher than that loaded on the outer surface of solid silica nanoparticles (SSN). **(B,C)** showed the pore structure of MSNs and **(D)** showed the circular dichroism (CD) spectrum of free lysozyme and the one loaded inside MSNs. Reproduced with permission from Kao et al. (2014), The American Chemical Society.

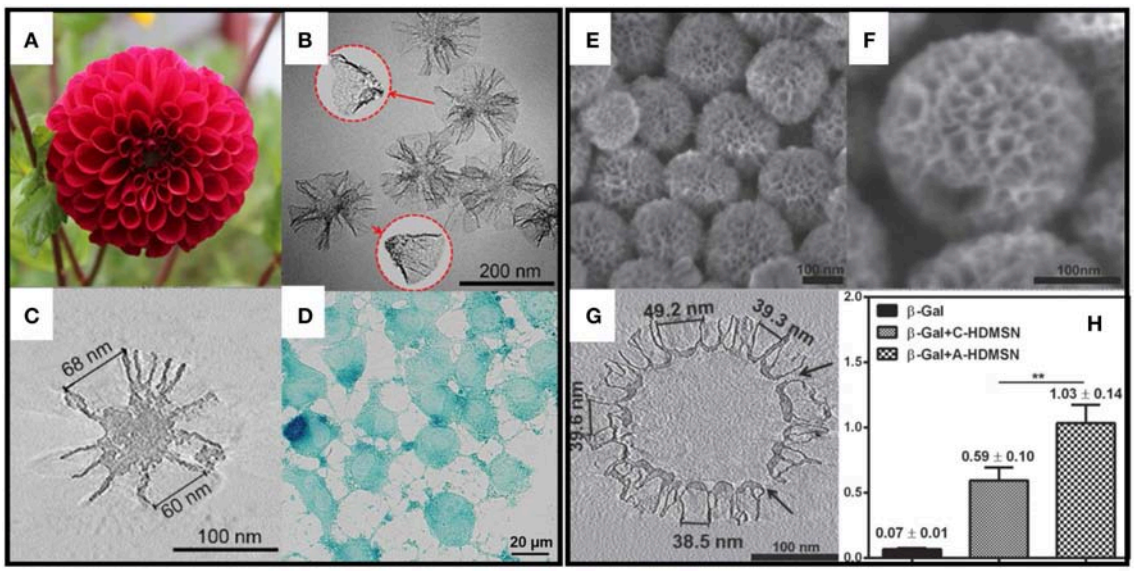

FIGURE 2 | MSNs with radial pore structure and their application for large protein (β-Gal) delivery. **(A–C)** showed the structure of MSN-CC and **(D)** shows the intracellular delivery of β-Gal. **(E–G)** showed the structure of amino group modified hollow MSNs with radial pores. **(H)** showed the highest β-Gal delivery efficacy ** $p < 0.01$. Reproduced with permission from Xu et al. (2015), The Wiley-VCH and Meka et al. (2016), The Wiley-VCH.

2015). For the first strategy, the most typical example is the synthesis of SBA-15 using amphiphilic block copolymers as templates, and the pore size can achieve up to 10 nm (Zhao et al., 1998). For the second strategy, 1,3,5-trimethylbenzene (TMB) is the most common pore-expanding agent (Huo et al., 1996; Feng et al., 2000) and the pore size of MSNs can be enlarged in a large range with addition of TMB. It is noted that excessive addition of swelling agents may result in the loss of structure (Knezevic and Durand, 2015). Very recently, MSNs with radial pore structures (Polshettiwar et al., 2010; Shen et al., 2014; Du and Qiao, 2015; Wang et al., 2019) provide another strategy in the synthesis of MSNs with large pores. The pore size can be expanded to 50 nm or even larger (Xu et al., 2015; Wang et al., 2019).

Surface Functionalization

The loading of drug into MSNs are usually achieved by the interaction between the protein molecules and surface of pore channels through non-covalent bindings such as

electrostatic interaction, hydrogen bonding, pi-pi stacking etc, (Yang et al., 2012). Chemical modification of MSNs with appropriate functional groups can provide specific interactions with proteins thus provide effective control over protein loading and release. The high density of silanol groups on the surfaces of MSNs and the large library of available organic silanes make the functionalization of MSNs quite easy through a simple post-grafting or co-condensation method (Manzano et al., 2008; Yang et al., 2008; Chang et al., 2010; Li et al., 2013; Bouchoucha et al., 2014; Jambhrunkar et al., 2014). With suitable surface functionalization, strong interaction between proteins and the pore channels by electrostatic force can be achieved, and protein loading amount can be increased while release rates are slowed. In pioneering studies, positively charged amino modified MCM-41 and SBA-15 showed a much higher loading capacity to IBU (a drug with carboxy groups, negative charged) compared to unmodified negative charged ones (Vallet-Regi, 2006). A slower release rate of IBU was also observed from the amino modified MSNs (Babonneau et al., 2003, 2004; Ramila et al., 2003; Song et al., 2005; Vallet-Regi, 2006). Tu et al. (2016) tested the encapsulation ability of negatively and positively charged MSNs with big pores (10 nm) toward a series of proteins with different molecular weights (from 12 to 250 kDa) and surface charges. It is concluded that the surface chemistry within the channels plays a dominant role in the loading of proteins. It is also notable that the protein loading process was quick, MSNs achieved 95% of maximum proteins loading ability within 20 min (Tu et al., 2016).

Another strategy of surface functionalization to control the protein loading and delivery behaviors is modification of MSNs with hydrophobic groups. Proteins are composed of many amino acids with different hydrophobic properties, a hydrophobic surface modification usually increases the protein loading and enhance the stability. Doadrio et al. (2006) modified SBA-15 with octyl (-C8) and octadecyl (-C18) groups and tested the drug release behaviors after loading with an antibiotic drug erythromycin. They found the MSNs modified with hydrophobic groups showed a slower release rate, the octadecyl-modified SBA-15 exhibited a one order of magnitude lower release rate compared to unmodified SBA-15. The observation was explained as the hydrophobic groups impeded the penetration of aqueous solution and prevented the fast release of the loaded drugs (Vallet-Regi et al., 2007). Bale et al. (2010) utilized n-octadecyltrimethoxysilane modified silica nanoparticles to deliver green fluorescent protein and RNase A into mammal cells. Results indicated that hydrophobic modification helped to preserve the biological activity of proteins and, more importantly, to achieve endosomal escape. Niu et al. (2016) studied the effects of hydrophobic modification (octadecyl-group) as well as surface roughness of silica nanoparticles on the loading capacity, release profile, cellular uptake and endosomal escape of RNase A. They concluded that the hydrophobic modification enhanced the protein loading capacity, achieved sustained release and improved the cellular uptake performance. Octadecyl-functionalized silica nanoparticles with rough surface showed the best performance in RNase A delivery which caused significant cancer cell inhibition. In addition, Zhang et al. (2018) reported that hydrophobic modification of silica vesicles (-C8 and -C18 groups) enhanced the insulin enrichment ability from PBS or artificial urine. They also found that the insulin which loaded inside alkyl modified silica vesicles showed less secondary structure's conformation change than that of hydrophilic ones.

Pore Structure

Various pore structures, in terms of pore geometry, are also reported to affect the protein loading and release properties. Xu et al. (2015) synthesized MSNs with cone shaped pores (MSN-CC, **Figures 2A–D**), which has a large pore size (45 nm) and a high pore volume (2.59 $cm^3\ g^{-1}$). They demonstrated that MSN-CC can achieve a high loading capacity of large proteins and successfully deliver active beta-galactosidase (β-Gal, 8*13*18 nm) into cells. Based on this work, Meka et al. (2016) designed an amine-functionalized hollow MSNs with cone shaped pores using one step synthesis. With the cationic groups, this hollow MSNs (**Figures 2E–H**) showed higher loading capacity toward negative proteins such as β-Gal and better cellular uptake performance by up to 40-fold and 5-fold compared to free protein or protein loaded in unmodified MSNs. In addition, β-Gal delivered by amine-modified MSNs retains its activity and catalytic functions. Andersson et al. (2004) also showed MSNs with cage-like pores provided a higher drug loading amount compared to those with cylindrical pores. The pore structure also influences the drug release behavior. Vallet-Regi et al. (2007) found that MCM-48 with a 3D cubic pore structure released loaded IBU faster than MCM-41 with 2D hexagonal pores (Izquierdo-Barba et al., 2009).

Surface Area

Usually the drug loading process was carried out by immersing MSNs in drug solutions with high concentration followed with separation. Vallet-Regi et al. (2007) compared the maximum loading amount of alendronate in MSNs with similar structure but different surface area. Results showed that under the same loading condition MCM-41 with surface area of 1,157 $m^2\ g^{-1}$ had a higher loading amount than SBA-15 with surface area of 719 $m^2\ g^{-1}$ (139 vs. 83 mg g^{-1}) (Vallet-Regi et al., 2007; Izquierdo-Barba et al., 2009). The pore surface provides the sites for the physical or chemical adsorption of the drugs, thus is an important factor for evaluating the drug loading capacity of MSNs. This conclusion is based on the studies of small molecular drugs. For proteins, large pore negative charged MSNs with different structures (with a core inside vs. hollow) but similar surface area have similar proteins loading capacity (Xu et al., 2015; Meka et al., 2016). More studies with rationale design are suggested to further test the effects the surface area on protein loading. It is noted that the contribution of different (e.g., micropore) surface area need to be considered corresponding influence on protein loading and release.

Pore Volume

Though the drug loading process is considered to be mainly happened on the surface of mesopores, the drug-drug interactions can happen under some conditions such as very high drug loading concentration, which could fulfill the pores. In those cases the pore volume is an important factor which affects the drug loading capacity. For example mesocellular

silica foams with a pore volume of 1.9 cm^3 g^{-1} showed a higher bovine serum albumin loading amount than SBA-15 with a pore volume of 1.1 cm^3 g^{-1} (Schmidt-Winkel et al., 1999). Yang and co-authors coated mesoporous silica foam (pore size > 10 nm) on the outside of solid magnetic oxide composites for protein adsorption. With the addition of several mesoporous silica layers, the pore volume increased to ∼0.49 cm^3 g^{-1} and high loading capacity toward BSA (113 mg g^{-1}) and cytochrome C (142–175 mg g^{-1}) were achieved without compromising the magnetic property (Yang et al., 2014). Xu et al. (2015) synthesized MSNs with cone shaped pores and the pore volume reached as high as 2.69 cm^3 g^{-1}, a ultra-high loading capacity toward large proteins (560 mg g^{-1} toward IgG and 190 mg g^{-1} toward β-Gal) was achieved (Xu et al., 2015; Meka et al., 2016). In general, MSNs with high pore volume can load more amount of proteins under the condition that the pore size is larger than the dimension of proteins. The effect of pore volume toward protein release has not been reported yet to our knowledge.

APPLICATION MSNs FOR INTRACELLULAR PROTEINS DELIVERY

Protein therapeutics are promising drugs to intervene cell functions more precisely due to their high target specificity. They are also considered to be safer compared to gene therapies as no genetic alteration happens. In many applications such as cancer therapy and immune therapy, protein therapeutics need to work inside the cells however bare protein cannot cross the cell membranes by themselves. In 2007, Slowing et al. (2007) first demonstrated the intracellular delivery of a small protein, native cytochrome c (with a size of 2.6*3.2*3.3 nm), into human cervical cancer cells (Hela cells) by MCM-41 type MSNs with 5.4 nm pore size. In this pioneer work, though the intracellular delivery of cytochrome c was proved, the function of the protein after deliver into cells was not tested. Later, Davis et al. (2008) employed PEI modified MSNs to delivery cytochrome c and induced programmed cell death of Hela cells (Huang et al., 2013). In addition to cytochrome c, ribonuclease A (RNase A, with the size of 2.2* 2.8*3.8 nm) is also widely used as a protein drug model to test the delivery efficacy and the intracellular functions. RNase A degraded RNA in the cytosol, after loaded into MSNs and delivered into cancer cells, they can inhabit protein production and cause cell death. Zhang et al. (2014) reported hollow silica vesicles for the intracellular delivery of RNase A. Results show a high protein loading capacity and high potency for cancer cell inhibition. Niu et al. (2016) demonstrated hydrophobic modification (C18-functionalization) of MSNs is an effective strategy for the intracellular delivery of RNase A. Benzene-bridged MSNs (with hydrophobic groups in the framework or silica) were also fabricated and applied for RNase A delivery (Yang Y. N. et al., 2015). In addition to small proteins, protein therapeutics with large molecular weight are also delivered into cells benefiting from the development of MSNs with large pores (Xu et al., 2015; Meka et al., 2016).

In addition to just delivery of proteins into cells, there were more designs on MSNs to achieve "on-demand" responsive intracellular release. For example, organic MSNs with disulfide bond can achieve glutathione (GSH) responsive release to selectively release proteins in cancer cells. Yang et al. (2016) designed disulfidebond-bridged and large-pored MSNs for intracellular RNase A delivery. This disulfide bond-bridged MSNs demonstrated a GSH responsive degradation behavior, which showed a higher degradation rate in cancer cells but a low rate in normal cells. Very recently, oxidative and redox dual-responsiveness organosilica nanoparticles were further developed to selectively deliver and release RNase A in cancer cells and the anticancer performance was evaluated *in vivo* (**Figure 3**, Shao et al., 2018). These diselenide-bridged MSNs with 10 nm pores can load RNase A inside the pore channels with electrostatic interaction and degrade upon exposure to redox or oxidative conditions to release the payload. The anti-cancer performance was also evaluated on nude mice bearing tumors. With surface medication with fragments from the cancer cell membrane, those MSNs showed longer blood circulation time, low toxicity and enhanced tumor inhabitation ability, suggesting dual responsive degradable MSNs with proper surface modification provides a promising strategy for the delivery of protein therapeutics into tumors (Shao et al., 2018).

MSNs are also widely used for immune therapy and to deliver vaccine into antigen presenting cells (Mody et al., 2013). Yang and collaborators reported the delivery of protein antigens using multi-shell dendritic mesoporous organosilica nanoparticles for cancer immunotherapy. The organosilica nanoparticles successfully loaded ovalbumin (OVA) and mediated endo/lysosome escape to macrophages. They evaluated the *in vivo* antitumor performance of organosilica nanoparticles to deliver B16F10 tumor cell fragments in a therapeutic vaccination model, showing better immunity for cancer therapy than pure silica nanoparticles. Their work provided us new insights for the design of MSNs for adjuvants delivery and vaccine developments (Yang Y. et al., 2017). MSNs are also used for oral vaccine delivery. Wang et al. (2012) loaded bovine serum albumin into MSNs with different particle size (130 nm, 450 nm, and 1–2 μm) and administrated orally to mice. They observed the immune response and found MSNs with small size triggered higher IgG antibody concentration in plasma (Wang et al., 2012).

In addition to cancer and immune therapy, MSNs are also used to for other protein therapies such as deliver proteasomes for the treatment of Azhamen's syndrome. Han et al. (2014) utilized MSNs to load and deliver therapeutic proteasomes to degrade tau aggregates for the management of Alzheimer's disease. MSNs were internalized and distributed in the cytosol after endosomes escaping. *In vitro* tests showed proteasomes loaded MSNs degraded the overexpressed tau in the cells more efficiently compared to the native proteasomes, and decreased the levels of the truncated tau which is considered as pathological hallmark of this disease (**Figure 4**).

APPLICATION OF MSNs FOR EXTRACELLULAR PROTEIN DELIVERY

For those protein therapeutics that works outside of cells, MSNs also provide a platform to protect their activity and achieve

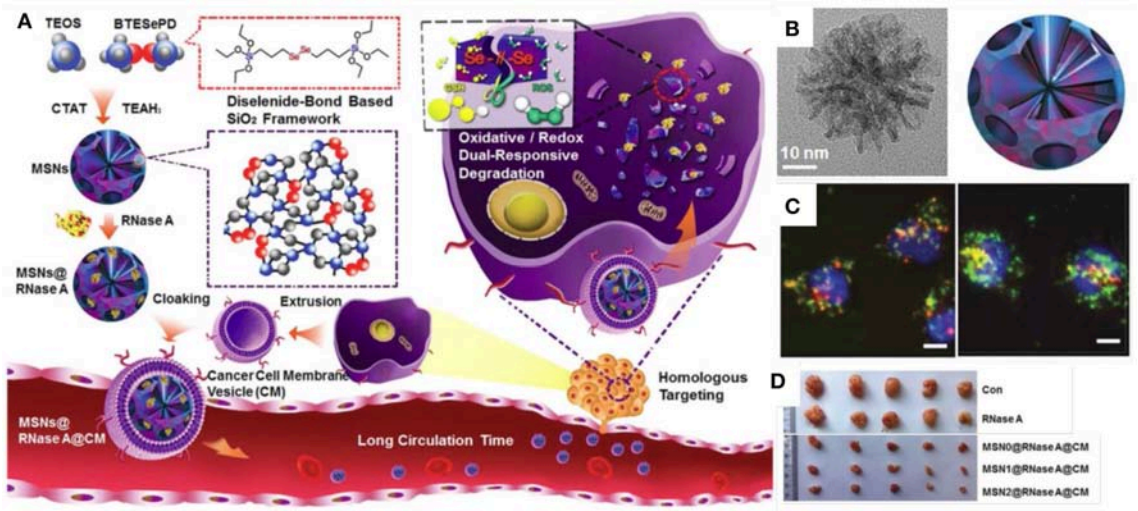

FIGURE 3 | Responsive MSNs based protein delivery system for cancer therapy. Schematic drawing **(A)** showed the synthesis of biodegradable diselenide-bridged MSNs [TEM images in **(B)**] with dual-responsive and cancer cell membrane mimetic surface modification was used to deliver RNase A into cancer cells **(C)** and inhibit tumor growth *in vivo* **(D)**. Reproduced with permission from Shao et al. (2018), The Wiley-VCH.

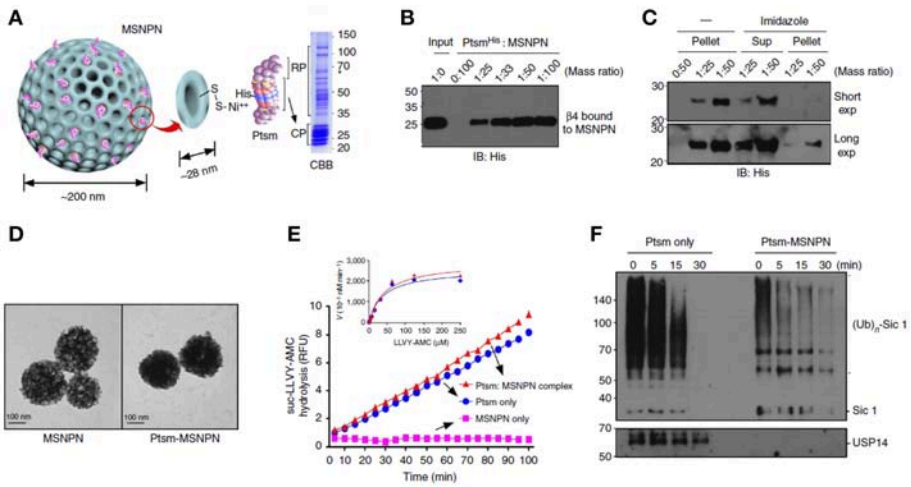

FIGURE 4 | MSNs delivered proteasome to degrade tau aggregates, a pathological hallmark of Alzheimer's disease. Panel **(A)** was the schematic illustration and **(B,C)** showed the SDS-polyacrylamide gel electrophoresis (PAGE) staining of MSNs- proteasome interaction. Panel **(D)** showed the TEM images of MSNs and proteasome loaded MSNs. Hydrolysis assay **(E)** and western blots studies **(F)** demonstrated the degradation of tau aggregates, indicating the delivery of active form of proteasomes by MSNs. Reproduced with permission from Han et al. (2014), The Nature Publishing Group.

responsive release. For example, insulin is widely used for the management of diabetes. However, the daily multiple insulin injections are quite painful, this discomfort can become a barrier to the use the insulin injections for many patients (Hunt et al., 1997; Zambanini et al., 1999). In addition, direct injection manner may cause hypoglycemia and result in serious problems such as unconsciousness or even death (Veiseh et al., 2015). Glucose responsive systems that release insulin automatically in a way that mimics physiological insulin secretion provide a better way and have the potential to change the way in which type 1 diabetes is managed.

Various MSN-based glucose responsive insulin release systems have been developed which take advantage of the high drug loading capacity, good biocompatibility and easy surface modification offered by MSNs (He and Shi, 2011; Zhao et al., 2011; Chen et al., 2013; Xu et al., 2017). In 2009, Zhao et al. (2009) reported boronic acid (one type of phenylboronic acid, PBA, which can form reversible covalent complexes with diol units of glucose) functionalized MSNs for glucose-responsive controlled release of insulin and cyclic adenosine monophosphate. The gluconic acid-modified insulin was immobilized on the exterior surface of MSNs, which also served as caps to encapsulate cAMP

molecules inside the mesopores. The release of both insulin and cAMP was triggered by the introduction of glucose, which competitively bounds to boronic-acid on the surface of MSNs, resulting in the loosening of insulin and the release of cAMP. However, in this work the insulin was modified by gluconic acid which may affect the biological function of this component. Sun et al. (2013) introduced another two PBA derivatives, 3-acrylamidophenylboronic acid and N-isopropylacrylamide for use as capping agents for insulin loaded MSNs. These PBA derivatives formed a dense layer which prevented the release of insulin and underwent swelling upon exposure to glucose to trigger insulin release. In this design unmodified insulin was used which eliminated the concern of denaturation of insulin.

Another design based on GOD mechanism was reported in 2011. Zhao et al. (2011) used MSNs with large pores (approx. 20 nm) for insulin loading, while the pore capping was achieved via a coating of GOD and catalase (CAT), an enzyme capable of catalyzing H_2O_2 into H_2O and oxygen to prevent the accumulation of H_2O_2, using layer-by-layer (LbL) method to control the insulin release. Up to 377 mg/g loading capacity of insulin was achieved using this method. The glucose responsive layers (enzyme layers) were coated onto the insulin loaded MSNs by Schiff base bond formation and functioned as "gates" to preventing insulin release in the absence of glucose. The enzymes (GOD and CAT) converted glucose into gluconic acid with oxygen and the production of gluconic acid decreased the local pH value. In the presence of glucose, the Schiff base bond was partially protonated and the enzyme layers were "loosened" which increased the permeability and triggered insulin release (Qi et al., 2009; Chen et al., 2011, 2012). With this design the insulin was released in response to glucose spontaneously and could achieve repeated on/off releases of insulin under the condition with/without glucose (Zhao et al., 2011).

It is noted that most of current glucose responsive insulin release systems (primarily GOD based systems) release more than half their loaded insulin at a glucose concentration either below 7 mM (De Geest et al., 2006; Ding et al., 2009; Qi et al., 2009; Wang et al., 2009; Zhao et al., 2009, 2011, 2012, 2013; Chen et al., 2011, 2012; Sato et al., 2011; Sun et al., 2013; Chou et al., 2015) or above 20 mM (Gu et al., 2013; Yu et al., 2015). However, the blood glucose levels are adjusted in the range of 3.9 ∼ 6.1 mM under normal physiological conditions, which means most of the glucose responsive systems are too sensitive, releasing more than half the loaded insulin content even under normal blood glucose concentrations. Recently, Xu et al. (2017) reported a glucose-responsive insulin release system based silica vesicles loaded with insulin with a layer-by-layer enzyme polymer coating (**Figure 5**). The insulin-release threshold can be adjusted by changing the polymer amount in the coating layers and the insulin release was switched "ON" in response to hyperglycemia and "OFF" to normal glucose levels. *In vivo* experiments in type I diabetes mice showed this MSNs based system regulated the glycemia levels in a normal range up to 84 h with a single administration while not affected the blood glucose concentration of normal mice. Those MSNs based systems have the potential to be developed as convenient and safe insulin delivery carriers for diabetes management.

For monoclonal antibodies generally working on the surface of cells, loading inside MSNs also enhanced their activity by providing protein and controlling release. For example, cytotoxic T-lymphocyte associated antigen 4 antibody (CTLA-4 Ab) can inhibit checkpoint receptor and has been used in patients with melanoma. Functionalized silica foam with a pore size of 30 nm was used to loaded CTLA-4 Ab and showed an ultra-high loading capacity (up to 800 mg g^{-1}). *In vivo* tests with tumor bearing mice (melanomas) model showed that CTLA-4 Ab loaded silica foam significantly enhanced antitumor activity compared to free

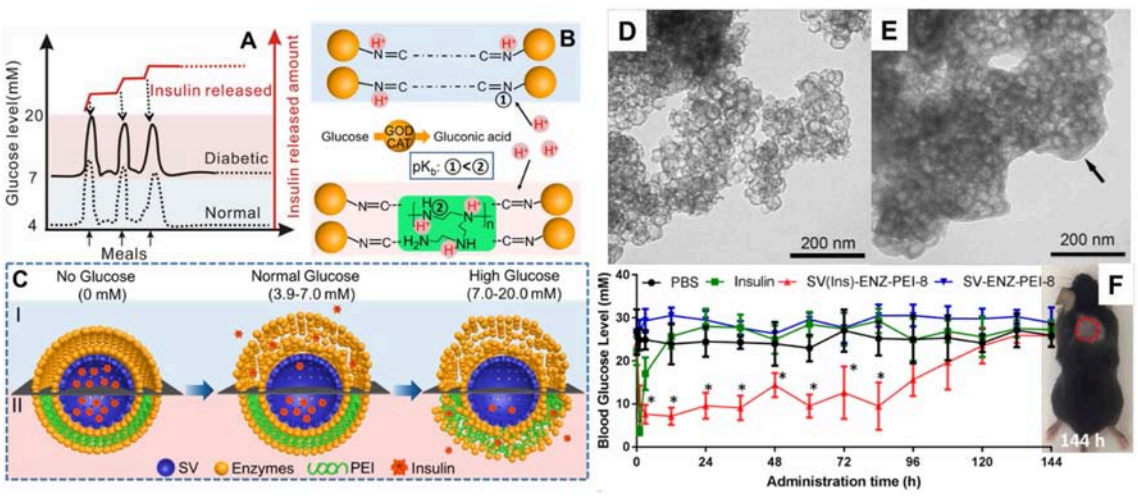

FIGURE 5 | MSNs based glucose responsive insulin delivery system **(A–C)**. Hollow MSNs **(D)** was used to loaded insulin and functionalized with glucose responsive layers through enzyme-polymer layer-by-layer coating strategy **(E)**. *In vivo* studies showed MSNs based nanosystem enables a fast glucose response insulin release and regulates the glycemia levels in a normal range up to 84 h with a single administration **(F)**. Reproduced with permission from Xu et al. (2017), The American Chemical Society.

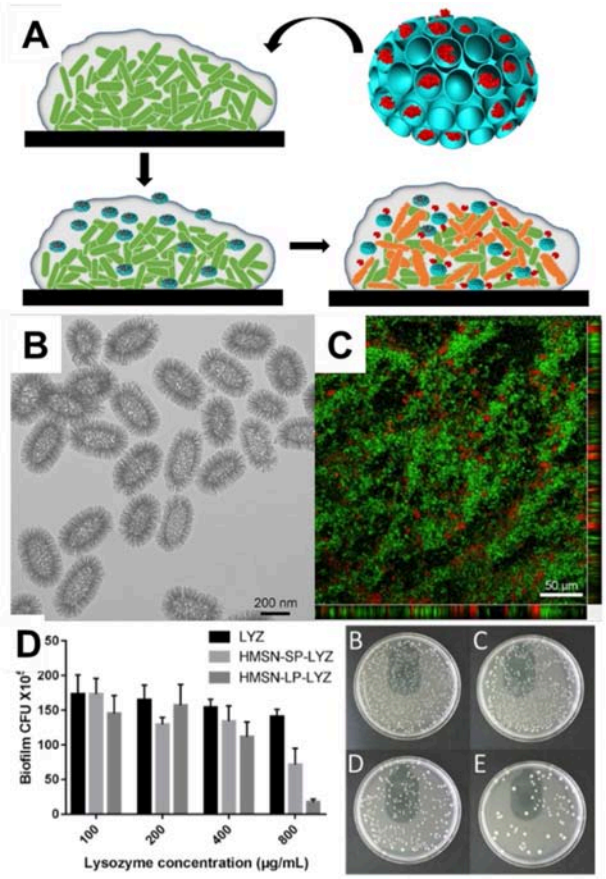

FIGURE 6 | Mesoporous silica nanoparticles for the delivery of antimicrobial protein into biofilm. MSNs for lysosome delivery. **(A)** the schematic drawing of MSNs delivery for biofilm. Panel **(B)** showed the TEM image of MSNs and **(C)** the penetration of MSNs into biofilm. The antibacterial performance was tested towards *E. coli* biofilm **(D)**. Reproduced from Xu et al. (2018) and by permission of The Royal Society of Chemistry.

antibodies, attributed to the prolonged release and protection of antibodies at tumor sites (Lei et al., 2010).

APPLICATION OF MSNs FOR ANTIBACTERIAL PROTEINS DELIVERY

The use of nanoparticles as delivery vehicles for antimicrobial proteins shows great potential for the treatment of bacterial infections. For example, lysozyme, a nature protein than can catalyze the hydrolysis of bacterial wall, was coated on the surface of MSN-41 which enhanced the interact with *Escherichia coli* (*E. coli*, one typical Gram-negative bacterium) and raised the local concentrations of lysozyme. The minimal inhibition concentration was 5-folds lower after conjugated with MSNs compared to free lysozyme (Li and Wang, 2013). To tackle the problem of exposure of lysozyme on the external surface, Song et al. (2016) prepared MSNs with large pores which had ability to load lysozyme inside, and demonstrated the enhanced the ability for the treatment of *E. coli in vitro* and in an *ex vivo* small intestine infection model. Wang et al. (2019) prepared dendritic mesoporous silica nanoparticles with pore sizes ranging from 2.7 to 22.4 nm for lysozyme loading. They found MSNs with large pores had a high lysozyme loading ability (244.5 mg g^{-1}) and showed a sustained release profile. Lysozyme loaded inside MSNs showed better antibacterial effect toward *E. coli,* reducing the minimum inhibitory concentration (MIC) from 2,500 mg mL^{-1} of free lysozyme to 500 μg mL^{-1}. Very recently, Xu et al. (2018) reported that MSNs could penetrate inside the biofilms (Biofilms are groups of microbial cells embedded in extracellular polymeric substances and bacteria in biofilms had higher resistance to antimicrobial drugs) and deliver lysozyme into biofilm to kill deeper bacteria (**Figure 6A**). Those hollow mesoporous silica nanoparticles with large cone-shaped pores (**Figure 6B**) had ability to loaded lysozyme inside and penetrated into biofilms (**Figure 6C**). Enhanced therapeutic activity toward E. coli biofilms was demonstrated with rational design of MSNs (**Figure 6D**).

APPLICATION OF MSNs FOR ENZYME MOBILIZATION AND CATALYSIS

MSNs are also of great significance for enzyme immobilization and catalysis by addressing the intrinsic issues of the native enzymes (Wang and Caruso, 2005; Popat et al., 2011; Yang T. et al., 2017). Wang and Caruso (2005) used a series of MSNs with pore sizes from 2 to 40 nm for the immobilization of various enzymes including lysozyme, peroxidase, catalase and cytochrome C. After loading inside MSNs, the enzymatic activity was retained in a wide range of pH and even after exposure to enzyme-degrading substances such as proteases. It is noted that MSNs-enzyme kept 70% of the initial activity after 25 batch of successive reactions. Very recently, Kalantari et al. (2018) also reported the application of dendritic mesoporous organosilica nanoparticles with benzene groups in the framework for an enzyme, lipase, and immobilization. It is interesting to note that after loaded into organosilica nanoparticles, lipase showed enhanced pH and thermal stability and also higher activity than free lipase. In addition, after 5 cycles lipase loaded in MSNs retained 94% catalytic activity, showing the advantage for reusability (Kalantari et al., 2018).

SUMMARY AND OUTLOOK

In conclusion, MSNs demonstrated high loading capacity and protective effects toward proteins, provided advantages in the intracellular, extracellular, antibacterial delivery, immobilization of various proteins with enhanced therapeutic/catalytic efficacy. With the rigid framework and well-defined pores, MSNs provide protection toward protein and preserve their activity. In addition, the fast development of novel MSNs especially those with radial pore structure and large pores promotes the application for protein delivery. We envision that significant progress will be made and new MSNs with rational design and tailored functionalization will be developed in the near future for better protein delivery.

For the future directions, targeted protein delivery and controlled protein release would be emerging technological

strategies to further improve the therapeutic effects. The recent works such as cloaked MSNs with red blood cell membranes or other targeting agents have shown longer circulation time and accumulation in target areas such as tumor (Xuan et al., 2018). The design of various responsive release system based MSNs are also receiving more attention. Many new studies have clearly demonstrated the feasibility and advantage of remote-controlled proteins release systems (Yang et al., 2013).

It is noted that the *in vivo* effects of MSNs based proteins delivery systems are less studied. More intensive preclinical explorations such as animal studies are needed to realize their potential in clinical applications. Currently the investigation of MSNs for the *in vivo* delivery of therapeutic proteins has not kept pace with advances in MSNs fabrication. More studies are expected to evaluated the biocompatibility, stability, efficacy and biological interactions of MSNs based protein delivery system. The close collaborations between materials scientists, biologist, pharmacist, and clinician would fasten this process.

AUTHOR CONTRIBUTIONS

CX, CL, and CY designed this study. CX and CL wrote the manuscript. CX and CY revised the manuscript.

ACKNOWLEDGMENTS

We thank the Australian National Fabrication Facility-Queensland Node (ANFFQ), The University of Queensland. CX acknowledges the support from National Health and Medical Research Council fellowship, CL acknowledges the support from Advance Queensland Fellowship.

REFERENCES

Andersson, J., Rosenholm, J., Areva, S., and Linden, M. (2004). Influences of material characteristics on ibuprofen drug loading and release profiles from ordered micro- and mesoporous silica matrices. *Chem. Mater.* 16, 4160–4167. doi: 10.1021/cm0401490

Angelos, S., Liong, M., Choi, E., and Zink, J. I. (2008). Mesoporous silicate materials as substrates for molecular machines and drug delivery. *Chem. Eng. J.* 137, 4–13. doi: 10.1016/j.cej.2007.07.074

Arruebo, M., Fernandez-Pacheco, R., Ibarra, M. R., and Santamaria, J. (2007). Magnetic nanoparticles for drug delivery. *Nano Today* 2, 22–32. doi: 10.1016/S1748-0132(07)70084-1

Babonneau, F., Camus, L., Steunou, N., Ramila, A., and Vallet-Regi, M. (2003). Encapsulation of ibuprofen in mesoporous silica: solid state NMR characterization. *Self-Assembled Nanostruct. Mater.* 775, 77–82. doi: 10.1557/PROC-775-P3.26

Babonneau, F., Yeung, L., Steunou, N., Gervais, C., Ramila, A., and Vallet-Regi, M. (2004). Solid state NMR characterisation of encapsulated molecules in mesoporous silica. *J. Sol-Gel Sci. Technol.* 31, 219–223. doi: 10.1023/B:Jsst.0000047991.73840.8b

Bale, S. S., Kwon, S. J., Shah, D. A., Banerjee, A., Dordick, J. S., and Kane, R. S. (2010). Nanoparticle-mediated cytoplasmic delivery of proteins to target cellular machinery. *ACS Nano* 4, 1493–1500. doi: 10.1021/nn901586e

Banting, F. G., Best, C. H., Collip, J. B., Campbell, W. R., and Fletcher, A. A. (1991). Pancreatic extracts in the treatment of diabetes-mellitus—preliminary-report. *Can. Med. Assoc. J.* 145, 1281–1286.

Bao, H. F., Yang, J. P., Huang, Y., Xu, Z. P., Hao, N., Wu, Z. X., et al. (2011). Synthesis of well-dispersed layered double hydroxide core@ordered mesoporous silica shell nanostructure (LDH@mSiO_2) and its application in drug delivery. *Nanoscale* 3, 4069–4073. doi: 10.1039/c1nr10718f

Bouchoucha, M., C-,Gaudreault, R., Fortin, M. A., and Kleitz, F. (2014). Mesoporous silica nanoparticles: selective surface functionalization for optimal relaxometric and drug loading performances. *Adv. Funct. Mater.* 24, 5911–5923. doi: 10.1002/adfm.201400524

Carino, I. S., Pasqua, L., Testa, F., Aiello, R., Puoci, F., Iemma, F., et al. (2007). Silica-based mesoporous materials as drug delivery system for methotrexate release. *Drug Delivery* 14, 491–495. doi: 10.1080/10717540701606244

Chang, B. S., Guo, J., Liu, C. Y., Qian, J., and Yang, W. L. (2010). Surface functionalization of magnetic mesoporous silica nanoparticles for controlled drug release. *J. Mater. Chem.* 20, 9941–9947. doi: 10.1039/c0jm01237h

Chen, M. J., Huang, C. S., He, C. S., Zhu, W. P., Xu, Y. F., and Lu, Y. F. (2012). A glucose-responsive controlled release system using glucose oxidase-gated mesoporous silica nanocontainers. *Chem. Commun.* 48, 9522–9524. doi: 10.1039/c2cc34290a

Chen, X. Y., Wu, W., Guo, Z. Z., Xin, J. Y., and Li, J. S. (2011). Controlled insulin release from glucose-sensitive self-assembled multilayer films based on 21-arm star polymer. *Biomaterials* 32, 1759–1766. doi: 10.1016/j.biomaterials.2010.11.002

Chen, Y., Chen, H. R., and Shi, J. L. (2013). *In vivo* bio-safety evaluations and diagnostic/therapeutic applications of chemically designed mesoporous silica nanoparticles. *adv. Mater.* 25, 3144–3176. doi: 10.1002/adma.201205292

Chou, D. H. C., Webber, M. J., Tang, B. C., Lin, A. B., Thapa, L. S., Deng, D., et al. (2015). Glucose-responsive insulin activity by covalent modification with aliphatic phenylboronic acid conjugates. *Proc. Natl. Acad. Sci. U.S.A.* 112, 2401–2406. doi: 10.1073/pnas.1424684112

Cirujano, F. G., Luz, I., Soukri, M., Van Goethem, C., Vankelecom, I. F. J., Lail, M., et al. (2017). Boosting the catalytic performance of metal-organic frameworks for steroid transformations by confinement within a mesoporous scaffold. *Angew. Chem. Int. Ed.* 56, 13302–13306. doi: 10.1002/anie.201706721

Dai, J.-T., Zhang, Y., Li, H.-C., Deng, Y.-H., Elzatahry, A. A., Alghamdi, A., et al. (2017). Enhancement of gemcitabine against pancreatic cancer by loading in mesoporous silica vesicles. *Chin. Chem. Lett.* 28, 531–536. doi: 10.1016/j.cclet.2016.11.008

Davis, M. E., Chen, Z., and Shin, D. M. (2008). Nanoparticle therapeutics: an emerging treatment modality for cancer. *Nat. Rev. Drug Discovery* 7, 771–782. doi: 10.1038/Nrd2614

De Geest, B. G., Jonas, A. M., Demeester, J., and De Smedt, S. C. (2006). Glucose-responsive polyelectrolyte capsules. *Langmuir* 22, 5070–5074. doi: 10.1021/la053368o

Ding, Z. B., Guan, Y., Zhang, Y. J., and Zhu, X. X. (2009). Synthesis of glucose-sensitive self-assembled films and their application in controlled drug delivery. *Polymer* 50, 4205–4211. doi: 10.1016/j.polymer.2009.07.001

Doadrio, J. C., Sousa, E. M. B., Izquierdo-Barba, I., Doadrio, A. L., Perez-Pariente, J., and Vallet-Regi, M. (2006). Functionalization of mesoporous materials with long alkyl chains as a strategy for controlling drug delivery pattern. *J. Mater. Chem.* 16, 462–466. doi: 10.1039/b510101h

Du, X., and Qiao, S. Z. (2015). Dendritic silica particles with center-radial pore channels: promising platforms for catalysis and biomedical applications. *Small* 11, 392–413. doi: 10.1002/smll.201401201

Duncan, R. (2006). Polymer conjugates as anticancer nanomedicines. *Nat. Rev. Cancer* 6, 688–701. doi: 10.1038/nrc1958

Elsabahy, M., and Wooley, K. L. (2012). Design of polymeric nanoparticles for biomedical delivery applications. *Chem. Soc. Rev.* 41, 2545–2561. doi: 10.1039/c2cs15327k

Feng, P. Y., Bu, X. H., Stucky, G. D., and Pine, D. J. (2000). Monolithic mesoporous silica templated by microemulsion liquid crystals. *J. Am. Chem. Soc.* 122, 994–995. doi: 10.1021/ja992921j

Gao, X. H., Cui, Y. Y., Levenson, R. M., Chung, L. W. K., and Nie, S. M. (2004). *In vivo* cancer targeting and imaging with semiconductor quantum dots. *Nat. Biotechnol.* 22, 969–976. doi: 10.1038/nbt994

Ghosh, P., Yang, X. C., Arvizo, R., Zhu, Z. J., Agasti, S. S., Mo, Z. H., et al. (2010). Intracellular delivery of a membrane-impermeable enzyme in active form

using functionalized gold nanoparticles. *J. Am. Chem. Soc.* 132, 2642–2645. doi: 10.1021/ja907887z

Gradishar, W. J., Tjulandin, S., Davidson, N., Shaw, H., Desai, N., Bhar, P., et al. (2005). Phase III trial of nanoparticle albumin-bound paclitaxel compared with polyethylated castor oil-based paclitaxel in women with breast cancer. *J. Clin. Oncol.* 23, 7794–7803. doi: 10.1200/Jco.2005.04.937

Greco, F., and Vicent, M. J. (2009). Combination therapy: opportunities and challenges for polymer-drug conjugates as anticancer nanomedicines. *Adv. Drug Delivery Rev.* 61, 1203–1213. doi: 10.1016/j.addr.2009.05.006

Gu, Z., Biswas, A., Zhao, M. X., and Tang, Y. (2011). Tailoring nanocarriers for intracellular protein delivery. *Chem. Soc. Rev.* 40, 3638–3655. doi: 10.1039/c0cs00227e

Gu, Z., Dang, T. T., Ma, M. L., Tang, B. C., Cheng, H., Jiang, S., et al. (2013). Glucose-responsive microgels integrated with enzyme nanocapsules for closed-loop insulin delivery. *Acs Nano* 7, 6758–6766. doi: 10.1021/nn401617u

Han, D. H., Na, H. K., Choi, W. H., Lee, J. H., Kim, Y. K., Won, C., et al. (2014). Direct cellular delivery of human proteasomes to delay tau aggregation. *Nat. Commun.* 5:5633. doi: 10.1038/ncomms6633

He, Q. J., and Shi, J. L. (2011). Mesoporous silica nanoparticle based nano drug delivery systems: synthesis, controlled drug release and delivery, pharmacokinetics and biocompatibility. *J. Mater. Chem.* 21, 5845–5855. doi: 10.1039/c0jm03851b

Huang, W. Y., Davies, G. L., and Davis, J. J. (2013). Engineering cytochrome-modified silica nanoparticles to induce programmed cell death. *Chem. Eur. J.* 19, 17891–17898. doi: 10.1002/chem.201303239

Hunt, L. M., Valenzuela, M. A., and Pugh, J. A. (1997). NIDDM patients' fears and hopes about insulin therapy—the basis of patient reluctance. *Diabetes Care* 20, 292–298. doi: 10.2337/diacare.20.3.292

Huo, Q. S., Margolese, D. I., and Stucky, G. D. (1996). Surfactant control of phases in the synthesis of mesoporous silica-based materials. *Chem. Mater.* 8, 1147–1160. doi: 10.1021/cm960137h

Izquierdo-Barba, I., Martinez, A., Doadrio, A. L., Perez-Pariente, J., and Vallet-Regi, M. (2005). Release evaluation of drugs from ordered three-dimensional silica structures. *Eur. J. Pharmaceut. Sci.* 26, 365–373. doi: 10.1016/j.ejps.2005.06.009

Izquierdo-Barba, I., Sousa, E., Doadrio, J. C., Doadrio, A. L., Pariente, J. P., Martinez, A., et al. (2009). Influence of mesoporous structure type on the controlled delivery of drugs: release of ibuprofen from MCM-48, SBA-15 and functionalized SBA-15. *J. Sol-Gel Sci. Technol.* 50, 421–429. doi: 10.1007/s10971-009-1932-3

Jambhrunkar, S., Qu, Z., Popat, A., Karmakar, S., Xu, C., and Yu, C. Z. (2014). Modulating *in vitro* release and solubility of griseofulvin using functionalized mesoporous silica nanoparticles. *J. Colloid Interface Sci.* 434, 218–225. doi: 10.1016/j.jcis.2014.08.019

Kalantari, M., Yu, M. H., Jambhrunkar, M., Liu, Y., Yang, Y. N., Huang, X. D., et al. (2018). Designed synthesis of organosilica nanoparticles for enzymatic biodiesel production. *Mater. Chem. Front.* 2, 1334–1342. doi: 10.1039/c8qm00078f

Kalantari, M., Yu, M. H., Yang, Y. N., Strounina, E., Gu, Z. Y., Huang, X. D., et al. (2017). Tailoring mesoporous-silica nanoparticles for robust immobilization of lipase and biocatalysis. *Nano Res.* 10, 605–617. doi: 10.1007/s12274-016-1320-6

Kao, K.-C., Lin, T.-S., and Mou, C.-Y. (2014). Enhanced activity and stability of lysozyme by immobilization in the matching nanochannels of mesoporous silica nanoparticles. *J. Phys. Chem. C* 118, 6734–6743. doi: 10.1021/jp4112684

Kim, T. H., Lee, S., and Chen, X. Y. (2013). Nanotheranostics for personalized medicine. *Expert Rev. Mol. Diagn.* 13, 257–269. doi: 10.1586/Erm.13.15

Knezevic, N. Z., and Durand, J. O. (2015). Large pore mesoporous silica nanomaterials for application in delivery of biomolecules. *Nanoscale* 7, 2199–2209. doi: 10.1039/c4nr06114d

Kura, A. U., Hussein, M. Z., Fakurazi, S., and Arulselvan, P. (2014). Layered double hydroxide nanocomposite for drug delivery systems; bio-distribution, toxicity and drug activity enhancement. *Chem. Central J.* 8:47. doi: 10.1186/s13065-014-0047-2

Leader, B., Baca, Q. J., and Golan, D. E. (2008). Protein therapeutics: a summary and pharmacological classification. *Nat. Rev. Drug Discov.* 7, 21–39. doi: 10.1038/nrd2399

Lei, C. H., Liu, P., Chen, B. W., Mao, Y. M., Engelmann, H., Shin, Y., et al. (2010). Local release of highly loaded antibodies from functionalized nanoporous support for cancer immunotherapy. *J. Am. Chem. Soc.* 132, 6906–6907. doi: 10.1021/ja102414t

Li, L. L., and Wang, H. (2013). Enzyme-coated mesoporous silica nanoparticles as efficient antibacterial agents *in vivo*. *Adv. Healthc. Mater.* 2, 1351–1360. doi: 10.1002/adhm.201300051

Li, Z. J., Zhang, Y. J., Zhang, H. W., and Fu, H. X. (2013). Long-lasting phosphorescence functionalization of mesoporous silica nanospheres by $CaTiO_3:Pr^{3+}$ for drug delivery. *Microporous Mesoporous Mater.* 176, 48–54. doi: 10.1016/j.micromeso.2013.02.050

Lind, A., Spliethoff, B., and Linden, M. (2003). Unusual, vesicle-like patterned, mesoscopically ordered silica. *Chem. Mater.* 15, 813–818. doi: 10.1021/Cm021243o

Liu, Z., Robinson, J. T., Tabakman, S. M., Yang, K., and Dai, H. J. (2011). Carbon materials for drug delivery & cancer therapy. *Mater. Today* 14, 316–323. doi: 10.1016/S1369-7021(11)70161-4

Manzano, M., Aina, V., Arean, C. O., Balas, F., Cauda, V., Colilla, M., et al. (2008). Studies on MCM-41 mesoporous silica for drug delivery: effect of particle morphology and amine functionalization. *Chem. Eng. J.* 137, 30–37. doi: 10.1016/j.cej.2007.07.078

Manzano, M., and Vallet-Regi, M. (2010). New developments in ordered mesoporous materials for drug delivery. *J. Mater. Chem.* 20, 5593–5604. doi: 10.1039/b922651f

Meka, A. K., Abbaraju, P. L., Song, H., Xu, C., Zhang, J., Zhang, H. W., et al. (2016). A vesicle supra-assembly approach to synthesize amine-functionalized hollow dendritic mesoporous silica nanospheres for protein delivery. *Small* 12, 5169–5177. doi: 10.1002/smll.201602052

Meng, H., Yang, S., Li, Z. X., Xia, T., Chen, J., Ji, Z. X., et al. (2011). Aspect ratio determines the quantity of mesoporous silica nanoparticle uptake by a small GTPase-dependent macropinocytosis mechanism. *Acs Nano* 5, 4434–4447. doi: 10.1021/nn103344k

Michalet, X., Pinaud, F. F., Bentolila, L. A., Tsay, J. M., Doose, S., Li, J. J., et al. (2005). Quantum dots for live cells, *in vivo* imaging, and diagnostics. *Science* 307, 538–544. doi: 10.1126/science.1104274

Mody, K. T., Popat, A., Mahony, D., Cavallaro, A. S., Yu, C. Z., and Mitter, N. (2013). Mesoporous silica nanoparticles as antigen carriers and adjuvants for vaccine delivery. *Nanoscale* 5, 5167–5179. doi: 10.1039/c3nr00357d

Muller, R. H., Radtke, M., and Wissing, S. A. (2002). Solid lipid nanoparticles (SLN) and nanostructured lipid carriers (NLC) in cosmetic and dermatological preparations. *Adv. Drug Delivery Rev.* 54, S131–S155. doi: 10.1016/S0169-409x(02)00118-7

Mura, S., and Couvreur, P. (2012). Nanotheranostics for personalized medicine. *Adv. Drug Delivery Rev.* 64, 1394–1416. doi: 10.1016/j.addr.2012.06.006

Naseri, N., Valizadeh, H., and Zakeri-Milani, P. (2015). Solid lipid nanoparticles and nanostructured lipid carriers: structure, preparation and application. *Adv. Pharmaceut. Bull.* 5, 305–313. doi: 10.15171/apb.2015.043

Niu, Y. T., Yu, M. H., Meka, A., Liu, Y., Zhang, J., Yang, Y. N., et al. (2016). Understanding the contribution of surface roughness and hydrophobic modification of silica nanoparticles to enhanced therapeutic protein delivery. *J. Mater. Chem. B* 4, 212–219. doi: 10.1039/c5tb01911g

Peer, D., Karp, J. M., Hong, S., Farokhzad, O. C., Margalit, R., and Langer, R. (2007). Nanocarriers as an emerging platform for cancer therapy. *Nat. Nanotechnol.* 2, 751–760. doi: 10.1038/nnano.2007.387

Polshettiwar, V., Cha, D., Zhang, X., and Basset, J. M. (2010). High-surface-area silica nanospheres (KCC-1) with a fibrous morphology. *Angew. Chem. Int. Ed.* 49, 9652–9656. doi: 10.1002/anie.201003451

Popat, A., Hartono, S. B., Stahr, F., Liu, J., Qiao, S. Z., and Lu, G. Q. (2011). Mesoporous silica nanoparticles for bioadsorption, enzyme immobilisation, and delivery carriers. *Nanoscale* 3, 2801–2818. doi: 10.1039/c1nr10224a

Qi, W., Yan, X. H., Fei, J. B., Wang, A. H., Cui, Y., and Li, J. B. (2009). Triggered release of insulin from glucose-sensitive enzyme multilayer shells. *Biomaterials* 30, 2799–2806. doi: 10.1016/j.biomaterials.2009.01.027

Ramila, A., Munoz, B., Perez-Pariente, J., and Vallet-Regi, M. (2003). Mesoporous MCM-41 as drug host system. *J. Sol-Gel Sci. Technol.* 26, 1199–1202. doi: 10.1023/A:1020764319963

Robinson, J. T., Tabakman, S. M., Liang, Y. Y., Wang, H. L., Casalongue, H. S., Vinh, D., et al. (2011). Ultrasmall reduced graphene oxide with high

near-infrared absorbance for photothermal therapy. *J. Am. Chem. Soc.* 133, 6825–6831. doi: 10.1021/ja2010175

Sato, K., Yoshida, K., Takahashi, S., and Anzai, J. I. (2011). pH- and sugar-sensitive layer-by-layer films and microcapsules for drug delivery. *Adv. Drug Delivery Rev.* 63, 809–821. doi: 10.1016/j.addr.2011.03.015

Schmidt-Winkel, P., Lukens, W. W., Zhao, D. Y., Yang, P. D., Chmelka, B. F., and Stucky, G. D. (1999). Mesocellular siliceous foams with uniformly sized cells and windows. *J. Am. Chem. Soc.* 121, 254–255. doi: 10.1021/Ja983218i

Shao, D., Li, M., Wang, Z., Zheng, X., Lao, Y. H., Chang, Z., et al. (2018). Bioinspired diselenide-bridged mesoporous silica nanoparticles for dual-responsive protein delivery. *Adv. Mater.* 30:e1801198. doi: 10.1002/adma.201801198

Shen, D. K., Yang, J. P., Li, X. M., Zhou, L., Zhang, R. Y., Li, W., et al. (2014). Biphase stratification approach to three-dimensional dendritic biodegradable mesoporous silica nanospheres. *Nano Lett.* 14, 923–932. doi: 10.1021/nl404316v

Shen, S. C., Ng, W. K., Chia, L. S. O., Dong, Y. C., and Tan, R. B. H. (2013). Applications of mesoporous materials as excipients for innovative drug delivery and formulation. *Curr. Pharmaceut. Des.* 19, 6270–6289. doi: 10.2174/1381612811319350005

Siefker, J., Karande, P., and Coppens, M. O. (2014). Packaging biological cargoes in mesoporous materials: opportunities for drug delivery. *Expert Opinion on Drug Delivery* 11, 1781–1793. doi: 10.1517/17425247.2014.938636

Slowing, I. I., Trewyn, B. G., and Lin, V. S. Y. (2007). Mesoporous silica nanoparticles for intracellular delivery of membrane-impermeable proteins. *J. Am. Chem. Soc.* 129, 8845–8849. doi: 10.1021/ja0719780

Song, H., Nor, Y. A., Yu, M. H., Yang, Y. N., Zhang, J., Zhang, H. W., et al. (2016). Silica nanopollens enhance adhesion for long-term bacterial inhibition. *J. Am. Chem. Soc.* 138, 6455–6462. doi: 10.1021/jacs.6b00243

Song, S. W., Hidajat, K., and Kawi, S. (2005). Functionalized SBA-15 materials as carriers for controlled drug delivery: influence of surface properties on matrix-drug interactions. *Langmuir* 21, 9568–9575. doi: 10.1021/la051167e

Sparreboom, A., Scripture, C. D., Trieu, V., Williams, P. J., De, T. P., Yang, A., et al. (2005). Comparative preclinical and clinical pharmacokinetics of a cremophor-free, nanoparticle albumin-bound paclitaxel (ABI-007) and paclitaxel formulated in cremophor (Taxol). *Clin. Cancer Res.* 11, 4136–4143. doi: 10.1158/1078-0432.Ccr-04-2291

Sun, C., Lee, J. S. H., and Zhang, M. Q. (2008). Magnetic nanoparticles in MR imaging and drug delivery. *Adv. Drug Delivery Rev.* 60, 1252–1265. doi: 10.1016/j.addr.2008.03.018

Sun, L., Zhang, X. G., Zheng, C., Wu, Z. M., and Li, C. X. (2013). A pH gated, glucose-sensitive nanoparticle based on worm-like mesoporous silica for controlled insulin release. *J. Phys. Chem. B* 117, 3852–3860. doi: 10.1021/jp400442x

Torchilin, V. P. (2005). Recent advances with liposomes as pharmaceutical carriers. *Nat. Rev. Drug Discovery* 4, 145–160. doi: 10.1038/nrd1632

Tu, J., Boyle, A. L., Friedrich, H., Bomans, P. H. H., Bussmann, J., Sommerdijk, N. A. J. M., et al. (2016). Mesoporous silica nanoparticles with large pores for the encapsulation and release of proteins. *ACS Appl. Mater. Interfaces* 8, 32211–32219. doi: 10.1021/acsami.6b11324

Urquhart, L. (2018). Market watch: top drugs and companies by sales in 2017. *Nat. Rev. Drug Discov.* 17, 232. doi: 10.1038/nrd.2018.42

Usmani, S. S., Bedi, G., Samuel, J. S., Singh, S., Kalra, S., Kumar, P., et al. (2017). THPdb: database of FDA-approved peptide and protein therapeutics. *PLoS ONE* 12:e0181748. doi: 10.1371/journal.pone.0181748

Vallet-Regi, M. (2006). Ordered mesoporous materials in the context of drug delivery systems and bone tissue engineering. *Chem. Eur. J.* 12, 5934–5943. doi: 10.1002/chem.200600226

Vallet-Regi, M., Balas, F., and Arcos, D. (2007). Mesoporous materials for drug delivery. *Angew. Chem. Int. Ed.* 46, 7548–7558. doi: 10.1002/anie.200604488

Vallet-Regi, M., Balas, F., Colilla, M., and Manzano, M. (2008). Bone-regenerative bioceramic implants with drug and protein controlled delivery capability. *Progr. Solid State Chem.* 36, 163–191. doi: 10.1016/j.progsolidstchem.2007.10.002

Veiseh, O., Tang, B. C., Whitehead, K. A., Anderson, D. G., and Langer, R. (2015). Managing diabetes with nanomedicine: challenges and opportunities. *Nat. Rev. Drug Discovery* 14, 45–57. doi: 10.1038/nrd4477

Villegas, M. R., Baeza, A., and Vallet-Regi, M. (2018). Nanotechnological strategies for protein delivery. *Molecules* 23:23051008. doi: 10.3390/molecules23051008

Wang, B. L., Ma, R. J., Liu, G., Li, Y., Liu, X. J., An, Y. L., et al. (2009). Glucose-responsive micelles from self-assembly of poly(ethylene glycol)-b-poly(acrylic acid-co-acrylamidophenylboronic acid) and the controlled release of insulin. *Langmuir* 25, 12522–12528. doi: 10.1021/la901776a

Wang, S. B. (2009). Ordered mesoporous materials for drug delivery. *Microporous Mesoporous Mater.* 117, 1–9. doi: 10.1016/j.micromeso.2008.07.002

Wang, T. Y., Jiang, H. T., Zhao, Q. F., Wang, S. L., Zou, M. J., and Cheng, G. (2012). Enhanced mucosal and systemic immune responses obtained by porous silica nanoparticles used as an oral vaccine adjuvant: effect of silica architecture on immunological properties. *Int. J. Pharmaceut.* 436, 351–358. doi: 10.1016/j.ijpharm.2012.06.028

Wang, Y., Du, X., Liu, Z., Shi, S., and Lv, H. (2019). Dendritic fibrous nano-particles (DFNPs): rising stars of mesoporous materials. *J. Mater. Chem. A* 7, 5111–5152. doi: 10.1039/C8TA09815H

Wang, Y. J., and Caruso, F. (2005). Mesoporous silica spheres as supports for enzyme immobilization and encapsulation. *Chem. Mater.* 17, 953–961. doi: 10.1021/cm0483137

Xiong, L., Du, X., Shi, B. Y., Bi, J. X., Kleitz, F., and Qiao, S. Z. (2015). Tunable stellate mesoporous silica nanoparticles for intracellular drug delivery. *J. Mater. Chem. B* 3, 1712–1721. doi: 10.1039/c4tb01601g

Xu, C., He, Y., Li, Z. H., Nor, Y. A., and Ye, Q. S. (2018). Nanoengineered hollow mesoporous silica nanoparticles for the delivery of antimicrobial proteins into biofilms. *J. Mater. Chem. B* 6, 1899–1902. doi: 10.1039/c7tb03201c

Xu, C., Lei, C., Huang, L., Zhang, J., Zhang, H., Song, H., et al. (2017). Glucose-responsive nanosystem mimicking the physiological insulin secretion via an enzyme–polymer layer-by-layer coating strategy. *Chem. Mater.* 29, 7725–7732. doi: 10.1021/acs.chemmater.7b01804

Xu, C., Niu, Y. T., Popat, A., Jambhrunkar, S., Karmakar, S., and Yu, C. Z. (2014). Rod-like mesoporous silica nanoparticles with rough surfaces for enhanced cellular delivery. *J. Mater. Chem. B* 2, 253–256. doi: 10.1039/c3tb21431a

Xu, C., Yu, M. H., Noonan, O., Zhang, J., Song, H., Zhang, H. W., et al. (2015). Core-cone structured monodispersed mesoporous silica nanoparticles with ultra-large cavity for protein delivery. *Small* 11, 5949–5955. doi: 10.1002/smll.201501449

Xuan, M. J., Shao, J. X., Zhao, J., Li, Q., Dai, L. R., and Li, J. B. (2018). Magnetic mesoporous silica nanoparticles cloaked by red blood cell membranes: applications in cancer therapy. *Angew. Chem. Int. Ed.* 57, 6049–6053. doi: 10.1002/anie.201712996

Yan, L., Chen, W., Zhu, X. Y., Huang, L. B., Wang, Z. G., Zhu, G. Y., et al. (2013). Folic acid conjugated self-assembled layered double hydroxide nanoparticles for high-efficacy-targeted drug delivery. *Chem. Commun.* 49, 10938–10940. doi: 10.1039/c3cc45714a

Yang, J. P., Shen, D. K., Wei, Y., Li, W., Zhang, F., Kong, B. A., et al. (2015). Monodisperse core-shell structured magnetic mesoporous aluminosilicate nanospheres with large dendritic mesochannels. *Nano Res.* 8, 2503–2514. doi: 10.1007/s12274-015-0758-2

Yang, J. P., Shen, D. K., Zhou, L., Li, W., Li, X. M., Yao, C., et al. (2013). Spatially confined fabrication of core-shell gold nanocages@mesoporous silica for near-infrared controlled photothermal drug release. *Chem. Mater.* 25, 3030–3037. doi: 10.1021/cm401115b

Yang, J. P., Zhang, F., Li, W., Gu, D., Shen, D. K., Fan, J. W., et al. (2014). Large pore mesostructured cellular silica foam coated magnetic oxide composites with multilamellar vesicle shells for adsorption. *Chem. Commun.* 50, 713–715. doi: 10.1039/c3cc47813k

Yang, P. P., Gai, S. L., and Lin, J. (2012). Functionalized mesoporous silica materials for controlled drug delivery. *Chem. Soc. Rev.* 41, 3679–3698. doi: 10.1039/c2cs15308d

Yang, P. P., Quan, Z. W., Lu, L. L., Huang, S. S., and Lin, J. (2008). Luminescence functionalization of mesoporous silica with different morphologies and applications as drug delivery systems. *Biomaterials* 29, 692–702. doi: 10.1016/j.biomaterials.2007.10.019

Yang, T., Wei, L., Jing, L., Liang, J., Zhang, X., Tang, M., et al. (2017). Dumbbell-shaped bi-component mesoporous janus solid nanoparticles for biphasic interface catalysis. *Angew. Chem. Int. Ed.* 56, 8459–8463. doi: 10.1002/anie.201701640

Yang, Y., Lu, Y., Abbaraju, P. L., Zhang, J., Zhang, M., Xiang, G., et al. (2017). Multi-shelled dendritic mesoporous organosilica hollow spheres: roles of composition and architecture in cancer immunotherapy. *Angew. Chem. Int. Ed.* 56, 8446–8450. doi: 10.1002/anie.201701550

Yang, Y. N., Niu, Y. T., Zhang, J., Meka, A. K., Zhang, H. W., Xu, C., et al. (2015). Biphasic synthesis of large-pore and well-dispersed benzene bridged mesoporous organosilica nanoparticles for intracellular protein delivery. *Small* 11, 2743–2749. doi: 10.1002/smll.201402779

Yang, Y. N., Wan, J. J., Niu, Y. T., Gu, Z. Y., Zhang, J., Yu, M. H., et al. (2016). Structure-dependent and glutathione-responsive biodegradable dendritic mesoporous organosilica nanoparticles for safe protein delivery. *Chem. Mater.* 28, 9008–9016. doi: 10.1021/acs.chemmater.6b03896

Yu, J. C., Zhang, Y. Q., Ye, Y. Q., DiSanto, R., Sun, W. J., Ranson, D., et al. (2015). Microneedle-array patches loaded with hypoxia-sensitive vesicles provide fast glucose-responsive insulin delivery. *Proc. Natl. Acad. Sci. U.S.A.* 112, 8260–8265. doi: 10.1073/pnas.1505405112

Zambanini, A., Newson, R. B., Maisey, M., and Feher, M. D. (1999). Injection related anxiety in insulin-treated diabetes. *Diabetes Res. Clin. Pract.* 46, 239–246.

Zhang, J., Karmakar, S., Yu, M. H., Mitter, N., Zou, J., and Yu, C. Z. (2014). Synthesis of silica vesicles with controlled entrance size for high loading, sustained release, and cellular delivery of therapeutical proteins. *Small* 10, 5068–5076. doi: 10.1002/smll.201401538

Zhang, J., Zhang, L., Lei, C., Huang, X., Yang, Y., and Yu, C. (2018). A concentration-dependent insulin immobilization behavior of alkyl-modified silica vesicles: the impact of alkyl chain length. *Langmuir* 34, 5011–5019. doi: 10.1021/acs.langmuir.8b00377

Zhao, D. Y., Feng, J. L., Huo, Q. S., Melosh, N., Fredrickson, G. H., Chmelka, B. F., et al. (1998). Triblock copolymer syntheses of mesoporous silica with periodic 50 to 300 angstrom pores. *Science* 279, 548–552. doi: 10.1126/science.279.5350.548

Zhao, L., Ding, J. X., Xiao, C. S., He, P., Tang, Z. H., Pang, X., et al. (2012). Glucose-sensitive polypeptide micelles for self-regulated insulin release at physiological pH. *J. Mater. Chem.* 22, 12319–12328. doi: 10.1039/c2jm31040f

Zhao, L., Xiao, C. S., Ding, J. X., He, P., Tang, Z. H., Pang, X., et al. (2013). Facile one-pot synthesis of glucose-sensitive nanogel via thiol-ene click chemistry for self-regulated drug delivery. *Acta Biomater.* 9, 6535–6543. doi: 10.1016/j.actbio.2013.01.040

Zhao, W. R., Zhang, H. T., He, Q. J., Li, Y. S., Gu, J. L., Li, L., et al. (2011). A glucose-responsive controlled release of insulin system based on enzyme multilayers-coated mesoporous silica particles. *Chem. Commun.* 47, 9459–9461. doi: 10.1039/c1cc12740c

Zhao, Y. N., Trewyn, B. G., Slowing, I. I., and Lin, V. S. Y. (2009). Mesoporous silica nanoparticle-based double drug delivery system for glucose-responsive controlled release of insulin and cyclic AMP. *J. Am. Chem. Soc.* 131, 8398. doi: 10.1021/ja901831u

Zhu, J. H., Niu, Y. M., Li, Y., Gong, Y. X., Shi, H. H., Huo, Q., et al. (2017). Stimuli-responsive delivery vehicles based on mesoporous silica nanoparticles: recent advances and challenges. *J. Mater. Chem. B* 5, 1339–1352. doi: 10.1039/c6tb03066a

Conflict of Interest Statement: The authors declare that the research was conducted in the absence of any commercial or financial relationships that could be construed as a potential conflict of interest.

Copyright © 2019 Xu, Lei and Yu. This is an open-access article distributed under the terms of the Creative Commons Attribution License (CC BY). The use, distribution or reproduction in other forums is permitted, provided the original author(s) and the copyright owner(s) are credited and that the original publication in this journal is cited, in accordance with accepted academic practice. No use, distribution or reproduction is permitted which does not comply with these terms.

Polymer Chemistry

Junwei Wu

Dr Junwei Wu obtained his BE and ME from University of Science & Technology Beijing (China) and PhD from West Virginia University. He is now an Associate Professor at the Harbin Institute of Technology, Shenzhen. His research concerns novel materials development for energy storage and conversion, such as Li/Na-ion batteries, full solid cell, and solid oxide fuel cell, etc. He also serves as the deputy secretary general of the Shenzhen Association for Vacuum Technology Industries. He has published more than 50 journal papers, and an invited reviewer of Advanced Materials, Energy Storage Materials, Advanced Functional Materials, etc.

Marianna Pannico

Marianna Pannico obtained her PhD in Materials and Structures Engineering at the University of Napoli Federico II in 2010, supervised by Professor C. Carfagna. In January 2011 she joined the laboratory of molecular spectroscopy as part of Professor P. Musto's research group at the ICTP-CNR, later becoming a Researcher there in 2013. Notably, from November 2014 to January 2015 she collaborated with Prof. Maria de Fátima V. Marques on the VAIKUTUS project at the Instituto de Macromoléculas (IMA-UFRJ), Brazil. Dr Pannico's research focuses primarily on polymer nanocomposites, additives diffusion phenomena in polymer matrices, infrared spectroscopy, Raman Spectroscopy, and Surface Enhanced Raman Spectroscopy (SERS).

Romina Rega

Dr Romina Rega graduated in Physics in 2009 at the University of Naples Federico II with the highest honors, with a focus on Organic Electronics. Later, she continued to deepen this field at the National Agency for New Technologies, Energy and Sustainable Economic Development. During her PhD activity in "Innovative Technologies for Materials, Sensors and Imaging", she studied the stability of the organic thin film transistors. In 2014, she joined CNR-ISASI (Institute of Applied Sciences and Intelligent Systems) where she deals with the manipulation of polymeric materials using the pyro-electro-hydrodynamic effect induced by pyroelectric crystals and the realization of polymeric microstructures for biological applications.

Zhanhua Wang

Zhanhua Wang obtained his PhD degree in 2011in Polymer Chemistry and Physics from Jilin University under the supervision of Prof. Bai Yang. After that, he worked as a postdoctoral fellow with Prof. Marek Urban at the University of Southern Mississippi and Clemson University. He then moved to Wageningen University as a postdoctoral researcher and worked with Prof. Han Zuilhof until 2016. Presently, he is an Associate Professor at the Polymer Research Institute of Sichuan University. His current scientific interests are focused on stimuli-responsive polymer materials, self-healing and anti-fouling materials, and 3D printing polymer or polymer composite materials.

Michele Galizia

Michele Galizia is an Assistant Professor of Chemical Engineering at the University of Oklahoma since August 2017. In 2006, when he was an undergraduate student at the University of Bologna, Italy, he was awarded a Graduate Fellowship from the Italian Ministry of Education. After obtaining his PhD in Chemical Engineering, he joined the University of Naples Federico II as a Post-Doc Researcher. Finally, in 2013, he joined the Benny Freeman-Don Paul Research Group at the University of Texas at Austin as a Research Associate. Prof. Galizia's research focuses on membrane science, with emphasis on gas separation and organic solvent nanofiltration.

Alberto Fina

Alberto Fina is active in the field of polymer nanocomposites (nanoclays, POSS, carbon nanotubes, graphene) mainly aiming at enhancing thermal conductivity and flame retardancy. His recent research focuses on the fundamental aspects behind thermal conductivity in polymer nanocomposites, including the study of heat transfer on individual nanoparticles and their networks, as well as on the design and manufacturing of interfaces between nanoparticles, *via* the covalent or non-covalent chemical functionalization of graphene and related materials. A. Fina is a full Professor of Chemistry at Politecnico di Torino (I) and, currently, co-author of 74 papers in peer-reviewed journals with an H-index of 26.

Orietta Monticelli

Orietta Monticelli obtained her Laurea degree with honors in Industrial Chemistry from the University of Genoa in 1992. In 1996, Orietta Monticelli obtained her PhD in Chemistry, working at Genoa University and at the Department of Chemical Engineering (Boulder, Colorado, USA). Between January 1997 and June 1998, she won two scholarships from the European Union (Marie Curie Research Training Grant) and worked at the Centrum voor Oppervlatechemie en Katalise of Leuven University (Leuven Belgium). Since 2014, Orietta Monticelli has been an Associate Professor at Genoa University. Her scientific activity is documented in more than 90 publications in international scientific journals (H-30 index, over 2000 citations, Scopus May 2019). Her recent scientific interest include the development of novel formulations based on bio-polymers, in particular on polylactic acid.

frontiers in Chemistry

REVIEW
published: 08 August 2019
doi: 10.3389/fchem.2019.00522

Review on Polymer-Based Composite Electrolytes for Lithium Batteries

Penghui Yao[1†], *Haobin Yu*[1†], *Zhiyu Ding*[1], *Yanchen Liu*[1], *Juan Lu*[1], *Marino Lavorgna*[2], *Junwei Wu*[1*] and *Xingjun Liu*[1]

[1] Shenzhen Key Laboratory of Advanced Materials, Department of Materials Science and Engineering, Harbin Institute of Technology, Shenzhen, China, [2] Institute of Polymers, Composite, and Biomaterials, National Research Council, Portici, Italy

Lithium-ion batteries have dominated the high performance and mobile market for last decade. Despite their dominance in many areas, the development of current commercial lithium-ion batteries is experiencing bottlenecks, limited by safety risks such as: leakage, burning, and even explosions due to the low-boiling point organic liquid electrolytes. Solid electrolyte is a promising option to solve or mitigate those issues. Among all solid electrolytes, polymer based solid electrolytes have the advantages of low flammability, good flexibility, excellent thermal stability, and high safety. Numerous researchers have focused on implementing solid polymer based Li-ion batteries with high performance. Nevertheless, low Li-ion conductivity and poor mechanical properties are still the main challenges in its commercial development. In order to tackle the issues and improve the overall performance, composites with external particles are widely investigated to form a polymer-based composite electrolyte. In light of their work, this review discusses the progress of polymer-based composite lithium ion's solid electrolytes. In particular, the structures, ionic conductivities, electrochemical/chemical stabilities, and fabrications of solid polymer electrolytes are introduced in the text and summarized at the end. On the basis of previous work, the perspectives of solid polymer electrolytes are provided especially toward the future of lithium ion batteries.

Keywords: polymer solid electrolytes, polymer, lithium-ion batteries, Li-ion conductivity, composite

OPEN ACCESS

Edited by:
Pellegrino Musto, Italian National Research Council (CNR), Italy

Reviewed by:
Helinando Pequeno De Oliveira, Universidade Federal do Vale do São Francisco, Brazil
Giuseppe Scherillo, University of Naples Federico II, Italy

***Correspondence:**
Junwei Wu
junwei.wu@hit.edu.cn

[†] *These authors have contributed equally to this work*

Specialty section:
This article was submitted to Polymer Chemistry, a section of the journal Frontiers in Chemistry

Received: *29 January 2019*
Accepted: *08 July 2019*
Published: *08 August 2019*

Citation:
Yao P, Yu H, Ding Z, Liu Y, Lu J, Lavorgna M, Wu J and Liu X (2019) Review on Polymer-Based Composite Electrolytes for Lithium Batteries. Front. Chem. 7:522. doi: 10.3389/fchem.2019.00522

INTRODUCTION

From the moment in 1991 when the SONY corporation launched the commercialization of lithium-ion batteries, lithium-ion batteries have thrived significantly and dominated in many different applications, such as electric vehicles, portable devices (Scrosati and Garche, 2010; Verma et al., 2010; Manthiram et al., 2017). Although lithium-ion batteries have many advantages such as high energy density and long cycle life, the potential safety issues and saturated high energy density have become bottlenecks which impedes further development.

Current commercial lithium-ion batteries use liquid organic electrolytes, which have significant advantages of high conductivity and excellent wettability on electrode surfaces. However, the obvious and inevitable drawbacks of liquid electrolytes are electrochemical instabilities and potential risks, plus low ion selectivity. Compared with liquid electrolytes, solid electrolytes have higher safety and thermal stability, since it can provide a physical barrier layer to separate positive

and negative electrodes and prevent thermal runaway under high temperature or impact. In addition, solid electrolyte makes it possible to use a lithium metal anode, due to its effective suppression of Li dendrite formation. Despite the significant advantages, some weaknesses still remain to be improved, such as low ionic conductivity and insufficient interface contact. Plenty of research is being conducted to conquer the weakness and develop new generation of solid lithium batteries (Tang et al., 2007; Zhao et al., 2012; Liu et al., 2013; Zhang Q. Q. et al., 2017). To meet the commercial requirements, high ionic conductivity, favorable mechanical properties, and outstanding interfacial stability with the electrodes are the most fundamental requirements for solid electrolytes (Fergus, 2010).

Inorganic solid electrolyte (ISE), solid polymer electrolyte (SPE), and composite electrolyte (CSE) are widely studied in lithium-ion batteries. Oxide group and sulfide group are two types widely used in ISE. Some of them [such as sulfide-based $Li_{10}GeP_2S_{12}$ (Kamaya et al., 2011)] exhibit high conductivity equivalent to that of organic liquid electrolytes, but the issues of high processing difficulty, high cost, and large interface impedance restricts its wide application (Knauth, 2009; Fergus, 2010). SPEs not only have excellent electrochemical performance and high safety, but are also good in flexibility and process ability, which has high possibilities for use in next-generation high-energy batteries (Dias et al., 2000; Stephan and Nahm, 2006; Yarmolenko et al., 2018). In the meantime, it avoids the danger of Li metal dendrite growth (Meyer, 1998; Agrawal and Pandey, 2008; Tikekar et al., 2016). SPEs, including polyethylene oxide (PEO) (Farrington and Briant, 1979; Watanabe et al., 1999; Siqueira and Ribeiro, 2006), polycarbonate (Forsyth et al., 1997; Sun et al., 2014; Liu et al., 2015), and polysiloxane (Sun et al., 1996; Fonseca and Neves, 2002) have been extensively investigated. However, the ionic conductivity and mechanical strength of SPEs are still not ideal, which is the major obstacle to hamper their wide applications (Chen et al., 2016).

Different methods are adopted for improving the polymer electrolyte system. Typically, they can be categorized into two approaches: (1) Polymer/polymer coordination and (2) Composite polymer electrolyte.

Copolymerization, crosslinking, interpenetration, and blending are widely used as polymer/polymer coordination; however, it does not significantly increase the mechanical properties of the electrolyte. Various composites had been mixed into polymers, as shown in **Figure 1**, including inert ceramic fillers (Agrawal and Pandey, 2008; Lin et al., 2016), fast-ion conductive ceramics (Aliahmad et al., 2016; Keller et al., 2017; Ling et al., 2018), lithium salts (Do et al., 1996), ionic liquid (Subianto et al., 2009), etc. With the synergistic effect of polymer and inorganic filler, the room temperature conductivity and mechanical strength of composite polymer electrolyte can be greatly improved, as well as the interface stability with the electrode. In my group, similar synergistic effects on composite electrolyte had been reported in inorganic fillers composite with Nafion membrane for direct methanol fuel cell applications (Cui et al., 2015, 2018), the corresponding mechanism is similar with the composite electrolyte with organic fillers. The used polymer matrices and properties for SPE are summarized in **Table 1**.

Solid polymer electrolytes (SPEs) currently have great application prospects in lithium batteries fabrication, numerous researchers also take great efforts to develop innovative SPEs and the successful applications will play a key role in developing lithium battery with excellent performance. **Figure 2** shows that the number of published sci-tech articles in the polymer-based solid electrolyte over a period of 19 years from 2000 to 2018. The trend shows the steady increase from about 750 in 2000 to the largest point around 2,400 in 2017. From the year of 2010, the number of essays in this field keep steady over 2000, which is the fact that polymer-based solid electrolyte will have excellent application prospects. A large number of reviews have summarized the research and development history of polymer electrolytes (Qiu et al., 2004; Dong and Wang, 2005; Srivastava and Tiwari, 2009; Fergus, 2010; Liu et al., 2013; Osada et al., 2016; Zhang Q. Q. et al., 2017). However, there is relatively few reviews on polymer-based solid electrolytes.

This review article highlights recent researches on SPEs for solid state lithium-ion batteries, in particular about the effects of composition with various filler materials. In this review, polymer based composite electrolytes, including polymer/inert ceramics, polymer/fast-ion conductive, polymer/ionic liquid, polymer/MOFs, and polymer/cellulose composite electrolytes. Furthermore, a perspective on the future research direction for developing safety, stable, and high energy density composite polymer electrolytes for solid-state batteries will be provided.

IONIC CONDUCTIVITY AND INTERFACE

Ionic Conductivity Mechanism

In order to develop SPEs with high lithium ion conductivity, the polymer should not only dissolve lithium salt, but also be able to couple with lithium ions. The polar groups in the polymer (—O—, —S—, etc.) are effective building blocks for dissolving lithium salts. Most of the research on all-SPEs is focused on polyethylene oxide (PEO) and its derivatives. The lone pair of oxygens on the PEO segment is coordinated to the lithium ion by Coulombic interaction, causing the anion and cation of the lithium salt to dissociate. In the process, PEO acts as solvent, and the lithium salt dissolves into the PEO matrix. In addition to the oxygen atom (—O—) on the PEO chain, other atoms such as the nitrogen in the imide (—NH—) and the sulfur in the thiol (—S—) also play a similar role. Under the electric field, the migration movement of Li^+ cations are from one coordination point to another along the polymer segment, or jump from one segment to another. The ion transport mechanism of polymer electrolytes such as PEO is shown in **Figure 3** (Xu, 2004).

In the polymer-lithium salt composite system, the ions are not free to move due to the huge size of the polymer chain plus the boundary effect of crystalline domains. The factors affecting the ionic conductivity are the number of lithium ions and the mobility of the polymer chain. The amount of ions that can be migrated depends on the ability of the polymer to dissociate the lithium salt, and thus the lithium salt of low lattice energy and the polymer of high dielectric constant can promote this dissociation (Young et al., 2014). Under steady state conditions, the ionic conductivity can be expressed by the

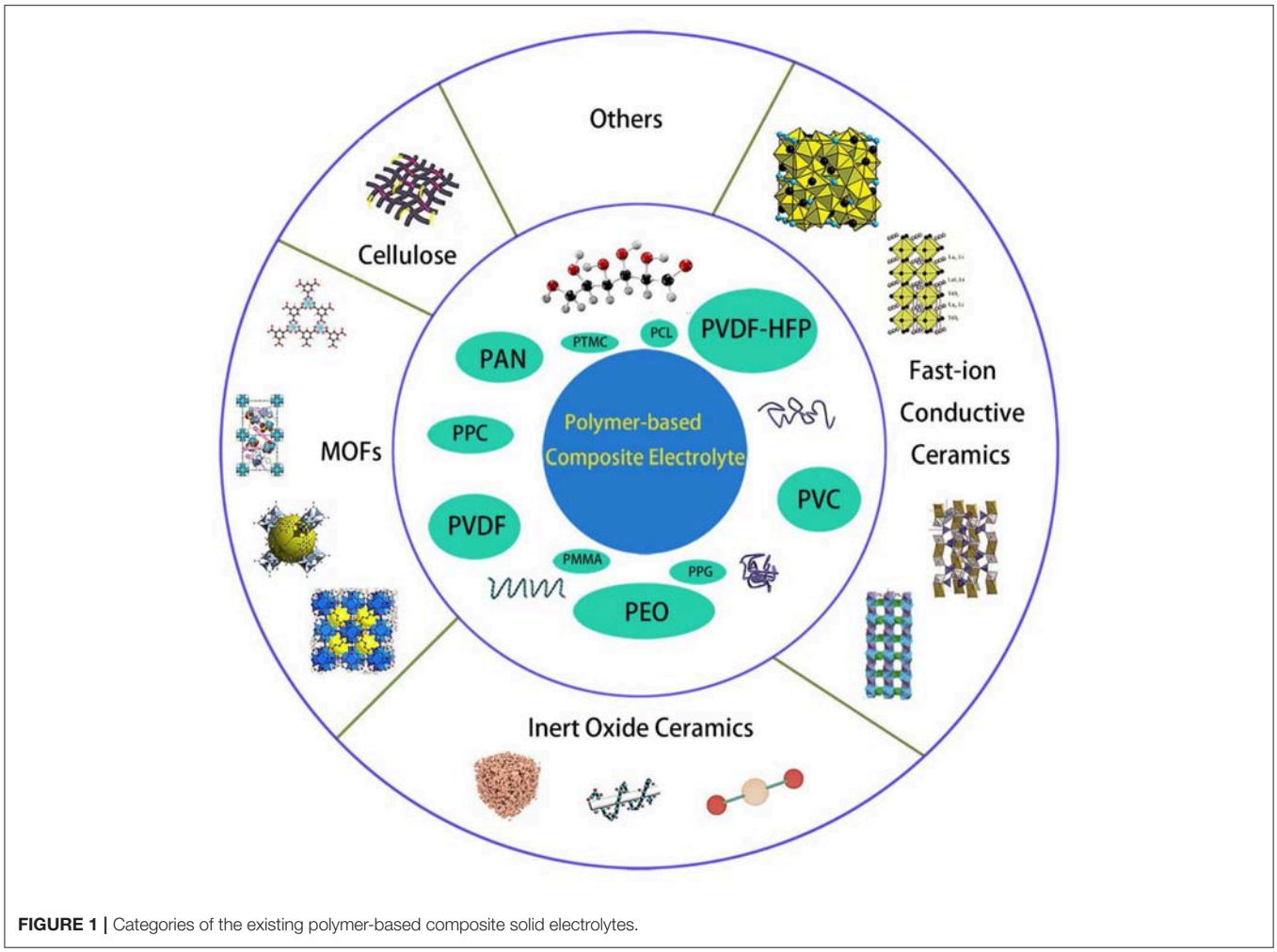

FIGURE 1 | Categories of the existing polymer-based composite solid electrolytes.

following equation (Wei-Min, 2012):

$$\sigma = \mathrm{F} \sum n_i q_i \mu_i \tag{1}$$

Here, F is the Faraday constant; n_i represents the number of free ions; q_i represents the number of charges, and μ_i is the mobility. Therefore, it can be seen that in the polymer electrolyte, the increasement of the concentration of the movable ions and the migration speed of the ions can increase the conductivity of the ions.

In SPEs, the most commonly used theory to explain the migration of ions in polymers includes Arrhenius theory, Vogel-Tammann-Fulcher (VTF) theory, William-Landel-Ferry (WLF) theory, and the combinations of above theories (Ratner et al., 2000; Quartarone and Mustarelli, 2011).

The classical Arrhenius theory explains the temperature relationship of ion migration caused by polymer segment motion, expressed as (Zhang Q. Q. et al., 2017):

$$\sigma = \sigma_0 \exp(\frac{-E_a}{KT}) \tag{2}$$

Here, E_a represents the activation energy for single molecules or groups of ions to migrate, σ_0 represents the pre-exponential factor, while T represents thermodynamic temperature.

Generally, ion jump motion and polymer chain relaxation and/or segmental motion together affect conductivity, so the vs. 1/T curve is generally non-linear (Agrawal and Pandey, 2008). The typical lg-1/T in polymers is usually based on the T_g-based equation, so VTF mainly describes the relationship between polymer electrolyte conductivity and temperature (Zhang Q. Q. et al., 2017):

$$\sigma = \sigma_0 T^{-\frac{1}{2}} \exp(-\frac{B}{T - T_0}) \tag{3}$$

Here, σ_0 is a pre-exponential factor, B is an action factor with dimension as the energy dimension, and T_0 is the reference temperature, which can be expressed in T_g, normally 10–50 K below the experimental glass transition temperature. At room temperature, if only the effect of the polymer segment on conductivity is considered, low glass transition temperature can play a positive role in the improvement of the conductivity.

Based on the study of PEO and PPO salt complexes, the ionic conductivity can be related to frequency and temperature

TABLE 1 | Common polymer matrix.

Polymer matrix	Molecular formula	Glass transition temperature T_g/°C	Melting point T_m/°C
PEO	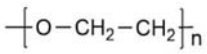	−64	65
PVC	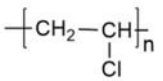	80	220
PAN	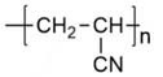	125	317
PMMA	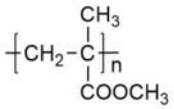	105	Amorphous
PVDF	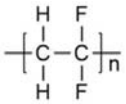	−40	171
PVDF-HFP	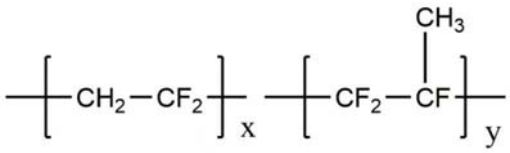	−90	135
PPG	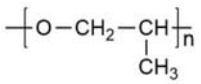	−60	Amorphous
PDMS	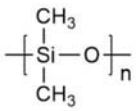	−127	−40
PEC	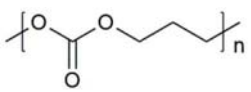	5	Amorphous
PPC	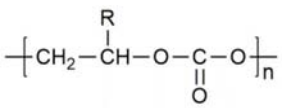	35	Amorphous
PCL	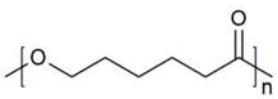	−60	Amorphous
PTMC	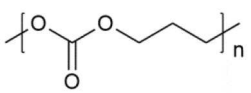	−15	Amorphous

by using the William-Landel-Ferry (WLF) equation, considering the relaxation process of polymer molecular chain motion in an amorphous system. The expression is:

$$\lg \frac{\sigma(\mathrm{T})}{\sigma(\mathrm{T_g})} = \frac{C_1(T - T_g)}{C_2 + (T - T_g)} \tag{4}$$

Here, $\sigma(T_g)$ is the conductivity of the relevant ions at glass transition temperature T_g, and C_1 and C_2 are the WLF parameters in the free volume equation of ion migration, respectively.

T_g is one of the most critical parameter of polymer electrolyte. The conductivity is very low as the temperature below T_g, and it

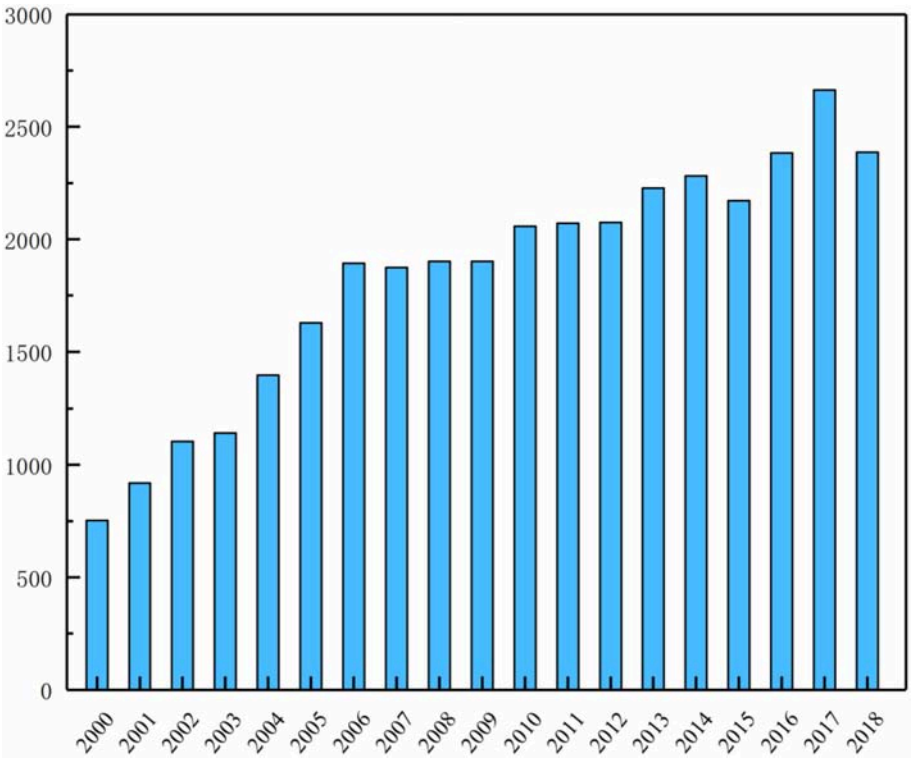

FIGURE 2 | The number of published sci-hech articles in the polymer-based solid electrolyte over a period of 19 years from 2000 to 2019.

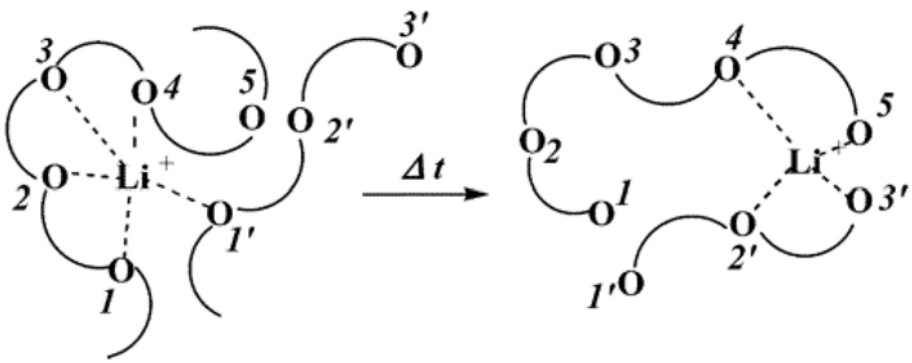

FIGURE 3 | Schematic diagram of lithium ion conduction mechanism of PEO-based polymer electrolyte. [Reproduction with permission from Xu (2004), Copyright 2004, American Chemical Society].

will be obviously improved above T_g. Therefore, to reduce T_g is beneficial to the improvement of conductivity.

The above three theories well-explain the conductive mechanism of the PEO-based electrolyte. The amorphous phase of the polymer is mainly effective for the migration of ions. The theory can also be applied to other polymer electrolytes.

Interface

In the solid lithium-metal battery, the cathode is typically $LiFePO_4$ or $LiCoO_2$. Metallic lithium is used as a negative electrode. The cathode/electrolyte interface requires a solid electrolyte with excellent flexibility to ensure low interface resistance, while the anode/electrolyte interface requires a strong solid electrolyte to withstand the puncture of the metal lithium dendrites (Camacho-Forero and Balbuena, 2018; Wang L. P. et al., 2018; Zhang et al., 2018). The good flexibility of the SPE makes the lower interface resistance possible, but the low mechanical properties are difficult to withstand the puncture of the metal lithium dendrites. In contrast, a rigid inorganic ceramic electrolyte can withstand the metallic lithium dendrites, but has a large interfacial resistance due to insufficient contact with the electrodes (Xu et al., 2018). Therefore, the flexible polymer

electrolyte or the rigid inorganic ceramic electrolyte has difficulty used in solid metal lithium battery separately. In order to take full advantage of polymer and inorganic ceramic electrolyte, polymer composite inorganic ceramic electrolyte offers an option. It is expected that the obtained solid metal lithium battery has both low interface resistance and the ability to inhibit lithium dendrite formation. In addition, the electrochemical instability of the interface easily leads to the occurrence of side reactions and thus the cover of the electrodes form a solid electrolyte interface (SEI), which may lead to a shortened cycle life of the cell (Xu et al., 2018).

SOLID POLYMER ELECTROLYTES WITH INERT OXIDE CERAMICS

In recent years, many studies have been addressed to incorporate inert oxide ceramics particles into polymer electrolyte, in order to improve the mechanical properties, reduce polymer crystallinity, and thus solve the problem of low ionic conductivity of SPE. Different types of inert ceramics had been incorporated into the polymer, such as SiO_2 (Nan et al., 2003; Ketabi and Lian, 2013), Al_2O_3 (Weston and Steele, 1982; Capuano et al., 1991; Tambelli et al., 2002; Liang et al., 2015), TiO_2 (Pal and Ghosh, 2018), zeolite, etc. The ionic conductivities of solid polymer composite electrolyte containing inert ceramic filler are showed in **Table 2**. In 1982, Weston and Steele (1982) mixed PEO with Al_2O_3 to form a composite. It was firstly proved that PEO doped with inert material particles exhibited an improvement of mechanical properties and ionic conductivity. Subsequently, Capuano et al. (1991) explored the contribution of the doping amount and particle size of $LiAlO_2$ powder on the conductivity of solid electrolyte. It was found that the conductivity reached the highest as the doping amount of $LiAlO_2$ was around 10 wt.%. It is also worth noting that particle size of the inert ceramic material affected the conductivity of the SPE, which increases with particle sizes as the size is $<10\,\mu m$. Tambelli et al. (2002) reported that Al_2O_3 can effectively reduce the crystallinity and glass transition temperature of PEO. This confirms that the decrease of polymer crystallinity promotes the improvement of ionic conductivity. The decrease in crystallinity can enlarge the number of free segments of the polymer and accelerate the movement of the segments, which can effectively promote the migration of lithium ions. Similar results were reported on PEO-PMMA-LiTFSI-Al_2O_3 composite electrolytes. They were prepared based on PEO-PMMA as a host matrix and nano Al_2O_3 as filler by solution casting technique (Liang et al., 2015). The composite electrolytes doped with Al_2O_3 exhibited an improvement of the ionic conductivity from 6.71×10^{-7} to 9.39×10^{-7} S/cm.

SiO_2 is also a common inert ceramic filler material used in the preparation of SPE. Lee et al. reported a composite of a PEO matrix and SiO_2 fillers containing ethylene carbonate (EC)/propylene carbonate (PC). The composite had an ionic conductivity of 2×10^{-4} S/cm at ambient temperature (Nan et al., 2003) with 2.5 wt.% filler loadings. In addition to powder, SiO_2 is also designed as a three-dimensional framework doped into the polymer. Lin et al. (2018) prepared a composite of PEO-Silica aerogel which exhibited high ionic conductivity 6×10^{-4} S/cm and high modulus 0.43 GPa. This study effectively solves the issue of poor mechanical properties and ionic conductivity of composite by controlling powder dispersion. SiO_2 aerogel skeleton has a good acidic surface. It can interact with lithium cations extensively and form a continuous channel in the composite material, beneficial to salt dissociation and improvement of ionic conductivity. Ion pairs are difficult to form because of the strong Lewis acid-base interaction of doped TiO_2 and the anion of lithium salt, resulting in more mobile charge carriers (Pal and Ghosh, 2018). Croce et al. (1998) studied a solid polymer electrode consisting of a nanosized TiO_2 particles, PEO, and $LiClO_4$. This hybrid exhibits a higher ionic conductivity of 10^{-5} S/cm. Pal and co-workers fabricated SPEs comprising of PMMA, $LiClO_4$, and TiO_2, by standard solution cast technique (Pal and Ghosh, 2018). The results showed that by composite nanosized-TiO_2 to the polymer electrolytes, the thermal stability can be improved as well. The conductivity reached 3×10^{-4} S/cm at 303 K. Moreover, specific capacity of such polymer electrolyte-based $LiCoO_2$/graphite at 30°C exhibited 30 mAh/g at room temperature in twelfth cycle. In addition, some studies have incorporated a variety of inorganic ceramics into the polymer, and the ionic conductivity has also been improved. For example, nanosized SiO_2, and nanoporous Al_2O_3 were combined with PVDF-HFP to obtain composite electrolytes that delivered moderate conductivity of 10^{-3} S/cm with 2.5 wt.% of fillers (Aravindan and Vickraman, 2008).

Liu et al. (2016) has the designed and fabricated a SPE comprising Y_2O_3 nanoparticle, ZrO_2 nanowire fillers, and PAN by electrospinning (**Figure 4A**). Y_2O_3-stabilized ZrO_2(YSZ) nanowire in PAN have a lot of positively charged oxygen vacancies with Lewis acid character, which may attract the anion of lithium salt and thus promote the dissociation of salts. The addition of YSZ nanoparticles or YSZ nanowires has a different degree of improvement in ionic conductivity compared to the absence of YSZ. The improvement effect of YSZ nanowires is better, and 7YSZ (7 mol% of Y_2O_3-doped ZrO_2 nanowires) had a high room-temperature ionic conductivity of 1.07×10^{-5} S/cm at 30°C with an enhancement of two orders of magnitude compared with pristine PAN electrolyte (**Figure 4B**). Recently, Tao et al. (Sheng et al., 2018) incorporated $Mg_2B_2O_5$ nanowires into PEO-LiTFSI-based solid electrolyte. The composite electrolytes exhibit good mechanical properties, outstanding electrochemical stability, and ionic conductivity, because of the fast ion motion on the surfaces of $Mg_2B_2O_5$ and interactions between the $Mg_2B_2O_5$ and $TFSI^-$ (**Figure 4C**). In addition, other inert oxide ceramics have also been reported to improve the SPE performance, such as $LiAlO_2$ (Gang et al., 1992; Hu et al., 2007), ZnO (Xiong et al., 2006), Fe_3O_4 (Reddy et al., 2006), and $BaTiO_3$ (Itoh et al., 2003a,b).

SOLID POLYMER ELECTROLYTES WITH FAST-ION CONDUCTIVE CERAMICS

Fast ion conductor ceramics, also known as active inorganic electrolytes, exhibit a high ionic conductivity of up to 10^{-2} S/cm

TABLE 2 | Summary of inert oxide Ceramics/polymer solid electrolytes.

Year	Polymer electrolyte ingredients	Ionic conductivity (S/cm)	References
1991	$LiAlO_2$-PEO-$LiClO_4$	10^{-4} (60°C)	Liu et al., 2013
1998	TiO_2-PEO-$LiClO_4$	10^{-5} (30°C)	Manthiram et al., 2017
2002	Al_2O_3-PEO-$LiClO_4$	10^{-2} (60°C)	Liu et al., 2017
2003	SiO_2-PEO-$LiClO_4$-EC/PC	2×10^{-4} (25°C)	Lin et al., 2016
2015	Al_2O_3-PEO-PMMA-LiTFSI	9.39×10^{-7} (25°C)	Liu et al., 2016
2016	SiO_2-Al_2O_3-PVDF-HFP-$LiPF_3(CF_3CF_2)_3$	10^{-3} (25°C)	Meyer, 1998
2016	Y_2O_3-doped ZrO_2 nanowire (YSZ)—PAN–$LiClO_4$	1.07×10^{-5} (30°C)	Mueller et al., 2006
2018	TiO_2_PMMA-$LiClO_4$	3×10^{-4} (30°C)	Liu et al., 2015
2018	Silica aerogel-PEO-LiTFSI	6×10^{-4} (30°C)	Liu et al., 2015
2018	$Mg_2B_2O_5$ Nanowire-PEO-LiTFSI	1.53×10^{-4} (40°C)	Nair et al., 2009

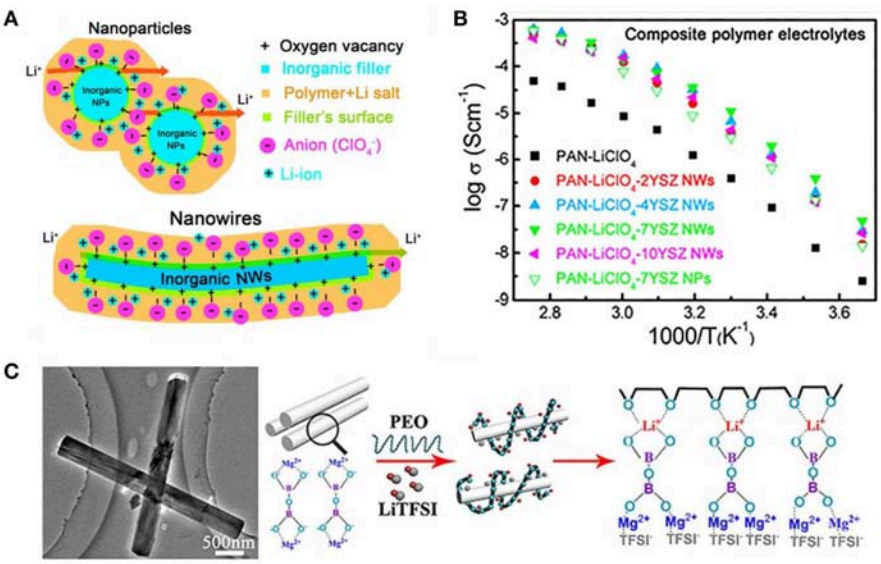

FIGURE 4 | (A) Li-ion transport in the composite polymer electrolytes with Y_2O_3 nanoparticle and ZrO_2 nanowire fillers. [Reproduction with permission from Liu et al. (2016) Copyright© 2016, American Chemical Society] **(B)** Relationship between the Y doping level and the conductivity, together with the conductivity of the YSZ bulk [Reproduction with permission from Liu et al. (2016) Copyright© 2016, American Chemical Society] **(C)** Schematics of lithium ion migration in $Mg_2B_2O_5$ enhanced composite SSEs. [Reproduction with permission from Sheng et al. (2018) Copyright© 2018, American Chemical Society].

at 25°C. Four structures of fast ion conductors are displayed in **Figure 5**.

However, the poor interfacial contact restricts their direct use as solid electrolytes. Thus, composite of fast ion conductor ceramics with polymer can take full advantages of both parts. Fast ionic conductors commonly have garnet-type, NASICON-type and LISICON-type ceramics etc. **Table 3** gives a summary of fast-ion conductive ceramics/polymer solid electrolytes.

Garnet-Type Composite Polymer Electrolytes

From the moment in 2007 when $Li_7La_3Zr_2O_{12}$ (LLZO) was first found, garnet-type Li solid-state electrolyte generates great interest in recent years. $Li_7La_3Zr_2O_{12}$ (LLZO), garnet-type Li solid-state electrolyte, has attracted much attention since it was first reported in 2007 (Xie H. et al., 2018). $Li_5La_3M_2O_{12}$ (M = Nb, Ta) is the first reported lithium ion conductor with a garnet structure (**Figure 5A**; Thangadurai et al., 2003; O'Callaghan et al., 2008). The traditional garnet chemical formula is $A_3B_2(XO_4)_3$ (A = Ca, Mg, Y, La or rare-earth elements; B = Al, Fe, Ga, Ge, Mn, Ni, or V). Garnet-type Li solid-state electrolyte has high ionic conductivity and wide electrochemical window (Wu et al., 2017). At room temperature, the ionic conductivity of $Li_5La_3M_2O_{12}$ (M = Nb, Ta) reached 10^{-3} S/cm and exhibits outstanding chemical stability over a wide temperature range. However, when the all-solid-state battery is assembled using garnet-type ceramics, the electrode/electrolyte interface always shows poor conductivity, resulting in deteriorated battery performance, as well as increased interface resistance and decreased ionic conductivity (Chen et al., 2018). Polymer/Garnet composite electrolytes offer an option of improving the overall electrochemical performances.

With a large specific surface area, nanoscale garnet ceramic fillers improve the transition rate of ions (Kumar and Scanlon, 2000). A composite electrolyte composed of PEO containing 52.5 wt.% $Li_7La_3Zr_2O_{12}$(LLZO) particles displays a conductivity

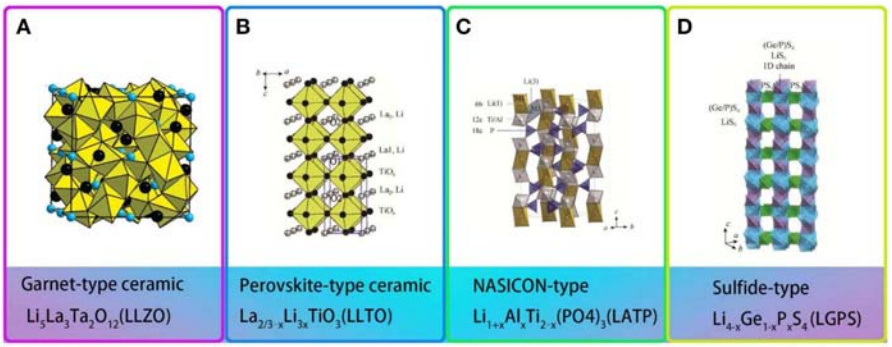

FIGURE 5 | Structures of different types of fast ion conductors **(A)** Framework of garnet-type ceramic [Reproduction with permission from O'Callaghan et al. (2008) Copyright© 2008, American Chemical Society] **(B)** Crystal structure of perovskite-type ceramic. [Reproduction with permission from Stramare et al. (2003) Copyright© 2003, American Chemical Society] **(C)** Crystal structure of NASICON-type ceramic. [Reproduction with permission from Perez-Estebanez et al. (2014) Copyright© 2015, The Royal Society of Chemistry] **(D)** Crystal structure of Sulfide-type ceramic. [Reproduction with permission from Kamaya et al. (2011) Copyright© 2011, nature].

TABLE 3 | Summary of fast-ion conductive ceramics/polymer solid electrolytes.

Year	Polymer electrolyte ingredients	Ionic conductivity (S/cm)	References
2003	$Li_5La_3M_2O_{12}$ (M = Nb, Ta)-PEO-$LiPF_6$	10^{-6} (25°C)	Ratner et al., 2000
2015	$Li_7La_3Zr_2O_{12}$(LLZO)-PEO-$LiClO_4$	4.42×10^{-4} (55°C)	Shi et al., 2017
2015	$Li_{0.33}La_{0.557}TiO_3$(LLTO) random nanowire-PAN-$LiClO_4$	2.4×10^{-4} (25°C)	Subianto et al., 2009
2015	$Li_{2.5}Al_{0.5}Ge_{1.5}(PO_4)_3$ (LAGP)-PEO-$LiClO_4$	2.6×10^{-4} (55°C)	Tikekar et al., 2016
2015	$Li_7La_3Zr_2O_{12}$(LLZO)-PEO-$LiClO_4$	4.42×10^{-4} (55°C)	Shi et al., 2017
2016	$Li_{6.4}La_3Zr_2Al_{0.2}O_{12}$(LLZO)-PEO-LiTFSI	2.5×10^{-4} (25°C)	Stavila et al., 2014
2016	$Li_{1.5}Al_{0.5}Ge_{1.5}(PO_4)_3$ (LAGP)-PEO-LiTFSI	6.76×10^{-4} (60°C)	Thokchom et al., 2008
2016	$Li_{10}GeP_2S_{12}$-PEO-LiTFSI	10^{-5} (25°C)	Verma et al., 2010
2017	$Li_{6.20}Ga_{0.30}La_{2.95}Rb_{0.05}Zr_2O_{12}$-PVDF-LiTFSI	1.62×10^{-3} (25°C)	Scrosati and Garche, 2010
2017	$Li_{6.75}La_3Zr_{1.73}Ta_{0.23}O_{12}$-PVDF-$LiClO_4$	5×10^{-4} (25°C)	Siqueira and Ribeiro, 2006
2017	$Li_{0.33}La_{0.557}TiO_3$(LLTO) aligned nanowire-PAN-$LiClO_4$	6.05×10^{-5} (30°C)	Srivastava and Tiwari, 2009
2017	$Li_{1.3}Al_{0.3}Ti_{1.7}(PO_4)_3$(LATP)-PEO-BPEG-LiTFSI	2.5×10^{-4} (60°C)	Thangadurai et al., 2003
2018	$Li_7La_3Zr_2O_{12}$ (LLZO)-PEO-LiTFSI	1.12×10^{-4} (25°C)	Quartarone and Mustarelli, 2011
2018	$Li_{6.4}La_3Zr_{1.4}Ta_{0.6}O_{12}$(LLZTO)-PEO-LiTFSI	10^{-4} (55°C)	Sheng et al., 2017
2018	$Li_{0.33}La_{0.557}TiO_3$-PEO-$LiClO_4$	2.4×10^{-4} (25°C)	Stramare et al., 2003
2018	3D-$Li_{0.35}La_{0.55}TiO_3$(LLTO)-PEO-LiTFSI	8.8×10^{-5} (25°C)	Sun et al., 2014

which reaches 4.42×10^{-4} S/cm at 55°C (Thokchom et al., 2008). $Li_{6.75}La_3Zr_{1.75}Ta_{0.25}O_{12}$ (LLZTO) is selected as an active filler and dispersed into PVDF matrix to fabricate PVDF/LLZTO hybrid electrolytes (Zhang X. et al., 2017). The hybrid electrolyte with 10 wt.% LLZTO loadings exhibited the highest ionic conductivity (5×10^{-4} S/cm), about seven times more than none LLZTO. It is attributed to that LLZTO particles react with Li^+ via acid-base interaction. Dissociation of the lithium salt will raise the carrier density for conduction. Furthermore, the garnet ceramic filler contributes to reduce the crystallinity of polymer and so to increase the ionic conductivity. Instead of simply mixing active ceramic particles into polymers, Goodenough et al. (Chen et al., 2018) introduced a novel approach of composite polymer into ceramic.

As a consequence, high ionic conductivity (10^{-4} S/cm at 55°C) were gained and the electrochemical window of 0–5.0 V. As used in the all-solid-state Li/$LiFePO_4$ cells, both "ceramic-in-polymer" and "polymer-in-ceramic" with a LiTFSI salt display remarkable cycling stability. The systems, "polymer-in-ceramic" provide higher mechanical strength and safety than "ceramic-in-polymer."

Morphologies of ceramics fillers such as particles, distribution of nanowire and 3D framework may affect the ionic conductivity of polymer composite electrolytes. Unlike particles and random nanowires, aligned nanowires combined with polymers can provide continuous transport pathways for Li^+ (**Figure 6**). Cui et al. (Liu et al., 2017) compares the different morphologies of LLZO to evaluate their benefits for ionic transport. They found that a composite polymer electrolyte with well-aligned inorganic nanowires (LLZO) shows an ionic conductivity of 6.05×10^{-5} S/cm at 30°C, which was increased by almost one order of magnitude than the composite with randomly aligned nanowires or nanoparticles. The appreciable conductivity

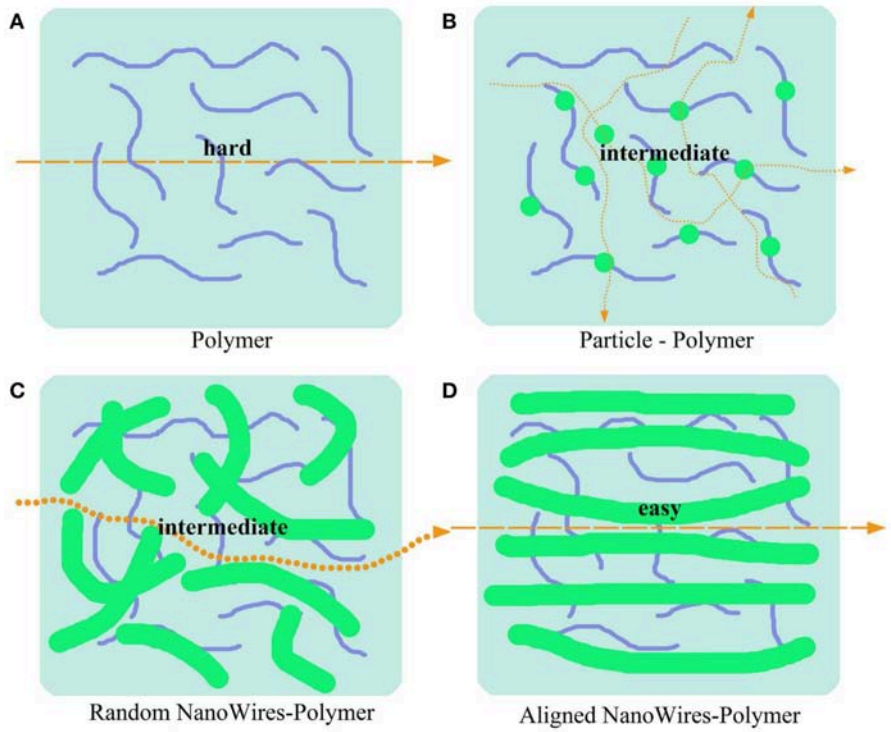

FIGURE 6 | Schematic of conduction mechanism in three kinds of morphologies solid polymer electrolytes. **(A)** Ionic transport path in pure polymer electrolytes. **(B–D)** Ionic transport path in polymer-based composite electrolytes with nanoparticles **(B)**, random nanowires **(C)** and aligned nanowires **(D)**.

improvement is due to Li^+ migration without crossing junctions on the nanowire surfaces.

In addition to 1D nanowires (Bae et al., 2018), prepared 3D ceramic $Li_{6.28}La_3Zr_2Al_{0.24}O_{12}$ networks by using hydrogel and mixed it into polymer solution to attain solid electrolyte. The designed structure is believed to have high conductivity (8.5×10^{-5} S/cm at 25°C) and good interfacial compatibility with electrodes. The integrated structure of 3D LLZO structure provides continuous 3D network of conduction pathways leading to highly improved ionic conductivity and mechanical properties. Similarly, 3D garnet nanofiber networks-polymer composite was also prepared (Fu et al., 2016). In this approach, the LLZO porous structure, composed of casually distributed and interconnected nanofibers, forms a continuous transport network for Li^+. The LiTFSI-PEO polymer is then filled into the porous 3D LLZO ceramic networks, forming the 3D garnet-polymer composite films. Then LiTFSI-PEO polymer and porous 3D Inorganic structure are combined to synthesize a 3D LLZO-polymer composite membrane which exhibited a high ionic conductivity of 2.5×10^{-4} S/cm at 25°C. The three-dimensional ion transport network offers a new option of designing composite electrolytes.

Perovskite-Type Composite Polymer Electrolytes

Perovskite-type solid electrolytes $Li_{3x}La_{2/3-x}TiO_3$ (LLTO) has a cubic structure with space group of P4/mmm and C-mmm (**Figure 5B**; Stramare et al., 2003). LLTO is well-known for its stable at high voltages. However, its preparation conditions are very strict and the ionic conductivity is also low. Recently, a polymer–ceramic composite electrolyte PEO/$LiClO_4$ has been studied by composite PEO with $Li_{0.33}La_{0.557}TiO_3$ nanowires. It exhibited extreme lithium-ion conductivity of 2.4×10^{-4} S/cm at 25°C (Zhu et al., 2018). Cui et al. (Liu et al., 2015) studied the effect of two different morphological LLTO materials on the ionic conductivity of polymer electrolytes, which are nanoscale particles and nanowire LLTO, respectively (**Figure 7**). The introduction of LLTO nanowire into PAN achieved higher ionic conductivity 2.4×10^{-4} S/cm at room temperature as compared to pristine PAN film. The composite electrolyte offers a 3D long distance Lithium-ion transmission network, which reduce the negative effect of agglomeration of inorganic ceramics in polymers relative to nanoparticles. This work opened a new way to develop one-dimensional fast ion conductive ceramic materials in solid electrolytes for lithium batteries.

The ionic conductivity has a strong relationship with the ceramic component loadings in the composite electrolyte. Generally, the higher the content, the lower the ionic conductivity will be, because nano-sized ceramic fillers are agglomerated and may block the percolation network around the phase interface. Meanwhile, in order to achieve high security of the composite electrolyte, it is necessary to reduce the proportion of combustible organic polymer content and increase the flame-retardant inorganic ceramic portion. Goodenough et al. (Bae et al., 2018) constructed a 3D-LLTO/PEO composite electrolyte using a hydrogel-derived method. The LLTO was incorporated into the hydrogel template, then it was cast with

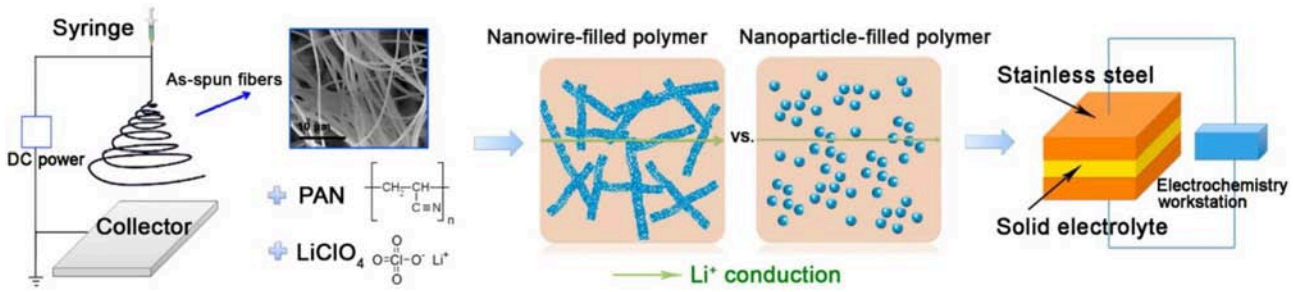

FIGURE 7 | Schematic illustration for the synthesis of ceramic nanowire-filled polymer-based composite electrolytes. [Reproduction with permission from Liu et al. (2015) Copyright© 2009, American Chemical Society].

PEO after removing the template. This artificial 3D infiltration network naturally avoids the agglomeration of nanofillers compared to the traditional simple dispersion process, and its ultra-high specific surface area provides a continuous phase interface network as lithium ion transport channel. Therefore, this composite electrolyte displayed a high ionic conductivity of 8.8×10^{-5} S cm^{-1} at room temperature.

NASICON-Type Composite Polymer Electrolytes

NASICON-type ceramics (aka "sodium super ion conductor") were firstly discovered in 1968 with composition of $NaM_2(PO_4)_3$ (M = Ge, Ti, Zr) (Epp et al., 2015). Surdrean et al. firstly reported NASICON-type solid electrolyte $LiZr_2(PO_4)_3$ at 1989. For formula $LiM_2(XO_4)_3$, $[M_2(XO_4)_3]$ constitutes the basic structure of NASICON. The MO_6 octahedron and the XO_4 tetrahedron are connected in a common angle to form Li-ion transmission channel. Aono et al. (1990) first reported doped trivalent ions into $LiTi_2(PO_4)_3$ and found that the ionic conductivity was improved. In 2014, Perez-Estebanez et al. (2014) achieved high conductivity in the $Li_{1+x}Al_xTi_{2-x}(PO_4)_3$ (LATP) of 6.76×10^{-4} S/cm at 60°C (**Figure 5C**). After that, research on NASICON-type electrolyte experienced fast growth because of its high ionic conductivity (over 10^{-3} S/cm) at ambient temperature and stable in the ambient atmosphere.

Pan group (Yang et al., 2017) fabricated $Li_{1.3}Al_{0.3}Ti_{1.7}(PO_4)_3$-PEO polymer electrolyte. The discharge specific capacity of $LiFePO_4$/Li using this polymer electrolyte was 158.2 and 94.2 mAh/g at 0.1 and 2 C, respectively. LATP can not only form pathways for lithium transportation in the interphase, leading to improved ionic conductivity, but also physically resist lithium dendrite growth. Lithium aluminum germanium phosphate (LAGP) is also a kind of NASICON-type fast ion conductor ceramic with relative high ionic conductivity ($>10^{-4}$ S/cm). Zhao et al. (2016a) similarly incorporated NASICON-type $Li_{1.5}Al_{0.5}Ge_{1.5}(PO_4)_3$ (LAGP) as Li^+ conductors into PEO matrix. The resultant polymer electrolyte displayed a wide electrochemical window of 0–5.3 V and an ion-conductivity of 6.76×10^{-4} S/cm at 60°C. More intriguingly, such polymer electrolyte based $LiFePO_4$/Li battery showed prominent cycling stability (90% after 50 cycles). Jung et al. (2015) designed a stretchable ceramic-polymer composite electrolyte membrane where NASICON-type LAGP were incorporated into a polymer-Li salt $LiCLO_4$ matrix, to synthesize a polyethylene oxide solid electrolyte membrane (**Figure 8A**). The PEO-$LiCLO_4$-LAGP composite electrolyte with 60–80 wt.% LAGP is still capable of providing enough mechanical modulus and good electrochemical performance. Li/$LiFePO_4$ cells initial discharge capacities reach 138.5 mAh/g and deliver good capacity retention.

Sulfide-Type Polymer Electrolytes

Sulfide-type electrolytes show supreme ion-conductivities in the magnitude of 10^{-2} S/cm at room temperature (Kamaya et al., 2011). However, they demonstrate instability due to reaction with water vapor in air. Sulfide-type ceramics can be divided into three categories: glasses, glass-ceramic, and ceramic. The entire types ion-conductivity can near or exceed liquid electrolyte. Glass/glass-ceramic Li_2S-P_2S_5 and ceramic thio-LISICON $Li_{4-x}Ge_{1-x}P_xS_4$ ($0 < x < 1$) are the most promising ones. $Li_{10}GeP_2S_{12}$ and PEO has been composited to prepare solid electrolyte membrane (Zhao et al., 2016b). The conductivity at room temperature reaches 10^{-5} S/cm, which is higher than other conventional PEO electrolyte at least one order of magnitude, and the electrochemical window spans between 0 and 5.7 V. It greatly expands the selection range of positive electrode materials and presents improved stability to lithium metal. The solid polymer batteries show capacity retentions approaching 92.5% after 50 cycles. Villaluenga et al. (2016) prepared a non-flammable composite electrolytes by fully mechanochemical reaction between hydroxy-terminated perfluoropolyether (PFPE-diol), LiTFSI and $75Li_2S{\cdot}25P_2S_5$ by ball milling for 2 h. The electrolyte containing 77 wt.% ($75Li_2S{\cdot}25P_2S_5$) and 23 wt.% PFPE-diol/LiTFSI displays a conductivity of 10^{-4} S/cm at room temperature (**Figure 8B**).

Solid Polymer Electrolytes With Ionic Liquid

An ionic liquid (IL) is a molten salt at low temperatures and generally consist of organic cations and inorganic anions (Zhao et al., 2016b). Due to the special state, ionic liquids have the characteristics of vapor pressure free, high electrochemical stability, and good thermal stability (Armand et al., 2009).

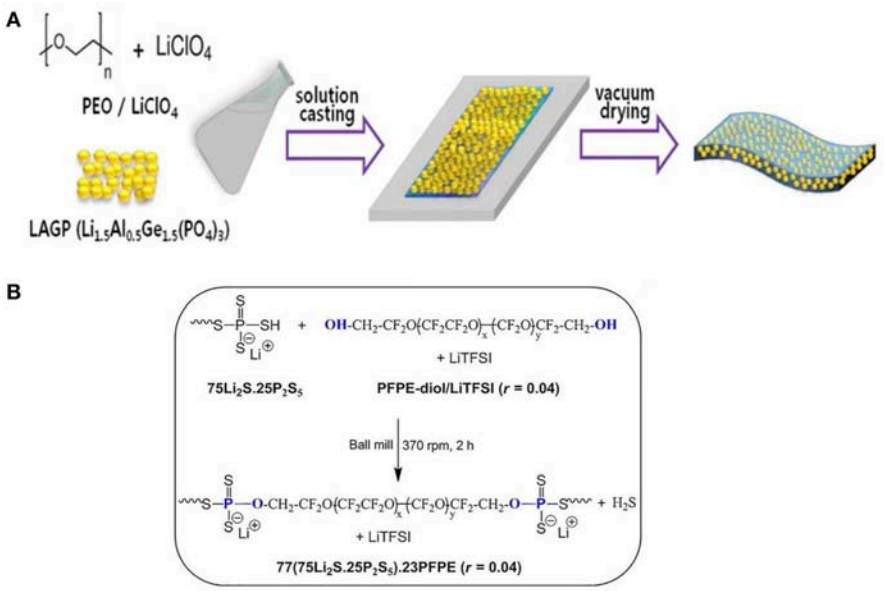

FIGURE 8 | (A) Schematic presentation of preparation for PEO-LiClO4-LAGP hybrid solid electrolyte. [Reproduction with permission from Jung et al. (2015) Copyright 2017, The Electrochemical Society.] **(B)** Synthesis of the hybrid electrolyte $77(75Li_2S.25P_2S_5).23PFPE$ ($r = 0.04$) by mechanochemical reaction. [Reproduction with permission from Villaluenga et al. (2016). Copyright 2016, National Academy of Sciences].

Although ionic liquids have high ionic conductivity, they are not suitable for direct use as electrolytes because of low viscosity. The combination of ionic liquid and polymer offers an option as solid electrolyte for lithium ion batteries.

The introduction of IL into the polymer results in higher ionic conductivity, but it is usually accompanied by a decrease in mechanical strength, especially at high temperature. Lower IL concentration leads to higher mechanical strength, and a smoother continuous electrolyte surface, which is more favorable for ion transport. Therefore, the amount of IL plays an important influence on the ionic conductivity and mechanical properties. Moreover, battery cycling at high temperatures usually causes decomposition of IL components, resulting in degraded performances. It added one more requirement of the polymer components to retain high IL contents.

IL-based polymer electrolytes are mainly classified into three categories. (1) polymer doped IL; (2) ILs/polymerizable monomers crosslinks; (3) polymeric ionic liquids (PILs). The first one is just IL added to the polymer solution or infused in the polymer film directly. For example, Subianto et al. (2009) prepared an electrolyte consisting of IL, silica nano-particles, and Nafion by using sulfonated polyhedral oligomeric silsesquioxane (S-POSS) modified Nafion membranes soaking with 1-butyl-3-methylimidazolium bis-(trifluoromethylsulfonyl)imide (BMI-BTSI) (**Figure 9**). The thermal stability of Nafion films was improved after ionic liquid infiltration. More importantly, the conductivity of the infiltrated films is increased by one to two orders of magnitude than that of the unmodified one. ILs/polymer monomer cross-linking is the mixing of ILs and polymerizable monomers to obtain electrolytes by means of thermal or photo polymerization. Polymeric ionic liquids (PILs) can be designed by the direct polymerization of polymerizable IL-based monomer or polymerizing a modified polymer and an IL monomer. By taking full advantages of the specific properties of ionic liquids and polymers, PIL membrane has generated great interest in recent years. By adopting solution cast technique, Karuppasamy et al. (2016) designed PIL synthesized solid electrolytes by preparing ionic liquids of lithium N, N-bis(trifluoromethanesulfonyl)imide (LiTFSI) in N-ethyl-N-methylimidazolium–bis(trifluoromethanesulfonyl) imide (EMImTFSI) IL with incorporated organic solvent and nanoparticle into PEO. The prepared PIL electrolyte exhibits high ionic conductivity of 10^{-2} S/cm and high electrochemical stability. Yang et al. (Li et al., 2011) designed a solid electrolyte by combining PIL with different anions such as BF_4^-, PF_6^-, ClO_4^-, and $N(CF_3\ SO_2)_2^-$. PILs electrolyte with 1g2-MA-BF_4/$LiBF_4$ exhibited ionic conductivity as high as 1.35×10^{-4} S/cm at 30°C. Starting from PEO, modified sepiolite (TPGS-S), LiTFSI, and 1-Butyl-1-methylpyrrolidinium bis(trifluoromethanesulfonyl)imide (PYR14TFSI) ionic liquid, electrolytes was synthesized via solvent free extrusion method (Gonzalez et al., 2018). The resultant polymer electrolyte displayed wide electrochemical window of 4.2 V and ion-conductivity of 5×10^{-4} S/cm at 60°C.

SOLID POLYMER ELECTROLYTES WITH MOFs

Metal–organic frameworks (MOFs) are a new kind of porous material, which are composed of metal ions and bridging organic ligands (Stavila et al., 2014; Indra et al., 2018; Xie X. C. et al.,

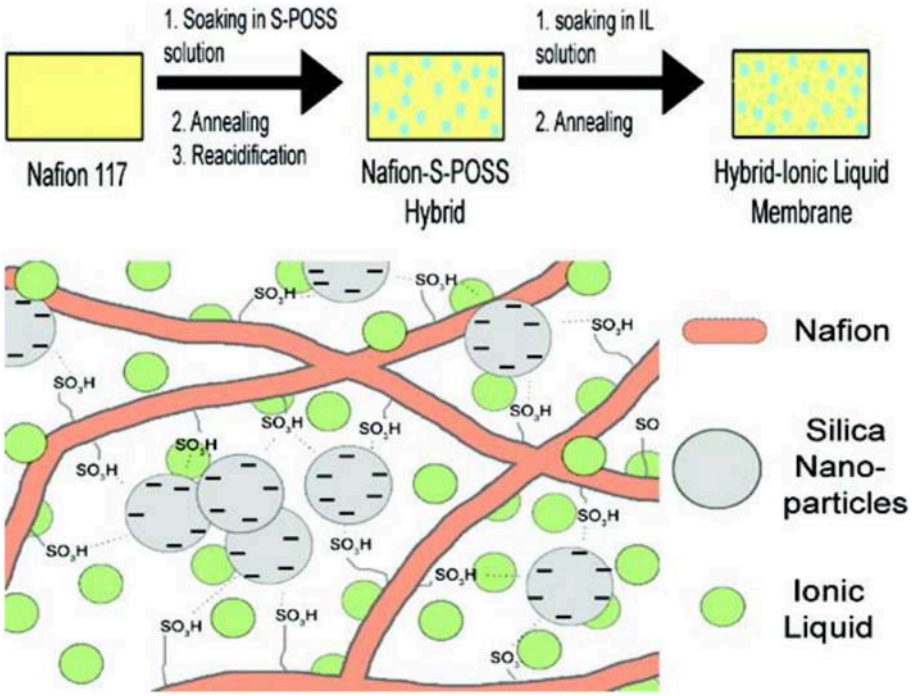

FIGURE 9 | Schematic illustration of the overall procedure for the preparation of Hybrid-Ionic liquid electrolyte. [Reproduction with permission from Subianto et al. (2009). Copyright© 2009, American Chemical Society].

2018). MOFs have many properties such as porosity, large specific surface area, and polymetallic sites (Yuan et al., 2013), so they are widely used in many fields including gas adsorption, molecular separation, drug delivery (Mueller et al., 2006; Kuppler et al., 2009; Li et al., 2009). Many investigations have indicated that MOFs also has positive effect on increased ionic conductivity due to high specific surface and the good adsorption property. Yuan et al. (2013) prepared a new SPE by the addition of Zn-based MOF-5 into PEO polymer electrolyte. The combination of MOFs and polymer showed positive effect on the mechanical and electrochemical properties as solid electrolyte. The ionic conductivity of these membrane can reach 3.16×10^{-5} S/cm at ambient temperature, which is attributed to two parts. Firstly, the interaction of the Lewis acidic sites on the MOF-5 with the PEO chain and the lithium salt hinder the crystallization of the PEO, and facilitate the formation of Li^+ conductive channels. Secondly, the isotropic open MOF-5 can adsorb solvent to accelerate the transport of ions. Gerbaldi et al. (2014) proposed a new filler material (aluminum-based MOF) (**Figure 10A**), which was successfully prepared and incorporated in a PEO-based polymer matrix. Ionic conductivity of the composite membrane is two orders of magnitude greater than that without mixed MOFs. lithium batteries ($Li/LiFePO_4$) with the electrolyte showed distinguished charge-discharge performance and high specific capacity. At 1 C rate, the battery can still cycle stably at 50°C, and the decay of specific capacity is not obvious when restored to 70°C. After 500 cycles, the capacity is almost maintained as the initial, and the Coulombic efficiency is only slightly decreased. This shows an excellent capacity retention capability and good cycle stability (**Figure 10B**). Recently, Wang Z. et al. (2018) synthesized a new chemically linked composite MOF-polymer electrolyte. The film was prepared by photopolymerization with post-synthetic modification of the MOF (M-UiO-66-NH_2), poly(ethylene glycol) diacrylate and LITFSI (**Figure 11**). The interface between MOF and polymer provides a fast channel for lithium-ion transport, accordingly the conductivity of the composite electrolyte (HSPE-1-8) is 4.31×10^{-5} S/cm at 30°C that is up to five times more than that of no composite MOF. The solid $Li/LiFePO_4$ cells assembled with these SPEs cycled at 60°C demonstrated excellent coulombic efficiencies.

SOLID POLYMER ELECTROLYTES WITH CELLULOSE

Cellulose is a non-toxic harmless, inexpensive, and natural eco-friendly materials with high mechanical strength and a large specific surface area (Baxter et al., 2009; Sheng et al., 2017) Due to the unique properties, cellulose can not only enhance the mechanical properties of polymers in electrolytes, but hinder the growth of lithium dendrites effectively acting as a physical barrier. The interface between cellulose and polymer behaves as a channel for ion transport, facilitating ion transport. In addition, polar groups in cellulose can improve salt dissociation (Shi et al., 2017). Nair et al. (2009) reported a polymer composite electrolyte with cellulose reinforcement. The reinforced electrolyte exhibited a high ionic conductivity (2.0×10^{-4} S/cm at 25°C) and

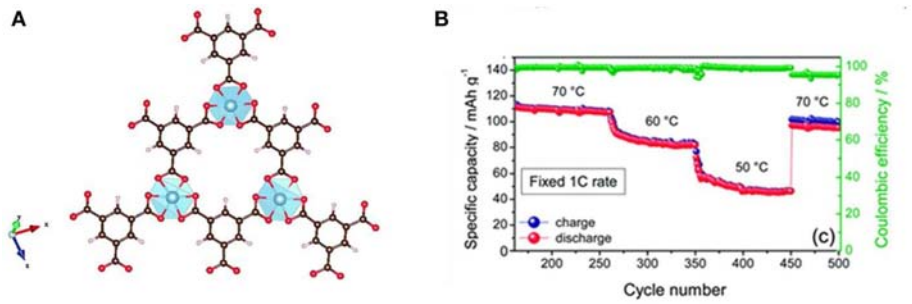

FIGURE 10 | (A) Schematic diagram of the ideal network structure of an aluminum(III)-1,3,5-benzenetricarboxylate (Al-BTC) metal organic framework. **(B)** Electrochemical characteristics of the $LiFePO_4$/S4-NCPE/Li cell at different temperatures and current regimes. [Reproduction with permission from Gerbaldi et al. (2014). Copyright© 2014, The Royal Society of Chemistry].

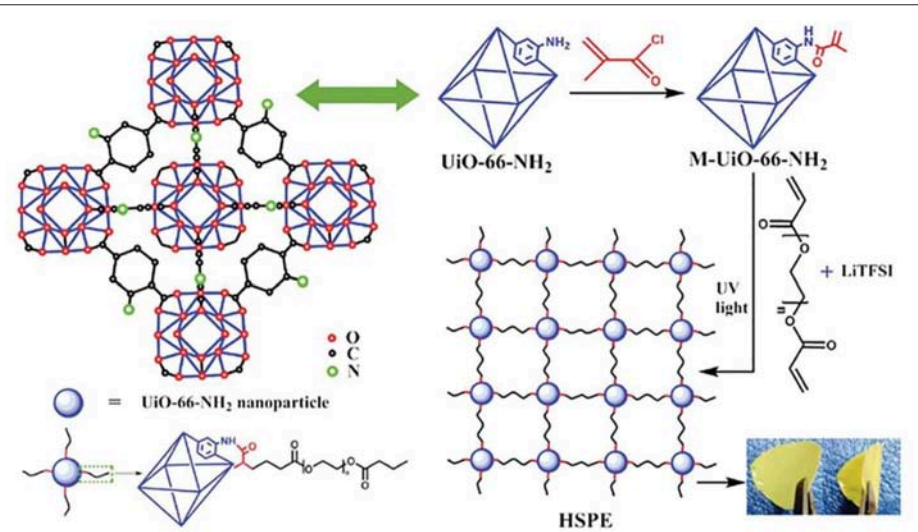

FIGURE 11 | Synthetic route of the hybrid covalently linked MOF-PEGDA-based all-solid-state electrolyte. [Reproduction with permission from Wang Z. et al. (2018). Copyright© 2018, The Royal Society of Chemistry].

an exceptional mechanical property, which is expected for flexible electronic devices applications. Furthermore, ionic liquid compounded with cellulose can solve the issues of IL leakage in the composite electrolyte. Shi et al. (2017) designed a new type of 3D self-assembled polymeric ionic liquid (PIL)-nano-cellulose to form polymer electrolyte. The structure not only enhances the mechanical properties of the SPE, but also forms strong lithium coordination to promote lithium salt dissolution. The dissolved lithium salt can combine with IL to form an ion-conducting domain, thereby promoting ion transport. Asghar et al. (2012) adequately utilizes the characteristics of networked cellulose (NC), with mechanical strength and adopted it to design quasi-solid PEG-LiClO4-NC polymer electrolyte. The resultant composite electrolyte with a 12.8 wt.% NC resulted in the highest ion conductivity (10^{-4} S/cm at 25°C) and is electrochemically stable up to 4.7 V. Similarly, Zhang et al. (2014) combined cellulose non-woven with PCA-PEO to fabricate a rigid-flexible coupling SPE, upgrading their comprehensive properties of the composite electrolyte significantly.

SUMMARY AND OUTLOOK

Although lithium-ion batteries have long been commercialized, the use of liquid electrolytes has some disadvantages such as poor safety and unstable electrochemical performance, which greatly limits its further development and wider applications. Solid composite polymer electrolyte in lithium-ion batteries has received a lot of attention lately because of its low flammability, good flexibility, excellent thermal stability, and high safety. In this review, we have provided fundamental understandings of the ionic conductivity mechanisms and interfaces for solid composite electrolytes, in the meantime, recent progresses on polymer-based composite electrolytes were summarized, including polymer/inert ceramics, polymer/fast-ion conductive, polymer/ionic liquid, polymer/MOFs, and polymer/cellulose composite electrolytes.

Although substantial researches have been dedicated to the polymer-based composite electrolytes, some fundamental issues still need to be solved urgently before commercialization. For

example, ionic conductivity of the composite solid electrolyte still differs by several orders of magnitude from the liquid counterpart; many polymer-based solid electrolytes exhibit high ionic conductivity at high temperatures, while it drops dramatically at lower temperatures; the conductivity mechanism and interfacial interaction need to be further clarified not accelerate further studies.

At present, the polymer/ionic liquid solid electrolyte inevitably causes a decrease in mechanical properties when obtaining high ionic conductivity, which has great safety hazards. The difficulty in polymer/inert ceramic solid electrolytes is how to construct a good dispersion and strengthen the interaction between the filler and the polymer, which restricts the further improvement of ionic conductivity. In comparison, polymer/fast ion conductors composite electrolytes have both high ionic conductivity at room temperature and good mechanical properties. The future development direction of polymer-based solid electrolytes is likely to be the combination of fast ion conductors and polymers, which can combine the advantages of high ion conductivity of fast ion conductors and solve the problem of poor interface contact. Of all the types of polymer-based composite solid electrolytes, SPEs with fast ion conductors have gained all the advantages and are the direction of development of commercial solid electrolytes.

The following aspects were recommended of focusing on solid electrolyte in future developments. Firstly, using materials genome database to analyze, guide, and design composite material can promote efficiency and cost savings. Material calculations facilitate an in-depth understanding of the material. The corresponding ionic mechanism can be simulated and interpreted by material calculations. Secondly, most of battery materials, such as electrodes, electrolytes, and SEI films, are sensitive to electron beams and difficult to observe under conventional transmission electron microscopy (TEM). Advanced characterization techniques can facilitate analysis of material mechanisms. For example, using cryo-electron microscopy, Zachman et al. (2018) reveals atomic structure of sensitive battery materials and interfaces. Similarly, Meng et al. (Wang et al., 2017) studied the interface of solid electrolytes via Cryogenic TEM, which has greatly promoted further research on the interface. Finally, struggling to find suitable composite electrolytes with high conductivities at low temperature always deserves more study. Commercial solid electrolytes require high ionic conductivity at room temperature, safety and easy processing to compete with the liquid counterpart.

AUTHOR CONTRIBUTIONS

PY, JW, and HY collected the data, performed the statistical analysis, interpretation of the results, and wrote the manuscript. ZD, YL, and JL carried out the bibliographical research and performed the inferential analyses together with other authors. ML and XL offered Suggestions and revisions in English for the article.

FUNDING

This work was financially supported by the Shenzhen International Collaboration project (GJHZ20180923193456903), and Shenzhen Fundamental Research Program of Subject Layout (JCYJ20170413102735544).

REFERENCES

Agrawal, R. C., and Pandey, G. P. (2008). Solid polymer electrolytes: materials designing and all-solid-state battery applications: an overview. *J Phys D Appl Phys.* 41:223001. doi: 10.1088/0022-3727/41/22/223001

Aliahmad, N., Shrestha, S., Varahramyan, K., and Agarwal, M. (2016). Poly(vinylidene fluoride-hexafluoropropylene) polymer electrolyte for paper-based and flexible battery applications. *AIP Adv.* 6:065206. doi: 10.1063/1.4953811

Aono, H., Sugimoto, E., Sadaoka, Y., Imanaka, N., and Adachi, G. (1990). Ionic-conductivity of solid electrolytes based on lithium titanium phosphate. *J. Electrochem. Soc.* 137, 1023–1027. doi: 10.1149/1.2086597

Aravindan, V., and Vickraman, P. (2008). Characterization of SiO_2 and Al_2O_3 incorporated PVdF-HFP based composite polymer electrolytes with LiPF3(CF3CF2)(3). *J. Appl. Polym. Sci.* 108, 1314–1322. doi: 10.1002/app.27824

Armand, M., Endres, F., MacFarlane, D. R., Ohno, H., and Scrosati, B. (2009). Ionic-liquid materials for the electrochemical challenges of the future. *Nat. Mater.* 8, 621–629. doi: 10.1038/Nmat2448

Asghar, A., Samad, Y. A., Lalia, B. S., and Hashaikeh, R. (2012). PEG based quasi-solid polymer electrolyte: mechanically supported by networked cellulose. *J. Memb. Sci.* 421, 85–90. doi: 10.1016/j.memsci.2012.06.037

Bae, J., Li, Y., Zhang, J., Zhou, X., Zhao, F., Shi, Y., et al. (2018). A 3D nanostructured hydrogel-framework-derived high-performance composite polymer Lithium-ion electrolyte. *Ange. Chem. Int. Ed.* 57, 2096–2100. doi: 10.1002/anie.201710841

Baxter, J., Bian, Z., Chen, G., Danielson, D., Dresselhaus, M. S., Fedorov, A. G., et al. (2009). Nanoscale design to enable the revolution in renewable energy. *Energy Environ. Sci.* 2, 559–588. doi: 10.1039/b821698c

Camacho-Forero, L. E., and Balbuena, P. B. (2018). Exploring interfacial stability of solid-state electrolytes at the lithium-metal anode surface. *J. Power Sources* 396, 782–790. doi: 10.1016/j.jpowsour.2018.06.092

Capuano, F., Croce, F., and Scrosati, B. (1991). Composite polymer electrolytes. *J. Electrochem. Soc.* 138, 1918–1922. doi: 10.1149/1.2085900

Chen, L., Li, Y., Li, S.-P., Fan, L.-Z., Nan, C.-W., and Goodenough, J. B. (2018). PEO/garnet composite electrolytes for solid-state lithium batteries: from "ceramic-in-polymer" to "polymer-in-ceramic". *Nano Energy* 46, 176–184. doi: 10.1016/j.nanoen.2017.12.037

Chen, R. J., Qu, W. J., Guo, X., Li, L., and Wu, F. (2016). The pursuit of solid-state electrolytes for lithium batteries: from comprehensive insight to emerging horizons. *Mater. Horizon.* 3, 487–516. doi: 10.1039/c6mh00218h

Croce, F., Appetecchi, G. B., Persi, L., and Scrosati, B. (1998). Nanocomposite polymer electrolytes for lithium batteries. *Nature* 394, 456–458.

Cui, Y., Baker, A. P., Xu, X., Xiang, Y., Wang, L., Lavorgna, M., et al. (2015). Enhancement of Nafion based membranes for direct methanol fuel cell applications through the inclusion of ammonium-X zeolite fillers. *J. Power Sources* 294, 369–376. doi: 10.1016/j.jpowsour.2015.06.078

Cui, Y., Liu, Y., Wu, J., Zhang, F., Baker, A. P., Lavorgna, M., et al. (2018). Porous silicon-aluminium oxide particles functionalized with acid moieties: an innovative filler for enhanced Nafion-based membranes of direct methanol fuel cell. *J. Power Sources* 403, 118–126. doi: 10.1016/j.jpowsour.2018.09.090

Dias, F. B., Plomp, L., and Veldhuis, J. B. J. (2000). Trends in polymer electrolytes for secondary lithium batteries. *J. Power Sources* 88, 169–191. doi: 10.1016/s0378-7753(99)00529-7

Do, J. S., Chang, C. P., and Lee, T. J. (1996). Electrochemical properties of lithium salt-poly(ethylene oxide)ethylene carbonate polymer electrolyte and discharge characteristics of Li/MnO_2. *Solid State Ionics* 89, 291–298. doi: 10.1016/0167-2738(96)00343-8

Dong, X. C., and Wang, L. (2005). Compositions, structures and properties of polymer electrolytes for lithium ion battery. *Progr. Chem.* 17, 248–253.

Epp, V., Ma, Q., Hammer, E.-M., Tietz, F., and Wilkening, M. (2015). Very fast bulk Li ion diffusivity in crystalline $Li_{1.5}Al_{0.5}Ti_{1.5}(PO_4)(3)$ as seen using NMR relaxometry. *Phys. Chem. Chem. Phys.* 17, 32115–32121. doi: 10.1039/c5cp05337d

Farrington, G. C., and Briant, J. L. (1979). Fast ionic transport in solids. *Science* 204, 1371–1379. doi: 10.1126/science.204.4400.1371

Fergus, J. W. (2010). Ceramic and polymeric solid electrolytes for lithium-ion batteries. *J. Power Sources* 195, 4554–4569. doi: 10.1016/j.jpowsour.2010.01.076

Fonseca, C. P., and Neves, S. (2002). Characterization of polymer electrolytes based on poly(dimethyl siloxane-co-ethylene oxide). *J. Power Sources* 104, 85–89. doi: 10.1016/s0378-7753(01)00902-8

Forsyth, M., Tipton, A. L., Shriver, D. F., Ratner, M. A., and MacFarlane, D. R. (1997). Ionic conductivity in poly(diethylene glycol-carbonate)/sodium triflate complexes. *Solid State Ionics* 99, 257–261. doi: 10.1016/s0167-2738(97)00115-x

Fu, K. K., Gong, Y., Dai, J., Gong, A., Han, X., Yao, Y., et al. (2016). Flexible, solid-state, ion-conducting membrane with 3D garnet nanofiber networks for lithium batteries. *Proc. Natl. Acad. Sci. USA.* 113, 7094–7099. doi: 10.1073/pnas.1600422113

Gang, W., Roos, J., Brinkmann, D., Capuano, F., Croce, F., and Scrosati, B. (1992). Comparison of NMR and conductivity in (PEO)(8)$LiCLO_4$+GAMMA-$LiALO_2$. *Solid State Ionics* 53, 1102–1105. doi: 10.1016/0167-2738(92)90297-3

Gerbaldi, C., Nair, J. R., Kulandainathan, M. A., Kumar, R. S., Ferrara, C., Mustarelli, P., et al. (2014). Innovative high performing metal organic framework (MOF)-laden nanocomposite polymer electrolytes for all-solid-state lithium batteries. *J. Mater. Chem. A* 2, 9948–9954. doi: 10.1039/c4ta01856g

Gonzalez, F., Tiemblo, P., Garcia, N., Garcia-Calvo, O., Fedeli, E., Kvasha, A., et al. (2018). High performance polymer/ionic liquid thermoplastic solid electrolyte prepared by solvent free processing for solid state lithium metal batteries. *Membranes* 8:55. doi: 10.3390/membranes8030055

Hu, L., Tang, Z., and Zhang, Z. (2007). New composite polymer electrolyte comprising mesoporous lithium aluminate nanosheets and PEO/LiClO4. *J. Power Sources* 166, 226–232. doi: 10.1016/j.jpowsour.2007.01.028

Indra, A., Song, T., and Paik, U. (2018). Metal organic framework derived materials: progress and prospects for the energy conversion and storage. *Adv. Mater.* 30:1705146. doi: 10.1002/adma.201705146

Itoh, T., Ichikawa, Y., Uno, T., Kubo, M., and Yamamoto, O. (2003a). Composite polymer electrolytes based on poly(ethylene oxide), hyperbranched polymer, $BaTiO_3$ and $LiN(CF_3SO_2)(2)$. *Solid State Ionics* 156, 393–399. doi: 10.1016/s0167-2738(02)00682-3

Itoh, T., Miyamura, Y., Ichikawa, Y., Uno, T., Kubo, M., and Yamamoto, O. (2003b). Composite polymer electrolytes of poly(ethylene oxide)/$BaTiO_3$/Li salt with hyperbranched polymer. *J. Power Sources* 119, 403–408. doi: 10.1016/s0378-7753(03)00261-1

Jung, Y.-C., Lee, S.-M., Choi, J.-H., Jang, S. S., and Kim, D.-W. (2015). All solid-state lithium batteries assembled with hybrid solid electrolytes. *J. Electrochem. Soc.* 162, A704–A710. doi: 10.1149/2.0731504jes

Kamaya, N., Homma, K., Yamakawa, Y., Hirayama, M., Kanno, R., Yonemura, M., et al. (2011). A lithium superionic conductor. *Nat. Mater.* 10, 682–686. doi: 10.1038/nmat3066

Karuppasamy, K., Rhee, H. W., Reddy, P. A., Gupta, D., Mitu, L., Polu, A. R., et al. (2016). Ionic liquid incorporated nanocomposite polymer electrolytes for rechargeable lithium ion battery: a way to achieve improved electrochemical and interfacial properties. *J. Ind. Eng. Chem.* 40, 168–176. doi: 10.1016/j.jiec.2016.06.020

Keller, M., Appetecchi, G. B., Kim, G.-T., Sharova, V., Schneider, M., Schuhmacher, J., et al. (2017). Electrochemical performance of a solvent-free hybrid ceramic-polymer electrolyte based on $Li_7La_3Zr_2O_{12}$ in P(EO)(15)LiTFSI. *J. Power Sources* 353, 287–297. doi: 10.1016/j.jpowsour.2017.04.014

Ketabi, S., and Lian, K. (2013). Effect of SiO2 on conductivity and structural properties of PEO-EMIHSO4 polymer electrolyte and enabled solid electrochemical capacitors. *Electrochim. Acta* 103, 174–178. doi: 10.1016/j.electacta.2013.04.053

Knauth, P. (2009). Inorganic solid Li ion conductors: An overview. *Solid State Ionics* 180, 911–916. doi: 10.1016/j.ssi.2009.03.022

Kumar, B., and Scanlon, L. G. (2000). Composite electrolytes for lithium rechargeable batteries. *J. Electroceramics* 5, 127–139. doi: 10.1023/a:1009958118260

Kuppler, R. J., Timmons, D. J., Fang, Q.-R., Li, J.-R., Makal, T. A., Young, M. D., et al. (2009). Potential applications of metal-organic frameworks. *Coord. Chem. Rev.* 253, 3042–3066. doi: 10.1016/j.ccr.2009.05.019

Li, J.-R., Kuppler, R. J., and Zhou, H.-C. (2009). Selective gas adsorption and separation in metal-organic frameworks. *Chem. Soc. Rev.* 38, 1477–1504. doi: 10.1039/b802426j

Li, M., Yang, L., Fang, S., and Dong, S. (2011). Novel polymeric ionic liquid membranes as solid polymer electrolytes with high ionic conductivity at moderate temperature. *J. Memb. Sci.* 366, 245–250. doi: 10.1016/j.memsci.2010.10.004

Liang, B., Tang, S., Jiang, Q., Chen, C., Chen, X., Li, S., et al. (2015). Preparation and characterization of PEO-PMMA polymer composite electrolytes doped with nano-Al2O3. *Electrochim. Acta* 169, 334–341. doi: 10.1016/j.electacta.2015.04.039

Lin, D., Liu, W., Liu, Y., Lee, H. R., Hsu, P.-C., Liu, K., et al. (2016). High ionic conductivity of composite solid polymer electrolyte via *in situ* synthesis of monodispersed SiO_2 nanospheres in poly(ethylene oxide). *Nano Lett.* 16, 459–465. doi: 10.1021/acs.nanolett.5b04117

Lin, D., Yuen, P. Y., Liu, Y., Liu, W., Liu, N., Dauskardt, R. H., et al. (2018). A silica-aerogel-reinforced composite polymer electrolyte with high ionic conductivity and high modulus. *Adv. Mater.* 30:e1802661. doi: 10.1002/adma.201802661

Ling, S.-G., Peng, J.-Y., Yang, Q., Qiu, J.-L., Lu, J.-Z., and Li, H. (2018). Enhanced ionic conductivity in LAGP/LATP composite electrolyte. *Chin. Phy. B,* 27:038201. doi: 10.1088/1674-1056/27/3/038201

Liu, J., Xu, J. Y., Lin, Y., Li, J., Lai, Y. Q., Yuan, C. F., et al. (2013). All-solid-state lithium ion battery: research and industrial prospects. *Acta Chim. Sin.* 71, 869–878. doi: 10.6023/a13020170

Liu, W., Lee, S. W., Lin, D., Shi, F., Wang, S., Sendek, A. D., et al. (2017). Enhancing ionic conductivity in composite polymer electrolytes with well-aligned ceramic nanowires. *Nat. Energy* 2:17035. doi: 10.1038/nenergy.2017.35

Liu, W., Lin, D., Sun, J., Zhou, G., and Cui, Y. (2016). Improved lithium ionic conductivity in composite polymer electrolytes with oxide-ion conducting nanowires. *ACS Nano* 10, 11407–11413. doi: 10.1021/acsnano.6b06797

Liu, W., Liu, N., Sun, J., Hsu, P. C., Li, Y. Z., Lee, H. W., et al. (2015). Ionic conductivity enhancement of polymer electrolytes with ceramic nanowire fillers. *Nano Lett.,* 15, 2740–2745. doi: 10.1021/acs.nanolett.5b00600

Manthiram, A., Yu, X. W., and Wang, S. F. (2017). Lithium battery chemistries enabled by solid-state electrolytes. *Nat. Rev. Mater.* 2:16103. doi: 10.1038/natrevmats.2016.103

Meyer, W. H. (1998). Polymer electrolytes for lithium-ion batteries. *Adv. Mater.* 10, 439-+. doi: 10.1002/(sici)1521-4095(199804)10:6<439::Aid-adma439>3.0.Co;2-i

Mueller, U., Schubert, M., Teich, F., Puetter, H., Schierle-Arndt, K., and Pastre, J. (2006). Metal-organic frameworks–prospective industrial applications. *J. Mater. Chem.* 16, 626–636. doi: 10.1039/b511962f

Nair, J. R., Gerbaldi, C., Chiappone, A., Zeno, E., Bongiovanni, R., Bodoardo, S., et al. (2009). UV-cured polymer electrolyte membranes for Li-cells: Improved mechanical properties by a novel cellulose reinforcement. *Electrochem. Commun.* 11, 1796–1798. doi: 10.1016/j.elecom.2009.07.021

Nan, C. W., Fan, L. Z., Lin, Y. H., and Cai, Q. (2003). Enhanced ionic conductivity of polymer electrolytes containing nanocomposite SiO_2 particles. *Phys. Rev. Lett.* 91:4. doi: 10.1103/PhysRevLett.91.266104

O'Callaghan, M. P., Powell, A. S., Titman, J. J., Chen, G. Z., and Cussen, E. J. (2008). Switching on fast lithium ion conductivity in garnets: The structure and transport properties of Li(3+x)Nd(3)Te(2-x)Sb(x)O(12). *Chem. Mater.* 20, 2360–2369. doi: 10.1021/cm703677q

Osada, I., de Vries, H., Scrosati, B., and Passerini, S. (2016). Ionic-liquid-based polymer electrolytes for battery applications. *Ange. Chem. Int. Ed.* 55, 500–513. doi: 10.1002/anie.201504971

Pal, P., and Ghosh, A. (2018). Influence of TiO2 nano-particles on charge carrier transport and cell performance of PMMA-$LiClO_4$ based nano-composite electrolytes. *Electrochim. Acta* 260, 157–167. doi: 10.1016/j.electacta.2017.11.070

Perez-Estebanez, M., Isasi-Marin, J., Toebbens, D. M., Rivera-Calzada, A., and Leon, C. (2014). A systematic study of Nasicon-type Li-i + XMXTi2 _ x(PO4)(3) (M: Cr, Al, Fe) by neutron diffraction and impedance spectroscopy. *Solid State Ionics* 266, 1–8. doi: 10.1016/j.ssi.2014.07.018

Qiu, W.-L., Yang, Q.-H., Ma, X.-h., Fu, Y.-B., and Zong, X.-F. (2004). Research on PEO-based dry solid polymer electrolytes for rechargeable lithium batteries. *Chin. J. Power Sources* 28, 440–448, 457.

Quartarone, E., and Mustarelli, P. (2011). Electrolytes for solid-state lithium rechargeable batteries: recent advances and perspectives. *Chem. Soc. Rev.* 40, 2525–2540. doi: 10.1039/c0cs00081g

Ratner, M. A., Johansson, P., and Shriver, D. F. (2000). Polymer electrolytes: ionic transport mechanisms and relaxation coupling. *Mrs Bullet.* 25, 31–37. doi: 10.1557/mrs2000.16

Reddy, M. J., Chu, P. P., Kumar, J. S., and Rao, U. V. S. (2006). Inhibited crystallization and its effect on conductivity in a nano-sized Fe oxide composite PEO solid electrolyte. *J. Power Sources,* 161, 535–540. doi: 10.1016/j.jpowsour.2006.02.104

Scrosati, B., and Garche, J. (2010). Lithium batteries: status, prospects and future. *J. Power Sources,* 195, 2419–2430. doi: 10.1016/j.jpowsour.2009.11.048

Sheng, J., Tong, S., He, Z., and Yang, R. (2017). Recent developments of cellulose materials for lithium-ion battery separators. *Cellulose* 24, 4103–4122. doi: 10.1007/s10570-017-1421-8

Sheng, O., Jin, C., Luo, J., Yuan, H., Huang, H., Gan, Y., et al. (2018). $Mg_2B_2O_5$ Nanowire enabled multifunctional solid-state electrolytes with high ionic conductivity, excellent mechanical properties, and flame-retardant performance. *Nano Lett.* 18, 3104–3112. doi: 10.1021/acs.nanolett.8b00659

Shi, Q. X., Xia, Q., Xiang, X., Ye, Y. S., Hai Yan, P., Xue, Z. G., et al. (2017). Self-assembled polymeric ionic liquid-functionalized cellulose nanocrystals: constructing 3D ion-conducting channels within ionic liquid-based composite polymer electrolytes. *Chem. Euro. J.* 23, 11881–11890. doi: 10.1002/chem.201702079

Siqueira, L. J. A., and Ribeiro, M. C. C. (2006). Molecular dynamics simulation of the polymer electrolyte poly(ethylene oxide)/LiClO4. II. Dynamical properties. *J. Chem. Phys.* 125:214903. doi: 10.1063/1.2400221

Srivastava, N., and Tiwari, T. (2009). New trends in polymer electrolytes: a review. *E-Polymers* 146, 1–17. doi: 10.1515/epoly.2009.9.1.1738

Stavila, V., Talin, A. A., and Allendorf, M. D. (2014). MOF-based electronic and optoelectronic devices. *Chem. Soc. Rev.* 43, 5994–6010. doi: 10.1039/c4cs00096j

Stephan, A. M., and Nahm, K. S. (2006). Review on composite polymer electrolytes for lithium batteries. *Polymer* 47, 5952–5964. doi: 10.1016/j.polymer.2006.05.069

Stramare, S., Thangadurai, V., and Weppner, W. (2003). Lithium lanthanum titanates: A review. *Chem. Mater.* 15, 3974–3990. doi: 10.1021/cm0300516

Subianto, S., Mistry, M. K., Choudhury, N. R., Dutta, N. K., and Knout, R. (2009). Composite polymer electrolyte containing ionic liquid and functionalized polyhedral oligomeric silsesquioxanes for anhydrous PEM applications. *ACS Appl. Mater. Interfaces* 1, 1173–1182. doi: 10.1021/am900020w

Sun, B., Mindemark, J., Edstrom, K., and Brandell, D. (2014). Polycarbonate-based solid polymer electrolytes for Li-ion batteries. *Solid State Ionics* 262, 738–742. doi: 10.1016/j.ssi.2013.08.014

Sun, J. Z., MacFarlane, D. R., and Forsyth, M. (1996). Ion conductive poly(ethylene oxide dimethyl siloxane) copolymers. *J. Polymer Sci. Polymer Chem.* 34, 3465–3470.

Tambelli, C. C., Bloise, A. C., Rosario, A., Pereira, E. C., Magon, C. J., and Donoso, J. P. (2002). Characterisation of PEO-Al2O3 composite polymer electrolytes. *Electrochim. Acta* 47, 1677–1682. doi: 10.1016/s0013-4686(01)00900-8

Tang, Z., Hu, L., Zhang, Z., and Su, F. (2007). Research progress of solid polymer electrolytes for lithium ion batteries. *J. Chin. Ceramic Soc.* 35, 123–128.

Thangadurai, V., Kaack, H., and Weppner, W. J. F. (2003). Novel fast lithium ion conduction in garnet-type $Li_5La_3M_2O_{12}$ (M = Nb, Ta). *J. Am. Ceramic Soc.* 86, 437–440. doi: 10.1111/j.1151-2916.2003.tb03318.x

Thokchom, J. S., Gupta, N., and Kumar, B. (2008). Superionic conductivity in a lithium aluminum germanium phosphate glass-ceramic. *J. Electrochem. Soc.* 155, A915–A920. doi: 10.1149/1.2988731

Tikekar, M. D., Choudhury, S., Tu, Z., and Archer, L. A. (2016). Design principles for electrolytes and interfaces for stable lithium-metal batteries. *Nat. Energy* 1, 1–7. doi: 10.1038/nenergy.2016.114

Verma, P., Maire, P., and Novak, P. (2010). A review of the features and analyses of the solid electrolyte interphase in Li-ion batteries. *Electrochim. Acta* 55, 6332–6341. doi: 10.1016/j.electacta.2010.05.072

Villaluenga, I., Wujcik, K. H., Tong, W., Devaux, D., Wong, D. H. C., DeSimone, J. M., et al. (2016). Compliant glass-polymer hybrid single ion-conducting electrolytes for lithium batteries. *Proc. Natl. Acad. Sci. USA.* 113, 52–57. doi: 10.1073/pnas.1520394112

Wang, L.-P., Zhang, X.-D., Wang, T.-S., Yin, Y.-X., Shi, J.-L., Wang, C.-R., et al. (2018). Ameliorating the interfacial problems of cathode and solid-state electrolytes by interface modification of functional polymers. *Adv. Energy Mater.* 8:1801528. doi: 10.1002/aenm.201801528

Wang, X., Zhang, M., Alvarado, J., Wang, S., Sina, M., Lu, B., et al. (2017). new insights on the structure of electrochemically deposited lithium metal and its solid electrolyte interphases via cryogenic TEM. *Nano Lett.* 17, 7606–7612. doi: 10.1021/acs.nanolett.7b03606

Wang, Z., Wang, S., Wang, A., Liu, X., Chen, J., Zeng, Q., et al. (2018). Covalently linked metal-organic framework (MOF)-polymer all-solid-state electrolyte membranes for room temperature high performance lithium batteries. *J. Mater. Chem. A* 6, 17227–17234. doi: 10.1039/c8ta05642k

Watanabe, M., Endo, T., Nishimoto, A., Miura, K., and Yanagida, M. (1999). High ionic conductivity and electrode interface properties of polymer electrolytes based on high molecular weight branched polyether. *J. Power Sources* 81, 786–789. doi: 10.1016/s0378-7753(99)00250-5

Wei-Min, W. (2012). Study on all solid-state composite polymer electrolyte. *Adv. Mat. Res.* 571, 13–16. doi: 10.4028/www.scientific.net/AMR.571.13

Weston, J. E., and Steele, B. C. H. (1982). Effects of inert fillers on the mechanical and electrochemical properties of lithium salt poly (ethylene-oxide) polymer electrolytes. *Solid State Ionics* 7, 75–79. doi: 10.1016/0167-2738(82)90072-8

Wu, J.-F., Pang, W. K., Peterson, V. K., Wei, L., and Guo, X. (2017). Garnet-type fast Li-ion conductors with high ionic conductivities for all-solid-state batteries. *ACS Appl. Mater. Interfaces* 9, 12461–12468. doi: 10.1021/acsami.7b00614

Xie, H., Yang, C., Fu, K., Yao, Y., Jiang, F., Hitz, E., et al. (2018). Flexible, scalable, and highly conductive garnet-polymer solid electrolyte templated by bacterial cellulose. *Adv. Energy Mater.* 8:1703474. doi: 10.1002/aenm.201703474

Xie, X.-C., Huang, K.-J., and Wu, X. (2018). Metal-organic framework derived hollow materials for electrochemical energy storage. *J. Mater. Chem. A* 6, 6754–6771. doi: 10.1039/c8ta00612a

Xiong, H. M., Wang, Z. D., Xie, D. P., Cheng, L., and Xia, Y. Y. (2006). Stable polymer electrolytes based on polyether-grafted ZnO nanoparticles for all-solid-state lithium batteries. *J. Mater. Chem.* 16, 1345–1349. doi: 10.1039/b514346b

Xu, K. (2004). Nonaqueous liquid electrolytes for lithium-based rechargeable batteries. *Chem. Rev.* 104, 4303–4417. doi: 10.1021/cr030203g

Xu, R. C., Xia, X. H., Zhang, S. Z., Xie, D., Wang, X. L., and Tu, J. P. (2018). Interfacial challenges and progress for inorganic all-solid-state lithium batteries. *Electrochim. Acta* 284, 177–187. doi: 10.1016/j.electacta.2018.07.191

Yang, L., Wang, Z., Feng, Y., Tan, R., Zuo, Y., Gao, R., et al. (2017). Flexible composite solid electrolyte facilitating highly stable "soft contacting" Li-electrolyte interface for solid state lithium-ion batteries. *Adv. Energy Mater.* 7:1701437. doi: 10.1002/aenm.201701437

Yarmolenko, O. V., Yudina, A. V., and Khatmullina, K. G. (2018). Nanocomposite polymer electrolytes for the lithium power sources (a Review). *Rus. J. Electrochem.* 54, 325–343. doi: 10.1134/s1023193518040092

Young, W. S., Kuan, W. F., and Epps, T. H. (2014). Block copolymer electrolytes for rechargeable lithium batteries. *J. Polymer Sci. B Polymer Phys.* 52, 1–16. doi: 10.1002/polb.23404

Yuan, C., Li, J., Han, P., Lai, Y., Zhang, Z., and Liu, J. (2013). Enhanced electrochemical performance of poly(ethylene oxide) based composite polymer electrolyte by incorporation of nano-sized metal-organic framework. *J. Power Sources* 240, 653–658. doi: 10.1016/j.jpowsour.2013.05.030

Zachman, M. J., Tu, Z., Choudhury, S., Archer, L. A., and Kourkoutis, L. F. (2018). Cryo-STEM mapping of solid-liquid interfaces and dendrites

in lithium-metal batteries. *Nature 560*, 345–349. doi: 10.1038/s41586-018-0397-3

Zhang, J., Yue, L., Hu, P., Liu, Z., Qin, B., Zhang, B., et al. (2014). Taichi-inspired rigid-flexible coupling cellulose-supported solid polymer electrolyte for high-performance lithium batteries. *Sci. Rep.* 4:6272. doi: 10.1038/srep06272

Zhang, Q. Q., Liu, K., Ding, F., and Liu, X. J. (2017). Recent advances in solid polymer electrolytes for lithium batteries. *Nano Res.* 10, 4139–4174. doi: 10.1007/s12274-017-1763-4

Zhang, X., Liu, T., Zhang, S., Huang, X., Xu, B., Lin, Y., et al. (2017). Synergistic Coupling between $Li_{6.75}La_3Zr_{1.75}Ta_{0.25}O_{12}$ and Poly(vinylidene fluoride) induces high ionic conductivity, mechanical strength, and thermal stability of solid composite electrolytes. *J. Am. Chem. Soc.* 139, 13779–13785. doi: 10.1021/jacs.7b06364

Zhang, X.-Q., Cheng, X.-B., and Zhang, Q. (2018). Advances in interfaces between Li metal anode and electrolyte. *Adv. Mater. Interfaces* 5:1701097. doi: 10.1002/admi.201701097

Zhao, Y., Huang, Z., Chen, S., Chen, B., Yang, J., Zhang, Q., et al. (2016a). A promising PEO/LAGP hybrid electrolyte prepared by a simple method for all-solid-state lithium batteries. *Solid State Ionics* 295, 65–71. doi: 10.1016/j.ssi.2016.07.013

Zhao, Y., Wu, C., Peng, G., Chen, X., Yao, X., Bai, Y., et al. (2016b). A new solid polymer electrolyte incorporating $Li_{10}GeP_2S_{12}$ into a polyethylene oxide matrix for all-solid-state lithium batteries. *J. Power Sources* 301, 47–53. doi: 10.1016/j.jpowsour.2015.09.111

Zhao, Y., Zhang, Y., Gosselink, D., Doan, T. N. L., Sadhu, M., Cheang, H.-J., et al. (2012). Polymer electrolytes for lithium/sulfur batteries. *Membranes* 2, 553–564. doi: 10.3390/membranes2030553

Zhu, P., Yan, C., Dirican, M., Zhu, J., Zang, J., Selvan, R. K., et al. (2018). $Li_{0.33}La_{0.557}TiO_3$ ceramic nanofiber-enhanced polyethylene oxide-based composite polymer electrolytes for all-solid-state lithium batteries. *J. Mater. Chem. A* 6, 4279–4285. doi: 10.1039/c7ta10517g

Conflict of Interest Statement: The authors declare that the research was conducted in the absence of any commercial or financial relationships that could be construed as a potential conflict of interest.

Copyright © 2019 Yao, Yu, Ding, Liu, Lu, Lavorgna, Wu and Liu. This is an open-access article distributed under the terms of the Creative Commons Attribution License (CC BY). The use, distribution or reproduction in other forums is permitted, provided the original author(s) and the copyright owner(s) are credited and that the original publication in this journal is cited, in accordance with accepted academic practice. No use, distribution or reproduction is permitted which does not comply with these terms.

frontiers in Chemistry

ORIGINAL RESEARCH
published: 24 April 2019
doi: 10.3389/fchem.2019.00275

Sorption of Water Vapor in Poly(L-Lactic Acid): A *Time-Resolved* FTIR Spectroscopy Investigation

Marianna Pannico and Pietro La Manna*

Institute of Polymers, Composites and Biomaterials, National Research Council of Italy, Pozzuoli, Italy

In this contribution the sorption of water vapor in Poly(L-lactic acid) (PLLA) was studied by time-resolved FTIR spectroscopy. The collected FTIR data were analyzed by complementary approaches such as difference spectroscopy, two-dimensional correlation spectroscopy (2D-COS), and least-squares curve-fitting analysis which provided information about the overall diffusivity, the nature of the molecular interactions among the polymer and the penetrant and the dynamics of the various molecular species. The diffusion coefficient were evaluated as a function of vapor activity and were found in good agreement with previously reported values. The system showed a Fickian behavior with diffusivity increasing with penetrant concentration. Two distinct water species (first-shell and second-shell layers) were detected and quantified by coupling FTIR and gravimetric measurements.

Keywords: water vapor, diffusion, FTIR spectroscopy, PLLA, molecular interaction

OPEN ACCESS

Edited by:
Gaetano Guerra,
University of Salerno, Italy

Reviewed by:
Letizia Verdolotti,
Institute of Polymers, Composite and Biomaterials, Italian National Research Counci, Italy
Giuseppe Scherillo,
University of Naples Federico II, Italy
Michele Galizia,
University of Oklahoma, United States

****Correspondence:***
Marianna Pannico
marianna.pannico@ipcb.cnr.it

Specialty section:
This article was submitted to Polymer Chemistry, a section of the journal Frontiers in Chemistry

Received: *27 December 2018*
Accepted: *03 April 2019*
Published: *24 April 2019*

Citation:
Pannico M and La Manna P (2019) Sorption of Water Vapor in Poly(L-Lactic Acid): A Time-Resolved FTIR Spectroscopy Investigation. Front. Chem. 7:275. doi: 10.3389/fchem.2019.00275

INTRODUCTION

Over the past decade, the use of polymeric biodegradable materials has increased substantially because of their versatility in a variety of applications as well as for the increasing environmental concern. They are widely used in the pharmaceutical, medical, and packaging fields due to their unique properties such as biocompatibility, biodegradability, eco-friendliness, and processability (Ikada and Tsuji, 2000; Temenoff and Mikos, 2000; Chen et al., 2002; Noda and Ozaki, 2004; Nair and Laurencin, 2007; Siracusa et al., 2008; Sabir et al., 2009; Armentano et al., 2010; Leja and Lewandowicz, 2010). Among the wide family of biopolymers, Poly(lactic acid) (PLA), and, in particular, its L-isomer, PLLA, has gained prominence owing to its excellent biocompatibility and good mechanical properties. Commercially, PLLA has been introduced in food packaging applications including oriented and flexible films, extruded and/or thermoformed packages for food and beverage containers, cups, overwrap, and blister packages (Tullo, 2000; Auras et al., 2004; Sagar et al., 2007; Tawakkal et al., 2014). In the realm of biomaterials, Dürselen et al. (2001) demonstrated that PLLA fibers are ideally suited for ligament and tendon reconstruction as well as stents for vascular and urological surgery. PLLA based microspheres were also used as injectable material in facial reconstructive surgery and in drug delivery systems (DDS) for the administration of a wide variety of medical agents (Imola and Schramm, 2002; Eppley et al., 2004; Tyler et al., 2016). PLLA contains flexible ester bonds whose hydrolytic degradation is caused by water diffusing into the bulk material. The hydrolytic products are non-harmful and non-toxic monomers/oligomers because they are metabolized via the citric acid (Krebs) cycle. For both medical and packaging applications, hydrolysis would be one of the most important degradation mechanism to account for. The PLLA hydrolysis behavior in biomedical devices such as implants and carriers in DDS, has

been widely investigated in different media at various temperatures (Göpferich, 1996; Li, 1999; Liu et al., 2000; Tsuji et al., 2000, 2003, 2011; Tsuji and Miyauchi, 2001; Fukuda et al., 2002; Kikkawa et al., 2002; Yuan et al., 2002). Literature data are mainly concerned with the effects of water in the liquid state. Only few studies have been reported on the PLLA hydrolysis carried out by water vapor (Ho et al., 1999; Copinet et al., 2004; Holm et al., 2006). Water sorption in PLA significantly affects the physico-chemical properties of the polymer matrix. Rocca-Smith et al. (2017) clearly showed that the stability of PLA was also influenced by the water physical state. It is evident that, in all the above applications, the diffusion of water in the bulk material represent one of the major issue to be considered. In this contribution, a molecular level description of water vapor diffusion in a fully amorphous PLLA matrix is reported. Among the different spectroscopic techniques employed for the investigation of water–polymer systems (Rothwell et al., 1984; Taylor et al., 2001) (Solid-state NMR, Raman, neutron scattering, light scattering) FTIR spectroscopy has been demonstrated to be very powerful because of its sensitivity toward H-bonding detection and its sampling flexibility (Cotugno et al., 2001; Scherillo et al., 2013).

We report on a *time-resolved* FTIR study performed at different relative pressures of water vapor. The spectral data have been analyzed by different and complementary approaches, namely, difference spectroscopy (DS), least-squares curve fitting (LSCF), and 2-D correlation spectroscopy (2DCOS) which allowed us to isolate the spectrum of the penetrant and to improve the resolution of its complex band profile in the ν(OH) frequency range. The above techniques, taken together, provided information on the nature, number, and dynamic behavior of the water species present in the investigated system. By coupling the spectroscopic data with gravimetric measurements, carried out in the same conditions of temperature and vapor pressure, we were able to quantify the water species population.

EXPERIMENTAL

Materials

PLLA was a commercial grade product (Ingeo Biopolymer 2003D) kindly provided by Nature Works (Minnetonka, MN, USA). It had $\overline{M}_n = (79.4+1.1)\,kDa$, $\overline{M}_w = (121.3+0.5)\,kDa$ and a polydispersity of 1.53 ± 0.02. The present PLLA resin, in the form of pellets, contains, according to the supplier, 4% D-lactic acid isomer; it has a density of 1.240 g/cm^3, a melting temperature of 145–170°C, a glass transition temperature (T_g) of 55–58°C, and a crystallinity (maximum attainable) of 35%. Chloroform, 99.8% purity, was purchased from Sigma-Aldrich (Milan, Italy) and used with no further purification.

Film Preparation

A 20 wt% solution of PLLA in chloroform was spread onto a glass plate with a Gardner knife to obtain a film thickness of 46 ± 5 μm. The PLLA film was kept overnight at room temperature to remove most of the solvent. Final drying was accomplished in a vacuum oven at 40°C for 10 days. No residual solvent was detected by spectroscopic (FTIR) and gravimetric (TGA) measurement.

FTIR Sorption Measurements

Time-resolved spectra were collected in transmission mode during sorption/desorption cycles of water vapor in the samples. The experiments were performed using a vacuum-tight FTIR sorption cell in which a free standing PLLA film is exposed from both sides to water vapor at constant temperature (35°C) and selectable relative pressures (p/p_0 = 0–0.5) of the penetrant. The sorption cell was accommodated in the sample compartment of a suitably modified FTIR spectrometer [Spectrum 100 from Perkin-Elmer (Norwalk, CT)], equipped with a Ge/KBr beam splitter and a wide-band DTGS detector. The cell was directly connected through service lines to a water reservoir, a turbo-molecular vacuum pump, a pressure transducer [MKS Baratron 121 (Andover, MA); full scale, 100 Torr; resolution, 0.01 Torr; accuracy, ± 0.5% of the reading] and a Pirani vacuometer. Full details of the experimental apparatus are reported in Cotugno et al. (2001). Before each sorption measurement, the sample was dried under vacuum, overnight, at 35°C in the same apparatus used for the test. The instrumental parameters for data collection were set as follows: resolution = 2 cm^{-1}; optical path difference (OPD) velocity = 0.2 cm/s; spectral range, 4,000–600 cm^{-1}. Spectra were acquired in the single-beam mode for subsequent data processing. Automated data acquisition was controlled by a dedicated software package for *time-resolved* spectroscopy (Timebase, from Perkin-Elmer).

Gravimetric Measurements

For calibration purposes, gravimetric measurements were performed using a microbalance Q5000 SA apparatus (produced by TA Instruments, New Castle, DE, USA) that is a fully automated gravimetric water vapor sorption analyzer, operating in the 5–85°C temperature range. The sample was exposed to

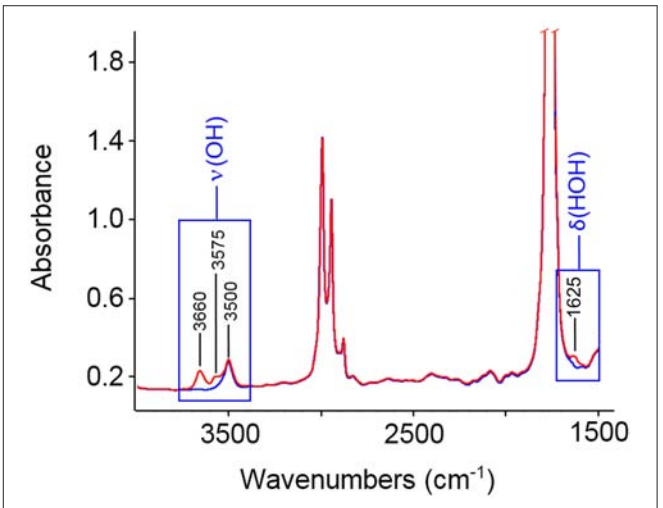

FIGURE 1 | FTIR spectra of: fully dried PLLA film (blue trace); the same film equilibrated at p/p_0 = 0.5 (red trace).

a series of humidity step changes at a constant temperature of 35°C. The relative humidity in the sample chamber is dynamically controlled in the 0–98% RH range, with an accuracy of ±1% RH, by mixing, in due proportion, a dry and a gaseous nitrogen stream saturated with water vapor by means of electronic mass flow controllers. Integral sorption runs were performed at four selected values of relative pressure, p/p_0, i.e., 0.202, 0.396, 0.582, and 0.764. Prior to each sorption test, the sample was dried in the microbalance under dry nitrogen steam until a constant weight was attained. Further details on the experimental apparatus and data treatment are reported in Scherillo et al. (2012b).

FTIR Data Analysis

Full absorbance spectra (i.e., sample plus absorbed water) were obtained using a background collected on the empty cell at the same relative pressure of water vapor used for the sorption measurement. The spectra representative of absorbed water were obtained by using the difference spectroscopy (DS) technique, i.e., by subtracting the spectrum of the dry sample from that of the sample equilibrated at different p/p_0 values:

$$A_d(\nu) = A_s(\nu) - k \cdot A_r(\nu) \quad (1)$$

where $A(\nu)$ is the absorbance at frequency ν and the subscripts d, s, and r denote, respectively, the difference spectrum, the sample spectrum (*wet* specimen), and the reference spectrum (*dry* specimen). k is an adjustable parameter which allows to compensate for thickness differences (if any) between the sample and the reference spectra. It was experimentally verified that negligible thickness changes take place during sorption; therefore, the k values were consistently taken as unity. The DS procedure allowed us to eliminate the interference of the polymer spectrum in the analytical ranges of interest [3,800–3,400 cm^{-1}, ν(OH), and 1,660–1,550 cm^{-1}, δ(HOH)]. Separation of multicomponent bands into individual peaks was achieved by a least-squares curve fitting (LSCF) algorithm based on the Levenberg–Marquardt method (Marquardt, 1963). The peak function was a mixed Gauss–Lorentz line-shape of the form:

$$f(x) = (1 - Lr)H \exp - \left[\left(\frac{x - x_0}{FWHH} \right)^2 (4 \ln 2) \right] + Lr \frac{H}{4\left(\frac{x - x_0}{FWHH}\right)^2 + 1} \quad (2)$$

where x_0 is the peak position; H the peak height; $FWHH$ the full-width at half height and Lr is the fraction of Lorentz character. In order to keep the number of adjustable parameters to a minimum, the baseline, the number of components and the band-shape (Lr parameter) were fixed, allowing the curve-fitting algorithm to optimize $FWHH$, H, and x_0 for the individual components.

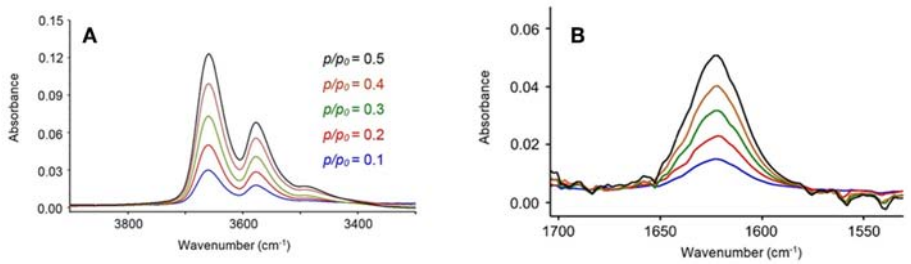

FIGURE 2 | Difference spectra in the 3,900–3,300 cm^{-1} range **(A)** and in the 1,700–1,540 cm^{-1} range **(B)** for the PLLA film equilibrated at different relative pressures of water vapor.

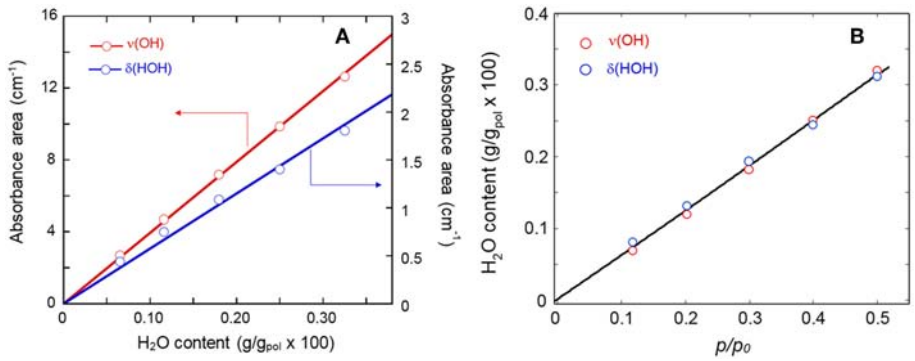

FIGURE 3 | (A) Calibration curves (Absorbance vs. gravimetric concentration) for the ν(OH) and the δ(HOH) bands of sorbed H_2O. **(B)** Sorption isotherm as evaluated from the two analytical signals.

Two-Dimensional Correlation Spectroscopy (2D-COS) Analysis

The experimental spectra for 2D-COS analysis were pre-processed to avoid the occurrence of artifacts due to baseline instabilities and other non-selective effects. The frequency region of interest (3,900–3,300 cm^{-1}) was isolated and offset to zero absorbance. Generalized 2D-IR analysis was performed by a script written in house with the MATLAB programming language (Mathworks, Natick, MA). The MATLAB environment also provided the tools for the graphical representation of the correlation spectra (contour plots, 3D images). The algorithm proposed by Noda relying on the Hilbert transform (Noda, 2000) was used for the numerical evaluation of the correlation intensities. The 2D correlation analysis was performed on an evenly spaced sequence of 100 spectra collected at a constant sampling interval of 0.98 s. The analyzed time-span (98 s) was sufficient to attain sorption equilibrium (vide infra). The notation adopted to identify the peaks appearing in the correlation spectra is that described in Musto et al. (2007).

RESULTS AND DISCUSSION

FTIR SPECTROSCOPY

In **Figure 1** are reported the FTIR spectra of the fully dried PLLA film (blue trace) and of the same film equilibrated at a relative pressure of water vapor, p/p_0, equal to 0.5 (red trace). Sorbed water displays characteristic bands around 3,660 cm^{-1} [ν(OH)] and 1,625 cm^{-1} [δ(HOH)]. Difference spectroscopy (DS) allows us to suppress the interference of the substrate and to isolate the spectrum of the penetrant. This is represented in **Figures 2A,B** in the 3,900–3,200 cm^{-1} range and in the 1,700–1,500 cm^{-1} range, respectively. The spectra were collected at the indicated relative pressures of water vapor. Both ν(OH) and δ(HOH) bands increase with relative pressure and the bandshapes are very reproducible, which suggests that, in the explored p/p_0 range the molecular interactions formed between the probe and the polymer substrate (and, eventually, the probe self-association) do not depend on H_2O concentration. The featureless and symmetrical profile of the δ(HOH) band reflects the very low sensitivity of the δ-mode to H-bonding (Murthy and Rao, 1968). This characteristic makes the bending peak suitable for analytical purposes. The stretching band is more complex, owing to the high sensitivity of these modes to the molecular environment.

Two well-defined maxima are observed at 3,660 and 3,578 cm^{-1}, suggesting the presence of multiple water species involved in different types of H-bonding interactions. These results confirm that in-depth analysis of the ν(OH) profile will provide molecular level information on the system under scrutiny. Preliminary attempts at curve resolution of the traces in **Figure 2A** by LSCF analysis using only two components were unsuccessful, regardless of the adopted bandshape.

This suggests a more complex structure of the experimental profile, which had to be explored by resolution-enhancement approaches.

In **Figure 3A** is represented the correlation between the absorbance area of the ν(OH) and the δ(HOH) bands with the amount of sorbed water measured gravimetrically. The linear trend through the origin confirms the validity of the Beer-Lambert relationship and allows us to use the photometric data for the quantitative monitoring of the diffusion kinetics and for measuring solubility vs. relative-pressure isotherms.

The sorption isotherm at 35°C in the p/p_0 range 0.1–0.5 is reported in **Figure 3B**, while **Figure 4** shows the sorption kinetics at $p/p_0 = 0.5$. As expected, data taken from the two analytical signals are essentially coincident; the isotherm is linear in the explored pressure range and the maximum mass uptake is 0.33 wt%. This value is low and only slightly higher than those for other semicrytalline polyesters of similar molecular structure

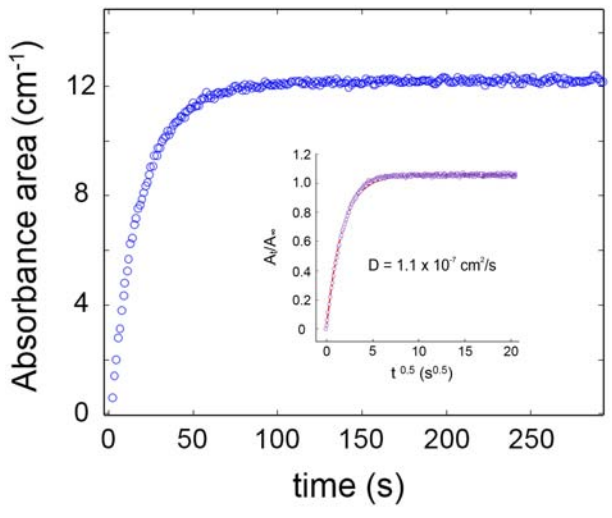

FIGURE 4 | Absorbance of the ν(OH) band of water as a function of time for a sorption experiment at $p/p_0 = 0.5$. The inset displays the Fick's diagram obtained therefrom. Open circles refer to experimental data points; the continuous line is the least-squares regression with model Equation (3).

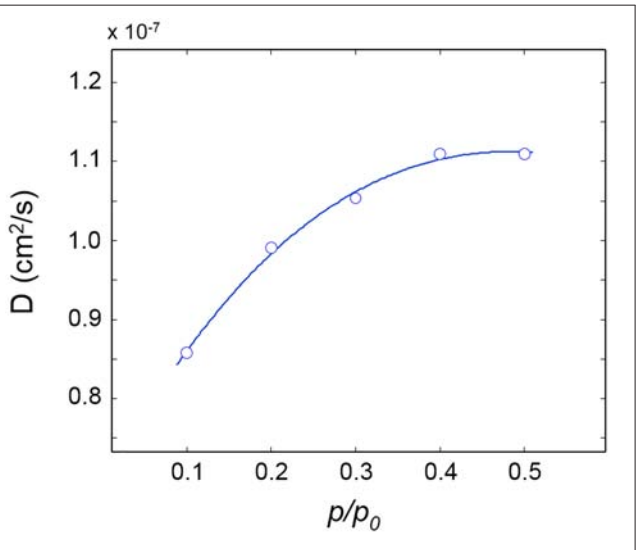

FIGURE 5 | Diffusivity of H_2O in PLLA as a function of relative pressure of water vapor. The connecting line is for eye guidance.

[PCL, poly(propylene sebacate)], on account of the hydrophobic character of these polymers. More on this later. The kinetic behavior was modeled by the Fick's second law of diffusion expressed in terms of absorbance, which, for the case of a plane sheet exposed to an equal penetrant activity on both sides, can be written as (Crank, 1975):

$$\frac{A(t)}{A_\infty} = \frac{M(t)}{M_\infty} = 1 - \frac{8}{\pi^2}\sum_{m=0}^{\infty}\frac{1}{(2m+1)^2}\,exp\left[\frac{-D\,(2m+1)^2\,\pi^2 t}{L^2}\right] \quad (3)$$

In Equation (3) $A(t)$ and A_∞ represent the integrated absorbance of the ν(OH) band at time t and at equilibrium, L is the film thickness and D is the mutual diffusivity.

The model consistently simulates the experimental data in the whole time range (see inset of **Figure 4**), and the $A(t)/A_\infty$ vs. $t^{0.5}$ curve is linear up to an ordinate value of 0.6, which demonstrates the Fickian behavior of the system. This result is in line with earlier literature reports on polyesters belonging to the same family (Musto et al., 2014; Scherillo et al., 2016).

Sorption kinetics were monitored at five p/p_0 values from 0.1 to 0.5 and the diffusion coefficients, D, evaluated therefrom are plotted as a function of p/p_0 in **Figure 5**.

The D-value reported in the literature (0.7×10^{-7} cm^2/s by gravimetry) (De Santis et al., 2015) is found in good agreement

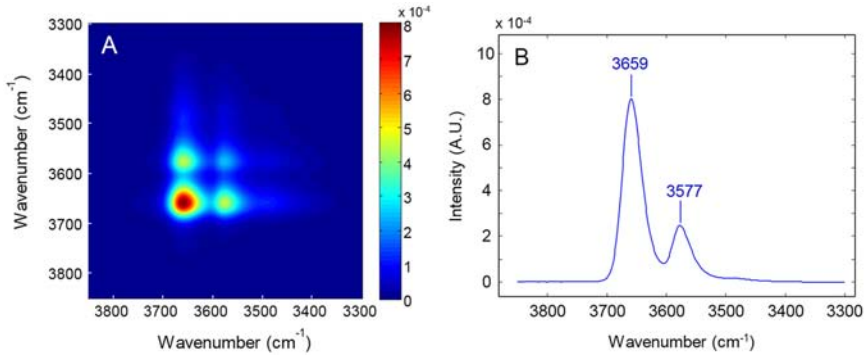

FIGURE 6 | (A) 2D-COS synchronous color-map obtained from the *time-resolved* spectra collected during the sorption experiment at $p/p_0 = 0.5$. **(B)** Power spectrum calculated therefrom.

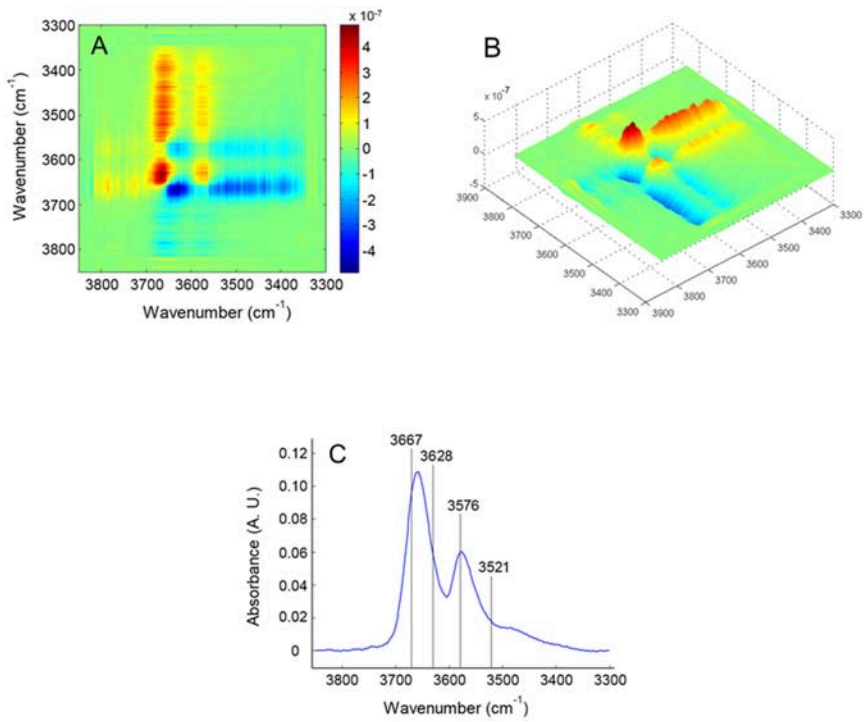

FIGURE 7 | 2D-COS asynchronous map obtained from the *time-resolved* spectra collected during the sorption experiment at $p/p0 = 0.5$. The map is represented as an intensity–color map **(A)** and as a 3-D image **(B)**; **(C)** presents the frequency spectrum with the position of the components identified by 2D-COS analysis.

with the present spectroscopic determinations; an increasing trend of D with the water vapor pressure is also noted in **Figure 5**, which indicates that the mutual diffusivity coefficient is a growing function of the penetrant concentration.

This behavior is generally associated to a swelling effect of the penetrant, which increases the available free volume, with the consequence of enhancing the mobility of the diffusing molecules. In the present case, no direct spectroscopic evidence is found for the swelling of the sample upon sorption. However, a possibility exists that, while the swelling is so small to remain below the limits of detection, it is still sufficient to produce a sizeable effect at the molecular level. The present diffusivity data only allow us a tentative interpretation; a deeper analysis supported by thermodynamic and/or MD modeling is currently underway.

2D-COS Analysis

The 2D-COS technique was shown to be a powerful method for studying molecular interactions that produce broad, poorly resolved features (Noda and Ozaki, 2004; Galizia et al., 2014). It is a perturbative technique by which a system initially at equilibrium is subjected to an external stimulus: a correlation analysis is performed on the spectral response (absorbance, in the present case) as a function of a third common variable related to the perturbing function (time, in the present case).

In **Figures 6A,B** are represented, respectively, the synchronous spectrum in the 3,800–3,300 cm^{-1} range, obtained from the time-resolved spectra collected during the sorption experiment performed at $p/p_0 = 0.5$ and the power spectrum, i.e., the autocorrelation profile taken across the main diagonal. The synchronous map displays the autopeaks (and the corresponding cross-peaks) already identified in the frequency profile; in the power-spectrum the two components are fully resolved and there is no evidence of further spectral features, in contrast with the results of the LSCF analysis.

TABLE 1 | Position, sign, and type of the correlation peaks appearing in the synchronous and asynchronous spectra.

ν_1 (cm^{-1})	ν_2 (cm^{-1})	Sign[a]	Type[b]	Trend[c]
SYNCHRONOUS				
3,659	3,659	+	A	> >
3,577	3,577	+	A	> >
3,659	3,577	+	C	> >
ν_1 (cm^{-1})	ν_2 (cm^{-1})	Sign[a]	Type[b]	Rate of change
ASYNCHRONOUS				
3,628	3,667	−	C	3,628 < 3,667
3,576	3,628	+	C	3,576 > 3,628
3,521	3,667	−	C	3,521 < 3,667
3,521	3,576	−	C	3,521 < 3,576

[a] *The sign refers to the cross-peaks in the lower side of the spectrum, with respect to the main diagonal. The sign of the cross-peaks in the upper side can be deduced on the basis of the symmetry properties of the respective matrices (synchronous, symmetric; asynchronous, antisymmetric).*

[b] *A, autopeak (along the main diagonal); C, cross-peak (off-diagonal).*

[c] *>, increasing peak; <, decreasing peak.*

In **Figure 7** is displayed the asynchronous spectrum in the form of a contour-map (**Figure 7A**) and as a 3D iso-intensity surface (**Figure 7B**) which highlights finer details on the shape of the correlation bands. The components identified in the asynchronous map are indicated in the frequency spectrum of **Figure 7C**. The results of the analysis are summarized in **Table 1**. The specificity and the resolution enhancement brought by asynchronous correlation allows us to identify two components in the main frequency peak at 3,659 cm^{-1}, located, respectively, at 3,667 and 3,628 cm^{-1}. These are readily recognized in the form of two well-developed cross-peaks (in the lower side of the map with respect to the main diagonal) at [3,628–3667 (–)], [3,576–3,628 (+)]. The shape of these two cross-peaks is typical of a correlation between two sharp signals. Two more correlation bands occur at [3,521–3,667 (–)] and [3,521–3,576 (–)]. These are less defined and display the elongated shape characteristic of a correlation between a sharp signal and a much broader band. In particular, the band at [3,521–3576 (–)] is only slightly above the noise level (see **Figures 7A,B**), reflecting the low intensity of the signal at 3,521 cm^{-1}. The two above features clearly identify the presence of a broad component approximately centered at 3,521 cm^{-1}, already suggested by the preliminary LSCF analysis. The asynchronous map displays a more detailed pattern and is richer of information than the synchronous.

This effect is related to the fact that in the former case resolution enhancement occurs via two distinct mechanisms, i.e., the spreading of the spectral data over a second frequency axis, and the vanishing of the asynchronous correlation intensity for signals evolving at the same rate. A detailed discussion of the latter effect is reported in Musto et al. (2018). In the synchronous spectrum only the first mechanism is operative.

To summarize, 2D-COS identified four components in the ν(OH) range: three are sharp and are located at 3,667, 3,628, and 3,576 cm^{-1}, the fourth is much broader and is so weak to be barely detectable in the frequency spectrum. Taking into account the correlation relationships from the 2D-COS maps, the following interpretation can be advanced: the four components are arranged pair-wise, the two signals centered at 3,667 and 3,576 cm^{-1} evolve synchronously and at a different rate with respect to the couple at 3,628–3,521 cm^{-1} that is also synchronously correlated. Applying the Noda correlation rules (Noda and Ozaki, 2004) the sign of the cross-peaks reveals that, in the sorption experiment the doublet at 3,655–3,562 cm^{-1} grows faster than the doublet at 3,611–3,486 cm^{-1}.

The above findings can be interpreted considering that a single water molecule produces two OH-stretching modes (in-phase at lower frequency and out-of-phase at higher frequency). Thus, the two couples of signals suggest the presence of two distinct water species. The doublet at 3,667–3,576 cm^{-1} is assigned, respectively, to the ν_{as} and the ν_s modes of isolated water molecules interacting with the PLLA carbonyls, while the second couple at 3,628–3,521 cm^{-1} originates from a self-associated water species. It has been demonstrated that, when aggregates of the type C=O....H–O–H (Iwamoto et al., 2003) are formed, the "free" O–H bonds in the complex produces a characteristic signature at 3,690 cm^{-1}. The absence of this feature, coupled with the 2D-COS results which detected only two H_2O species,

provides support for the conclusion that in the present system the amount of H_2O molecules forming an H-bonding interaction with a single carbonyl group is negligible. The stoichiometry of the carbonyl-to-water interaction is thus 2:1, i.e., of the type:

–C=O....H–O–H....O=C–.

Of the two components belonging to the self-associated species, the one at 3,628 cm^{-1} originates (predominantly) from a "free" O–H bond, while that at 3,521 cm^{-1} is due to the O–H bond forming the self-interaction. In fact, the breadth of the latter band, around four times larger than the other three signals (see the forthcoming paragraph on LSCF analysis), is characteristic of water-to-water H-bonding, with the associated distribution of bond-lengths and geometries. The two water species identified spectroscopically with the signals they produce are schematically represented in **Figure 8**.

LSCF Analysis

The 2D-COS results were used as a benchmark to guide the LSCF analysis. Thus, a Gaussian component at 3,520 cm^{-1} was added to the model; the high-frequency peak was maintained as single component because no evidence of a fine structure was discernible. The regression of the spectrum representative of water sorbed at equilibrium in PLLA at $p/p_0 = 0.5$ is reported in **Figure 9**.

The adopted model afforded a satisfactory and consistent simulation of all the experimental profiles collected at the different p/p_0 values. The intensity of the resolved components can be converted into absolute concentration of the two water species provided that the values of the relative molar absorptivities, ε_i, are known or can be estimated. In the present case, a method based on coupling the Beer-Lambert expression for the total concentration of sorbed water with the mass-balance relationship (Musto et al., 2014) was adopted. In brief,

$$C_{tot} = \frac{A_{bc}}{\varepsilon_{bc} L} + \frac{A_{sa}}{\varepsilon_{sa} L} \quad (4)$$

$$C_{tot} = C_{bc} + C_{sa} \quad (5)$$

$$\frac{A_{bc}}{C_{tot}} = \varepsilon_{bc} L - \frac{\varepsilon_{bc}}{\varepsilon_{sa}} \cdot \frac{A_{sa}}{C_{tot}} \quad (6)$$

In Equations (4–6) A is the integrated absorbance, C the volumetric concentration and L the sample thickness. The subscripts *bc* and *sa* refer, respectively, to the H_2O molecules bound to carbonyls and to those self-associated (see **Figure 8**); *tot*

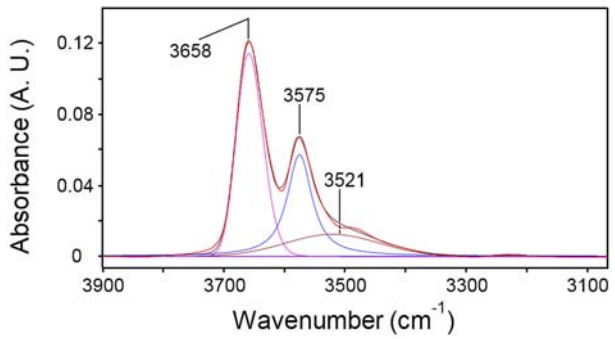

FIGURE 9 | Curve fitting analysis of the spectrum representative of H_2O sorbed in PLLA ($p/p_0 = 0.5$). The figure displays the experimental profile (red trace), the best-fitting curve (black trace) and the resolved components.

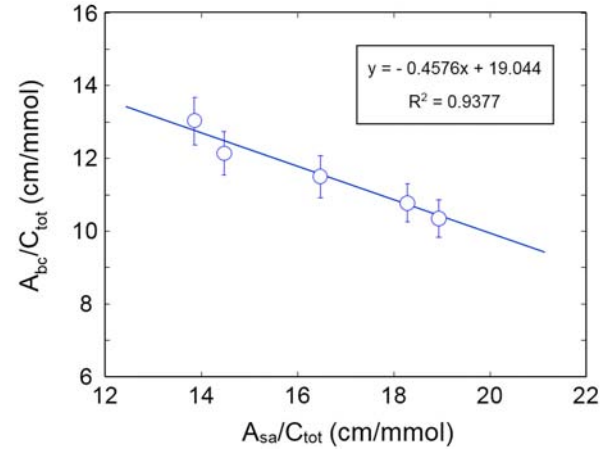

FIGURE 10 | Plot of $\frac{A_{bc}}{C_{tot}}$ as a function of $\frac{A_{sa}}{C_{tot}}$.

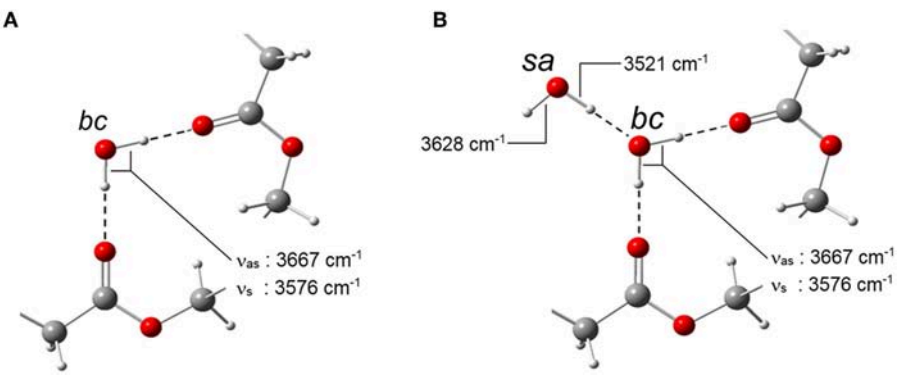

FIGURE 8 | Schematic representation of the two water species identified in the H_2O/PLLA system. **(A)** *bc* stands for *bound to carbonyls;* **(B)** *sa* stands for *self-associated*.

stands for total. The C_{tot} values were taken from the gravimetric measurements as a function of p/p_0. The density of PLLA (1.240 g/cm^3), assumed invariant with H_2O sorption, was employed to convert gravimetric weight ratios into volumetric concentration values. The components at 3,575 and 3,521 cm^{-1} were selected as analytical peaks for the *bc* and the *sa* species, respectively, because of the unresolved, two-component structure of the 3,658 cm^{-1} peak.

The plot of $\frac{A_{bc}}{C_{tot}}$ vs. $\frac{A_{sa}}{C_{tot}}$ is displayed in **Figure 10**: the data exhibit the expected behavior. The absorptivity values calculated from the slope and the intercept of regression line are: $\varepsilon_{bc} = 41.3$ km/mol and $\varepsilon_{sa} = 90.2$ km/mol. These values compare favorably with those obtained for the system H_2O/PCL ($\varepsilon_{bc} = 72.2$ km/mol and $\varepsilon_{sa} = 98.2$ km/mol) (Musto et al., 2014) and the system H_2O/polyetherimide ($\varepsilon_{bc} = 34.5$ km/mol and $\varepsilon_{sa} = 89.7$ km/mol) (Musto et al., 2014; de Nicola et al., 2017).

In **Figure 11** are reported the absolute concentrations (mmol/cm^3) of the two water species (calculated from the respective Lambert-Beer relationships) as a function of relative pressure of water vapor. In the same plot, for comparison, are also reported the total concentration of sorbed water (C_{tot}) and the excess C_{bc} values, i.e., $C_m = C_{bc} - C_{sa}$.

In the light of the proposed structures of the H_2O/PLLA molecular aggregates, C_{sa} corresponds to the concentration of H_2O dimers and C_m to the concentration of isolated (monomeric) species in the system. The change of monomer concentration is modest, with a slight decreasing trend at high p/p_0 values. In the whole pressure range the dimers represent the prevailing species. The C_{sa} curve displays an upward concavity not observed in the C_{bc} curve, which suggests an intersection of the two curves just above 0.6. At the intersection the isolated species are no longer present ($C_m = 0$) and all the H_2O molecules bound to carbonyls are self-associated. If the C_{sa} offsets the C_{bc}, aggregates of more than two water molecules are being formed in the system, which indicates the onset of the clustering process. In the present system this point lies above $p/p_0 = 0.5$ and has not been reached (Musto et al., 2012; Scherillo et al., 2012a, 2014; Galizia et al., 2014).

It is informative to compare the sorption behavior of the H_2O/PLLA and H_2O/PCL systems (Musto et al., 2014) (see **Figure 11B**). Both substrates are aliphatic polyesters with a very close molecular structure (the only difference being in the aliphatic chain, comprising five CH_2 groups for PCL and one –C(CH_3)– unit for PLLA). PCL is semicrystalline with a crystallinity degree of 58% (DSC); the PLLA sample used in the present investigation is fully amorphous. The amount of water sorbed at equilibrium is significantly higher in PLLA than in PCL in the whole p/p_0 range. This can be partially attributed to the higher interactive character of PLLA (higher density of C=O groups). The main effect is however related to the absence, in PLLA, of a crystalline phase impervious to the penetrant.

In PCL the analysis of the two-species population indicated that up to 0.6 p/p_0 values only dimers are formed, while at higher relative pressures of H_2O vapor, clustering takes place (Musto et al., 2014). In PLLA, dimers are still the prevailing species, but monomeric water is present up to $p/p_0 = 0.5$ and beyond. This result is again to be related to the higher number of proton acceptors (C=O) per unit volume in PLLA compared to PCL, which increases the probability for the penetrant of finding two close carbonyls in the right configuration for forming the aggregate represented in **Figure 8A**. The increased relevance of

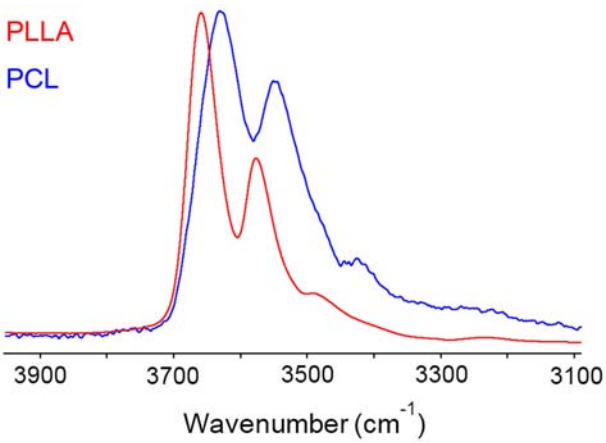

FIGURE 12 | Spectra representative of water sorbed in PLLA (red trace) and in PCL (blue trace) in the ν(OH) region (3,900–3,100 cm^{-1}).

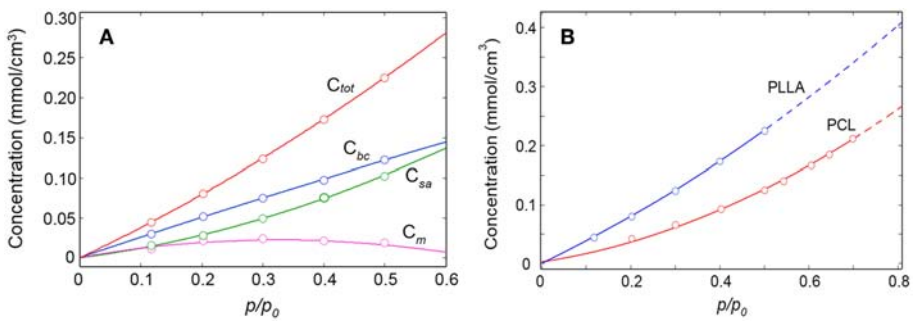

FIGURE 11 | C_{tot}, C_{bc}, C_{sa}, and C_m as a function of the relative pressure of water vapor **(A)**; comparison between the sorption isotherms of the H_2O/PLLA and H_2O/PCL systems **(B)**.

self-association in PCL is clearly reflected in the appearance of the penetrant spectrum (see **Figure 12**) where the broad component at lower frequency (self-associated O–H bond) is significantly larger than in PLLA.

CONCLUSIONS

In the present contribution the sorption of water vapor in PLLA has been studied by FTIR spectroscopy. Data gathered at sorption equilibrium and during the diffusion process have been analyzed by different techniques, namely, difference spectroscopy, two-dimensional correlation spectroscopy and least-squares curve fitting, which provided complementary information. Two distinct molecular species were detected in the system: single H_2O molecules bound to the PLLA carbonyls via a –C=O....H–O–H....O=C– stoichiometry and self-associated H_2O molecules forming second- shell layers. No evidence was found of the presence of C=O....H–O–H species.

Coupling the spectroscopic data with gravimetric measurements, it was possible to evaluate the population of the two water species. It was found that, in the explored p/p_0 range (0–0.5) dimers represent the prevailing species, but monomeric water remains well-detectable. In the present system the onset of the clustering process (i.e., when aggregates of more than two water molecules are formed) lies above $p/p_0 = 0.5$ and has not been reached. The diffusion coefficient were measured as a function of water activity and is in good agreement with literature values. The diffusivity was found to increase with water concentration possibly due to a swelling effect.

AUTHOR CONTRIBUTIONS

MP: conceptualization, formal analysis, supervision, writing—review and editing. MP and PL: investigation. MP and PL: methodology.

REFERENCES

Armentano, I., Dottori, M., Fortunati, E., Mattioli, S., and Kenny, J. M. (2010). Biodegradable polymer matrix nanocomposites for tissue engineering: a review. *Polym. Degrad. Stab.* 95, 2126–2146. doi: 10.1016/j.polymdegradstab.2010.06.007

Auras, R., Harte, B., and Selke, S. (2004). An overview of polylactides as packaging materials. *Macromol. Biosci.* 4, 835–864. doi: 10.1002/mabi.200400043

Chen, G., Ushida, T., and Tateishi, T. (2002). Scaffold design for tissue engineering. *Macromol. Biosci.* 2, 67–77. doi: 10.1002/1616-5195(20020201)2:2<67::AID-MABI67>3.0.CO;2-F

Copinet, A., Bertrand, C., Govindin, S., Coma, V., and Couturier, Y. (2004). Effects of ultraviolet light (315 nm), temperature and relative humidity on the degradation of polylactic acid plastic films. *Chemosphere* 55, 763–773. doi: 10.1016/j.chemosphere.2003.11.038

Cotugno, S., Larobina, D., Mensitieri, G., Musto, P., and Ragosta, G. (2001). A novel spectroscopic approach to investigate transport processes in polymers: the case of water–epoxy system. *Polymer* 42, 6431–6438. doi: 10.1016/S0032-3861(01)00096-9

Crank, J. (1975). *The Mathematics of Diffusion*. Oxford: Clarendon Press.

de Nicola, A., Correa, A., Milano, G., La Manna, P., Musto, P., Mensitieri, G., et al. (2017). Local structure and dynamics of water absorbed in poly(ether imide): a hydrogen bonding anatomy. *J. Phys. Chem. B* 121, 3162–3176. doi: 10.1021/acs.jpcb.7b00992

De Santis, F., Gorrasi, G., and Pantani, R. (2015). A spectroscopic approach to assess transport properties of water vapor in PLA. *Polym. Test.* 44, 15–22. doi: 10.1016/j.polymertesting.2015.03.015

Dürselen, L., Dauner, M., Hierlemann, H., Planck, H., Claes, L. E., and Ignatius, A. (2001). Resorbable polymer fibers for ligament augmentation. *J. Biomed. Mater. Res.* 58, 666–672. doi: 10.1002/jbm.1067

Eppley, B. L., Morales, L., Wood, R., Pensler, J., Goldstein, J., Havlik, R. J., et al. (2004). Resorbable PLLA PGA plate and screw fixation in pediatric craniofacial surgery: clinical experience in 1883 patients. *Plast. Reconstr. Surg.* 114, 850–856. doi: 10.1097/01.PRS.0000132856.69391.43

Fukuda, N., Tsuji, H., and Ohnishi, Y. (2002). Physical properties and enzymatic hydrolysis of poly(l-lactide)–CaCO3 composites. *Polym. Degrad. Stab.* 78, 119–127. doi: 10.1016/S0141-3910(02)00125-8

Galizia, M., La Manna, P., Mensitieri, G., Pannico, M., and Musto, P. (2014). Diffusion in polymers as investigated by two-dimensional correlation spectroscopy: the H2O/PCL system. *J. Mol. Struct.* 1069, 290–298. doi: 10.1016/j.molstruc.2014.02.045

Göpferich, A. (1996). Mechanisms of polymer degradation and erosion. *Biomaterials* 17, 103–114. doi: 10.1016/0142-9612(96)85755-3

Ho, K.-L. G., Pometto, A. L., and Hinz, P. N. (1999). Effects of temperature and relative humidity on polylactic acid plastic degradation. *J. Environ. Polym. Degrad.* 7, 83–92. doi: 10.1023/A:1021808317416

Holm, V. K., Ndoni, S., and Risbo, J. (2006). The stability of poly(lactic acid) packaging films as influenced by humidity and temperature. *J. Food Sci.* 71, E40–E44. doi: 10.1111/j.1365-2621.2006.tb08895.x

Ikada, Y., and Tsuji, H. (2000). Biodegradable polyesters for medical and ecological applications. *Macromol. Rapid Commun.* 21, 117–132. doi: 10.1002/(SICI)1521-3927(20000201)21:3<117::AID-MARC117>3.0.CO;2-X

Imola, M. J., and Schramm, V. L. (2002). Resorbable internal fixation in pediatric cranial base surgery. *Laryngoscope* 112, 1897–1901. doi: 10.1097/00005537-200210000-00038

Iwamoto, R., Matsuda, T., Sasaki, T., and Kusanagi, H. (2003). Basic interactions of water with organic compounds. *J. Phys. Chem. B* 107, 7976–7980. doi: 10.1021/jp030561n

Kikkawa, Y., Abe, H., Iwata, T., Inoue, Y., and Doi, Y. (2002). Crystallization, stability, and enzymatic degradation of poly(l-lactide) thin film. *Biomacromolecules* 3, 350–356. doi: 10.1021/bm015623z

Leja, K., and Lewandowicz, G. (2010). Polymer biodegradation and biodegradable polymers - a review. *Pol. J. Environ. Stud.* 19, 255–266.

Li, S. (1999). Hydrolytic degradation characteristics of aliphatic polyesters derived from lactic and glycolic acids. *J. Biomed. Mater. Res.* 48, 342–353. doi: 10.1002/(SICI)1097-4636(1999)48:3<342::AID-JBM20>3.0.CO;2-7

Liu, L., Li, S., Garreau, H., and Vert, M. (2000). Selective enzymatic degradations of poly(l-lactide) and poly(ε-caprolactone) blend films. *Biomacromolecules* 1, 350–359. doi: 10.1021/bm000046k

Marquardt, D. W. (1963). An algorithm for least-squares estimation of nonlinear parameters. *J. Soc. Indust. Appl. Math.* 11, 431–441.

Murthy, A. S. N., and Rao, C. N. R. (1968). Spectroscopic studies of the hydrogen bond. *Appl. Spectrosc. Rev.* 2, 69–191. doi: 10.1080/05704926808050887

Musto, P., Galizia, M., Pannico, M., Scherillo, G., and Mensitieri, G. (2014). Time-resolved fourier transform infrared spectroscopy, gravimetry, and thermodynamic modeling for a molecular level description of water sorption in poly(ε-caprolactone). *J. Phys. Chem. B* 118, 7414–7429. doi: 10.1021/jp502270h

Musto, P., La Manna, P., Pannico, M., Mensitieri, G., Gargiulo, N., and Caputo, D. (2018). Molecular interactions of CO2 with the CuBTC metal organic framework: an FTIR study based on two-dimensional correlation spectroscopy. *J. Mol. Struct.* 1166, 326–333. doi: 10.1016/j.molstruc.2018.04.058

Musto, P., Mensitieri, G., Lavorgna, M., Scarinzi, G., and Scherillo, G. (2012). Combining gravimetric and vibrational spectroscopy measurements to quantify first- and second-shell hydration layers in polyimides with different molecular architectures. *J. Phys. Chem. B* 116, 1209–1220. doi: 10.1021/jp2056943

Musto, P., Ragosta, G., Mensitieri, G., and Lavorgna, M. (2007). On the molecular mechanism of H2O diffusion into polyimides: a vibrational spectroscopy investigation. *Macromolecules* 40, 9614–9627. doi: 10.1021/ma071385+

Nair, L. S., and Laurencin, C. T. (2007). Biodegradable polymers as biomaterials. *Prog. Polym. Sci.* 32, 762–798. doi: 10.1016/j.progpolymsci.2007.05.017

Noda, I. (2000). Determination of two-dimensional correlation spectra using the Hilbert transform. *Appl. Spectrosc.* 54, 994–999. doi: 10.1366/0003702001950472

Noda, I., and Ozaki, Y. (eds.). (2004). "Other types of two-dimensional spectroscopy," in *Two-Dimensional Correlation Spectroscopy - Applications in Vibrational and Optical Spectroscopy* (Chichester: John Wiley & Sons Ltd.), 95–110. doi: 10.1002/0470012404.ch7

Rocca-Smith, J. R., Whyte, O., Brachais, C.-H., Champion, D., Piasente, F., Marcuzzo, E., et al. (2017). Beyond biodegradability of poly(lactic acid): physical and chemical stability in humid environments. *ACS Sustain. Chem. Eng.* 5, 2751–2762. doi: 10.1021/acssuschemeng.6b03088

Rothwell, W. P., Holecek, D. R., and Kershaw, J. A. (1984). NMR imaging: study of fluid absorption by polymer composites. *J. Polymer Sci.* 22, 241–247. doi: 10.1002/pol.1984.130220501

Sabir, M. I., Xu, X., and Li, L. (2009). A review on biodegradable polymeric materials for bone tissue engineering applications. *J. Mater. Sci.* 44, 5713–5724. doi: 10.1007/s10853-009-3770-7

Sagar, J., Chaib, B., Sales, K., Winslet, M., and Seifalian, A. (2007). Role of stem cells in cancer therapy and cancer stem cells: a review. *Cancer Cell Int.* 7:9. doi: 10.1186/1475-2867-7-9

Scherillo, G., Carbone, M. G. P., Petretta, M., La Manna, P., Panayiotou, C., Bikiaris, D. N., et al. (2016). Water sorption thermodynamics in poly(propylene sebacate). *Polymer* 97, 346–361. doi: 10.1016/j.polymer.2016.05.047

Scherillo, G., Galizia, M., Musto, P., and Mensitieri, G. (2013). Water Sorption thermodynamics in glassy and rubbery polymers: modeling the interactional issues emerging from FTIR spectroscopy. *Ind. Eng. Chem. Res.* 52, 8674–8691. doi: 10.1021/ie302350w

Scherillo, G., Petretta, M., Galizia, M., La Manna, P., Musto, P., and Mensitieri, G. (2014). Thermodynamics of water sorption in high performance glassy thermoplastic polymers. *Front. Chem.* 2:25. doi: 10.3389/fchem.2014.00025

Scherillo, G., Sanguigno, L., Galizia, M., Lavorgna, M., Musto, P., and Mensitieri, G. (2012a). Non-equilibrium compressible lattice theories accounting for hydrogen bonding interactions: modelling water sorption thermodynamics in fluorinated polyimides. *Fluid Phase Equilib.* 334, 166–188. doi: 10.1016/j.fluid.2012.06.030

Scherillo, G., Sanguigno, L., Sansone, L., Di Maio, E., Galizia, M., and Mensitieri, G. (2012b). Thermodynamics of water sorption in poly(s accounting for hydrogen bonding interactions: modelling water sorption thermodynamics in fluorinated *Fluid Phase Equilib.* 313, 127–139. doi: 10.1016/j.fluid.2011.10.012

Siracusa, V., Rocculi, P., Romani, S., and Dalla Rosa, M. (2008). Biodegradable polymers for food packaging: a review. *Trends Food Sci. Technol.* 19, 634–643. doi: 10.1016/j.tifs.2008.07.003

Tawakkal, I. S., Cran, M. J., Miltz, J., and Bigger, S. W. (2014). A review of poly(lactic acid)-based materials for antimicrobial packaging. *J. Food Sci.* 79, R1477–R1490. doi: 10.1111/1750-3841.12534

Taylor, L. S., Langkilde, F. W., and Zografi, G. (2001). Fourier transform Raman spectroscopic study of the interaction of water vapor with amorphous polymers. *J. Pharm. Sci.* 90, 888–901. doi: 10.1002/jps.1041

Temenoff, J. S., and Mikos, A. G. (2000). Review: tissue engineering for regeneration of articular cartilage. *Biomaterials* 21, 431–440. doi: 10.1016/S0142-9612(99)00213-6

Tsuji, H., Daimon, H., and Fujie, K. (2003). A new strategy for recycling and preparation of poly(l-lactic acid): hydrolysis in the melt. *Biomacromolecules* 4, 835–840. doi: 10.1021/bm034060j

Tsuji, H., Eto, T., and Sakamoto, Y. (2011). Synthesis and hydrolytic degradation of substituted poly(DL-lactic acid)s. *Materials* 4, 1384–1398. doi: 10.3390/ma4081384

Tsuji, H., and Miyauchi, S. (2001). Enzymatic hydrolysis of poly(lactide)s: effects of molecular weight, l-lactide content, and enantiomeric and diastereoisomeric polymer blending. *Biomacromolecules* 2, 597–604. doi: 10.1021/bm010048k

Tsuji, H., Mizuno, A., and Ikada, Y. (2000). Properties and morphology of poly(L-lactide). III. Effects of initial crystallinity on long-term in vitro hydrolysis of high molecular weight poly(L-lactide) film in phosphate-buffered solution. *J. Appl. Polymer Sci.* 77, 1452–1464. doi: 10.1002/1097-4628(20000815)77:7<1452::AID-APP7>3.0.CO;2-S

Tullo, A. (2000). Plastic found at the end of the maize. *Chem. Eng. News Arch.* 78:13. doi: 10.1021/cen-v078n003.p013

Tyler, B., Gullotti, D., Mangraviti, A., Utsuki, T., and Brem, H. (2016). Polylactic acid (PLA) controlled delivery carriers for biomedical applications. *Adv. Drug Deliv. Rev.* 107, 163–175. doi: 10.1016/j.addr.2016.06.018

Yuan, X., Mak, A. F. T., and Yao, K. (2002). Comparative observation of accelerated degradation of poly(l-lactic acid) fibres in phosphate buffered saline and a dilute alkaline solution. *Polym. Degrad. Stab.* 75, 45–53. doi: 10.1016/S0141-3910(01)00203-8

Conflict of Interest Statement: The authors declare that the research was conducted in the absence of any commercial or financial relationships that could be construed as a potential conflict of interest.

The reviewer LV declared a shared affiliation, with no collaboration, with the authors, MP and PL, to the handling editor at the time of review.

The reviewer GS declared a past co-authorship with one of the authors MP to the handling editor.

Copyright © 2019 Pannico and La Manna. This is an open-access article distributed under the terms of the Creative Commons Attribution License (CC BY). The use, distribution or reproduction in other forums is permitted, provided the original author(s) and the copyright owner(s) are credited and that the original publication in this journal is cited, in accordance with accepted academic practice. No use, distribution or reproduction is permitted which does not comply with these terms.

frontiers in Chemistry

ORIGINAL RESEARCH
published: 19 June 2019
doi: 10.3389/fchem.2019.00429

Pyro-Electrification of Freestanding Polymer Sheets: A New Tool for Cation-Free Manipulation of Cell Adhesion *in vitro*

Romina Rega[1], Oriella Gennari[1], Laura Mecozzi[1], Vito Pagliarulo[1], Martina Mugnano[1], Emilia Oleandro[1,2], Filomena Nazzaro[3], Pietro Ferraro[1] and Simonetta Grilli[1]*

[1] Institute of Applied Sciences and Intelligent Systems, National Research Council (CNR-ISASI), Pozzuoli, Italy, [2] Department of Mathematics and Physics, University of Campania "L. Vanvitelli", Caserta, Italy, [3] Institute of Food Sciences, National Research Council (CNR-ISA), Avellino, Italy

Localized electric fields have become, in recent years, a source of inspiration to researchers and laboratories thanks to a huge amount of applications derived from it, including positioning of microparticles as building blocks for electrical, optical, and magnetic devices. The possibility of producing polymeric materials with surface charge thus opens new perspectives for applications where process simplicity and cost-effectiveness of flexible electronics are of fundamental importance. In particular, the influence of surface charges is widely studied and is a critical issue especially when new materials and functional technologies are introduced. Here, we report a voltage-free pyro-electrification (PE) process able to induce a permanent dipole orientation into polymer sheets under both mono- and bipolar distribution. The technique makes use of the pyroelectric effect for generating electric potentials on the order of kilovolts by an easy-to-accomplish thermal treatment of ferroelectric lithium niobate (LN) crystals. The PE allows us to avoid the expensive and time-consuming fabrication of high-power electrical circuits, as occurs in traditional generator-based techniques. Since the technique is fully compatible with spin-coating-based procedures, the pyro-electrified polymer sheets are easily peeled off the surface of the LN crystal after PE completion, thus providing highly stable and freestanding charged sheets. We show the reliability of the technique for different polymers and for different applications ranging from live cell patterning to biofilm formation tests for bacteria linked to food-processing environments.

Keywords: dipoles orientation, pyro-electrification, pyroelectric effect, lithium niobate, cell patterning and manipulation, bacteria biofilm

OPEN ACCESS

Edited by:
Pellegrino Musto, Italian National Research Council (CNR), Italy

Reviewed by:
Guoqing Pan, Jiangsu University, China
Rocktotpal Konwarh, Addis Ababa Science and Technology University, Ethiopia

****Correspondence:***
Romina Rega
r.rega@isasi.cnr.it

Specialty section:
This article was submitted to Polymer Chemistry, a section of the journal Frontiers in Chemistry

Received: *29 January 2019*
Accepted: *27 May 2019*
Published: *19 June 2019*

Citation:
Rega R, Gennari O, Mecozzi L, Pagliarulo V, Mugnano M, Oleandro E, Nazzaro F, Ferraro P and Grilli S (2019) Pyro-Electrification of Freestanding Polymer Sheets: A New Tool for Cation-Free Manipulation of Cell Adhesion in vitro. Front. Chem. 7:429. doi: 10.3389/fchem.2019.00429

INTRODUCTION

The possibility of tailoring the material surface properties has allowed an increasingly active field for a wide variety of researches and applications ranging from materials science, nanotechnology, and electronics to biological and medical systems (Stuart et al., 2010). One possibility for functionalizing surfaces and thus tuning interfacial properties is to use specific chemical treatment or to design and induce the electrostatic charges in specific locations. In particular, materials that show net electrostatic charges have been the key issue for fruitful applications in electronics, mechanics, and

biological systems. Supports with localized charges are widely used to control the behavior of thin-film electronic devices (Jacobs and Whitesides, 2001). Moreover, obtaining templates with a pattern of electrostatic charges becomes very useful in applications including sorting and self-assembling of micro- and nano-particles (Palleau et al., 2011; Zhao et al., 2011), macromolecules (Seemann et al., 2007; Zhao et al., 2011; Xi et al., 2012), or other building blocks (Cole et al., 2010). Recently, the programming and patterning of electric charges have been widely demonstrated by simple and effective processes in ferroelectric substrates (Grilli et al., 2008b; Esseling et al., 2013; Gennari et al., 2013; Carrascosa et al., 2015; Chen et al., 2016) devoting much attention to the possibility of using polymeric materials thanks to their ability to be economically produced on a large scale and with the further advantage of flexible thin-film technology. The techniques for charging polymeric surfaces are numerous and are quite well-established. The most common approaches require an external voltage source as in the case of contact poling (Hill et al., 1994) or corona poling (Rychkov et al., 2011). However, these techniques present severe limitations. In the case of contact poling, a large charge injection could produce a detrimental dielectric breakdown of the films (Hill et al., 1994; DeRose et al., 2006), while in the case of corona poling, the good homogeneity of the polarization is not guaranteed due to the difficult control of the high field intensity required. In addition, the poled films present often several surface damages due to various reactive and energy species, such as ozone or nitrogen oxides, that are produced by the corona discharge (Sprave et al., 1996).

Here, we propose a simple and voltage-free process based on pyro-electrification (PE), capable of producing polar orientation and 2D polar patterning in freestanding polymer sheets. Compared to conventional electrification techniques, the PE is electrode-free and is able to produce high voltages by a simple thermal treatment in ferroelectric crystals of lithium niobate (LN), thus simplifying the whole process significantly. Moreover, we can produce both homogeneous and bipolar charge distributions simply by using one-domain or homemade periodically poled LN crystals obtaining pyro-electrified polymer sheets with a net surface charge. Recently, we investigated the presence of such charge by analyzing the second harmonic signal and by observing the adhesion and spreading of eukaryotic cells on PE polymers that would be otherwise cytophobic surfaces (Rega et al., 2016a,b; Lettieri et al., 2017). Moreover, we evaluated *in vitro* the ability of bacteria to form biofilms very rapidly (Gennari et al., 2018).

It is recognized that the adhesion and proliferation of different types of cells on polymeric materials depend on surface characteristics and can be significantly influenced by the surface charge on that material (Robertus et al., 2010; Li et al., 2018; Liu et al., 2018; Ma et al., 2019).

Polystyrene (PS) and poly (methyl methacrylate) (PMMA) are materials typically used in labware equipment. They are cytophobic and require a chemical or physical treatment to promote cell adhesion. The most common treatments make use of sulfuric acid, or chromic acid, which can produce different kinds of functional groups on the surface, such as sulfonate, hydroxyl, or carboxyl. Another family of techniques makes use of protein adsorption, such as fibronectin, laniline, and Arginylglycylaspartic acid (RGD) peptide that chemically mimic the extracellular microenvironment and alter the structure of the surface. On the other hand, physical treatments able to activate the surface of traditional cytophobic surfaces by mild oxidation involve ultraviolet light or corona discharge stimulation. Regardless of the method, the cell adhesion promotion requires an electrostatically charged surface. All of these treatments are well-established but are laborious and expensive with additional drawbacks related to potentially polluting materials.

Here, we show the possibility of obtaining charged polymeric surfaces capable of interacting electrostatically with cell cultures under safe conditions by an easy and economical procedure, tracing the route as an alternative tool for all those applications in which the use of chemical agents or complicated physical treatments can be detrimental for both environment and cell cultures.

MATERIALS AND METHODS

The ferroelectric LN is a rhombohedral crystal belonging to the point group 3 m that exhibits pyroelectricity at room temperature. The spontaneous polarization P_s changes according to $\Delta P_i \alpha p_i \Delta T$, where P_i is the coefficient of the polarization vector, p_i is the pyroelectric coefficient, and ΔT is the temperature variation. At room temperature, the equilibrium condition makes the charge of the spontaneous polarization P_s to be balanced fully by the environmental screening charges, and no electric field exists (Grilli et al., 2008a). The temperature variation changes the polarization magnitude and perturbs this equilibrium, causing a lack or excess of surface screening charge (Bhowmick et al., 2017). As a consequence, an electrostatic state appears and generates a high-intensity electric field at the crystal surface (Bhowmick et al., 2017) with mono- or bipolar properties depending on the nature of the LN crystal, mono-domain in the first case and periodically poled (PPLN) in the second one. The PPLN crystals were homemade by standard electric field poling onto photoresist patterned samples (Detrait et al., 1998; Huang et al., 2012; Pagliarulo et al., 2018) and consisted of an array of ferroelectric domains with opposite polarization. The pyroelectric effect generates an array of surface charges with opposite sign, following the pattern of the reversed domains. Recently, we demonstrated for the first time the possibility of using the pyroelectric effect for a wide variety of applications ranging from biological to soft matter manipulation application (Ferraro et al., 2010; Mecozzi et al., 2016, 2017; Rega et al., 2019).

The PE exploits this electric field during an appropriate thermal treatment. The PE induces a permanent orientation of the dipoles when exceeding the glass transition temperature of the polymer, namely, when the dipole molecules can be easily oriented. This technique guarantees simplicity and cost-effectiveness since only a polymeric solution is needed, spin coated on an LN crystal and thermal treated on conventional hotplates. The fundamental role is played by the LN crystal since it supports, heats, and polarizes the polymer layer, which, at the

end of the process, is easily removed, obtaining a freestanding charged sheet.

THE PYRO-ELECTRIFICATION

Figure 1 shows the schematic view of the procedure.

The LN crystal sample is spin coated with a polymer solution at room temperature and then heated by a digitally controlled hotplate according to a thermal treatment based on three steps identified here by the following labels: slow heating (Stuart et al., 2010), holding (Jacobs and Whitesides, 2001), and fast cooling (Palleau et al., 2011). The slow heating induces a temperature rise from room temperature (T_i) up to the glass transition temperature of the polymer (T_f) at a rate of 1°C/min. The holding step keeps the sample at the final temperature T_f for 10 min. In the fast cooling step, the polymer-coated crystal is moved to a second hotplate set at a lower temperature T_l ∼50°C. The slow rate of temperature increase in the first step and the holding state are of crucial importance for keeping the electrostatic equilibrium between the slight polarization change of the LN and the screening charges on the surface, prior to reaching the glass transition of the polymer. Once this state is reached, the polymer becomes very amorphous and the dipole molecules can orient easily under the action of the strong electric field generated onto the surface of the crystal by the pyroelectric effect. The monotonic cooling step is necessary to provide large ΔT that generates a steady and strong electric field capable of poling the polymer and, simultaneously, freezing the poled state into the polymer itself. The poled polymer layer can be peeled off from the surface of the crystal proving a freestanding sheet with the same polarization orientation of the LN crystal that drove the PE process.

The technique can be performed under two different configurations and with different polymer solutions. The single-domain PE (SD-PE) uses a single domain crystal, while the multi-domain PE (MD-PE) makes use of a periodically poled crystal PPLN with different geometries. In the case of the SD-PE configuration, the polymer layer exhibits a polarization charge with single orientation, while in the case of the MD-PE configuration, the polymer shows the pattern of domains with reversed polarization according to the ferroelectric domain pattern of the driving PPLN crystal. The driving crystal can be re-used indefinitely after appropriate solvent cleaning.

THE POLYMER SOLUTIONS

Solid-state polymers were used as received, without further purification (Sigma-Aldrich, Milan, Italy). Polysulfone (PSU) transparent pellets (M_w 35,000) were dissolved at 80% w/w in anisole and stirred at 70°C for 3 h. PS powder (M_w 350,000)

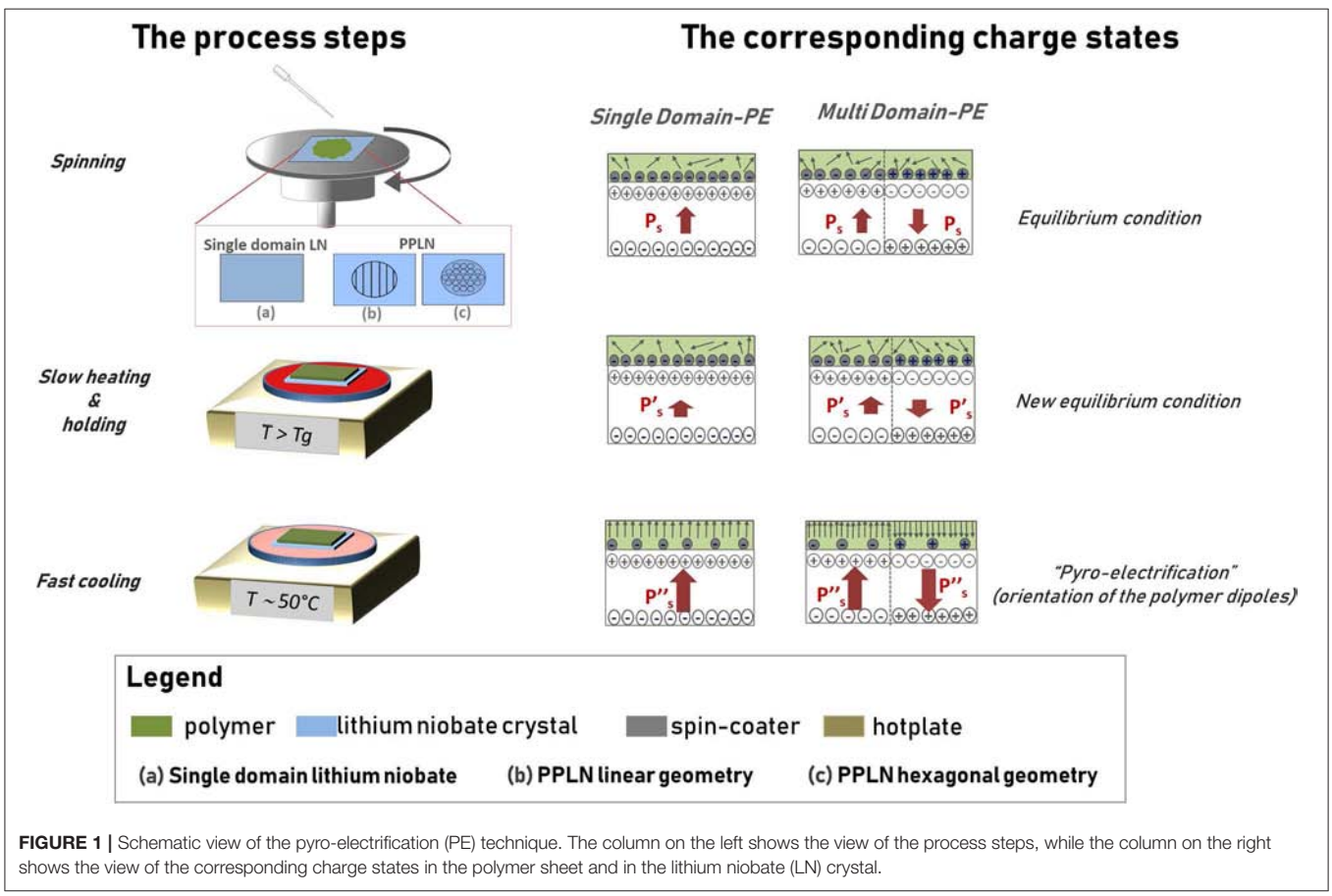

FIGURE 1 | Schematic view of the pyro-electrification (PE) technique. The column on the left shows the view of the process steps, while the column on the right shows the view of the corresponding charge states in the polymer sheet and in the lithium niobate (LN) crystal.

was dissolved at 60% w/w in anisole and stirred at 70°C for 6 h. PMMA (M_w 996,000) was dissolved at 15% w/w in anisole and stirred at 70°C for 3 h. The resulting polymer solutions of PSU, PS, and PMMA were stored at 4°C.

THE PERIODICALLY POLED LN CRYSTALS

The LN crystals were bought from Crystal Technology Inc., Palo Alto, California, in the form of both sides polished into 500 μm-thick c-cut 3-inch. wafers and were cut into square samples (2 × 2 cm^2) by a standard diamond saw. The PPLNs were obtained by standard electric field poling onto photoresist-patterned samples (Huang et al., 2012; Bhowmick et al., 2017; Pagliarulo et al., 2018). Two geometries were considered: linear (period, 200 μm) and square array of hexagons (period, 200 μm).

THE BARE SHEETS (CONTROL)

The freestanding PSU, PS, and PMMA bare sheets were obtained by spin coating a 2 × 2 cm^2 sized glass coverslip at 4,000 RPM for 2 min with the polymer solution and by peeling off the slide accurately just after solvent evaporation.

THE SH-SY5Y HUMAN NEUROBLASTOMA AND THE NIH-3T3 MOUSE EMBRYONIC FIBROBLAST CELLS

The SH-SY5Y and NIH-3T3, cells lines were purchased from European Collection of Authenticated Cell Cultures (ECACC) (Sigma-Aldrich, Milan, Italy). They were routinely grown in Dulbecco's modified Eagle's medium (DMEM) containing 4.5 g/L D-glucose and supplemented with 2 mM L-glutamine, penicillin (100 units/ml), and streptomycin (100 μg/ml), and containing 20% (v/v) fetal bovine serum (FBS) (GIBCO, Gaithersburg, MD, USA). For the cell culture experiments, the SH-SY5Y and NIH-3T3 were detached by means of Trypsin/Ethylenediaminetetraacetic acid dipotassium salt dihydrate (EDTA) solution (Sigma, Milan, Italy), resuspended in DMEM−20% FBS, seeded at a concentration of 1.0 × 10^5 cells/ml on the MD-PE sheets (immersed in DMEM medium at 37°C for 1 h prior to use), and then incubated into conventional 30 mm-diameter Petri dishes at 37°C and in a saturated humidity atmosphere containing 95% air and 5% CO_2. Cells were allowed to grow in DMEM−20% FBS on different substrates for 24 h. Cell adhesion and spreading were observed over 24 h under a standard inverted optical microscope (AxioVert, Carl Zeiss, Jena, Germany).

IMMUNOFLUORESCENCE

The cells were cultured 24 h on the surface of interest and then fixed by standard procedures. The cells were then stained by Alexa Fluor 488 phalloidin and by blue fluorescent Hoechst 33,342 dye and trihydrochloride trihydrate (Molecular Probes Invitrogen) for visualizing nuclei and actin filaments.

BACTERIAL STRAIN AND CULTURE CONDITIONS

In the present study, we used the Gram-positive Listeria innocua (strain DSMZ 20649) provided by the Deutsche Sammlung von Mikroorganismen und Zellkulturen, Braunschweig, Germany. The bacteria strains were plated and incubated on Luria-Bertani (LB) agar plates (10 g/l NaCl, 10 g/l tryptone, 5 g/l yeast extract, and 15 g/l agar, Thermo Fisher Scientific). One day before the experiments, a single bacterial colony was picked up and cultured in LB broth medium at 37°C in a shaker incubator at 225 RPM for 16–18 h to achieve saturation conditions. A 1:5 volumetric dilution of the cell culture was then grown in LB until reaching the log phase. Then, the growth was stopped and bacteria were harvested by centrifugation at 7.200 g (Beckman Coulter tj-25 centrifuge, California, USA) for 10 min in order to separate the cells from the medium. Sterilized LB broth was measured (3 ml) into sterile tubes. The bacteria concentration was evaluated by the spectrophotometric measurement (Bio-Rad SmartSpecTM Plus Spectrophotometer, California, USA) of the suspension absorbance at 600 nm (optical density at 600 nm, i.e., OD_{600}), considering that 8 × 10^8 cells/ml have an $OD_{600} = 1$.

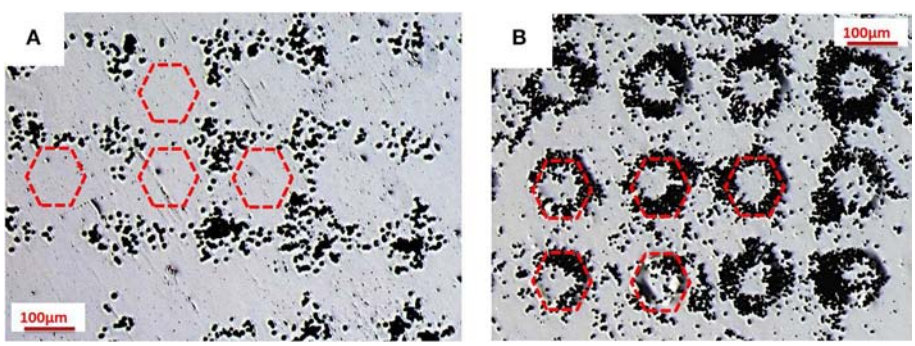

FIGURE 2 | Optical microscope images of decoration technique: toner distribution on two polystyrene (PS) sheets after pyro-electrification (PE) by a periodically poled lithium niobate (PPLN) crystal, where the hexagons exhibit **(A)** positive and **(B)** negative charge polarity. The hexagons are indicated by the schematic drawings with the red dotted line.

MICROTITER-PLATE TEST

In order to quantify the biofilm formation, we use the crystal violet assay (Stepanović et al., 2000). This technique involves fixing the bacterial film with methanol, staining with crystal violet, releasing the bound dye with 33% glacial acetic acid, and measuring the optical density (OD) of the solution at 600 nm by spectrophotometric measurement (Bio-Rad SmartSpecTM Plus Spectrophotometer, CA, USA).

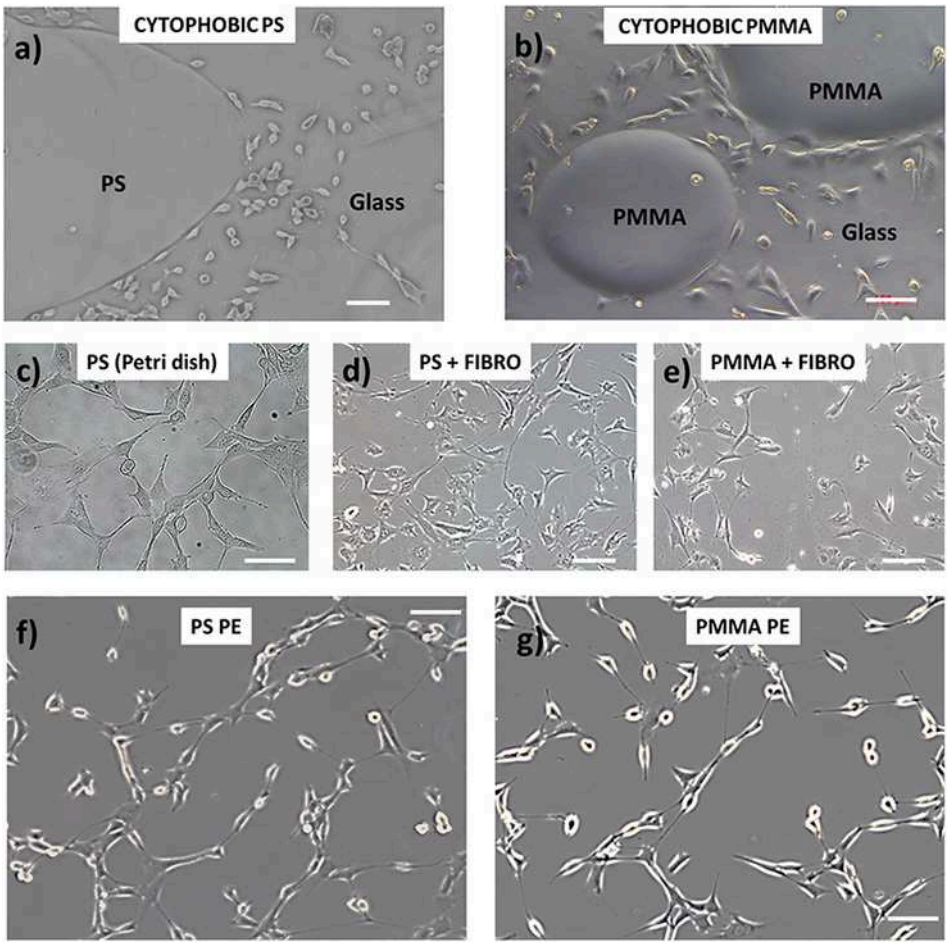

FIGURE 3 | NIH-3T3 cell adhesion behavior on **(a,b)** bare PS and poly(methyl methacrylate) (PMMA) polymer (respectively) spotted on a glass coverslip where it shows the cytophobic behavior of the materials; **(c–e)** conventional PS Petri dish (generally treated with UV light), PS coated with fibronectin protein, and PMMA coated with fibronectin protein, respectively; **(f,g)** NIH-3T3 cells grown on the pyro-electrified PS and PMMA, respectively. Scale bar, 100 μm.

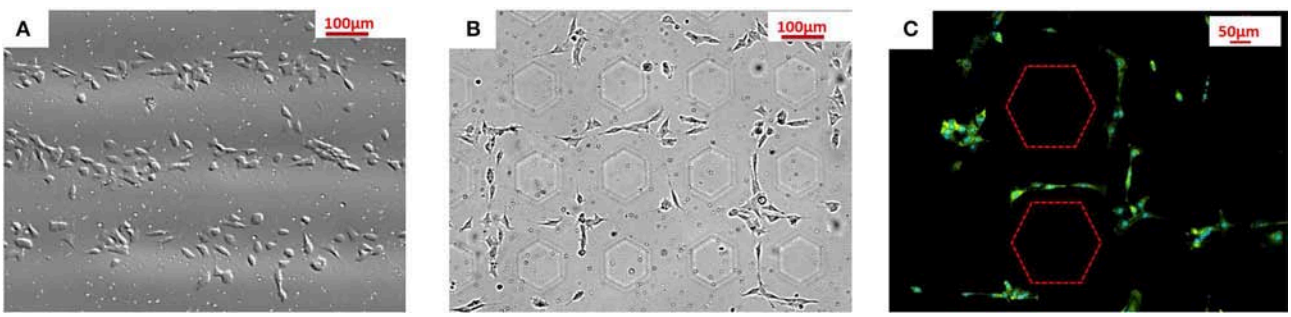

FIGURE 4 | SH-SY5Y cell adhesion behavior on **(A)** PS sheet pyro-electrified linearly at 200 μm; **(B)** cell patterning on PMMA (15% in anisole w/w) sheet pyro-electrified by an array of hexagons at 200 μm; **(C)** immunofluorescence images of cells cultured after 24 h incubation on PS sheets pyro-electrified by an array of hexagons at 200 μm. The dashed lines correspond to the boundaries between regions with opposite polarities.

THE VIABILITY TEST

The viability of the bacterial strain (*L. innocua*) was tested through the live/dead viability/cytotoxicity assay kit (Live/Dead *Bac*Light bacterial viability kit, Thermo Fisher Scientific, Waltham, MA, USA). The easy-to-use live/dead kit is utilized for monitoring the viability of the bacterial populations as a function of the sheet integrity of the cell. The live/dead BacLight Bacterial Viability Kits utilize mixtures of our SYTO® 9 green-fluorescent nucleic acid stain and the red fluorescent nucleic acid stain, propidium iodide. These stains differ both in their spectral characteristics and in their ability to penetrate healthy bacterial cells. Cells with a compromised sheet that are considered to be dead or dying will stain red, whereas cells with an intact sheet will stain green. The cells were incubated on each substrate for 24 h. After incubation, each substrate was immersed in 8 μl of 1,000-fold diluted live/dead kit solution and was incubated for 15 min in the dark. The fluorescence micrographs were acquired by an inverted laser scanning confocal microscope (Zeiss LSM 700, Germany), equipped with a 20× objective.

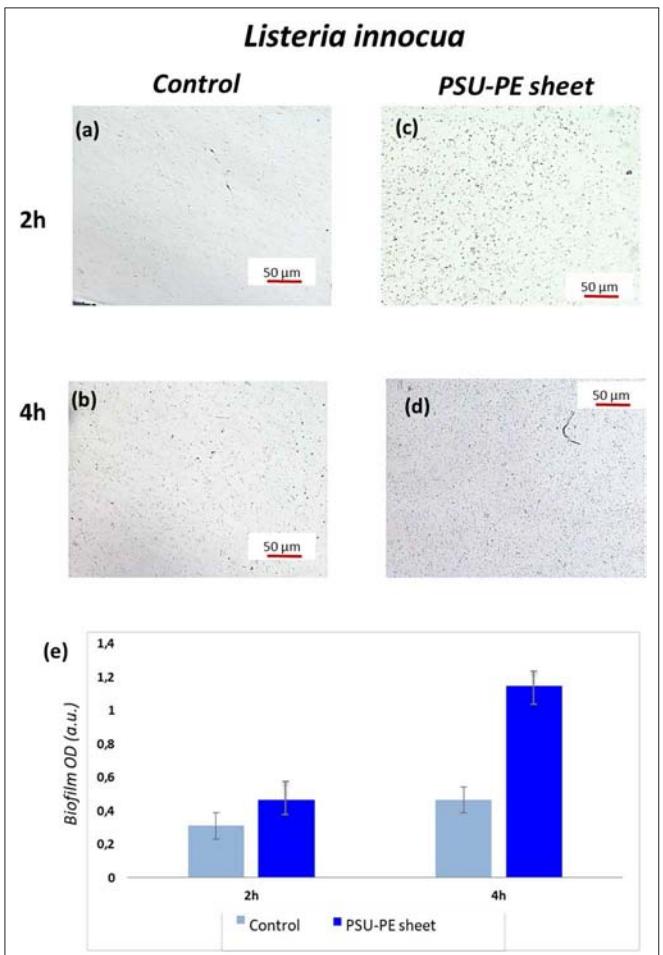

FIGURE 5 | (a,b) Optical microscopy images of *L. innocua* bacterial adhesion at two different time points on control and **(c,d)** on the polysulfone pyro-electrified (PSU-PE) sheet; **(e)** histogram of bacteria biofilm OD (optical density) on the control and the PSU-PE sheet at two different time points.

RESULTS AND DISCUSSION

Two PMMA sheets were subjected to PE by using a PPLN crystal (see **Figure 1** for the multi-domain procedure). A faster test to verify the presence of the charges on the PE sheet is the decoration technique. The polymer solution was spun on one face of the crystal and, in the second experiment, on the other face of the PPLN. As a consequence, we produced two freestanding PS sheets with a bipolar polarization pattern following the pattern of reversed domains of the PPLN. The hexagonal regions of the PS sheets exhibited positive and negative polarity, respectively. **Figures 2A,B** shows the typical optical microscope images of these two PS sheets after gentle sprinkling of toner dust on the surface.

These images show clearly that the particles of toner, bringing a negative charge, are attracted electrostatically by the hexagonal regions (positive charge) in the first case (see **Figure 2A**) and by the surrounding regions (positive charge) in the second case (see **Figure 2B**), thus demonstrating the non-negligible electric field generated on the surface of the pyro-electrified PS sheets.

We demonstrate here the possibility of using the permanent electric field on the PE sheet for guiding live cell adhesion *in vitro*. PS and PMMA labware equipment have been used for cell culture since about 1965. Many cell types adhere to and move on the surfaces of such materials and present a morphology that is very similar to that seen when the cells are grown on glass. However, it has long been known that these materials must be subjected to a surface treatment to render their surface suitable for cell attachment. Bare PS and PMMA are unsuitable for cell attachment, meaning that cells seeded and incubated onto surfaces made of such polymers cannot find adhesion cues and remain suspended. This has been attributed to the surface chemistry of the materials, and many different specific surface treatments have been made to change the chemistry involved in the non-adhesive nature of these polymers (Klemperer and Knox, 1977; Maroudas, 1977; Grinnell, 1978; Lee et al., 1994; Buttiglione et al., 2007).

Here, we demonstrate the cytophilic capability of PE polymer for cultured NIH-3T3 cells (see Materials and Methods for details) on PS and PMMA sheets pyro-electrified on a single domain crystal. **Figure 3** shows the optical microscope images of the sheets after 24 h incubation with NIH-3T3 cells. In particular, the image in **Figures 3a,b** show the cytophobic behavior of bare PS and PMMA polymer spotted on a glass coverslip where it is clearly seen that the cells are not able to adhere and spread. These materials are often treated in a chemical or physical way in order to permit cell adhesion and spreading. **Figures 3c–e** show the adhesion of NIH-3T3 cells on a conventional PS Petri dish (generally treated with UV light), PS coated with fibronectin protein, and PMMA coated with fibronectin protein, respectively. **Figures 3f,g** show

the NIH-3T3 cells grown on the pyro-electrified PS and PMMA, respectively.

On substrates treated with fibronectin, the cellular conformation and their spatial distribution are characterized by a more compact organization and a more spread cellular shape, indicating a stronger cell–cell interaction than the interaction with the adhesion surface. The cellular distribution on the pyro-electrified sheets shows, on the other hand, an elongated shape of the nuclei and cellular filopodes, typical of cells polarized along one preferential direction. This characteristic is an indication of a strong interaction with the contact surface, which is predominant with respect to the cell–cell interaction.

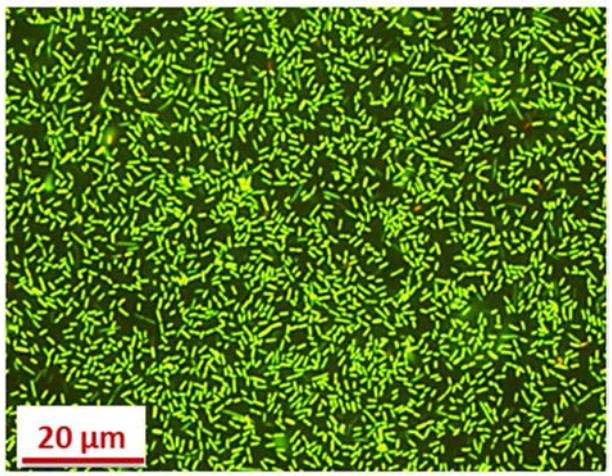

FIGURE 6 | Fluorescence microscopy images of *L. innocua* forming biofilms onto the PSU-PE sheet after 24 h incubation and live/dead staining.

Moreover, as already shown in our previous paper (Rega et al., 2016a,b), it is possible to have a cell pattern configuration when seeded on sheets pyro-electrified by a multi-domain crystal with a bipolar configuration of the charge distribution on the sheet surface. Here, we demonstrate the reliability of the technique with other periods and different concentrations of the polymer.

Figure 4A shows that SH-SY5Y cells adhered selectively on the positive region of PS sheet with bipolar domains having linear geometry with a 200 µm period, while **Figure 4B** corresponds to a PMMA (15% in anisole w/w) sheet, with bipolar domains having two-dimensional distributions at a 200 µm period. Moreover, in order to better elucidate the material–cytoskeleton cross-talk during adhesion, we fixed the cells after 24 h incubation on PS sheets pyro-electrified by PPLN crystals with hexagonal domains, and we performed immunofluorescence reactions (**Figure 4C**) (see Materials and Methods for details). The cells appear clearly to adhere selectively on the regions with positive polarity in the case of linear domains as well as in the case of two-dimensional domains. In fact, the cells bring a negative net charge on the external sheet (Ohgaki et al., 2001) and, as a consequence,

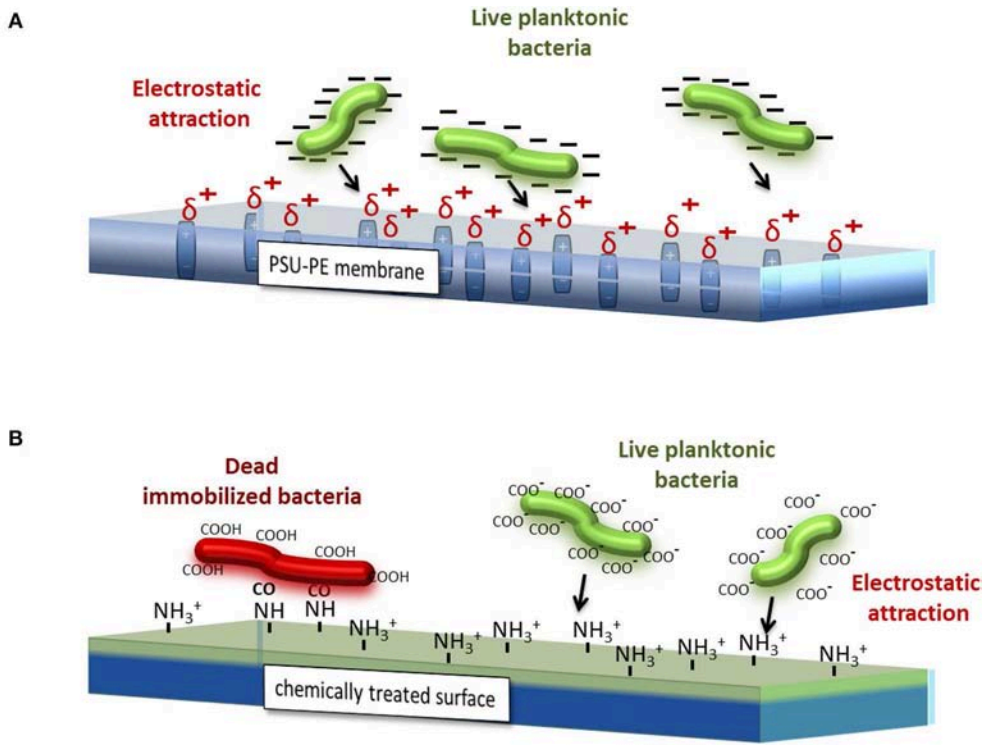

FIGURE 7 | Simplified schematic views of the different interaction mechanisms between bacteria, the cytomembrane, and **(A)** the PSU-PE sheet and **(B)** a generic chemical-coated sheet.

are attracted electrostatically by the regions of the sheet exposing a net positive polarization charge.

The PE allows us to achieve cell patterning results through a cation-free method, avoiding time-consuming and expensive lithographic-based procedures and moreover directly onto freestanding, and cheap polymer sheets. The relatively easy-to-accomplish procedure, which makes use simply of LN crystals and conventional hotplates, would be easily implementable in biology laboratories for routine cell biology experiments where selective cell adhesion configurations are of crucial importance. For example, in the case of electric-field-sensitive cells, we envisage the possibility of using PE for developing pre-defined neuronal networks for deep studies on their physiology and morphology behavior.

Recently, we demonstrated the possibility of using pyro-electrified sheets and fibers for rapid and reliable "biofilm electrostatic test" (Gennari et al., 2018) of *Escherichia coli* and *Staphylococcus epidermidis*, with potential applications in the field of biomedicine. In fact, the rapid biofilm formation promoted by our sheets would have a significant impact on health service when a fast response to an antibiogram test can save lives. Here, we show how the pyro-electrified sheets promote a rapid biofilm formation also in the case of *L. innocua*, a non-pathogenic species closely related to *L. monocytogenes* (Scifò et al., 2009; Tajkarimi et al., 2016; Jeon et al., 2018; Sheng et al., 2018). We use an SD-PE sheet as a tool for simple, rapid, and cost-effective evaluation of biofilm formation, through the electrostatic interaction of planktonic bacteria with a pyro-electrified carrier (Asadishad et al., 2011; Gennari et al., 2018). The fact that biofilms have a multidisciplinary impact that includes environmental, industrial, and clinical characteristics, and that over 60% of all human bacterial infections and up to 80% of all chronic infections are related to bacterial biofilms, is of fundamental importance in assessing how different environmental factors may affect the bacterial vitality. The cellular mechanisms underlying microbial biofilm formation and behavior are beginning to be understood and are targets for novel specific intervention strategies to control bacteria colonies formation in different fields and in particular for the food-processing environment (Dickson and Koohmaraie, 1989; Sahm et al., 1994; Linke and Goldman, 2011; Bianco et al., 2017; Bruslind, 2017; Mandracchia et al., 2019).

Here, we demonstrate that SD-PE carrier provides a polarization field able to immobilize the *L. innocua* bacteria and test their ability to form live biofilms within 2 h, avoiding time-consuming and laborious incubations and/or intermediate chemical treatments. PSU sheets (about 100 μm thickness and 2 × 2 cm^2 sized) were produced: (Stuart et al., 2010) a bare sheet that represents the control and (Jacobs and Whitesides, 2001) polysulfone pyro-electrified (PSU-PE), where the positive side was in contact with the bacterial suspension. These sheets were incubated at different times (2 and 4 h) at 37°C in two different Petri dishes (35 mm) covered with 1 ml of *L. innocua* bacterial suspension (Gram-positive) and 2 ml of phosphate-buffered saline (PBS). The control and the SD-PE sheets were observed under an optical microscope, and **Figure 5** shows the corresponding typical images.

These microscope images show the immobilized and biofilm forming bacteria on the control and PSU-PE sheet at different time intervals. The number of adhesion bacteria on the PSU-PE sheet appeared clearly higher than that on the control at each observation time. These results are confirmed by the quantitative evaluation of biofilm formation obtained by the microtiter-plate test (see Materials and Methods for details). The diagram in **Figure 5e** shows results averaged over five measures of biofilm OD (optical density) formation and shows evidence of the larger population of bacteria on the PE sheet.

To verify the viability of the biofilms, the PSU-PE sheet was mounted onto a glass slide in a well after 24 h incubation with planktonic bacteria in order to perform the reaction with the live/dead staining kit (see Material and Methods for details). After 24 h incubation, we found that the viability of the high-density biofilms formed onto the PSU-PE sheet was clearly evident (**Figure 6**). The PSU-PE sheet immobilized planktonic bacteria more rapidly than the control and favored biofilm formation without damaging the bacterial cytomembrane even after 24 h incubation, thus demonstrating biocompatiblity.

On the contrary, chemical coatings could immobilize planktonic bacteria, but could even destroy the bacterial cytomembrane causing their death. Cationic surfaces are obtained usually by the covalent attachment of different chemical compounds, such as quaternary ammonium organo-silanes (Isquith et al., 1972; Gottenbos et al., 2002; Li et al., 2006), antimicrobial peptides (Gabriel et al., 2006; Gao et al., 2011), polyethylenimines (PEI) (Lin et al., 2003), and many others. The mechanism of interaction, as already explained in Gennari et al. (2018), is schematized in **Figure 7**. The PE process provides a sheet (in this case, the PSU-PE sheet) with δ^+ charge due to the permanent dipole generated during the process. Those charges attract the negative net charge onto the bacterial cytomembrane (COO^- groups), thus leading to bacteria immobilization and promoting the biofilm formation. In contrast, the cationic groups $NH3^+$, generally formed on the chemically treated surface, form an electrostatic bond with the COO^- groups onto the cytomembrane of bacteria adhered, thus displacing the divalent cations forming the lipopolysaccharide network. This causes the disruption of the cytomembrane and then microorganism death.

The PE of freestanding polymer sheets could find applications in the food processing field as a quality check tool. The ultimate goal is the development of a rapid and easy PE assay for a quantitative analysis of a food sample, enabling food technologists to detect the contaminant agents in fresh products that represent a serious risk for all the consumers. In fact, it would be desirable having a compact and efficient system that could be used, for example, in an industry outside the laboratory. However, to develop and to design industrial applications for food processing, more data on the interaction between the process and the target organism are required. PE assay approaches will help to close this gap in the future, because they have the potential to be used as a method to control bacteria contamination and to ensure fresh food safety.

CONCLUSION

Here, we show an innovative PE technique capable of inducing a permanent dipole charge into freestanding polymer sheets by exploiting the pyroelectric properties of LN crystals, under both single- and multi-domain configurations. The resulting sheets can correspondingly have a mono- and bipolar charge with a magnitude able to selectively promote the adhesion of both eukaryotic and prokaryotic cells. The innovative use of the pyroelectric effect allows us to avoid expensive and time-consuming fabrication of electrodes and high-voltage circuits, since the appropriate thermal treatment of LN generates electrical potentials on the order of kilovolts. The same LN crystal can be used indefinitely for different PE cycles. The technique is free from lithography-based procedures and free from the use of cation-based chemicals, eventually detrimental for specific cell sheet structures. We show how these sheets can be used for cell patterning as well as for rapid biofilm formation. The relatively easy implementation makes PE implementable in a biology laboratory, opening the route to a novel generation of platforms for manipulating cell adhesion *in vitro* through non-invasive polarization charges, with the additional advantage of being flexible, freestanding, and cheap.

AUTHOR CONTRIBUTIONS

RR planned, conducted experiments and wrote the manuscript. OG, MM, FN and EO prepared the biological cultures. VP made the PPNL samples. PF and SG supervised the project. All authors discussed the results and contributed to the manuscript.

FUNDING

The authors acknowledge the EU funding within the Horizon 2020 Program, under the FET-OPEN Project SensApp, Grant Agreement No. 829104.

REFERENCES

Asadishad, B., Ghoshal, S., and Tufenkji, N. (2011). Method for the direct observation and quantification of survival of bacteria attached to negatively or positively charged surfaces in an aqueous medium. *Environ. Sci. Technol.* 45, 8345–8351. doi: 10.1021/es201496q

Bhowmick, S., Iodice, M., Gioffrè, M., Breglio, G., Irace, A., Riccio, M., et al. (2017). Investigation of pyroelectric fields generated by lithium niobate crystals through integrated microheaters. *Sens. Actuators A Phys.* 261, 140–150. doi: 10.1016/j.sna.2017.05.010

Bianco, V., Mandracchia, B., Nazzaro, F., Marchesano, V., Gennari, O., Paturzo, M., et al. (2017). "Food quality inspection by speckle decorrelation properties of bacteria colonies," in *Optical Methods for Inspection, Characterization, and Imaging of Biomaterials III* (San Francisco, CA).

Bruslind, L. (2017). *Chapter 4: Microbiology*. Corvallis, OR: Open Oregon State.

Buttiglione, M., Vitiello, F., Sardella, E., Petrone, L., Nardulli, M., Favia, P., et al. (2007). Behaviour of SH-SY5Y neuroblastoma cell line grown in different media and on different chemically modified substrates. *Biomaterials* 28, 2932–2945. doi: 10.1016/j.biomaterials.2007.02.022

Carrascosa, M., García-Cabañes, A., Jubera, M., Ramiro, J. B., and Agulló-López, F. (2015). LiNbO3: a photovoltaic substrate for massive parallel manipulation and patterning of nano-objects. *Appl. Phys. Rev.* 2:040605. doi: 10.1063/1.4929374

Chen, L., Li, S., Fan, B., Yan, W., Wang, D., Shi, L., et al. (2016). Dielectrophoretic behaviours of microdroplet sandwiched between LN substrates. *Sci. Rep.* 6:29166. doi: 10.1038/srep29166

Cole, J. J., Barry, C. R., Wang, X., and Jacobs, H. O. (2010). Nanocontact electrification through forced delamination of dielectric interfaces. *ACS Nano* 4, 7492–7498. doi: 10.1021/nn1016692

DeRose, C. T., Enami, Y., Loychik, C., Norwood, R. A., Mathine, D., Fallahi, M., et al. (2006). Pockel's coefficient enhancement of poled electro-optic polymers with a hybrid organic–inorganic sol-gel cladding layer. *Appl. Phys. Lett.* 89:131102. doi: 10.1063/1.2357157

Detrait, E., Lhoest, J. B., Knoops, B., Bertrand, P., and de Aguilar, P. V. D. B. (1998). Orientation of cell adhesion and growth on patterned heterogeneous polystyrene surface. *J. Neurosci. Methods* 84, 193–204. doi: 10.1016/S0165-0270(98)00114-9

Dickson, J. S., and Koohmaraie, M. (1989). Cell surface charge characteristics and their relationships to bacterial attachment to meat surfaces. *App. Environ. Microbiol.* 55, 832–836.

Esseling, M., Zaltron, A., Sada, C., and Denz, C. (2013). Charge sensor and particle trap based on z-cut lithium niobate. *Appl. Phys. Lett.* 103:061115. doi: 10.1063/1.4818143

Ferraro, P., Coppola, S., Grilli, S., Paturzo, M., and Vespini, V. (2010). Dispensingnano–pico droplets and liquid patterning by pyroelectrodynamic shooting. *Nat. Nanotechnol.* 5, 429–435. doi: 10.1038/nnano.2010.82

Gabriel, M., Nazmi, K., Veerman, E. C., Nieuw Amerongen, A. V., and Zentner, A. (2006). Preparation of LL-37-grafted titanium surfaces with bactericidal activity. *Bioconjug. Chem.* 17, 548–550. doi: 10.1021/bc050091v

Gao, G., Lange, D., Hilpert, K., Kindrachuk, J., Zou, Y., Cheng, J. T. J., et al. (2011). The biocompatibility and biofilm resistance of implant coatings based on hydrophilic polymer brushes conjugated with antimicrobial peptides. *Biomaterials* 32, 3899–3909. doi: 10.1016/j.biomaterials.2011.02.013

Gennari, O., Grilli, S., Coppola, S., Pagliarulo, V., Vespini, V., Coppola, G., et al. (2013). Spontaneous assembly of carbon-based chains in polymer matrixes through surface charge templates. *Langmuir* 29, 15503–15510. doi: 10.1021/la403603d

Gennari, O., Marchesano, V., Rega, R., Mecozzi, L., Nazzaro, F., Fratianni, F., et al. (2018). Pyroelectric effect enables simple and rapid evaluation of biofilm formation. *ACS Appl. Mater. Interfaces* 10, 15467–15476. doi: 10.1021/acsami.8b02815

Gottenbos, B., van der Mei, H. C., Klatter, F., Nieuwenhuis, P., and Busscher, H. J. (2002). *In vitro* and *in vivo* antimicrobial activity of covalently coupled quaternary ammonium silane coatings on silicone rubber. *Biomaterials* 23, 1417–1423. doi: 10.1016/S0142-9612(01)00263-0

Grilli, S., Paturzo, M., Miccio, L., and Ferraro, P. (2008a). *In situ* investigation of periodic poling in congruent LiNbO3 by quantitative interference microscopy *Meas. Sci.Technol.* 19:074008. doi: 10.1088/0957-0233/19/7/074008

Grilli, S., Vespini, V., and Ferraro, P. (2008b). Surface-charge lithography for direct PDMS micro-patterning. *Langmuir* 24, 13262–13265. doi: 10.1021/la803046j

Grinnell, F. (1978). "Cellular adhesiveness and extracellular substrata," in *International Review of Cytology, Vol. 53*, eds G. H. Bourne, J. F. Danelli, and K. W. Jeon (San Francisco, CA: Academic Press), 65–144.

Hill, R. A., Knoesen, A., and Mortazavi, M. A. (1994). Corona poling of nonlinear polymer thin films for electro-optic modulators. *Appl. Phys. Lett.* 65, 1733–1735. doi: 10.1063/1.112899

Huang, S., Luo, J., Yip, H. L., Ayazi, A., Zhou, X. H., and Jen, A. K. Y. (2012). Efficient poling of electro-optic polymers in thin films and silicon slot waveguides by detachable pyroelectric crystals. *Adv. Mater.* 24:42. doi: 10.1002/adma.201102874

Isquith, A. J., Abbott, E. A., and Walters, P. A. (1972). Surface-bonded antimicrobial activity of an organosilicon quaternary ammonium chloride. *Appl. Microbiol.* 24, 859–863.

Jacobs, H. O., and Whitesides, G. M. (2001). Submicrometer patterning of charge in thin-film electrets. *Science* 291, 1763–1766. doi: 10.1126/science.1057061

Jeon, H. R., Kwon, M. J., and Yoon, K. S. (2018). Control of *Listeria innocua* biofilms on food contact surfaces with slightly acidic electrolyzed water and the risk of biofilm cells transfer to duck meat. *J. Food Prot.* 81, 582–592. doi: 10.4315/0362-028X.JFP-17-373

Klemperer, H. G., and Knox, P. (1977). Attachment and growth of BHK and liver cens on polystyrene: effect of surface groups introduced by treatment with chromic acid. *Lab. Pratt.* 26, 179–180.

Lee, J. H., Jung, H. W., Kang, I. K., and Lee, H. B. (1994). Cell behaviour on polymer surfaces with different functional groups. *Biomaterials* 15, 705–711. doi: 10.1016/0142-9612(94)90169-4

Lettieri, S., Rega, R., Pallotti, D. K., Gennari, O., Mecozzi, L., Maddalena, P., et al. (2017). Direct evidence of polar ordering and investigation on cytophilic properties of pyroelectrified polymer films by optical second harmonic generation analysis. *Macromolecules* 50, 7666–7671. doi: 10.1021/acs.macromol.7b00794

Li, W., Yan, Z., Ren, J., and Qu, X. (2018). Manipulating cell fate: dynamic control of cell behaviors on functional platforms. *Chem. Soc. Rev.* 47, 8639–8684. doi: 10.1039/C8CS00053K

Li, Z., Lee, D., Sheng, X., Cohen, R. E., and Rubner, M. F. (2006). Two-level antibacterial coating with both release-killing and contact-killing capabilities. *Langmuir* 22, 9820–9823. doi: 10.1021/la0622166

Lin, J., Qiu, S., Lewis, K., and Klibanov, A. M. (2003). Mechanism of bactericidal and fungicidal activities of textiles covalently modified with alkylated polyethylenimine. *Biotechnol. Bioeng.* 83, 168–172. doi: 10.1002/bit.10651

Linke, D., and Goldman, A. (2011). *Bacterial Adhesion, Chemistry, Biology and Physics*. Springer.

Liu, L., Tian, X., Ma, Y., Duan, Y., Zhao, X., and Pan, G. (2018). A versatile dynamic mussel-inspired biointerface: from specific cell behavior modulation to selective cell isolation. *Angew. Chem. Int. Ed.* 57, 7878–7882. doi: 10.1002/anie.201804802

Ma, Y., Tian, X., Liu, L., Pan, J., and Pan, G. (2019). Dynamic synthetic biointerfaces: from reversible chemical interactions to tunable biological effects. *Acc. Chem. Res*. doi: 10.1021/acs.accounts.8b00604. [Epub ahead of print]

Mandracchia, B., Palpacuer, J., Nazzaro, F., Bianco, V., Rega, R., Ferraro, P., et al. (2019). Biospeckle decorrelation quantifies the performance of alginate-encapsulated probiotic bacteria. *IEEE J. Sel. To. Quantum Electron.* 25, 1–6. doi: 10.1109/JSTQE.2018.2836941

Maroudas, N. G. (1977). Sulphonated polystyrene as an optimal substratum for the adhesion and spreading of mesenchymal cells in monovalent and divalent saline solutions. *J. Cell. Physiol.* 90, 511–519. doi: 10.1002/jcp.1040900314

Mecozzi, L., Gennari, O., Rega, R., Battista, L., Ferraro, P., and Grilli, S. (2017). Simple and rapid bioink jet printing for multiscale cell adhesion islands. *Macromol. Biosci.* 17:1600307. doi: 10.1002/mabi.201600307

Mecozzi, L., Gennari, O., Rega, R., Grilli, S., Bhowmick, S., Gioffrè, M. A., et al. (2016). Spiral formation at the microscale by μ-pyro-electrospinning. *Soft Matter* 12, 5542–5550. doi: 10.1039/C6SM00156D

Ohgaki, M., Kizuki, T., Katsura, M., and Yamashita, K. (2001). Manipulation of selective cell adhesion and growth by surface charges of electrically polarized hydroxyapatite. *J. Biomed. Mater. Res A* 57, 366–373. doi: 10.1002/1097-4636(20011205)57:3<366::AID-JBM1179>3.0.CO;2-X

Pagliarulo, V., Gennari, O., Rega, R., Mecozzi, L., Grilli, S., and Ferraro, P. (2018). Twice electric field poling for engineering multiperiodic Hex-PPLN microstructures. *Opt. Lasers Eng.* 104, 48–52. doi: 10.1016/j.optlaseng.2017.08.015

Palleau, E., Sangeetha, N. M., Viau, G., Marty, J. D., and Ressier, L. (2011). Coulomb force directed single and binary assembly of nanoparticles from aqueous dispersions by AFM nanoxerography. *ACS Nano* 5, 4228–4235. doi: 10.1021/nn2011893

Rega, R., Gennari, O., Mecozzi, L., Grilli, S., Pagliarulo, V., and Ferraro, P. (2016a). Bipolar patterning of polymer sheets by pyroelectrification. *Adv. Mater.* 28, 454–459. doi: 10.1002/adma.201503711

Rega, R., Gennari, O., Mecozzi, L., Pagliarulo, V., Bramanti, A., Ferraro, P., et al. (2019). Maskless arrayed nanofiber mats by bipolar pyroelectrospinning. *ACS Appl. Mater. Interfaces* 11, 3382–3387. doi: 10.1021/acsami.8b12513

Rega, R., Gennari, O., Mecozzia, L., Grilli, S., Pagliarulo, V., and Ferraro, P. (2016b). "Pyro-electrification of polymer membranes for cell patterning," in *AIP Conference Proceedings* (Ischia: AIP Publishing), 020042.

Robertus, J., Browne, W. R., and Feringa, B. L. (2010). Dynamic control over cell adhesive properties using molecular-based surface engineering strategies. *Chem. Soc. Rev.* 39, 354–378. doi: 10.1039/B906608J

Rychkov, D., Kuznetsov, A., and Rychkov, A. (2011). "Electret properties of polyethylene and polytetrafluoroethylene films with chemically modified surface," in *Proceedings of the 14th International Symposium on Electrects* (Montpellier: IEEE), 8–14.

Sahm, D. F., Weissfeld, A., and Trevino, E. A. (1994). *Baily and Scott's Diagnostic Microbiology, 9th Edn*. St. Louis, MO: Mosby.

Scifò, G. O., Randazzo, C. L., Restuccia, C., Fava, G., and Caggia, C. (2009). *Listeria innocua* growth in fresh cut mixed leafy salads packaged in modified atmosphere. *Food Control* 20, 611–617. doi: 10.1016/j.foodcont.2008.08.017

Seemann, L., Stemmer, A., and Naujoks, N. (2007). Local surface charges direct the deposition of carbon nanotubes and fullerenes into nanoscale patterns. *Nano Lett.* 7, 3007–3012. doi: 10.1021/nl0713373

Sheng, L., Hanrahan, I., Sun, X., Taylor, M. H., Mendoza, M., and Zhu, M. J. (2018). Survival of *Listeria innocua* on Fuji apples under commercial cold storage with or without low dose continuous ozone gaseous. *Food Microbiol.* 76, 21–28. doi: 10.1016/j.fm.2018.04.006

Sprave, M., Blum, R., and Eich, M. (1996). High electric field conduction mechanisms in electrode poling of electro-optic polymers. *Appl. Phys. Lett.* 69, 2962–2964. doi: 10.1063/1.117744

Stepanović, S., Vuković, D., Dakić, I., Savić, B., and Švabić-Vlahović, M. (2000). A modified microtiter-plate test for quantification of staphylococcal biofilm formation. *J. Microbiol. Methods* 40, 175–179. doi: 10.1016/S0167-7012(00)00122-6

Stuart, M. A. C., Huck, W. T., Genzer, J., Müller, M., Ober, C., Stamm, M., et al. (2010). Emerging applications of stimuli-responsive polymer materials. *Nat. Mater.* 9, 101–113. doi: 10.1038/nmat2614

Tajkarimi, M., Harrison, S. H., Hung, A. M., and Graves, J. L. Jr. (2016). Mechanobiology of antimicrobial resistant *Escherichia coli* and *Listeria innocua*. *PLoS ONE* 11:e0149769. doi: 10.1371/journal.pone.0149769

Xi, X., Zhao, D., Tong, F., and Cao, T. (2012). The self-assembly and patterning of thin polymer films on pyroelectric substrates driven by electrohydrodynamic instability. *Soft Matter* 8, 298–302. doi: 10.1039/C1SM06434G

Zhao, D., Martinez, A. D., Xi, X., Ma, X., Wu, N., and Cao, T. (2011). Self-organization of thin polymer films guided by electrostatic charges on the substrate. *Small* 7, 2326–2333. doi: 10.1002/smll.201100245

Conflict of Interest Statement: The authors declare that the research was conducted in the absence of any commercial or financial relationships that could be construed as a potential conflict of interest.

Copyright © 2019 Rega, Gennari, Mecozzi, Pagliarulo, Mugnano, Oleandro, Nazzaro, Ferraro and Grilli. This is an open-access article distributed under the terms of the Creative Commons Attribution License (CC BY). The use, distribution or reproduction in other forums is permitted, provided the original author(s) and the copyright owner(s) are credited and that the original publication in this journal is cited, in accordance with accepted academic practice. No use, distribution or reproduction is permitted which does not comply with these terms.

frontiers in Chemistry

ORIGINAL RESEARCH
published: 11 February 2019
doi: 10.3389/fchem.2019.00059

Ultrasound Reversible Response Nanocarrier Based on Sodium Alginate Modified Mesoporous Silica Nanoparticles

Xiaochong Li, Zhanhua Wang and Hesheng Xia*

State Key Laboratory of Polymer Materials Engineering, Polymer Research Institute, Sichuan University, Chengdu, China

Mesoporous silica nanoparticles (MSN) covered by polymer coatings, cross-linked by weak coordination bonds were expected to present a reversible responsiveness under on-off ultrasound stimuli. Herein, we prepared a sodium alginate (SA) modified MSN with carboxyl-calcium (COO^{-}-Ca^{2+}) coordination bonds in the modified layer, which could block the mesopores of MSN and effectively prevent the cargo from pre-releasing before stimulation. The coordination bonds would be destroyed under the stimulation of low intensity ultrasound (20 kHz) or high intensity focused ultrasound (HIFU, 1.1 MHz), leading to a rapid and significant cargo release, and then they could be reformed when ultrasound was turned off, resulting in an instant cargo release stopping. The reversible cleavage and reformation of this coordination bonds under on-off ultrasound stimulus were confirmed by the gel-sol transition behaviors of the SA-$CaCl_2$ gels. An excellent real-time control of rhodamine B (RhB) release performance was obtained under the ultrasound stimuli. Obviously, the cargo release ratio could reach to nearly 40% when HIFU (80 W) was turned on for 5 min, and remained basically constant when ultrasound was turned off, which would finally reach to nearly 100% within 30 min under this on-off pulsatile status. These hybrid MSN based nanoparticles with excellent reversible ultrasound on-off responsiveness were of great interest in on-demand drug delivery applications in the future.

Keywords: mesoporous silica nanoparticles, sodium alginate, reversible, ultrasound response, controlled drug delivery

OPEN ACCESS

Edited by:
Pellegrino Musto, Italian National Research Council (CNR), Italy

Reviewed by:
Nicolas Hans Voelcker, Monash University, Australia
Guoqing Pan, Jiangsu University, China

****Correspondence:***
Zhanhua Wang
zhwangpoly@scu.edu.cn

Specialty section:
This article was submitted to Polymer Chemistry, a section of the journal Frontiers in Chemistry

Received: *04 December 2018*
Accepted: *21 January 2019*
Published: *11 February 2019*

Citation:
Li X, Wang Z and Xia H (2019) Ultrasound Reversible Response Nanocarrier Based on Sodium Alginate Modified Mesoporous Silica Nanoparticles. Front. Chem. 7:59. doi: 10.3389/fchem.2019.00059

INTRODUCTION

During recent decades, with the development of nanotechnology, nanoparticles have been widely applied and well-developed in the field of biomedicine for drug delivery. The most important reason behind this revolution is that nanomaterials as drug carriers can overcome the shortcomings of the conventional small molecule drugs, such as the short half-life, the fast metabolism, and concentration reduction, which consequently decrease the therapeutic effects and increase the toxic side effects on the human body (Hubbell and Chilkoti, 2012). In fact, nanomaterials can make drugs accumulated at the tumor site and reduce the drug concentration in the normal tissue cell sites, thereby improving the anticancer effect as well as reducing the side effects (Panyam and Labhasetwar, 2003; Allen and Cullis, 2004; Farokhzad and Langer, 2009). Moreover, traditional anticancer drugs are usually very small in size and are quickly cleared in the blood so that the

effective concentration at the site of the tumor will be reduced. By loading these small anticancer drugs into the appropriate nanocarriers, the circulation time of the drug molecules in the blood can be extended (Bae et al., 2011; Bogart et al., 2014).

Among various nanomaterials employed for drug delivery applications, the fast-growing attention to mesoporous silica nanoparticles (MSN) has been vastly highlighted due to their outstanding properties, such as large specific surface areas, uniform pores with adjustable structures, excellent biocompatibility, and thermal stability, as well as a facile modification on surface (Trewyn et al., 2007; Chang et al., 2013; Argyo et al., 2014; Paris et al., 2015). However, conventional bare MSN cannot effectively prevent the drugs from being pre-released because of their open mesopores, therefore they cannot achieve an accurate controlled therapeutic efficacy. One alternative that has been proposed to date is the study of the smart drug delivery system, which allows the elaborate surface modifications based on MSN and endows one or more stimuli responsiveness onto them (Chen et al., 2010; Li Z. et al., 2012; Mura et al., 2013; Argyo et al., 2014; Baeza et al., 2015; Wen et al., 2017). Smart drug delivery systems can make mesoporous entrance open or close under exposure to various single internal stimulus [i.e., pH (Li et al., 2014; Cheng et al., 2017; Zeng et al., 2017], redox substances Zhao et al., 2009; Sauer et al., 2010, and enzymes Bernardos et al., 2010; Sun et al., 2013), single external stimulus [i.e., light (Ferris et al., 2009; Martínez-Carmona et al., 2015), temperature (Chung et al., 2008; Schlossbauer et al., 2010), magnetic field (Chen et al., 2011; Xuan et al., 2018), and ultrasound (Chen Y. et al., 2014; Paris et al., 2015; Anirudhan and Nair, 2018)] or a combination of multiple stimuli (Chen X. et al., 2014; Li et al., 2015, 2018). Among all of the studied stimuli, ultrasound attracts great attention due to its robust and unique advantages, especially for the high intensity focused ultrasound (HIFU). Generally, ultrasound has two kinds of categories according to the frequency: low intensity ultrasound (20–200 kHz) and HIFU (>200 kHz). Both types of ultrasound can easily realize a spatiotemporal control of drug release at the targeted location and can easily regulate the penetrate depth by tuning the frequency, power density, and duration (Mura et al., 2013; Boissenot et al., 2016). Additionally, ultrasounds are also appealing because of their non-invasiveness, non-ionizing and cost effectiveness, as well as the enhanced cell membrane permeability. More importantly, compared with low intensity ultrasound, HIFU can focus the intense ultrasonic wave in a targeted small spot, while in other areas the intensity of the wave is relatively low and can be accepted by the human body. So HIFU is effective and safe as a promising stimulus, which has been widely used in human drug delivery applications (Schroeder et al., 2009; Xia et al., 2016).

In general, ultrasound has two main effects which are thermal effect and acoustic cavitation effect; both can play a role in triggering the release of drugs from nanocarriers (Sirsi and Borden, 2014; Xia et al., 2016). When acoustic waves are passing through a tissue the attenuation is generated. The attenuation energy will be converted into thermal effect. Acoustic cavitation is a process where plenty of microbubbles form, grow and collapse during a very short period of time when ultrasound is applied. Cavitation threshold is easily realized by low intensity ultrasound while the thermal effect is more significant when high intensity focused ultrasound (HIFU) is used. Indeed, although both thermal effect and acoustic cavitation effect can make polymers unstable or even destroyed, the latter factor is usually considered as the main reason for ultrasound-induced drug release by bond cleavage of hybrid nanocarriers (Tong et al., 2013; Chen X. et al., 2014; Paris et al., 2015; Li et al., 2016; Anirudhan and Nair, 2018). The strong physical forces associated with the collapse of cavitation bubbles can induce some cleavages of mechano-labile bonds and scission of polymer chains, which is termed as mechano-chemistry. Therefore, for those hybrid nanocarriers that are introduced with the mechano-labile bonds, they will have ultrasonic responsiveness and the modified structure will be broken up when ultrasound is on and, eventually, the inner drugs can be released (Li et al., 2017).

Previously, there have been many studies on ultrasound-induced cleavage of some chemical bonds, such as covalent bonds (ester bond, disulfide bond, Diels-Alder linkage) and supramolecular interaction (hydrogen bond, metal coordination, electrostatic interaction, and π-π interaction) in well-designed polymers, which were applied to ultrasound responsive drug delivery (Li et al., 2010, 2018; Xuan et al., 2012; Tong et al., 2013; Liang et al., 2014) and self-healing/shape memory materials (Li G. et al., 2012; Lu et al., 2014). However, most of the covalent bond cleavages in solution are irreversible, which cannot be applied to the drug delivery field in combination with nanocarriers, and cannot effectively reserve residual drugs after ultrasound stopping. On the contrary, metal coordination, one of the supramolecular interactions, can meet the above requirements well due to its reversibility (Beck and Rowan, 2003; Vermonden et al., 2003; Paulusse and Sijbesma, 2004). It has been widely demonstrated that many metal coordination complexes could achieve reversibility under certain stimulation, such as Fe(III)-polyphenols complexes (Ju et al., 2015), Cu(II)–terpyridine complexes (Liang et al., 2014), Pd(II)-phosphane complexes (Paulusse and Sijbesma, 2004), Ca(II)-carboxyl complexes (Huebsch et al., 2014), and borate-PEGylated coordination complexes (Liu et al., 2018). Reversible ultrasonic responsive hybrid nanocarriers based on metal coordination interaction and combined with MSN are expected to be achieved and applied in the field of drug delivery. To this aim, dynamic metal coordination bonds formed between carboxyl groups (COO^-) and calcium ions (Ca^{2+}) come into our view. The labile metal coordination bonds, formed by Ca^{2+} and COO^- of SA, may be cleavable when ultrasound is turned on and also can be reformed after ultrasound is turned off. Porous nanoparticles covered by cross-linked polymer coatings through coordination bonds formed between Ca^{2+} and COO^- could successfully open the pores and release the loaded cargoes by breaking up the cross-linking structure under low intensity ultrasound or HIFU. In order to verify our hypothesis and obtain a novel kind of reversible ultrasound responsive drug carrier, we prepared a novel kind of hybrid MSN by grafting sodium alginate (SA) polymer onto the MSN surface, which was further cross-linked by $CaCl_2$ solution after cargo loading. Preparation and each step surface modification of MSN particles were

fastidiously characterized. The hypothesis that COO^{-}-Ca^{2+} coordination bonds are dynamically reversible was tested by the gel-sol transition of the SA-$CaCl_2$ gels under ultrasound. The responsive cargo release pattern and the possible mechanism behind that were further investigated by using different two kinds of ultrasound (low intensity ultrasound or HIFU). Almost no drug release behavior under heating at 100°C suggested that the acoustic cavitation was the primary reasons of release. This research may provide an effective method to achieve an on-demand drug release pattern by using remote ultrasound stimulation and build up the frame for advancing future therapeutic applications.

EXPERIMENTAL

Materials

Cetyltrimethylammonium bromide (CTAB, 99.9%), tetraethyl orthosilicate (TEOS, 99.99%), sodium alginate (SA), and N-hydroxysuccinimide (NHS) were purchased from Aladdin (China). 3-aminopropyltriethoxysilane (APTES, 98%) was obtained from Adamas Reagent Co. Ltd. The model drug, Rhodamine B, and 1-ethyl-3-(3-(dimethylamino)- propyl) carbodiimide (EDC·HCl) were purchased from Best Reagent Co. Ltd (Chengdu, China). Methanol, ethanol, toluene, sodium hydroxide (NaOH), hydrochloric acid (HCl), ethyl acetate (EtOAc), and anhydrous calcium chloride ($CaCl_2$) were all analytical chemicals supplied by Kelon Chemical Reagent Co. Ltd (Chengdu, China). Toluene was dried by refluxing in the presence of calcium hydride (CaH_2) prior to use. All of the other regents were used as received.

Synthesis of Mesoporous Silica Nanoparticles (MSN)

The preparation procedure was followed on a previously reported method with a little modification (Lee et al., 2010; Chang et al., 2013). Cetyltrimethylammonium bromide (CTAB, 1 g) was absolutely dissolved in 500 mL of deionized water (DI water) in a three-necked flask. Then, 2.0 M NaOH (3.5 mL) as the base catalyzer of the sol-gel reaction was added. Under the heating of water bath, the above mixture was mechanically stirred at 300 rpm for 2 h when the temperature raised to 70°C. Thereafter, tetraethyl orthosilicate (TEOS, 5 mL) and ethyl acetate (5 mL) were added sequentially at intervals of 1 min. The mixture was stirred for another 30 s and immediately stopped to keep at 70°C for 2 h. The solvent was removed by centrifugation and the precipitate was washed with a large amount of DI water and ethanol in turn. Finally dried the product under vacuum at 60°C overnight and collected before using.

In order to make MSN possess internal mesoporous structure, the reflux process with acid methanol solution was applied. The as-prepared particles (1.0 g) were extracted by refluxing in methanol (100 mL) and concentrated hydrochloric acid (1 mL) at 60°C for 6 h. After centrifugation and washing with DI water and ethanol three times, respectively, the template-removed mesoporous silica nanoparticles (MSN) were dried at 60°C in a vacuum overnight.

Synthesis of Amino-Modified MSN (MSN-NH_2)

As-synthesized MSN (1.0 g) and anhydrous toluene (75 mL) were placed into a round bottom flask which had been purged with high pure N_2, and then 3-aminopropyltriethoxysilane (APTES, 4 mL) was added. This mixture was stirred under an inert atmosphere at 85°C for 24 h. The particles were separated by centrifugation and washed with anhydrous toluene and ethanol three times, respectively. The final product was obtained through drying under vacuum at 60°C overnight.

Synthesis of Alginate-Grafted MSN (MSN-SA)

Firstly, a solution of sodium alginate (SA, 0.2%, w/v) at pH 5.0 was prepared, which was adjusted by adding 1 M HCl solution. Next, 1-ethyl-3-(3-(dimethylamino)- propyl) carbodiimide (EDC, 5.8 g) was dissolved in the above SA solution (50 mL) in a round-bottom flask and stirred at room temperature for a while, followed by the addition of MSN-NH_2 particles (0.30 g) and N-hydroxysuccinimide (NHS, 3.5 g). After stirring the reaction mixture for 24 h at room temperature, the solution was centrifuged and washed with an excessive amount of DI water. The alginate-grafted MSN (MSN-SA) was dried in a vacuum oven at 60 °C overnight.

Cargo Loading and Ionic Coordinated Cross-Linking via $CaCl_2$

The model cargo, Rhodamine B (RhB), was loaded into the channels of MSN-SA by soaking the MSN-SA particles (40 mg) in an aqueous solution of RhB (24 mL, 3 mM) at room temperature. After stirring in the dark for 24 h, the saturated $CaCl_2$ solution (50 mL) was added and the reaction solution was continuously stirred for another 24 h, leading to the cross-link reactions between Ca^{2+} and the COO^{-}. The RhB-loaded, Ca^{2+} cross-linked MSN were separated by centrifugation and washed with DI water more than 3 times until the supernatant was nearly colorless to remove the unloaded cargoes, and the supernatant was collected for loading capacity calculation. Finally, the resulting materials (RhB@MSN-SA@Ca^{2+}) were dried in a vacuum oven at 60°C overnight. The loading amount of RhB was quantitatively evaluated by UV-vis spectroscopy and calculated by the following equation with the collected supernatant:

$$\text{Loading Capacity} = \frac{\textit{initial weight of RhB} - \textit{supernatant weight of RhB}}{\textit{total weight of cargo loaded particles}} \times 100\%$$

The Ca^{2+} cross-linked MSN without RhB loaded (MSN-SA@Ca^{2+}) was prepared by the method as same as the previously mentioned.

Cargo Release

The cargo release experiment from RhB@MSN-SA@Ca^{2+} nanocarriers was operated as follows: particles (5 mg) were soaked in 5 mL of Dulbecco's PBS (dPBS, pH 7.4, with an additional 15 mM Ca^{2+}) and transferred into a dialysis bag

(MWCO 3500), which was maintained in 45 mL of dPBS buffer and shaken at 37°C. To measure the concentration of the released cargo, 3 mL external dPBS buffer was withdrawn and tested by UV-vis spectroscopy, with replenishing subsequently the same volume of dPBS buffer to keep a constant release medium.

To study the ultrasound (US) responsiveness of RhB@MSN-SA@Ca^{2+} nanoparticles, the sample dispersion was exposed to low intensity US (20 kHz) or high intensity focused ultrasound (HIFU, 1,1 MHz). Two different types of ultrasound devices are depicted in **Figure S1**. Before applying US irradiation, the RhB@MSN-SA@Ca^{2+} (5 mg) was ultrasonicated widely in dPBS solution (1 mL) for a short time. In the case of HIFU exposure, the suspension was sealed in a dialysis bag (MWCO 3500), which was immersed in a custom-built glassware containing another dPBS solution (10 mL). At every point of studied time, 3 mL of outer releasing medium was withdrawn to test the cargo release amount by UV-vis and replenished with the equal volume of fresh dPBS. As to the low intensity US, the double jacketed beaker was used to hold the nanoparticle suspension and the outer layer is filled with condensed water (<26°C). After a certain irradiation period of US, the suspension was transferred into a dialysis bag and then processed in the same way as before. The release property of hybrid nanoparticles treated with low intensity ultrasound was compared with those treated under HIFU condition.

Pre-experiment of Ultrasonic Reversible Responsiveness

For *in vitro* ultrasound stimulation experiments, the gel was obtained by dropwise adding 50 mM $CaCl_2$ solution to a stirred sodium alginate (SA) solution in a bottle. The intensity and duration of low intensity ultrasound were 9.02 W/cm^2 and 5 min at 20 kHz. Low intensity ultrasound was carried out in an environment with condensed water, whose temperature was kept <26°C. As to HIFU stimulation, the gel was formed in the mouth of a tube and then the tube was placed upside down on the focal of HIFU wave. The power and application time of HIFU was 40 W and 5 min at 1.1 MHz. HIFU irradiation was carried out in a water bath, so the influence of focal thermo effect on the cross-linked structure should be studied. After that, gels were kept under different heating conditions (70, 100, 120°C) for an hour as control experiments, observing whether gel-sol transformation occurred, to exclude the thermo effect of HIFU.

In vitro Cytotoxicity Assay

The cytotoxicity of MSN-SA and MSN-SA@$CaCl_2$ was assessed by the standard MTT assay using HeLa cells. Five replicates were set in each test group. Firstly, Hela cells were seeded into a 96-well plate and the cell density was adjusted to 6×10^3 cells/well. After overnight incubation, the cells were incubated with different concentrations of MSN-SA and MSN-SA@$CaCl_2$ for 48 h, and then 0.5 mg/mL MTT (200 μ L) solution was added to incubate each well for another 4 h at a constant temperature of 37°C and 5% CO_2. Then, the supernatant was removed, and the obtained crystals were dissolved in dimethyl sulfoxide (150 μ L). After gently shaking in the dark for 10 min, the average absorbance was analyzed by a microplate reader (Rayto, Rt2100c) at a wavelength of 492 nm.

Characterizations

Cargo release profiles were obtained by a Cary 60 UV-Vis spectrophotometer (Agilent, USA). Fourier transform infrared (FT-IR) analysis was operated on a Nicolet-560 spectrometer. The morphology and mesoporous structures were visualized using a scanning electron microscopy (SEM) on a Quanta 250 instrument (FEI Co. Ltd, USA) and transmission electron microscopy (TEM) on Tecnai G2 F20 S-TWIN (FEI Co. Ltd, USA), respectively. Zeta-potential was measured by a Zetasizer Nano-ZS (Malvern) at 25°C. N_2 adsorption–desorption isotherms were obtained on an Autosorb-IQ2 Fully Automatic Analyzer. Thermogravimetric analysis (TGA) was carried out on a PerkinElmer TGA4000 from 100 to 800°C (10°C/min) in N_2 atmosphere. Powder small-angle X-ray diffraction (XRD) measurements were implemented using an Empyrean powder diffractometer. X-ray photoelectron spectroscopy (XPS) was carried out with a KRATOS XSAM800 spectrometer.

RESULTS AND DISCUSSION

Preparation and Characterization of Hybrid Mesoporous Silica Nanocomposites

Schematic illustration of our designed hybrid nanoparticles with reversible ultrasonic responsiveness and the preparation route were demonstrated in **Figure 1**. First, 3-aminopropyltriethoxysilane (APTES) was used to modify the MSN surface with -NH_2 groups. Then, sodium alginate (SA) polymers were grafted onto the amino modified MSN (MSN-NH_2), which was then cross-linked by $CaCl_2$ solution to form the COO^--Ca^{2+} coordination bonds. As depicted in **Figure 2**, SEM and TEM images could intuitively confirm the particle morphology and pore structure. The pure MSN had a regular, spherical shape with an average diameter of 134 ± 14 nm, which was manually counted from 110 particles (**Figures 2a,c**). The channel structure of pure MSN could be clearly seen from the TEM image (**Figure 2b**). After a few steps of surface modifications, the average diameter of obtained particles increased to around 147 ± 19 nm (**Figures 2d,f**). The structure of channels became blurred and so did the edge of MSN materials which become less smooth (**Figure 2e**) proving that the polymer was successfully grafted and cross-linked on the surface of MSN.

The successful modifications of SA polymer onto the MSN surface were characterized by various spectroscopy means. Powder small-angle XRD analysis was employed to characterize the 2D hexagonal pore array structure of pure MSN, which was indicated as (100), (110), and (200) characteristic diffraction peaks (**Figure 3A**). After modifications, the three Bragg peaks of MSN-NH_2 and MSN-SA showed a decreased intensity compared to the pure MSN curve, which resulted from the successful introduction of SA polymer on the surface of particles. Fourier transform infrared (FT-IR) spectroscopy was used to characterize each modification step performed on the surface of pure MSN, as displayed in **Figure 3B**. Firstly, the hydrocarbon vibrational peaks of the methyl and methylene groups at 2850 and 2920 cm^{-1} disappeared with the removal of the CTAB template, leaving a Si-O-Si vibration peak near 1100 cm^{-1} and

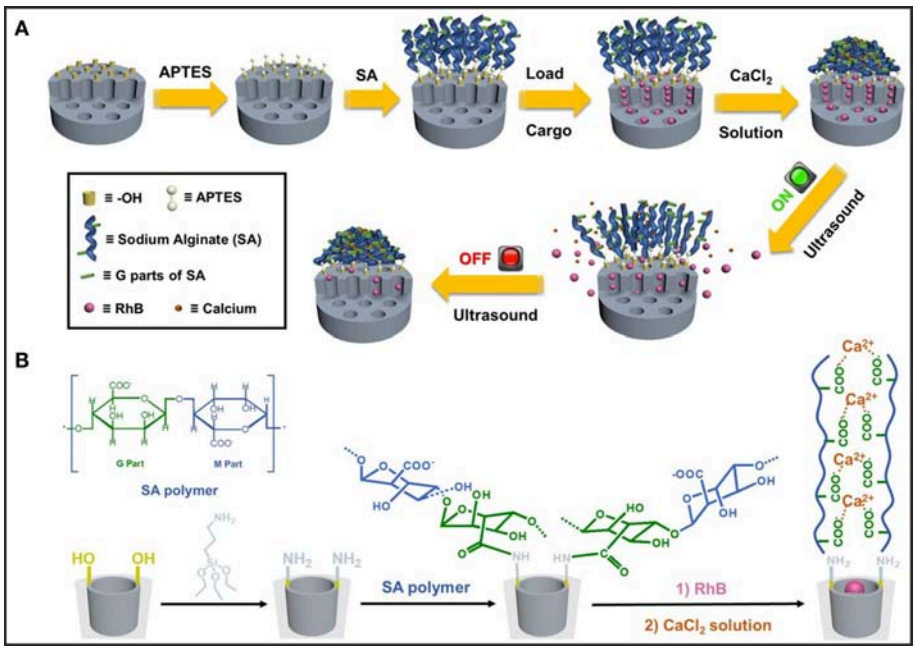

FIGURE 1 | (A) Schematic illustration of the preparation process and ultrasonic reversible responsive behavior of the dynamic cross-linked network on hybrid MSN nanoparticles. **(B)** Molecular structure of sodium alginate (SA) and the synthetic route of calcium ion cross-linked MSN-SA.

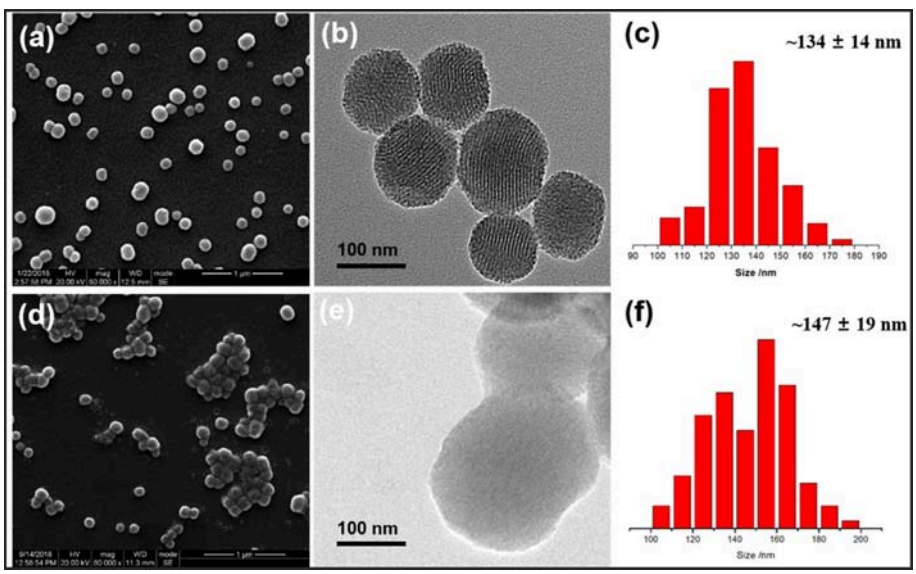

FIGURE 2 | SEM images, TEM images, and size distribution of **(a–c)** MSN and **(d–f)** cross-linked MSN-SA@Ca^{2+}, respectively.

a silicon hydroxyl peak near 3400 cm^{-1} which belonged to the neat MSN. A high intensity at 1630 cm^{-1} of MSN was ascribed to absorbed water bending vibration. Next, the amino groups (-NH_2) were immobilized on the surface of MSN in the presence of 3-aminopropyltriethoxysilane (APTES), which was confirmed by the characteristic peak of MN-NH_2 at 1560 cm^{-1}. After the reaction between -NH_2 and SA, two peaks at 1640 and 1370 cm^{-1} of MSN-SA assigned to the amide group (–CONH–) and carboxylic acid group (–COOH), respectively. This observation was proof that SA polymer had been successfully linked to the MSN surface, in line with the previous SEM, TEM, and XRD results (**Figures 2**, **3A**).

To further verify the accomplishment of each step modification, the MSN-based samples were characterized by X-ray photoelectron (XPS) spectroscopy. As displayed in **Figure 3C** and **Table S1**, a new peak appeared at 404 eV

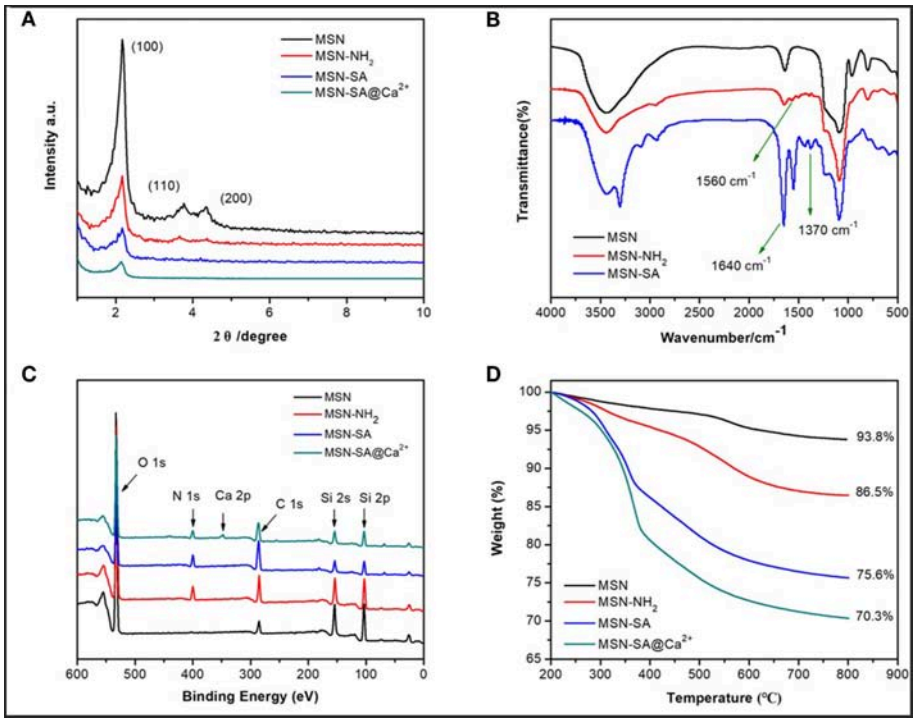

FIGURE 3 | (A) Power small-angle XRD patterns of MSN, MSN-NH_2, MSN-SA, and MSN-SA@Ca^{2+}; **(B)** FTIR spectra of MCM (before CTAB template removal), MSN, MSN-NH_2, and MSN-SA; **(C)** XPS spectra of MSN, MSN-NH_2, MSN-SA, and MSN-SA@Ca^{2+}; **(D)** TGA curves of MSN, MSN-NH_2, MSN-SA, and MSN-SA@Ca^{2+}.

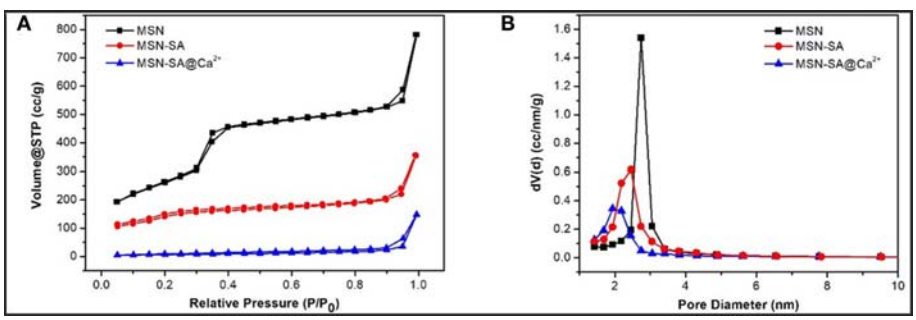

FIGURE 4 | (A) Nitrogen adsorption-desorption isotherms and **(B)** pore size distribution of MSN, MSN-SA, and MSN-SA@Ca^{2+}, respectively.

TABLE 1 | N_2 adsorption-desorption results of MSN and hybrid MSN particles in brief.

Sample	BET surface area (m^2/g)	BJH pore size (nm)
MSN	970.42	2.74
MSN-NH_2	548.96	2.45
MSN-SA@Ca^{2+}	252.36	1.93

ascribed to the N element from MSN-NH_2 result (red curve in **Figure 3C**), which confirmed the successful reaction between silanol groups and APTES. The percentage of N element of MSN-NH_2 was estimated to be 5%, whereas before modification only O, C, Si elements could be detected in the composition of MSN (black curve). Comparing the spectra of MSN-SA (blue curve in **Figure 3C**) with that of MSN-NH_2 (red curve in **Figure 3C**), the intensity of C element increased, while the intensity of Si decreased due to the polymer shielding effect after SA polymer modification. The presence of Ca 2p peak at 347 eV of MSN-SA@Ca^{2+} spectra (green curve in **Figure 3C**), whose percentage of Ca element was calculated to be 2.23%, indicated the successful cross-linking of SA polymer by $CaCl_2$ substance.

The weight loss percentage of various MSN-based samples was characterized by the thermogravimetric analysis (TGA), which were presented in **Figure 3D**. The final weight loss of MSN, MSN-NH_2, MSN-SA, and MSN-SA@Ca^{2+} were 6.2, 13.5, 24.4 and 30%, respectively. Increasing weight losses indicated

the successful immobilizations of APTES, SA polymer and cross-linked agent $CaCl_2$ on MSN particles. There is about 4.56 mmol/g amino on MSN-NH_2 as calculated from an extra 7.3% weight loss after being modified. The percentage of SA and $CaCl_2$ on particles was about 11 and 5.6%, which further demonstrated the reaction of SA polymer and $CaCl_2$. Beyond this, the average surface zeta potentials of all MSN-based materials were detected, and the data were shown in **Figure S2** and **Table S2**. The zeta potential of MSN-NH_2 was +38.09 mV, which indicated the introduction of amino groups compared with −27.56 mV of MSN. The zeta potential of MSN-SA was lowered to −34.10 mV since SA polymer has a large number of carboxyl groups. As to cross-linked nanoparticles, the zeta potential increased mainly due to the introduction of cationic calcium.

In addition, the surface area and pore size distribution of pure MSN and modified MSN nanoparticles were measured by the N_2 adsorption-desorption isotherms (**Figure 4** and **Table 1**). Clearly, the curve of pure MSN analyzed by the Brunauer–Emmett–Teller (BET) method showed a relatively sharp adsorption step at ∼ 0.3 P/P_0, which was classified as a typical IV behavior (Chang et al., 2013). This phenomenon was mainly due to the well-ordered mesoporous structure of MSN. It was worth noting that there were narrow H1-type hysteresis loops in the isotherms, which were mainly attributed to the capillary condensation. A narrow pore size distribution for each nanoparticle could be obtained by the Barrett–Joyner–Halenda (BJH) method. Nevertheless, the isotherms of MSN-SA and cross-linked MSN became flattered after modifications, and the pore diameter also decreased apparently. As summarized in **Table 1**, the surface area and the pore size of MSN was 970.42 m^2/g and 2.74 nm, respectively. As to MSN-SA@Ca^{2+}, these parameters were reduced to 252.36 m^2/g and 1.93 nm, respectively, resulting from the successful surface modification of pure MSN which limited the absorption of N_2.

Exploration of Ultrasound Reversible-Responsiveness

Before investigating whether there was the ultrasonic reversible response of designed hybrid MSN materials, cross-linked SA-$CaCl_2$ gel under ultrasound irradiation was studied first. According to the literature reported (Huebsch et al., 2014), ultrasound could break the complexation of divalent cations (e.g., Ca^{2+}) and SA, while the presence of Ca^{2+} in physiological fluids would allow re-crosslinking after removal of the stimulus, therefore achieving a reversible on-demand response. To emphasize the role of ultrasound in

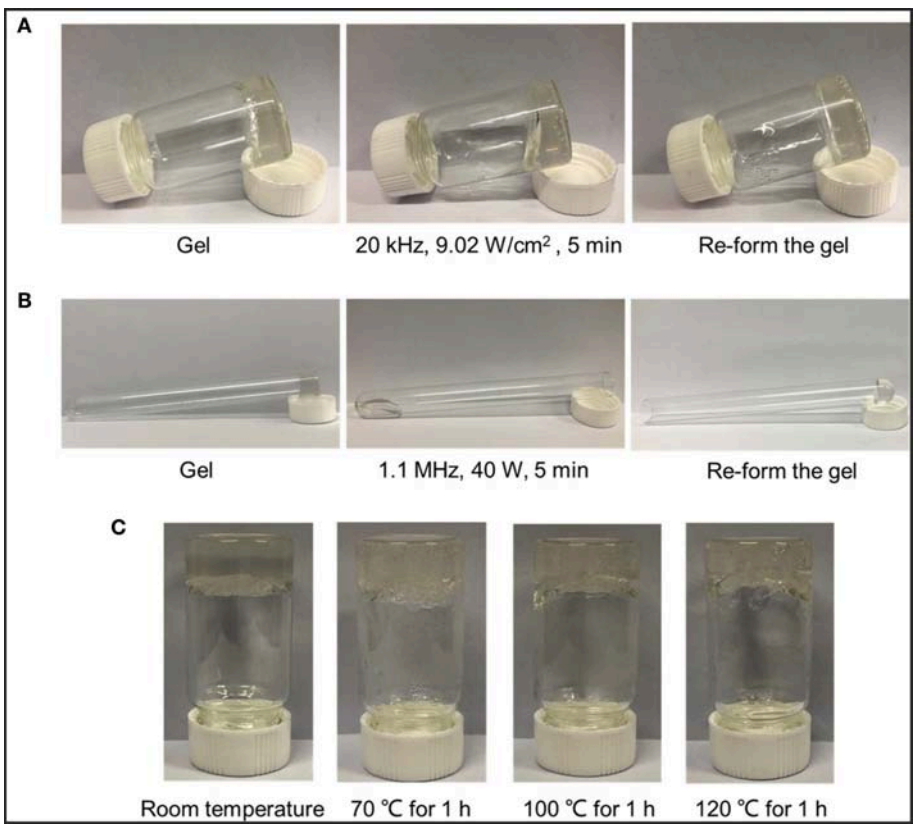

FIGURE 5 | Ultrasound induced disruption and reformation of ionically cross-linked gels. Macroscopic images of the proposed ability of **(A)** low intensity ultrasound and **(B)** HIFU to induce temporary disruption of cross-linked structure by $CaCl_2$ with SA polymer; **(C)** Macroscopic images of gels' status before and after treatment at different heating temperatures.

the cross-linked network, two different intensity ultrasounds were applied and the reversible gel-sol transition behaviors were studied.

As shown in **Figure 5**, ultrasounds and heating conditions were applied to the collected gel, respectively. A series of macroscopic photographs clearly illustrated the reversible nature of the calcium-alginate cross-linking system and its response to the activation effect of ultrasounds. From **Figures 5A,B**, the original gel state would become a flowing liquid state after activating either by low intensity ultrasound or HIFU, which was named as a gel-sol transition. After removal of ultrasound, the sol state could subsequently return to the original gel state. Since the test of cross-linked gel stimulated by low intensity ultrasound was carried out in condensed water which the environmental temperature was maintained lower than 26°C, so the thermal effect could be eliminated and only the acoustic cavitation of low intensity ultrasound had an influence on the cross-linked structure. As to the HIFU, the thermal effect was stronger than that of low intensity ultrasound, so it was necessary to test which of the two effects was the main reason. A control experiment that gels were put into the different heating environment for an hour to test the main ultrasonic effect was designed. **Figure 5C** showed the images of SA-$CaCl_2$ gel before and after thermal treatment. Only the content of water decreased and no gel-sol transition occurred. This phenomenon excluded the thermal effect from influence factors and concluded that the ultrasonic cavitation did play a major role in disrupting the ion-cross-linked structure of the gel (Paulusse and Sijbesma, 2004, 2008; Karthikeyan et al., 2008).

Cargo Loading and Release

The feasibility of applying this ultrasonic reversible response ion-crosslinked structure to the on-demand cargo delivery was investigated by using Rhodamine B (RhB) as a model drug. There was about 14.3% of RhB loaded in the mesopores of MSN-SA, which was determined by a pre-established calibration curve (**Figure S3A**) using UV-vis spectroscopy. To investigate the US responsive release of cross-linked nanoparticles, the low intensity ultrasound and HIFU were both applied. Similarly, the releasing content of RhB was calculated using a standard calibration cure in **Figure S3B**. HIFU-triggered RhB releasing profiles under different power (40, 60, and 80 W) were firstly studied. For the first six hours, the sample was placed in the 37°C environment without irradiation. Immediately after 5 min of HIFU stimulation, the sample was continuously placed in the 37°C constant water bath shaker and the released cargo was collected at the specific time. As shown in **Figure 6A**, without stimulation, the cumulative release percentage was nearly zero for the initial several hours. However, a sudden increase in the release profile could be obtained by stimulating samples with HIFU. Upon exposure to HIFU, the percentage of final release of RhB could reach as high as 25, 48, and 78% at the output power of 40, 60, and 80 W, respectively. It has been demonstrated that the effects of ultrasound, both thermo effect and cavitation, could cause the sonodynamic shear to break the weak bonds, such as covalent bond, non-covalent π-π bond, metal coordination interaction, and hydrogen bond, therefore, damaging the integrity of structure network and discharge the embedded drugs (Li et al., 2010, 2018; Tong et al., 2013; Xia et al.,

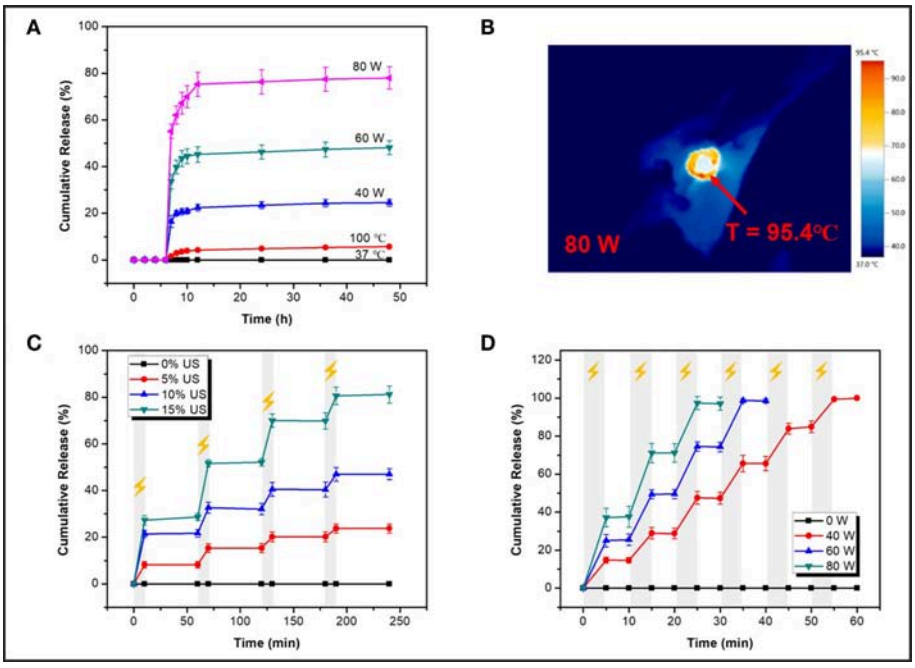

FIGURE 6 | (A) Nature release profiles (release at 37°C) after different treatments for 5 min (40, 60, 80 W of HIFU and heating at 100°C); **(B)** The maximum temperature of latex membrane at the focal of HIFU wave recorded by an Infrared Thermal Imager at 80 W; **(C)** On-off releasing profiles at different outputs of low intensity ultrasound (0, 5, 10, and 15% of power, 10 min irradiation); **(D)** On-off releasing profiles at different power of HIFU (40, 60, 80 W, 5 min irradiation).

2016). In the previous part, thermo effects had been concluded that ould not make a major impact on the gel-sol transition of SA-$CaCl_2$ gel (**Figure 5C**). It still needed to be determined for cross-linked MSN particles whether acoustic cavitation dominates the destruction of SA-Ca^{2+} cross-linked structure and the promotion of cargo release. The Infrared Thermal Imager was used to record the maximum temperature of latex membrane at the focal of the HIFU wave under different power outputs, the images were presented in **Figure 6B** and **Figure S4**. The temperature could reach to 61.3, 77.8, 95.4°C after irradiation for 5 min at 40, 60, and 80 W, respectively. 100°C, which was higher than the maximum temperature corresponding to the maximum power, was chosen to do the control experiment. After heating at 100°C for 5 min, the RhB releasing process was operated at 37°C, which was the same as the HIFU-triggered releasing experiment condition that was previously mentioned. In the end, the final percentage of RhB release was about 6%, which, although higher than that of untreated samples, was still much lower than that of HIFU exposed samples. These results further confirmed that cavitation effect rather than thermal effect of HIFU broke the SA-Ca^{2+} cross-linked structure and promoted the cargo release.

Figures 6C,D were cargo release profiles under the different power of low intensity ultrasound and HIFU. As depicted in **Figure 6C**, upon exposure to pulsatile ultrasound, cross-linked nanoparticles showed an obvious responsive release compared to non-stimulated samples (0% US). When ultrasound was turned on for 10 min, cargoes' releasing performance was apparent and when ultrasound was turned off, cargoes' releasing behavior stopped as well. Upon this pulsatile ultrasound (10 min-exposure per hour), the total RhB-releasing percentage could reach as high as 24, 47, and 81% at different powers (5%, 10%, 15% of total power) over 240 min. Then, the releasing profile was further studied under HIFU irradiation. A significantly increased release percentage was observed in an on/off pattern at a different output power of HIFU (**Figure 6D**). Ultrasonic stimulation was on for 5 min, then off for next 5 min, and nearly 100% of the RhB could be released in 60 min upon HIFU exposure. As an illustration, within a short duration of 55 min, the RhB-releasing percentage could reach up to 99% at the output power of 40 W. And yet it took only 30 min to obtain nearly 98% RhB-releasing at the output power of 80 W. All RhB cargoes could be released within 60 min upon HIFU exposure. What's important is that from the release pattern, the amount of RhB release was minor, even nil when either low intensity ultrasound or HIFU was off, proving from the side that the previously proposed SA-Ca^{2+} cross-linked structure indeed had the property of reversible self-recovery under ultrasound exposure. Comparing the time of releasing 80% of RhB, HIFU with no doubt had a shorter time (∼22 min for 80 W) and, in other words, higher efficiency than low intensity ultrasound (∼190 min for 15% of power) for the releasing stimulation. On the other hand, the maximum power of the above HIFU (80 W) was definitely safer than that of low intensity ultrasound (15% of total power) in practical human drug delivery because the latter would do harm to other healthy organizations in the body due to its strong cavitation effect. Thus, ultrasound, especially HIFU, could be an ideal external stimulation to realize a fast response releasing behavior with an on/off pattern, and these designed hybrid nanocarriers with reversible open/close responsiveness were intriguing candidates for effective drug delivery.

In vitro Cytotoxicity Assay

The investigation on the cytotoxicity of blank hybrid nanoparticles of MSN-SA and MSN-SA@$CaCl_2$ was also necessary before using them as drug carriers for future therapeutic application. The *in vitro* cytotoxicity experiment against HeLa cells was carried out with a standard MTT assay. As clearly illustrated in **Figure 7**, with the increase concentration of two nanoparticles, the cell viabilities performed a decrease trend. Nevertheless, MSN-SA and MSN-SA@ $CaCl_2$ nanoparticles did not show high cytotoxicity even up to a concentration of 60 μg/mL, indicating these two nanoparticles both had good biocompatibilities and were suitable as drug carriers in therapeutic application.

CONCLUSIONS

In summary, we developed a kind of hybrid organic-inorganic nanoparticles composed of MSN and SA-$CaCl_2$ cross-linked coatings which possess a reversible ultrasonic responsiveness with an apparent on/off release pattern. The sodium alginate (SA) polymer was successfully grafted onto the surface of mesoporous silica nanoparticles (MSN) through an amino terminated silane coupling agent, then $CaCl_2$ was introduced to cross-link the SA polymer layer which acted as a gatekeeper to prevent the RhB from premature releasing. The obtained hybrid nanoparticles presented a reversible-responsiveness to both low intensity ultrasound and high intensity focused ultrasound (HIFU), which was proved by calcium alginate gel-sol transformation experiments under ultrasound. The cargo loaded nanoparticles showed a fast ultrasound-induced release behavior and performed a good on/off release pattern under a pulsatile ultrasonic status. The mechanism of ultrasound-induced disruption was investigated and concluded that it

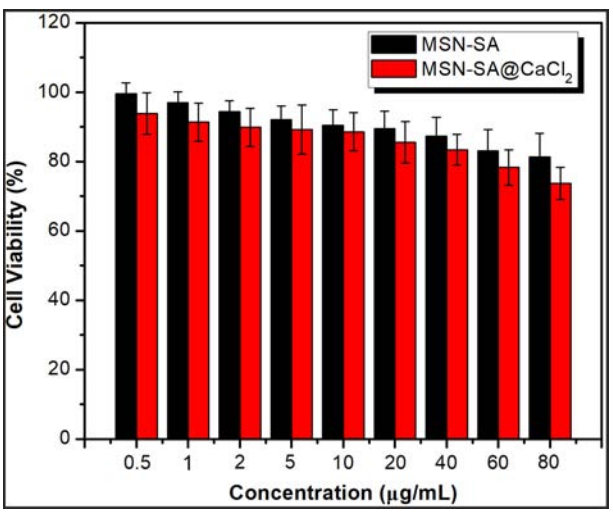

FIGURE 7 | Cell viability of Hela cells in MSN-SA, MSN-SA@$CaCl_2$ dispersion at different concentrations (0.5, 1, 2, 5, 10, 20, 40, 60, 80 μg/mL) by the standard MTT assay ($n = 5$).

was indeed the cavitation effect that dominated the process of breaking the metal coordination interaction. This study envisions that these new ultrasound stimulus reversible responsive organic-inorganic hybrid nanoparticles may possess potential applications in building on-demand drug delivery for timing-specific stimulation.

AUTHOR CONTRIBUTIONS

All authors listed have made a substantial, direct and intellectual contribution to the work, and approved it for publication.

ACKNOWLEDGMENTS

We are grateful to acknowledge the financial support from the National Natural Science Foundation of China (51473094, 51703143). The authors also thank to the State Key Laboratory of Polymer Materials Engineering (Grant No. sklpme2017-3-04).

SUPPLEMENTARY MATERIAL

The Supplementary Material for this article can be found online at: https://www.frontiersin.org/articles/10.3389/fchem.2019.00059/full#supplementary-material

REFERENCES

Allen, T. M., and Cullis, P. R. (2004). Drug delivery systems: entering the mainstream. *Science* 303, 1818–1822. doi: 10.1126/science.1095833

Anirudhan, T. S., and Nair, A. S. (2018). Temperature and ultrasound sensitive gatekeepers for the controlled release of chemotherapeutic drugs from mesoporous silica nanoparticles. *J. Mater. Chem. B* 6, 428–439. doi: 10.1039/C7TB02292A

Argyo, C., Weiss, V., Bräuchle, C., and Bein, T. (2014). Multifunctional mesoporous silica nanoparticles as a universal platform for drug delivery. *Chem. Mater.* 26, 435–451. doi: 10.1021/cm402592t

Bae, K. H., Chung, H. J., and Park, T. G. (2011). Nanomaterials for cancer therapy and imaging. *Mol. Cells* 31, 295–302. doi: 10.1007/s10059-011-0051-5

Baeza, A., Colilla, M., and Vallet-Regí, M. (2015). Advances in mesoporous silica nanoparticles for targeted stimuli-responsive drug delivery. *Expert Opin. Drug Deliv.* 12, 319–337. doi: 10.1517/17425247.2014.953051

Beck, J. B., and Rowan, S. J. (2003). Multistimuli, multiresponsive metallo-supramolecular polymers. *J. Am. Chem. Soc.* 125, 13922–13923. doi: 10.1021/ja038521k

Bernardos, A., Mondragon, L., Aznar, E., Marcos, M. D., Martinez-Mañez, R., Sancenón, F., et al. (2010). Enzyme-Responsive intracellular controlled release using nanometric silica mesoporous supports capped with "Saccharides". *ACS Nano* 4, 6353–6368. doi: 10.1021/nn101499d

Bogart, L. K., Pourroy, G., Murphy, C. J., Puntes, V., Pellegrino, T., Rosenblum, D., et al. (2014). Nanoparticles for imaging, sensing, and therapeutic intervention. *ACS Nano* 8, 3107–3122. doi: 10.1021/nn500962q

Boissenot, T., Bordat, A., Fattal, E., and Tsapis, N. (2016). Ultrasound-triggered drug delivery for cancer treatment using drug delivery systems: from theoretical considerations to practical applications. *J. Control. Release* 241, 144–163. doi: 10.1016/j.jconrel.2016.09.026

Chang, B., Chen, D., Wang, Y., Chen, Y., Jiao, Y., Sha, X., et al. (2013). Bioresponsive controlled drug release based on mesoporous silica nanoparticles coated with reductively sheddable polymer shell. *Chem. Mater.* 25, 574–585. doi: 10.1021/cm3037197

Chen, C., Geng, J., Pu, F., Yang, X., Ren, J., and Qu, X. (2010). Polyvalent nucleic acid/mesoporous silica nanoparticle conjugates: dual stimuli-responsive vehicles for intracellular drug delivery. *Angew. Chem. Int. Ed.* 50, 882–886. doi: 10.1002/anie.201005471

Chen, P. J., Hu, S. H., Hsiao, C. S., Chen, Y. Y., Liu, D. M., and Chen, S. Y. (2011). Multifunctional magnetically removable nanogated lids of Fe3O4–capped mesoporous silica nanoparticles for intracellular controlled release and MR imaging. *J. Mater. Chem.* 21, 2535–2543. doi: 10.1039/C0JM02590A

Chen, X., Soeriyadi, A. H., Lu, X., Sagnella, S. M., Kavallaris, M., and Gooding, I. J. (2014). Dual bioresponsive mesoporous silica nanocarrier as an "AND" logic gate for targeted drug delivery cancer cells. *Adv. Funct. Mater.* 24, 6999–7006. doi: 10.1002/adfm.201402339

Chen, Y., Meng, Q., Wu, M., Wang, S., Xu, P., Chen, H., et al. (2014). Hollow mesoporous organosilica nanoparticles: a generic intelligent framework-hybridization approach for biomedicine. *J. Am. Chem. Soc.* 136, 16326–16334. doi: 10.1021/ja508721y

Cheng, W., Nie, J., Xu, L., Liang, C., Peng, Y., Liu, G., et al. (2017). pH-Sensitive delivery vehicle based on folic acid-conjugated polydopamine-modified mesoporous silica nanoparticles for targeted cancer therapy. *ACS Appl. Mater. Interfaces* 9, 18462–18473. doi: 10.1021/acsami.7b02457

Chung, P.-W., Kumar, R., Pruski, M., and Lin, V. S. Y. (2008). Temperature responsive solution partition of organic–inorganic hybrid poly(N-isopropylacrylamide)-coated mesoporous silica nanospheres. *Adv. Funct. Mater.* 18, 1390–1398. doi: 10.1002/adfm.200701116

Farokhzad, O. C., and Langer, R. (2009). Impact of nanotechnology on drug delivery. *ACS Nano* 3, 16–20. doi: 10.1021/nn900002m

Ferris, D. P., Zhao, Y. L., Khashab, N. M., Khatib, H. A., Stoddart, J. F., and Zink, J. I. (2009). Light-Operated mechanized nanoparticles. *J. Am. Chem. Soc.* 131, 1686–1688. doi: 10.1021/ja807798g

Hubbell, J. A., and Chilkoti, A. (2012). Nanomaterials for drug delivery. *Science* 337, 303–305. doi: 10.1126/science.1219657

Huebsch, N., Kearney, C. J., Zhao, X., Kim, J., Cezar, C. A., Suo, Z., et al. (2014). Ultrasound-triggered disruption and self-healing of reversibly cross-linked hydrogels for drug delivery and enhanced chemotherapy. *Proc. Natl. Acad. Sci. U.S.A.* 111, 9762–9767. doi: 10.1073/pnas.1405469111

Ju, Y., Cui, J., Müllner, M., Suma, T., Hu, M., and Caruso, F. (2015). Engineering low-fouling and pH-Degradable capsules through the assembly of metal-phenolic networks. *Biomacromolecules* 16, 807–814. doi: 10.1021/bm5017139

Karthikeyan, S., Potisek, S. L., Piermattei, A., and Sijbesma, R. P. (2008). Highly efficient mechanochemical scission of silver-carbene coordination polymers. *J. Am. Chem. Soc.* 130, 14968–14969. doi: 10.1021/ja806887k

Lee, J. E., Lee, N., Kim, H., Kim, J., Choi, S. H., Kim, J. H., et al. (2010). Uniform mesoporous dye-doped silica nanoparticles decorated with multiple magnetite nanocrystals for simultaneous enhanced magnetic resonance imaging, fluorescence imaging, and drug delivery. *J. Am. Chem. Soc.* 132, 552–557. doi: 10.1021/ja905793q

Li, F., Lu, J., Kong, X., Hyeon, T., and Ling, D. (2017). Dynamic nanoparticle assemblies for biomedical applications. *Adv. Mater.* 29:1605897. doi: 10.1002/adma.201605897

Li, F., Xie, C., Cheng, Z., and Xia, H. (2016). Ultrasound responsive block copolymer micelle of poly(ethylene glycol)–poly(propylene glycol) obtained through click reaction. *Ultrason. Sonochem.* 30, 9–17. doi: 10.1016/j.ultsonch.2015.11.023

Li, G., Fei, G., Xia, H., Han, J., and Zhao, Y. (2012). Spatial and temporal control of shape memory polymers and simultaneous drug release using high intensity focused ultrasound. *J. Mater. Chem.* 22, 7692–7696. doi: 10.1039/C2JM30848G

Li, Q. L., Sun, Y., Sun, Y. L., Wen, J., Zhou, Y., Bing, Q. M., et al. (2014). Mesoporous silica nanoparticles coated by layer-by-layer self-assembly using Cucurbit[7]uril for *in vitro* and *in vivo* anticancer drug release. *Chem. Mater.* 26, 6418–6431. doi: 10.1021/cm503304p

Li, Q. L., Xu, S. H., Zhou, H., Wang, X., Dong, B., Gao, H., et al. (2015). pH and glutathione dual-responsive dynamic cross-linked supramolecular network on mesoporous silica nanoparticles for controlled anticancer drug release. *ACS Appl. Mater. Interfaces* 7, 28656–28664. doi: 10.1021/acsami.5b10534

Li, X., Xie, C., Xia, H., and Wang, Z. (2018). pH and ultrasound dual-responsive polydopamine-coated mesoporous silica nanoparticles for controlled drug delivery. *Langmuir* 34, 9974–9981. doi: 10.1021/acs.langmuir.8b01091

Li, Y., Tong, R., Xia, H., Zhang, H., and Xuan, J. (2010). High intensity focused ultrasound and redox dual responsive polymer micelles. *Chem. Commun.* 46, 7739–7741. doi: 10.1039/C0CC02628J

Li, Z., Barnes, J. C., Bosoy, A., Stoddart, J. F., and Zink, J. I. (2012). Mesoporous silica nanoparticles in biomedical applications. *Chem. Soc. Rev.* 41, 2590–2605. doi: 10.1039/C1CS15246G

Liang, B., Tong, R., Wang, Z., Guo, S., and Xia, H. (2014). High intensity focused ultrasound responsive metallo-supramolecular block copolymer micelles. *Langmuir* 30, 9524–9532. doi: 10.1021/la500841x

Liu, S., Pan, J., Liu, J., Ma, Y., Qiu, F., Mei, L., et al. (2018). Dynamically PEGylated and borate-coordination-polymer-coated polydopamine nanoparticles for synergetic tumor-targeted, chemo-photothermal combination therapy. *Small* 14:1703968. doi: 10.1002/smll.201703968

Lu, X., Fei, G., Xia, H., and Zhao, Y. (2014). Ultrasound healable shape memory dynamic polymers. *J. Mater. Chem. A* 2, 16051–16060. doi: 10.1039/C4TA02726D

Martínez-Carmona, M., Baeza, A., Rodriguez-Milla, M. A., García-Castro, J., and Vallet-Regí, M. (2015). Mesoporous silica nanoparticles grafted with a light-responsive protein shell for highly cytotoxic antitumoral therapy. *J. Mater. Chem. B* 3, 5746–5752. doi: 10.1039/C5TB00304K

Mura, S., Nicolas, J., and Couvreur, P. (2013). Stimuli-responsive nanocarriers for drug delivery. *Nat. Mater.* 12, 991–1003. doi: 10.1038/nmat3776

Panyam, J., and Labhasetwar, V. (2003). Biodegradable nanoparticles for drug and gene delivery to cells and tissue. *Adv. Drug Deliv. Rev.* 55, 329–347. doi: 10.1016/S0169-409X(02)00228-4

Paris, J. L., Cabañas, M. V., Manzano, M., and Vallet-Regí, M. (2015). Polymer-Grafted mesoporous silica nanoparticles as ultrasound-responsive drug carriers. *ACS Nano* 9, 11023–11033. doi: 10.1021/acsnano.5b04378

Paulusse, J. M., and Sijbesma, R. P. (2008). Selectivity of mechanochemical chain scission in mixed palladium(ii) and platinum(ii) coordination polymers. *Chem. Commun.* 4416–4418. doi: 10.1039/B806978F

Paulusse, J. M. J., and Sijbesma, R. P. (2004). Reversible mechanochemistry of a PdII coordination polymer. *Angew. Chem.* 116, 4560–4562. doi: 10.1002/ange.200460040

Sauer, A. M., Schlossbauer, A., Ruthardt, N., Cauda, V., Bein, T., and Bräuchle, C. (2010). Role of endosomal escape for disulfide-based drug delivery from colloidal mesoporous silica evaluated by live-cell imaging. *Nano Lett.* 10, 3684–3691. doi: 10.1021/nl102180s

Schlossbauer, A., Warncke, S., Gramlich, P. M. E., Kecht, J., Manetto, A., Carell, T., et al. (2010). A programmable DNA-based molecular valve for colloidal mesoporous silica. *Angew. Chem. Int. Ed.* 49, 4734–4737. doi: 10.1002/anie.201000827

Schroeder, A., Kost, J., and Barenholz, Y. (2009). Ultrasound, liposomes, and drug delivery: principles for using ultrasound to control the release of drugs from liposomes. *Chem. Phys. Lipids* 162, 1–16. doi: 10.1016/j.chemphyslip.2009.08.003

Sirsi, S. R., and Borden, M. A. (2014). State-of-the-art materials for ultrasound-triggered drug delivery. *Adv. Drug Deliv. Rev.* 72, 3–14. doi: 10.1016/j.addr.2013.12.010

Sun, Y. L., Zhou, Y., Li, Q. L., and Yang, Y. W. (2013). Enzyme-responsive supramolecular nanovalves crafted by mesoporous silica nanoparticles and choline-sulfonatocalix[4]arene [2]pseudorotaxanes for controlled cargo release. *Chem. Commun.* 49, 9033–9035. doi: 10.1039/C3CC45216F

Tong, R., Xia, H., and Lu, X. (2013). Fast release behavior of block copolymer micelles under high intensity focused ultrasound/redox combined stimulus. *J. Mater. Chem. B* 1, 886–894. doi: 10.1039/C2TB00222A

Trewyn, B. G., Slowing, I. I., Giri, S., Chen, H. T., and Lin, V. S. Y. (2007). Synthesis and functionalization of a mesoporous silica nanoparticle based on the sol–gel process and applications in controlled release. *Acc. Chem. Res.* 40, 846–853. doi: 10.1021/ar600032u

Vermonden, T., van der Gucht, J., de Waard, P., Marcelis, A. T. M., Besseling, N. A. M., Sudhölter, E. J. R., et al. (2003). Water-Soluble reversible coordination polymers: chains and rings. *Macromolecules* 36, 7035–7044. doi: 10.1021/ma030353t

Wen, J., Yang, K., Liu, F., Li, H., Xu, Y., and Sun, S. (2017). Diverse gatekeepers for mesoporous silica nanoparticle based drug delivery systems. *Chem. Soc. Rev.* 46, 6024–6045. doi: 10.1039/C7CS00219J

Xia, H., Zhao, Y., and Tong, R. (2016). "Ultrasound-Mediated Polymeric Micelle Drug Delivery," in *Therapeutic Ultrasound,* eds. J.M. Escoffre and A. Bouakaz. (Cham: Springer International Publishing), 365–384.

Xuan, J., Boissière, O., Zhao, Y., Yan, B., Tremblay, L., Lacelle, S., et al. (2012). Ultrasound-responsive block copolymer micelles based on a new amplification mechanism. *Langmuir* 28, 16463–16468. doi: 10.1021/la303946b

Xuan, M., Shao, J., Zhao, J., Li, Q., Dai, L., and Li, J. (2018). Magnetic mesoporous silica nanoparticles cloaked by red blood cell membranes: applications in cancer therapy. *Angew. Chem. Int. Ed.* 57, 6049–6053. doi: 10.1002/anie.201712996

Zeng, X., Liu, G., Tao, W., Ma, Y., Zhang, X., He, F., et al. (2017). A drug-self-gated mesoporous antitumor nanoplatform based on pH-sensitive dynamic covalent bond. *Adv. Funct. Mater.* 27:1605985. doi: 10.1002/adfm.201605985

Zhao, Y., Trewyn, B. G., Slowing, I. I., and Lin, V. S. Y. (2009). Mesoporous silica nanoparticle-based double drug delivery system for glucose-responsive controlled release of insulin and cyclic AMP. *J. Am. Chem. Soc.* 131, 8398–8400. doi: 10.1021/ja901831u

Conflict of Interest Statement: The authors declare that the research was conducted in the absence of any commercial or financial relationships that could be construed as a potential conflict of interest.

Copyright © 2019 Li, Wang and Xia. This is an open-access article distributed under the terms of the Creative Commons Attribution License (CC BY). The use, distribution or reproduction in other forums is permitted, provided the original author(s) and the copyright owner(s) are credited and that the original publication in this journal is cited, in accordance with accepted academic practice. No use, distribution or reproduction is permitted which does not comply with these terms.

frontiers in Chemistry

REVIEW
published: 23 October 2018
doi: 10.3389/fchem.2018.00511

Advances in Organic Solvent Nanofiltration Rely on Physical Chemistry and Polymer Chemistry

Michele Galizia and Kelly P. Bye*

School of Chemical, Biological and Materials Engineering, The University of Oklahoma, Norman, OK, United States

The vast majority of industrial chemical synthesis occurs in organic solution. Solute concentration and solvent recovery consume ∼50% of the energy required to produce chemicals and pose problems that are as relevant as the synthesis process itself. Separation and purification processes often involve a phase change and, as such, they are highly energy-intensive. However, novel, energy-efficient technologies based on polymer membranes are emerging as a viable alternative to thermal processes. Despite organic solvent nanofiltration (OSN) could revolutionize the chemical, petrochemical, food and pharmaceutical industry, its development is still in its infancy for two reasons: (i) the lack of fundamental knowledge of elemental transport phenomena in OSN membranes, and (ii) the instability of traditional polymer materials in chemically challenging environments. While the latter issue has been partially solved, the former was not addressed at all. Moreover, the few data available about solute and solvent transport in OSN membranes are often interpreted using inappropriate theoretical tools, which contributes to the spread of misleading conclusions in the literature. In this review we provide the state of the art of organic solvent nanofiltration using polymeric membranes. First, theoretical models useful to interpret experimental data are discussed and some misleading conclusions commonly reported in the literature are highlighted. Then, currently available materials are reviewed. Finally, materials that could revolutionize OSN in the future are identified. Among the possible applications of OSN, isomers separation could open a new era in chemical engineering and polymer science in the years to come.

Keywords: OSN, sorption, diffusion, transport, polymers

OPEN ACCESS

Edited by:
Pellegrino Musto, Consiglio Nazionale Delle Ricerche (CNR), Italy

Reviewed by:
Gloria Huerta-Angeles, Contipro Inc., Czechia
Nonappa, Aalto University, Finland

****Correspondence:***
Michele Galizia
mgalizia@ou.edu

Specialty section:
This article was submitted to Polymer Chemistry, a section of the journal Frontiers in Chemistry

Received: *01 August 2018*
Accepted: *04 October 2018*
Published: *23 October 2018*

Citation:
Galizia M and Bye KP (2018) Advances in Organic Solvent Nanofiltration Rely on Physical Chemistry and Polymer Chemistry. Front. Chem. 6:511. doi: 10.3389/fchem.2018.00511

INTRODUCTION

Polymer technology is of paramount importance in several fields. Petrochemical, materials, food and tissue engineering, as well as medicine, optics and microelectronics are some of the areas were polymers endowed with specific structural or functional properties are sought (Haupt and Mosbach, 2000; Ma et al., 2002; Ulbricht, 2006). In this review we discuss the use of functional polymers to achieve molecular separations in liquid phase.

The vast majority of industrial organic synthesis occurs in solution. Downstream processes, such as solute concentration and solvent recovery, play a crucial role in the chemical industry and pose problems that are as relevant as the synthesis process itself (Marchetti et al., 2014). Often, especially in the food or pharmaceutical industry, traditional thermal separation processes, such as

distillation, cannot be exploited, since exposure to high temperatures would permanently damage thermally labile molecules, such as drugs, active principles and aromas (Kim et al., 2016; Priske et al., 2016). Liquid chromatography may represent, especially on small scales, an alternative to distillation, however it requires large volumes of solvent to be processed (Liang et al., 2008).

Nowadays, separations consume 15% of the energy produced in the world. Specifically, 80% of the energy demanded to separate chemicals is used for distillation (Lively and Sholl, 2017). Membrane separations operate at relatively mild conditions and do not require a phase change, which makes them less energy demanding relative to thermal processes (Galizia et al., 2017a). Moreover, while distillation requires very large equipment and huge investment costs, membrane modules are compact and much easier to assemble and operate. As a case study, let us consider one cubic meter of acetone solution containing a generic solute. Concentrating by a factor 10 this solution by distillation would require an amount of energy equal to 850 MJ. If the same separation is performed at room temperature and 25 bar using a membrane module, the energy consumption would be 2.2 MJ.

The separations mentioned above are generally classified as organic solvent nanofiltration (OSN) and organic solvent reverse osmosis (OSRO) (Koh et al., 2016; Koros and Zhang, 2017). OSN refers to situations in which a bulky solute, whose molecular mass is in the range 200–1000 g/mol, has to be separated from a solvent. OSN membranes generally operate based on the size sieving mechanism (Marchetti et al., 2014). First, the mixture to be separated is compressed to 30–40 atm and fed to the membrane: bulky solute molecules diffuse slowly through the membrane and, for entropic reasons, tend to be sorbed to a small extent by the membrane materials so, based on the solution-diffusion model (cf. section Solution-Diffusion model), they are rejected by the membrane and concentrated in the retentate side. Conversely, small solvent molecules preferentially permeate through the membrane (Marchetti et al., 2014). During the process, the downstream side of the membrane is kept at atmospheric pressure, so the pressure difference across the membrane drives the selective permeation of the solvent over the solute. OSRO refers to membrane separation of two or more liquids of like size. Since the currently available polymer materials cannot accomplish the latter separation, OSRO research efforts are being directed toward inorganic membranes based on carbon molecular sieves (Koros and Zhang, 2017; Lively and Sholl, 2017). Such materials separate molecules of like size based on the so-called entropic selectivity (Singh and Koros, 1996; Koros and Zhang, 2017).

There are several incentives for using OSN in the industrial practice. First, membrane filtration can be used either alone or in combination with traditional processes, such as distillation or liquid chromatography, giving rise to the so-called process intensification. As demonstrated by several techno-economic studies, such practice would reduce significantly the energy consumption of traditional processes, while ensuring high separation efficiency (White, 2006; Van der Bruggen, 2013; Marchetti et al., 2014; Szekely et al., 2014). Another advantage for using membrane filtration is its flexibility. Indeed, three operating modes are possible for OSN membranes, namely concentration, purification, and solvent exchange. Concentration processes involve the separation of a single solute from a solvent. As mentioned above, solute is concentrated in the retentate side, and solvent is recovered in the permeate side. Purification processes consist in separating two or more solutes, for example the main product of a chemical reaction from the byproduct. Finally, solvent exchange is used to enrich a solution in the solvent B by removing the solvent A.

Although ceramic materials have been also explored, polymers appear more suitable for OSN applications. The large amount of energy required to fabricate defect-free ceramic membranes, as well their intrinsic brittleness, represent the most relevant drawbacks for using ceramics in membrane manufacturing (Li, 2007).

Although OSN membranes are supposed to work based on the size exclusion mechanism, several factors, such as chemical-physical properties of the solute, solute-membrane interactions, solvent-membrane interactions, and membrane structure influence the membrane performance (Tsarkov et al., 2012; Postel et al., 2013; Volkov et al., 2014, 2015; Ben Soltane et al., 2016; Marchetti et al., 2017). However, little research efforts have been devoted to the analysis of these fundamental aspects.

The first attempt to use polymer membranes for organic liquid separation dates back to 1964, when Sourirajan used cellulose acetate to separate xylene from ethanol (Sourirajan, 1964). For almost 30 years, cellulose acetate was considered the standard material for separations involving organic liquids (Kopecek, 1970; Fang et al., 1992). The lack of materials capable to withstand chemically challenging environments has represented, for a long time, the real roadblock to progress in OSN (Cook et al., 2018). Indeed, organic solvents are sorbed to a significant extent by glassy and rubbery polymers. Such very high sorption, which often exceeds 50% by weight, may prejudice the membrane stability. Sometime, polymers can even dissolve in the presence of organic solvents. Several stable materials were developed in the last two decades, so the issue of membrane stability can be considered partially solved. Among these materials, cross-linked Lenzing P84 polyimide (White, 2001, 2002) has been particularly successful and it made possible small scale industrial applications of OSN in dewaxing of lube oil, homogeneous catalyst recovery, and enrichment of aromatics.

In the last decade, research has been focusing on tough polymers. This class of materials includes glassy polymers made of condensed aromatic rings with superior stability in solvents, such as polybenzimidazoles (Vogel and Marvel, 1961; Valtcheva et al., 2014, 2015; Borjigin et al., 2015) and polymers of intrinsic microporosity (PIMs) (Budd et al., 2004; Fritsch et al., 2012; Gorgojo et al., 2014; Ogieglo et al., 2017). Perfluorinated polymers (Chau et al., 2018), polyether ether ketone (PEEK) (Da Silva Burgal et al., 2015, 2017), and polyarylates (Jimenez-Salomon et al., 2016) also received significant attention for separations in harsh environments. In this review, we provide a detailed discussion of these materials, including synthesis routes, transport properties and property-structure correlations.

New interesting applications of OSN are in the pharmaceutical industry and, more specifically, in the downstream processing

of drugs, peptides and oligonucleotides. Noteworthy, membrane filtration in pharmaceutical industry can be exploited for separations, extractions, drying and also for particles formation (i.e., crystallization) (Buonomenna and Bae, 2015). For example, oligonucleotides and peptides are synthesized in solution and require a thorough purification before use. OSN represents a valid alternative to other processes, such as distillation or solvent extraction, which could potentially damage thermally and chemically labile biomolecules. Membranes based on cross-linked polybenzimidazole were successfully used to purify peptides and oligonucleotides, opening a new avenue in the area of oligo therapeutics (Kim et al., 2016).

Although membrane separation of organics has been indicated as one of the seven molecular separations that could change the world in the next decades (Lively and Sholl, 2017), OSN is currently one of the most poorly understood processes at a fundamental level. Specifically, the lack of fundamental knowledge about molecular factors governing solute and solvent transport in OSN membranes hampers OSN to take off the ground. Fundamental understanding of transport phenomena in OSN membranes would help not only to develop guidelines for the rational design of materials with pre-assigned transport properties, but also to select the optimal operative conditions to maximize the productivity and selectivity of existing membranes. Such aspect constitutes an essential prerequisite to make OSN competitive with traditional processes.

In this review we provide the state of the art of OSN using polymeric membranes. First, theoretical models useful to interpret experimental data are discussed and some misleading conclusions commonly reported in the literature are highlighted. The correct interpretation of OSN data is an essential pre-requisite to identify the key factors affecting solute and solvent transport in OSN membranes. Specifically, the individuation of a general framework to interpret transport data in OSN membranes represents the first step toward the development of structure-property correlations useful for the rational design of OSN membranes. A general theoretical framework for OSN is presented in section Transport Phenomena is OSN Membranes: Mechanism and Challenges. Then, currently available materials are reviewed. Finally, materials that could revolutionize OSN in the future are identified. For each of them, synthesis routes and structure-property correlations are presented and discussed.

TRANSPORT PHENOMENA IS OSN MEMBRANES: MECHANISM AND CHALLENGES

Solution-Diffusion Model

The solution-diffusion model sets the mechanism by which gases, vapors, liquids, and ions diffuse through dense (i.e., non-porous) polymers (Paul, 1973, 2004; Wijmans and Baker, 1995). Leveraging on an elegant series of experiments and a purposely built theory, Paul and coworkers, in the early 70's, demonstrated that the solution-diffusion mechanism rules the pressure driven transport of organic liquids in rubbery polymers (Paul and Ebra-Lima, 1971). The pioneering studies conducted by Paul can be considered the first attempt to understand OSN at a fundamental level, although, at the time, OSN was not recognized as such.

According to the solution-diffusion model, penetrant molecules first partition between the feed and the upstream face of the membrane. Then, sorbed molecules diffuse through the membrane thickness, down a concentration (or chemical potential) gradient. Finally, they desorb from the downstream face of the membrane. When considering the transport of liquids through dense polymer membranes, the permeability coefficient, which is an intrinsic property of the membrane material, is defined as the pressure and thickness normalized flux (Paul, 1973):

$$P_1 = \frac{n_1 l}{\rho_1 \Delta p} \tag{1}$$

where subscripts 1 and 2 stand for the penetrant and the membrane species, respectively. In Equation 1, n_1 is the steady-state penetrant mass flux relative to the fixed frame reference, i.e., the membrane, ρ_1 is the penetrant density, Δp is the pressure difference across the membrane, and $\boldsymbol{l}$ is the membrane thickness. To simplify the matter, let us consider the diffusion of a pure liquid through a polymer. To quantitatively describe this phenomenon, it is necessary to define a frame of reference. Two frames of reference can be used, namely fixed or moving (Paul, 1973; Kamaruddin and Koros, 1997; Galizia et al., 2016). In the moving framework, the diffusional flux is defined with respect to the center of mass of the polymer-penetrant system, which, in turn, moves with its own bulk velocity. Within this framework, the diffusional velocity relative to the bulk velocity causes the penetrant flux through the membrane. In the fixed or stationary frame of reference, the membrane itself is used as the frame of reference. The penetrant mass flux through the membrane, n_1, with respect to the fixed frame is expressed as follows (Paul, 1973; Kamaruddin and Koros, 1997; Galizia et al., 2016):

$$n_1 = n_1^{diff} + n_1^{conv} = j_1 + \omega_1 (n_1 + n_2) \tag{2}$$

where j_1 is the diffusive mass flux, i.e., the mass flux of species 1 relative to the center of mass of the polymer-penetrant system, ω_1 is the penetrant mass fraction in the membrane, and n_2 is the membrane flux (cf. **Figure 1**). This result can be extended to multicomponent permeation, so that, with respect to the fixed frame of reference, the mass flux of each permeating species is given by the convective flux resulting from the bulk motion of the permeating mixture (second term at the right-hand side in Equation 2), plus the diffusive flux (first term at the right-hand side in Equation 2).

In case of Fickian diffusion, j_1 is expressed as follows:

$$j_1 = -\rho D_1 \frac{d\omega_1}{dx} \tag{3}$$

where D_1 is the effective, concentration averaged penetrant diffusion coefficient through the membrane, ρ is the density of polymer-penetrant mixture, and x is the generic abscissa through the membrane thickness. Combining Equations 2, 3 and remembering that at steady state the polymer flux, n_2, is zero,

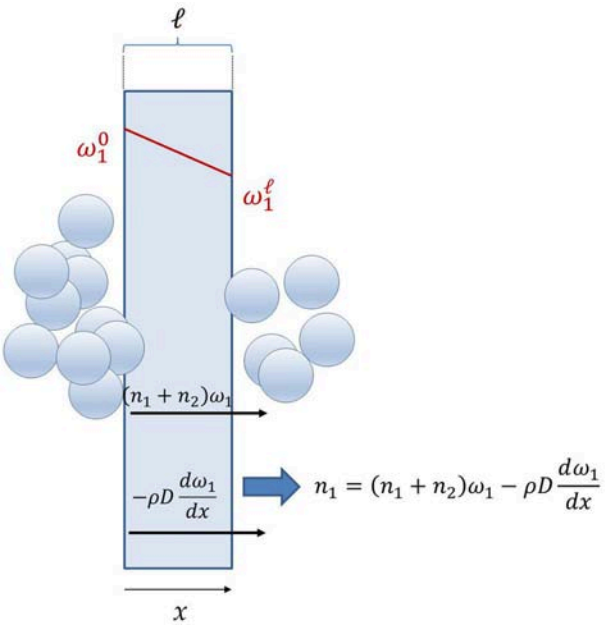

FIGURE 1 | Schematic of small molecule transport through dense polymer membranes.

leads to the following expression for the penetrant mass flux with respect to the fixed frame of reference:

$$n_1 = -\left(\frac{\rho D_1}{1-\omega_1}\right)\frac{d\omega_1}{dx} \tag{4}$$

During a permeation experiment, penetrant flux is measured with respect to the membrane, i.e., the experimentally measured flux is n_1 (Paul, 1973). However, when considering gas and vapor transport in polymers, ω_1 is vanishing, so that $1-\omega_1 \cong 1$. In this situation, the experimentally measured flux, n_1, is essentially equal to the diffusive flux, j_1. In contrast, liquid solvent uptake by polymers may be significant, so $1-\omega_1 \ll 1$, which means that n_1 significantly departs from j_1. In the latter situation, neglecting the factor $1/(1-\omega_1)$ in Equation 4 would cause significant errors in the estimation of the diffusion coefficient (Paul, 1973).

As the approach presented above can be generalized to the diffusion of multicomponent mixtures, Equation 4 should be used to describe solvent and solute transport in OSN membranes. Interestingly, such approach can be further generalized to account for the effects of osmotic pressure and concentration polarization (Peeva et al., 2004). Details about integration of Equation 4 were reported by Dinh (Dinh et al., 1992) and Paul (Paul, 1973). Integration of Equation 4 requires that the penetrant concentration profile in the membrane is known. As reported in previous studies (Paul, 2004; Galizia et al., 2016), the ω_1 profile can be considered linear, so that $\omega_1 = \omega_1^0\left(1-\frac{x}{l}\right)$, where ω_1^0 is the penetrant concentration in the upstream face of the membrane, which can be estimated from liquid sorption experiments.

Correcting the Fick's law for the frame of reference is not sufficient. When considering a membrane separating two solutions with different compositions, the chemical potential gradient across the membrane is the driving force for penetrant diffusion (Bird et al., 1960). However, as concentration is much easier to measure than chemical potential, often the concentration gradient across the membrane is assumed as the actual driving force for penetrant transport. Indeed, in writing Equation 4, we followed the latter approach. When the driving force is expressed in terms of concentration gradient, the diffusion coefficient appearing in Equation 4, D_1, is the product of a purely kinetic quantity, i.e., the mobility coefficient, L_1 , which accounts for the frictional resistance offered by the polymer matrix to penetrant diffusion, and the thermodynamic factor, $\frac{1}{RT}\frac{\partial\mu_1}{\partial ln\omega_1}$, related to polymer-penetrant interactions (Doghieri and Sarti, 1997; Galizia et al., 2011):

$$D_1 = L_1\left(\frac{1}{RT}\frac{d\mu_1}{dln\omega_1}\right) \tag{5}$$

In Equation 5, μ_1 is the penetrant chemical potential in the polymer-penetrant mixture and ω_1 is the penetrant mass fraction in the polymer. When polymer-penetrant mixing is ideal (i.e., no special interactions take place), the factor $\left(\frac{1}{RT}\frac{d\mu_1}{dln\omega_1}\right)$ is equal to one. Conversely, when polymer-penetrant mixing is non-ideal, which happens frequently, the thermodynamic factor deviates from one. Specifically, when the polymer and penetrant exhibit like physical-chemical properties and their mutual interactions are thermodynamically favorable, $\left(\frac{1}{RT}\frac{d\mu_1}{dln\omega_1}\right) > 1$. Conversely, when polymer-penetrant interactions are thermodynamically unfavorable, $\left(\frac{1}{RT}\frac{d\mu_1}{dln\omega_1}\right) < 1$ (Doghieri and Sarti, 1997; Galizia et al., 2011). This aspect complicates significantly the analysis of diffusion coefficients, which need to be corrected also for thermodynamic non-idealities. While the latter issue has been addressed by Paul for rubbery membranes, based on the Flory-Huggins theory (Paul, 1973), no general solution has been proposed so far for glassy membranes. Such aspect represents a potential research topic *per se*, since polymers used for OSN are typically glassy. A very simple method to correct diffusion coefficients in glassy polymer for thermodynamic non-idealities relies on vapor sorption data. Gas and vapor sorption isotherms in glassy polymers can be described using the dual mode sorption model (Koros et al., 1976), which provides the following analytic expression for the thermodynamic factor (Merkel et al., 2000):

$$\frac{1}{RT}\frac{d\mu_1}{dln\omega_1} = \frac{k_D + \frac{C_H' b}{1+bp}}{k_D + \frac{C_H' b}{(1+bp)^2}}\left[1 + \frac{M_w}{22414\rho_p}\left(k_D p + \frac{C_H' bp}{1+bp}\right)\right] \tag{6}$$

where k_D, C_H' and b are the three dual mode parameters, which can be estimated by fitting vapor sorption isotherms, p is the vapor partial pressure, M_w is the penetrant molecular mass and ρ_p is the polymer density. If vapor sorption data are available, the thermodynamic factor can be calculated as a function of activity using Equation 6, and then it can be extrapolated at activity 1, i.e., to the case of liquid sorption. However, such very simple method does not always work. For example, lower alcohols

(e.g., methanol and ethanol) sorption is some glassy polymers, such as polyacetylenes, cannot be described by the dual mode model, due to the occurrence of significant penetrant clustering (Galizia et al., 2011, 2012). For this reason, advanced methods based on more fundamental models are under development. For example, the non-equilibrium lattice fluid model provides a general, analytic expression for the penetrant chemical potential in mixture with a glassy polymer (Doghieri and Sarti, 1996), from which the derivative appearing in Equation 5 can be calculated analytically.

For rubbery polymers, the diffusion coefficient corrected for the frame of reference and thermodynamic non-idealities is given by (Paul, 1973):

$$L_1 = D_1 \left(1-\phi_1\right)^2 \left(1 - 2\chi_1\phi_1\right) \tag{7}$$

where D_1 is the experimentally determined diffusion coefficient, ϕ_1 is the penetrant volume fraction in the membrane, and χ_1 is the polymer-penetrant Flory-Huggins interaction parameter (Flory, 1942).

Paul (1973) successfully used this approach to describe a set of experimental diffusion data presented by White (1960). White measured pure liquid water transport through rubbery polyacrylamide membranes whose water content was about 70% vol. Interestingly, water diffusion coefficient through the membrane, calculated as the ratio of permeability to sorption coefficients, resulted one order of magnitude larger than water self-diffusion coefficient (i.e., 2.8×10^{-5} cm^2/s). To explain this unexpected result, White speculated that, for such highly swollen membrane, water transport occurs by pore flow. Paul demonstrated that the results presented by White could be rationalized using Equations 4 and 7 (Paul, 1973). Indeed, since the polyacrylamide membrane was highly swollen, neglecting the term $1/(1-\omega_1)$ in Equation 4, as well as thermodynamic non-idealities, led White to overestimate the diffusion coefficient by orders of magnitude. After correction for the effect of the frame of reference and thermodynamic non-ideality, water diffusion coefficients in polyacrylamide were far below the liquid water self-diffusion coefficient. So, invoking pore flow to describe water transport in polyacrylamide membranes was inappropriate.

In recent years, similar conclusions were drawn by Volkov et al. (1996) when assessing the suitability of glassy poly(trimethylsilyl propyne) (PTMSP) for OSN application. They observed that liquid ethanol diffusion coefficient in PTMSP (i.e., 1.27×10^{-8} cm^2/s) was larger than ethanol self-diffusion coefficient (i.e., 1.10×10^{-9} cm^2/s) and speculated occurrence of pore flow transport. This conclusion is dramatically altered if the experimental data are analyzed using the Paul's approach. From swelling experiments, ethanol volume fraction in PTMSP at room temperature resulted 0.46. If one assumes, in first approximation, the Flory-Huggins theory to account for thermodynamic non-ideality, the χ parameter can be estimated from liquid ethanol sorption data. Doing so, gives $\chi = 0.813$. Finally, from Equation 7, the ethanol diffusion coefficient in PTMSP corrected for the frame of reference and thermodynamic non-idealities is 9.30×10^{-10} cm^2/s, which is below the ethanol self-diffusion coefficient and fifteen times smaller relative to the value calculated by Volkov. The dual mode approach, although more appropriate for glassy PTMSP, cannot be used to correct ethanol diffusion coefficient for thermodynamic non-idealities, since ethanol sorption is PTMSP is not dual-mode type (Doghieri and Sarti, 1997).

The examples discussed above show how poor has been, so far, the fundamental analysis of transport phenomena in OSN membranes, and how this issue continues to generate misleading interpretations of experimental data.

The solution-diffusion model links penetrant permeability, solubility and diffusion coefficients in the membrane as follows (Wijmans and Baker, 1995):

$$P_1 = D_1 \times S_1 \tag{8}$$

When considering the permeation of a binary mixture through a membrane, the selectivity for the component *i* vs. the component *j* is defined as follows (Wijmans and Baker, 1995):

$$\alpha_{ij} = \frac{P_i}{P_j} = \frac{D_i}{D_j} \times \frac{S_i}{S_j} = \alpha_D \times \alpha_S \tag{9}$$

where α_D and α_S are the diffusivity-selectivity and the solubility-selectivity, respectively. The diffusivity-selectivity is believed to control the selective permeation of solvent over solute through OSN membranes. Indeed, since diffusivity decreases markedly with increasing penetrant size, solute molecules are expected to be rejected by the membrane due to their very slow diffusion in the membrane material. However, deviations from this rule of thumb have been observed. For example, Postel reported that during removal of non-polar hydrocarbon solutes (e.g., alkanes) from polar solvents (e.g., isopropanol) using rubbery PDMS membranes, solute permeability through the membrane largely exceeds solvent permeability (Postel et al., 2013). As a consequence, the solute is enriched in the permeate side relative to the feed side (i.e., the membrane is solute-selective instead of solvent-selective, cf. **Figure 2**). Postel hypothesized that preferential solute sorption in PDMS, caused by its higher thermodynamic affinity with the polymer, is responsible for this phenomenon, even though no direct proof of this hypothesis has been provided (Postel et al., 2013).

As we will see in the forthcoming sections, often commercial membranes are made by a thin active layer, which actually performs the separation, cast onto a porous support. Since the thickness of the active layer cannot be measured accurately, application of Equation 1 to calculate permeability is not straightforward. So, the performance of these composite membranes is expressed in terms of permeance instead permeability. Permeance is the thickness normalized permeability and, as such, it is not an intrinsic property of the membrane, since it depends on its geometry. Likewise, in practical applications, rejection is used instead selectivity. Rejection of species *i* is defined as follows (Marchetti et al., 2014, 2017):

$$R_i = 1 - \frac{C_i^p}{C_i^f} \tag{10}$$

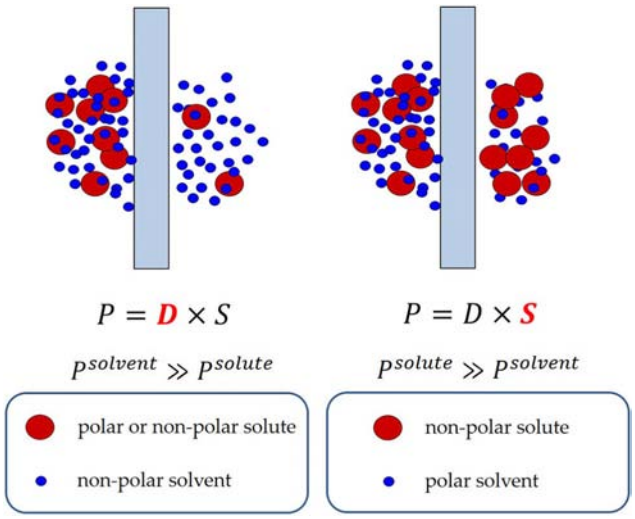

FIGURE 2 | Solvent and solute transport in PDMS-based membranes. On the right is reported the case where solute permeability exceeds solvent permeability. Solute preferential sorption is believed to be the cause of this behavior (Postel et al., 2013).

where C_i^p and C_i^f are the concentrations of species i in the permeate and feed, respectively. Rejection is related to selectivity as follows:

$$\alpha_{ij} = \frac{1 - R_i}{1 - R_j} \tag{11}$$

Plasticization

Membrane plasticization indicates an increase in chain mobility caused by penetrant sorption (Chiou et al., 1985). Such improved chain mobility reduces the energy penalty required to open gaps between polymer chains, thus enhancing penetrant diffusivity and permeability. However, such an increase in permeability is accompanied by a loss in membrane selectivity. OSN membranes must exhibit adequate resistance to plasticization, as they face directly organic liquids during their operation. Methods to mitigate membrane plasticization rely essentially on polymer chemistry: covalent or ionic cross-linking, as well as use of rigid monomers with limited rotation freedom are some relevant examples (Vanherck et al., 2013; Valtcheva et al., 2014, 2015).

Physical Aging

Rigid materials, such as glassy polymers, are sought in OSN applications. Glassy polymers contain an excess free volume trapped in their structure and, as such, they are non-equilibrium materials. Excess free volume is *per se* unstable and tends to be relaxed over time, producing a progressive densification of the polymer matrix. This process is referred to as physical aging (Huang and Paul, 2004, 2006). Loss of free volume significantly affects transport properties of glassy membranes, as it reduces small molecule permeability and enhances selectivity. Paul and co-workers demonstrated that the physical aging rate of glassy polymer films is inversely proportional to their square thickness, which justifies the accelerated aging exhibited by thin films typically used in membrane applications (Huang and Paul, 2004, 2006). Membranes 1 μm thick or less lose 25% of their permeability within a few days after manufacturing. Another 25% of their permeability is lost in the following 15 days (Galizia et al., 2017a). For example, asymmetric membranes based on cross-linked Lenzing P84 polyimide, the current standard material for OSN, exhibit solvent permeance ranging from 1 to 2 L/(m^2 h bar). Thermal annealing at 200°C decreases solvent permeance to zero, due to polymer densification (See See-Toh et al., 2007a). The issue of physical aging becomes dramatic during operation at medium-high temperatures, as polymer chains motion, who is ultimately responsible for physical aging of glassy polymers, becomes faster with increasing temperature.

Strategies to mitigate this issue have been devised, which rely on covalent cross-linking and use of rigid monomers with frustrated rotation freedom. While the former strategy was sometimes successful, the latter did not always guarantee good results, as rigid polymers, such as PIMs (Bernardo et al., 2017) and thermally rearranged (TR) polymers (Wang et al., 2014) also exhibit physical aging when manufactured as thin films.

Recently, Livingston and co-workers reported negligible aging in poly(ether ether ketone) (PEEK) membranes for OSN (Da Silva Burgal et al., 2015, 2017). PEEK is a fully aromatic, semi-crystalline polymer made by hydroquinone and benzophenone segments. Physical aging of bulky membranes (10–50 μm) typically used in the academia is a slow process and its effects do not show up within experimentally accessible timescales (Galizia et al., 2017a). To accelerate physical aging, Da Silva Burgal annealed thick films made by PEEK, Lenzing P84 polyimide and polybenzimidazole at 120°C for 48 h (Da Silva Burgal et al., 2017). Polyimide and PBI samples became very brittle after thermal annealing, due to the accelerated free volume relaxation, which reduced polymer chain mobility. Their Young's modulus could not be measured after annealing. In contrast, PEEK didn't show any brittleness and its Young's modulus increased from 61 MPa to 108 MPa after annealing at 120°C. The unusual stability exhibited by PEEK is likely due to the presence of ultra-rigid crystalline domains, which freeze polymer chains in the amorphous domain in their original position (Da Silva Burgal et al., 2017).

Three dimethylformamide (DMF) filtration experiments were run with PEEK, polyimide P84 and PBI membranes at 30, 85, and 140°C, respectively, followed by a fourth run at 30°C. Permeance of P84 decreased by a factor 6 from 30 to 85°C. At 140°C, cross-linking thermal scission caused the membrane failure. PEEK and PBI permeance increased by a factor 20 and 2.5, respectively, from 30 to 140°C. Interestingly, during the fourth filtration cycle, when temperature was returned to 30°C, PEEK exhibited the same permeance as in the first run, and PBI lost 25% of its original permeance (cf. **Figure 3**). This result was justified by invoking negligible aging in PEEK (Da Silva Burgal et al., 2017).

Permeability-Selectivity Trade-Off

The existence of a trade-off between permeability and selectivity in polymer membranes for gas separation was reported on empirical bases by Robeson (Robeson, 1991, 2008), and it was explained theoretically by Freeman (1999). Generally, highly permeable membranes exhibit poor selectivity, and vice-versa. As a consequence, the performance of polymer membranes is

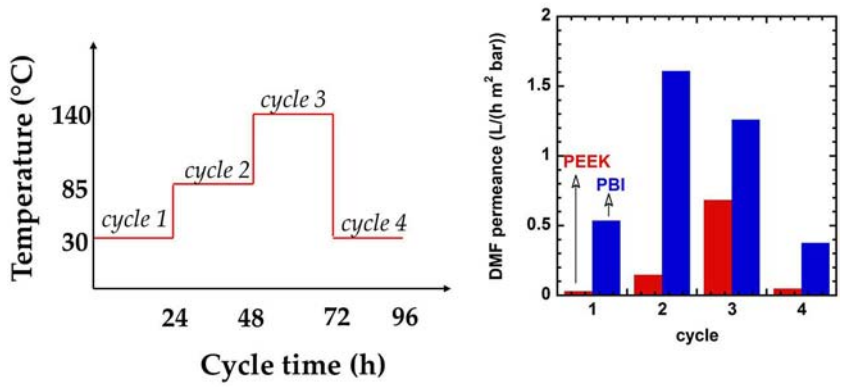

FIGURE 3 | Effect of physical aging on poly (ether ether ketone) and polybenzimidazole membranes. Adapted from Da Silva Burgal et al. (2017), with permission of *Elsevier*.

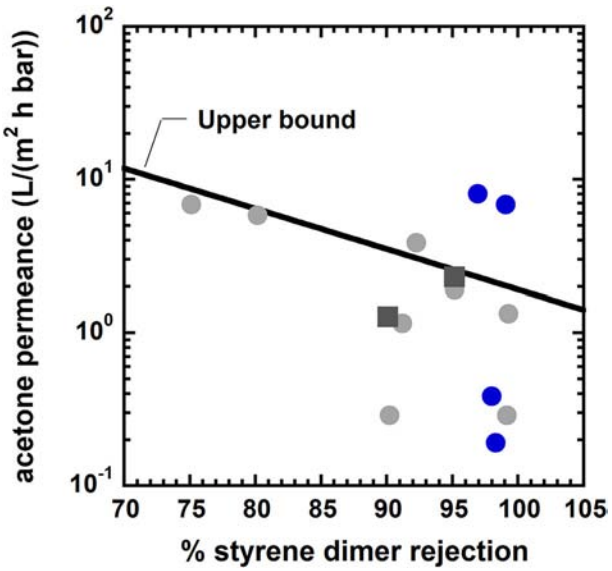

FIGURE 4 | Upper bound diagram for styrene dimers (molecular mass 236 g/mol) separation from acetone at room temperature. Solid gray circles: conventional asymmetric membranes. Solid black square: conventional composite membranes. Solid blue circles: nanoporous polyarylates synthesized by Jimenez-Salomon et al. (2016). Blue circles above the upper bound refer to polyarylates obtained using contorted, non-planar monomers [i.e., 9,9-bis(4-hydroxyphenyl)fluorine]. Blue circles below the upper bound refer to polyarylates obtained using planar, non-contorted monomers (i.e., dihydroxyanthraquinone). Adapted from Jimenez-Salomon et al. (2016), with permission of *NatureResearch*.

limited to stay below the upper bound defined by the best performing materials. Conversely, inorganic materials, such as zeolites, often surpass the upper bound, as they exhibit high levels of permeability and selectivity. Recently, a permeability-selectivity trade-off for OSN membranes was reported by Marchetti (Marchetti et al., 2017). Such finding strongly supports the idea that the solution-diffusion mechanism rules solute and solvent transport in OSN membranes. An example of permeance/rejection upper bound for OSN is reported in **Figure 4**.

Effect of Pressure on Solvent Flux

One of the most controversial aspects in OSN is the dependence of solvent flux on the upstream pressure. Several authors observed that flux is linear with Δp (i.e., the pressure difference across the membrane), and it declines at high pressures. Membrane compaction caused by the upstream pressure has been invoked to explain this behavior (Machado et al., 1999; Grekhov et al., 2012; Ben Soltane et al., 2013). However, while this explanation could be physically sound for soft, rubbery membranes, such as PDMS (elastic modulus < 4 MPa), it seems unrealistic for rigid glassy polymers typically used in OSN (elastic modulus $\cong 4$ GPa), especially if we consider that flux decline often starts at relatively low pressures, such as 10–12 bar. We believe the right explanation of this phenomenon should be found in the pioneering studies from Paul and co-workers (Paul and Ebra-Lima, 1970, 1971; Paul, 1973). Paul demonstrated that the driving force for liquid transport through a swollen membrane is the swelling gradient between the upstream and the downstream face of the membrane, $\phi_1^0 - \phi_1^l$, where ϕ is the liquid volume fraction in the membrane material (Paul, 1973). While ϕ_1^0 (i.e., the liquid volume fraction in the upstream face) is constant, as it does not depend on the applied pressure, ϕ_1^l (i.e., the liquid volume fraction in the downstream face) decreases with increasing upstream pressure. When the upstream pressure is high enough, ϕ_1^l can become zero. In this situation, the maximum driving force is available, which means that flux cannot further increase with increasing pressure (cf. **Figure 5**). Paul derived the following expression for solvent mass flux as a function of applied Δp (Paul, 1976, 2004):

$$n_1 = \frac{C_1^0 D_1}{l\left(1-\omega_1^0\right)}\left[1 - exp\left(-\frac{\tilde{V}_1 \Delta p}{RT}\right)\right] \tag{12}$$

where C_1^0 and ω_1^0 are the solvent concentration and mass fraction at the upstream face of the membrane, respectively, $\tilde{V}_1$ is

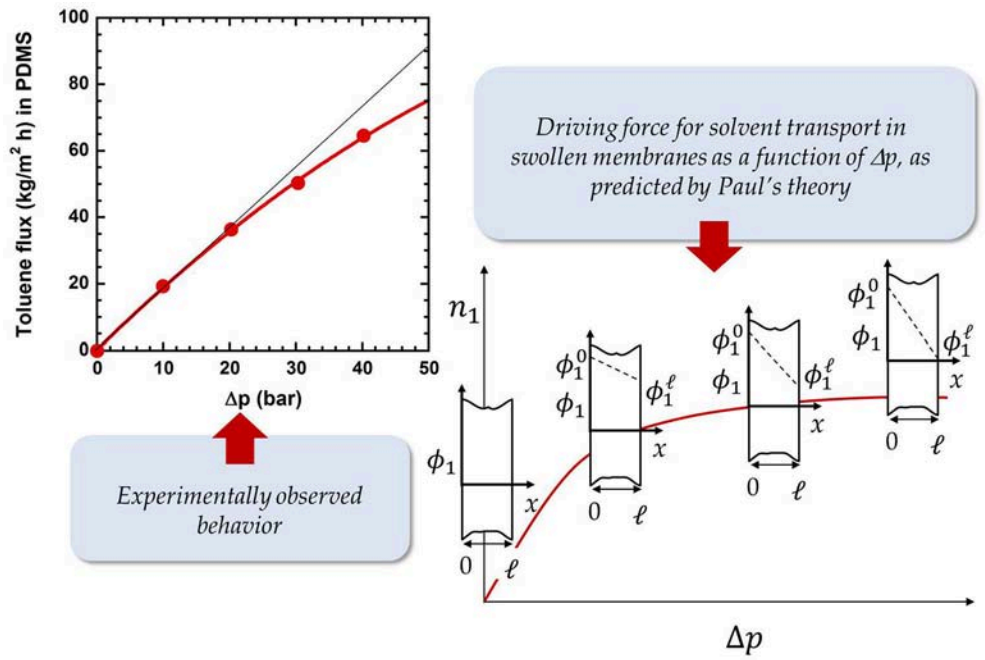

FIGURE 5 | Toluene flux through PDMS as a function of Δp at room temperature. Data were taken from Postel et al. (2013). The evolution of driving force for solvent transport as a function of Δp is reported as well, adapted from Paul (2004), with permission of *Elsevier*.

the solvent molar volume and Δp is the pressure difference across the membrane. Equation 12 states that the ceiling flux is attained more rapidly with increasing permeant molar volume.

Machado and co-workers (Machado et al., 1999) measured the permeability of pure liquid alcohols and hydrocarbons as a function of applied pressure in MPF-50, a commercial membrane made by cross-linked silicon rubber. They observed, especially for higher alcohols (i.e., isopropanol, butanol, and pentanol) and large hydrocarbons (n-pentane), a severe flux decline starting at 15 atm. For methanol such decline was less pronounced. To justify this behavior, Machado and co-workes invoked membrane compaction. However, in doing so, the authors recognized that flux decline at high pressures was significant especially for bulky solvents, i.e., solvent endowed with large molecular size. We believe their conclusions are somehow misleading, since membrane compaction is a purely mechanical effect that should take place regardless of penetrant size. Machado used the following empirical expression to fit flux vs. pressure curves:

$$n_1 = n_1^0 exp\left(-\alpha_p \Delta p\right) \tag{13}$$

where n_1^0 is a pre-exponential factor and α_p is an empirical parameter that measures membrane compaction: the higher the membrane compaction, the higher α_p. So, flux decline becomes faster with increasing α_p (that is, flux decline starts at lower pressures with increasing α_p). Paul's theory can be used to rationalize this behavior, without invoking membrane compaction. Indeed, Equation 12 states that (i) at low Δp flux is linear, as it can be demonstrated by replacing the exponential term with a first order Taylor expansion (i.e., $1 - exp\left(-\frac{\tilde{V}_1 \Delta p}{RT}\right) \cong \frac{\tilde{V}_1 \Delta p}{RT}$ when Δp is small), and (ii) at sufficient high Δp, the downward curvature of the flux-pressure curve becomes more pronounced as the solvent molar volume increases. **Figure 6A** shows the dimensionless flux, n_1^{dim} , (i.e., $n_1^{dim} = \left[1 - exp\left(-\frac{\tilde{V}_1 \Delta p}{RT}\right)\right]$) as a function of Δp, for different values of $\tilde{V}_1$. The downward curvature of the flux-pressure curves becomes more pronounced with increasing permeant molecular size, as observed by Machado.

Interestingly, for any given couple of solvents, i and j, the α_p^i/α_p^j ratio matches very well with the molar volumes ratio, $\tilde{V}^i/\tilde{V}^j$ (cf. **Figure 6B**). This analysis points out that the parameter α_p in the empirical Machado's model does not account for membrane compaction, as the authors state. According to Paul's theory, α_p is a measure of penetrant molecular size. So, occurrence of flux decline is not sign of membrane compaction, as commonly believed in the literature. Flux decline simply indicates that the system is approaching a condition where the driving force for solvent transport is maximum. When this maximum is reached, the flux attains its ceiling value. Moreover, the magnitude of flux decline increases with increasing permeant molecular size. So, the empirical Machado's model, if interpreted correctly, coincides with the rigorous Paul's model.

CURRENT OSN MATERIALS

OSN is a relatively young process, but with enormous potential for growth. Small scale applications of OSN are today in the

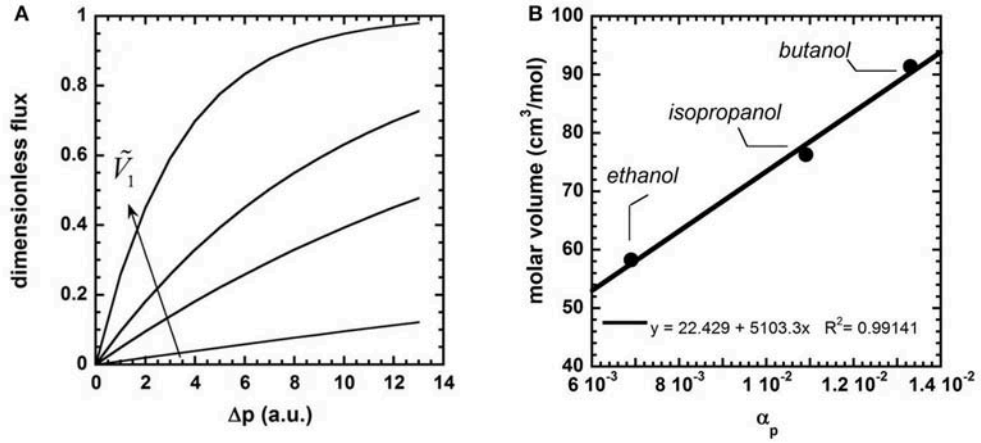

FIGURE 6 | (A) Solvent dimensionless flux vs. Δp at various solvent molar volumes, as predicted by the Paul theory (Paul, 1973). **(B)** Solvent molar volume, $\tilde{V}_1$, vs. α_p in silicone rubber MPF-50 (Machado et al., 1999).

pharmaceutical and cosmetic industry, as well as in refinery (dewaxing of lube oil) (Marchetti et al., 2014, 2017; Buonomenna and Bae, 2015). Composite membranes, consisting of a very thin (<1 μm thick) active layer supported onto a porous backing, are often considered in the academic research and industrial practice (cf., **Figure 7**). The active layer and the backing support are made by different materials and have different structures and properties. They are combined together exploiting interfacial polymerization, as well as well-established spin coating or dip coating techniques. The support is generally made by polysulfone, polypropylene, polyimide or polybenzimidazole, depending on the environment the membrane has to face with. The active layer, which performs the separation, is generally made by cross-linked Lenzing P84 polyimide or cross-linked silicon rubber (PDMS) (Marchetti et al., 2014). The chemical structure of P84 polyimide and PDMS and their relevant chemical-physical properties are reported in **Table 1**. Alternatively, asymmetric membranes can be used (cf., **Figure 7**). Asymmetric membranes exhibit a dense skin, which performs the separation, supported onto a porous medium, made of the same material as the skin itself. They are prepared via phase-inversion, a process originally developed by Loeb and Sourirajan (Loeb and Sourirajan, 1963). A dilute solution of the membrane material in an appropriate solvent is cast onto a fabric backing. Then, the freshly cast membrane is soaked in a non-solvent bath where phase separation occurs. The polymer-rich phase generates the dense active layer, and the polymer-poor phase generates the porous support. Compared to composite membranes, asymmetric membranes exhibit lower resistance to physical aging and less stable properties during operation.

Standard membrane materials for OSN are polyimides (White, 2002) and cross-linked silicone rubber (Postel et al., 2013), even though new materials, such as polybenzimidazole and PIMs, are emerging as promising candidates (Valtcheva et al., 2014, 2015). Unlike gas separation, OSN currently relies on a limited number of membrane materials, since polymers capable to withstand organic environments are rare.

Since the pioneering studies conducted by White in the early 2000's (White, 2001, 2002), Lenzing P84, a polyimide obtained by the condensation of 2,4-diidocyanato-1-methylbenzene and 1,1′-methylenebis(4-isocyanatobenzene) with 5,5′-carbonylbis(1,3-isobenzofurandione), is currently the standard membrane material for OSN (Silva et al., 2005; See-Toh et al., 2007a, 2008). Lenzing P84 films can be fabricated via solution casting from DMF, NMP, DMSO and DMAc solutions. Due to its fully aromatic, rigid structure, Lenzing P84 exhibits long lasting resistance to several solvents, such as hydrocarbons, toluene, alcohols and ketones. White prepared asymmetric membranes based on Lenzing P84 to separate linear from branched alkanes in toluene solutions. He showed that pristane, a saturated hydrocarbon bearing 19 carbon atoms, exhibited lower flux through Lenzing P84 relative to n-docosane, a linear saturated hydrocarbon bearing 22 carbon atom. This behavior is interesting, since pristane has lower molecular weight and molar volume relative to docosane. White attributed this behavior to the larger cross-section area of pristane, which increases the frictional resistance offered by the polymer to molecular diffusion. Based on this picture, pristane is better rejected than docosane due to its slower diffusion through the membrane material (White, 2002).

Afterwards, White used Lenzing P84 to separate aromatic from aliphatic aromas: interestingly, aromatic compounds exhibited higher fluxed than aliphatic ones. This behavior was attributed to the sorption contribution. Indeed, aromatic compounds interact more favorably with the aromatic polymer backbone than aliphatic species do. Such favorable thermodynamic interaction enhances the solubility of aromatic over aliphatic species in the membrane, which, based on the solution-diffusion model, justifies the experimental findings (White, 2002).

To improve the stability in aggressive aprotic solvents (e.g., THF, DMF and NMP), in which polyimides are soluble, Livingston and co-workers crosslinked Lenzing P84 using aliphatic diamines (ethylenediamine, propanediamine,

FIGURE 7 | Structure of composite **(A)** and asymmetric **(B)** membranes for OSN.

TABLE 1 | Current standard materials for OSN: Lenzing P84 polyimide and PDMS.

	P84 polyimide	**PDMS**
	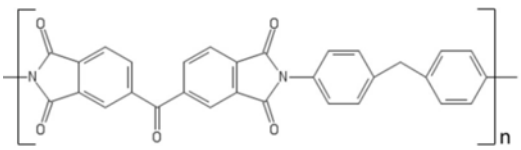	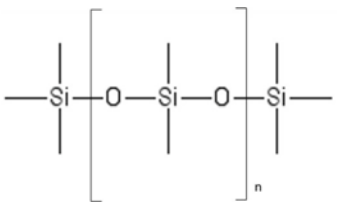
Glass transition temperature (°C)	329	−123
Young's modulus (GPa)	2.50	0.004
Methanol permeance* [L/(h m^2 bar)]	5.48	0.619
Source	(P84 product data, http://www.hppolymer.com/pdfs/Dimond%20wheel%20brochure.pdf; Darvishmanesh et al., 2010)	Lotters et al., 1997; Postel et al., 2013

*At room temperature.

hexanediamine, and octanediamine) in methanol solution. The cross-linking mechanism was described in detail by Liu et al. (2001). Specifically, the amino groups available on the cross-linker react with the imide groups on the polymer backbone to form amide moieties. The matrix swelling induced by methanol sorption is an essential pre-requisite for the formation of cross-linking. Indeed, if the polymer is not swollen enough, the reaction between the amino and the imide groups can be very slow. The method devised by Livingston produces uniform cross-linking throughout the whole membrane thickness. Other methods based on the radical-initiated cross-linking cannot be exploited, since they would effectively cross-link just the membrane surface, thus causing the membrane failure in aprotic acids. Cross-linked Lenzing P84 exhibited excellent stability in tetrahydrofuran (THF), N-methyl pyrrolidone (NMP), and dimethylformamide (DMF). FTIR analysis demonstrated that no morphological changes occurred in the membrane after soaking in these solvents for 120 h (See-Toh et al., 2007b). Obviously, the gain in stability upon cross-linking is accompanied by a decrease in permeability, caused by the enhanced chain packing.

Cross-linked PDMS has been tested to concentrate dyes from organic solutions and remove solvents from vegetable oils (Subramanian et al., 2001, 2003; Koike et al., 2002; de Morais Coutinho et al., 2009). The main drawback for using PDMS is its poor resistance to aggressive solvents. Indeed, due to the high chain flexibility and weak rigidity, PDMS sorbs a significant amount of solvent (Favre et al., 1994; Whu et al., 2000; Sheth et al., 2003; Vankelecom et al., 2004), which prejudices the membrane stability.

Both Lenzing polyimide and PDMS suffer of several limitations. Lenzing PI exhibits, indeed, modest fluxes but high resistance to aggressive environments. In contrast, PDMS exhibits high fluxes but poor chemical resistance. So, new materials are sought to overcome such limitations.

In recent years, polybenzimidazole (PBI), commercially available under the trade name of Celazole®, emerged as a promising material for OSN. PBI, first synthesized by Vogel and Marvel (Vogel and Marvel, 1961), is prepared from isophthalic acid and 3-3′-diaminobenzidine. It exhibits a rigid, aromatic structure with frustrated chain mobility. Moreover, intermolecular hydrogen bonding acts as a cross-link and contributes to mitigate swelling and plasticization in the presence of organic liquids. PBI exhibits also unusual thermal stability, with a negligible mass loss (< 5%) upon exposure to 570°C. Such

unique combination of rigidity, high glass transition temperature and unprecedented chemical and thermal resistance, makes PBI suitable for separations in chemically challenging environments (Borjigin et al., 2015). However, the lack of solubility in most of organic solvents makes it difficult manufacturing thin membranes based on PBI. This polymer is only soluble in aggressive solvents, such as dimethylacetamide (DMAc). To further improve solubility in DMAc, LiCl is added to the dope solution, which complicates the post-processing treatment of the membranes as, after fabrication, LiCl has to be removed. These issues hamper the use of PBI in the industrial practice.

Livingston and co-workers developed cross-linked asymmetric membranes based on PBI with superior resistance in acid environments (Valtcheva et al., 2014). PBI was cast from a DMAc solution onto a non-woven polypropylene support. The nascent membrane was then soaked in water to generate phase separation and induce the asymmetric structure. Following this protocol, membranes were cross-linked upon immersion in a hot solution of dibromobenzene in acetonitrile (cf., **Figure 8**). Interestingly, the resulting cross-linked membranes exhibited good separation performance for several PEG markers in acetonitrile and dimethylformamide, as well as excellent dimensional stability even in hydrochloric acid solutions.

Since the pioneering work by Sourirajan in the early 60s, cellulose acetate and its derivatives have been, for at least two decades, the most studied materials for OSN applications. However, due to its poor resistance to aggressive solvents, cellulose acetate could only be used to separate a limited number of mixtures, such as water/alcohol. Moreover, due to the presence of crystalline domains, solvent flux through cellulose acetate membranes is relatively low. Recently, Vanherck et al. developed a new strategy to enhance the permeability of cellulose acetate OSN membranes without sacrificing the selectivity (Vanherck et al., 2011). They exploited the principle of photothermal heating by embedding gold nanoparticles (GNPs) into a cellulose acetate membrane. In this way it is possible to increase the local temperature in the membrane during operation by light irradiation, which, in turn, significantly enhances solvent flux. Such increase in solvent transport rate is essentially ascribable to an increase in diffusion coefficient. Indeed, solvent mobility coefficient through the membrane increases exponentially with increasing temperatures, due to the reduction of frictional resistance offered by polymer chains to penetrant diffusion. In contrast, the effect of temperature on the sorption coefficient is much weaker. The same principle was exploited by Nakai to improve by 37% CO_2 permeability through cellulose acetate (Nakai et al., 2002).

The method proposed by Vanherck leverages on the gold nanoparticles ability to absorb light and convert it into heat (Daniel and Astruc, 2004). Such an effect becomes especially efficient at specific wavelengths, where surface plasmon resonance occurs. Golden nanoparticles were generated directly into a pre-made cellulose acetate membrane using the protocol reported by Huang (Huang et al., 2005). The amount of nanoparticles in the membrane was varied between 0 and 2% wt. To run nanofiltration experiments, Vanherck modified a dead-end filtration cell by building a glass window on top of it, to allow an argon-ion laser beam (wavelength = 514 nm) to irradiate the active membrane area (Vanherck et al., 2011).

Interestingly, water and alcohol permeability increased up to 15 and 400%, respectively, upon laser irradiation, with no detectable effects on solute (bromothymol blue) rejection. Moreover, solvent permeability returned to its original value after the laser was turned off, indicating that the observed change in transport properties was only due to the reversible membrane heating and not to permanent structural modifications. The much larger permeability improvement observed for alcohols was attributed to the lower specific heat of alcohols relative to water, which permits a more rapid heating of the swollen membrane. Likewise, alcohols exhibit lower thermal conductivity relative to water, so, while flowing through the membrane, they remove less heat.

MOLECULAR FACTORS AFFECTING SOLUTE AND SOLVENT TRANSPORT IN OSN MEMBRANES

The vast majority of research efforts on OSN focused, so far, on applications: commercially available or newly synthesized materials were used to measure solvent flux and solute rejection and such measurements helped to assess the suitability of those materials for specific applications. However, little information is available about molecular factors affecting solute and solvent transport in OSN membranes. The transport mechanism itself is object of discussion, as some researchers assume a solution-diffusion mechanism, others a pore-flow mechanism (Marchetti and Livingston, 2015; Ben Soltane et al., 2016). However, many factors, above all the existence of a permeability-selectivity trade-off, suggest that OSN membranes work based on the solution-diffusion mechanism. This conclusion was confirmed unequivocally by a series of simple but effective experiments performed by Paul in the early 70s. Specifically, Paul measured solvent permeability through a stack of several membranes. After reaching steady-state, the membranes were rapidly removed from the permeation cell and weighed. The experimental solvent concentration profile in the stack was in excellent agreement with that predicted assuming a solution-diffusion transport mechanism (cf. **Figure 5**, Paul and Ebra-Lima, 1971).

Fundamental structure-property correlations are available for gas separation membranes, which makes it possible to design polymers with pre-assigned transport properties. For example, use of polyethers for CO_2 separation leverages on the high thermodynamic affinity between CO_2 molecules and polar ether groups, which enhances CO_2 sorption and, according to Equation 8, CO_2 selective permeability (Bondar et al., 1999). So, membranes for gas separation are engineered by properly tuning solubility and diffusivity of the target penetrant in the membrane material. This goal is achieved, in turn, by tuning the polymer chemistry, that is, using monomers bearing specific functional groups.

The lack of information about the role of sorption and diffusion coefficients on solvent and solute transport is actually a roadblock toward the rational design of smart OSN membranes.

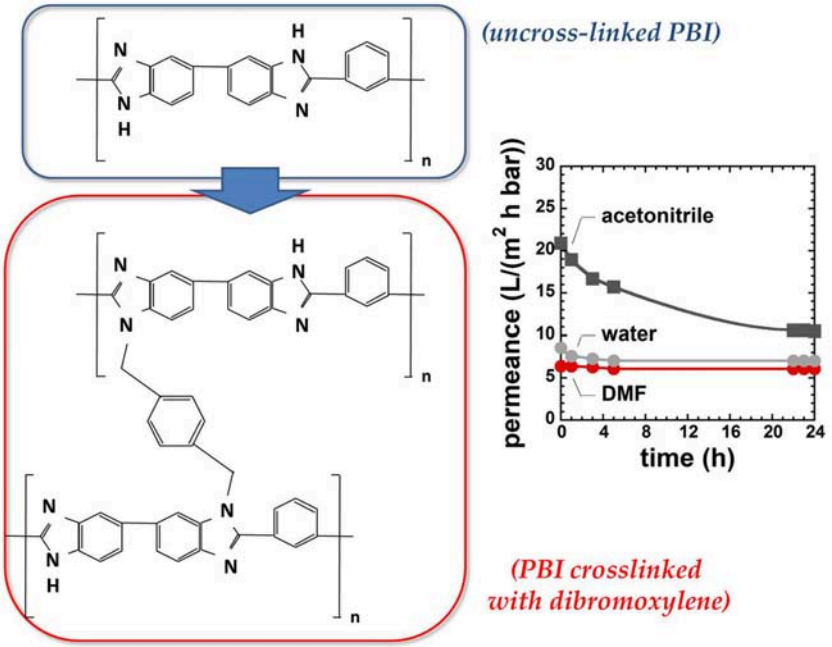

FIGURE 8 | Structure and properties of novel PBI membranes cross-linked with dibromoxylene. Adapted from Valtcheva et al. (2014), with permission of *Elsevier*.

Nevertheless, in this section we identify, based on the few data available, the main molecular factors that influence solute and solvent transport in OSN membranes.

From a theoretical standpoint, small molecule sorption in polymers is a phase equilibrium problem (Galizia et al., 2012). Sorption equilibrium is reached when penetrant chemical potential in the external fluid phase equates that in the polymer mixture. As chemical potential contains, by its definition, an enthalpic (i.e., energetic) and an entropic contribution, small molecules sorption in polymers is influenced by these two effects (Galizia et al., 2012). Enthalpic effects are related to polymer-penetrant interactions and, as a rule of thumb, favorable interactions translate in high penetrant solubility in the membrane material. Entropic effects are related to penetrant size. As general rule, sorption decreases with increasing penetrant size. Indeed, absent specific interactions, it is less and less likely to accommodate bulkier penetrant molecules in the polymer matrix than smaller penetrant molecules.

Vankelecom et al. (1997) and Cocchi et al. (2015a) reported sorption and diffusion coefficients of several liquids in rubbery PDMS. Alkanes solubility in PDMS decreases linearly with the number of carbon atoms, indicating that sorption is affected essentially by entropic factors. In contrast, solubility of polar alcohols in PDMS follows a non-monotonous trend with the number of carbon atoms, as it increases moving from ethanol to 1-butanol, and then decreases linearly going from 1-butanol to higher alcohols, following the same trend observed for alkanes. This phenomenon was justified based on the interplay between enthalpic and entropic effects. Indeed, PDMS exhibits poor thermodynamic affinity with lower polar alcohols. The strong repulsive interactions between –OH polar groups and the non-polar PDMS backbone strongly oppose to alcohol dissolution in the polymer. When the length of the alkyl tail increases, the affinity between alcohols and PDMS increases, which justifies the increase in solubility observed going from methanol to 1-butanol. When the alkyl tail is long enough, the polar –OH group is sterically shielded, so alcohols start to behave as alkanes and their solubility in PDMS decreases with increasing penetrant size. So, the increase in solubility from methanol to 1-butanol is driven by enthalpic (i.e., energetic) effects, and the subsequent decrease is driven by entropic effects.

Vankelecom demonstrated that the solubility of organic liquids in PDMS decreases linearly with increasing the difference between the penetrant and polymer Hildebrandt solubility parameter, $\delta - \delta_{PDMS}$ (Vankelecom et al., 1997). Afterwards, Cocchi showed that a better linear correlation is obtained if penetrant solubility in PDMS is plotted against $M_w^{0.75}(\delta - \delta_{PDMS})^2$, where M_w is the penetrant molecular weight (Cocchi et al., 2015a). Indeed, while the correlation reported by Vankelecom accounts just for energetic factors, that reported by Cocchi accounts for both energetic (through δ) and entropic (through M_w) factors. Doing so, sorption data for hydrocarbons, alcohols and several other organic liquids fall on a master curve. Unfortunately, such analysis is fairly absent in the literature for glassy polymers. Cocchi et al. (2015b) also reported mixed solvent-solute solubility data in PDMS. In mixed conditions, solute solubility in the membrane is greatly enhanced, up to 25 times, compared to pure solute solubility, which indicates that real solvent-to-solute solubility-selectivity is lower than that predicted on the basis of pure component sorption data. The

large enhancement in solute sorption in mixed conditions was justified based of the high degree of membrane swelling induced by the solvent.

Diffusivity-selectivity data for solute-solvent mixtures are virtually absent in the literature. Small molecules diffusion coefficients in polymers generally decrease with increasing penetrant size (Galizia et al., 2017b). The critical volume, as well as the kinetic diameter or squared kinetic diameter have been used as a measure of penetrant size. Interestingly, diffusion coefficients of liquid penetrants in PDMS do not always correlate to penetrant size. For example, as reported by Cocchi et al. (2015a), acetone diffusivity in PDMS is larger than water diffusivity, despite water (kinetic diameter = 0.265 nm) is a smaller molecule than acetone (kinetic diameter = 0.50 nm). This behavior was explained considering that acetone is sorbed to a greater extent than water by PDMS, so acetone diffusion occurs in a much more swollen membrane, which offers a lower frictional resistance to penetrant transport. However, subtle interactional effects influence penetrant diffusion in polymers. As discussed above, penetrants diffusion coefficient in polymers is the product of a purely kinetic quantity, i.e., the mobility coefficient, L_1, which quantifies the frictional resistance offered by the polymer matrix to penetrant diffusion, and a thermodynamic factor, related to polymer-penetrant interactions. The thermodynamic factor is higher than one when polymer-penetrant interactions are thermodynamically favorable, and less than one when such interactions are thermodynamically unfavorable. Due to the strong hydrophobicity of PDMS, acetone-PDMS affinity is much higher than water-PDMS affinity, so the thermodynamic contribution to acetone diffusion in PDMS is expected to largely exceed that of water (Favre et al., 1994; Singh et al., 1998), which would justify the experimental findings reported by Cocchi.

RECENT ADVANCES AND FUTURE DIRECTIONS IN OSN

Polybenzimidazoles

In this section, we identify new generation materials for OSN and outline applications that will likely drive OSN research in the next decades. As mentioned in section Current OSN Materials, polybenzimidazole exhibits unprecedented thermal, mechanical and chemical stability, however, some drawbacks limit its use in the industrial practice. Above all, the poor chain mobility caused by the rigid diaminobenzidine segments, combined with the efficient chain packing produced by intermolecular hydrogen bonds, reduces small molecule permeability in PBI. As a matter of fact, PBI exhibits quite low fluxes (i.e., low productivity), which makes it unappealing for practical applications. To circumvent these issues, Riffle and coworkers synthesized a substituted PBI with improved processability and higher permeability relative to commercial PBI (Borjigin et al., 2015). They replaced the linear, rigid diaminobenzidine monomer with 3,3′, 4,4′ tetraaminodiphenylsulfone (TADPS). Such monomer exhibits higher flexibility relative to diaminobenzidine, due to the presence of the sulfonyl linkage between diaminophenyl groups (cf. **Table 2**). Moreover, the kinked structure of TADPS-PBI induced by sulfonyl groups frustrates chain packing and enhances small molecules sorption and transport. Interestingly, substituted PBI exhibits improved solubility in solvents (DMAc, DMSO, NMP), while maintaining chemical, mechanical and thermal stability comparable to those exhibited by commercial PBI. H_2 and CO_2 permeability coefficients in TADPS-PBI and in commercial PBI were fairly similar, but TADPS-PBI exhibited higher H_2/CO_2 selectivity. This fact is significant, since the improved flexibility induced by sulfonyl groups did not sacrifice the membrane performance. Investigation of substituted PBI for OSN application is underway.

Polymers of Intrinsic Microporosity (PIMs)

The most known member of this family of polymers, PIM-1, first synthesized by Budd and McKeown in 2004, is prepared by the nucleophilic substitution reaction of tetrafluoro-phathalonitrile with 5,5,6,6-tetrahydroxy-3,3,3,3-tetramethyl-1,1′-spirobisindane. The spiro-center of 5,5,6,6-tetrahydroxy-3,3,3,3-tetramethyl-1,1′-spirobisindane is responsible for the contorted structure exhibited by this polymer. PIM-1 exhibits a glass transition temperature above 450°C and a three-dimensional ladder structure, which frustrates chain packing and produces interconnected free volume cavities whose dimension is < 2 nm. Consistently, the BET surface area is very high, up to 800 m^2/g. Due to this ladder-type, rigid structure, PIMs are poorly soluble in solvents, except THF and chloroform (Budd et al., 2004).

A drawback for using PIMs in OSN is their tendency to swell in the presence of solvents (Ogieglo et al., 2017), such as acetone and toluene, which produces very high flux but poor solute rejection. Several attempts have been made to synthesize alternative PIMs, but only a limited number of monomers is able to give polymers with a sufficiently high molecular weight (Sanders et al., 2013). Combining PIM-1 with other polymers could be, in principle, another route to improve its properties, but serious compatibility issues were reported. Gao et al. coated a PVDF support with a thin PIM-1 layer, but the adhesion of the active layer to the substrate was poor (Gao et al., 2017).

Currently, research efforts are underway to improve PIMs resistance to solvents by cross-linking or chemical modification. Fritsch (Fritsch et al., 2012) blended PIM-1 with polyethyleneimine (PEIm) in THF solution. Then, poly(ethylene glycol diglycidyl ether) (PEGDEG) was added to the solution. PEGDEG cross-linked the blend by reacting with the PEIm amino groups. Cross-linked PIM-1-PEIm membranes exhibited much better dimensional stability in solvents. Moreover, blending with rubbery PEIm reduced significantly the PIM-1 brittleness.

Livingston and coworkers developed composite membranes made of a 140 nm thick PIM-1 layer supported on PAN or alumina, which exhibited excellent resistance to physical aging after annealing for several hours at 150°C (Gorgojo et al., 2014). Remarkably, solvent permeability was almost 2 orders of magnitude higher than in commercial membranes based on Lenzing P84 polyimide. Unexpectedly, solvent permeance decreased with decreasing the active layer thickness below 140 nm. Indeed, as demonstrated by light interferometry, chain packing is enhanced in ultrathin films.

TABLE 2 | New materials for OSN application.

Material	Structure
PBI	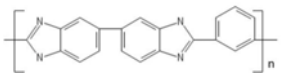
TADPS-PBI	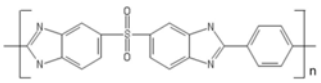
PIM-1	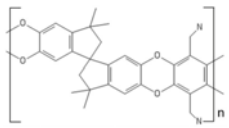
PIM-8	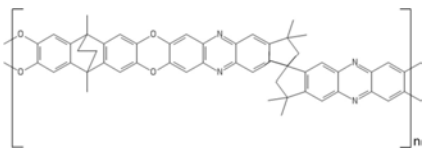
PTMSP	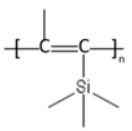
Teflon® AF	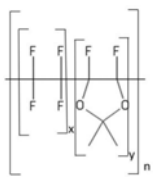
Pebax	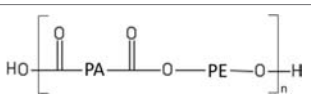
Polyarylates	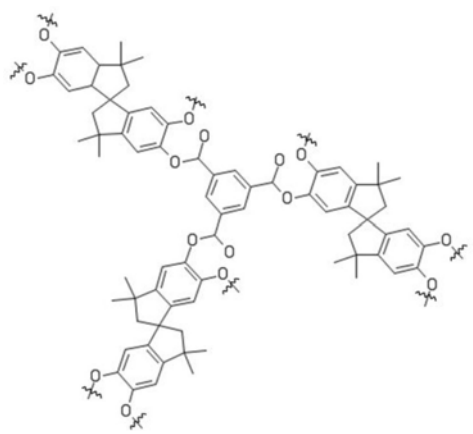

Very recently, PIMs emerged as promising materials for isomer separation. The latter is among the most challenging separations, as isomers exhibit like size and very similar chemical-physical properties, which makes it difficult developing membranes with adequate levels of selectivity. Such separations are highly demanded in the pharmaceutical industry, where isomers of a given compound often exhibit different therapeutic properties. Intrinsically chiral materials exhibited high selectivity for chiral separations. Weng and coworkers (Weng et al., 2015) synthesized intrinsically chiral PIMs with spectacular selectivity for several isomers of practical deal. Chiral ladder (+)PIM-CN was prepared by condensation reaction between enantiomerically pure 5,5′,6,6′-tetrahydroxy-3,3,3′,3′-tetramethyl-1,1′-spirobisindane and 2,3,5,6-tetrafluorophthalonitrile in DMF, in the presence of K_2CO_3. Selectivities as high as 14 were observed for some chiral separations (e.g., the resolution of R,S mandelic acid and R,S-binol). Interestingly, sorption experiments revealed that solubility-selectivity is equal to one, so the selective permeation of isomers through this material is solely driven by the diffusion contribution. However, the fundamental origin of this behavior is still unknown.

Future research efforts will likely focus on PIMs different than PIM-1. For example, PIM-8 was synthesized by Ghanem et al. by polymerization of 2,3,6,7-tetrahydroxy-9,10-dimethyl-9,10-ethanoanthracene (Ghanem et al., 2008). PIM-8 exhibited a 50% higher selectivity for linear vs. branched alkanes relative to PIM-1. Cook and coworker attributed this behavior to a narrower and much regular size distribution of free volume cavities in PIM-8 (Cook et al., 2018).

Perfluorinated Glassy Polymers

Perfluorinated polymers are soluble in a limited number of fluorinated liquids and exhibit excellent resistance to the vast majority of organic solvents. Recently, Chau reported solvent permeability and solute rejection data for a series of perfluorodioxole copolymers, such as Hyflon® AD and Cytop® (Chau et al., 2018). Solvent (methanol, hydrocarbons, aromatics, THF) sorption in perfluorodioxole copolymers is about 1% wt, which is much lower than in other glassy polymers. Interestingly, n-heptane sorption in perfluorodioxole copolymers is much larger, 2.5% wt, which enhances n-heptane flux far above that of other organic solvents and reduces substantially solute rejection. The molecular origin of this behavior was tentatively attributed to the higher matrix dilation induced by bulky n-heptane molecules. This explanation, however, appears not convincing on the basis of the relatively low n-heptane sorption level. This example demonstrates the urgent need of fundamental transport studies in glassy OSN membranes.

Block Copolymers With Hard and Soft Segments

Poly(ether block amide), commercially available under the trade name Pebax®, is a thermoplastic block copolymer made by rigid polyamide segments, which provide mechanical rigidity, interspaced with highly permeable, rubbery polyether segments.

Pebax® has shown superior performance in gas separation (Bondar et al., 2000), and recently it raised attention in OSN (Aburabie and Peinemann, 2017). The relative amount of glassy and rubbery segments can be tuned, resulting in different Pebax® grades exhibiting different transport and mechanical properties (Bondar et al., 1999, 2000). The role of the glassy segments consists in providing mechanical strength, reducing the swelling of the highly permeable rubbery blocks and maintaining good levels of dimensional stability and selectivity. Pebax® can be cross-linked upon immersion in toluene diisocyanate (TDI) solutions, which promotes the formation of urethane linkages between the hydroxyl groups on the polyether segments and the carbonyl groups of TDI (Aburabie and Peinemann, 2017). The cross-linking mechanism proposed by Aburabie was confirmed via DSC analysis. Compared to the pristine, uncross-linked sample, the endothermic peak attributed to the fusion of polyether blocks in the cross-linked sample shifted from 50 to 80°C, whereas the peak assigned to the polyamide blocks did not show any change. This result confirms that the cross-linking is produced by the reaction of TDI with the polyether blocks, as explained above (Aburabie and Peinemann, 2017).

Aburabie showed that ethanol permeance of composite membranes fabricated by coating a PAN support with Pebax® was 8 times reduced relative to the PAN support alone (Aburabie and Peinemann, 2017). Moreover, the Pebax® active layer was not able to reject brilliant blue in ethanol solution, due to the excessive membrane swelling. A significant enhancement in separation performance was observed after cross-linking. The best results were obtained using a 2% wt cross-linker concentration and a reaction time of 30 min. In this condition, rejection of brilliant blue was about 95% and ethanol permeance was 0.1 L/(m^2 h bar). When the reaction time was larger than 30 min, the membrane assumed a strongly packed structure, likely due to a very high degree of cross-linking. In this condition, ethanol flux was fairly zero even at pressures of 20 bar.

Interestingly, Pebax®/PAN membranes cross-linked with 2% TDI for 30 min exhibit 100% rejection of olive oil from a 10% wt olive oil solution in acetone (Aburabie and Peinemann, 2017). Thus, Pebax® appears suitable for application in the food industry, where organic solvents are often used to extract vegetable oils from seeds. Currently, solvent recovery from edible oils is performed by distillation, which can alter the organoleptic properties of oils.

The main drawback for using Pebax® in OSN is its tendency to swell in water and alcohols, which leads to lower selectivities. Water flux through uncross-linked Pebax® membranes increases by almost 50% after 20 h of soaking in water. In contrast, membranes cross-linked with TDI do not exhibit any increase in water flux after swelling in water for 20 h (Aburabie and Peinemann, 2017). So, cross-linking with TDI appears a viable route to produce stable Pebax® membranes for OSN applications.

High Free Volume Polyacetylenes

Substituted polyacetylenes, such as poly(trimethylsilyl propyne) (PTMSP) and poly(methylpentyne) (PMP), exhibit a rigid, glassy structure and bulky functional groups that produce inefficient chain packing, with fractional free volume levels up to 30% (Tanaka et al., 1985; Merkel et al., 2000; Galizia et al., 2014). Composite PTMSP membranes exhibited ethanol permeances as high as 17 L/(m^2 h bar), which is one of the highest values reported in the literature so far (Grekhov et al., 2012; Volkov et al., 2013). However, freshly cast PTMSP membranes exhibit an accelerated physical aging even when they are fabricated as bulky films (Nagai et al., 2000). This behavior is due to the strong departure of this material from equilibrium conditions, as witnessed by the high free volume level. Recently, Lau and co-workers discovered that physical aging of PTMSP and PMP can be stopped upon addition of microporous PAFs (Porous Aromatic Frameworks) (Lau et al., 2014). Specifically, microporous PAFs exert a chain threading effect by partially sorbing the polymer in their pores, which freezes the polymer structure and keeps the polymer chains in their original position. Such beneficial effect completely stops compaction and densification of high free volume polyacetylenes. This result represents a breakthrough and could bring the scientific community to reconsider application of polyacetylenes in OSN. In principle, to further improve its stability in chemically aggressive environments and delay physical aging, PTMSP can be cross-linked with 3,3′-diazidodiphenylsulfone. However, as noted by Kelman et al., chemical cross-linking reduces gas permeability by 70% relative to uncross-linked PTMSP, which makes this material no longer attractive for industrial applications (Kelman et al., 2007). As a matter of fact, no systematic study about the use of cross-linked PTMSP in OSN is available in the literature.

Isoporous Membranes

Developing isoporous membranes for OSN, i.e., membranes with a very uniform size and distribution of free volume cavities (improperly defined "pores"), will be an important goal over the next years (Yu et al., 2014). While this approach is under investigation for gas separation membranes (Abetz, 2014), a few authors attempted to exploit it for OSN. The actual challenge is that free volume architecture can be disrupted upon exposure to aggressive solvents, thus thwarting the efforts made to synthesize materials with specifically-sized free volume cavities.

Recently, Jimenez-Salomon exploited interfacial polymerization to fabricate highly permeable and selective polyarylate nanofilms, <20 nm thick, onto cross-linked polyimide nanofiltration membranes (Jimenez-Salomon et al., 2016). They used contorted monomers, such as 5,5′,6,6′-tetrahydroxy-3,3,3′,3′-tetramethylspirobisindane (TTSBI) and 9,9-bis(4-hydroxyphenyl)fluorine (BHPS) to prepare polyarylates with controlled and specifically-sized free volume elements. During polymerization, TTSBI units acquire a non-coplanar orientation, which leads to polymers having three-dimensional structures and interconnected free volume elements. This picture was confirmed by molecular simulations. For comparison, they also synthesized polyarylates with planar, non-contorted monomers, such as dihydroxyanthraquinone and 1,3-benzenediol, which exhibited much lower permeance but similar selectivity relative to materials containing contorted

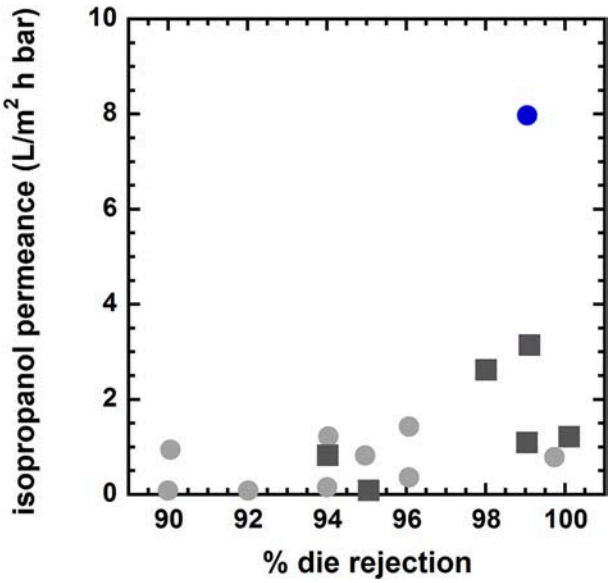

FIGURE 9 | Isopropanol permeance vs. rose Bengal rejection at room temperature and $\Delta p = 30$ bar. Solid gray circles: conventional asymmetric membranes. Solid black squares: conventional composite membranes. Solid blue circle: polyarylate synthesized using non-planar, contorted monomers (Jimenez-Salomon et al., 2016). Adapted from Jimenez-Salomon et al. (2016), with permission of *NatureResearch*.

monomers. Interestingly, isoporous polyarylates surpass abundantly the upper bound in several applications. As shown in **Figure 9**, isopropanol permeance exhibited by polyarylates is twice that of conventional asymmetric and composite membranes for OSN, and dye (rose Bengal) rejection is over 99%.

Another possible approach for the design of polymers with controlled free volume architecture relies on using monomers bearing triptycene moieties. Recently, this approach has been successfully used to design gas separation membranes (Luo et al., 2016, 2018; Weidman and Guo, 2017; Weidman et al., 2017) endowed with unprecedented levels of permeability and selectivity. Triptycenes are three-dimensional, paddlewheel-like structures formed by three aromatic rings arranged at 120° on three different planes. Once incorporated into the polymer backbone, trypticenes disrupt chain packing and introduce an ultra-fine microporosity which enables for superior size-sieving ability. Specifically, the microporosity is provided via the internal free volume associated to each triptycene moiety. Moreover, unlike ordinary glassy polymers, whose free volume is purely conformational, the internal free volume of triptycene units is configurational and, as such, it is not collapsible. According to this physical picture, iptycene-based polymers exhibit uncommon resistance to physical aging (Luo et al., 2016, 2018; Weidman and Guo, 2017; Weidman et al., 2017). Potential use of such materials in OSN is fairly unexplored. The advantages for using iptycene-based polymers in OSN could be twofold. First, the fine and homogeneous internal free volume provided by triptycenes is inaccessible to solute molecules, but it is potentially accessible to solvent molecules whose diameter is <4Å, which should guarantee high solvent flux and high solute rejection. Moreover, tough glassy polymers, such as polybenzoxazoles modified introducing triptycene moieties, would also guarantee outstanding resistance in harsh environments, which is an essential condition for applications in OSN.

Hybrid Materials

The most revolutionary application of OSN in the future will likely be the separation of isomeric solutes from organic solutions. This application is relevant in the pharmaceutical and petrochemical industry. For example, separation of hexane isomers is crucial to enhance gasoline octane number. Mixed matrices formed by selective fillers embedded in polymer membranes could make this application a reality. For example, ZIF-77 has been identified as a good candidate for isomer separations (Dubbeldam et al., 2012; Krishna and van Baten, 2017), but, surprisingly, no publication dealing with mixed matrix membranes containing ZIF-77 is available in the literature.

Recently, a new MOF with hydrophobic quadrilateral channels was synthesized via a solvothermal process from $[Fe_3(\mu_3\text{-}O)(COO)_6]$ and 2,2-bis(4-carboxyphenyl)-hexafluoropropane (6FDA) and tested for separation of hexane isomers (Lv et al., 2018). The successful separation of n-hexane from its branched isomers relies essentially on solubility-selectivity, as linear n-hexane can be selectively sorbed by the $[Fe_3(\mu_3\text{-}O)(COO)_6]$-6FDA MOF, while sorption of branched isomers is sterically hindered. The sorption selectivity exhibited by the $[Fe_3(\mu_3\text{-}O)(COO)_6]$-6FDA MOF is 20 times higher than that of other sorbents, such as ZIF-8, zeolite 5A and zeolite β (Luna-Triguero et al., 2017). Moreover, this smart MOF exhibits very stable sorption capacity and selectivity after several sorption-desorption cycles.

Significant research efforts are being devoted to the fabrication of hybrid materials that surpass the permeability-selectivity upper bound. For example, Wu and coworkers incorporated MXenes nanosheets in hydrophilic poly(ethyleneimine) (PEIm) and hydrophobic silicon rubber (PDMS) (Wu et al., 2016). MXenes, first reported by Naguib et al. in 2014, are 2-D inorganic structures consisting of a thin layer of transition metals (Naguib et al., 2014). The resulting membranes were mechanically robust and exhibited higher alcohol permeability and much higher alcohol selectivity relative to neat polymers, thus surpassing the permeability-selectivity upper bound. Specifically, MXenes nanosheets contain polar -OH groups which enhance alcohol sorption and, based on the solution-diffusion model, alcohol permeability (Wu et al., 2016). For example, isopropanol permeability in PDMS-MXenes membranes is 162% higher than in neat PDMS. Moreover, the MXenes nanosheets block solute (e.g., PEG oligomers whose molecular weight ranged from 200 to 1000 Da) transport through the membrane, by making their diffusional pathway more tortuous, which produces a significant increase in solute rejection.

The isopropanol flux and PEG1000 rejection of the PEim-MXenes membrane at room temperature and 10 bar was tracked for 12 h (cf. **Figure 10**). Isopropanol flux declined by 20% (i.e.,

from 33.5 to 28 L/m^2 h) in the first 4 h and then reached a pseudo-steady state value for the following 8 h. PEG1000 rejection changed from 98.8 to 99.2% within the same time frame. The flux decline was explained invoking membrane compaction and pore blockage by solvent molecules (Wu et al., 2016).

Membranes Based on Preassembled Nanoparticles

The phase separation process leads to membranes exhibiting a relatively broad distribution of free volume size. The possibility of tailoring the membrane microstructure so as to impart a well-defined free volume architecture has been explored is several ways. As discussed above, one possibility consists in using isoporous membranes. An alternative route to control the free volume architecture and create "manipulated" permeation pathways consists in preparing membranes based on preassembled nanoparticles. Several attempts have been made to deposit polymer nanoparticles on porous supports (Siddique et al., 2011). Nanoparticles can assemble in regular arrays, whose geometry influences the final transport properties of the membrane. Interstitial space between nanoparticles provides preferential permeation pathways. The "pore" size of these membranes can be controlled by tuning the nanoparticles size: if the nanoparticles size distribution is very uniform, the size of the interstitial channels is also uniformly distributed, which is an essential prerequisite to fabricate highly selective membranes (Siddique et al., 2011).

Siddique et al. deposited several layers of NIPAM (N-isopropylacrylamide)-HEMA(2-hydroxyethyl methacrylate) nanoparticles, whose diameter was 120 or 300 nm, onto a porous support via spin coating (Siddique et al., 2011). NIPAM-HEMA nanoparticles were first modified with acryloyl chloride to create polymerizable vinyl groups on their surface. The coating was then stabilized by UV cross-linking via radical polymerization. The support was prepared by casting a P84 polyimide solution onto a non-woven polyester backing. Phase separation of P84 was then induced upon immersion in a water bath. Following this step, the polyimide support was cross-linked upon soaking into a 1,6-hexanediamine-isopropanol solution. Finally, spin coating from methanol solutions was exploited to deposit a nanoparticle layer whose thickness ranged from 1 to 23 μm.

TEM micrographs show that moderate nanoparticle deformation takes place after deposition and UV cross-linking. Moreover, nanoparticles partially occupy the pores of the support membrane. Such observations are crucial to explain the results of nanofiltration experiments. Indeed, based on geometrical considerations, the theoretical pore size should be in the range 9–23 nm, so membranes coated with nanoparticles should not be able to separate molecules in the nanofiltration range (Siddique et al., 2011). However, rejection of styrene oligomers from toluene and acetone solutions was close to 100%, indicating that molecular separation in the nanofiltration range took place. The authors speculated that nanoparticle deformation is responsible for this behavior. As mentioned above, TEM analysis confirms

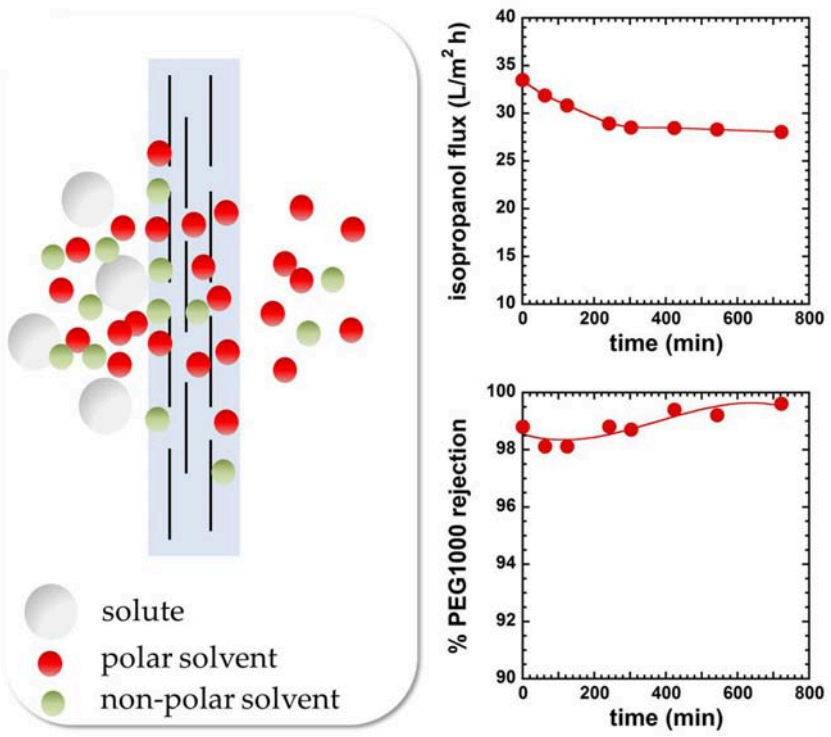

FIGURE 10 | Structure and properties of mixed matrix membranes based on PEIm and MXenes (Wu et al., 2016). OSN experiments were run at room temperature and 10 bar using an isopropanol/PEG1000 solution. Adapted from Wu et al. (2016), with permission of *Elsevier*.

this hypothesis. Interesting, solvent fluxes as high as 55 L/(m^2 h) were measured, which led the authors to hypothesize that polystyrenes transport occurs in the interstitial spaces only, while solvent permeates through both the interstitial spaces and the nanoparticles (Siddique et al., 2011). Such hypothesis is consistent with the typical behavior exhibited by swollen NIPAM nanogels, which are highly permeable to small molecules, and practically impermeable to bulky solutes (Schild, 1992).

Interestingly, polystyrenes rejection increases with increasing the thickness of the nanoparticle layer, due to the narrower pore size distribution, and decreases with increasing nanoparticle diameter, due to the formation of larger interstitial spaces. So, the best membranes are obtained upon deposition of a relatively thick layer of small nanoparticles (Siddique et al., 2011). Deposition of nanoparticles exhibiting different sizes further improves solute rejection. Specifically, the mean pore size can be decreases by coating the support with larger nanoparticles first, and then with smaller nanoparticles.

Nanopapers

Manufacturing of polymer nanofiltration membranes often requires the use of large amounts of toxic solvents and chemicals. Use of membranes made of cellulose or nanocellulose would provide a solution to the above mentioned issue, as these materials can be processed in aqueous solution (Mautner et al., 2014; Sukma and Culfaz-Emecen, 2018). Nanofibrillated cellulose in the paper form, also called nanopaper, exhibits outstanding mechanical properties and thermal stability, other than good barrier properties (Klemm et al., 2011; Mautner et al., 2014). Moreover, nanopapers exhibit nanopores whose size is comparable to that of a single molecule and, for this reason, they would be ideal candidates for OSN applications (Mautner et al., 2014). Recently, Mautner et al. prepared solvent stable OSN membranes from aqueous suspension of (2,2,6,6-tetramethylpiperidin-1-yl)oxy (TEMPO) oxidized nanofibrillated cellulose (Mautner et al., 2014). Addition of trivalent salts, such as $AlCl_3$, to the aqueous suspension induces the flocculation of nanofibrils by changing their surface charge. Specifically, trivalent cations are sorbed on the negatively charged nanofibrils surface, causing a decrease of the ζ-potential (Mautner et al., 2014). Nanofibrils compaction leads to the formation of self-standing membranes that have shown organic solvents permeances up to 100 L/(h m^2 MPa) and retention of polystyrene close to 100%.

Interestingly, organic liquids (n-hexane, tetrahydrofuran) permeance was larger than that of water, irrespective of the hydrophilic behavior of nanocellulose (Mautner et al., 2014). The molecular origin of this behavior is still unknown, since permeability coefficients were not deconvoluted into their elemental sorption and diffusion contributions. Moreover, water permeance decreased from 47 to 5 L/(h m^2 MPa) after 1 h of operation (Mautner et al., 2014). The authors attributed this behavior to membrane compaction under pressure.

Interestingly, the average pore size is equal to the nanofibrils diameter, so the porosity of these membranes can be finely tuned by changing the size of the cellulose nanofibrils (Mautner et al., 2014).

CONCLUSIONS

Organic solvent nanofiltration is a new paradigm in the chemical industry. Despite it is intrinsically safe, energy efficient and scalable, OSN is today one of the most poorly understood processes at a fundamental level. Factors that limit its exploitation in the industry are:

i) The lack of fundamental knowledge about solute and solvent transport mechanism. Moreover, the few elemental transport data available are often interpreted in a too simplistic way, which contributes to the spread of misleading conclusions in the literature.
ii) The lack of materials capable to tolerate chemically challenging environments.

While recent research efforts contributed to address the latter point, fundamental understanding of OSN remains poor and incomplete. For example, diffusion coefficients in solvent swollen membranes have to be estimated carefully, by accounting for the effects of the frame of reference and thermodynamic non-idealities. Not taking into account these effects, hampers the possibility of developing structure-property correlations to be used for the rational design of OSN membranes.

The most important recent advances in OSN are the introduction of polymers and hybrid materials with improved permeability, selectivity, and long term stability. Polybenzimidazoles, PIMs, block copolymers with hard and soft segments, hybrid materials containing MOFs and ZIFs and membranes based on pre-assembled nanoparticles appear as the best candidates for future developments.

The most challenging application in the next decades will likely be the separation of isomers. Solving this problem will open a new era in chemical, petrochemical, food, and pharmaceutical industry. Joined efforts from polymer chemistry (to synthesize and modify materials) and physical chemistry (to understand and define optimal transport properties) are necessary to make such new era a reality.

AUTHOR CONTRIBUTIONS

MG conceived and wrote the manuscript. KB contributed to select the contents, prepared the figures and run calculations.

FUNDING

Financial support from the UROP Program sponsored by the University of Oklahoma is gratefully acknowledged.

ACKNOWLEDGMENTS

MG wishes to dedicate this work to his mentor and friend, Prof. Donald R. Paul, with whom he worked for some years. His brilliant scholar inspired some of the ideas discussed in this paper.

REFERENCES

Abetz, V. (2014). Isoporous block copolymer membranes. *Macrom. Rapid Comm.* 36, 10–22. doi: 10.1002/marc.201400556

Aburabie, J., and Peinemann, K. V. (2017). Crosslinked poly(ether block amide) composite membranes for organic solvent nanofiltration applications. *J. Membr. Sci.* 523, 264–272. doi: 10.1016/j.memsci.2016.09.027

Ben Soltane, H., Roizard, D., and Favre, E. (2013). Effect of pressure on the swelling and fluxes of dense PDMS membranes in nanofiltration: an experimental study. *J. Membr. Sci.* 435, 110–119. doi: 10.1016/j.memsci.2013.01.053

Ben Soltane, H., Roizard, D., and Favre, E. (2016). Study of the rejection of various solutes in OSN by a composite polydimethylsiloxane membrane: investigation of the role of the solute affinity, Sep. *Purif. Tech.* 161, 193–201. doi: 10.1016/j.seppur.2016.01.035

Bernardo, P., Bazzarelli, F., Tasselli, F., Clarizia, G., Mason, C. R., Maynard-Atem, L., et al. (2017). Effect of physical aging on the gas transport and sorption in PIM-1 membranes. *Polymer* 113, 283–294. doi: 10.1016/j.polymer.2016.10.040

Bird, R. B., Stewart, W. E., and Lightfoot, E. N. (1960). *Transport Phenomena*. New York, NY: John Wiley & Sons.

Bondar, V. I., Freeman, B. D., and Pinnau, I. (1999). Gas sorption and characterization of poly(ether-b-amide) segmented block copolymers. *J. Polym. Sci. B.* 37, 2463–2475.

Bondar, V. I., Freeman, B. D., and Pinnau, I. (2000). Gas transport properties of poly(ether-b-amide) segmented block copolymers. *J. Polym. Sci. B*38, 2051–2062. doi: 10.1002/1099-0488(20000801)38:15<2051::AID-POLB100>3.0.CO;2-D

Borjigin, H., Stevens, K. A., Liu, R., Moon, J. D., Shaver, A. T., Swinnea, S., et al. (2015). Synthesis and characterization of polybenzimidazoles derived from tetraaminodiphenylsulfone for high temperature gas separation membranes. *Polymer* 71, 135–142. doi: 10.1016/j.polymer.2015.06.021

Budd, P. M., Ghanem, B. S., Makhseed, S., McKeown, N. B., Msayib, K. J., and Tattershall, C. E. (2004). Polymers of intrinsic microporosity (PIMs): robust, solution-processable, organic nanoporous materials. *Chem. Commun.* 230–231. doi: 10.1039/b311764b

Buonomenna, M. G., and Bae, J. (2015). Organic solvent nanofiltration in pharmaceutical industry. *Sep. Purif. Rev.* 44, 157–182. doi: 10.1080/15422119.2014.918884

Chau, J., Basak, P., Kaur, J., Hu, Y., and Sirkar, K. K. (2018). Performance of a composite membrane of a perfluorodioxole copolymer in organic solvent nanofiltration. *Sep. Purif. Tech.* 199, 233–241. doi: 10.1016/j.seppur.2018.01.054

Chiou, J. S., Barlow, J. W., and Paul, D. R. (1985). Plasticization of glassy polymers by CO2. *J. Appl. Polym. Sci.* 30, 2633–2342. doi: 10.1002/app.1985.070300626

Cocchi, G., De Angelis, M. G., and Doghieri, F. (2015a). Solubility and diffusivity of liquids for food and pharmaceutical applications in crosslinked polydimethylsiloxane (PDMS) films: I. Experimental data on pure organic components and vegetable oil. *J. Membr. Sci.* 492, 600–611. doi: 10.1016/j.memsci.2015.04.063

Cocchi, G., De Angelis, M. G., and Doghieri, F. (2015b). Solubility and diffusivity of liquids for food and pharmaceutical applications in crosslinked polydimethylsiloxane (PDMS) films: I. Experimental data on mixtures. *J. Membr. Sci.* 492, 612–619. doi: 10.1016/j.memsci.2015.04.062

Cook, M., Gaffney, P. R. J., Peeva, L. G., and Livingston, A. G. (2018). Roll-to-roll dip coating of three different PIMs for organic solvent nanofiltration. *J. Membr. Sci.* 558, 52–63. doi: 10.1016/j.memsci.2018.04.046

Da Silva Burgal, J., Peeva, L., Kumbharkar, S., and Livingston, A. G. (2015). Organic solvent resistant poly(ether-ether-ketone) nanofiltration membranes. *J. Membr. Sci.* 479, 105–116. doi: 10.1016/j.memsci.2014.12.035

Da Silva Burgal, J., Peeva, L., and Livingston, A. G. (2017). Negligible ageing in poly(ether-ether-ketone) membranes widens application range for solvent processing. *J. Membr. Sci.* 525, 48–56. doi: 10.1016/j.memsci.2016.10.015

Daniel, M. C., and Astruc, D. (2004). Gold nanoparticles: assembly, supramolecular chemistry, quantum-size-related properties, and applications toward biology, catalysis, and nanotechnology. *Chem. Rev.* 104, 293–346. doi: 10.1021/cr030698+

Darvishmanesh, S., Degreve, J., and Van der Bruggen, B. (2010). Mechanisms of solute rejection in solvent resistant nanofiltration: the effect of solvent on solute rejection. *Phys. Chem. Chem. Phys.* 12, 13333–13342. doi: 10.1039/c0cp00230e

de Morais Coutinho, C., Chiu, M. C., Correa Basso, R., Badan Ribeiro, A. P., Guaraldo Gonçalves, L. A., and Viotto, L. A. (2009). State of art of the application of membrane technology to vegetable oils: a review. *Food Res. Int.* 42, 536–550. doi: 10.1016/j.foodres.2009.02.010

Dinh, S. M., Berner, B., Sun, Y. M., and Lee, P. I. (1992). Sorption and transport of ethanol and water in poly(ethylene-co-vinyl-acetate) membranes. *J. Membr. Sci.* 69, 223–234. doi: 10.1016/0376-7388(92)80041-H

Doghieri, F., and Sarti, G. C. (1996). Nonequilibrium lattice fluids: a predictive model for the solubility in glassy polymers. *Macromolecules* 29, 7885–7896.

Doghieri, F., and Sarti, G. C. (1997). Solubility, diffusivity, and mobility of n-pentane and ethanol in poly(1-trimethylsilyl-1-propyne). *J. Polym. Sci. B* 35, 2245–2258.

Dubbeldam, D., Krishna, R., Calero, S., and Yazaydin, A. O. (2012). Computer-assisted screening of ordered crystalline nanoporous adsorbents for separation of alkane isomers. *Angew. Chem. Int. Ed.* 51, 11867–11871. doi: 10.1002/anie.201205040

Fang, Y., Sourirajan, S., and Matsuura, T. (1992). Reverse osmosis separation of binary organic mixtures using cellulose acetate butyrate and aromatic polyamide membranes. *J. Appl. Polym. Sci.* 44, 1959–1969. doi: 10.1002/app.1992.070441111

Favre, E., Schaetzel, P., Nguygen, Q. T., Clement, R., and Neel, J. (1994). Sorption, diffusion and vapor permeation of various penetrants through dense poly(dimethylsiloxane) membranes: a transport analysis. *J. Membr. Sci.* 92, 169–184. doi: 10.1016/0376-7388(94)00060-3

Flory, P. J. (1942). Thermodynamics of high polymer solutions. *J. Chem. Phys.* 10, 51–61. doi: 10.1063/1.1723621

Freeman, B. D. (1999). Basis of Permeability/Selectivity Tradeoff Relations in Polymeric Gas Separation Membranes. *Macromolecules* 32, 375–380. doi: 10.1021/ma9814548

Fritsch, D., Merten, P., Heinrich, K., Lazar, M., and Priske, M. (2012). High performance organic solvent nanofiltration membranes: development and thorough testing of thin film composite membranes made of polymers of intrinsic microporosity (PIMs). *J. Membr. Sci.* 401–402, 222–231. doi: 10.1016/j.memsci.2012.02.008

Galizia, M., Chi, W. S., Smith, Z. P., Merkel, T. C., Baker, R. W., and Freeman, B. D. (2017a). 50th Anniversary perspective: polymers and mixed matrix membranes for gas and vapor separation: a review and prospective opportunities. *Macromolecules* 50, 7809–7843. doi: 10.1021/acs.macromol.7b01718

Galizia, M., De Angelis, M. G., Messori, M., and Sarti, G. C. (2014). Mass transport in hybrid PTMSP/silica membranes. *Ind. Eng. Chem. Res.* 53, 9243–9255. doi: 10.1021/ie4035225

Galizia, M., De Angelis, M. G., and Sarti, G. C. (2011). Sorption and transport of hydrocarbons and alcohols in addition-type poly(trimethyl silyl norbornene). I: Experimental data. *J. Membr. Sci.* 385–386, 141–153. doi: 10.1016/j.memsci.2011.09.032

Galizia, M., De Angelis, M. G., and Sarti, G. C. (2012). Sorption of hydrocarbons and alcohols in addition-type poly(trimethyl silyl norbornene) and other high free volume glassy polymers. II: NELF model predictions. *J. Membr. Sci.* 405–406, 201–211. doi: 10.1016/j.memsci.2012.03.009

Galizia, M., Paul, D. R., and Freeman, B. D. (2016). Liquid methanol sorption, diffusion and permeation in charged and uncharged polymers. *Polymer* 102, 281–291. doi: 10.1016/j.polymer.2016.09.010

Galizia, M., Stevens, K. A., Paul, D. R., and Freeman, B. D. (2017b). Modeling gas permeability and diffusivity in HAB-6FDA polyimide and its thermally rearranged analogs. *J. Membr. Sci.* 537, 83–92. doi: 10.1016/j.memsci.2017.05.015

Gao, L., Alberto, M., Gorgojo, P., Szekely, G., and Budd, P. M. (2017). High flux PIM-1/PVDF thin film composite membranes for 1-butanol/water pervaporation. *J. Membr. Sci.* 529, 207–214. doi: 10.1016/j.memsci.2017.02.008

Ghanem, B. S., McKeown, N. B., Budd, P. M., and Fritsch, D. (2008). Polymers of intrinsic microporosity derived from bis(phenazyl) monomers. *Macromolecules* 41, 1640–1646. doi: 10.1021/ma071846r

Gorgojo, P., Karan, S., Wong, H. C., Jimenez-Salomon, M. F., Cabral, J. T., and Livingston, A. G. (2014). Ultrathin polymer films with intrinsic microporosity: anomalous solvent permeation and high flux membranes. *Adv. Func. Mater.* 24, 4729–4737. doi: 10.1002/adfm.201400400

Grekhov, A., Belogorlov, A., Yushkin, A., and Volkov, A. (2012). New express dynamic technique for liquid permeation measurement in a wide

range of transe-membrane pressures. *J. Membr. Sci.* 390–391, 160–163. doi: 10.1016/j.memsci.2011.11.038

Haupt, K., and Mosbach, K. (2000). Molecularly imprinted polymers and their use in biomimetic sensors. *Chem. Rev.* 100, 2495–2504. doi: 10.1021/cr990099w

Huang, Y., and Paul, D. R. (2004). Physical aging of thin glassy polymer films monitored by gas permeability. *Polymer* 45, 8377–8393. doi: 10.1016/j.polymer.2004.10.019

Huang, Y., and Paul, D. R. (2006). Physical aging of thin glassy polymer films: free volume interpretation. *J. Membr. Sci.* 277, 219–229. doi: 10.1016/j.memsci.2005.10.032

Huang, Y. J., Li, D., He, P., Sun, C. Y., Wang, M. J., and Li, J. H. (2005). Semipermeable membrane embodying noble metal nanoparticles and its electrochemical behaviors. *J. Electroanal. Chem.* 579, 277–282. doi: 10.1016/j.jelechem.2005.02.020

Jimenez-Salomon, M. F., Song, Q., Jelfs, K. E., Munoz-Ibanes, M., and Livingston, A. G. (2016). Polymer nanofilms with enhanced microporosity by interfacial polymerization. *Nat. Mater.* 15, 760–767. doi: 10.1038/nmat4638

Kamaruddin, H. D., and Koros, W. J. (1997). Some observations about the application of the Fick's first law for membrane separation of multicomponent mixtures. *J. Membr. Sci.* 135, 147–159.

Kelman, S. D., Matteucci, S., Bielawski, C. W., and Freeman, B. D. (2007). Crosslinking poly(1-trimethylsilyl-1-propyne) and its effect on solvent resistance and transport properties. *Polymer* 48, 6881–6892. doi: 10.1016/j.polymer.2007.08.063

Kim, J. F., Gaffney, P. R. J., Valtcheva, I. B., Williams, G., Buswell, A. M., Anson, M. S., et al. (2016). Organic solvent nanofiltration (OSN): a new technology platform for liquid-phase oligonucleotide synthesis (LPOS). *Org. Proc. Res. Dev.* 20, 1439–1452. doi: 10.1021/acs.oprd.6b00139

Klemm, D., Kramer, F., Moritz, S., Lindstroem, T., Ankerfors, M., Gray, D., et al. (2011). Nanocelluloses: a new family of nature-based materials. *Angew. Chem. Int. Ed.* 50, 5438–5466. doi: 10.1002/anie.201001273

Koh, D. Y., McCool, B. A., Deckman, H. W., and Lively, R. P. (2016). Reverse osmosis molecular differentiation of organic liquids using carbon molecular sieve membranes. *Science* 353, 804–807. doi: 10.1126/science.aaf1343

Koike, S., Subramanian, R., Nabetani, H., and Nakajima, M. (2002). Separation of oil constituents in organic solvents using polymeric membranes. *J. Am. Oil Chem. Soc.* 79, 937–942. doi: 10.1007/s11746-002-0582-7

Kopecek, J. (1970). Performance of porous cellulose acetate membranes for the reverse osmosis separation of mixtures of organic liquids. *Ind. Eng. Chem. Proc. Des. Dev.* 9, 5–12. doi: 10.1021/i260033a002

Koros, W. J., Paul, D. R., and Rocha, A. A. (1976). Carbon dioxide sorption and transport in polycarbonate. *J. Polym. Sci.: Polym. Phys. Ed.* 14, 687–702. doi: 10.1002/pol.1976.180140410

Koros, W. J., and Zhang, C. (2017). Materials for next generation molecularly selective synthetic membranes. *Nature Mat.* 16, 289–297. doi: 10.1038/nmat4805

Krishna, R., and van Baten, J. M. (2017). Screening metal–organic frameworks for separation of pentane isomers. *Phys. Chem. Chem. Phys.* 19, 8380–8387. doi: 10.1039/C7CP00586E

Lau, C. H., Nguyen, P. T., Hill, M. R., Thornton, A. W., Konstas, K., Doherty, C. M., et al. (2014). Ending aging in super glassy polymer membranes. *Angew. Chem.* 53, 5322–5326. doi: 10.1002/anie.201402234

Li, K. (2007), *Ceramic Membranes for Separation and Reaction*. Chichester: John Wiley & Sons.

Liang, P., Xu, J., and Li, Q. (2008). Application of dispersive liquid-liquid microextraction and high performance liquid chromatography for the determination of three phthalate esters in water samples. *Anal. Chim. Acta* 609, 53–58. doi: 10.1016/j.aca.2007.12.025

Liu, Y., Wang, R., and Chung, T. S. (2001). Chemical cross-linking modification of polyimide membranes for gas separation. *J. Membr. Sci.* 189, 231–239. doi: 10.1016/S0376-7388(01)00415-X

Lively, R. P., and Sholl, D. S. (2017). From water to organics on membrane separations. *Nature Mat.* 16, 276–279. doi: 10.1038/nmat4860

Loeb, S., and Sourirajan, S. (1963). "Sea water demineralization by means of an osmotic membrane," in *Advances in Chemistry Series,* ed R. F. Gould (Washington, DC: ACS), 117–132.

Lotters, J. C., Olthuis, W., Veltink, P. H., and Bergveld, P. (1997). The mechanical properties of the rubber elastic polymer polydimethylsiloxane for sensor applications. *J. Micromech. Microeng.* 7, 145–147. doi: 10.1088/0960-1317/7/3/017

Luna-Triguero, A., Gomez-Alvarez, P., and Calero, S. (2017). Adsorptive process design for the separation of hexane isomers using zeolites. *Phys. Chem. Chem. Phys.* 19, 5037–5042. doi: 10.1039/C6CP08025A

Luo, S., Wiegand, J. R., Kazanowska, B., Doherty, C. M., Konstas, K., Hill, A. J., et al. (2016). Finely tuning the free volume architecture in iptycene-containing polyimides for highly selective and fast hydrogen transport. *Macromolecules* 49, 3395–3405. doi: 10.1021/acs.macromol.6b00485

Luo, S., Zhang, Q., Zhu, L., Lin, H., Kazanowska, B. A., Doherty, C. M., et al. (2018). Highly selective and permeable microporous polymer membranes for hydrogen purification and CO_2 removal from natural gas. *Chem. Mater.* 30, 5322–5332. doi: 10.1021/acs.chemmater.8b02102

Lv, D., Wang, H., Chen, Y., Xu, F., Shi, R., Liu, Z., et al. (2018). Iron-based metal–organic framework with hydrophobic quadrilateral channels for highly selective separation of hexane isomers. *ACS Appl. Mater. Interfaces* 10, 6031–6038. doi: 10.1021/acsami.7b18620

Ma, H., Jen, A. K. Y., and Dalton, L. R. (2002). Polymer-based optical waveguides: materials, processing, and devices. *Adv. Mater.* 14, 1339-1365. doi: 10.1002/1521-4095(20021002)14:19<1339::AID-ADMA1339>3.0.CO;2-O

Machado, D. R., Hasson, D., and Semiat, R. (1999). Effect of solvent properties on permeate flow through nanofiltration membranes. Part I: investigation of parameters affecting solvent flux. *J. Membr. Sci.* 163, 93–102. doi: 10.1016/S0376-7388(99)00158-1

Marchetti, P., Jimenez Salomon, M. F., Szekely, G., and Livingston, A. G. (2014). Molecular separation with organic solvent nanofiltration: a critical review. *Chem. Rev.* 114, 10735–10806. doi: 10.1021/cr500006j

Marchetti, P., and Livingston, A. G. (2015). Predictive membrane transport models for organic solvent nanofiltration: how complex do we need to be? *J. Membr. Sci.* 476, 530–553. doi: 10.1016/j.memsci.2014.10.030

Marchetti, P., Peeva, L., and Livingston, A. G. (2017). The selectivity challenge in organic solvent nanofiltration: membrane and process solutions. *Ann. Rev. Chem. Biomol. Eng.* 8, 473–497. doi: 10.1146/annurev-chembioeng-060816-101325

Mautner, A., Lee, K. Y., Lahtinen, P., Hakalahti, M., Tammelin, T., Li, K., et al. (2014). Nanopapers for organic solvent nanofiltration. *Chem. Comm.* 50, 5778–5781. doi: 10.1039/C4CC00467A

Merkel, T. C., Bondar, V., Nagai, K., and Freeman, B. D. (2000). Sorption and transport of hydrocarbon and perfluorocarbon gases in poly(1-trimethylsilyl-1-propyne). *J. Polym. Sci. B: Polym. Phys.* 38, 273–296. doi: 10.1002/(SICI)1099-0488(20000115)38:2<273::AID-POLB1>3.0.CO;2-X

Nagai, K., Freeman, B. D., and Hill, A. J. (2000). Effect of physical aging of poly(1-trimethylsilyl-1-propyne) films synthesized with $TaCl_5$ and $NbCl_5$ on gas permeability, fractional free volume, and positron annihilation lifetime spectroscopy parameters. *J. Polym. Sci. B: Polym. Phys.* 38, 1222–1239. doi: 10.1002/(SICI)1099-0488(20000501)38:9<1222::AID-POLB14>3.0.CO;2-P

Naguib, M., Mochalin, V. M., Barsoum, M. W., and Gogotsi, Y. (2014). 25th anniversary article: MXenes: a new family of two-dimensional materials. *Adv. Mater.* 26, 992–1005. doi: 10.1002/adma.201304138

Nakai, Y., Tsujita, Y., and Yoshimizu, H. (2002). Control of gas permeability for cellulose acetate membrane by microwave irradiation. *Desalination* 145, 375–377. doi: 10.1016/S0011-9164(02)00439-3

Ogieglo, W., Rahimi, K., Rauer, S. B., Ghanem, B., Ma, H., Pinnau, I., et al. (2017). How do organic vapors swell ultrathin films of polymer of intrinsic microporosity PIM-1? *J. Phys. Chem. B* 121, 7210–7220. doi: 10.1021/acs.jpcb.7b03891

Paul, D. R. (1973). Relation between hydraulic permeability and diffusion in homogeneous swollen membranes. *J. Polym. Sci.* 2, 289–296.

Paul, D. R. (1976). The solution-diffusion model for swollen membranes. *Sep. Purif. Methods* 5, 33–50. doi: 10.1080/03602547608066047

Paul, D. R. (2004). Reformulation of the solution-diffusion theory of reverse osmosis. *J. Membr. Sci.* 241, 371–386. doi: 10.1016/j.memsci.2004.05.026

Paul, D. R., and Ebra-Lima, O. M. (1970). Pressure-induced diffusion of organic liquids through highly swollen polymer membranes. *J. Appl. Polym. Sci.* 14, 2201–2224. doi: 10.1002/app.1970.070140903

Paul, D. R., and Ebra-Lima, O. M. (1971). The mechanism of liquid transport through swollen polymer membranes. *J. Appl. Polym. Sci.* 15, 2199–2210. doi: 10.1002/app.1971.070150912

Peeva, L. G., Gibbins, E., Luthra, S. S., White, L. S., Stateva, R. P., and Livingston, A. G. (2004). Effects of concentration polarization and osmotic pressure on flux in organic solvent nanofiltration. *J. Membr. Sci.* 236, 121–136. doi: 10.1016/j.memsci.2004.03.004

Postel, S., Spalding, G., Chirnside, M., and Wessling, M. (2013). On negative retentions in organic solvent nanofiltration. *J. Membr. Sci.* 447, 57–65. doi: 10.1016/j.memsci.2013.06.009

Priske, M., Lazar, M., Schnitzer, C., and Baumgarten, G. (2016). Recent applications of organic solvent nanofiltration. *Chem. Ing. Tech.* 88, 39–49. doi: 10.1002/cite.201500084

Robeson, L. M. (1991). Correlation of separation factor versus permeability for polymeric membranes. *J. Membr. Sci.* 62, 165–185. doi: 10.1016/0376-7388(91)80060-J

Robeson, L. M. (2008). The upper bound revisited. *J. Membr. Sci.* 320, 390–400. doi: 10.1016/j.memsci.2008.04.030

Sanders, D. F., Smith, Z. P., Guo, R., Robeson, L. M., McGrath, J. E., Paul, D. R., et al. (2013). Energy-efficient polymeric gas separation membranes for a sustainable future: a review. *Polymer* 54, 4729–4761. doi: 10.1016/j.polymer.2013.05.075

Schild, H. G. (1992). Poly (N-isopropylacrylamide): experiments, theory and application. *Progr. Polym. Sci.* 17, 163–249. doi: 10.1016/0079-6700(92)90023-R

See-Toh, Y. H., Ferreira, F. C., and Livingston, A. G. (2007a). The influence of membrane formation parameters on the functional performance of organic solvent nanofiltration membranes. *J. Membr. Sci.* 299, 236–250. doi: 10.1016/j.memsci.2007.04.047

See-Toh, Y. H., Lim, F. W., and Livingston, A. G. (2007b). Polymeric membranes for nanofiltration in polar aprotic solvents. *J. Membr. Sci.* 301, 3–10. doi: 10.1016/j.memsci.2007.06.034

See-Toh, Y. H., Silva, M., and Livingston, A. G. (2008). Controlling molecular weight cut off curves for highly solvent stable organic solvent nanofiltration (OSN) membranes. *J. Membr. Sci.* 324, 220–232. doi: 10.1016/j.memsci.2008.07.023

Sheth, J. P., Qin, Y., Sirkar, K. K., and Baltzis, B. C. (2003). Nanofiltration-based diafiltration process for solvent exchange in pharmaceutical manufacturing. *J. Membr. Sci.* 211, 251–261. doi: 10.1016/S0376-7388(02)00423-4

Siddique, H., Peeva, L. G., Stoikos, K., Pasparakis, G., Vamvakaki, M., and Livingston, A. G. (2011). Membranes for organic solvent nanofiltration based on preassembled nanoparticles. *Ind. Eng. Chem. Res.* 52, 1109–1121. doi: 10.1021/ie202999b

Silva, P., Han, S., and Livingston, A. G. (2005). Solvent transport in organic solvent nanofiltration membranes. *J. Membr. Sci.* 262, 49–59. doi: 10.1016/j.memsci.2005.03.052

Singh, A., Freeman, B. D., and Pinnau, I. (1998). Pure and mixed gas acetone/nitrogen permeation properties of polydimethylsiloxane [PDMS]. *J. Polym. Sci. B.* 36, 289–301. doi: 10.1002/(SICI)1099-0488(19980130)36:2<289::AID-POLB8>3.0.CO;2-M

Singh, A., and Koros, W. J. (1996). Significance of entropic selectivity for advanced gas separation membranes. *Ind. Eng. Chem. Res.* 35, 1231–1234. doi: 10.1021/ie950559l

Sourirajan, S. (1964). Separation of hydrocarbon liquids by flow under pressure through porous membranes. *Nature* 203, 1348–1349. doi: 10.1038/2031348a0

Subramanian, R., Raghavarao, K. S. M. S., Nabetani, H., Nagajima, M., Kimura, T., and Maekawa, T. (2001). Differential permeation of oil constituents in nonporous denser polymeric membranes. *J. Membr. Sci.* 187, 59–69. doi: 10.1016/S0376-7388(00)00673-6

Subramanian, R., Raghavarao, K. S. M. S., Nakajima, M., Nabetani, H., Yamaguchi, T., and Kimura, T. (2003). Application of dense membrane theory for differential permeation of vegetable oil constituents. *J. Food Eng.* 60, 249–256. doi: 10.1016/S0260-8774(03)00045-1

Sukma, F. M., and Culfaz-Emecen, P. Z. (2018). Cellulose membranes for organic solvent nanofiltration. *J. Membr. Sci.* 545, 329–336. doi: 10.1016/j.memsci.2017.09.080

Szekely, G., Jimenez-Salomon, M. F., Marchetti, P., Kim, J. F., and Livingston, A. G. (2014). Sustainability assessment of organic solvent nanofiltration: from fabrication to application. *Green Chem.* 16, 4440–4473. doi: 10.1039/C4GC00701H

Tanaka, K., Matsuya, H., Masuda, T., and Higashimura, T. (1985). Gas permeability of polyacetylenes carrying substituents. *J. Appl. Polym. Sci.* 30, 1605–1616. doi: 10.1002/app.1985.070300426

Tsarkov, S., Khotimskiy, V., Budd, P. M., Volkov, V., Kukushkina, J., and Volkov, A. (2012). Solvent nanofiltration through high permeability glassy polymers: effect of polymer and solute nature. *J. Membr. Sci.* 423–424, 65–72. doi: 10.1016/j.memsci.2012.07.026

Ulbricht, M. (2006). Advanced functional polymer membranes. *Polymer* 47, 2217–2262. doi: 10.1016/j.polymer.2006.01.084

Valtcheva, I. B., Kumbharkar, S. C., Kim, J. F., Bhole, Y., and Livingston, A. G. (2014). Beyond polyimide: crosslinked polybenzimidazole membranes for organic solvent nanofiltration (OSN) in harsh environments. *J. Membr. Sci.* 457, 62–72. doi: 10.1016/j.memsci.2013.12.069

Valtcheva, I. B., Marchetti, P., and Livingston, A. G. (2015). Crosslinked polybenzimidazole membranes for organic solvent nanofiltration (OSN): Analysis of crosslinking reaction mechanism and effects of reaction parameters. *J. Membr. Sci.* 493, 568–579. doi: 10.1016/j.memsci.2015.06.056

Van der Bruggen, B. (2013). Integrated membrane separation processes for recycling of valuable wastewater streams: nanofiltration, membrane distillation, and membrane crystallizers revisited. *Ind. Eng. Chem. Res.* 52, 10335–10341. doi: 10.1021/ie302880a

Vanherck, K., Hermans, S., Verbiest, T., and Vankelecom, I. (2011). Using the photothermal effect to improve membrane separations via localized heating. *J. Mater. Chem.* 21, 6079–6087. doi: 10.1039/c0jm03932b

Vanherck, K., Koeckelberghs, G., and Vankelecom, I. F. J. (2013). Crosslinking polyimides for membrane application: a review. *Progr. Polym. Sci.* 38, 874–896. doi: 10.1016/j.progpolymsci.2012.11.001

Vankelecom, I. F. J., De Beukelaer, S., and Uytterhoeven, J. B. (1997). Sorption and pervaporation of aroma compounds using zeolite-filled PDMS membranes. *J. Phys. Chem. B* 101, 5186–5190. doi: 10.1021/jp962273f

Vankelecom, I. F. J., De Smet, K., Gevers, L. E. M., Livingston, A. G., Nair, D., Aerts, S., et al. (2004). Physio-chemical interpretation of the SRNF transport mechanism for solvents through dense silicone membranes. *J. Membr. Sci.* 231, 99–108. doi: 10.1016/j.memsci.2003.11.007

Vogel, H., and Marvel, C. S. (1961). Polybenzimidazoles, new thermally stable polymers. *J. Polym. Sci.* 50, 511–539. doi: 10.1002/pol.1961.1205015419

Volkov, A., Yushkin, A., Grekhov, A., Shutova, A., Bazhenov, S., Tsarkov, S., et al. (2013). Liquid permeation through PTMSP: One polymer for two different membrane applications. *J. Membr. Sci.* 440, 98–107. doi: 10.1016/j.memsci.2013.03.067

Volkov, A., Yushkin, A., Kachula, Y., Khotimskiy, V., and Volkov, V. (2014). Application of negative retention in organic solvent nanofiltration for solutes fractionation. *Sep. Purif. Tech.* 124, 43–48. doi: 10.1016/j.seppur.2013.12.044

Volkov, A. V., Stamatialis, D. F., Khotimsky, V. S., Volkov, V. V., Wessling, M., and Plate, N. A. (1996). Poly[1-(trimethylsilyl)-1-propyne] as a solvent resistance nanofiltration membrane material. *J. Membr. Sci.* 281, 351–357. doi: 10.1016/j.memsci.2006.04.004

Volkov, A. V., Tsarkov, S. E., Gilman, A. B., Khotimskiy, S. V., Roldughin, V., and Volkov, V. V. (2015). Surface modification of PTMSP membranes by plasma treatment: asymmetry of transport in organic solvent nanofiltration. *Adv. Coll. Interf. Sci.* 222, 716–727. doi: 10.1016/j.cis.2014.11.005

Wang, H., Chung, T. S., and Paul, D. R. (2014). Physical aging and plasticization of thick and thin films of the thermally rearranged ortho-functional polyimide 6FDA-HAB. *J. Membr. Sci.* 458, 27–35. doi: 10.1016/j.memsci.2014.01.066

Weidman, J. R., and Guo, R. (2017). The use of iptycenes in rational macromolecular design for gas separation membrane applications. *Ind. Eng. Chem. Res.* 56, 4220–4236. doi: 10.1021/acs.iecr.7b00540

Weidman, J. R., Luo, S., Zhang, Q., and Guo, R. (2017). Structure manipulation in triptycene-based polyimides through main chain geometry variation and its effect on gas transport properties. *Ind. Eng. Chem. Res.* 56, 1868–1879. doi: 10.1021/acs.iecr.6b04946

Weng, X., Baez, J. E., Khiterer, M., Hoe, M. Y., Bao, Z., and Shea, K. J. (2015). Chiral polymers of intrinsic microporosity: selective membrane permeation of enantiomers. *Angew. Chem. Int. Ed.* 54, 11214–11218. doi: 10.1002/anie.201504934

White, L. S. (2001). *Polyimide Membranes for Hyperfiltration Recovery of Aromatic Solvents*. US patent 6.180.008.

White, L. S. (2002). Transport properties of a polyimide solvent resistant nanofiltration membrane. *J. Membr. Sci.* 205, 191–202. doi: 10.1016/S0376-7388(02)00115-1

White, L. S. (2006). Development of large-scale applications in organic solvent nanofiltration and pervaporation for chemical and refining processes. *J. Membr. Sci.* 286, 26–35. doi: 10.1016/j.memsci.2006.09.006

White, M. L. (1960). The permeability of an acrylamide polymer gel. *J. Phys. Chem.* 64, 1563–1565. doi: 10.1021/j100839a055

Whu, J. A., Baltzis, B. C., and Sirkar, K. K. (2000). Nanofiltration studies of larger organic microsolutes in methanol solutions. *J. Membr. Sci.* 170, 159–172. doi: 10.1016/S0376-7388(99)00374-9

Wijmans, J. G., and Baker, R. W. (1995). The solution-diffusion model: a review. *J. Membr. Sci.* 107, 1–21. doi: 10.1016/0376-7388(95)00102-I

Wu, X., Hao, L., Zhang, J., Zhang, X., Wang, J., and Liu, J. (2016). Polymer-$Ti_3C_2T_X$ composite membranes to overcome the trade-off in solvent resistant nanofiltration for alcohol-based system. *J. Membr. Sci.* 515, 175–188. doi: 10.1016/j.memsci.2016.05.048

Yu, H., Qiu, X., Nunes, S. P., and Peinemann, K. V. (2014). Self-assembled isoporous block copolymer membranes with tuned pore sizes. *Angew. Chem. Int. Ed.* 53, 10072–10076. doi: 10.1002/anie.20140449

Conflict of Interest Statement: The authors declare that the research was conducted in the absence of any commercial or financial relationships that could be construed as a potential conflict of interest.

Copyright © 2018 Galizia and Bye. This is an open-access article distributed under the terms of the Creative Commons Attribution License (CC BY). The use, distribution or reproduction in other forums is permitted, provided the original author(s) and the copyright owner(s) are credited and that the original publication in this journal is cited, in accordance with accepted academic practice. No use, distribution or reproduction is permitted which does not comply with these terms.

frontiers in Chemistry

ORIGINAL RESEARCH
published: 29 March 2019
doi: 10.3389/fchem.2019.00176

Stereocomplexation of Poly(Lactic Acid)s on Graphite Nanoplatelets: From Functionalized Nanoparticles to Self-assembled Nanostructures

Matteo Eleuteri[1], *Mar Bernal*[1], *Marco Milanesio*[2], *Orietta Monticelli*[3]* *and Alberto Fina*[1]*

[1] Dipartimento di Scienza Applicata e Tecnologia, Sede di Alessandria, Politecnico di Torino, Alessandria, Italy, [2] Dipartimento di Scienze e Innovazione Tecnologica, Università degli Studi del Piemonte Orientale, Alessandria, Italy, [3] Dipartimento di Chimica e Chimica Industriale, Università di Genova, Genova, Italy

The control of nanostructuration of graphene and graphene related materials (GRM) into self-assembled structures is strictly related to the nanoflakes chemical functionalization, which may be obtained via covalent grafting of non-covalent interactions, mostly exploiting π-stacking. As the non-covalent functionalization does not affect the sp^2 carbon structure, this is often exploited to preserve the thermal and electrical properties of the GRM and it is a well-known route to tailor the interaction between GRM and organic media. In this work, non-covalent functionalization of graphite nanoplatelets (GnP) was carried out with *ad-hoc* synthesized pyrene-terminated oligomers of polylactic acid (PLA), aiming at the modification of GnP nanopapers thermal properties. PLA was selected based on the possibility to self-assemble in crystalline domains via stereocomplexation of complementary poly(L-lactide) (PLLA) and poly(D-lactide) (PDLA) enantiomers. Pyrene-initiated PLLA and PDLA were indeed demonstrated to anchor to the GnP surface. Calorimetric and X-ray diffraction investigations highlighted the enantiomeric PLAs adsorbed on the surface of the nanoplatelets self-organize to produce highly crystalline stereocomplex domains. Most importantly, PLLA/PDLA stereocomplexation delivered a significantly higher efficiency in nanopapers heat transfer, in particular through the thickness of the nanopaper. This is explained by a thermal bridging effect of crystalline domains between overlapped GnP, promoting heat transfer across the nanoparticles contacts. This work demonstrates the possibility to enhance the physical properties of contacts within a percolating network of GRM via the self-assembly of macromolecules and opens a new way for the engineering of GRM-based nanostructures.

Keywords: PLA stereocomplex, graphite nanoplatelets, interfacial thermal resistance, thermal bridging, non-covalent functionalization

OPEN ACCESS

Edited by:
Pellegrino Musto, Italian National Research Council (CNR), Italy

Reviewed by:
Tadeusz Antoni Biela, Polish Academy of Sciences, Poland
Vincenzo Venditto, University of Salerno, Italy

***Correspondence:**
Orietta Monticelli
orietta.monticelli@unige.it
Alberto Fina
alberto.fina@polito.it

Specialty section:
This article was submitted to Polymer Chemistry, a section of the journal Frontiers in Chemistry

Received: *31 January 2019*
Accepted: *06 March 2019*
Published: *29 March 2019*

Citation:
Eleuteri M, Bernal M, Milanesio M, Monticelli O and Fina A (2019) Stereocomplexation of Poly(Lactic Acid)s on Graphite Nanoplatelets: From Functionalized Nanoparticles to Self-assembled Nanostructures. Front. Chem. 7:176. doi: 10.3389/fchem.2019.00176

INTRODUCTION

Graphene and graphene-related materials (GRM) are one of the most intensively explored nanoparticles family in materials science owing to their superior properties (Geim and Novoselov, 2007; Gómez-Navarro et al., 2007; Lee et al., 2008; Stoller et al., 2008; Balandin and Nika, 2012). In particular, graphene oxide (GO), reduced graphene oxide (RGO), multilayer graphene (MLG), and

graphite nanoplatelets (GnP) attracted a wide research attention in the last decade (Ferrari et al., 2015). Their peculiar mechanical, electrical and thermal properties make GRM ideal platforms for the construction of sophisticated nanostructured systems, which fabrication requires precise control of graphene chemistry, including chemical modifications with specific functional groups (Rodriguez-Perez et al., 2013). In this field, the organic functionalization of GRM has led to the manufacturing of high-performance multifunctional graphene-based materials where covalent and non-covalent bonding provides bridges between adjacent layers (Meng et al., 2013; Wan et al., 2018). However, the covalent attachment of any functional group affects the thermal and electronic properties of GRM because of the perturbation of their aromatic character. Therefore, the supramolecular functionalization is often preferable as it may preserve the structure and properties of non-oxidized GRM, while it simultaneously enables the attachment of specific organic moieties, through π-stacking or hydrophobic and electrostatic interactions (Zhang et al., 2007; Choi et al., 2010; Liu et al., 2010; Cheng et al., 2012; Hsiao et al., 2013; Ji et al., 2015; Georgakilas et al., 2016). In particular, π-π stacking interactions between GRM and polyaromatic hydrocarbons, such as pyrene, perylene, hexabenzocoronene, have been widely investigated and validated for the preparation of GRM-based materials (Björk et al., 2010; Georgakilas et al., 2012; Parviz et al., 2012; Hirsch et al., 2013; Wang et al., 2014). Non-covalent functionalization of GRM may indeed be exploited to tailor interfaces between nanoplatelets and the surrounding organic media or to control interfaces within GRM networks.

Compatibilization between GRM nanoplatelets and organic polymers have been widely studied to promote dispersion in the preparation of nanocomposites as well as to tailor their physical properties (Kuilla et al., 2010; Potts et al., 2011; Mittal, 2014; Papageorgiou et al., 2017). Polyaromatic derivatives, mostly based on pyrene or perylene substituted with a dangling chain able to compatibilize toward the organic polymer have been largely studied, including the functionalization of GRM with polymers bearing pyrene groups (Liu et al., 2010; Liang et al., 2012; Tong et al., 2013; Wang et al., 2015; Fina et al., 2018).

On the other hand, the modification of interfaces between GRM nanoplatelets within their percolating network is currently of high interest to enhance mechanical, electrical, and thermal performance in GRM aerogels, foams and nanopapers. In particular, thermal properties of GRM nanopapers have attracted a significant research interest for the application as flexible heat spreaders (Shen et al., 2014; Song et al., 2014; Xin et al., 2014; Renteria et al., 2015; Bernal et al., 2017, 2018). However, the application of GRM based nanopapers is typically limited by their low mechanical resistance and brittleness. The incorporation of a limited amount of polymers into GRM nanopapers may enhance their toughness and deformability, while decreasing the heat transfer efficiency of the nanopaper, as polymers are well-known for their typically low thermal conductivity. However, as the thermal conductivity of polymers is strongly dependent on chain orientation (Singh et al., 2014; Chen et al., 2016) and crystallinity (Choy et al., 1993; Ronca et al., 2017), the possibility to control local orientation and crystallization of macromolecules at the surface of GRM currently appears as a fascinating route to produce mechanically strong and high thermal conductivity nanostructures.

Several polymers have been shown to effectively nucleate on GRM (Ferreira et al., 2013; Manafi et al., 2014; Bidsorkhi et al., 2017; Colonna et al., 2017b), despite the self-organization of highly ordered crystalline domains onto the surface of GRM remains challenging. An interesting option to self-assemble crystalline domains is via stereocomplexation of complementary polymer enantiomers. For instance, polylactic acid (PLA) has two optically active enantiomers because of the chiral nature of the monomer: poly(L-lactide) (PLLA) and poly(D-lactide) (PDLA). PLLA and PDLA are able to co-crystallize into racemic stereocomplexes (SC), which have been studied mostly for their higher thermal stability and superior physical properties than the homocrystals of the homopolymers (Tsuji et al., 1992; Tsuji, 2005; Hirata and Kimura, 2008). The incorporation of small amounts of GRM and functionalized GRM in PLLA/PDLA blends was also shown to promote the intermolecular coupling between the enantiomers, thus acting as nucleating agents for the stereocomplex (Sun and He, 2012; Wu et al., 2013; Gardella et al., 2015; Xu et al., 2015, 2016; Yang et al., 2016; Zhang et al., 2017).

In this work, we report a facile approach to promote PLA SC formation onto the surface of GnP, exploiting the denser chain packing in the SC structure (Anderson and Hillmyer, 2006; Xu et al., 2006) to modify the physical properties of the contact between graphite nanoplatelets. Pyrene-end functionalized enantiomeric PLAs with low molecular weight were synthesized and used to supramolecularly modify GnP. Then, stereocomplexation of the PLLA and PDLA anchored to the GnP surface was carried out, to produce highly crystalline domains acting as junctions between nanoplatelets. Results obtained demonstrated the promotion of the intermolecular coupling between the enantiomeric PLAs adsorbed on the surface of the nanoplatelets, leading to the efficient stereocomplexation of the systems. More importantly, the presence of highly crystalline domains from PLLA/PDLA stereocomplexation delivered nanopapers with a higher through-plane efficiency in heat transfer, acting as efficient thermal bridges between overlapped GnP.

EXPERIMENTAL SECTION

Materials

L-lactide and D-lactide (purity ≥98%) were purchased from Sigma-Aldrich. Before polymerization, both monomers, L-lactide and D-lactide, were purified by three successive re-crystallizations from 100% (w/v) solution in anhydrous toluene and dried under vacuum at room temperature. 1-Pyrenemethanol (Pyr-OH) (purity 98%) and stannous octanoate, tin(II) 2-ethylhexanoate ($Sn(Oct)_2$, purity ∼95%) were purchased from Sigma-Aldrich and used as received. All solvents, toluene (anhydrous, purity 99.8%), chloroform (purity ≥99.5%), methanol (purity ≥99.8%), N-N-dimethylformamide (DMF) (anhydrous, purity 99.8%) and dimethyl ether (DME) (purity ≥99.0%) were purchased

from Sigma Aldrich and used without further purifications. Graphite nanoplatelets (GnP) were synthesized by Avanzare (Navarrete, La Rioja, Spain) according to a previously reported procedure (Colonna et al., 2017a). In brief, overoxidized-intercalated graphite was prepared starting from natural graphite, followed by rapid thermal expansion of at 1,000°C, to produce a worm-like solid, and then mechanically milled to obtain GnP.

Synthesis of Pyrene-End Functionalized PLLA and PDLA (Figure 1A)

Pyrene-end functionalized poly(L-lactic acid) (Pyr-L) and pyrene-end functionalized poly(D-lactic acid) (Pyr-D) were synthesized by the ring-opening polymerization (ROP) of monomers, L-lactide and D-lactide, initiated with Pyr-OH and catalyzed by $Sn(Oct)_2$ in bulk at 140°C, as previously reported (Eleuteri et al., 2018). In detail, L-lactide or D-lactide (5.5 g, 38 mmol) were charged under argon flow into the reactor (i.e., a 50-ml two-neck round-bottomed flask equipped with a magnetic stirrer). Pyr-OH (220 mg, 0.94 mmol) was introduced under argon flow and the flask was evacuated for 15 min and purged with argon; these vacuum/argon cycles were repeated three times in order to thoroughly dry the reactants. The monomer-to-Pyr-OH molar ratio was calculated to obtain an average theoretical molecular weight (M_{nth}) for Pyr- L or Pyr- D of 7,000 g/mol. Then, the reactor vessel was immersed in an oil bath at 140°C under stirring. Once the reactants were completely melted and homogenized, a freshly prepared solution of $Sn(Oct)_2$ in toluene (271 μL, $[lactide]/[Sn(Oct)_2] = 10^3$) was added under argon and the reaction was allowed to proceed under inert atmosphere for 24 h. After cooling to room temperature, the reaction was quenched in an ice bath and the crude products were dissolved in chloroform and poured into an excess of cold methanol (2°C). The solid residue was filtered and dried in vacuum at 40°C. Then, Pyr-L was dissolved in DMF (15 mg mL^{-1}) at 65°C for 15 min. The solvent was allowed to evaporate at 25°C for 48 h and the residual solvent was removed by drying at 60°C for 3 h.

Preparation of Pyr-L/Pyr-D Stereocomplex

Equivalent amounts of Pyr-L and Pyr-D were separately dissolved in DMF (15 mg mL^{-1}) at 65°C. The solutions were then mixed and stirred at 65°C for 15 min. The mixed solution was casted on a Petri dish. The solvent was allowed to evaporate at 25°C for 48 h and the residual solvent was removed by drying at 60°C for 3 h. The above-described blends were denoted as Pyr-L/Pyr-D SC. It is worth mentioning that both parallel and antiparallel stereocomplex structures may be obtained from the blend of Pyr-L and Pyr-D, as previously reported for similar pyrene-terminated PLA oligomers (Danko et al., 2018). However, the two structures have very limited differences in cell dimensions (Brizzolara et al., 1996) and interaction energies, so that the two cannot be distinguished by XRD data and thermal analyses and, most importantly, are expected to deliver very similar material properties.

Preparation of Functionalized GnP Pyr-L (Figure 2A)

One hundred milligram GnP were added to a 100 mL solution of Pyr-L in DMF (0.5 mg·mL^{-1}) and sonicated in pulsed mode (30 s ON and 30 s OFF) for 15 min with power set at 30% of the full output power (750 W) by using an ultrasonication probe (Sonics Vibracell VCX-750, Sonics & Materials Inc.) with a 13 mm diameter Ti-alloy tip. After that, the suspension was left to stand for 24 h to ensure the adsorption of the stereoisomer on the basal plane of GnP. Then, the suspension was filtered through a Nylon Supported membrane (0.45 μm nominal pore size, diameter 47 mm, Whatman) and the filtrate analyzed by UV-Vis. The filtered cake was re-dispersed in DMF (50 mL), sonicated in an ultrasonication bath for 10 min, filtered and the filtrate analyzed by UV-Vis. The dispersion-filtration cycle was repeated a second time to ensure the completely disappearance of the Pyr-L on the filtrate. Finally, the functionalized GnP were washed with methanol (50 mL) and diethyl ether (50 mL) and dried at 60°C for 24 h.

Preparation of Functionalized GnP Pyr-L/Pyr-D SC (Figures 2B,C)

Functionalized GnP Pyr-L/Pyr-D SC were prepared following two different methods. In the first method (**Figure 2B**), 100 mg GnP was added to a 100 mL DMF solution containing equivalent masses of Pyr-L (25 mg) and Pyr-D (25 mg). The procedure previously described for sonication, filtration and purification of the functionalized GnP Pyr-L was followed and the modified GnP obtained by this method are coded as GnP Pyr-L/Pyr-D SC_A. In the second method (**Figure 2C**), two suspensions of GnP Pyr-L and GnP Pyr-D (25 mg of enantiomer and 50 mg GnP in 50 mL DMF) prepared as described previously for GnP Pyr-L were mixed together to obtain a final solution with the same concentrations of enantiomers and GnP as in GnP Pyr-L/Pyr-D SC_A. The procedure previously described for sonication, filtration and purification was followed and the modified GnP obtained by this method are coded as GnP Pyr-L/Pyr-D SC_B.

Preparation of GnP and Functionalized GnP Nanopapers

GnP nanopapers were prepared by suspension of GnP in DMF at a concentration of 0.2 mg mL^{-1} and the solutions were sonicated as described previously for the preparation of functionalized GnP. Then, GnP nanopapers were prepared by vacuum filtration, dried and mechanically pressed, following the procedure previously reported (Bernal et al., 2017).

GnP nanopapers containing the stereocomplexes were prepared following the method described previously for GnP Pyr-L/Pyr-D SC_A. The total concentrations of Pyr-L and Pyr-D in DMF were 0.1 mg mL^{-1}, while the final concentration of GnP in the solutions was 0.2 mg mL^{-1}. For comparison purposes, two additional nanopapers were prepared for the formation of the stereocomplex, increasing the concentrations of the stereoisomers to 0.2 and 0.4 mg mL^{-1}, denoted as GnP Pyr-L/Pyr-D SC_A′ and GnP Pyr-L/Pyr-D SC_A″, respectively.

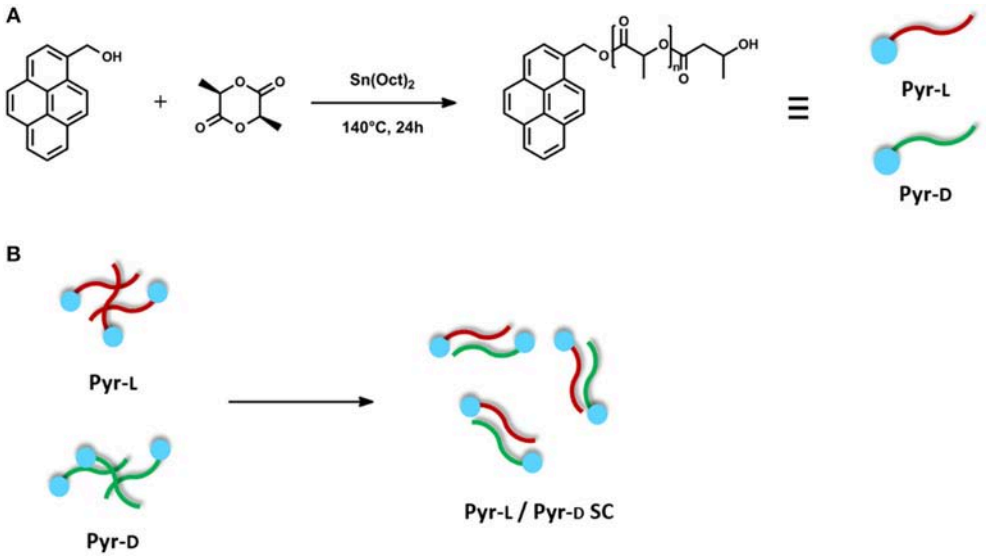

FIGURE 1 | (A) Synthesis of Pyr-L and Pyr-D. **(B)** Schematic illustration of stereocomplex formation from equivalent amounts of Pyr-L and Pyr-D.

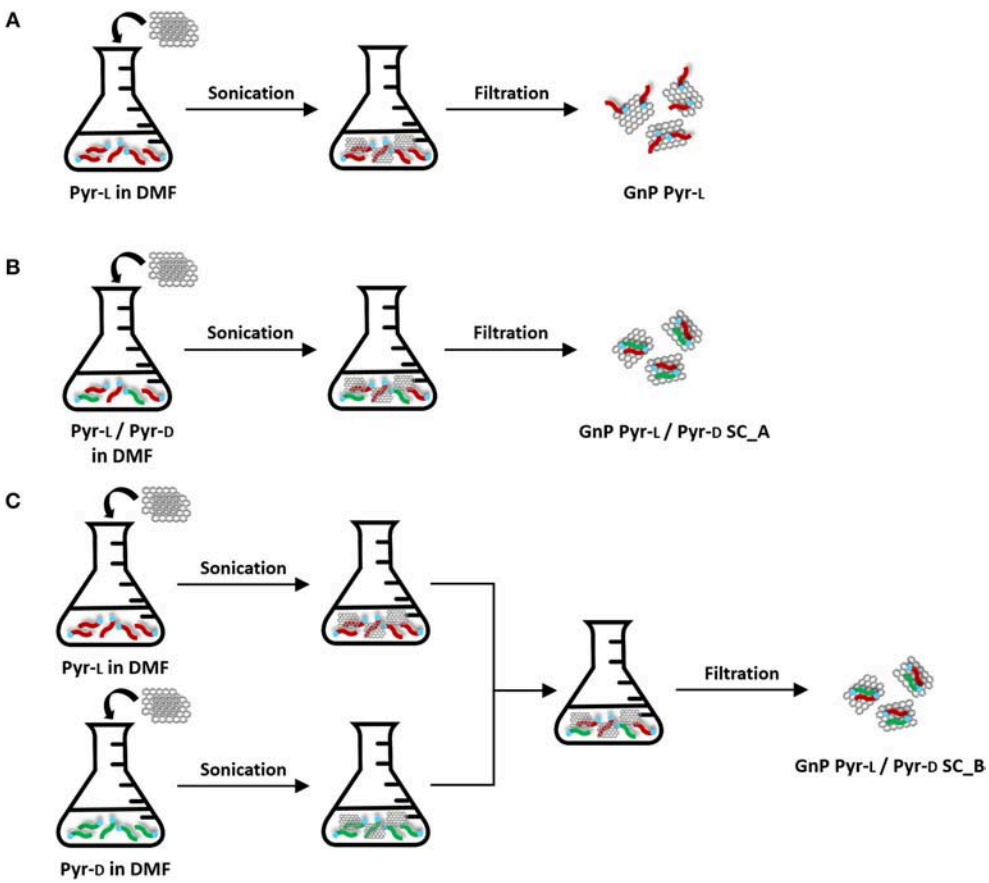

FIGURE 2 | Preparation of functionalized GnP: **(A)** GnP Pyr-L, **(B)** GnP Pyr-L/Pyr-D SC_A, and **(C)** GnP Pyr-L/Pyr-D SC_B.

Characterization Methods

All ^{1}H Nuclear Magnetic Resonance (NMR) spectra were recorded on a NMR Varian Mercury Plus 300 MHz. Samples were dissolved in deuterated chloroform ($CDCl_3$) with TMS as internal reference (chemical shifts δ in ppm).

Differential scanning calorimetry (DSC) measurements were performed on a DSC Q20 (TA Instruments, USA). Approximately 5 mg of sample were placed in the aluminum pans. The samples were heated from 25 to 250°C at a heating rate of 10°C min^{-1} and kept for 1 min to erase the thermal history. Afterwards, the specimens were cooled down to 25°C, and finally reheated to 250°C at 10°C min^{-1} to evaluate the crystallization and melting behavior of the samples. For functionalized GnP, the reference aluminum pan was filled with pristine GnP to facilitate the observation of the thermal transitions arising from the Pyr-L and Pyr-L/Pyr-D SC.

Powder X-ray diffraction (XRD) measurements for the stereoisomers, the SC crystallites and functionalized GnP were carried out using an X-ray diffractometer (PANalytical X'Pert Pro MPD, Philips PW3040/60) with a Cu Kα radiation source with a wavelength of 1.542 Å. The measurements were operated at 40 kV and 40 mA with scan angles from 5 to 25° at a scan step of 0.026°. XRD measurements on nanopapers were carried out also with a 2D detector, exploiting a Gemini R Ultra diffractometer. All data were collected using Cu Kα radiation. Data collection and reduction was carried out with CrysAlisPro software, version 1.171.35.11 (Agilent Technologies UK Ltd. Oxford, UK). 2D images were collected with a time from 10 to 30 s depending on the 2θ. The 2D data were then reduced to intensity vs. 2θ profiles by the same software, to investigate preferential orientations in the nanopapers and well as to obtain averaged XRD profiles over the whole possible orientations.

Thermal gravimetrical analysis (TGA) were performed using a TGA Discovery (TA Instruments, USA) under nitrogen atmosphere from 50 to 800°C at 10°C min^{-1}. The thermal degradation temperatures were defined as the temperatures corresponding to the maximum DTG peaks, obtained from the first derivative curve of the TGA thermogram.

Fourier-transform infrared (FT-IR) spectra were recorded on a Perkin Elmer Perkin Elmer Frontier spectrometer (Waltham, MA, USA) in the range of 400–4,000 cm^{-1} with 16 scans at a resolution of 4 cm^{-1}.

X-ray photoelectron spectroscopy (XPS) were performed on a VersaProbe5000 Physical Electronics X-ray photoelectron spectrometer with a monochromatic Al source and a hemispherical analyzer. Survey scans and high-resolution spectra were recorded with a spot size of 100 μm. The samples were prepared by depositing the GnP powders onto adhesive tape and keeping the samples under vacuum for 15 h prior to the measurement. A Shirley background function was employed to remove the background of the spectra.

The morphology of the graphene papers was characterized by a high resolution Field Emission Scanning Electron Microscope (FESEM, ZEISS MERLIN 4248).

The density (ρ) of the nanopapers was calculated according to the formula $\rho = m/V$, where m is the mass of the nanopaper, weighed at room temperature using the TGA microbalance (Sensitivity: < 0.1 μg) and V is calculated from a well-defined disk film using the average thicknesses measured by FESEM.

The in-plane thermal diffusivity ($\alpha_{\parallel}$) and cross-plane diffusivity ($\alpha_{\perp}$) were measured using the xenon light flash technique (LFT) (Netzsch LFA 467 *Hyperflash*). The samples were cut in disks of 23 mm and the measurement of the $\alpha_{\parallel}$ was carried out in a special in-plane sample holder while the $\alpha_{\perp}$ was measured in the standard cross-plane configuration. Each sample was measured five times at 25°C.

RESULTS AND DISCUSSION

Synthesis of Pyr-L and Pyr-D by ROP and Formation of Pyr-L/Pyr-D SC

The Pyr-L and Pyr-D synthesized by the ring-opening polymerization of L-lactide and D-lactide using Pyr-OH as initiator have been first characterized for their molar masses. The number average molecular weight (M_{nNMR}) of Pyr-L and Pyr-D was estimated based on the ^{1}H-NMR spectra (**Figure S1**), using the integral area of the methine protons signals in the PLA chain and next to the terminal hydroxyl group, at δ = 5.16 ppm and δ = 4.35 ppm, respectively. The M_{nNMR} is *ca.* 7,000 g mol^{-1}, which is in accordance to the theoretical number average molecular weight (M_{nth}) calculated from the monomer-to-Pyr-OH molar ratio, thus confirming the controlled polymerization reaction. Furthermore, the characteristic absorption bands of pyrene (**Figure S2**) confirm the presence of the cromophore group in the enantiomers.

Crystallization of as-synthesized Pyr-L or Pyr-L/Pyr-D SC was obtained after dissolving the product in N,N-dimethylformamide (DMF) and left to crystallize. DMF was chosen in this study, allowing for the formation of stereocomplex crystallites and providing sufficient affinity for the subsequent dispersion of graphene nanoplatelets, as the surface tension of DMF (37.1 mJ m^{-2}) is similar to that of graphene (Hernandez et al., 2008; Coleman et al., 2011). Given the influence of the solvent on the polymorphic crystalline structure of poly(L-lactide) (Marubayashi et al., 2012, 2013) and stereocomplex crystallization of PLA (Tsuji and Yamamoto, 2011; Yang et al., 2017) have been previously reported, for comparison purposes, Pyr-L or Pyr-L/Pyr-D SC crystallizations were also performed in chloroform, being the most common solvent for PLA (result comparison in **Supporting Information**).

The structures of the Pyr-L and Pyr-L/Pyr-D SC after crystallization from DMF were corroborated by FTIR spectroscopy (**Figure 3**). The ν(C=O) band, which is sensitive to the morphology and the conformation of PLA (Kister et al., 1998), changed after the stereocomplexation, showing a downshift of the signal which is related to the weak hydrogen bond formation between the CH_3 groups and the C=O group in the Pyr-L/ Pyr-D SC (Kister et al., 1998; Zhang et al., 2005; Gonçalves et al., 2010). Furthermore, the CH_3 and CH bending region, between 1,250 and 1,400 cm^{-1}, showed asymmetric and broad bands for Pyr-L compared to Pyr-L/Pyr-D SC, being the δ(CH) band high-frequency shift for the stereocomplex (∼10 cm^{-1}), as previously observed by Kister et al. (1998).

The band at 920 cm^{-1}, observed in Pyr-L and assigned to the α-helix of an enantiomeric PLA, disappeared in and Pyr-L/Pyr-D SC and a new band appeared at 909 cm^{-1}, corresponding to β-helix, characteristic of the stereocomplex, accordingly to previous report by Michalski et al. (2018). Finally, after stereocomplexation the ν(C-COO) stretching mode at 872 cm^{-1} is shifted at higher frequency and appears less asymmetric compared to the corresponding band in Pyr-L spectrum, thus further confirming the successful formation of the stereocomplex crystallites.

The stereocomplexation of pyrene-based PLA systems were analyzed by DSC (**Figure 4A**) and XRD (**Figure 4B**). The stereoisomers, Pyr-L and Pyr-D, were confirmed to crystallize in the stereocomplex form as demonstrated by the increase of the melting temperature (T_m), from 152.2°C for Pyr-L to 207.5°C for Pyr-L/Pyr-D SC. Moreover, the formation of the Pyr-L/Pyr-D SC leads to both higher enthalpy of melt crystallization (ΔH_m) and high T_m in DMF compared to the stereocomplex formed in chloroform (see **Figure S3** and **Table S1**), evidencing for the crucial role of the solvent in promoting stereocomplexation. Interestingly, no crystallization peak (T_{cc}) at around 100°C was observed during the formation of Pyr-L/Pyr-D SC in DMF, which is ascribed to the crystallization during the previous cooling scan (Bao et al., 2016). Hence, the π-π interactions between pyrene groups in low molecular weight Pyr-L and Pyr-D did not hinder the stereocomplex crystallization (de Arenaza et al., 2013), as exclusive stereocomplex crystallites are formed in DMF (Yang et al., 2017). The effect of DMF on the crystallization of Pyr-L and the formation of SC crystallites in Pyr-L/Pyr-D SC were also confirmed by XRD (**Figure 4B**). In fact, Pyr-L shows the typical diffraction peaks of the stereoisomer at 2θ 14.8, 16.7, 19.1, and 22.4°, corresponding to the (010), (110)/(200), (203), and (210) planes. Additionally, the crystalline complex ε-form, induced by the formation of complexes in specific solvents with five-membered ring structure such as DMF (Marubayashi et al., 2012, 2013), is evidenced by the peak observed at 2θ ≈ 12.4°. Pyr-L/Pyr-D SC formed in DMF exhibits only the diffraction peaks of SC crystallites at 12.1, 21.1, and 24.0°, thus indicating the exclusive formation of SC crystallites, due to the low vapor pressure of DMF and the dissimilar solubility parameter between solvent and polymer (Tsuji and Yamamoto, 2011; Yang et al., 2017).

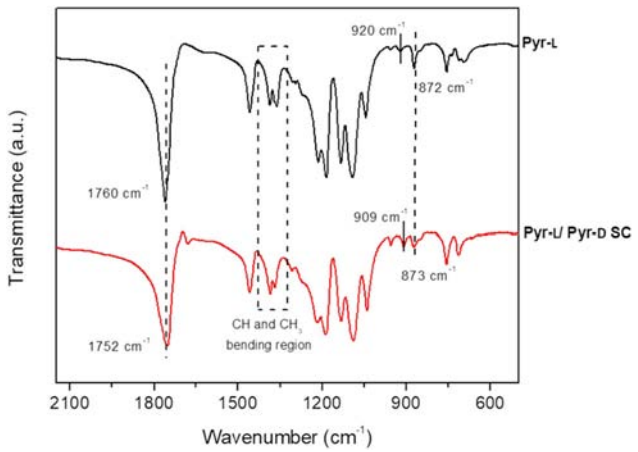

FIGURE 3 | FTIR spectra (500–2,250 cm^{-1} region) of Pyr-L (black) and Pyr-L/Pyr-D SC (red) after crystallization in DMF.

Supramolecular Functionalization of GnP With Pyrene-End Functionalized PLAs

The formation of the stereocomplex in the presence of GnP was investigated using two different approaches: (i) sonicating the nanoplatelets in a solution containing both Pyr-L and Pyr-D (**Figure 2B**) and (ii) sonicating separately the GnP with each of the stereoisomers, Pyr-L or Pyr-D, before mixing them to form the stereocomplex (**Figure 2C**). After that, the products were washed thoroughly to remove any DMF-soluble oligomers unbound to GnP (See **Figure S4** in the Supporting Information).

The modification of GnP was investigated by XPS (**Figure S5**), which provides information about the elemental composition

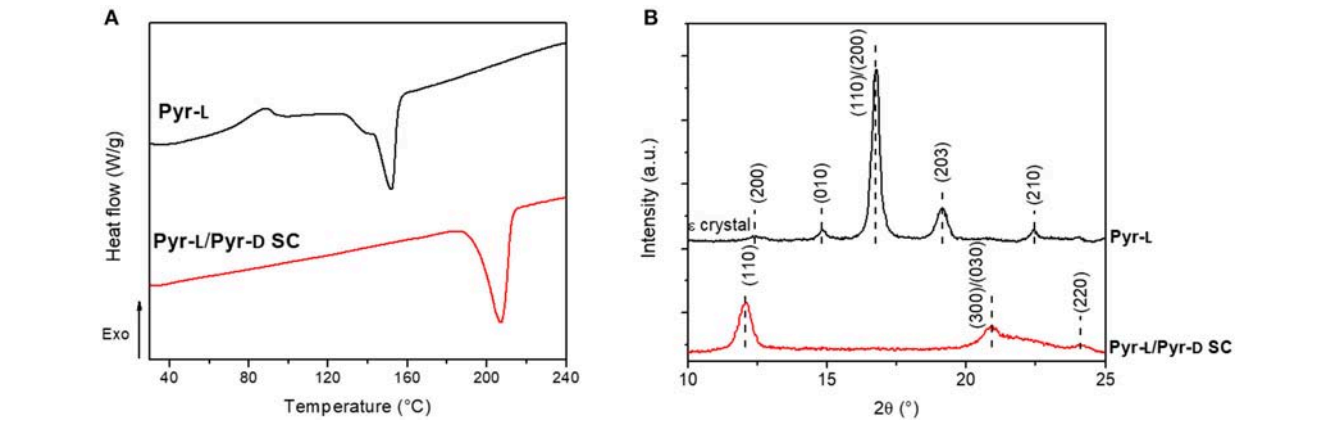

FIGURE 4 | (A) DSC thermograms of Pyr-L and Pyr-L/Pyr-D SC recorded during the second heating (10°C min^{-1}). **(B)** Powder XRD patterns of Pyr-L and Pyr-L/Pyr-D SC.

and chemical binding states of the samples. Pyr-L and Pyr-L/Pyr-D SC were first analyzed, showing signals at ∼284.9 eV attributed to aliphatic carbons (–CH_2, –CH_3), at 285.5 eV (C-OH), the C-O-C peak at 286.8 eV and the 288.9 eV binding energy of the –C=O. The deconvolution of the C_{1s} spectra of the functionalized GnP are dominated by the peak at 284.4 eV, related to the sp^2 C-C bonds and thus the differentiation of the additional aliphatic carbons of the polymer backbone was difficult, suggesting for a limited fraction of PyrL or PyrD onto GnP. However, the O_{1s} spectra (**Figure S5B**) showed the three bands typical of the composition of PLA (O-C=O at 531.5 eV, C-O-C at 533.0 eV and C-OH at 534.2 eV) reflected in GnP Pyr-L and GnP Pyr-L/Pyr-D SC, evidencing significant differences compared to pristine GnP and directly evidencing for grafted PLA chains. The fitting of XPS spectra, with additional comments and atomic ratios for each oxygen functional group are reported in Supporting Info, **Figure S5** and **Table S2**.

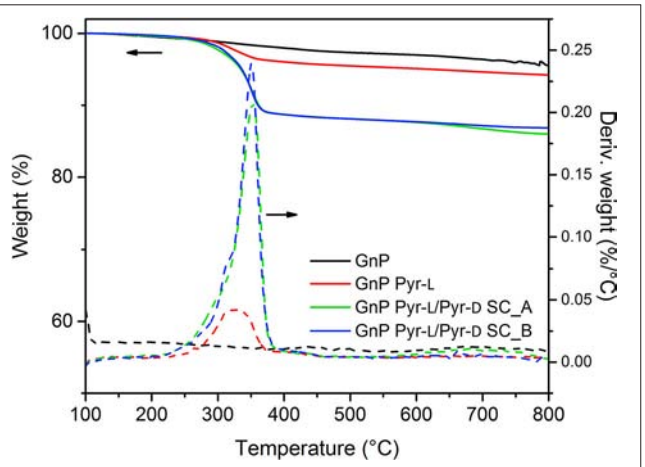

FIGURE 5 | TGA curves of GnP and functionalized GnP.

The functionalization of GnP by the stereoisomers and the formation of the stereocomplex on the basal plane of GnP was also corroborated by thermal analysis (**Figure 5**). Pristine GnP showed a 3.0% weight loss until 600°C under N_2 atmosphere, because of the decomposition of organic impurities and or elimination of the few oxidized groups obtained during the synthesis process of such nanoplatelets (Colonna et al., 2017a). On the other hand, the major weight loss for PLA-functionalized GnP is observed between 200 and 400°C, corresponding to the decomposition of the polymer chains. In this temperature range, GNP Pyr-L showed a small weight loss ∼ 3 wt.% (after subtraction of the weight loss corresponding to the pristine GnP), which corresponds to an adsorption concentration of 0.0535 mmol g^{-1} or adsorption density of ∼1,400 chains μm^{-2}. The adsorption of the stereoisomers in the surface of GnP can be explained by (i) the π-π interactions between pyrene moieties and GnP and (ii) the intermolecular CH-π interactions between the –CH groups of PLLA and GnP (Hu et al., 2009; Arenaza et al., 2015), the former assumed to be more significant. Therefore, the limited adsorption of Pyr-L is mainly ascribed to the low content of pyrene anchoring units, as each oligomeric PLA chain is end capped with a single pyrene group. This observation is consistent with previous studies on the non-covalent functionalization of carbon nanoparticles with pyrene containing polymers, where lower pyrene/polymer ratios showed a weakening of the polymer-carbon nanoparticle interactions (Meuer et al., 2008, 2009).

GnP Pyr-L/Pyr-D SCs, prepared with the two different methodologies, were also investigated for their thermal decomposition. GnP Pyr-L/Pyr-D SCs exhibited a higher thermal stability, as observable from the onset temperature of 353.0°C, compared to 322.3°C for GnP Pyr-L to. Most interestingly, the amount of polymer chains adsorbed on the nanoplatelets is in both cases *ca.* 10 wt.%, (20 wt.% of the total initial amount of polymer) that corresponds to an adsorption concentration and density of 0.190 mmol g^{-1} and ∼12,000 chains μm^{-2},

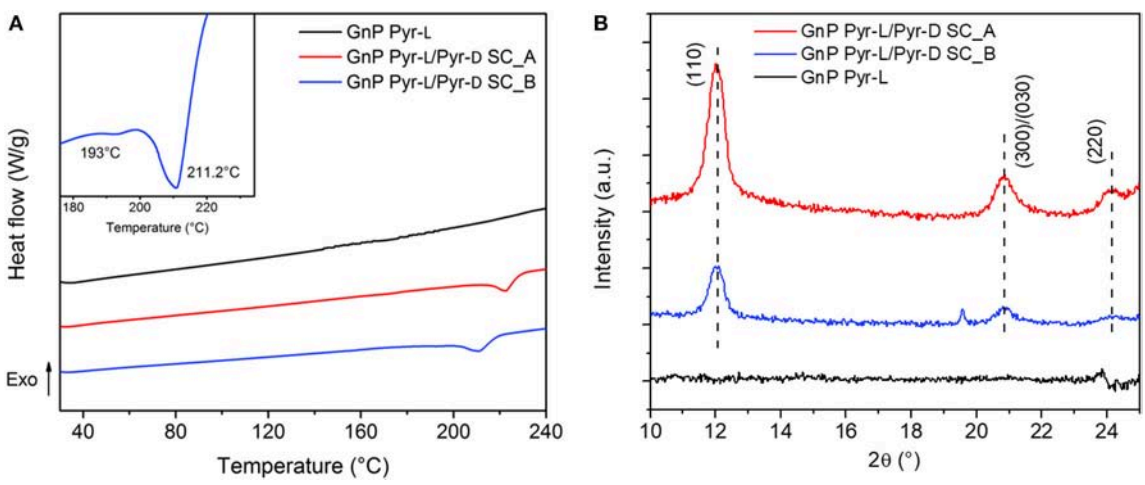

FIGURE 6 | (A) DSC thermograms of GnP Pyr-L and GnP Pyr-L/Pyr-D SC recorded during the second heating (10°C min^{-1}). Inset shows the melting region of GnP Pyr-L/Pyr-D SC_B. **(B)** Powder XRD patterns of GnP Pyr-L and GnP Pyr-L/Pyr-D SC.

respectively. These values are one order of magnitude higher than those calculated for the GnP functionalized with only Pyr-L. The strong ability of carbon-based nanoparticles to induce the stereocomplex crystallization of PLA (Hu et al., 2009; Xu et al., 2010; Yang et al., 2016) together with the formation of SC precursors in the presence of DMF adsorbed on the GnP during the sonication process, favors the supramolecular functionalization of GnP with the SC.

DSC heating curves and XRD patterns of functionalized GnP (**Figure 6**) were further performed to discern the phenomena related to the adsorption of the stereoisomers on the GnP and the formation of the SC crystallites. The DSC thermogram of GnP Pyr-L did not show any clear melting peak of the homocrystals (**Figure 6A**) and no diffraction peaks of Pyr-L could be observed on the XRD pattern (**Figure 6B**). These results confirm the low amount of stereoisomer adsorbed on the basal plane of GnP, as already evidenced from TGA. On the other hand, GnP Pyr-L/Pyr-D SC exhibited clear evidences of PLA stereocomplexation, with significant differences as a function of the preparation method (**Figure 6A** inset). GnP Pyr-L/Pyr-D SC_A, prepared sonicating GnP in a mixed solution of the stereoisomers in DMF, showed a single T_m at 222.8°C, which is 15.3°C higher than the T_m of the SC in the absence of GnP, while showing the typical diffraction peaks (**Figure 6B**) of the SC crystallites at $2\theta = 12.0$, 20.8, and 24.1°, assigned to the (110), (300)/(030), and (220) planes (Tsuji, 2005; Bao et al., 2016). On the other hand, GnP Pyr-L/Pyr-D SC_B, where GnP was separately sonicated in the presence of one of the stereoisomers before mixing them to form the SC, exhibited two partially overlapped melting peaks at about 193 and 211°C (**Figure 6A**, inset), while displaying a XRD signal at the same position but with lower intensities, when compared to GnP Pyr-L/Pyr-D SC_A. The double melting peak has been previously observed in the precipitates of PDLA + PLLA mixtures of the stereoisomers in solution and explained by melting of less perfect crystallites and recrystallization into more stable crystallites (Tsuji et al., 1992). It is worth noting that the main melting point of SCs in GnP Pyr-L/Pyr-D SC_B was found at a temperature (211.2°C) that is significantly lower than the T_m of GnP Pyr-L/Pyr-D SC_A. These differences highlight the role of both GnP and interactions of pyrene-terminated PLA oligomers to its surface. Indeed, in GnP Pyr-L/Pyr-D SC_B, the stereoisomers anchored onto the basal plane of GnP through pyrene terminals clearly affects the nucleation and growth of the SC crystallites. Hence, the probability of the intermolecular contact between the stereoisomers in solution and those on GnP increases, enhancing the stereocomplex crystallization from the surface of the nanoparticles (Hu et al., 2009; Yang et al., 2016). However, the mobility of Pyr-L and Pyr-D chains adsorbed on the GnP is limited, organizing the SC crystallites in a poorly stable state, as observed by the DSC

TABLE 1 | Density (ρ) and in-plane ($\alpha_{\parallel}$) and cross-plane ($\alpha_{\perp}$) thermal diffusivities of nanopapers.

Nanopaper	ρ (g cm^{-3})	SC content	$\alpha_{\parallel}$ (mm^{2}s^{-1})	$\alpha_{\perp}$ (mm^{2}s^{-1})
GnP	1.03 ± 0.02	-	221.6 ± 4.2	0.96 ± 0.02
GnP Pyr-L/Pyr-D SC_A	0.40 ± 0.06	7.0	163.9 ± 3.6	0.53 ± 0.01
GnP Pyr-L/Pyr-D SC_A′	0.35 ± 0.06	9.1	148.0 ± 2.3	2.85 ± 0.05
GnP Pyr-L/Pyr-D SC_A″	0.32 ± 0.07	16.3	116.0 ± 15.8	4.50 ± 0.01

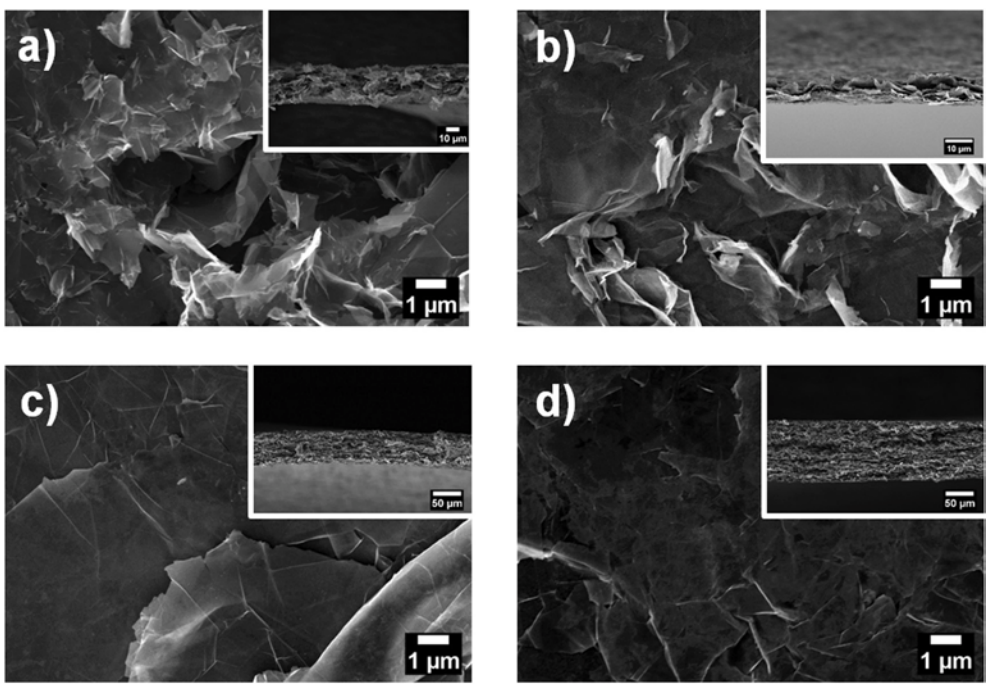

FIGURE 7 | Top view FESEM images of GnP nanopapers: **(a)** GnP, **(b)** GnP Pyr-L/Pyr-D SC_A, **(c)** GnP Pyr-L/Pyr-D SC_A′, and **(d)** GnP Pyr-L/Pyr-D SC_A″. Insets are the corresponding cross-sectional FESEM images of the nanopapers.

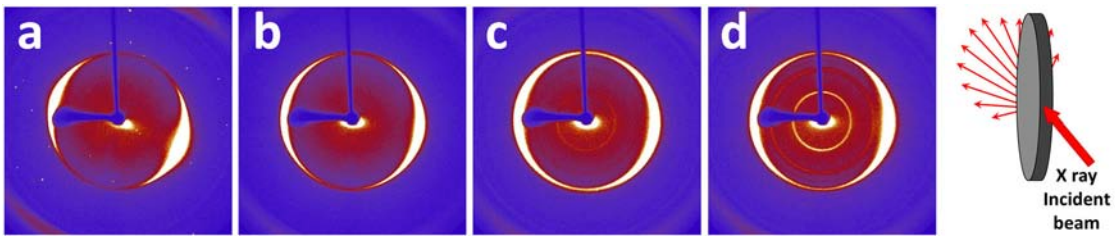

FIGURE 8 | 2D XRD patterns measured via transmission geometry on nanopapers of pristine GnP **(a)** GnP Pyr-L/Pyr-D SC_A **(b)**, GnP Pyr-L/Pyr-D SC_A′ **(c)**, and GnP Pyr-L/Pyr-D SC_A″ **(d)**. A schematic of pattern collection is also reported.

results. In GnP Pyr-L/Pyr-D SC_A, two competing effects are occurring simultaneously: the anchoring of the polymer chains to the nanoplatelets and the formation of the SC crystallites from enantiomers in solution. Here, the mobility of the polymer chains is promoted by sonication in solution together with the GnP, enhancing the stereocomplexation process, while the pyrene groups favor their adsorption on the basal planes of the GnP. As a direct consequence, more organized and stable crystallites are obtained in GnP Pyr-L/Pyr-D SC_A.

Functionalized GnPs were used to prepare nanopapers, to assess the effect of the modification with Pyr-D/Pyr-L on the thermal transfer properties. In particular, the nanopapers have been prepared following the method described for GnP Pyr-L/Pyr-D SC_A, that has been previously confirmed that this strategy forms better SC crystallites. Furthermore, two nanopapers with increasing concentration of the stereoisomers were prepared to investigate the effect of the SC content on the properties of the nanopapers.

Nanopapers density was significantly decreased by the presence of Pyr-L/Pyr-D SC, in the range of 0.3 ÷ 0.4 g cm^{-3}, compared to 1.0 g cm^{-3} for the pristine GNP nanopaper (**Table 1**). Despite the density is slightly decreasing with increasing the enantiomer concentration, the strong reduction in density is not consistent with the simple presence of the SC phase, based on the organic content, as determined by residue at 600°C in thermogravimetric analyses (**Table 1** and **Figure S6**). Therefore, the nanopaper density appears to be mainly dependent on a different organization of the flakes, driven by the organic functionalization with Pyr-L/Pyr-D.

To investigate the microstructure of the nanopapers, FESEM analyses were carried out; top-view and cross-sectional images of the nanopapers are shown in **Figure 7**. The presence of the organic phase, corresponding to the Pyr-L/Pyr-D SC (**Figures 7b–d**), can be observed on the top-view images as thin coating onto the GnP flakes. The cross-sectional images of the nanopapers (**Figure 7** insets) suggest the presence of the polymer chains, indeed modifies the structural organization of the GnP flakes. To further investigate the self-assembly of GnP flakes in the nanopaper, 2D-XRD measurements were carried out to qualitatively evaluate the degree of in-plane orientation. In **Figure 8**, 2D XRD patterns for the nanopapers of pristine GnP and GnP Pyr-L/Pyr-D SC are reported. As expected for nanopapers prepared by vacuum filtration from suspensions of 2D nanoparticles, a very high degree of in-plane

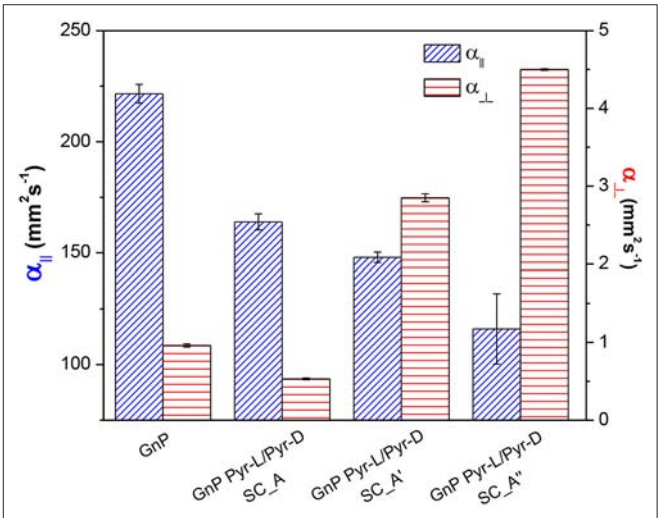

FIGURE 9 | In-plane ($\alpha_{\parallel}$) and cross-plane ($\alpha_{\perp}$) thermal diffusivities for pristine and functionalized GnP nanopapers, with different contents of Pyr-L/Pyr-D SC.

preferential orientation was observed for pristine GnP. This is evidenced by the strongly variable intensity distribution of the 002 basal plane for graphite *vs.* the azimuthal angle, with the characteristic two maxima is opposite positions, confirming a very large fraction of the GnP flakes is oriented parallel to the plane of the nanopaper. In the presence of Pyr-L/Pyr-D SC, a slightly lower degree of orientation is generally observed, as suggested by a weaker orientation of the diffraction signal for 002 graphitic planes. This limited loss of orientation is particularly clear with in the cases of GnP Pyr-L/Pyr-D SC_A′ and GnP Pyr-L/Pyr-D SC_A″, suggesting that higher concentrations of SC have a role in the self-assembly of GnP nanoflakes during filtration. Furthermore, for GnP Pyr-L/Pyr-D inner diffraction circles are visible, corresponding to the XRD diffraction signals from the SC (**Figure S7**), with no significant preferential orientation (**Figures 8c,d**) and intensity proportional to the SC concentration determined by TGA.

The thermal diffusivity of the nanopapers were analyzed in both cross-plane and in-plane directions. Results reported in **Table 1** and **Figure 9** show a clear reduction of in-plane diffusivity in the presence of SC, which is expected, based on the low thermal conductivity of polymers. Furthermore, this reduction is a direct function of the fraction of SC in the

nanopaper. Conversely, the cross plane diffusivity showed only a slight reduction at the lowest SC content, whereas at higher SC content the diffusivity is increased by a factor of 3 in GnP Pyr-L/Pyr-D SC_A′ and 4.5 in GnP Pyr-L/Pyr-D SC_A″, despite the increasing fraction of the polymeric phase.

The increase in cross-plane diffusivity may partially be related to a loss in nanoflakes orientation. As the fractions of flakes lying on direction tilted with respect to the nanopaper plane are expected to contribute more to the heat transfer across the nanopaper, owing to the well-known anisotropy of graphitic materials. However, in this case, the above commented differences in preferential orientation are not sufficient to explain the change in cross-plane diffusivity. Indeed, the lower degree of orientation was observed for GnP Pyr-L/Pyr-D SC_A, compared to pristine GnP, does not correspond to a better cross plane diffusivity. Furthermore, the significant differences between diffusivities for GnP Pyr-L/Pyr-D SC_A′ and GnP Pyr-L/Pyr-D SC_A″ are not reflected in terms of preferential orientations, proven to be comparable. Therefore, the enhanced efficiency on cross-plane heat transfer appears to be related to the organization of the SC phase, acting as thermal bridge between GnP flakes. In fact, crystallinity and orientation of the macromolecules are well-known to dramatically affect the thermal conductivity of the polymeric materials (Choy et al., 1980, 1993; Singh et al., 2014) and the organization of a thermally stable and highly crystalline SC phase, strongly interacting to the surface of GnP via the pyrene terminal groups, appears to have an effective role in promoting heat transfer between overlapped GnP flakes.

CONCLUSIONS

Non-covalent functionalization of graphite nanoplatelets (GnP) was obtained with *ad hoc* synthesized pyrene chain-ended oligomers of stereoregular polylactic acid (Pyr-L and Pyr-D), exploiting the π-π stacking interactions with GnP surface. Stereocomplexation of Pyr-L and Pyr-D onto GnP was obtained both *via* one-pot preparation from a mixture of GnP/Pyr-L/Pyr-D, as well as by mixing of GnP/Pyr-L and GnP/Pyr-D suspensions, with the former procedure allowing the preparation of better organized SC domains. Nanopapers were prepared at different SC fraction, evidencing the dominant role of the polymeric functionalization in the self-assembly of the GnP flakes. In particular, lower densities and reduced orientations of the nanopapers were induced by the presence of SC, acting as a polymeric cross-linkers between different GnP moieties. Most interestingly, the presence of PLA SC between GnP flakes was found to enhance cross-plane heat transfer in GnP Pyr-L/Pyr-D SC nanopapers, explained in terms of the contribution of local crystallinity to the reduction of thermal resistance at the interface between GnP flakes. Therefore, the possibility to control the thermal conductivity anisotropy of GnP nanostructures, by the self-assembly of organic polymeric functionalization, was demonstrated. The proposed approach can be generally applied to the physical properties modification of engineered nanostructures based on graphene and graphene related materials.

DATA AVAILABILITY

The datasets generated for this study are available on request to the corresponding author.

AUTHOR CONTRIBUTIONS

AF and OM conceived this research work and the experiments within, interpreted the experimental results and led the research activities. ME carried out the synthesis of Pyr-L/Pyr-D, nanopapers, and characterization. MB contributed to the synthesis, data analysis and interpretation of results. MM carried out 2D XRD measurement, data treatment and interpretation. Manuscript was mainly written by MB and AF.

ACKNOWLEDGMENTS

This work has received funding from the European Research Council (ERC) under the European Union's Horizon 2020 research and innovation programme grant agreement 639495 — INTHERM — ERC-2014-STG.

The authors gratefully acknowledge Dr. Julio Gomez (Avanzare Innovación Tecnólogica, E) for providing GnP, Dr. Mauro Raimondo (Politecnico di Torino, I) for FESEM analyses, Dr. Salvatore Guastella (Politecnico di Torino, I) for XPS measurements and Dr. Domenica Marabello (University of Turin and CRISDI, Italy) for 2D XRD measurements.

SUPPLEMENTARY MATERIAL

The Supplementary Material for this article can be found online at: https://www.frontiersin.org/articles/10.3389/fchem.2019.00176/full#supplementary-material

REFERENCES

Anderson, K. S., and Hillmyer, M. A. (2006). Melt preparation and nucleation efficiency of polylactide stereocomplex crystallites. *Polymer* 47, 2030–2035. doi: 10.1016/j.polymer.2006.01.062

Arenaza, I. M., d., Obarzanek-Fojt, M., Sarasua, J. R., Meaurio, E., Meyer, F., et al. (2015). Pyrene-end-functionalized poly(L-lactide) as an efficient carbon nanotube dispersing agent in poly(L-lactide): mechanical performance and biocompatibility study. *Biomed. Mater.* 10:045003. doi: 10.1088/1748-6041/10/4/045003

Balandin, A. A., and Nika, D. L. (2012). Phononics in low-dimensional materials. *Mater. Today* 15, 266–275. doi: http://doi.org/10.1016/S1369-7021(12)70117-7

Bao, J., Chang, X., Shan, G., Bao, Y., and Pan, P. (2016). Synthesis of end-functionalized hydrogen-bonding poly(lactic acid)s and preferential stereocomplex crystallization of their enantiomeric blends. *Polymer Chem.* 7, 4891–4900. doi: 10.1039/C6PY00976J

Bernal, M. M., Di Pierro, A., Novara, C., Giorgis, F., Mortazavi, B., Saracco, G., et al. (2018). Edge-grafted molecular junctions between graphene nanoplatelets: applied chemistry to enhance heat transfer in nanomaterials. *Adv. Funct. Mater.* 28:1706954. doi: 10.1002/adfm.201706954

Bernal, M. M., Tortello, M., Colonna, S., Saracco, G., and Fina, A. (2017). Thermally and electrically conductive nanopapers from reduced graphene oxide: effect of nanoflakes thermal annealing on the film structure and properties. *Nanomaterials* 7:428. doi: 10.3390/nano7120428

Bidsorkhi, H. C., D'Aloia, A. G., De Bellis, G., Proietti, A., Rinaldi, A., Fortunato, M., et al. (2017). Nucleation effect of unmodified graphene nanoplatelets on PVDF/GNP film composites. *Mater. Today Commun.* 11, 163–173. doi: 10.1016/j.mtcomm.2017.04.001

Björk, J., Hanke, F., Palma, C.-A., Samori, P., Cecchini, M., and Persson, M. (2010). Adsorption of aromatic and anti-aromatic systems on graphene through π-π stacking. *J. Phys. Chem. Lett.* 1, 3407–3412. doi: 10.1021/jz101360k

Brizzolara, D., Cantow, H. J., Diederichs, K., Keller, E., and Domb, A. J. (1996). Mechanism of the stereocomplex formation between enantiomeric poly(lactide)s. *Macromolecules* 29, 191–197. doi: 10.1021/ma951144e

Chen, H., Ginzburg, V. V., Yang, J., Yang, Y., Liu, W., Huang, Y., et al. (2016). Thermal conductivity of polymer-based composites: fundamentals and applications. *Progr. Polymer Sci.* 59, 41–85. doi: 10.1016/j.progpolymsci.2016.03.001

Cheng, Q.-Y., Zhou, D., Gao, Y., Chen, Q., Zhang, Z., and Han, B.-H. (2012). Supramolecular self-assembly induced graphene oxide based hydrogels and organogels. *Langmuir* 28, 3005–3010. doi: 10.1021/la204558f

Choi, E.-Y., Han, T. H., Hong, J., Kim, J. E., Lee, S. H., Kim, H. W., et al. (2010). Noncovalent functionalization of graphene with end-functional polymers. *J. Mater. Chem.* 20, 1907–1912. doi: 10.1039/B919074K

Choy, C. L., Chen, F. C., and Luk, W. H. (1980). Thermal conductivity of oriented crystalline polymers. *J. Polymer Sci.* 18, 1187–1207. doi: doi: 10.1002/pol.1980.180180603

Choy, C. L., Fei, Y., and Xi, T. G. (1993). Thermal conductivity of gel-spun polyethylene fibers. *J. Polymer Sci. Part B Polymer Phys.* 31, 365–370. doi: doi: 10.1002/polb.1993.090310315

Coleman, J. N., Lotya, M., O'Neill, A., Bergin, S. D., King, P. J., Khan, U., et al. (2011). Two-dimensional nanosheets produced by liquid exfoliation of layered materials. *Science* 331, 568–571. doi: 10.1126/science.1194975

Colonna, S., Bernal, M. M., Gavoci, G., Gomez, J., Novara, C., Saracco, G., et al. (2017a). Effect of processing conditions on the thermal and electrical conductivity of poly (*butylene terephthalate*) nanocomposites prepared via ring-opening polymerization. *Mater. Design* 119(Suppl. C), 124–132. doi: 10.1016/j.matdes.2017.01.067

Colonna, S., Pérez-Camargo, R. A., Chen, H., Liu, G., Wang, D., Müller, A. J., et al. (2017b). Supernucleation and orientation of Poly(*butylene terephthalate*) crystals in nanocomposites containing highly reduced graphene oxide. *Macromolecules* 50, 9380–9393. doi: 10.1021/acs.macromol.7b01865

Danko, M., Hrdlovic, P., Brzezinski, M., Duda, A., and Biela, T. (2018). Real-time monitoring of stereocomplex formation of poly(L-lactide) and poly (D-lactide) decorated with a pyrene derivative as a fluorescence probe. *Polymer* 156, 76–84. doi: 10.1016/j.polymer.2018.09.041

de Arenaza, I. M., Sarasua, J. R., Amestoy, H., Lopez-Rodriguez, N., Zuza, E., Meaurio, E., et al. (2013). Polylactide stereocomplex crystallization prompted by multiwall carbon nanotubes. *J. Appl. Poly. Sci.* 130, 4327–4337. doi: 10.1002/app.39721

Eleuteri, M., Pastorino, L., and Monticelli, O. (2018). On the degradation properties of electrospun fibers based on PLLA: the effect of a drug model modification. *Poly. Degr. Stabil.* 153, 109–117. doi: 10.1016/j.polymdegradstab.2018.04.013

Ferrari, A. C., Bonaccorso, F., Fal'ko, V., Novoselov, K. S., Roche, S., Boggild, P., et al. (2015). Science and technology roadmap for graphene, related two-dimensional crystals, and hybrid systems. *Nanoscale* 7, 4598–4810. doi: 10.1039/c4nr01600a

Ferreira, C. I., Dal Castel, C., Oviedo, M. A. S., and Mauler, R. S. (2013). Isothermal and non-isothermal crystallization kinetics of polypropylene/exfoliated graphite nanocomposites. *Thermochimica Acta* 553, 40–48. doi: 10.1016/j.tca.2012.11.025

Fina, A., Colonna, S., Maddalena, L., Tortello, M., and Monticelli, O. (2018). Facile and low environmental impact approach to prepare thermally conductive nanocomposites based on polylactide and graphite nanoplatelets. *ACS Sustain. Chem. Eng.* 6, 14340–14347. doi: 10.1021/acssuschemeng.8b03013

Gardella, L., Furfaro, D., Galimberti, M., and Monticelli, O. (2015). On the development of a facile approach based on the use of ionic liquids: preparation of PLLA (sc-PLA)/high surface area nano-graphite systems. *Green Chem.* 17, 4082–4088. doi: 10.1039/C5GC00964B

Geim, A. K., and Novoselov, K. S. (2007). The rise of graphene. *Nat. Mater.* 6, 183–191. doi: 10.1038/nmat1849

Georgakilas, V., Otyepka, M., Bourlinos, A. B., Chandra, V., Kim, N., Kemp, K. C., et al. (2012). Functionalization of Graphene: covalent and non-covalent approaches, derivatives and applications. *Chem. Rev.* 112, 6156–6214. doi: 10.1021/cr3000412

Georgakilas, V., Tiwari, J. N., Kemp, K. C., Perman, J. A., Bourlinos, A. B., Kim, K. S., et al. (2016). Noncovalent functionalization of graphene and graphene oxide for energy materials, biosensing, catalytic, and biomedical applications. *Chem. Rev.* 116, 5464–5519. doi: 10.1021/acs.chemrev.5b00620

Gómez-Navarro, C., Weitz, R. T., Bittner, A. M., Scolari, M., Mews, A., Burghard, M., et al. (2007). Electronic transport properties of individual chemically reduced graphene oxide sheets. *Nano Lett.* 7, 3499–3503. doi: 10.1021/nl072090c

Gonçalves, C. M. B., Coutinho, J.,o,.A. P., and Marrucho, I.M. (2010). "Optical Properties," in *Poly(Lactic Acid)* eds R. Auras, L.-T. Lim, Susan E. M. Selke, H. Tsuji (Hoboken, NJ: John Wiley and Sons, Inc.), 97–112.

Hernandez, Y., Nicolosi, V., Lotya, M., Blighe, F. M., Sun, Z., De, S., et al. (2008). High-yield production of graphene by liquid-phase exfoliation of graphite. *Nat. Nanotechnol.* 3:563. doi: 10.1038/nnano.2008.215

Hirata, M., and Kimura, Y. (2008). Thermomechanical properties of stereoblock poly(lactic acid)s with different PLLA/PDLA block compositions. *Polymer* 49, 2656–2661. doi: 10.1016/j.polymer.2008.04.014

Hirsch, A., Englert, J. M., and Hauke, F. (2013). Wet Chemical Functionalization of Graphene. *Accounts Chem. Res.* 46, 87–96. doi: 10.1021/ar300116q

Hsiao, S.-T., Ma, C.-C. M., Tien, H.-W., Liao, W.-H., Wang, Y.-S., Li, S.-M., et al. (2013). Using a non-covalent modification to prepare a high electromagnetic interference shielding performance graphene nanosheet/water-borne polyurethane composite. *Carbon* 60, 57–66. doi: 10.1016/j.carbon.2013.03.056

Hu, X., An, H., Li, Z.-M., Geng, Y., Li, L., and Yang, C. (2009). Origin of carbon nanotubes induced Poly(l-Lactide) crystallization: surface induced conformational order. *Macromolecules* 42, 3215–3218. doi: 10.1021/ma802758k

Ji, L., Wu, Y., Ma, L., and Yang, X. (2015). Noncovalent functionalization of graphene with pyrene-terminated liquid crystalline polymer. *Composites Part A Appl. Sci. Manufact.* 72, 32–39. doi: 10.1016/j.compositesa.2015.01.009

Kister, G., Cassanas, G., and Vert, M. (1998). Effects of morphology, conformation and configuration on the IR and Raman spectra of various poly(lactic acid)s. *Polymer* 39, 267–273. doi: 10.1016/S0032-3861(97)00229-2

Kuilla, T., Bhadra, S., Yao, D., Kim, N. H., Bose, S., and Lee, J. H. (2010). Recent advances in graphene based polymer composites. *Progr. Poly. Sci.* 35, 1350–1375. doi: 10.1016/j.progpolymsci.2010.07.005

Lee, C., Wei, X., Kysar, J. W., and Hone, J. (2008). Measurement of the elastic properties and intrinsic strength of monolayer graphene. *Science* 321, 385–388. doi: 10.1126/science.1157996

Liang, C., Jingquan, L., Rui, W., Zhen, L., and Wenrong, Y. (2012). A facile "graft from" method to prepare molecular-level dispersed graphene–polymer composites. *J. Poly. Sci. Part A Poly. Chem.* 50, 4423–4432. doi: 10.1002/pola.26264

Liu, J., Yang, W., Tao, L., Li, D., Boyer, C., and Davis, T. P. (2010). Thermosensitive graphene nanocomposites formed using pyrene-terminal polymers made by RAFT polymerization. *J. Poly. Sci. Part A Poly. Chem.* 48, 425–433. doi: 10.1002/pola.23802

Manafi, P., Ghasemi, I., Karrabi, M., Azizi, H., and Ehsaninamin, P. (2014). Effect of graphene nanoplatelets on crystallization kinetics of Poly (lactic acid). *Soft Mater.* 12, 433–444. doi: 10.1080/1539445X.2014.959598

Marubayashi, H., Asai, S., and Sumita, M. (2012). Complex crystal formation of Poly(l-lactide) with solvent molecules. *Macromolecules* 45, 1384–1397. doi: 10.1021/ma202324g

Marubayashi, H., Asai, S., and Sumita, M. (2013). Guest-induced crystal-to-crystal transitions of Poly(l-lactide) complexes. *J. Phys. Chem. B* 117, 385–397. doi: 10.1021/jp308999t

Meng, Y., Wang, K., Zhang, Y., and Wei, Z. (2013). Hierarchical porous graphene/polyaniline composite film with superior rate performance for flexible supercapacitors. *Adv. Mater.* 25, 6985–6990. doi: doi: 10.1002/adma.201303529

Meuer, S., Braun, L., and Zentel, R. (2008). Solubilisation of multi walled carbon nanotubes by [small alpha]-pyrene functionalised PMMA and their liquid crystalline self-organisation. *Chem. Commun.* 27, 3166–3168. doi: 10.1039/B803099E

Meuer, S., Braun, L., and Zentel, R. (2009). Pyrene containing polymers for the non-covalent functionalization of carbon nanotubes. *Macromol. Chem. Phys.* 210, 1528–1535. doi: 10.1002/macp.200900125

Michalski, A., Socka, M., Brzezinski, M., and Biela, T. (2018). Reversible supramolecular polylactides gels obtained via stereocomplexation. *Macromol. Chem. Phys.* 219:1700607. doi: 10.1002/macp.201700607

Mittal, V. (2014). Functional polymer nanocomposites with graphene: a review. *Macromol. Mater. Eng.* 299, 906–931. doi: 10.1002/mame.201300394

Papageorgiou, D. G., Kinloch, I. A., and Young, R. J. (2017). Mechanical properties of graphene and graphene-based nanocomposites. *Progr. Mater. Sci.* 90, 75–127. doi: 10.1016/j.pmatsci.2017.07.004

Parviz, D., Das, S., Ahmed, H. S. T., Irin, F., Bhattacharia, S., and Green, M. J. (2012). Dispersions of non-covalently functionalized graphene with minimal stabilizer. *ACS Nano* 6, 8857–8867. doi: 10.1021/nn302784m

Potts, J. R., Dreyer, D. R., Bielawski, C. W., and Ruoff, R. S. (2011). Graphene-based polymer nanocomposites. *Polymer* 52, 5–25. doi: 10.1016/j.polymer.2010.11.042

Renteria, J. D., Ramirez, S., Malekpour, H., Alonso, B., Centeno, A., Zurutuza, A., et al. (2015). Strongly anisotropic thermal conductivity of free-standing reduced graphene oxide films annealed at high temperature. *Adv. Funct. Mater.* 25, 4664–4672. doi: 10.1002/adfm.201501429

Rodriguez-Perez, L., Herranz, M.,a,.A., and Martin, N. (2013). The chemistry of pristine graphene. *Chem. Commun.* 49, 3721–3735. doi: 10.1039/C3CC38950B

Ronca, S., Igarashi, T., Forte, G., and Rastogi, S. (2017). Metallic-like thermal conductivity in a lightweight insulator: solid-state processed ultra high molecular weight polyethylene tapes and films. *Polymer* 123, 203–210. doi: 10.1016/j.polymer.2017.07.027

Shen, B., Zhai, W., and Zheng, W. (2014). Ultrathin flexible graphene film: an excellent thermal conducting material with efficient EMI shielding. *Adv. Funct. Mater.* 24, 4542–4548. doi: 10.1002/adfm.201400079

Singh, V., Bougher, T. L., Weathers, A., Cai, Y., Bi, K., Pettes, M. T., et al. (2014). High thermal conductivity of chain-oriented amorphous polythiophene. *Nat. Nanotechnol.* 9, 384. doi: 10.1038/nnano.2014.44

Song, N.-J., Chen, C.-M., Lu, C., Liu, Z., Kong, Q.-Q., and Cai, R. (2014). Thermally reduced graphene oxide films as flexible lateral heat spreaders. *J. Mater. Chem. A* 2, 16563–16568. doi: 10.1039/C4TA02693D

Stoller, M. D., Park, S., Zhu, Y., An, J., and Ruoff, R. S. (2008). Graphene-Based Ultracapacitors. *Nano Lett.* 8, 3498–3502. doi: 10.1021/nl802558y

Sun, Y., and He, C. (2012). Synthesis and stereocomplex crystallization of Poly(lactide)–graphene oxide nanocomposites. *ACS Macro Lett.* 1, 709–713. doi: 10.1021/mz300131u

Tong, X.-Z., Song, F., Li, M.-Q., Wang, X.-L., Chin, I.-J., and Wang, Y.-Z. (2013). Fabrication of graphene/polylactide nanocomposites with improved properties. *Comp. Sci. Technol.* 88, 33–38. doi: 10.1016/j.compscitech.2013.08.028

Tsuji, H. (2005). Poly(lactide) stereocomplexes: formation, structure, properties, degradation, and applications. *Macromol. Biosci.* 5, 569–597. doi: 10.1002/mabi.200500062

Tsuji, H., Hyon, S. H., and Ikada, Y. (1992). Stereocomplex formation between enantiomeric poly(lactic acids). 5. Calorimetric and morphological studies on the stereocomplex formed in acetonitrile solution. *Macromolecules* 25, 2940–2946. doi: 10.1021/ma00037a024

Tsuji, H., and Yamamoto, S. (2011). Enhanced stereocomplex crystallization of biodegradable enantiomeric Poly(lactic acid)s by repeated casting. *Macromol. Mater. Eng.* 296, 583–589. doi: 10.1002/mame.201000397

Wan, S., Li, Y., Mu, J., Aliev, A. E., Fang, S., Kotov, N. A., et al. (2018). Sequentially bridged graphene sheets with high strength, toughness, and electrical conductivity. *Proc. Natl. Acad. Sci. U.S.A.* 115:21. doi: 10.1073/pnas.1719111115

Wang, H., Bi, S.-G., Ye, Y.-S., Xue, Y., Xie, X.-L., and Mai, Y.-W. (2015). An effective non-covalent grafting approach to functionalize individually dispersed reduced graphene oxide sheets with high grafting density, solubility and electrical conductivity. *Nanoscale* 7, 3548–3557. doi: 10.1039/C4NR06710J

Wang, J., Chen, Z., and Chen, B. (2014). Adsorption of polycyclic aromatic hydrocarbons by graphene and graphene oxide nanosheets. *Environ. Sci. Technol.* 48, 4817–4825. doi: 10.1021/es405227u

Wu, D., Cheng, Y., Feng, S., Yao, Z., and Zhang, M. (2013). Crystallization behavior of polylactide/graphene composites. *Industr. Eng. Chem. Res.* 52, 6731–6739. doi: 10.1021/ie4004199

Xin, G., Sun, H., Hu, T., Fard, H. R., Sun, X., Koratkar, N., et al. (2014). Large-area freestanding graphene paper for superior thermal management. *Adv. Mater.* 26, 4521–4526. doi: 10.1002/adma.201400951

Xu, H., Feng, Z.-X., Xie, L., and Hakkarainen, M. (2016). Graphene oxide-driven design of strong and flexible biopolymer barrier films: from smart crystallization control to affordable engineering. *ACS Sust. Chem. Eng.* 4, 334–349. doi: 10.1021/acssuschemeng.5b01273

Xu, H., Teng, C., and Yu, M. (2006). Improvements of thermal property and crystallization behavior of PLLA based multiblock copolymer by forming stereocomplex with PDLA oligomer. *Polymer* 47, 3922–3928. doi: 10.1016/j.polymer.2006.03.090

Xu, H., Wu, D., Yang, X., Xie, L., and Hakkarainen, M. (2015). Thermostable and impermeable "nano-barrier walls" constructed by Poly(lactic acid) stereocomplex crystal decorated graphene oxide nanosheets. *Macromolecules* 48, 2127–2137. doi: 10.1021/ma502603j

Xu, J.-Z., Chen, T., Yang, C.-L., Li, Z.-M., Mao, Y.-M., Zeng, B.-Q., et al. (2010). Isothermal crystallization of Poly(l-lactide) induced by graphene nanosheets and carbon nanotubes: a comparative study. *Macromolecules* 43, 5000–5008. doi: 10.1021/ma100304n

Yang, S., Xu, J.-Z., Li, Y., Lei, J., Zhong, G.-J., Wang, R., et al. (2017). Effects of solvents on stereocomplex crystallization of high-molecular-weight polylactic acid racemic blends in the presence of carbon nanotubes. *Macromol. Chem. Phys.* 218:1700292-n/a. doi: 10.1002/macp.201700292

Yang, S., Zhong, G.-J., Xu, J.-Z., and Li, Z.-M. (2016). Preferential formation of stereocomplex in high-molecular-weight polylactic acid racemic blend induced by carbon nanotubes. *Polymer* 105, 167–171. doi: 10.1016/j.polymer.2016.10.034

Zhang, D., Lin, Y., and Wu, G. (2017). Polylactide-based nanocomposites with stereocomplex networks enhanced by GO-g-PDLA. *Comp. Sci. Technol.* 138, 57–67. doi: 10.1016/j.compscitech.2016.11.016

Zhang, J., Sato, H., Tsuji, H., Noda, I., and Ozaki, Y. (2005). Infrared spectroscopic study of CH3···OC interaction during Poly(l-lactide)/Poly(d-lactide) stereocomplex formation. *Macromolecules* 38, 1822–1828. doi: 10.1021/ma047872w

Zhang, Y., Liu, C., Shi, W., Wang, Z., Dai, L., and Zhang, X. (2007). Direct measurements of the interaction between pyrene and graphite in aqueous media by single molecule force spectroscopy: understanding the π-π Interactions. *Langmuir* 23, 7911–7915. doi: 10.1021/la700876d

Conflict of Interest Statement: The authors declare that the research was conducted in the absence of any commercial or financial relationships that could be construed as a potential conflict of interest.

Copyright © 2019 Eleuteri, Bernal, Milanesio, Monticelli and Fina. This is an open-access article distributed under the terms of the Creative Commons Attribution License (CC BY). The use, distribution or reproduction in other forums is permitted, provided the original author(s) and the copyright owner(s) are credited and that the original publication in this journal is cited, in accordance with accepted academic practice. No use, distribution or reproduction is permitted which does not comply with these terms.

Supramolecular Chemistry

David Margulies

David Margulies has been an Associate Professor at the Weizmann Institute of Science in Israel within the Organic Chemistry Department since 2017. Dr Margulies obtained his Master's and PhD degrees in Organic Chemistry at the Weizmann Institute of Science between 1998 and 2006, under the supervision of Professor Abraham Shanzer. He then moved to Yale University for a Post-doctoral Associate position from 2006 to 2009, before returning to the Weizmann Institute of Science as a Senior Scientist in 2009. Dr Margulies has received numerous honors and awards throughout his research career, including the 2019 NCK Prize for a Young Outstanding Medicinal Chemistry, and the 2018 MSMLG Czarnik Emerging Investigator Award (6th International Conference of Molecular Sensors and Molecular Logic Gates).

Suying Xu

Dr Suying Xu has been an Associate Professor at the Beijing University of Chemical Technology since 2015. Her research focuses on the design of fluorescent probes, the fabrication of nanostructures, as well as the preparation of multifunctional nanomaterials for bioimaging and disease treatment.

Ross S. Forgan

Dr Ross Forgan has been a Royal Society University Research Fellow since 2012 and Reader in Chemistry at the University of Glasgow since 2016. His research into the application of metal-organic frameworks in biomimetic catalysis and nanoscale drug delivery is underpinned by fundamental studies into molecular recognition and self-assembly processes inside nanoporous materials. In 2016 he won a highly prestigious ERC Starting Grant, and he was awarded the Sessler Early Career Researcher Prize in 2018. He is a Fellow of the Royal Society of Chemistry and a founding member of the Royal Society of Edinburgh Young Academy of Scotland.

Meng Li

Meng Li now is an Associate Professor at the North China Electric Power University. She obtained her BSc in 2011 at the East China University of Science and Technology, and completed a combined Master's and PhD degree from 2011 to 2012 with Prof. Weihong Zhu in China. She then worked with Prof. Tony D James to obtain another PhD degree at University of Bath from October 2012 to July 2015. She attended many major international conferences such as the Molecular Sensor and Molecular Logic gates. Her research interests comprise many aspects of supramolecular chemistry, electrochemistry and materials chemistry, including molecular recognition and materials fabrication.

Tsuyoshi Minami

Tsuyoshi Minami obtained his PhD from Tokyo Metropolitan University in 2011, under the direction of Professor Yuji Kubo. During his PhD studies he worked with Professor Tony D. James of the University of Bath on collaborative projects. He was a Postdoctoral Researcher from 2011 to 2013 and a Research Assistant Professor in 2013 at Bowling Green State University, working with Professor Pavel Anzenbacher Jr. He then joined Yamagata University as an Assistant Professor from 2014 to 2016. He has been a lecturer at The University of Tokyo since 2016. His interests include supramolecular analytical chemistry, self-assembled materials, and organic transistors for sensing applications.

Xiao-Peng He

Xiao-Peng He obtained his BSc in Applied Chemistry in 2006 and his PhD in Pharmaceutical Engineering in 2011 from ECUST. He completed a co-tutored doctoral program at ENS Cachan (France) from July 2008 to February 2009. He then carried out his postdoctoral research with Prof. Kaixian Chen (SIMM, CAS) at ECUST from 2011 to 2013. He is now a Professor at the Feringa Nobel Prize Scientists Joint Research Center, School of Chemistry and Molecular Engineering, ECUST, where his research interests span from chemical glycobiology to fluorescent molecular probes and functional materials of different dimensions for disease diagnostics and theranostics.

Robert B. P. Elmes

Rob graduated with a BA Mod (1st Class) in Medicinal Chemistry from Trinity College Dublin in 2007 before he was awarded an IRCSET Embark Scholarship to undertake his PhD under the supervision of Prof. Thorri Gunnlaugsson at TCD. In 2011 Rob moved to The University of Sydney as a Postdoctoral Fellow under the guidance of Prof. Kate Jolliffe before returning to Ireland in late 2014 as a Lecturer in the Department of Chemistry at Maynooth University. Rob's research interests lie in the fields of Supramolecular Chemistry and Chemical Biology where the group is using supramolecular chemistry to develop new drug delivery vehicles, diagnostic tools, therapeutics and chemosensors.

Lupei Du

Lupei Du is currently an Associate Professor at the School of Pharmacy, Shandong University. She obtained her PhD degrees from China Pharmaceutical University in 2006, and her postdoctoral training at the Department of Chemistry, Georgia State University from 2006 to 2009. She joined Shandong University in 2009. Her main research interests include the rational design and synthesis of medicinal molecules and bioactive probes.

frontiers in Chemistry

ORIGINAL RESEARCH
published: 16 April 2019
doi: 10.3389/fchem.2019.00243

Molecular Logic as a Means to Assess Therapeutic Antidotes

*Linor Unger-Angel, Leila Motiei and David Margulies**

Department of Organic Chemistry, Weizmann Institute of Science, Rehovot, Israel

An emerging direction in the area of molecular logic and computation is developing molecular-scale devices that can operate in complex biological environments, such as within living cells, which are beyond the reach of conventional electronic devices. Herein we demonstrate, at the proof-of-principle level, how concepts applied in the field of molecular logic gates can be used to convert a simple fluorescent switch (YES gate), which lights up in the presence of glutathione s-transferase (GST), into a medicinally relevant INHIBIT gate that responds to both GST and beta-cyclodextrin (β-CD) as input signals. We show that the optical responses generated by this device indicate the ability to use it as an enzyme inhibitor, and more importantly, the ability to use β-CD as an "antidote" that prevents GST inhibition. The relevance of this system to biomedical applications is demonstrated by using the INHIBIT gate and β-CD to regulate the growth of breast cancer cells, highlighting the possibility of applying supramolecular inputs, commonly used to control the fluorescence of molecular logic gates, as antidotes that reverse the toxic effect of chemotherapy agents. We also show that the effect of β-CD can be prevented by introducing 1-adamantanecarboxylic acid (Ad-COOH) as an additional input signal, indicating the potential of obtaining precise, temporal control over enzyme activity and anticancer drug function.

Keywords: molecular logic gates, fluorescent molecular probes, supramolecular chemistry, enzyme inhibitors, thiazole orange-based protein identifiers (TOPIs), glutathione s-transferase (GST), cyclodextrin host, adamantyl guest

OPEN ACCESS

Edited by:
Tony D. James,
University of Bath, United Kingdom

Reviewed by:
David C. Magri,
University of Malta, Malta
Adam Charles Sedgwick,
University of Texas at Austin, United States

****Correspondence:***
David Margulies
david.margulies@weizmann.ac.il

Specialty section:
This article was submitted to Supramolecular Chemistry, a section of the journal Frontiers in Chemistry

Received: *20 January 2019*
Accepted: *26 March 2019*
Published: *16 April 2019*

Citation:
Unger-Angel L, Motiei L and Margulies D (2019) Molecular Logic as a Means to Assess Therapeutic Antidotes. Front. Chem. 7:243. doi: 10.3389/fchem.2019.00243

INTRODUCTION

Molecular logic gates constitute a wide range of molecular switches that respond to diverse input signals according to the rules of Boolean logic. Since the inception of the first molecular AND logic gate (de Silva et al., 1993), a wide range of "digital" optical switches (de Ruiter and van der Boom, 2011; de Silva and Uchiyama, 2011; Magri and Mallia, 2013; Ling et al., 2015; Akkaya et al., 2017; Katz, 2017; Erbas-Cakmak et al., 2018; Pilarczyk et al., 2018) and related pattern-generating devices (Rout et al., 2012, 2013, 2014; Sarkar et al., 2016; Hatai et al., 2017; Lustgarten et al., 2017; Pode et al., 2017) have been developed and used for various applications, including information processing (de Ruiter and van der Boom, 2011; de Silva and Uchiyama, 2011; Ling et al., 2015; Akkaya et al., 2017; Katz, 2017; Erbas-Cakmak et al., 2018; Pilarczyk et al., 2018), user identification (Rout et al., 2013; Lustgarten et al., 2017; Andréasson and Pischel, 2018), cryptography (Sarkar et al., 2016; Lustgarten et al., 2017), and sensing (Ling et al., 2015; Wu et al., 2017; Erbas-Cakmak et al., 2018; Magri, 2018). These input-dependent systems were initially considered as potential alternatives to conventional transistors and circuits (de Silva et al., 1993). However, as the area of molecular computing progressed, and as the challenges associated with building molecule-based circuits revealed, this field has undergone a paradigm shift. It is now believed that although

molecular logic gates may not be able to compete with the speed and power of silicon, a key advantage of using such systems lies in their molecular scale, which enables them to target and sense small biomolecules (e.g., proteins) and to operate in living cells and tissues, where silicon-based devices cannot access (de Silva, 2013). Examples of such systems include molecular logic gate-based photodynamic therapy agents designed to be less harmful to neighboring healthy tissue (Erbas-Cakmak and Akkaya, 2013; Erbas-Cakmak et al., 2013, 2015; Turan et al., 2018), as well as "digitally activated" drug models (Amir et al., 2005; Wang et al., 2010; You et al., 2015; Pode et al., 2017) that release an active pharmaceutical in response to combinations of biomarkers. We have recently shown that "digital" control over prodrug activation can also be achieved by controlling communication between proteins, rather than modifying the prodrug itself (Peri-Naor et al., 2015a,b). The "smart" therapeutic models mentioned before (Amir et al., 2005; Wang et al., 2010; de Silva, 2013; Erbas-Cakmak and Akkaya, 2013; Erbas-Cakmak et al., 2013, 2015; Peri-Naor et al., 2015a,b; You et al., 2015; Pode et al., 2017; Turan et al., 2018) demonstrate how concepts developed in the area of molecular logic may ultimately lead to the generation of highly selective anti-cancer drugs. The latter may not only minimize the severe side effects of current chemotherapies—these drugs may also prevent the increasing incidence of patients' death when inappropriate doses are mistakenly used.

An alternative approach to preventing the lethal effects of improper chemotherapy treatment has recently emerged. Rather than developing more selective drugs, this approach relies on "chemotherapy antidotes" that compete with the binding of chemotherapy agents to their protein targets and consequently, arrest their fatal effects. Vistogard (uridine triacetate), for example, is an antidote that has recently been approved for treating life-threatening toxicity patients subjected to an overdose of the chemotherapy medication capecitabine (5-fluorouracil or 5-FU) (Cada et al., 2016). Reversing the effect of therapeutic agents can also be achieved by using synthetic agents that interact with the synthetic agonist/antagonist themselves, rather than with their biological target. Such systems could allosterically change the structure of an inhibitor (Taylor et al., 2009; Zhou et al., 2017; Mukherjee et al., 2018) or encapsulate it via supramolecular host-guest interactions (Bom et al., 2002). We have recently developed an allosteric inhibitor that reversibly controls the activity of glutathione s-transferase (GST), and we have used Boolean logic to analyze the inhibitor's function (Peri-Naor et al., 2015a). In parallel, we developed "turn-on" fluorescent molecular probes (i.e., YES gates), termed thiazole-orange-based protein identifier (TOPIs), which detect GST by generating a light output signal. Herein, we show that digital analysis of the response of one of these probes (TOPI-4) to GST and an additional chemical input (β-CD) converts this probe from a simple fluorescent YES gate into an INHIBIT gate. Previous studies have demonstrated the ability to obtain molecular INHIBIT gates that respond to supramolecular hosts as inputs (de Silva et al., 1999; Pischel et al., 2010). In this study, we show that such digital optical responses can be used to monitor GST binding interactions and, as a result, indicate whether β-CD could prevent the molecular logic gate from binding and inhibiting GST. Bearing in mind the wide interest in creating chemotherapy antidotes (Cada et al., 2016), we demonstrate, at the proof-of-principle level, how the toxic effect of this inhibitor on cancer cells can be regulated using external input signals.

MATERIALS AND METHODS

All reagents and solvents were obtained from commercial suppliers and used without further purification. Recombinant human GST P1-1 was obtained from the Israel Structural Proteomics Center (Weizmann Institute of Science, Rehovot, Israel). 1-Adamantanecarboxylic acid and β- cyclodextrin were purchased from Sigma-Aldrich. Enzymatic assays were carried out using a BioTek synergy H4 hybrid multiwell plate reader in clear flat-bottom polystyrene 384-well microplates (Corning). Fluorescence measurements were carried out using a BioTek synergy H4 hybrid multiwell plate reader in clear and black flat-bottom polystyrene NBS 384-well microplates (Corning).

GST Activity Measurements

The GST activity was measured spectrophotometrically in aqueous phosphate buffer (5 mM, pH 6.5) using chloro-2,4-dinitrobenzene (CDNB) and Glutathione (GSH) as substrates. The concentrations of GST-P1-1, GSH, and CDNB were 20 nM, 350 μM, and 700 μM, respectively. In a typical experiment, TOPI-4 and various concentrations of β-CD were incubated in microplate wells and then GST-P1-1, GSH, and CDNB were subsequently added. The formation of S-(2,4-dinitrophenyl)-glutathione was monitored using a microplate reader at $\lambda = 340$ nm.

Controlling GST Activity With β-CD and Ad-COOH

TOPI-4 (500 nM) was incubated with various concentrations of β-CD and Ad-COOH for 10 min and then GST-P1 (20 nM) was added. Finally, GSH (350 μM) and CDNB (720 μM) were added and the initial kinetic velocities (V_0) were measured. Data are expressed as mean values ± std. deviation of triplicate measurements.

Controlling the Fluorescence Response With β-CD and Ad-COOH

TOPI-4 (100 nM) was incubated with various concentrations of β-CD and Ad-COOH for 10 min and then GST-P1 (90 nM) was added. The fluorescence measurements were recorded after 30 min of incubation in aqueous phosphate buffer (5 mM, pH = 6.5) using a microplate reader and an excitation wavelength of 500 nm. Data are expressed as mean values ± std. deviation of triplicate measurements.

MTT Cytotoxicity Assays

MDA-MB-231 cells were cultured in RPMI (Roswell Park Memorial Institute) media supplemented with 10% FBS (Fetal Bovine Serum), L-glutamine, and antibiotics. Cells (9×10^3 cells/well) were seeded in 96-well plates. The next day, the cells

were incubated with different concentrations of TOPI-4 (100 nM-40 μM) for 24 h, after which, MTT reagent (5 mg/mL) was added and the cells were incubated at 37°C for another 5 h. Then, the medium was slowly removed without breaking the formazan crystals. Next, 100 μL of SDS-DMF solution (80 g of SDS in 400 mL of 1:1 DMF:H_2O) was added to stop the reduction reaction. Finally, the absorbance values at 570 nm were recorded, the data were analyzed using Graphpad Prism 7.0 and fitted to a sigmoidal dose response plot. The ED_{50} value of TOPI-4 was estimated to be 10.3 ± 0.1 μM and this concentration was used in further experiments to test the ability of β-CD to reverse the cell toxicity effect of TOPI-4.

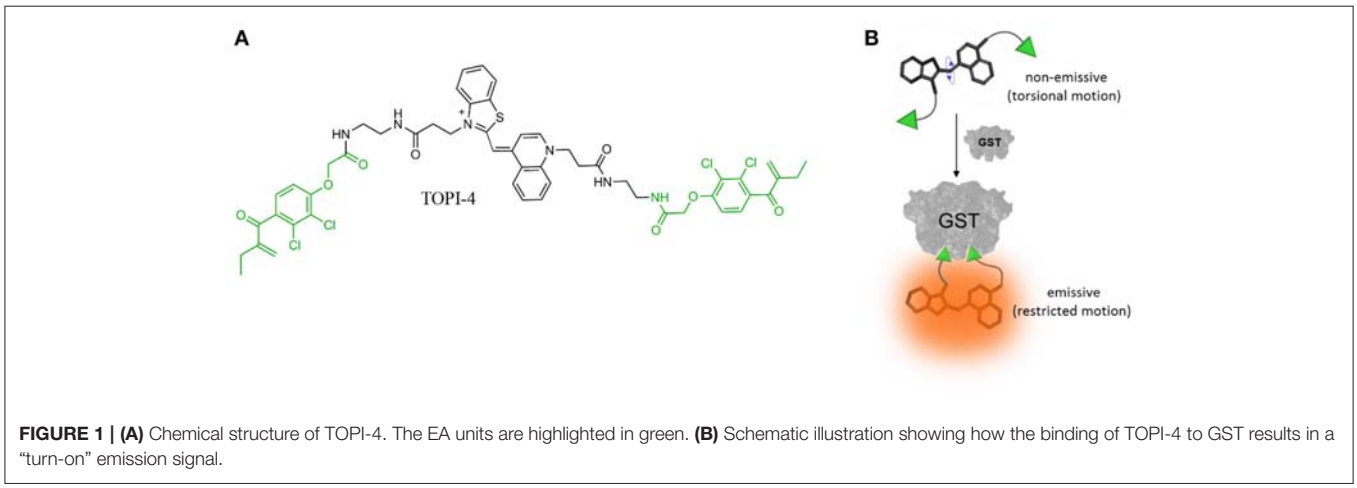

FIGURE 1 | (A) Chemical structure of TOPI-4. The EA units are highlighted in green. **(B)** Schematic illustration showing how the binding of TOPI-4 to GST results in a "turn-on" emission signal.

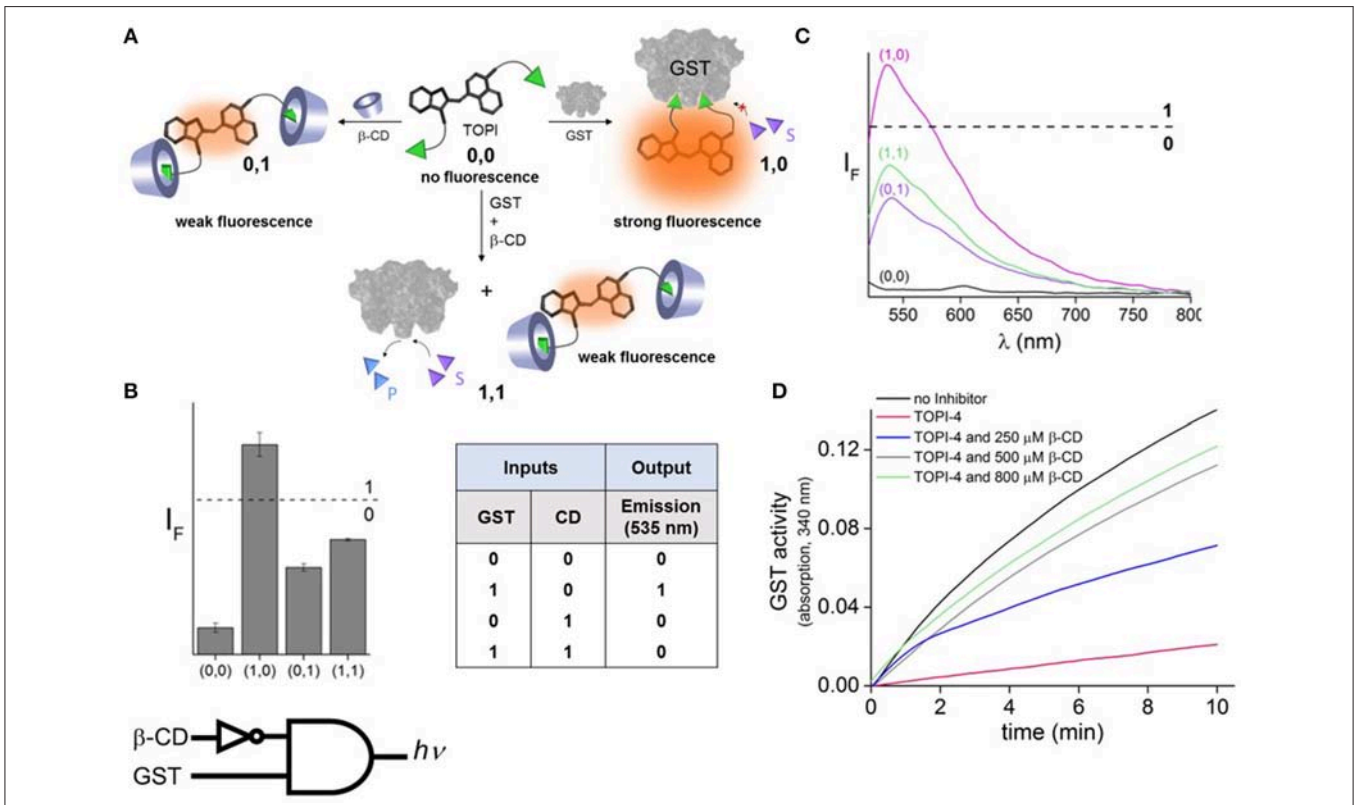

FIGURE 2 | (A) Schematic illustration showing how the binding of TOPI-4 to GST and/or β-CD inputs affects the catalytic activity of GST and the emission of the probe, which results in an optical INHIBIT gate function. S and P correspond to the substrate and product, respectively. **(B)** The corresponding bar plot and truth table. The results are expressed as the mean values ± std. deviation of the triplicate measurements. **(C)** The fluorescence response of TOPI-4 (100 nM) to different combinations of the GST (90 nM) and/or β-CD (1 mM) inputs. **(D)** Enzymatic activity of GST (20 nM) in the absence and presence of TOPI-4 (500 nM) and with increasing concentrations of β-CD. $\lambda_{ex}/\lambda_{em}$ = 500/535 nm.

RESULTS AND DISCUSSIONS

To demonstrate the feasibility of creating molecular logic gate-based chemotherapy antidotes, we exploited the inhibitory effect of bivalent, "turn-on" fluorescent molecular probes, termed TOPIs, recently developed by our group. In an earlier study, we showed that the binding of the two ethacrynic amide (EA) units of TOPI-4 (**Figure 1A**) to the two active sites of GST restricts the torsional motion of the probe, which leads to a "turn-on" emission signal (**Figure 1B**; Unger-Angel et al., 2015). This enhanced emission was selectively observed in biofluids and cancer cells with elevated levels of GSTs, indicating the potential of using such probes in medical diagnosis (Unger-Angel et al., 2015). GSTs are well-known targets for cancer therapy, and ethacrynic acid-based inhibitors have been considered as anti-cancer drug candidates (Allocati et al., 2018). This prompted us to investigate whether the fluorescent TOPI-4 probe could also act as a switchable GST inhibitor that, in addition to sensing GST and cancer cells (Unger-Angel et al., 2015), could be used to regulate GST activity and consequently, cancer cell death. In particular, we expected that analyzing the optical response of TOPI-4 to GST and an additional supramolecular host that interacts with TOPI-4 would indicate the host's ability to disrupt the GST-TOPI-4 binding interactions and the consequent inhibition of GST activity (**Figure 2A**). To prevent the inhibitory effect of TOPI-4 by a supramolecular "antidote," we selected

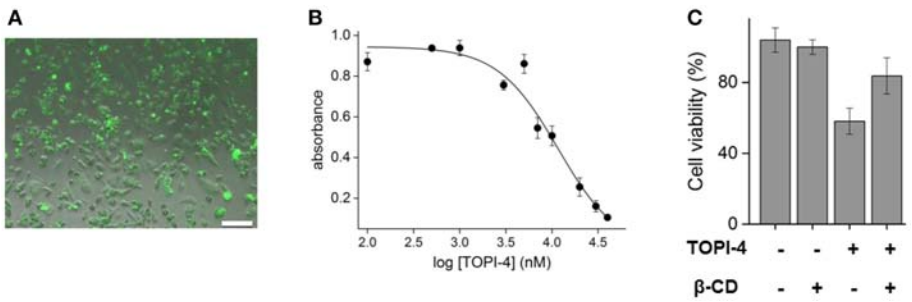

FIGURE 3 | (A) Fluorescence image of MDA-MB-231, overexpressing GST, incubated with TOPI-4 (10 μM). The scale bar is 100 μm. **(B)** Results of an MTT assay that measures the viability of MDA-MB-231 cells under increasing concentrations of TOPI-4. The absorption at 570 nm reflects the number of viable cells. **(C)** Cell viability scores of MDA-MB-231 cells treated with TOPI-4 (10 μM) and/or β-CD (750 μM).

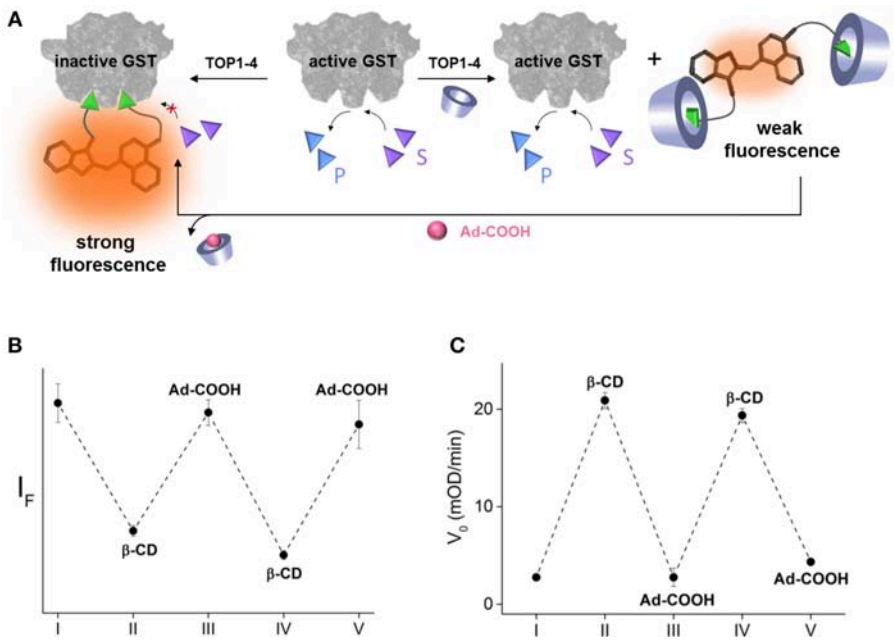

FIGURE 4 | (A) Schematic representation of the way GST activity can be controlled by using Ad-COOH as an additional input that competes with the binding of β-CD to the TOPI-4 inhibitor. **(B)** Emission intensity measured by combining TOPI-4 with GST-P1-1 and different combinations of β-CD and Ad-COOH: (I) no input, (II) β-CD (1 mM), (III) β-CD (1 mM) and Ad-COOH (1.5 mM), (IV) β-CD (3 mM), and Ad-COOH (1.5 mM), and (V) β-CD (3 mM) and Ad-COOH (5 mM). **(C)** Initial velocity (V_0) measured by combining TOPI-4 with GST-P1-1 and different combinations of β-CD and Ad-COOH: (I) no input, (II) β-CD (800 μM), (III) β-CD (800 μM), and Ad-COOH (1 mM), (IV) β-CD (2.5 mM) and Ad-COOH (1 mM), and (V) β-CD (2.5 mM) and Ad-COOH (3.3 mM). $\lambda_{ex}/\lambda_{em}$ = 500/535 nm.

beta-cyclodextrin (β-CD) as the external input. β-CD was chosen as an input for two main reasons. First, this supramolecular host is known to form complexes with a variety of hydrophobic guests, about the size of the EA groups (Crini, 2014). Therefore, we expected that β-CD would form a complex with TOPIs, disrupt their binding to GST, and possibly limit their ability to penetrate cells. Second, β-CD is a non-toxic agent that has been tested for various medical applications (Bom et al., 2002; Del Valle, 2004; Loftsson et al., 2005). Hence, by using β-CD as an "antidote," we aimed to demonstrate the relevance of this study to real-life applications. **Figure 2A** shows the way this additional β-CD input should convert TOPI-4 from a simple fluorescence switch (i.e., a YES gate), which previously responded to GST only (Unger-Angel et al., 2015), into a molecular INHIBIT gate whose fluorescence output depends on the combinations of GST and β-CD as inputs. Importantly, because the GST-TOPI-4 interaction should always be accompanied by enzyme inhibition, we expected that obtaining an optical INHIBIT function would indicate the ability of β-CD to serve as an "antidote" that prevents GST inhibition by TOPI-4 (**Figure 2A**, state 1, 1 vs. 1, 0). For simplicity, **Figure 2A** illustrates the formation of a 1:2 TOPI-4: β-CD complex. Note, however, that other modes of interaction that can prevent inhibition (e.g., binding of β-CD to the TO core) may also occur. The rationale behind the different optical states (**Figure 2A**) and the corresponding truth table (**Figure 2B**) is as follows: In the absence of the GST and β-CD inputs (state: 0, 0), TOPI-4 is not fluorescent (output: 0), owing to an intramolecular motion between the benzothiazole and the quinoline rings. The binding of TOPI-4 to GST (state: 1, 0), however, inhibits the enzyme and concomitantly restricts the intramolecular motion, which leads to a strong fluorescence response (output: 1). The interaction of TOPI-4 with β-CD alone (state: 0, 1) less significantly affects the intramolecular twisting of TOPI-4, which results in a weaker fluorescence signal (output: 0). Finally, when both GST and β-CD inputs are present (state: 1, 1), β-CD prevents the EA groups of TOPI-4 from binding to the two active sites of the GST dimer. Consequently, the probe remains in a low fluorescence state (outputs: 0) and GST remains active. The anticipated optical responses were measured experimentally (**Figure 2C**). As expected, the maximal fluorescence intensity obtained upon adding GST alone was not observed when other combinations of inputs were present in the solution. Importantly, the INHIBIT gate responses revealed similar fluorescence outputs for states (0, 1) and (1, 1), which indicates the possibility of using β-CD as an "antidote" that prevents the formation of the GST-TOPI-4 complex. Note that although this digital analysis of TOPI-4's optical responses provides an efficient analytical tool to distinguish among bimolecular interactions, the relatively small differences between the fluorescence intensity values generated for state (1, 1) (55%), state (1, 0) (100%), and (0, 1) (41%) would complicate using this INHIBIT gate to construct advanced molecular computation devices. For example, it would complicate integrating this gate with another gate that responds to light as an input. This research direction, however, is beyond the scope of this study.

The effect of β-CD on GST inhibition was confirmed by performing an enzymatic assay that follows the conjugation of two GST-specific substrates: chloro-2,4-dinitrobenzene (CDNB) and glutathione (GSH) (**Figure 2D**; Peri-Naor et al., 2015a). With this assay, the formation of the product (GSH-CDNB conjugate) was followed by monitoring the absorbance at 340 nm in the presence and absence of TOPI-4, as well as in the presence of TOPI-4 and increasing concentrations of β-CD. The results show that whereas 500 nM of TOPI-4 strongly inhibited the enzyme, in the presence of β-CD (800 μM) GST remained active, confirming that the supramolecular interactions between the β-CD host and the TOPI-4 guest disrupt the function of the TOPI-4 inhibitor.

To demonstrate the relevance of these results to therapeutic applications, breast cancer cells (MDA-MB-231) overexpressing GST were treated with increasing doses of TOPI-4, imaged using a fluorescence microscope, and their viability was measured by using a MTT assay following ∼24 h of incubations. The results show that TOPI-4 exhibits good cell permeability (**Figure 3A**) and that it inhibits cancer cell growth (**Figure 3B**) with an ED_{50} value of 10 μM. In the next step, we investigated whether, in addition to regenerating GST activity (**Figure 2D**), β-CD can serve as an "antidote" that reduces the TOPI-4-induced cell toxicity. **Figure 3C** shows the viability scores obtained upon subjecting breast cancer cells to 10 μM TOPI-4 with and without β-CD (750 μM). As a control, the number of viable cells was also measured in the presence of only β-CD. The results show that whereas TOPI-4 eradicated nearly 50% of the viable cells, in the presence of β-CD the cell viability increased to ∼85%, indicating the potential of using supramolecular inputs of this class as "antidotes". Notably, the β-CD "antidote" did not fully reverse the effect of the inhibitor on cells. Although this incomplete recovery of cell viability is consistent with the incomplete reactivation of GST in the enzymatic assay (**Figure 2D**), it could also result from non-specific interactions between the GST-TOPI-4 complex and other proteins, which leads to partial dissociation of the inhibitor-antidote complex in a cellular environment. Alternatively, it may indicate that, in addition to GST inhibition, other factors contribute to the TOPI-4-induced cytotoxicity.

In addition to demonstrating a model of a drug-antidote system, these results demonstrate a potential means to establish precise, temporal control over enzyme function. Inspired by the way that enzyme activities were reversibly controlled using DNA-based devices (Saghatelian et al., 2002; Harris et al., 2011; Peri-Naor et al., 2015a), we investigated the possibility of making our system reversible by introducing an adamantane (Ad) derivative as another chemical input. We expected that a water-soluble 1-adamantanecarboxylic acid (Ad-COOH) would compete with the binding of β-CD to the EA binders of TOPI-4, which would release the caged inhibitor and enable it to inhibit GST (**Figure 4A**). Ad-COOH was chosen for this goal, owing to the ability of Ad-derivatives to bind β-CD strongly and selectively (Wenz et al., 2006). In addition, Ad derivatives, similar to β-CDs, are generally non-toxic and have been tested as therapeutics (Štimac et al., 2017). The ability to obtain precise, supramolecular control over the binding of TOPI-4 to GST was demonstrated by adding GST to TOPI-4 incubated with increasing concentrations of β-CD and Ad-COOH and measuring the fluorescence

responses (**Figure 4B**). The results show that the successive addition of an excess of β-CD and Ad-COOH led to a sequential decrease and increase in the fluorescence of TOPI-4, respectively, which is expected from the changes in the interaction between the fluorescent probe and the GST enzyme (**Figure 4A**). Next, we measured the initial velocity (V_0) of the GST-catalyzed reaction measure after adding GST to a solution containing the CDNB and GSH substrates and increasing concentrations of β-CD and Ad-COOH (**Figure 4C**). Strikingly, whenever one of these inputs was introduced in excess, the effect of the other input was reversed, confirming the ability to control GST activity by using a supramolecular host-guest switching mechanism (**Figure 4A**). We believe that regulating intracellular enzymatic activities with similar mechanisms could also provide a means to establish precise, temporal control over cell growth. Research in this direction is underway in our laboratory.

CONCLUSIONS

In conclusion, we have shown how the optical responses of a molecular logic gate revealed the possibility of using it to regulate enzyme function and consequently, cytotoxicity. Although much progress needs to be made in terms the inhibitor's affinity and selectivity in order to apply this system as therapeutics, this model system demonstrates a unique, supramolecular approach to achieving chemotherapy antidotes and switchable enzyme functions. Most importantly, it shows how concepts developed in the area of molecular logic gates, such as the use of supramolecular hosts as inputs that control the fluorescence responses of molecular logic gates (de Silva et al., 1999; Pischel et al., 2010), could be used to construct assays that track biomolecular interactions. Our results show the potential of using such assays for the generation of "smart" therapeutics, in which the function of enzymes and/or drugs can be controlled with external, non-toxic input signals. We hope that this study will inspire the development of other molecular computation devices that can operate in a complex biological environment, such as within living cells, and consequently, can perform tasks that are beyond the ability of conventional electronic computers.

AUTHOR CONTRIBUTIONS

LU-A, LM, and DM designed the project. LU-A synthesized the probe, performed the experiments, and analyzed the data. LM and DM wrote the manuscript.

ACKNOWLEDGMENTS

This work was supported by the European Research Council Starting Grant 338265.

REFERENCES

Akkaya, E. U., Katz, E., and Pischel, U. (2017). Molecular logic: from single logic gates to sophisticated logic circuits, from fundamental science to practical applications. *ChemPhysChem* 18, 1665–1666. doi: 10.1002/cphc.201700602

Allocati, N., Masulli, M., Di Ilio, C., and Federici, L. (2018). Glutathione transferases: substrates, inhibitors and pro-drugs in cancer and neurodegenerative diseases. *Oncogenesis* 7:8. doi: 10.1038/s41389-017-0025-3

Amir, R. J., Popkov, M., Lerner, R. A., Barbas, C. F., and Shabat, D. (2005). Prodrug activation gated by a molecular "OR" logic trigger. *Angew. Chem Int. Ed.* 44, 4378–4381. doi: 10.1002/anie.200500842

Andréasson, J., and Pischel, U. (2018). Molecules for security measures: from keypad locks to advanced communication protocols. *Chem. Soc. Rev.* 47, 2266–2279. doi: 10.1039/C7CS00287D

Bom, A., Bradley, M., Cameron, K., Clark, J. K., van Egmond, J., Feilden, H., et al. (2002). A novel concept of reversing neuromuscular block: chemical encapsulation of rocuronium bromide by a cyclodextrin-based synthetic host. *Angew. Chem Int. Ed.* 41, 265–270. doi: 10.1002/1521-3773(20020118)41:2<265::AID-ANIE265>3.0.CO;2-Q

Cada, D. J., Mbogu, U., Bindler, R. J., and Baker, D. E. (2016). Uridine triacetate. *Hosp. Pharm.* 51, 484–488. doi: 10.1310/hpj5106-484

Crini, G. (2014). Review: a history of cyclodextrins. *Chem. Rev.* 114, 10940–10975. doi: 10.1021/cr500081p

de Ruiter, G., and van der Boom, M. E. (2011). Surface-confined assemblies and polymers for molecular logic. *Acc. Chem. Res.* 44, 563–573. doi: 10.1021/ar200002v

de Silva, A. P. (2013). "Improved therapy," in *Molecular logic-Based Computation* (Cambridge: RSC), 364.

de Silva, A. P., Dixon, I. M., Gunaratne, H. Q. N., Gunnlaugsson, T., Maxwell, P. R. S., and Rice, T. E. (1999). Integration of logic functions and sequential operation of gates at the molecular-scale. *J. Am. Chem. Soc.* 121, 1393–1394. doi: 10.1021/ja982909b

de Silva, A. P., Gunaratne, H. Q. N., and McCoy, C. P (1993). Molecular photoionic AND gate based on fluorescent signalling. *Nature* 364, 42–44. doi: 10.1038/364042a0

de Silva, A. P., and Uchiyama, S. (2011). "Molecular logic gates and luminescent sensors based on photoinduced electron transfer," in *Luminescence Applied in Sensor Science,* eds L. Prodi, M. Montalti, and N. Zaccheroni (Berlin: Springer Berlin Heidelberg), 1–28.

Del Valle, E. M. M. (2004). Cyclodextrins and their uses: a review. *Process Biochem.* 39, 1033–1046. doi: 10.1016/S0032-9592(03)00258-9

Erbas-Cakmak, S., and Akkaya, E. U. (2013). Cascading of molecular logic gates for advanced functions: a self-reporting, activatable photosensitizer. *Angew. Chem Int. Ed.* 52, 11364–11368. doi: 10.1002/anie.201306177

Erbas-Cakmak, S., Bozdemir, O. A., Cakmak, Y., and Akkaya, E. U. (2013). Proof of principle for a molecular 1 : 2 demultiplexer to function as an autonomously switching theranostic device. *Chem. Sci.* 4, 858–862. doi: 10.1039/C2SC21499G

Erbas-Cakmak, S., Cakmak, F. P., Topel, S. D., Uyar, T. B., and Akkaya, E. U. (2015). Selective photosensitization through an AND logic response: optimization of the pH and glutathione response of activatable photosensitizers. *Chem. Commun.* 51, 12258–12261. doi: 10.1039/C5CC01261A

Erbas-Cakmak, S., Kolemen, S., Sedgwick, A. C., Gunnlaugsson, T., James, T. D., Yoon, J., et al. (2018). Molecular logic gates: the past, present and future. *Chem. Soc. Rev.* 47, 2228–2248. doi: 10.1039/C7CS00491E

Harris, D. C., Saks, B. R., and Jayawickramarajah, J. (2011). Protein-binding molecular switches via host–guest stabilized DNA Hairpins. *J. Am. Chem. Soc.* 133, 7676–7679. doi: 10.1021/ja2017366

Hatai, J., Motiei, L., and Margulies, D. (2017). Analyzing amyloid beta aggregates with a combinatorial fluorescent molecular sensor. *J. Am. Chem. Soc.* 139, 2136–2139. doi: 10.1021/jacs.6b10809

Katz, E. (2017). Enzyme-based logic gates and networks with output signals analyzed by various methods. *ChemPhysChem* 18, 1688–1713. doi: 10.1002/cphc.201601402

Ling, J., Daly, B., Silverson, V. A., and de Silva, A. P. (2015). Taking baby steps in molecular logic-based computation. *Chem. Commun.* 51, 8403–8409. doi: 10.1039/C4CC10000J

Loftsson, T., Jarho, P., Másson, M., and Järvinen, T. (2005). Cyclodextrins in drug delivery. *Expert Opin. Drug Deliv.* 2, 335–351. doi: 10.1517/17425247.2.1.335

Lustgarten, O., Motiei, L., and Margulies, D. (2017). User authorization at the molecular scale. *ChemPhysChem* 18, 1678–1687. doi: 10.1002/cphc.201700506

Magri, D. C. (2018). Recent progress on the evolution of Pourbaix sensors: molecular logic gates for protons and oxidants. *Chemosensors* 6:48. doi: 10.3390/chemosensors6040048

Magri, D. C., and Mallia, C. J. (2013). "CHAPTER 3 metal ion sensing for biomedical uses," in *Supramolecular Systems in Biomedical Fields*, ed H. J. Schneider (The Royal Society of Chemistry), 38–67.

Mukherjee, P., Leman, L. J., Griffin, J. H., and Ghadiri, M. R. (2018). Design of a DNA-programmed plasminogen activator. *J. Am. Chem. Soc.* 140, 15516–15524. doi: 10.1021/jacs.8b10166

Peri-Naor, R., Ilani, T., Motiei, L., and Margulies, D. (2015a). Protein–protein communication and enzyme activation mediated by a synthetic chemical transducer. *J. Am. Chem. Soc.* 137, 9507–9510. doi: 10.1021/jacs.5b01123

Peri-Naor, R., Motiei, L., and Margulies, D. (2015b). Artificial signal transduction therapy: a futuristic approach to disease treatment. *Future Med. Chem.* 7, 2091–2093. doi: 10.4155/fmc.15.147

Pilarczyk, K., Wlazlak, E., Przyczyna, D., Blachecki, A., Podborska, A., Anathasiou, V., et al. (2018). Molecules, semiconductors, light and information: towards future sensing and computing paradigms. *Coord. Chem. Rev.* 365, 23–40. doi: 10.1016/j.ccr.2018.03.018

Pischel, U., Uzunova, V. D., Remón, P., and Nau, W. M. (2010). Supramolecular logic with macrocyclic input and competitive reset. *Chem. Commun.* 46, 2635–2637. doi: 10.1039/b927595a

Pode, Z., Peri-Naor, R., Georgeson, J. M., Ilani, T., Kiss, V., Unger, T., et al. (2017). Protein recognition by a pattern-generating fluorescent molecular probe. *Nat. Nanotechnol.* 12, 1161–1168. doi: 10.1038/nnano.2017.175

Rout, B., Milko, P., Iron, M. A., Motiei, L., and Margulies, D. (2013). Authorizing multiple chemical passwords by a combinatorial molecular keypad lock. *J. Am. Chem. Soc.* 135, 15330–15333. doi: 10.1021/ja4081748

Rout, B., Motiei, L., and Margulies, D. (2014). Combinatorial fluorescent molecular sensors: the road to differential sensing at the molecular level. *Synlett* 25, 1050–1054. doi: 10.1055/s-0033-1340639

Rout, B., Unger, L., Armony, G., Iron, M. A., and Margulies, D. (2012). Medication detection by a combinatorial fluorescent molecular sensor. *Angew. Chem. Int. Ed.* 21, 12477–12481. doi: 10.1002/anie.201206374

Saghatelian, A., Guckian, K. M., Thayer, D. A., and Ghadiri, M. R. (2002). DNA detection and signal amplification via an engineered allosteric enzyme. *J. Am. Chem. Soc.* 125, 344–345. doi: 10.1021/ja027885u

Sarkar, T., Selvakumar, K., Motiei, L., and Margulies, D. (2016). Message in a moleule. *Nat. Commun.* 7, 11374–11382. doi: 10.1038/ncomms11374

Štimac, A., Šekutor, M., Mlinarić-Majerski, K., Frkanec, L., and Frkanec, R. (2017). Adamantane in drug delivery systems and surface recognition. *Molecules* 22:E297. doi: 10.3390/molecules22020297

Taylor, S. K., Pei, R., Moon, B. C., Damera, S., Shen, A., and Stojanovic, M. N. (2009). Triggered release of an active peptide conjugate from a DNA device by an orally administrable small molecule. *Angew. Chem Int. Ed.* 48, 4394–4397. doi: 10.1002/anie.200900499

Turan, I. S., Gunaydin, G., Ayan, S., and Akkaya, E. U. (2018). Molecular demultiplexer as a terminator automaton. *Nat. Commun.* 9, 805. doi: 10.1038/s41467-018-03259-z

Unger-Angel, L., Rout, B., Ilani, T., Eisenstein, M., Motiei, L., and Margulies, D. (2015). Protein recognition by bivalent, 'turn-on' fluorescent molecular probes. *Chem. Sci.* 6, 5419–5425. doi: 10.1039/C5SC01038A

Wang, J., Katz, E. J. A., and Chemistry, B. (2010). Digital biosensors with built-in logic for biomedical applications—biosensors based on a biocomputing concept. *Anal. Bioanal. Chem.* 398, 1591–1603. doi: 10.1007/s00216-010-3746-0

Wenz, G., Han, B. H., and Müller, A. (2006). Cyclodextrin rotaxanes and polyrotaxanes. *Chem. Rev.* 106, 782–817. doi: 10.1021/cr970027+

Wu, D., Sedgwick, A. C., Gunnlaugsson, T., Akkaya, E. U., Yoon, J., and James, T. D. (2017). Fluorescent chemosensors: the past, present and future.*Chem. Soc. Rev.* 46, 7105–7123. doi: 10.1039/C7CS00240H

You, M., Zhu, G., Chen, T., Donovan, M. J., and Tan, W. (2015). Programmable and multiparameter DNA-based logic platform for cancer recognition and targeted therapy. *J. Am. Chem. Soc.* 137, 667–674. doi: 10.1021/ja509263k

Zhou, X., Su, X., Pathak, P., Vik, R., Vinciguerra, B., Isaacs, L., et al. (2017). Host–guest tethered DNA transducer: ATP fueled release of a protein inhibitor from cucurbit[7]uril. *J. Am. Chem. Soc.* 139, 13916–13921. doi: 10.1021/jacs.7b07977

Conflict of Interest Statement: The authors declare that the research was conducted in the absence of any commercial or financial relationships that could be construed as a potential conflict of interest.

Copyright © 2019 Unger-Angel, Motiei and Margulies. This is an open-access article distributed under the terms of the Creative Commons Attribution License (CC BY). The use, distribution or reproduction in other forums is permitted, provided the original author(s) and the copyright owner(s) are credited and that the original publication in this journal is cited, in accordance with accepted academic practice. No use, distribution or reproduction is permitted which does not comply with these terms.

frontiers in Chemistry

ORIGINAL RESEARCH
published: 01 February 2019
doi: 10.3389/fchem.2019.00032

A Near-Infrared Ratiometric Fluorescent Probe for Highly Selective Recognition and Bioimaging of Cysteine

Xuan Zhang[1,2], Li Zhang[1†], Wei-Wei Ma[1†], Yong Zhou[1], Zhen-Ni Lu[1] and Suying Xu[3]**

[1] *Key Laboratory of Science and Technology of Eco-Textiles, Ministry of Education, College of Chemistry, Chemical Engineering & Biotechnology, Donghua University, Shanghai, China,* [2] *State Key Laboratory of Fine Chemicals, Dalian University of Technology, Dalian, China,* [3] *Department of Biochemistry, Faculty of Science, Beijing University of Chemical Technology, Beijing, China*

OPEN ACCESS

Edited by:
Tony D. James,
University of Bath, United Kingdom

Reviewed by:
Youjun Yang,
East China University of Science and Technology, China
Jiangli Fan,
Dalian University of Technology (DUT), China

****Correspondence:***
Xuan Zhang
xzhang@dhu.edu.cn
Suying Xu
syxu@mail.buct.edu.cn

† These authors have contributed equally to this work

Specialty section:
This article was submitted to Supramolecular Chemistry, a section of the journal Frontiers in Chemistry

Received: *29 November 2018*
Accepted: *14 January 2019*
Published: *01 February 2019*

Citation:
Zhang X, Zhang L, Ma W-W, Zhou Y, Lu Z-N and Xu S (2019) A Near-Infrared Ratiometric Fluorescent Probe for Highly Selective Recognition and Bioimaging of Cysteine. Front. Chem. 7:32. doi: 10.3389/fchem.2019.00032

A benzothiazole-based near-infrared (NIR) ratiometric fluorescent probe (**HBT-Cys**) was developed for discriminating cysteine (Cys) from homocysteine (Hcy) and glutathione (GSH). The probe was designed by masking phenol group in the conjugated benzothiazole derivative with methacrylate group that could be selectively removed by Cys, and therefore an intramolecular charge transfer (ICT) fluorescence was switched on in the NIR region. In the absence of Cys, the probe exhibited a strong blue fluorescence emission at 431 nm, whereas a NIR fluorescence emission at 710 nm was significantly enhanced accompanied by a decrease of emission at 431 nm in the presence of Cys, allowing a ratiometric fluorescence detection of Cys. The fluorescence intensity ratio (I_{710nm}/I_{431nm}) showed a good linear relationship with Cys concentration of 1–40 μM with the detection limit of 0.5 μM. The sensing mechanism was explored based on MS experimental analysis and DFT theoretical calculation. Moreover, the fluorescent probe was successfully used for fluorescence bioimaging of Cys in living cells.

Keywords: NIR ratiometric fluorescent probe, cysteine, benzothiazole derivative, living cells imaging, intramolecular charge transfer

INTRODUCTION

It has been known that small molecular biothiols, such as L-cystein (Cys), homocysteine (Hcy), and glutathione (GSH) played vital roles in the maintenance of redox homeostasis, intracellular signal transduction, and human metabolism (Shahrokhian, 2001; Giles et al., 2003). Cys is a metabolic product of Hcy and a precursor of the antioxidant GSH, and its normal intracellular level remains to be 30–200 μM (Liu et al., 2014). The deficiency of Cys could cause edema, leucocyte loss, liver damage as well as neurotoxicity, whereas the excess levels of Cys might relate to cardiovascular and Alzheimer's diseases (Lipton et al., 2002; Shao et al., 2012; Dorszewska et al., 2016; Qi et al., 2018). Hence, it has attracted intense interest in the development of novel strategy for detection and imaging of the intracellular Cys, which will further contribute to the better understanding the pathology of associated diseases and their early diagnosis and treatment.

Design and synthesis of small molecule-based fluorescent probe received much attention in molecule recognition and fluorescence signaling in living biosystems due to many advantages of fluorescence technique, such as high sensitivity and selectivity, simplicity, *in vivo* bioimaging (De Silva et al., 1997; Chen et al., 2010, 2016; Chan et al., 2012; Yang et al., 2013; Li et al., 2014; Niu et al., 2015). For bioimaging application, the development of fluorescent probes with near-infrared (NIR, 650–900 nm) emission is more promising due to the merits of deeper tissue penetration and minimum interference from the indigenous fluorescence background of biosystem (Escobedo et al., 2010; Nolting et al., 2011; Yuan et al., 2013; Guo et al., 2014). Additionally, the ratiometric fluorescent probes could provide an inherent reliability originating from its effective self-calibration advantage by monitoring two well-resolved emissions (Kikuchi et al., 2004; Demchenko, 2010; Lee et al., 2015). Although a number of fluorescent probes for Cys detection and imaging have been reported, most of them could not discriminate Cys from Hcy/GSH due to their similar molecular structures and reactivity (Chen et al., 2017, 2018; Li et al., 2017; Liu X. et al., 2017; Nawimanage et al., 2017; Wang F. et al., 2017; Wang Q. et al., 2017, 2018a; Wu et al., 2017; Yin et al., 2017; Yue et al., 2017a,b; Zhang et al., 2017, 2018a,b; Hou et al., 2018; Kim et al., 2018; Ren et al., 2018; Song et al., 2018; Tian et al., 2018; Wang et al., 2018b; Wang J. et al., 2018; Wang L. et al., 2018; Sheng et al., 2019). Several ratiometric fluorescent probes for Cys have been developed (Lv et al., 2014; Feng et al., 2017; Liu G. et al., 2017; Wang F. et al., 2017; Wang L. et al., 2018 Wu et al., 2018; Yue et al., 2018; Zhu et al., 2018), but only a few of them showed the fluorescence emission in NIR region (Feng et al., 2017; Zhu et al., 2018). Therefore, the development of NIR ratiometric fluorescent probe for selective detection of Cys is still a challenging task.

Recently, we have found that the π-conjugation extended benzothiazole derivatives exhibited short-wavelength fluorescence emission in non-polar solvent but the NIR emission in polar solvent, where the NIR fluorescence originated from the deprotonation of phenol group switching on an intramolecular charge transfer (ICT) process (Zhang et al., 2016b). In this work, we envisaged that the masking of phenol group in conjugated benzothiazole derivatives with methacrylate moiety, a Cys-selective recognition site, will result in a short-wavelength emission but a NIR fluorescence will appear in the presence of Cys due to the Cys-selectively induced deprotection, and therefore will allow a NIR ratiometric fluorescence detection of Cys. Accordingly, a new conjugated benzothiazole derivative (**HBT-Cys**, **Scheme 1**) was synthesized and developed as a novel NIR ratiometric fluorescent probe for Cys detection. The probe distinguished Cys well from GSH/Hcy in a ratiometric manner in aqueous solution and successfully applied in living cells imaging.

MATERIALS AND METHODS

All the chemicals are analytical grade that was used without purification and purchased from Sinopharm Chemical Reagents Corp. (Shanghai, China). Phosphate buffered saline (PBS, pH = 7.4) was prepared from K_2HPO_4 (0.1 M) and KH_2PO_4 (0.1 M). The stock solution of the probe **3** was prepared in DMF and all of others species solutions were prepared in deionized water. ^{1}H NMR and ^{13}C NMR spectra were recorded on a Bruker AVANCE III 400 MHz spectrometer. Mass spectra were obtained on AB Sciex MALDI-TOF/TOF^{TM} MS. Fluorescence spectra were measured on Edinburgh FS5 spectrofluorometer with Ex/Em slit widths of 5 nm. The absolute fluorescence quantum yields were obtained on Edinburgh FS5 spectrofluorometer equipped with an integrating sphere (EI-FS5-SC-30). Absorption spectra were obtained on a SHIMADZU UV-1800 spectrophotometer. Confocal fluorescence imaging experiments in living Hela cells were carried out with a Carl Zeiss LSM 700 microscope. Theoretical calculations were performed based on the Gaussian 09 package (Frisch et al., 2010). The ground state and the first singlet excited state geometries of the compounds were optimized in the gas phase using density functional theory (DFT) and time-dependent density functional theory (TDDFT) at the B3LYP/6-31+G(d) level, respectively. The fluorescence emission properties were calculated using TDDFT based on the optimized first singlet excited state geometries, respectively.

HeLa cells were cultured in Dulbecco's Modified Eagle Medium (DMEM) supplemented with 10% fetal bovine serum at 37°C in a 95% humidity atmosphere under 5% CO_2 environment. Then the cells were seeded in confocal microscope culture dishes with a density of 2×10^5 cells per well. The cells were then incubated with probe **HBT-Cys** (20 μ M) for 120 min at 37°C, washed with PBS buffer (10 mM) three times to remove free probe. In the control experiments, the cells were pretreated with NEM (1 mM) for 30 min at 37°C, followed by washing with PBS for three times, and incubated with probe **HBT-Cys** (20 μM) for 120 min at 37°C. In another control experiment, the cells were pretreated with NEM (1 mM) for 30 min at 37°C, followed by washing with PBS three times, then incubated with Cys (200 μM) for 30 min, and further incubated with probe **HBT-Cys** (20 μ M)

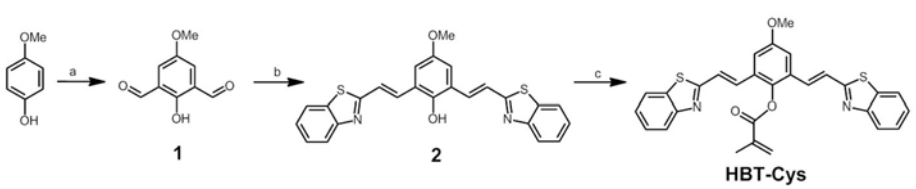

SCHEME 1 | Synthesis of **1**, **2**, and **HBT-Cys**. Reagents and conditions: **(a)** hexamethylenetetramine, TFA, 110○C, 72 h; **(b)** 2-methylbenzothiazole, AcO_2, 145°C, 56 h; pyridine, 115°C, 2 h; water, 100°C, 6 h; and **(c)** methacryloyl chloride, acetone, K_2CO_3, r.t., 8 h.

for 120 min at 37°C, respectively. All the cells were washed with PBS three times to remove free probe and then imaged at blue and red channels, respectively in a Carl Zeiss LSM 700 microscope.

The synthesis procedures are illustrated in **Scheme 1**. The compound **1** was facilely synthesized according to the similar procedure described previously (Zhang and Liu, 2016a). Briefly, under an N_2 atmosphere, 4-methoxylphenol (20 mmol) and hexamethylenetetramine (60 mmol) were dissolved in TFA (15 mL) and refluxed at 110°C for 72 h. The mixture was then cooled down to room temperature and poured into a 3 M HCl solution (120 mL). The crude product was obtained by filtration and further purified by column chromatography (silica gel, CH_2Cl_2) to give **1** as a yellow solid (**Figures S3, S4**). Yield: 19%. ^{1}H NMR (400 MHz, DMSO-d_6), δ (ppm): 11.09 (s, 1H), 10.24 (s, 2H), 7.60 (s, 2H), 3.82 (s, 3H). ^{13}C NMR (100 MHz, DMSO-d_6), δ (ppm): 55.89, 121.34, 124.31, 152.12, 156.45, 191.70.

Under an N_2 atmosphere, compound **1** (4 mmol) and 2-methylbenzothiazole (16 mmol) were refluxed in acetic anhydride (3 mL) at 145°C for 56 h. After cooling to room temperature, the solid was obtained by filtration and thoroughly washed by water. The obtained solid was further dissolved in pyridine (19 mL) and refluxed at 115°C for 2 h, then water (10 mL) was added and stirred at 100°C for another 6 h. After cooling down to room temperature, the crude product was collected by filtration and thoroughly washed by CH_2Cl_2 to give **2** as a yellow solid (**Figures S5, S6**). Yield: 72%. ^{1}H NMR (400 MHz, DMSO-d_6), δ (ppm): 9.55 (s, 1H), 8.12 (d, J = 4 Hz, 2H), 8.02-7.98 (m, 4H), 7.68 (d, J = 16 Hz, 2H), 7.53 (t, J = 8 Hz, 2H), 7.45 (t, J = 8 Hz, 4H), 3.86 (s, 3H); ^{13}C NMR (100 MHz, DMSO-d_6), δ (ppm): 55.60, 113.19, 122.12, 122.19, 122.42, 125.32, 125.90, 126.44, 132.05, 133.93, 147.90, 153.12, 153.40, 166.72. MALDI-TOF-MS: m/z calcd for $C_{25}H_{18}N_2O_2S_2$, 442.08; found 442.8298 $[M + H]^+$ (**Figure S9**).

Compound **2** (0.1 mmol) was dissolved in acetone (200 mL) and methacryloyl chloride (0.13 mmol in 5 mL acetone) was slowly added dropwise under stirring at 0°C in the presence of K_2CO_3 (2.0 mmol). Then the mixture was warmed to room temperature and stirred for another 8 h. The reaction mixture was filtrated and the filtrate was concentrated in vacuum. The residue was dissolved in CH_2Cl_2 and then washed with water and the organic layer was dried with $MgSO_4$. After removing $MgSO_4$ by filtration, the crude product was obtained by evaporation under reduced pressure and then purified by column chromatography (silica gel, CH_2Cl_2/ethyl acetate = 30:1 v/v) to give **HBT-Cys** as yellow solid (**Figures S7, S8**). Yield: 45%. ^{1}H NMR (400 MHz, $CDCl_3$), δ (ppm): 8.03 (d, J = 8 Hz, 2H), 7.86 (d, J = 8 Hz, 2H), 7.52-7.46 (m, 6H), 7.41 (t, J = 8 Hz, 2H), 7.28 (s, 2H), 6.61 (s, 1H), 5.99 (s, 1H), 3.92 (s, 1H), 2.20 (s, 3H). ^{13}C NMR (100 MHz, $CDCl_3$), δ (ppm): 18.67, 55.81, 112.86, 121.59, 123.13, 124.90, 125.86, 126.61, 128.52, 130.24, 130.99, 134.14, 135.07, 141.26, 153.31, 157.64, 165.86, 166.61. MALDI-TOF-MS: m/z calcd for $C_{29}H_{22}N_2O_3S_2$, 510.11; found 511.2485 $[M + H]^+$, 533.2472 $[M + Na]^+$ (**Figure S10**).

RESULTS AND DISCUSSIONS

Design and Synthesis

To design a selective fluorescent probe for Cys, a methacrylate group was chosen as the recognition site which can specifically react with Cys *via* conjugate addition/cyclization reaction (Yang et al., 2011; Ma et al., 2017). The conjugated benzothiazole derivatives displayed the large Stokes' shifted NIR fluorescence emission in deprontonated phenolate anion form due to the strong electron-donating ability of phenolate anion induced

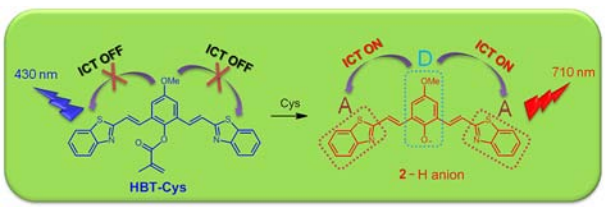

SCHEME 2 | The proposed sensing mechanism of the probe **HBT-Cys** toward Cys.

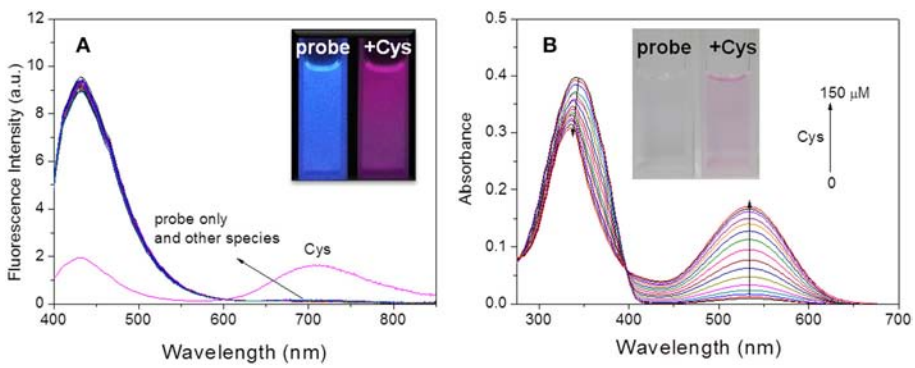

FIGURE 1 | Fluorescence spectra of **HBT-Cys** (10 μM) in the absence and presence of 15 equiv. of various amino acids and biologically relevant species **(A)**. Absorption spectra of **HBT-Cys** (10 μM) upon addition of 0–150 μM Cys **(B)**. Insets are the fluorescence **(A)** and solution **(B)** color change of the probe in the absence and presence of Cys, where the fluorescence in **(A)** was obtained by exposing the solution under UV lamp at 365-nm. The measurements were performed in aqueous PBS buffer solution (pH = 7.4, 50% DMF) and the excitation wavelength was 396 nm for fluorescence measurement.

an occurrence of ICT (Karton-Lifshin et al., 2012; Zhang et al., 2016b), but showed a short-wavelength fluorescence in the neutral phenol form, which allowed a ratiometric detection manner based on two emissions. The novel fluorescent probe **HBT-Cys** was thus readily synthesized by combining methacrylate group into conjugated benzothiazole derivative. As shown in **Scheme 1**, the 2,6-diformyl-4-methoxylphenol (**1**) was firstly synthesized from commercially available 4-methoxylphenol *via* Duff reaction, then the conjugated benzothiazole derivative (**2**) was obtained by a direct condensation reaction between **1** and commercially available 2-methylbenzothiazole, and finally the probe **HBT-Cys** was easily afforded by treating **2** with methacryloyl chloride in acetone. The chemical structures of the probe **HBT-Cys** and intermediate compounds were characterized by ^{1}H NMR, ^{13}C NMR, and MALDI-TOF-MS.

Spectral Properties

The conjugated benzothiazole derivative **2** showed a short-wavelength emission at 500 nm in $CHCl_3$ but a NIR emission at 730 nm in DMF with fluorescence quantum yield of 0.36 and 0.24, respectively (**Figure S1**). The NIR fluorescence emission was observed at 710 nm with a fluorescence quantum yield of 0.085 even in the PBS buffer solution (pH = 7.4, containing 50% DMF). These excellent fluorescence properties allowed compound **2** as a suitable platform to construct the fluorescent probe. As expected, the probe **HBT-Cys** showed a short-wavelength emission at 431 nm in the PBS buffer solution (pH = 7.4, containing 50% DMF), but a NIR fluorescence located at 710 nm appeared with decrease of the short-wavelength emission in the presence of Cys (**Figure 1A**). In contrast, the fluorescence spectra of the probe **HBT-Cys** showed no distinct change upon addition of others species such as common amino acids (GSH, Cys, Hcy, Asp, Asn, Ser, Pro, Ala, Gly, Val, Leu, lle, Thr, Arg, Glu, Gln, Tyr, His, Met, Phe, Trp, Lys, Tau), cations (Na^+, K^+, Ca^{2+}, Mg^{2+}), anions (SO_4^{2-}, NO_3^-, Cl^-), Na_2S, mercaptoacetic acid and glucose. An obvious fluorescence color change from blue to red was observed in the presence of Cys (**Figure 1A**). This indicates that the probe **HBT-Cys** exhibited a high selectivity toward Cys in aqueous solution. Meanwhile, the probe **HBT-Cys** only displayed a strong absorption at 343 nm in the PBS buffer solution (pH = 7.4, containing 50% DMF), and the peak at 343 nm gradually

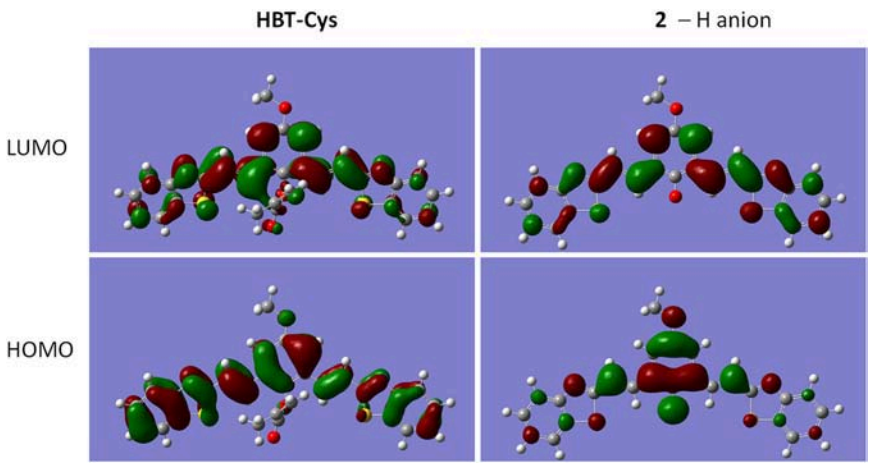

FIGURE 2 | LUMO and HOMO orbitals of **HBT-Cys** and **2**–H anion in the ground state.

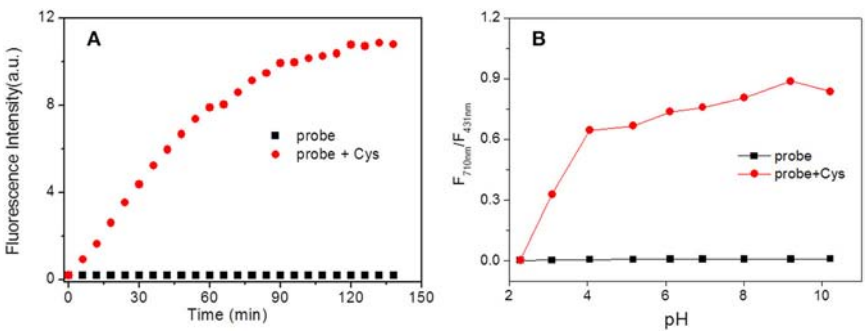

FIGURE 3 | Time **(A)** and pH **(B)** effect on fluorescence intensity of **HBT-Cys** in the absence and presence of Cys. The fluorescence intensity measured at 710 nm in **(A)**. The measurements were performed in aqueous PBS buffer solution (pH = 7.4, 50% DMF) and the excitation wavelength was 396 nm for fluorescence measurement.

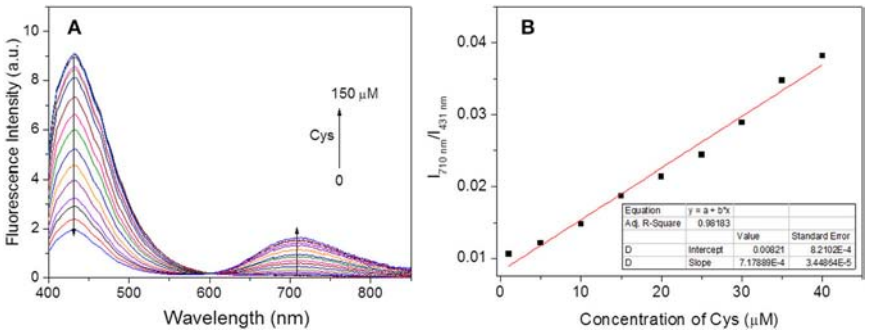

FIGURE 4 | Evolution of fluorescence spectra of **HBT-Cys** (10 μM) with addition of various amount of Cys (0–150 μM) **(A)** and the corresponding linear relationship of fluorescence intensity ratio (I_{710nm} /I_{431nm}) vs. concentration of Cys (0–40 μM) **(B)**. The measurements were performed in aqueous PBS buffer solution (pH = 7.4, 50% DMF) and the excitation wavelength is 396 nm for fluorescence measurement.

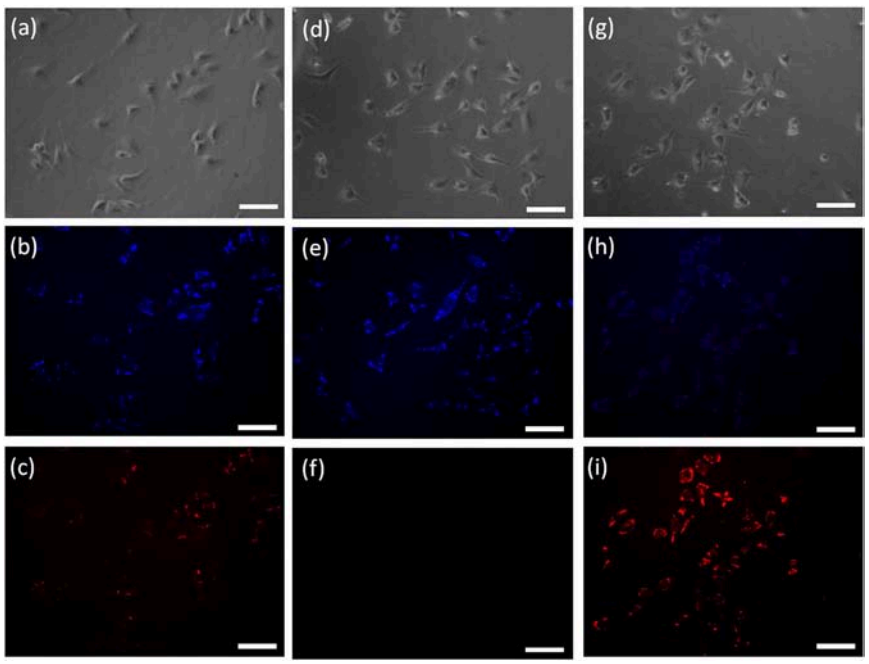

FIGURE 5 | Confocal fluorescence images of living Hela cells incubated with the probe **HBT-Cys** (20 μM) for 120 min at 37°C: cells without treatment **(a–c)**, cells with pre-treatment of NEM (1 mM) **(d–f)**, and cells with pre-treatment of NEM (1 mM) and further addition of 200 μM Cys **(g–i)**. **(a,d,g)** are the bright-field images; **(b,c,e,f,h,i)** are the fluorescence images at blue and red channels, respectively. The scale bar represented 100 μm.

decreased with a significant increase of the absorption at 533 nm upon addition of various amounts of Cys, where an isosbestic point was observed at 396 nm and the solution color turned pink from colorless (**Figure 1B**). No significant absorption spectral change was observed in the presence of others species. These spectral properties suggested that the **HBT-Cys** could serve as a NIR ratiometric fluorescent probe for high selective detection of Cys over Hcy/GSH.

Sensing Mechanism

To confirm that probe **HBT-Cys** has been transformed into **2** in the presence of Cys as shown in **Scheme 2**, ESI-MS mass analysis of a mixture solution of the probe **HBT-Cys** (10 μM) with 10 equiv. Cys was conducted. A prominent peak at m/z = 441 corresponding to the $[\mathbf{2}–H]^-$ anion was observed (**Figure S2**), suggesting the fact that Cys took the methacrylate moiety away from probe **HBT-Cys**. The DFT calculation was further performed to gain better insights into the NIR fluorescence and signaling mechanism. **Figure 2** presented the optimized ground state structures of both the probe **HBT-Cys** and **2**–H anion. Obviously, the π electrons of the probe **HBT-Cys** were well-delocalized on the whole molecular skeleton on both the lowest unoccupied molecular orbital (LUMO) and the highest occupied molecular orbital (HOMO). When the π electrons of **2**–H anion

were still delocalized on the whole molecular skeleton on the LUMO, they mainly localized on the phenolate group on the HOMO, implying a potential ICT process from the phenolate donor (D) to two benzothiazole acceptors (A) as shown in . It has been known that the phenol moiety is a latent electron donor but acts as a strong electron donor when it transformed into phenolate, and could therefore switch on an ICT emission (Karton-Lifshin et al., 2012; Zhang et al., 2016b). Based on the TD-DFT calculation on the excited state, the fluorescence emission wavelengths were predicted to be 739 nm for the **2**–H anion. The well-reproduction of the experimental result implied that the reliability of present theoretical calculation level. Thus, the signaling mechanism could be rationalized as Cys induced removal of methacrylate group and switch on of ICT emission, shown in **Scheme 2**.

Response Time and pH Influence

The time-dependent fluorescence response of the probe **HBT-Cys** with and without Cys was performed, respectively. As shown in **Figure 3A**, the NIR fluorescence intensity at 710 nm was dramatically increased over 60 min and leveled off after about 120 min in the presence of Cys. Without Cys, the NIR fluorescence of the probe **HBT-Cys** displayed no significant changes, suggesting that the probe itself is stable enough under experimental condition. Thus, the spectral measurements of **HBT-Cys** were carried out after 120 min upon addition of Cys in the solution.

The pH influence on the fluorescence of the probe both in the absence and presence of Cys were investigated. Without Cys, the fluorescence intensities ratio (I_{710nm}/I_{431nm}) displayed negligible changes over the range of pH 2.0–10.0 (**Figure 3B**). However, in the presence of Cys, the I_{710nm}/I_{431nm} ratio showed a drastic enhancement after pH $>$ 3 and remained to be almost constant over whole pH region examined. This revealed that the present probe could work in a broad pH region (pH 3.0–10.0) and suitable for imaging under physiological conditions.

Ratiometric Fluorescence Detection and Imaging of Cys

Under the optimal experimental conditions, the ratiometric fluorescence titrations toward Cys were performed. With excitation at 396 nm (an isosbestic point in absorption spectra, **Figure 1B**), it could be seen that the fluorescence emission gradually decreased at 431 nm and increased at 710 nm with increasing Cys amounts up to 150 μM (**Figure 4A**). The I_{710nm}/I_{431nm} ratios followed a good linear relationship ($R^2 = 0.9818$) with Cys concentration ranging from 1–40 μM (**Figure 4B**). The detection limit was estimated to be 0.5 μM according to S/N = 3. Hence, the probe **HBT-Cys** could detect Cys quantitatively by ratiometric fluorescence method with excellent sensitivity.

To evaluate the potential practical applications of probe **HBT-Cys**, the fluorescence imaging of Cys in living HeLa cells were also performed with a Carl Zeiss LSM 700 microscope, where dual blue and red channels were monitored, respectively (**Figure 5**). When HeLa cells were incubated with the probe **HBT-Cys** (20 μM) for 120 min at 37°C, both blue and red fluorescence emissions were observed in two channels (**Figures 5b,c**), where the NIR emission resulted from the intracellular Cys induced removal of methacrylate group in the probe. In the control experiment, HeLa cells were pretreated with N-ethylmaleimide (NEM, a known scavenger for Cys, 1 mM for 30 min), and thereafter incubated with probe **HBT-Cys** (20 μM) for another 120 min. While the blue fluorescence remained, there was no fluorescence in the red channel (**Figures 5e,f**). Then the NEM-pretreated HeLa cells were further sequentially incubated with Cys (200 μM) for 30 min, the probe **HBT-Cys** (20 μM) for 120 min at 37°C. As a result, a bright fluorescence in the red channel was again observed inside cells accompanied by a weak fluorescence in the blue channel (**Figures 5h,i**). These results suggested that the probe **HBT-Cys** can serve as a promising fluorescent probe for Cys imaging in living cells.

CONCLUSIONS

In summary, a benzothiazole-based NIR ratiometric fluorescent probe **HBT-Cys** was developed for selective detection of Cys over Hcy and GSH in aqueous solution. The probe was designed by masking the phenol group in the conjugated benzothiazole derivative through methacrylate group that acts both as a trigger of the ICT fluorescence and recognition site for Cys. Upon addition of Cys, the NIR fluorescence emission at 710 nm was significantly increased with decrease of the fluorescence emission at 431 nm. The fluorescence intensity ratio (I_{710nm}/I_{431nm}) showed a linear relationship with Cys concentration of 1–40 μM with the detection limit of 0.5 μM. Based on mass analysis and DFT calculation, the signaling mechanism of Cys induced removal of methacrylate group and switch-on of the ICT fluorescence was proposed. The fluorescent probe was also successfully used for bioimaging of Cys in living cells, which would provide guidelines for design of novel ratiometric fluoresencent probes in future.

AUTHOR CONTRIBUTIONS

LZ and W-WM were responsible for designing and performing the experiments. YZ and Z-NL were responsible for the characterization of compounds. SX and XZ were responsible for drafting and discussing the manuscript.

FUNDING

This work was financially supported by the State Key Laboratory of Fine Chemicals, Dalian University of Technology (KF 1715), Shanghai Municipal Natural Science Foundation (16ZR1401700), and the Fundamental Research Funds for the Central Universities (PYBZ1827).

SUPPLEMENTARY MATERIAL

The Supplementary Material for this article can be found online at: https://www.frontiersin.org/articles/10.3389/fchem.2019.00032/full#supplementary-material

REFERENCES

Chan, J., Dodani, S. C., and Chang, C. J. (2012). Reaction-based small-molecule fluorescent probes for chemoselective bioimaging. *Nat. Chem.* 4, 973–984. doi: 10.1038/NCHEM.1500

Chen, C., Zhou, L., Liu, W., and Liu, W. (2018). Coumarinocoumarin-based two-photon fluorescent cysteine biosensor for targeting lysosome. *Anal. Chem.* 90, 6138–6143. doi: 10.1021/acs.analchem.8b00434

Chen, H., Tang, Y., and Lin, W. (2016). Recent progress in the fluorescent probes for the specific imaging of small molecular weight thiols in living cells. *Trends Anal. Chem.* 76, 166–181. doi: 10.1016/j.trac.2015.11.014

Chen, X., Zhou, Y., Peng, X., and Yoon, J. (2010). Fluorescent and colorimetric probes for detection of thiols. *Chem. Soc. Rev.* 39, 2120–2135. doi: 10.1039/B925092A

Chen, Z., Sun, Q., Yao, Y., Fan, X., Zhang, W., and Qian, J. (2017). Highly sensitive detection of cysteine over glutathione and homo-cysteine: new insight into the Michael addition of mercapto group to maleimide. *Biosens. Bioelectron.* 91, 553–559. doi: 10.1016/j.bios.2017.01.013

De Silva, A. P., Gunaratne, H. Q. N., Gunnlaugsson, T., Huxley, A. J. M., McCoy, C. P., Rademacher, J. T., et al. (1997). Signaling recognition events with fluorescent sensors and switches. *Chem. Rev.* 97, 1515–1566. doi: 10.1021/cr960386p

Demchenko, A. P. (2010). The concept of λ-ratiometry in fluorescence sensing and imaging. *J. Fluoresc.* 20, 1099–1128. doi: 10.1007/s10895-010-0644-y

Dorszewska, J., Prendecki, M., Oczkowska, A., Dezor, M., and Kozubski, W. (2016). Molecular basis of familial and sporadic Alzheimer's disease. *Curr. Alzheimer Res.* 13, 952–963. doi: 10.2174/1567205013666160314150501

Escobedo, J. O., Rusin, O., Lim, S., and Strongin, R. M. (2010). NIR dyes for bioimaging applications. *Curr. Opin. Chem. Biol.* 14, 64–70. doi: 10.1016/j.cbpa.2009.10.022

Feng, S., Fang, Y., Feng, W., Xia, Q., and Feng, G. (2017). A colorimetric and ratiometric fluorescent probe with enhanced near-infrared fluorescence for selective detection of cysteine and its application in living cells. *Dyes Pigm.* 146, 103–111. doi: 10.1016/j.dyepig.2017.07.002

Frisch, M. J., Trucks, G. W., Schlegel, H. B., Scuseria, G. E., Robb, M. A., Cheeseman, J. R., et al. (2010). *Gaussian 09, Revision C.01*. Wallingford, CT: Gaussian Inc.

Giles, N. M., Watts, A. B., Giles, G. I., Fry, F. H., Littlechild, J. A., and Jacob, C. (2003). Metal and redox modulation of cysteine protein function. *Chem. Biol.* 10, 677–693. doi: 10.1016/S1074-5521(03)00174-1

Guo, Z., Park, S., Yoon, J., and Shin, I. (2014). Recent progress in the development of near-infrared fluorescent probes for bioimaging applications. *Chem. Soc. Rev.* 43, 16–29. doi: 10.1039/c3cs60271k

Hou, X., Li, Z., Li, B., Liu, C., and Xu, Z. (2018). An "off-on" fluorescein-based colormetric and fluorescent probe for the detection of glutathione and cysteine over homocysteine and its application for cell imaging. *Sens. Actuators B Chem.* 260, 295–302. doi: 10.1016/j.snb.2018.01.013

Karton-Lifshin, N., Albertazzi, L., Bendikov, M., Baran, P. S., and Shabat, D. (2012). "Donor-two-acceptor" dye design: a distinct gateway to NIR fluorescence. *J. Am. Chem. Soc.* 134, 20412–20420. doi: 10.1021/ja308124q

Kikuchi, K., Takakusa, H., and Nagano, T. (2004). Recent advances in the design of small molecule-based FRET sensors for cell biology. *Trends Anal. Chem.* 23, 407–415. doi: 10.1016/S0165-9936(04)00608-9

Kim, Y., Choi, M., Mulay, S. V., Jang, M., Kim, J. Y., Lee, W.-H., et al. (2018). Aqueous red-emissive probe for the selective fluorescent detection of cysteine by deprotection/cyclization cascade resulting in large stokes' shift. *Chem. Eur. J.* 24, 5623–5629. doi: 10.1002/chem.201706073

Lee, M. H., Kim, J. S., and Sessler, J. L. (2015). Small molecule-based ratiometric fluorescence probes for cations, anions, and biomolecules. *Chem. Soc. Rev.* 44, 4185–4191. doi: 10.1039/C4CS00280F

Li, X., Gao, X., Shi, W., and Ma, H. (2014). Design strategies for water-soluble small molecular chromogenic and fluorogenic probes. *Chem. Rev.* 114, 590–659. doi: 10.1021/cr300508p

Li, Y., Liu, W., Zhang, P., Zhang, H., Wu, J., Ge, J., et al. (2017). A fluorescent probe for the efficient discrimination of Cys, Hcy and GSH based on different cascade reactions. *Biosens. Bioelectron.* 90, 117–124. doi: 10.1016/j.bios.2016.11.021

Lipton, S. A., Choi, Y. B., Takahashi, H., Zhang, D., Li, W., Godzik, A., et al. (2002). Cysteine regulation of protein function - as exemplified by NMDA-receptor modulation. *Trends Neurosci.* 25, 474–480. doi: 10.1016/S0166-2236(02)02245-2

Liu, G., Liu, D., Han, X., Sheng, X., Xu, Z., Liu, S., et al. (2017). A hemicyanine-based colorimetric and ratiometric fluorescent probe for selective detection of cysteine and bioimaging in living cell. *Talanta* 170, 406–412. doi: 10.1016/j.talanta.2017.04.038

Liu, J., Sun, Y.-Q., Huo, Y., Zhang, H., Wang, L., Zhang, P., et al. (2014). Simultaneous fluorescence sensing of cys and GSH from different emission channels. *J. Am. Chem. Soc.* 136, 574–577. doi: 10.1021/ja409578w

Liu, X., Tian, H., Yang, L., Su, Y., Guo, M., and Song, X. (2017). An ESIPT-based fluorescent probe for sensitive and selective detection of Cys/Hcy over GSH with a red emission and a large Stokes shift. *Tetrahedron Lett.* 58, 3209–3213. doi: 10.1016/j.tetlet.2017.06.082

Lv, H., Yang, X.-F., Zhong, Y., Guo, Y., Li, Z., and Li, H. (2014). Native chemical ligation combined with spirocyclization of benzopyrylium dyes for the ratiometric and selective fluorescence detection of cysteine and homocysteine. *Anal. Chem.* 86, 1800–1807. doi: 10.1021/ac4038027

Ma, W.-W., Wang, M.-Y., Yin, D., and Zhang, X. (2017). Facile preparation of naphthol AS-based fluorescent probe for highly selective detection of cysteine in aqueous solution and its imaging application in living cells. *Sens. Actuators B* 248, 332–337. doi: 10.1016/j.snb.2017.03.169

Nawimanage, R. R., Prasai, B., Hettiarachchi, S. U., and McCarley, R. L. (2017). Cascade reaction-based, near-infrared multiphoton fluorescent probe for the selective detection of cysteine. *Anal. Chem.* 89, 6886–6892. doi: 10.1021/acs.analchem.7b01384

Niu, L.-Y., Chen, Y.-Z., Zheng, H.-R., Wu, L.-Z., Tung, C.-H., and Yang, Q.-Z. (2015). Design strategies of fluorescent probes for selective detection among biothiols. *Chem. Soc. Rev.* 44, 6143–6160. doi: 10.1039/C5CS00152H

Nolting, D. D., Gore, J. C., and Pham, W. (2011). Near-infrared dyes: probe development and applications in optical molecular imaging. *Curr. Org. Synth.* 8, 521–534. doi: 10.2174/157017911796117223

Qi, Y., Huang, Y., Li, B., Zeng, F., and Wu, S. (2018). Real-time monitoring of endogenous cysteine levels *in vivo* by near-infrared turn-on fluorescent probe with large stokes shift. *Anal. Chem.* 90, 1014–1020. doi: 10.1021/acs.analchem.7b04407

Ren, X., Tian, H., Yang, L., He, L., Geng, Y., Liu, X., et al. (2018). Fluorescent probe for simultaneous discrimination of Cys/Hcy and GSH in pure aqueous media with a fast response under a single-wavelength excitation. *Sens. Actuators B Chem.* 273, 1170–1178. doi: 10.1016/j.snb.2018.04.163

Shahrokhian, S. (2001). Lead phthalocyanine as a selective carrier for preparation of a cysteine-selective electrode. *Anal. Chem.* 73, 5972–5978. doi: 10.1021/ac010541m

Shao, J., Sun, H., Guo, H., Ji, S., Zhao, J., Wu, W., et al. (2012). A highly selective red-emitting FRET fluorescent molecular probe derived from BODIPY for the detection of cysteine and homocysteine: an experimental and theoretical study. *Chem. Sci.* 3, 1049–1061. doi: 10.1039/C2SC00762B

Sheng, H., Hu, Y., Zhou, Y., Fan, S., Cao, Y., Zhao, X., et al. (2019). A highly selective ESIPT-based fluorescent probe with a large Stokes shift for the turn-on detection of cysteine and its application in living cells. *Dyes Pigm.* 160, 48–57. doi: 10.1016/j.dyepig.2018.07.036

Song, H., Zhang, J., Wang, X., Zhou, Y., Xu, C., Pang, X., and Peng, X. ,(2018). A novel "turn-on" fluorescent probe with a large stokes shift for homocysteine and cysteine: performance in living cells and zebrafish. *Sens. Actuators B Chem.* 259, 233–240. doi: 10.1016/j.snb.2017.12.010

Tian, Y., Zhu, B., Yang, W., Jing, J., and Zhang, X. (2018). A fluorescent probe for differentiating Cys, Hcy and GSH via a stepwise interaction. *Sens. Actuators B Chem.* 262, 345–349. doi: 10.1016/j.snb.2018.01.181

Wang, F., Feng, C., Lu, L., Xu, Z., and Zhang, W. (2017). A ratiometric fluorescent probe for rapid and sensitive detection of biothiols in fetal bovine serum. *Talanta* 169, 149–155. doi: 10.1016/j.talanta.2017.03.080

Wang, J., Niu, L., Huang, J., Yan, Z., Zhou, X., and Wang, J. (2018). Thiazolyl substituted NBD as fluorescent probe for the detection of homocysteine and cysteine. *Dyes Pigm.* 158, 151–156. doi: 10.1016/j.dyepig.2018.05.039

Wang, L., Zhuo, S., Tang, H., and Cao, D. (2018). An efficient fluorescent probe for rapid sensing of different concentration ranges of cysteine with two-stage ratiometric signals. *Dyes Pigm.* 157, 284–289. doi: 10.1016/j.dyepig.2018.05.004

Wang, Q., Ma, F., Tang, W., Zhao, S., Li, C., and Xie, Y. (2018a). A novel nitroethylene-based porphyrin as a NIR fluorescence turn-on probe for

biothiols based on the Michael addition reaction. *Dyes Pigm.* 148, 437–443. doi: 10.1016/j.dyepig.2017.09.046

Wang, Q., Wang, H., Huang, J., Li, N., Gu, Y., and Wang, P. (2017). Novel NIR fluorescent probe with dual models for sensitively and selectively monitoring and imaging Cys in living cells and mice. *Sens. Actuators B Chem.* 253, 400–406. doi: 10.1016/j.snb.2017.06.166

Wang, Q., Wei, X., Li, C., and Xie, Y. (2018b). A novel p-aminophenylthio- and cyano-substituted BODIPY as a fluorescence turn-on probe for distinguishing cysteine and homocysteine from glutathione. *Dyes Pigm.* 148, 212–218. doi: 10.1016/j.dyepig.2017.09.020

Wu, Q., Mao, M., Liang, W., and Stadler, F. J. (2018). Quinoline-derived fluorescent probes for the discrimination of Cys from Hcys/GSH and bioimaging in living cells. *Talanta* 186, 110–118. doi: 10.1016/j.talanta.2018.04.044

Wu, Q., Wu, Y., Yu, C., Wang, Z., Hao, E., and Jiao, L. (2017). A highly selective visible light excitable boron dipyrromethene probe for cysteine over homocysteine and glutathione based on a Michael addition reaction. *Sens. Actuators B Chem.* 253, 1079–1086. doi: 10.1016/j.snb.2017.07.028

Yang, X.-F., Guo, Y.-X., and Strongin, R. M. (2011). Conjugate addition/cyclization sequence enables selective and simultaneous fluorescence detection of cysteine and homocysteine. *Angew. Chem. Int. Ed.* 50, 10690–10693. doi: 10.1002/anie.201103759

Yang, Y., Zhao, Q., Feng, W., and Li, F. (2013). Luminescent chemodosimeters for bioimaging. *Chem. Rev.* 113, 192–270. doi: 10.1021/cr2004103

Yin, C.-X., Xiong, K.-M., Huo, F.-J., Salamanca, J. C., and Strongin, R. M. (2017). Fluorescent probes with multiple binding sites for the discrimination of Cys, Hcy, and GSH. *Angew. Chem. Int. Ed.* 56, 13188–13198. doi: 10.1002/anie.201704084

Yuan, L., Lin, W., Zheng, K., He, L., and Huang, W. (2013). Far-red to near infrared analyte-responsive fluorescent probes based on organic fluorophore platforms for fluorescence imaging. *Chem. Soc. Rev.* 42, 622–661. doi: 10.1039/c2cs35313j

Yue, P., Yang, X., Ning, P., Xi, X., Yu, H., Feng, Y., et al. (2018). A mitochondria-targeted ratiometric two-photon fluorescent probe for detecting intracellular cysteine and homocysteine. *Talanta* 178, 24–30. doi: 10.1016/j.talanta.2017.08.085

Yue, Y., Huo, F., Li, X., Wen, Y., Yi, T., Salamanca, J., et al. (2017a). pH-dependent fluorescent probe that can be tuned for cysteine or homocysteine. *Org. Lett.* 19, 82–85. doi: 10.1021/acs.orglett.6b03357

Yue, Y., Huo, F., Ning, P., Zhang, Y., Chao, J., Meng, X., et al. (2017b). Dual-site fluorescent probe for visualizing the metabolism of Cys in living cells. *J. Am. Chem. Soc.* 139, 3181–3185. doi: 10.1021/jacs.6b12845

Zhang, H., Feng, W., and Feng, G. (2017). A simple and readily available fluorescent turn-on probe for cysteine detection and bioimaging in living cells. *Dyes Pigm.* 139, 73–78. doi: 10.1016/j.dyepig.2016.12.011

Zhang, J., Ji, X., Ren, H., Zhou, J., Chen, Z., Dong, X., et al. (2018a). Meso-heteroaryl BODIPY dyes as dual-responsive fluorescent probes for discrimination of Cys from Hcy and GSH. *Sens. Actuators B Chem.* 260, 861–869. doi: 10.1016/j.snb.2018.01.016

Zhang, J., Ji, X., Zhou, J., Chen, Z., Dong, X., and Zhao, W. (2018b). Pyridinium substituted BODIPY as NIR fluorescent probe for simultaneous sensing of hydrogen sulphide/glutathione and cysteine/homocysteine. *Sens. Actuators B Chem.* 257, 1076–1082. doi: 10.1016/j.snb.2017.10.133

Zhang, X., and Liu, J.-Y. (2016a). Solvent dependent photophysical properties and near-infrared solid-state excited state intramolecular proton transfer (ESIPT) fluorescence of 2,4,6-trisbenzothiazolylphenol. *Dyes Pigm.* 125, 80–88. doi: 10.1016/j.dyepig.2015.10.002

Zhang, X., Liu, J.-Y., Ma, W.-W., and Yang, M.-L. (2016b). Near-infrared fluorescence of p-conjugation extended benzothiazole and its application for biothiol imaging in living cells. *J. Mater. Chem. B* 4, 6662–6669. doi: 10.1039/c6tb01465h

Zhu, X., Yuan, L., Hu, X., Zhang, L., Liang, Y., He, S., et al. (2018). Construction of a fluorine substituted chromenylium-cyanine near-infrared fluorophore for ratiometric sensing. *Sens. Actuators B Chem.* 259, 219–225. doi: 10.1016/j.snb.2017.12.008

Conflict of Interest Statement: The authors declare that the research was conducted in the absence of any commercial or financial relationships that could be construed as a potential conflict of interest.

Copyright © 2019 Zhang, Zhang, Ma, Zhou, Lu and Xu. This is an open-access article distributed under the terms of the Creative Commons Attribution License (CC BY). The use, distribution or reproduction in other forums is permitted, provided the original author(s) and the copyright owner(s) are credited and that the original publication in this journal is cited, in accordance with accepted academic practice. No use, distribution or reproduction is permitted which does not comply with these terms.

frontiers in Chemistry

ORIGINAL RESEARCH
published: 31 January 2019
doi: 10.3389/fchem.2019.00036

Uncovering the Structural Diversity of Y(III) Naphthalene-2,6-Dicarboxylate MOFs Through Coordination Modulation

Sarah L. Griffin[1,2], *Claire Wilson*[1] *and Ross S. Forgan*[1]*

[1] WestCHEM School of Chemistry, University of Glasgow, Glasgow, United Kingdom, [2] EPSRC Centre for Innovative Manufacturing in Continuous Manufacturing and Crystallisation, University of Strathclyde Technology and Innovation Centre, Glasgow, United Kingdom

Metal-organic frameworks (MOFs)—network structures built from metal ions or clusters and connecting organic ligands—are typically synthesized by solvothermal self-assembly. For transition metal based MOFs, structural predictability is facilitated by control over coordination geometries and linker connectivity under the principles of isoreticular synthesis. For rare earth (RE) MOFs, coordination behavior is dominated by steric and electronic factors, leading to unpredictable structures, and poor control over self-assembly. Herein we show that coordination modulation—the addition of competing ligands into MOF syntheses—offers programmable access to six different Y(III) MOFs all connected by the same naphthalene-2,6-dicarboxylate ligand, despite controlled synthesis of multiple phases from the same metal-ligand combination often being challenging for rare earth MOFs. Four of the materials are isolable in bulk phase purity, three are amenable to rapid microwave synthesis, and the fluorescence sensing ability of one example toward metal cations is reported. The results show that a huge variety of structurally versatile MOFs can potentially be prepared from simple systems, and that coordination modulation is a powerful tool for systematic control of phase behavior in rare earth MOFs.

Keywords: metal-organic frameworks, yttrium, coordination modulation, microwave synthesis, fluorescent sensing

OPEN ACCESS

Edited by:
Tony D. James,
University of Bath, United Kingdom

Reviewed by:
Guzman Gil-Ramirez,
University of Lincoln, United Kingdom
Adam Charles Sedgwick,
University of Texas at Austin, United States

***Correspondence:**
Ross S. Forgan
Ross.Forgan@glasgow.ac.uk

Specialty section:
This article was submitted to Supramolecular Chemistry, a section of the journal Frontiers in Chemistry

Received: *27 November 2018*
Accepted: *14 January 2019*
Published: *31 January 2019*

Citation:
Griffin SL, Wilson C and Forgan RS (2019) Uncovering the Structural Diversity of Y(III) Naphthalene-2,6-Dicarboxylate MOFs Through Coordination Modulation. Front. Chem. 7:36. doi: 10.3389/fchem.2019.00036

INTRODUCTION

Research revolving around metal-organic frameworks (MOFs)—network structures wherein metal ions or clusters are connected by organic linkers into diverse topologies (Furukawa et al., 2013)—has rapidly increased in recent years following publication of landmark materials in the late 1990s (Chui et al., 1999; Li et al., 1999), with there being ~70,000 MOF structures reported in the Cambridge Structural database as of 2016 (Moghadam et al., 2017). The reason for this interest can be attributed to the permanent porosity and vast range of structural and chemical properties that can be imparted on MOFs, leading to an array of applications from gas storage and separation (Yang and Xu, 2017) to drug delivery and biosensing (Abánades Lázaro and Forgan, 2019). As more MOFs are discovered it is becoming apparent that there is a large range of fascinating topologies accessible, showing diversities in their coordination, solvation, and porosity.

A considerable amount of research focuses on the discovery and synthesis of new frameworks, utilizing a wide range of metals—most commonly transition metals—and organic linkers. We have studied the modulated self-assembly of Zr(IV) (Marshall et al., 2016) and Sc(III) (Marshall et al., 2018) MOFs in detail, yet studies into the synthesis of new yttrium materials appear to be somewhat limited. Whilst yttrium is a *d* block metal, it is considered as a rare earth (RE) metal and displays coordination chemistry similar to the lanthanides when in the Y(III) oxidation state. As such, there are several reports of lanthanide doped Y-MOFs, for example MIL-78 (Serre et al., 2004) and MIL-92 (Surblé et al., 2005), with the possibility of utilizing the inherent luminescence of europium and terbium to impart nitroaromatic detection and tunable photoluminescence properties on the otherwise non-luminescent materials (Singha et al., 2015; Zheng et al., 2015). Of the single metal Y-MOFs reported, several exhibit permanent porosity and high thermal and water stability, leading to a range of potential applications (Weng et al., 2006; Luo et al., 2008; Jiang et al., 2010; Gong et al., 2012; Duan et al., 2013; Kim et al., 2015; Bezrukov and Dietzel, 2017; Mohideen et al., 2018). For example, a 1,2,4,5-tetrakis(4-carboxyphenyl)benzene based Y-MOF has been utilized for indoor moisture control (Abdulhalim et al., 2017), whilst a framework based on a hexa-carboxylate linker showed selective adsorption of C_2H_2 and CO_2 over CH_4 (Liu et al., 2017).

Much like in the synthesis of many other MOFs, coordination modulation—the addition of monotopic linkers as capping agents or crystallization promotors (McGuire and Forgan, 2015)—has been used in the synthesis of Y-MOFs in order to achieve highly crystalline material. Coordination modulation is routinely implemented in the synthesis of MOFs, most commonly enhancing crystallinity and allowing the isolation of single crystals, although under certain conditions, coordination modulation can also control particle size, allowing for the synthesis of nanomaterials (Guo et al., 2012; Chen et al., 2018), or introduce defects throughout a structure whilst maintaining the overall topology (Wu et al., 2013). It should be noted that the use of different modulators in syntheses does not tend to have an effect on the topology of the resultant material. For example, in the case of Zr-MOFs of the UiO topology, the use of different modulators, such as L-proline, benzoic and acetic acid, still results in the formation of the UiO structure, merely with different physical or chemical properties (Schaate et al., 2011; Marshall et al., 2016). Unlike their transition element counter parts however, RE elements have less predictable coordination geometries, resulting in a greater variety of coordination geometries. As a result there is much more difficulty in the prediction of rare earth MOF structures compared to transition metal-based MOFs (Pagis et al., 2016), with coordination modulation potentially perturbing self-assembly to allow isolation of new structures (Decadt et al., 2012). For example, Eddaoudi et al. have introduced 2-fluorobenzoic acid as an efficient modulator of RE MOFs, isolating for example Y-MOFs containing hexanuclear (**Figure 1A**) (Xue et al., 2013, 2015; Luebke et al., 2015) and nonanuclear (**Figure 1B**) (Guillerm et al., 2014; Abdulhalim et al., 2017; Chen et al., 2017) secondary building units (SBUs).

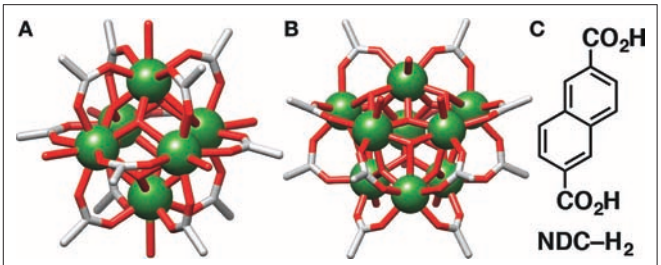

FIGURE 1 | Examples of 12-connected **(A)** $[Y_6(OH)_8(RCO_2)_{12}(H_2O)_6]^{2-}$ and **(B)** $[Y_9(O)_2(OH)_{14}\ (RCO_2)_{12}(H_2O)_7]^{3-}$ SBUs accessible through coordination modulation. **(C)** Chemical structure of the naphthalene-2,6-dicarboxylic acid (NDC-H_2) linker.

Herein, we report an extensive study into the effects of coordination modulation on the crystallization of naphthalene-2,6-dicarboxylic acid (NDC-H_2, **Figure 1C**) Y-MOFs. Contrary to many modulated syntheses in which modulation does not affect overall topology, in this case the use of different modulators led to the crystallization of a range of phases containing Y(III) and 2,6-NDC^{2-}, each exhibiting different coordination, solvation, and void space. The selected modulators ranged in pH, size and functionality. Several of the Y-MOFs were synthesized in bulk with phase purity via solvothermal synthesis, with multiple syntheses also successfully being carried out via microwave assisted heating, considerably reducing synthesis time. The luminescent properties of one of the MOFs were also examined, studying the sensing abilities of the framework in the presence of a variety of metals ions.

RESULTS AND DISCUSSION

Use of different modulators allowed isolation of six different framework structures wherein Y^{3+} cations are linked by 2,6-NDC^{2-} units (see SI, section Synthesis). A summary of synthetic conditions is given in **Table 1**.

Subjecting YCl_3 and 2,6-NDC-H_2 to solvothermal synthesis in DMF at 120°C resulted in the isolation of $\mathbf{[Y_2(NDC)_3(C_3H_7NO)_2]_n}$ **(1)**. **1** is a 3D coordination polymer, which crystallizes in the monoclinic space group $P2_1/c$. The asymmetric unit contains two crystallographically independent Y^{3+} ions having the same connectivity, three 2,6-NDC^{2-} linkers and two DMF molecules. One dimensional chains of Y^{3+} cations running down the crystallographic *c* axis (**Figure 2A**) are connected by carboxylate units of the linkers, with three NDC^{2-} units bridging adjacent metal ions in the $(\eta^1{:}\eta^1{:}\mu_2)$ motif seen in the related $Sc_2(BDC)_3$ MOF (Miller et al., 2005; Perles et al., 2005). The larger size of Y^{3+} compared to Sc^{3+} leads to coordination of one DMF molecule, making the Y^{3+} molecules seven-coordinate (**Figure 2B**), and distancing them further from one another along the chain (Y···Y ∼4.8 Å) than in $Sc_2(BDC)_3$ (Sc···Sc ∼4.4 Å). The chains connect into a net with diamond-shaped pores into which the DMF molecules protrude (**Figure 2C**).

TABLE 1 | Summary of synthetic conditions used to prepare single crystals of Y-NDC MOFs **1**–**6**.

MOF	Y source	Modulator	Solvent	T	Time
1	$YCl_3{\cdot}6H_2O$[a]	None	DMF	120°C	24 h[b]
2	$Y(NO_3)_3{\cdot}6H_2O$	H_2O (2 equiv)	DMF	120°C	24 h
3	$Y(NO_3)_3{\cdot}6H_2O$	HNO_3 (16 equiv)	DMF	120°C/16°C	24 h/72 h
4	$Y(NO_3)_3{\cdot}6H_2O$	Acetic Acid (40 equiv)	DMF	120°C	24 h[c]
5	$Y(NO_3)_3{\cdot}6H_2O$	2-Fluorobenzoic acid (8 equiv)/HNO_3 (40 equiv)	DMF/H_2O (5:1)	120°C	2 h[c]
6	$Y(NO_3)_3{\cdot}6H_2O$	Tartaric acid (0.5 equiv)	DMF/H_2O/EtOH (2:1:1)	80°C	24 h

[a] *Can also be synthesized using* $Y(NO_3)_3{\cdot}6H_2O$.
[b] *Alternatively 1 h in a microwave reactor.*
[c] *Alternatively 2 h in a microwave reactor.*

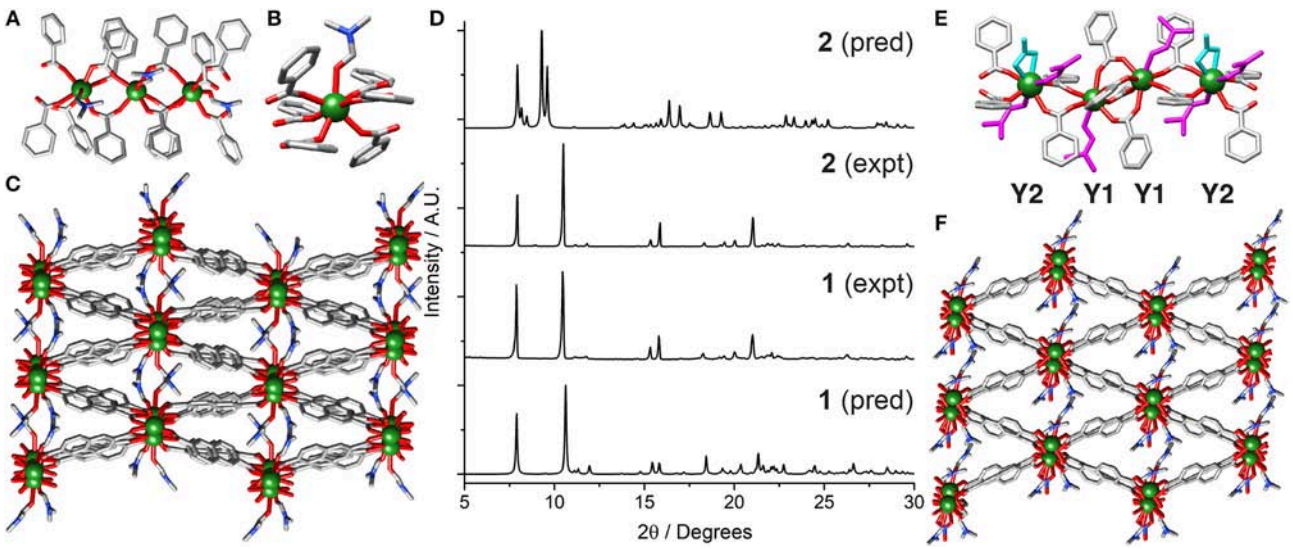

FIGURE 2 | Crystal structure of **1**. **(A)** The one-dimensional chain SBU. **(B)** The coordination sphere of Y1. **(C)** The overall packing structure showing potential porosity. **(D)** Stacked PXRD patterns of bulk samples of **1** and **2** compared to their predicted patterns, confirming crystals of **2** were isolated from material with bulk composition of **1**. Crystal structure of **2**. **(E)** One-dimensional chain SBU with coordinating nitrate (cyan) and DMF (magenta). **(F)** Packing structure showing structural relationship with **1**. H atoms and disorder removed for clarity in all crystal structure images.

The synthesis of **1** can be successfully scaled up to produce the material in bulk with high crystallinity and phase purity, as shown by powder X-ray diffraction (PXRD), which was carried out on a washed and dried sample, showing a close match to the pattern predicted from the crystal structure (**Figure 2D**). Rapid microwave synthesis (Lin et al., 2012) of **1** is also possible. Yttrium chloride was used rather than yttrium nitrate in order to produce single crystals suitable for structure determination X-ray diffraction, however the same structure is produced when using yttrium nitrate (**Figure S1**).

In a synthesis using $Y(NO_3){\cdot}6H_2O$ and NDC-H_2 doped with two additional equivalents of water, it was possible to isolate crystals of $\mathbf{[Y_3(NDC)_4(C_3H_7NO)_4(NO_3)]_{\mathit{n}}}$ **(2)**, from a bulk solid that was shown by PXRD to comprise almost entirely **1** (**Figure 2D** and **Figure S2**). Structure **2** crystallizes in the triclinic space group $P\bar{1}$, with the asymmetric unit containing one and a half Y^{3+} ions, two 2,6-NDC^{2-} linkers, one and a half coordinated nitrate molecules and two coordinated DMF molecules. The unit cell contains two crystallographically independent Y^{3+} centers, one of which is disordered across two crystallographically equivalent positions through an inversion center. The structure is related to **1**; it is comprised of 1D chains of single metal ions, repeating in a $[Y1{\cdots}Y1{\cdots}Y2]_n$ fashion over the independent Y^{3+} ions (**Figure 2E**). The Y1 centers are linked by four bridging NDC^{2-} units with carboxylate groups in the $(\eta^1{:}\eta^1{:}\mu_2)$ motif, with each Y1 linked to an adjacent Y2 by two carboxylates in the same $(\eta^1{:}\eta^1{:}\mu_2)$ motif and the seven-coordinate geometry completed by a DMF solvent molecule. As such, the Y2 centers coordinate to four carboxylate oxygen atoms (two bridging from each Y1 center) with the coordination sphere filled by two DMF molecules and one bidentate nitrate anion, making it eight-coordinate. The Y2 ions are disordered across an inversion center, resulting in two distinct positions 1.3213(3) Å apart with associated disorder of the coordinated ligands. Along the chain, which has the sequence Y1Y1Y2Y1Y1Y2, the Y1···Y1 distance is 4.1635(1) Å,

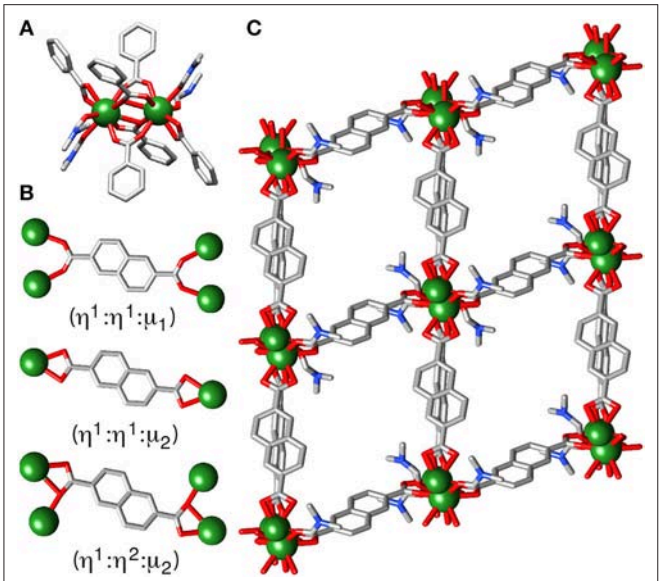

FIGURE 3 | The crystal structure of **3**. **(A)** The dimeric SBU. **(B)** The differing coordination modes of the crystallographically independent NDC^{2-} ligands. **(C)** The packing structure viewed down the *a* axis. H atoms removed for clarity.

while the Y1···Y2 distances are longer and asymmetric, with one Y1···Y2 distance of 5.1434(2) Å and the other of 5.4725(2) Å, likely because Y1···Y1 are connected via four carboxylate groups from four linkers whereas Y1···Y2 are connected by only two carboxylate groups from two linkers. The overall structure looks similar to **1**, with diamond-like pores containing DMF and nitrate ligands pointing into potential pore space (**Figure 2F**).

Attempts to produce phase pure samples of **2**, by deliberate addition of 16 equivalents of nitric acid as a source of nitrate into solvothermal syntheses, resulted in the isolation of $\mathbf{[Y_2(NDC)_3(C_3H_7NO)_4]_n}$ **(3)**, which has a significantly different structure but contains no nitrate. The structure, which crystallizes in the triclinic $P\bar{1}$ space group, has discrete dimeric SBUs (**Figure 3A**) rather than 1D chains of Y^{3+} ions. The asymmetric unit consists of a nine-coordinate Y^{3+} ion, one and a half 2,6-NDC^{2-} linkers and two coordinated DMF molecules. Four NDC^{2-} linkers bridge the binuclear SBU, two with the $(\eta^1{:}\eta^1{:}\mu_2)$ motif and two with the $(\eta^1{:}\eta^2{:}\mu_2)$ motif, with adjacent pairs of Y^{3+} ions in the SBU separated by 3.9933(2) Å and related by an inversion center. The Y^{3+} ions also coordinate to a linker in a terminal bidentate $(\eta^1{:}\eta^2{:}\mu_1)$ motif (**Figure 3B**) and two DMF molecules, making them nine-coordinate. The bridging linkers form square grid-like sheets along the *bc* plane, with the terminal linkers connecting the sheets in an offset manner to form a 3D net with a calculated void space [N_2 probe, Mercury 3.10.3 (Macrae et al., 2008)] of 31.9%, with continuous channels running through the framework along the *a* axis (**Figure 3C**). A discrete complex, $[Y_2(3,5\text{-DHB})_2(CH_3CO_2)_4(H_2O)_4]$ (DHB = dihydroxybenzoate), with a closely related coordination arrangement to the dimeric SBU in **3**, has been observed previously (Dan et al., 2006).

The synthesis of **3** differs from the others in that crystallization occurs at room temperature after the reaction solution has been heated to 120°C for 24 h. Upon removing the reaction jar from the oven, the clear yellow solution (previously colorless) was left undisturbed in a chilled room for a further 3 days, wherein crystallization of block crystals occurred. The reaction was successfully scaled up, proven both visually and by SCXRD, however the framework is not stable to solvent loss as demonstrated by a change in PXRD pattern, highlighting the decomposition (**Figure S3**). Structurally analogous MOFs have been prepared from Ce, Eu, and Tb, which also decompose in air (Wang et al., 2002), although a Nd derivative has shown sufficient stability to allow gas uptake, with $S_{BET} = 150\ m^2g^{-1}$ (Wang et al., 2015).

Subsequently, carboxylate-based modulators were examined. Incorporation of 40 equivalents of acetic acid into the synthesis resulted in the isolation of $\mathbf{[Y(NDC)(CH_3CO_2)(C_3H_7NO)]_n}$ **(4)** as a phase pure material. **4** crystallizes in the triclinic space group $P\bar{1}$, with the asymmetric unit containing an eight-coordinate Y^{3+} ion, one 2,6-NDC^{2-} linker, a coordinated acetate and a DMF molecule. The structure is related to **1**, with one-dimensional chains of Y^{3+} ions bridged by NDC^{2-} linkers, but one NDC^{2-} ligand is replaced by two acetate ligands (**Figure 4A**). The structure can be thought of as containing chains of dimers; two equivalent Y^{3+} ions, related by an inversion center, are bridged by carboxylate units from two NDC^{2-} ligands in the $(\eta^1{:}\eta^1{:}\mu_2)$ motif and two acetates in the $(\eta^1{:}\eta^2{:}\mu_2)$ motif. These dimers are linked to one another by two further NDC^{2-} carboxylates, also in the $(\eta^1{:}\eta^1{:}\mu_2)$ motif, with the Y^{3+} coordination sphere being completed by a DMF molecule. The Y···Y distance within the "dimer" is 3.8689(9) Å, while the Y···Y distance to the adjacent "dimer" in the chain is 5.570(1) Å. **4** has a similar packing arrangement to **1**, with diamond-shaped pores down the *b* axis filled with DMF molecules (**Figure 4B**). Unlike **2**, the sample can be prepared in bulk, with phase purity confirmed by PXRD (**Figure 4C**).

The combination of 2-fluorobenzoic acid, nitric acid, and water as co-modulators for RE MOFs has previously resulted in isolation of MOFs with UiO-66 (Xue et al., 2013) and MIL-88 (Wei et al., 2017) nets, as well as novel topologies (Guillerm et al., 2014). With Y^{3+} and NDC^{2-}, a structure related to MIL-88C is formed, $\mathbf{(CH_3)_2NH_2[Y_3(NDC)_3(HCOO)_3(OH)]_n}$ **(5)**. Structure **5** crystallizes as hexagonal plates (**Figure 4D**) in the $P\bar{3}$ space group, with the asymmetric unit containing one seven-coordinate Y^{3+} ion, one 2,6-NDC^{2-} linker, one formate and one third of a dimethylammonium ion (both generated by decomposition of DMF), and one third of a hydroxyl ion. The framework is comprised of $[Y_3(\mu_3\text{-OH})(RCO_2)_6]$ trimeric SBUs [**Figure 4E**, Y1···O1C = 2.2986(3) Å] linked by NDC^{2-} linkers into the MIL-88C topology (**Figure 4F**). The SBUs, which lie in the *ab* plane, are further connected via two bridging formates per Y^{3+} ion to form a 2D sheet; the distance between neighboring clusters, measured between the oxygen atoms of adjacent bridging μ_3-OH ligands (O1C), is

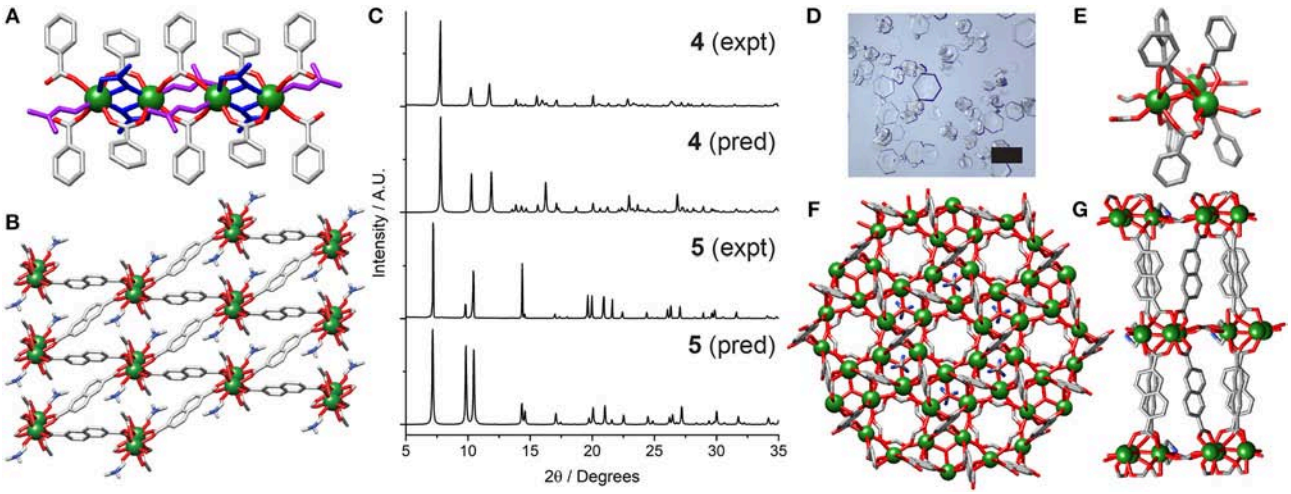

FIGURE 4 | Crystal structure of **4**. **(A)** One dimensional chain SBU, with coordinated acetate (blue) and DMF (magenta). **(B)** Packing structure viewed down the *b* axis. **(C)** Stacked PXRD patterns of **4** and **5** compared to their predicted patterns. **(D)** Optical image of the hexagonal plates of **5**, which give rise to preferred orientation related peak height discrepancies in the PXRD pattern of bulk samples. Scale bar 500 μm. Crystal structure of **5**. **(E)** Trigonal SBU showing bridging formates. **(F)** Packing structure showing solvent inaccessible voids between SBUs. **(G)** Hexagonal packing arrangement viewed down the *c* axis.

10.376(2) Å. Disordered dimethylammonium ions sit in the plane of the clusters, forming NH···O hydrogen bonds to oxygen atoms of the linking formates [N1S···O1F = 3.0180(5) Å] and NDC^{2-} linkers [N1S···O1 = 3.0100(3) Å]. The overall structural formula can be confirmed by ^1H NMR spectroscopic analysis of digested samples, clearly showing the presence of dimethylammonium cations and formate anions with integral ratios consistent with the overall formula (**Figure S6**). The structure has pockets of void space totaling 20.3% of the framework, with the bridging formates preventing a continuous solvent accessible pore (**Figure 4G**). Whilst similar to MIL-88C type structures, the higher coordination number of Y compared to transition metals results in the additional coordination of the formate groups to link the SBUs, expected to limit the breathing nature of **5**, a property associated with transition metal linked MIL-88C materials (Horcajada et al., 2011). The crystal structure of the analogous Er-MOF has recently been reported, with the Y-MOF identified by PXRD (Wei et al., 2017).

Tartaric acid has previously been shown to be an efficient modulator in the synthesis of a mixed metal Y-BDC MOF in a mixed EtOH/water solvent system (Abdelbaky et al., 2014), and so conditions (heating to 80°C for 24 h) inspired by this were implemented with Y^{3+} and NDC^{2-}. Single crystals of $\mathbf{[Y_2(NDC)_3(C_2H_5OH)(H_2O)_3]_n{\cdot}3(C_3H_7NO)}$ **(6)** could be isolated from the resulting gel. **6** crystallizes in the triclinic space group $P\bar{1}$; the crystal structure was determined from a selected crystal and does not represent the bulk material, which, after washing and drying, PXRD analysis confirms to be predominantly **1** (**Figure S7**). The asymmetric unit of **6** contains two Y^{3+} ions, three 2,6-NDC^{2-} linkers, a coordinated ethanol molecule and three coordinated water molecules. Chains of single Y^{3+} ions run along the *bc* plane throughout the framework (**Figure 5A**), alternating in a -Y1-Y1-Y2-Y2- fashion. Each Y^{3+} is bridged by two NDC^{2-} carboxylates in the (η^1:η^1:μ_2) motif and is also bridged by a bidentate NDC^{2-} carboxylate in a (η^1:η^1:μ_1) arrangement. The difference between Y1 and Y2 lies in coordinated solvents; Y1 is coordinated to one water molecule and one ethanol molecule, whilst Y2 is coordinated to two water molecules. Within the linear metal chain there are three different but similar Y-Y distances—Y1···Y1 = 4.742(2) Å, Y2···Y2 = 4.731(2) Å, and Y1···Y2 = 4.8846(2) Å,—highlighting the similarity of the eight-coordinate Y^{3+} ions.

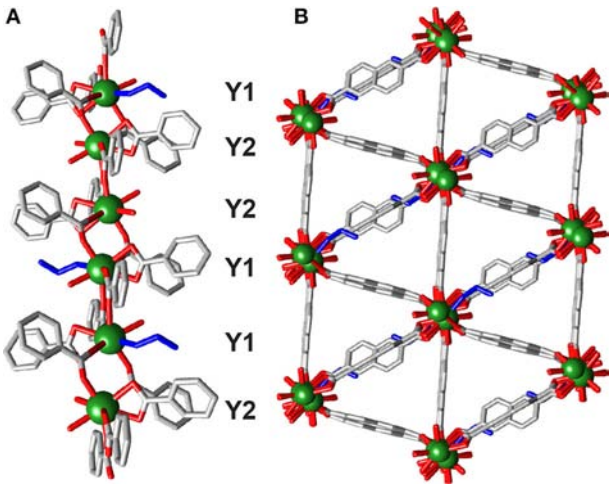

FIGURE 5 | The crystal structure of **6**. **(A)** One dimensional chain SBU, with coordinating ethanol colored blue. **(B)** Packing structure showing significant void space, with ordered DMF guests removed for clarity.

The chains are connected in an approximately hexagonal manner by the NDC^{2-} ligands to form a framework with a 29% void space [N_2 probe, Mercury 3.10.3 (Macrae et al.,

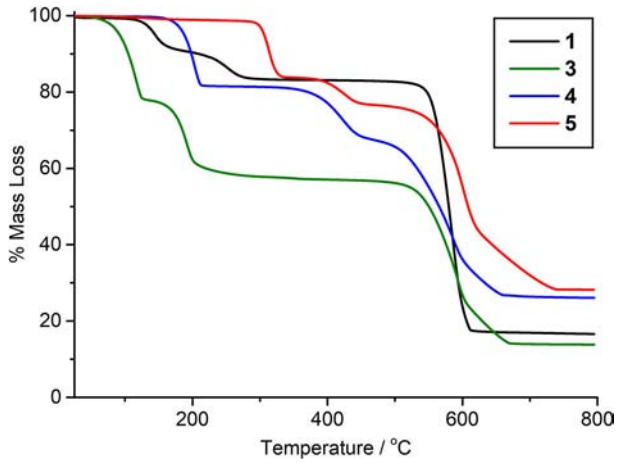

FIGURE 6 | Thermogravimetric analysis in air of **1**, **3**, **4**, and **5**.

2008)], running in disconnected sheets along the *bc* plane (**Figure 5B**) and containing ordered DMF solvent molecules. It was unfortunately not possible to prepare a phase-pure sample of **6**.

By simple modification of synthetic conditions, six different MOFs have been characterized from a single metal-ligand system, with counterions, solvents, and most importantly modulators playing key roles in directing structure formation. Of the six, the syntheses of frameworks **1**, **4,** and **5** were successfully scaled up to produce the materials in bulk with high crystallinity and phase purity, as shown by PXRD which was carried out on washed and dried samples. The predicted and experimental powder patterns show good overlap, while minor discrepancies in peak intensities can be attributed to preferential orientation of the packed powder samples. These three frameworks were also successfully produced through microwave-assisted synthesis. Each was carried out on the same scale as that of the bulk solvothermal synthesis and produced crystalline, phase pure material in 2 h and under compared to 24 h solvothermally (**Figures S4** and **S5**). Compounds **2** and **6** crystallize alongside **1** under specific conditions, while **3** can also be scaled up, but appears to be unstable to drying.

1, **4**, and **5** can be produced in bulk and have potential voids if solvents can be successfully removed. As such, thermogravimetric analysis was carried out on bulk samples (**Figures S8** and **S9**), along with an undried sample of **3**, which is unstable to solvent removal, to assess its bulk composition (**Figure 6**). The TGA profile of **1** shows the stepwise loss of its two DMF molecules, with a mass loss of 8.6% followed by another of 7.5% between 115°C and 290°C. The final weight loss of 66.2% between 525°C and 618°C can be attributed to the organic linkers. Analysis of **4** shows a similar initial loss of coordinated DMF between 154°C and 214°C, followed by a stepped 55.3% mass loss between 340°C and 670°C arising from the loss of acetate and linkers. **5** shows a first weight loss of 16.2% between 287°C and 336°C which closely correlates with the loss of dimethylammonium cations and formate anions.

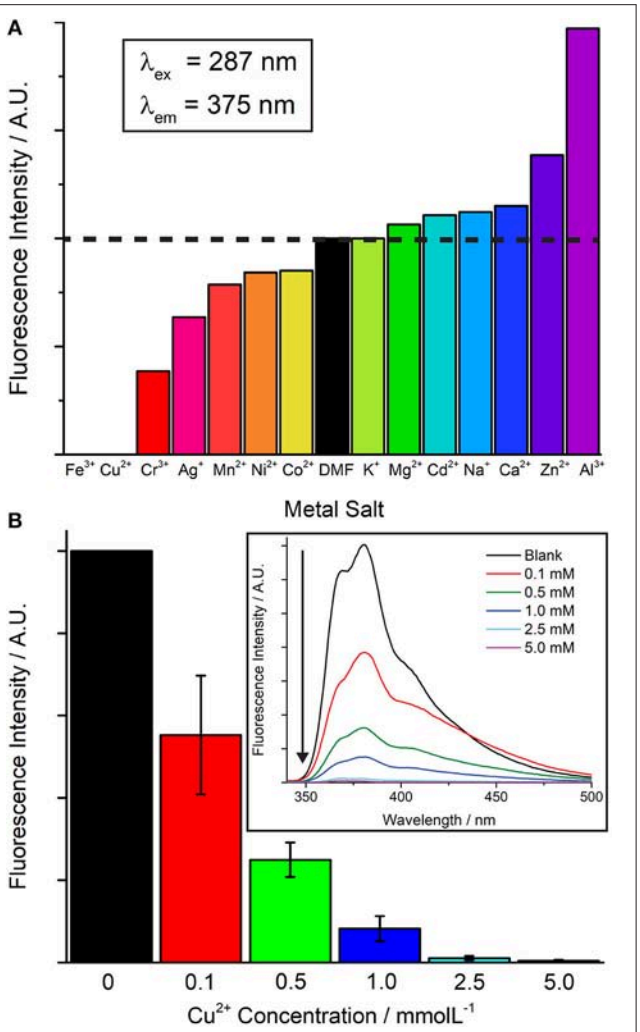

FIGURE 7 | (A) Changes in luminescence of samples of **5** when contacted with 5 mM DMF solutions of metal nitrates. **(B)** Concentration dependence of turn-off sensing of Cu^{2+}. Experiments carried out in triplicate, typical spectra for Cu^{2+} sensing shown as an inset.

The following two-step loss of 55.5% can be attributed to the loss of NDC^{2-} linkers and hydroxide. Due to decomposition of **3** on solvent removal, the material was not fully dried before analysis. As such, the initial 22.1% weight loss between 55°C and 126°C arises from encapsulated DMF. The subsequent mass loss of 20.2% correlates with the loss of coordinated DMF, and is followed by a 43.7% mass loss due to organic linkers, confirming the bulk composition suggested by the single crystal structure.

Despite the ability to remove solvent molecules from the materials, none were found to be porous to N_2 at 77 K. Removal of coordinated DMF from **1** and **4** presumably results in framework collapse, although it is noted that during the peer review period, a Ce(III) analog of **1** was reported which could be desolvated at 300°C to a phase that was porous to CO_2 (Atzori et al., in press). For **5**, whilst the framework does show void space, it is possible that access

to the void channels is blocked due to charge-balancing dimethylammonium ions lying in the cluster layer of the framework.

The luminescence properties of **5** were investigated in DMF solution in the presence of a variety of metal nitrates, with differing extents of cation exchange with the dimethylammonium ions a possible mechanism for fluorescent sensing. The excitation of the free NDC-H_2 linker at $\lambda = 287$ nm leads to an emission maximum at $\lambda = 375$ nm, with a shoulder at $\lambda = 364$ nm, dictating the excitation wavelength for **5**. Finely ground framework **5** (2 mg) was immersed in 5 ml of 5 mM DMF solutions of $M^{x+}(NO_3)_x$ ($M = Ag^+$, Al^{3+}, Cd^{2+}, Ca^{2+}, Cr^{3+}, Co^{2+}, Cu^{2+}, Fe^{3+}, Mn^{2+}, Mg^{2+}, Ni^{2+}, K^+, Na^+, Zn^{2+}) and sonicated for 30 min. The luminescence of **5** can be seen to vary to some degree in the presence of all the metal nitrates (**Figure 7A**). Soaking in Fe^{3+} and Cu^{2+} solutions led to complete quenching of luminescence, whereas Al^{3+} and Zn^{2+} solutions gave rise to a considerable increase in luminescence. The presence of Cd^{2+} and Zn^{2+} notably leads to a shift in the intensity ratio between the 364 and 375 nm peaks, along with the appearance of a new shoulder peak at 350 nm (**Figure S10**).

To examine any potential structural changes, the crystallinity of **5** was examined via PXRD after soaking of the samples for 3 days in the metal nitrate solutions. The crystallinity of **5** is retained in the presence of all metals except Fe^{3+}, where the sample becomes completely amorphous (**Figure S11**). The concentration dependence of Cu^{2+} turn-off sensing was examined, with significant quenching still observed at 0.1 mM concentrations of Cu^{2+} (**Figure 7B**).

CONCLUSIONS

Through the use of a range of different modulators, a series of six yttrium frameworks with the naphthalene-2,6-dicarboxylate linker have been synthesized, each exhibiting different coordination, solvation, and void space. Unlike transition metal frameworks in which coordination modulation can be used to enhance crystallinity or impart structural properties whilst maintaining topology, the same technique when used with yttrium leads to a range of polymorphs, with the modulator instead acting as a structural director. The resultant frameworks show considerable structural diversity and high thermal stabilities, with framework **5** presenting interesting luminescence properties in the presence of metal nitrate solutions. This technique could unlock a vast myriad of new yttrium frameworks, with this work generating six structures resulting from just one linker, and a seventh recently published using 2,6-difluorobenzoic acid as modulator (Liu et al., 2018). The combination of modulation along with alternative linkers, varying in their functionality, length, and connectivity, could lead to diverse further interesting frameworks.

DATA AVAILABILITY STATEMENT

The data which underpin this work are available at http://dx.doi.org/10.5525/gla.researchdata.728.

AUTHOR CONTRIBUTIONS

RSF and SLG devised the Project. SLG carried out the research, CW carried out crystallographic analysis, and RSF supervised the project. All authors contributed to the writing of the manuscript.

FUNDING

RSF thanks the Royal Society for receipt of a URF. We thank EPSRC (EP/K503058, EP/L50497X, EP/M506539, and EP/M508056/1) and the EPSRC Centre for Innovative Manufacturing in Continuous Manufacturing and Crystallisation (EP/K503289/1) for funding this work.

ACKNOWLEDGMENTS

We thank the EPSRC National Crystallographic Service for single crystal data collections (Coles and Gale, 2012). We thank Dr. Ross Marshall for his early contribution to the project, conducting preliminary syntheses and providing useful discussion.

SUPPLEMENTARY MATERIAL

The Supplementary Material for this article can be found online at: https://www.frontiersin.org/articles/10.3389/fchem.2019.00036/full#supplementary-material

REFERENCES

Abánades Lázaro, I., and Forgan, R. S. (2019). Application of zirconium MOFs in drug delivery and biomedicine. *Coord. Chem. Rev.* 380, 230–259. doi: 10.1016/j.ccr.2018.09.009

Abdelbaky, M. S. M., Amghouz, Z., García-Granda, S., and García, J. R. (2014). A metal–organic framework assembled from Y(III), Li(I), and terephthalate: hydrothermal synthesis, crystal structure, thermal decomposition and topological studies. *Dalton Trans.* 43, 5739–5746. doi: 10.1039/c3dt53415d

Abdulhalim, R. G., Bhatt, P. M., Belmabkhout, Y., Shkurenko, A., Adil, K., Barbour, L. J., et al. (2017). A fine-tuned metal–organic framework for autonomous indoor moisture control. *J. Am. Chem. Soc.* 139, 10715–10722. doi: 10.1021/jacs.7b04132

Atzori, C., Lomachenko, K. A., Øien-Ødegaard, S., Lamberti, C., Stock, N., Barolo, C., and Bonino, F. (in press). Disclosing the Properties of a New Ce(III)-Based MOF: $Ce_2(NDC)_3(DMF)_2$. *Cryst. Growth Des.* doi: 10.1021/acs.cgd.8b01369

Bezrukov, A. A., and Dietzel, P. D. C. (2017). A permanently porous yttrium–organic framework based on an extended tridentate phosphine containing linker. *Inorg. Chem.* 56, 12830–12838. doi: 10.1021/acs.inorgchem.7b01574

Chen, Y., Zhang, S., Chen, F., Cao, S., Cai, Y., Li, S., et al. (2018). Defect engineering of highly stable lanthanide metal-organic frameworks by particle modulation for coating catalysis. *J. Mater. Chem. A* 6, 342–348. doi: 10.1039/C7TA09036F

Chen, Z., Weseliński, Ł. J., Adil, K., Belmabkhout, Y., Shkurenko, A., Jiang, H., et al. (2017). Applying the power of reticular chemistry to finding the missing

alb-MOF platform based on the (6,12)-coordinated edge-transitive net. *J. Am. Chem. Soc.* 139, 3265–3274. doi: 10.1021/jacs.7b00219

Chui, S. S. Y., Lo, S. M. F., Charmant, J. P. H., Orpen, A. G., and Williams, I. D. (1999). A chemically functionalizable nanoporous material $[Cu_3(TMA)_2(H_2O)_3]_n$. *Science* 283, 1148–1150. doi: 10.1126/science.283.5405.1148

Coles, S. J., and Gale, P. A. (2012). Changing and challenging times for service crystallography. *Chem. Sci.* 3, 683–689. doi: 10.1039/C2SC00955B

Dan, M., Cheetham, A. K., and Rao, C. N. (2006). Diverse structures and dimensionalities in hybrid frameworks of strontium and lanthanum with isomeric dihydroxybenzoates. *Inorg. Chem.* 45, 8227–8238. doi: 10.1021/ic060917k

Decadt, R., Van Hecke, K., Depla, D., Leus, K., Weinberger, D., Van Driessche, I., et al. (2012). Synthesis, crystal structures, and luminescence properties of carboxylate based rare-earth coordination polymers. *Inorg. Chem.* 51, 11623–11634. doi: 10.1021/ic301544q

Duan, J., Higuchi, M., Foo, M. L., Horike, S., Rao, K. P., and Kitagawa, S. (2013). A family of rare earth porous coordination polymers with different flexibility for CO_2/C_2H_4 and CO_2/C_2H_6 separation. *Inorg. Chem.* 52, 8244–8249. doi: 10.1021/ic401157n

Furukawa, H., Cordova, K. E., O'Keeffe, M., and Yaghi, O. M. (2013). The chemistry and applications of metal-organic frameworks. *Science* 341:1230444. doi: 10.1126/science.1230444

Gong, H. Y., Rambo, B. M., Nelson, C. A., Cho, W., Lynch, V. M., Zhu, X., et al. (2012). Multi component self-assembly: supramolecular organic frameworks containing metal–rotaxane subunits (RSOFs). *Dalton Trans.* 41, 1134–1137. doi: 10.1039/C1DT11495F

Guillerm, V., Weselinski, Ł. J., Belmabkhout, Y., Cairns, A. J., D'elia, V., Wojtas, Ł., et al. (2014). Discovery and introduction of a (3,18)-connected net as an ideal blueprint for the design of metal–organic frameworks. *Nat. Chem.* 6, 673–680. doi: 10.1038/nchem.1982

Guo, H., Zhu, Y., Wang, S., Su, S., Zhou, L., and Zhang, H. (2012). Combining coordination modulation with acid–base adjustment for the control over size of metal–organic frameworks. *Chem. Mater.* 24, 444–450. doi: 10.1021/cm202593h

Horcajada, P., Salles, F., Wuttke, S., Devic, T., Heurtaux, D., Maurin, G., et al. (2011). How linker's modification controls swelling properties of highly flexible iron(III) dicarboxylates MIL-88. *J. Am. Chem. Soc.* 133, 17839–17847. doi: 10.1021/ja206936e

Jiang, H. L., Tsumori, N., and Xu, Q. (2010). A series of (6,6)-connected porous lanthanide–organic framework enantiomers with high thermostability and exposed metal sites: scalable syntheses, structures, and sorption properties. *Inorg. Chem.* 49, 10001–10006. doi: 10.1021/ic101294s

Kim, Y., Yang, T., Yun, G., Ghasemian, M. B., Koo, J., Lee, E., et al. (2015). Hydrolytic transformation of microporous metal–organic frameworks to hierarchical micro- and mesoporous MOFs. *Angew. Chem. Int. Ed.* 54, 13273–13278. doi: 10.1002/anie.201506391

Li, H., Eddaoudi, M., O'Keeffe, M., and Yaghi, O. M. (1999). Design and synthesis of an exceptionally stable and highly porous metal-organic framework. *Nature* 402, 276–279. doi: 10.1038/46248

Lin, Z. J., Yang, Z., Liu, T. F., Huang, Y. B., and Cao, R. (2012). Microwave-assisted synthesis of a series of lanthanide metal–organic frameworks and gas sorption properties. *Inorg. Chem.* 51, 1813–1820. doi: 10.1021/ic202082w

Liu, C., Eliseeva, S. V., Luo, T. Y., Muldoon, P. F., Petoud, S., and Rosi, N. L. (2018). Near infrared excitation and emission in rare earth MOFs via encapsulation of organic dyes. *Chem. Sci.* 9, 8099–8102. doi: 10.1039/C8SC03168A

Liu, K., Li, X., Ma, D., Han, Y., Li, B., Shi, Z., et al. (2017). A microporous yttrium metal-organic framework of an unusual nia topology for high adsorption selectivity of C_2H_2 and CO_2 over CH_4 at room temperature. *Mater. Chem. Front.* 1, 1982–1988. doi: 10.1039/C7QM00164A

Luebke, R., Belmabkhout, Y., Weseliński, L. J., Cairns, A. J., Alkordi, M., Norton, G., et al. (2015). Versatile rare earth hexanuclear clusters for the design and synthesis of highly-connected ftw-MOFs. *Chem. Sci.* 6, 4095–4102. doi: 10.1039/C5SC00614G

Luo, J., Xu, H., Liu, Y., Zhao, Y., Daemen, L. L., Brown, C., et al. (2008). Hydrogen adsorption in a highly stable porous rare-earth metal-organic framework: sorption properties and neutron diffraction studies. *J. Am. Chem. Soc.* 130, 9626–9627. doi: 10.1021/ja801411f

Macrae, C. F., Bruno, I. J., Chisholm, J. A., Edgington, P. R., Mccabe, P., Pidcock, E., et al. (2008). Mercury CSD 2.0 - new features for the visualization and investigation of crystal structures. *J. Appl. Cryst.* 41, 466–470. doi: 10.1107/S0021889807067908

Marshall, R. J., Hobday, C. L., Murphie, C. F., Griffin, S. L., Morrison, C. A., Moggach, S. A., et al. (2016). Amino acids as highly efficient modulators for single crystals of zirconium and hafnium metal-organic frameworks. *J. Mater. Chem. A* 4, 6955–6963. doi: 10.1039/C5TA10401G

Marshall, R. J., Lennon, C. T., Tao, A., Senn, H. M., Wilson, C., Fairen-Jimenez, D., et al. (2018). Controlling interpenetration through linker conformation in the modulated synthesis of Sc metal–organic frameworks. *J. Mater. Chem. A* 6, 1181–1187. doi: 10.1039/C7TA09699B

McGuire, C. V., and Forgan, R. S. (2015). The surface chemistry of metal–organic frameworks. *Chem. Commun.* 51, 5199–5217. doi: 10.1039/C4CC04458D

Miller, S. R., Wright, P. A., Serre, C., Loiseau, T., Marrot, J., and Férey, G. (2005). A microporous scandium terephthalate, $Sc_2(O_2CC_6H_4CO_2)_3$, with high thermal stability. *Chem. Commun.* 30, 3850–3852. doi: 10.1039/b506677h

Moghadam, P. Z., Li, A., Wiggin, S. B., Tao, A., Maloney, A. G. P., Wood, P. A., et al. (2017). Development of a cambridge structural database subset: a collection of metal–organic frameworks for past, present, and future. *Chem. Mater.* 29, 2618–2625. doi: 10.1021/acs.chemmater.7b00441

Mohideen, M. I. H., Belmabkhout, Y., Bhatt, P. M., Shkurenko, A., Chen, Z., Adil, K., et al. (2018). Upgrading gasoline to high octane numbers using a zeolite-like metal–organic framework molecular sieve with ana-topology. *Chem. Commun.* 54, 9414–9417. doi: 10.1039/C8CC04824J

Pagis, C., Ferbinteanu, M., Rothenberg, G., and Tanase, S. (2016). Lanthanide-based metal organic frameworks: synthetic strategies and catalytic applications. *ACS Catal.* 6, 6063–6072. doi: 10.1021/acscatal.6b01935

Perles, J., Iglesias, M., Martín-Luengo, M. Á., Monge, M. Á., Ruiz-Valero, C., and Snejko, N. (2005). Metal–organic scandium framework: useful material for hydrogen storage and catalysis. *Chem. Mater.* 17, 5837–5842. doi: 10.1021/cm051362e

Schaate, A., Roy, P., Godt, A., Lippke, J., Waltz, F., Wiebcke, M., et al. (2011). Modulated synthesis of zr-based metal–organic frameworks: from nano to single crystals. *Chem. Eur. J.* 17, 6643–6651. doi: 10.1002/chem.201003211

Serre, C., Millange, F., Thouvenot, C., Gardant, N., Pellé, F., and Férey, G. (2004). Synthesis, characterisation and luminescent properties of a new three-dimensional lanthanide trimesate: $M((C_6H_3)–(CO_2)_3)$ (M = Y, Ln) or MIL-78. *J. Mater. Chem.* 14, 1540–1543. doi: 10.1039/B312425H

Singha, D. K., Majee, P., Mondal, S. K., and Mahata, P. (2015). Visible detection of explosive nitroaromatics facilitated by a large stokes shift of luminescence using europium and terbium doped yttrium based MOFs. *RSC Adv.* 5, 102076–102084. doi: 10.1039/C5RA22599J

Surblé, S., Serre, C., Millange, F., Pelle, F., and Férey, G. (2005). Synthesis, characterisation and properties of a new three-dimensional Yttrium–Europium coordination polymer. *Solid State Sci.* 7, 1074–1082. doi: 10.1016/j.solidstatesciences.2005.04.015

Wang, C. C., Yeh, C. T., Ke, S. Y., Cheng, Y. T., Yang, C. C., Lee, G. H., et al. (2015). Assembly of three Nd(III) 2,6-naphthalenedicarboxylates (ndc^{2-}) 3D coordination polymers based on various secondary building units (SBUs): structural diversity and gas sorption properties. *RSC Adv.* 5, 92378–92386. doi: 10.1039/C5RA10799G

Wang, Z., Jin, C. M., Shao, T., Li, Y. Z., Zhang, K. L., Zhang, H. T., et al. (2002). Syntheses, structures, and luminescence properties of a new family of three-dimensional open-framework lanthanide coordination polymers. *Inorg. Chem. Commun.* 5, 642–648. doi: 10.1016/S1387-7003(02)00515-4

Wei, N., Zuo, R. X., Zhang, Y. Y., Han, Z. B., and Gu, X. J. (2017). Robust high-connected rare-earth MOFs as efficient heterogeneous catalysts for CO_2 conversion. *Chem. Commun.* 53, 3224–3227. doi: 10.1039/C7CC00363C

Weng, D., Zheng, X., and Jin, L. (2006). Assembly and upconversion properties of lanthanide coordination polymers based on hexanuclear building blocks with (μ_3-OH) bridges. *Eur. J. Inorg. Chem.* 2006, 4184–4190. doi: 10.1002/ejic.200600491

Wu, H., Chua, Y. S., Krungleviciute, V., Tyagi, M., Chen, P., Yildirim, T., et al. (2013). Unusual and highly tunable missing-linker defects in zirconium metal–organic framework UiO-66 and their important effects on gas adsorption. *J. Am. Chem. Soc.* 135, 10525–10532. doi: 10.1021/ja404514r

Xue, D. X., Belmabkhout, Y., Shekhah, O., Jiang, H., Adil, K., Cairns, A. J., et al. (2015). Tunable rare earth fcu-MOF platform: access to adsorption kinetics driven gas/vapor separations via pore size contraction. *J. Am. Chem. Soc.* 137, 5034–5040. doi: 10.1021/ja5131403

Xue, D. X., Cairns, A. J., Belmabkhout, Y., Wojtas, L., Liu, Y., Alkordi, M. H., and Eddaoudi, M. (2013). Tunable rare-earth fcu-MOFs: a platform for systematic enhancement of CO_2 adsorption energetics and uptake. *J. Am. Chem. Soc.*135, 7660–7667. doi: 10.1021/ja401429x

Yang, X., and Xu, Q. (2017). Bimetallic metal–organic frameworks for gas storage and separation. *Cryst. Growth Des.* 17, 1450–1455. doi: 10.1021/acs.cgd.7b00166

Zheng, Y., Liu, K., Sun, X., Guan, R., Su, H., You, H., et al. (2015). A series of nano/micro-sized metal–organic frameworks with tunable photoluminescence properties. *CrystEngComm* 17, 2321–2326. doi: 10.1039/C4CE02456G

Conflict of Interest Statement: The authors declare that the research was conducted in the absence of any commercial or financial relationships that could be construed as a potential conflict of interest.

Copyright © 2019 Griffin, Wilson and Forgan. This is an open-access article distributed under the terms of the Creative Commons Attribution License (CC BY). The use, distribution or reproduction in other forums is permitted, provided the original author(s) and the copyright owner(s) are credited and that the original publication in this journal is cited, in accordance with accepted academic practice. No use, distribution or reproduction is permitted which does not comply with these terms.

frontiers in Chemistry

ORIGINAL RESEARCH
published: 20 June 2019
doi: 10.3389/fchem.2019.00447

Clustering-Triggered Emission of Carboxymethylated Nanocellulose

Meng Li[1,2]*, *Xiaoning Li*[1,2], *Xuefei An*[1,2], *Zhijun Chen*[3]* and *Huining Xiao*[4]*

[1] Hebei Key Lab of Power Plant Flue Gas Multi-Pollutants Control, Department of Environmental Science and Engineering, North China Electric Power University, Baoding, China, [2] MOE Key Laboratory of Resources and Environmental Systems Optimization, Ministry of Education, Beijing, China, [3] Key Laboratory of Bio-based Material Science and Technology of Ministry of Education, Northeast Forestry University, Harbin, China, [4] Department of Chemical Engineering, University of New Brunswick, Fredericton, NB, Canada

Non-conjugated polymers with luminescence emission property have recently drawn great attention due to their promising applications in different areas. Most traditional organic synthetic non-conjugated polymers required complicated synthesis. Herein, we report a non-conjugated biomass material, carboxymethylated nanocellulose (C-CNC), which is found to be practically non-luminescent in dilute solutions, while being highly emissive when aggregated as nanosuspensions. We propose that the luminescence of C-CNC originates from the through-space conjugation of oxygen atoms and carboxyl groups of C-CNC. Thus, a clearer mechanism of clusteroluminescence was provided with the subsequent experiments. The effects of concentration of C-CNC, solvent, temperature and pH have also been investigated. In addition, ethylenediamine (EDA) has been employed to "lock" C-CNC material via the bonding of amide groups with carboxylic groups. As prepared C-CNC/EDA confirmed that the clusteroluminescence was attributed to the amide moieties and through-space conjugation between oxygen and carbonyl moieties. Density functional theory (DFT) calculations have also been employed to confirm the luminescence mechanism. It is believed that such clustering-triggered emission mechanism is instructive for further development of unconventional luminogens.

Keywords: carboxymethylated nanocellulose, clustering-triggered emission, carboxyl groups, space conjugation, nanomaterials

OPEN ACCESS

Edited by:
Tony D. James,
University of Bath, United Kingdom

Reviewed by:
Lei Cui,
Shanghai University, China
Shaomin Ji,
Guangdong University of Technology, China

***Correspondence:**
Meng Li
princessviola@163.com
Zhijun Chen
chenzhijun@nefu.edu.cn
Huining Xiao
huiningxiao@hotmail.com

Specialty section:
This article was submitted to Supramolecular Chemistry, a section of the journal Frontiers in Chemistry

Received: *01 May 2019*
Accepted: *03 June 2019*
Published: *20 June 2019*

Citation:
Li M, Li X, An X, Chen Z and Xiao H (2019) Clustering-Triggered Emission of Carboxymethylated Nanocellulose. Front. Chem. 7:447. doi: 10.3389/fchem.2019.00447

INTRODUCTION

Over several decades, fluorescent organic molecules and nanomaterials have attracted much attention and interest due to their special photophysical properties and wide applications in areas such as bioimaging, organic light-emitting diodes (OLEDs), light-emitting electrochemical cells (LECs), and phototherapy reagents, etc (Schwartz et al., 2007; Qin et al., 2012; Wang et al., 2012; Cheng et al., 2015; Li et al., 2018c). Initially, fluorescent organic molecules are widely employed in inorganic ion detection, drug analysis, etc (Bian et al., 2014; Li et al., 2018b). However, most of the reported probe molecules have suffered from the aggregation-caused quenching (ACQ) effect and faced the problem of poor solubility, biocompatibility, and solid-state luminescence, which has greatly limited their potential applications (O'Brien et al., 2010; Wu and Butt, 2016; Huang et al., 2019). Until 2001, Tang and co-workers raised the concept of aggregation-induced emission (AIE), and reported AIE luminogens (Luo et al., 2001). Compared to ACQ molecules, AIE luminogens could turn from non-luminescent or weak fluorophors into strong emitters when they are aggregated into nanoparticles in poor solvents or fabricated into thin films in solid state

(Xing et al., 2007; Yamaguchi et al., 2017). Therefore, many AIE luminogens have been synthesized to understand the luminous mechanism due to their unique luminescence (Chen et al., 2013; Qiu et al., 2018). Most AIE luminogens are generally constructed by aromatic groups and conjugated subunits, which function as chromophore centers (Yuan et al., 2014). However, achieving organic fluorescent nanomaterials with aggregation-induced emission is not an easy task as lots of aggregation-induced emission luminogens required complicated synthesis or toxic starting materials.

Recently, some non-conventional luminogens such as non-conjugated polymers, which are free of aromatic building blocks, have been reported due to their unique clustering-triggered emission (CTE) (Yuan and Zhang, 2017; Chen et al., 2018a). Compared to the conventional AIE luminogens, the CTE luminogens are generally more hydrophilic, easy to prepare, and biocompatible, making them ideal for biological and medical applications (Qin et al., 2017; Dou et al., 2018). Typically, these polymers have electron-rich heteroatoms, such as nitrogen (N), oxygen (O), sulfur (S), phosphorus (P) (Zhao et al., 2015; Zhou et al., 2016; Shang et al., 2017). Therefore, the luminescence mechanism may be attributed to clustering of these electronics-rich atoms and subsequent electron cloud overlaps to form extend conjugation to rationalize the unique AIE properties (Shen et al., 2012; Zhu et al., 2015). Moreover, it is found that some natural products also have visible light in concentrated and solid state conditions, such as dendrimers, starch, amino acids and sodium alginate, etc (Wang and Imae, 2004; Ye et al., 2017; Dou et al., 2018; He et al., 2018). Such CTE materials have huge potential in sensing and cell imaging technologies, which could contribute to the development of nano-luminescence materials (Jin et al., 2016; Ma et al., 2016; Li et al., 2017).

Most clustering-triggered emission (CTE) luminogens have been fabricated by precipitation of precursor organic molecules and polymers (Mohamed et al., 2015; Li et al., 2017; Lu et al., 2017). However, few works have explored the luminescence of natural products with low cost and good biocompatibility (Zhao et al., 2016). In this work, we studied the luminescence behavior of carboxymethylated nanocellulose (C-CNC) with rich carboxyl groups (Dong and Roman, 2007; Yang et al., 2016). The as-prepared C-CNC showed excitation/polarity-dependent fluorescence emission, indicating their potential in differentiating solvents with different polarities. Additionally, the effects of concentration of C-CNC, solvent, temperature, pH and amination with EDA have been investigated. Density functional theory (DFT) calculations have also been employed to understand the clusteroluminescent emission that could be attributed to through-space conjugation between oxygen atoms and carbonyl groups (Miao et al., 2016; Zhu et al., 2016). These results should be highly implicative for further understanding the emission of CTE luminogens.

EXPERIMENTAL SECTION

Chemicals and Instruments

The experimental reagents used in this research were isopropyl alcohol, methano, ethanol absolute, N,N-dimethylformamide, tetrahydrofuran, ethylenediamine, monochloroacetic acid, hydrochloric acid, degreased cotton, sodium chloride, sodium hydroxide, sodium carbonate, sodium perborate, and pH buffer. All these materials were AR grade and purchased from Tianjin Kermel Chemical Reagent. Ethanol absolute, N,N-dimethylformamide and tetrahydrofuran were analytical of chromatographic grade. The water used in all experiments was ultrapure water, produced using a Smart-RO ultrapure water system (Hitech Instruments Co., Ltd., Shanghai, China).

The instruments were used as follows: mass flow meter; F97Pro fluorescence spectrophotometer; DF-101S heat collection-constant temperature type magnetic stirrer, Mettler Toledo electronic balance; SHENGYANG Ultrasonic Cleaner, TH21 Heating thermostat.

Characterization

The scanning electron microscopy (SEM) images on the C-CNC were observed with the magnification of 2500–100 000 times via the HitachiS-4800 SEM. After the samples were sonicated for 10–15 min and then dripped onto the conductive adhesive film, the acceleration voltage of this process was 0.5–30 kV. The crystal structure of the sample at an acceleration voltage of 200 kV was observed using a JEM-2100 transmission electron microscope (TEM).

The crystalline phase of the sample was characterized by X-ray diffraction (XRD, Bruker D8 advance) at a wide angle (10–90°) scan in steps of 0.01 degrees. And the functional group on the surface of C-CNC was measured by Fourier transform infrared spectrometer (FT/IR-200, JASCO, Japan), and for each sample, a scan of 50 mg of the sample in the range of 4,000–500 cm^{-1} was recorded with a wave number accuracy of 0.01 cm^{-1}. The X-ray photoelectron spectrum (XPS) of the sample was measured on a MultiLab 2000 XPS (Thermo VG Scientific). ^1H NMR spectra were recorded on an AVANCE III HD 500 MHz spectrometer (Bruker Corp., Karlsruhe, Germany) with D_2O. Theoretical calculations were carried out using the B3LYP/6-31G(d) basis set and density functional theory (DFT). The fluorescence lifetimes of C-CNC were measured on a FLS980 spectrometer (Edinburgh Instruments, UK). The quantum yield (Φ) was determined by a FLS920 spectrometer with an excitation wavelength of 360 nm at 25°C (Edinburgh Instruments, UK). Dynamic light scattering (DLS) was measured on a ZEN3700 (Malvern, UK).

The Preparation of C-CNC

C-CNC was synthesized according to the reported methods (Hebeish et al., 2010). Three gram finely degreased cotton was dispersed in 180 mL isopropanol and mechanically stirred at 25°C for 30 min. A calculated volume of 8 mL 50% NaOH (w/v) was added dropwise over about 10 min and the mixture was continuously stirred at 25°C for 60 min. Monochloroacetic acid (0.4 g) dissolved in 15 mL of isopropyl alcohol and then neutralized with the equivalent amount of Na_2CO_3. After the temperature rose to 60°C, the above mixture continued to stir for 60 min. At the end of this process, the mixture was filtered and suspended in 150 mL of 80% methanol and then neutralized with acetic acid. After the reaction, the sample was washed three times with methanol and dried to obtain C-CNC.

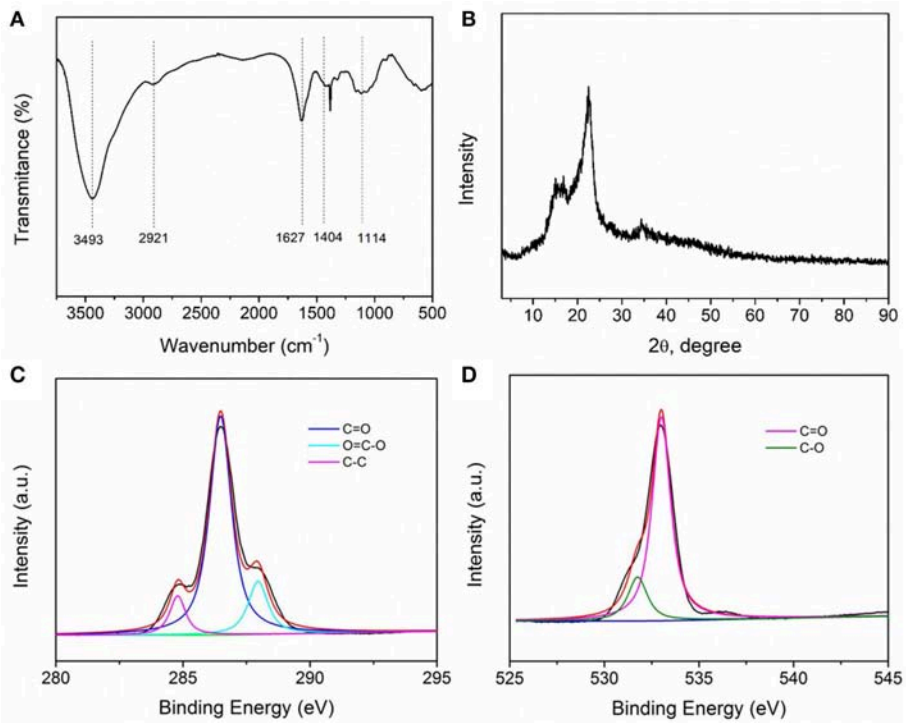

FIGURE 1 | (A) FTIR spectra of C-CNC, **(B)** X-ray diffraction pattern of C-CNC, **(C)** C 1s XPS spectrum of C-CNC, **(D)** O 1s XPS spectrum of C-CNC.

Subsequently, C-CNC was purified by precipitation and freeze dried for further use. The carboxyl group content measured by conductivity was 0.6 mmol/g (**Figure S1**).

The Preparation of C-CNC/EDA

C-CNC (100 mg) and EDA (4 μL) were dissolved in deionized water (50 mL) and mixed uniformly. Then the solution was transferred to a pressure bottle (100 mL) and heated at 100°C for 8 h in a vacuum oven. After the reaction, the reactors were cooled down to room temperature naturally. The prepared sample was directly measured using a fluorescence spectrophotometer.

RESULTS AND DISCUSSION

Characterizations

Fourier Transform Infra-Red (FTIR) spectroscopy was initially employed to understand the structure of C-CNC (**Figure 1A**). A plurality of broad peaks in the 1,000–1,200 cm^{-1} region correspond to -C-O-C- stretching vibration. For the bending vibration mode of -CH_2, the spectrum of C-CNC showed a peak at 2,921 cm^{-1}. The broad peaks in the 3,200–3,600 cm^{-1} region correspond to -OH stretching vibrations. For C-CNC, the main spectra of the peaks at about 1,404 cm^{-1} corresponds to COO- symmetrical stretching vibrations and the peaks at about 1,627 cm^{-1} ascribed to the asymmetric stretching vibrations of COO-. A peak at 3,493 cm^{-1} appeared in the spectrum, ascribed to the -OH stretching vibrations for C-CNC.

As shown in **Figure 1B**, XRD characterization of the C-CNC was performed to investigate the phase structure of the sample. The diffraction peaks of C-CNC at 15.1°, 16.8°, 22.5°, and 34.3° corresponding to the (1-10), (100), (200), (004) crystallographic planes, which indicates the C-CNC belongs to the typical type of cellulose I (Li and Renneckar, 2011; Rafieian and Simonsen, 2014; Du et al., 2016). XPS measurement was examined to further study the chemical state changes of the C-CNC. It can be seen from **Figure 1C** that the high-resolution C 1s XPS spectra of the sample. For the C-CNC, the peak at 288.9 eV (C1) is typically ascribed to the sp^2-bonded carbon (O-C=O). The peak at 287.8 eV (C2) is considered to C=O bond. And the peak at 284.6 eV (C3) could be ascribed to sp^2 C-C bonds. These results confirm the existence of carboxyl groups in C-CNC. The XPS O 1s spectra can be seen from **Figure 1D** with peaks at 530.78 eV and 532.88 eV, corresponding to C-O and C=O bond in the carboxyl group of C-CNC (You et al., 2017). A representative SEM image of the C-CNC can be seen from **Figure S2a**, which shows a rugged surface (Querejeta-Fernandez et al., 2014). **Figure S2b** shows a typical transmission electron microscope (TEM) image of C-CNC. The C-CNCs in water show a substantially clear dispersion with a rod-like morphology (Habibi et al., 2010; Majoinen et al., 2014). The Raman spectrum of C-CNC presents that there is no visible raman peaks with large slits of C-CNC, which may be due to the poor fluorescent intensity of C-CNC solutions (**Figure S3**).

Fluorescent Tests of C-CNC

As a starting point for our research, excitation-dependent fluorescence emission of C-CNC was observed (**Figure S4**). We could see that the bathochromic shift in fluorescence

when the excitation wavelength was increased from 320 to 360 nm. Additionally, it found a slight difference at 320 nm, which might be attributed to the cluster size of C-CNC. Upon addition of organic solvent, C-CNC might form aggregates in different sizes. Aggregates in different size might have different through-space conjugated structures, which made these aggregates with different excitation and emission wavelengths. Additionally, these through-space conjugated structures had a high molecular energy gap and were mainly located in deep UV region, as they cannot form a big conjugated area. As a result, exposure of the sample to different wavelengths meant different energy-matched aggregates would be excited. However, the shape of fluorescence emission did not substantially change with excitation wavelength for normal molecularly dispersed organic chromophores. This result might be attributable to polydisperse through-space-conjugation units consisting of carbonyl moieties (Dou et al., 2018; Ma et al., 2018). Moreover, the 360 nm was selected as the

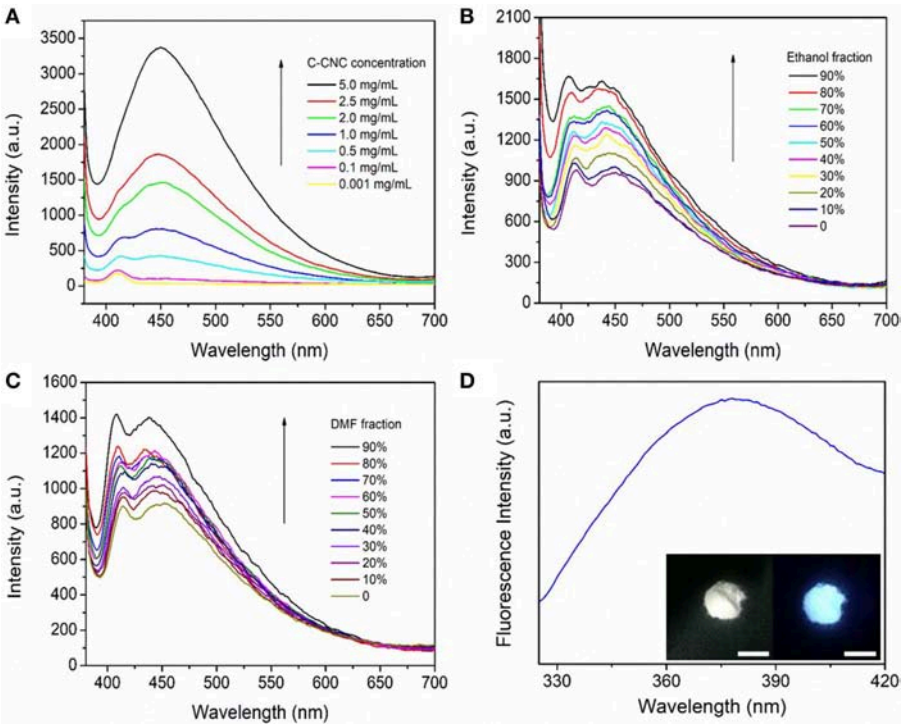

FIGURE 2 | (A) Fluorescence emission of C-CNC at different concentrations in water (excitation wavelength = 360 nm), **(B)** Fluorescence emission of C-CNC (0.5 mg/mL) in mixtures of ethanol and water (excitation wavelength = 360 nm), **(C)** Fluorescence emission of C-CNC (0.5 mg/mL) in mixtures of DMF and water (excitation wavelength = 360 nm), **(D)** Fluorescence emission of C-CNC in the solid state (excitation wavelength = 300 nm). Inset: images of C-CNC powder in bright field and upon excitation at 365 nm. Scale bar = 1 cm.

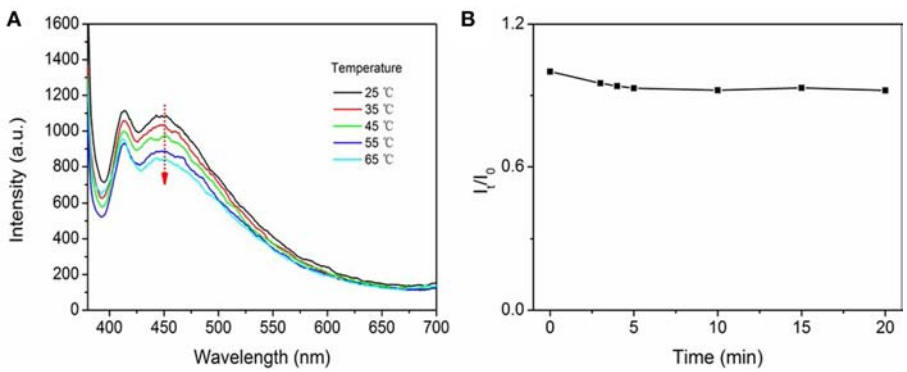

FIGURE 3 | (A) Fluorescence of C-CNC (0.5 mg/mL) in water at different temperatures (25–65°C), (excitation wavelength = 360 nm), **(B)** Fluorescence intensity of C-CNC (excitation wavelength = 360 nm), I_t is fluorescence intensity after UV irradiation and I_0 is fluorescence intensity without UV irradiation.

excitation wavelength with its nice emission intensity in the subsequent experiments.

To get insight into the clustering of C-CNC, the absorption spectra of different concentrations of C-CNC were examined (Qin et al., 2017; Chen et al., 2018b). At low concentrations, we could only see the single maximum absorption peak of C-CNC. With the concentration of C-CNC slowly increasing, a new red-shifted peak appears at 340 nm (**Figure S5a**) (Ma et al., 2018). When the C-CNC reached an optimum concentration of 0.5 mg/mL, the peak intensity increased significantly (**Figure S5a**). These results provide a likelihood for the presence of aggregation in concentrated solutions of C-CNC (Chen et al., 2018b). And the apparent peak of C-CNC around 340 nm was found under excitation (**Figure S5b**). As shown in **Figure 2A**, there was a similar trend between fluorescence and UV-vis spectra of C-CNC solutions. Enhancement of fluorescence was also observed when the concentration of C-CNC was increased, with higher concentrations triggering constant fluorescence enhancement. When the C-CNC concentration reached 5.0 mg/mL, the fluorescence was significantly enhanced, indicating a positive correlation and fluorescence emission of C-CNC (**Figure S5c**). It can be seen from **Figure 2B** that the fluorescence was very low when C-CNC was dissolved in good solvent water. However, the fluorescence intensity gradually increased, as the poor solvent ethanol was added to the C-CNC aqueous solution (Zhou et al., 2016; Qin et al., 2017; Yang et al., 2017). When the fraction of ethanol is 90%, the fluorescence of C-CNC is increased by 1.6 times, which provides conclusive evidence that C-CNC produces cluster-induced luminescence. Moreover, other organic solvents such as N,N-dimethylformamide (DMF) and tetrahydrofuran (THF) had also been employed to verify the clustering-triggered emission. The C-CNC showed fluorescence enhancement as the DMF and THF concentration increased, indicating an interaction between the fluorophore and the solvent (**Figures 2C** and **S5d**), namely, the polarity of the solvent affected the fluorescence emission (Zhao et al., 2015; Miao et al., 2016; Gu et al., 2018). C-CNC showed strong fluorescence emission in the solid state with a quantum yield of 7.8% (**Figure 2D**), meanwhile, the C-CNC aqueous solution exhibited a quantum yield of 12.3% (Crosby and Demas, 1971). Furthermore, the excited state of C-CNC is a double exponential decay process with an average fluorescence lifetime of 3.16 ns, demonstrating its excellent optical properties (**Figure S6**). In the control experiment, the nanocellulose did not show fluorescence enhanced with the

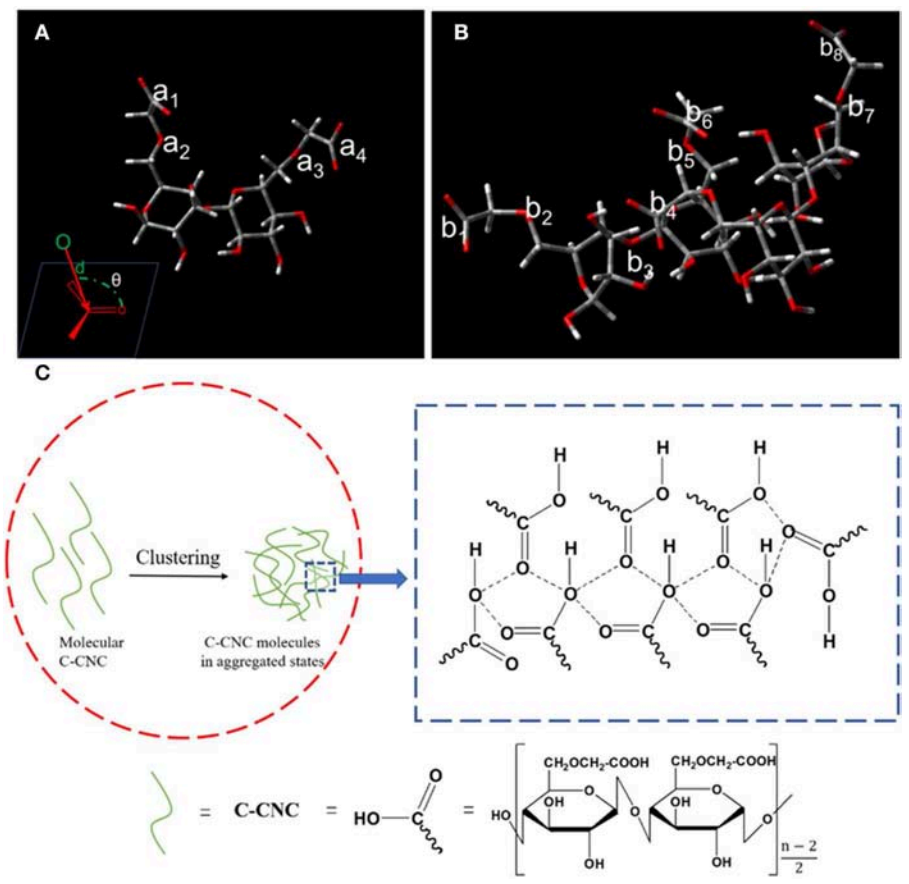

FIGURE 4 | Optimized conformations of C-CNC **(A)**, inset: proposed model of n → π* interaction and C-CNC dimer, **(B)** in water, red sticks = oxygen atoms, gray sticks = carbon atoms, **(C)** Schematic illustration of the emission mechanism of C-CNC.

ethanol concentration increased, which suggested the carboxyl groups were the luminance center of C-CNC (**Figure S7**).

In order to further understand the interactions of carboxyl groups on C-CNC, acid-base stability of C-CNC was also investigated at different pH solutions. Generally, C-CNC showed nice stability in an acidic environment (**Figure S8a**). However, it was found that the fluorescence intensity decreased slightly in an alkaline environment of C-CNC (**Figure S8b**). As shown in **Figure S8c**, the fluorescence intensity of C-CNC was highest at pH = 4, which may be ascribed to the through-space conjugation of carbonyl groups, especially hydrogen bonds increase, leading to the fluorescence enhancement. However, in basic environment, the interactions of carbonyl groups diminished due to the electrostatic repulsion, which resulted in reduced clustering of C-CNC. These results further verify the CTE mechanism of C-CNC.

Subsequently, the emission of C-CNC was measured at different temperatures to determine the effect of temperature. When the temperature was raised from 25 to 65°C, a slight decrease was observed in fluorescence emission (**Figure 3A**). Additionally, the prepared C-CNC was measured by the DLS. It was found that the mean diameter of C-CNC at 25°C was 7.8 nm, however, the mean diameter was decreased to 6.2 nm at 65°C, indicating that the aggregates were reduced after heating (**Figure S9**). This slight change could be ascribed to the fact that an increase in temperature would disturb the interaction of the carbonyl groups, resulting in the interruption of C-CNC clusters, which is consistent with the literature (Ma et al., 2018). In addition, the photostability of C-CNC was examined. Compared with the traditional dyes, fluorescence materials with AIE properties generally show better photostability (Ma et al., 2018). After 20 min of UV irradiation, the fluorescence intensity of C-CNC decreased by about 8% (**Figure 3B**). These results demonstrate that C-CNC possess good anti-photobleaching ability, which is of great importance for further applications.

To further decipher the emission mechanism, DFT calculations were used to investigate the clusteroluminescence. A two-molecule unit was used as the model for calculations. The configurations of C-CNC and C-CNC dimers in water were optimized using DFT, B3LYP/6-31G(d) (**Figures 4A,B**). The intramolecular distance (d) (a_1-a_2, a_3-a_4, **Figure 4A**, inset) of adjacent oxygen and carbonyl moieties was 2.54 Å and 2.54 Å, respectively. The Bürgi-Dunitz trajectory (a_1-a_2 and a_3-a_4) for nucleophilic addition (θ, **Figure 4A**, inset) was about 143° and 88° in individual C-CNC molecules. This indicated that the lone pair (n) on the oxygen atom did not effectively interpenetrate the empty π* orbital of the carbonyl group and through-space conjugation did not occur (Feng et al., 2016; Wang et al., 2017). In **Figure 4B**, the DFT simulation illustrated that the intramolecular distance between adjacent oxygen and carbonyl moieties did not change a lot after formation of the C-CNC dimer. The intramolecular distance between b_1-b_2, b_3-b_4, b_5-b_6, b_7-b_8 was 2.54 Å, 2.47 Å, 2.50 Å and 2.50 Å, respectively. However, the Bürgi-Dunitz trajectory for nucleophilic addition (θ) changed a lot. The θ of b_1-b_2, b_3-b_4, b_5-b_6, b_7-b_8 was 100°, 113°, 119° and 111°, respectively. These results indicated a sub-van der Waals contact (d < 3.22 Å), with the carbon of the acceptor carbonyl group along the Bürgi-Dunitz trajectory for nucleophilic addition (95° < θ < 125°), which caused effective n → π* interaction and through-space electronic interactions. As a result, LUMO orbitals were lowed. The theoretical calculations confirmed that clusteroluminescence can be attributed to through-space conjugation of oxygen atoms and carbonyl moieties caused by clustering of C-CNC (**Figure 4C**).

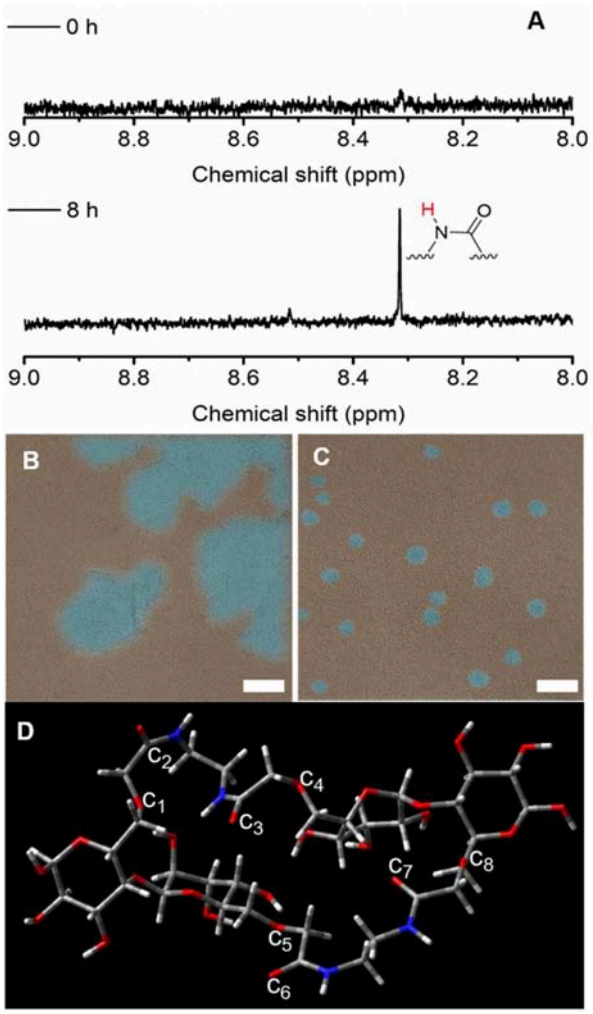

FIGURE 5 | (A) Partial ^{1}H NMR spectra of C-CNC and ethylenediamine in D_2O before (top) and after (bottom) reaction, **(B)** TEM images of aqueous solution of C-CNC and ethylenediamine before and **(C)** after reaction, scale bars = 10 nm, **(D)** Optimized conformation of C-CNC/EDA, red sticks = oxygen atoms, gray sticks = carbon atoms.

Encouraged by this result, we continued our experiment to further confirm the interaction of carboxyl groups for the CTE phenomenon. In this experiment, we used ethylenediamine to react with carboxyl groups on C-CNC in water with

different reaction time (Gómez et al., 2017). The prepared C-CNC/EDA was monitored by ^{1}H NMR. In **Figure 5A**, it was found that no peaks were observed in the region of 8.2–8.4 ppm, but a new peak at ∼8.32 ppm, which was attributed to amide units, indicating that C-CNC/EDA was successfully prepared. In a control experiment, ^{1}H NMR of C-CNC did not show a change in the region of 8.2–8.4 ppm in the absence of ethylenediamine (**Figure S10**). TEM images before the reaction showed only dried random C-CNC aggregates and no nanodots (**Figure 5B**). After the reaction, TEM images of samples that had not undergone any separation or purification clearly showed nanodots with an average diameter of 5 nm (**Figure 5C**). This is further evidence for the amidation reaction between C-CNC and ethylenediamine. As expected, the fluorescence of C-CNC/EDA enhanced with the increase of reaction time compared with C-CNC and ethylenediamine (**Figure S11**). The chemical reactions occurred between the amino group of ethylenediamine and the carboxyl group of C-CNC, which were used to "lock" C-CNC, resulting in promoting the clustering of C-CNC. The results further demonstrate that the enhanced emission of C-CNC may be due to the interactions of carboxyl groups on C-CNC. To further verify the mechanism, DFT, B3LYP/6-31G(d) calculation was used. The distance (d) of c_1-c_2 c_3-c_4, c_5-c_6, and c_7-c_8 was 2.46 Å, 2.44 Å, 2.44 Å and 2.46 Å, respectively (**Figure 5D**). The Bürgi-Dunitz trajectory (θ) of c_1-c_2 c_3-c_4, c_5-c_6, and c_7-c_8 was 125°, 124°, 89° and 91°, respectively. Compared with the C-CNC cluster, it was surprisingly found that less O and carbonyl C couples formed effective $n \rightarrow \pi^*$ interaction in the C-CNC/EDA, which was inconsistent with our hypothesis. Therefore, such high fluorescence intensity may be attributed to the introduction of amide units, leading to through-space interaction of amide groups electrons resembling to those of aromatic structure caused by hydrogen bond (Feng et al., 2016). These results demonstrate that the enhanced fluorescence was caused by through-space conjugation of amide introduced. Furthermore, C-CNC was also investigated for its chiroptical properties. Interestingly, both C-CNC and C-CNC/EDA showed chirality (**Figure S12**), neither C-CNC nor C-CNC/EDA induced significant changes at detected concentrations, indicating that the chirality can be maintained very well after chemical modifications (Li et al., 2018a). The chirality of C-CNC could be further investigated for chiral sensing applications in future research.

CONCLUSION

Biomass material, C-CNC, was used to prepare CTE nanomaterials via a chemical carboxylation method. The C-CNC had a good quantum yield of 7.8% and 12.3% in solid state and aqueous solutions, respectively. It also had a lifetime of 3.16 ns and showed excitation/polarity-dependent emission. Both experimental and DFT calculations have been employed to confirm that the clusteroluminescent emission originates from the intermolecular through-space conjugation between oxygen atoms and carbonyl groups on C-CNC. In addition, the prepared C-CNC/EDA also confirmed that the clusteroluminescence was attributed to the amide moieties and through-space conjugation between oxygen and carbonyl moieties. We believe our work not only provides an easy and green preparation of CTE nanomaterials, but gives a new possible mechanism of fluorescence emission of non-conjugated materials.

DATA AVAILABILITY

The raw data supporting the conclusions of this manuscript will be made available by the authors, without undue reservation, to any qualified researcher.

AUTHOR CONTRIBUTIONS

ML designed the experiments, analyzed experimental results, and wrote the manuscript. XL and XA carried out the experiments. ZC and HX analyzed experimental results and provided guidance.

FUNDING

The present work is supported by the National Natural Science Foundation of China (Grant #: 21607044). This work was also supported by Natural Science Foundation of Hebei Province (Grant #: B2017502069) and the Fundamental Research Funds for the Central Universities (Grant #: 2018MS113).

SUPPLEMENTARY MATERIAL

The Supplementary Material for this article can be found online at: https://www.frontiersin.org/articles/10.3389/fchem.2019.00447/full#supplementary-material

REFERENCES

Bian, L., Ji, X., and Hu, W. (2014). A novel single-labeled fluorescent oligonucleotide probe for silver(I) ion detection in water, drugs, and food. *J. Agric. Food Chem.* 62, 4870–4877. doi: 10.1021/jf404792z

Chen, X., Liu, X., Lei, J., Xu, L., Zhao, Z., Kausar, F., et al. (2018a). Synthesis, clustering-triggered emission, explosive detection, and cell imaging of nonaromatic polyurethanes. *Mol. Syst. Des. Eng.* 3, 364–375. doi: 10.1039/C7ME00118E

Chen, X., Luo, W., Ma, H., Peng, Q., Yuan, W. Z., and Zhang, Y. (2018b). Prevalent intrinsic emission from nonaromatic amino acids and poly(amino acids). *Sci. Chi. Chem.* 61, 1–9. doi: 10.1007/s11426-017-9114-4

Chen, Y., Lin, J., Yuan, W., Yu, Z., Lam, J. W., and Tang, B. Z. (2013). 1-((12-Bromododecyl)oxy)-4-((4-(4-pentylcyclohexyl)phenyl)ethynyl) benzene: liquid crystal with aggregation-induced emission characteristics. *Sci. Chi. Chem.* 56, 1191–1196. doi: 10.1007/s11426-013-4950-5

Cheng, J., Li, Y., Sun, R., Liu, J., Gou, F., Zhou, X., et al. (2015). Functionalized Salen ligands linking with non-conjugated bridges: unique and colorful aggregation-induced emission, mechanism, and applications. *J. Mater. Chem. C* 3, 11099–11110. doi: 10.1039/C5TC02555A

Crosby, G. A., and Demas, J. N. (1971). Measurement of photoluminescence quantum yields. *Review. J. Phys. Chem.* 75, 991–1024. doi: 10.1021/j100678a001

Dong, S., and Roman, M. (2007). Fluorescently labeled cellulose nanocrystals for bioimaging applications. *J. Am. Chem. Soc.* 129, 13810–13811. doi: 10.1021/ja076196l

Dou, X., Zhou, Q., Chen, X., Tan, Y., He, X., Lu, P., et al. (2018). Clustering-triggered emission and persistent room temperature phosphorescence of sodium alginate. *Biomacromolecules* 19, 2014–2022. doi: 10.1021/acs.biomac.8b00123

Du, H., Liu, C., Mu, X., Gong, W., Lv, D., Hong, Y., et al. (2016). Preparation and characterization of thermally stable cellulose nanocrystals via a sustainable approach of FeCl3-catalyzed formic acid hydrolysis. *Cellulose* 23, 2389–2407. doi: 10.1007/s10570-016-0963-5

Feng, L., Fei, H., Liu, B., Yang, G., Gai, S., Yang, P., et al. (2016). g-C_3N_4 coated upconversion nanoparticles for 808 nm near-infrared light triggered phototherapy and multiple imaging. *Chem. Mater.* 28, 7935–7946. doi: 10.1021/acs.chemmater.6b03598

Gómez, F. N., Combariza, M. Y., and Blanco-Tirado, C. (2017). Facile cellulose nanofibrils amidation using a 'one-pot' approach. *Cellulose* 24, 717–730. doi: 10.1007/s10570-016-1174-9

Gu, X., Zhang, X., Ma, H., Jia, S., Zhang, P., Zhao, Y., et al. (2018). Corannulene-incorporated AIE nanodots with highly suppressed nonradiative decay for boosted cancer phototheranostics *in vivo*. *Adv. Mater.* 30:1801065. doi: 10.1002/adma.201801065

Habibi, Y., Lucia, L. A., and Rojas, O. J. (2010). Cellulose nanocrystals: chemistry, self-assembly, and applications. *Chem. Rev.* 110, 3479–3500. doi: 10.1021/cr900339w

He, Z., Ke, C., and Tang, B. Z. (2018). Journey of aggregation-induced emission research. *ACS Omega* 3, 3267–3277. doi: 10.1021/acsomega.8b00062

Hebeish, A. A., El-Rafie, M. H., Abdel-Mohdy, F. A., Abdel-Halim, E. S., and Emam, H. E. (2010). Carboxymethyl cellulose for green synthesis and stabilization of silver nanoparticles. *Carbohydr. Polym.* 82, 933–941. doi: 10.1016/j.carbpol.2010.06.020

Huang, Y., Xing, J., Gong, Q., Chen, L. C., Liu, G., Yao, C., et al. (2019). Reducing aggregation caused quenching effect through co-assembly of PAH chromophores and molecular barriers. *Nat. Commun.* 10, 1–9. doi: 10.1038/s41467-018-08092-y

Jin, G., Feng, G., Qin, W., Tang, B. Z., Liu, B., and Li, K. (2016). Multifunctional organic nanoparticles with aggregation-induced emission (AIE) characteristics for targeted photodynamic therapy and RNA interference therapy. *Chem. Commun.* 52, 2752–2755. doi: 10.1039/c5cc07818k

Li, D., Qin, W., Xu, B., Qian, J., and Tang, B. Z. (2017). AIE Nanoparticles with high stimulated emission depletion efficiency and photobleaching resistance for long-term super-resolution bioimaging. *Adv. Mater.* 29, 3643–3651. doi: 10.1002/adma.201703643

Li, F., Li, Y., Yang, X., Han, X., Jiao, Y., Wei, T., et al. (2018a). Highly fluorescent chiral N-S-doped carbon dots from cysteine: affecting cellular energy metabolism. *Angew. Chem.* 57, 2377–2382. doi: 10.1002/anie.201712453

Li, M., Liu, Z., Wang, H.-C., Sedgwick, A. C., Gardiner, J. E., Bull, S. D., et al. (2018b). Dual-function cellulose composites for fluorescence detection and removal of fluoride. *Dyes Pigment* 149, 669–675. doi: 10.1016/j.dyepig.2017.11.033

Li, M., Liu, Z., Wang, S., Calatayud, D. G., Zhu, W. H., James, T. D., et al. (2018c). Fluorescence detection and removal of copper from water using a biobased and biodegradable 2D soft material. *Chem. Commun.* 54, 184–187. doi: 10.1039/c7cc08035b

Li, Q., and Renneckar, S. (2011). Supramolecular structure characterization of molecularly thin cellulose I nanoparticles. *Biomacromolecules* 12, 650–659. doi: 10.1021/bm101315y

Lu, H., Hu, Z., and Feng, S. (2017). Nonconventional luminescence enhanced by silicone induced aggregation. *Chem. Asian J.* 12, 1213–1217. doi: 10.1002/asia.201700234

Luo, J., Xie, Z., Lam, J. W. Y., Cheng, L., Tang, B. Z., Chen, H., et al. (2001). Aggregation-induced emission of 1-methyl-1,2,3,4,5-pentaphenylsilole. *Chem. Commun.* 0, 1740–1741. doi: 10.1039/b105159h

Ma, H., Yang, Z., Cao, H., Lei, L., and Lei, Z. (2016). One bioprobe: a fluorescent and AIE-active macromolecule; two targets: nucleolus and mitochondria with long term tracking. *J. Mater. Chem. B* 5, 655–660. doi: 10.1039/C6TB02844F

Ma, Z., Liu, C., Niu, N., Chen, Z. J., Li, S. J., Liu, S. X., et al. (2018). Seeking brightness from nature: j aggregation-induced emission in cellulolytic enzyme lignin nanoparticles. *ACS Sustainable Chem. Eng.* 6, 3169–3175. doi: 10.1016/j.dyepig.2016.04.036

Majoinen, J., Haataja, J. S., Appelhans, D., Lederer, A., Olszewska, A., Seitsonen, J., et al. (2014). Supracolloidal multivalent interactions and wrapping of dendronized glycopolymers on native cellulose nanocrystals. *J. Am. Chem. Soc.* 136, 866–869. doi: 10.1021/ja411401r

Miao, X., Liu, T., Zhang, C., Geng, X., Meng, Y., and Li, X. (2016). Fluorescent aliphatic hyperbranched polyether: chromophore-free and without any N and P atoms. *Phys. Chem. Chem. Phys.* 18, 4295–4299. doi: 10.1039/c5cp07134h

Mohamed, M. G., Hsu, K. C., Hong, J. L., and Kuo, S. W. (2015). Unexpected fluorescence from maleimide-containing polyhedral oligomeric silsesquioxanes: nanoparticle and sequence distribution analyses of polystyrene-based alternating copolymers. *Polym. Chem.* 7, 135–145. doi: 10.1039/c5py01537e

O'Brien, J., Wilson, I., Orton, T., and Pognan, F. (2010). Investigation of the Alamar Blue (resazurin) fluorescent dye for the assessment of mammalian cell cytotoxicity. *Eur. J. Biochem.* 267, 5421–5426. doi: 10.1046/j.1432-1327.2000.01606.x

Qin, A., Lam, J. W. Y., and Tang, B. Z. (2012). Luminogenic polymers with aggregation-induced emission characteristics. *Prog. Polym. Sci.* 37, 182–209. doi: 10.1016/j.progpolymsci.2011.08.002

Qin, Z., Mao, Q., Cong, S., Chen, Y. N., Xin, P., Tan, H., et al. (2017). Simple aliphatic oximes as nonconventional luminogens with aggregation-induced emission characteristics. *J. Mater. Chem. C* 5, 3699–3705. doi: 10.1039/C7TC00783C

Qiu, Z., Liu, X., Lam, J. W. Y., and Tang, B. Z. (2018). The marriage of aggregation-induced emission with polymer science. *Macromol. Rapid Commun.* 40, 1800568. doi: 10.1002/marc.201800568

Querejeta-Fernandez, A., Chauve, G., Methot, M., Bouchard, J., and Kumacheva, E. (2014). Chiral plasmonic films formed by gold nanorods and cellulose nanocrystals. *J. Am. Chem. Soc.* 136, 4788–4793. doi: 10.1021/ja501642p

Rafieian, F., and Simonsen, J. (2014). Fabrication and characterization of carboxylated cellulose nanocrystals reinforced glutenin nanocomposite. *Cellulose* 21, 4167–4180. doi: 10.1007/s10570-014-0305-4

Schwartz, G., Pfeiffer, M., Reineke, S., Walzer, K., and Leo, K. (2007). Harvesting triplet excitons from fluorescent blue emitters in white organic light-emitting diodes. *Adv. Mater.* 19, 3672–3676. doi: 10.1002/adma.200700641

Shang, C., Wei, N., Zhuo, H., Shao, Y., Zhang, Q., Zhang, Z., et al. (2017). Highly emissive poly(maleic anhydride-alt-vinyl pyrrolidone) with molecular weight-dependent and excitation-dependent fluorescence. *J. Mater. Chem. C* 5, 8082–8090. doi: 10.1039/C7TC02381B

Shen, X. Y., Yuan, W. Z., Liu, Y., Zhao, Q., Lu, P., Ma, Y., et al. (2012). Fumaronitrile-based fluorogen: red to near-infrared fluorescence, aggregation-induced emission, solvatochromism, and twisted intramolecular charge transfer. *J. Phys. Chem. C* 116, 10541–10547. doi: 10.1021/jp303100a

Wang, D., and Imae, T. (2004). Fluorescence emission from dendrimers and its pH dependence. *J. Am. Chem. Soc.* 126, 13204–13205. doi: 10.1021/ja0454992

Wang, J., Mei, J., Hu, R., Sun, J. Z., Qin, A., and Tang, B. Z. (2012). Click synthesis, aggregation-induced emission, E/Z isomerization, self-organization, and multiple chromisms of pure stereoisomers of a tetraphenylethene-cored luminogen. *J. Am. Chem. Soc.* 134, 9956–9966. doi: 10.1021/ja208883h

Wang, X., Valiev, R. R., Ohulchanskyy, T. Y., Åqren, H., Yang, C., and Chen, G. (2017). Dye-sensitized lanthanide-doped upconversion nanoparticles. *Chem. Soc. Rev.* 46, 4150–4167. doi: 10.1039/c7cs00053g

Wu, S., and Butt, H. J. (2016). Near-infrared-sensitive materials based on upconverting nanoparticles. *Adv. Mater.* 28, 1208–1226. doi: 10.1002/adma.201502843

Xing, C. M., Lam, J. W. Y., Qin, A. J., Dong, Y. Q., Haussler, M., Yang, W. T., et al. (2007). Unique photoluminescence from nonconjugated alternating copolymer poly[(maleic anhydride)-alt-(vinyl acetate)]. *Polym. Mater. Sci. Eng.* 96, 418–419.

Yamaguchi, M., Ito, S., Hirose, A., Tanaka, K., and Chujo, Y. (2017). Control of aggregation-induced emission versus fluorescence aggregation-caused quenching by bond existence at a single site in boron pyridinoiminate complexes. *Mater. Chem. Front.* 1, 1573–1579. doi: 10.1039/c7qm00076f

Yang, L., Wang, L., Cui, C., Lei, J., and Zhang, J. (2016). Stöber strategy for synthesizing multifluorescent organosilica nanocrystals. *Chem. Commun.* 52, 6154–6157. doi: 10.1039/c6cc01917j

Yang, T., Dai, S., Yang, S., Chen, L., Liu, P., Dong, K., et al. (2017). Interfacial clustering-triggered fluorescence-phosphorescence dual solvoluminescence of metal nanoclusters. *J. Phys. Chem. Lett.* 8, 3980–3985. doi: 10.1021/acs.jpclett.7b01736

Ye, R., Liu, Y., Zhang, H., Su, H., Zhang, Y., Xu, L., et al. (2017). Non-conventional fluorescent biogenic and synthetic polymers without aromatic rings. *Polym. Chem.* 8, 1722–1727. doi: 10.1039/C7PY00154A

You, R., Dou, H., Chen, L., Zheng, S., and Zhang, Y. (2017). Graphitic carbon nitride with S and O codoping for enhanced visible light photocatalytic performance. *RSC Adv.* 7, 15842–15850. doi: 10.1039/c7ra01036b

Yuan, W. Z., and Zhang, Y. M. (2017). Nonconventional macromolecular luminogens with aggregation-induced emission characteristics. *J. Polym. Sci. Part A: Polym. Chem.* 55, 560–574. doi: 10.1002/pola.28420

Yuan, Y., Kwok, R. T., Feng, G., Liang, J., Geng, J., Tang, B. Z., et al. (2014). Rational design of fluorescent light-up probes based on an AIE luminogen for targeted intracellular thiol imaging. *Chem. Commun.* 50, 295–297. doi: 10.1039/c3cc47585a

Zhao, E., Lam, J. W. Y., Meng, L., Hong, Y., Deng, H., Bai, G., et al. (2015). Poly[(maleic anhydride)-alt-(vinyl acetate)]: A pure oxygenic nonconjugated macromolecule with strong light emission and solvatochromic effect. *Macromolecules* 48, 64–71. doi: 10.1021/ma502160w

Zhao, W., Simmons, B., Singh, S., Ragauskas, A., and Cheng, G. (2016). From lignin association to nano-/micro-particle preparation: extracting higher value of lignin. *Green Chem.* 18, 5693–5700. doi: 10.1039/c6gc01813k

Zhou, Q., Cao, B., Zhu, C., Xu, S., Gong, Y., Yuan, W. Z., et al. (2016). Clustering-triggered emission of nonconjugated polyacrylonitrile. *Small* 12, 6586–6592. doi: 10.1002/smll.201601545

Zhu, Q., Zhang, Y., Nie, H., Zhao, Z., Liu, S., Wong, K. S., et al. (2015). Insight into the strong aggregation-induced emission of low-conjugated racemic C6-unsubstituted tetrahydropyrimidines through crystal-structure-property relationship of polymorphs. *Chem. Sci.* 6, 4690–4697. doi: 10.1039/c5sc01226k

Zhu, S., Song, Y., Shao, J., Zhao, X., and Yang, B. (2016). Non-conjugated polymer dots with crosslink-enhanced emission in the absence of fluorophore units. *Cheminform* 47, 14626–14637. doi: 10.1002/chin.201606250

Conflict of Interest Statement: The authors declare that the research was conducted in the absence of any commercial or financial relationships that could be construed as a potential conflict of interest.

Copyright © 2019 Li, Li, An, Chen and Xiao. This is an open-access article distributed under the terms of the Creative Commons Attribution License (CC BY). The use, distribution or reproduction in other forums is permitted, provided the original author(s) and the copyright owner(s) are credited and that the original publication in this journal is cited, in accordance with accepted academic practice. No use, distribution or reproduction is permitted which does not comply with these terms.

frontiers in Chemistry

ORIGINAL RESEARCH
published: 25 February 2019
doi: 10.3389/fchem.2019.00049

A Saccharide Chemosensor Array Developed Based on an Indicator Displacement Assay Using a Combination of Commercially Available Reagents

*Yui Sasaki, Zhoujie Zhang and Tsuyoshi Minami**

Institute of Industrial Science, University of Tokyo, Tokyo, Japan

Herein, a very simple colorimetric chemosensor array is reported for saccharides (D-glucose, D-fructose, D-xylose, D-galactose, D-mannose, L-rhamnose, and *N*-acetyl-D-gluosamine). While various types of chemosensors for saccharides have been investigated extensively to-this-date, tremendous additional efforts are still required on a regular basis for the syntheses of new chemosensors. Complicated syntheses would be a bottleneck, given that artificial receptor-based chemosensing systems are not so popular in comparison to biomaterial-based (e.g., enzyme-based) sensing systems. Toward this end, chemosensor array systems using molecular self-assembled materials can avoid the abovementioned synthetic efforts and achieve simultaneous qualitative and quantitative detection of a number of guest saccharides. Using a practical approach, we focus on an indicator displacement assay (IDA) to fabricate a chemosensor array for colorimetric saccharide sensing. On this basis, 3-nitrophenylboronic acid (3-NPBA) spontaneously reacts with catechol dyes such as alizarin red S (ARS), bromopyrogallol red (BPR), pyrogallol red (PR), and pyrocatechol violet (PV), and yields boronate ester derivatives with color changes. The addition of saccharides into the aqueous solution of the boronate esters induces color recovery owing to the higher binding affinity of 3-NPBA for saccharides, thus resulting in the release of dyes. By employing this system, we have succeeded in discriminating saccharides qualitatively and quantitatively with a classification success rate of 100%. Most importantly, our chemosensor array has been fabricated by only mixing low cost commercially available reagents *in situ*, which means that complicated synthetic processes are avoided for saccharide sensing. We believe this simple colorimetric assay that uses only commercially available reagents can create new, user-friendly supramolecular sensing pathways for saccharides.

Keywords: saccharide, chemosensor array, phenylboronic acid, indicator displacement assay, colorimetric sensing, regression analysis

OPEN ACCESS

Edited by:
Tony D. James,
University of Bath, United Kingdom

Reviewed by:
Robert Elmes,
Maynooth University, Ireland
David C. Magri,
University of Malta, Malta

****Correspondence:***
Tsuyoshi Minami
tminami@iis.u-tokyo.ac.jp

Specialty section:
This article was submitted to Supramolecular Chemistry, a section of the journal Frontiers in Chemistry

Received: *29 November 2018*
Accepted: *18 January 2019*
Published: *25 February 2019*

Citation:
Sasaki Y, Zhang Z and Minami T (2019) A Saccharide Chemosensor Array Developed Based on an Indicator Displacement Assay Using a Combination of Commercially Available Reagents. Front. Chem. 7:49. doi: 10.3389/fchem.2019.00049

INTRODUCTION

To-this-date, the analysis of monosaccharides has been proven particularly important in the field of food chemistry because the monitoring of foodstuff quality and the investigation of illegal additions of saccharides into fruit juices or honey are highly required (Tůma et al., 2011). Monosaccharides, such as D-(+)-glucose (Glc), D-(−)-fructose (Fru), D-(+)-xylose (Xyl), D-(+)-galactose (Gal),

D-(+)-mannose (Man), L-(+)-rhamnose (Rha) and *N*-acetyl-D-(+)-glucosamine (NAcGlc) are generally contained in food or beverages (Martínez Montero et al., 2004), and are conventionally analyzed using instrumental methods (e.g., high-performance liquid chromatography (HPLC) (Schmid et al., 2016) and/or mass spectrometry (MS) (Žídková and Chmelík, 2001) owing to their increased accuracy and reliability. Unfortunately, these methods are associated with increased-costs that incur owing to the use of expensive equipment, relatively complicated procedures, and the necessity of trained personnel. In the efforts to simplify the detection of saccharides, optical chemosensors have been researched extensively (Sun and James, 2015; You et al., 2015). Chemosensors exhibit color and/or fluorescence changes by capturing guest molecules. Accordingly, we can easily recognize the evoked results by simple visual inspection. However, conventional methods used to develop a single chemosensor require a complicated multi step synthesis process (Liu et al., 2015). The latter would prevent the increase of the popularity of the chemosensors in the field of analytical science and industry. In this regard, a molecular self-assembly (Bull et al., 2013) inspired by nature is utilized to prepare saccharide chemsensors *in situ* (Miyaji and Sessler, 2001; Strongin et al., 2001; Sasaki et al., 2017). Herein, we only used a combination of commercially available and inexpensive reagents for the preparation of saccharide chemosensors. This means that 3-nitrophenylboronic acid (3-NPBA) (Hall, 2011) is employed as the saccharide receptor and a catechol dye, such as alizarin red S (ARS), bromopyrogallol red (BPR), pyrogallol red (PR), and pyrocatechol violet (PV), is used as the indicator (Minami et al., 2016) (**Figure 1**). First, mixing the 3-NPBA and catechol dyes yields boronate esters accompanied by color changes (Springsteen and Wang, 2001; Kubo et al., 2005). Subsequently, a color recovery can be observed by the addition of saccharides because of the dissociation of boronate esters between 3-NPBA and dyes (Ma et al., 2009). This indicator displacement assay (IDA) (Nguyen and Anslyn, 2006), that is used as a sensor array, provides a finger print-like response to saccharides and leads to excellent discrimination results (Maximilian Bojanowski et al., 2017). These results indicate that the smart and appropriate combination of general reagents minimizes synthetic efforts in laboratories, thereby allowing a simplified and easy preparation of supramolecular chemosensors.

MATERIALS AND METHODS

Materials

ARS, Fru, Glc, Xyl, and NAcGlc, were purchased from FUJIFILM Wako Pure Chemical Corporation (Osaka, Japan). Additionally, 3-NPBA, BPR, PR, PV, Gal, Man, and Rha, were purchased from the Tokyo Chemical Industry Co. Ltd. (Tokyo, Japan). Disodium hydrogenphosphate dodecahydrate and sodium dihydrogenephosphate dihydtare were purchased from the Kanto Chemical Co. Inc. (Tokyo, Japan). Diluted solutions used for all photophysical experiments were prepared using Mill-Q water (18.4 MΩ).

Measurements

UV-vis spectra were measured by a Shimadzu UV-2600 spectrophotometer. UV-vis spectra were recorded within the wavelength range from 350 to 800 nm. Scans were acquired under ambient conditions at 25°C. Saccharide titrations were conducted in a phosphate buffer solution (100 mM) with a pH of 7.4 at 25°C. Titration isotherms were obtained from the changes in the absorption maximum at 455 nm for ARS, 540 nm for BPR, 535 nm for PR, and at 497 nm for PV, respectively. Titration curves, obtained by plotting the change in absorption, were analyzed using non-linear least-squares methods and the equations for the one to one binding model and the IDA model (Hargrove et al., 2010). Equations 1 and 2 were used to fit the UV-vis measurement results,

$$[H]_t = [H] + \frac{K_G\,[H]}{1+K_G\,[H]}\,[G]_t + \frac{K_I\,[H]}{1+K_I\,[H]}\,[I]_t \quad (1)$$

$$A = \frac{[I]_t}{1+K_I\,[H]}\left(\varepsilon_I\, b + \varepsilon_{HI}\, b\, K_I\,[H]\right) \quad (2)$$

where $[G]_t$, $[H]_t$, $[I]_t$, are the total concentrations of saccharides (as the guests), 3-NPBA (as the host), and for the catechol dyes (as the indicators), respectively. Moreover, K_I and K_G are the binding constants of the indicator to the host and the guest to the host, respectively. Furthermore, [H] donates the unknown concentration of the host. The [H] value could be determined using K_I and K_G, and with the use of the experimentally obtained values $[G]_t$, $[H]_t$, and $[I]_t$. Additionally, ε_I and ε_{HI} are the molar absorptivities of the indicator and the complex of the host and the indicator, respectively. Equivalently, A and b are the saccharide concentration-dependent absorbance and the thickness of the cuvette, respectively.

The array experiment for qualitative and quantitative analyses was performed in 384-well microplates. The fluids [phosphate buffer (100 mM) at pH 7.4, ARS, BPR, PR and PV (40 μM), 3-NPBA (6 mM), and the analyte solutions (100 mM)], were eliminated with a contact-free dispenser as follows. Each experiment was carried out in 24 repetitions. Each well received 90 μL of the buffer solution which contained the catechol dyes and 3-NPBA. Subsequently, 10 μL of analyte solutions or water were dispensed. After this period, the plate was shaken for 3 min. UV-vis spectra were measured by a Biotek SYNERGY H1 microplate reader. The UV-vis spectra were recorded from 400 to 620 nm. The resulting absorption data were applied to the Student's *t*-test to exclude four outlier data points (from the total of 24 repetitions) (Minami et al., 2012). The coefficient of variability of the data was lower than 6%. In the case of qualitative analyses, the obtained data was analyzed using linear discriminant analyses (LDA) (Anzenbacher et al., 2010) without any further pretreatment. The semi quantitative analyses were conducted using LDA after an analysis-of-variance (ANOVA) test. A support vector machine with a principal component analysis preprocessing (PCs = 3) was used for the quantitative assay of the Glc and Fru mixtures.

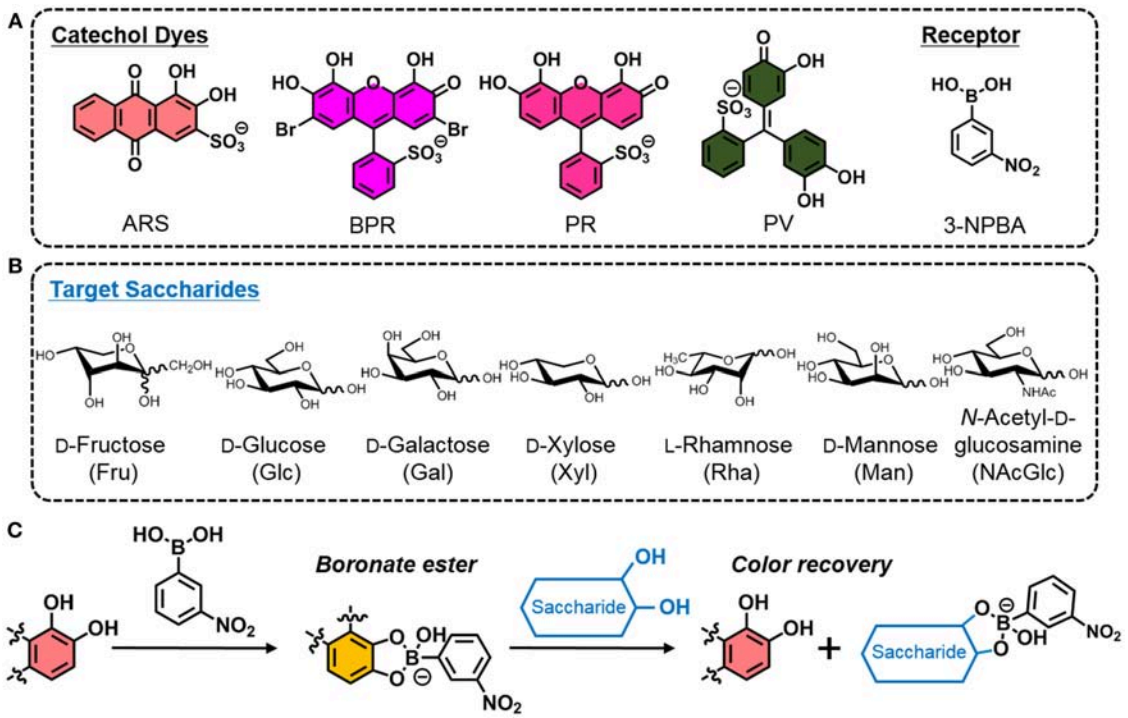

FIGURE 1 | (A) Chemical structures of ARS, BPR, PR, PV, and 3-NPBA. **(B)** List of target saccharides. **(C)** Illustrated scheme of the indicator displacement assay utilizing the building blocks (i.e., a catechol dye and 3-NPBA) for the easy preparation of colorimetric sensing.

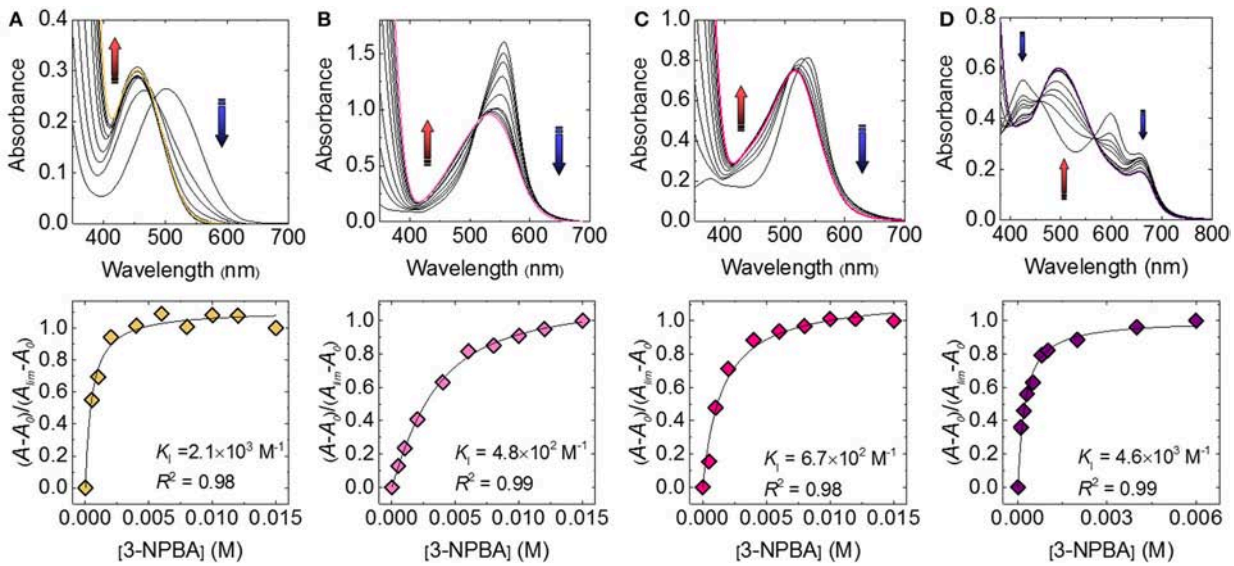

FIGURE 2 | UV-vis spectra of the catechol dye (40 μM) upon the addition of 3-NPBA in a phosphate buffer solution (100 mM) at a pH of 7.4 at 25°C for **(A)** ARS, **(B)** BPR, **(C)** PR, and **(D)** PV.

RESULTS AND DISCUSSION

First, the complexation of catechol dyes and 3-NPBA in a phosphate buffer (100 mM) at pH 7.4 at 25°C was investigated using UV-vis titration experiments. As shown in **Figure 2**, the absorption spectra of the catechol dyes were shifted as a function of increasing the concentration of 3-NPBA. For example, a significant blue shift ($\Delta\lambda = 46$ nm) was observed in the case of ARS. These responses indicate the formation of the dynamic covalent bond (i.e., boronate esterification), which is identified by fast-atom-bombardment (FAB) mass spectrometry (see the **Supplementary Material**). The associated constants (K_Is) of

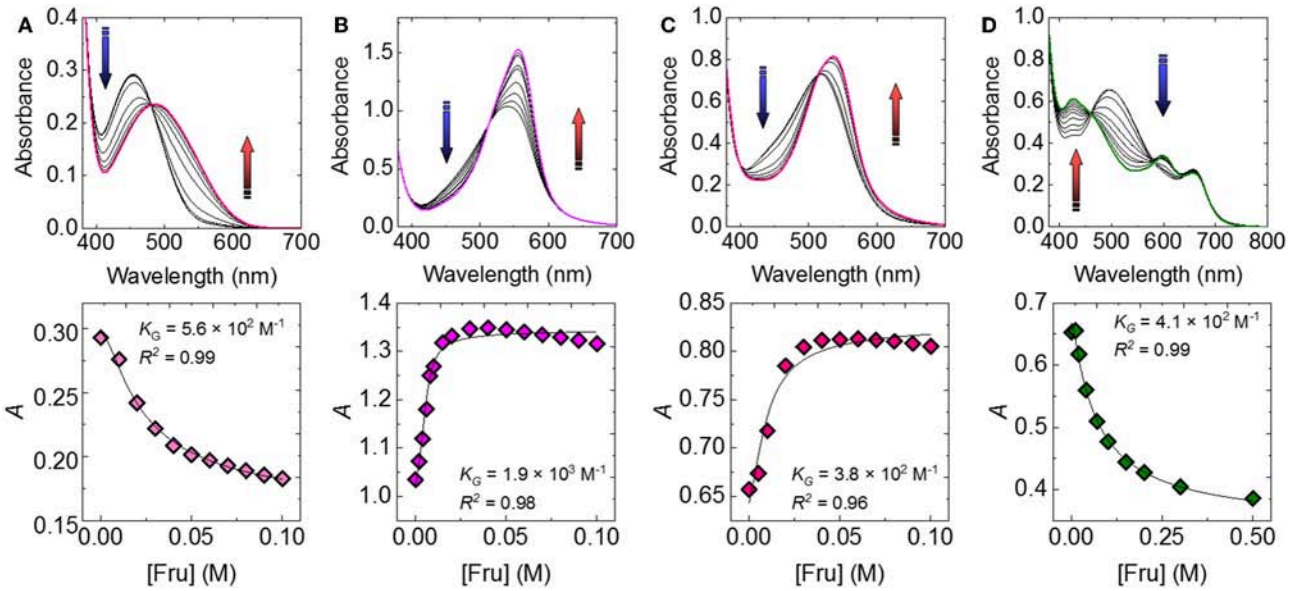

FIGURE 3 | UV-vis spectra of the catechol dye (40 μM)-3-NPBA (6 mM) complex upon the addition of Fru in a phosphate buffer solution (100 mM) at a pH of 7.4 and at 25°C for **(A)** ARS-3-NPBA, **(B)** BPR-3-NPBA, **(C)** PR-3-NPBA, and **(D)** PV-3-NPBA.

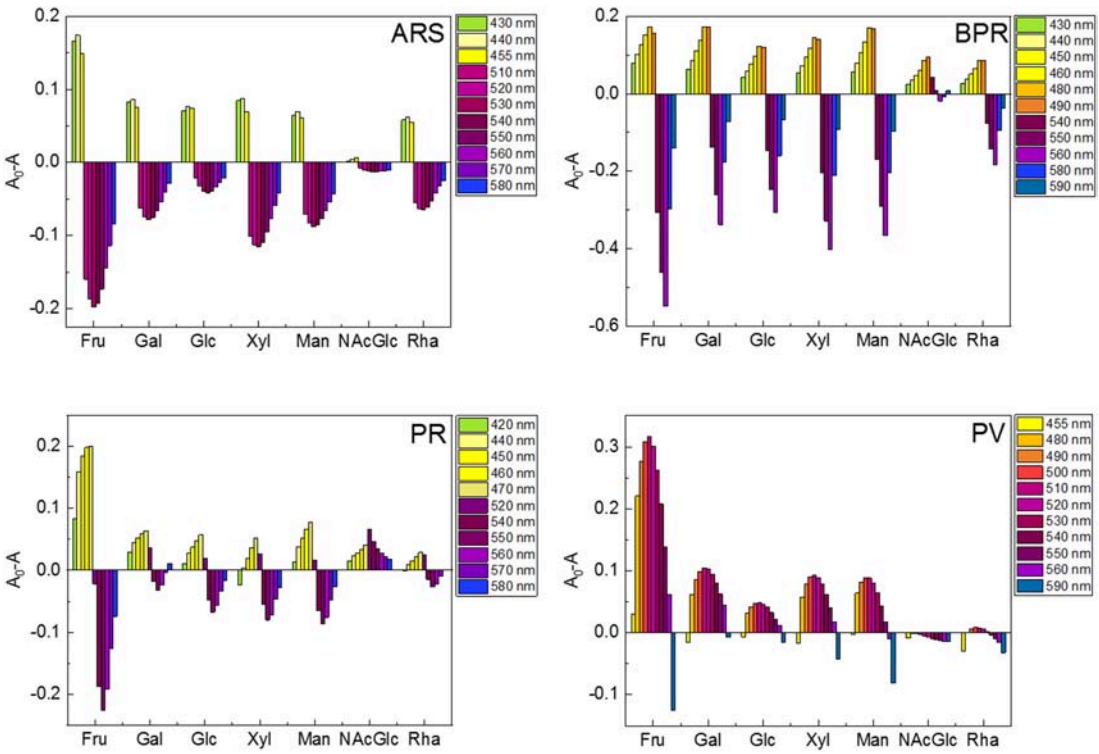

FIGURE 4 | Colorimetric finger print-like response patterns obtained from changes in each absorption wavelength of the catechol dye (40 μM)-3-NPBA (6 mM) complex upon the addition of saccharides (100 mM). **(A)** ARS-3-NPBA, **(B)** BPR-3-NPBA, **(C)** PR-3-NPBA, and **(D)** PV-3-NPBA.

these complexes were estimated to be 2.1 × 10^3 M^{-1} for ARS, 4.8 × 10^2 M^{-1} for BPR, 6.7 × 10^2 M^{-1} for PR, and 4.6 × 10^3 M^{-1} for PV.

Subsequently, we attempted to detect seven types of monosaccharides (Fru, Glc, Xyl, Gal, Man, Rha, and NAcGlc) which are generally contained in food or beverages. **Figure 3**

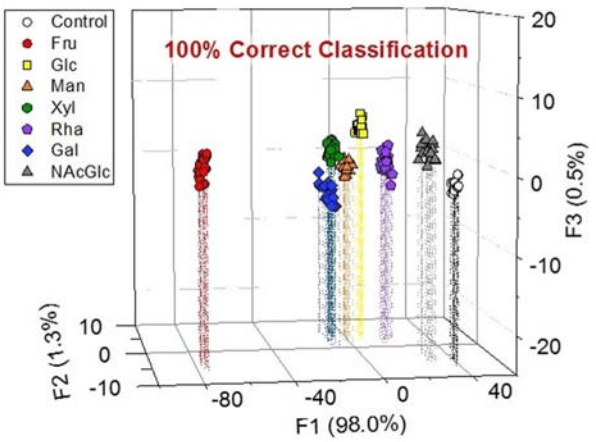

FIGURE 5 | LDA plot for the response of the colorimetric chemosensor array showing the seven types of saccharides (and control) in a phosphate buffer solution at a pH of 7.4 at 25°C. [Saccharide] = 100 mM. Twenty repetitions were measured for each analyte. The cross-validation routine shows a classification success rate of 100%.

shows the UV-vis titration results of Fru as example. The spectral shift by the incremental Fru concentration was observed to be accompanied by the recovery of the color. The observed recovery suggests that the complexation of 3-NPBA and saccharide occurred on the basis of IDA. Importantly, colorimetric finger print-like responses were obtained by changing the combination of catechol dyes and saccharides (**Figure 4**). The binding constants between 3-NPBA and saccharides in the presence of catechol dyes are summarized in **Table 1**. The calculate K_Gs were comparable to previously reported colorimetric saccharide chemosensors based on PBAs (Koumoto and Shinkai, 2000; Springsteen and Wang, 2002). From the standpoint of the pattern recognition algorithm, the cross-reactive selectivity is very useful in discriminating various analytes with a high classification accuracy.

Because the finger print-like response encouraged us to fabricate the chemosensor array, we decided to attempt a high-throughput saccharide sensing test. Among the pattern recognition algorithms, we employed LDA as one of the available supervised methods to a) reduce the dimensionality and b) classify the multivariate data. To discriminate analyte patterns, a mathematical model is firstly constructed using a training dataset, which is subsequently evaluated by cross-validation protocols. In our case, a leave-one-out cross-validation protocol (i.e., the jackknife method) was conducted to evaluate the level of correct classification of the observations within the clusters (Anzenbacher et al., 2010). In this assay, 20 repetitions were conducted to confirm reproducibility. We succeeded in discriminating eight clusters (control and seven saccharides, with a total of 160 data points) with a classification success rate of 100% (**Figure 5**). Interestingly, the position of the Fru cluster is far from the control cluster, most probably owing to the fact that Fru induced the strongest colorimetric response among the tested saccharides. Thus, we can conclude that the LDA plots reflect appropriately the colorimetric responses of the tested saccharides. According to the result of ANOVA (**Supplementary Figure 15**), the contribution of BPR for discrimination is much higher than the other three dyes. It seems that the relatively high contribution of BPR caused the high F1 value. However, the contribution of the other three dyes is not ignorable. In the absence of ARS, PR or PV, we could not achieve 100% correct classification. Therefore, LDA using four dyes with 3-NPBA is required to discriminate target saccharides.

Although Musto et al., previously reported a qualitative discrimination of saccharides with the use of a colorimetric assay (Musto et al., 2009), quantitative assays for saccharides have not been fully investigated. We thus attempted to apply a semi quantitative assay for Fru and Glc. Beverages, such as fruit juices and wines, generally contain saccharides at concentrations in the range of several tens to hundreds of mM (Han et al., 2016). The LDA was also conducted as the pattern recognition in the semi quantitative assay. This means that the LDA score plots for concentrations in the range of several tens of mM of Fru and Glc were clearly discriminated with classification success rates of 100% (**Figure 6**). The notable point of the assay is that these cluster positions possess significant trends depending on the saccharide concentrations, which is in agreement with the results of the UV-vis spectroscopic titrations.

From the viewpoint of practical sensing applications, a regression assay for complexed media is necessary. Finally, we demonstrated a quantitative assay for a mixture of Fru and Glc. In this assay, various mixture samples containing eight different concentrations of each saccharide were prepared and were injected in the colorimetric sensor chip. The concentration of Fru was adjusted to gradually decrease, while the concentration of Glc was gradually increased relative to Fru. Owing to the complicated optical responses of the chemosensor array, we employed a support vector machine algorithm (SVM) (Hamel, 2009). The SVM is a powerful analytical method for a quantitative assay, such as the simultaneous prediction of species and concentrations. This method enables the creation of a linear regression line even though an original inset dataset does not show a linear correlation (e.g., analysis of mixed components). The measured UV-vis spectra of chemosensors were analyzed by the SVM, and then unknown concentrations of saccharides in the mixtures were predicted (**Supplementary Figure 20**). The predicted concentrations (circle dots in **Supplementary Figure 20**) closely exist on the calibration regression linear line. This indicates that we predicted successfully the saccharide concentrations in the mixtures. The relatively low values of the root-mean-square errors (RMSEs) also indicate the high accuracy of the model and its predictive capacity. To the best of our knowledge, this is the first example that accomplishes colorimetric regression analyses of saccharides in mixtures using only a simple and an appropriate combination of commercially available reagents.

CONCLUSION

In summary, we demonstrated the qualitative and quantitative detection of monosaccharides with a simple colorimetric chemosensor array. Owing to the reduced complexity of

TABLE 1 | Binding constants (K_G M^{-1})[a] on the basis of the indicator displacement assay.

Dye	Fru	Gal	Glc	Xyl	Man	NAcGlc	Rha
ARS	560 ± 71	110 ± 11	52 ± 4	41 ± 6	<10	<10	17 ± 2
BPR	1900 ± 39	230 ± 24	150 ± 6	110 ± 5	110 ± 13	<10	46 ± 4
PR	380 ± 38	<10	<10	<10	<10	<10	<10
PV	410 ± 49	33 ± 6	16 ± 1	12 ± 2	<10	<10	<10

[a]*Binding constants were calculated using the change in the UV-vis absorption upon the addition of the analyte in a phosphate buffer solution (100 mM) at a pH of 7.4 at 25°C. All the errors of the binding constants are <19%. Five repetitions were measured for each analyte.*

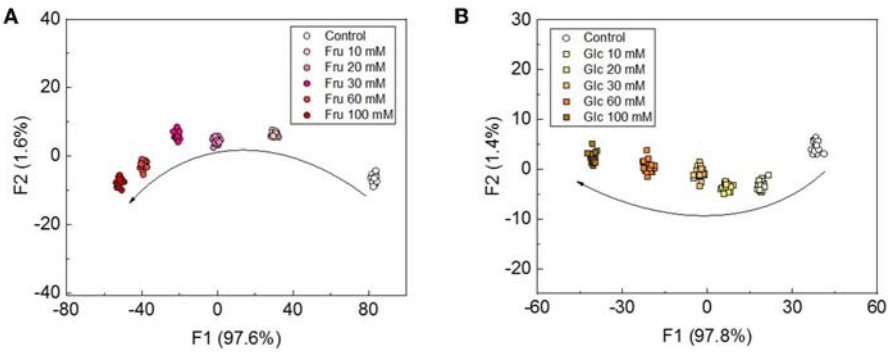

FIGURE 6 | LDA plots for the semi-quantitative assay for **(A)** Fru and **(B)** Glc at the concentration range of 0-100 mM. Twenty repetitions were measured for each concentration.

conventional complicated synthetic methods, the molecular self-assembled system was employed to prepare chemosensors *in situ*. Accordingly, the chemosensor array was fabricated by mixing low-cost, commercially available reagents, such as 3-NPBA, and four types of catechol dyes. The various combinations of these compounds with saccharides generated multi-color response patterns based on the IDA. In the case of the qualitative assay based on the LDA, we succeeded in discriminating of eight distinct groups (control and seven types of saccharides) with a classification success rate of 100%. Furthermore, semi quantitative and quantitative assays for Fru and Glc were conducted and resulted in highly accurate discrimination and prediction. We believe that the simple methods proposed here can be readily conducted by specialists and non-specialists of supramolecular and analytical chemistry, and could contribute to the increase in popularity of chemosensors.

AUTHOR CONTRIBUTIONS

YS performed the spectroscopic and the high-throughput array experiments and wrote the manuscript. ZZ performed the spectroscopic experiments and calculated the binding constants. SVM was also performed by ZZ. TM conceived the entire project.

FUNDING

YS and TM thank the financial support from the Japan Society for the Promotion of Science (JSPS, Grant-in-Aid for Scientific Research, Nos. 18J21190 and 17H04882).

ACKNOWLEDGMENTS

We thank Prof. H. Houjou and I. Yoshikawa of The University of Tokyo for their technical support regarding the FAB–mass spectrometry.

SUPPLEMENTARY MATERIAL

The Supplementary Material for this article can be found online at: https://www.frontiersin.org/articles/10.3389/fchem.2019.00049/full#supplementary-material

REFERENCES

Anzenbacher, P., Jr., Lubal, P., Buček, P., Palacios, M. A., and Kozelkova, M. E. (2010). A practical approach to optical cross-reactive sensor arrays. *Chem. Soc. Rev.* 39, 3954–3979. doi: 10.1039/B926220M

Bull, S. D., Davidson, M. G., van den Elsen, J. M. H., Fossey, J. S., Jenkins, A. T. A., Jiang, Y.-B., et al. (2013). Exploiting the reversible covalent bonding of boronic acids: recognition, sensing, and assembly. *Acc. Chem. Res.* 46, 312–326. doi: 10.1021/ar300130w

Hall, D. G. (ed.). (2011). "Boronic acids: preparation and applications in organic synthesis medicine and materials" *2nd Edn,* (Weinheim: Wiley-VCH Verlag GmbH and Co. KGaA).

Hamel, L. H. (2009). *Knowledge Discovery with Support Vector Machines.* (Hoboken: John Wiley and Sons, Ltd).

Han, J., Bender, M., Seehafer, K., and Bunz, U. H. F. (2016). Identification of white wines by using two oppositely charged poly(*p*-phenyleneethynylene)s individually and in complex. *Angew. Chem. Int. Ed.* 55, 7689–7692. doi: 10.1002/anie.201602385

Hargrove, A. E., Zhong, Z., Sessler, J. L., and Anslyn, E. V. (2010). Algorithms for the determination of binding constants and enantiomeric excess in complex host : guest equilibria using optical measurements. *New J. Chem.* 34, 348–354. doi: 10.1039/B9NJ00498J

Koumoto, K., and Shinkai, S. (2000). Colorimetric sugar sensing method useful in "neutral" aqueous media. *Chem. Lett.* 29, 856–857. doi: 10.1246/cl.2000.856

Kubo, Y., Ishida, T., Kobayashi, A., and James, T. D. (2005). Fluorescent alizarin–phenylboronic acid ensembles: design of self-organized molecular sensors for metal ions and anions. *J. Mater. Chem.* 15, 2889–2895. doi: 10.1039/B501243K

Liu, S., Bai, H., Sun, Q., Zhang, W., and Qian, J. (2015). Naphthalimide-based fluorescent photoinduced electron transfer sensors for saccharides, *RSC Adv.* 5, 2837–2843. doi: 10.1039/C4RA13414A

Ma, W. M. J., Pereira Morais, M. P., D'Hooge, F., van den Elsen, J. M. H., Cox, J. P. L., James, T. D., et al. (2009). Dye displacement assay for saccharide detection with boronate hydrogels. *Chem. Commun.* 532–534. doi: 10.1039/B814379J

Martínez Montero, C., Rodríguez Dodero, M. C., Guillén Sánchez, D. A., and Barroso, C. G. (2004). Analysis of low molecular weight carbohydrates in food and beverages: a review. *Chromatographia* 59, 15–30.

Maximilian Bojanowski, N., Bender, M., Seehafer, K., and Bunz, U. H. F. (2017). Discrimination of saccharides by a simple array. *Chem. Eur. J.* 23, 12253–12258. doi: 10.1002/chem.201700831

Minami, T., Emami, F., Nishiyabu, R., Kubo, Y., and Anzenbacher, Jr., P. (2016). Quantitative analysis of modeled ATP hydrolysis in water by a colorimetric sensor array. *Chem. Commun.* 52, 7838–7841. doi: 10.1039/C6CC02923J

Minami, T., Esipenko, N. A., Zhang, B., Kozelkova, M. E., Isaacs, L., Nishiyabu, R., et al. (2012). Supramolecular sensor for cancer-associated nitrosamines. *J. Am. Chem. Soc.* 134, 20021–20024. doi: 10.1021/ja3102192

Miyaji, H., and Sessler, J. L. (2001). Off-the-shelf colorimetric anion sensors. *Angew. Chem. Int. Ed.* 40, 154–157.

Musto, C. J., Lim, S. H., and Suslick, K. S. (2009). Colorimetric detection and identification of natural and artificial sweeteners. *Anal. Chem.* 81, 6526–6533. doi: 10.1021/ac901019g

Nguyen, B. T., and Anslyn, E. V. (2006). Indicator–displacement assays. *Coord. Chem. Rev.* 250, 3118–3127. doi: 10.1016/j.ccr.2006.04.009

Sasaki, Y., Minamiki, T., Tokito, S., and Minami, T. (2017). A molecular self-assembled colourimetric chemosensor array for simultaneous detection of metal ions in water. *Chem. Commun.* 53, 6561–6564. doi: 10.1039/C7CC03218H

Schmid, T., Baumann, B., Himmelsbach, M., Klampfl, C. W., and Buchberger, W. (2016). Analysis of saccharides in beverages by HPLC with direct UV detection. *Anal. Bioanal. Chem.* 408, 1871–1878. doi: 10.1007/s00216-015-9290-1

Springsteen, G., and Wang, B. (2001). Alizarin Red S. as a general optical reporter for studying the binding of boronic acids with carbohydrates. *Chem. Commun.* 1608–1609. doi: 10.1039/b104895n

Springsteen, G., and Wang, B. (2002). A detailed examination of boronic acid–diol complexation. *Tetrahedron* 58, 5291–5300. doi: 10.1016/S0040-4020(02)00489-1

Strongin, R. M., Cabell, L. A., Luce, N. S., Lewis, P. T., He, M., Escobedo, J. O., et al. (2001). *Colorimetric and Fluorimetric Analysis of Carbohydrates*. U.S. Patent No US6534316B2. Washington, DC: U.S. Patent and Trademark Office.

Sun, X., and James, T. D. (2015). Glucose sensing in supramolecular chemistry. *Chem. Rev.* 115, 8001–8037. doi: 10.1021/cr500562m

Tůma, P., Málková, K., and Samcová, E., Štulík, K. (2011). Rapid monitoring of mono- and disaccharides in drinks, foodstuffs and foodstuff additives by capillary electrophoresis with contactless conductivity detection. *Anal. Chim. Acta* 698, 1–5. doi: 10.1016/j.aca.2011.04.055

You, L., Zha, D., and Anslyn, E. V. (2015). Recent advances in supramolecular analytical chemistry using optical sensing. *Chem. Rev.* 115, 7840–7892. doi: 10.1021/cr5005524

Žídková, J., and Chmelík, J. (2001). Determination of saccharides in fruit juices by capillary electrophoresis and matrix-assisted laser desorption/ionization time-of-flight mass spectrometry. *J. Mass Spectrom.* 36, 417–421. doi: 10.1002/jms.144

Conflict of Interest Statement: The authors declare that the research was conducted in the absence of any commercial or financial relationships that could be construed as a potential conflict of interest.

Copyright © 2019 Sasaki, Zhang and Minami. This is an open-access article distributed under the terms of the Creative Commons Attribution License (CC BY). The use, distribution or reproduction in other forums is permitted, provided the original author(s) and the copyright owner(s) are credited and that the original publication in this journal is cited, in accordance with accepted academic practice. No use, distribution or reproduction is permitted which does not comply with these terms.

frontiers in Chemistry

ORIGINAL RESEARCH
published: 08 May 2019
doi: 10.3389/fchem.2019.00294

Self-Assembled Thin-Layer Glycomaterials With a Proper Shell Thickness for Targeted and Activatable Cell Imaging

Chao Zhang[1†], Guanzhen Wang[2,3†], Hai-Hao Han[4†], Xi-Le Hu[4], Robert A. Field[5], Guo-Rong Chen[4], Jia Li[2], Bing Ye[1], Xiao-Peng He[4*] and Yi Zang[2*]*

[1] Emergency Department, Jinan Children's Hospital, Jinan, China, [2] State Key Laboratory of Drug Research, National Center for Drug Screening, Chinese Academy of Sciences, Shanghai Institute of Materia Medica, Shanghai, China, [3] University of Chinese Academy of Sciences, Beijing, China, [4] Key Laboratory for Advanced Materials and Feringa Nobel Prize Scientist Joint Research Center, School of Chemistry and Molecular Engineering, East China University of Science and Technology, Shanghai, China, [5] Department of Biological Chemistry, John Innes Centre, Norwich Research Park, Norwich, United Kingdom

OPEN ACCESS

Edited by:
Tony D. James, University of Bath, United Kingdom

Reviewed by:
Lin Yuan, Hunan University, China
Juyoung Yoon, Ewha Womans University, South Korea

***Correspondence:**
Bing Ye
13583184890@163.com
Xiao-Peng He
xphe@ecust.edu.cn
Yi Zang
yzang@simm.ac.cn

[†] These authors have contributed equally to this work

Specialty section:
This article was submitted to Supramolecular Chemistry, a section of the journal Frontiers in Chemistry

Received: *12 March 2019*
Accepted: *10 April 2019*
Published: *08 May 2019*

Citation:
Zhang C, Wang G, Han H-H, Hu X-L, Field RA, Chen G-R, Li J, Ye B, He X-P and Zang Y (2019) Self-Assembled Thin-Layer Glycomaterials With a Proper Shell Thickness for Targeted and Activatable Cell Imaging. Front. Chem. 7:294. doi: 10.3389/fchem.2019.00294

The construction of targeted and activatable materials can largely improve the precision of disease diagnosis and therapy. However, the currently developed systems either target a transmembrane antigen or are activatable to release imaging and/or therapeutic reagents intracellularly. Here, we develop a simple thin-layer glycomaterial through the self-assembly between fluorescent glycoprobes, in which the carbohydrate-targeting reagent and the fluorophore are linked to each other by polyethylene glycol with a suitable chain length, and thin-layer manganese dioxide. The fluorogenic material developed is both capable of targeting a transmembrane glycoprotein receptor and fluorescently activatable by intracellular biothiols. The shell thickness of the material was determined to be important for achieving the biothiol-induced activation of fluorescence. This research might provide insight into the development of precision-enhanced self-assembled materials for disease theranostics.

Keywords: fluorescence, precision, imaging, activatable, receptor

INTRODUCTION

Carbohydrate–protein interactions are responsible for the activation of many biological and disease-relevant signaling pathways (Lee and Lee, 1995). During the process of a certain number of diseases, transmembrane receptors that are selective for carbohydrates (monosaccharides or oligosaccharides) are overexpressed (Kampen, 2011). As a result, glycomaterials, which are prepared by covalently or non-covalently conjugating carbohydrates to a variety of different material substrates including polymers, nanoparticles, and thin-layer materials, have been developed for targeted disease diagnosis and therapy (Ji et al., 2016; Zhang et al., 2017; Fu et al., 2018).

Recently, the use of thin-layer materials, such as graphene oxide and graphene-like materials, for biomedical applications has emerged as a topical research area (Chung et al., 2013; Shareena et al., 2018). Among the advanced materials developed, thin-layer molybdenum disulfides and oxides have been proven to be of good biocompatibility with low *in vitro* and *in vivo* toxicity to construct theranostic materials (Liu et al., 2014, 2015; He and Tian, 2016; Yadav et al., 2019).

Thin-layer manganese dioxide (MnO_2), which can be readily degraded to form manganese ions, has been extensively used to construct activatable sensing and therapeutic materials in response to the reducing microenvironments or low pH inside cancer cells (Zhao et al., 2014; Fan et al., 2015; Chen et al., 2016).

While previous studies mainly focused on the development of materials that can target a transmembrane antigen or are activatable for controlled release of imaging and therapeutic agents, here we develop a thin-layer glycomaterial for both targeted and activatable imaging of cells. Self-assembly between fluorescent glycoprobes and thin-layer MnO_2 produces fluorogenic glycomaterials, which can target a transmembrane glycoprotein receptor to deliver the glycoprobes inside cells. Then, degradation of the thin-layer MnO_2 backbone by intracellular biothiols activates the glycoprobe fluorescence, enabling the targeted, activatable functional cell imaging.

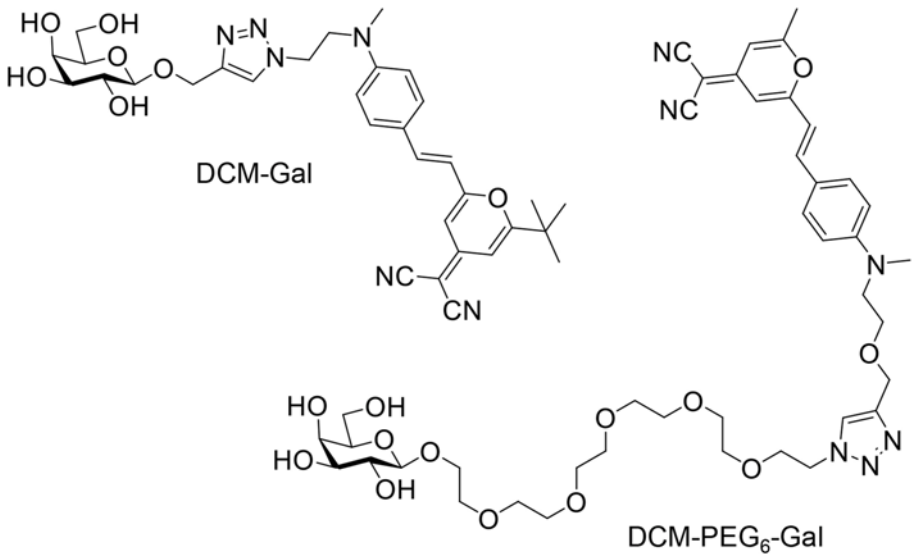

FIGURE 1 | Structure of the glycoprobes used for self-assembly with thin-layer MnO_2.

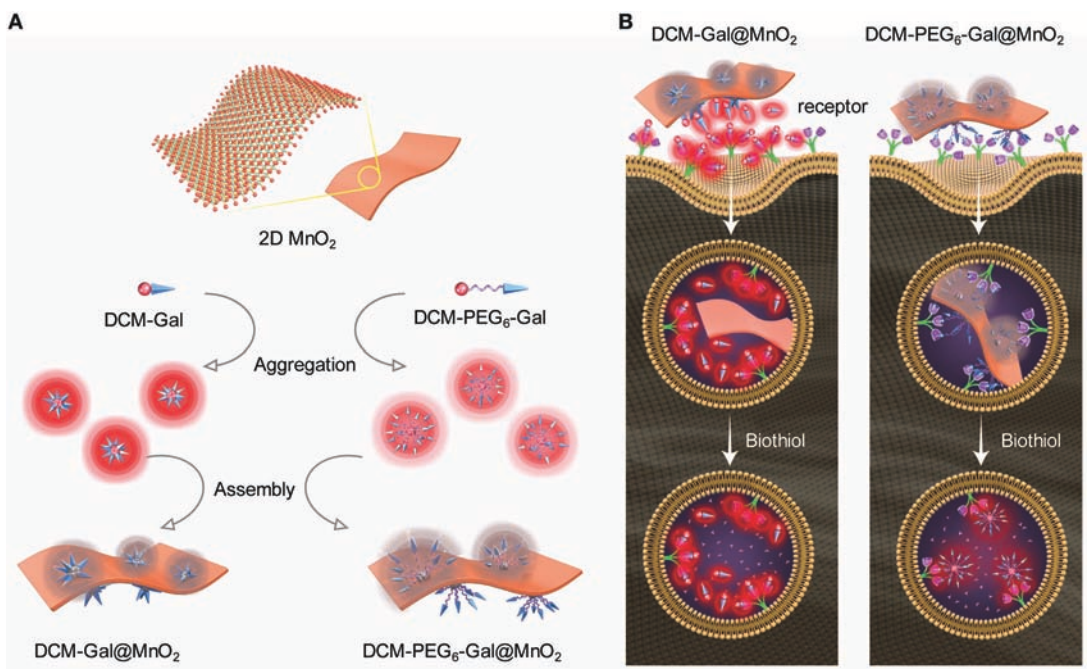

FIGURE 2 | Schematic illustration of **(A)** aggregation and then self-assembly of the glycoprobes with thin-layer MnO_2, producing the thin-layer glycomaterials with different shell thicknesses, and **(B)** the different fluorescence activation mode of the glycomaterials after endocytosis by cells that express asialoglycoprotein receptors.

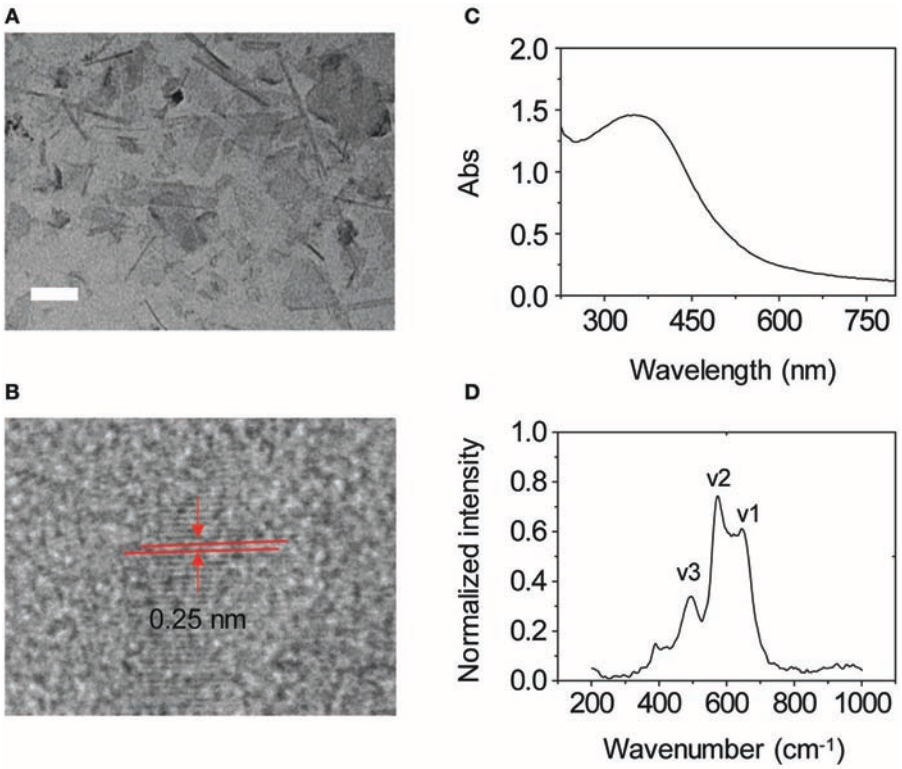

FIGURE 3 | (A) Representative high-resolution transmission electron microscopic (HRTEM) image of thin-layer MnO_2 (scale bar = 50 nm). **(B)** An enlarged view of an HRTEM image of thin-layer MnO_2. **(C)** UV–vis absorption spectrum of thin-layer MnO_2 (100 μg ml^{-1} dissolved in Tris-HCl buffer). **(D)** Raman spectrum of thin-layer MnO_2 (100 μg ml^{-1} dissolved in Tris-HCl buffer).

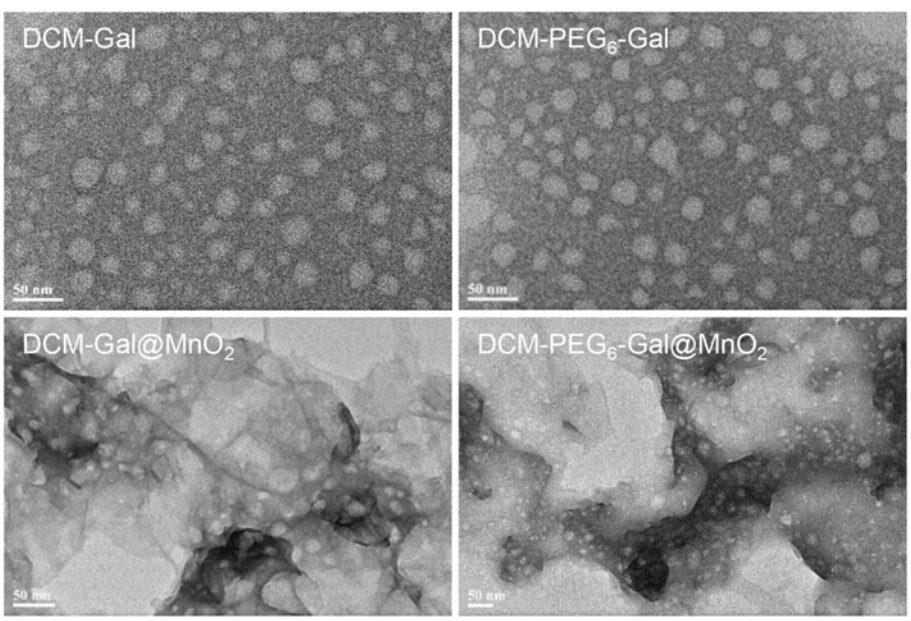

FIGURE 4 | Representative HRTEM images of DCM-Gal, DCM-PEG_6-Gal, DCM-Gal@MnO_2 (DCM-Gal/MnO_2 = 10 μM/10 μg ml^{-1} dissolved in Tris-HCl buffer), and DCM-PEG_6-Gal@MnO_2 (DCM-PEG_6-Gal/MnO_2 = 10 μM/10 μg ml^{-1} dissolved in Tris-HCl buffer).

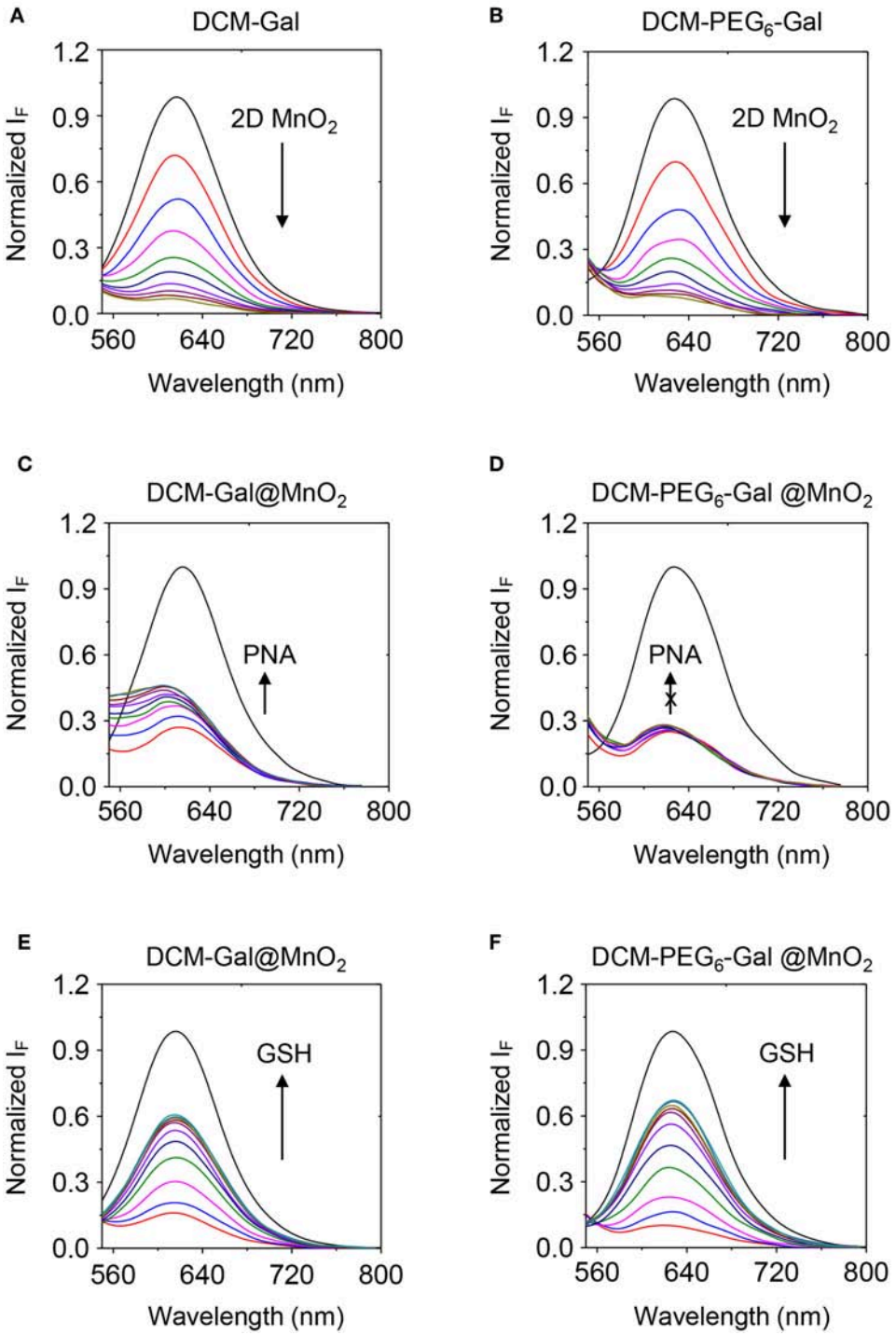

FIGURE 5 | Fluorescence spectra of **(A)** DCM-Gal (10 μM) and **(B)** DCM-PEG_6-Gal (10 μM) with increasing thin-layer MnO_2 (from top to bottom curve: 0–40 μg ml^{-1}, interval: 4 μg ml^{-1}). Fluorescence spectra of **(C)** DCM-Gal@MnO_2 (DCM-Gal/MnO_2 = 10 μM/40 μg ml^{-1}) and **(D)** DCM-PEG_6-Gal@MnO_2 (DCM-PEG_6-Gal/MnO_2 = 10 μM/20 μg ml^{-1}) with increasing PNA (peanut agglutinin, from bottom to top curve: 0–40 μM, interval: 5 μM). Fluorescence spectra of **(E)** DCM-Gal@MnO_2 (DCM-Gal/MnO_2 = 10 μM/40 μg ml^{-1}) and **(F)** DCM-PEG_6-Gal@MnO_2 (DCM-PEG_6-Gal/MnO_2 = 10 μM/40 μg ml^{-1}) with increasing GSH (γ-glutathione, from bottom to top curve: 0–500 μM, interval: 50 μM).

Importantly, we demonstrate that the shell thickness is crucial for achieving the biothiol-responsive fluorescence activation of the thin-layer glycomaterials.

RESULTS AND DISCUSSION

Two DCM (dicyanomethylene-4H-pyran)-based glycoprobes [DCM-Gal (Ji et al., 2016) and DCM-PEG_6-Gal] with linkers of different lengths connecting a DCM and a galactose epitope were used (**Figure 1**). An experimental section and original NMR spectral copies of new compounds are presented in **Supplementary Material**. The presence of a hexa-PEG linkage in the structure of DCM-PEG_6-Gal could facilitate the formation of a PEG shell on the surface of thin-layer materials in order to enhance the stability of the material in complex biological environments (**Figure 2A**). We envision that while the material composite formed between DCM-Gal and thin-layer MnO_2 might dissociate directly after interaction with the asialoglycoprotein receptor (ASGPr) that selectively recognizes galactoconjugates, that formed between DCM-PEG_6-Gal and thin-layer MnO_2 could be more stable during receptor-mediated endocytosis for stimuli-activated fluorescence imaging (**Figure 2B**).

To prove our hypothesis, the glycoprobes were used for self-assembly in Tris-HCl buffer with thin-layer MnO_2 prepared by the previously reported method (Zhao et al., 2014). In its representative high-resolution transmission electron microscopy (HRTEM) images, we observed thin-flake objects, suggestive of the formation of thin-layer MnO_2 (**Figure 3A**). The orthogonal distance (~0.25 nm) between two consecutive slabs of [MnO_6] is characteristic of the typical birnessite-type MnO_2 (**Figure 3B**; Kim et al., 2017). In the UV spectrum of the thin-layer MnO_2, a predominant absorbance peak at ca. 380 nm was detected (**Figure 3C**), which is attributable to the d–d transition of Mn ions in the MnO_6 octahedra of the thin-layer material (Kai et al., 2008). Raman spectroscopy was also used for material characterization. Three typical bands at 647, 575, and 497 cm^{-1} were observed, which are characteristic of the ν_1 (the symmetric stretching vibration of the Mn–O bond in the MnO_6 octahedral plane), ν_2 (the stretching vibration mode of Mn–O in the MnO_6 octahedral basal plane), and ν_3 (the deformation mode of the metal–oxygen chain of Mn–O–Mn in the MnO_2 octahedral lattice) vibrational features of thin-layer MnO_2, respectively (**Figure 3D**; Julien et al., 2003, 2004). We also observed that both DCM-Gal and DCM-PEG_6-Gal form nanoparticles (**Figure 4**), whereas after assembly, the particles were determined to be adhered onto the surface of thin-layer MnO_2 (**Figure 4**).

Subsequently, fluorescence spectroscopy was used for the analysis of the self-assembly. We observed a gradually decreased fluorescence of both DCM-Gal (**Figure 5A**) and DCM-PEG_6-Gal

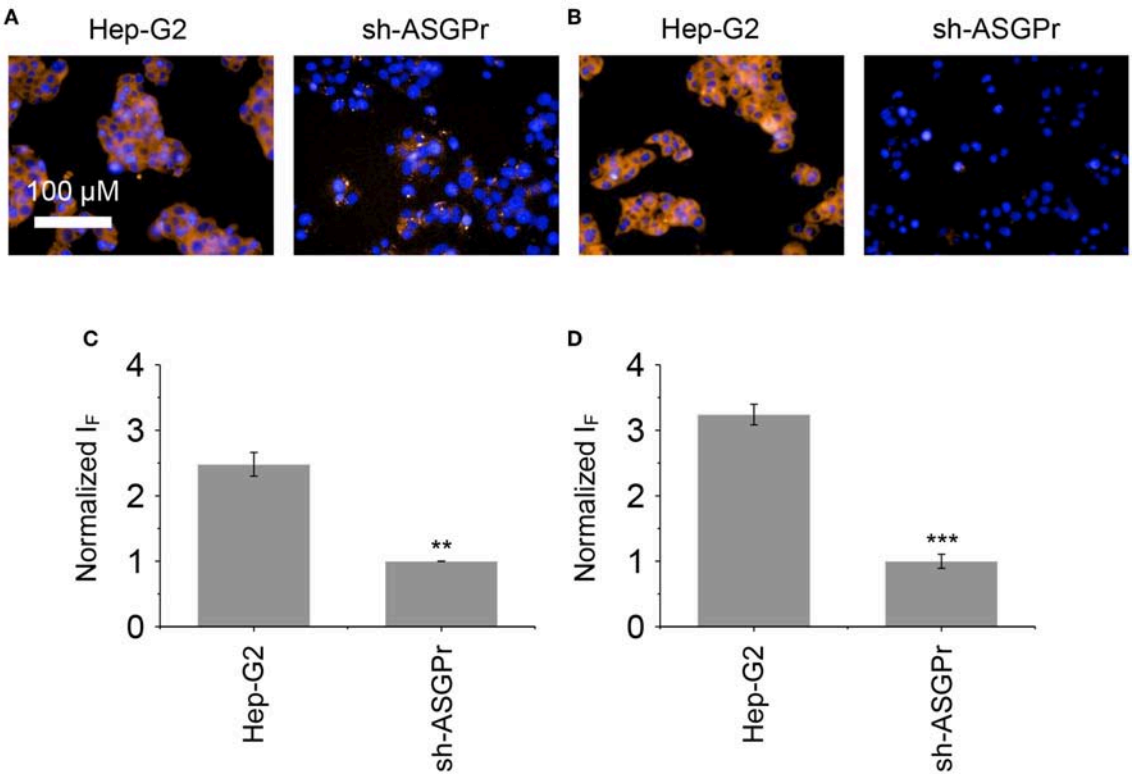

FIGURE 6 | Fluorescence imaging **(A)** and quantification **(C)** of Hep-G2 and sh-ASGPr cells after incubation with DCM-Gal@MnO_2 (DCM-Gal/MnO_2 = 10 μM/32 μg ml^{-1}). Fluorescence imaging **(B)** and quantification **(D)** of Hep-G2 and sh-ASGPr cells after incubation with DCM-PEG_6-Gal@MnO_2 (DCM-PEG_6-Gal/MnO_2 = 10 μM/32 μg ml^{-1}). $^{**}P < 0.01$, $^{***}P < 0.005$. Error bars mean S. D. ($n = 3$). Excitation and emission channels used were 460–490 and 560–630 nm, respectively. Cell nuclei were stained by Hoechst 33342 (excitation and emission channels were 360–400 and 410–480 nm, respectively).

(**Figure 5B**) in the presence of increasing thin-layer MnO_2. This suggests the adsorption of the glycoprobes onto the surface of the material, leading to fluorescence quenching (Zhao et al., 2014). To test its stability toward a carbohydrate-binding protein, we added peanut agglutinin (PNA) that selectively recognizes the galactose epitopes on the surface of the material composite. Interesting, while a gradual fluorescence enhancement was observed for the DCM-Gal@MnO_2 group with increasing PNA (**Figure 5C**), which is in accordance with our previous observations that complexation between glycoprobe and PNA competitively removes the probe molecules from the surface of the quenching material, the quenched fluorescence of DCM-PEG_6-Gal remained almost unchanged (**Figure 5D**). This suggests the importance of the hexa-PEG shell for the protection of the material composite from disassociation upon interaction with a galactose-selective lectin. In contrast, the fact that the presence of GSH led to the fluorescence enhancement of both glycomaterials, which is the result of degradation of the thin-layer MnO_2 backbone, suggests their ability for activatable fluorescence sensing and imaging (**Figures 5E**,**F**).

Next, the glycomaterials were used for cell imaging. Hep-G2 cells that highly express ASGPr as well as GSH, and a previously established Hep-G2 cell line with a reduced ASGPr expression by gene transfection (Fu et al., 2018), were used to test the receptor-targeting capacity of the materials. We determined that the fluorescence of both materials was produced mainly in Hep-G2 rather than in sh-ASGPr cells, suggesting their good receptor-targeting property because of the exposure of galactose epitopes on the surface (**Figure 6**; Burgess et al., 1992). Then, we used Hep-G2 cells with a depleted GSH concentration by pretreatment with NEM (a known GSH scavenger) to measure the fluorescence activity of the materials. A similar level of fluorescence was determined in Hep-G2 cells with or without GSH for the DCM-Gal@MnO_2 group (**Figures 7A**,**C**). In contrast, the fluorescence of DCM-PEG_6-Gal@MnO_2 in Hep-G2 cells with endogenous GSH was much stronger than in those with depleted GSH (**Figures 7B**,**D**). These results preliminarily suggest that while the DCM-Gal@MnO_2 ensemble disassociates upon interaction with ASGPr, DCM-PEG_6-Gal@MnO_2, because of the presence of a hexa-PEG shell, remained much more stable upon receptor-mediated endocytosis. However, the subsequent presence of a high concentration of intracellular GSH led to material degradation, thus enabling activatable fluorescence imaging (**Figure 2B**).

CONCLUSIONS

We have shown in this research that by properly modulating the shell thickness of self-assembled, thin-layer glycomaterials can enable targeted and activatable imaging of cells. The glycomaterial coated with a hexa-PEG shell can effectively protect the material ensemble from disassociation after incubation with a lectin that selectively recognizes the carbohydrate epitopes on the material surface. In the subsequent cell imaging assay, we also observed that the fluorescence activation of the thickly shelled glycomaterial was dependent on the presence intracellular

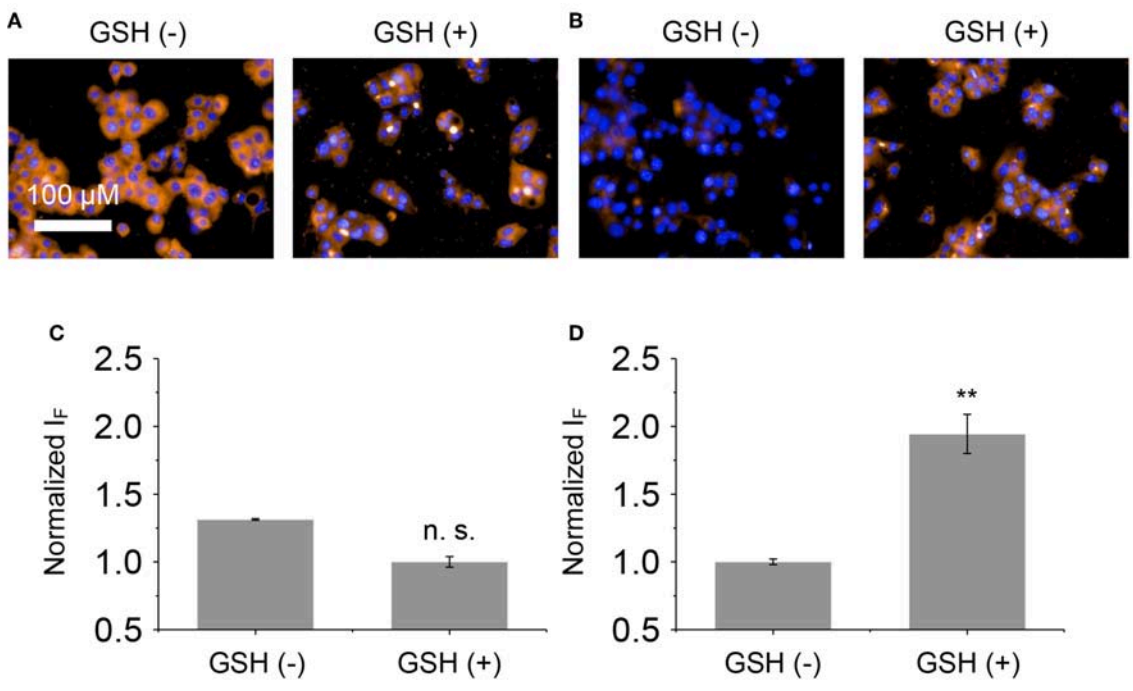

FIGURE 7 | Fluorescence imaging **(A)** and quantification **(C)** of Hep-G2 treated with DCM-Gal@MnO_2 (DCM-Gal/MnO_2 = 10 μM/32 μg ml^{-1}) pretreated with NEM (N-ethylmaleimide is a known GSH quencher, 500 μM) or GSH (300 μM). Fluorescence imaging **(B)** and quantification **(D)** of Hep-G2 treated with DCM-PEG_6-Gal@MnO_2 (DCM-PEG_6-Gal/MnO_2 = 10 μM/32 μg ml^{-1}) pretreated with NEM (500 μM) or GSH (300 μM). n.s., not significant; $^{**}P < 0.01$. Error bars mean S. D. ($n = 3$). Excitation and emission channels used were 460–490 and 560–630 nm, respectively. Cell nuclei were stained by Hoechst 33342 (excitation and emission channels were 360–400 and 410–480 nm, respectively).

biothiols, while that which lacks the protective shell was directly dependent on the expression of transmembrane glycoprotein receptors irrespective of the intracellular GSH concentration. This implies the importance of properly adjusting the shell thickness of self-assembled thin-layer materials in order to enhance the precision of functional cell imaging. We are currently using this concept for the construction of other thin-layer MnO_2-based materials for the analysis of the biothiol level in different types of cancer cells such as leukemia cells.

DATA AVAILABILITY

The raw data supporting the conclusions of this manuscript will be made available by the authors, without undue reservation, to any qualified researcher.

AUTHOR CONTRIBUTIONS

All authors listed have made a substantial, direct and intellectual contribution to the work, and approved it for publication.

FUNDING

This research is supported by the National Natural Science Foundation of China (21722801, 21776078, 81671739, 81673489, and 81125023), the Shanghai Municipal Science and Technology Major Project (grant no. 2018SHZDZX03), and the International Cooperation Project (no. 16430724100).

ACKNOWLEDGMENTS

Ya-Wen Cheng is thanked for her help in compound synthesis and spectroscopic measurements.

SUPPLEMENTARY MATERIAL

The Supplementary Material for this article can be found online at: https://www.frontiersin.org/articles/10.3389/fchem.2019.00294/full#supplementary-material

REFERENCES

Burgess, J. B., Baenziger, J. U., and Brown, W. R. (1992). Abnormal surface distribution of the human asialoglycoprotein receptor in cirrhosis. *Hepatology* 15, 702–706.

Chen, Q., Feng, L., Liu, J., Zhu, W., Dong, Z., Wu, Y., et al. (2016). Intelligent albumin–MnO_2 nanoparticles as pH-/H_2O_2-responsive dissociable nanocarriers to modulate tumor hypoxia for effective combination therapy. *Adv. Mater.* 28, 7129–7136. doi: 10.1002/adma.201601902

Chung, C., Kim, Y. K., Shin, D., Ryoo, S. R., Hong, B. H., and Min, D. H. (2013). Biomedical applications of graphene and graphene oxide. *Acc. Chem. Res.* 46, 2211–2224. doi: 10.1021/ar300159f

Fan, W., Bu, W., Shen, B., He, Q., Cui, Z., Liu, Y., et al. (2015). Intelligent MnO_2 Nanosheets anchored with upconversion nanoprobes for concurrent pH-/H_2O_2-responsive UCL imaging and oxygen-elevated synergetic therapy. *Adv. Mater.* 27, 4155–4161. doi: 10.1002/adma.201405141

Fu, Y. X., Han, H. H., Zhang, J. J., He, X. P., Feringa, B. L., and Tian, H. (2018). Photocontrolled fluorescence "double-check" bioimaging enabled by a glycoprobe-protein hybrid. *J. Am. Chem. Soc.* 140, 8671–8674. doi: 10.1021/jacs.8b05425

He, X. P., and Tian, H. (2016). Photoluminescence architectures for disease diagnosis: from graphene to thin-layer transition metal dichalcogenides and oxides. *Small* 12, 144–160. doi: 10.1002/smll.201502516

Ji, D. K., Zhang, Y., Zang, Y., Li, J., Chen, G. R., He, X. P., et al. (2016). Targeted intracellular production of reactive oxygen species by a 2D molybdenum disulfide glycosheet. *Adv. Mater.* 28, 9356–9363. doi: 10.1002/adma.201602748

Julien, C., Massot, M., Baddour-Hadjean, R., Franger, S., Bach, S., and Pereira-Ramos, J. P. (2003). Raman spectra of birnessite manganese dioxides. *Solid State Ionics* 159, 345–356. doi: 10.1016/S0167-2738(03)00035-3

Julien, C. M., Massot, M., and Poinsignon, C. (2004). Lattice vibrations of manganese oxides—Part 1. Periodic structures. *Spectrochim. Acta Part A* 60, 689–700. doi: 10.1016/S1386-1425(03)00279-8

Kai, K., Yoshida, Y., Kageyama, H., Saito, G., Ishigaki, T., Furukawa, Y., et al. (2008). Room-temperature synthesis of manganese oxide monosheets. *J. Am. Chem. Soc.* 130, 15938–15943. doi: 10.1021/ja804503f

Kampen, K. R. (2011). Membrane proteins: the key players of a cancer cell. *J. Membr. Biol.* 242, 69–74. doi: 10.1007/s00232-011-9381-7

Kim, H., Watthanaphanit, A., and Saito, N. (2017). Simple solution plasma synthesis of hierarchical nanoporous MnO_2 for organic dye removal. *ACS Sust. Chem. Eng.* 5, 5842–5851. doi: 10.1021/acssuschemeng.7b00560

Lee, Y. C., and Lee, R. T. (1995). Carbohydrate–protein interactions—basis of glycobiology. *Acc.Chem. Res.* 28, 321–327.

Liu, T., Shi, S. X., Liang, C., Shen, S. D., Cheng, L., Wang, C., et al. (2015). Iron oxide decorated MoS_2 nanosheets with double PEGylation for chelator-free radio labeling and multimodal imaging guided photothermal therapy. *ACS Nano* 9, 950–960. doi: 10.1021/nn506757x

Liu, T., Wang, C., Gu, X., Gong, H., Cheng, L., Shi, X. Z., et al. (2014). Drug delivery with PEGylated MoS_2 nano-sheets for combined photothermal and chemotherapy of cancer. *Adv. Mater.* 26, 3433–3440. doi: 10.1002/adma.201305256

Shareena, T. P. D., McShan, D., Dasmahapatra, A. K., and Tchounwou, P. B. (2018). A review on graphene-based nanomaterials in biomedical applications and risks in environment and health. *Nano Micro Lett.* 10:53. doi: 10.1007/s40820-018-0206-4

Yadav, V., Roy, S., Singh, P., Khan, Z., and Jaiswal, A. (2019). 2D MoS_2-based nanomaterials for therapeutic, bioimaging, and biosensing applications. *Small* 15:e1803706. doi: 10.1002/smll.201803706

Zhang, J., Fu, Y., Han, H. H., Zang, Y., Li, J., He, X. P., et al. (2017). Remote light-controlled intracellular target recognition by photochromic fluorescent glycoprobes. *Nat. Commun.* 8:987. doi: 10.1038/s41467-017-01137-8

Zhao, Z. L., Fan, H. H., Zhou, G. F., Bai, H. R., Liang, H., Wang, R. W., et al. (2014). Activatable fluorescence/MRI bimodal platform for tumor cell imaging *via* MnO_2 nanosheet–aptamer nanoprobe. *J. Am. Chem. Soc.* 136, 11220–11223. doi: 10.1021/ja5029364

Conflict of Interest Statement: The authors declare that the research was conducted in the absence of any commercial or financial relationships that could be construed as a potential conflict of interest.

Copyright © 2019 Zhang, Wang, Han, Hu, Field, Chen, Li, Ye, He and Zang. This is an open-access article distributed under the terms of the Creative Commons Attribution License (CC BY). The use, distribution or reproduction in other forums is permitted, provided the original author(s) and the copyright owner(s) are credited and that the original publication in this journal is cited, in accordance with accepted academic practice. No use, distribution or reproduction is permitted which does not comply with these terms.

frontiers in Chemistry

ORIGINAL RESEARCH
published: 22 May 2019
doi: 10.3389/fchem.2019.00354

Squaramide—Naphthalimide Conjugates as "Turn-On" Fluorescent Sensors for Bromide Through an Aggregation-Disaggregation Approach

*Lokesh K. Kumawat[1], Anthony A. Abogunrin[1], Michelle Kickham[1,2], Jyotsna Pardeshi[2], Orla Fenelon[1], Martina Schroeder[2,3] and Robert B. P. Elmes[1,3]**

[1] Department of Chemistry, Maynooth University, National University of Ireland, Maynooth, Ireland, [2] Department of Biology, Maynooth University, National University of Ireland, Maynooth, Ireland, [3] Maynooth University Human Health Research Institute, Maynooth University, National University of Ireland, Maynooth, Ireland

OPEN ACCESS

Edited by:
Tony D. James, University of Bath, United Kingdom

Reviewed by:
Valeria Amendola, University of Pavia, Italy
Philip A. Gale, University of Sydney, Australia

***Correspondence:**
Robert B. P. Elmes
robert.elmes@mu.ie

Specialty section:
This article was submitted to Supramolecular Chemistry, a section of the journal Frontiers in Chemistry

Received: 15 February 2019
Accepted: 29 April 2019
Published: 22 May 2019

Citation:
Kumawat LK, Abogunrin AA, Kickham M, Pardeshi J, Fenelon O, Schroeder M and Elmes RBP (2019) Squaramide—Naphthalimide Conjugates as "Turn-On" Fluorescent Sensors for Bromide Through an Aggregation-Disaggregation Approach. Front. Chem. 7:354. doi: 10.3389/fchem.2019.00354

The syntheses of two new squaramide-naphthalimide conjugates (**SQ1** and **SQ2**) are reported where both compounds have been shown to act as selective fluorescence "turn on" probes for bromide in aqueous DMSO solution through a disaggregation induced response. **SQ1** and **SQ2** displayed a large degree of self-aggregation in aqueous solution that is disrupted at increased temperature as studied by ^{1}H NMR and Scanning Electron Microscopy (SEM). Moreover, the fluorescence behavior of both receptors was shown to be highly dependent upon the aggregation state and increasing temperature gave rise to a significant increase in fluorescence intensity. Moreover, this disaggregation induced emission (DIE) response was exploited for the selective recognition of certain halides, where the receptors gave rise to distinct responses related to the interaction of the various halide anions with the receptors. Addition of F^- rendered both compounds non-emissive; thought to be due to a deprotonation event while, surprisingly, Br^- resulted in a dramatic 500–600% fluorescence enhancement thought to be due to a disruption of compound aggregation and allowing the monomeric receptors to dominate in solution. Furthermore, optical sensing parameters such as limits of detection and binding constant of probes were also measured toward the various halides (F^-, Cl^-, Br^-, and I^-) where both **SQ1** and **SQ2** were found to sense halides with adequate sensitivity to measure μM levels of halide contamination. Finally, initial studies in a human cell line were also conducted where it was observed that both compounds are capable of being taken up by HeLa cells, exhibiting intracellular fluorescence as measured by both confocal microscopy and flow cytometry. Finally, using flow cytometry we were also able to show that cells treated with NaBr exhibited a demonstrable spectroscopic response when treated with either **SQ1** or **SQ2**.

Keywords: supramolecular chemistry, squaramide, 1, 8-naphthalimide, fluorescent sensor, anion recognition

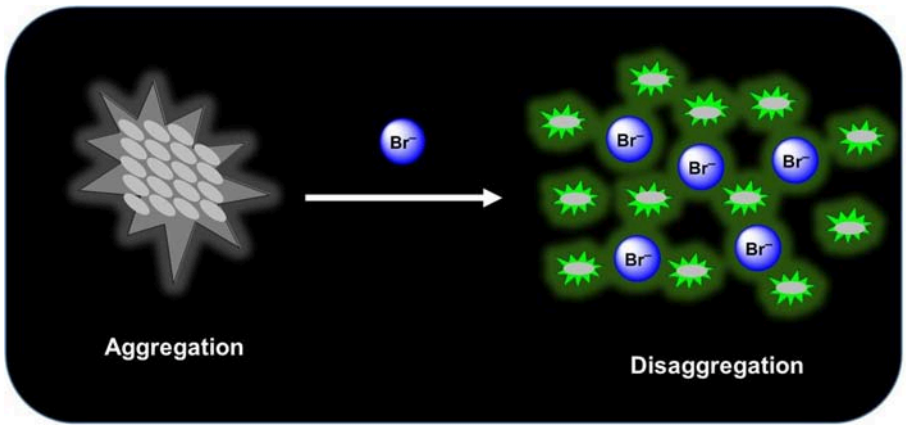

GRAPHICAL ABSTRACT |

INTRODUCTION

Anion sensing has been a key area of supramolecular chemistry since the introduction of the field in the early 1970's (Beer and Gale, 2001; Gunnlaugsson et al., 2006; Duke et al., 2010; Busschaert et al., 2015; Gale et al., 2016; Langton et al., 2016). In particular the recognition and sensing of halides has garnered considerable research interest due to their prevalence in biological and ecological settings (Verkman, 1990; Cametti and Rissanen, 2009, 2013; Evans and Beer, 2014; Ashton et al., 2015). While chloride and fluoride have captivated much of the research interest due to their major roles in cellular homeostasis, acid/base equilibria, and pollution concerns other halides such as bromide have been largely ignored. This is surprising given the clinical symptoms of bromide intoxication (also known as bromism), a once common disease where large doses of bromide were found to impair neuronal transmission and cause nausea and vomiting, abdominal pain, coma, and paralysis (Olson and System, 2004). Although now rare, bromism cases continue to be reported due to non-prescription bromide-based medications being available over the counter where a recent case resulted in extremely high levels of bromide intoxication (serum bromide level of 1,717 mg/L) (Hoizey et al., 2003). Moreover, from an environmental standpoint, bromide pollution can result in reaction between chlorine and naturally occurring organic matter in drinking-water, forming brominated, and mixed chloro-bromo by products such as trihalomethanes or halogenated acetic acids (Gribble, 2004). Indeed, the World Health Organization reports that while low levels of bromide pollution do not seem to have detrimental effects on humans or animals (World Health Organization, 2009), bromate (formed in water during ozonation) is a known carcinogen (World Health Organization, 2005). However, the selective binding and sensing of bromide is made challenging by its intermediate size and hydration energy between chloride and iodide (Marcus, 1991), and reported examples in the literature remain scarce (Kang and Kim, 2005; Suksai et al., 2005; Vlascici et al., 2018). One of the few examples, reported by Qian and co-workers, developed a rhodamine based fluorescent probe capable of selective sensing of iodide and bromide in aqueous solution based on a metal ion removal and anion ligand exchange mechanism (Xu et al., 2012). Nyokong and co-workers reported the use of GSH-capped quantum dots (QDs) covalently linked to a nickel tetraamino-phthalocyanine complex where the covalent binding of the QDs to the Ni complex induced fluorescence quenching before with introduction of Br– restoring the fluorescence (Adegoke and Nyokong, 2013). Most recently, Beer and co-workers developed a redox-active ferrocene functionalized rotaxane with a halogen bonding anion binding site that was capable of selective Br^- sensing over Cl^- in the presence of water as measured by ^1H NMR and electrochemical measurements (Lim and Beer, 2019).

Much of the literature surrounding anion sensors relies on a binding event that disrupts/enhances some type of electron transfer mechanism such as photoinduced electron transfer (PET), internal charge transfer (ICT), excited state intramolecular proton transfer (ESIPT), fluorescence resonance energy transfer (FRET), etc. to yield a measurable fluorescence response (de Silva et al., 1997; Wu et al., 2011; Fan et al., 2013; Lee et al., 2015; Kumawat et al., 2017; Sedgwick et al., 2018). Some more recent reports take advantage of aggregation induced emission (AIE) (Hong et al., 2011), whereby recognition of an anion causes aggregation of the sensor thereby reducing molecular rotation and inducing large fluorescence perturbations (Peng et al., 2009; Ma et al., 2019). The opposite sensing mechanism, disaggregation induced emission (DIE), where dis-assembly of a non-fluorescent aggregate releases individual fluorescent molecules has received much less attention even though the process from aggregation to disaggregation generally causes a recovery or enhancement of fluorescence signals, and thus provides a useful method to design "turn-on" probes (Zhai et al., 2014). Recognition events that induce a fluorescence increase are preferable from the perspective of industrial/medical application where such a facile "turn-on" response can give naked-eye real-time information. Indeed, a recent report from O'Shea and co-workers detailed the use of an amphiphilic BF_2-azadipyrromethene (NIR-AZA) DIE probe

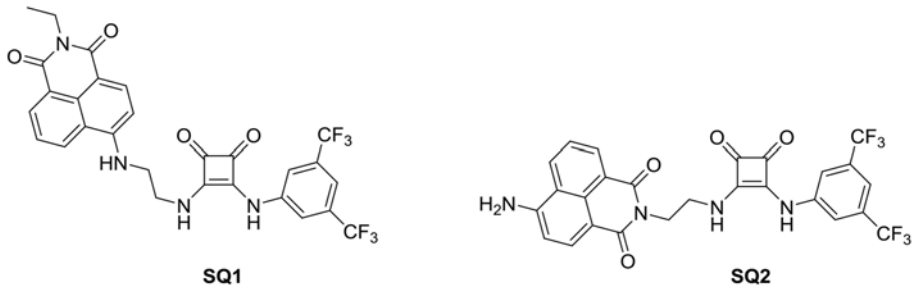

FIGURE 1 | Chemical structures of probes **SQ1** and **SQ2**.

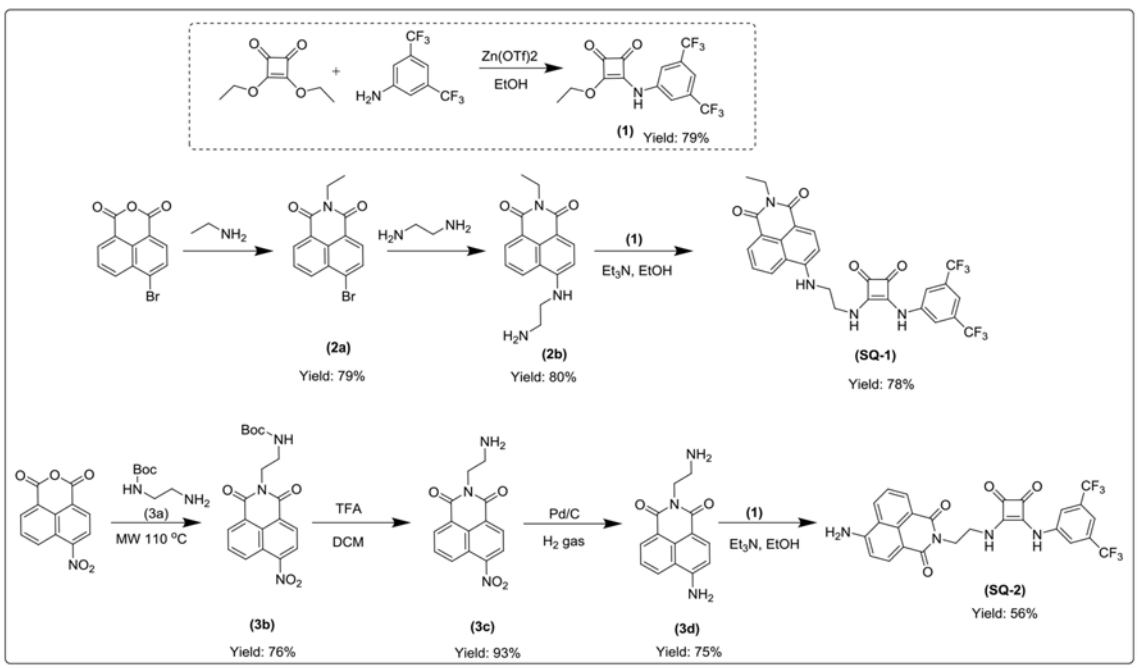

SCHEME 1 | Syntheses of **SQ1** and **SQ2**.

where a membrane selective fluorescence "off to on" switching event allowed visualization of dynamic cellular events in real-time (Wu et al., 2018). Here the authors exemplify how DIE can be exploited to produce a signal in response to a biological event specific to the plasma membrane, allowing real-time visualization of cell-cell contacts through pairs of filopodia.

From our work on squaramides we are familiar with the self-assembly/aggregation of these molecules due to bidirectional H-bonding interactions in addition to π-π stacking brought about by the aromatic cyclobutenedione ring (Elmes et al., 2013, 2014, 2015; Busschaert et al., 2014; Elmes and Jolliffe, 2014; Qin et al., 2016; Marchetti et al., 2018). Moreover, we have also gained considerable experience working with the naphthalimide fluorophore which has fluorescence properties that are highly dependent upon aggregation (Elmes and Gunnlaugsson, 2010; Elmes et al., 2012; Ryan et al., 2012, 2015; Ao et al., 2017). Indeed, Scanlan, Gunnlaugsson and co-workers have recently shown glycosylated naphthalimide and naphthalimide Tröger's bases that act as fluorescent aggregation probes for the Con A protein where both structures self-assemble in solution to form supramolecular structures by head-to-tail π-π stacking and extended hydrogen bonding interactions (Calatrava-Pérez et al., 2019). Inspired by this work, we envisaged that a naphthalide-squaramide conjugate may also aggregate efficiently in solution and such aggregation behavior may be modulated upon anion recognition where a disruption of a H-bonding network would reverse self-assembly. Thus, we set about designing a small family of squaramide-naphthalimide conjugates in which we wished to vary the position of the squaramide in relation to the naphthalimide to place the squaramide at either the "head" or the "tail" of the structure (**Figure 1**). As shown in **Scheme 1** our design incorporated a short linker with a significantly hydrophobic side arm that we expected may aid in the aggregation behavior of the sensors in polar solvents.

Herein, we report the synthesis of compounds **SQ1** and **SQ2** where we have exploited their aggregation behavior and found

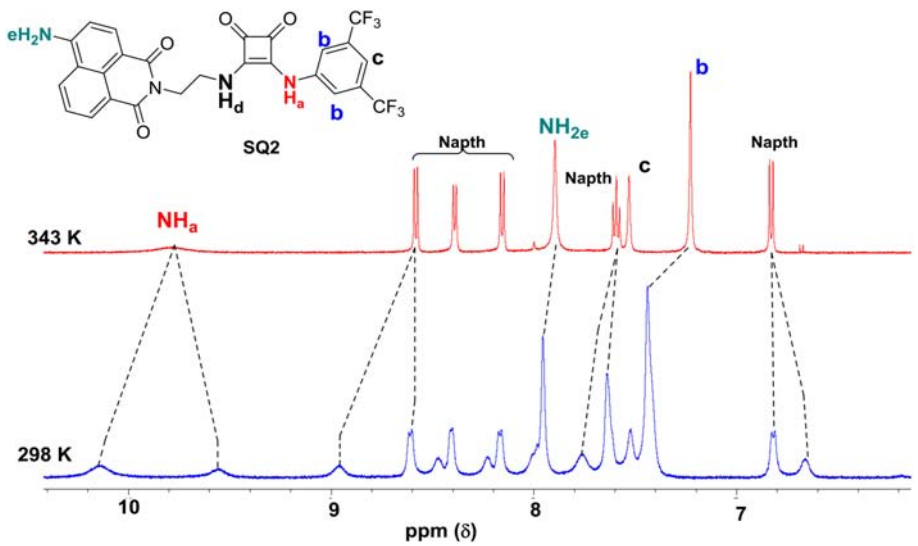

FIGURE 2 | Disaggregation response of probes **SQ2** (5.0×10^{-3} M) at different temperatures. in DMSO-d_6.

differing fluorescence responses to various halides in solution. We have discovered that both **SQ1** and **SQ2** behave as DIE based sensors in solution show differing responses to various anions but with an unexpectedly selective fluorescence "turn on" response to bromide. Moreover, initial results obtained with the HeLa cell line demonstrate that the effect can also be observed in the complex biological environment of a human cell.

RESULTS AND DISCUSSIONS

Synthesis

The syntheses of compounds **SQ1** and **SQ2** were achieved using the synthetic pathway outlined in **Scheme 1**. Briefly, **SQ1** was synthesized by amination of 4-bromo-1,8-naphthalimide **2a** using ethylenediamine before nucleophilic addition of the resulting intermediate **2b** to 3,5-bis(trifluoromethyl)phenyl squarate monoester **1** to yield **SQ1** in 78% yield. Similarly, **SQ2** was formed from an initial reaction of 4-nitro-1,8-naphthalic anhydride **3** with *N*-Boc-ethylenediamine **3a** to yield intermediate **3b** before subsequent TFA mediated deprotection of the Boc group **3c** and catalytic reduction of the nitro group yielded compound **3d** that was also reacted with 3,5-bis(trifluoromethyl)phenyl squarate monoester **1** to yield **SQ2** in 56% yield. All compounds and intermediates were fully characterized by ^{1}H NMR, ^{13}C NMR, HRMS and IR spectroscopy (see **Supporting Information**). However, during NMR characterization it was noted that the ^{1}H NMR spectra of both **SQ1** and **SQ2** gave rise to complex spectra exhibiting significantly broadened peaks. Indeed, as discussed above, it is well-known that squaramides benefit from several characteristics that make them amenable for use in self-assembled materials, in particular their structural rigidity, aromaticity and ability to form strong two-dimensional hydrogen bonds (Storer et al., 2011; Wurm and Klok, 2013). Similarly, naphthalimides, with their extended planar, aromatic structure are well known to partake in π-π stacking; a characteristic that renders the photophysical properties of napthalimides sensitive to such stacking events (Duke et al., 2010; Banerjee et al., 2013). In order to investigate the self-assembly behavior of **SQ1** and **SQ2** several techniques such as ^{1}H NMR, fluorescence measurements and SEM were utilized.

Aggregation Behavior Measured by ^{1}H NMR and SEM Spectroscopy

The ^{1}H NMR spectra of **SQ1** and **SQ2** in *d6*-DMSO was measured at both 298 and 343 K. Both spectra clearly showed substantial differences between room and high temperatures where the spectra of **SQ1** and **SQ2** at 298 K appear broad and complex, as discussed above, signifying some degree of aggregation is occurring. Conversely, upon heating the samples to 343 K large changes in the spectra are observed whereby the signals become sharp and well-resolved allowing complete characterization of all ^{1}H signals at this temperature. For example, **Figure 2** exemplifies the apparent differences between the ^{1}H NMR spectrum of **SQ2** at 298 and 343 K. Interestingly, signals associated with the naphthalimide moiety appear to resolve from two broad signals per proton to become one well-resolved signal for each proton. Moreover, the signals associated with the 3,5-bis(trifluoromethyl)phenyl portion of the molecule appear to undergo significant chemical shift changes, particularly the protons at the 2 and 6 position (H_b) ($\Delta\delta = 105$ Hz. Similarly, the CH_2 directly attached to the squaramide moiety also resolves from two signals to one but does not fully resolve to the expected multiplicity and remains broad (**Figure S20**). Perhaps most striking is the fact that the squaramide NH signals appear as two distinct signals in the ^{1}H NMR (10.1 and 9.56 ppm) at 298 K but are resolved to one broad signal at 9.78 ppm at 343 K. Taken together the evidence from the above study suggests that the entire molecule is taking part in aggregation behavior with the

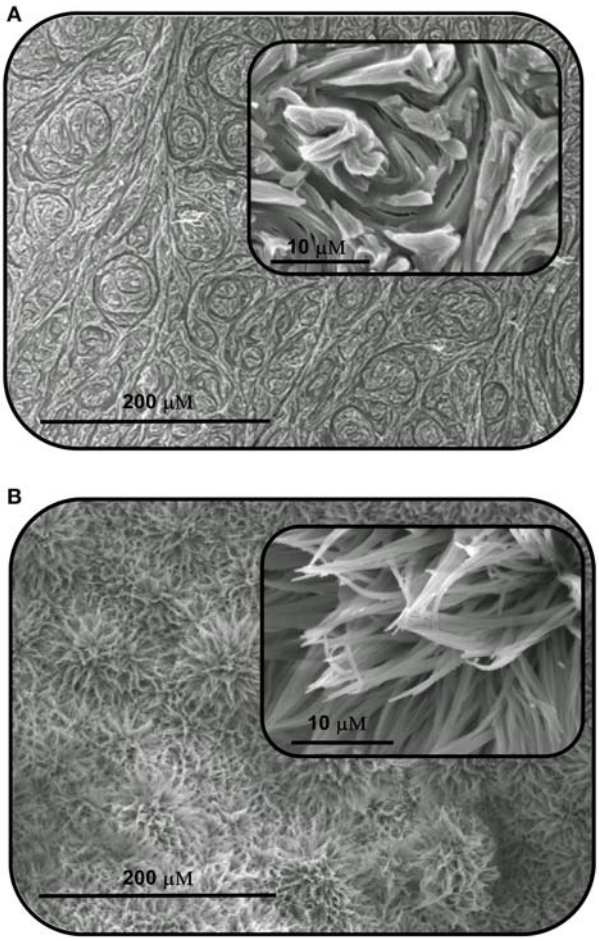

FIGURE 3 | Scanning electron microscopy (SEM) images of the aggregates formed by self-assembly of **(A) SQ1** and **(B) SQ2** in DMSO.

squaramide, naphthalimide and 3,5-bis(trifluoromethyl)phenyl portions all playing a role. Similar behavior was observed in the cases of both **SQ1** and **SQ2** (**Figure S19**).

In order to further probe the aggregation characteristics of both compound, attempts were made to grow crystals from concentrated DMSO solutions. Unfortunately, in our hands the compounds did not crystallize and instead formed what appeared to be amorphous solids. The morphological features of these solids were thus analyzed by scanning electron microscopy (SEM), and as shown in **Figure 3**, the SEM images exhibit interesting and distinct morphology on the nanoscale. **SQ1** appeared as "swirls" that propagate throughout the entire material. Conversely, **SQ2** formed showed a sponge like structure that at higher magnification appears to be composed of small nanofilaments. Although firm conclusions cannot be drawn on the exact molecular interactions that give rise to such interesting morphology it is clear that a high degree of aggregation is occurring that appears to be in an ordered fashion to give rise to such patterns.

Both **SQ1** and **SQ2** were examined using UV/Vis spectroscopy and fluorescence emission spectroscopy. The UV/Vis absorption spectrum of **SQ1** in DMSO showed three absorption maxima at 280, 340, and 445 nm with extinction coefficient values of 32,642, 19,559, and 15,439 M^{-1} respectively. Similarly, **SQ2** showed an almost identical spectrum to **SQ1** with maxima also at 280, 340, and 445 nm and with extinction coefficients of 34,785, 20,405, and 13,717 M^{-1}, respectively. Furthermore, both compounds exhibited fluorescence emission at *ca.* 525 nm. With the aggregation behavior observed in the previous section, we also undertook a thermal study to investigate if the fluorescence of **SQ1** and **SQ2** could be modulated by disaggregation. A temperature dependent fluorescence study was thus undertaken in 5% aq. DMSO. As seen in **Figure 4**, both **SQ1** and **SQ2** exhibited a sharp increase in fluorescence 220–300% as a function of temperature. These results support the ^{1}H NMR results above where we suggest that both **SQ1** and **SQ2** aggregate in solution but, upon heating, disassemble thus allowing the fluorescence intensity to increase. Interestingly, upon cooling the emission does not decrease to its original value. This may suggest that once disrupted the self-aggregation behavior is not reversible under these conditions (**Figure S23**). A fluorescence dilution study was also conducted, where it was observed that the fluorescence intensity of both **SQ1** and **SQ2** at 525 nm is linear to concentration (from 0.05 to 5 μM) and suggests that aggregation occurs at very low concentrations (**Figure S24**).

With the observed properties exhibited by **SQ1** and **SQ2** and the known propensity of squaramides to bind strongly to halides and other anionic species (Prohens et al., 1998, 2001; Piña et al., 2008; Amendola et al., 2010; Busschaert et al., 2012; Delgado-Pinar et al., 2012; Jin et al., 2013), we expected that introduction of anionic analytes may also disrupt the self-aggregation of the **SQ1** and **SQ2**. If indeed disruption was to occur, we expected some modulation of their photophysical properties would result and potentially give rise to a new class of anion sensors based on disaggregation.

Anion Induced Disaggregation

To investigate the ability of anions to disrupt the self-aggregation of **SQ1** and **SQ2** a series of ^{1}H NMR experiments were carried out. Initial qualitative measurements were undertaken using a screening experiment in which 30 equiv. of several anions (AcO^-, $H_2PO_4^-$, SO_4^{2-}, F^-, Cl^-, Br^-, and I^- as their tetrabutylammonium salts) were added to the receptors in solution (0.5% H_2O in DMSO-d_6). These preliminary results showed significant changes of the spectra of both **SQ1** and **SQ2**. Dramatic changes were observed in the ^{1}H NMR spectra of both receptors in the presence of AcO^-, F^-, $H_2PO_4^-$, and SO_4^{2-} where addition of these anions led to the disappearance of the NH signal (H_a) as shown in **Figure 5** for **SQ2** and also either broadened (AcO^- and F^-) or sharpened ($H_2PO_4^-$ and SO_4^{2-}).

Stark color changes of the solutions of **SQ1** and **SQ2** were observed upon the addition of F^- from yellow to red. The disappearance of the NH signal (H_a) and the stark color change suggests that deprotonation of the squaramide/naphthalimide may be responsible. We further confirmed this deprotonation behavior by observation of bifluoride (HF_2^-) in the ^{1}H NMR spectra of **SQ1** and **SQ2** upon the addition of F^- as shown in **Figure 5** for receptor **SQ1**. Moreover, distinct changes were

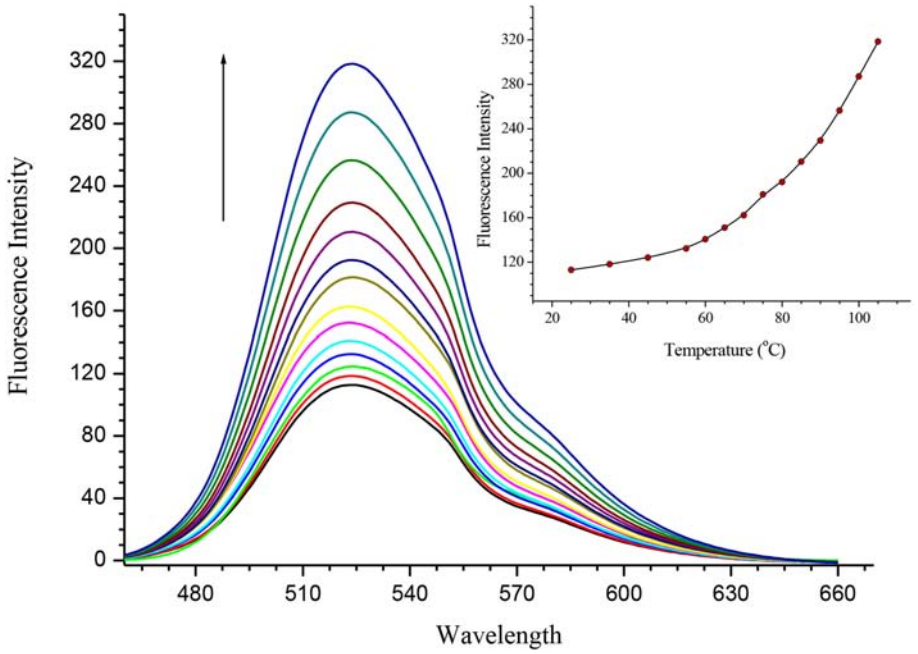

FIGURE 4 | Fluorescence temperature study demonstrating the disaggregation response of **SQ2** (5.0×10^{-6} M) in 5% aq. DMSO from 25° to 110°C.

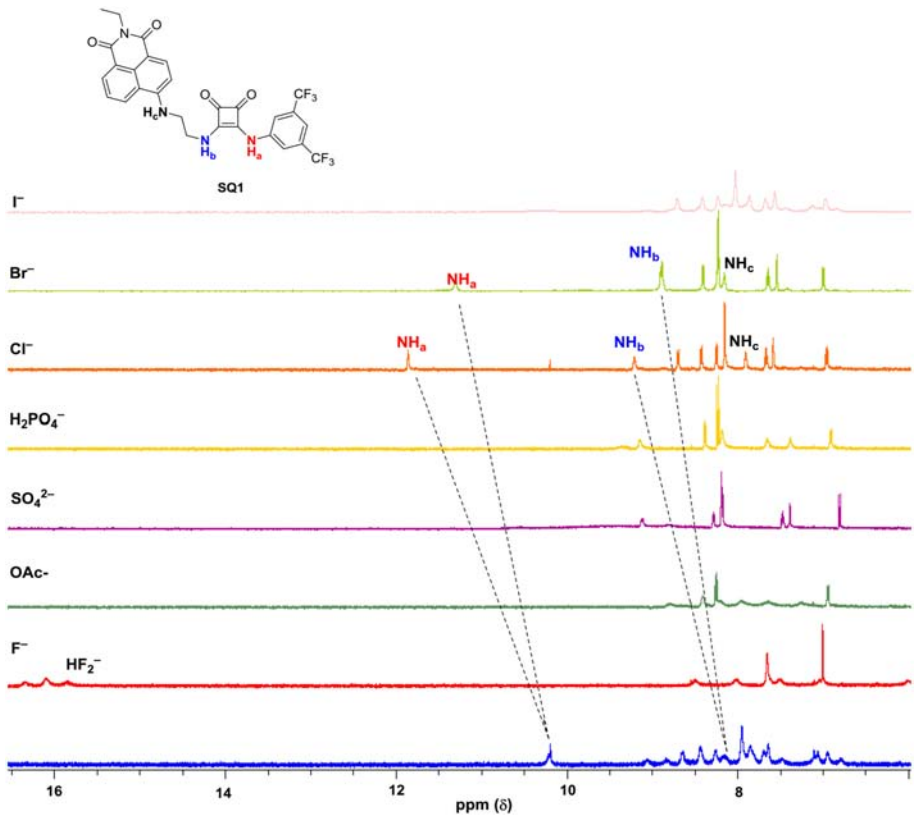

FIGURE 5 | ^{1}H NMR stackplot of **SQ1** with various anions (30 equivalents) in 0.5% H_2O in DMSO-d_6 at 298 K.

observed in the ^{1}H NMR spectra of **SQ1** and **SQ2** upon the addition of Cl^- and Br^-. For example, with **SQ2** these halides led to a large downfield shift of the NH signal (H_a) from 10.2 to 12.1 ppm for Cl^- and to 11.1 ppm for Br^- coupled with a significantly sharpened signal. Similar behavior was observed for **SQ1** (see **Figure S25**). The large downfield shift of the NH signal suggests a classical H-bonding interaction between Cl^- and Br^- and the NH protons of the squaramides. To further investigate the binding interaction of halides with **SQ1** and **SQ2** more detailed ^{1}H NMR spectroscopic titrations were carried out with halides F^-, Cl^-, Br^-, and I^- as their tetrabutylammonium salts with the resulting data fit to a 1:1 binding model using the open access BindFit software program (Thordarson, 2011; Lowe et al., 2012; Brynn Hibbert and Thordarson, 2016) to provide the apparent stability constants (K_a), which are summarized in **Table 1**.

TABLE 1 | Summary of the halide association constants K_a (M^{-1}) of receptors **SQ1** and **SQ2** in DMSO-d_6 at 273 K according to the ^{1}H NMR titration data.

Receptor	K_a (M^{-1}) (% Error)			
	F^-	Cl^-	Br^-	I^-
SQ1	–[a]	489 (6%)	165 (10%)	–[b]
SQ2	–[a]	221 (9%)	99 (9%)	–[b]

[a] *Addition of F^- resulted in deprotonation and prevented an association constant from being determined.*

[b] *Spectral changes were too minor to provide an accurate association constant. A series of equilibria may occur in solution under the reported conditions (e.g., aggregate disruption, anion binding to the monomer; anion binding to the aggregate etc.) thus these data, that have been fitted to a 1:1 binding model, are included to give a comparison of analogous squaramide anion receptors previously reported Busschaert et al., 2012; Bao et al., 2018.*

As an example, **Figure 6** shows the changes observed in the ^{1}H NMR spectrum of **SQ1** upon the addition of Cl^- (20 equiv.). A gradual downfield shift of the NH signal (H_a) from 10.2 to 11.8 ppm in the ^{1}H NMR spectrum was observed upon the increasing concentration of Cl^-. These changes together with increased spectral resolution observed over the entire spectrum upon the addition of Cl^-, clearly support a classical H-bonding interaction between Cl and the NH protons (H_a) of the receptors.

Overall, both **SQ1** and **SQ2** were found to bind to Cl^- and Br^- with moderate affinities with **SQ1** showing a slightly increased affinity for both anions compared to **SQ2** where the position of the squaramide at the "tail" of the naphthalimide seems to be optimal for both anions. Similarly, both receptors exhibited a preference for Cl^- over Br^- while I^- showed an almost complete lack of binding in both cases. Conversely, as previously discussed F^- resulted in receptor deprotonation thus the data could not be fit to a suitable ^{1}H NMR binding model. Analysis of the ^{1}H NMR spectra of the complexes also provided further evidence for the disaggregation of **SQ1** and **SQ2** in the presence of Cl^- and Br^- where the bound receptors gave rise to a well-resolved spectrum with sharp signals that could be clearly attributed to the proposed target structures. In addition, the signal for the CH_2 protons directly attached to the squaramide moiety in both

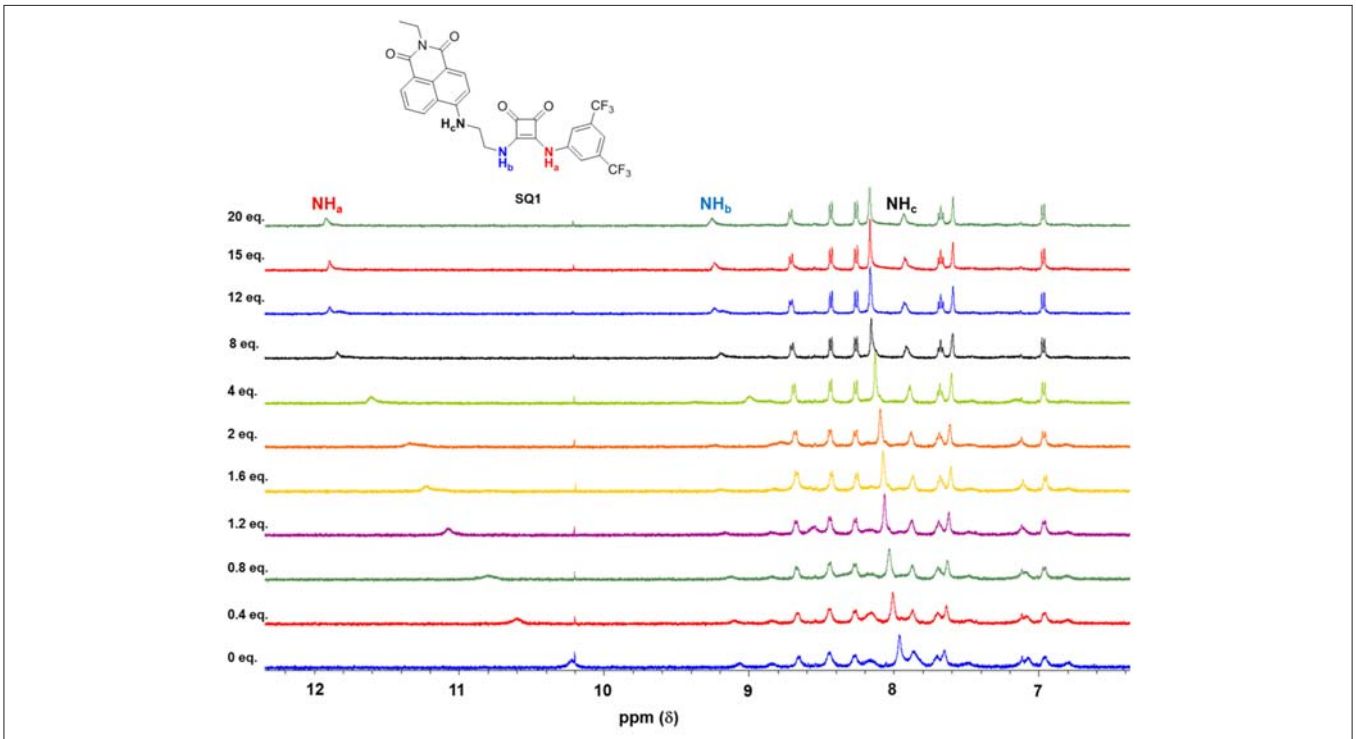

FIGURE 6 | Changes in the ^{1}H NMR spectrum (NH_a, NH_b, NH_c identified) of **SQ1** upon the addition 0–20 equivalents of anions as tetrabutylammonium (TBA) chloride in DMSO-d_6.

cases resolved from two broad signals to one single signal with significantly improved resolution (**Figures S20, S21**).

While conducting the ^{1}H NMR experiments we also noticed samples containing Cl^- and Br^- exhibited significantly more intense fluorescence than the parent receptors in solution when irradiated with UV light. This chance observation led us to investigate the fluorescence behavior of **SQ1** and **SQ2** upon titration with the halides in more detail.

Having observed such stark changes in the ^{1}H NMR titrations of **SQ1** and **SQ2** in the presence of halides we next wished to investigate their excited state properties in the presence of F^-, Cl^-, Br^-, and I^-. Titrations were performed in 5% aq. DMSO with addition of aliquots of the anions as their tetrabutylammonium salts. Both receptors exhibited emission with maxima at ca. 525 nm in solution. As shown in **Figure 7** additions of the halides resulted in varying effects. In the presence of I^- minor changes were observed where a small increase in emission intensity (20–25%) was observed up to a concentration of 20 mM. Addition of F^-, on the other hand, was found to result in a large decrease in emission intensity (80–85%) culminating in the both **SQ1** and **SQ2** largely appearing as non-fluorescent. We ascribe this behavior to the deprotonation observed in the NMR titrations and similar behavior was also observed in the presence of basic non-halide anions such as AcO^-, $H_2PO_4^-$, SO_4^{2-}. Most strikingly, however, was the observation of large fluorescence increases in the presence of both Cl^- and Br^- where the addition of Cl^- resulted in a 98 and 170% enhancement of emission from **SQ1** and **SQ2,** respectively, while, unexpectedly, Br^- resulted in a 500 and 600% enhancement of emission from **SQ1** and **SQ2,** respectively. From the previous temperature dependent fluorescence study, we suggest that the emission enhancement is as a result of the disaggregation of **SQ1** and **SQ2** in solution where aggregation induced self-quenching is disrupted allowing the release of monomers in solution and thus a recovery in fluorescence. Moreover, these responses were also clearly visible to the naked eye under UV illumination (**Figure 7B**). In order to investigate the effect of water on the fluorescence response, qualitative titrations were also performed in non-aqueous DMSO and in 20% aq. DMSO. We observed that the selective response to Br^- in pure DMSO was similar to that seen in 5% aq DMSO while in 20% aq. DMSO the response was considerably less defined. These results suggest that water concentration has a significant effect on the aggregation behavior of both **SQ1** and **SQ2** and thus their ability to act as halide sensors in fully aqueous environments (**Figures S27**, **28**).

Nevertheless, in order to investigate the sensing responses of **SQ1** and **SQ2** in more detail, fluorescence titrations were performed with 0.0–100.0 equivalent increments of halides in 5% aq. DMSO. As seen in the qualitative experiments the fluorescence intensity of both receptors is quenched by 80–85% upon addition of F^- while minor fluorescence enhancements are observed for I^-. However, a larger degree of enhancement (98–170%) is observed upon addition of Cl^- and, most interestingly, we observed a 500–600% increase in fluorescence intensity centered at 525 nm upon addition of Br^- (**Figure 8**).

These results demonstrate that both **SQ1** and **SQ2** show a selective fluorescence response toward Br^- when compared against other halides. This result is particularly unexpected given the NMR studies above where the binding of **SQ1** and **SQ2** to Cl^- appears to be considerably stronger when measured by ^{1}H NMR titration. Moreover, the desired "OFF-ON" fluorescence response paves the way for **SQ1** and **SQ2** to be used as selective bromide sensors with potential industrial/medical application. Limit of detection (LOD) values were estimated using a standard deviation method (LOD) = (3 S/m, in which S is the standard deviation of blank measurements, n = 11, and m is the slope of the linear equation) (Kumar et al., 2016), where **SQ1** and **SQ2** were found to exhibit LOD values in the μM range; values that are adequate to measure trace levels of halide contamination. A summary of the fluorescence quenching/enhancement characteristics and LOD values for **SQ1** and **SQ2** in the presence of the halides are listed in **Table 2**.

Evaluation of SQ1 and SQ2 in a Human Cell Line

With the observed spectroscopic responses and the potential application of **SQ1** and **SQ2** as bromide sensors we also

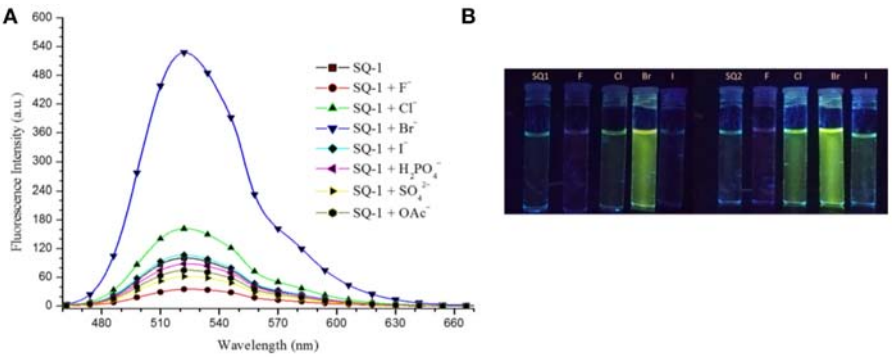

FIGURE 7 | (A) Fluorescence response of **SQ1** (5 μM) in 5% aq. DMSO toward different TBA anions (20 mM). (λ_{ex}. 435 nm). **(B)** Fluorescence response of **SQ1** and **SQ2** toward various halides in 5% aq DMSO after UV illumination as seen by the naked eye.

wished to evaluate their biocompatibility in a human cell line. Gale and co-workers have recently reported analogous naphthalimide-squaramide conjugates for use as anion receptors and transmembrane anion transporters where they found that the most active anion transporter [which also contained a 3,5-bis(trifluoromethyl)phenyl squaramide moiety] was readily internalized in human lung carcinoma A549 cells and exhibited no toxicity up to a concentration of 100 μM as determined using a CCK-8 assay (Bao et al., 2018). Thus we set out to conduct an initial evaluation of **SQ1** and **SQ2** uptake and behavior in cells. Firstly, the ability of **SQ1** and **SQ2** to be internalized into cells was assessed using confocal microscopy in HeLa cells, a widely-used cervical carcinoma cell line. HeLa cells (0.5×10^5) were incubated with either **SQ1** or **SQ2** (either 20, 5, or 1 μM) at 37°C for 1 h before the cells were fixed, and mounted for microscopy. **Figure 9** shows examples of cells incubated with **SQ1** and **SQ2** at 5μM, demonstrating successful uptake, as all cells in the sample emitted strong green fluorescence. **SQ1** and **SQ2** appear to localize in the cytoplasm as co-localization studies with the nucleic acid stain DAPI (blue) suggest that neither **SQ1** nor **SQ2** enter the nucleus. Uptake of both compounds was also investigated in a more quantitative manner using flow cytometry where, again, both **SQ1** and **SQ2** were rapidly taken up by HeLa cells. Resulting histogram plots show an increase in mean fluorescence intensity in a concentration-dependent manner and a clear shift for the entire cell population, demonstrating that all cells successfully internalized the compounds (**Figure 9**).

Cellular viability in the presence of **SQ1** and **SQ2** was measured using an MTT assay where the results showed that the % viability of HeLa cells decreased in a dose-dependent manner in the presence of **SQ1** and **SQ2,** with **SQ2** showing higher levels of cytotoxicity compared to **SQ1**. **SQ1** appeared to be largely non-toxic up to 1 μM while **SQ2** at 1 μM showed % cell viability at 28% (±20%) (see **Figure S42**). Gale and co-workers reported no toxicity up to a concentration of 100 μM for their 1,8-naphthalimide–squaramide conjugates, while **SQ1,** which is structurally very similar to the compounds reported by Gale, was shown to be considerably more cytotoxic under these conditions (Bao et al., 2018). Finally, we wished to determine whether the Br^- sensing abilities of these compounds could be measured *in cellulo*. As mentioned above O'Shea (Wu et al., 2018) and others (Zhai et al., 2014) have already exploited a disaggregation approach to sensing in a biological environment, thus we sought to investigate if **SQ1** and **SQ2** could measure bromide contamination in cells. Indeed, as shown in **Figure 10**, flow cytometry analysis was able to show a further increase in fluorescence intensity for cells incubated with **SQ1** or **SQ2** in the presence of sodium bromide (50 mM) compared to those incubated with the squaramide receptors in the absence of sodium bromide.

CONCLUSIONS

The field of molecular recognition continues to grow with ever more elegant receptors being reported that are capable of selective recognition for various anions using a diverse set of

TABLE 2 | Summary of the fluorescence quenching/enhancement characteristics and the Limit of Detection (LOD) values obtained for **SQ1** and **SQ2** in the presence of halides.

Probe	Anions	Fluorescence response	Detection limit (LOD = 3σ/slope)
SQ1	F^-	80% Quenching	6.25×10^{-6} M
	Cl^-	98% Enhancement	9.65×10^{-5} M
	Br^-	500% Enhancement	1.33×10^{-5} M
	I^-	20% enhancement	8.03×10^{-4} M
SQ2	F^-	85% Quenching	5.58×10^{-6} M
	Cl^-	170% Enhancement	7.86×10^{-5} M
	Br^-	600% Enhancement	1.92×10^{-5} M
	I^-	25% enhancement	5.51×10^{-4} M

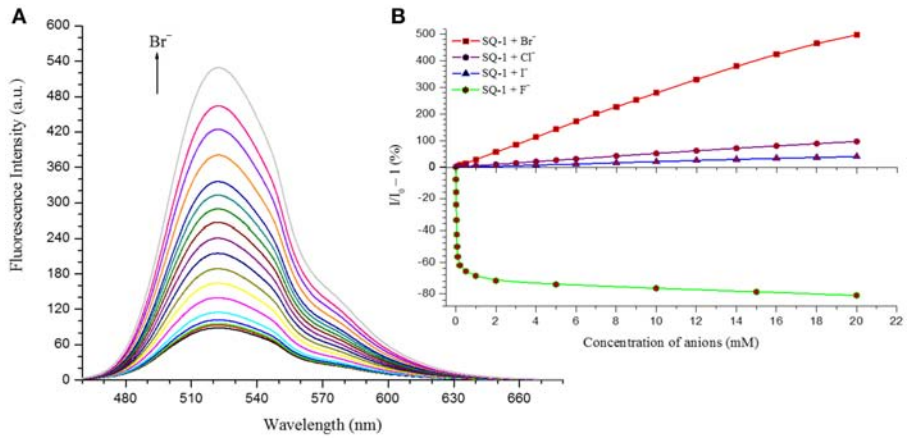

FIGURE 8 | (A) Changes in the fluorescence response of **SQ1** in the presence of Br^- in 5% aq. DMSO **(B)** Relative fluorescence enhancement and quenching response of **SQ1** with different halides in 5% aq. DMSO.

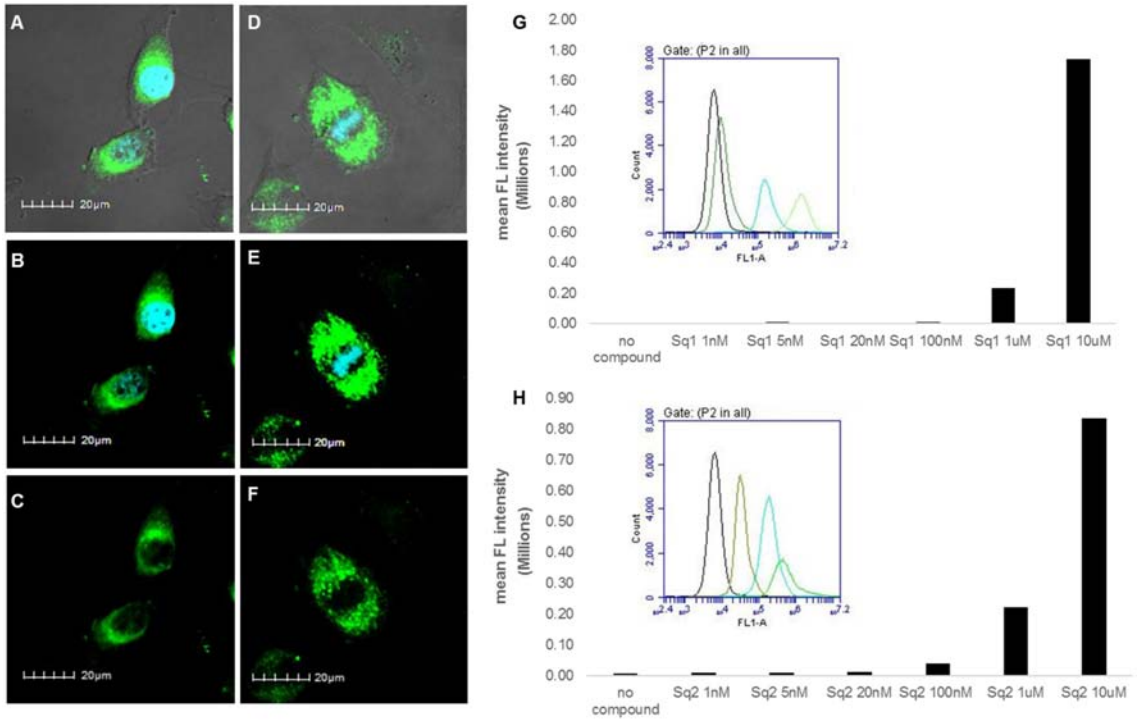

FIGURE 9 | Uptake of **SQ1** and **SQ2** (5 μM) by HeLa cells. **(A–F)** shows images obtained by confocal microscopy. **(A)** shows an overlay of the bright field image of treated cells with the DAPI (4′,6-diamidino-2-phenylindole) signal (blue) and **SQ1** (green), **(B)** shows overlay of **SQ1** (green) and nuclear co-stain DAPI (blue), **(C)** shows **SQ1** fluorescence alone (green), **(D)** shows an overlay of the bright field image of treated cells with the DAPI signal (blue) and **SQ2** (green), **(B)** shows overlay of **SQ2** (green) and nuclear co-stain DAPI (blue), **(C)** shows **SQ2** fluorescence alone (green). Scale bars: 20 μm. Additional images displayed in the Supporting Information. **(G,H)** shows flow cytometry data for **SQ1** and **SQ2,** respectively. Bar charts show the mean fluorescence intensity (FL-1) obtained in a representative experiment (out of two) with cells treated with **SQ1** or **SQ2** over a wide range of concentrations (1 nm−10 μM). In addition, histogram plots for FL-1 are also shown to illustrate the clear shift in FL-1 for the entire cell population (untreated cells (black), 100 nM, 1, 10 uM).

approaches. Indeed, with our experience of studying squaramide based probes we have attempted to uncover an alternative approach for selective detection of a somewhat neglected halide; Br^-. In this study we have reported the synthesis of two new squaramide-naphthalimide conjugates based on a "head to head" or "head to tail" design. We initially discovered that both probes **SQ1** and **SQ2** displayed a large degree of self-aggregation in aqueous DMSO solution that could be disrupted at increased temperature as studied by ^1H NMR and SEM. Moreover, we also discovered that the fluorescence behavior of both receptors was highly dependent upon the aggregation state and disruption of aggregation by increasing temperature gave rise to a significant increase in fluorescence intensity. We therefore exploited this disaggregation induced emission response for the recognition of halides, where we discovered that the receptors gave rise to distinct responses related to the interaction of the various halide anions with the receptors. Addition of F^- rendered both compounds non-emissive; thought to be due to a deprotonation event while, surprisingly, Br^- resulted in a dramatic 500–600% fluorescence enhancement thought to be due to a disruption of compound aggregation and allowing the monomeric receptors to dominate in solution. Furthermore, optical sensing parameters such as limits of detection and binding constant of probes were also measured toward the various halides (F^-, Cl^-, Br^-, and I^-) where both **SQ1** and **SQ2** were found to sense halides with adequate sensitivity to measure μM levels of halide contamination. Finally, initial studies in a human cell line were also conducted where it was observed that both compounds are easily taken up by HeLa cells, exhibiting strong intracellular fluorescence as measured by both confocal microscopy and flow cytometry. We were also able to demonstrate that **SQ1**- or **SQ2**- containing Hela cells treated with NaBr exhibited increased fluorescence intensity. While the observed increases in fluorescence intensity were modest in relation to those observed in the spectroscopic titrations described above, cell cytometry analysis allowed some distinction to be made. Given the complex environment of the cellular cytoplasm, the fully aqueous environment and the presence of intracellular Cl^- at high concentrations (ranging from 5 to 80 mM in mammalian cells) (Andersen, 2013) it is not surprising that the response is considerably less pronounced. Solvent effects are also likely to play a major role in the anion response. To the best of our knowledge, **SQ1** and **SQ2** are the first such fluorescent sensors capable of sensing Br^- *in cellulo* and we are currently working toward sensors with an improved bromide sensitivity and cellular cytotoxicity profile.

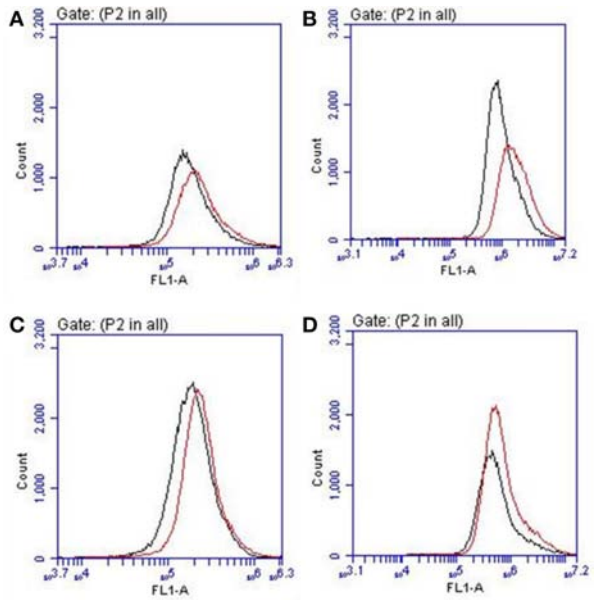

FIGURE 10 | Flow cytometry histogram plots for HeLa cells incubated with **(A) SQ1** (1 μM), **(B) SQ1** (10 μM), **(C) SQ2** (1 μM), and **(D) SQ2** (10 μM) in the absence (black) or presence of NaBr (red).

EXPERIMENTAL SECTION

3-((3,5-bis(trifluoromethyl)phenyl)amino)-4-ethoxycyclobut-3-ene-1,2-dione (1)

A solution of 3,5-bis(trifluoromethyl)aniline (1.835 mL, 11.75 mMol, 1eq) in EtOH (5 mL) was slowly added to a mixture of diethyl squarate (1.74 mL, 11.75 mMol, 1 eq) and zinc triflate (0.85 g, 2.35 mMol, 0.2 eq) in 5 mL EtOH. The reaction was stirred at room temperature overnight. The precipitate was collected by suction filtration and washed with EtOH and Et_2O to yield the product as an off-white amorphous solid (3.28 g, 79%). **^{1}H NMR,** (DMSO-d_6, 500.13 MHz) δ (ppm), J (Hz): 1.41 (t, J = 7.1, 3H, CH_3), 4.79 (q, J = 7.1, 2H, CH_2), 7.78 (s, 1H, phenylene H), 8.03 (s, 2H, phenylene H), 11.19 (br, 1H, NH); **^{13}C NMR** (DMSO-d_6, 125.76 MHz): δ (ppm): 184.9, 179.7, 140.6, 131.7, 131.4, 131.2, 126.8, 124.6, 122.4, 119.9, 116.8, 70.5, 15.8; **HRMS** (ESI) calcd. for $C_{14}H_{10}F_6NO_3$ $[M + H]^+$ 354.056, found 354.0554; **ν_{max} (KBr)/cm^{-1}:** 3,254, 3,185, 3,100, 3,062, 3,004, 1,816, 1,717, 1,603, 1,476, 1,453, 1,278, 1,233, 1,170, 1,101, 1,042, 997, and 936.

6-bromo-2-ethyl-1H-benzo[de]isoquinoline-1,3(2H)-dione (2a)

4-Bromo-1,8-naphthalic anhydride (2.0 g, 7.33 mMol, 1 eq) was mixed with ethylamine (0.57 mL, 8.66 mMol, 1.2 eq) in EtOH (10 mL). The reaction mixture was refluxed at 80°C for 24 h. The precipitate was collected by suction filtration and washed with EtOH and Et_2O to yield the product as a light tan amorphous solid (1.74 g, 79%). **^{1}H NMR,** (DMSO-d_6, 500.13 MHz) δ (ppm), J (Hz): 1.21 (t, J = 7.0, 3H, CH_3), 4.06 (q, J = 7.0, 2H, CH_2), 7.99 (t, J = 8.0, 1H, phenylene H), 8.21 (d, J = 7.8, 1H, phenylene H), 8.32 (d, J = 7.8, 1H, phenylene H), 8.55 (q, J = 7.8, 2H, phenylene H); **^{13}C NMR** (DMSO-d_6, 125.76 MHz): δ (ppm): 163.1, 163.1, 133.0, 132.0, 131.8, 131.4, 130.3, 129.5, 129.3, 128.8, 123.3, 122.5, 35.4, 13.5; **HRMS** (ESI) calcd. for $C_{28}H_{20}Br_2N_2NaO_4$ $[2M + Na]^+$ 628.968, found 628.9599; **ν_{max} (KBr)/cm^{-1}:** 3,086, 2,979, 2,939, 1,921, 1,779, 1,740, 1,693, 1,612, 1,587, 1,568, 1,505, 1,456, 14,35, 1,401, 1,371, 1,354, 1,339, 1,325, 1,244, 1,227, 1,201, 1,170, 1,150, 1,095, 1,061, 1,044, 1,021, and 961.

6-((2-aminoethyl)amino)-2-ethyl-1H-benzo[de]isoquinoline-1,3(2H)-dione (2b)

6-bromo-2-ethyl-1H-benzo[de]isoquinoline-1,3(2H)-dione (1 g, 3.288 mMol, 1 eq) was stirred at room temperature overnight in neat ethylenediamine (10 mL, excess) to yield a dark orange liquid. The crude product was slowly added to deionized water (50 mL) and left to stir at room temperature for 2 h. The precipitate was collected by suction filtration and washed with H_2O to yield the product as a yellow amorphous solid (0.748 g, 80%). **^{1}H NMR,** (DMSO-d_6, 500.13 MHz) δ (ppm), J (Hz): 1.11 (t, J = 7.0, 3H, CH_3), 2.82 (t, J = 6.4, 2H, CH_2), 3.32 (t, J = 6.4, 2H, CH_2), 3.97 (q, J = 7.1, 2H, CH_2), 6.73 (d, J = 8.5, 1H, phenylene H), 7.60 (m, 1H, phenylene H), 8.18 (d, J = 8.5, 1H, phenylene H), 8.36 (dd, 1H, phenylene H), 8.63 (dd, 1H, phenylene H); **^{13}C NMR,** (DMSO-d_6, 125.76 MHz) δ (ppm): 13.7, 34.7, 46.7, 104.3, 108.1, 120.6, 122.3, 124.6, 129.0, 129.8, 131.0, 134.6, 151.3, 163.1, 164.0; **HRMS** (ESI) calcd. for $C_{16}H_{18}N_3O_2$ $[M + H]^+$ 284.139, found 284.1389; **ν_{max} (KBr)/cm^{-1}:** 3,358, 2,979, 1,676, 1,612, 1,586, 1,550, 1,461, 1,430, 1,396, 1,370, 1,349, 1,249, 1,188, 1,152, 1,121, 1,104, 1,066, 965, and 918.

Tert-butyl(2-aminoethyl)carbamate (3a)

To a 500 mL round bottom flask was added ethylenediamine (13.4 mL, 161.86 mMol, 10 eq) in $CHCl_3$ (100 mL). A solution of di-tert-butyl dicarbonate (4.4 g, 37.56 mMol, 1 eq) in $CHCl_3$ (50 mL) was added dropwise over 2 h at 0°C and stirred at room for 24 h. The reaction mixture was washed with brine, the organic layer was washed with de-ionized H_2O and dried over $MgSO_4$. The filtrate was concentrated in vacuo to yield an off-white liquid. (2.012 g, 34%). **^{1}H NMR,** (DMSO-d_6, 500 MHz) δ (ppm), J (Hz): 1.36 (s, 9H, CH_3), 2.51 (d, J = 6.5, 2H, CH_2), 2.90 (d, J = 5.8, 2H, CH_2), 6.71 (s, 1H, NH); **^{13}C NMR** (DMSO-d_6, 125.76 MHz): δ (ppm): 28.7, 31.7, 42.0, 44.1, 77.8, 79.6, 156.1.

Tert-butyl(2-(6-nitro-1,3-dioxo-1H-benzo[de]isoquinolin-2(3H)-yl)ethyl)carbamate (3b)

Tert-butyl (2-aminoethyl) carbamate (0.565 mL, 3.54 mMol, 1 eq) was slowly added dropwise to a solution of 4-Nitro-1,8-naphthalic anhydride (0.86 g, 3.54 mMol, 1 eq) in EtOH (20 mL). The reaction mixture was left to react in a 35 mL microwave tube for 1 h at 110°C, 1 mbar and 300 watts. The precipitate was collected by suction filtration and washed with EtOH and Et_2O to yield the product as a peach amorphous solid (1.047 g, 76%). **^{1}H NMR,** (DMSO-d_6, 500.13 MHz) δ (ppm), J (Hz): 1.22 (s, 9H, CH_3), 3.27 (t, J = 6.0, 2H, CH_2), 4.14 (t, J = 6.0, 2H, CH_2), 6.88 (t, J = 6.3, 1H, NH), 8.09 (t, J = 8.1, 1H, phenylene H), 8.55 (d, J = 8.0, 1H, phenylene H), 8.62 (m, 2H, phenylene H), 8.71 (d, J = 8.4, 1H, phenylene H); **^{13}C NMR** (DMSO-d_6, 125.76 MHz): δ (ppm): 28.5, 38.0, 77.9, 123.1, 123.5, 124.6, 127.3, 128.9, 129.0,

129.9, 130.5, 132.0, 149.5, 156.2, 162.8, 163.6; **HRMS** (ESI) calcd. for $C_{19}H_{19}N_3NaO_6$ $[M + Na]^+$ 408.117, found 408.1144; **ν_{max} (KBr)/cm^{-1}:** 3,401, 3,070, 2,977, 2,935, 1,714, 1,702, 1,623, 1,593, 1,584, 1,523, 1,447, 1,410, 1,365, 1,341, 1,272, 1,233, 1,255, 1,192, 1,169, 1,148, 1,064, 992, and 968.

2-(2-aminoethyl)-6-nitro-1H-benzo[de]isoquinoline-1,3(2H)-dione (3c)

Tert-butyl (2-(6-nitro-1,3-dioxo-1H-benzo[de]isoquinolin-2(3H)-yl)ethyl)carbamate (1.02 g, 2.647 mMol, 1 eq) was dissolved in (TFA: DCM, 50: 50) (6 mL) and was stirred at room temperature overnight. The solvent was removed under reduced pressure to yield a beige amorphous solid (0.70 g, 93%). **^{1}H NMR,** (DMSO-d_6, 500 MHz) δ (ppm), *J* (Hz): 3.17 (q, *J* = 5.6, 2H, CH_2), 4.33 (t, *J* = 5.6, 2H, CH_2), 7.81 (br, 2H, NH_2), 8.13 (m, 1H, phenylene H), 8.58 (d, *J* = 7.9, 1H, phenylene H), 8.66 (m, 2H, phenylene H), 8.76 (dd, 1H, phenylene H); **^{13}C NMR** (DMSO-d_6, 125 MHz): δ (ppm): 37.9, 38.2, 123.2, 123.4, 124.7, 127.2, 128.9, 129.4, 130.1, 130.6, 132.2, 149.7, 163.3, 164.0; **HRMS** (ESI) calcd. for $C_{14}H_{12}N_3O_4$ $[M + H]^+$ 286.082, found 286.0800; **ν_{max} (KBr)/cm^{-1}:** 3,078, 1,712, 1,595, 1,525, 1,465, 1,437, 1,384, 1,348, 1,247, 1,151, 1,093, 1,058, 1,020, and 981.

6-amino-2-(2-aminoethyl)-1H-benzo[de]isoquinoline-1,3(2H)-dione (3d)

Pd/C (∼0.2 g) was added to a solution of 2-(2-aminoethyl)-6-nitro-1H-benzo[de]isoquinoline-1,3(2H)-dione (1.00 g, 3.50 mMol) dissolved in MeOH (40 mL). The reaction was placed under a H_2 atmosphere and left to stir at room temperature for 3 h. The reaction was filtered through a pad of celite and washed with excess MeOH, the filtrate was removed under reduced pressure to yield a mustard amorphous solid (0.673g, 75%). **^{1}H NMR,** (DMSO-d_6, 500.13 MHz) δ (ppm), *J* (Hz): 3.12 (s, 2H, CH_2), 4.27 (t, *J* = 6.0, 2H, CH_2), 6.86 (d, *J* = 8.4, 1H, phenylene H), 7.48 (s, 2H, NH_2), 7.67 (m, 1H, phenylene H), 7.77 (br, 2H, NH_2), 8.21 (d, J = 8.4, 1H, phenylene H), 8.44 (dd, 1H, phenylene H), 8.63 (dd, 1H, phenylene H); **^{13}C NMR,** (DMSO-d_6, 125.76 MHz) δ (ppm): 37.62, 38.36, 108.01, 108.63, 119.84, 122.43, 124.46, 129.94, 130.46, 131.52, 134.52, 153.40, 163.89, 164.96; **HRMS** (ESI) calcd. for $C_{14}H_{14}N_3O_2$ $[M + H]^+$ 256.108, found 256.1055; **ν_{max} (KBr)/cm^{-1}:** 3,419, 3,362, 3,259, 3,017, 1,636, 1,582, 1,531, 1,485, 1,429, 1,402, 1,378, 1,353, 1,311, 1,247, 1,203, 1,172, 1,128, 1,016, 964, and 907.

6-((2-((2-((3,5-Bis(Trifluoromethyl)Phenyl)Amino)-3,4-Dioxocyclobut-1-en-1-yl)Amino)Ethyl)Amino)-2-Ethyl-1H-Benzo[de]Isoquinoline−1,3-(2H)-Dione (SQ-1)

A solution of 3-((3,5-bis(trifluoromethyl)phenyl)amino)-4-ethoxycyclobut-3-ene-1,2-dione (0.436 g, 1.235 mMol, 1 eq) in EtOH (8 mL) was added slowly to a mixture of 6-((2-aminoethyl)amino)-2-ethyl-1H-benzo[de]isoquinoline-1,3(2H)-dione (0.35 g, 1.235 mM, 1 eq) and Et_3N (0.689 mL, 4.94 mMol, 4 eq) in EtOH (12 mL). The reaction was stirred at room temperature overnight. The precipitate was collected by suction filtration and washed with EtOH and ether. Product as a yellow amorphous solid with 78% yield (0.575 g). ^{1}H NMR at 343K, (DMSO- d_6, 500 MHz) δ (ppm), *J* (Hz): 1.18 (t, *J* = 7.0, 3H, CH_3), 3.70 (q, *J* = 5.5, 2H, CH_2), 3.95 (t, *J* = 5.5, 2H, CH_2), 4.04 (q, *J* = 7.0, 2H, CH_2), 6.91 (d, *J* = 8.5, 1H, phenylene H), 7.47 (s, 1H, phenylene H), 7.63 (m, 2H, phenylene H), 7.80 (br, 2H, NH), 7.89 (s, 1H, phenylene H), 8.25 (d, *J* = 8.5, 1H, phenylene H), 8.39 (d, J = 7.0, 1H, phenylene H), 8.58 (d, *J* = 8.3, 1H, phenylene H), 9.68 (br, 1H, NH); ^{13}C NMR at 343K, (DMSO-d_6, 125.76 MHz) δ (ppm): 13.6, 30.9, 34.6, 43.2, 44.2, 104.6, 109.1, 114.7, 118.3, 120.8, 122.5, 124.7, 128.6, 129.8, 130.9, 134.2, 141.5, 150.7, 163.1, 163.9, 171.2, 181.3; HRMS (ESI) calcd. for $C_{28}H_{21}F_6N_4O_4$ $[M + H]^+$ 591.146 found 591.1439; ν_{max} (KBr)/cm-1: 3,292 (broad), 3,086, 2,982, 1,796, 1,687, 1,581, 1,548, 1,459, 1,348, 1,278, 1,249, 1,180, 1,130, 1,067, 999, and 932.

6-amino-2-(2-((2-((3,5-bis(trifluoromethyl)phenyl)amino)-3,4-dioxocyclobut-1-en-1-yl)amino)ethyl)-1H-benzo[de]isoquinoline-1,3(2H)-dione (SQ-2)

A solution of 3-((3,5-bis(trifluoromethyl)phenyl)amino)-4-ethoxycyclobut-3-ene-1,2-dione (0.14 g, 0.39 mMol, 1 eq) in EtOH (8 mL) was slowly added to a mixture of 6-amino-2-(2-aminoethyl)-1H-benzo[de]isoquinoline-1,3(2H)-dione (0.1 g, 0.39 mmol, 1 eq) and Et3N (0.217 mL, 1.56 mMol, 4 eq) in EtOH (10 mL). The reaction was stirred at room temperature overnight. The precipitate was collected by suction filtration and washed with EtOH and Et2O to yield the product as an olive green amorphous solid (0.123 g, 56%). ^{1}H NMR at 343K, (DMSO-d_6, 500.13 MHz) δ (ppm), *J* (Hz): 3.90 (s, 2H, CH_2), 4.31 (t, *J* = 6.0, 2H, CH_2), 6.82 (d, *J* = 8.4, 1H, phenylene H), 7.22 (s, 2H, NH_2), 7.52 (s, 1H, phenylene H), 7.58 (t, *J* = 8.0, 1H, phenylene H), 7.89 (s, 2H, phenylene H), 8.15 (d, *J* = 8.4, 1H, phenylene H), 8.37 (d, *J* = 7.1, 1H, phenylene H), 8.57 (d, *J* = 8.4, 1H, phenylene H), 9.77 (br, 1H, NH); ^{13}C NMR at 343K, (DMSO-d_6, 125.76 MHz) δ (ppm): 27.9, 42.9, 108.7, 114.8, 118.4, 119.9, 120.3, 122.2, 122.5, 124.2, 124.7, 129.0, 130.3, 131.3, 134.3, 141.7, 153.3, 163.3, 164.6, 171.4, 181.3; HRMS (ESI) calcd. for $C_{52}H_{33}F_{12}N_8O_8$ $[2M + H]^+$ 1125.223, found 1125.2226; ν_{max} (KBr)/cm^{-1}: 371, 3,254, 1,796, 1,692, 1,636, 1,599, 1,528, 1,476, 1,434, 1,378, 1,308, 1,276, 1,250, 1,184, 1,129, 1,068, 1,000, and 933.

DATA AVAILABILITY

The datasets generated for this study are available on request to the corresponding author.

AUTHOR CONTRIBUTIONS

RE, LK, and MS designed the study and wrote the manuscript. RE and MS supervised the study. AA and LK synthesized and characterized the compounds and

carried out all spectroscopic titrations. OF performed the SEM studies. MS, MK, and JP carried out the biological studies. All authors discussed the results and commented on the manuscript.

ACKNOWLEDGMENTS

LK wishes to acknowledge the Irish Research Council for a Government of Ireland Postdoctoral Research Fellowship (GOIPD/2017/1091). MK also acknowledges the Irish Research Council for a Government of Ireland Postgraduate Scholarship (GOIPG/2015/3488). JP thanks Maynooth University for the award of a Hume Scholarship. Science Foundation Ireland are acknowledged for the funding of a Clariostar plate reader and Mass Spec facilities through the Opportunistic Infrastructure Fund (16/RI/3399).

SUPPLEMENTARY MATERIAL

The Supplementary Material for this article can be found online at: https://www.frontiersin.org/articles/10.3389/fchem.2019.00354/full#supplementary-material

REFERENCES

Adegoke, O., and Nyokong, T. (2013). Fluorescence "turn on" probe for bromide ion using nanoconjugates of glutathione-capped CdTe@ZnS quantum dots with nickel tetraamino-phthalocyanine: characterization and size-dependent properties. *J. Photochem. Photobiol. A* 265, 58–66. doi: 10.1016/j.jphotochem.2013.05.013

Amendola, V., Bergamaschi, G., Boiocchi, M., Fabbrizzi, L., and Milani, M. (2010). The squaramide versus urea contest for anion recognition. *Chem. Eur. J.* 16, 4368–4380. doi: 10.1002/chem.200903190

Andersen, O. S. (2013). "Cellular electrolyte metabolism," in *Encyclopedia of Metalloproteins,* eds R. H. Kretsinger, V. N. Uversky, and E. A. Permyakov (New York, NY: Springer New York), 580–587. doi: 10.1007/978-1-4614-1533-6_223

Ao, X., Bright, S. A., Taylor, N. C., and Elmes, R. B. P. (2017). 2-Nitroimidazole based fluorescent probes for nitroreductase; monitoring reductive stress in cellulo. *Org. Biomol. Chem*. 15, 6104–6108. doi: 10.1039/C7OB01406F

Ashton, T. D., Jolliffe, K. A., and Pfeffer, F. M. (2015). Luminescent probes for the bioimaging of small anionic species *in vitro* and *in vivo*. *Chem. Soc. Rev.* 44, 4547–4595. doi: 10.1039/C4CS00372A

Banerjee, S., Veale, E. B., Phelan, C. M., Murphy, S. A., Tocci, G. M., Gillespie, L. J., et al. (2013). Recent advances in the development of 1,8-naphthalimide based DNA targeting binders, anticancer and fluorescent cellular imaging agents. *Chem. Soc. Rev.* 42, 1601–1618. doi: 10.1039/c2cs35467e

Bao, X., Wu, X., Berry, S. N., Howe, E. N. W., Chang, Y.-T., and Gale, P. A. (2018). Fluorescent squaramides as anion receptors and transmembrane anion transporters. *Chem. Commun.* 54, 1363–1366. doi: 10.1039/C7CC08706C

Beer, P. D., and Gale, P. A. (2001). Anion recognition and sensing: the state of the art and future perspectives. *Angew. Chem. Int. Ed.*, 40, 486–516. doi: 10.1002/1521-3773(20010202)40:3<486::AID-ANIE486>3.0.CO;2-P

Brynn Hibbert, D., and Thordarson, P. (2016). The death of the Job plot, transparency, open science and online tools, uncertainty estimation methods and other developments in supramolecular chemistry data analysis. *Chem. Commun*. 52, 12792–12805. doi: 10.1039/C6CC03888C

Busschaert, N., Caltagirone, C., Van Rossom, W., and Gale, P. A. (2015). Applications of supramolecular anion recognition. *Chem. Rev.* 115, 8038–8155. doi: 10.1021/acs.chemrev.5b00099

Busschaert, N., Elmes, R. B. P., Czech, D. D., Wu, X., Kirby, I. L., Peck, E. M., et al. (2014). Thiosquaramides: pH switchable anion transporters. *Chem. Sci.* 5, 3617–3626. doi: 10.1039/C4SC01629G

Busschaert, N., Kirby, I. L., Young, S., Coles, S. J., Horton, P. N., Light, M. E., et al. (2012). Squaramides as potent transmembrane anion transporters. *Angew. Chem. Int. Ed.* 51, 4426–4430. doi: 10.1002/anie.201200729

Calatrava-Pérez, E., Delente, J. M., Shanmugaraju, S., Hawes, C. S., Williams, C. D., Gunnlaugsson, T., et al. (2019). Glycosylated naphthalimides and naphthalimide Tröger's bases as fluorescent aggregation probes for Con A. *Org. Biomol. Chem*. 17, 2116–2125. doi: 10.1039/C8OB02980F

Cametti, M., and Rissanen, K. (2009). Recognition and sensing of fluoride anion. *Chem. Commun.* 2809–2829. doi: 10.1039/b902069a

Cametti, M., and Rissanen, K. (2013). Highlights on contemporary recognition and sensing of fluoride anion in solution and in the solid state. *Chem. Soc. Rev.* 42, 2016–2038. doi: 10.1039/C2CS35439J

de Silva, A. P., Gunaratne, H. Q. N., Gunnlaugsson, T., Huxley, A. J. M., McCoy, C. P., Rademacher, J. T., et al. (1997). Signaling recognition events with fluorescent sensors and switches. *Chem. Rev.* 97, 1515–1566.

Delgado-Pinar, E., Rotger, C., Costa, A., Pina, M. N., Jimenez, H. R., Alarcon, J., et al. (2012). Grafted squaramide monoamine nanoparticles as simple systems for sulfate recognition in pure water. *Chem. Commun.* 48, 2609–2611. doi: 10.1039/c2cc17798f

Duke, R. M., Veale, E. B., Pfeffer, F. M., Kruger, P. E., and Gunnlaugsson, T. (2010). Colorimetric and fluorescent anion sensors: an overview of recent developments in the use of 1,8-naphthalimide-based chemosensors. *Chem. Soc. Rev.* 39, 3936–3953. doi: 10.1039/b910560n

Elmes, R. B. P., Busschaert, N., Czech, D. D., Gale, P. A., and Jolliffe, K. A. (2015). pH switchable anion transport by an oxothiosquaramide. *Chem. Commun.* 51, 10107–10110. doi: 10.1039/C5CC03625A

Elmes, R. B. P., Erby, M., Bright, S. A., Williams, D. C., and Gunnlaugsson, T. (2012). Photophysical and biological investigation of novel luminescent Ru(ii)-polypyridyl-1,8-naphthalimide Tröger's bases as cellular imaging agents. *Chem. Commun.* 48, 2588–2590. doi: 10.1039/c2cc17274g

Elmes, R. B. P., and Gunnlaugsson, T. (2010). Luminescence anion sensing via modulation of MLCT emission from a naphthalimide-Ru(II)-polypyridyl complex. *Tet. Lett.* 51, 4082–4087. doi: 10.1016/j.tetlet.2010.05.127

Elmes, R. B. P., and Jolliffe, K. A. (2014). Amino acid-based squaramides for anion recognition. *Supramol. Chem.* 27, 321–328. doi: 10.1080/10610278.2014.976221

Elmes, R. B. P., Turner, P., and Jolliffe, K. A. (2013). Colorimetric and luminescent sensors for chloride: hydrogen bonding vs deprotonation. *Org. Lett.* 15, 5638–5641. doi: 10.1021/ol402500q

Elmes, R. B. P., Yuen, K. K. Y., and Jolliffe, K. A. (2014). Sulfate-selective recognition by using neutral dipeptide anion receptors in aqueous solution. *Chem. Eur. J.* 20, 7373–7380. doi: 10.1002/chem.201400292

Evans, N. H., and Beer, P. D. (2014). Advances in anion supramolecular chemistry: from recognition to chemical applications. *Angew. Chem. Int. Ed.* 53, 11716–11754. doi: 10.1002/anie.201309937

Fan, J., Hu, M., Zhan, P., and Peng, X. (2013). Energy transfer cassettes based on organic fluorophores: construction and applications in ratiometric sensing. *Chem. Soc. Rev.* 42, 29–43. doi: 10.1039/C2CS35273G

Gale, P. A., and Howe, E. N. W., Wu, X. (2016). Anion receptor chemistry. *Chemistry* 1, 351–422. doi: 10.1016/j.chempr.2016.08.004

Gribble, G. W. (2004). Amazing organohalogens: although best known as synthetic toxicants, thousands of halogen compounds are, in fact, part of our natural enviornment. *Am. Sci.* 92, 342–349. doi: 10.1511/2004.48.937

Gunnlaugsson, T., Glynn, M., Tocci, G. M., Kruger, P. E., and Pfeffer, F. M. (2006). Anion recognition and sensing in organic and aqueous media using luminescent and colorimetric sensors. *Coord. Chem. Rev.* 250, 3094–3117. doi: 10.1016/j.ccr.2006.08.017

Hoizey, G., Lamiable, D., Millart, H., and Trenque, T. (2003). Bromism from daily over intake of bromide salt AU - Frances, C. *J. Toxicol.* 41, 181–183. doi: 10.1081/CLT-120019135

Hong, Y., Lam, J. W. Y., and Tang, B. Z. (2011). Aggregation-induced emission. *Chem. Soc. Rev.* 40, 5361–5388. doi: 10.1039/c1cs15113d

Jin, C., Zhang, M., Wu, L., Guan, Y., Pan, Y., Jiang, J., et al. (2013). Squaramide-based tripodal receptors for selective recognition of sulfate anion. *Chem. Commun.* 49, 2025–2027. doi: 10.1039/c3cc00196b

Kang, J., and Kim, J. (2005). Bromide selective fluorescent anion receptor with glycoluril molecular scaffold. *Tet. Lett.* 46, 1759–1762. doi: 10.1016/j.tetlet.2004.09.065

Kumar, M., Kumawat, L. K., Gupta, , V. K., and Sharma, A. (2016). Novel furochromenone based dual channel sensors for selective detection of Cu2+ with potential applications in sample monitoring, membrane sensing and photo–printing. *Chem. Select* 1, 277–284. doi: 10.1002/slct.201500023

Kumawat, L. K., Asif, M., and Gupta, V. K. (2017). Dual ion selective fluorescence sensor with potential applications in sample monitoring and membrane sensing. *Sens. Actuators B. Chem.* 241, 1090–1098. doi: 10.1016/j.snb.2016.10.031

Langton, M. J., Serpell, C. J., and Beer, P. D. (2016). Anion recognition in water: recent advances from a supramolecular and macromolecular perspective. *Angew. Chem. Int. Ed.* 55, 1974–1987. doi: 10.1002/anie.201506589

Lee, M. H., Kim, J. S., and Sessler, J. L. (2015). Small molecule-based ratiometric fluorescence probes for cations, anions, and biomolecules. *Chem. Soc. Rev.* 44, 4185–4191. doi: 10.1039/C4CS00280F

Lim, J. Y. C., and Beer, P. D. (2019). Electrochemical bromide sensing with a halogen bonding [2]Rotaxane. *Eur. J. Org. Chem*. doi: 10.1002/ejoc.201801571. [Epub ahead of print].

Lowe, A. J., Pfeffer, F. M., and Thordarson, P. (2012). Determining binding constants from 1H NMR titration data using global and local methods: a case study using [n]polynorbornane-based anion hosts. *Supramol. Chem.* 24, 585–594. doi: 10.1080/10610278.2012.688972

Ma, H., Yang, M., Zhang, S., Yin, P., Wang, T., Yang, Y., et al. (2019). Two aggregation-induced emission (AIE)-active reaction-type probes: for real-time detecting and imaging of superoxide anions. *Analyst* 144, 536–542. doi: 10.1039/C8AN01811A

Marchetti, L. A., Mao, N., Krämer, T., Kitchen, J. A., and Elmes, R. B. P. (2018). A long wavelength colourimetric chemosensor for fluoride. *Supramol. Chem.* 30, 795–805. doi: 10.1080/10610278.2018.1461873

Marcus, Y. (1991). Thermodynamics of solvation of ions. Part 5.—Gibbs free energy of hydration at 298.15 K. *J. Chem. Soc. Faraday Transac.* 87, 2995–2999.

Olson, K. R., and System, C. P. C. (2004). *Poisoning and Drug Overdose; Lange Medical.* New York, NY: Books/McGraw-Hill.

Peng, L., Wang, M., Zhang, G., Zhang, D., and Zhu, D. (2009). A fluorescence turn-on detection of cyanide in aqueous solution based on the aggregation-induced emission. *Org. Lett.* 11, 1943–1946. doi: 10.1021/ol900376r

Piña, M. N., Soberats, B., Rotger, C., Ballester, P., Deyà, P. M., and Costa, A. (2008). Selective sensing of competitive anions by non-selective hosts: the case of sulfate and phosphate in water. *New J. Chem.* 32, 1919–1923. doi: 10.1039/b809454c

Prohens, R., Martorell, G., Ballester, P., and Costa, A. (2001). A squaramide fluorescent ensemble for monitoring sulfate in water. *Chem. Commun.* 1456–1457. doi: 10.1039/b104172j

Prohens, R., Tomàs, S., Morey, J., Deyà, P. M., Ballester, P., and Costa, A. (1998). Squaramido-based receptors: Molecular recognition of carboxylate anions in highly competitive media. *Tet. Lett.* 39, 1063–1066. doi: 10.1016/S0040-4039(97)10728-6

Qin, L., Hartley, A., Turner, P., Elmes, R. B. P., and Jolliffe, K. A. (2016). Macrocyclic squaramides: anion receptors with high sulfate binding affinity and selectivity in aqueous media. *Chem. Sci.* 7, 4563–4572. doi: 10.1039/C6SC01011C

Ryan, G. J., Elmes, R. B. P., Quinn, S. J., and Gunnlaugsson, T. (2012). Synthesis and photophysical evaluations of fluorescent quaternary bipyridyl-1,8-naphthalimide conjugates as nucleic acid targeting agents. *Supramol. Chem.* 22, 175–188. doi: 10.1080/10610278.2011.638381

Ryan, G. J., Poynton, F. E., Elmes, R. B. P., Erby, M., Williams, D. C., Quinn, S. J., et al. (2015). Unexpected DNA binding properties with correlated downstream biological applications in mono vs. bis-1,8-naphthalimide Ru(ii)-polypyridyl conjugates. *Dalton Trans.* 44, 16332–16344. doi: 10.1039/C5DT00360A

Sedgwick, A. C., Wu, L., Han, H.-H., Bull, S. D., He, X.-P., James, T. D., et al. (2018). Excited-state intramolecular proton-transfer (ESIPT) based fluorescence sensors and imaging agents. *Chem. Soc. Rev.* 47, 8842–8880. doi: 10.1039/C8CS00185E

Storer, R. I., Aciro, C., and Jones, L. H. (2011). Squaramides: physical properties, synthesis and applications. *Chem. Soc. Rev.* 40, 2330–2346. doi: 10.1039/c0cs00200c

Suksai, C., Leeladee, P., Jainuknan, D., Tuntulani, T., Muangsin, N., Chailapakul, O., et al. (2005). A new heteroditopic receptor and sensor highly selective for bromide in the presence of a bound cation. *Tet. Lett.* 46, 2765–2769. doi: 10.1016/j.tetlet.2005.02.156

Thordarson, P. (2011). Determining association constants from titration experiments in supramolecular chemistry. *Chem. Soc. Rev.* 40, 1305–1323. doi: 10.1039/C0CS00062K

Verkman, A. S. (1990). Development and biological applications of chloride-sensitive fluorescent indicators. *Am. J. Physiol. Cell Physiol.* 259, C375–C388. doi: 10.1152/ajpcell.1990.259.3.C375

Vlascici, D., Plesu, N., Fagadar-Cosma, G., Lascu, A., Petric, M., Crisan, M., et al. (2018). Potentiometric sensors for iodide and bromide based on Pt(II)-Porphyrin. *Sensors* 18:E2297. doi: 10.3390/s18072297

World Health Organization (2005). *Bromate in Drinking-Water: Background Document for Development of WHO Guidelines for Drinking-Water Quality*. Geneva.

World Health Organization (2009). *Bromide in Drinking-Water: Background Document for Development of WHO Guidelines for Drinking-Water Quality*. Geneva.

Wu, D., Cheung, S., Sampedro, G., Chen, Z.-L., Cahill, R. A., and O'Shea, D. F. (2018). A DIE responsive NIR-fluorescent cell membrane probe. *Biochim. Biophys. Acta* 1860, 2272–2280. doi: 10.1016/j.bbamem.2018.09.006

Wu, J., Liu, W., Ge, J., Zhang, H., and Wang, P. (2011). New sensing mechanisms for design of fluorescent chemosensors emerging in recent years. *Chem. Soc. Rev*. 40, 3483–3495. doi: 10.1039/c0cs00224k

Wurm, F. R., and Klok, H.-A. (2013). Be squared: expanding the horizon of squaric acid-mediated conjugations. *Chem. Soc. Rev.* 42, 8220–8236. doi: 10.1039/c3cs60153f

Xu, L., Xu, Y., Zhu, W., Xu, Z., Chen, M., and Qian, X. (2012). Fluorescence sensing of iodide and bromide in aqueous solution: anion ligand exchanging and metal ion removing. *New J. Chem.* 36, 1435–1438. doi: 10.1039/c2nj40102a

Zhai, D., Xu, W., Zhang, L., and Chang, Y.-T. (2014). The role of "disaggregation" in optical probe development. *Chem. Soc. Rev.* 43, 2402–2411. doi: 10.1039/c3cs60368g

Conflict of Interest Statement: The authors declare that the research was conducted in the absence of any commercial or financial relationships that could be construed as a potential conflict of interest.

Copyright © 2019 Kumawat, Abogunrin, Kickham, Pardeshi, Fenelon, Schroeder and Elmes. This is an open-access article distributed under the terms of the Creative Commons Attribution License (CC BY). The use, distribution or reproduction in other forums is permitted, provided the original author(s) and the copyright owner(s) are credited and that the original publication in this journal is cited, in accordance with accepted academic practice. No use, distribution or reproduction is permitted which does not comply with these terms.

frontiers in Chemistry

ORIGINAL RESEARCH
published: 08 February 2019
doi: 10.3389/fchem.2019.00054

Aggregation-Induced Emission: Lighting Up hERG Potassium Channel

*Xiaomeng Zhang, Tingting Liu, Qi Li, Minyong Li and Lupei Du**

Key Laboratory of Chemical Biology (MOE), Department of Medicinal Chemistry, School of Pharmacy, Shandong University, Jinan, China

Based on the scaffold of astemizole and E-4031, four AIE light-up probes (**L1–L4**) for Human Ether-a-go-go-Related Gene (hERG) potassium channel were developed herein using AIE fluorogen(TPE). These probes showing advantages such as low background interference, superior photostability, acceptable cell toxicity, and potent inhibitory activity, which could be used to image hERG channels at the nanomolar level. These AIE light-up probes hoped to provide guidelines for the design of more advanced AIE sensing and imaging hERG channels to a broad range of applications.

Keywords: AIE light-up probes, hERG channel, cell imaging, fluorophore, pharmacophore

OPEN ACCESS

Edited by:
Tony D. James,
University of Bath, United Kingdom

Reviewed by:
Adam Charles Sedgwick,
University of Texas at Austin, United States
Xiao-Yu Hu,
Nanjing University of Aeronautics and Astronautics, China

****Correspondence:***
Lupei Du
dulupei@sdu.edu.cn

Specialty section:
This article was submitted to Supramolecular Chemistry, a section of the journal Frontiers in Chemistry

Received: *05 December 2018*
Accepted: *21 January 2019*
Published: *08 February 2019*

Citation:
Zhang X, Liu T, Li Q, Li M and Du L (2019) Aggregation-Induced Emission: Lighting Up hERG Potassium Channel. Front. Chem. 7:54. doi: 10.3389/fchem.2019.00054

INTRODUCTION

The potassium channels encoded by the hERG (human ether-a-go-go related gene) mediate the rapidly activating delayed rectifier K+ current (I_{Kr}), which plays a key role in repolarization of the ventricular action potential (Perrin et al., 2008). A number of drugs were withdrawn from the market because of their blockade on the hERG channel, such as Cissapride, Tefenadine, Astemisole, and Grepafloxacin (Roden, 2004; Du et al., 2007; Yamakawa et al., 2012). They can induce long QT syndrome, which may degenerate into ventricular fibrillation and sudden death (Roden, 2004; Babcock and Li, 2013). Therefore the study of hERG inhibition has become an important part of modern safety pharmacology. Today, FDA guidelines expect that all drugs should be measured the affinity with hERG channel to evaluate their cardiotoxicity (Brown, 2004). Recently, many studies have shown that various cancer cell lines express hERG channels, whereas, corresponding normal cell lines do not express significant hERG protein, such as neuroblastoma, breast cancer, and colon cancer cells (Bianchi et al., 1998; Cherubini and Crociani, 2000; Pillozzi et al., 2002). hERG channels are in connection with some progresses, such as increasing tumor cell proliferation, invasion and lymphatic spread, reducing cell differentiation (Jehle et al., 2011). In these tumor cells, the hERG protein can be used as a biomarker for malignant transition.

In order to analyze the hERG channels, there is a stringent demand for a simple and safe method to image hERG channels. Such studies will conduce to a better understanding of the role of hERG channels in cancer cells and further improve the diagnosis and treatment of cancer. Among imaging technologies, fluorescence imaging is considered as one of the most significant methods in the medical research and life science field. Using fluorescence imaging, it is possible to directly visualize hERG channels. What counts is that fluorescent probe is a significant factor in fluorescence imaging. Nowadays, there have various fluorescent probes using in living cells and biological system by scientists from the fluorescence imaging field (Liu et al., 2016, 2017). However, many fluorescent probes show different fluorescent behaviors in dilute and concentrated solutions. The fluorescence intensity is often weakened or quenched at high concentrations, which is mechanistically related with the "formation of aggregates,"

a phenomenon widely known as "aggregation-caused quenching" (ACQ) (Ding et al., 2013). Although scientists have made great efforts to overcome this phenomenon, ACQ effect is still an obstacle to the application of fluorescent probes to image biological target.

Tang's group found a novel fluorescent effect in 2001, a phenomenon named as "aggregation-induced emission," (AIE) which was completely opposite to the ACQ effect. They discovered there was no fluorescence when hexaphenylsilole (HPS) was dissolved in a fine solvent but there was strong fluorescence when it was dissolved in a poor solvent (Hong et al., 2011). When hexaphenylsilole is in free state, intramolecular rotation occurs, and there is no emission, but intramolecular rotation is restricted when it is in aggregated state, leading to fluorescence. Since then, quite a number of AIEgens have emerged and have been used in biological imaging, chemical sensing, smart materials and optoelectronic devices. Among the AIEgens, tetraphenylethene (TPE) derivatives (Shi et al., 2012; Ding et al., 2013) have been widely applied in rational design of AIE probes. AIE light-up probes offer superior photostability

TABLE 1 | Photophysical properties of synthesized probes.

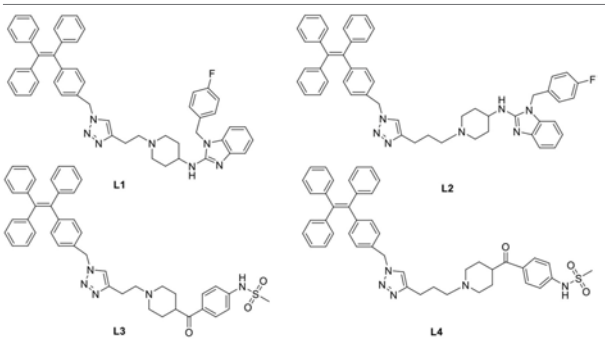

Compd	λ_{max}(nm)	λ_{ex}(nm)	λ_{em}(nm)	Φ (%)
L1	331	325	465	23
L2	329	325	465	25
L3	337	330	465	29
L4	336	330	465	25

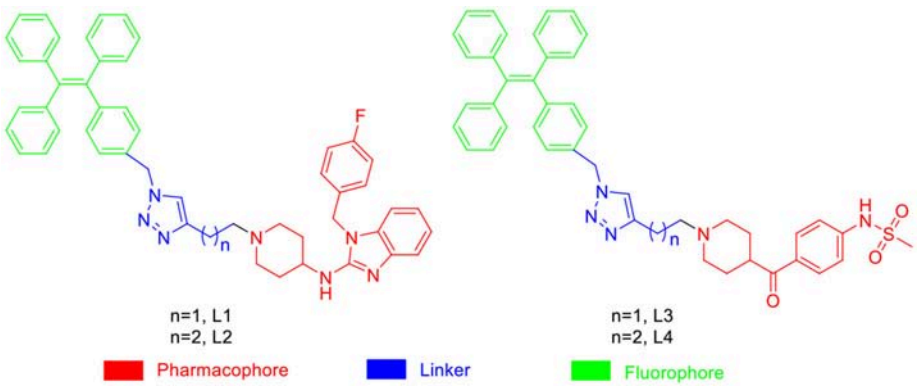

SCHEME 1 | Design Strategy of the Fluorescent probes.

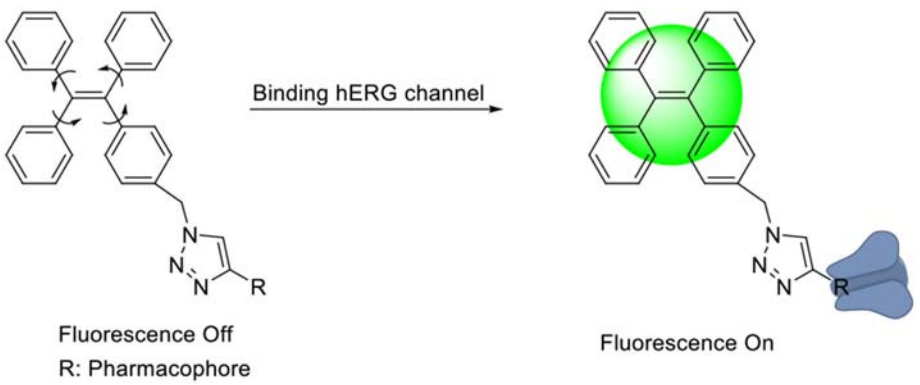

SCHEME 2 | The "Off-On" Mechanism of the Fluorescent Probes.

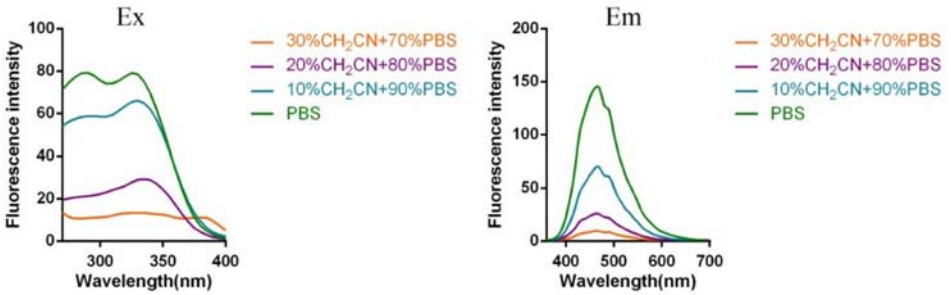

FIGURE 1 | Fluorescent excitation (the emission wavelength was 465 nm) and emission spectra (the excitation wavelength was 325 nm) of probe **L1** in solution with different ratio of acetonitrile and PBS.

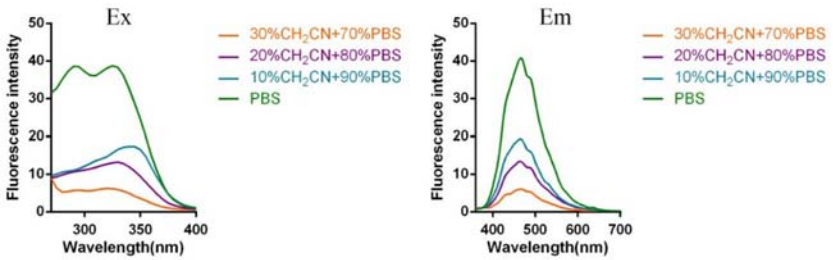

FIGURE 2 | Fluorescent excitation (the emission wavelength was 465 nm) and emission spectra (the excitation wavelength was 325 nm) of probe **L2** in solution with different ratio of acetonitrile and PBS (Fluorescent excitation and emission spectra of probe **L3** and **L4** can be found in **Supplementary Material**).

TABLE 2 | Inhibitory activity of the synthesized probes against the hERG potassium channel[a].

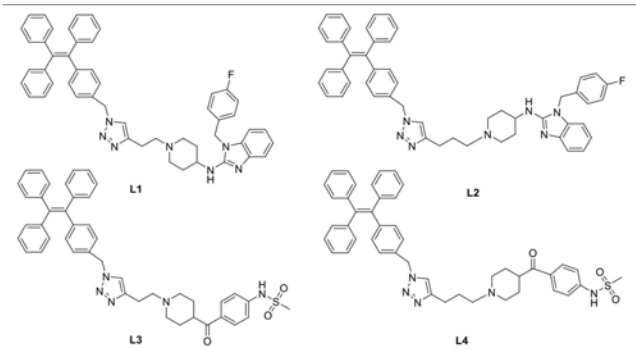

Compd	IC_{50} (nM)	K_i^b (nM)
L1	102.50	57.58
L2	155.90	87.58
L3	0.32	0.18
L4	1.05	0.59
Astemizole	11.25	6.32

[a]*see supporting information.* [b]*the inhibition constant (K_i) was calculated from each IC_{50} value using the Cheng–Prusoff equation.*

TABLE 3 | Cytotoxicity results for probes.

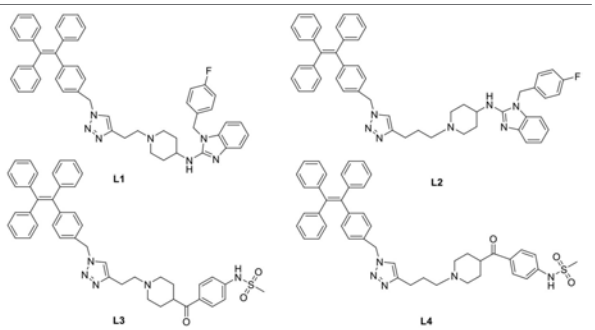

Compd	IC_{50} (μM)
L1	20.74 ± 0.68
L2	8.56 ± 0.32
L3	39.99 ± 1.94
L4	17.37 ± 1.06
Astemizole	17.37 ± 1.07

and higher signal reliability comparing with conventional probes because of their higher resistance to photobleaching (Wang et al., 2016b).

RESULTS AND DISCUSSION

Chemistry

In general, the typical fluorescent probe consists of three parts: a fluorophore, a pharmacophore, and a linker (Cohen et al., 2002; Chen et al., 2014; Mizukami et al., 2014). In consideration of

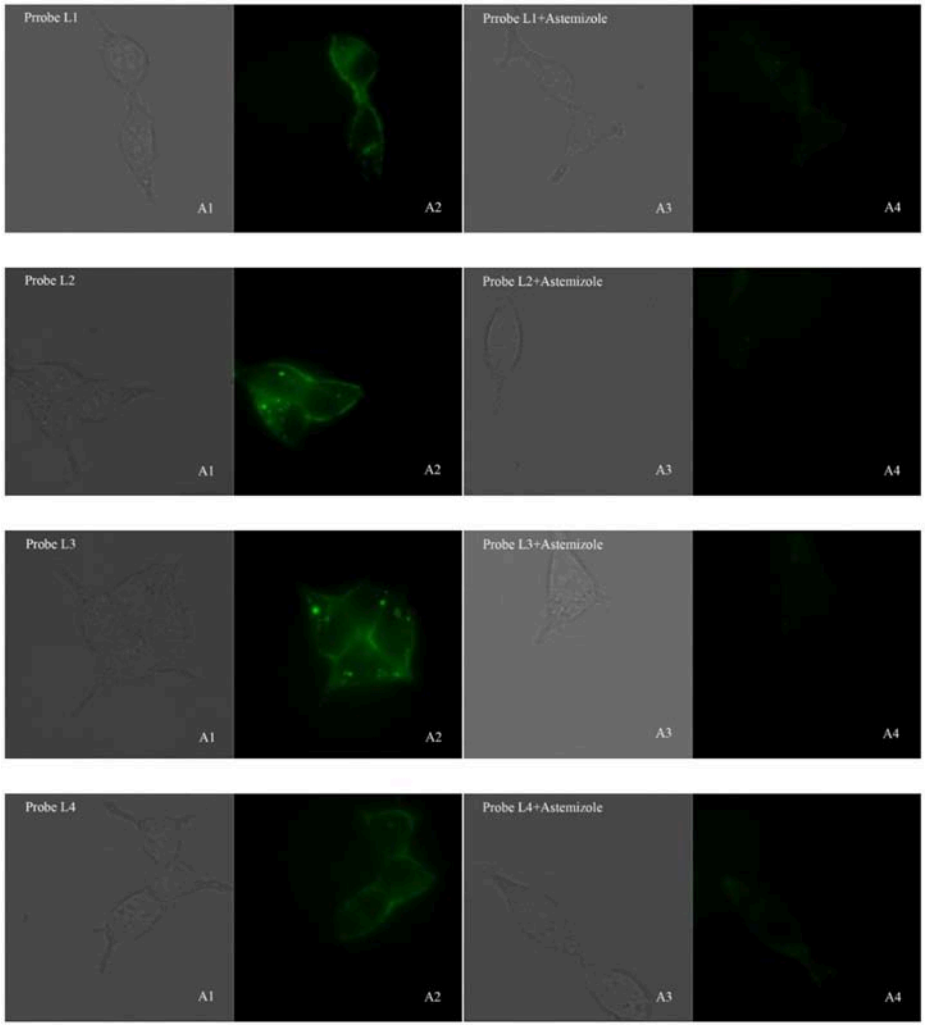

FIGURE 3 | Fluorescence microscopy imaging of hERG transfected HEK293 cells incubated with 5 μM probe **L1**, 5 μM probe **L2**, 1 μM probe **L3**, 5 μM probe **L4** (A1, bright field; A2, GFP channel), respectively. The imaging of inhibition of the hERG channels was accomplished by incubating astemizole (50, 50, 10, 50 μM) with probe **L1** (5 μM), **L2** (5 μM), **L3** (1 μM), and **L4** (5 μM) (A3, bright field; A4, GFP channel). All cells were incubated with each probe at 37°C for 10 min and washed immediately. The background was adjusted by ImageJ software. Imaging was performed using a Zeiss Axio Observer A1 microscope with a 63 × objective lens.

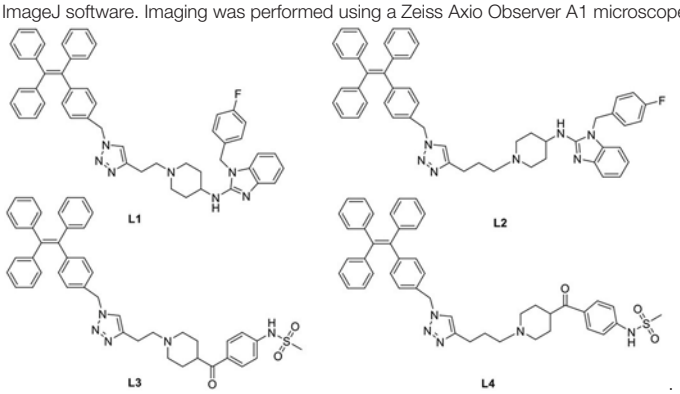

good fluorescent properties of TPE, it has been chosen as the fluorophore in the rational design for hERG channels probe. For pharmacophore, Astemizole and E-4031, the potent inhibitors of hERG channel, were chosen (Yamakawa et al., 2012; Wang et al., 2016a). For purpose of keeping the inhibitory activity of the probe, the major interaction sites of inhibitor's bonding were retained. Then the "click" reaction between the azoyl group on the fluorescence group and the acetylene group on

the recognition group was carried out by copper (I) in order to generate the turn-on probe (Liang et al., 2015). The small molecule fluorescent probes (**L1–L4**) for the hERG channels were illustrated in **Scheme 1**. When the probe is in freestate, the benzene ring can rotate freely, and the molecules in excited state release energy in a nonradiative manner. However, the free rotation of the benzene rings is limited after the probe binding hERG channel, and the excited molecules mostly release energy as fluorescence (**Scheme 2**).

Spectroscopic Properties of the Probes

Subsequently, the spectroscopic properties of the probes (**L1, L2, L3, L4**) were measured in 10 μM solution in PBS (pH = 7.4). The results indicated that all probes had similar fluorescent properties because of the same fluorophore (**Table 1**, **Figures 1**, **2**).

Binding Affinity of Probes

Afterwards, the inhibitory activities of the probes against the hERG potassium channel were evaluated utilizing radio-ligand binding assays by hERG transfected HEK293 cells. The results showed that probe **L3** displayed best inhibitory activity against the hERG channel, and the calculated IC_{50} and K_i values are 0.32 and 0.18 nM, respectively, which are slightly lower than astemizole (11.25 and 6.32 nM). Probe **L4** also showed lower inhibitory activity than astemizole, with IC_{50} values of 1.05 nM. Probes **L1** and **L2** showed potent inhibitory activity against hERG channel, with IC_{50} values of 120.50 and 155.90 nM, respectively, although lower than that of astemizole (See **Table 2**).

Cytotoxicity Assay

The cytotoxicity of these probes was evaluated by CCK-8 assays using hERG transfected HEK293 cells. The results indicated that the IC_{50} of probes **L1–L4** were 3.55 ± 0.28, 2.43 ± 0.12, and 7.03 ± 0.14 μM in hERG-HEK293 cells (See **Table 3**).

Fluorescent Image Assay

In consideration of their good fluorescent properties, acceptable cell toxicity, and potent inhibitory activity, probes **L1–L4** were utilized to image living cell in order to assess the capability of our probes for screening hERG channel. hERG transfected HEK293 cells were used to the imaging of probes **L1–L4** for hERG channels. Before we used probe to image cells, cell autofluorescence, and the effect of astemizole on cell autofluorescence were conducted (see **Supplementary Material**). The imaging results make clear that the autofluorescence of cells could be negligible in both the presence and absence of astemizole (**Figure S9**), which indicated the autofluorescence of the cells and astemizole would not interfere with the imaging of cells using probes **L1–L4**. The fluorescent imaging results demonstrated that these probes can label hERG-HEK293 cells with rapid responses and strong fluorescence to image hERG channels (**Figure 3**). Meanwhile, we chose a potent inhibitor of the hERG channels (astemizole) to incubate the cells with each probe. The fluorescence intensity was significantly decreased when the cells were co-incubated with astemizole and probe because of the inhibition of hERG channels by astemizole, which indicated that the hERG channels can be selectively labeled by the probe. Particularly, a complex washing procedure is not required because of their turn-on mechanism, which facilitated the experimental process. In conclusion, the results indicated that these probes all possess superior selectivity for hERG channels and could be used in the detection of hERG potassium channel.

CONCLUSIONS

AIEgens are an emerging class of fluorophore with unique photophysical properties whose applications are attracting increasing attention. We designed four fluorescent probe for hERG channels based on AIE effect, with good fluorescent properties and acceptable cytotoxicity. The affinity for the hERG channel showed that the probes **L1–L4** have higher affinity for the hERG channel, especially the probe molecule **L3** (IC_{50} = 1.05 nM, K_i = 0.59 nM), which has a stronger affinity for the hERG potassium channel than the positive drug astemizole (IC_{50} = 11.25 nM, K_i = 6.32 nM). The probes **L1–L4** can be utilized to the localization and visualization of hERG channel, and they have been successfully utilized to label the hERG channels in hERG- HEK293 cells at the nanomolar level. These probes are anticipated to set up a screening system for hERG channels. But two aspects are deemed essential for these AIE light-up probes for hERG channels, these AIE light-up probes used blue green emissive TPE fluorogens, which have limited application in *in vivo* studies that require deep penetration and low autofluorescence. One choice is to design red or FR/NIR emissive AIEgens with desirable functionalities. The alternative option is to choose red or FR/NIR emissive fluorophore which can greatly widen the scope of fluorescent probe for hERG channels *in vivo* applications.

AUTHOR CONTRIBUTIONS

XZ, ML, and LD conceived and designed the experiments. XZ, TL, and QL performed the experiments. XZ, ML, and LD analyzed the data. XZ wrote the manuscript. LD retouched the document.

FUNDING

The present project was supported by grants from the Shandong Natural Science Foundation (No. ZR2017MH101) and the Key Research and Development Project of Shandong Province (No. 2017CXGC1401).

SUPPLEMENTARY MATERIAL

The Supplementary Material for this article can be found online at: https://www.frontiersin.org/articles/10.3389/fchem.2019.00054/full#supplementary-material

REFERENCES

Babcock, J. J., and Li, M. (2013). hERG channel function: beyond long QT. *Acta Pharmacol. Sin.* 34, 329–335. doi: 10.1038/aps.2013.6

Bianchi, L., Wible, B., Arcangeli, A., Taglialatela, M., Morra, F., Castaldo, P. (1998). herg encodes a K+ current highly conserved in tumors of different histogenesis: a selective advantage for cancer cells? *Cancer Res.* 58, 815–822. doi: 10.1002/cphy.cp050111

Brown, A. M. (2004). Drugs, hERG and sudden death. *Cell Calcium* 35, 543–547. doi: 10.1016/j.ceca.2004.01.008

Chen, L., Li, J., Du, L., and Li, M. (2014). Strategies in the design of small-molecule fluorescent probes for peptidases. *Med. Res. Rev.* 34, 1217–1241. doi: 10.1002/med.21316

Cherubini, T. G. L., and Crociani, O. (2000). HERG potassium channels are more frequently expressed in human endometrial cancer as compared to non-cancerous endometrium. *Br. J. Cancer* 83, 1722–1729. doi: 10.1054/bjoc.2000.1497

Cohen, B. E., McAnaney, T. B., Park, E. S., Jan, Y. N., Boxer, S. G., and Jan, L. Y. (2002). Probing protein electrostatics with a synthetic fluorescent amino acid. *Science* 296, 1700–1703. doi: 10.1126/science.1069346

Ding, D., Li, K., Liu, B., and Tang, B. Z. (2013). Bioprobes based on AIE fluorogens. *Acc. Chem. Res.* 46, 2441–2453.doi: 10.1021/ar3003464

Du, L., Li, M., You, Q., and Xia, L. (2007). A novel structure-based virtual screening model for the hERG channel blockers. *Biochem. Biophys. Res. Commun.* 355, 889–894. doi: 10.1016/j.bbrc.2007.02.068

Hong, Y., Lam, J. W. Y., and Tang, B. Z. (2011). Aggregation-induced emission. *Chem. Soc. Rev.* 40, 5361–5388. doi: 10.1039/c1cs15113d

Jehle, J., Schweizer, P. A., Katus, H. A., and Thomas, D. (2011). Novel roles for hERG K(+) channels in cell proliferation and apoptosis. *Cell Death Dis.* 2:e193. doi: 10.1038/cddis.2011.77

Liang, J., Tang, B. Z., and Liu, B. (2015). Specific light-up bioprobes based on AIEgen conjugates. *Chem. Soc. Rev.* 44, 2798–2811. doi: 10.1039/c4cs00444b

Liu, T., Jiang, Y., Liu, Z., Li, J., Fang, K., Zhuang, C., et al. (2017). Environment-sensitive turn-on fluorescent probes for p53–MDM2 protein–protein interaction. *Medchemcomm* 8, 1668–1672. doi: 10.1039/c7md00287d

Liu, Z., Jiang, T., Wang, B., Ke, B., Zhou, Y., Du, L., et al. (2016). Environment-sensitive fluorescent probe for the human ether-a-go-go-related gene potassium channel. *Anal. Chem.* 88, 1511–1515. doi: 10.1021/acs.analchem.5b04220

Mizukami, S., Hori, Y., and Kikuchi, K. (2014). Small-molecule-based protein-labeling technology in live cell studies: probe-design concepts and applications. *Acc. Chem. Res.* 47, 247–256. doi: 10.1021/ar400135f

Perrin, M. J., Subbiah, R. N., Vandenberg, J. I., and Hill, A. P. (2008). Human ether-a-go-go related gene (hERG) K+ channels: function and dysfunction. *Prog. Biophys. Mol. Biol.* 98, 137–148. doi: 10.1016/j.pbiomolbio.2008.10.006

Pillozzi, S., Brizzi, M. F., Balzi, M., Crociani, O., Cherubini, A., Guasti, L., et al. (2002). HERG potassium channels are constitutively expressed in primary human acute myeloid leukemias and regulate cell proliferation of normal and leukemic hemopoietic progenitors. *Leukemia* 16, 1791–1798. doi: 10.1038/sj.leu.2402572

Roden, D. M. (2004). Drug-induced prolongation of the QT interval. *N. Engl. J. Med.* 350, 1013–1022. doi: 10.1056/NEJMra032426

Shi, H., Kwok, R. T., Liu, J., Xing, B., Tang, B. Z., and Liu, B. (2012). Real-time monitoring of cell apoptosis and drug screening using fluorescent light-up probe with aggregation-induced emission characteristics. *J. Am. Chem. Soc.* 134, 17972–17981.doi: 10.1021/ja3064588

Wang, B., Liu, Z., Ma, Z., Li, M., and Du, L. (2016a). Astemizole derivatives as fluorescent probes for hERG potassium channel imaging. *ACS Med. Chem. Lett.* 7, 245–249. doi: 10.1021/acsmedchemlett.5b00360

Wang, Y. F., Zhang, T., and Liang, X. J. (2016b). Aggregation-induced emission: lighting up cells, revealing life! *Small* 12, 6451–6477. doi: 10.1002/smll.201601468

Yamakawa, Y., Furutani, K., Inanobe, A., Ohno, Y., and Kurachi, Y. (2012). Pharmacophore modeling for hERG channel facilitation. *Biochem. Biophys. Res. Commun.* 418, 161–166. doi: 10.1016/j.bbrc.2011.12.153

Conflict of Interest Statement: The authors declare that the research was conducted in the absence of any commercial or financial relationships that could be construed as a potential conflict of interest.

Copyright © 2019 Zhang, Liu, Li, Li and Du. This is an open-access article distributed under the terms of the Creative Commons Attribution License (CC BY). The use, distribution or reproduction in other forums is permitted, provided the original author(s) and the copyright owner(s) are credited and that the original publication in this journal is cited, in accordance with accepted academic practice. No use, distribution or reproduction is permitted which does not comply with these terms.

Theoretical and Computational Chemistry

Vera Krewald

Vera Krewald obtained her PhD under the supervision of Prof. F. Neese and Dr D. A. Pantazis at the MPI for Chemical Energy Conversion in Mülheim/Ruhr, Germany, having worked on the water splitting reaction in natural photosynthesis. After a Marie-S.-Curie postdoctoral stay in Prof. L. González's group at the University of Vienna, Austria, she began independent research as a 50th Anniversary Prize Fellow at the University of Bath, UK, in 2017. Since December 2018, she is a tenure track Professor at TU Darmstadt, Germany. Research in her group focusses on the electronic structure analysis of open-shell transition metal complexes for reactions such as nitrogen activation, water oxidation and oxygen reduction.

Manuel Hitzenberger

Manuel Hitzenberger was born in Innsbruck in 1984 and is currently a postdoctoral researcher at the Technical University of Munich at the chair of Theoretical Biophysics - Molecular Dynamics. He studied Chemistry at the Leopold-Franzens University Innsbruck, where he graduated in 2012 from the Institute of General, Inorganic and Theoretical Chemistry. In 2017 he obtained his PhD, also at the University of Innsbruck, specializing in QM/MM-MD simulations of biomacromolecules. Today, his main research interests lie in the fields of membrane protein dynamics, protein – ligand docking, and multi-scale approaches to molecular dynamics.

Heather J. Kulik

Heather J. Kulik is an Assistant Professor in Chemical Engineering at MIT. She received her BE in Chemical Engineering from Cooper Union in 2004 and her PhD in Materials Science and Engineering from MIT in 2009. Following postdocs at Lawrence Livermore and Stanford, she returned to MIT. Her work has been recognized by a Burroughs Wellcome Fund Career Award at the Scientific Interface, an Office of Naval Research Young Investigator Award, a DARPA Young Faculty Award, an AAAS Marion Milligan Mason Award, the NSF CAREER, the ACS OpenEye Award for Outstanding Junior Faculty in Computational Chemistry, and the Journal of Physical Chemistry Lectureship, among others.

Jane R. Allison

Jane obtained a BSc (Hons) from the University of Canterbury in 2003 and a PhD from Cambridge University in 2008, where she worked with Prof. Chris Dobson. After working as a postdoc with Prof. Wilfred van Gunsteren at ETH Zürich, she returned to New Zealand in 2012 to become a Lecturer at Massey University. She was awarded a Rutherford Discovery Fellowship in 2015, and in 2018, moved to the University of Auckland, where she is an Associate Professor and an Associate Investigator with the Maurice Wilkins Centre for Molecular Biodiscovery and the Biomolecular Interaction Centre at the University of Canterbury.

Krzysztof B. Beć

Krzysztof B. Beć obtained his PhD degree in 2014 in Physical and Theoretical Chemistry from the University of Wrocław. His research involved thin-film IR spectroscopy, optical constants, and computational methods. He worked with Professor Yukihiro Ozaki as a Postdoctoral Fellow and Research Assistant Professor at Kwansei Gakuin University, Japan where he developed applications for simulation of NIR spectra and contributed to the development of ATR-FUV spectroscopy and its applications (polymer-carbon nanostructure composites). He continues his work in basic and applied spectroscopy in Prof. Christian W. Huck's team at University of Innsbruck, Austria.

Matthew G. Quesne

Dr Matthew George Quesne obtained his PhD from Manchester University, under the supervision of Dr Samuel de Visser, for modelling homogeneous catalysts. In 2014, he joined Dr Tomasz Borowski's group (Krakow, Poland) where he used MD, QM/MM and cluster model techniques to simulate enzyme catalyzed reactions. In 2016, Dr Quesne moved to Prof. Richard Catlow's group at Cardiff University where he studied CO2 activation by various materials and in March he started a position at the UK Catalysis Hub. Dr Quesne has published 29 high impact peer reviewed articles as well as three book chapters. He has over 800 citations and an H-index of 18.

frontiers in Chemistry

ORIGINAL RESEARCH
published: 16 May 2019
doi: 10.3389/fchem.2019.00352

Steric Switching From Photochemical to Thermal N_2 Splitting: A Computational Analysis of the Isomerization Reaction $\{(Cp^*)(Am)Mo\}_2(\mu\text{-}\eta^1\text{:}\eta^1\text{-}N_2) \rightarrow \{(Cp^*)(Am)Mo\}_2(\mu\text{-}N)_2$

*Vera Krewald**

Theoretische Chemie, Fachbereich Chemie, TU Darmstadt, Darmstadt, Germany

A μ-η^1:η^1-N_2-bridged Mo dimer, $\{(\eta^5\text{-}C_5Me_5)[N(Et)C(Ph)N(Et)]Mo\}_2(\mu\text{-}N_2)$, cleaves dinitrogen thermally resulting in a crystallographically characterized bis-μ-N-bridged dimer, $\{(\eta^5\text{-}C_5Me_5)[N(Et)C(Ph)N(Et)]Mo\}_2(\mu\text{-}N)_2$. A structurally related Mo dimer with a bulkier amidinate ligand, ([N(^{i}Pr)C(Me)N(^{i}Pr)]), is only capable of photochemical dinitrogen activation. These opposing reactivities were rationalized as steric switching between the thermally and photochemically active species. A computational analysis of the geometric and electronic structures of intermediates along the isomerization pathway from $Mo_2(\mu\text{-}\eta^1\text{:}\eta^1\text{-}N_2)$ to $Mo_2(\mu\text{-}\eta^2\text{:}\eta^1\text{-}N_2)$ and $Mo_2(\mu\text{-}\eta^2\text{:}\eta^2\text{-}N_2)$, and finally $Mo_2(\mu\text{-}N)_2$, is presented here. The extent to which dispersion affects the thermodynamics of the isomers is evaluated, and it is found that dispersion interactions play a significant role in stabilizing the product and making the reaction exergonic. The concept of steric switching is further explored with theoretical models with sterically even less demanding ligands, indicating that systematic ligand modifications could be used to rationally design the N_2 activation energy landscape. An analysis of electronic excitations in the computed UV-vis spectra of the two complexes shows that a particular type of asymmetric excitations is only present in the photoactive complex.

Keywords: nitrogen fixation, molybdenum, density functional theory, isomerization thermodynamics, theoretical UV-vis spectroscopy

OPEN ACCESS

Edited by:
Sam P. De Visser,
University of Manchester,
United Kingdom

Reviewed by:
Lawrence Sita,
University of Maryland, United States
Jose Oscar Carlos Jimenez-Halla,
University of Guanajuato, Mexico

***Correspondence:**
Vera Krewald
krewald@chemie.tu-darmstadt.de

Specialty section:
This article was submitted to Theoretical and Computational Chemistry, a section of the journal Frontiers in Chemistry

Received: *04 March 2019*
Accepted: *29 April 2019*
Published: *16 May 2019*

Citation:
Krewald V (2019) Steric Switching From Photochemical to Thermal N_2 Splitting: A Computational Analysis of the Isomerization Reaction $\{(Cp^*)(Am)Mo\}_2(\mu\text{-}\eta^1\text{:}\eta^1\text{-}N_2) \rightarrow \{(Cp^*)(Am)Mo\}_2(\mu\text{-}N)_2$. Front. Chem. 7:352. doi: 10.3389/fchem.2019.00352

INTRODUCTION

Catalytic nitrogen fixation with well-defined molecular complexes remains a grand challenge despite decades of research in this field. The research field is driven by the vision that a molecular catalyst capable of catalytically transforming nitrogen atoms from the dinitrogen molecule into ammonia or chemicals of higher economic value would contribute to a more sustainable chemical industry not dependent on fossil resources (Crossland and Tyler, 2010; Broda et al., 2013; Tanabe and Nishibayashi, 2013; Lee et al., 2014; Burford and Fryzuk, 2017; Burford et al., 2017; Connor and Holland, 2017; Creutz and Peters, 2017; Eizawa and Nishibayashi, 2017; Kuriyama and Nishibayashi, 2017; Roux et al., 2017). Industrial

ammonia production with the Haber-Bosch process is overall energy efficient, but relies on fossil H_2 for the steam reforming step (Schlögl, 2008). While a molecular catalyst for NH_3 production may never be efficient enough to replace the highly optimized Haber-Bosch process, research in this area results in valuable insights into the fundamental principles and electronic structure requirements for N_2 activation. This in turn may not only be relevant for fertilizer production, but also for alternative fuels that are based on nitrogen instead of carbon (Schlögl, 2010) (Grinberg et al., 2016; Chen et al., 2018). Catalysts that produce ammonia from dinitrogen are based on molybdenum, iron and cobalt (Roux et al., 2017), with many more elements known to be capable of binding N_2 and activating the strong N-N bond (Burford and Fryzuk, 2017; Klopsch et al., 2017). Strategies toward the development of molecular N_2 fixation catalysts operating at ambient or close to ambient conditions encompass a better understanding of the nitrogenase cofactor in nature (Lancaster et al., 2011; Spatzal et al., 2011; Sippel and Einsle, 2017), the development of molecular complexes and catalysts that activate or split N_2 (Dance, 2010; MacLeod and Holland, 2013; MacLeod et al., 2016; Djurdjevic et al., 2017; Eizawa et al., 2017; Sickerman et al., 2017), and the elucidation of the electronic structure of such complexes with computational and spectroscopic studies (Himmel and Reiher, 2006; Studt and Tuczek, 2006; Christian et al., 2007; Huss et al., 2013; Weymuth and Reiher, 2014). Ideally, the complexes will either fully cleave the N_2 molecule or activate the bond sufficiently that the nitrogen atoms are prepared for subsequent chemical reactions, and be part of a complete catalytic cycle with reasonable turnover numbers and turnover frequencies.

Over the past decade, Sita et al. have synthesized and characterized an extensive isostructural series of dinitrogen-bridged dimers which are capable of thermal or photochemical dinitrogen activation (Hirotsu et al., 2007a). The M-(μ-N_2)-M cores, where M = Ti (Fontaine et al., 2010), V (Keane et al., 2014); Zr (Hirotsu et al., 2007b), Nb (Keane et al., 2014), Mo (Fontaine et al., 2010); Hf (Hirotsu et al., 2007b), Ta (Hirotsu et al., 2007a; Keane et al., 2014), W (Fontaine et al., 2010), are stabilized by a common ligand sphere composed of a Cp* ligand and an amidinate ligand on each metal, see **Figure 1A** (Yonke et al., 2011a,b; Keane et al., 2013; Farrell et al., 2016; Duman and Sita, 2017). The amidinate ligand can be functionalized at the N-donor atoms or central carbon. Common N-functionalizations are Et and ^{i}Pr, and common C-functionalizations are Me, NMe_2 (i.e., a guanidinate), and Ph. In this paper, the ligand modifications will be denoted as {C-functionalization–N-functionalization}, e.g., {Me–^{i}Pr} for the ligand {N(^{i}Pr)C(Me)N(^{i}Pr)}$^-$. The M-(μ-N_2)-M cores are side-on bridging with a non-planar diamond core for Zr and Hf, and end-on bridging with a linear or near-linear core for Ti, V, Nb, Ta, Mo, and W (Keane et al., 2014).

Most of the complexes in Sita's series are thermally active, i.e., activate or split the N-N bond to yield monomeric metal nitride or dimeric μ-N-bridged complexes initially (Fontaine et al., 2010; Keane et al., 2015; Duman and Sita, 2017). Two complexes based on Mo and W are photoactive, i.e., result in complexes with M_2(μ-N) and M_2(μ-N)$_2$ cores upon irradiation with a mercury pressure lamp, see **Figure 1B** (Keane et al., 2015).

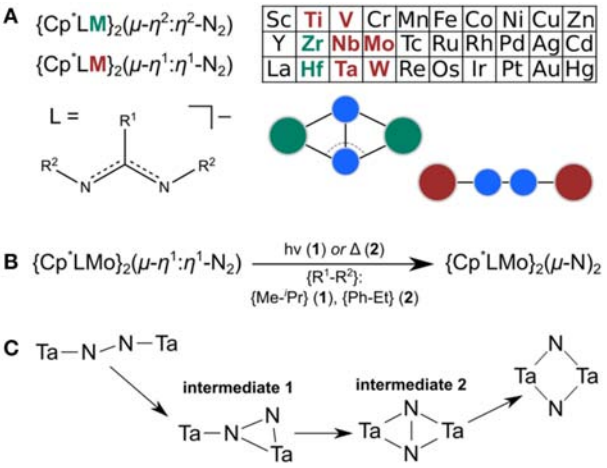

FIGURE 1 | (A) Overview of Sita's series of N_2-bridged complexes; Zr and Hf complexes are non-planar μ-η^2:η^2-N_2-bridged whereas all other known complexes have linear μ-η^1:η^1-N_2-bridged cores. **(B)** Capacity of the molybdenum complexes **1** and **2** for thermal or photochemical dinitrogen activation. **(C)** Isomerization path predicted computationally (Zhang et al., 2011) for the Ta congener using a simplified ligand framework.

Photochemical activation of N_2 (Krewald, 2018) in a well-defined molecular complex was first observed in 2001 (Solari et al., 2001), and has since been shown in several N_2-bridged dimers based on Mo (Curley et al., 2008; Miyazaki et al., 2014; Keane et al., 2015), W (Keane et al., 2015), Re (Schendzielorz et al., 2019), and Os (Kunkely and Vogler, 2010). Nitrogen photoactivation itself is currently not well-understood with only one time-resolved spectroscopy (Huss et al., 2013) and few computational investigations (Reiher et al., 2004; Krewald and González, 2018) available. The appeal of a light-driven step in nitrogen splitting lies in high spatio-temporal reaction control, high selectivity by depositing a well-defined amount of energy into the catalyst, and potentially the use of sunlight as a free and green source of energy.

For the Mo and W complexes with the {Me–^{i}Pr} ligand, Sita et al. showed that they are thermally stable at up to 100°C in hydrocarbon solution, but are sensitive to irradiation from a Rayonet carousel of medium-pressure Hg lamps (Keane et al., 2015). Through photolysis in the presence of a Group 14 alkyl- or aryl-substituted chloride (i.e., R_3ECl, E = C, Si, Ge), terminal imido products and metal dichloride precursors of the starting complexes are formed. The imido product can react with CO_2 to form isocyanate derivatives $R_3EN{=}C{=}O$ and a metal oxo complex, which can be transformed into the metal dichloride precursor, thus completing the chemical cycle (Keane et al., 2015). Although the photochemical activation of N_2 is in principle a desirable reaction, the authors noted that for these particular complexes the reactions were slow and suffered from poor energy efficiency and atom economy. Because the underlying photophysics and photochemistry of nitrogen photofixation are poorly understood in general (Krewald, 2018), Sita et al. subsequently sought to enable the thermal pathway by reducing the steric demands of the {Me–^{i}Pr} ligand in the photochemically active Mo and W dimers (Duman et al., 2016).

Steric hindrance as a design feature has been exploited in dinitrogen activation before, e.g., by Cummins et al., who have shown that an undesired mono-μ-N product of their $[(N(^tBu)(Ar))_3Mo(\mu\text{-}N_2)Mo(N(^tBu)(Ar))_3]$ complex is avoided (Laplaza and Cummins, 1995; Johnson et al., 1997), unlike in other dinitrogen-splitting complexes (Solari et al., 2001). Similarly, a well-established body of work by Power et al. among others exploits the cumulative effects of dispersion interactions in sterically crowded systems to stabilize otherwise energetically unfavorable complexes (Liptrot et al., 2016; Liptrot and Power, 2017). Seminal work by Grimme has provided the computational basis to explore these effects *in silico* (Grimme, 2004, 2011; Grimme et al., 2011b).

For the Ta, Nb, and Hf congeners an extensive study focused on the link between steric demand and nitrogen activation capacity (Fontaine et al., 2010; Keane et al., 2014). Expanding on these principles, thermal dinitrogen activation in both the Mo and W complexes could indeed be achieved by modifying the amidinate ligand substitution pattern from {Me–^{i}Pr} to {Ph–Et} (Duman et al., 2016). Again, the isomerization from a linear to a diamond-shaped core was observed and some of the resulting products were crystallized (Duman et al., 2016). It is not immediately obvious whether the difference in reactivity is mainly due to steric or electronic factors. The set of $M_2(\mu\text{-}\eta^1\text{:}\eta^1\text{-}N_2)$ complexes with M = Mo, W are experimentally characterized as having singlet ground states for both the {Me–^{i}Pr} and the {Ph–Et} ligands (Fontaine et al., 2010; Keane et al., 2015; Duman et al., 2016). For the $M_2(\mu\text{-}N)_2$ cores, diamagnetic character is also dominant; however for the molybdenum dimer with {Me–^{i}Pr} ligands strong paramagnetic shifting of the ^{1}H resonances in the NMR spectra is observed in solution despite SQUID magnetometry data on the solid state sample supporting a closed-shell configuration (Keane et al., 2015). Overall, the crystallographic core geometries and electronic structure properties of the starting complexes are rather similar, warranting a more detailed look at their isomerization reactions.

The isomerization of the Ta dimer from a linear to a diamond-shaped core originally suggested by Fontaine et al. (2010) was explored computationally by Morokuma et al. with a simplified ligand system (Cp instead of Cp*; {H–Me} amidinate ligands) (Zhang et al., 2011). According to this study, the linear core, $M_2(\mu\text{-}\eta^1\text{:}\eta^1\text{-}N_2)$, transforms into an end-on/side-on bridging core, $M_2(\mu\text{-}\eta^2\text{:}\eta^1\text{-}N_2)$, then into a side-on/side-on bridging dimer, $M_2(\mu\text{-}\eta^2\text{:}\eta^2\text{-}N_2)$, before fully breaking the N-N bond and forming a diamond-shaped core, $M_2(\mu\text{-}N)_2$; see **Figure 1C** (Zhang et al., 2011).

In this contribution, computational analyses based on density functional theory are used to elucidate the ground state geometries and electronic structures of the linear molybdenum complexes $\{(\eta^5\text{-}C_5Me_5)[N(^iPr)C(Me)N\text{-}(^iPr)]Mo\}_2(\mu\text{-}N_2)$ (**1**) and $\{(\eta^5\text{-}C_5Me_5)[N(Et)C(Ph)N\text{-}(Et)]Mo\}_2(\mu\text{-}N_2)$ (**2**). The relevant intermediates along the isomerization paths to molybdenum dimers with diamond-shaped cores are identified and characterized to evaluate the idea of steric switching along the isomerization paths. The relevance of dispersion corrections for all intermediates is discussed, and suggestions for complexes with further reduced steric bulk are made. To gain some insight into the photoactivity of the complex with bulkier ligands, the electronic UV-vis absorption spectra are predicted and differences to the spectrum obtained for the thermally active compound are discussed. It is found that a group of transitions with asymmetric MLCT and LMCT character is present in the photoactive, but absent in the thermally active compound. This contribution aims to provide computational insight into the previously unclear ground state electronic structure of the complexes with linear Mo-N-N-Mo cores and identifies possible reasons for the observed differences in reactivity of these structurally similar complexes which may be of relevance for future experimental studies on the complexes' thermodynamic and kinetic properties as well as their photophysical and photochemical processes.

MATERIALS AND METHODS

All calculations were performed with the ORCA program package as unrestricted Kohn-Sham calculations (Neese, 2012). Geometries were optimized with the BP86(Perdew, 1986; Becke, 1988) density functional using the resolution of the identity approximation, the def2-TZVP basis set for molybdenum and nitrogen atoms with def2-ECP for molybdenum atoms, the def2-SVP basis for carbon and hydrogen atoms, and the def2/J auxiliary basis (Andrae et al., 1990; Weigend and Ahlrichs, 2005; Weigend, 2006). The grid size was increased to 7 in ORCA nomenclature, and the integration accuracy was set to 7.0. Tight SCF and optimization convergence criteria were chosen. The CPCM implicit solvent model with benzene ($\varepsilon = 2.28$) was used. Grimme's atom-pairwise dispersion correction with Becke-Johnson damping (D3BJ) was used (Grimme et al., 2010, 2011a), except where explicitly excluded as mentioned in the main text.

For the relative energies of spin states, single point energy calculations were performed with the density functionals PBE0 (Adamo and Barone, 1999), TPSSh (Staroverov et al., 2003), B3LYP (Lee et al., 1988; Becke, 1993), M06 (Zhao and Truhlar, 2008), including the chain-of-spheres approximation and the def2/JK basis set (Weigend, 2008; Neese et al., 2009b). To confirm the predicted geometries along the isomerization paths as true minima, the absence of any imaginary frequencies was verified with frequency calculations using the same computational details as for the geometry optimizations, except for the omission of the CPCM solvent model. To obtain a full thermodynamic picture, enthalpies, entropies and Gibbs free enthalpies were taken from these calculations, supplemented with electronic energy calculations with the B3LYP or PBE0 functional using the RIJCOSX approximation with the def2/JK auxiliary basis set.

The UV-vis spectra of the linear complexes were predicted with TD-DFT using various density functionals due to the absence of a calibration study for similar molybdenum dimers. Even though compared with the experimental spectrum of $\{(\eta^5\text{-}C_5Me_5)[N(^iPr)C(Me)N\text{-}(^iPr)]Mo\}_2(\mu\text{-}N_2)$, the predicted spectra are shifted to higher energies by ca. 1 eV, the main features are reproduced satisfactorily. Using otherwise identical settings for the electronic structure calculations as for the single point calculations above, the density functionals tested are BP86

(Perdew, 1986; Becke, 1988), TPSS (Tao et al., 2003), TPSSh (Staroverov et al., 2003), B3LYP (Lee et al., 1988; Becke, 1993), PBE0 (Adamo and Barone, 1999), CAM-B3LYP (Yanai et al., 2004), LC-BLYP (Iikura et al., 2001), and ωB97X (Chai and Head-Gordon, 2008). The Tamm-Dancoff approximation(Hirata and Head-Gordon, 1999) was used and 100 roots were calculated (Neese and Olbrich, 2002). The solvent modeled was methyl cyclohexane ($\varepsilon = 2.071$). All line spectra are generated with the ORCA utility program *orca_mapspc* with spectral broadening of 2,500 cm^{-1}.

RESULTS

Geometries and Electronic Structures of Molybdenum Dimers With Linear and Diamond-Shaped Cores

The starting complexes are $\{(\eta^5\text{-}C_5Me_5)[N(^i Pr)C(Me)N\text{-}(^i Pr)]Mo\}_2(\mu\text{-}N_2)$, $\mathbf{1}_{lin}$, which is photoactive, and $\{(\eta^5\text{-}C_5Me_5)[N(Et)C(Ph)N\text{-}(Et)]Mo\}_2(\mu\text{-}N_2)$, $\mathbf{2}_{lin}$, which is thermally active. They may be formally viewed as two Mo(II), d^4, with a neutral N_2 bridge, or as two Mo(IV), d^2, with a N_2^{4-} bridge (Fontaine et al., 2010). A crystal structure is only available for $\mathbf{2}_{lin}$, where the N-N bond length of 1.288 Å corresponds approximately to a dinitrogen double bond (Holland, 2010). As noted by Fontaine et al., the true electronic configuration probably lies somewhere in-between the oxidation states that can be assigned formally (Fontaine et al., 2010).

The crystal structures of the product complexes $\{(\eta^5\text{-}C_5Me_5)[N(^i Pr)C(Me)N\text{-}(^i Pr)]Mo\}_2(\mu\text{-}N)_2$, $\mathbf{1}_{dia}$, and $\{(\eta^5\text{-}C_5Me_5)[N(Et)C(Ph)N\text{-}(Et)]Mo\}_2(\mu\text{-}N)_2$, $\mathbf{2}_{dia}$, show diamond-shaped Mo_2N_2 cores. Formally, the molybdenum ions are now oxidized to Mo(V), d^1, implying that in principle a singlet and a triplet ground state are accessible. In the solid state, magnetic data obtained from SQUID magnetometry indicate a closed-shell electronic structure for $\mathbf{1}_{dia}$. Notably, the ^1H NMR resonances of solutions of $\mathbf{1}_{dia}$ are subject to paramagnetic shifting whereas for $\mathbf{2}_{dia}$ no indication for open-shell character is found (Keane et al., 2015; Duman et al., 2016). The N-N distances are >2.5 Å and thus no residual bonding interaction is to be expected. The crystallographic Mo-Mo distances on the other hand are slightly shorter than twice Pauling's covalent bond radius for Mo (1.371 Å). At 2.676 and 2.648 Å, respectively, they are in the range of distances expected for a Mo-Mo single or double bond (Pauling and Kamb, 1986; Shin and Parkin, 1998; Neary and Parkin, 2017). Both diamond cores are to some extent asymmetric: the molybdenum ions in $\mathbf{1}_{dia}$ have different bond lengths with the bridging nitrogen atoms ($Mo^1\text{-}N^{1,2}$: 1.850 Å, $Mo^2\text{-}N^{1,2}$: 1.964 Å), whereas each molybdenum in $\mathbf{2}_{dia}$ has two different bond lengths with the nitrogen bridges (1.892, 1.927 Å) (Keane et al., 2015; Duman et al., 2016). From a purely structural point of view, the two complexes have strikingly similar geometries that do not indicate any major influence of the ligand sphere on the geometry of the Mo_2N_2 core.

The structural parameters obtained for $\mathbf{1}_{lin}$ from a geometry relaxation are in good agreement with those of related complexes such as $\mathbf{2}_{lin}$ (**Figure 3**). In the absence of a crystal structure for $\mathbf{1}_{lin}$, no direct comparison to experimental data is possible. The geometry optimization of $\mathbf{2}_{lin}$ results in excellent agreement with the available crystal structure. The N-N distance is found to be 1.247 Å (exp.: 1.288 Å) and the Mo-N bond lengths are predicted to within 0.03 Å. In both linear molybdenum dimers, the Mayer bond orders indicate a N-N double bond (1.64) and bonds that are in-between single and double bonds for the M-N interaction (1.39, see **Table 1**).

TABLE 1 | Computed Mayer bond orders along the isomerization coordinate of **1** and **2**, including for the singlet (s) and triplet (t) configurations of $\mathbf{1}/\mathbf{2}_{dia}$.

Cpd.	Mo-Mo	Mo-N	Mo-N	Mo-N	Mo-N	N-N
1_{lin}	0.32	1.39	0.12	1.39	0.12	1.60
1_{int-1}	0.26	1.31	0.14	1.23	0.36	1.24
1_{int-2}	0.35	1.14	0.69	1.12	0.61	0.88
1_{dia} (s)	0.70	1.23	1.23	1.23	1.23	<0.1
1_{dia} (t)	0.43	1.56	1.53	1.00	1.02	<0.1
2_{lin}	0.31	1.39	0.11	1.39	0.11	1.64
2_{int-1}	0.27	1.19	0.17	1.15	0.51	1.14
2_{int-2}	0.33	1.13	0.68	1.09	0.64	0.89
2_{dia} (s)	0.73	1.13	1.36	1.36	1.13	<0.1
2_{dia} (t)	0.42	1.47	1.66	1.11	0.94	<0.1

For the product $\mathbf{1}_{dia}$, the geometry relaxation with a singlet electronic configuration yields a symmetric diamond core with a Mo-Mo distance of 2.633 Å, a N-N distance of 2.744 Å, and Mo-N bond lengths of 1.901 Å. This structure is clearly at odds with the crystallographically determined asymmetry of the core, in which the two molybdenum ions have different bond lengths with the bridging nitrogen atoms. Therefore, a separate geometry relaxation was performed using the triplet state of $\mathbf{1}_{dia}$. This resulted in a geometry that contains one Mo center with shorter Mo-N bond lengths (1.818, 1.821 Å) and one Mo center with longer Mo-N bond lengths (1.978, 1.980 Å). While overall an improvement in relation to the experimentally found structure, the Mo-Mo distance is now somewhat overestimated (calc: 2.770 Å, exp: 2.676 Å, **Figure 3A**).

The singlet and triplet geometries of $\mathbf{1}_{dia}$ are energetically separated by 7.4 kcal/mol at the level of theory of the geometry optimization, which would indicate that the higher-lying triplet state is not significantly populated. Although without careful calibration it is uncertain whether any given density functional yields accurate spin state energetics, hybrid functionals may be considered as somewhat more suitable in this case. Single point energy calculations show a consistently smaller separation between the singlet and triplet state geometries, with the singlet state remaining lower in energy (PBE0: 1.9 kcal/mol, TPSSh: 4.1 kcal/mol, B3LYP: 2.0 kcal/mol, M06: 3.9 kcal/mol). It must be stressed, however, that a reliable estimate of the energy separation could only be achieved with highly accurate methods such as DLPNO-CCSD(T) in combination with a large basis set (Neese et al., 2009a; Paulechka and Kazakov, 2017; Saitow et al., 2017). The Mayer bond orders of the singlet state are reflective of the symmetric core (Mo-Mo: 0.70, all Mo-N: 1.23). The triplet state features a significantly reduced Mo-Mo bond strength (0.43) and asymmetry in the Mo-N bond orders (1.53, 1.56; 1.02, 1.00). The

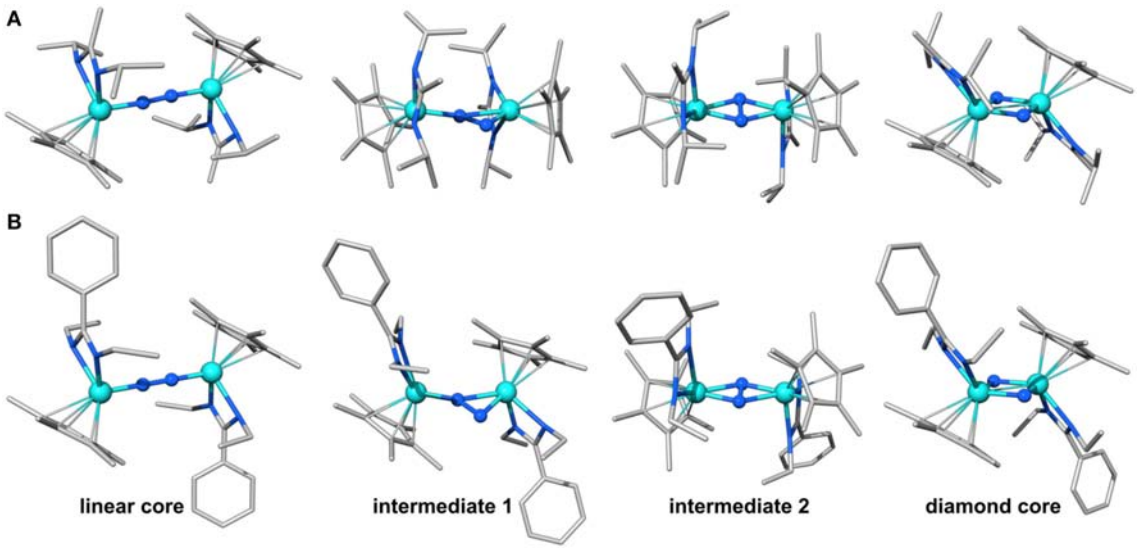

FIGURE 2 | Geometries predicted along the isomerization path of **1 (A)** and **2 (B)**. Color code for atoms is Mo: light blue, N: blue, C: gray, H omitted for clarity.

Mulliken spin populations of the triplet state are 0.50 and 1.43, which is indicative of a degree of spin delocalization between a Mo(VI) center and a Mo(IV) center, respectively.

For the product $\mathbf{2}_{dia}$, a geometry optimization with an electronic singlet state configuration reproduces the crystal structure parameters very well, see **Figure 3B**. The distortion of the diamond core is accompanied by different bond distances to the amidinate-N donor atoms (2.200, 2.220 Å), all of which are longer than in the starting complex $\mathbf{2}_{lin}$ (2.130–2.137 Å). The Mayer bond orders indicate a single bond between the two metals (0.73) and strong Mo-N interactions that mirror the asymmetry of the core (1.13, 1.36 for each Mo).

Naturally, the question arises whether a triplet state can also be found for $\mathbf{2}_{dia}$, and what its energetic separation from the singlet state would be. There is no experimental indication for any open-shell character of this complex. Nevertheless, the geometric and electronic structure resulting from the triplet state relaxation of $\mathbf{2}_{dia}$ is surprisingly similar to that of $\mathbf{1}_{dia}$ in its triplet state. The Mo-Mo distance is elongated to 2.762 Å, and asymmetric Mo centers with respect to their interaction with the bridging nitrogen atoms are found (1.812, 1.835, 1.998, 1.966 Å). Similarly, the Mo-Mo Mayer bond order is reduced to 0.42, and the Mo center with short M-N bonds has higher bond orders (1.47, 1.66) than that with longer M-N bonds (1.11, 0.94). The Mulliken spin populations (0.46, 1.38) match those found for the triplet state of $\mathbf{1}_{dia}$. The relative total energies of the singlet and triplet state of $\mathbf{2}_{dia}$ are increased compared with $\mathbf{1}_{dia}$ with the singlet state again remaining the more stable one (BP86: 8.3 kcal/mol, PBE0: 4.0 kcal/mol, TPSSh: 5.5 kcal/mol, B3LYP: 4.01 kcal/mol, M06: 6.15 kcal/mol). Although a clear differentiation between the relative abundance of singlet and triplet state for the diamond cores in **1** and **2** will require further experimental information coupled to high accuracy computations, the present results corroborate that a triplet state may be more readily accessible in $\mathbf{1}_{dia}$ than in $\mathbf{2}_{dia}$. The small energy differences between singlet and triplet states are furthermore in agreement with the experimental observation that changes in the environment, e.g., crystal structure vs. solution phase, may well be sufficient to introduce a spectroscopically significant amount of the higher spin state in $\mathbf{1}_{dia}$ (Keane et al., 2015).

Isomerization Paths

The structures of the molybdenum dimers with the same multiplicity are strikingly similar, regardless of the ligand sphere. Merely from the inspection of their geometries and electronic structures it is therefore not obvious why $\mathbf{1}_{lin}$ requires activation with light to achieve the transformation to the diamond-shaped core whereas $\mathbf{2}_{lin}$ is capable of thermal isomerization. The next step toward elucidating this difference in reactivity was therefore to identify intermediates along the isomerization pathway. This may also lead to a better understanding of the atomic-level realization of "steric switching" (Duman et al., 2016) from the photochemical to the thermal process. Morokuma et al. evaluated a four-step isomerization path for the Ta complexes with a simplified ligand sphere ({H–Me}, i.e., R^1: H, R^2: Me), as sketched in **Figure 1C** (Zhang et al., 2011). It involves a change in dinitrogen coordination from $Ta_2(\mu\text{-}\eta^1\text{:}\eta^1\text{-}N_2)$ to $Ta_2(\mu\text{-}\eta^2\text{:}\eta^1\text{-}N_2)$ in intermediate 1 and subsequently to $Ta_2(\mu\text{-}\eta^2\text{:}\eta^2\text{-}N_2)$ in intermediate 2 with a residual N-N bond, before fully breaking the N-N interaction in $Ta_2(\mu\text{-}N)_2$. Given that the geometries and reactivities of the complexes in the Sita series are largely similar, these intermediates represent a reasonable starting point for an investigation of the isomerization paths of the Mo dimers.

Indeed, the analogous intermediates were identified for both dimers (**Figures 2**, **3**). Overall, their respective geometries are of striking similarity. Upon formation of $\mathbf{1}/\mathbf{2}_{int-1}$ with a $\mu\text{-}\eta^2\text{:}\eta^1\text{-}N_2$ bridge, the N-N distance increases to ca. 1.30 Å in

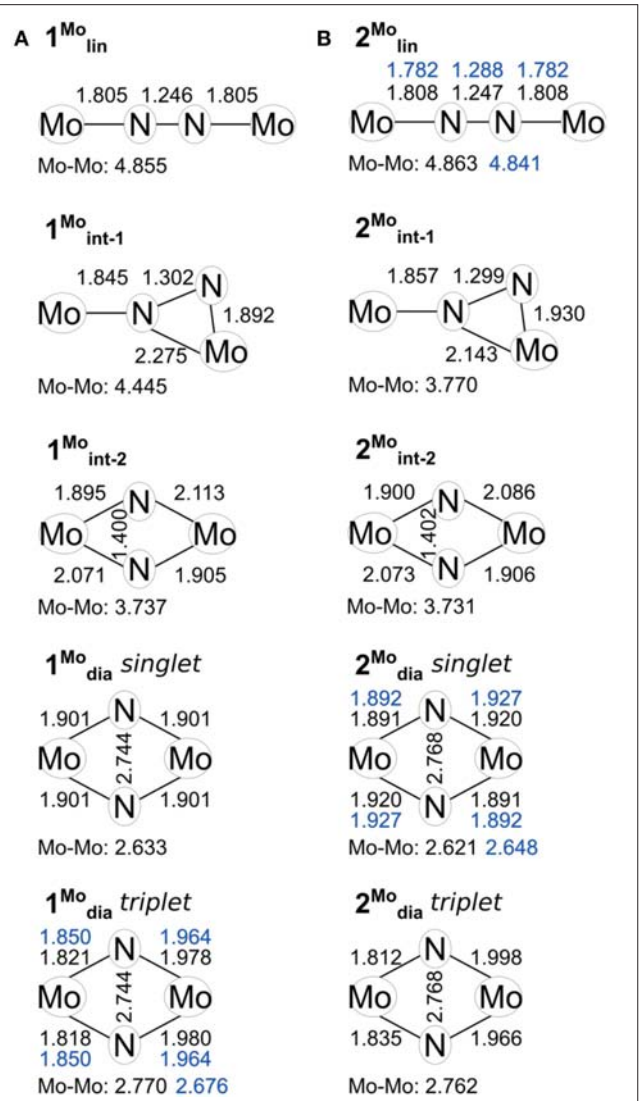

FIGURE 3 | Key geometric parameters computed for the isomers of **1 (A)** and **2 (B)**, including the core geometries of **1**/**2**$_{dia}$ in their triplet states. Values found in crystal structures where available are given in blue.

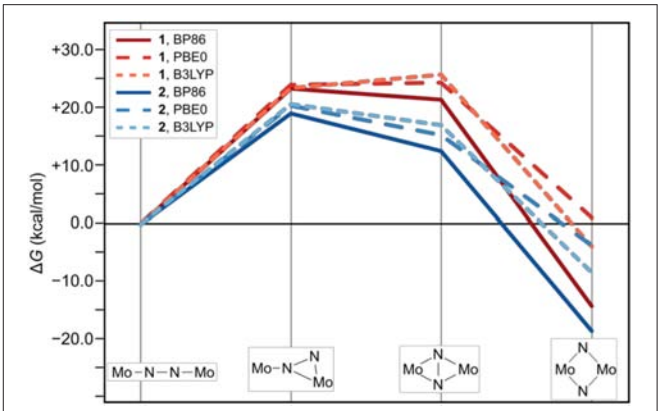

FIGURE 4 | Thermodynamic profile of the isomerization paths for **1** (red) and **2** (blue). Data points for which the electronic structures are calculated with PBE0 and B3LYP are long-dashed and short-dashed, respectively.

both complexes, concomitant with a significant reduction in N-N bond order (**Table 1**). The Mo-N bond lengths of the η^1-coordinated Mo are 1.845 Å (**1**$_{int-1}$) and 1.857 Å (**2**$_{int-1}$), thus increased by only ca. 0.05 Å compared to the linear precursors. As expected, the η^2-coordinated Mo-N interactions are significantly longer than the previous η^1-distances at now 1.892 Å (**1**$_{int-1}$) and 1.930 Å (**2**$_{int-1}$) for the 'short' and 2.275 Å (**1**$_{int-1}$) and 2.143 Å (**2**$_{int-1}$) for the "long" interactions. Despite the latter distances being relatively long, the bond orders support a very weak bond (**Table 1**). In the second intermediates, **1**/**2**$_{int-2}$ with a μ-η^2:η^2-N_2 unit, the nitrogen-nitrogen distances are ca. 1.40 Å and the Mayer bond orders indicate that a single N-N bond is still present (0.88, 0.89). Both Mo_2N_2 cores show asymmetry in the Mo-μ-N bond lengths: similar to the singlet form of **2**$_{dia}$, each Mo ion has a short (ca. 1.9 Å) and a long (ca. 2.1 Å) separation from the bridges. The bond orders show a discrepancy in the interaction strength of less than half a single bond.

The thermodynamic profiles of the isomerization paths in **Figure 4** show that the formation of all intermediates is endergonic. At the level of theory used for optimizing the geometries and obtaining the Hessians, the first intermediates are predicted at ΔG values of 23.5 kcal/mol (**1**$_{int-1}$) and 19.1 kcal/mol (**2**$_{int-1}$). The formation of the second intermediates is only slightly less endergonic for **1**$_{int-2}$ at 21.7 kcal/mol, but significantly less so for **2**$_{int-2}$ at 12.5 kcal/mol. Finally, the driving force for the overall isomerization appears to be the formation of the dimers with diamond-shaped cores at −14.3 kcal/mol for **1**$_{dia}$ and −18.7 kcal/mol for **2**$_{dia}$ according to the ΔG values predicted at this level of theory. To verify whether the electronic structure description would have a significant influence on the overall profiles, single point energy calculations with the two hybrid functionals PBE0 and B3LYP were carried out. The resulting reaction profiles, using the thermodynamic data calculated with the BP86 density functional, shows that the change in ΔG for **1**/**2**$_{int-1}$ is <2 kcal/mol while **1**/**2**$_{int-2}$ are predicted to be 3–5 kcal/mol less stable. More importantly, however, the product with a diamond-shaped Mo_2(μ-N)$_2$ core for **1** is calculated to be significantly less exergonic (−3.9 kcal/mol with B3LYP) or even endergonic (+1.0 kcal/mol for PBE0). In contrast, while the product of the isomerization reaction for **2** is also less stabilized with hybrid functionals it is clearly still exergonic at −8.5 kcal/mol with B3LYP or −3.8 kcal/mol with PBE0.

The reaction profiles thus show that isomerization can in principle occur in both complexes, albeit at higher cost for intermediate formation and a significantly lower driving force in complex **1** compared with complex **2**. Comparison with the experimental kinetic data would require the identification of transition states along the isomerization path, which is beyond the scope of this work. The core geometries are strikingly similar and do not readily explain the thermodynamic differences, therefore any attempt to analyze and rationalize the underlying reasons for the experimentally observed "steric switching" must inspect the interactions between the two halves of the ligand

sphere. Indeed, an interesting point was noted when analyzing the contributions from the dispersion correction.

Influence of Dispersion on the Isomerization Path Energetics

Initially, the number and distance of pairs of hydrogen atoms will serve as a measure for steric interactions in the intermediates. This provides an intuitive picture of the steric clashes while at the same time facilitating a quantitative comparison along the isomerization paths. As reference values, hydrogen atoms of the same methyl group are usually <1.8 Å apart; distances between hydrogen atoms attached to adjacent carbon atoms in phenyl and ethyl groups are ∼2.5 Å. **Figure 5** shows the number of H-H distances for the species along the isomerization coordinate in bins of 0.4 Å width between 1.8 and 4.2 Å. The precise numbers, average values and combined lengths for the H-H pairs are given in the SI. Generally, complex **1** has more H-H pairs than complex **2**, in line with the chemical expectations for the "bulky" {Me-^{i}Pr} and "sterically reduced" {Ph-Et} ligand systems. For both complexes the number of H-H contacts increases during the overall isomerization process from $\mathbf{1/2}_{lin}$ to $\mathbf{1/2}_{dia}$ (286 to 330 for **1**, 210 to 236 for **2**). For **1**, the increase stems largely from longer distances (+36 for 3.4–4.2 Å, orange and red in **Figure 5**, cf. +6 for **2** in this range), whereas for **2** the number of shorter distances increases most (+16 for 1.8–2.6 Å, dark and medium blue in **Figure 5**; cf. +15 for **1** in this range). The inter-hydrogen distances between ligands coordinated at different metals in the bins 1.8–2.2 Å (dark blue), 2.2–2.6 Å (middle blue), and 2.6–3.0 Å (light blue) are visualized in **Figure 6** for the linear and diamond-shaped complexes of **1** and **2**. In terms of absolute numbers, these fall in the range of 2.03–2.73 Å for $\mathbf{1}_{lin}$ and 2.15–2.98 Å for $\mathbf{2}_{lin}$; 2.03–2.78 Å for $\mathbf{1}_{dia}$ and 1.96–2.84 Å for $\mathbf{2}_{dia}$.

The effect of these interactions on the relative energetics are expected to be dominated by two factors: destabilization due to closer nuclei positions, and stabilization due to dispersion interactions. Since dispersion interactions are always attractive (Grimme, 2011), and a larger number of interhydrogen contacts is built up along the reaction coordinate, it is clear that dispersion interactions should stabilize the products to a significant extent. In terms of single point energies, dispersion corrections account for a stabilization of ca. −23 kcal/mol for $\mathbf{1/2}_{dia}$ relative to $\mathbf{1/2}_{lin}$, i.e. the energy gain in both complexes is practically identical. The stabilization of intermediates $\mathbf{1/2}_{int-1}$ and $\mathbf{1/2}_{int-2}$ due to dispersion is also almost identical in the two complexes and <10 kcal/mol relative to the linear starting compounds. Therefore, despite an overall larger number of H-H pairs <4.2 Å apart, complex **1** benefits only as much as complex **2** from stabilization through dispersion, implying that each H-H pair in **1** has a smaller effect. The absolute dispersion corrections in all intermediates of **1** are ca. 5 kcal/mol less than for those of **2** (see SI for details).

The effect of omitting dispersion effects can be tested *in silico* by removing the dispersion corrections in the geometry optimizations, which is presented exemplarily for complex **2** starting from the fully optimized structures that included dispersion corrections. As an aside, it is noted that upon removal of dispersion corrections the geometry of intermediate $\mathbf{1}_{int-1}$ could not be optimized despite several attempts; instead the molecule relaxed to a linear Mo–(μ-η^1:η^1-N$_2$)–Mo core. Likewise the optimization of $\mathbf{1}_{dia}$ without dispersion corrections resulted in a frequency analysis with significant imaginary entries that could not be removed, indicating that the structures obtained are not a proper minima on the potential energy surface. For complex **2** with its starting complex, intermediates and product, the changes in geometry range from barely visible by eye inspection to subtle in many of the isomers, while in some the phenyl group rotates (see SI for Cartesian coordinates of all geometries). Comparing the total number of H contacts in the structures optimized with and without dispersion corrections

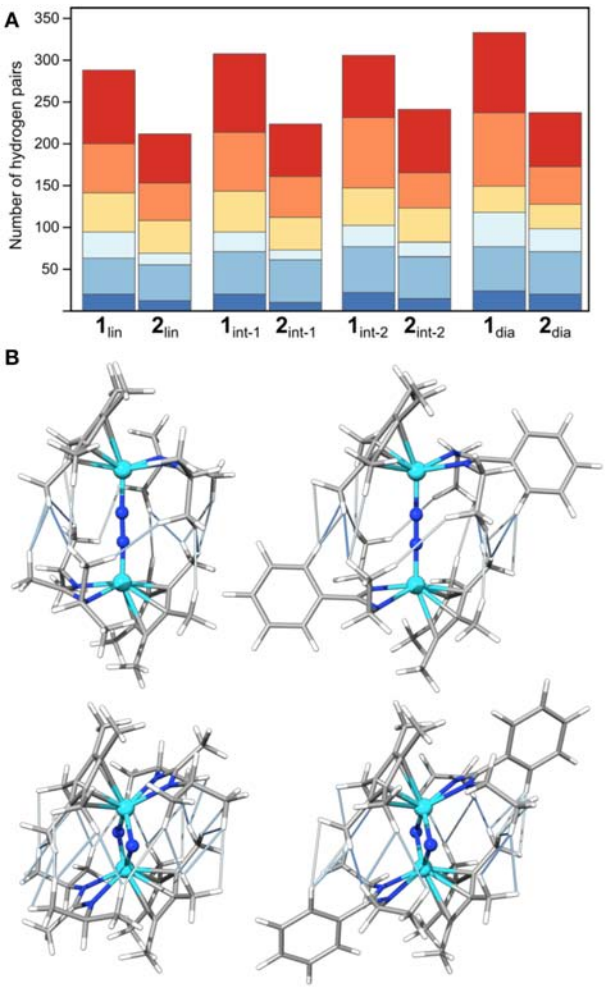

FIGURE 5 | Visualization of the number of hydrogen pairs along the isomerization pathway of **1** and **2, (A)** in terms of absolute numbers in bins of 1.8–2.2 Å (dark blue), 2.2–2.6 Å (middle blue), 2.6–3.0 Å (light blue), 3.0–3.4 Å (yellow), 3.4–3.8 Å (orange), 3.8–4.2 Å (red), and **(B)** as a representation of the actual geometric interactions in $\mathbf{1}_{lin}$ (top left), $\mathbf{1}_{dia}$ (top right), $\mathbf{2}_{lin}$ (bottom left) and $\mathbf{2}_{dia}$ (bottom right); H-H interactions are shown as thin lines in dark blue (1.8–2.2 Å), middle blue (2.2–2.6 Å), and light blue (2.6–3.0 Å). Color code for atoms is Mo: light blue N: blue, C: gray, H light gray.

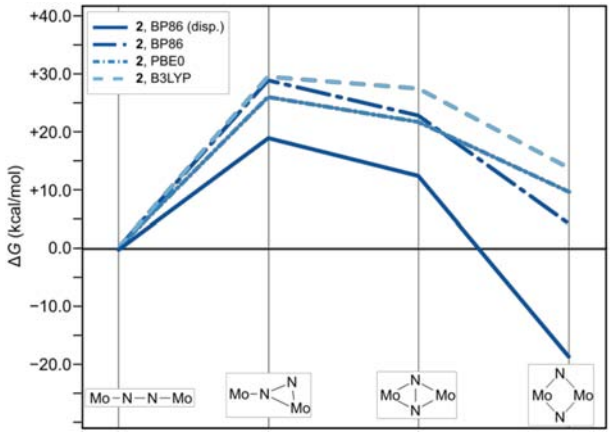

FIGURE 6 | Effect of omitting dispersion corrections on the thermodynamic profile of the isomerization paths of **2**. The thermodynamic profile including dispersion is shown as a solid line for reference; data points for which the electronic structures are calculated with BP are long-dashed-dotted (dark blue), with PBE0 are short-dash-dotted (mid-blue), and with B3LYP short-dashed (light blue).

shows that **2** loses 18 pairs in its linear form and 12 pairs in its diamond form (see **Supporting Information**).

The thermodynamic profiles for all forms of **2** optimized without dispersion corrections show that the isomerization path is significantly destabilized. Dispersion interactions thus have a more pronounced stabilizing effect on the dimer with a diamond-shaped core compared to the starting complex with a linear core, consistent with the increase in H-H pairs with distances smaller than 4.2 Å. The isomerization product of **2** has a ΔG value of 4.1 kcal/mol using the BP86 electronic structure description. An even more distinct destabilization is predicted with the PBE0 ($\mathbf{2}_{dia}$: 9.6 kcal/mol) and B3LYP ($\mathbf{2}_{dia}$: 13.7 kcal/mol) density functionals.

In silico Modifications

With the above information on the isomerization paths for **1** and **2** at hand, *in silico* modifications of the amidinate ligand are carried out. The leading question is whether any further reduction of the steric demands of the ligands would lead to lower energy intermediates. The ligand systems considered are {Me-Et} (**3**) and {Ph-H} (**4**). While a substitution pattern of {H-H} would obviously represent the sterically least demanding amidinate ligand, and thus serve as a sort of base line, geometry optimizations with this ligand were unsuccessful for all steps of the isomerization except intermediate 2. All energetic minima identified showed negative frequencies of significant magnitude ($>>100\ cm^{-1}$) in their Hessians, indicating that these hypothetical structures would not be stable.

The starting compound **3** has a linear core with key geometric parameters that are almost identical to that of the original compounds **1** and **2**. In contrast, the optimized geometry of **4** has a "pre-bent" core with Mo-N-N angles of 163.5 and 163.3°, compared with 177.2–179.1° for the other three complexes discussed here. None of the other key geometric parameters

TABLE 2 | Key interatomic distances in Å of the Mo_2N_2 cores in the hypothetical compounds **3** and **4**.

Cpd.	Mo-Mo	Mo-N	Mo-N	Mo-N	Mo-N	N-N
$\mathbf{3}_{lin}$	4.86	1.81	3.05	1.81	3.05	1.25
$\mathbf{3}_{int-1}$	3.66	1.85	3.08	1.93	2.12	1.31
$\mathbf{3}_{int-2}$	3.72	1.89	2.08	1.89	2.08	1.41
$\mathbf{3}_{dia}$ (s)	2.62	1.91	1.90	1.91	1.90	2.77
$\mathbf{4}_{lin}$	4.83	1.81	3.03	1.81	3.03	1.24
$\mathbf{4}_{int-1}$	3.55	1.84	3.10	1.94	2.16	1.29
$\mathbf{4}_{int-2}$	3.72	1.90	2.06	1.90	2.06	1.40
$\mathbf{4}_{dia}$ (s)	2.63	2.03	1.85	1.80	1.95	2.72

show a great variation between the four substitution patterns, see **Table 2**. Likewise, the degree of N-N bond activation as judged by bond length and Mayer bond order is basically unchanged by different amidinate substitution patterns. The only exception to this is intermediate 1 where the bond order is 1.05 for **3** and 1.07 for **4** vs. 1.24 in **1** and 1.14 in **2**, indicating that a lower steric demand or fewer attractive dispersion interactions allow for a greater weakening of the N-N bond.

As expected from the design concept of lowering the steric bulk, both changes in ligand sphere result in thermodynamic profiles that lie overall energetically below those of the original systems, see **Figure 7**. The isomerization path of complex **3** with the {Me-Et} substitution pattern is consistently situated 1–3 kcal/mol below that of complex **2**. Thus, the formation of intermediate **1** is still the most costly in terms of relative free energies. For complex **4**, however, intermediate 1 lies distinctly lower than intermediate 2, by 2.5 kcal/mol for the PBE0 density functional (2.9 kcal/mol for BP86, 4.2 kcal/mol for B3LYP), therefore achieving a markedly different topology of the isomerization energy surface.

UV-vis Spectra and Photoactivity

The molecular orbital pattern of the starting compounds is largely as expected for linear M-N-N-M complexes based on a ligand field picture. The d and p valence orbitals of Mo and N form σ, π and δ combinations with alternating bonding and antibonding character between adjacent nuclei, i.e., σ-σ-σ, σ-σ*-σ, σ*-σ-σ*, σ*-σ*-σ*, and similarly for the other molecular orbitals (Krewald and González, 2018). The HOMO and HOMO-1 correspond to δ-orbitals dominated by Mo(d) atomic orbital contributions. The LUMO is of π*-π-π* character, i.e., dominated by a π-interaction between μ-N(p) orbitals and π*-interaction between μ-N(p) and Mo(d) orbitals. **Figure 8** shows the π and δ manifold of the Mo_2N_2 core schematically.

To determine any electronic structure differences that may lead to the differences in thermal and photo-reactivity observed for **1** and **2**, their UV-vis spectra are computed and analyzed. While an experimental UV-vis spectrum of $\mathbf{1}_{lin}$ is published, for $\mathbf{2}_{lin}$ no literature reference is available. The UV-vis spectra for $\mathbf{1}_{lin}$ and $\mathbf{2}_{lin}$ were computed with TD-DFT, testing various GGA, meta-GGA, hybrid and range-separated density functionals to achieve a close agreement with the experimental spectrum (see computational details and **Supporting Information**).

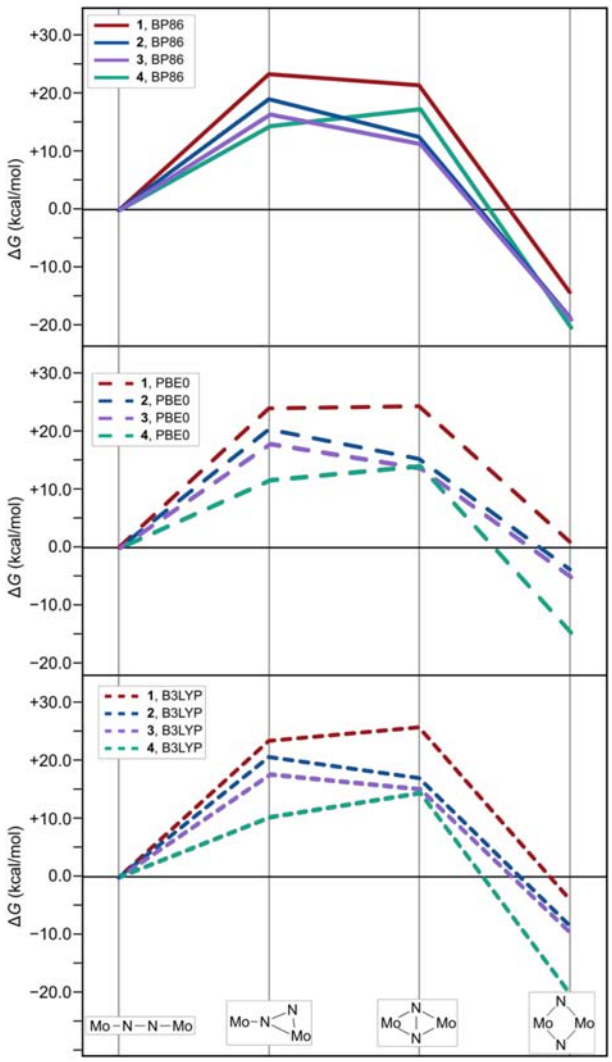

FIGURE 7 | Thermodynamic profiles for **1**, **2**, and {Me-Et} (**3**) and {Ph-H} (**4**) as two systems with further reduced steric bulk. The top, middle and bottom panel show data for electronic structures calculated with the density functionals BP86, PBE0, and B3LYP, respectively.

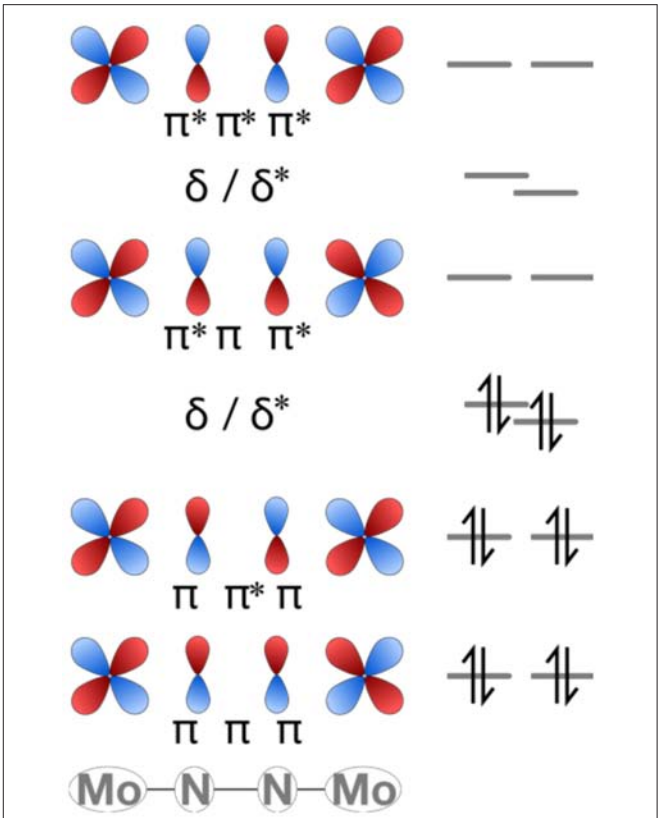

FIGURE 8 | Partial MO diagram of the π and δ manifold for the linear cores of complexes **1** and **2**.

The best visual agreement between the experimental spectrum of $\mathbf{1}_{lin}$ and a calculated counterpart was achieved with the range-separated functional LC-BLYP, although it must be recognized that all spectra obtained with TD-DFT are significantly blue-shifted. To facilitate a visual comparison with the digitized experimental spectrum, a gray line spectrum of the experimental data is also blue-shifted by 7,869 cm^{-1} in **Figure 9A**. It can be seen that the relative energies and intensities of the spectral features at ca. 29,000 cm^{-1} (calc.; exp.: 22,000 cm^{-1}) and 37,500 cm^{-1} (calc.; exp.: 30,000 cm^{-1}) are reproduced well. The signal at 42,500 cm^{-1} (calc.) would then correspond to the shoulder at 35,800 cm^{-1} (exp.) in the experimental spectrum. The second high-intensity signal at ca. 38,800 cm^{-1} in the experimental spectrum cannot be assigned firmly to the calculated spectral features of $\mathbf{1}_{lin}$. The predicted spectrum for $\mathbf{2}_{lin}$ shows overall similar features with a slightly altered intensity distribution.

In the middle and lower panel of **Figure 9A**, the energies and oscillator strengths of the individual transitions predicted for $\mathbf{1}_{lin}$ and $\mathbf{2}_{lin}$ are depicted. At first glance, the line spectra are almost identical. A subtle difference worth noting is a cluster of excitations just below 40,000 cm^{-1} in the calculated spectrum of $\mathbf{1}_{lin}$, in contrast to a solitary transition at slightly lower energy in the calculated spectrum of $\mathbf{2}_{lin}$. In both complexes, the low-energy feature at ca. 29,000 cm^{-1} is due to a metal-to-ligand charge transfer excitation from Mo to the amidinate ligand, as assigned based on the difference density (**Figure 9B**). The first high-intensity feature at ca. 37,500 cm^{-1} in $\mathbf{1}_{lin}$ can be assigned to an LMCT transition from the dinitrogen bridge to the metal ions (14). In contrast, both intense transitions (15, 16) at the same energy in the spectrum of $\mathbf{2}_{lin}$ are due to core-to-amidinate excitations. The second intense signal at 42,500 cm^{-1} is dominated by excitations from a π-π*-π orbital to molybdenum d and amidinate ligand orbitals. A similar character can be assigned to the corresponding feature in the spectrum of $\mathbf{2}_{lin}$.

A possibly very relevant difference between the two complexes is found when assessing the character of the six transitions below 40,000 cm^{-1} in the spectrum of $\mathbf{1}_{lin}$, i.e., transitions 17–22. The first five excitations have difference densities that are distinctly asymmetric. All of them are LMCT transitions, with excitations originating from both amidinate and Cp* ligands.

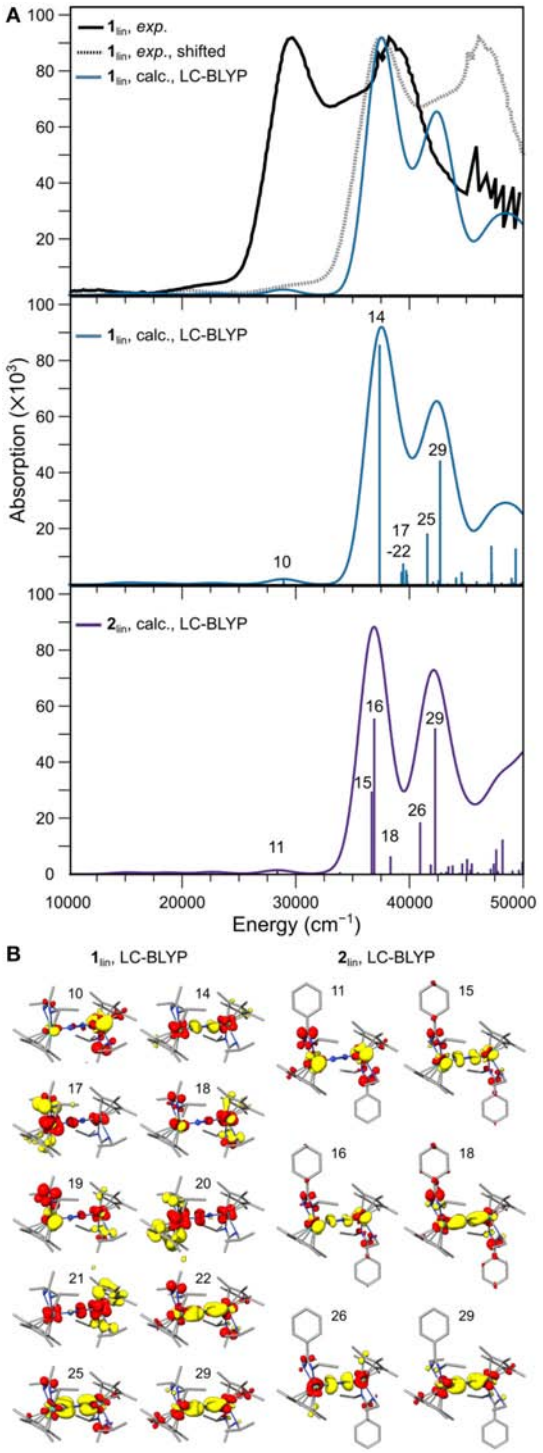

FIGURE 9 | (A) Experimental UV-vis spectrum of $\mathbf{1}_{lin}$ (black: digitized, gray: digitized and blue-shifted) and the broadened line spectrum predicted with TDDFT using the LC-BLYP density functional (top), calculated oscillator strengths and intensities of the individual transitions and broadened line spectrum for $\mathbf{1}_{lin}$ (middle) and $\mathbf{2}_{lin}$ (bottom). **(B)** Difference densities for the individual transitions labeled in **(A)**; yellow and red isosurfaces correspond to density loss and gain, respectively.

The sixth transition is a core-to-amidinate excitation, similar to the transitions assigned to the higher-energy feature. It is important to stress that the character of the features is not dependent on the density functional chosen for the analysis, but that similar characteristics can be assigned based on other density functionals. As can be seen from a comparison of the difference densities of states 22 ($\mathbf{1}_{lin}$) and 18 ($\mathbf{2}_{lin}$), the character of that solitary excitation in the sub-40,000 cm^{-1} energy region in the spectrum of complex $\mathbf{2}_{lin}$ is almost identical. This difference in the spectra of $\mathbf{1}_{lin}$ and $\mathbf{2}_{lin}$, i.e., the fact that there are asymmetric excitations in one complex that are entirely absent in the other, may be the reason that only $\mathbf{1}_{lin}$ is photoactive (Duman et al., 2016). Sita et al. had put forward the idea that during the photo-driven isomerization and/or dissociation of $\mathbf{1}_{lin}$, a ligand may have to temporarily detach (Duman et al., 2016). The asymmetric character of the excitations assigned above align with this hypothesis.

DISCUSSION AND CONCLUSIONS

The Sita complexes are the most complete series of isostructural dinitrogen-bridged compounds that span groups 4–6 across all transition metal rows: Ti, V; Zr, Nb, Mo; Hf, Ta, W (Hirotsu et al., 2007a,b; Fontaine et al., 2010; Yonke et al., 2011a; Keane et al., 2013, 2014, 2015; Duman et al., 2016; Duman and Sita, 2017). The only missing complex is the Cr dimer, which has been attributed to its much smaller covalent radius than the other early transition metals. Besides a Cp* ligand, one guanidinate or amidinate ligand in one of their five variations, with ^{i}Pr or Et at the N-donor atoms and NMe_2, Me, H or Ph at the central carbon, is bound at each metal. This series is of great value for a systematic insight into the fundamental concepts of nitrogen activation due to the variety of metals that is stabilized by ligands of the same family. Comparison of the similarities and differences in this series allows for systematic comparisons of electronic and structural effects in dinitrogen activation. With two members of the series, Sita et al. have shown that by reducing the steric bulk of the substituents in the photochemically active {(η^5-C_5Me_5)[N(^{i}Pr)C(Me)N-(^{i}Pr)]Mo}$_2$(μ-N_2) (**1**) complex to {(η^5-C_5Me_5)[N(Et)C(Ph)N-(Et)]Mo}$_2$(μ-N_2) (**2**), a thermal pathway to dinitrogen splitting becomes accessible (Keane et al., 2015; Duman et al., 2016). In this paper, computational predictions for likely isomerization intermediates were presented and the thermodynamics of the isomerization reaction were analyzed.

It was confirmed that steric bulk has a significant influence on the thermodynamic profile of the isomerization reactions. The ΔG values for the formation of the intermediates during the isomerization of complex **1** with bulkier ligands were found to be several kcal/mol above those for complex **2** with a sterically less demanding ligand sphere. Furthermore, dispersion interactions along the reaction path appear to be highly relevant factor in the overall driving force of the reaction. In geometry optimizations that omitted dispersion effects, the isomerization of **2** was seen to be energetically disfavored, while no stable

intermediates and products were found for the isomerization of **1** without consideration of dispersion effects. In other words, the rearrangement of bonds from approximate double bonds in the linear cores of the starting complexes (Mo-N ca. 1.4, N-N ca. 1.6) and strong single bonds in the diamond-shaped cores of the products (Mo-N ca. 1.2, Mo-Mo ca. 0.7) appears to be almost isoenergetic or perhaps even disfavored. The reactions become overall favorable through the greater dispersion stabilization of the product compared to the starting compound. Since the differences in dispersion correction are approximately equivalent between $\mathbf{1}_{lin}/\mathbf{1}_{dia}$ and $\mathbf{2}_{lin}/\mathbf{2}_{dia}$, the remaining difference in reactivity must be attributed to repulsive effects. Based on experimental observations, it is clear that in at least one intermediate along the isomerization pathway of **1**, dispersion effects are not sufficient to overcome steric hindrances. This will be addressed in forthcoming work.

To further explore the concept of reducing the steric requirements of the ligand sphere, *in silico* modifications with {Me-Et} and {Ph-H} were considered. Indeed, the thermodynamics of the reaction path become even more favorable than for the thermally active system {Ph-Et}. For {Ph-H}, the overall energy landscape of the reaction was even altered. However, this also means that changing the ligand substitution pattern can drastically alter the picture that is generated computationally. Especially for reactions with subtle changes in relative energy caution is in order when truncating the ligand system to lower the computational cost. It appears advisable to test the results for artifacts. The change in relative ΔG values for the intermediates 1 and 2 obtained with different ligand substitutions shows that this approach can be highly effective in engineering an ideal energy landscape for dinitrogen activation. Besides steric tunic, a future target of computational and experimental studies on this isostructural series will likely be electronic tuning through electron-donating or electron-withdrawing substituents.

To better understand the photoactivity of complex **1**, the UV-vis spectra of $\mathbf{1}_{lin}$ and $\mathbf{2}_{lin}$ were computed. Even though the line spectra appear very similar at first glance, the first intense feature is assigned to transitions with different excitation character. In the photoactive complex **1**, there is a single excitation with high oscillator strength due to a LMCT from the bridging N_2 to the molybdenum ions, i.e., shifting electron density away from the N_2 unit and hence likely weakening the dinitrogen bond further. In the photochemically inactive complex **2**, there are two transitions of similar MLCT character shifting electron density from the entire Mo_2N_2 core to the amidinate ligand. While little is known about the photoactive states in dinitrogen photoactivation complexes, a recent study on a rhenium dimer with a PNP pincer ligand (Schendzielorz et al., 2019) identified states in the photoactive region of μ-N_2-to-metal character, i.e., similar to the high-intensity excitation in complex **1**. A similar excitation character was also found for a N_2-bridged photoactive molybdenum pincer complex by Nishibayashi et al. (Miyazaki et al., 2014). If it were confirmed experimentally that irradiation of *only* the first signal results in photoactivation of complex **1**, a general pattern regarding the requirements for successful N_2 photoactivation could emerge that is independent of the ligand platform and metal chosen.

However, the spectrum of complex $\mathbf{1}_{lin}$ also contains a cluster of medium-high intensity transitions that are *not* predicted for the photo-inactive complex $\mathbf{2}_{lin}$. These are due to asymmetric excitations that originate from the ligand sphere of only one molybdenum ion and shift density into the Mo-N-N-Mo π system. The character of these excitations is in line with Sita's hypothesis of a temporary, photo-induced ligand detachment being required for isomerization of the molybdenum dimer and splitting of the N-N bond (Duman et al., 2016).

A better understanding of dinitrogen photoactivation in general will require more spectroscopic studies on the character of the photoactive states and the excited state decay. Additionally, an exhaustive comparison of the photo-activation and thermal activation pathways for the isostructural complexes in Sita's series requires the character(s) of the specific photoactive state(s) to be known so that its features can be related to the transition state structure of the thermal path. However, already at this point, it is interesting to see that despite the geometric similarities of the two complexes, the ligand sphere appears to have a distinct influence on their electronic structures that is mapped in the computed excitation spectra. Further computational and experimental studies, especially in terms of time-resolved spectroscopy, are required to fully elucidate these subtle differences.

DATA AVAILABILITY

The raw data supporting the conclusions of this manuscript will be made available by the author, without undue reservation, to any qualified researcher.

AUTHOR CONTRIBUTIONS

VK designed the research, carried out the required calculations and analyses, and wrote the paper.

ACKNOWLEDGMENTS

A 50th Anniversary Prize Fellowship from the University of Bath (01/2017-11/2018), and the Balena High Performance Computing (HPC) Service at the University of Bath are gratefully acknowledged. Mr. George Nichols is acknowledged for the computation of preliminary UV-vis spectra.

SUPPLEMENTARY MATERIAL

The Supplementary Material for this article can be found online at: https://www.frontiersin.org/articles/10.3389/fchem.2019.00352/full#supplementary-material

REFERENCES

Adamo, C., and Barone, V. (1999). Toward reliable density functional methods without adjustable parameters: the PBE0 model. *J. Chem. Phys.* 110, 6158–6170. doi: 10.1063/1.478522

Andrae, D., Haussermann, U., Dolg, M., Stoll, H., and Preuss, H. (1990). Energy-adjusted Ab initio pseudopotentials for the 2nd and 3rd row transition-elements. *Theor. Chim. Acta* 77, 123–141.

Becke, A. D. (1988). Density-functional exchange-energy approximation with correct asymptotic-behavior. *Phys. Rev. A* 38, 3098–3100.

Becke, A. D. (1993). Density-functional thermochemistry.3. The role of exact exchange. *J. Chem. Phys.* 98, 5648–5652. doi: 10.1063/1.464913

Broda, H., Hinrichsen, S., and Tuczek, F. (2013). Molybdenum(0) dinitrogen complexes with polydentate phosphine ligands for synthetic nitrogen fixation: geometric and electronic structure contributions to reactivity. *Coord. Chem. Rev.* 257, 587–598. doi: 10.1016/j.ccr.2012.05.010

Burford, R. J., and Fryzuk, M. D. (2017). Examining the relationship between coordination mode and reactivity of dinitrogen. *Nat. Rev. Chem.* 1:0026. doi: 10.1038/s41570-017-0026

Burford, R. J., Yeo, A., and Fryzuk, M. D. (2017). Dinitrogen activation by group 4 and group 5 metal complexes supported by phosphine-amido containing ligand manifolds. *Coord. Chem. Rev.* 334, 84–99. doi: 10.1016/j.ccr.2016.06.015

Chai, J.-D., and Head-Gordon, M. (2008). Systematic optimization of long-range corrected hybrid density functionals. *J. Chem. Phys.* 128:084106. doi: 10.1063/1.2834918

Chen, J. G., Crooks, R. M., Seefeldt, L. C., Bren, K. L., Morris Bullock, R., Darensbourg, M. Y., et al. (2018). Beyond fossil fuel–driven nitrogen transformations. *Science* 360:aar6611. doi: 10.1126/science.aar6611

Christian, G., Stranger, R., Yates, B. F., and Cummins, C. C. (2007). Rationalizing the different products in the reaction of N_2 with three-coordinate MoL_3 complexes. *Dalton Trans.* 2007, 1939–1947. doi: 10.1039/B701050H

Connor, G. P., and Holland, P. L. (2017). Coordination chemistry insights into the role of alkali metal promoters in dinitrogen reduction. *Catal. Today* 286, 21–40. doi: 10.1016/j.cattod.2016.08.014

Creutz, S. E., and Peters, J. C. (2017). Exploring secondary-sphere interactions in Fe-N_xH_y complexes relevant to N_2 fixation. *Chem. Sci.* 8, 2321–2328. doi: 10.1039/C6SC04805F

Crossland, J. L., and Tyler, D. R. (2010). Iron–dinitrogen coordination chemistry: dinitrogen activation and reactivity. *Coord. Chem. Rev.* 254, 1883–1894. doi: 10.1016/j.ccr.2010.01.005

Curley, J. J., Cook, T. R., Reece, S. Y., Müller, P., and Cummins, C. C. (2008). Shining light on dinitrogen cleavage: structural features, redox chemistry, and photochemistry of the key intermediate bridging dinitrogen complex. *J. Am. Chem. Soc.* 130, 9394–9405. doi: 10.1021/ja8002638

Dance, I. (2010). Mimicking nitrogenase. *Dalton Trans.* 39, 2972–2983. doi: 10.1039/b922606k

Djurdjevic, I., Einsle, O., and Decamps, L. (2017). Nitrogenase cofactor: inspiration for model chemistry. *Chem. Asian J.* 12, 1447–1455. doi: 10.1002/asia.201700478

Duman, L. M., Farrell, W. S., Zavalij, P. Y., and Sita, L. R. (2016). Steric switching from photochemical to thermal reaction pathways for enhanced efficiency in metal-mediated nitrogen fixation. *J. Am. Chem. Soc.* 138, 14856–14859. doi: 10.1021/jacs.6b09789

Duman, L. M., and Sita, L. R. (2017). Closing the loop on transition-metal-mediated nitrogen fixation: chemoselective production of $HN(SiMe_3)_2$ from N_2, Me_3SiCl, and X-OH (X = R, R_3Si, or silica gel). *J. Am. Chem. Soc.* 139, 17241–17244. doi: 10.1021/jacs.7b08859

Eizawa, A., Arashiba, K., Tanaka, H., Kuriyama, S., Matsuo, Y., Nakajima, K., et al. (2017). Remarkable catalytic activity of dinitrogen-bridged dimolybdenum complexes bearing NHC-based PCP-pincer ligands toward nitrogen fixation. *Nat. Commun.* 8:14874. doi: 10.1038/ncomms14874

Eizawa, A., and Nishibayashi, Y. (2017). "Catalytic nitrogen fixation using molybdenum-dinitrogen complexes as catalysts," in *Nitrogen Fixation. Topics in Organometallic Chemistry*, Vol. 60, ed Y. Nishibayashi (Cham: Springer).

Farrell, W. S., Yonke, B. L., Reeds, J. P., Zavalij, P. Y., and Sita, L. R. (2016). Small-molecule activation within the group 6 Complexes (η^5-C_5Me_5)[$N(^iPr)C(Me)N(^iPr)$]M(CO)(L) for M = Mo, W and L = N_2, NCMe, η^2-alkene, SMe_2, C_3H_6O. *Organometallics* 35, 1132–1140. doi: 10.1021/acs.organomet.6b00131

Fontaine, P. P., Yonke, B. L., Zavalij, P. Y., and Sita, L. R. (2010). Dinitrogen complexation and extent of N=N activation within the group 6 "end-on-bridged" dinuclear complexes, {(η^5-C_5Me_5)M[N(i-Pr)C(Me)N(i-Pr)]}$_2$(μ-η^1:η^1-N_2) (M = Mo and W). *J. Am. Chem. Soc.* 132, 12273–12285. doi: 10.1021/ja100469f

Grimme, S. (2004). Accurate description of van der Waals complexes by density functional theory including empirical corrections. *J. Comput. Chem.* 25, 1463–1473. doi: 10.1002/jcc.20078

Grimme, S. (2011). Density functional theory with London dispersion corrections. *Wiley Interdiscipl. Rev. Comput. Mol. Sci.* 1, 211–228. doi: 10.1002/wcms.30

Grimme, S., Antony, J., Ehrlich, S., and Krieg, H. (2010). A consistent and accurate ab initio parametrization of density functional dispersion correction (DFT-D) for the 94 elements H-Pu. *J. Chem. Phys.* 132, 154104–154119. doi: 10.1063/1.3382344

Grimme, S., Ehrlich, S., and Goerigk, L. (2011a). Effect of the damping function in dispersion corrected density functional theory. *J. Comput. Chem.* 32, 1456–1465. doi: 10.1002/jcc.21759

Grimme, S., Huenerbein, R., and Ehrlich, S. (2011b). On the importance of the dispersion energy for the thermodynamic stability of molecules. *ChemPhysChem* 12, 1258–1261. doi: 10.1002/cphc.201100127

Grinberg, D. A., Elishav, O., Bardow, A., Shter, G. E., and Grader, G. S. (2016). Nitrogen-based fuels: a power-to-fuel-to-power analysis. *Angewan. Chem. Int. Ed.* 55, 8798–8805. doi: 10.1002/anie.201510618

Himmel, H. J., and Reiher, M. (2006). Intrinsic dinitrogen activation at bare metal atoms. *Angewan. Chem. Int. Ed.* 45, 6264–6288. doi: 10.1002/anie.200502892

Hirata, S., and Head-Gordon, M. (1999). Time-dependent density functional theory within the Tamm–Dancoff approximation. *Chem. Phys. Lett.* 314, 291–299. doi: 10.1016/s0009-2614(99)01149-5

Hirotsu, M., Fontaine, P. P., Epshteyn, A., Zavalij, P. Y., and Sita, L. R. (2007a). Dinitrogen activation at ambient temperatures: new modes of H_2 and $PhSiH_3$ additions for an "End-On-Bridged" [Ta(IV)]$_2$(μ-η^1:η^1-N_2) complex and for the bis(μ-nitrido) [Ta(V)(μ-N)]$_2$ product derived from facile N-N bond cleavage. *J. Am. Chem. Soc.* 129, 9284–9285. doi: 10.1021/ja072248v

Hirotsu, M., Fontaine, P. P., Zavalij, P. Y., and Sita, L. R. (2007b). Extreme N-N bond elongation and facile N-atom functionalization reactions within two structurally versatile new families of group 4 bimetallic "side-on-bridged" dinitrogen complexes for zirconium and hafnium. *J. Am. Chem. Soc.* 129, 12690–12692. doi: 10.1021/ja0752989

Holland, P. L. (2010). Metal-dioxygen and metal-dinitrogen complexes: where are the electrons? *Dalton Trans.* 39, 5415–5425. doi: 10.1039/C001397H

Huss, A. S., Curley, J. J., Cummins, C. C., and Blank, D. A. (2013). Relaxation and dissociation following photoexcitation of the (μ-N_2)[Mo(N[t-Bu]Ar)$_3$]$_2$ dinitrogen cleavage intermediate. *J. Phys. Chem. B* 117, 1429–1436. doi: 10.1021/jp310122x

Iikura, H., Tsuneda, T., Yanai, T., and Hirao, K. (2001). A long-range correction scheme for generalized-gradient-approximation exchange functionals. *J. Chem. Phys.* 115, 3540. doi: 10.1063/1.1383587

Johnson, M. J. A., Lee, P. M., Odom, A. L., Davis, W. M., and Cummins, C. C. (1997). Atom-bridged intermediates in N- and P-Atom transfer reactions. *Angewan. Chem. Int. Ed.* 36, 87–91. doi: 10.1002/anie.199700871

Keane, A. J., Farrell, W. S., Yonke, B. L., Zavalij, P. Y., and Sita, L. R. (2015). Metal-mediated production of isocyanates, $R_3EN{=}C{=}O$ from dinitrogen, carbon dioxide, and R_3ECl. *Angewan. Chem. Int. Ed.* 54, 10220–10224. doi: 10.1002/anie.201502293

Keane, A. J., Yonke, B. L., Hirotsu, M., Zavalij, P. Y., and Sita, L. R. (2014). Fine-tuning the energy barrier for metal-mediated dinitrogen N-N bond cleavage. *J. Am. Chem. Soc.* 136, 9906–9909. doi: 10.1021/ja505309j

Keane, A. J., Zavalij, P. Y., and Sita, L. R. (2013). N-N bond cleavage of mid-valent Ta(IV) hydrazido and hydrazidium complexes relevant to the Schrock cycle for dinitrogen fixation. *J. Am. Chem. Soc.* 135, 9580–9583. doi: 10.1021/ja402804k

Klopsch, I., Yuzik-Klimova, E. Y., and Schneider, S. (2017). "Functionalization of N2 by mid to late transition metals via N-N bond cleavage," in *Nitrogen Fixation. Topics in Organometallic Chemistry*, Vol. 60, ed Y. Nishibayashi (Cham: Springer).

Krewald, V. (2018). Dinitrogen photoactivation: status quo and future perspectives. *Dalton Trans.* 47, 10320–10329. doi: 10.1039/c8dt00418h

Krewald, V., and González, L. (2018). A Valence-Delocalised Osmium dimer capable of dinitrogen photocleavage: Ab initio insights into its electronic structure. *Chem. Eur. J.* 24, 5112–5123. doi: 10.1002/chem.201704651

Kunkely, H., and Vogler, A. (2010). Photolysis of aqueous [(NH3)5Os(mu-N2)Os(NH3)5]5+: cleavage of dinitrogen by an intramolecular photoredox reaction. *Angewan. Chem. Int. Ed.* 49, 1591–1593. doi: 10.1002/anie.200905026

Kuriyama, S., and Nishibayashi, Y. (2017). "Catalytic transformations of molecular dinitrogen by iron and cobalt-dinitrogen complexes as catalysts," in *Nitrogen Fixation. Topics in Organometallic Chemistry*, Vol. 60, ed Y. Nishibayashi (Cham: Springer).

Lancaster, K. M., Roemelt, M., Ettenhuber, P., Hu, Y., Ribbe, M. W., Neese, F., et al. (2011). X-ray emission spectroscopy evidences a central carbon in the nitrogenase iron-molybdenum cofactor. *Science* 334, 974–977. doi: 10.1126/science.1206445

Laplaza, C. E., and Cummins, C. C. (1995). Dinitrogen cleavage by a three-coordinate molybdenum(III) complex. *Science* 268, 861–863. doi: 10.1126/science.268.5212.861

Lee, C., Yang, W., and Parr, R. G. (1988). Development of the Colle-Salvetti correlation-energy formula into a functional of the electron-density. *Phys. Rev. B* 37, 785–789. doi: 10.1103/PhysRevB.37.785

Lee, C. C., Ribbe, M. W., and Hu, Y. (2014). Cleaving the N-N triple bond: the transformation of dinitrogen to ammonia by nitrogenases. *Met. Ions Life Sci.* 14, 147–176. doi: 10.1007/978-94-017-9269-1_7

Liptrot, D. J., Guo, J. D., Nagase, S., and Power, P. P. (2016). Dispersion forces, disproportionation, and stable high-valent late transition metal alkyls. *Angewan. Chem. Int. Ed.* 55, 14766–14769. doi: 10.1002/anie.201607360

Liptrot, D. J., and Power, P. P. (2017). London dispersion forces in sterically crowded inorganic and organometallic molecules. *Nat. Rev. Chem.* 1:0004. doi: 10.1038/s41570-016-0004

MacLeod, K. C., and Holland, P. L. (2013). Recent developments in the homogeneous reduction of dinitrogen by molybdenum and iron. *Nat. Chem.* 5, 559–565. doi: 10.1038/nchem.1620

MacLeod, K. C., Menges, F. S., McWilliams, S. F., Craig, S. M., Mercado, B. Q., Johnson, M. A., et al. (2016). Alkali-controlled C–H cleavage or N–C bond formation by N_2-derived iron nitrides and imides. *J. Am. Chem. Soc.* 138, 11185–11191. doi: 10.1021/jacs.6b04984

Miyazaki, T., Tanaka, H., Tanabe, Y., Yuki, M., Nakajima, K., Yoshizawa, K., et al. (2014). Cleavage and formation of molecular dinitrogen in a single system assisted by molybdenum complexes bearing ferrocenyldiphosphine. *Angewan. Chem. Int. Ed.* 53, 11488–11492. doi: 10.1002/anie.201405673

Neary, M. C., and Parkin, G. (2017). reactivity of cyclopentadienyl molybdenum compounds towards formic acid: structural characterization of $CpMo(PMe_3)(CO)_2H$, $CpMo(PMe_3)_2(CO)H$, $[CpMo(\mu\text{-}O)(mu\text{-}O_2CH)]_2$, and $[Cp^*Mo(\mu\text{-}O)(\mu\text{-}O_2CH)]_2$. *Inorg. Chem.* 56, 1511–1523. doi: 10.1021/acs.inorgchem.6b02606

Neese, F. (2012). The ORCA program system. *Wiley Interdisciplinary Reviews: Computational Molecular Science* 2, 73–78. doi: 10.1002/wcms.81

Neese, F., Hansen, A., and Liakos, D. G. (2009a). Efficient and accurate approximations to the local coupled cluster singles doubles method using a truncated pair natural orbital basis. *J. Chem. Phys.* 131:064103. doi: 10.1063/1.3173827

Neese, F., and Olbrich, G. (2002). Efficient use of the resolution of the identity approximation in time-dependent density functional calculations with hybrid density functionals. *Chem. Phys. Lett.* 362, 170–178. doi: 10.1016/s0009-2614(02)01053-9

Neese, F., Wennmohs, F., Hansen, A., and Becker, U. (2009b). Efficient, approximate and parallel Hartree–Fock and hybrid DFT calculations. A "chain-of-spheres" algorithm for the Hartree–Fock exchange. *Chem. Phys.* 356, 98–109. doi: 10.1016/j.chemphys.2008.10.036

Paulechka, E., and Kazakov, A. (2017). Efficient DLPNO–CCSD(T)-based estimation of formation enthalpies for C-, H-, O-, and N-containing closed-shell compounds validated against critically evaluated experimental data. *J. Phys. Chem. A* 121, 4379–4387. doi: 10.1021/acs.jpca.7b03195

Pauling, L., and Kamb, B. (1986). A revised set of values of single-bond radii derived from the observed interatomic distances in metals by correction for bond number and resonance energy. *Proc. Natl. Acad. Sci.* 83, 3569–3571.

Perdew, J. P. (1986). Density-functional approximation for the correlation-energy of the inhomogeneous electron-gas. *Phys. Rev. B* 33, 8822–8824. doi: 10.1103/PhysRevB.33.8822

Reiher, M., Kirchner, B., Hutter, J., Sellmann, D., and Hess, B. A. (2004). A photochemical activation scheme of inert dinitrogen by dinuclear Ru^{II} and Fe^{II} complexes. *Chem. Eur. J.* 10, 4443–4453. doi: 10.1002/chem.200400081

Roux, Y., Duboc, C., and Gennari, M. (2017). Molecular catalysts for N_2 reduction: state of the art, mechanism, and challenges. *ChemPhysChem* 18, 2606–2617. doi: 10.1002/cphc.201700665

Saitow, M., Becker, U., Riplinger, C., Valeev, E. F., and Neese, F. (2017). A new near-linear scaling, efficient and accurate, open-shell domain-based local pair natural orbital coupled cluster singles and doubles theory. *J. Chem. Phys.* 146:164105. doi: 10.1063/1.4981521

Schendzielorz, F., Finger, M., Abbenseth, J., Wurtele, C., Krewald, V., and Schneider, S. (2019). Metal-ligand cooperative synthesis of benzonitrile by electrochemical reduction and photolytic splitting of dinitrogen. *Angewan. Chem. Int. Ed.* 58, 830–834. doi: 10.1002/anie.201812125

Schlögl, R. (2008). "Ammonia synthesis," in *Handbook of Heterogeneous Catalysis*, eds G. Ertl, H. Knözinger, F. Schüth, and J. Weitkamp, 2501–2575. doi: 10.1002/9783527610044.hetcat0129

Schlögl, R. (2010). The role of chemistry in the energy challenge. *ChemSusChem* 3, 209–222. doi: 10.1002/cssc.200900183

Shin, J. H., and Parkin, G. (1998). Phosphorus–carbon bond activation of PMe_3 at a dimolybdenum center: synthesis and structure of $[Cp^*Mo(\mu\text{-}O_2CMe)]_2(\mu\text{-}PMe_2)(\mu\text{-}Me)$. *Chem. Commun.* 1998, 1273–1274. doi: 10.1039/a801835i

Sickerman, N. S., Tanifuji, K., Hu, Y., and Ribbe, M. W. (2017). Synthetic analogues of nitrogenase metallocofactors: challenges and developments. *Chem. Eur. J.* 23, 12425–12432. doi: 10.1002/chem.201702496

Sippel, D., and Einsle, O. (2017). The structure of vanadium nitrogenase reveals an unusual bridging ligand. *Nat. Chem. Biol.* 13, 956–960. doi: 10.1038/nchembio.2428

Solari, E., Da Silva, C., Iacono, B., Hesschenbrouck, J., Rizzoli, C., Scopelliti, R., et al. (2001), Photochemical activation of the N?N bond in a dimolybdenum-dinitrogen complex: formation of a molybdenum nitride. *Angew. Chem. Int. Ed.* 40, 3907–3909. doi: 10.1002/1521-3773(20011015)40:20<3907::AID-ANIE3907>3.0.CO;2-%23

Spatzal, T., Aksoyoglu, M., Zhang, L., Andrade, S. L., Schleicher, E., Weber, S., et al. (2011). Evidence for interstitial carbon in nitrogenase FeMo cofactor. *Science* 334:940. doi: 10.1126/science.1214025

Staroverov, V. N., Scuseria, G. E., Tao, J., and Perdew, J. P. (2003). Comparative assessment of a new nonempirical density functional: molecules and hydrogen-bonded complexes. *J. Chem. Phys.* 119, 12129–12137. doi: 10.1063/1.1626543

Studt, F., and Tuczek, F. (2006). Theoretical, spectroscopic, and mechanistic studies on transition-metal dinitrogen complexes: implications to reactivity and relevance to the nitrogenase problem. *J. Comput. Chem.* 27, 1278–1291. doi: 10.1002/jcc.20413

Tanabe, Y., and Nishibayashi, Y. (2013). Developing more sustainable processes for ammonia synthesis. *Coord. Chem. Rev.* 257, 2551–2564. doi: 10.1016/j.ccr.2013.02.010

Tao, J., Perdew, J. P., Staroverov, V. N., and Scuseria, G. E. (2003). Climbing the density functional ladder: nonempirical meta-generalized gradient approximation designed for molecules and solids. *Phys. Rev. Lett.* 91:146401. doi: 10.1103/PhysRevLett.91.146401

Weigend, F. (2006). Accurate coulomb-fitting basis sets for H to Rn. *Phys. Chem. Chem. Phys.* 8, 1057–1065. doi: 10.1039/B515623H

Weigend, F. (2008). Hartree-Fock exchange fitting basis sets for H to Rn. *J. Comput. Chem.* 29, 167–175. doi: 10.1002/jcc.20702

Weigend, F., and Ahlrichs, R. (2005). Balanced basis sets of split valence, triple zeta valence and quadruple zeta valence quality for H to Rn: design and assessment of accuracy. *Phys. Chem. Chem. Phys.* 7, 3297–3305. doi: 10.1039/b508541a

Weymuth, T., and Reiher, M. (2014). Gradient-driven molecule construction: an inverse approach applied to the design of small-molecule fixating catalysts. *Int. J. Quantum Chem.* 114, 838–850. doi: 10.1002/qua.24686

Yanai, T., Tew, D. P., and Handy, N. C. (2004). A new hybrid exchange–correlation functional using the Coulomb-attenuating method (CAM-B3LYP). *Chem. Phys. Lett.* 393, 51–57. doi: 10.1016/j.cplett.2004.06.011

Yonke, B. L., Keane, A. J., Zavalij, P. Y., and Sita, L. R. (2011a). Mononuclear tantalum(IV, d^1) imido complexes supported by the monocyclopentadienyl, amidinate and guanidinate ligand sets as models to explore dinitrogen fixation by "end-on-bridged" dinuclear $\{[Ta(IV, d^1)]\}_2(\mu\text{-}\eta^1\text{:}\eta^1\text{-}N_2)$ complexes. *Organometallics* 31, 345–355. doi: 10.1021/om200961r

Yonke, B. L., Reeds, J. P., Zavalij, P. Y., and Sita, L. R. (2011b). Catalytic degenerate and nondegenerate oxygen atom transfers employing N_2O and CO_2 and a M(II)/M(IV) cycle mediated by Group 6 M(IV) terminal oxo complexes. *Angewan. Chem. Int. Ed.* 50, 12342–12346. doi: 10.1002/anie.201106074

Zhang, W., Tang, Y., Lei, M., Morokuma, K., and Musaev, D. G. (2011). Ditantalum dinitrogen complex: reaction of H_2 molecule with "end-on-bridged" $[Ta(IV)]_2(\mu\text{-}\eta^1\text{:}\eta^1\text{-}N_2)$ and Bis(μ-nitrido) $[Ta(V)]_2(\mu\text{-}N)_2$ complexes. *Inorg. Chem.* 50, 9481–9490. doi: 10.1021/ic201159z

Zhao, Y., and Truhlar, D. G. (2008). The M06 suite of density functionals for main group thermochemistry, thermochemical kinetics, non covalent interactions, excited states, and transition elements: two new functionals and systematic testing of four M06-class functionals and 12 other functionals. *Theor. Chem. Acc.* 120, 215–241. doi: 10.1007/s00214-007-0310-x

Conflict of Interest Statement: The author declares that the research was conducted in the absence of any commercial or financial relationships that could be construed as a potential conflict of interest.

Copyright © 2019 Krewald. This is an open-access article distributed under the terms of the Creative Commons Attribution License (CC BY). The use, distribution or reproduction in other forums is permitted, provided the original author(s) and the copyright owner(s) are credited and that the original publication in this journal is cited, in accordance with accepted academic practice. No use, distribution or reproduction is permitted which does not comply with these terms.

frontiers in Chemistry

ORIGINAL RESEARCH
published: 04 January 2019
doi: 10.3389/fchem.2018.00640

γ-Secretase Studied by Atomistic Molecular Dynamics Simulations: Global Dynamics, Enzyme Activation, Water Distribution and Lipid Binding

Manuel Hitzenberger and Martin Zacharias*

Physics Department T38, Technical University of Munich, Garching, Germany

γ-secretase, an intramembrane-cleaving aspartyl protease is involved in the cleavage of a large number of intramembrane proteins. The most prominent substrate is the amyloid precursor protein, whose proteolytic processing leads to the production of different amyloid Aβ peptides. These peptides are known to form toxic aggregates and may play a key role in Alzheimer's disease (AD). Recently, the three-dimensional structure of γ-secretase has been determined via Cryo-EM, elucidating the spatial geometry of this enzyme complex in different functional states. We have used molecular dynamics (MD) simulations to study the global dynamics and conformational transitions of γ-secretase, as well as the water and lipid distributions in and around the transmembrane domains in atomic detail. Simulations were performed on the full enzyme complex and on the membrane embedded parts alone. The simulations revealed global motions compatible with the experimental enzyme structures and indicated little dependence of the dynamics of the transmembrane domains on the soluble extracellular subunits. During the simulation on the membrane spanning part a transition between an inactive conformation (with catalytic residues far apart) toward a putatively active form (with catalytic residues in close proximity) has been observed. This conformational change is associated with a distinct rearrangement of transmembrane helices, a global compaction of the catalytically active presenilin subunit a change in the water structure near the active site and a rigidification of the protein fold. The observed conformational rearrangement allows the interpretation of the effect of several mutations on the activity of γ-secretase. A number of long-lived lipid binding sites could be identified on the membrane spanning surface of γ-secretase which may coincide with association regions of hydrophobic membrane helices to form putative substrate binding exosites.

Keywords: γ-secretase, familial Alzheimer's disease (fAD), Molecular dynamics (MD), presenilin, nicastrin, amyloid, intramembrane aspartyl proteases, intramembrane proteolysis

OPEN ACCESS

Edited by:
Sam P. De Visser,
University of Manchester,
United Kingdom

Reviewed by:
Arnab Mukherjee,
Indian Institute of Science Education and Research, India
Dingguo Xu,
Sichuan University, China

****Correspondence:***
Manuel Hitzenberger
manuel.hitzenberger@tum.de

Specialty section:
This article was submitted to Theoretical and Computational Chemistry, a section of the journal Frontiers in Chemistry

Received: *28 September 2018*
Accepted: *07 December 2018*
Published: *04 January 2019*

Citation:
Hitzenberger M and Zacharias M (2019) γ-Secretase Studied by Atomistic Molecular Dynamics Simulations: Global Dynamics, Enzyme Activation, Water Distribution and Lipid Binding. Front. Chem. 6:640. doi: 10.3389/fchem.2018.00640

INTRODUCTION

The protein complex γ-secretase (g-sec) is the only known intramembrane protease requiring an elaborate interplay between four different proteins: nicastrin (NIC), presenilin (PS), anterior pharynx-defective-1 (APH-1) and presenilin enhancer-2 (PEN-2) (Bai et al., 2015a,b; Langosch et al., 2015; Langosch and Steiner, 2017), rendering it the structurally most complex member of this

functional family and due to its proposed role in Alzheimer's disease (AD) also the most studied one (De Strooper et al., 2012; Fukumori and Steiner, 2016). It has been established that g-sec is able to process a large number of substrates (Beel and Sanders, 2008; Haapasalo and Kovacs, 2011; Langosch et al., 2015) (as of today more than 90 potential substrate molecules are known Langosch et al., 2015) indicating that one role of this protein complex is the removal of partially degraded proteins from the membrane, thereby preventing their accumulation.

The most thoroughly investigated (Langosch et al., 2015; Langosch and Steiner, 2017) target of g-sec mediated cleavage is C99, containing a single-span transmembrane alpha-helix. C99 is the C-terminal fragment of the amyloid precursor protein (APP) and results from the removal of large parts of the APP ectodomain (Zhang et al., 2011). This preprocessing step, in the case of APP mediated by β-secretase (Vassar et al., 1999), is necessary for sterical reasons: Proteins possessing large soluble extracellular domains are unable to get into close contact with the active site of g-sec (Bai et al., 2015b; Langosch et al., 2015; Langosch and Steiner, 2017). The biological role of APP is mostly in the dark (Deyts et al., 2016) but it is well established that sequential C99 processing results in an intracellular peptide (AICD), several short (mostly three amino acid long) peptides and the Aβ40/42/43/46 fragments (Bolduc et al., 2016).

In patients not suffering from familial Alzheimer's disease (FAD), Aβ40 peptides are the main product of C99 cleavage while the longer variants are yielded in much lower quantities (Zhang et al., 2011). This balance, however, seems to be rather delicate and can be shifted toward the production of longer amino acid chains (predominantly Aβ42) by several factors, such as mutations and changes of bilayer composition or temperature (Holmes et al., 2012; Szaruga et al., 2017). The A$\beta > 40$ fragments are known to be more prone to aggregation than the shorter variants and thus have been found to be the main components of amyloid deposits in the brains of AD patients (Hardy and Higgins, 1992; De Strooper et al., 2012; Langosch et al., 2015; Langosch and Steiner, 2017). Over 200 pathogenic Alzheimer's disease related PS mutations have been reported on www.alzforum.org (affecting 135 different amino acids), as well as over 20 that are situated on C99. Another well studied substrate for g-sec is the Notch ligand/receptor complex, which upon cleavage releases an intracellular fragment leading to the expression of various genes. Aberrant activation of this Notch signaling pathway has been found to promote tumor cell proliferation and is linked to several types of cancer (Rao et al., 2009; Krop et al., 2012).

Structurally, g-sec adopts an N_{in} topology, forming a complex with 1:1:1:1 stoichiometry (Bai et al., 2015a,b; Langosch et al., 2015). Because there are two different PS and APH-1 genes - PS-1, PS-2, APH-1a, and APH1b, four different complexes can be formed. PS-1 and APH-1a, however, are the prevalent variants of the respective proteins (Bai et al., 2015b), resulting in NIC:PS-1:APH-1a:PEN-2 being the most common g-sec complex.

Nicastrin (green structure in **Figure 1**), a 709 amino acid (AA) long protein, consisting of one transmembrane helix and a large globular extracellular ectodomain (ECD) is believed to play the role of gatekeeper for g-sec, blocking the access to

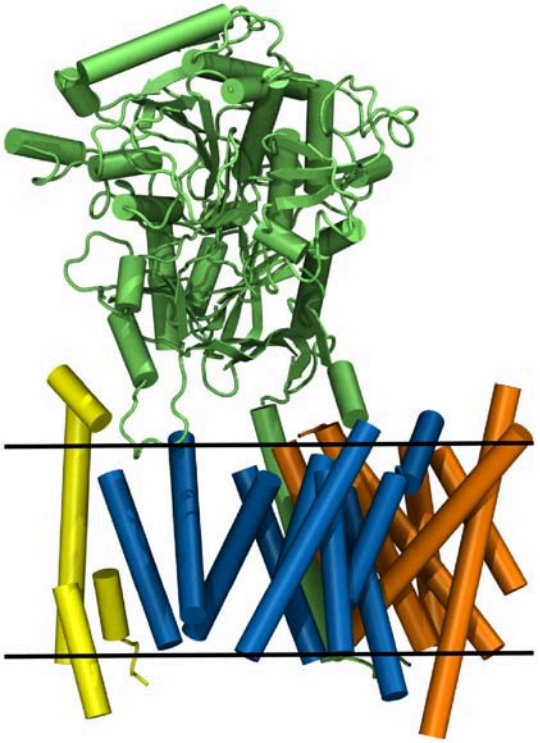

FIGURE 1 | The g-sec complex. Nicastrin (green), presenilin (blue), anterior pharynx-defective-1 (orange), and presenilin enhancer-2 (yellow). The approximate location of the lipid bilayer is indicated by two black lines.

PS for potential substrates with its bulky soluble domain (Bai et al., 2015a; Langosch et al., 2015; Langosch and Steiner, 2017). Presenilin-1 (blue protein in **Figure 1**), a 467 AA long aspartyl protease, contains the two catalytically active residues D257 and D385 (Wolfe et al., 1999). APH-1a (orange in **Figure 1**) consists of 265 residues, functions as a scaffolding protein and binds the transmembrane domain (TMD) of nicastrin (Lee et al., 2004). PEN-2 (yellow in **Figure 1**) has been shown to play a role in the autoproteolytic cleavage of the long cytosolic loop between the transmembrane domains 6 and 7, taking place upon maturation of the g-sec complex (Bai et al., 2015b). With only 101 AA (Francis et al., 2002) it is also the smallest of the four proteins. Even though a lot of insight into the structural and biochemical properties of g-sec has been gained in the last couple of years (De Strooper et al., 2012; Bai et al., 2015a,b; Holmes et al., 2012; Kong et al., 2015; Langosch et al., 2015; Fukumori and Steiner, 2016; Somavarapu and Kepp, 2016; Xu et al., 2016; Langosch and Steiner, 2017; Szaruga et al., 2017), many questions still remain unanswered:

Most soluble proteases cleave their substrates on a (sub)second timescale, whereas g-sec operates much less efficiently, taking minutes to process a single molecule (Kamp et al., 2015; Langosch et al., 2015). Since the chemical process of bond hydrolysis itself takes less than a second in most soluble proteases (Grossman et al., 2011; Langosch et al., 2015), the low turnover rate of g-sec must be the result of a

slow process that is necessary to initiate the actual substrate cleavage. The nature of this process is unknown and could involve substrate positioning, conformational rearrangements, frequent enzyme/ligand dissociations or any combination of the aforementioned. Another interesting question associated with the hydrolysis is raised by the fact that the active site of PS is situated deeply inside the membrane region, usually considered to be highly hydrophobic—a property presumably obstructive to a process involving water molecules.

The mechanism of substrate recognition and discrimination is unknown as well. As of now, no structural or dynamical profile attributable to all known g-sec substrates could be identified (Langosch et al., 2015; Langosch and Steiner, 2017). Since g-sec seems to play a major role in familial Alzheimer's disease (FAD), influencing its behavior and thereby forcing it into an Aβ production line where only the more benign 40AA long variant is produced looks to be a very promising endeavor. While complete g-sec inhibition has been shown to have a detrimental effect on health (De Strooper, 2014), preliminary g-sec modulation studies have shown some promise (De Strooper and Chávez Gutiérrez, 2015). Gaining further insight into the exact physico-chemical processes steering C99 processing will aid rational, structure-based approaches to drug design as well as the development of novel gene-therapeutic strategies.

A milestone in the investigation of g-sec was achieved by Bai et al. reporting three-dimensional structures of the complete γ-secretase complex (Bai et al., 2015a,b). These Cryo-EM experiments also uncovered that g-sec exists in a remarkable conformational diversity: Three distinctively different conformational states of the complex have been discovered. They are mainly differing in the distance of the TMDs 6 and 7—bearing the catalytically active side chains and the relative positioning of PEN-2 to PS-1 (Bai et al., 2015b).

Based on the Cryo-EM structures an anisotropic network model (ANM) has recently been constructed to analyze sterically possible large scale motions of the g-sec complex. These studies identified several hinge sites in g-sec and suggested large scale motions of the nicastrin domain relative to the PS-1 that could be involved in positioning of the substrate and promoting cleavage (Lee et al., 2017). Such large scale domain motions were also found in a combination of atomistic and coarse-grained (CG) Molecular Dynamics (MD) simulations of g-sec structures (Aguayo-Ortiz et al., 2017). In addition, the CG simulations suggested transitions between an inactive conformation with a large distance between two Asp residues involved in catalysis and states with the two Asp residues in a geometry compatible with a catalytically active arrangement that was not observed in shorter atomistic simulations (Somavarapu and Kepp, 2017). In the current study we conducted long time scale atomistic MD simulations starting from Cryo-EM derived structures to investigate local and global g-sec mobility and how it might be related to function but focusing also on water and lipid distribution surrounding the g-sec complex. In simulations of the membrane spanning part of g-sec the studies indicate a transition from an inactive arrangement (large distance between Asp residues involved in catalysis) to a potentially active form with a close distance of the Asp residues including also transient binding of water molecules in the active site. It also gives insight into the sterically possible motions of the PS1 TM helices mediating the transition. The active site but also other regions between TM helices appear to be accessible to water several Angstroms away from the boundary between membrane and the aqueous phase. Analysis of the lipid mobility around the g-sec complex revealed several stable binding regions that indicate binding regions for hydrophobic substrate helices. Finally, we interpret the simulation results in light of the potential role of some known mutations in γ-secretase that interfere with activity due to a putative influence on transitions toward the active conformation.

MATERIALS AND METHODS

Both simulations (henceforth referred to as system 1 and system 2, respectively) that have been conducted for this study were based on the PDB structure 5FN2 (Bai et al., 2015b) since it is the most complete of all available g-sec structures. In 5FN2, not only transmembrane domain 2 (TMD 2) is fully resolved, also a large patch of the loop 2 region connecting TMD 6 to TMD 7 is visible. All other available g-sec PDB structures miss this loop 2 domain spanning from residue 264 to 278. This region is very close to the putative binding site, therefore its structure and dynamics may be important to the functioning of the enzyme. Unfortunately, structural data on the largest part of this intracellular loop 2 region is still missing because it is outside of the membrane and very mobile. Therefore, this 89 amino acid long region (residues 289 to 377) was restored by CHARMM-GUI and cleaved to enable the simulation of the matured complex.

To enable the physically correct positioning of the proteins in the POPC membrane bilayer, the PDB file was submitted to the PPM (Lomize et al., 2012) server. The starting structure and the simulation protocol was then generated by uploading the reoriented structure to the CHARMM-GUI (Jo et al., 2008; Wu et al., 2014) web server.

Since aspartyl proteases require one active aspartate to function as a base and the other one as an acid (Singh et al., 2008), D257 has been protonated. Bai et al. (Bai et al., 2015b) have reported a hydrogen bond between E280 and H163, holding the loop region situated underneath the putative substrate binding site, in place. Because mutation of E280 is the most common cause leading to FAD (Lemere et al., 1996), this structural feature has been stabilized by protonating H163 in the simulations. The rest of the titratable side chains have been left in protonation states, assumed to be the predominant ones under physiological pH. The proteins were embedded in a bilayer consisting of 300 POPC molecules and placed in a periodic simulation box containing 0.15M KCl and approx. 33,000 or 55,000 water molecules, respectively. The target temperature was set to 303.15K, using Langevin dynamics (Goga et al., 2012) with a collision frequency of $1ps^{-1}$ while the system pressure was kept at 1bar by the Berendsen barostat (Berendsen et al., 1984) and a relaxation time of 0.5 ps. By applying the SHAKE algorithm (Ryckaert et al., 1977), the systems could be propagated by 2.0fs every time step. Non-bonded interactions have been calculated explicitly until a distance of 8Å after which long range effects were accounted for by the particle mesh Ewald method (Darden et al., 1993). Prior to simulation, the aqueous layers have been relaxed by

geometry optimization. Preceding a 500ns equilibration phase, the simulation boxes were heated to the target temperature while simultaneously applying pressure and slowly lowering/removing the positional restraints placed on the amino acids and lipid molecules. The proteins were described by the AMBER14SB (Maier et al., 2015) force field, whereas for lipid molecules and water the Lipid14 (Dickson et al., 2014) and TIP3P (Mark and Nilsson, 2001) force fields were used. All simulations were performed utilizing the CUDA (Nickolls et al., 2008) version of the pmemd program, provided with the AMBER16 package (Case et al., 2016). Trajectory analysis and calculation of principle components of motion (PCA) were carried out using cpptraj, which is part of the AMBER16 package (Case et al., 2016) and the results were visualized by VMD (Humphrey et al., 1996). The only difference between the simulations is the absence of the nicastrin ectodomain in system 2 (the TMD of nicastrin was included in both simulations). Due to the bulky nature of the NIC ectodomain, its removal permits a large reduction of simulated amino acids and water molecules. Besides an increase in sampling time due to reduced number of atoms, the putative influence of the NIC ECD to g-sec dynamics could be studied as well. System 1 has been sampled for 1 μs while the evaluation trajectory of system 2 has a length of 3.5 μs.

RESULTS AND DISCUSSION

System 1: Complete γ-Secretase Complex

Atomistic MD simulations were started from the best resolved Cryo-EM structure (pdb entry 5FN2). Root mean square deviations (RMSDs) calculated for the *Cα* atoms of several parts of g-sec compared to the PDB structure indicate that the protein remained close to the experimental structure throughout the simulation (see also **Figure S1**). During the simulation, the membrane spanning parts fluctuated but on average remained within ∼ 2Å of the reference structure (first frame of the sampling trajectory). Since the NIC ECD consists of many mobile loop regions, it naturally exhibits larger deviations than the TMDs situated in the lipid bilayer (which is also more viscous than water). **Figure 2A** depicts the RMSDs associated with system 1.

In the experimental apo conformation of the PDB-entries 5FN3, 5FN4 and 5FN5 the region beyond residues L262, C263 or P264 of TMD 6 in PS1 (depending on the chosen structure) is not resolved, presumably because of high mobility. However, in the inhibitor bound structure (5FN2) the helix kinks at P264 and goes on for several more residues. According to Bai et al., the presence of the inhibitor rigidifies the structure of g-sec, compared to its apo-form. (Bai et al., 2015b). In the simulation, which was started from 5FN2, an unfolding of the helical region beyond C263 was observed and the chain took on a far more mobile structure in the form of a loop region (**Figure S2**). This fits very well to the reported apo-structures of g-sec and confirms that the absence of a binding partner near the active site of PS-1 destabilizes this region.

In order to capture coupled global motions occurring during the MD study, principal component analysis (PCA) has been performed on the 1 μs long sampling trajectory of the complete γ-secretase complex. The most pronounced motions are shown in **Figures 2B–D**. The first principal component revealed that the nicastrin ectodomain consists of two independently moving sub-domains—a small and a large lobe: Most of the TMDs of g-sec and the smaller lobe of the NIC ectodomain are concertedly moving away from the larger globular nicastrin extracellular domain. This behavior indicates potential plasticity of the NIC ectodomain when acting as a binding site for the extracellular terminus of potential substrate proteins (see **Figure 2B**).

Principal component 2 (**Figure 2C**) showed that the complex exhibits an opening and closing motion, changing the size of the cavity formed by the ectodomain and the intracellular TMDs. This behavior has previously been reported in coarse grained simulations (Aguayo-Ortiz et al., 2017), elastic network model calculations (Lee et al., 2017) or by experiment (Elad et al., 2015) and may ensure that a broader range of substrate molecules can be processed: The NIC extracellular region has been indicated as a substrate binding site (Fukumori and Steiner, 2016) and in order to play this role it probably has to be close enough to the lipid bilayer to bind and stabilize the membrane-bound substrate. At the same time, however, the cavity has to remain spacious enough to incorporate a sufficiently large part of the substrate's ectodomain—this is necessary to ensure that the intramembrane domain of the substrate can come into close contact with the active site of presenilin. If the cavity formed by nicastrin and the TMDs was of constant size the number of g-sec substrates would very likely be much lower, since fixed NIC-membrane surface distances would allow for only little variety in substrate ectodomain size.

The third largest combined motion of the g-sec complex was a lateral ectodomain movement with respect to the TMDs (see **Figure 2D**). Upon closer inspection of the mobility of the PS-1 TMD residues in the principal components, it is apparent that TMD2 and the directly connected N-terminal region of TMD3 are very mobile. This finding was not surprising as TMD2 due to its mobility is not visible in many Cryo-EM structures (Bai et al., 2015b), suggesting that TMD2 could function as a possible gate for substrate entry. The video clips of the first three principal components (included as **Supplementary Material**) depict the relative movement of the different domains and helices of g-sec more clearly.

The PCA also showed that the conducted simulation reproduced the relative movement of PS-1 and Pen-2, reported by experiments (Bai et al., 2015b) (Bai et al. used the Pen-2 - PS-1 tilting angles in tandem with the active-inactive conformational change to group the reported Cryo-EM structures into three different structural classes). Similar tilting motions with respect to PS-1 can also be reported for Aph-1a. The extend of these motions observed in the simulation has been compared to the PDB structures: The tilt reported in the Cryo-EM structures (5FN2, 5FN3, 5FN4, and 5FN5) has been evaluated by first, aligning them according to the positions of the C*α* atoms of PS1 TMDs 4, 5, 7, 8, and 9 and then calculating for each structure, the standard deviation of the angles between helix 3 of PEN-2 and the arbitrarily chosen (yet mutual to all structures) z-axis. In the simulation, the sampled angle changes have been measured by aligning TMDs 4, 5, 7, 8, and 9 in each frame of the trajectory and subsequent calculation of the standard deviation of the PEN-2 - z-axis angle as above. The resulting standard

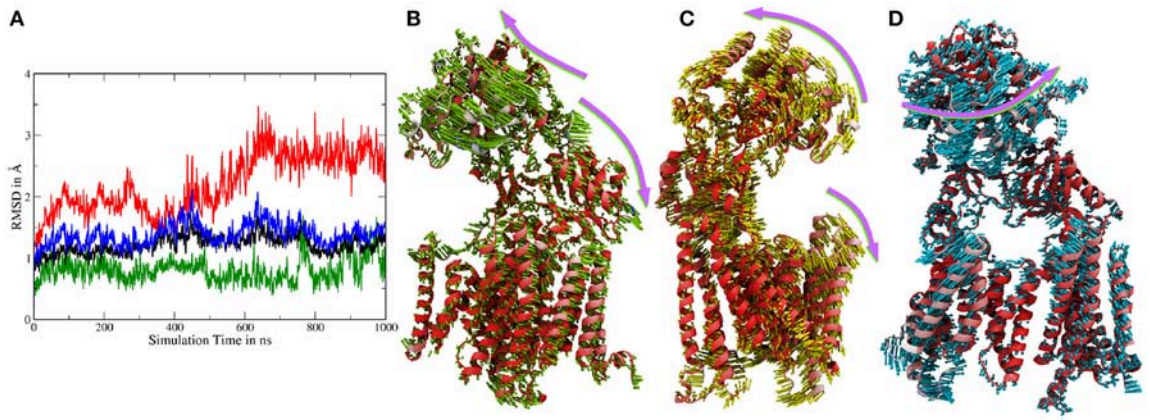

FIGURE 2 | (A) Cα-RMSDs calculated for system 1, with the first frame in the trajectory used as reference. Red: RMSD of complete nicastrin; green: TMD of nicastrin; black: all TMDs; blue: PS-1 TMDs. **(B–D)** Principal component analysis of simulation 1 (full g-sec). The mobility of each residue is depicted by the coloring scheme, ranging from red (least movement) via white to blue. The direction and extend of the movement is indicated by small arrows. Due to its high mobility, the intracellular loop 2 was not included in this evaluation in order to emphasize on nicastrin movement. **(B)**: Mode 1. **(C)**: Mode 2. **(D)**: Mode 3.

deviations obtained for the PDB files and the simulation were in good agreement with each other (2,47° for the PDB structures and 2.24° for system 1). The deviations of the APH-1a tilting were obtained by the same approach, however, this time the vector used to measure the APH-1a angle with respect to the z-axis was defined by calculating the centers of mass of (i) all the extracellular topside C_α atoms of the APH-1a TMDs and (ii) of their intracellularly oriented counterparts. This way a mean tilting angle of all the APH-1a TMDs has been determined. The resulting standard deviations of 0.67° (PDB) and 1.71° were in satisfying agreement with each other but suggested that the relative movement between PS-1 and APH-1a was slightly increased in the simulation, compared to the Cryo-EM structures. Plots showing tilting angles vs. simulation time can be found in the supplementary section (**Figure S3**). **Figures 3A,B** depict representative snapshots from the simulation, highlighting the sampled protein conformations in the simulated complex that compare well with arrangements observed in the PDB structures 5FN3 and 5FN5 (classes 1 and 3, respectively, shown in **Figures 3C,D**).

The first three principal components account for 49% of all motions in the simulations. While the fourth component, being a combination of the motions represented by modes 1 and 3, still represented global movement, all other eigenvectors of the covariance matrix referred to very localized loop rearrangements or fluctuations of terminal TMD regions (see **Figure S3** indicating the contribution of the first 20 modes).

The independent motions of the two nicastrin ectodomain lobes relative to PS-1 was further confirmed by a measurement of the distances and angles between amino acids, located either in the large lobe, the small lobe or the active site of PS-1 (see **Figure 4**). The distance between the large lobe (V328) and the active site of PS-1 (D257) showed two different types of variations: smaller, short lived fluctuations and a much slower but more distinct global movement (indicated by the running average in **Figure 4B**). The mean extend of this distance change witnessed during the simulation lies in the region of 3 to 4Å. It agrees quite well with the distance variation observed in the high-resolution Cryo-EM structures of Bai et al. (2015b), featuring V328-D257 distance deviations of the same magnitude. However, the larger scale changes reported by Elad et al. (2015) (up to 5 nm) have not been observed in our simulation, it is possible that larger scale global motions may require longer simulations beyond the scale of the present study. The angle defined by V328, L121 (in the small lobe) and D257 changes at exactly the same time as the fluctuations between V328 and D257 take place, clearly showing that this relative large lobe - PS-1 movement is decoupled from the movement of the smaller extracellular subdomain.

The distance changes between the small lobe and the PS-1 active site on the other hand, were of severely reduced extend, only exhibiting relatively low fluctuations and virtually no slow relative movement (**Figure 4C**). Another indication of decoupled subdomain dynamics of the ectomonain lobes is represented by **Figure 4D**, where a variation in L88-V295 distance is visible, indicating a conformational change in the nicastrin ectodomain.

It has been reported (Bai et al., 2015b; Aguayo-Ortiz et al., 2017) that PS-1 can adopt two distinct states: One, where the catalytically active side chains are relatively close to each other and a state, characterized by larger D257-D385 distances. For an aspartyl protease to cleave a peptide, besides the presence of the substrate, a water molecule at the right position, as well as two aspartates in a certain (proximal) geometry are required (Singh et al., 2008). During the sampling phase of system 1, PS-1 occupied the active state with a very low distance between both active site aspartates (approx. 8Å). This is surely aided by the fact that D257 was protonated, enabling the formation of a hydrogen bond between both side chains which remains stable for the duration of the simulation. For completion it should be noted that during the equilibration phase, also a different conformation was adopted, where D257 and D385 were separated by a larger margin (= inactive conformation).

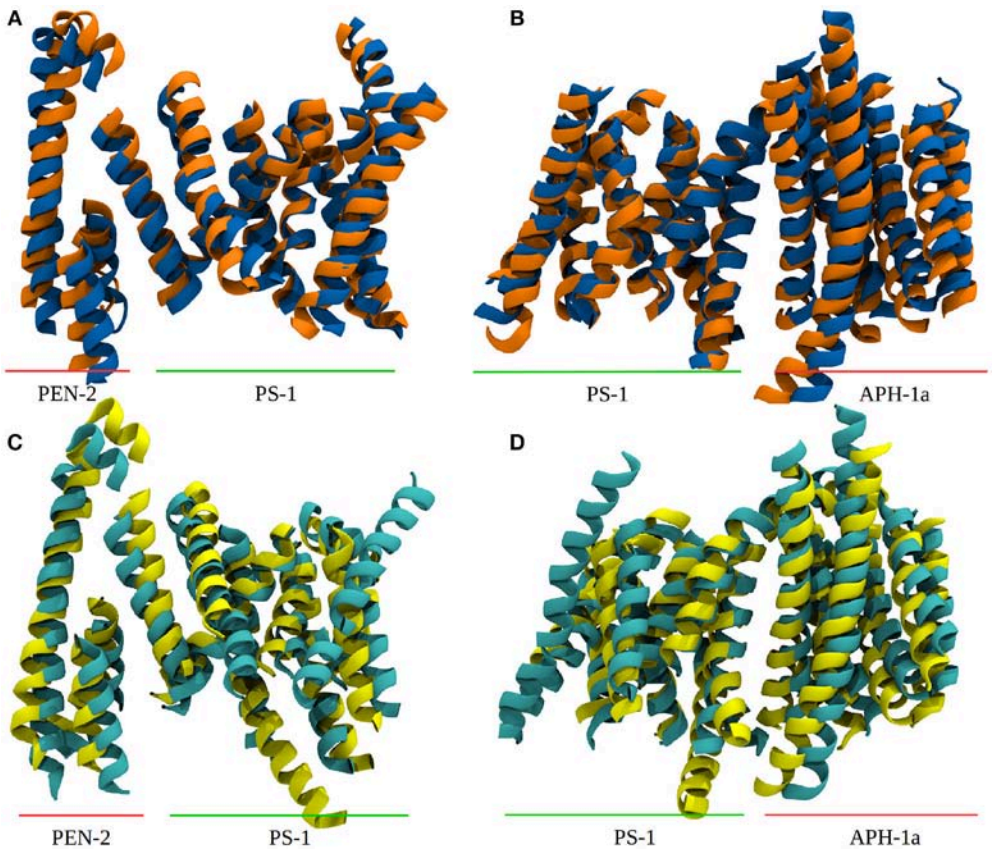

FIGURE 3 | Comparison between system 1 and experimental data. **(A)** Snapshots from system 1, depicting the "in" (blue) and "out" (orange) orientation of Pen-2 by superposition. **(B)** APH-1a tilting with respect to PS-1 in system 1. **(C,D)** Depiction of PDB structures 5FN3 (cyan, class 1) and 5FN5 (yellow, class 3) exhibiting very similar structural diversity. The structures were aligned at the C_α atoms of PS-1 TMDs 1, 5, 8, and 9.

System 2: γ-Secretase Without Ectodomain

In order to improve the sampling of the simulation and to investigate the influence of the ectodomain to γ-secretase dynamics, a 3.5 μs (+500 ns equilibration) long simulation of g-sec without the NIC ECD was conducted. The starting structure was taken from a snapshot of system 1 during equilibration. The NIC ECD was removed and the TMDs were embedded in a lipid bilayer consisting of 300 POPC molecules. During the 3.5 μs sampling phase, PS-1 changed its conformation from inactive to active at around the 1.75 μs mark. The mean active-site aspartate (D385 and D257) separations in the inactive state were found to be 9.1 ± 0.6Å (Cα-Cα, with distances up to 11.6Å) and 8.0 ± 0.7Å (Cγ-Cγ). Plots are shown on **Figure 5A**. The active conformation, on the other hand, was characterized by average Cα-Cα and Cγ-Cγ distances of 8.3 ± 0.6Å and 6.0 ± 1.0Å, respectively (see also **Figure 5A**, where the red and black solid lines denote the mean aspartate distances in active state, while the dashed lines represent mean values for the inactive conformation). Simultaneously with the putative activation of the enzyme, the separation between the TMDs 2 and 3 increased, indicating a conformational change affecting more than one PS-1 TMD.

If one takes a closer look at the catalytic aspartates, it becomes apparent that in active state they can either form a direct hydrogen bond, leading to Cα-Cα distances of 7.5 ± 0.3Å (in 26% of all sampled frames in active conformation) or can be bridged by one water molecule, increasing Cα-Cα separation to 8.6 ± 0.4Å. Snapshots of these respective conformations are shown in **Figures 5B,C**. The observed D257-D385 separations were in good agreement with the experimental data reported by Bai et al. (finding that active site Cα-Cα distances range from 8.0 to 12.7Å) (Bai et al., 2015b). Another interesting structural aspect can be uncovered by comparing the mean conformation of the first 1,000 ns (inactive state) of simulation 2, the mean conformation of the last 1,000 ns (active state) of system 2 and the mean structure resulting from the 1000ns trajectory obtained for system 1 (active state): The respective structures are shown superimposed on **Figure 5D** and indicate that transitioning from inactive to active state coincides with the repositioning of TMDs 1, 6, 7, 8, and 9 while TMD 2 and 3 adopt conformational diverse arrangements. The average structures have been generated by aligning the respective trajectories along the heavy atoms of the proteins and subsequently calculating the mean position of each atom in the simulations. This concerted rearrangement of some of the PS-1 TMDs could be further highlighted by calculating

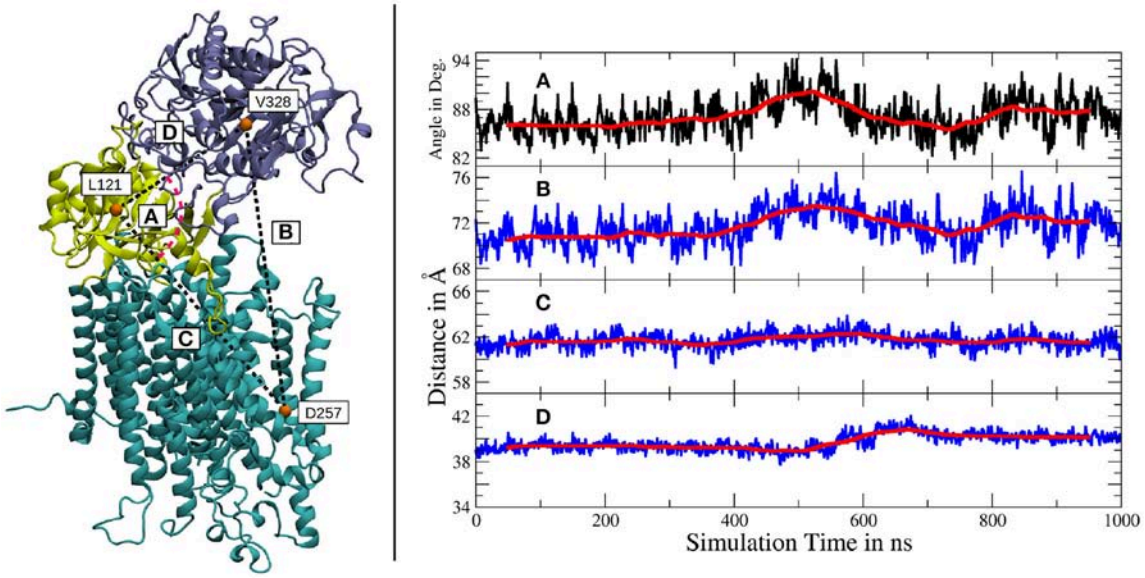

FIGURE 4 | Left panel: Location of the amino acids used for subdomain distance measurements. The large lobe is colored in iceblue, the small lobe in yellow and the intramembrane domains of g-sec are depicted in cyan. Right panel: **(A)** Angle between V328, L121 and D257. **(B)** Distance between V328, situated in the large lobe and D257, one of the catalytically active aspartates. **(C)** Distance change between the small lobe (L121) and the PS-1 active site (D257). **(D)** Distance change between the two ectodomain lobes (L121 and V328). The scaling is the same for all distance plots and a running average (100 points averaging window) has been added for greater clarity (red lines).

RMSDs for every residue in the TMDs in every frame. This was achieved by comparing their positions at each frame to their average position while being in the inactive conformation (the first 1,000 ns of the simulation were taken to calculate the mean inactive structure). The "per-residue RMSDs" depicted on the left hand panel of **Figure 6** indicate that the positional shifts of TMDs 1, 3, 6, 7, 8, and 9 coincided with the inactive to active transition of PS-1. From the positions of the Cα atoms of the active aspartates, it seems as if two different principal rearrangements were leading to distances favorable for substrate cleavage: A slight repositioning and rotation of the N-terminal region of TMD 7 (where D385 is located) and TMD 6 (where D257 is located) moving toward the center of PS-1. Transmembrane domain 2 displayed significant mobility throughout the entire simulation that agreed with the experimental observation that the structure of TMD 2 cannot be resolved in several Cryo-EM structures.

Recording the radius of gyration of PS-1 (right-hand panel on **Figure 6**) demonstrates that the TMD rearrangement upon inactive to active transition was associated with a contraction of PS-1, as the mean radius changed from 14.71Å to 14.46Å.

The contraction of the intracellular side of PS-1 could also be witnessed by a principal component analysis performed on the 3.5μs sampling trajectory including the TMDs of PS-1 and PEN-2: In mode 1 (**Figures 7A,B**) TMDs 1, 6, 7, 9 of PS-1 and the PEN-2 α-helices were moving toward each other, thereby reducing the intra-domain distances (and with them also the separation between D257 and D385). PS-1 TMD 8, on the other hand, moved away from the rest of the presenilin helices.

The second most important of the concerted movements is depicted in **Figures 7C,D**: The distance between the catalytic aspartates remained constant but PS-1 TMDs 4, 5 and to a lesser extend 3 along with PEN-2 moved in different directions than the other PS-1 TMDs. This conformational change was decoupled from the transition between the active and inactive states and confirmed the structural classes reported by Bai et al where PEN-2 tilting also seemed to be independent from the D257-D385 distance (Bai et al., 2015b). Movie clips showing the coupled motions are provided as **Supplementary Material**. The first two modes of the PCA accounted for 47% of the overall mobility sampled by the evaluation trajectory. The remaining modes, however, emphasized strongly on fluctuations of terminal TMD domains, mainly involving TMD 2 (**Figure S4** depicts the contribution of the first 20 modes to the total mobility).

Known pathogenic mutations in PS-1 lead to different results regarding g-sec activity: A change of overall substrate processivity—mainly a decrease, sometimes even to the point of inactivation, or a shift of the ratio of product amyloids (very often increasing Aβ42 levels). Frequently, also a combination of the above effects is witnessed (Sun et al., 2016). Many of the mutations resulting in reduced or abolished g-sec activity are located at the interface of adjacent TMDs. Such mutations can be expected to destabilize presenilin or even prevent correct positioning of the respective TMDs during protein synthesis or folding. It is, however, likely that some of the mutations have a more subtle effect on the PS-1 structure and simply interfere with the relative positioning of the catalytic residues, thereby influencing important conformational changes. One such mutation site is F386, situated on TMD 7, right next to D385. As illustrated in **Figure 8**, the side chain of this residue is very close to five other known mutation sites (Sun et al., 2016;

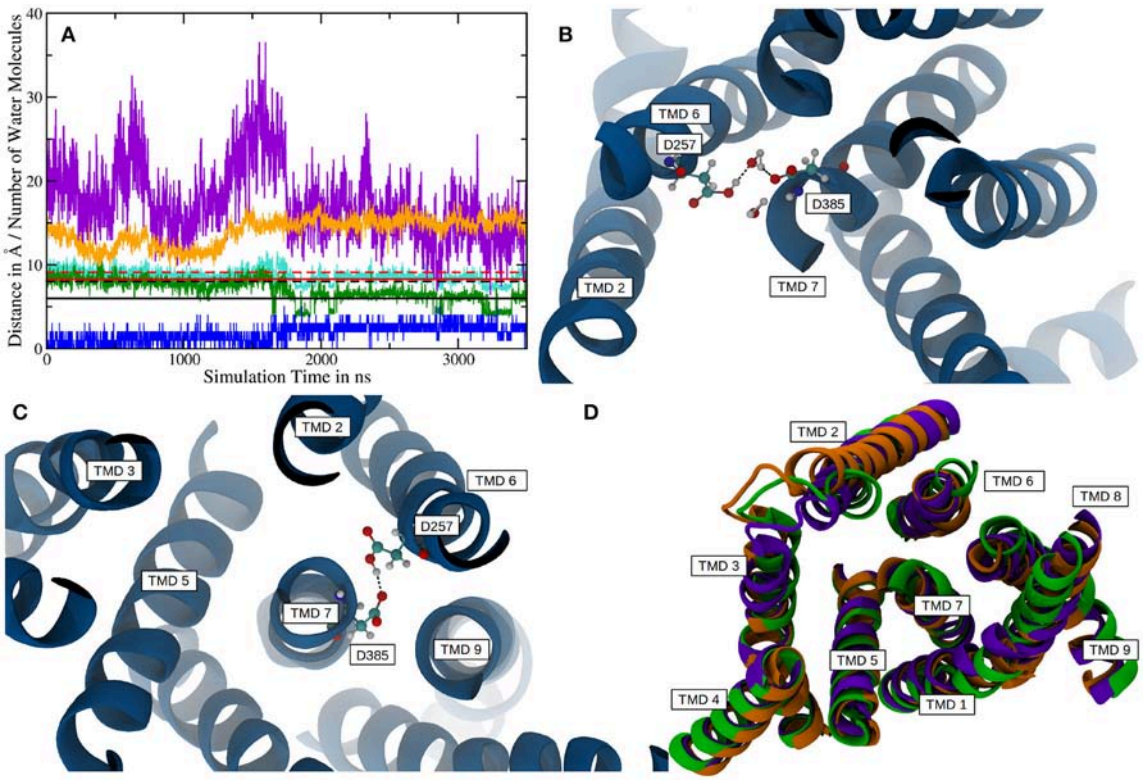

FIGURE 5 | (A) Plot depicting distances between certain residues and the number of water molecules within PS-1 in system 2. The Cα distance between D257 and D385 is shown in cyan with the mean distances for the active (solid line) and inactive (dashed line) given in red. The green plot represents the sampled distances between the Cγ atoms of the catalytic aspartates and the black lines indicate the mean separation in the inactive (dashed) and active (solid) states. The distance between V142 (TMD 2) and S169 (TMD 3) is depicted in orange. The blue line is the number of water molecules within 4Å of D257 and D385 and the purple plot indicates the number of water molecules inside the putative substrate binding area of PS-1. Please note, that the purple graph has been scaled down by a factor of two in order to increase comparability. **(B)** The active site aspartates are bridged via a water molecule at Cα distances of 8.6 ± 0.4Å. **(C)** At a Cα separation of 7.5 ± 0.3Å the two catalytic side chains are forming a hydrogen bond. **(D)** Superposition of the mean structures of inactive PS-1 (system 2, green), active PS-1 (system 2, purple) and system 1 (orange). View from the intracellular side.

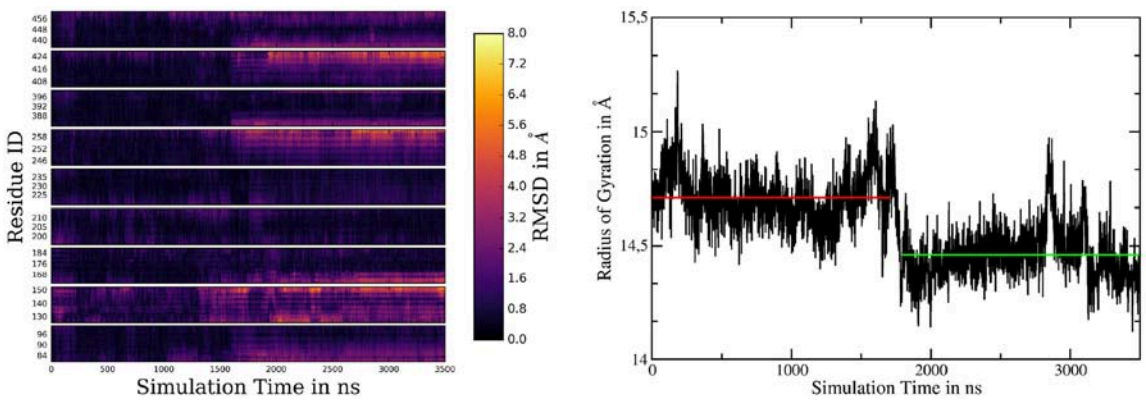

FIGURE 6 | (Left panel) Heatmap of per-residue RMSDs of the simulation of system 2, comparing the mean structure of the first 1,000 ns (=inactive conformation) to every frame of the trajectory. **(Right panel)** Radius of gyration of system 2 calculated by considering the Cα atoms of TMDs 1, 6, 7, 8, and 9. The red and green lines denote the mean radii of the inactive and active conformations, respectively.

Szaruga et al., 2017), S390, S230, C92, V89, and P88. While residues P88, V89, C92, and S230 outline the binding pocket of F386, S390 helps to position C92 by acting as a hydrogen bond acceptor. During the simulation, upon activation of the enzyme, F386 "plugged" into the binding cavity, and anchored TMD 7 to TMD 1, thereby impacting the positioning of D385 (see

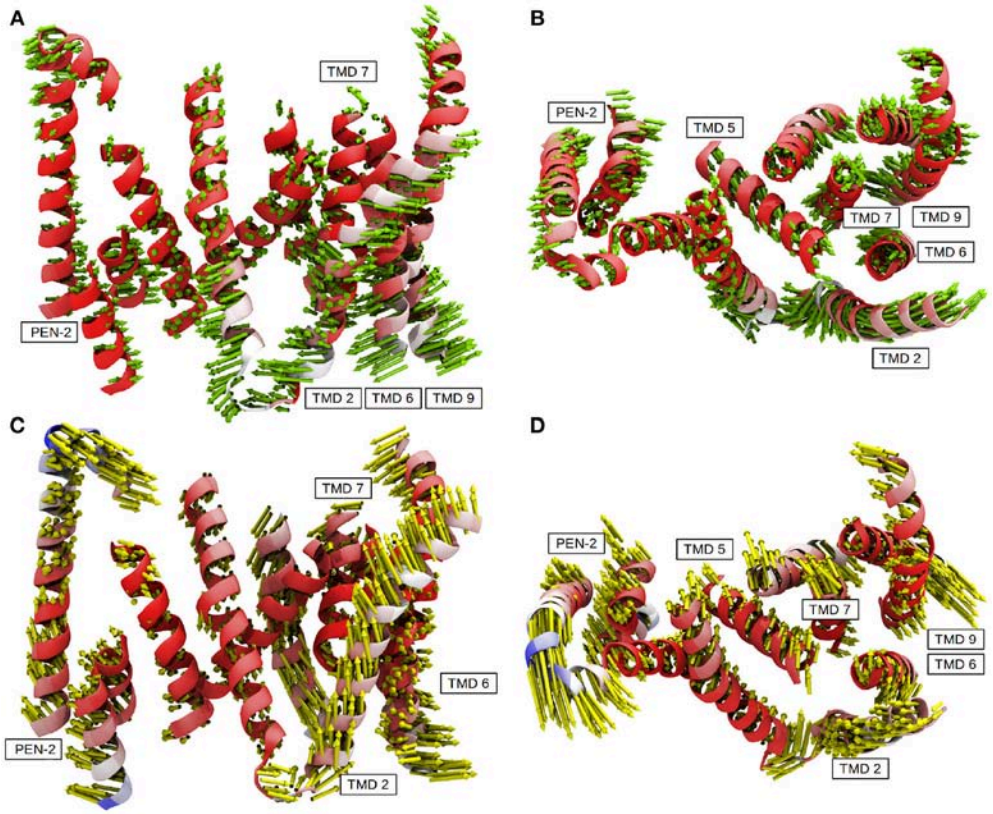

FIGURE 7 | The first two principal components calculated from system 2. **(A)** Mode 1 side view. **(B)** Mode 1 top view (from extracellular side). **(C)** Model 2 side view. **(D)** Mode 2 top view (from extracellular side). Residues colored in red exhibit low mobility while blue indicates strong fluctuations.

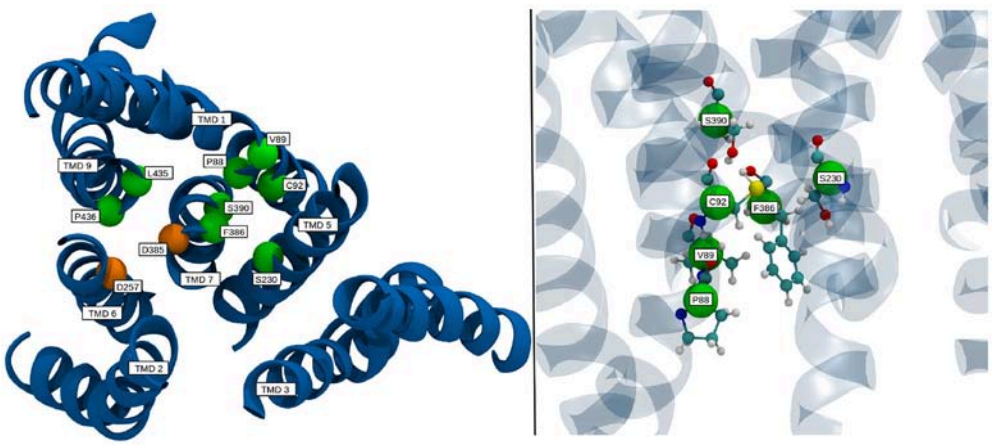

FIGURE 8 | Location of select mutation sites on the TMDs of PS-1 which are known to severely reduce the catalytic activity of γ-secretase. TMDs are colored in blue, mutation sites are depicted as green spheres, while the catalytic residues are shown in orange.

also **Figure 6**). Changing the sterical properties of this binding site or mutating F386 to a serine can be expected to have an impact on this behavior, hinting at why these mutation sites severely lower the catalytic capabilities of g-sec. Residues P88, V89 and C92 are located on TMD 1 which explains why the positioning of parts of TMD 1 is connected to the inactive-active conformation change of PS-1 (see also right panel on **Figure 6**). Other residues that may directly influence the positioning of the catalytically active aspartates are L435 and P436. While the mutation of L435 to a phenylalanine can increase the sterical barrier for TMD 7 twisting, changing P436 into a serine might influence the catalytic capabilities of D257 and D385 because

S436 would be capable of forming hydrogen bonds with their side chains.

In order to assess the stability of the protein complex and compare it to system 1, several C_α RMSDs have been calculated. As can be seen in **Figure 9A**, the fluctuations of the TMDs were considerably higher in system 2, compared to system 1. To isolate the contribution leading to this increased mobility and to improve the comparability to the shorter system 1 simulation, the 3,500 ns long trajectory has been split into two 1,000 ns long trajectories: One trajectory where PS-1 is in inactive state and a second with PS-1 in the (presumably) catalytically active conformation. The transitory part in the middle of the complete trajectory has been left out in order to remove the TMD rearrangements from the dataset (as such a conformational change was not occurring in system 1). The RMSDs resulting from the analysis of these new trajectories showed that the deviations were of the same magnitude as in system 1, with the only exception being the non-PS-1 TMDs in the first 1,000 ns (= inactive state) of the simulation (see **Figure 9B**), suggesting that the inactive conformation of PS-1 may lead to a slightly less stable protein complex.

The primary (known) role of the ectodomain of nicastrin is gate keeping the g-sec complex, thereby prohibiting the processing of substrate TMDs before the shedding of their ectodomains. It is also known that nicastrin plays an essential role in stabilizing the g-sec complex (Zhang et al., 2005). To assess the complex stability compared to the simulation of full γ-secretase, PEN-2 and APH-1a tilting motions have been calculated with the same method as for system 1 and with a standard deviation of 2.68° for PEN-2 and 1.68° for APH-1a the results suggest that the absence of the NIC ECD does not destabilize the rest of the protein assembly (values for system 1 are: 2.24° and 1.71°, respectively). Therefore it seems very likely that the stabilizing effect of NIC is due to its transmembrane helix. To further elucidate the role of the ectodomain of nicastrin, the structure and dynamics of PS-1 in systems 1 and 2 have been evaluated and compared to each other. One way of comparing structural features is through per-residue RMSDs, calculated for each frame in the trajectory. The heatmap plot in **Figure 10A** has been generated by first calculating the RMSDs of all residues in the simulation of system 1 (against the mean structure) in order to establish the "natural" fluctuations of the system (i.e., the noise). In a second step the per-residue RMSDs of simulation 1 were calculated against the mean structure of the last 1,000 ns of simulation 2 (= the active conformation). Subsequently, the per-residue RMSDs of the first step were subtracted from the second data set in order to plot only the (absolute) deviations that occur in addition to the "natural" fluctuations. This plot showed that for the most part, structurally the two simulations were very similar, again with TMD 2 and the N-terminal end of TMD 3 being the exception (and to an extend also TMD 6).

A similar comparison this time, between the inactive conformation of system 2 and simulation 1 resulted in **Figure 10B**. In this case, the heatmap plot indicated larger deviations between the two instances of PS-1: Additionally to TMD 2 (and 3), also the lower parts (= pointing toward the intracellular region) of TMDs 6, 7, 8, and 9 showed significant aberration throughout the trajectory. This structural evaluation fits nicely to the superposition of the mean structures of trajectories 1, 2 (active) and 2 (inactive) in **Figure 5D**, indicating the same structural differences. The dynamics of the two systems can be assessed by calculating B-factors for all PS-1 residues (excluding the very mobile loop 2 region). The resulting plots for systems 1 and 2 are shown on **Figure 10C**.

Evidently, the B-factors of all the TMDs are very low and approximately of the same magnitude in all compared trajectories. The only obvious exception is TMD 2 in the complete trajectory of system 2 where the Cα atoms clearly exhibited heightened mobility. Another difference between the (shorter) simulation including the NIC ECD and the complete trajectory of system 2 was the mobility of the loops connecting the C-terminal TMDs 7, 8, and 9. Upon closer inspection, however, also TMDs 6, 7, 8, and 9 displayed slightly increased dynamics in the complete trajectory of system 2. To put these results into perspective one has to consider the fact that the simulation of system 2 is more than twice as long as the one of system 1 and as has already been discussed, PS-1 undergoes a conformational change including the (relative) rearrangement of several TMDs. Furthermore, TMD 2 is known to be highly mobile, so increased positional fluctuations in this part of the protein are not really surprising. For a more balanced comparison between the shorter and the longer simulation, trajectory 2 has been divided into a 1,000 ns inactive conformation state and a 1,000 ns long active conformation state, while the TMD rearrangements taking place in approx. the middle of the simulation were omitted from the data (these trajectories were exactly the same as those that have been used to generate the additional RMSD plots above). The B-factors corresponding to these new trajectories are shown of **Figure 10C** as green and blue lines, respectively. These split-trajectories lead to the verdict that the mobility of PS-1 TMDs is not affected by the presence or absence of the NIC ECD: The resulting B-factors of the shorter system 2 trajectories fit nicely to the B-factors calculated for the TMDs in the simulation with complete nicastrin. The case of the loop regions is a bit more complex: The data suggested that (i) the active form of PS-1 exhibits lower fluctuations compared to the inactive conformation, (ii) the loop (and adjacent TMD regions) connecting TMDs 2 and 3 seemed to be of greatly reduced mobility in the simulations without the NIC ECD if inactive-active conformational changes are taken out of the picture. Since, however, the evaluation of the complete simulation 2 trajectory showed greatly increased mobility in this exact region, differences in B-factors concerning the region connecting TMDs 2 and 3 are insufficient to be taken as prove for external influences. These aberrations were very likely just of statistical nature and due to the fact that not all evaluation windows used for the respective B-factor calculations caught the same extent of the configurational changes. Altogether, the available data suggest only a small influence of the ECD of NIC on the structure and dynamics of PS-1.

Apart from conformational transitions, one of the questions in the context of intramembrane proteolysis is the availability of a sufficient number of water molecules, not only to facilitate the hydrolysis but also to stabilize putative transition states and the (putative) unwinding of the alpha helical substrate molecule.

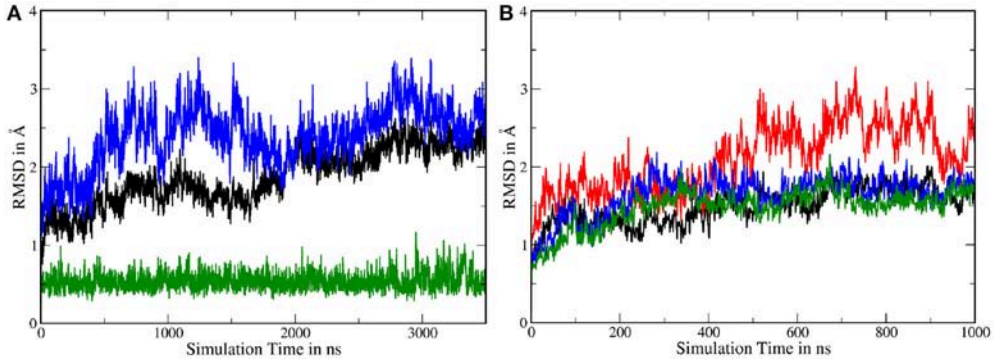

FIGURE 9 | (A) Backbone RMSD with respect to the first frame in the trajectory. Green: nicastrin TMD; black: PS-1 TMDs; blue: all TMDs. **(B)** Backbone RMSDs of the split trajectory. Black: PS-1 TMDs (inactive conformation); red: all TMDs (inactive conformation); green: PS-1 TMDs (active conformation); blue: all TMDS (active conformation).

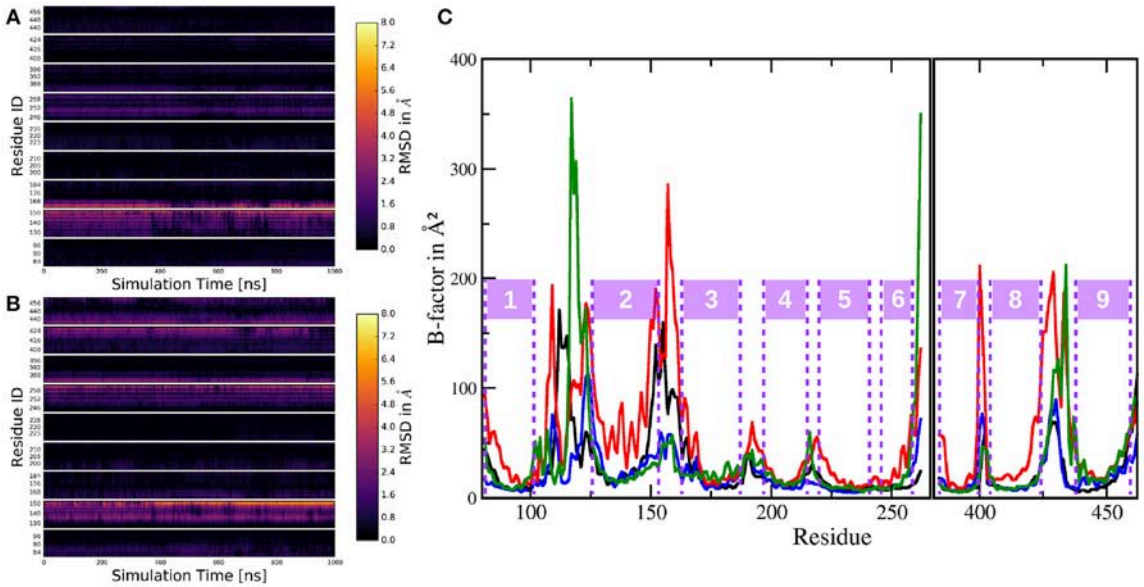

FIGURE 10 | Per-residue RMSD heatmap plots comparing: **(A)** The simulation of system 1 to the mean structure of the active conformation of system 2. **(B)** The trajectory of system 1 to the mean structure of the inactive conformation trajectory of system 2. **(C)** Cα B-factors of the residues in PS-1, excluding the highly mobile loop 2 region. Black: system 1; red: system 2 (complete trajectory); blue: system 2, active conformation (last 1,000 ns of system 2 sim.); green: system 2, inactive conformation (first 1,000 ns of system 2 sim.).

In order to investigate its hydration properties PS-1 has been approximated by a box with a volume of approx. 30,200Å^3. Subsequently, the mean number of water molecules within that cube was calculated by averaging over all 3,500 sampling frames. This evaluation showed that a mean number of 123.2 (with 87 being the lowest count and 167 the highest) water molecules were situated somewhere between the TMDs of PS-1 and with that also inside the membrane. The water distribution, depicted by **Figure 11** is not homogeneous and the number of solvent molecules rapidly diminishes in the vertical center of the protein.

Since the active-site aspartates are situated at the intracellular side of the g-sec complex, the water molecules located in this region can be expected to play a larger role in processing and stabilizing the substrate. Therefore, the number of water molecules residing inside the area around the active site—presumably coinciding with the region where the C-terminal part of a substrate molecule is located, has been ascertained as well. The box chosen to represent the putative binding and processing site was approx. 7,800 Å^3 in size and incorporated a mean value of 34.8 water molecules, ranging from 13 to 73 (see also **Figure 12**).

Intriguingly, if the number of water molecules is plotted against simulation time, an abrupt change is apparent (purple line in **Figure 5A**). This change in number of water molecules coincided with the transition from inactive to active state PS-1. Since the box volume remained constant, a change of water accessibility to the binding region must be responsible for

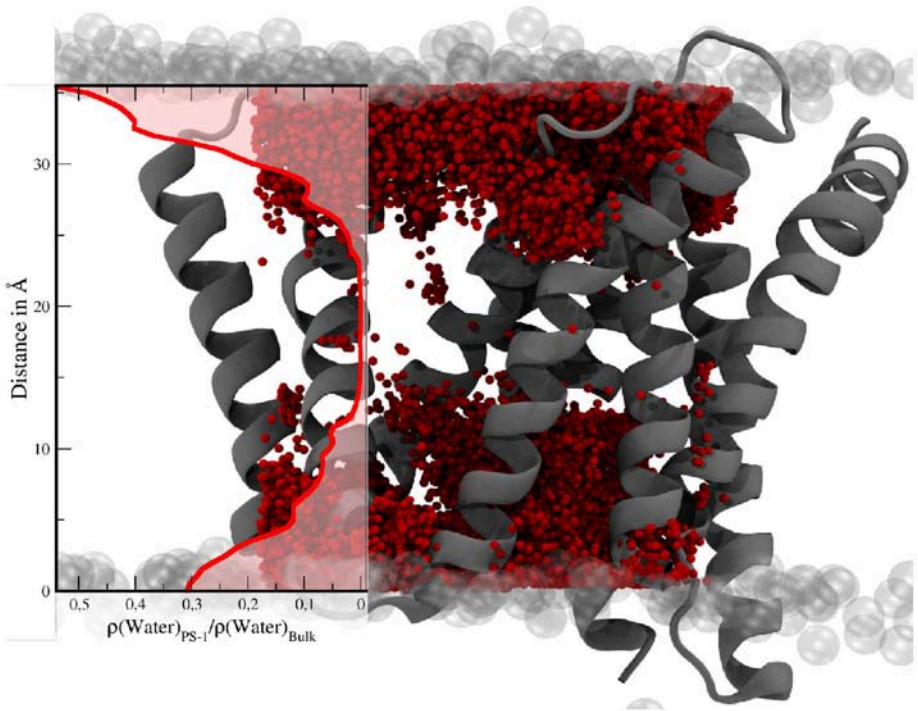

FIGURE 11 | Water molecules within a box of 30 × 28 × 36Å in the TM region of PS-1. The transparent gray spheres indicate the edge of the membrane domain. The red spheres are water molecules. The visualization of the water distribution has been generated by superimposing the positions of all water molecules within the given boundaries at every tenth evaluation frame of the simulation. The graph on the left shows the mean water density (N_{water}/*Volume*) in PS-1, relative to the bulk region.

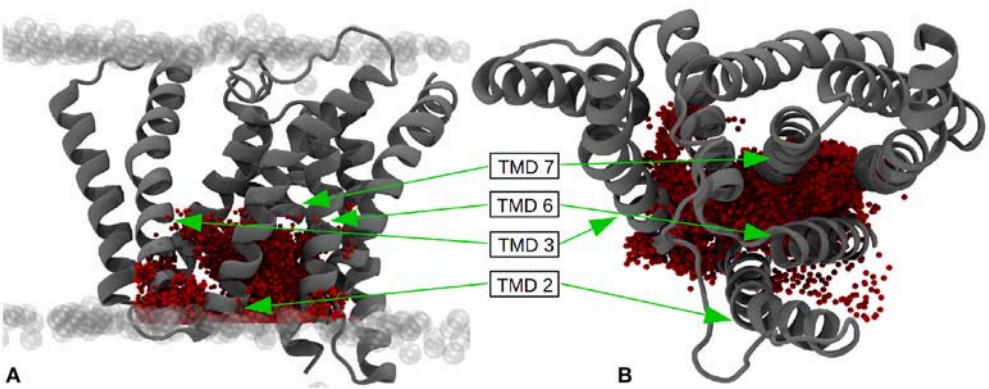

FIGURE 12 | (A) Water molecules within the putative binding region of the substrates (27 × 18 × 16Å) - side view. **(B)** Top view of the putative binding region. The pictures have been generated by superimposing the positions of all water molecules within the given boundaries at every tenth evaluation frame of the simulation. The extracellular side is at the top.

this behavior. This finding can be explained by the proposed contraction of the TMDs during the conformational transition of PS-1 to the active form. The plot also highlights that the fluctuation of the number of water molecules close to the cleavage site was distinctly lower in the active conformation, again suggesting a more rigid conformational state (the standard deviation changes from 4.4 to 3.0). The water molecules directly responsible for the hydrolysis of the substrate are of course those that are very close to both catalytic aspartates. As shown by the blue line in **Figure 5A**, the number of water molecules within 4Å of both D257 and D385, changed from a mean 1.0 (inactive conformation) to 2.6 (active conformation), indicating structural properties more favorable for substrate processing.

One of the open questions regarding g-sec and its processing of single-span TMDs is the location of the substrate binding site(s). In addition to the active site (leading to immediate cleavage), the existence of several exosites responsible for the recognition and recruitment of substrate TMDs has been heavily

indicated by a number of experimental studies (Esler al., 2002; Tian et al., 2002; Kornilova et al., 2005; Fukumori and Steiner, 2016). The identification of such sites could help to elucidate the path along which C99 and other substrates enter the active site of PS-1, thereby enabling the analysis of the role played by many of the known PS-1 FAD mutations. Although fatty acid chains of POPC lipids differ quite substantially from TMD α-helices, their main mode of interaction with transmembrane proteins is similar—namely through dispersion effects in the apolar bilayer region and polar interactions at the lipid-water interface. Simple apolar interactions are rather unspecific (especially when compared to hydrogen bonds or salt bridges) and it can be argued that protein regions that are able to immobilize and bind POPC lipids should also be able to form substantial interactions with transmembrane α-helices. Insight into the number and position of such interaction patches was gained by measuring the mobility of all lipids in the simulation box. The ones that showed a very small deviation from their mean position can be regarded as situated at a protein region favorable for binding hydrophobic species (with polar headgroups). In order to achieve this, all subsequent frames of trajectory 2 have been aligned to the first frame with respect to the Cα atoms of the protein TMDs. Subsequently, the heavy-atom B-factors of all fatty acid chains have been calculated.

The resulting positional deviations indicated that lipid mobility in the system was very diverse. Generally, most POPC molecules were able to freely travel around the bilayer in the simulation box, however, some lipids were evidently held in place by interactions with one ore more of the g-sec subunits. These lipids have been identified by their low B-factor and the immobilization of their fatty acid chains has been confirmed by visual inspection of the trajectory. The left panel on **Figure 13** shows the seventeen lipids that exhibited the lowest B-factors in the simulation. All of the depicted fatty acid chains remained trapped in position and did not diffuse through the bilayer.

The four fatty acids showing the lowest B-factor (157–250Å^2) depicted in cyan, were situated at two different positions: One lipid (consisting of two fatty acid chains) was bound between the TMDs of nicastrin and APH-1a but since this patch is very far away from the active site it is unlikely that a putative substrate entry path starts from there (let alone it being the active site). The second binding site was intriguingly coinciding with the cavity formed by TMD 2, TMD 3, and TMD 5 in which a co-purified helix had been identified by Bai et al. (2015b). This cavity (see also **Figure 13**, right panel) remained stable for the duration of all the conducted simulations and is outlined by many of the known mutations reportedly leading to early onset Alzheimer's disease (cf. www.alzforum.org). These circumstances make a strong case for this region being an important substrate binding site, perhaps even the active site.

Another area often suspected to be involved in substrate adoption consists of TMDs 2, 6, and 9 (Tomita and Iwatsubo, 2013; Fukumori and Steiner, 2016). This suggestion is also supported by the present data as two fatty acids chains belonging to the same lipid were binding to that specific region. However, the color scheme (green: B-factor between 405 and 519 Å^2; purple: B-factor between 785 and 1025 Å^2 in **Figure 13** indicates that the immobilizing effect was lower and one of the two chains was bound with higher affinity than the other. Upon visual inspection of the simulation it became evident that most of the time only one of the two fatty acids was interfacing with the protein, with very few instances where both were able to bind simultaneously. This hints at slightly unfavorable conditions for binding larger entities at this position. Nevertheless, this location is easier to access than the cavity at TMD 2, 3, and 5, as there is a cytosolic loop connecting TMDs 2 and 3, requiring deformation of the substrate helix upon entering. A potential substrate helix bound at either of the two positions would be very close to the active site. Another interesting accumulation of lipids was situated at PEN-2 and PS-1 TMD 4 where a number of immobilized fatty acid could can be found, indicating that this region might play a role as an exosite, capturing potential substrates moving freely in the membrane.

CONCLUSIONS

Two atomistic (1 to 3.5 μs long) simulations of the γ-secretase complex have been conducted. with evaluation trajectories that were up to 3.5 μs in length. To our knowledge these are the longest purely atomistic computer simulations of the complete g-sec complex conducted to date. All simulations exhibited modest positional deviations throughout the sampling phase, indicating that the employed force fields were able to maintain stable conditions and keep the structure of the protein complex close to its native Cryo-EM-deduced structure. The existence of different conformational classes with respect to the distance between the active site aspartates and the relative position of PS-1 and PEN-2, as predicted by experimental means (Bai et al., 2015b), were also observed in the simulations. Additionally, similar tilting motion as exhibited by PEN-2 were also witnessed for APH-1a in agreement with available high resolution Cryo-EM structures.

Evaluation of the dynamical aspects of the complete complex in a POPC bilayer further confirmed the existence of a pronounced "up/down" and "left/right" movement exhibited by the NIC ECD. This sort of relative ecto-TMD movement has previously been suggested by simulations conducted with coarse grained (Aguayo-Ortiz et al., 2017) or elastic network models (Lee et al., 2017) of g-sec.

Since g-sec has been simulated with and without the bulky nicastrin ectodomain it was possible to investigate the influence on the dynamical and structural properties of the catalytic subunit of the complex. On the time scale of the present simulations no significant effect of the ectodomain on the structure and dynamics of presenilin-1 has been observed.

In one of the simulations a conformational change leading from catalytically inactive PS-1 to the active conformation has been sampled and the associated distinct motions characterizing the transition have been identified: A reduction of the distance between TMD 6 and 7 by an inward movement on the part of TMD 6, as well as a rotation of the N-terminus of TMD 7, leading D385 to face D257. Also, the observation of an active conformational arrangement over μs time scale indicated that such a state is at least transiently accessible also in the apo state of the enzyme. RMSD, mobility and water hydration data strongly suggested that the active conformation of g-sec is more rigid than the inactive form. It has recently been speculated

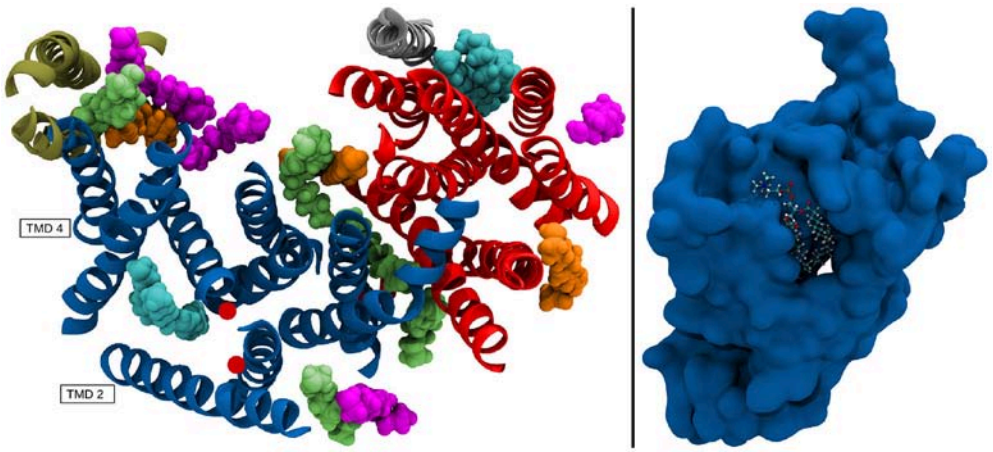

FIGURE 13 | (Left panel) TMDs of γ-secretase with strongly immobilized lipids. The TMDs of PS-1 are colored in dark blue, PEN-2 is depicted in beige, APH-1 in red and nicastin in gray. The lipids are colored according to their B-factor: Cyan: 156 to 250Å^2; orange: 405 to 519Å^2; green: 610 to 732Å^2; purple: 785 to 1026Å^2. The active site residues D257 and D385 are marked by red dots. **(Right panel)** Van der Waals surface depiction of presenilin-1 with the strongly bound POPC molecule in the cavity.

that some FAD mutations may lead to a destabilization of the protein fold which in turn could have an impact on its proteolytic capabilities (Szaruga et al., 2017). The conformational change sampled in this study suggests that even the wildtype of γ-secretase exists in conformational states with differing rigidity. Mutations at neuralgic positions can be expected to shift the balance between these states also in the direction of the state with more loosely associated TMDs. This could have an impact on both, the enzyme-substrate complex stability and the length of the interval between two processing steps (because g-sec is more likely to be in a state where it is not capable to cleave the APP fragment).

The hydration properties of PS-1 have been elucidated by counting the water molecules present at specific locations, leading to the conclusion that there is an ample amount of water molecules present in and around the active site of PS-1. The high number of polar solvent molecules in the putative binding site also hinted at the possible destabilization of a hydrophobic substrate helix, not only in the location of the scissile bond but also further downstream up to the substrate C-terminus.

The prime suspect to be the main substrate binding site is the cavity located between TMDs 3 and 5. Not only has it been stable throughout all simulations, it was large enough to bind a substrate TMD (Bai et al., 2015b), outlined by several FAD mutation sites (cf. www.alzforum.org) and strongly immobilized hydrophobic chains as shown by the lipid mobility computation for system 2. If C99 or other substrates bind in this groove, it would also be very likely that they formed additional interactions with the nicastrin loop extending from residue S241 to C248. What speaks against TMDs 2 and 3 forming the portal to the active site is the presence of a very short loop connecting both helices at the intracellular side, thus forcing a potential (uncleaved) substrate molecule to be kinked in order to fit. On the other hand, the gathered simulation data strongly suggests, that the protein is very flexible in exactly this region. Such high plasticity is of course very beneficial for the hypothetical entry of a sterically demanding substrate molecule. Future simulation studies in the presence of a substrate TM helix may help to elucidate putative substrate binding sites as well as entry pathways to the active site and also provide insight into how the flexibility of γ-secretase is affected by substrate binding.

AUTHOR CONTRIBUTIONS

MH performed research, analyzed data, and wrote the article. MZ designed research and wrote the article.

FUNDING

Financial support by the DFG (German Research Foundation) grant FOR 2290 (project P7) is gratefully acknowledged. Computer resources for this project have been provided by the Gauss Centre for Supercomputing /Leibniz Supercomputing Centre under grant pr27a.

ACKNOWLEDGMENTS

We thank Dieter Langosch, Christina Scharnagl, and Harald Steiner for many helpful discussions.

SUPPLEMENTARY MATERIAL

The Supplementary Material for this article can be found online at: https://www.frontiersin.org/articles/10.3389/fchem.2018.00640/full#supplementary-material

REFERENCES

Aguayo-Ortiz, R., Chávez-Garcia, C., Straub, J. E., and Dominguez, L. (2017). Characterizing the structural ensemble of γ-secretase using a multiscale molecular dynamics approach. *Chem. Sci.* 8, 5576–5584. doi: 10.1039/C7SC00980A

Bai, X., Rajendra, E., Yuang, G., Shi, Y., and Scheres, S. H. W. (2015b). Sampling the conformational space of the catalytic subunit of human γ-secretase. *eLife* 4:pii:e11182. doi: 10.7554/eLife.11182

Bai, X., Yan, C., Yan, G., Lu, P., Ma, D., Sun, L., et al. (2015a). An atomic structure of human γ-secretase. *Nature* 525, 212–218. doi: 10.1038/nature14892

Beel, A. J., and Sanders, C. R. (2008). Substrate specificity of gamma-secretase and other intramembrane proteases. *Cell Mol. Life Sci.* 65, 1311–1334. doi: 10.1007/s00018-008-7462-2

Berendsen, H. J. C., Postma, J. P. M., van Gunsteren, W. F., DiNola, A., and Haak, J. R. (1984). Molecular dynamics with coupling to an external bath. *J. Phys. Chem.* 81, 3684–3690. doi: 10.1063/1.448118

Bolduc, D. M., Montagna, D. R., Seghers, M. C., Wolfe, M. S., and Selkoe, D. J. (2016). The amyloid beta forming tripeptide cleavage mechanism of γ-secretase. *eLife* 5:e17578. doi: 10.7554/eLife.17578

Case, D. A., Betz, R. M., Cerutti, D. S., Cheatham, T. E. III., Darden, T. A., Duke, R. E., et al. (2016). *Amber 2016*. San Francisco, CA: University of California.

Darden, T., York, D., and Pedersen, L. (1993). Particle mesh ewald: an n log (n) method for ewald sums in large systems. *J. Chem. Phys.* 98, 10089–10092. doi: 10.1063/1.464397

De Strooper B. (2014). Lessons from a failed γ-secretase alzheimer trial. *Cell* 159, 721–726. doi: 10.1016/j.cell.2014.10.016

De Strooper, B., and Chávez Gutiérrez, L. (2015). Learning by failing: ideas and concepts to tackle γ-secretases in alzheimer's disease and beyond. *Ann. Rev. Pharmacol. Toxicol.* 55, 419–437. doi: 10.1146/annurev-pharmtox-010814-124309

De Strooper, B., Iwatsubo, T., and Wolfe, M. S. (2012). Presenilins and γ-secretase: structure, function and role in alzheimer's disease. *Cold Spring Harb. Perspect. Med.* 2:a006304. doi: 10.1101/cshperspect.a006304

Deyts, C., Thinakaran, G., and Parent, A. T. (2016). App receptor? To be or not to be. *Trends Pharmacol. Sci.* 37, 390–411. doi: 10.1016/j.tips.2016.01.005

Dickson, C. J., Madej, D. M., Skjevik, Å. A., Betz, R. M., Teigen, K., Gould, I. R., et al. (2014). Lipid14: the amber lipid force field. *J. Chem. Theory Comput.* 10, 865–879. doi: 10.1021/ct4010307

Elad, N., De Strooper, B., Lismont, S., Hagen, W., Veugelen, S., Arimon, M., et al. (2015). The dynamic conformational landscape of γ-secretase. *J. Cell Sci.* 128, 589–598. doi: 10.1242/jcs.164384

Esler, W. P., Kimberly, W. T., Ostaszewski, B. L., Ye, W., Diehl, T. S., Selkoe, D. J., et al. (2002). Activity-dependent isolation of the presenilin–γ-secretase complex reveals nicastrin and a γ substrate. *Proc. Natl. Acad. Sci. U.S.A.* 99, 2720–2722. doi: 10.1073/pnas.052436599

Francis, R., McGrath, G., Zhang, J., Ruddy, D. A., Sym, M., Apfeld, J., et al. (2002). aph-1 and pen-2 are required for notch pathway signaling, γ-secretase cleavage of βapp, and presenilin protein accumulation. *Dev. Cell* 3, 85–97. doi: 10.1016/S1534-5807(02)00189-2

Fukumori, A., and Steiner, H. (2016). Substrate recruitment of γ-secretase and mechanism of clinical presenilin mutations revealed by photoaffinity mapping. *EMBO J.* 35, 1628–1643. doi: 10.15252/embj.201694151

Goga, N., Rzepiela, A. J., De Vries, A. H., Marrink, S. J., and Berendsen, H. J. C. (2012). Efficient algorithms for langevin and dpd dynamics. *J. Chem. Theory Comput.* 8, 3637–3649. doi: 10.1021/ct3000876

Grossman, M., Born, B., Heyden, M., Tworowsky, D., Fields, G., Sagi, I., et al. (2011). Correlated structural kinetics and retarded solvent dynamics at the metalloprotease active site. *Nat. Struct. Mol. Biol.* 18, 1102–1108. doi: 10.1038/nsmb.2120

Haapasalo, A., and Kovacs, D. M. (2011). The many substrates of presenilin/gamma-secretase. *J. Alzheimers Dis.* 25, 3–28. doi: 10.3233/JAD-2011-101065

Hardy, J. A., and Higgins, G. A. (1992). Alzheimer's disease: the amyloid cascade hypothesis. *Science* 256, 184–185. doi: 10.1126/science.1566067

Holmes, O., Paturi, S., Wenjuan, Y., Wolfe, M. S., and Selkoe, D. J. (2012). Effects of membrane lipids on the activitiy and processivity of purified γ-secretase. *J. Biochem.* 52, 3565–3575. doi: 10.1021/bi300303g

Humphrey, W., Dalke, A., and Schulten, K. (1996). Vmd - visual molecular dynamics. *J. Mol. Graphics* 14, 33–38. doi: 10.1016/0263-7855(96)00018-5

Jo, S., Iyer, V. G., and Im, W. (2008). Charmm-gui: a web-based graphical user interface for charmm. *J. Comput. Chem.* 29, 1859–1865. doi: 10.1002/jcc.20945

Kamp, F., Winkler, E., Trambauer, J., Ebke, A., Fluhrer, R., and Steiner, H. (2015). Intramembrane proteolysis of β-amyloid precursor protein by γ-secretase is an unusually slow process. *Biophys. J.* 108, 1229–1237. doi: 10.1016/j.bpj.2014.12.045

Kong, R., Chang, S., Xia, W., and Wong, S. T. C. (2015). Molecular dynamics simulation study reveals potentials substrate entry path into γ-secretase/presenilin-1. *J. Struct. Biol.* 191, 120–129. doi: 10.1016/j.jsb.2015.07.001

Kornilova, A. Y., Bihel, F., Das, C., and Wolfe, M. S. (2005). The initial substrate-binding site of γ-secretase is located on presenilin near the active site. *Proc. Natl. Acad. Sci. U.S.A.* 102, 3230–3235. doi: 10.1073/pnas.0407640102

Krop, I., Demuth, T., Guthrie, T., Wen, P. Y., Mason, W. P., Chinnaiyan, P., et al. (2012). Phase i pharmacologic and pharmacodynamic study of the gamma secretase (notch) inhibitor mk-0752 in adult patients with advanced solid tumors. *J. Clin. Oncol.* 30, 2307–2313. doi: 10.1200/JCO.2011.39.1540

Langosch, D., Scharnagl, C., Steiner H., and Lemberg, M. K. (2015). Understanding intramembrane proteolysis: from protein dynamics to reaction kinetics. *Trends Biochem. Sci.* 40, 318–327. doi: 10.1016/j.tibs.2015.04.001

Langosch, D., and Steiner, H. (2017). Substrate processing in intramembrane proteolysis by –secretasethe role of protein dynamics. *Biol. Chem.* 398, 441–453. doi: 10.1515/hsz-2016-0269

Lee, J. Y., Feng, Z., Xie, X. Q., and Bahar, I. (2017). Allosteric modulation of intact γ-secretase structural dynamics. *Biophys. J.* 113, 2634–2649. doi: 10.1016/j.bpj.2017.10.012

Lee, S. F., Shah, S., Yu, C., Wigley, W. C., Li, H., Lim, M., et al. (2004). A conserved gxxxg motif in aph-1 is critical for assembly and activity of the γ-secretase complex. *J. Biol. Chem.* 279, 4144–4152. doi: 10.1074/jbc.M309745200

Lemere, C. A., Lopera, F., Kosik, K. S., Lendon, C. L., Ossa, J., Saido, T. C., et al. (1996). The e280a presenilin 1 alzheimer mutation produces increased aβ42 deposition and severe cerebellar pathology. *Nat. Med.* 2, 1146–1150. doi: 10.1038/nm1096-1146

Lomize, M. A., Pogozheva, I., Joo, H., Mosberg, H. I., and Lomize, A. L. (2012). Opm database and ppm web server: resources for positioning of proteins in membranes. *Nucleic Acids Res.* 40, D370–D376. doi: 10.1093/nar/gkr703

Maier, J. A., Martinez, C., Kasavajhala, K., Wickstrom, L., Hauser, K., and Simmerling, C. (2015). ff14sb: improving the accuracy of protein side chain and backbone parameters from ff99sb. *J. Chem. Theory Comput.* 11, 3696–3713. doi: 10.1021/acs.jctc.5b00255

Mark, P., and Nilsson, L. (2001). Structure and dynamics of the tip3p, spc, and spc/e water models at 298 k. *J. Phys. Chem. A* 105, 9954–9960. doi: 10.1021/jp003020w

Nickolls, J., Buck, I., Garland, M., and Skadron, K. (2008). Scalable parallel programming with cuda. *ACM Queue* 6, 40–53. doi: 10.1145/1365490.1365500

Rao, S. S., O'Neil, J., Liberator, C. D., Hardwick, J. S., Dai, X., Zhang, T., et al. (2009). Inhibition of notch signaling by gamma secretase inhibitor engages the rb pathway and elicits cell cycle exit in t-cell acute lymphoblastic leukemia cells. *Cancer Res.* 69, 3060–3068. doi: 10.1158/0008-5472.CAN-08-4295

Ryckaert, J. P., Ciccotti, G., and Berendsen, H. J. C. (1977). Numerical integration of the cartesian equations of motion of a system with constraints: molecular dynamics of n-alkanes. *J. Comput. Phys.* 23, 2327–2341. doi: 10.1016/0021-9991(77)90098-5

Singh, R., Barman, A., and Prabhakar, R. (2008). Computational insights into aspartyl protease activity of presenilin 1 (ps1) generating alzheimer amyloid β-peptides (aβ40 and aβ42). *J. Phys. Chem. B.* 113, 2990–2999. doi: 10.1021/jp811154w

Somavarapu, A. K., and Kepp, K. P. (2016). The dynamic mechanism of presenilin-1 function: sensitive gate dynamics and loop unplugging control protein access. *Neurobiol. Dis.* 89, 147–156. doi: 10.1016/j.nbd.2016.02.008

Somavarapu, A. K., and Kepp, K. P. (2017). Membrane dynamics of γ-secretase provides a molecular basis for aβ binding and processing. *ACS Chem. Neurosci.* 8, 2424–2436. doi: 10.1021/acschemneuro.7b00208

Sun, L. Zhou, R., Yang, G., and Shi, Y. (2016). Analysis of 138 pathogenic mutations in presenilin-1 on the *in vitro* production of aβ42 and aβ40

peptides in γ-secretase. *Proc. Natl. Acad. Sci. U.S.A.* 114:E476–E485. doi: 10.1073/pnas.1618657114

Szaruga, M., Munteanu, B., Lismont, S., Veugelen, S., Horré, K., Mercken, M. (2017). Alzheimer's-causing mutations shift aβ length by destabilizing γ-secretase aβn interactions. *Cell* 170, 443–456. doi: 10.1016/j.cell.2017.07.004

Tian, G., Sobotka-Briner, C. D., Zysk, J., Liu, X., Birr, C., Sylvester, M. A., et al. (2002). Linear non-competitive inhibition of solubilized human γ-secretase by pepstatin a methylester, l685458, sulfonamides, and benzodiazepines. *J. Biol. Chem.* 277, 31499–31505. doi: 10.1074/jbc.M112328200

Tomita, T., and Iwatsubo, T. (2013). Structural biology of presenilins and signal peptide peptidases. *J. Biol. Chem.* 288, 14673–14680. doi: 10.1074/jbc.R113.463281

Vassar, R., Bennett, B. D., Babu-Khan, S., Kahn, S., Mendiaz, E., Denis, P., et al. (1999). β-secretase cleavage of alzheimer's amyloid precursor protein by the transmembrane aspartic protease bace. *Science* 286, 735–741. doi: 10.1126/science.286.5440.735

Wolfe, M. S., Xia, W., Ostaszewski, B. L., Diehl, T. S., Taylor K. W., and Selkoe, D. J. (1999). Two transmembrane aspartates in presenilin-1 required for presenilin endoproteolysis and γ-secretase activity. *Nature* 398:513. doi: 10.1038/19077

Wu, E. L., Cheng, X., Jo, S., Rui, H., Song, K. C., Dvila-Contreras, E. M., et al. (2014). Charmm-gui membrane builder toward realistic biological membrane simulations. *J. Comput. Chem.* 35, 1997–2004. doi: 10.1002/jcc.23702

Xu, T., Yan, Y., Kang, Y., Jiang, Y., Melcher, K., and Xu, H. E. (2016). Alzheimer's disease-associated mutations increase amyloid precursor protein resistance to γ-secretase cleavage and the aβ40/aβ42 ratio. *Cell Discov.* 1:16026. doi: 10.1038/celldisc.2016.26

Zhang, Y., Luo, W., Wang, H., Lin, P., Vetrivel, K. S., Liao, F., et al. (2005). Nicastrin is critical for stability and trafficking but not association of other presenilin/γ-secretase components. *J. Biol. Chem.* 280, 17020–17026. doi: 10.1074/jbc.M409467200

Zhang, Y., Thompson, R., Zhang, H., and Xu, H. (2011). App processing in alzheimer's disease. *Mol. Brain* 4:3. doi: 10.1186/1756-6606-4-3

Conflict of Interest Statement: The authors declare that the research was conducted in the absence of any commercial or financial relationships that could be construed as a potential conflict of interest.

Copyright © 2019 Hitzenberger and Zacharias. This is an open-access article distributed under the terms of the Creative Commons Attribution License (CC BY). The use, distribution or reproduction in other forums is permitted, provided the original author(s) and the copyright owner(s) are credited and that the original publication in this journal is cited, in accordance with accepted academic practice. No use, distribution or reproduction is permitted which does not comply with these terms.

frontiers in Chemistry

ORIGINAL RESEARCH
published: 16 April 2019
doi: 10.3389/fchem.2019.00219

Bridging the Homogeneous-Heterogeneous Divide: Modeling Spin for Reactivity in Single Atom Catalysis

Fang Liu[1], *Tzuhsiung Yang*[1], *Jing Yang*[1], *Eve Xu*[1], *Akash Bajaj*[1,2] *and Heather J. Kulik*[1]*

[1] *Department of Chemical Engineering, Massachusetts Institute of Technology, Cambridge, MA, United States,* [2] *Department of Materials Science and Engineering, Massachusetts Institute of Technology, Cambridge, MA, United States*

Single atom catalysts (SACs) are emergent catalytic materials that have the promise of merging the scalability of heterogeneous catalysts with the high activity and atom economy of homogeneous catalysts. Computational, first-principles modeling can provide essential insight into SAC mechanism and active site configuration, where the sub-nm-scale environment can challenge even the highest-resolution experimental spectroscopic techniques. Nevertheless, the very properties that make SACs attractive in catalysis, such as localized *d* electrons of the isolated transition metal center, make them challenging to study with conventional computational modeling using density functional theory (DFT). For example, Fe/N-doped graphitic SACs have exhibited spin-state dependent reactivity that remains poorly understood. However, spin-state ordering in DFT is very sensitive to the nature of the functional approximation chosen. In this work, we develop accurate benchmarks from correlated wavefunction theory (WFT) for relevant octahedral complexes. We use those benchmarks to evaluate optimal DFT functional choice for predicting spin state ordering in small octahedral complexes as well as models of pyridinic and pyrrolic nitrogen environments expected in larger SACs. Using these guidelines, we determine Fe/N-doped graphene SAC model properties and reactivity as well as their sensitivities to DFT functional choice. Finally, we conclude with broad recommendations for computational modeling of open-shell transition metal single-atom catalysts.

Keywords: density functional theory, catalysis, single atom catalysis, spin state crossover, transition metal chemistry

OPEN ACCESS

Edited by:
Sam P. De Visser,
University of Manchester,
United Kingdom

Reviewed by:
Daniel Glossman-Mitnik,
Advanced Materials Research Center,
Mexico
Matthew George Quesne,
Cardiff University, United Kingdom

***Correspondence:**
Heather J. Kulik
hjkulik@mit.edu

Specialty section:
This article was submitted to Theoretical and Computational Chemistry, a section of the journal Frontiers in Chemistry

Received: *20 December 2018*
Accepted: *20 March 2019*
Published: *16 April 2019*

Citation:
Liu F, Yang T, Yang J, Xu E, Bajaj A and Kulik HJ (2019) Bridging the Homogeneous-Heterogeneous Divide: Modeling Spin for Reactivity in Single Atom Catalysis. Front. Chem. 7:219. doi: 10.3389/fchem.2019.00219

INTRODUCTION

Single atom catalysts (SACs) (Yang et al., 2013) are emergent catalytic materials (Yang et al., 2013; Liang et al., 2015, 2017) that have the promise of merging the scalability of heterogeneous catalysts with the high activity and atom economy of homogeneous catalysts, but the reactivity of SACs is poorly understood (**Figure 1**). Fe/N-doped graphene SACs have been demonstrated for critical transformations such as selective hydrocarbon oxidation (Liu et al., 2017), including ambient methane to methanol conversion (Cui et al., 2018), and as non-Pt oxygen reduction reaction (ORR) electrocatalysts (Li et al., 2016; Chen et al., 2017; Yang et al., 2018). The short-lived, variable

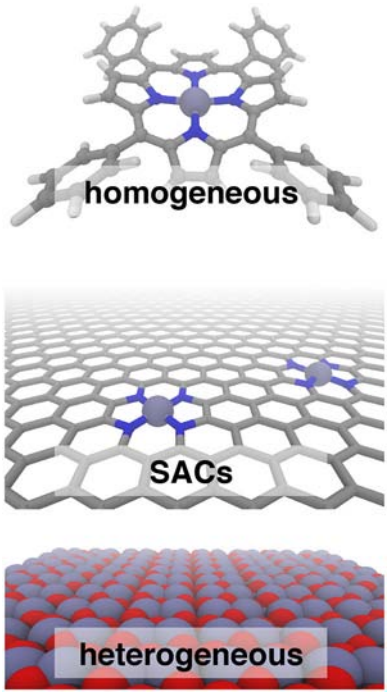

FIGURE 1 | Iron catalysts in three classes: homogeneous tetraphenyl porphyrin **(Top)**, N-doped graphene single atom catalysts (SACs, **Middle**), and heterogeneous hematite **(Bottom)**. In all cases, carbon is shown in gray, nitrogen in blue, iron in purple, and oxygen in red.

SAC active sites that are fundamentally sub-nm-scale challenge the resolution of spectroscopic techniques (Fei et al., 2015; Wang and Zhang, 2016), making first-principles modeling essential to mechanistic study.

For these emerging catalysts, changing synthesis (Liu et al., 2017) or reaction (Li et al., 2016; Zitolo et al., 2017) conditions changes the distribution of SAC coordination geometries, and the most reactive species for key reactions (e.g., ORR or selective partial hydrocarbon oxidation) remain under debate (Zitolo et al., 2015; Zhu et al., 2017; Yang et al., 2018). In selective partial hydrocarbon oxidation, spin-state-dependent reactivity of Fe/N-doped graphene SACs has been observed, with an intermediate, five-coordinate Fe(III)-N-C catalyst more reactive and selective (Liu et al., 2017) than low-spin or high-spin Fe active sites with four- or six-fold coordination. The fundamental source of this spin-state dependent reactivity remains unknown. In SAC electrocatalysts (Fei et al., 2015; Qiu et al., 2015; Zitolo et al., 2015, 2017; Back et al., 2017; Chen et al., 2017; Cheng et al., 2017; Zhang et al., 2017a,b; Zhu et al., 2017; Gao et al., 2018; Jiang et al., 2018; Wang et al., 2018; Zhang et al., 2018), changes in applied potential (e.g., in ORR) have been suggested to change the Fe SAC active site, possibly through a change in spin state (Zitolo et al., 2017).

Although perhaps surprising in the context of heterogeneous catalysis, strong spin-state dependence in reactivity is well-known in homogeneous catalyst (Schröder et al., 2000) analogs. Thus, it follows that paradigms that work in coordination chemistry might apply to SACs as well. The near-octahedral coordination environment around a metal center produces distinct quantum mechanical spin states (i.e., local metal magnetic moments) that are determined by the ligand-field strength as well as oxidation state and metal identity (Tsuchida, 1938). Different spin states often have distinct reaction barriers (Schröder et al., 2000; Schwarz, 2017) in a paradigm known as two-state reactivity (TSR) (Shaik et al., 1995; Schröder et al., 2000; Schwarz, 2017). TSR was first identified for Fe^+ ions, where oxidation of H_2 or CH_4 to H_2O or CH_3OH, respectively, is limited by spin inversion from a steep ground state, high spin (HS) surface to a more reactive but excited state low spin (LS) surface. For cases such as iron-oxo porphyrin systems that have nearly degenerate spin states, different pathways can indeed lead to distinct products (Kamachi and Yoshizawa, 2003; Ji et al., 2015).

In minimal model single-site catalysts, we recently demonstrated (Gani and Kulik, 2018) that bond elongation or compression has an effect similar to modulating ligand field strength, which could also alter ground state spin and reactivity in an interconnected manner. Most Fe(II)/N complexes have near degenerate HS and LS states because nitrogen ligands are of intermediate field strength, but small changes in the N-N separation of bidentate ligands that make up the octahedral complex are known to tune the experimental ground state of the material (Phan et al., 2017). In metal-doped graphene, strain has been predicted to change the ground state spin (Huang et al., 2011). Even changes in orientation of ligands (i.e., one equatorial swapped with one axial) have been experimentally observed to change the favored ground state spin of related molecular complexes (Andris et al., 2016).

The confined nature of metal *d* states and interactions with localized *p* orbitals from organic ligand atoms impart properties to open-shell SACs in a manner more closely resembling the chemical bonding of homogeneous catalysts than bulk metal counterparts. These very features, i.e., quantum size effects (Yang et al., 2013) at an open shell, high-valent metal atom, that make SACs reactive for essential catalytic transformations (Qiao et al., 2011; Yang et al., 2013; Zitolo et al., 2015, 2017; Zhang et al., 2018) also make conventional computational tools used in heterogeneous catalysis (i.e., plane wave, semi-local density functional theory, or DFT) ill-suited to predictive SAC study. Well-localized electrons are disproportionately affected by self-interaction error in approximate DFT (Cohen et al., 2011; Kulik, 2015), leading to an imbalanced treatment of differing spin and oxidation states (Ganzenmüller et al., 2005; Kulik et al., 2006; Droghetti et al., 2012; Ioannidis and Kulik, 2015, 2017; Mortensen and Kepp, 2015; Gani and Kulik, 2017).

Despite evidence of the importance of spin in homogeneous (Abram et al., 2014; Zhu et al., 2016; Schwarz, 2017) and SAC catalysts (Liu et al., 2017), most first-principles studies of SACs (Chu et al., 2015; Ma et al., 2016; Xu et al., 2018) have avoided directly quantifying the role of metal center spin in reactivity, with few exceptions (Impeng et al., 2014; Fong et al., 2018; Sirijaraensre and Limtrakul, 2018). In most studies, the magnetic moment is calculated with a semi-local DFT functional known to produce erroneous magnetic moments (Kulik, 2015; Ioannidis and Kulik, 2017; Janet et al., 2017; Wilbraham et al.,

2017) and the magnetization is often allowed to vary along the reaction coordinate (Xu et al., 2018). However, in confined metal centers, spin states are well defined and transitions between spin states occur with low probability because they are quantum mechanically forbidden. Spin state transitions can become kinetically limiting (Shaik et al., 1995; Schröder et al., 2000; Schwarz, 2017), explaining unexpected experimental reactivity (Andris et al., 2016). Within the homogeneous catalysis community (Harvey, 2014; Hernández-Ortega et al., 2015), significant effort has been made to develop tools to assess whether spin crossover is kinetically limiting, but this is not the case in SACs.

Unfortunately, given the importance of spin in predicting reactivity, spin state ordering is highly sensitive to the exchange-correlation functional employed in approximate DFT (Ganzenmüller et al., 2005; Kulik et al., 2006; Droghetti et al., 2012; Ioannidis and Kulik, 2015, 2017; Mortensen and Kepp, 2015). Semi-local (e.g., generalized gradient approximation, GGA) DFT functionals widely employed for their good cost/accuracy balance for many properties consistently stabilize overly-delocalized, covalent states (Autschbach and Srebro, 2014). GGAs thus favor the increased bonding in low-spin over high-spin states (Kulik, 2015; Gani and Kulik, 2017; Ioannidis and Kulik, 2017; Janet et al., 2017; Wilbraham et al., 2017). Hybrid functionals, which incorporate an admixture of HF exchange, are employed in organic chemistry to correct delocalization errors (Kümmel and Kronik, 2008). In transition metal catalysis, the fraction of HF exchange required, as judged by comparison to experiment or accurate correlated wavefunction theory (WFT) reference, is strongly system dependent (Bruschi et al., 2004; Ganzenmüller et al., 2005; Smith et al., 2005; Bowman and Jakubikova, 2012; Droghetti et al., 2012; Ioannidis and Kulik, 2015; Verma et al., 2017).

Thus, in this work, we carry out highly accurate correlated wavefunction theory calculations to develop benchmarks for transition metal complex spin state ordering with ligands that model the environment observed in single atom catalysts. Using these benchmarks, we identify trends in DFT functional performance, and then we evaluate how these observations influence predictions of the stability, reactivity, and ground state identity in models of Fe(II)/N-doped graphene SACs. Finally we provide our conclusions and outlook, including recommendations for computational modeling in this emergent space of single atom catalysis.

COMPUTATIONAL DETAILS

Octahedral Transition Metal Complexes

Initial structures of octahedral transition metal (TM) complexes with H_2O, NH_3, pyridine, and pyrrole ligands were built with the molSimplify toolkit (Ioannidis et al., 2016) with both ligand force-field pre-optimization and trained metal-ligand bond length features enabled. For the hexa-aqua and hexa-ammine complexes, M(II) Ti-Ni and M(III) V-Cu ions were studied, but the pyrrole and pyridine ligands were only studied in complex with Fe(II) or Fe(III). The formal charges assigned to the ligands were neutral in all cases except for pyrrole, which was deprotonated and given a −1 charge. High-spin (HS)-low-spin (LS) states studied in this work were defined as: triplet-singlet for d^2 Ti(II)/V(III) and d^8 Ni(II)/Cu(III), quartet-doublet for d^3 V(II)/Cr(III) and d^7 Co(II)/Ni(III), quintet-singlet for d^4 Cr(II)/Mn(III) and d^6 Fe(II)/Co(III), and sextet-doublet for d^5 Mn(II)/Fe(III). Intermediate-spin (IS) states were also studied: triplet d^4 Cr(II)/Mn(III) or d^6 Fe(II)/Co(III) and quartet d^5 Mn(II)/Fe(III).

Fe/N-Doped Graphene SAC Finite Models

Two possible Fe(II) coordination environments in finite graphitic SAC models were investigated with DFT, and in both the metal is coordinated by four nitrogen atoms substituted in the graphene structure. In both cases, we employed a hydrogen-atom-terminated graphene flake to avoid increasing computational cost in accordance with prior SAC computational studies that used finite models (Xu et al., 2018). First, a FeN_4C_{10} compound (chemical formula: $C_{36}N_4H_{16}Fe$) was studied in which all coordinating nitrogen atoms were in six-membered rings (i.e., pyridinic N). This structure is formed by removing two adjacent C atoms from $C_{42}H_{16}$ and replacing the four C atoms surrounding the vacancy with N atoms. This active site would correspond to two adjacent point defects in graphene, as has been observed experimentally (Banhart et al., 2011). A second compound, FeN_4C_{12} (chemical formula: $C_{40}N_4H_{16}Fe$), was also studied in which all coordinating nitrogen atoms were in five-membered rings (i.e., pyrrolic N). This structure was formed by removing two C atoms from a $C_{46}H_{16}$ structure, which contains two seven-membered rings in the center surrounded by four five-membered rings. Thus, this structure would require vacancy migration that has also been experimentally observed (Banhart et al., 2011). The two C atoms were removed from where the seven membered rings are joined, and the four inward-facing C atoms that are part of the five-membered rings were replaced with N atoms. All initial coordinates were generated by drawing the 2D structures with ChemDraw and converting the xml structures to 3D coordinates with the molSimplify (Ioannidis et al., 2016) interface to OpenBabel (O'Boyle et al., 2011) followed by force field optimization with the universal force field (Rappé et al., 1992). Singlet, triplet, and quintet spin states were studied, and all simulations had zero net charge.

Fe/N-Doped Graphene SAC Periodic Models

Periodic analogs to the flake models were studied starting from a 4×4 supercell of graphene at its experimental lattice parameter (Trucano and Chen, 1975). A smaller supercell than suggested (i.e., 7×7) in previous work (Krasheninnikov et al., 2009) was used for computational efficiency, and future work should focus on the effect of supercell size on dopant properties. The pyridinic (chemical formula: FeN_4C_{18}) SAC model was created following the same vacancy/N-atom replacement approach as in the finite case. For the pyrrolic (chemical formula: FeN_4C_{20}) SAC model, we started from the pyridinic case, inserting C atoms into the five-membered FeN_2C_2 ring. Next, we adjusted the adjacent six-membered rings into five-membered rings to create pyrrolic N atoms. In this small supercell, an eight-membered C ring was

then formed next to the five membered rings. Neutral systems were studied by spin polarized, fixed magnetization periodic calculations in singlet, triplet, and quintet states.

Localized Basis Set DFT Calculations

Transition Metal Complexes

All LS, IS, and HS complexes were geometry optimized with DFT using the PBE0 (default 25% exchange) global hybrid GGA functional (Adamo and Barone, 1999) with the def2-TZVP basis set (Weigend and Ahlrichs, 2005) in ORCA v.4.0 (Neese, 2018). Singlet states were calculated in a restricted formalism, whereas all remaining calculations were open shell and required level shifting (Saunders and Hillier, 1973) in select cases to aid self-consistent field convergence typically with a value of 1.0 eV but as large as 100.0 eV in one case ($[Mn(NH_3)_6]^{2+}$). The optimizations were carried out using the BFGS algorithm in redundant internal coordinates implemented to the default tolerances of 3×10^{-4} hartree/bohr for the maximum gradient and 5×10^{-6} hartree for the change in self-consistent field (SCF) energy between steps. All calculations at other levels of theory or with differing functional definitions were obtained as single point energies on these optimized geometries. The effect of Hartree-Fock (HF) exchange fraction choice on spin-state energetics within DFT was investigated by altering the fraction in a modified form of the PBE0 global hybrid. The HF exchange fraction was varied from as low as 0% [i.e., a pure PBE GGA (Perdew et al., 1996)] to as high as 100% HF exchange in increments of 10–20%, as indicated in the text, again using the def2-TZVP basis set. In previous work (Gani and Kulik, 2016), we found tuning range-separation parameters in range-corrected hybrids to have a comparable effect on density and energetics of transition metal complexes to global exchange tuning, and therefore we focus on only global exchange tuning in this work.

Fe/N-Doped Graphene Flake Models

Geometry optimizations and single-point energy calculations were performed with ORCA v4.0. All DFT methodology was kept the same as for transition metal complexes, including geometry optimizing at PBE0 (25% exchange) and carrying out single points at modified exchange fractions in PBE0 in 10% increments in conjunction with the def2-TZVP basis set, except as noted below. All singlet, triplet, and quintet calculations were carried out in an unrestricted formalism. All calculations employed the resolution of the identity (RI) (Baerends et al., 1973; Whitten, 1973; Dunlap et al., 1979; Eichkorn et al., 1995, 1997; Kendall and Fruchtl, 1997) and the chain-of-sphere (COSX)(Neese et al., 2009) approximations with the auxiliary basis set def2/J (Weigend, 2006) and def2-TZVP/C (Hellweg et al., 2007) for all atoms to accelerate the calculations while introducing marginal errors (Kossmann and Neese, 2009). Molecular structures and orbitals were visualized and plotted with VESTA (Momma and Izumi, 2011).

Periodic DFT Calculations

All systems were calculated with both the PBE (Perdew et al., 1996) semi-local GGA functional and the HSE06 (Heyd et al., 2003, 2006) local, range-separated GGA hybrid using the plane wave, periodic boundary condition Quantum-ESPRESSO (Paolo et al., 2009) code. Norm-conserving pseudopotentials for C, N, and Fe were generated with OPIUM (Rappe et al., 1990). The wavefunction and charge density cutoffs employed were 50 Ry and 200 Ry, respectively. A Monkhorst-Pack k-point grid of 8 $\times$ 8 $\times$ 1 was used for efficiency after confirming convergence of total energies with k-point mesh size. Total energies were converged to 0.1 meV and forces were converged to 1 meV/Å. Quantum-ESPRESSO post-processing tools were employed to visualize the spin density and projected density of states. Variable cell relaxation was employed to obtain final lattice parameters with PBE GGA for the pyridinic (result: 8.34 Å $\times$ 7.55 Å) and pyrrolic (result: 8.35 Å) models. A vacuum between each SAC layer of 10 Å was included along with a dipole correction to limit periodic image effects (Bengtsson, 1999). The HSE06 calculations were obtained as single point energies applied to these structures.

Correlated WFT

Complete active-space second-order perturbation theory (CASPT2) (Andersson et al., 1992) calculations were performed with OpenMolcas[1] (Aquilante et al., 2016) on M(II)/M(III) hexa-aqua and hexa-ammine octahedral complexes. Calculations were carried out with two active space definitions: the standard active space and an extended active space. For the standard active space, we followed literature recommendations for TM complexes (Pierloot, 2003; Veryazov et al., 2011) to include five orbitals with TM 3*d* character, two σ bonding orbitals describing covalent metal-ligand bonding, and five double-shell *d* orbitals for mid-row and later transition metals [i.e., Mn(II/III) and later]. For n 3*d* electrons, the standard active space is (n + 4, 7) (i.e., for Sc-Cr) or (n + 4, 12) (i.e., for Mn-Cu). In the extended active space, we followed additional literature recommendations (Wilbraham et al., 2017) to include the metal 3*s* orbital and an unoccupied counterpart, giving an active space of (n + 6, 9) (i.e., for Sc-Cr) or (n + 6, 14) (i.e., for Mn-Ni). Relativistic atomic natural orbital (ANO-rcc) basis sets (Roos et al., 2004, 2005) contracted to [7s6p5d3f2g1h] for the metal center, [4s3p2d1f] for O and N, and [3s1p] for H were used together with the scalar relativistic Douglas-Kroll Hamiltonian (Douglas and Kroll, 1974; Hess, 1986). The 10 core orbitals were frozen in all calculations. An imaginary level shift (Forsberg and Malmqvist, 1997) of 0.1 was used, and a zeroth-order Hamiltonian empirical correction, i.e., the IPEA shift (Ghigo et al., 2004), was set as 0.5 a.u. or varied as described in the main text to identify the effect on spin state energetics. For difficult to converge complete active space self-consistent field iterations, a level shift was applied to the Hamiltonian with shift value 1.0.

RESULTS AND DISCUSSION

Spin State Ordering in Model Complexes

Correlated WFT Results

We first conducted correlated wavefunction theory (WFT) calculations to generate reference spin-splitting energies of model

[1]OpenMolcas. Available online at: https://gitlab.com/Molcas/OpenMolcas.git (accessed June 6, 2018).

first row octahedral transition metal complexes. Our focus is on weak field hexa-aqua and hexa-ammine complexes that are small (i.e., 19–25 atoms in size) and of comparable ligand field strength to the coordination environment in SACs. Although CASPT2 is often the method of choice for predicting spin state energetics for molecules that are either too large or multireference in character to be comfortably treated with CCSD(T) (Pierloot et al., 2017), a number of calculation parameters can strongly influence the CASPT2 predictions. Specifically, spin state energetics can be influenced by the active space choice and the formulation of the zeroth-order Hamiltonian, i.e., the value of the IPEA shift (Ghigo et al., 2004). Here, we investigate the effects of both of these factors and then select reference results for DFT calculations.

Several studies (Kepenekian et al., 2009; Lawson Daku et al., 2012; Vela et al., 2016; Pierloot et al., 2017) have shown that the standard IPEA shift of 0.25 a.u. in CASPT2 overstabilizes high spin states. However, there is no universal agreement about the best solution to this problem. Some (Kepenekian et al., 2009; Lawson Daku et al., 2012; Vela et al., 2016) have recommended increasing the IPEA shift to 0.5–0.7 a.u. based on comparison with experimental or MRCI results, whereas others (Pierloot et al., 2017) recommend the standard IPEA value because increased IPEA can reduce the high spin bias but only at the expense of deteriorating the CASPT2 description of valence correlation. To understand the effect of IPEA shift, we obtained CASPT2 spin-splitting energies with IPEA shifts of 0.0, 0.50, and 1.5 a.u. and standard active spaces (**Figure 2** and see Computational Details). For all complexes, increasing IPEA shifts the high-spin/low-spin splitting toward more positive values, reducing high spin stabilization. The range of energetics calculated with different IPEA values for each complex provides a measure of IPEA sensitivity of each transition metal complex's spin-splitting energy (**Figure 2**). The IPEA sensitivity is consistently largest for cases where the high spin state has four more unpaired electrons than the low spin state (i.e., Cr^{2+} through Co^{3+}).

To focus only on spin state definitions in which the high spin state has two more unpaired electrons, we compare the high spin/low spin splitting, ΔE_{H-L}, for early and late TMs with the high spin/intermediate spin splitting, ΔE_{H-I}, for mid-row TMs. For these two electron differences, we observe similar sensitivities, with a ca. 10–20 kcal/mol positive shift when the IPEA is changed from 0.0 to 1.5 a.u. (**Figure 2**). This observation excludes only very early or late TM complexes that have smaller sensitivities. In comparison, the 4 electron-difference cases have higher sensitivities of around 30 kcal/mol or more (**Figure 2**). Overall, most early- and mid-row complexes remain high spin regardless of the IPEA shift (i.e., below the zero axis in **Figure 2**). The smaller energetic differences between states in later TM complexes [e.g., hexa-aqua Ni(III)] mean that the IPEA shift can change the ground state from high spin to low spin for very large IPEA shifts. For subsequent calculations, we selected the 0.5 a.u. IPEA shift but note that variation across the commonly employed range of 0.0–0.5 a.u. can shift the predicted ΔE_{H-L} (ΔE_{H-I}) spin-splitting for mid-row [e.g., Fe(II/III)] complexes by around 10 (3) kcal/mol (**Figure 2**).

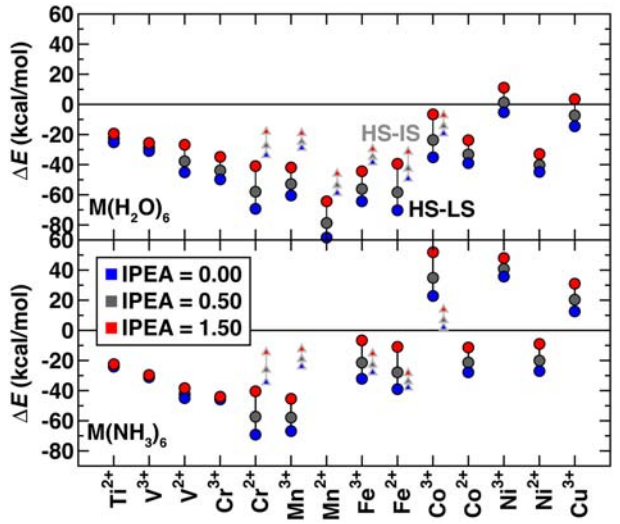

FIGURE 2 | CASPT2 spin splitting energetics in kcal/mol for ΔE_{H-L} (circles) and ΔE_{H-I} (triangles), as indicated in inset, of hexa-aqua (top) and hexa-ammine (bottom) transition metal complexes. Results are shown for 3 IPEA shifts: 0.00 (blue symbols), 0.50 (dark gray symbols), and 1.50 (red symbols) a.u.. Both M(II) and M(III) complexes are shown sorted by the number of 3*d* electrons, from Ti^{2+} to Cu^{3+}.

We next investigated the effect of use of a standard active space vs. a more extended active space in the CASPT2 calculations of ΔE_{H-L} and ΔE_{H-I} using the 0.5 a.u. IPEA shift (**Supplementary Table 1**). For most complexes, the energetic difference due to active space change is on the order of a few kcal/mol, which suggests that the calculation is converged with respect to active space size, as motivated in previous work (Wilbraham et al., 2017). The major outlier identified is $[Mn(NH_3)_6]^{2+}$, which is strongly low-spin in the standard active space but becomes high-spin like hexa-aqua Mn(II) with the extended active space, exhibiting greater active space dependence than had been observed in Mn(II) porphyrins (Yang et al., 2016) (**Supplementary Table 1**). This discrepancy is likely caused by orbital rotation of some active orbitals into the inactive metal 3*s*/4*s* orbitals, as suggested in recent work (Radoń and Drabik, 2018) on aqua complexes. After removing this outlier, the mean absolute difference between the standard and extended active space results for all ΔE_{H-L} and ΔE_{H-I} combinations is 3.3 kcal/mol for the hexa-aqua and 5.9 kcal/mol for the hexa-ammine complexes. The mean signed error is near zero for the hexa-aqua cases, and weakly negative (ca. −3 kcal/mol) for the hexa-ammines (**Supplementary Table 1**). Generally, discrepancies are smallest for the hexa-aqua complexes throughout and especially small for the early or late TMs (e.g., Ti^{2+}-V^{2+} and Ni^{3+}-Cu^{3+}), typically as little as 0–2 kcal/mol (**Supplementary Table 1**). In mid-row cases, there is no universal preference as to whether ΔE_{H-L} or ΔE_{H-I} has more active space dependence.

Given the small size of the studied octahedral complexes, we selected the extended active space calculations as reference values for comparison to DFT. Use of the larger active space changed some ground state spin assignments. When calculated

with the extended active space, almost all hexa-aqua complexes are high spin, excluding only weakly low spin $[Ni(H_2O)_6]^{3+}$ with a ΔE_{H-L} of 0.49 kcal/mol. The slightly stronger ligand field in the hexa-ammine complexes produces some additional LS late-TM complexes [e.g., Co(III) and Cu(III)] along with the analogous Ni(III) complex. Examining isoelectronic metals generally reveals that the later, more oxidized metal has only a weak high-spin-stabilizing effect that is smaller than the ligand-field effect in cases where the two metals converge to similar electronic states (**Figure 2** and **Supplementary Table 1**).

DFT Functional Performance

Despite the high accuracy of CASPT2 for treating spin state energetics in TM complexes, the high computational cost and sensitivity to active space definition and parameters limit its application on SACs. We thus sought to identify the extent to which DFT functionals can be selected or tuned to reproduce the spin-splitting energetics obtained with CASPT2. We focused on the exchange fraction within the global hybrid PBE0 (Adamo and Barone, 1999), motivated by previous observations of comparable behavior in tuning range-separated hybrids (Gani and Kulik, 2016), global hybrids with a different correlation functional (Ioannidis and Kulik, 2015), or those that incorporate meta-GGA exchange (Ioannidis and Kulik, 2017).

From all complexes studied with CASPT2, we narrowed our focus to those containing nominally 3–7 3*d* electrons (i.e., V^{2+} to Ni^{3+}) that are most likely to be good candidates for understanding spin-state dependent single atom catalysis. We determined the effect of varying PBE0 exchange fraction on both ΔE_{H-L} and ΔE_{H-I} for the relevant subset (i.e., 4–6 3*d* electrons). In accordance with prior work (Droghetti et al., 2012; Ioannidis and Kulik, 2015), we anticipated the sensitivity of these quantities to exchange fraction and the optimal exchange fraction to minimize error with respect to CASPT2 to be chemistry dependent. However, we aimed to identify if these trends can be readily rationalized (Gani and Kulik, 2017) or learned (Janet and Kulik, 2017) for use in SAC modeling.

As expected (Droghetti et al., 2012; Ioannidis and Kulik, 2015; Zhao and Kulik, 2018), spin-state energetics vary linearly with exchange fraction over a wide range (i.e., 0–50%) and high-spin states are stabilized with increasing exchange fraction for all transition metal complexes studied (**Supplementary Tables 2–3**). We quantified the exchange sensitivity of the spin-splitting energetics (Ioannidis and Kulik, 2015) by an approximate linear fit:

$$\frac{\partial \Delta E_{H\text{-}L/I}}{\partial a_{HF}} \approx \frac{\Delta \Delta E_{H\text{-}L/I}}{\Delta a_{HF}} \quad (1)$$

We use the unit notation HFX corresponding to the variation from 0 to 100% exchange. To maximize correspondence in quantities compared, we evaluate exchange sensitivity of all spin states that differ by two paired electrons: ΔE_{H-L} for V(II)/Cr(III) and Co(II)/Ni(III) and ΔE_{H-I} for the remaining complexes (ΔE_{H-L} values are also tabulated in **Supplementary Table 3**). The exchange sensitivity of two-electron-difference spin-state ordering for $[M(H_2O)_6]^{2+}$ complexes is relatively invariant to

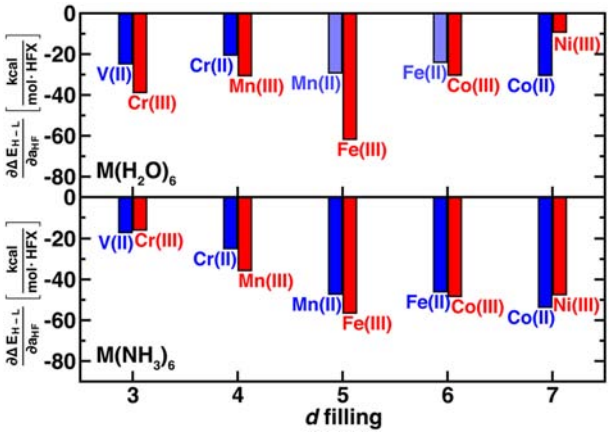

FIGURE 3 | Sensitivity of spin-state splitting with respect to HF exchange (i.e., $\partial \Delta E_{H-L}/\partial a_{HF}$, in kcal/mol·HFX) for hexa-aqua (top) and hexa-ammine (bottom) transition metal complexes. Both M(II) and M(III) complexes are shown grouped by their nominal *d* filling from 3 to 7 3*d* electrons for V(II) to Ni(III). For the 4, 5, and 6 *d*-electron cases, the energy gap corresponds to high-spin/intermediate-spin rather than high-spin/low-spin. Shaded bars indicate that spin contamination could not be eliminated for both spin states and sensitivity may not be reliable.

3*d* filling (i.e., varying only 2–4 kcal/(mol·HFX), see **Figure 3**). Conversely, hexa-ammine Mn(II), Fe(II), and Co(II) complexes have increased spin-splitting exchange sensitivity over the earlier TM complexes (**Figure 3**). For both ligand fields, the M(III) complexes are even more varied, with the least exchange sensitivity being observed in either late or early transition metal complexes (**Figure 3**). These observations are consistent with the fact that these complexes should have the least difference in electron delocalization between the two spin states, reducing exchange sensitivity (Gani and Kulik, 2017). Although M(III) complexes are more variable, isoelectronic +2/+3 complexes do have somewhat comparable exchange sensitivity (**Figure 3**). In comparing ΔE_{H-L} for all complexes, exchange sensitivity is universally higher for these mid-row cases due to the enhanced sensitivity of the four-electron difference energetics (e.g., $[M(H_2O)_6]^{2+}$: −57 kcal/(mol·HFX) for Mn vs. −25 kcal/(mol·HFX) for V, see **Supplementary Figure 1**).

The remaining question is whether the exchange fraction can be appropriately tuned within a modified form of PBE0 to obtain ΔE_{H-L} and ΔE_{H-I} values that match CASPT2 results. Comparing the range of spin-splitting energies obtained from 0 to 100% exchange to the CASPT2 extended active space values generally reveals that high exchange fractions (c.a. 40%) are required to reproduce CASPT2 results (**Figure 4** and ΔE_{H-L}-only results shown in **Supplementary Figure 2**). With the exception of Ni(III) or V(II)/Cr(III) hexa-ammines, pure PBE GGA ΔE values are much more positive (i.e., low-spin biased) than the WFT results (**Figure 4**). Increasing exchange thus in most cases improves agreement with WFT, but the optimal exchange fraction for reproducing the CASPT2 result varies significantly for the different complexes (**Figure 4**). For five of the cases [e.g., midrow $Mn(II)(H_2O)_6$, $Fe(II)(NH_3)_6$, and $Co(II)(H_2O)_6$], the optimal exchange fraction is larger than

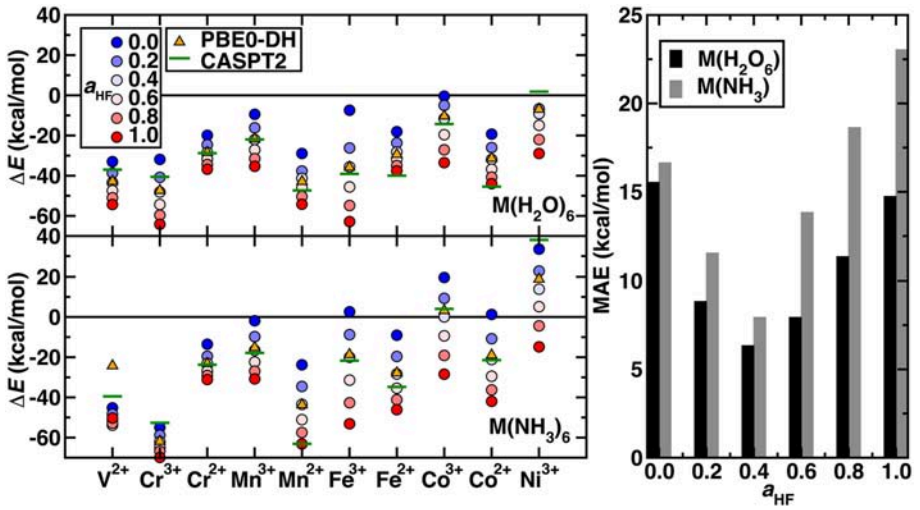

FIGURE 4 | (Left) Spin-splitting energetics (in kcal/mol) corresponding to ΔE_{H-l} for Cr^{2+}-Co^{3+} and ΔE_{H-L} for all other cases shown for hexa-aqua **(Top)** and hexa-ammine **(Bottom)** complexes. Modified PBE0 GGA hybrid results are shown as circles. The exchange fraction, a_{HF}, is colored from blue for 0.0 (pure GGA) to red for 1.0 (full HF exchange), according to the inset legend. Reference CASPT2 results with the extended active space and IPEA shift of 0.5 a.u. are shown as green horizontal lines. The PBE0-DH results are shown as orange triangles. **(Right)** MAE (in kcal/mol) at several exchange fractions for the hexa-aqua and hexa-ammine complexes indicated at left.

0.4, whereas the majority of the remaining complexes would require exchange fractions of 0.0-0.4 to recover the CASPT2 value (**Figure 4**). Only three complexes [i.e., V(II)$(H_2O)_6$, Cr(III)$(H_2O)_6$, and Ni(III)$(H_2O)_6$] have an optimal exchange fraction corresponding to typically applied (Ioannidis and Kulik, 2015) values of around 10–30%.

Considering overall performance on the 20 TM complexes, incorporating any exact exchange reduces the mean absolute error (MAE) of spin-splitting energies with respect to WFT. From PBE to 20% to 40% exchange, the MAE decreases monotonically from 17 to 12 to 8 kcal/mol for hexa-ammines and comparably (i.e., 16 to 9 to 6 kcal/mol) for hexa-aquas (**Figure 4**). Increasing HF exchange higher than 40% increases the MAE again for both ligand fields. For these two weak ligand fields, the optimal exchange fraction is more metal dependent than ligand field dependent, producing comparable optimal exchange values for fixed metal and oxidation state (**Figure 4**). Recent work (Wilbraham et al., 2018) has suggested double hybrids (DH, i.e., with MP2 long-range correlation) could improve predictions of spin-state ordering. We selected the PBE0-DH, which contains 50% global HF exchange for comparison to GGA global hybrid results (**Figure 4**). The PBE0-DH results are comparable to those obtained with a modified PBE0 global hybrid GGA with 40% exchange (i.e., MAE of 8 kcal/mol for hexa-ammine complexes and 6 kcal/mol for hexa-aqua complexes, see **Supplementary Table 4**). Given the higher computational cost and scaling of the double hybrids, tuned GGA hybrids would remain a preferable choice for modeling larger systems.

Comparison of Nitrogen-Containing Ligands

So far, we have studied model complexes and confirmed the importance of incorporating exact exchange in DFT functionals to reproduce correlated WFT reference spin-splitting energetics. We next considered the transferability of exchange sensitivity of DFT spin-splitting energetics to octahedral transition metal complexes that contain coordination environments similar to Fe/N-doped graphene SAC models. The two ligands we used to represent these environments were pyridine (py) in which the coordinating nitrogen is in a six membered carbon-containing ring and pyrrole (pyr) in which the coordinating nitrogen is in a five membered carbon-containing ring (**Figure 5** inset and see Computational Details). With a pure PBE GGA, all complexes except for hexa-pyr Fe(II) are low spin, whereas exchange fractions above ∼15% instead result in all ground states being assigned as high spin (**Figure 5**). The trend with exchange is again linear as in the hexa-ammine complexes, although the linearity is slightly reduced for Fe(II) vs. Fe(III) complexes (**Figure 5**).

The ΔE_{H-L} values are within ∼7 kcal/mol for all complexes of the same oxidation state across the full range of exchange due to the relatively similar ligand field strengths of the N-containing ligands and comparable metal-ligand bond lengths (**Supplementary Table 5**). However, the hexa-ammines are generally the most low-spin-favoring, whereas the SAC-like nitrogen complexes have a slightly increased high-spin bias. In analogy to ligand field arguments for ΔE_{H-L}, exchange sensitivities, $\frac{\partial \Delta E_{H-L}}{\partial a_{HF}}$, of spin splitting are also comparable for ammonia, pyridine and pyrrole complexes (**Figure 5**). For $\frac{\partial \Delta E_{H-L}}{\partial a_{HF}}$, NH_3 and pyrrole are very similar in both Fe(II) [−72 and −77 kcal/(mol·HFX)] and Fe(III) [−88 and −85 kcal/(mol·HFX)], whereas pyridine has slightly larger slope of −92 kcal/(mol·HFX) in both oxidation states. These observations are consistent with the previously observed greater sensitivity to the ligand identity than to oxidation state for Fe(II)/Fe(III) (Ioannidis and Kulik, 2015). Due to the similar spin-splitting

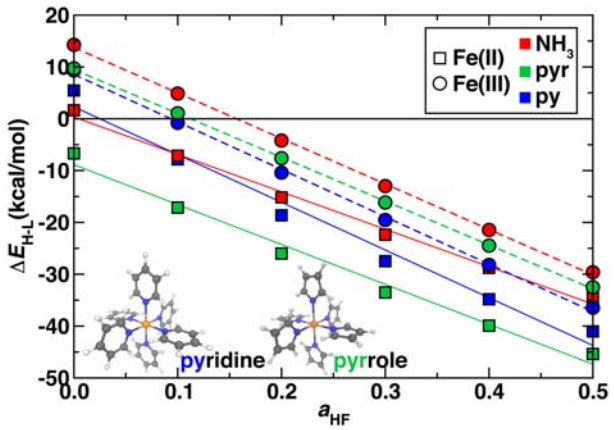

FIGURE 5 | Sensitivity to HF exchange fraction (a_{HF}) of high-spin/low-spin splitting (ΔE_{H-L}, in kcal/mol) for Fe(II) (squares) and Fe(III) (circles) homoleptic octahedral transition metal complexes with NH_3 (red symbols), pyridine (blue symbols), and pyrrole (green symbols) ligands. The structures of pyridine and pyrrole compounds are shown in inset in ball and stick (gray carbon, blue nitrogen, white hydrogen, and orange for iron). A zero axis is shown that indicates change in favored ground state spin.

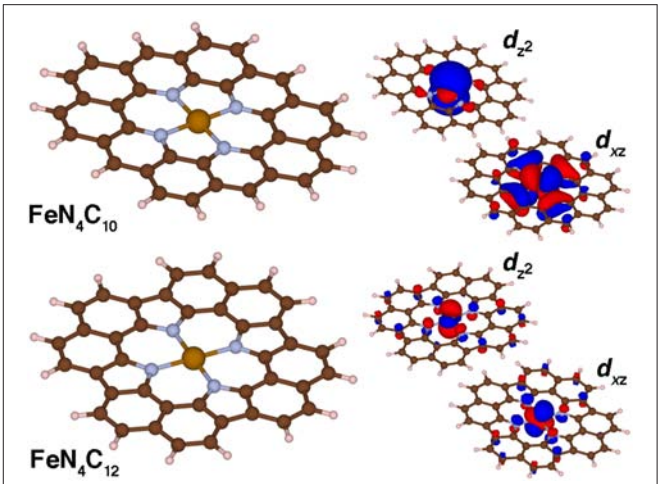

FIGURE 6 | Molecular structures (left) and singly occupied d_{xz} and $d_z{}^2$ spin-up molecular orbitals (right) for FeN_4C_{10} and FeN_4C_{12} graphene flake SAC models in the triplet state. The positive and negative phases of the wavefunction are shown in red and blue, respectively. An isosurface of 0.01 e/Bohr^3 was used for the orbitals of FeN_4C_{10} and of 0.03 e/Bohr^3 for those of FeN_4C_{12} for clarity. All structures are shown in ball and stick representation with carbon in brown, hydrogen in white, nitrogen in light blue, and iron in orange.

energetics and sensitivities to exchange, we expect that our observations on hexa-ammine complexes are applicable to pyridinic and pyrrolic nitrogen-containing complexes and materials as well. Thus, for larger SAC models, we recommend either typical exchange fractions for qualitative ground state spin assignment (i.e., high spin) or higher exchange fractions (ca. 40–50%) that were needed in the hexa-ammine cases to reproduce WFT results quantitatively.

Graphene Flake Models of SACs

Fe/N-doped graphitic SACs are expected on the basis of experimental spectroscopic characterization (Zitolo et al., 2015; Chen et al., 2017; Liu et al., 2017) to consist of Fe metal centers coordinated by pyridinic or pyrrolic nitrogen atoms. These experimental observations come from a combination of aberration corrected scanning tunneling electron microscopy to confirm well-isolated metal sites as well as numerous spectroscopic techniques (e.g., X-ray absorption spectroscopy) to confirm the metal coordination (Zitolo et al., 2015; Chen et al., 2017; Liu et al., 2017). Although the most reactive SAC active site remains an open question, we consider in this work two limits in finite graphene flake SAC models that contain either four pyridinic (FeN_4C_{10}) or pyrrolic (FeN_4C_{12}) N atoms (**Figure 6**). Due to the rigidity of the graphene flakes, singlet Fe(II) pyridinic (py) and pyrrolic (pyr) Fe-N bond lengths are shorter than the corresponding py or pyr octahedral complexes (py: 1.90 vs. 2.08 Å or pyr: 1.97 Å vs. 2.11 Å, see **Supplementary Tables 5–6**). This rigidity in the SAC models without any displacement of iron from the plane that has been observed in porphyrins (Sahoo et al., 2015) also leads to average Fe-N distances being invariant to spin state. There is a marginal (ca 0.01 Å) increase from singlet to quintet spin states for the FeN_4C_{10} SAC in comparison to large (ca. 0.16–0.20 Å) bond length increases from singlet to quintet in the $Fe(II)(py)_6$ complex (**Supplementary Tables 5–6**). The Fe-N distances are shorter in pyridinic FeN_4C_{10} than in pyrrolic FeN_4C_{12} (i.e., 1.90 Å vs. 1.96 Å) due to smaller N-N separations (FeN_4C_{10}: 2.61 Å and 2.75 Å, FeN_4C_{12}: 2.75 Å). Despite this difference in N-N separation, which has previously been noted to influence experimental spin state ordering (Phan et al., 2017), the PBE0 ground state spin is triplet in both models (**Supplementary Table 7**).

The two singly occupied orbitals in both triplet SAC models correspond to the d_{xz} and $d_z{}^2$ orbitals consistent with expectations for square-planar coordinated triplet Fe(II) (**Figure 6**). Small differences are observed in the orbital character due to the lower symmetry for the pyridinic FeN_4C_{10} flake: in this case, d_{xz} and d_{yz} degeneracy is broken (**Figure 6**). The longer N-N separation along the x-axis leads to a pure d_{xz} orbital vs. d_{xz} and d_{yz} mixing for the case of pyrrolic FeN_4C_{12} (**Figure 6**). In both cases, weak coupling is observed between the metal-centered orbitals and p-orbitals of both the N and C atoms in the graphene flake (**Figure 6**).

For both SAC models at the PBE0 level of theory, singlet and quintet states reside ∼4–6 kcal/mol and 12 kcal/mol above the triplet ground state, respectively, and thus singlet-quintet ΔE_{H-L} is around +6–8 kcal/mol (**Supplementary Table 7**). These observations contrast with the octahedral models: ΔE_{H-L} for $Fe(II)(py)_6$ is −15 kcal/mol and is −30 kcal/mol for $Fe(II)(pyr)_6$ (**Supplementary Table 4**). These differences can be traced to several factors, including the coordination number (4 vs. 6) in the models as well as rigidity of the graphene flakes that compress Fe-N bonds to values more commensurate with equilibrium low-spin geometries. Finally, examining the electronic structure of the SAC models reveals distribution

of spin not just on the metal but also on the flake in the high spin states, particularly for the pyrrolic FeN_4C_{12} models (**Supplementary Tables 8, 9**). Even in the triplet ground state this is apparent with a magnetic moment of 2.2 μ_B, close to that expected (i.e., 2 μ_B) for FeN_4C_{10}, but with a larger 2.7 μ_B on Fe for FeN_4C_{12} (**Supplementary Tables 8, 9**). The singlet FeN_4C_{12} is also open shell with a 1.4–2.0 μ_B magnetic moment on Fe (**Supplementary Table 9**). In contrast with the molecular complexes, the quintets are particularly poorly described by a localized metal spin, with a reduced Fe moment vs. the triplet state of around 2.4 μ_B on Fe for FeN_4C_{12} and a comparable one of 2.2 μ_B on Fe for FeN_4C_{10}. Although spin contamination can be expected with increasing HF exchange fraction, comparison of these moments across 0–50% exchange does not ever produce a pure 4 μ_B moment on Fe for the quintet FeN_4C_{12} (**Supplementary Table 9**). This observation could be due to low-lying unoccupied states on graphene that are populated instead of the metal states, especially in these models and at this level of theory, as is known to occur in porphyrins as well (Fujii, 2002).

Beyond PBE0 (25%) results on the graphene SAC models, we considered properties over a range that spans from typical values in periodic catalysis modeling (i.e., 0%) to larger values (40%) motivated by our octahedral complex studies (see section Spin State Ordering in Model Complexes). Over this 0–40% range of exchange fractions, singlet and triplet states become destabilized with respect to high-spin quintet states (**Figure 7**). The reduced dependence of spin-state ordering observed here on exchange fraction in comparison to the octahedral complexes is due to differences in coordination number and rigidity of the SAC models. Intermediate Fe spin states were observed experimentally (Liu et al., 2017) for N-doped graphitic SACs using Mössbauer spectroscopy. Although high HF exchange fractions favoring quintet states for both SAC models would suggest inconsistencies with experiment, it is important to recall that the magnetic moments of the Fe metal are intermediate in both triplet and quintet states. Therefore, high HF exchange fractions are in fact stabilizing the simultaneous presence of spin on the graphene coupled to an intermediate Fe center (**Supplementary Tables 8, 9**). In both FeN_4C_{12} at low exchange fractions and FeN_4C_{10} over a larger range of 0-100% exchange, higher order than typically linear sensitivities are observed to % exchange (**Supplementary Figure 3**). For FeN_4C_{12}, the anti-ferromagnetically coupled metal spin on Fe varies significantly (i.e., 0.6 μ_B) and discontinuously, leading to less smooth energetic variations (**Figure 7**). For the FeN_4C_{10} model where spin states are more well defined, the variations are instead linear over the expected range of HF exchange (Droghetti et al., 2012; Ioannidis and Kulik, 2015; Zhao and Kulik, 2018).

High-valent Fe(IV)=O intermediates are expected to be essential for catalytic transformations at N-doped graphitic SACs (Liu et al., 2017). Thus, we examined the spin-state-, model-, and exchange-fraction-dependence of reaction energetics for Fe(IV)=O formation. Here, we employed N_2O as a model oxidant, but results are comparable when assuming the oxygen atom comes from triplet O_2 (**Figure 8** and **Supplementary Figures 4–6**). Overall, pyridinic SACs form more stable oxo species across the range of HF exchange and spin states than pyrrolic SACs (**Figure 8**). Although activation energies would be needed to make firmer statements about relative active site model reactivity, the endothermic reaction energies for the intermediate spin FeN_4C_{12} above 20% exchange (ca. +10 kcal/mol at 40% exchange) suggest that the pyrrolic model could potentially be unreactive with N_2O oxidant (**Figure 8**). Regardless of spin state or model, increasing exchange fraction makes formation of oxo intermediates less favorable due to the penalty for delocalization (Gani and Kulik, 2017).

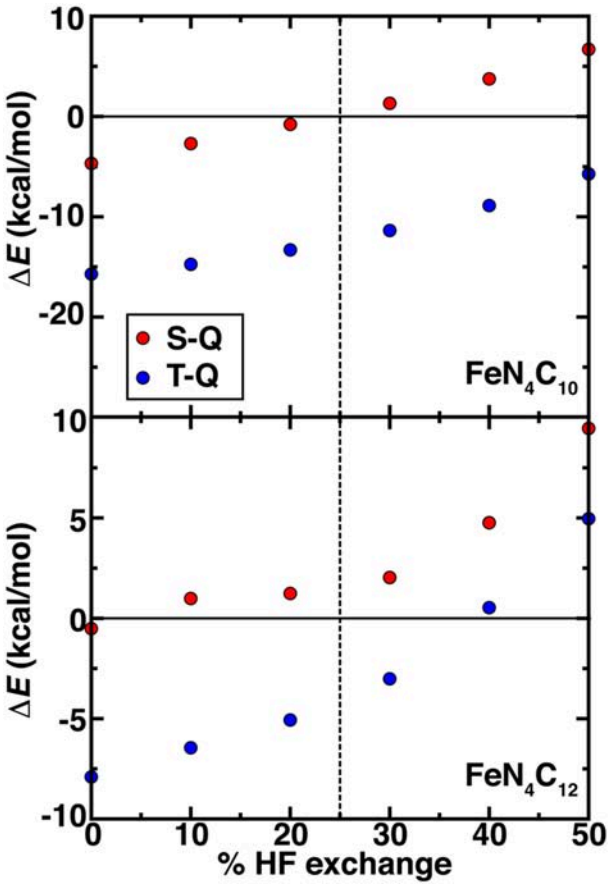

FIGURE 7 | Spin-splitting energetics (in kcal/mol) for singlet-quintet (S-Q, red circles) or triplet-quintet (T-Q, blue circles) spin states vs. % HF exchange for pyridinic (FeN_4C_{10}, top) and pyrrolic (FeN_4C_{12}, bottom) SAC models. The 25% exchange in standard PBE0 is indicated as a vertical dashed line.

Determination of ground state spin from DFT of the pristine Fe(II)/N SAC model and the Fe(IV)=O intermediate should be carried out with caution, noting that spin (ca. 0.5–1.0 μ_B) arises on the O atom in triplet and quintet states of both Fe(IV)=O SAC models but not in the singlet states (**Supplementary Tables 8, 9**). Although spin on the oxo species can be expected and even linked to catalytic efficiency (Liu et al., 2009; Quesne et al., 2014), these states cannot readily be described within a single Kohn-Sham determinant in DFT (Koch and Holthausen, 2015). Overall, spin state ordering of the bare Fe(II) SAC is largely preserved in the Fe(IV)=O intermediate, with singlet and triplet Fe(IV)=O states being weakly stabilized

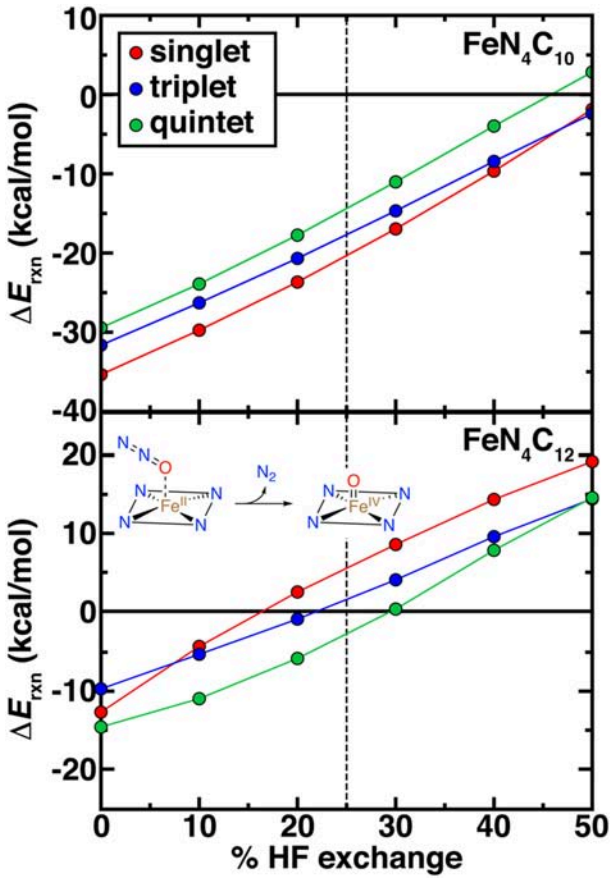

FIGURE 8 | Reaction energetics (ΔE_{rxn}, in kcal/mol) for oxo formation from N_2O oxidant vs. % HF exchange for pyridinic (FeN_4C_{10}, top) and pyrrolic (FeN_4C_{12}, bottom) SAC models. The reaction is shown in inset. In each case, singlet (red circles), triplet (blue circles), and quintet (green circles) oxo formation energies are shown. The 25% exchange in standard PBE0 is indicated as a vertical dashed line.

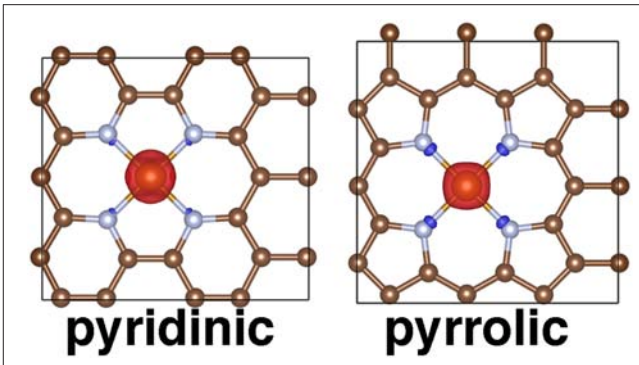

FIGURE 9 | Periodic structures for pyridinic and pyrrolic periodic SAC models in the triplet state with spin density shown. Positive spin density is shown in red and negative spin density is shown in blue, with an isosurface value of 0.03 e/Bohr^3. All structures are shown in ball and stick representation with carbon in brown, nitrogen in light blue, and iron in orange.

by around 3–5 kcal/mol with respect to the bare Fe(II) case for the pyridinic SACs (**Supplementary Figure 4**). In the pyrrolic case, the opposite occurs, potentially due to the loss of spin on the ring in triplet pyrrolic Fe(IV)=O (**Supplementary Table 9** and **Figure 4**). Nevertheless, further investigation of kinetic barriers is merited in future work, as close spin state ordering of both the Fe(IV)=O and pristine Fe(II) intermediates combined with comparable differences of around 5–10 kcal/mol between reaction energetics in each spin state could give rise to spin-state dependent reactivity with distinct product formation (Kamachi and Yoshizawa, 2003; Ji et al., 2015). Finally, it is noteworthy that at 0% exchange (i.e., pure PBE), singlet FeN_4C_{12} is predicted to produce a slightly more stable Fe(IV)=O than the triplet, the same ordering that is observed for FeN_4C_{10} albeit at −10 to −15 kcal/mol in the former case vs. −30 to −35 kcal/mol in the latter case (**Figure 8**). At the 40% exchange motivated by our careful CASPT2 characterization of Fe-N bonds (see section Comparison of Nitrogen-Containing Ligands), or even at the 25% exchange fraction motivated in stronger ligand field cases (Ioannidis and Kulik, 2017), conclusions are different. Namely, at these higher exchange fractions: (i) the triplet oxo is more stable for pyrrolic SACs than the singlet, whereas the ordering remains the same for the pyridinic case, and (ii) neither form exothermically for the pyrrolic case at these exchange fractions.

Periodic Modeling of SACs

We validated our choice of finite SAC flakes by comparing to periodic models of both pyridinic and pyrrolic SAC active sites (**Figure 9**). We focused on the triplet intermediate spin state favored both in our finite models and in experiment (Liu et al., 2017). Shorter Fe-N 1.91 Å vs. 1.97 Å Fe-N bond lengths are observed for the pyridinic model than for the pyrrolic models, consistent with the finite models. It is more straightforward to localize the magnetic moment to the metal in these periodic systems than was observed for the molecular models (**Supplementary Table 10** and **Supplementary Figure 7**). For the triplet cases, spin density is nearly exclusively observed on the metal center (**Figure 9**). In both pyridinic and pyrrolic periodic models, use of the hybrid functional leads to less electron density on the Fe center than when a GGA is employed, consistent with prior observations (Gani and Kulik, 2016; Zhao and Kulik, 2018) (**Supplementary Table 10**).

We compared the electronic structure of the pyridinic and pyrrolic SAC active site models by determining the projected density of states (PDOS) decomposed by N 2*p*, C 2*p*, and Fe 3*d* contributions with the HSE06 hybrid functional (**Figure 10**). Qualitatively, the occupied orbitals and symmetries confirm observations made on the finite graphene flake models with PBE0, which may be expected if short range effects dominate as HSE06 and PBE0 both incorporate 25% exchange in the short range mixed with pure PBE exchange. That is, the pyridinic system again has singly occupied d_z^2 and d_{xz} orbitals and no occupation of the d_{xy} state. The pyrrolic system also differs from the pyridinic by having degenerate d_{xz} and d_{yz} states, consistent with the molecular flakes (**Figure 10**). Generally, agreement is more variable for other spin states, where convergence of the magnetic state is sensitive to starting conditions in the periodic calculation (**Supplementary Figures 8–9**). In the pyridinic case,

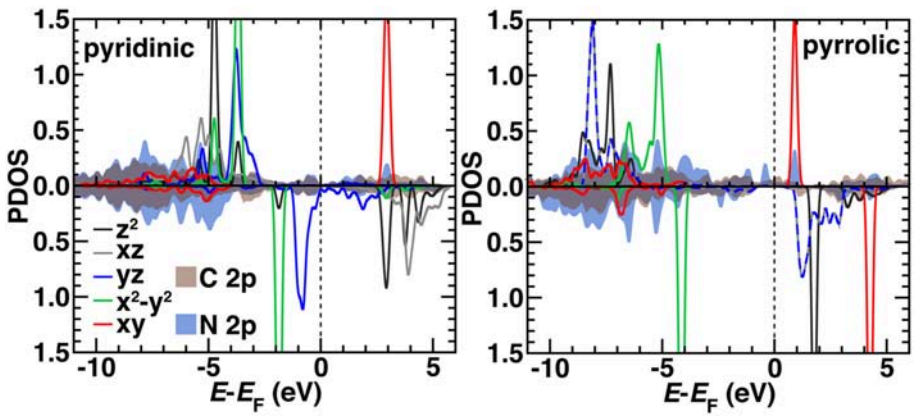

FIGURE 10 | The HSE06 projected density of states (PDOS) for spin up **(Top)** and down (**Bottom**, reflected curves) triplet pyridinic **(Left)** and pyrrolic **(Right)** SAC models. The 3*d* Fe orbital PDOS are shown as indicated in inset legends as solid curves except for *yz* and *xz* in the pyrrolic case, which are shown as dashed lines due to their degeneracy. The average PDOS for a 2*p* orbital from C (brown) or N (dark blue) are shown as translucent shaded regions. All energy levels (in eV) are aligned to the Fermi level (E_F), which is shown as a vertical dashed line. Some *d* levels have been truncated by the *y*-axis range to be able to compare to the broader C 2*p* and N 2*p* features.

d_{yz} states span the Fermi level, whereas the 3*d* states are well separated in the pyrrolic SAC (**Figure 10**). The pyrrolic 3*d* states also mix more deeply into the C and N 2*p* bands, whereas in the pyridinic case, most 3*d* states sit at the top of the occupied C/N 2*p* bands (**Figure 10**). Overall, these observations support the use of finite models at higher levels of theory for consistent modeling, due to the unique challenges of modeling periodic systems with such methods (Janet et al., 2017). More analysis in larger supercells with variable graphene defects will be necessary in future work to strengthen this conclusion.

CONCLUSIONS AND OUTLOOK

We have presented an overview of the effect of computational model choice on the properties of octahedral transition metal complexes and emergent single atom catalyst (SAC) materials made from Fe centers in N-doped graphene. The octahedral transition metal complexes chosen mimic the ligand field environment observed in the SAC models but remain tractable for study with multi-reference wavefunction theory. Observations from the hexa-aqua and hexa-ammine complex studies revealed that spin state ordering of mid-row complexes could be sensitive both to the IPEA shift chosen and whether an extended active space was used, whereas late and early transition metals were far less sensitive. Then using these extended active space CASPT2 results as a benchmark, we observed that nearly all transition metal complexes benefitted from increased HF exchange. In fact, errors with respect to exchange fraction chosen monotonically decreased from 0 to 40% but with no improvement for higher exchange fractions. The 40% exchange hybrid results had comparable accuracy to the more computationally demanding double hybrid PBE0-DH.

The HF exchange tuning study confirmed the comparable behavior of Fe(II) complexes with ammonia, pyridine, and pyrrole ligands due to the overriding role of the metal, oxidation state, and ligand connecting atom in determining functional sensitivity. Comparison to CASPT2 results on the hexa-ammine system motivated us to propose higher exchange fractions (ca. 40% rather than 25% in PBE0) to be essential to counteract the low-spin bias in semi-local DFT. Using these benchmarks, we then evaluated the effect of DFT functional tuning on finite graphitic SAC models with pyridine or pyrrole nitrogen atoms. In these square planar SAC geometries, rigid structures compressed the Fe-N bond length, reducing exchange sensitivity of spin state ordering but otherwise confirming the observations in the octahedral complexes (i.e., favoring higher spin configurations and destabilizing singlet states). We observed that at the recommended higher exchange fractions, the formation of an oxo intermediate from N_2O became unfavorable at the pyrrolic SAC active site. We also observed changes in spin state ordering of the most stable oxo intermediates. Thus, incorporation of exchange can alter predictions of reactivity at SAC active sites. Finally, we confirmed that these observations were not sensitive to choice of a finite SAC model by comparing to periodic SAC models where similar electron configurations were observed.

Overall, predictions of reactivity and spin state ordering are highly sensitive to the functional employed. We have shown that this sensitivity is broadly transferable across different ligand environments as long as the metal and direct ligating atom are kept constant. This observation can be leveraged to obtain DFT functional performance on smaller models where correlated WFT is tractable. Additionally, smaller flake models may be amenable to direct WFT calculation with methods not covered in this work. Spin state exchange sensitivity can be expected to be depressed in cases where the SAC is fully rigid and prevents expansion of the metal-ligand bond when the spin state changes. The highly ordered, symmetric cases here are expected to be the limit in this rigidity argument, and more disordered SAC models

or more flexible active sites (e.g., graphitic carbon nitride) are expected to be more sensitive. Still, some outstanding challenges remain in understanding the extent to which spin arising on the graphene itself could be physical and also impart reactivity or whether it arises due to increased static correlation error for hybrid DFT. Furthermore, in periodic simulations with larger supercells than studied in this work it will become essential to employ range-separated hybrids with HF exchange only in the short range, and the comparison to CASPT2 results to range-separated hybrid tuning will be essential here. Overall, modeling in SACs will continue to benefit from this multi-level approach in assessing method accuracy and sensitivity and how method choice impacts predictions of active site geometry and reactivity.

AUTHOR CONTRIBUTIONS

HK designed the research. FL, TY, JY, EX, and AB carried out the research. FL, TY, JY, and HK wrote and revised the manuscript.

FUNDING

The authors acknowledge support by the Department of Energy under grant number DE-SC0018096 for the work on density functional theory and the support of FL and AB. The authors also acknowledge the National Science Foundation under grant number CBET-1704266 for the support of TY. HK holds a Career Award at the Scientific Interface from the Burroughs Wellcome Fund.

ACKNOWLEDGMENTS

The authors thank Adam H. Steeves for providing a critical reading of the manuscript.

SUPPLEMENTARY MATERIAL

The Supplementary Material for this article can be found online at: https://www.frontiersin.org/articles/10.3389/fchem.2019.00219/full#supplementary-material

REFERENCES

Abram, S.-L., Monte-Pérez, I., Pfaff, F. F., Farquhar, E. R., and Ray, K. (2014). Evidence of two-state reactivity in alkane hydroxylation by lewis-acid bound copper–nitrene complexes. *Chem. Commu.* 50, 9852–9854. doi: 10.1039/C4CC03754E

Adamo, C., and Barone, V. (1999). Toward reliable density functional methods without adjustable parameters: the PBE0 model. *J. Chem. Phys.* 110, 6158–6170. doi: 10.1063/1.478522

Andersson, K., Malmqvist, P. Å., and Roos, B. O. (1992). Second-order perturbation theory with a complete active space self-consistent field reference function. *J. Chem. Phys.* 96, 1218–1226. doi: 10.1063/1.462209

Andris, E., Jašík, J., Gómez, L., Costas, M., and Roithová, J. (2016). Spectroscopic characterization and reactivity of triplet and quintet iron (IV) oxo complexes in the gas phase. *Angewandte Chemie Int. Ed.* 55, 3637–3641. doi: 10.1002/anie.201511374

Aquilante, F., Autschbach, J., Carlson, R. K., Chibotaru, L. F., Delcey, M. G., De Vico, L., et al. (2016). Molcas 8: new capabilities for multiconfigurational quantum chemical calculations across the periodic table. *J. Comput. Chem.* 37, 506–541. doi: 10.1002/jcc.24221

Autschbach, J., and Srebro, M. (2014). Delocalization error and "functional tuning" in Kohn–Sham calculations of molecular properties. *Acc. Chem. Res.* 47, 2592–2602. doi: 10.1021/ar500171t

Back, S., Lim, J., Kim, N.-Y., Kim, Y.-H., and Jung, Y. (2017). Single-atom catalysts for CO2 electroreduction with significant activity and selectivity improvements. *Chem. Sci.* 8, 1090–1096. doi: 10.1039/C6SC03911A

Baerends, E. J., Ellis, D. E., and Ros, P. (1973). Self-consistent molecular Hartree-Fock-Slater calculations - I. the computational procedure. *Chem. Phys.* 2, 41–51. doi: 10.1016/0301-0104(73)80059-X

Banhart, F., Kotakoski, J., and Krasheninnikov, A. V. (2011). Structural defects in graphene. *ACS Nano* 5, 26–41. doi: 10.1021/nn102598m

Bengtsson, L. (1999). Dipole correction for surface supercell calculations. *Phys. Rev. B* 59, 12301–12304. doi: 10.1103/PhysRevB.59.12301

Bowman, D. N., and Jakubikova, E. (2012). Low-spin versus high-spin ground state in pseudo-octahedral iron complexes. *Inorg. Chem.* 51, 6011–6019. doi: 10.1021/ic202344w

Bruschi, M., De Gioia, L., Zampella, G., Reiher, M., Fantucci, P., and Stein, M. (2004). A theoretical study of spin states in Ni-S4 complexes and models of the [NiFe] hydrogenase active site. *J. Biol. Inorgan. Chem.* 9, 873–884. doi: 10.1007/s00775-004-0588-2

Chen, Y., Ji, S., Wang, Y., Dong, J., Chen, W., Li, Z., et al. (2017). Isolated single iron atoms anchored on N-doped porous carbon as an efficient electrocatalyst for the oxygen reduction reaction. *Angewandte Chemie* 129, 7041–7045. doi: 10.1002/ange.201702473

Cheng, Q., Yang, L., Zou, L., Zou, Z., Chen, C., Hu, Z., et al. (2017). Single cobalt atom and N codoped carbon nanofibers as highly durable electrocatalyst for oxygen reduction reaction. *ACS Catal.* 7, 6864–6871. doi: 10.1021/acscatal.7b02326

Chu, M., Liu, X., Sui, Y., Luo, J., and Meng, C. (2015). Unique reactivity of transition metal atoms embedded in graphene to CO, NO, O2 and O adsorption: a first-principles investigation. *Molecules* 20, 19540–19553. doi: 10.3390/molecules201019540

Cohen, A. J., Mori-Sánchez, P., and Yang, W. (2011). Challenges for density functional theory. *Chem. Rev.* 112, 289–320. doi: 10.1021/cr200107z

Cui, X., Li, H., Wang, Y., Hu, Y., Hua, L., Li, H., et al. (2018). Room-temperature methane conversion by graphene-confined single iron atoms. *Chem 4*, 1902–1910. doi: 10.1016/j.chempr.2018.1005.1006

Douglas, M., and Kroll, N. M. (1974). Quantum electrodynamical corrections to the fine structure of helium. *Ann. Phys.* 82, 89–155. doi: 10.1016/0003-4916(74)90333-9

Droghetti, A., Alfè, D., and Sanvito, S. (2012). Assessment of density functional theory for iron (II) molecules across the spin-crossover transition. *J. Chem. Phys.* 137:124303. doi: 10.1063/1.4752411

Dunlap, B. I., Connolly, J. W. D., and Sabin, J. R. (1979). Some approximations in applications of X-alpha theory. *J. Chem. Phys.* 71, 3396–3402. doi: 10.1063/1.438728

Eichkorn, K., Treutler, O., Ohm, H., Haser, M., and Ahlrichs, R. (1995). Auxiliary basis-sets to approximate coulomb potentials. *Chem. Phys. Lett.* 240, 283–289. doi: 10.1016/0009-2614(95)00621-A

Eichkorn, K., Weigend, F., Treutler, O., and Ahlrichs, R. (1997). Auxiliary basis sets for main row atoms and transition metals and their use to approximate Coulomb potentials. *Theor. Chem. Acc.* 97, 119–124. doi: 10.1007/s002140050244

Fei, H., Dong, J., Arellano-Jiménez, M. J., Ye, G., Dong Kim, N., Samuel, E. L. G., et al. (2015). Atomic cobalt on nitrogen-doped graphene for hydrogen generation. *Nat. Commun.* 6:8668. doi: 10.1038/ncomms9668

Fong, A., Vandervelden, C., Scott, S. L., and Peters, B. (2018). Computational support for Phillips catalyst initiation via Cr–C bond

homolysis in a chromacyclopentane site. *ACS Catal.* 8, 1728–1733. doi: 10.1021/acscatal.7b03724

Forsberg, N., and Malmqvist, P.-Å. (1997). Multiconfiguration perturbation theory with imaginary level shift. *Chem. Phys. Lett.* 274, 196–204. doi: 10.1016/S0009-2614(97)00669-6

Fujii, H. (2002). Electronic structure and reactivity of high-valent oxo iron porphyrins. *Coord. Chem. Rev.* 226, 51–60. doi: 10.1016/S0010-8545(01)00441-6

Gani, T. Z. H., and Kulik, H. J. (2016). Where does the density localize? convergent behavior for global hybrids, range separation, and DFT+U. *J. Chem. Theory Comput.* 12, 5931–5945. doi: 10.1021/acs.jctc.6b00937

Gani, T. Z. H., and Kulik, H. J. (2017). Unifying exchange sensitivity in transition metal spin-state ordering and catalysis through bond valence metrics. *J. Chem. Theory Comput.* 13, 5443–5457. doi: 10.1021/acs.jctc.7b00848

Gani, T. Z. H., and Kulik, H. J. (2018). Understanding and breaking scaling relations in single-site catalysis: methane-to-methanol conversion by Fe(IV)=O. *ACS Catal.* 8, 975–986. doi: 10.1021/acscatal.7b03597

Ganzenmüller, G., Berkaïne, N., Fouqueau, A., Casida, M. E., and Reiher, M. (2005). Comparison of density functionals for differences between the high- (T2g5) and low- (A1g1) spin states of iron(II) compounds. IV. Results for the ferrous complexes [Fe(L)('NHS4')]. *J. Chem. Phys.* 122:234321. doi: 10.1063/1.1927081

Gao, Z.-Y., Yang, W.-J., Ding, X.-L., Lv, G., and Yan, W.-P. (2018). Support effects on adsorption and catalytic activation of O 2 in single atom iron catalysts with graphene-based substrates. *Phys. Chem. Chem. Phys.* 20, 7333–7341. doi: 10.1039/C7CP08301G

Ghigo, G., Roos, B. O., and Malmqvist, P.-Å. (2004). A modified definition of the zeroth-order hamiltonian in multiconfigurational perturbation theory (CASPT2). *Chem. Phys. Lett.* 396, 142–149. doi: 10.1016/j.cplett.2004.08.032

Harvey, J. N. (2014). Spin-forbidden reactions: computational insight into mechanisms and kinetics. *Wiley Interdiscip. Rev. Comput. Mol. Sci.* 4, 1–14. doi: 10.1002/wcms.1154

Hellweg, A., Hattig, C., Hofener, S., and Klopper, W. (2007). Optimized accurate auxiliary basis sets for RI-MP2 and RI-CC2 calculations for the atoms Rb to Rn. *Theor. Chem. Acc.* 117, 587–597. doi: 10.1007/s00214-007-0250-5

Hernández-Ortega, A., Quesne, M. G., Bui, S., Heyes, D. J., Steiner, R. A., and, Scrutton, N. S., et al. (2015). Catalytic mechanism of cofactor-free dioxygenases and how they circumvent spin-forbidden oxygenation of their substrates. *J. Am. Chem. Soc.* 137, 7474–7487. doi: 10.1021/jacs.5b03836

Hess, B. A. (1986). Relativistic electronic-structure calculations employing a two-component no-pair formalism with external-field projection operators. *Phys. Rev. A* 33:3742. doi: 10.1103/PhysRevA.33.3742

Heyd, J., Scuseria, G. E., and Ernzerhof, M. (2003). Hybrid functionals based on a screened Coulomb potential. *J. Chem. Phys.* 118, 8207–8215. doi: 10.1063/1.1564060

Heyd, J., Scuseria, G. E., and Ernzerhof, M. (2006). Erratum: hybrid functionals based on a screened coulomb potential. *J. Chem. Phys.* 124:219906. doi: 10.1063/1.2204597

Huang, B., Yu, J., and Wei, S.-H. (2011). Strain control of magnetism in graphene decorated by transition-metal atoms. *Phys. Rev. B* 84:075415. doi: 10.1103/PhysRevB.84.075415

Impeng, S., Khongpracha, P., Warakulwit, C., Jansang, B., Sirijaraensre, J., Ehara, M., et al. (2014). Direct oxidation of methane to methanol on Fe–O modified graphene. *RSC Adv.* 4, 12572–12578. doi: 10.1039/C3RA47826B

Ioannidis, E. I., Gani, T. Z., and Kulik, H. J. (2016). molSimplify: A toolkit for automating discovery in inorganic chemistry. *J. Comput. Chem.* 37, 2106–2117. doi: 10.1002/jcc.24437

Ioannidis, E. I., and Kulik, H. J. (2015). Towards quantifying the role of exact exchange in predictions of transition metal complex properties. *J. Chem. Phys.* 143:034104. doi: 10.1063/1.4926836

Ioannidis, E. I., and Kulik, H. J. (2017). Ligand-field-dependent behavior of meta-GGA exchange in transition-metal complex spin-state ordering. *J. Phys. Chem. A* 121, 874–884. doi: 10.1021/acs.jpca.6b11930

Janet, J. P., and Kulik, H. J. (2017). Predicting electronic structure properties of transition metal complexes with neural networks. *Chem. Sci.* 8, 5137–5152. doi: 10.1039/C7SC01247K

Janet, J. P., Zhao, Q., Ioannidis, E. I., and Kulik, H. J. (2017). Density functional theory for modelling large molecular adsorbate-surface interactions: a mini-review and worked example. *Mol. Simul.* 43, 327–345. doi: 10.1080/08927022.2016.1258465

Ji, L., Faponle, A. S., Quesne, M. G., Sainna, M. A., Zhang, J., Franke, A., et al. (2015). Drug metabolism by cytochrome P450 enzymes: what distinguishes the pathways leading to substrate hydroxylation over desaturation? *Chem. A Euro. J.* 21, 9083–9092. doi: 10.1002/chem.201500329

Jiang, K., Siahrostami, S., Zheng, T., Hu, Y., Hwang, S., Stavitski, E., et al. (2018). Isolated Ni single atoms in graphene nanosheets for high-performance CO_2 reduction. *Energy Environ. Sci.* 11, 893–903. doi: 10.1039/C7EE03245E

Kamachi, T., and Yoshizawa, K. (2003). A theoretical study on the mechanism of camphor hydroxylation by compound I of cytochrome P450. *J. Am. Chem. Soc.* 125, 4652–4661. doi: 10.1021/ja0208862

Kendall, R. A., and Fruchtl, H. A. (1997). The impact of the resolution of the identity approximate integral method on modern ab initio algorithm development. *Theor. Chem. Acc.* 97, 158–163. doi: 10.1007/s002140050249

Kepenekian, M., Robert, V., and Le Guennic, B. (2009). What zeroth-order hamiltonian for CASPT2 adiabatic energetics of Fe (II) N 6 architectures? *J. Chem. Phys.* 131:114702. doi: 10.1063/1.3211020

Koch, W., and Holthausen, M. C. (2015). *A Chemist's Guide to Density Functional Theory*. Weinheim: John Wiley & Sons.

Kossmann, S., and Neese, F. (2009). Comparison of two efficient approximate Hartree-Fock approaches. *Chem. Phys. Lett.* 481, 240–243. doi: 10.1016/j.cplett.2009.09.073

Krasheninnikov, A. V., Lehtinen, P. O., Foster, A. S., Pyykkö, P., and Nieminen, R. M. (2009). Embedding transition-metal atoms in graphene: structure, bonding, and magnetism. *Phys. Rev. Lett.* 102:126807. doi: 10.1103/PhysRevLett.102.126807

Kulik, H. J. (2015). Perspective: treating electron over-delocalization with the DFT+U method. *J. Chem. Phys.* 142:240901. doi: 10.1063/1.4922693

Kulik, H. J., Cococcioni, M., Scherlis, D. A., and Marzari, N. (2006). Density functional theory in transition-metal chemistry: a self-consistent hubbard U approach. *Phys. Rev. Lett.* 97:103001. doi: 10.1103/PhysRevLett.97.103001

Kümmel, S., and Kronik, L. (2008). Orbital-dependent density functionals: theory and applications. *Rev. Mod. Phys.* 80, 3–60. doi: 10.1103/RevModPhys.80.3

Lawson Daku, L. V. M., Aquilante, F., Robinson, T. W., and Hauser, A. (2012). Accurate spin-state energetics of transition metal complexes. 1. CCSD (T), CASPT2, and DFT study of [M (NCH) 6] 2+(M= Fe, Co). *J. Chem. Theory Comput.* 8, 4216–4231. doi: 10.1021/ct300592w

Li, J., Ghoshal, S., Liang, W., Sougrati, M.-T., Jaouen, F., Halevi, B., et al. (2016). Structural and mechanistic basis for the high activity of Fe-N-C catalysts toward oxygen reduction. *Energy Environ. Sci.* 9, 2418–2432. doi: 10.1039/C6EE01160H

Liang, J. X., Wang, Y. G., Yang, X. F., Xing, D. H., Wang, A. Q., Zhang, T., et al. (2017). "Recent advances in single-atom catalysis," in *Encyclopedia of Inorganic and Bioinorganic Chemistry*, ed R. A. Scott (Hoboken, NJ: Wiley).

Liang, S., Hao, C., and Shi, Y. (2015). The power of single-atom catalysis. *ChemCatChem* 7, 2559–2567. doi: 10.1002/cctc.201500363

Liu, H. N., Llano, J., and Gauld, J. W. (2009). A DFT study of nucleobase dealkylation by the DNA repair enzyme AlkB. *J. Phys. Chem. B* 113, 4887–4898. doi: 10.1021/jp810715t

Liu, W., Zhang, L., Liu, X., Liu, X., Yang, X., Miao, S., et al. (2017). Discriminating catalytically active FeNx species of atomically dispersed Fe–N–C catalyst for selective oxidation of the C–H bond. *J. Am. Chem. Soc.* 139, 10790–10798. doi: 10.1021/jacs.7b05130

Ma, D. W., Wang, Q., Yan, X., Zhang, X., He, C., Zhou, D., et al. (2016). 3d transition metal embedded C2N monolayers as promising single-atom catalysts: a first-principles study. *Carbon* 105, 463–473. doi: 10.1016/j.carbon.2016.04.059

Momma, K., and Izumi, F. (2011). VESTA 3 for three-dimensional visualization of crystal, volumetric and morphology data. *J. Appl. Crystallogr.* 44, 1272–1276. doi: 10.1107/S0021889811038970

Mortensen, S. R., and Kepp, K. P. (2015). Spin propensities of octahedral complexes from density functional theory. *J. Phys. Chem. A* 119, 4041–4050. doi: 10.1021/acs.jpca.5b01626

Neese, F. (2018). Software update: the ORCA program system, version 4.0. *Wiley Interdiscip. Rev. Comput. Mol. Sci.* 8:e1327. doi: 10.1002/wcms.1327

Neese, F., Wennmohs, F., and Hansen, A. (2009). Efficient and accurate local approximations to coupled-electron pair approaches: an attempt to revive the pair natural orbital method. *J. Chem. Phys.* 130:114108. doi: 10.1063/1.3086717

O'Boyle, N. M., Banck, M., James, C. A., Morley, C., Vandermeersch, T., and Hutchison, G. R. (2011). Open babel: an open chemical toolbox. *J. Cheminform.* 3:33. doi: 10.1186/1758-2946-3-33

Paolo, G., Stefano, B., Nicola, B., Matteo, C., Roberto, C., Carlo, C., et al. (2009). QUANTUM ESPRESSO: a modular and open-source software project for quantum simulations of materials. *J. Phys. Conden. Matter* 21:395502. doi: 10.1088/0953-8984/21/39/395502

Perdew, J. P., Burke, K., and Ernzerhof, M. (1996). Generalized gradient approximation made simple. *Phys. Rev. Lett.* 77:3865. doi: 10.1103/PhysRevLett.77.3865

Phan, H., Hrudka, J. J., Igimbayeva, D., Lawson Daku, L. v. M., and Shatruk, M. (2017). A simple approach for predicting the spin state of homoleptic Fe (II) tris-diimine complexes. *J. Am. Chem. Soc.* 139, 6437–6447. doi: 10.1021/jacs.7b02098

Pierloot, K. (2003). The CASPT2 method in inorganic electronic spectroscopy: from ionic transition metal to covalent actinide complexes. *Mol. Phys.* 101, 2083–2094. doi: 10.1080/0026897031000109356

Pierloot, K., Phung, Q. M., and Domingo, A. (2017). Spin state energetics in first-row transition metal complexes: contribution of (3s3p) correlation and its description by second-order perturbation theory. *J. Chem. Theory Comput.* 13, 537–553. doi: 10.1021/acs.jctc.6b01005

Qiao, B., Wang, A., Yang, X., Allard, L. F., Jiang, Z., Cui, Y., et al. (2011). Single-atom catalysis of CO oxidation using Pt 1/FeO x. *Nat. Chem.* 3:634–641. doi: 10.1038/nchem.1095

Qiu, H. J., Ito, Y., Cong, W., Tan, Y., Liu, P., Hirata, A., et al. (2015). Nanoporous graphene with single-atom nickel dopants: an efficient and stable catalyst for electrochemical hydrogen production. *Angewandte Chem Int. Edit.* 54, 14031–14035. doi: 10.1002/anie.201507381

Quesne, M. G., Latifi, R., Gonzalez-Ovalle, L. E., Kumar, D., and de Visser, S. P. (2014). Quantum mechanics/molecular mechanics study on the oxygen binding and substrate hydroxylation step in AlkB repair enzymes. *Chem. Euro. J.* 20, 435–446. doi: 10.1002/chem.201303282

Radoń, M., and Drabik, G. (2018). Spin states and other ligand-field states of aqua complexes revisited with multireference ab initio calculations including solvation effects. *J. Chem. Theory Comput.* 14, 4010–4027. doi: 10.1021/acs.jctc.8b00200

Rappé, A. K., Casewit, C. J., Colwell, K., Goddard, I. I. I. W. A., and Skiff, W. (1992). UFF, a full periodic table force field for molecular mechanics and molecular dynamics simulations. *J. Am. Chem. Soc.* 114, 10024–10035. doi: 10.1021/ja00051a040

Rappe, A. M., Rabe, K. M., Kaxiras, E., and Joannopoulos, J. D. (1990). Optimized pseudopotentials. *Phys. Rev. B* 41, 1227–1230. doi: 10.1103/PhysRevB.41.1227

Roos, B. O., Lindh, R., Malmqvist, P.-Å., Veryazov, V., and Widmark, P.-O. (2004). Main group atoms and dimers studied with a new relativistic ANO basis set. *J. Phys. Chem. A* 108, 2851–2858. doi: 10.1021/jp031064+

Roos, B. O., Lindh, R., Malmqvist, P.-Å., Veryazov, V., and Widmark, P.-O. (2005). New relativistic ANO basis sets for transition metal atoms. *J. Phys. Chem. A* 109, 6575–6579. doi: 10.1021/jp0581126

Sahoo, D., Quesne, M. G., de Visser, S. P., and Rath, S. P. (2015). Hydrogen-bonding interactions trigger a spin-flip in iron (III) porphyrin complexes. *Angewandte Chem Int. Edit.* 54, 4796–4800. doi: 10.1002/anie.201411399

Saunders, V. R., and Hillier, I. H. (1973). A 'Level-Shifting' method for converging closed shell Hartree-Fock wave functions. *Int. J. Quantum Chem.* 7, 699–705. doi: 10.1002/qua.560070407

Schröder, D., Shaik, S., and Schwarz, H. (2000). Two-state reactivity as a new concept in organometallic chemistry. *Acc. Chem. Res.* 33, 139–145. doi: 10.1021/ar990028j

Schwarz, H. (2017). Ménage-à-trois: single-atom catalysis, mass spectrometry, and computational chemistry. *Catal. Sci. Technol.* 7, 4302–4314. doi: 10.1039/C6CY02658C

Shaik, S., Danovich, D., Fiedler, A., Schröder, D., and Schwarz, H. (1995). Two-state reactivity in organometallic gas-phase ion chemistry. *Helv. Chim. Acta* 78, 1393–1407. doi: 10.1002/hlca.19950780602

Sirijaraensre, J., and Limtrakul, J. (2018). Theoretical investigation on reaction pathways for ethylene epoxidation on Ti-decorated graphene. *Struct. Chem.* 29, 159–170. doi: 10.1007/s11224-017-1015-y

Smith, D. M., Dupuis, M., and Straatsma, T. (2005). Multiplet splittings and other properties from density functional theory: an assessment in iron–porphyrin systems. *Mol. Phys.* 103, 273–278. doi: 10.1080/00268970512331317309

Trucano, P., and Chen, R. (1975). Structure of graphite by neutron diffraction. *Nature* 258:136–137. doi: 10.1038/258136a0

Tsuchida, R. (1938). Absorption spectra of co-ordination compounds. *I. Bull. Chem. Soc. Jpn.* 13, 388–400. doi: 10.1246/bcsj.13.388

Vela, S., Fumanal, M., Ribas-Ariño, J., and Robert, V. (2016). On the zeroth-order hamiltonian for CASPT 2 calculations of spin crossover compounds. *J. Comput. Chem.* 37, 947–953. doi: 10.1002/jcc.24283

Verma, P., Varga, Z., Klein, J. E., Cramer, C. J., Que, L., and Truhlar, D. G. (2017). Assessment of electronic structure methods for the determination of the ground spin states of Fe (II), Fe (III) and Fe (IV) complexes. *Phys. Chem. Chem. Phys.* 19, 13049–13069. doi: 10.1039/C7CP01263B

Veryazov, V., Malmqvist, P. Å., and Roos, B. O. (2011). How to select active space for multiconfigurational quantum chemistry? *Int. J. Quantum Chem.* 111, 3329–3338. doi: 10.1002/qua.23068

Wang, A., and Zhang, T. (2016). Water splitting: taking cobalt in isolation. *Nat. Energy* 1:15019. doi: 10.1038/nenergy.2015.19

Wang, J., Zhang, H., Wang, C., Zhang, Y., Wang, J., Zhao, H., et al. (2018). Co-synthesis of atomic Fe and few-layer graphene towards superior ORR electrocatalyst. *Energy Storage Mater.* 12, 1–7. doi: 10.1016/j.ensm.2017.11.004

Weigend, F. (2006). Accurate coulomb-fitting basis sets for H to Rn. *Phys. Chem. Chem. Phys.* 8, 1057–1065. doi: 10.1039/b515623h

Weigend, F., and Ahlrichs, R. (2005). Balanced basis sets of split valence, triple zeta valence and quadruple zeta valence quality for H to Rn: design and assessment of accuracy. *Phys. Chem. Chem. Phys.* 7, 3297–3305. doi: 10.1039/b508541a

Whitten, J. L. (1973). Coulombic potential-energy integrals and approximations. *J. Chem. Phys.* 58, 4496–4501. doi: 10.1063/1.1679012

Wilbraham, L., Adamo, C., and Ciofini, I. (2018). Communication: evaluating non-empirical double hybrid functionals for spin-state energetics in transition-metal complexes. *J. Chem. Phys.* 148:041103. doi: 10.1063/1.5019641

Wilbraham, L., Verma, P., Truhlar, D. G., Gagliardi, L., and Ciofini, I. (2017). Multiconfiguration pair-density functional theory predicts spin-state ordering in iron complexes with the same accuracy as complete active space second-order perturbation theory at a significantly reduced computational cost. *J. Phys. Chem. Lett.* 8, 2026–2030. doi: 10.1021/acs.jpclett.7b00570

Xu, H., Cheng, D., Cao, D., and Zeng, X. C. (2018). A universal principle for a rational design of single-atom electrocatalysts. *Nat. Catal.* 1, 339–348. doi: 10.1038/s41929-018-0063-z

Yang, L., Cheng, D., Xu, H., Zeng, X., Wan, X., Shui, J., et al. (2018). Unveiling the high-activity origin of single-atom iron catalysts for oxygen reduction reaction. *Proc. Natl. Acad. Sci.* 115:6626. doi: 10.1073/pnas.1800771115

Yang, T., Quesne, M. G., Neu, H. M., Cantú Reinhard, F., n,. G., Goldberg, D. P., et al. (2016). Singlet versus triplet reactivity in an Mn (v)–oxo species: testing theoretical predictions against experimental evidence. *J. Am. Chem. Soc.* 138, 12375–12386. doi: 10.1021/jacs.6b05027

Yang, X.-F., Wang, A., Qiao, B., Li, J., Liu, J., and Zhang, T. (2013). Single-atom catalysts: a new frontier in heterogeneous catalysis. *Acc. Chem. Res.* 46, 1740–1748. doi: 10.1021/ar300361m

Zhang, C., Sha, J., Fei, H., Liu, M., Yazdi, S., Zhang, J., et al. (2017a). Single-atomic ruthenium catalytic sites on nitrogen-doped graphene for oxygen reduction reaction in acidic medium. *ACS Nano* 11, 6930–6941. doi: 10.1021/acsnano.7b02148

Zhang, L., Jia, Y., Gao, G., Yan, X., Chen, N., Chen, J., et al. (2018). Graphene defects trap atomic Ni species for hydrogen and oxygen evolution reactions. *Chem* 4, 285–297. doi: 10.1016/j.chempr.2017.12.005

Zhang, Z., Gao, X., Dou, M., Ji, J., and Wang, F. (2017b). Biomass derived n-doped porous carbon supported single fe atoms as superior

electrocatalysts for oxygen reduction. *Small* 13:1604290. doi: 10.1002/smll.201604290

Zhao, Q., and Kulik, H. J. (2018). Where does the density localize in the solid state? divergent behavior for hybrids and DFT+U. *J. Chem. Theory Comput.* 14, 670–683. doi: 10.1021/acs.jctc.7b01061

Zhu, B., Guan, W., Yan, L.-K., and Su, Z.-M. (2016). Two-state reactivity mechanism of benzene C–C activation by trinuclear titanium hydride. *J. Am. Chem. Soc.* 138, 11069–11072. doi: 10.1021/jacs.6b02433

Zhu, C., Fu, S., Shi, Q., Du, D., and Lin, Y. (2017). Single-atom electrocatalysts. *Angewandte Chemie Int. Edit.* 56:13944. doi: 10.1002/anie.201703864

Zitolo, A., Goellner, V., Armel, V., Sougrati, M.-T., Mineva, T., Stievano, L., et al. (2015). Identification of catalytic sites for oxygen reduction in iron- and nitrogen-doped graphene materials. *Nat. Mater.* 14:937. doi: 10.1038/nmat4367

Zitolo, A., Ranjbar-Sahraie, N., Mineva, T., Li, J., Jia, Q., Stamatin, S., et al. (2017). Identification of catalytic sites in cobalt-nitrogen-carbon materials for the oxygen reduction reaction. *Nat. Commun.* 8:957. doi: 10.1038/s41467-017-01100-7

Conflict of Interest Statement: The authors declare that the research was conducted in the absence of any commercial or financial relationships that could be construed as a potential conflict of interest.

Copyright © 2019 Liu, Yang, Yang, Xu, Bajaj and Kulik. This is an open-access article distributed under the terms of the Creative Commons Attribution License (CC BY). The use, distribution or reproduction in other forums is permitted, provided the original author(s) and the copyright owner(s) are credited and that the original publication in this journal is cited, in accordance with accepted academic practice. No use, distribution or reproduction is permitted which does not comply with these terms.

frontiers in Chemistry

METHODS
published: 05 June 2019
doi: 10.3389/fchem.2019.00400

CherryPicker: An Algorithm for the Automated Parametrization of Large Biomolecules for Molecular Simulation

Ivan D. Welsh[1,2] *and Jane R. Allison*[1,2,3,4]*

[1] School of Biological Sciences, University of Auckland, Auckland, New Zealand, [2] Centre for Theoretical Chemistry and Physics, Institute of Natural and Computational Sciences, Massey University, Auckland, New Zealand, [3] Biomolecular Interaction Centre, University of Canterbury, Christchurch, New Zealand, [4] Maurice Wilkins Centre for Molecular Biodiscovery, University of Auckland, Auckland, New Zealand

Molecular simulations allow investigation of the structure, dynamics and thermodynamics of molecules at an atomic level of detail, and as such, are becoming increasingly important across many areas of science. As the range of applications increases, so does the variety of molecules. Simulation of a new type of molecule requires generation of parameters that result in accurate representation of the behavior of that molecule, and, in most cases, are compatible with existing parameter sets. While many automated parametrization methods exist, they are in general not well suited to large and conformationally dynamic molecules. We present here a method for automated assignment of parameters for large, novel biomolecules, and demonstrate its usage for peptides of varying degrees of complexity. Our method uses a graph theoretic representation to facilitate matching of the target molecule to molecular fragments for which reliable parameters are available. It requires minimal user input and creates parameter files compatible with the widely-used GROMACS simulation software.

Keywords: automated parametrization, fragment matching, biomolecules, molecular dynamics, graph theory, GROMOS force field

OPEN ACCESS

Edited by:
Thomas S. Hofer,
University of Innsbruck, Austria

Reviewed by:
Arnab Mukherjee,
Indian Institute of Science Education and Research, India
Sam P. De Visser,
University of Manchester, United Kingdom
Krzysztof Bernard Bec,
University of Wrocław, Poland

***Correspondence:**
Jane R. Allison
j.allison@auckland.ac.nz

Specialty section:
This article was submitted to Theoretical and Computational Chemistry, a section of the journal Frontiers in Chemistry

Received: *27 October 2018*
Accepted: *17 May 2019*
Published: *05 June 2019*

Citation:
Welsh ID and Allison JR (2019) CherryPicker: An Algorithm for the Automated Parametrization of Large Biomolecules for Molecular Simulation. Front. Chem. 7:400. doi: 10.3389/fchem.2019.00400

1. INTRODUCTION

Molecular simulations provide a means to investigate molecular interactions at or near atomistic detail. Such simulations are becoming increasingly important in areas ranging from biomedical to materials science. The accuracy of molecular simulations is in large part dependent on the quality of the parameters used to describe the inter- and intra- molecular interactions; that is, the force field. Within the realm of biomolecular simulations, force fields such as AMBER (Weiner et al., 1984, 1986; Cornell et al., 1995; Duan et al., 2003), CHARMM (Brooks et al., 1983; Reiher, 1985; MacKerell et al., 1998, 2000; Foloppe and MacKerell, 2000) and GROMOS (Schuler et al., 2001; Oostenbrink et al., 2004; Poger et al., 2010; Schmid et al., 2011) are widely used. These contain highly optimized parameters for proteins, and to varying degrees, nucleic acids, lipids and sugars. However, when it comes to simulating novel molecules, such as drug molecules, toxins, non-ribosomal peptides, post-translational modifications to proteins, or certain lipids, parameters are unlikely to be included in a given force field, necessitating parametrization.

Over the decades, a range of automated parametrization methods have been developed, such as MKTOP (Kaminski et al., 2001; Ribeiro et al., 2008), Antechamber (Wang et al., 2004, 2006),

PRODRG (Schüttelkopf and van Aalten, 2004), the ATB (Malde et al., 2011; Canzar et al., 2013; Koziara et al., 2014), Paramfit (Betz and Walker, 2015), GENRTF (Miller et al., 2008), RED (Vanquelef et al., 2011) and LigParGen (Dodda et al., 2017). Such methods generally rely on performing quantum chemical calculations and deriving atomic partial charges and bonded parameters from the resultant electronic information.

As the size of the molecule to be parameterized increases, such quantum chemical based methods become impractical. Firstly, quantum chemical methods scale at least as poorly as N^3, where N is the number of basis functions, with many scaling even more poorly. As such, the required computational effort quickly becomes intractable as molecule size increases. Additionally, it is well known that charge distributions are highly conformationally dependent (Stouch and Williams, 1992, 1993; Urban and Famini, 1993; Koch and Stone, 1996). As a consequence, derivation of reliable force field parameters capable of describing the full conformational space of the molecule requires quantum chemical calculations to be carried out for multiple conformations. This conformational dependence applies to both non-bonded and, to a lesser extent, bonded parameters.

Historically, biomolecule force fields were constructed by careful parametrization of small model chemicals, for example, compounds representative of each amino acid side chain. A similar approach could conceivably be taken to generate parameters for novel molecules. Proteins have a very limited chemical space, comprising just 20 unique amino acids that are joined together in a linear fashion, and which themselves mostly contain an identical "backbone." In comparison, the chemical space available to drug molecules is extremely large. For example, the ZINC15 database (Sterling and Irwin, 2015) contains over 100 million unique molecules. This greatly increased chemical space makes it implausible to define a finite set of model compounds. However drug molecules are typically relatively small, and are often conformationally constrained, making automated parameterisation schemes both tractable and best suited to their parameterisation. Biomolecules besides proteins and other well-studied cases present a different scenario, however. Their chemical space is much more limited, but their size can extend well beyond the reaches of quantum chemical calculations. Additionally, they are likely to undergo significant conformational motion.

We have therefore developed a fragment-based approach, reminiscent of the construction of biomolecular force fields, to parameterisation of novel biomolecules. Our approach utilizes graph theoretic representation and methodology. In contrast to other existing parameterisation methods, our approach avoids the use of expensive quantum chemical calculations. Our implementation is split into two parts: an Athenaeum, a library of molecular fragments, and CherryPicker, an algorithm for parameterisation based on matching portions of a target molecule to fragments in an Athenaeum. The code is written in C++, with Python bindings to enable ease of use provided by pybind11 (Jakob et al., 2017), and is available on GitHub at https://git.io/fp4Fr.

2. ALGORITHM DESCRIPTION

An overview of the procedures carried out in parameterizing a novel molecule using CherryPicker and one or more Athenaeums is provided in **Figure 1**. Parameterizing a novel molecule using CherryPicker proceeds as follows. A target molecule is submitted to CherryPicker and parameters are determined by comparing the target with molecular fragments contained in one or more Athenaeums. We use a graph theoretic framework in which molecules are represented as condensed molecular graphs, and matching between the target molecule and the fragments in the Athenaeum is done using subgraph isomorphism. A default parameterisation scheme is provided where parameters assigned to the target molecule are the mean (point charges) or mode (all other parameters) of the set of parameter values obtained from the pool of matching fragments. The set of assigned parameters is written to file in a format suitable for use in a simulation engine such as GROMACS (Abraham et al., 2015).

Below, we describe the implementation details of the Athenaeum library and CherryPicker algorithm. For clarity, we assume the use of the GROMOS force field and the GROMACS simulation engine. This entails the parameter values for each force field term, such as the parameters of the Lennard-Jones term for atomic centers or harmonic force constants for bonds, being identified by an integer type code. The only exception is the atomic partial charges, for which the actual parameter value is used throughout. The implementation is designed such that adding support for additional force fields or simulation engines is straightforward, however.

2.1. Data Input and Output

We provide a number of file input and output methods for handling chemical structure and parameter data.

To build an Athenaeum, both the chemical structure and the associated parameters of one or more molecules are required. Supported input file formats are the MTB format used by the GROMOS simulation engine (Christen et al., 2005), and the ITP format used by GROMACS (Abraham et al., 2015). It is also possible to supply a PDB file alongside the MTB or IFP file. ITP parsing currently assumes a GROMOS-style force field. As MTB and, in many cases, ITP files use force field type codes rather than specifying the actual parameter values, the force field itself, i.e., the parameter values associated with each force field type code, is also required. Currently only the GROMOS IFP file format is able to be parsed, but a hard-coded implementation of the GROMOS 54A7 force field (Schmid et al., 2011) is also provided.

The chemical structure of the target molecule for parameterisation must be provided in PDB format, including CONECT records. Chemical structures can be output in either PDB or GROMACS GRO formats, and the associated assigned parameters can be output in MTB or IFP format.

2.2. Condensed Molecular Graph

The target molecule and all fragments in the Athenaeum are represented as *molecular graphs* or *condensed molecular graphs*. A *molecular graph* is a labeled graph whose vertices correspond to the atoms of a molecule and edges correspond to the chemical

bonds. Generally, vertices are labeled with the element type of the atom, and edges are labeled with the type of the bond, i.e., its bond order. Such graphs often contain a large number of leaves, which can cause combinatorial explosion of search algorithms. This is particularly true of the subgraph isomorphism mappings used here. To alleviate this problem we introduce the concept of a *condensed molecular graph*.

A condensed molecular graph is a molecular graph where leaves are removed and the label of the leaf's parent vertex modified to indicate the absence. A leaf is only removed if its corresponding atom has a formal charge of 0, is either hydrogen or a halogen, and the edge that would be removed is labeled with a bond order of one. In this way, we ensure that any potentially important chemical information is explicitly maintained while reducing the computational cost.

Another reason for the use of condensed molecular graphs is their increased information density. Bit manipulation is utilized to compress multiple pieces of information into a single integer value for labeling both the vertices and edges. Doing so means that when performing subgraph isomorphism matching, the comparison between two potentially matching vertices or edges can be executed in a single CPU instruction.

2.2.1. Vertex Labels

The vertices of the condensed molecular graph carry ten distinct pieces of information. Bit manipulation means that each vertex label requires just 32 bits, as shown in **Figure 2** and detailed below.

$2^0 \rightarrow 2^6$

These seven bits represent the atomic number, in binary form, of the element associated with the vertex. Currently, there are 118 elements in the periodic table, meaning they can all be represented by the seven available bits.

$2^7 \rightarrow 2^9$

These three bits give the magnitude of the formal charge on the atom associated with the vertex, again in binary form. The use of

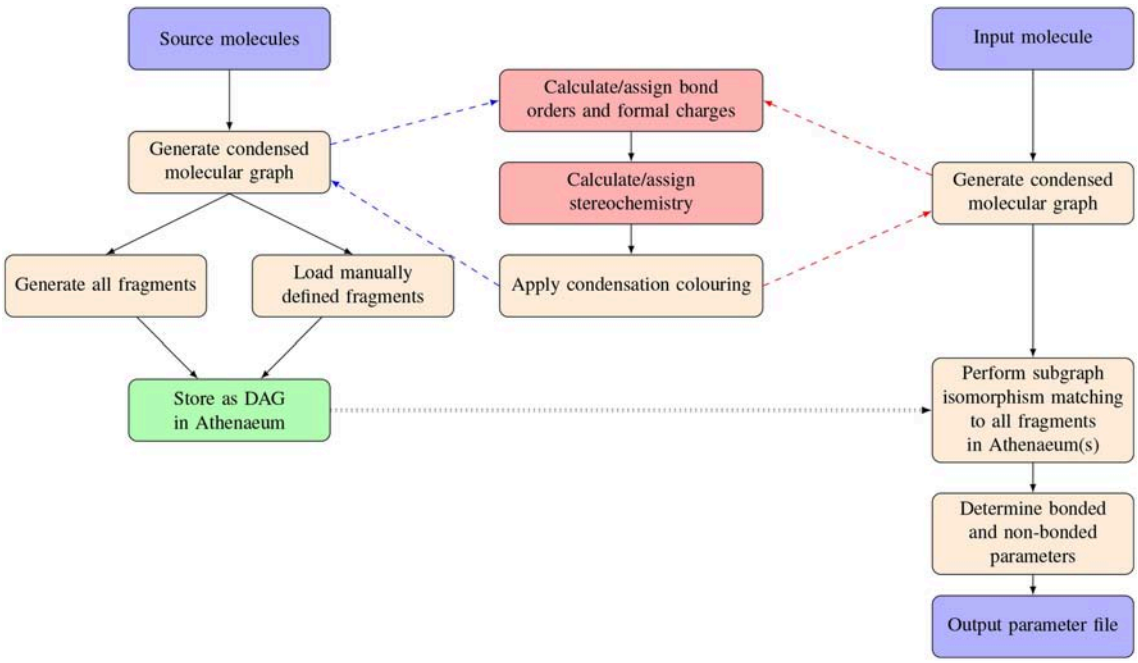

FIGURE 1 | Schematic of the process of automated parameterisation carried out by CherryPicker. The two red boxes indicate procedures described elsewhere (Welsh and Allison, 2019).

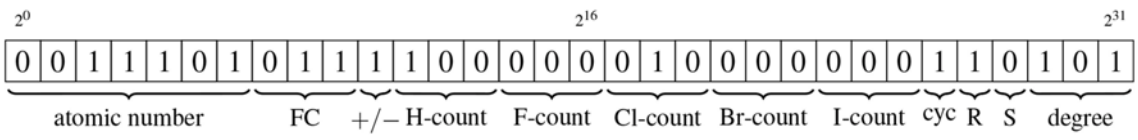

FIGURE 2 | Schematic illustrating how bit manipulation allows all information associated with a vertex to be stored using just 32 bits. The types of information are, from left to right: atomic number of the element associated with the vertex; magnitude of the formal charge of the atom associated with the vertex; sign of the formal charge; the counts of each of the five different elements that can be condensed into a vertex; whether the vertex is part of a cycle of size up to eight; the chirality (R/S) of the vertex; the degree of the vertex. All items are stored by converting the positive numeric values to binary format, other than the sign of the formal charge and the cycle and chirality indicators, for which the binary encodings are described in the text.

three bits allows for formal charge magnitudes of between zero and seven, which covers all formal charge values likely to occur in the context of molecular simulation. An automated means of determining formal charge, such as that previously described by us (Welsh and Allison, 2019), can be utilized.

2^{10}
This bit gives the sign of the formal charge. It is set to `0` if the formal charge is zero or positive and `1` if it is negative.

$2^{11} \rightarrow 2^{13}$, $2^{14} \rightarrow 2^{16}$, $2^{17} \rightarrow 2^{19}$, $2^{20} \rightarrow 2^{22}$, $2^{23} \rightarrow 2^{25}$
These five groups of three bits represent the counts of each of the five different elements that could be condensed into a vertex in the transition from a molecular graph to a condensed molecular graph, which are limited to hydrogen or halogen atoms. While in most molecular contexts, no more than three vertices of the same element would be condensed into the same parent vertex, we allow three bits per element rather than just two so as to allow for cases such as methane where there are four condensed vertices. The value of each bit is the binary value of the integer count of that element, with the first group being for condensed hydrogen atoms, the second for condensed fluorine and so forth down the halogen column of the periodic table.

2^{26}
This bit is set if the vertex is part of a cycle of size up to eight.

$2^{27} \rightarrow 2^{28}$
These two bits are used to represent any chirality associated with the atom represented by a vertex. Bit 2^{27} is set when the atom has *R* chirality, and bit 2^{28} is set when the atom has *S* chirality.

$2^{29} \rightarrow 2^{31}$
These final three bits represent the degree, in binary representation, of the vertex within the molecular graph.

2.2.2. Edge Labels

Edge labels utilize 12 bits to store four distinct pieces of information, again making use of bit manipulation, as shown in **Figure 3** and detailed below.

$2^{0} \rightarrow 2^{2}$
These three bits contain the bond order of the associated bond, with each value matching the integer value of the bond order, so that single to quadruple bonds carry values of $1 - 4$, an aromatic bond has a value of 5, a one-and-a-half bond has a value of 6 and a two-and-a-half bond has a value of 7.

$2^{3} \rightarrow 2^{4}$
These two bits are used to represent any stereochemistry associated with the bond represented by an edge. Bit 2^{3} is set when the bond is the central bond of an *E* isomer, and 2^{4} is set when the bond is the central bond of a *Z* isomer.

2^{5}
This bit is set if the edge is part of a cycle with a size of up to eight.

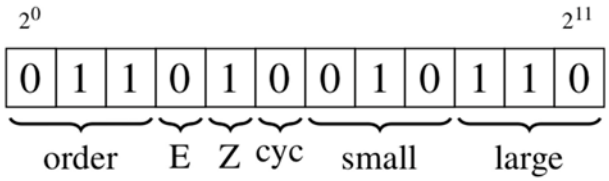

FIGURE 3 | Schematic showing the edge information, which is stored using 12 bits. The types of information are, from left to right: bond order of the associated bond; stereochemistry (E/Z) of the associated bond; whether the edge is part of a cycle with a size of up to eight; the smallest and largest degree of the vertices on either side of the edge. The numeric values of the bond order and degree are converted to binary format; the binary encodings of the stereochemistry and cycle indicators are described in the text.

$2^{6} \rightarrow 2^{8}$, $2^{9} \rightarrow 2^{11}$
These two groups contain the degree of the vertices on either side of the edge, with the first group containing the lowest degree value, and the second the highest. The three bits in each group are set to match the binary value of the integer degree.

2.3. Athenaeum

The CherryPicker algorithm utilisers one or more Athenaeums, each of which is a collection of already-parameterized molecules and the fragments derived from them. Fragmentation can be user-directed or fully automated, as outlined below.

An Athenaeum can be marked as *self-consistent*. This label is intended for use in Athenaeums constructed from fragment sources, such as the amino acids, for which the parameter values assigned to a given functional group are consistent. Being labeled as such indicates that all matching fragments that the CherryPicker algorithm finds within the Athenaeum will carry the same parameter values. If any cases where this is not the case are discovered, an error will be thrown.

2.3.1. Fragments

A fragment is a connected induced subgraph of a condensed molecular graph, consisting of two regions defined by non-intersecting vertex sets. The first region is the *core region*, from which parameters will be extracted. The vertex set of this region must also induce a connected subgraph of the overall condensed molecular graph. The second region is the *overlap region*. The overlap region does not contribute parameters; rather, it is used to ensure that the core region of a fragment and the portion of the target to which it matches have similar chemical environments. See the **Supplementary Materials** for a discussion on choosing the overlap size.

Fragments are stored within an Athenaeum in a tree like structure on a per molecule basis. A fragment is a vertex superset of another (smaller) fragment if the set of vertices in the smaller fragment are a subset of those in the larger fragment. Each fragment stores a reference to each of its immediate vertex supersets. However if multiple fragments are vertex subsets of another larger fragment, the larger fragment is only referenced by the first such smaller fragment.

2.3.2. User-Specified Fragment Generation

User-specified fragment generation involves providing a molecule, and a list of the core and overlap atoms that will form a fragment. The fragment specification file format allows for the user to specify any number of fragments to generate from a given molecule. Examples are provided in the GitHub repository. The only restriction on user-specified fragments is that the core atoms and core + overlap atoms must form induced subgraphs of the molecule's condensed molecular graph. Unlike automatically generated fragments, the overlap regions of each fragment are specified individually, and may contain different numbers of atoms.

2.3.3. Fully Automated Fragment Generation

For fully automated fragment generation, the only input required is a molecule. The overlap size is a property of the Athenaeum to which the fragments formed from this molecule will be added. Fragments of all possible sizes are generated. The user has the option to specify minimum and/or maximum fragment sizes, as well as choose which Athenaeum(s) to match against, when running CherryPicker.

For each provided molecule, all connected induced subgraphs $G' = (V', E')$ of the molecule's condensed molecular graph, $G = (V, E)$, are generated and tested against the three criteria outlined below to determine whether they are valid fragments, with each subgraph forming the core region of a fragment. The overlap region is then all vertices of the subgraph G' within a path length k of the core region, where k is the overlap length. Each Athenaeum generated fully automatically has a separate value of k.

The three criteria used to determine if a fragment is valid are:

1. Given a subgraph $G' = (V', E')$ of G, and edge $e = (u, v)$ incident on G', that is, $(u \in V \wedge v \in V') \vee (u \in V' \wedge v \in V)$, e must be labeled as representing a bond of order one or aromatic. Allowing aromatic bonds here enables fused cyclic systems to be fragmented.
2. Any edge $e = (u, v)$ incident on G' must have at least one of its vertices labeled as being carbon.
3. Let the subgraph $G'' = (V'', E'')$ be the induced subgraph of G containing the union of the core region vertex set and overlap region vertex set. Every leaf of G'' that belongs to the overlap region vertex set must have a path length of at least k to all vertices of the core region.

The user can choose which of these rules to activate when generating an Athenaeum, and the implementation also makes it straightforward to add additional rules as desired.

2.4. CherryPicker

The CherryPicker algorithm assigns parameters to a target molecule by iterating through a list of Athenaeums. The user can determine the minimum and/or maximum size of the core region of the fragments to test, defaulting to a minimum size of four and no maximum size. At each iteration, all fragments within the current Athenaeum are checked for subgraph isomorphism with the target condensed molecular graph. If the fragment is found to match a portion of the target molecule, the values of the fragment's atom, bond, angle and dihedral parameters are tallied against the corresponding vertices and edges of the target condensed molecular graph. This process is repeated until all Athenaeums have been exhausted, or the target molecule has a parameter pool for all its terms. The resulting *target molecule parameter pool* is then returned.

CherryPicker allows the concept of *dangling* bonded parameters. This refers to the case where, when a fragment is matched to a target molecule, at least half of the atoms involved in a given bond, angle or dihedral term are within the core region of the fragment, and the remainder are in the overlap region. Parameters can be assigned from the dangling bonded term, effectively enabling the core region be to edge terminated rather than vertex terminated. The criteria for allowing a bonded term to dangle is that one of the two atoms defining a bond, two of the atoms defining an angle, or two neighboring atoms defining a dihedral must be in the core region.

Being NP-complete, the subgraph isomorphism problem is inherently difficult. A number of heuristic methods have been developed for solving this problem. Here, we have implemented and tested two algorithms for subgraph isomorphism: the VF2 algorithm (Cordella et al., 2004), as implemented in the Boost Graph Library (Siek et al., 2002), and the RI algorithm (Bonnici et al., 2013). The latter is the default setting as it is more efficient. Both algorithms allow for labeled vertices and edges of graphs. As the labels used here are single integer values, a *mask* is created prior to performing the subgraph isomorphism search that dictates the pieces of information in the label to consider. For example, vertex matches could be based upon only the element and formal charge components of the label without having to modify the label, and thus the Athenaeum, itself. Additionally, to further speed up the parameterisation time, we exploit the tree-like way in which fragments are stored in an Athenaeum. The smaller fragments are tested for subgraph isomorphism first. If a small fragment does not match the target molecule, all larger fragments of which the small fragment is a subgraph will also not match, and therefore do not need to be tested.

Athenaeums are searched in a first-in first-out manner. Ideally they are provided in an order running from most to least reliable. Once all fragments within an Athenaeum have been compared to the target molecule, all components of the target molecule which mapped to a fragment are marked. These regions are excluded from any subsequent searches through additional Athenaeums, thus ensuring that the most reliable parameters identified from the early-stage Athenaeums are not replaced by less reliable parameters from later Athenaeums. Additionally, if an Athenaeum is marked as self-consistent, once all fragments in that Athenaeum have been tested, the mapped parameters are checked to ensure that they are indeed self-consistent. If they are not, CherryPicker ceases execution and the user is alerted.

The target molecule parameter pool is a distinct representation of a molecule containing all parameter values mapped to it during the subgraph isomorphism searches through an Athenaeum. For atoms, the parameter pool consists of counts of the type of each mapped atom, and the list of partial atomic charges of each mapped atom. For bonds, angles and dihedrals

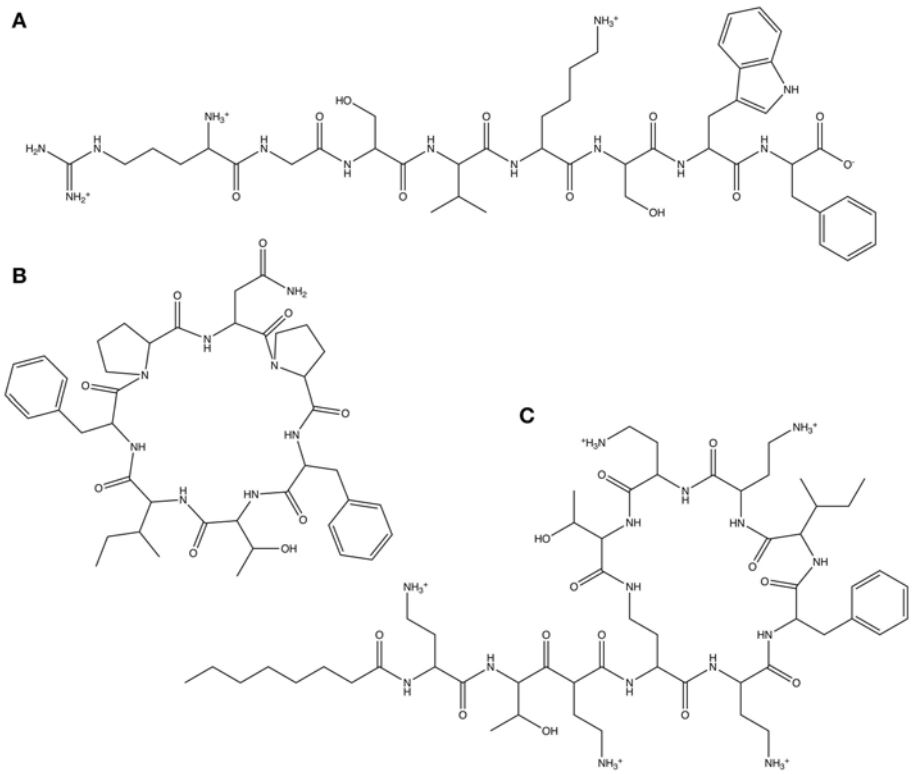

FIGURE 4 | The three peptides used to illustrate the performance of CherryPicker using user-specified and automatically-generated Athenaeums. **(A)** The randomly generated amino acid sequence Arg-Gly-Ser-Val-Lys-Ser-Trp-Phe, **(B)** the cyclic peptide Axinellin A, which has the amino acid sequence cyclo(Asn-Pro-Phe-Thr-Ile-Phe-Pro), **(C)** the non-ribosomal cyclic lipopeptide Polymyxin B3, which has the amino acid sequence octanoyl-Dab-Thr-Dab-Dab(1)-Dab-D-Phe-Leu-Dab-Dab-Thr-(1).

the parameter pool consists of counts of the corresponding mapped types.

Once each Athenaeum has been searched, the target molecule parameter pool is distilled down to a set of *assigned parameter values* for the marked components of the target molecule. Partial charges for atoms are set to the mean of the distribution of mapped partial charges. Preliminary tests revealed that for fragments with an overlap size of at least two atoms, the partial charges are approximately normally distributed, thus the mean is appropriate (see **Figures S1**, **S2**). All other parameter values are set to the mode of the mapped types.

Once all Athenaeum's have been searched, the partial charges are checked. Adding the means of partial atomic charges from matched fragments is likely to result in a non-integer total charge on the target molecule. We therefore implement a simple scheme to avoid this physically unreasonable situation. We assume that the difference between the expected total charge of the target molecule and that obtained with CherryPicker is small. As such, the difference between the assigned and expected charge is added to the atom with the most negative (assigned charge $>$ expected charge) or positive (assigned charge $<$ expected charge) partial charge. Atoms whose parameters were determined by mapping to a self-consistent Athenaeum are excluded from charge adjustment.

CherryPicker outputs both the assigned parameter values and the entire molecule parameter pool. The latter given as comments so that the provided MTB or ITP files could be used without further modification. Providing the entire molecule parameter pool allows the user to check and, if desired, adjust the assigned parameters, as well as gain a deeper understanding of the performance of the CherryPicker algorithm and suitability of the Athenaeums.

3. ALGORITHM TESTING

To illustrate the effectiveness of this fragment based method for parameterisation we present a few simple test molecules, focusing on the well studied peptide space. In future work we will explore much larger and more diverse chemical spaces.

As our first test, we use a linear octapeptide with the randomly generated amino acid sequence Arg-Gly-Ser-Val-Lys-Ser-Trp-Phe (**Figure 4A**). The second test molecule is the cyclic peptide *Axinellin A*, a bioactive cyclic heptapeptide isolated from the marine sponge *Axinella carteri* (Randazzo et al., 1998), which has been chemically synthesized (Fairweather et al., 2010) and has the amino acid sequence *cyclo*(Asn-Pro-Phe-Thr-Ile-Phe-Pro) (**Figure 4B**). Finally, we look at the non-ribosomal peptide *Polymyxin B3* (Zavascki et al., 2007), a lipopeptide antibiotic

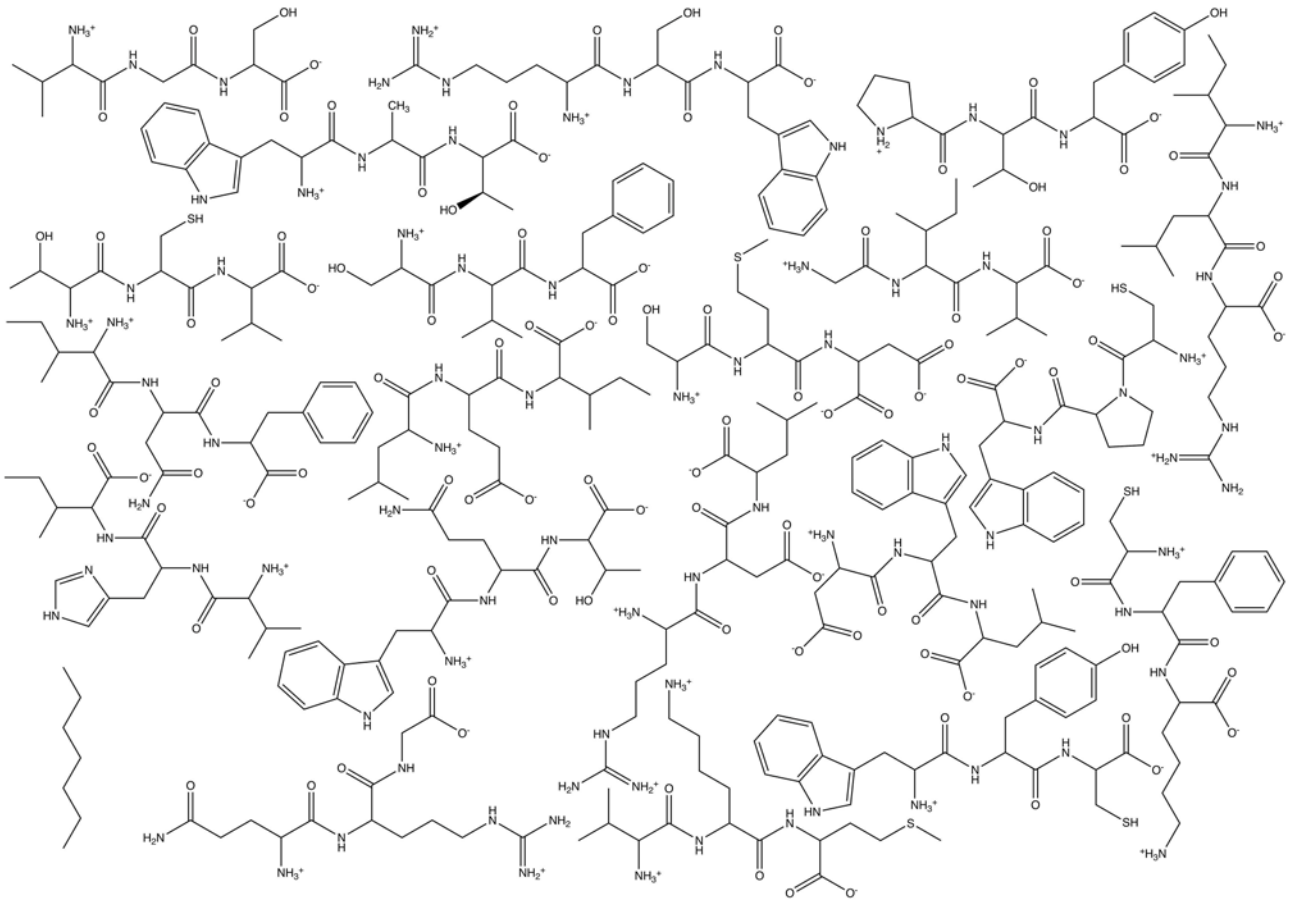

FIGURE 5 | Chemical structures of the molecules used to generate the two Athenaeums used here: 20 tripeptides plus heptane.

isolated from *Bacillus polymyxa*. Polymyxin B3 comprises a cyclic polypeptide with a tripeptide side chain and a fatty acid tail and has the amino acid sequence octanoyl-Dab-Thr-Dab-Dab(1)-Dab-D-Phe-Leu-Dab-Dab-Thr-(1) (**Figure 4C**). The parameters obtained for each test molecule using CherryPicker are provided in the **Supplementary Material**.

The CherryPicker algorithm was run with masked vertex and edge labels. Vertices were masked such that only the element type, formal charge, condensed vertices, and degree were used for matching. Edge labels were masked such that only bond order, and the source/target degree were used. For the automatically generated Athenaeums, the minimum fragment size, that is, the size of the core region in a fragment graph, was two.

3.1. Athenaeums

For these tests, we utilized simple Athenaeums to better illustrate the effects of Athenaeum content and the choices that a user can make in fragment generation and in running CherryPicker. Two different Athenaeums were generated from a set of 21 small molecules. For each of the 21 natural amino acids, a tripeptide was generated, with charged N- and C- termini and the amino acid flanked by two random amino acids. Generating these 20 random molecules resulted in the following sequences: Val-Gly-Ser, Trp-Ala-Thr, Arg-Ser-Trp, Pro-Thr-Tyr, Thr-Cys-Val, Ser-Val-Phe, Ile-Leu-Arg, Gly-Ile-Val, Ser-Met-Asp, Cys-Pro-Trp, Cys-Phe-Lys, Trp-Tyr-Cys, Asp-Trp-Leu, Leu-Glu-Ile, Ile-Asn-Phe, Trp-Gln-Thr, Val-His-Ile, Val-Lys-Met, and Gln-Arg-Gly. Of note is that the amino acids Asp and Glu were in their deprotonated, negatively charged state, Lys and Arg were in their protonated, positively charge state, and His was neutral and protonated at the NE2 position. The final molecule was heptane. Structures of the molecules used for Athenaeum generation are given in **Figure 5**. All molecules were in GROMOS united-atom format and parameterized using the standard GROMOS 54A7 force field (Schmid et al., 2011).

The first Athenaeum was built from a simple set of user-specified fragments. For each of the 20 random peptides, the central amino was defined as the core region of a fragment, and each instance of a terminal amino acid was also defined as the core region of a fragment. In all cases, the overlap region comprised the neighboring amine and/or carboxo group. This resulted in 44 fragments. **Figure 6** shows an example of one such fragment from one of the peptides. From heptane, two fragments were defined. The core of the first fragment comprises the three carbon atoms from a methyl terminal, and

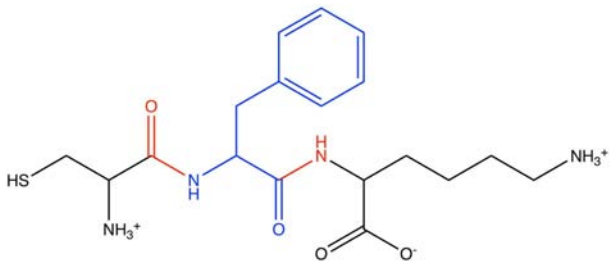

FIGURE 6 | Example of a fragment in the user-specified Athenaeum: the phenylalanine-centered tripeptide Cys-Phe-Lys, showing (blue) the core atoms of the phenylalamine fragment and (red) the overlap regions.

its overlap region is the next carbon in the chain. The core of the second fragment comprises the three carbon atoms in the center of the heptane molecule, with the overlap region comprising a single carbon atom on either side. This Athenaeum was marked as being self-consistent. While this Athenaeum is sufficient for the test cases presented here, we note that it will not be able to parameterize all possible linear proteins/peptides containing only the natural 20 amino acids as, for example, not all protonation states of side chains are present. However, this is easily resolved by adding more source molecules. On the flip side, a user-specified Athenaeum has the advantage of allowing prior knowledge, such as which functional groups or connections between functional groups are most transferable, to be included.

The second Athenaeum was automatically generated. The 21 molecules listed above were passed through the fully-automated fragment generation method (see above) using an overlap length of $k = 1$, which gave rise to an Athenaeum containing 134799 fragments. It is not marked as being self-consistent, as not all fragments created in this way will provide the same parameters to a given functional group.

3.2. Linear Octapeptide

Parameterisation of linear peptides/proteins is already well supported by all molecular dynamics simulation engines. We use this example to illustrate that CherryPicker produces the same results as existing methods, such as the GROMACS (Abraham et al., 2015) tool *pdb2gmx*, which generates parameter files for proteins from a coordinate (PDB) file. Using only the user-specified Athenaeum, CherryPicker exactly reproduces the parameters that *pdb2gmx* provides for the linear octapeptide using the GROMOS 54A7 force field. While it would generally be ill-advised to use CherryPicker in such a manner, as existing tools are more than capable of performing the same task, CherryPicker does have some advantages. For example, *pdb2gmx* uses a database to identify amino acids based on the amino acid names in the input coordinate file. If any of the amino acids are misnamed, *pdb2gmx* is unable to determine which parameters to assign. As CherryPicker uses a chemical structure-matching algorithm, it does not require the input amino acids to be correctly named.

3.3. Axinellin A

Axinellin A is a cyclic peptide, parameterisation of which is not explicitly supported by *pdb2gmx*. While it is relatively simple to generate parameters for the corresponding linear peptide and then manually modify the resultant parameter file to create a cyclic peptide, this requires detailed understanding of both the parameter file format and the correct parameters to select. CherryPicker, in contrast, handles cyclic and linear systems equivalently.

Using only the user-specified Athenaeum, CherryPicker is unable to completely parameterize *axinellin A*. Specifically, it fails to parameterize the two residues that precede proline residues, that is, the asparagine residue and the penultimate phenylalanine residue. This is not unexpected, as the cyclic nature of the proline side chain means that its backbone amine group is tertiary as opposed to secondary as it is for all the other residues. The simple user-specified Athenaeum does not contain fragments for all the different amino acids preceding a proline, and is thus unable to parameterize all Xxx-Pro combinations.

This failure of the user-specified Athenaeum provides an opportunity to showcase the use of an automatically-generated Athenaeum. From the molecules used to generate the Athenaeums (**Figure 5**), it is clear that parameters for the two unparameterized residues are available, but the necessary fragments are not included in the user-specified Athenaeum. Adding the automatically-generated Athenaeum, which is searched only after the user-specified Athenaeum and so only used to parameterize regions of the target molecule not parameterized by the user-specified Athenaeum, does result in complete parameterisation of *axinellin A*. The automatically-generated Athenaeum also results in self-consistent parameters in this instance, which are consistent with those generated by manually cyclising a parameter file for a linear version of Axinellin A generated using *pdb2gmx*.

3.4. Polymyxin B3

Our final test case is *polymyxin B3*, a peptide that is both cyclic and branched, which makes it difficult to handle with a tool like *pdb2gmx*. Additionally, it contains non-natural amino acids and a lipidated amino acid, parameters for which are not included in the standard force field parameter files provided with molecular dynamics engines and searched by tools like *pdb2gmx*. It is therefore an ideal case for illustration of the functionality of CherryPicker.

For this molecule we ignore the stereochemistry of the C_α backbone carbon, i.e., both L- and D-amino acids are considered equivalent. This is easily adjusted by the user after parameter generation, but can also be solved by generating an Athenaeum that includes L- and D-amino acids and using a mask that includes stereochemistry matching.

With the user-directed Athenaeum, CherryPicker is only able to extract parameters for the naturally occurring amino acids, threonine, phenylalanine, and leucine, as expected given the nature of this Athenaeum. It also extracts parameters for the majority of the fatty acid, excluding the peptide bond that joints it to the remainder of the polymyxin. The natural amino acids are

correctly identified, and the presence of heptane fragments allows for the identification of straight chain alkane fragments.

After exhausting the fragments in the manual Athenaeum, the remaining unparametrized portions of *polymyxin B3* are mainly the diaminobutyric acid residues. Structurally, these are similar to lysine residues, except with a shorter carbon chain length. As such, an Athenaeum containing fragments of lysine would be expected to be able to parameterize the diaminobutyric acid residues. This is what is observed when using the automatically-generated Athenaeum. All atoms, bonds and angles, except those involving the carboxy group joining the fatty acid tail to the peptide chain, are assigned consistent parameters.

The unmatched atoms, bonds and angles involving the carboxy group of the fatty acid indicate a deficiency of the Athenaeum, rather than a deficiency of the matching algorithm. This can easily be overcome by building additional Athenaeums that incorporate a wider range of already-parameterized molecules, such as lipids. Our purpose here, however, was to illustrate how much can be achieved with even a very simple Athenaeum that requires only molecules already available in standard biomolecular force fields.

Parameters were also not assigned to the dihedral terms for rotation about the central bond of the diaminobutyric acid side chains. This is because the fragments that matched to these side chains had a maximum (core plus overlap) size of three, whereas a core+overlap size of four is required for dihedral terms to be included in a fragment, even utilizing dangling bonds. Again, this would be alleviated by using a broader Athenaeum that covered more chemical groups.

In the current implementation of CherryPicker, placeholder parameters are inserted in the output parameter file when parameters are not assigned after parsing all available Athenaeums, giving the user a clear indication that parameters were not assigned from the Athenaeum. In the future, it will be possible to automatically identify unmatched regions and extract them as separate molecules, capped as necessary to maintain appropriate chemistry, for parameterisation by other means. As these regions are likely to be individually fairly small, parameterisation using automated web servers that carry out quantum chemical calculations will be possible. Once parameterized, these molecules will then be able to be added to the Athenaeum, thus plugging its gaps and broadening the scope of molecules that can be parameterized.

3.5. Limitations

As with all automated parameterisation schemes, there are limitations to the approach presented here. Firstly, the quality of parameters obtained for the target molecule is highly dependent on the nature and parameters of the source molecules from which fragments are generated. If molecular dynamics simulations of the source molecules give incorrect emergent properties, simulations of target molecules parameterized by CherryPicker will likely also give incorrect properties. Additionally, deficiencies in the Athenaeum, i.e., Athenaeums that do not provide fragments to cover all regions of a target molecule, will become apparent, as was shown with the parameterisation of *polymyxin B3* discussed above. Finally, the choice of overlap size will have a potentially pronounced effect on the parameters attained, especially in the fully automated use case. A smaller overlap will lead to more of a target molecule being parameterized, but risks loss of the chemical environment selectivity that a larger overlap region enables, and thus poorer quality parameters.

4. CONCLUSIONS

The CherryPicker algorithm, combined with one or more Athenaeums, provides a simple to use yet widely applicable method for rapidly generating parameters for novel biomolecules. By assembling parameters derived from fragments of molecules that are already parameterized according to a particular biomolecular force field, we ensure that the resultant parameter set for the novel molecule is by design compatible with an existing force field. The user is able to specify the nature and number of Athenaeums used, including how the already-parameterized molecules are fragmented. This provides control over, for instance, the reliability and consistency of the parameters that are assigned to the target molecule. In demonstrating the application of CherryPicker to a series of peptides of varying degrees of complexity, we illustrate how even very simple Athenaeums are able to parameterize a wider range of molecules than would be possible with existing parameter generation tools. Target molecules are input to CherryPicker in the standard and commonly-used PDB format, and coordinate and parameter files are output in the formats required for the popular GROMACS simulation software, making it straightforward to integrate CherryPicker into established simulation pipelines. This will in turn act to facilitate the use of molecular simulations across a broad range of scientific fields.

AUTHOR CONTRIBUTIONS

IW co-designed, coded, and tested the software and co-wrote the manuscript. JA co-designed the software and tests, and co-wrote the paper.

FUNDING

JA is supported by a Rutherford Discovery Fellowship (15-MAU-001). IW was supported by a Marsden Fast Start grant to JA (13-MAU-039) and by Massey University Doctoral Completion and Dissemination grants.

ACKNOWLEDGMENTS

The authors are extremely grateful for inspiration and advice from Prof. Alan Mark, Dr Alpesh Malde, Dr Martin Stroet, and Bertrand Caron, University of Queensland.

SUPPLEMENTARY MATERIAL

The Supplementary Material for this article can be found online at: https://www.frontiersin.org/articles/10.3389/fchem.2019.00400/full#supplementary-material

REFERENCES

Abraham, M. J., Murtola, T., Schulz, R., Páll, S., Smith, J. C., Hess, B., et al. (2015). Gromacs: high performance molecular simulations through multi-level parallelism from laptops to supercomputers. *SoftwareX* 1–2:19–25. doi: 10.1016/j.softx.2015.06.001

Betz, R. M., and Walker, R. C. (2015). Paramfit: automated optimization of force field parameters for molecular dynamics simulations. *J. Comput. Chem.* 36, 79–87. doi: 10.1002/jcc.23775

Bonnici, V., Giugno, R., Pulvirenti, A., Shasha, D., and Ferro, A. (2013). A subgraph isomorphism algorithm and its application to biochemical data. *BMC Bioinformat.* 14:S13. doi: 10.1186/1471-2105-14-S7-S13

Brooks, B. R., Bruccoleri, R. E., Olafson, B. D., States, D. J., Swaminathan, S., and Karplus, M. (1983). Charmm: a program for macromolecular energy, minimization, and dynamics calculations. *J. Comput. Chem.* 4, 187–217.

Canzar, S., El-Kebir, M., Pool, R., Elbassioni, K., Malde, A. K., Mark, A. E., et al. (2013). Charge group partitioning in biomolecular simulation. *J. Comput. Biol.* 20, 188–198. doi: 10.1089/cmb.2012.0239

Christen, M., Hünenberger, P. H., Bakowies, D., Baron, R., Bürgi, R., Geerke, D. P., et al. (2005). The gromos software for biomolecular simulation: Gromos05. *J. Comput. Chem.* 26, 1719–1751. doi: 10.1002/jcc.20303

Cordella, L. P., Foggia, P., Sansone, C., and Vento, M. (2004). A (sub)graph isomorphism algorithm for matching large graphs. *IEEE Trans. Pattern Anal. Mach. Intell.* 26, 1367–1372. doi: 10.1109/TPAMI.2004.75

Cornell, W. D., Cieplak, P., Bayly, C. I., Gould, I. R., Merz, K. M., Ferguson, D. M., et al. (1995). A second generation force field for the simulation of proteins, nucleic acids, and organic molecules. *J. Am. Chem. Soc.* 117, 5179–5197.

Dodda, L. S., Cabeza de Vaca, I., Tirado-Rives, J., and Jorgensen, W. L. (2017). Ligpargen web server: an automatic opls-aa parameter generator for organic ligands. *Nucleic Acids Res.* 45, W331–W336. doi: 10.1093/nar/gkx312

Duan, Y., Wu, C., Chowdhury, S., Lee, M. C., Xiong, G., Zhang, W., et al. (2003). A point-charge force field for molecular mechanics simulations of proteins based on condensed-phase quantum mechanical calculations. *J. Comput. Chem.* 24, 1999–2012.

Fairweather, K. A., Sayyadi, N., Roussakis, C., and Jolliffe, K. A. (2010). Synthesis of the cyclic heptapeptide axinellin a. *Tetrahedron* 66, 935–939. doi: 10.1016/j.tet.2009.11.090

Foloppe, N., and MacKerell, A. D. Jr. (2000). All-atom empirical force field for nucleic acids: I. parameter optimization based on small molecule and condensed phase macromolecular target data. *J. Comput. Chem.* 21, 86–104.

Jakob, W., Rhinelander, J., and Moldovan, D. (2017). *Pybind11–Seamless Operability Between c++11 and Python.* Available online at: https://github.com/pybind/pybind11 (accessed September 11, 2018).

Kaminski, G. A., Friesner, R. A., Tirado-Rives, J., and Jorgensen, W. L. (2001). Evaluation and reparametrization of the opls-aa force field for proteins via comparison with accurate quantum chemical calculations on peptides. *J. Phys. Chem. B* 105, 6474–6487. doi: 10.1021/jp003919d

Koch, U., and Stone, A. J. (1996). Conformational dependence of the molecular charge distribution and its influence on intermolecular interactions. *J. Chem. Soc. Faraday Trans.* 92, 1701–1708. doi: 10.1039/ft9969201701

Koziara, K., Stroet, M., Malde, A., and Mark, A. (2014). Testing and validation of the automated topology builder (atb) version 2.0: prediction of hydration free enthalpies. *J. Comput. Aided Mol. Design* 28, 221–233. doi: 10.1007/s10822-014-9713-7

MacKerell, A. D., Banavali, N., and Foloppe, N. (2000). Development and current status of the charmm force field for nucleic acids. *Biopolymers* 56, 257–265. doi: 10.1002/1097-0282(2000)56:4<257::AID-BIP10029>3.0.CO;2-W

MacKerell, A. D., Bashford, D., Bellott, M., Dunbrack, R. L., Evanseck, J. D., Field, M. J., et al. (1998). All-atom empirical potential for molecular modeling and dynamics studies of proteins. *J. Phys. Chem. B* 102, 3586–3616.

Malde, A. K., Zuo, L., Breeze, M., Stroet, M., Poger, D., Nair, P. C., et al. (2011). An automated force field topology builder (atb) and repository: Version 1.0. *J. Chem. Theory Comput.* 7, 4026–4037. doi: 10.1021/ct200196m

Miller, B. T., Singh, R. P., Klauda, J. B., Hodošček, M., Brooks, B. R., and Woodcock, H. L. (2008). Charmming: a new, flexible web portal for charmm. *J. Chem. Inform. Model.* 48, 1920–1929. doi: 10.1021/ci800133b

Oostenbrink, C., Villa, A., Mark, A. E., and Van Gunsteren, W. F. (2004). A biomolecular force field based on the free enthalpy of hydration and solvation: the gromos force-field parameter sets 53a5 and 53a6. *J. Comput. Chem.* 25, 1656–1676. doi: 10.1002/jcc.20090

Poger, D., Van Gunsteren, W. F., and Mark, A. E. (2010). A new force field for simulating phosphatidylcholine bilayers. *J. Comput. Chem.* 31, 1117–1125. doi: 10.1002/jcc.21396

Randazzo, A., Dal Piaz, F., Orrù, S., Debitus, C., Roussakis, C., Pucci, P., et al. (1998). Axinellins a and b: New proline-containing antiproliferative cyclopeptides from the vanuatu sponge axinella carteri. *Eur. J. Organ. Chem.* 1998, 2659–2665.

Reiher, W. E. (1985). *Theoretical Studies of Hydrogen Bonding.* Ph.D. thesis, Harvard University. "Theoretical Studies of Hydrogen Bonding."

Ribeiro, A. A. S. T., Horta, B. A. C., and de Alencastro, R. B. (2008). Mktop: a program for automatic construction of molecular topologies. *J. Brazil. Chem. Soc.* 19, 1433–1435. doi: 10.1590/S0103-50532008000700031

Schmid, N., Eichenberger, A., Choutko, A., Riniker, S., Winger, M., Mark, A., et al. (2011). Definition and testing of the gromos force-field versions 54a7 and 54b7. *Eur. Biophys. J.* 40, 843–856. doi: 10.1007/s00249-011-0700-9

Schuler, L. D., Daura, X., and van Gunsteren, W. F. (2001). An improved gromos96 force field for aliphatic hydrocarbons in the condensed phase. *J. Comput. Chem.* 22, 1205–1218. doi: 10.1002/jcc.1078.abs

Schüttelkopf, A. W., and van Aalten, D. M. F. (2004). Prodrg: a tool for high-throughput crystallography of protein–ligand complexes. *Acta Crystallogra. Sect. D* 60, 1355–1363. doi: 10.1107/S0907444904011679

Siek, J., Lee, L.-Q., and Lumsdaine, A. (2002). *The Boost Graph Library: User Guide and Reference Manual.* Boston, MA: Addison-Wesley Longman Publishing Co., Inc.

Sterling, T., and Irwin, J. J. (2015). Zinc 15–ligand discovery for everyone. *J. Chem. Inform. Model.* 55, 2324–2337. doi: 10.1021/acs.jcim.5b00559

Stouch, T., and Williams, D. E. (1992). Conformational dependence of electrostatic potential derived charges of a lipid headgroup: Glycerylphosphorylcholine. *J. Comput. Chem.* 13, 622–632.

Stouch, T. R., and Williams, D. E. (1993). Conformational dependence of electrostatic potential-derived charges: Studies of the fitting procedure. *J. Comput. Chem.* 14, 858–866.

Urban, J. J., and Famini, G. R. (1993). Conformational dependence of the electrostatic potential-derived charges of dopamine: ramifications in molecular mechanics force field calculations in the gas phase and in aqueous solution. *J. Comput. Chem.* 14, 353–362.

Vanquelef, E., Simon, S., Marquant, G., Garcia, E., Klimerak, G., Delepine, J. C., et al. (2011). R.e.d. server: a web service for deriving resp and esp charges and building force field libraries for new molecules and molecular fragments. *Nucleic Acids Res.* 39(Suppl-2):W511–W517. doi: 10.1093/nar/gkr288

Wang, J., Wang, W., Kollman, P. A., and Case, D. A. (2006). Automatic atom type and bond type perception in molecular mechanical calculations. *J. Mol. Grap. Model.* 25, 247–260. doi: 10.1016/j.jmgm.2005.12.005

Wang, J., Wolf, R. M., Caldwell, J. W., Kollman, P. A., and Case, D. A. (2004). Development and testing of a general amber force field. *J. Comput. Chem.* 25, 1157–1174. doi: 10.1002/jcc.20035

Weiner, S. J., Kollman, P. A., Case, D. A., Singh, U. C., Ghio, C., Alagona, G., Profeta, S., et al. (1984). A new force field for molecular mechanical simulation of nucleic acids and proteins. *J. Am. Chem. Soc.* 106, 765–784.

Weiner, S. J., Kollman, P. A., Nguyen, D. T., and Case, D. A. (1986). An all atom force field for simulations of proteins and nucleic acids. *J. Comput. Chem.* 7, 230–252.

Welsh, I. D., and Allison, J. R. (2019). Automated simultaneous assignment of bond orders and formal charges. *J. Cheminformat.* 11:18. doi: 10.1186/s13321-019-0340-0

Zavascki, A., Goldani, L., Li, J., and Nation, R. (2007). Polymyxin b for the treatment of multidrug-resistant pathogens: a critical review. *J. Antimicrob. Chemother.* 60, 1206–1215. doi: 10.1093/jac/dkm357

Conflict of Interest Statement: The authors declare that the research was conducted in the absence of any commercial or financial relationships that could be construed as a potential conflict of interest.

Copyright © 2019 Welsh and Allison. This is an open-access article distributed under the terms of the Creative Commons Attribution License (CC BY). The use, distribution or reproduction in other forums is permitted, provided the original author(s) and the copyright owner(s) are credited and that the original publication in this journal is cited, in accordance with accepted academic practice. No use, distribution or reproduction is permitted which does not comply with these terms.

frontiers in Chemistry

REVIEW
published: 22 February 2019
doi: 10.3389/fchem.2019.00048

Breakthrough Potential in Near-Infrared Spectroscopy: Spectra Simulation. A Review of Recent Developments

Krzysztof B. Beć and Christian W. Huck*

Center for Chemistry and Biomedicine, Institute of Analytical Chemistry and Radiochemistry, Leopold-Franzens University, Innsbruck, Austria

OPEN ACCESS

Edited by:
Sam P. De Visser, University of Manchester, United Kingdom

Reviewed by:
Ramiro Arratia-Perez, Universidad Andrés Bello, Chile
Daniel Glossman-Mitnik, Centro de Investigación en Materiales Avanzados (CIMAV), Mexico

****Correspondence:***
Krzysztof B. Beć
krzysztof.bec@gmail.com

Specialty section:
This article was submitted to Theoretical and Computational Chemistry, a section of the journal Frontiers in Chemistry

Received: *06 December 2018*
Accepted: *18 January 2019*
Published: *22 February 2019*

Citation:
Beć KB and Huck CW (2019) Breakthrough Potential in Near-Infrared Spectroscopy: Spectra Simulation. A Review of Recent Developments. Front. Chem. 7:48. doi: 10.3389/fchem.2019.00048

Near-infrared (12,500–4,000 cm^{-1}; 800–2,500 nm) spectroscopy is the hallmark for one of the most rapidly advancing analytical techniques over the last few decades. Although it is mainly recognized as an analytical tool, near-infrared spectroscopy has also contributed significantly to physical chemistry, e.g., by delivering invaluable data on the anharmonic nature of molecular vibrations or peculiarities of intermolecular interactions. In all these contexts, a major barrier in the form of an intrinsic complexity of near-infrared spectra has been encountered. A large number of overlapping vibrational contributions influenced by anharmonic effects create complex patterns of spectral dependencies, in many cases hindering our comprehension of near-infrared spectra. Quantum mechanical calculations commonly serve as a major support to infrared and Raman studies; conversely, near-infrared spectroscopy has long been hindered in this regard due to practical limitations. Advances in anharmonic theories in hyphenation with ever-growing computer technology have enabled feasible theoretical near-infrared spectroscopy in recent times. Accordingly, a growing number of quantum mechanical investigations aimed at near-infrared region has been witnessed. The present review article summarizes these most recent accomplishments in the emerging field. Applications of generalized approaches, such as vibrational self-consistent field and vibrational second order perturbation theories as well as their derivatives, and dense grid-based studies of vibrational potential, are overviewed. Basic and applied studies are discussed, with special attention paid to the ones which aim at improving analytical spectroscopy. A remarkable potential arises from the growing applicability of anharmonic computations to solving the problems which arise in both basic and analytical near-infrared spectroscopy. This review highlights an increased value of quantum mechanical calculations to near-infrared spectroscopy in relation to other kinds of vibrational spectroscopy.

Keywords: near-infrared, NIRS, spectra simulation, theoretical spectroscopy, anharmonic methods

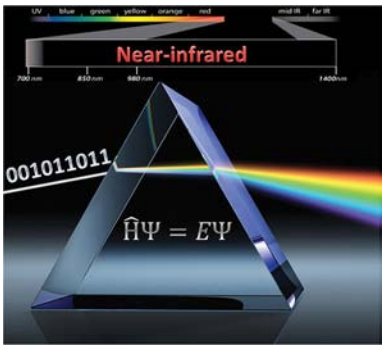

Graphical Abstract | The properties of near-infrared spectroscopy create unique synergy with quantum mechanical spectra simulations.

INTRODUCTION

Near-infrared spectroscopy (commonly abbreviated as NIRS) has distinguished itself by a remarkable evolution from an undervalued section of vibrational spectroscopy to one of the presently most widespread modern analytical techniques with strong prospects for further expansion (Ciurczak and Drennen, 2002; Siesler et al., 2002; Cozzolino, 2014; Huck, 2014, 2016a; Ozaki et al., 2017). The second major application field taking advantage of the potential embodied in NIRS is hyperspectral imaging (Ozaki et al., 2017; Türker-Kaya and Huck, 2017; Dorrepaal and Gowen, 2018; He et al., 2018), which enjoys a rapidly growing interest in the biomedical applications (He et al., 2015; Türker-Kaya and Huck, 2017) and is a subject of focused development nowadays (He et al., 2015; Sun et al., 2017; Wong et al., 2019). As will be discussed further on, most of the distinctiveness of NIRS results from the specificity of the corresponding spectral region located between visible and infrared (near-infrared or NIR; 800–2,500 nm; 12,500–4,000 cm^{-1}). From the point of view of the present review, the foremost aspect worth emphasizing is the molecular mechanisms standing behind the absorption of electromagnetic radiation in NIR, which involves excitations of non-fundamental vibrations, overtones and combination modes. The primary parameters of the resulting bands, wavenumbers and intensities are ruled by anharmonic effects with inter-mode anharmonicity playing the most substantial role. In this sense, NIRS distinctively sets itself apart from the other kinds of vibrational spectroscopy (mid-infrared, MIR; far-infrared, FIR; Mantsch and Naumann, 2010[1] and Raman) in which the major chemical information originates from fundamental vibrational transitions. Unlike these latter ones, which put the harmonic approximation into good use, theoretical NIRS unequivocally requires computationally intensive anharmonic approaches. Hence, NIR spectral simulations have remained rather rare in literature until the recent advances in theory and computer technology made such studies feasible for the molecules extending beyond a few atoms in complexity. It can be stated that this is an emerging field, as the entirety of literature reporting on theoretical NIR simulations of the molecules relevant for applied studies has emerged in the current decade.

The aim of the present review is to provide a comprehensive introduction to theoretical NIRS and to expound its distinctiveness and exceptional significance for the contemporary progress of applied spectroscopy (**Graphical Abstract**). In order to fully apprehend a remarkable synergy arising between the theoretical and experimental NIRS, far outweighing the analogous relation existing in the other kinds of vibrational spectroscopy, the present article includes brief information on the specificity of basic and analytical NIRS. Throughout the following sections, the underlying phenomena and key correspondences are thoroughly explained, together with a brief history sketch reaching the most recent accomplishments and future prospects, outlining a complete overview of the highly promising and boundary-crossing development currently taking place in the field of NIRS.

NEAR-INFRARED SPECTROSCOPY. THE TALE OF AN UGLY DUCKLING

Early Developments

Near-infrared light has been the first kind of non-visible electromagnetic radiation discovered as early as in year 1800 in the famous experiment of Herschel. Although this happened by observing that NIR light is absorbed by matter, it may be considered a peculiar plot twist of scientific history that the actual development of NIR spectroscopy has lagged behind the techniques resorting to other spectral regions, e.g., ultra-violet (UV), visible (VIS) or MIR. By the time these other kinds of optical spectroscopy have reached reasonable levels of maturity (ca. 1950–1960s), instrumentation capable of working in the NIR region was still being used only as an add-on unit to the major optical devices. The potential of NIR region remained not recognized at that time for several reasons. First, in basic research the lack of stimulus resulted primarily from the competition from MIR spectroscopy. The chemical information derived from the fundamental bands has always seemed more specific and readily available. The absorption occurring in the NIR region of the vast majority of both organic and inorganic matter is relatively weak. An example of a common and relatively strongly absorbing medium is liquid water, whose NIR absorption coefficient values remain at least two orders of magnitude lower than in the MIR region (**Figure 1**). At that time, before the era of Fourier-transform (FT) optical spectrometers, the relatively primitive dispersive devices have, by design, been less potent in capturing weaker signals. Both the registered peak positions and absorption intensity values have been rather unreliable because of the imperative instrument calibration and also due to analog electronics (Davies, 2011). The spectra collection was a time-consuming and manpower-intensive process. Additionally, weak and broad structures resulting from multiple overlaying bands are typically found in this spectral region. Hence, NIR absorption

[1]This includes terahertz (THz) spectroscopy; despite differences in the instrumentation, FIR and THz spectroscopy both elucidate the same information from the analyzed sample (Mantsch and Naumann, 2010).

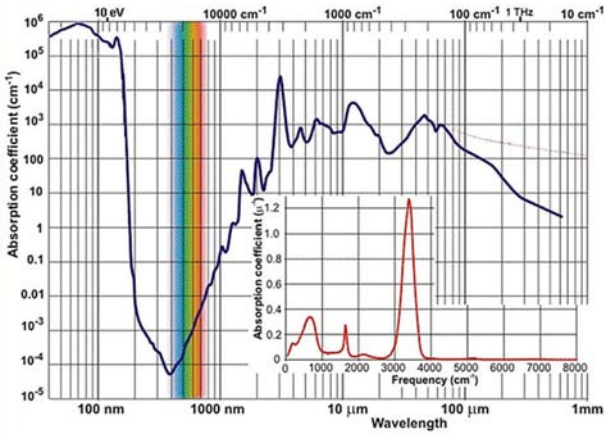

FIGURE 1 | The spectrum of absorption coefficient of liquid water[2].

was troublesome in measurement and analysis and its potential has long remained undervalued (Davies, 2011).

In this context, the fact that analytical chemistry first reached to the unique favors of NIR spectroscopy may be unexpected. Briefly during the 1950s, the NIR region attracted limited attention in measurements of moisture in hazardous materials, where MIR spectroscopy found limited applicability due to strong absorption of water (**Figure 1**). However, other emerging analytical techniques (e.g., chromatography) proved to be even more superior for such a task and soon took over. Much has changed when an engineer K. Norris working for the United States Department of Agriculture re-invoked NIR spectroscopy for the analysis of moisture in grains and oilseeds (Davies, 2011). This required the designing of an instrument featuring a very high light efficiency. Over the next years, Norris and collaborators further developed early analytical NIRS, often facing scientific and engineering challenges, as well as straight opposition from some part of the spectroscopic community. Although early instrumentation has initially been troublesome and barely reliable enough for analytical applications, the unique advantages of applied NIR spectroscopy have been recognized and this activity marked the beginning of the evolution path leading to the present state-of-the-art NIRS (Davies, 2011).

Analytical NIRS Today

Nowadays NIRS is being widely used in modern analytical applications due to a uniquely synergistic combination of qualities. Its universality, wide applicability, uncomplicated instrumentation, low time-to-result and low cost factors are prominent advantages from the point of view of qualitative and quantitative analysis (Ciurczak and Drennen, 2002; Siesler et al., 2002; Cozzolino, 2014; Huck, 2014, 2016a; Ozaki et al., 2017). It enables the non-invasive, non-destructible analysis of a variety of samples while maintaining a good balance between its cost, time, and analytical performance. The mentioned typical low absorptivity in NIR (**Figure 1**) results in the ability of examining a bulk sample in high volume with no limitation to the sample surface, as often encountered in optical spectroscopy. NIRS has found its way to quality control laboratories dealing with, e.g., food (Smyth and Cozzolino, 2013; Henn et al., 2016; Ringsted et al., 2017; Chapman et al., 2018) and natural products (Pezzei et al., 2017a), agriculture-related items (Pezzei et al., 2017b), pharmaceuticals (Kirchler et al., 2017a; Yan and Siesler, 2018a), phytopharmaceuticals (Stecher et al., 2003) and phytoanalysis in general (Huck, 2017a), polymers (Huck, 2016b; Unger et al., 2016; Yan and Siesler, 2018b) fuel (Lutz et al., 2014a), cosmetics (Blanco et al., 2007), biomedical applications (Jue and Masuda, 2013), general industry (Huck, 2017b) and environmental studies (Altinpinarn et al., 2013; Roberts and Cozzolino, 2016, 2017), among others (Ciurczak and Drennen, 2002; Siesler et al., 2002; Iwamoto, 2009; Cozzolino, 2014; Huck, 2014, 2016a; Ozaki et al., 2017; Power et al., 2018; Yan and Siesler, 2018c). In response to strong demand from the industry the instrumentation has been undergoing continuous development. One of the most recent milestones in this evolution path was the introduction of portable spectrometers (Herberholz et al., 2010; O'Brien et al., 2012; Alcalà et al., 2013), which marked the beginning of truly on-site capability of NIRS analysis (Wiedemair et al., 2018). Within the next decade, strong prospects exist for this technique to ultimately achieve wide-spread use even at consumer level due to the development of inexpensive mobile phone-attachable spectrometers and highly autonomous software for data analysis (Klakegg et al., 2016; Watanabe et al., 2016). The cost factor should not be underestimated, as it is a crucial factor for wide utilization; this is a subject of focused development (Saranwong et al., 2013). It may be reasonably envisioned that the next major breakthrough will be accomplished by the successful design and implementation of single-chip *in-silicon* spectrometers; the era of such devices in MIR spectroscopy is approaching (Wang et al., 2013; Ribessi et al., 2016; Sieger and Mizaikoff, 2016) and similar evolution in NIRS should be anticipated.

Analytical NIRS relies extensively on various methods of statistical analysis, which are commonly grouped under the well-established term of chemometrics (Beebe et al., 1998; Marini, 2013). These methods may be roughly divided into three classes. (1) Exploratory Data Analysis (EDA) includes techniques of data mining (e.g., Cluster Analysis, PCA-Principal Component Analysis) which are used for gaining deeper insights into high-volume complex data such as a large set of NIR spectra. (2) Regression analysis groups the methods used for the prediction/quantification of chemical content (predictive models); it finds extensive use in detection and quantification of selected chemical components. The most utilized techniques include Multiple Linear Regression (MLR), Principal Component Regression (PCR) and Partial Least Squares Regression (PLSR). (3) Classification techniques are used for the separation and sorting as well as grouping of samples with regard to a selected property. Classification approaches include supervised (e.g., SIMCA, Soft Independent Modeling of Class Analogy; LDA, Linear Discriminant Analysis; PLS-DA, Partial Least Squares Discriminant Analysis or SVMC, Support Vector Machine

[2](http://www1.lsbu.ac.uk/water/water_vibrational_spectrum.html#k) under Creative Commons license. Attribution-NonCommercial-NoDerivs 2.0 UK: England & Wales (CC BY-NC-ND 2.0 UK).

Classification) and unsupervised approaches (e.g., K-mean and K-median methods, Hierarchical Cluster Analysis or PCA, this time in its classification role). Classification methods allow e.g., group samples in accordance with their source of origin, level of authenticity, or even the region or conditions of cultivation in the case of agricultural products. Within the set content rule, the classification methods may be used, for example, for the separation of contaminated samples from the pure ones.

At present, analytical NIRS is an active research field with a considerably wide scientific and professional community involved, as evidenced by the narrowly scoped and highly attended international conferences (to list only the few: meetings of International Council for Near-Infrared Spectroscopy [ICNIRS]; International Diffuse Reflectance Conference [IDRC]; Asian NIR Symposia [ANS]), and scientific journals (e.g., *Journal of Near Infrared Spectroscopy*; *NIR News*). The development of the data analytical/statistical methods (i.e., chemometrics Burns and Ciurczak, 2007), which are essential in analytical NIRS, has grown to become another largely independent field of research (e.g., *Journal of Chemometrics*; *Chemometrics and Intelligent Laboratory Systems*; *Journal of Multivariate Analysis*). On the other hand, a rapid expansion of applied NIRS has resulted in its detachment from basic spectroscopy, physical chemistry, and molecular science. This fact, in turn, creates hindrances in the further advancement of this field, as will be explained in detail below.

The stimulated development of applied NIRS created focus on relatively narrow, short-reaching goals suiting specific analytical applications. This pragmatic demeanor has led to a detachment of analytical NIRS from its physicochemical background. Basic NIR investigations of the chemical structure, molecular vibrations, and intra- and inter-molecular interactions remain limited in relation to the exceedingly active field of applied studies (Huck, 2014). Due to an intrinsic complexity of NIR spectra, reflecting the anharmonic nature of molecular vibrations (Huck, 2014; Ozaki et al., 2017) the observed spectral outline typically emerges from multiple overlapping contributions. The resulting broad and non-homogeneous bands create significant difficulties in the comprehensive association of the observed spectral variability and physicochemical background. For this reason, in NIR analytical routines, spectral data is often used without any attempt to interpret the chemical information embodied within. Chemometrics allows the correlation of subtle spectral variability with the sample composition and thus yields effective chemical content detection and quantification. However, it lacks in providing a physicochemical interpretation for the information it delivers. In this context, the analytical NIRS is often effectively limited to a "black-box tool."

NIRS in Physical Chemistry

The value of NIRS to basic research stems from specific physicochemical features differing from those of the fundamental region (IR, Raman) (Czarnecki et al., 2015). NIR spectra remain the most natural and rich source of information on the anharmonicity of molecular vibrations. The absorptivity of NIR transitions gradually decreases toward the higher tones and higher order combinations. The co-existence of various bands (e.g., first, second, and third overtones Gonjo et al., 2011; Futami et al., 2012; Chen et al., 2014) within the same spectra is a key advantage here. Low band intensities enable systematic studies of the molecules in solution with a widely spread concentration range. This provides the possibility of a comprehensive investigation of intermolecular interactions, association mechanisms, solvent effects, molecular self-organization, and the structure of liquid phase (Czarnecki et al., 2015; Wrzeszcz et al., 2016a,b). In the NIR region, the bands originating from X-H (e.g., C-H, O-H, N-H) vibrations are strongly articulated. These chemical groups are most commonly responsible for the formation of hydrogen bonding. This enhances the potential of exploring the nature of hydrogen bonding and molecular interactions (Czarnecki et al., 2015). In the NIR region, particular types of bands are being enhanced in their intensity. The bands due to non-associated species usually are much more intense than those of aggregated molecules (Czarnecki et al., 2015). The NIR band heights often carry valuable information on themselves. For example, the prominence of the first overtone band of C=O stretching mode (5,260–5,130 cm^{-1}) varies strongly among different molecular systems (Czarnecki et al., 2015). On the other hand, the second overtone of C=C stretching mode is not commonly observed in NIR spectra. One can conclude on this mode by investigating the spectral shift of its first overtone band or the combination band with the modes of a C-H group connected directly to the C=C moiety. Another relevant example may be provided in the form of the first overtone of C≡N stretching mode, or the second overtone of C=N mode. Contrary to the respective fundamentals, these transitions have very low absorptivity and have not yet been identified in the NIR region.

The specificity of such vibrational effects in NIR, different from those observed in MIR spectra, create a large amount of independent spectral information of high value for physical chemistry. However, NIR spectral analysis remains prone to ambiguities due to overlapping, anharmonicity, and the omni-presence of coexisting effects, which translate to convoluted spectral changes. Similar reasons have also been forming a hindrance in analytical NIRS. The intrinsic complexity of the spectra has forced the extensive usage of spectral pretreatment methods and advanced data analysis, for example, two-dimensional correlation spectroscopy (2D-COS) (Noda, 1989; Noda et al., 1995; Noda and Ozaki, 2004). The 2D-COS technique allows the expanding of the spectral information onto two-dimensions, basically elucidating the correlations in the spectral variations and visualizing straightforwardly the complex dependencies which would be otherwise difficult to trace in linear NIR spectra. It finds an extreme value in the analysis of spectral variations, as not only the changes are illuminated, but their direction and sequence can also be elucidated. 2D-COS also gains a better resolution through the simplification of the spectral data, the possibility of a more distinct assignment of bands, and exploration of the sequential order of changes occurring in the sample. Therefore, the different inter- and intramolecular behavior of samples can be investigated through the peaks visible in the synchronous (*syn*) and asynchronous (*asyn*) spectra, which are obtained by spreading spectral information as a function of

two independent wavenumber axes over the second dimension (Noda and Ozaki, 2004).

A brief note on NIRS in biophysical chemistry should be made here as well (Huck, 2016a). In addition to the advantages outlined above, low absorptivity of NIR radiation also promotes its value when applied for the purpose of hyper spectral imaging (Huck, 2016a; Ozaki et al., 2017; Türker-Kaya and Huck, 2017; He et al., 2018). The resulting relatively deep penetration of NIR light plays a key role here, allowing an effective in-depth probing of the sample, a fact which finds an exceptional applicability in biophysical and biomedical studies (Huck, 2016a; Sun et al., 2017; Türker-Kaya and Huck, 2017). This currently remains a strongly developing area (He et al., 2015; Dorrepaal and Gowen, 2018; Wong et al., 2019), ultimately aiming at multi-modal imaging (He et al., 2018), which gives rise to an intriguing question of how in the nearest future this may be hyphenated with a similarly rapidly growing theoretical NIRS. This review will also include a short exploration of this topic.

THEORETICAL NEAR-INFRARED SPECTROSCOPY–AN OVERVIEW OF THE EMERGING FIELD

Fundamentals of Theoretical NIRS

As mentioned earlier, the simplistic harmonic approximation of molecular vibration brings substantial practical advantages from the point-of-view of computational complexity. The Newton equations of molecular oscillation lead to a matrix eigenvalue equation in which the harmonic vibrational frequencies are obtained through diagonalization of the matrix of mass-weighted second derivatives of the potential energy (mass-weighted Hessian). Consequently, the transition intensity is calculated from the derivative of dipole moment over the normal coordinates. Since Hessian is given as a straightforward output of the geometry optimization procedure, harmonic frequencies are calculated with a relatively minor additional cost. A commonplace overestimation of harmonic frequencies is being routinely addressed with a simple empirical scaling, thus yielding cost-effective theoretical MIR or Raman spectra (Wilson et al., 1955). However, NIR modes unequivocally require to step beyond harmonic approximation. While di-atomic anharmonicity remains relatively easy to account for, the problem arises in complexity for polyatomic molecules, mostly due to mode-mode couplings. A variety of anharmonic approaches has been proposed in the literature. However, in practical terms these methods have been prohibitively expensive and thus, until recently, have not been employed for the prediction of NIR spectra of reasonably complex molecules. The computational affordability is the primary factor from the point of view of applied spectroscopy. The anharmonic approaches may thus be categorized by their accuracy vs. cost ratio. In this sense, variational methods may be omitted due to extreme expense. This holds, in spite of their capability to yield an exact solution, limited only by the quality of potential energy evaluation. Variational methods are practically applicable to the simplest systems only (Polyansky et al., 2003). In contrast, applied spectroscopy relies on reasonably efficient anharmonic methods with the ability to treat complex molecules at a controlled penalty of a less accurate description of certain non-essential factors. For example, the Vibrational Self-Consistent Field (VSCF) method, which has fairly often been used for anharmonic simulation of MIR spectra (Gerber et al., 2005; Lutz et al., 2014b), assumes full factorizability of vibrational wavefunction into a set of normal mode wavefunctions. However, the VSCF scheme requires reasonably accurate probing of the vibrational potential; it is commonly based on a 16-point grid. The key economical feature here is the approximate treatment of inter-modal anharmonicity, effectively in which any given mode feels an averaged effect resulting from all other modes. This approximation has often been too severe; a number of refinements in the approach appeared, in which the cost-accuracy balance has frequently been skewed toward accuracy. For example, an improved variant, perturbation-corrected VSCF (PT2-VSCF) uses the second-order perturbation theory to correct the VSCF level couplings, yielding a higher certainty (Jung and Gerber, 1996). Concurrently, a number of reported attempts have been aimed at increasing the method's affordability, e.g., by reducing the grid-density for potential evaluations (Lutz et al., 2014c) or by employing more efficient ways for the determination of the electronic structure underlying the layer of anharmonic vibrational analysis [e.g., the resolution of the identity (RI) approximation in connection with the Moller-Plesset second order perturbation, i.e., RI-MP2; (Lutz et al., 2015)]. Interestingly, the precision penalty of basic VSCF decreases as the molecule complexity increases. This occurs due to a more effective averaging with the increasing numbers of modes within the VSCF mean-field approximation and has been exploited, for example, in biomolecule studies (Pele and Benny Gerber, 2010).

Another class of anharmonic methods is based on the vibrational second-order perturbation theory (VPT2) (Nielsen, 1951; Clabo et al., 1988). In principle, these include the anharmonic correction of vibrational potential in the form of cubic and quartic force constants yielded through the numerical differentiation of the harmonic Hessian at molecular geometries only slightly displaced from the equilibrium; very few energy evaluations are needed in this case. VPT2 methods are known for being computationally cost-effective; this is particularly evident if only bi-modal correlations are included in the calculations. However, the applicability of these methods has typically been hindered by their tendency to produce meaningless results in case of tightly-coupled modes (close degeneracies, i.e., vibrational resonances). The appearance of such singularities does not follow any consecutive pattern. Instead, their presence depends on a particular molecule; consequently, customized solutions have typically been needed almost each time. This fact severely restricted VPT2 usage in applied spectroscopy. Attempts have been made to develop an automated treatment of close degeneracies (Barone, 2005). For example, deperturbed (DVPT2) and generalized (GVPT2) schemes have appeared recently. These methods identify and remove close degeneracies from the perturbative treatment (in DVPT2 scheme) and reintroduce the removed terms through the variational approach (only in GVPT2 approach) (Barone,

2005). Essential for applied spectroscopy, these methods are suitable for any general molecule, effectively creating a robust and generally applicable tool for anharmonic calculations of even fairly complex molecules. Investigations into the solution phase often find a useful addition of computationally affordable implicit solvation model. Several different approaches may be found in recent literature, e.g., Polarizable Continuum Model (PCM) and derivatives; conductor-like polarizable continuum model (CPCM) or integral equation formalism variant (IEF-PCM); these approximate description of solvation allow for efficient increase in the quality of simulations performed in solution phase (Beć et al., 2016a, 2017).

Other anharmonic methods may also be mentioned, e.g., vibrational configuration interaction (VCI) (Whitehead and Handy, 1975) and vibrational coupled-cluster (VCC) (Christiansen, 2004) methods. These computationally highly expensive approaches are rarely found in the literature being used for the simulation of MIR spectra of simple molecules, particularly in cases where certain vibrational intricacies cannot be omitted (Oschetzki et al., 2013). Ongoing development in high-power computing may result in an increased application of these methods in the future. A final remark may be aimed at anharmonic calculations of macromolecules and biomolecules. As is known, anharmonic effects are sometimes substantial in those cases; certain biomolecules, e.g., proteins or nucleic acids, exhibit strong anharmonicity expressed in low-barrier bond torsions, low-energy vibrations in the THz region, ring modes in large ring systems, or hydrogen-bonded complexes (Hamm and Hochstrasser, 2001; Walther et al., 2002). In these applications, even a basic account for anharmonicity may yield significant gains. Due to the complexity of such molecules, the computational cost factor remains the center of attention. A number of efficiency-oriented methodological studies aimed at large molecular systems has emerged; this challenging research area meets strong stimulus from various fields and remains very active (Levy et al., 1984; Pele and Benny Gerber, 2010; Schlick, 2010; Krasnoshchekov and Stepanov, 2015).

Recent times have seen a progressing amount of quantum mechanical (QM) simulations of NIR spectra. Such studies, so far, have mostly utilized either VSCF or VPT2 routes, as those possess the required balance between accuracy and computing cost, essential in applied spectroscopy. Various examples of such studies will be overviewed beneath.

Basic Molecules

A number of QM studies on NIR spectra of basic molecules have been reported over the last few years (Beć et al., 2016a, 2018a; Grabska et al., 2017a,b). Vibrational studies of these systems are relatively important for our understanding of the general spectra-structure correlations (Czarnecki et al., 2000; Wojtków and Czarnecki, 2006; Michniewicz et al., 2007, 2008; Haufa and Czarnecki, 2010) and the role of conformational isomerism (Czarnecki et al., 2006; Wojtków and Czarnecki, 2006), structure and dynamics of hydrogen-bonding, self-association mechanisms and intermolecular interactions (Czarnecki and Ozaki, 1999; Czarnecki et al., 2000, 2010; Czarnecki, 2003; Czarnecki and Wojtków, 2004; Michniewicz et al., 2007; Haufa and Czarnecki, 2010), in particular the interactions with solvent molecules (e.g., water, nonpolar solvents) (Gonjo et al., 2011; Tomza and Czarnecki, 2015), or chiral discrimination (Czarnecki, 2003); the temperature influence on the above effects was often also examined (Czarnecki and Ozaki, 1999; Iwahashi et al., 2000; Šašić et al., 2002; Wojtków and Czarnecki, 2005, 2006, 2007; Grabska et al., 2017a). In the above contexts, alcohol molecules have remained among those investigated most frequently in physicochemical NIRS; often, the lack of QM spectra simulations hindered full comprehension therein. Beć et al. recently investigated basic alcohols; methanol, ethanol and 1-propanol by experimental and theoretical NIRS, demonstrating the potential of such approach in gaining a deep understanding of these spectra (Beć et al., 2016a). A good agreement between the experimental (solution; 3 10^{-5} M in CCl_4) and calculated spectra has been achieved, including the reproduction of finer bands (**Figures 2**–**3**) and the manifestation of conformational isomerism. This demonstrated well the potential of QM spectra simulation in explaining the spectra-forming factors in NIR (**Figure 2**) far surpass that achievable by classical spectroscopic methods even for an elementary molecule such as methanol (Weyer and Lo, 2002). Ethanol and 1-propanol feature more vibrational bands, and additionally, have conformational isomers which results in distinct spectral signatures (**Figure 3**). Beć et al. have shown that with QM simulations it is possible to unambiguously follow the contributions from conformational isomers in the NIR region (Beć et al., 2016a). They also reproduced the bandshape details of the 2νOH band, a major peak in NIR spectra of alcohols. A homogenous structure of methanol is clearly set apart from ethanol and 1-propanol, accounting for their conformational flexibility. The simulation reflected well an increasing complexity of 2νOH bandshape due to the separation of the contributions stemming from different conformers (Beć et al., 2016a).

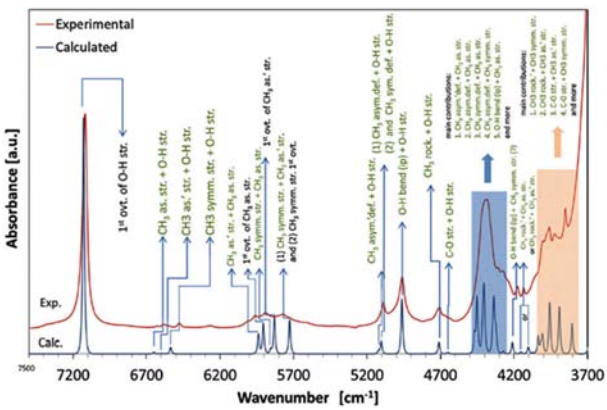

FIGURE 2 | NIR spectra of diluted methanol; experimental (5 10^{-3} M CCl_4) and simulated by the use of anharmonic calculations (GVPT2 scheme on DFT-B2PLYP/SNST level of electronic theory and CPCM solvation model of CCl_4) (Beć et al., 2016a). Reproduced by permission of the PCCP Owner Societies.

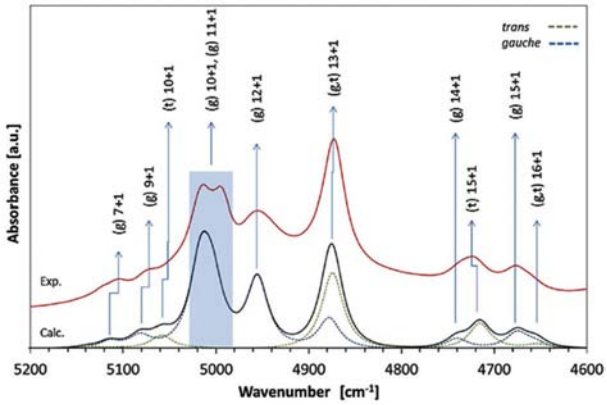

FIGURE 3 | Band assignments in the experimental and calculated NIR spectra of low concentration (5 10^{-3} M CCl_4) ethanol. The calculated NIR spectrum is based on the CPCM-B2PLYP-D/SNST level of theory. Details of the 5,200–4,600 cm^{-1} region (Beć et al., 2016a). Reproduced by permission of the PCCP Owner Societies.

TABLE 1 | An exemplary comparison of total computational time for methanol molecule (including geometry optimization, harmonic calculations and VPT2 treatment).

Method	Solvent model	CPU time[a] [s]	Wall time[a] [s]	Wall time relative ratio
B3LYP/6-31G(d,p)	–	117	353	1
B3LYP/6-31G(d,p)	CPCM	135	375	1.1
B3LYP/6-31G(d,p)	IEF-PCM	147	409	1.2
B3LYP/6-31G(d,p)	SMD	151	422	1.2
B3LYP/N07D	–	157	466	1.3
B3LYP/SNST	–	246	1,345	3.8
B3LYP-D3/SNST	–	246	1,351	3.8
MP2/SNST	–	305	878	2.5
B2PLYP/N07D	–	370	1,060	3.0
B2PLYP/SNSD	–	660	1,860	5.3
B2PLYP/SNST	–	886	2,534	7.2
B2PLYP-FC/SNST	–	887	2,448	6.9
B2PLYP-D/SNST	–	891	2,520	7.1
B2PLYP/SNST	CPCM	928	2,515	7.1
B2PLYP-D/SNST	CPCM	938	2,644	7.5
B2PLYP/SNST	SMD	957	2,580	7.3
B2PLYP/SNST	IEF-PCM	971	2,623	7.4
MP2/aVTZ	–	2,512	6,553	18.6
MP2/aVQZ	–	46,083	119,288	337.9

[a] *The CPU time and wall time depend on the hardware platform. The presented values are for 24 core Intel Haswell architecture computing node. Reprinted with permission from Beć et al. (2016b).*

In the study of simple alcohol molecules, the deperturbed/generalized vibrational second-order perturbation theory (DVPT2/GVPT2) has been used at several levels of electronic theory (Beć et al., 2016a). A number of basis sets have been considered, as well as a selection of three different solvation models within self-consistent reaction field (SCRF) formalism. This allowed for an effective method validation accounting to their feasibility in accurate reflection of NIR modes; similar comparisons assembled for fundamental (IR) modes are frequent in literature yet remain very rare for non-fundamentals. Beć et al. concluded that the density functional theory (DFT) should be prioritized in applied spectroscopic studies. DFT offers a good cost-precision balance, this being a primary factor since anharmonic vibrational analysis is notably expensive in itself (**Table 1**). Post Hartree-Fock approaches, e.g., the Møller-Plesset second order perturbation (MP2) method may find limited use due to unfavorable accuracy/computing time factor. DFT with a carefully selected density functional, matching the complexity of the calculated molecule, may be considered the best choice here. For the treatment of molecules in solution, B3LYP and B2PLYP functionals are recommended, even more with the addition of empirical correction for dispersion improving the description of non-covalent and long-range interactions at a moderate cost. The conclusion was that double-hybrid functionals, e.g., B2PLYP, offer better consistency of NIR frequencies albeit when short-time of the simulation is prioritized, single-hybrid B3LYP is sufficiently good. A more detailed evaluation of the computational demands of different electronic approaches used inVPT2 calculation has been reported by the same authors (Beć et al., 2016b). Calculations employing the B2PLYP functional were roughly twice as expensive as those with B3LYP; a triple-ζ SNST basis set versus a small double-ζ N07D basis increases the computing time by a factor of two, at least in the case of methanol molecule. Contrarily, an addition of the empirical dispersion correction and implicit solvation model (CPCM, IEF-PCM or SMD) introduce only a meager overhead (**Table 1**). Therefore, including these two supplementary calculation steps may be recommended; the former is applicable in general, while the latter is applicable to molecules in the solution phase (Beć et al., 2016a).

The influence of temperature on the structure and association mechanisms of alcohols and similar molecules has always been a primary scientific problem studied in physicochemical NIRS. It has been well-known that in diluted alcohols the 2νOH band undergoes a temperature-induced spectral shift and intensity variation. Additionally, bandshape changes have been closely monitored by second derivation and two-dimensional correlation analyses (2D-COS); the latter technique has proven to be particularly powerful in these studies. In this context, examinations of butyl alcohols were helpful due to the differences among these isomeric molecules (Maeda et al., 1999; Czarnecki et al., 2015). A change of the 2νOH bandshape and a peakshift is observed in the case of 1-butanol, 2-butanol, and *iso*-butanol; however, *tert*-butanol spectrum features only a peak shift. Accordingly, 1-butanol, 2-butanol and *iso*-butanol feature conformational flexibility; on the contrary, *tert*-butyl alcohol is inflexible. These observations suggested that conformational isomerism should be responsible for the respective temperature-dependent NIR spectra inconsistency; yet, no decisive explanations could be provided at that time (Maeda et al., 1999). This problem has recently been reinvestigated by Grabska et al. this time

with the solid support of QM simulations (Grabska et al., 2017a). Their attempt to theoretically reproduce the temperature induced spectral variations in the NIR region of butanols was successful. To improve the accuracy/cost balance in the anharmonic treatment of these larger molecules, they applied a hybrid approach in vibrational analysis; the harmonic and anharmonic steps were performed on different levels of electronic theory (B2PLYP/def2-TZVP and B3LYP/SNST; respectively), maximizing the efficiency of the calculation. The obtained simulated NIR spectra have resembled the experimental ones remarkably well (**Figure 4**), including the reproduction of subtle effects, e.g., minor bands between 5,200 and 4,500 cm^{-1} for all four butyl alcohols (**Figure 4**). Detailed and reliable band assignment and full comprehension of the NIR spectra of diluted butanols was achieved (Grabska et al., 2017a). In the next step, Grabska et al. investigated the temperature dependence of the conformational population of butyl alcohols (Grabska et al., 2017a). By calculating the Boltzmann coefficients corresponding to all conformational isomers of 1-butanol, 2-butanol and *iso*-butanol and subsequent use of these values in spectra simulation, including theoretical 2D-COS plots, they have succeeded in reproducing the temperature-dependent spectral shift and bandshape changes observed experimentally. This comparison has confirmed that the relative changes in the conformational populations contribute, at least partially, to the observed spectral variability. Hence, the background for the experimental observations was decisively explained and the old and never fully explained scientific problem was solved. Grabska et al. has adequately demonstrated the usefulness of QM simulations in bringing definite answers to the problems which have often been difficult to become unequivocally resolved by means of classical NIR spectroscopy (Grabska et al., 2017a).

A number of open questions related to NIR spectroscopy and physical chemistry of alcohols still remain. In example, Beć, Grabska and Czarnecki examined 1-hexanol, cyclohexanol, and phenol (Beć et al., 2018a). They focused on the spectra-structure correlations in NIR due to the vibrations of an OH group attached to a molecular skeleton of three different kinds; linear and cyclic aliphatic, and aromatic ring. It is well known that the bands due to X-H modes and particularly OH vibration, are enhanced in NIR spectra. Hence, OH vibrations belong to the primary spectra-forming factors; in this context, investigating how a molecular structure affects the NIR spectrum brings long-awaited answers (Beć et al., 2018a). Those three molecules manifest remarkable dissimilarity in NIR spectra; 1-hexanol remains similar to shorter chain linear alcohols. However, cyclohexanol, and even more phenol, had substantial differences (**Figure 5**). Detailed band assignments and the elucidation of distinct trends in NIR spectra could be carried out with the aid of

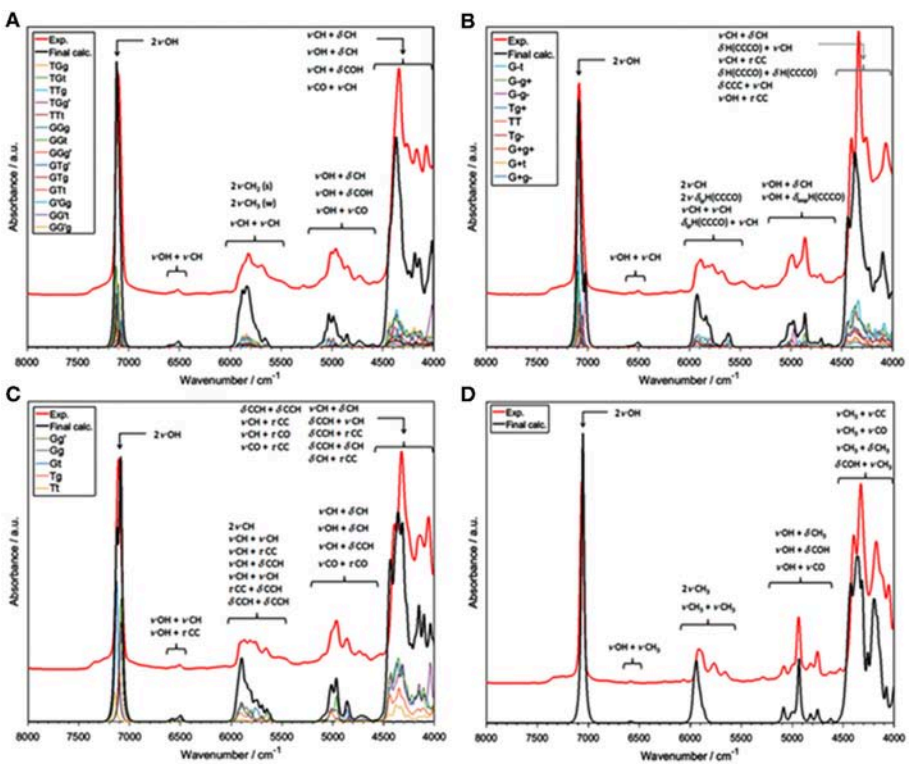

FIGURE 4 | Experimental and simulated (harmonic: B2PLYP/def2-TZVP; VPT2: B3LYP/SNST; CPCM) NIR spectra of butyl alcohols; **(A)** 1-butanol; **(B)** 2-butanol; **(C)** *iso*-butanol; **(D)** *tert*-butyl alcohol. The contributions of the spectral lineshapes corresponding to conformational isomers presented as well (colored lines). Reprinted with permission from Grabska et al. (2017a). Copyright 2017 American Chemical Society.

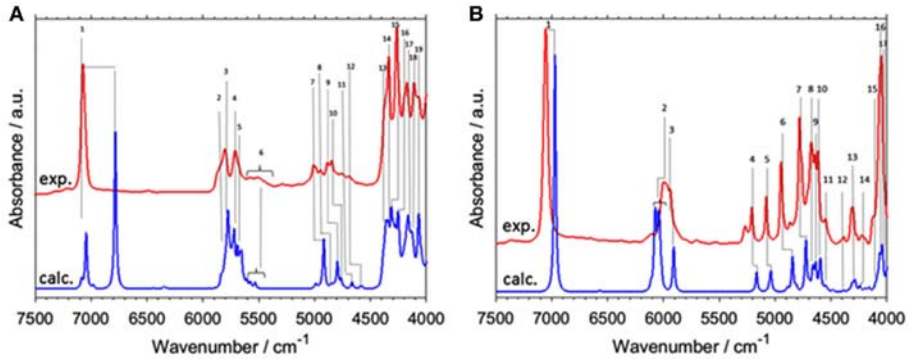

FIGURE 5 | Experimental (0.2 M; CCl_4) and simulated (VPT2//B3LYP/SNST+CPCM) NIR spectra of **(A)** cyclohexanol and **(B)** phenol. Reprinted with permission from Elsevier (Beć et al., 2018a).

QM simulations. The peculiarities of combination bands of νOH mode could be noted. This mode couples strongly to a number of other modes and gives a distinct spectral signature between 5,500 and 4,000 cm^{-1} (**Figure 5**). The specificity of phenol ring modes was also concluded. Good separation of the fundamental bands in the MIR region translates into NIR features with well-resolved sharp peaks appearing throughout lower wavenumbers (5,500–4,000 cm^{-1}). This should be considered an uncommon observation in NIR spectra and also in elementary molecules e.g., methanol rather manifest broadened bands (**Figure 2**). The established signature allows to discriminate easily between different kinds of alcohols (aliphatic, aromatic) and to identify an OH group attached to an aromatic ring (Beć et al., 2018a). It should be noted that the accuracy of VPT2 simulation is lower for the 2νOH peak in general, but in the case of cyclohexanol it was by far inadequate (**Figure 5A**). The reasons for this are well-understood and will be discussed in detail in the present review.

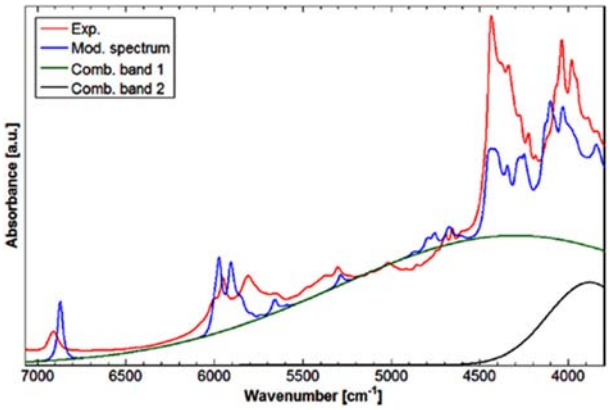

FIGURE 6 | Experimental (solution; CCl_4) and modeled spectrum of acetic acid. Band fitting results for the two combination bands involving OH stretching modes of acetic acid cyclic dimer. Reprinted with permission from Beć et al. (2016c). Copyright 2016 American Chemical Society.

Investigations of Intermolecular Interactions

NIRS manifests unique suitability for investigating intermolecular interactions, e.g., hydrogen-bonding. Not without reason, this aspect is strongly focused in physicochemical NIRS (Czarnecki and Ozaki, 1999; Czarnecki et al., 2000, 2010; Czarnecki, 2003; Czarnecki and Wojtków, 2004; Michniewicz et al., 2007; Gonjo et al., 2011; Tomza and Czarnecki, 2015). The potential of QM simulations has long been utilized in MIR and Raman studies. On the contrary, NIRS lacked such powerful support due to practical limitations, as explained earlier. The cyclic dimer of carboxylic acids, e.g., formic acid or acetic acid, has frequently been considered a prototypic system of the hydrogen bonded complex. Beć et al. have recently presented a combined experimental and computational NIRS study of acetic acid in a CCl_4 solution (Beć et al., 2016c). The focus was on the spectroscopic properties of the cyclic dimer, which is strongly stabilized and persist as the major form throughout a widely variable concentration. The QM simulation has reproduced the majority of experimental NIR bands; however, a distinct exception was observed. The binary combination bands involving the stretching and bending of OH modes had a very strong calculated intensity, resulting in the appearance of two sharp and well-resolved peaks in the simulated spectrum. In contrast these are clearly absent in the experimental NIR lineshape. However, prominent elevation of the baseline is apparent in the NIR spectrum of soluted acetic acid, visible between 6,500 and 4,000 cm^{-1} and extending below. The following hypothesis was proposed in the article; the aforementioned combination bands undergo a spectral shift and broadening as a hydrogen-bonding effect; similar effects are well-known in MIR spectra. These two particular simulated combination bands were then fitted to the experimental spectrum to reflect the baseline contribution. Such treatment significantly improved the agreement with the experimental NIR spectrum (**Figure 6**). This investigation focused attention on the possibility of hydrogen bonding being manifested in the NIR spectrum through the baseline elevation (Beć et al., 2016c); such spectral feature is frequently observed in the NIR spectra of complex samples.

The basic study of acetic acid yielded a good understanding of NIR properties of simple carboxylic acids, which was helpful

in the further exploration of fatty acids. These fundamental biomolecules can be grouped into short- (SCFAs), medium- (MCFAs) and long-chain fatty acids (LCFAs). Fatty acids manifest various properties interesting from the point of view of physical chemistry, e.g., association mechanisms and hydrogen bonding properties (Iwahashi et al., 1995a,b; Matsuzawa et al., 2013). These systems are also extremely important in applied NIR studies involving any kind of biological samples, e.g., in hyperspectral imaging and analytical applications (Ishigaki et al., 2016a,b; Puangchit et al., 2017). For these reasons, SCFAs and MCFAs were examined by Grabska et al. in their two following studies (Grabska et al., 2017c,d). The former one focused on five SCFAs; saturated: propionic and butyric acid; and unsaturated ones: acrylic, crotonic and vinylacetic acid (Grabska et al., 2017c). These carboxylic acids are reasonably more complex than acetic acid, and are thus appropriate test subjects for verifying if the conclusions on acetic acids can be generalized onto larger carboxylic acids. Additionally, their complexity and mutual differences in the structure are perfect for investigating the NIR manifestations of the aliphatic chain structure and the existence of C=C bonds (Grabska et al., 2017c). Grabska et al. have selected these objects to capture the principle structural features of FAs (**Figure 7**). Those included: the difference between saturated and unsaturated SCFAs, impact of the location of C=C bond (medium-chain: crotonic acid; terminal: acrylic and vinylacetic acid), exclusive existence of either of the three following structural features: methyl (crotonic acid), sp^3 or sp^2 (terminal; acrylic acid, vinylacetic acid), methylene group (Grabska et al., 2017c).

The DVPT2 anharmonic vibrational analysis performed at the B3LYP/SNST+CPCM level of electronic theory involved full conformational analysis for each of SCFAs in the spectra simulation procedure (Grabska et al., 2017c). The final agreement between the simulated and experimental spectra as measured in the solution phase (0.05 M; CCl_4) was of high quality (**Figure 9**). The SCFAs case confirmed the previous observation; a baseline elevation phenomenon similar to that observed for acetic acid was clearly noticed (Beć et al., 2016c). Specific combination bands had higher intensities by orders of magnitude than those of the other NIR bands. Those combinations ($a + b$ and $a + c$) result from the following modes: (a) out-of-phase (or opposite phase) stretching and (b) in-plane bending modes, each time combined with (c) in-phase stretching mode of hydrogen-bonded OH groups. Through a band-fitting procedure analogous to that performed for acetic acid, a much better reproduction of the experimental spectra was accomplished. The stimulus for attempting the band fitting resulted from an undoubtful absence of any intensive sharp peaks in the experimental spectra, which were suspected to form the baseline elevation through band broadening. Grabska et al. also observed consecutive trends throughout several NIR subregions of SCFAs. Specific disparities in overtone and combination intensities were observed; the elucidated contribution of the CH_3 group was found to be fully consistent with experimental studies found in the literature. Unsaturated SCFAs revealed a specific impact on the NIR spectrum of the localization of C=C bond; e.g., terminal C=C imposing an appearance of sp^2 CH_2 group leads yields extremely specific, well-defined and intense NIR bands, observed at 6,172/6,131, 4,746/4,734, and 4,483/4,489 cm^{-1} for acrylic/vinylacetic acids, respectively. It was concluded that these bands are excellent structural markers because of high intensity and positioning in wavenumber regions where the bands of other structures remain absent (Grabska et al., 2017c).

A continuation of the above overviewed study was published soon after, in which the NIR features of two MCFAs, saturated hexanoic and unsaturated sorbic acid, were examined (Grabska et al., 2017d). Those molecules exhibit distinct differences in the NIR region observable from a very high dilution (minimal self-association) to a more concentrated solution (with the domination of the spectral bands from cyclic dimers; **Figure 7**). For both cases, accurate spectra simulation yielded a comprehensive explanation of the observed features. Evidence showed that the shape of NIR spectra is similar through a widely varying concentration; this holds even in neat liquid (hexanoic acid) and powder (sorbic acid) (Grabska et al., 2017d). These findings were consistent with previous ones, as reported for acetic acid and SCFAs (Beć et al., 2016c; Grabska et al., 2017c). The three discussed studies (Beć et al., 2016c; Grabska et al., 2017c,d) indicated that theoretical NIR biospectroscopy may become

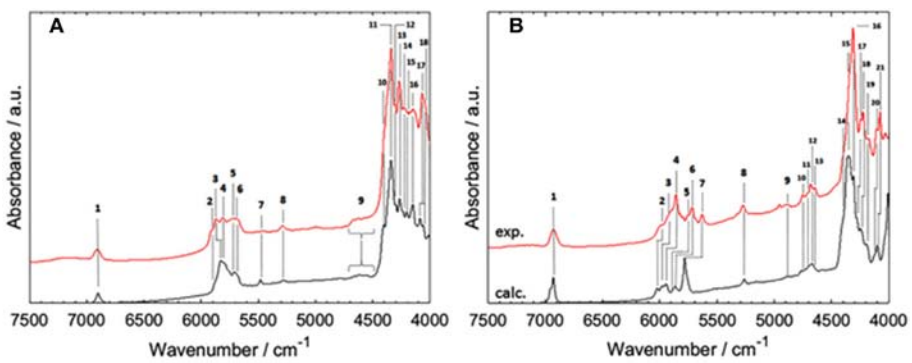

FIGURE 7 | Band assignments proposed for NIR spectra of MCFAs in medium to high concentration (CCl_4); **(A)** hexanoic acid, **(B)** sorbic acid. Reprinted with permission from Elsevier (Grabska et al., 2017d).

feasible as small and medium-sized biomolecules are within the potential for accurate NIR simulations. Further expansion onto more complex objects (e.g., LCFAs, lipids, proteins, nucleic acids) may be anticipated in the foreseeable future. So far, the reported accomplishments in theoretical NIRS of small biomolecules were successfully employed for the interpretation of NIR images of biosamples (Puangchit et al., 2017).

Other Examples of NIR Simulations in Physical Chemistry

Isotopic substitution has definitely been a key phenomenon remaining in the center of attention of vibrational spectroscopy. It gives a prominent spectral signature; primarily significant spectral shifts (Jaffe, 1987; Davis et al., 1996; Workman and Weyer, 2007). For this reason, it has been one of the most potent tools of classical spectroscopy used for band assignments. One can relatively easily follow the spectral changes resulting from specifically arranged isotopic substitutions, e.g., through the deuteration of an OH or other functional groups in simple molecules. In this way, the corresponding spectral variability may be comprehended relatively easily even in the NIR region. However, an imperfect partial substitution (e.g., the existence of CX_3 groups, where X=H,D are distributed randomly) resulting from a spontaneous isotope equilibration or faulty synthesis leads to significant difficulties in interpreting an NIR spectrum. Such random forms are impossible to be isolated from the sample, and thus, no reference spectrum of any of such forms can be recorded. In this case, spectra simulation is an extremely potent tool, as recently demonstrated by Grabska et al. In their comprehensive study of methanol and its deuterated derivatives, they examined all isotopomers of methanol molecule by simulating their NIR spectra (**Figure 8**; Grabska et al., 2017b). Through this, they successfully identified randomly substituted species found in two commercial samples of CH_3OD, and they directly monitored different levels of contamination by random isotopomers of methanol molecule in NIR spectra. Such an achievement would be out of reach in classical spectroscopy. Additionally, the anharmonic QM simulation yielded comprehensive band assignments in the NIR spectra of the four major methanol isotopomers, CH_3OH, CH_3OD, CD_3OH, and CD_3OD. These compounds have routinely been employed in physicochemical NIRS. Grabska et al. also included vibrational transitions up to three quanta in their computational study. The resulting simulated spectra included first and second overtones as well as binary and ternary combinations (Grabska et al., 2017b). This move gave an opportunity to confirm an earlier assumed non-essential loss of spectral information in NIR spectra modeling when only first overtones and binary combinations are considered. The conclusion that a practical restriction of the simulation to two quanta transitions (first overtones, binary combinations) could earlier been only assumed, e.g., such simplification in the simulated spectra of butanols did not prevent an excellent agreement with the experimental bands (**Figure 4**). On this occasion, the study of methanol and deuterated derivatives confirmed that the loss of up to ca. 20% of spectral information may be anticipated. This estimation

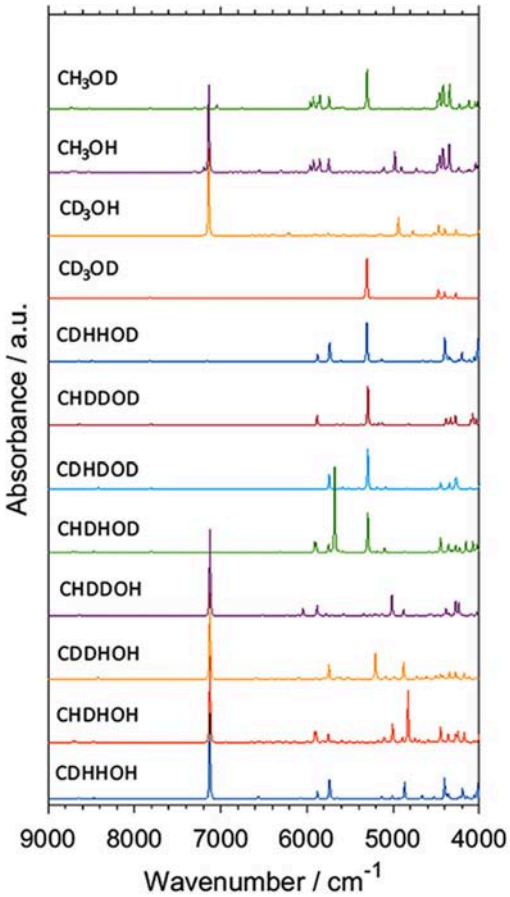

FIGURE 8 | Simulated NIR spectra of CXXXOX (X = H, D) molecules. Reprinted with permission from Grabska et al. (2017b). Copyright 2017 American Chemical Society.

was based on the relationship between the summed integral intensity of the calculated bands. The lost (or omitted) calculated spectral information is distributed among multiple yet weak bands and remains effectively "diffused" over the wavenumber axis. Hence, second overtones and ternary combinations are not essential for NIR spectra comprehension. This approximation holds unless ones would want to examine the upper NIR region, over 7,000 cm^{-1}. These wavenumbers have typically been rather rarely focused on in both physicochemical and analytical NIRS. However, upper NIR is the working region of some new miniaturized NIR instruments (Kirchler et al., 2017b). Thus, an additional ability to model second overtones and ternary combinations should be of increasing importance in the upcoming studies.

Worth emphasizing is the fact that QM calculations deliver a clear image of the intrinsically complex nature of NIR spectra. Although it has long been known, nowadays simulated spectra reproduce it accurately and visualize it straightforwardly. A good example of the NIR band overlay was provided by Grabska et al. in the case of vinylacetic acid (**Figure 9**; Grabska et al., 2017c). A common intensity scale of all bands depicted in **Figure 9**

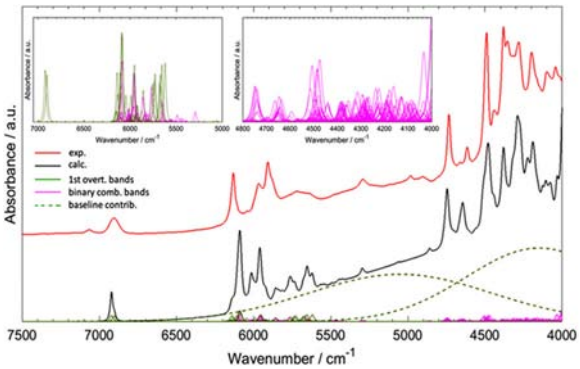

FIGURE 9 | Convolution of NIR bands on the example of spectra simulation for vinylacetic acid. All bands are presented in common intensity, note an extensive band overlay. Reprinted with permission from Grabska et al. (2017c). Copyright 2017 American Chemical Society.

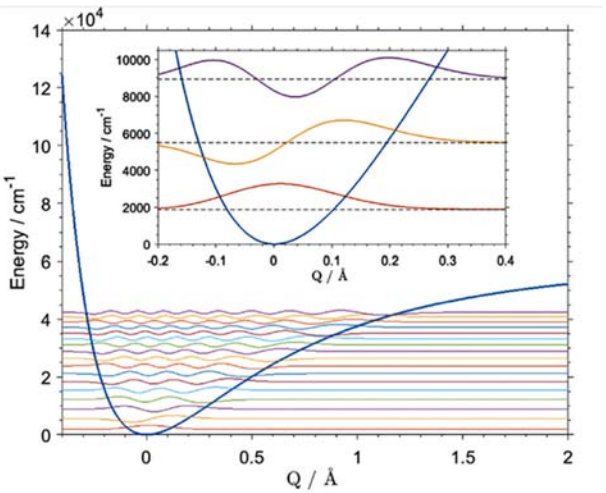

FIGURE 10 | Vibrational potential and vibrational states [B3LYP/6-311G(d,p)] of the OH stretching mode of the main (equatorial-gauche) conformer of cyclohexanol. Reprinted with permission from Elsevier (Beć et al., 2018a).

adequately demonstrates the extensity of band overlapping. Despite the complexity of that and similar NIR spectra, QM simulation reproduced it accurately including very complex region of 5,000–4,000 cm^{-1}, where the maximum overlay occurs due to appearance of the majority of binary combinations therein (Grabska et al., 2017c).

Highly Accurate Modeling of Single-Mode Anharmonicity

Generally applicable anharmonic computational schemes, e.g., VPT2 or VSCF, through simplifications are affordable enough to be used for the calculation of a large number of transitions, e.g., first overtones and binary combinations of all modes (Beć et al., 2017). The general methods are highly useful in the simulation of an entire NIR spectra as overlapping of the manifold bands in this region would make it extremely difficult to rely on any arbitrary selection of particular modes. Exceptions can be found though, e.g., 2νOH band most often appears as a single peak at least in the absence of molecular association (Czarnecki et al., 2015; Beć et al., 2016a). At the same time, as a highly anharmonic mode it is frequently described inadequately by VSCF or VPT2 approaches. These methods acquire their efficiency by approximating the anharmonic potential on a possibly lowest number of energy evaluations. Thus, effectively they "capture" a limited amount of anharmonicity, which may be enough in most cases, but not necessarily, e.g., when the mode deviates from the harmonic oscillator to a certain degree (Beć et al., 2017). Several attempts to improve accuracy have been made e.g., by transformation of the vibrational coordinates; this remains an active field of research (Yagi et al., 2012; Thomsen et al., 2014). The application of VSCF or VPT2 calculations to highly anharmonic modes may yield unreliable results. Particularly troublesome cases may be addressed through a detailed study of the single-mode anharmonicity through multi-point energy evaluations, and solving the corresponding time-independent Schrödinger equation. With an adequately large number of evaluation points, the vibrational levels can be derived with very high accuracy (Gonjo et al., 2011; Yagi, 2016; Schuler et al., 2017).

A number of approaches to the described vibrational problem exist. The differences between them often results from various numerical methods being employed for solving the matrix differential equation in the eigenvalue problem (Schuler et al., 2017). These computations are often used in NIR physicochemical studies, where the precision of the calculation of a certain mode is essential. For example, Beć et al. recently showcased the potential of improving the quality of simulation of cyclohexanol in NIR (**Figure 10**; Beć et al., 2018a). In that case, the VPT2 method erroneously reproduced the 2νOH band, yielding a very high error on the wavenumber of the equatorial-*trans* form, the major conformer of the molecule. Consequently, a splitting of the 2νOH band appeared in simulation while it is absent in the experimental spectrum (Beć et al., 2018a). Dense grid-point probing [B3LYP/6-311G(d,p)+CPCM(CCl_4)] of the vibrational potential along the OH stretching normal coordinate was carried out for the two leading conformers of cyclohexanol (Beć et al., 2018a). The generalized matrix Numerov method was used in solving the time-independent Schrödinger equation. By capturing the majority of anharmonicity, the vibrational levels were obtained with effectively absolute accuracy (<1 cm^{-1}). This means that vibrational analysis was not a source of any meaningful error in itself. A reduction in the anharmonic vibrational analysis imprecision is essential, as it is sometimes a source of significant error (Schuler et al., 2017). However, the final inaccuracy vs. the experimental value is still affected by a number of other unavoidable factors, e.g., error on electronic energy or simplification of the molecular model such as single molecule calculations, implicit solvent models, etc. (Schuler et al., 2017). Luckily, that kind of error is frequently equal between similar molecules, e.g., the two cyclohexanol conformers. Effectively, high accuracy in relative sense in comparative studies is possible due to precise reproduction of the wavenumber differences existing between those systems.

Beć et al. evidenced this circumstance well as they obtained an exact match of the splitting between 2νOH among the two conformers of cyclohexanol (calculated 30 cm^{-1}, experimental 27 cm^{-1}). By contrast, that value was predicted erroneously by VPT2 as 260 cm^{-1} (Beć et al., 2018a). Obviously, such quality of prediction requires large computing expense. The grid density may, however, be flexibly adjusted, which would allow for e.g., the affordable examination of larger molecules.

A highly accurate determination of vibrational states and transition intensities was performed e.g., in systematic examinations of subtle spectral variations due to certain substituents (Takahashi and Yabushita, 2013) or solvent effects (Futami et al., 2011, 2012; Gonjo et al., 2011) in NIR and MIR. For example, Gonjo et al. studied solvent effects in vibrational spectra of phenol and 2,6-dihalogenated derivatives (Gonjo et al., 2011). In this particular case, a high environmental sensitivity of the OH stretching mode delivered valuable spectral information; however, because of a high anharmonicity, this information is difficult for elucidation and accurate computations are essential. They examined fundamental, first-, second-, and third overtones by including broad spectral region, VIS, NIR, and MIR (15,600–2,500 cm^{-1}). Such a wide aim necessarily required an accurate solution, particularly for the higher overtones. Therefore, the νOH vibrational potential was probed with a dense step (0.02 q_0; −0.7 to 1.0 q_0) using a relatively high level of electronic theory [B3LYP/6-311++G(3df,3pd)] for accurate energy evaluations; the vibrational problem was solved through Johnson's approach (Johnson, 1977). Implicit solvation by means of the Isodensity Polarizable Continuum Model (IPCM) allowed the reproduction of the experimental effects observable for phenol, 2,6-difluorophenol, 2,6-dichlorophenol, and 2,6-dibromophenol in different solvents (*n*-hexane, CCl_4, $CHCl_3$, CH_2Cl_2). Gonjo et al. concluded a "parity" in relative intensities over the sequences of transitions and they suggested that an intermolecular OH...Cl hydrogen bond between phenols and the solvent is responsible for that phenomenon (Gonjo et al., 2011). A similar problem was further investigated by Futami et al. for pyrrole (Futami et al., 2011). An accurate modeling of single-mode anharmonicity also enabled studies on the influence of the solvent's dielectric constant on X-H stretching mode in the solution phase, as reported by Futami et al. on the example of HF as a prototypic polar molecule (Futami et al., 2012). The computations [B3LYP/6-311++G(3df,3pd) and CCSD/aug-cc-pVQZ levels; IPCM solvent approximation] elucidated the potential and dipole moment function variations in response to the changing solvent's dielectric constant. The investigation of the solvent effect in NIR and IR was continued by Chen et al. (2014); in this case, C=O stretching vibrations in acetone and 2-hexanone were examined.

The formation of X-H...B hydrogen bonding induces significant changes to the potential curve, vibrational states and transition intensities of the stretching X-H vibration. Due to the high anharmonicity of this mode, accurate theoretical methods as discussed in this section are essential. This was demonstrated by Futami et al. on the example of the pyrrole, pyridine, and pyrrole–pyridine complexes (Futami et al., 2009). The experimental observation of non-bonded pyrrole reveals a well-resolved 2νNH peak at 6,856 cm^{-1}; yet, the band is absent in the pyrrole–pyridine complex. A computational study explained that, in the complex the transition dipole moment is remarkably reduced for the first overtone mode of the hydrogen-bonded NH group (Futami et al., 2009). Continued further by Futami et al., other complexes featuring NH...π hydrogen bonding, e.g., pyrol-ethylene and pyrrole-acetylene systems, were evidenced to follow the above pattern (Futami et al., 2014).

Toward Feasible Modeling of NIR Spectra of Complex Systems and Biomolecules

Biomolecules feature a largely increasing importance in current spectroscopy in response to the strong stimulus for boundary-crossing research e.g., with focus on medicinal applications Jue and Masuda (2013). This also holds for NIRS, which is useful for investigations of biomaterial owing to its capability of studying moist samples. As it was well-explained throughout this review so far, biomolecules are complex systems which prove to be a particular challenge for theoretical NIRS. It is, therefore, of high importance to advance toward efficient NIR simulations of biomolecules. Because of this, recently matured VPT2 routines (DVPT2/GVPT2) seem to be the most promising due to their favorable cost-to-accuracy ratio (see section Fundamentals of Theoretical NIRS). Among the major kinds of biomolecules, long-chain fatty acids (LCFAs) have the advantage of forming better-defined structures, due to the tendency of carboxyl groups to form cyclic dimers strongly stabilized through dual hydrogen-bond (see section Investigations of Intermolecular Interactions). LCFAs feature protracted aliphatic chains (13–22 carbons); those most commonly appearing (e.g., oleic acid or palmitic acid) have chains with 15 to 22 carbons. They exist in all kinds of biological matter, either as the constituents of lipids or as free fatty acids (FFAs). They are the second energy source of the animal body and are also part of the chemical composition of several vegetable oils (Zielinska, 2014). They also suit a wide range of industrial applications, thus remaining the focus of NIRS in pharmaceutical (Ahmad, 2017), cosmetics (Białek et al., 2016), and food industries (Wood et al., 2003). For these reasons, the relevancy of these biomolecules in the context of NIRS is very high. Hence, LCFA molecules suited as perfect objects for the breakthrough study as reported recently by Grabska et al. (2018). A selection of six compounds, saturated (palmitic, stearic, arachidic) and unsaturated (linolenic, linoleic, oleic) acids, was investigated by experimental/theoretical NIRS. These examinations were aimed at providing an in-depth explanation of the spectral origins, their relationships to the chemical structure, in particular the impact of alkyl chain's saturation, as well as deeper insights into anharmonicity of the most important vibrational modes in these molecules (Grabska et al., 2018). Two separate computational approaches were used in this study. The first one, DVPT2, was an effective way to reproduce the entire NIR spectra and proved that the cost-effectiveness of the method is adequate even for biomolecular studies (Ozaki et al., 2017). The accurate reproduction of

the NIR lineshapes proved that the approximation of inter-modal anharmonicity, i.e., coupling between vibrational modes, in DVPT2 retains adequate quality even for the molecular systems with an overwhelming number of such couplings; the number of binary combinations surpassed 66,000 for the dimeric molecules of LCFAs (Beć and Grabska, 2018; Grabska et al., 2018). This fact also reflects the exponentially increasing complexity of the NIR spectra with the size of a molecule. The resulting combination band overlay creates substantial difficulty in elucidating certain spectra-forming factors and comparing specific features, e.g., the impact of the saturation of LCFAs. For this reason, Grabska et al. presented a clearer and more accessible illustration of the spectral contributions in the form of heatmap (**Figure 11**). These maps reflect the level-of-influence of selected modes of interest, arbitrarily grouped in such a way that the important factors could be easily assessed. The quality of simulation allowed for unambiguous assignment of all NIR bands and also to differentiate clearly between saturated and unsaturated LCFAs. Further progress in this field is strongly promoted as it finds immediate application in NIR biospectroscopy and imaging (Grabska et al., 2017c,d; Puangchit et al., 2017).

Theoretical NIRS in Aid of Analytical Applications

Bio-significant molecules remain near the center of attention of applied NIRS. Qualitative and quantitative analysis of natural products (e.g., raw biomaterials, intermediate and final products) is a strongly developing field of applications (Huck, 2014, 2016a); this fact focuses attention on biomolecules. NIRS in hyphenation with chemometrics (multivariate analysis; MVA) uses rich chemical information entangled in the NIR spectrum of complex samples and correlates it with the chosen property of sample (Ozaki et al., 2006). Despite practical effectiveness, the procedure is performed in black-box from the point of view of physical chemistry. Molecular and vibrational background phenomena remain transparent in this routine. It has been a necessity for analytical NIRS to evolve despite such hindrance. The concept of incorporating chemical band assignments into chemometrics appeared in literature (Westad et al., 2008) with the aim to improve the analytical performance of NIRS. However, this idea has not been truly employed further. The lack of readily available high-resolution deconvolution of the spectra, which would additionally offer an ability to assign the resolved contributions was the major problem here. QM simulation of NIR spectra bears a strong potential to finally reactivate this extremely promising line of research. Recent time has seen attempts to adopt theoretical NIRS for the benefit of analytical studies (Schmutzler et al., 2013; Lutz et al., 2014a; Kirchler et al., 2017a; Kirchler et al., 2017b).

The first of such an example appeared in 2014 as Schmutzler et al. reported their design of an analytical pathway which employs NIRS/MVA for the effective quality control of apples (Schmutzler et al., 2013). This contribution had a substantial impact on the quality control of food/agricultural products, as it proposed entirely automatic, non-destructive

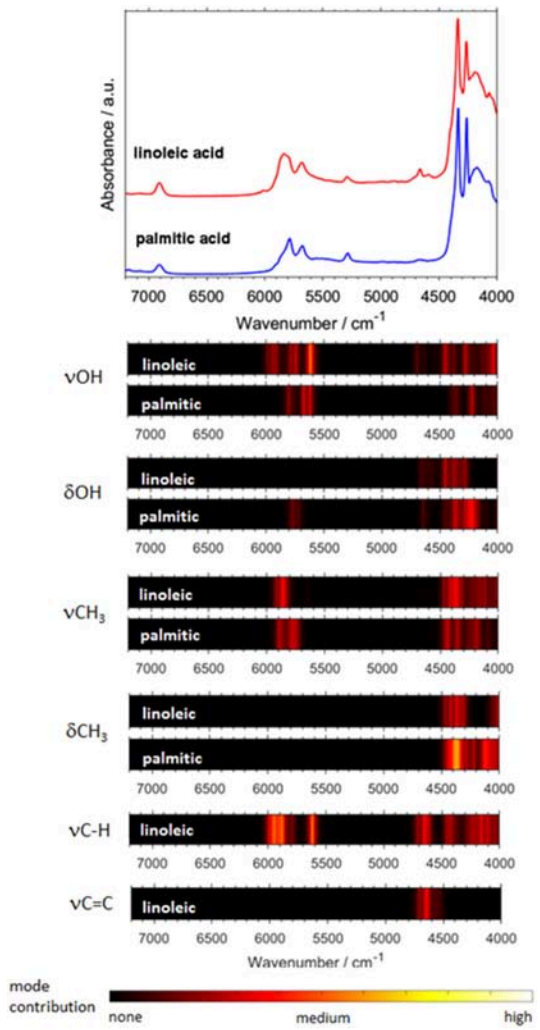

FIGURE 11 | Generalized contributions into NIR spectra of the selected types of modes involved in the binary combinations as uncovered by quantum mechanical spectra simulation of linoleic and palmitic acid. (Reprinted with permission from Grabska et al. (2018). Copyright (2018) American Chemical Society).

NIRS instrumentation for the analysis of apples. It utilized the principle of surface scanning in order to average the sample's surface inhomogeneity and a fiber probe for the convenient arrangement of the analytical instrumentation. From the point of view of the present review, it should be emphasized that this work also employed QM spectra simulation in the procedure, resulting in a first attempt of creating a computer-aided NIRS analytical spectroscopy. In this study, the point of interest was put on malic acid, a dicarboxylic acid existing on apple surface, which is a highly informative marker of the fruit's general condition (Schmutzler et al., 2013).

For the anharmonic vibrational analysis of malic acid, Schmutzler et al. used PT2-VSCF, a second-order perturbation corrected VSCF scheme, which features an improved quality of prediction of inter-modal anharmonicity (Schmutzler et al.,

2013). The electronic structure was determined at the Møller-Plesset MP2 level of theory with a 6-31G(d,p) basis set; an implicit approximation of aqueous solution through CPCM solvation model of water was included. L- and D- chiral isomers of malic underwent anharmonic treatment and theoretical bands up to three quanta, second overtones and ternary combinations, were obtained. Simulated bands compared to the experimental NIR spectrum are presented in **Figure 12**. The experimental features were reflected in the simulation qualitatively, correctly yielding comprehensive band assignments. According to the authors, the assumed simplifications i.e., quartic force field approximation, relatively simple basis set, implicit solvation model, could decrease the accuracy of their simulation. They also concluded that the PT2-VSCF approach involves only moderate computational efficiency which is further lowered by unfavorable scaling with molecule size. As they pointed out, this considerably hinders the feasibility of studying larger molecules using similar methods (Schmutzler et al., 2013). Notwithstanding this, simpler molecules such as malic acid may successfully undergo PT2-VSCF treatment in aid of analytical NIRS. Accordingly, Lutz et al. applied a similar computations scheme in their development of miniaturized NIRS for gasoline content analysis and quantification (Lutz et al., 2014a). Several kinds of compounds were needed to be considered, in order to represent the chemical residents in gasoline. Consequently, they examined ethanol (oxygenated fuel additive), *n*-octane (linear alkane representative), toluene (aromatic and branched/alkyl-substituted aromatic hydrocarbons) and ethyl *tert*-butyl ether (ethers and branched/alkyl-substituted aliphatic hydrocarbons and also oxygenated fuel additive). These systems retain relative simplicity and are suitable for PT2-VSCF anharmonic analysis without an apparent need for simplifications. This even allowed for the employment of the post-Hartree-Fock method for the determination of electronic energy, as the MP2 method together with TZVP basis set were used. Thus, the level of electronic theory was considerably higher than in the study of malic acid. In this case, Lutz et al. succeeded in inserting QM simulation into their analytical study, and the benefits included comprehensive band assignments, vastly improving the qualitative discrimination of the gasoline residents (Lutz et al., 2014a).

Phytoanalysis is one of the fields in which analytical NIRS becomes the tool-of-choice in qualitative and quantitative analysis (Huck, 2014, 2016a). The phytopharmaceutical industry requires highly robust methods of analysis as natural products are complex and susceptible to content variation. Hence, an independent insight from the NIR simulation brings in a substantial value, e.g., by allowing the qualitative evaluation of analyzed data or the comprehension of chemical factors influencing chemometric analysis. Recently, Kirchler et al. showcased the potential of combined theoretical/analytical NIRS in two of their subsequent feasibility studies on the analytical performances of miniaturized NIRS in quantifying rosmarinic acid (RA) in *Rosmarini folium* (Kirchler et al., 2017a,b). In various traditional plant medicines, RA is the primary active compound with therapeutic and antioxidant properties. As a relatively complex molecule (42 atoms; 188 electrons), it is somewhat expensive to obtain the anharmonic force field. For a similar reason, the resulting NIR spectrum involves numerous convoluted bands. This stems from a high number of binary combinations (7,140 in total), and naturally, a similarly substantial amount of intermodal couplings required to simulate the NIR spectrum of RA. To achieve the best cost/accuracy balance, the DVPT2 approach at the B3LYP/N07D level of electronic theory were employed for this task (**Figure 13**). This selection offers good efficiency without any essential accuracy compromise. As showcased in the case of RA, it delivered a qualitatively correct result and may be useful in simulating large molecules. A simplified treatment of the RA molecule in a vacuum did not reduce the quality of simulation exceedingly; manifestations of intermolecular interactions e.g., 2νOH band broadenings could be easily identified in the experimental spectrum with the availability of a clear image resolved from QM simulation. Additionally, the

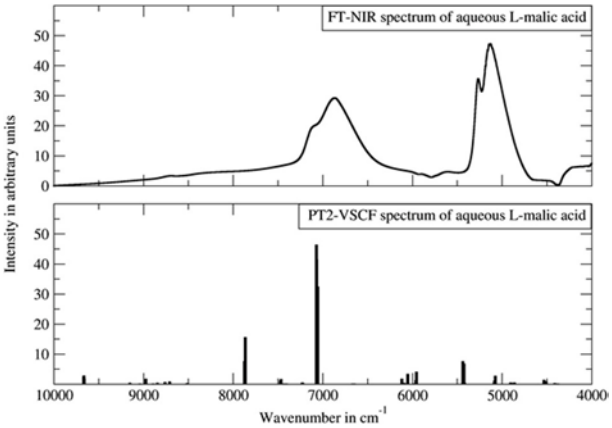

FIGURE 12 | The experimental FT-NIR spectrum of aqueous malic acid in comparison with the PT2-VSCF derived line spectrum. Reprinted from Schmutzler et al. (2013). Reprinted with permission from Nova Science Publishers, Inc.].

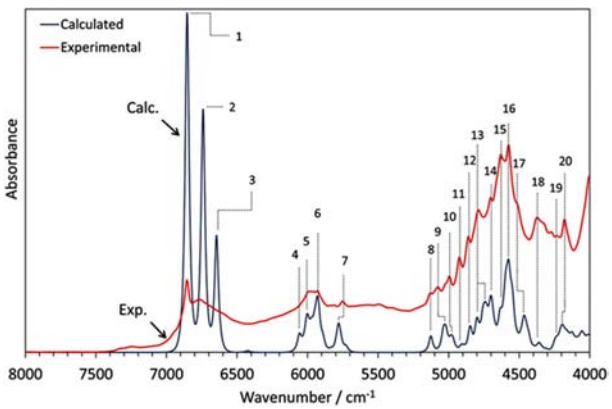

FIGURE 13 | The experimental (powder) and theoretical NIR spectrum of rosmarinic acid obtained in anharmonic GVPT2//DFT-B3LYP/N07D simulation (Kirchler et al., 2017b). Reproduced by permission of The Royal Society of Chemistry.

baseline elevation effects could also be understood, much like the effects observed previously for carboxylic acids (Grabska et al., 2017c,d). These accomplishments yielded full comprehension of the NIR spectrum of RA, leading to detailed band assignments (**Figure 13** and **Table 2**). These findings could then be used by Kirchler et al. for gaining a better understanding of the variability of PLS regression coefficients vectors assembled for the data originating from different NIR spectrometers with particular attention paid to miniaturized devices (Kirchler et al., 2017b). Different instruments yield different calibration curves, and different wavenumber regions manifest varying levels of influence in the regression. Kirchler et al. presented a state-of-the-art multi-method approach combining QM simulations, chemometrics (involving wavenumber discriminant methods, e.g., Moving-Window PLSR, MW-PLSR), and advanced methods of spectral analysis (Two Dimensional Correlation, 2D-COS; in particular, heterocorrelation elucidating spectral differences due to instrumental factors), indicating how modern analytical NIRS may be evolving in the foreseeable future (Kirchler et al., 2017b).

A more recent study confirmed the feasibility of the concept outlined above and went a step further in exploring how QM spectra simulations can be used to obtain new insight and physicochemical interpretation of the predictive models benefitting analytical applications (Beć et al., 2018b). Beć et al. investigated NIR properties of thymol with a handful of highly informative findings which would be otherwise unobtainable without accurate NIR simulation. Thymol is a phenolic constituent commonly found in a number of herbal plants, e.g., in a traditional plant medicine Thymi herba. Thymol strongly contributes to the general therapeutic properties of these herbs; e.g., by its anti-oxidant, anti-inflammatory, antiseptic (antifungal and antibacterial), antispasmodic, and immunomodulatory properties. Beyond its pharmaceutical significance, thymol is also an interesting molecule for spectroscopic investigations because of its vibrational features. The side groups attached to an aromatic ring may provide plentiful information on the spectra-structure correlations. An OH group commonly manifests a strong tendency to interact with the chemical neighborhood,

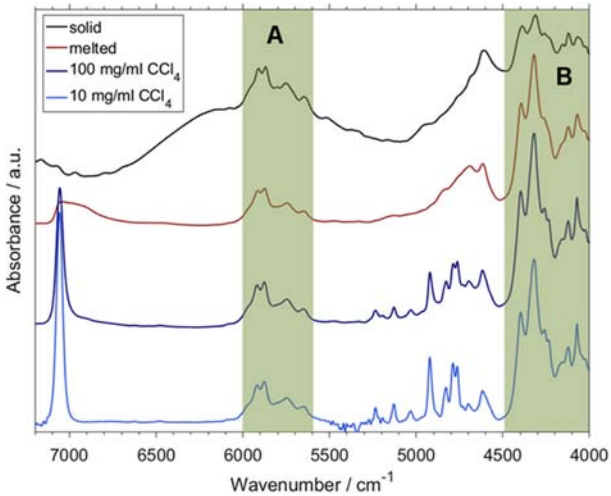

FIGURE 14 | A set of the experimental NIR spectra of thymol; solid state and melted (neat liquid, 333 K) as well as diluted in CCl_4 (100 and 10 mg mL^{-1} CCl_4). Highlighted are the wavenumber regions qualitatively independent of sample phase and concentration; **(A)** 6,000–5,600 cm^{-1}; **(B)** 4,490–4,000 cm^{-1} (Reprinted with permission from Beć et al., 2018b).

TABLE 2 | Band assignments in NIR spectrum of rosmarinic acid, based on GVPT2//DFT-B3LYP/N07D calculation.

	Wavenumber/cm^{-1}		Major contributions
	Exp.	Calc.	
1	6854.9	6,853	2νOH (ar)
2	6767.2	6,741	2νOH (ar)
3	~6680	6,645	2νOH (carboxyl)
4	~6044	6,056	2νCH (ar, aliph, in-phase)
5	5986.5	6,001	2νCH (ar, aliph, opp.-phase); 2νCH (ar)
6	5929.7	5,930	2νCH (ar); 2νCH (ar)
7	5752.5	5,780	[$\nu_{as}CH_2$, νCH (ar)] + [ν_{as} CH_2, νCH (ar)];
8	5128.0	5,126	[ν C=O, δ_{ip}OH (carboxyl)] + [νOH (carboxyl)]
9	5075.8	5,027	[δ_{ring}, δ_{ip}OH (ar)] + [νOH (ar, para-)]; [δ_{ring}, δ_{ip}OH (ar)] + [νOH (ar, para-)]; [δ_{ring}] + [νOH (ar, para-)]
10	4994.9	4,980	[δ_{ring}, δ_{ip}OH (ar)] + [νOH (ar, meta-)]; [δ_{ring}, δ_{ip}OH (ar)] + [νOH (ar, meta-)]
11	4923.8	4,906	[δ_{ring}, δ_{ip}OH (ar)] + [νOH (ar, para-)]; [δ_{ring}, δ_{ip}OH (ar)] + [νOH (ar, para-)]
12	4860.0	4,847	[δ_{ring}, δ_{ip}OH (ar)] + [νOH (ar, meta-)]; [δ_{ring}, δ_{ip}OH (ar)] + [νOH (ar, meta-)]
13	4788.3	4,798	[νCC] + [νOH (ar, para-)]; [νCC] + [νOH (ar, para-)]; [νCC] + [νOH (ar, meta-)]; [δCCH (carboxyl)] + [νOH (carboxyl)]; [δCH (ar), δ_{ip}OH (ar)] + [νOH (ar, para-)]; [δCH (ar), δ_{ip}OH (ar)] + [νOH (ar, para-)]
14	4701.0	4,701	[δCH (aliph)] + [νOH (ar, meta-)]; [δCH (ar), δ_{ip}OH (ar)] + [νOH (ar, meta-)]
15	4629.4	4,632	[δCH (ar), δ_{ring}, δ_{ip}OH (ar)] + [νOH (ar, meta-)]; [δCH (ar), δ_{ring}, δ_{ip}OH (ar)] + [νOH (ar, para-)]; [δ_{ip}OH (ar), δCH (ar), δ_{ring}] + [νOH (ar, para-)]
16	4575.7	4,757	[δCH (ar), δ_{ring}, δ_{ip}OH (ar)] + [νOH (ar, meta-)]; [δ_{ip}OH (ar), δCH (ar), δ_{ring}] + [νOH (ar, meta-)]
17	~4,508	4,465	[δ_{ring}, δ_{ip}OH (ar)] + [νCH (ar)]; [δ_{ring}] + [νCH (ar)]; [δ_{ring}, δ_{ip}OH (ar)] + [νCH (ar)]; [νC-O (carboxyl), δ_{ip}OH (carboxyl)] + [νOH (carboxyl)]; [δ_{ring}] + [νCH (ar)]; [δ_{ring}, δ_{ip}OH (ar)] + [νCH (ar)]
18	4372.3	4,360	[δ_{ring}] + [νCH (ar)]; [δ_{ring}] + [νCH (ar)]
19	4233.3	4,237	[$\delta_{sciss}CH_2$] + [$\nu_{as}CH_2$, νCH (ar)]; [$\delta_{sciss}CH_2$] + [$\nu_{as}CH_2$, νCH (ar)]
20	4179.4	4,194	[δCH (aliph)] + [νCH (ar, aliph, opp.-phase)]; [δ_{sciss} CH_2] + [$\nu_s CH_2$]; [δCH (aliph)] + [νCH (ar, aliph, in-phase)]

Kirchler et al. (2017b)-Reproduced by permission of The Royal Society of Chemistry.

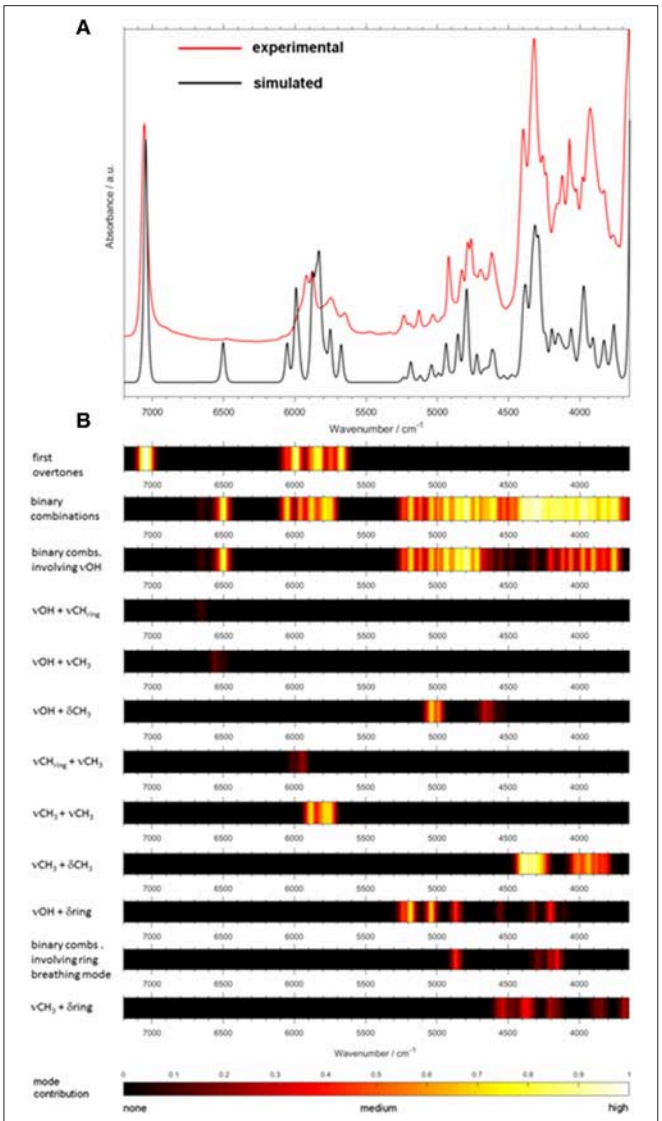

FIGURE 15 | The analysis of mode contribution into NIR spectrum of thymol (solution; 100 mg mL^{--1} CCl_4) based on the simulated data (DVPT2//DFT-B3LYP/SNST+CPCM). **(A)** Experimental and simulated outlines. **(B)** Contributions of selected modes as described on the figure (Reprinted with permission from Beć et al., 2018b).

e.g., to form a hydrogen-bond network. Due to this fact, and also because of the high anharmonicity of its vibrations, the existence of an OH group is a major spectrum-forming factor in NIR. For these reasons, the OH group has frequently been in the center of attention of NIR physicochemical as found in the literature (Czarnecki et al., 2015). The examination by Beć et al. elucidated a pattern of spectral variability following the sample state (solid and melted, neat liquid) and concentration (neat liquid and diluted in an inert solvent; CCl_4). Certain spectral regions in NIR manifested strong insensitivity to those properties of the sample (**Figure 14**; regions highlighted as A and B), while some others were observed to be clearly affected (**Figure 14**; all bands outside regions A and B). By QM simulations, the modes which stand behind that consecutive pattern could be fully identified (**Figure 15**). It was then observed that there exists a clear division between the highly relevant factors from the point of view of NIRS. Vibrations which are the most essential in shaping the NIR spectrum, and also sensitive to the changes in the sample property, were found to be consecutively discriminated by the PLS regression while quantifying the thymol content in a natural sample. Upon confronting these influential wavenumbers with the major features in the PLSR coefficients vector, it was found that the entirety of the spectral features identified as decisive in the PLSR model (5,860, 5,760; falling into the region A; **Figure 14** and 4,476, 4,418, 4,392, 4,368, 4,220, 4,128, and 4,092; cm^{-1}; belonging in the region B; **Figure 14**) originate from two insensitive to the concentration and sample state NIR sub-regions of thymol. These "invariant" regions contain CH_3 and aromatic CH bands. Surprisingly, the νOH mode, which is otherwise the most influential spectrum-forming factor (**Figure 15**), was largely omitted in the chemometric model. It was suggested that the sensitivity of the νOH mode to intermolecular interactions, manifested in NIR through significant band broadening, may be one of the responsible factors (Beć et al., 2018b). That promising study demonstrated well the need to further explore through a systematic investigation the underdeveloped area which appears at the connection between physical chemistry, theoretical NIRS and applied spectroscopy.

Other Applications, Arising Possibilities, and Remaining Challenges

As explored so far in the present review, the advent of feasible NIR spectra simulations has brought substantial gains to physical and analytical chemistry, both in basic and applied studies. The benefits for biomedical applications, e.g., NIR hyperspectral imaging (mapping) of biosamples could be evidenced as well (e.g., Huck, 2016a; Ozaki et al., 2017; Türker-Kaya and Huck, 2017). Deep penetration of the sample by NIR light, a consequence of the typically low absorptivity in this spectral region (see section Near-Infrared Spectroscopy. The Tale of an Ugly Duckling), forms a perfectly synergistic effect with the other values of NIRS (e.g., non-invasive character, low cost factor, wide applicability, superior time-to-result ratio), creating a strong stimulus for further development at the foundations of this technique (He et al., 2018; Wong et al., 2019). A question may arise on how in the nearest future theoretical and computational methods may become useful in these developments.

Several topics of the highest importance for spectral imaging presently remain a subject of intensive research, with the ultimate goal of introducing a feasible multi-modal imaging technique (He et al., 2018). A good example is the recent development of NIR radiation sources (He et al., 2015; Sun et al., 2017; Wong et al., 2019), with aim of being used in NIR fluorescence imaging, as thoroughly reviewed by He et al. (2018). The development studies for novel sources utilizing small-molecule fluorophores by Sun et al. (2017), high-efficiency NIR emitting materials coming from Wong et al. (2019), or ultralow-intensity NIR radiation source for drug delivery using upconverting particles

by He et al. (2015), could potentially see substantial gains from readily available theoretical and computational approaches. The new radiation sources which yield their superior capabilities from novel applications of bioinorganic chemistry, e.g., heavy transition metal and lanthanide complexes, could potentially benefit from computational simulations of the vibrational and electronic properties of such materials. At present, this remains a challenge, due to the complex electronic structure of transition metal atoms. Anharmonic simulations of vibrational spectra of such materials are prohibitively expensive; the computational expense associated with solving the vibrational problem in anharmonic approximation of advanced materials requires well-thought simplifications applied at several potential levels, ranging from the vibrational analysis itself (e.g., through reducing the grid density for total energy evaluations; Lutz et al., 2014c) to ingenious approaches to the electronic structure itself (e.g., Messner et al., 2014; Lutz et al., 2015). Vibrational spectra simulations of the metaloorganic complexes involving lighter metal ions can be found in recent literature.

As a good example, Lutz et al. have succeeded in the accurate reproduction of vibrational properties of the bioinorganic complex, trans-bis(glycinato)copper(II) (*cis* and *trans* isomers), in an aqueous solution (Lutz et al., 2013). They conducted quantum mechanical charge field molecular dynamics (QMCF-MD) studies, reporting the first QM simulations of organometallic complexes by this method. In hyphenation with experimental MIR spectroscopic data, they yielded accurate structural details of the investigated isomers as well as novel dynamic data, which has successfully been confirmed and extended by subsequent mid-infrared measurements. Although still being limited to a scaled harmonic approximation, according to Lutz et al. (2013), the spectroscopic results, critically assessed by adjacent multivariate data analysis (chemometrics), indicated an isomeric stability at ambient conditions, vanishing at elevated temperatures. Chemical systems containing metal ion significantly increase the computational complexity of the simulation procedure. Often, while maintaining careful error control, simplifications in the determination of the electronic structure may bring substantial gains in this regard. As recently demonstrated by Messner et al. in their investigation of the hydration of immobilized Fe(III), complexes of Fe(III) with methyl substituted iminodiacetate ($[Fe(MSIDA)(H_2O)_3]+$), as well as with methyl substituted nitrilotriacetate ($[Fe(MSNTA)(H_2O)_2]$) in aqueous solutions (Messner et al., 2014) by QMCF-MD, ingenious balancing between the cost-accuracy of the applied electronic method brings notable advantages, e.g., allowing to expand the parameters of molecular dynamics in return. By choosing a relatively fundamental Hartree-Fock (HF) approach, even over a much more robust MP2 method, Messner et al. accomplished essential progress in our understanding of the hydration structure and dynamics of metaloorganic complexes. Their effort has also been aimed at vibrational properties, while MIR spectroscopic data has been used as the reference. The understanding of the dynamics of metal cations and metaloorganic complexes in aqueous solution progressed further with ongoing studies continued within the same research group, e.g., as reported by Tirler et al. (2015) who once again applied, with high success, the quantum dynamic QMCF-MD simulation for the exploration of the stability of aqueous hexacyanoferrate(II) ion, in isolation as well as in the presence of potassium counterions. Further progress has been achieved in understanding the structure and dynamics of solvated metaloorganic complexes, when Tirler and Hofer investigated [MgEDTA]2– and [CaEDTA]2– systems (Tirler and Hofer, 2015). Furthermore, even more sophisticated systems, such as the aqueous 18-crown-6 (18C6) and strontium(II)-18-crown-6 (18C6–Sr) have been proven (Canaval et al., 2015) to be applicable to QMCF-MD treatment.

So far, simulation studies have repeatedly been evidenced to be of high value to metaloorganic chemistry, by delivering unique and highly desired information on the structure, vibrational features, dynamics, solvation, interactions, and stability of these important constituents of novel materials. It may be anticipated that these accomplishments will result in further progress in the computer-aided material design, which could find immediate application in the development of novel chromophores and enhancing NIR spectral imaging. On the other hand, the evolution toward anharmonic approximation may bring feasible studies of the properties of such materials in the NIR region. Currently, this remains hindered by the computational complexity introduced through anharmonic approximation, which indirectly also makes it difficult to fully incorporate a number of other effects, (e.g., relativistic effects Kondo et al., 2018; Madhu Trivikram et al., 2018), spin-orbit interaction (Gans et al., 2013), or vibronic coupling (Bloino et al., 2016). On the other hand, the exploration of the possible ways to increase the affordability of the relevant computational approaches (e.g., Lutz et al., 2014c, 2015; Messner et al., 2014) is ongoing, as explained above, and substantial advancements may be anticipated to occur in the near future.

FINAL REMARKS AND FUTURE PROSPECTS

Analytical NIRS relies on correlating the spectral variability with sample properties. The tools used for this purpose do not provide any understanding of these correlations, e.g., the parameters of the chemometric models have no immediately available physical interpretation. This creates a serious hindrance for applied NIRS from a conceptual, but also from a practical, point of view. For example, it has been shown that the structure of the PLS regression coefficients vector changes, e.g., between different spectrometers. Sensitivity to a multitude of different factors makes it difficult to elucidate the vibrational background of the analyzed spectral variability and the role of anharmonic effects. Theoretical spectroscopy offers substantial aid in answering the principle questions, which would be beneficial for both basic NIRS in the physicochemical context and in applied analytical spectroscopy.

Theoretical NIRS currently stands in a unique spot, where its usefulness to applied spectroscopy is far superior than the analogous relationships present in other kinds of vibrational spectroscopy. Nowadays, theoretical NIRS is still at a relatively early stage of development. It is an emerging field, which only

recently became more explored as the associated computational complexity had long been prohibitive. It was the current decade which witnessed advances in anharmonic theories, aided by ever-growing computer technology, which has enabled the feasible theoretical NIRS in connection with applied spectroscopy. As the number of studies in this area develops, the link between analytical and theoretical NIRS is being further strengthened; a clear trend in this evolution path is marking the anticipated further advancement. Focus of applied spectroscopy is on complex samples in which molecules remain under constant influence of the chemical neighborhood througha variety of intermolecular interactions, e.g., as in the discussed case of malic acid-water complex (Schmutzler et al., 2013). One should anticipate that in the near future research will be oriented to this direction, with more complex and interacting molecular systems, large biological systems and direct applications of theoretical NIRS in analytical routines. An even more coherent growth of theoretical near-infrared spectroscopy in close connection to analytical applications may be envisioned.

AUTHOR CONTRIBUTIONS

KB designed the article and wrote the manuscript. CH co-designed the general outline of the article. Both authors discussed the details of the review.

REFERENCES

Ahmad, M. (ed.). (2017). *Fatty Acids*. Oxford: Academic Press; AOCS Press.

Alcalà, M., Blanco, M., Moyano, D., Broad, N. W., O'Brien, N., Friedrich, D., et al. (2013). Qualitative and quantitative pharmaceutical analysis with a novel handheld miniature near-infrared spectrometer. *J. Near Infrared Spectrosc.* 21, 445–447. doi: 10.1255/jnirs.1084

Altinpinarn, S., Sorak, D., and Siesler, H. W. (2013). Near infrared spectroscopic analysis of hydrocarbon contaminants in soil with a hand-held spectrometer. *J. Near Infrared Spectrosc.* 21, 511–521. doi: 10.1255/jnirs.1079

Barone, V. (2005). Anharmonic vibrational properties by a fully automated second-order perturbative approach. *J. Chem. Phys.* 122, 14108–14118. doi: 10.1063/1.1824881

Beć, K. B., Futami, Y., Wójcik, M. J., Nakajima, T., and Ozaki, Y. (2016c). Spectroscopic and computational study of acetic acid and its cyclic dimer in the near-infrared region. *J. Phys. Chem. A* 120, 6170–6183. doi: 10.1021/acs.jpca.6b04470

Beć, K. B., Futami, Y., Wójcik, M. J., and Ozaki, Y. (2016a). A spectroscopic and theoretical study in the near-infrared region of low concentration aliphatic alcohols. *Phys. Chem. Chem. Phys.* 18, 13666–13682. doi: 10.1039/C6CP00924G

Beć, K. B., and Grabska, J. (2018). Quantum mechanical simulations of near-infrared spectra of biomolecules–Long-chain fatty acids. *NIR News* 29, 13–19. doi: 10.1177/0960336018788631

Beć, K. B., Grabska, J., and Czarnecki, M. A. (2018a). Spectra-structure correlations in NIR region: spectroscopic and anharmonic DFT study of n-hexanol, cyclohexanol and phenol. *Spectrochim. Acta A* 197, 176–184. doi: 10.1016/j.saa.2018.01.041

Beć, K. B., Grabska, J., Kirchler, C., and Huck, C. W. (2018b). NIR spectra simulation of thymol for better understanding of the spectra forming factors, phase and concentration effects and PLS regression features. *J. Mol. Liq.* 268, 895–902. doi: 10.1016/j.molliq.2018.08.011

Beć, K. B., Grabska, J., and Ozaki, Y. (2017). "Advances in anharmonic methods and their applications to vibrational spectroscopies," in *Frontiers of Quantum Chemistry*, eds M. J. Wójcik, H. Nakatsuji, B. Kirtman, and Y. Ozaki (Singapore: Springer). 483–512.

Beć, K. B., Wójcik, M. J., and Nakajima, T. (2016b). Quantum chemical calculations of basic molecules: alcohols and carboxylic acids. *NIR News* 27, 15–21. doi: 10.1255/nirn.1650

Beebe, K. R., Pell, R. J., and Seasholtz, M. B. (1998). *Chemometrics: A Practical Guide*. New York, NY: Wiley.

Białek, A., Białek, M., Jelinska, M., and Tokarz, A. (2016). Fatty acid profile of new promising unconventional plant oils for cosmetic use. *Int. J. Cosmet. Sci.* 38, 382–388. doi: 10.1111/ics.12301

Blanco, M., Alcalá, M., Planells, J., and Mulero, R. (2007). Quality control of cosmetic mixtures by NIR spectroscopy. *Anal. Bioanal. Chem.* 389, 1577–1583. doi: 10.1007/s00216-007-1541-3

Bloino, J., Baiardi, A., and Biczysko, M. (2016). Aiming at an accurate prediction of vibrational and electronic spectra for medium-to-large molecules: an overview. *Int. J. Quantum Chem.* 116, 1543–1574. doi: 10.1002/qua.25188

Burns, D. A., and Ciurczak, E. W. (eds.). (2007). *Handbook of Near-Infrared Analysis*. 3rd Edn. Boca Raton, FL: CRC Press.

Canaval, L. R., Hadisaputra, S., and Hofer, T. S. (2015). Remarkable conformational flexibility of aqueous 18-crown-6 and its strontium(II) complex–ab initio molecular dynamics simulations. *Phys. Chem. Chem. Phys.* 17, 16359–16366. doi: 10.1039/C5CP01977J

Chapman, J., Power, A. C., Chandra, S., and Cozzolino, D. (2018). Meat consumption and green gas emissions: a chemometrics analysis. *Food Anal. Methods* 1, 1–6. doi: 10.1007/s12161-018-1378-8

Chen, Y., Morisawa, Y., Futami, Y., Czarnecki, M. A., Wang, H.-S., and Ozaki, Y. (2014). Combined IR/NIR and density functional theory calculations analysis of the solvent effects on frequencies and intensities of the fundamental and overtones of the C=O stretching vibrations of acetone and 2-hexanone. *J. Phys. Chem. A* 118, 2576–2583. doi: 10.1021/jp411855b

Christiansen, O. (2004). A second quantization formulation of multimode dynamics. *J. Chem. Phys.* 120, 2140–2148. doi: 10.1063/1.1637578

Ciurczak, E. W., and Drennen, J. K. III. (2002). *Pharmaceutical and Medical Applications of Near-Infrared Spectroscopy*. Boca Raton, FL: CRC Press.

Clabo, D. A., Allen, W. D., Remington, R. B., Yamaguchi, Y., and Schaefer, H. F. III. (1988). A systematic study of molecular vibrational anharmonicity and vibration-rotation interaction by self-consistent-field higher-derivative methods–asymmetric-top molecules. *Chem. Phys.* 123, 187–239. doi: 10.1016/0301-0104(88)87271-9

Cozzolino, D. (ed.). (2014). *Infrared Spectroscopy: Theory, Developments and Applications*. New York, NY: Nova Science Pub Inc.

Czarnecki, M. A. (2003). Near-infrared spectroscopic study of hydrogen bonding in chiral and racemic octan-2-ol. *J. Phys. Chem. A* 107, 1941–1944. doi: 10.1021/jp0270102

Czarnecki, M. A., Czarnik-Matusewicz, B., Ozaki, Y., and Iwahashi, M. (2000). Resolution enhancement and band assignments for the first overtone of OH(D) stretching modes of butanols by two-dimensional near-infrared correlation spectroscopy. 3. Thermal dynamics of hydrogen bonding in butan-1-(ol-d) and 2-methylpropan-2-(ol-d) in the pure liquid states. *J. Phys. Chem. A* 104, 4906–4911. doi: 10.1021/jp991753e

Czarnecki, M. A., Morisawa, Y., Futami, Y., and Ozaki, Y. (2015). Advances in molecular structure and interaction studies using near-infrared spectroscopy. *Chem. Rev.* 115, 9707–9744. doi: 10.1021/cr500013u

Czarnecki, M. A., Muszynski, A., and Troczynska, H. (2010). Molecular structure and hydrogen bonding in liquid cyclohexanol and cyclohexanol/water mixtures studied by FT-NIR spectroscopy and DFT calculations. *J. Mol. Struct.* 974, 60–67. doi: 10.1016/j.molstruc.2009.12.012

Czarnecki, M. A., and Ozaki, Y. (1999). The temperature-induced changes in hydrogen bonding of decan-1-ol in the pure liquid phase studied by two-dimensional Fourier transform near-infrared correlation spectroscopy. *Phys. Chem. Chem. Phys.* 1, 797–800. doi: 10.1039/a808699k

Czarnecki, M. A., and Wojtków, D. (2004). Two-dimensional FT-NIR correlation study of hydrogen bonding in the butan-1-ol/ water system. *J. Phys. Chem. A* 108, 2411–2417. doi: 10.1021/jp035820n

Czarnecki, M. A., Wojtków, D., and Haufa, K. (2006). Rotational isomerism of butanols: infrared, near-infrared and DFT study. *Chem. Phys. Lett*. 431, 294–299. doi: 10.1016/j.cplett.2006.09.096

Davies, T. (2011). Happy 90th Birthday to Karl Norris, Father of NIR Technology. *NIR News* 22, 3–16. doi: 10.1255/nirn.1247

Davis, S., Anderson, D. T., Farrell, J. T. Jr., and Nesbitt, D. J. (1996). Isotopic substitution of a hydrogen bond: a near infrared study of the intramolecular states in (DF)2. *J. Chem. Phys*. 104:8197. doi: 10.1063/1.471604

Dorrepaal, R., and Gowen, A. (2018). Identification of magnesium oxychloride cement biomaterial heterogeneity using raman chemical mapping and NIR hyperspectral chemical imaging. *Sci. Rep*. 8:13034. doi: 10.1038/s41598-018-31379-5

Futami, Y., Morisawa, Y., Ozaki, Y., Hamada, Y., Wójcik, M. J., and Ozaki, Y. (2012). The dielectric constant dependence of absorption intensities and wavenumbers of the fundamental and overtone transitions of stretching vibration of the hydrogen fluoride studied by quantum chemistry calculations. *J. Mol. Struct*. 1018, 102–106. doi: 10.1016/j.molstruc.2012.01.029

Futami, Y., Ozaki, Y., Hamada, Y., and Ozaki, Y. (2014). Frequencies and absorption intensities of the fundamental and the first overtone of NH stretching vibrations of pyrrole acetylene and pyrrole ethylene complexes studied by density-functional-theory calculation. *Vib. Spectrosc*. 72, 124–127. doi: 10.1016/j.vibspec.2014.03.001

Futami, Y., Ozaki, Y., Hamada, Y., Wójcik, M. J., and Ozaki, Y. (2009). Frequencies and absorption intensities of fundamentals and overtones of NH stretching vibrations of pyrrole and pyrrole–pyridine complex studied by near-infrared/infrared spectroscopy and density-functional-theory calculations. *Chem. Phys. Lett*. 482, 320–324. doi: 10.1016/j.cplett.2009.09.063

Futami, Y., Ozaki, Y., Hamada, Y., Wójcik, M. J., and Ozaki, Y. (2011). Solvent dependence of absorption intensities and wavenumbers of the fundamental and first overtone of NH stretching vibration of pyrrole studied by near-infrared/infrared spectroscopy and DFT calculations. *J. Phys. Chem. A* 115, 1194–1198. doi: 10.1021/jp108548r

Gans, B., Grassi, G., and Merkt, F. (2013). Spin–Orbit and vibronic coupling in the ionic ground state of iodoacetylene from a rotationally resolved photoelectron spectrum. *J. Phys. Chem. A* 117, 9353–9362. doi: 10.1021/jp310241d

Gerber, R. B., Chaban, G. M., Brauer, B., and Miller, Y. (2005). "First principles calculations of anharmonic vibrational spectroscopy of large molecules," in *Theory and Applications of Computational Chemistry: The First 40 Years*, eds C. E. Dykstra, K. S. Kim, G. Fleming, and G. E. Scuseria (Amsterdam: Elsevier Publications), 165–193.

Gonjo, T., Futami, Y., Morisawa, Y., Wójcik, M. J., and Ozaki, Y. (2011). Hydrogen bonding effects on the wavenumbers and absorption intensities of the OH fundamental and the first, second and third overtones of phenol and 2,6-dihalogenated phenols studied by visible/near-infrared/infrared spectroscopy and density functional theory calculations. *J. Phys. Chem. A* 115, 9845–9853. doi: 10.1021/jp201733n

Grabska, J., Beć, K. B., Ishigaki, M., Huck, C. W., and Ozaki, Y. (2018). NIR spectra simulations by anharmonic DFT-saturated and unsaturated long-chain fatty acids. *J. Phys. Chem. B* 122, 6931–6944. doi: 10.1021/acs.jpcb.8b04862

Grabska, J., Beć, K. B., Ishigaki, M., Wójcik, M. J., and Ozaki, Y. (2017d). Spectra-structure correlations of saturated and unsaturated medium-chain fatty acids. Near-infrared and anharmonic DFT study of hexanoic acid and sorbic acid. *Spectrochim. Acta, A* 185, 35–44. doi: 10.1016/j.saa.2017.05.024

Grabska, J., Beć, K. B., Ozaki, Y., and Huck, C. W. (2017a). Temperature drift of conformational equilibria of butyl alcohols studied by near-infrared spectroscopy and fully anharmonic DFT. *J. Phys. Chem. A* 121, 1950–1961. doi: 10.1021/acs.jpca.7b00646

Grabska, J., Czarnecki, M. A., Beć, K. B., and Ozaki, Y. (2017b). Spectroscopic and quantum mechanical calculation study of the effect of isotopic substitution on NIR spectra of methanol. *J. Phys. Chem. A* 121, 7925–7936. doi: 10.1021/acs.jpca.7b08693

Grabska, J., Ishigaki, M., Beć, K. B., Wójcik, M. J., and Ozaki, Y. (2017c). Correlations between structure and near-infrared spectra of saturated and unsaturated carboxylic acids. An insight from anharmonic DFT calculations. *J. Phys. Chem. A* 121, 3437–3451. doi: 10.1021/acs.jpca.7b02053

Hamm, P., and Hochstrasser, R. M. (2001). "Structure and dynamics of proteins and peptides: femtosecond two-dimensional infrared spectroscopy," in *Practical Spectroscopy*, Vol. 26, ed M. D. Fayer (Boca Raton, FL: CRC Press).

Haufa, K., and Czarnecki, M. A. (2010). Molecular structure and hydrogen bonding of 2-aminoethanol, 1-amino-2-propanol, 3-amino-1-propanol, and binary mixtures with water studied by Fourier transform near infrared spectroscopy and density functional theory calculations. *Appl. Spectrosc*. 64, 351–358. doi: 10.1366/000370210790918445

He, S., Krippes, K., Ritz, S., Chen, Z., Best, A., Butt, H.-J., et al. (2015). Ultralow-intensity near-infrared light induces drug delivery by upconverting nanoparticles. *Chem. Commun*. 51, 431–434. doi: 10.1039/C4CC07489K

He, S., Song, J., Qu, J., and Cheng, Z. (2018). Crucial breakthrough of second near-infrared biological window fluorophores: design and synthesis toward multimodal imaging and theranostics. *Chem. Soc. Rev*. 47, 4258–4278. doi: 10.1039/C8CS00234G

Henn, R., Schwab, A., and Huck, C. W. (2016). Evaluation of benchtop versus portable near-infrared spectroscopic method combined with multivariate approaches for the fast and simultaneous quantitative analysis of main sugars in syrup formulations. *Food Contr*. 68, 97–104. doi: 10.1016/j.foodcont.2016.03.037

Herberholz, L., Kolomiets, O., and Siesler, H. W. (2010). Quantitative analysis by a portable near infrared spectrometer: can it replace laboratory instrumentation for in situ analysis? *NIR News* 21, 1–8. doi: 10.1255/nirn.1185

Herschel, W. (1800). XIV. Experiments on the refrangibility of the invisible rays of the sun. *R. Soc*. 90, 284–292. doi: 10.1098/rstl.1800.0015

Huck, C. W. (2014). "Near-Infrared (NIR) Spectroscopy in Natural Product Research," in *Handbook of Chemical and Biological Plant Analytical Methods*, eds K. Hostettman, S. Chen, A. Marston, H. Stuppner (Hoboken, NJ: John Wiley & Sons). 1–18.

Huck, C. W. (2016a). *Infrared Spectroscopy in Near-infrared/Infrared Bioanalysis Including Imaging*. Chichester, UK: John Wiley & Sons; Encyclopedia of Analytical Chemistry.

Huck, C. W. (2016b). The future role of near infrared spectroscopy in polymer and chemical analysis. *NIR News* 27, 17–23. doi: 10.1255/nirn.1577

Huck, C. W. (2017a). Selected latest applications of molecular spectroscopy in natural product analysis. *Phytochem. Lett*. 20, 491–498. doi: 10.1016/j.phytol.2016.12.028

Huck, C. W. (2017b). Theoretical and technical advancements of near-infrared spectroscopy and its operational impact in industry. *NIR News* 28, 17–21. doi: 10.1177/0960336017738174

Ishigaki, M., Kawasaki, S., Ishikawa, D., and Ozaki, Y. (2016a). Near-infrared spectroscopy and imaging studies of fertilized fish eggs: *in vivo* monitoring of egg growth at the molecular level. *Sci. Rep*. 6:20066. doi: 10.1038/srep20066

Ishigaki, M., Yasui, Y., Puangchit, P., Kawasaki, S., and Ozaki, Y. (2016b). In vivo monitoring of the growth of fertilized eggs of medaka fish (Oryzias latipes) by near-infrared spectroscopy and near-Infrared imaging—a marked change in the relative content of weakly hydrogen-bonded water in egg yolk just before hatching. *Molecules* 21, 1003–1017. doi: 10.3390/molecules21081003

Iwahashi, M., Hachiya, N., Hayashi, Y., Matsuzawa, H., Liu, Y., Czarnecki, M. A., et al. (1995a). Self-association of cis-9-octadecen-1-ol in the pure liquid state and in decane solutions as observed by viscosity, self-diffusion, nuclear magnetic resonance, electron spin resonance and near-infrared spectroscopic measurements. *J. Phys. Chem*. 99, 4155–4161. doi: 10.1021/j100012a041

Iwahashi, M., Suzuki, M., Czarnecki, M. A., Liu, Y., and Ozaki, Y. (1995b). Near-IR molar absorption coefficient for the OH-stretching mode of cis-9-octadecenoic acid and dissociation of the acid dimers in the pure liquid state. *J. Chem. Soc. Faraday Trans*. 91, 697–701. doi: 10.1039/ft9959100697

Iwahashi, M., Suzuki, M., Katayama, N., Matsuzawa, H., Czarnecki, M. A., Ozaki, Y., et al. (2000). Molecular self-assembling of butan-1-ol,butan-2-ol, and 2-methylpropan-2-ol in carbon tetrachloride solutions as observed by near-infrared spectroscopic measurements. *Appl. Spectrosc*. 54, 268–276. doi: 10.1366/0003702001949203

Iwamoto, R. (2009). Near-infrared spectroscopy as a useful tool for analysis in solution in common organic solvents. *Appl. Spectrosc.* 63, 354–362. doi: 10.1366/000370209787598942

Jaffe, D. (1987). FT-I.R. spectra of acetic acid and deuterated analogs in the monomer O–H and O–D regions. *Spectrochim. Acta A* 43, 1393–1396. doi: 10.1016/S0584-8539(87)80017-X

Johnson, B. R. (1977). New numerical methods applied to solving the one-dimensional eigenvalue problem. *J. Chem. Phys*. 67:4086. doi: 10.1063/1.435384

Jue, T., and Masuda, K. (2013). (eds.). *Application of Near Infrared Spectroscopy in Biomedicine.* New York, NY: Springer Science & Business Media.

Jung, J. O., and Gerber, R. B. (1996). Vibrational wave functions and spectroscopy of $(H_2O)n$, n= 2, 3, 4, 5: vibrational self-consistent field with correlation corrections. *J. Chem. Phys.* 105, 10332–10348. doi: 10.1063/1.472960

Kirchler, C. G., Pezzei, C. K., Beć, K. B., Henn, R., Ishigaki, M., Ozaki, Y., et al. (2017a). Critical evaluation of NIR and ATR-IR spectroscopic quantifications of rosmarinic acid in rosmarini folium supported by quantum chemical calculations. *Planta Med.* 83, 1076–1084. doi: 10.1055/s-0043-107032

Kirchler, C. G., Pezzei, C. K., Beć, K. B., Mayr, S., Ishigaki, M., Ozaki, Y., et al. (2017b). Critical evaluation of spectral information of benchtop vs. portable near-infrared spectrometers: quantum chemistry and two-dimensional correlation spectroscopy for a better understanding of PLS regression models of the rosmarinic acid content in *Rosmarini folium. Analyst* 142, 455–464. doi: 10.1039/C6AN02439D

Klakegg, S., Luo, C., Gonçalves, J., Hosio, S., and Kostakos, V. (2016). "Instrumenting smartphones with portable NIRS," *Proceedings of the 2016 ACM International Joint Conference on Pervasive and Ubiquitous Computing: Adjunct*. (New York, NY: ACM), 618–623.

Kondo, Y., Kobayashi, M., Akama, T., Noro, T., and Taketsugu, T. (2018). Comput. Chem. All-electron relativistic computations on the low-lying electronic states, bond length, and vibrational frequency of CeF diatomic molecule with spin–orbit coupling effects. *Comput. Chem.* 39, 964–972. doi: 10.1002/jcc.25171

Krasnoshchekov, S. V., and Stepanov, N. F. (2015). Nonempirical anharmonic vibrational perturbation theory applied to biomolecules: free-base porphin. *J. Phys. Chem. A* 119, 1616–1627. doi: 10.1021/jp5077092

Levy, R. M., Srinivasan, A. R., Olson, W. K., and McCammon, J. (1984). A quasi-harmonic method for studying very low frequency modes in proteins. *Biopolymers* 23, 1099–1112. doi: 10.1002/bip.360230610

Lutz, O. M. D., Bonn, G. K., Rode, B. M., and Huck, C. W. (2014a). Towards reproducible quantification of ethanol in gasoline via a customized mobile NIR spectrometer. *Anal. Chim. Acta* 826, 61–68. doi: 10.1016/j.aca.2014.04.002

Lutz, O. M. D., Meßner, C. B., Hofer, T. S., Canaval, L. R., Bonn, G. K., and Huck, C. W. (2014b). Computational vibrational spectroscopy of glycine in aqueous solution-fundamental considerations towards feasible methodologies. *Chem. Phys.* 43, 521–528. doi: 10.1016/j.chemphys.2014.03.003

Lutz, O. M. D., Messner, C. B., Hofer, T. S., Glätzle, M., Huck, C. W., Bonn, G. K., et al. (2013). Combined Ab initio computational and infrared spectroscopic study of the cis- and trans-Bis(glycinato)copper(II) complexes in aqueous environment. *J. Phys. Chem. Lett.* 4, 1502–1506. doi: 10.1021/jz400288c

Lutz, O. M. D., Rode, B. M., Bonn, G. K., and Huck, C. W. (2014c). Largely reduced grid densities in a vibrational self-consistent field treatment do not significantly impact the resulting wavenumbers. *Molecules* 19, 21253–21275. doi: 10.3390/molecules191221253

Lutz, O. M. D., Rode, B. M., Bonn, G. K., and Huck, C. W. (2015). The performance of RI-MP2 based potential energy surfaces in a vibrational self-consistent field treatment. *Chem. Phys. Lett.* 619, 66–70. doi: 10.1016/j.cplett.2014.11.050

Madhu Trivikram, T., Schlösser, M., Ubachs, W., and Salumbides, E. J. (2018). Relativistic and QED effects in the fundamental vibration of T2. *Phys. Rev. Lett.* 120, 163002–163004. doi: 10.1103/PhysRevLett.120.163002

Maeda, H., Wang, Y., Ozaki, Y., Suzuki, M., Czarnecki, M. A., and Iwahashi, M. (1999). A near-infrared study of hydrogen bonds in alcoholscomparison of chemometrics and spectroscopic analysis. *Chemom. Intell. Lab. Syst.* 45, 121–130. doi: 10.1016/S0169-7439(98)00096-3

Mantsch, H. H., and Naumann, D. (2010). Terahertz spectroscopy: the renaissance of far infrared spectroscopy. *J. Mol. Struct.* 964, 1–4. doi: 10.1016/j.molstruc.2009.12.022

Marini, F. (ed.). (2013). *Chemometrics in Food Chemistry*, Vol. 28. 1st Edn. Oxford; Amsterdam: Elsevier.

Matsuzawa, H., Tsuda, M., Minami, H., and Iwahashi, M. (2013). Dynamic molecular behavior and cluster structure of octanoic acid in its liquid and CCl4 solution. *Food Nutr. Sci.* 4, 25–32. doi: 10.4236/fns.2013.49A1005

Messner, C. B., Lutz, O. M. D., Rainer, M., Huck, C. W., Hofer, T. S., Rode, B. M., et al. (2014). Bonn. Structure and dynamics of chromatographically relevant Fe(III)-Chelates. *J. Phys. Chem. B* 118, 12232–12238. doi: 10.1021/jp505193y

Michniewicz, N., Czarnecki, M. A., and Hawranek, J. P. (2007). Near infrared spectroscopic study of liquid propanols. *J. Mol. Struct.* 844–845, 181–185. doi: 10.1016/j.molstruc.2007.04.001

Michniewicz, N., Muszynski, A., Wrzeszcz, W., Czarnecki, M. A., Golec, B., Hawranek, J. P., et al. (2008). Vibrational spectra of liquid 1-propanol. *J. Mol. Struct.* 887, 180–186. doi: 10.1016/j.molstruc.2008.03.020

Nielsen, H. H. (1951). The vibration-rotation energies of molecules. *Rev. Mod. Phys.* 23, 90–136.

Noda, I. (1989). Two-dimensional infrared spectroscopy. *J. Am. Chem. Soc.* 111, 8116–8118. doi: 10.1021/ja00203a008

Noda, I., Liu, Y., Ozaki, Y., and Czarnecki, M. A. (1995). Two-dimensional Fourier transform near-infrared correlation spectroscopy studies of temperature-dependent spectral variations of oleyl alcohol. *J. Phys. Chem.* 99, 3068–3073. doi: 10.1021/j100010a016

Noda, I., and Ozaki, Y. (2004). *Two-Dimensional Correlation Spectroscopy: Applications in Vibrational and Optical Spectroscopy*. Hoboken, NJ: John Wiley & Sons.

O'Brien, N. A., Hulse, C. A., Friedrich, D. M., Van Milligen, F. J., von Gunten, M. K., Pfeifer, F., et al. (2012). "Miniature near-infrared (NIR) spectrometer engine for handheld applications," in *Proceedings* of *SPIE 8374, Next-Generation Spectroscopic Technologies*, Vol. 837404 (Baltimore, MD). doi: 10.1117/12.979220

Oschetzki, D., Zeng, X., Beckers, H., Banert, K., and Rauhut, G. (2013). Azidoacetylene–interpretation of gas phase infrared spectra based on high-level vibrational configuration interaction calculations. *Phys. Chem. Chem. Phys.* 15, 6719–6725. doi: 10.1039/c3cp50268f

Ozaki, Y., Huck, C. W., and Beć, K. B. (2017). "Near infrared spectroscopy and its applications," in *Molecular and Laser Spectroscopy*, ed V. P. Gupta (Amsterdam: Elsevier), 11–38.

Ozaki, Y., McClure, W. F., and Christy, A. A., (eds.). (2006). *Near-Infrared Spectroscopy in Food Science and Technology*. Hoboken, NJ: Wiley-Interscience.

Pele, L., and Benny Gerber, R. (2010). On the mean accuracy of the separable VSCF approximation for large molecules. *J. Phys. Chem. C* 114, 20603–20608. doi: 10.1021/jp105066a

Pezzei, C. K., Schönbichler, S. A., Hussain, S., Kirchler, C. G., Huck-Pezzei, V. A., Popp, M., et al. (2017a). Near-infrared and mid-infrared spectroscopic techniques for a fast and nondestructive quality control of *Thymi herba*. *Planta Med.* 83, 1–8. doi: 10.1055/s-0043-121038

Pezzei, C. K., Schönbichler, S. A., Kirchler, C. G., Schmelzer, J., Hussain, S., Huck-Pezzei, V. A., et al. (2017b). Application if benchtop and portable near-infrared spectrometers for predicting the optimum harvest time of *Verbena officinalis*. *Talanta* 169, 70–76. doi: 10.1016/j.talanta.2017.03.067

Polyansky, O. L., Császár, A. G., Shirin, S. V., Zobov, N. F., Barletta, P., Tennyson, J., et al. (2003). High-Accuracy ab initio rotation-vibration transitions for water. *Science* 299, 539–542. doi: 10.1126/science.1079558

Power, A. C., Chapman, J., Chandra, S., and Roberts, J. J. D. (2018). Cozzolino. Illuminating the flesh of bone identification–An application of near infrared spectroscopy. *Vib. Spectrosc.* 98, 64–68. doi: 10.1016/j.vibspec.2018.07.011

Puangchit, P., Ishigaki, M., Yasui, Y., Kajita, M., Ritthiruangdej, R., and Ozaki, Y. (2017). Non-staining visualization of embryogenesis and energy metabolism in medaka fish eggs using near-infrared spectroscopy and imaging. *Analyst* 142, 4765–4772. doi: 10.1039/C7AN01575E

Ribessi, R. L., Neves Tde, A., Rohwedder, J. J., Pasquini, C., Raimundo, I. M., Wilk, A., et al. (2016). iHEART: a miniaturized near-infrared in-line gas sensor using heart-shaped substrate-integrated hollow waveguides. *Analyst* 141, 5298–5303. doi: 10.1039/C6AN01027J

Ringsted, T., Siesler, H. W., and Engelsen, S. B. (2017). Monitoring the staling of wheat bread using 2D MIR-NIR correlation spectroscopy. *J. Cereal Sci.* 75, 92–99. doi: 10.1016/j.jcs.2017.03.006

Roberts, J. J., Cozzolino, D. (2016). Wet or dry? The effect of sample characteristics on the determination of soil properties by near infrared spectroscopy. *Trends Analyt. Chem.* 83B, 25–30. doi: 10.1016/j.trac.2016.08.002

Roberts, J. J., and Cozzolino, D. (2017). Wet or dry? The challenges of NIR to analyse soil samples. *NIR News* 28, 3–5. doi: 10.1177/0960336017707884

Saranwong, S., Kawano, S., Ikehata, A., Noguchi, G., Park, S., Sashida, K., et al. (2013). Development of a low-cost NIR instrument for minced meat analysis: part 1-Spectrophotometer and sample presentations. *Am. J. Agric. Sci. Technol.* 2, 61–68. doi: 10.7726/ajast.2013.1005

Šašić, S., Segtnan, V. H., and Ozaki, Y. (2002). Self-modeling curve resolution study of temperature-dependent near-infrared spectra of water and the investigation of water structure. *J. Phys. Chem. A* 106, 760–766. doi: 10.1021/jp013436p

Schlick, T. (2010). *Force Fields in Molecular Modeling and Simulation: An Interdisciplinary Guide An Interdisciplinary Guide*. New York, NY: Springer-Verlag.

Schmutzler, M., Lutz, O. M. D., and Huck, C. W. (2013). "Analytical pathway based on non-destructive NIRS for quality control of apples," in *Infrared Spectroscopy: Theory, Developments and Applications*, ed D. Cozzolino (New York, NY: Nova Science Publisher), 1–21.

Schuler, M. J., Hofer, T. S., and Huck, C. W. (2017). Assessing the predictability of anharmonic vibrational modes at the example of hydroxyl groups–*ad hoc* construction of localised modes and the influence of structural solute–solvent motifs. *Phys. Chem. Chem. Phys*. 19, 11990–12001. doi: 10.1039/C7CP01662J

Sieger, M., and Mizaikoff, B. (2016). Toward on-chip mid-infrared sensors. *Anal. Chem*. 88, 5562–5573. doi: 10.1021/acs.analchem.5b04143

Siesler, H. W., Ozaki, Y., Kawata, S., and Heise, H. M., (eds.). (2002). *Near-Infrared Spectroscopy*. Weinheim: Wiley-VCH.

Smyth, H., and Cozzolino, D. (2013). Instrumental methods (spectroscopy, electronic nose, and tongue) as tools to predict taste and aroma in beverages: advantages and limitations. *Chem. Rev*. 113, 1429–1440. doi: 10.1021/cr300076c

Stecher, G., Huck, C. W., Stöggl, W. M., and Bonn, G. K. (2003). Phytoanalysis: a challenge in phytomics. *Trends Anal. Chem*. 22, 1–14. doi: 10.1016/S0165-9936(03)00108-0

Sun, Y., Ding, M., Zeng, X., Xiao, Y., Wu, H., Zhou, H., et al. (2017). Novel bright-emission small-molecule NIR-II fluorophores for in vivo tumor imaging and image-guided surgery. *Chem. Sci*. 8, 3489–3493. doi: 10.1039/C7SC00251C

Takahashi, J., and Yabushita, S. (2013). Theoretical analysis of weak adjacent substituent effect on the overtone intensities of XH (X = C, O) stretching vibrations. *J. Phys. Chem. A* 117, 5491–5502. doi: 10.1021/jp312674r

Thomsen, B., Yagi, K., and Christiansen, O. (2014). A simple state-average procedure determining optimal coordinates for anharmonic vibrational calculations. *Chem. Phys. Lett.* 610–611, 288–297. doi: 10.1016/j.cplett.2014.07.043

Tirler, A. O., and Hofer, T. S. (2015). A Comparative study of [CaEDTA]2– and [MgEDTA]2–: structural and dynamical insights from quantum mechanical charge field molecular dynamics. *J. Phys. Chem. B* 119, 8613–8622. doi: 10.1021/acs.jpcb.5b03938

Tirler, A. O., Persson, I., Hofer, T. S., and Rode, B. M. (2015). Is the Hexacyanoferrate(II) anion stable in aqueous solution? A Combined Theoretical and Experimental Study. *Inorg. Chem*. 54, 10335–10341. doi: 10.1021/acs.inorgchem.5b01701

Tomza, P., and Czarnecki, M. A. (2015). Microheterogeneity in binary mixtures of propyl alcohols with water: NIR spectroscopic, twodimensional correlation and multivariate curve resolution study. *J. Mol. Liq*. 209, 115–120. doi: 10.1016/j.molliq.2015.05.033

Türker-Kaya, S., and Huck, C. W. (2017). A review of mid-infrared and near-infrared imaging: principles, concepts and applications in plant tissue analysis. *Molecules* 22, 168–188. doi: 10.3390/molecules22010168

Unger, M., Pfeifer, F., and Siesler, H. W. (2016). Comparative variable temperature studies of polyamide II with a benchtop fourier transform and a miniature handheld near-infrared spectrometer using 2D-COS and PCMW-2D analysis. *Appl. Spectrosc*. 70, 1202–1208. doi: 10.1177/0003702816652365

Walther, M., Plochocka, P., Fischer, B., Helm, H., and Uhd Jepsen, P. (2002). Collective vibrational modes in biological molecules investigated by terahertz time-domain spectroscopy. *Biopolymers* 67, 310–313. doi: 10.1002/bip.10106

Wang, X., Antoszewski, J., Putrino, G., Lei, W., Faraone, L., and Mizaikoff, B. (2013). Mercury–cadmium–telluride waveguides –a novel strategy for on-chip mid-infrared sensors. *Anal. Chem*. 85, 10648–10652. doi: 10.1021/ac4025544

Watanabe, T., Sekine, R. R., Mizuno, T., and Miwa, M. (2016). Development of portable, wireless and smartphone controllable near-infrared spectroscopy system. *Adv. Exp. Med. Biol*. 923, 385–392. doi: 10.1007/978-3-319-38810-6_50

Westad, F., Schmidt, A., and Kermit, M. (2008). Incorporating chemical band-assignment in near infrared spectroscopy regression models. *J. Near Infrared Spectrosc*. 16, 265–273. doi: 10.1255/jnirs.786

Weyer, L. G., and Lo, S. C. (2002). "Spectra-structure correlations in the near-infrared," in *Handbook of Vibrational Spectroscopy*, Vol. 3, eds J. M. Chalmers and P. R. Griffiths (Chichester: Wiley). 1–21.

Whitehead, R. J., and Handy, N. C. (1975). Variational calculation of vibration-rotation energy levels for triatomic molecules. *J. Mol. Spec*. 55, 356–373. doi: 10.1016/0022-2852(75)90274-X

Wiedemair, V., De Biasio, M., Leitner, R., Balthasar, D., and Huck, C. W. (2018). Application of design of experiment for detection of meat fraud with a portable near-infrared spectrometer. *Curr. Anal. Chem*. 14, 58–67. doi: 10.2174/1573411013666170207121113

Wilson, E. B. Jr., Decius, J. C., and Cross, P. C. (1955). *Molecular Vibrations: The Theory of Infrared and Raman vibrational Spectra*. New York, NY: McGraw-Hill.

Wojtków, D., and Czarnecki, M. A. (2005). Effect of temperature and concentration on the structure of tert-butyl alcohol/water mixtures: near-infrared spectroscopic study. *J. Phys. Chem. A* 109, 8218–8224. doi: 10.1021/jp052833n

Wojtków, D., and Czarnecki, M. A. (2006). Effect of temperature and concentration on the structure of sec-butyl alcohol and isobutyl alcohol/water mixtures: near-infrared spectroscopic study. *J. Phys. Chem. A* 110, 10552–10557. doi: 10.1021/jp062307b

Wojtków, D., and Czarnecki, M. A. (2007). Two-dimensional attenuated total reflection infrared and near-infrared correlation study of the structure of butyl alcohol/water mixtures. *Appl. Spectrosc*. 61, 928–934. doi: 10.1366/000370207781745900

Wong, W.-Y. R., Zhang, Y., Chen, Z., Song, J., He, J., Wang, X., et al. (2019). Rational design of high efficiency green to deep red/near-infrared emitting materials based on isomeric donor-acceptor chromophores. *J. Mater. Chem. C*. doi: 10.1039/C8TC05383A

Wood, J. D., Richardson, R. I., Nute, G. R., Fisher, A., Kasapidou, P. R., and Sheard, M. E. (2003). Effects of fatty acids on meat quality: a review. *Meat. Sci*. 66, 21–32. doi: 10.1016/S0309-1740(03)00022-6

Workman, J. Jr., and Weyer, L. (2007). *Practical Guide to Interpretive Near-Infrared Spectroscopy*. Boca Raton, FL: CRC Press.

Wrzeszcz, W., Tomza, P., Kwaśniewicz, M., Mazurek, S., and Czarnecki, M. A. (2016b). Microheterogeneity in binary mixtures of aliphatic alcohols and alkanes: ATR-IR/NIR spectroscopic and chemometric studies. *RSC Adv*. 6, 94294–94300. doi: 10.1039/C6RA18692K

Wrzeszcz, W., Tomza, P., Kwaśniewicz, M., Mazurek, S., Szostak, R., and Czarnecki, M. A. (2016a). Microheterogeneity in binary mixtures of methanol with aliphatic alcohols: ATR-IR/NIR spectroscopic, chemometrics and DFT studies. *RSC Adv*. 6, 37195–37202. doi: 10.1039/C6RA04595B

Yagi, K. (2016). Development of molecular vibrational structure theory with an explicit account of anharmonicity. *Mol. Sci*. 10:A0085. doi: 10.3175/molsci.10.A0085

Yagi, K., Keçeli, M., and Hirata, S. (2012). Optimized coordinates for anharmonic vibrational structure theories. *J. Chem. Phys*. 137:204118. doi: 10.1063/1.4767776

Yan, H., and Siesler, H. W. (2018a). Quantitative analysis of a pharmaceutical formulation: performance comparison of different handheld near-infrared spectrometers. *J. Pharm. Biomed. Anal*. 160, 179–186. doi: 10.1016/j.jpba.2018.07.048

Yan, H., and Siesler, H. W. (2018b). Identification performance of different types of handheld near-infrared (NIR) spectrometers for the recycling of polymer commodities. *Appl. Spectrosc*. 72, 1362–1370. doi: 10.1177/0003702818777260

Yan, H., and Siesler, H. W. (2018c). Identification of textiles by handheld near infrared spectroscopy: Protecting customers against product counterfeiting. *J. Near Infrared Spectrosc*. 26, 311–321. doi: 10.1177/0967033518796669

Zielinska, I. N. (2014). Fatty acids in vegetable oils and their importance in cosmetic industry. *Chemik* 68, 103–110. Available online at: http://www.chemikinternational.com/year-2014/year-2014-issue-2/fatty-acids-in-vegetable-oils-and-their-importance-in-cosmetic-industry/

Conflict of Interest Statement: The authors declare that the research was conducted in the absence of any commercial or financial relationships that could be construed as a potential conflict of interest.

Copyright © 2019 Beć and Huck. This is an open-access article distributed under the terms of the Creative Commons Attribution License (CC BY). The use, distribution or reproduction in other forums is permitted, provided the original author(s) and the copyright owner(s) are credited and that the original publication in this journal is cited, in accordance with accepted academic practice. No use, distribution or reproduction is permitted which does not comply with these terms.

frontiers in Chemistry

REVIEW
published: 12 April 2019
doi: 10.3389/fchem.2019.00182

Advances in Sustainable Catalysis: A Computational Perspective

Matthew G. Quesne, Fabrizio Silveri, Nora H. de Leeuw and C. Richard A. Catlow*

School of Chemistry, Cardiff University, Cardiff, United Kingdom

The enormous challenge of moving our societies to a more sustainable future offers several exciting opportunities for computational chemists. The first principles approach to "catalysis by design" will enable new and much greener chemical routes to produce vital fuels and fine chemicals. This prospective outlines a wide variety of case studies to underscore how the use of theoretical techniques, from QM/MM to unrestricted DFT and periodic boundary conditions, can be applied to biocatalysis and to both homogeneous and heterogenous catalysts of all sizes and morphologies to provide invaluable insights into the reaction mechanisms they catalyze.

Keywords: green chemistry, computational chemistry, density functional theory, QM/MM, homogeneous catalysis, heterogeneous catalysis

OPEN ACCESS

Edited by:
Sam P. De Visser,
University of Manchester,
United Kingdom

Reviewed by:
Laura Masgrau,
Universidad Autónoma de Barcelona,
Spain
Kara Elizabeth Ranaghan,
University of Bristol, United Kingdom

****Correspondence:***
Matthew G. Quesne
quesnem@cardiff.ac.uk

Specialty section:
This article was submitted to Theoretical and Computational Chemistry, a section of the journal Frontiers in Chemistry

Received: *30 January 2019*
Accepted: *07 March 2019*
Published: *12 April 2019*

Citation:
Quesne MG, Silveri F, de Leeuw NH and Catlow CRA (2019) Advances in Sustainable Catalysis: A Computational Perspective. Front. Chem. 7:182. doi: 10.3389/fchem.2019.00182

INTRODUCTION

The challenge of moving toward a greener and more sustainable society will inevitably require the drastic transformation of many aspects of modern culture and economy, with all areas of resource management and production needing radical overhaul (Liu et al., 2015; Little et al., 2016; Bakshi et al., 2018). From a green chemistry standpoint this means the reengineering of chemical pathways that: (i) make the most efficient use of natural resources (Hellweg and Canals, 2014; Bakshi et al., 2015, 2018; Jaramillo and Destouni, 2015), (ii) reduce the volume of hazardous/polluting reagents and solvents (Clark et al., 2015; Clarke et al., 2018), and (iii) promote the substitution of fossil fuel resources with renewable alternatives (Gallezot, 2012; Wettstein et al., 2012; Sheldon, 2014, 2016; Den et al., 2018; Talebian-Kiakalaieh et al., 2018). Achieving all these goals will require the design of novel and efficient catalysts that are active under mild conditions and can be produced sustainably without leading to unacceptably high levels of toxic pollutants (Beletskaya and Kustov, 2010; Polshettiwar and Varma, 2010; Chua and Pumera, 2015; Egorova and Ananikov, 2016). However, before any of these new catalysts can be developed a fundamental understanding of the properties of the currently most efficient and environmentally sustainable options has to be obtained, in order to enable the design of their replacement (Campbell et al., 2016; Hutchings et al., 2016; Pelletier and Basset, 2016; Friend and Xu, 2017; Chen et al., 2018; Kornienko et al., 2018; Caddell Haatveit et al., 2019). Computational models have proved to be one of the most efficient and least resource heavy ways of obtaining such information and have now become an invaluable component in the field as a whole (Nørskov et al., 2009; Hansgen et al., 2010; Medford et al., 2015; Sutton and Vlachos, 2015; Greeley, 2016; Grajciar et al., 2018). In recent years, joint experimental and theoretical catalytic studies have become routine and have proven crucial to any fundamental understanding of catalysis at the molecular level, which will be underscored in detail in the proceeding example sections of this perspective (Hirunsit et al., 2015; Van Speybroeck et al., 2015; Yu et al., 2017; Kulkarni et al., 2018; Zhu et al., 2018).

Quantum Mechanical/Molecular Mechanics

Computational chemistry really came of age during the 1960s, with the advent of mainframe computers; however, early breakthroughs in approximating the wavefunction of many electron systems date back almost 30 years earlier with the development of the Møller-Plesset second-order perturbation wavefunction theory (MP2) (Møller and Plesset, 1934). One major and much more recent development was the applicability of density functional theory (DFT), especially after the incorporation of the gradient approximations into the exchange correlation function (Becke, 1993). However, not all DFT functionals are created equally and at the turn of the millennium John Perdew proposed a climbing scale coined the "Jacob's ladder" with pure GGA functional near the bottom and hybrid functionals close to the top (Perdew and Schmidt, 2001; Sousa et al., 2007). In practice, this often means that *in silico* homogenous catalytic systems, which are often modeled with hybrid functionals (Green et al., 2014; Wójcik et al., 2016; Wojdyła and Borowski, 2016; Delarmelina et al., 2017; Dabral et al., 2018), produce results that are closer to experimental values then those obtained when modeling heterogenous catalysts, where pure GGA are frequently the only efficient functionals to be implemented periodically (Hammond et al., 2012; Zhao et al., 2015; Ishikawa et al., 2017; Kunkel et al., 2018; Morales-Gar et al., 2018; Fang et al., 2019; Wang et al., 2019). Unfortunately, there is no universal functional and the most appropriate exchange–correlation term must be assessed on a system specific basis by benchmarking theoretically obtained electronic or catalytic properties to those observed experimentally (Laurent and Jacquemin, 2013; de Visser et al., 2014; Hickey and Rowley, 2014; Cantú Reinhard et al., 2016); additionally, the amount of Hartree–Fock component included in the exchange component of the most commonly used hybrid functionals can be modified to produce a better match between experimental and *in silico* values (Reiher et al., 2001; Walker et al., 2013). Increasingly, the importance of systematically benchmarking the functional of choice to experimentally determined properties of heterogenous catalysts is also becoming widely understood (Janthon et al., 2013, 2014; Quesne et al., 2018; Zhang et al., 2018). Implementing such well-benchmarked quantum mechanical techniques, has led to an explosion in studies that highlight fundamental aspects of the reaction mechanisms catalyzed by (i) enzymatic biocatalysts (Meunier et al., 2004; Li et al., 2012; Quesne et al., 2013; Blomberg et al., 2014; de Visser et al., 2014), (ii) homogenous catalysts (Kumar et al., 2010; Prokop et al., 2011; Neu et al., 2014; Sahu et al., 2014; Yang et al., 2016), and (iii) heterogenous catalytic materials (Alfredsson and Catlow, 2002; Sun and Liu, 2011; Cadi-Essadek et al., 2015, 2016; Quesne et al., 2018; Schilling and Luber, 2018; Silveri et al., 2019). Moreover, when such techniques are combined with classical molecular mechanics or dynamics, hybrid QM/MM cluster models can be constructed that act as relatively computationally inexpensive methods for studying large catalysts from microporous and mesoporous materials (O'Malley et al., 2016; Catlow et al., 2017b; Nastase et al., 2019) to heterogenous nanocatalysts (Xie et al., 2017; Lu et al., 2019) and are often especially useful during the study of enzymatic reaction mechanisms (Gao and Truhlar, 2002; Senn and Thiel, 2007, 2009; van der Kamp and Mulholland, 2013). Indeed, one of the initial motivations for the development of the QM/MM method in the 1970s was to investigate such biocatalyzed reaction (Warshel and Levitt, 1976); although, despite the techniques early development, it was not until much later that the methodology really came into its own and the technique started to become widely applied (Field et al., 1990; Rothlisberger et al., 2000). As previously mentioned, QM/MM methods are now being increasingly used to model heterogenous catalysts, for example in modeling catalytic process in zeolites (Nastase et al., 2019) and supported nano-catalysts (Xie et al., 2017; Lu et al., 2019). An illustrative example of one such ionic catalyst is shown in **Figure 1**, where a QM region with a circumference of 10 Å has been applied to a slab of magnesium oxide.

Most QM/MM studies begin with a crystal structure that is often deposited and stored online, whereby database of everything from zeolites (Baerlocher and McCusker, 2010) to enzymes (Berman et al., 2000) as well as the primitive cells of ionic material (Hellenbrandt, 2014) are available to researchers. Heterogeneous catalysts tend to be very ordered with relatively small primitive cells that can be optimized using a 3D periodic scheme (Ghorbanpour et al., 2014); as incorporated in codes such as VASP (Kresse and Furthmüller, 1996a), CASTEP (Clark et al., 2005), and CRYSTAL (Dovesi et al., 2014), prior to the preparation of a larger supercell for QM/MM treatment. However, even with heterogenous catalysts, there may be a need for some post-optimization modification of the crystal structure to introduce defects and active sites; as is often the case with zeolites whereby Brønsted acid sites need to be included, which involves substitution of silicon atoms by aluminum and charge compensation by protons (Sastre et al., 2002; O'Malley et al., 2016; Nastase et al., 2019). Conversely, large catalysts with disordered tertiary structures often require a far more extensive preparation protocol, which is especially true for enzymatic catalysts, since it is often impossible to crystallize an active enzyme/substrate complex and heavy atom positions need to be modified to create reactant starting structures (Quesne et al., 2014). Additionally, all residues need to be protonated because hydrogen atoms do not have enough electron density to be resolved accurately; which is typically done to a specific pH value with a PROPKA server (Dolinsky et al., 2007). Finally, since most crystallization techniques reduce the water content inside the protein core, a detailed molecular dynamics protocol needs to be run to solvate the model using one of the biomolecular force fields designed specifically for proteins (Oostenbrink et al., 2004; Wang et al., 2004; Brooks et al., 2009).

Once a working model of the catalyst and substrate is obtained, the large system needs to be split into a minimum of two regions. Typically, the much smaller region contains all the atoms that need to be describe quantum mechanically (QM region) and the other much larger region contains all the remaining atoms (MM region); which are described at a much lower level of theory, often with classical molecular mechanics. Since creating these regions may necessitate the breaking of either covalent or ionic bonds, an accurate description of the

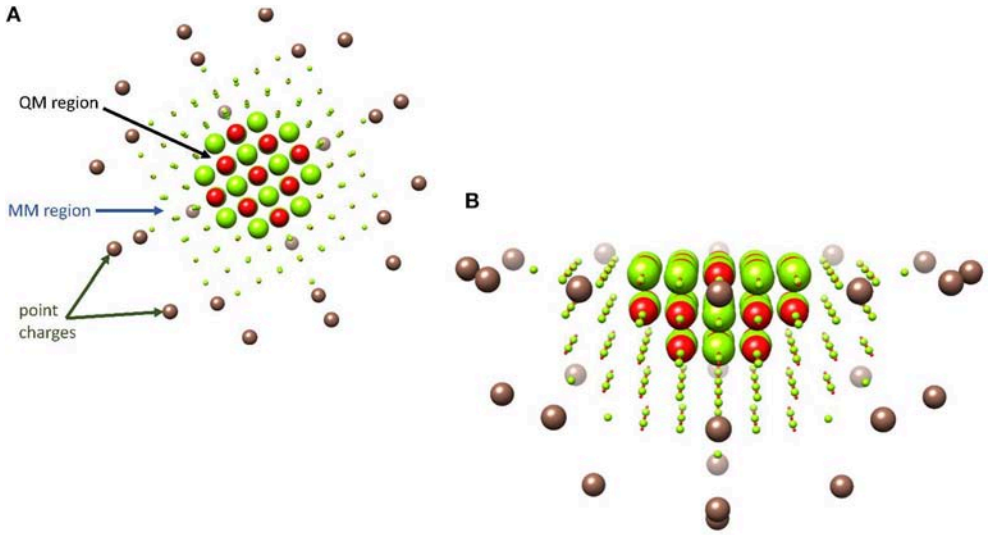

FIGURE 1 | Illustrative representation of a typical QM/MM set-up of an example metal–oxide, MgO. A QM region with a circumference of 10 Å is shown with large red and green spheres, with point charges colored brown. **(A)** Top–view from above the slab, **(B)** side–on from the slab edge.

interactions between different regions is critical for the correct electronic structure of the QM region. Currently the most common method for dealing with the valence issue in covalent systems, such as zeolites and biocatalysts, requires capping boundary atoms with hydrogen linkers (Senn and Thiel, 2009; Catlow et al., 2017a). When modeling ionic catalysts, interatomic potentials are often used to describe the MM region and an electrostatic embedding protocol is used to provide a countering polarizing environment to the ions at the border of the QM region (Bredow et al., 1996; Sokol et al., 2004).

Although, electrostatic embedding is also commonly applied to QM/MM models of covalent catalysts (Field et al., 1990) there is also the possibility of using a reduced mechanical embedding approach (Maseras and Morokuma, 1995). Both techniques model electrostatic interactions between atoms either side of the QM/MM boundary; however, MM charges are only included in the QM Hamiltonian with electrostatic embedding, which makes it the only appropriate methodology for ionic catalysts. In mechanical embedding protocols, electrostatic interaction between the two regions are assigned classically and so changes in the polarization of QM atoms due to electron transport (i.e., during a chemical reaction) is unaccounted for by changes in charge distribution (Chung et al., 2015). Importantly, the use of an electrostatic embedding protocol often produces results that are very sensitive to the choice of a given QM region, with convergence studies reporting that the absolute mean deviation between 40 different QM regions increased from 1.7 kcal mol^{-1} to ∼5 kcal mol^{-1} when moving from a mechanical to an electrostatic embedding protocol (Hu et al., 2011). Therefore, the use of an electrostatic embedding protocol may lead to less accurate results for the study of covalent catalysts in cases where the boundaries of the QM/MM regions are chosen poorly. This problem is negated in for example QM/MM case study reported here, where ChemShell was used as a platform to create quickly create several different QM regions for benchmarking and the boundary regions were very carefully chosen to only cut through sp^3 hybridized C–C bonds (Sherwood et al., 2003; Lu et al., 2019).

After a model of the catalyst is created, there are two major schemes for calculating the reaction landscape. Subtractive protocols are very commonly used in the study of reaction landscapes catalyzed by covalent catalysts, such as zeolites (Namuangruk et al., 2004; Vreven and Morokuma, 2006) and enzymes (Quesne et al., 2014; Wojdyla and Borowski, 2018). In two-layer subtractive protocols, only the QM region is capped with linker atoms because the whole system is also calculated at the MM level of theory, which would means that the MM energy of the QM region needs to be subtracted [$E_{MM}(\mathrm{QM_{region}})$] from the total energy to avoid double counting (see Equation 1). The QM/MM case study presented in this perspective utilizes the alternative additive approach, shown in Equation (2), whereby, only the MM region is calculated at the MM level of theory (E_{MM}). This negates the need for a subtraction step but requires the addition of a specific coupling term to describe the QM/MM border region (E_{border}), which includes bonding, electrostatic and Van der Waals interactions between the two regions (Sherwood et al., 2003). Importantly, when calculating using a mechanical embedding approach to calculate energy landscapes for covalent catalysts, it has been reported that both protocols should provide identical results (Cao and Ryde, 2018).

$$E^{total}_{QM/MM} = E^{whole}_{MM} + E_{QM}\left(QM_{region}\right) - E_{MM}\left(QM_{region}\right) \quad (1)$$

$$E^{total}_{QM/MM} = E_{MM} + E_{QM}\left(QM_{region}\right) + E_{border} \quad (2)$$

Other Computational Techniques

One of the main alternatives to the QM/MM technique for the study of reaction mechanisms catalyzed by enzymes involves the use of QM cluster models that focus on the biocatalyst's active site region and immediate surroundings. The models can consist of dozens to hundreds of atoms, which are all treated with a highly accurate level of computational theory. Generally, the majority of the substrate binding pocket is included with priority given to charged hydrophylic residues that form strong hydrogen bonds or π-staking interactions with either the substrate or co-factors, which inevitably are also included (Siegbahn and Crabtree, 1997; Borowski et al., 2004; Hernández-Ortega et al., 2014, 2015; Miłaczewska et al., 2018). Thus, these models should faithfully mimic substrate position as well as the enzyme's catalytic activity; however, the need to add geometric constraints to these models can sometime restrict substrate mobility. Of course there are many advantages and disadvantages to both techniques, which have been well discussed elsewhere (Blomberg et al., 2014; de Visser et al., 2014; Borowski et al., 2015; Quesne et al., 2016a). Molecular cluster approaches have also been used successfully to calculate adsorbate energies and simulate frequencies for many heterogenous catalysts (Haase and Sauer, 1994; Pelmenschikov et al., 1995, 1998; Zygmunt et al., 1998; Dangi et al., 2010); however, the neglecting of long-range Coulomb interactions as well as the lack of realistic steric constraints can reduce the effectiveness of such techniques for calculating reaction pathways. Dynamical approaches such as metadynamics (Barducci et al., 2011; Qian, 2012), umbrella sampling (Kästner, 2011), transition path sampling (Bolhuis et al., 2002) as well as many others (Meliá et al., 2012; Roca et al., 2012), can also be applied to catalyst reactivity, where they can be very advantageous in the study of free energy landscapes and rare-events, which is especially true for large systems where there are many degrees of freedom to be considered along with many energetically close "representative" transition states (Tsai et al., 2002). Metadynamics aims to sample the three–dimensional free energy surface of a reaction landscape using one of several "collective" variable associated with the transfer atom(s) (Laio and Parrinello, 2002; Iannuzzi et al., 2003; Ensing et al., 2005; Laio et al., 2005) and has been extensively applied to zeolite (Moors et al., 2013; Van Der Mynsbrugge et al., 2014; Dewispelaere et al., 2015; Hajek et al., 2016; Cnudde et al., 2017) and enzyme (Petersen et al., 2009; McGeagh et al., 2011; Lira-Navarrete et al., 2014; Raich et al., 2016; O'Hagan et al., 2019) catalyzed reaction. Such techniques work best when a reaction coordinate can be assigned to a simple set of collective variables that apply to distinct groups inside the reactant(s); however, in cases where the reaction path is uncertain more degrees of freedom can be explored using a transition path sampling protocol. Such methods incorporate Monte Carlo techniques into a molecular dynamical algorithm to locate a number of potential transition states connecting different minima (Bolhuis et al., 2002; Petersen et al., 2009) and have also been extensively applied to both enzyme (Swiderek et al., 2014; Althorpe et al., 2016) and zeolite (Lo et al., 2005; Bucko et al., 2009) catalyzed reaction pathways. Of course, the holy-grail of modeling is to drive the first-principles design of these very large macro-catalysts from the ground up using knowledge about their functional building blocks and related existing catalysts to predict the three-dimensional structure of the whole *in silico*. Exciting developments in this field are being developed for both microporous (Wells and Sartbaeva, 2015; Nearchou et al., 2018) and biological catalysts (Zanghellini et al., 2006; Kiss et al., 2013) and aim to explore a much larger structural space than exists in the naturally occurring catalysts, opening up the potential for novel route toward sustainable chemical reactions (Muñoz Robles et al., 2015; Rodríguez-Guerra et al., 2018).

Neither QM/MM methods nor large restricted cluster model techniques are required for small homogenous catalysts, where a reasonable gas phase system can often be created using all of the catalyst and substrate atoms (Draksharapu et al., 2015; Sahoo et al., 2015; Greer et al., 2019). However, this is often not the case for the computational study of heterogenous catalysts, which are most commonly investigated using a periodic treatment to enable proper description of the band structure of a solid (Blöchl et al., 1994; Kresse and Furthmüller, 1996a,b). Notwithstanding the increased use of many of the advanced techniques as mentioned above, for these materials it is still extremely common to use periodic boundary conditions to simulate an infinite solid surface (Grau-Crespo et al., 2003, 2006; Janthon et al., 2013). It is also important to note that QM/MM approaches can be especially unsuitable for calculating metallic catalysts that have extended states that are not localized to and extend beyond the QM boundary. Examples of such systems are discussed in the final section of this perspective, whereby, the electronic properties and catalytic activity of various transition metal carbides are modeled in reciprocal rather the real space. The only cases where an unrestricted, molecular, DFT type protocol may be warranted is either when the number of atoms in the solid state catalyst are too few for banding to occur (Abuelela et al., 2012; Liu and Lee, 2012; Feng et al., 2018; Zheng et al., 2018), or when a specific geometric feature such as an edge site in a strongly ionic or covalent catalyst is under investigation (Pelmenschikov et al., 1996; Chieregato et al., 2014; Pasini et al., 2014; Geng et al., 2018). The example sections that follow, provide case studies where all these techniques have been applied to a wide range of different catalysts and work to highlight the potential for improving the sustainability of various chemical protocols by computationally led "catalysis by design."

APPLICATIONS OF QUANTUM MECHANICS/MOLECULAR MECHANICS (QM/MM)

Green Biocatalysis of Terminal Olefins From Fatty Acids

It is widely recognized that there is an urgent need for the development of sustainable replacements to crude oil (Kerr, 2007; Shafiee and Topal, 2009; Murray and King, 2012). Sustainable generation of bio-fuels utilizing biocatalytic pathways from fatty acid feedstocks has been identified as a promising area of research (Stephanopoulos, 2007; Kung et al., 2012; Peralta-Yahya et al., 2012; Straathof, 2014). However, much of these biosynthetic

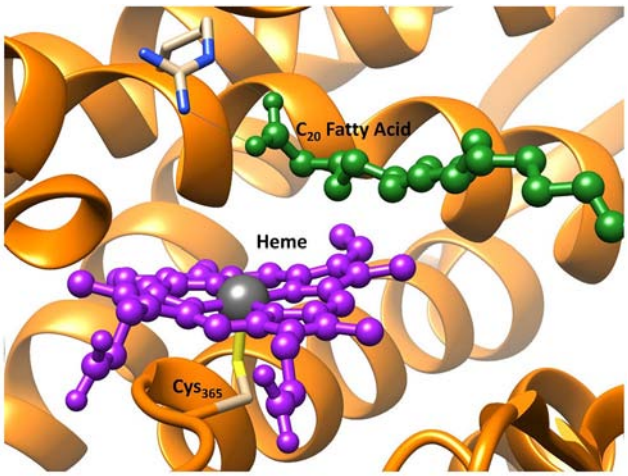

FIGURE 2 | Active site region of P450 OleT, from PDB 4L40 (Belcher et al., 2014) with heme in purple and the fatty acid substrate in dark green. Figure modified using atomic coordinate reported previously (Ji et al., 2015; Faponle et al., 2016).

processes require whole cell techniques that reduce efficiency. Many of the alternative chemical synthesis protocols, used to transform fatty acids into terminal alkenes, are very far from green and require palladium catalysts and high temperatures (Gooßen and Rodríguez, 2004; Liu et al., 2014). In recent years, it has been reported that the bacterial P450 peroxygenases $OleT_{JE}$ is able to catalyze the conversion of fatty acids to olefins without the need for additional cellular electron transfer machinery, since H_2O_2 and not O_2 is used as the oxidant (Rude et al., 2011; Wang et al., 2014; Dennig et al., 2015; Grant et al., 2015). These medium-chain terminal olefins make excellent feedstocks for biofuels because they can be substituted for diesel without major engine modification and have improved temperature tolerance as well as a high energy content (Peralta-Yahya et al., 2012; Lennen and Pfleger, 2013). However, whilst such research does offer the possibility of an environmentally friendly route for the production of bio-fuels, at present, industrial application are limited by the abundance of side-products (alcohols). Therefore, before industrial applications can proceed there needs to be a more fundamental understanding into the origin of the bifurcation of the olefin and alcohol pathways. Two combined DFT and QM/MM studies have recently been published that investigate this bifurcation in depth, with the aim of steering bio-engineering of $OLeT_{JE}$ to improve product selectivity (Ji et al., 2015; Faponle et al., 2016), and these studies will be discussed in our first example section.

As mentioned above $OleT_{JE}$ is a cytochrome P450, a family of enzymes that are ubiquitous and highly conserved throughout nature (Groves, 2003; Meunier et al., 2004; Ortiz de Montellano, 2004; Denisov et al., 2005; de Montellano, 2010; Kadish et al., 2010). Importantly, this enzyme family exhibits an extreme functional diversity in the reaction mechanisms they catalyze: from the metabolism of harmful drug molecules in the liver (Ji et al., 2015), to hormone biosynthesis (Guengerich, 2001; Posner and O'Neill, 2004; Munro et al., 2007) and they have also been commercially implemented in the cosmetics industry (Reinhard and de Visser, 2017). The active site region of OleT is depicted in **Figure 2**, and highlights the conserved thiolate linkage (Cys_{365}) coordinated to an iron center of the heme co-factor, which are common features of all P450s (Poulos et al., 1985; Schlichting et al., 2000; Auclair et al., 2001). This resting state is primed to activate hydrogen peroxide via a hydrogen atom isomerization to form, the highly active iron(IV)-oxo heme cation radical species, Compound I (Cpd I) (de Visser et al., 2003; Shaik et al., 2005; Rittle and Green, 2010). Whilst there is significant structural homogeneity amongst the P450s, they often diverge in the residues close to their active sites; in general those enzyme that possess relatively tight binding pockets such as $P450_{cam}$ oxidizing smaller substrate and those who incorporate more open active regions such as $P450_{BM3}$ catalyzing larger substrate, like fatty acids (Gelb et al., 1982; Atkins and Sligar, 1987; Ruettinger et al., 1989; Davydov et al., 1999). In addition to the reduction in energy and toxic material consumption, many P450 isozymes demonstrate improved product regioselectivity over more conventional catalysts; therefore, their industrial application could lead to a reduced volume of wasteful side-products and therefore the biotechnological approach can be considered superior in terms of environmental sustainability (Grogan, 2011; O'Reilly et al., 2011). The question then concerns which aspects of $OleT_{JE}$ causes its atypical product infidelity and can an in-depth computational investigation of its activity drive future bio-engineering of this enzyme toward selective bio-fuel production.

Biofuel Production: What Drives Enzymatic Regioselective Toward the Olefin

The bifurcated reaction mechanism proposed in **Scheme 1**, has been previously validated by computational models that predict the initial formation of a Cpd I species that exhibits spin-state selective product distribution (de Visser et al., 2001; Kamachi and Yoshizawa, 2003; Kumar et al., 2004b; Shaik et al., 2005; Quesne et al., 2016b). Computational studies that modeled only the first coordination sphere of Cpd I are in very good agreement with experimental observations (Rettie et al., 1987; Loch et al., 1995; Forkert and Lee, 1997; Sadeque et al., 1997; Lee et al., 1998; Wen et al., 2001; Gunes et al., 2007), whereby in general these models showed that Cpd I in the doublet spin state predominantly catalysis alcohol formation via small hydroxyl rebound barriers, whilst the quartet species can destabilize the radical intermediate and catalyze a broader range of products (de Visser et al., 2001, 2013). However, in order to confirm the veracity of this proposed mechanism for $OleT_{JE}$ and to provide a deeper understanding of the effect of the protein environment on product specificity a combination of DFT and QM/MM techniques were required (Ji et al., 2015; Faponle et al., 2016).

These studies initially relied on small DFT models in order to evaluate the extent to which product specificity was driven by substrate properties, since *in vitro* experiments had shown that a member of this enzyme family catalyzes the exclusive

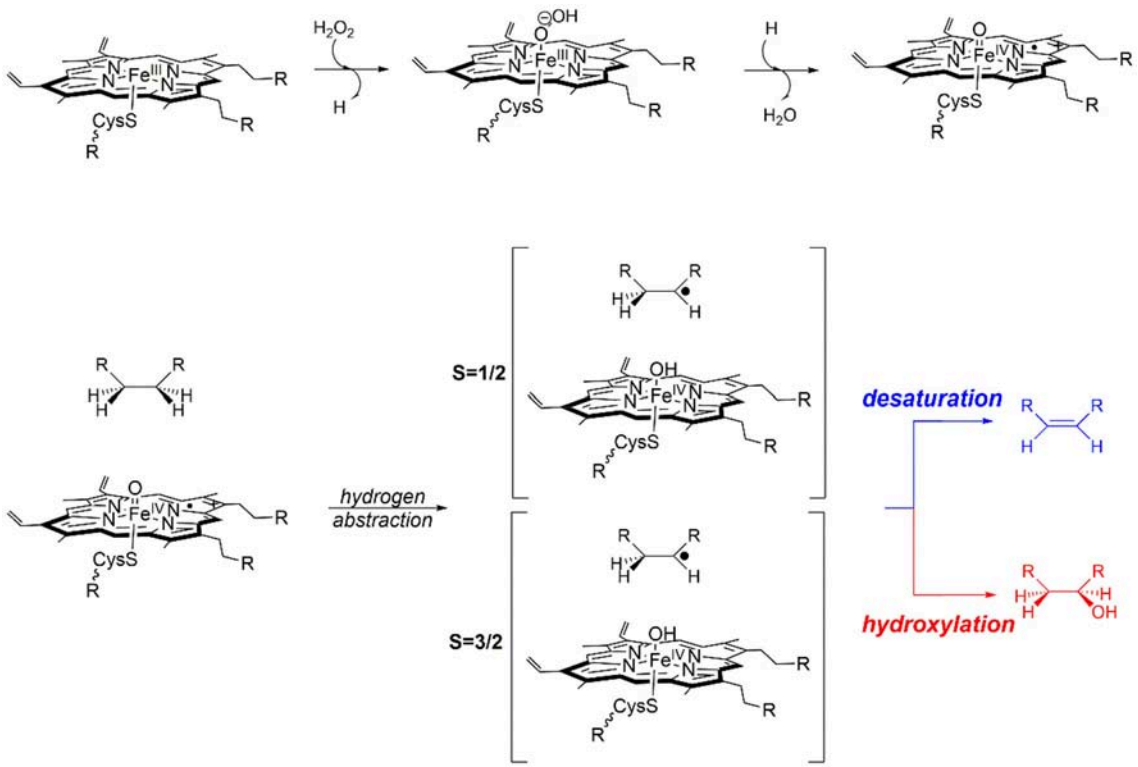

SCHEME 1 | Proposed hydroxylation and desaturation pathways, as catalyzed by P450 OleT.

hydroxylation of ethane (ET) to ethanol and the desaturation of dihydroanthracene (DHA), whilst valpronic acid (VA) can go through either pathway (Groves and McClusky, 1976). However, whilst the minimal DFT models did manage to predict the exclusive production of ethanol from ET, both DHA and VA showed similar reaction profiles, whereby, the doublet spin state catalyzed a combination of products via barrierless reaction mechanisms, whilst the quartet spin state catalyzed only the alcohol production via much lower hydroxyl rebound barriers. Therefore, the kinetic control exhibited by this active site model has proven insufficient for the understanding the different product selectivity reported for DHA and VA (Groves and McClusky, 1976). Importantly, this observation indicates that such a minimal model system may also be insufficient for the study of regioselectivity in product formation, as catalyzed by $OleT_{JE}$. Excitingly, if product selectivity in these cases can be assigned to environmental factors remote from the first coordination sphere of the co-factor, then it may be possible to modify product selectivity through bio-engineering of $OleT_{JE}$.

Therefore, to investigate the origin of the lack of fidelity in product regioselectivity vis-a-vis desaturation vs. α-hydroxylation of long chain fatty acids, as catalyzed by $OleT_{JE}$, a detailed QM/MM protocol was initiated. The QM/MM model was designed starting from the crystal structure coordinates of the enzyme/substrate complex (see **Figure 2**) (Belcher et al., 2014). These crystal coordinates represent the enzymes resting state and therefore were modified to approximate the heavy atoms of the Cpd I active species, in a manner previously reported (Porro et al., 2009; Postils et al., 2018). Finally, the active enzyme/substrate reactant species was solvated, protonated, equilibrated and split into QM and MM regions before the reaction coordinates could be followed, using a well-established protocol (Kumar et al., 2011; Quesne et al., 2014). The QM/MM calculations employ a combination of the CHARMM27 force field (Brooks et al., 2009), as implemented in DL_POLY (Smith et al., 2002) and UB3LYP/SV(P) method as implemented in TURBOMOLE (Ahlrichs et al., 1989) with a solvent sphere of 35Å placed around the whole enzyme/substrate complex. All calculations were performed using the ChemShell code (Sherwood et al., 2003) as a platform to run an electrostatically embedded, additive QM/MM scheme. As hoped, this model did show that the presence of the protein environment had a major impact on product selectivity; whereby the ground state switched from the doublet, found in the small DFT model, to a quartet. More importantly, the product selectivity also flips with the decarboxylation barrier reduced from 17.8 to 5.1 kcal mol^{-1}, which is below the 6.6 kcal mol^{-1} found for the hydroxyl rebound step. Thus, the ordering of the two barriers is reversed from that seen with the DFT model, where the alcohol production was favored by >10 kcal mol^{-1}. A more detailed study found that this reversal in the barrier ordering was strongly dependent on the position of the hydrogen atom that was to be abstracted (Faponle et al., 2016). The energy

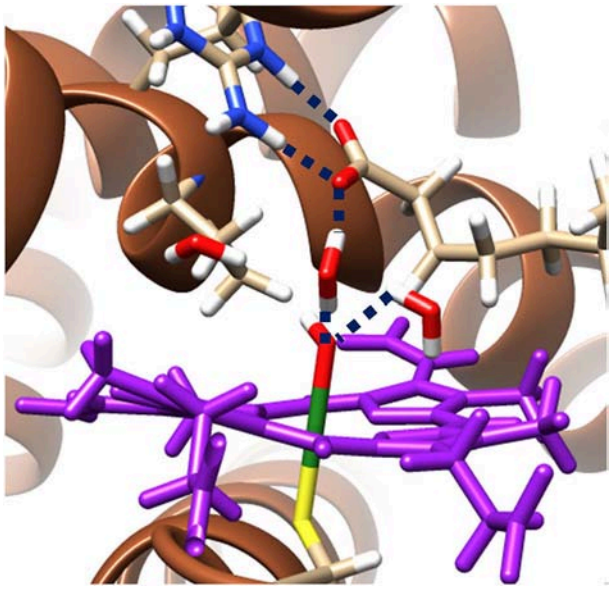

FIGURE 3 | QM/MM model of the ground state radical intermediate of hydrogen atom abstraction catalyzed by $OleT_{JE}$. Hydrogen bonding networks are linked with blue dashed lines and the heme co–enzyme is colored purple. The MM region is shown as brown secondary structure alpha–helices and beta–sheets; whilst, all atoms specifically highlighted are included in the QM region. Figure modified using atomic coordinate reported previously (Ji et al., 2015; Faponle et al., 2016).

barriers for hydrogen atom abstraction from the beta carbon of the fatty acid was very slightly lower than that seen with the alpha carbon. Importantly, hydrogen abstraction at the alpha position favored the alcohol production, whilst olefin production was dominant in the slightly more favorable beta radical intermediate. Intriguingly, while olefin production is favored using the QM/MM methodology, the two barriers are within the margin of error of the theory, which could help explain the mix product distribution seen experimentally (Rude et al., 2011; Wang et al., 2014,Dennig et al., 2015; Grant et al., 2015).

The hydrogen bonding networks present in the ground state radical hydroxyl-intermediate are highlighted in **Figure 3** and provide an insight into the origin of the reversal of product selectivity seen between the two methods. Often the use of a well-designed QM/MM protocol is the only way faithfully to replicate the local solvation environment surrounding an enzymes active region (Borowski et al., 2015; Quesne et al., 2016a). This phenomenon is evident here, with water networks surrounding the iron(IV)-hydroxo of the radical intermediate forming a bridge to a guanidine group of Arg_{245}, which in turn increases the energy required for the rotation of the hydroxyl group, which is required to position the correct orbital overlap to initiate a rebound of the hydroxyl-group toward the substrate radical. Importantly, $OleT_{JE}$ has an especially large binding pocket, allowing greater solvation of its active site. The effect of this is obvious when comparing the active site region of $OleT_{JE}$ to other P450s such as $P450_{cam}$, which tend to exclude much of the water from their active site (Poulos et al., 1987; Auclair et al., 2001). Thus, these results indicate that $OleT_{JE}$ is able to effectively elevate the hydroxyl rebound barrier for radical recombination and therefore enable the pathway toward olefin production to become competitive. These results taken together are very encouraging with regard to the potential of directed bioengineering of a OleT based isoenzymes that is able to sustainably and selectively produce biofuels from terminal olefins, without the need for harsh reaction conditions or wasteful redox partners.

ACTIVE SITE CLUSTER MODELS

The Promise of Sustainable Routes for the Catalysis of Spin Forbidden O_2 Activation

Activating molecular oxygen in its triplet ground state is a very important step in many industrial processes (Wang et al., 2001; Liang et al., 2011; Suntivich et al., 2011). However, currently harsh conditions are generally required along with the use of a precious metal cofactor, which are in low-earth abundance and whose extraction has high environmental cost (Murthi et al., 2004; Zhang et al., 2007; Kotobuki et al., 2009; Widmann and Behm, 2014). This is due to the high stability and low reactivity of triplet O_2, whose oxidation of substrates is often spin forbidden. Therefore, it is important to look at nature in order to develop more sustainable chemical pathway for oxygen reduction, which also drastically reduces the heavy metal component of the catalyst (Solomon and Stahl, 2018). However, most biocatalysts not only require metal cofactors but also organic co-enzymes, which in turn require the use of whole cell cultures to be regenerated, and these limitations reduce the utility of such enzymes in industrial processes (Solomon et al., 2000; Bugg and Ramaswamy, 2008; Quesne et al., 2015; de Visser, 2018). There is however, a small subgroup of these dioxygenases that are able to direct the spin-forbidden triplet to singlet conversion of molecular oxygen without the need of either a redox active metal co-factor or a sacrificial organic co-enzyme (Fetzner and Steiner, 2010). One of the few examples of this type of enzyme is the (1H)-3-hydroxy-4-oxoquinaldine 2,4-dioxygenase (HOD), which catalyzes dioxygenation of (1*H*)-3 hydroxy-4-oxoquinaldine (QND), leading to cleavage of the *N*-heteroaromatic ring (Bauer et al., 1996). Therefore, in our second example section, HOD was chosen as the subject of a couple of detailed studies (Hernández-Ortega et al., 2014, 2015), based on the DFT cluster model approach, into the basis of co-factor and flavin free activation of O_2. It is anticipated that a detailed first-principles understanding of the origin of this activity could help direct the future design of industrial catalysts that can more environmentally perform spin-forbidden oxygenation reactions.

Biocatalytic Activity of Metal-Independent Dioxygenases

These studies employed variable sized DFT models, shown in **Figure 4**, where enzyme thermodynamics and kinetics were determined by models of only the substrate and molecular oxygen (highlighted in red). Of the two larger active site cluster

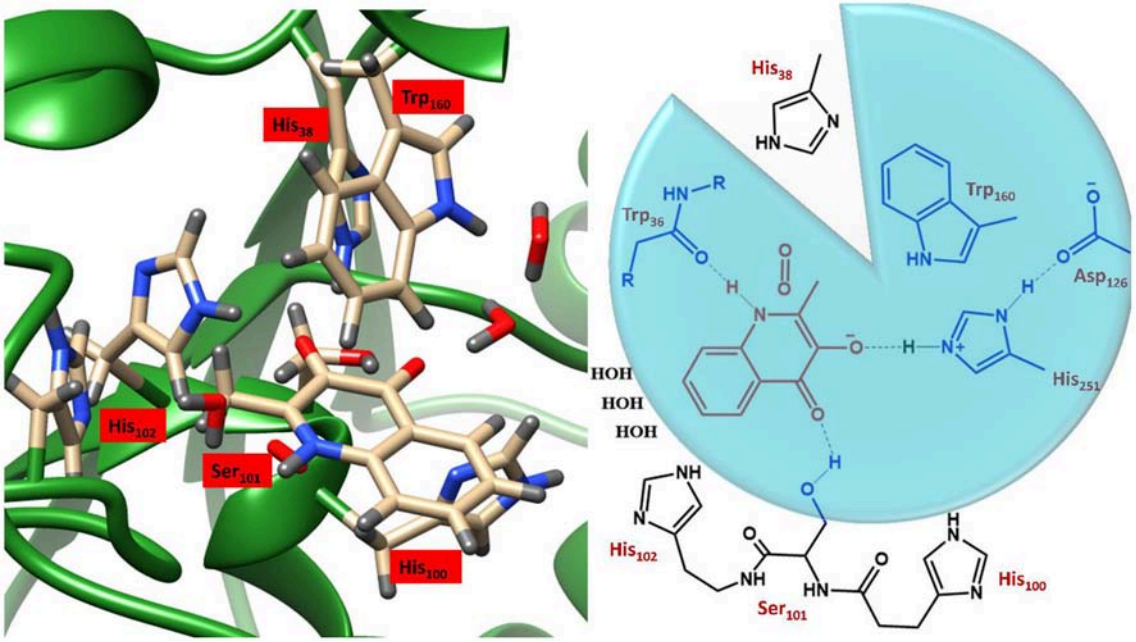

FIGURE 4 | Illustration of the active site region of HOD and a schematic representation of the three DFT cluster models. Model A (red) simply contains the substrate and O_2, Model B (blue circle) also the residues in blue, and Model B includes all residues depicted. Figure modified using atomic coordinate reported previously (Hernández-Ortega et al., 2014, 2015).

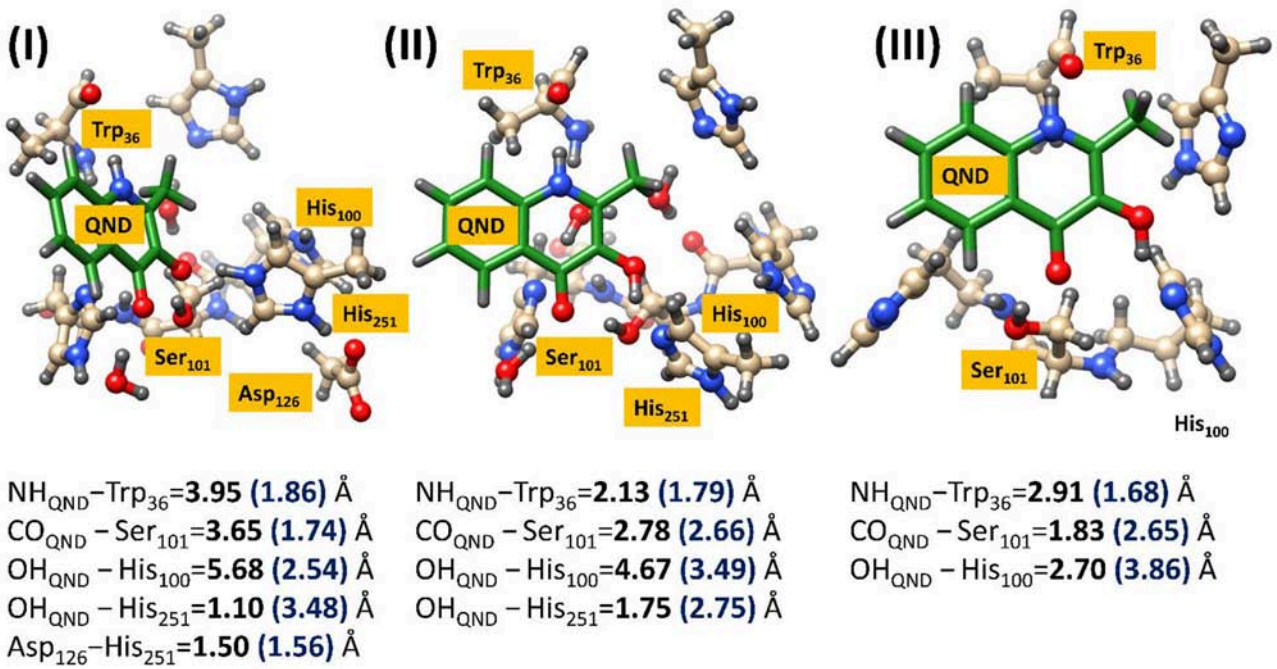

FIGURE 5 | Comparison of the geometric changes between the initial QM/MM optimized structures and those obtained using a DFT cluster model, for three HOD variants. **(I)** Wild type HOD, **(II)** D126A, and **(III)** H251A. All systems were optimized at B3LYP/6-31+G*/Cluster//QMMM level of theory with important atomic distances from DFT (left) and QMMM (right) optimization given in Å. Figure modified using atomic coordinate reported previously (Hernández-Ortega et al., 2014, 2015).

models, the smaller one incorporated only the atoms in the blue circle, whereby, truncated versions of His_{251}, Asp_{126}, Ser_{101}, and Trp_{160} and the backbone of Trp_{36} were added. The largest cluster model included all the atoms of the smaller ones as well as three water molecules and three additional imidazole groups, representing His_{38}, His_{100}, and His_{102} (black). Since the initial study focused purely on the formation of a substrate anion by a proton abstraction (Hernández-Ortega et al., 2014), oxygen was only present in the cluster models of the second study into the rate-limiting spin-forbidden activation of triplet oxygen, by the activated QND (Hernández-Ortega et al., 2015). The protocol for setting up the cluster models was very similar to that discussed in the previous section, whereby, the crystal structure was initially protonated, solvated, equilibrated and optimized. The crystal structure of the wild type enzyme was taken from the protein data bank (PDB) file 2WJ4 (Steiner et al., 2010), whilst the mutant variants were prepared *in silico* by modifying either a carboxylate or an imidazole group. As is shown in **Figure 4**, the QM regions of the two mutants lacked atoms for either a carboxylate or a carboxylate and imidazole group, for D126A and H251A, respectively. These structures were then equilibrated and optimized in the same manner described for $OleT_{JE}$ (above), whereby a solvent sphere of 35 Å was placed around the whole system and the functional UB3LYP (Lee et al., 1988; Becke, 1993) in combination with the 6–31G(3d,p) basis set was used for the QM region. Therefore, whilst for this example QM/MM was not employed to investigate the kinetics of QND oxidation by HOD, it was used to obtain cluster model starting structures that represented protonated, solvated and optimized coordinates.

This approach was required to obtain reasonable starting structures for the cluster models, which were also calculated using the same UB3LYP/6–31G(3d,p) methodology, only this time implemented in the Gaussian software package (Frisch et al., 2009). However, after the large cluster models were excised and optimized it became evident that the two technique gave radically different geometries, as can be seen in **Figure 5**. Much of these effects can be attributed to changes in substrate orientation that might to some extent be constrained by residues remote from the active site region. The precise position of the substrate seems to be significantly model dependent, although, there does appear to be a general migration away from hydrogen bonding networks with Trp_{36} and Ser_{101}, in all models. Even though it could be argued that either increasing the cluster size or putting more constraints on the substrate might increase the match between the reactant geometries obtained by the two techniques, it was decided that such techniques would be too costly and could lead to unphysically high barriers along the reaction path. It is also important to note that the initial QM/MM optimized starting structures show there to be barely any effect of residue modification on substrate positioning, which may indicate that the QM/MM models are too inflexible to accurately simulate point-mutations. Alternatively, it is very possible that these two point-mutations would not be expected to produce a large amount of tertiary structure changes, and even if they did would require much more intensive molecular dynamics simulations to replicate *in silico*. In either case, as demonstrated below, it was shown that the cluster models were sufficient to provide important electronic insights into the origin of the experimentally observed differences in catalytic activity between the different variants.

TABLE 1 | QND deprotonation by His residues, using active site models of different HOD variants and minimal models of the His/Asp dyad.

	$\Delta E + ZPE$	ΔG
WT	−0.9	−0.8
D126A	13.1	14.0
H251A	28.0	27.8
His251-H	13.4	13.3
His251-Asp126	1.8	1.8

All Zero point (ZPE) and Gibbs free energies for QND deprotonation were obtained at UB3LYP/6–31G(3d,p) level of theory. All energies are given in kcal mol^{-1} and relate the deprotonated QND to reactant species.

The first study used a combined experimental and theoretical (cluster model) approach in order to investigate the preliminary proton abstraction step, which forms the active substrate anion. This combination technique underscored the importance of the histidine/aspartate dyad, since on its own His_{251} is not basic enough to abstract a proton from QND. Therefore, a strong hydrogen bond with Asp_{126} is required to catalyze QND deprotonation, which is evident by the >13 kcal mol^{-1} endothermicity of the smallest model shown in **Table 1**. These findings were replicated experimentally with the production of two mutant variants D126A and H251A, which each targeted one of the dyad residues with a point-mutation to an alanine. Each mutation caused a substantial drop in enzyme activity. Stop-flow experiments assessed deprotonation rate constants (k_H) that were 5- to 40-fold lower in D126A and too low to measure in the H251A variant. Importantly, initial optimizations with both cluster and QM/MM models of wild-type HOD showed spontaneous proton transfer from the substrate; whilst, a stable hydrogenated QND species was found in both mutant clusters. The driving force for these different initial states is validated by the theoretical models, whereby, the wild-type models were the only ones to show exothermic deprotonation steps, with the thermodynamics of the D126A and H251A models pointing the equilibrium toward (QND)–OH (see **Table 1**). These substrate deprotonation energies report the bond formation energy of the $His_{(x)}$–H, where His_{100} substitutes His_{251} in the H251A variant, minus the bond dissociation energy of the (QND)-H bond that is broken. As shown in **Table 1**, when these energies are calculated the slightly exothermic nature of the wild-type cluster model is set against endothermic energies of >10 kcal mol $^{-1}$ for D126A and $\sim$30 kcal mol $^{-1}$ for H251A. Finally, it was determined that the origin of the loss in proton abstraction ability seen in the D126A variant was an increase in the proton affinity of His_{251} by 12 kcal mol $^{-1}$ upon coordination with Asp_{126}.

At the time of publication, the computational results of the second study were somewhat controversial (Thierbach et al., 2014; Silva, 2016). This study focused on the spin-forbidden

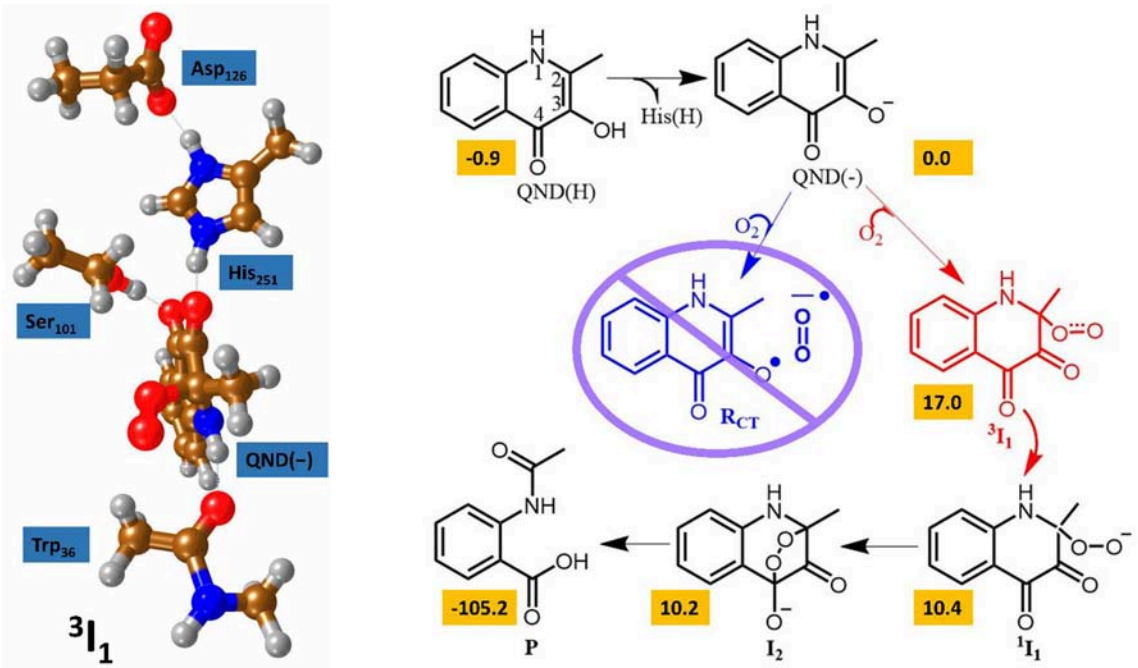

FIGURE 6 | The two calculated reaction mechanisms for the oxidation of QND. The proposed pathway (blue) was assessed as less favorable than the alternative (red). A graphical representation of the alternative triplet intermediate is also shown (left). Figure modified using atomic coordinate reported previously (Hernández-Ortega et al., 2014, 2015).

incorporation of triplet oxygen into the singlet product, the mechanism of which has wide implications for green chemistry. In this study the authors concluded that the rate-limiting oxygen activation step proceeded via an initial short lived oxygen bond triplet intermediate (Hernández-Ortega et al., 2015). Spin trapping experiments had been used to propose an alternative mechanism, whereby an initial long range electron transfer created a superoxo radical species that was then able to recombine with the substrate radical (see **Figure 6**) (Müller et al., 1987; Thierbach et al., 2014; Kralj et al., 2015). However, the authors of this theoretical study determined that their calculations indicated the experimentally observed radical could be more correctly assigned to the radical rearrangement that transformed the QND(−) substrate into the $^3\mathbf{I_1}$ intermediate with the aid of an elongation of the C2–C3 bond and the rehybridization of these two carbon centers from sp^2 to sp^3. The theoretical findings were additionally strengthened by transient state stop-flow experiments, which were completely unable to detect any signature that could have been assigned to the proposed $\mathbf{R}_{CT}$ intermediate. These studies provided a greater fundamental knowledge of this novel class of dioxygenases that could have important implications for future development of novel green catalytic routes to spin forbidden oxygen activation. These results indicate that the stabilization of a short-lived triplet intermediate, which last long enough for spin state crossing, could be key to future catalyst design.

HOMOGENOUS CATALYSTS MODELED WITH UNRESTRICTED DFT

Oxidation of Methane to Methanol

Using density functional theory (DFT) methodology to characterize and rationally tune bioinorganic, earth-abundant and environmentally compatible homogenous catalysts, is a major field of combined computational and experimental research (Kumar et al., 2010; Prokop et al., 2011; Neu et al., 2014; Sahu et al., 2014; Yang et al., 2016). DFT techniques have been used to study the selective halogenation (Quesne and de Visser, 2012), nitrogenation (Timmins et al., 2018), and oxygenation (Jastrzebski et al., 2014) abilities of many such catalysts. Indeed, work on the selective dioxygenation of catechol by tris(2-pyridylmethyl)amine (TPA) has shown promise for the potential of a sustainable, green-catalytic route for nylon production via dimethyl adipate (Jastrzebski et al., 2013, 2014). Homogenous catalysts are often able to catalyze reaction mechanisms selectively at far lower temperatures and pressures then conventional routes. Indeed, selectivity can be one of the most important environmental benefits of choosing homogenous catalysts because of the increased yields and lower side-products. However, it is important to consider the potential of homogeneous catalysts increasing the volumes of contamination and waste, as well as the excess energy required for product separation and catalyst recycling, which is often

greater than observed using heterogenous catalysts (Lam et al., 2010; Tan et al., 2013). Therefore, it is crucial to consider to what extent there could be an overall environmental benefit to using homogenous catalysis over the more conventional heterogenous routes (Corma and García, 2003; Astruc, 2007; Baroi and Dalai, 2015). The example catalyst presented here, is very novel for possessing the ability of converting methane to methanol at low temperatures and ambient pressures (Kudrik and Sorokin, 2008; Sorokin et al., 2008, 2010; Isci et al., 2009; Kudrik et al., 2012). Whilst the reactivity of this bio-mimetic catalyst has been well characterized, the origin of its efficiency was poorly understood. Therefore, a detailed an in-depth computational study was undertaken to understand the aspects of its catalysis that enabled such high activity toward methane hydroxylation, so that such a fundamental understanding of reactivity could be used to further improve the activity of this or related catalysts (Quesne et al., 2016b).

As discussed in the olefin production section, the P450 super family of enzymes are amongst the most efficient and powerful catalysts for oxidizing C-H bonds. However, despite the extreme amount of substrate diversity, there is no natural pathway that utilized a P450 isoenzyme and is also powerful enough to activate the 104.9 kcal mol $^{-1}$ strong C–H bond of methane. In fact, under guest/host activation conditions, methane was the only short chain alkane that $P450_{BM3}$ was unable to oxidize (Kawakami et al., 2011, 2013; Zilly et al., 2011). Bioengineering does a little better than nature with CYP_{153A6} actually showing some oxidation activity toward methane, although, with an extremely slow turnover frequency of 0.02–0.05 (Chen et al., 2012). These observations are in stark contrast with the μ-nitrido-bridged diiron-oxo porphyrin catalyst discussed in this section, which has demonstrated high oxidative activity toward methane and is based on a dimer of two of the co-enzymes found in P450s (Kudrik and Sorokin, 2008; Sorokin et al., 2008, 2010; Isci et al., 2009; Kudrik et al., 2012). The active site of P450 enzymes consists of thiolate linked iron-oxo porphyrin (see **Figure 1**). Importantly, the observation that the use of perfluoro-carboxylic acid to enable alkane activation by $P450_{BM3}$ proved insufficient for methane oxidation provides evidence against a mechanism whereby the lack of P450 activity is simply due to the absence of a isoenzyme that is able to accommodate methane in its active site (Kawakami et al., 2011, 2013). An alternative explanation for the inferior activity, toward the oxidation of methane, demonstrated by P450s over the diiron porphyrin catalysts is seen in the numerous studies into the effect of different axial ligands in the catalytic activity of iron-porphyrins (Gross and Nimri, 1994; Czarnecki et al., 1996; Song et al., 2005; Takahashi et al., 2012). Regardless of the relative importance of either of these affects, the origin of the massive improvement seen in the diiron porphyrin dimer above the mono-porphyrin bio-catalyst is of crucial important for the future design of the next generation of powerful oxidants for sustainable methanol production.

Origin of the Catalytic Activity of Diion(IV)oxo Porphyrinod

Over the years, a minimum model of Compound I (see **1**, **Figure 7**) has been extensively tested and proved to be sufficient for explaining the first coordination sphere P450s (Yoshizawa et al., 2001; de Visser et al., 2004; Shaik et al., 2005), which is the same model ([FeIV(O) (Por^+) −SH]) that was mentioned in our first example section and consisted of an iron-porphyrin coordinated by an oxo group *trans* to an SH, representing the axial cysteine. The μ-nitrido-bridged diiron-oxo porphyrin model (see **2**, **Figure 7**) replaces the SH group for a nitrogen, which became a linker for a second iron-porphyrin. The DFT calculations were performed without any geometric restrictions on any of the atoms in the model systems and full optimizations were undertaken for each minima using UB3LYP (Lee et al., 1988; Becke, 1993), in combination with the initial double-ζ basis set 6–31G (Ditchfield et al., 1971) on all atoms except for Fe where LACVP with a Neon core potential was implemented (BS1). Subsequently, single point gas-phase and solvent corrected calculation were run using the same functional in combination with the polarizable and defuse triple-ζ basis sets 6–311+G(d,p) and LACV3P+ (BS2). Free energy values were calculated at 298.15K and 1 atmosphere of pressure, with such a protocol being well benchmarked previously (de Visser, 2010).

Figure 7 shows the free energy landscapes for the methane to methanol reaction as catalyzed by both model catalysts. Since the energy barriers associated with the hydrogen atom transfer (HAT) on both the doublet and quartet spin state surfaces are the same to the first decimal place for catalyst **1**, the energy landscapes of both are considered. This spin state derived bifurcation in the pathways catalyzed by CpdI is in excellent agreement with multiple different studies (de Visser et al., 2003, 2014; Kumar et al., 2004a,b) and stands in sharp contrast to the diiron porphyrin dimer catalyst (**2**), which exhibits a doublet ground state with a rate-limiting step that is well separated (by >40 kcal mol $^{-1}$) from the hydrogen atom abstraction barrier on the quartet energy landscape. Such a dominant doublet ground state is also in excellent agreement with previous work on **2** (Silaghi-Dumitrescu et al., 2011; Ansari et al., 2015; Işci et al., 2015). Therefore, only the low spin state surface of **2** is included in **Figure 7**. The reaction mechanism for both catalysts proceeds via a rate-limiting hydrogen atom abstraction transition state ($\mathbf{TS}_{HA}$) leading to a radical hydroxyl intermediate ($\mathbf{I}_H$), which is capable of forming methanol ($\mathbf{P}_{OH}$) through radical recombination with the methyl radical following a hydroxyl rebound barrier ($\mathbf{TS}_{OH}$). The decrease in the free energy barrier for $\mathbf{TS}_{HA}$ of 13.6 kcal mol $^{-1}$ for **2** over **1** corresponds to a rate enhancement of $\sim 10^{10}$. Indeed, such a low barrier would imply that **2** was able to catalyze the oxidation of methane at room temperature, which has been observed experimentally (Sorokin et al., 2008). The bond length shown in **Figure 7** show that the high energy $\mathbf{TS}_{HA}$ seen in **1** is considerably more product like with a shorter O-H and a longer C-H distance than is the case for $\mathbf{2TS}_{HA}$. Notwithstanding these differences, both transition states are generally product like, which was expected and is a consistent trend in methane

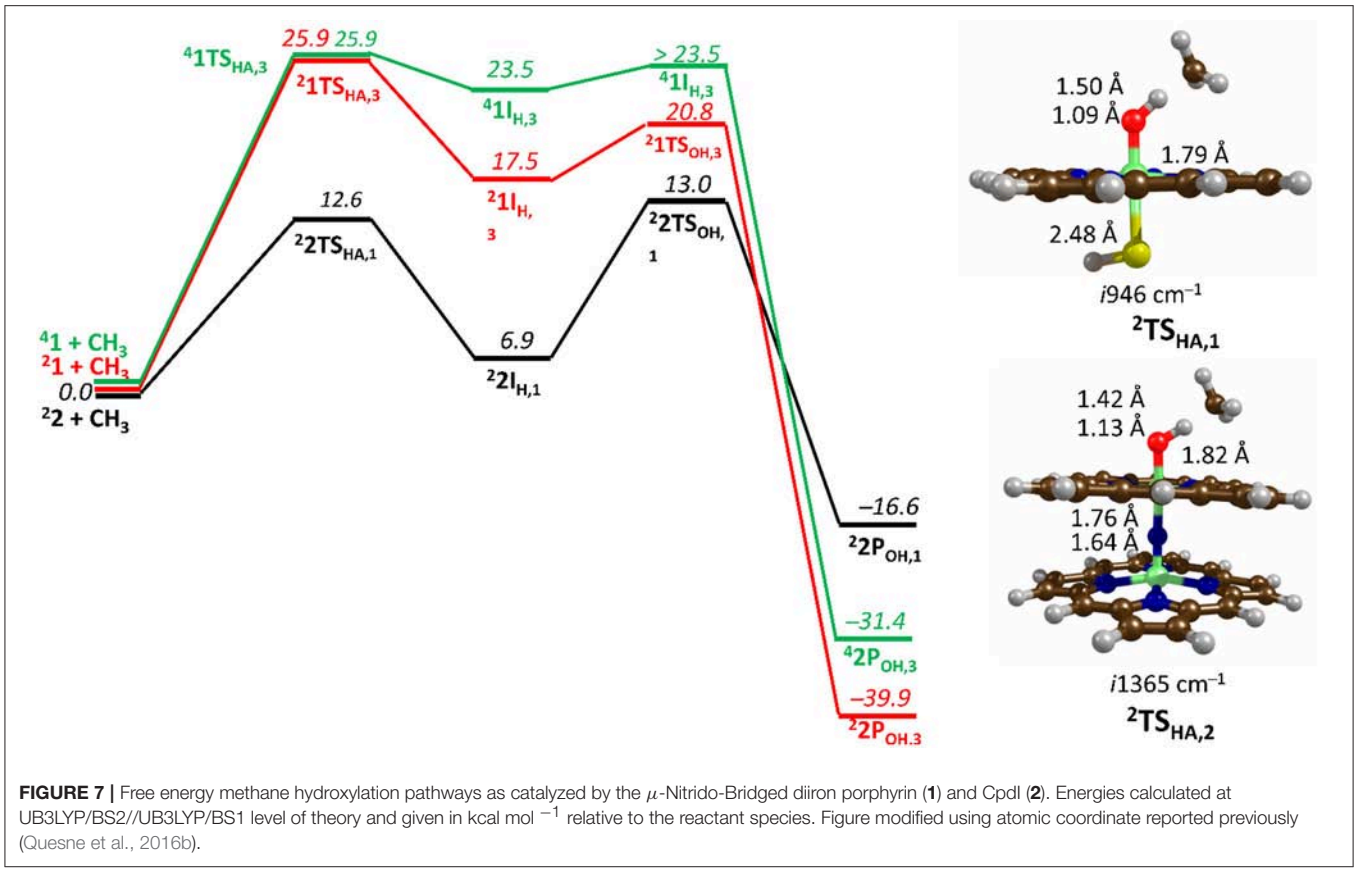

FIGURE 7 | Free energy methane hydroxylation pathways as catalyzed by the μ-Nitrido-Bridged diiron porphyrin (**1**) and CpdI (**2**). Energies calculated at UB3LYP/BS2//UB3LYP/BS1 level of theory and given in kcal mol $^{-1}$ relative to the reactant species. Figure modified using atomic coordinate reported previously (Quesne et al., 2016b).

hydroxylation barriers (Yoshizawa et al., 2001; de Visser et al., 2004; Shaik et al., 2008).

The divergence in the performance of these two catalysts can be explained by differences in the electronic structure with regard to the location of valence electrons, as shown in **Figure 8**. The valence electrons for CpdI (**1**) are shown on the left and have an occupancy of π^2_{xz}, π^2_{yz}, π^{*1}_{xz}, π^{*1}_{yz} dominated by the Fe(IV)oxo combined with a singly occupied a^1_{2u} on the heme cation radical. Therefore, CpdI has a ground state with a total of three unpaired electrons and the close lying doublet and quartet spin state only diverge electronically by either anti-ferromagnetically or ferromagnetically coupled heme and FeO orbitals (de Visser et al., 2003; Porro et al., 2009). In **2** the eight valence electrons of an axial Fe(IV)-nitrido mix with the seven of the Fe(IV)oxo and the energy of the a_{2u} orbitals of both porphyrins are lowered to give an occupancy of π^2_{x1}, π^2_{y1}, π^2_{x2}, π^2_{y2}, $a^2_{2u,1}$, $a^2_{2u,2}$, π^{*2}_{x3}, π^{*1}_{y3}. For simplicity only the two occupied anti-bonding π– orbitals as well as the highest lying a_{2u} orbital is included in **Figure 8**. In retrospect such a change is not unexpected since it has been determined that mixing between the $3P_Z$ orbital on the axial Sulfur atom, which is absent in **2**, and the a_{2u} porphyrin orbital raises the latter's energy above that of the π FeO orbitals and leads to the porphyrin radical in **1** (Ogliaro et al., 2001). However, the degree to which this change affects the electron and proton affinities of **2** is somewhat more surprising, since research has indicated that the kinetics of HAT reactions is usually correlated to the thermodynamics of hydrogen atom binding ($\mathbf{BDE_{OH}}$) (Friedrich, 1983; Bordwell and Cheng, 1991; Mayer, 1998). **Figure 9** breaks down the $\mathbf{BDE_{OH}}$ of both catalysts into electron (**EA**) and proton ($\mathbf{\Delta_{acid}}$) affinity components. Therefore, for each catalyst $\mathbf{BDE_{OH}} = \mathbf{\Delta_{acid}} - \mathbf{EA} - \mathbf{IE_H}$, whereby ($\mathbf{IE_H}$) describes the ionization energy of a hydrogen atom. It is clear from **Figure 9** that whilst the electron affinity of the FeO is greater by ∼ 29 kcal mol^{-1} in the CpdI mimic this is more than compensated by the >35 kcal mol^{-1} increase basicity of the anionic species of **2**, which is consistent with other studies that show the dominance of $\mathbf{\Delta_{acid}}$ in $\mathbf{BDE_{OH}}$ (Green et al., 2004; Parsell et al., 2009). Therefore, it is the increase basicity of the μ-nitrido-bridged diiron-oxo porphyrin that is the origin of its increased activity and any attempt to further design this powerful oxidant will have to consider carefully the consequences of attempting to improve the election affinity by addition of axial ligands, which could lead to a loss in the orbital reorganization that is critical to increasing $\mathbf{\Delta_{acid}}$.

HETEROGENOUS CATALYSIS MODELED WITH PERIODIC BOUNDARY CONDITIONS

Catalytic Activity of Transition Metal Carbides

Transition metal carbides (TMCs) are a class of material known for their catalytic activity since 1973 (Levy and Boudart, 1973).

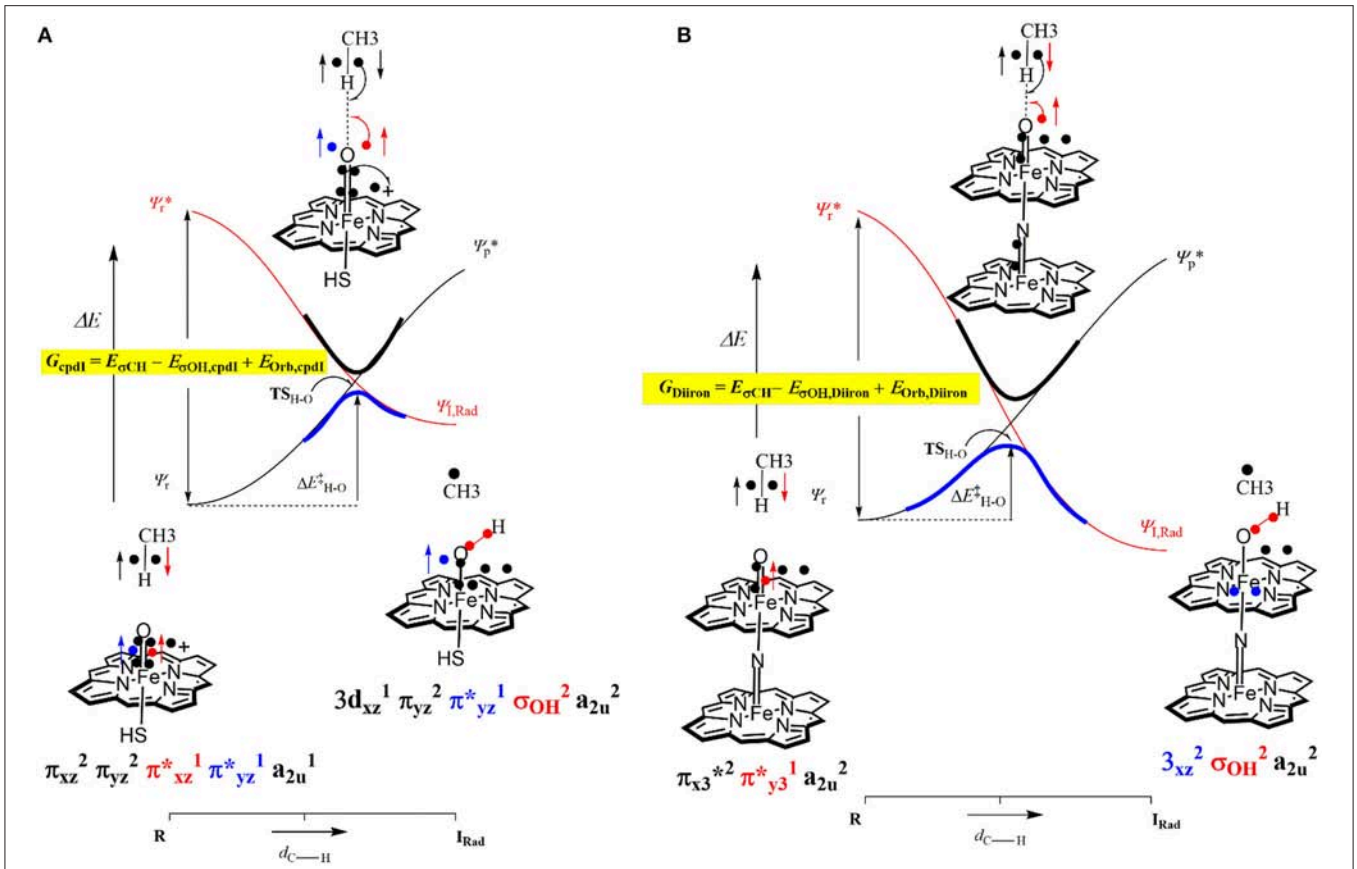

FIGURE 8 | Valence bond diagram of methane hydroxylation by models of P450 CpdI **(A)** and the Diiron porphyrin catalyst **(B)**.

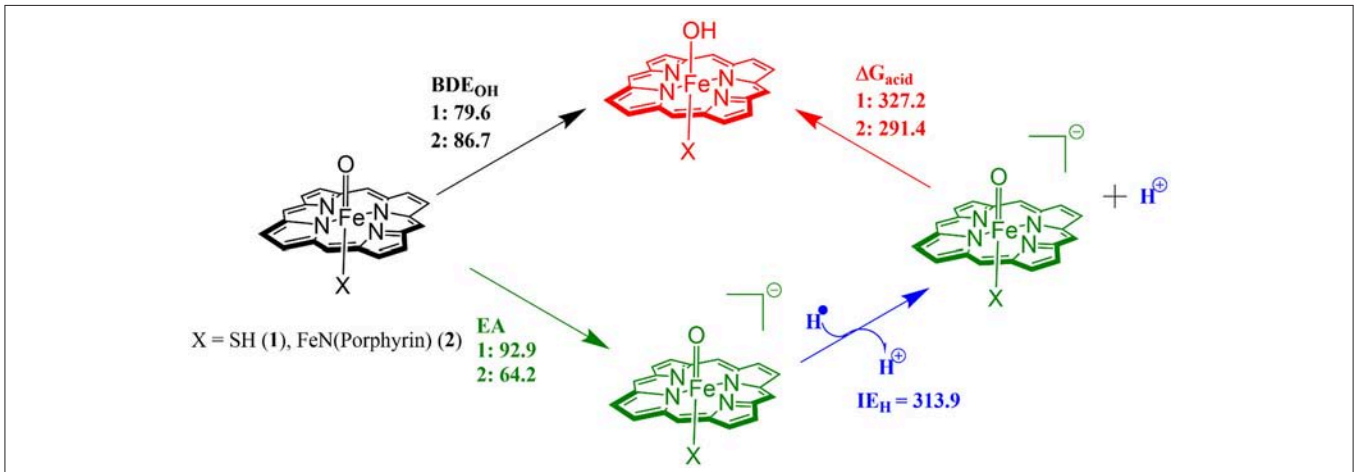

FIGURE 9 | Theoretically determined free energy values for the hydrogenation of catalysts **1** and **2**. All solvent corrected free energies were obtained at UB3LYP/BS2//UB3LYP/BS1 level of theory and are given in kcal mol^{-1}.

These materials present different stoichiometries and structures depending on the position of the metal in the periodic table: Ti and Zr, on the left-hand side of the d-series, form stable and non-defective monocarbides, while metals toward the center of the periodic table present a lower carbon content, as seen in the widely studied case of Fe_3C (Häglund et al., 1993; Oyama, 2008). All these materials, however, are considered valuable for industrial applications because of their relatively low cost, high durability and melting points as well as their catalytic activity (Hwu and Chen, 2005; Qi et al., 2013). TMCs have been tested for

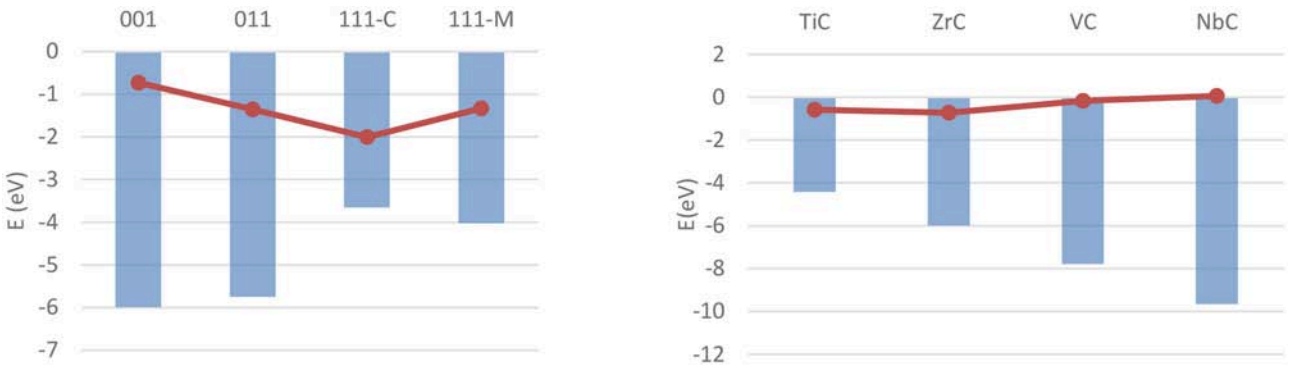

FIGURE 10 | Correlation between ΔE_{ads} of a single hydrogen molecule (red dots) and the d-band centers (blue columns) on different carbides and surfaces. **(Left)** Shows the values for ZrC over the four investigated surfaces, **(Right)** shows the values for (001) surfaces over the four carbides.

a wide variety of catalytic reactions, especially hydrogenation and dehydrogenation reactions for which their activity has proved to be qualitatively similar to that of Pt (Levy and Boudart, 1973; Delannoy et al., 2000). One such avenue of research, that exploits TMCs as catalysts for the hydrogen evolution reaction (HER), is particularly relevant to environmentally sustainable chemistry, as it is considered to be a key element in the transition from a fossil fuel-based to a hydrogen-based economy. The HER is the focus of a large amount of research interest worldwide for its role in alkaline water electrolysis, which produces highly pure H_2, and in hydrogen fuel cells; both these applications make use of Pt as a catalyst to lower the overpotential required to perform the reaction down to appropriately 0.2 eV, but the cost and scarcity of the element (Yang, 2009), as well as the questionable environmental sustainability of Pt mining (Maboeta et al., 2006; Saurat and Bringezu, 2008; Glaister and Mudd, 2010) have driven the research toward catalysts composed of more earth-abundant elements such as TMCs. A related application, is the catalytic reduction of CO_2 with H_2, which usually aims at the production of CO or CH_3OH, often requiring a surface-mediated proton transfer to transform CO_2 into COOH (Posada-Pérez et al., 2017a).

The bulk and surface properties of TMCs have been well characterized in the past few years (Vines et al., 2005; Quesne et al., 2018), but fewer computational studies have been performed on their catalytic activity. Adsorption and activation studies have been performed for both H_2 and CO_2 for a wide range of early- and mid-series TMCs, with all of these studies modeling low-index surfaces of the catalysts using periodic boundary conditions. The (001) surfaces of MoC and Mo_2C, the latter being either Mo- or C-terminated, have been the focus of a work from Posada-Pérez et al. on hydrogen adsorption (Posada-Pérez et al., 2017b), which found stable, dissociative adsorption of H_2 on all three materials with no activation barrier when dispersion interaction correction is taken into account. The adsorption is found to occur primarily on top of surface carbon atoms on both materials, with adsorption energies calculated with the Perdew–Burke–Ernzerhof (PBE) (Perdew et al., 1996) functional in the −1 to −2.5 eV range, whilst consistently higher on the metal-rich carbide. Similarly, a study from Silveri et al. (2019) investigated the adsorption of H_2 on TiC, VC, ZrC, and NbC, using a combination of periodic boundary conditions and the PBE functional, found adsorption to be exothermic on these systems' (001) surfaces as well. Unlike the former, however, this study was extended to the (011) and (111) surfaces as well, in order to obtain a more complete picture of the reactivity of the material. These data highlighted how the stability of the (001) surface is correlated with a lower reactivity on all carbides. More generally, all monocarbides show similar geometric and electronic properties of the adsorption, with the only major difference between the carbides being the strength of the adsorption in most cases. The exceptions are the carbon termination of the (111) surfaces of TiC and VC, which are found to be unstable in presence of hydrogen. However, the availability of adsorption energy data for all low-index surfaces across four carbides allowed these to be correlated with surface properties such as work function and *d*-band center position, as shown for the latter in **Figure 10**.

Higher coverage states have also been investigated, observing a decrease in the adsorption energy per atom as well as a similar, although not linear, decrease in work function, attributable to the electron transfer from the adsorbed hydrogens to the metallic slab. The coverage states of each surface of the four carbides were also predicted at a wide range of temperatures and pressures, and correlated with the tendency of the hydrogen either to adsorb on or desorb from the surface. As a result, it was shown how the strength of the C–H and M–H bonds on the (011) and (111) surfaces is predicted to hinder the feasibility of catalytic reactions such as HER on all higher-index surfaces. Conversely, the (001) surface - previously shown to be the lowest energy termination, shows a rapidly changing coverage state, suggesting its potential as an active termination for catalytic reactions involving a surface mediated hydrogenation and further elucidating the mechanistic details of the catalytic activity of the carbides. **Figure 11** shows the hydrogen coverage states as a function of the H_2 chemical potential for the TiC (001) surface.

MoC and Mo_2C have also been studied computationally for their capability to adsorb CO_2 and dissociate it to CO (Posada-Pérez et al., 2014). These studies show how both materials effectively activate carbon dioxide and in the case of the far more

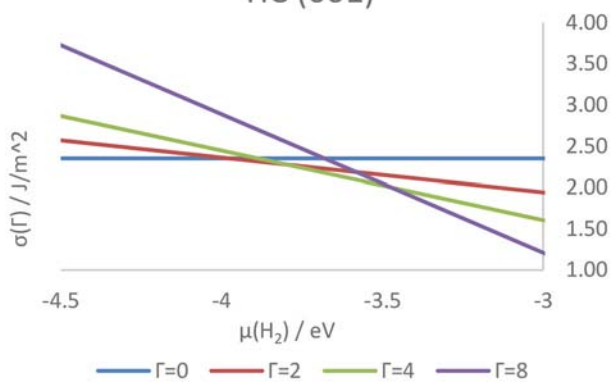

FIGURE 11 | Surface free energies of surfaces in different hydrogenation states as a function of the chemical potential of gaseous hydrogen above the TiC (001) surface. The letter Γ indicates the number of atoms on the surface of the catalyst, with $\Gamma = 0$ and $\Gamma = 8$ corresponding, respectively to a coverage of 0 ML and 1 ML.

active Mo_2C material, it is also possible to observe spontaneous dissociation. These studies, albeit not elucidating the catalytic behavior of early- and mid-series transition metal carbides completely, provide a powerful basis for further theoretical and experimental work on the catalytic activity of these materials for reactions such as HER, CO_2 reduction and inverse water-gas shift and demonstrate the power of the periodic DFT approach to highlight fundamental properties of heterogenous catalyst. The elucidations of the mechanistic aspects of such reactions will help greatly in the development of the sustainable generation of fuels and chemicals as well as guiding the future design of the catalytic component of the hydrogen fuel cell—a challenge for which innovative catalysis is of paramount importance.

SUMMARY AND CONCLUSIONS

The urgent need for society to move toward a greener and more sustainable future presents a very exciting opportunity for catalytic chemists. Many of the necessary changes in resource management and increased energy efficiency will be propelled by the directed design of new catalysts, for which a detailed theoretical understanding of the activity of current catalysts is a crucial part. Many very different computational techniques are being applied to the characterization of novel catalysts as a preliminary step to the engineering of new and much greener chemical route to important products. The implementation of a QM/MM protocol to the challenge of bioengineering the enzyme $OleT_{JE}$, in order to increase its selectivity toward olefin production is explored in the first case study. This study indicates that the enzyme was able to effectively elevate a hydroxyl radical recombination barrier which leads to the alternative olefin pathway becoming competitive. This process is modulated by changes in the local solvation environment so there could be the potential to bioengineer an OleT isoenzyme to selectivity produce olefin for a sustainable route to bio-fuel production. The next case study used restricted cluster model calculations to investigate the ability of HOD to catalyze spin-forbidden oxygen activation. Interestingly, this study did not confirm the experimentally proposed reaction mechanism, but instead offered the potential for a novel green catalytic route for the activation of molecular oxygen via the stabilization of a triplet intermediate dioxygen species. The third case study explored the reactivity of a novel μ-nitrido-bridged diiron-oxo porphyrin that was able to catalyze the methane to methanol reaction under very mild conditions. This study used unrestricted DFT methods to determine that the acidity of the FeO anion was mostly responsible for its increased activity over the related mono-oxygen porphyrin catalysts. These results indicated that any improvement of the catalyst could not be made by sacrificing the novel orbital mixing along the Z-axis. Therefore, simply increasing the electron affinity of the FeO by binding a strong electron withdrawing group in the axial position is likely to be counterproductive. Finally, we consider several periodic DFT studies into the electronic properties and catalytic abilities of the low-index facets of early transition metal carbides. These studies point to the possibility of green catalytic routes toward the production of fuels and useful chemicals from the utilization of the green-house gas carbon dioxide; as well as the potential for these materials to be used as catalysts in hydrogen fuel cells.

AUTHOR CONTRIBUTIONS

All authors listed have made a substantial, direct and intellectual contribution to the work, and approved it for publication.

FUNDING

This work was funded by both Cardiff University and an EPSRC under the Low Carbon Fuels initiative.

ACKNOWLEDGMENTS

The authors thank Stefan Nastase for his help and expertise in the area of Zeolite computational chemistry.

REFERENCES

Abuelela, A. M., Mohamed, T. A., and Prezhdo, V. O. (2012). DFT simulation and vibrational analysis of the IR and Raman spectra of a CdSe quantum dot capped by methylamine and trimethylphosphine oxide ligands. *J. Phys. Chem. C.* 116, 14674–14681. doi: 10.1021/jp30x‘3275v

Ahlrichs, R., Bar, M., Haser, M., Horn, H., and Kölmel, C. (1989). Electronic structure calculations on workstation computers: the program system Turbomole. *Chem. Phys. Lett.* 162, 165–169.

Alfredsson, M., and Catlow, C. R. A. (2002). A comparison between metal supported C-ZrO2 and CeO2. *Phys. Chem. Chem. Phys.* 4, 6100–6108. doi: 10.1039/b204680f

Althorpe, S. C., Ananth, N., Angulo, G., Astumian, R. D., Beniwal, V., Blumberger, J. et al. (2016). Non-adiabatic reactions: general discussion. *Faraday Discuss.* 195, 311–344. doi: 10.1039/C6FD90078J

Ansari, M., Vyas, N., Ansari, A., and Rajaraman, G. (2015). Oxidation of methane by an N-bridged high-valent diiron–oxo species: electronic structure implications on the reactivity. *Dalt. Trans.* 44, 15232–15243. doi: 10.1039/C5DT01060H

Astruc, D. (2007). Palladium nanoparticles as efficient green homogeneous and heterogeneous carbon-carbon coupling precatalysts: a unifying view. *Inorg. Chem.* 46, 1884–1894. doi: 10.1021/ic062183h

Atkins, W. M., and Sligar, S. G. (1987). Metabolic switching in cyctochrome P-450cam: deuterium isotope effects on regiospecificity and the monooxygenase/oxidase ratio. *J. Am. Chem. Soc.* 109, 3754–3760. doi: 10.1021/ja00246a038

Auclair, K., Moënne-Loccoz, P., and de Montellano, P. R. (2001). Roles of the proximal heme thiolate ligand in cytochrome P450cam. *J. Am. Chem. Soc.* 123, 4877–4885. doi: 10.1021/ja0040262

Baerlocher, C., and McCusker, L. B. (2010). *Database of Zeolite Structures.* Available online at: http://www.iza-structure.org/databases/ (accessed March 24, 2019).

Bakshi, B. R., Gutowski, T. G., and Sekulic, D. P. (2018). Claiming sustainability: requirements and challenges. *ACS Sustain. Chem. Eng.* 6, 3632–3639. doi: 10.1021/acssuschemeng.7b03953

Bakshi, B. R., Ziv, G., and Lepech, M. D. (2015). Techno-ecological synergy: a framework for sustainable engineering. *Environ. Sci. Technol.* 49, 1752–1760. doi: 10.1021/es5041442

Barducci, A., Bonomi, M., and Parrinello, M. (2011). Metadynamics. *Wiley Interdiscip. Rev. Comput. Mol. Sci.* 1, 826–843. doi: 10.1002/wcms.31

Baroi, C., and Dalai, A. K. (2015). Process sustainability of biodiesel production process from green seed canola oil using homogeneous and heterogeneous acid catalysts. *Fuel Process. Technol.* 133, 105–119. doi: 10.1016/j.fuproc.2015.01.004

Bauer, I., Max, N., Fetzner, S., and Lingens, F. (1996). 2,4-Dioxygenases catalyzing N-heterocyclic-ring cleavage and formation of carbon monoxide. purification and some properties of 1H-3-hydroxy-4-Oxoquinaldine 2,4-dioxygenase from *Arthrobacter* sp. Ru61a and comparison with 1H-3-Hydroxy-4-Oxoquinoline 2,4-Dio. *Eur. J. Biochem.* 240, 576–583. doi: 10.1111/j.1432-1033.1996.0576h.x

Becke, A. D. (1993). Density-functional thermochemistry. III. The role of exact exchange. *Chem. Phys.* 98, 5648–5652.

Belcher, J., McLean, K. J., Matthews, S., Woodward, L. S., Fisher, K., Rigby, S. E. J., et al. (2014). Structure and biochemical properties of the alkene producing cytochrome P450 OleTJE (CYP152L1) from the Jeotgalicoccus sp. 8456 bacterium. *J. Biol. Chem.* 289, 6535–6550. doi: 10.1074/jbc.M113.527325

Beletskaya, I. P., and Kustov, L. M. (2010). Catalysis as an important tool of green chemistry. *Russ. Chem. Rev.* 79, 441–461. doi: 10.1070/RC2010v079n06ABEH004137

Berman, H. M., Westbrook, J., Feng, Z., Gilliland, G., Bhat, T. N., Weissig, H., et al. (2000). The protein data bank nucleic acids research. *Nucleic Acids Res.* 28, 235–242. doi: 10.1093/nar/28.1.235

Blöchl, P. E., Jepsen, O., and Andersen, O. K. (1994). Improved tetrahedron method for Brillouin-zone integrations. *Phys. Rev. B.* 49, 16223–16233. doi: 10.1103/PhysRevB.49.16223

Blomberg, M. R., Borowski, T., Himo, F., Liao, R.-Z., and Siegbahn, P. E. (2014). Quantum chemical studies of mechanisms for metalloenzymes. *Chem. Rev.* 114, 3601–3658. doi: 10.1021/cr400388t

Bolhuis, P. G., Chandler, D., Dellago, C., and Geissler, P. L. (2002). Transition path sampling : throwing ropes over rough mountain passes, in the dark. *Annu. Rev. Phys. Chem.* 53, 291–318. doi: 10.1146/annurev.physchem.53.082301.113146

Bordwell, F. G., and Cheng, J. (1991). Substituent effects on the stabilities of phenoxyl radicals and the acidities of phenoxyl radical cations. *J. Am. Chem. Soc.* 113, 1736–1743. doi: 10.1021/ja00005a042

Borowski, T., Bassan, A., and Siegbahn, P. E. M. (2004). 4-Hydroxyphenylpyruvate dioxygenase: a hybrid density functional study of the catalytic reaction mechanism. *Biochemistry.* 43, 12331–12342. doi: 10.1021/bi049503y

Borowski, T., Quesne, M., and Szaleniec, M. (2015). "QM and QM/MM methods compared: Case studies on reaction mechanisms of metalloenzymes". *Advances in Protein Chemistry and Structural Biology,* Vol. 100 ed T. Karabencheva-Christova (Oxford: Elsevier), 187–224.

Bredow, T., Geudtner, G., and Jug, K. (1996). Embedding procedure for cluster calculations of ionic crystals. *J. Chem. Phys.* 105, 6395–6400. doi: 10.1063/1.472492

Brooks, B. R. III., Brooks, C. L. III, Mackerell, A. D., Nilson, L., Petrella, R. J., Roux, B., et al. (2009). CHARMM: the biomolecular simulation program. *J. Comput. Chem.* 30, 1545–1614. doi: 10.1002/jcc.21287

Bucko, T., Benco, L., Dubay, O., Dellago, C., and Hafner, J. (2009). Mechanism of alkane dehydrogenation catalyzed by acidic zeolites: Ab initio transition path sampling. *J. Chem. Phys.* 131:214508. doi: 10.1063/1.3265715

Bugg, T. D., and Ramaswamy, S. (2008). Non-heme iron-dependent dioxygenases: unravelling catalytic mechanisms for complex enzymatic oxidations. *Curr. Opin. Chem. Biol.* 12, 134–140. doi: 10.1016/j.cbpa.2007.12.007

Caddell Haatveit, K., Garcia-Borràs, M., and Houk, K. N. (2019). Computational protocol to understand P450 mechanisms and design of efficient and selective biocatalysts. *Front. Chem.* 6:663. doi: 10.3389/fchem.2018.00663

Cadi-Essadek, A., Roldan, A., and de Leeuw, N. H. (2015). Ni deposition on yttria-stabilized ZrO_2 (111) surfaces: a density functional theory study. *J. Phys. Chem. C.* 119, 6581–6591. doi: 10.1021/jp512594j

Cadi-Essadek, A., Roldan, A., and de Leeuw, N. H. (2016). Density functional theory study of the interaction of H_2O, CO_2 and CO with the ZrO_2 (111), Ni/ZrO_2 (111), YSZ (111) and Ni/YSZ (111) surfaces. *Surface Sci.* 653, 153–162. doi: 10.1016/j.susc.2016.06.008

Campbell, C., van Santen, R., Stamatakis, M., Collis, N., Freund, J. H., Plaisance, C., et al. (2016). Catalyst design from theory to practice: general discussion. *Faraday Discuss.* 188, 279–307. doi: 10.1039/C6FD90016J

Cantú Reinhard, F. G., Faponle, A. S., and De Visser, S. P. (2016). Substrate sulfoxidation by an Iron(IV)-Oxo complex: benchmarking computationally calculated barrier heights to experiment. *J. Phys. Chem. A.* 120, 9805–9814. doi: 10.1021/acs.jpca.6b09765

Cao, L., and Ryde, U. (2018). On the difference between additive and subtractive QM/MM calculations. *Front. Chem.* 6:89. doi: 10.3389/fchem.2018.00089

Catlow, C. R. A., Buckeridge, J., Farrow, M. R., Logsdail, A. J., and Sokol, A. A. (2017a). "Quantum Mechanical/Molecular Mechanical (QM/MM) Approaches," in *Handbook of Solid State Chemistry*, eds R. Dronskowski, S. Kikkawa, and A. Stein (Weinheim: Wiley-VCH Verlag GmbH & Co. KGaA), 647–680.

Catlow, C. R. A., Van Speybroeck, V., and van Santen, R. (2017b). *Modelling and Simulation in the Science of Micro- and Mesoporous Materials.* (Oxford: Elsevier).

Chen, M. M., Coelho, P. S., and Arnold, F. H. (2012). Utilizing terminal oxidants to achieve P450-catalyzed oxidation of methane. *Adv. Synth. Catal.* 354, 964–968. doi: 10.1002/adsc.201100833

Chen, W. J., Xu, R.-N., Lin, W., Sun, X., Wang, B., Wu, Q.-H., et al. (2018). DFT studies on Ni-mediated C-F cleavage for the synthesis of cyclopentadiene derivatives. *Front. Chem.* 6:319. doi: 10.3389/fchem.2018.00319

Chieregato, A., Fornasari, G., Cavani, F., Mella, M., Bandinelli, C., and Velasquez Ochoa, J. (2014). On the chemistry of ethanol on basic oxides: revising mechanisms and intermediates in the lebedev and guerbet reactions. *ChemSusChem.* 8, 377–388. doi: 10.1002/cssc.201402632

Chua, C. K., and Pumera, M. (2015). Carbocatalysis: the state of metal-free catalysis. *Chem. A Eur. J.* 21, 12550–12562. doi: 10.1002/chem.201501383

Chung, L. W., Sameera, W. M. C., Ramozzi, R., Page, A. J., Hatanaka, M., Petrova, G. P., et al. (2015). The ONIOM method and its applications. *Chem. Rev.* 115, 5678–5796. doi: 10.1021/cr5004419

Clark, J. H., Farmer, T. J., Hunt, A. J., and Sherwood, J. (2015). Opportunities for bio-based solvents created as petrochemical and fuel products transition towards renewable resources. *Int. J. Mol. Sci.* 16, 17101–17159. doi: 10.3390/ijms160817101

Clark, S. J., Segall, M. D., Pickard, C. J., Hasnip, P. J., Probert, M. I. J., Refson, K., et al. (2005). First principles methods using CASTEP. *Zeitschrift fur Krist.* 220, 567–570. doi: 10.1524/zkri.220.5.567.65075

Clarke, C. J., Tu, W.-C., Levers, O., Bröhl, A., and Hallett, J. P. (2018). Green and sustainable solvents in chemical processes. *Chem. Rev.* 118, 747–800. doi: 10.1021/acs.chemrev.7b00571

Cnudde, P., De Wispelaere, K., Van der Mynsbrugge, J., Waroquier, M., and Van Speybroeck, V. (2017). Effect of temperature and branching on the nature and

stability of alkene cracking intermediates in H-ZSM-5. *J. Catal.* 345, 53–69. doi: 10.1016/j.jcat.2016.11.010

Corma, A., and García, H. (2003). Lewis acids: from conventional homogeneous to green homogeneous and heterogeneous catalysis. *Chem. Rev.* 103, 4307–4366. doi: 10.1021/cr030680z

Czarnecki, K., Nimri, S., Gross, Z., Proniewicz, L. M., and Kincaid, J. R. (1996). Direct resonance Raman evidence for a trans influence on the ferryl fragment in models of compound I intermediates of heme enzymes. *J. Am. Chem. Soc.* 118, 2929–2935. doi: 10.1021/ja952177c

Dabral, S., Engel, J., Mottweiler, J., Spoehrle, S. S. M., Lahive, C. W., and Bolm, C. (2018). Mechanistic studies of base-catalysed lignin depolymerisation in dimethyl carbonate. *Green Chem.* 20, 170–182. doi: 10.1039/C7GC03110F

Dangi, G. P., Pillai, R. S., Somani, R. S., Bajaj, H. C., and Jasra, R. V. (2010). A density functional theory study on the interaction of hydrogen molecule with MOF-177. *Mol. Simul.* 36, 373–381. doi: 10.1080/08927020903487404

Davydov, D. R., Hui Bon Hoa, G., and Peterson, J. A. (1999). Dynamics of protein-bound water in the heme domain of P450BM3 studied by high-pressure spectroscopy: comparison with P450cam and P450 2B4. *Biochemistry.* 38, 751–761. doi: 10.1021/bi981397a

de Montellano, P. R. O. (2010). Hydrocarbon hydroxylation by cytochrome P450 enzymes. *Chem. Rev.* 110, 932–948. doi: 10.1021/cr9002193

de Visser, S., Ogliaro, P. F., and Shaik, S. (2001). How does ethene inactivate cytochrome P450 en route to its epoxidation? a density functional study. *Angew. Chem. Int. Ed.* 40, 2871–2874. doi: 10.1002/1521-3773(20010803)40:15<2871::AID-ANIE2871>3.0.CO;2-R

de Visser, S., Shaik, P. S., Sharma, P. K., Kumar, D., and Thiel, W. (2003). Active species of horseradish peroxidase (HRP) and cytochrome P450: two electronic chameleons. *J. Am. Chem. Soc.* 125, 15779–15788. doi: 10.1021/ja0380906

de Visser, S. P. (2010). Trends in substrate hydroxylation reactions by heme and nonheme iron(IV)-oxo oxidants give correlations between intrinsic properties of the oxidant with barrier height. *J. Am. Chem. Soc.* 132, 1087–1097. doi: 10.1021/ja908340j

de Visser, S. P. (2018). Mechanistic insight on the activity and substrate selectivity of nonheme iron dioxygenases. *Chem. Rec.* 18, 1501–1516. doi: 10.1002/tcr.201800033

de Visser, S. P., Kumar, D., Cohen, S., Shacham, R., and Shaik, S. (2004). A predictive pattern of computed barriers for C-H hydroxylation by compound I of cytochrome p450. *J. Am. Chem. Soc.* 126, 8362–8363. doi: 10.1021/ja048528h

de Visser, S. P., Porro, C. S., Quesne, M. G., Sainna, M. A., and Munro, A. W. (2013). Overview on theoretical studies discriminating the two-oxidant versus two-state-reactivity models for substrate monoxygenation by cytochrome p450 enzymes. *Curr. Top. Med. Chem.* 13, 2218–2232. doi: 10.2174/15680266113136660155

de Visser, S. P., Quesne, M. G., Martin, B., Comba, P., and Ryde, U. (2014). Computational modelling of oxygenation processes in enzymes and biomimetic model complexes. *Chem. Commun.* 50, 262–282. doi: 10.1039/C3CC47148A

Delannoy, L., Giraudon, J. M., Granger, P., Leclercq, L., and Leclercq, G. (2000). Group VI transition metal carbides as alternatives in the hydrodechlorination of chlorofluorocarbons. *Catal. Today.* 59, 231–240. doi: 10.1016/S0920-5861(00)00289-3

Delarmelina, M., Marelli, E., de M Carneiro, J. W., Nolan, S. P., Bühl, M. (2017). Mechanism of the catalytic carboxylation of alkylboronates with CO_2 Using Ni–NHC complexes: a DFT Study. *Chem. A Eur. J.* 23, 14954–14961. doi: 10.1002/chem.201703567

Den, W., Sharma, V. K., Lee, M., Nadadur, G., and Varma, R. S. (2018). Lignocellulosic biomass transformations via greener oxidative pretreatment processes: access to energy and value-added chemicals. *Front. Chem.* 6:141. doi: 10.3389/fchem.2018.00141

Denisov, I. G., Makris, T. M., Sligar, S. G., and Schlichting, I. (2005). Structure and chemistry of cytochrome P450. *Chem. Rev.* 105, 2253–2277. doi: 10.1021/cr0307143

Dennig, A., Kuhn, M., Tassoti, S., Thiessenhusen, A., Gilch, S., Bülter, T., et al. (2015). Oxidative decarboxylation of short-chain fatty acids to 1-alkenes. *Angew. Chemie Int. Ed.* 54, 8819–8822. doi: 10.1002/anie.201502925

Dewispelaere, K., Ensing, B., Ghysels, A., Meijer, E. J., and Vanspeybroeck, V. (2015). Complex reaction environments and competing reaction mechanisms in zeolite catalysis: insights from advanced molecular dynamics. *Chem. A Eur. J.* 21, 9385–9396. doi: 10.1002/chem.201500473

Ditchfield, R., Hehre, W. J., and Pople, J. A. (1971). Self-consistent molecular-orbital methods. IX. An extended gaussian-type basis for molecular-orbital studies of organic molecules. *J. Chem. Phys.* 54, 724–728. doi: 10.1063/1.1674902

Dolinsky, T. J., Czodrowski, P., Li, H., Nielsen, J. E., Jensen, J. H., Klebe, G., et al. (2007). PDB2PQR: expanding and upgrading automated preparation of biomolecular structures for molecular simulations. *Nucleic Acids Res.* 35, W522–W525. doi: 10.1093/nar/gkm276

Dovesi, R., Orlando, R., Erba, A., Zicovich-Wilson, C. M., Civalleri, B., Casassa, S., et al. (2014). CRYSTAL14: a program for the ab initio investigation of crystalline solids. *Int. J. Quantum Chem.* 114, 1287–1317. doi: 10.1002/qua.24658

Draksharapu, A., Angelone, D., Quesne, M. G., Padamati, S. K., Gómez, L., Hage, R., et al. (2015). Identification and spectroscopic characterization of nonheme iron (III) hypochlorite intermediates. *Angew. Chem. Int. Ed.* 54, 4357–4361. doi: 10.1002/anie.201411995

Egorova, K. S., and Ananikov, V. P. (2016). Which metals are green for catalysis? *comparison of the toxicities of Ni, Cu, Fe, Pd, Pt, Rh, and Au Salts. Angew. Chem. Int. Ed.* 55, 12150–12162. doi: 10.1002/anie.201603777

Ensing, B., Laio, A., Parrinello, M., and Klein, M. L. (2005). A recipe for the computation of the free energy barrier and the lowest free energy path of concerted reactions. *J. Phys. Chem. B.* 109, 6676–6687. doi: 10.1021/jp045571i

Fang, H., Roldan, A., Tian, C., Zheng, Y., Duan, X., Chen, K., et al. (2019). Structural tuning and catalysis of tungsten carbides for the regioselective cleavage of C–O bonds. *J. Catal.* 369, 283–295. doi: 10.1016/j.jcat.2018.11.020

Faponle, A. S., Quesne, M. G., and de Visser, S. P. (2016). Origin of the regioselective fatty-acid hydroxylation versus decarboxylation by a cytochrome P450 Peroxygenase: what drives the reaction to biofuel production? *Chemistry.* 22, 5478–5483. doi: 10.1002/chem.201600739

Feng, J. X., Wu, J. Q., Tong, Y. X., and Li, G. R. (2018). Efficient hydrogen evolution on cu nanodots-decorated Ni3S2 nanotubes by optimizing atomic hydrogen adsorption and desorption. *J. Am. Chem. Soc.* 140, 610–617. doi: 10.1021/jacs.7b08521

Fetzner, S., and Steiner, R. A. (2010). Cofactor-independent oxidases and oxygenases. *Appl. Microbiol. Biotechnol.* 86, 791–804. doi: 10.1007/s00253-010-2455-0

Field, M. J., Bash, P. A., and Karplus, M. (1990). A combined quantum mechanical and molecular mechanical potential for molecular dynamics simulations. *J. Comput. Chem.* 11, 700–733. doi: 10.1002/jcc.540110605

Forkert, P.-G., and Lee, R. P. (1997). Metabolism of ethyl carbamate by pulmonary cytochrome P450 and carboxylesterase isozymes: involvement of CYP2E1 and hydrolase A. *Toxicol. Appl. Pharmacol.* 146, 245–254. doi: 10.1006/taap.1997.8233

Friedrich, L. E. (1983). The two hydrogen-oxygen bond-dissociation energies of hydroquinone. *J. Org. Chem.* 48, 3851–3852. doi: 10.1021/jo00169a062

Friend, C. M., and Xu, B. (2017). Heterogeneous catalysis: a central science for a sustainable future. *Acc. Chem. Res.* 50, 517–521. doi: 10.1021/acs.accounts.6b00510

Frisch, M. J., Trucks, G. W., Schlegel, H. B., Scuseria, G. E., Robb, M. A., Cheeseman, J. R., et al. (2009). *Gaussian 09, Revis. B.01.* Gaussian, Inc. Wallingford, CT.

Gallezot, P. (2012). Conversion of biomass to selected chemical products. *Chem. Soc. Rev.* 41, 1538–1558. doi: 10.1039/C1CS15147A

Gao, J., and Truhlar, D. G. (2002). Quantum mechanical methods for enzyme kinetics. *Annu. Rev. Phys. Chem.* 53, 467–505. doi: 10.1146/annurev.physchem.53.091301.150114

Gelb, M. H., Heimbrook, D. C., Malkonen, P., and Sligar, S. G. (1982). Stereochemistry and deuterium isotope effects in camphor hydroxylation by the cytochrome P450cam monooxygenase system. *Biochemistry.* 21, 370–377. doi: 10.1021/bi00531a026

Geng, C., Weiske, T., Li, J., Shaik, S., and Schwarz, H. (2018). On the intrinsic reactivity of diatomic 3d transition-metal carbides in the thermal activation of methane: striking electronic structure effects. *J. Am. Chem. Soc.* 141, 599–610. doi: 10.1021/jacs.8b11739

Ghorbanpour, A., Rimer, J. D., and Grabow, L. C. (2014). Periodic, vdW-corrected density functional theory investigation of the effect of Al siting in H-ZSM-5 on

chemisorption properties and site-specific acidity. *Catal. Commun.* 52, 98–102. doi: 10.1016/j.catcom.2014.04.005

Glaister, B. J., and Mudd, G. M. (2010). The environmental costs of platinum–PGM mining and sustainability: Is the glass half-full or half-empty? *Miner. Eng.* 23, 438–450. doi: 10.1016/j.mineng.2009.12.007

Gooßen, L. J., and Rodríguez, N. (2004). A mild and efficient protocol for the conversion of carboxylic acids to olefins by a catalytic decarbonylative elimination reaction. *Chem. Commun.* 35, 724–725. doi: 10.1039/B316613A

Grajciar, L., Heard, C. J., Bondarenko, A. A., Polynski, M. V., Meeprasert, J., Pidko, E. A., et al. (2018). Towards operando computational modeling in heterogeneous catalysis. *Chem. Soc. Rev.* 47, 8307–8348. doi: 10.1039/C8CS00398J

Grant, J. L., Hsieh, C. H., and Makris, T. M. (2015). Decarboxylation of fatty acids to terminal alkenes by cytochrome P450 compound I. *J. Am. Chem. Soc.* 137, 4940–4943. doi: 10.1021/jacs.5b01965

Grau-Crespo, R., De Leeuw, N. H., and Catlow, C. R. A. (2003). Cation distribution and magnetic ordering in FeSbO4. *J. Mater. Chem.* 13, 2848–2850. doi: 10.1039/b309796j

Grau-Crespo, R., Moreira, I. D. P. R., Illas, F., De Leeuw, N. H., and Catlow, C. R. A. (2006). The effect of cation coordination on the properties of oxygen vacancies in FeSbO4. *J. Mater. Chem.* 16, 1943–1949. doi: 10.1039/b518219k

Greeley, J. (2016). Theoretical heterogeneous catalysis: scaling relationships and computational catalyst design. *Annu. Rev. Chem. Biomol. Eng.* 7, 605–635. doi: 10.1146/annurev-chembioeng-080615-034413

Green, A. G., Liu, P., Merlic, C. A., and Houk, K. N. (2014). Distortion/interaction analysis reveals the origins of selectivities in iridium-catalyzed C-H borylation of substituted arenes and 5-membered heterocycles. *J. Am. Chem. Soc.* 136, 4575–4583. doi: 10.1021/ja411699u

Green, M. T., Dawson, J. H., and Gray, H. B. (2004). Oxoiron(IV) in chloroperoxidase compound II is basic: implications for P450 chemistry. *Science.* 304, 1653–1656. doi: 10.1126/science.1096897

Greer, A., Taylor, S. F. R., Daly, H., Quesne, M. G., Catlow, R., Jacquemin, J., et al. (2019). Investigating the effect of NO on the capture of CO2 using superbase ionic liquids for flue gas applications. *ACS Sustain. Chem. Eng.* 7, 567–3574. doi: 10.1021/acssuschemeng.8b05870

Grogan, G. (2011). Cytochromes P450: exploiting diversity and enabling application as biocatalysts. *Curr. Opin. Chem. Biol.* 15, 241–248. doi: 10.1016/j.cbpa.2010.11.014

Gross, Z., and Nimri, S. (1994). A pronounced axial ligand effect on the reactivity of oxoiron(Iv) porphyrin cation radicals. *Inorg. Chem.* 33, 1731–1732. doi: 10.1021/ic00087a001

Groves, J. T. (2003). The bioinorganic chemistry of iron in oxygenases and supramolecular assemblies. *Proc. Natl. Acad. Sci. U.S.A.* 100, 3569–3574. doi: 10.1073/pnas.0830019100

Groves, J. T., and McClusky, G. A. (1976). Aliphatic hydroxylation via oxygen rebound. Oxygen transfer catalyzed by iron. *J. Am. Chem. Soc.* 98, 859–861. doi: 10.1021/ja00419a049

Guengerich, F. P. (2001). Common and uncommon cytochrome P450 reactions related to metabolism and chemical toxicity. *Chem. Res. Toxicol.* 14, 611–650. doi: 10.1021/tx0002583

Gunes, A., Bilir, E., Zengil, H., Babaoglu, M. O., Bozkurt, A., and Yasar, U. (2007). Inhibitory effect of valproic acid on cytochrome P450 2C9 activity in epilepsy patients. *Basic Clin. Pharmacol. Toxicol.* 100, 383–386. doi: 10.1111/j.1742-7843.2007.00061.x

Haase, F., and Sauer, J. (1994). 1H NMR chemical shifts of ammonia, methanol, and water molecules interacting with broensted acid sites of zeolite catalysts: Ab-initio calculations. *J. Phys. Chem.* 98, 3083–3085. doi: 10.1021/j100063a006

Häglund, J., Fernndez Guillermet, A., Grimvall, G., and Körling, M. (1993). Theory of bonding in transition-metal carbides and nitrides. *Phys. Rev. B.* 48, 11685–11691. doi: 10.1103/PhysRevB.48.11685

Hajek, J., Van Der Mynsbrugge, J., De Wispelaere, K., Cnudde, P., Vanduyfhuys, L., Waroquier, M., et al. (2016). On the stability and nature of adsorbed pentene in Brønsted acid zeolite H-ZSM-5 at 323 K. *J. Catal.* 340, 227–235. doi: 10.1016/j.jcat.2016.05.018

Hammond, C., Forde, M. M., Ab Rahim, M. H., Thetford, A., He, Q., Jenkins, R. L., et al. (2012). Direct catalytic conversion of methane to methanol in an aqueous medium by using copper-promoted Fe-ZSM-5. *Angew. Chemie Int. Ed.* 51, 5129–5133. doi: 10.1002/anie.201108706

Hansgen, D. A., Vlachos, D. G., and Chen, J. G. (2010). Using first principles to predict bimetallic catalysts for the ammonia decomposition reaction. *Nat. Chem.* 2, 484–489. doi: 10.1038/nchem.626

Hellenbrandt, M. (2014). The inorganic crystal structure database (ICSD)—present and future. *Crystallogr. Rev.* 10, 17–22. doi: 10.1080/08893110410001664882

Hellweg, S., and Canals, L. M. I. (2014). Emerging approaches, challenges and opportunities in life cycle assessment. *Science* 344, 1109–1113. doi: 10.1126/science.1248361

Hernández-Ortega, A., Quesne, M. G., Bui, S., Heuts, D. P., Steiner, R. A., Heyes, D. J., et al. (2014). Origin of the proton-transfer step in the cofactor-free 1-H-3-hydroxy-4-oxoquinaldine 2,4- dioxygenase: Effect of the basicity of an active site His residue. *J. Biol. Chem.* 289, 8620–8632. doi: 10.1074/jbc.M113.543033

Hernández-Ortega, A., Quesne, M. G., Bui, S., Heyes, D. J., Steiner, R. A., Scrutton, N. S., et al. (2015). Catalytic mechanism of cofactor-free dioxygenases and how they circumvent spin-forbidden oxygenation of their substrates. *J. Am. Chem. Soc.* 137, 7474–7487. doi: 10.1021/jacs.5b03836

Hickey, A. L., and Rowley, C. N. (2014). Benchmarking quantum chemical methods for the calculation of molecular dipole moments and polarizabilities. *J. Phys. Chem. A.* 118, 3678–3687. doi: 10.1021/jp502475e

Hirunsit, P., Luadthong, C., and Faungnawakij, K. (2015). Effect of alumina hydroxylation on glycerol hydrogenolysis to 1,2-propanediol over Cu/Al2O3: combined experiment and DFT investigation. *RSC Adv.* 5, 11188–11197. doi: 10.1039/C4RA14698K

Hu, L., Söderhjelm, P., and Ryde, U. (2011). On the convergence of QM/MM energies. *J. Chem. Theory Comput.* 7, 761–777. doi: 10.1021/ct100530r

Hutchings, G. J., Catlow, C. R. A., Hardacre, C., and Davidson, M. G. (2016). Catalysis making the world a better place: satellite meeting. *Philos. Trans. R. Soc. A Math. Phys. Eng. Sci.* 374:20150358. doi: 10.1098/rsta.2015.0358

Hwu, H. H., and Chen, J. G. (2005). Surface chemistry of transition metal carbides. *Chem. Rev.* 105, 185–212. doi: 10.1021/cr0204606

Iannuzzi, M., Laio, A., and Parrinello, M. (2003). Efficient exploration of reactive potential energy surfaces using car-parrinello molecular dynamics. *Phys. Rev. Lett.* 90:238302. doi: 10.1103/PhysRevLett.90.238302

Isci, U., Afanasiev, P., Millet, J. M., Kudrik, V. E., Ahsen, V., and Sorokin, A. B. (2009). Preparation and characterization of mu-nitrido diiron phthalocyanines with electron-withdrawing substituents: application for catalytic aromatic oxidation. *Dalt. Trans.* 7410–7420. doi: 10.1039/b902592h

Işci, Ü., Faponle, A. S., Afanasiev, P., Albrieux, F., Briois, V., Ahsen, V., et al. (2015). Site-selective formation of an iron(iv)-oxo species at the more electron-rich iron atom of heteroleptic μ-nitrido diiron phthalocyanines. *Chem. Sci.* 6, 5063–5075. doi: 10.1039/C5SC01811K

Ishikawa, S., Jones, D. R., Iqbal, S., Reece, C., Morgan, D. J., Willock, D. J., et al. (2017). Identification of the catalytically active component of Cu-Zr-O catalyst for the hydrogenation of levulinic acid to γ-valerolactone. *Green Chem.* 19, 225–236. doi: 10.1039/C6GC02598F

Janthon, P., Kozlov, S. M., Viñes, F., Limtrakul, J., and Illas, F. (2013). Establishing the accuracy of broadly used density functionals in describing bulk properties of transition metals. *J. Chem. Theory Comput.* 9, 1631–1640. doi: 10.1021/ct3010326

Janthon, P., Luo, S. A., Kozlov, S. M., Viñes, F., Limtrakul, J., Truhlar, D. G., et al. (2014). Bulk properties of transition metals: a challenge for the design of universal density functionals. *J. Chem. Theory Comput.* 10, 3832–3839. doi: 10.1021/ct500532v

Jaramillo, F., and Destouni, G. (2015). Comment on 'planetary boundaries: guiding human development on a changing planet'. *Science* 348:1217. doi: 10.1126/science.aaa9629

Jastrzebski, R., Quesne, M. G., Weckhuysen, B. M., De Visser, S. P., and Bruijnincx, P. C. A. (2014). Experimental and computational evidence for the mechanism of intradiol catechol dioxygenation by non-heme iron(III) complexes. *Chem. A Eur. J.* 20, 15686–15691. doi: 10.1002/chem.201404988

Jastrzebski, R., Weckhuysen, B. M., and Bruijnincx, P. C. A. (2013). Catalytic oxidative cleavage of catechol by a non-heme iron(III) complex as a green route to dimethyl adipate. *Chem. Commun.* 49, 6912–6914. doi: 10.1039/c3cc42423e

Ji, L., Faponle, A. S., Quesne, M. G., Sainna, M. A., Zhang, J., Franke, A., et al. (2015). Drug metabolism by cytochrome P450 enzymes: what distinguishes the

pathways leading to substrate hydroxylation over desaturation? *Chem. Eur. J.* 21, 9083–9092. doi: 10.1002/chem.201500329

Kadish, K. M., Smith, K. M., and Guilard, R. (2010). *Handbook of Porphyrin Science*. Singapore: World Scientific.

Kamachi, T., and Yoshizawa, K. (2003). A theoretical study on the mechanism of camphor hydroxylation by compound I of cytochrome P450. *J. Am. Chem. Soc.* 125, 4652–4661. doi: 10.1021/ja,0208862

Kästner, J. (2011). Umbrella sampling. *Wiley Interdiscip. Rev. Comput. Mol. Sci.* 1, 932–942. doi: 10.1002/wcms.66

Kawakami, N., Shoji, O., and Watanabe, Y. (2011). Use of perfluorocarboxylic acids to trick cytochrome P450BM3 into initiating the hydroxylation of gaseous alkanes. *Angew. Chemie Int. Ed.* 50, 5315–5318. doi: 10.1002/anie.201007975

Kawakami, N., Shoji, O., and Watanabe, Y. (2013). Direct hydroxylation of primary carbons in small alkanes by wild-type cytochrome P450BM3 containing perfluorocarboxylic acids as decoy molecules. *Chem. Sci.* 4, 2344–2348. doi: 10.1039/c3sc50378j

Kerr, R. A. (2007). Global warming is changing the world. *Science.* 316, 188–190. doi: 10.1126/science.316.5822.188

Kiss, G., Çelebi-Ölçüm, N., Moretti, R., Baker, D., and Houk, K. N., (2013). Computational enzyme design. *Angew. Chemie Int. Ed.* 52, 5700–5725. doi: 10.1002/anie.201204077

Kornienko, N., Heidary, N., Cibin, G., and Reisner, E. (2018). Catalysis by design: development of a bifunctional water splitting catalyst through an operando measurement directed optimization cycle. *Chem. Sci.* 9, 5322–5333. doi: 10.1039/C8SC01415A

Kotobuki, M., Leppelt, R., Hansgen, D. A., Widmann, D., and Behm, R. J. (2009). Reactive oxygen on a Au/TiO2 supported catalyst. *J. Catal.* 264, 67–76. doi: 10.1016/j.jcat.2009.03.013

Kralj, M., Uzelac, L., Wang, Y.-H., Wan, P., Tireli, M., Mlinarić-Majerski, K., et al. (2015). Enhancement of antiproliferative activity by phototautomerization of anthrylphenols. *Photochem. Photobiol. Sci.* 14, 1082–1092. doi: 10.1039/C5PP00099H

Kresse, G., and Furthmüller, J. (1996a). Efficient iterative schemes for *ab initio* total-energy calculations using a plane-wave basis set. *Phys. Rev. B.* 54, 11169–11186. doi: 10.1103/PhysRevB.54.11169

Kresse, G., and Furthmüller, J. (1996b). Efficiency of ab-initio total energy calculations for metals and semiconductors using a plane-wave basis set. *Comput. Mater. Sci.* 6, 15–50. doi: 10.1016/0927-0256(96)00008-0

Kudrik, V. E., Afanasiev, P., Alvarez, L. X., Dubourdeaux, P., Clemancey, M., and Sorokin, A. B. (2012). An N-bridged high-valent diiron-oxo species on a porphyrin platform that can oxidize methane. *Nat. Chem.* 4, 1024–1029. doi: 10.1038/nchem.1471

Kudrik, V. E., and Sorokin, A. B. (2008). N-bridged diiron phthalocyanine catalyzes oxidation of benzene with H2O2 via benzene oxide with NIH shift evidenced by using 1,3,5-[D3]benzene as a probe. *Chemistry* 14, 7123–7126. doi: 10.1002/chem.200800504

Kulkarni, A., Siahrostami, S., Patel, A., and Nørskov, J. K. (2018). Understanding catalytic activity trends in the oxygen reduction reaction. *Chem. Rev.* 118, 2302–2312. doi: 10.1021/acs.chemrev.7b00488

Kumar, A., Goldberg, I., Botoshansky, M., Buchman, Y., and Gross, Z. (2010). Oxygen atom transfer reactions from isolated (oxo) manganese (V) corroles to sulfides. *J. Am. Chem. Soc.* 132, 15233–15245. doi: 10.1021/ja1050296

Kumar, D., De Visser, S. P., and Shaik, S. (2004a). Oxygen economy of cytochrome P450: what is the origin of the mixed functionality as a dehydrogenase-oxidase enzyme compared with its normal function? *J. Am. Chem. Soc.* 126, 5072–5073. doi: 10.1021/ja0318737

Kumar, D., de Visser, S. P., Sharma, P. K., Cohen, S., and Shaik, S. (2004b). Radical clock substrates, their C-H hydroxylation mechanism by cytochrome P450, and other reactivity patterns: what does theory reveal about the clocks' behavior? *J. Am. Chem. Soc.* 126, 1907–1920. doi: 10.1021/ja039439s

Kumar, D., Thiel, W., and de Visser, S. P. (2011). Theoretical study on the mechanism of the oxygen activation process in cysteine dioxygenase enzymes. *J. Am. Chem. Soc.* 133, 3869–3882. doi: 10.1021/ja107514f

Kung, Y., Runguphan, W., and Keasling, J. D. (2012). From fields to fuels: recent advances in the microbial production of biofuels. *ACS Synth. Biol.* 1, 498–513. doi: 10.1021/sb300074k

Kunkel, C., Vin, F., and Illas, F. (2018). Biogas upgrading by transition metal carbides. *ACS Appl. Energy Mater.* 1, 43–47. doi: 10.1021/acsaem.7b00086

Laio, A., and Parrinello, M. (2002). Escaping free-energy minima. *Proc. Natl. Acad. Sci. U.S.A.* 99, 12562–12566. doi: 10.1073/pnas.202427399

Laio, A., Rodriguez-Fortea, A., Gervasio, F. L., Ceccarelli, M., and Parrinello, M. (2005). Assessing the accuracy of metadynamics. *J. Phys. Chem. B.* 109, 6714–6721. doi: 10.1021/jp045424k

Lam, M. K., Lee, K. T., and Mohamed, A. R. (2010). Homogeneous, heterogeneous and enzymatic catalysis for transesterification of high free fatty acid oil (waste cooking oil) to biodiesel: a review. *Biotechnol. Adv.* 28, 500–518. doi: 10.1016/j.biotechadv.2010.03.002

Laurent, A. D., and Jacquemin, D. (2013). TD-DFT benchmarks: a review. *Int. J. Quantum Chem.* 113, 2019–2039. doi: 10.1002/qua.24438

Lee, C., Yang, W., and Parr, R. G. (1988). Development of the Colle-Salvetti correlation-energy formula into a functional of the electron density. *Phys. Rev. B.* 37, 785–789. doi: 10.1103/PhysRevB.37.785

Lee, R. P., Parkinson, A., and Forkert, P. G. (1998). Isozyme-selective metabolism of ethyl carbamate by cytochrome P450 (CYP2E1) and carboxylesterase (hydrolase A) enzymes in murine liver microsomes. *Drug Metab. Dispos.* 26, 60–65.

Lennen, R. M., and Pfleger, B. F. (2013). Microbial production of fatty acid-derived fuels and chemicals. *Curr. Opin. Biotechnol.* 24, 1044–1053. doi: 10.1016/j.copbio.2013.02.028

Levy, R. B., and Boudart, M. (1973). Platinum-like behavior of tungsten carbide in surface catalysis. *Science.* 181, 547–549. doi: 10.1126/science.181.4099.547

Li, D., Wang, Y., and Han, K. (2012). Recent density functional theory model calculations of drug metabolism by cytochrome P450. *Coord. Chem. Rev.* 256, 1137–1150. doi: 10.1016/j.ccr.2012.01.016

Liang, Y., Li, Y., Wang, H., Zhou, J., Wang, J., Regier, T., et al. (2011). Co3O4 nanocrystals on graphene as a synergistic catalyst for oxygen reduction reaction. *Nat. Mater.* 10, 780–786. doi: 10.1038/nmat3087

Lira-Navarrete, E., Iglesias-Fernández, J., Zandberg, W. F., Compañón, I., Kong, Y., Corzana, F., et al. (2014). Substrate-guided front-face reaction revealed by combined structural snapshots and metadynamics for the polypeptide n -acetylgalactosaminyltransferase 2. *Angew. Chemie Int. Ed.* 53, 8206–8210. doi: 10.1002/anie.201402781

Little, J. C., Hester, E. T., and Carey, C. C. (2016). Assessing and enhancing environmental sustainability: a conceptual review. *Environ. Sci. Technol.* 50, 6830–6845. doi: 10.1021/acs.est.6b00298

Liu, H., and Lee, J. Y. (2012). Electric field effects on the adsorption of CO on a graphene nanodot and the healing mechanism of a vacancy in a graphene nanodot. *J. Phys. Chem. C.* 116, 3034–3041. doi: 10.1021/jp210719r

Liu, J., Mooney, H., Hull, V., Davis, S. J., Gaskell, J., and Hertel, T. et al. (2015). Systems integration for global sustainability. *Science* 347:1258832. doi: 10.1126/science.1258832

Liu, Y., Kim, K. E., Herbert, M. B., Fedorov, A., Grubbs, R. H., and Stoltz, B. M. (2014). Palladium-catalyzed decarbonylative dehydration of fatty acids for the production of linear alpha olefins. *Adv. Synth. Catal.* 356, 130–136. doi: 10.1002/adsc.201301109

Lo, C. S., Radhakrishnan, R., and Trout, B. L. (2005). Application of transition path sampling methods in catalysis: a new mechanism for C-C bond formation in the methanol coupling reaction in chabazite. *Catal. Today.* 105, 93–105. doi: 10.1016/j.cattod.2005.04.005

Loch, J. M., Potter, J., and Bachmann, K. A. (1995). The influence of anesthetic agents on rat hepatic cytochromes P450 *in vivo*. *Pharmacology.* 50, 146–153. doi: 10.1159/000139276

Lu, Y., Farrow, M. R., Fayon, P., Logsdail, A. J., Sokol, A. A., Catlow, C. R. A., et al. (2019). Open-source, python-based redevelopment of the chemshell multiscale QM/MM environment. *J. Chem. Theory Comput.* 15, 1317–1328. doi: 10.1021/acs.jctc.8b01036

Maboeta, M. S., Claassens, S., van Rensburg, L., and van Rensburg, P. J. J. (2006). The effects of platinum mining on the environment from a soil microbial perspective, *water. Air. Soil Pollut.* 175, 149–161. doi: 10.1007/s11270-006-9122-1

Maseras, F., and Morokuma, K. (1995). Imomm: a new ab initio+ molecular mechanics geometry optimization scheme of equilibrium structures and transition states. *J. Comp. Chem.* 16, 1170–1179. doi: 10.1002/jcc.540160911

Mayer, J. M. (1998). Hydrogen atom abstraction by metal– oxo complexes: Understanding the analogy with organic radical reactions. *Acc. Chem. Res.* 31, 441–450. doi: 10.1021/ar970171h

McGeagh, J. D., Ranaghan, K. E., and Mulholland, A. J. (2011). Protein dynamics and enzyme catalysis: insights from simulations. *Biochim. Biophys. Acta Proteins Proteomics.* 1814, 1077–1092. doi: 10.1016/j.bbapap.2010.12.002

Medford, A. J., Vojvodic, A., Hummelshøj, J. S., Voss, J., Abild-Pedersen, F., Studt, F., et al. (2015). From the Sabatier principle to a predictive theory of transition-metal heterogeneous catalysis. *J. Catal.* 328, 36–42. doi: 10.1016/j.jcat.2014.12.033

Meliá, C., Ferrer, S., Moliner, V., Tuñõn, I., and Bertrán, J. (2012). Computational study on hydrolysis of cefotaxime in gas phase and in aqueous solution. *J. Comput. Chem.* 33, 1948–1959. doi: 10.1002/jcc.23030

Meunier, B., De Visser, S. P., and Shaik, S. (2004). Mechanism of oxidation reactions catalyzed by cytochrome P450 enzymes. *Chem. Rev.* 104, 3947–3980. doi: 10.1021/cr020443g

Miłaczewska, A., Kot, E., Amaya, J. A., Makris, T. M., Zajac, M., Korecki, J., et al. (2018). On the structure and reaction mechanism of human acireductone dioxygenase. *Chem. A Eur. J.* 24, 5225–5237. doi: 10.1002/chem.201704617

Møller, C., and Plesset, M. S. (1934). Note on an approximation treatment for many-electron systems. *Phys. Rev.* 46, 618–622. doi: 10.1103/PhysRev.46.618

Moors, S. L. C., De Wispelaere, K., Van Der Mynsbrugge, J., Waroquier, M., and Van Speybroeck, V. (2013). Molecular dynamics kinetic study on the zeolite-catalyzed benzene methylation in ZSM-5. *ACS Catal.* 3, 2556–2567. doi: 10.1021/cs400706e,

Morales-Gar, A., Fernández-Fernández, A., Viñes, F., and Illas, F. (2018). CO_2 abatement using two-dimensional MXene carbides, *J. Mater. Chem. A.* 6, 3381–3381. doi: 10.1039/C7TA11379J

Müller, K., Wiegrebe, W., and Younes, M. (1987). Formation of active oxygen species by dithranol, III dithranol, active oxygen species and lipid peroxidation *in vivo*. *Arch. Pharm.* 320, 59–66. doi: 10.1002/ardp.19873200110

Muñoz Robles, V., Ortega-Carrasco, E., Alonso-Cotchico, L., Rodriguez-Guerra, J., Lledós, A., and Maréchal, J. D. (2015). Toward the computational design of artificial metalloenzymes: from protein-ligand docking to multiscale approaches. *ACS Catal.* 5, 2469–2480. doi: 10.1021/acscatal.5b00010

Munro, A. W., Girvan, H. M., and McLean, K. J. (2007). Variations on a (t) heme–novel mechanisms, redox partners and catalytic functions in the cytochrome P450 superfamily. *Nat. Prod. Rep.* 24, 585–609. doi: 10.1039/B604190F

Murray, J., and King, D. (2012). Climate policy: Oil's tipping point has passed, *Nature.* 481, 433–435. doi: 10.1038/481433a

Murthi, V. S., Urian, R. C., and Mukerjee, S. (2004). Oxygen reduction kinetics in low and medium temperature acid environment: correlation of water activation and surface properties in supported Pt and Pt alloy electrocatalysts. *J. Phys. Chem. B.* 108, 11011–11023. doi: 10.1021/jp048985k

Namuangruk, S., Pantu, P., and Limtrakul, J. (2004). Alkylation of benzene with ethylene over faujasite zeolite investigated by the ONIOM method. *J. Catal.* 225, 523–530. doi: 10.1016/j.jcat.2004.04.016

Nastase, S. A. F., O'Malley, A. J., Catlow, C. R. A., and Logsdail, A. J. (2019). Computational QM/MM investigation of the adsorption of MTH active species in H-Y and H-ZSM-5. *Phys. Chem. Chem. Phys.* 21, 2639–2650. doi: 10.1039/C8CP06736H

Nearchou, A., Raithby, P. R., and Sartbaeva, A. (2018). Systematic approaches towards template-free synthesis of EMT-type zeolites. *Microporous Mesoporous Mater.* 255, 261–270. doi: 10.1016/j.micromeso.2017.08.036

Neu, H. M., Yang, T., Baglia, R. A., Yosca, T. H., Green, M. T., Quesne, M. G., et al. (2014). Oxygen-atom transfer reactivity of axially ligated Mn (V)–Oxo complexes: evidence for enhanced electrophilic and nucleophilic pathways. *J. Am. Chem. Soc.* 136, 13845–13852. doi: 10.1021/ja507177h

Nørskov, J. K., Bligaard, T. R. J., and Christensen, C. H. (2009). Towards the Computational Design of Solid Catalysts. *Nat. Chem.* 1, 37–46. doi: 10.1038/nchem.121

Ogliaro, F., de Visser, S. P., Cohen, S., Kaneti, J., and Shaik, S. (2001). The experimentally elusive oxidant of cytochrome P450: a theoretical "trapping" defining more closely the "real" species. *ChemBioChem.* 2, 848–851. doi: 10.1002/1439-7633(20011105)2:11<848::AID-CBIC848>3.0.CO;2-0

O'Hagan, M., Duchi, M., Morales, J. C., Galan, M. C., Mulholland, A., Oliver, T., et al. (2019). A photoresponsive stiff-stilbene ligand fuels the reversible conformational unfolding of G-quadruplex DNA. *Angew. Chemie Int. Ed.* doi: 10. 1002/anie.201900740

O'Malley, J., Logsdail, A. J., Sokol, A. A., and Catlow, C. R. A. (2016). Modelling metal centres, acid sites and reaction mechanisms in microporous catalysts. *Faraday Discuss.* 188, 235–255. doi: 10.1039/C6FD00010J

Oostenbrink, C., Villa, A., Mark, A. E., and Van Gunsteren, W. F. (2004). A biomolecular force field based on the free enthalpy of hydration and solvation: the GROMOS force-field parameter sets 53A5 and 53A6. *J. Comput. Chem.* 25, 1656–1676. doi: 10.1002/jcc.20090

O'Reilly, E., Köhler, V., Flitsch, S. L., and Turner, N. J. (2011). Cytochromes P450 as useful biocatalysts: addressing the limitations. *Chem. Commun.* 47, 2490–2501.

Ortiz de Montellano, P. R. (2004). *Cytochrome P450: Structure, Mechanism, and Biochemistry*. New York, NY: Springer.

Oyama, S. T. (2008). "High-surface transition metal carbides and nitrides," in *Preparation of Solid Catalysts,* G. Ertl, H. Knözinger, and J. Weitkamp (New York, NY: Wiley), 139–150.

Parsell, T. H., Yang, M.-Y., and Borovik, A. S. (2009). C– H bond cleavage with reductants: re-investigating the reactivity of monomeric MnIII/IV– oxo complexes and the role of oxo ligand basicity. *J. Am. Chem. Soc.* 131, 2762–2763. doi: 10.1021/ja8100825

Pasini, T., Lolli, A., Albonetti, S., Cavani, F., and Mella, M. (2014). Methanol as a clean and efficient H-transfer reactant for carbonyl reduction: scope, limitations, and reaction mechanism. *J. Catal.* 317, 206–219. doi: 10.1016/j.jcat.2014.06.023

Pelletier, J. D. A., and Basset, J. M. (2016). Catalysis by design: well-defined single-site heterogeneous catalysts. *Acc. Chem. Res.* 49, 664–677. doi: 10.1021/acs.accounts.5b00518

Pelmenschikov, A. G., Morosi, G., Gamba, A., and Coluccia, S. (1995). A check of quantum chemical molecular models of adsorption on oxides against experimental infrared data. *J. Phys. Chem.* 99, 15018–15022. doi: 10.1021/j100041a016

Pelmenschikov, A. G., Morosi, G., Gamba, A., Coluccia, S., Martra, G., and Paukshtis, E. A. (1996). Single and multiple Lewis sites of MgO: a combined IR and ab initio study with CD3CN as a molecular probe. *J. Phys. Chem.* 100, 5011–5016. doi: 10.1021/jp952720b

Pelmenschikov, G., Morosi, G., Gamba, A., and Coluccia, S. (1998). Unimportance of the surrounding lattice in the adsorption of CO on low-coordinated mg Sites of MgO. *J. Phys. Chem. B.* 102, 2226–2231. doi: 10.1021/jp9731765

Peralta-Yahya, P. P., Zhang, F., S., del Cardayre, B., and Keasling, J. D. (2012). Microbial engineering for the production of advanced biofuels, *Nature.* 488, 320–328. doi: 10.1038/nature11478

Perdew, J. P., Burke, K., and Ernzerhof, M. (1996). Generalized gradient approximation made simple. *Phys. Rev. Lett.* 77, 3865–3868. doi: 10.1103/PhysRevLett.77.3865

Perdew, J. P., and Schmidt, K. (2001). "Jacob's ladder of density functional approximations for the exchange-correlation energy," in *AIP Conference Proceedings*, Vol. 577, (AIP), 1–20.

Petersen, L., Ardèvol, A., Rovira, C., and Reilly, P. J. (2009). Mechanism of cellulose hydrolysis by inverting GH8 endoglucanases: a QM/MM metadynamics study. *J. Phys. Chem. B.* 113, 7331–7339. doi: 10.1021/jp811470d

Polshettiwar, V., and Varma, R. S. (2010). Green chemistry by nano-catalysis. *Green Chem.* 12, 743–754. doi: 10.1039/b921171c

Porro, C. S., Sutcliffe, M. J., and de Visser, S. P. (2009). Quantum mechanics/molecular mechanics studies on the sulfoxidation of dimethyl sulfide by compound i and compound 0 of cytochrome P450: which is the better oxidant? *J. Phys. Chem. A.* 113, 11635–11642. doi: 10.1021/jp9023926

Posada-Pérez, S., Gutiérrez, R. A., Zuo, Z., Ramírez, P. J., Viñes, F., Liu, P., et al. (2017a). Highly active Au/δ-MoC and Au/β-Mo $_2$ C catalysts for the low-temperature water gas shift reaction: effects of the carbide metal/carbon ratio on the catalyst performance. *Catal. Sci. Technol.* 7, 5332–5342. doi: 10.1039/C.7C. Y.00639J.

Posada-Pérez, S., Viñes, F., Ramirez, P. J., Vidal, A. B., Rodriguez, J. A., and Illas, F. (2014). The bending machine: CO2 activation and hydrogenation on δ-MoC(001) and β-Mo2C(001) surfaces. *Phys. Chem. Chem. Phys.* 16, 14912–14921 doi: 10.1039/C4CP01943A

Posada-Pérez, S., Viñes, F., Valero, R., Rodriguez, J. A., and Illas, F. (2017b). Adsorption and dissociation of molecular hydrogen on orthorhombic β-Mo 2C and cubic δ-MoC (001) surfaces. *Surf. Sci.* 656, 24–32. doi: 10.1016/j.susc.2016.10.001

Posner, G. H., and O'Neill, P. M. (2004). Knowledge of the proposed chemical mechanism of action and cytochrome P450 metabolism of antimalarial trioxanes like artemisinin allows rational design of new antimalarial peroxides. *Acc. Chem. Res.* 37, 397–404. doi: 10.1021/ar020227u

Postils, V., Saint-André, M., Timmins, A., Li, X.-X., Wang, Y., Luis, J. M., et al. (2018). Quantum mechanics/molecular mechanics studies on the relative reactivities of compound I and II in cytochrome P450 enzymes. *Int. J. Mol. Sci.* 19:E1974. doi: 10. 3390/ijms19071974

Poulos, T. L., Finzel, B. C., Gunsalus, I. C., Wagner, G. C., and Kraut, J. (1985). The 2.6-A crystal structure of *Pseudomonas putida* cytochrome P-450, *J. Biol. Chem.* 260, 16122–16130.

Poulos, T. L., Finzel, B. C., and Howard, A. J. (1987). High-resolution crystal structure of cytochrome P450cam. *J. Mol. Biol.* 195, 687–700. doi: 10.1016/0022-2836(87)90190-2

Prokop, K. A., Neu, H. M., de Visser, S. P., and Goldberg, D. P. (2011). A manganese(V)-oxo pi-cation radical complex: influence of one-electron oxidation on oxygen-atom transfer. *J. Am. Chem. Soc.* 133, 15874–15877. doi: 10.1021/ja2066237

Qi, K. Z., Wang, G. C., and Zheng, W. J. (2013). A first-principles study of CO hydrogenation into methane on molybdenum carbides catalysts. *Surf. Sci.* 614, 53–63. doi: 10.1016/j.susc.2013.04.001

Qian, X. (2012). Mechanisms and energetics for brønsted acid-catalyzed glucose condensation, dehydration and isomerization reactions. *Top. Catal.* 55, 218–226. doi: 10.1007/s11244-012-9790-6

Quesne, M. G., Borowski, T., and De Visser, S. P. (2016a). Quantum mechanics/molecular mechanics modeling of enzymatic processes: caveats and breakthroughs. *Chem. A Eur. J.* 22, 2562–2581. doi: 10.1002/chem.201503802

Quesne, M. G., and de Visser, S. P. (2012). Regioselectivity of substrate hydroxylation versus halogenation by a nonheme iron (IV)–oxo complex: possibility of rearrangement pathways. *JBIC J. Biol. Inorg. Chem.* 17, 841–852. doi: 10.1007/s00775-012-0901-4

Quesne, M. G., Faponle, A. S., Goldberg, D. P., and Visser, S. P. D. (2015). "Catalytic function and mechanism of heme and nonheme iron(IV)-oxo complexes in nature," in *Spin States in Biochemistry and Inorganic Chemistry: Influence on Structure and Reactivity* eds M. Swart and M. Costas (New York, NY: Wiley), 185–202.

Quesne, M. G., Latifi, R., Gonzalez-Ovalle, L. E., Kumar, D., and De Visser, S. P. (2014). Quantum mechanics/molecular mechanics study on the oxygen binding and substrate hydroxylation step in AlkB repair enzymes. *Chem. A Eur. J.* 20, 435–446. doi: 10.1002/chem.201303282

Quesne, M. G., Roldan, A., de Leeuw, N. H., and Catlow, C. R. A. (2018). Bulk and surface properties of metal carbides: implications for catalysis. *Phys. Chem. Chem. Phys.* 20, 6905–6916. doi: 10.1039/C7CP06336A

Quesne, M. G., Senthilnathan, D., Singh, D., Kumar, D., Maldivi, P., Sorokin, A. B., et al. (2016b). Origin of the enhanced reactivity of μ-nitrido-bridged diiron(IV)-oxo porphyrinoid complexes over cytochrome P450 compound i. *ACS Catal.* 6, 2230–2243. doi: 10.1021/acscatal.5b02720

Quesne, M. G., Ward, R. A., and de Visser, S. P. (2013). Cysteine protease inhibition by nitrile-based inhibitors: a computational study. *Front. Chem.* 1, 39. doi: 10.3389/fchem.2013.00039

Raich, L., Nin-Hill, A., Ardèvol, A., and Rovira, C. (2016). "Enzymatic Cleavage of Glycosidic Bonds: Strategies on How to Set Up and Control a QM/MM Metadynamics Simulation," in *Methods in Enzymology,* Vol. 577 ed G. A. Voth (Oxford: Elsevier), 159–183.

Reiher, M., Salomon, O., and Hess, B. A. (2001). Reparameterization of hybrid functionals based on energy differences of states of different multiplicity. *Theor. Chem. Acc.* 107, 48–55. doi: 10.1007/s00214-001-0300-3

Reinhard, F. C., and de Visser, S. (2017). Biodegradation of cosmetics products: a computational study of cytochrome P450 metabolism of phthalates. *Inorganics.* 5:77. doi: 10.3390/inorganics5040077

Rettie, A. E., Rettenmeier, A. W., Howald, W. N., and Baillie, T. A. (1987). Cytochrome P-450–catalyzed formation of delta 4-VPA, a toxic metabolite of valproic acid. *Science.* 235, 890–893. doi: 10.1126/science.3101178

Rittle, J., and Green, M. T. (2010). Cytochrome P450 compound I: capture, characterization, and CH bond activation kinetics. *Science.* 330, 933–937. doi: 10.1126/science.1193478

Roca, M., Aranda, J., Moliner, V., and Tuñón, I. (2012). Modeling methods for studying post-translational and transcriptional modifying enzymes. *Curr. Opin. Chem. Biol.* 16, 465–471. doi: 10.1016/j.cbpa.2012.10.014

Rodríguez-Guerra, J., Jan-E. B., Lledós, A., Maréchal, J.-D., Alonso-Cotchico, L., Sciortino, G., et al. (2018). "Computational Studies of Artificial Metalloenzymes: From Methods and Models to Design and Optimization 99," in *Artificial Metalloenzymes and MetalloDNAzymes in Catalysis* eds M. Diéguez, J.E. Bäckvall and O. Pámies (New York, NY: Wiley), 99–136.

Rothlisberger, U., Carloni, P., Doclo, K., and Parrinello, M. (2000). A comparative study of galactose oxidase and active site analogs based on QM/MM Car-Parrinello simulations. *J. Biol. Inorg. Chem.* 5, 236–250. doi: 10.1007/s007750050368

Rude, M. A., Baron, T. S., Brubaker, S., Alibhai, M., Del Cardayre, S. B., and Schirmer, A. (2011). Terminal olefin (1-alkene) biosynthesis by a novel P450 fatty acid decarboxylase from Jeotgalicoccus species. *Appl. Environ. Microbiol.* 77, 1718–1727. doi: 10.1128/AEM.02580-10

Ruettinger, R. T., Wen, L.-P., and Fulco, A. J. (1989). Coding nucleotide. 5'regulatory, and deduced amino acid sequences of P-450BM-3, a single peptide cytochrome P-450: NADPH-P-450 reductase from *Bacillus megaterium*. *J. Biol. Chem.* 264, 10987–10995.

Sadeque, A. J., Fisher, M. B., Korzekwa, K. R., Gonzalez, F. J., and Rettie, A. E. (1997). Human CYP2C9 and CYP2A6 mediate formation of the hepatotoxin 4-ene-valproic acid. *J. Pharmacol. Exp. Ther.* 283, 698–703.

Sahoo, D., Quesne, M. G., De Visser, S. P., and Rath, S. P. (2015). Hydrogen-bonding interactions trigger a spin-flip in iron(III) porphyrin complexes. *Angew. Chem. Int. Ed.* 54, 4796–4800. doi: 10.1002/anie.201411399

Sahu, S., Quesne, M. G., Davies, C. G., Durr, M. M, Ivanović-Burmazović, I., Siegler, M. A., et al. (2014). Direct observation of a nonheme iron (IV)–oxo complex that mediates aromatic C–F hydroxylation. *J. Am. Chem. Soc.* 136, 13542–13545. doi: 10.1021/ja507346t

Sastre, G., Fornes, V., and Corma, A. (2002). On the preferential location of Al and proton siting in zeolites: a computational and infrared study. *J. Phys. Chem. B.* 106, 701–708. doi: 10.1021/jp013189p

Saurat, M., and Bringezu, S. (2008). Platinum group metal flows of europe, part 1. *J. Ind. Ecol.* 12, 754–767. doi: 10.1111/j.1530-9290.2008.00087.x

Schilling, M., and Luber, S. (2018). Computational modeling of cobalt-based water oxidation: current status and future challenges. *Front. Chem.* 6:100. doi: 10.3389/fchem.2018.00100

Schlichting, I., Berendzen, J., Chu, K., Stock, A. M., Maves, S. A., Benson, D. E., et al. (2000). The catalytic pathway of cytochrome P450cam at atomic resolution. *Science.* 287, 1615–1622. doi: 10.1126/science.287.5458.1615

Senn, H. M., and Thiel, W. (2007). QM/MM studies of enzymes. *Curr. Opin. Chem. Biol.* 11, 182–187. doi: 10.1016/j.cbpa.2007.01.684

Senn, H. M., and Thiel, W. (2009). QM/MM methods for biomolecular systems. *Angew. Chemie Int. Ed.* 48, 1198–1229. doi: 10.1002/anie.200802019

Shafiee, S., and Topal, E. (2009). When will fossil fuel reserves be diminished? *Energy Policy.* 37, 181–189. doi: 10.1016/j.enpol.2008.08.016

Shaik, S., Kumar, D., and de Visser, S. P. (2008). A valence bond modeling of trends in hydrogen abstraction barriers and transition states of hydroxylation reactions catalyzed by cytochrome P450 enzymes. *J. Am. Chem. Soc.* 130, 14016. doi: 10.1021/ja806917f

Shaik, S., Kumar, D., de Visser, S. P., Altun, A., and Thiel, W. (2005). Theoretical perspective on the structure and mechanism of cytochrome P450 enzymes. *Chem. Rev.* 105, 2279–2328. doi: 10.1021/cr030722j

Sheldon, R. A. (2014). Green and sustainable manufacture of chemicals from biomass : state of the art several books on catalysis as well. *Green Chem.* 16, 950–963. doi: 10.1039/C3GC41935E

Sheldon, R. A. (2016). Green chemistry, catalysis and valorization of waste biomass. *J. Mol. Catal. A Chem.* 422, 3–12. doi: 10.1016/j.molcata.2016.01.013

Sherwood, P., de Vries, A. H., Guest, M. F., Schreckenbach, G., Catlow, C. R. A., French, A. A., et al. (2003). QUASI: a general purpose implementation of the QM/MM approach and its application to problems in catalysis. *J. Mol. Struct. Theochem.* 632, 1–28. doi: 10.1016/S0166-1280(03)00285-9

Siegbahn, E. M., and Crabtree, R. H. (1997). Mechanism of C–H activation by diiron methane monooxygenases: quantum chemical studies. *J. Am. Chem. Soc.* 119, 3103–3113. doi: 10.1021/ja963939m

Silaghi-Dumitrescu, R. V., Makarov, S., Uta, M.-M., Dereven'kov, I. A., and Stuzhin, P. A. (2011). Redox non-innocence of a nitrido bridge in a methane-activating dimer of iron phthalocyanine. *N. J. Chem.* 35, 1140–1145. doi: 10.1039/c0nj00827ct

Silva, P. J. (2016). Refining the reaction mechanism of O2 towards its co-substrate in cofactor-free dioxygenases. *PeerJ*. 4:e2805. doi: 10.7717/peerj.2805

Silveri, F., Quesne, M. G., de Leeuw, N. H.., and Richard A, C. (2019). Hydrogen adsorption on transition metal carbides: a DFT study. *Phys. Chem. Chem. Phys*. 21, 5335–5343. doi: 10. 1039/c8cp05975f

Smith, W., Yong, C. W., and Rodger, P. M. (2002). DL_POLY: application to molecular simulation. *Mol. Simul.* 28, 385–471. doi: 10.1080/08927020290018769

Sokol, A. A., Bromley, S. T., French, S. A., Catlow, C. R. A., and Sherwood, P. (2004). Hybrid QM/MM embedding approach for the treatment of localized surface states in ionic materials. *Int. J. Quantum Chem*. 99, 695–712. doi: 10.1002/qua.20032

Solomon, E. I., Brunold, T. C., Davis, M. I., Kemsley, J. N., Lee, S. K., Lehnert, N., et al. (2000). Geometric and electronic structure/function correlations in non-heme iron enzymes. *Chem. Rev*. 100, 235–350. doi: 10.1021/cr9900275

Solomon, E. I., and Stahl, S. S. (2018). Introduction: oxygen reduction and activation in catalysis. *Chem. Rev*. 118, 2299–2301. doi: 10.1021/acs.chemrev.8b00046

Song, W. J., Ryu, Y. O., Song, R., and Nam, W. (2005). Oxoiron(IV) porphyrin pi-cation radical complexes with a chameleon behavior in cytochrome P450 model reactions. *J. Biol. Inorg. Chem.* 10, 294–304. doi: 10.1007/s00775-005-0641-9

Sorokin, A. B., Isci, U., Dumoulin, F., and Ahsen, V. (2010). Preparation of N-bridged diiron phthalocyanines bearing bulky or small electron-withdrawing substituents. *J. Porphyr. Phthalocyanines.* 14, 324–334. doi: 10.1142/S1088424610002069

Sorokin, A. B., Kudrik, V. E., and Bouchu, D. (2008). Bio-inspired oxidation of methane in water catalyzed by N-bridged diiron phthalocyanine complex, *Chem Commun.* 2562–2564. doi: 10.1039/b804405h

Sousa, S. F., Fernandes, P. A., and Ramos, M. J. (2007). General performance of density functionals. *J. Phys. Chem. A*. 111, 10439–10452. doi: 10.1021/jp0734474

Steiner, R. A., Janssen, H. J., Roversi, P., Oakley, A. J., and Fetzner, S. (2010). Structural basis for cofactor-independent dioxygenation of N-heteroaromatic compounds at the / -hydrolase fold. *Proc. Natl. Acad. Sci. U.S.A*. 107, 657–662. doi: 10.1073/pnas.0909033107

Stephanopoulos, G. (2007). Challenges in engineering microbes for biofuels production. *Science.* 315, 801–804. doi: 10.1126/science.1139612

Straathof, A. J. J. (2014). Transformation of biomass into commodity chemicals using enzymes or cells. *Chem. Rev*. 114, 1871–1908. doi: 10.1021/cr400309c

Sun, Q., and Liu, Z. (2011). Mechanism and kinetics for methanol synthesis from CO2/H2over Cu and Cu/oxide surfaces: recent investigations by first principles-based simulation. *Front. Chem. China* 6, 164–172. doi: 10.1007/s11458-011-0250-9

Suntivich, J., Gasteiger, H. A., Yabuuchi, N., Nakanishi, H., Goodenough, J. B., and Shao-Horn, Y. (2011). Design principles for oxygen-reduction activity on perovskite oxide catalysts for fuel cells and metal–air batteries. *Nat. Chem.* 3, 546–550. doi: 10.1038/nchem.1069

Sutton, J. E., and Vlachos, D. G. (2015). Building large microkinetic models with first-principles[U+05F3] accuracy at reduced computational cost. *Chem. Eng. Sci.* 121, 190–199. doi: 10.1016/j.ces.2014.09.011

Swiderek, K., Javier Ruiz-Pernía, Moliner, V., and Tuñón, I. (2014). Heavy enzymes-experimental and computational insights in enzyme dynamics. *Curr. Opin. Chem. Biol.* 21, 11–18. doi: 10.1016/j.cbpa.2014.03.005

Takahashi, A., Yamaki, D., Ikemura, K., Kurahashi, T., Ogura, T., Hada, M., et al. (2012). Effect of the axial ligand on the reactivity of the oxoiron (IV) porphyrin π-cation radical complex: higher stabilization of the product state relative to the reactant state. *Inorg. Chem.* 51, 7296–7305. doi: 10.1021/ic,3006597

Talebian-Kiakalaieh, A., Amin, N. A. S., Najaafi, N., and Tarighi, S. (2018). A review on the catalytic acetalization of bio-renewable glycerol to fuel additives. *Front. Chem.* 6:573. doi: 10.3389/fchem.2018.00573

Tan, H. W., Abdul Aziz, A. R., and Aroua, M. K. (2013). Glycerol production and its applications as a raw material: a review. *Renew. Sustain. Energy Rev.* 27, 118–127. doi: 10.1016/j.rser.2013.06.035

Thierbach, S., Bui, N., Zapp, J., Chhabra, S. R., Kappl, R., and Fetzner, S. (2014). Substrate-assisted O2 activation in a cofactor-independent dioxygenase. *Chem. Biol.* 21, 217–225. doi: 10.1016/j.chembiol.2013.11.013

Timmins, A., Quesne, M. G., Borowski, T., and de Visser, S. P. (2018). Group transfer to an aliphatic bond: a biomimetic study inspired by nonheme iron halogenases. *ACS Catal.* 8685–8698. doi: 10.1021/acscatal.8b,01673

Tsai, C.-J., Nussinov, R., Kumar, S., Ma, B., and Hu, Z. (2002). Transition-state ensemble in enzyme catalysis: possibility, reality, or necessity? *J. Theor. Biol.* 203, 383–397. doi: 10.1006/jtbi.2000.1097

van der Kamp, M. W., and Mulholland, A. J. (2013). Combined quantum mechanics/molecular mechanics (QM/MM) methods in computational enzymology. *Biochemistry* 52, 2708–2728. doi: 10.1021/bi400215w

Van Der Mynsbrugge, J., Moors, S. L. C., De Wispelaere, K., and Van Speybroeck, V. (2014). Insight into the formation and reactivity of framework-bound methoxide species in h-zsm-5 from static and dynamic molecular simulations. *ChemCatChem.* 6, 1906–1918. doi: 10.1002/cctc.201402146

Van Speybroeck, V., Hemelsoet, K., Joos, L., Waroquier, M., Bell, R. G., and Catlow, C. R. A. (2015). Advances in theory and their application within the field of zeolite chemistry. *Chem. Soc. Rev.* 44, 7044–7111. doi: 10.1039/C5CS00029G

Vines, F., Sousa, C., Liu, P., Rodriguez, J. A., and Illas, F. (2005). A systematic density functional theory study of the electronic structure of bulk and (001) surface of transition-metals carbides. *J. Chem. Phys.* 122:174709. doi: 10.1063/1.1888370

Vreven, T., and Morokuma, K. (2006). Chapter 3 hybrid methods: ONIOM(QM:MM) and QM/MM. *Annu. Rep. Comput. Chem.* 2, 35–51. doi: 10.1016/S1574-1400(06)02003-2

Walker, M., Harvey, A. J. A., Sen, A., and Dessent, C. E. H. (2013). Performance of M06, M06-2X, and M06-HF density functionals for conformationally flexible anionic clusters: M06 functionals perform better than B3LYP for a model system with dispersion and ionic hydrogen-bonding interactions. *J. Phys. Chem. A*. 117, 12590–12600. doi: 10.1021/jp408166m

Wang, C., Liu, Y., Li, S., Guan, W., Lu, X., Yan, J., et al. (2014). Hydrogen peroxide-independent production of α-alkenes by OleTJE P450 fatty acid decarboxylase. *Biotechnol. Biofuels.* 7:28. doi: 10.1186/1754-6834-7-28

Wang, F., Xia, C., De Visser, S. P., and Wang, Y. (2019). How does the oxidation state of palladium surfaces affect the reactivity and selectivity of direct synthesis of hydrogen peroxide from hydrogen and oxygen gases? *A Density Functional Study. J. Am. Chem. Soc.* 141, 901–910. doi: 10.1021/jacs.8b10281

Wang, J., Wolf, R. M., Caldwell, J. W., Kollman, P. A., and Case, D. A. (2004). Development and testing of a general amber force field. *J. Comput. Chem.* 25, 1157–1174. doi: 10.1002/jcc.20035

Wang, Z. H., Wang, C. Y., and Chen, K. S. (2001). Two-phase flow and transport in the air cathode of proton exchange membrane fuel cells. *Power Sources J.* 94, 40–50. doi: 10.1016/S0378-7753(00)00662-5

Warshel, A., and Levitt, M. (1976). Theoretical studies of enzymic reactions: dielectric, electrostatic and steric stabilization of the carbonium ion in the reaction of lysozyme. *J. Mol. Biol.* 103, 227–249. doi: 10.1016/0022-2836(76)90311-9

Wells, S. A., and Sartbaeva, A. (2015). GASP: software for geometric simulations of flexibility in polyhedral and molecular framework structures. *Mol. Simul.* 41, 1409–1421. doi: 10.1080/08927022.2015.1032277

Wen, X., Wang, J. S., Kivisto, K. T., Neuvonen, P. J., and Backman, J. T. (2001). *In vitro* evaluation of valproic acid as an inhibitor of human cytochrome P450 isoforms: preferential inhibition of cytochrome P450 2C9 (CYP2C9). *Br. J. Clin. Pharmacol.* 52, 547–553. doi: 10.1046/j.0306-5251.2001.01474.x,

Wettstein, S. G., Martin Alonso, D., Gürbüz, E. I., and Dumesic, J. A. (2012). A roadmap for conversion of lignocellulosic biomass to chemicals and fuels. *Curr. Opin. Chem. Eng.* 1, 218–224. doi: 10.1016/j.coche.2012.04.002

Widmann, D., and Behm, R. J. (2014). Activation of Molecular Oxygen and the nature of the active oxygen species for CO oxidation on oxide supported Au catalysts. *Acc. Chem. Res.* 47, 740–749. doi: 10.1021/ar400203e

Wójcik, A., Radon, M., and Borowski, T. (2016). Mechanism of O_2 activation by α-ketoglutarate dependent oxygenases revisited. *A Quantum Chemical Study. J. Phys. Chem. A.* 120, 1261–1274. doi: 10.1021/acs.jpca.5b12311

Wojdyła, Z., and Borowski, T. (2016). DFT study of the mechanism of manganese quercetin 2,3-dioxygenase: quest for origins of enzyme unique nitroxygenase activity and regioselectivity. *J. Biol. Inorg. Chem.* 21, 475–489. doi: 10.1007/s00775-016-1356-9

Wojdyła, Z., and Borowski, T. (2018). On how the binding cavity of AsqJ dioxygenase controls the desaturation reaction regioselectivity: a QM/MM study. *J. Biol. Inorg. Chem.* 23, 795–808. doi: 10.1007/s00775-018-1575-3

Xie, Z., Sui, Y., Buckeridge, J., Catlow, C. R. A., Keal, T. W., Sherwood, P., et al. (2017). Demonstration of the donor characteristics of Si and O defects in GaN using hybrid QM/MM. *Phys. Status Solidi Appl. Mater. Sci.* 214:1600445. doi: 10.1002/pssa.201600445

Yang, C.-J. (2009). An impending platinum crisis and its implications for the future of the automobile. *Energy Policy.* 37, 1805–1808. doi: 10.1016/j.enpol.2009.01.019

Yang, T., Quesne, M. G., Neu, H. M., Reinhard, F. G. C., Goldberg, D. P., and De Visser, S. P. (2016). Singlet versus triplet reactivity in an Mn(V)-oxo species: testing theoretical predictions against experimental evidence. *J. Am. Chem. Soc.* 138, 12375–12386. doi: 10.1021/jacs.6b05027

Yoshizawa, K., Kamachi, T., and Shiota, Y. (2001). A theoretical study of the dynamic behavior of alkane hydroxylation by a compound I model of cytochrome P450. *J. Am. Chem. Soc.* 123, 9806–9816. doi: 10.1021/ja010593t

Yu, J., Xie, L. H., Li, J. R., Ma, Y., Seminario, J. M., et al. (2017). CO2 capture and separations using MOFs: computational and experimental studies. *Chem. Rev.* 117, 9674–9754. doi: 10.1021/acs.chemrev.6b00626

Zanghellini, A., Jiang, L., Wollacott, A. M., Cheng, G., Meiler, J., and Althoff, E. A. et al. (2006). New algorithms and an in silico benchmark for computational enzyme design. *Protein Sci.* 15, 2785–2794. doi: 10.1110/ps.062353106

Zhang, G. X., Reilly, A. M., Tkatchenko, A., and Scheffler, M. (2018). Performance of various density-functional approximations for cohesive properties of 64 bulk solids. *N. J. Phys.* 20:063020. doi: 10.1088/1367-2630/aac7f0

Zhang, J., Sasaki, K., Sutter, E., and Adzic, R. A. (2007). Science and U. Stabilization of platinum oxygen-reduction electrocatalysts using gold clusters, *Science.* 315, 220–222. doi: 10.1126/science.1134569

Zhao, Z. J., Chiu, C. C., and Gong, J. (2015). Molecular understandings on the activation of light hydrocarbons over heterogeneous catalysts. *Chem. Sci.* 6, 4403–4425. doi: 10.1039/C5SC01227A

Zheng, L., Su, H., Zhang, J., Walekar, L. S., Vafaei Molamahmood, H., Zhou, B., et al. (2018). Highly selective photocatalytic production of H2O2on sulfur and nitrogen co-doped graphene quantum dots tuned TiO2. *Appl. Catal. B Environ.* 239, 475–484. doi: 10.1016/j.apcatb.2018.08.031

Zhu, C. R., Gao, D., Ding, J., Chao, D., and Wang, J. (2018). TMD-based highly efficient electrocatalysts developed by combined computational and experimental approaches. *Chem. Soc. Rev.* 47, 4332–4356. doi: 10.1039/C7CS00705A

Zilly, F. E., Acevedo, J. P., Augustyniak, W., Deege, A., Hausig, U. W., and Reetz, M. T. (2011). Tuning a p450 enzyme for methane oxidation. *Angew. Chem. Int. Ed.* 50, 2720–2724. doi: 10.1002/anie.201006587

Zygmunt, S. A., Mueller, R. M., Curtiss, L. A., and Iton, L. E. (1998). An assessment of density functional methods for studying molecular adsorption in cluster models of zeolites. *J. Mol. Struct. Theochem.* 430, 9–16. doi: 10.1016/S0166-1280(98)90205-6

Conflict of Interest Statement: The authors declare that the research was conducted in the absence of any commercial or financial relationships that could be construed as a potential conflict of interest.

Copyright © 2019 Quesne, Silveri, de Leeuw and Catlow. This is an open-access article distributed under the terms of the Creative Commons Attribution License (CC BY). The use, distribution or reproduction in other forums is permitted, provided the original author(s) and the copyright owner(s) are credited and that the original publication in this journal is cited, in accordance with accepted academic practice. No use, distribution or reproduction is permitted which does not comply with these terms.

Advantages of publishing in Frontiers

OPEN ACCESS
Articles are free to read for greatest visibility and readership

FAST PUBLICATION
Around 90 days from submission to decision

HIGH QUALITY PEER-REVIEW
Rigorous, collaborative, and constructive peer-review

TRANSPARENT PEER-REVIEW
Editors and reviewers acknowledged by name on published articles

Frontiers
Avenue du Tribunal-Fédéral 34
1005 Lausanne | Switzerland

Visit us: www.frontiersin.org
Contact us: info@frontiersin.org | +41 21 510 17 00

REPRODUCIBILITY OF RESEARCH
Support open data and methods to enhance research reproducibility

DIGITAL PUBLISHING
Articles designed for optimal readership across devices

FOLLOW US
@frontiersin

IMPACT METRICS
Advanced article metrics track visibility across digital media

EXTENSIVE PROMOTION
Marketing and promotion of impactful research

LOOP RESEARCH NETWORK
Our network increases your article's readership